Proceedings Third International Conference on Scour and Erosion

November 1 - 3, 2006

Amsterdam, The Netherlands

Contents Full paper

A Laboratory Study on Incipient Motion of Nonuniform Sediment Mixtures
M.Monowar Hossain, Liton Kumar Sarker

Protecting canal banks and pipeline crossings against scour in the Hartelkanaal, Rotterdam
G. van der Hout, T. Blokland

Design of granular bed protections using a RANS 3D-flow model
T.H.G. Jongeling, dr. H.R.A. Jagers, and C. Stolker

Application of Sacrificial Piles to Control Scouring Around Bridge Piers
Ş.Y. Kayatürk and M. Göğüş

Experimental study of flow field and sediment transport around bridge abutments
A. Khosronejad, and C.D. Rennie

Interaction of horseshoe vortex, detached shear layers, and near-wall turbulence during scour at a bridge pier
G. Kirkil, G. Constantinescu and R. Ettema

Trial and Scour; Scour and Bed Protection at the Discharge Sluices in the Afsluitdijk, The Netherlands
W.C.D. Kortlever

Riprap Design Criteria, Specifications,
P.F. Lagasse, L.A. Arneson, P.E. Clopper and L.W. Zevenbergen

Flow Patterning Associated with Three-Dimensional Obstacles: a Proxy for Scour
D.O. Lambkin, J.K. Dix and S.R. Turnock

Characterization of Leaching Behavior of Recycled Concrete Used for Scour Prevention
Juhyung LEE, Kiseok KWAK, Jaehyun PARK and Moonkyung CHUNG

Automatic Non-intrusive Measurement of Scour-Hole Geometry
O. Link, F.Pfleger and U. Zanke

Unsteady bridge scour monitoring in Taiwan
J.Y. Lu, J.H. Hong, J.J. Lee and C.C. Su

Pairing riverbanks instability and fluvial hydraulics for the prediction of risk zones on a river undergoing dam break flooding
Mahdi T

Foreshore erosion and scour induced failures of sea dikes
C.V. Mai, K.W. Pilarczyk[2] and P.H.A.J.M. van Gelder

Depth of Scour at Groups of Two Bridge Piers
M.B. Mashahir, A.R. Zarrati, and E. Mokallaf

Time Development of Scour in a Cohesive Material due to a Submerged Circular Turbulent Impinging Jet
K.A. Mazurek, N. Rajaratnam and D.C. Sego

Empirical Modeling of the Evolution of the Coastline behind the Breakwaters (Tunisia)
MEDHIOUB. Samir, RONDAY. François

Riprap protection of Spill-through Abutments on Laterally Sloping Foodplains
Bruce Melville, Leighton Fletcher

Barbs (Submerged Groynes) for River Bend Bank Protection: Application of a Three-Dimensional Numerical Model
B. Minor, C. D. Rennie and D. R. Townsend

Field Study on Bank Erosion due to a Crank Flow in a River Channel which has Divergence Convergence Meandering System
Tomokazu MISHINA and Nyosen SUGA

Development of the Fully Functional Stilling Basin in Extreme Geological and Spatial Conditions
- HPP Moste III
Jure Mlacnik, Sabina Misigoj

Study on Local Scour around Spur Dikes in the Akashi River
A. Morita, K. Kanda and M. Kishihara

Considerations and Model Tests on the Design of River Barrages with Respect to Piping

M. Achmus*, B.G.S. Mansour**

* Institute of Soil Mechanics, Foundation Engineering and Waterpower Engineering, University of Hannover, Germany
** Director of Works, Reservoir and Grand Barrages Sector, Ministry of Water Resources and Irrigation, Cairo, Egypt

The exit gradient method is the state-of-the-art method for the design of river barrages with respect to piping. This method is compared with other methods. Questions arise concerning the magnitude of the admissible exit gradients to be considered in the design. Model tests are presented, in which favourable conditions for the beginning and the progress of a piping process under a river barrage were simulated by disturbance of the downstream soil bed. It is shown that under such conditions piping can occur with hydraulic exit gradients, determined from a two-dimensional model, significantly lower than the theoretically critical exit gradient.

I. INTRODUCTION

Piping is an erosion mechanism which is very relevant for river barrages as well as for dams and dikes. The under-seepage of such structures in soils sensitive to erosion (e.g. fine-grained, but non-cohesive soils like fine or medium sand) can lead to the development of a pipe, in which soil material is transported. Such processes usually begin at the downstream exit of the seepage flow, with the pipe development progressing from the downstream to the upstream side. At the end of this process the total failure of the barrage or dam occurs.

In Fig. 1 a schematic sketch of a piping channel developing at a river barrage is shown. The erosion begins at the downstream exit of the seepage. Here the seepage direction is nearly vertical, so that the start of the process corresponds to a local hydraulic uplift failure. In principle, this means that the hydraulic gradient at the seepage exit has to be limited in a way to avoid hydraulic failure with a sufficient safety factor. One problem in this respect is that possible disturbances in the subsoil (heterogeneities or scour holes) may lead to locally increased hydraulic gradients, which means that piping begins at lower gradients than expected based on calculations using a non-disturbed soil profile. In 1961 Terzaghi & Peck [7] already stated that piping erosion under dams can occur at water level differences much lower than to be expected due to hydraulic failure calculations.

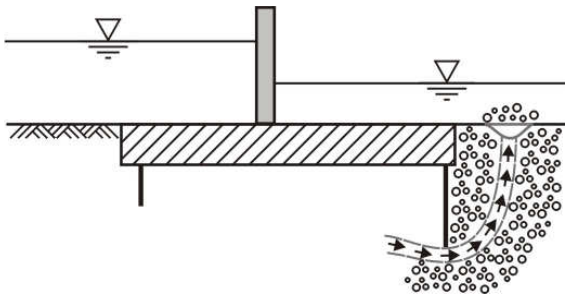

Figure 1. Schematic sketch of a piping channel occurring at the downstream end of a river barrage

Since the consideration of spatial effects of soil heterogeneity in design is usually not suitable due to limited knowledge of the subsoil conditions, admissible exit gradients have to cover such effects by means of high required safety factors.

In this paper design approaches for the consideration of piping are presented and compared for the case of a river barrage. The results of model tests are presented, which were carried out to quantify critical exit gradients under consideration of soil disturbances.

II. DESIGN METHODS FOR PIPING

The first design approach for considering piping stems from Bligh [1], who defined a seepage coefficient as follows:

$$C_B = L / H \geq C_{B,requ} \tag{1}$$

Here L is the seepage length around the structure and H is the water head. The required minimum values $C_{B,requ}$ given in Table 1 are dependent on the soil type and were derived from experience.

With theoretical considerations Sellmeijer [6] derived an equation for the critical gradient H/L which leads to piping failure. With this approach the dependence of the critical seepage coefficient on the soil type assumed by Bligh was confirmed.

Lane [3] modified the Bligh equation. He analyzed data from a large number of dams, of which a few failed due to piping, and he found out that a large vertical portion of the seepage length acts favourably. He proposed weighting the vertical portion three times higher than the horizontal one, defining the seepage coefficient as follows:

$$C_L = \frac{L_v + L_h / 3}{H} \geq C_{L,requ} \tag{2}$$

Consequently, the required values $C_{L,requ}$ are different from those given by Bligh (see Table I).

TABLE I.
REQUIRED SEEPAGE COEFFICIENTS ACCORDING TO BLIGH AND LANE

Soil type	$C_{B,requ}$ from Bligh	$C_{L,requ}$ from Lane
Very fine sand, Silt	18	8.5
Fine sand	15	7
Coarse sand	12	5
Sand and Gravel, Fine gravel	9	4

With Lane's and Bligh's methods the exact boundary conditions of the under-seepage cannot be taken into account. The actual hydraulic gradients in the subsoil are influenced, for instance, by the height of the percolated soil layer and by the locations and depths of vertical cut-offs (e.g. sheet pile walls, see Fig. 2).

Tschugajew [8] proposed to assess piping by means of a control gradient

$$I_c = \frac{H}{T\sum \zeta_i} \le I_{c,crit} \,. \qquad (3)$$

The resistance coefficients ζ_i are to be calculated for the different sections of the seepage region (for details see [4]). With this the geometry of the under-seepage situation is taken into account. On the basis of a data evaluation from more than 170 dams, of which several failed due to piping, Tschugajew recommended the critical control gradients given in Table II.

With the three methods mentioned an estimation is possible for assessing the danger of piping erosion. However, in cases where piping is decisive for the design, a more exact consideration of the problem is necessary.

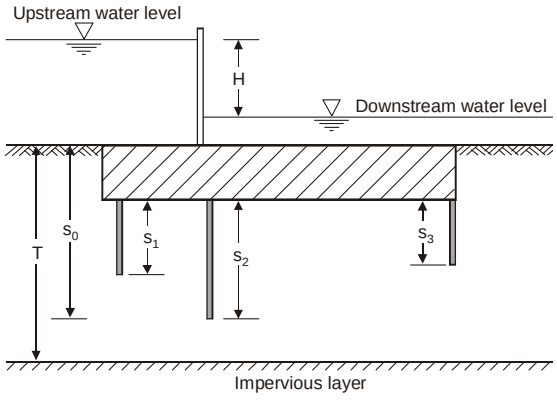

Figure 2. Geometric parameters of under-seepage flow

TABLE II.
CRITICAL CONTROL GRADIENTS ACCORDING TO TSCHUGAJEW

Soil type	$I_{c,crit}$ for cases with single cut-off	$I_{c,crit}$ for other cases
Fine sand	0.15 to 0.20	0.12 to 0.16
Medium sand	0.20 to 0.26	0.15 to 0.20
Coarse sand	0.30 to 0.39	0.25 to 0.33

As mentioned above, the process of piping erosion begins at the downstream exit of the under-seepage flow. This means that the actual hydraulic gradient at this location is decisive for the erosion design. With the exit gradient method, the hydraulic exit gradients i_{exit} are determined by means of a flow net and compared with admissible values $i_{exit,adm}$, which are again dependent on the type of subsoil. Schematically this is shown in Fig. 3.

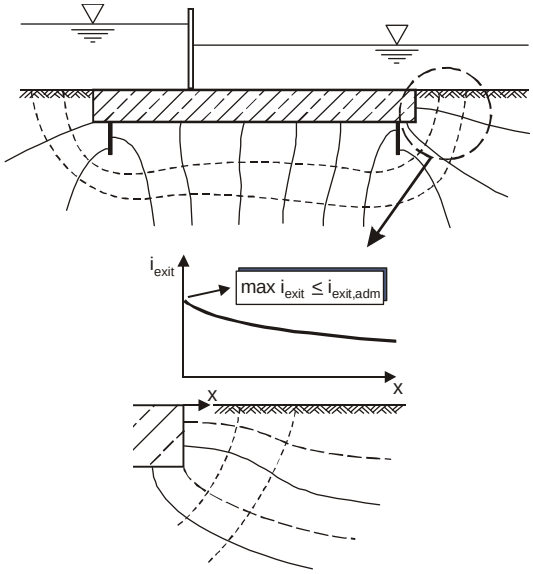

Figure 3. Exit gradient method

With numerical methods the effect of the boundary conditions of the under-seepage, e.g. different soil layers or anisotropy of the soil permeability, can be considered. Using parametric studies with a variation of input parameters a risk estimation can also be carried out, taking the uncertainties in the design parameters into account.

Instead of required seepage coefficients or a critical control gradient, admissible exit gradients have to be applied. Such values proposed by Novak et al. [5] are given in Table III.

TABLE III.
ADMISSIBLE EXIT GRADIENTS ACCORDING TO NOVAK ET AL.

Soil type	$i_{exit,adm}$
Fine sand	0.14 to 0.17
Coarse sand	0.17 to 0.20
Gravel	0.20 to 0.25

For the example of the Old Assiut Barrage on the River Nile in Egypt [4] the admissible or critical water heads have been calculated by use of the methods mentioned. The location of cut-offs (sheet piles) was varied. The results are shown in Fig. 4.

Tschugajew's method gives high water heads, because this method obviously implies no factor of safety. Admissible water heads in a similar range are obtained from Lane's and Bligh's method and from the exit gradient method. However, only the latter registers the different effectivities of the upstream and downstream cut-

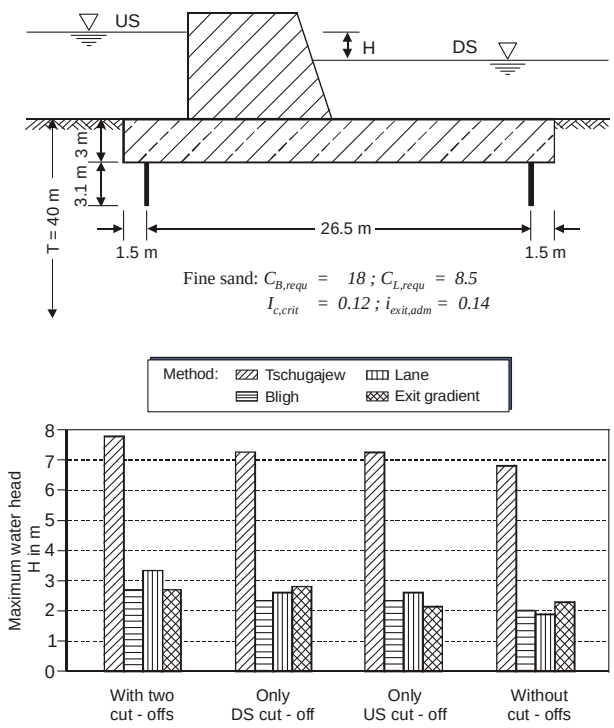

Figure 4. Comparison of calculation results for the Old River Nile Barrage at Assiut

offs. Furthermore, it is the only method which is capable of considering more complex conditions like soil layering or anisotropic permeability, which often have to be accounted for in practice.

III. CRITICAL EXIT GRADIENT

For vertical upwards-directed seepage flow the critical hydraulic gradient, for which the volume-specific seepage force equals the soil unit weight, is

$$i_{crit} = \frac{\gamma'}{\gamma_w} . \qquad (4)$$

Here γ' and γ_w are the buoyant unit soil weight and the unit weight of water, respectively. Since at the under-seepage flow exit no overburden pressure acts, local hydraulic failure and with that the start of the erosion process occurs when the exit gradient reaches this critical gradient. For non-cohesive soils the buoyant unit weight normally lies in the range 9 kN/m^3 $\leq \gamma' \leq$ 11 kN/m^3, dependent on the relative density. Thus, the bandwidth for the critical exit gradient is $0.9 \leq i_{crit} \leq 1.1$. With the introduction of a safety factor η, the admissible exit gradient is

$$i_{exit,adm} = \frac{i_{crit}}{\eta} . \qquad (5)$$

Novak et al. [5] derived the admissible exit gradients given in Table III from (5) using safety factors of 5 to 6. This may be justified by the fact that, at least for the example shown above, this safety factor leads to admissible water heads which are similar to the values obtained with Lane's and Bligh's methods based on experience. However, such safety factors are unusual even in geotechnical engineering and need clarification.

The background to the low admissible exit gradient is that piping erosion is a local, three-dimensional effect, whereas the exit gradients are calculated using a two-dimensional model or at least a model with homogeneous soil layers. In reality, local soil heterogeneities or disturbances (like e.g. scour holes) have to be considered, which lead to locally increased hydraulic gradients. Since it is normally impossible to take such disturbances into account, the uncertainty has to be covered by the use of high required safety factors.

However, to assess the real level of safety it should be known which are the actual critical gradients valid for most unfavourable conditions. For this reason, model tests have been carried out, in which the soil at the downstream end of a model barrage was disturbed systematically.

IV. MODEL TESTS

A. Model test set-up

In 1922 Terzaghi carried out model tests to study piping under a shallow foundation and found out that Bligh's design method incorporates high factors of safety compared with his test results. In the 1930s Davidenkoff carried out similar tests, but he inserted a small glass tube in the foundation bed to produce an artificial weak point. He established that the water head at which piping occurred was nearly halved by this measure [2].

In the tests reported here disturbance of the downstream river bed was achieved by means of a small needle which was pricked into the soil at different locations to favour the start of the erosion process.

The test set-up used is shown in Fig. 5. A model of the Old Assiut Barrage foundation on the River Nile with a scale of about 1:100 was investigated. Two foundation models, one with two cut-offs at the upstream and downstream end of the foundation and one without cut-offs, were used. Also, the depth T of the sand subsoil layer was varied between 10 cm and 25 cm.

The soil used was a uniform fine to medium sand. The grain size distribution of this material is shown in Fig. 6. The following parameters apply for the sand:

- Minimum void ratio: $e_{min} = 0.67$
- Maximum void ratio: $e_{max} = 1.09$

In two test series the sand was placed in the box once with an average void ratio of $e = 0.92$, which corresponds to a loose to medium dense state (relative density $D_r = 0.40$) and once with $e = 0.72$, corresponding to a dense state ($D_r = 0.88$). The loose to medium dense state was achieved by pouring the sand gently into the water, and the dense state by vibrating the box with the help of a plate vibrator whilst pouring the sand.

Starting from a constant water level, the level on the upstream side of the model barrage was increased stepwise. After each step of initially 4, later on 2 and finally 1 cm increase the evolution of stationary seepage conditions was waited for. For this the seepage discharge

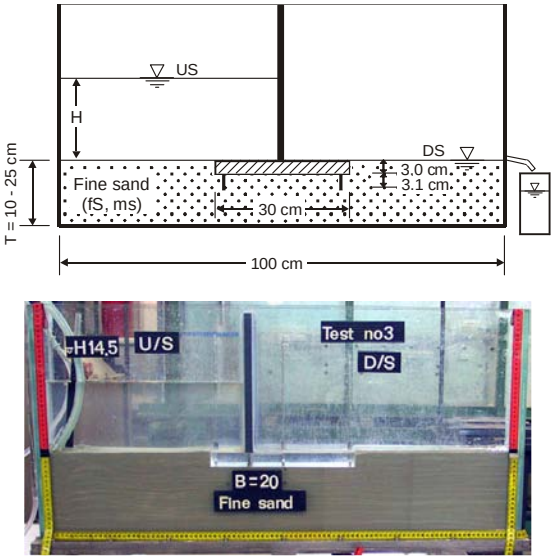

Figure 5. Model tests set-up: schematically, with cut-offs (top), photographic view (bottom, without cut-offs)

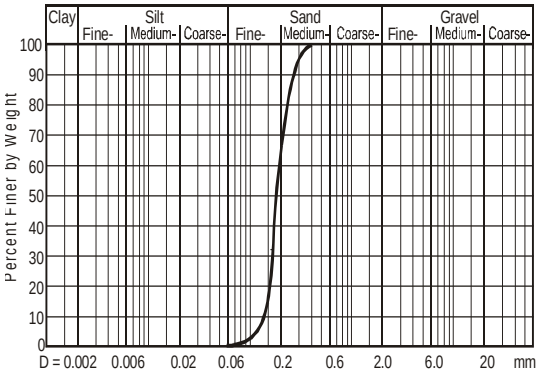

Figure 6. Grain size distribution of the sand used

and, by means of piezometers, the water pressures beneath the foundation were measured. Then the downstream soil bed was disturbed with the help of a thin needle to simulate disturbance and to create favourable conditions for the start of piping erosion. The disturbance was made at the middle and at both sides just beside the downstream end of the foundation with depths ranging from 3 to 7 cm. When this was done, at a certain water head a local 'boiling' zone indicating the start of the erosion process was observed. Afterwards, the time interval till the next water head increase of 1 cm was raised to 40 minutes in order to observe carefully the ongoing process until complete foundation failure occurred.

B. Observed phenomena

After reaching a certain water head on the upstream side, for both cases with and without vertical cut-offs a local erosion funnel evolved at the downstream end of the foundations. In this region the seepage force equalled the soil weight, so that the soil grains were moving around. Since this looks like as if the sand is boiling, the zone is called the 'boiling zone'. This state is stable, i.e. transportation of soil grains and a further progress of the piping channel only occurs when the water head is increased further. This was also observed in experiments by Sellmeijer [6].

Further increase of the water head leads to erosion. Due to transportation of the soil grains a small elevation in the downstream bed occurs. The boiling sometimes stopped, possibly due to blockage caused by the deposition of the sand grains, but after another disturbance with the needle it continued again. During the test, ejected sand was continuously removed to simulate the transport to be expected by the downstream water flow and to keep the erosion process in progress.

With the ongoing increase of the water head difference, in the case without cut-offs a small piping channel formed in the contact surface between the soil and the foundation, progressing towards the upstream side. This could be observed in tests using a transparent foundation model. In the top view given in Fig. 7, the boiling zone and the piping channel observed in one test are shown. During the ongoing process, a depression in the soil bed upstream of the model barrage could be observed.

For the cases with cut-offs, firstly a small depression formed at the upstream side of the downstream cut-off. Due to the depression, in the upper layer of sand between the two cut-offs the transport of soil particles to the downstream side took place. At a later stage, this material loss leads to a depression of the sand bed at the upstream end of the foundation (Fig. 7 bottom).

Finally, in all tests a complete failure of the foundation occurred with a drastic outflow of the soil beneath the foundation and a more or less instant equalization of the water levels upstream and downstream. In the tests, the

Figure 7. Observed phenomena during piping erosion: system without (top) and with cut-offs (bottom)

foundations stayed in their positions, because to avoid seepage beside the foundation, a silicone seal had been arranged between the foundation and the model box (Fig. 8). In nature, complete failure would lead to high displacements and rotations of the foundation.

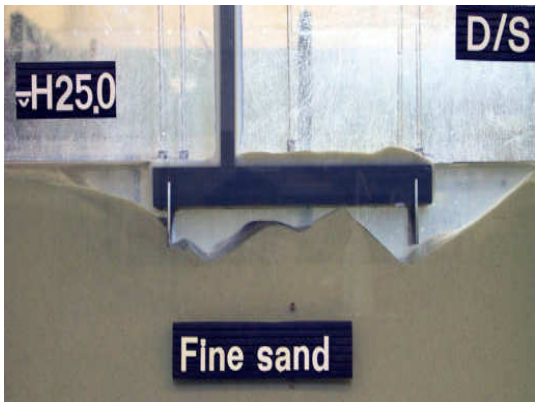

Figure 8. Final situation after complete failure

C. *Test results and analysis*

The water head differences acting at the beginning of the piping process, i.e. the first evolution of a boiling zone, and at the end of the tests reaching the ultimate failure are given in Table IV.

On one hand there is a clear influence of the relative density of the sand. For the cases with dense sand higher water heads apply than for loose to medium dense sand. On the other hand there is also a tendential influence of the depth of the sand layer. The higher the subsoil depth, the lower is the water head necessary for the begin of and the failure due to piping. This agrees with results from the exit gradient method, since a larger subsoil depth leads to higher exit gradients.

TABLE IV.
WATER HEAD DIFFERENCES MEASURED IN THE TESTS

Test case	Depth of sand layer *T* in cm	Water head difference *H* in cm	
		Piping start	Failure
Loose to medium dense sand, no cut-offs	10	13	16
	15	11	15
	20	13	14
	25	10	13.5
Dense sand, no cut-offs	10	15.5	18
	15	15	17
	20	14.7	16.5
	25	14	16
Loose to medium dense sand, with cut-offs	10	17	22
	15	14	22
	20	14	21
	25	14	20
Dense sand, with cut-offs	10	22	27
	15	20	25
	20	21	26
	25	19	25

To determine the critical exit gradients from the experimental tests, back-calculations using flow nets established for the model test cases were carried out. A homogeneous subsoil with isotropic permeability was assumed. Thus, the exit gradients belonging to the water heads measured could be calculated. In Figs. 9 and 10 the exit gradients belonging to the start of piping and determined at ultimate failure are given. The results for dense sand and for loose to medium dense sand are depicted separately.

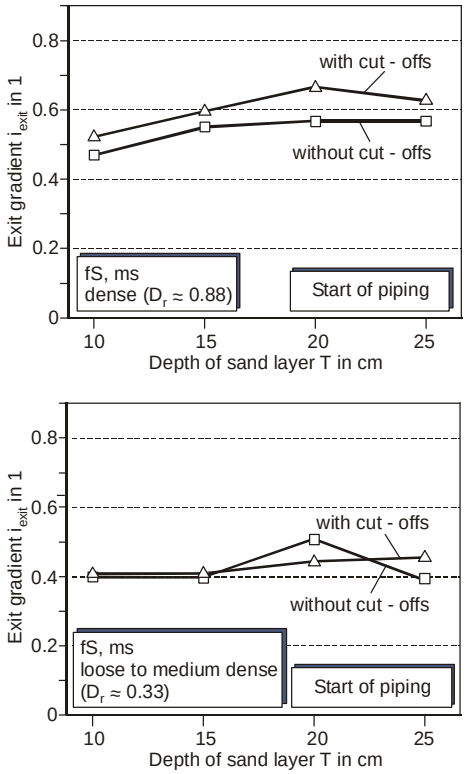

Figure 9. Exit gradients at the start of piping determined for dense sand (top) and for loose to medium dense sand (bottom)

There is a tendency, at least for dense sand, that in cases with vertical cut-offs higher critical exit gradients apply. For dense sand and a small sand layer depth of 10 cm slightly lower exit gradients are also determined.

From the experimental tests, exit gradients belonging to the start of piping between 0.5 and 0.65 are found for dense sand and between 0.4 and 0.5 for loose to medium dense sand. To induce the ultimate failure, exit gradients between 0.55 and 0.85 for dense sand and between 0.5 and 0.65 for loose to medium dense sand were determined.

V. CONCLUSIONS

The exit gradient method is the only method capable of accounting for complex boundary conditions in the design of river barrages with respect to piping. In cases where piping is decisive for the design of a structure, this method should be used.

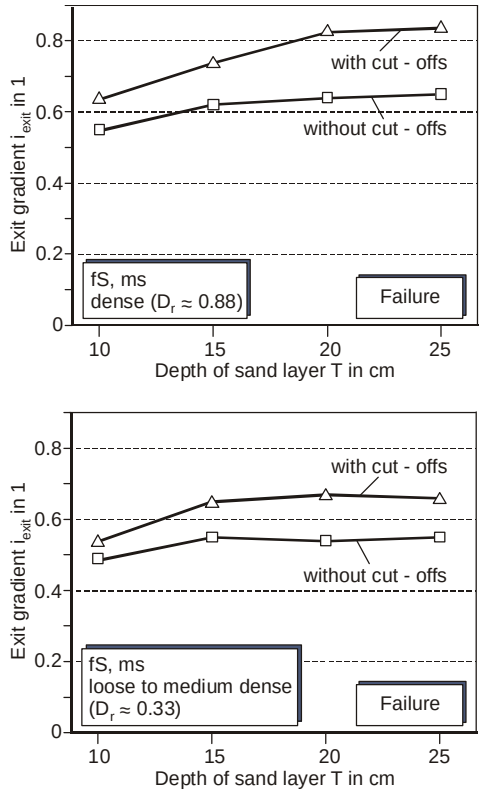

Figure 10. Exit gradients at ultimate failure determined for dense sand (top) and for loose to medium dense sand (bottom)

However, at which water head difference piping starts and failure of the structure occurs, depends strongly on soil heterogeneities or on the existence of disturbed zones in the subsoil. Thus empirical values of the admissible exit gradient are used, which imply a safety factor between 5 and 6 to the theoretically critical hydraulic gradient of about 0.9 to 1.1.

The model tests reported here make it clear that under extremely unfavourable conditions, i.e. very favourable conditions for piping, the erosion can begin at hydraulic gradients – calculated by means of a two-dimensional model – much lower than the theoretical value. Piping in fine sand was observed to begin at water head differences belonging to calculated exit gradients of about 0.4 for the loose to medium dense state and of about 0.5 for the dense state. Assuming these values to be the real critical exit gradients, the admissible exit gradients proposed by Novak et al. imply a real safety factor of about 3. Higher exit gradients are necessary to induce failure of the structure, leading to safety factors of 4 and higher.

The installation of vertical cut-offs tends to increase the critical exit gradient. The reason for this might be that the direction of seepage flow near the exit point is not really vertical but inclined for the cases without cut-offs. Also, without cut-offs, piping channels can easily course in the interface between foundation and soil. In the tests the foundation surface was relatively smooth, and the foundation pressure was relatively low.

Due to German regulations, a safety factor against hydraulic failure of 1.5 is usually required. Considering this, higher exit gradients seem to be admissible with respect to piping. However, it has to be pointed out that the critical exit gradients found should not be applied directly to practical problems. It is yet not clear to which degree the simulated disturbance of the soil bed is realistic and really covers most unfavourable conditions in nature. It must also be considered that the magnitude of soil pressures in the model tests was much smaller than in reality, which is at least of influence for the progress of the erosion after occurrence of the first boiling zone.

Thus, many questions concerning admissible exit gradients are still open. This justifies the relatively low admissible values used in practice at the present time. However, it is felt that in many cases the design with these values implies higher safety factors than necessary. To use this potential for optimization, further research has to be carried out.

REFERENCES

[1] W.G. Bligh, *The practical design of irrigation works*, Constable, London, 1912.

[2] R. Davidenkoff, *Unterläufigkeit von Stauwerken*, Werner Verlag, Düsseldorf, 1970.

[3] E.W. Lane, "Security from under-seepage masonry dams on earth foundations", *Proceedings ASCE, Transactions No. 100*, pp. 1235-1272, 1934.

[4] B.G.S. Mansour, *Investigations on design and rehabilitation options for river barrages with special respect to piping*, Mitteilungen des Instituts für Grundbau, Bodenmechanik und Energiewasserbau, Universität Hannover, Heft 62, 2005.

[5] P. Novak, A.I.B. Moffat, C. Nalluri, R. Narayanan, *Hydraulic Structures*, 3rd edition, Spon Press, London/New York, 2001.

[6] J.B. Sellmeijer, *On the mechanism of piping under impervious structures*, Technical University of Delft, The Netherlands, 1988.

[7] K. Terzaghi, R.B. Peck, *Die Bodenmechanik in der Baupraxis*, Springer Verlag, Berlin, 1961.

[8] R. Tschugajew, *A new method for the calculation of seepage flow* (in Russian), Gidrotechniceskoe stroitel'stvo 26, Moscow, 1956.

Bank Erosion Mitigation Red River Vietnam, Towards an Anticipating River Training Strategy

G.J. Akkerman [*], E. Mosselman[**], G.J. Schiereck [***], Pham An Tuyet [****], Pham Dinh[*****]
[*] Royal Haskoning, Nijmegen, The Netherlands
[**] Delft University of Technology & WL | Delft Hydraulics , Delft, The Netherlands
[***] Ministry of Transport and Public Works , The Hague, The Netherlands
[****] Vietnam Institute for Water Resources Research, Hanoi, Vietnam
[*****] Vietnam Institute for Water Resources Research, Hanoi, Vietnam

I. INTRODUCTION

Bank protection, as a means of mitigation of bank erosion along rivers, may serve different goals and may take different forms. The different goals are not always addressed well in bank protection design. In addition, bank protection works may themselves induce more severe erosion, when not properly designed within the total concept of river training. These issues will be dealt with in this paper. The ideas are illustrated for the Red River system in Vietnam, for which the authors analyzed the erosion problems and reviewed the current practices regarding planning, implementation and monitoring of bank protection works.

II. BACKGROUND

One of the most prominent issues in current river training is the control of bank erosion. Bank erosion may cause major loss of land and property and may endanger the stability of structures such as embankments. Apart from the settlements at the river banks that need to be protected, flood plains may be inhabited or used economically. In the latter case severe bank erosion has to be controlled there as well. At the other hand, bank erosion is a natural manifestation of river dynamics. By introducing extensive bank protection works, the natural dynamics of rivers is suppressed and adverse effects may arise, such as the creation of very sharp bends, as shown in Fig. 1 below.

FIGURE 1. EFFECT OF LOCAL FIXATION OF MEANDER BEND

Man-made bank protection works may even change the course of the main channel, such as in Pakistan where spurs built in Punjabi rivers are attracting head-on attack during floods. These examples show that bank protection works should be considered within the total framework of river training. Such a framework, as presented hereafter, may help river managers in placing bank protection in the wider context of integrated river management and to formulate an anticipating river training strategy.

III. OBJECTIVES AND FUNCTIONS

The objectives and functions of bank protection works show a hierarchy:

Type A = first type of protection: protection of higher grounds from erosion and to provide safety against flooding. In addition, critical infrastructure can be protected, i.e. bridge abutments and pipeline crossings.

Type B = second type of protection: protection of flood plains to mitigate erosion and to provide safety against erosion and (frequent) flooding of the floodplain.

Type C = third type of protection: promotion of navigation by fixation/constriction of the main channel.

The spatial appearance of these types of protection levels is illustrated in Fig. 2 below.

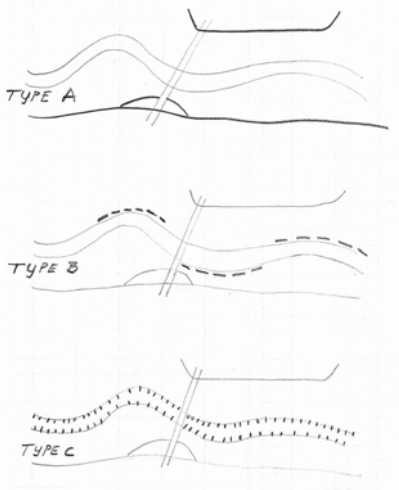

FIGURE 2. ILLUSTRATION OF DIFFERENT TYPES OF PROTECTION

The different types of protection can be combined, e.g. starting from Type A, proceeding with Type B and ending up with Type C, as was the case in the Netherlands' Rhine river system. As a result, the whole river system has gradually been trained and controlled. In contrast, Type A will leave maximum river dynamics and maximum natural development. The three types are sometimes three successive stages in the training of the river, but not necessarily because they serve different purposes: flood protection, erosion protection and navigation. Hence, e.g. combinations of Types A and C, without Type B are also possible. Type C, serving the development of inland navigation can also be applied in absence of Types A and B, e.g. in natural river systems with minor interventions, such as seasonal training works to influence the sediment distribution. At present there is a strong tendency for the Rhine rivers to allow the river more space and dynamics and to restore natural assets. This implies reducing Type B protection, while maintaining Types A and C.

The different protection levels require different types of bank protection structures:

Type A requires high structures and high safety levels → massive and solid bank protection works.

Type B requires intermediate structures and intermediate safety levels

→ less massive and less solid bank protection works.

Type C requires low structures and minor safety levels

→ (usually) modest or provisional bank protection works, focused on constriction of the fairway and/or sediment management.

It should be remarked that only in case of extreme navigational demands, e.g. at the Waal river in the Netherlands, the protection works of Type C will have to be extensive, such as a continuous groyne system in the Waal river, shown in Fig. 3.

IV. Overall Situation of Bank Protections along the Red River

The authors of this paper participated in a mission for evaluation of bank erosion and current protection works in the Red River in Vietnam [1]. The location was upstream of Hanoi (up to Viet Tri) and downstream of Hanoi (up to Hung Yen). In addition distributaries, the Duong River, the Thai Binh and the Luoc, have been surveyed.

The protection levels of these river stretches are typically of Types A and B. Training works for navigation are in a premature stage yet. Type A is evident from the high flood embankments surrounding the meander belt and the densely populated areas to be protected. These embankments have to be protected from outflanking of the main channel during high river flows. At many locations, the main channel approaches the primary embankments and there the focal point is laid on the bank protection works. However, the flood plains are also widely occupied: large and small settlements and intensive economic activities (e.g. sand mining, agriculture). At the larger villages Type A protection is used, leading to encroachments of the flood plains. Generally, however, Type B protection applies, mainly concentrated near sharp outer bends.

FIGURE 3. AREAL VIEW OF GOYNES AT THE WAAL RIVER

The encroachment of the natural flood plains can have adverse effects, with effects comparable to Fig. 1, as shown in Fig. 4. This will, together with the other occupation in and usage of the flood plains, increase flooding risk. From this example, it can be seen that river management should in the first place be spatially oriented with due consideration of the dynamic character of the river. Given the situation as it is now, with a strongly utilized and tamed river, the Type A and Type B protections may need to be continued. This is acknowledged and practiced in present bank protection design for the Red River.

In spite of the river training works already applied, the Red River locally still has some dynamic character. This can be seen from Fig. 5. Herein the plan form upstream of Hanoi is shown in 1990 as well as in 2000 (white lines) from satellite images. In recent years and in the years to come, however, more and more bank protection works do contribute to further fixation of the main channel. Yet after every flood season, new endangered locations arise which have to be urgently protected.

Some of the river authorities showed an inclination towards full protection of the main channel by means of groynes. It should be kept in mind, however, that this protection is of Type C, which would not be justified from navigational point-of-view at present. Navigation is coming up as an economical factor, but is still modest. Another item arises here: the large difference in low water levels and flood levels. As a consequence, it would suffice to keep the protection works (e.g. groynes) of Type C modest, which is also important from an economical point-of-view. In that case, however, these works will not provide sufficient protection for the flood plains (Type B), let alone for the higher grounds (Type A). The sparse groynes that have already been constructed near the primary embankments do not seem to be very effective up to now. Groyne construction, as compared to direct strengthening of the banks is not economical, as the material usage increases strongly with increasing heights. Hence, groynes should not be applied as a protection for the primary embankments.

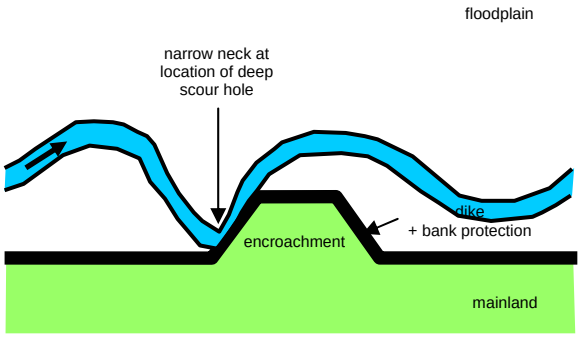

FIGURE 4. 'FOLDING' OF CHANNEL NEAR ENCROACHMENT

The planning and execution of bank protection works is mainly reactive-based, i.e. as an instant reaction upon the observation of strong bank erosion after the flood season. At those locations, the bathymetry is measured and a decision is made on the necessity for bank protection works. If deemed necessary, these works are initiated shortly after a positive decision. The respective departments are dealing with this approach effectively. This approach is also highly cost-effective on the short-term, which is inevitable with the limited funds available at present.

V. REVIEW OF LOCATIONS ALREADY PROTECTED

Bank erosion has been intense along the Red River. Over the years, the reactive response resulted in relatively long stretches of protected banks of the main channel. This followed from an inventory, including field visits, during the mission of the authors. A typical illustration is shown in Fig. 6 for the section of the Red River upstream of Hanoi.

This example shows that the dynamics of the Red River near Ha Noi is strongly reduced nowadays by the presence of these protection works. Also in other stretches nearly every outer bend is provided with some protection. This can be well-understood from the demand for Type B protection (floodplains). However, some dynamics still remains and in future new critical bank sections will certainly continue to appear.

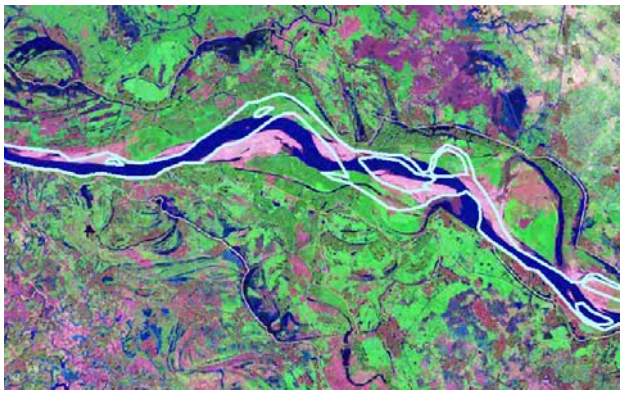

FIGURE 5. PLAN FORM CHANGES FROM SATELLITE IMAGES

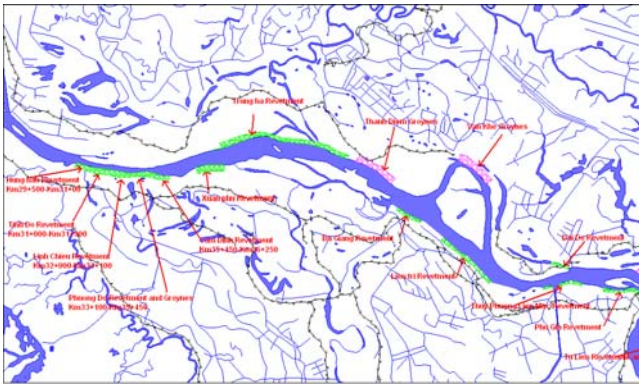

FIGURE 6. ILLUSTRATION OF BANK PROTECTION WORKS

VI. STRUCTURAL DESIGN OF BANK PROTECTION

During floods the flow velocities in the Red River are large and, as a consequence, the tractive forces on the slopes are large as well. Hence, the banks need to be protected in a robust way. To cope with this requirement, the Red River authority developed a special type of protection: concrete or masonry grids, filled up with a neatly placed rockfill stone pitching. This type of protection is called 'Tsu Phan' and is shown in Fig. 7 below. This rockfill layer is provided with a filter layer underneath of crushed gravel. The use of geotextiles, as separation between gravel layer and soil, was observed at some places, but was absent at other places.

Below the waterline, rubble is dumped to fill up the slope to the desired angle or gabions or bamboo-packed stone sausages ('dragons') are applied. Before placing the stabilization, the slope above the waterline is re-adjusted to the desired slope angle (usually around 1: 2.5) by removing or replenishing the soil.

There are quite some advantages to this method, such as easy visual construction without measuring equipment after the grids have been installed. Another advantage is that the stone pitching is enclosed by the concrete or masonry grids, what adds to the stiffness of the pitching. Initially, drainage ditches can be made first. They are accurately positioned and provide a reference position for the subsequent construction of the grids.

The stone pitching is able to withstand large flow velocities, in spite of the small stones used, and is far more preferable than a loose rockfill revetment in this situation (scarcity of large rockfill scarce, abundant relatively cheap labour).

FIGURE 7. STONE PITCHING GRID ('TSU PHAN')

VII. DISCUSSION

Bank erosion is a major threat to safety and occupied areas in the floodplains of the Red River. Hence, the efforts and costs of bank protection works is substantial. The mission team felt that the approach of the Red River authorities (Dike Departments) to combat bank erosion is highly cost-effective and adequate. The reactive strategy is fitting well into the present budget framework.

Additional budget, however, may give the opportunity to arrive at a more anticipating river training strategy. Such a strategy would allow a more preventive approach and would possibly minimize bank protection works in future.

Bank erosion is just one phenomenon of the complex morphodynamic behaviour of the river. A better understanding of the morphodynamics is important for a sustainable long-term river management strategy. This is especially important while at present hydraulic and morphological data are scarce. At the same time, the Red River experiences large changes, e.g. a strong decrease of the forest cover of the Da River (a major upstream tributary) [2] over the last decades, excessive sand mining from the river (poorly recorded) and ongoing occupation of flood plain areas. In addition, the morphodynamic behaviour of the river is complicated by the large difference between discharges in the flood and in the dry season (factor 20).

It is very important to maintain safety levels against flooding in future. This requires a better understanding, a better monitoring of plan form changes and improved predictions on the morphodynamic development of the Red River system.

Such knowledge can be used very well for introducing a more anticipating bank protection strategy, which will also contribute to safety and cost-effectiveness.

For the short-term the mission team recommended to monitor plan form changes by satellite image analysis, to increase bathymetric monitoring and to perform 1-D morphodynamic modeling, so as to anticipate better on bed and bank erosion. A second recommendation is to set-up a Best Practice Guide on bank protections, so as to unify and improve, where necessary, current bank protection design. Another issue is to study the changing morphology of the bifurcation of the Red River and Duon River at Hanoi.

ACKNOWLEDGMENT

The authors thank the Vietnam Ministry of Agriculture and Rural Development for their invitation and hospitality and the Asian Development Bank for their funding. Thanks are also due to the Second Red River Basin Sector Project, that identified this mission [3] and hosted our mission team. The Dutch authors are especially grateful for the pleasant cooperation with the counterpart experts: the co-authors of this article.

REFERENCES

[1] G.J. Schiereck, G.J. Akkerman & E. Mosselman, “Bank Erosion and River Training (BERT) –Mission, Second Red River Basin Sector Project, 2005.

[2] G.J. Klaassen, K.W. Pilarcyk and D.C. San, “River Bank Erosion and Mitigation Strategies in Vietnam”. Paper presented at the ISFD-Congress, Nijmegen, The Netherlands, 2005, pp.269-279.

[3] C.J. Sloff et al., “Inception Report, Strategic flood management”, Second Red River Basin Sector Project, 2005.

Quantification of the Erosive Capacity of Water

George W. Annandale*
* Engineering and Hydrosystems Inc., Denver, Colorado, USA

When expressing average flow velocity, wall shear stress and available stream power as a function of hydraulic roughness it is found that flow velocity decreases, wall shear stress increases and stream power remains constant [2]. These three parameters are often used as indicators of the relative magnitude of the erosive capacity of water, and the differing trends provide practicing engineers with a practical problem. The trend characteristics imply that it is unknown whether the erosive capacity of water will increase, decrease or remain constant when using conventional parameters for quantifying the relative magnitude of the erosive capacity of flowing water subject to varying hydraulic roughness.

This paper addresses the apparent dichotomy by using boundary layer theory to quantify turbulent boundary shear stress and applied boundary stream power as a function of hydraulic roughness. By making use of findings by [4] and the conclusions from the boundary layer analysis [1], it is concluded that either turbulent boundary shear stress or applied boundary stream power can be used to quantify the relative magnitude of the erosive capacity of water. Using applied boundary stream power is preferred because it resembles turbulence intensity and therefore quantifies the relative magnitude of pressure fluctuations in turbulent flow, which is the principal agent leading to incipient motion [1]. It is shown that average flow velocity is an undesirable indicator of the relative magnitude of the erosive capacity of water because it provides contradictory results.

I. INTRODUCTION

The term "erosive capacity of water" is an elusive concept. From empirical experience it is known that the potential for incipient motion of earth materials, and thus the potential for scour, increases as the "flow intensity" of water increases. The concept of increased flow intensity can take on different meanings, dependent on the observer. Some observers prefer to express it in terms of average flow velocity, while others prefer to express it as shear stress or stream power. It has been found that use of these three indicator parameters to quantify the relative magnitude of the erosive capacity of flowing water results in inconsistent conclusions [1].

The paper illustrates that this inconsistency can be resolved by quantifying the relative magnitude of the erosive capacity of turbulent flowing water when taking full account of flow processes in the near-boundary region.

II. FLOW CONDITIONS AT INCIPIENT MOTION

Reference [4] has shown that incipient motion under laminar flow conditions is a function of wall shear stress, while the same under turbulent flow conditions depends purely on fluctuating turbulent pressures when flow conditions in the near boundary region is characterized as smooth turbulent flow. The analysis by [4] also demonstrates that turbulent fluctuating pressures combined with a transverse force of water along the bed results in concurrent lifting and rotation of particles at the point of incipient motion when flow conditions in the near boundary region changes to rough turbulent flow. The validity of these proposed mechanisms were illustrated by making use of basic principles of hydraulics and the Shields diagram.

Reference [3] showed that fluctuating pressures in turbulent flow play the dominant role in scour of rock, regardless of whether it scours by means of dynamic impulsion (block removal), brittle fracture or fatigue failure. Methods for quantifying the magnitude of fluctuating pressures resulting from turbulent plunging jets are available (see e.g. [1] and [3]).

Methods for quantifying the magnitude of turbulent fluctuating pressures for most other flow conditions, such as flow around bridge piers, past bridge abutments, around channel bends, underneath hydraulic jumps, etc. are not generally known. Practicing engineers therefore prefer to use indicator parameters to quantify the relative magnitude of such pressure fluctuations, and thus the magnitude of the erosive capacity of water in turbulent flow.

III. INDICATOR PARAMETERS

The objective of using indicator parameters in scour technology is to quantify the relative magnitude of the erosive capacity of water. Typical indicator parameters that are generally used in engineering practice include average flow velocity, wall shear stress and available stream power.

Average flow velocity $\bar{u}$ can be expressed as,

$$\bar{u} = 18\log\left(\frac{12\cdot R}{k_s}\right)\cdot\sqrt{R\cdot s_f} \qquad (1)$$

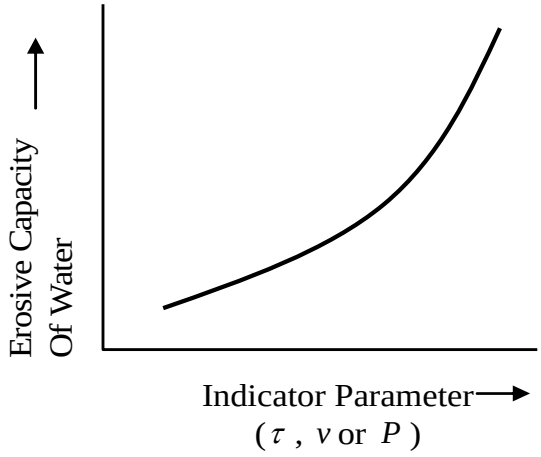

Figure 1. Desired relationship between indicator parameters and the actual magnitude of the erosive capacity of water.

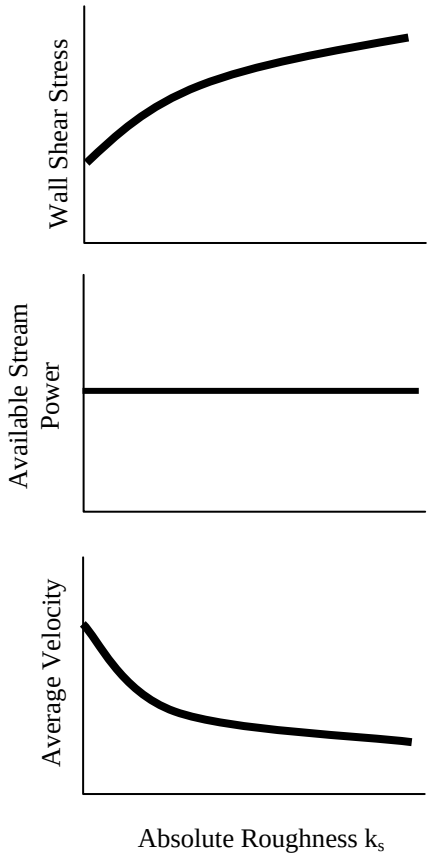

Figure 2. Actual behavior of commonly used indicator parameters for quantifying the relative magnitude of the erosive capacity of water, expressed as a function of absolute roughness.

Where R = hydraulic radius; s_f = energy slope; k_s = absolute roughness.

Wall shear stress $\overline{\tau}_w$ is calculated as,

$$\overline{\tau}_w = \rho \cdot g \cdot R \cdot s_f \qquad (2)$$

Where ρ = mass density of water; g = acceleration due to gravity.

Available stream power P is expressed as,

$$P = \tau \cdot u \qquad (3)$$

Due to the fact that indicator parameters do not quantify the exact magnitude of the erosive capacity of water, but only its relative magnitude, these parameters should be characterized by internal consistency. The behavior of indicator parameters is internally consistent if the relative change in parameter value resembles the actual change in the erosive capacity of flowing water. This means that the magnitude of an indicator parameter must consistently increase when the actual magnitude of the erosive capacity of the water increases. Similarly, the values of the indicator parameters must consistently decrease when the actual magnitude of the erosive capacity of water decreases (Fig. 1).

References [1] and [2] show that the conventional indicator parameters used in engineering (i.e. average flow velocity, wall shear stress and available stream power) are not internally consistent. When expressing the relative change in indicator value as a function of hydraulic roughness, it is found that wall shear stress increases, available stream power remains constant, and average flow velocity decreases (Fig. 2). The inconsistency in these trends provides practicing engineers with a dilemma.

IV. Near-Boundary Processes

In order to explain the relevance of near-boundary processes in quantifying the relative magnitude of the erosive capacity of water it is necessary to first consider the distribution of stream power of flowing water in a water column. Such consideration provides an indication of the spatial variation of the rate of energy dissipation, which is directly related to turbulence production, and thus the relative magnitude of fluctuating pressures.

Reference [1] illustrates that the distributions of available and applied stream power differ. Available stream power is the stream power that is made available to the flowing water to overcome internal and boundary resistance. Applied stream power is the stream power that is used by the flowing water to overcome internal resistance. The latter represents the distribution of the rate of energy dissipation in the flowing water.

The difference in distribution between available and applied stream power can be explained by using an analogy of a simply supported beam bending under its own weight. The beam weight is equivalent to the available stream power, i.e. it makes a force available to bend the beam. The stresses developing within the beam re-distributes this force to overcome internal resistance offered by the beam. The distribution of the internal stresses in the beam differs from the distribution of the applied load.

Fig. 3 illustrates the distribution of available and applied stream power [1]. The available stream power has its maximum value at the water surface and is zero at the bed, while the applied stream power's maximum value is at the bed and it is zero at the water surface elevation.

This makes sense because the greatest resistance against flow is encountered at the boundary.

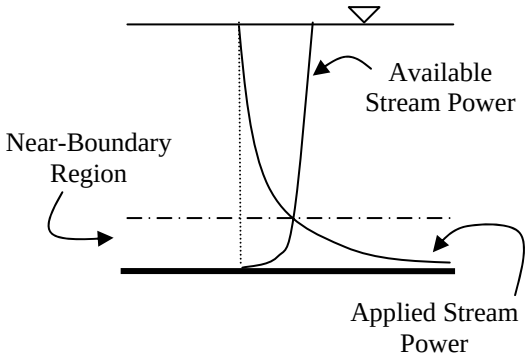

Figure 3. Distribution of available and applied stream power in flowing water.

Fig. 3 illustrates that the available stream power equals the applied stream power at the upper limit of the near-boundary region. It also shows that, theoretically, the applied stream power at the bed approaches a value of infinity. This is obviously not possible and is a limitation of the far-field equations used to derive the distribution of the applied stream power [1].

It is therefore necessary to investigate the actual distribution of the applied stream power at the boundary. Applied stream power is also known as turbulence production and its distribution within the near-boundary region is shown in Fig. 4.

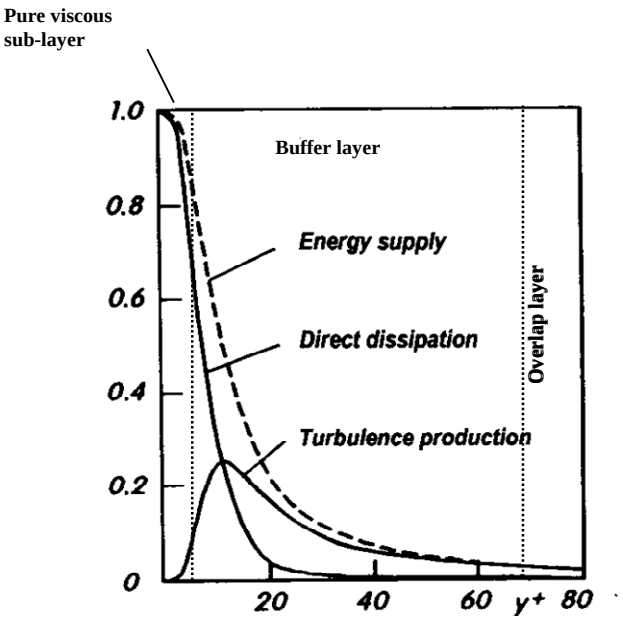

Figure 4. Dimensionless distribution of energy supply, direct dissipation and turbulence production in the near-boundary region [6]

Our principal interest for the topic under discussion is to quantify the applied stream power, and therefore the turbulence production, in the vicinity of the boundary, i.e. within the near-boundary region. Reference [5] expresses the dimensionless form of turbulence production TP as,

$$TP = \tau_t^+ \cdot \frac{du^+}{dy^+} \tag{4}$$

where $\tau_t^+ = \frac{\tau_t}{\rho u_*^2}$; τ_t = turbulent boundary shear stress; $u_* = \sqrt{\frac{\overline{\tau}_w}{\rho}}$ = shear velocity; $\overline{\tau}_w$ = average wall shear stress; $u^+ = \frac{\overline{u}}{u_*}$; $\overline{u}$ = average velocity.

Therefore, in order to quantify the magnitude of the turbulence production in this region it is necessary to integrate the expression for dimensionless turbulence production between zero and the upper limit of this region. The near-boundary region occupies a space close to the boundary that equals about $70y^+$, where $y^+ = \delta = \nu/u_*$, and ν = kinematic viscosity of the water; and δ = Prandtl's wall layer thickness. Therefore, quantification of the total amount of applied stream power within this region requires integration between $y = 0$ and $y = 70y^+$.

By fitting a curve to the dimensionless distribution of turbulence production within the near-boundary region [1] shows that,

$$\int_0^{70y^+} \tau_t^+ \frac{du^+}{dy^+} dy^+ = 7.853 \tag{5}$$

By integrating Eq. (5) it is shown that the applied stream power at the boundary, i.e. within the near-boundary region, can be expressed as,

$$\tau_t \overline{u} = 7.853 \cdot \rho u_*^3 = 7.853\rho \left(\sqrt{\frac{\overline{\tau}_w}{\rho}} \right)^3 \tag{6}$$

and that the turbulent boundary shear stress can be expressed as,

$$\tau_t = 7.853 \left(\frac{u_*}{\overline{u}} \right) \overline{\tau}_w \tag{7}$$

Eq. (7) indicates that the total amount of turbulent shear stress at the boundary, resulting from turbulence production within the near-boundary region, is a function of the shear and average velocities. This equation is interpreted as representing the amount of shear stress actually applied to the boundary.

The difference between turbulent boundary shear stress and wall shear stress is similar to the difference between applied and available stream power. The wall shear stress is the amount of shear that is made available for the water to overcome internal and boundary resistance. The turbulent shear stress is the shear stress that is applied to actually overcome the internal resistance within the flow

and at the boundary. Eq. (7) expresses the magnitude of the turbulent boundary shear stress within the near-boundary region.

When using Eq.'s (6) and (7) as indicator parameters to quantify the relative magnitude of the erosive capacity of flowing water the trends are similar. Fig. 5 shows the relationships between turbulent boundary shear stress and applied boundary stream power as a function of absolute roughness.

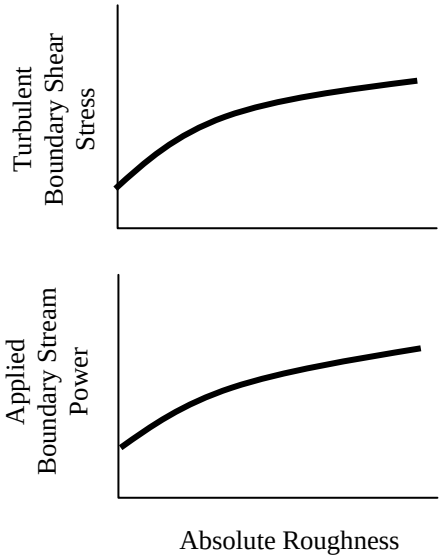

Figure 5. Trends in turbulent boundary shear stress and applied stream power to the boundary as a function of absolute roughness [1]

V. RELEVANCE

The mere fact that the trends in turbulent boundary shear stress and applied stream power at the boundary are similar, as such, does not justify their use as indicator parameters. The finding that fluctuating turbulent pressure play a dominant role in incipient motion under turbulent flow conditions requires justification that these variables are related to fluctuating turbulent pressures.

Reference [6] found that the root mean square of fluctuating turbulent pressures p' is correlated to shear stress as,

$$p' = 3 \cdot \tau_t \tag{8}$$

While [7] found that the maximum value of fluctuating turbulent pressures p'_{max} can be as high as $6 \cdot p'$, which means that

$$p'_{max} = 18 \cdot \tau_t \tag{9}$$

These correlations can be used as justification that a relationship between turbulent boundary shear stress and the magnitudes of fluctuating pressure exists. However, when using turbulent boundary shear stress as an indicator of the relative magnitude of the erosive capacity of turbulent flowing water it is necessary to recall that incipient motion under such conditions is not a shear process.

As applied stream power is equivalent to turbulence production and reflects the rate of energy dissipation in turbulent flowing water, it is considered to provide a good indication of the relative magnitude of fluctuating turbulent pressures. Fig. 6 shows a relationship between the rate of energy dissipation (stream power) at the base of a hydraulic jump and the standard deviation (root mean square) of fluctuating pressures.

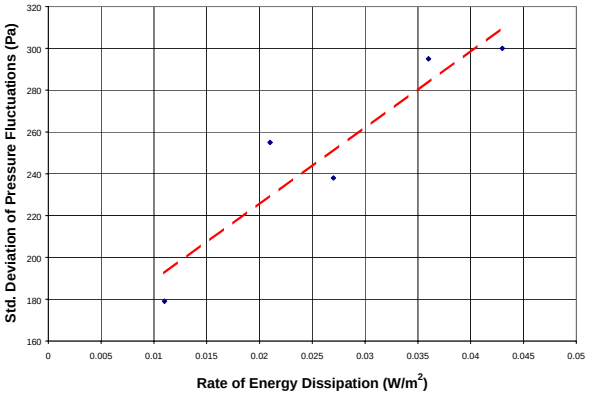

Figure 6. Relationship between stream power (rate of energy dissipation) and the standard deviation (rms) of turbulent fluctuating pressures [1]

It is therefore considered reasonable to use either turbulent boundary shear stress or applied stream power at the boundary to quantify the relative magnitude of the erosive capacity of water in turbulent flow. However, the use of stream power is considered more representative because it is a direct reflection of turbulence production and the rate of energy dissipation, and therefore the relative magnitude of turbulent pressure fluctuations.

VI. CONCLUSION

Incipient motion under laminar flow conditions is directly dependent on shear stress, whereas incipient motion under turbulent flow conditions is principally dependent on turbulent pressure fluctuations. Laminar flow in the near-bed region requires greater effort to move a particle than is the case during turbulent flow due to the fact that shear is the principal agent leading to this motion.

When the flow conditions in the near-boundary layer is characterized as smooth turbulent flow, incipient motion is solely dependent on pressure fluctuations. If near-boundary layer flow conditions convert to rough turbulent flow, incipient motion is initiated by a combination of pressure fluctuations and horizontal flow. This results in rotation of particles during the process of incipient motion, which requires more effort to entrain particles than when smooth turbulent flow conditions exist.

When assessing incipient motion under turbulent flow conditions, the most common scenario, it is required to either quantify the actual magnitude of fluctuating pressures or use indicator parameters quantifying its relative magnitude. The actual magnitudes of fluctuating pressures are often not easily determined in practice. The preferred method for quantifying the relative magnitude of the erosive capacity of turbulent flow therefore entails the use of indicator parameters.

The preferred indicator parameters conventionally used to quantify the relative magnitude of the erosive capacity

of water are average flow velocity, wall shear stress and available stream power. However, it has been shown that these variables are inconsistent indicators of the relative magnitude of the erosive capacity of water ([1] and [2]).

This paper presents equations that can be used to quantify the magnitude of turbulent boundary shear stress and applied boundary stream power. These parameters quantify the shear and power within the near-boundary region and are considered appropriate for quantifying the relative magnitude of the erosive capacity of water leading to incipient motion. It has also been found that the turbulent boundary shear stress and applied stream power at the boundary display consistent trends when expressed as a function of absolute hydraulic roughness.

It is concluded that turbulent boundary shear stress and applied stream power at the boundary can be used to quantify the relative magnitude of the erosive capacity of water. The use of average flow velocity to accomplish the same is not defensible, nor is the use of available stream power.

REFERENCES

[1] G.W. Annandale, *Scour Technology*, McGraw-Hill, New York, 2006.

[2] G.W. Annandale, Erosive Capacity, Resistance and Process, *Proc. Second International Conference on Scour and Erosion*, Singapore, 2004.

[3] E. Bollaert, *Transient Water Pressures in Joints and Formation of Rock Scour due to High-Velocity Jet Impact*, Communication No. 13. Laboratory of Hydraulic Constructions, Ecole Polytechnique Federale de Lausanne, Switzerland, 2002.

[4] R.N. Croad, *Physics of Erosion of Cohesive Soils*, PhD Thesis, Department of Civil Engineering, University of Auckland, Auckland, New Zealand. 1981.

[5] H. Schlicthing and K. Gersten, *Boundary Layer Theory*, 8th Revised and Enlarged Edition, Springer-Verlag, New York, 2000.

[6] J.D. Hinze, Turbulence, 2nd Edition, McGraw-Hill, New York, 1975.

[7] R. Emmerling, *The instantaneous fluctuation of the wall pressure under a turbulent boundary layer flow*, Max-Planck-Institut fur Stromungsforschung, Rep. No. 9, 1973.

Bridges in Critical Condition

San Benito River Gravel Mining and the Hospital Road Bridge

Catherine M.C. Avila, P.E., D.WRE, MSCE, MBA
Avila and Associates Consulting Engineers, Inc., Walnut Creek, CA, USA

I. Abstract

The bridges on the San Benito River provide excellent examples of many of the issues of keen interest today in scour research including 1) the impact of gravel mining on channel bed degradation and lateral channel migration, 2) successful and unsuccessful scour countermeasures, and 3) the impact of complex pier shapes and large diameter piers.

Gravel operations on the San Benito River have included both the bed (instream extraction) and the bank (terrace) operations for the last 50 years. The extraction rates have exceeded the replenishment rates by 2 to 7 times. This mining of the river has caused 2-4 meters of channel bed degradation and bank erosion undermining bridge structures and adjacent land. This paper illustrates the need for regulatory or approving authorities to assure that appropriate and effective environmental mitigation measures and funding guarantees are in place prior to approving gravel mining operations in or adjacent to rivers.

II. Overview

The San Benito River has been mined commercially for gravel since the 1950's. According to past reports [1], [2] and [3], the riverbed has degraded due in large part to past gravel mining activities conducted without adequate replenishment i.e. riverbed degradation which removes vital cover protecting bridge foundations from local scour.

The rapid urbanization occurring throughout California has increased the demand for sand and gravel used in construction activities. The California Department of Conservation estimates that 20 percent of construction aggregate comes from in-stream sources. In 1996, 289 in-stream operations produced 22.8 million tons of sand and gravel valued at $114 million [4]. It is estimated; however, that average annual bedload sediment yield for all the rivers in California is only about 13 million metric tons [5]. Thus, instream operators extract almost twice the sediment yield in an average year.

Aggregate is primarily used for construction—predominately for road base and concrete components. The California Department of Transportation (Caltrans) is a major aggregate consumer in California, utilizing approximately 20 million tons of sand and gravel in 1991 [6].

A. Location of Bridges

The project site is located just outside of the City of Hollister located San Benito County in Central California as shown in Figure 1.

Figure 1. Location Map within California

There are 5 bridges located on the main stem of the San Benito River as shown in Figure 2 below.

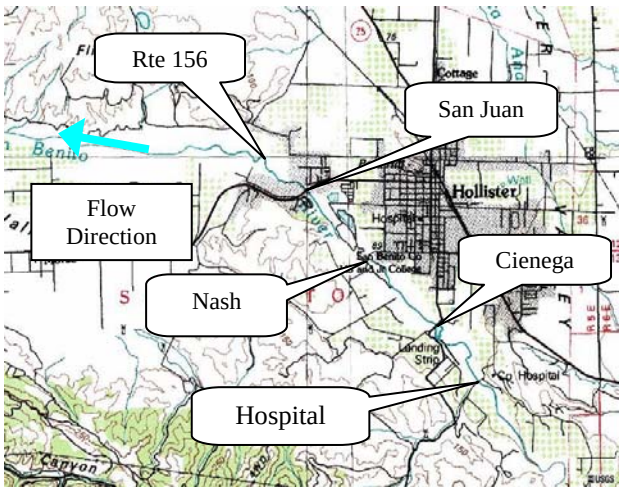

Figure 2. Location of bridges crossing San Benito River near Hollister

B. Gravel Mining Operations and Challenges

The riverbed of the San Benito River has been a major source for sand and gravel for the region since the 1950's. According to the County Planning Department, most of the permits issued to extract gravel from the river were issued between 1959 and the mid 1970's (Rob Mendiola, Former San Benito County Planning Department, Personal Communication). According to a recent study

[7], however, the actual gravel extraction since 1952 has ranged from 87,000 m^3 to 132,000 m^3.

Operations on the San Benito River and Tres Pinos Creek have decreased to only 5 operations in recent years (Mary Paxton, Former San Benito County Planning Department, Personal Communication). These 5 operations are permitted to extract a total of 428,000 cubic meters of material. Two of the operations are located downstream below the San Juan Road bridge (also known as the old 156 Bridge) approximately 5 km downstream and are unlikely to have an adverse impact this far upstream. These downstream operations account for 200,000 cubic meters of the permitted extraction. Two of the operations are located in Tres Pinos Creek which feeds into the San Benito River. One of these is considered an "off-channel" operation since it is in the current terraces, however, it is unknown if these terraces are a sufficient distance from the active channel to avoid pit capture. The terrace operation accounts for 100,000 cubic meters of material. The last active operation is a proposed in-stream gravel extraction operation between the Nash Road and Cienega Road Bridges and is currently in litigation with the local agency.

There are also 4 off-channel and semi-off-channel pits upstream of Hospital Road and downstream to the Cienega Road Bridge as shown in Figure 3 which have ceased operation and are in the process of "reclamation." One operation (the McClatchy Pit) is a "reclaimed" gravel pit.

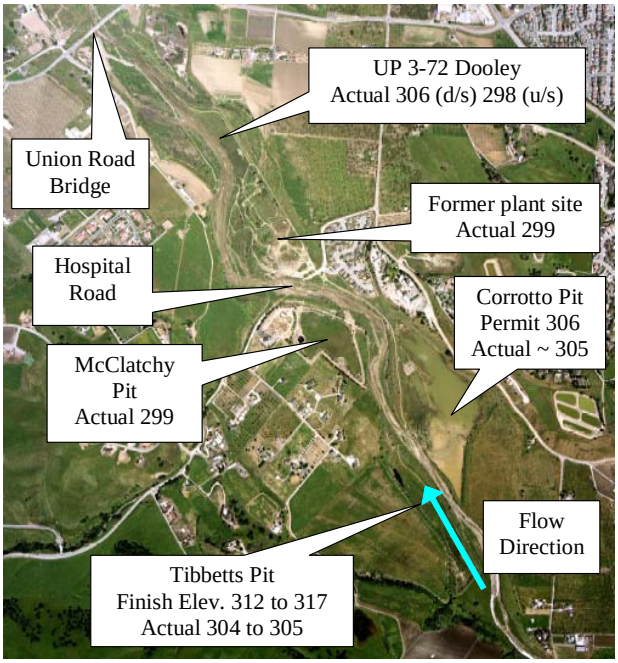

Figure 3: Existing and historic gravel mining operations near Hospital Road

One of the challenges with the "off channel" operations is that they are only out of the currently active riverbed, but within the meander belt of the historic channel. As part of the analysis for the Hospital Road Bridge replacement, Avila and Associates compared the riverbank location through time [8]. The earliest available aerial photograph (1947) shows the riverbed to be approximately 460 meters wide at the Hospital Road crossing; this had decreased to 400 meters wide in 1974 and 260 meters wide in 2005 as shown in Figure 4. This information was used in the bridge design to minimize potential loss of the abutment fill.

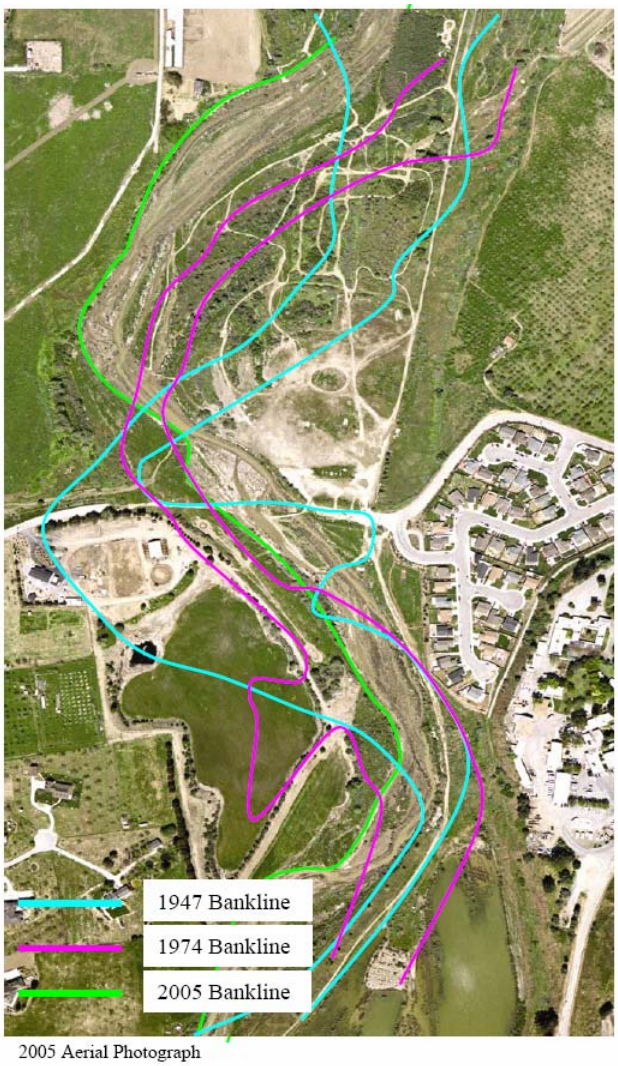

Figure 4. Bankline analysis near the Hospital Road Bridge from 1947, 1974 and 2005 aerial photographs.

In addition, some of the pits are up to 3.7 meters below their permitted mining depths and 2 to 2.5 meters below the current river thalweg adjacent to the pit as shown in Figure 5 below.

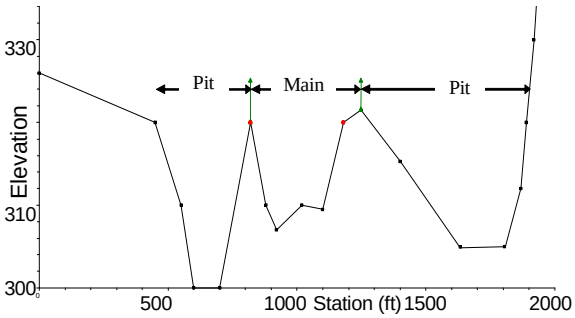

Figure 5: "perched channel" situated between a reclaimed gravel pit (McClatchy) and soon to be reclaimed pit (Corrotto).

Although the Corotto and Tibbetts Pits were both anticipated to be "off-channel pits", in the 1998 storms, the setback of the Corotto Pit was breached (east bank) and Tibbetts Pit eroded. In 2003, the operator amended their Reclamation Plan for these Pits in order to make

these “off channel pits” part of the river. This proposal is still being reviewed by the San Benito County Planning Department.

III. Physical Consequences

There is a significant sediment imbalance in the San Benito River. Annual replenishment estimates vary from 18,000 m^3 to 53,000 m^3 in various studies by Ayres Associates and Golder Associates in the 1990’s [1], [2], [3]. That means the average annual gravel extraction of 87,000 m^3 to 132,000 m^3 [7] exceeds the replenishment by almost 2 to over 7 times.

A. Channel bed degradation

Avila and Associates documented degradation at bridge locations based upon maintenance inspection records kept for the bridges and updated channel cross sections taken by Avila and Associates [9]. Approximately 3 meters of degradation was shown at the Cienega Road Bridge between 1960 and 2005 as shown in Figure 6. Almost 5 meters of degradation occurred at the San Juan Road Bridge between 1950 and 2005 as shown in Figure 7.

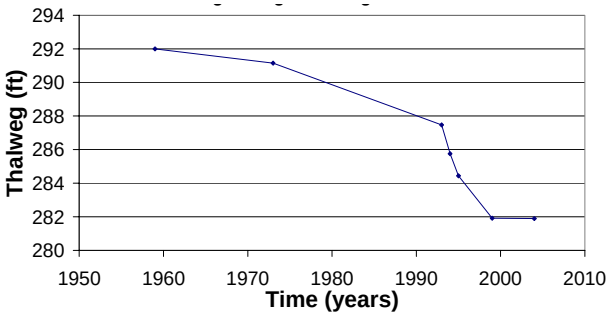

Figure 6: Cienega Bridge Thalweg over time

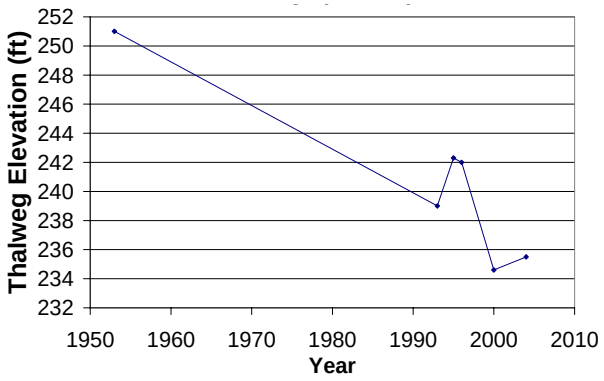

Figure 7. San Juan Road Bridge Thalweg over time

In a recent study [3], Ayres Associates relocated historical channel bed thalweg information along the river from upstream of the Hospital Road Bridge to downstream of the new Route 156 Bridge as shown in Figure 8. Their study documented the channel bed degradation which averaged 2-4 m of degradation at critical infrastructure crossing the river [7]. A maximum of 6 meters was documented at the new Route 156 Bridge and approximately 3 meters upstream at the Hospital Road Bridge.

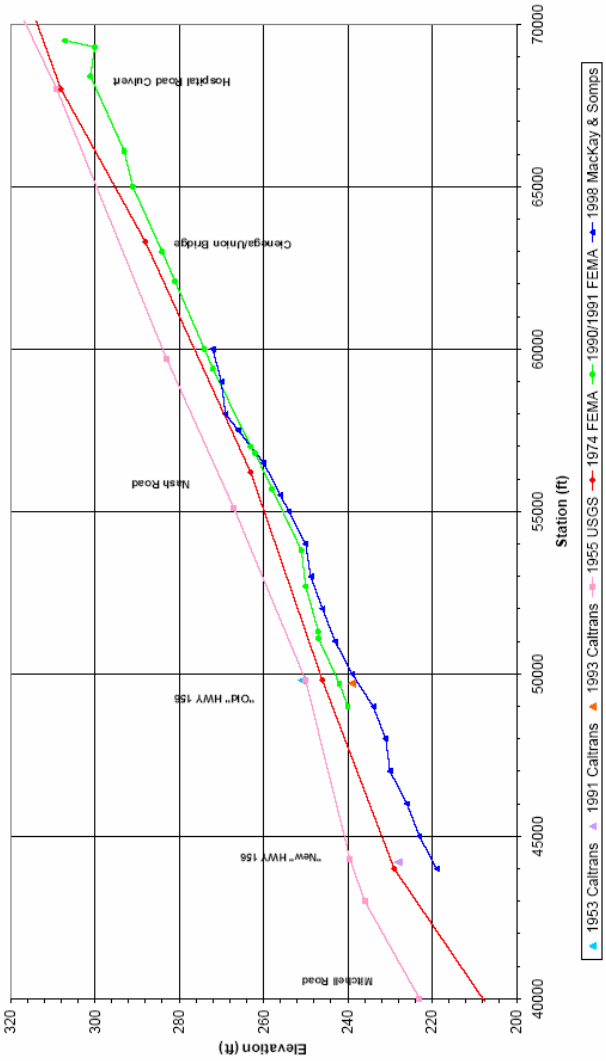

Figure 8. Channel bed degradation along the San Benito River

B. Lateral channel migration

Lateral channel migration has also proven a significant challenge for property adjacent to the San Benito River. The channel bed degradation on the river has destabilized the riverbanks inducing lateral channel erosion. This migration undermined the foundations of the house shown in Figure 9. The house was moved to another part of the property away from the river (Dale Rosskamp, San Benito County Public Works Department, Personal Communication).

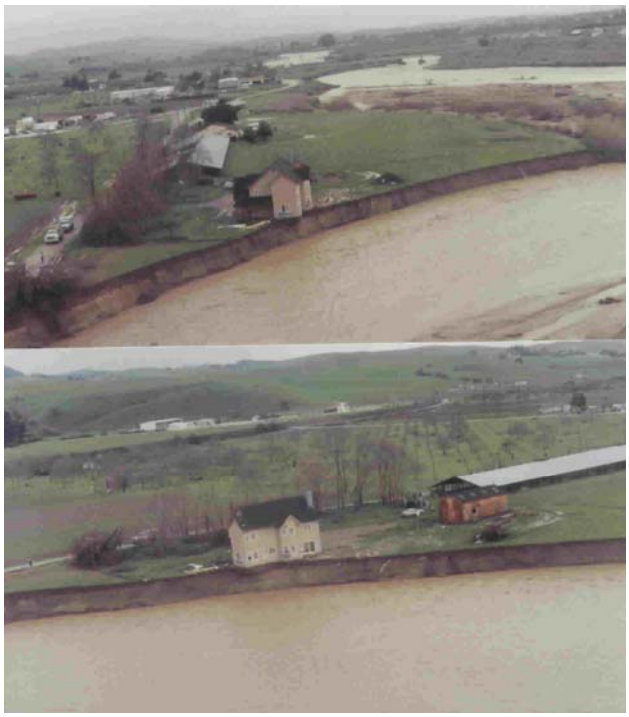

Figure 9: Lateral channel erosion undermined the foundations of a house on the San Benito River (photo by San Benito County Public Works Department)

C. Scour countermeasures

The channel bed degradation and lateral channel erosion noted above have caused all of the bridges on the main stem to be repaired or replaced in the past 10 years. Following is a description of the countermeasures and the cost of future degradation starting from downstream and moving upstream.

The most downstream bridge (Route 156) was constructed in 1997 and accounted for almost 8 meters of channel bed degradation in addition to local pier scour caused by the 2.4 meter single column Cast-in-Drill-Hole (CIDH) piles.

The New Route 156 bridge replaces the "old 156" (now called San Juan Road) bridge which will be relinquished to the City of Hollister. Caltrans does not consider the bridge to be scour critical because it is currently protected from local pier scour by rock riprap which was replaced in 2002 at an estimated cost of $188,000 for four piers as shown in Figure 10.

The next bridge upstream is the Nash Road Bridge. It is currently considered a low water crossing which is rebuilt after significant discharges almost every winter. An 86.9 meter long bridge is currently being constructed to replace the low water crossing. The Nash Road Bridge accounted for an estimated 10.7 meters of future channel bed degradation [9].

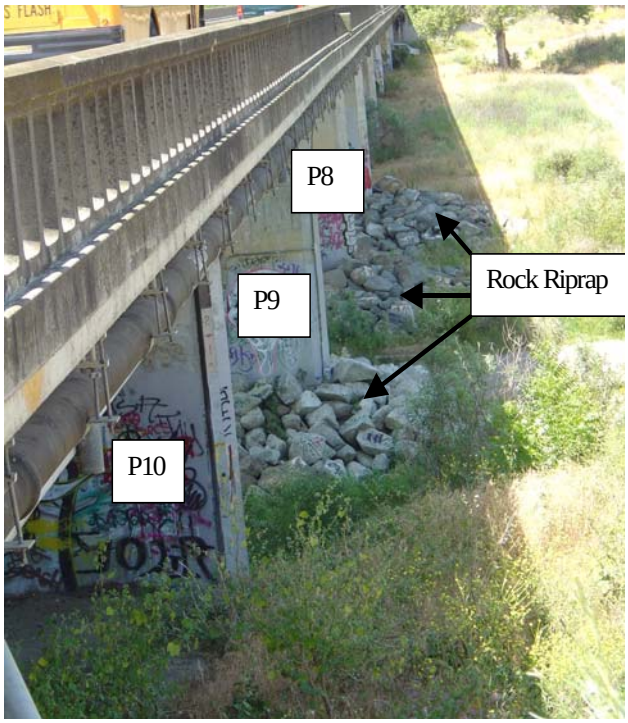

Figure 10. Rock riprap placed at Piers 7 through 10 of the San Juan Road Bridge.

The next bridge upstream is the Cienega Road Bridge. Scour countermeasures consisting of cable tied blocks were installed at the bridge piers in approximately 1989. These cable tied blocks failed during the 1993 storms on the San Benito River as shown in Figure 11.

Figure 11: Pier #5 undermining and failure of "scour protection" installed in 1989 (photograph by Caltrans)

Storms in March of 1995 undermined piers 3 though 6 exposing approximately 2 meters of Raymond piles as shown in Figure 12. The bridge was closed to traffic until scour countermeasures could be installed. Raymond piles provides some unique challenges because it is only reinforced in the first 3.7 meters or ¼ of its length (whichever is greater).

Figure 12. Pile Exposure following March 1995 Storms (note failed scour protection) (photo by Boyle)

The County hired an engineering consultant who designed a scour countermeasure consisting of sheet pile coffer dams and rock riprap which were constructed to elevation 260 at piers 5 through 8 at a cost of $600,000 as shown in Figure 13.

Figure 13. Coffer dams and rock rip rap placed following 1995 Storms (photo by Musseter Engineering, Inc.)

The bridge was re-opened to traffic in May of 1995 but a subsequent scour evaluation by Caltrans rated the bridge as scour critical. The bridge scour countermeasure complicated the pier scour analysis significantly with a 0.6 meter wide pier and a 3 meter wide exposed footing. Following storms in 1998, most of the rock rip rap washed away from the bridge and almost none remains today as shown in Figure 14 below.

Figure 14: Cienega Road Bridge looking upstream at the sheet pile cofferdams (photo by Author)

The most upstream bridge on the San Benito River is the Hospital Road Bridge. It is currently a low water crossing consisting of a series of six-0.9 meter diameter corrugated plastic pipes as shown in Figure 15below.

Figure 15: Existing low water crossing at Hospital Road (photo by Author)

The low water crossing is replaced each year as shown in Figure 16 below. According to the Public Works Department, the cost of the installation (including labor and materials) was estimated to be approximately $35,000 to $45,000 annually in 1998 dollars (Dale Rosskamp, San Benito County Public Works Department, Personal Communication).

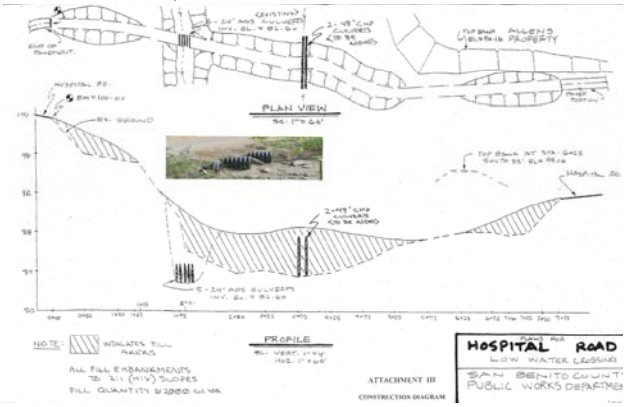

Figure 16: Hospital Road Low Water Crossing Installation plan

The low water crossing is proposed to be replaced with a 5-span reinforced concrete bridge which will be 185 meter long and have 2.1 to 2.4 meter wide single column bents. The bridge is designed to account for 3.6 to 4.3 meters of degradation in addition to 3.6 to 4 meters of local pier scour.

IV. Economic Consequences

There is significant economic cost associated with channel bed degradation and lateral channel migration. This includes not only the cost of repairing or replacing the bridge, but also the lost opportunity cost associated with significant detours and/or traffic delays.

A recent study by Avila and Associates [10] estimated the cost of 1.5 meters of degradation caused by one gravel mining operation on the San Benito River. One countermeasure considered to arrest degradation was constructing a check dam at the upstream limits of the gravel operation (downstream of Nash Road) to arrest

potential headcutting from propagating upstream. The low and high estimated cost of constructing the approximately 183 m check dam is shown in Table 1. Because the check dams would inhibit fish passage, it is likely that fish ladders would also be required

Table 1. Low and High estimated cost to construct a check dam at the upstream limits of the Gravel Operation in 2003 dollars $K.

Infra-structure	Foundation Abutment Walls	Design, permitting, right of way acquisition, roadwork, etc.	Total Cost (+/- 30%)
183 m long Structure	$1,100 to $1,300	$275 to $325	$1,375 to $1,625
Fish Ladder	$80 to $800	$20 to $200	$100 to $1,000
Total Cost 183 m long	$1,180 to $2,100	$295 to $525	$1,475 to $2,625

An approximately 244 m long check dam would also be required downstream of the San Juan Road bridge to mitigate potential scour downstream at that bridge as shown in Table 2.

Table 2. Low and High estimated cost to construct a check dam downstream of the San Juan Road Bridge in 2003 $K.

Infrastructure	Foundation Abutment Walls	Design, permitting, right of way acquisition, roadwork, etc.	Total Cost (+/- 30%)
244 m long Structure	$1,600 to $1,900	$400 to $475	$2,000 to $2,400
Fish Ladder	$80 to $800	$20 to $200	$100 to $1,000
Total Cost 244 m long	$1,700 to 2,700	$420 to $675	$2,000 to $3,400

An alternative to a check dam at the existing San Juan Bridge which has less environmental challenges is to construct Outrigger Bents to support the bridge with the anticipated degradation. A typical outrigger bent is shown in Figure 17.

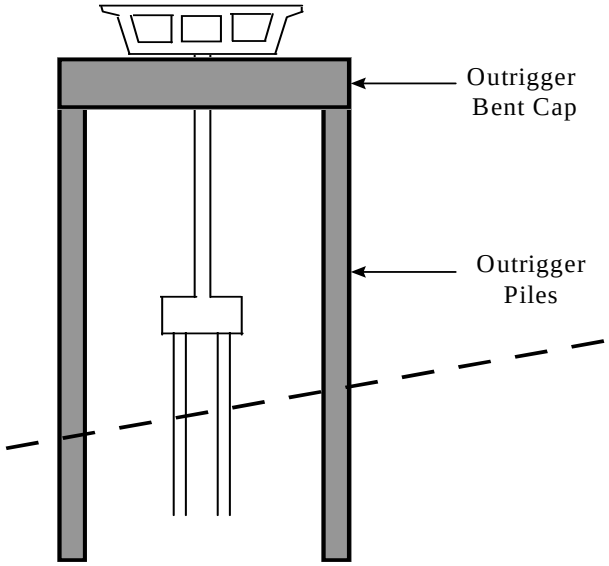

Figure 17. Typical Outrigger Bent

The cost of constructing outrigger bents at each pier foundation is shown in Table 3 below.

Table 3: Low and High Estimated cost to construct Outrigger Bents at all piers on the bridge (in 2003 $K)

Infrastructure	Outrigger Bent (Constr-uction Cost)	Design, permitting, right of way acquisition, roadwork, etc.	Total Cost (+/- 30%)
San Juan Bridge	$2,000 to $3,900	$520 to $970	$2,600 to $4,900
Cienega Road Bridge	$1,800 to $3,500	$500 to $900	$2,300 to $4,400

Replacing the bridges becomes the countermeasure of last resort. Costs of constructing three bridges on the reach are available. These range from $1,700/square meter to $2,100/square meter as shown in Table 4.

Table 4: Bridge Replacement Costs for bridges crossing the San Benito River in square meters in 2003 $.

Infrastructure	Length (m)	Width (m)	Cost (2003 $K)	Cost ($/sq m)
New 156 Bridge	246	13.3	$5,660	$1,733
Nash Rd Bridge	86.9	12.8	$1,892	$1,701
Hospital Rd Bridge	244	9.8	$5,040	$2,119

Square foot costs were used to estimate to project the cost of replacing the Cienega Road and San Juan Road Bridges as shown in Table 5.

Table 5: Estimated range of Replacement Cost (based on square foot cost from Table above) in 2003 $K

Infra-structure	Replacement (Construction Cost)	Design, permitting, right of way acquisition, roadwork, etc.	Estimated Total Cost (+/- 30%)
Cienega Road	$4,400 to $5,500	$1,100 to $1,400	$5,500 to $6,900
San Juan Bridge	$4,700 to $5,900	$1,200 to $1,500	$5,900 to $7,400

In 2003, the cost of constructing countermeasures at the Cienega Road Bridge range from a low estimate of $2 million (M) to construct a check dam to a high estimate of $6.9M to replace the bridge. Countermeasure costs for the San Juan Bridge range from $2.6M to place a check dam to $7.4 M to replace the bridge.

A. Detour costs

If the bridges fail in a flood due to foundation instability, there is a detour "cost" to the traveling public. The cost can be illustrated by the loss of three spans of the Route 1 Bridge over the Carmel River in Monterey County, California, in the floods of March 1995. Due to the bridge wash out, the trip from Carmel Highlands to Carmel was increased from approximately 15 minutes to 6.5 hours. This increased the cost to an individual driver from Carmel Highlands to Carmel from $2.40 to $62.40 per trip. During the 6 days between the bridge collapse and the temporary bridge erection, the only alternative to the detour was a helicopter ride that took less than 5 minutes and cost $50 each way (in 1995 dollars) validating the $60 trip estimate [11].

A recent study by Rister and Graves [12] updated the delay costs from the estimates used in the study above to $12.1 per vehicle-hour for passenger cars and $30 per vehicle-hour for a truck in 1998 dollars. When updated to 2003 dollars, these estimates are increased to $16.1 per vehicle-hour for passenger cars and $39.9 per vehicle-hour for a truck.

During the winter, the Nash and Hospital Road crossings are currently unavailable. Table 6 shows the detour length, Average Daily Traffic (ADT), the year the ADT is for and the percentage of the ADT that accounts for truck traffic as shown in Table 6.

Table 6: Detour Length and Average Daily Traffic (ADT) for infrastructure (from Caltrans Maintenance Records)

Bridge name	Detour Length (miles)	ADT	Year of ADT	% Trucks
San Juan	4	13,822	1997	10
Nash	3.5	2730	1992 (county)	35
Cienega	3	1000	1998	15
Hospital (existing)	n/a low water xing	750	1998	5

Through a review of the maintenance records, it does not appear that the ADT has changed considerably since the 1995 storms. Because it is not scour critical, it is assumed that the San Juan Bridge would be open during winter floods as it was in 1995 when the Cienega Road Bridge was closed to traffic for 60 days while the scour countermeasure was installed. The detour time is the estimated time it would take to cross the San Juan Road Bridge rather than the bridge noted as shown in Table 7 below.

Table 7: Estimated Detour Cost Caused by Closure of the Cienega Road Bridge in 1995 (in 2003 $K)

Bridge name	Detour Time (min.)	Cars	Trucks
Nash	15	1775	955
Cienega	20	850	150
Hospital	25	712	38
Total Cost			

Bridge name	60 day detour "cost" cars	60 day detour "cost" trucks	Total cost
Nash	$424	$572	$995
Cienega	$274	$12	$286
Hospital	$286	$38	$324
Total Cost			$1,600

The estimated "delay cost" caused by the closure of the Cienega Road Bridge in 1995 is $1.6M. If the Cienega Road Bridge is closed to traffic again, the delay costs could increase depending upon the amount of time it would take to reopen the bridge.

V. Conclusion

The bridges on the San Benito River either have been constructed in the past 10 years or likely will be replaced in the next 10 years. Rehabilitating or replacing infrastructure on this actively-mined river has been costly to the tax payers who have borne the burden of replacing the bridges. Specifically, in the United States, eligible bridges are often replaced under the Highway Bridge Rehabilitation and Replacement Program (HBRRP). Historically, the Federal Government has paid 80% of the replacement cost with the local agency picking up the remaining 20%.

These future expenditures could have been avoided or deferred for several more decades if local regulatory agencies would have required that the gavel mine operators adequately mitigated their impacts as part of the environmental review process (California Environmental Quality Act in California) and required financial guarantees for their implementation.

VI. Acknowledgment

Special thanks to the following: Tom Smith, Ayres Associates; Mike Harvey, Mussetter Engineering Inc., Nick Burmas, Marwan Siagian, and Robert Zezoff, Caltrans, Mary Paxton and Rob Mendiola, (formerly) San Benito County Planning Department, Dale Rosskamp, San Benito County Public Works Department.

Most of the information related to the bridges for this report was obtained from the California Department of Transportation (Caltrans) Bridge Maintenance Records (Caltrans, 2004). Under the Code of Federal Regulation,

bridges must be inspected at regular intervals not to exceed 2 years (CFR 650.305). The guidelines for maintenance inspections are found in the Federal Highway Administration (FHWA) "Recording and Coding Guide for the Structure Inventory and Appraisal of the Nation's Bridges" Report No. FHWA-PD-96-001. (FHWA, 2001). These records are kept at the Office of Structure Maintenance and Investigations (OSM&I) office in Sacramento.

VII. References

[1] Ayres Associates, "Phase I Investigation of Erosion and Scour Problems on the San Benito River in San Benito County", 1995.

[2] Golder Associates, 1997 "Quantitative and Qualitative Analyses of Degradation of the San Benito River" prepared for the City of Hollister.

[3] Ayres Associates "Letter Report, Geomorphic and Sediment Delivery Assessment San Benito River and Tres Pinos Creek Watersheds, San Benito County, California", 1999.

[4] Avila, Catherine Crossett, "Managing Impacts of Gravel Mining on Bridges in California (Overmining causes Undermining)" submitted in partial fulfillment of a Master of Science Degree, University of Calif. at Davis, 1998.

[5] Kondolf, G. Mathias, "Managing Bedload Sediment in Regulated Rivers: Examples from California, U.S. A.", American Geophysical Union, 1995.

[6] Crossett, Catherine M., "Overmining Causes Undermining (It's a Mad Mad River)" in the ASCE Hydraulic Engineering Conference, 1993.

[7] Harvey, M.D. and Smith, T.W., 1998. "Gravel mining Impact on San Benito River, California", in Proceedings of the 1998 International Water Resources Engineering Conference, Hydraulics Division, ASCE, Memphis, Tennessee, August 3-5.

[8] Avila and Associates Consulting Engineers, Inc. "Bridge Hydrologic and Hydraulic Analysis for the Hospital Road Bridge crossing in the San Benito River, San Benito County, California" Draft Report dated July 2005.

[9] Schaff & Wheeler, Consulting Engineers, December 23, 2002 "Draft Bridge Hydraulics Study, Nash Road Bridge at San Benito River" prepared for Mark Thomas & Company.

[10] Avila and Associates Consulting Engineers, Inc., 2004, "Potential impact of sandman's Reclamation Plan 2003-16 on San Benito River Infrastructure." Prepared for the Cassidy, Shimko and Dawson.

[11] Avila, Catherine, "Cost of Caltrans Countermeasures" in ASCE Hydraulic Engineering Conference, 1998.

[12] Rister, Brad W., and Graves, Clark, March 2002 "The Cost of Construction Delays and Traffic Control for Life-Cycle Cost Analysis of Pavements." Prepared by the Kentucky Transportation Center.

.

Modelling Interrill Erosion by Means of a Laboratory Model

G. Balacco, A. Di Santo, U. Fratino and F.M. Renna
Technical University of Bari/Dep. of Hydraulic Engineering and Chemistry - Bari, Italy

I. Introduction

The erosive process plays, nowadays, an important role in the process of degradation and it is strongly influenced by the temporal and spatial variability of the parameters from which it depends [25].

The erosion rate of a soil exceeds the formation rate of the same, as result of the excessive exploitation of the ground and its productivity. This disparity between accelerated erosion and soil formation can be attributed "*in toto"* to the anthropic activity. The remarkable demographic increase in the twentieth century has drastically emphasized the risk and the extension of the degradation process of soil components [19].

A possible interpretation of this phenomenon is given by the consideration that to the economic development in a country often follows a change of the soil utilization.

In the last five decades several studies were focused on the erosion process starting from the plot scale to the global scale. A wide number of assessment models have been adopted to gather and process data, even if many doubts still remain in analyzing them [16].

The paper presents the first results of an extensive laboratory campaign in order to define the influence that the wet-dry climate regime carries out on erosion process.

The preliminary work was pointed for defining initial conditions and laboratory methodologies to achieve a reliable simulation. The first experimental results were compared with estimated values obtained by the WEPP model.

The purpose of this last analysis was to provide a first response of the capability of the WEPP model for simulating soil loss during a rainfall event.

II. Interril Erosion: State of the art

Literature data evidence that rainfall is certainly the most important factor into erosion process phenomena. Erosion due to the rain action is correlated to its characteristics time, drop diameters and rain intensities; the modality succession of the events determines two underlying fundamental parameters: kinetic energy and the momentum.

The first kind of erosion, due to the rain impact, is linked to the rainfall characteristics, slope soil, water depth and the land nature. The uncohesive soils have a different behaviour regarding the cohesive ones. In the first case the soil particles are tied only by contact forces and their breakages are due to gravitational actions [1,22]. In the case of cohesive soils there are chemical ties, known as chemical gel [1,22]; their breakage is due to the overcoming of the rain drop force. Starting from this moment the particles, scattered by the rain, are carried on by water. This action depends on the morphologic characteristics (slope, length, roughness and profile shape), from soil characteristics and hydrogeological ones (hydraulic conductivity and filtration).

These considerations show the complexity of the process and, at the same time, justify the numerous literature studies.

In the following some experimental results obtained in laboratory are summarized. Salles and Poesen [23] leaded laboratory tests on a sandy plot to estimate the incident action of rain, varying the rainfall intensity. The collected data have been used to define an erosion index of the rain that takes into account the amount of material removed with the momentum and the diameter of particles. Jayawardena and Bhuiyan [15] generated laminar flow on a plot with fixed slope and sandy soil to define a physical approach that could separate the contribute given by the action of the rain from the transport. The collected data evidence the strong contribution to the erosive process that derives from the impact of the rain on the soil.

The splash erosion depends also on the land slope. Wan and al. [26] leaded experiences varying the slope and setting the intensity of rain on a silty clay plot. It is evident that the rain erosion prevails on runoff for slopes higher than 9%, whereas under this value the behaviour seems to be inverted. This data have been confirmed from Jayawardena and Bhuiyan [15] tests.

Romkens and al. [20] highlighted the influence of the rainfall performing a experiment on a parcel of silt loam soil, scarcely erodible, and with several slope. The results shows that, as slope increases, a succession of events of decreasing intensity produces greater erosions. Moreover, the authors observe that erosion increases with roughness. Gomez and Nearing [10] attained the same conclusions studying a silty on a variable slope plot.

The system has undergone a rain set with increasing intensity and it has been observed that the roughness influences significantly the beginning of the phenomenon. According to Fox and Bryan [8], also sandy loam lands present the same behaviour. The roughness influence increases for higher slopes becoming constant for flat slope. Moreover, by means of tracers, they have observed that the erosion and the average speed change with the slope square root. Chaplot and Le Bissonnais [7] have obtained the same results thank to a parcel of silty loam with different slope. They evidence that the interril measures are connected to the size of a plot. These aspects are in agreement with the Hairsine and Rose [12] and Rose [21] cinematic analytical model. Gabriels [9]

performed experiments on two plots of sandy and sandy loam soils, deducing that the influence of plot length is not very important for flat slopes; instead on a steep slope a sandy soil presents an erosion process for unit of length different from the sandy loam plot. The reduction of the interril erosion for loamy sand is confirmed from the Stomph e al. [24] experiences. Using a modular plot with fixed slope they found, in presence of hortonian flows, a scale effect due to the length of the profile. In fact, modules of 1.5 m, subjected to a short rainfalls, are characterised from a length unit runoff greater than that of multiple modules. This behaviour seems attenuated for rains of equal intensity and short time. Recently, Hancock and al. [11] have correlated the slope to the shape of land profile. They considered a particle of fixed sizes and have reproduced three profiles using mixture of flying ashes with a low cohesion and poor infiltration capacity. They found that an half of a rain intensity produces an half of erosion on a single profile, beside an increase of the slope, for a fixed intensity, produces an increase of eroded material of one order of magnitude higher. These aspects highlight the presence of a threshold in the slope value, which, once exceeded, leads to a remarkable increase of shear stress. These results was similar to Romkens and al. [20], Jayawardena and Bhuiyan [15] and Wan and al. [27].

The experiences leaded from Huang and al. [13], using a dual-box system with silty loam soil, have lead to the same results concerning the role of the slope and the rain intensity.

A dual-box model simulates vertical flow movement in a soil from the top to the bottom and vice versa or it assures a constant hydraulic level to a given depth in a soil. Data collected during these experiences show that the last plot, object of the analysis, in condition for free drainage and with a 5% slope, presents the formation of little concavities on surface as the rainfall intensity increases. This phenomenon already starts with a low intensity and with 10% slope profile and it evolves gradually through reciprocal connections, up to generating rills of higher intensity. In the same conditions, but adding filtration flow from the bottom, we can observe a precocious appearance of rills and a sediment production in the order of three or six times higher than the previous. This situation tends to attenuate itself following the formation of rill canalized erosion.

This aspect was confirmed by Owoputi and Stolte [18] experiences on sandy loam and sandy clay soils. The results show that vertical ascending flow does not influence the erosion. However, with the simultaneous presence of the rain, it was observed greater erosion in comparison to the case of rain only. Moreover, the experiment highlights that the soil erodibility is connected to the filtration from the bottom and manages indirectly the formation and the evolution of the canalized erosion.

Runoff cannot be used for the study of erosion when the contribution of the filtration is not very important. Although the behaviours of two lands are similar, a great profile erosion of the with sandy loam, uncohesive lands, implies a great influence of the regimes of flow from the bottom. The soil erodibility is connected both to soil characteristics and regime of established underground motion.

III. LABORATORY SET-UP AND MEASUREMENTS PROCEDURES

At the literary review, above mentioned highlights the opportunity to better analyze the role of the wet-dry climatic regime and the concomitant action driven by the infiltration process in the interrill erosion phenomenon.

The soil behavior, related to the intensity of the rainfall, depends on the length of the previous dry period. From the increase of this length a loss of the water content ratio takes place, until a water deficit threshold is achieved. The latter situation brings a mechanical modification in the soil characteristics, which is manifested by cracks and fractures. The formation of these erosion structures enhances the soil bent to erosion and transportation.

This is a typical condition of the southern Italian soils, where frequent and intense rainfalls and long and dry period alternate. It appears interesting to focus the attention on such aspect.

This paper summarizes and highlights some recent researches, above mentioned, which examines the role of the main parameters that affect soil erosion. The goal is to provide more details thanks to carefully controlled laboratory experiences.

Experimental tests were conducted with a slope-adjustable plot equipped with a rainfall simulator, a tensiometric system, a solar irradiation system, a profile meter, an outlet flume to collect runoff and sediment load and, finally, a graduate tank to measure infiltration volume (figure 1). A brief description of the equipment and soil preparation are reported below.

Figure 1. The experimental set-up.

A. Experimental set-up

The laboratory experimental setup was built in the Large Model Laboratory of the Department of Water Engineering and Chemistry, Technical University of Bari. The main purpose of the 2.0 x 1.0 x 0.5 m (l x b x h) plot was to simulate as closely as possible the sediment transport, deposition and detachment that occur on the soil during or after a rainfall event. In order to accomplish this, the following design variables and restraints was taken into account:

- the slope of the plot should be variable from 0 to 14%
- free infiltration on the bed and the bottom of the plot

- the end of the plot should have an endplate which can be adjustable to different heights to allow natural erosion on the bottom

B. Soil preparation

The sediment chosen for all the experimental runs was a sandy loam (13.5 clay, 16.5% silt, 70 % sand) and was taken from a slope of Rendina dam, in Basilicata region (Southern Italy).

Laboratory measurements were made to provide correct information about soil properties, in particular the soil has a dry unit weight of 1.46 g/cm^3, a void ratio of 0.45 and a volumetric water content 1.95%.

The Rendina reservoir is a pilot river basin on which, during the last few years, various investigations were conducted [3,4,5,], nevertheless, for its same history, it represents a singular and, at the same time, representative case for the analysis of the interrill erosion process.

The soil was air-dried and coarsely grinded and finally blended, before to be settled into the plot over the perforated bed and covered by geotextile material above which five subsequent layers of 10 cm each one were spread out. The layers were gently tamped with a steel straight roller and by hands.

C. Tensiometric system

Four water pressure devices were placed along the plot respectively at 70 cm and 180 cm apart the upstream edge of the plot on two different height, 15 cm and 35 cm from the bottom respectively.

The purpose of these sensors, mod. 2100F produced by Soilmosture Equipment Corp, was to test the possibility of measuring water height when no infiltration is present in the soil and to identify infiltration trends when infiltration occurs. They are able to acquire suction values in a range from 0 to 85 KPa and to transfer data in continuous to a data acquisition board for their management and treatment.

D. Rainfall simulator

The plot was provided with a rainfall simulator consisting of several spray sprinkler, series PS Hunter, performing different rainfall intensities with a fall height of 5.40 m. They were supplied by a pressurized pipeline. The head pressure was controlled by throttle valve and checked by a Bourdon pressure gauge.

The properties of generated storms are very similar to the natural storms of corresponding intensities. In particular, drops, supplied by sprinklers, have as a average diameter of 4 mm, is in agreement with Hudson [14] and Ferro [2].

In this experience a fixed rainfall volume was supplied at four different intensity levels but each one having the same amount of rain. The rain unit volume applied in every test was 60 mm and the relative intensities were approximately 120, 60, 30 and 15 mm h^{-1}

Rainfall was measured during each experiment to check if there was spatial homogeneous distribution over the plot.

E. Solar irradiation simulation

Two high pressure sodium vapours lamps, produced from Leuci series NA-T, of 400W, generating a light flux of about 48000 lumen each, was used in order to reproduce the effect of the solar radiation.

In this earlier stage of the test the goal was to simulate in very short time the effects of irradiation on the southern Italy soils at the end of summer season. In this period of the year the soils are characterized from a cracking process (fig.2), that in the following winter season often determines a trigger of erosive process. For this purpose the lamps were settled in such way to achieve the maximum possible radiation, checked by a ground temperature measurement.

In particular, the lamps lit up 11 hours per day catching up on the land a temperature of approximately 55 °C. Once caught up a typical representative condition of the end of summer, made evident by the suction pressures measured by tensiometric system, the plot underwent a wash away effect due to high intensity rain event.

In a second future phase, after estimated the total entity of the phenomena, the experiences will continue through the reproduction of the solar irradiation in more adherent way to the reality, taking into account the daily excursion.

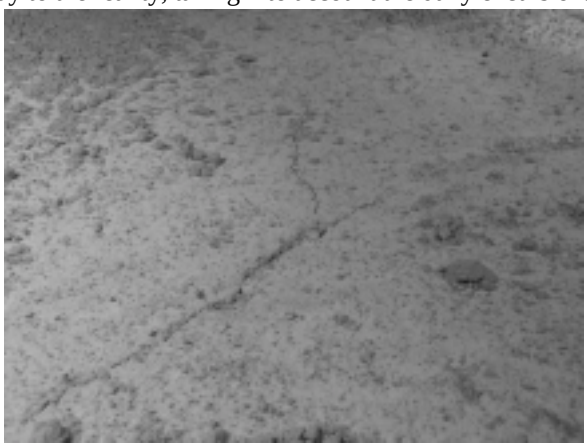

Figure 2. A typical cracking due to solar irradiation effect.

F. Soil loss measuremnts

Variation in sediment yield during plot evolution was measured by collecting sediment samples from the outlet flume at regular intervals depending on the length of the run. The volume of water and sediments derived during each sample interval was determined by means of a graduated scale on the bottle and, after the water was driven off by placing the collected sample in a oven at 105°C, the mass of dry sediments was measured.

Moreover the infiltrated water, was collected by hopper, stored in a transparent glass tank and measured by means a graduated scale.

After each rainstorm event a profile meter with a graduate rod was used to assess the variation level of plot surface, defining the erosion process evolution. In this way the surface topography was analysed to define erosion and drainage network patterns.

IV. RESULTS AND DISCUSSION

This paper presents the results of the first laboratory experiments. Long time was spent to define initial conditions measuring some parameters as bulk density, water content etc. So, a set of four different rain intensity was tested on a slope steepness of 7%. Every simulation

presents the same condition in terms of rainfall volume and crusting effect on the plot surface, obtained using the solar irradiation simulation system.

In particular, it was interesting comparing measure data with the numerical results estimated by using the WEPP model, *a physical based model considered to possess state-of-the-art knowledge of erosion science* [6], aiming to evaluate reliability of the model.

A. Hydraulic Conductivity

To prepare the plot for the tests, a preliminary rain with a 15 mm/h intensity was applied. Sprinklers used for the preliminary phase had the aim to reach a proper soil humidity. In order to obtain it, the sprinklers adopted were designed to minimize the effect of rainsplash reducing the drop size.

The first operation was to define the value of hydraulic conductivity parameter. In order to compare the measure data obtained by laboratory experiences and simulated data by WEPP, the value of hydraulic conductivity parameter was evaluated in both cases.

Infiltration in WEPP model is calculated using a solution of the Green–Ampt-Mein-Larson equation by means of the effective hydraulic conductivity parameter (K_e) definition, in order to obtain reliable evaluation of infiltration and runoff. The Green-Ampt equation is a widely used equation for modelling one dimensional vertical flow of water into soil. It was developed from an integration of Darcy's law by assuming infiltration from a ponded surface into a deep homogenous soil of uniform antecedent water content. The value of K_e estimated for the plot using the above mentioned modified Green-Ampt equation was equal to 8.11 E-06 m/s.

Using measured data in the initial unsaturated stage and by visual observation of wetting front velocity, during the first preparatory rainfall simulation of 15 mm/h, the effective hydraulic conductivity parameter (K_e) was calculated using the classical expression of the same Green-Ampt equation, without any adjustment. The value was assessed equal to 3.28E-07 m/s which corresponds to the equilibrium value as shown in the fig. 4.

Figure 3. Photograph of the plot with the position of the wetting front after 1h of experiment.

The value estimated with the WEPP model is higher than the measured data. The difference between these values can be ascribed to the several calibrations and adjustment of the equation in the WEPP model and the great dependence of the same from soil granulometry and management.

Another simplification of WEPP model is that the value of K_e, entered in soil input file of the model, was used as an effective conductivity for each of the storms within the entire simulation and settled as a constant. This assumption doesn't match reality because of the fact that the hydraulic conductivity is a variable quantity, as a non-linear function of the volumetric water content (θ). Starting from this consideration and using the infiltration volumes, collected during that first experience at regular time range, the hydraulic conductivity at saturation (K_s) was estimated by means of a simplified procedure such as the infiltration velocity. The value defined by the above-mentioned procedure was equal to 3.20E-06 m/s.

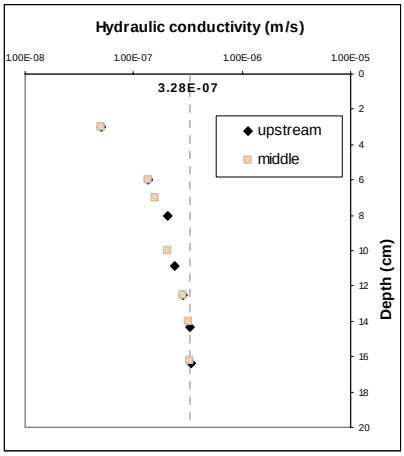

Figure 4. Evolution of hydraulic conductivity.

B. Discussion

During each rainfall simulation, overland flow samples were taken at the flume outlet at several time defined as a function of the run length and its rain intensity, in order to reproduce a fixed rainfall volume on the plot.

After each of the rainfall simulation or after solar irradiation, a survey of the plot surface was made, verifying the expected shape erosions by counting the number of appeared rills; pictures were taken to compare the situation before and after each experience (fig. 5).

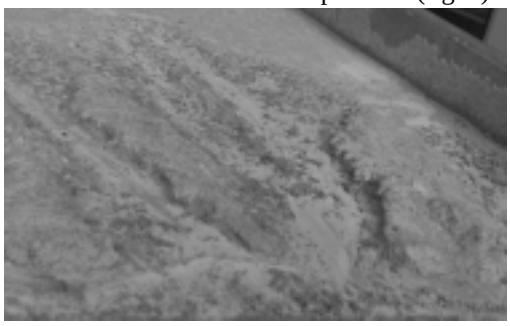

Figure 5. Example of the final surfaces after a rainfall simulation of 120 mm/h.

At the end of each experience lamps for solar irradiation simulation were lit for several days to reproduce crusting effect on the plot surface and a new rainfall simulation was carried on later.

Table I resumes the amount of eroded materials and runoff in each rainfall simulation. For the first two simulation: rainfall events of 15 and 30 mm/h, there was no reply of the plot in terms of runoff and sediment load. Figure 6 illustrates, the runoff only for rain intensity of 60 and 120 mm/h each. At shown in fig. 6 high rainfall intensity caused a reduction in infiltration and, after the first minute, was produced runoff, that was higher than the previous one.

The high rainfall intensity substantially produced about 2.7 kg sediments, this quantity is about one order of magnitude higher than that produced by the low rainfall intensity.

TABLE I.
TOTAL RUNOFF AND SOIL LOSS FOR EACH RAINFALL EVENT

Rainfall intensity (mm/h)	Soil loss (kg)	Runoff (mm)
15	0.00	0.00
30	0.00	0.00
60	0.15	8.98
120	2.75	28.44

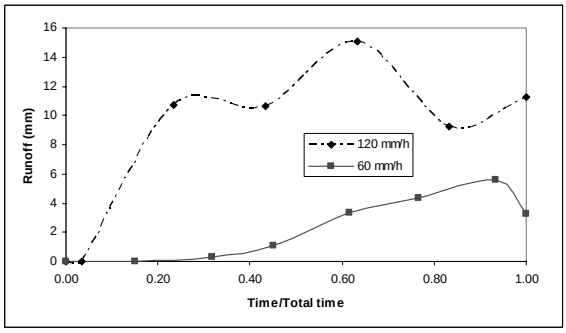

Figure 6. Runoff output data versus dimensionless time..

Figure 7 shows the sediment concentration relationship as a function of cumulative rainfall during, respectively, a simulated rainstorm of 60 mm/h and 120 mm/h. This relationship shows the rapid rise in the sediment concentration and, at the same time, the reaching of a stable equilibrium condition. This behavior was related to different type of events, because during the early stage of a rainfall, the soil erosion is dominated by soil detachment due to drops impact. Upon ponding, runoff rate and solid load rapidly increase until the local compacted soil lead to a constant contribute of sediment concentration, due mainly to runoff effect.

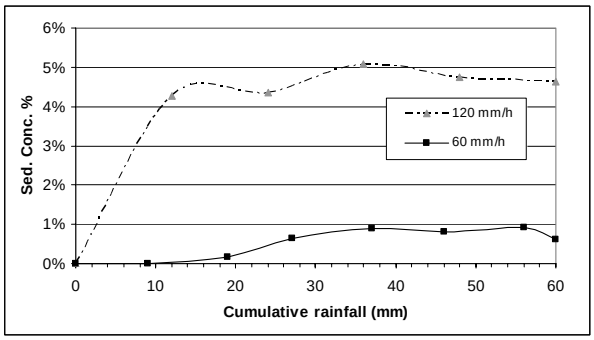

Figure 7. Sediment concentration as a function of the accumulative rainfall.

In a second phase these data were compared with simulated data, obtained from the WEPP model application. This model is able to evaluate runoff and erosion from a daily basis scale to a annual one. Erosion process can be simulated at hillslope or watershed scale. The present simulation, however, was restricted to a hillslope profile identical to experimental plot.

The main discrepancy between WEPP model simulation and measured data was the entity of soil loss and predicted runoff volume. Figure 8 and 9 illustrate this behavior, in particular the plot and the model do not provide a answer in terms of runoff or soil loss for an rain intensity of 15 and 30 mm/h, whereas in the other cases WEPP over-predicts runoff and soil loss.

This results was in agreement with those observed by Nearing [17]. In particular, he wrote that soil erosion models tend to over-predict erosion for a small measured values and under-predict erosion for large measured values. This discrepancy is due to fact that the models have a deterministic in nature and the measured data has a significant random component for which the models cannot account. That fact is a practical and, at the same time, unavoidable limitation in defining a prediction model function of numerous parameters; e.g. local variation in rainfall intensities from plot to plot, or microtopography or different erosion or sedimentation location.

Observing the comparison between measured and simulated data it can be supposed that the hypothesis of Nearing is correct and that small changes into the behavior of a plot, during a rainfall in terms of runoff and soil loss, can modify its answer on the contrary of the conclusion of study by Bowen et al. [6].

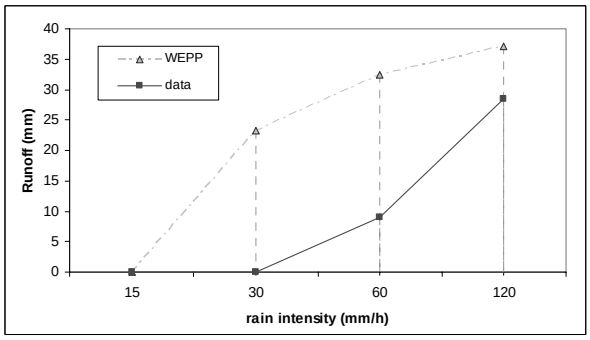

Figure 8. Runoff rate comparison between WEPP and experimental data for each rainfall simulation

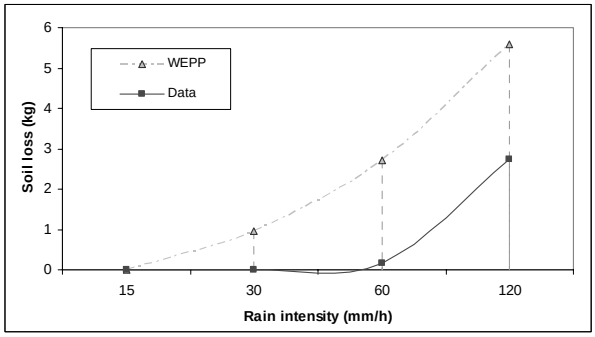

Figure 9. Total soil loss comparison between WEPP and experimental data for each rainfall simulation.

V. CONCLUSION

This paper represents only the first stage of a large laboratory campaign with the aim to evaluate the dependence of soil erosion process on wet-dry climatic regime. This aspect, which seems to have not been

examined in a complete way by technical literature, is crucial for many southern Italian soils, where long dry season is followed by a intense rainfall period.

In order to prepare the physical model and the numerical one as backgrounds to this experimental study, a slope-adjustable plot was built.

A long preliminary study was conducted to define the geometrical scale, instrumental devices and soil features.

This chosen soil was a sandy loam soil for simulating a real soil texture, present in southern Italy, which behavior is well known. The first results allow to assess the effective hydraulic conductivity parameter (3.28E-07 m/s) and hydraulic conductivity at saturation (3.20E-06 m/s).

The first value does not match the value provided by the WEPP model, as expected by the empirical nature of WEPP algorithm.

Further, the rainfall-runoff and runoff-soil loss relationship were investigated. For a constant slope, the sediment concentration achieves a constant value at low rainfall intensity. Moreover the soil loss seems to be strongly related to rainfall at different intensities.

The numerical simulation, by WEPP models, shows a similar trend even if meaningfully over-predict the measure values.

In a second phase planned for next future the experiences will continue through the reproduction of the daily solar excursion in order to add further informations and experimental evidences.

ACKNOWLEDGMENT

The research has been supported by funds of the Italian Ministry for Research. and the University (MIUR) within the PRIN 2005 program.

REFERENCES

[1] Annandale G.V. "*Scour Technology* ", McGraw-Hill, (2006).

[2] Bagarello V, Ferro V., Giordano G., "*Trasporto d' acqua e sedimenti a scala di versante*", Editoriale BIOS, 2001 (italian).

[3] Balacco G., Di Santo A., Fratino U., Piccinni A. F.: "*Valutazione della potenziale erodibilitá di un bacino a differenti scale di applicazione*", Giornata di studio su "La Gestione degli invasi artificiali: monitoraggio batimetrico, recupero di capacità e riutilizzo dei sedimenti", Potenza (2002) (italian).

[4] Balacco G., Santaloia F., Fratino U., Cotecchia F., Castorani A. "*I processi di erosione nel bacino della diga di Abate Alonia: analisi fenomenologica e modelli di previsione*" - 28° Convegno di Idraulica e Costruzioni Idrauliche; Potenza (2002) (italian).

[5] Balacco G., "*Modelli interpretativi del processo erosivo nei bacini idrografici*", Phd Thesis, National Libraries of Rome and Florence, (2003) (italian).

[6] Bowen W., Baigorria G., Barrera V., Cordova J., Muck P. and Pastor R., "*A process-based Modell (WEPP) for simulating soil erosion in Andes*", p. 403-408. CIP Program Report 1997-1998. International Potato Center, Lima, Peru.

[7] Chaplot, V., Le Bissonnais, Y., "*Field measurment of interrill erosion under different slopes and plots*", Earth Surf. Process. Landforms 25, (2000), pp. 145-153.

[8] Fox, D.M., Rorke, B.B., "*The relationship of soil loss by interrill erosion to slope gradient*", Catena 38, (1999), pp. 211-222.

[9] Gabriels, D "*The effect of slope length on the amount and size distribuzion of eroded silt loam soils: short slope laboratory experiments on interrill erosion"*, Geomorfology 28 (1998), pp. 169-172.

[10] Gόmez, J.A., Nearing, M.A. "*Runoff and sediment losses from rough and smooth soil surfaces in a laboratory experiment"*, Catena 59 (2005), pp. 253-266.

[11] Hancock, G.R., Nuake, J., Fityus, S.G., "*Modelling of sediment dynamics in a laboratory-scale experimental catchment*", Hydrological processes DOI:10.1002/hyp.5899 (2005).

[12] Hairsine P.B. and Rose C.W., "*Modeling water erosion due to overland flow using physical priciples,1. Sheet flow*" Water Resources Research, 28, 237-243 (1992).

[13] Huang,C., Wells, L.K., Norton, D.L., "*Sediment transport capacity and erosion processes: model concept and reality*", Earth Surf. Process. Landforms 24, (1999) pp. 503-516.

[14] Hudson N. W., *"Field measurement of soil erosion and runoff"*, Food and Agriculture Organization of the United Nations - Rome, 1993.

[15] Jayawardena, A.W., Bhuiyan, R.R., "*Evaluation of an interrill soil erosion model erosion using laboratory catchment data*", Hydrological processes 13, (1999), pp. 89-100.

[16] Lal R., "*Soil Degradation by Erosion*", Land Degradation and Development 12: 519-539 (2001).

[17] Nearing M.A., "Why soil erosion models over-predict small soil losses and under-predict large soil losses", Catena 32 (1998), pp. 15-22.

[18] Owoputi, L.O., Stolte, W.J., "*The role of seepage in erodibility*", Hydrological processes 15, (2001), pp 13-22.

[19] Richards J.F., "*Land Transformation*", in The hearth as Transformed by Human Action: Global and Regional Changes in Biosphere Over the Past 300 Years, Turner B.L., Clark W.C., Kate R.W., Richards J.F., Mathews J.T., Mayer W.B. Cambridge University Press: New York; 163-178 (1991).

[20] Rӧmkens, M.J.M., Helmig, K., Prasad, S.N. "*Soil erosion under different rainfall intensites, surface roughness, and soil water regime*", Catena 46 (2001), pp. 103-123.

[21] Rose, C.W. 1993. "*Erosion and sedimentation*" pp. 301-343. In: M. Bonell, M.M. Hufschmidt and J.S. Gladwell (eds), "Hydrology and Water Management in the Humid Tropics - Hydrological Research Issues and Strategies for Water Management" (Cambridge University Press, Cambridge).

[22] Rucker M.L. "*Percolation Theory Approach to Quantify Geo-Material Density - Modulus Relationship*", 9Th ASCE Specialty Conference on Prabablistic Mechanics and Structural Reliability, (2004).

[23] Salles C.and Poesen J., " *Rain properties controlling soil splash detachment*", Hydrological processes 14:, (2000), pp. 271-282.

[24] Stomph, T.J., De Ridder, N. Steenhuis, T.S., Van De Giesen, N.C., "*Scale effect of hortonian overland flow and rainfall-runoff dynamics: laboratory validation of a process-based model*", Earth Surf. Process. Landforms 27, (2002) pp. 847-855.

[25] Toy T. J., Foster G.R., Renard K.G., *"Soil Erosion – Processes, Prediction, Measuremnet and Control"*, J. Wiley & Sons, (2002).

[26] Wan, Y., El-Swaify, S.A., Sutherland, R.A.,"*Partitioning interrill splash and wash dynamics: a novel laboratory approach*", Soi L Technology 9, (1996), pp. 55-69.

[27] Wang X. and Wang Z.Y. "*Effect of land use change on runoff and sediment yield "*, International Journal of Sediment Research, Vol.14, No.4, (1999).

.

Transient wave induced pore pressures in a stratified seabed

F.B.J. Barends
GeoDelft & TUDelft, Delft, The Netherlands

The transient pore pressure generation in a stratified seabed due to waves is not trivial. The variance in permeability and compressibility of submerged soil layers may give rize to locally unexpected effective stress changes and in some locations excess pore pressures that exceed common limits and seem to have a negative retardation [12]. It may reduce the local seabed stability and resistance against erosion or liquefaction. This paper explains these phenomena and discusses observations which show peculiar effects.

I. Introduction

The paper addresses special aspects of cyclic consolidation, not commonly described in standard textbooks. After introduction of the fundamentals the attention is focussed on special effects and practical aspects.

II. Multi-Dimensional Consolidation

Consider the storage equation in the process of porous flow in a deforming porous medium

$$\nabla \cdot q = - \partial \varepsilon / \partial t \tag{1}$$

where $\nabla\cdot$ is the divergence operator, q the specific discharge (bulk flow velocity), ε the volumetric strain of the porous medium and t the time. The left hand side expresses the net outflow (fluid volume per time) out of a unit bulk volume, and the right hand side the volumetric storage change per time. The minus sign expresses that loss of mass by outflow should match the shrinkage of storage (volumetric strain = volume change per unit volume). As such the equation is just a mass balance for an incompressible pore fluid. Introduction of Darcy's law

$$q = - (\kappa/\mu) \nabla p \tag{2}$$

with ∇ the gradient operator, κ the intrinsic permeability[1], μ the pore fluid dynamic viscosity and p the excess pore pressure (in the absence of the hydrostatic component) and the introduction of Hooke's law for the porous medium

$$\varepsilon = - \sigma'/K_s = - (\sigma - p)/K_s \tag{3}$$

with σ' the effective (isotropic) stress, σ the total (isotropic) stress and K the bulk modulus[2], renders the storage equation (1) into

$$\nabla \cdot \kappa/\mu \nabla p = - (1/K_s)(\partial \sigma/\partial t - \partial p/\partial t) \tag{4}$$

If the medium is homogeneous (κ, μ and K_s are uniform) this becomes

$$\nabla \cdot \nabla p = (1/c)(\partial p/\partial t - \partial \sigma/\partial t) \tag{5}$$

with $c = \kappa K_s/\mu = k K_s/\gamma$, referred to as the consolidation coefficient for incompressible pore water. The compressibility of the porous fluid β can be encountered in c, according to [1]

$$c = k K_s/(\gamma(1+n\beta/K_s) \tag{6}$$

Then, also the compressibility factor a is involved, see (28). Equation (5) is the so-called storage equation, which together with equilibrium equations, boundary conditions, initial state and constitutive soil behaviour describes the process of multi-dimensional consolidation.

III. Averaged Cyclic Consolidation

A. The Simple Method; Boundary Loading.

If the total stress σ is uniform and constant in time, the field response (5) is described by

$$c \nabla^2 p = p_{,t} \tag{7}$$

At the drained boundary A_1 harmonic loading is applied

$$p_1 = H \cos[\omega t] \quad \text{at} \quad A_1 \tag{8}$$

The harmonic solution, employing complex algebra, seeks the real part of the complex response according to (7) subjected to the complex extension of the loading

$$p_1 = H \exp[i\omega t] \tag{9}$$

[1] Hydraulic permeability k is related to the intrinsic permeability κ by $k = \kappa\gamma/\mu$, where γ represents the fluid volumetric weight. It appears in Darcy's law when expressed in terms of the piezometric head: $q = -k\nabla\phi$.

[2] The choice of the bulk modulus K_s in expressing the state of the porous medium implies a constraint to the type of loading, i.e. an isotropic state. For other states corresponding parameters are to be introduced, i.e. for a laterally confined state K_s should be replaced by $K_s + {}^4/_3 G$.

Since a harmonic response is considered, everywhere the pore pressure has identical frequency. Thus

$$p = P \exp[i\omega t] \tag{10}$$

where P is only a function of space. Equation (7) becomes

$$c\nabla^2 P = i\omega P \tag{11}$$

A simple solution is sought by averaging over space, referred to as *the simple method* [11], rendering (11) into,

$$c\iiint \nabla^2 P dV = i\omega \iiint P dV \tag{12}$$

Introduction of average field pressures

$$\mathbf{P} = \iiint P dV / V \quad \text{and} \quad \mathbf{p} = \iiint p dV / V \tag{13}$$

and assuming an approximate 2D parabolic distribution of the field pressure, see sketch underneath,

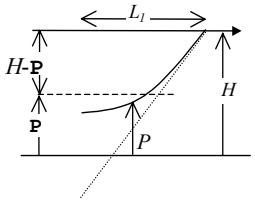

so that

$$\iiint \nabla^2 P dV = \iint \nabla P dA = 3(H - \mathbf{P}) A_1 / L_1 \tag{14}$$

where, A_1 is the drained surface and L_1 the relevant flow path, renders (12) into

$$\mathbf{P} = H(1 - i\alpha)/(1 + \alpha^2) \tag{15}$$

with $\alpha = \omega L_1 L_2 / 3c$ and $L_2 = V/A_1$, a hydraulic radius expressing the drainage capacity. The total harmonic response is therefore

$$\mathbf{p} = \mathbf{P} \exp[i\omega t] = H \exp[i\omega t](1 - i\alpha)/(1 + \alpha^2) \tag{16}$$

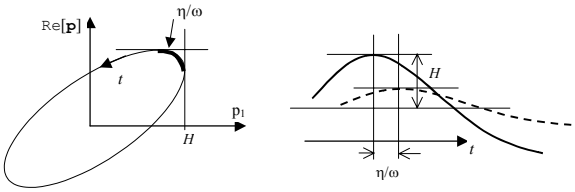

Figure 1. Harmonic response to cyclic boundary loading

The real part of this expression, the response we are looking for, becomes after some elaboration

$$Re[\mathbf{p}] = H \cos[\omega t - \eta] / \sqrt{[1 + \alpha^2]} \tag{17}$$

where $\eta = \arctan[\alpha]$. Solution (17) presents a response with a decay of $1/\sqrt{[1+\alpha^2]}$ and a delay of η/ω, as shown in Figure 1.

B. The Simple Method; Total Loading.

If boundary pressure p is constant (zero), but total stress σ is uniform and harmonic in time

$$\sigma = H \exp[i\omega t] \tag{18}$$

then the field response (5) is described by

$$c\nabla^2 p = p_{,t} - \sigma_{,t} \tag{19}$$

The pore pressure will be harmonic with the same frequency. Thus, (10) applies and (19) becomes

$$c\nabla^2 P = i\omega (P - H) \tag{20}$$

Volume average yields

$$c\iiint \nabla^2 P dV = i\omega \iiint (P - H) dV \tag{21}$$

Introduction of average field pressures according to (13), and assuming an approximate 2D parabolic distribution of the field pressure, see sketch underneath,

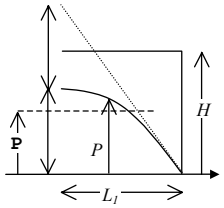

gives

$$\iiint \nabla^2 P dV = \iint \nabla P dA = -3\mathbf{P} A_1 / L_1 \tag{22}$$

This renders (22) into

$$\mathbf{P} = H i\alpha (1 - i\alpha)/(1 + \alpha^2) \tag{23}$$

The total harmonic response is therefore

$$\mathbf{p} = \mathbf{P} \exp[i\omega t] = H \exp[i\omega t]\, i\alpha (1 - i\alpha)/(1 + \alpha^2) \tag{24}$$

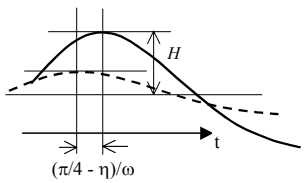

Figure 2. Harmonic response to cyclic total loading

The real part of this expression yields

$$Re[\mathbf{p}] = H \alpha \cos[\omega t + \pi/4 - \eta] / \sqrt{[1 + \alpha^2]} \tag{25}$$

Solution (25) presents a response with a decay of $\alpha/\sqrt{[1+\alpha^2]}$, and a delay of $(-\pi/4 + \eta)/\omega$, which is a *negative delay* for $\eta > \pi/4$, see Figure 2. The condition $\eta > \pi/4$ complies with $\alpha = \omega L_1 L_2 /3c < 1$. For a sandy seabed, under cyclic loading with a period in the order of $T = 10$s or $\omega = 2\pi/T = 0.63$, and length scales L_1 and L_2 in the order of decimeters (which is rather likely, see chapter IV), the condition of negative delay, i.e. $\alpha < 1$, is met for a seabed consolidation coefficient c larger than the order of $\omega L_1 L_2 /3 = 2\ 10^{-3}$ m^2/s, which is also likely in many cases.

For a soft clayey seabed, the length scales L_1 and L_2 are normally in the order of decameters and the corresponding consolidation coefficient c is usually in the order of 10^{-5} m^2/s, or smaller. In this case the condition of negative delay, i.e. $\alpha < 1$, is met for slower waves, like tidal waves, where ω is in the order of 10^{-4} rad/s.

The observed transient excess pore pressure response in coastal zones due to tidal water level changes shows a damped response with, indeed, a negative delay (the peak response occurs earlier than the peak loading). Already in 1904 Honda [2] noticed a negative delay in the potential tidal response in Yokohama and in 1916 Friedrich [3] observed the same in Lubeck. Unknown subsoil water streams were thought to be the cause! In 1933 Franx noticed a similar behavior during construction of the Park sluice in Rotterdam, and in the same year Steggewentz wrote a PhD-thesis on the tidal response [4]. No explanation was offered. Later, De Lange and Maas [5] found an explanation for the negative delay based on the principle of superposition for rivers with a limited width. The phenomenon was finally understood after a close inspection of the physical process that takes place, in fact, as a consequence of the effective stress principle [6] [7] [12].

The understanding that the maximum induced pore pressure under the leeside of a dike may occur without any delay or even earlier than maximum river level, was important for the decision when, after critical high riverwaters in 1995, evacuated inhabitants of the Dutch cities in danger of inundation could safely return to their homes.

IV. 1D-Unform Cyclic Consolidation

A. Homogneous Case

Consider a typical case of a cyclic loaded seabed. The loading is in terms of total stress

$$\sigma = \sigma_0 \cos(\omega t) \tag{26}$$

can be decomposed into pore pressure and effective stress, using Terzaghi's effective stress rule, according to

$$p = \lambda\sigma_0 \cos(\omega t) \quad \text{and} \quad \sigma' = (1-\lambda)\,\sigma_0 \cos(\omega t) \tag{27}$$

where λ is a value between 0 and 1, and as such covering all practically possible situations. For λ=1 it refers to free waves on a seabed, for λ=0 to a cyclic loaded shallow submerged foundation on a drained layer, see Figure 3.

The consolidation process in the soil is according to (5) and (6) described by

$$cp_{,zz} = p_{,t} - a\sigma_{,t} \quad \text{with} \quad a = (1+n\beta/\alpha_s)^{-1} \tag{28}$$

where α_s represents the laterally confined compressibility, equal to $1/K + {}^4/_3 G$, and c is defined by $k/(\gamma(\alpha_s + n\beta)$.

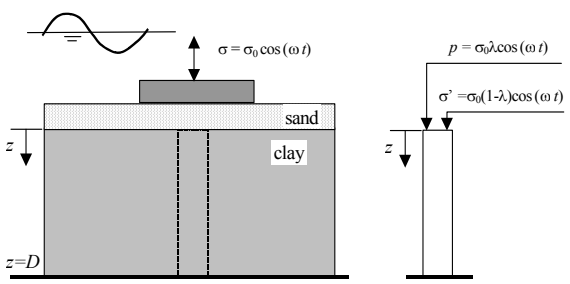

Figure 3. Cylcic consolidation on a seabed

Equilibrium at the bottom yields $\sigma = \sigma_0 \cos(\omega t)$. At the bottom both phases do not move relatively. The flow term becomes zero, which yields, applying (28)

$$p_{,t} - a\sigma_{,t} = 0 \quad \text{or} \quad p = a\sigma + \text{constant} \tag{29}$$

The constant can be identified with the effect of volumetric weight (hydrostatic pressure). Because, here, excess pore pressures are considered, this constant is zero. The internal stress state at the bottom becomes

$$p = a\sigma_0 \cos(\omega t) \quad \text{and} \quad \sigma' = (1-a)\,\sigma_0 \cos(\omega t) \tag{30}$$

Introduction of the variable $w = a\sigma - p$ yields for (28), keeping in mind that σ is only a function of t and not of z

$$cw_{,zz} = w_{,t} \tag{31}$$

with boundary conditions

$$z = 0: \qquad w = a\sigma - p = (a-\lambda)\,\sigma_0 \cos(\omega t) \tag{32a}$$

$$z = D \text{ (bottom):} \qquad w = a\sigma - p = 0 \tag{32b}$$

An harmonic solution is found by considering the response of the system to the complex excitation: $\exp(i\omega t)$, by stating that

$$w(z,t) = W(z)\,\exp(i\omega t) \tag{33}$$

Inserting this into equation (31) yields

$$cW_{,zz} = i\omega W \tag{34}$$

which has a general solution according to

$$W = (a-\lambda)\,\sigma_0 \exp[-z\sqrt{(i\omega/c)}] \tag{35}$$

It is assumed that the layer is relatively thick, which implies a condition that there $z\sqrt{(i\omega/c)}$ is large, or the seabed layer $D >> \sqrt{(c/\omega)}$. The total solution is found by combining (33) and (35)

$$w = (a-\lambda)\,\sigma_0 \exp[-z\sqrt{(i\omega/c)} + i\omega t] \tag{36}$$

Splitting this formula into a real and an imaginary part yields with $\sqrt{i} = (1+i)/\sqrt{2}$

$$w = (a\text{-}\lambda)\,\sigma_0 \exp[-\zeta + i(\omega t - \zeta)] \quad \text{with} \quad \zeta = z\sqrt{(\omega/2c)} \quad (37)$$

or

$$w = (a\text{-}\lambda)\,\sigma_0 \exp(-\zeta)\,[\cos(\omega t\text{-}\zeta) + i\sin(\omega t\text{-}\zeta)] \quad (38)$$

The real part is the response to the real part of the loading according to (26), which is $w_{(z=0)}=(a\text{-}\lambda)\ \sigma_0\ \cos(\omega t)$. Hence, the final solution becomes

$$w = (a\text{-}\lambda)\,\sigma_0 \exp(-\zeta)\,\cos(\omega t\text{-}\zeta) \quad (39)$$

The corresponding pore pressure and effective stress become, using $w = a\sigma - p$ and (26)

$$p = a\sigma\text{-w} = a\sigma_0\,[\cos(\omega t) - (1\text{-}\lambda/a)\exp(-\zeta)\cos(\omega t\text{-}\zeta)] \quad (40)$$

$$\sigma' = \sigma\text{-}p = \sigma_0\,[(1\text{-}a)\cos(\omega t)+(1\text{-}\lambda/a)\exp(-\zeta)\cos(\omega t\text{-}\zeta)] \quad (41)$$

For the investigation of the behaviour of pore pressure and effective stress, formula (40) is rewritten in the form of an amplitude P and a phase shift ψ, according to

$$p = P\cos(\omega t + \psi) \quad (42)$$

With

$$\xi = 1\text{-}\lambda/a \quad (43a)$$

$$A = 1\text{-}\xi\exp(-\zeta)\cos(\zeta) \quad (43b)$$

$$B = \xi\exp(-\zeta)\sin(\zeta) \quad (43c)$$

$$\psi = \text{atan}\,(B/A) \quad (43d)$$

equation (40) becomes

$$p = a\sigma_0\,[A\cos(\omega t) - B\sin(\omega t)] \quad (44)$$

which can be elaborated into

$$p = a\sigma_0\,\sqrt{(A^2+B^2)}\,\cos(\omega t + \psi) \quad (45)$$

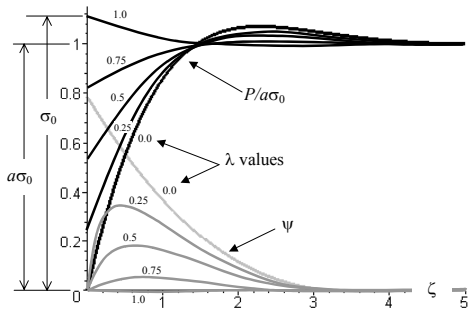

Figure 4. Pore pressure amplitudes P and (negative phase) shifts ψ

Finally, using (42) and (43), the amplitude and phase shift become

$$P = a\sigma_0\,\sqrt{(1 - 2\xi\exp(-\zeta)\cos(\zeta) + \xi^2\exp(-2\zeta))} \quad (46a)$$

$$\psi = \text{atan}[\xi\sin(\zeta)/\{\exp(\zeta) - \xi\cos(\zeta)\}] \quad (46b)$$

The graphical representation of these formulas is given in Figure 4 for the cases λ = 0, 0.25, 0.5, 0.75 1.0, and a = 0.9.

In Figure 5, the case: λ=0 (ξ=1), which refers to a shallow submerged foundation on a filterbed, subjected to a effective cyclic loading, is shown separately.

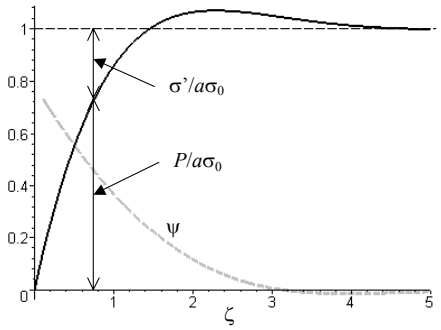

Figure 5. Pore-pressure amplitude and phase shift, case: λ=0, a=0.9

The case λ = 0, shown in Figure 5, reveals that at certain depth $\zeta > 1.45$ or $z > 2.06\sqrt{(c/\omega)}$ the amplitude P becomes *larger* than the partial loading $a\sigma_0$. A maximum is found at $z = 3.25\sqrt{(c/\omega)}$ of $1.07a\sigma_0$. In case of incompressible water, the pore pressure is there 7% larger than the total loading σ_0. The phase shift ψ shows that in the area $0 < z < \pi\sqrt{(2c/\omega)}$ the local maximum of p arrives before the maximum of the loading, in fact a *negative* phase shift or a negative delay. For z = 0 this negative phase shift is at maximum $\pi/4$, with a local amplitude equal to zero. The negative phase shift is small, about 0.03π, when p reaches its maximum at $z = 3.25\sqrt{(c/\omega)}$, see Figure 4 and 5. Hence, the maximum pore pressure response and the maximum loading will hardly show any phase shift. For A set of isochrones for the induced pore pressure for the case of a fully drained surface (λ = 0) including the effect of pore fluid compressibility, i.e. for a = 0.9 or $n\beta = 0.1\alpha_s$, is presented in Figure 6.

The value $\sqrt{(c/\omega)}$ has dimension of length. For sand: $c \approx 0.01$ and for clay: $c \approx 10^{-5}$ m^2/s. For tidal loading, $\omega \approx 1.45\ 10^{-4}$ 1/s, this length becomes for sand: $\sqrt{(c/\omega)}$ = 8.3m, and clay: $\sqrt{(c/\omega)}$ = 0.26m. For large waves with a period of T=10s this becomes ($\omega = 2\pi/T = 0.63$ rad) for sand: $\sqrt{(c/\omega)}$ = 0.13m, and for clay: $\sqrt{(c/\omega)}$ = 0.003m. Hence, consolidation takes place neart the seabed surface, and the assumption of a 1-D schematization is valid, because the wave length is in both cases much larger than the consolidating zone. The effective stress σ' can be treated in the same way. The amplitude is the counterpart of p because at any moment their sum is equal to the loading amplitude $a\sigma_0$. Hence. the effective stress amplitude σ' is also presented in the graph of P of Figure 5. In a zone beyond $z = 2.06\sqrt{(c/\omega)}$ the induced effective stress becomes negative

(tensile). Because of hydrostatic stress (gravity is not included in this analysis) tensile stresses may not occur, but lower effective stress does occur.

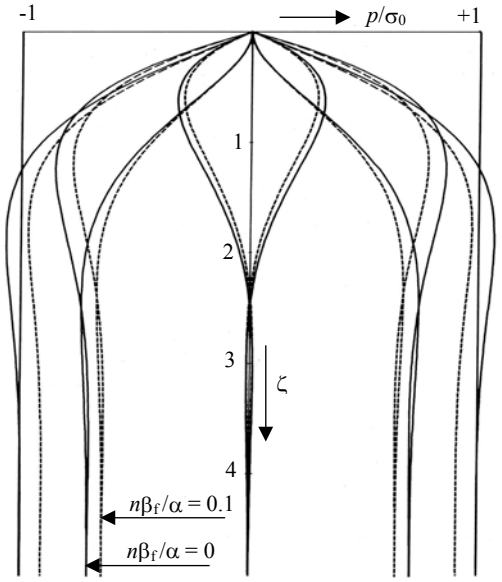

Figure 6. 1D-isochrones of pore pressures due to cyclic loading

This particular example shows three typical effects of cyclic consolidation: (1) the maximum pore pressure at some moments may exceed the maximum total loading, (2) the generated effective stresses may become tensile, and (3) there is a negative delay in the response. Moreover, these phenomena may take place in a relatively small zone near the border, which with regard to the wavelength supports the validity of the 1-D approach.

B. Heterogeneous Case

Next, consider a stratified subsoil, i.e. a two-layer system. The upper layer is defined in the range $0 < z < D$, and the second layer in the range $z > D$. At the boundary $z = 0$ a cyclic loading is imposed, according to (27). Solution (40) can be applied to both layers. However, at the layer separation, $z = D$, two physical conditions have to be satisfied. The pore pressure is continuous and the flux across the interface is preserved. Therefore, the solution of a finite layer is required in the upper layer. In terms of w, following (39) the solution for the upper layer becomes

$$w = w_0 \exp(-\zeta_1) \cos(\omega t - \zeta_1) + w_1 \exp(\zeta_1) \cos(\omega t + \zeta_1) \quad (47)$$

with $\zeta_1 = z\sqrt{(\omega/2c_1)}$ and $0 < z < D$. At the boundary, $z = 0$, the following holds

$$w_0 + w_1 = \lambda a \sigma_0 \quad (48)$$

In the second layer, solution (39) applies, as

$$w = w_2 \exp(-\zeta_2) \cos(\omega t - \zeta) \quad (49)$$

with $\zeta_2 = z\sqrt{(\omega/2c_2)}$ and $z > D$. The two conditions at the interface and boundary condition (48) determine uniquely the integration constants w_0, w_1 and w_2.

To avoid lengthy computations here, just the solution for the case of a fully drained seabed, i.e. $\lambda = 0$, and an incompressible pore fluid, i.e. $\beta = 0$ ($a = 1$), is presented

$0 < z < D$:

$$p = \sigma_0(\cos(\omega t) - ((1-\delta) \exp(\chi_1) \cos(\omega t + \chi_1 - \psi) + (1+\delta) \exp(-\chi_1) \cos(\omega t - \chi_1 - \psi)) / 2N) \quad (50a)$$

$z > D$:

$$p = \sigma_0(\cos(\omega t) - \exp(-\chi_2) \cos(\omega t - \chi_2 - \psi) / N \quad (50b)$$

with

$$\chi_1 = (z-D)\sqrt{(\omega/2c_1)} \quad \text{and} \quad \chi_2 = (z-D)\sqrt{(\omega/2c_2)}$$

$$\delta = (k_2\sqrt{(\omega/2c_2)}) / (k_1\sqrt{(\omega/2c_1)})$$

$$\psi = \arctan(A/B) \quad \text{and} \quad N = \sqrt{(A^2+B^2)}$$

$$A = \cos(D\sqrt{(\omega/2c_1)})(\cosh(D\sqrt{(\omega/2c_1)}) + \delta \sinh(D\sqrt{(\omega/2c_1)}))$$

$$B = \sin(D\sqrt{(\omega/2c_1)})(\sinh(D\sqrt{(\omega/2c_1)}) + \delta \cosh(D\sqrt{(\omega/2c_1)}))$$

In Figure 7 two situations are presented for incompressible pore water. Note, that the maximum pore pressure occurs at the layer separation and is in the order of $1.11\sigma_0$, exceeding the loading by 11%, in this case.

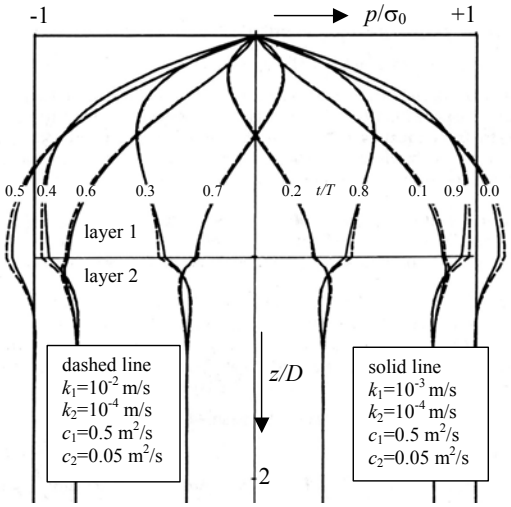

Figure 7. 1D-isochrones of cyclic pore pressures in a 2-layer system

The gradient $p_{,z}$ in the second layer at the interface is of particular interest concerning internal stability (filter stability and suffosion). It is expressed by

$$p_{,z} = \sigma_0\sqrt{(\omega/c_2)} \cos(\omega t - \psi + \pi/4) / N \quad (51)$$

This particular example shows (1) that, in a two-layered stratified porous medium, maximum cyclic pore pressures take place at the interface and they may exceed the total loading up to ~20%, and (2) local pore fluid gradients at the interface in the finer bed are relatively large.

V. 2D-Effects of Cyclic Consolidation on Seabeds

A. Free Running Waves

In the previous chapters it is outlined that special local pore pressure effects occur in zones near the boundary or interfaces in layered seabed soils. These zones are small in comparison to the wavelength. Hence, the 1-D approach is valid. However, 2-D effects may be significant, which is elucidated by the following example.

Consider a three-layered submerged soil profile, which is subjected to sea waves. The waves produce a running cyclic water pressure at the sea bottom, as a total loading since at the sea bottom the effective stress is zero, $\sigma' = 0$. This loading is characterised by a pore pressure with an amplitude H, wavelength L and wave period $T = 2\pi/\omega$. The first layer consists of silty sand, the second of stiff sea-gravel and the third of sandy clay. The geometry and relevant soil properties are presented in Figure 8.

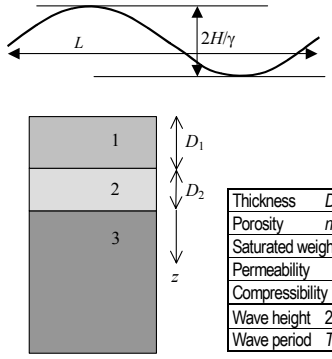

	1	2	3
Thickness D [m]	3	5	> 20
Porosity n [-]	0.3	0.4	0.35
Saturated weight γ [kN/m³]	19.5	18.0	16.5
Permeability k [m/s]	10^{-5}	10^{-3}	10^{-7}
Compressibility α_s [m²/MN]	0.1	0	1
Wave height $2H/\gamma$ [m]	5		
Wave period T [s]	15		

Figure 8. Three-layered seabed and its characteristic parameters

Assuming incompressible water, i.e. $a = 1.0$, application of (40) and (41) for free waves, i.e. $\lambda = 1$, for the first layer results in

$$p = \sigma_0 \cos(\omega t) \quad \text{and} \quad \sigma' = 0 \tag{52}$$

Hence, the water pressure at the sea bottom is transferred to the second layer without any change. Because of the relatively rigid and permeable condition of the second layer, the induced pore pressures will spread in this layer almost instantaneously; the wave top and wave trough are significantly damped. In the extreme case, the pore pressure in the second layer is just the average of the wave loading. This phenomenon causes to effects: (1) the pore pressure changes will invoke a local consolidation effect in the lower part of the top layer, restricted to a narrow zone in the order of $\sqrt{(\omega/c_1)}$ (for the data given in Figure 8, some centimeters), and (2) in the second layer the effective stress σ' will change as to comply with the total loading; thus

$$p = 0 \quad \text{and} \quad \sigma' = \sigma_0 \cos(\omega t) \tag{53}$$

This represents a condition for the third layer, according to (40) and (41) with $a = 1.0$ and $\lambda = 0$, and hence the pore pressure response in layer 3 complies with

$$p = \sigma_0 [\cos(\omega t) - \exp(-\zeta)\cos(\omega t - \zeta)] \tag{54}$$

$$\sigma' = \sigma_0 \exp(-\zeta)\cos(\omega t - \zeta) \tag{55}$$

Figure 5 describes the situation in layer 3 precisely. In conclusion, one may expect little to no effects in layer 1 and layer 2, but in layer 3 local excess pore pressures and high local gradients at the interface will occur. Figure 9 shows the result of corresponding maximum pore pressures at the wave top and wave trough. As discussed before, there will be hardly any phase shift. Hence, the seabed is subjected to serious local wave induced effects, particularly at the layer interfaces, which may jeopardise the internal filter stability.

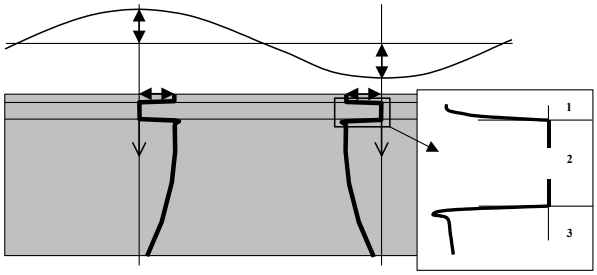

Figure 9. Pore pressure amplitude response and local effects (inset)

B. Rocking Rigid Foundations

A semi-submerged coastal structure, founded on a filter bed and subjected to wave loading, will rock on its foundation. These movements will cause deformation in the seabed and hence water pressures in the subsoil, distinguished as induced pore pressures. Free (standing) waves before the structure may also generate induced pore pressures in the subsoil. Thus, the situation at the edges of the foundation involves two phenomena; in fact, a combination of the cyclic pore pressure generation, as presented in Figure 3, for $\lambda = 1$ (free-wave loading) and $\lambda = 0$ (effective drained loading), in a 2-D setting, see Figure 10. Although the cyclic character of this induced phenomenon will probably not create serious pore water flow, large local pore water gradients may occur occasionally, which invokes migration of particles, and without proper precautionary measures it can affect the stability of the structure.

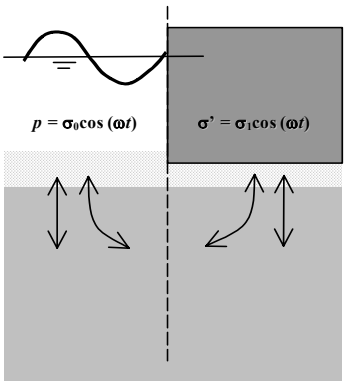

Figure 10. Combined conditions at the edge of a coastal structure

An example of a numerical simulation of a 2-D consolidation process involving the previously described condition at the edge of a rocking coastal structure, on a shallow foundation and subjected to wave loading, is presented in Figure 11 and 12. Figure 11 shows a soft seabed with on top one coarse, relatively stiff and permeable filter layer, and Figure 12 shows a soft seabed, with on top a two-layer filter bed consisting of coarse and finer and softer material. The pore water is assumed compressible, as air intrusion due to wave action is rather likely.

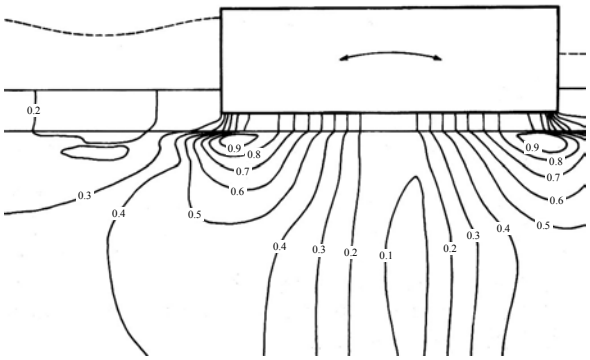

Figure 11. Rocking coastal structure on a single layer filter bed [7] [8]

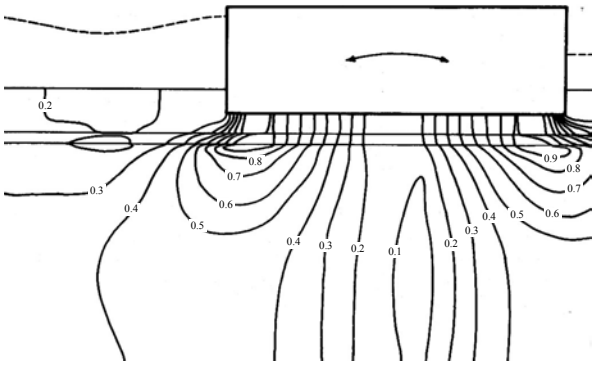

Figure 12. Rocking coastal structure on a two-layer filter bed [7] [8]

In above pictures iso-porepressure lines are presented, tagged with a number that shows the excess pore pressure relative as a fraction of the maximum loading by the rocking structure. Local zones of high pressures are observed, in agreement with aspects discussed in Chapter IV and V. Proper modeling of local gradients in these zones near interfaces of the filter bed is achieved by a fine FEM mesh. These gradients are essential in the design of a stable filter bed under extreme loading conditions.

VI. Field Observations

At Zeebrugge, situated on the Belgium coast, an outer harbour has been constructed with breakwaters of rubble mound type founded on a dumped sand layer. In order to gather information about the pore pressure distribution in the dumped sand layer and in the top zone of the underlying natural seabed layers, and about the pore pressure changes due to tides and waves, special field measurements have been conducted by means of electrical pore pressure measuring devices, mounted at 7 levels in the shaft of a cone shaped steel probe of 13m length (Figure 13). The submerged soil profile – local normal mean sea level is about 5m above the seabed – contains several layers of coarse sand with some bolders, together about 10m Thick, dumped on the original seabed, which consists of a small layer of clayey sand on top of a thick clay deposit (Bartoon clay).

Some of the reported measurments [9] are shown (Figure 13), one referring to tides and one referring to waves.

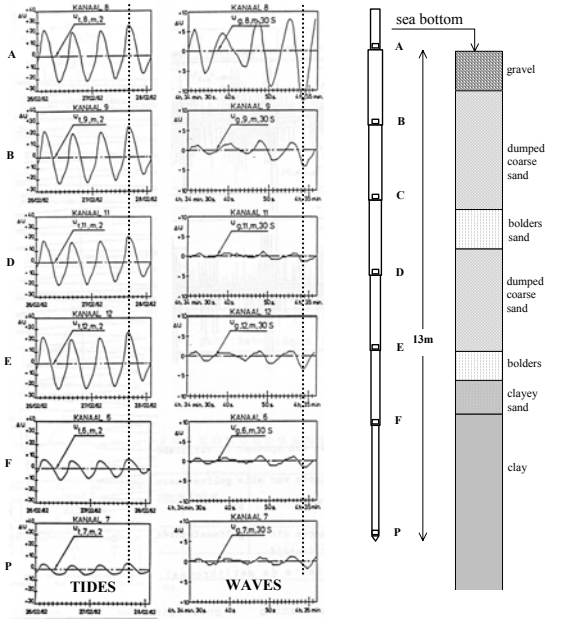

Figure 13. Field data of tidal and wave pore pressure response [9] [10]

The difference in amplitude damping is clearly observed. Tides do not damp in the coarse layers; they do in the clay seabed, probably due to the effect of air or gas bubbles. Waves are damped significantly, probably due to local differences in compressibility. Note, the local decrease of amplitude at level *C*, which is due to local gas bubbles or to horizontal averaging effects discussed in Chapter V. It is remarkable that, for both cases, there is no phase shift at all for the tides and a very small phase shift for the waves, which support the theory discussed in the previous chapters.

VII. Conclusion

In practice, one commonly interpretes cyclic pore pressures, such as shown in Figure 13, by applying the well-known formula for cyclic-damped response from the theory of heat conduction, which states

$$p = p_0 \exp(-\zeta)\cos(\omega t-\zeta)] \tag{56}$$

This is not correct, since it violates the principle of effective stress and the fact that the total loading by waves, tides or rocking submerged structures is transferred as a body force instead of a boundary force. Moreover, one will miss in this way specific phenomena, such as relatively large excess pore pressures and large local gradients, which may be important for the design. This paper explains which approach is proper and which effects can be expected.

LIST OF SYMBOLS

Symbol	*Unit*	*Formula*	*Definition*
a	-	$1/(1+n\beta_f/\alpha_s)$	coefficient
A	-		parameter, constant
A_1	m^2		boundary surface
B	-		parameter, constant
c	m^2/s	$ka/\gamma\alpha_s$	consolidation coefficient
D	m		soil layer thickness
g	m/s^2		gravity acceleration
G	N/m^2		shear modulus
H	N/m^2		wave pressure amplitude
$2H/\gamma$	m		wave height
k	m/s	$\kappa\gamma/\mu$	hydraulic permeability
K_s	N/m^2		bulk modulus
L	m		wavelength
L_1	m		average flow path, length scale
L_2	m	V/A_1	drainage capacity, length scale
n	-		porosity
N	-		parameter, constant
p	N/m^2		pore pressure, field variable
p_1	N/m^2		boundary pore pressure
P	N/m^2		spacial pore pressure
$\mathbf{p}$	N/m^2		average pore pressure
$\mathbf{P}$	N/m^2		spacial average pore pressure
q	m/s		bulk velocity
t	s		time coordinate
V	m^3		(bulk) volume
T	s	$2\pi/\omega$	wave period
w	N/m^2	$a\sigma - p$	stress variable
W	N/m^2		spacial stress variable
z	m		space coordinate
α_s	m^2/N	$1/(K_s + {}^4/_3 G)$	laterally confined compressibility
α	-	$\omega L_1 L_2/3c$	coefficient
β	m^2/N		pore fluid compressibility
γ	N/m^3	ρg	specific (water) weight
η	rad	$\mathrm{atan}(\alpha)$	delay; phase shift
ε	-		strain
δ	-	$(K_2\sqrt{(\omega/2c_2)}) / (K_1\sqrt{(\omega/2c_1)})$	parameter, constant
κ	m^2	kv/g	intrinsic permeability
λ	-		coefficient
μ	N/sm	$\nu\rho$	dynamicfluid viscosity
ν	m^2/s		kinematic fluid viscosity
ρ	kg/m^3		fluid density
σ	N/m^2		total stress
σ'	N/m^2	$\sigma' + p$	effective stress
σ_0 , σ_1	N/m^2		loading (total) stress amplitude
ψ	rad		delay; phase shift
χ	-	$(z-D)\sqrt{(\omega/2c)}$	relative space coordinate
ω	rad/s	$2\pi/T$	angular velocity
ξ		$1 - \lambda/a$	coefficient
ζ, ζ_1, ζ_2	-	$z\sqrt{(\omega/2c)}$	relative space coordinate

REFERENCES

[1] Verruijt, A., 1969, The completeness of Biot's solution of the coupled thermo-elastic problem, *Jl Quart Applied Math, Vol XXVI-4, p:485-490.*

[2] Honda, K., 1904, Daily periodic change in the level in the artesian wells in Yokohama, Yosgiwara and Okubo, *Proc Tokyo Physico-Math. Soc., Vol 9, p:123-127*.

[3] Friedrich, P., 1916, Groundwater phenomena in the city Lubeck and its surroundings (German), *Mitt. Geografische Gesellschaft und Nature Historisch Museum*, *Lubeck, 2(27), p:67-83*.

[4] Steggewentz, J.H., 1993, *The influence of tidal seas and rivers on groundwater levels* (Dutch), Ph-T thesis TUDelft, Meinema, Delft.

[5] De Lang, W.J. and Maas, C., (1986), About forerunning of groundwater tides on tidal motion in the river Ijssel near Gouderak,(Dutch), *H2O 19, p:24-29*.

[6] Bauduin, C.M.H.L. and Barends, F.B.J., 1987, Tydal response under dutch dikes (Dutch), *H_2O 21, p:25-28*.

[7] Barends, F.B.J., (1978) Advanced methods in groundwater flow computation, *LGM-Mededelingen, XIX, p:65-75*.

[8] Barends, F.B.J. and Thabet, R., 1978, Groundwater flow and dynamic gradients, *Proc. Int Symp. on Foundation Aspects of Coastal Struct, GeoDelft, Vol 6(1), p:1-13*.

[9] De Rouck, J., 1991, *The stability of rubble-mound breakwaters*, Ph-D Thesis Univ Leuven, UDC627.325, 525 pages.

[10] De Wolf, P., Carpentier, R., Verdonck, W., Boulart, L., De Rouck, J., De Saint Aubain, T. and De Voghel, J., 1983, In situ pore pressure measurements for the construction of the breakwater of the new outer harbour at Zeebrugge, *Proc. Harbour Congres, Antwerpen, 13 pages.*

[11] Verruijt, A. 1980 A simple formula for the estimation of pore pressures and their dissipation, *Jl Appl Ocean Research, Vol 2, p:57-62.*

[12] Barends, F.B.J., 2005, Associating with Advancing Insight. Terzaghi Oration, *Proc XVI-ICSMGE Osaka, Millpress Rotterdam, Vol 1, p217-248*.

Design of Bridge Abutment Scour Countermeasures

B. D. Barkdoll[1], B. W. Melville[2], and R. Ettema[3]

[1]Civil & Environmental Engineering Department, Michigan Tech University, Houghton, MI 49931; PH: (906) 487-1981; FAX: (906) 487-2943; email: barkdoll@mtu.edu
[2]Civil & Environmental Engineering Department, University of Auckland, New Zealand; PH: 64 9 373-7599 x88165; FAX: (64) (9) 3737462 ; email: b.Melville@auckland.ac.nz
[3] Civil & Environmental Engineering Department, University of Iowa; PH: 319-335-5224; FAX: 319-335-5660; email: robert-ettema@uiowa.edu

INTRODUCTION

Bridge scour, both at piers and abutments, is one of the leading causes of bridge failure. Scour can lead to the undermining of pier and abutments that, when below the foundation, can lead to the collapse of the structure. Bridge collapse results in costly repairs, disruption of traffic, and possible death of passengers traveling on the bridge when collapse occurs.

Abutments come in various shapes, orientations, and set-back distances, thereby making it difficult to analyze all possible abutment conditions. Abutments can have vertical walls or be of the spill-through variety. The skew angle of the abutment to the waterway can be perpendicular or angled upstream or downstream. In addition, the abutment can encroach out into the waterway, thereby blocking the flow, or be set back from the waterway well onto the floodplain.

The objective of this paper is to review the selection and design of existing bridge abutment countermeasures for older bridges that tend to have vertical walls and be located flush with the main channel banks and be perpendicular to the waterway [1].

SCOUR-INDUCING FLOW PATTERNS

To understand the rationale behind countermeasure design, it is helpful to first review the flow patterns at abutments that cause scour. With reference to Fig. 1, the principle scour-inducing flow patterns are (1) a downward-moving roller caused by impact with the flow striking the leading abutment corner that combines with (2) return flow from the floodplain into the main channel, (3) a secondary vortex following the downward flow mentioned above whose axis as near the bed and parallel to the abutment, (4) increased main-channel velocity due to the contraction caused by the abutment, and (5) a tornado-like wake vortex downstream of the abutment. Shear layer vortices are formed that play a less substantial role in scour as well.

BANK-HARDENING COUNTERMEASURES

Bank-hardening countermeasures are comprised of various hard materials located on the bed and banks in the vicinity of the abutment to increase the ability of the bad or bank to resist scour by the flow. The flow strength is not altered in any significant way. The three methods covered here are riprap, cable-tied blocks, and geobags.

Riprap

Riprap is the most common countermeasure employed and consists of large rocks arranged flush with the bed and banks in several layers of thickness. Failure of riprap beds has been observed due to (1) dislodging of the individual rocks due to excessive stream velocity, (2) dislodging of individual rocks at the edge of the riprap blanket due to the flow undermining and lifting the rocks up and into direct contact with the flow, and (3) sinking of the riprap blanket due to winnowing of the fine bed material up through the rocks where it is carried away by the flow.

Design consists of the specification of the rock size to avoid direct dislodging, riprap blanket thickness, the lateral extent of the blanket to avoid edge failure, the gradation of riprap, and a filter material to avoid winnowing of the fines.

To size the riprap stone the method of [2]:

$$D_{50} = \left(\frac{1.064 U^2 Y^{0.23}}{(S_s - 1) g} \right)^{0.81}$$

where D_{50}=the median riprap size, U=the cross-sectionally averaged water velocity, Y=flow depth, S_s=specific gravity of the riprap material, and g=gravitational constant.

The thickness of the riprap blanket, $t=1.5D_{100}$, or where D_{100} is the largest size of riprap stone [3]).

The lateral extent of the riprap blanket can be found by

$$W_{\min} = C_1 (d_s - d_b + D_{50})$$

where W_{min}=the minimum riprap blanket extent across the channel, C_1 = 1.68 and 1.19 at the upstream and downstream corners of the riprap layer, respectively, d_s= depth of equilibrium scour, and d_b= the depth of the riprap blanket bottom below the average channel bed level (Fig. 2). d_s can be found for bedform-dominated cases by

$$d_s = C_2 H$$

where H is maximum bed-form height and C_2 = 1.2 and 1.0 for the upstream and downstream corners of the riprap layer, respectively (van Ballegooy et al. 2005). Otherwise, add other scour components to d_s.

The proper gradation of riprap can be found using the criteria of [4] summarized in Table 1.

Table1. Riprap gradation for bridge protection

Stone Size Range	**Percentage of Gradation Smaller than**
$1.5D_{50}$ to $1.7D_{50}$	100
$1.2D_{50}$ to $1.4D_{50}$	85
$1.0D_{50}$ to $1.1D_{50}$	50
$0.4D_{50}$ to $0.6D_{50}$	15

To design the filter material the pore space should be finer than the natural riverbed material. See [5] and [6] for more details

Cable-tied Blocks

Cable-tied block consist of a series of blocks linked together with cable to hold them together as a coherent mat. Design issues include primarily the block size, lateral extent, and edge treatment.

Block size can be estimated by the following equation:

$$\frac{H_b}{y} = \left[\frac{a_{cb}\rho}{(\rho_{cb} - \rho)(1-p)}\right] Fr^2$$

in which H_b=the height of the block, y=flow depth, a_{cb} = 0.1, ρ_{cb} is the block density, ρ is the fluid density, and Fr=the Froude Number.

CTB blocks are typically manufactured as a truncated pyramid shape with a square base and top. The spacing between CTB units should be adequate to allow the mattress to have a sufficient degree of flexibility, and that block shape should not inhibit mat flexibility.

Typically, synthetic filters are used beneath CTB mats.

Lateral extent of the cable-tied block mattress can be determined from

$$W = 1.55(d_s - d_b)$$

where W is apron width, d_s is scour depth (= mat settlement depth) at the outer edge of the mat, and d_b is the placement (burial) depth of the mat. See Fig. 3.

To prevent the uplifting of the leading edge blocks the size can be determined by

$$\frac{H_b}{Y} = \frac{158}{(S_{cb} - 1)} Fr^2 \frac{n^2}{Y^{0.33}}$$

where S_{cb} is the specific gravity of the blocks and n is the Manning coefficient. Care needs to be taken to ensure that the leading edge of the mat remains buried.

Geobags

Geobags are bags of pervious material that are filled with a pervious granular material (sand or gravel) that are used as bank hardening elements, thereby possessing enough weight to hold sediment in place, but allowing the flow of water through them to reduce uplifting pressure to reduce the likelihood of uplifting of the bag or winnowing of the fines underneath. The bag material can be a geosynthetic fabric such as the filter layer of riprap discussed above.

Design considerations include sizing, linking of bags, angle of placement and placement extent [7].

Minimum sizing can be determined by that of equivalent riprap as mentioned above. The individual bags should be tied together to help them function as a single mattress thereby allowing flexibility to conform to the irregular bed shape. The geobag mattress should have a maximum slope of 2H:1V with a toe extending a downward length equal to at least 2 bags into the riverbed.

FLOW-ALTERING COUNTERMEASURES

Three new flow-altering countermeasures are described next that do not attempt to increase the bank's ability to resist erosion, but to reduce the flow's energy to scour. These methods are (1) parallel walls, (2) spur dikes, and (3) abutment collars.

Parallel Wall Countermeasure

The design parameters for the parallel wall scour countermeasure are the wall length, width and protrusion into the main channel [8]. Each of these is discussed next. See Fig. 4 for a sketch of the design dimensions.

The length of the parallel wall should be 0.5_aL, where L_a is the abutment length (perpendicular to flow direction). The maximum steepness of the side wall angle should be the angle of repose for the rock employed. The height of the wall should be sufficient to have the top of the wall be above the top of the lowest portion of the bridge decking. The wall width

should be wide enough to accommodate the wall height and the sidewall angle of the rock wall. The bottom of the rock wall should be even with the abutment such that no part of the wall should protrude out into the main channel. The wall should be parallel to the river banks. Thus, if the river section is straight, then the wall should be straight as well, but if the river section is curved, then the wall should also be curved and parallel to the river banks. See Fig. 5 for a sketch of a curved wall. The thickness of the apron should be at least two times the diameter of the size of rocks used for the wall. The width of the apron should be at least 4 times the wall height. The apron should extend the full length of the wall. At the upstream end, the apron should join the floodplain.

Spur Dike Countermeasure

The design parameters for spur dikes as abutment scour countermeasures are dike length, spacing, and width [9]. See Fig. 6 for a definition sketch.

There should be at least three dikes used: two shorter dikes at the upstream and downstream corners of the abutment and a longer dike located upstream of the abutment. For wide abutments (parallel to the flow) there may need to be additional short dikes as well (see discussion on dike spacing below).

The top length of the dike (perpendicular to flow direction) should be equal to the abutment length, L_a, (perpendicular to the flow). For the shorter dikes this length extends from the abutment face out into the main channel. For the longer dike upstream of the abutment, the length is longer than L_a. The dike should extend the same distance into the river that the shorter dikes do and extend back onto the floodplain a distance sufficiently far to not affect the river flow. The bottom dike length is determined by the angle of the wall face. Care should be taken, however, on narrower rivers not to block too much of the river width with the dikes. Therefore, the dikes should not extend further out into the main channel than one-fourth of the river width.

Dikes should be located at the abutment corners and extending out into the main channel. Since dike spacing should be less than the abutment length, L_a, an intermediate dike may be needed depending if the abutment width (parallel to flow direction) is longer then the abutment length, L_a.

The maximum steepness of the side wall angle should be the angle of repose for the rock employed.

Dike width is determined by the dike face angle, which should be less than the angle of repose of the rock used to construct the dike.

Abutment Collar Countermeasure

The design parameters for abutment collars are the elevation, upstream, downstream, and lateral extents [9] and [10]. See Fig. 7 for a definition sketch.

The collar should be located at an elevation of $0.08y_m$ below the mean main channel bed level, where y_m is the main channel bankful flow depth (Fig. 7).

The minimum collar width should be $0.23L_a$, where L_a is the abutment length perpendicular to the flow direction (Fig. 7).

The collar should extend to a location $0.6L_a$ upstream from the upstream abutment corner, where L is the abutment length perpendicular to the flow direction (Fig. 7).

The collar should extend at least as far downstream as the downstream end of the abutment.

ACKNOWLEDGMENTS

This work was performed under the National Academy of Sciences, Transportation Research Board, National Cooperative, Highway Research Project # 24-18A.

REFERENCES

[1] Barkdoll, B. D. Melville, B. W. and Ettema, R. 2006, A Review of Bridge Abutment Scour Countermeasures, *Proceedings of the 2006 World Environmental and Water Resources Congress, May 21-25, 2006, Omaha, Nebraska*.

[2] Pagan-Ortiz, J.E. (1991) "Stability Of Rock Riprap For Protection At The Toe Of Abutments Located At The Flood Plain," *Report No. FHWA-Rd-91-057*, Federal Highway Administration, U.S. Department Of Transportation, Washington, D.C., U.S.A.,125 pp.

[3] Lagasse, P. F., Zevenbergen, L. W., Schall, J. D., Clopper, P. E. (2001). Bridge Scour and Stream Instability Countermeasures. Publication No. FHWA NHI 01-003, Hydraulic Engineering Circular No. 23, U. S. Department of Transportation, Federal Highway Administration. Pages 2.7, 2.9, 4.6, 6.16 - 6.18, Design Guidelines 1, 9, 10.

[4] Brown and Clyde 1989 "Design of riprap revetment," Hydraulic Engineering Circular 11 (HEC-11), Report No. FHWA-IP-89-016, Federal Highway Administration, U.S. Department of Transportation, Washington, D.C., U.S.A.

[5] Melville, B., van Ballegooy, S., Coleman, S., and Barkdoll, B. (2006) Countermeasure Toe Protection at Spill-Through Abutments, ASCE *J. Hydraulic Engineering* Vol. 132, No. 3, March 2006, pp. 235-245

[6] Melville, B., van Ballegooy, S., Coleman, S., and Barkdoll, B. (2005). "Scour Countermeasures for Wing-wall Abutments", ASCE *J. Hydraulic Engineering*, Vol. 132, No. 6, June 2006, pp. 563-574.

[7] Korkut,R., Martinez, E.J., Ettema, R., and Brian Barkdoll (2006) "Geobag Performance As Scour Countermeasure For Wingwall Abutments." ASCE J. Hydraulic Engineering, in press.

[8] Li, H., Barkdoll, B.D., Kuhnle, R., and Alonso, C. (2006) "Parallel Walls as an Abutment Scour Countermeasure" ASCE *J. Hydraulic Engineering*, Vol. 132, No. 5, May 2006, pp. 510-520.

[9] Li, H., Kuhnle, R., and Barkdoll, B.D. (2006) "Spur Dikes and Collars as Abutment Scour Countermeasures: An Experimental Study" ASCE J. Hydraulic Engineering, accepted.

[10] Hua Li, Brian Barkdoll, and Roger Kuhnle, 2005, Bridge Abutment Collar as a Scour Countermeasure, Proceedings of the 2005 World Water and Environmental Resources Congress, May 15-19, 2005, Anchorage, Alaska.

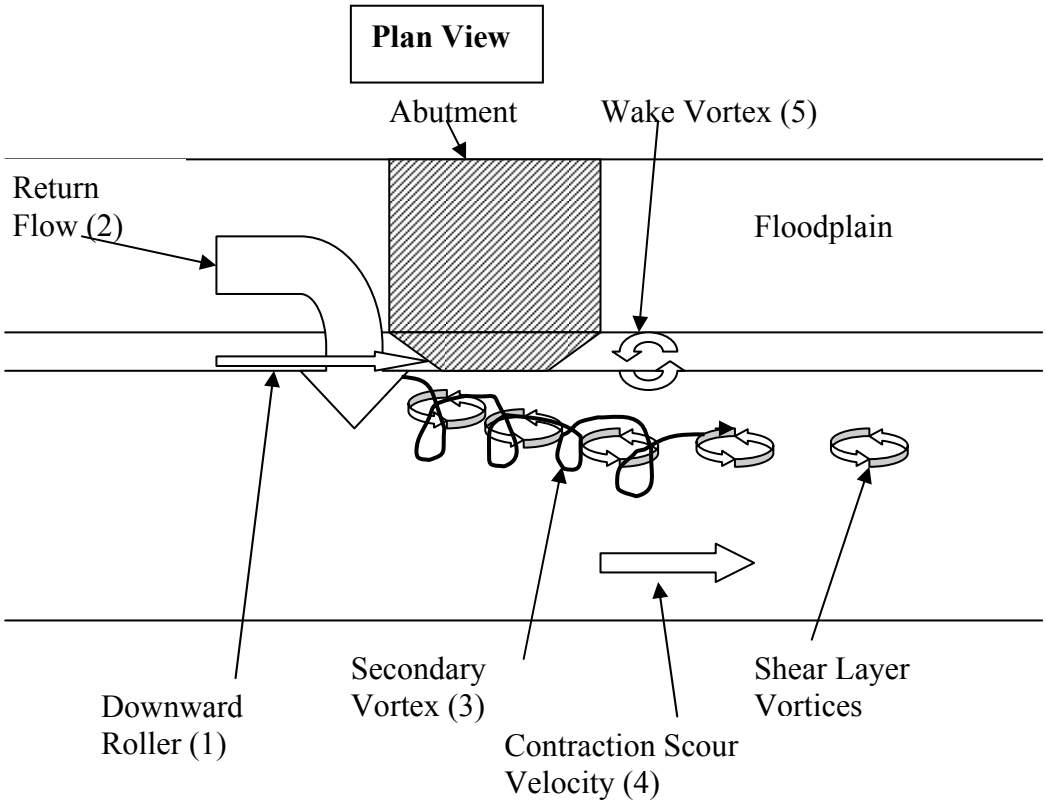

Fig. 1. Scour inducing flow patterns.

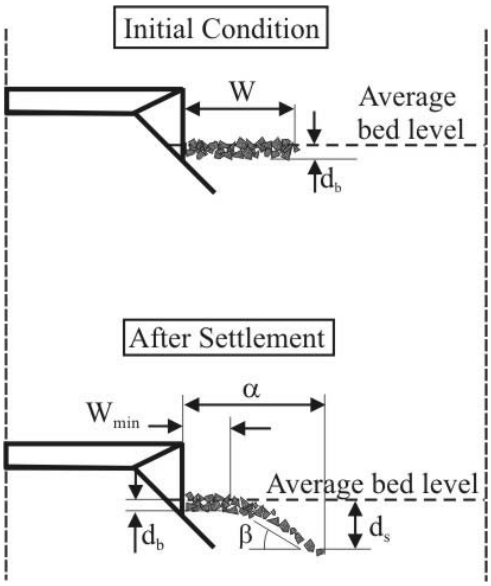

Fig. 2. Riprap apron settlement

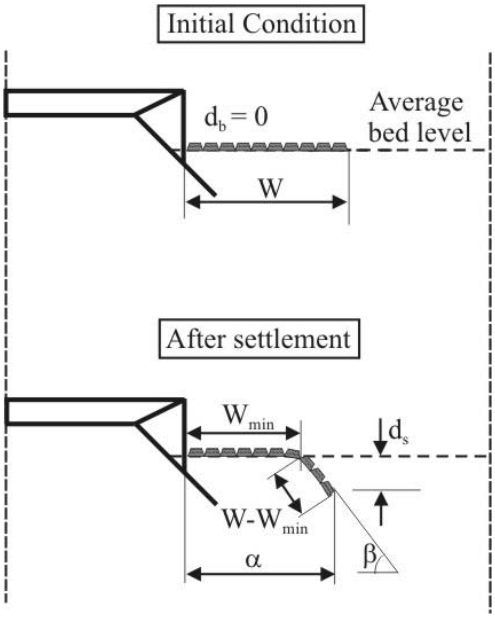

Fig. 3. CTB apron settlement

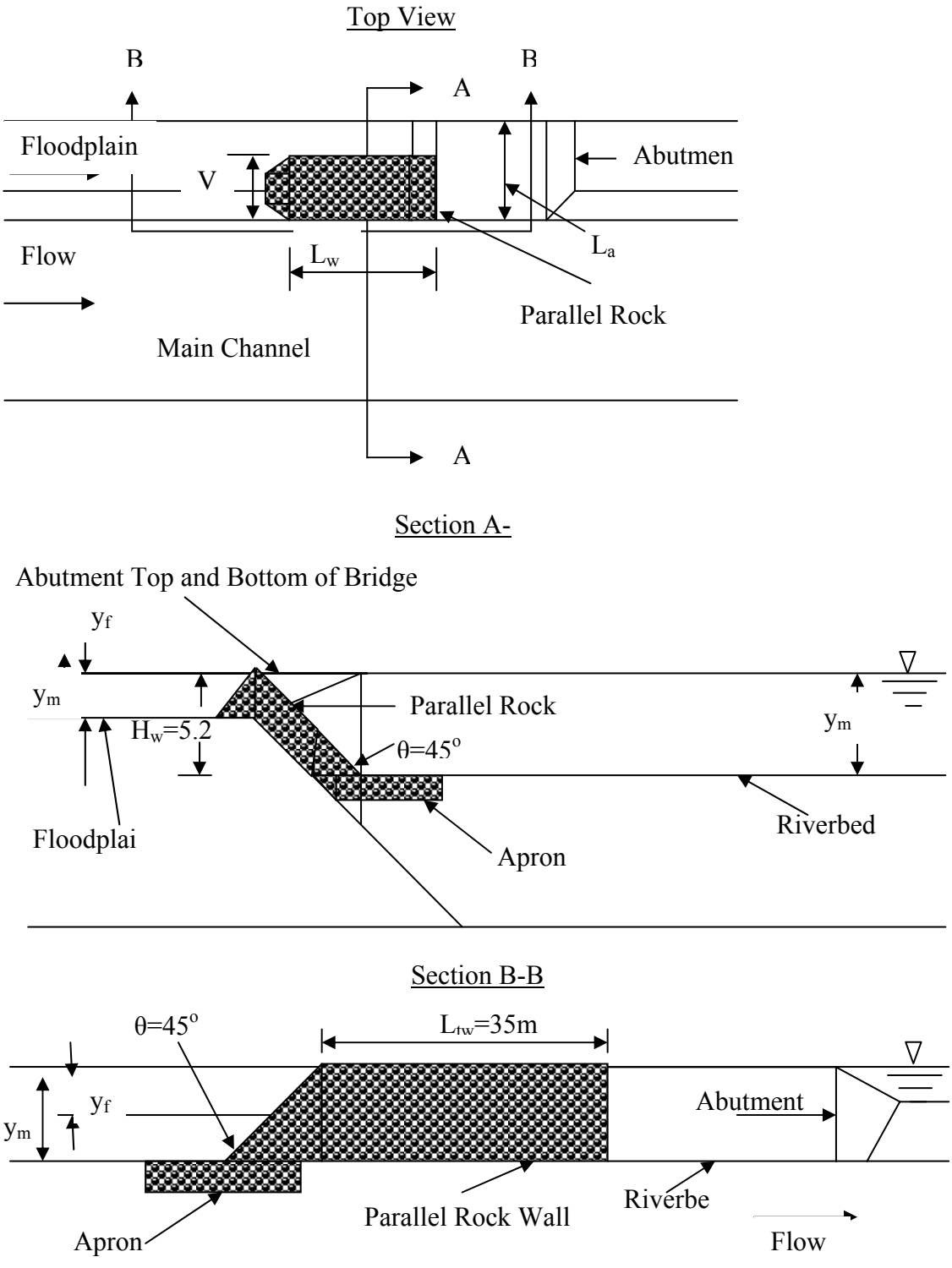

Fig. 4. Design dimensions for parallel rock wall.

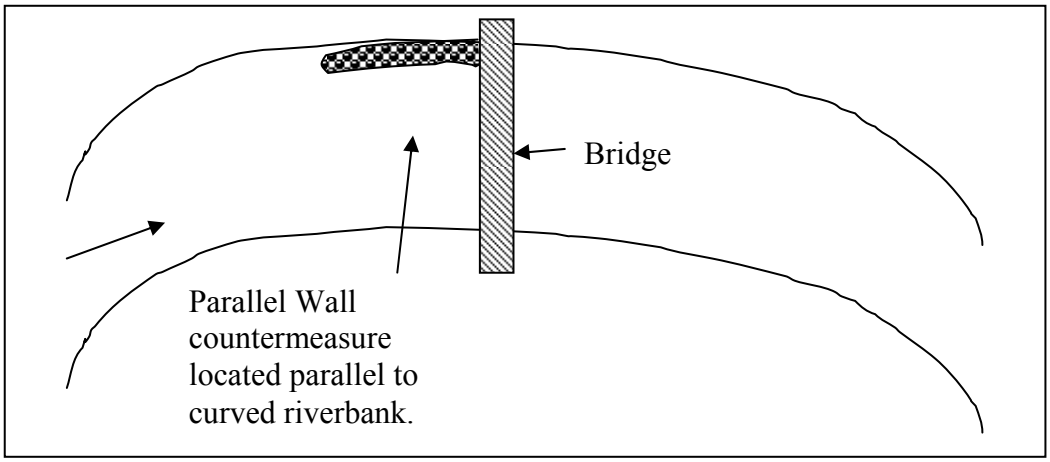

Fig. 5. Parallel Wall countermeasure located on river bend. Wall kept parallel to riverbank.

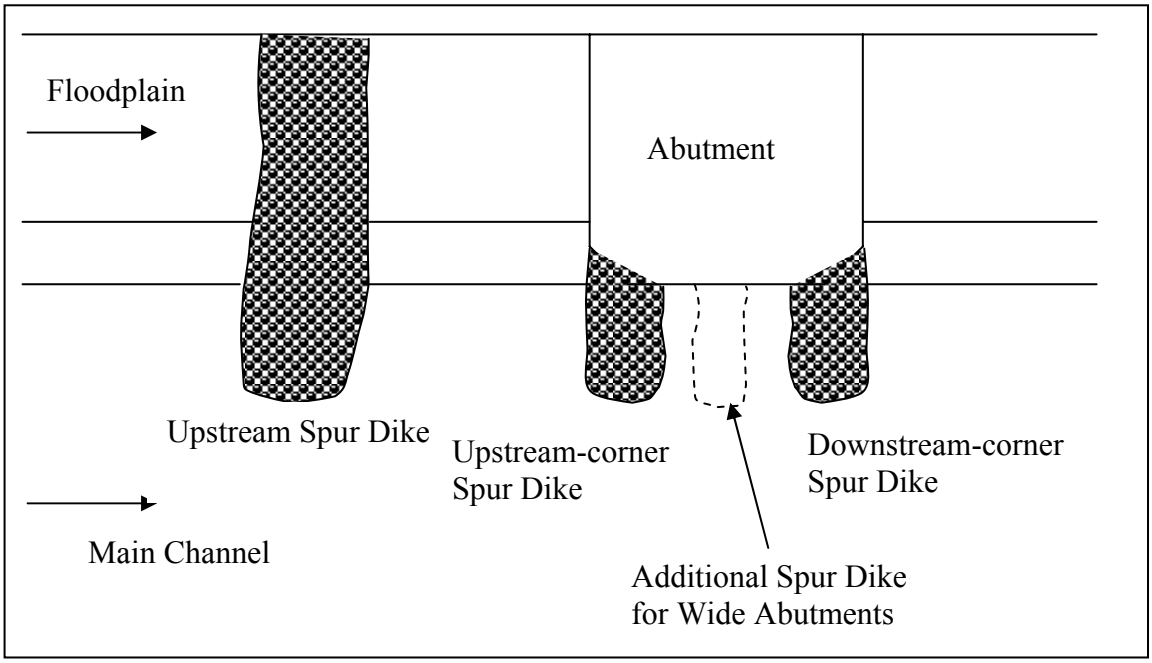

Fig. 6. Definition sketch for spur dike countermeasure design

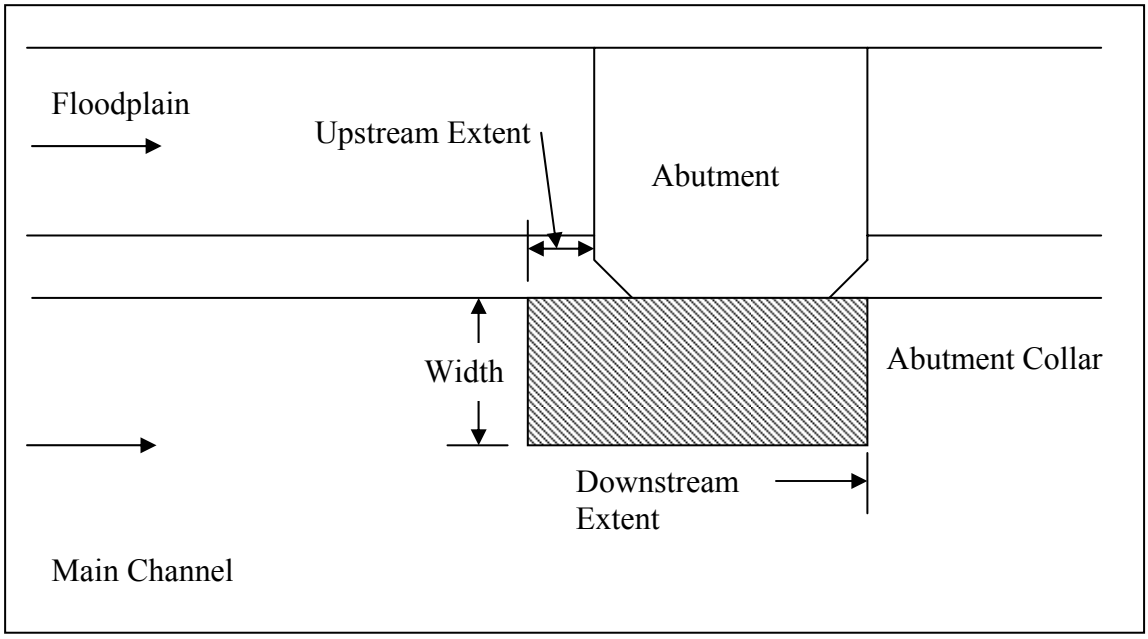

Fig. 7. Definition sketch of abutment collar countermeasure.

Temporal evolution of local scour in bridge piers: a Morphodynamic Approach

A.Bateman*; M. Fernández*; G. Parker**
* Thecnical University of Catalonia /Hydraulic, Marine & Environmental Engineering Department , Barcelona-Spain
** University of Illinois, Urbana Champain, USA
e-mail 1st author: allen.bateman@upc.edu

ABSTRACT: Until today, few researchers have worked on the temporal evolution of local scour at bridge piers from the physical point of view, this question was not taken into account, until recent works like [12]. Usually functional dimensionless models using the maximum equilibrium values (maximum scour depth or equilibrium time magnitudes) registered in a physical model, [7], [8], [9] were studied. The present work introduces you to a solution in which a series of physical hypothesis take into account the processes that occur during the formation and evolution of local scour at bridge piers. The relationship that exists between the active action of the horseshoe vortices formed in the upstream face of the pier and the passive action of the crumbled bed wall of the pit predetermines the temporal evolution of the scour in three clear different stages during time. Both phenomena feeding back one to each other forming a quasi chaotic system that evolves in time until it reaches the final equilibrium, behavior that is shown by the Poincaré graphs [10]. This is the starting point to make the formulation of a system of two non linear equations in total derivatives to evaluate with great accuracy the temporal evolution of the local scour for square bridge piers that can be easily extended to other geometries. A set of 4 experiments of long duration have been carried out in square bridge piers at a reduced physical model at the laboratory of the University of Catalonia and have been compared with the proposed mathematical model. Three of the four experiments arrived without problems to the equilibrium condition. The results demonstrate the existence of a physical limit for the temporal evolution and show clearly the phases that take place during the scour processes. To analyze the scour processes, the concept of velocity of dissipation of energy that needs a free vortex in a fluid to pass from a high energy to a low energy state, before dissipated in viscosity [1] and a simple hydrological concept to recreate continuous crumbling of the wall of the pit, was used and implemented. These circumstances form a set of equations independent of the final stabilization value of the variables that permits to evaluate a quasi steady state of the local scour processes without knowing the final condition. This kind of formulation allows to evaluate local scour during a flood using the concept of quasi steady state with clear water flow as a strong hypothesis. An example presented here shows the simple calculation.

I. INTRODUCTION

The local temporal scour at bridge piers processes in steady state regime has a beginning and an end, the beginning is not so clear due to the fact that in the reality the flood discharge is not steady and furthermore it has very different stages. Nevertheless, in the laboratory the conditions can be established much more controlled than in reality and allow to understand the phenomenon with some more detail. In the laboratory it is easy to control the sediment size, the mean velocity, the flow direction and other variables that influence the local scour processes. The first step in the local scour is very difficult to measure because the initial velocity of scour is very high. The final stage is equilibrium and no scour occurs.

Two different phenomena act at the same time, are coupled and depend on each other. This kind of process controls the three different stages that the scour goes through during time. One of them is the action of the vortex that is created in front of the pier due to the shock of the flow with the pier. The other phenomenon is the crumbling of the wall of the pit due to geotechnical instabilities. This last phenomenon occurs in frequent collapses that lead the sediment to the zone where the vortex acts. From now in advance the two phenomena are known as active the first and passive the last.

The final stage occurs when the particles of sediment are in equilibrium, that is no sediment is transported out of the pit, and then no more scour is detected. This equilibrium, as we can see depends on one more phenomena, the seepage flow that occurs in front of the pier. The influence of the seepage can be very strong to divert the final equilibrium scour in more than twice its value without seepage.

In this work, all the local scour stage processes are analyzed by formulating a morphodynamic model to predict its evolution and by understanding the different phenomena that take place during the scouring. The morphodynamic model takes into account the vortex energy and the crumbled pit walls as a hydrological model. Two total differential equations are derived and solved with the Runge Kutta model.

All the numerical data are compared with experimental data, obtained during a set of runs realized at the Hydraulic, Marine and Environmental Department Laboratory of the Technical University of Catalonia. Other experiments realized at Saint Anthony Falls Laboratory are also presented, the last

ones were conduced to obtain the influence of seepage in local scour. An empirical relationship between the geometry of the pit conduces to the Golden Relationship; the coincidence is surprisingly high.

II. EXPERIMENTAL SET UP.

A. *Hydraulic, Marine and Environmental Department Laboratory runs*

Experiments were carried out at a flume of 8 m length and 2.5 m width which is divided into three different parts. The middle one is formed by a ditch of 2.5 m length and 0.5 m depth in which the piers were placed. The slope of the bed is nearly 0.6%. Figure 1 shows the schema of the experimental set up. Discharges around of 58, 92 and 140 l/s were used to determine three different configurations in which the threshold of movement was found. All the tests were made in this condition, in which the relationship between nominal and critical velocity is of the order of one, always a little bit less than one.

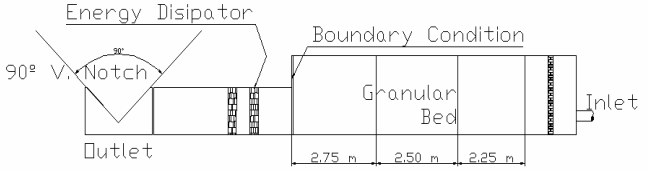

Figure 1. Experimental flume that consists in a length of 50 cm depth.

beginning of each test the flow boundary condition was closed enough using a huge amount of bricks that were extracted slowly one by one to reach the previous determined threshold condition. To avoid initial scour without arriving to the final discharge a plastic plate was placed around the pier and was taken off when the flow conditions were set up. The time zero starts when the last brick is extracted from the boundary section and the plastic protection at the pier is taken out. This task has to be done delicately to control the level of water at each instant to avoid a flood that destroys the experiment. The Manning coefficient of the granular zone was determined to be 0.016. The threshold of movement was determined for all the tests.

Square piers of 3, 4, 6, and 9 cm where used. The last pier was transparent with the only purpose to put a web cam and to be able to register what happens in the active zone. The occurrence of the intermittent collapses was verified with the registration. Those collapses that transport the sediment from the passive to the active zone were also described by Miller (2003). The normal water depth was performed for all tests with a 0.0368 m^2/s. Three of the four runs arrive to an equilibrium state. Those experiments where sufficient to prove the behavior of the local

, the normal flow depth, q unit discharge, Rh hydraulic stress y τ_c critical stress

	y_0	(l/s/m)	Rh (m)	Sf	v* (m/s)	$\tau 0=\gamma \cdot Sf \cdot Rh$ (N/m^2)	$\tau_{C(N/m^2)}$	τ_0/τ_C
Pier 3	9.41	.6	0.088	0.00099	0.0292	0.85	0.96	0.89
Pier 4	9.55	.6	0.089	0.00095	0.0288	0.83	0.96	0.86
Pier 6	9.48	.7	0.088	0.00097	0.0290	0.84	0.96	0.88
Pier 9	9.47	.5	0.088	0.00097	0.0290	0.84	0.96	0.87

Discharge was measured by using the 90º V-notch whose discharge relation is $Q=1.366.(h+0.008)^{2.5}$. In all the tests the discharge level was controlled to check the constant discharge during the tests. Mechanical meters were used to determine the levels at

different control points, upstream and downstream the pier, it was because of the 0% slope of the bed that never a normal depth of the flow was developed. A uniform sediment of γs=2.6 Ton/m3 was used with a size distribution of d_{16}=0.957 mm, d_{50}=1.617 mm, d_{84}=1.94 mm y d_{90}=1.975 mm with σ_g=1.36. The zero level print of the scour was measured to know the form of the erosion in order to compare with a numerical model in a future. Temporal scour at different points was taken both with manual and automatic measurements. The automatic ones were realized with an echo sound sensor constructed by the Signal Process Department of the UPC, [2]. The boundary condition was achieved by using rectangular bricks of two different widths. At the

temporal scour. The entire tests were run

in clear water flow that is the more erosive condition. This is the starting time.

Near and around the pier a set of gages to control bed level were tested, the important one was the one at the front of the pier at the active zone and which serves to contrast the morphodynamic model. The other points were considered as control points. The bed level measurement was taken with ultrasonic gages with a 1 minute frequency; the test conditions are presented in table 1. The water level was chosen to avoid the grain size influence and the threshold of movement conditions was set.

B. Saint Anthony Falls Laboratory runs

A Flume 18 m long, 0.90 m wide and 80 cm deep was used to do the runs. In the middle of the flume a sand terrace was placed, a smooth slope transition was made at its entrance and at its final part. The terrace was leveled with a slope of about 0.5% and in the middle a plastic pier of 9 cm width was installed.

The terrace was leveled with a slope of about 0.5% and in the middle a plastic pier of 9 cm width was placed. A drifting screw downstream gate was used to get control of the water level and to be able to adjust the normal depth in the zone of interest. Below the terrace, as a base of the pier, a system of 1 mm tubes was placed to measure the pressure distribution at the bed level in the pit zone, the tubes were placed in some chosen points.

Also the pressure in the faces of the pier and its surroundings was measured, with special attention to the front and to the back of the pier. The Figures 2 and 3 show the situation of the tubes. The tubes were put at level with the sediment bed simply by pulling them until their mouths coincide with the bed level. The tubes didn't disturb nor the flow neither the bed. Connecting the tubes to a gage level panel and with a photographic camera, the pressure level at all points was measured.

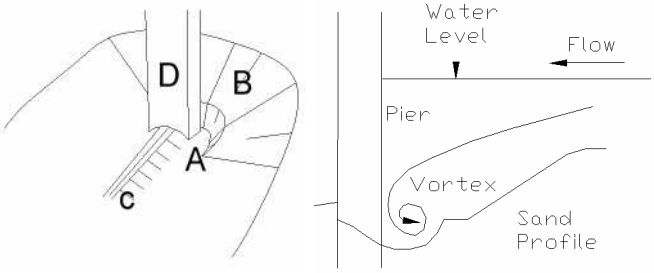

Figure 4. The different zones of the scour pits. A the little active pit and B the passive zone or crumbling zone.

Figure 5. Longitudinal profile of the bed and the position of the vortex.

III. DETAILED OBSERVATION NOTES

The scour pit was created by a denominated frontal horseshoe vortex that has a power capable to raise the sediment particles from the bed at the active zone. Figure 4 shows the principal zones of the scour pit (Figure 4 is a drawing based on a photo of one of the experiments), at least those observed during the tests and those that coincide very well with observations of other researchers who were studying the phenomena. Figure 4 shows three zones of interest in the scour phenomena. The zone A, that is little scour at the front of the pier that is well observed at square piers and less at circular piers; the zone B is the pit that for its size is easy to observe

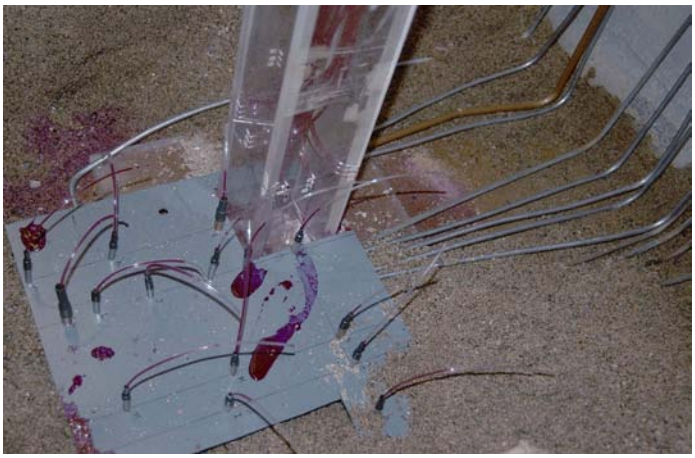

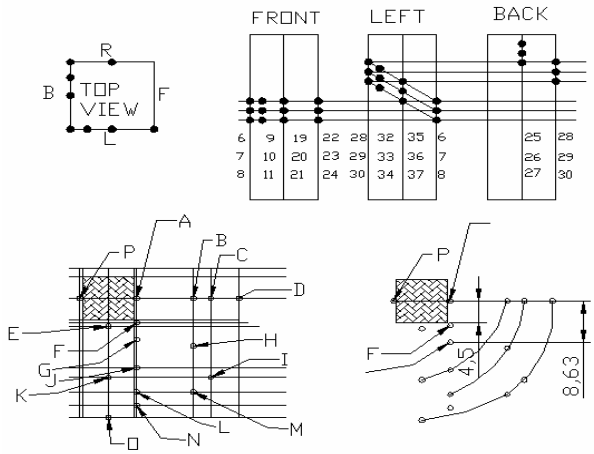

Figure 3. Distribution of the gages

and is commented by the different authors as it has a geometry like an inverted cone. Nevertheless, the difference between both pits is substantial, the zone A will be the active zone where the vortex concentrates its energy and does the work of scour. The B pit, is formed by the intermittent collapses or crumbling of the wall of the B pit to the A zone. The relationship between both pits is fundamental in the scour history. The vortex raises the sediment and throws it upstream. The sediment forms a little terrace over which the sediment runs away first laterally (to both sides of the pier) and finally downstream. The action of the vortex supports the bank of the active pit in high slopes, but the losses of sediment of the active zone finally destabilize the passive pit conducing it to crumble. The zone C is formed by the sedimentation or low transport capacity of the flow, just downstream the pier and only the Von Karman vortices (vertical axis vortex) are active.

The maximum scour occurs in the active zone, and its evolution is not continuously growing as announced by Franzetti, but the contrary, in some determined moment the process stops. Figure 6 shows an example of the temporal evolution of the local scour in the point in which the maximum scour

is produced. This figure shows the result of the 4 cm square pier test, for better observation a normal-log plot it used. It is possible to distinguish clearly what happens at the beginning and at the final stage in the same graph. The graph can be divided into three different parts, as observed by [3] at bridge abutments. The three phases can be named by the kind of processes that occur in them; the initial one or active phase, the principal one or passive phase and finally the equilibrium phase.

The more interesting phenomenon that occurs during the scour evolution is the continuous collapse of the wall; it is possible to distinguish it plotting a Poincare Map of the process. Figure 7 shows two examples of this map, velocity of scour vs. the scour, mapped for a short period of time to see the process in detail. A series of collapses, as a chaotic behavior, is detected in the figure. Each dot represented in the figure is a measured point; you can see the movement of the sediment, sometimes eroded and sometimes deposited. The high scour velocity at initial instants avoids the collapses of the wall pit and no chaotic behavior is present, when the vortex loses some of the energy the collapses start. The collapses are bigger the bigger is the pit, and for this reason the graph becomes thicker.

IV. MORPHODYNAMIC MODEL

A short description of the theoretical model is presented here. It consists of the explanation of the different processes that occur during the scour evolution and its possible evaluation.

a) Vortex scours power. It is obvious that the power of the vortex in front of the pier is proportional to the mean flow velocity, *V*. The vortexes contain an energy that is dissipated in the following form, after [1], as:

$$\text{Power per unit mass} = \frac{dv^2}{dt} = A_p \frac{v_v^3}{l_v} \qquad \textbf{(1)}$$

in which, v is the mean velocity of the vortex; l_v is a length defined as the integral scale or vortex size; A_p is a constant of the order of one, independent of the Reynolds number, [5] and [1]. The relationship (1) defines the velocity of energy dissipation per unit mass for a free vortex, but the relationship can be valid for a confined vortex as that formed in front of the pier. The difference is that the flow continuously feeds energy to the vortex body. In this way the vortex only is the transmission belt to dredge the sediment. The relation (1) can be expressed in terms of mean flow velocity, just changing the local velocity v of the vortex by U, the length is of the order of the size of the vortex. [11], show that the relationship between the vortex velocity and the flow velocity U is nearly constant as shown by their experiments in a circular pier. The same authors show that the size of the vortex is of the order of 80% of the water depth. The mean velocity of the flow can be expressed as, $U = q/(y_0 + d_s)$ and the mean vortex length l can be written as $l_v \propto (d_s + y_0)$. In which y_0 is the water depth; d_s the scour depth measured from the bed level; l_v vortex integral scale or mean vortex diameter, U mean flow velocity and q unit flow discharge.

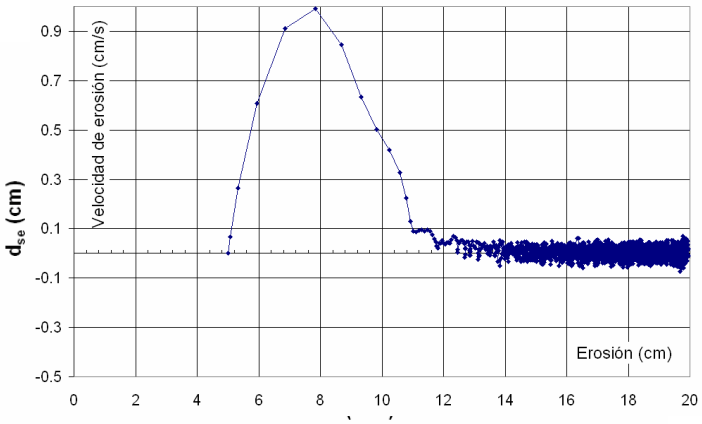

Figure 7. Evolution of the crumbling process. Look how at final stages the scour and deposits are bigger than the previous.

Figure 6. The different parts of the local scour evolution at rectangular bridge piers.

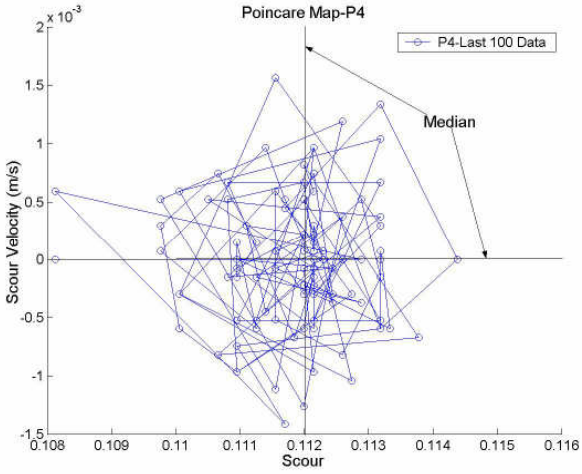

Figure 8. A zoom of the Poincare Map of figure 7 for the last 100 data or instants. Take into account that between two dots one minute passes. A prechaotic behavior is present.

b) Power Scour. In order that erosion takes place, the power of the vortex has to have at least the sufficient power to move the sediment. In other words:

$$\text{Power necesary to move the sediment} = W_s \frac{d}{dt}(d_s) = \text{Force} \cdot \text{Velocity} \qquad \textbf{(2)}$$

in which W_s is the submerged weight of the sediment expressed as $W_s = \rho g(S_s - 1)\forall = \rho g R \forall$; $\forall$ the net volume of the sediment; ρ the water unit weight; $(S_s - 1) = R$; in which S_s is the relative density of the sediment.

c) Scour capacity. One of the important issues is that the vortex always exists independently of the size of the pit. The vortex loses energy because more

water is involved in the process as scour increases and less energy per unit mass is available. Equations (1) and (2) can be equated to give the following relationship:

$$A_a \frac{d}{dt}(d_s) = A_a \left(\frac{(1-\lambda) q^3}{g R a (y_0 + d_s)^4} \right) \quad \textbf{(3)}$$

in which, λ is the porosity of the material and α is a proportionality coefficient that indicates that the vortex does not occupy the whole volume and that the power of the vortex is less than the power provided by the mean flow. A_a, is the area in which the vortex acts and produces erosion. This area depends strongly on the pier geometry because each flow line can be converted into a vortex and concentrates the energy to produce scour. Flow lines that pass directly without vortex formation do not contribute to the scour process but to the sediment transport. This phenomenon differentiates scour depths for different piers geometry.

Equation (3) is very active by its own, because no sediment collapses from the passive zone to the recent formed pit. This equation coincides with the first minutes of the processes, but later the wall of the pit begins to collapse into the active pit. In this moment the process is going to be decelerated. The sediment begins to flow into the pit diminishing the scour velocity. Using a sediment conservation equation between both zones A and B and the energy of the vortex or equation (3), the general situation can be expressed as:

$$\frac{A_a}{(1-\lambda)} \frac{d(d_s)}{dt} = -Q_s + \frac{q^3 A_a}{g R a (y_0 + d_s)^4} \quad \textbf{(4)}$$

d) <u>Collapses as continuous phenomenon</u>. Assuming that the sediment flows from the zone B to zone A in a continuous form, a hydrological relationship can be assumed to model this kind of flow. The particles situated in the pit walls are in imminent motion, because they stay in a friction slope condition. When the vortex erodes the active zone, the wall of the pit collapses in a complex phenomenon, a chaotic situation starts. The simple solution is the hydrological model that is presented here. Assume Q_s is the discharge of sediment that passes from one zone to the other, B to A, and assume that it is proportional to the volume (V_c) contained in the zone B susceptible to be collapsed, because the particles of the wall of the pit are in their threshold of movement. This hydrological equation can be formulated as:

$$Q_s = K \, V_c^n \quad \textbf{(5)}$$

in which *K* is a proportional factor and *n* an exponent, that distinguishes some kind of rheological response or non-linearity response of the particle system. The factor *n* differentiates the sand particle system from water behaviour. Per unit time it can be written as:

$$\frac{dQ_s}{dt} = n K^{1/n} (Q_s)^{(1-1/n)} \left(\frac{dV_c}{dt} \right) \quad \textbf{(6)}$$

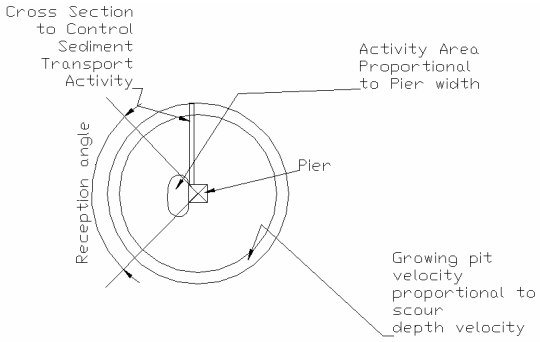

Figure 9. Geometrical sketch of the pit.

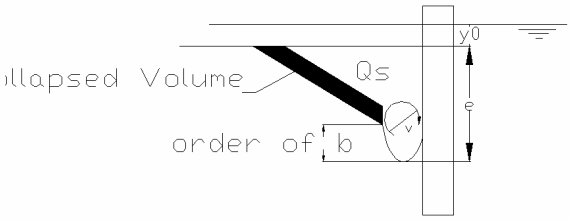

Figure 10. Geometrical sketch of the pit.

As it is shown in Figure 9 it is possible to say that the volume susceptible to be collapsed at some instant is the difference between the potential volume, V_e, and the volume eroded until this instant, V_h. That is per unit time:

$$\frac{dV_c}{dt} = \frac{d}{dt}(V_e - V_h) \quad \textbf{(7)}$$

After defining the geometrical volumes using Figure 9 and evaluate the pit as an inverted cone, it is possible to define the following relations between the variables involved:

$$V_e = G(d_s - e_0)^3 \qquad \text{with}$$
$$G = \frac{1}{2} q \sqrt{\frac{1}{\tan^2(f)} + 1} \quad \textbf{(8)}$$

Combined with equations 5, 6 and 7 it is easy to obtain the second differential equation, that is written as:

$$\frac{dQ_s}{dt} = n K^{1/n} (Q_s)^{(1-1/n)} \left(3G (d_s - e_0)^2 \frac{d(d_s)}{dt} - Q_s \right) \quad \textbf{(9)}$$

in which d_s and e_0 are the local scour depth at instant *t* and scour depth at the instant in which the collapses begin, respectively. e_0, stays with the same value during the entire scour process and its value is of the order of the width of the pier. In Figure 9 is defined the angle of reception of material θ, which limits the area of collapse from the passive zone to the active pit and ϕ the friction angle or repose angle.

Equations, 4 and 9, constitute a system of total differential equation in terms of scour depth, d_s, and

total solid discharge, Q_s. This pair of equations can be solved by four order Runge Kutta method or similar, in an easy way. The total solid discharge controls the velocity of scour.

e) Boundary Conditions: To start to integrate the equations it is important to distinguish the three phases, each of them require a physical real condition. They are the active, the passive and the equilibrium phase. In the initial instants only the active scour is present and evolves continuously just until the scour depth is of the order of y_0, only the equation (3) is active. In this moment the collapses of the bed begin to crumble and the system of equations 4 and 9 becomes active. The process stops when some threshold condition is established. The present work tries to show how this condition has to have a link with the non-hydrostatic pressure that acts around the pier near the bed.

Integration of equation (3) gives equation (10) as follows:

$$d_s = \left(\frac{5(1-l)q^3}{gRa}\right)^{1/5} t + y_0^{5/5} - y_0 \qquad \textbf{(10)}$$

In the beginning of the process, equation (10) governs the scour evolution. Scour depends on the one fifth power of time and maintains this behaviour just until the collapses from the bed start. It can be seen that for time zero scour is really zero. The porosity, unit discharge and specific gravity are the parameters that intervene in the initial process and the scour is independent of the pier size. Figure 11 shows the initial evolution with some initial data, the central line is with α equal 1 and certain discharge q. The line below is for α equal 1.4 and the upper one for 10% more discharge. As α acts the same as the submerged specific gravity, a variation of 40% of R contributes nearly the same as a variation of 10% of discharge q.

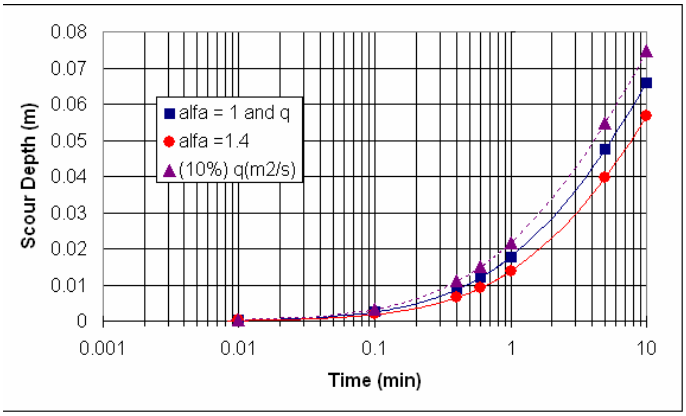

Figure 11. Scour at the initial instants. The evolution of the scour does not depend on the width of the pier but in the vortex power.

The area A_a, is the area in which the vortex, formed by the shock of the flow against the pier, acts. It is assumed that some flow lines shock and other lines pass away without forming a vortex. In the rectangular piers almost all the lines of the flow are intercepted by the pier width, in circular piers this does not occur, at least only in a reduced area or angle in which the flow can be reflected. This concept is shown in figure 12. A_a is smaller in the circular pier than in the rectangular one.

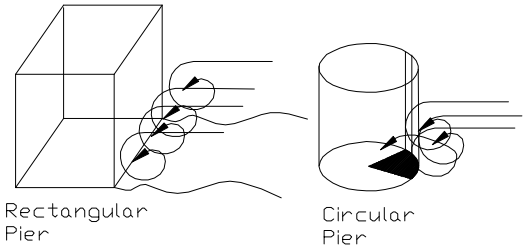

Figure 12. The schemas show how the vortices only act in some restricted area; it depends on the geometry of the flow. At equality of flow conditions, the vortex in the square and circular pier has the same power, but in the rectangular pier the vortex acts in a more extensive area.

F) golden ratio relationship: accidentally it is found, that the scour process has always the same relationship between the parts of its geometry and it coincides with the golden ratio. Figure 13 shows the first measurements that were taken to evaluate the golden ratio. In table 2 the rest of tests is shown, the measurements were carried out before this idea occurred.

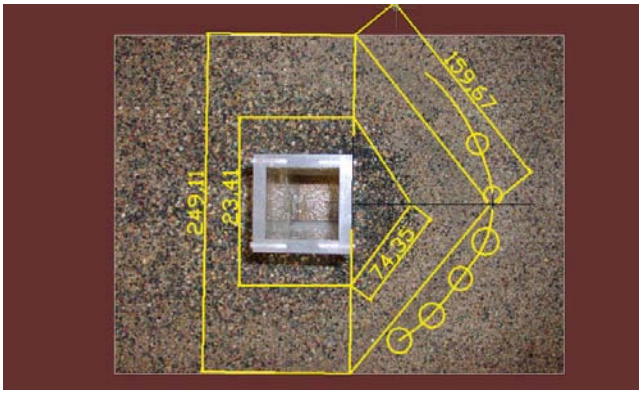

Figure 13. Photography of the local scour in a 9 cm bridge pier. It shows two triangles that correspond to both pits, the active and the passive one.

Table 2. Golden Ratio obtained in the 4 experiments. The last experiment didn't arrive to the final equilibrium.

	H(cm)	L(cm)	D/H
Pier 3 cm	34.8	22	1.55
Pier 4 cm	27.0	17	1.55
Pier 6	18.3	10.5	1.64

cm			
Pier 9 cm	44.4	28	1.55

The relationship is found by simple inspection of the local scour. Tracing the pit border just until the plane that contains the face of the pier, it is possible to construct a triangle. The first distance is the diagonal of the triangle containing the face of the pier and is limited by its intersection with the border of the pits. The second distance is formed by the union of the apex of the border of the pit with the intersection mentioned above. Dividing the first distance by the second a value near the Golden Ratio is obtained. This relationship is maintained in every instant during the entire test, except for the initial process in which there is no data available. The Golden Ratio is a number about $\varphi = 1.61\ldots$, and is a known relationship from ancient Greece, [6]. Based on Figure 14 the equations 11, 12, 13 and 14 can be formulated, which contribute to evaluate the geometry of the pit at any instant.

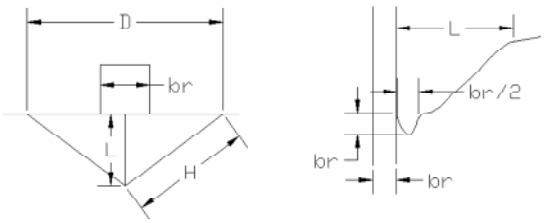

Figure 14. Geometrical definition of the pit and its relationship with the Golden Ratio.

The geometrical variables of these equations are defined in Figure 14. W_f is the lateral width of the scour in the same plane of the face of the pier. This distance is useful to control the threshold of movement and the sediment transport out of the active pit, also to affront the equilibrium phase.

$$H = \frac{L}{\sqrt{1 - \left(\frac{\varphi}{2}\right)^2}} \qquad \textbf{(11)}$$

$$L = \frac{\frac{b_r}{2}(tg(\varphi) - 1) + d_s}{tg(\varphi)} \qquad \textbf{(12)}$$

$$D = \frac{j\,L}{\sqrt{1 - (j/2)^2}} \qquad \textbf{(13)}$$

$$W_f = \frac{D - b_r}{2} \qquad \textbf{(14)}$$

g) Non hydrostatic Pressure distribution. In order to understand the maximum scour process or the equilibrium phase, at the Saint Anthony Falls Laboratory a set of runs to determine the pressure distribution at the sediment bed around the pier were carried out. As explained above, a set of gage levels were installed to read the pressure value. Figure 15 shows the levels at the final equilibrium in one of the tests.

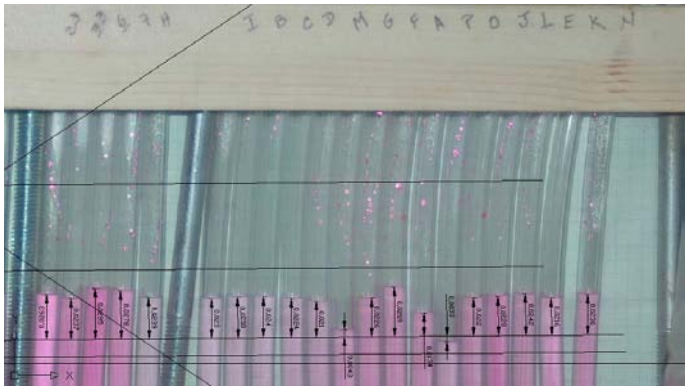

Figure 15. Pressure distribution at gages in the selected points around the pier and near the bed.

Figures 2 and 3 show the position of the level gages, a plot of the pressure distribution along the line that contains the pier face normal to the flow is shown in Figure 16.

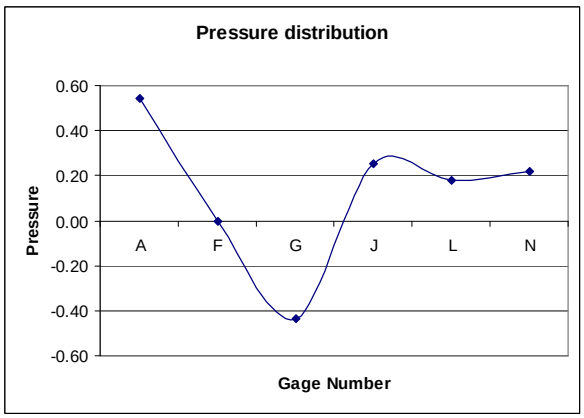

Figure 16. Pressure distribution at a line normal to the flow at the level of the upstream face of the pier.

The maximum pressure difference is located between the axe of the pier or point A and the point G. Point G lies in the central zone of the active pit. The difference of pressure between the points A and G is about 1 cm of water and the distance between them is 8.63 cm. The Darcy's law shows that there is a seepage flow from A to G, [4] due to the difference of pressure as shown above. The flow exits in the minimum pressure zone and pushes the sediment with a pressure normal to the bed and proportional to:

$$P_{nh} = g\frac{\partial h}{\partial z}\,D_m \qquad \textbf{(15)}$$

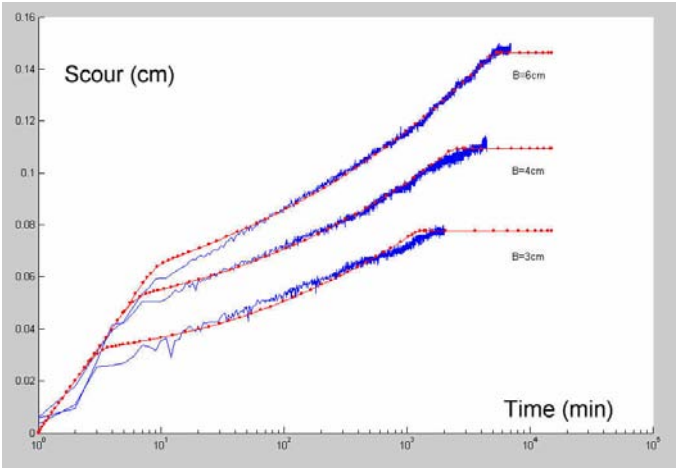

Figure 17. Temporal evolution of local scour at bridge piers.

In which, P_{nh} is the pressure done by the seepage flow, *h* the hydraulic head between two points, *z* the direction of the flow and D_m the mean diameter of the sediment. This pressure is the same as a buoyant force and can be expressed in this same form. The result of this thought is like the sediment loses weight. In the case that occupies our attention, the energy seepage gradient is about 11%, the mean diameter of the sediment is about 1mm. Then the pressure due to the seepage flow is about 1.13 N/m^2 which is comparable with the critical stress at the threshold of movement, 0.96 N/m^2, except that the first of this forces acts in the same direction as the weight. The seepage pressure represents a lost in weight particle, in this case, from about 10%.

V. RESULTS

In Figure 17 it can be observed, how the model forecasts the temporal evolution of the local erosion for the three experiments with piers with 3, 4 and 6 cm of width. In order to obtain the results shown in the figure, the following parameters have been considered: reception angle 120 degrees, $K=1$, α = 1,13, e_0 is in the range of the width of the pier b_r, $A_a=b_r^2/2$. The other values are a result of the experiment. All the parameters have been adjusted manually without the previous realisation of an optimisation study of these parameters. The scour equilibrium phase has been adjusted manually, currently the phenomena of distribution of non-hydrostatic pressures is studied. The distribution of pressures in the bed and along a line parallel to the face upstream of the pier has been measured. This is why this phenomenon is thought to be related to the seepage phenomenon. As an advance to the study in progress, in Figure 16 the distribution of pressures in the section parallel to the face upstream of the pier is shown.

It exists a maximum pressure in the central point A of the pier above the hydrostatic, in the corner F of the pier the pressure is low, even below the value of the hydrostatical. At the middle of the active pit, point G, the pressure is even lower. The maximum difference of pressure found is about 1 cm in only 8.6 cm length, about 11% grade line slope. The lost of weight for this flow is of the order of 10%.

Figure 18 shows the comparison between the Melville Formulation, Franzetti formulation, the experimental data and the actual model. The scour axe is normalized. The maximum scour evaluated by the formula of [9] agrees perfectly with the experiments. Nor Franzetti neither Melville adjust the initial scour process. This is the big difference between the present model and the other formulation.

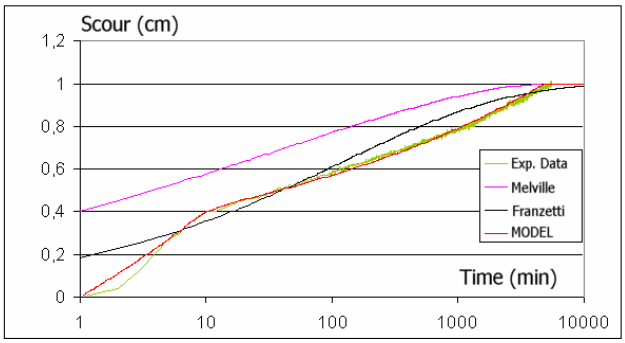

Figure 18. Comparison between experimental data (4 cm pier width), Melville, Franzetti and the present Model for the 4 cm pier. The data are in dimensionless form. Here is shown that it is necessary the use of two different behaviour to forecast the experimental data.

VI. CONCLUSIONS

The following aspects can be highlighted: The vortex dynamic applications have good results in scour time evolution analysis.

Three different phases are distinguished, the active, the passive and the equilibrium one. The active is controlled by the vortex dynamics, the passive appears due to the crumbling of material into the active pit. The equilibrium phase depends on the non-hydrostatic pressure distribution.

A non linear system of two total differential equations is presented, which agree very well with experimental data, by using a vortex dynamic equation and an hydrological type equation.

Without the knowledge of the final condition state it is possible to evaluate the local scour and also it is possible to introduce a non steady state of flow discharge and sediment discharge. For the last one no experimental data exists to prove its kindness.

A deeper study about the parameters involved has to be carried out to know more about their sensibility in the process of scour evaluation.

The Golden Ratio relationship seems to be a useful tool to evaluate the geometry of the pit and the stress

condition in the outlet surface area to control the equilibrium phase.

A simple non-hydrostatic pressure distribution study has been presented. It seems to be very important phenomena that can control the equilibrium phase. The non-hydrostatic pressure distributions in the bed surface increase the mobility of the grains around the pier.

VII. AKNOWLEDGMENTS

The work presented was funded by CICYT under the following projects BTE2002-00375, NCED National Center on Earth Dynamics (Minneapolis), Ren2000-1013, HID96-0971.

VIII. BIBLIOGRAPHY

[1] Batchelor G.K. (1953). “The theory of homogeneous turbulence”. Cambridge Science Classics.

[2] Bateman, A. & Torres, A. Experimental Study on Local Scour at Accompanied Pier Systems. 3rd Symposium on River Costal and Estuarine Morphodynamics. Barcelona. Sánchez Arcilla-Bateman.

[3] Cardoso, A. H., Bettess, R. (1999). “Effects of time and channel geometry on scour at bridge abutments.” J. Hydr. Engrg., ASCE, 125(4), 388-399.

[4] Cheng & Chiew (1999). “Incipient Sediment Motion With Upward Seepage”. Journal of hydraulic Research. Vol 37. No.5 pp 665-680.

[5] Dryden H.L. (1943) A review of the statistical theory of turbulence. Quart. Appl. Math. I, 7.

[6] Euclides de Alejandría. (300 a.c.) “The Thirteen Books of The Elements” Translated by Sir Thomas L. Heath (1956). Cambridge University.

[7] Franzetti S.; Malavasi, S.; Piccinin, C. (1994) “Sulle erosione alla base de pile de ponte in acque chiare”, Procedings 24 convegnodi idraulica e construzione idrauliche, Napoli vol II. T4-13-24.

[8] Melville, B. W., (1997). “Pier and abutment scour: integrated approach.” J. Hydr. Engrg., ASCE, 123(2), 125-134.

[9] Melville, Bruce W.; Chiew, Yee-Meng. (1999) Time Scale For Local Scour At Bridge Piers. Journa lof Hydraulic Engineering, Vol. 125, No. 1

[10] Moon F.C. (2004). Chaotic Vibrations. New Jersey. John Wiley & sons. Inc. Hoboken.

[11] M. Muzzammil, T. Gangadhariah, (2003). The mean characteristics of horseshoe vortex at a cylindrical pier. Journal of Hydraulic Research Vol. 41, No. 3, pp. 285–297.

[12] William Miller, Jr. (2003). Model For The Time Rate Of Local Sediment Scour At a Cylindrical Structure. University Of Florida.

Scour Reduction Using Collar around Piers Group

Mubeen Beg*, Mohd. Jamil**
Sr. Lecturer Department of civil Engineering, Z.H. College of Engg. & Tech., AMU, Aligarh, U.P. India

***Professor Department of civil Engineering, Z.H. College of Engg. & Tech., AMU, Aligarh, U.P. India*

Several methods have been attempted to reduce scour depth around bridge piers, such as sacrificial piles placed upstream of the pier, slots through the pier, riprap and gabion placed around the pier and collar around the pier. Following successful application of collar on circular and rectangular piers for reduction of scouring, the present study examines experimentally the effectiveness of a collar on a group of circular cylindrical piers. The experiments were carried out in clear-water scour condition with flow intensity 0.95 and the group of piers aligned in line with the flow, and skewed at 7.5°, 10° and 15° to the flow, without collar and with a collar fixed at sediment bed level. It is worth to mention that application of collar on the group of the piers studied in this work is extremely successful in producing 100 percent reduction in the scour depth up-to 7.5°angles of attack of flow. At 15° angle of attack, application of collar gives 79.3 percent reduction in scour depth.

INTRODUCTION

Scour is the process of lowering of river -bed due to removal of the bed material by erosive action of flowing water. The presence of an obstruction like a pier in an alluvial channel leads to the formation of horseshoe vortex at upstream and sides of the pier and also wake vortices at the downstream side of the pier because of flow separation at the sides. As a result, the flow gets modified, bed shear stress increases around the pier and scour takes place in the vicinity of the pier. Enlargement of the flow cross-section due to the scour eventually reduces the shear stress around the pier. The term ' local scour' is used to emphasize the fact that the lowering of the river- bed occurs only in the vicinity of the pier.

Scour around bridge piers as a result of flooding is the most common cause of bridge failure (Richardson and Davis, 1995; Johnson and Dock, 1996; Melville and Coleman, 2000). The potential cost including human toll and monetary cost of bridge failure due to scour damage has highlighted the need for better scour prediction and protection methods. A large depth of foundation is required for bridge piers to overcome the effect of scour which is a costly proportion. Therefore, for safe and economical design, scour around the bridge piers is required to be controlled.

Various methods have been attempted to control scouring around bridge piers, such as using riprap around the pier, slots through piers, sacrificial piles in front of a pier, piers group and collars. Countermeasures to control the local scour at bridge piers can be grouped in two categories;

(1) Armoring devices:

In this device, the streambed resistance is increased by placing the riprap and gabions around the piers. Several researchers (Parola,1993; Yoon et al., 1995; Chiew, 1995;Worman 1989, (Lim and Chiew, 1996 and 1997); Lim, 1998; Chiew and Lim, 2000; Lim and Chiew, 2001), Maynord, S.T. (1995),' have attempted to determine the size and extent of the riprap layer.

(2) Flow altering devices:

Using flow altering devices, the shear stresses on the riverbed, in the vicinity of pier, are reduced by altering the flow pattern around a pier which in turn reduces the scour depth at the pier.

Attempts have been made by several investigators to reduce the depth of scour around a pier using armoring and flow altering devices i.e., by placing the riprap around the pier (Brice et al., 1978;Croad, 1993; Parola,1993; Yoon et al., 1995; Worman 1989, (Lim and Chiew, 1996 and 1997); Lim, 1998; Chiew and Lim, 2000; Lim and Chiew, 2001), providing an array of piles in front of the pier(Chabert and Engeldinger, 1956 and Melville and Hadfield,1999), a collar around the pier (Schneible, 1951;Thomas 1967; Tanaka and Yano 1967; Ettema 1980; Chiew, 1992; Kumar et al., 1999, Zarrati et al. 2004), submerged vanes(Odgard and Wang 1987), a delta-wing-like fin in front of the pier (Gupta and Gangadharaiah, 1992), a slot through the pier(Chiew, 1992, Kumar et a., 1999) and partial pier-groups (Vittal et al. 1994)

Flow altering devices can be more economical, especially when the riprap material in required amount is not available near the bridge site or is expensive.

Flow pattern and Mechanism of Scouring:

The performance of any scour protection device around bridge piers depends on how does the device counter the scouring process. Flow mechanism of scouring around a bridge pier is very complex and has been investigated by various researchers (Chabert and Engeldinger, 1956; Hjorth, 1975; Melville, 1975; Melville and Raudkivi, 1977; Dargahi, 1990; Ahmed and Rajaratnam, 1998 and Graf and Istiarto, 2002).

As the approach flow velocity goes to zero at the leading face of the pier, it causes an increase in pressure. As the flow velocity decreases from the surface to the

bed, the dynamic pressure on the pier face also decreases downwards. As a result, a vertically downward pressure gradient is developed on the leading face of the pier which drives the flow down the pier, like a vertical jet. When this down-flow impinges the streambed, it digs a hole in front of the pier, and rolls up and by interaction with the coming flow forms a complex vortex system and a scour hole forms around the pier.

The horseshoe vortex deepens the scour hole in front of the pier until the shear stress on the bed material at the base of the pier becomes less than the critical shear stress. The separation of the flow at the sides of the pier causes so-called wake vortices. These vortices are unstable and shed alternatively. These vortices act as little tornadoes, lifting the sediment from the bed.

Application of Collar:

Reduction of scouring by indirect method can be achieved by using a slot in the pier (Chiew, 1992;Vittal et al., 1994; Kumar et al., 1999. However, a slot may be blocked by floating debris. In addition to this, its construction is difficult. A collar around the pier diverts the down flow and shields the streambed from its direct impact.

The scour reduction efficiency of collars has already been established in earlier studies (Zarrati et al., 2004; Kumar et al., 1999;Chiew, 1992; Ettema, 1980;Tanaka and Yano, 1967; Thomas 1967; Schneible, 1951). Kumar et al. (1999) performed a series of experiments on effectiveness of collar for control of scouring around circular bridge piers. Zarrati et al.(2004) conducted a series of experiments using a collar for control of scouring around rectangular pier having a collar with the same width all around the pier. The piers are sensitive to the angle of attack of flow and scour depth around them increases rapidly with an increase in angle of attack (Laursen and Toch, 1956; Ettema et al., 1998). Zarrati et al. (2004) conducted experiments on rectangular piers with varying angles of attack. A scanty information however, is available in literature about the application of collars on group of piers.

Following successful application of collar plates on piers for reduction of scouring, in this paper the effectiveness of collar plate on a group of piers was studied experimentally

EXPERIMENTAL PROGRAMME

It is well known that experimental methods are helpful in understanding and analyzing the behavior of complex flow situations which otherwise cannot be subjected to purely theoretical analysis. Therefore, it was planned to conduct laboratory experiments to study the application of collar on piers group for scour depth reduction.

Experiments were conducted in a rectangular re-circulating tilting flume, 11.0 m long, 75.6 cm wide and 55.0 cm deep located in the Hydraulics laboratory of Civil Engineering Department, Z.H. College of Engineering and Technology, AMU Aligarh, India. Water was supplied to the flume from a constant head overhead tank, which got its supply from the laboratory water supply system. Flow straightners were provided at the upstream end of flume to ensure uniformly distributed flow across the width of the flume and minimum turbulence in the flow. Water supply into the flume was regulated by operating a valve in the water supply pipeline. A calibrated bend meter was used for measuring discharge passing through the flume. Water surface level and bed level in flume were measured using a point gauge mounted on a trolley which could be moved over adjustable rails mounted on the two walls of the flume. The rails were kept parallel to the flume bed. A tailgate was provided at the downstream end of the flume, which was operated to adjust the depth of flow in the flume. A transition of wooden block was fitted tightly at the entrance of the flume to ensure smooth flow without disturbing the sediment bed in the flume. A sediment trap was provided at the downstream end to collect sediment coming from the upstream bed.

Sediment was filled in the flume to a constant thickness of 25 cm in the rest section. At the entrance of the flume, graded layers of glass beads, followed by a transition block of wood, were placed to obtain a smooth flow without disturbing sediment bed in the flume. A sediment trap was provided at the outlet of the sand bed. As such, water flowing out of the flume was clear and virtually sediment free.

The piers group model was comprised on five galvanized iron smooth circular cylinders, one cylinder of 4.15 cm at the center and two cylinders of 3.3 cm and 2.15cm on either side of 4.15 cm cylinder. All the five cylinders were joined in a group to give a form similar to lenticular pier. The aspect ratio (length/width) of this piers group was equal to 3.61. The size of the piers group was so selected that the blockage effect on scour depth in the flume was insignificant. Experiments were conducted in uniform non-ripple forming sediment bed of median diameter d_{50} equal to 0.95 mm and standard deviation (σ_g = 1.15) in steady state clear-water scour condition at flow intensity (U/U_c) of 0.95. The experiments were conducted in three phases. In first phase, a series of experiments was conducted with 4.15 cm diameter single isolated cylinder to form the basis for comparison with the piers group model at 0^o angle of attack. In second phase, the experiments were conducted at piers group model without collar aligned at 0^o, 7.5oand 15^o to the flow. In third phase the experiments were conducted with same piers group model fixed with collar plate at bed level at the same angles of attack as in phase second. All the experiments were conducted under same hydraulic and sediment conditions.

Water was allowed to flow over the level sediment bed slowly and the flow was adjusted using the inlet valve and the tailgate to achieve steady and uniform flow condition. Before the start of each experiment, the pier was inserted in the test section vertically in desired positions. The area around the piers models was leveled.

The scour depths were measured with the help of point gauge at various time intervals. It was observed during the experimental runs that the water depth was maintained at a sensibly constant elevation. All the experiments were conducted under same hydraulic and sediment condition. The experiments were run for sufficient time.

The range of variables used in the present study is given in Table 1.

TABLE: 1

SEDIMENT AND HYDRAULIC DETAILS

Pier type	Size of pier (cm)	Pier aspect ratio	H (cm)	U (m/s)	D_{50} (mm)
Circular	4.15	-	14	0.40	0.95
Piers Group model	-	3.61	14	0.40	0.95

Temporal measurements of scour depth at nose and other point at the pier mode were made during the experimental runs. After the completion of the experimental run, the flow was gradually stopped and the flume was drained off very carefully so that the scour hole and scour patterns developed by the flow around the pier were not disturbed. Thereafter, the scoured area was surveyed with a point gauge. The curves for temporal variation of scour depth and maximum scour depth versus angles of attack curves were plotted for the two phases of experiments. The mathematical models were also developed to predict the maximum scour depth. To overcome the difficulty of observing the development of the scour hole, strong light source was used which permitted the observation of the phenomenon as it progressed.

Experiments were performed in the following phases:

Phase I: Isolated Pier:

A series of experiments was first performed on 4.15 cm diameter single cylinder to form a basis against which the scour depth at piers group could be compared.

Phase II: Piers group without collar:

Experiments were conducted using a piers group model, comprising on five galvanized iron smooth circular cylinders, one cylinder of 4.15 cm at the center and two cylinders of 3.3 cm and 2.15cm on either side of 4.15 cm cylinder as shown in Fig. 1. In this phase, the experiments were performed on piers group aligned at 0°, 7.5oand 15° to the flow without using collar plate.

Phase III: Piers group with collar:

In this phase, experiments were conducted by applying a collar plate around the piers group as shown in Fig.1.

Fout! Objecten kunnen niet worden gemaakt door veldcodes te bewerken.

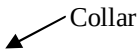

Fig. 1 Piers group with and without collar

The collar was fixed at the sediment bed level. Before the start of each experimental run, the pier model was located centrally and vertically into the sediment bed in the flume. The pier model was installed at a distance of 3.5.metres from the inlet of the flume projecting well above the water surface. The area around the pier model was leveled. The water from the supply pipe line was allowed to flow over the leveled sediment bed slowly with the help of the inlet valve in the supply line. As steady uniform flow conditions were established, the experimental run was started

During the experimental runs ,the scour depth was measured at the nose of the pier and at other points around the model pier at regular time intervals of 5,10,15,30,60,120,180,240, 300,360,420 and 480 minutes with the point gauge. The mean approach flow depth was kept constant as 14 cm throughout the experiments. At the end of the experimental run, the water supply was gradually stopped and the water was drained off from the flume with extreme care that there was no disturbance in the scour hole and the scour patterns around the pier. Detailed measurements of scoured area around the pier were then made in static condition. Finally, the photographs of the scoured area around the pier were taken

Results and Discussion

The temporal development of scour depth around piers group with and without collar aligned at different angles of attack, are presented in figures 2 and 3 respectively. It is evident from these figures that application of collar around piers group, not only causes reduction in the maximum scour depth but also the rate of scouring is also reduced considerably. Reduction in the rate of scouring reduces the risk of pier failure when the duration of flood is low.

The variation of scour depth around piers group with and without collar versus angles of attack has been plotted in figure 4 which shows that at piers group without having collar around it the scour depth remains

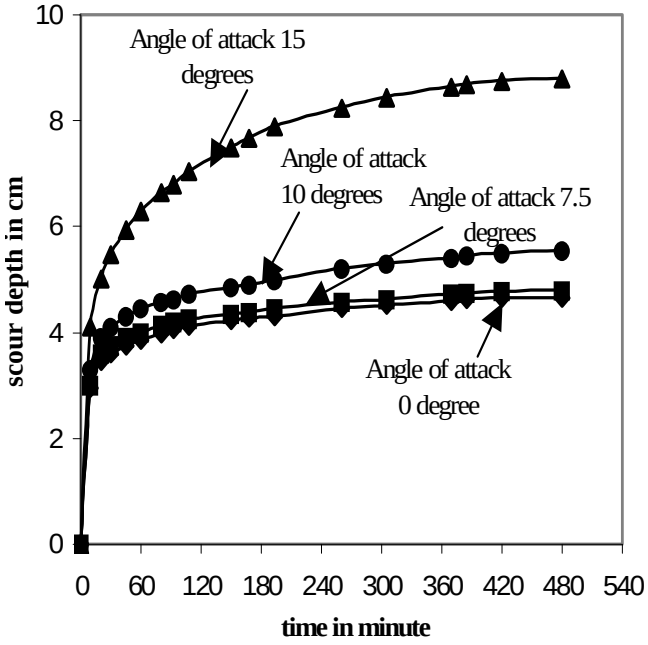

Fig.2 Temporal variation of scour depth at piers group without collar.

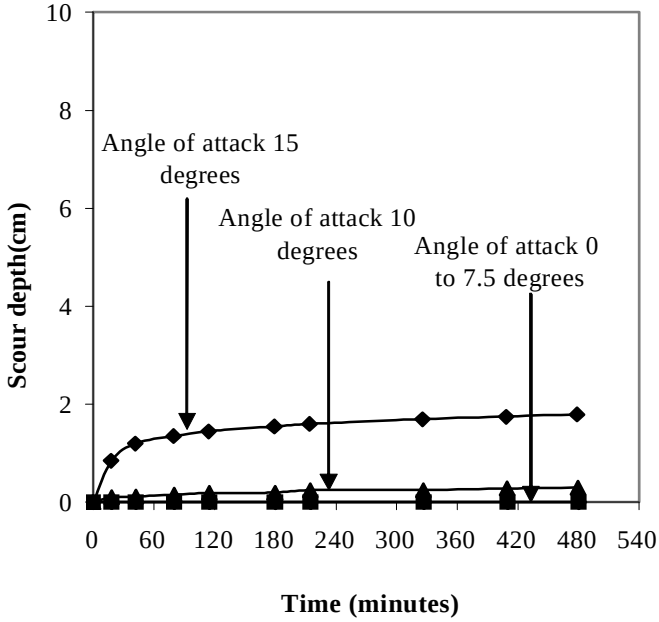

Fig. 3 temporal variation of scour depth at piers group with collar

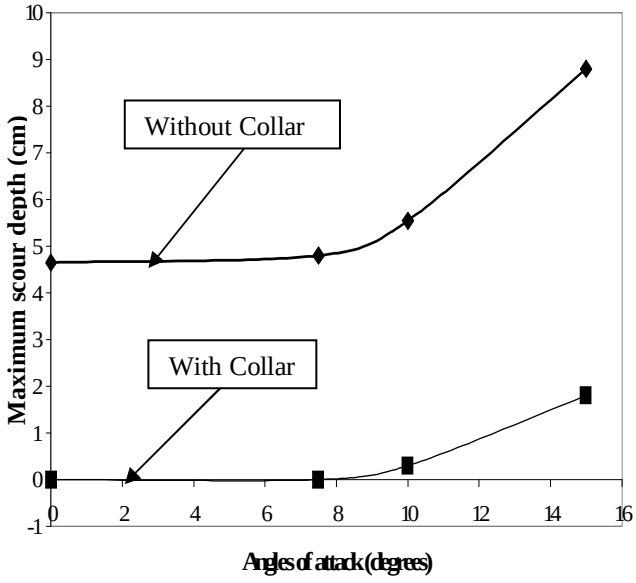

Fig. 4 Angle of attack versus maximum scour depth with and without collar at piers group

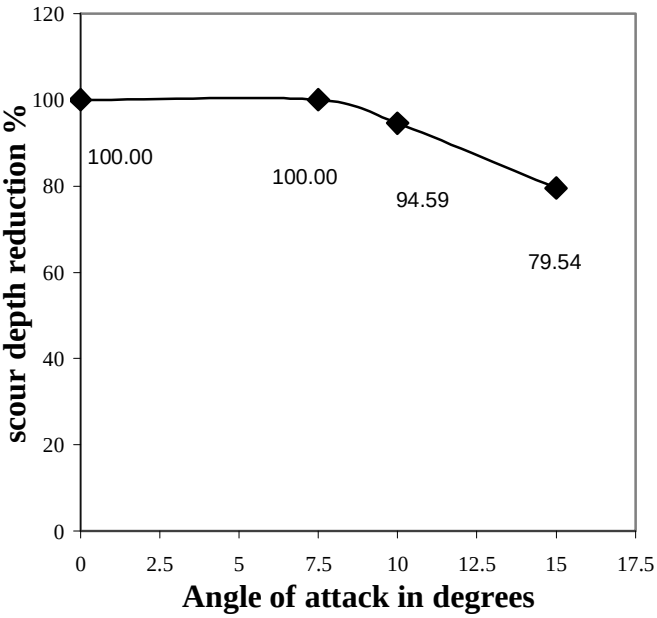

Fig. 5 - Scour depth reduction using collar around piers group

almost constant up-to 7.5 degree angle of attack. From 7.5 to 10 degrees of angles of attack, there is small increase in scour depth. Beyond 10-degree angle of attack, the scour depth increases rapidly. In figure 4 similar trends can be seen in the variation of scour depth around piers group having collar around it.

The efficiency of collar in reducing the depth of scour around pier group can be observed in figure 5. It is worth to mention that application of collar around piers group for angles of attack 0 to 7.5 degrees produces 100 percent reduction in scour depth. As shown in figure 5, the reduction in scour depth at 10 and 15 degrees angles of attack, is 94.59 percent and 79.54 percent respectively.

The use of piers group having no collar around it and aligned at 0 degree angle of attack with the flow yields about 35 percent reduction in scour depth as compared to the scour depth at single isolated 4.15 cm cylinder which has been used in formation of piers group.

Chabert and Engeldinger (1956) conducted experiments on piers group of three circular cylinders at different angles of attack. The piers group had a cylinder of 15 cm diameter at the center and one cylinder of 7.5 cm diameter on either sides of the 15cm cylinder placed at a distance of 15cm from the outer face of the 15 cm cylinder. The aspect ratio of this piers group was equal to 4. The b/d_{50} was equal to 50 where b= diameter of the cylinder at the center of the piers group.

The geometrical form of the piers group, b/d_{50} ratio and piers group aspect ratio used in present study are almost same as that of Chabert and Engeldinger.

The values of relative scour depth (i.e., scour depth at piers group/ scour depth at single isolated central cylinder) obtained from curve of Chabert and Engeldinger from present study, were compared for the case of zero degree angle of attack. A good agreement has been observed. The present study can be very useful in economical design of bridge pier.

Conclusions

Following conclusions are drawn from present study Piers group without having collar around it gives about 35 percent reduction in scour depth as compared to the scour depth around a single isolated maximum size cylinder used in forming the piers group. Application of collar around the piers group produces 100 percent reduction in scour depth at angles of attack up-to 7.5 degrees, 94.79 percent reduction at 10 degree angle of attack and 79.54 percent reduction at 15 degree angle of attack as compared to scour depth at corresponding angles of attack without collar around it. The reduction in scour depth using piers group in present study is in good agreement with the piers group used by Laursen and Toch at zero degree and 15 degree angles of attack The present study can be very useful in economical design of bridge piers.

Acknowledgement

The authors are highly thankful to The Department of Civil Engineering Z.H. College of Engineering and Technology, Aligarh Muslim University, U.P., India, for providing the necessary facilities in hydraulics laboratory for the successful completion of this work.

References:

[1] Ahmed, F., and Rajaratnam N. (1998). ' Flow around bridge Piers', Am. Soc. Civ. Engrg., J. Hydr. Engrg., 124(3),288-300.

[2] Brice, J. C., Bloggett, J.C. and others (1978)." Countermeasures for Hydraulic Problems at Bridge piers", Vol. 1 and 2,FHWA-78-162 & 163, Federal Highway Administration, U.S. Department of transportation, Washington, D.C.

[3] Breusers, N.H.C. and Raudkivi, A.J.(1991). "Scouring", 2nd Hydraulic Structures Design Manual, IAHR, A.A. BALKEMA/ROTTERDAM, The Netherlands.

[4] Chabert, J. and Engeldinger, P. (1956). Etude des affouillement autour des Piles des ponts (Study on Scour around bridge piers), Laboratoire National d'Hydraulique, Chatou, France.

[5] Chiew Y.M. (1995),' Mechanics of riprap failure at bridge piers', j. of Hydraulic Engineering, ASCE, vol. 121,No. 9, pp. 635-643.

[6] Chiew, Y.M.(1992), Scour Protection at Bridge Piers", J. Hydr. Engrg., ASCE, 118(9), 1260-1269.

[7] Chiew Y.M. and Lim, F. H. (2000), 'Failure Behavior of riprap layer at bridge piers under live-bed conditions," J. Hydr. Engrg., ASCE, 126(1),43-55.

[8] Croad, R.N. (1993), ' bridge pier scour protection using riprap,' central laboratories report no. PR3-0071, works consultancy services, N.Z.

[9] Dargahi, B.(1990), " Controlling Mechanism of Local Scouring", J. Hydr. Engrg., ASCE, 116(10), 1197-1214.

[10] Dey, S. (1997)."Local Scour at Piers", part I: a review of developments of research,' IRTCES, Int. J. Sediment Res., 12(2),23-44.

[11] Dey, S., Bose, S.K., and Sastry, G.L.N. (1995). 'Clear Water scour at circular piers: a model.,' Am. Soc. Civ. Eng., J. Hydr. Engrg., 121(12), 869-876.

[12] Ettema, R.(1980). Scour at Bridge Piers, Report No. 216, School of Engrg., University of Auckland, Auckland, New Zeeland.

[13] Ettema, R., Mostafa, E.A., Melville, B.W. and Yassin, A.A.(1998),"Local Scour at Skewed Piers," J. Hydr. Engrg.,ASCE, 124(7), 756-759.

[14] Graf, W.H. and ISTIARTO, (2002), 'Flow pattern in the scour hole around a cylinder', journal of hydraulic research, vol. 40, No v. 1, pp. 13-20.

[15] Graf, W. H.,and Yulistiyanto, B.(1998)" Experiments on flow around a cylinder; the velocity and vorticity fields, Int. Ass. Hydr. Res., J. Hydr. Res., 36(4), 637-653.

[16] Gupta, A.K., and Gangadharaiah, T. (1992). "Local scour reduction by a delta wing-lick passive device." *Proc., 8th Congr. of Asia and Pacific Reg. Div.*, 2, CWPRS, Pune, India, B471-B481.

[17] Hjorth, P.(1975). Study on the Nature of Local Scour, Dept. Water Resources, Lund Inst. Of Tech., Bulletin Series A, No. 46.

[18] Istiarto,I.(2001). 'Flow around a cylinder on a mobile channel bed.' Ph.D. Thesis, no. 2368, EPFL., Lausanne, Switzerland.

[19] Johnson, P.A. and Dock, D.A. (1996). " Prababilistic Bridge Scour Estimates", J. Hydr. Engrg., ASCE, 124(7), 750-754.

[20] Kumar, V, Ranga Raju, K.G. and Vittal, N.(1999)."Reduction of Local Scour around Bridge Piers Using Slot and Collar", Technical Note, J. Hydr. Engrg., ASCE, 125(12), 1302-1305.

[21] Laursen, E.M. and Toch, A.(1956)."Scour around Bridge Piers and Abutments, Iowa Highway Research Board, Bulletin No. 4, Ames, iowa, U.S.A.

[22] Lim and Chiew, (2001). Parametric study of riprap failure around bridge Piers, J of Hyd Research, Vol. 30, No. 1, pp. 61-72.

[23] Lim, F.H. (1998),'Riprap protection and its failure mechanisms', A thesis submitted to the School of civil and structural enginerring, Nanyang technological university,sigapore in fulfillment of the requirements for the degree of doctor of philosophy.

[24] Lim F.H. and Chiew, Y.M.(1996),stability of riprap layer under live-bed conditions' proc., Ist Inter. Conf. On new/emerging concepts for rivers, RiverTech'96, Vol.2, 830-837.

[25] Lim, F.H. and Chiew, Y.M. (1997),' Failure behavior of riprap layer around bridge piers,' proc., 27th conf. of IAHR, Managing water, coping with scaracity and abundance, 184-189.

[26] Maynord, S.T. (1995),"Gabion mattress channel protection design", J. of Hydraulic Engineering, ASCE, vol. 121, No. 7, pp. 519-522.

[27] Melville, B.W. and Coleman, S.E., (2000)," Bridge Scour", Water Resources publications, LLC, Highlands Ranch,CO,572 pp.

[28] Melville, B.W. and Raudkivi, A.J.(1997)." Flow characteristics in Local Scour at Bridge Piers", J. Hydr. Research IAHR, 15, 373-380.

[29] Melville, B.W. (1975). 'Local scour at bridge sites.' Report No. 117, University of Auckland, School of Engineering, New Zeeland.

[30] Melville, B.W. and Raudkivi, A.J.(1977).' Flow characteristics in local scour at bridge piers.' Am.Soc. Civ. Eng., J. Hydr. Engrg., 15(4), 373-380.

[31] Melville, B.W. and Hadfield, A.C.(1999)., "Use of Sacrificial Piles as Pier Countermeasures", J. Hydr. Engrg., Vol. 125, No. 11 , pp 1221-1224.

[32] Odgaard, A.J., and Wang, Y. (1987). "Scour prevention at bridge piers." *Hydr. Engrg.* 87, R.M. Ragan, ed., National Conference, Virginia, 523-527.

[33] Parola, A.C.(1993),"Stability of riprap at bridge piers", J. Hydr. Engrg. ASCE, 119, 1080-1093.

[34] Posey, C.J. (1974),'tests of scour protection for bridge piers,' J. Hydr. Engrg., ASCE, 100(12),1773-1783.

[35] Raudkivi, A.J. (1991).' Scour at bridge piers.' In Scouring, Ed. H. Breusers and A.J.

[36] Raudkivi, A.A. Balkema, Rotterdam. NL.

[37] Richardson, E.V. and S.R. Davis (1995). "Evaluating scour at Bridges," Hydraulic Engineering Circular No. 18 (HEC-18), Publication No. FHWA-IP-90-017, Third Edition, Federal Highway Administration, Washington, D.C.

[38] Schneible, D.E. (1951). "An investigation of the effect of bridge pier shape on the relative depth of scour." M.Sc. thesis. Graduate College of the State, University of Iowa, Iowa City, Iowa.

[39] Tanaka, S. and Yano, M.(1967). " Local Scour around a Circular Cylindere", Proc. 12the IAHR congress, delft, The Netherlands,3,193-201.

[40] Vittal, N., Kothyari, U.C. and Haighghat, m.(1994)." Clear water scour around Bridge piers Group", ", J. Hydr. Engrg. ASCE, 120(11), 1309-1318.

[41] Worman, A. (1989)," Riprap Protection Without Filter Layers", ", J. Hydr. Engrg. ASCE, 115(12), 1615-1629.

[42] Yoon, T.H., Yoon, S.B. and Yoon, K.S. (1995)." Design of riprap for Scour Protection around Bridge Piers", 26th IAHR Congress, U.K., Vol. 1., pp. 105-110

Determination of local scours near platforms at Piltun-Astohskoye and Lunskoye oil and gas field during joined action of waves and currents

B.V. Belyajev*, M.E. Mironov*
* Vedeneev VNIIG, St. Petersburg, Russia

The paper suggests a procedure for evalution of local scours in front of large Gravity Based Structures (GBS) under joined effect of waves and currents. Given are expressions and relationships for determination of scour depths. Results of evalution of local scours near GBS for the two "Sakhalin-II" locations, site "Piltun-Astohskoye" and site "Lunskoye", is presented as an example.

INTRODUCTION

Gravity Based Structures (GBS), installed at the sea bottom are known to substantially affect the wave pattern together with the superimposed flows. Vortex zones appear in the vicinity of the structure and the summary velocities of flow particles usually tend to surpass the critical values for various bed soils. As a result, local scours are appearing at the substructure units and this is leading to deterioration of normal operating conditions.

Judging from the consequences, two main failure models of soil foundation were selected for a structure during seabed scour. In the first case the holes appear directly near the borders of the GBS. If the height of a protective skirt is insufficient then intensive washing out of soils begins below the foundation resulting in additional deposits and tilts of the structure. The washing out of this kind is not admissible and accordingly the depths of local scours abutted to the GBS should not be more than the height of the skirt (usually 2.0-2.5 m).

In the second case the seabed scours occur at a distance from the structure and are not influenced directly by the contact of GBS with the soil but they sufficiently decrease stability of the soil foundation to shear. To estimate the marginal resistance to shear it is required to have information about dimensions in plan and depths of local scours.

At present the task of defining local scours near GBS with cross sections of large size under joint action of waves and current is far from final solution. Only separate publications are known, which are based on the results of laboratory researches of local scours near some types of structures basically from current [1 – 3 etc.] and also both from separate and joint action of waves and current [4 – 7]. The results of experimental researches of local scours of seabed at a barrier of the large cross sections and partial height in conditions of the North Sea are presented in work [2].

The review and the analysis of the relevant literature indicates that the problem of assessment of local scours, even at the simplest vertical cylindrical substructure units has no exact theoretical solution. All the known publications are mainly based on the data of laboratory tests. The performance of such tests presents difficulties of modelling structurally non-uniform foundation soils and especially their grain-size analysis.

METHOD PROPOSED

The authors of the present publication suggest the following set of special approaches for the determination of local scours at the substructure units of ice resistant structures. First, the locations of most intensive local bed scours (accounting for joint action of waves and flows) are identified in the laboratory on a physical model. Subsequently, the maximum bed velocities are determined in places most vulnerable to scours. Then the suggested engineering expressions are used for the evaluation of depths of local scours (with account of the known elements of waves and flows, characteristics of soil conditions and parameters of lithodynamic processes, known dimensions of substructure foundation, design of bed scour protection arrangements, etc.). Finally, the obtained data is compared with the permitted values (e.g. with the design height of stone layer).

Depths of local scours under the joint action of waves and currenst

Calculation of depth d_s of local seabed scour at depth of water d under the joint action of waves and currents was carried out on the proposed in [1, 2] general approach based on the following formulation:

$$d_S/d = f(t)\prod_1^6 f_i, \qquad (1)$$

where $f(t)$ – the function accounting for changes of local scour depths with time,

$$f(t) = 1 - \exp(-t/A), \qquad (2)$$

$$A = 0,2 + 60d_{50}, \qquad (3)$$

t – time, hour; d_{50} – sediment size by which 50% by weight is finer than, м.

For function f_1, accounting for the influence of waves on scour depth the following formula is proposed [7]

$$f_1 = 0,044\mathrm{KC}^*, \qquad (4)$$

where KC* – the modified Keulegan-Carpenter number is calculated by

$$\mathrm{KC}^* = \frac{V_w T_w}{d}. \qquad (5)$$

Here V_w – the maximum horizontal component of orbital wave velocity at a level of seabed; T_w – waves period accepted equal to average period of waves T_{av}; d – water depth.

The function f_2, accounting for the influence of current on scour depth is to be defined by formula [8]

$$f_2 = \frac{a\tanh\left[3,5\left(V_{cw}-b\right)\right]+1,9-a}{a\tanh\left(-3,5b\right)+1,9-a}, \quad (6)$$

$$a = \frac{0,95}{1+0,005\mathrm{KC}},\ b = \frac{0,8}{1+0,005\mathrm{KC}^2}, \quad (7)$$

$$\mathrm{KC} = \frac{V_w T_w}{D}, \quad (8)$$

where D – characteristic length of the structure, V_{cw} – effective dynamic flow velocity should be defined according to formula [9]

$$V_{cw} = \sqrt{\lambda/2}\left(V_c + \alpha_w V_w\right). \quad (9)$$

Here λ – the coefficient of hydraulic friction,

$$\lambda = 8g/C^2, \quad (10)$$

where g – acceleration of gravity, C – Shezy coefficient determined according to formula [4]

$$C = 5.75\sqrt{g}\log_{10}\left(\frac{12d}{k_S}\right), \quad (11)$$

where k_S – equivalent roughness height,

$$\left.\begin{aligned} k_S &= 2d_{50} \quad \text{for smooth conditions} \\ k_S &= 3d_{90} \quad \text{for rough conditions} \end{aligned}\right\}, \quad (12)$$

where d_{50} and d_{90} – sediment size by which 50% and 90% by weight is finer than, m.

In the formula (9) also it is accepted: V_c – averaged in depths current velocity; α_w – the coefficient accounting for pulsation character of wave velocities at a level of seabed.

The coefficient α_w should be defined according to condition of equivalence of scour ability of wave and current,

$$\alpha_w = \frac{V_{cr,c}}{V_{cr,w}}. \quad (13)$$

Here $V_{cr,c}$ – critical flow velocity for current above homogeneous non-cohesion soil foundation defined by formula [10]

$$V_{cr,c} = \log\left(\frac{8.8d}{d_{50}}\right)\sqrt{\frac{2}{0.44k_n\rho_w}\left[\left(\rho_s-\rho_w\right)gd_{50}+2c_y k_0\right]}, \quad (14)$$

where k_n – the coefficient accounting the pulsation character of current velocity within the seabed is defined by formula

$$k_n = 1+\frac{1}{0.3+\left(\frac{\nu^2}{gd_{50}^3}\right)^{1/3}}, \quad (15)$$

ρ_w – water density, ρ_s – soil density, c_y – fatigue rupture strength for non-cohesion fine-grained soil,

$$c_y = 8\rho\nu\frac{\left(g\nu\right)^{1/3}}{d_{50}}, \quad (16)$$

k_0 – the coefficient accounting for deviation of cohesion forces from their average values (it is possible to take $k_0 = 0.5$).

In the formula (13) also it is accepted: $V_{cr,w}$ – critical flow velocity for wave above homogeneous non-cohesion soil foundation defined by formula [11, 12]

$$\left.\begin{aligned} V_{cr,w} &= 3.25\sqrt{gd_{50}} \quad \text{for } d_{50} < 3.38\times10^{-3} \\ V_{cr,w} &= 3.25\sqrt{gd_{50}}\left(\frac{3.38\times10^{-3}}{d_{50}}\right)^{0.17} \quad \text{for } d_{50} \ge 3.38\times10^{-3} \end{aligned}\right\}. \quad (17)$$

The function f_3, accounting for the influence of the critical flow velocity for wave on the soil foundation is to be defined by formula [1, 2]

$$f_3 = \frac{V_{cw}}{V_{cr}^*}, \quad (18)$$

where V_{cr}^* – critical dynamic flow velocity for wave,

$$V_{cr}^* = \frac{V_{cr,w}\sqrt{g}}{C}. \quad (19)$$

The function f_4, accounting for the influence of the structure height on scour depth is recommended in [2] to take equal to 1 for $h_{pr}/d \ge 1$, where h_{pr} is the structure height above the seabed level, and for $h_{pr}/d < 1$

$$f_4 = \tanh\left[3,5V_{cw}\left(\frac{h_{pr}}{d}-1,4\right)\right]+1. \quad (20)$$

The function f_5, accounting for the influence of the structure shape on scour depth is to be taken in [2]: for circular structures – 1,0; for a square structures (90° orientation) – 2,0; for a square structures (45° orientation) – 2,8.

For the function f_6, accounting for the influence of the relationship of characteristic length of the structure D to water depth d, the following relation is recommended [1]:

$$f_6 = 1,5\left(D/d\right)^{0,65}. \quad (21)$$

The analysis of the scour depths according to (1 – 21) is based using a number of assumptions: directions of waves and current are accepted agreed; seabed soils are considered homogeneous, non-cohesion and nonlaminar in occurrence; the form of GBS is assumed symmetrical relative to the longitudinal axis; slope of the head edges of GBS are not considered.

VALIDATIONS

The developed fotmulas to predict the scour depth has been verified with other relevant data sets available. They are summarised in Table I, Table II.

TABLE I. VALIDATION DATA FOR CYLINDER WITHOUT CURRENT FROM [13]

Region of Russia	D, m	d, m	Boundary conditions			Scour depth d_s, m	
			H_w, m	T_w, s	d_{50}, m	Calc.	Meas.
Sea of Azov	8.0	5.5	1.4	5.0	0.00007	1.0	1.5
	8.0	5.5	2.0	5.0	0.00007	1.7	
	8.0	5.5	2.2	5.0	0.00007	2.1	
Black Sea	1.2	3.0	1.0	4.0	0.00020	0.6	0.6

TABLE II. VALIDATION DATA FOR GBS WITH CURRENT FROM [2]

GBS	D, m	d, m	Boundary conditions				Scour depth d_s, m	
			H_S, m	T_P, s	d_{50}, m	V_c, m/s	Calc.	Meas.
F3	80.0	42.3	9.5	13.3	0.00015	0.64	3.0	3.0
F3	80.0	42.3	9.5	13.3	0.00015	0.82	4.0	

It can be concluded that for both model and prototype data are within 20%. These results confirm the reliability of the developed fotmulas to predict the scour depth, although the amount of data is very limited.

PRACTICAL APPLICATIONS

This section presents the information about the results of test verification of constructions for scour protection of bottom soils under simultaneous action of waves and currents used in the projects of reinforced concrete gravity substructures for the GBS "Piltun-Astokhskoye B" (PA-B) and GBS "Lunskoye A" (Lun-A) at the licensed sites of the "Sakhalin-II" Project (Fig. 1).

The main goal of this results is to make expert estimation of the accepted constructions for scour protection of bottom soils under simultaneous action of waves and currents in compliance with the data received from the Russian designing practice.

The basic initial data used in designing and verification of constructions for scour protection of bottom soils around the substructures of the GBS PA-B and GBS Lun-A are presented in Table III.

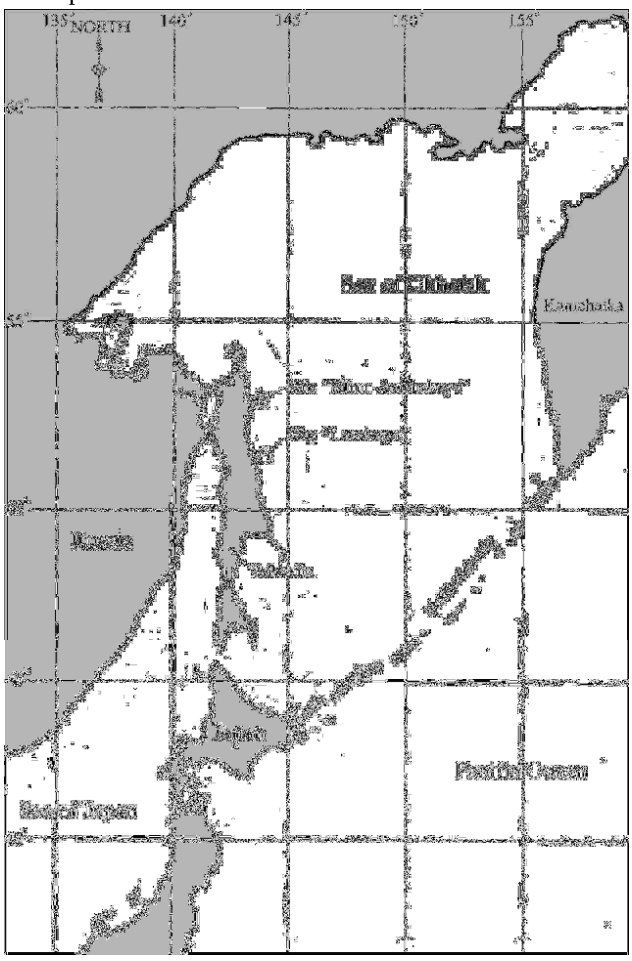

Figure 1. Situational scheme of site "Piltun-Astohskoye" and site "Lunskoye"

TABLE III. INITIAL DATA FOR DESIGNING AND VERIFICATION OF CONSTRUCTIONS FOR SCOUR PROTECTION OF BOTTOM SOILS AROUND OF THE GBS PA-B AND GBS LUN-A

GBS	PA-B	Lun-A
Sea depths		
Maximum sea depth (m)	34.78	53.63
Minimum sea depth (m)	29.50	47.70
Elements of waves independently of the angle of their approach in a storm of a 100 year return period		
Maximum wave height H_{max} (m)	18.0	18.8
Height of significant waves H_s (m)	9.7	9.9
Height of mean waves H_{av} (m)	6.1	6.2
Period of maximum waves T_{max} (s)	13.5	13.6
Spectrum peak period T_p (s)	14.2	14.3
Mean wave period T_z (s)	10.6	10.6
Velocities of currents of a 100 year return period independently of their direction		
On water surface (m/s)	1.78	1.59
At mid depth (m/s)	1.61	1.44
1 m above seabed (m/s)	1.07	0.91
Bottom soils		
Upper layer	Sand of average density, d_{50} = 0.30 mm	Sand: fine, medium, loose and of average density, d_{50} = 0.20 mm
Thickness of upper layer	Up to 0.5 m	Up to 0.8 m
Underlayer	Sand: fine, medium, hard with streaks of clay and gravel inclusions in the bottom of the layer d_{50} = 0.70 mm	Clay with streaks of silty and sandy soils
Thickness of underlayer	Up to 23.0 m	Up to 8.0 m

Platform descriptions

1) PA-B Platform

The PA-B combined drilling/production topside facilities will rest on a GBS at site "Piltun-Astohskoye". The base of the GBS PA-B consists of a concrete base caisson of 94 m x 91.5 m and 11.5 m in height (Fig. 2). Four conical concrete shafts rise 39 m in height from the base caisson to support the topside facilities.

2) Lun-A Platform

The Lun-A combined drilling/production topside facilities will rest on GBS at site "Lunskoye". The base of the GBS Lun-A consists of a concrete base caisson of 105 m x 88 m and 13.5 m in height (Fig. 3). Four conical concrete shafts rise 55.7 m in height from the base caisson to support the topside facilities.

Maximum bed wave velocities

Wave velocities around the faces of the support caissons of the platforms were observed near vertical walls of restricted width and incomplete height at the arbitrary angle of approach of interfered waves with allowance for non-linear effects by the 3rd order of approximation (3-D problem) [14].

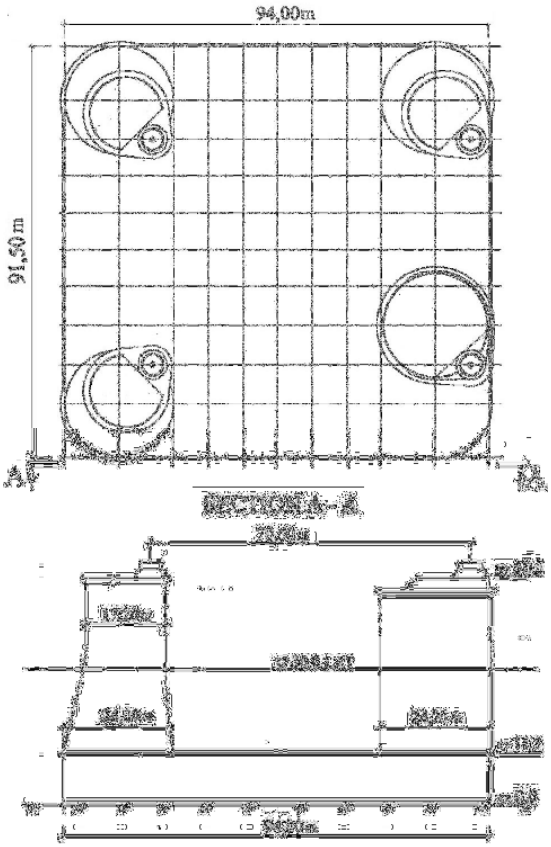

Figure 2. Plan and cross section of the substructure of the GBS PA-B

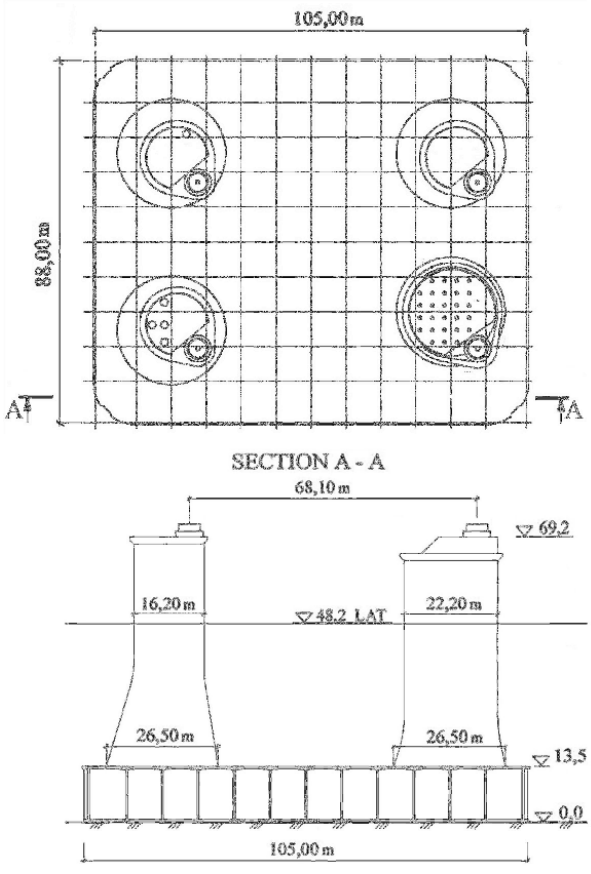

Figure 3. Plan and cross section of the substructure of the GBS Lun-A

Tables IV and V show the results of wave velocities at the seabed level near the front faces of the support caissons of the GBS PA-B and GBS Lun-A along the axis and at the corners of the vertical walls of restricted width and incomplete height with frontal approach of interfered waves with allowance for non-linear effects by the 3rd order of approximation.

TABLE IV. WAVE VELOCITIES ALONG THE AXIS OF THE GBS PA-B AND GBS LUN-A

Distance from frontal face along platform axis, m	Wave velocities around GBS, m/s	
	PA-B	Lun-A
1.0	1.05	0.82
5.0	1.05	0.82
15.0	1.20	0.88
20.0	1.30	0.93

TABLE V. WAVE VELOCITIES AT THE CORNERS OF THE GBS PA-B AND GBS LUN-A

Distance from the corners of the GBS, м	Wave velocities around GBS, m/s	
	PA-B	Lun-A
1.0	1.53	1.08
5.0	1.53	1.08
15.0	1.53	1.08
20.0	1.53	1.08

The results of calculation of local scour depths of bottom soils by the method according to the formulas (1 – 21) with the account of the combined effects of waves and currents are presented in Table VI.

TABLE VI. DEPTH OF SCOUR PITS IN BOTTOM SOILS AROUND THE GBS PA-B AND GBS LUN-A

Method	Depths of local scour in bottom soils around GBS, m	
	PA-B	Lun-A
Formulas (1 – 21)	8.43	4.86

The depths of local scour determined by the formulas (1 – 21) under simultaneous action of waves and currents exceed considerably the thickness of upper layers of bottom soils. This fact confirms that it is necessary to protect the seabed around the GBS PA-B and GBS Lun-A from scour.

From the data of the projects it follows that after installation of the platforms on the spot it is planning to erect protection fillings around the perimeter of the support caissons from stone with average size d_{50} = 0.25m with layers of 2.5 – 3.5m thick for the GBS PA-B and 2.0m for the GBS Lun-A. The width of the bottom of the protection filling makes up about 19.0m for the GBS PA-B and 15.0m for the GBS Lun-A. The filters from broken stone with average size d_{50} = 0.04m, 0.5m thick are arranged between the stone protection fillings and the seabed. The width on the bottom of the reverse filters makes up about 21.0m for the GBS PA-B and 17.0m for the GBS Lun-A.

The depths of local scour in the upper layer of the protection fillings calculated by the method according to

the formulas (1 – 21) with the account of simultaneous action of waves and currents are presented in Table VII.

TABLE VII. DEPTHS OF SCOUR PITS AROUND THE GBS PA-B AND GBS LUN-A

Method	Depths of local scour of stone layer around GBS, m	
	PA-B	Lun-A
Formulas (1 – 21)	0.18	0.12

From the analysis of the data of Table VII it may be concluded that the accepted in the project protection filling with the stone size d_{50} = 0.25 m for the GBS PA-B and for the GBS Lun-A it is sufficient.

CONCLUSION

On the basis of the work presented in this paper the following is concluded and recommended:

- The improved design formulas has been offered for offshore structures subjected to wave or joined effect of waves and currents.
- Using the formulas the maximum local scour depths can be predicted.
- The design size of the constructions for scour protection for the GBS PA-B and GBS Lun-A are as a whole substantiated and valid.

REFERENCES

[1] Breusers H.N.C., Nicolett G, Shen H.W. Local scour around cylindrical piers // J. Hydraulic Researh, 15, No. 3, pp. 211-252, 1977.

[2] Bos K.J., Verheij H.J., Kant G., Kruisbrink A.C.H. Scour protection around gravity based structures using small size rock // Proc. First Int. Conf. on Scour of Foundations (ICSF-1), Texas A@M University, College Station, Texas, USA, pp. 567-581, 2002.

[3] Escarameia M., May R.W.P Scour around structures in tidal flows // HR Wallingford report SR 521, 1999.

[4] Hoffmans G.J.C.M., Verheij H.J. Scour manual. A.A. Balkema/Rotterdam/ Brookfield, 1997.

[5] Khalfin I.S.H. Local scour around ice-resistant structures caused by waves and current effect // POAC-symposium 28, Helsinki, Vol. 2, pp. 992-1002, 1983.

[6] Sumer B.M., Christiansen N., Fredsoe J. Influence of cross section on wave scour around piles // J. Waterway, Port, Coastal and Ocean Eng., ASCE, 119(5), pp. 477-495, 1993.

[7] Sumer B.M., Fredsoe J. Wave scour around Large Vertical Cylinder // J. Waterway, Port, Coastal and Ocean Eng., ASCE, pp. 125-134, 2001.

[8] Sumer B.M., Fredsoe J. Scour around a pile in combined waves and current // J. Hydr. Eng., pp. 403-411, 2001.

[9] Devis M.Kh., Mishchenko S.M. Experimental investigations of local scour of bed adjacent to foundations of offshore hydraulic structures // Izvestia, B. E. Vedeneev VNIIG, V. 236, pp. 140-151, (in Russian), 2000.

[10] Mirtskhoulava Ts. Ye. Scouring by flowing water of cohesive and noncohesive beds // J. Hydraulic Res., IAHR, 29(3), 1991.

[11] SNiP 2.06.04-82*. Loads and impacts on hydrotechnical structures (from waves, ice and ships) / Minstroy RF. M.: GP TsPP, (in Russian), 1995.

[12] R 31.3.07-01. Instructions on calculations of loads and impacts rom waves, ships and ice on offshore hydrotechnical structures. Additions and refinements of SNiP 2.06.04-82*. M.: Ed. Soyuzmorniiproyekt, (in Russian), 2001.

[13] Khalfin I. Sh. Actions of waves on sea gas-and-oil production structures. M.: Nedra, (in Russian), 1990.

[14] Mironov M.E. Non-linear waves and their impact on flat walls. – Vedeneev VNIIG, 126 p. (in Russian), 2001.

Role of fluid structures in a two-dimensional scour holes

Alex Bey[1], M.A.A. Faruque[1], Ram Balachandar[2] and B.B. Budkowska[2]
[1]Research Associate, Department of Civil & Environmental Engineering, University of Windsor, Windsor, Ontario, Canada.
[2]Professor, Department of Civil & Environmental Engineering, University of Windsor, Windsor, Ontario, Canada.

An experimental program was carried out to understand the role of fluid structures in a scour hole generated by a plane wall jet. A laser Doppler anemometer was used to characterize the velocity field at various locations in the scour hole region. Observations indicate that different types of fluid structures influence scour at different time periods. Based on the present tests, the entire test duration is divided into five time zones. Following vigorous scour caused principally by jet shear forces and impingement at the start of the test and during early time periods, the flow was characterized by the presence of longitudinal axial vortices, turbulent bursts and movement of the jet impingement point during the later stages. Attempts were made to distinguish the fluid structures at asymptotic conditions. The scour hole region was characterized by the presence of randomly forming and disappearing streaks, laterally located concave shaped depressions, rolling and ejection of the bed material. Through analysis of higher order moments, sweep and ejection type events were observed, which can potentially contribute to scour.

I. INTRODUCTION

Laboratory studies of the interaction of plane wall jets with non-cohesive sand beds and other forms of two-dimensional jet scour have been carried out to understand the mechanisms of scour. As rightly pointed out by Ref. [5], a comprehensive understanding of the scour mechanisms remains elusive because of the complex nature of the flow field. The hydrodynamic characteristics of the jet flow, and the concave shape of the eroded bed further increases the complexity. The physical properties of the sediment as well as the turbulent flow field characteristics are equally responsible for the entrainment, suspension, transportation and deposition of the sediment. Details of several other previous studies involving two-dimensional jet scour are available in Ref. [3] and avoided here for brevity. Recently, Ref. [1] noted the need to understand the role of turbulent fluctuations in scour analysis.

In a recent study, Ref. [6] suggest that sediment transport, and the resulting scouring mechanism was due to turbulence created by Görtler vortices as a result of the destabilization of the turbulent wall layer by the concave curvature of the water sediment interface. They also proposed new scaling laws relating time and the attainment of the quasi-steady scour depth.

Concurrent with the development and evaluation of mathematical models, it is necessary to understand the flow features that influence the scour process. The present study was carried out to obtain the velocity field in the scoured region and to further understand the role of turbulent flow structures that influence scour. To this end, velocity measurements were conducted within the scour region at asymptotic conditions. Besides the mean flow, the higher order velocity moments were evaluated to understand the role of turbulent events.

II. EXPERIMENTAL SETUP AND PROCEDURE

The experiments were performed in a recirculating open channel flume which is 15 m long, 0.4 m wide and 0.9 m deep. The nozzle width is 0.4 m wide with an opening b_o = 25 mm, and is set flush with a horizontal non-cohesive bed (0.3 m deep, 0.4 m wide and 2.5 m long). The median grain diameter, d_{50} is 2.15 mm with a geometric standard deviation σ_g of 1.28. The bed material can be classified as very fine gravel. The bed was fully saturated prior to the start of the tests. The flow conditions were maintained to obtain local scour and there was no net transport of material beyond the edge of the bed.

Two tests were conducted uninterrupted at a tailwater depth (H_t), corresponding to $20b_o$. The present tests can be classified to be under the high submergence flow regime. The jet exit velocity (U_o) for the two tests (denoted as A and B) was held constant at 1.0 m/s and 1.27 m/s, respectively. These correspond to jet exit Reynolds numbers ($Re_j = U_o b_o/\nu$) of 25,000 and 32,000 respectively. The densimetric Froude numbers $F_o = U_o \Big/ \sqrt{g(\Delta\rho/\rho)d_{50}}$ are 5.4 and 6.8, respectively. It should be remarked that the test at U_o = 1.0 m/s (Test A) was repeated thrice, mainly to ensure repeatability and also to obtain confirmation of flow features that were noticed. The scour profiles were obtained using a digital point gauge having a resolution of ±0.01 mm.

The test duration extended over a period of 8-12 days even though an asymptotic state of scour was noted to be attained earlier on. Based on the rate of growth of the scour hole and mound, one can define an asymptotic condition as a state beyond which no significant changes in geometry occur. Sectional and plan view of the scour region along with the definition of variables is shown in Figure 1a. Figure 1b shows the variation of the important scour parameters with time. Depending on the scour hole/mound geometric parameter chosen, the time to achieve an asymptotic state can be as low as t = 24 hours. For example, the total length of the scour affected region (L_T) attains an asymptotic state at t = 24 hours, while the change in the maximum depth of the

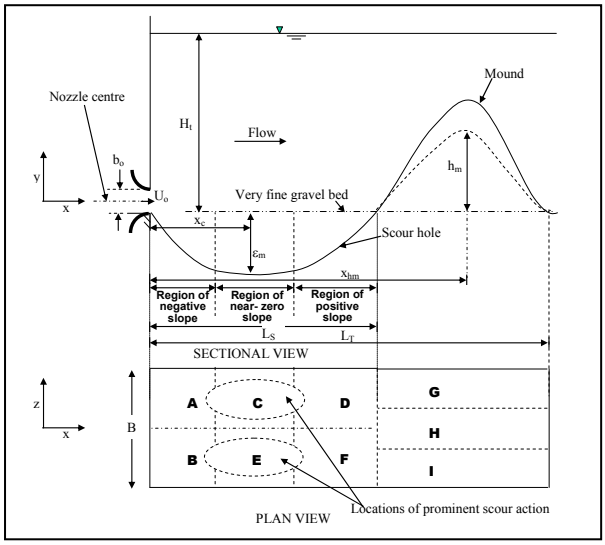

Figure 1a: Definition sketch.

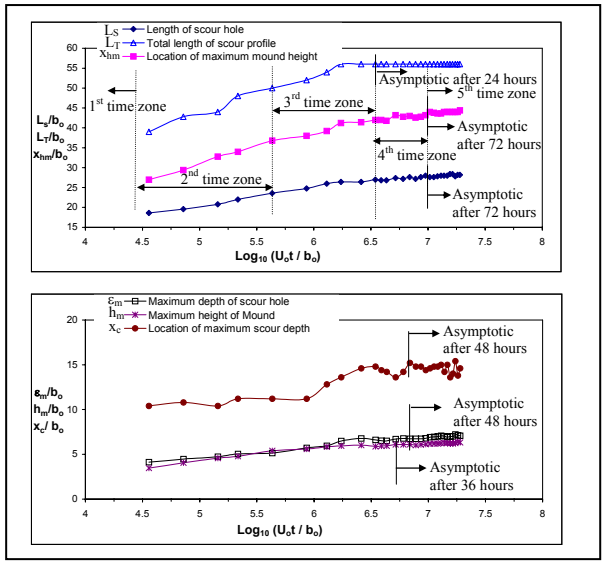

Figure 1b: Variation of scour parameters with time.

scour hole (ε_m) is less than 5 % from t = 48 hours and beyond. However, it should be noted that beyond 72 hours, there is the presence of the turbulent bursts which cause local changes in the location of the maximum depth of scour hole (x_c) but no significant changes in the mean scour profile. In this study, the asymptotic condition has been defined as a state when no significant change in any of the scour parameters is noticed. Detailed velocity measurements were conducted well beyond the 72-hour period.

For each test, the uniformity of the velocity distribution across the nozzle exit was verified. Further, constancy in test conditions was ensured by monitoring the velocity at the nozzle exit over the entire test duration (8 ~ 12 days). The velocity measurements were carried out with a non-intrusive two component fiber-optic LDA operated in backward scatter mode. The presence of glass side walls of the flume provided optical access to the laser beams. Details of the LDA system are available elsewhere (Ref. [4]) and not included here for brevity. At asymptotic conditions, velocity profiles were obtained along the flume axis at various axial stations covering a range $2 \le x/b_o \le 50$.

The scour hole shape as a function of time, sediment movement in the scour hole and its variation across the width of the channel was studied with a video imaging system. Dye injection was used to enhance flow visualization. In this study, U and V denote the velocity in the x and y direction respectively, while u and v denote the fluctuations about the mean. The time averaged quantities are denoted by an over bar.

III. RESULTS AND DISCUSSION

Effect of time:

The following observations were made with the aid of dye injection and observing the movement of bed particles at various locations in the flow field. Distinct types of scour phenomena were observed in five different time ranges. These time zones were chosen based on a detailed review of the video tapes and observations made during repeated experiments. A time scale, defined by $T = L_s/U_o$ is defined in the present study and is used to non-dimensionalize the time zones. Here, L_s is the length of the scour hole at asymptotic conditions (Figure 1a). It should be remarked that another parameter such as ε_m or x_c could have been chosen to represent length scale. However, on repeated viewing of the tapes, L_s was found to be consistently easier to measure and more sensitive as an indicator of asymptotic state. Figure 1b also depicts the five time zones and one can notice that the rate of change of scour (for example, see change in slope of L_s vs. time or x_{hm} vs. time) more-or-less can be correlated with the time zones. The five time zones are described below:

a) $t/T \le 850$: When the plane wall jet exits the nozzle, the flow is initially parallel to the bed and following a very short duration, scour commences. Scour is very vigorous and a negative slope region is quickly established (see Figure 1a). A hole is formed downstream of the nozzle and the very fine gravel particles are deposited as a mound further downstream. In this time zone, the scour hole and mound are fairly two dimensional. The size of the hole is gradually increased with the increase in the length of the negative slope region. Due to the jet impingement action, most of the downstream grain movement occurs in the near-zero or positive bed slope region. As the scour hole progresses in the longitudinal direction, the jet impingement on the downstream slope of the hole causes a large scale suspension of bed material into the flow. An example of this suspension at early stages of the scouring process is shown in Figure 2a. Though not shown in the figures, video images indicate that grains are suspended all the way to the free surface (~ 20 b_o). The particles are predominantly transported in the downstream direction though some fall back into the scour hole.

b) $850 \le t/T \le 15 \times 10^3$: With progress in time (t > 600 s for Test A), the jet expands into a larger space (due to the presence of a larger and deeper scour hole). The jet is confined by the bed on one side and can be considered to be relatively free on the other side. The large scale suspension of the bed material seen earlier is reduced significantly (Figure 2b). In this time zone, the bed particles are carried in the vertical direction up to about 6 ~ 8 b_o. There is very little scour that occurs in the negative slope region. It has been reported in previous

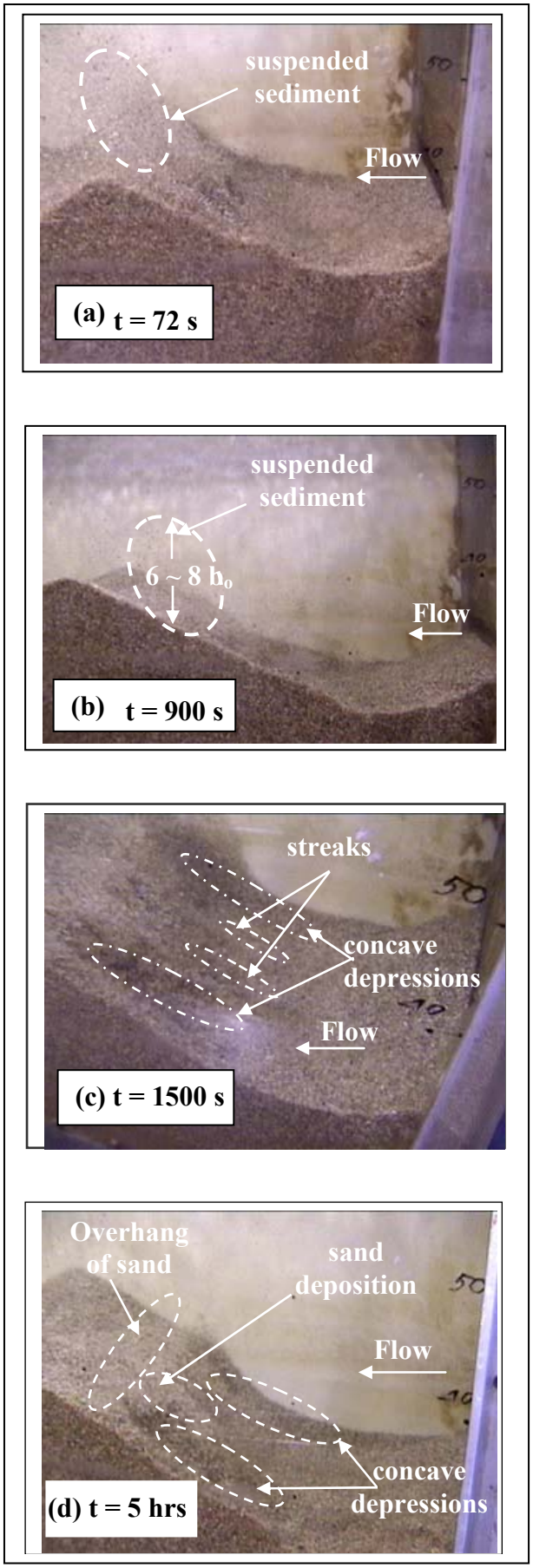

Figure 2: Images illustrating scour process.

studies that the negative slope quickly attains an equilibrium condition while most of the scour occurs downstream. In the negative slope region, the bed material moves towards the nozzle due to the formation of a recirculating flow. The grains also roll down the negative slope but no major scour occurs in this region. Most of the downstream grain movement continues to occur in the near-zero or positive bed slope region. Two well defined concave shaped lateral depressions stretching from region C into region D (and from E to F, Figure 1a) are formed. One can also observe two to three longitudinal streaks, that form and disappear rapidly in the scour hole region accompanied by lateral motion of bed particles. The presence of these streaks cause the very fine gravel to be deposited as small longitudinal ridges. Figure 2c shows the scour hole at t = 1500 s with two streaks and two concave depressions. The streaks are very similar to that noticed by Ref. [6]. However, Ref. [6] did not report the presence of the concave shaped depressions. The concave depressions on either side of the streaks are very prominent. The formation and disappearance of the streaks continue for a relatively significant period. Ref. [6] observed loose sediment streaks or longitudinal ridges on the positive bed slope in the scour hole while in the present tests, the streaks were observed mostly in the near-zero bed slope and at the beginning of positive bed slope. They mentioned that streaks or longitudinal ridges represented signature of intense longitudinal vortices which lift up the sediment. They attributed these vortices to Görtler instability and have shown that the flow conditions favour such instability. In the present tests, systematic formation of loose streaks was not observed although there was the tendency for the formation of one or two very unstable short streaks. It is important to point out that Ref.[6] conducted their experiments in the submergence range of 2.75 to 8.8, which is much lower than that used in the present study. As indicated earlier, tests in this range of submergence have been noted to be strongly influenced by flicking of the jet towards the bed and free surface in an alternate manner (Ref. [2]).

c) $15 \times 10^3 \leq t/T \leq 125 \times 10^3$: After about 3 hours when scour had progressed sufficiently, the streak like features became less prominent. On either side of the flume axis, there appeared a 'scoop and throw' like scouring action which caused longitudinal concave shaped depressions and is represented in Figure 2d. This is once again in the region C-D and E-F in Figure 1a. The bed appears to be fluidized at the end of these concave shaped depressions and particles are carried by the flow downstream into the mound region. A portion of the bed particles accumulate on the upstream face of the mound and in between the two concave shaped depressions and eventually slide back into the depressions when their apparent weight is greater than the sweeping force of the fluid. The 'scoop and throw' like action is then momentarily arrested.

One can also observe a lifting spiraling motion of bed particles near the end of concave shaped depression, indicative of some type of vortex activity. Dye visualization in the near bed region confirms vortex like structures and the sudden acceleration of the flow at the end of the scooped region. The presence of the vortices was also confirmed by observing the motion of individual grains.

d) $125 \times 10^3 \leq t/T \leq 375 \times 10^3$: 'Scoop and throw' like scouring action slowed down after 24 hours. Progress of scour continues but at a slower pace. Concave shaped depression caused by 'scoop and throw' mechanism is not that apparent at this stage but small scale suspension of bed material provides evidence of 'scoop and throw' action. One can notice small scale bed suspension on one side of the flume axis in Figure 2e (which shows the near-bed region only). The suspension of a very few grains extends to about 1 ~ 2 b_o. This subsided 'scoop and throw' action continues up to 72 hours. Dye injection confirmed the presence of spiral motions during this time period. Figures 2f to 2h show images of the flow field in the near-bed region at $x/b_o = 10$. The dye is injected by a 'L' shaped tube with the exit port facing the near wall of the flume. In Figure 2f, the dye initially flow towards the near side wall (out of the picture) and spirals towards the upstream direction. In Figure 2g, the dye injection is shown 2 s later than that in Figure 2f. The dye now exits the port and flows towards the far wall. In Figure 2h (which is acquired 4 s later than Figure 2g), the dye flows in the downstream at a slight angle to the streamwise direction. Collectively, using images such as Figure 2f to 2h and several video frames, a clear spiraling motion can be deciphered.

e) $t/T > 375 \times 10^3$: About 72 hours into the scour process, when the scour hole attains an asymptotic state, what can be described as turbulent bursts were noticed to occur in the near-bed region across the cross-section of the flume. Figure 2i and 2j show images with and without turbulent bursts separated by a time interval of 2 s. The effect of the burst can be noticed by the suspension of bed particles. These bursts were frequent and occurred randomly. Furthermore, they caused the movement of bed particles close to the bed region in all directions. The transport in the vertical direction is less than b_o. This type of activity is visible in a section beyond the maximum scour depth location (x_c in Figure 1a). In addition, at asymptotic conditions, two prominent scour mechanisms were observed to occur on either side of the flume axis and as shown in Figure 2k. As a consequence of these mechanisms, bed particles were laterally moved from the region. Particles appeared to be spiraled towards the side walls and the flume axis. However, no longitudinal particle movement was observed along the nozzle axis. These two scour mechanisms occurred quite frequently and as measured by the movement of bed particles, the two fluid structures causing the scour appear to be identical in strength as the bed contour was symmetrical about the flume axis. Occasionally, one would note that one of the two structures was stronger than the other, and this caused lateral movement towards the weaker side. This momentarily caused the bed contour to become asymmetrical. No preferential occurrence on one or the other side of the flume axis of the stronger structure was noted. It should be remarked that at asymptotic conditions, the back and forth movement of the impingement point (discussed in a later section), the frequent but random turbulent bursts and the two prominent scour mechanisms, all occurred at one time or the other. The jet impingement tends to cause a limited suspension and lifting of the bed particles into the flow stream where they are picked up and transported by the higher velocity fluid parcels. In addition, the fluid structures caused lateral particle movement. It is however note worthy that in spite of these actions, any changes in the instantaneous bed profile was a local phenomenon and did not cause significant change in the overall mean

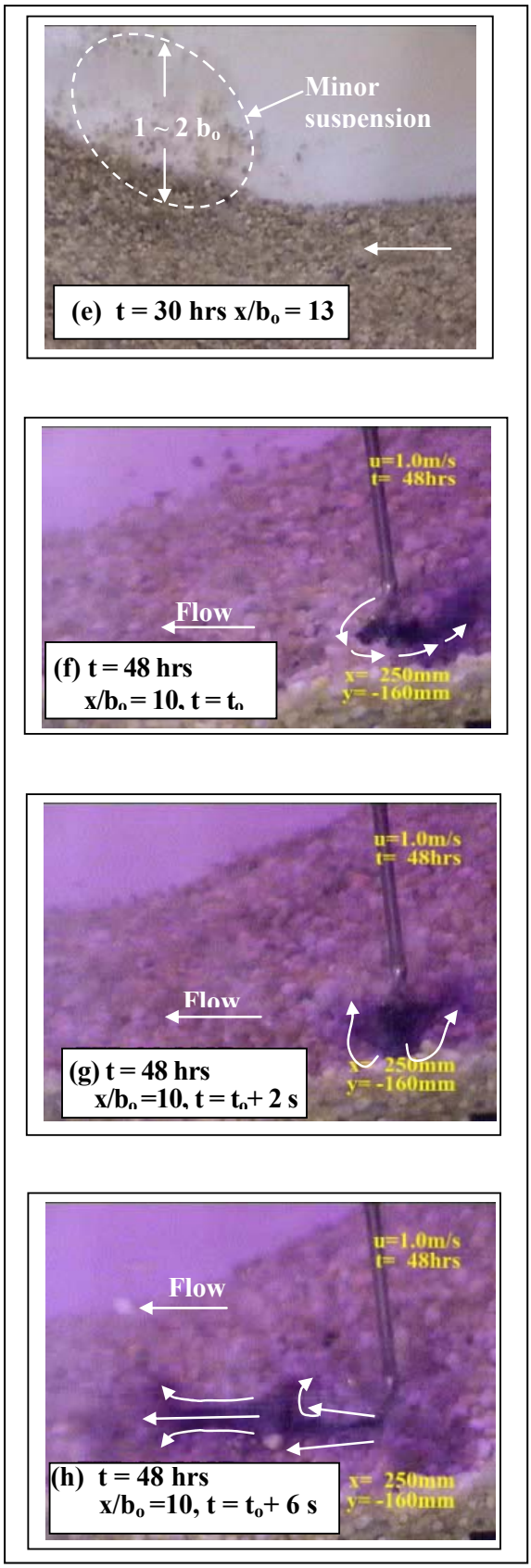

Figure 2 (cont'd): Images illustrating scour process.

bed profile. It should also be noted that at the asymptotic state, scour profile in the hole region is nominally two-dimensional across the width of the flume. However, at the mound region, the lateral profile is not two-dimensional and has two distinct peaks (Region G and I of Figure 1a). These peaks occur closer to the side walls leaving a trough in center portion of the mound (Region H of Figure 1a).

Presence of vortex in 'scoop and throw' regime:

As indicated in the previous section, two counter rotating vortices were seen to occur in the scour region (for the time period $15 \times 10^3 \leq t/T \leq 375 \times 10^3$). The presences of the vortices were confirmed by dye visualization and movement of fine gravel particles in the scour hole. Figures 3a to 3d shows the vertical component velocity histogram at $x/b_o = 14$ for Test A. Negative V will indicate downward directed motion. Since the laboratory is equipped only with a two-dimensional LDA system, the third velocity component (W) could not be directly obtained. Additional measurements were made by placing the LDA probe at an angle with the streamwise direction and the arrangement is indicated as an insert in Figure 3e to obtain an estimate of velocity in the z direction. Figures 3e to 3h show the velocity histogram obtained in the plane of measurement indicated in the inset of Figure 3e. Negative value of this histogram indicates motion towards the near side wall and positive value of the same indicates motion towards the far side wall. As indicated in the histograms, the number of negative measurements decreased as one goes up from the near-bed location. These measurements are only qualitative and used to evaluate the fluid motion towards the wall. Together with the vertical velocity measurement (Figures 3a to 3d), one can clearly see a rotational type motion that is directed towards the inner side wall in the bottom regions and away from the inner side wall for the upper locations and serves to confirm the presence of a vortex structure.

Asymptotic conditions:

As indicated earlier, detailed velocity measurements were conducted at an asymptotic state when there was no significant change in the scour conditions. The impingement of the jet on the bed is first discussed followed by the variation of the mean velocity and higher-order moments.

Jet Impingement: During the progress of the scour hole, visual observation indicates that the jet impingement point moves back and forth. This can be confirmed by the presence of upstream and downstream movement of particles near the bed in the range $0 < x/b_o < 16$. Figure 4 shows the histogram of streamwise velocity along the scoured bed for Test B at various locations ($10 < x/b_o \leq 20$). These locations extend from the end of the negative bed slope region to the start of the positive bed slope region as indicated in Figure 4b. One can note from the graphs that, for $10 < x/b_o \leq 13$ (Figures 4a, 4c to 4e), although the streamwise mean velocity is very low near the bed, the instantaneous velocity varies over a wide range from -0.8 m/s to 1.0 m/s. The histograms have two distinct peaks and one can also note that the negative instantaneous velocity constitutes a significant percent of the total realizations, which is a

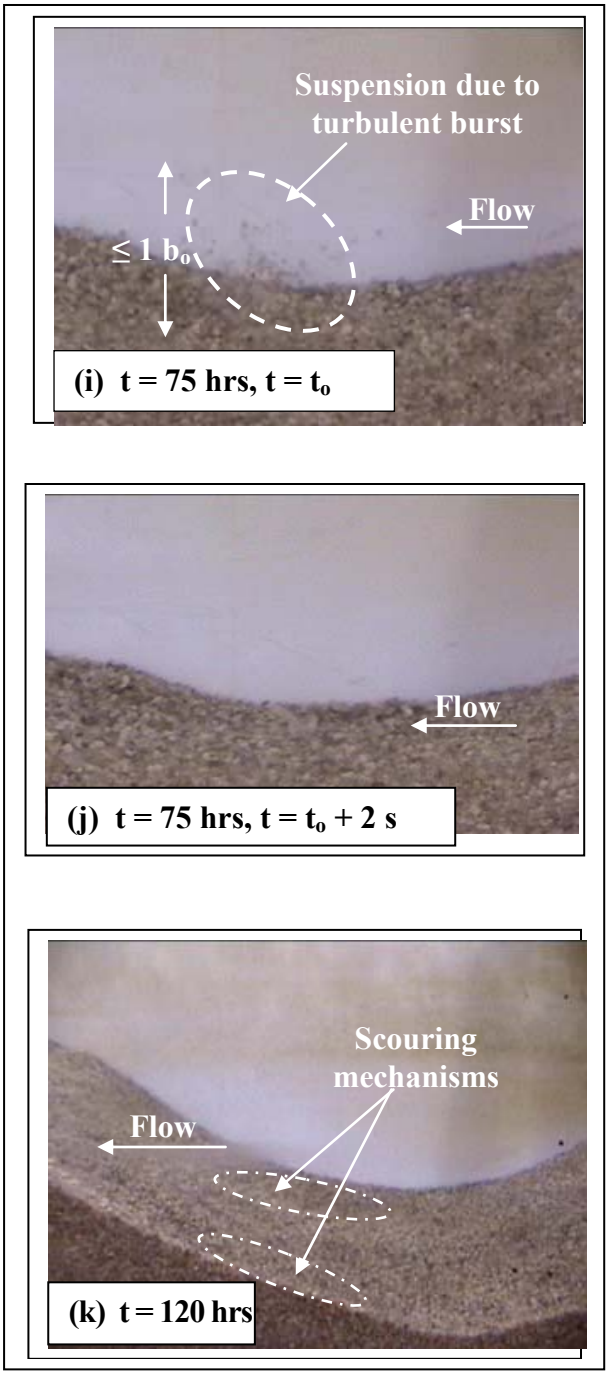

Figure 2 (cont'd): Images illustrating scour process.

clear indication of back and forth movement of jet impingement point. For $x/b_o \geq 14$ (Figures 4f to 4h), the value of mean streamwise velocity increases and the negative instantaneous velocity count decreases. For the location of $x/b_o = 20$ (Figure 4i), the negative instantaneous velocity count is less than 10%, and the overall histogram tends to have a single peak with more turbulence like fluctuations rather than back and forth jet movement. This is an indication that the jet impingement point extends up to about $x/b_o \approx 18$ with a mean location (defined as the location where 50% of velocity realizations are negative) occurring around $x/b_o \approx 13$.

Mean velocity profiles: Figure 5 shows the velocity vector plots for test A in the scour hole region at

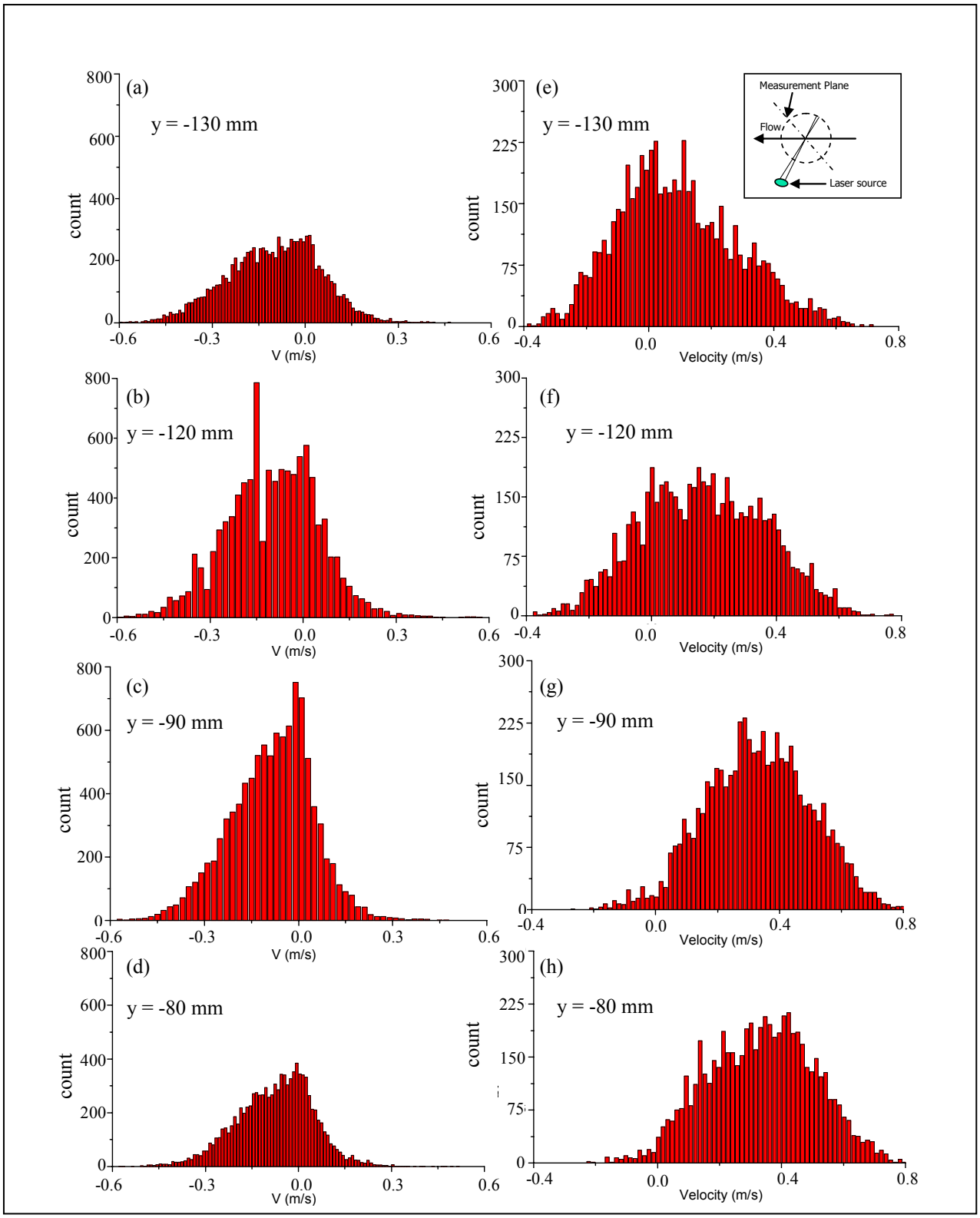

Figure 3: V histogram and estimate of W histogram at $x/b_o = 14$.

asymptotic conditions. One can clearly see from the vector plots that the jet expands and interacts with the bed. In the region above the jet, there is a large scale recirculating region which extends to about $35b_o$ downstream. The center of this region is located at about $16b_o$ along the x axis and about $10b_o$ along the y axis. It is important to recognize that this recirculation region provides for a significant downward velocity component near the nozzle. The impingement of the jet also generates a recirculating flow in the bed region close to the nozzle. A similar velocity plot was obtained for Test B which is qualitatively similar to that obtained in Test A. The mean impingement point in Test B occurs farther from the nozzle and consequently has a larger near-bed recirculation zone.

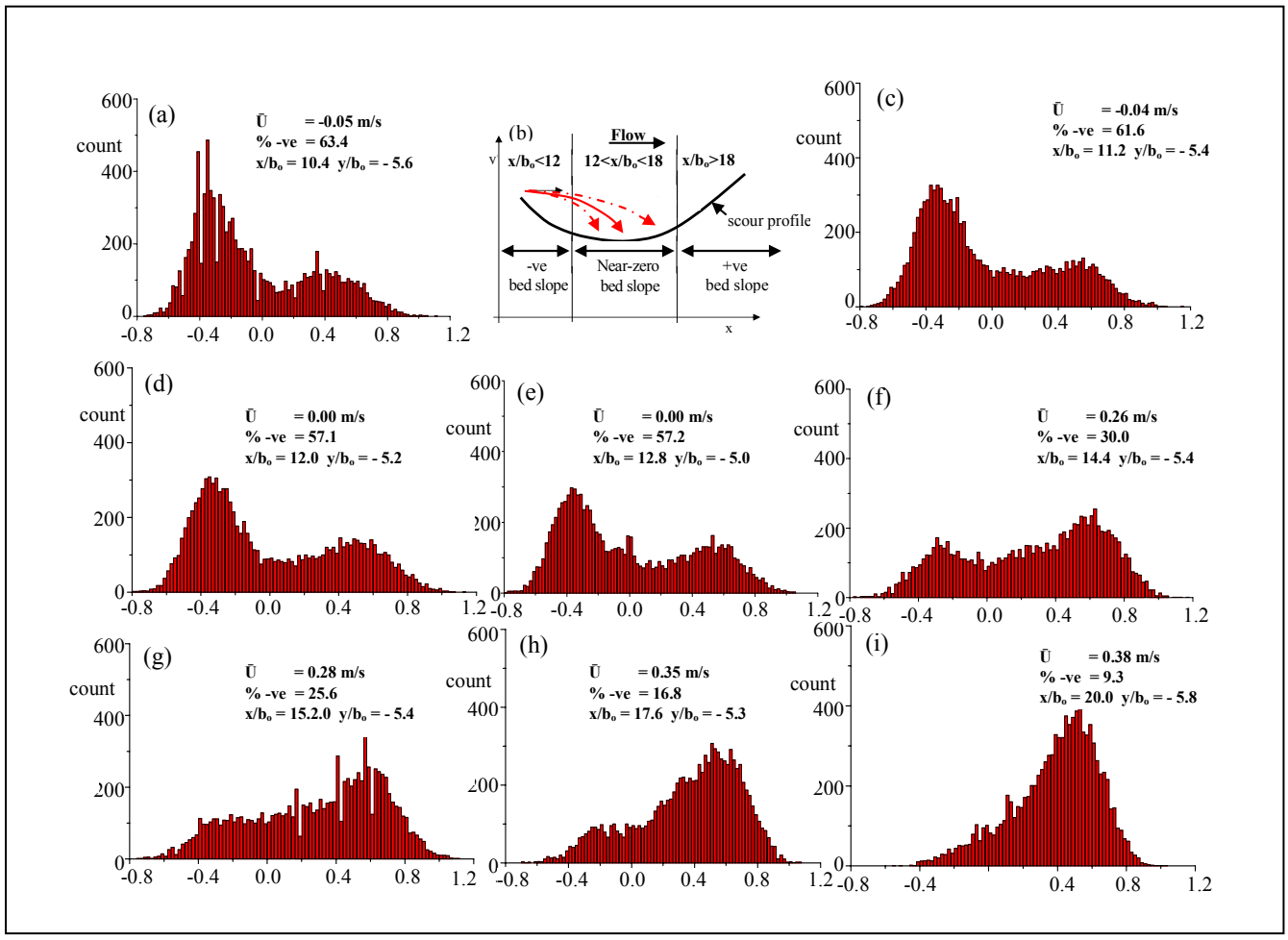

Figure 4: Histogram of streamwise velocity distributions along the scour bed for Test B.

In progressing from near the nozzle to several downstream stations, the jet expands. The locus of the maximum velocity moves downwards away from the nozzle axis which is indicative of the jet bending. Clearly, the jet expands asymmetrically and the computed rate of expansion was found to be higher than free jets. The bottom half of the jet displays a greater half-width than the upper half of the jet. Moreover, it is clear that, the jet begins to bend very early on and is different from a free jet. This is different from the observation of Ref. [7] who noted the jet characteristic to be similar to that of a free jet up to the point of maximum scour.

Higher order moments: Figure 6 shows the variation of turbulent diffusion in the y direction, $D_v = \overline{u^2 v}$ and the variation of $\overline{u^3}$ which can be thought as the streamwise flux of the turbulent kinetic energy $\overline{u^2}$ at various axial stations. The values for $\overline{u^2 v}$ and $\overline{u^3}$ above y/b$_o$ = 3 are close to zero and therefore makes no significant contribution to the discussion on the effect of turbulence on scour. The nine sets of profiles are divided into 3 rows, depending on the location with respect to the maximum scour depth. Figures 6a to 6c are in region of negative bed slope, Figures 6d to 6g are in the region of

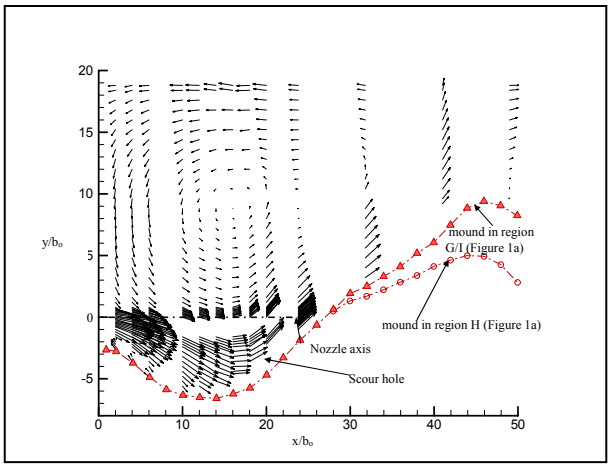

Figure 5: Velocity vector plot for Test A.

near-zero scour slope, while Figures 6h and 6i are in the region of positive bed slope.

Figure 6a shows that both D_v and $\overline{u^3}$ are close to zero near the bed. As one progresses from the bed towards the free surface, absolute values of both D_v and $\overline{u^3}$ increase and attain local peaks at almost the same level (y/b$_o$ = -1.6) but with opposite signs. D_v has a negative peak

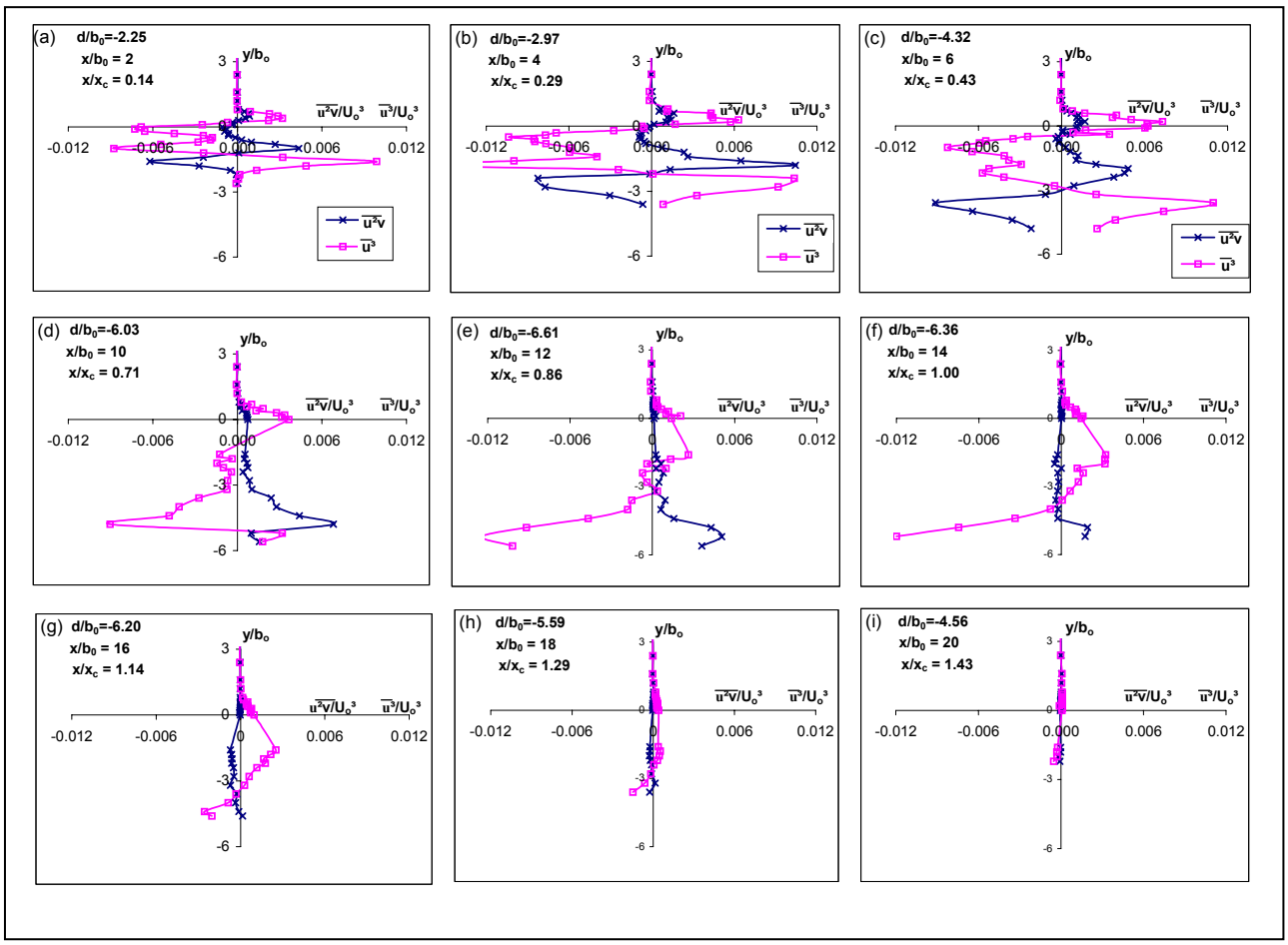

Figure 6: Variation of $\overline{u^2v}$ and $\overline{u^3}$ at various axial stations (Test A).

whereas $\overline{u^3}$ has a positive peak. The peak value of $\overline{u^3}$ is larger than that of D_v. This indicates strong sweeping type motion in the flow direction that is partly directed towards the bed. If one were to extrapolate this flow process to earlier time periods, such sweeping motions could influence scour significantly. For locations farther up ($y/b_o \geq -1.6$), absolute values of both D_v and $\overline{u^3}$ decrease and become zero at almost the same level ($y/b_o = -1.2$). This has significance as the changeover of sign indicates change in type of motion (ejection vs. sweep). Beyond this point, again absolute values of both D_v and $\overline{u^3}$ increase and attain local peak values at $y/b_o = -1.0$, but once again with opposite sign. This time, D_v has a positive peak whereas $\overline{u^3}$ has a negative peak. Similar to the earlier peak values, the peak value of $\overline{u^3}$ is larger than peak value of D_v. This indicates an upward transport of u momentum, where as $\overline{u^3}$ is negative, indicating a slower moving fluid parcel. With further increasing y/b_o, both the variables approach zero. At $y/b_o = -0.4$ (which is also the location of maximum $\overline{U}$), $\overline{u^2v}$ attains a zero value. Further increase in y/b_o (≈ -0.1) indicates that both variables attain local peak values and both are negative. This indicates fluid particles enter the jet as entrainment from above the jet centerline. Just above the nozzle centerline ($y/b_o = 0.4$), $\overline{u^2v}$ and $\overline{u^3}$ both are positive, albeit slightly. This indicates that the fluid particle is being ejected and simultaneously moving a bit faster in the flow direction. Above this point, the value of both the variables reduces to almost zero and remains so for the rest of the depth. These have no direct influence on the effect of turbulence on scour.

Figure 6b shows characteristics, which are similar to that shown in Figure 6a. However, the magnitudes of the peaks are larger, which is indicative of larger level of turbulence activity. Figure 6c shows characteristics, which are similar to that shown in Figures 6a and 6b. Figure 6d shows both positive peak values (albeit very low) for $\overline{u^2v}$ and $\overline{u^3}$ near the bed ($y/b_o = -5.6$). This is an indication of tendency for the fluid parcels to move in an upward direction. At this station, for $y/b_o = -4.8$, both D_v and $\overline{u^3}$ attain peak values. D_v attains a positive peak whereas $\overline{u^3}$ attains a negative peak. Similar to the earlier peak values, the peak value of $\overline{u^3}$ is larger than peak value of D_v. This indicates an upward transport of u momentum, where as $\overline{u^3}$ is negative indicates a slower fluid parcel motion. Together, $\overline{u^2v}$ and $\overline{u^3}$ indicate ejection of low speed fluid parcels that would be entrained into the jet. This type of motion can potentially

contribute to suspending individual grains that can be transported by the mean flow. Farther from the bed and towards the free surface, the absolute value of both $\overline{u^2v}$ and $\overline{u^3}$ reduces and have no direct influence on the effect of turbulence on scour. Figures 6e and 6f shows characteristics similar to that shown in Figure 6d and are all in the region of near-zero bed slope. Comparing Figure 6d with Figure 6e and 6f, one can note that the magnitude of peak for $\overline{u^3}$ increases and the magnitude of peak for $\overline{u^2v}$ decreases with increasing distance from nozzle and the jet-like characteristics diminish starting at Figure 6f and beyond. As one is close to the mean attachment point of the jet on the bed, the impingement causes large scale motion in all directions. This is reflected in the reduction of $\overline{u^2v}$ and $\overline{u^3}$ values. Figures 6h and 6i show the profiles in the positive slope region and indicate that the values for $\overline{u^2v}$ are close to zero throughout the depth of flow. This indicates very low turbulent diffusion in the y direction. For this region, there is a reduction in the streamwise turbulent flux with increasing distance from nozzle and eventually reaches zero, indicating a reduction in turbulent activities.

The ejection and sweeping type activities described above confirm the visual observations noted earlier. At the location of two prominent fluid structures (at asymptotic conditions), there is very large negative $\overline{u^3}$ values with low turbulent diffusion. This may be one of the causes for particle movement at this location.

IV. CONCLUSIONS

An experimental study was carried out to further understand the role of fluid structures in causing scour by plane jets. The study indicates the presence of different types of flow structures during various time periods. Both visual observation and velocity measurements aided in deciphering the role of the fluid structures. Even for regions near the nozzle, the present jet did not demonstrate free jet like characteristics as indicated by the velocity measurements. This is to be expected due to bed confinement on one side and the large scale recirculation zone situated above the jet on the other side. The growth rate of the jet is larger towards the bed due to the excess turbulence created by the water-bed interaction. The following are the main conclusions that can be drawn from the study:

1. The entire test duration, from the start of flow to the attainment of asymptotic conditions, can be divided in to five time zones. A time scale, denoted by the ratio of the length of the scour hole at asymptotic conditions to the jet exit velocity is used to normalize the five regimes. Each of the time zones had certain dominant flow features. The first time zone was accompanied by intense digging due to the direct shear action of the jet. Two or three longitudinal streaks and very prominent concave depressions were observed in the second time zone. A scoop and throw type event was noticed in the third and fourth of the time zones, while turbulent bursts were active during asymptotic conditions.

2. At asymptotic conditions, besides the turbulent bursts, two prominent scour mechanisms were also observed occurring on either side of the flume axis. Bed particles appeared to be spiraled towards the side walls and the flume axis due to this motion. It should be remarked that the back and forth movement of the impingement point, the frequent but random turbulent bursts and the two prominent scour mechanisms, all occurred at one time or the other.

3. At the asymptotic state, scour profile in the hole region is nominally two-dimensional across the width of the flume. However, in the mound region, the lateral profile is not two-dimensional and has two distinct peaks. These peaks occur closer to the side walls leaving a trough in center portion of the mound.

4. Jet impingement point on the bed moves back and forth and the mean location of impingement is close to the maximum scour depth. Wide range of variation in instantaneous velocity from positive to negative values is a clear indication of back and forth movement of jet.

5. Most of the turbulence activity occurs at the end of negative slope and continues till the start of positive bed slope region. Analysis of the triple correlations indicates sweep type events in the region which can contribute to scour. Ejection type activity also occur which suspend the bed particles and can be carried away by mean flow. Though the velocity measurements were conducted at asymptotic conditions, one can extrapolate to other time periods and conclude than the sweep and ejection contribute significantly to the scour process.

REFERENCES

[1] Annandale, G.W. (2004). Keynote address, Second International Conference on Scour and Erosion. Singapore.

[2] Balachandar, R., Kells, J.A., and Thiessen, R.J. (2000). "The effect of tailwater depth on the dynamics of local scour." *Canadian Journal of Civil Engineering*, 27(1),138-150.

[3] Bey, A (2005), "Two-dimensional scour hole problem". M. A. Sc., thesis, Department of Civil and Environmental Engineering, University of Windsor, Canada.

[4] Faruque, M. A. A. (2004). "Transient local scour by submerged three dimensional wall jets: Effect of tailwater depth." M. A. Sc., thesis, University of Windsor, Canada

[5] Hogg, A. J., Huppert, H. E. and Dade, W.B. (1997). "Erosion by planar turbulent wall jets." *Journal of Fluid Mechanics, 338, 317-340.*

[6] Hopfinger, E.J., Kurniawan, A., Graf, W. H., and Lemmin, U. (2004) "Sediment erosionby Götler vortices: the scour problem." *Journal of Fluid Mechanics,* 520, 327-342.

[7] Rajaratnam, N. and Berry, B. (1977). "Erosion by circular turbulent wall jets." *Journal of Hydraulic Research*, 15(3), p 277-289.

Large-scale scour of the seafloor and the influence of bed material gradation Maasvlakte 2, Port of Rotterdam

S. Boer*, J.A. Roelvink** and T. Vellinga***

* Infram , PO Box 16, 8316 ZG Marknesse, The Netherlands, Tel. +31 (527) 241120, sander.boer@infram.nl
** UNESCO-IHE and WL | Delft Hydraulics, P.O. Box 3015, 2601 DA Delft, The Netherlands, Tel. +31 (15) 2151715, d.roelvink@unesco-ihe.org
*** Delft University of Technology and Port of Rotterdam, P.O. Box 6622, 3002 AP Rotterdam, The Netherlands, Tel +31 (15) 2521309, t.vellinga@portofrotterdam.com

ABSTRACT

Morphological predictions on the basis of uniform (non-graded) sediment revealed an unrealistically strong development of scour hole in the area directly to west of Maasvlakte 2. Additional computations with a state-of-the-art graded sediment transport model have shown that armouring effects do indeed reduce the depth and extent of the scour hole. By means of sensitivity calculations the impact of armouring on the scour development has been examined. The sensitivity tests confirm that the incorporation of armouring processes strongly reduces the development of the scour hole, suggesting an approximately 30% decrease in terms of the area below the -20m depth contour.

I. INTRODUCTION

Rotterdam is creating a prime new European location for port activities and industries which will be reclaimed from the sea, linking directly to the current port and industrial zone. The total land reclamation known as Maasvlakte 2 will consist of 1,000 hectares of commercial sites for deep sea container handling, chemical industry and distribution (figure 1).

The most obvious spot for the new port is situated in an area known as Natura 2000 site Voordelta, a Special Area of Conservation (SAC) (figure 2). Safeguarding the natural values of the Voordelta was one of the leading principles on which the design of Maasvlakte 2 is based.

Figure 1. Design of Maasvlakte 2

The effects of the construction, presence and uses of Maasvlakte 2 have been determined by means of an Environmental Impact Assessment (EIA) and an Appropriate Assessment (AP) of the effects on the SAC. The Maasvlakte 2 project includes compensation projects for the natural values which will or may be lost. Compensation will be found in the realization of a 25.000 ha marine reserve and 35 ha new dunes. In this way the foundation is laid for the construction of a functional and optimal accessible port area, while impact on the natural features and the environment is limited and compensated to the greatest possible extent.

Within the framework of the Maasvlakte 2 project extensive studies have been executed to determine the impact of Maasvlakte 2 on the existing current pattern and the transport of sand and silt, and the resulting morphological changes.

Figure 2. Natura 2000 site Voordelta

Ín this paper specific attention is given on the issue of large scale scour of the surrounding seafloor, which is important from various perspectives, viz.:

- environmental affects: erosion of the seafloor below NAP -20m needs to be compensated in view of loss of habitat and loss of potential feeding area, for protected birds that tend to feed not deeper than -20m.
- maintenance need of the sandy sea defence of Maasvlakte 2: extent and location of the scour hole may cause additional erosion of the beach and dunes.
- dredging requirements: sand originating from the scour hole may cause additional accretion of the existing access channel to the port of Rotterdam (Maasgeul)

II. SCOUR DEVELOPMENT PRESENT SITUATION

The present port entrance dates from the period 1968-1976. Regular bathymetrical surveys have been carried out during construction and after completion of the works. Surveys were executed both in the immediate vicinity of the works in progress (Zuiderdam and Noorderdam) and in a larger sea area to the west of the Maasvlakte (figure 3).

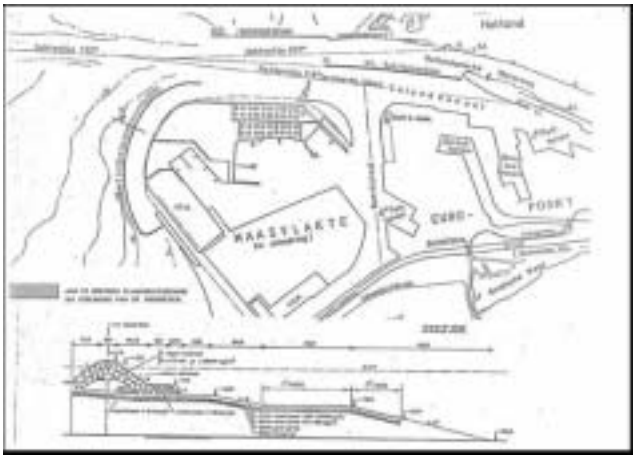

Figure 3. Original situation

During construction local erosion was observed along the Zuiderdam moving along with the temporary head of the structure. At two locations the erosion remained present during a longer period: along the southern bend of the Zuiderdam, at the transition from the rock protection to the sandy beach, and 2 km northward of it, approximately along the middle part of the Zuiderdam (figure 3).

During construction only limited erosion was observed at a larger scale: erosion rates between 1970 and 1976 were approximately 0.1 to 0.2m per year in the sea area to the west of Maasvlakte. Locally, also areas with some accretion were found: accretion rates were less than 0.1m per year.

After completion of the port entrance erosion in the sea area to the west of the Maasvlakte has continued. However, successive bathymetrical surveys indicate that the erosion process gradually slowed down over the years. Presently, the scour hole has reached more or less an equilibrium state (figure 4). The scour hole exists nearly along the whole outer contour of the Zuiderdam covering an area of approximately 160 hectares. The maximum bottom depth is approximately NAP -18m. This implies that since 1970 a maximum erosion of approximately 6 m has occurred (based on the initial depth of NAP -12m).

The design of Maasvlakte 2 shows much agreement with the present situation. Computations for Maasvlakte 2 indicate that the main flow characteristics in the future situation will undergo only little changes as compared to the present situation. Therefore, it is reasonable to expect that the development of scour in the new situation with Maasvlakte 2 will show much resemblance with the scour hole in the present situation.

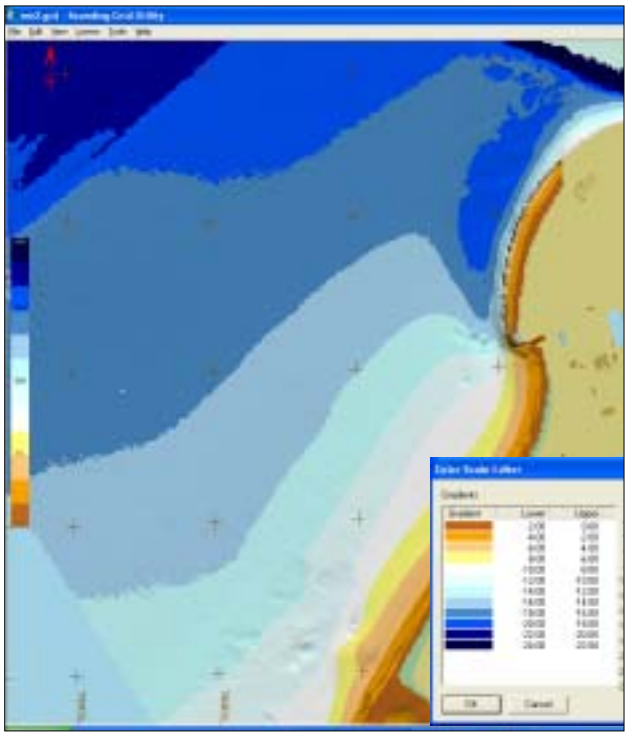

Figure 4. Bathymetrical survey (2006)

III. MORPHODYNAMIC COMPUTATIONS

The morphological impact of Maasvlakte 2, including the issue of large scale scour of the surrounding seafloor, has been determined on the basis of morphodynamic computations. Thereby use has been made of the integrated modelling system Delft3D developed by WL|Delft Hydraulics, including the modules Delft2D-RAM, Delft2D-MOR and Delft3D-ONLINE (Table I).

For the various investigations, which were carried out in the course of time, always modules with latest functionalities and improved usability have been used.

TABLE I.
APPROACHES MORPHODYNAMIC MODELS

DELFT2D-MOR: this process based module which is a subset of DELFT3D system is designed to simulate sediment transports and morphological developments in coastal, river and estuarine areas (Roelvink and Van Banning, 1994). The 'standard' morphodynamic method involves a coupled simulation of waves, currents, transport and bottom changes. A morphological process is built up from morphological time steps, which consist of a simulation of wave-current interaction over a tidal cycle, followed by a number of intermediate steps where transport is computed and averaged over a tidal cycle, and the bottom is updated. The transport and bottom computations are repeated a number of times using "continuity correction" (= constant discharge trough cells), until bottom changes are so large that a full hydrodynamics computation is required. The method requires full transport computations through tidal cycle, which can be time-consuming especially when suspended-load transport induced by waves and currents in shallow areas is to be accounted for.
DELFT2D-RAM: this hybrid module which is also a subset of DELFT3D system can be applied for Rapid Assessment of Morphology (Roelvink et al., 2001). The RAM module can be characterized as a 'quick-and-dirty' bottom updating scheme (based on the "continuity correction') in combination with repeated detailed computations of hydrodynamics and sediment transport using DELFT2D-MOR.
DELFT3D-ONLINE: this module which is the latest refinement of Delft3D system can operate in 2DH and in 3D mode. The module is characterized by online coupling between hydrodynamic and transport/bottom modules which enables simultaneous computation of flows and transports and simultaneous feedback to bottom changes. Therefore, hydrodynamic flow calculations are always carried out using the correct bathymetry. Only the wave model is executed separately. Acceleration of the morphological developments is achieved by up-scaling the bottom developments during each time step by means of a so-called morphological scaling factor. In this project the Delft3D-ONLINE module was used in 2DH mode. The Maasvlakte 2 computations have been carried using a recently developed calculation scheme in which the simulation is split into a number of parallel processes, which all represent different conditions; at a given frequency all processes provide bottom changes to the merging process, which returns a weighted average bottom change to all processes which then continue the simulation (Roelvink, 2006).

In this paper only results will be presented derived from the most recent studies which were carried out in 2005 and 2006 for the current lay-out of Maasvlakte 2 (figure 1).

A. Study 2005 (Roelvink and Aarninkhof, 2005)

The set-up and execution of this study elaborated as much as possible on earlier investigations in order to be able to compare the results (e.g. wave- and current conditions, bed material characteristics, roughness size). However, the most important shortcomings of the previously used Delft2D-RAM/MOR module were overcome by:

- use of the wave propagation model SWAN and the DELFT3D-ONLINE approach which was required for a realistic reproduction of bottom changes in the shallow areas of the Voordelta site.
- incorporation of wave effects which was considered to be important for the development of the scour hole and the maintenance of the sandy beach and dunes.

In figure 5 a typical example of the morphological development is given after 20 years. Both (a) the erosion-sedimentation pattern and (b) the final bottom geometry are shown. It appears that a scour hole will develop almost along the entire north-westerly coastline of Maasvlakte 2. A depth of NAP-25m is exceeded in a rather large area. Sand originating from the scour hole is mainly deposited in the access channel but also in the area to the north of Maasvlakte 2 some accretion can be observed.

The location of the scour hole agrees very well with the area with maximum tidal current velocities during flood phase (figure 6).

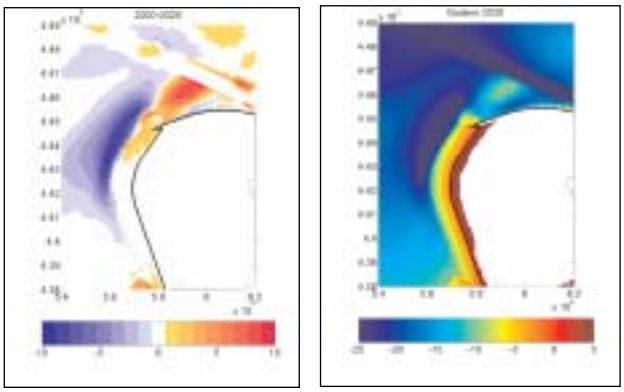

(a) bottom changes (b) bottom geometry

Figure 5. Computation DELFT3D-Online (2005)

In Figure 7 the time development of the scouring is shown in terms of (a) the area subjected to erosion with a depth larger than 1 m, (b) the area which is eroded below NAP-20m and (c) the maximum erosion depth. The applied model and the associated input parameters result in a scour hole with a size of 1420 hectare after 20 years. The area below NAP -20m which is calculated is about 760 ha and the maximum depth is about NAP-27m.

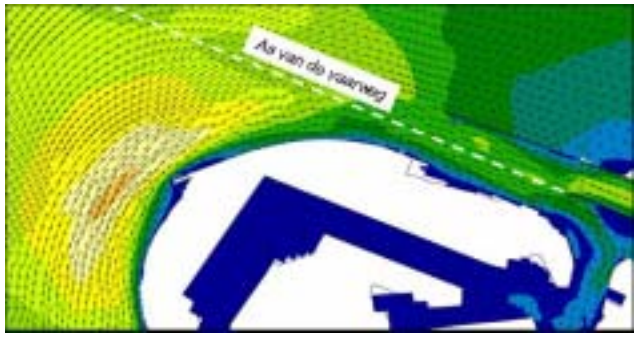

Figure 6. Flow pattern during maximum flood

From these figures it can be seen that the process of scour continues after 20 years and that equilibrium is not yet reached. A similar calculation for the existing situation (autonomous situation) also showed a persistent scour for the next 20 years. These unrealistically strong developments do not correspond with the experiences from the existing Maasvlakte. The observer scour is much smaller that the calculated scour. The calculated size and depth of the scour hole are therefore considered as rather conservative estimates.

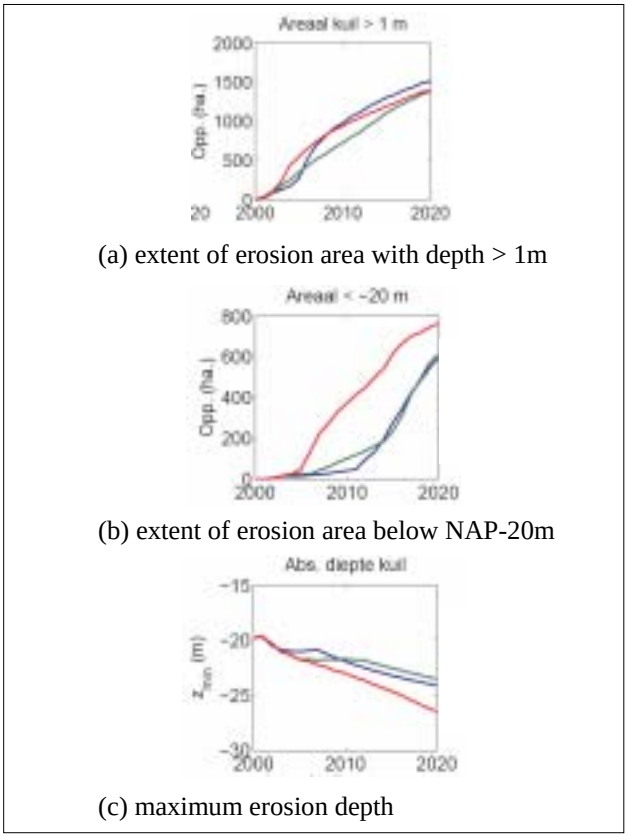

(a) extent of erosion area with depth > 1m

(b) extent of erosion area below NAP-20m

(c) maximum erosion depth

Figure 7. Computation DELFT3D-Online (2005)

t25 = autonomous situation
t26 = intermediate lay-out (850 hectare)
t27 = final lay-out (1000 hectare)

B. Study 2006 (Elias et al., 2006)

Further analysis revealed that the overestimation could be related to the schematization of the seafloor by means of uniform non-graded sediment with a mean particle size of 160 micron.

From literature it is known that sorting of graded bed material and natural armouring of the surface layer may result in a strong reduction of the scouring process. Also a heterogeneous composition of the sub-seafloor may have a strong impact. Until recently experience with the modelling of graded material was mainly restricted to river applications; for coastal areas such applications were still rare. However, with the latest version of DELFT3D this process can be simulated in a schematized way by distinguishing several sediment fractions and bottom layers.

Within the framework of the Maasvlakte 2 project the graded sediment model has been applied to carry out sensitivity computations. The computations are of a comparative nature not aiming at providing an accurate prediction of the location and extent of the scour hole. The latter can only be achieved by extensive calibration and verification of the model and the incorporation of the effect of both wave-induced and flow- induced sediment transports.

1) IJmuiden case

Because only little experience with the model existed, a concise investigation for the scour hole near the harbour moles of IJmuiden has been conducted firstly. The underlying reasoning is that this scour hole is well measured and documented. Also some studies with DELFT3D for the area have been carried out in the past (Roelvink et al., 1994; Lesser et al., 2004).

From these computations the correct functioning of the model was demonstrated. The sorting process of bed material in the scour hole by erosion of finer fractions and lagging behind coarser fractions could be reproduced in a satisfactory manner (figure 8). Also a lot of experience was obtained about the best way of schematisation, viz.: number of layers, layer thickness and fractional partition of bed material.

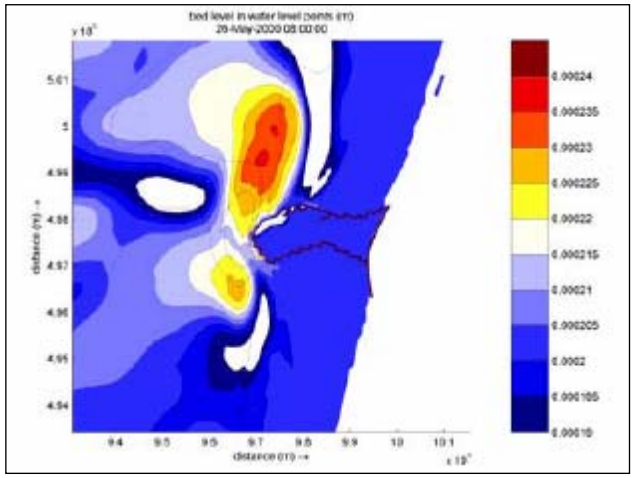

Figure 8. IJmuiden case, spatial distribution of mean grainsize (after 20 years)

2) Maasvlakte 2 case

Subsequently, computations have been performed for the situation of Maasvlakte 2 using the graded sediment model. The set-up of the model was, wherever possible, chosen in accordance with the study of 2005.

Computations were carried out for uniform and graded bed material. For the computations with uniform sediment a number of mean particle sizes have been distinguished, viz: 160 and 200 micron (overall values entire area) and

160/285 micron (with a distinction between the characteristics of seabed and cross-shore profile of Maasvlakte 2). The characteristics of the graded material have been derived from grading curves determined from soil drilling samples wich were collected in the area during a survey in 2005 (figure 9).

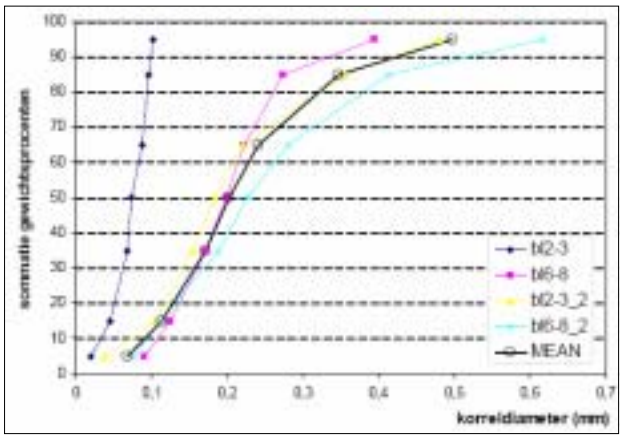

Figure 9. Grading curves from soil drilling samples collected in the area

The bed material is schematized using the average grading curve represented by 5 sediment fractions (table II).

TABLE II.
SEDIMENT FRACTIONS

Fraction	D50 (micron)	relative distribution (%)
1	91	20
2	171	30
3	242	30
4	347	10
5	487	10

It appears that the average D50 of the bed material is 200 micron. This is considerably larger than the value of 160 micron which was used in all previous computations of Maasvlakte 2 (as a representative mean value of the whole study area). Further on it is shown that this difference in particle size will already have some impact on the development of the scour hole.

In the original computations several schematizations for the sub-seafloor were used. The results presented in this paper only refer to the schematization with 15 bottom layers each having a thickness of 1 m.

In figure 10 the calculated bottom geometry after 20 years is shown for the various simulations with uniform and graded bed material. From this figure the difference between graded and uniform material can be seen very clearly. With graded material the maximum erosion depth and the extent of the erosion area are strongly reduced. The results of the cases with uniform material are very similar to the results of previous studies. Some differences in extent and depth of the scouring hole can be observed, depending on the particle size. However, the general shape of the scouring hole remains the same in these cases.

In figure 11 a comparison is made between the computational results with graded bed material and uniform bed material (with a D50 of 200 micron). The differences between these two cases are both related to the maximum scour depth and the extent of the erosion area. With uniform bed material a maximum depth of more than 10m below the original bottom level is reached after 20 years (NAP -26.5m). With graded material this is reduced to 4m (NAP-20.5m). With the effect of graded material incorporated the development of the scour hole is strongly reduced; an approximately 30% reduction in terms of the area below the NAP-20m depth contour is suggested.

IV. CONCLUSIONS

Morphological predictions on the basis of uniform (non-graded) sediment revealed an unrealistically strong development of a scour hole in the area directly west of Maasvlakte 2. Additional computations with a state-of-the-art graded sediment transport model have shown that armouring effects do indeed reduce the depth and extent of the scour hole. By means of sensitivity calculations the impact of armouring on the scour development has been examined. For that purpose the existing Maasvlakte 2 model was extended with a graded sediment schematisation based on the composition of the sub seafloor. The sensitivity tests confirm that the incorporation of armouring processes strongly reduces the development of the scour hole, suggesting an approximately 30% decrease in terms of the area below the NAP-20m depth contour.

In summary, the use of an innovative, graded sediment transport model has shown the potential for improved prediction of the morphological evolution of scour holes. These techniques enable the Port of Rotterdam to anticipate well on the expected scour hole development, the resulting access channel maintenance and additional compensation for the scour below NAP-20m in the planned marine reserve. Additionally the model can contribute importantly to future EIA's for large-scale coastal interventions.

ACKNOWLEDGMENT

We thank the Port of Rotterdam Authority giving this opportunity to publish and to present the results of the research in question at the ICSE 2006.

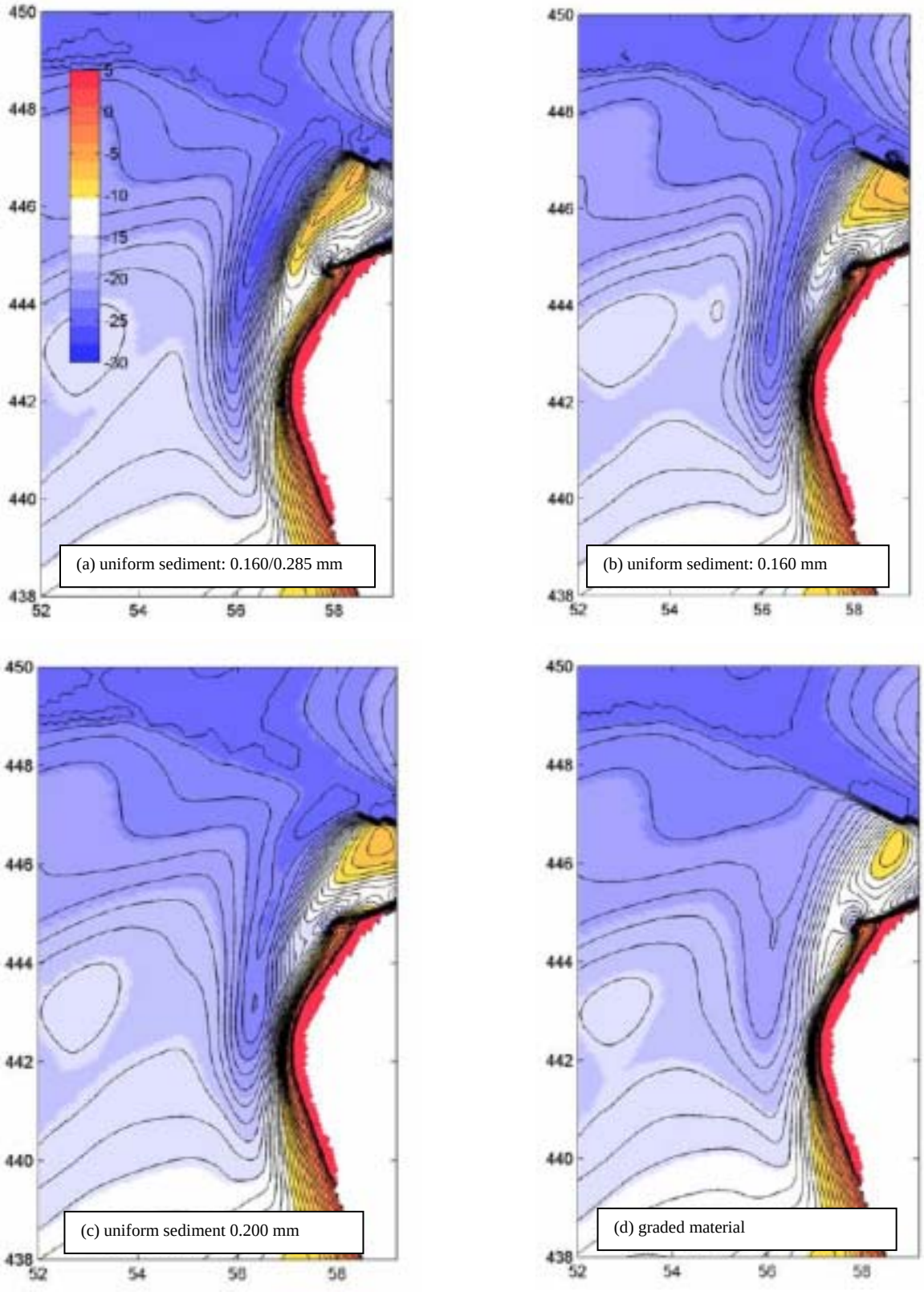

Figure 10. Example DELFT3D-Online (2006)

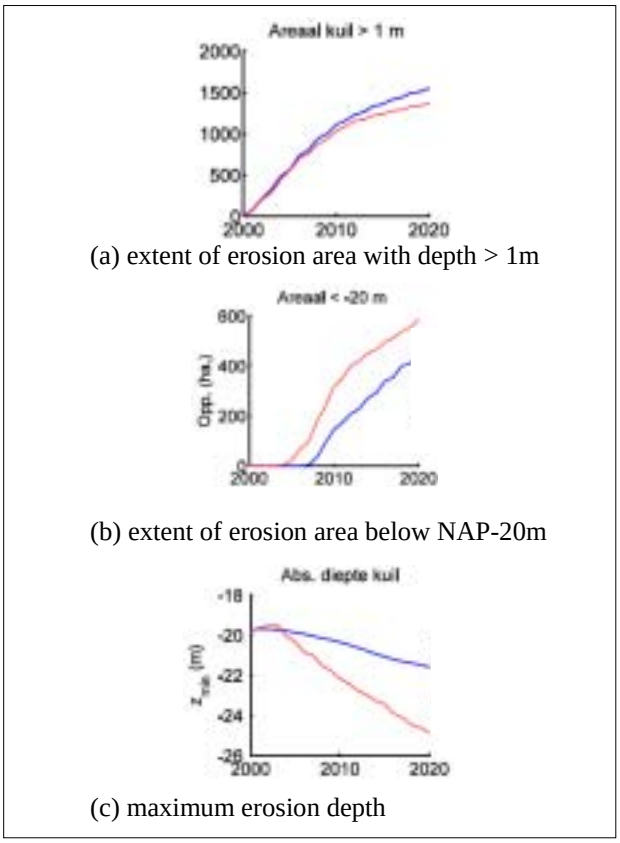

(a) extent of erosion area with depth > 1m

(b) extent of erosion area below NAP-20m

(c) maximum erosion depth

Figure 11. Example DELFT3D-Online (2006) (red: uniform; blue: graded)

REFERENCES

Elias, E., Aarninkhof, S.., Roelvink, J.A. (2006). Ontwikkeling Ontgrondingskuil bij Maasvlakte 2, Z4114.00, WL| Delft Hydraulics.

Lesser, G.R., Roelvink, J.A., van Kester, J.A.T.M., Stelling, G.S., (2004). Development and validation of a threedimensional model, Coastal Engineering 51, pp. 883915.

Roelvink, J.A. and Banning, G.K.F.M. van (1994). Design and development of Delft3D and application to coastal morphodynamics, Hydroinformatics 94, Verwey, Minns, Babovic & Maksimovic (eds), Balkema, Rotterdam, 1994, pp. 451-455.

Roelvink, D., Boutmy, A., Stam, J.M. (1998). A simple method to predict longterm morphological changes. Proceedings of the 26th International Conference on Coastal, Engineering, Copenhagen. ASCE, New York, pp. 3224–3237.

Roelvink, J.A., Jeuken, M.C.J.L., van Holland, G., Aarninkhof, S.G.J. and Stam, J.M.T. (2001). Long-term, process-based modelling of complex areas. Proceedings of Coastal Dynamics ’01, Lund, Sweden, June 2001. New York, ASCE, 383–92.

Roelvink, J.A., Aarninkhof, S.G.J. (2005). Onderbouwend onderzoek MER Maasvlakte2. Onderdeel Morfologie. Z3959, WL/Delft Hydraulics.

Roelvink, J.A. (2006). Overview of coastal morphodynamic evolution techniques, Coastal Engineering, Volume 53, Issue 2-3, 1 February 2006, Pages 277-287

Waterloopkundig Laboratorium, Scouring near the Port of IJmuiden, WL-report H460, 1988 (in Dutch).

Application of a physics based scour prediction model to Tucurui Dam Spillway (Brazil)

E.F.R. Bollaert* and B. Petry**
* AquaVision Engineering Ltd., Lausanne, Switzerland
** Engineering Consultant, Delft, The Netherlands

I. INTRODUCTION

This paper presents the application of a recently developed physics based model for the prediction of scour formation downstream of large dam spillways (Bollaert, 2004). The model is based on experiments with air-water jets impinging on jointed media and related numerical modeling of involved physical phenomena. It predicts ultimate scour depth and time evolution of scour formation in different types of fissured media. It is under continuous development and has been applied to several scour cases worldwide. The model includes several physics based modules for scour prediction that are based on the resistance of the medium to fissure initiation and propagation, as well as on the resistance of individual blocks to sudden ejection.

The real case example of Tucurui Dam Spillway, located on the Tocantins River in northern Brazil is presented here (Petry et al., 2002). The spillway facilities were designed to handle a design discharge of up to 100,000 cms. Model tests using non-cohesive and cohesive representations of the plunge pool were conducted during the design process to verify scouring. They resulted in the forecast of a satisfactory scour behavior. During the operation period, underwater surveys confirmed the occurrence of only minor effects caused by the recorded floods.

The 17 year long period of record (1984-2001) included several large flood occurrences but did not contain an extreme flood event. The numerical model described above was first calibrated based on the prototype observations of the plunge pool resistance and then design discharge conditions were applied to forecast the plunge pool behavior with regard to scour formation under such an extreme event. The Paper presents the details of the modeling process and provides an account of results obtained for the case of such an extreme occurrence.

Tucurui Dam Spillway is located on the Tocantins River in northern Brazil, in operation since 1984 (Petry et al., 2002) The uncommonly large dimensions of the Tucurui Spillway facilities have practically no precedence in the history of large Dams. As illustrated in Figure 1, they are characterized by: an ogee type gate-controlled surface overflow structure topped by 23 radial gates (20.75m high x 20m wide); a compact flip bucket; and a 50m deep plunge pool extending over the entire length of the structure, pre-excavated in the downstream rock. The spillway facilities were designed to handle an un-precedent design discharge of up to 110,000 cms under a gross head of 60 to 70 m. Extensive and detailed Hydraulics Laboratory model tests using different non-cohesive and cohesive representations of the plunge pool area were conducted during the design process to verify scouring. They resulted in the forecast of a satisfactory and controlled scouring behavior for a pre-excavated plunge pool at an elevation of – 40 m a.s.l. At a later stage, during the operation period, underwater surveys were conducted by the Owner to verify such scour behavior. This confirmed the occurrence of only minor effects caused by the actually recorded sequence of flood discharges.

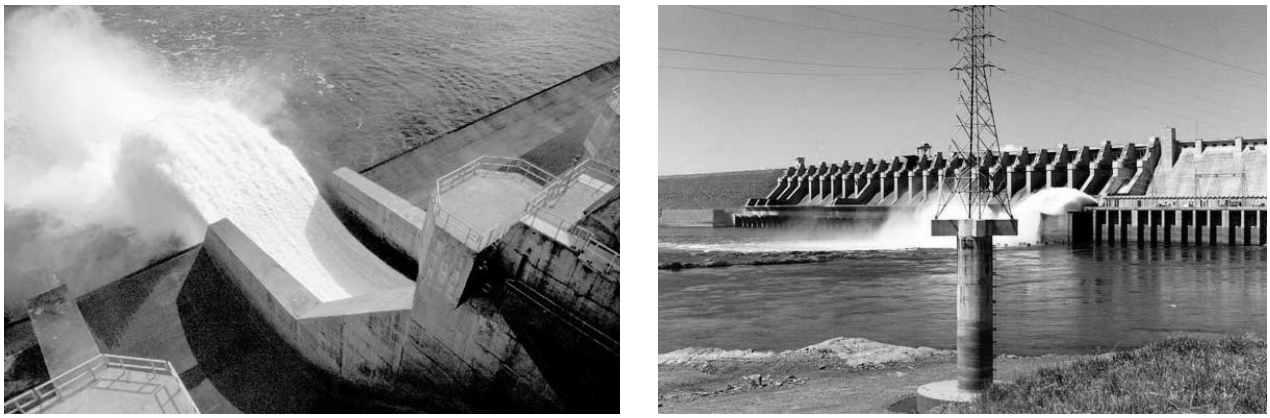

Figure 1. a) Detailed view of flip bucket spillway; b) General view of spillway and plunge pool

II. HISTORY OF FLOODING AND SCOUR FORMATION AT TUCURUI DAM

Tucurui Dam has a well-described and amazing flood history. Floods and water levels of the Tocantins River have been recorded since 1969. Initially, extreme flood discharge values were determined based on a statistical analysis of the data of Tucurui and Itupiranga about 175 km upstream of the dam site. Between 1978 and 1980, however, three major flood events occurred, resulting in a redefinition and calibration of the flow rating curve at Tucurui. This allowed defining the 1980 peak flood at 68'400 m^3/s, the largest value ever recorded on the Tocantins River.

More detailed subsequent flood studies showed that the initially assumed extreme flood values for the dam spillway had been significantly underestimated. As a function of meteorological and drainage conditions, the PMF event was increased from 90'000 m^3/s to 110'000 m^3/s, in agreement with the maximum possible capacity of the spillway under construction at that time. This increase, however, would need the construction of an additional auxiliary spillway with 3 additional gates during phase 2 of the power house construction (1994).

Flood records made since dam construction have shown that the PMF value of 110'000 m^3/s is slightly conservative. For example, the maximum peak discharge recorded between 1984 and 2001 was of only 43'400 m^3/s in January 1990. Hence, in conjunction with economic considerations, it has finally been decided to not construct the auxiliary spillway and to keep the initial spillway design.

Second, scour formation in the downstream plunge pool has been described by a series of bathymetric surveys and underwater inspections between 1984 and 2001. The first inspection took place in 1984 and allowed detecting sedimentation along the right hand side of the plunge pool due to 3 years of continuous river flow through the diversion outlets at time of dam construction. The second survey took place in 1985, but had to be restricted to the most left part of the plunge pool, due to turbulent vortices in the basin.

The third survey occurred in 1986, after two years of continuous spillway operation. This showed that all former sediment deposits had been washed away and that, as predicted by the laboratory model, only two areas along the pool bottom were slightly eroded. The maximum observed scour formation was of only 5 m. It was assumed that this erosion is related to removal of partially detached rock blocks during initial spillage. These blocks were fractured and detached by blasting during dam construction and their removal does not represent any risk to the structure.

This satisfactory plunge pool performance, together with a progressive reduction of flood discharges and spillage periods, allowed reporting the fourth bathymetric survey to 1997. This survey showed erosion in the same areas than the ones detected during previous surveys. The maximum scour depth was still situated around – 45m.

Hence, as a conclusion, it may be stated that the pre-excavated plunge pool behaves like expected during dam construction. For a recorded period of 17 years, incorporating 6 flood events of more than 31'000 m^3/s and a maximum value of 43'400 m^3/s, no significant scour formation could be observed. Nevertheless, since the extreme flood event of 68'000 m^3/s during dam construction, no major flood events have been recorded.

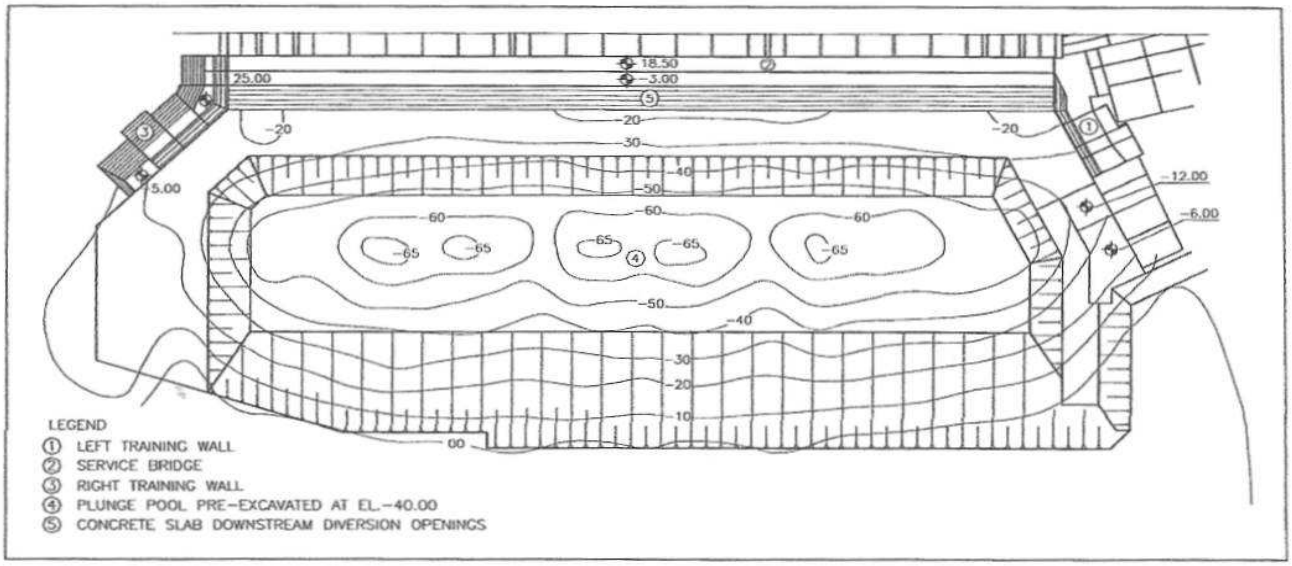

Figure 2. Scour formation in plunge pool following laboratory test with gravel and 100'000 cms (Large Brazilian Spillways, ICOLD, Petry et al. 2002)

III. Detailed Spillway and Plunge Pool Characteristics

The spillway and plunge pool of Tucurui Dam are presented in Figures 2 and 3. The spillway consists of 23 bays with radial gates of 20 m width by 20.75 m height. The spillway crest has a Creager profile. Its detailed design was based on two-and three-dimensional hydraulic model tests at a maximum scale of 1/50. The chute of the spillway ends with a compact flip bucket. The bucket has a radius of 35 m, an elevation of 30 m and an exit angle of 32°, resulting in minimum and maximum jet throw distances of 80 m respectively 130 m.

Plunge pool design has been optimized by means of hydraulic model tests. Tests have been performed for discharges between 15'000 and 100'000 m^3/s and for pool bottom elevations of -15, -25 and -40 m a.s.l. The latter pool depth has been retained because significantly reducing return currents in the modeled basin and avoiding substantial erosion for discharges of up to 50'000 m^3/s. For a design discharge of about 100'000 m^3/s, the model tests predicted scour formation down to –65m, i.e. 25 m of additional scour formation compared to the pre-excavated bottom level of the pool. This result was obtained by using non-cohesive gravel and might thus be considered as slightly conservative.

The choice of a flip bucket together with a pre-excavated plunge pool has been influenced by the very high unitary discharges (up to 228 m^2/s at maximum capacity) and by the valley's geomorphology. Also, pre-excavation of the rock allowed to re-utilize this material for the concrete of the spillway.

IV. Comprehensive Scour Model (CSM, Bollaert 2004)

A new and physics based scour prediction model has been developed at the Laboratory of Hydraulic Constructions of the Swiss Federal Institute of Technology in Lausanne, Switzerland (Bollaert, 2002 and 2004; Bollaert & Schleiss, 2005). The model uses physical laws and phenomena that have been simplified to allow its application to practical engineering projects. It is based on experimental and numerical investigations of dynamic water pressures in rock joints (Bollaert, 2002).

The model comprises two methods that describe failure of fractured rock. The first one, the Comprehensive Fracture Mechanics (CFM) method, determines the ultimate scour depth by expressing instantaneous or time-dependent joint propagation due to water pressures jacking inside the joint. The second one, the Dynamic Impulsion (DI) method, describes the ejection of rock blocks from their mass due to sudden uplift pressures.

The structure of the Comprehensive Scour Model consists of three modules: the falling jet, the plunge pool and the rock mass. The latter module implements the two aforementioned failure criteria. More details can be found in Bollaert (2004) or Bollaert & Schleiss (2005).

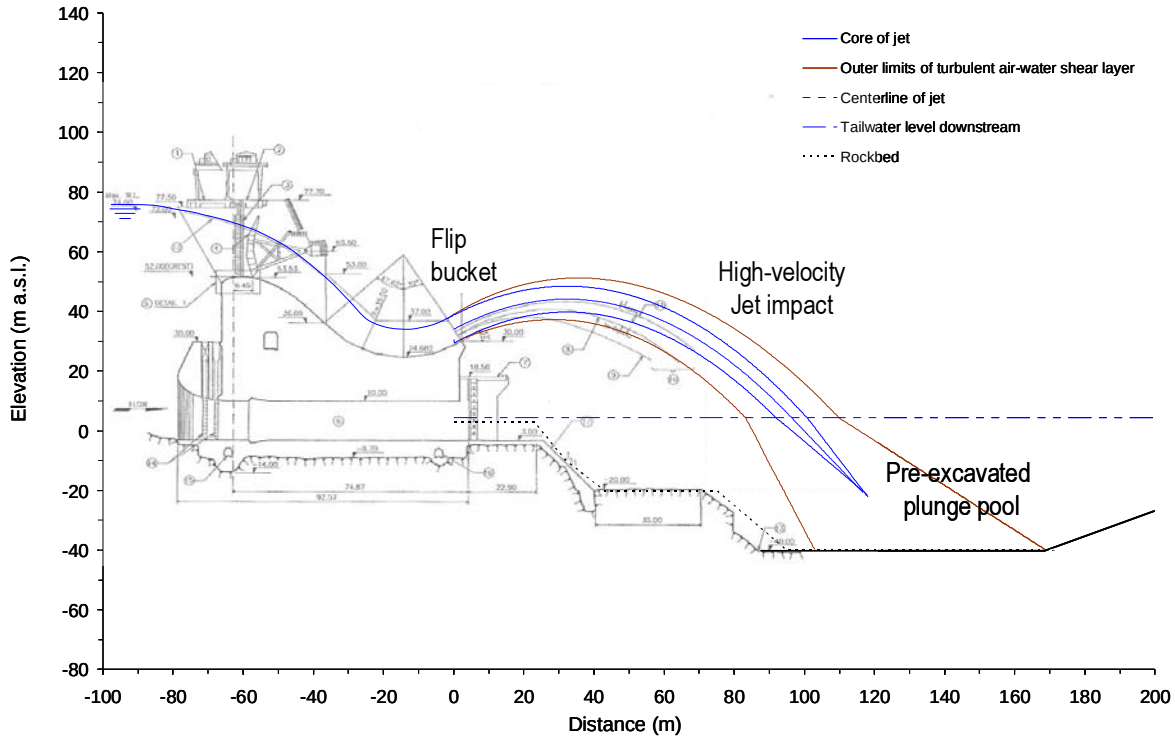

Figure 3. Cross-sectional view of spillway and pre-excavated plunge pool.

A. *Falling jet Module*

This module describes how the hydraulic and geometric characteristics of the jet are transformed from dam issuance down to the plunge pool (Figure 3). Three parameters characterize the jet at issuance: the velocity V_i, the diameter (or width) D_i and the initial turbulence intensity Tu, defined as the ratio of velocity fluctuations to the mean velocity.

The jet trajectory is based on ballistics and air drag and will not be further outlined. The jet module computes the longitudinal location of impact, the total trajectory length L and the velocity and diameter at impact V_j and D_j. The turbulence intensity is presented in the next paragraph and defines the spread of the jet δ_{out} (Ervine et al., 1997). Superposition of the outer spread to the initial jet diameter D_i results in the outer jet diameter D_{out}, which is used to determine the extent of the zone at the water-rock interface where severe pressure damage may occur. Relevant mathematical expressions are written:

$$Tu = u'/U \tag{1}$$

$$\frac{\delta_{out}}{X} = 0.38 \cdot Tu \tag{2}$$

$$D_j = D_i \cdot \sqrt{\frac{V_i}{V_j}} \tag{3}$$

$$V_j = \sqrt{V_i^2 + 2gZ} \tag{4}$$

$$D_{out} = D_i + 2 \cdot \delta_{out} \cdot L \tag{5}$$

in which δ_{out} is the half angle of outer spread, X the longitudinal distance from the point of issuance and Z the vertical fall distance of the jet. Typical outer angles of jet spread are 3-4 % for roughly turbulent jets (Ervine & Falvey, 1987). The corresponding inner angles of jet spread are 0.5 - 1 %.

The angle of the jet at impact is neglected, which is reasonable for impingement angles that are close to the vertical (70-90°). For smaller impingement angles, it is proposed to redefine the water depth Y as the exact trajectory length of the jet through the water cushion, and not as the vertical difference between water level and pool bottom.

B. *Plunge Pool Module*

This module describes the hydraulic and geometric characteristics of the jet when traversing the plunge pool and defines the water pressures at the water-rock interface. The plunge pool water depth Y is essential. For near-vertically impacting jets, it is defined as the difference between the water level and the bedrock level at the point of impact. The water depth increases with discharge and scour formation. Initially, Y equals the tailwater depth t (Figure 4). During scour formation, Y has to be increased with the depth of the formed scour h. Prototype observations indicate possible mounding at the downstream end of the pool. This mounding results from detached rock blocks that are swept away and that deposit immediately downstream. This can raise the tailwater level. The effect is not directly described in the model but can easily be added to the computations by appropriate modification of the water depth during scour.

The water depth Y and jet diameter at impact D_j determine the ratio of water depth to jet diameter at impact Y/D_j. This ratio is directly related to jet diffusion. Precaution should be taken when applying this parameter. Significant differences may exist in practice due to the appearance of vortices or other surface disturbing effects, which can change the effective water depth in the pool. Again, engineering judgment is required on a case-by-case basis.

Dynamic pressures acting at the water-rock interface can be generated by core jet impact, appearing for small water depths Y, or by developed jet impact (shear layer), appearing for Y/D_j higher than 4 to 6 (for plunging jets) (Figure 4). The most relevant pressure characteristics are the mean dynamic pressure coefficient C_{pa} and the root-mean-square (rms) coefficient of the fluctuating dynamic pressures C'_{pa}, both measured directly under the centerline of the jet. These coefficients correspond to the ratio of pressure head (in [m]) to incoming kinetic energy of the jet ($V^2/2g$) and are defined as follows:

$$C'_{pa} = 0.00022 \cdot \left(\frac{Y}{D_j}\right)^3 + 0.0079 \cdot \left(\frac{Y}{D_j}\right)^2 + 0.0716 \cdot \left(\frac{Y}{D_j}\right) + \eta \tag{6}$$

$$C_{pa} = 38.4 \cdot (1 - \alpha_i) \cdot \left(\frac{D_j}{Y}\right)^2 \quad \text{for } Y/D_j > 4\text{-}6 \tag{7}$$

$$C_{pa} = 0.85 \quad \text{for } Y/D_j < 4\text{-}6 \tag{8}$$

$$\alpha_i = \frac{\beta}{1+\beta} \tag{9}$$

Eqs. (7)-(9) are based on Ervine et al. (1997). The air concentration at jet impact α_i is defined as a function of the volumetric air-to-water ratio β. Plausible prototype values for β are 1-2. For a given α_i, mean and fluctuating dynamic pressures are defined as a function of Y, D_j and Tu. Similar expressions are proposed at locations radially outwards from the jet's centerline and can be found in Bollaert (2002). Tu is assumed representative for low-frequency fluctuations, which define the stability of the jet during its fall. Hence, Tu can be related to the rms values of the pressure fluctuations at the pool bottom. This is essential because these fluctuations generate peak pressures inside underlying rock joints.

Following eq. (6), the rms values of the pressure fluctuations at the pool bottom (C'_{pa}) depend on Y/D_j and Tu. The parameter η of eq. (6) represents the degree of jet stability: η is equal to 0 for compact jets and goes up to 0.15 for highly turbulent and unstable jets. Compact jets

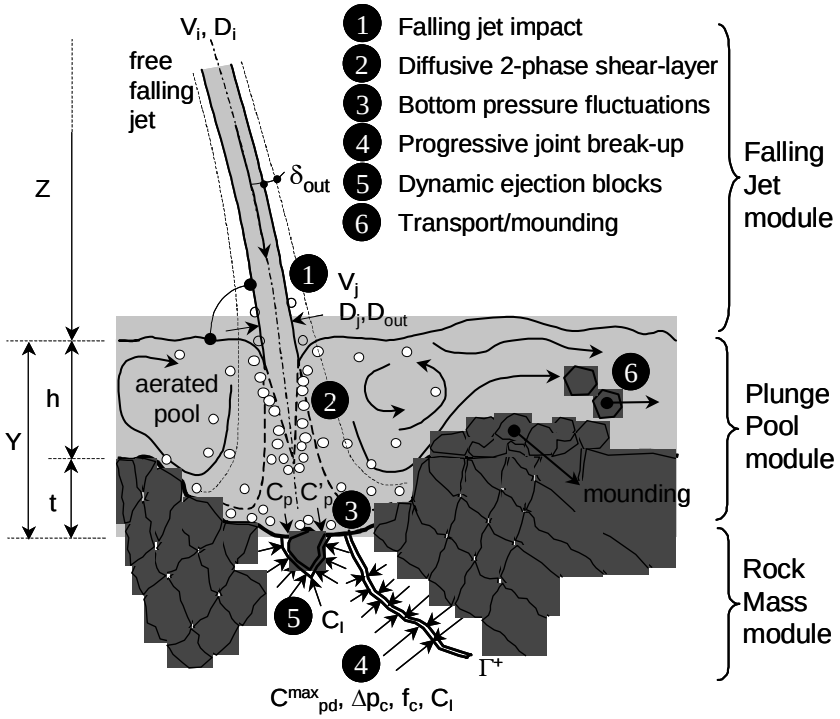

Figure 4. Main parameters of scour and its physical phenomena (Bollaert, 2004)

(Tu < 1%) are smooth-like during their fall, without any instability. Highly turbulent jets have a Tu > 5%. In between, for 1% < Tu < 5%, η has to be chosen between 0 and 0.15 as a function of jet stability effects.

Generally, Tu is unknown. Under such circumstances, estimation can be made based on the type of outlet structure (Bollaert et al., 2002). As such, a free overfall jet has an estimated Tu of 1-3 %, a ski jump 3-5 %, and intermediate or bottom outlets 5-8 %. However, Tu may largely depend on the outlet geometry, the flow pattern upstream, etc. These aspects should be accounted for by appropriate engineering judgment.

C. Rock Mass Module

The pressures defined at the bottom of the pool are used for determination of the transient pressures inside open-end or closed-end rock joints. The parameters are:

1. maximum dynamic pressure coefficient C^{max}_p
2. characteristic amplitude of pressure cycles Δp_c
3. characteristic frequency of pressure cycles f_c
4. maximum dynamic impulsion coefficient C^{max}_I

The first parameter is relevant to brittle propagation of closed-end rock joints. The second and third parameters express time-dependent propagation of closed-end rock joints. The fourth parameter is used to define dynamic uplift of rock blocks formed by open-end rock joints.The maximum dynamic pressure C^{max}_p is obtained through multiplication of the rms pressure C'_{pa} with an amplification factor Γ^+, and by superposition with the mean dynamic pressure C_{pa}. Γ^+ expresses the ratio of the peak value inside the rock joint to the rms value of pressures at the pool bottom and has been determined based on prototype-scaled experiments (Bollaert, 2004).

The product of C'_{pa} times Γ^+ results in a maximum pressure, written as (Bollaert, 2002):

$$P_{\max}[Pa] = \gamma \cdot C_p^{\max} \cdot \frac{V_j^2}{2g} = \gamma \cdot \left(C_{pa} + \Gamma^+ \cdot C'_{pa}\right) \cdot \frac{V_j^2}{2g} \quad (10)$$

The main uncertainty of eq. (10) lies in the Γ^+ factor. The characteristic amplitude of the pressure cycles, Δp_c, is determined by the maximum and minimum pressures of the cycles. The characteristic frequency of pressure cycles f_c follows the assumption of a perfect resonator system and depends on the air concentration in the joint α_i and on the length of the joint L_f.

Beside the dynamic pressure inside rock joints, the resistance of the rock also has to be determined. The cyclic character of the pressures generated by the impact of a high-velocity jet makes it possible to describe joint propagation by *fatigue* stresses occurring at the tip of the joint. This can be described by Linear Elastic Fracture Mechanics (LEFM).

A simplified methodology is used (Bollaert, 2004). It is called the *Comprehensive Fracture Mechanics (CFM) method* and applicable to any type of partially jointed

rock. Pure tensile pressure loading inside rock joints is described by a stress intensity factor K_I, which represents the amplitude of the stresses that are generated by the water pressures at the tip of the joint. The corresponding resistance of the rock mass against joint propagation is expressed by its fracture toughness K_{Ic}.

Joint propagation distinguishes between brittle (or instantaneous) joint propagation and time-dependent joint propagation. The former happens for a stress intensity factor that is equal to or higher than the fracture toughness of the material. The latter is occurring when the maximum possible water pressure results in a stress intensity that is inferior to the material's resistance. Joints may then be propagated by fatigue. Failure by fatigue depends on the frequency and the amplitude of the load cycles. The fracture mechanics implementation of the hydrodynamic loading consists of a transformation of the water pressures in the joints into stresses in the rock. These stresses are characterized by K_I as follows:

$$K_I = P_{\max} \cdot F \cdot \sqrt{\pi \cdot L_f} \qquad (11)$$

in which K_I is in MPa$\sqrt{m}$ and P_{max} in MPa. The boundary correction factor F depends on the type of crack and on its persistency, i.e. its degree of cracking defined as a/B or b/W in Figure 5. This figure presents two basic configurations for partially jointed rock. The choice of the most relevant geometry depends on the type and the degree of jointing of the rock.

The first crack is of semi-elliptical shape and partially sustained by the surrounding rock mass in two horizontal directions. Corresponding stress intensity factors should be used in case of low to moderately jointed rock. The second crack is single-edge notched and of two-dimensional nature. Support from the surrounding rock mass is only exerted perpendicular to the plane of the notch and, as a result, stress intensity factors will be substantially higher. Thus, it is appropriate for significantly to highly jointed rock.

For practice, F values of 0.5 or higher are considered to correspond to completely broken-up rock, i.e. the DI method becomes more applicable than the CFM method. For values of 0.1 or less, a tensile strength approach is more plausible. However, most of the values in practice can be considered between 0.20 and 0.40, depending on the type and number of joint sets, the degree of weathering, joint interdistances, etc.

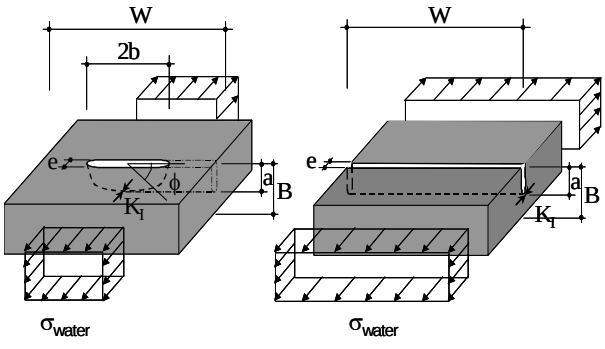

Figure 5. Rock joint parameters (Bollaert, 2004)

The fracture toughness K_{Ic} has been related to the mineralogical type of rock and to the unconfined compressive strength UCS. Furthermore, corrections are made to account for the loading rate and the in-situ stress field. The corrected fracture toughness is defined as the in-situ fracture toughness $K_{I,ins}$ and is based on a linear regression of available literature data.

$$K_{I\,ins,\,UCS} = (0.008\text{-}0.010)\cdot UCS + (0.054\sigma_c) + 0.42 \qquad (12)$$

in which σ_c represents the confinement horizontal in-situ stress and T, UCS and σ_c are in MPa. Instantaneous joint propagation will occur if $K_I \geq K_{I,ins}$. If this is not the case, joint propagation is expressed by an equation as originally proposed to describe fatigue growth in metals:

$$\frac{dL_f}{dN} = C_r \cdot \left(\Delta K_I / K_{Ic}\right)^{m_r} \qquad (13)$$

in which N is the number of pressure cycles. C_r and m_r are material parameters that are determined by fatigue tests and ΔK_I is the difference of maximum and minimum stress intensity factors. To implement time-dependent joint propagation into the model, m_r and C_r have to be known. They represent the vulnerability of rock to fatigue and can be derived from available literature data on quasi-steady break-up by water pressures in joints (Atkinson, 1987). A first-hand calibration for granite (Cahora-Bassa Dam; Bollaert, 2002) resulted in C_r = 1E-8 for m_r = 10.

The fourth dynamic parameter is the maximum dynamic impulsion $C^{max}{}_I$ in an open-end rock joint (underneath single block), obtained by time integration of net forces on the block:

$$I = \int_0^{\Delta tpulse} \left(F_u - F_o - G_b - F_{sh}\right)\cdot dt = m \cdot V_{\Delta tpulse} \qquad (14)$$

in which F_u and F_o are the forces under and over the block, G_b is the immerged weight of the block and F_{sh} represents the shear and interlocking forces. The shape of a block and the type of rock define the immerged weight. Shear and interlocking forces depend on the joint pattern and the in-situ stresses. As a first approach, they can be neglected. The pressure field over the block is governed by jet diffusion. The pressure field under the block corresponds to transient pressure waves. The first step is to define the maximum net impulsion I^{max}. I^{max} is defined as the product of a net force and a time period. The corresponding pressure is made non-dimensional by the jet's kinetic energy $V^2/2g$. This results in a net uplift pressure coefficient C_{up}. The time period is non-dimensionalized by the travel period that is characteristic for pressure waves inside rock joints, i.e. $T = 2\cdot L_f/c$. This results in a time coefficient T_{up}. Hence, the non-dimensional impulsion coefficient C_I is defined by the

product $C_{up} \cdot T_{up} = V^2 \cdot L/g \cdot c$ [m·s]. The maximum net impulsion I^{max} is obtained by multiplication of C_I by $V^2 \cdot L/g \cdot c$. Prototype-scaled analysis of uplift pressures resulted in the following expression for C_I:

$$C_I = 0.0035 \cdot \left(\frac{Y}{D_j}\right)^2 - 0.119 \cdot \left(\frac{Y}{D_j}\right) + 1.22 \qquad (15)$$

Failure of a block is expressed by the displacement it undergoes due to the net impulsion C_I. This is obtained by transformation of $V_{\Delta tpulse}$ in eq. (14) into a net uplift displacement h_{up}. The net uplift displacement that is necessary to eject a rock block from its matrix is difficult to define. It depends on the protrusion and the degree of interlocking of the blocks. A first-hand calibration on Cahora-Bassa Dam (Bollaert, 2002) resulted in a critical net uplift displacement of 0.20.

V. Application of CSM model to Tucurui Dam

The Comprehensive Scour Model has been applied to Tucurui Dam spillway and plunge pool. The model has first of all been calibrated based on the assumption that, for flood events of up to 50'000 m^3/s, no significant scour forms at the plunge pool bottom.

Second, the model has been applied to a fictitious design event with a discharge of 110'000 m^3/s. The different steps performed are explained hereafter for each module of the scour model.

A. *Falling Jet at Tucurui Dam*

The jet at Tucurui Dam is issuing from a chute with flip bucket. As such, numerical computations have first been performed of the air-water flow characteristics along the chute. The water surface line for a 110'000 m^3/s is presented in Figure 3.

The flow velocity at the lip of the flip bucket equals 27.8 m/s, for a total flow depth of about 8 m. The upstream water level is 75.3 m a.s.l. and the downstream plunge pool water level is at 4.4 m a.s.l. The jet is thus of rectangular shape with a width of 20m and an issuance thickness of 8m.

Second, the jet characteristics at impact in the tailwater depth have been defined based on ballistics accounting for air drag. As such, the jet velocity at impact has been computed at 37.9 m/s for an inner jet core diameter of about 6.9 m. Its turbulence intensity has been estimated at 8 % and its air concentration at impact at 40 %, corresponding to very turbulent air-water jets.

B. *Plunge Pool Diffusion at Tucurui Dam*

The diffusion of the jet through the pool water depth is presented in Figure 3. Significant spread of the jet is computed, with an outer jet diameter at impact in the pool of about 20m. The jet core vanishes before impacting the plunge pool bottom, corresponding to fully developed jet conditions.

Very little information is available regarding the type and quality of the rock mass at Turcurui Dam. As a first-hand approach, and based on the initial model calibration for lower discharges, the following table of values has been used for the computations:

Table 1. Rock mass characteristics used for the numerical computations at Tucurui Dam

	Property	Symbol	CONSERV	AVERAGE	BENEF	Unity
Rock mass	Unconfined Compressive Strength	UCS	50	75	100	MPa
	Density rock	γ_r	2600	2700	2800	kg/m3
	Ratio horizontal/vertical stresses	K_0	2-3	2-3	2-3	-
	Typical maximum joint length	L	1	1	1	m
	Vertical persistence of joint	P	0.25	0.25	0.25	-
	Form of rock joint	-	single-edge	elliptical	circular	-
	Tightness of joints	-	tight	tight	tight	-
	Total number of joint sets	N_j	3+	3	2+	-
	Typical rock block length	l_b	1	1	1	m
	Typical rock block width	b_b	1	1	1	m
	Typical rock block height	z_b	0.5	0.75	1	m
	Joint wave celerity	c	150	125	100	m/s
	Fatigue sensibility	m	8	9	10	-
	Fatigue coefficient	C	1.00E-07	1.00E-07	1.00E-07	-

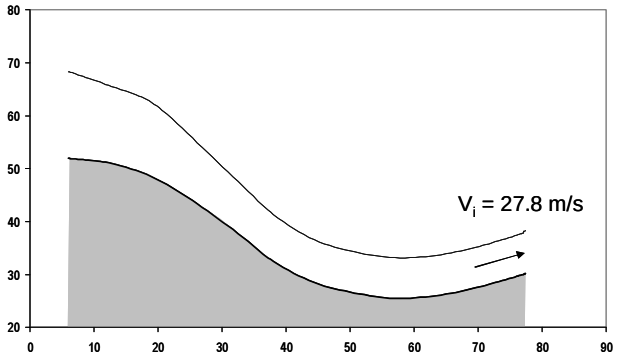

Figure 6. Numerical computation of flow characteristics along chute and flip bucket

Distinction has been made between conservative, average and beneficial assumptions on the different geomechanic parameters. A UCS strength between 50 and 100 MPa has been assumed.

C. Comprehensive Fracture Mechanics (CFM) Results

When applying the Comprehensive Fracture Mechanics (CFM) model under the centerline of the jet impacting in the plunge pool, Table 2 shows that beneficial parametric assumptions result in no scour formation.

For the most conservative parametric assumptions, scour formation down to a plunge pool bottom level of about – 65 m for a flood duration of 2 months has been computed. This is very close to the results obtained on the laboratory model using gravel. This is not so surprising given the fact that, for the single-edge rock joints that are assumed under conservative parametric conditions, the rock is considered almost completely broken up into distinct blocks and thus quite similar to gravel under laboratory conditions.

Second, on the long term (= after 80 months of design flood), maximum scour elevations between -47 m and -74 m have been computed. For only 8 months of design flood, which seems much more plausible during the lifetime of the dam, the corresponding plunge pool scour elevations are between -41 m and -67 m. In other words, even during very long periods of design discharge at Tucurui Dam, potential scour formation would still remain within controllable limits. This is especially true given the fact that, based on Figure 3, for such high floods, the jet impacts at about 130 m from the toe of the dam and thus no risk is apparent for the dam.

D. Dynamic Impulsion (DI) Results

Based on the Dynamic Impulsion model, the scour computed under the centerline of the jet becomes more important than for the Comprehensive Fracture Mechanics model, with scour elevations at – 63 m for beneficial parametric assumptions and down to – 94 m for conservative parametric assumptions. While the former value is again very close to the laboratory results, the latter seems much more pessimistic regarding future scour formation during the design flood event.

Nevertheless, it has to be kept in mind that the DI model results largely depend on the assumed ratio of rock block height to side length. Under conservative assumptions at Table 2, this ratio has been taken equal to 0.5. This means that only flat and completely detached rock blocks.

Table 2. Scour elevations as a function of time duration of flood following a 100'000 m^3/s flood event at Tucurui Dam (CSM model)

SCOUR ELEVATION COMPUTATIONS									
TIME				CFM			DI		
Hours	Days	Months	Years	BENEF	AVER	CONS	CONS	AVER	BENEF
96	4	0.1	0.01	-40.4	-53.6	-61.6	-93.9	-78.9	-63.2
192	8	0.3	0.02	-40.4	-53.6	-62.6	-93.9	-78.9	-63.2
720	30	1.0	0.08	-40.4	-54.3	-64.1	-93.9	-78.9	-63.2
1500	62.5	2.1	0.17	-40.4	-54.9	-65.0	-93.9	-78.9	-63.2
5760	240	8.0	0.67	-41.3	-56.4	-67.2	-93.9	-78.9	-63.2
57600	2400	80.0	6.67	-47.5	-59.2	-74.3	-93.9	-78.9	-63.2

VI. CONCLUSIONS

This Paper presents a new and physics based scour prediction model applicable to high-head hydraulic structures. The basics of the model are briefly outlined. The model has been applied to the Tucurui Dam spillway and plunge pool in Brazil, for which almost no scour has been observed in-situ after 17 years of moderate floods events. The model has first been calibrated based on these moderate flood events.

Then, the design flood of 110'000 m^3/s has been tested. Depending on the applied rock failure criteria and the assumptions made on the rock mass quality, scour elevations are situated between – 40 m and – 94 m.

However, when only applying the most plausible parametric combinations, scour would extend down to about – 55 m for partially broken up rock and down to -80 m in case of completely broken up rock at the dam site.

Considering the fact that all detached rock blocks have been washed out of the plunge pool immediately after dam construction, it may be stated that the ultimate scour depth following the design flood event would be situated around – 55 m. This is reasonably close to the laboratory model test result of – 65 m by using gravel to represent the rock mass.

REFERENCES

[1] Atkinson, B.K. (1987). Fracture Mechanics of Rock. Academic Press Inc., London.

[2] Bollaert, E.F.R. (2002). Transient water pressures in joints and formation of scour due to high-velocity jet impact. Communication 13, Laboratory of Hydraulic Constructions, Lausanne, Switzerland.

[3] Bollaert, E.F.R. (2004). A comprehensive model to evaluate scour formation in plunge pools. Int. J. Hydropower & Dams, 2004, 2004(1), pp. 94-101.

[4] Bollaert, E.F.R. and Schleiss, A.J. (2005), A physically-based model for evaluation of rock scour due to high-velocity jet impact, Journal of Hydraulic Engineering, March 2005.

[5] Ervine, D.A. and Falvey, H.R. (1987). "Behavior of turbulent jets in the atmosphere and in plunge pools." Proceedings of the Institution of Civil Engineers. Part 2, Vol. 83, 295-314.

[6] Ervine, D.A., Falvey, H.T., Withers, W. 1997. "Pressure fluctuations on plunge pool floors". Journal of Hydraulic Research, Vol. 35, 2, 257-279.

[7] Petry, B.et al. (2002), Tucurui Spillway on the Tocantins River-Performance during 17 years of Operation, in "Large Brazilian Spillways--An Overview of Brazilian Practice and Experience in Designing and Building Spillways for Large Dams", International Commission on Large Dams/Brazilian Committee on Dams, 2002.

Extreme Scour Prediction at High-Head Concrete Dam and Stilling Basin (United States)

E.F.R. Bollaert*, B. Vrchoticky ** and H.T. Falvey***
* AquaVision Engineering Ltd., Lausanne, Switzerland
** US Army Corps of Engineers, United States
*** H.T. Falvey & Associates, Colorado, United States

I. INTRODUCTION

This paper presents the application of a recently developed physics based model that predicts scour formation downstream of large dam spillways (Bollaert, 2004). The model is based on experiments with air-water jets impinging on jointed media and related numerical modeling of involved physical phenomena. It predicts the ultimate scour depth and the time development of scour formation in different types of fissured media. The model is under continuous development and has been applied to several scour cases worldwide. The model includes several physics based modules for scour prediction that are based on the resistance of the medium to fissure initiation and propagation, as well as on the resistance of individual blocks to sudden ejection.

A case study of a High-Head Concrete Dam and Stilling Basin as shown in figure 1, located in the United States, is presented here. The dam in question has experienced several large storm events during the last twenty years, with maximum spillway releases of up to about 4,000 m^3/s. The latest hydrology developed in lieu of these events indicates that for the Probable Maximum Flood (PMF), releases from the dam could exceed 22,700 m^3/s, while the original design PMF was only 15,600 m^3/s.

Hence, modifications to the outlet works are being studied to increase the flood discharge capacity by increasing the gate size and adding two additional gates. The larger jets issuing from the modified outlet works impact against a stilling basin that was originally designed mainly as a hydraulic jump energy dissipater. There is no true plunge pool for the jets and tailwater is relatively shallow.

The present paper describes detailed numerical computations made to predict the ultimate possible scour depth in the rock formation downstream of the dam following a failure of the concrete lining of the stilling basin. The computations have been made for both the emergency design flood through the 3 emergency spillway gates (8,500 m^3/s) and for the new PMF event (22,700 m^3/s). A 3D assessment of scour hole formation and its time development in the rock mass downstream of the dam has been obtained. The computations indicate that, during the design flood, scour will remain quite local, while for the PMF event, failure of the concrete lining might result in severe scour formation of the rocky foundation just downstream of the dam.

a) General view of dam and stilling basin

b) Downstream view of stilling basin and channel

Figure 1.

II. MAIN CHARACTERISTICS OF DAM AND STILLING BASIN

The geometry of the dam and downstream stilling basin is shown in Figure 2. The dam is a concrete gravity dam equipped with 5 service spillway gates and 3 emergency spillway gates. In addition to these gates, the dam also incorporates 10 intermediate outlet works, with dimensions of 3m by 4m (4 lower tiers) and 3m by 4.5 m (6 upper tiers) The dam is able to pass excess water from the reservoir in two different ways: by means of crest overflows along the downstream face (chute) of the dam and by means of a series of pressurized outlets (jet flow) through the dam body. The jets from the outlets impact the downstream stilling basin.

The stilling basin floor consists of concrete slabs and sidewalls and measures about 75 m wide by 110 m long. The upstream boundary is formed by a smooth curve at the dam toe, while the downstream boundary is formed by an end sill. The concrete slabs have a thickness of about 1.5 m, with horizontal dimensions of 15m by 15m (square slabs) or 6m by 15m (rectangular slabs).

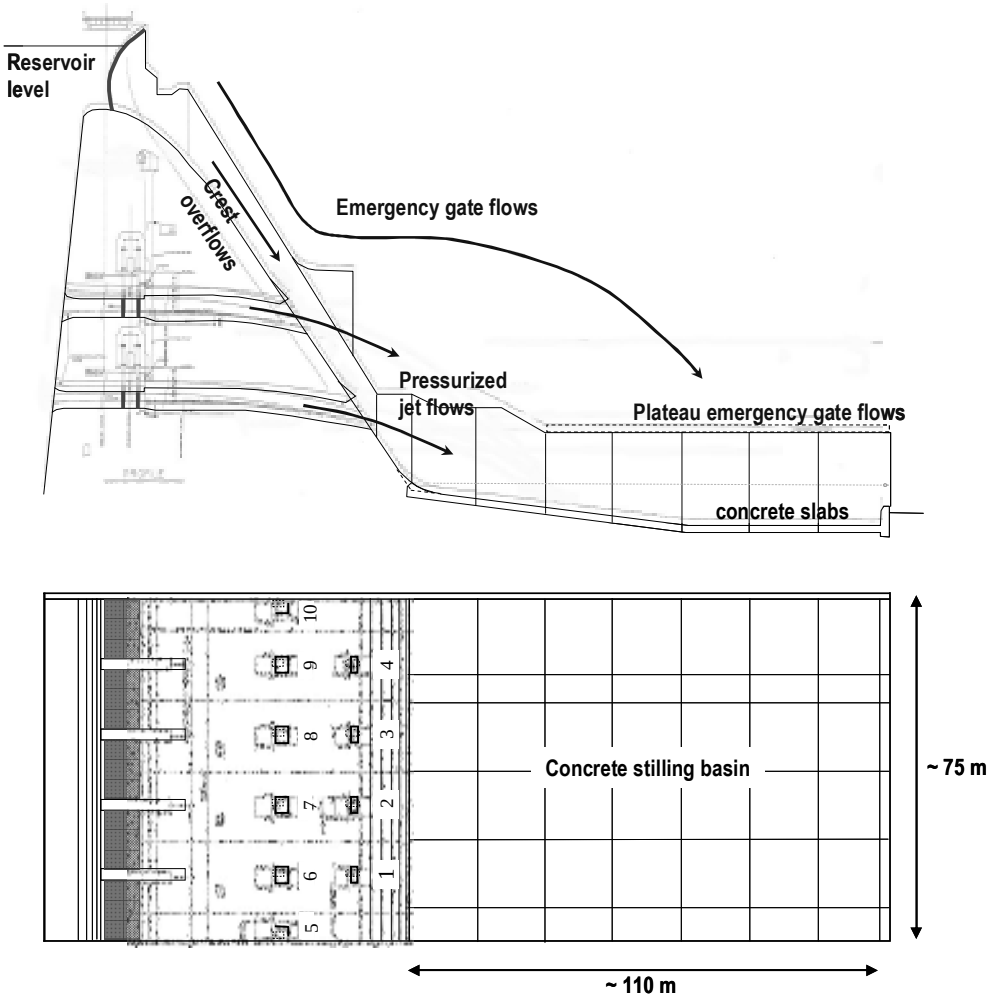

Figure 2. Plan view and cross-sectional view of high-head dam and stilling basin

III. ROCK MASS CHARACTERISTICS

The rock mass at the dam site is described as a hard and durable Sierra granite/quartz diorite, medium to coarse grained, with an Unconfined Compressive Strength (UCS) of about 130 MPa. Based on drainage gallery core drilling, the RQD (Rock Quality Designation) has been estimated at 75-90 %. The rock is slightly to moderately weathered and is generally considered to provide a good erosion resistant surface. Nevertheless, one of the most serious problems encountered during dam construction was the depth of weathering. This depth depends on the average joint spacing and on micro fracturing of the grains. Most weathering was found to start by alteration along the joints, due to water flowing through these planes. Moreover, the rock is intersected by faults, shear zones and different main joint sets. Zones of sheared rock of up to more than 1m thick are also present. These zones are nearly vertical, but most probably do not interfere with the stilling basin rocky foundation.

IV. Comprehensive Scour Model (Bollaert, 2004)

A new and physics based scour prediction model was developed at the Laboratory of Hydraulic Constructions of the Swiss Federal Institute of Technology in Lausanne, Switzerland (Bollaert, 2002 and 2004; Bollaert & Schleiss, 2005). The model uses physical laws and phenomena that have been simplified to allow its application to practical engineering projects. It is based on experimental and numerical investigations of dynamic water pressures in rock joints (Bollaert, 2002).

The model comprises two methods that describe failure of fractured rock. The first one, the Comprehensive Fracture Mechanics (CFM) method, determines the ultimate scour depth by expressing instantaneous or time-dependent joint propagation due to water pressures jacking inside the joint. The second one, the Dynamic Impulsion (DI) method, describes the ejection of rock blocks from their mass due to sudden uplift pressures.

The structure of the Comprehensive Scour Model consists of three modules: the falling jet, the plunge pool and the rock mass. The latter module implements the two aforementioned failure criteria. More details can be found in Bollaert (2004) or Bollaert & Schleiss (2005).

A. Falling jet Module

This module describes how the hydraulic and geometric characteristics of the jet are transformed from the free falling jet down to the plunge pool as shown in Figure 3. Three parameters characterize the falling jet: the velocity V_i, the diameter (or width) D_i and the initial turbulence intensity Tu, defined as the ratio of velocity fluctuations to the mean velocity.

The jet trajectory is based on ballistics and air drag and will not be further outlined. The jet module computes the longitudinal location of impact, the total trajectory length L and the velocity and diameter at impact V_j and D_j. The turbulence intensity is presented in the next paragraph and defines the spread of the jet δ_{out} (Ervine et al., 1997). Superposition of the outer spread to the initial jet diameter D_i results in the outer jet diameter D_{out}, which is used to determine the extent of the zone at the water-rock interface where severe pressure damage may occur. The relevant relationships are:

$$Tu = u'/U \tag{1}$$

$$\frac{\delta_{out}}{X} = 0.38 \cdot Tu \tag{2}$$

$$D_j = D_i \cdot \sqrt{\frac{V_i}{V_j}} \tag{3}$$

$$V_j = \sqrt{V_i^2 + 2gZ} \tag{4}$$

$$D_{out} = D_i + 2 \cdot \delta_{out} \cdot L \tag{5}$$

in which δ_{out} is the half angle of outer spread, X the longitudinal distance from the point of issuance and Z the vertical fall distance of the jet. Typical outer angles of jet spread are 3-4 % for roughly turbulent jets (Ervine & Falvey, 1987). The corresponding inner angles of jet spread are 0.5 - 1 %.

The angle of the jet at impact is neglected, which is reasonable for impingement angles that are close to the vertical (70-90°). For smaller impingement angles, the water depth Y is defined as the exact trajectory length of the jet through the water cushion, and not as the vertical difference between water level and pool bottom.

B. Plunge Pool Module

This module describes the hydraulic and geometric characteristics of the jet when traversing the plunge pool and defines the water pressures at the water-rock interface. The plunge pool water depth Y is essential. For near-vertically impacting jets, it is defined as the difference between the water level and the bedrock level at the point of impact. The water depth increases with discharge and scour formation. Initially, Y equals the tailwater depth t as shown in Figure 4. During scour formation, Y has to be increased with the depth of the formed scour h. Prototype observations indicate possible mounding at the downstream end of the pool. This mounding results from detached rock blocks that are swept away and that deposit immediately downstream. This can raise the tailwater level. The effect is not directly described in the module but can easily be added to the computations by appropriate modification of the water depth during scour.

The water depth Y and jet diameter at impact D_j determine the ratio of water depth to jet diameter at impact Y/D_j. This ratio is directly related to jet diffusion. Precaution should be taken when applying this parameter. Significant differences may exist in practice due to the appearance of vortices or other surface disturbing effects, which can change the effective water depth in the pool. Again, engineering judgment is required on a case-by-case basis.

Dynamic pressures acting at the water-rock interface are generated by core jet impact for small water depths Y, or by developed jet impact (shear layer), for Y/D_j greater than 4 to 6 (for plunging jets) as shown in Figure 4. The most relevant pressure characteristics are the mean dynamic pressure coefficient C_{pa} and the root-mean-square (rms) coefficient of the fluctuating dynamic pressures C'_{pa}, both measured directly under the centerline of the jet. These coefficients correspond to the ratio of pressure head (in [m]) to incoming kinetic energy of the jet ($V^2/2g$) and are defined as follows:

$$C'_{pa} = 0.00022 \cdot \left(\frac{Y}{D_j}\right)^3 + 0.0079 \cdot \left(\frac{Y}{D_j}\right)^2 + 0.0716 \cdot \left(\frac{Y}{D_j}\right) + \eta \tag{6}$$

$$C_{pa} = 38.4 \cdot (1 - \alpha_i) \cdot \left(\frac{D_j}{Y}\right)^2 \quad \text{for } Y/D_j > 4\text{-}6 \tag{7}$$

$$C_{pa} = 0.85 \qquad \text{for } Y/D_j < 4\text{-}6 \tag{8}$$

$$\alpha_i = \frac{\beta}{1+\beta} \tag{9}$$

Equations 7 through 9 are based on Ervine et al. (1997). The air concentration at jet impact α_i is defined as a function of the volumetric air-to-water ratio β. Plausible prototype values for β are 1-2. For a given α_i, mean and fluctuating dynamic pressures are defined as a function of Y, D_j and Tu. Similar expressions are proposed at locations radially outwards from the jet's centerline and can be found in Bollaert (2002). Tu is assumed representative for low-frequency fluctuations, which define the stability of the jet during its fall. Hence, Tu can be related to the root-mean-square (rms) values of the pressure fluctuations at the pool bottom. This is essential because these fluctuations generate peak pressures inside underlying rock joints.

From equation 6, the rms values of the pressure fluctuations at the pool bottom (C'_{pa}) depend on Y/D_j and Tu. The parameter η of equation 6 represents the degree of jet stability: η is equal to 0 for compact jets and goes up to 0.15 for highly turbulent and unstable jets. Compact jets

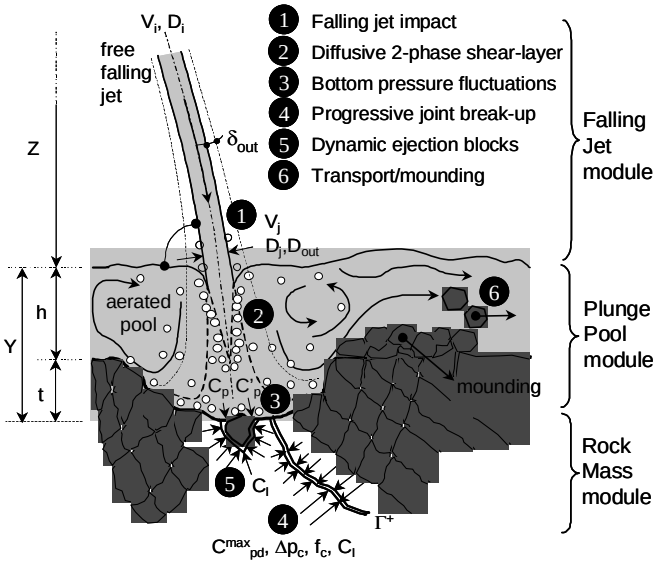

Figure 3. Main parameters of scour and its physical phenomena (Bollaert, 2004)

(Tu < 1%) are smooth during their fall, without any instability. Highly turbulent jets have a Tu > 5%. In between, for 1% < Tu < 5%, η has to be chosen between 0 and 0.15 as a function of jet stability effects.

Generally, Tu is unknown. Under such circumstances, estimation can be made based on the type of outlet structure (Bollaert et al., 2002). For example, a free overfall jet has an estimated Tu of 1-3 %, a ski jump 3-5 %, and intermediate or bottom outlets 5-8 %. However, Tu may largely depend on the outlet geometry, the flow pattern upstream, etc. These aspects should be accounted for by appropriate engineering judgment.

C. Rock Mass Module

The pressures defined at the bottom of the pool are used for determination of the transient pressures inside open-end or closed-end rock joints. The parameters are:

1. maximum dynamic pressure coefficient C^{max}_p
2. characteristic amplitude of pressure cycles Δp_c
3. characteristic frequency of pressure cycles f_c
4. maximum dynamic impulsion coefficient C^{max}_I

The first parameter is relevant to brittle propagation of closed-end rock joints. The second and third parameters express time-dependent propagation of closed-end rock joints. The fourth parameter is used to define dynamic uplift of rock blocks formed by open-end rock joints. The maximum dynamic pressure C^{max}_p is obtained through multiplication of the rms pressure C'_{pa} with an amplification factor Γ^+, and by superposition with the mean dynamic pressure C_{pa}. Γ^+ expresses the ratio of the peak value inside the rock joint to the rms value of pressures at the pool bottom and has been determined based on prototype-scaled experiments (Bollaert, 2004).

The product of C'_{pa} times Γ^+ results in a maximum pressure, written as (Bollaert, 2002):

$$\boldsymbol{P}_{\max}[\boldsymbol{Pa}] = \gamma \cdot \boldsymbol{C}_{\boldsymbol{p}}^{\max} \cdot \frac{\boldsymbol{V}_{\boldsymbol{j}}^2}{2\boldsymbol{g}} = \gamma \cdot \left(\boldsymbol{C}_{\boldsymbol{pa}} + \Gamma^+ \cdot \boldsymbol{C}'_{\boldsymbol{pa}}\right) \cdot \frac{\boldsymbol{V}_{\boldsymbol{j}}^2}{2\boldsymbol{g}} \tag{10}$$

The main uncertainty of equation 10 lies in the Γ^+ factor. The characteristic amplitude of the pressure cycles, Δp_c, is determined by the maximum and minimum

pressures of the cycles. The characteristic frequency of pressure cycles f_c follows the assumption of a perfect resonator system and depends on the air concentration in the joint α_i and on the length of the joint L_f.

Beside the dynamic pressure inside rock joints, the resistance of the rock also has to be determined. The cyclical character of the pressures generated by the impact of a high-velocity jet makes it possible to describe joint propagation by ***fatigue*** stresses occurring at the tip of the joint. This can be described by Linear Elastic Fracture Mechanics (LEFM).

A simplified methodology is used (Bollaert, 2004). It is called the ***Comprehensive Fracture Mechanics (CFM) method*** and applicable to any type of partially jointed rock. Pure tensile pressure loading inside rock joints is described by a stress intensity factor K_I, which represents the amplitude of the stresses that are generated by the water pressures at the tip of the joint. The corresponding resistance of the rock mass to joint propagation is expressed by its fracture toughness K_{Ic}.

Joint propagation distinguishes between brittle (or instantaneous) joint propagation and time-dependent joint propagation. The former happens for a stress intensity factor that is equal to or higher than the fracture toughness of the material. The latter is occurring when the maximum possible water pressure results in a stress intensity that is inferior to the material's resistance. Joints may then be propagated by fatigue. Failure by fatigue depends on the frequency and the amplitude of the load cycles. The fracture mechanics implementation of the hydrodynamic loading consists of a transformation of the water pressures in the joints into stresses in the rock. These stresses are characterized by K_I as follows:

$$\boldsymbol{K_I = P_{\max} \cdot F \cdot \sqrt{\pi \cdot L_f}} \qquad (11)$$

in which K_I is in MPa$\sqrt{m}$ and P_{max} in MPa. The boundary correction factor F depends on the type of crack and on its persistency, i.e. its degree of cracking defined as a/B or b/W in Figure 5. This figure presents two basic configurations for partially jointed rock. The choice of the most relevant geometry depends on the type and the degree of jointing of the rock.

The first crack is of semi-elliptical shape and partially sustained by the surrounding rock mass in two horizontal directions. Corresponding stress intensity factors should be used in case of low to moderately jointed rock. The second crack is single-edge notched and of two-dimensional nature. Support from the surrounding rock mass is only exerted perpendicular to the plane of the notch and, as a result, stress intensity factors will be substantially higher. Thus, it is appropriate for significantly to highly jointed rock.

In practice, F values of 0.5 or higher are considered to correspond to completely broken-up rock, i.e. the DI method becomes more applicable than the CFM method. For values of 0.1 or less, a tensile strength approach is more plausible. However, most of the values in practice can be considered between 0.20 and 0.40, depending on the type and number of joint sets, the degree of weathering, distances between joints, etc.

The fracture toughness K_{Ic} has been related to the mineralogical type of rock and to the unconfined compressive strength UCS. Furthermore, corrections are made to account for the loading rate and the in-situ stress field. The corrected fracture toughness is defined as the in-situ fracture toughness $K_{I,\ ins}$ and is based on a linear regression of available literature data.

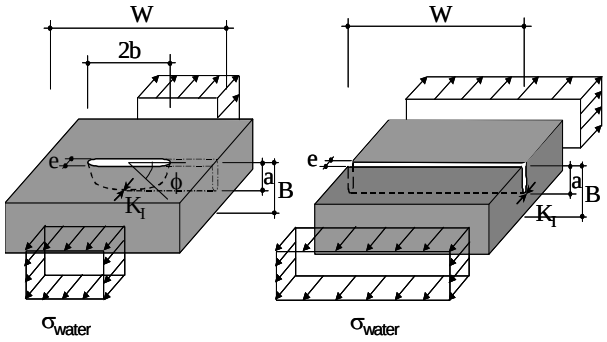

Figure 4. Rock joint parameters (Bollaert, 2004)

$$K_{I\ ins,\ UCS} = (0.008\text{-}0.010)\cdot UCS + (0.054\cdot\sigma_c) + 0.42 \qquad (12)$$

in which σ_c represents the confinement horizontal in-situ stress and T, UCS and σ_c are in MPa. Instantaneous joint propagation will occur if $K_I \geq K_{I,ins}$. If this is not the case, joint propagation is expressed by an equation as originally proposed to describe fatigue growth in metals:

$$\frac{\boldsymbol{dL_f}}{\boldsymbol{dN}} = \boldsymbol{C_r \cdot \left(\Delta K_I / K_{Ic}\right)^{m_r}} \qquad (13)$$

in which N is the number of pressure cycles. C_r and m_r are material parameters that are determined by fatigue tests and ΔK_I is the difference of maximum and minimum stress intensity factors. To implement time-dependent joint propagation into the model, m_r and C_r have to be known. They represent the vulnerability of rock to fatigue and can be derived from available literature data on quasi-steady break-up by water pressures in joints (Atkinson, 1987). A calibration for granite (Cahora-Bassa Dam; Bollaert, 2002) resulted in C_r = 1E-8 for m_r = 10.

The fourth dynamic parameter is the maximum dynamic impulsion $C^{max}{}_I$ in an open-end rock joint (underneath single block), obtained by time integration of net forces on the block:

$$\boldsymbol{I} = \int_0^{\Delta tpulse} \left(\boldsymbol{F_u - F_o - G_b - F_{sh}}\right)\cdot \boldsymbol{dt} = \boldsymbol{m \cdot V_{\Delta tpulse}} \qquad (14)$$

in which F_u and F_o are the forces under and over the block, G_b is the submerged weight of the block and F_{sh} represents the shear and interlocking forces. The shape of a block and the type of rock define the immerged weight. Shear and interlocking forces depend on the joint pattern and the in-situ stresses. As a first approach, they can be neglected. The pressure field over the block is governed by jet diffusion. The pressure field under the block corresponds to transient pressure waves. The first step is to define the maximum net impulsion I^{max}. I^{max} is defined as the product

of a net force and a time period. The corresponding pressure is made non-dimensional by the jet's kinetic energy $V^2/2g$. This results in a net uplift pressure coefficient C_{up}. The time period is made non-dimensional by the travel period that is characteristic for pressure waves inside rock joints, i.e. $T = 2 \cdot L_f/c$. This results in a time coefficient T_{up}. Hence, the non-dimensional impulsion coefficient C_I is defined by the product $C_{up} \cdot T_{up} = V^2 \cdot L/g \cdot c$ [m·s]. The maximum net impulsion I^{max} is obtained by multiplication of C_I by $V^2 \cdot L/g \cdot c$. Prototype-scaled analysis of uplift pressures resulted in the following expression for C_I:

$$C_I = 0.0035 \cdot \left(\frac{Y}{D_j}\right)^2 - 0.119 \cdot \left(\frac{Y}{D_j}\right) + 1.22 \qquad (15)$$

Failure of a block is expressed by the displacement it undergoes due to the net impulsion coefficient C_I. This is obtained by transformation of $V_{\Delta tpulse}$ in equation 14 into a net uplift displacement h_{up}. The net uplift displacement that is necessary to eject a rock block from its matrix is difficult to define. It depends on the protrusion and the degree of interlocking of the blocks. A calibration on Cahora-Bassa Dam (Bollaert, 2002) resulted in a critical net uplift displacement of 0.20.

V. APPLICATION OF CSM MODEL

The Comprehensive Scour Model has been applied to the stilling basin of this case study. The model has applied parametric values as presented in Table 1 to estimate scour formation in the rocky foundation following failure of the concrete slabs of the stilling basin. The time development of scour has been defined at time intervals of 1h, 6h, 12h, 24h, 4 days, 8 days, 100 and finally 200 days of discharge.

TABLE I. MAIN GEOMECHANICAL PARAMETERS USED BY THE CSM MODEL

	Parameter	Symbol	Unit	VALUE
Fracture Mechanics	Type of rock	-	-	granite
	Unconfined Compressive Strength	UCS	MPa	131
	In-situ stress ratio	K_0	-	0
	Joint wave celerity for break-up	c	m/s	150
	Amplification factor G	-	-	2
	Number of joint sets	N_j	-	3
	Typical maximum joint length	L	m	1
	Initial break-up of joint	P	-	varies
	Form of joints	-	-	varies
	Fatigue sensibility	m_f	-	10
	Fatigue coefficient	C_f	-	1.00E-07
Dynamic Impulsion	Ratio height/side length of block	h_b/l_b	-	0.25
	Density rock	γ_r	kg/m^3	2650
	Joint wave celerity for uplift	c	m/s	100

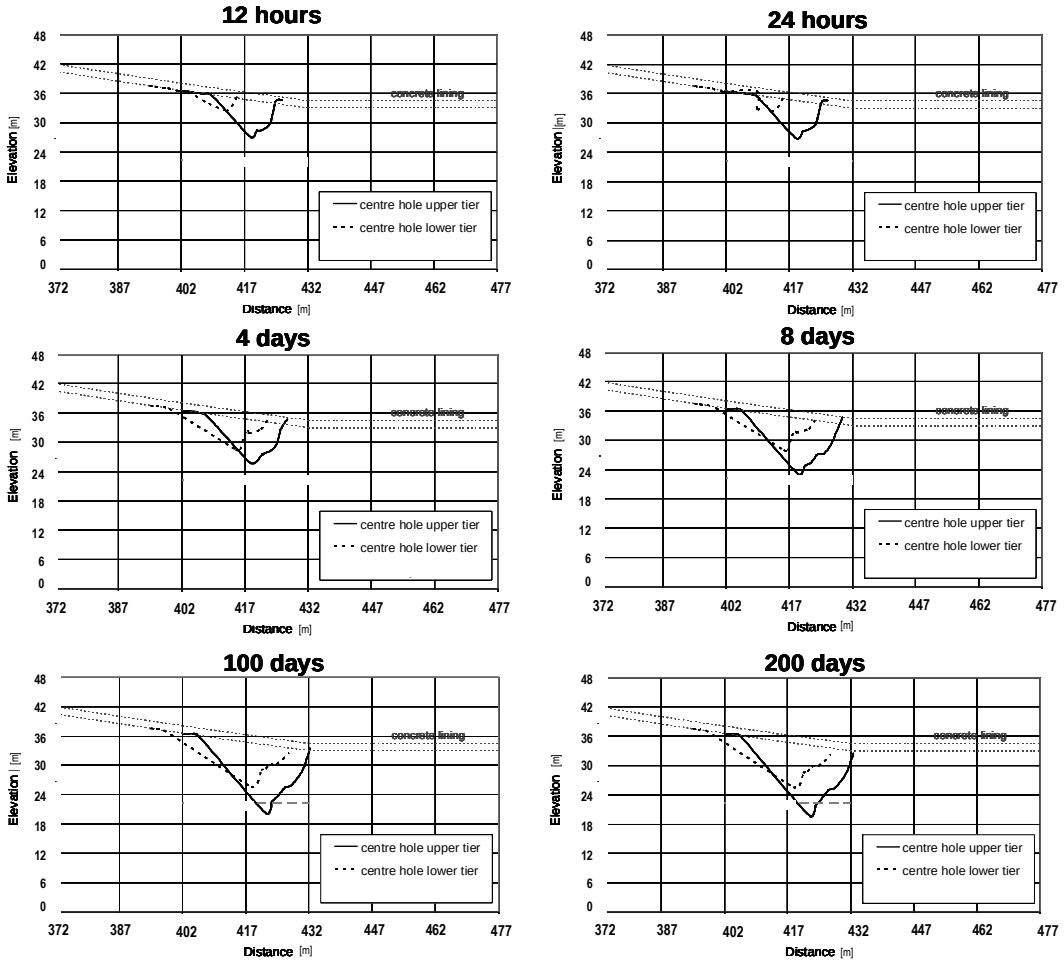

Figure 5. Scour formation as a function of time in stilling basin for a constant discharge of 3,300 cms and following the parametric assumptions of Table 1 (Comprehensive Fracture Mechanics Model, Bollaert 2004).

A. Scour formation for flood event of 3,300 cms

First, potential scour formation in the stilling basin and following failure of the concrete slabs has been estimated for a regular flood event that is transferred towards downstream via the pressurized outlet works. The flood discharge is assumed constant and defined at 3,300 cms.

Figure 5 presents scour formation as a function of the time duration of the flood event. Each of the figures represents a longitudinal section of the stilling basin, showing the initial elevation of the concrete slabs and the depth and the general shape of the formed scour hole. Based on the Comprehensive Fracture Mechanics Model, it can be seen that scour rapidly forms during the first few days and that subsequent scour takes much more time to happen. After 200 days of constant discharge, the scour hole has attained a maximum depth of 15 m. Figure 6 presents the corresponding three-dimensional perspective view, showing the shape of the scour holes formed in the rock mass underneath the stilling basin. The part of the stilling basin that is represented on this figure corresponds to the sloped (upstream) part, with a total length of about 60 m. When applying the Dynamic Impulsion Model, the ultimate scour depth for the same constant discharge is situated at 15.5 m, i.e. very close to the former results after 200 days of discharge.

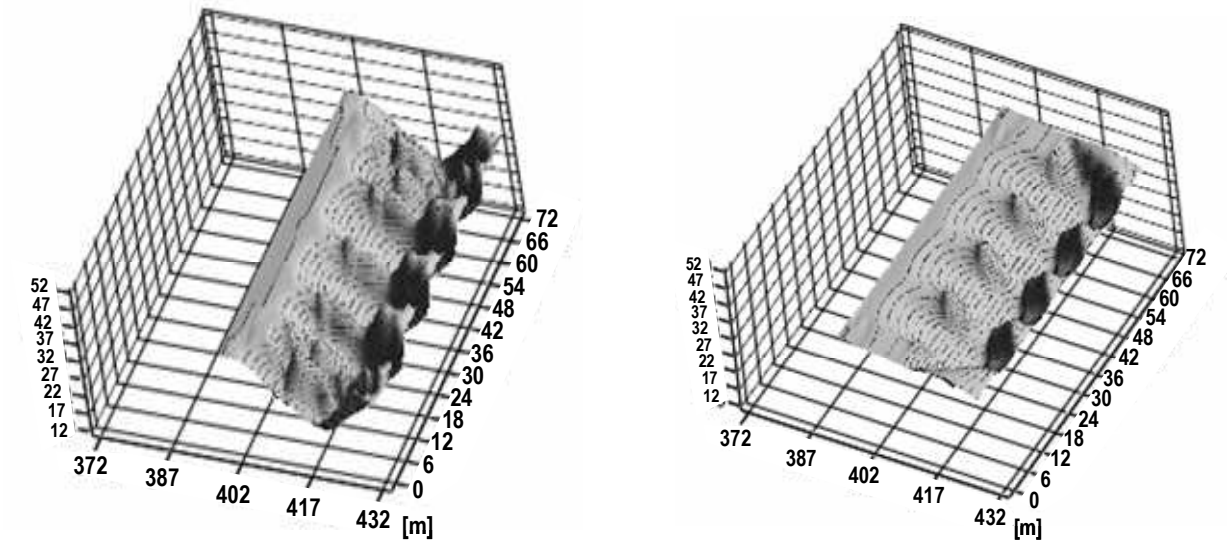

UPPER OUTLET WORKS LOWER OUTLET WORKS

Figure 6. 3D-shape of scour hole along the sloping part of the stilling basin bottom following a discharge of 3,300 cms and due to upper or lower pressurized outlet works functioning during 200 days (ultimate depth).

B. Emergency spillway flow scour formation

Potential scour formation downstream of the three emergency spillways has been determined for an extreme flood event of 8,500 cms (through these three gates only). Each emergency spillway gate has dimensions of 12 m by 15 m and generates a high-velocity free surface flow along a chute that ends with a flip bucket (Figures 1a & 2).

The flow from the flip bucket generates a rectangular shaped jet with a thickness of 8 m and a width of 15 m. The jet velocity at the flip is about 24 m/s. The jets are assumed to remain rectangular shaped during their fall and impact onto the downstream slab.

This slab is situated about 25-30 m higher than the stilling basin bottom and consists of a 1m thick concrete lining placed on dredge tailings of granular material between the left-sidewall of the stilling basin and the rock mass as shown in Figure 2. The tailings have a triangular cross-sectional shape that stays more or less constant in the longitudinal (flow) direction. The downstream part of the concrete lining of the slab has been partially damaged during past operation of the emergency spillways and has been repaired by placing a 3 m thick layer of lean concrete onto the dredge tailings, with a new reinforced concrete slab above that repair.

As the emergency jets might partially impact upstream of the repaired zone, and the concrete might fail or be uplifted more easily than the surrounding rock, this local reinforcement has not been accounted for in the present computations.

The results of the scour computations are summarized at Table 2 for that part of the slab that is located directly next to the stilling basin sidewall. Based on the Comprehensive Fracture Mechanics Model (CFM), scour formation only occurs after very long periods of extreme flooding (100 days or more) and consists of a very local destruction of the rock mass over a length of about 15-20 m. Nevertheless, for such periods of discharge, the

ultimate scour depth extends about 10 m beyond the elevation of the concrete slabs of the stilling basin. Its three-dimensional shape is presented in Figure 7. The scour hole has a length of about 15-20 m and a lateral width of 15 m.

The Dynamic Impulsion Model (DI) predicts much deeper scour than the Fracture Mechanics model, but this method uses the hypothesis that the rock mass consists of fully broken up rock blocks. This assumption is probably not plausible at large depths and not fully representative for the state of the rock mass.

Similar results for that part of the slab that is located further away from the sidewall of the stilling basin, at distances of more than 30 m, are summarized at Table 3. It can be noticed that the Fracture Mechanics approach indicates almost no scour formation, while the Dynamic Impulsion approach again results in significant scour formation. The same remark as for the first part of the plateau is valid here.

TABLE II. SCOUR RESULTS AT PLATEAU BENEATH EMERGENCY SPILLWAYS AND CLOSE TO THE STILLING BASIN SIDEWALL

	Flood duration h	Ultimate Scour Elevation m a.s.l.	Depth of Scour m
Fracture Mechanics Model	24 192 4800	no scour (50-55) 46 24.5	0 4-9 26-31
Dynamic Impulsion Model	infinity	17	33-38

TABLE III. SCOUR RESULTS AT PLATEAU BENEATH EMERGENCY SPILLWAYS AT 30 M DISTANCE FROM THE STILLING BASIN SIDEWALL

	Flood duration h	Ultimate Scour Elevation m a.s.l.	Depth of Scour m
Fracture Mechanics Model	24 192 4800	no scour (64) 64 61.5	0 0 2.5
Dynamic Impulsion Model	infinity	22.5	41.5

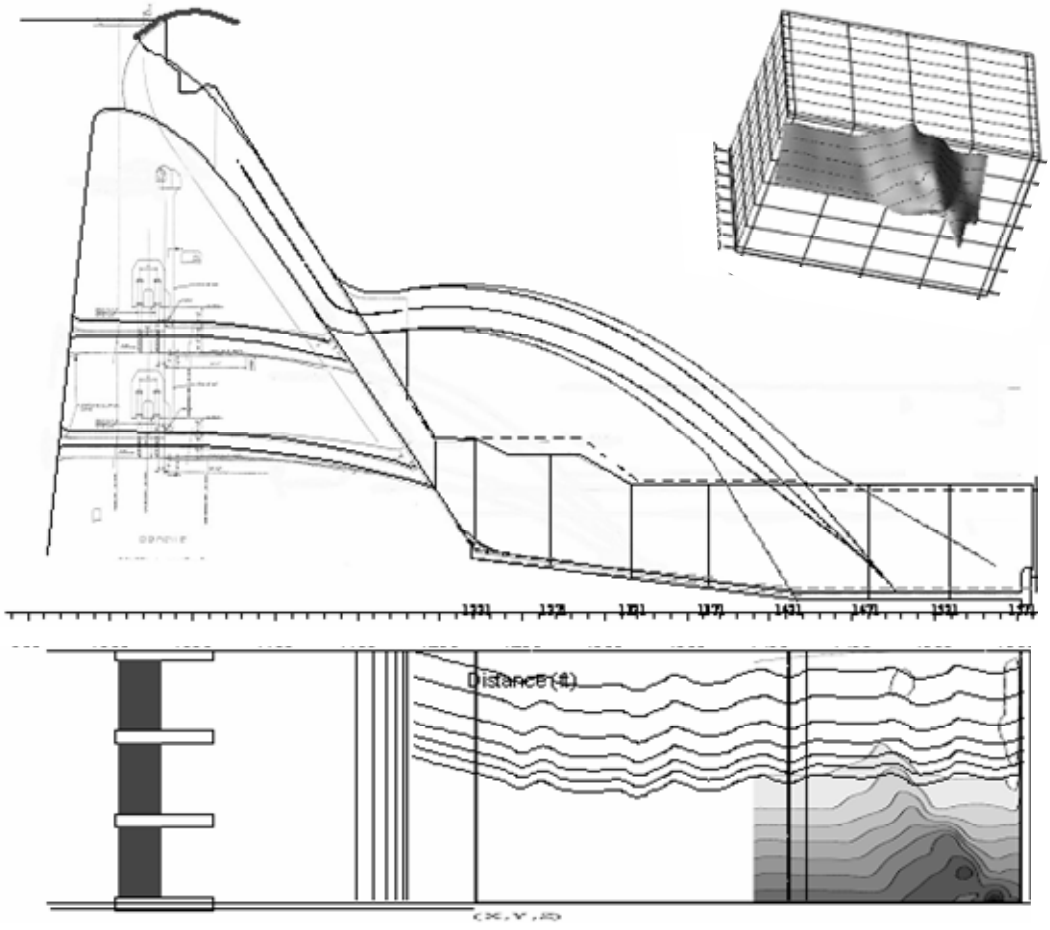

Figure 7. Emergency spillway scour: jet trajectory, zone of impact on the downstream concrete plateau and ultimate scour elevation for the parametric assumptions presented at Table 1.

VI. CONCLUSIONS

This Paper presents a new and physics based scour prediction model applicable to high-head hydraulic structures. The basics of the model are briefly outlined. The model has been applied to a High-Head Dam and Stilling Basin located in the United States.

The scour computations are based on the assumption that, during the flood event, one or more concrete slabs of the stilling basin fail. Scour is then computed in the underlying rocky foundation. The results of the scour computations indicate that, for a normal flood discharge of 3,300 cms, passing through the upper and lower tiers of the outlet works, only minor scour forms along the sloped (upstream) part of the stilling basin bottom. This scour forms almost completely within the first few days of the event. Subsequent scour formation takes much more time to happen. No danger for dam stability is apparent.

Second, scour formation following an operation of the three emergency spillway gates has been computed for a total discharge through these gates of 8,500 cms. The computations based on Fracture Mechanics result in scour depths of about 26-31 m after very long times of discharge (hundreds of days). This scour only forms locally, directly next to the left sidewall of the stilling basin, but may extend deeper than the concrete slabs of the stilling basin. Application of the Dynamic Impulsion Model indicates a scour hole of about 40 m deep. This model, however, assumes fully broken up rock at all depths and thus is too conservative.

Hence, it may be stated that, for an emergency flood through the emergency spillway gates, no significant scour will form into the downstream concrete plateau during the lifetime of the dam. Nevertheless, local minor scour may form and generate damage to the plateau.

REFERENCES

[1] Atkinson, B.K. (1987). Fracture Mechanics of Rock. Academic Press Inc., London.

[2] Bollaert, E.F.R. (2002). Transient water pressures in joints and formation of scour due to high-velocity jet impact. Communication 13, Laboratory of Hydraulic Constructions, Lausanne, Switzerland.

[3] Bollaert, E.F.R. (2004). A comprehensive model to evaluate scour formation in plunge pools. Int. J. Hydropower & Dams, 2004, 2004(1), pp. 94-101.

[4] Bollaert, E.F.R. and Schleiss, A.J. (2005), A physically-based model for evaluation of rock scour due to high-velocity jet impact, Journal of Hydraulic Engineering, March 2005.

On Modelling of the Hole Erosion Test

S.Bonelli*, N. Benahmed* and O. Brivois*,**
* Cemagref/Hydraulics Engineering and Hydrology Research Unit, Aix-en-Provence, France
** CNRS/Mechanics and Acoustics Laboratory, Marseille, France

I. Introduction

Internal erosion of soil induced by seepage flow is the main cause of major hydraulic works failures (dykes, dams). The issue is defined by the risk of flooding of areas located downstream. When internal erosion is suspected to occur or is already detected in situ, the amount of warning time before failure is difficult to predict. The development of effective emergency action plans which will lead to prevent heavily loss of life and property damage is strongly linked to the knowledge of a characteristic time.

During the last decades, several investigations were carried out to study the internal erosion on the laboratory. Four types of this process were, particularly, identified [4], [5]: 1) evolution of defect (cracks or microfissures) in the soil matrix, 2) regressive erosion, 3) internal suffusion which modifies the soil structure, 4) external suffusion between two soils. This study concerns the first mechanism: the enlargement of a crack which leads to an internal erosion called "piping" in soil mechanics.

Numerous experimental methods have been performed in order to reproduce the internal erosion process in the laboratory and different types of equipment were developed with particular attention focussed on the hole erosion tests [3], [12], [13]. However, few attempts have been made to model these tests. The purpose of this paper is to propose a useful model for the interpretation of the hole erosion test.

On the first part, equations of diphasic flow and equations of jump with erosion are presented. On the second part, a model is developed from spatial integration of a set of simplified equations obtained from asymptotic developments in the case of a circular hole. Some comparison of modelling with experiments are finally shown on the third part.

II. Two-phase Flow Equation with Interface Erosion

We study the surface erosion phenomenon of a fluid/soil interface under a flow parallel to the interface. The soil, considered here as saturated, is eroded by the flow which then transports the eroded particles. As far as the particles are smaller enough compared to the characteristic length scale of the flow, this two-phase flow can be considered as a continuum. We note Ω the two-phase mixture volume and Γ the fluid/soil interface. For simplification, sedimentation and deposition processes are neglected. The mass conservation equations for the water-particles mixture and for the mass of particles as well as the balance equation of momentum of the mixture within Ω can be written as follows in an Eulerian framework [6], [10]:

$$\frac{\partial \rho}{\partial t} + \vec{\nabla} \cdot (\rho \vec{u}) = 0 \tag{1}$$

$$\frac{\partial \rho Y}{\partial t} + \vec{\nabla} \cdot (\rho Y \vec{u}) = -\vec{\nabla} \cdot \vec{J} \tag{2}$$

$$\frac{\partial \rho \vec{u}}{\partial t} + \vec{\nabla} \cdot (\rho \vec{u} \otimes \vec{u}) = \vec{\nabla} \cdot \boldsymbol{\sigma} \tag{3}$$

In these equations, ρ is the density mixture, depending on the particles mass fraction Y; $\vec{u}$ is the mass-weighted average velocity; $\vec{J}$ is the mass diffusion flux of particles; $\boldsymbol{\sigma}$ is the Cauchy stress tensor in the mixture.

The two media, i.e. the soil and the two-phase fluid, are separated by the interface Γ. The water particles mixture is assumed to flow as a fluid above Γ, while a solid-like behaviour is considered underneath. As erosion occurs, a mass flux crosses this interface and so undergoes a transition from solid-like to fluid-like behaviour. As a consequence, Γ is not a material interface: at differents moments, Γ is not defined by the same particles. We assume that Γ is a purely geometric separation and has no thickness. Let us denote by $\vec{n}$ the normal unit vector of Γ oriented outwards the soil, and $\vec{v}_\Gamma$ the normal velocity of Γ. The jump equations over Γ are [9]:

$$\left[\!\left[\rho(\vec{v}_\Gamma - \vec{u}) \cdot \vec{n} \right]\!\right] = 0 \tag{4}$$

$$\left[\!\left[\rho Y(\vec{v}_\Gamma - \vec{u}) \cdot \vec{n} \right]\!\right] = \left[\!\left[\vec{J} \cdot \vec{n} \right]\!\right] \tag{5}$$

$$\left[\!\left[\rho \vec{u}(\vec{v}_\Gamma - \vec{u}) \cdot \vec{n} \right]\!\right] = -\left[\!\left[\boldsymbol{\sigma} \cdot \vec{n} \right]\!\right] \tag{6}$$

This project was sponsored by the Région Provence Alpes Côte d'Azur. This research effort is continuing under the sponsorship of the French National Research Agency under grant 0594C0115 (ERINOH).

where $[\![a]\!] = a_g - a_b$ is the jump of any physical variable a across the interface, and a_g and a_b stands for the limiting value of a from the solid and fluid sides of the interface, respectively. The soil is supposed homogeneous, rigid and without seepage. The co-ordinate system is linked to the soil. In this case, the total flux of eroded material (both particles and water) crossing the interface is $\dot{m} = -\rho_g \vec{v}_\Gamma \cdot \vec{n}$ where ρ_g is the density of the soil.

Erosion laws, dealing with soil surface erosion by a tangential flow, are often written as threshold laws such as [2]:

$$\dot{m} = k_{er}(\left|\tau_b\right| - \tau_c) \text{ if } \left|\tau_b\right| > \tau_c,\ 0 \text{ otherwise} \quad (7)$$

where τ_c is the critical (threshold) shear stress for erosion, k_{er} is the coefficient of soil erosion, and $\left|\tau_b\right|$ is the tangential shear stress at the interface defined by

$$\left|\tau_b\right| = \sqrt{(\boldsymbol{\sigma}\cdot\vec{n})^2 - (\vec{n}\cdot\boldsymbol{\sigma}\cdot\vec{n})^2}\Big|_b \quad (8)$$

This complete set of equations (1-3) were already used to study different situations of permanent flow (boundary layer and free surface flow) over an erodable ground [1]. Here, these equations can be extended to the study of internal erosion by mean of a spatial integration over Ω.

III. APPLICATION TO PIPING EROSION

We consider a cylinder Ω of length L and radius R (with initial value R_0) (Fig. 1). Reference velocity is $V_{fl} = Q_{fl} / \pi R_0^2$ where Q_{fl} is the initial entrance flow, and flow time is $t_{fl} = R_0 / V_{fl}$. By assuming an axisymmetrical flow, we eliminate one momentum equation. We introduce the small parameter R_e^{-1} to simplify the dimensionless equations in a boundary layer theory spirit [8],[11]. Reynolds number $R_e = V_{fl} R_0 / \nu_f$ is assumed to be large, where ν_f is the kinematic viscosity. Navier-Stokes equations are written with the time scaled by t_{fl}, the axial coordinate by $R_0 R_e$, the radial coordinate by R_0, the axial velocity by V_{fl}, the radial velocity by V_{fl} / R_e, and stresses scaled by $\rho_f V_{fl}^2$. Supposing turbulent stress viscosity and diffusivity, we make regular asymptotic expansion of unknown and we neglect the terms of order $\mathrm{O}(R_e^{-1})$ in (1) and (2) (as in [1]). As a result, we have now only one momentum equation, and the pressure is uniform across a section.

Therefore, we integrate the obtained system first on a cross section, and secondly along the axis. We denote the mean value of a in a cross section as $< a >_R$, and the mean value in Ω as $< a >_\Omega$. The mean longitudinal velocity is $V =< u >_R$. The mean density of the fluid is $\overline{\rho} =< \rho >_\Omega$. Some assumptions are made: A1) the tangential velocities are supposed continuous across Γ (no-slip condition on the interface), A2) the radial profile of the velocity field is given by the Nikuradze approximation, A3) the concentration is uniform in a section, A4) we introduce a phenomenological friction coefficient f_b by $\tau_b = f_b \overline{\rho} V^2$, A5) the radius R is axially uniform (as a consequence, $V =< u >_\Omega$). This leads to an ordinary differential system with unknowns $(R, \overline{\rho}, V)$ which can be solved numerically.

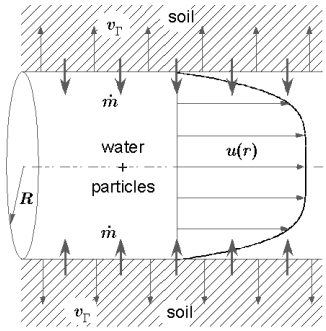

Figure 1. Sketch of the axisymmetrical flow with erosion of the soil and transport of the eroded particles

If the erosional time scale is chosen, dimensionnal analysis reveals that the four basic dimensionless parameters of the system are:

$$\tilde{a}_\phi = \frac{\alpha R_0 \rho_g}{2 f_b L \rho^f},\ \tilde{b}_\phi = \left(\frac{< u^2 >_\Omega}{< u >_\Omega^2} - 1\right)\left(1 - \frac{\rho^f}{\rho_g}\right) \quad (9)$$

$$\tilde{k}_{ref} = \frac{k_{er} V_{fl}}{1 + k_{er} V_{fl}},\ \tilde{\tau}_c = \frac{\tau_c}{P_{fl}} \quad (10)$$

The stress $P_{fl} = R_0(p_{in} - p_{out}) / 2L$ represents the hydraulic gradient and depends on the input and output pressures, respectively p_{in} and p_{out}. The positive dimensionless number $\alpha = (\rho_{out} - \rho_f) / (\overline{\rho} - \rho_f)$ represents the fact that the input fluid is pure water, while the output fluid is a two-phase mixture ($\rho_f < \overline{\rho} < \rho_{out}$).

The erosional velocity appears to be $V_{er} = k_{er} P_{fl} / (1 + k_{er} V_{fl}) \rho_g$. The eroded flow is thus $Q_{er} = 2\pi R_0 L V_{er}$ and the erosional time is $t_{er} = R_0 / V_{er}$. As a consequence, the erosional flow scale ratio is $Q_{er} / Q_{fl} = \alpha \tilde{k}_{ref} \tilde{a}_\phi^{-1}$, the erosional time scale ratio is $t_{fl} / t_{er} = \tilde{k}_{ref} f_b \rho^f / \rho_g$ and the maximum volumic concentration is $c_{ref} = (1 - n) / (1 + \tilde{a}_\phi \tilde{k}_{ref}^{-1})$ where n is the porosity of the soil.

Now we assume that $\tilde{a}_\phi \geq \mathrm{O}(1)$ and $\tilde{b}_\phi \approx \mathrm{O}(1)$, which is the case in the experiments described below. We call $\tilde{k}_{ref}$ the kinetics of erosion (dimensionless) number. If $\tilde{k}_{ref} \ll 1$ is a small parameter, then asymptotic analysis

leads to important conclusions: 1) the concentration is low and becomes a secondary unknown as it does not influence the density, the inertia, the velocity nor the stress, 2) the flow is quasisteady, 3) the interface velocity is low and does not contribute to inertia. We call this case, which arises when $k_{er} \ll V_{fl}^{-1}$, the situation of low kinetics of erosion.

Starting from initial condition $(R(0) = R_0, V(0) = 0)$, and under constant hydraulic gradient $P_{fl} > \tau_c$, the solution of the system can be written as:

$$\frac{R(t)}{R_0} = 1 + \left(1 - \frac{\tau_c}{P_{fl}}\right)\left[\exp\left(\frac{t}{t_{er}}\right) - 1\right] \qquad (10)$$

$$\frac{Q(t)}{Q_{fl}} = \left(\frac{R(t)}{R_0}\right)^{5/2} \qquad (11)$$

$$t_{er} = \frac{2L\rho_g}{k_{er}(p_{in} - p_{out})} \qquad (12)$$

The shear stress at the interface and the velocity are given by

$$\frac{\tau_b(t)}{P_{fl}} = \frac{R(t)}{R_0}, \quad \frac{V(t)}{V_{fl}} = \sqrt{\frac{R(t)}{R_0}} \qquad (13)$$

It is important to note that the limiting case $\tilde{k}_{ref} \to 1$ (corresponding to $k_{er} \to \infty$) may be of interest. In this case, the concentration can be high, and even more close to the compacity of the soil $c_{ref} = (1-n)/(1+\tilde{a}_\phi)$. The erosional law (3) leads to $\tau_b = \tau_c$, but the rheological law depends strongly upon the concentration [7] (assumption A4 has to be modified) so the velocity remains unknown. Moreover, the concentration influences most probably the velocity profil: assumptions A2 and A4 are not relevant anymore. To our knowledge, radial profil of concentration in pipe flow with erosion remains to be investigated.

IV. COMPARISON WITH EXPERIMENT

According to the logic of the derivation given above, the obtained scaling laws (10) and (11) should hold in all past and future experiments performed in erosional pipe flow with constant pressure drop, in the situation of low kinetics of erosion. The ultimate justification is a comparison with experiment.

The Hole Erosion Test has been designed to reproduce piping flow erosion in a hole [3]. The soil specimen is compacted inside a standard mould used for the Standard Compaction Test. A hole is drilled along the longitudinal axis of the soil sample. An eroding fluid is driven through the soil sample to initiate erosion of the soil along the pre-formed hole. The test result is described by the flow rate versus time curve under constant pressure drop. For further details on this test, see [3], [12], [13].

The predicted scaling law is now compared to avalaible data produced by [3]. Scaling were performed on 18 tests, concerning 10 different soils (clay, sandy clay, clayey sand or silty sand). Table I contains geological origin, particle size distribution and particle density of soils samples. Table II contains geotechnical properties of soil samples. Table III contains parameters of 18 the hole erosion tests. Table IV contains results of the modelling of these tests with the scaling law (10) and (11). The initial radius and the length of the pipe were R_0=3 mm and L=117 mm. The range of $\tilde{a}_\phi$ numbers is 2.37 to 4.82, and the range of $\tilde{k}_{er}$ numbers is 7.54 10^{-5} to 1.19 10^{-2}, so all cases correspond to the situation of low kinetics of erosion.

Fig. 2 shows the increase of the flow in $Q \propto R^{5/2}$ and shows that the use of t_{er} leads to an efficient dimensionless scaling. In Fig. 3, we plot the experimental data of [3] in the $(R(t)/R_0 - \tau_c/P_{fl},\ t/t_{er} + \ln(1 - \tau_c/P_{fl}))$ plane. We observe that all the data except for few fall on a single curve. Taking into account the many simplifying assumptions, the agreement with the scaling law (4) speaks for itself: in spite of the large range of k_{er} (three orders of magnitude), no further manipulation is needed to bring its consequences into line with the experimental data.

TABLE I.
GEOLOGICAL ORIGIN, PARTICLE SIZE DISTRIBUTION AND PARTICLE DENSITY OF SOIL SAMPLES

Soil	Geological Origin	%Gravel	%Sand	%Fines	%Finer than 0.002mm	Soil Particle Density
Bradys	Residual	1	24	75	48	2.74
Fattorini	Colluvial	3	22	75	14	2.68
Hume	Alluvial	0	19	81	51	2.71
Jindabyne	Residual	0	66	34	15	2.68
Lyell	Residual	1	70	29	13	2.61
Matahina	Residual	7	43	50	25	2.67
Pukaki	Glacial	10	48	42	13	2.70
Shellharbour	Residual	1	11	88	77	2.75
Waranga	Alluvial	0	21	79	54	2.69

TABLE II.
GEOTECHNICAL PROPERTIES OF SOIL SAMPLES

Soil		Test Name	Optimum Water Content (%)	Test Water Content (%)	Optimum Porosity	Test Porosity
Bradys	high plasticity sandy clay	BDHET001	35.0	35.8	0.52	0.52
		BDHET002	35.0	35.9	0.52	0.52
Fattorini	medium plasticity sandy clay	FTHET010	18.5	15.6	0.37	0.37
Hume	low plasticity sandy clay	HDHET001	21.0	21.4	0.39	0.40
		HDHET005	21.0	17.9	0.39	0.40
		HDHET006	21.0	22.6	0.39	0.40
		HDHET007	21.0	22.4	0.39	0.40
		HDHET009	21.0	22.7	0.39	0.40
Jindabyne	clayey sand	JDHET001	16.0	15.7	0.35	0.35
		JDHET005	16.0	13.8	0.35	0.35
		JDHET013	16.0	16.2	0.35	0.35
		JDHET016	16.0	18.3	0.35	0.35
Lyell	silty sand	LDHET014	10.0	8	0.25	0.25
Matahina	low plasticity clay	MDHET006	16.5	14.3	0.32	0.32
Pukaki	silty sand	PDHET003	8.5	8.6	0.20	0.20
Shellharbour	high plasticity clay	SHHET005	41.0	38.7	0.55	0.55
		SHHET009	41.0	37.9	0.55	0.55

V. CONCLUSION

Many laboratory tests are commonly used to study internal erosion in a soil. One of them, the hole erosion test appears to be efficient and simple to quantify the rate of piping erosion, but few attempts have been made to model this test. We started from the field equations of diphasic flow with diffusion, and the equations of jump with erosion. After many simplifying assumptions, from asymptotic developments and dimensionnal analysis, we proposed some characteristic numbers, among which the two most significant are the kinetics of erosion dimensionless number and the erosional time.

We defined a particular case: the situation of low kinetics of erosion. This situation arises when kinetics of erosion is much small than one. In this case, the influence of both concentration and inertial effects can be neglected. We obtained an analytical scaling law for the interpretation of the hole erosion test with constant pressure drop. We made comparison with available experimental data on seventeen tests concerning nine different soils. This comparison has confirmed the validity of our scaling law, which can be used for the interpretation of the hole erosion test.

More research works are needed to investigate if this characteristic time could be used in practical situations to predict the developpement of internal erosion on hydraulic works.

ACKNOWLEDGMENT

The authors wish to thanks Pr. Robin Fell and Dr. Chi Fai Wan for their valuable experimental data.

REFERENCES

[1] O. Brivois, *Contribution to strong slope erosion by a two-phase turbulent flow*, PhD, University of Aix-Marseille II, 2005.

[2] H. Chanson, *The Hydraulics of Open Channel Flows: An Introduction*, Butterworth-Heinemann, Oxford, UK, 1999.

[3] R. Fell and C.F. Wan , *Investigation of internal erosion and piping of soils in embankment dams by the slot erosion test and the hole erosion test* UNICIV Report No R-412, The University of New South Wales Sydney ISSN 0077 880X, 2002.

[4] M. A. Foster and R. Fell, Assessing embankment dam filters that do not satisfy design criteria. *Journal of Geotechnical and Geoenvironmental Engineering*, 127(5), 398–407, 2001.

[5] J.-J. Fry , *Internal Erosion: Typology, Detection, Repair*, Barrages and Reservoirs No. 6. French Comitee of Large Dams, Le Bourget-du-lac Cedex, 1997.

[6] P. Germain, Q.S. Nguyen and P. Suquet, Continuum Thermodynamics, *Journal of Applied Mechanics*, 50, 1010-1020, 1983.

[7] P.-Y. Julien, *Erosion and Sedimentation*, Cambridge University Press, 1995.

[8] P.-Y. Lagrée and S. Lorthois, The RNS/Prandtl equations and their link with other asymptotic descriptions. Application to the computation of the maximum value of the Wall Shear Stress in a pipe, *International Journal of Engineering Science* , 43(3), 352-378, 2005.

[9] L. W. Morland and S. Sellers, Multiphase mixtures and singular surfaces, *International Journal of Non-Linear Mechanics*, 36, 131-146, 2001.

[10] R.I. Nigmatulin, *Dynamics of multiphase media*, Book News, Inc. Portland, 1990.

[11] H. Schlichting, *Boundary layer theory* , 7th ed Mc Graw Hill, New York, 1987.

[12] C.F. Wan and R. Fell, Investigation of rate of erosion of soils in embankment dams, *Journal of Geotechnical and Geoenvironmental Engineering*, 30(4), 373-380, 2004.

[13] C.F. Wan and R. Fell, Laboratory Tests on the Rate of Piping Erosion of Soils in Embankment Dams, *Journal of Geotechnical Testing Journal,* 27(3), 2004.

TABLE III.
PARAMETERS OF THE HOLE EROSION TEST

Test	P_{fl} (Pa)	V_{fl} (m/s)	t_{fl} (10^{-3} s)	f_b (10^{-2})	R_e	$\tilde{a}_\phi$
BDHET001	79.96	2.20	1.36	1.65	6610	2.84
BDHET002	53.22	1.87	1.61	1.52	5606	3.07
FTHET010	93.78	2.57	1.17	1.42	7721	3.61
HDHET001	92.87	2.43	1.23	1.57	7298	3.30
HDHET005	66.13	2.22	1.35	1.34	6663	3.75
HDHET006	79.30	2.29	1.31	1.51	6875	3.46
HDHET007	79.43	2.33	1.29	1.47	6981	3.56
HDHET009	79.57	2.15	1.39	1.72	6452	3.04
JDHET001	77.74	2.26	1.33	1.53	6769	3.47
JDHET005	9.65	0.71	4.25	1.94	2115	2.68
JDHET013	53.22	1.52	1.98	2.32	4548	2.29
JDHET016	6.91	0.63	4.73	1.72	1904	3.15
LDHET014	7.96	0.81	3.70	1.21	2433	4.57
MDHET006	129.00	2.93	1.03	1.51	8779	3.57
PDHET003	16.43	1.02	2.93	1.57	3067	3.87
SHHET005	106.30	2.68	1.12	1.48	8038	3.05
SHHET009	102.39	2.71	1.11	1.39	8144	3.23
WBHET001	105.91	2.71	1.11	1.44	8144	3.58

TABLE IV.
RESULTS OBTAINED WITH THE SCALING LAW

Test	τ_c (Pa)	V_{er} (10^{-5} m/s)	t_{er} (s)	c_{ref} (10^{-5})	k_{er} (10^{-4} s/m)	$k_{er}V_{fl}$ (10^{-4})
BDHET001	76.07	1.35	223	11	3.02	6.65
BDHET002	50.93	1.43	210	14	4.80	8.97
FTHET010	6.63	4.10	73	39	8.57	22.05
HDHET001	92.87	0.94	319	9	2.01	4.88
HDHET005	66.13	1.00	299	10	2.93	6.50
HDHET006	76.00	0.18	1712	2	0.44	1.01
HDHET007	79.41	0.50	600	5	1.26	2.93
HDHET009	74.42	0.14	2183	1	0.35	0.75
JDHET001	72.32	2.26	133	25	5.89	13.30
JDHET005	6.92	0.46	647	16	9.59	6.76
JDHET013	49.66	0.79	380	13	3.03	4.59
JDHET016	6.42	0.26	1165	10	7.73	4.90
LDHET014	7.95	5.22	57	185	139.19	112.86
MDHET006	128.22	0.71	424	6	1.13	3.31
PDHET003	13.85	0.71	424	21	10.05	10.28
SHHET005	106.20	1.98	152	13	3.22	8.63
SHHET009	99.77	0.31	975	2	0.52	1.40
WBHET001	105.81	1.41	213	12	2.62	7.12

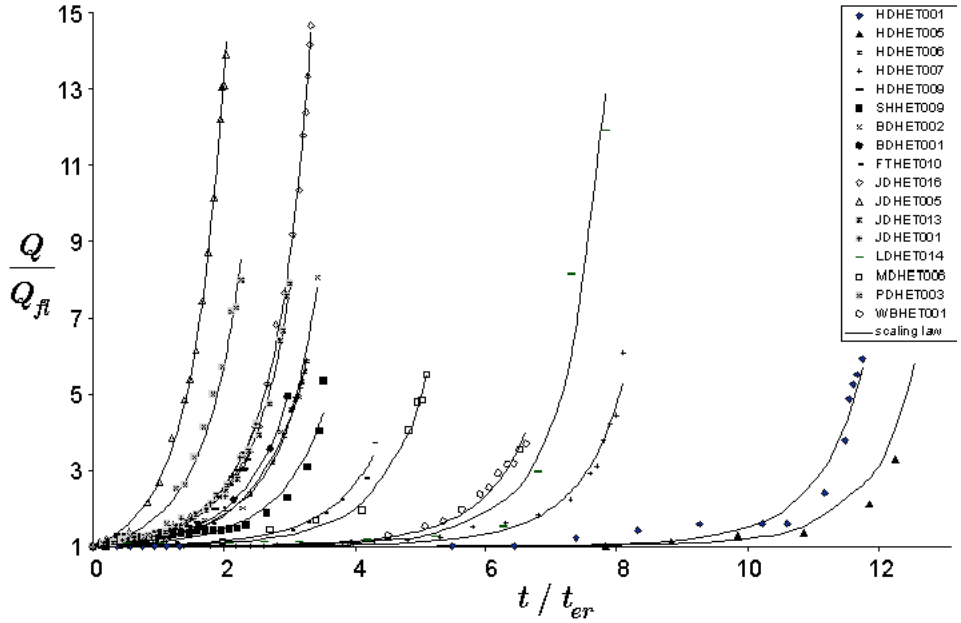

Figure 2. Hole Erosion Test, data(symbols)/ scaling law (continuous lines) comparison, dimensionless flow as a function of dimensionless time. The experimental data are taken from [2].

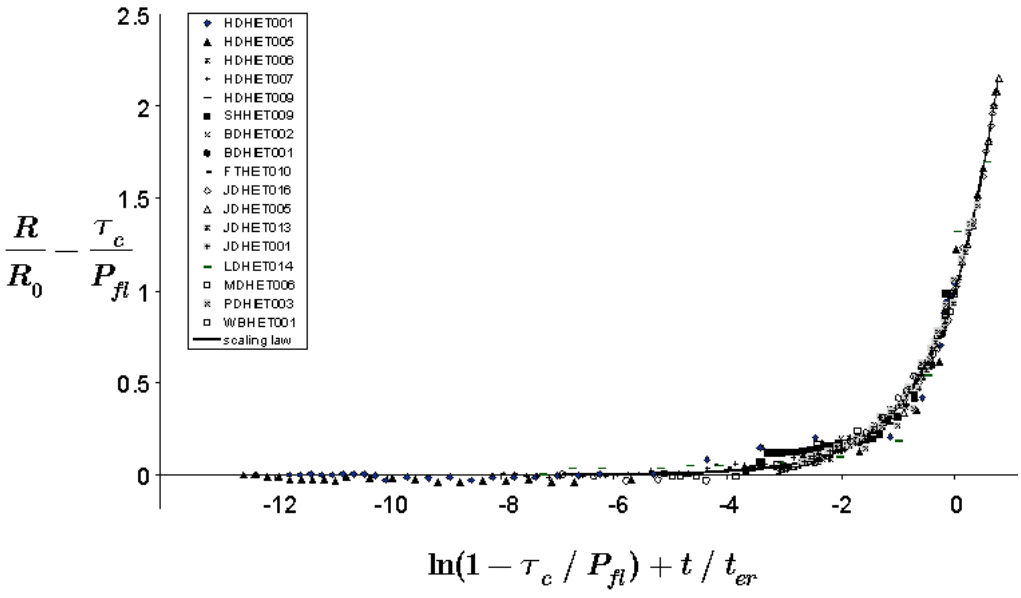

Figure 3. Hole Erosion Test, data(symbols)/scaling law(continuous lines) comparison, dimensionless radius as a function of dimensionless time. The experimental data are taken from [2].

SCOUR AT BRIDGES DUE TO DEBRIS ACCUMULATION: A REVIEW

Jean-Louis BRIAUD[1], Hamn-Ching CHEN[2], Kuang-An CHANG[3], Xingnian CHEN[4], Seung Jae OH[4]

ABSTRACT

Ten percent of all bridges over rivers in the USA are subjected to debris scour. This debris is principally made of tree trunks and other types of vegetation. The debris accumulates at bridges, mostly around piers; this increases the effective size of the pier and leads to a larger scour hole around the pier. Predicting such an increase in scour depth is still very difficult because the research ahs been limited. This article presents the results of a review of the existing knowledge on this topic. It addresses three topics: How much debris comes down rivers? How much debris accumulates at bridges? How deep will the debris scour be?

INTRODUCTION

The problem of debris scour is serious throughout the world (Figs. 1 to 4). Debris, in particular tree trunks, accumulates at bridges and creates a larger obstacle to the flow. The water needs to compensate for that decrease in flow area and erodes the river bottom: this is debris scour. In the USA, it is estimated that about 10% of all bridges over water are subjected to debris scour. This number comes from the database developed by Dave Mueller at the USGS (http://ky.water.usgs.gov/Bridge_Scour/BSDMS/). Indeed in this 507 bridge case histories database, 49 are classified as having debris problems. Doheny (1993) also indicates that for 876 highway bridges surveyed in Maryland, the number of bridges with debris blockage was 120 or 13.7%. Other countries have similar problems as was exposed at the First International Conference on Scour of Foundations organized at Texas A&M University in November 2002 (http://tti.tamu.edu/conferences/scour). This article is a review of the existing knowledge on debris scour. It addresses the following topics. 1. How much debris comes down the rivers? 2. How much of the debris coming down the river accumulates at bridges and what is the shape of the accumulation? 3. Knowing the quantity and shape of the debris, how deep will the scour hole be? 4. Common practice for debris scour calculations. 5. Case histories are then listed and discussed.

Fig. 1 – Example 1 (From Beucler, 2003)

Fig. 2 – Example 2 (From Diehl, 1997)

1. Professor and Holder of the Buchanan Chair, Dpt. of Civil Engineering, Texas A&M University, College Station, Texas, 77843-3136, USA, (briaud@tamu.edu).
2. Professor, Dpt. of Civil Engineering, Texas A&M University, College Station, Texas, 77843-3136, USA.
3. Assistant Professor, Dpt. of Civil Engineering, Texas A&M University, College Station, Texas, 77843-3136, USA.
4. Graduate Student, Dpt. of Civil Engineering, Texas A&M University, College Station, Texas, 77843-3136, USA.

Fig. 3 – Example 3 (From Benn, 2003)

Fig. 4 – Example 4 (Diehl, 1997)

HOW MUCH DEBRIS COMES DOWN RIVERS?

Debris can be classified and HEC-9 (Reihsen and Harrison, 1971) presents such a classification. The most common debris is vegetation (tree trunks and limbs) and ice (in the Northern parts of the country). Ice debris scour is studied at CRREL (Cold Region Research Engineering Laboratory) by Leonard Zabilansky including a case history (monitoring a bridge) and flume tests. Trees falling into rivers represent the most common source of debris however. The debris in rivers is either fresh debris or old debris, but old debris represents the majority. Indeed Chang and Shen (1979) state that floating debris are composed mostly of old plants and trees that are scattered along stream channel banks and on channel bars for 10 or more years. Even during the catastrophic flood of 1969 in Nelson County, Virginia, where many landslides were reported, only about 50 percent of the floating debris was found to be fresh (Chang and Shen, 1979).

The factors influencing the loading of debris into the river (Keller, Tally, 1979, Hogan, 1987) include geology, valley slope, bank erosion, landslide activity, wind-throw, channel width, channel sinuosity, discharge, upstream drainage area, and floatation from upstream. The events leading to tree collapse can be chronic or episodic. Chronic mechanisms include the regular introduction of wood as a result of natural tree mortality or gradual bank undercutting. These processes tend to add small amounts of wood at frequent intervals. In contrast, episodic inputs, including catastrophic wind-throw, fire or severe flood, occur infrequently but can add large amounts of wood to the channel network. The zone which contributes most of the debris is located within 30 m of the river bank (Fetherston et al., 1995).

To quantify debris, Downs and Simon (2001) presented steps to get the necessary input data in the model. **1**. Delineate plots on either bank of the river stretching from the waters edge. **2**. Within each plot measure all trees with a diameter greater than 0.05m at breast height. **3**. Estimate tree height using an angular reading from a known horizontal distance. **4**. Calculate the average tree diameter and tree height. **5**. Calculate the average density of trees in the survey area. Various correlations have been attempted on the basis of local databases. Bilby and Ward (1989) developed such correlations for streams in Western Washington (Fig. 5)**.** Robinson and Beshta (1990) for streams in Southern Alaska also attempted correlations (Fig. 6).

Nakamura and Swanson (1993) observed the interaction between woody debris and channel morphology at mountain streams in Western Oregon and presented the results in tabular form. Braudrick et al. (1997) observed that there were essentially three types of debris transport in rivers (Fig. 7): 1. un-congested transport, 2. congested transport, 3. semi-congested transport.

HOW MUCH DEBRIS ACCUMULATES AT BRIDGES?

Diehl (1997) points out that most debris accumulations form at the water surface as a raft. Logs and smaller pieces of debris accrete to the upstream edge of the raft. The accumulation can grow toward the river bed through accretion of logs on the underside of the raft as they are washed under it by the plunging flow at the upstream edge. Alternatively, the raft can

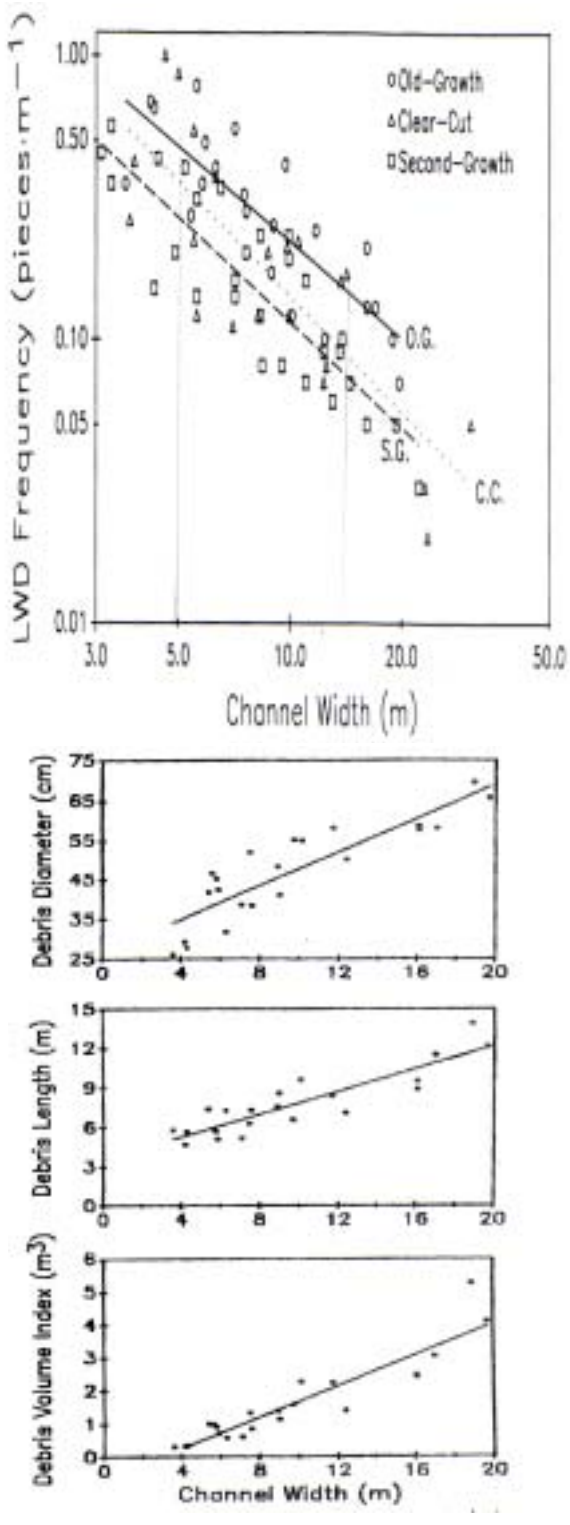

Fig. 5 – Observations from Bilby and Ward (1989) for Streams in Western Washington. (LWD = Large Woody Debris. Frequency = Number of Debris Pieces Divided by the Length of River Containing Those Debris Pieces, Debris Volume Index = Volume of the Debris Piece, L x $\pi D^2/4$)

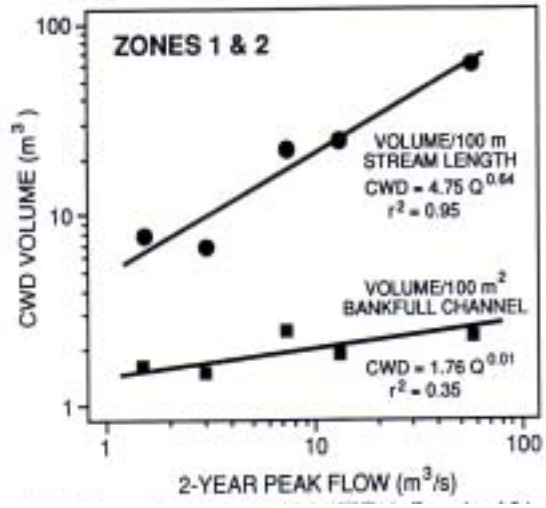

Fig. 6–Observations from Robinson and Beshta (1990) for Streams in Southern Alaska (CWD = Coarse Woody Debris)

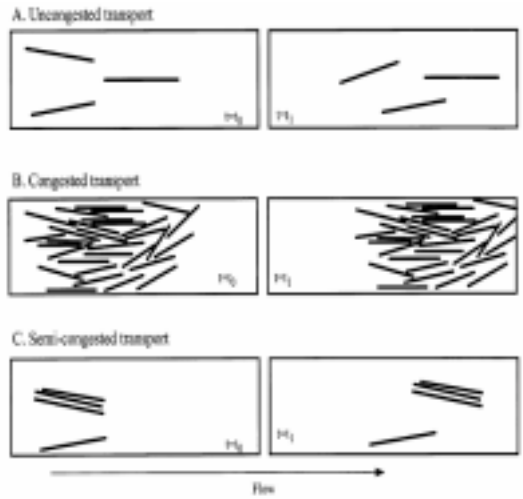

Fig. 7–Debris Transport (Braudrick et al., 1997)

forces on the raft exceed its compressive strength (Kennedy,1962). Most observed debris accumulations fall into two classes: single-pier accumulations (Fig. 4) and span blockages (Fig. 1).

Diehl and Bryan (1993) found that debris jams contained 23 percent of the total debris volume found in the river. Most of the rest of the debris occurred along short reaches of relatively unstable channel.

The shape and size of the accumulation depends on a number of factors. Accumulations may be irregular, but most large accumulations are similar in shape. In the process of formation, logs are added parallel to the upstream edge of the raft. Accumulation is often with a curved

upstream edge, and with the upstream nose of the raft near the thalweg. Single-pier accumulations often take on a form roughly resembling the inverted half-cone shape implied by New Zealand's design criteria (Dongol, 1989). The depth of a blockage is limited by the depth of flow. Debris accumulations can extend up to the maximum flood stage even after the flood recedes. The maximum vertical extent of drift observed is about 12 m, but a larger vertical extent of debris seems possible (Diehl, 1997). The maximum width of the common types of debris accumulation is determined by the length of the longest pieces of drift. The width of the channel influences the length of drift delivered to the bridge, and therefore helps to determine accumulation potential and characteristics (Diehl, 1997).

The factors affecting debris accumulation at bridges include: properties of the debris, flow conditions (velocity and depth), channel characteristics, bridge geometry (pier placement, type of pier, span). The properties of the debris refer to the rate of decay of the woody debris; this rate varies within the range of 1% to 3% of mass per year; this means that woody debris can persist for years in the river environment. Many have worked on this problem including Keller and Tally (1979) , Harmon et al. (1986); Andrus et al. (1988), Murphy and Koski (1989); Gippel et al. (1992), Ward and Aumen (1986); Golladay and Webster (1988), Hauer (1989), Sedell et al. (1988). The length of the longest pieces of drift determines the maximum width of the common types of drift accumulation. Throughout much of the United States, the maximum sturdy-log length is 24 m, and may be as long as about 45 m in parts of northern California and the Pacific Northwest.

As shown by Lyn et al. (2003) high flow velocities carry a lot of debris but low flow depths are most favorable to accumulation. The channel width plays an important role in debris accumulation by controlling the maximum size of log that can transported. Correlation work by Diehl and Bryan (1993) and by Diehl (1997) shows the relationship between debris width and channel width (Figs. 8, 9, and 10). With regard to pier placement, Diehl also observes that among 3,581 selected bridges in Tennessee, those with one pier in the channel were several times more likely to have single-pier drift accumulations than bridges with two piers on the banks and none in the channel. The river geometry (a bend for example) also influences the judicious location of the pier to minimize debris accumulation. The type of pier also affects debris. Multiple column piers and piers with exposed pile caps and piles accumulate debris more than single column piers. The span length needs to be compared with the longest log length for the area. A method to estimate the potential for debris accumulation has been devised by Diehl (1997). It consists of two convenient flow charts based on the concept of the design log length and envelopes recommended for design shown below. Methods for estimating a maximum drift-accumulation size for use in bridge design have been recommended for Australia and New Zealand, but not for the United States (American Association of State Highway and Transportation Officials, 1989). Australian design practice assumes that the potential width of drift at a pier is equal to the average

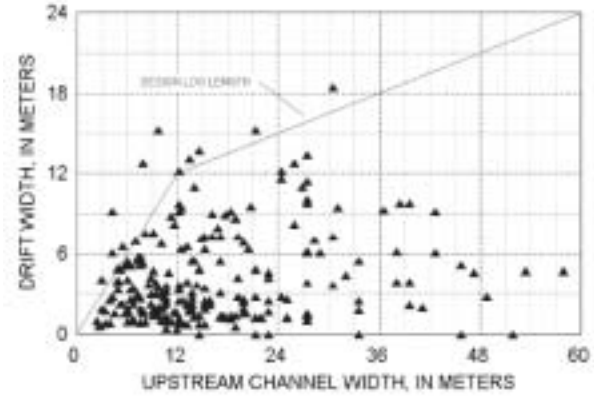

Fig. 8 - Indiana Data (Diehl, 1997)

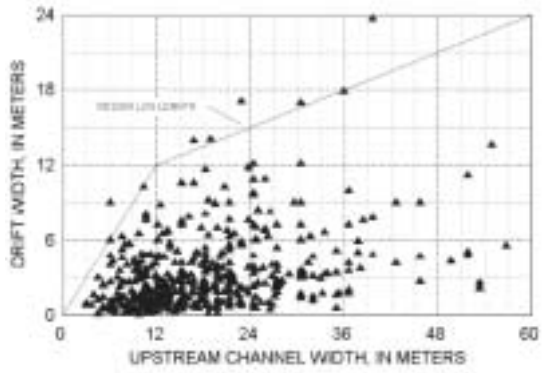

Fig. 9 - Tennessee Data (Diehl, 1997)

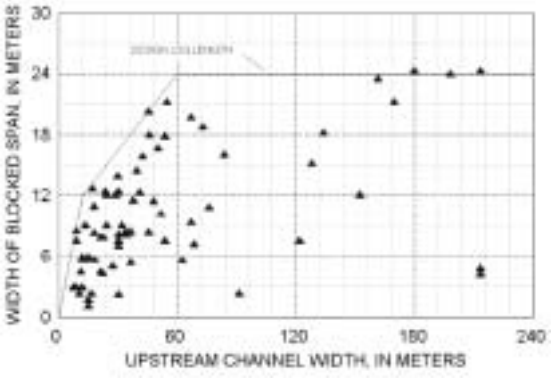

Fig. 10 - Pacific Northwest Data (Diehl, 1997)

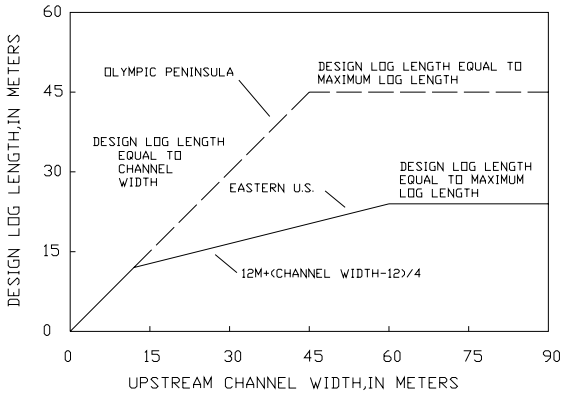

Fig. 11 - Design Chart (Diehl, 1997)

of the adjacent span lengths, up to a maximum of 20 m, and that the minimum assumed vertical depth is 1.2 m (National Association of Australian State Road Authorities, 1976; Wellwood and Fenwick, 1990). The potential width of drift on a submerged bridge superstructure is assumed to be the length of the superstructure. In developed river basins, the assumed minimum potential vertical depth of a drift accumulation is 1.2 m greater than the vertical extent of the submerged superstructure (typically, from low steel to the top of the parapet). The assumed maximum potential vertical depth is 3 m, unless local information indicates that it should be greater. New Zealand's design practice is similar to Australian design practice. A draft design specification states that the potential drift accumulation at a pier can be assumed to be triangular in cross section perpendicular to the approaching flow .The triangle's greatest width (at the water surface) is half the sum of the adjacent span lengths up to a maximum of 15 m. The triangle extends vertically downward along the pier nose to a depth equal to half the total water depth or 3 m, whichever is less (Fig. 12). Diehl (1997) found in his study that the maximum width and depth of drift accumulations exceeded the values used in design in Australia and New Zealand.

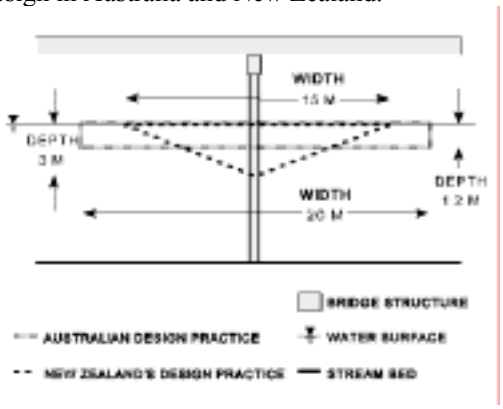

Fig. 12 - Vertical Cross Section of Assumed Maximum Drift Accumulations on Single Piers. (Diehl, 1997)

HOW DEEP WILL THE DEBRIS SCOUR BE?

Once the debris size has been established, then the additional depth of scour created by the debris needs to be estimated. Two methods presently exist in the literature; the HEC-18 Appendix method and the Melville-Dongol method. The HEC-18 Appendix method is quite conservative in that it takes the width of the debris as the pier width (Fig. 13). In another words it assumes that the debris width is constant and extends all the way down to the bottom of the river. Then the regular equations of HEC-18 are used with the new dimensions.

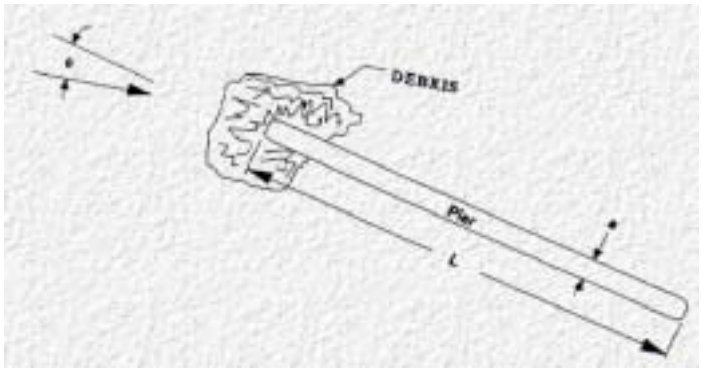

Fig. 13 - HEC-18 Approach (Richardson and Davis (2001)

The Melville Dongol method (1992) was developed from flume tests done at the University of Auckland. For piers without debris, they give:

$$\frac{d_s}{D_e} = 1.872\left(\frac{y}{D_e}\right)^{0.255} \quad \frac{d_s}{D_e} = 2.4$$

$$(y/D_e < 2.6) \qquad (y/D_e > 2.6)$$

Where, d_s is the total scour depth (pier plus debris), D_e is the equivalent pier diameter, and y is water depth. The equivalent pier diameter is calculated by using an equivalent area concept as follows; the effective diameter of the pier with debris accumulation, D_e is given by

$$D_e = \frac{T_d^* D_d + (y - T_d^*)D}{y}$$

where, T_d^* is effective thickness of debris and $T_d^* = 0.52T_d$. The factor 0.52 was determined by evaluating the limits of T_d and D_d / D for the hypothetical case where D is assumed to be zero and the debris is assumed to extend to the base of the scour hole. The diagram indicates that the calculated scour depth for piers with debris

accumulation given by the design curve is always more than the measured values.

Other factors such as clear water scour, relative flow depth, bed sediment size, pier shape and approach flow alignment are included using modification factors

$$\frac{d_s}{D} = K_I K_y K_d K_\sigma K_s K_\alpha$$

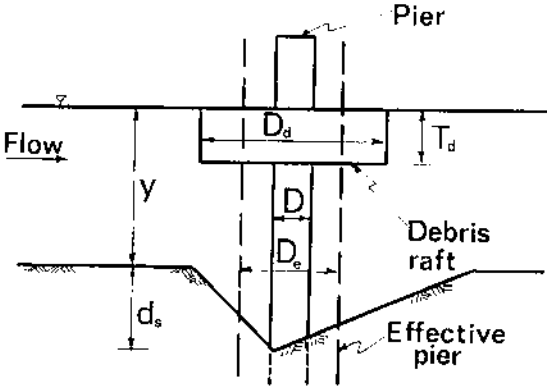

Fig. 14 - Melville and Dongol Method (1992)

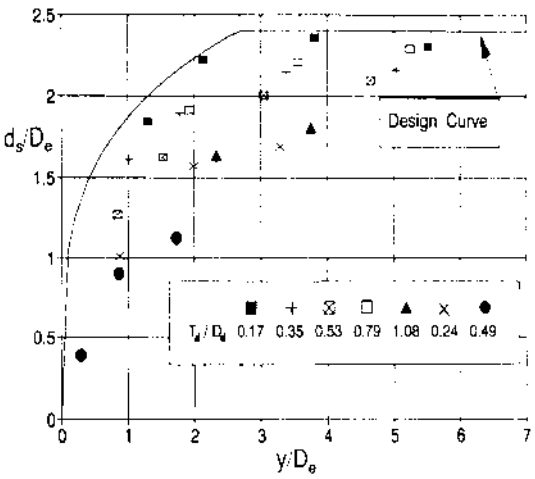

Fig. 15- Melville and Dongol Curve (1992)

where

K_I	Flow intensity factor	K_d	Sediment size factor
K_y	Flow depth factor	K_s	Pier shape factor
K_σ	Sediment gradation factor	K_α	Pier alignment factor

Additional contributions to the prediction of debris scour have been made by Manga and Kirchner (2000) on the shear stress on the river bottom due to the existence of debris around a pier and by Wallerstein and Thorne (1995, 1996, 1997).

CONCLUSIONS

A review of existing knowledge on debris scour at bridge piers was presented. The questions addressed were: How much debris comes down rivers? How much debris accumulates at bridges? How deep will the debris scour be? The answers to those questions found in existing knowledge remain vague. The guidelines in Australia and in New Zealand seem to be the most advanced.

REFERENCES

1. American Association of State Highway and Transportation Officials (1989)., "Standard specifications for highway bridges (14th ed.)" *Washington D.C., American Association of State Highway and Transportation Officials*, 420
2. Andrus, C.W., Long, B.A., and Froehlich, H.A.(1988). "Woody debris and its contribution to pool formation in a coastal stream 50 years after logging" *Canadian Journal of Fisheries and Aquatic Sciences*, 45 (12), 2080-2086.
3. Benn J., 2003, personal communication.
4. Beucler B.L., 2003, http://www.cflhd.gov/design/hyd/S11_P29.pdf
5. Bilby, R. E. and Ward, J. W. (1989). "Changes in characteristics and function of woody debris in with increasing size of streams in Western Washington." *Transactions of the American Fisheries Society*, 118, 368-378.
6. Braudrick, C. A., Grant, G. E., Ishikawa, Y. and Ikeda, H. (1997). "Dynamics of woody transport in streams: a flume experiment." *Earth surface processes and land forms*, 22, 669-683.
7. Chang F.F.M. and Shen, H.W. (1979). "Debris problems in the river environment." *Federal Highway Administration,* Report No. FHWA-RD-79-62.
8. Diehl, T. H. and Bryan, B. A. (1993). "Supply of large woody debris in a stream channel." *U. S. Geological Survey,* 810 Broadway, Suite 500, Nashville, TN., U.S.A., unpublished paper.
9. Diehl, T.H. (1997). "Potential drift accumulation at bridges." *Federal Highway Administration Report* No.FHWA-RD-97-028, 1997.
10. Doheny, E. J. (1993). "Relation of channel stability to scour at highway bridges over waterways in Maryland." *Hydraulic* Engineering '93, 2, 2243-2248.

11. Dongol, D.M. (1989). "Effect of debris rafting on local scour at bridge piers." ***Department of Civil Engineering University of Auckland.***

12. Downs, P. W. and Simon, A. (2001). "Fluvial geomorphological analysis of the recruitment of large woody debris in the Yalobusha River network, Central Mississippi, USA." *Geomorphology, 37*, 65-91.
13. Fetherston, K. L., Naiman, R. J. and Bilby, R. E. (1995). "Large woody debris, physical process, and riparian forest development in montane river networks of the Pacific Northwest." *Geomorphology,* 13, 133-144.
14. Gippel, C. J., O'Neil, I. C. and Finlayson B. L. (1992). "The hydraulic basis of snag management." *Department of Geography, University of Melbourne,* Australia.
15. Golladay, S.W., and Webster, J.R (1988) "Effects of clear-cut logging on wood breakdown in Appalachian mountain streams." *American Midland Naturalist*, 119(1), 143-155.
16. Harmon, M.E., Franklin, J.F., Swanson, F.J., Sollins, P., Gregory, S.V., Lattin, J.D., Anderson, N.H., Cline, S.P., Aumen, N.G., Sedell, J.R., Lienkaemper, G.W., Cromack, K., Jr., and Cummins, K.W. (1986) "Ecology of coarse woody debris in temperate ecosystems" *Advances in Ecological Research,* 15, 133-302.

17. Hauer, F.R. (1989). "Organic matter transport and retention in a blackwater stream recovering from flow augmentation and thermal discharge." *Regulated Rivers Research and Management*, 4 (4), 371-380

18. Hogan, D. L. (1987). "The influence of large organic debris on channel recovery in the Queen Charlotte Islands, British Columbia, Canada." *Erosion & Sedimentation in the Pacific Rim, Proceedings of the Corvallis Symposium,* IAHS, 165, 343-355.
19. Keller, E. A. and Tally, T. (1979). "Effects of large organic debris on channel form and fluvial process in the coastal redwood environment." *Adjustments to the fluvial system,* Kendall Hunt, Dudque, Iowa, 167-197.
20. Kennedy, R.J. (1962) "The forces involved in pulpwood holding grounds: Montreal, Canada" *Pulp and Paper Research Institute of Canada*, Technical Report No. 292, 207.
21. Lyn, D.A., Cooper, T., Yi, Y.-K., Sinha, R. and Rao, A.R. (2003). "Laboratory and field study of single-pier debris accumulation" *TRB 2003 Annual Meeting CD-ROM*
22. Manga, M. and Kirchner, J.W. (2000). "Stress partitioning in streams by large woody debris" *Water resources research,* 36(8), 2373-2379
23. Melville B. W. and Dongol D. M. (1992). "Bridge Pier Scour with Debris Accumulation" *Journal of Hydraulic Engineering, ASCE*, 118(9), 1306-1310
24. Murphy, M.L., and Koski, K.V. (1989). "Input and depletion of woody debris in Alaska streams and implications for streamside management" *North American Journal of Fisheries Management*, 9 (4), 427-436.
25. Nakamura, F. and Swanson, F. J. (1993). "Effects of coarse woody debris on morphology and sediment storage of a mountain stream system in Western Oregon" *Earth surface process and landform,* 18, 43-61
26. National Association of Australian State Road Authorities (1976) "NAASRA bridge design specification: Sydney" *National Association of Australian State Road Authorities*.
27. Reihsen G., Harrison L.J., 1971, "Debris Control Structures", Hydraulic Enginering Circular No. 9, FHWA report EPD-86-106, Federal Highway Administration, Wahington, D.C., USA
28. Richardson, E. V., and Davis, S. R, (2001). "Evaluating scour at bridges", *Washington, D.C. Federal Highway Administration,* Report No. FHWA-NHI-01-001, Hydraulic Engineering Circular No. 18, (4th edition).
29. Robinson, E.G., and Beschta, R. L. (1990). "Characteristics of Coarse Woody Debris for Several Coastal Streams of Southeast Alaska, USA" *Canadian Journal of Fish and Aquatic Science*, 47, 1684-1693
30. Sedell, J.R., Bisson, P.A., Swanson, F.J., and Gregory, S.V. (1988) "What we know about large trees that fall into streams and rivers, *Chapter 3 of* Maser, C., Tarrant, R.F., Trappe, J.M., and Franklin, J.F., eds., From the forest to the sea: A story of fallen trees" *U.S. Department of Agriculture Forest Service General Technical Report PNW-GTR-229*, 47-81.
31. Wallerstein, N. and Thorne, C.R. (1995). "Impacts of wood debris on fluvial processes and channel morphology in stable and unstable streams" *U.S. Army Research,* Development and Standardization Group-UK.
32. Wallerstein, N. and Thorne, C.R. (1996). "Debris control at hydraulic structures – management of woody debris in natural channels and at hydraulic structures" *U.S.*

Corps of Engineers, Waterways Experiment Station.

33. Wallerstein, N., Thorne, C.R., Abt S.R. (1997). "Debris control at hydraulic structures in selected areas of the United States and Europe" *U.S. Army Engineer Waterways Experiment Station.*

34. Ward, G.M., and Aumen, N.G. (1986) "Woody debris as a source of fine particulate organic matter in coniferous forest stream ecosystems" *Canadian Journal of Fisheries and Aquatic Sciences*, 43 (8), 1635-1642

35. Wellwood, N., and Fenwick, J. (1990). "A flood loading methodology for bridges" *Proceedings, 15th Australian Road Research Board Conference, August 1990*: Australian Road Research Board, p. 315-341.

Numerical model for wave-induced scour below a piggyback pipeline

L. Cheng[1], M. Zhao[1], F. Li[2] and H.W. An[1]
[1] School of Civil and Resource Engineering, The University of Western Australia, 35 Striling Highway, Crawley, WA 6009, Australia
[2] CSIRO Petroleum, 26 Dick Perry Ave, Kensington, WA 6151,Australia

Local scour below a piggyback pipeline due to wave action is investigated numerically. The piggyback pipeline consists of two pipelines of different diameters with the small one being located directly at the top of the large one (as shown in Fig. 1). Wave-induced flow around the pipeline is assumed to be sinusoidal oscillatory flow. The Reynolds averaged Navier-Stokes equations and the *k-ω* turbulent equations are solved using a finite element method. The conservation of the sediment mass is solved for predicting the bed scour profile. The model is firstly validated against the scour below a single pipeline under waves, where the experimental data are available. Then the model is employed to simulate the scour below a piggyback pipeline in waves. Computations are carried out for the diameter ratio of the small pipe diameter (*d*) to the larger one (*D*) equal 0.2 and the KC number, based on the large pipeline diameter, equals 12. The gap between the two pipelines ranges from 0.05*D* to 0.5*D*. The effects of the gap ratio *G*/*D* on the scoured bed profile are investigated numerically.

I. INTRODUCTION

Scour below a pipeline in currents has been investigated both experimentally and numerically in the past decades. It is well understood that the scour hole behind the pipeline is much gentler than that in front of the pipeline. The experiments showed that the scour can be classified into two stages [1, 2]. In the early stage of the scour development there is no vortex shedding behind the pipeline. The jet flow through the gap between the pipeline and the bed plays an important role in the scour process. This is called tunnel scouring [2]. As the scour depth under the pipe increases to a certain value and the gap between the pipe and bed becomes large enough, the vortex shedding occurs. The vortex shedding dominates the scour process from this moment onwards. This type of scour is called lee-wake scour [2].

Numerical models were also established for simulating the local scour below pipelines in currents in the past. It had been demonstrated that the models based on the potential flow can not predict the vortex shedding induced gentle slope behind the pipe [3, 4]. The turbulent flow model is mainly used in recent years to resolve the flow field in the scour models. Several scour models based on the turbulence model were established [4-7].

Investigations of scour below pipelines in waves are rarer than in currents. Sumer and Fredsøe [8] investigated the scour below pipelines in waves by physical experiments. They found that the scour process is mainly governed by the Keulegan-Carpenter (KC) number. The KC parameter is defined by $KC=U_mT/D$, where U_m is the velocity amplitude of the oscillatory flow, T is the period of the flow and D is the pipeline diameter. Liang and Cheng [9] simulated the scour below pipelines in waves numerically using a finite difference method (FDM). They found that the steady streaming always exists and directs away from the pipeline.

In this study, a finite element model (FEM) is established for simulating the scour below a piggyback pipeline in waves. It is expected that the FEM model offers more flexibility in handling the irregular computational domain created by local scour of the seabed. In the present model, the flow is simulated by solving the Navier-Stokes equations. The *k-ω* model is applied to simulate the turbulence of the flow. The sediment transport rates (includes bed load and suspended load) are calculated. The bed profile evolution is predicted by solving the conservation equation of the sediment mass. The model is firstly validated against wave scour below a single pipeline. The computed scour profiles are compared with the experimental data. Then the scour model is applied to simulate the scour below a piggyback pipeline under wave action. The piggyback pipeline consists of two pipelines of different diameters with the small one is located directly at the top of the large one (as shown in Fig. 1). Computations are carried out for the diameter ratio of the small pipe diameter (d) to the larger one (D) equal 0.2 and KC number based on the large pipeline diameter equal 12. The gap between the two pipelines ranges from 0.05D to 0.5D.

II. NUMERICAL METHOD

Local scour below a piggyback pipeline in waves (as shown in Fig. 1) is considered. The piggyback pipeline consists of two pipelines of different diameters. The small pipe is placed on top of the large one. The large pipeline is initially mounted on the sandy sea bed. In this study, the wave motion is assumed to be sinusoidal oscillatory flow [9]. The numerical model comprises of a flow model, a sediment transport model and a morphological model.

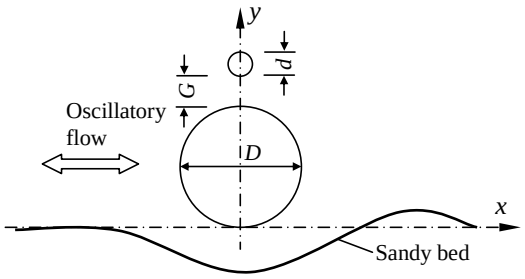

Fig. 1 Sketch of flow wave scour below a piggyback pipeline

The flow is simulated by solving a set of Reynolds-averaged Navier-Stokes equations. The turbulence of the flow is simulated by the *k-ω* turbulent model. The Reynolds-averaged Naiver-Stokes equations and the *k-ω* equations are solved by the finite element model proposed by Zhao et al. [10]. The details on the model can be found in reference [10].

A rectangular computational domain is employed in the computation. The pipeline is placed at the center of the domain. At the left and right boundaries, the vertical velocity component is set to be zero, and the profiles for the horizontal velocity, turbulent quantities are obtained based on the equilibrium profiles obtained from a separate calculation of oscillatory flow in a channel with a flat bed using the same program. Pressure at the right boundary is given a reference value of zero. At the upper boundary, vertical velocity component is set to be zero and zero normal gradient condition is applied to the turbulent quantities and pressure. On the wall boundaries, the standard wall function boundary condition is implemented [5].

The transport of sediment particles by a flow are generally in the form of bed-load and suspended load. The bed-load is the transport of sediment particles in a thin layer of about 2 sediment particle diameters thick above the bed by sliding, rolling and sometimes jumping with a longitudinal distance of a few particle diameters [11]. In this paper the bed load transport rate is calculated by the following equation proposed by Engelund and Fredsøe [12]:

$$q_b = \frac{1}{6}\pi d_{50}^3 d P_{EF} U_b \tag{1}$$

where d_{50} is the median grain diameter, P_{EF} is the percentage of particles in motion in the surface layer of the bed, U_{b} is the mean transport velocity of a particle moving along the bed. The U_{b} and P_{EF} are calculated by the following empirical formulae [12]:

$$U_b = a u_f (1 - 0.7\sqrt{\theta/\theta_c}) \tag{2}$$

$$P_{EF} = \left[1 + \left(\frac{1}{6}\frac{\pi\mu_d}{\theta - \theta_c}\right)^4\right]^{1/4} \tag{3}$$

where $u_f = \sqrt{\tau/\rho}$ is the friction velocity, τ is the bed shear stress, $a = 10$ is an experimental constant, $\theta = u_f^2/[g(s-1)d_{50}]$ is the Shields parameter, θ_c the threshold Shields parameter, μ_d is the dynamic friction coefficient, taken as 0.51 [13]. For sand on a slope bed, the threshold Shields parameter is modified as [14] $\theta_c = \theta_{c0}(\cos\alpha + \sin\alpha/\tan\phi)$, where θ_{c0} is the threshold Shields parameter on a flat bed, α is the bed slope angle, ϕ is the angle of repose of the sediment.

The suspended load transport rate is calculated according to the suspended sediment concentration. The volumetric concentration *c* of the suspended sediment is calculated by solving the following transport equation.

$$\frac{\partial c}{\partial t} + u_1\frac{\partial c}{\partial x_1} + (u_2 - w_s)\frac{\partial c}{\partial x_2} = \frac{\partial}{\partial x_j}\left(\frac{\nu_t}{\sigma_c}\frac{\partial c}{\partial x_j}\right) \tag{4}$$

where w_{s} is the settling velocity of the sediment in the water, σ_c is the turbulent Schmidt number which is taken to be 0.8 in present study. The settling velocity in clear water w_{s0} is computed by [15]:

$$w_{s0} = (\nu/d_{50})[(10.36^2 + 1.049D_*^3)^{1/2} - 10.36] \tag{5}$$

In order to consider the reduction of the settling velocity due to the interaction of the sediment grains, the w_{s} is modified by [16] $w_s = w_{s0}(1-c)^m$, where *m* is a constant which is set to be 5. The sediment concentration at the interface of the bed load and the suspended load, which is $2d_{50}$ above the wall, is specified based on the experimental formula [17]

$$c_a = [0.331(\theta - 0.045)^{1.75}]/[1 + 0.72(\theta - 0.045)^{1.75}] \tag{6}$$

Following Zyserman and Fredsøe [17], the threshold Shields parameter for computing the reference concentration is set to be 0.045 as shown in Eq. (10). If the bed Shields parameter is smaller than the threshold Shields parameter, the zero normal gradient of the sediment concentration is applied [6]. Eq. (5) is also solved by a finite element method in a same mesh of the flow calculation.

The suspended transport rate (q_s) is calculated by $q_s = \int_{z_b+\Delta_b}^{z_s} u_1 c dz$, where z_{s} is the water surface level, $\Delta_b = 2d_{50}$ is the reference level below which the sediment is transported as the bed load and above which the sediment transported as suspended load.

The time averaged bed load ($\bar{q}_{\mathrm{s}}$) and suspended load ($\bar{q}_b$) is calculated by averaging them over a wave period. The following conservation equation of the sediment mass is solved for modeling the bed profile evolution.

$$\frac{\partial z_b}{\partial t} = -\frac{1}{1-\lambda}\frac{\partial}{\partial x}(\bar{q}_b + \bar{q}_s) \tag{7}$$

where z_b is the bed elevation, λ is the sediment porosity.

In scour calculations, the computational mesh needs to be updated in each morphological time step. After the bed level is updated, the nodal points of the mesh are adjusted according to the updated bed profile. In this study, the fluid domain is considered as an imaginary elastic solid [18] when updating the mesh. The displacement of the mesh is governed by the equilibrium equations of elasticity by specifying the displacement along the bed. In order to avoid excessive deformations of small size elements, variable Lame elastic constants of the elastic solid are applied to elements to provide more

stiffness to small elements [18].

The computational procedure can be summarized as follows:

(1) Solve the Reynolds-averaged Navier-Stokes equations, the turbulent equations and the convection-diffusion equation of the sediment concentration. If the flow calculation reaches the equilibrium state (the flow velocity, the turbulent quantities and the sediment concentration in two successive periods are almost same), the scour computation is started.

(2) Calculate the bed load and the suspended load in one wave period, while solving the flow and turbulent equations.

(3) Average the bed load and the suspended load over one wave period to obtain the time averaged transport rates.

(4) Calculate the bed profile at next morphological time step according to Eq. (7). The morphological time step is selected to be much larger than the flow time step in order to speed up the calculation.

(5) Sand-slide model [5] is applied to guarantee the slope angle of the bed is not larger than the repose angle of the sediment grain.

(6) Update the mesh according to the updated bed profile.

(7) Keep bed profile constant and solve the flow equations for a number of wave periods to allow the equilibrium state being reached after the bed change.

(8) Iterate from step (2) to (7) until the bed change rate approaches to zero.

III. WAVE SCOUR BELOW A SINGLE PIPELINE

The scour model is firstly applied to simulate the local scour below a single pipeline in waves in order to validate the model. The wave motion is modeled by a sinusoidal oscillatory flow [4]. The scour process for KC = 7 in the experiments of Sumer and Fredsøe [8] is simulated. In order to make a direct comparison with the experimental results, the computation is carried out under the conditions which are the same as those specified in the physical experiment [8]. In the experiment, the pipeline diameter was 0.05 m. The amplitude of the oscillatory flow is 0.228 m/s. The median sediment grain size was d_{50} = 0.58 mm. The Reynolds number is 1.1×10^4. In the present computation, the pipeline diameter and the sediment grain size are selected to be same as those used in the experiment. A computational domain of a width of 60D and a height of 6D is used. The pipeline is located at the middle cross-section of the domain. The depth-averaged velocity amplitude is 0.228 m/s.

The pipeline is originally placed on a flat sandy bed. Fig. 2 shows the initial computational mesh near the pipe. An initial scour hole of a depth of 0.1D beneath the pipeline is introduced to avoid a complete re-meshing during the calculation. It has been demonstrated in early studies that the introduction of the initial scour hole has negligible effect on the modeled subsequent scour developments [5]. Fine structural quadrilateral elements are employed near the pipeline surface and the bed. The pipeline surface is discretized using 120 nodes. The total number of nodal points in the mesh shown in Fig. 2 is 18534.

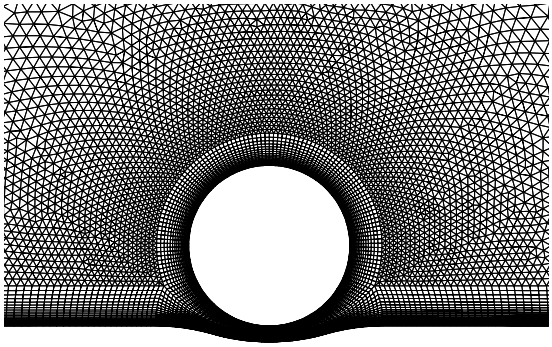

Fig. 2 Initial computational mesh for a single pipeline

Fig. 3 shows the comparison of the bed profiles at three instants after the initiation of the scour. The computed results agree well with the experimental data [8]. Two small sand dunes form at the beginning of the scour. These two dunes are transported away from the pipeline and their heights decrease with time. At t = 55 min, the scour rate approaches to zero. In the early stage of the scour, both the measured and the computed bed profiles are almost symmetric with respect to the pipeline center. The measured bed profile becomes asymmetric at the equilibrium state (See Fig. 3 (c)). However, the computed bed profile keeps symmetric throughout the duration of the scour. The asymmetry of the bed profile observed in the experiment likely attributes to the fact that the oscillation of the wave particle velocity in the experiment is not exactly sinusoidal due to the nonlinearity.

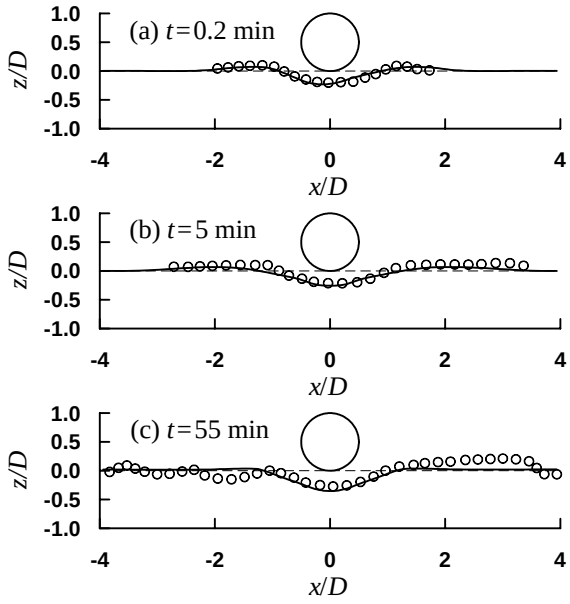

Fig. 3 Comparison of the bed profiles. ○○○, experimental [8]; ——, numerical

Fig. 4 shows the distribution of the period averaged bed load and suspended load sediment transport rates. It is seen that the directions of the sediment transport rates are away from the pipeline. The high transport rate occurs in the vicinity of the pipeline. The period averaged sediment transport rates far away from the pipeline approach to zero because the effect of the pipeline on the flow is weak. The bed load transport rate is much larger than the suspended load transport rate in the study case. Both bed load and suspended load transport rates decrease with time. At $t = 55$ minutes, the variation of the sediment transport rate with x is rather weak. It is also observed that the variation of the bed profile with time approaches to zero at $t = 55$ minutes.

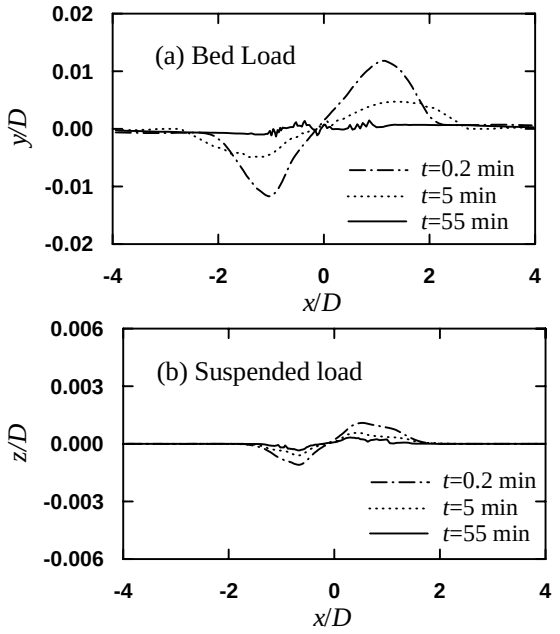

Fig. 4 Distribution of the period averaged sediment transports

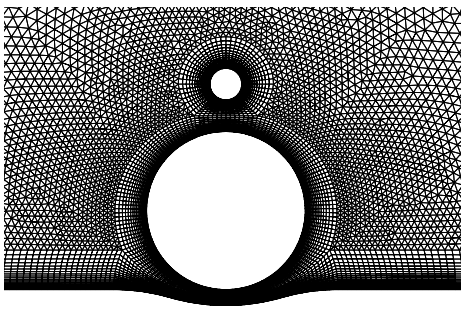

Fig. 5 Finite element mesh for $G/D = 0.2$

IV. WAVE SCOUR BELOW A PIGGYBACK PIPELINE

The finite element model is applied to simulate the wave-induced scour below a piggyback pipeline. The piggyback pipeline comprises of two pipelines of different diameters as shown in Fig. 1. The large pipeline diameter is 0.25 m. The diameter ratio d/D is kept to be 0.2. The gap between the small pipeline and the large one is G. The sediment grain diameter is $d_{50} = 0.5$ mm. The wave is modeled by sinusoidal oscillatory flow. The wave period is 6 s. The amplitude of the depth averaged velocity (U_m) is 0.5 m/s. The KC number and the Reynolds number (both based on the large pipeline diameter) are 12 and 1.25×10^5 respectively. The computational domain with a depth of $6D$ and a width of $30D$ is divided into unstructured finite elements. Fig. 5 is an example of the finite element mesh in the vicinity of the pipeline for $G/D = 0.2$. Computations are carried out for $G/D = 0.1$, 0.15, 0.2, 0.3, 0.4 and 0.5. The effect of G/D on the scour depth is investigated numerically.

Computations are carried out until two hours after scour. Fig. 6 shows the comparison of the time history of the scour depth just below the large pipeline centre (S_0). The S_0 in the single large pipeline case is also plotted in Fig. 6 for comparison. It can be seen from Fig. 6 that the scour rate at the beginning of the scour is very large, it decreases with time. At the moment of $t = 2$ hours, the scour rate for all cases has become very small. It is seen that the scour depths at $GD = 0.15$ and 0.20 are larger than that of the single pipeline case. The scour rate for $G/D = 0.10$ is close to those for $GD = 0.15$ and 0.20 before $t = 1$ hour. After $t = 1$ hour the scour rate for $G/D = 0.10$ is almost zero. At the S_0 for $G/D = 0.30$, 0.40 and 0.50 approaches to that in single pipeline case. It is expected that the effect of the small pipeline on the large one becomes weak in these two cases.

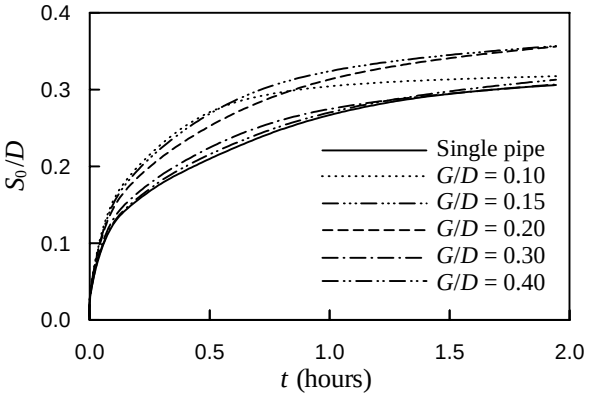

Fig. 6 Time histories of the scour depth just below the pipeline center

Fig. 7 shows the variation of the scour depth below the pipeline center versus G/D ratio at $t = 2$ hours. The scour depth in Fig. 7 is normalized by that of single pipeline (S_{01}) case. It is seen that at $G/D = 0.15$ and 0.20 the scour depth is about 1.17 times of that in single pipeline case.

For all different G/D cases, two sand dunes forms at the two sides of the pipeline after the onset of the scour. The sand dunes move away from the pipeline and their heights decreases with time. Fig. 8 shows the scour profiles at $t = 2$ hours for different values of G/D. It is seen from Fig. 8 that the bed shape is similar to that in single pipeline case except the case of $G/D = 0.10$. For $G/D = 0.10$, the two sand dunes are still not far way from the pipeline. It is found that the sand dunes are still moving away from the pipeline at a very slow speed. But the scour depth below the pipeline center for $G/D = 0.10$ has reached a constant at $t = 2$ hours (as shown in Fig. 6).

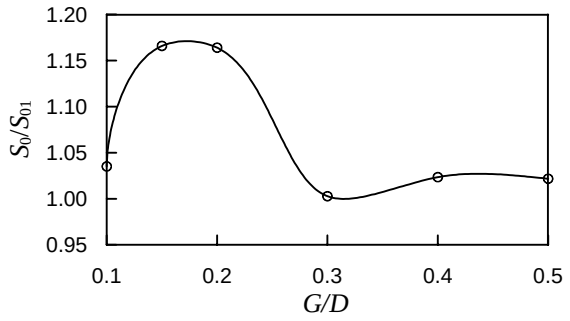

Fig. 7 Variation of scour depth below pipeline center versus G/D ($t = 2$ hours)

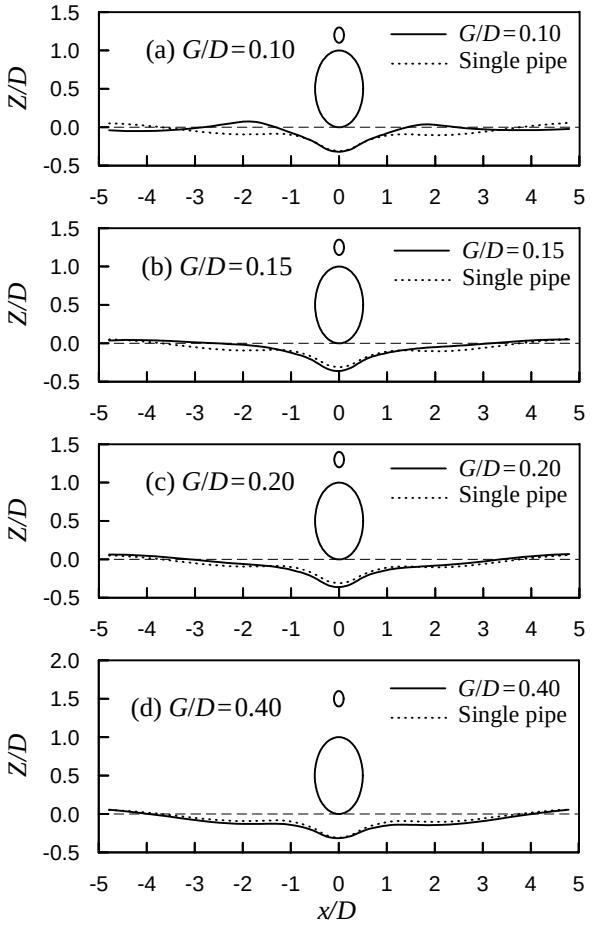

Fig. 8 Scour profiles for different values of G/D ($t = 2$ h)

The gentle slopes of the scour hole at both sides of the pipeline in Fig. 8 are similar to lee-wake induced scour in steady current case. Mao [1] had demonstrated that the gentle slope in the wake of the pipeline is due to the vortex shedding. Zhao and Cheng [7] also reproduced the lee-wake scour process by numerical method. In case of wave scour, the vortex shedding occurring in each half of wave period is similar to that in the steady current case. If the KC number is large, more vortices will be shed from the pipeline in a half of a period. The larger the KC number is, the further away from the pipelines they will be transported. It is expected that the increase of KC number will lead to gentler slopes of the scour hole at both sides of the pipelines. It can be demonstrated by comparing the scour hole at lower KC in Fig. 8 with that studied in Section III (Fig. 3).

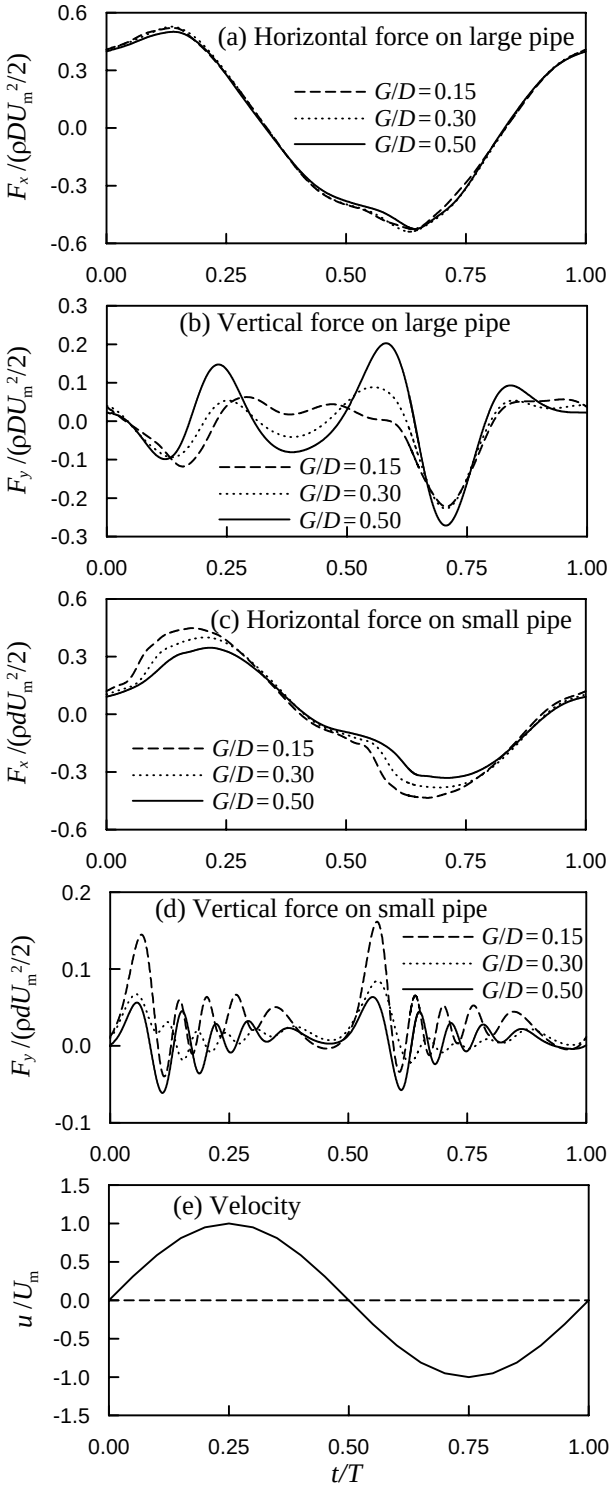

Fig. 9 Time histories of the hydrodynamic forces on the pipelines

Fig. 9 shows the time history of the hydraulic force on the large and the small pipelines after $t = 2$ hours. The $t/T = 0$ instant in Fig. 9 corresponds to $t = 2$ hours. T is wave period. It can be seen that effect of the gap ratio (G/D) on the hydraulic force is significant. The amplitudes of the fluctuating in-line forces on both large pipeline and the

small pipeline decrease with the increase of G/D. The decrease rate of the large pipeline is much smaller than that of the small pipeline. It is seen from Fig. 9 (a) and (c) that the maximum in-line forces reach their maximum values prior to the velocity. The phase shift between the maximum in-line force and the maximum velocity is about 30 degree.

The fluctuation of the lift force on the pipelines is due to the flow reverse and the vortex shedding [19]. The frequency of the lift force on the small pipeline is much larger than that on the large pipeline. The KC number based on the small pipeline is 60, which is 5 times that based on the large pipeline. It is observed that the number of vortices shed from the small pipeline in one wave period is much more than the number shed from the large pipeline. The frequency of the lift force on the large pipeline is about three times of the wave frequency. The frequency of the lift on the small pipeline is ten times of the flow frequency.

The drag and inertia coefficient on each pipeline is obtained by fitting the computed in-line force with the Morison equation using the least square method. The Morison equation is

$$F_x = \frac{1}{4}\rho\pi D^2 C_M \frac{du}{dt} + \frac{1}{2}\rho D C_D u|u| \qquad (8)$$

where C_D and C_M are the drag and inertia coefficients respectively. The drag and inertia coefficients on the small pipeline are also calculated by Eq. (8) based on the small pipeline diameter. Two lift coefficients are examined. The lift coefficients C_{L+} and C_{L-} on the large pipeline are defined as

$$C_{L+} = \max(F_y / \rho D U_m^2 / 2) \qquad (9)$$

$$C_{L-} = \min(F_y / \rho D U_m^2 / 2) \qquad (10)$$

The lift coefficients C_{L+} and C_{L-} on the small pipeline are also calculated by Eqs. (9) and (10) by replacing D with d.

Fig. 10 shows the variation of the force coefficients versus G/D after 2 hours of scour. Both the drag coefficient and the inertia coefficient on the large pipeline are smaller than their counterparts on the small pipeline. This is because that part of the large pipeline is immerged in the boundary layer of the flow in which the flow velocity is very small. The effects of G/D on C_D and C_M of large pipeline are weaker than those of small pipeline. The C_D and C_M on the small pipeline decreases with the increase of G/D. The C_D on the large pipeline changes little with G/D except a slight decrease as G/D increase from 0.1 to 0.15. The C_M on the large pipeline does not change with G/D either.

The C_{L+} on the large pipeline increases with the increase of G/D but decreases with the increase of G/D on the small pipeline. The change rates of the C_{L-} on both pipelines are small relative to those of C_{L+}. The vector of average lift coefficient ($\overline{C}_L = (C_{L+} + C_{L-})/2$) is away from bed and that on the large pipeline is towards the bed when G/D is small. It approaches zero at $G/D > 0.40$. It can be seen From Fig. 10 (c) that the absolute value C_{L-} is almost the same as C_{L+} with $G/D = 0.50$ for both pipelines. The symmetry of the lift coefficients can also be found in Fig. 9 (d). The symmetry is because the interaction between the two pipelines becomes weak at large value of G/D.

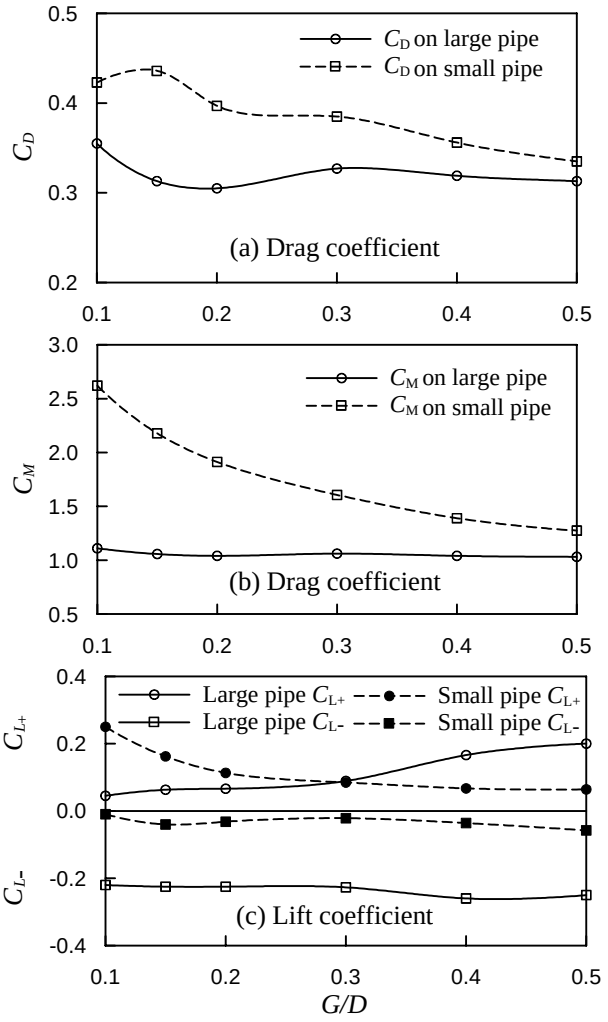

Fig. 10 Variation of the force coefficient versus G/D (t = 2 h)

CONCLUSIONS

The wave-induced scour below a piggyback pipeline is investigated numerically. The vertical two-dimensional finite element model is established for simulating the scour. The turbulent flow is simulated by solving the Reynolds-averaged Navier-Stokes equations with the k-ω turbulent model. The bed evolution is updated by solving the sediment mass conservation equation. In order to speed up the computational speed the morphological time step is selected to be much larger than the flow time step. The model is firstly used to simulate the scour below a single pipeline under waves. The pipeline is initially placed on a flat sandy bed. The wave motion is modeled by a sinusoidal oscillatory flow. The predicted scour holes agree well with Sumer and Fredsøe [8] experimental results (KC=7 case).

The scour below a piggyback pipeline is then investigated. The calculations are carried out for KC=12 and the gap ratio G/D ranging from 0.1 to 0.5. It is found that the maximum scour depth just below the pipeline occurs in the intermediate gap ratio $G/D = 0.15$ and 0.20. The scour profiles for $G/D \geq 0.30$ are similar to those of

the single pipeline case. The KC number affects the slope of the scour hole. The slope is steep for small KC number and gentle for large KC number.

The force coefficients on the pipelines above the scoured bed are also studied. The effect of the gap on the force on the small pipeline is much stronger than that on the large pipeline. The C_D and C_M on the small pipeline decrease with the increase of G/D. The change rates of the C_{L-} on both pipelines are small relative to those of C_{L+}. The averaged lift coefficient $\overline{C}_L$ is away from the bed and that on the large pipeline is towards the bed when G/D is small. It approaches zero when $G/D > 0.40$.

ACKNOWLEDGMENT

The authors would like to acknowledge the supports from Australia Research Council through ARC Discovery Projects Program Grant No. DP0557060.

REFERENCES

[1]. Mao, Y., 1986, The interaction between a pipeline and an erodible bed, Ser. Paper 39, Institute of Hydrodynamics and Hydraulic Engineering, Technical University of Denmark, Lyngby, Denmark.

[2]. Sumer, B.M. and Fredsøe J., 2002, The mechanics of scour in the marine environment, World Scientific, pp 15 - 138.

[3]. Sumer, B.M., Jensen, H.R. and Fredsøe, J, 1988, Effect of lee-wake on scour below pipelines in current, J. Waterw. Port Coast. Ocean Eng., Vol 114, No 5, pp 599-614.

[4]. Li, F. and Cheng, L., 2001, Prediction of lee-wake scouring of pipelines in currents, J. Waterw. Port Coast. Ocean Eng. Vol 127, No 2, pp 106-112.

[5]. Liang, D., Cheng, L. and Li, F., 2005, Numerical modeling of flow and scour below a pipeline in currents Part II. Scour simulation, Coastal Eng. Vol 52, pp 43-62.

[6]. Brørs, B., 1999 Numerical modeling of flow and scour at pipelines, J. Hydraul. Eng, Vol 125, No 5, pp 511-523.

[7]. Zhao M. and Cheng L., 2006. Numerical modeling of local scour below a piggyback pipeline in currents. Submitted to Journal of Hydraulic Engineering.

[8]. Sumer, B.M. and Fredsøe J., 1990, Scour below pipelines in waves, J. Waterw. Port Coast. Ocean Eng., Vol 116, No 3, pp 307-323.

[9]. Liang, D., and Cheng, L., 2005, Numerical model for wave-induced scour below a submarine pipeline, J. Waterw. Port Coast. Ocean Eng. Vol 131, No 5, pp 193-202.

[10]. Zhao, M., Cheng, L., Teng, B., Dong, G., 2005, Hydrodynamic forces on dual cylinders of different diameters in steady currents, Submitted to Journal of Fluids and Structures.

[11]. Einstein, H.A., 1950, Bed-load function for sediment transportation in open channel flow, United States Department of Agriculture, Washington D.C., Technical Bulletin, No. 1026, pp. 25.

[12]. Engelund, F. and Fredsøe, J., 1976, A sediment transport model for straight alluvial channels, Nordic Hydrol., Vol. 7, pp. 293-306.

[13]. Fredsøe, J., Deigaard, R., 1992, Mechanics of Coastal Sediment Transport, Advanced Series on Ocean Engineering 3. Word Scientific, Singapore.

[14]. Allen, J. R. L., 1982, Simple models for the shape and symmetry of tidal sand waves: I. Statically stable equilibrium forms, Mar. Geol. Vol. 48, pp. 31-49.

[15]. Soulsby, R., 1997, Dynamics of Marine Sands. Tomas Telford, London.

[16]. Richardson, J.F., Zaki, W. N., 1954, Sedimentation and fluidisation: Part I, Trans. Inst. Chem. Eng., Vol. 32, No. 1, pp. 35-53.

[17]. Zyserman, J.A., Fredsøe, J., 1990, Data analysis of bed concentration of suspended sediment, J. Hydraulic Engineering, Vol. 120, No. 9, pp. 1021-1042.

[18]. Johnson, A.A., Tezduyar, T, E., 1994, Mesh update strategies in parallel finite element computations of flow problems with moving boundaries and interfaces, Comput. Methods Appl. Mech. Engrg, Vol. 119, pp. 73-94.

[19]. Williamson, C.H.K. 1985. Evolution of a single wake behind a pair of bluff bodies, Journal of Fluid Mechanics, 159, 1-18.

Thoughts on Riprap Protection around Bridge Piers

Y. M. Chiew*
* School of CEE, Nanyang Technological University, Singapore 639798

ABSTRACT

Using riprap stones as an armoring countermeasure to protect bridge piers against scour has been used by hydraulic engineers for over a century. Its success, however, is not always guaranteed, and bridges sometimes are found wanting under certain flood conditions. Recent experimental studies over the past 25 years have revealed five main failure mechanisms associated with riprap protection around bridge piers. They are (1) Edge failure; (2) Shear induced failure; (3) Winnowing failure; (4) Bedform-induced failure; and (5) Bed-degradation induced failure. In order to ensure riprap as an effective scour countermeasure, each of these failure mechanisms must be addressed. This paper presents recent research findings in addressing how these failure mechanisms are tackled. Additionally, it also offers innovative ideas for additional research to eliminate or at least reduce the extent of the failure mechanisms.

I. INTRODUCTION

The formation of a pier-scour hole around bridge foundations has been the cause of many failures. Published data have unequivocally supported the correlation between bridge failure and pier-scour [1]. Because of the important relationship between scour hole formation and bridge failure, engineers have adopted various protection methods with the intention of either eradicating or at least minimizing the size of the scour hole. Whenever plausible, some engineers have avoided piers in their design such that pier-scour hole is eliminated altogether. When the construction of piers is inevitable, design considerations of bridge foundations must include pier-scour prediction for without which, the integrity of the bridge may easily be compromised.

Engineering methods developed to deal with pier-scour problems are unsophisticated and they generally can be categorized into two distinctive groups: flow-altering and armoring countermeasures. References [1] and [2] provide excellent descriptions of both these two types of scour countermeasures. Considering the frequency of use between these two types of scour countermeasure in practice, it appears that practitioners have endowed more confidence in armoring rather than flow-altering countermeasure. The principle behind an armoring countermeasure is the provision of a more resistant sediment bed to withstand the pier-induced flow field in the form of the downflow and horseshoe vortex. A host of devices, for example, riprap stones, cabled-tied blocks, Reno Mattresses, concrete-filled mats and bags, concrete apron, dolos, tetrapods, etc. have been used as armoring countermeasure with varying degrees of success. One of the main reasons for their often unpredictable behavior under field conditions may be attributed to the lack of systematic research on their performance. This deficiency has, to a large extent, been addressed in the past two and a half decades when systematic research investigations were carried out in many parts of the world. Results from these studies have provided an improved understanding on the performance of armoring countermeasure used to protect against pier-scour. The use of riprap stones as a pier-scour countermeasure has particularly been tested. With these studies, we now can better understand how riprap stones around a bridge pier fail under both clear-water and live-bed conditions.

II. FAILURE MECHANISMS

Based on numerous experimental studies conducted in a wide range of flow conditions [3~7], we now can identify five different failure mechanisms associated with riprap failure around bridge piers. They are:

1. Edge failure: rocks at the edge of the riprap layer are eroded, which affected its stability;
2. Shear failure: riprap stones are entrained by the local pier-induced flow field due to their inadequate resistance;
3. Winnowing failure: the underlying finer bed material are winnowed through the voids or interstices of the riprap stones;
4. Bedform-induced failure: riprap stones are disturbed by the fluctuation of the bed level due to the propagation of bedforms such as dunes past the pier; and
5. Bed-degradation induced failure: riprap failure associated with general scour.

Edge Failure

While the above five failure mechanisms were deduced primarily from studies conducted with riprap stones, it will not be erroneous to surmise that the same failure mechanisms apply to all types of armoring countermeasure, such as the devices stated above. A classical example of edge failure can be seen at a bridge in Taichung, Taiwan where a thick concrete apron was

placed around the bridge pier (Fig. 1a). This is coupled with placement of tetrapods immediately downstream of the apron. Figures 1(b) and (c) show how edge failure effectively eroded all the tetrapods. With the total failure of the tetrapods at this bridge, the concrete apron has become extremely venerable and the integrity of the bridge may be seriously compromised. This example clearly shows how edge failure can be extremely detrimental to armoring countermeasure.

Figure 1(a). Concrete apron as a pier-scour countermeasure at a bridge in Taichung, Taiwan

Figure 1(b). Edge failure leading to erosion of the tetrapods

Figure 1(c). Eroded tetrapods downstream of bridge

Edge failure is also found in many other scour protection schemes apart from piers. It is often inadvertently induced by placing a layer of rocks or riprap mattress over the bed material around some hydraulic structures. Reference [8] described the close correlation of edge failure and the eventual demise of an offshore submarine pipeline. Similar failures were also observed downstream of many tidal gates in certain parts of Malaysia and Singapore.

Experimental studies [3] have shown that edge failure occurs at the periphery or edge of the coarse riprap stones and fine bed sediment interface, an occurrence that is not uncommon in flume experiments involving a rigid-loose bed interface. At such a location, a scour hole inevitably forms on the downstream erodible bed. With riprap protection around a bridge pier, edge failure can occur when the coarse riprap stones remain intact or stable. With the intact riprap layer in place, the downstream finer sediment particles are entrained by the flow because of their lower critical shear stress. When this happens, a local depression forms and the larger riprap stones are exposed. The stones at the edge thus roll or slide into the depression, as shown in Figure 2.

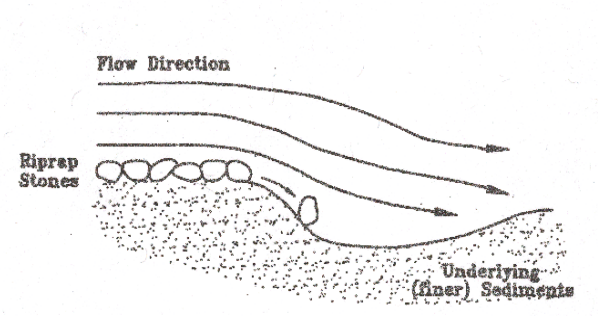

Figure 2. Schematic illustration of edge failure [3]

With a riprap layer placed around a bridge pier, edge erosion generally occurs at the downstream end of the riprap layer. It takes place at low velocity ratio where shear and winnowing erosion are normally absent, and often constitutes the first sign of failure of the riprap layer. With the erosion of some of the larger riprap stones due to edge erosion, shear erosion and subsequently winnowing erosion may set in. Using a series of six photographs, ref [3] described how riprap failure begins with edge failure at the downstream of the riprap layer. How the riprap layer would progress beyond edge failure is very much dependent on its aerial coverage and thickness. This aspect of scour research is still not thoroughly investigated.

Edge failure was also observed at the upstream end of the bridge pier. Describing this type of occurrence, ref [9] stated that “as the scour (at the upstream location) progresses deeper, edge stones in the riprap layer begin to experience undercutting, causing them to subside into the scour region. With the edge stones removed the inner riprap is exposed. These stones gradually subside as sand is winnowed from beneath them”.

Edge failure, whether it occurs at the upstream or downstream end of the bridge pier, serves as an important function in weakening the riprap layer. By itself, edge

failure will not render the demise of the riprap layer because it does not have a direct impact on the foundation of the hydraulic structure. Its role is indirect in that it

(a) Exposes the larger stones in the coarse-fine sediment interface, rendering them more susceptible to erosion; and
(b) Reduces the thickness of the riprap layer, thereby promoting winnowing failure.

In summary, edge failure hastens the eventual demise of the riprap layer as it enhances either winnowing or shear failure. The former leads to embedment while the latter enhances disintegration of the riprap layer.

Shear Failure

Shear failure, which is the most studied of all the failure mechanisms to-date, can similarly cause bridge failure. It refers to the entrainment of riprap stones or other armoring countermeasure devices by the pier-induced flow field. Its occurrence simply means that the stones or other armoring devices used are just not large or heavy enough to withstand the local flow filed. To properly account for this failure mechanism is rudimentary; all one needs to do is to select a device with larger or heavier units to resist erosion. Theoretically, this refers to the condition where the critical shear stress of the device is larger than the applied shear stress. Studies over the past quarter century have provided many empirical and semi-empirical equations for the selection of the appropriate riprap stone size to withstand the designed flow field. A list of these equations was compiled by [7], who also compared each of their performance under given flow conditions. Some of these equations and their efficiency can be found in [1, 6, 7].

While the principle behind carrying out a design against shear failure is straightforward, engineers have sometimes adopted the use of gabions or Reno mattresses as an armoring countermeasure device. One of the reasons is the possibility of using smaller size rocks placed within a cage rather than the larger and often more expensive rocks. While this can satisfy the designed condition with reference to the threshold or critical shear stress of the gabions as a unit, it will fail if the steel cages break as they deteriorate with time. This is especially important if the gabions are in contact with seawater. With such breakages, shear failure inevitably takes place as the smaller rocks within the cage are not designed for the local flow field.

Winnowing Failure

Another important failure mechanism has been identified as winnowing failure, which refers to the situation where the underlying finer bed material is winnowed through the voids or interstices of the coarser riprap stones. The same process of winnowing can also be observed in natural alluvial channel, especially for beds consisting of sediments with different strata in which a layer of coarse particles overlay that of finer sediments. Under this condition, erosion of the underlying finer sediment particles through the voids of the coarser ones may occur. The extent of winnowing is dependent on the magnitude and type of flow, and the relative size of the overlying coarse and underlying fine sediment particles. Reference [3] described some experiments conducted in a 2-dimensional flow where winnowing is the dominant mode of erosion. In a 3-dimensional flow field, as is the case of flow around a bridge pier, winnowing is even more conducive because of the high level of turbulence. This is especially apparent if there are less than three layers of coarse stones making up the riprap layer. Experimental observations [3, 4, 9] have clearly revealed the importance of winnowing on the degradation of a riprap layer. Under such a condition, the riprap stone is large enough to resist shear failure, but the underlying finer sediments were entrained through the process of winnowing. The effectiveness of a riprap layer or other armoring countermeasure devices can easily be compromised if winnowing failure becomes excessive. It can lead to significant degradation of the riprap mattress or *embedment failure*, which can have dire consequences on the performance of the riprap layer. To this end, ref [3] has published a figure, which is reproduced in this paper as Figure 3 to demarcate embedment failure (caused primarily by winnowing failure) from total disintegration failure (caused primarily by shear failure).

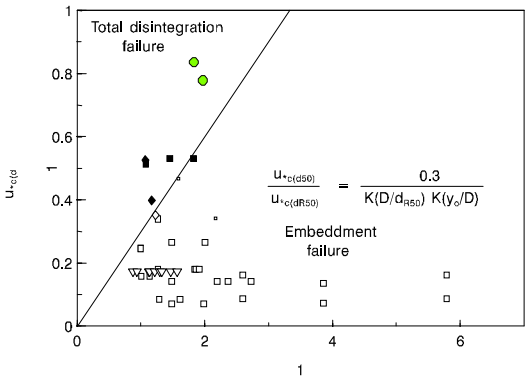

Figure 3. Classification of failure mode of riprap layer [3]

Bedform-Induced Failure

The above three failure mechanisms occurs under both clear-water and live-bed conditions. The last two, vis-à-vis bedform-induced and bed-degradation induced failure occur under live-bed conditions only. Bedform-induced failure can be especially important in terms of its impact on the effectiveness of riprap layer as a pier-scour countermeasure. This is especially so if large dunes are present on the approaching bed as bedform-induced failure is closely related to the fluctuating bed level due to the propagation of ripples or dunes past the riprap layer. Two important effects can be identified with reference to this correlation. First, the fluctuating bed level causes the riprap stones to lose support, and therefore stability. Second, when the trough of the dunes arrives at the riprap layer, high level of turbulence is generated at the reattached zone of the flow over the dune crest. These two occurrences combine with the pier-induced flow field to pluck and erode the riprap stones. Once these stones

are eroded, the degraded layer becomes thinner and is further loosened, which gives an impetus for winnowing, resulting in the embedment of the riprap layer.

Reference [4] has devised and conducted an experiment to differentiate bedform-induced failure from the other three types of failure discussed earlier. It involves two tests which were both conducted under transition flat bed conditions at a velocity ratio, U/U_c = 4.5. All the other test conditions were identical except that in the first test, the flow velocity was increased as quickly as practicable so that transition flat bed was formed immediately after the onset of the test. The objective of such a procedure is to avoid the formation of ripples or dunes on the approaching bed so as to negate any bedform-induced failure at the riprap layer before the test was conducted. With the second test, velocity was increased incrementally, thus allowing ripples and dunes to form prior to the final test with U/U_c = 4.5.

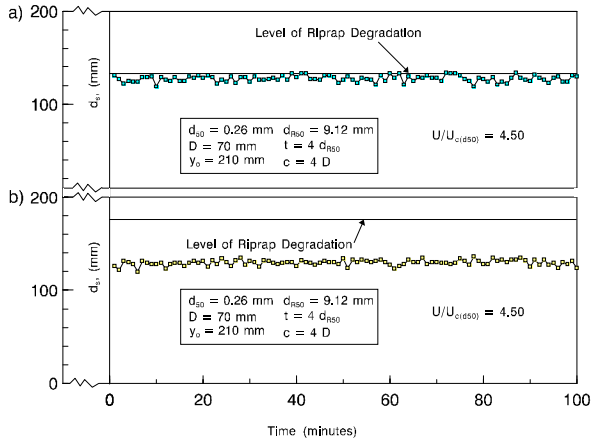

Figure 4. Temporal variation of scour depth in transition flat bed regime with different antecedent bedforms: (a) Immobile plane bed; (b) Immobile plane bed, ripples and dunes [4]

Figure 4 shows the results of the two tests, and it depicts the temporal scour depth fluctuation at U/U_c = 4.5 where transition flat bed was present on the approaching bed. The horizontal lines in the figures depict the depth of the riprap layer degradation, d_{rp} – the level to which the riprap layer has degraded. It shows that d_{rp} for Tests (a) and (b) = 133 mm and 176 mm, respectively. In Test (a), the scour depth expectedly fluctuates with time, which is due to avalanches of the sediment particles on the upstream slope of the scour hole. The result shows that the riprap layer has clearly degraded to the same level as the maximum scour depth. On the other hand, d_{rp} associated with Test (b) is deeper by 43 mm when compared to that associated with Test (a). The reason for the deeper d_{rp} is because of the antecedent condition where ripples and dunes were present. The difference of 43 mm (difference between 176 and 133 mm) is caused by bedform-induced failure. These tests clearly highlight the importance of bedform-induced failure, as it will amplify the extent of riprap layer degradation.

The importance of bedform-induced failure at riprap layers is also highlighted in [2, 9]. In the latter study, the authors concluded that destabilization of a riprap layer by the progression of bedforms past the pier is the dominant failure mode under live-bed conditions, whereas shear, winnowing and edge failures play a secondary role.

Bed-Degradation Induced failure

The fifth mechanism affecting riprap failure at bridge piers is bed-degradation induced failure [11, 12]. Unlike the other four, this type of failure will only occur under a condition when general scour is present. Under this condition, there is a net loss of sediment over the section of the river in which the bridge is founded.

If the riprap stones around a bridge pier remain intact in a river subjected to general scour, a mound, as shown in Fig. 5, will form around the pier. Although it appears to serve its function in protecting the pier against erosion, the study shows that additional floods with large dunes translating past the pier can have dire consequences its integrity as a pier-scour countermeasure. Observations in [11] showed that the riprap layer had disintegrated significantly when two floods of similar magnitude were allowed on the riprap layer cum bridge pier. This result suggests that recurrent maintenance is necessary to enhance the effectiveness of the riprap layer in protecting the pier against scour in a degrading channel.

Figure 5. Formation of riprap mound around bridge pier in a degrading bed

III. PIER-SCOUR PROTECTION

In order to have a riprap layer or other armoring countermeasure devices that effectively protect bridge piers against scour, it is imperative that all the above failure mechanisms be attended to. Although many auxiliary designs have been added to a pier-riprap layer in practice, its performance is still not absolute or certain. Field results have shown that many bridges do fail as a result of the scour hole that forms at their foundation despite riprap protection with or without such auxiliary addendum.

This paper presents two recent ideas developed at the Nanyang Technological University, Singapore on how

some of the failure mechanisms described earlier can be tackled by incorporating a complementary or stand-alone method to augment the effectiveness of pier-scour protection. Understanding on how these methods perform is still in its infancy stage, but preliminary research offers promising results. It is hoped that with more systematic research, the performance of these methods can be better understood so that field deployment may be implemented with more certainty and assurance of success. The two new methods are:

(1) Incorporation of suction with a riprap layer; and
(2) Use of tetrahedron frames.

Incorporation of Suction with Riprap Protection

The possible use of suction to augment the performance of a riprap layer around bridge piers arises from results obtained from an extensive research program on seepage effects on turbulent open-channel flow and sediment transport carried out at the Nanyang Technological University by the author and his co-workers. Those studies show that the turbulent characteristics of the flow are significantly modified even though the seepage flow rates, either as suction or injection, are only a small fraction of the main flow rates in the channel. Additionally, the studies also show that the incipient sediment motion and the dune geometry change with seepage. Arising from these findings, it is surmised that utilization of seepage can likewise modify the behavior of both the flow and sediment transport around a bridge pier. If such changes in flow and sediment transport pattern could be exploited, the performance of the riprap layer may be enhanced to counteract some or all the failure mechanisms associated with pier-riprap failure.

A series of tests was conducted using uniform sediment with a median grain size, d_{50} = 2.2 mm as the bed material. A cylindrical pier made from a 50-mm diameter Perspex tube was placed in the test section. A riprap layer, made from uniform coarse gravel with median grain size = 30 mm and density = 2,650 kg/m^3 was placed around the cylindrical pier. The cover and thickness of the riprap layer are 14 cm and 5 cm, respectively. Figure 6 shows how seepage was introduced upstream of the riprap layer by means of three pipes embedded beneath the sediment bed. The streamwise distance between the pipes was 58 mm and identical holes with diameter = 6 mm were drilled around the pipe.

Three sets of experiments were conducted to explore how suction affects the performance of the riprap layer. In Series A, tests were conducted without suction, and the results form the basis for comparison. In the second Series B, only pipe 1 was in operation while all three pipes were used to produce suction for Series C. Moreover, three shear stress excess at u_*/u_{*c} = 1.1, 1.4 and 1.8 were used in the tests. The experimental results are summarized in Table 1.

The experimental data in Table 1 are plotted in terms of %RDP as a function of Q_s/Q_o. The former is defined as the reduction ratio of the depth of riprap layer with (d_{rs}) and without suction (d_{ro})

$$\%RDP = \frac{d_{rs} - d_{ro}}{d_{ro}} x100\% \qquad (1)$$

On the other hand, Q_o and Q_s are defined as the undisturbed main flow rate in the channel and the suction flow rate, respectively. Figure 7 shows how the ratio of suction rates affects degradation of the riprap layer.

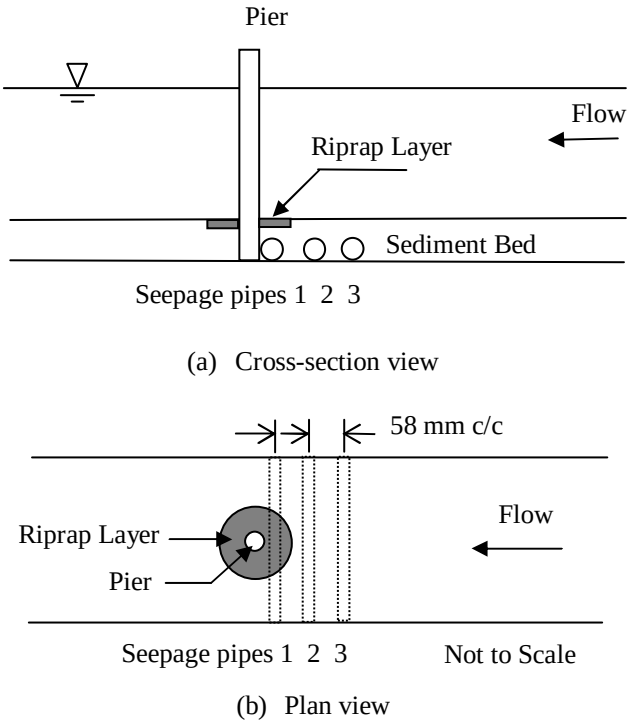

Figure 6. Experimental setup of seepage tests with pier- riprap

TABLE 1.
Summary of Experimental Results

No of Pipes	Q m^3/h	Q_s m^3/h	d_r mm	Q_s/Q %	% RDP
u/u_c = 1.1					
1	220	0	21	0	0
1	220	1.125	14	0.51	33.3
1	220	1.8	10	0.82	52.4
u/u_c = 1.4					
1	275.4	0	30	0	0
1	275.4	1.125	23	0.41	23.3
1	275.4	1.8	17	0.65	43.3
u/u_c = 1.8					
3	367	0	51	0	0
3	367	0.4	35	0.11	31.4
3	367	0.52	36	0.14	29.4
3	367	0.69	40	0.19	21.6
3	367	1.5	44	0.41	13.7
3	367	1.8	42	0.49	17.7

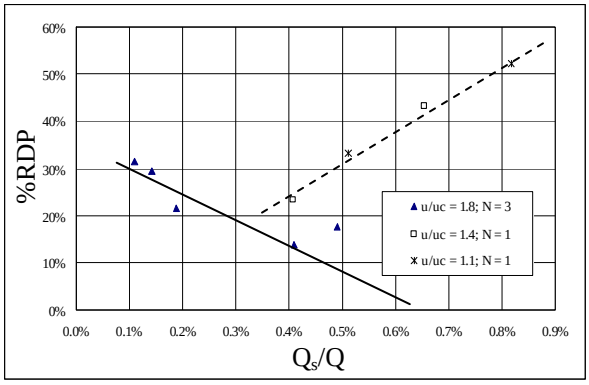

Figure 7. Effect of suction on riprap layer degradation

The results in Fig. 7 clearly show that suction does have a significant effect on the riprap layer degradation. In all the tests, the %DRP exceeds 0, reaching a maximum value of 52.4% when only one pipe with suction ratio, Q_s/Q_o = 0.82% is in operation. The result is clearly promising with reference to suction effects on riprap protection against pier-scour. The reduction in riprap layer degradation is attributed to the reduction in the local turbulence intensity in the flow. This in turns impedes winnowing failure resulting in a significant reduction in d_{rs}.

The data in Fig. 7 also show a decreasing trend, which is associated with tests conducted with u_*/u_{*c} = 1.8, where dunes with a measurable height were present. Under this condition, the dominant mode of failure is no longer winnowing but that of bedform-induced failure. Under this condition, the critical variable is the size of the dune propagating past the riprap layer, and suction has the unfortunately effect of increasing the dune height [13]. The overall impact on riprap layer degradation is due to the combined influence of both a reduction in turbulence intensity and an increase in dune height. The experimental results appear to show that the effect of the latter surpasses that of the former, resulting in a reduction in %RDP, as shown in Fig. 7.

While no definitive conclusions can be drawn presently due to the limited data we have, the results show that seepage application does offer a positive improvement on riprap protection at bridge piers.

Use of Tetrahedron Frame

The use of tetrahedron frame as a pier-scour countermeasure was first advocated by researchers from the College of water Conservancy and Hydropower Engineering at the Hohai University in Nanjing, China. This new scour countermeasure was tested in the laboratory and subsequently used for river bank protection. Extension of its use as a pier-scour countermeasure was discussed and later tested at the Nanyang Technological University (NTU) under a collaborative research program between these two Universities.

The results from the tests conducted at NTU are reported in another paper presented in this conference, and they will not be repeated here. Suffice to say that the results also offer an extremely promising trend in that the problem of edge failure appears to have been addressed. If proven to be effective, this method will offer a most important advancement on using armoring countermeasure at bridge piers.

IV. CONCLUSIONS

Research investigations from around the world over the past quarter century have revealed that a pier-riprap layer is subjected to five different failure mechanisms. They can act singly or combine to cause embedment or total disintegration of the riprap layer. These five failure mechanisms are edge failure, shear failure, winnowing failure, bedform-induced failure and bed-degradation induced failure. In order to provide an effective means to protect against pier-scour, it is imperative that the scour countermeasure must be able to withstand all these failure mechanisms. Based on understanding of these failure mechanisms, this paper presents two new and innovative pier-scour protection devices. The results so far show an extremely promising trend in that they arrest directly or indirectly edge failure, winnowing failure and bedform-induced failure. If proven to be effective when more experimental data become available, these methods may be used with more confidence in the field as a reliable pier-scour countermeasure around bridge piers. They may even be extended for use in other hydraulic or coastal structures.

REFERENCES

[1] B. W. Melville, and S. E. Coleman, *Bridge Scour*, Water Resources Publication, LLC, CO., USA, 2000.

[2] G. Parker, C. Toro-Escobar, and R. L. Voigt, "Countermeasures to Protect Bridge Piers from Scour." Final Report prepared for National Highway Research Program, Transportation Research Board, National Research Council, University of Minnesota, Minneapolis, December, 360pp, 1998.

[3] Y. M. Chiew, "Mechanics of riprap failure at bridge piers", *Journal of Hydraulic Engineering*, ASCE, Vol. 121, No. 9, 1995, pp.635-643.

[4] Y. M. Chiew., and F. H. Lim, "Failure Behavior of Riprap Layer at Bridge Piers under Live-Bed Conditions", *Journal of Hydraulic Engineering*, ASCE, Vol. 126, No. 1, 2000, pp.43-55.

[5] Y. M. Chiew, "Local Scour and Riprap Stability at Bridge Piers in a Degrading Channel". Journal of Hydraulic Engineering, ASCE, vol. 130, no. 3, 218-226, 2004.

[6] Y. M. Chiew, "Failure Mechanisms of Riprap Layer around Bridge Piers". *Invited Paper* (Plenary Section) in Proceedings of First International Conf. on Scour of Foundations (ICSF-1), Vol. 1, 70-91, 2002.

[7] C. S. Lauchlan, "Countermeasure for pier scour", phD Thesis, The University of Auckland, Auckland, New Zealand, 1999.

[8] G. Annandale, B. W. Melville, and Y. M. Chiew, "Scour Case Studies". Report of Federal Waterways Engineering and Research Institute (Bundesanstalt fur Wasserbau), Karlsruhe, Number 85, 43-58, December 2002.

[9] C. S. Lauchlan, and B. W. Melville, B. W., "Riprap Protection at Bridge Piers", Journal of Hydraulic Engineering, ASCE, Vol. 127, No. 5, pp. 412-418, 2001.

[10] C. S. Lauchlan, and B. W. Melville, B. W., "Effect of Bed Degradation on Riprap Protection at Bridge Piers", Proceedings of the Institution of Civil Engineers, Water and Maritime Engineering, Vol. 154, Issue 1, pp. 19-27, 2002.

[11] Y. M. Chiew, "Local Scour and Riprap Stability at Bridge Piers in a Degrading Channel". Journal of Hydraulic Engineering, ASCE, vol. 130, no. 3, 218-226, 2004.

[12] C. S. Lauchlan, and B. W. Melville, “Effect of Bed Degradation on Riprap Protection at Bridge Piers”, Proceedings of the Institution of Civil Engineers, Water and Maritime Engineering, Vol. 154, Issue 1, pp. 19-27, 2002.

[13] Y. Lu, and Y. M. Chiew, “Using Seepage as an Auxiliary Method for Pier-Scour Countermeasure”, Proc. 2nd Int. Conf. on Scour and Erosion (ICSE-2), 14-17 November, 70-77.2004.

Countermeasures to Protect Bridge Piers from Scour

P.E. Clopper*, P.F. Lagasse*, L.W. Zevenbergen*, and C.I. Thornton**
*Ayres Associates Inc, 3665 JFK Parkway, Bldg. 2, Ste 200, Fort Collins, CO, USA
**Colorado State University, Fort Collins, CO, USA

I. Introduction

Scour causes 60% of bridge failures in the United States. National studies by the Federal Highway Administration (FHWA) of bridge failures caused by floods have shown the threat to bridge foundations is approximately equally distributed between scour at bridge piers and scour at bridge abutments. This paper presents the methods and results of NCHRP Project 24-07(2), "Countermeasures to Protect Bridge Piers from Scour." [1]

Approximately 83% of the 583,000 bridges in the National Bridge Inventory (NBI) are built over waterways. To cite just one example of the magnitude of the threat to bridges over water, in the 1994 flooding from a single storm (tropical storm Alberto) in Georgia, more than 500 state and locally owned bridges experienced damage attributed to scour. Thirty-one state owned bridges experienced scour depths ranging from 4 to 6 meters. Those 31 bridges had to be replaced.

Based on technical advisories and guidance from FHWA, most bridge owners have implemented comprehensive programs, inspections, and operational procedures to make their bridges less vulnerable to damage or failure from scour. New bridges are designed to resist damage from scour, while existing bridges are inspected regularly and evaluated to determine if a present or potential condition exists that may render the bridge vulnerable to damage during a future flood. When such a condition is found to exist, the bridge is rated as scour critical, and further evaluations are made to determine the best way to address the problem. Where pier scour is a problem, installation of pier scour countermeasures can be considered as one option in a comprehensive Plan of Action to reduce the vulnerability of the bridge.

Countermeasures for scour and stream instability problems are measures incorporated into a highway-stream crossing system to monitor, control, inhibit, change, delay, or minimize stream instability and bridge scour problems. While considerable research has been dedicated to development of countermeasures for scour and stream instability, many countermeasures have evolved through a trial and error process and lack definitive design guidance. In addition, some countermeasures have been applied successfully in one area, but have failed when installations were attempted under different geomorphic or hydraulic conditions. This is particularly true of pier scour countermeasures. In the mid-1990s, FHWA guidance to the state DOTs cautioned that pier scour countermeasures, such as riprap, may not provide adequate long-term protection, primarily because selection criteria, design guidelines, and specifications were not available.

By the late 1990s, progress had been made in developing selection, design, and installation guidelines for pier scour countermeasures. For example, the publication of the first edition of Hydraulic Engineering Circular HEC-23 in 1997 was a first step toward identifying, consolidating, and disseminating information on countermeasure guidance [2]. In addition, the first phase of NCHRP Project 24-07 provided the initial results of laboratory and field research to evaluate the performance of pier scour countermeasures and develop design and implementation guidance [3].

From the review of the literature, it is apparent that local scour at bridge piers is a potential safety hazard to the traveling public and is a major concern to transportation agencies. Bridge-pier scour is a dynamic phenomenon that varies with water depth, flow velocity, flow angle, pier shape and width, and other factors. If it is determined that scour at a bridge pier can adversely affect the stability of a bridge, scour countermeasures to protect the pier should be considered. Because of their critical role in ensuring bridge integrity, and their potentially high cost, it is important that the most appropriate countermeasures be selected, designed, and constructed.

The objectives of NCHRP Project 24-07(2) were to develop and recommend: (a) practical selection criteria for bridge pier scour countermeasures, (b) guidelines and specifications for design and

construction, (c) guidelines for inspection, maintenance, and performance evaluation. The countermeasures considered included:

- Riprap
- Partially grouted riprap
- Articulating concrete blocks
- Gabion mattresses
- Grout-filled mats

In addition, issues related to riprap at skewed piers and mounded riprap were investigated.

II. Laboratory Testing

NCHRP Project 24-07(2) was initiated in April 2001 to refine the results of earlier work, test additional pier scour countermeasures, and develop selection criteria and detailed guidelines and specifications. Laboratory testing for an initial set of countermeasures (riprap, articulating concrete blocks, and indoor tests of partially grouted riprap) was conducted in the hydraulics laboratory at the Colorado State University (CSU) Engineering Research Center. Testing began in August 2003 and was completed in December 2004. Continuation funding for additional countermeasure testing (gabion mattresses, grout-filled mattresses, riprap at skewed piers, mounded riprap, and prototype-scale tests of geotextile bags and partially grouted riprap) was authorized in December 2004 and testing of these countermeasures was completed in December 2005.

A. Developing the Testing Program

Items identified as gaps in the current state of the practice were reviewed and a specific test, or series of tests, was designed to address each deficiency. Merits and deficiencies of each countermeasure were considered in developing the testing program, including:

- Selection criteria
- Design methods and guidelines
- Construction specifications and guidelines
- Maintenance and inspection guidelines
- Performance evaluation guidelines

Dominant-process design models that accurately reflect the mode of failure associated with the particular countermeasure were reviewed in order to size the armor elements for the laboratory conditions. Typically, these models included local hydraulic conditions characterized by a combination of velocity and shear stress. It was decided to size all countermeasure armor for a design velocity of 2 times the critical velocity of the 0.6 mm sand comprising the bed material, resulting in an approach velocity of 0.6 m/s for countermeasure design.

The laboratory tests were not designed to replicate any particular prototype scale conditions. For example, a $2V_{crit}$ run (using a 20-cm square pier) was not intended to represent specific scale ratio of a prototype pier or flow condition. The intent of the testing program was to provide valid comparisons of countermeasure types to each other and to the unprotected condition. In each case, the test countermeasure was "designed" to withstand the $2V_{crit}$ hydraulic condition. For example, the riprap size was selected such that particle dislodgement or entrainment was not anticipated during the $2V_{crit}$ run. This did not mean that the riprap (or any other countermeasure) would not fail due to other factors, such as settling, edge undermining, or winnowing of substrate material. Selected runs utilizing an approach velocity greater than $2V_{crit}$ were intended to take each system to failure by particle dislodgement.

Criteria for rating performance was consistent between countermeasures, but was not necessarily identical for all countermeasures. A countermeasure was considered to have failed if the countermeasure (or its component particles) was dislodged, lifted, or entrained. Relative performance was gauged by whether the countermeasure functioned as intended. Specifically, if settling along the countermeasure edge was expected, actual settlement was not considered poor performance. Maximum scour anywhere within the limits of the countermeasure or along the edge of the countermeasure was documented.

The testing program also addressed stability and performance issues associated with the extent of the countermeasure placement around the pier, and the termination details at the pier and around the periphery of the installation. Lastly, various filter types and extents were investigated by varying this aspect for selected test runs.

B. Testing Protocol – Indoor Flume

Testing conducted for Research Project 24-07(2) utilized the largest of the CSU laboratory's sediment recirculating flumes. The flume is 2.6 m wide by 1.4 m deep by 60 m long, and is capable of recirculating water and sediment over a range of slopes up to 2%. The maximum discharge in the flume is 2.8 cubic meters per second (cms).

A mobile data acquisition cart traverses the flume and provides flexibility in data collection. A wide variety of point gages and velocity probes can be mounted to the cart. The data acquisition cart can

then be positioned to collect data at any given location in the flume. The cart also has the capacity to provide space and power for a personal computer for data collection.

Three piers were placed along the centerline of the testing flume. Square piers 20 cm long by 20 cm wide were used. Spacing between the piers was a minimum of 13 m to ensure the formation of uniform flow lines upstream of each pier. Sand with a d_{50} of approximately 0.6 mm was placed in the flume to a depth of approximately 45 cm. Figure 1 provides a schematic of the flume, data acquisition cart, pier layout, and ancillary components.

A matrix of flume tests was developed for the research program and approved by the NCHRP research panel prior to initiating the tests. Each clear water test consisted of a series of two discharges. Discharge rates were predetermined to correspond to flow velocities of V_{crit} and $2V_{crit}$ where V_{crit} is the calculated critical velocity of the 0.6 mm sediment size utilized throughout the testing program (0.3 m/s). The V_{crit} and $2V_{crit}$ runs were performed without sediment recirculation. Separate runs on selected countermeasure configurations were performed at velocities greater than $2V_{crit}$ with sediment recirculation, therefore, clear water, live bed, and sediment-deficient conditions were examined.

During the live bed runs, bed form type, length, and height were recorded. Flow duration was sufficient to ensure that bed forms migrated through the system. One baseline run was performed at velocities up to $3V_{crit}$ to determine the performance of standard, loose riprap under conditions where particle dislodgement or entrainment is anticipated.

Data collected during each test included pre-test surveys, approach flow velocity, local pier velocity, flow depth and post-test surveys. In addition, non-professional photographic and video footage was recorded for each test. Water surface elevations were collected every 1.3 m along the flume, and local and approach flow velocities collected at each pier. Water surface elevations were determined by a point gage accurate to ± 1.5 mm. Velocities were collected with an 3-D acoustic doppler velocimeter, accurate to ± 2%. Approach velocities were collected at 20, 60, and 80% of the flow depth. Local velocity profile measurements were collected at each pier. Pre- and post- test surveys were conducted with a point gage and total station survey equipment. Survey resolution was sufficient to accurately map each scour hole and document system performance.

Prior to each test, the tailgate was closed and the flume slowly filled with water until the target flow depth of 30.5 cm was established. Flow was introduced very slowly to ensure no local scour occurred during start-up. During the slow filling process, air was allowed to escape from the sand bed. With the flume full of water, discharge was slowly increased to the target discharge, while simultaneously opening the tailgate until steady flow at the target depth of 30.5 cm relative to the initial bed surface was obtained. This process ensured a gradual acceleration of flow until the target velocity was achieved and maintained.

Each run then proceeded for a duration of approximately 2.5 hours while velocity and water surface data was collected at each pier, and at designated locations between piers. For tests utilizing live-bed conditions with sediment feed, the duration was increased to 8 hours per run. After each test, the discharge was gradually decreased and the tailgate adjusted to ensure that no additional scour occurred during the drain-out period. Typically, the flume was allowed to drain out overnight, and the sand bed around each pier was mapped the next day. Figure 2 provides an example of the general testing procedure and results.

C. Riprap

Most of the early work on the stability of pier riprap is based on the size of the riprap stones and their ability to withstand high approach velocities and buoyant forces. Parola [4] noted that secondary currents induced by bridge piers cause high local boundary shear stresses, high local seepage gradients, and sediment diversion from the streambed surrounding the pier, and that the addition of riprap also changes the boundary stresses. His study recommended that the stone size should be determined for plane bed conditions, which were the most severe conditions found in model studies to that point.

However, a subsequent study of the causes of riprap failure at model bridge piers conducted by Chiew [5] under clear-water conditions with gradually increasing approach flow velocities defined three modes of failure:

1. Riprap shear failure – whereby the riprap stones cannot withstand the downflow and horseshoe vortex associated with the pier scour mechanism.
2. Winnowing failure – whereby the underlying finer bed material is removed through voids or interstices in the riprap layer.
3. Edge failure – whereby instability at the edge of the coarse riprap layer initiates a scour hole beginning at the perimeter and working inward that ultimately destabilizes the entire layer.

Lim and Chiew [6] conducted experiments to evaluate the stability of pier riprap under live-bed conditions with migrating bed forms. Subsequent research [3, 7, 8, 9, 10, 11, 12] indicated that bed-form undermining is the controlling failure mechanism at bridge piers on rivers where mobile bed forms are present during high flows, especially sand bed rivers. Figure 3 shows typical photographs of riprap tests under clear-water and live-bed conditions in the CSU indoor flume.

D. Partially-Grouted Riprap

Current practice in the United States discourages the use of grouted riprap, primarily because the voids within the riprap are often nearly completely filled with grout in most cases, which creates rigidity and impermeability that often leads to failure. Guidelines on the construction of grouted riprap in the United States are associated almost entirely with riprap bed and bank protection (e.g., [13]). Total grouting converts a flexible revetment material like a riprap layer into a rigid mass and reduces the permeability of the layer. This may cause the entire riprap layer to fail as a result of either undermining or uplift and thus negates the natural benefit caused by raveling of loose riprap into the scour hole or trough of migrating bed forms.

Partially grouted riprap provides a more suitable alternative to total grouting because it alleviates the concerns and problems associated with complete filling of the voids with grout. Partial grouting increases the stability of the riprap unit without sacrificing flexibility and allows for the use of smaller rock and thinner riprap layers in areas where the required stone size for loose riprap is expensive or unavailable.

A target for grout placement is that the voids within a riprap layer should contain about 75% grout in the upper third of the layer, 50% grout in the middle third, and 25% grout in the lower third [2]. No grout should penetrate deep enough to come into contact with any underlying filter. Construction methods must be closely monitored to ensure that the appropriate voids and surface openings are provided. Contractors in Germany have developed techniques and special equipment to achieve the desired grout coverage and the right grout penetration.

Heibaum [14] indicates that grouting has proven its long-term stability and ability to keep costs low, and notes that laboratory tests at Braunshweig University in Germany proved that partially grouted riprap is stable up to a flow velocity of 8 m/s. Since the riprap is dumped or placed as needed and only then is the layer grouted, a close contact to structural elements such as bridge piers can be achieved. Figure 4 shows typical photographs of the partial grout tests in the indoor flume.

E. Articulating Concrete Blocks

Articulating concrete block systems (ACBs) can be used to provide a flexible armor layer as a pier scour countermeasure. These systems consist of preformed units which interlock, are held together by steel rods or cables, are bonded to a geotextile or filter fabric, or abut together to form a continuous blanket or mat. Data sheets for a number of the more common proprietary ACB revetment systems can be found in [16], while [3] provides a brief review of the limited studies conducted on the use of ACBs for pier scour protection.

There is limited experience with the use of articulating block systems as a scour counter-measure for bridge piers alone. More frequently, these systems have been used for bank revetments and channel armoring where the mat is placed across the entire channel width and keyed into the abutments or bank protection. For this reason, guidelines for placing articulating block systems along banks and in channels are well documented (e.g., [15]), but there are few published guidelines on the installation of these systems around bridge piers.

Where ACB systems have been installed as a countermeasure for scour at bridge piers, cable-tied concrete block mats are used most often. There are two failure mechanisms for ACBs: (1) overturning and rollup of the leading edge of the mat where it is not adequately anchored or toed in, and (2) uplift at the center of the mat where the leading edge is adequately anchored. In the absence of a filter or geotextile, winnowing can still occur and can result in subsidence of all or a portion of the ACB mat. Studies conducted on the effectiveness of ACBs as a countermeasure have determined that the use of a filter fabric or geotextile is essential to the overall effectiveness and stability of the ACB system unless the substrate is coarse enough to prevent winnowing through the open cells of the blocks.

Although cables can prevent the loss of individual blocks or group of blocks from the matrix, the Factor of Safety design method presented in [15] does not attribute any additional stability benefit to cables. For the cable to provide a restraining force, tension must be mobilized in the cable, thus implying that blocks have already begun to uplift and therefore loss of intimate contact, which constitutes failure, has already occurred. Tests of ACB systems in the

indoor flume were conducted using no cables; the critical shear stress for the blocks was determined in a smaller flume prior to placement around the test piers. Figure 5 shows typical photographs of ACB testing in the indoor flume.

F. Gabion Mattresses

Gabion mattresses are containers constructed of wire mesh or welded wire and filled with loose stones or other similar material. The stones used to fill the containers can be either angular rock or large cobbles, although angular rock is preferred due to higher degree of interlock between stones.

Gabions have been used for streambank protection for more than 100 years in Europe and have gained increasing popularity in the United States, especially in the desert Southwest. Like riprap, they are porous, being composed of loose rock, and are not susceptible to uplift forces. They can be stacked to form a wall or joined together to form a large mattress. If the configuration is undermined or becomes unstable, the inherent flexibility of the wire mesh allows them to deform to the bed or bank. In addition, the use of a wire mesh allows for the use of relatively small stones, which can yield the same amount of protection as much larger particles in a loose configuration.

It may seem intuitive that gabions should be effective as pier scour countermeasures, especially if they are installed with an underlying filter or geotextile and a seal to the pier is provided. However, rivers carrying coarse bedload can abrade the wire comprising the baskets. The passage of large bed forms can cause the wire mesh to break under tension during deformation of the gabion, allowing the fill stones to be lost. The gabion mattress may pull away from the pier face if there is significant edge settlement associated with winnowing or the passage of bed forms. These factors appear to have contributed to the failure of the gabions used to counter pier scour at the Whakatane River Bridge on State Highway 30 in New Zealand [10]. Anchoring the gabion to the bed with long steel rods may alleviate some of these problems. Figure 6 shows photographs of typical tests of gabion mattresses conducted in the indoor flume.

G. Grout-Filled Mats

The grout-filled mat is a single, continuous layer of strong synthetic fabric sewn into a series of bags or compartments that are connected internally by ducts. The compartments are then filled with a concrete grout that, when set, forms a mat comprised of a grid of connected pillow-shaped units. While the individual blocks may articulate within the mat and the mat remains structurally sound, the general design approach is to consider the mat as a rigid monolithic layer. In some cases, the mat may be strengthened with cables installed similar to those used in articulating concrete blocks. Filter points or weep holes allow for pressure relief across the mat.

Grout-filled mat systems can range from very smooth, uniform surface conditions approaching cast-in-place concrete in terms of surface roughness, to extremely irregular surfaces exhibiting substantial projections into the flow, resulting in boundary roughness approaching that of moderate size rock riprap. Because this type of armor is fairly specialized, comprehensive technical information on specific mat types and configurations is available from a number of manufacturers.

The primary failure mechanisms for grout-filled mats consist of rolling, undercutting, and scouring at gaps [16]. Rolling, the most severe form of failure, is related to uplift forces created by flow over the mat. This allows the mat at midsection to be "lifted up" slightly and then pushed loose by the force of the current or allows the edges of the mat to be rolled back. Undercutting is a gradual process arising from local scour at the mat edges and from the main horseshoe vortex. Scouring at the gaps between the mat and the pier wall allows the horseshoe vortex to generate a scour hole beneath the front edge or side sections of the mat.

The research to date on the use of grout-filled mats as a bridge scour countermeasure found that placement is extremely important for successful performance and effectiveness. Properly placed grout mats extending 1.5 to 2 pier widths were found to provide significant protection to bridge piers. Recommendations in [16] are that grout mats should be placed at bed level and that toeing in the edges of the mat may increase stability with regard to potential rolling failure and undercutting, especially under live-bed conditions. Further recommendations [17] are that anchors should be used to protect the leading edge against uplift forces when the mat is placed on the surface of a loose, erodible channel bed. References [18] and [19] stress the importance of a tight seal around the pier-mat interface to inhibit scour and undermining beneath the mat. Mat selection and sizing criteria based on analysis of sliding stability are provided in [2]. Figures 7 and 8 show installation and testing of materials used to simulate rigid and flexible grout-filled mats, respectively.

H. Outdoor Tests: Partially Grouted Riprap

Two tests were conducted to quantify performance of partially grouted riprap at essentially prototype

scale. Installation of the countermeasure was performed at a rectangular pier measuring 0.45 m wide by 1.4 m long. A pre-formed scour hole around the pier was partially filled with sand-filled geotextile containers to serve as the filter beneath the armor stone. The containers were constructed using a nonwoven needlepunched fabric. Each container measured 1.2 m x 0.5 m x 0.1 m and was filled with 91 kg of sand.

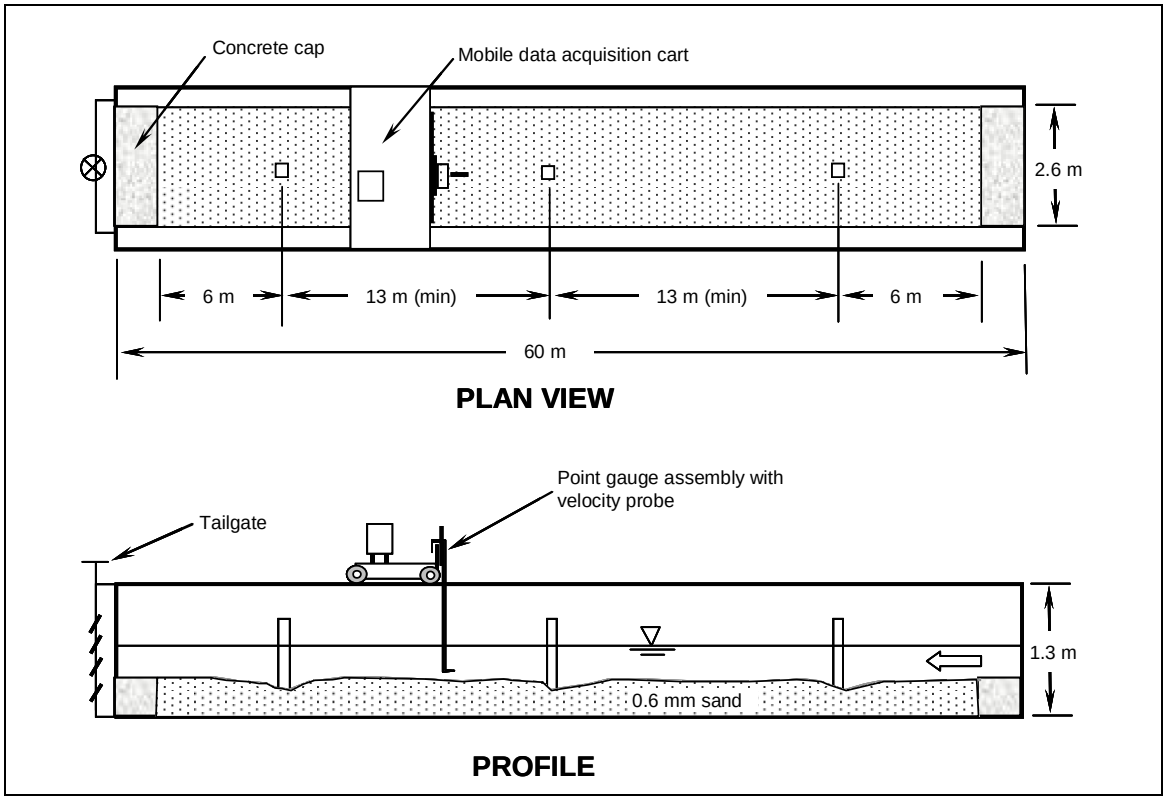

Figure 1. Schematic diagram of indoor flume showing data acquisition.

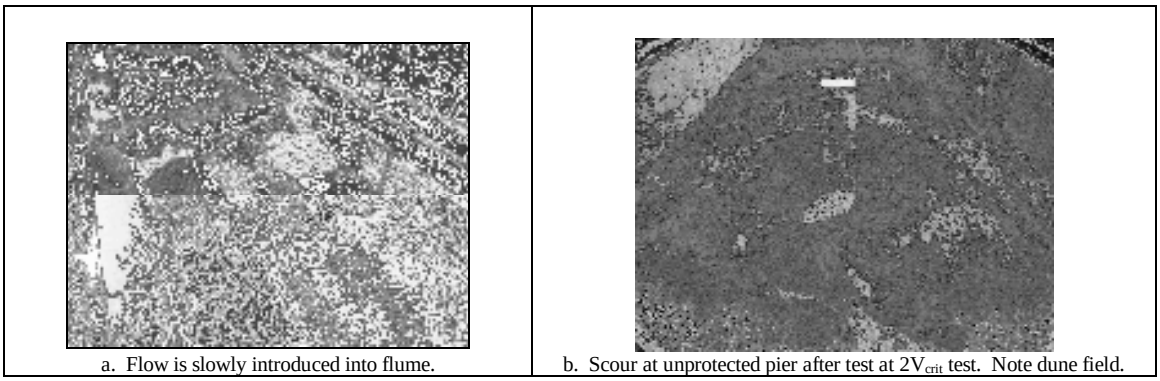

a. Flow is slowly introduced into flume.

b. Scour at unprotected pier after test at $2V_{crit}$ test. Note dune field.

Figure 2. Indoor flume tests showing typical initial and final conditions.

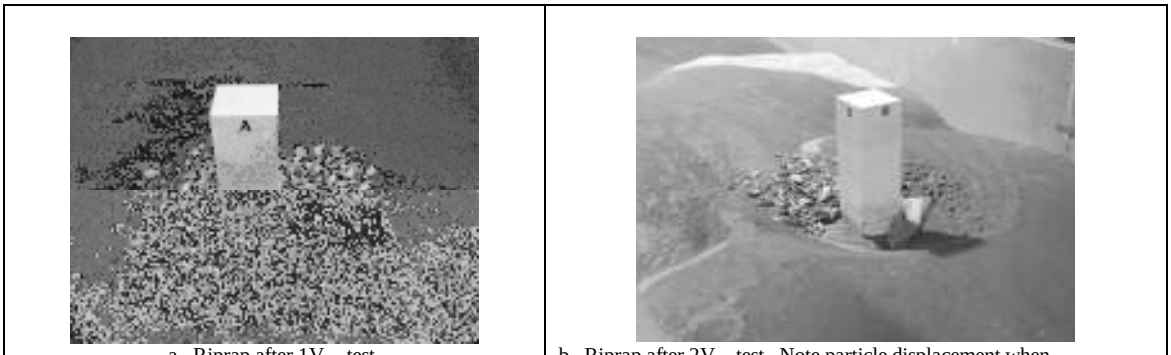

a. Riprap after $1V_{crit}$ test.

b. Riprap after $2V_{crit}$ test. Note particle displacement when areal extent is insufficient.

Figure 3. Indoor flume tests of standard riprap.

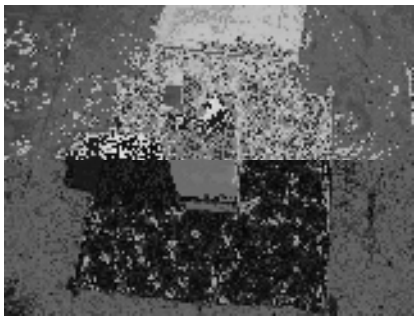

a. Placing partially-grouted riprap. Note spot-grouting technique.

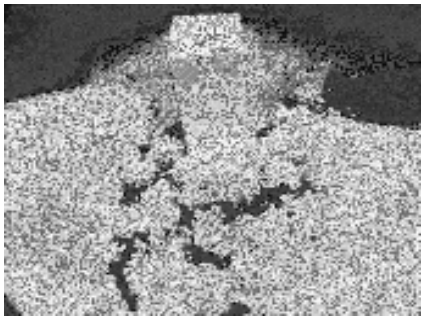

b. Partial grout after $2V_{crit}$ test.

Figure 4. Indoor flume tests of partially grouted riprap.

a. Placing articulating concrete blocks. Note toedown depth at perimeter of system.

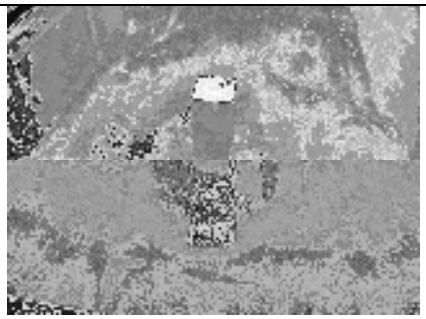

b. Articulating concrete blocks after 2 V_{crit} run. Note dune field and loss of blocks on the right side of pier.

Figure 5. Indoor flume tests of articulating concrete blocks.

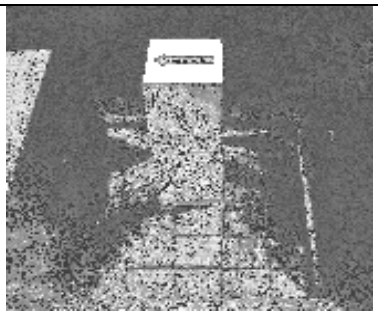

a. Placing gabion mattresses. Note toedown depth at perimeter of system.

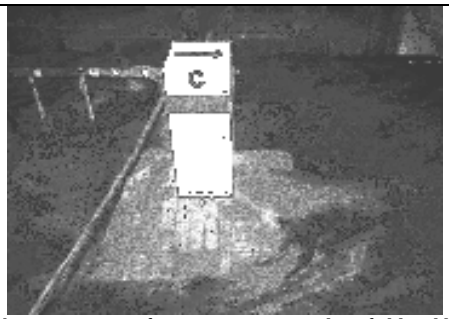

b. Gabion mattresses after 2 V_{crit} run. Note dune field and loss of blocks on the right side of pier.

Figure 6. Indoor flume tests of gabion mattresses.

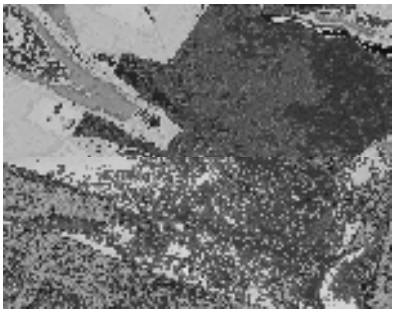

a. Placing rigid grout-filled mat.

b. Rigid grout-filled mat after $2V_{crit}$ test. Note undermining around periphery of mat.

Figure 7. Indoor flume tests of rigid grout-filled mats.

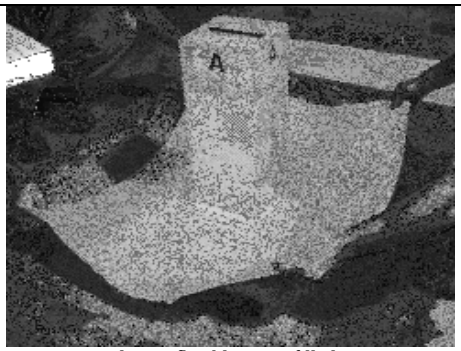

a. Placing flexible grout-filled mat.

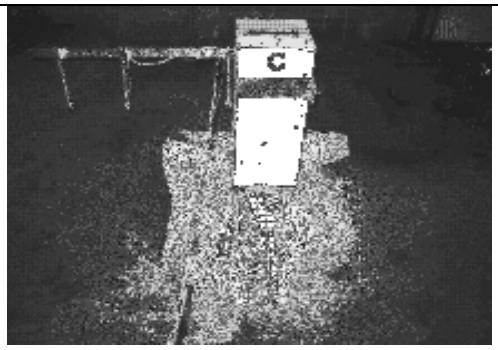

b. Flexible grout-filled mat after $2V_{crit}$ test.

Figure 8. Indoor flume tests of flexible grout filled mat.

The geocontainers were dumped into flowing water (0.5 m/s velocity and 0.5 m depth) using a standard backhoe bucket equipped with a grapple. Durable sandstone rock with a d_{50} of 15 cm was dumped onto the geocontainers using the same piece of equipment.

The first test examined potential constructability and environmental issues associated with underwater application of grout (Figure 9). Because of concerns voiced by permitting agencies involved with in-stream construction, water quality was monitored with a series of In-Situ Troll 9000 Profilers placed in stream at seven locations. The Troll 9000 Profilers continually recorded measurements of pH, conductivity, turbidity, and temperature. Baseline conditions were established prior to initiation of the grout placement 3.6 m upstream of the pier along the centerline of the flume. Figure 10 provides an illustration of pH measurements from the continuous monitors.

The second test was conducted to examine the stability performance of partially grouted riprap (right side of pier) compared to standard (loose) riprap of the same size and gradation (left side of pier). After 2 hours of flow with an approach velocity of 1.95 m/s, the loose riprap had scoured adjacent to the pier, whereas the partially grouted riprap remained intact. Figure 11 shows the installation after completion of the test.

III. Results

NCHRP Project 24-07(2) resulted in the development of a unified set of guidelines, specifications, and procedures that can be accepted by the State DOTs in the U.S. for the design, installation, and inspection of a variety of armoring-type countermeasures to protect bridge piers from scour.

To guide the practitioner in developing appropriate designs and ensuring successful installation of pier scour countermeasures, a countermeasure selection method was developed. Five factors comprise the model, and a numerical Selection Index (SI) is calculated. A higher value of SI indicates that the countermeasure type is more appropriate from both suitability and economic perspectives. The five factors are:

S1: Bed material size and transport
S2: Severity of debris or ice loading
S3: Constructability constraints
S4: Inspection and maintenance requirements
LCC: Life cycle costs

The Selection Index is calculated as:

$SI = (S1xS2xS3xS4)/LCC$

The findings and recommendations of the study are being combined into guidelines for each countermeasure type as stand-alone appendices. These guidelines are presented in a standard three-part format using the Federal Highway Administration's Hydraulic Engineering Circular (HEC) 23 [2] as a guide. Each guideline includes:

- Part 1 – Design and Specification
- Part 2 – Construction
- Part 3 – Inspection, Maintenance, and Performance Evaluation

Individual guidelines are currently being finalized and will contain specific recommendations for the following items: Material requirements, extent of system placement, thickness, filter requirements, transitions and termination details, and countermeasure sizing equations.

Acknowledgment

This work was sponsored by the American Association of State Highway and Transportation Officials, in cooperation with the Federal Highway Administration (FHWA), and was conducted through the National Cooperative Highway Research Program (NCHRP), which is administered by the Transportation Research Board (TRB) of the National Research Council (NRC).

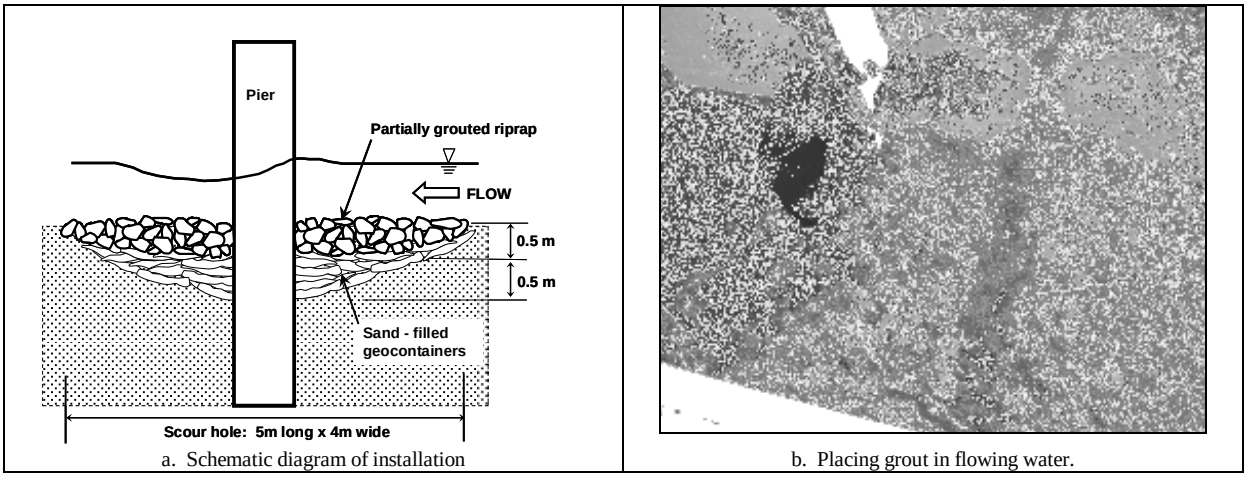

a. Schematic diagram of installation

b. Placing grout in flowing water.

Figure 9. Prototype-scale test of partially-grouted riprap in the outdoor flume.

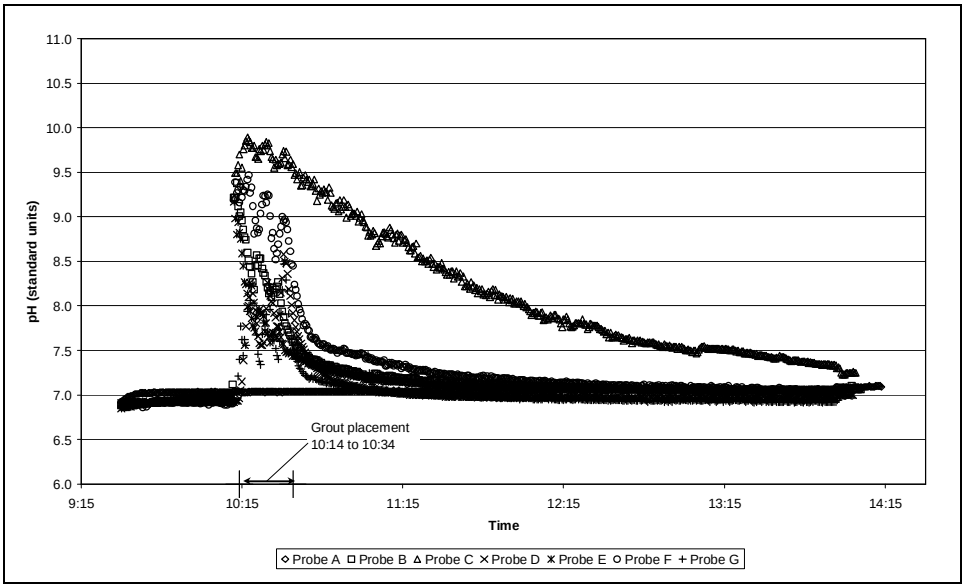

Figure 10. Graph of pH versus time during partial grout installation. Probe C (triangles) was located directly downstream of the pier at the edge of the grouting area.

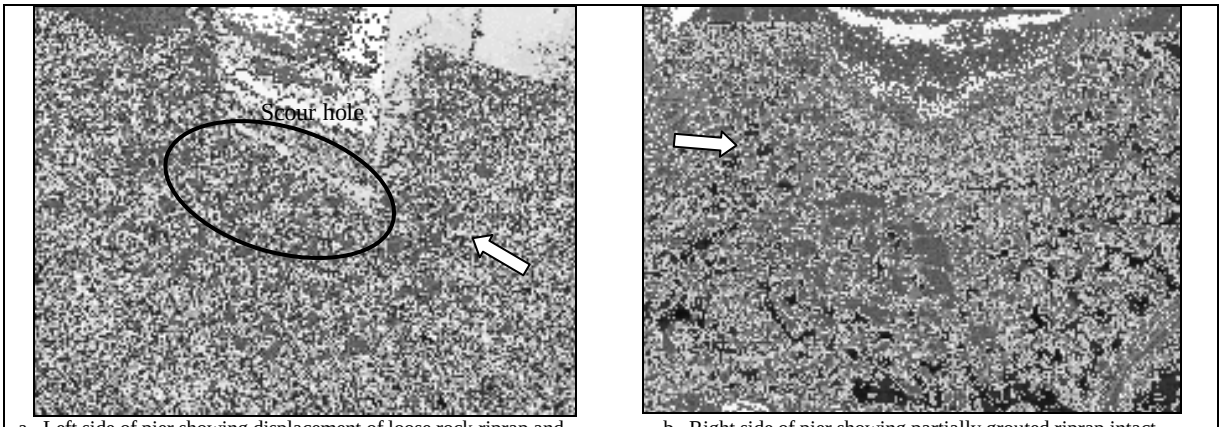

a. Left side of pier showing displacement of loose rock riprap and scour adjacent to pier.

b. Right side of pier showing partially grouted riprap intact.

Figure 11. Comparison of standard riprap vs. partially grouted riprap.

This paper is based on an uncorrected draft report under development for submittal by the authors to the TRB. The opinions and conclusions expressed or implied in the report are those of the authors. They are not necessarily those of the Transportation Research Board, the National Research Council, the Federal Highway Administration, the American Association of State Highway and Transportation Officials, or the individual states participating in the National Cooperative Highway Research Program.

REFERENCES

[1] P.F. Lagasse, P.E. Clopper, and L.W. Zevenbergen, "Countermeasures to Protect Bridge Piers from Scour," Preliminary Draft Final Report, NCHRP Project 24-07(2), Transportation Research Board, National Academy of Science, Washington, D.C., 2006.

[2] Lagasse, P.F., Zevenbergen, L.W., Schall, J.D., and Clopper, P.E., "Bridge Scour and Stream Instability Countermeasures," Hydraulic Engineering Circular No. 23 (HEC-23, Second Edition), FHWA NHI 01-003, Federal Highway Administration, Washington, D.C. (2001).

[3] Parker, G., Toro-Escobar, C., and Voigt, R.L. Jr. "Countermeasures to Protect Bridge Piers from Scour," Users Guide (revised 1999) and Final Report, NCHRP Project 24-7, prepared for Transportation Research Board by St. Anthony Falls Laboratory, University of Minnesota, MN, 360 pp. (1998).

[4] Parola, A.C. "Stability of Riprap at Bridge Piers," In: Thorne, C.R., Abt, S.R., Barends, F.B.J., Maynord, S.T., and Pilarczyk, K.W. (Eds.), River, Coastal, and Shoreline Protection: Erosion Control Using Riprap and Armourstone, John Wiley & Sons Ltd., Chichester, pp. 149-158 (1995).

[5] Chiew, Y.M. "Mechanics of Riprap Failure at Bridge Piers," ASCE Journal of Hydraulic Engineering, Vol. 121, No. 9, pp. 635-643 (1995).

[6] Lim, F.H. and Chiew, Y.M. "Stability of Riprap Layer Under Live-Bed Conditions," In: Maxwell, W.H.C., Preul, H.C., and Stout, G.E. (Eds.), Proceedings Rivertech96: 1st International Conference on New/Emerging Concepts for Rivers, Volume 2, Chicago, IL, pp. 830-837 (1996).

[7] Melville, B,W., Lauchlan, C.S., and Hadfield, A.C. "Bridge Pier Scour Countermeasures," In: Wang, S.S.Y., Langendoen, E.J., and Shields, F.D., Jr. (Eds.), Proceedings of the Conference on Management of Landscapes Disturbed by Channel Incision: Stabilization, Rehabilitation, Restoration, Oxford, MS (1997).

[8] Lim, F.H. and Chiew, Y.M. "Failure Behavior of Riprap Layer Around Bridge Piers," In: Holly, F.M., Jr., Alsaffar, A., English, M., and Szollosi-Nagy, A. (Eds.), Managing Water: Coping with Scarcity and Abundance, Proceedings of Theme A, 27th IAHR Congress, San Francisco, CA, pp. 185-189 (1997).

[9] Lim, F.H. and Chiew, Y.M. "Parametric Study of Riprap Failure Around Bridge Piers," ASCE Journal of Hydraulic Research, Vol. 39, No. 1, pp. 61-72 (2001).

[10] Lauchlan, C.S. "Pier Scour Countermeasures," Ph.D. Thesis, University of Auckland, Auckland, New Zealand (1999).

[11] Chiew, Y.M. and Lim, F.H. "Failure Behavior of Riprap Layer at Bridge Piers Under Live-Bed Conditions," ASCE Journal of Hydraulic Engineering, Vol. 126, No. 1, pp. 43-55 (2000).

[12] Lauchlan, C.S. and Melville, B.W. "Riprap Protection at Bridge Piers," ASCE Journal of Hydraulic Engineering, Vol. 127, No. 5, pp. 412-418 (2001).

[13] Brown, S.A. and Clyde, E.S. "Design of Riprap Revetment, Hydraulic Engineering Circular No. 11" (HEC-11), FHWA-IP-016, Federal Highway Administration, Washington, D.C. (1989).

[14] Heibaum, M.H., "Scour Countermeasures using Geosynthetics and Partially Grouted Riprap," Transportation Research Record 1696, Vol. 2, Paper No. 5B0106, pp. 244-250 (2000).

[15] Ayres Associates, "Articulating Concrete Block Design Manual," prepared for the Harris County Flood Control District, Houston, TX (2001).

[16] Fotherby, L.M. "Footings, Mats, Grout Bags, and Tetrapods; Protection Methods Against Local Scour at Bridge Piers," MS Thesis, Colorado State University, Fort Collins, CO (1992).

[17] Bertoldi, D.A., Jones, J.S., Stein, S.M., Kilgore, R.T., and Atayee, A.T., "An Experimental Study of Scour Protection Alternatives at Bridge Piers," FHWA-RD-95-187, Federal Highway Administration, Washington, D.C. (1996).

[18] Jones, J.S., Bertoldi, D. and Stein, S. "Alternative Scour Countermeasures," Proceedings ASCE 1st International Conference Water Resources Engineering, Vol.2, 14-18 August 1995, San Antonio, TX, pp. 1819-1823 (1995).

[19] Stein, S., Jones, J.S., Bertoldi, D., and Umbrell, E. "Alternatives to Riprap as a Scour Countermeasure," In: Richardson, E.V., and Lagasse, P.F. (eds.), Stream Stability and Scour at Highway Bridges, Compendium of Papers ASCE Water Resources Engineering Conferences 1991 to 1998, pp. 893-904 (1998).

Comparison of Long-Term Streambed Scour Monitoring Data with Modeled Values at the Knik River, Alaska

J.S. Conaway

U.S. Geological Survey, Alaska Science Center, Anchorage, Alaska, USA. jconaway@usgs.gov

Streambed-scour monitoring at selected bridge sites in Alaska is being used to assess real-time hazards, but also illustrates the complexities of streambed scour and the difficulty of predicting scour using existing methods. Four years of stage and bed-elevation data at the Knik River near Palmer, Alaska show an annual cycle of channel aggradation and degradation to an equilibrium level that is punctuated by shorter periods of scour and fill. The annual vertical bed-elevation change exceeds 6 meters and is an interplay of sediment supply, discharge, and the influence of instream hydraulic structures. Channel contraction at this site is nearly four to one at high flows and upstream guide banks direct flow through the bridge reach.

Data from a pier-mounted sonar together with hydraulic variables measured during high flows and variables computed with a multi-dimensional hydrodynamic model were used to evaluate seven predictive equations for live-bed contraction scour and two abutment scour computations. Two scour events were simulated with the hydrodynamic model; one related to rainfall, the other owing to a period of increased glacial melting. Streambed scour for these two events varied considerably in timing and duration although both had similar streamflow discharges. Total computed scour exceeded measured values by 40 to 60 percent depending on the equations selected. The long-term monitoring data indicate the scour at this site is not only a reaction to changes in hydraulic variables, but is also affected by the timing and duration of streamflow as well as the source of the high flow, factors not typically included in the engineering assessment of streambed scour.

I. Introduction

Streambed scour followed by fill after a flood passage is a well documented process at locations where regular cross-section measurements are made. Data describing the timing and duration of this process are limited by the frequency of field visits. To better understand this process and to monitor bed elevation at bridge piers, the U.S. Geological Survey and the Alaska Department of Transportation and Public Facilities operate a network of streambed scour-monitoring stations in Alaska. Currently 16 bridges are instrumented with sonars to measure distance to streambed and river stage. These stations provide state engineers with near real-time bed elevation data to remotely assess scour at bridge piers during high flows. The data also provide a nearly continuous record of bed elevation in response to changes in discharge and sediment supply. Seasonal changes as well as shorter duration scour and fill have been recorded. In addition to the near real-time data, channel bathymetry and velocity profiles are collected at each site several times per year. This paper focuses on 4 years of hydraulic and sonar data collected at the Knik River. These data are compared to results from predictive scour calculations using variables generated by a hydrodynamic model.

There are two bridges that cross the Knik River on the Old Glenn Highway (Fig. 1). The upstream most bridge, which is no longer open to vehicular traffic, is 610 m long and is supported by six piers. Approximately 30 m downstream of this structure is the active bridge that was built in 1975 and is 154 m in length and supported by two piers. The roadway approaches to this bridge significantly contract the channel. Two guide banks extend upstream of both bridges and route flow through the rip-rap lined bridge reach. All piers are approximately aligned with the flow.

The right-bank pier of the new bridge was instrumented with a retractable, pier-mounted 235 kilohertz echosounder in 2002. Stage data were measured by a U.S. Geological Survey stream gage (Station number 15281000). The echosounder was mounted at an angle on the side of pier near the nose in order to collect data just upstream of the pier footing and subfooting. Data are collected every 30 minutes and transmitted every 6 hours. When bed elevation or stage thresholds are exceeded, data transmissions increase in frequency. These near real-time data for the Knik River and other sites in Alaska are available on the web at http://ak.water.usgs.gov/usgs_scour. Streambed elevation and stage data accuracies are ±0.15 m and ±0.03 m, respectively. All elevations reported here are referenced to the North American Vertical Datum of 1988.

II. Streambed Scour at the Knik River

The Knik River near Palmer was the only site within the monitoring network that had large changes in bed elevation each year. Annual scour ranged from 5.2 m to 6.0 m. The Knik River is a braided sand and gravel channel that transports large quantities of sediment from the Knik Glacier. The braided channel narrows from approximately 4.8 km wide at the glacier mouth to 0.12

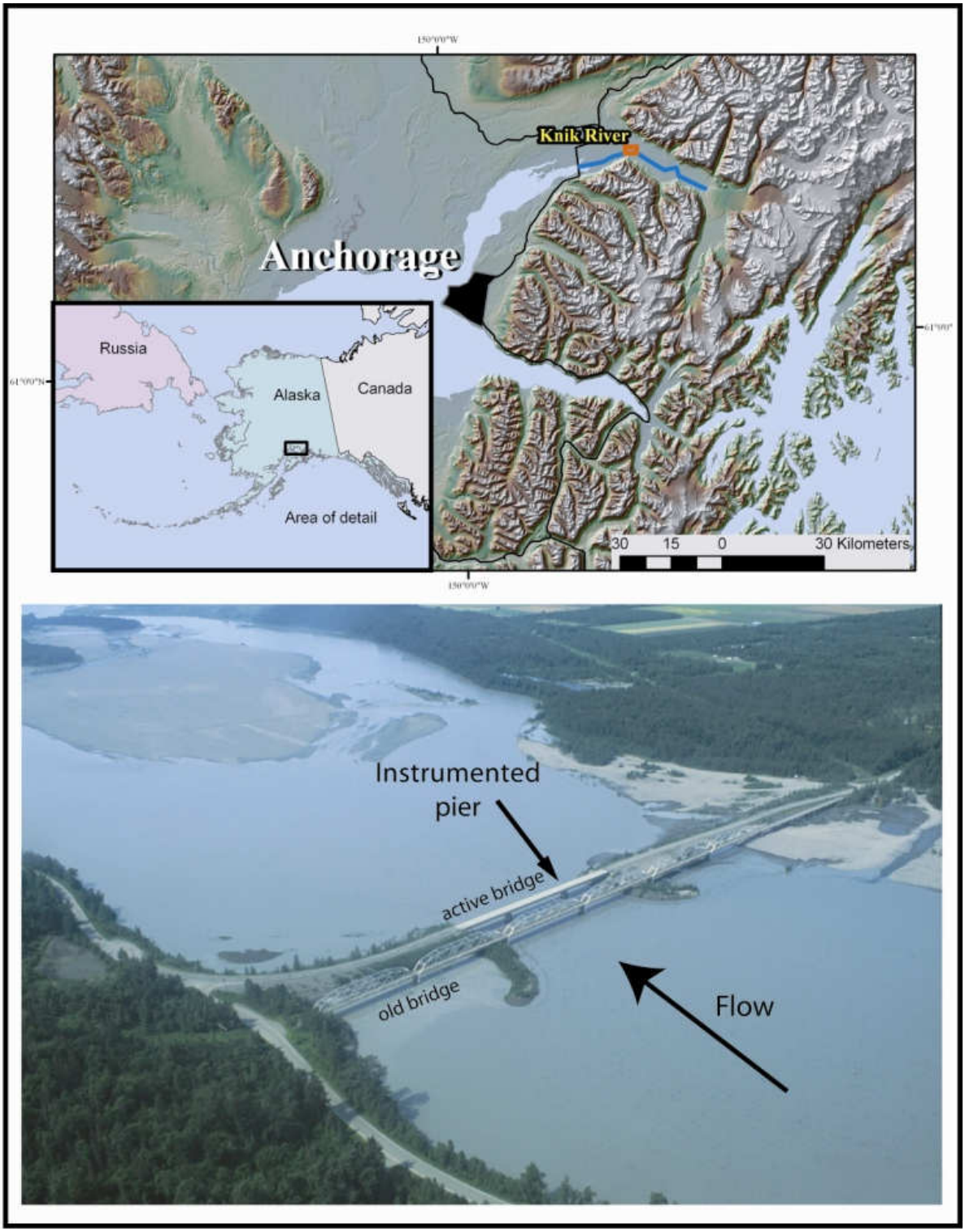

Figure 1. Location of the Knik River Old Glenn Highway bridge and oblique aerial photo of the study reach during a summer high flow.

km at the Old Glenn Highway bridge where the channel is subject to a 4:1 contraction during summer high flows. It drains an area of approximately 3,100 km^2, over half of which consists of glaciers. At a discharge of 850 m^3/s on July 12, 2003, suspended sediment-concentration was measured at 711 mg/L and bedload discharge was 8,160 metric tons/d. Median grain size of the bedload was 2.0 mm. Scour at this site is a complex interaction of seasonal bed elevation changes, flow hydraulics associated with upstream guide banks, and bed armoring associated with the complex pier shape. The current morphological and alluvial characteristics of the river can be partially attributed to large glacial-outburst floods that occurred nearly every year from 1914-1966. The maximum measured discharge from these events was 10,200 m^3/s.

These outburst floods no longer occur because of recession and thinning of the Knik Glacier.

Streambed scour at the Knik River was initially investigated by Norman [1]. His study focused on data collected in 1965 and included measurements made during a glacial outburst flood with a discharge of 6,680 m^3/s. At this time only the upstream bridge was present and there was no significant channel contraction. Reference [1] measured no appreciable contraction scour and 1.15 m of local pier scour.

A. Discussion of Monitoring Data

Since the installation of the monitoring equipment, discharge at the Knik River has ranged from 17 m^3/s to 1,710 m^3/s for water years 2002-2005. During the winter months, the streambed at the monitored bridge pier aggraded to an elevation of between 9.8 and 10.4 m each year (Fig. 2). From the beginning of data collection each year in early May until the latter part of June, the bed degraded at an average rate of 0.06 m/day, about 2.4 m each year. Over this same period of time, the stage increased at a rate of 0.02 m/day, 0.03 m/day, and 0.02 m/day for 2003, 2004, and 2005, respectively. Following this period of seasonal channel degradation the bed elevation at the pier remains relatively stable at an elevation of 7.8 m (equilibrium elevation), with brief periods of scour and fill during high flows. The channel begins to aggrade each year in September as stage decreases.

The mean bed elevation at a river cross section is not only dependent upon discharge, but is also related to changes in width, depth, velocity, and sediment load during the passage of a flood [2]. Streambed scour in the bridge reach is an interplay of discharge, sediment transport and the flow hydraulics associated with the channel contraction, upstream guide banks, and piers. Although the sonar only measures the bed elevation in front of the right-bank pier, the measured changes in bed elevation represent channel change from all the above factors. The cross section defined by the upstream bridge opening was surveyed periodically to document changes in bed elevation across the channel (Fig. 3). These cross sections and the sonar data show an annual cycle in channel change. Scour at this site is not uniformly distributed across the channel and is a combination of live-bed contraction and abutment scour along the guide banks. Vortices that develop as flow is routed around the guide banks erode the right and left portions of the channel and there is little bed-elevation change in the middle except at high flows. Increases in stage result in larger flow vortices and progressive deepening of the channel from the banks towards the center of the channel.

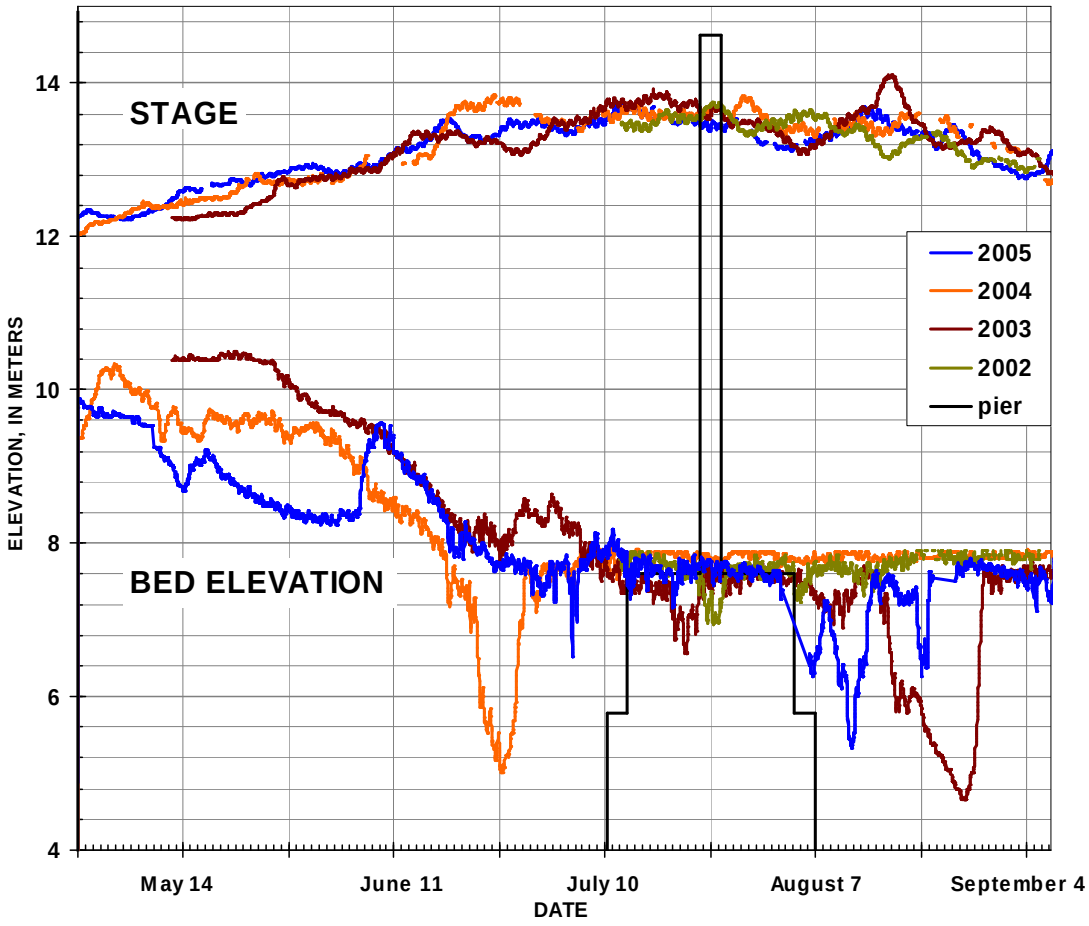

Figure 2. Stage and bed elevation at the monitored bridge pier for 2002-2005 at the Knik River near Palmer, Alaska. The bridge pier and footings are plotted for reference.

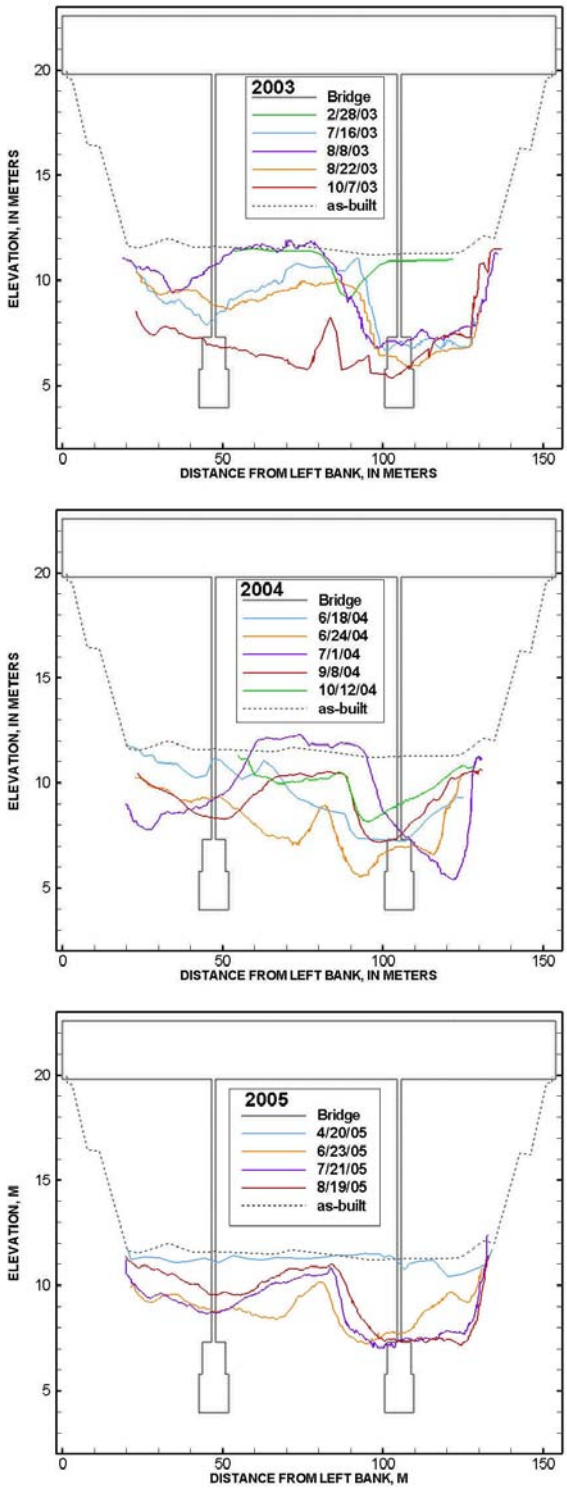

Figure 3. Upstream bridge cross sections at the Knik River for 2003-2005.

At higher stages, this scour along the channel margin overrides the effects of local scour at the pier where the sonar is mounted. The pier is supported by a 7.3 m wide footing and 9.1 m wide sub footing. These footings appear to armor the local bed and bed elevation remained near the elevation of the top of the footing for extended periods (Fig. 2). These observations agree with those of Parola et al. [3], who found that rectangular pier footings protect the streambed from the scouring of vortex systems formed by the pier until the streambed is below the footing then vortices from the footing induce scour. Local scour at the right-bank pier was not distinguishable from the contraction and abutment scour in surveyed bridge cross sections (Fig. 3). A depression in the cross section at the pier would indicate local scour.

The channel at the Knik River scours vertically and laterally towards the center to accommodate increased summer discharge. Vertical and lateral scour are concurrent until the footing of the pier is reached, at which point vertical scour is limited and increases in channel area are made by lateral scour. This process is illustrated in the successive cross sections plotted in Fig. 3. The lateral scour then proceeds until the channel width intersects vortices that are shed from a pier supporting the upstream bridge. These vortices weaken downstream of the old bridge pier and deposit sediment that was scoured locally from the upstream pier. A bar that formed downstream of the pier is visible in the middle of the channel in soundings from 2003 and 2004 (Fig. 3).

Two distinct scour and fill events from 2003 and 2004 highlight differences in timing and duration of scour (Fig. 4). Both scour events were associated with a period of high temperatures and subsequent increased glacial melt, but in 2003 the warm weather was followed by 10 days of rainfall and cooler temperatures. Scour magnitude for both events was approximately 3 m from the equilibrium bed elevation. The maximum scour occurred slightly after the peak in stage in 2003 and in 2004 maximum scour was concurrent with peak stage. The duration of scour, measured from when the bed elevation begins to decrease until fill begins, was 11.5 days in 2003 and 4 days in 2004. The scour in 2003 was of greater duration because the discharge and sediment supply from the glacier was reduced by the cooler temperatures. The channel infilled 3 m in 2 days after warmer temperatures resumed, likely accompanied by an increase in sediment load. In 2004, stage increased rapidly prior to scour and was then steady with diurnal fluctuations. The scour began after the bed had degraded to the elevation of the top of the pier footing. Filling of the channel began before the stage began to decrease. Since bed elevation changes in alluvial systems are the response to changes in sediment supply and flow hydraulics, and flow hydraulics were relatively constant during this event, an increase in sediment supply from the glacial melt water is thought to have initiated the filling.

III. HYDRODYNAMIC MODELING

The U.S. Geological Survey's Multi-Dimensional Surface Water Modeling System (MD_SWMS) [4] was selected to simulate hydraulic conditions for the 2003 and 2004 scour events. MD_SWMS is a pre- and post-processing application for computational models of surface-water hydraulics. MD_SWMS uses a multi-dimensional steady-state model of flow, FaSTMECH [5].

The model was calibrated to surveyed water-surface elevations and two-dimensional velocity vectors

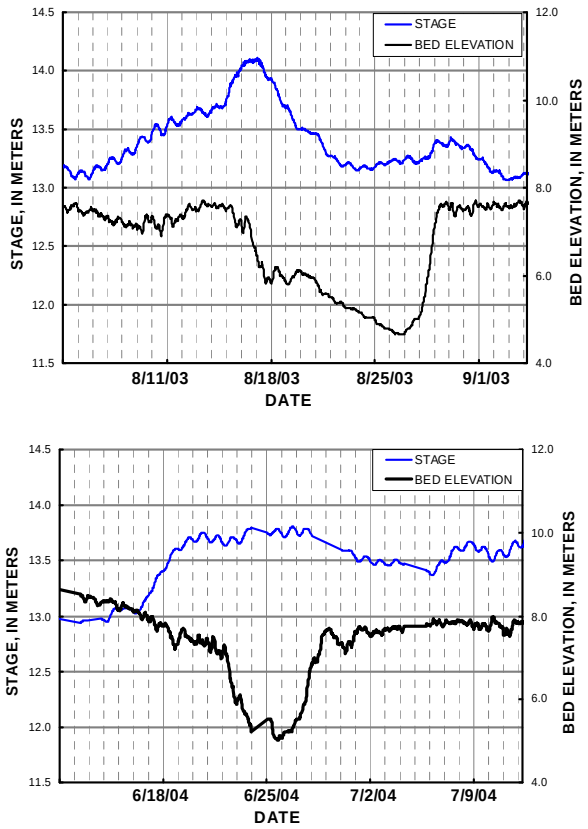

Figure 4. Stage and bed elevation at monitored bridge pier from two scour and fill events on the Knik River near Palmer, Alaska. Stage increases were the result of rainfall (2003, upper plot) and glacial melting from a prolonged period of warm weather (2004, lower plot).

measured with an acoustic Doppler current profiler. The peak discharge for each scour event was then simulated with the calibrated model. Hydraulic variables needed for the computation of predictive contraction and abutment scour were extracted from model results and are discussed below. A multi-dimensional model was required to properly simulate the flow routing around the guide banks and to accurately determine the area of active flow that was obstructed by the embankments.

IV. Computation of Scour

Total scour at the Knik River is a combination of scour at the piers, abutment scour along the guide banks, and contraction scour. Separating the individual components of scour from the monitoring and field data is difficult. Local scour at the bridge piers was not observed in cross section bathymetery at high flows and was not included in the computation of total scour. The contraction scour component was separated from the abutment scour along the guide banks by measuring the bed elevation change in the center of the channel. For this assessment, scour along the right and left banks is considered purely abutment scour. Actual conditions are likely a combination of all three components.

A. Contraction Scour

Contraction and abutment scour at the Knik River are considered live-bed. Under live-bed conditions, contraction scour in the bridge section reaches a minimum when sediment transport into the contracted section equals sediment transport out or when the mean velocity equals the critical velocity of the mean-diameter bed material. An equilibrium is reached when the transport capacity in the contracted section decreases because of increasing channel area and the attendant decrease in flow velocity. The banks of the river in the bridge reach are armored with rip-rap, so increases in channel area occur through a combination of vertical scour and lateral scour towards the center of the channel. Contraction scour does not occur uniformly across the channel (Fig 3.). There are two active areas of scour along the right and left banks through the bridge.

Predictive contraction-scour equations do not directly compute the depth of scour, but rather the depth of flow in the contracted section for equilibrium conditions. The most widely used equations are semi-empirical and based on formulas of sediment transport and uniform flow. The equations evaluated here all incorporate flow depths and ratios of discharge and channel width in the contracted and uncontracted sections. At this site, the volume of flow in the active channel in the approach is always equal to the flow through the bridge. The discharge ratio factor is therefore not needed and the common form of the contraction scour equation is simplified to:

$$y_{CS} = y_1 \left(\frac{w_1}{w_2} \right)^{Ew} - y_1 \qquad (1)$$

where,

y_{CS} is scour depth in the contracted section, in meters;

y_1 is the average depth in the upstream main channel, in meters;

w_1 is the width of the main-channel of the approach section, in meters;

w_2 is the width of the of the main-channel in the contracted section, in meters; and

E_w is a coefficient that accounts for the method of sediment transport. Values are presented in Table 1.

The estimated contraction-scour depth is the difference between the flow depth in the contracted section after scour has occurred and the flow depth that existed prior to any scour. Estimation of the flow depth prior to scour is difficult. The channel geometry in the contracted section, when the channel bathymetry was collected for the hydrodynamic model, had already been modified to some degree by abutment and contraction scour. A reference surface from which the total scour can be subtracted must be established. This surface typically is determined either from the channel geometry of the upstream uncontracted section or by interpreting a surface along a longitudinal profile that spans the contracted section. The monitoring data show that the bed aggrades annually to an average elevation of 10.1 m during the lower winter discharges when there is no contraction of the channel. This elevation also agrees with the elevation determined using the longitudinal profile method.

Live-bed contraction scour was estimated for the 2003 and 2004 scour events using several predictive equations. The equations are all similar in form to (1), but use different sediment-transport exponents (E_w) that are

TABLE I. CONTRACTION SCOUR VARIABLES AND COMPUTED SCOUR

Variables		2004	2003
Q	Discharge	934 m^3/s	1180 m^3/s
w_1	Width of approach section	450 m	450 m
w_2	Width of contracted section	120 m	120 m
y_1	Average depth of approach section	1.9 m	2.2 m
y_s	Observed scour depth	2.7 m	2.9 m

Sediment Transport Coefficients (E_w)		Computed Scour (y_s)	
Laursen [6]	0.59	2.2 m	2.5 m
Straub [7]	0.43	1.5 m	1.6 m
Straub [7]	0.642	2.5 m	2.9 m
Komura [8]	0.85	3.9 m	4.5 m
Komura [8]	0.667	2.7 m	3.0 m
Culbertson et al. [9]	0.667	2.7 m	3.0 m
Griffith [10]	0.637	2.5 m	2.8 m

summarized in Table 1 along with the computed scour values. The values range from 1.5-3.9 m and 1.6-4.5 m for the 2004 and 2003 scour events. Measured scour in the center of the channel from the reference elevation was 2.7 m in 2004 and 2.9 m in 2003.

B. Abutment Scour

Abutment scour is dependent upon the amount of flow obstructed by the abutment, shape and alignment of the abutment, sediment characteristics, and flow hydraulics. The guide banks that extend upstream of the bridge were designed to route flow through the contracted bridge reach. As flow is routed around the guide banks into the bridge reach horizontal vortices develop at the nose and scour the channel along two zones adjacent to each abutment (Fig. 5). The guide banks and abutments themselves are all lined with riprap and protected from scour. As discharge increases, more flow is routed around the guide banks and the magnitude of the vortices and depth of scour increases until an equilibrium is reached for the flow conditions. Scour is greater along the right bank because more flow is conveyed on this side of the channel. Abutment scour was estimated for the right bank only.

The two recommended equations in the Hydrologic Engineering Circular 18 [11] are based predominately on laboratory data. Froehlich [12] developed the following equation from a regression analysis of laboratory flume data:

$$y_s = y_f \left[2.27 K_1 K_2 \left(\frac{L'}{y_f} \right)^{0.43} Fr^{0.61} + 1 \right] \qquad (2)$$

where,

y_s is scour depth at the abutment, in meters;

y_f is the average depth of flow on the flood plain, in meters;

K_1 is a coefficient for abutment shape;

K_2 is a coefficient for angle of abutment to flow;

L' is the length of active flow obstructed by the embankment, in meters, and

Fr is the Froude number of the approach flow upstream of the abutment.

The second recommended equation is based on field data collected on spur dikes on the Mississippi and is applicable when the ratio of the projected abutment length to the flow depth is greater than 25, a condition that is satisfied for the Knik River. This equation is referred to as the HIRE (Highways in the River Environment) [13] equation:

$$y_s = y_f \left(4 Fr^{0.33} \frac{K_1}{0.55} K_2 \right) \qquad (3)$$

where,

y_s is scour depth at the abutment, in meters;

y_f is the average depth of flow on the flood plain, in meters;

K_1 is a coefficient for abutment shape;

K_2 is a coefficient for angle of abutment to flow, and

Fr is the Froude number of the approach flow upstream of the abutment.

In both equations, the area defined as flood plain was the area of the channel between the nose of the guide bank and the right bank shoreline. These equations typically result in overly conservative estimates of scour because they were developed using the abutment and roadway approach length as one of the variables. At this site, the discharge intercepted by the abutment is a function of stage not abutment length. Sturm [14] addressed this concern by evaluating the discharge intercepted by the abutment rather than length of the abutment, but his equations were developed for clear-water scour and extension to live-bed conditions is tentative. The variables and computed scour results from (2) and (3) are summarized in Table 2.

TABLE II. ABUTMENT SCOUR VARIABLES AND COMPUTED SCOUR.

Variables		2004	2003
Q	Discharge	934 m^3/s	1180 m^3/s
y_f	Average depth of flow on the floodplain	3 m	3.2 m
K_1	Spill through abutment shape coefficient	0.55	0.55
K_2	Coefficient for 90 degree angle of abutment into flow	1	1
Fr	Froude number of approach flow	0.22	0.26

Abutment Scour Equation	Computed Scour (y_s)	
Froehlich [12]	7.6 m	8.4 m
HIRE [13]	7.3 m	8.2 m

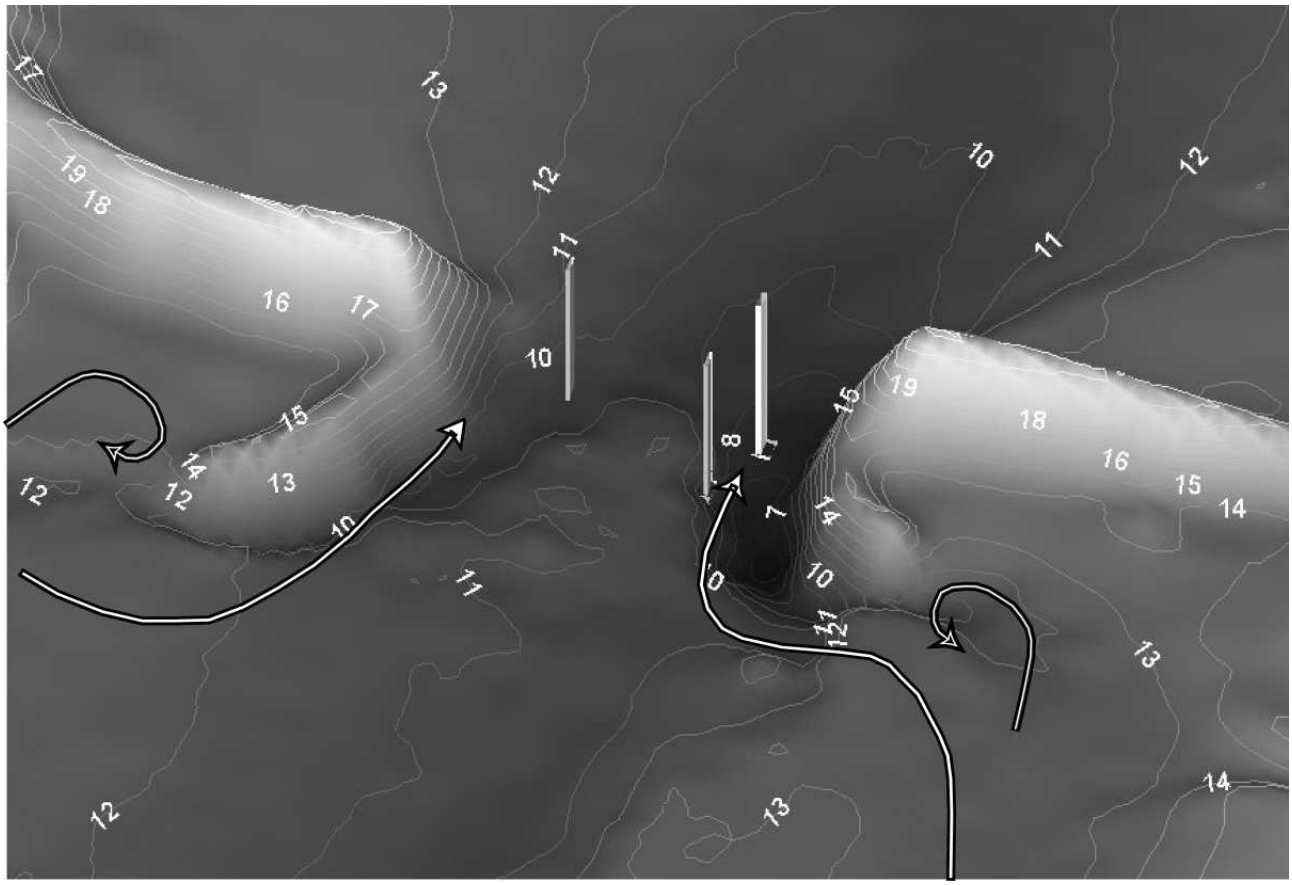

Figure 5. Topography and bathymetry at the Knik River with approximate lines of flow. Contours elevations are in meters, North American Vertical Datum of 1988.

The total measured scour at the right-bank pier as measured from the reference surface elevation of 10.1 m for the 2003 and 2004 scour events was 5.3 m and 5.1 m, respectively. The results from (2) and (3) overestimated scour for the 2003 event by 55 percent and 60 percent, respectively. The results from (2) and (3) for the 2004 scour event overestimated scour by 43 percent and 50 percent respectively. This overestimation would be greater if the estimated contraction scour were included for the right side of the channel.

V. SUMMARY

Long-term streambed-scour monitoring data from a bridge pier on the Knik River illustrate an annual pattern of channel aggradation and degradation that is punctuated by shorter periods of scour and fill. Observed scour over 4 years of study averaged 6 m. Scour at this site is complex and is a combination of pier, contraction, and abutment scour, with abutment scour being the primary factor. The duration and magnitude of streambed scour was dependent on the source and timing of high flows. Two scour events with similar discharges were modeled with a multi-dimensional hydrodynamic model and results were used to calculate contraction and abutment scour with recommended predictive equations. Computed contraction scour over and under calculated the scour that was observed. The computed abutment scour over estimated by 43 to 60 percent. Pier scour was not computed because it was not observed at high flows.

Long-term monitoring data are necessary to distinguish seasonal scour from short-term scour and to determine the components of scour and their individual influence. The over prediction of computed abutment scour illustrates the need for further refinement of these equations for live-bed conditions. Data collected at this site will contribute to the need for field data at sites with significant abutment scour.

REFERENCES

[1] V.W. Norman, "Scour at selected bridge sites in Alaska", *U.S. Geological Survey Water-Resources Investigations Report* 32-75, 1975, 160 p.

[2] L.B. Leopold, M.G. Wolman, and J.P. Miller, J.P., *Fluvial Processes in Geomorphology*: San Francisco, CA, W.H. Freeman and Company, 1964, 522 p.

[3] A.C. Parola, S.K Mahavadi,., B.M Brown,.and A. El Khoury**,** "Effects of rectangular foundation geometry on local pier scour", *Journal of Hydraulic Engineering*, v. 122, no. 1, 1996, p. 35-40.

[4] R.R McDonald, J.M Nelson, P.J Kinsel,., and J.S. Conaway, "Modeling surface-water flow and sediment mobility with the multi-dimensional surface water modeling system", *U.S. Geological Survey Fact Sheet 2005-3078*, 2006, 6 p.

[5] J.M. Nelson, J.P. Bennett, and S.M. Wiele, "Flow and sediment transport modeling" in *Tools in Fluvial Geomorphology*, England, Wiley, 2003, p. 539-576.

[6] E.M. Laursen, "Scour at bridge crossings", *Transactions of the American Society of Civil Engineers*, v. 127, part 1, 1962, p. 166-209.

[7] L.G. Straub, "Missouri River report", U.S. Department of the Army to 73rd United States congress, 2nd Session, House of Representatives document 238, Appendix XV, 1935, 1156 p.

[8] S. Komura, “Equilibrium depth of scour in long constrictions”, *American Society of Civil Engineers Journal of the Hydraulics Division*, v. 89, no. HY3, 1963, p. 17-37.

[9] D.M. Culbertson, L.E. Young, and J.C. Brice, “Scour and fill in alluvial channels”, *U.S. Geological Survey Professional Paper 462-A*, 1964, 47 p.

[10] W.M. Griffith, “A theory of silt transportation”, *Transactions of the American Society of Civil Engineers*, v. 104, 1939, p. 1733-1786.

[11] E.V. Richardson, and S.R. Davis, “Evaluating scour at bridges”, *Federal Highway Administration Hydraulic Engineering Circular no. 18*, FHWA NHI 01-001, 2001, p. 378.

[12] D.C. Froehlich, “Abutment scour prediction”, presentation to the Transportation Research Board, 1989.

[13] E.V. Richardson, D.B. Simons, and P.F. Lagasse, “Highways in the river environment”, *Federal Highway Administration Hydraulic Series no. 6*, FHWANHI 01-004, 2001, p. 644.

[14] T.W. Sturm, “Enhanced abutment scour studies for compound channels”, U.S. Department of Transportation, Federal Highway Administration, 2004, p. 144.

Experimental analysis of instabilities in very loose sands

A. Daouadji[1], H. AlGali[1], and F. Darve[2]
[1]Laboratoire de Physique et Mécanique des Matériaux, UMR CNRS 7554
Université Paul Verlaine - Metz -France
[2]Laboratoire Sols, Solides, Structures RNVO, Alert Geomaterials
Institut National Polytechnique de Grenoble, UJF, CNRS - France

Abstract:

In this paper, the influence of strain and stress loading paths on the behavior of very loose sand is analyzed with particular attention to potential instabilities. A particular stress path, i.e. a quasi constant shear undrained path, is presented and comparisons are made with data from literature. Experimental results show that diffuse mode failure occurs before the Mohr-Coulomb failure surface is reached. It is shown for these undrained tests that excess pore pressure results from collapse and it is not a trigger parameter. Moreover, stress ratios at collapse and corresponding mobilized angle of friction are very close for classical consolidated undrained tests, constant shear drained tests and quasi constant shear undrained tests. The onset of collapse is thus independent of the loading path under drained and undrained conditions but depend on the direction of the stress increment.

I. INTRODUCTION

Several studies have shown that collapse can occur before reaching the plastic limit criterion, such the Mohr-Coulomb criterion ([1], [2], [6], [9], [15], [16] and [17]). This phenomenon is related to the bifurcation of the response of the material and to the loss of stability. At the bifurcation point, the sample should behave of in several ways. If considering the response curve, the sample can follow the fundamental branch and thus remain stable. Depending on the wavelength of the eigenmode comparatively to the characteristic length of the sample or the structure, two principal cases should occur. If the eigenvector is (very) small, localization of the strains occurs and shear band will appear. If the wavelength is close to or greater than the characteristic length, a diffuse mode of failure will then take place. The first type of behaviour have been thoroughly studied and simulated by using of the vanishing determinant of the acoustic tensor. The second type of response of the material after bifurcation will experimentally explored in this paper. Diffuse mode of failure manifests itself by a collapse of the sample strictly inside the Mohr-Coulomb plastic limit criterion and a sudden increase of strains. In this case, no more localization of strains appears and conventional failure analysis cannot explain them. Recent study ([1]) has shown that results obtained for clayey sands are very close to those obtained for very loose sands. Conclusions made for the very loose tested sand can thus be extrapolated to clayey sands containing a percentage of fine content up to 10 or 15 percent by weight. This work proposes a new test which follows a particular path: quasi constant shear stress undrained test (C.S.U.) in order to check if excess pore pressure is the consequence of collapse. In other words, is excess pore pressure a trigger parameter under undrained conditions? It is analytically established that collapse occurs inside a domain which is include in the Mohr – Coulomb limit criterion (a necessary condition) and that collapse depend on the direction of the increment of the loading [4]. A definition of an unstable domain is also proposed for classical undrained compression triaxial tests (ICU), for constant shear drained tests (CSD) and for quasi constant shears undrained tests (CSU). All tests have the same stress increment direction at collapse and are isotropically consolidated.

II. EXPERIMENTAL SETUP

This section presents the experimental apparatus developed to impose both axial loading (stress and strain controlled) and constant shear stress on the soil specimen under drained and undrained conditions. Unlike in previous experimental studies on dry sand [16] and on drained saturated sands ([6] and [9]) a particular loading path (detailed in section 4) is applied under undrained conditions. First, the components of the entire experimental setup will be presented, then the testing procedure and the characteristics of the sand used will described.

A. Testing apparatus

Axial displacement is imposed by a Whykeham Farrance ® Tritech (100 KN) displacement-controlled apparatus. The displacement rate is chosen by selecting a velocity in the range of 0.00001 to 5.99999 mm/mn. However, the loading can be completely applied via a piston type cylinder which can be assembled on the apparatus. With this arrangement mixed loading (i. e. displacement-controlled then load controlled) can be applied. Two digital pressure / volume controllers (DPVC) are used to perform isotropic consolidated drained tests. Back pressure is measured with a pore pressure transducer. During testing, the measured value is compared to the applied pressure. Axial

displacement is measured by an external LVDT and changes in volume are measured by the piston displacement into and out of the DPVC. The forces are measured by an internal submersible load cell with the capacity of 1 or 5 KN depending of the initial density and the effective mean pressure. All tests variables are stored in a microcomputer.

B. Sample preparation

- Specimen preparation: The moist tamping (MT) method is used to prepare the specimen. The sand has a moisture content of about 3-4% in order to reach near maximal void ratio before and after isotropic consolidation of about the maximum void ratio $e_{max} \approx 1$ (TABLE 1). In order to obtained homogeneous samples, sand was carefully placed in five layers in the mould [1]. The membrane is sealed at the base of the cell and at a top cap. Saturated porous stones are placed in enlarged end plates to minimize friction and to allow homogeneous deformations at large strains. A small vacuum (10KPa) is applied to permit the removal of the split mould. The cell is then put into the testing apparatus and filled with water. A small confining pressure (20KPa) is then applied and reached a value of 30KPa when the vacuum is nil.

- Saturation process: A de-aerated water percolation is carried out to ensure sample saturation. Both cell pressure and back pressure are increased simultaneously in steps of 30KPa. During this process the B-Skempton coefficient is checked and samples are assumed to be saturated if $B \geq 96\%$.

- Void ratios: By drying the sample, the final void ratio is calculated. This void ratio is the same as the void ratio after consolidation e_c (as the test is undrained). The void ratio before consolidation (e_o) is obtained from the measured volume variation during isotropic consolidation and by assuming that grains and water are incompressible. Comparison of the initial void ratio e_i (accounting for the membrane thickness) and e_o shows that e_i is slightly higher than e_o due to strain that occur during the saturation phase and also during consolidation (see table 1).

TABLE 1 : CHARACTERISTICS OF THE UNDRAINED TESTS ON HOSTUN SAND S28

Test #	p'_0 (KPa)	e_i	e_o	e_c	q/p'_0
6	100	1.159	1.086	0.974	-
42	300	1.140	1.060	1.025	-
7	750	1.196	1.083	1.000	-
31	100	1.180	1.136	1.085	0.285
26	300	1.147	1.070	0.996	0.218
41	300	1.132	1.101	1.026	0.305
27	750	1.154	1.136	1.005	0.210

C. Tested material

The sand used for this study is Hostun S28 sand. The quartzic grains are sub-angular and the grain size distribution is uniform (Figure 1). The principal characteristics are summarized in TABLE 2.

TABLE 2 : BASIC PROPERTIES OF HOSTUN S28 SAND

Type	Mean Size (mm)	Cu	Specific gravity	Max void ratio	Min void ratio	Frictional angle (°)
Quartzic	0.3 - 0.35	2	2.65	1	0.656	32

D. Testing program

For a given void ratio, three effective mean pressures are used: p'_o = 100, 300 and 750KPa. The first series concern classical undrained triaxial tests (section III), the second series are constant shear drained tests (section IV) and the third series are quasi constant shear undrained tests (section V).

III. CLASSICAL LAOD AND DISPLACEMENT CONTROLLED UNDRAINED TESTS

Results obtained for load-controlled tests are compared with those obtained by Matiotti [13] and by Doanh et al. [7] for displacement-controlled tests. Results obtained for displacement-controlled tests are also compared to those obtained on same sand with a very close density by Desrues et al. [5]. The experimental device used in their study is a displacement-controlled apparatus which was modified to permit application of a constant force corresponding to peak shear stress. The constant force results from a spring attached to the displacement controlled device and the force is therefore proportional to the spring stiffness. As shown in Figure 2, it is noted at the peak of stress that $\eta = q/p' = 0.6$ which corresponds to a mobilized angle of friction of approximately 16°.

Good agreement is shown in this figure and these results validate both the experimental device and also the sample preparation (TABLE 1).

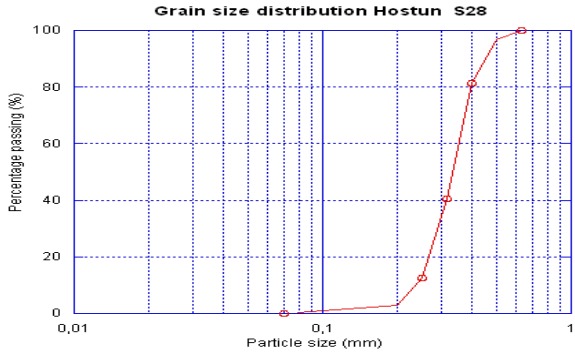

Figure 1 Hostun fine sand grain size distribution.

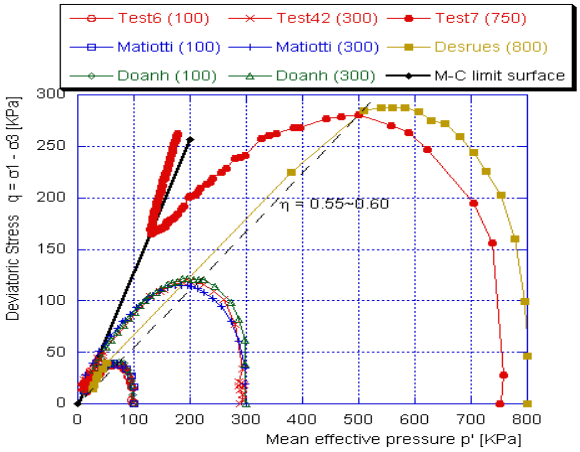

Figure 2 : Comparison of our results with those of Matiotti and al. ([13]), Doanh and al. ([7]) and of Desrues and al. [5] for p'_o = 100, 300, 750 KPa.

IV. CONSTANT SHEAR DRAINED TEST

This test was originally developed by Sasitharan et al. [15] on saturated loose Ottawa sand sheared under drained conditions with dead load. This special stress path was performed to simulate the loading of soil within a slope or an embankment subjected to a low increase in pore pressure. Di Prisco and Imposimato [6] and Gajo [9] have performed similar tests on Hostun's sand for approximately the same void ratio as in our experiments. The constant shear stress is also applied using dead load. Our main results are presented in Figure 3 either by increasing the pore pressure (tests # 58 and 61) or by decreasing total stresses (tests # 51 and 60).

V. QUASI CONSTANT SHEAR UNDRAINED TEST

An original test is presented in this section. The practical applications of this test correspond to the construction of a structure under undrained conditions on loose sand when boundary conditions prevent the drainage (retaining walls without drainage for example). It should be noticed that these tests also correspond to those obtained for denser sands containing 10 or 15 % (by mass) of fines (clayey sand for example). Practical application examples for such studies include the analysis of landslides and deep foundations.

A. Quasi Constant Shear Undrained test

In these tests, isotropically consolidated samples (point A in Figure 4) are submitted to either displacement- or stress-controlled loading (Point B). It important to emphasize that it is difficult to maintain the shear stress constant during these tests. Indeed, a similar reduction in shear stress is noted in tests conducted by Lade [11] on closure of the drainage valve which corresponds to the undrained phase of the classical drained then undrained test and by Chu et al. [2] for constant shear drained (CSD) tests**.** Undrained conditions are maintained and the sample is then sheared along a quasi constant deviator stress path by decreasing the total axial stress (σ_1) and the total radial stresses (σ_3) from point C to point D for which an increase of the axial deformation is noticed (Figure 7). The deviatoric stress is then maintained quasi constant up to the point E. Nevertheless, at this point, it is no longer possible to maintain the constant shear stress as on CE. Indeed, it decreases continuously; the test becomes non-controllable as defined by Nova [14].

B. Experimental results

Figure 4 shows results of a constant deviatoric undrained test on an isotropic consolidated sample ($p'_0 = (\sigma'_1 + 2\ \sigma'_3)/3 = 750$ KPa) with a void ratio before isotropic consolidation of $e_0 = 1.136$. The deviatoric stress - effective mean pressure response is shown in this figure. After undrained loading, the stress deviator ($q = \sigma_1 - \sigma_3$) was maintained approximately constant up to 157.5 KPa which corresponds to an anisotropic stress state $q/p' = 0.210$. To study the influence of the effective mean normal pressure, results obtained for p'_0 = 100, 300 and 750 KPa are presented in Figure 5. Figure 6 presents results obtained for two tests carried out with the same effective mean normal pressure of 300 KPa and for two values of constant deviatoric stress. Figure 7 shows the deviatoric stress and the excess pore pressure, the axial deformation as well as the second order work versus time which is defined in section VI.C.

VI. RESULTS AND DISCUSSION

A. Onset of collapse

Experimental collapse points obtained from C.U., C.S.D. and C.S.U. tests are plotted in Figure 8. Herein, collapse means that the sample is no more controllable [14]. The loading program, with the correct control parameters, can thus not be maintained. One can see that the stress ratios and the corresponding mobilized angles of friction at collapse are very close (Tab. 3). It is relevant to note that collapse occurs strictly inside a domain which is included in the Mohr-Coulomb limit surface. Taking into account experimental uncertainties, the unstable line seems to be unique for all the considered loading paths. This result is of course not generally valid and could be induced here by the fact that, at collapse, stress increments are parallel as depicted in Figure 9.

B. Diffuse mode of failure

The deformation of all the samples seems to be homogeneous even for large strains (after collapse): no strain localization neither by a single shear band nor by shear bands pattern were noted. One can observe in Figure 7 that pore pressure monotonically decreases after the application of constant shear stress (between the points C and D). Moreover, the analysis of pore pressure variation at the time of collapse highlights two points:

- Collapse occurs while the pore pressure decreases meaning that the increase in pore pressure is related to collapse (see Figure 7). Therefore, pore pressure is not a trigger parameter for collapse.

- The increase in pore pressure during collapse is more than likely the result of a diffuse mode of deformation rather than a localized one since, upon localized deformation, no notable change in pore pressure should be observed.

C. Characteristic of the constant shear undrained test

The sign of the second order work, based on the local condition of stability defined by Hill [10], can be used to study the stability of the tested material. In axisymmetric conditions second order work is defined ([3], [4], and [17]):

$$d^2 W = d\sigma_{ij}\, d\varepsilon_{ij} = d\sigma_1 d\varepsilon_1 + 2\, d\sigma_3 d\varepsilon_3 \quad (1)$$

which can be re-arranged to give:

$$d^2 W = dq\, d\varepsilon_v + d\sigma_3 d\varepsilon_v \quad (2)$$

with $dq = d\sigma_1 - d\sigma_3$ and $d\varepsilon_v = d\varepsilon_1 + 2\, d\varepsilon_3$.

Along the C.S.U (isochoric condition and q = constant) $d\varepsilon_v = 0$ and $dq = 0$ which implies that $d^2W = 0$.

It is not possible to apply this path as showing in Table 4. As no volume variation is imposed, it is not possible to impose also no variation of shear stress. For this reason, a very small variation of the shear stress

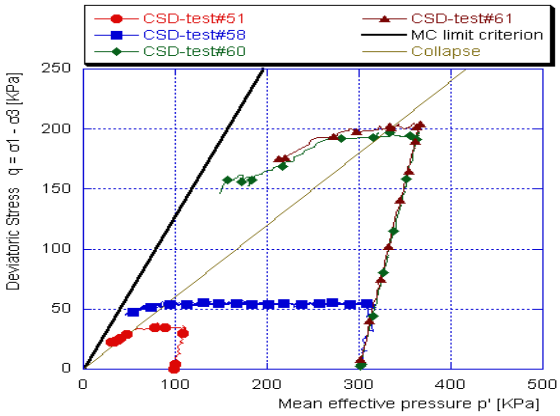

Figure 3. Constant shear drained tests on Hostun's sand

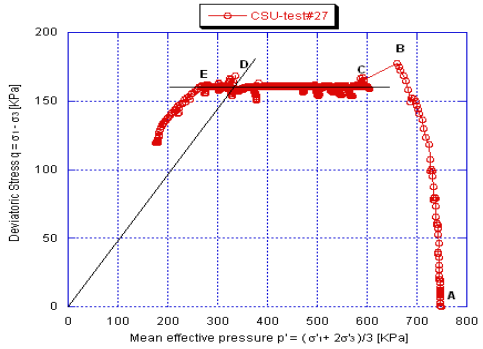

Figure 4 Quasi constant shear undrained test

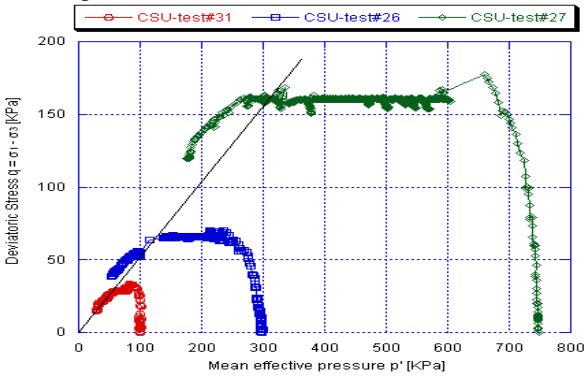

Figure 5 Quasi constant shear undrained test p'_o = 100, 300, 750 KPa

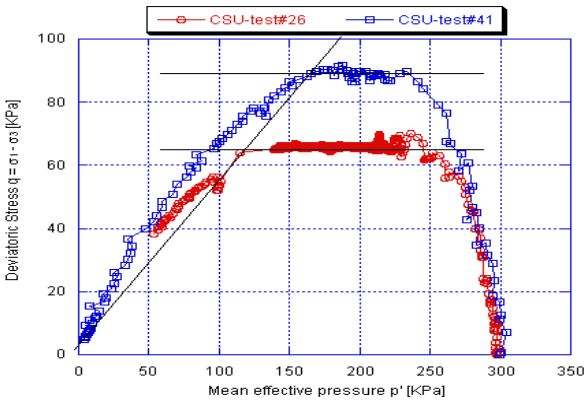

Figure 6 Quasi constant shear undrained test p'_o = 300 KPa, q_{const} = 65.26 and 91.55 KPa.

TABLE 3 : MOBILIZED ANGLE OF FRICTION AND STRESS RATIO AT COLLAPSE DURING C.U. ,C.S.D. AND C. S. U. TRIAXIAL TESTS ON HOSTUN SAND

Type of test	Test #	p'_0 (KPa)	e_o	ϕ_{mob} (°)	$(q/p')_{coll}$
I.C.U.	6	100	1.086	15.26	0.58
	42	300	1.060	15.67	0.59
	7	750	1.083	14.89	0.56
C.S.D.	51	100	1.192	15.06	0.57
	58	300	1.068	14.49	0.55
	60	300	1.161	16.53	0.62
C.S.U.	31	100	1.136	13.91	0.52
	26	300	1.070	14.72	0.56
	41	300	1.101	13.64	0.51
	27	750	1.136	15.36	0.58

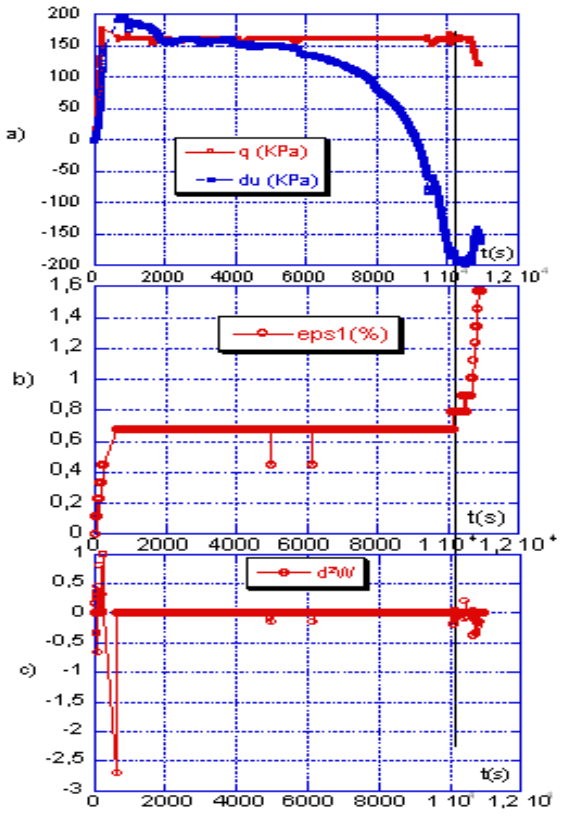

Figure 7 Constant shear undrained test (p'_o = 750 KPa): deviatoric and excess pore pressure, axial displacement and second order work versus time (test 27).

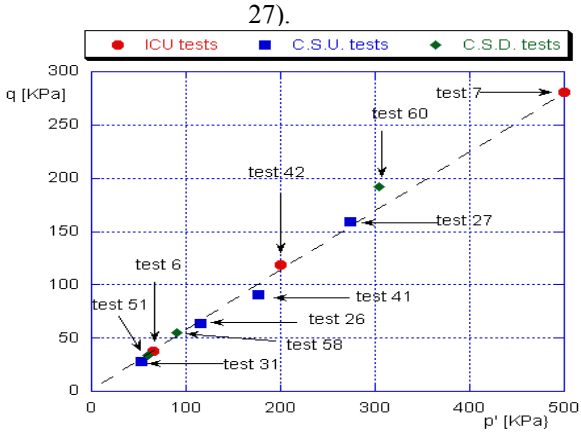

Figure 8 Comparison between stress ratios obtained from CU, CSD and CSU tests

$$\begin{cases} d\varepsilon_v = 0 \\ dq = \eta \end{cases} \quad (3)$$

Table 4: Available equations for load-controlled tests under undrained conditions.

Conditions	Stresses	Strains
Axisymmetry	$d\sigma_2 = d\sigma_3$	$d\varepsilon_2 = d\varepsilon_3$
Isochoric	/	$d\varepsilon_v = 0$
p′ and q decrease	$d\sigma_1 < 0$	/
	$d\sigma_3 < 0$	/
Constitutive relation	$\boldsymbol{\sigma} = C^{ep}\,\boldsymbol{\varepsilon}$	
q constant	impossible	/

dq = η is needed. Figure 7 illustrates that, the second order work is negative when collapse occurs.

$$\begin{bmatrix} dq \\ d\varepsilon_v \end{bmatrix} = \begin{bmatrix} A & C \\ D & B \end{bmatrix} \begin{bmatrix} d\varepsilon_1 \\ d\sigma_3 \end{bmatrix} \quad (4)$$

$$\begin{cases} Ad\,\varepsilon_1 + Cd\,\sigma_3 = \eta \\ Dd\,\varepsilon_1 + Bd\,\sigma_3 = 0 \end{cases} \quad (5)$$

$$d\sigma_3 = \frac{D}{CD - AB}\eta \quad (d\sigma_3 < 0 \; if \; \eta > 0) \quad (6)$$

$$d\sigma_1 = \left(1 + \frac{D}{CD - AB}\right)\eta \quad (d\sigma_1 < 0 \; if \; \eta > 0) \quad (7)$$

$$d\varepsilon_1 = \frac{B}{AB - CD}\eta \quad (d\varepsilon_1 > 0 \; if \; \eta > 0) \quad (8)$$

$$d\varepsilon_3 = \frac{B}{2(CD - AB)}\eta \quad (d\varepsilon_3 < 0 \; if \; \eta > 0) \quad (9)$$

The parameter η takes the successively the value:

$$\eta = \pm k \quad (10)$$

where k is imposed and depends on the test (0.5 or 1 KPa). The second order work is then given by:

$$d^2W = \eta d\varepsilon_1 = \frac{B}{AB - CD}\eta^2 \quad (11)$$

At the bifurcation point, which corresponds to the peak of the shear stress in the classical undrained test, we have:

$$\begin{cases} \eta = 0 \\ AB - CD = 0 \\ d^2W = 0 \end{cases} \quad (12)$$

Amplitude of the second order work goes to infinity in the vicinity of the bifurcation point. However, it was experimentally noted that the second order work value is finite as depicted in Figure 7.

Sometimes, sample collapse can occur before reaching the unstable domain. This behavior can be explained by an imperfection of the experimental device or by a disturbance in the loading. This observation is important for the study of slope instability because such disturbances can occur that lead to failure on slopes smaller than 10° and can be shown as trigger factors.

VII. CONCLUSIONS

In this work, classical consolidated undrained (C.U.) tests, constant shear stress drained tests (C.S.D.) and quasi constant shear stress undrained tests (C.S.U.) were applied to very loose sand. Results obtained are presented and discussed. Analysis of pore pressure evolution highlights a diffuse mode of deformation during collapse. Moreover, the break in the pore pressure evolution slope makes it possible, during the test, to locate the instant when collapse occurs. The increase in the pore pressure is thus the consequence of collapse and not a triggering factor.

Collapse of samples occurs for closed values of stress ratios and mobilized angles of friction. It can thus be stated that the onset of collapse is not dependant of the loading conditions under drained and undrained cases but depend on the direction of the stress increment.

Second order work calculated from the experimental results becomes negative at the time of collapse and can be a valuable tool for identifying collapse.

One should notice that this collapse always occurs strictly inside the Mohr-Coulomb limit surface of plasticity and that explain certain ruptures which can not be explained by the classical theory of plasticity.

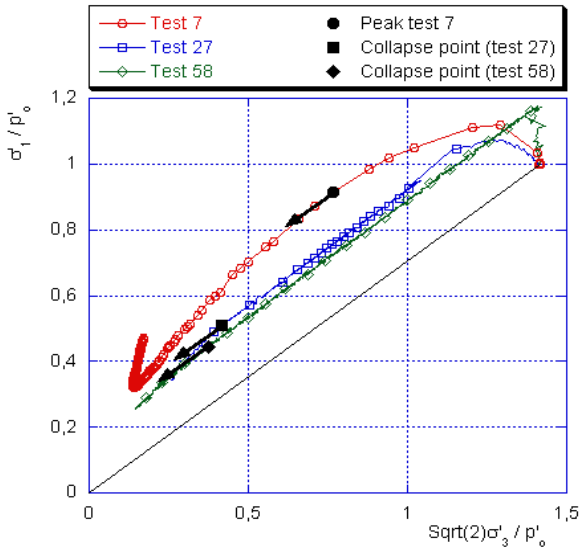

Figure 9. Orientation of stress increments for ICU, CSD and CSU tests.

ACKNOWLEDGMENT

Authors wanted to thanks the “Région Lorraine” for its support.

REFERENCES

[1] CHU J. and LEONG W.K. Effect of fines on instability behaviour of loose sand. *Geotechnique*, 52(10):751–755, 2002.

[2] Chu J., Leroueil S., and Leong W.K., Unstable behaviour of sand and its implication for slope instability. *Can. Geotech. J.* 40: 873–885 (2003)

[3] DARVE F. and LAOUAFA F. Instabilities in granular materials and application to landslides. *Mech. Cohes. Frict. Mater.*, 5(8):627–652, 2000.

[4] DARVE F., SERVANT G., LAOUAFA F., and KHOA H.D.V. Failure in geomaterials: continuous and discrete analyses. *Comp.Methods Appl.Mech. Engrg*,

193:3057–3085, 2004.

[5] DESRUES J. and GEORGOPOULOS I.O. unpublished.

[6] DI PRISCO C. and IMPOSIMATO S. Experimental analysis and theoretical interpretation of triaxial load controlled loose sand specimen collapses. *Mech. Cohes. Frict. Mater.*, 2:93–120, 1997.

[7] DOANH T., IBRAIM E., and MATIOTTI R. Undrained instability of very loose hostun sand in triaxial compression and extension. part 1: experimental observations. *Mech. Cohes. Frict. Mater.*, 2:47–70, 1997.

[8] ECKERSLEY J.D. Instrumented laboratory flowslides. *Geotechnique*, 40(3):489–502, 1990.

[9] GAJO A. The influence of system compliance on collapse of triaxial sand samples. *Can. Geotech. J.*, 41:257–273, 2004.

[10] HILL R. A general theory of uniqueness and stability in elastic-plastic solids. *J. Mech. Phys. Solids*, 6:239–249, 1958.

[11] LADE P.V. Instability, shear banding, and failure in granular materials. *Int. J. of Solids and Structures*, 39:3337–3357, 2002.

[12] LAOUAFA F. and DARVE F. Modelling of slope failure by a material instability mechanism. *Comp. Geotechn*, 29:301–325, 2001.

[13] MATIOTTI R. and DI PRISCO C., and NOVA R. Experimental observations on static liquefaction of loose sand. *In Earthquake Geotechnical Engineering, Ishihara editions, Balkema*, pages 817–822, 1995.

[14] NOVA R. Controllability of the incremental response of soil specimens subjected to arbitrary loading programmes. *J. Mech. behav. Mater.*, 5, N◦2:193–201, 1994.

[15] Sasitharan, S., Robertson, P.K., Sego, D.C., and Morgenstern, N.R.. Collapse behavior of sand. *Canadian Geotechnical Journal,* 30: 569–577,1993.

[16] SKOPEK P. and MORGENSTERN N.R. and ROBERTSON P.K. and SEGO D.C. Collapse of dry sand. *Can. Geotechn. J.*, 31:1008–1014, 1994.

[17] SERVANT G., DARVE F., DESRUES J., and GEORGOPOULOS I.O. Diffuse modes of failure in geomaterials. *In Di Benedetto, editor, Deformation characteristics of geomaterials. Swets & Zeitlinger*, pages 181–198, 2005.

Intelligent Estimation of the Maximum Depth of Scour Hole around Bridge Piers in cohesive sediment using Artificial Neural Network

A. A. Dehghani* S. A. Salamatian* and M. Ghodsian*
* Tarbiat Modares University/Department of Civil engineering, Tehran, Iran

Determination of local scour at bridge piers is one of the critical problems in the design of bridge foundations to resist the erosive action of oncoming flows. Estimation of local pier scour depth has been studied by large numbers of researchers in noncohesive alluvial materials but very little effort has been devoted to the study of pier scour in cohesive materials. Artificial neural network (ANN) is one such technique with flexible mathematical structure which is capable of identifying complex non-linear relationship between input and output data without attempting to reach understanding in to the nature of the phenomena. In this study a multiplayer perceptron neural network is used for estimation the maximum scour depth around bridge piers in cohesive sediment. The performances of this network were compared with estimated results by available experimental relation. The results show the best agreement between the estimated results by neural network and experimental data.

I. INTRODUCTION

The estimation of scour depth around bridge piers is a major concern of bridge engineers. Underestimation of depth of scour and it's a real extend results in design of too shallow a function which may consequently get exposed to the flow endangering the safety of the bridge [1]. Overestimation of the scour depth results in uneconomical design the most common cause of bridge failures is scouring at bridge piers and abutments mainly during flood events [2]. As a consequence, local scour at bridge functions has long concerned engineers. Local scour around a bridge pier is affected by large number of variables primarily the flow, fluid, sediment and pier characteristics. The process of local scour has been studied extensively for cohesive less alluvial materials [3]. However, often riverbeds and banks are found to be composed of mixture of bars of gravel, sand, clay and silt. Little is known so far about the effect of the presence of cohesive material on pier scour [4]. A literature review indicates that the Scour depth estimation at bridge piers has attracted considerable research interest, and numbers of prediction methods exists at present. Since piers are important infrastructural components of bridges transmitting loads superimposed on slabs to the function, the phenomenon of scouring around these elements has long been studied. Although there is a need to define accurately the scour around bridge piers [5]. Aware of the lack of accurate methods to predict local scour at bridge piers, several studies have been completed since the beginning of the 1980s (e.g., at Auckland University).

Artificial Neural Network (ANN) is a mathematical tool, which tries to represent low-level intelligence in natural organisms and it is a flexible structure, capable of making a non-linear mapping between input and output spaces [6].

In this study the maximum scour depth around bridge piers were obtained by using the multiplayer perceptron (MLP) neural network.

II. DIMENSIONAL ANALYSIS

Dimensional analysis that has been used for correlating the variables affecting the local scour depth at bridge piers has been extended to include cohesive soil properties in order to account for the cohesive bed material. The variables used in the analysis are parameters defining the soil, the fluid, and the geometry of the modeled system. Depth of pier scour, *Ds*, which is the dependent variable in this analysis, can be expressed as a function of the following independent variables:

$$D_s = f(Y,b,V,D_{50},\sigma_g,\phi,\rho_s,t,g,\rho,\nu, S,CC,Mn,C,IWC) \quad (1)$$

In which *Ds* = depth of scour; *Y* = depth of approach flow; *b* = pier width; *V* = velocity of approach flow; *D50* = mean sediment diameter; σ*g* = standard deviation of sediment size; ϕ = pier shape factor; ρs=density of sediment particles; *t*= time; *g* = gravitational acceleration; ρ = fluid density; ν = fluid kinematics viscosity; *S* = soil shear strength; *CC*= clay content; *Mn* = origin of clay minerals (e.g. Kaolinite, Illite, Montmorillonite); *C* = degree of compaction; and *IWC* = initial water content.
Applying the dimensional analysis using *b, V,* and ρ as repeating variables, and using appropriate simplifications, the following set of dimensionless parameters can be Obtained [7]:

$$D_s / b = f(F_r, IWC, S/\rho V^2, C) \quad (2)$$

In which *Fr* is the approach Froude number ($=V/\sqrt{gY}$). In deriving equation 2, the clay content (*CC*) was eliminated as a variable since the effects of this parameter was found to be an independent factor only up to 12 percent clay content. In the cohesive pier scour experiments in Montmorillonite clays, the clay content was kept constant at 32 percent.

III. ARTIFICIAL NEURAL NETWORK

Artificial Neural Network (ANN) is a mathematical tool, which tries to represent low-level intelligence in natural organisms [6], and it is a flexible structure, capable of making a non-linear mapping between input and output spaces.

Neural network processing is based on performance of many simple processing units called neuron, cell, node or PE. Each neuron in each layer is connected to all elements in the previous and the next layer with links, each has an associative weight. The general ability of an ANN is to learn and to simulate the natural and complex phenomena.

If we consider the X=[x1, x2 …, xn] as input vector and W= [w1, w2 …, wn] as network parameter (weight) vector and if the goal is approximating the multi variate function $f(x)$, the learning procedure is to find the best weight vector (W) to have the best approximation of the $f(x)$. In this paper, Multi layer perceptron (MLP)

With back propagation learning rule is used.

A. *Multi layer perceptron (MLP)*

The MLP network (Sometimes is called Back Propagation (BP) network) is shown in Figure 1 is probably the most popular ANN in engineering problems in the case of non-linear mapping and is called "Universal Approximator". The learning process is performed using the well-known BP algorithm [8]. In this study, the standard BP algorithm based on the delta learning rule is used.

Two main processes are performed in a BP algorithm, a forward pass and a backward pass. In the forward pass an output pattern is presented to the network and its effect propagated through the network, layer by layer. For each neuron, the input value is calculated as follows:

$$net_i^n = \sum_{j=1}^{m} w_{ji}^n . O_j^{n-1} \quad (3)$$

Where

net_i^n is the input value of ith neuron in nth layer;

w_{ji}^n is the connection weight between ith neuron in nth layer and jth neuron in the (n-1)th layer;

O_j^{n-1} is the output of jth neuron in the (n-1)th layer;

M is the number of neurons in the (n-1)th layer.

In each neuron, the value calculated from Eq. (3) is transferred by an activation function. The common function for this purpose is the sigmoid function, is given by:

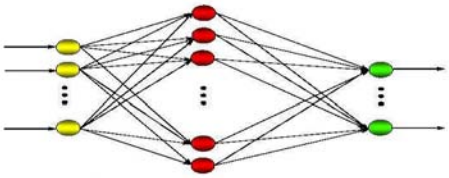

Figure1. Multi Layer Perceptron Neural Network Learning in ANNs

$$Sig(net_j^n) = 1/(1 + Exp(-net_j^n)) \quad (4)$$

Hence the output of each neuron is computed and propagated through the next layer until the last layer. Finally, the computed output of the network is prepared to compare with the target output. In this regard, an appropriate objective function such as the Sum of Square Error (SSE) or Root Mean Square Error (RMSE) is calculated as follows:

$$SSE = \sum_{i=1}^{n_p} \sum_{j=1}^{n_o} (T_{pj} - O_{pj})^2 \quad (5)$$

$$RMSE = \sqrt{\frac{\sum_{i=1}^{n_p} \sum_{j=1}^{n_o} (T_{pj} - O_{pj})}{n_p . n_o}} \quad (6)$$

Where

T_{pj} is the jth element of the target output related to the pth pattern;

O_{pj} is the computed output of jth neuron related to the pth pattern;

n_p is the number of patterns;

n_o is the number of neurons in the output layer.

After calculating the objective function, the second step of the BP algorithm, i.e. the backward process is started by back propagation the network error to the previous layers. Using the gradient descent technique, the weights are adjusted to reduce the network error by performing the following equation [8]:

$$\Delta w_{ji}^n (m+1) = \eta . \frac{\partial (E)}{\partial w_{ji}^n} + \alpha . \Delta w_{ji}^n (m) \quad (7)$$

Where:

$\Delta w_{ji}^{n}(m+1)$ is the weight increment at the (m+1)th iteration (Epoch);

η is the learning rate (Rumelhart & McClelland, 1986)

α is the momentum term $(0 \le \eta, \alpha \le 1)$

This process is continued until the allowable network error occurred.

IV. TRAINING THE NETWORK AND VERIFICATION OF RESULTS

For designing the artificial neural network, the experimental data obtained by reference [7], were used. The experiments were conducted in Colorado State University for the Federal Highway Administration. In the experiments, 1-m long cylindrical piers made of clear Plexiglas with 0.152- m and 0.102-m diameters were used. The scour depth development was measured against time utilizing three measuring tapes attached to the interior wall of each pier and a periscope manufactured by the use of a small inclined mirror. Also a homogeneous soil containing clay, silt, and fine sand particles, in which cohesion plays a predominant role, was used. Utilizing the X-Ray Diffraction Test, the dominant clay mineral was found to be Montmorillonite. The cohesive soil was also classified as medium plasticity clay and the texture as clay loam. Pier scour analysis was conducted under two major categories:

1) Unsaturated Montmorillonite clay scour and 2) saturated Montmorillonite clay scour. The distinction is made since for saturated cohesive materials, parameters such as Torvane shear strength and compaction have no physical significance; whereas these parameters are important in unsaturated cohesive material scour. The experimens limited itself to conditions in which the oncoming flows do not scour the approach reach (clear water conditions). The duration of experiments in the study was long enough to maintain the equilibrium condition for at least 4 hours. The detail of experimental arrangement is presented in reference [7].The number of available data collected for this study is 58. The data set were shuffled; 33 of them were used for the learning process, the 15 sets were used for testing and the 10 set were used for verification respectively. The range of variables is summarized in table 1. The network was designed with two parameters of Equation (2) as input pattern, and the scour depth dimensionless (ds/b) as output pattern. The configuration of designed neural networks is shown in figure 2.

The number of neurons in the hidden layer and the parameter α were determined by calibration through several run tests. Figure 3 shows the comparison between measured and estimated values of ds/b for Train pattern. Here the number of neurons in the hidden layer is 7. Figure 4 shows the best agreement between measured and estimated values for test pattern and figure 5 shows the best agreement between measured and estimated values for verification pattern.

TABLE 1.
RANGE OF USED VARIABLES.

Variable	Ranges
C	58-87
F_r	0.161-1.76

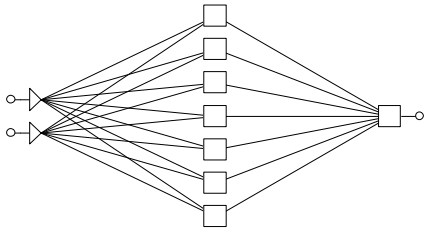

Figure2. Multi Layer Perceptron Neural Network Learning in ANNs

Figures 3, 4, 5 shows that the designed neural network is giving acceptable result. Hence one can conclude that the ANN is suitable tool for predicting scour depth.

V. COMPARISON WITH PREVIOUS STUDIES

In order to compare the results of designed neural network with previous empirical equation, the following equation which was given by Reference [7] was used:

The maximum scour depth around bridge piers in cohesive sediment with unsaturated condition is as follow:

$$\frac{d_s}{b} = 24{,}715(IWC)^{0.36} F_r^{\,1.92} C^{-1.62} \qquad (8)$$

Where the initial water content (IWC) and compaction (C) are in percent. In deriving this expression, the initial water content ranged from 15 to 50 percent, and compaction ranged from 50 to 100 percent. The development of equation 8 is based on laboratory tests in which Froude numbers ranged from 0.18 to 0.37, and soil shear strength values ranged from 0.1 to 0.45 kg/cm2.

For saturated Montmorillonite clay soils, equation 2 can be simplified further by eliminating the dimensionless soil shear strength parameter, (S/ ρV2), since this term has no physical meaning for saturated clays at high initial water contents (it approaches to 0). Also, for saturated conditions the compaction of cohesive soils, C, is mainly related to the water content and can therefore be removed from the list of independent variables.

Introducing the pier scour initiating Froude number, Fi, to define threshold conditions for pier scour and replacing Fr by the excess Froude number, (Fr-Fi), equation 2 becomes:

$$\frac{d_s}{b} = f(F_r - F_i, IWC) \qquad (9)$$

Using the results of experimental study, Fi and Ds / b are determined as:

$$F_i = \frac{350}{(IWC)^2} \tag{10}$$

And

$$\frac{d_s}{b} = 0.0288(IWC)^{1.14}(F_r - F_i)^{0.6} \tag{11}$$

For approach Froude numbers less than the pier scour initiating Froude number (i.e., Fr <Fi), depth of scour is zero. For supercritical approach conditions, the value of experimental coefficient 0.0288 was found to be 0.0131.

Figure 6, 7, 8 shows the agreement between measured and estimated values by above equation for train, test and verification patterns.

For comparison the results, a discrepancy ratio $ds/b = (ds/b)c/(ds/b)_m$ was used. The mean value and the standard deviation for test pattern are presented in table 2. If the mean value and standard deviation are close to 0 and 1 respectively, the estimated results are closer to experimental results. Thus it maybe concluded that the present model gives better results than available experimental relation.

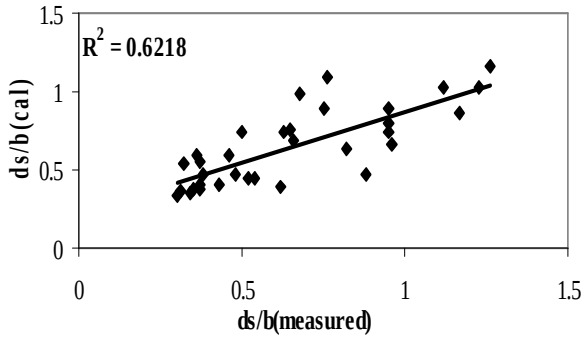

Figure 3. Comparison between measured and ANN estimated values for Train patterns.

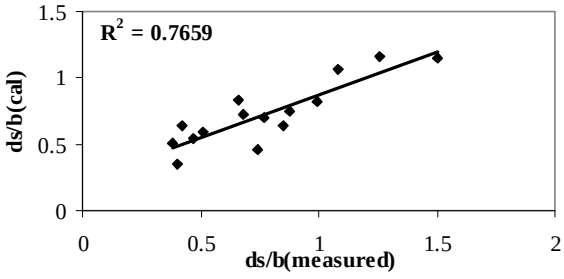

Figure5. Comparison between Measured and ANN estimated values for test patterns.

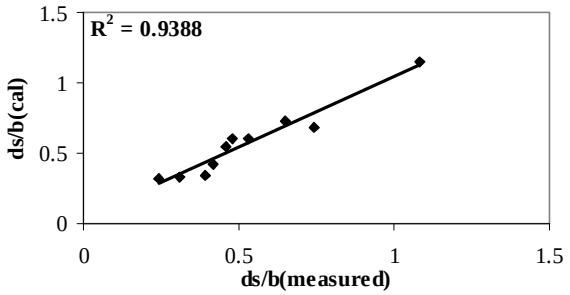

Figure3. Comparison between measured and ANN estimated values for verification patterns.

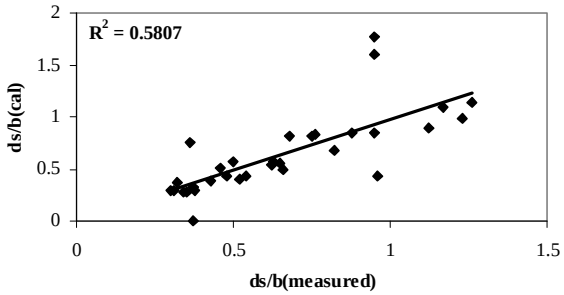

Figure6. Comparison between measured and estimated values for train patterns.

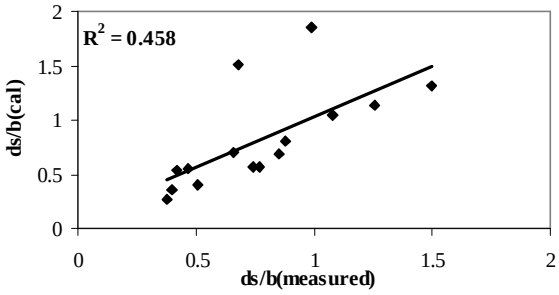

Figure7. Comparison between Measured and estimated values for test patterns.

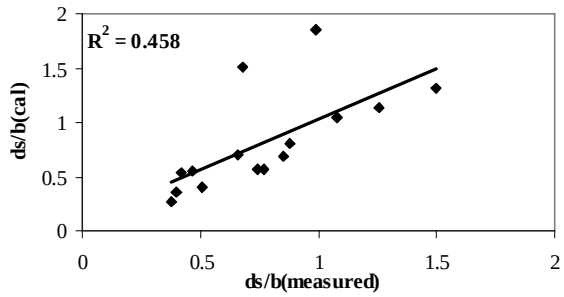

Figure8. Comparison between Measured and estimated values for verification patterns.

TABLE 2.
ACCURACY OF FORMULA FOR SCOUR DEPTH.

Method	Mean	Standard deviation
Federal Highway Administration(2003)	1.06284	0.43052
Presented ANN Model	1.00182	0.24574

Figure 9 shows the variation of estimated results ($\frac{d_s}{b}$) by artificial neural networks against two input parameters (C, F_r). It maybe concluded that the maximum depth of scour is increased by decreasing the Compaction (C) and increasing the Froud number (F_r).

VI. CONCLUSION

The application of ANNs for prediction of scour depth around bridge piers in cohesive sediment is introduced. It was shown that the neural network model can be successfully applied for the prediction of scour depth around bridge piers.

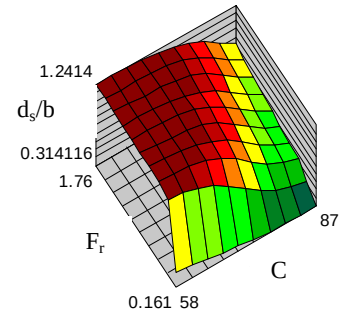

Figure9. the area of result by neural network

References

[1] G. Ahmed, Rajaratnam, N., "Flow around bridge piers," *J. Hydr. Engrg. A.S.C.E.*, Vol. 124, No. 3, pp. 228-299, March 1998.

[2] A.H. Cardoso, and R Bettess., "Effects of Time and Channel geometry on Scour at Bridge abutments," *J. Hydr. Engrg*, Vol. 125, No. 4, pp. 388-399, April 1999.

[3] C. Kuuijper, M. Cornelisse, and C. Winterwerp,. "Research on Erosive properties of Cohesive sediment," *J. of Geophysical Res*., vol. 94, No. 10, pp. 14341-14350, October 1989.

[4] S. A. Ansari, K. G. RANGA RAJU, "Influence of Cohesion on Scour around Bridge piers," Journal of Hydraulic Research, Vol. 40, No. 6, pp. 717-729, March 2002.

[5] B.W. Melville, and A.J. Sutherland, "Design method for Local scour at Bridge piers", *J. Hydr. Engrg*. Vol. 114, No. 10, pp. 1210-1226., 1988.

[6] M.B. Gorzalczany, "Computational Intelligence Systems and Applications", Physica-Verlag Company, Heidelberg: Germany (2002).

[7] A. Molinas, "Bridge Scour in Nonuniform sediment mixtures and in Cohesive materials:synthesis report, " Federal Highway Administration,FHWA-RD-03-083,2003.

[8] D.E. Rumelhart, J.L McClelland, & the PDP research group. "Parallel recognition in Modern computers. In processing: Explorations in the Microstructure of cognition". VOL 1. Foundations, MIT Press/Bradford Books, Cambridge Mass, 1986.

Effect of Sill on Local Scour at Lateral Intake in 180 Degree Curved Channel

A.A. Dehghani[*], M. Ghodsian[**], S. A. A. Salehi Neyshabouri[**] and M. Shafiefar[*]
[*] Tarbiat Modarres University/Department of Civil Engineering, Tehran, Iran

The lateral intake causes that the streamlines near the lateral intake are curved and diverted to lateral intake, therefore some vortex are formed and local scour observed near the lateral intake. Due to secondary flow in river bend, the scour develops near the outer bank and sediment moves toward the inner bank from outer bank of the bend, thus the outer bank of the bend is best location for lateral intake. Since floodwater carries a large amount of sediment, the sediment enters to lateral intake situated even in outer bank of the bend. As a result the channel conveyance decreases. There are several methods of sediment control in lateral intakes. One of the most common methods is use of sill in entrance of intake. In this study, the sill structure is used for sediment control at lateral intake in 180 degree curved channel. The effect of sill height on depth of scour hole at lateral intake under clear water condition has been studied experimentally. The experiments showed that two scour holes, one in the upstream and the other in the downstream edge of lateral intake, formed near the lateral intake. Moreover it was found that by increasing the height of sill the maximum depth of scour increases.

I. INTRODUCTION

The mechanics of sediment in channel bends, frequently appearing in natural rivers, is much more complex than that in straight channels. In a natural channel bend, the flow is turbulent and strongly three dimensional and channel topography is irregular. A characteristics feature of flow in a curved open channel is a strongly helical flow (also known as spiral flow, secondary current or transverse circulation) due to difference of centrifugal forces between the upper and lower layer of flow. This helical flow plays a significant role in the development of the transverse profile of bed and shear stress at the bottom. Due to secondary current, the lateral transport of sediment across the channel bend is observed. The inner bank is subjected to deposition, while the outer bank is subjected to scour. Due to the fact that one of the primary goals of diversion structures is to minimize the amount of sediment diversion, thus the outer bank of the channel bend can be used as the best location for lateral diversion.

Since floodwater carries a large amount of sediment, the sediment enters to lateral intake situated even in outer bank of the bend. As a result the channel conveyance decreases. There are several methods of sediment control in lateral intakes. One of the most common methods of sediment control at lateral intake is use of the sill in front of intake. The level of the sill is critical. It should be set at such a height above the bed of the river so that the sediment load is excluded at high river flows. But at the same time the crest of the sill must be low enough to enable the water demand to discharge over the sill at low river levels [1]. Wang have used sill for sediment control at front of lateral intake in straight channel [2]. Reference [3] is also, based on other works suggested using sill in front of intake for sediment control [3].

Despite the fact that lateral diversion should be located in an outer bank of a river bend; little information is available about the height of sill on local scour at lateral intake.

In this study an attempt has been made to investigate such effect experimentally. The effect of sill height on scour depth at lateral intake in clear water condition has been studied.

II. EXPERIMENTAL ARRANGEMENT

Experiments have been conducted in a re-circulating flume having a central angle of 180º; radius of channel center line 2.6 m, width of 0.6 m and height of 0.6 m. Figure 1 shows a plane view of the flume. The bend is connected to an upstream straight reach having length of 7.2 m and a downstream straight reach having length of 5.2 m. The bed and sides of flume was made of Plexiglas supported by metal frame. Measurement of discharge was done using an ultrasonic flow meter located in supply pipe and checked with a sharp crested weir in downstream return channel. Bed profile was recorded using bed profiler, which senses bed elevation by means of electromagnetic signals. Water was supplied from a sump into the entrance tank. Water level in the flume was controlled by tail gate situated at the end of flume. A 20 cm layer of uniform sand, with d_{50}=1.28 mm, was placed on the bed and covered the total length of the flume. The channel was equipped with two rails on which an instrument carriage was mounted. The sand bed surface was properly leveled by a plate attached to the instrument carriage. The Lateral intake, located at outer bank in section 115 degree, was 1.5 m long and 0.25 m wide. Discharge was kept constant at 40 l/s with a uniform depth of 0.173 m in upstream straight section. For this flow condition, the mean velocity in upstream channel is 0.85 times sediment threshold velocity. Different sill height (i.e 0, 4.5 and 6 cm) were used. Experiments were carried out until the condition of equilibrium bathymetry was observed, i.e. when the maximum scour depth is approximately time invariant. This time was about 4-5 hours. The bed topography in the main channel was measured at the end of each experiment.

III. RESULTS

Figure 2 shows a typical bed contour at lateral intake for clear water condition. It is clear that two scour holes form in the main channel at upstream and downstream of the lateral intake. Some of the scoured material is transported to the lateral intake and some part of the scoured material is accumulated to form a ridge at the downstream of second scour hole. The crest of this ridge is inclined to inner bank of the bend. This inclination is due to secondary flow in downstream of lateral intake.

Figure 3 shows a typical 3D view of bed topography for sill height equal to 6 cm. It is clear that the maximum depth of scour at upstream scour hole is less than the maximum depth of scour at the downstream scour hole. The inclination of crest of the ridge toward the inner bank of the bend is also shows in Figure 3.

For considering the effect of sill height on scour depth at lateral intake, the longitudinal section of bed near the outer bank of the bend is plotted in figure 4. in this figure z is the bed elevation and x is the distance from start of the bend. Figure 4 shows that by increasing the ratio of sill height (hs) to water depth in upstream channel (h), the maximum scour depth in upstream scour hole decreases while in the downstream scour holes decreases.

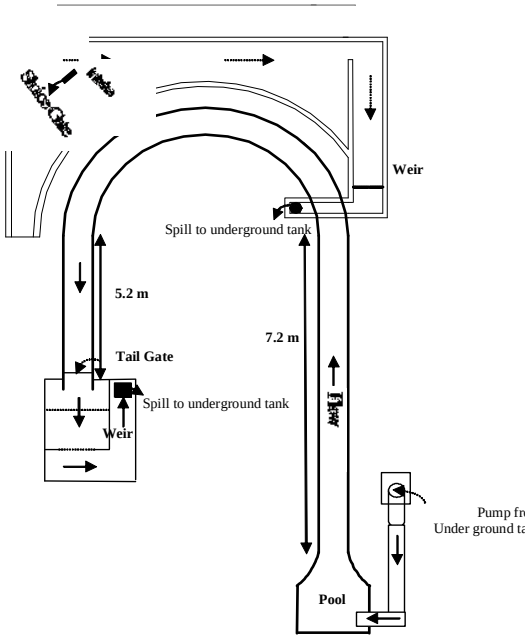

Figure1. Plane view of the flume and lateral intake.

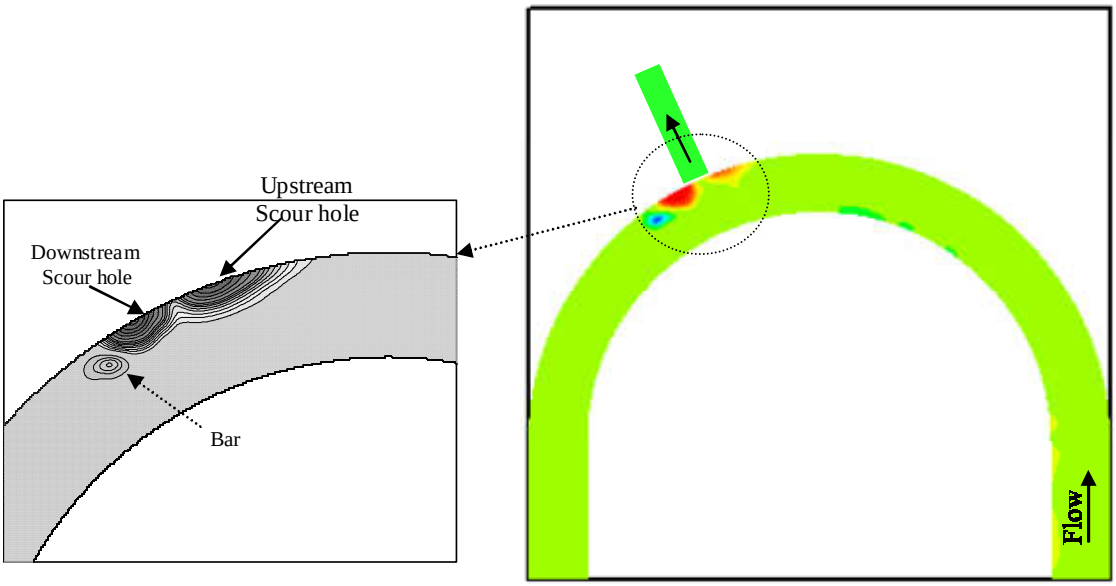

Figure2. Typical bed contour for scouring around lateral intake.

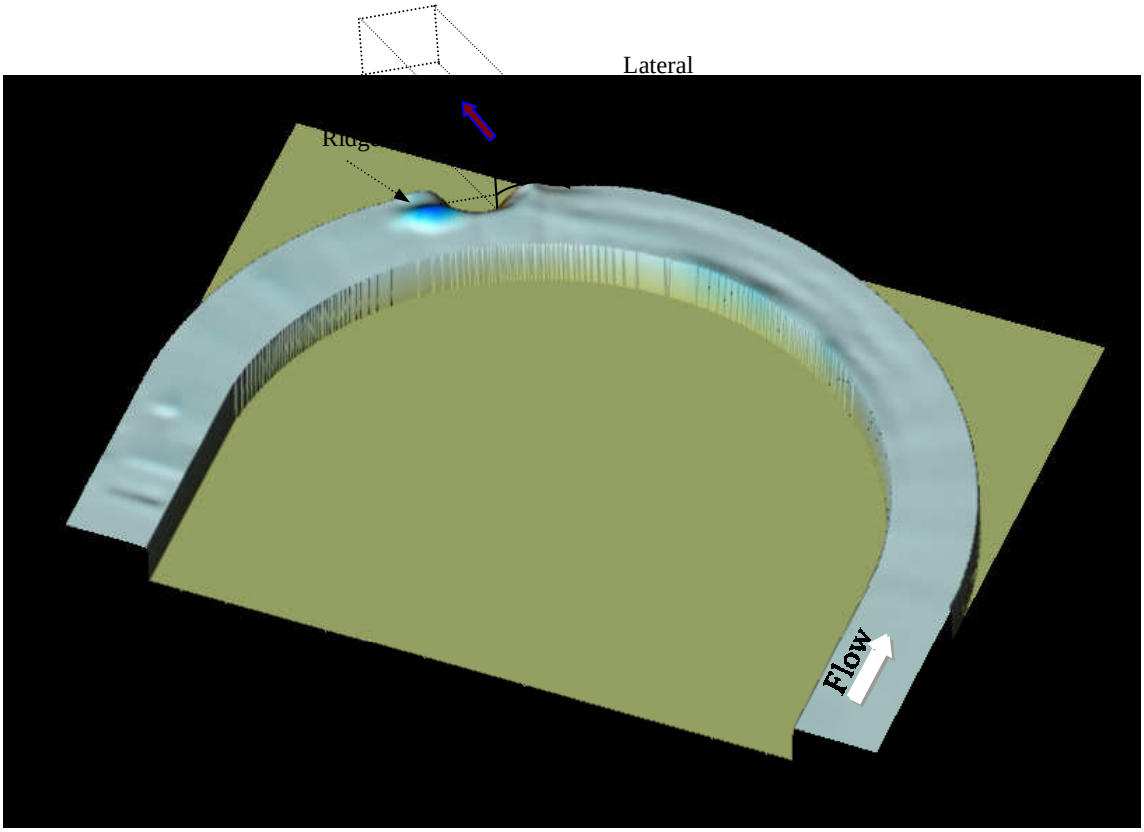

Figure3. 3D view of bed topography for scouring around lateral intake.

It is clear that the hs/h the height of ridge increase due to increase of part of the scoured material.

Figure 5 shows the variation of (ds/h) against (hs/h) for upstream scour hole, where ds is the maximum scour depth. Using the least square methods, the following equation was obtained for relative scour depth ds/h with the correlation coefficient (R^2) of 0.997.

$$ds/h = -6.1226(hs/h) + 3.555 \quad (1)$$

Figure 6 shows the variation of (ds/h) against (hs/h) for downstream scour hole.

Using the least square methods, the following equation was obtained for relative scour depth ds/h with the correlation coefficient (R^2) of 0.948.

$$ds/h = 3.701(hs/h) + 3.9132 \quad (2)$$

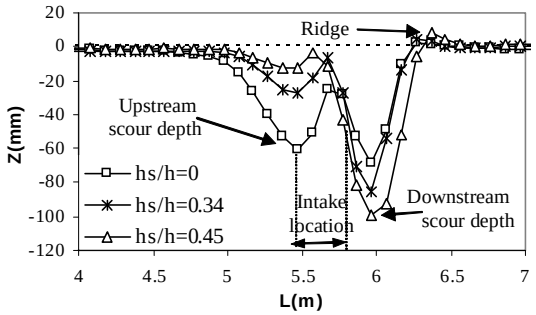

Figure4. Longitudinal section of bed near the outer bank of the bend.

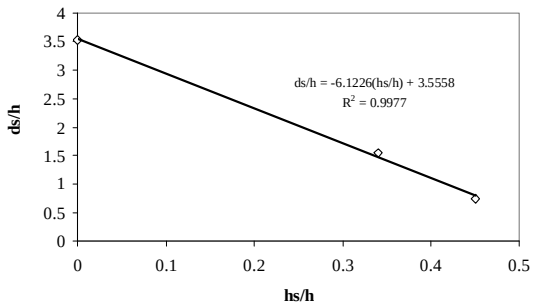

Figure5. Variation of (ds/h) against (hs/h) for upstream scour hole.

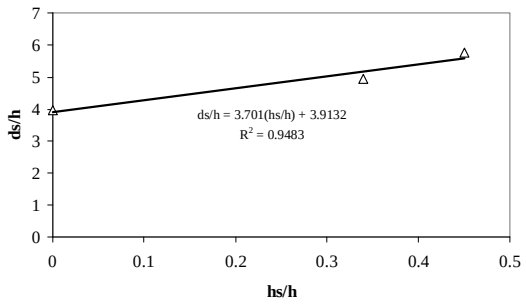

Figure6. variation of (ds/h) against (hs/h) for downstream scour hole.

IV. CONCLUSION

The following results can be obtained from this experimental study:

- Two scour holes form at the upstream and the downstream of lateral intake in clear water condition.
- A ridge is also form at the downstream of second scour hole.
- Due to secondary flow, the crest of ridge is inclined to inner bank of the bend.
- By increasing the sill height, the maximum depth of scour in upstream scour hole decreases.
- By increasing the sill height, the maximum depth of scour in downstream scour hole increases.
- New equations for maximum scour depth at lateral intake are developed.

REFERENCES

[1] P. Avery, *Sediment control at Intake; a design guide*, BHRA., The Fluid Engineering Center, England, 1989.

[2] X. Wang, R. Zhang, and X. Zhang, "Test study on hydraulic and sediment problem for diversion and intake channel," *20 th congress of IAHR*, Tokyo, Japan, pp. 439–446, 1993.

[3] A. J. Raudkivi, *Sedimentation, exclusion and Removal of Sediment from Diverted water*, Hydraulic Structure Design Manual, No.6, Balkema Publ., 1993, 161 p.

Control of Scour around Circular Piles under Waves and Current

Subhasish Dey*, B. Mutlu Sumer** and Jørgen Fredsøe**
* Indian Institute of Technology, Department of Civil Engineering, Kharagpur, India
** Technical University of Denmark, MEK, Coastal, Maritime & Structural Engineering Section (formerly ISVA), Lyngby, Denmark

I. INTRODUCTION

When a pile is embedded vertically in a sediment bed, scour takes place near the pile by the action of waves or current. Determination of the magnitude of scour is of immense practical importance from viewpoint of the safety of the foundation of marine and river structures, such as offshore platforms, subsea templates, bridges etc, as excessive scour at piles is harmful for the structures. Scour at piles under waves has been studied by Chiew [1], Sumer et al. [2, 3], and Sumer and Fredsøe [4]. Alternatively, scour at piles under steady current has been well explored [5-12]. Review of the important experiments and field studies on scour at piers or piles under waves and currents was put forward by Breusers et al. [13], Breusers and Raudkivi [14], Dey [15], Melville and Coleman [16] and Sumer and Fredsøe [17].

Efforts have been given in finding consistent ways to control scour depth at piles. For instance, armoring techniques include riprap, cable-tied blocks, tetrapods etc. placed at the pier or pile base [18]; and flow alteration techniques are adopted by sacrificial piles in front of piers [5, 19], circular collars around piers [20], submerged vanes [21] and slot through piers [22]. Importantly, the existing scour-control measures seem to be expensive.

The aim of the present study is to find out the effectiveness of the splitter-plate attached to the pile and the threaded pile (helical wires or cables wrapped spirally on the pile) for controlling scour at circular piles under waves. In addition, in steady current, the scour reduction efficiency of threaded piles was explored.

II. EXPERIMENTAL SETUP AND PROCEDURE

A. *Experiments in Wave Flume*

Experiments were conducted in a wave flume of 0.6 m wide, 0.8 m depth and 26.5 m length. The mean water depth was maintained constant at 0.40 m for all the tests with waves. Piles of diameters 4 cm and 6 cm were tested for scouring in a uniform bed sand of median diameter 0.2 mm. The critical Shields parameter θ_c for the bed sand was 0.056; and the wave experiments were run for live-bed scour condition. Two types of scour control devices studied were: (a) splitter-plate attached to the pile along the vertical plane of symmetry [Fig. 1(a)]; and (b) threaded pile (helical wires or cables wrapped spirally on the pile) [Fig. 1(b)]. Splitter-plate was 0.45 m wide attached vertically to the pile facing the flow. For threaded piles, helical wires of diameters 2 cm and 3 cm were wrapped spirally on the pile surface to form circular thread. The thread angles α for piles of diameters 4 cm and 6 cm were 65° and 60°, respectively. Only the single threaded case was tested in waves. In the experiments, programmable piston-type wave generator generated the monochromatic waves. To avoid wave breaking, care was taken so that the wave height did not exceed 40 % of the mean flow depth. A Dutch-beach type wave absorber placed at the downstream end of the flume was used to absorb the reflection of the waves. Experiments were started with leveled sediment beds, and the tests continued for a period of 30 - 45 min until the scour process generated an equilibrium scour hole. In order to have a comparative study, for each test, scour at an unprotected pile was performed simultaneously with the protected piles. A micro-propeller meter was placed 10 cm above the leveled sand bed to measure the instantaneous oscillatory flow velocity over a period of time. A miniature underwater video camera was held near the sand bed to visualize the flow and the scouring process at the pile. The bed sand acted as a tracer to visualize the flow.

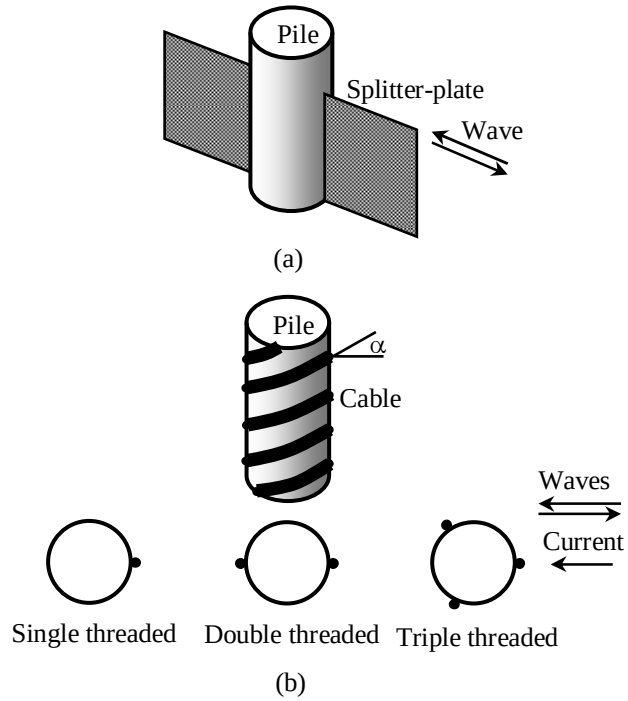

Figure 1. (a) Splitter-plate attached to the pile along the vertical plane of symmetry; and (b) threaded pile (helical wires or cables wrapped spirally on the pile to form thread)

B. Estimation of Parameters Related to Waves

Wave period T was put up in the experiments through a programmable piston-type wave generator. The maximum value of the outer oscillatory velocity U_m was detected by a micro-propeller meter. Therefore, the maximum value of undisturbed shear velocity U_{fm} is calculated by

$$U_{fm} = U_m (f/2)^{0.5} \tag{1}$$

where f is the friction coefficient. In steady currents, U_{fm} and U_m are replaced by the undisturbed shear velocity V_f and the average approaching flow velocity V, respectively. According to Fredsøe and Deigaard [23], the friction coefficient f can be given by

$$f(a/\varepsilon > 50) = 0.04(a/\varepsilon)^{-0.25} \tag{2}$$

$$f(a/\varepsilon > 50) = 0.4(a/\varepsilon)^{-0.75} \tag{3}$$

where a is the amplitude of wave; ε is the equivalent roughness height of Nikuradse, assumed as $2d_{50}$; and d_{50} is the median diameter of sand. The amplitude a can be estimated as a first approximation from

$$a = U_m T/(2\pi) \tag{4}$$

The Shields parameter θ is given by

$$\theta = U_{fm}^2/(\Delta g d_{50}) \tag{5}$$

where Δ is $s - 1$; s is the relative density of sand; and g is the gravitational acceleration. The Shields parameter θ becomes critical Shields parameter θ_c, when U_{fm} approaches critical value for the initial movement of bed sand. For scour at piles under wave, the scour depth is characterized by the Keulegan-Carpenter (KC) number [2, 3], which is defined by

$$KC = U_m T/D \tag{6}$$

where D is the pile diameter.

C. Experiments in Current Flume

The experiments were carried out in a current flume of 20 m long, 0.9 m wide and 0.7 m deep. A circular pile of 20 cm diameter was placed in a sand recess of 2.4 m long, 0.9 m wide and 0.3 m deep, which contained uniform sand (median diameter, d_{50} = 0.26 mm). The critical Shields parameter θ_c for the bed sand was 0.048. Synthetic cables of diameter 1 cm, 1.5 cm and 2 cm were wrapped spirally on the surface of the pile to form circular threads. The thread angles provided were 15° and 30°. For each combination of cable size and thread angle, single, double and triple threaded piles were tested [Fig. 1(b)]. The sand recess was located at 10 m downstream of the flume inlet. In order to maintain the same level of the sand-bed (in the sand recess), a false floor was constructed at an elevation of 0.3 m from the flume bottom through out the length of the flume. Uniform sand having same size as that used for the scouring test was glued over the false floor. A calibrated V-notch weir, fitted at the inlet of the flume, was used to measure the flow discharge. In the flume, the flow depth was controlled by a tailgate. During the experiments, the approaching flow depth was kept constant as 0.30 m; and the average approaching flow velocity V was set as 0.262 m/s, which satisfied a clear-water scour condition for which $V = 0.9V_c$; where V_c = critical average velocity for sand particles (= 0.291 m/s, for d_{50} = 0.26 mm). Unlike the wave case, the maximum scour depth, in steady current, is obtained under clear-water condition, when $V \rightarrow V_c$. As, in the experiment, it was difficult to maintain undisturbed upstream bed for $V = V_c$, the tests were conducted for $V = 0.9V_c$. The experiments were run under a clear-water scour condition for a period of 48 h when an equilibrium state of scour reached. For unprotected pile (without thread), equilibrium scour depth S measured was 9.5 cm.

The instantaneous 3D velocity components were detected by a SonTek made 5 cm downlooking acoustic Doppler velocimeter (ADV). The ADV functioned on a pulse-to-pulse coherent Doppler shift to provide instantaneous 3D velocity components at a rate of 50 Hz. Output data from ADV was filtered using spike removal algorithm. The ADV readings were taken along the upstream plane of symmetry of the pile to recognize the effect of the spirally wrapped cables around the piles on the vortex flow field.

III. Results and Discussions

A. Scour under Wave

The main parameter to govern the equilibrium scour depth at a pile under waves is the KC number [2]. For $6 < KC < 100$, the vortex shedding is the principal mechanism of scour process [2, 3]. The mechanism of scour under waves is based on the vortex shedding that each shed vortex sweeps the sediment as if it were a tornado carrying sediment particles into its core to deposit them away from the pile, while it is convected downstream. As a result of which, a net scour around the pile is formed in each half period. Sumer et al. [3] reported that no vortex shedding takes place, when $KC < 6$ for circular piles. Therefore, for $KC \geq 6$, scour occurs near the pile and attains an equilibrium stage through a transition period being approximately 30 - 45 min. The scour depth that corresponds to this stage is termed equilibrium scour depth S. The underwater video photographs reveal that the equilibrium scour depth in live-bed scour slightly fluctuates (about 5 %) over a period of time due continuous change of bed morphology, particularly at small and moderate values of θ_c.

Unlike for steady current, the horseshoe vortex does not exist when $KC < 6$ [24]. For $KC \geq 6$, the horseshoe vortex starts to develop gradually due to the separation of approaching flow under the action of the adverse pressure gradient induced by the pile. However, for small values of KC (= 6 to 30), the effect of the horseshoe vortex on scour is insignificant, as its strength and life period is very small [24]. With an increase in KC number, the scour process is gradually influenced by the extended life period of the horseshoe vortex, which eventually

becomes dominate mechanism of scour process for $KC >$ 100 [2]. Sumer et al. [2] gave the following empirical equation of scour depth at circular piles under waves:

$$S(KC \geq 6) = 1.3D\{1 - \exp[-0.03(KC - 6)]\} \qquad (7)$$

The idea here is to change the local flow and to interrupt the vortex shedding so that the development of the scour depth at piles under waves is controlled. To do this, splitter-plates were attached to the pile along the vertical plane of symmetry [Fig. 1(a)], and the threaded pile [Fig. 1(b)] were used. The splitter-plate helped to divide the flow by the two sides of the pile. Thus, the process of alternate vortex shedding was interrupted, as they were separated by the splitter-plate. On the other hand, in case of threaded piles, the projection of the helical wires that formed the threads disrupts the vortex shedding [25]. However, the use of larger thread angles α (= 60° and 65°) that can encounter well with the wave motion as the line of flow separation on the pile surface is almost vertical, were observed to be efficient in interrupting vortex shedding. Figs. 2(a-c) display the video photographs of different stages of vortex formations at unprotected pile, pile with splitter-plate and threaded pile. Fig. 2(a) presents (from left to right) the stages of the formation of well-defined vortex before shedding from the unprotected pile. A strong swirl is formed to carry the bed sand into its core. Fig. 2(b) shows the formation of a vortex, which is initially well-defined, but unable to shed in presence of the splitter-plate and finally breaks down. In Fig. 2(c), the vortex is unable to grow to its full form due to the helical wires. Finally, a diffused vortex, which has little sand carrying capacity, is observed.

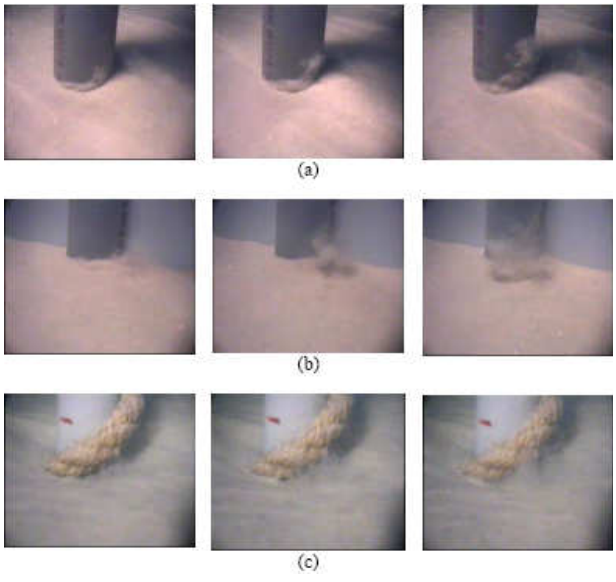

Figure 2. Video photographs of different stages of vortex formation: (a) unprotected pile, where vortex is well-defined before shedding; (b) pile with splitter-plate, where vortex grows initially and finally breaks down; and (b) threaded pile, where vortex is unable to grow in its full form and finally diffuses

The experiments were performed for the range of Shields parameter θ = 0.14 - 0.191 and KC = 8.3 - 33.8. Sumer et al. [2] reported that the horseshoe vortex, being the sole mechanism of scour process for $KC >$ 100, acts along with vortex shedding to form scour hole for 30 < KC < 100. The average reduction of scour depth by the splitter-plate was 61.6 %. For threaded piles, different combinations of cable and pile sizes were tested, and the most efficient combination was found for cable-pile diameter ratio of 0.75, in which average scour depth reduction was observed as 51.1 %. The average reductions of scour depths for other cable-pile diameter ratios b/D = 0.33 and 0.5 were obtained as 43.2 and 48.1 %, respectively. Fig. 3 shows the nondimensional scour depth S/D as a function of KC number for unprotected and protected piles. The experimental results of unprotected piles and the curve of Sumer et al. [2] collapse. Here, the reduction of scour depth for protected piles is obvious; as the data plots for protected piles are quite below the curve of Sumer et al. [2].

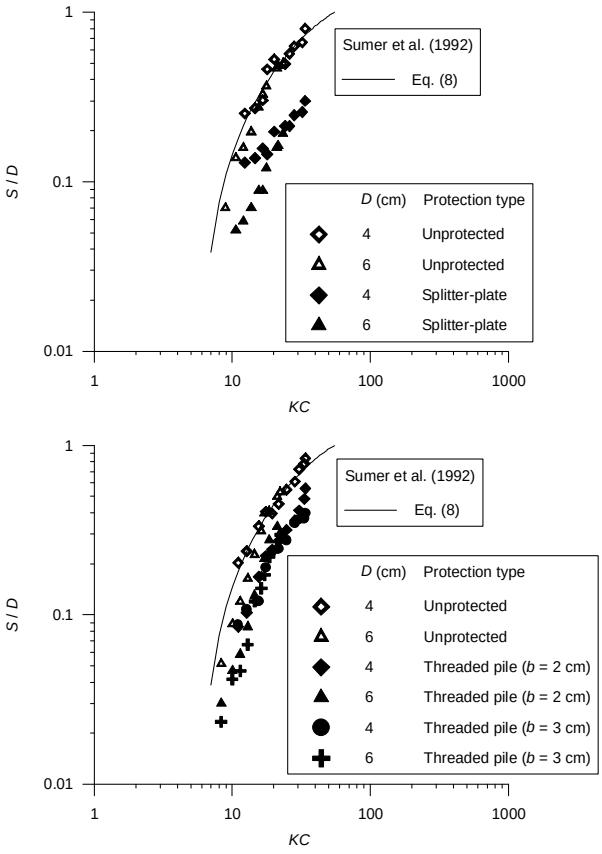

Figure 3. Nondimensional scour depth S/D as a function of KC number for unprotected and protected piles under waves

B. Scour under Current

Melville [26] and Dey et al. [10] studied the flow field around a pile. The main component features of the flow field are the downflow, horseshoe vortex and wake vortices. The approaching flow becomes stagnant at the upstream face of the pile. Since the approaching flow has maximum magnitude at the free surface and decreases to zero at the bed, the stagnation pressure decreases in the downward direction causing the flow to be driven down along the upstream face of the pile. To be more explicit, the boundary layer at the pile upstream overcomes a strong adverse pressure gradient set up by the pile, separating the approaching flow and forming the horseshoe vortex. The downflow and horseshoe vortex

dislodge the bed sand at the pier. Once the scour hole is developed, the flow separates from the upstream edge of the scour hole. The horseshoe vortex, thus formed, migrates downstream by the sides of the pile for a couple of pile-diameters before losing its existence becoming a part of general flow. The stagnation pressure also accelerates the flow by the sides of the pile, resulting in a separation of flow at the sides and creating of wake vortices at the interfaces to the main flow. The wake vortices, which act as a vacuum cleaner to dislodge the bed sand, travel downstream with the flow.

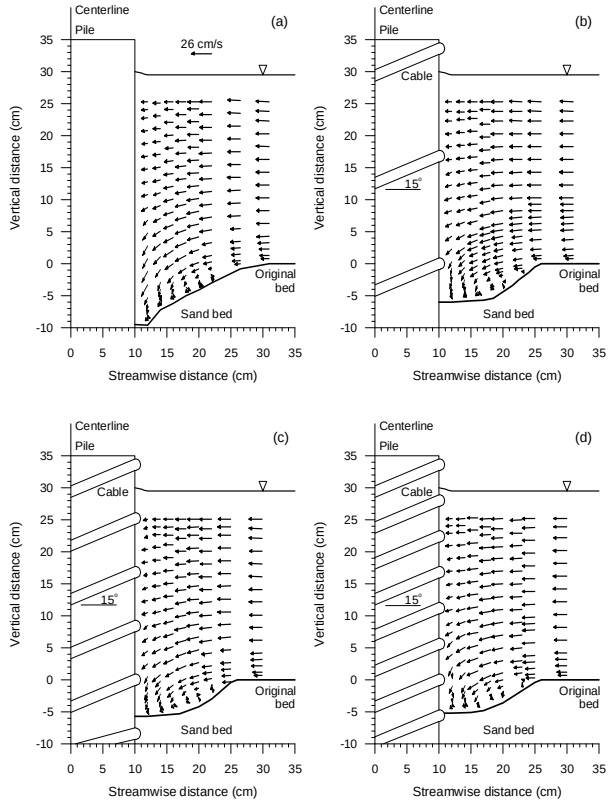

Figure 4. Vortex flow fields at the upstream plane of symmetry of the piles: (a) unprotected pile; (b) single threaded pile; (c) double threaded pile; and (d) triple threaded pile

For aforementioned reasons, one possible way of controlling scour depth is to weaken and possibly interrupt the formation of the downflow and horseshoe vortex being achieved by using three types of threaded piles (single, double and triple threaded piles) which were tested [Fig. 1(b)] under clear-water scour condition for $V/V_c = 0.9$. In steady current, relatively less thread angles α (= 15° and 30°) that can encounter with the downflow and horseshoe vortex at the upstream face of the pile, were provided. In order to recognize the influence of threaded piles on the vortex flow field, the flow field in equilibrium stage of scour was measured by the ADV. The vector plots of the flow fields at the upstream plane of symmetry of the piles are shown in Figs. 4(a-d). The downflow and the horseshoe vortex are significant for the unprotected pile [Fig. 4(a)]. The groove at the upstream base of the pile forms by the action of the strong downflow. It is evident from Figs. 4(b-d) that there is a consistent decrease in magnitude downflow with an increase in number of threads formed by wrapping cables on the piles. A close observation of the flow field reveals that the cable not only reduces the magnitude of downflow, but also deflects the horseshoe vortex further upstream, resulting in a relatively flat base of the scour hole without any groove. Therefore, the scour depth reduces to a great extent.

The outcome of these tests was to identify the importance of various geometrical parameters towards reduction of scour depth. The maximum reduction of scour depth obtained was 46.3 % by using a triple threaded pile having thread angle of 15° and cable diameter $b = 0.1D$. Fig. 5 shows the dependency of nondimensional scour depth (ratio of scour depth at protected pile to scour depth at unprotected pile) on cable-pile diameter ratio b/D for different threaded piles and thread angles. The scour depth consistently decreases with an increasing in cable diameter and number of threads. The reduction of scour depth by a triple threaded pile is very effective. Moreover, the thread angle of a cable wrapped on the pile has a significant role towards reduction of scour depth. A relatively less thread angle (it is 15° in this study) is found to be more efficient than a greater thread angle (it is 30° in this study), as the cable can encounter well with the downflow and horseshoe vortex to weaken them at relatively less thread angle. However, further reduction of thread angle or increase of cable diameter with respect to pile diameter is not a practicable.

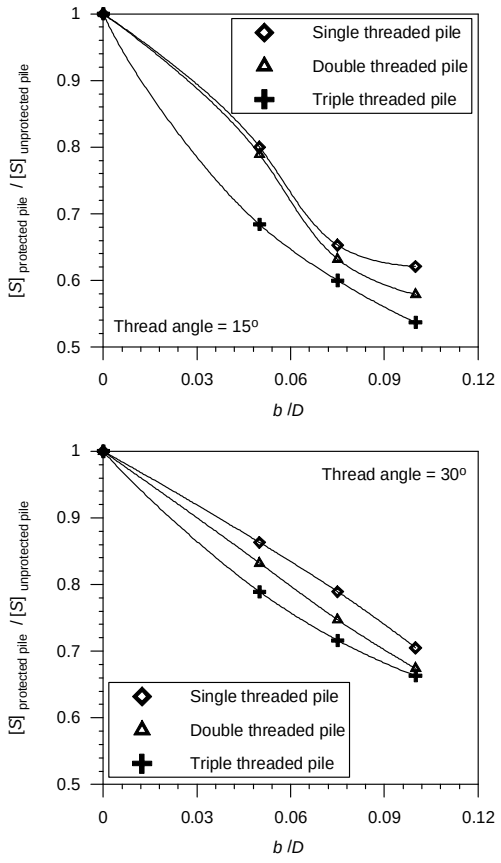

Figure 5. Dependency of nondimensional scour depth (ratio of scour depth at protected pile to scour depth at unprotected pile) on cable-pile diameter ratio b/D for different threaded piles and thread angles under steady current

IV. CONCLUSIONS

Methods for reduction of scour depth at vertical circular piles under monochromatic waves and steady current have been proposed. For scour under waves, splitter-plate attached to the pile along the vertical plane of symmetry and threaded pile were useful to reduce the scour depth at piles. For $6 < KC < 100$, the vortex shedding is the primary mechanism of scour under waves. The average reduction of scour depth by splitter-plate was obtained as 61.6 %. For threaded piles, various cable-pile diameter ratios were tested and the most efficient cable-pile diameter ratio was observed as 0.75, which decreased scour depth by an average 51.1 %. The average reductions of scour depths for other cable-pile diameter ratios of 0.33 and 0.5 were 43.2 and 48.1 %, respectively. The splitter-plate separates the flow by the two sides of the pile and interrupts the vortex shedding from its natural frequency, while for threaded piles, the helical wires that form the threads disturbs the vortex shedding. On the other hand, in steady current, threaded pile found to be a useful means to reduce scour depth at piles to a sizeable extent. Cables wrapped spirally on the pile help to weaken the strengths of the downflow and horseshoe vortex. The experimental results revealed that the scour depth decreases with an increase in cable diameter and number of threads, and with a decrease in thread angle. In this study, the maximum reduction of scour depth obtained was 46.3 % by using a triple threaded pile having thread angle of 15° and cable-pile diameter ratio of 0.1. These methods to control scour are easy to implement and inexpensive.

REFERENCES

[1] Y. M. Chiew, "Local scour at vertical piles under wave action," *Proc. 9th Australian Conf. on Coast. and Ocean Eng.*, Adelaide, Australia, 1989, pp. 393-396.

[2] B. M. Sumer, J. Fredsøe and N. Christiansen, "Scour around vertical pile in waves," *J. Waterw., Port, Coastal, Ocean Eng.*, vol. 118, pp. 15-31, January/February 1992.

[3] B. M. Sumer, N. Christiansen and J. Fredsøe, "Influence of cross section on wave scour around piles," *J. Waterw., Port, Coastal, Ocean Eng.*, vol. 119, pp. 477-495, September/October 1993.

[4] B. M. Sumer and J. Fredsøe, "Wave scour around a large vertical circular cylinder," *J. Waterw., Port, Coastal, Ocean Eng.*, vol. 127, pp. 125-134., May/June 2001.

[5] J. Chabert and P. Engeldinger, "Etude des affouillements autour des piles de ponts," Laboratoire National d'Hydraulique, Chatou, France, 1956.

[6] A. J. Raudkivi and R. Ettema, "Clear-water scour at cylindrical piers," *J. Hydraul. Eng*., vol. 109, pp. 338-350, March 1983.

[7] B. W. Melville, "Live-bed scour at bridge piers," *J. Hydraul. Eng*., vol. 110, pp. 1234-1247, September 1984.

[8] A. J. Raudkivi, "Functional trends of scour at bridge piers," *J. Hydraul. Eng*., vol. 112, pp. 1-13, January 1986.

[9] B. W. Melville and A. J. Sutherland, "Design method for local scour at bridge piers," *J. Hydraul. Eng*., vol. 114, pp. 1210-1226, October 1988.

[10] S. Dey, S. K. Bose and G. L. N. Sastry, "Clear water scour at circular piers: a model," *J. Hydraul. Eng*., vol. 121, pp. 869-876, December 1995.

[11] S. Dey, "Time variation of scour in the vicinity of circular piers," *Proc. Inst. Civ. Eng., Water, Maritime Energ*., vol. 136, pp. 67-75, June 1999.

[12] B. W. Melville and Y. M. Chiew, "Time scale for local scour at bridge piers," *J. Hydraul. Eng*., vol. 125, pp. 59-65, January 1999.

[13] H. N. C. Breusers, G. Nicollet and H. W. Shen, "Local scour around cylindrical piers," *J. Hydraul. Res.*, vol. 15, pp. 211-252, June 1977.

[14] H. N. C. Breusers and A. J. Raudkivi, *Scouring*. IAHR Hydraulic Structures Design Manual, vol. 2, A. A. Balkema, Rotterdam, The Netherlands, 1991.

[15] S. Dey, "Local scour at piers, part I: a review of development of research," *Int. J. Sediment Res*., vol. 12, pp. 23-44, June 1997.

[16] B. W. Melville and S. E. Coleman, *Bridge scour*, Water Resources Publications, Fort Collins, Colorado, 2000.

[17] B. M. Sumer and J. Fredsøe, *The mechanics of scour in the marine environment*, World Scientific, Singapore, 2002.

[18] P. F. Lagasse, L. W. Zevenbergen, J. D. Schall and P. E. Clopper, "Bridge scour and stream instability countermeasures," *HEC23 FHWA NHI 01-003*, Federal Highway Administration, US Department of Transportation, Washington, DC, 2001.

[19] B. W. Melville and A. C. Hadfield, "Use of sacrificial piles as pier scour countermeasures." *J. Hydraul. Eng*., vol. 125, pp. 1221-1224, November 1999.

[20] Z. Thomas, "An interesting hydraulic effect occurring at local scour," *Proc. 12th Cong. of IAHR*, Fort Collins, vol. 3, pp. 125-134, 1967.

[21] A. J. Odgaard and Y. Wang, "Scour prevention at bridge piers," *Proc. Nat. Conf. on Hydraul. Eng*., Virginia, pp. 523-527, 1987.

[22] Y. M. Chiew, "Scour protection at bridge piers," *J. Hydraul. Eng*., vol. 118, pp. 1260-1269, September 1992.

[23] J. Fredsøe and R. Deigaard *Mechanics of coastal sediment transport*, World Scientific, Singapore, 1992.

[24] B. M. Sumer, N. Christiansen and J. Fredsøe, "Horseshoe vortex and vortex shedding around a vertical wall-mounted cylinder exposed to waves," *J. Fluid Mech*., vol. 332, pp. 41-70, 1997.

[25] B. M. Sumer and J. Fredsøe, *Hydrodynamics around cylindrical structures*. World Scientific, River Edge, NJ, 1997.

[26] B. W. Melville, "Scour at bridge sites." *Rep. No. 117*, School of Engineering, University of Auckland, Auckland, New Zealand, 1975.

Scour Protection around Bridge Piers Using Tetrahedron Frames

B. Ding*, Y. M. Chiew**and H. W. Tang*

*College of Water Conservancy and Hydropower Engineering, Hohai University, Nanjing, China

**School of CEE, Nanyang Technological University, Singapore

ABSTRACT

Armoring countermeasure such as riprap stones has been extensively used as a means to protect bridge piers against scour. In this study, an innovative armoring device in the form of tetrahedron frames is tested for its effectiveness as a pier-scour countermeasure. Although the device has previously been used as a protection method against bank and beach erosion, it has not been tested as a pier-scour countermeasure. This study aims to investigate the mechanism of using tetrahedron frames as a pier-scour countermeasure, and to explore its effectiveness. Experimental data show that the frame can effectively protect the foundation of bridge piers against scour. The equilibrium scour depth first increases almost linearly with velocity, then decreases at velocities just above the threshold for bed sediment entrainment until a minimum is reached at about 1.1 times the threshold velocity. The presence of the frames significantly dissipates the energy associated with the downflow and horseshoes vortex. Two-dimensional tests without bridge piers were also conducted and the results show that edge failure, which often occurs at the interface of a riprap stone layer and the finer bed material, does not occur at the periphery of the tetrahedron-frame layer. This observation is confirmed by 3D-tests conducted with a bridge pier.

I. INTRODUCTION

The formation of scour holes around bridge piers is common in rivers and canals. Bridge damages at a river crossing often can be attributed to scouring at its foundations [1]. The protection of the foundation of bridge piers is important since there is an important relationship between bridge failure and scour at bridge foundations.

There are many armoring devices such as riprap, cabled-tied blocks, Reno mattresses, gabion mattresses, concrete-filled mats and bags, concrete apron, dolos, tetrapods, etc. Despite using riprap, which is the most commonly used countermeasure to protect pier foundation against scour, failures still occur. Based on published studies [1~3], there are five failure mechanisms associated with riprap protection: shear failure, winnowing failure, edge failure, bedform-induced failure and bed-degradation induced failure. Each of these failure mechanisms plays a role in causing the eventual demise of the riprap layer.

As a new scour countermeasure, tetrahedron frames was first used to protect riverbank against erosion. It can change a scouring state to a deposition state near dikes or river bank slopes through a change in the velocity distribution resulting in a reduction in local velocity [4]. Knowledge on how a tetrahedron frame affects bridge pier scour is very limited. A thorough understanding of the mechanism of tetrahedron frame protection around bridge piers is necessary before engineers can adopt this method as a pier-scour protection device. The aim of the study is to investigate the mechanism associated with using tetrahedron frames as a pier-scour countermeasure, and to explore its effectiveness.

II. EXPERIMENTS SETUP AND PROCEDURE

Cohesionless uniform bed material with a median particle size of 0.40 mm and a specific gravity, S_s, of 2.65 was used in this study. The geometric standard deviation of the bed material was 1.35. Figure 1 shows the particle size distribution of the sediment.

The specific gravity of the tetrahedron frame was 2.45, and the cross-section of rods making up the frame is 1.7 mm × 1.7 mm with a length = 17 mm. Figure 2 shows the sketch of a single tetrahedron frame and the photograph of two tetrahedron frames stacked on top of each other.

The Shields diagram was used to calculate the critical shear velocity, $u_{*c,}$ of the bed sediment, which is 0.01486 m/s. The corresponding critical mean flow velocity, U_c, was determined using (1), which is similar to the formula given in Chiew [2]

$$\frac{U_c}{u_{*c}} = 5.75\log(\frac{y_0}{1.3d_{50}}) + 6 \qquad (1)$$

Two adjustable flumes with dimensions = 6 m length, 0.176 m width and 0.2 m depth (Flume1) and 16 m length, 0.6 m width and 0.6 m depth, (Flume2), respectively, were used in this study. Flume 1 has a feed system while Flume 2 is a sediment- recirculating type flume. For both flumes, water stored in a downstream water tank was recycled using a centrifugal pump, through a PVC pipe into the stilling basin at the upstream end of the flumes. A settling tank at the downstream end of Flume 2 collects the sediment into a steep-sided hopper over the sediment recirculation pump intake. A separate constant speed pump is used to recirculate the sediment, which is collected before the water reaches the water tank. An adjustable weir is located at the downstream end of the settling tank; it acts as a water level controller and prevents sediment particles from entering the main pump intake. The flow rate was monitored using an electromagnetic flow meter, and regulated using the combination of a butterfly valve and a speed inverter.

In Flume 2, there is a 1-m-long recess in which sediment was placed to reduce the amount of bed sediment needed for the test. A cylindrical pier, which was made from a 70-mm-diameter clear Perspex tube, was located at the centre of sediment recess. A bed, consisting of 7-cm thick sediment that has the same property as the sediment particles in the recess，was placed along the bed of the flume,

Figure 3 shows how the Tetrahedron frames were placed around the pier. The extent of a tetrahedron frame layer was defined by its cover, *C*, which is the border length of the square. The placement cover, *C/D*, used in this study is 5.

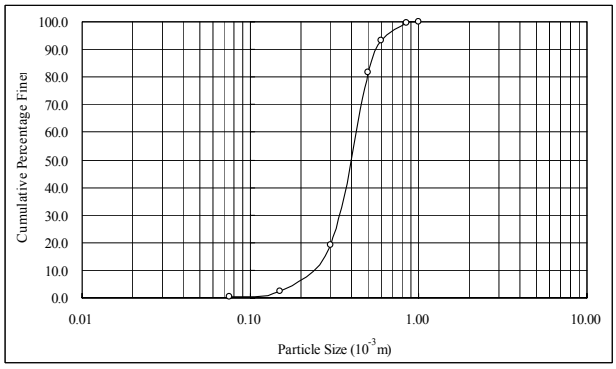

Figure 1. Particle size distribution of sediment

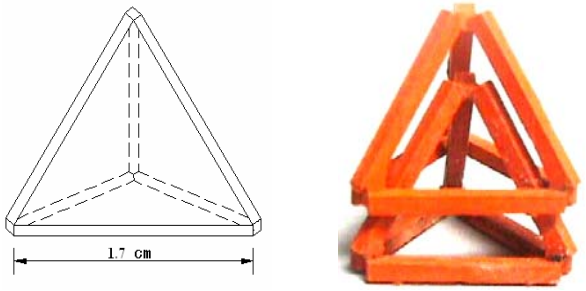

Figure 2. Sketch of tetrahedron frames

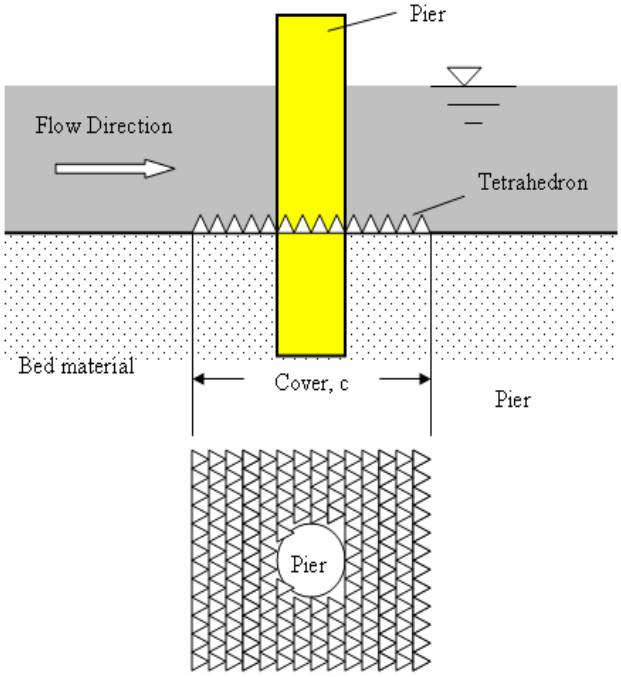

Figure 3. Definition sketch of placement of frames

Before starting the experiments, the bed sediments were well compacted to prevent any presence of air voids which will cause settlement when water was introduced. The next step in the procedure was to level the sediment bed before the tetrahedron frames were carefully placed around the pier. After preparation of the tetrahedron frame layer, the flume was slowly filled with water in order to avoid any undesirable disturbance on the sediment bed. Once the desired flow depth was reached, the flow was slowly increased to its predetermined rate. The stability of the tetrahedron frame layer was observed and development of the scour hole monitored. Two types of tests were conducted. The first was a 2-dimensional test (without pier) conducted in Flume 1. The undisturbed approach flow depth was set at 50 mm. The objective of the tests was to examine whether edge failure will occur with the tetrahedron frame protection. A clear-water condition was used in the test because the flume did not allow for sediment recirculation. The second test was conducted in Flume 2 with a pier surrounded by tetrahedron frames, similar to that shown in Fig. 3. The undisturbed approach flow depth was set at 250 mm. The test aimed to investigate the mechanisms associated with using tetrahedron frames as a pier-scour countermeasure, and to explore its effectiveness. The scour depths were measured using a periscope. The near equilibrium criteria used was that proposed by Melville and Chiew [5], i.e., that the tests were stopped when the change in scour depth did not exceed 0.05*D* (5% of the pier diameter) during a 24-hour period.

III. Bed Erosion with Tetrahedron Frame Protection without Pier

Earlier studies have shown that riprap protection is subjected to a number of failure mechanisms that can destabilize the stones and lead to a complete disintegration of the protective armor. The failure mechanisms under clear-water conditions are shear failure, winnowing failure and edge failure. It is expected that shear failure will also occur with tetrahedron frames when the shear velocity exceeds the critical shear velocity for the entrainment of tetrahedron frames.

Edge failure, as documented in Chiew [2], occurs at the periphery of the coarse riprap stones and fine bed sediment interface. He attributed it to the high shear stress experienced by the finer sediment particles as water flow from the coarse to the fine bed boundary. The downstream finer sediment particles are entrained by the flow because of their lower critical shear stress. When this happens, a local depression, which exposes the larger riprap stones, will form. The stones at the edge will roll or slide into the depression. Chiew stated that such erosion takes place at low velocity ratio where shear and winnowing erosion are normally absent, and constitutes the first sign of failure of the riprap layer. Edge failure hastens the eventual demise of the riprap layer as it enhances either winnowing or shear failure. The former leads to embedment while the latter enhances disintegration of the riprap layer.

A series of tests were conducted without a bridge pier in Flume 1 to eliminate the complex 3D flow field associated with bridge pier scour. Its aim was to examine whether winnowing failure and edge failure will occur with tetrahedron frames protection. Figure 4 shows the layout of the tetrahedron frame layer, which spans the full width of the flume during the test. The purpose of such a layout is to exclude sidewall effects and to ensure a 2D failure behavior. For the tests, the sediment used was 0.4 mm, the approach flow depth = 50 mm and the velocity ratio < 1. The length of the tetrahedron frame layer along the flow direction is 400 mm. It may be inferred from the velocity ratios used in the study that any movement of the sediment is not directly due to the flow velocity.

Observations showed that sediment was scoured at the upstream section of the tetrahedron frame layer and then settled further downstream (see Fig. 5). Tang et al. [4] showed that when flow passes through the frames, different types of vortices are generated and turbulent intensity increase around the rods of the frames due to disturbances induced by the rods. All these cause the scour to form at the upstream section of the tetrahedron frames. The velocity behind a single frame is re-distributed and velocity near the bottom is reduced, causing sediment deposition. The pattern of sediment erosion and deposition observed in this study supports the description by Tang et al. [4].

Scour also occurs at the location downstream of the tetrahedron frame layer. The flow velocity at this location can be sub-divided into two parts: vertical velocity, V_0, which is sensitive to the scour depth and horizontal velocity, U_0, which is sensitive to the position of the scour hole (see Fig. 6). The maximum scour depth, d_{se2}, downstream of the tetrahedron frames layer is highly sensitive to U/U_c. Figure 7 shows that the maximum scour depth increases almost linearly with velocity ratios under clear-water conditions. Obviously, the larger the velocity, the larger the momentum of the flow impinging on the bed is. Figure 8 shows that the position at which the maximum scour depth is located is also related to the velocity ratio.

During the tests, troughs (see Fig. 4) were observed to form downstream of the tetrahedron frames. When water flows over the tetrahedron layer, a large portion of it passes through the tetrahedron frames before impinging onto the bed downstream, thereby causing erosion. A smaller portion impinges on the rods of the tetrahedron frame causing vortex formation within the frame. The former causes sediment erosion resulting in the formation of the trough. The latter, however, causes a reduction of velocity; this resulted in no-erosion in certain locations downstream of the tetrahedron frame layer, as is shown in Fig. 4.

In summary, a tetrahedron frame layer can avoid edge failure for the following reasons:

1. When the water flows through the tetrahedron frames, the velocity can be significantly reduced; and
2. Due to the disturbance induced by the rods, different types of vortices are generated and the velocity is re-distributed. The flat portion and trough that form downstream of the tetrahedron frame layer is an indication of the velocity distribution.

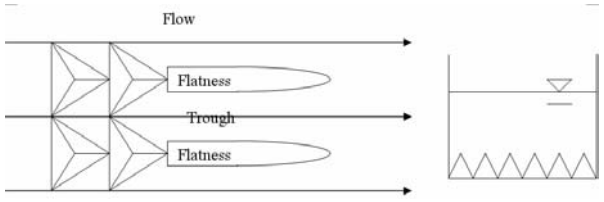

Figure 4. Sketch of trough downstream of frames

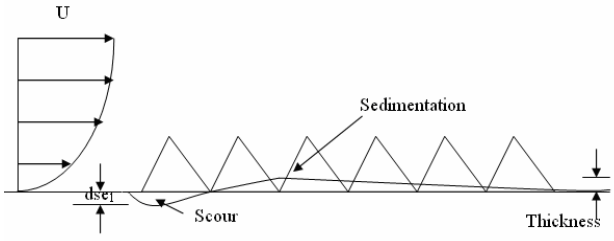

Figure 5. Sketch of the scour and sedimentation within frame layer

Figure 6. Sketch of the flatness and scour hole formed downstream of the tetrahedron frame layer

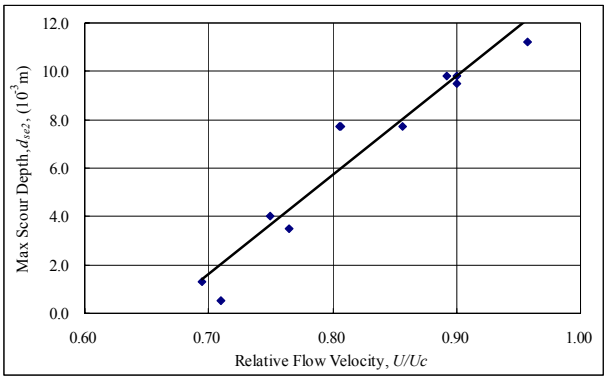

Figure 7. Maximum scour depths (d_{se2}) downstream of tetrahedron layer as a function of flow velocity ratio

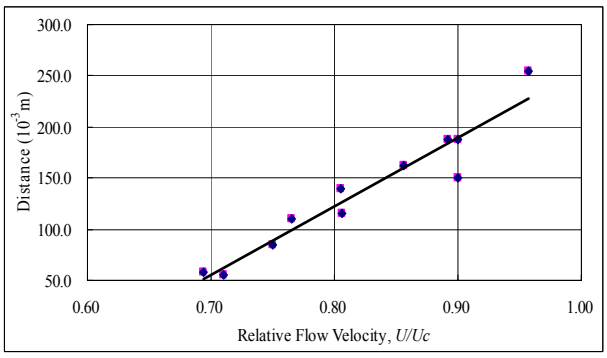

Figure 8. The distance between maximum scour position and end of tetrahedron frame layer as a function of flow velocity ratio

IV. SCOUR AT BRIDGE PIERS WITH TETRAHEDRON FRAME PROTECTION

During the test, the number of tetrahedron frame layers was 1 and 2 (see Fig. 2). The undisturbed approach flow depth = 250mm, with pier diameter D and median sediment size d_{50} = 70 mm and 0.4 mm, respectively. Based on previous studies on local scour at bridge piers [6-7], the equilibrium scour depth becomes independent on the depth of flow relative to pier-width, y_0/D, and the pier width relative to sediment median size, D/d_{50}, when they are larger than 3 and 50, respectively. This effect can also be applied to the present study. Since the flow shallowness and sediment coarseness are negligible, the present study aims to investigate the relationship between equilibrium scour depth and the flow intensity.

Under live-bed conditions, the maximum pier-scour depth occurs when the trough of a bed feature is at the pier. At this juncture, the scour depth includes not only scour due to the pier but also that due to bed form. As a result, it is more pertinent to present scour depth as a temporal rather than the absolute value. To this end, the temporal mean scour depth is obtained from

$$d_{av} = \frac{\sum_{i=1}^{N} d_{si}}{N} \tag{2}$$

where N= 100, measured at intervals of 1 minutes.

Scour depth and width

Early experimental studies on scour around a cylindrical bridge pier have shown that the relative equilibrium scour depth is highly sensitive to the undisturbed approach mean flow velocity, U. Tests were conducted in this study to examine the effect of U/U_c on the formation of the equilibrium scour depth around a bridge pier with the protection of tetrahedron frame layer. Table 1 contains the experimental results obtained in this study. Figure 9 shows how U/U_c affects the relative equilibrium scour depth, d_{av}/D. The experimental data show that d_{av}/D increases almost linearly with the velocity ratio under clear-water conditions. The maximum dimensionless equilibrium scour depth approximately occurs when the relative flow velocity is unity, which corresponds to the critical condition for bed material entrainment.

In live-bed scour, the data show decreasing sour depth until a local minimum is reached, after which the scour depth increase again. This trend is similar to that of local scour at bridge piers without countermeasures [6-7].

The shape of d_{av}/D versus U/U_c curve is related to the bed features translating past the scour hole. When the approach velocity exceeds the critical velocity of the bed sediment, general sediment movement begins and causes a new equilibrium between scour hole development and sediment supply from upstream. For this reason, the shape of d_{av}/D versus U/U_c curve is no longer linear under live-bed conditions. Due to the complement of sediment from upstream, the scour depth decreases after the approach velocity exceeds critical velocity until a local minimum is reached. When the relative flow velocity increases further, the scour depth increases from the minimum depth to larger depths. The data of one tetrahedron frame layer show that the scour depth increasing quickly when the relative flow velocity is larger than 1.3. Actually some of the tetrahedron frames were washed away because their critical velocity was exceeded. When the relative flow velocity reached 1.5, the tetrahedron frame layer was almost totally destroyed due to shear failure such that the scour depth is almost equal to that without any countermeasure. A curve following the trend of the data if the frames were intact is superimposed with a broken line in Fig. 9; this shows the possible trend of the scour depth when the velocity is larger than 1.3. More studies are needed to substantiate this hypothesis.

Figure 10 shows the effect of velocity ratio on the relative equilibrium scour width, L/D, where L is the distance between the nose of the pier and the un-scoured point along the flow direction. The curve has a similar trend as that of scour depth under clear-water condition.

Effect of tetrahedron frame protection

The data of the present study, along with those collected by Chiew [6] and Ettema [8] are plotted in Figs. 9 and 10. The data of Chiew and Ettema were used because their tests were conducted with tests conducted using median grain size = 0.24 and 0.38 mm, respectively; $y_0/D \geq 3$ and $D/d_{50} \geq 50$. Tests conducted in this study have the same general condition.

TABLE 1. SUMMARY OF EXPERIMENTAL RESULTS IN FLUME 2

Test Number	Layer Number	U (m/s)	U/U_c	u_*/u_{*c}	Time (hour)	d_{se} (mm)	d_{se}/D	L/D
A1	0	0.189	0.593		56	52	0.743	1.143
A2	0	0.259	0.815		50	117	1.671	2.571
B1	1	0.275	0.866	1.001	42	59	0.843	1.193
B2	1	0.223	0.702	0.759	71	48.5	0.693	1.043
B3	1	0.166	0.522	0.518	24	9	0.129	0.129
B4	1	0.187	0.588	0.547	46	22	0.314	0.571
B5	1	0.192	0.603	0.601	48	25.5	0.364	0.643
B6	1	0.250	0.787	0.897	63	59.5	0.850	1.143
B7	1	0.237	0.746	0.833	70	51	0.729	1.029
B8	1	0.207	0.651	0.654	94	40	0.571	0.786
C1	2	0.248	0.780	0.881	114	46	0.657	0.929
C2	2	0.167	0.524	0.527	40	8.5	0.121	0.286
C3	2	0.185	0.581	0.578	15	11	0.157	0.314
C4	2	0.209	0.656	0.643	31.5	25	0.357	0.517
C5	2	0.226	0.711	0.777	30	34.5	0.493	0.729
C6	2	0.236	0.742	0.830	25	38	0.543	0.771
C7	2	0.265	0.834	0.939	27	48	0.686	0.929
C8	2	0.285	0.896	1.023	23	53	0.757	1.000
D1	1	0.309	0.969		34	58	0.829	1.143
D2	1	0.338	1.063		36	56	0.800	
D3	1	0.320	1.005		30	55	0.786	
D4	1	0.372	1.168		20	58	0.829	
D5	1	0.404	1.269		28	63	0.905	
D6	1	0.430	1.350		22	78	1.116	
D7	1	0.461	1.449		48	101	1.443	

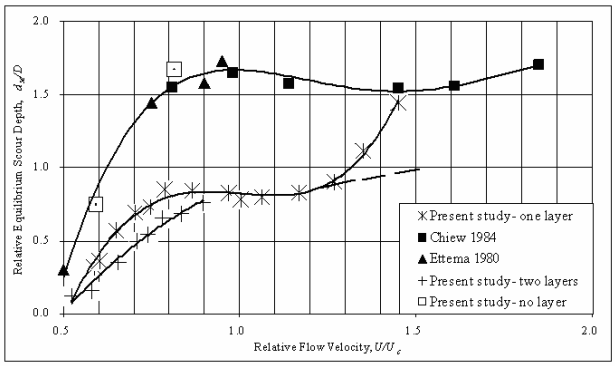

Figure 9. Effects of flow velocity ratio on relative equilibrium scour depth

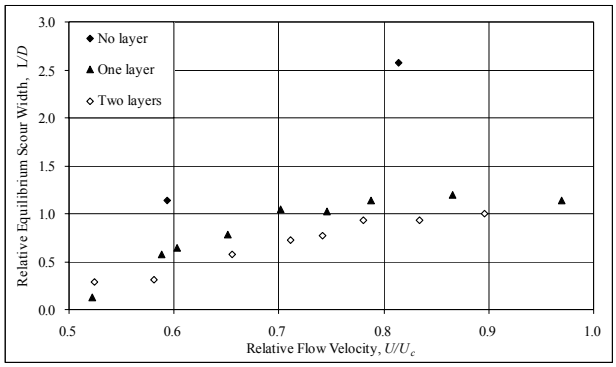

Figure 10. Effects of flow velocity ratio on relative equilibrium scour width

Compared with the experiment data obtained from published studies, the following inferences are drawn:

1. The relative scour depth decreases significantly when tetrahedron frames protection is placed around a pier. When only one layer of tetrahedron frame is placed, the relative equilibrium scour depth is almost half of that without any countermeasures. The relative scour depth associated with two layers is marginally smaller than that with one layer;
2. The tetrahedron frames increases the critical velocity needed for the initiation for scour hole development. This is due to a reduction of the near-bed velocity;
3. The minimum scour depth is reached at a lower flow velocity ratio when compared to that without placement of the tetrahedron frames. Under live-bed conditions, the minimum scour depth occurs at $U/U_c \approx 1.1$ while that without any countermeasure at approximately 1.5; and
4. The relative equilibrium scour width reduces significantly with tetrahedron frames protection. The frames reduce the velocity near the bottom effectively and prevent the scour hole from becoming wider.

Mechanism of tetrahedron frame protection at bridge piers

The two primary mechanisms that cause scour at bridge piers without any countermeasure are downflow and horseshoes vortex. Erosion by the downflow is due to the momentum of a stream of fluid impinging onto the bed at the base of the pier. The stream of fluid acts somewhat like a vertical jet in eroding the bed material, causing the scour hole to deepen. At a certain depth the downflow attains peak strength and thereafter, it gradually decreases as the scour hole deepens. Ettema [8] stated that the downflow velocity reaches its maximum when the scour depth ratio is between 0.8 and 1. The relative scour depth of the present study when the tetrahedron frame layers were intact was all less than 1. This is because the presence of the tetrahedron frame has, to a certain extent, prevented the sediment from erosion by the downflow. Tang et al. [4, 9], conducted a series of experiments on the resistance characteristic of tetrahedron frames and concluded that the velocity can be significantly reduced when water flows over a layer of tetrahedron frame. They stated that "when frames are placed in water, turbulent intensity is enlarged and turbulence energy is dissipated". After the downflow has interacted with the tetrahedron frame, its momentum has been dissipated and significantly weakened before impinging onto the sediment bed. This resulted in reduced erosion.

When a hole around a bridge pier is excavated by the downflow, the horseshoe vortex develops and enhances bed erosion together with the downflow. In the presence of the tetrahedron frames, the energy of the horseshoe vortex is also dissipated, resulting in the formation of a smaller scour hole compared to that without the scour countermeasure.

V. CONCLUSIONS

Based on results from the experiments conducted in the study, the following conclusions are drawn:

1. The scour depth with tetrahedron frame protection at bridge piers increases almost linearly with flow velocity ratio under clear-water conditions, and reaches a peak at the critical conditions of sediment entrainment. Under live-bed conditions, the data show decreasing scour depths above the threshold condition until a local minimum is reached, after which the scour depth increases again, but at a decreasing rate.
2. The tetrahedron frame layer has a positive effect in protecting the pier foundation against scour. It can dissipate the energy of the downflow and horseshoe vortex, thus reducing the pier-scour depth when compared to that without any countermeasure. When one tetrahedron frame layer was placed, the relative equilibrium scour depth is almost half of that without any countermeasures. Two layers provide a marginal improvement.
3. Results conducted in 2-dimensional tests with a tetrahedron frame layer show that it can prevent edge failure. This observation is substantiated by tests conducted with a bridge pier. In the upstream end of the tetrahedron frame layer, erosion occurs but downstream of it, sediment deposition takes place, preventing the formation of edge failure.

REFERENCES

[1]. Y. M. Chiew, "Failure Mechanisms of Riprap Layer Around Bridge Piers", *First International Conference on Scour of Foundations*, Texas, USA, pp. 70-91, 2002.

[2]. Y. M. Chiew, "Mechanics of Riprap Failure at Bridge piers", in *Journal of Hydraulic Engineering*, ASCE, Vol. 121, No. 9, 1995, pp.635-643.

[3]. Y. M. Chiew., and F. H. Lim, "Failure Behavior of Riprap Layer at Bridge Piers under Live-Bed Conditions", in *Journal of Hydraulic Engineering*, ASCE, Vol. 126, No. 1, 2000, pp.43-55.

[4]. H. W. Tang, Y. Xiao, X. R. Xu, and Z. Gao, "Experimental Resistance Characteristics of Penetrating Frame Tetrahedron-Like", *XXX IAHR Congress*, AUTh, Thessaloniki, Greece， pp.823-830, 2003.

[5]. B. W. Melville, and Y. M. Chiew, "Time Scale for Local Scour at Bridge Piers", in *Journal of Hydraulic Engineering*, ASCE, Vol. 125, No.1, 1999, pp.59-65.

[6]. Y. M. Chiew, *Local Scour at Bridge Piers*, PhD thesis, Auckland University, Auckland, New Zealand, 1984.

[7]. Y. M. Chiew, and B. W. Melville, "Local Scour around Bridge Piers", in *Journal of Hydraulic Research*, Vol. 25, No. 1, 1987, pp. 15-26.

[8]. R. Ettema., *Scour at Bridge Piers*, PhD thesis, Auckland University, Auckland, 1980.

[9]. H. W. Tang, F. T. Li., and Y. Xiao, X. R. Xu. Z. L. Wang, and C. T. Zhou, "Experimental Study on Effect of Scour Prevention and Sedimentation Promotion of Bank Protection of Tetrahedron Penetrating Frame Groups", in *Port & Waterway Engineering*, Total 344, No. 9, 2002, pp.25-28.

The Design and Application of Scour anticipated Designs in River Related and Coastal Structures in various Countries and their Effectiveness

J. (Hans) Van Duivendijk
Delft University of Technology, Delft, Netherlands

I. INTRODUCTION

Various types of scour can confront the engineer, who has to design and construct a hydraulic structure in a marine environment. The engineer is interested in the magnitude of the scour to be expected and its development in time. He hopes that such information, if at all available, is accurate and that he can base his design and construction method on such information without meeting any unexpected hydr-aulic response.

In principle the engineer can react differently, according to the situation:

1 he accepts that scour will develop after completion of the structure and, given its extent and rate of development, he takes measures to prevent (or limit) damage to the structure and loss of stability;
2 he tries to prevent the scour or, in any case, takes measures to keep it away from the structure;
3 he is aware of the possibility that the works will be only exposed to scour during construction and he takes temporary measures to limit the damage;
4 he completely under-estimates or is not aware of any danger of scour and must repair the damage afterwards against high cost.

In my long professional life I have encountered scour in many different projects and I was always able to act in accordance with one of the first three options. Luckily, I did not come in the last situation during my professional career but, as a trainee, I saw how serious the consequences can be of non-envisaged scour.

Below, I will elaborate on the said situations, as encountered by my colleagues and myself, by presenting five case histories. They will be presented in chronological order as one learns always from mistakes. Moreover, one starts usually by having responsibility for small projetcs and ends up doing large projects.

II. CASE HISTORY ONE: FAILURE OF TIDAL CLOSURE JUST AFTER COMPLETION (NETHERLANDS)

A. Prologue

Tidal closures require a very special skill of hydraulic engineering. The risks are not always fully recognized and this may lead easily to a complete failure. Such failure is very serious in the sense that many months of preparation might be lost in less than one hour. In the example given below the situation no. 4, described in the Introduction, of not being aware of the threat of scour is demonstrated.

B. Closure Concept

In 1954 a tidal inlet in the south western part of The Netherlands, called 'Dijkwater', would be closed.

The closure concept was:

(a) protect bed of 55 m wide tidal channel by means of fascine mattresses;
(b) construction of sand body of future polder dyke on the mudflats (which became dry during low tide);
(c) protect temporarily slopes of sand body in and near axis of future closure bund at both sides of tidal channel by means of brushwood bank protection works ballasted with stone (Fig. 1);
(d) construct jetty across tidal channel and close this channel in one neap tide by transforming jetty into cofferdam filled with clay.

On 26th August the closure works started at low tide at 07.30 hours. At 11.00 hours a 70 m long cofferdam had been formed having a maximum height of 4 m by nailing boards to the jetty piles and bracings and dumping clay inside the cofferdam from side tipping narrow gauge railway wagons crossing the jetty from both sides (Fig. 2).

At that point in time the closure appeared to have been successful.

.

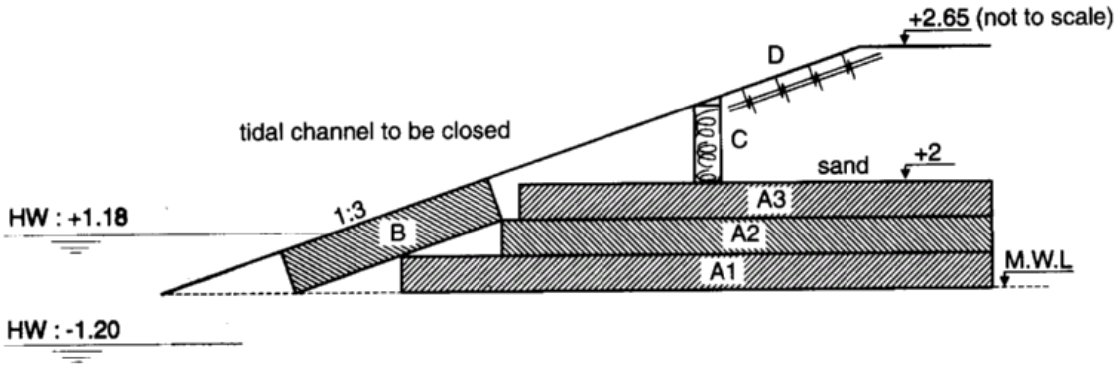

Figure 1. Layer of three horizontally placed fascine mattresses (A1-A3) at east abutment, bordered by bed / bank protection mattress (B), reed 'wall' (C) and light slope protection of brushwood (D)

Figure 2. The tidal closure, effected by means of a cofferdam filled up with clay during the rising tide

C. The Failure due to Scour

At one side of the channel it had been neglected, however, to remove the aforementioned bank protection (Fig. 1) prior to start of closure. When outside high water reached its peak it was roughly 1.5 m higher than the water level in the closed-off tidal inlet. Meanwhile the water had started to flow through the brushwood layer, thick 0.3 m from outside to inside and the adjacent layer of three mattresses (B and A in Fig. 1). The head difference had become 1.5 m over 4 m distance. The through-flow took the sand out of the adjacent sand body (Fig. 3). Within 30 minutes a 40 m wide breach had formed and all works for the closure which had been prepared during a period of 5 months could be considered as total loss. Ultimately, the width of the breach became 140 m. A new attempt was made 1½ months later at considerable cost by constructing a combined vertical and horizontal closure using shales (a waste product of Dutch coal mining operations).

Figure 3. Breach of the clay-filled cofferdam at the east abutment a few minutes prior to High Water [4].

III. CASE HISTORY TWO : CLOSURE OF A TIDAL INLET (GHANA)

A. Prologue

The project[1] described in this Section is a typical example of situation no. 3: the designer knows that the works will be only exposed to scour during construction and he takes temporary measures to limit the damage. Moreover, the project illustrates very well the concept of appropriate technology. Last but not least, a lack of quantitive data is normal in that kind of situations and the engineer has to use his intuition, common sense and and knowledge of well-known hydraulic and morphologic phenomena to find daily a solution to new problems.

B. Outline of the Problem

The town of Keta is situated in the south- east of Ghana, near the delta of the Volta River. Keta, a town of 18,000 inhabitants, is built on the small sand ridge between the Gulf of Guinee and the Keta Lagoon. The water level of this lagoon (area 300 km^2, which is 115 square miles) varies with the seasons.

As the water levels are determined by nature, the rate of increase of water levels as well as the maximum water level reached vary from year to year. The sand ridge between lagoon and sea is relatively narrow, the lands around the lagoon are swampy. Therefore most of the population lives on the sand ridge and on its slopes at the side of the lagoon (Fig. 4)

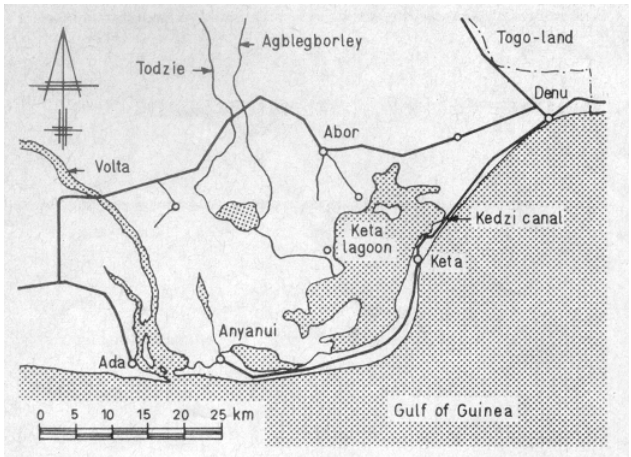

Figure 4. Situation of the gap (called Kedzi Canal) in the sand ridge

Each year the water level of the lagoon will rise and again each year there is a chance that the water level will become so high that houses and crops are inundated. In most cases, such inundation, though inconvenient, is accepted. In certain years, however, (and this happened for instance in 1963 and 1968) the water level becomes so high (i.e. 0.5 to 1 m of water in houses and on roads) that the situation is very dangerous (danger of many people being drowned, epidemics, transport of food

[1] The only publication is in the Dutch language: [6]

hampered). Consequently, it was decided in 1963 as well as in 1968 to make a small cut in the aforementioned sand ridge.

In both cases the excess water was discharged succesfully into the sea and, within five days, the water level had dropped 1 m (1963) and 1.2 m (1968). However, as a consequence of this mass evacuation of floodwater, a tidal inlet had formed (width of opening 250 m, depth 4.5 m).

The inlet formed in November 1963 (apart from some human assistance) closed after 11 months. This was mainly due to the littoral drift along the coast.

The gap made in August 1968 behaved differently. It "travelled" over a distance of 350 m and there were no signs after nine months that it would close itself. Therefore the Government of Ghana requested my employer to "give general advice to the staff of the Public Works Department (P.W.D.) on problems relating to the closure of the gap".

After two short visits to the site, during which the gap was surveyed, cross sections made and the flow pattern during ebb and f lood was studied, an advice on closure of the gap was prepared. P.W.D. agreed in principle with the plans and it was agreed that the State Construction Corporation, S.C.C., would carry out the work on a daywork basis under our supervision.

C. The Closure Concept

The plan for closure and subsequently also the execution was based on the use of local materials (sand, sandbags, mats of reed for bed and slope protection) as well as on the availability of road building plant (scrapers and bulldozers).

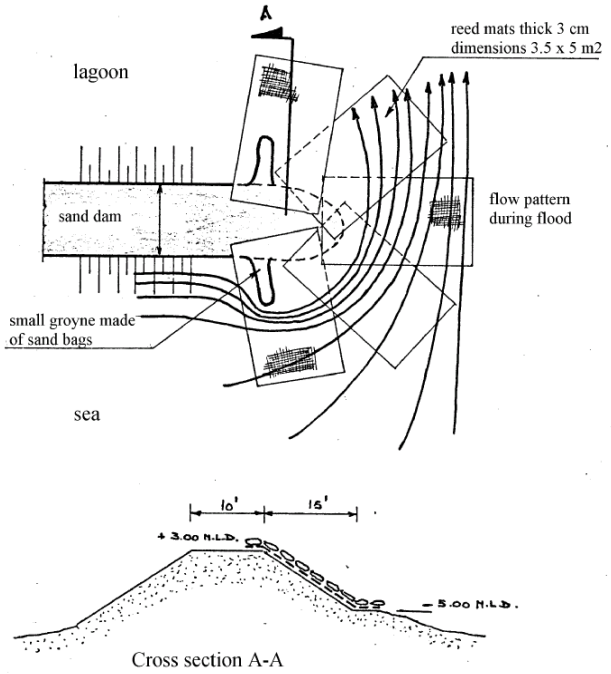

Figure 5. Daily slope protection at end of sand dam using reed mats and sand bags

Though the tidal differences were moderate (0.6 m at neap tide to 1.5 m at spring tide), the tidal prism (5 million m^3), the extent of the gap (depth 3 m, width 200 m) and, finally, the fact that all soil in bed and banks of the gap was (coarse) sand, made the job not an easy one. The main principle followed throughout has been the intermediate protection by means of reed mats of slopes and embankments made of sand against the scouring force of the tides. Sandbags (weight 250 kg each) were placed neatly on the mats to a depth of 1.8 m under water by local f ishermen (Fig. 8).

During the gradual narrowing of the gap velocities were measured of 2 to 3 m/sec and once, after a line squall, as high as 4 m/sec.

D. How Scour during Construction was being dealt with

An important parameter for scour in sand is the average grain size. At Keta the grain size of the soil particles in and around the gap varied beteen 0.5 and 2 mm which signifies coarse sand and this is of prime importance for the success of the closure.

The width of the gap during the first visit was 200 m and the max. current velocities measured varied between 1 and 1.5 m/s. The ebb current turned out to be stronger than the flood current. The main current during ebb crossed the gap more or less diagonally and tended to erode the eastern side of the gap even further. The first objective was therefore to stop erosion at the eastern shore of the gap. Accordigly, during low tide, a strip of shore, wide 3 to 30 m (the last in axis of closure) and long 200 m was protected by placing bags of sand on reed mats. An under water sill (level 2 m below average water level) was formed by placing reed mats in the axis of closure over a length of 30 m (perpendicular to the current) and a width of 3.6 m. In this manner a sill of 50 m length (width 3.6 to 30 m) would be available for the final closure (see Fig. 6).

Subsequently, the gap was narrowed by bulldozers, pushing out sand from the western shore into the gap. During the construction of the sand dam it turned out to be necessary to protect the end of the heap of sand each afternoon to avoid serious scour during the night. These protection works became more and more sophisticated as the gap narrowed and velocities increased. A sketch of the protection.is given in Fig. 5. In general, such protection works were carried out during a period of 3 hours prior to darkness (at 6 p.m.) the exact timing depended also on the tide. Thirty to forty men and women were involved in filling, transporting and placing the heavy bags (200 to 250 in number) over an area 80 to 120 m^2 of mats, most of it under water. In general such protection could withstand velocities of 1.5 to 3 m/s.

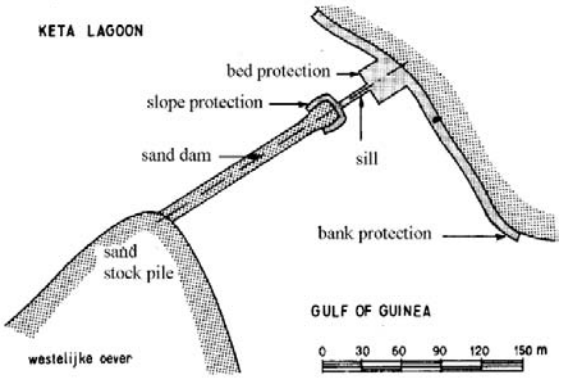

Figure 6. Over view of closure plan

The sand dam was ultimately pushed out over a distance of 160 m during a period of 10 days. Obviously daily progress slowed down when the gap became narrower and current velocities increased. During the last days the daily progress was not more then 10 m and sand losses amounted to more than 50 %. During the night scour in front of the protected underwater slope was 1.5 m.

E. The Closure Works

Preparatory works started during the second half of August. Plant started to move into site on 1st September and on 5th September the first works to be done (protection of bed and slope of gap, stockpiling of sand) were in full progress.

On the 23rd September the actual closure works commenced by pushing a sand dam forward across the gap. On the 2nd of October this work had progressed sofar that the last move for closure could be made. At that time a sand dam having a length of 160 m had been constructed. The gap which was left measured 40 m in width and was closed successfully on the 3rd of October 1969 by placing appr. 6,000 sandbags in the gap. This was done by 250 persons during a period of four hours (Fig. 9).

F. Evaluation

No doubt, the weakest point in the closure concept was the very narrow (3.6 m wide) sill. If deep scour had developed at one or both sides of the sill it would have collapsed. Another point of concern was scour, which could develop in the unprotected stretch between end of sand dam and end of sill. It helped that the narrowing of the gap coïncided in time with a decrease in tidal amplitude. Obviously, the day selected for closure was close (i.e. two days prior) to a neaptide.

The reed mats turned out to be strong and sandtight. Nevertheless, the daily returning afternoon exercise of protecting the end of the sand dam became more and more difficult (Fig. 7).

Rainstorms (lasting only a few hours) tended to induce wind set up which in turn resulted in high current velocities (up to 4 m /s).

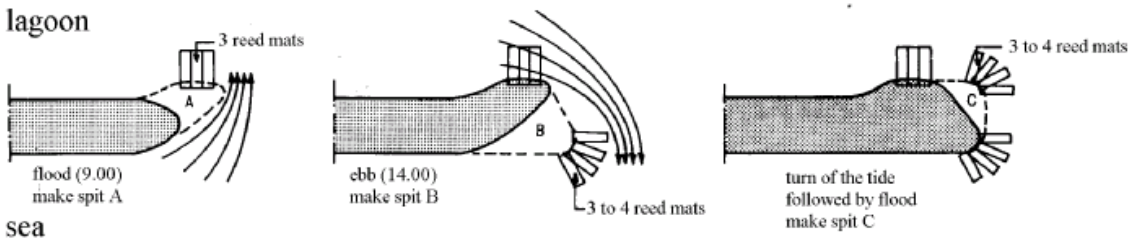

Figure 7. Construction of sand dam in relation to tidal currents

Figure 8. Slope protection at end of dam

Figure 9. Closure in progress

IV. CASE HISTORY THREE : DESIGN AND CONSTRUCTION OF SEA DEFENCES (GUYANA)

A. Prologue

Polders on the coast are normally protected against high tides and salt water intrusion by means of embankments. These embankments, locally called sea dykes, sea defences or sea walls, not only have to withstand high water levels but must also resist wave attack and remain stable when the foreshore is eroded by wave action or by the marine currents along the coast. Because of this multi-purpose function sea dykes are not always just earth embankments but are provided in many places with revetments, copings, sea side toe protection and internal drainage.

In this Section some significant design and construction aspects of sea dykes built and still to be built along the coast of Guyana and related to scour will be discussed [7].
It is a typical example of situation 1: accept the scour and take measures to prevent damage and loss of stability to the structure.

B. Some Particulars of the Coastal Plain and Near-Shore Belt

The coast of Guyana is part of a much larger unity, the some 1,500 km long coast between the Amazon and Orinoco Rivers which has everywhere equal environmental conditions and similar geographical features. The area which is roughly enclosed by the Amazon River, the Orinoco River and the Atlantic Ocean has been known as the Guianas since about 1500 A.D. The length of the coast of Guyana, between Punta Playa (Venezuelan border) and the Courentyne River (Surinam border) is about 425 kms .
The fertile coastal plain of Guyana is a comparitively narrow, low-lying area which consists of soft clayey soils. The area slopes very gently down to the sea. Along the shore line groundlevels vary between 0.3 m below and appr. 0.5 m above mean sea level (MSL). The tides, however, normally rise to some 1.5 m above MSL. Consequently, occupation and cultivation on the coast is only possible when there is a natural or man-made protection against higher sea levels.
Agricultural development started with the creation of plantations laid out perpendicular to the coastline. When there were no natural sand reefs, flooding was checked by earthdams built some distance inland and parallel to the coastline. At the start earth embankments could be kept low because of their location and the natural protection provided by mangrove and gourida bush.

Now the coast forms a unity with the shallow near-shore belt of the oceanic shelf which presents a pattern of wave-like mud shoals moving slowly from east to west. On the coast the pattern manifests itself in the natural situation by a periodic occurrence of accretion and erosion. During the past 200 years the resulting effect has been a general regression of the coast.
The vulnerable earth dams mentioned above will provide the required protection against high water levels but cannot withstand the attack of waves which reach the embankments as soon as the vegetation on the foreshore has been destroyed by the erosion forces following the passing of a mud shoal.
In the past the solution was to accept the regression of the coast-line and to build a new earth dam further inland.

During the 20th century, however, it has become practice in the relatively densely populated and more developed agricultural areas to strengthen the earth embankments against wave attack by revetments and copingwalls. This was done in order to stop locally a further regression of the coastline. But the system turned out not to be successful. In the late sixties of the last century this situation was not any longer accepted and it was decided to try to design sea defences which do not collapse, which can permanenetly resist erosion and check regression of the coast line.
During the studies, made to enable a feasible design to be developed, values for various parameters had to be determined such as: erosion depth of foreshore, duration of an erosion cycle, rates of the resulting regression of the unprotected coast line, soil characteristics, wave attack, etc. Apart from the study of these typical design parameters an inventory and analysis was also made as regard the existing sea defences (some 320 km of which 50 % without any slope protection) and why they always failed as soon as the mud shoal had passed.

It is relevant here to summarize the studies regarding the earlier mentioned traveling mud shoals. The large mud banks, travelling along the coast at regular intervals, are the most striking feature of the offshore hydrography of the Guyana coast. The average length of a bank is about 45 kilometers. The pattern of mud fades away at a depth of about 18 meters, at a distance of about 25 kilometers from the coast. This is also the place where the muddy bottom of the coastal belt changes to the harder and coarser surface of the continental shelf.
The mud banks travelling along the coast show a more or less cyclic development of the shore at each place on the coast. Generally, a large mud flat can be observed in an area where the crest of a mud bank is situated off the coast. The drying line may lie some kilometres seaward from the high water mark which also shifts seaward by sedimentation. The shoal apparently protects the coast against the attack of waves and currents. Some time later mangroves of the species Avicennia Nitida start growing on the soft mud when its surface rises above MSL. The occurrence of young growth of this type of vegetation is a clear indication of accretion. The fringe of the bush of Avicennia trees gradually moves seaward over the mud flat in the course of time. It starts later and its rate of advance is smaller than is the case with the growing mud flat.
Meanwhile, the mud shoal is attacked by erosion, gradually it becomes narrower, and it attains the appearance of an abrasion plain. The vegetation stops advancing. Later, when the abrasion reaches the bush fringe and no fresh sidements are any more deposited in the bush area, the vegetation is affected and trees are seen dying; even farther landward. Dead trees are found on the shore in front of the old vegetation when the erosion cuts into the vegetated coast. The offshore bottom becomes steep in the area where the trough between two mud banks meets the shore. Often, in the absence of much sand, this part of the eroding shore shows a succession of typical small bays.

Erosion has formed a specific pattern of small gullies in front of the steep edge of the eroding mud plain. These phenomena characterize an eroding coast.
In this period swell penetrates up to the coast and breaks on or near the shore. The erosion of the coast proceeds until, suddenly, another mud flat starts forming in front of the eroded shore.
Fixation of a shore by a sea defence will prevent a recession of the shore but of course it cannot prevent the erosion of mud from the offshore bottom of the sea.

C. Scope of the Problem

Between the passing of two travelling mudbanks the shore in front of the sea defence erodes and the average level of the foreshore is lowered significally. This in turn results in higher waves reaching the sea defence and, consequently, in heavier wave attack and higher wave run-up on the sea defence. This was acted upon during the past by protecting the earth dam with a revetment and by placing a concrete wall (called coping), 0.5 - 2 metres high, on top of the earthdam (Figure 10). The latter was introduced when it was experienced that an earth dam having a height of 4 to 5 metres lost its stability on the soft clay layers. The erosion of the foreshore however increases the height of the sea defence in relation to the level of the foreshore and practically everywhere the sea defence collapsed and had to be abandoned during the period (5-10 years) lapsing between the passing of two mudbanks. The authorities then had only one option left: accept the regression of the coast and to place the sea defence further inland..

The team, of which the writer was a member, had the task to prepare a new design for the sea defence taking into account:

- expected erosion of the foreshore
- wave attack and wave run-up
- sub-soil constraints
- economy of construction
- local capabilities for construction
- limited requirements for maintenance

D. Design of a New Cross-Section for Sea Defences.

It turned out to be quite a challenge to prepare a new design for the cross-section of the sea defences in Guyana.
An important issue was, for instance the wave attack. The seaward slope of a seawall is subject to continuous attack by waves. The zone of attack shifts up and down with the tide. The effect of the waves on the slope depends on the gradient of the slope and from this point of view a gentle slope is preferable. However, length of slope and volume of sea defence increase with a flattening of the slope. Consequently, the slope's gradient is a compromise

between hydraulic, structural and economic considerations.
Assuming that a sea defence is sufficiently high to prevent overtopping during high water levels, overtopping will then only take place by wave action. In Guyana design water levels or water levels of 0.3 m below design water level are much more frequent than in the Netherlands. But frequent overtopping with saline water is detremental to the grassed (land side) slopes and will also increase the salt content in the acquifer in the polder. Loss of the grass cover on the slopes (especially in the tropics) will utlimately result in a dryed-out cracked clay layer which is easily weakened by rain and seawater and this in turn may lead to soil- mechanical failure of the slope. Bearing this in mind a (rather low) design criterion of 0.1 liter per m per sec. for overtopping was taken.
All these considerations led to a design height of the seadefence (measured from level of eroded foreshore up to level of the crest) of 7.2 m (24 ft).
.

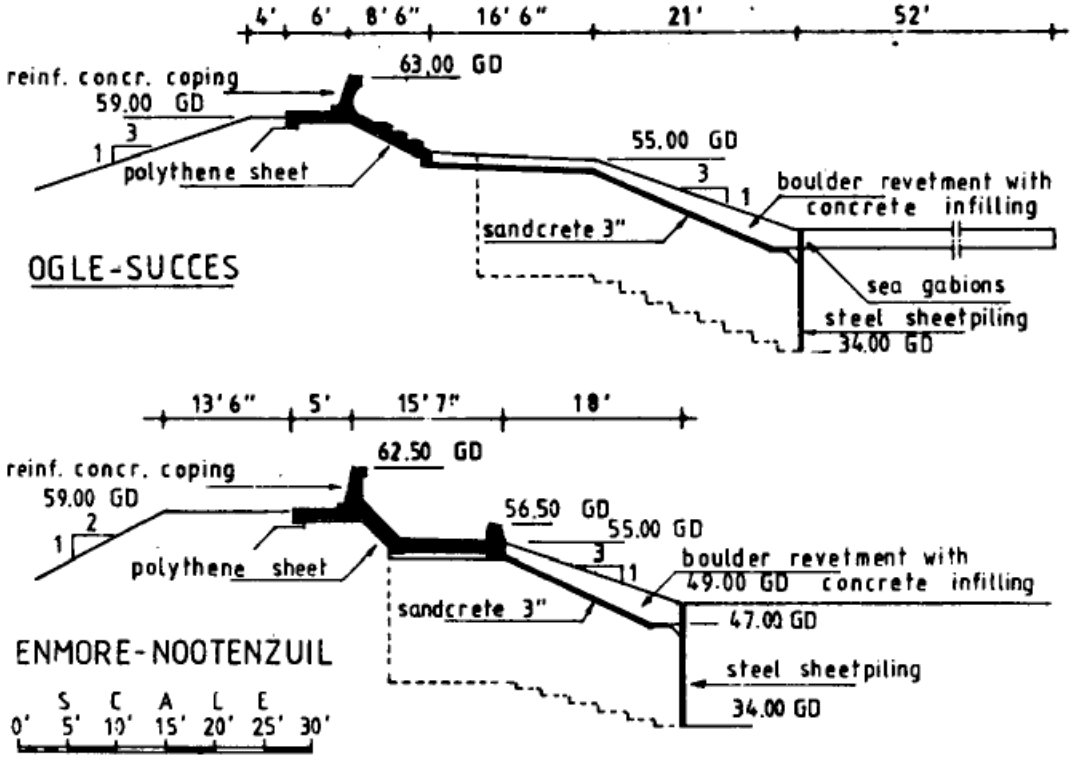

Figure 10. Typical cross sections of Sea Defences prior to 1970

But it was known from experience, soil mechanical tests and slope stability calculations that such an embankment would loss its stability as soon as the foreshore erosion had progressed significantly!
Apart from this loss of stability because of erosion near the toe, sea defences had collapsed in the past due to overtopping, damage to the coping or damage to the revetment. This meant that a lower crest was no solution to the problem and that also the coping and revetment needed improvement.
A survey of existing and (partly) collapsed embankments learned that all revetments made in the past were of the rigid type placed on rather soft and not always well compacted clay. It was therefore decided to introduce a new type of revetment: sand-mastic grouted stone. The latter not only provides high flexibility combined with physical strength, water tightness and durability but also turned out to be the most economical solution.
During construction special care would be required for connection to the revetment and to the use of flexible joints between coping elements.

To overcome the stability problem two elements were introduced into the cross section:
- a 15 m (50 ft) m long berm at the average level of low water (50.00 GD)[2] between actual upper embankment and lower embankment (toe structure)
- a rip rap layer on the slope of the upper embankment; this limited wave run up and, consequently, the height of the crest.

[2] GD = Georgetown datum, levels are in ft.

The toe structure is required between the berm at a level of 50 GD and the foreshore, the level of which may vary but for oceanic coasts can be considered to be at a lowest level of 40 GD.
In addition to its primary purpose to stop the cyclic erosion undermining the sea defence the toe structure should resist eroding forces of wave action and the downward rush of water following the breaking of waves at lower tidal levels. Moreover, the design should allow for possible differences between the pore pressure inside the sea defence and the water level outside, when the tide is out.

After due consideration of various alternatives it was concluded that a graded filter type toe protection would meet fully the design criteria and would also be cheapest to construct. The new cross-section as developed is shown in Fig. 11.

Though copings in general cannot be recommended for incorperation in sea defences. It was felt that use of a coping of limited height would reduce the cost of construction of the sea defence significantly. It was therefore decided to present an alternative cross-section. for the sea defence incorporating a coping (Fig. 12).

E. Construction and Monitoring

The design as developed during the studies and briefly reviewed in the foregoing sections was applied in practice for the sea defence in front of the capital, Georgetown. The existing sea defence was re-constructed during the period 1973-1976. Hydraulic studies had indicated that erosion of the foreshore was due to start in 1973. In fact erosion started during 1974 and the foreshore gradually eroded from an average level of 54 GD during the period 1936-1969 at 30 metres from the toe of the defence down to 49 GD (1976).

Now, in 2006, the re-constructed sea defence has been in operation for thirty years and so far has fully satisfied the design criteria. This cannot be said about adjacent sections of sea defence, which were also re-constructed during the sixties and early seventies (but in accordance with the designs in use up to 1970). In these sections oversplash still poses problems occasionally and the rigid concrete slab revetments on the outer slope tend to deteriorate quickly.

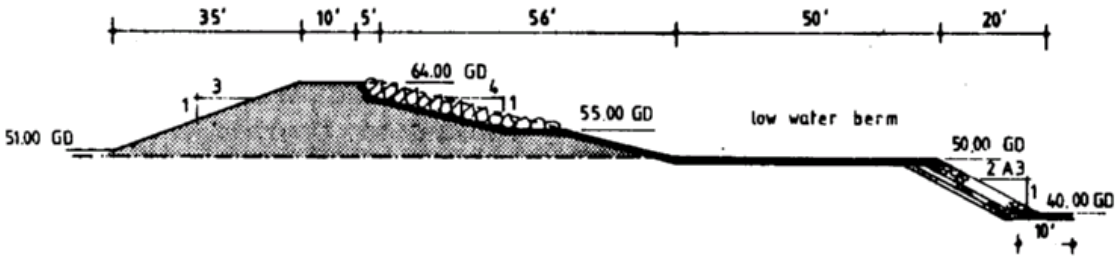

Figure 11. Cross- section of new design

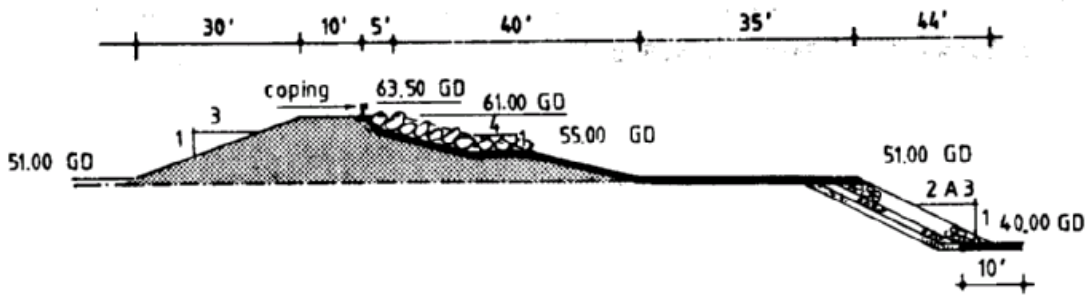

Figure 12. Cross- section of new design: alternative with coping and reduced width of berm

V. CASE HISTORY FOUR: SCOUR DURING CONSTRUCTION OF THE FENI DAM (BANGLADESH)

A. Prologue

The design and construction of the Feni Dam in Bangladesh (1984-1985) is considered internationally as an outstanding example of the use of appropriate technology in hydraulic engineering. The actual final tidal closure was effected for the greater part by utilizing manpower at a large scale. This can best be illustrated by giving some figures about the construction of the closure bund on the day of closure (28th February 1985): on that day the estuary was closed during ebb tide by means of a 800 long, 2.5 m high dam in which 650,000 bags filled with clay were placed by 12,000 labourers in a period of six hours.
Particulars of design and construction can be found in various publications[3] while National Geographic included the project in their publication [3].

Reference is made to these publications for details of the Project. Here, only the problems caused by scour will be discussed. The situations 2 and 3, as described in Section I, apply.

B. Site Conditions

Tides with large amplitudes occur at the closure site. In the axis of closure, the shoals are at a level[4] of SOB +0 to +1.00 m. The low water level at the closure dam site is more or less constant, during both spring and neap tides, and is essentially governed by the bathymetry at the site and the quantity of upland discharge. It can be considered to be at SOB. During the dry season the high water levels will be at its lowest by the end of February, i.e. during neap tide at SOB + 1.80 m and during springtide at SOB + 4.0 m. During the wet season spring tide levels are considerably higher.
A remarkable aspect of the tide in the Feni Estuary is the uneven distribution between flood en ebb. On the average the flood lasts less than three hours, while the ebb lasts approx. 8 hrs. 30 min. The current reversal at the end of ebb time is almost instantaneous and is often accompanied by a tidal bore.

In the natural situation (before the construction of any closure work) the maximum current velocities occur during flood and reach values of approx. 2 m/s.

The subsoil at the closure dam site consists mainly of sandy silt and silty sand, with occasional clay layers. At several locations the sand/silt is very loosely packed and has densities below the critical level. This implies that the soil can be subject to liquefaction if unsuitable loadings occur. 'Unsuitable' loadings may result from earthquakes or from scour of the riverbed prior to the closure operations; after closure no further scour can take place. The loose packing of the subsoil also implies high erodability. Substantial changes of the riverbed are to be expected once the current patterns at the closure site would be disturbed by the closure works.

C. Bed Protection Works

The site conditions as described above determined the need for an extensive bed protection at and near the axis of closure. The main function of the bed protection is to stabilize the riverbed, so that any activities related to the closure operations do not result in appreciable scour. The bed protection would cover a strip along the axis of closure (1,300 m) over a width of 150 m.

The required width followed from the expected scour which could develop immediately downstream of a bed protection mattress followed by possible liquefaction in (part of) the subsoil underneath the mattress.

The bed protection was constructed by means of so-called fascine mattresses consisting of a grid of bamboos and reed rolls fixed to a polypropylene filter-cloth and ballasted with river boulders. A filter-cloth is also necessary for geotechnical reasons, namely to spread the load of the (future) dam over the subsoil and to prevent (or at least limit) local subsoil failure during construction. For the gully along the left bank the mattresses were pre-fabricated on the riverbank and floated to the correct location around the time of high water. They were subsequently ballasted with boulders and sunk to the riverbed. Dimensions of these mattresses were approximately 60 by 30 m^2.

On the shoals the mattresses were assembled in-situ during low tide (Fig. 13). Dimensions of these mattresses varied but were maximum 80 by 50 m^2. The expected scour downstream of mattresses placed on the shoals was much less than expected.

The highest current velocities occur in the gullies (2.6 m/s). The gully mattresses (30 m * 60 m) were placed in rows of three in the direction of the current, so that it took at least three days to proceed 30 m measured along the axis of the future dam. During this time the edges of the mattresses (especially those, parallel to the currents) constituted a change to the bed-roughness, which induced extra turbulence. This resulted in substantial scour along the edges of the mattresses (Figure 14), so that it became more difficult to place the next row of mattresses.

[3] Mentioned are in this respect: [1], [8] and [9].
[4] SOB is an abbreviation of Survey of Bangladesh

Figure 13. Making a bed protection mattress on the shoals at low tide

.

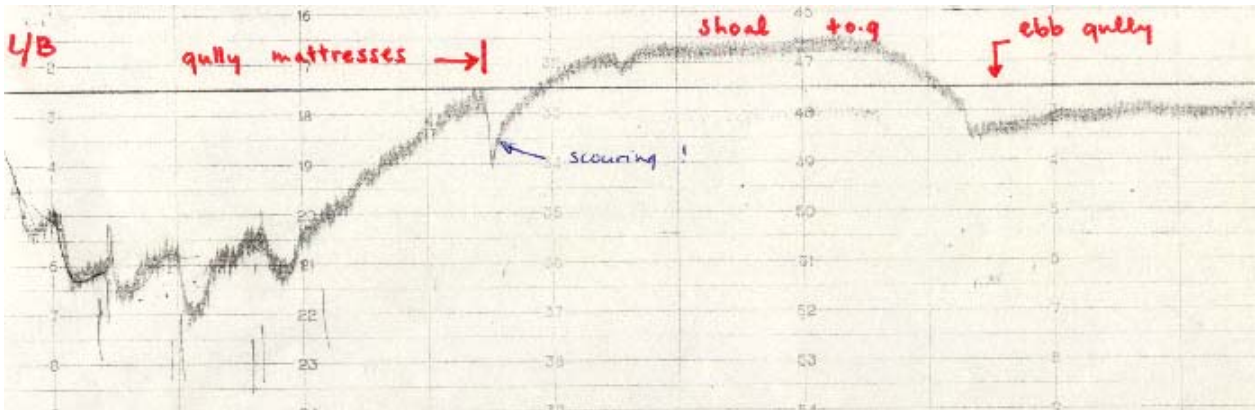

Figure 14. Scour along mattresses successively placed in gully along the Left Bank (L/B)

The difficulties can be described as follows:

(1) The scoured hole (or rather channel) along (a series of) mattresses prevented that the next series of mattresses could be placed with a properly connected overlap: the ballast on the mattress-section over and above the scoured channel resulted in protruding of the reedrolls above the earlier placed mattress (because the reed roll1s were rather stiff). On the other hand it was not possible to reduce the stiffness of the reedrolls, because in that case the whole sinking operation would come in jeopardy. It is suspected that at some locations the lack of a proper overlap has resulted in further scour between the mattresses, though this could not be verified by soundings.

(2) The additional roughness to the riverbed introduced by the mattresses has probably a1so led to a concentration of the currents in the unprotected parts

of the gully. As the river bed material in this location was rather loosely packed fine sand and silt, it was casily erodable. Substantial erosion was recorded between the time of commencement of the bed protection works in the gully and the time it was completed.

From the above it follows that production and placing of mattresses had to be done during the shortest possible period. In fact in the gully along the left bank 22 mattresses were placed during a period of 27 days. This gully tended to become deeper (from SOB – 1.00 m to -3.5 m) as the mattress operations progressed.

The gully along the right bank never became that deep but reacted at the placing of mattresses by shifting its course towards the as yet unprotected shoals (Fig. 15). After both banks and gullies had been protected mattresses were placed on the shoals. The overall number of mattresses ultimately placed was 123 in a period of 77 days. The overall area thus protected was 195 000 m^2.

D. Concluding Remarks

Fact is that the bed protection, after its completion, has prevented deep scour to develop along the axis of closure. During its construction, however, it was in fact the placing of mattresses which prompted scour.

Before the tidal closure, as mentioned earlier, could be effected, the contractor had to construct the sill in the gullies , on top of the bed protection. This turned out to be a difficult and critical operation but ultimately the sill was ready a few days before the day of closure.

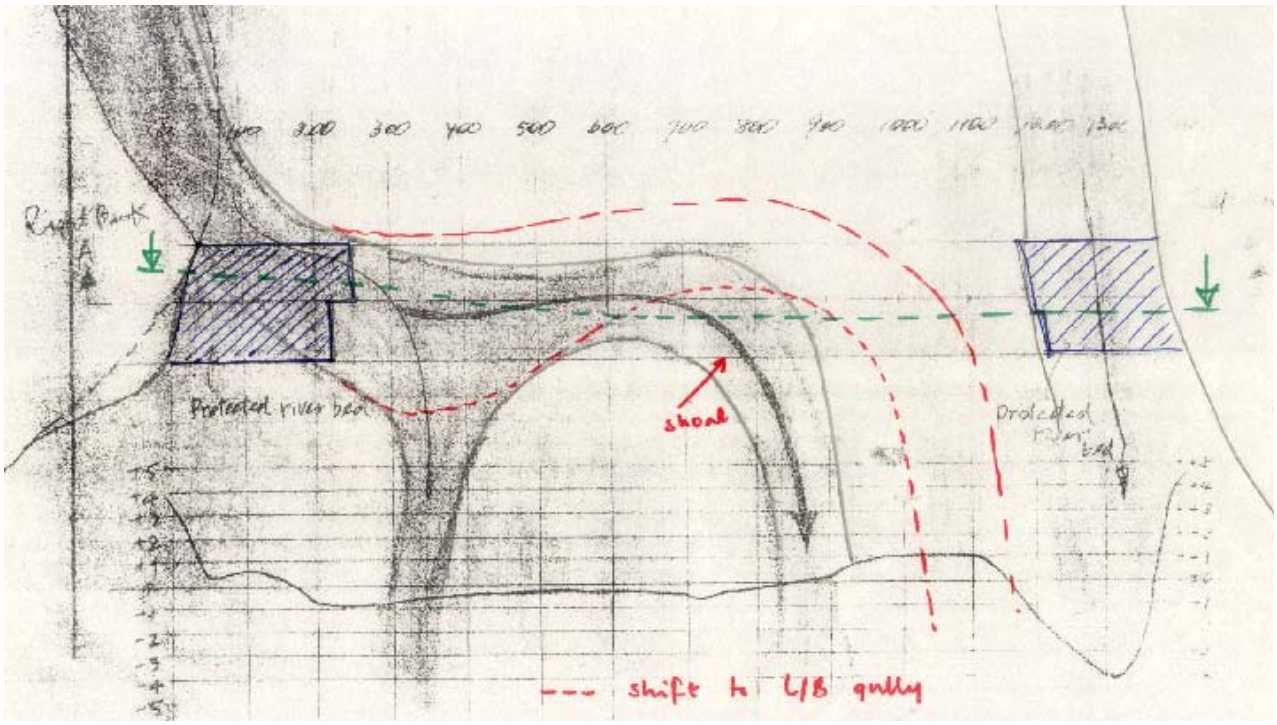

Figure 15. Sketch showing shifting of the gully near right bank as a consequence of progressing bed protection

.

VI CASE HISTORY FIVE : THE RIVER TRAINING WORKS FOR THE JAMUNA BRIDGE IN BANGLADESH

A. Prologue

The Jamuna river, known as the Brahmaputra in India, is one of the world's great rivers. With its vast catchment area covering the eastern Himalayas, it ranks as the world's fourth largest in terms of peak discharge and second largest in sediment load. The Jamuna runs in the north-south direction dividing Bangladesh in two before its confluence with the Ganges and final discharge into the Bay of Bengal.

The Jamuna is a braided river with its channels continuously changing course within the braid belt, which is flooded in most monsoon seasons and measures as much as 40 km wide in some places. Even at its narrowest point the braid belt is 15 to 20 km wide.
The people of this area have long desired a bridge across the Jamuna that would bring social, political and econonomic integration and development to the region. Studies for a road and rail crossing were commissioned as long ago as 1964. The studies which, ultimately, resulted

in the construction of the Jamuna Bridge were commissioned in 1986.

B. The Challenge

The provision of a fixed bridge crossing of the Jamuna is a major engineering task of unusual technical complexity. The primary technical issues addressed in the engineering development of schemes for this project were:

- the size and nature of the braided Jamuna river
- the weakness of the foundation material and the seismicity of the area
- the requirement of having the project operational within three and a half years of contract signing.

In this contribution focus will be only on the control of the river[5].

C. Control of the River

The control of the Jamuna river is a major engineering undertaking. The maximum river discharge during flood (average 65,000 m^3/s), the shifting deeply-scoured channels (40-45 m during flood conditions), the seasonal river level range (from +6 m to +14 m PWD) and the width (15 km at flood stage and 5 km at low water at its narrowest point) all imposed considerable demands on the design and construction of the river training works. The 8m range in river levels led to a seasonal construction period of 6.5 months for the river training works.

A key issue in this respect was the relation between project cost and bridge length. Costings were made for the total crossing of 15 km within which the bridge length varied from the full 15 km to 3 km. The hydraulic studies indicated that the risk of outflanking the training works with a 3 km opening was not acceptable. The solution selected was a bridge length of approximately 4.8 km with river training works (guide bunds) of 3.1 km and 3.2 km on the east and west banks, respectively (Fig. 16). Existing 'hard'points were strengthened some distance upstream of the bridge on both banks

D. Layout River Training Works

The layout of the river training works as determined at the feasibility stage in 1986 was based on the comparatively stable situation south of Serajganj of one main river channel, where only limited shifting of the river banks had been observed for some years. Later, in 1987-1989, it became apparent that the extreme floods in the Jamuna of 1987 and 1988 had considerably distorted the equilibrium which had previously existed in the selected bridge corridor.

As can be seen in Fig..17, a second major channel developed along the west bank while both the east and the west channel tended to move east and west, respectively. In the period 1987-1992 the banks at the proposed bridge axis moved 1 km to the east and 1.5 km to the west, respectively. This completely distorted the idea of having a 5 km long bridge with guide bunds built in the flood plains at both sides. As a longer bridge meant additional cost, it was decided to study the possibility of constructing one of the guide bunds on a mid-river char (the local name for a sandbank) or in a shallow river channel during the dry season. This could turn out to be costly, depending on the level of the riverbed and/or the location of the char. However, at the time of construction an effort would be made to find an optimum between:

(a) extending the length of the bridge in order to build the guide bund on a char

(b) constructing a more expensive guide bund in a shallow channel without extending the bridge length.

It is one of the major achievements that this unusual approach proposed by the consultants was accepted by the employer and co-financiers and proved most successful. The final location of the west guide bund could only be determined by the Consultants on 15 October 1995 as the river levels fell, i.e. 19 months after award of the major construction contracts. This approach resulted in no additional project costs and the relevant provisional sums for contingencies were not required.

E. Cross-Section of Guide Bunds

The cross-sectional design of the guide bunds as adopted during the design stage was based on the following principal considerations:

- extreme bend scour
- a depth of bund that is capable of being dredged having due regard to economic considerations
- slope stabifity
- protection of slope
- economic considerations

In the period that the designs were made the knowledge about the morphology of the river Jamuna was still very limited[6].

During the feasibility studies ground investigations, mathematical and physical modelling, analysis by means of remote sensing and river surveys (in so far as funds were available for that purpose) had provided valuable information but much 'engineering judgement' was still required in developing the design. On the basis of hydrographic surveys and discharge measurements various scour formulas were developed by Delft Hydraulics.

[5] For a more general and broader description of the Project see [5] and [10].

[6] Since then, this situation has improved thanks to the river studies carried out after the flood of 1988 in the context of the Flood Action Plan (FAP).

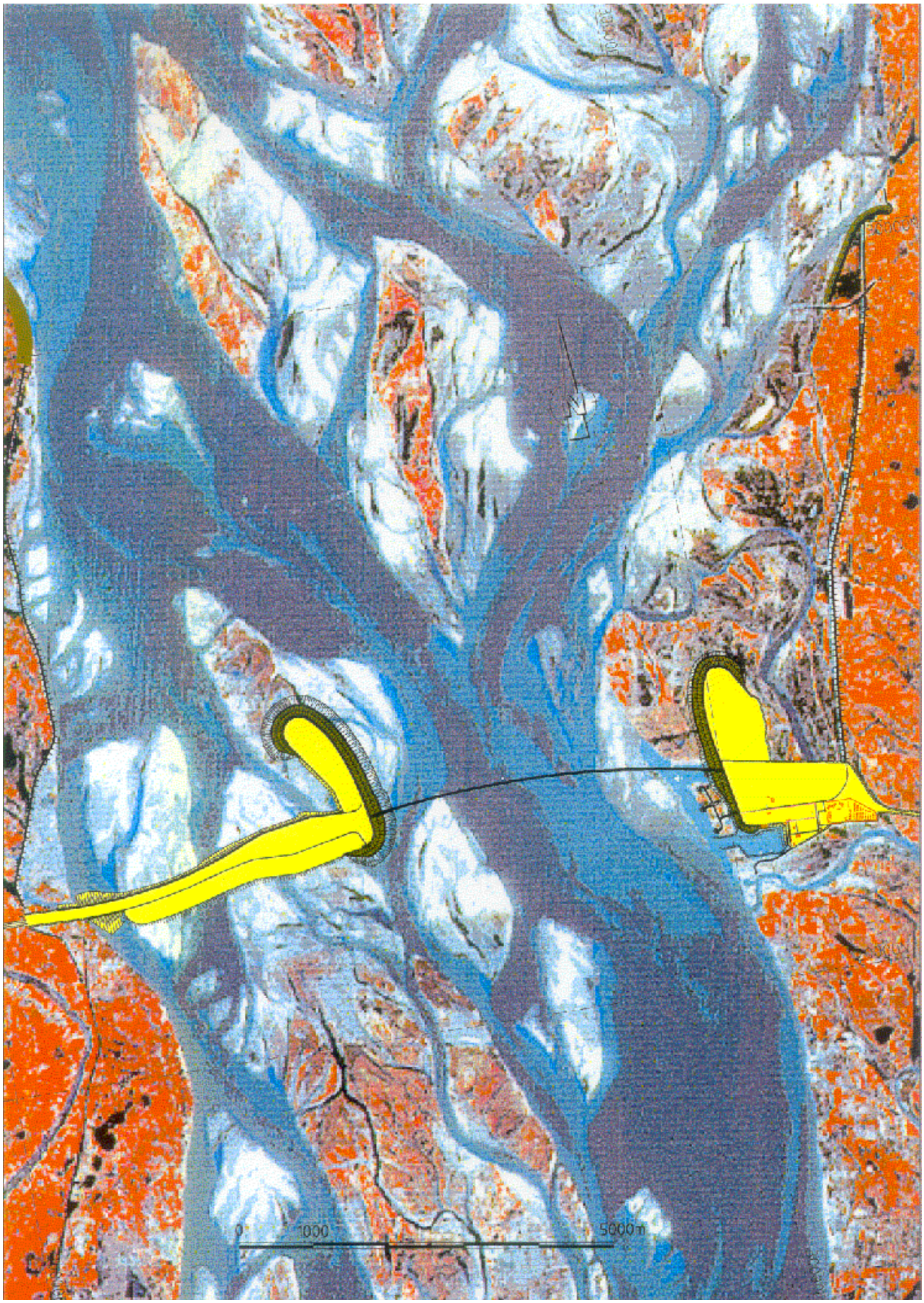

Figure 16. Satellite image with superimposed guide bunds and reclamation for Jamuna Multipurpose Bridge

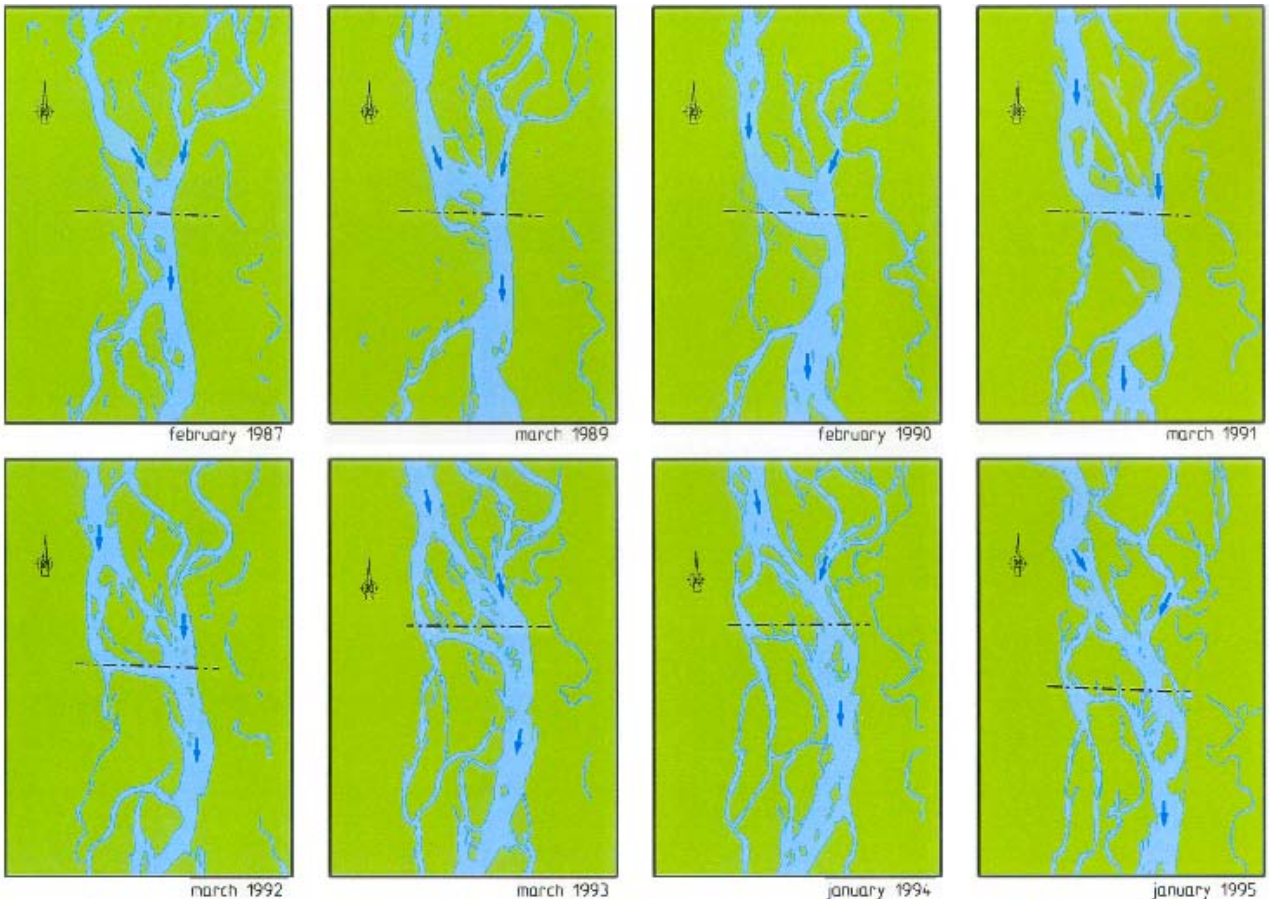

Figure 17. Low water channels of the river Jamuna near the bridge axis during the period 1987-1995

In order to limit construction cost probabilistic design methods were used to determine maximum permissible scour depths for which the design would be made.

Extreme scour is a typical feature of the Jamuna: river branches flow in thick, loosely packed, alluvial depositions of, predominantly silty sand. These river branches change continuously (direction, location). The river transports much sediment, especially during the high water period. When the water level goes down, the channels are silting up. Scouring (and the related bank erosion) takes place during channel shifting and during the increase in river flow in the high water season. Extreme scour is due to local disturbances in the cross-section (for instance by guide bunds and bridge piers), in outer bends of channels and at the confluence of river branches.

Scour is an important technical parameter for the level of the toe of the underwater slope as well as for the foundation depth of the bridge piling. It also determines the magnitude of the dredging to be carried out.

The scour to be expected along a guide bund can be of the order of 40 m, relative to the level of the flood plain (PWD + 12 m). Two extreme avenues are open to provide protection against currents to such depths:

(a) Provide a sufficient quantity of erosion resistant material along the perimeter of the guide bund, and leave it to "nature" to deposit this material at the anticipated depth during the scour process. If the erosion resistant material is provided at original ground level (flood plain level), no dredging work will be required for the guide bund. The principle discussed is known as the "falling apron" sometimes referred to as the "launched apron". This principle has been adopted for the guide bund at the Hardinge bridge (Bangladesh) and also at the bridge across the Brahmaputra near Kaliabhomora (India).

(b) Dredge a trench to full (expected scour) depth and cover one side of the trench with an erosion resistant protection; the covered slope will become the river side of the guide bund.

Ideally, gentle slopes extending down to the full expected erosion depth are preferred. Unfortunately, in the case of the Jamuna Bridge dredging to full depth would:

- lead to very large dredging volumes (order of 22 million m^3 per guide bund); such volumes would be very difficult to handle within the short construction season available for the guide bund.
- require very specialized dredging equipment, of which it is doubtful that it would be available in the market.
- be very expensive.

Cost comparisons have been made for combinations of dredging to a certain depth (with proper slope protection on the dredged slope) and a falling apron over the "remaining" height.

The total cost increases with increasing depth. For this increased cost it is obvious that a higher degree of safety of behaviour of the guide bund would be achieved.

During the design stage the Consultants proposed for both guide bunds to adopt everywhere a 'toe' level of PWD -18m as the initial level of the falling apron for the following reasons:

- the "remaining" falling height (10 m) for the apron is large, but not too large to implement any additional measures to protect the slope should this become necessary.
- the dredging depth is very substantial (up to 30m, measured from the level of the flood plain), but can be dredged with equipment which is available in the market or which can easily be adapted.
- though requiring a major effort, it is possible to complete an entire guide bund within one working season.

F. Design Adaptations during Construction

It should be anticipated for a project of this nature that design adaptations would be required during construction. These adaptations could be, among other things, due to one or more of the following circumstances:

- erosion of river banks resulting in changed bank lines and another site configuration
- major shifting of river channels
- increased flow through secondary creeks and floodways
- discovery during construction of sub-soil conditions not known at the time of design (despite extensive site investigation)
- delays in the start of the construction period.

In practice, nearly all the above circumstances occurred during the construction period. This meant that the design of both guide bunds and the Bhuapur hard point had to be adapted with regard to location, plan form and cross-section. The change in location and plan form was on the one hand due to channel shifting and on the other to land acquisition constraints. The change in cross section in the first instance was due to difficulties encountered during construction of the west guide bund. It became evident that the soil during and after dredging was very sensitive to slight dynamic disturbances[7]. It was therefore decided to adopt a more gentle gradient (see below).

G. Construction of River Training Works

Construction of the river training works, commencing with the east guide bund, started on 15 October 1994 in accordance with the revised works programme. During this period it was necessary to dredge the work harbour and to reclaim areas in the flood plain using the sand dredged from the harbour basin. These areas were required by the two major contracts (bridge and river training works) for offices, workshops, working areas and residential areas for the site staff. One year after start of construction, the location of the west guide bund was fixed. It was the intention to complete this guide bund, including all reclamation and closure of the western river channel as well as some secondary channels, in a period of 6.5 months. This became impossible, mainly due to the unforeseen behaviour of the sub-soil. In November-December 1995 a number of minor and major slips occurred in rapid succession in the dredged 1-in-3.5 slope. This prompted the consultant to change the slope gradient to1-in- 5 down to a level of PWD - 4 m and to 1-in-6 between PWD -4 m and the toe (Fig. 18).

The gradient of the slope in the amended design is considerably more gentle than in the original design. This led to an adjustment (outside the bridge corridor) of the toe level of the protection works (PWD -15 m instead of -18 m) because model tests carried out in the context of the Flood Action Plan [2] had demonstrated that a more gentle slope reduces extreme bend scour.

H. The Application of Fascine Mattresses

Despite the slips at the west guide bund, the slope protection works in general were carried out as planned. This was due to the application of a modernized version of the old Dutch fascine mattress. A Dutch fascine matfress historically was of 0.5 m thick brushwood construction in units of 1000 to 2000 m2 which, after fabrication during low tide, were floated to the site. After positioning, they would be ballasted and sunk at the turn of the tide and a final ballast layer placed by dumping stones from flat top barges.

[7] This sensitivity is due to the presence of mica in combination with a relative density which is lower than 0.50 to 0.55. The low relative density in turn is caused by the rapid silting up of channels at the end of the flood season.

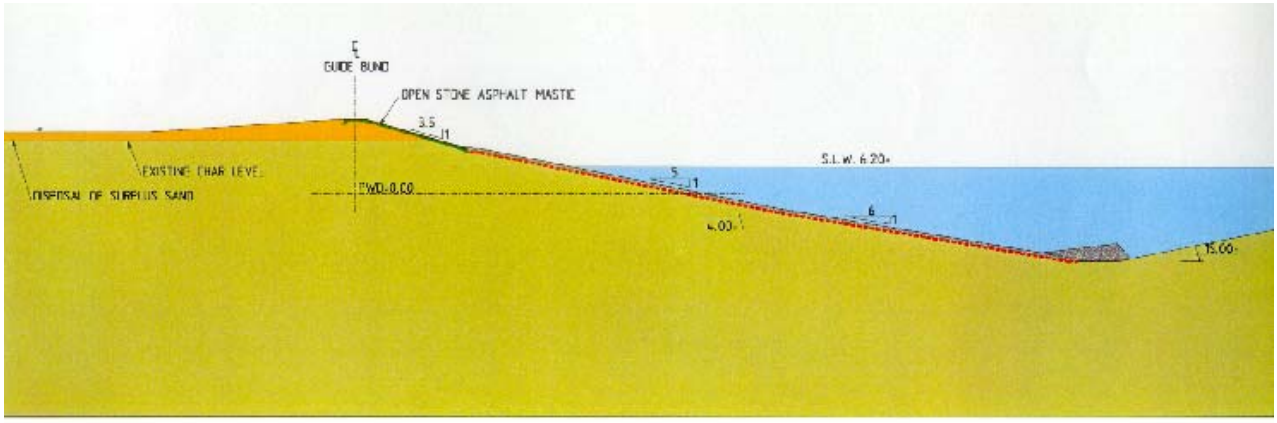

Figure 18. Cross section of guide bund outside bridge corridor

The fascines had a triple function. They acted as a filter layer, provided a rigid framework to the mattress and provided buoyancy. With current designs, the filter function has been taken over by a composite geotextile. In Bangladesh this geotextile is attached to a rigid framework of split bamboos which also provide buoyancy. For the Jamuna river training works the largest mattress dimensions were 30 m by 155 M (4,650 m^2). After positioning, the floating mattress was gradually sunk by ballasting with boulders. Final ballasting, by placing rock up to 100 kg, was effected by means of a side stone-dumping vessel. This vessel, with capacity of up to 1300 t of rock, was positioned by means of satellites (GPS) and its combined movements and dumping rate controlled by computers.

At the west guide bund, 141 mattresses having an overall area of 480,000 m^2 were placed in a period of 146 days. At the east guide bund 93 mattresses measuring 400,000 m^2 were placed in 121 days. The side stone-dumping vessel was operated 24 hours a day and reached dumping productions of 10 000 t a day. The guide bunds, which were constructed in trenches, required a total of 26 million m^3 of dredging.

I. Concluding Comments

Through co-operation by all the parties involved, including the Bangladesh govermnent, the co-financiers, the consultants and the contractors, the political, economic and technical challenges of the project have been successfully managed. The river training works were completed in June 1997 (Fig. 19) and the last span of the bridge was completed in March 1998. The bridge opened for traffic on 23 June 1998 and has, since then, more than satisfied the expectations.

During the high water season of the year 2000 scour in front of the toe of the guide bund was locally 5 m (water depth 33 m) below level of the toe (PWD -15 m) and the falling apron prevented slides or undercutting of the slope. So far, the river training works have successfully passed the attack by nine annual floods without any damage.

In 2001 the designer (Royal Haskoning.), contractor (HAM-Van Oord ACZ) and employer (Jamuna Multipurpose Bridge Authority) jointly received the Prof. Dr. Ir J.F. Agema Award for the design and construction of the river training works for the Jamuna Bridge.

Figure 19. The western, 3.2 km long, guide bund, seen from the North (upstream) after its completion (April 1997). The 5 km long bridge is still under construction in the background. The picture is dominated by the wide, 27 m deep, trench, especially dredged to enable construction of the gentle (1V:5H to 1V:6H) under water rip rap slope. Above water on the slope one can see , intersected by a narrow berm, the black strip of the open stone asphalt and the hand-placed riprap

REFERENCES

[1] CUR/RWS, 1995, Manual on the Use of Rock in Hydraulic Engineering, CUR, Gouda, The Netherlands.

[2] FAP 21/22, 1996, Bank Protection and River Training (AFPM) Pilot Project (Tech. Rep. No 5, Additional Model Tests), Flood Plan Coordination Organization, Bangladesh.

[3] National Geographic Society, 1992, The Builders, Marvels of Engineering, Washigton DC, USA.

[4] Rijkswaterstaat, 1961, Verslag over de Stormvloed van 1953, (Report on the Storm Surge of 1953), Staatsdrukkerij, 's Gravenhage, The Netherlands.

[5] Tappin R.G.R., J.Van Duivendijk and M. Haque, 1998, The Design and Construction of the Jamuna Bridge in Bangladesh, Proc. Institution of Civil Engineers, 126, Nov, 150-162 (Paper 11704), London, UK.

[6] Van Duivendijk J. 1970, Sluiting van een stroomgat in Ghana, (Closure of a tidal inlet in Ghana), De Ingenieur, nr 20, The Hague Netherlands.

[7] Van Duivendijk J. and J.R. Pieters, 1982, Design and Construction of the Sea Defences of Guyana, Papers International Symposium Polders of the World, Vol. 2, ILRI, Wageningen, The Netherlands.

[8] Van Duivendijk J. and B. Te Slaa, 1987, The Feni River Closure Dam, Int. Water Power and Dam Construction, January, UK.

[9] Van Duivendijk H. 1987, They Stopped the Sea, Nat. Geographic, Vol. 172, No 1, July, Washington DC, USA.

[10] Van Duivendijk H. 1997, Building the Jamuna Bridge in Bangladesh, Land and Water International 89, The Hague, The Netherlands.

Design Estimation of Abutment Scour Depths

R. Ettema*, A. Yorozuya*, M. Muste*, and T. Nakato *
* The University of Iowa/Department of Civil & Environmental Engineering, Iowa City, USA

ABSTRACT

Considerable uncertainty and debate surround scour-depth estimation for abutments, to the extent that the existing estimation relationships are not well accepted. The crux of the concern is that existing relationships tend to predict scour depths that seem excessive. The present paper introduces a practical design approach to scour depth estimation. The approach is still in development, its estimation relationships are being formed using the findings from an extensive laboratory study.

I. INTRODUCTION

Abutment scour involves hydraulic erosion with consequent slope-stability failure of the earth-fill embankment at the abutment. Many bridge abutments are located in compound channels whose geometry is rather complex. Additionally, many abutments are located where the channel is formed of several bed materials, occupying different locales within a bridge site; sands may form the bed of a main channel, silts and clay may predominate in riverbanks and underlying floodplains, and rocks may have been placed as riprap protection for the abutment, as well sometimes along adjoining riverbanks. Early work on abutment scour focused on the simpler and perhaps idealized situations of scour. Commensurately, the existing relationships and guidelines apply to simplified abutment situations, such as an abutment placed in a straight rectangular channel, and can only be extended with considerable uncertainty to actual field conditions. Often extrapolation causes existing scour relationships to predict substantially greater extents of scour than actually may occur at many actual bridge sites.

A common feature of abutment scour suggests a reasonably straightforward approach to obtaining design estimates of scour-depth at abutments. The feature is abutment and embankment contraction of flow through a bridge waterway. The flow locally around the abutment is part of the overall field of constricted flow through a bridge waterway, to the extent that it can be difficult to distinguish between what conventionally are termed "local scour" and "contraction scour." The fresh approach adumbrated in this paper treats abutment scour as a local amplification of contraction scour. Only when flow erodes and passes through an approach embankment, then fully exposing an abutment as if it were a pier, does local scour occur at an abutment. The writers currently are further developing the approach.

II. ABUTMENT CONSTRUCTION

Though many studies have focused on the several of the component scour processes at play, and have delineated sets of important parametric trends, few studies have considered the usual construction features of abutments and their approach embankments in compound channels:

1. Most abutments comprise an abutment structure, such as the standard-stub abutment used for spill-through abutments (Figure 1), and that structure is a pile-founded structure (the other common type of abutment is a "wing-wall" abutment used typically for smaller bridges);
2. The earthfill embankment approaching the abutment structure is erodible and subject to geotechnical instabilities (Figure 2);
3. The portion of the embankment near the abutment usually is riprap protected;
4. The floodplain (often extensively comprising cohesive soils) may be much less readily eroded than the main-channel bed;

The fact that most abutments usually are piled structures with an earthfill embankment influences scour depths at abutments. Most scour case-studies show that the embankment fails before the abutment's foundation fails (e.g., Ettema et al. 2002).

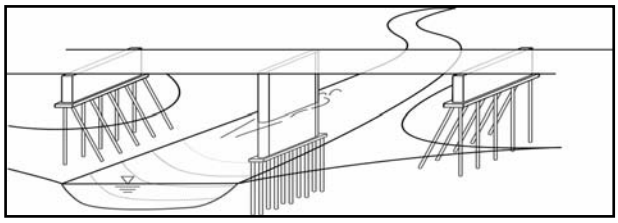

Figure 1. Many abutments are pile-supported and have an earthfill embankment

Figure 2. Failure of earthfill embankment at abutment

III. EXPERIMENTS

The writers conducted experiments with abutments in a compound channel subject to several conditions of embankment and floodplain erodibility: fixed embankment and floodplain (such as a floodplain formed of largely cohesive soil); erodible floodplain and riprap-protected embankment; and erodible floodplain with

erodible embankment. The main channel had a bed of uniform sand. Figure 3 shows the scour that developed for one configuration of fixed abutment on a fixed floodplain. The scour, by lowering the bed near the abutment, potentially could make the channel bank and embankment face unstable.

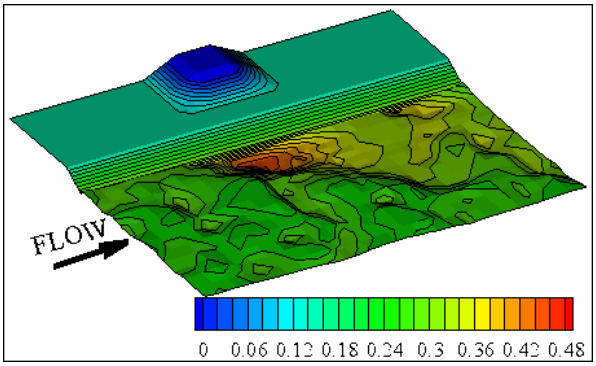

Figure 3. Bathymerty of scour zone at abutment (lab)

Most embankments are erodible, and it is common for the approach embankment near the abutment to fail and breach before the abutment itself fails, if indeed the abutment does fail. This observation is borne out by the writers' laboratory experiments, which were conducted with a floodplain simulated with sand, as shown in Figure 3. Observations from case studies in the field and from the writers' laboratory experiments show that, as abutment scour develops, the channel bank erodes eventually causing the embankment side-slope to undergo a slope-stability failure. Failure and erosion of the embankment isolates the abutment, practically exposing it as if it were a pier. Also, embankment failure may somewhat relax contraction scour.

Moreover, the experiments show that maximum scour depth may not occur at the abutment. As the width of floodplain increases, and flow contraction concomitantly increases, the location of deepest scour can shift downstream of the abutment. Figure 3 depicts one scour condition resulting from the writers' experiments with an erodible wingwall abutment – though the embankment failed partially, the deepest scour occurred a short distance downstream of the abutment. Evidently, the location of deepest scour varies with the flow field developed around the abutment. Figure 4 depicts the deepest scour condition occurring at the abutment structure itself – this condition occurred when the embankment was eroded through such that the abutment structure became exposed, and scour developed as if the abutment were a form of pier.

For some configurations of intact embankment, depending on the approach flow orientation and flow field generated by the embankment and abutment, the maximum scour depth may occur right at the abutment. Based on observations from the writers' experiments, and a review of published data, it would seem that the maximum scour depth occurs right at the abutment in cases where the abutment and its embankment are taken to be a fixed, solid body that extends deeply into the bed of a channel; this form of abutment and embankment have been extensively tested in prior flume studies.

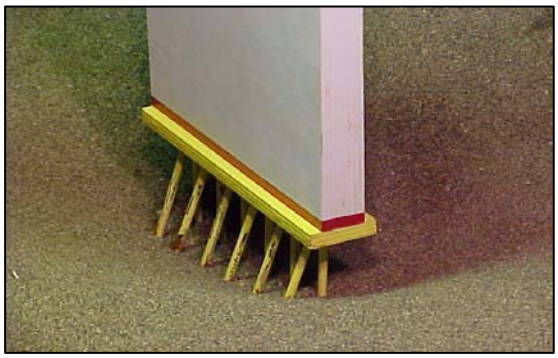

Figure 4. deepest scout at abutment base occurs when embankment washed out

IV. ABUTMENTS NEAR MAIN CHANNEL

The existing relationships for scour-depth estimation treat abutments and approach embankments as fixed, solid structures extending deep into the bed. However, few abutments are built like that. Illustrations like Figures 1 and 2, as well as the writers' observations of scour development at piled-supported abutments and earthfill embankments, suggest the need for a practical estmation approach to scour-depth estimation. The practical approach offered here focuses on estimates of maximum flow depth associated with two primary scour forms:

1. *Maximum scour as near-abutment amplification of contraction scour*. The writers suggest that, especially for spill-through abutments, the deepest scour develops essentially as a near-abutment amplification of contraction scour, with the amplification caused by the increased flow velocity and turbulence local to the abutment and its approach embankment. This depth occurs when an abutment's embankment is either fully or largely intact, such that the flow is constricted through the bridge opening. The term "embankment largely intact" here means that the flow has not broken through the approach embankment.

Actually, for an abutment on a compound channel, deepest scour should be checked at two locations: in the main channel if the abutment is close to the main channel; and, on the floodplain if the abutment well set back from the main channel.

2. *Maximum scour as local scour at fully exposed abutment structure*. This scour form occurs when the embankment has eroded so that the abutment structure (e.g., standard stub or wingwall) is fully exposed as if it were a pier.

Because contraction scour integrates the influences of several variables (e.g., approach-flow depths and discharge, bed sediment), it is meaningful and convenient to relate maximum scour depth Y_{max} to contraction-scour depth Y_C: i.e., for a fixed embankment and floodplain,

$$Y_{\max} = \alpha Y_C \qquad (1)$$

The factor α amplifies Y_C near the abutment. The magnitude of α depends on flow velocity distribution at the bridge site, and it must account for turbulence. Site

morphology, along with the presence of vegetation, and sundry physical peculiarities complicate estimation of flow distribution and scour depth for sites. In particular, it is difficult to identify precisely where flow velocity will be largest, turbulence greatest, and scour depth likely deepest. The relationship α has yet to be determined. The writers suggest that (1) be expressed as

$$\left(\frac{Y_{\max}}{Y_1}\right) = C_T\left(\frac{q_{\max}}{q_1}\right)^{6/7} \tag{2}$$

In which q_{max} is the unit discharge coinciding with the location of deepest scour in the main channel. If all the floodplain flow entered the main channel, in the situation of a long abutment extending practically across the floodplain, $q_{\max} = m\bar{q}_2$; $\bar{q}_2 = (Q_{1m} + Q_F)/B_2$; Q_{1m} is approach flow in the main channel, and Q_F is approach flow over the floodplain. Values of m and C_T have to be determined from laboratory or numerical-simulation data.

An approximate relationship for flow depth at the site of maximum scour is

$$Y_{MAX} = Y_1 C_T m^{6/7}\left(\frac{\bar{q}_2}{\bar{q}_1}\right)^{6/7} \tag{3}$$

in which $\bar{q}_1 = Q_{1m}/B_1$. For a long contraction, $m \approx 1$, $C_T \approx 1$, and thus (3) simplifies to

$$Y_{MAX} = Y_1\left(\frac{\bar{q}_2}{\bar{q}_1}\right)^{6/7} = Y_C \tag{4}$$

which essentially is the relationship proposed by Laursen (1960) for estimating the scour depth associated with live-bed flow through a long contraction. Comparison of (1), (3), and (4) indicates that

$$Y_{MAX} = \alpha Y_C = C_T m^{6/7} Y_C \tag{5}$$

The main difficulty to be overcome for design estimation of scour depth, therefore, is estimation m and C_T.

V. ABUTMENTS SET-BACK ON FLOODPLAIN

This condition of abutment failure is of primary concern for abutments on wide floodplains, and set well back from the main channel. Because clear-water flow predominantly occurs on floodplains, it is assumed herein that scour of a floodplain at an abutment occurs as clear-water scour. Moreover, it is assumed that the scour development is not affected by flow or scour of the main-channel bed. Analysis leads to

$$\left(\frac{Y_{\max}}{Y_F}\right) = C_T m^{6/7}\left(\frac{\tau'_F}{\tau_C}\right)^{3/7}\left(\frac{\bar{q}_2}{\bar{q}_F}\right)^{6/7} \tag{6}$$

in which τ'_F and τ_C are boundary shear stress on the floodplain, and critical for boundary sediment entrainment, respectively. Ettema et al. (2005) provide details as to the derivation and use of (6), as well as (1) through (5).

VI. EXPERIMENT RESULTS

The scour data are being obtained for three states of floodplain and embankment erodibility:

1. Fixed floodplain and embankment;
2. Erodible floodplain and riprap-protected embankment; and,
3. Erodible floodplain and an unprotected embankment.

To assess the depth-amplification factor $\alpha = C_T m^{6/7}$ expressed in (5), Figure 5 plots the ratio Y_{MAX}/Y_C versus $\bar{q}_2/\bar{q}_1$ for fixed floodplain and embankment.

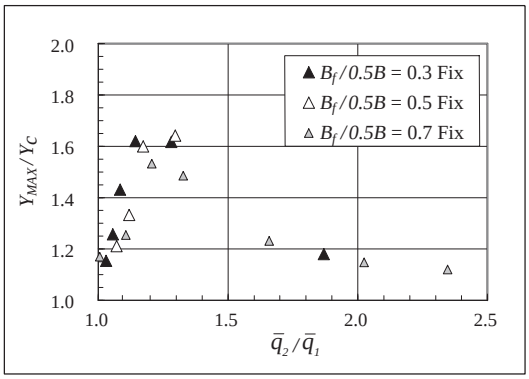

Figure 5. Variation flow-depth increase, Y_{MAX}/Y_C, with $\bar{q}_2/\bar{q}_1$; spill-through abutments on fixed (erosion-resistant) floodplain

This figure provides some important insights:

1. The data appear to conform to a reasonably consistent trend;
2. At the lesser values of $\bar{q}_2/\bar{q}_1$ (and flow contraction), Y_{MAX} substantially exceeds Y_C. Eventually as the bridge waterway becomes more contracted, $\bar{q}_2/\bar{q}_1$ increases, and values Y_{MAX} of approach Y_C. This portion of the trend reflects the dominance of scour caused primarily by flow contraction as opposed to that attributable the local change in bed form height in the contraction combined with the turbulence generated by flow passing around the abutment and over the edge of the main-channel bank;
3. It is intriguing that the values of Y_{MAX}/Y_C attain a maximum value of around 1.5~1.6 when $\bar{q}_2/\bar{q}_1 \approx$ 1.2~1.3;
4. It also is intriguing that the values of Y_{MAX}/Y_C decline quite markedly after the maximum. The values then asymptote to a level of about 1.1; and,
5. The parameter floodplain width divided by channel half width, $B_f/0.5B$, exerts a small influence, especially in the maximum values of Y_{MAX}/Y_C. The maximum value of Y_{MAX}/Y_C is larger for the smaller value of $B_f/0.5B$. This influence is attributable to the fact that, in absolute lengths, the abutment is closer to the main channel, thereby causing more of the

turbulence generated by the abutment to be diffused to the main channel. Here B_F is floodplain width, 0,5B is half width of main channel, and L is abutment length.

Figure 6 plots the ratio Y_{MAX}/Y_C versus $\bar{q}_2/\bar{q}_1$ for the erodible floodplain and riprap-protected embankment.

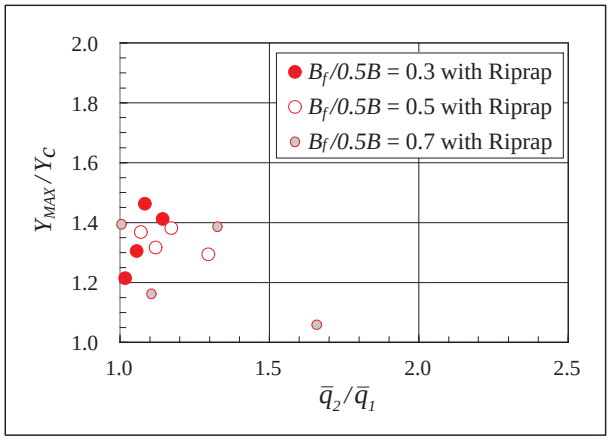

Figure 6. Variation flow-depth increase, Y_{MAX}/Y_C, with $\bar{q}_2/\bar{q}_1$; spill-through abutments (armored with riprap) on erodible floodplain

This figure combines the data trends obtained for scour conditions 1 and 2:

1. For the lesser values of $\bar{q}_2/\bar{q}_1$ (and flow contraction), Y_{MAX} substantially exceeds Y_C. Moreover, for some experiments, the value of Y_{MAX}/Y_C exceeds that obtained when the floodplain was fixed. For these latter experiments, Scour Condition 2 prevailed and produced a deeper scour than did Scour Condition 1.
2. As values of $\bar{q}_2/\bar{q}_1$ increased, scour conditions 1 and 2 jointly increased the flow cross-sectional area at the abutment, and thereby relaxed the flow contraction, thereby resulting in a leveling off of flow depths at the scour location.

Figure 7 includes data obtained with the wing-wall abutments for this scour condition; i.e., for the cases $B_f/0.5B$ = 0.3, 0.5, and 0.7; note that L/B_f = 1. When the floodplain and the embankment are erodible, the three scour conditions occurred. When the flow breached the embankment, the abutment itself becomes exposed, so that scour-depth estimation must treat the abutment as if it were a pier-like structure. The writers are completing a design relationship for this condition. It is interesting to see that $Y_{MAX}/Y_C \approx 1$, when the floodplain and embankment were fixed. This finding suggests that, the scour was largely due to flow contraction, and was not much affected by turbulence generated by flow around the abutment. The flow field observations and measurements taken in the lab support this finding.

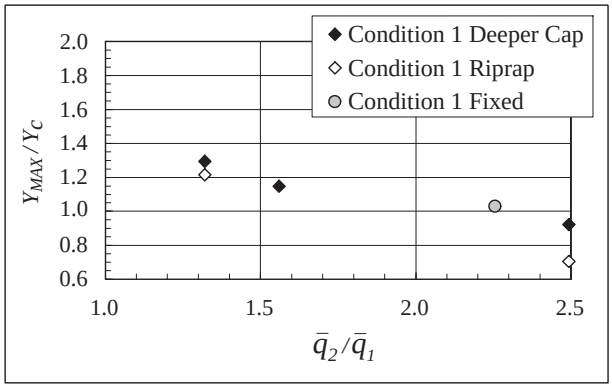

Figure 7. Variation flow-depth increase, Y_{MAX}/Y_C, with $\bar{q}_2/\bar{q}_1$; wing-wall abutments on fixed or erodible floodplain

VII. Design Approach

The observations and data indicate that a practical, and adequately reasonable, approach to estimating scour depth at an abutment can be obtained using (4), (5), and (6). To use these equations entails determining the unit discharge ratio $\bar{q}_2/\bar{q}_1$ along with m and C_T. A 2-dimensional, numerical flow model can be used to estimate $\bar{q}_2/\bar{q}_1$ along with m, though C_T will have to remain empirically derived (with field verification) from laboratory data. The present data, though, suggest that approximate estimation can be made for scour of the main channel:

$$Y_{MAX} = C_T m^{6/7} Y_C \approx \alpha Y_C = 1.75 Y_C \qquad (7)$$

In which Y_c is the flow depth associated with maximum unit discharge through the bridge waterway. This relationship is applicable to spill-through and wing-wall abutments. The suggestion of using α = 1.75 requires further verification, but results to date indicate it to be quite appropriate for design estimation. If no contraction scour is estimated to occur, (7) gives Y_{max} as twice the design flow depth through the bridge waterway.

VIII. Conclusions

The new and practical approach for scour-depth estimation pursued by the writers holds good promise of being practicable and providing scour-depth estimates closer to those observed in the field. This paper outlines the approach. The writers presently are conducting further experiments towards determining the relationships expressed in (2) through (4). The outcome of the experiments may place the estimation approach on a suitably practical and reasonably accurate footing.

IX. Acknowledgment

The work presented here is being conducted under project NCHRP 24-20 of the U.S. Transportation Research Board.

Scour by submerged three-dimensional wall jets

M.A.A. Faruque[1], Partha Sarathi[2] and Ram Balachandar[3]

[1]Research Associate, Department of Civil & Environmental Engineering, University of Windsor, Windsor, Ontario, Canada.

[2]Graduate Student, Department of Civil Engineering, University of Western Ontario, London, Ontario, Canada.

[3]Professor, Department of Civil & Environmental Engineering, University of Windsor, Windsor, Ontario, Canada.

The characteristics of scour caused by submerged square jets were studied by varying the densimetric Froude number, sediment grain size and tailwater conditions. Velocity measurements were conducted using a laser Doppler anemometer. Progressing from the start of the test towards asymptotic conditions, the geometric parameters used to describe scour are found to be sensitive to tailwater conditions and the ratio of the nozzle size-to-grain size. The present results indicate that the effect of nozzle size-to-grain size ratio can be important and needs to be incorporated in the interpretation of scour. This effect is reduced as asymptotic conditions are reached. Turbulent bursts were noted to have an important role in the scour process, and are more distinguishable with the finer bed material. At low values of the relative tailwater depth, the flow and the corresponding scour pattern tends to be non-symmetrical. Moreover, at low values of tailwater depth and higher densimetric Froude number, the scour pattern is quite different from the other test conditions.

I. INTRODUCTION

The prediction and control of scour is considered to be very important in hydraulic engineering practice. Flow through a hydraulic structure often issues in the form of a jet. To better understand the scouring process, jets interacting with sand beds have been studied by previous researchers and empirical relations have been proposed to predict scour. The jet configurations have varied from two-dimensional plane conditions to more complex geometry. Scour by three-dimensional (3-D) wall jets has not been studied as extensively as that caused by plane wall jets. Ref. [8] studied the scour produced by circular wall jets interacting with erodible sand and polystyrene beds. Using both air and water jets, they concluded that the main geometric characteristics of the scour hole are function of the densimetric Froude number ($F_o = U_o \Big/ \sqrt{g(\Delta\rho/\rho)d_{50}}$). Here, g is the acceleration due to gravity, ρ is the mass density of water, $\Delta\rho$ is mass density difference between the bed particle and fluid, and d_{50} is the median bed particle grain size. Using circular jets, Ref. [9] performed experiments with low tailwater depths. Noting the ridge to be flat at low tailwater depths, they concluded that the relative tailwater depth and width of the downstream channel do not affect the maximum depth of scour, whereas the location of the maximum scour was affected. The effect of tailwater depth has also been studied by Ref. [2]. They noted that tailwater has an influence on the maximum depth of scour at asymptotic conditions in the range $2.9 < F_o < 12$. They recognized a critical tailwater condition beyond which a decrease or increase in tailwater causes an increase in the maximum depth of scour. In addition, their data indicates that this critical value increases with increasing F_o and the effect of tailwater becomes insignificant when H/b_o is beyond 16. Sediment non-uniformity also has an effect on scour development by 3-D jets. In studying scour of the non-uniform sand beds, Ref. [7] noted that during early stages of the scouring process, the finer particles become suspended while the coarser particles move in sliding and saltation modes. These types of motions cause the formation of an armor surface that protects the bed as the scour hole develops.

Ref. [6] studied the effect of the channel width-to-nozzle width ratio (expansion ratio) on the scour development and observed that the scour depth was not affected when the expansion ratio is ten or greater. Ref. [4] studied local scour by deeply submerged circular jets of both air and water. They expected that the ratio of the size of the nozzle to the sand particle size should have an influence on the scour profiles, but did not elaborate further.

Ref. [1] compiled data from thirteen different sources including their own study and further highlighted F_o as a characteristic parameter to describe the scour profile. They noted that the tailwater depth had a pronounced effect on asymptotic scour depth for $F_o > 10$. The maximum depth of scour was larger at deeper submergences and higher values of F_o. It was also noted that to attain an asymptotic state at higher values of F_o, a longer time was required. Ref. [5] studied the effect of tailwater depth on local scour by wall jets using a 76 mm square nozzle. The tailwater depth varied from two to six times of nozzle opening and the nozzle expansion ratio was 14.5. In addition, a few exploratory tests were conducted at a nozzle expansion ratio of 41.3. Their data indicates that the maximum depth of scour tends to be larger at a lower submergence. At their lowest tailwater depth, they observed the formation of a secondary ridge that was attributed to secondary flow and proximity of the channel wall to the scour region. They suggested a series of scaling parameters consisting of nozzle size, sand grain size, and densimetric Froude number to describe the scour parameters. Finally, they concluded that the densimetric Froude number, tailwater depth and nozzle size-to-grain size ratio, all have an influence on the extent of scour caused by 3-D jets. They speculated about the dominance of each parameter at different flow conditions.

It is clear that the effects of tailwater depth, nozzle size, jet expansion ratio and grain size have to be clarified. Particularly the effect of nozzle size-to-grain size ratio has not been explicitly considered in previous analysis. In this paper, an effort is made to better understand the scouring process using the data from a

series of experiments with square wall jets. The variables of interest are the densimetric Froude number (F_o), tailwater depth (H) and sediment size (d_{50}). To this end, three different values of F_o (= 3.9, 6.6 and 10.0), a range of H/b_o ($1 \le H/b_o \le 18$) and two different values of b_o/d_{50} (= 10.8 and 37.5) were chosen.

II. Experimental Setup and Procedure

Experiments were carried out in a rectangular open channel flume at the University of Windsor. The nozzle was positioned near the upstream end of the flume. Flow straightners were used at the entrance to the nozzle to reduce the turbulence level and condition the flow. The square nozzle exit was 26.6 mm x 26.6 mm, which provides a nozzle area contraction of 131:1. The ratio of the channel width to the nozzle width was 41.3, which is well above the recommended value of ten to avoid side wall effects. Two types of sand were used in the experiments. The gradation measurements of the sands are tabulated in Table 1 and the bed material can be considered to be uniform.

TABLE 1: GRADATION MEASUREMENTS

Parameter	Sand 1	Sand 2
d_{50} (mm)	2.46	0.71
$\sigma_g = \sqrt{d_{84}/d_{16}}$	1.24	0.9

Table 2 provides the details of the experimental conditions. For measuring velocity, a single-component fiber-optic LDA was used. Due to the restrictions imposed by the geometry of the transmitting optics and the channel support structures, no measurements were possible at locations closer than a distance of one b_o (26.6 mm) downstream of the nozzle exit. Velocity measurements were conducted along the centerline of the nozzle at various stations ($1 \le x/b_o \le 25$). To measure the volume of the scour hole at asymptotic conditions, the procedure suggested by Ref. [2] was used. This involved neatly spreading out a thin sheet of plastic in the scour hole region and pouring known volumes of water until the water surface touched the tip of the point gauge, which was adjusted to the original sand bed level.

III. Results and Discussion

Visual observation:

Fig. 1 shows the schematic of the scour hole and ridge that is formed downstream of the nozzle. A general description of the scour process observed during the Test no. 318 (H/b_o = 18, d_{50} = 2.46 mm at F_o = 10) is first presented. Variations from this case at other flow conditions are described as the discussion progresses.

Once the pump was started, a vigorous scour action occurred close to the nozzle and formed a hole. At the early stages of the scouring process, the nearly elliptical scour hole grew longitudinally with a moving ridge formed downstream of the scour hole. The infant ridge moved forward with a rolling motion of sand particles and with time, the ridge became larger in size. The particles, which have already reached the crest of the ridge, slide down the downstream slope of the ridge. For the large tailwater, at no point, there was large scale suspension of sand particles into the flowing stream. Occasionally, particles could be seen to be thrown from the near bed region into the higher fluid velocity region away from the bed at the early stages of the experiment. In time, the scour hole and the ridge grew in size and the ridge was transported in the streamwise direction. For this grain size (d_{50} = 2.46 mm), after about 15 hours from the start of the test, the rate of change in the scour field was very much reduced and the geometry tended towards an asymptotic state.

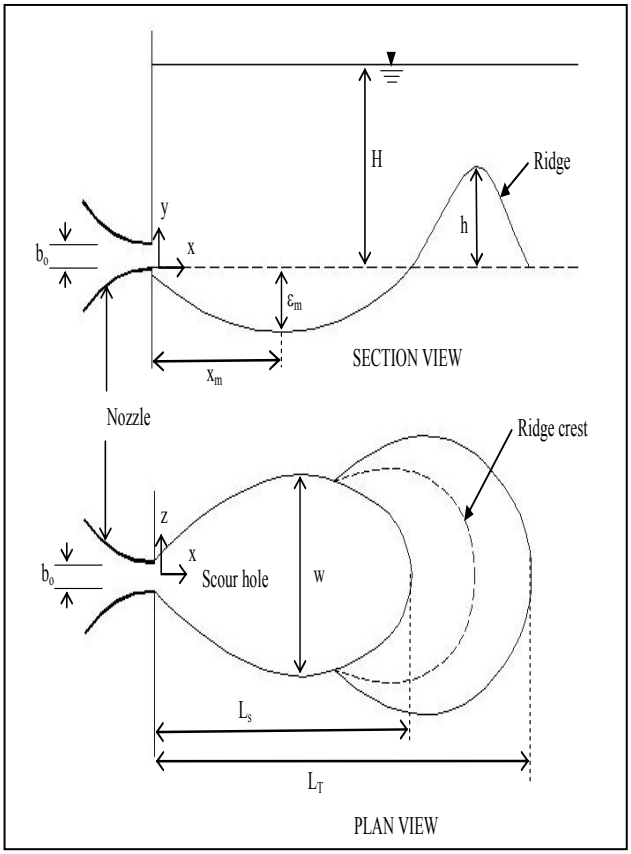

Fig. 1: Definition of scour parameters.

Fig. 2 provides a pictorial representation of the top view of the asymptotic scour hole and the ridge at different tailwater depths for F_o = 10. At the higher tailwater depths ($H/b_o \ge 4$), the scour hole and the ridge were almost symmetrical about the nozzle axis (Figs. 2a, 2b and 2c). With a decrease of tailwater depth ($H/b_o < 3$), the ridge crest disappeared and a plateau was formed on the ridge (Figs. 2e and 2f). At the lower values of H/b_o, confinement effects became important as the jet was constrained in the vertical motion. Due to this confinement, the jet expands more freely in the lateral direction, causing a larger sized hole in this direction and consequently, the ridge was also spread out more laterally. Dye visualization indicated higher velocity on the top portion of the ridge, compared to the other tailwater depths. As a result, the ridge tended to become flatter as the flow exerts sufficient shear stress to cause further movement of sand particles on the ridge. Moreover, at the lower tailwater depths, the scour hole and the ridge became non-symmetrical. This non-symmetrical nature was observed to be prevalent in the experiments with lower densimetric Froude numbers (F_o).

TABLE 2: DETAIL OF EXPERIMENTS

Test no.	U_o (m/s)	F_o	d_{50} (mm)	b_o (mm)	H/b_o	Run time (h)	$\varepsilon_{m\alpha}$ (mm)	w_α (mm)	$L_{s\alpha}$ (mm)	V_s (x 10^3 mm^3)
101	0.78	3.9	2.46	26.6	1	24	45.5	194	385	980
102	0.78	3.9	2.46	26.6	2	24	29.7	135	288	340
103	0.78	3.9	2.46	26.6	3	24	27.8	140	330	400
104	0.78	3.9	2.46	26.6	4	24	31.3	154	355	490
106	0.78	3.9	2.46	26.6	6	24	30.1	145	370	490
112	0.78	3.9	2.46	26.6	12	24	29.3	132	370	560
115	0.78	3.9	2.46	26.6	15	24	28.4	127	376	390
118	0.78	3.9	2.46	26.6	18	24	27.5	128	371	325
201	1.31	6.6	2.46	26.6	1	24	75.4	340	600	3340
202	1.31	6.6	2.46	26.6	2	24	69.9	259	585	3010
203	1.31	6.6	2.46	26.6	3	24	61.5	246	563	2320
204	1.31	6.6	2.46	26.6	4	24	60.1	228	546	2440
206	1.31	6.6	2.46	26.6	6	24	57.2	255	525	2320
212	1.31	6.6	2.46	26.6	12	24	61.9	248	550	2720
215	1.31	6.6	2.46	26.6	15	24	61.7	240	550	2600
218	1.31	6.6	2.46	26.6	18	24	58.7	234	539	2285
301	2.0	10.0	2.46	26.6	1	24	106.4	534	840	13370
302	2.0	10.0	2.46	26.6	2	24	106.1	420	830	11135
303	2.0	10.0	2.46	26.6	3	24	103.6	400	820	10500
304	2.0	10.0	2.46	26.6	4	24	95.7	410	795	9090
306	2.0	10.0	2.46	26.6	6	24	91.0	390	783	8950
312	2.0	10.0	2.46	26.6	12	24	93.9	368	780	8850
315	2.0	10.0	2.46	26.6	15	24	90.2	355	780	7830
318	2.0	10.0	2.46	26.6	18	24	92.4	367	790	8740
402	1.08	10.0	0.71	26.6	2	96	94.9	445	850	10000
404	1.08	10.0	0.71	26.6	4	96	89.0	454	810	9920
406	1.08	10.0	0.71	26.6	6	96	92.0	403	795	9490
418	1.08	10.0	0.71	26.6	18	96	90.1	397	783	8520
506	0.71	6.6	0.71	26.6	6	96	57.8	246	545	2600
518	0.71	6.6	0.71	26.6	18	96	58.0	238	570	2610
606	0.42	3.9	0.71	26.6	6	96	29.1	124	355	495

Note: The last two digits in the Test no. represent the tailwater ratio (H/b_o).

For the lower tailwater depths, the jet initially tended to move laterally to one side. However, with time the flow tended to become symmetrical about the nozzle axis and the scour hole and the ridge changed in response to the jet movement. Fig. 3 shows the scour pattern at $F_o = 6.6$ and $H/b_o = 2$. For this flow, the jet initially moved to the right of the centerline and then moved slowly towards the nozzle axis. The corresponding scour pattern reflects this phenomenon where the ridge is clearly non-symmetrical. Ref. [5] reported the presence of two secondary ridges on both sides of the main ridge in the experiment with a larger size nozzle ($b_o = 76$ mm) at $H/b_o = 2$, which was noted to be an effect of the jet expansion ratio (B/b_o). However, in the present study no secondary ridge was observed on either side of the main ridge. In their study, the jet expansion ratio was 14.5, whereas, for the present study, it is 41.3.

Visual observations also indicate the presence of turbulent bursts, which occurred frequently in the region downstream of the maximum depth of the scour hole. The importance of these burst events in scour studies have been pointed out recently by Ref. [3]. Few scattered bursts were also observed in the region upstream of the maximum depth of the scour hole. For experiments with the coarser sand ($d_{50} = 2.46$ mm), the turbulent bursts did not play a considerable role in sediment transport. The bursts were not strong enough to transport the larger particles and only a sweeping motion of the finer particles occurred. However, for the experiments with the finer sand ($d_{50} = 0.71$ mm), the frequency of the turbulent bursts was higher and visually appeared to play a considerable role in sediment transport. With the finer sand bed, in addition to the longitudinal growth of the scour hole and formation of the ridge, some particles were also transported as suspended load and were deposited past the ridge at the beginning of the experiment, and formed a rippled bed past the ridge. However, with time the scour hole and the ridge covered the uneven bed. After the formation of the ridge, a small

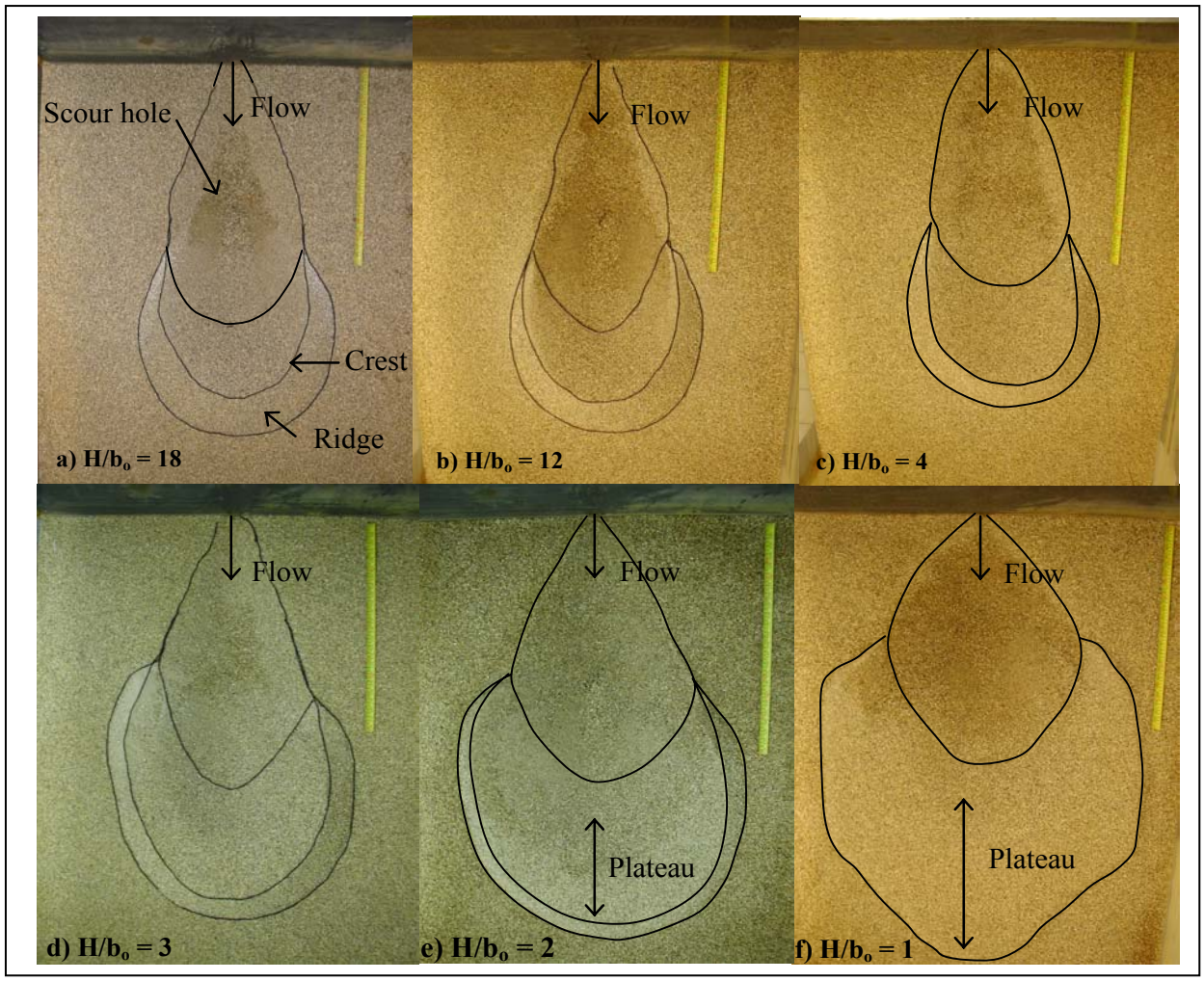

Fig.2: Top view of the scour hole and the ridge (F_o = 10).

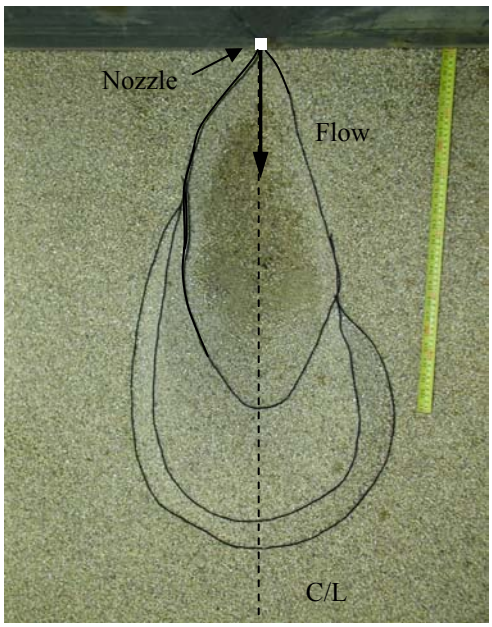

Fig. 3: Top view of the scour profile of Test no. 202 (F_o = 6.6, H/b_o = 2).

dune with a lateral curvature formed on the upstream slope of the ridge (see Fig. 4a). Over time, this dune migrates towards the crest (Figs. 4b, 4c) and falls off the crest. Soon, a second dune forms and begins to migrate up the ridge. Occasionally, due to the occurrence of turbulent bursts, the dune broke up (Fig. 4d) and rolled down to the ridge towards the scour hole. The bursts were strong enough to cause rolling motion of particles in all directions. Some of the particles were seen to roll down towards the scour hole, while others were thrown past the ridge crest. The migrating dunes were not observed in the experiments with the coarser sand.

Scour progress with time:

Figs. 5a - c show the variation of maximum depth of the scour hole with increasing time at various tailwater and F_o values. In these figures, the data of Ref. [5] and Ref. [2] have also been included to enable comparison. Ref. [2] conducted experiments with a 51 mm square nozzle (F_o = 4.4, H/b_o = 1.57, b_o/d_{50} = 62.5, and B/b_o = 12). It should be remarked that the value of b_o/d_{50} in the present study is 10.8 and 37.5 for the coarser and the finer sand, respectively. Considering the three sets of data, it should be noted that the overall range of b_o/d_{50} and H/b_o are quite large. Furthermore, the range of expansion ratio

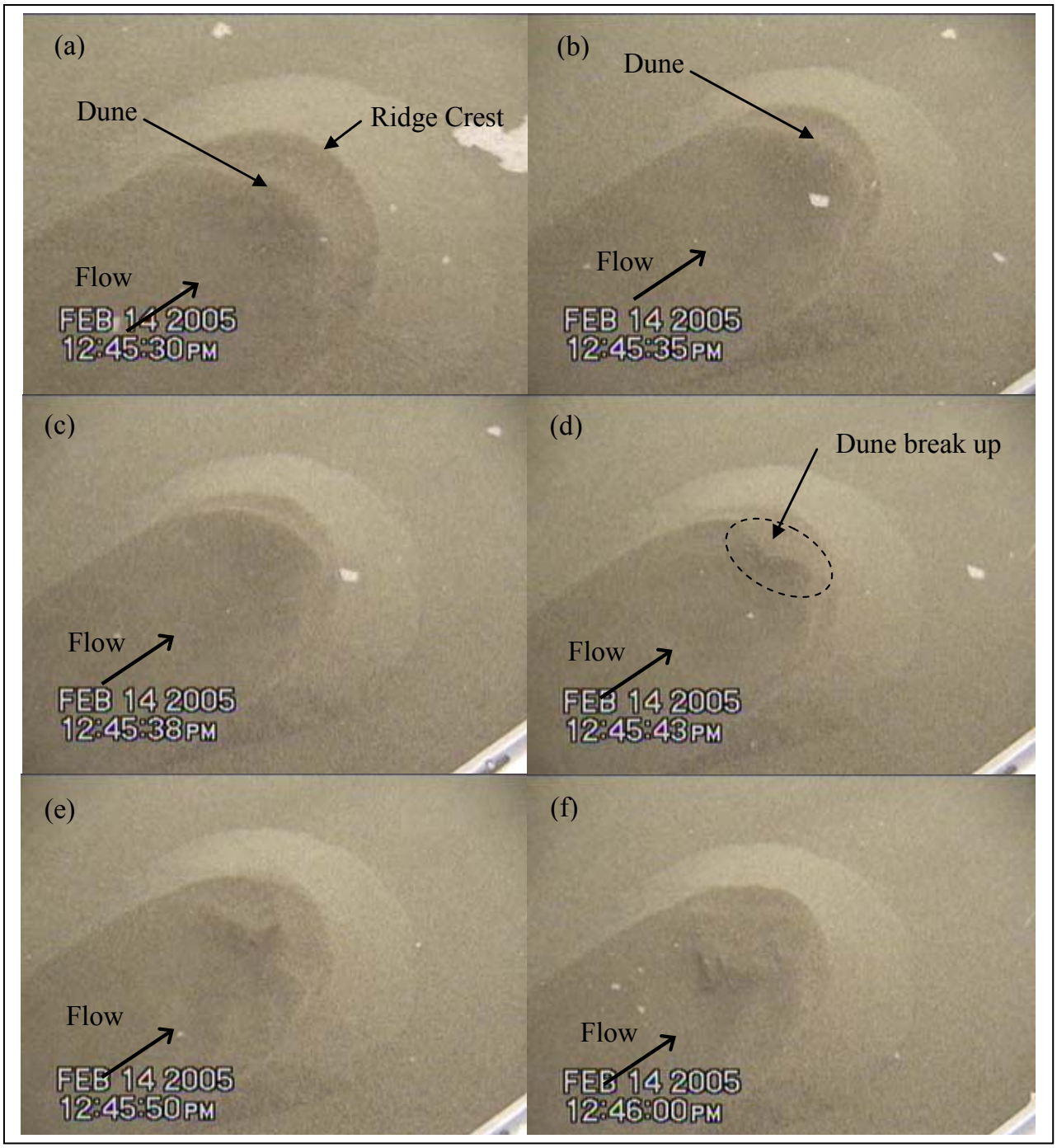

Fig. 4: Formation and rolling down of the small dune (Test no. 418).

is also quite varied ($12 \leq B/b_o \leq 41.3$). The present data at the lower value of F_o (= 3.9) is in agreement with that of Ref. [2] and Ref. [5], indicating that tailwater depth has no significant effect on the maximum depth of scour at low F_o, barring the data at the lowest tailwater condition ($H/b_o = 1$). For $H/b_o = 1$, it should be remarked that it was not visually possible to actually obtain the maximum depth of the scour during the progress of the test. Consequently, only the data at an asymptotic condition after the flow was stopped is shown in the figure. In fact, the present and previous data indicate that for $F_o < 5$, the influence of b_o/d_{50} is important during the early stages of scour and the maximum depth of the scour hole becomes almost independent of all other parameters at an asymptotic state (merging of curves A and B).

Fig. 5b shows the time variation of scour at $F_o = 6.6$. It can be seen from Fig. 5b that for $H/b_o \geq 3$, the data is more or less collapsed on to a single line (curve C). For $H/b_o \leq 2$, the maximum depth of scour is higher (curve D). This is principally due to the effect of tailwater as all other parameters are the same as in curve C and the value of B/b_o is very large in the present experiments. For $H/b_o \leq 2$, since the expansion of the jet and entrainment of ambient fluid is limited in the vertical direction towards the free surface, the jet diffusion is reduced and has more

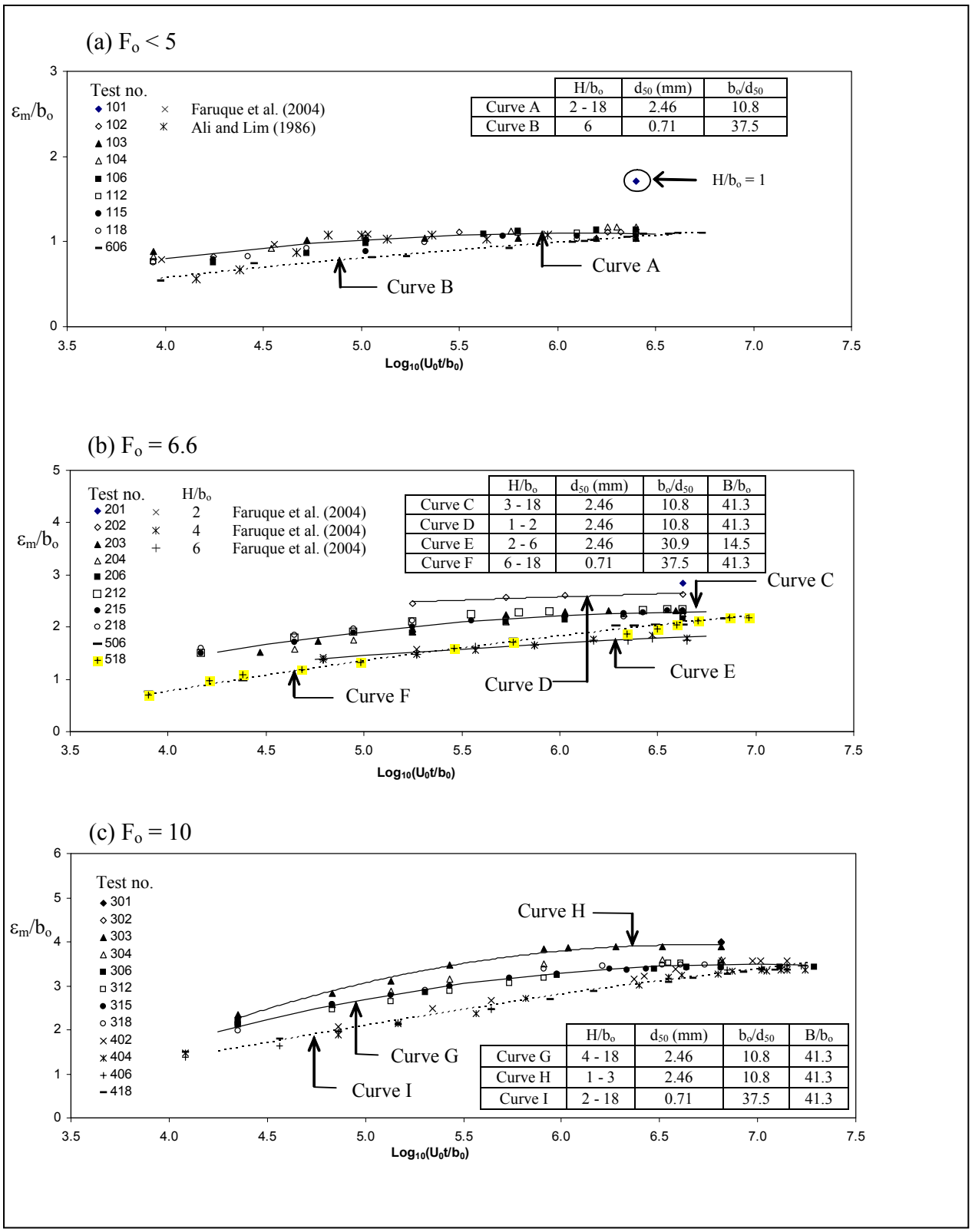

Fig. 5: Variation of maximum depth of the scour with time.

potential to cause scour. It is important to note that the data of Ref. [5] obtained with a 76 mm square nozzle and b_o/d_{50} = 30.9, though collapsed together (curve E), are different from the present set of data. This could be due to the change in b_o/d_{50} or due to the expansion ratio (B/b_o), as both values are different from the present data set. Also shown in Fig. 5b is the data of the tests conducted with the smaller sand (d_{50} = 0.71 mm) and the trend is indicated by curve F (H/b_o = 6 and 18). Clearly, the evolution of scour with the finer sand follows a

distinct trend different from the larger sand. However, at asymptotic conditions, the maximum depth of scour is quite similar for both grain sizes. Since the expansion ratio is held constant and the tailwater depths are large, and only the sand bed is changed, one can conclude that the difference noted between curves C and F is principally due to b_o/d_{50}. Comparing curves E and F, one can note that there is 21% change in b_o/d_{50}, whereas there is a 185% change in B/b_o. The difference noted in the two curves is more likely due to the changes in b_o/d_{50} as the expansion ratio is greater than ten and should have a minimal effect (Ref. [6]). Given that all the data presented in Fig. 5b are from tests conducted at larger values of B/b_o, one is tempted to conclude that the effect of b_o/d_{50} can be quite important in the interpretation of the results. Previous studies have qualitatively speculated on the importance of b_o/d_{50} (Ref. [4]). This is perhaps, the first quantitative study to identify the role of b_o/d_{50}. With increasing b_o/d_{50}, one can note that the time to attain an asymptotic state is increased.

Fig. 5c shows the present data at $F_o = 10$ and illustrates that for the experiments with larger grain size and $H/b_o > 3$, the data are collapsed together on to a single line (curve G). The data of the experiments with smaller sand size are collapsed on to a different line (curve I). Since the value of F_o (= 10) is constant, the larger grain size tests were conducted at a higher velocity, which proportionally causes higher shear stresses near the bed and increases scour. It is important to recognize that as the expansion ratio is held constant in the tests denoted by curves G and I (but different b_o/d_{50}), the differences in the two curves can be attributed to the effect of nozzle size-to-grain size ratio.

Overall, one can note from Figs. 5a - c that there is a dependence of ε_m on tailwater depth, but it is limited to $H/b_o \leq 1$ for $F_o = 3.9$, $H/b_o \leq 2$ for $F_o = 6.6$, and at the highest value of F_o, the effect of tailwater is prominent for $H/b_o \leq 3$. Furthermore, Fig. 5 clearly shows that the effect of b_o/d_{50} can be important at all values of F_o.

The variation of the maximum width of the scour hole and the variation of the length of the scour hole with time for three values of F_o is available in Ref. [10] and details are avoided here for brevity.

Scour geometry at asymptotic conditions:

Fig. 6a shows the asymptotic scour profiles along the centerline of the nozzle for the experiments having different tailwater conditions at $F_o = 10$. In this figure, both the axes are normalized by the width of the nozzle (b_o). Only some of the profiles are shown to avoid cluttering. The profiles indicate that the location of maximum depth of the scour hole tends to be closer to the nozzle with decreasing tailwater depth. The height of the ridge was found to be larger with a sharp crest at the higher tailwater conditions ($H/b_o \geq 4$), while the ridge tends to flatten out with the decreasing tailwater depth. It is note worthy that at asymptotic conditions, the profiles for $H/b_o \geq 4$ are all collapsed together. Not only is the maximum depth of scour the same at the larger tailwater depths, but the entire scour profiles are similar.

The normalized asymptotic perimeter of the scour hole is shown in Fig. 6b. The location of maximum width of the scour hole tends to be closer to the nozzle and is wider at lower tailwater depths. The inability of the jet to expand in the vertical direction (towards the free surface) causes the jet to expand laterally. This results in the scour hole width being larger at $H/b_o = 1$ than at any other conditions. Fig. 6c shows the normalised asymptotic perimeter of the ridge for the experiments shown in the earlier figures. The ridge is wider at lower tailwater depths. Moreover, the shape of the ridge is different at $H/b_o = 1$. Initially, at the start of the test with low H/b_o, the shape of the ridge is very similar to that of the other tailwater depths. However, with increased lateral spreading of the jet, the scour hole widens laterally and correspondingly, the ridge also widens. This later formed wider ridge pushes forward the earlier formed narrow ridge downstream, resulting in the shape shown in Fig. 6c that is different from that noticed at larger H/b_o. Fig. 6d shows the normalised asymptotic perimeter of the ridge for a series of experiments having $F_o = 3.9$. One can note that all the data at higher tailwater conditions ($H/b_o \geq 4$) are closely spaced. The ridge is wider at $H/b_o = 1$ and non-symmetrical at low tailwater depths.

The asymptotic shape of the scour bed profiles for different densimetric Froude numbers (F_o) at $H/b_o = 18$ are presented in Fig. 6e. It can be seen that the depth and the distance of the maximum depth of the scour hole from the nozzle (x_m) increases with increasing F_o. Correspondingly, the height and location of the ridge increases with increasing F_o. Fig. 6f shows the profiles at three values of F_o for $H/b_o = 2$. At the lower value of F_o, the ridge crest is sharper while at $F_o = 10$, the ridge is flat and directly related to the prevailing local velocity (hence the shear stress). Fig. 6g shows the profiles at different F_o for $H/b_o = 1$. It is clear that the size and shape of the ridge is clearly dependent on densimetric Froude number (F_o) and tailwater depth. At very low tailwater depths, the ridge tends to be flat for all F_o.

Fig. 6h shows the variation of the ridge height with tailwater depth. With increasing tailwater depth, the ridge height increases quite rapidly and stabilizes to a near constant value beyond $H/b_o = 6$. Moreover, the effect of F_o is clearly distinct in the figure. Grain size has no significant effect on the relative height of the ridge at asymptotic conditions. It should be noted that at $F_o = 10$, the height of the ridge is slightly greater than the prevailing downstream depth of the flow at $H/b_o = 1$, which can also be found in the results of Ref. [9] for low H/b_o. Ref. [1] categorized the relative ridge height according to submergence. On re-interpretation of their data, one can note that at higher F_o (> 10), there is a critical tailwater depth beyond which an increase or decrease in tailwater depth causes an increase in ridge height.

Sediment deposition:

In the series of experiments conducted one could visually observe a differential deposition of fine and coarse particles at different locations in the scour hole and ridge. For example, fine particles were deposited at the side of the scour hole (see region "A" in inset of Fig. 7a). Also, coarser particles were noted at the bottom of the scour hole just downstream of the maximum scour depth. This layer of coarser particles was only about a grain size in thickness and is located between $0.55L_s$ to $0.75L_s$. This distribution of coarser particles resembles an "armoring layer" which forms when larger particles are

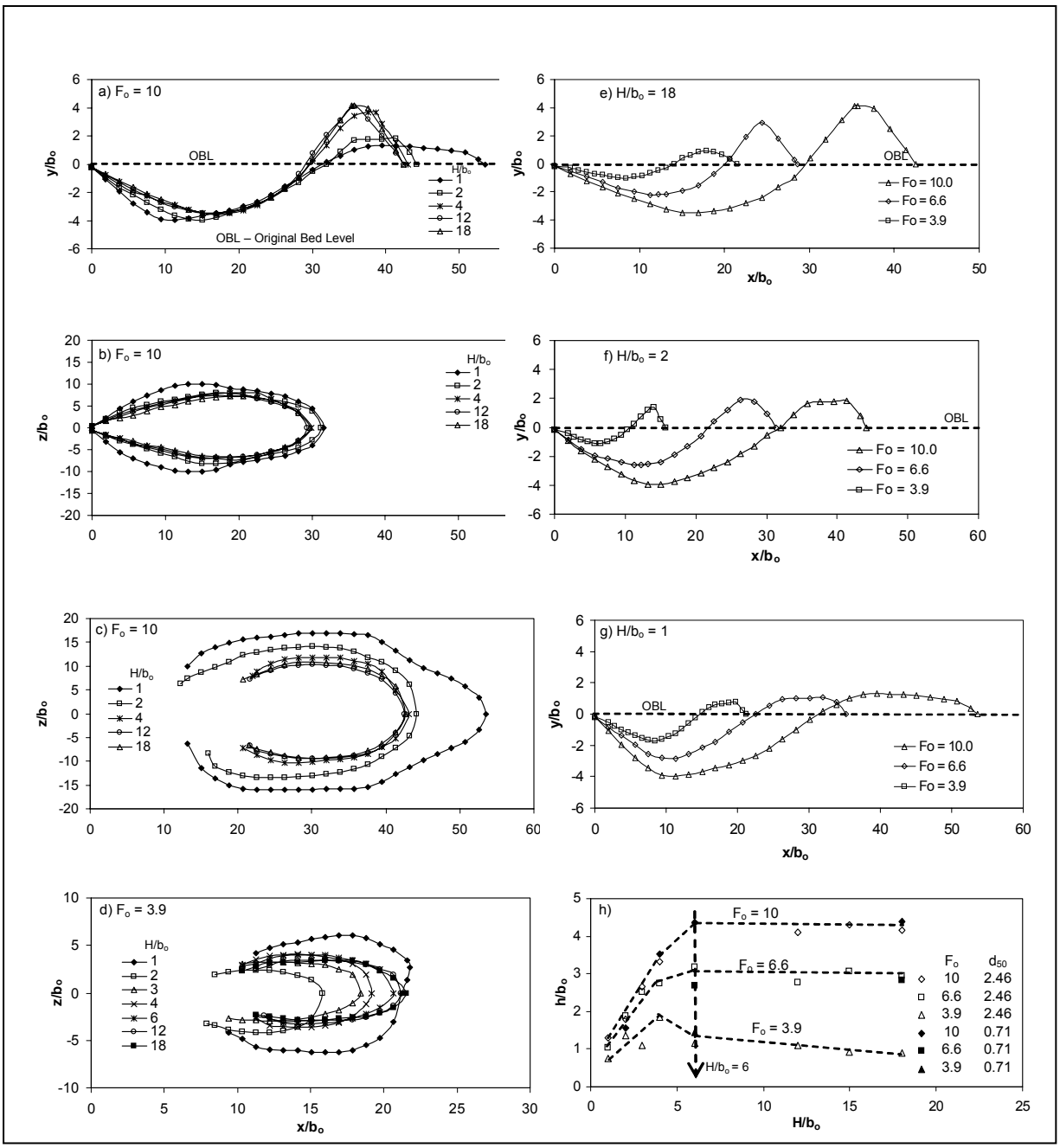

Fig. 6: Scour geometry at asymptotic conditions.

less susceptible to be transported (Ref. [7]). As the layer of sand is very thin and distributed over a small area, grain size sample was not collected from this region. The sand samples were collected for grain size analysis from three different locations, which are shown in an inset in Fig. 7a. Region "A" is the location where the fine particles are deposited. Region "B" is the downstream slope of the ridge and region "C" is the upstream slope of the ridge. Fig. 7a shows the result of sieve analysis of the experiments with F_o = 10 and H/b_o = 2. From this figure, one can note that the sand deposited on the downstream slope of the ridge is slightly coarser than that on upstream slope. This deposition pattern supports the earlier observation by Ref. [9]. A plausible explanation can be provided as follows. At the very beginning of the experiments, the fluid flows in a straight path and the particles tend to follow the fluid path due to the high jet momentum. With the gradual formation of the scour hole and the ridge, the fluid changes its straight path and follows a curvilinear path shown in the Fig. 7b. The larger particles, which are not able to follow the curvilinear path of the fluid because of their inertia, follow their original course and get transported straight up the ridge and then slide down. The relatively finer particles, which tend to follow the fluid more closely, get transported and deposited at the start of the ridge (zone "A"). Zone "A" also includes a part of the scour hole region and some finer particles are also observed on both the sides of the scour hole, which is caused by the sweeping motion originating in the turbulent burst.

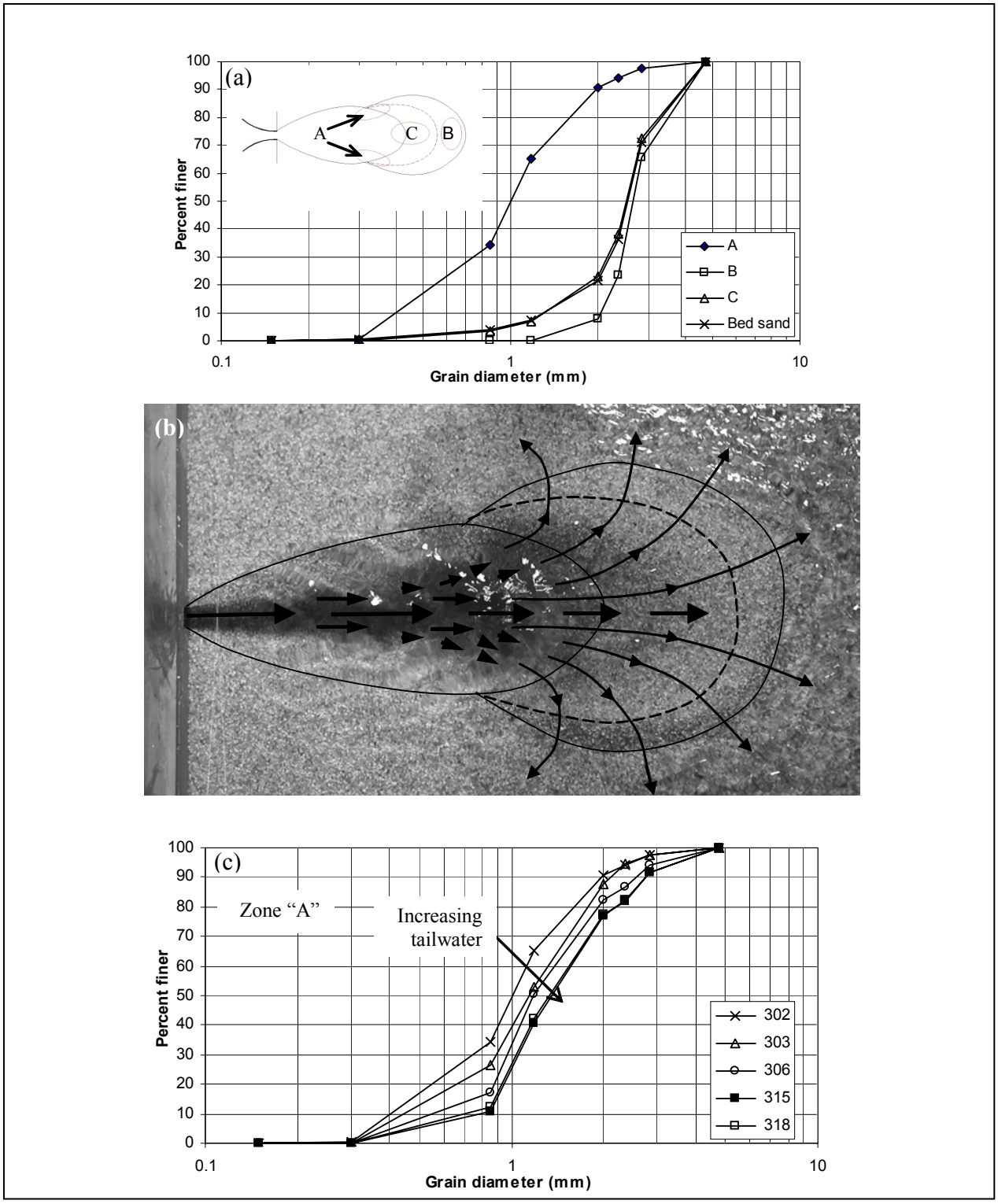

Fig. 7: a) Particle size distribution for Test no. 302, b) Curvilinear flow pattern near the ridge, c) Particle size distribution for experiments having different tailwater conditions.

Fig. 7c shows the particle size distribution at various tailwater depths in zone "A". The median diameter (d_{50}) of the fine particles increases with increasing tailwater depth and at high values of H/b_o, d_{50} remains nearly constant. At the low tailwater depths, dye visualization shows that the effect of the secondary flow becomes stronger. This enhances the scouring process of the sediment and results in the finest deposition at region "A". No systematic variation in grain size distribution with tailwater was observed for regions "B" and "C".

IV. Conclusions

The present study deals with local scour caused by three-dimensional square jets interacting with non-cohesive sand beds. The series of experiments cover a

range of tailwater conditions, densimetric Froude numbers and nozzle size-to-grain size ratios.

Previous studies have recognized that the densimetric Froude number (F_o) is the most important parameter that influences scour. The present study quantitatively identified the role of nozzle size-to-grain size ratio and tailwater depth. It has been observed that at a certain F_o, the evolution of scour with time depends on nozzle size-to-grain size ratio, however, at the asymptotic state, the scour hole parameters were found to be more-or-less independent of grain size. It was found that there is a dependence of maximum depth of the scour hole (ε_m) on tailwater depth but it is limited to $H/b_o \leq 1$ for $F_o = 3.9$, at $F_o = 6.6$ it is limited to $H/b_o \leq 2$, and at the highest value of F_o, the effect of tailwater is significant for $H/b_o \leq 3$. Tailwater was found to have a minimal effect on the maximum width of the scour hole. The length of the scour hole was found to be sensitive to the tailwater depth at shallower conditions. However, the trend at $F_o = 3.9$ is found to be different from that at higher values of F_o.

At an asymptotic state, the depth, width, and length of the scour hole initially decrease with increasing tailwater depth, and after a certain tailwater depth, the values tend to increase slightly and attain constancy. This effect is more prominent at low F_o. It should be noted that the trend seen in the present study is similar to earlier observation made by Ref. [2]. However, the changes with tailwater are not as prominent as that noted by them.

In an effort to provide useful but simplified scour predicting equations at asymptotic conditions, it was assumed that the role of grain size was completely absorbed by densimetric Froude number. The present data supports this assumption. The relationships for predicting the geometric parameters of the scour hole have been proposed in terms of densimetric Froude number (F_o) and tailwater depth. It has been found that the predictions based on the present study are more appropriate for a wide range of test conditions.

In this study, a differential deposition of fine and coarser particles at different locations in the scour hole and ridge was observed. Relatively coarser particles were transported in a straight path to downstream locations because of their larger inertia, whereas, the finer particles were carried by the secondary curvilinear flow around the ridge and were deposited on both the sides of the scour hole and also near the start of the ridge. The formation of migrating dunes and break up of the dunes by turbulent bursts was found to occur in the tests with the finer sand.

REFERENCES

[1] Ade, F. and Rajaratnam, N. (1998). "Generalized study of erosion by circular horizontal turbulent jets." *J. of Hydraulic Research, IAHR,* 36(4), 613-635.

[2] Ali, K. H. M. and Lim, S. Y. (1986). "Local scour caused by submerged wall jets." *Proc. of the Inst. of Civil Engrs.*, Part 2, 81, 607-645.

[3] Bey, A., Faruque, M. A. A. and Balachandar, R. (2005). "Two dimensional scour hole problem: Role of fluid structures." Submitted to the *J. of Hydraulic Engineering*.

[4] Chiew, Y. M. and Lim, S. Y. (1996). "Local scour by a deeply submerged horizontal circular jet." *J. of Hydraulic Engineering*, 122(9), 529-532.

[5] Faruque, M.A.A., Sarathi, P., and Balachandar, R. (2004). "Transient local scour by submerged three-dimensional wall jets: Effect of tailwater depth." *Second International Conference on Scour and Erosion, November 14 – 17, 2004, Singapore*, 2, 309-316.

[6] Lim, S. Y. (1995). "Scour below unsubmerged full-flowing culvert outlets." *Proc. of the Institution of Civil Engineers, Water Maritime and Energy*, 112(2), 136-149.

[7] Lim, S. Y. and Chin, C. O. (1992). "Scour by circular wall jets with non-uniform sediments." *Advances in Hydro-science and Engrg.,* 1, 1989-1994.

[8] Rajaratnam, N. and Berry, B. (1977). "Erosion by circular turbulent wall jets." *J. of Hydraulic Research*, 15(3), 277-289.

[9] Rajaratnam, N. and Diebel, M. (1981). "Erosion below culvert-like structure." *Proc., 5th Canadian Hydrotechnical Conf.,* May26–27, CSCE, 469-484.

[10] Sarathi, P. (2005). "Scour by submerged square wall jets at low densimetric Froude numbers." M. A. Sc. Thesis, Dept. of Civil and Environmental Engineering, University of Windsor, Ontario, Canada.

Dynamic behavior of bridges affected by scouring: numerical simulations and experimental evidence

S. Foti*, D. Sabia*
* Politecnico di Torino, DISTR, Torino, Italy

The dynamical behavior of a bridge is influenced by the conditions of its foundation system. In the present paper, the possibility of detecting the presence of scour of foundations on the basis of dynamical monitoring of the bridge is assessed using numerical simulations and experimental data from a case history. The results show a very promising correspondence between scouring and the global dynamical response of the piers, allowing for promising applications of traffic induced vibrations in monitoring and field investigations.

I. INTRODUCTION

Dynamic tests are often used to infer the conditions of existing structures or to verify the validity of structural models. Advanced data processing methods allow the identification of natural frequencies and experimental modal shapes from the response of the structure to external loading [1][2][3]. The use of ordinary traffic loads as excitation is particularly interesting because it allows the study of the structure in service, with no need for traffic interruptions, which are always very difficult to manage [4].

In the present study the possibility of using the response of the bridge to external loading to investigate the existence of scouring phenomena is proposed. The study is focused on a real case history concerning a five-span bridge having one of the piers affected by serious scouring problems. The possibility of testing the structure before and after retrofitting has been particularly valuable. The experimental data used in the present study are part of larger testing datasets collected primarily for modal identification of the whole bridge (spans and piers) before and after the retrofitting [5].

In order to have a greater insight on the experimental results, also some numerical simulations have been performed using a FEM model to reproduce, at least qualitatively, the global dynamic behavior of the structure.

II. CASE HISTORY

The bridge (Figure 1) is located in the nearby of Turin (Northern Italy) on the Dora Baltea River, an affluent of the Po River characterised by heavy seasonal flows caused by snow thawing in the nearby mountains during spring or by heavy rains, typically in autumn. It is located along the road connecting the two towns of Strambino (on the West side) and Piverone (Figure 2). The bridge, which was built in 1965, has five 30m spans constituted of simply supported prestressed reinforced concrete decks. The foundation system of each one of the 4 piers in the water bed was originally constituted by a mat on 24 piles having 600mm diameter and 15m length. As a countermeasure for scour, a series of 55 piles with diameter 400mm and length 8m was placed all around the perimeter of the foundation mat in the 1980s.

The local stratigraphy beneath the piers is composed essentially of two geologic formations: a first alluvial layer composed of sands and gravels with variable thickness (5m to 20m going from Strambino to Piverone), underlain by a very soft silty clay likely of lacustral origin.

Figure 1 The bridge before retrofitting (Downstream view)

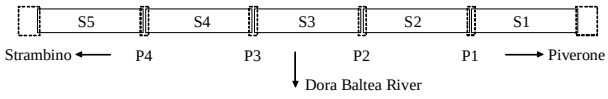

Figure 2 Conventional numbering of piers and spans

At the time of construction, the riverbed was at the same level of the top of the foundation mat. General and local erosion caused over the years a considerable scour of pier foundations, so that in 1982 the top 2-3 meters of the piles were above the riverbed. At that time it was decided to use a cement injection to realize a single foundation block delimited by the edge piles.

The flood of year 2000 caused further scour in the foundation of the piers. A bathymetry of the riverbed after the flood event evidenced generalized erosion, with a particularly marked scour of foundation for one of the pier (P2) where the riverbed was 6 meters beneath the top of the foundation mat (the top 5 meters of piles were without lateral constrain). As a safety measure, a limitation of the traffic on the bridge was decided at that time. Moreover a continuous monitoring of the pier was started in order to plan emergency actions on the intense traffic. The monitoring plan consisted in topographical measurements to detect rotations of the piers and the installation of a permanent inclinometer for the critical pier. The relative movements of reference points on the upstream and

downstream side of each pier are reported in Figure 3. A very marked settlement is detected for pier P2, which moreover underwent a marked rotation with the two sides of the pier showing respectively a vertical displacement of 16mm and 44mm as of March 2004. Settlements of the other piers are instead very limited and do not show marked differences between upstream and downstream side of each pier. The measurements also show a later stabilization, likely due in part to the restrictions in traffic and to the stabilization the phenomenon with a partial filling in of the scour hole.

Because of budget restrictions, it was decided to retrofit the bridge by substituting pier P2 only, whereas other piers would remain unaltered. The retrofitting has taken place in the spring of 2004. The old foundation mat has been incorporated in a larger one founded on 6 large diameter piles with length 47m. Two columns founded on the new foundation mat carry the bridge spans, whereas the old pier has been disconnected from the bridge spans, so that no load is transferred to the old foundation (Figure 4).

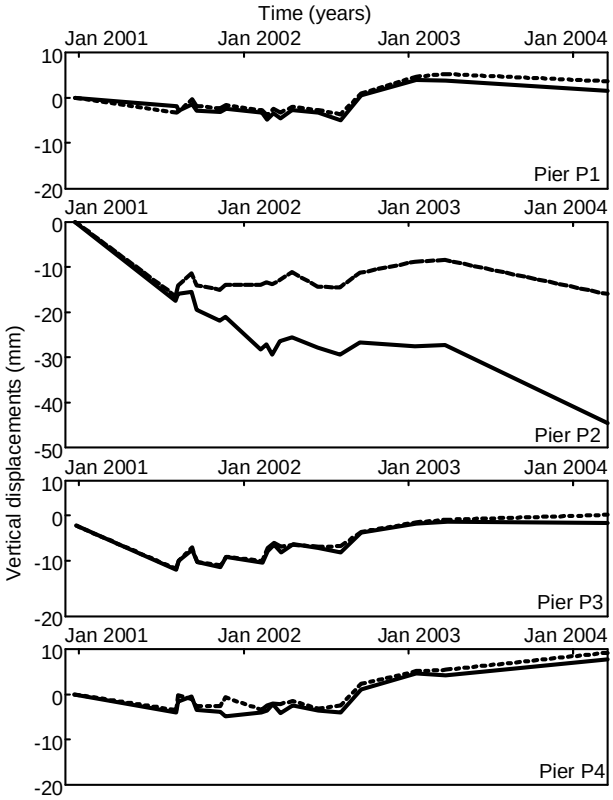

Figure 3 Topographical monitoring on bridge piers (solid line: upstream reference point; dotted line: downstream reference point)

Figure 4 The bridge after retrofitting of pier P2 (Downstream view)

III. SIGNAL PROCESSING

Scouring is expected to reduce the global stiffness of the foundation system, so that the effect of the same load is different if compared to the unaltered situation. The difference in stiffness is sometimes used in order to identify the type of foundation [6]. Since experimental data in the present study are collected under ordinary traffic load and measurements on different piers have been collected at different time, a direct comparison is not possible, because the entity of the load is unknown.

Considering the typical manifestation of localized erosion with scour holes concentrated on the upstream side, a pier affected by scour of foundations is expected to show a markedly asymmetric dynamic behavior. In the present work reference is made to signals collected along a straight line on the foundation mat using an array of receivers. In this case it is expected that the motion at each reference point will be different because of rotations of the foundation caused by uneven support conditions. Since the receivers more often used in dynamical tests are accelerometers, in the present work accelerations will be considered as motion parameters, but similar conclusions could be obtained also in terms of velocity or displacements.

Several possibilities can be devised in terms of signal analysis to evidence the asymmetric response of the pier. Reference can be made to relative levels of maximum acceleration along the receiver array or to cross-correlation of the signals with respect to reference receivers placed on the bridge deck [7].

In the present study the choice has been to refer to the covariance matrix of the signals. Considering a discrete set of discrete signals $s_n(t)$, the covariance matrix **COV** is defined as [8]:

$$COV_{ij}=E[(s_i(t)-\mu_i)(s_j(t)-\mu_j)] \qquad \text{for } i=1\ldots n;\ j=1\ldots n$$

where E[...] represents the mathematical expectation and $\mu_j=E[s_j(t)]$. The diagonal terms of the covariance matrix coincide with variances of single signals and, in terms of signal analysis, with the maximum value of their autocorrelations [9]. This value can be considered a more robust indicator of the motion for each receiver than the maximum acceleration since it takes into account the whole duration of the signal.

IV. NUMERICAL SIMULATIONS

A. FEM Model

Some numerical simulations have been performed in order to assess the sensibility of the overall dynamic response of the system to scour of foundations [10]. In this respect a FEM model has been built using the code Cosmos/m ™ [11]. The model is not aimed at reproducing exactly the existing bridge since several details of the bridge and its foundations system are not known, as for example material parameters both of the superstructure and of the foundation soil.

Considering the static scheme of the bridge, it is sufficient to reproduce a single pier and the two spans supported by it. A view of the FEM model is shown in Figure 5. The superstructure and the foundation mat are reproduced using Shell elements, while pile foundations are reproduced using 3D Beam elements.

The interaction between the pile and the surrounding soil is modeled with distributed vertical and horizontal springs [12]. Considering the low strains induced by traffic loads, the springs are linear elastic.

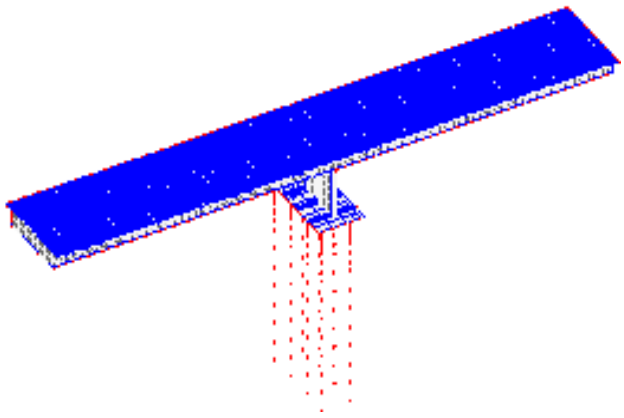

Figure 5 FEM Model

The effect of scour has been modeled by suppressing the springs in the top portion of selected piles. In particular several configurations of the scour hole have been modeled by suppressing the springs for one or more rows of piles and for different depths.

A modal analysis of the bridge in its unaltered and scoured configurations showed moderate differences in natural frequencies and modal shapes [10].

The model has then been used to asses the response of the bridge to external excitation using modal superposition. Considering the scope of the analysis a simple impulsive time history of vertical external forces has been applied on top of the bridge deck.

In order to reproduce the typical setup used in the experiments (described in the following sections) a set of 8 reference points along the foundation mat have been selected (Figure 6) and the acceleration time histories have been computed in the different configurations of the model (with and without scouring). A sample synthetic time history is reported in Figure 7.

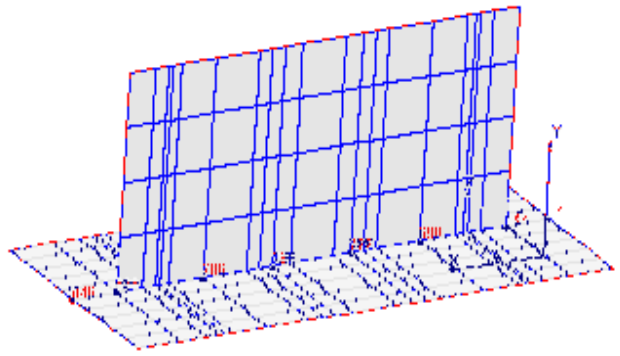

Figure 6 Reference points on the foundation mat of the FEM Model

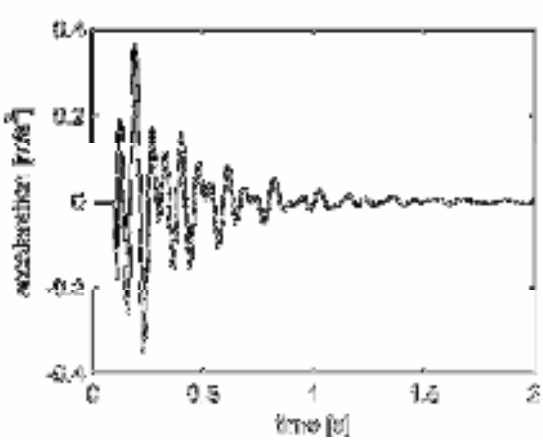

Figure 7 Sample synthetic acceleration time history from FEM simulations

B. Numerical Results

The synthetic signals obtained from the FEM model have been analyzed following the procedure outlined in Section III. Figure 8 reports the diagonal terms of the covariance matrix of the synthetic signals computed for the reference points of Figure 6. Three different situations are compared: the initial FEM model with unaltered springs and two models in which localized scouring has been modeled suppressing part of the springs for the two rows of piles on the upstream side of the foundation. In this case the external impulsive load is placed on the upstream carriageway. The effect of scouring is neatly indicated from the progressive asymmetric behavior with increasing scour depth.

In order to verify the influence of the load position, the same numerical simulations have been performed switching the load to the downstream carriageway, so that in this case the load is applied on the opposite side of the scour hole. The results are reported in Figure 9. Also in this case the progressive erosion lead to an asymmetric behavior of the pier, but the phenomenon is much less marked as clearly shown in Figure 10, where the global responses for the case of 6m scour with different position of the external load are compared.

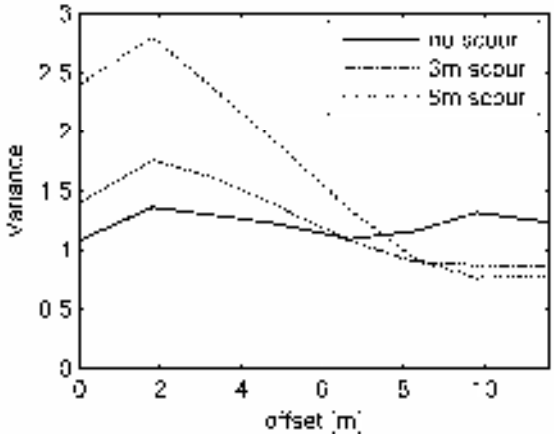

Figure 8 Numerical simulations: global dynamic response of the pier for different level of scour (load applied on the same side of scour hole)

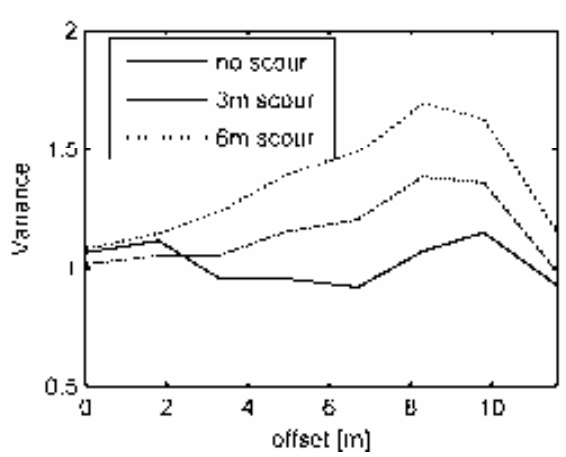

Figure 9 Numerical simulations: global dynamic response of the pier for different level of scour (load applied on the opposite side of scour hole)

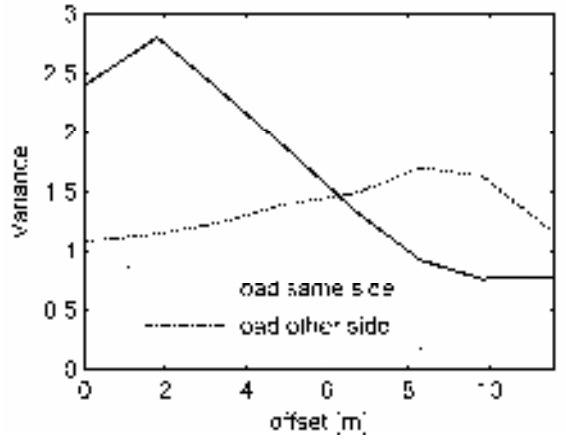

Figure 10 Numerical simulations: influence of the load position on the global dynamic response of the pier in presence of scour

These numerical results show that not only the global dynamic response of the pier is sensitive to erosion in the top portion of the foundations pile, but also that it is possible to locate the scour hole beneath the foundation by comparing the results for different positions of the external load.

V. Experimental Results

A. Data Acquisition

Experimental data have been collected in ordinary traffic conditions, using the passage of heavy vehicles as external source. The data have been collected using a 14 channels data-logger and low frequency accelerometers. The tests were performed before and repeated after the retrofitting of pier P2, using slightly different acquisition setups. In both cases 12 receivers were placed on top of the foundation mat, while the other 2 receivers were placed on the bridge deck as reference points. A sample experimental setup for the 12 receivers placed on the foundation mat is reported in Figure 11, showing the orientation of each receiver. The choice of the acquisition setup was such that the experimental data could be used for modal identification, which was the primary purpose of the investigation [5].

For the present study only the vertical components along a straight line of the mat foundation are considered (e.g. receivers 3, 4, 5, 6 in Figure 11). A sample experimental acceleration time history for a point on the foundation mat is reported in Figure 12. The vibration induced by the passage of the truck is easily located in the first part of the signal.

In order to assess the influence of load position, the signals related to trucks passing on each of the two carriageways have been analyzed separately.

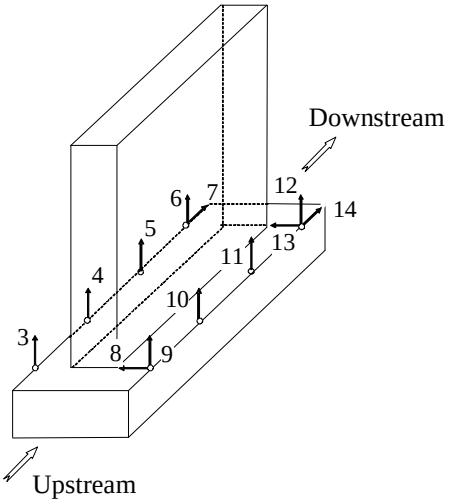

Figure 11 Experimental setup (arrows identify the orientations of accelerometers)

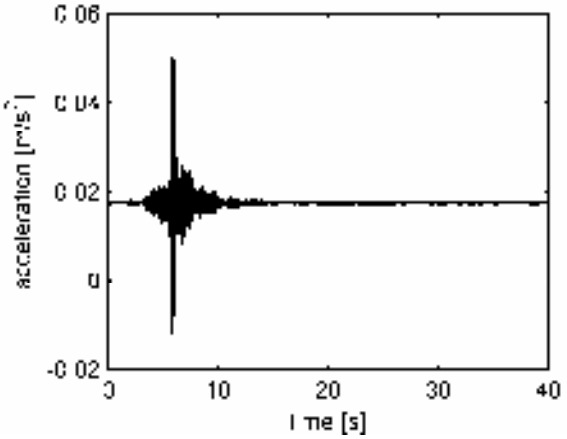

Figure 12 Example of experimental acceleration time history on the foundation mat

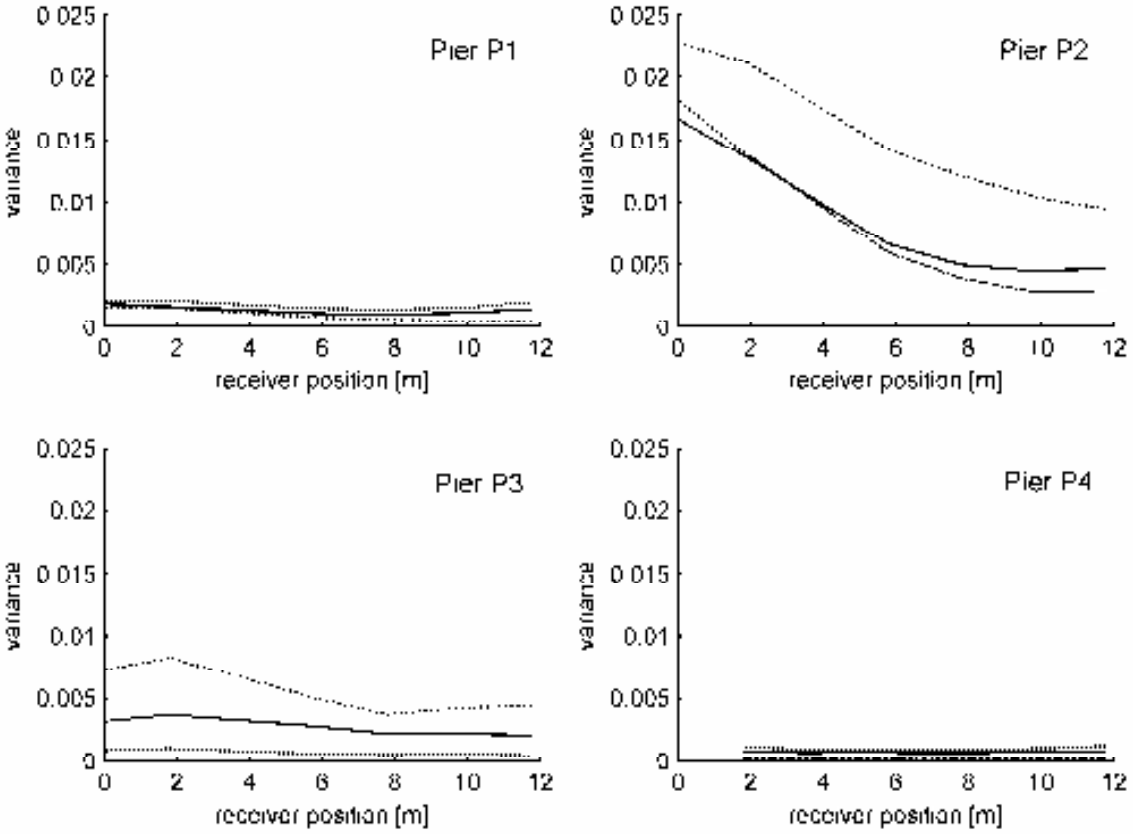

Figure 13 Experimental results: dynamic response of piers before the retrofitting (traffic on the upstream carriageway)

B. Experimental evidence

The first testing session was conducted in July 2003 prior to the retrofitting of pier P2. The test was primarily aimed at modal identification, which evidenced a different behavior of the spans supported by pier P2, likely associated to the different support conditions due to scouring [5].

The experimental data have been analyzed considering the parameters described in Section III and used for the analysis of synthetic signals in Section IV. The experimental signals have been filtered to remove the high frequency noise, using a band-pass filter 1-10Hz, which has been chosen on the basis of the results of modal identification of the piers in order to include the contribution of all the significant modes [5]. Figure 13 reports the results obtained for each pier of the bridge on the first testing session (before retrofitting of pier P2). For each pier, three repetitions of the test are reproduced (i.e. the elaboration of the signals associated to the passage of three different trucks). All the experimental data reported in this figure are related to traffic passing on the upstream carriageway of the bridge.

The comparison of the results clearly shows the different global dynamic response of pier P2, likely associated to the scour phenomenon evidenced by previous independent measurements (Figure 3). In particular the detected asymmetry is very similar to the one obtained from the numerical simulations (Figure 8).

It is noteworthy the fact that apart from the asymmetry of the response, the values of variance obtained on pier P2 are much larger than the ones on the other piers. Similarly it is also interesting that apart from pier P2 the highest levels of variance are obtained for pier P3 which is the other central pier, considering the geometrical symmetry of the bridge, hence more likely interested by erosion phenomena (see also Figure 3). Although these observations are only qualitative, since the traffic induced vibrations are associated to different vehicles having different (and not controlled) weight and velocity, they can be very interesting for subsequent investigations in which a controlled load could be used and a simultaneous acquisition on the different piers could lead to more comparable results.

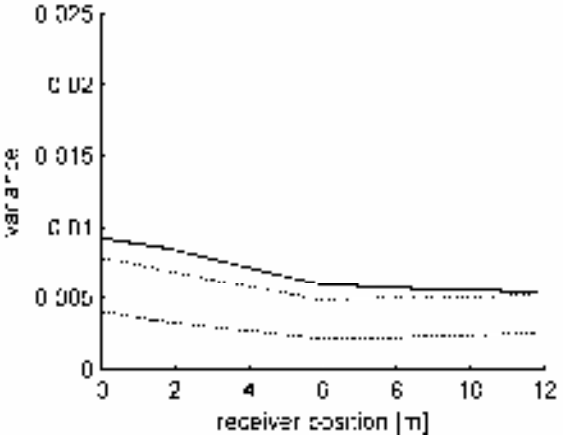

Figure 14 Experimental results for pier P2 (traffic load on the downstream carriageway)

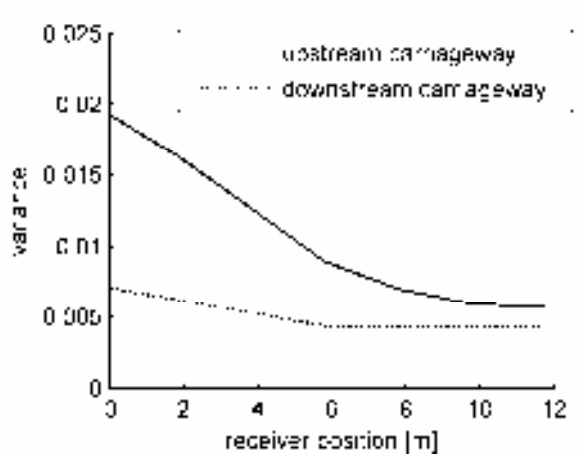

Figure 15 Experimental results: influence of the load position

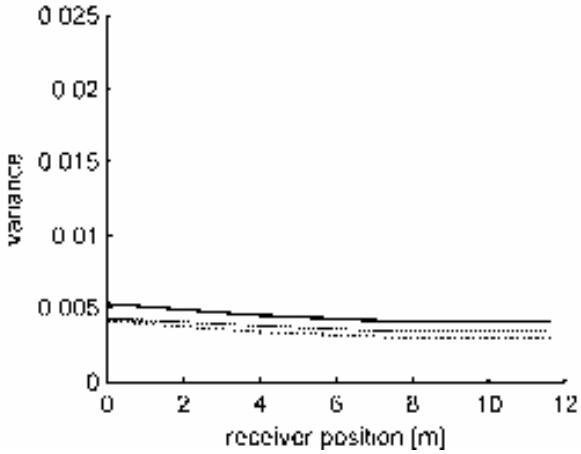

Figure 16 Experimental results: Pier P2 after retrofitting

In order to confirm the influence of load position, which has been evidenced by numerical analysis (Section IV), the data related to traffic on the downstream carriageway have been analyzed separately. Figure 14 reports the relative results for pier P2. In this case only a slight asymmetry is detected and the absolute values of the signal variances are much lower. The comparison between average experimental results obtained for the traffic load on the two carriageway (Figure 15) confirms this observation and are in line with the results obtained with the numerical simulation (Figure 10).

The conclusion that can be drawn from these experimental results is that pier P2 is affected by a localized scour below the upstream portion of the foundation mat. This result is good agreement with topographical monitoring (Figure 3).

As detailed in Section II, pier P2 underwent a major retrofitting with a completely new foundation on 6 large diameter piles. The experimental tests were repeated in September 2004 after the retrofitting, in order to assess the overall modifications in the dynamic behavior of the bridge. As for the first testing session, the tests were primarily aimed at the modal identification of the bridge (spans and piers). Experimental modes for the different bridge spans were in this case more similar and the peculiar features for the spans supported by pier P2 were not anymore more present [5].

Also in this case the experimental data have been subsequently analysed on the basis of parameters identified in Section III.

The results for piers P1, P3 and P4 did not show marked differences with respect to the first testing campaign and are not reported in the present paper. In fact these piers were unaltered.

The results for pier P2 are reported in Figure 16. As expected the behavior of the pier is now significantly different and it is characterized by an overall symmetry.

C. Snapshots of foundation displacements

An additional interpretation of the experimental data is introduced in the following, based on the displacement time histories obtained by double integration of the original acceleration data. Indeed considering the uneven support condition induced by scouring it is expected that a significant rotational component be introduced, while piers not affected by scouring are expected to have a predominant vertical translation.

Considering the set of signals related to vertical displacements of the foundation mat it is possible to obtain snapshots of the foundation motion at different times. Figure 17 and Figure 18 have been obtained assuming as reference time the one in which the vertical displacements at the center of the foundation mat was at its maximum.

The comparison of results before and after the retrofitting shows the influence of scouring on the behavior of pier P2 before the retrofitting, which is characterized by a marked rotational component.

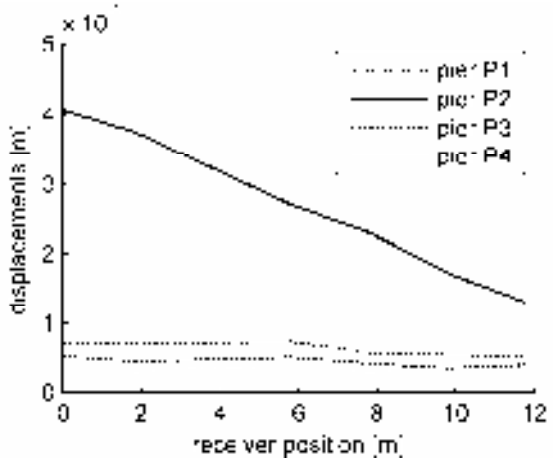

Figure 17 Vertical displacement of the foundation mat at a reference time (before retrofitting of pier P2)

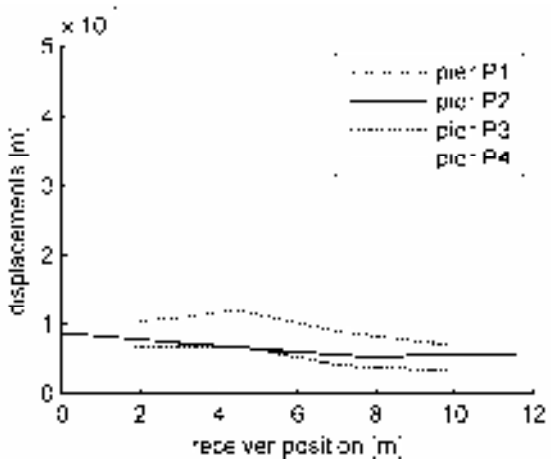

Figure 18 Vertical displacement of the foundation mat at a reference time (before retrofitting of pier P2)

VI. FINAL REMARKS

The experimental results confirm the potential of traffic induced vibrations as a tool for monitoring scour of foundations. In particular the data reported in the present paper show that also with very simple and fast processing it is possible to obtain useful indications about the presence of scouring.

The significance of the present case history is related to previous evidence of scouring for a single pier of a multi-span bridge. The direct comparison of the results for different piers is in good qualitative agreement with the results obtained on a numerical model, demonstrating the possibility of detecting the presence of scour holes and their position beneath the foundation.

The tools presented in the paper can be profitably used for monitoring bridges, programming simple testing campaign at different times in the lifespan of the structure. Advantages of such monitoring are that it is directly associated to the structural conditions and that test can be run under ordinary traffic conditions.

It is anticipated that the potential of such monitoring be even greater if the piers are founded on shallow foundations. Indeed in those cases the influence of scouring on the foundation stiffness is expected to be more pronounced.

On the other hand, since the experimental evidence is mainly related to asymmetric behavior of the foundation caused by scour holes, it is likely not able to produce significant results in presence of global and local erosion phenomena which produce uniform scouring condition for the whole group of piles.

ACKNOWLEDGMENT

The experimental part of the work has been funded by the Torino County Authority (Provincia di Torino), to whom the authors are also grateful for additional data on the bridge. Authors are grateful to the following individuals for the precious help in acquiring and processing experimental data and in performing numerical simulations: Diego Rivella, Paolo Occelli, Marco Raviolo and Andrea Toselli.

REFERENCES

[1] Juang J.N., Applied system identification, Prentice-Hall, Englewood Cliffs, USA, 1994

[2] Liung L, System Identification: Theory for user, 2nd ed., Prentice-Hall, Englewood Cliffs, USA, 1999

[3] Maia N.M.M., Silva J.M.M., Theoretical and experimental modal analysis, Research Studies Press, ltd, Baldock, UK, 1997

[4] De Stefano A., Sabia D., Sabia L. (1997) "Structural identification using ARMAV models from noisy dynamic response under unknown random excitation", ***Proc. Int. Conf. DAMAS,*** 1997, 419-428

[5] Foti S., Sabia D., ***Influence of scour of foundations on the dynamic response of bridges***, unpublished

[6] Olson L.D., Jalinoos F., Aouad M.F., ***Determination of unknown subsurface bridge foundations***, Geotechnical Guideline No. 16, FHWA,

[7] M. Raviolo, ***Experimental analysis of the dynamic behaviour of river crossings in presence of scouring***, Master Thesis, Politecnico di Torino, Italy, 2005 (In Italian)

[8] Marple L. Jr., ***Digital Spectral Analysis with Applications***., Prentice Hall, Englewood Cliffs. 1987.

[9] Santamarina J.C., Fratta D., ***Discrete signals and inverse problems in civil engineering***, ASCE Press, New York, 1998

[10] A. Toselli, ***Numerical analysis of bridges affected by scour of foundations***, Master Thesis, Politecnico di Torino, Italy, 2005 (In Italian)

[11] SRAC, ***Cosmos/m 2.5 User's guide***, Santa Monica, USA, 1999

[12] Roesset J.M., Stiffness and damping coefficients for foundation, in ***Dynamic response of pile foundations: analytical aspects***, ASCE nat. conv, O'Neil and Dodry, ed., New York (USA), 1980, 1-27

Internal erosion as failure mechanism of inner dike slope by wave overtopping - Analysis of Wissekerke tests by means of piping theory

M. Galiana
Cetmef, Compiègne, France

I. INTRODUCTION

During overflow or wave overtopping, breaching of river dikes or coastal defence structure is mainly caused by erosion of the inner slope of dikes. As a result, catastrophic flooding, followed by significant damage and loss of life are likely to occur. Such a disaster was experienced in the Netherlands in 1953. Since this date, significant improvements have been made in the conception of dikes, particularly in the revetment of the outer slope. Nowadays, the understanding of phenomena at stake during waves attack is better but it is still difficult to evaluate resistance to erosion of inner slope of dikes confronted with continuous water flow by overflow or discontinuous water flow by wave overtopping.

In the coming decades, global warming will make sea and river level increase and dikes will be more likely to experience overtopping waves or overflow events. It is also important to improve knowledge in failure mechanisms of the inner slope of dikes, in order to find the better way to test this part of dikes and to give prediction.

The present study within the Delft Cluster framework "Safety against Flooding" is focused on the resistance of the inner slope to wave overtopping, regarding aspects of erosion, in particular for dikes with a (vegetated) cover layer of clay material. The objective of this study is to contribute to the development of a prediction model for erosion of vegetated clay cover of inner dike slope by overtopping waves. This paper is an extract from a Master's thesis [1] and it focuses on one of the failure mechanisms which affect inner slope of dikes, namely the internal erosion mechanism which was observed during flooding of 1953 and during a large scale field test in Wissekerke in 1995.

The first part highlights general considerations and an overview of failure mechanisms which may occur on the inner slope of dike after overtopping or overflow are presented. These mechanisms are internal erosion, surface erosion, superficial sliding and deep sliding. Then, Wissekerke tests, which are in situ tests aimed at simulating overflow conditions on inner slopes of dikes, are described.

The second part starts with an analysis of different mechanisms which composed the main process of internal erosion. Creation of a crack at the top of the dike combined with soil deformation and creation of a well at the toe of the dike are likely to lead to erosion of soil from the sandy core. Our study is focused on the residual strength of the dike, namely process of soil erosion once a well had been formed at the toe of the dike. Sellmeijer's sophisticated model for piping is adapted to create a prediction model for the pipe phenomenon occurring under the cover layer of inner slope.

The third part is focused on results from this prediction model. Method followed during our calculation and some modellings are presented. Modellings with horizontal pipe formed through the dike and with pipe formed under the cover layer of the inner slope of dikes are performed. Comparisons with Sellmeijer's model for piping are made.

II. GENERAL

A. Background

The dike studied is composed of a vegetated clay cover and a sandy core (Fig 1). The upper layer of about 0.3m consists of material on which vegetation can develop well; the under layer consists of erosion-resistant clay [2]. The dike is experiencing overflow or overtopping waves. Overflow occurs if the water level exceeds the crest level, while wave overtopping may occur if the water level is still below the crest of the dike. So, overflow has a (quasi-)steady character, while wave overtopping is a non-steady water movement [3]. As a consequence of these two phenomena, grass cover layers on the crest and inner slope of dikes are potentially exposed to hydraulic loading. This hydraulic loading is said to generate erosion of the cover layer, and is a possible mechanism for initiation of breach development in the flood defence system [4]. Erosion of material depends on the flow velocity and the embankment material. If the material is not resistant enough to water flow, the time required, until a breach has formed is very important. Up to now this extra time is not taken into account when considering the strength of a dike because hardly any knowledge is available on this subject [5]. The residual strength of a dike is defined as the water retaining capacity of the dike after initial damage. This can be expressed in the amount of time from the moment of initial damage until the moment when an increasing flow of water runs into the polder (dike breach). If this residual strength is larger than the duration of the storm, the initial damage will not lead to inundation [6].

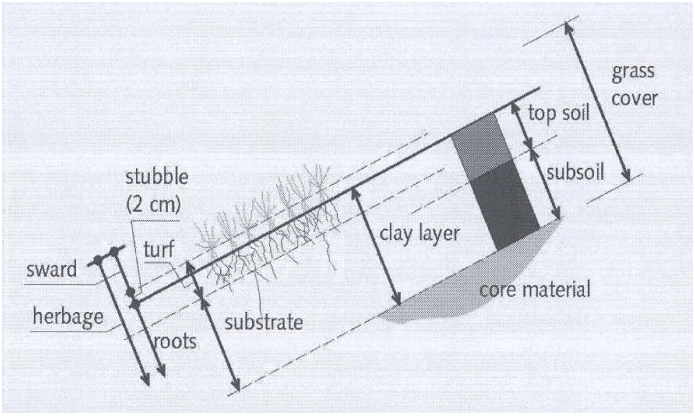

Figure 1. Grass cover layer [7]

B. Failure mechanisms on the inner slope of dike

Due to overtopping or overflow, four failure mechanisms may affect the inner slope of dikes. Three of these mechanisms induce erosion of the cover layer of the dike whereas another one induces entire erosion of the inner slope. We can distinguish: internal erosion, surface erosion, superficial and deep sliding, depending on whether there is creation of a cover layer crack at the top of the dike or not. Here is definition in arbitrary order of importance.

1. Internal erosion

Internal erosion, like surface erosion and superficial sliding, is likely to occur after the creation of a cover layer crack at the top of the dike. During water seepage in the dike, two processes can appear depending on the structure of the dike [5]:

- If the core of the dike consists of clay, a well occurs at the dike toe and soil is carried away. Within the cover layer a small channel is formed and grows. When channel dimensions become too high, the top layer collapses;
- if the core of the dike is sand, water pressures become so high at the dike toe, that soil of the top layer is pushed away and a gate occurs. Then, water flow makes the gate grow and the remaining cover layer fails. In this case, the phenomenon is close to the micro instability[1] mechanism [5].

2. Surface erosion

Surface erosion appears as a consequence of water flow on the surface of the top layer. Depending on hydraulic conditions and on cover layer properties, soil is carried out more or less quickly. After, the inner slope steepens and erodes gradually.

3. Superficial sliding

Mainly, two processes occur during superficial sliding: decrease of shear strength as a function of saturation and increase in weight of the layer (which depends on thickness). Most of the time, superficial sliding is initiated by the creation of a crack in the cover layer at the top of the dike, and water infiltrates directly by the crack into the soil, provoking soil saturation. Strength of the top layer decreases with saturation and the increase of the thickness of the saturated layer is getting so high that a superficial sliding occurs.

4. Deep sliding

Contrary to the three previous mechanisms, deep sliding can appear without any crack of the cover layer. Water flow directly infiltrates in the inner slope of the dike and saturates the soil. At a time when the soil has been saturated enough, a deep sliding may occur.

C. Presentation of Wissekerke tests [8]

1. Description of overflow tests and field

Wissekerke tests are well-instrumented full scale field tests, which were performed at an old sea embankment in Wissekerke (in the South-West of the Netherlands) in August 1995. These tests were aimed at analyzing the way that water infiltrates into the dike and at studying failure mechanisms on the inner slope of dike due to overflow events.

Overflow conditions were simulated by spraying the inner slope of the dike with partly salty water. Pipes were situated at the crest of the dike and water was pumped from a small ditch situated at the toe of the dike. Ditch level stayed constant during all the tests, because other pumps added water taken from a small canal, located not so far from test site. Four tests were conducted; three of them were not instrumented, whereas one was instrumented. Before these four overflow tests, preliminary identification tests were performed and some quick calculations were made. These calculations predicted that one part of the top layer of the inner slope should slide and the depth of the top layer sliding was expected to be between 0.5 and 1 meter. Instruments were then placed in function of these results.

In situ tests and laboratory tests were executed to determine soil characteristics before overflow tests, at different times. Each time, geophysical tests, borings, triaxial tests, and grass strength tests[2] were performed. By this way, soil parameters were determined and a geotechnical profile of the cover layer and the core of the dike core was drawn. Cover layer is mainly composed by clay and silt and the core of the dike is sand. Top layer is more permeable than deeper layers. Top layer permeability is about 10^{-3}-10^{-4} m/s between 0 and 0.5 meters deep, core permeability is about 10^{-6}m/s between 0.5 and 2 meters deep and 10^{-7}-10^{-8}m/s between 2 and 4 meters deep. Tests were performed on a 10*15m^2 square area and inner slope was about 1:1.5.

Tests were performed during summer and soil was very dry. That's why for three of the four tests, soil was sprayed before the beginning of the test. During the four overflow tests, two failure mechanisms were observed: superficial sliding and internal erosion.

2. Description of failure mechanisms

At the beginning of the test, water infiltrates into the inner slope. Half an hour later, a crack occurs at the top of the inner slope, near the crest. As a consequence, water infiltrates by this crack and saturation is getting higher at the top of the inner slope. Effective shear stress is also becoming lower. A stick can be easily put half a meter deep into the soil from the top of the inner slope, whereas the same stick can be hardly put a few centimeters deep into the soil at the toe of the inner slope. At a time when inner slope becomes saturated enough, soil deformations occur and two scenarios, which depend on top layer strength, are possible:

- If strength of top layer is large.

  The top layer can resist to initial water pressures. Water hardly flows on the inner slope and saturates soil from top layer. At the toe of the inner slope, air bubbles are observed, which means that soil is getting saturated. Due to high water pressures, cover layer is getting softer, so that a sliding occurs. One part of the top layer, one meter deep and a few meters large slides and it takes 5 minutes to come down at the toe of the inner slope. Soil from this sliding is so soft, that it is very difficult to walk on it just after the sliding.

- If top layer has nearly no strength.

  Water can go out the top layer and water pressures in the top layer decrease: a well also occurs. This

[1] Micro-instability on dikes is a phenomenon in which the lower part of a dike becomes instable due to seeping water.

[2] This test consists of determining the maximal strength and maximal traction tension of grass in function of applied displacement and time of application.

well is initially small, but after a while and with erosion development, more soil goes away and erosion flow rate increases. Top layer is more and more saturated and grass mate is damaged by a few cracks, which pave the way for ditches. Then, erosion mechanism becomes more important, and ditches become larger and soil is pushed away at the dike toe.

During these two scenarios, a large amount of sand is carried away at the dike toe.

3. Description of the instrumented test

As far as the instrumented test is concerned, it lasted 3 hours and water was sprayed before the beginning of the test. Initial flow rate was about 1.7l/m/s and final flow rate was about 3.6l/m/s. About 1h20min after the beginning of the test, a plastic sheet had been put at the top of the dike, under the spray equipments, to avoid erosion.

The core of the dike was instrumented with different kinds of sensors: flow meter sensors, water pressure sensors, tensiometers, displacement sensors, inclinometers. A video camera was used too, and in order to determine the sliding depth, 6 clay columns, 2 meters length, had been put in the inner slope. Water infiltrated very quickly during the test (after 30min, water depth was about 1.25 meters) and infiltration values were higher than expected. As a consequence, some data given by water infiltration sensors were not always right, because these sensors were not adapted at such high values of infiltration very much. Water pressures varied very much locally and their values were higher than expected. No relation has been found between these water pressures and the creation of wells. First deformations observed are located near the crest and then on the entire inner slope. Clay columns deformations had shown that sliding thickness was about 1 meter deep.

III. Development of a prediction model

A. *Analysis of internal erosion mechanism*

According to observations made during Wissekerke tests, internal erosion mechanism can be divided into four sub-mechanisms:

- creation of a crack at the top of the dike;
- saturation of the dike and deformation;
- cracking of top layer at the toe of the dike and creation of a well;
- soil erosion.

1. Creation of a crack at the top of the dike

Overtopping waves or overflow will cause water to flow at the inner slope of the dike. Water will infiltrate into the dike, provoking soil saturation. After a while, a crack is also likely to occur near the crest of the dike. According to observations made during Wissekerke tests, this crack is the starting point of internal erosion. Moreover, observations made during flooding in 1953, back up this hypothesis. During flooding in 1953, most dikes were confronted with overtopping. And dikes, which were covered by a waterproofed canvas after creation of a crack at their top, didn't experience any kinds of internal erosion, nor sliding of the cover layer. In the book "The disaster" [9], the writer has assembled 200 eye witness reports of flooding in 1953. It is written (p324) that people "have dragged the canvas covers over the crack and loaded the cover with sandbags.[…] In this way this night improvising with covers and bags several cracks were filled or covered and as a result prohibited breaching."

However, even if current observations make it obvious that creation of a crack at the top of the dike is a necessary condition for internal erosion, we can't say for sure that internal erosion won't appear without this crack. Indeed, creation of a crack at the top of the dike enables water to saturate more easily and more quickly the top layer and the ground layer of soil. In our opinion, this crack has mainly an influence on the speed of internal erosion mechanism. So, for further modelling or tests, it could be interesting to determine the real effect of crack at the top of the dike on internal erosion mechanism.

2. Saturation of the dike and deformation

Once a crack at the top of the dike had occurred, soil is getting saturated faster. To explain deformation observed during the phenomenon, we could refer to knowledge from unsaturated soil mechanics. Indeed, if we consider that soil is unsaturated before the beginning of the test, two possibilities can occur when soil is sprayed, that is to say when suction decreases:

- soil collapses, when pressures are higher than swell pressures;
- soil swells, when pressures are lower than swell pressures.

In our case, soil is expected to swell when it is sprayed. In order to go further in the modelling of internal erosion mechanism, it could be interesting to determine these deformations, which could have an impact on the limit traction of grass and clay.

Another important question is what parts of the clay dike will get saturated and what the location of the phreatic surface will be: Will the clay cover layer become saturated? Will the whole sand core become saturated? Will the phreatic surface in the sand core rise to the crest? A corresponding question is how the pore pressure distribution will develop. If the sand core becomes saturated to a high level yielding a high phreatic surface, no hydrostatic pressure distribution is possible without immediate instability of the clay cover layer. A non-hydrostatic pressure distribution in the sand core requires drainage either through the sub soil or through the clay cover layer or through pipes (or slits or rabbit holes) with an opening (crack) at the toe.

3. Cracking of top layer at the toe of the dike and creation of a well

Before any erosion may occur, a crack has to been created at the toe of the dike. Indeed, we could refer to knowledge from piping, defined as development of a pipe through the dike from downstream to upstream side. Conditions for creation of a crack are similar to our case of internal erosion. If a covering clay layer is present, cracking is a necessary condition for the creation of sand boils. If they are no cracks there will be no piping, unless open channels are already present, for example as a result of dead tree roots, digging and, depending on the groundwater situation, cracks in the clay [10]. When the covering layer is so heavy that cracking cannot occur, neither can the erosion mechanism as no sand can be borne away. The soil configuration is then insensitive to piping.

Cracks in the covering layer can occur due to uplift, through which the seepage water finds its way to the surface. Flow

gradient have to be large enough to uplift soil. And the following condition can be written to check if a crack can occur:

$$i_{upward} \geq \frac{\gamma_{sat} - \gamma_w}{\gamma_w} \quad (1)$$

where:

i_{upward}: upward gradient[-]

γ_{sat} : unit weight of saturated soil from the cover layer [kN/m^3]

γ_w : unit weight of water [kN/m^3]

4. Soil erosion

For development of erosion, two scenarios are likely to occur. Either soil is pushed away in relatively large units through the crack or, after creation of a pipe, the individual soil particles are eroded from the pipe boundaries by the flow.

a) No pipe : discharge of water through porous medium

In order to know if soil is likely to be pushed away without creation of a pipe but as a result of water infiltration through porous media, a simple modelling has been performed. For this modelling, which is based on data taken from the instrumented test of Wissekerke, it is assumed that there is no pipe in soil during erosion process. Detailed explanations and calculations can be found in [1].

Soil erosion is supposed to be a consequence of water flow through porous media. Soil is also supposed to be fully saturated and water infiltrates through a thin layer of soil. The infiltration velocity is given by Darcy's formula.

The amount of flow rate given by this modelling is much lower than the flow rate approximately measured at the exit of the well during the instrumented test of Wissekerke. So, it is deduced that water infiltration through porous media is not sufficient enough to observe an internal erosion mechanism as observed during Wissekerke tests and soil erosion is due to the presence of a pipe in the soil.

A few minutes after the creation of the well, it can be legitimately assumed that soil erosion is caused by a piping phenomenon. That's the reason why the next parts from our report are focused on piping. However, some comments must be added about presence of a pipe when the well is created. Indeed, according to previous part, piping can only occur if a sandboil or a well is present. This means, that a pipe can't be present in soil before creation of the well. A pipe can't also appear a few seconds after creation of the well, because it takes a certain time before creation of a pipe. So, it is impossible to have a pipe before creation of a well, which is contradictory with results given by our modelling. If more attention is focused on what happened just before the creation of the well, the conundrum can be partly solved.

According to the movie from Wissekerke tests, a light swell can be observed before creation of the well at the toe of the dike. So, it can be assumed that a cavity or a rabbit hole was already present before the well was created. Research on phenomena at stake and initial conditions required for creation of such a well in case of Wissekerke tests are beyond the scope of this thesis.

b) Erosion due to piping

After creation of the crack, two other conditions must be fulfilled to get piping [11]:

- Condition for pipe in sand: there must be a ''roof'' of clay, concrete otherwise.
- The groundwater flow discharge per unit dike length, Dc, must be strong enough to erode the soil and let the pipe grow until the length l for which equilibrium is just reached: $Dc = Dc_{critical.for.pipe.length}$

For checking piping, different calculation models and calculation rules are available:

- Simple (empirical) calculation rules. One general characteristic of these rules is that they are simple and that a few parameters are necessary. Bligh and Lane rules are also such classical rules. They read:

  $L/H=E$ (2)

  where

  H: head across the structure

  E : erosion factor (different for Bligh and Lane),

  L : length of structure ($L=L_{vertical}+\frac{1}{3} L_{horizontal}$ for Lane and $L=L_{horizontal}$ for Bligh)

- Complex calculation models. More parameters are necessary for a precise calculation. Sellmeijer designed such a model, by using basically analytical methods and numerical methods to refine the results. His model, which is essentially two-dimensional, takes into account the transportation of grains through an already formed channel. His formula, which is equation (3), relates the hydraulic head H, the volumetric weight ratio γ'_p / γ_w, the particle diameter d_{70}, the intrinsic permeability κ, the bedding angle $\hat{\Theta}$, the drag factor $\hat{C}$ (coefficient of White), the thickness of the sand layer D, the length of the seepage line L.

  $$\frac{H}{L} = \lambda b \frac{\gamma'_p}{\gamma_w} \tan\hat{\Theta}\left(0.68 - 0.1\ln b\right) \quad (3)$$

  where

  $$\lambda = \left(\frac{D}{L}\right)^{\left(\frac{0.28}{\left(\frac{D}{L}\right)^{2.8}-1}\right)} \quad (4)$$

  $$b = \hat{C} d_{70}\left(\frac{1}{\kappa L}\right)^{1/3} \quad (5)$$

The following parts will focus on residual strength of the dike. So, it is supposed that a well had been created and a pipe had started to be formed. A modelling based on the same method as Sellmeijer [12] is proposed.

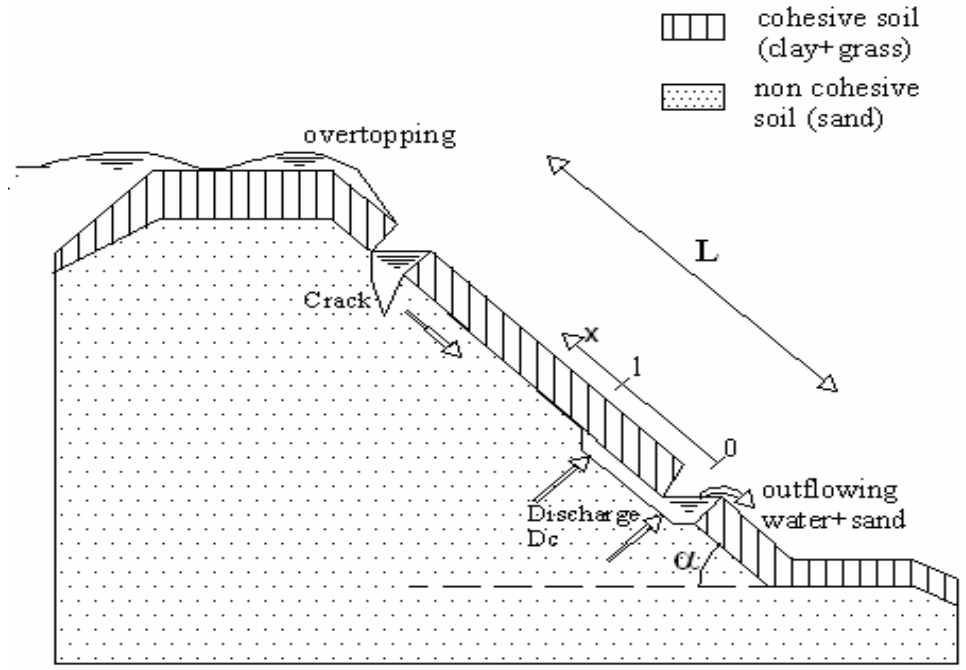

Figure 2. Piping under the cover layer of inner dike slope of dikes (flow direction from left to right)

B. Proposition of a modelling

In his thesis, Sellmeijer [12] modeled piping for a horizontal pipe. His model is sophisticated, but also fairly complicated. In this part, the equations found by Sellmeijer will be changed in order to take into account the inner slope of dike and some assumptions will be made in order to proceed at easier calculations.

Piping can be considered as the combined effect of three interacting processes:

- flow through the slit combined with stability,
- groundwater flow through the soil in the direction of the slit,
- flow through the sand boil including sand fluidization.

Here, the third process "flow through the sand boil including sand fluidization" is not considered. Indeed, according to Sellmeijer's results [12], influence exerted by parameters of the sandboil is minimal. The interaction between groundwater flow and slit flow is modeled as in Sellmeijer's thesis. Head gradient and discharge along the slit-soil interface, as functions of the place, are defined:

- p(x,y)=p(x), component of gradient which is parallel to the slit
- q(x,y)=q(x) component of gradient which is perpendicular to the slit
- $Dc(x)$ discharge through slit per unit dike length (m^2/s) defined as follow:

$$Dc(x) = kQ(x) = k(l - x)q(x) \qquad (6)$$

where
Q : vertical potential [m]
k : hydraulic permeability [m/s]
x:parallel coordinate to the slit
l: slit length [m]

1. Flow through the slit combined with stability

a) Flow in the slit

We first assume that the perpendicular gradient to the slit q is constant:

$$\frac{\partial q}{\partial x}(0 < x < l) = 0 \qquad (7)$$

This assumption appears justified for the interesting cases of just critical grain stability, at least for 90% of the slit: 0<x<0.9l. Indeed, according to intermediate results of Sellmeijer [12], deviations are to be expected in the very beginning of the slit 0.9l<x<l. So, it can be considered that q=q(x=0).

It is supposed that flow in the slit is laminar. In this case, results from Sellmeijer [12] can be used and flow can be described by the following equations:

- the continuity of flow:

$$12\kappa Q = a^3 p \qquad (8)$$

where
Q: vertical potential [m]
p : horizontal gradient [-]
a: depth of the slit [m]
κ : intrinsic permeability coefficient [m^2]

- the drag force τ along the bottom of the slit:

$$\tau = \frac{1}{2}\gamma_w pa \qquad (9)$$

By using previous equations, the condition of continuity of flow can be written as follows:

$$\tau(x) = \frac{6\rho_w \nu Dc(x)}{a^2} \qquad (10)$$

b) Erosion stability

The diameter of all particles is chosen equal and denoted by d. Four forces are applied on a particle at the top of the interface. These forces are:

- the weight of a particle :

$$F_1 = \gamma'_p \frac{\pi}{6} d^3 \qquad (11)$$

- the force associated with the perpendicular seepage gradient (uplift force) :

$$F_2 = Cq\gamma_w \frac{\pi}{6} d^3 \qquad (12)$$

- the drag force due to channel flow :

$$F_3 = \hat{C}\tau \frac{\pi d^2}{4} = \hat{C}\left(\frac{1}{2} pa\gamma_w\right)\frac{\pi d^2}{4} \qquad (13)$$

- the force associated with the parallel seepage gradient :

$$F_4 = p\gamma_w \frac{\pi}{6} d^3 \qquad (14)$$

In order to facilitate the handling of the equations considerably, a second assumption is made : the force associated with the parallel seepage gradient F_4 is neglected as compared to the drag force F_3 [1]. Indeed, the ratio of these two forces is written:

$$\frac{F_3}{F_4} = \frac{3}{4}\hat{C}\frac{a}{d} \qquad (15)$$

and everywhere in any slit of interesting dimensions, $\frac{3}{4}\hat{C}\frac{a}{d} >> 1$, thus $F_3 >> F_4$

The equilibrium for rotation of the grain yields the following relationship at the junction point J of two particles (Fig 3) :

$$F_3 \frac{d}{2}\cos\hat{\Theta} + F_2 \frac{d}{2}\sin\hat{\Theta} = F_1 \frac{d}{2}\sin(\hat{\Theta} - \alpha) \qquad (16)$$

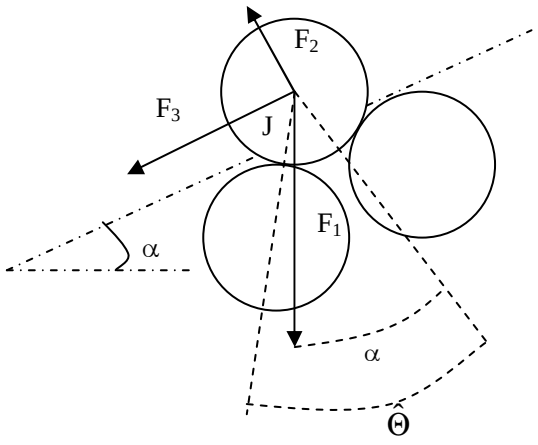

Figure 3. Grains equilibrium

By using expression of the three forces, the critical shear stress τ_{cr} can be determined.

$$\tau_{cr} = \frac{\gamma'_p\, d \sin(\hat{\Theta} - \alpha) - Cq\gamma_w d \sin\hat{\Theta}}{\frac{3}{2}\hat{C}\cos\hat{\Theta}} \qquad (17)$$

Then expressions for the critical depth of the slit a_{cr}, the critical discharge through slit per unit dike length Dc_{cr}, and the critical component of gradient parallel to the slit p_{cr} can be found as functions of x. Expressions found allow us to characterize the situation by just the values at the end of the slit, where x=0 [1]. Assuming that κ, $\hat{C}$, $\hat{\Theta}$, d, γ_p are known constants, we have the following five parameters describing the slit and the flow through it: l, $a_{0,cr}$, q_{cr}, $Dc_{0,cr}$, $p_{0,cr}$.

2. Groundwater flow through the soil in the direction of the slit

Given a certain l, we need four relationships to find the four critical values, whereas we have only three relationships given expressions for a_{cr}, Dc_{cr}, p_{cr} [1]. So we need an additional relationship and we make a third assumption.

Sellmeijer finds an implicite relationship between q_{cr} and p_{cr} by making his groundwater calculation. Here a relationship between q_{cr}, p_{cr} and l, is assumed in agreement with the following likely tendency of the interaction between groundwater flow and slit flow : increasing slit length l and associated increasing slit height, $a_{0,cr}$, yields a decreasing flow resistance in the slit, whereas the flow resistance in the ground does not change significantly. Thus, the direction of the groundwater flow at the soil-slit interface, which can be considered equal to $\frac{q}{p}$, changes from nearly parallel to the slit $\left(\frac{q}{p} = 0\right)$ to dominantly perpendicular to the slit $\left(\frac{q}{p} > 1\right)$. This can be expressed by :

$$\frac{q_{cr}}{p_{0,cr}} = C_0\left(\frac{l}{L_0}\right)^{C1} \qquad (18)$$

where
C_0 and C_1: "empirical" positive coefficients [-]
L_0 : characteristic dimension for the groundwater flow [m]

If we suppose that the uplift gradient is very small as compared to the weight of a particle, namely $\frac{\gamma'_p}{\gamma_w} >> Cq_{cr}$, we can roughly determine evolution of p_{cr} and q_{cr} in function of the slit length l :

- If C_1=1, $p_{0,cr}$ is proportional to $\frac{1}{l^{2/3}}$ and q_{cr} is proportional to $l^{2/3}$.
- If C_1=0.5, q would not increase with increasing l, which does not seem very likely
- If C_1=2, p would be proportional to 1/l and q would be proportional to l, which does not seem very likely either.

So C_1=1 seems a reasonable first estimate. In case of the flow as studied by Sellmeijer, L_0=L seems a reasonable assumption. Then, C_0=5 can be adopted, as $\frac{q_{cr}}{p_{0,cr}} = 2$ is

found by Sellmeijer for l=0.4L. So for flow through an infinite thick layer:

$$\frac{q_{cr}}{p_{0,cr}} = 5\frac{l}{L_0} \qquad (19)$$

After calculations, a relationship between $p_{o,cr}$ and others parameters, supposed as known, is found. Then the critical head in the slit P_{cr} is calculated :

$$P_{cr}(x) - P_{cr}(0) = \int_0^x p_{cr}\,dx \qquad (20)$$

$$P_{cr}(x) = P(0) + 2p_{0,cr}l\left(1 - \left(\frac{l-x}{l}\right)^{1/2}\right) \qquad (21)$$

As a result from this modelling, the slit depth, which is supposed constant along the slit, is independent of the inner slope [1].

IV. Model and Results

We continue to focus on the residual strength of the dike. It is assumed that a well has developed and a pipe gradually increases under the cover layer of the dike due to overtopping. In order to know more about this residual strength, our piping model must be able to answer the specific question: Is the discharge through the sand, as induced by overtopping, sufficient to cause an ever increasing pipe length? In other words, given a certain pipe-length and given a certain slope angle α, what is the critical discharge $Dc_{0,cr}$ (per unit length of the dike) .

A. Method

In order to answer our specific question, we compare the critical discharge through the slit $Dc_{0,cr}$ with the load discharge from the sand into the slit Dc_{load}.

1. Calculation of critical discharge $Dc_{0,cr}$

With the help of equations from the previous part, a spreadsheet, is created. The critical discharge $Dc_{0,cr}$ is calculated as follows:

- It is supposed as known parameters describing soil properties and values recommended by Sellmeijer [12] are retained (Table 1);
- a value of the slit length l is assumed;
- The ratio $q_{cr}/p_{0,cr}$ is calculated;
- $p_{0,cr}$ and q_{cr} are calculated**;**
- the critical discharge Dc_{0cr} is calculated.

Table 1. Values of soil parameters

Submerged unit weight of particles γ'_p	16.5 kN/m^3
Particle diameter d	2.10^{-4} m
Bedding angle of sand $\hat{\Theta}$	54 degrees
Surface factor C	0.4
Drag factor $\hat{C}$	4
Sand permeability	2.10^{-4}m/s
Kinematic viscosity υ	1.10^{-6}m^2/s

2. Calculation of load discharge Dc_{load}

In order to calculate load discharge, we make a groundwaterflow calculation by using the program MSeep. This program analyses two-dimensional stationary groundwaterflow for a cross section in layered soil structures, or for phreatic aquifers. The Finite Element Method is used to solve the differential equation of Laplace (Darcy+continuity) which represents the stationary groundwaterflow. A built-in meshgenerator creates an element mesh for the geometry [13].

In this modelling, we focus on the interface between the core of the dike and the cover layer. That's why we don't draw any cover layer in our modelling. In MSeep, after having entered geometry and values for parameters describing soil properties, we consider limit boundaries:

- At the upstream side and the downstream side, a boundary with potential is applied. The value at the downstream side will be kept constant and equal to the height level. The value at the upstream side will be made vary in order to observe influence of the head difference on results.
- At the slit location, a boundary with potential is also applied. Two different modelling are performed to model the slit :
  - First, the flow resistance in the slit is taken into account. In this case, the potential between the beginning and the end of the slit is equal to the potential at the downstream side plus the critical head difference in the slit given by the following equation.

$$\Delta P = P(l) - P(0) = 2p_{0,cr}l \qquad (22)$$

  - Secondly, the flow resistance in the slit is ignored. In this case, the potential between the beginning and the end of the slit is equal to the potential at the downstream side. The head difference in the slit is equal to zero :

$$\Delta P = P(l) - P(0) = 0 \qquad (23)$$

- Everywhere else, closed boundaries are chosen.

The program MSeep gives us velocities inside each finite element. As we know the length of each element, we determine the discharge through each element and then the total discharge, Dc_{load}, through the supposed slit [1]. On the same graph, the curves representing the critical discharge Dc_{0cr} and the load discharge Dc_{load} are then drawn as functions of the slit length.

B. Some modellings

1. Application to horizontal piping through the dike

a) Modelling and discussion

We have first made some calculation on the classical case of piping, namely by supposing that piping is formed through the core of the dike between the upstream and the downstream side. A simple geometry is chosen (Fig 4): the dike width (distance between points 2 and 3) equals 8

meters at its basis. The calculation are performed by considering an inner slope equals to 0 degree and a characteristic dimension for the groundwater flow L_0 equal to 8 meters. The slit is supposed to be situated between the points 2 and 7.

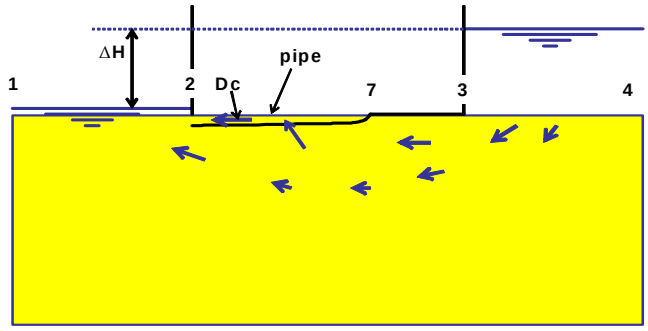

Figure 4. Geometry-Modelling with MSeep piping module (α=0)

After having used Mseep and our spreadsheet as explained previously, Fig 5 and Fig 6 are obtained, depending on whether we consider flow resistance or not. These figures show relations between the discharge through the slit Dc and the slit length l. By using these curves and comparing the critical discharge Dc_{0cr} with the load discharge from the sand into the slit Dc_{load}, we can conclude that the erosion process takes place.

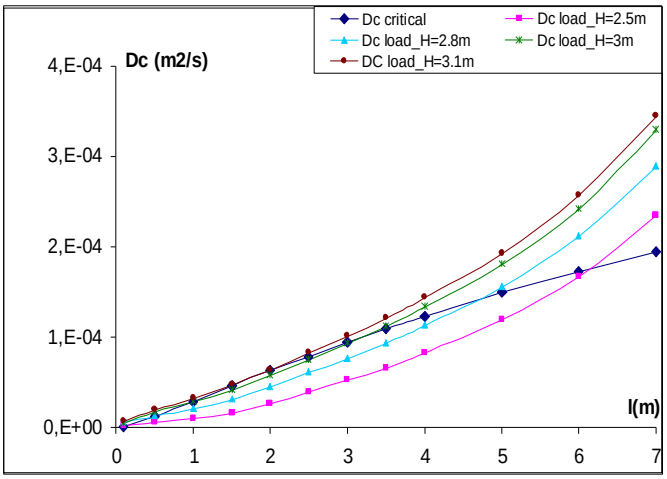

Figure 5. Relation between Dc and l (α=0deg, $\Delta P=2p_{0,cr}l$)

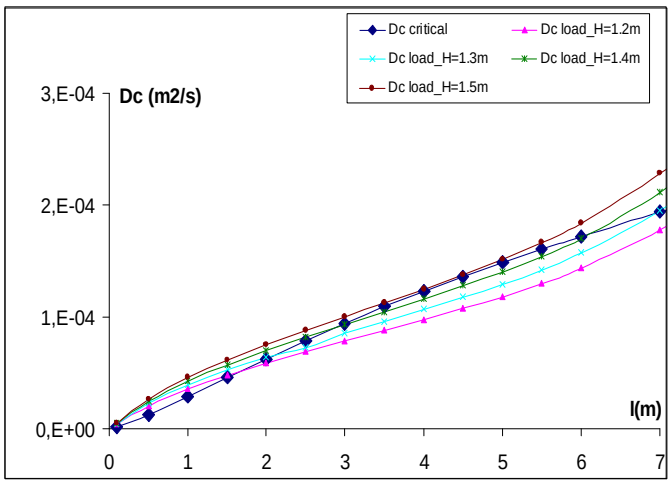

Figure 6. Relation between Dc and l (α=0deg, ΔP=0)

When the head drop H is higher than a critical value H_{cr}, the load discharge Dc_{load} is always higher than the critical discharge Dc_{0cr}. As a consequence erosion process starts after creation of the slit and as equilibrium cannot be reached, the slit can develop between the upstream and downstream side of the dike. The total collapse of the dike becomes also unavoidable.

In these modellings, the critical head drop is approximately equal to 3 meters when flow resistance is taken into account ($\Delta P=2p_{0,cr}l$) and is roughly equal to 1.4 meters when flow resistance is ignored (ΔP=0).

Given a certain head drop, lower than the critical value H_{cr}, we are in the following situation. At the beginning of the process, the load discharge is beyond the critical discharge, which is necessary for initiation of the phenomenon. The slit develops until the load discharge becomes equal to the critical discharge. When this condition is fulfilled, equilibrium is reached and the slit stops growing. If the head drop remains constant, the erosion process stops here. If the head drop increases, the erosion process starts again and the slit develops until a new equilibrium is reached. This process continues until the head drop equals the critical value, which means that equilibrium cannot be reached anymore.

In order to go deeper into the understanding of this process and to compare the results with Sellmeijer's model after, we focus on the relation between the head drop H and the slit length l. The critical curve representing the head drop H as a function of the slit length l is drawn (Fig 7). Points taken for this curve satisfy the condition: $Dc_{0cr} = Dc_{load}$ (junction points in Fig 5 and Fig 6). The shape of this curve is quite the same when flow resistance is considered and ignored. But values found are totally different. The critical head drop is higher when flow resistance is considered and the slit length is lower. The slit length is about 2 meters when flow resistance is considered and 4 meters otherwise.

It is obvious that a critical value of the head drop H exists. Beyond that value, equilibrium cannot be reached. To the left of the critical H the erosion length l is stable. Here a fluctuation in H is compensated for by a small increase in l. But to the right of the critical head a variation in l demands a subsequent decrease of H. If the hydraulic head stays constant a progressive process of erosion is set in motion, resulting in the total collapse of the dike.

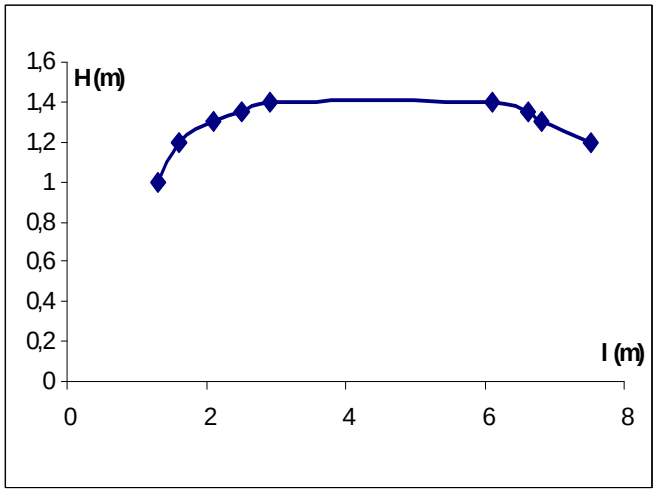

Figure 7. Relation between H and l (α=30deg, ΔP=0)

b) Comparison with Sellmeijer's model

Results from Sellmeijer's model are obtained by using directly the MSeep piping module. This module deals with piping as Sellmeijer did it in his thesis. However, only two forces and not four forces are considered for grains equilibrium, namely the drag force and the weight of the particles. Indeed, further calculation, made by Sellmeijer after his thesis, shown that forces associated with seepage gradient didn't play a great role in the phenomenon. As a comparison with our method, we consider three forces for grains equilibrium and the relationship between the two components of the gradient is found by making an empirical assumption and not after calculation.

Contrary to our modelling, where the slit is modeled by applying a boundary with potential, the use of the piping module requires to draw a dike over the supposed slit. Values are the same as in our modelling and the only difference is the presence of the dike. Vertical permeability of clay is equal to 10^{-5}m/s and horizontal permeability of clay is equal to 10^{-6} m/s.

MSeep gives us the critical curve representing the head drop as a function of the slit length. The shape of this curve is quite the same as ours (Fig 7). The critical head equals 1.2 meters and the critical slit length is equal to 3.5 meters. Values found fit well with value from our model when flow resistance is ignored. When flow resistance is considered, there is a factor 2 between values found by our model and values found by Sellmeijer's model. So, our model which ignores flow resistance, seems more suitable to deal with the horizontal case of piping.

2. Application to piping under the cover layer of the inner slope of dike (inner slope of 30 degrees)

For this modelling, we focus on pipe formed under the cover layer of the inner slope of dike. Geometry entered in MSeep is the same as in Wissekerke test. Inner slope is about 1:1.5 and length slope (between points 2 and 3 in Fig 8) is 8 meters. Calculation are performed by considering an inner slope of 30 degrees and a characteristic dimension for the groundwater flow L_0 of 8 meters. The thickness of the clay cover layer at the toe of the dike is 40 cm. Vertical permeability of clay is 10^{-5}m/s and horizontal permeability of clay is 10^{-6} m/s. The erosion process is the same as in our first modelling, when the pipe is horizontal. Curves shape is quite the same as in our first modelling but values for the discharge and the head drop are different.

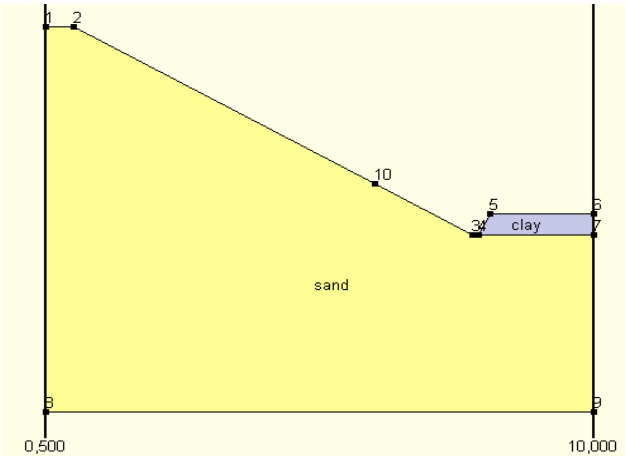

Figure 8. Geometry entered in MSeep for a slope of 30 deg

When flow resistance is ignored, the critical slit length is about 6.5 meters and the critical head drop is about 1.3 meters. When flow resistance is not ignored, the critical slit length is approximately 5 meters and the critical head drop is 1.8 meters. So, flow resistance has less influence on critical values when the pipe makes an angle of 30 degrees with the horizontal line.

A comparison with Sellmeijer's model is made. Sellmeijer's model gives a critical head of 0.35 meters and a critical slit length of 4.1 meters. So, a large difference exists between these values and critical values from our model. However, for both models, process can be described by the same way. Beyond a critical value of the head drop, equilibrium cannot be reached anymore and pipe can't but develop continuously. When the head drop is lower than this critical value, the slit develops as explained in our previous part.

So our model is sufficient to describe process but any conclusion can't be drawn as far as values are concerned. In order to refine it, assumption 3 should be reconsidered. The equation (19) should be revised and different values for empirical coefficients C_0 and C_1 should be chosen.

Although the critical values may deviate, some conclusions can be drawn about internal erosion phenomenon, which occurs during Wissekerke test. According to these models, a head drop much lower than the height difference between the toe and the crest of the dike is sufficient to engender continuous piping erosion and the collapse of the dike. Even the higher value found for the critical head, which equals to 1.8 meters, is twice as low as the height difference between the toe and the crest of the dike, which is equal to 4 meters. This result means that the dike doesn't need to be fully saturated to experience such an internal erosion phenomenon. In other words, once a well had occurred at the toe of the dike and pipe had started to be created; the inner slope of the dike can't but collapse.

V. CONCLUSION

Due to overtopping waves or overflow, four failure mechanisms may affect inner slope of dikes: internal erosion, surface erosion, superficial sliding and deep sliding. This communication sheds light on internal erosion mechanism occurring on sandy dike with a vegetated clay cover layer.

According to results from a large scale field test performed in 1995 in Wissekerke, internal erosion mechanism can be divided into four sub-mechanisms: creation of a crack at the top of the dike, deformation of the inner slope, creation of a well at the toe of the dike and soil erosion. As far as creation of a crack at the top of the dike is concerned, we think that its influence is mainly on saturation time of the dike. So for further research on the topic, it could be interesting to proceed at a sophisticated modelling of water infiltration into inner slope with and without a crack at the top of the dike; and depending on results, in-situ tests could be performed. More investigation could also be pursued in the understanding of phenomena and boundary conditions at stake during creation of well similar to Wissekerke tests.

In this communication, data and observations from the in-situ overflow test of Wissekerke are used to show, that water infiltrated in the dike cannot induce internal erosion

only by porous medium. Pipe flow is needed to explain internal erosion. The hypothesis of piping occurring between the cover layer and the sandy core of the dike is justified and retained for development of a prediction model of soil erosion.

Our model, a simplification of Sellmeijer's model, aims at determining the slit (or pipe) length at which the discharge through the slit is just sufficient to cause limit of equilibrium of sand particles. The load discharge through the sand into the slit is calculated with the program MSeep and is compared to the critical discharge through the slit, which is determined by using equations from our model. Calculations performed with our model are easier than those performed with Sellmeijer's model and some more assumptions are made. Particularly, the direction of the groundwater flow at the soil-slit interface is supposed to be given by the equation (19).

Modellings for different values of pipe slope are performed. Piping process is well described but critical values found are not always good, as compared to Sellmeijer's model for piping and observations from Wissekerke tests. So, for further investigation, we advice to refine equation (19). Other values for "empirical'' positive coefficients, different from values taken in this thesis, should be chosen. Comparisons between the model presented in this paper, the Sellmeijer's model and results from in situe or laboratory tests should be done too.

ACKNOWLEDGMENTS

The author wish to acknowledge Dr Andre Koelewijn, Ir Maarten de Groot, Dr Stan Schoofs for their valuable advice.

Thanks are also extended to Dr. Hans Sellmeijer and Dr Henk den Adel, for their listening and their helpness from time to time with different aspects of this study, and to the whole staff of Geodelft for his kindness.

REFERENCES

[1] M. Galiana, *Internal erosion as failure mechanism of inner dike slope clay cover by wave overtopping*, Extensive report of MSc-internship at GeoDelft/Delft Cluster, GeoDelft report no CO-418010/5, Delft Cluster project CT04.30, 2005, 80p.

[2] Technical Advisory Committee for Flood Defence TAW, *Clay for dikes*, Delft, 1996, 58p.

[3] J. H. De Vroeg, G. A. M. Kruse, M. R .A. Van Gent, *Processes related to breaching of dike; Erosion due to overtopping and overflow*, Delft Cluster-WL | Delft Hydraulics Project DC 030202/H3803, Delft, 2002.

[4] R. Hassan, M. Young, *Part D4.1 – Failures Mode: Grass Cover Layers on Dikes*, Floodsite Project Report, Contract No:GOCE-CT-2004-505420, 2005, 19p.

[5] J. G. Knoeff, H. J. Verheij, *Residual strength after initial failure by overflow/overtopping*, Delft Cluster-WL | Delft Hydraulics Project 02.02.01-57, Delft, 2003, 45p.

[6] M. Klein Breteler, J. G. Knoeff, A. Bizzarri, *Residual strength of dike after failure of cover layer*, ICCE, Lisbon, 2004, 13p

[7] Technical Advisory Committee for Flood Defence TAW, *Grass cover as a dike revetment*, Nivo, Drukkerij & DTP Service, 1999, 18p.

[8] A. J. M. Peters, J. K. Van Deen, *Eindrapportage veld- en laboratoriumonderzoek dijkoverslagproef*, CO-342770/121, Grondmechanica Delft, 1995, 52p .

[9] K. Slager, De Ramp een reconstructie (the disaster, a reconstruction), Leiden, 1992, pp319-324.

[10] Technical Advisory Committee for Flood Defence TAW, *Technical report on Sand Boils (piping)*, Delft, 1999, 108p.

[11] IHE (2003), *Revetments and dikes*, Delft, 2003, pp142-147.

[12] J. B Sellmeijer, *On the mechanism of piping under impervious structures*, LGM – Medelling, No 96, Delft, 1988, 56p.

[13] Geodelft , *MSeep User Manual-Release 6.7*, Delft, 2002, 75p.

Scour Caused by Rectangular Impinging Jet in Cohesiveless Beds

Masoud Ghodsian *, Bruce Melville ** and Stephen Coleman ***

* Professor, Water Engineering Research Center, Tarbiat Modares University, Tehran, Iran

** Professor, Department of Civil and Environmental Engineering, The University of Auckland, New Zealand

*** Associate Professor, Department of Civil and Environmental Engineering, The University of Auckland, New Zealand

I. Abstract

In this paper result of experiments on scour due to impinging rectangular jet in uniform cohesive bed material is presented. The effect of the tailwater depth, water and sediment discharge on the depth of scour was investigated. It was found that the depth of scour is a function of the densimetric Froude number, the ratio of drop height to tailwater depth and the ratio of sediment discharge to water discharge. Increasing the sediment load in the water jet leads to a decrease in the scour depth. It was found that the depth of scour increases with increasing the discharge. The depth of scour initially increases by increasing the tailwater depth and then decreases.

II. Introduction

Flow over and through hydraulic structures often occurs in the form of jets. The jet velocities are usually high enough to produce sizeable, even dangerous, scour holes. Several investigators have studied the scour due to a free overfall jet, including Damle (1966), Doddiah (1953), Robinson (1971), Rajaratnam and Beltaos(1977), Rajaratnam(1980), Abt et al. (1984), Mason (1989), Mason and Arumugam (1985), Ruff et al. (1987), Blaisdell and Anderson (1988), Amanian (1993), Afify and Gilberto (1994), Doehring and Abt (1994), Stein and Julien (1994), Azar (1998), Hoffmans (1998), Martins (1999), Ojha (1999), Mahboubi (2000), Ghodsian and Azar (2001,2002), Ghodsian (2002), Najafi (2003), Ghodsian and Najafi (2003), Tajkarimi (2004) and Bombardelli and Gioia (2005).

The results of an experimental study on depth of scour due to a free overfall jet are presented in this paper

III. Dimensional analysis

The scour depth d_s due to a free-falling jet depends on many variables, including unit discharge of flow q, velocity of outflow jet V, unit discharge of sediment load in the jet q_s, drop height H_c (measured from the centre of the jet to the bed), cross-sectional dimensions of the jet, density of water ρ, median sediment size d_{50}, density of sediment ρ_s, tailwater depth Y_t and acceleration due to gravity g. In this study, the hydraulic radius R of the jet cross section used to characteristic the jet size. Therefore:

$$d_s = f\left(R, Y_t, d_{50}, \rho, \rho_s, g, V, H_c, q, q_s\right) \qquad (1)$$

Using dimensional analysis, Eq. 1 can be written in the following form:

$$\frac{d_s}{Y_t} = f\left(\frac{Y_t}{H_c}, Fr_d \frac{R}{H_c}, \frac{q_s}{q}\right) \qquad (2)$$

in which Fr_d is the densimetric Froude number given by:

$$Fr_d = \frac{V}{\sqrt{g d_{50}(S_s - 1)}} \qquad (3)$$

where S_s is specific gravity of the sediment.

IIV. Experiments

The experiments were conducted in a re-circulating flume with a length of 40m, width of 0.83m and depth of 1.0m. A rectangular free overfall jet of 0.072m width was established 5m from the upstream end of the flume (Figure 1). The bed of the flume downstream from the jet was raised in order to create a 0.3m deep and 3m long test section. The test section was filled with a uniformly-graded sediment with a median diameter of d_{50}=0.62 mm. A sluice gate was used to control the tailwater depth. Discharge was measured by a calibrated sharp-crested triangular weir at the entrance to the jet approach channel. Initially, a thin protective metal sheet was placed on the sediment bed downstream of the jet. The flume was slowly filled until the desired tailwater level was reached. The jet-scour experiments were started when the protective sheet was rapidly removed. At the end of the experiments, the scour profile was measured using the depth sounder.

Initially, experiments were run with a clear-water jet flow and thereafter with a successively-increased sediment load to the jet. Sediment having the same size as that of the bed material (d_{50} = 0.62mm) was added to the jet using a hopper (see Fig. 1). Experiments were run for varying water and sediment discharges and tailwater conditions. The duration of experimental runs was set to 2hr. It was observed that most of the scour had occurred after 2hr. Table 1 shows the range of data studied.

TABLE 1. RANGE OF EXPERIMENTAL DATA

Parameter	Range
Y_t	9.4-20.3
Fr_d	7.19 – 9.36
Q_s	0 - 14
d_s/Y_t	0.11 – 1.3

V. RESULTS

In all the experiments it was observed that the scour hole is roughly circular in plan with most of the eroded material being deposited as a ridge downstream from the scour hole. However limited deposition occurs also on the sides of the scour hole (Fig.2). The effect of discharge on longitudinal and lateral scour profile, for Q_s=0, is shown in Figs. 3 and 4, respectively. These figures show that under the stronger flow of Q = 2.97L/s, which is associated with more longitudinal flow velocity, more sediment is transported downstream with deposition on the sides of the scour hole being sparse. It is evident that by increasing discharge the dimensions of scour hole and ridge formed at the downstream of scour hole increases.

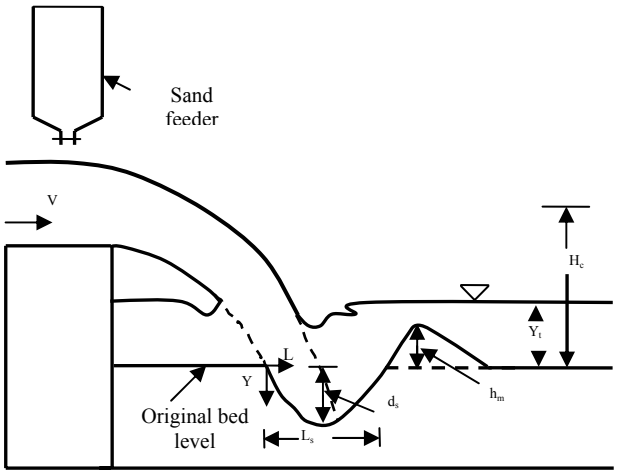

Fig 1. Schematic view of scour due to impinging jet

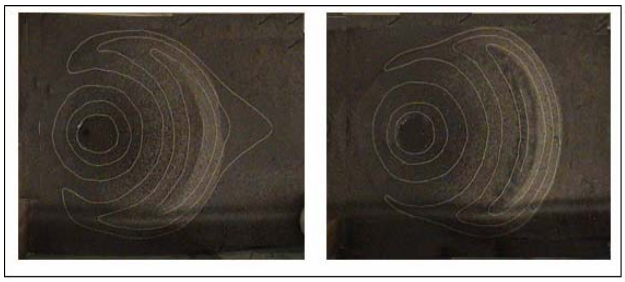

a) Q=1.45(L/s) b)Q=2.97 (L/s)

Fig. 2 Typical scour hole formed for two values of discharge; Y_t=9.4cm and Q_s=0

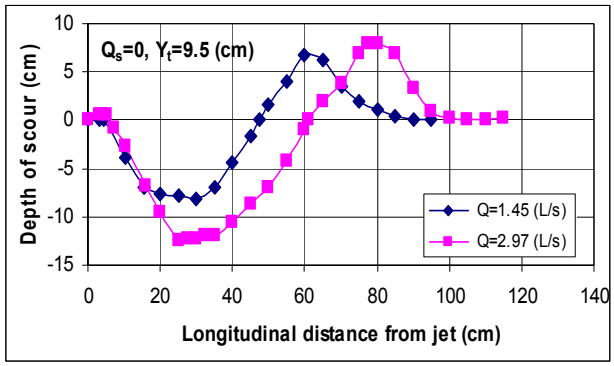

Fig. 3 Effect of discharge on longitudinal scour profile

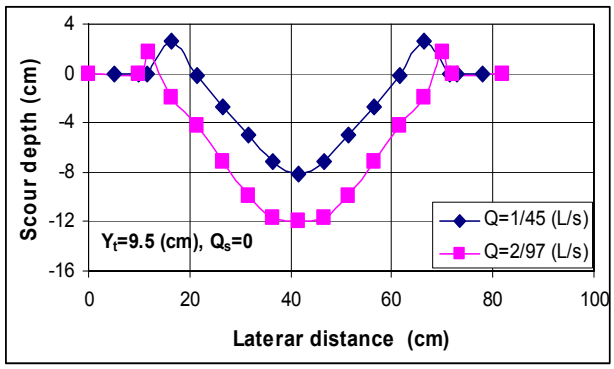

Fig. 4 Effect of discharge on lateral scour profile

The influence of the tailwater depth Y_t and discharge Q on the depth of scour d_s is demonstrated in Fig. 5, for which drop height H_c=27.6cm and sediment transport rate Q_s = 0. It is evident from these figures that increasing tail

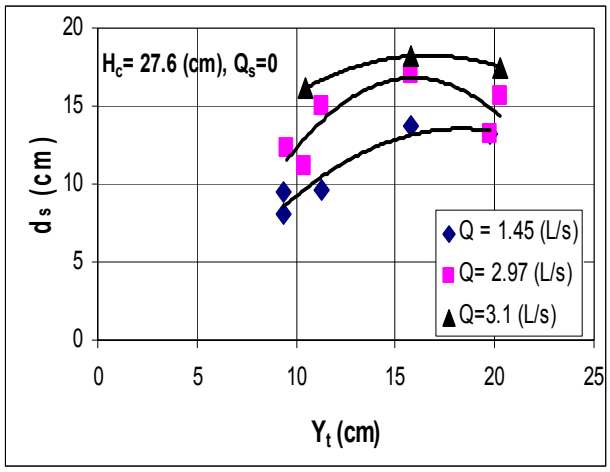

Fig. 5 Effect of tailwater depth and discharge on depth of scour

water depth increases the scour depth initially, reaches to a maximum and then decreases. For low values of tailwater depth, the scour depth is governed by the tailwater depth, increasing with larger depth. The decreasing depth of scour at high values of tailwater depth is attributed to the increasing dissipation of the energy of the jet flow for this case.

The influence of the sediment load of the jet on the scour depth is depicted in Fig. 6 for Q = 1.45L/s and three values of tailwater depth, Y_t=9.45cm, 11.3cm and 15.8cm respectively. When the jet is carrying sediment ($Q_s > 0$), the scouring potential of the jet is reduced, and the depth of the scour decrease.

The influences of the parameters q_s/q and Y_t/H_c on relative scour depth d_s/Y_t are shown in Fig. 7 for $Fr_d.R/H_c$= 0.357. The effect of q_s/q in reducing scour depth is clear from this figure. In summary, the scour depth developed below a free-falling jet is reduced in size when the jet carries a sediment load.

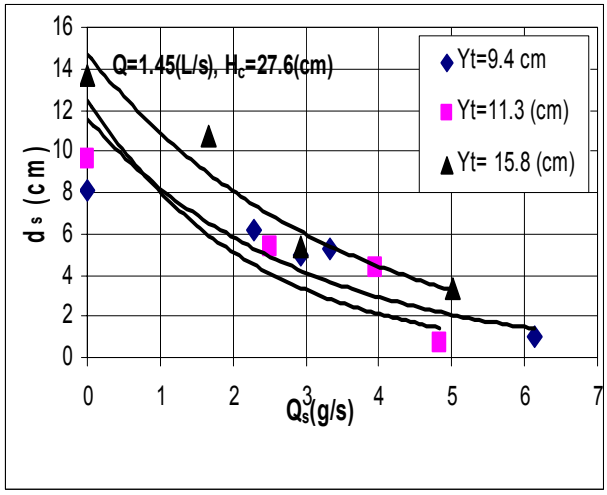

Fig. 6 Effect of sediment load on depth of scour

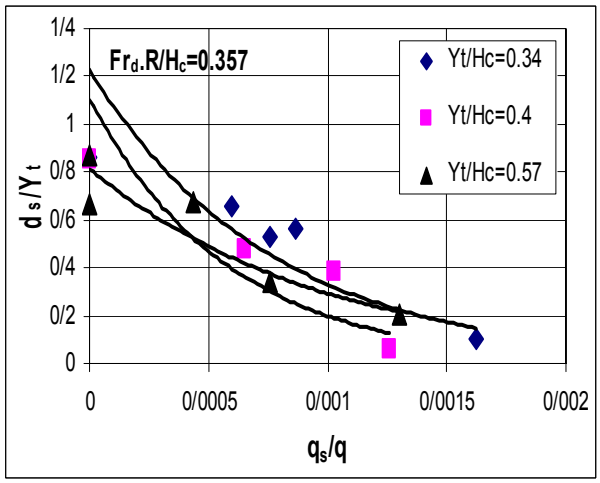

Fig. 7 Variations of d_s/Y_t with q_s/q for different values of Y_t/H_c

VI. CONCLUSIONS

The conclusions from this experimental study are:

- The sediment carried by a jet reduces the scouring potential of the jet as compared to a clear-water jet, as a result, the depth of scour decreas.
- With increasing tailwater depth, the depth of scour initially increases, reach a maximum value and thereafter decrease.
- With increasing discharge, the dimensions of scour hole and ridge height increases.
- With increasing sediment load in the jet flow, depth of scour decreases.
- Depth of scour is influenced by the parameters Fr_dR/H_c, Y_t/H_c and q/q_s.

References

[1] Abt S.R., Kloberdanz R.L. and Mendoza C., 1984, Unified culvert scour determination, *J. Hydr. Engrg.*, *ASCE*, 110(10), 1363-1367.

[2] Afify, M. and Gilberto E. U., 1994, Plunge pool scour by inclined jets, Hydraulic engineering 94- 1040-1044.

[3] Amanian, N., 1993, Scour below a flip bucket spillway, PHD dissertation, civil and environmental engineering, Utah state university, Logan, Utah, 250.

[4] Azar, F.A., 1998, Scour downstream of pipe culvert, M.S. Thesis, Tarbiat Modares University, Tehran, Iran, 120.

[5] Blaisdell F.W. and Anderson C.L., 1988, A comprehensive generalized study of scour at cantilevered pipe outlets, *J. Hydr. Res.*, IAHR, 26(4), 357-376.

[6] Bombardelli, F. A. and Gioia, G., 2005, Towards a theoretical model of localized turbulent scouring, Proc. of the 4th IAHR sypms. on river, costal and estuarine morph dynamics-RCEM, Urbana, Illinois, USA, 931-936.

[7] Damle, P.M., 1966, Evaluation of scour below ski-jump buckets of spillways, Proc. golden jubilee symp., Poona, India., 154-164.

[8] Doddiah, D., 1953, Scour from jets, proc. IAHR/ASCE conference, Minnesota; 161-169.

[9] Doehring, F., and Abt, S.R., 1994, Drop height influence on outlet scour, *J. Hydr. Engrg., ASCE*, 120(12), 1470-1476.

[10] Ghodsian, M., 2002, Scour hole geometry downstream of a culvert, 13th APD-IAHR Conference, Singapore, 272-275.

[11] Ghodsian, M. and Azar F.A., 2001, Effect of sediment gradation on scour below free over fall spillway, 3 rd

International Symposium on Environmental Hydraulics, Arizona State University, USA, on CD Ram.
[12] Ghodsian, M. and Azar F.A., 2002, Scour hole characteristics below free over fall spillway, *Int. J. of Sediment Research*, 17(4), 304-313.
[13] Ghodsian, M., and Najafi, J., 2003, Maximum depth of scour by impinging circular turbulent jet, 30th congress of IAHR, Greece, 353-359.
[14] Hoffmans, G. J. C. M., 1998, Jet scour in equilibrium phase, *J. Hydr. Engrg., ASCE*, 124(4), 430-437.
[15] Mahboubi, E., 2000, Effect of sediment size on scour due to free falling jet, M.S. Thesis, University of Science and Technology, Tehran, Iran, 130.
[16] Martins, K. J., 1999, Scour caused by rectangular impinging jets, Ph.D Thesis, Colorado State University, Forth Collins, USA, 403.
[17] Mason, P.J., 1989, Effects of air entrainments on plunge pool scour, *J. Hydr. Engrg., ASCE*, 115(3), 385-399.
[18] Mason, P.J., and Arumugam, K., 1985, Free jet scour below dams and flip buckets, *J. Hydr. Engrg., ASCE*, 111(2), 220-235.
[19] Najafi, J., 2003, Scour downstream of pipe culvert, M.S. Thesis, Tarbiat Modares University, Tehran, Iran. 110.
[20] Ojha, C.S.P., 1999, Outlet scour modeling for drop height influence, *J. Hydr. Engg., ASCE*, 125(1), 83-85.
[21] Rajaratnam, N., 1980, Erosion by plane turbulent jet, *J. Hydr. Res., IAHR*, 19(4), 339-358.
[22] Rajaratnam, N., and Beltaos, S. , 1977, Erosion by impinging circular turbulent jets, *J. Hydr. Div., ASCE*, 103(10), 1191-1205.
[23] Robinson A.R., 1971, Model study of scour from cantilevered outlets, *Trans., ASAE*, 14, 571-581.
[24] Ruff, J.F., Abt, S.R., Doehring, F.K., and Donnell, C.A., 1987, Influence of culvert shape on outlet scour, *J. Hydr. Engrg.*, ASCE. 113(3), 393-400.
[25] Stein, O.R., and Julien, P.Y., 1994, Sediment concentration below free overfall, *J. Hydr. Engrg., ASCE*, 120(9), 1043-1059.
[26] Tajkarimi, D., 2004, Analysis of scour due to free falling jet and application of neural network.", M.S. Thesis, Tarbiat Modares University, Tehran, Iran.

Keywords: scour, jet, densimetric Froude number, tailwater depth.

Local Scour at the Elliptical Guide Banks

B. Gjunsburgs*, R.R. Neilands* and E. Govsha*
* Riga Technical University/Water Engineering and Technology Department, Riga, Latvia

Scour development in time at the elliptical guide banks during the floods was studied. The dimensions of the upper part of the elliptical guide banks, namely the turn and length, were calculated by the Latishenko method. The length of the lower part of elliptical guide banks was half of the calculated upper part. The differential equation of the bed sediment movement in clear water is used, and a method for calculating the development of depth, width, and volume of scour hole with time during the floods at the head of the elliptical guide banks is elaborated and confirmed by experimental data. A new method for computing the equilibrium depth, width, and volume of a scour hole at the elliptical guide banks is presented. A comparison of the depth of scour computed after multiple floods with the equilibrium depth of scour allows us to estimate the stability of the elliptical guide banks during the maintenance period.

I. INTRODUCTION

Multiple floods lead to formation of local scour holes at bridge piers, abutments, and guide banks. It is important to predict the current stage of scour hole parameters at the bridge constructions and to estimate its stability after multiple floods during the maintenance period or at the design stage. The next unexpected flood can be the reason for bridge failure and transport infrastructure destruction. The local scour at the elliptical guide banks has not yet been studied.

Elliptical guide banks are used to guide the flow and sediments in and out the bridge opening, to reduce the flow separation at the alignment of the bridge, and to remove the scour hole from the abutment and embankment. The flow pattern and the scour hole values at the abutments and the elliptical guide banks are different.

The concentration of streamlines, a local increase in velocity, and the development of a scour hole were observed at the upstream head of the elliptical guide banks.

The differential equation of equilibrium of the bed sediment movement in clear water is used, and a method for calculating the development of depth, width, and volume of scour hole with time at the head of the elliptical guide banks during the floods is elaborated and confirmed by experimental data.

According to the tests and the method suggested, it was found that the scour starts when the floodplain is flooded over and usually stops at the peak of the flood. The scour development depends on the hydraulics of the flow, the river-bed parameters, and the flood duration. At the peak of the flood, a scour hole is usually formed. Although the scour process can be continued further, it stops, because the flood is time-restricted. The time of the scour is always less than the duration of the flood. At the next flood of the same probability, the scour process does not start at the moment when the floodplain is flooded, but at the later time step, closer to the peak of the flood. It happens because of the scour hole developed in the previous flood. The duration of the scour process at the second and forthcoming floods is less than that at the previous floods.

By using this method, it is possible to compute the current scour hole stage after multiple floods during the maintenance period or at the stage of designing the elliptical guide banks.

Based on the method suggested, the “ERoBo” computer program was elaborated and used in our calculations.

A new method for computing the equilibrium depth, width, and volume of the scour hole is presented. The equilibrium depth, width, and volume of the scour hole are achieved when the local velocity calculated at the flood peak becomes equal to the velocity at which the sediment movement starts. The parameters of a scour hole computed after multiple floods can be compared with its equilibrium parameters calculated by the equations suggested. The risk factor which estimates the stability of the elliptical guide banks can be determined as a ratio between the depth, width, and volume of the scour hole computed in time for a certain stage after several floods and the equilibrium scour hole parameters.

II. EXPERIMENTAL SETUP

The tests were carried out in a flume 3.5 m wide and 21 m long.

Different forms of guide banks were studied by Latishenko [1], and he recommended using elliptical guide banks as most acceptable in practice. The dimensions of the upper part of the elliptical guide bank, namely the turn and the length, were calculated according to the Latishenko method [1], and they were found to depend on the contraction of the flow and the width of the main channel. The length of the lower part of the guide bank was assumed to be half of the calculated upper part.

The tests were carried out in the open flow conditions for studying the flow distribution between the channel and the floodplain.

The tests with a rigid bed were performed for different flow contractions and Froude numbers in order to investigate the velocity and the changes in water level in the vicinity of the embankment, along it, and near a modeled elliptical guide bank.

The aim of the tests with a sand bed was to study the scour processes, the changes in the velocity with time, the influence of different hydraulic parameters, the

contraction rate of the flow, the grain size of the bed material, and the scour development in time.

The openings of the bridge model were 50, 80, 120 and 200 cm. The contraction rate of the flow Q/Q_b (where Q was the discharge of the flow and Q_b was the discharge of the flow in a bridge opening in open-flow conditions) varied respectively from 1.56 to 5.69 at a depth of floodplain of 7 and 13 cm, and the Froude numbers varied from 0.078 to 0.134; the slope of the flume was 0.0012.

The tests with a sand bed were carried out in the clear-water conditions. The sand was placed 1 m up and down the contraction of the flume. The mean size of grains was 0.24 and 0.67 mm. The condition that $Fr_R = Fr_f$ was fulfilled, where Fr_R and Fr_f were the Froude numbers for the plain river and for the flume, respectively. The tests in the flume lasted for 7 hours, the vertical scale was 50 and the time scale was 7. With respect to the real conditions, the test time was equal to 2 days. This was the mean duration of time steps into which the flood hydrograph was divided.

The development of a scour was examined with different flow parameters in time intervals within one 7-h step and within two steps of the hydrograph, 7 hours each.

The tests were carried out with one floodplain model and one side contraction of the flow and with two equal or different floodplain models and two side contractions. The position of the main channel was varied for different tests.

III. METHOD

The differential equation of equilibrium of the bed sediment movement for clear water conditions at the head of elliptical guide bank has the form

$$\frac{dW}{dt} = Q_S , \tag{1}$$

where W is a volume of the scour hole; t is a time; and Q_s is a sediment discharge out of the scour hole.

In different tests, it was found that the shape of a scour hole is not changing and can be found by the equation

$$W = \frac{1}{5}\pi m^2 h_s^3 , \tag{2}$$

where m is a steepness of the scour hole; and h_s is a depth of scour.

The left-hand part of (1) can be written in the form

$$\frac{dW}{dt} = \frac{3}{5}\pi m^2 h_s^3 \frac{dh_S}{dt} = a h_s^2 \frac{dh_S}{dt} , \tag{3}$$

where $a = (3/5)\pi m^2$.

The sediment discharge was determined by the Levi formula [2]

$$Q_S = ABV_l^4 , \tag{4}$$

where $B = mh_s$ is a width of a scour hole; V_l is a local velocity at the head of elliptical guide bank; and A is a parameter in the Levi formula [2].

The sediment discharge upon development of the scour is given by

$$Q_S = Amh_s V_l^4 = b\frac{h_s}{1+\frac{h_s}{2h_f}} , \tag{5}$$

where $b = AmV_l^4$.

Taking into account (1), (3) and (5), formula can be written in the form

$$a h_s^2 \frac{dh_s}{dt} = b\frac{h_s}{1+\frac{h_s}{2h_f}} . \tag{6}$$

After separating and integrating the variables, we have

$$t = D_i \int_{x_1}^{x_2} h_s \left(1+\frac{h_s}{2h_f}\right)^4 dh_s . \tag{7}$$

After integration with new variables, $x = 1 + h_s/2h_f$, $h_s = 2h_f(x - 1)$, and $dh_s = 2h_f dx$, we have

$$N_i = \frac{t_i}{4D_i h_f^2} + N_{i-1} , \tag{8}$$

where $N = 1/6x_i^6 - 1/5x_i^5$; and t_i is a time interval.

Calculating the value of N_i, we find x_i and the depth of scour at the end of time interval

$$h_s = 2h_f (x-1)\cdot k_m \cdot k_s \cdot k_\alpha , \tag{9}$$

where k_m is a coefficient depending on the side-wall slope of the guide bank [3]; k_s is a coefficient depending on the guide bank shape; and k_α is a coefficient depending on the angle of flow crossing [4].

To determine the development of scour depth during the flood, the hydrograph was divided into time steps with duration of 1 or 2 days, and each time step was divided into time intervals up to several hours. In the laboratory tests, the time steps were divided into 20 time intervals. For each time step, the following parameters must be determined: depth of water in the floodplain, contraction rate of the flow, maximum backwater, grain size, thickness of the bed layer with d, and specific weight of the bed material. As a result, we have V_l, V_0, A, D, N_i, N_{i-1}, and h_s at the end of time intervals and finally at the end the time step. For the next time step, the flow parameters changed because of the flood and the scour developed during the previous time step. Thus, the depth, width, and volume of the scour hole can be computed after several

floods both at the design stage and during the maintenance of bridge crossings.

Based on the method suggested, the "ERoBo" computer program was elaborated and used in our calculations.

Equation for equilibrium scour depth at the elliptical guide banks was elaborated. Scour at the elliptical guide banks stops when local velocity becomes equal to the velocity at which starts sediment movement.

The velocity V_{lt} is decreasing and V_{0t} is increasing with development of the scour hole. The scour ceases when V_{lt} becomes equal to βV_{0t}.

$$\frac{V_l}{1+\frac{h_{equil}}{2h_f}} = \beta V_0 \cdot \left(1+\frac{h_{equil}}{2h_f}\right)^{0.25}. \qquad (10)$$

The equilibrium depth of scour can be determined from (10) as follows:

$$h_{equil} = 2h_f\left[\left(\frac{V_l}{\beta V_0}\right)^{0.8} - 1\right]\cdot k_m \cdot k_s \cdot k_\alpha, \qquad (11)$$

where k_m is a coefficient depending on the side-wall slope of the guide bank [3], k_s is a coefficient depending on the guide bank shape, and k_α is a coefficient depending on the angle of flow crossing [4].

The velocity of sediment movement V_0 can be found from the Studenitcnikov formula [5].

Each flood of the designed probability increases the depth, width, and volume of the scour hole until, in hundreds of years, the equilibrium depth of scour can be reached.

IV. Results

The local velocity at the head of guide bank was studied in tests with a rigid bed, at different contraction rates, and for different Froude numbers of the flow. The local velocity was found from the formula:

$$V_l = \varphi_{el}\sqrt{2g\Delta h}, \qquad (12)$$

where φ_{el} is a velocity coefficient for the elliptical guide banks; g is a gravitational acceleration; and Δh is a maximum backwater determined by the Rotenburg formula [6].

The coefficient φ_{el} as a function of the contraction of the flow is showed in Figure 1.

During the scour at the steady flow conditions local velocity at the elliptical guide banks is decreasing and can be computed by formula

$$V_{lt} = \frac{V_l}{1+\frac{h_s}{2h_f}}. \qquad (13)$$

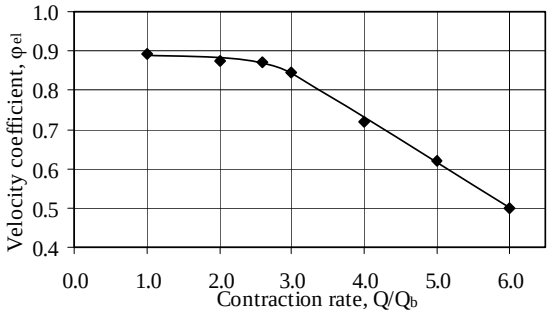

Figure 1. The velocity coefficient φ_{el} versus the contraction rate of the flow for elliptical guide banks

Velocity at which starts sediment movement is increasing during the scour development and can be found by formula

$$V_{0t} = \beta V_0\left(1+\frac{h_s}{2h_f}\right)^{0.25}. \qquad (14)$$

In Fig. 2 is presented local velocity V_{lt} and velocity V_{0t} changes in tests at steady flow conditions.

Comparison of the experimental and computed data for local velocity is presented in Table I.

The values of the depth of scour development with time obtained in tests and calculated by the method presented under the steady and unsteady flow conditions are given in Figs. 3 and 4. The development of scour depth measured in tests and determined by calculations is much the same, namely the rapid beginning of the process and its gradual reduction with time.

The development of the depth, width, and volume of scour after three floods of the same probability is shown in Figs. 5, 6, and 7, respectively. The most rapid development of the scour hole was observed in the first flood. In the following floods, the scour started later and closer to the peak of the flood. The time of scour and the rate of scour hole development in time reduced with every subsequent flood.

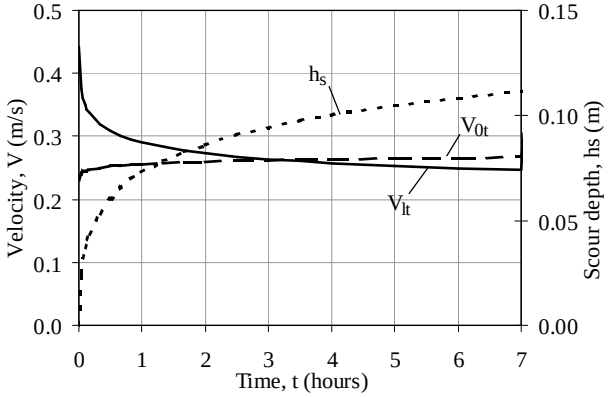

Figure 2. Velocity V_{lt} and V_{0t}, and scour depth h_s changes in tests at steady flow conditions

TABLE I.
COMPARISON BETWEEN THE EXPERIMENTAL AND CALCULATED DATA FOR LOCAL VELOCITIES AT THE ELLIPTICAL GUIDE BANKS

Test	Q/Q_b	Δh (cm)	$V_{l.test}$ (cm/s)	$V_{l.calc}$ (cm/s)	$\frac{V_{l.calc}}{Vl.test}$
EL1	5.27	2.220	39.1	36.2	1.080
EL2	5.69	3.620	46.4	46.8	0.991
EL3	5.55	3.950	49.7	52.1	0.954
EL4	3.66	1.189	36.9	35.1	1.051
EL5	3.87	1.795	44.0	45.2	0.973
EL6	3.78	2.350	51.0	53.9	0.946
EL7	2.60	0.557	28.4	26.7	1.064
EL8	2.69	0.993	37.8	37.5	1.008
EL9	2.65	1.280	43.0	51.2	0.840
EL10	1.56	0.380	23.9	22.3	1.072
EL11	1.66	0.455	26.1	23.0	1.135
EL12	1.67	0.530	28.2	30.7	0.919
EL13	4.05	1.420	38.2	32.5	1.177
EL14	3.99	1.800	43.4	37.5	1.157
EL15	4.05	2.700	52.7	49.4	1.067
EL16	3.66	1.189	36.9	35.1	1.051
EL17	3.87	1.795	44.0	45.2	0.973
EL18	3.78	2.350	51.0	53.9	0.946
EL19a	4.46	1.476	36.5	33.0	1.106
EL19b	3.21	0.769	31.4	28.3	1.110
EL20a	4.47	1.795	40.8	40.8	1.000
EL20b	3.24	0.950	34.8	34.4	1.012

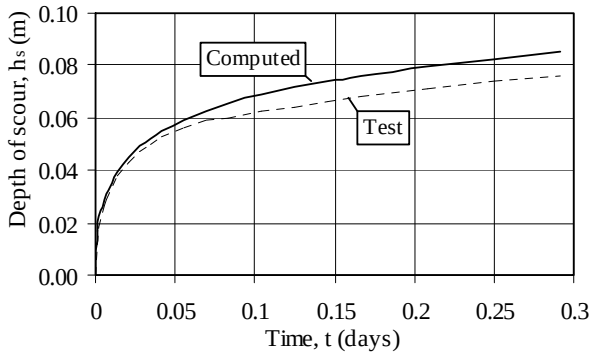

Figure 3. Scour development in time under steady flow conditions at the elliptical guide bank in test EL4

The scour depth at the elliptical guide banks measured after 7 and 14 hours in tests and calculated by the method suggested is presented in Table II.

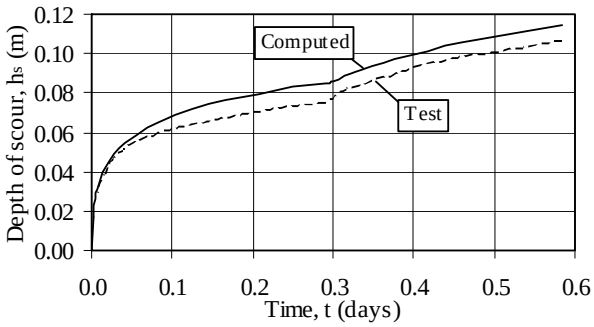

Figure 4. Development of scour in time under unsteady flow conditions at the elliptical guide bank in test ETL1

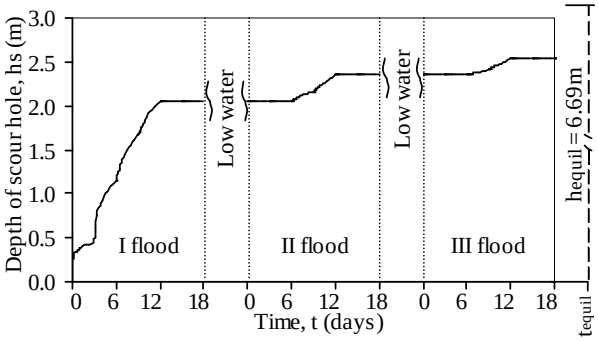

Figure 5. Development of scour depth in time within the limits of three floods of the same probability at the elliptical guide banks

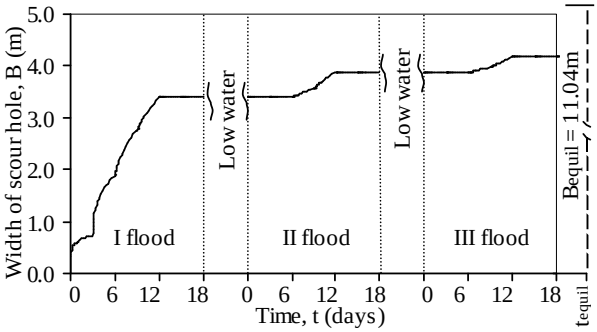

Figure 6. Development of scour hole width in time within the limits of three floods of the same probability at the elliptical guide banks

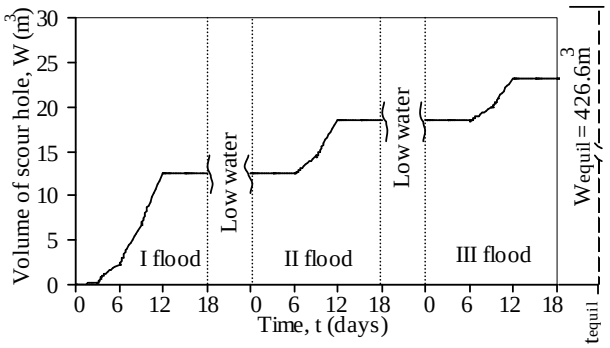

Figure 7. Development of scour hole volume in time within the limits of three floods of the same probability at the elliptical guide banks

TABLE II.
COMPARISON BETWEEN THE EXPERIMENTAL AND CALCULATED DEPTH OF SCOUR AT THE ELLIPTICAL GUIDE BANKS

Test	l_b (cm)	Q/Q_b	h_f (cm)	d (mm)	t (h)	$h_{s.test}$ (cm)	$h_{s.calc}$ (cm)	$\frac{h_{s.calc}}{h_{s.test}}$
EL1	50	5.27	7	0.24	7	9.40	9.20	1.022
EL2	50	5.69	7	0.24	7	12.20	11.90	1.025
EL3	50	5.55	7	0.24	7	14.30	13.00	1.100
EL4	80	3.66	7	0.24	7	7.60	8.40	0.905
EL5	80	3.87	7	0.24	7	11.00	11.00	1.000
EL6	80	3.78	7	0.24	7	14.00	13.51	1.036
EL7	120	2.60	7	0.24	7	5.20	5.00	1.040
EL8	120	2.69	7	0.24	7	8.30	8.80	0.943
EL9	120	2.65	7	0.24	7	11.50	10.70	1.075
EL10	200	1.56	7	0.24	7	2.40	3.00	0.800
EL11	200	1.66	7	0.24	7	3.70	4.11	0.900
EL12	200	1.67	7	0.24	7	4.70	4.90	0.959
EL13	80	4.05	13	0.67	7	6.40	6.80	0.941
EL14	80	3.99	13	0.67	7	9.10	9.60	0.948
EL15	80	4.05	13	0.67	7	14.00	14.20	0.986
EL16	80	3.66	7	0.67	7	6.10	5.60	1.089
EL17	80	3.87	7	0.67	7	8.40	8.20	1.024
EL18	80	3.78	7	0.67	7	12.20	10.50	1.162
EL19a	80	4.46	7	0.24	7	6.20	6.30	0.984
EL19b	80	3.21	7	0.24	7	6.40	7.30	0.877
EL20a	80	4.47	7	0.24	7	8.70	9.70	0.897
EL20b	80	3.24	7	0.24	7	8.20	7.60	1.079
ETL1	80	3.66	7	0.24				
	80	4.05	13	0.24	14	10.70	11.41	0.938
ETL2	80	3.87	7	0.24				
	80	3.99	13	0.24	14	13.70	14.80	0.926
ETL3	80	3.77	7	0.24				
	80	4.05	13	0.24	14	20.30	18.86	1.076

V. CONCLUSIONS

The differential equation of equilibrium of the bed sediment movement in clear water was used, and a method for calculating the development of depth, width, and volume of scour hole with time at the head of the elliptical guide banks during the floods was elaborated and confirmed by experimental data.

By using this method, it is possible to compute the current scour hole stage after multiple floods during the maintenance period or at the stage of designing the elliptical guide banks.

A new method for computing the equilibrium depth, width, and volume of the scour hole was presented. The equilibrium depth, width, and volume of the scour hole were achieved when the local velocity calculated at the flood peak became equal to the velocity at which the sediment movement starts.

The parameters of a scour hole computed after multiple floods can be compared with its equilibrium parameters calculated by the equations suggested.

Based on the method suggested, the "ERoBo" computer program was elaborated and used in our calculations.

The risk factor which estimates the stability of the elliptical guide banks can be determined as a ratio between the depth, width, and volume of the scour hole computed in time for a certain stage after several floods and the equilibrium scour hole parameters.

REFERENCES

[1] A. M. Latishenko, *Questions of artificially contracted flow,* Moscow: Gostroizdat, 1960 (in Russian).

[2] I. I. Levi, *Dynamics of River Flow.* Moscow: Gidrometeoizdat, 1969 (in Russian).

[3] I. A. Yaroslavcev, *Calculation of local scour at bridge piers*. Moscow: Bulletin of TCNIIS N80, 1956 (in Russian).

[4] E. V. Richardson and S. R. Davis, *Evaluating Scour at Bridges*, 3rd ed., Washington, DC, Federal Highway Administration Hydraulic Engineering Circular No. 18, FHWA-IP-90-017, 1995.

[5] V. I. Studenitcnikov, *Flow Erosion Capacity and River-Bed Calculation Methods*. Moscow: Engineering Literature Press, 1964 (In Russian).

[6] I. S. Rotenburg and V. S. Volnov, *Project Examples of Bridge Crossing*. Moscow: Vishaja Shkola, 1969 (in Russian).

A Model of Scouring around Structures including Stability Analysis of the Bottom

O. Goethel*, W. Zielke*
* University of Hannover, Hannover, Germany

I. Introduction

When the process of scouring is examined in a numerical model, flow and sediment transport are simulated in order to achieve knowledge of the temporal evolution and final scour depth. The modeling is limited to fluid flow, sediment transport at the bottom surface layer and resulting bottom evolution. Additional bottom movements are reduced to sliding sediment at the developing slopes. Less attention has until now been drawn to the modeling of the inner stability and the response of the bottom to shear stress and sediment transport. In order to gain more knowledge about the bottom and its behavior while the scouring process takes place, a finite element model for solids was implemented. The bottom surface geometry resulting from the sediment transport and the near-bed shear stress are taken into account as boundary conditions.

II. Model Description

A. Flow

To simulate a scouring processs the sediment transport model needs the input from a flow model, which calculates the near-bed shear stresses. Considering a cylinder in a steady current, the relevant flow effects for the scouring process are the horseshoe vortex, the increased flow velocities at the side of the pile and the vortex shedding. Especially the horseshoe vortex is a truly three-dimensional flow effect and therefore the incompressible Reynolds-averaged Navier-Stokes equations are solved for all three dimensions. Turbulence modeling is done by the k-ω model derived by [22]. The modifications of [10] were applied because of their advantage in simulating flow with a boundary layer and adverse pressure gradients.

The Reynolds equations are solved on a mesh of prismatic elements, which are obtained by duplicating a two-dimensional base mesh of triangles in the vertical direction. The mesh is refined in the vicinity of the cylinder and near the bottom, so that element edges have a minimum length of 1mm. Diffusion terms are solved implicitly and advection is done by the streamline upwind Petrov-Galerkin method [6].

B. Sediment Transport

The sediment transport is calculated as bed-load transport, which takes place at the bottom surface. In order to calculate a new bottom geometry, the bottom evolution equation (1) is being solved. The data for the necessary transport rate in (1) is determined by solving (2), which was found by [19].

$$\frac{\partial z_B}{\partial t} + \mathrm{div}\vec{q}_S = 0 \tag{1}$$

$$q_S = 0.25 d_{50} U_f D_*^{-0.3} \left(\frac{\tau - \tau_{cr}}{\tau_{cr}} \right) \tag{2}$$

$$\text{with } D_* = \left[\frac{(\rho_S / \rho - 1) g}{\nu^2} \right]^{1/3} d_{50} \tag{3}$$

D_* is a dimensionless particle parameter in which ν is the kinematic viscosity and d_{50} the medium grain diameter. In (2) U_f is the effective bed-shear velocity.

Sediment transport takes place, when the actual shear stress exceeds a critical value which can be expressed by the Shields mobility parameter θ_{cr} [15]. This is calculated by a parametrization of the Shields curve (4) done by [19]. Shear stress and mobility parameter are related by $\tau = \theta(\rho_S - \rho) g d_{50}$.

Steep slopes will occur as the scour developes, whereas most transport rate equations were derived for nearly horizontal beds. Experimental data shows that the transport rate [16] and threshold conditions change on a sloping bed. The differing values are caused by the influence of gravity on the sediment particles (Fig. 1). Therefore a correction of sediment transport rate and mobility parameter has to be done in order to take the slope effect into account.

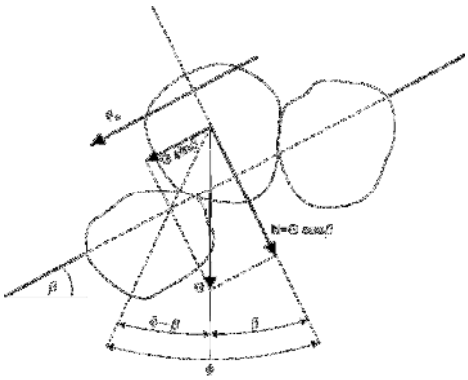

Figure 1. Sediment Particles on a Slope

The result for the Shields parameter on a horizontal bed is adjusted by (6) and (7) for longitudinal and transversal slopes based on the direction of the bed-shear velocity. Equation (6) was derived from the equilibrium of forces on a single particle on a sloping bed and was first presented by [13]. Comparison with experimental data shows good agreements [21]. The adjustment of the critical Shields parameter for transversal slopes (7) was first presented by [8] and was also derived by [7] and [3]. In (6) and (7) φ is the angle of repose and β is the actual slope angle.

$$\begin{aligned}
\theta_{cr} &= 0.24D_*^{-1} && \text{for} && 1 < D_* \le 4 \\
\theta_{cr} &= 0.14D_*^{-0.64} && \text{for} && 4 < D_* \le 10 \\
\theta_{cr} &= 0.04D_*^{-0.1} && \text{for} && 10 < D_* \le 20 \\
\theta_{cr} &= 0.013D_*^{-0.29} && \text{for} && 20 < D_* \le 150 \\
\theta_{cr} &= 0.055 && \text{for} && D_* > 150
\end{aligned} \tag{4}$$

$$\theta_{cr,slope} = \alpha_L \alpha_T \theta_{cr} \tag{5}$$

$$\alpha_L = \sin(\varphi - \beta_L)/\sin\varphi \tag{6}$$

$$\alpha_T = \cos\beta_T \left[1 - \tan^2\beta_T / \tan^2\varphi\right]^{0.5} \tag{7}$$

The sediment transport rate is treated in a smiliar way as the mobility parameter. Increasing the transport rate on a downward slope is taken into account by different equations for a longitudinal and a transversal slope. Equation (8) was found by [19] based on the equation of [16]. It predicts the amplification of the transport rate for a slope with decreasing elevation. In (8) C is the Chézy coefficient.

$$k_L = 0.5g^{-0.5}\left(\frac{d_{90}}{d_{30}}\right)^{0.2} C\tan^{0.6}\beta_L\left(\frac{\tau_b}{(\tau_b - \tau_{b,cr})}\right)^{0.5} \tag{8}$$

For slopes with increasing elevation no correction of the sediment transport rate is done. From experiments [1] found that the bed-load on an upward slope is adequately described by taking into account the modification of the critical Shields parameter.

The bed-load transport in the transverse direction was studied by [2], [4], [5] and [14]. The approach of [4] was chosen and implemented in the sediment transport model. The transport rate in cross direction is described by:

$$q_{s,T} = \left[\tan(u_{b,T}/u_{b,L}) + 1.5\left(\frac{\tau_{cr}}{\tau}\right)^{0.5}\tan\left(\frac{\partial z_B}{\partial T}\right)\right] \tag{9}$$

in which u_b is the near-bed velocity.

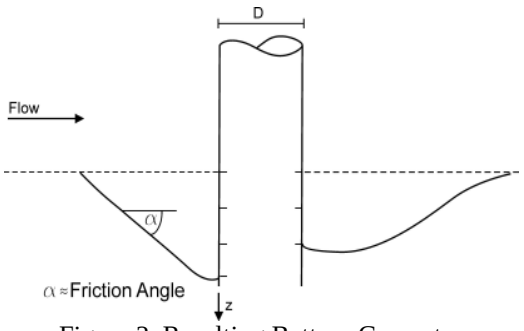

Figure 2. Resulting Bottom Geometry

When the scour develops in a sandy bed and the slope angle reaches the angle of repose, the slope will destabilize and sediment slides down in direction of the highest gradient. This effect must be taken into account in order to obtain a reasonable bottom geometry. The effect was implemented in a numerical model by initiating a sediment transport in direction of the gradient if the slope angle exceeds the angle of repose [11][12]. Hence the bottom evolution equation needs to be solved when a sandslide is executed. Sediment transport stops when the slope angle falls below the angle of repose. A slightly different way to model a sandslide is to shift the sediment in a mass conservative way from the higher meshpoints to the lower [20]. The criterion for initiating and stopping a sandslide is again the angle of repose. The resulting bottom geometry is therefore limited to the choice of this soil parameter (Fig. 2).

C. Bottom

Modeling the bottom with a finite element model provides the oppurtunity to examine its response to a changing geometry and to the shear stresses affecting the surface layer. The developing scour leads to steep slopes which become unstable when the angle of repose is reached. With the finite element model the mentioned behaviour can be simulated. Location and depth of instabilities can be analyzed.

The finite element model includes a linear-elastic as well as a visco-plastic (initial strain) method [23] with the failure criterions of Mohr-Coulomb and von Mises. In both cases the equations for equilibrium (10), strain-displacement relation (12) and the constitutive soil model are solved (11).

$$\begin{aligned}
\frac{\partial\sigma_x}{\partial x} + \frac{\partial\tau_{xy}}{\partial y} + \frac{\partial\tau_{xz}}{\partial z} &= 0 \\
\frac{\partial\sigma_y}{\partial y} + \frac{\partial\tau_{xy}}{\partial x} + \frac{\partial\tau_{yz}}{\partial z} &= 0 \\
\frac{\partial\sigma_z}{\partial z} + \frac{\partial\tau_{xz}}{\partial x} + \frac{\partial\tau_{yz}}{\partial y} &= 0
\end{aligned} \tag{10}$$

$$\begin{Bmatrix}\sigma_x\\ \sigma_y\\ \sigma_z\end{Bmatrix}=\frac{E}{1-\nu^2}\begin{bmatrix}1 & \nu & \nu\\ \nu & 1 & \nu\\ \nu & \nu & 1\end{bmatrix}\begin{Bmatrix}\varepsilon_x\\ \varepsilon_y\\ \varepsilon_z\end{Bmatrix}$$

$$\begin{Bmatrix}\tau_{xy}\\ \tau_{yz}\\ \tau_{xz}\end{Bmatrix}=\frac{E}{1-\nu^2}\begin{bmatrix}\frac{1-\nu}{2} & 0 & 0\\ 0 & \frac{1-\nu}{2} & 0\\ 0 & 0 & \frac{1-\nu}{2}\end{bmatrix}\begin{Bmatrix}\gamma_x y\\ \gamma_{yz}\\ \gamma_{xz}\end{Bmatrix} \qquad (11)$$

$$\begin{Bmatrix}\varepsilon_x\\ \varepsilon_y\\ \varepsilon_z\\ \gamma_{xy}\\ \gamma_{yz}\\ \gamma_{xz}\end{Bmatrix}=\begin{bmatrix}\frac{\partial}{\partial x} & & \\ & \frac{\partial}{\partial y} & \\ & & \frac{\partial}{\partial z}\\ \frac{\partial}{\partial y} & \frac{\partial}{\partial x} & \\ & \frac{\partial}{\partial z} & \frac{\partial}{\partial y}\\ \frac{\partial}{\partial z} & & \frac{\partial}{\partial x}\end{bmatrix}\begin{Bmatrix}u\\ v\\ w\end{Bmatrix} \qquad (12)$$

In (10)-(12) σ and τ are the stress components, ε and γ are the strains and (u,v,w) are the displacements. The soil paramters E and ν denote Young's modulus and Poisson's ratio. Solving (10)-(12) on a finite element mesh leads to a linear system of equations.

The case of a collapsing slope or sand slide is not an elastic problem. Irrecoverable strains occur when a failure of soil material takes place. In order to separate stresses causing elastic from those causing plastic deformations, a yield surface (failure criterion) is defined. For frictional materials, such as sand, the Mohr-Coulomb criterion can be applied. It has the form of an irregular hexagonal cone, as shown in Fig. 3.

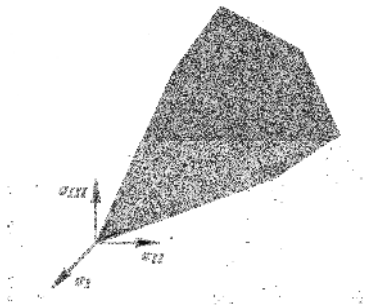

Figure 3. Mohr-Coulomb Yield Surface

The failure criterion is then given by

$$F=\sigma_m\sin\varphi+\bar{\sigma}\left(\frac{\cos\theta}{\sqrt{3}}-\frac{\sin\theta\sin\varphi}{3}\right)-c\cos\varphi\,. \qquad (13)$$

The friction angle is denoted with φ and c is the cohesion. The three invariants σ_m, $\bar{\sigma}$ and θ represent the mean stress, the deviator stress and the Lode angle.

$$\sigma_m=\sigma_x+\sigma_y+\sigma_z \qquad (14)$$

$$\bar{\sigma}=\left[(\sigma_x-\sigma_y)^2+(\sigma_y-\sigma_z)^2+(\sigma_z-\sigma_x)^2+6\tau_{xy}^2+6\tau_{yz}^2+6\tau_{xz}^2\right]^{0.5} \qquad (15)$$

$$\theta=1/3\left(\frac{-3\sqrt{6}J_3}{(\bar{\sigma}\sqrt{3})^3}\right) \qquad (16)$$

The invariants (14)-(16) are related to the principal stress space through:

$$\begin{aligned}\sigma_1&=\sigma_m+2/3\bar{\sigma}\sin(\theta-2/3\pi)\\ \sigma_2&=\sigma_m+2/3\bar{\sigma}\sin(\theta+2/3\pi)\\ \sigma 3&=\sigma_m+2/3\bar{\sigma}\sin\theta\end{aligned} \qquad (17)$$

The non-linearity of the process is taken into account by iteratively modifying the load vector and keeping the stiffness matrix constant. Each iteration is a linear-elastic analysis as described above. The plastic parts of the result are self-equilibrating loads which are applied to the load vector to redistribute the stress within the system [17].

The bottom surface geometry exists as a mesh of triangles. In order to obtain a three-dimensional mesh, a horizontal layer of triangles with the same element coordinates as the surface layer is created (Fig. 4). It is located 20% underneath the height of the lowest surface mesh point. The Space in between those layers is filled with a constant number of prismatic elements in the vertical direction.

The bottom finite element model has different degrees of freedom at the boundaries. No displacements are allowed at the bottom layer, whereas the surrounding boundary faces and the nodes at the cylinder are allowed to move in vertical direction.

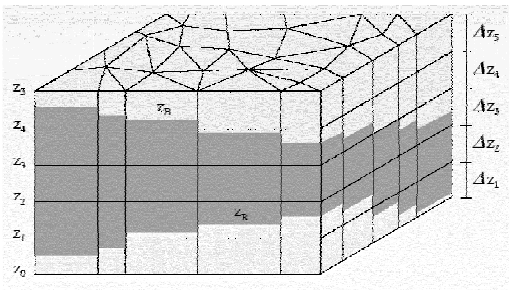

Figure 4. Bottom Mesh Structure [9]

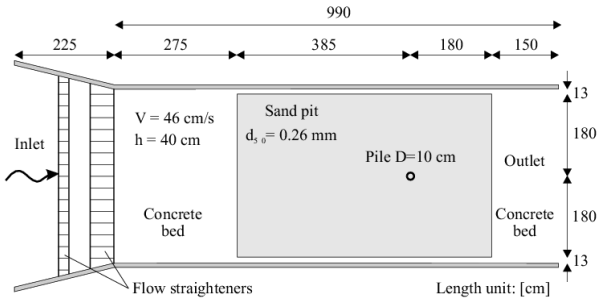

Figure 5. Scour Experiment [11]

III. MODELING RESULTS

A. Flow and Scour

The experimental results of [11] were used for verification of the flow and sediment transport model. The experiments were carried out in a flume with a width of 3.6m and a length of 9.90m (Fig. 5). A cylinder with a diameter of 10cm was placed within the sand pit. The sediment particles had a medium diameter of 0.26mm and the undisturbed flow velocity was 0.46cm/s at a water depth of 0.4m. The angle of repose for the given material wa defined as 32 degrees.

The flow around a vertical pile leads to vortex shedding (Fig. 6), known as the von Karman vortex street, and the horseshoe vortex (Fig. 7). The latter is caused by the difference in the vertical pressure, which occurs when a flow with a logarithmic velocity profile approaches the cylinder. Both flow effects are reproduced by the numerical model. The influence of the horseshoe vortex on the direction of the near-bed flow velocities can be seen in Fig. 8. In the upstream part of the cylinder the near-bed velocity points against the direction of the approaching flow. The contraction of the flow leads to increased velocities at the cylinder sides and therefore to an increased shear stress. In the numerical simulations the maximum value reaches eight times of that in the undisturbed areas as can be seen in Fig. 9.

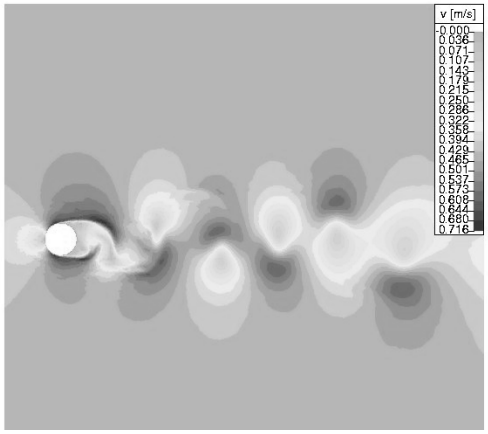

Figure 6. von Karman Vortex Street

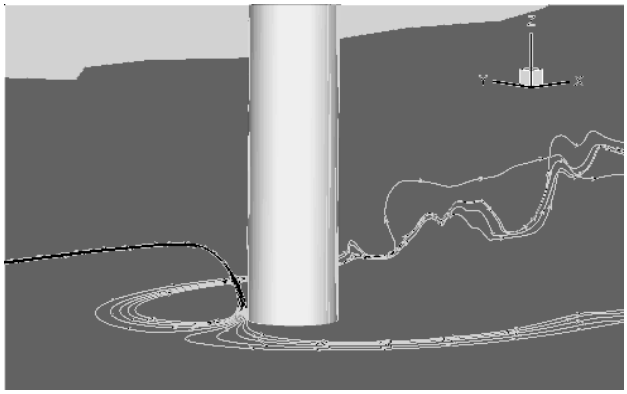

Figure 7. Horseshoe vortex

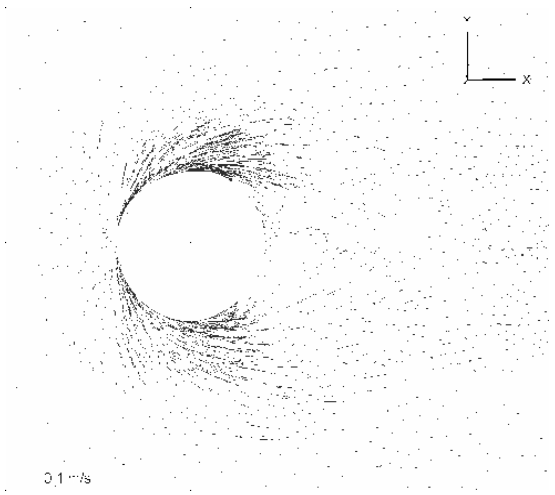

Figure 8. Near-bed Flow Velocities

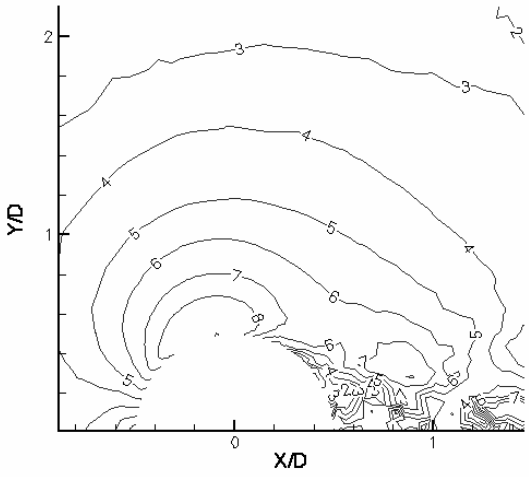

Figure 9. Amplification of Shear Stress

The high shear stresses around the cylinder lead to an intensive sediment transport and therefore the scour develops. Taking into account the transversal sediment transport at a slope leads to a resulting transport vector which no longer points in the direction of shear stress. In Fig. 10 the white arrows denote the direction of shear stress while the grey point in the direction of sediment transport. It can be seen that the latter is less radial after the correction.

After two hours of simulation the scour reaches a depth of approximately 14cm. The temporal evolution (Fig. 11) and the resulting shape of the scour (Fig. 12) are in a good agreement with the experimental results. The scour depth after two hours of simulation is not exactly met.

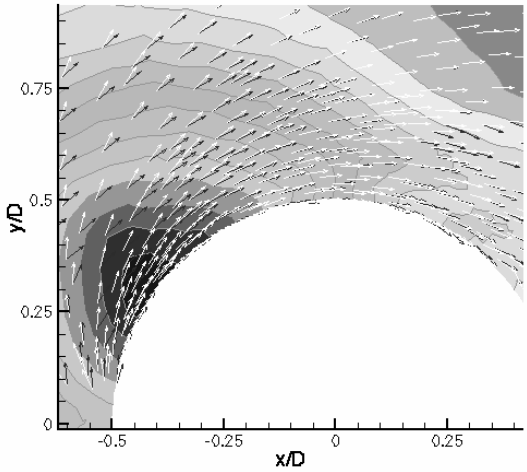

Figure 10. Sediment Transport Rates at a Slope

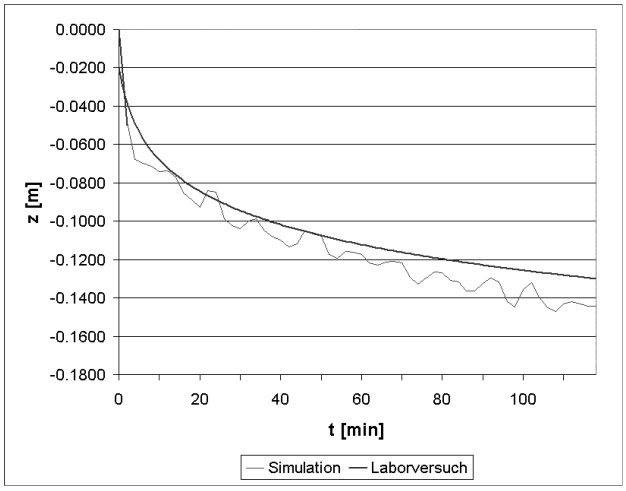

Figure 11. Temporal Evolution of Scour

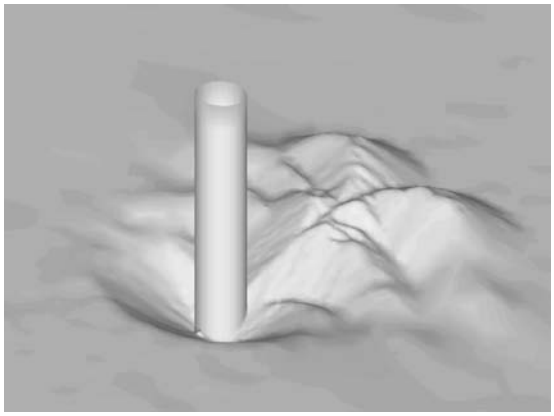

Figure 12. Scour after 2 Hours

B. Bottom

Simulations with the bottom finite element model were carried out in order to analyse the slope stability. At the present state of development the shear stress and dynamic flow pressure have not been taken into account (this will be included in the final version of the paper).

The scour geometry was held constant whereas the friction angle was altered. Other parameters used were Young's modulus $E = 1 \cdot 10^{-4}$ kN/m² and Poisson's ratio $\nu = 0.3$. The unit weight of the material was given as $\gamma = 10 \mathrm{kN/m^3}$. It is assumed that the upper layer is loose sand and therefore cohesion is not effective. After ten minutes of sediment transport the scour has reached a depth of 7cm. For this point in time the finite element simulations were carried out.

The plastic strains γ_{xz} are shown in Fig. 13 and Fig. 14. As a result from experiments in [11] sandslides were initiated when the slope angle was two degrees higher than the friction angle. Fig. 13 shows that with the difference of two degrees between slope and friction angle, strong plastic strains occur on the upstream as well as on the downstream slope. These can be expected to be the areas where most of the sandsliding takes place.

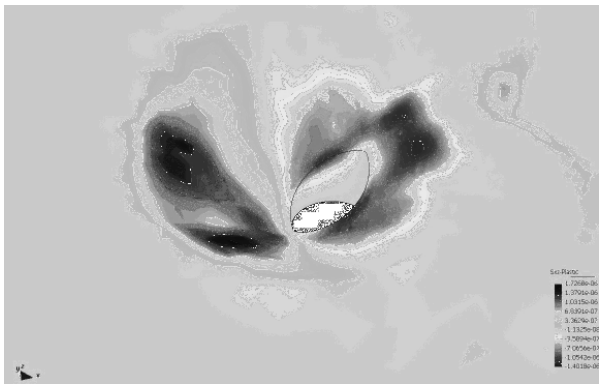

Figure 13. Plastic Strains at $\varphi - 2°$

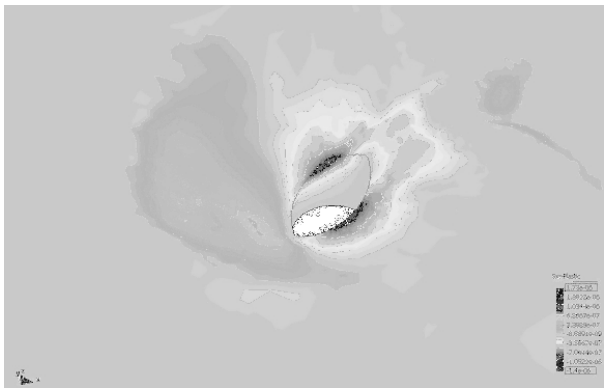

Figure 14. Plastic Strains at φ

IV. SUMMARY

The numerical model described is capable of calculating flow and sediment transport around structures as well as analyzing the bottom stability during scouring with a finite element model. High shear stress in the vicinity of the structure leads to an intensive sediment transport. Steep slopes occur as the scour develops. The change of threshold conditions and sediment transport rates at steep slopes are taken into account by modifying the values for a horizontal bed. Furthermore it is necessary to consider bottom movements which are a result of instabilities and which are independent from shear stress affecting the bottom. The sand slide algorithm is capable of simulating these movements, taken into account the friction angle as the only soil parameter.

The results of the scour simulation met the measured scour depth and the temporal evolution. Using the calculated bottom geometry for an analysis with the finite element model for the bottom leads to information where failure of stability occurs.

REFERENCES

[1] J.S. Damgaard, R.J.S. Whitehouse, R.L. Soulsby, "Bed-load Sediment Transport on Steep Longitudinal Slopes," *J. Hydr. Eng*., Vol. 123 (12), 1997.

[2] F. Engelund, "Flow and Bed Topography in Channel Bends," *J. Hydra. Div*., ASCE, Vol. 100 (11), 1974.

[3] S. Ikeda, "Incipient Motion of Sand Particles on Side Slopes," *J. Hydra. Div*., ASCE, Vol. 108 (1), 1982.

[4] S. Ikeda, "Lateral Bed-Load Transport on Side Slopes," *J. Hydra. Div*., ASCE, Vol. 108 (11), 1982.

[5] S. Ikeda, "Lateral Bed-Load Transport on Side Slopes," In: Civil Engineering Practice 2, Technomic Publishing Company, USA, 1988.

[6] Jacek A. Jankowski, "A non-hydrostatic model for free surface flows," Institute of Fluid Mechanics, University of Hannover, Report No. 56, 1999.

[7] E.W. Lane, "Design of Stable Channels," *Trans*., ASCE, Vol. 120, 1955.

[8] O. Leiner, "Zur Erforschung der Geschiebe und Sinkstoffbewegung," Zeitschrift für Bauwesen, Vol. 62, 1912.

[9] A. Malcherek, F. Piechotta,"Mathematical Module SediMorph," Federal Waterways Engineering and Research Institute, Germany, Technical Report, 2004.

[10] F.R. Menter, "Improved two-equation k-omega turbulence models for aerodynamic flows," NASA technical memorandum 103975, NASA, Ames Research Center, California, 1992.

[11] A. Roulund, "Three-dimensional Numerical Modelling of Flow around a Bottom-mounted Pile and its Application to Scour," Ph.D. thesis, Department of Hydrodynamics and Water Resources, Technical University of Denmark, Series Paper No. 74, 2000.

[12] A. Roulund, M. Sumer, J. Fredsøe, J. Michelsen, "Numerical and experimental investigation of flow and scour around a circular pile," *J. Fluid Mech*., Vol. 534, 2005.

[13] A. Schoklitsch, "Über Schleppkraft und Geschiebebewegung," Leipzig und Berlin, W. Engelmann, 1914.

[14] M. Sekine, G. Parker, "Bed-load transport on transverse slope. I.," *J. Hydr. Eng.* Vol. 118, No. 4, 1992.

[15] A. Shields, "Anwendung der Ähnlichkeitsmechanik und der Turbulenzforschung auf die Geschiebebewegung," Mitt. der Preussischen Versuchsanstalt für Wasserbau und Schiffbau, Vol. 26, 1936.

[16] G.M. Smart, "Sediment Transport Formula for Steep Channels," *J. Hydr. Eng*,. ASCE, Vol. 110, No3, 1984.

[17] I.M. Smith, D.V. Griffiths, „Programming the Finite element Method," John Wiley & Sons Ltd., 3rd Edition, 1998.

[18] M. Sumer, J. Fredsøe, "The Mechanics of Scour in the Marine Environment," Advanced Series in Ocean Engineering Vol. 17, World Scientific Publishing Co. Pte. Ltd., Singapore, 2002.

[19] L.C. van Rijn, "Principles of Sediment Transport in Rivers, Estuaries and Coastal Seas," Aqua Publications, Amsterdam, 1993.

[20] H. Weilbeer, "Numerische Simulation von Strömung und Kolkung an Wasserbauwerken," Institute of Fluid Mechanics, University of Hannover, Report No. 66, 2001.

[21] R.J.S. Whitehouse, J. Hardisty, "Experimental Assessment of Two Theories for the Effect of Bed Slope on the Threshold of Bed Load Transport," *Marine Geology*, Vol 79, 1988.

[22] D.C. Wilcox, "Turbulence Modeling for CFD," DCW Industries, California, USA, 2nd Edition, 1993.

[23] O.C. Zienkiewicz, R.L. Taylor, "The Finite Element Method," Butterworth-Heinemann, Oxford, 5th Edition, 2000.

Development of a scour monitoring system

J. Grabe*, S. Kinzler* and C. Miller **
* Technische Universität Hamburg-Harburg, Hamburg, Germany
** Hamburg Port Authority, Hamburg, Germany

The present paper reflects the new development of a scour monitoring system. The basic idea is to install two buoys, one has a density between the base failure load and fuidized soil "sink", the other between fluidized soil and water "float". The design of shape, guideway and data-logging will be illustrated.

I. Introduction

Container handling in the large sea and domestic ports is increasing very fast during the last years. In the wake of this evolution the ship size is also accretive. The growing engine power entail an accession of stress of wharfage and seabed as a result of docking and undocking maneuvers. This problem is especially relevant for self-docking ferries, RoRo ships and container cargo ships, which dispose normally high capacity bow stream or stern stream rudders.

During application of the propellers appear special erosion appearances at the seabed which are called *scours*. Scouring is the result of local raising stream velocity which disperse soil substratum. The result is a residual deepening of the seabed.

Extent, depth and durability of scouring are not known a priori. Based on the mechanism of bed erosion caused by exceedance of a critical shear stress by taking the *Bernoulli* equation [1] for the stern drive respectively according to *Römisch* [8] for the bow drive the scour mechanism can be calculated approximately. This computation should be judged critically because the empiric nature of equations is not considering specialized constraints.

To prevent endangering of water structures different strategies exist:

- Securing of seabed using scour protection systems: Scour protection systems are composed of loose or composite embankments. Accepted constructions prevent the erosion only by using large stone diameters;
- Integration of jet disposers in quay constructions Application of steam disposing elements as components of the sheet piling or installation of an erosion decreasing bed slab;
- Allowance of scour depth during design During the static design process a scour depth, based on careful estimates, is considered.

All strategies have in common that they require significant capital appropriations and, caused by the estimation on the safe side, seem inefficient.

It is necessary to develop a scour monitoring system to get to cost-effective and safe quay constructions. The monitoring system needs to be able to verify and examine the basis of the statical calculation. The monitoring system enables the observing engineer to log the characteristics of scouring during the whole docking and undocking maneuver. Subsequently the critical case can be certified or modified.

The Technical University Hamburg-Harburg, Institute of Geotechnical and Construction Management has developed such a monitoring system after observing scour procedures and has proved its effectiveness under laboratory conditions. Presently it will be installed together with the Hamburg Port Authority at berth 1, Hamburg Predöhlkai.

II. Scours

A. Formation of scours

Cause of the formation of scouring are high flow rates at the seabed. Especially drifts induced by engine propellers or bow stream rudders form finite but considering nearby standing harbor constructions like quay walls or dolphins particularly observant exposures.

Estimations for calculation of scour depths are given in the corresponding literature [4], [7].

Appearance of scours can lead to a local instability of a line shaped construction (e.g. a quay wall) or to global loss of stability of a point shaped construction (e.g. a monopile foundation). The loads are transferred on line shaped constructions in longitudinal direction. Scours occurring repeatedly on the same location can highly constrict the serviceability of the structure because deformations accumulate during each load relocation.

As avoidance of endangerment of water constructions by scours protection systems shall be provided. An exact acquaintance of the local conditions together with monitoring of the effective arising mechanisms permits an exact planning and dimensioning of scour protection systems and in the course of the structural analysis an accurate estimation of scour depths.

B. Experiences at Hamburg Port

At Hamburg port scours were discovered the first time during the bearing of the sea bed in front of quay walls 15 years ago. These scours were refilled with sand or flint.

A systematic investigation of the scour situation was made from 1988 until 1993 at one specific berth. On-site varying scour depths from about 2 meters up to 4 meters were observed in the monitoring time. Penetration tests

result significant lower stabilities of the seabed until a penetration depth of 6 meters.

There upon reduced static soil parameters were estimated in the design process of quay walls.

Advanced and more comprehensive studies and their results were performed during the years 1994 – 1996 and described below.

C. *Experiments at Leichtweiß and Franzius Institute*

Within the framework of an advice, commissioned by Hamburg Port Authority, in investigation of arrangements against slip stream erosion at ship berth, Leichtweiß-Institute of hydraulic engineering at Technical University Braunschweig as well as Franzius Institute at Technical University of Hanover have analyzed scour formation at harbor bed in the front of quay walls [3]. By means of a three-dimensional physical model the flow caused by stern propeller bow propeller were watched and analyzed.

Via hydraulic models under variation of definite hydrological and ship conditional framework, structural alteration of quay walls as well as characteristic situations of ship movement specific nature alike simulations accomplished. The model ships used to accord in their measurements and regarding the equipage with propulsion oars to modern container ships of 4. generation scale 1:45, geometry and flow conditions were given following similar laws. The Material of the bed was set to d_{85} = 0,04 m under consideration of scaling laws so that it suits the in-situ material at 5. and 6. berth of Burchardkai, Hamburg.

By varying significant parameters like machine speed or under keel height the dependency no the scour process is determined. The analysis of these experiments enables an estimation of the scour depth by known bed velocity.

By investigation of scour stability of unsecured seabed the bow stream induced scours are located directly at the quay construction while the stern stream induced scours occur minimum 5 meters away. It is imperative that static loads lead to larger scour depths than intermitting load.

Based on the enforced analysis a qualitative prediction of appearing scours is possible. A substantiated determination of scour depths depends on geometric boundary conditions, subsoil and flow behavior and thereby in particular case not or only approximately possible.

Taking the model scale under consideration the scour depth straight in front of the quay construction can reach slightly several meters. Scour depths in these categories lead to a decrease of bearing strength of wharfage and therefore to an exposure to loss of stability. A permanent control of scour depths is essential for apprehending specific arrangements of scour covering or scour reconstruction.

III. NEW MONITORING SYSTEM

Already acquainted procedures used for measuring scour depth during scour formation like e.g. sonar methods and optical systems are inapplicable due to occurring turbulent particle streams of whirled sediments. Supersonic measurements are not applicable because of the air bubbles running by screw cavitation. A demand for a new measurement and monitoring system for investigation of changes in seabed profiling is immanent.

Beside the ascertainable depth of seabed before the beginning and after ending the docking respectively the undocking maneuver using existing methods it is obvious that the critical load case of wharfage arises during interstages. Alterations in compactions of packing in subsoil located in scour and backfilling areas are due to comprehension of soil static approaches in the calculation of stability will be of great interest. Results of the in situ measurements could be adducted to control the *Froude* similar criteria which forms the basis of the model experiments.

In combination with an online protocol about the characteristics of scouring and a transmittance to the bridge of the docking or undocking ship the scour monitoring system can be used as assistance in maneuver free of failure for self landing ships. Concerning commitment liabilities the documentation of the scour logging may be helpful for allocate the scour origin to a certain ship or maneuver.

A measurement system that meets the requirements was developed at the Technical University Hamburg - Harburg, Institute of Geotechnical and Construction Management and applied for a patent [2].

A. *Description of the system*

The evolved system used for scour monitoring consists of two positively-driven swim respectively sink parts which measure the depth of the seabed at least at one measuring point close to the considered construction. The simple mechanic design of the procedure enables the operator to achieve reliable results under difficult conditions like turbulent flow an contrary weather.

The gained results depend of the specific weight of the measurement buoys. To make safe predictions concerning the stability of the considered construction a system with two buoys is recommended.

The two buoys differ in their specific weights. If the bulk density of the corpus is chosen superior than the density of the sediment it sinks downwards during the scour progress at the regarded location and rests at the maximum scour depth, unattached of an eventual refill of the scour. This compound is called “sink” hereafter. During the dimensioning of the sink the base failure load is to be considered.

If the specific weight is chosen between the weight of water and the weight of the mixed water soil suspension, originated by the turbulent flow at the seabed, the measuring result is the particular depth of the refilled seabed. If additional soil material sediments the buoy remains above the seabed. The illustrated body is called “float” hereafter because it floats on the seabed.

The described construction is illustrated in Fig. 1. The sink is working as drag indicator which shows the maximum scour depth ever whilst the float indicates the actual depth of the seabed at each measuring time step.

Shape and specific weight of the buoys are significant factors which are decisive for calibration of the mechanisms described above. Regarding the shape a double cone characteristic especially for the float is proved particularly favorable because bodies shaped that way will lift easier from the sediment.

An evaluation unit to record, analyze and/or indicate the actual scour depth in combination with a wireless transmission unit enables a monitoring of the docking and

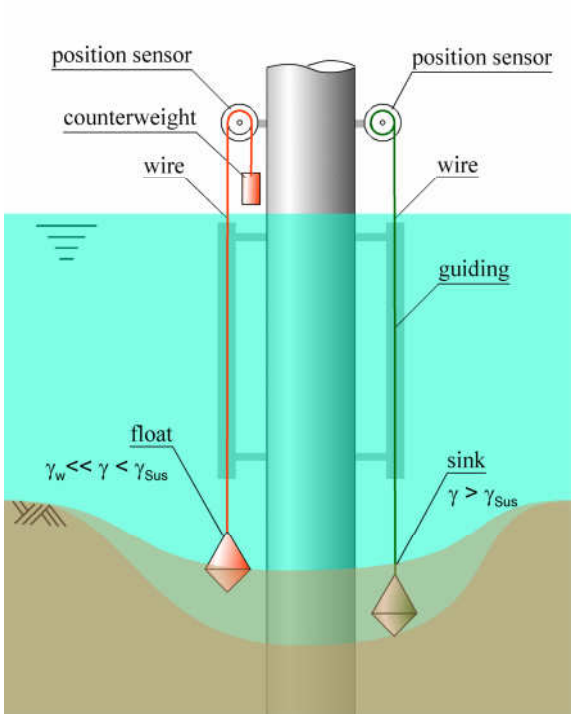

Figure 1. Schematic depiction od the measuring system

undocking maneuver. Among taking preliminary thresholds as a basis immediate protection arrangements can be taken. For an additional measurement of the extents of the scours it might be reasonable to collocate multiple scour measure units in a row . In this manner it is possible, assumed an appropriate concentration of measurement points, to gather the scour formation alongside a quay wall.

B. *Design of the float*

The scour monitoring system described in the section above was tested and precised under laboratory conditions. Beside the tests described hereafter some experiments with rings, bars, cuboid and cylindric shaped buoys were made. The most satisfactory results have been achieved with the double cylindric float thus only these tests will be described in detail.

Determining regarding the shaping of sink and float are slight penetration an lifting in respectively up from the suspension or sediment. The lowest resistance shows the double cylindric shaped buoys, whose base areas are directed against each other. All further geometries prove themselves as improper.

Figure 2. Investigated geometries for the floats

The laboratory buoys were turned out of different kinds of wood which possess varying densities, see Fig. 2.

The type of wood was chosen by assuming that the specific weight of the floats lies between the density of water and the density of the water soil suspension. We used olive, which has a density under laboratory conditions from 1,05 kg/dm3. The sinks are wooden, too. Therefore we choosed Cocobolo. It has a density of 1,1 kg/dm3 under laboratory conditions.

IV. PROVING THE SCOUR MONITORING SYSTEM

A. *Laboratory tests*

In the course of the developing of the scour monitoring system the Technical University Hamburg - Harburg Institute of Geotechnical and Construction Management performed small scaled model experiments. The results of these tests are listed in [5], [6].

The scour measuring system was tested in a box with dimensions h / w / d = 40 / 20 / 10 cm. The box is filled with water and up to the half of its height with soil. Using an inlet at the bottom of the box we derive a vertical flow, directed from bottom to top. Therefore the soil in the top layer is existent as suspension. A scour is generated.

The measurement buoys are fixed on bars which are moveable in vertical direction. In the initial state both matters rest on the seabed. As the tests are performed in a geometric tight box the whirling soil material sediments at the original place. The procedure is equivalent to the real maneuver operation and has nothing in common with the static loading. A respective test passage is shown in Fig. 3.

The sequence shows clearly the desired behavior of the measurement device. During the initial situation both buoys are lying on the seabed in the same depth. After finishing the experiment the sink is out of sight in contrast to the float which lies still on the top of the newly formed water bed. The maximum scour depth during the trial is shown by the sink position; an indication to the final depth of the sea bed after ending the maneuver could be given by regard the position of the float.

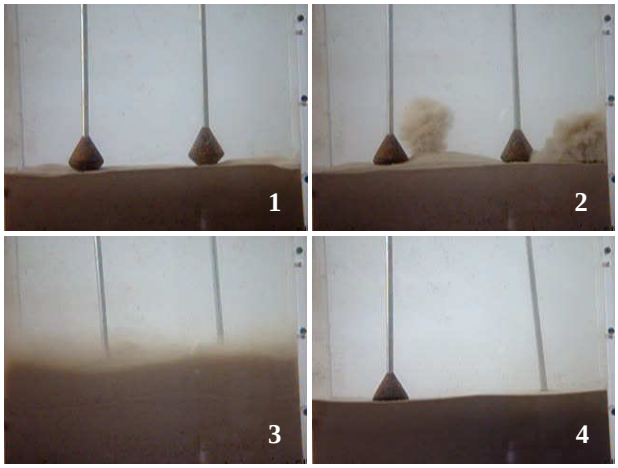

Figure 3. Experiment sequel scour measuring

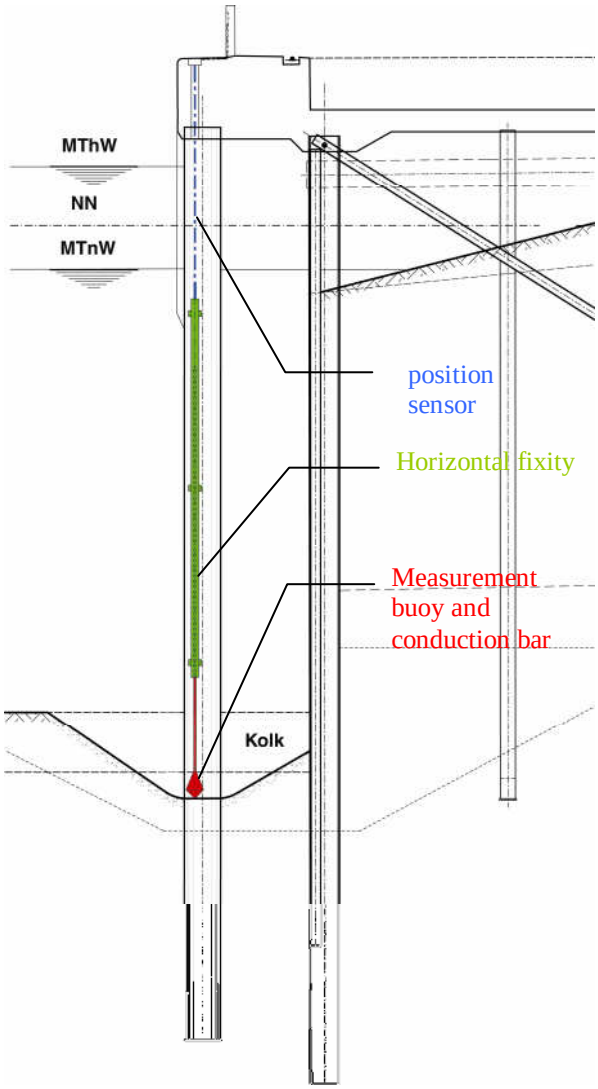

Figure 4. Installation of the scour monitoring system at Predöhlkai, Hamburg

B. Planned measuring program at Predöhlkai, Hamburg

The container handling in Hamburg is increasing very fast. Additional to the fairway deepening of the river Elbe and the construction of the 1.4 km long container terminal Altenwerder Hamburg Port Authority intends to build three new large ship berths for containerships with an overall length of 1035 m at Predöhlkai.

During the first phase of construction the executive company Hochtief, Hamburg Port Authority and Technical University Hamburg - Harburg agreed upon the installation of the described scour monitoring system. The berth is operating since November 2005. Because disturbances are feared during ice drift in winter it is planned to install the scour monitoring system in spring-time 2006.

The measurement buoys are manufactured in steel and are fixed to a conduction bar. The bar is vertical free and horizontal fixed via plates in the other directions on the friction pile. Using a cable winch coupled with position sensors the measure signals will be submitted to a data logger and recorded with a frequency between 20 Hz and 2 kHz. Thus a complete and real time documentation of scour formation during docking and undocking maneuver is possible.

A graphic of the planned installation is shown on Fig. 4.

REFERENCES

[1] Bollrich, G., 2000, Technische Hydromechanik Band 1 und 2 Verlag Bauwesen, Berlin.

[2] Deutsche Patentanmeldung „ Messverfahren und Vorrichtung zur Bestimmung der Tiefe eines sich ausbildenden Kolkes“, DE10 2004 047 529.

[3] Dücker, H.P., Miller, C., 1996, Harbour bottom erosions barths due to propeller jets, 11th Harbour Congress, Antwerp.

[4] Empfehlungen des Arbeitskreises “Ufereinfassungen” Häfen und Wasserstraßen, EAU 2004, Ernst & Sohn, Berlin.

[4] Grabe, J., 2005, Phänomene an der Grenzschicht Wasser und Boden. Tagungsband zum Workshop „Grenzschicht Wasser und Boden – Phänomene und Ansätze“, Veröffentlichungen des Arbeitskreises Geotechnik und Baubetrieb der TU Hamburg-Harburg, Heft 9, S. 3 – 30, Hamburg.

[6] Grabe, J., 2005, Untersuchungen zum Tragverhalten von Monopiles, HTG-Kongress 2005, Bremen.

[7] Hoffmans, G.J.C.M. and H.J. Verheij, 1997, Scour Manual, Balkema, Rotterdam.

[8 Römisch, K., 1994, Propellerstrahlinduzierte Erosionserscheinungen, HANSA – Schiffahrt – Schiffbau – Hafen, Nr. 9, S. 231-234, HTG Hamburg.

Kariba Dam Plunge Pool Scour

M.F. George*, G.W. Annandale**
* Engineering & Hydrosystems, Inc., Denver, USA
** Engineering & Hydrosystems, Inc., Denver, USA

Determination of the extent of scour is an important factor in the design of dams and spillways. The case study presented herein for Kariba Dam provides a practical application of the total dynamic pressure coefficient with Annandale's Erodibility Index Method (EIM) and Bollaert's Comprehensive Fracture Mechanics (CFM) and Dynamic Impulsion (DI) models. The total dynamic pressure coefficient has been developed to incorporate the effects of jet break up on the average and fluctuating dynamic pressures. The maximum scour depth predicted using the above methods shows very good agreement with the scour observed at the site to date.

I. INTRODUCTION

Determination of the extent of scour is an important factor in the design of a dam whether it be during an overtopping event or from flows discharged through the spillway. Often times a plunge pool is used as a cushion to dissipate energy from the falling jet of water.

Previous work by Bollaert [1] attempted to quantify pressures within a plunge pool when subject to an impacting jet by use of a dynamic pressure coefficient. This coefficient accounts for the average dynamic pressure associated with the impacting jet, the fluctuating dynamic pressure, as well as any amplification that may occur in rock joints due to resonance, but does not account for the degree of jet break up. Advancements regarding the effects of jet breakup on the mean and fluctuating dynamic pressures have been made by Castillo [2] and Ervine, Falvey and Withers [3], respectively. This has lead to the development of a total dynamic pressure coefficient.

The case study presented herein for Kariba Dam shows practical application of the total dynamic pressure coefficient using Annandale's Erodibility Index Method (EIM) [4,5] and Bollaert's Comprehensive Fracture Mechanics (CFM) and Dynamic Impulsion (DI) [1] in the verification of extent of plunge pool scour witnessed to date on site.

II. PROJECT BACKGROUND

Kariba Dam is double curvature concrete arch dam located on the Zambesi River between Zambia and Zimbabwe. The dam itself extends 130 m above its bedrock foundation comprised of granitic gneiss [6]. The dam spillway contains six rectangular shaped gates with openings of 8.8 m by 9.1 m [7]. Since 1959 after the dam's construction, several large flows passed through the spillway and resulted in the formation of a downstream plunge pool (Figure 1). The largest flow occurred in 1981 with a peak discharge of 9444 m^3/s, after which the scour hole reached a maximum depth of approximately 85 m below the original ground surface to an elevation of about 305 m [6].

This case study has been performed using the same initial assumptions made by Bollaert when he preformed a similar study at the dam [7]. For Bollaert's analysis a single gate was analyzed assuming an average opening of 75 %. Typical outlet velocities were approximated at 21.5 m/s, with a maximum elevation in the reservoir at 487.5 m and an average tailwater elevation of 400 m [7].

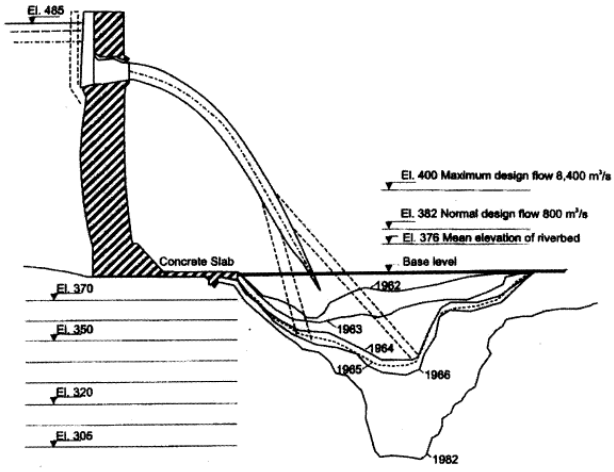

Figure 1. Scour hole formation at Kariba Dam [6]

III. SCOUR PROCESSES

Three mechanisms have been identified that lead to the break-up and removal of a rock mass when subjected to the forces associated with a falling jet of water. These include [1]:

- dynamic impulsion,
- brittle fracture, and
- sub-critical (fatigue) failure.

Dynamic impulsion refers to the ejection or "plucking" of individual rock blocks from their matrix due to pressure imbalances between the top and bottom of the block caused by the impinging jet. This mechanism is only applicable when the rock mass is already completely broken into individual rock blocks or when the rock mass has been completely fractured by brittle fracture or fatigue failure [1].

Brittle fracture refers to the instantaneous break-up of a rock mass along existing close-ended fissures. A close-ended fissure refers to a discontinuity that is not persistent through the rock mass. Scour progression in this failure mode generally occurs very rapidly and in an "explosive" manner. The pressure from the falling jet applied to the

rock joint can be amplified as much as 20 times due to resonance that can occur in a close-ended fissure [1].

Fatigue failure refers to the time-dependent break-up of a rock mass along existing close-ended fissures. Failure by fatigue is generally slower, occurring over an extended period of time as is the case for Kariba Dam. Cyclic pulses generated by the impinging jet propagate fractures bit by bit until the rock mass is completely broken-up into individual rock blocks [1]. The time to propagate a fissure through a certain distance of rock may be calculated by [8]:

$$\frac{dL}{dN} = C(\Delta K)^m \tag{1}$$

Where:

N = number of pressure cycles or "pulses" that will lead to fatigue failure,

C, m = rock properties,

ΔK = range of stress intensities within the rock joint due to the impinging jet, and

L = distance of fissure growth required for failure (m).

IV. Total Dynamic Pressure Coefficient

Recent research by Castillo [2] and Ervine, Falvey and Withers [3] regarding the effects of jet break up on the average dynamic pressure and fluctuating dynamic pressure, respectively, has been combined with that from Bollaert [1] to form the total dynamic pressure coefficient. This may be written as:

$$C_t = C_p + \Gamma \cdot RF \cdot C`_p \tag{2}$$

Where:

C_p = average dynamic pressure coefficient [2].

$C`_p$ = fluctuating dynamic pressure coefficient [1].

G = amplification factor for resonance that can occur in close-ended rock joints applied to $C`_p$ [1].

RF = reduction factor dependent on the degree of jet breakup applied to $C`_p$ based on research by Ervine, Falvey and Withers [3].

A. Average Dynamic Pressure Coefficient (Cp)

Recent research by Castillo [2] compares the effects of varying degrees of jet break up on the average dynamic pressure coefficient for rectangular jets. Castillo compares the average dynamic pressure coefficient to the ratio of plunge pool depth (Y) to jet impact thickness (d) for varying jet break up ratios (Figure 2). The degree of jet break up is determined by the ratio of the jet trajectory length (L) to the jet break up length (L_b). As the jet break up ratio (L/L_b) increases the average dynamic pressure coefficient decreases.

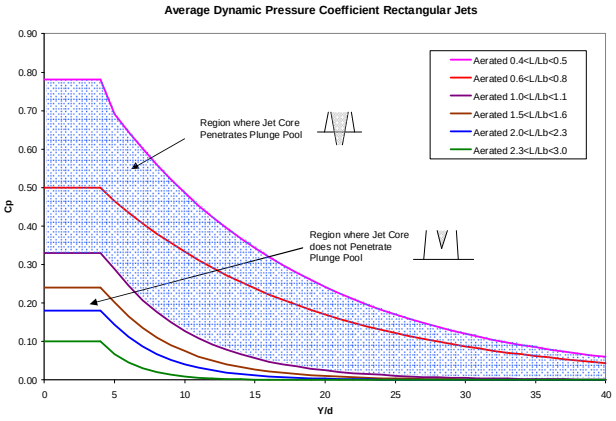

Figure 2. Calculation of C_p [2]

The length of the jet, calculated by Annandale [5], may be expressed as:

$$L = \int_0^x \sqrt{1 + \left[\tan(\theta) - \frac{2x}{K\left[4(d + \frac{v^2}{2g})\cos(\theta)^2\right]}\right]^2} \cdot dx \tag{3}$$

Where:

x = horizontal distance to impact (m).

θ = the angle of issuance.

d = the depth/thickness of the jet at issuance (m).

v = the initial velocity of the jet at issuance (m/s)

K = a coefficient representing energy loss of the jet.

Two separate equations to calculate the jet break up length are used depending on the method being utilized to determine the erosive capacity of the jet. Case studies have shown that the equation developed by Horeni [9] for rectangular nappes yields best results when used with Annandale's method. However, an equation developed from experimental testing on round jets by Ervine, Falvey and Withers [3] provides best results when used with Bollaert's method. The two equations are provided below.

Fout! Objecten kunnen niet worden gemaakt door veldcodes te bewerken. (4)

Where:

q = the unit discharge (m^2/s).

$$L_b(Ervine) = \frac{1}{2} \cdot d \cdot Fr^2 \cdot \frac{\frac{-1}{2} \cdot C + 1 + \frac{1}{2} \cdot (C^2 + 4 \cdot C)^{\frac{1}{2}}}{C} \tag{5}$$

Where:

d = the depth/thickness of the jet at issuance (m).

Fr = the Froude number at issuance.

$C = 1.07 \cdot T_u \cdot Fr^2$, where T_u is the turbulence intensity.

B. Fluctuating Dynamic Pressure Coefficient (C`p)

The fluctuating dynamic pressure coefficient relates the variation in pressure fluctuations with respect to the average dynamic pressure. $C`_p$ is calculated from the following graph (Figure 3) based on research conducted by Bollaert [1].

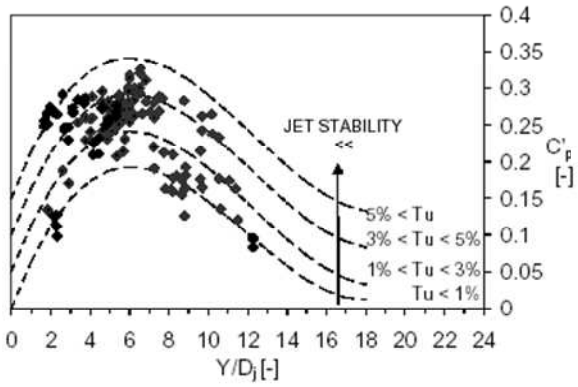

Figure 3. Determination of $C`_p$ [1]

As indicated, peak pressure fluctuations occur for plunge pool to jet thickness ratios (Y/D_j) of approximately six. For clarification, D_j in Figure 3 refers to the inner core thickness of the jet at impact. This is opposed to Castillo's research which uses the outer thickness of the jet at impact (this accounts for jet spread due to aeration).

Two scaling factors are also applied to the fluctuating dynamic pressure coefficient to account for amplification in close-ended rock joints as well as for varying degrees of jet break up.

Amplification in close-ended ended can occur due to resonance, thus causing significant pressure spikes at the tip of the fissure. These pressure spikes may be quantified by applying an amplification factor, G, developed by Bollaert (Figure 4) [1].

As indicated, peak amplification of nearly 8 to 20 times the original signal occurs for Y/D_j ratios of approximately 8 to 10.

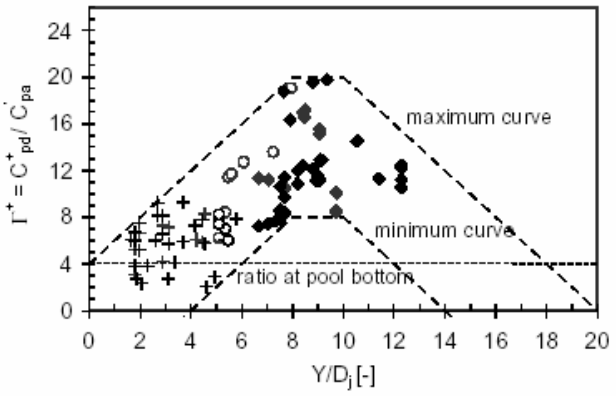

Figure 4. Determination of G [1]

Additionally, the erosive capacity of the jet needs to account for the response of the fluctuating pressures to the degree of jet break up. Similar to the average dynamic pressure, the fluctuating dynamic pressure decreases with increasing degrees of jet break up, ultimately resulting in diminished erosive capacity. Figure 5 shows a relationship developed by Ervine, Falvey and Withers [3] between the fluctuating dynamic pressure coefficient and the jet length to jet break up length ratio (L/L_b).

Based on this relationship, a reduction factor (*RF*) was determined and applied to Bollaert's fluctuating dynamic pressure coefficient ($C`_p$) depending on the degree of jet break up [5].

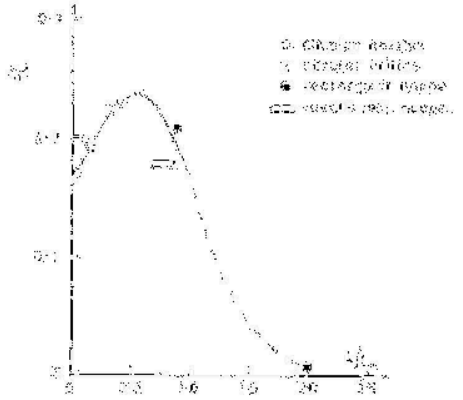

Figure 5. Relation of $C`_p$ to break up length ratio (L/L_b) [3]

V. Scour Prediction Methods

Two methods are used to predict the amount of scour likely to occur for a given discharge. These are Annandale's EIM [4,5] and Bollaert's CFM and DI models [1]. In general, the EIM is used to determine a total scour depth, while the CFM and DI model are used to give insight to the type of failure (i.e., brittle fracture, fatigue, or dynamic impulsion) occurring over that total depth, in addition to providing a total scour depth. For Kariba Dam, the scour depths predicted by the EIM as well as the CFM (namely fatigue failure) are of most importance.

A. Rock Resistance

The resisting power of the rock material is calculated for Annandale's method by assigning an empirical geo-mechanical index to the rock mass known as the Erodibility Index [5]. This is defined as:

$$EI = M_s \cdot K_b \cdot K_d \cdot J_s \qquad (6)$$

Where:

M_s = mass strength number,

K_b = particle/block size number,

K_d = discontinuity or inter-particle bond shear strength number, and

J_s = relative ground structure number.

The resisting power of the rock material (kW/m^2) is then calculated from the equation below [5]:

$$P_{rock} = EI^{0.75} \qquad (7)$$

When the erosive power of the jet is greater than the resisting power of the rock, scour shall occur. When the resisting power of rock is greater than that of the jet, scour will not occur.

B. Jet Erosive Capacity

Two methods are used to determine the erosive capacity of the impinging jet. The first method, by Annandale, describes erosive capacity in terms of unit stream power (W/m^2), while the second method, by Bollaert, relates erosive capacity in terms of pressure (Pa). The total dynamic pressure coefficient has been applied to both methods to account for variations in the average and fluctuating dynamic pressures due to jet break up.

The stream power of the impinging jet (W/m^2) for the EIM may be expressed as [5]:

$$SP_{jet} = \frac{\gamma \cdot Q \cdot H}{A} \cdot C_{t\_avg} \quad (8)$$

Where:

g = unit weight of water (N/m^3),

Q = discharge over the top of the dam (m^3/s),

H = head associated with the falling jet (m),

A = impact area of the jet (m^2), and

C_{t_avg} = average total dynamic pressure coefficient [5], which can be defined as: $C_{t\_avg} = C_{t\_1} + C_{t\_max}$, where C_{t_1} = total dynamic pressure coefficient not accounting for amplification in fissures (i.e., $\Gamma = 1$) and C_{t_max} = total dynamic pressure coefficient accounting for amplification with Γ defined by Figure 4.

For use with Bollaert's CFM and DI models, three separate pressure calculations are required. The first is the calculation of the pressure at the rock/water interface (i.e., the joint opening). This is the pressure used to calculate the amount of dynamic impulsion, which assumes fissures are open-ended and hence there is no amplification that may occur. This may be expressed as:

$$P = \gamma \cdot C_{t\_1} \cdot \phi \cdot \frac{v_j^2}{2g} \quad (9)$$

Where:

g = unit weight of water (N/m^3),

C_{t_1} = total dynamic pressure coefficient (not accounting for amplification, i.e., $\Gamma = 1$),

ϕ = energy coefficient (usually assumed = 1),

v_j = impact velocity of the jet (m/s), and

g = acceleration of gravity (m/s^2).

The second is the calculation of the maximum pressure that can be found in a close-ended fissure. This is similar to Equation 9 except that the total dynamic pressure coefficient has been adjusted to account for amplification that may occur due to resonance.

$$P_{\max\_fracture} = \gamma \cdot C_{t\_\max} \cdot \phi \cdot \frac{v_j^2}{2g} \quad (10)$$

Finally, the average pressure within a close-ended fissure may be calculated by making use of the previous two equations. This is defined as [1]:

$$P_{avg\_fracture} = 0.36 \cdot P + 0.64 \cdot P_{\max\_fracture} \quad (11)$$

The average pressure within close-ended fissure is used when calculating the amount of brittle fracture as well as fatigue failure time with Bollaert's CFM model.

VI. Scour At Kariba Dam

Scour calculations for Kariba Dam were performed for the peak discharge observed during the 1981 event and "average" rock mass parameters assumed by Bollaet [7]. These values are summarized in Table 1 below. Additional rock mass assumptions for the EIM are also included in Table 1 based on engineering judgment.

TABLE I. Rock Mass Parameters

Parameter	Value
Unconfined Compressive Strength (UCS)	125 MPa
Joint Persistency	25%
Maximum Joint Length	1 m
Joint Tightness	Tight
Joint Alteration/Filling*	None
Joint Roughness*	Rough & Undulating/Planar
Number of Joint Sets	3
Rock Quality Designation (RQD)*	80
Fatigue Coefficient, m	10
Fatigue Coefficient, C	1.3×10^{-6}

*Value assumed for EIM

Given the rock parameters above, a rock resistance of approximately 600 kW/m^2 was calculated for the EIM. Figures 6 and 7 show the maximum scour depths predicted for fatigue failure and the EIM.

Figure 6. Scour by fatigue failure using CFM model.

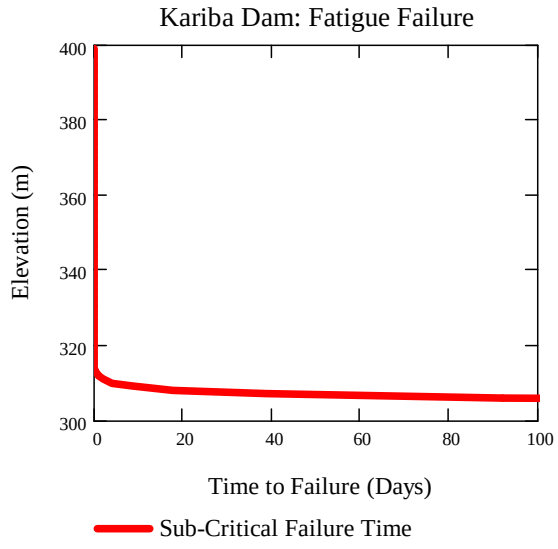

Figure 7. Scour prediction with the EIM

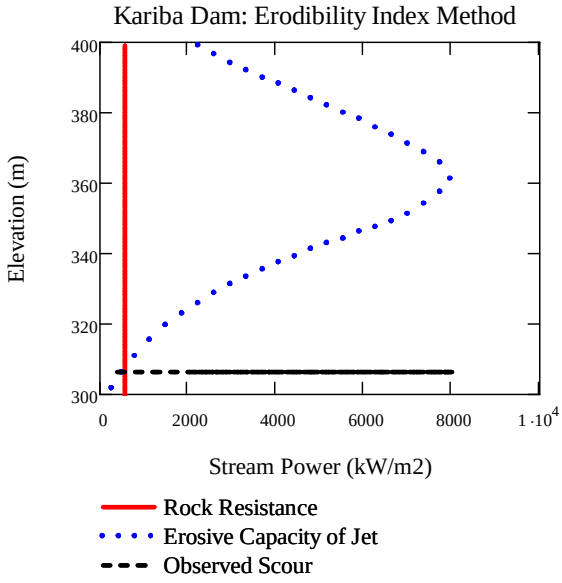

In Figure 6, the scour extent is shown as a function of time. Note that at about an elevation of 310 m (i.e., a plunge pool depth of nearly 90 m), the time it takes to fail the rock mass by fatigue begins to increase exponentially. It is just below this elevation that it is believed that scour progression would cease.

Figure 7 relates the scour extent by the use of a threshold value. At an elevation approximately a few meters above the observed scour elevation (305 m), the erosive capacity of the jet (measured by stream power) becomes less than the resisting capacity of the rock mass, suggesting no further scour.

As indicated, both methods produce nearly spot-on results in predicting the ultimate scour depth. This gives good promise to the use of the total dynamic pressure coefficient with the EIM, CFM and DI models.

VII. CONCLUSIONS

The application of the total dynamic pressure coefficient to Annandale's EIM and Bollaert's CFM and DI models appears to produce accurate representations of the maximum scour depth witnessed at Kariba Dam. The total dynamic pressure coefficient incorporates the effects of jet break up on the average and fluctuating dynamic pressures likely to result in a plunge pool from an impinging jet based on research by Castillo and Ervine, Falvey and Withers.

Incorporating the effects of jet break up is key when determining the extent of scour likely to occur for a given discharge as for increased degrees of break up, less scour is to be expected. This is an important factor when designing a plunge pool or plunge pool protection in the sense that huge costs could be alleviated if the extent of scour predicted is less than what would have been calculated not accounting for jet break up.

VIII. REFERENCES

[1] Bollaert, E. 2002. *Transient Water Pressures in Joints and Formation of Rock Scour due to High-Velocity Jet Impact, Communication No. 13*. Laboratory of Hydraulic Constructions, Ecole Polytechnique Federale de Lausanne, Switzerland.

[2] Castillo, L.G. 2003. Contribution to discussion of Bollaert and Schleiss' paper "Scour of rock due to the impact of plunging jet Part 1: A state-of-the-art review". *Journal of Hydraulic Research*. 41: 451-464.

[3] Ervine, D.A., H.T. Falvey, and W. Withers. 1997. Pressure Fluctuations on Plunge Pool Floors. *Journal of Hydraulic Research*. 35: 257-279.

[4] Annandale, G.W. 1995. Erodibility. *Journal of Hydraulic Research*. 33: 471-494.

[5] Annandale, G.W. 2006. *Scour Technology*. 1st ed. New York: McGraw-Hill.

[6] International Commission On Large Dams (ICOLD). 2002. Large Brazilian Spillways. 193-196.

[7] Bollaert, E. 2002. Erodibility of Fractured Media: Case Studies.

[8] Paris, P.C., M.P. Gomez, and W.E. Anderson. 1961. *Trend Engineering*. 13: 9-14.

[9] Horeni, P. 1956. Disintegration of a Free Jet of Water in Air. *Sesit 93*. Praha, Pokbaba.

KEY WORDS

Scour, plunge pool, Erodibility Index Method, jet break up, dynamic pressures, prediction, case study, Kariba Dam, Comprehensive Fracture Mechanics, Dynamic Impulsion.

Scour hole slope instability in sandy soil

M.B. de |Groot*, and D.R Mastbergen**
* GeoDelft, Delft, the Netherlands
** WL|Delft Hydraulics, Delft, the Netherlands

The development of a scour hole and in particular its upstream slope is determined by several morphological and geotechnical processes. Simple sliding and liquefaction flow slides are traditionally considered to be responsible for any slope instability. The process of breaching and slope erosion by density current was only recently recognised as another potentially important process. Its relevance for the stability of scour hole slopes is discussed in this paper.

I. INTRODUCTION

Scour holes near bridge piers, sluices, barriers and other structures in sandy rivers and estuaries may endanger the structure stability. A bed protection is usually required to protect the sand against the most turbulent flow and to keep the scouring far away from the structure (Figure 1).

Dimensioning of the bed protection requires the answer to such questions as:

- What reduction of scour hole depth, D, and slope angle, β, are caused by increasing the length, L, of the bed protection?
- What value of β and value of D guarantee the slope to remain stable in case of dense sand? Idem in case of loose sand?
- What length, L, need to be chosen to guarantee that the structure foundation remains stable in the unhoped case that slope instability occurs?

The answers require knowledge of the physical processes. Traditionally only morphological processes are considered to be relevant for the answer to the first question and only geotechnical processes for the other questions. Recently, however, a combination of partly morphological and geotechnical processes was recognized to play an important role in slope instability: breaching and the successive erosion by a sand-water mixture density or turbidity current that is produced by a breach [1, 10].

The consequences of this combination of processes for the design of bed protections will be discussed and illustrated with the design for the Oosterschelde barrier.

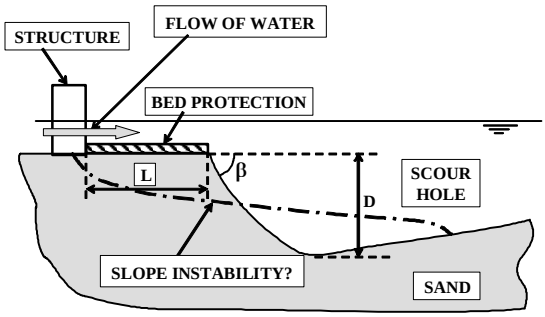

Figure 1. Dimensioning bed protection in view of scour hole

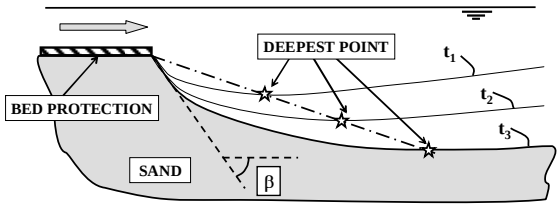

Figure 2. Scour hole shape is constant during increase of scour hole depth.

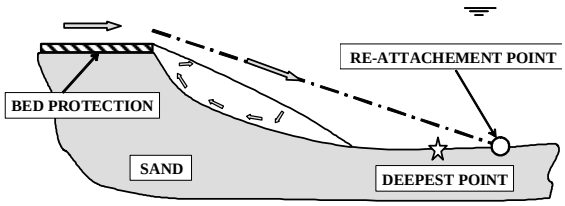

Figure 3. Flow pattern in scour hole

II. PHYSICAL PROCESSES

A. *Scouring*

The development of a scour hole is largely determined by erosion, which is a purely morphological process. A general description is presented by Pilarczyk in [2]. The deceleration of the flow after passage of the structure goes along with large velocity gradients and the development of additional turbulence. Thus, the downstream flow has a much larger sand transport capacity than the upstream flow and causes erosion of the bed as soon as the flow passes over the unprotected sand bed.

Four phases of scour hole development can be distinguished: initiation, development, stabilization and equilibrium. The second phase, which may take many

years, is of special importance for design. The scour hole depth increases rapidly in the beginning of this phase and more slowly in course of time. The scour hole shape, however, remains nearly unchanged: the deepest point remains on the same line through the end of the bed protection and the upstream slope angle, β, remains constant (Figure 2).

The flow pattern remains the same as well: detachment of the flow at the end of the bed protection, a main stream similar to a jet type flow [3] and re-attachment close to the deepest point of the scour hole, where most of the scour occurs (Figure 3). The moderate upward flow in the wake causes also some scour along the lower part of the upstream slope. The scour along the higher part of this slope is very limited.

The larger the flow velocity at the end of the bed protection the higher the speed of scouring. A similar influence has the turbulence at the end of the bed protection. This turbulence, however, has also another effect: the larger the turbulence the steeper the upstream slope of the scour hole, β.

A relationship between a turbulence parameter and β has been found by systematic scale model investigation. See section 2.4.9.7 of [2]. The scaling had been performed with polystyreen grains with such dimensions and under water weight that conformity could be approximated with respect to the most important morphological aspects: flow pattern, fall velocity of the grains and angle of repose. However, the approximation was not completely satisfactory and conformity with respect to geotechnical soil properties such as angle of shearing resistance and dilatancy is uncertain, whereas certainly no conformity had been arrived with respect to the permeability of the modelled sand.

Comparison between full scale and small scale tests with high turbulence [3] made clear that the average value of β along the bed protection edge found in the full scale tests agreed well with the value found in the small scale tests, but that the slope was significantly steeper at some locations, resulting in several slope instabilities.

The full scale tests illustrated another limitation of scale tests: natural soil usually consists of layers, some of which may be cohesive and cause a significant temporal delay of the scouring process.

Finally, the question may be raised whether the development of a scour hole, and in particular the steepest slopes, may also be influenced by the process of breaching and slope erosion by density current (see below under D). If so, this process will be underestimated in any scale model. Indeed the sand properties responsible for any process of breaching and the generation of an erosive turbidity current are not modelled correctly in the scale model

B. Simple sliding as cause of slope instability

A simple undeep sliding occurs as soon as the upstream slope in non-cohesive soil becomes steeper than the slope corresponding to the angle of shearing resistance, i.e. a slope of $\beta \approx 30^{\circ}$. Sliding with more complicated rupture surfaces may occur if cohesive layers are present. The shear strength in natural cohesive soils is nearly everywhere sufficient, however, to avoid sliding when the slope is more gentle than 1 : 2.

Temporarily steeper slopes, up to vertical, may be present in the case of shear in densely packed sand due to dilatancy. In that case temporary negative pore pressures will occur in the sand body with inflow of water from outside into the soil. This will be discussed under 'breaching' below.

C. Liquefaction flow slide

Loose sand has the tendency to contract, i.e. to decrease in volume during shear. Pore water flow resists such decrease, in case the sand is saturated and undrained and excess pore water pressures arise, causing a decrease in effective stress and in shear strength. This may be called liquefaction or, at least, partial liquefaction.

Some results of undrained, strain controlled Direct Simple Shear test on saturated sand samples are schematised in Figure 4. The test on medium dense sand shows a gradually increasing shear stress, τ, with increasing shear strain, γ. The test on loose sand, however, shows decrease in shear stress after the shear strain has reached a certain value. This decrease corresponds to a significant increase in excess pore water pressure to a value higher than 50% of the vertical stress σ_v, which means that the sand may be called (partially) liquefied.

The point where the shear stress starts to decrease may be called a point of 'meta-stability'. This means that any very small load change would lead to a sudden collapse of the sample (at least a very large shear deformation and sudden large increase in pore pressure) when the shear stress has reached this value in a stress-controlled test.

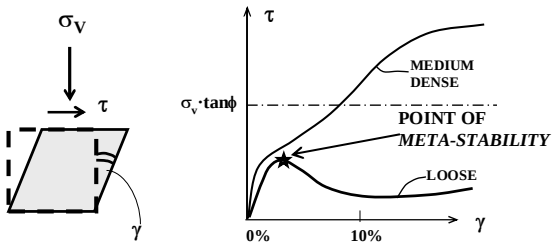

Figure 4. Result of direct simple shear test on undrained saturated sand

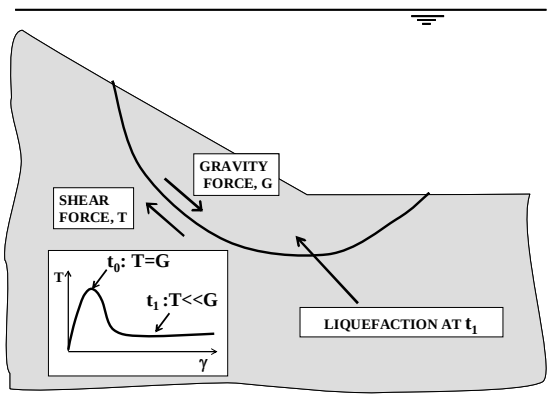

Figure 5. Liquefaction flow slide in case of meta-stable sand

A large part of the sand mass underneath a slope may be in a similar state of meta-stability (Figure 5) if the sand is loose and fine enough and if the slope is steep and high enough [5]. The sand in a slope at such location experiences monotonic shear loading due to gravity and the corresponding shear deformation does not yield any reduction of the loading. Consequently the sand is in a similar situation as in a stress controlled shear test. Much of the sand is in a nearly undrained condition if the sand mass is large enough, e.g. because the slope is relatively high, and if the sand is fine enough to have a relative low permeability.

Then any small change in loading, e.g. by a local erosion or a sudden decrease in water level, may disturb this meta-stability and cause the collapse of the sand mass, characterised by large excess pore pressures: the sand is 'liquefied' and starts to flow.

The sand is not completely undrained and some pore water is expelled, whereas the excess pore pressure reduces to zero when the sand has contracted enough. Then the sand flow stops as well [6]. The time needed for this process depends on the permeability of the sand and the thickness of the liquefied layer. The lower the permeability and the larger the thickness, the longer takes the liquefaction flow slide and the larger is the resulting slope deformation.

D. Breaching and slope erosion by density current

No liquefaction flow slide is to be expected in dense or medium dense sand. Slope instability may occur by 'simple sliding', but also by the combination of breaching and the erosion due to the sand-water mixture density current that is produced by the breach [1, 8].

A breach is a steep superficial sand slope disturbance that gradually retrogrades upward along the slope with the so-called wall velocity, defined by permeability and porosity of the sand bed. The slope of the breach is so steep that no long-time equilibrium is possible (Figure 6). Gravity induces a shear deformation of the sand at the breach surface. The tendency to dilate causes the development of negative excess pore water pressures at a small distance from the breach surface, where the sand behaves semi-undrained. The negative pore water pressures induce a temporary increase in shear strength of the sand, which keeps the sand stable for some time.

The negative pore water pressures cause an influx of water into the pores yielding an increase in pore volume of the sand. As soon as the pore volume has increased enough and the negative pore pressures have nearly disappeared, failure occurs and the grains fall downwards along the slope surface, resulting in the retrogression of the breach. The falling sand grains mix with the water outside the soil which is called entrainment.

Dependent on the height and the retrogression velocity of the breach, the initial flow velocity may be sufficient to keep the sand grains suspended and the breaching process results in a turbulent sand-water mixture flow at the toe of the breach. This mixture flows downward as a density current. Dependent on slope angle and height the density current will accelerate or decelerate.

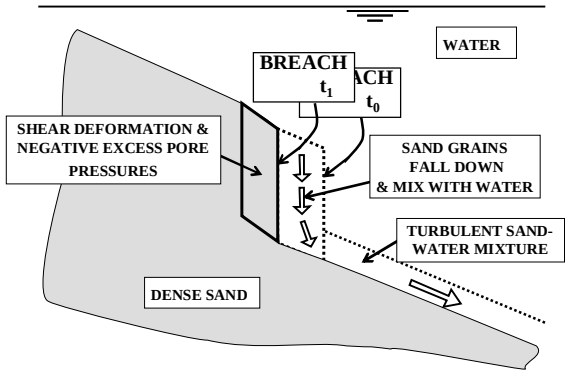

Figure 6. Gradual upward movement of breach and resulting sand water mixture

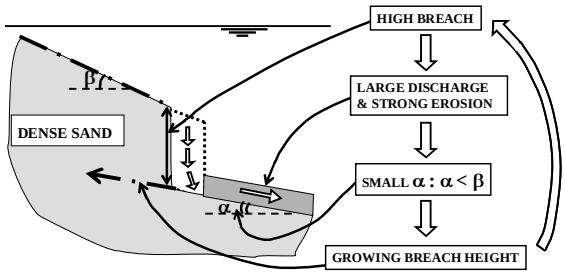

Figure 7. 'Ignitive' breach growth if initial breach height is larger than critical value

Erosion and sedimentation take place at the interface of the flow with the sand bed. Sedimentation dominates if the flow velocity of the density current is relatively small, due to a gentle slope of the sand bed or if the sand is particularly coarse. Erosion dominates, however, if the slope is steep enough and the sand relatively fine. Due to the increasing density and sand transport rate the flow velocity will increase further, resulting in even more erosion A so-called ignitive or self-accelerating turbidity current has developed (Figure 7). All the eroded sand will be transported downward and meanwhile the breach will retrograde upward until the original estuary bed with the bed protection has been reached. This breaching process is generally recognized as a slope failure or slope instability during or after dredging in sand pits and in submarine canyons [1, 8].

The minimum required time to establish a fully developed flow over the full slope height is defined by the breach retrogression or wall velocity and the slope height and is generally several hours.

The conditions for establishment of an erosive self-accelerating sand-water mixture flow resulting in a slope instability therefore are in the first place a steep sand slope and sufficient slope height in relation to the sand properties and an initiating event creating a breach which is high enough to suspend the sand. Moreover, a necessary condition to maintain the erosive flow and slope retrogression is the transport rate of the sand transported to the toe of the slope. Elsewhere, the sand will settle

eventually and a gentle slope will be created on which the flow will gradually extinguish.

The question needs to be considered under what circumstances these conditions can be met in a scour hole. The first condition, a relatively steep slope, β, can be present with large turbulence at the downstream end of the bed, as discussed above. A slope of 1:3 over 5 m or more is certainly steep enough for sand of about 200-300 μm, according to computations and field observations [1, 8]. The second condition, the initiation of a relatively high breach, however, requires a special composition of the subsoil and the interaction with other processes, as will be discussed below. The third condition, the transport rate of the sand at the toe can be provided by flow of the sand into deeper parts down slope or pick up by the main flow in the zone of flow re-attachment (Figure 3).

E. Interaction of processes: conditions for breaching slope instability

Slope instability due to a strong erosive breach induced self-accelerating turbidity current requires an initial high breach, i.e. the presence at any moment during the scouring process of a significant part of the slope that is so steep that it is only temporarily stable. The breach will not be very high during the normal scour hole development process if the subsoil consists of homogeneous (medium) dense sand. Then the scour hole shape develops regularly as illustrated in Figure 2, although some minor bank retrogression and bed protection damage is expected .

The presence of a clay layer, however, may bring about a more irregular scouring process. The layer may temporarily keep up a steep part of the slope. After undermining of the layer it may break off and cause a high breach in the sand above (Figure 8). An additional effect of the sudden sliding in clay and sand is the large increase in sand transport rate. Although this large transport rate does not continue for a long time, it may be sufficient to cause a strong local erosion process just below the slide due to a self-accelerating density current and initiate a retrogressive breaching process.

The presence of a layer of loose sand may cause a local flow slide and a subsequent breaching process (Figure 9) with a similar slope development.

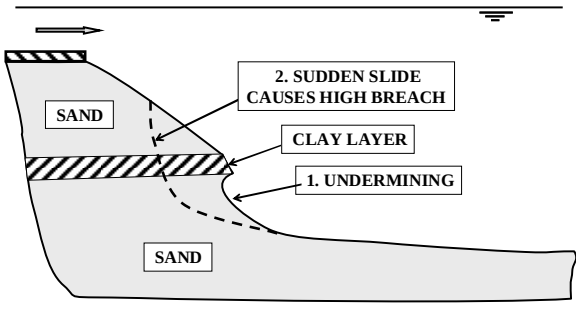

Figure 8. Clay layer as condition for high initial breach

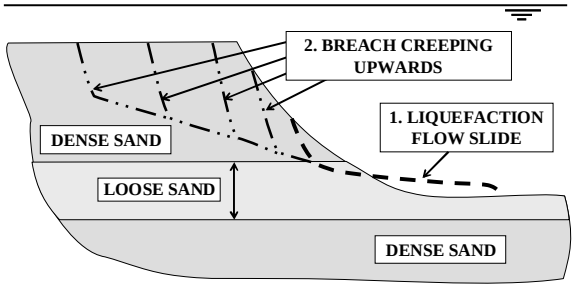

Figure 9. 'Ignitive' breach growth after liquefaction flow in layer of loose sand

III. REVISION NEEDED OF TRADITIONAL DESIGN PROCEDURE?

The 'traditional' design procedure is described in [2]. Two requirements could be formulated for a safe design:

1. The scour hole slopes should remain stable according to the best prediction method
2. If a slope instability occurs nevertheless, it should not endanger the structure

Both requirements can be reached by making the bed protection long enough. The longer the bed protection the less turbulence at its downstream end, which has two positive effects: the upstream slope angle, β, remains small, a guarantee against slope instability and the scour hole depth remains limited, a guarantee for the second requirement.

In case of loose sand and the risk of a liquefaction flow slide, however, an extremely long bed protection might be needed to meet both requirements and other measures could be considered, as discussed below for the example of the for the Oosterschelde barrier.

According to the traditional design procedure only the mechanism of simple sliding endangers slope stability if no loose sand is present. This would mean that slope instability could only occur in slopes steeper than 1 : 2 and any slope instability would not endanger the structure if the bed protection length is slightly longer than the expected scour hole depth.

Another traditional assumption, in case of a loose sand layer of limited thickness, was that the slope resulting after an instability would only be gentle at the level of this layer and would remain steep in other layers.

Slope instability due to breaching and erosion through density current was not considered. This is an omission and the following revision of the design procedure seems to be justified:

- Consider the risk of breaching and erosion in case of non-homogeneous subsoil. Compute the expected slope development given sand properties and expected scour hole depth.
- Estimate the geometric characteristics of local slides resulting after erosion near clay- or silt layers and in particular the resulting initial

breach height and the resulting temporary soil transport rate

- Estimate the geometry resulting after a local liquefaction flow slide in case of the presence of a loose sand layer amidst more dense sand layers and in particular the resulting initial breach height
- Predict the slope that results after the above predicted initial breach height or temporary soil transport rate due to the process of breaching and erosion through a density current.

IV. EXAMPLE OF OOSTERSCHELDE BARRIER

The Oosterschelde is a sandy estuary of around 80 km^2 of high ecological value. A barrier with gates was constructed in the mouth to guarantee the safety of the surrounding land against flooding in the early 1980's. The gates are closed only in case of extreme high water in order to keep the tidal variation during most of the time. The barrier has been designed such that the tidal variation is now 80% of the original variation. This could be reached by reducing the flow opening to about 20% of the original opening of the open Oosterschelde.

The flow opening with gates has been concentrated in the three largest estuary channels The flow opening reduction causes flow velocities in the opening of the barrier which are roughly 4 to 5 times the flow velocities up- and downstream the barrier. This causes a significant increase in turbulence downstream of the barrier in these three channels. This has resulted in 6 large scour holes, 3 on the estuary side (flood) and 3 on the sea side (ebb) downstream of the bed protection. The design with respect to the bed protection length and the scour holes is described in [7] .

The estuary side scour hole in the largest channel will be considered in more detail. The original depth in the 1 km wide central part of the channel varies from 40 m in the South to 25 m in the North. A channel bed protection until 650 m outside the axis of the barrier was placed before the construction of the actual barrier. The speed of scouring at the estuary side of this bed protection edge increased significantly after the start of this construction..

Scale modelling for these bed protections resulted in a prediction of the scour hole shape which can be characterised in the direction parallel to the bed protection edge by two deep parts, one in the South of the central channel part and the other in the North [8]. The predicted shape in the flow direction can be characterised (Figure 2) by tan β = 1 : 2 and the deepest point at 1 : 4 from the bed protection edge at the location of these deepest parts of the scour hole. More gentle slopes were expected in between. Inspection of the present scour hole shows that these predictions were quite correct.

The predicted depth in the two deep parts of the scour holes was roughly the same, but it was considered to be rather uncertain in view of a number of uncertainties in the boundary conditions and the model uncertainty. The predicted depth varied between 30 m and 80 m for the year 2004, roughly 20 years after the start of the barrier construction. Now, the most optimistic prediction appears to be correct for the Northern deepest part, where a depth of 30 m was measured in 2004, and appears to be even too pessimistic in the Southern part, where a depth of 20 m was observed.

The risk of liquefaction flow slides was analysed extensively as most of the sand in the subsoil above the level 30 m below mean sea level is loose [7 and 8]. A typical flow slide starting in the upstream slope would destroy the bed protection over a length of approximately 2 times to 5 times the scour hole depth. The risk analysis made clear that special measures were needed to reduce the risk. Two measures were applied:

- compaction of the sand underneath the downstream edges of the bed protections as illustrated in Figure 2.4.9.11 of [2]
- fixing by means of stone dumping of the upstream scour hole slope as soon as it had reached a certain slope angle, β, over a certain height (Figure 10).

The first 30 m to 60 m of stone dumping was accomplished before completion of the barrier. The area of the stone dumping reaches now more than 100 m from the edge of the bed protection close to the deepest part of the scour hole.

The measures appear successful: no damage to the original bed protection was observed up to now. The need for such measures seems to be illustrated by a very large failure of the Northern side slope of the scour hole which occurred just outside the bed protection between early 2004 and early 2005. The profiles before and after the slope failure are sketched in Figure 11.

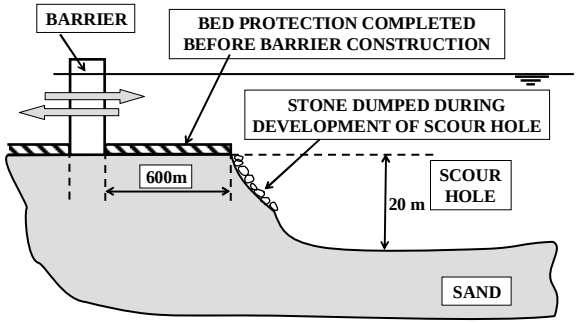

Figure 10. Design Oosterschelde Barrier

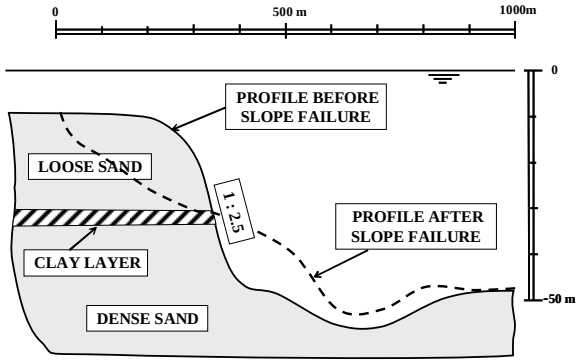

Figure 11. Slope failure in side slope of Oosterschelde scour hole

The situation just before the slide looks similar to the one sketched in Figure 8 and the question is raised whether the slope development in the sand above the clay layer may have been determined by breaching and slope erosion by density current. There seems to be one important difference: this sand was rather loose with the tendency to contract, rather than dilate, whereas breaching requires dilative sand. Nevertheless, if sand is not extremely loose, it shows some dilation after the contraction, which might enable breaching. This is assumption is made for the Oosterschelde sand above the clay layer in order to investigate, by means of calculations, if breaching may have been the cause for the observed slope development in the top 20 m of the upstream scour hole slope.

Therefore it is assumed that the subsoil consists of dominantly moderately packed fine sand of 200 μm, interrupted by a thin clay layer or by a 3 m thick layer of loose sand at a depth of 20 m underneath the original estuary bed as shown in Figure 11.

Then, an 'initial' breach with a height of about 3 m could have occurred after so much scouring that the scour hole was more than 20 m deep. Calculation of the process of breaching and erosion through density current results in the profiles given in Figure 12. The computed profiles represent the stationary retrograding situation when all the sand eroded from the slope is transported downstream into the scour hole or tidal current. Besides the sand properties the sand transport rate at the toe, which is active during at least several hours after initiation, determines the slope development and the retrogression rate. The larger the rate, the more gentle the resulting slope. If the sand is not transported at the toe sufficiently it will accumulate and the breaching process will gradually stop. The transport rate is estimated to be 15 to 60, kg/ms.

For comparison a slope of 1:2.5 and a slope of 1:10 are given in Figure 12. It can be concluded that due to the breaching process a maximum bank regression of about 100 to 300 m can be expected. The slope is steep at the top and very gentle just above the clay layer at a depth of 20 m below the original 'sea' bed.

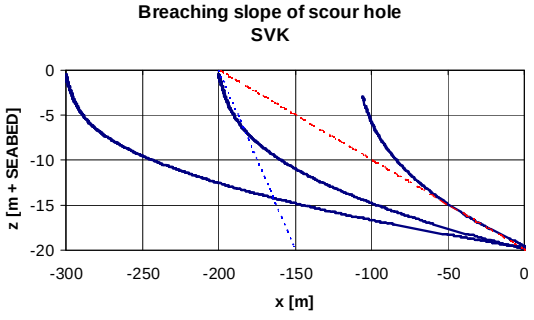

Figure 12. Computed slope development in the loose sand above the clay layer of Figure 11, assuming breaching in 200 μm sand for sand transport rate of respectively 60, 30 and 15 kg/sm

V. CONCLUSIONS

Only erosion, a purely morphological process, is usually considered to be responsible for the development of a scour hole, as long as no clear slope instabilities occur. The possibility should be considered, however, that the gradual development of the upstream scour hole slope is partly determined by breaching and erosion by a sand-water mixture density current.

Instability of the upstream scour hole slope is determined by mainly geotechnical processes in case of a subsoil of homogeneous sand. If densely packed the stability is determined by simple sliding; if loosely packed by liquefaction flow sliding.

In many cases, however, the subsoil is inhomogeneous: layers of densely packed sand are interrupted by layers of clay or loosely packed sand. Then, the slope instability may be determined by a combination of geotechnical instability and breaching with erosion by density current, resulting in a considerable bank regression.

This illustrated by a hindcast of a very large slope failure observed in the inhomogeneous soil adjacent to a scour hole near the Oosterschelde Barrier.

The measures taken to avoid slope failure of the upstream slope of the Oosterschelde Barrier scour holes appeared to be successful up to now. The failure observed in the side slope illustrates the need for such measures.

ACKNOWLEDGMENT

Mr. Jan Slagers of the 'Directie Zeeland' is acknowledged for collecting information about the present state of the Oosterschelde Barrier scour holes.

REFERENCES

[1] D.R. Mastbergen and J.H. van den Berg, "Breaching in fine sands and the generation of sustained turbidity currents in submarine canyons," *Sedimentology*, No 50, pp.635-637, 2003.

[2] K.W. Pilarczyk, "Local scour," in *The closure of tidal basins*, section 2.4.9, J.C. Huis in't Veld et al, Delft, Delft University Press, 1984, pp. 387–405.

[3] G.J.C.M. Hoffmans, "Jet Scour in Equilibrium Phase," *J. Hydraulic Engrg*., ASCE, vol 124, pp.430-436, April 1998.

[4] A.F.F. de Graauw and K.W. Pilarczyk, "Model-prototype conformity of local scour in non-cohesive sediments beneath overflow-dam," *Proc. IAHR-congress New Delhi*, or *WL/Delft Hydraulics*, publication 242, 1981.

[5] T.P. Stoutjesdijk, M.B. de Groot and J. Lindenberg, "Flow slide prediction method: influence of slope geometry," *Can. Geotechn. J*., No 35, pp 34 –5, 1998.

[6] A. Bezuijen and D.R. Mastbergen, "On the construction of sand-fill dams – part 2: soil mechanical aspects, " *Modelling Soil-Water –Structure Interactions*, P. Kolkman et al(eds), Balkema, Rotterdam, pp 363 - 371, 1988.

[7] Ministry of Public Works, Directie Zeeland "Deelnota 9 Bodembescherming," part of: *Ontwerpnota Stormvloedkering Oosterschelde, boek 2 de Waterbouwkundige werken*, pp 215-223, 1991.

[8] Ministry of Public Works, Deltadienst, "Stand van Zaken Rand bodembescherming," 22 RABO-N-82009, June 1982.

[9] P.G.J. Davis and M.B. de Groot, "Economic scour-protection, with adequate guarantee for structural safety," *Proc. XXth IAHR Congress, Moscow*, vol.III-B.d.4, 10 pp, September 1983.

[10] L.C. van Rijn, "Sand transport along pit slopes due to turbidity currents" *in SANDPIT, Sand Transport and Morphology of Offshore Sand mining pits*, Aqua Publications, 2005.

Innovative Scour Protection with Geotextile Sand Containers for Offshore Monopile Foundations of Wind Energy Turbines

J. Grüne*, U. Sparboom*, R. Schmidt-Koppenhagen*, H. Oumeraci*,
A. Mitzlaff**, J. Uecker**, K. Peters**

* Coastal Research Centre (FZK), Hannover, Germany
** IMS-Ingenieurgesellschaft mbH, Hamburg, Germany

I. INTRODUCTION

Creating renewable energy with wind turbines has increased rapidly in the previous years. This was mainly caused by environmental aspects with respect to carbon dioxide accumulation (greenhouse effect). But now also economical reasons become an important factor due to increasing prices and to shortage of fossil fuels as a consequence of increasing global energy consumption.

In some countries areas with effective wind conditions for wind turbines on land are restricted and increasingly occupied by wind turbines already. Thus, offshore areas become increasingly important for installing new wind parks. Otherwise technical and consequently economic boundary conditions for offshore wind parks are much more complex and difficult compared to the conditions of landside wind parks.

One of these complex and difficult offshore conditions relates to the foundation of the support structure, mostly designed as monopile structures. Such monopile support structures for offshore wind turbines in areas with movable sand beds may be affected by local scour processes due to wave and current action.

An innovative solution for monopile scour protection was proposed by using geotextile sand containers. Fig.1 shows a sketch of such a scour protection and the proposed model set-up for large-scale tests in the GWK . In comparison to a rubble mound design the sand containers are made from soft materials minimizing the danger of cable and monopile damage during the construction period. The knowledge about design criteria for such geotextile sand containers [1] is poor and needs to be improved.

In order to investigate the stability of such alternative scour protection around a monopole structure with geotextile sand containers, a research programme has been started recently at the FZK. In this programme physical large-scale model experiments in the Large Wave Channel (GWK) of the Coastal Research Centre (FZK) are being performed to minimise scale effects occurring both with simulation of wave induced hydrodynamic processes and especially with the scaling of natural fine sands, which

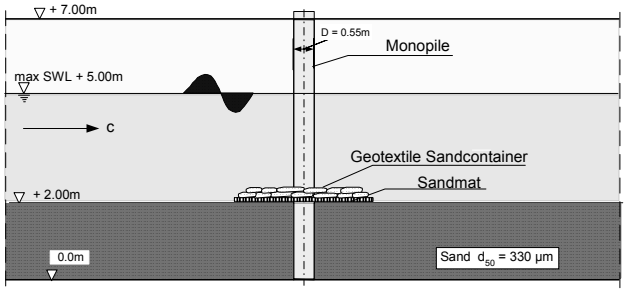

Figure 1.
Sketch of a scour protection with geotextile sand containers and proposed model set-up for large-scale tests in the GWK

both prevail at the proposed offshore areas. In the first part of the investigations pilot experiments on the stability of single geotextile sand containers and of container groups were performed. The results of these experiments are presented in the following and have been used for dimensioning the scour protection for the proposed main tests with a complete scour protection array around a monopile in the GWK.

II. EXPERIMENTS

In the beginning of the pilot experiments some few pilot tests were performed with 4 different geotextile sand containers sizes to get a first approach for dimensioning. All sand containers were placed on a horizontal sand bed. The sand bed was covered with a geotextile filter layer (sand mat) which is normally used as sublayer filter for scour protection. A longitudinal section of the GWK with the installed sand bed is given in Fig. 2. The sand containers were placed in an area on the horizontal sand bed around the proposed monopole.

A few additional tests were performed both with totally and with partly filled sand containers. The results showed a surprising strong influence of the percentage of filling, which means that the stability of sand containers not only is a function of the total weight. A trend was found that sand containers with lower total weights and high percentage of filling are more stable compared to those with higher weights and low percentage of filling.

Based on these first results, it was necessary to perform more comprehensive basic tests on the stability of sand containers before performing tests with a complete scour protection design around a monopile. For these basic test programme the sand containers were varied in size and percentage of filling, which results in 12 different container weights (Table I). Four different container sizes were used, the dimensions length (l) and width (w) in flat unfilled conditions are listed in the first row of Table I. Each of this four container sizes were charged with three percentages of filling: 56%, 80% and 100%, the relevant weights G and the dimensions length (l), width (w) and height (h) under filled conditions are given in Table I.

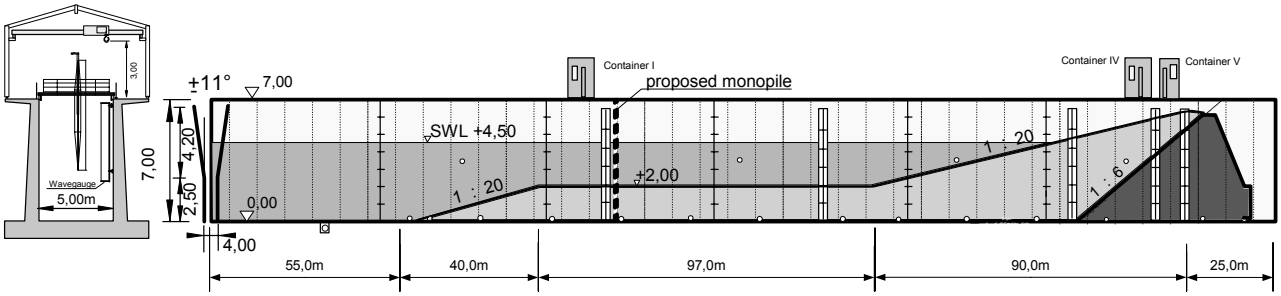

Figure 2. Longitudinal section of Large Wave Channel (GWK) with installed sand bed and proposed monopile

TABLE I

DIMENSIONS OF THE GEOTEXTILE SAND CONTAINERS

Geotextile Container Size (unfilled) l x w [cm]	Percentage of Filling [%]											
	56				80				100			
	Weight G [kg]	Dimension [cm]			Weight G [kg]	Dimension [cm]			Weight G [kg]	Dimension [cm]		
		l	w	h		l	w	h		l	w	h
29.5 x 14.5	1.71	28.2	14.4	3.3	2.45	27.2	13.6	5.0	3.06	27.3	13.3	6.6
36.0 x 18.5	3.34	35.6	17.7	3.9	4.78	34.2	17.2	6.0	5.97	35.4	16.9	7.5
47.0 x 23.0	7.24	45.2	22.8	5.2	10.33	44.0	22.1	7.8	12.91	43.9	22.3	10.2
48.0 x 26.0	10.25	51.3	24.8	6.9	14.64	51.3	25.3	9.0	18.31	48.7	25.2	11.8

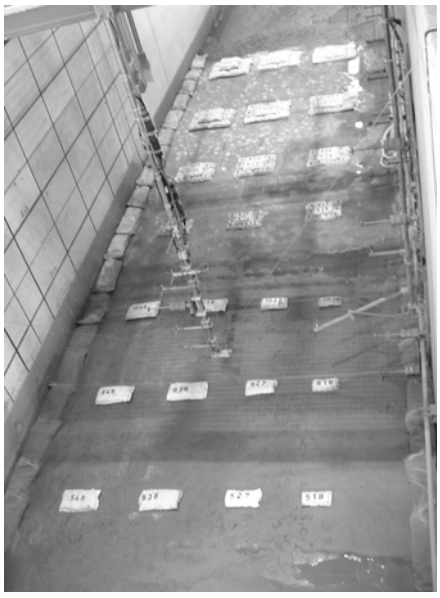

Sand containers placed transverse before tests

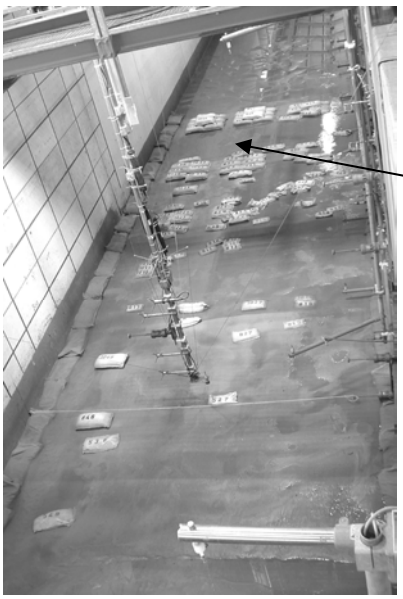

Displacements of sand containers after a test with $H_{1/3}$ = 1.0 m, T_p = 5 s

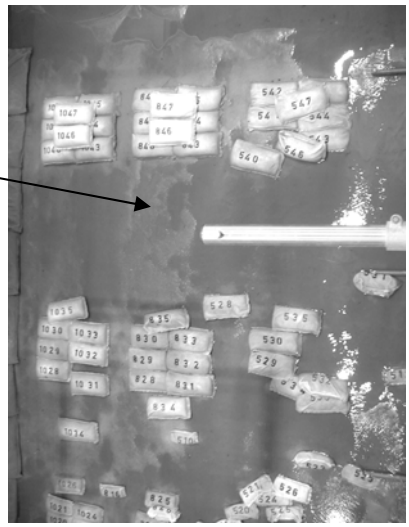

Detail for the container groups

Figure 3. Model set-up of the geotextile sand containers placed on a horizontal sand bed covered with a geotextile filter layer

The different container sizes were placed on the geotextile sublayer both as single containers and as a group of 8 containers in two layers, which results in totally 108 containers for each test. The lower layer of each group consists of 6 containers (3 times 2) and the upper layer of 2 containers, lying in the midst of the lower layer (see definition sketch in Figs. 7 and 8). The container group array should give first results on the interacting effect in a container array. Furthermore, the containers were placed inline and transverse to the wave approach direction. The test configuration transverse to the wave attack is shown in Fig. 3 (left hand photo).

The water depth above the sand bed was kept constant with 2.5 m. Irregular wave trains (Jonswap-spectra) of 120 waves with wave heights between $H_{1/3}$ = 0.6 m to 1.13 m and a peak period of T_p = 5 s were generated. After each test the GWK was drained in order to measure the displacements of each container (middle and right photos in Fig. 3) and to re-establish the test configuration.

III. RESULTS

In the following first results from the basic stability tests are reported. Some results are shown exemplarily in Figs. 5 to 8, where the displacements measured after a test with $H_{1/3}$ = 1.13 m are plotted in the plan views of the test area in the GWK. The Y-axis is along the GWK in wave approach direction (inline) with zero point at the proposed monopole position, the X-axis is transverse to the wave approach direction over the total width (5 m) of the GWK with zero point at the left wall of the channel.

The open squares give the container positions before the test, the dashed ones the position after the test. The displacements are recorded after each test accordingly to the definitions in Fig. 4. Each displaced sand container was replaced in its original position before the next test. The results for the single containers are given in Fig. 5 (inline wave approach) and Fig. 6 (transverse wave approach) and the ones for the container groups in Fig. 7 (inline) and Fig. 8 (transverse).

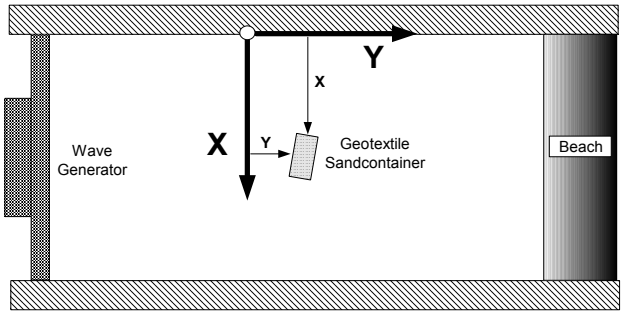

Figure 4. Definition of measured displacements

The displacement data in Fig. 5 for the single containers with inline wave approach demonstrate clearly the influence of the percentage of filling: There is a distinct trend of increasing stability with increasing percentage of filling. For example the 3.05 kg sand container with a filling of 100% is stable, whereas the 7.23 kg container with a filling of 56% is unstable. The data in Fig. 6 for the single containers with transverse wave approach show a similar but not so pronounced trend.

Results from the tests with the container groups are shown exemplarily in Fig. 7 and 8, where measured displacement data are plotted for one container size (l = 36 cm, w = 18.5 cm, unfilled) with 3 different percentages of filling. The wave approach in Fig. 7 is inline, the one in Fig. 8 is transverse. As well as for the data of the single containers the influence of the percentage of filling comes out clearly.

The reason for this effect may be explained by the following hypothesis: Partly filled containers may change their shape due to interior movement of the sand particles which may be caused from the wave-induced currents. With changing shape consequently the shape resistance increases. Thus, the stability decreases due to increasing acting force from the wave-induced currents and this results in a beginning of movement. The movement then may be amplified by further increasing shape resistance.

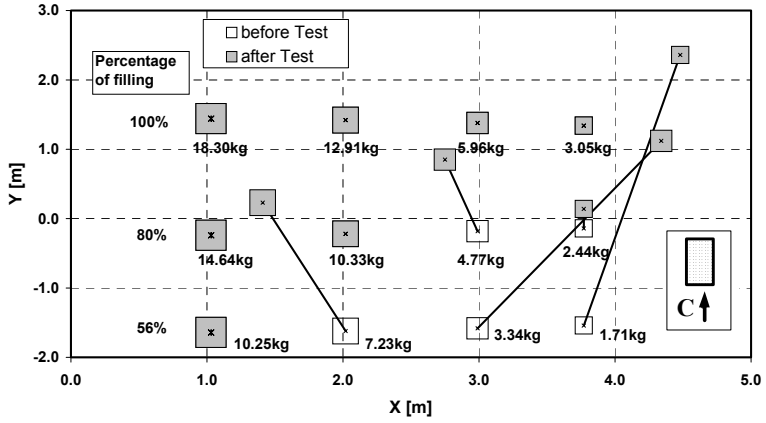

Figure 5. Displacements measured after a test with wave attack inline to single containers

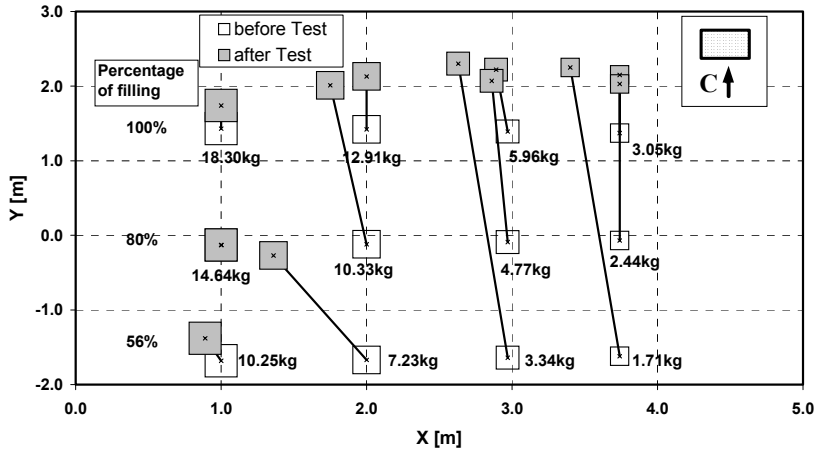

Figure 6. Displacements measured after a test with wave attack transverse to single containers

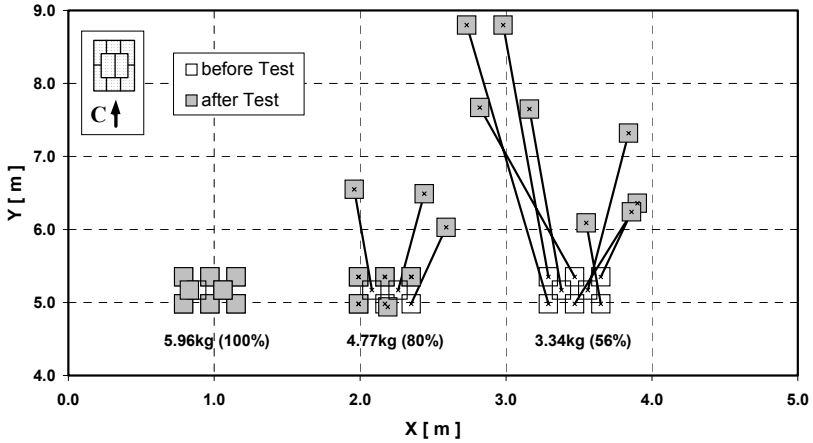

Figure 7. Displacements measured after a test with wave attack inline to container groups

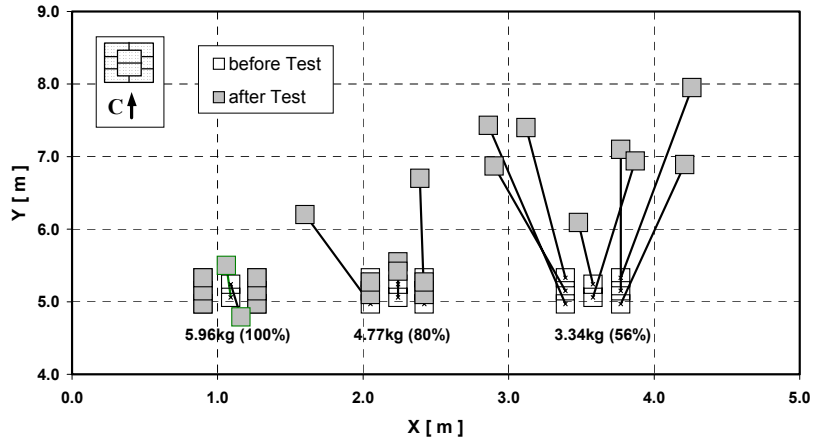

Figure 8. Displacements measured after a test with wave attack transverse to container groups

The inline displacements measured in the test series with the single containers placed inline to the wave approach, as shown in Fig. 5, are plotted in Fig. 9 versus the wave heights $H_{1/3}$. The data confirm that the percentage of filling has also an important influence on the stability of the sand containers.

The data in Fig. 10 give the same trend for the container groups with inline wave approach. The solid line in Fig. 10 stands for the mean inline displacement of all 8 containers in each group and the dotted lines for the maximum inline displacement in each group. Mostly strong differences occur between mean and maximum displacements. This results from the fact that the containers support one another especially in the lower layer. Thus, only the upper layer containers were displaced often (see Fig. 3).

The influence of wave approach direction comes out exemplarily from comparing the results in the upper part of Fig. 11 with the data in the middle part of Fig. 9 (both for single containers with 80% of filling). Inline displacements for single containers attacked with inline wave approach starts with much smaller wave heights $H_{1/3}$ compared to transverse wave approach. It must be mentioned that for container groups the differences between inline and transverse wave approach are much less, which is shown in Fig. 13.

As the waves generated in the GWK are long crested (two-dimensional), wave induced currents in transverse direction are generally very small and negligible.

Nevertheless, transverse displacements of the sand containers were recorded as shown exemplarily in the lower plot of Fig. 11. It was found that the transverse displacements generally increase with increasing inline displacements

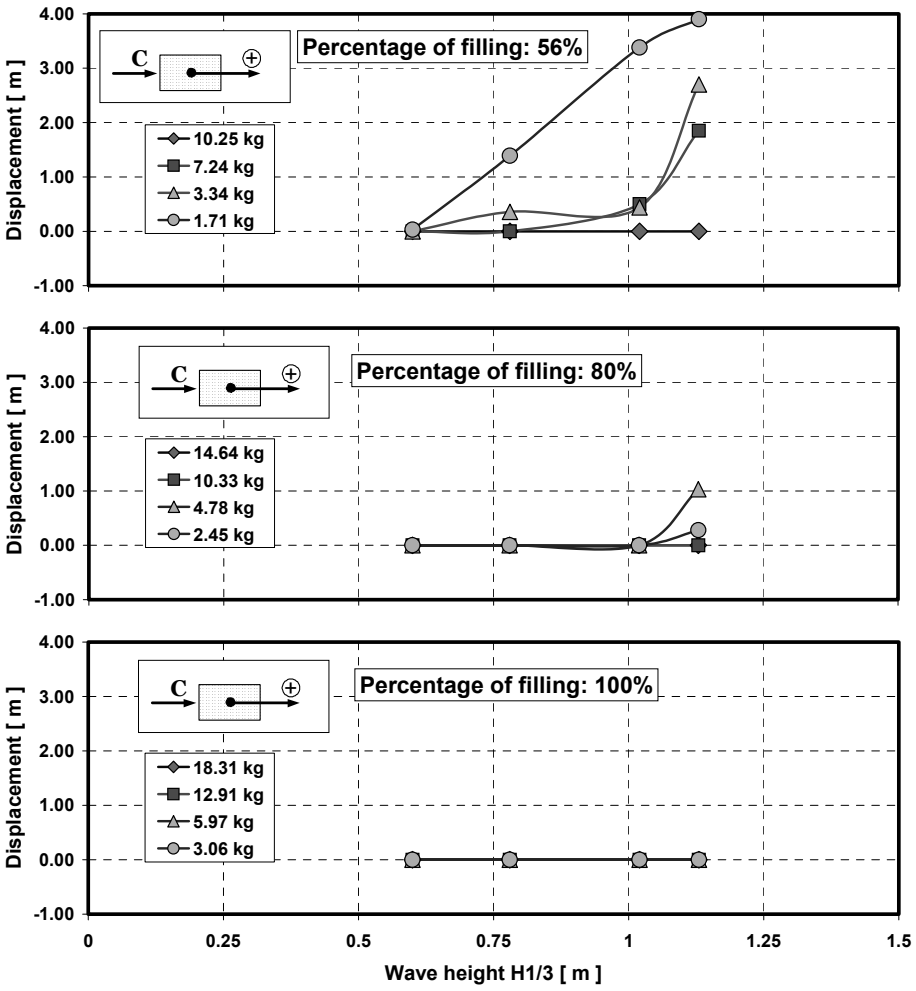

Figure 9. Displacements versus wave heights (single containers with inline wave attack)

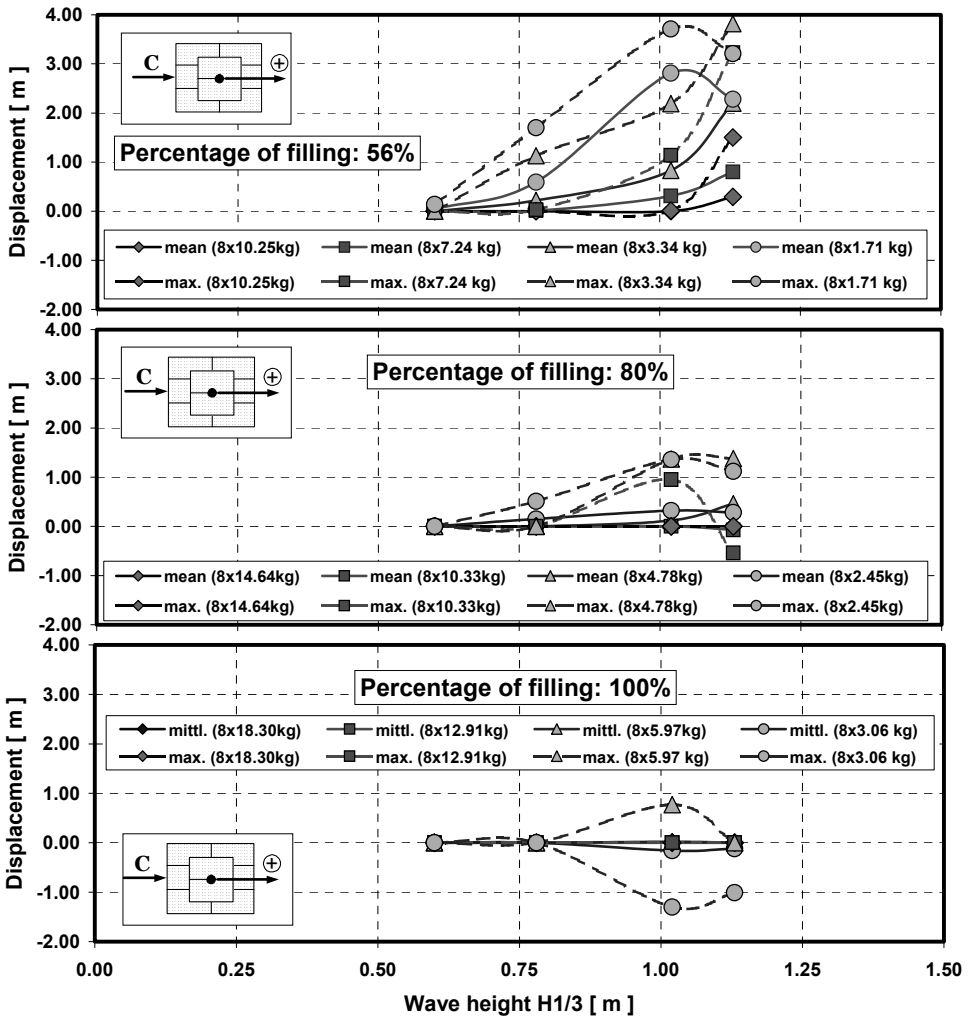

Figure 10. Displacements versus wave heights (container groups with inline wave attack)

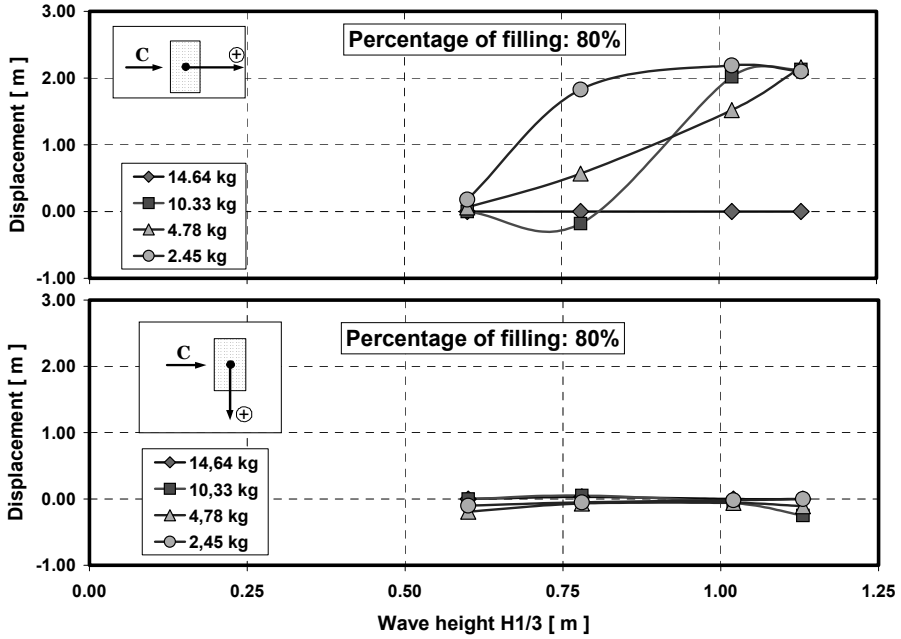

Figure 11. Inline and transverse displacements versus wave heights (single containers with transverse wave attack)

It must be considered, that the displacements were measured after the tests. Thus, these displacement data may represent only the impact of the last waves in the total wave train and may be overlapped by movements in any direction before. Consequently, there might have been larger displacements due to higher impacts from waves during the test. Hence there is no direct correlation between displacements and wave heights, nevertheless a distinct trend is identifiable. But at least the displacement data can describe two ultimate conditions: Stable (displacement = 0) or unstable (displacement > 0).

Some test results in the sense of stable or unstable are given exemplarily in Fig. 12, where the data of container groups with inline wave attack are plotted in a matrix of container weights G versus measured wave heights $H_{1/3}$. The straight lines represent a first approximation of the borderline between stable and unstable conditions. The solid line stands for a filling of 80%, the dotted ones for a filling of 56% and of 100%, respectively.

These borderlines of all test data result in a first dimensional empirical approximation:

$$G\,[kg] > A\,[-] + 25\,H_{1/3}\,[m]$$

with the coefficient A depending on the percentage of filling. It must be noted that this first step approach is only valid for a period T_p = 5 s referred to the experimental conditions. To create a dimensionless approach the research work will be continued by further analysis of the experimental data considering the wave-induced current data measured on the sand bed.

The empirical coefficients A estimated from all tests are given in Fig. 13 versus the percentage of filling. It is obvious that the dependence on wave approach direction is less for container groups compared to single containers as well as the dependence on the percentage of filling. Otherwise, the definition of the criteria stable – unstable is not comparable directly as even one displaced container in one group of totally 8 leads to the mode "unstable".

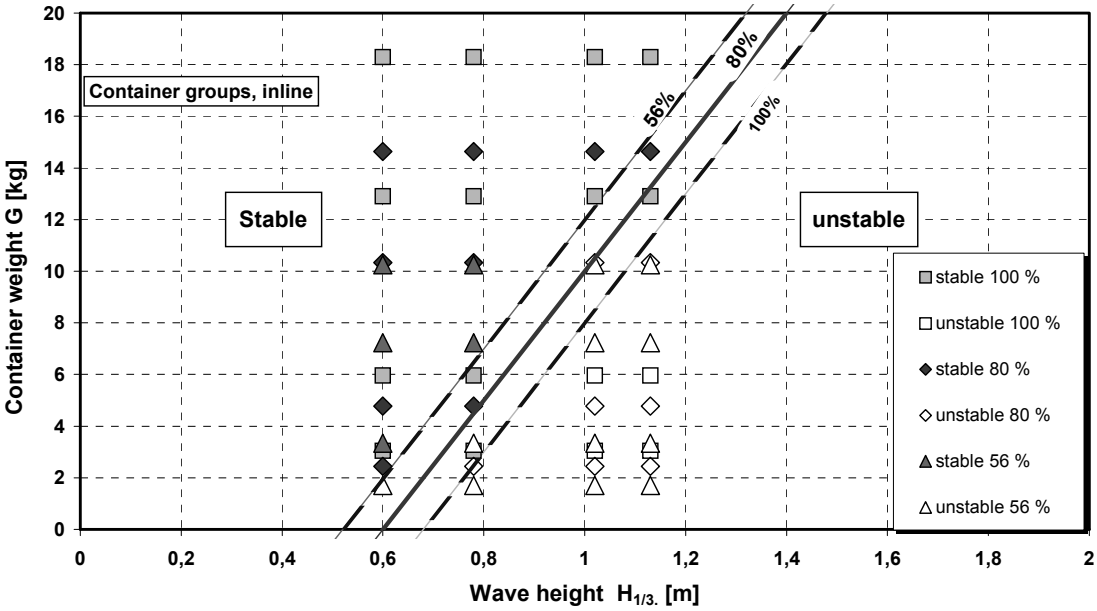

Figure 12. Stability conditions recorded from tests with container groups, inline wave attack

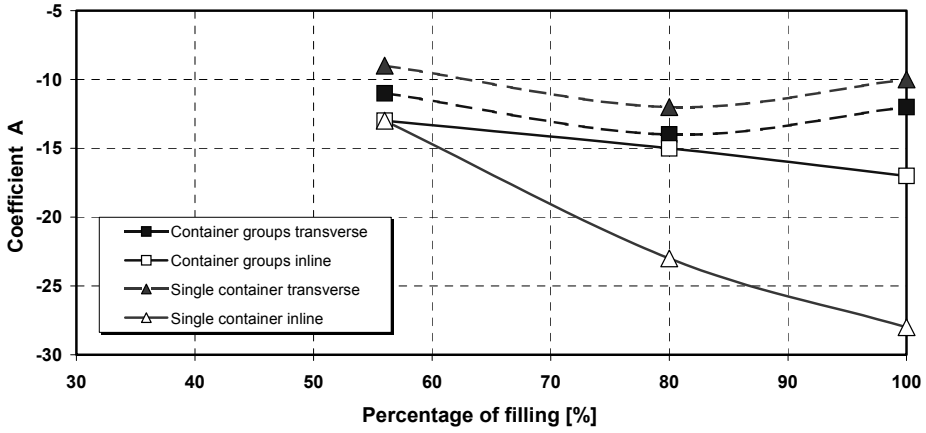

Figure 13. Coefficients A versus percentage of filling for single containers and container groups and for inline and transverse wave attack

IV. Concluding Remarks And Outlook

Investigations on the stability of an innovative scour protection design for monopile support structures using geotextile sand containers have been started in the Large Wave Channel (GWK) of the Coastal Research Centre (FZK). Basic test series were performed with single containers and container groups with different container weights, varied in sizes and percentages of filling. The first results lead to the following general statements:

- The stability of sand containers is not only a function of the total weight.
- Other influences are the percentage of filling and the direction of wave approach, which are smaller for container groups compared to single containers due to interaction effects in a group.
- The stability increases with increasing percentage of filling.

A first approximation from the measured data is estimated in an empirical approach on the stability depending on the wave height and the percentage of filling.

The investigation will be continued both by executing further analysis of the recent basic tests considering the wave-induced currents measured on the sand bed and by performing tests with a complete scour protection design around a monopile. The scour protection design consists of two layers of geotextile sand containers placed around a monopile structure (diameter of 5.5 m and water depth of 21 m in prototype) which is scaled down to 1:10 in the GWK (Fig. 14). Fig. 15 shows the 1:10 model of the monopile installed in the GWK under wave attack.

Figure 14. 1:10 model of the scour protection with sand containers in the GWK.

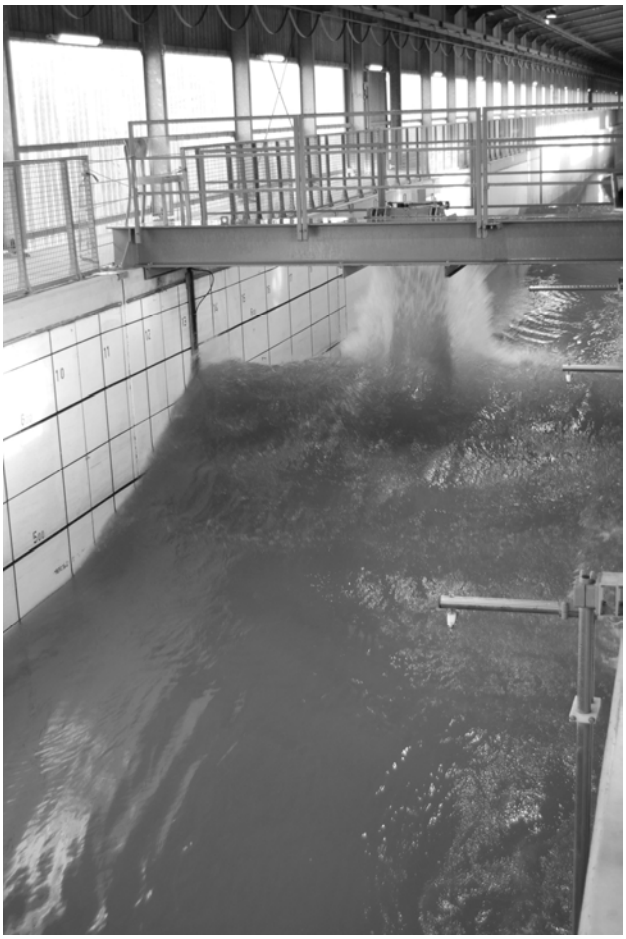

Figure 15. 1:10 model of the monopile under wave attack in the GWK.

Acknowledgment

The support of the research project (No. 0329973) by the *BUNDESMINISTERIUM FÜR UMWELT, NATURSCHUTZ UND REAKTORSICHERHEIT (BMU)* and the *OSB OFFSHORE – BÜRGER - WINDPARK BUTENDIEK GMBH & CO KG* is gratefully acknowledged. The geotextile materials for the sand containers are thankfully provided by the *NAUE FASERTECHNIK GMBH & CO KG.*

Reference

[1] K.W. Pilarczyk, *Geosynthetics and Geosystems in Hydraulic and Coastal Engineering*, A.A. Balkema, Rotterdam, 2000.

The Use of Morphological Models as a Tool for Assessing The Long-term Impact of Structures in Estuaries

J.M. Harris* and A.P. Wright*
* ABP Marine Environmental Research Ltd, Southampton, SO14 2AQ, UK

A systematic study has been undertaken to assess the suitability of using a morphological model in assessing the longer-term impact of placing structures in an estuary. The approach adopted uses a real estuary. In the area chosen to place the structure the bathymetry has been flattened continuing upstream to the tidal limit whilst maintaining the bed slope. The model has then been forced using different forcing drivers and parameter settings and different combinations of drivers and parameters the results compared to test the response of the model in both the short- (daily) and longer-term (yearly). An assessment of the channel formation with and without the structures in place has then been undertaken to determine the level of impact that the structures have on the system.

I. INTRODUCTION

The form an estuary takes is influenced by a range of physical processes that operate over varying temporal and spatial scales. In terms of the morphology of an estuary, and in particular the sediment transport, the principal hydrodynamic forcing mechanisms are tidal flow, fluvial flow, waves and density driven circulation. In order to implement works within these systems it is necessary to understand the impact any such scheme will have on that system and how it will interact with the physical processes driving that system. Even with the technology and understanding at our disposal today this is still no mean feat.

The objective of this study was to assess the extent to which a process-based morphological model can be used to investigate the longer-term impact of placing structures within an estuary. In the current study the structures are representative of bridge piers. The approach adopted makes use of the 'online' morphological model, which is part of the Delft3D suite of modelling tools. A real estuary has been chosen as the location for the investigation, specifically the Mersey Estuary.

The Mersey Estuary, Figure 1, is located on the west coast of England. The outer estuary forms Liverpool Bay, a generally shallow region containing large areas of sandbanks that are exposed at low water. Liverpool Bay is bounded to the east by the Lancashire coast, from Seaforth to Formby Point; and to the south by the Wirral Peninsula, from Hilbre Point at the mouth of the Dee Estuary, to New Brighton at the mouth of the River Mersey. At New Brighton the width of the Mersey is 1.5km, approximately, and at Pier Head the river narrows to about half this width (hence its name the Narrows). Beyond this point the river opens up to a large tidal basin, generally termed the 'inner estuary', which widens to a maximum width of about 5.5km. Beyond this is the upper estuary, which extends for a distance of about 42km from the Dingle to Howley Weir. At low water almost all of the tidal basin dries out leaving three channels, Garston, Middle Deep and Eastham. In the upper estuary, the low water channels meander through large areas of sand and mud banks. The primary sources of freshwater into the Mersey are at the tidal limit at Howley weir and over the sluices of the Weaver navigation

II. MODELLING APPROACH

In current study a fully calibrated and validated hydrodynamic model has been set up using the Delft3D suite of modelling tools, developed by WL | Delft Hydraulics. The numerical model is based on the Delft3D 'online' module, which solves the shallow water and transport equations using a finite difference scheme applied over a curvilinear grid. The software simulates hydrodynamic and sediment transport conditions simultaneously. At selected time-steps the bed is updated morphologically. A scaling factor (MORFAC) can be applied to the simulation to allow the model run to be predict change over longer periods of time. However, in particularly dynamic systems it is questionable if a scaling parameter can be applied due to the rapidly changing morphology.

Two models grids have been used in the study, the first covers the extents of the Mersey out into part of Liverpool Bay (Figure 2). The second grid starts at Gladstone Dock and extends to the tidal limits at Howley Weir (Figure 3). In the first grid the model's offshore boundary was driven with astronomic tidal constituents derived from a high-resolution model of the Irish Sea. In the second model, the seaward boundary was driven with either astronomic tidal constituents derived from real tidal records at Gladstone Docks or a real times series of water levels, again from Gladstone Docks.

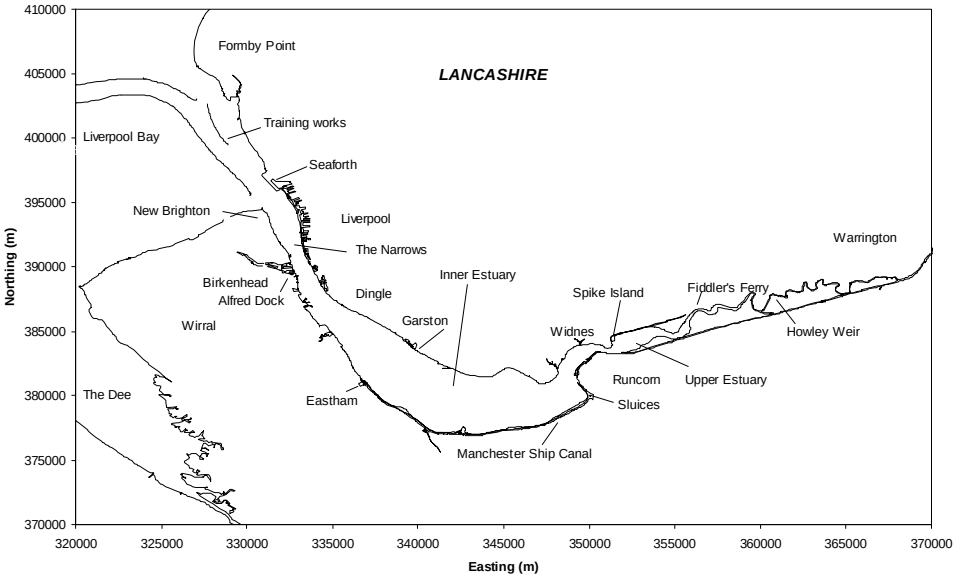

Figure 1: Plan of the Mersey Estuary.

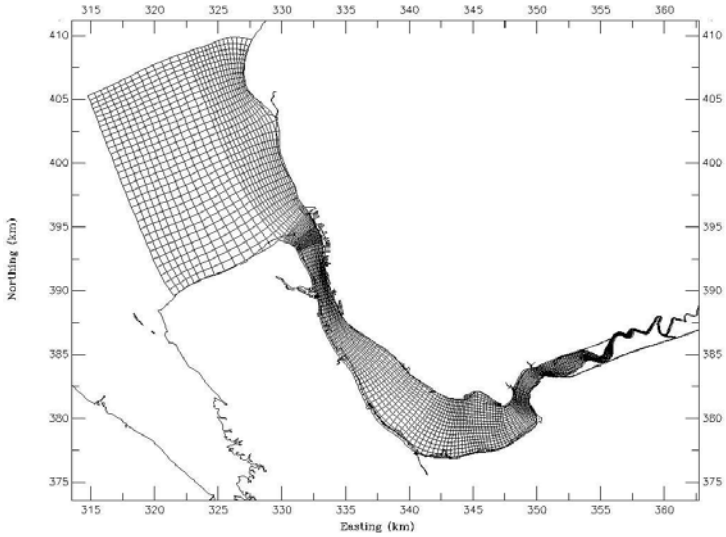

Figure 2: First curvilinear grid extending into Liverpool Bay.

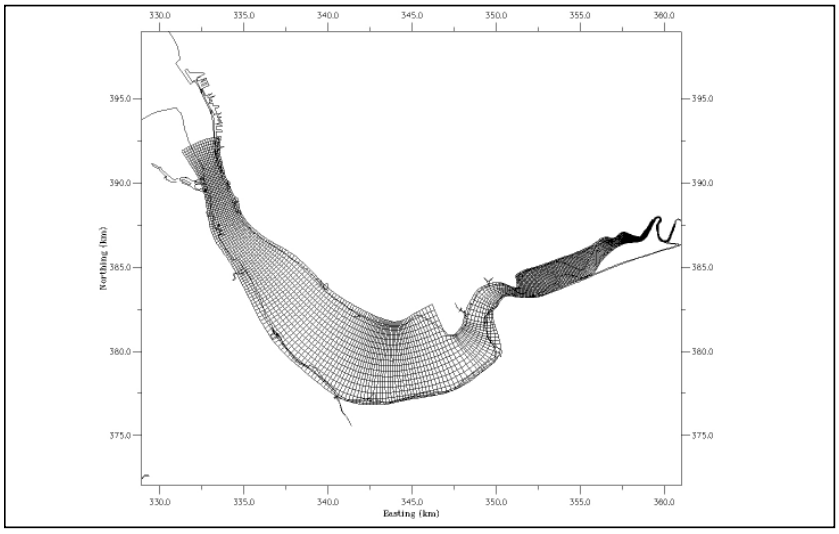

Figure 3: Second curvilinear grid starting at Gladstone Dock.

III. PHYSICAL AND NUMERICAL MODELS

Historically, modelling the interaction of the sediments with structures has always been carried out using physical models. Provided the measured parameters in the model are related to their corresponding prototype quantities by scaling laws that satisfy the rules of similitude then this approach is valid (Yalin, 1971). Physical models have been in use for a considerable time. In fact, in 1890 Professor Vernon-Harcourt read a paper to the Royal Society, London, entitled "Effects of Training Walls in an Estuary". In this paper he described a series of physical modelling experiments undertaken to investigate the impact of various engineering schemes would have on the Mersey Estuary. Around the same period Professor Osborne Reynolds, working at the University of Manchester was also undertaking experiments of a similar nature. Both of these engineers were pioneers in the use of models to aid the understanding of the physics of estuaries and the use of models as tools to investigate the impact of engineering schemes if placed within such environments.

More recently it has become possible to apply numerical processed based morphological models to look at the impact of engineering works in estuaries. However, as Hibma (2004) has recognized, understanding and predicting the morphodynamic evolution of estuaries is still limited by their complexity both spatially and temporally. However, it is possible to demonstrate that these processed based models have evolved sufficiently to reproduce similar behaviour to their physical counterparts.

Figures 4 and 5 show sketches of the bathymetric survey of the Mersey Estuary of 1881 and the results of Vernon-Harcourt's physical model simulation, respectively. The model used for the investigations represented the Mersey estuary from a little below Warrington out into Liverpool Bay beyond the bar, made to a horizontal scale of 1:30000 and a vertical scale of 1:500. The tidal period was calculated to be about 32.66 seconds with the maximum tidal rise of 9.45m at Liverpool amounting to 1.89cm in the model. Fine Bagshot sand was used to represent the bed of the estuary in the model (for further details see Vernon-Harcourt, 1890). A comparison of Vernon-Harcourt's results with the 1881 bathymetric survey shows that the general features of the estuary are fairly reproduced. An exact correspondence would not be expected due to the constantly shifting channels particularly in the upper reaches. In addition, a hydrographic survey of the whole estuary could not be taken rapidly enough to obtain the exact condition of the estuary at any given time.

Figure 3 shows the results of a numerical simulation using the 'online' morphological module within Delft3D modelling suite. The simulation starts from an initial flat bed condition (no initial slope applied) and assumes a uniform distribution of sand (median grain size diameter of 150μm). Typically, sand fractions within the estuary vary from between 700μm - 125μm, but the majority of deposits range between about 125μm and 250μm. Within the model set up the initial sediment thickness was set at 30m and the bed level was set at 8m below OD(Newlyn). The offshore boundary conditions used in the model were described by the use of astronomic tidal constituents. The model was set up to run in depth-average mode. Freshwater flow was applied at the tidal limit at Howley Weir ($30m^3/s$) and over the Weaver sluices ($10m^3/s$). Salinity was set at 27ppt along the offshore boundary and 0.01ppt at the points of fluvial input into the model.

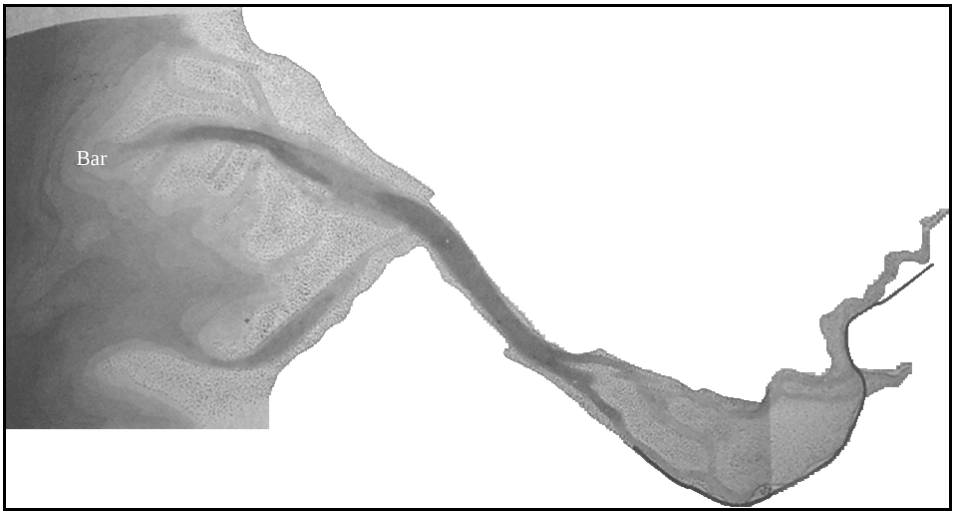

Figure 4: 1881 bathymetric survey of the Mersey Estuary (After Vernon-Harcourt, 1890).

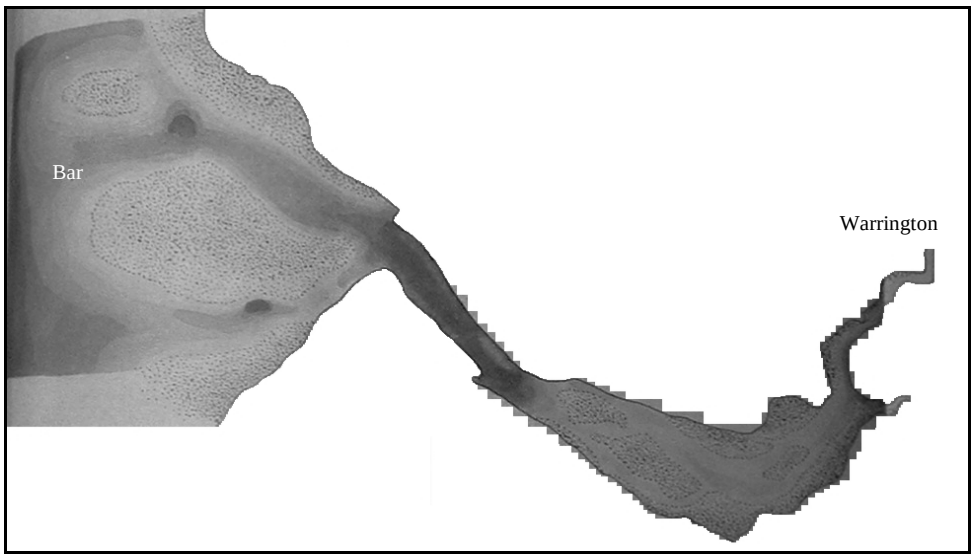

Figure 5: Results of physical model simulation of the Mersey Estuary (After Vernon-Harcourt, 1890).

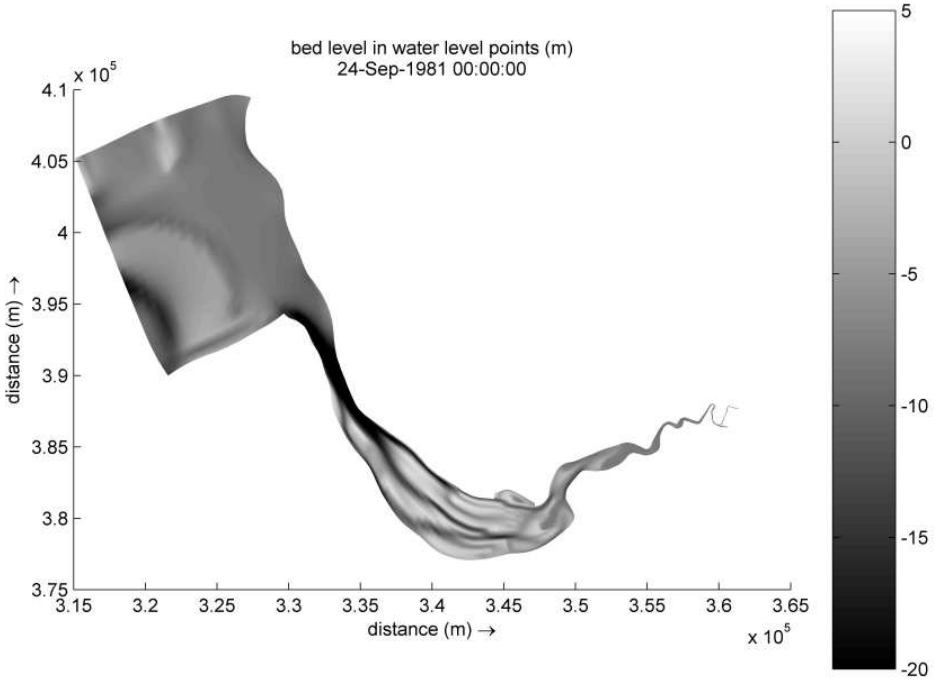

Figure 6: Numerical simulation of morphological evolution of the Mersey Estuary from a flat bed

From Figure 6 it can be see be seen that the numerical model is capable of reproducing the general features of the estuary: the development of channels within the estuary; a channel along the Wirral foreshore and the start of bank formation within Liverpool Bay. The model was run in real time with no morphological scaling applied and the figure represents the morphological evolution of the estuary after about 21 months. The system has still not reached equilibrium, and based on the results of a 'single element' model it will take about 41years (real time) for equilibrium to be reached (Townend, 2006). However, a comparison of the results from the physical and numerical models against the actual bathymetric survey of 1881 show reasonable agreement in respect of the main features.

Therefore, based on these results the morphological model is deemed suitable for exploring the impact of placing structures into the system.

IV. Model Simulations

The Mersey Estuary has again been used for the second part of this study. Within the estuary the area chosen for placing the bridge crossing is in the upper estuary (above Runcorn) and consists of low-water channels that meander through large areas of sand and mud banks and is characterized by a highly mobile and

active riverbed. The tidal action in this part of the estuary creates strong currents (>2m/s on spring tides), which are an important part of this process. In addition, historically the position of the low water channel in the estuary has shown considerable movement over the period of existing records.

The principal aim of these tests is to simulate channel formation in the upper estuary without and with the bridge piers in place and to observe the differences in predicted channel formation. The grid used for these investigations is shown in Figure 3 and is relatively coarse with a grid cell size of about 80m x 80m in the area of interest. The grid resolution has been adopted primarily to allow longer time-scale simulations to be undertaken within a reasonable time-frame.

The starting point for the study was a bathymetric and LIDAR survey undertaken of the estuary in 2002. Upstream of Runcorn (see Figure 1) the bathymetry was flattened (excluding hard points such as quay walls) whilst maintaining the general channel slope along the length of this portion of the model. A series of model runs were undertaken for the 'baseline' case, that is, with no bridge piers in place but with the flattened bathymetry. The model was run for a period of a year and the morphology allowed to develop over that period. No morphological scaling factor was applied so all the simulations were run in model real time. The model was driven with different conditions and combination of conditions together with different parameter settings in the morphological set up such as grain size and initial sediment thickness. Table 1 shows the various model settings applied for each run for the baseline case.

TABLE I.
MODEL SETTINGS FOR BASELINE CASE

Run number	Sediment type	Tidal boundary	Fluvial flow	Wind	Initial sediment depth (m)
1	Sand - 150μm	Harmonic constituents	Constant mean annual	None	1
2	Sand - 150μm	Harmonic constituents	Mean daily	None	1
3	Sand - 150μm	Real time-series	Constant mean annual	None	1
4	Sand - 150μm	Real time-series	Mean daily	None	1
5	Sand - 100μm	Real time-series	Constant mean annual	None	1
6	Sand – 64μm	Real time-series	Constant mean annual	None	1
7	Sand - 300μm	Real time-series	Constant mean annual	None	1
8	Sand - 300μm	Real time-series	Constant mean annual	None	4
9	Sand - 300μm	Real time-series	Constant mean annual	Real (hourly)	4

For the bridge pier scenario two tests were undertaken (Table II). The first test (run 1s) represented the bridge piers as solid structures, whilst the second test (run 2s) represented the piers as added friction terms. The additional friction is applied as a loss term in the model equations. In both scenarios three bridge piers were placed within the upper estuary. The initial run represents an extreme scenario as the piers each occupy a single model cell making them of the order of 80m in diameter. The second run represents the piers as 10m diameter structures.

TABLE II.
MODEL SETTINGS FOR BRIDGE PIER SCENARIOS

Run number	Sediment type	Tidal boundary	Fluvial flow	Wind	Initial sediment depth (m)
1s	Sand - 150μm	Real time-series	Constant mean annual	None	1
2s	Sand - 150μm	Real time-series	Constant mean annual	None	1

V. RESULTS

The morphological model proved to be unstable for different model forcing conditions and combination of forcings. This made comparison difficult for some of the scenarios tested. Figures 7 to 10 shows the variation in channel formation over several months for 64μm, 100μm, 150μm and 300μm median sands (runs 6, 5, 3 and 7, respectively). In all four tests the freshwater flow was kept constant, whilst the seaward boundary was forced using a real water level time-series. Overall, the difference in sediment size has little effect on the formation and position of the channels, only in the time required to form them. There are subtle differences in between the morphology formed using the various grain sizes, however, in general the patterns of channel formation are identical. This would suggest that sediment size is not a primary driver in the formation of the channels.

Figure 11 shows the variation in channel formation over a 6 months period for 150μm sand using astronomical tidal constituents to force the model on the offshore boundary and a constant annual mean freshwater flow (run 1). Initially, a channel is formed in the location of an existing channel along the north bank. However, this channel does not develop and is eventually cut off. There is no significant difference between the channel formed under these boundary forcing conditions and those formed using a real time-series and shown in Figure 9.

Figure 12 shows the results for the baseline case were the model boundaries have been forced using astronomical tidal constituents at the seaward end and a varying real mean daily flow has been applied at the tidal limit (run 2). The results represent the

morphological change over a four months period. The model proved to be unstable as a result of applying the varying daily mean discharge. As previously, over the duration of the simulation the model results show the development of a single main channel and there appears to be no significant difference between the channel formed under these forcing conditions and that observed in the previous scenarios presented (Figures 7 to 11).

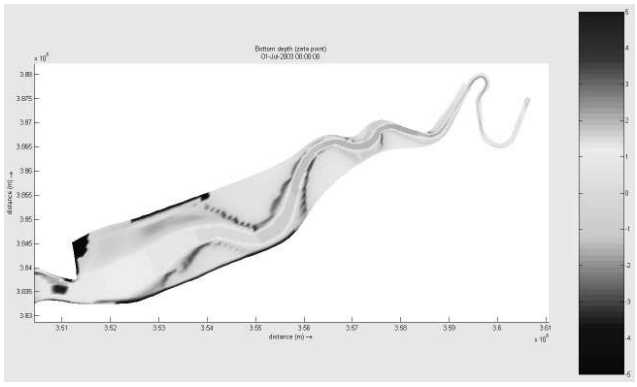

Figure 7: Bathymetric change after 6 months for 64μm sediment, using a real tidal time-series driver and a constant mean annual fluvial flow.

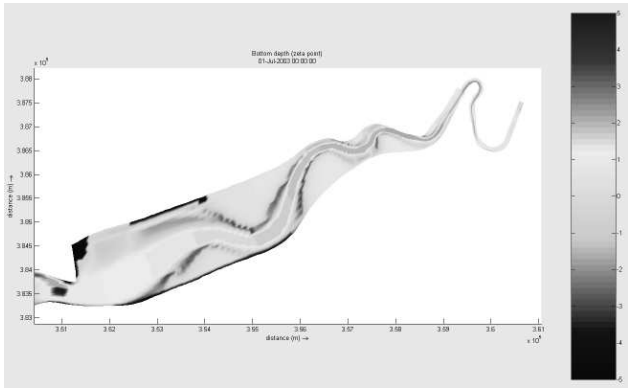

Figure 8: Bathymetric change after 6 months for 100μm sediment, using a real tidal time-series driver and a constant mean annual fluvial flow.

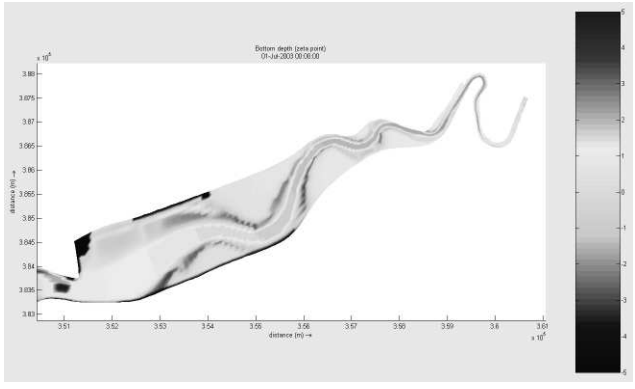

Figure 9: Bathymetric change after 6 months for 150μm sediment, using a real tidal time-series driver and a constant mean annual fluvial flow.

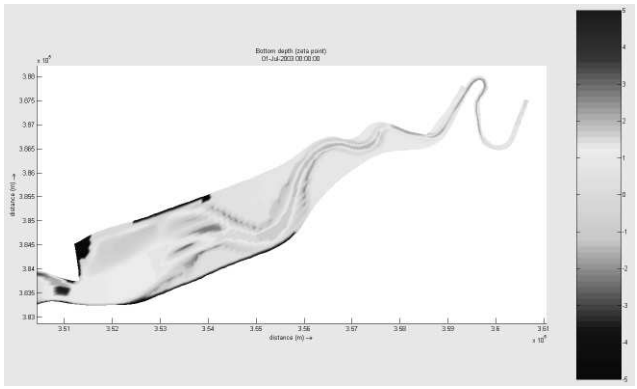

Figure 10: Bathymetric change after 6 months for 300μm sediment, using a real tidal time-series driver and a constant mean annual fluvial flow.

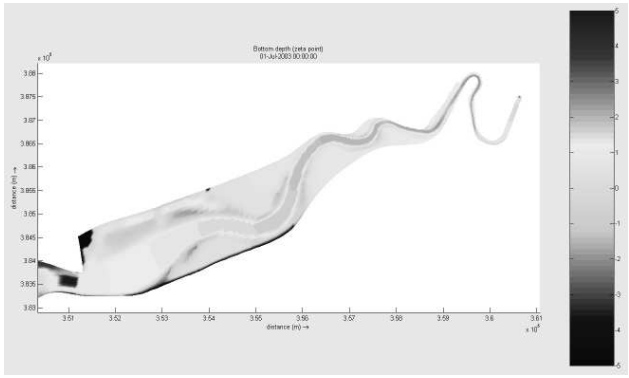

Figure 11: Bathymetric change after 6 months for 150mm sediment, using harmonic tidal constituents and a constant mean annual fluvial flow.

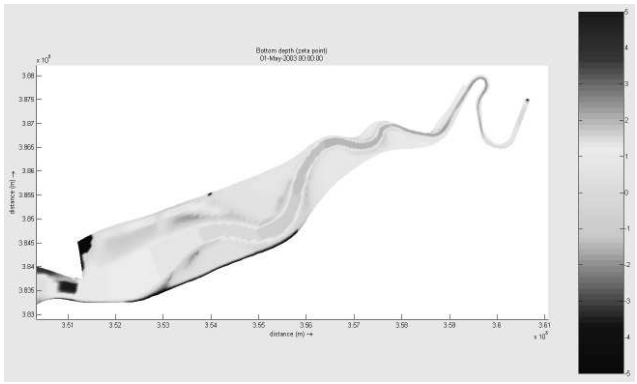

Figure 12: Bathymetric change after 4 months for 150mm sediment, using harmonic tidal constituents and a daily mean fluvial flow.

Running the same scenario but replacing the seaward boundary condition with a real time-series of water levels instead of the using astronomical tidal constituents led to instabilities developing after a month (run 4). Therefore, the results for this simulation have not been presented.

Figure 13 shows the results of a simulation using 300μm sand using a real time-series of water levels along the seaward boundary and a constant mean annual discharge at the tidal limit. In addition, the initial depth

of sediment was set at 4m (run 8) rather than the 1m initial depth used in all the previous results reported earlier. From the figure it is evident that the initial depth of sediment applied in the model leads to a different morphological outcome than that observed in the series of tests presented up to this point. Whilst there is still a principal channel formed there are also channels formed, initially, along both the south and north sides of the estuary. Towards Runcorn (refer to Figure 1) the main channel is deeper and narrower than that formed previously. Interestingly, the formation of the channels towards the sides of the estuary show some similarity to the existing situation.

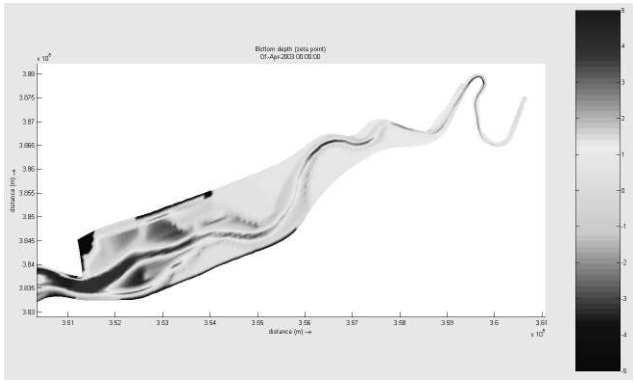

Figure 13: Bathymetric change after 3 months for 300mm sediment, using a real tidal time-series driver, a constant mean annual fluvial flow and an initial 4m depth of sediment.

The final test carried out with the baseline case used the same set up as for run 8 except with the addition of a wind stress over the model, which varied hourly in both speed and direction. The data applied was recorded at the seaward boundary of the model. Figure 14 shows the results from this simulation. The imposition of a wind stress over the model has no major impact on the model results.

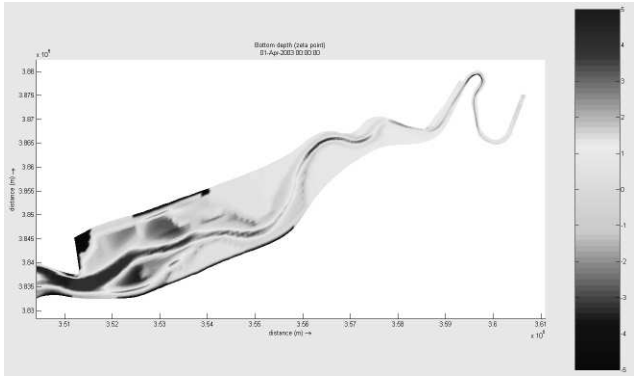

Figure 14: Bathymetric change after 3 months for 300mm sediment, using a real tidal time-series driver, a constant mean annual fluvial flow an initial 4m depth of sediment and an hourly wind speed and direction.

The final series of model runs were undertaken for the two bridge pier scenarios. Figure 15 shows the results of the simulation of three 80m diameter structures. There is an evident response of the system to having these structures within the estuary. Initially, the model shows a series of channels formed next to the piers (Figure 15a). However, over time these sperate channels become less marked (Figure 15b).

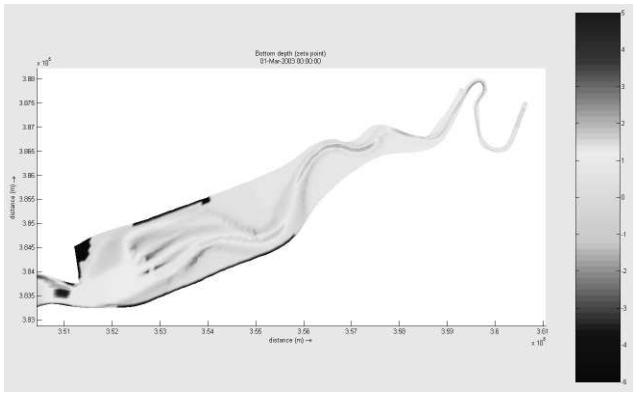

Figure 15a: Bathymetric change after 2 months with three 80m x 80m structures in place for 150mm sediment, using a real tidal time-series driver and a constant mean annual fluvial flow.

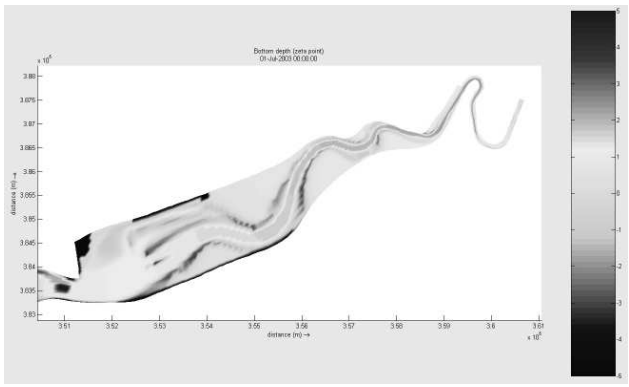

Figure 15b: Bathymetric change after 6 months with three 80m x 80m structures in place for 150mm sediment, using a real tidal time-series driver and a constant mean annual fluvial flow.

Figure 16 shows the response of the upper estuary to having three 10m diameter structures placed across the channel section. The results from this scenario show a very similar morphological pattern to that obtain with no structures in place (compare Figure 16 with Figure 9).

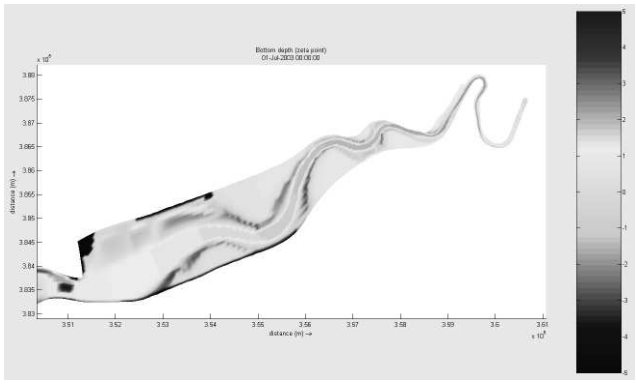

Figure 16: Bathymetric change after 6 months with three 10m diameter structures in place (represented using added friction terms) for 150mm sediment, using a real tidal time-series driver and a constant mean annual fluvial flow.

Over a longer time-scale the morphological changes in response to the piers may be reduced. However, the initial results from these last series of simulations demonstrates that the size of the structures placed within the cross-section of the estuary and thus the blockage effect that they represent in respect to the cross-sectional area is very important in respect to the effect of morphological development.

VI. Discussion

The initial morphological modelling exercise to 'mimic' the behaviour of a physical model has demonstrated the ability of such models to reproduce realistic channel–shoal systems. This would suggest that the numerical model possesses the requisite processes necessary to allow these estuarine channel-shoal systems to evolve. These results have supported the application of such models to the investigation of practical engineering issues such as the long-term impact of placing a structure, in this case a bridge, within an estuary system. There are limitations though, primarily the time required to simulate such problems is prohibitive, particularly if the model grid is particularly refined and if the model is run in 3D mode. The introduction of multiple sediment fractions will also have an impact on model run times. For estuary systems where the morphology is slow in adjusting then this may not be too limiting as the use of a scaling factor in the morphological simulations (MORFAC) may allow longer time-frames to be simulated. However, in estuary systems that are particularly dynamic then the use of such factors is highly questionable.

The results from the sensitivity tests have demonstrated that the model, when run in 'real time' (i.e. no morphological updating is applied) is generally insensitive to most model parameter settings. Changing the parameters such as grain size (within a reasonable range) do not appear to influence the eventual morphological pattern obtained only the time-scale taken for the pattern to form or the length-scale of the pattern formed. The exception to this is the initial depth of sediment, which has a much greater influence on the channel-shoal formation. This would suggest that this is a key parameter if the model is to have any chance of reproducing real morphological change. Therefore, the imposition of the Holocene surface as the initial depth of sediment may be important. However, this still neglects any change in sediment composition with depth.

The differences in water depth and the corresponding changes in the velocity distribution in response to the morphological updating in the model lead to the development of small perturbations in the morphology. These perturbations can become unstable and grow exponentially and cause the model to 'blow-up'.

More surprising is the effect of various boundary forcings applied to the morphological model such as tide-surge conditions, wind and varying freshwater flows. From the model tests undertaken the results suggest that the model is insensitive to such conditions, at least in a time-scale corresponding to the morphological change imposed when running the model with no applied scaling. Based on the results obtained the greatest limitation of the model is an apparent inability to create any form of dynamic equilibrium even when applying a varying wind speed and direction. The model results all show the development of a static equilibrium.

With respect to the simulations undertaken with bridge structures in place within the estuary, the model results enable limited conclusions to be drawn as to the longer-term effects. The model provides insight into the effects any significant loss in flow cross-section may have on morphological development. In addition, some inference can be made, based on the results, that if the simulation with the structures in place shows the same result as that with no structures present then the impact will be not be significant on the estuary system as a whole. However, the model currently appears incapable of reproducing any form of dynamic equilibrium and, therefore, has implications for longer-term impacts. For example, what would be the long-term outcome should a channel locate itself through the position of one or more of the bridge piers. Will the channel remain 'locked on' to the pier or will it be free to carry on meandering? In an estuary system like the Mersey where the sandbanks can be eroded by more than 1m in a single day such questions are important to the long-term evolution of the system. Early studies of the estuary by Cashin (1949) and Price and Kendrick (1963) have demonstrated that anthropogenic changes in the estuary have already altered the ability of the channel to meander freely. For example, construction of the training walls in Liverpool Bay, started in 1901, to fix the position of the main navigation channel to the Port of Liverpool suppressed channel meandering and confined more of the ebb tide to the trained channel. This in turn led to a strengthening of the flood tide along the Lancashire and North Wirral coastlines. Enhancement of the flood tide would have contributed to an increase in siltation in both the trained navigation channel and the estuary itself. On this basis, Price and Kendrick suggested that where meandering in the estuary is suppressed there is a resulting loss in volume. Although Inglis (1964) pointed out that channel stabilization only caused deterioration if it led to a loss of flow energy. The ability to model such effects is essential if numerical morphological models are to have a wider-applicability to such studies.

More recent studies (Haigh *et al.*, 2005) have suggested that the use of morphological models to predict channel switching using our current understanding of the mechanisms causing these events are unable to predict a channel switch. This could be be due to the correct processes not being represented in the modelling system, or that our understanding of the nature of such events is flawed. However, a principal mechanism of erosion in the estuaries such as the Mersey, where there are extensive areas of drying banks is block failure, this is a mechanism that is not incorporated into our sediment transport models.

Therefore, there is already a built in limitation in the numerical morphological tools being applied.

VII. CONCLUSIONS

The objective of the study was to assess the suitability of a process-based morphological model to be applied to the investigation of the long-term impact of placing structures within an estuary. An initial modelling investigation compared a numerical simulation with that of a physical model. From this initial study it was concluded that:

- A processed-based morphological model has demonstrated the ability to reproduce realistic channel–shoal systems. This would suggest that the numerical model possesses the requisite processes necessary to allow these estuarine channel-shoal systems to evolve.

From these modelling results it was concluded that such models can be applied to the investigation of practical engineering issues such as the long-term impact of placing a structure, in this case a bridge, within an estuary system. However, before undertaking any comparison of an estuary without and with structures in place a series of sensitivity tests were carried out. From these tests it was concluded that:

- When run in 'real time' (i.e. no morphological updating is applied) the results are generally insensitive to most model parameter settings. Changing the parameters such as grain size (within a reasonable range) do not appear to influence the eventual morphological pattern obtained only the time-scale taken for the pattern to form or the length-scale of the pattern formed.

- However, the initial depth of sediment, appears to have a much greater influence on the channel-shoal formation. This would suggest that this is a key parameter if the model is to have any chance of reproducing real morphological change. Therefore, the imposition of the Holocene surface as the initial depth of sediment may be important.

- From the model tests undertaken the results suggest that the model is insensitive to the effect of various boundary forcing applied to the morphological model such as tide-surge conditions, wind and varying freshwater flows., at least in a time-scale corresponding to the morphological change imposed when running the model with no morphological scaling.

- Based on the results obtained the greatest limitation of the model is an apparent inability to create any form of dynamic equilibrium even when applying a varying wind speed and direction. The model results all show the development of a static equilibrium.

From the simulations with bridge piers in place the model results enable limited conclusions to be drawn as to the longer-term effects. In general:

- The model provides insight into the effects any significant loss in flow cross-section may have on morphological development.

- Some inference can be made, based on the results, that if the simulation with the structures in place shows the same result as that with no structures present then the impact will be not be significant on the estuary system as a whole.

However, the model currently appears incapable of reproducing any form of dynamic equilibrium and, therefore, has implications for modelling longer-term impacts. As our understanding of the physics behind estuary processes continues to improve and as our ability to model them also advances then morphological models will become more valuable tools. However, there will always be limitations with such approaches due to the uncertainties present in the natural system.

VIII. REFERENCES

[1] Yalin, M.S. (1971). *Theory of hydraulic models*. MacMillan, London.

[2] Hibma, A. (2004). *Morphodynamic modelling of estuarine channel-shoal systems*. Ph.D thesis, Technical University of Delft.

[3] Vernon-Harcourt, L.F. (1890). Effect of training walls in an estuary. *Paper read to the Royal Society, London, January 30*.

[4] Townend, I.H. (2006). Personal communication.

[5] Cashin, J. A. (1949) "Engineering Works for the Improvement of the Estuary of the Mersey", *Journal of the Institution of Civil Engineers*, No. 7, 296-368.

[6] Price, W.A. and Kendrick, M.P. (1963). Field and model investigation into the reasons for siltation in the Mersey Estuary. Proc. Inst. Civil Engrs., April, Vol 24, pp 473-518.

[7] Inglis, C. (1964). In: Field and model investigation into the reasons for siltation in the Mersey estuary, Price, W.A. and Kendrick M.P., Reply to the Discussions, Proc. Inst. Of Civil Engrs., Vol. 27, March, pp. 613-647.

[8] Haigh I.D., Norton P.A. & Townend I. H. (2005). Understanding and Predicting Morphological Change in the Inner Humber Estuary. In: *Coastal Engng. 2004, Proc. of 29 Int. Conf.*, Lisbon, Portugal, 19 –24 Sept, 2004.

Cover Stones/Riprap over Liquefiable Soil

F. Hatipoglu[*], B.M. Sumer[**] and J. Fredsøe[**]

[*] Coastal, Maritime and Structural Engineering Section (formerly ISVA), Technical University of Denmark, MEK, Building 403, DK-2800 Kgs. Lyngby, Denmark, on leave from Istanbul Technical University, Maslak, Istanbul, Turkey

[**] Coastal, Maritime and Structural Engineering Section (formerly ISVA), Technical University of Denmark, MEK, Building 403, DK-2800 Kgs. Lyngby, Denmark

The present paper describes the results of an experimental study on cover stones/riprap on a liquefiable soil bed. The soil was silt with d_{50}=0.098 mm. Stones, the size 4 cm, were used as cover material. Various configurations of the cover stones were tested: One-layer deep, loose packing; One-layer deep, dense packing; Two-layers deep, loose packing; Three-layers deep, loose packing. Also, a test was carried out without a cover layer (the reference case). The experiments show that the soil liquefaction is dependent on the packing density of the cover stones; and the number of stone layers. The experiments also show that, when the soil is liquefied, stones penetrate/sink deep in the soil. Mechanisms related to the process of liquefaction of soil and that of sinking/penetration of cover material are described, and recommendations are made as to how cover stones can be used as a counter measure to protect soil against liquefaction.

I. INTRODUCTION

Surface protection by cover stones/riprap over a liquefiable soil (e.g., backfill soil, silt or fine sand, in a trench) is a method to protect the soil against scouring. Although a fairly substantial amount of knowledge has been gained on the behaviour of cover stones/riprap on a "liquefaction-resistant" sand bed (see e.g. References [1] and [2]), no study is yet available, investigating such protection systems over a liquefiable soil except Reference [3]. Using centrifuge wave testing, the latter authors studied the behaviour of a liquefiable soil covered (completely or partially) with gravel. Although limited to four tests (two tests with gravel covering the entire soil surface and two tests with that covering the soil surface only partially), the experiments in Reference [3] indicated that the soil was not liquefied when it was fully covered with the gravel.

The purpose of the present work is to study the behaviour of cover stones and underlying soil, addressing to the following questions (1) Can a liquefaction-prone soil underneath a stone protection system be liquefied even if it is fully covered? (2) Can cover stones/riprap be used as a counter measure against liquefaction? (3) What is the effect of packing density of the cover stones/riprap? (4) What is the effect of the number of cover-stones layers? (5) What is the behaviour of the cover stones/riprap if/when the soil underneath is liquefied (penetration distance)?

II. EXPERIMENTAL SETUP

The experiments were carried out in a wave flume, 0.6 m in width, 0.8 m in depth and 26.5 m in length. The water depth was maintained at 40 cm. The soil was placed in a 0.165 m deep, 0.56 m wide and 0.84 m long perspex box, located at 12 m from the wave generator. The box was placed in the flume so that the soil surface was flush with the false bottom of the flume (Fig. 1).

Two kinds of measurements were carried out: pore-water pressure measurements, and water-surface elevation measurements (at the same section as the pressure measurements). The pressure measurements were made in the middle of the silt box at five depths, z=0, 5, 10, 13 and 16 cm, in which z is the vertical distance measured downwards from the mudline (Fig. 1). The pore-pressure measurements were made, using Honeywell RS395 pressure transducers.

The soil used in the tests was silt. d_{50}, the grain size where 50% of soil is finer, is 0.098 mm; Specific gravity of sediment grains, $s=\gamma_s/\gamma$=2.65; Ratio between horizontal and vertical effective stresses, K_0=0.50; Maximum void ratio, e_{max}=0.90; Minimum void ratio, e_{min}=0.44.

Stones the size D=4 cm were used as cover stones in the tests. D was obtained from

$$D = (\sum_{i=1}^{N_s} D_i) / N_S \quad . \tag{1}$$

in which $D_i = \frac{1}{3}(D_x + D_y + D_z)$ in which $D_{x,y,z}$ are the dimensions measured in three major axes of an individual stone, and N_s the sample size, which was 40.

The stones were laid in one layer, two layers and three layers. Two kinds of stone packing were tested: loose packing and dense packing. In the loose packing, stones were placed in such away that the porosity was rather large while, in the dense packing arrangement, they were placed so that the porosity was quite small (stones being arranged like in a "jigsaw puzzle" exercise). The degree/density of packing was measured in terms of weight of cover stones per unit area of the bed, per stone layer, w. The larger the value of w, the denser the packing.

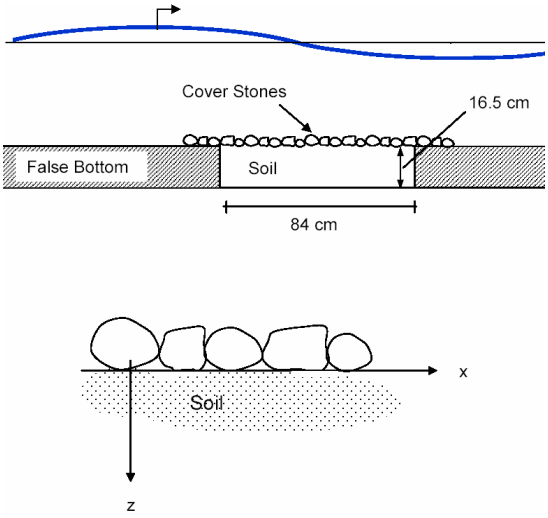

Figure 1. Test set-up and the coordinate system.

The stones initially lying on the entire bed were collected at the end of each test and weighed to get the quantity w. In the case of the loose packing, w was w=0.31-0.36 kPa per layer, and, in the case of the dense packing, it was w=0.53 kPa per layer. From w, the porosity of cover stones is obtained by

$$n = 1 - \frac{w}{s\gamma \overline{D_z}} . \qquad (2)$$

in which s is the specific gravity of the cover stones (2.65), γ the specific weight of water, and $\overline{D_z}$ the mean stone height when stones are placed in a cover layer. The latter was found to be 3.2±0.7 cm (the figure 0.7 cm being the standard deviation). The porosity values obtained in this way are n=0.57-0.63 for the loose-packing tests, and n=0.36 for the dense-packing tests.

The design of the tests was determined on the basis of the results of the one-layer stones tests. These tests showed that the soil was not liquefied with the dense-packing arrangement, as will be detailed later, and therefore no test was carried out with two and three layers of stones with the dense packing as no liquefaction would have occurred in these cases. Hence experiments were conducted with two and three layer stones with only the loose packing density. No test was conducted with four layers, as the three-layer test with the loose packing showed that no liquefaction occurred (as will be detailed later), and therefore it was concluded that liquefaction would not occur in the case of the four-layers cover stones even with the loose packing.

The number of tests conducted: 3 tests for the case of the loosely-packed stones, one layer deep; 1 test for the case of the loosely-packed stones, two-layers deep; 1 test for the case of the loosely-packed stones, one-layer deep; 2 tests for the case of the densely-packed stones, one-layer deep; and finally 1 test for the case of no stones (reference case).

The test conditions for the wave climate are: Wave height, H=17 cm; Wave period, T=1.6 s, Water depth, h=40 cm, Maximum value of orbital velocity at the bed (measured), U_m=31.2 cm/s; Maximum value of friction velocity (calculated from the wave friction factor, Reference [4]), U_{fm}=2.5 cm/s; Grain Reynolds number, $d_{50}U_{fm}/\nu$=2.4; and the Shields parameter, θ=0.4.

The way in which the soil was placed in the silt box was the same as in References [6]. The test duration (from the instant where the waves were switched on to that where the waves were stopped) was 30 minutes. This covered the entire liquefaction-compaction process. The latter process is described in References [5] and [6].

III. Results and Discussion

A. *Soil response with loosely-packed cover stone*

Fig. 2 presents the pore-pressure time series measured at depth z=16 cm where p is the pore-water pressure in excess of the static pore-water pressure at this depth, the excess pore pressure. Fig. 2 a represents the undisturbed case with no cover stones (the reference case), Fig. 2 b with the one-layer cover stones, Fig. 2 c with the three-layers cover stones. (The time series of the excess pore pressure for the two-layers cover stones case is similar to that of the one-layer situation, and is not shown here for reasons of space).

With the introduction of waves, the excess pore pressure begins to build up (Figs. 2 a-c). The buildup of excess pore pressure can be explained as follows (see e.g. Reference [2], Chapter 10). The waves generate cyclic shear strains in the soil. If the soil grains are initially loosely packed, the previously mentioned cyclic shear strains in the soil will gradually rearrange the soil grains at the expense of the pore volume of the soil. The latter effect will "pressurize" the water in the pores, and presumably lead to a buildup of excess pore pressure in the case of an undrained soil. As the wave action continues, the excess pore pressure will continue to accumulate.

First, consider the reference case (no stones, Fig. 2 a). It is seen that the accumulated period-averaged excess pore pressure eventually reaches a constant value, p_{max}. Liquefaction occurs when

$$p_{\max} = p' . \qquad (3)$$

in which p' is the initial mean normal effective stress,

$$p' = \gamma' z \frac{1+2K_0}{3} . \qquad (4)$$

in which $\gamma'=\gamma_t-\gamma$ is the submerged specific weight of soil, γ_t the specific weight of soil and γ the specific weight of water. (It is to be noted that the precise form of the criterion for the onset of liquefaction is, as of yet, not understood very well. Reference [6] discussed this issue in

detail. The latter authors concluded that the above criterion may, to a first approximation, be used for the

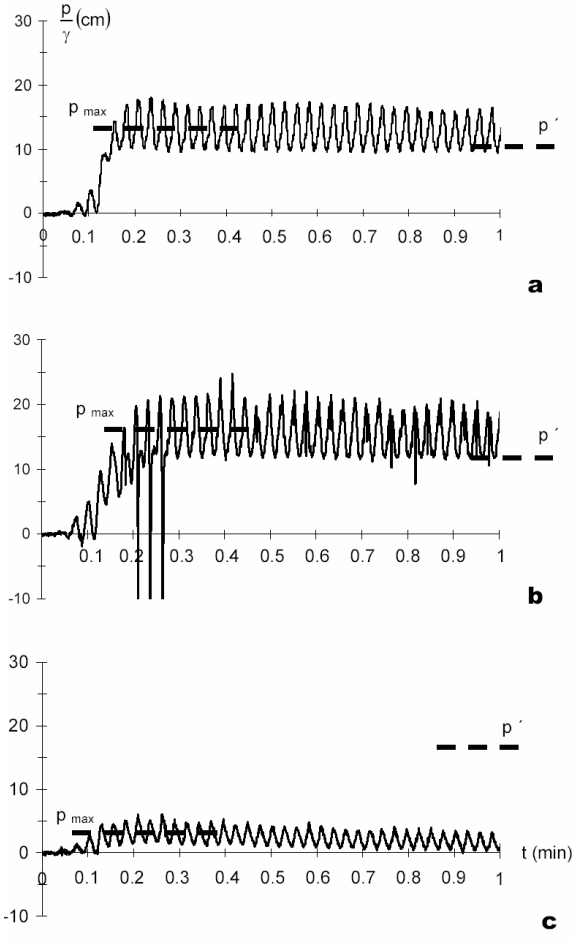

Figure 2. Time series of excess pore pressure in the soil at z=16 cm. (a) No cover stones (Liquefaction); (b) Loosely-packed, one-layer cover stones (Liquefaction); (c) Loosely-packed, three-layers cover stones (No liquefaction).

onset of liquefaction for most practical purposes, [7] and [2].)

Although not shown here, the pressure time series obtained for the other depths (z=0, 5, 10 and 13 cm) showed that the liquefaction occurred first at the surface of the soil and then progressed downwards, in agreement with the previous research, [5], [6], [8] and [9].

Figs. 2 b and c present the time series of the excess pore pressure for the cases with cover stones with one layer and three layers, respectively, at the same depth as in Fig. 2 a, i.e., z=16 cm. (The time series of the excess pore pressure for the two-layers cover stones case is similar to that of the one-layer situation, as pointed out earlier.)

The initial mean normal effective stress, p', will now have to be calculated by

$$p' = (\gamma' z + p_s)\frac{1+2K_0}{3}. \qquad (5)$$

in which p_s is the surface loading (also termed the surcharge) corresponding to the cover stones. This is actually the submerged weight of the stones per unit area of the bed, and given by

$$p_s = wN - (1-n)\overline{D_z}\gamma. \qquad (6)$$

in which N is the number of stone layers. The values of p' are calculated from Eqs. 5 and 6 and plotted in Figs. 2 b and c. The following conclusions are drawn from Fig. 2.

1. Fig. 2 b indicates that the soil under the cover stones is liquefied in the case of the one-layer cover. Although not shown here, the soil under the cover stones is also liquefied in the case of the two-layers cover stones. By contrast, there was no liquefaction in the case of the three-layers cover stones (Fig. 2 c). This implies that, although covered by stones, the soil in the case of the one- and two-layers cover stones was subject to cyclic shear strains which would gradually rearrange the soil grains at the expense of the pore volume of the soil, and the latter effect would "pressurize" the water in the pores, and presumably lead to a buildup of excess pore pressure, in exactly the same fashion as in the case of no stones, and this pressure buildup reaches such levels that it would eventually liquefy the soil.

2. Although there is a buildup of excess pore pressure in the three-layers cover stones case (Fig. 2 c), this accumulation of pressure is not enough to liquefy the soil (cf. p_{max}/γ=3 cm and p'/γ=16.3 cm, the latter figure calculated from Eqs. 5 and 6).

3. The measured pressure time series at the other soil depths (z=5, 10 and 13 cm) also reveal the same behaviour as in Fig. 2.

4. Finally, stones sink in the liquefied soil. The process of sinking is described in Section III.D.

B. Soil response with densely-packed cover stones

Fig. 3 displays the pressure time series obtained in the case of the densely-packed stones at z=16 cm. Two tests were conducted with the densely packed stones, and the results were practically the same.

Fig. 3 shows that although there is a buildup of pressure, the accumulated excess pore pressure is not large enough to liquefy the soil (p_{max}=3 cm versus p'/γ =12.5 cm). Comparison of Fig. 3 and Fig. 2 c (the case of the loosely-packed cover stones, three-layers deep) shows that the pressure responses in the two cases are quite similar. The pressure accumulates in both cases but the soil is not liquefied. The time series for the other depths where the pressure measurements were made behaved in much the same way as that at z=16 cm (Fig. 3).

Although the soil was not liquefied, the cover stones experienced some downward displacement/sinking (O(0.5-1 cm)) throughout the test. This is due to suction removal (winnowing) of the base sediment from between the stones. The sediment removed in this way is brought

into suspension near the bed just above the stones, and subsequently transported in the offshore direction by the steady streaming of the wave boundary layer (see, e.g.,

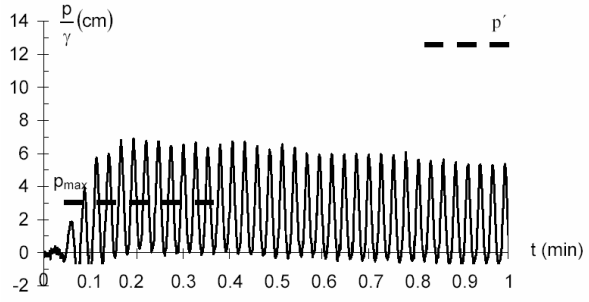

Figure 3. Time series of excess pore pressure in the soil at z=16 cm. Densely-packed, one-layer cover stones (No liquefaction).

Reference [4], for steady streaming), and as a result of this process, they sink, in precisely the same fashion as described in Reference [10] where the base sediment brought into suspension from between armour blocks/stones is transported by steady current, the flow environment studied in [10]. Since this is outside the scope of the present investigation, the subject will not be pursued further.

The present results generally agree with the centrifuge wave-testing results of [3]. The latter authors also observed no liquefaction when a liquefaction-prone soil was covered fully with gravel while they observed liquefaction when the soil was partially covered with gravel.

C. Mechanism of soil liquefaction under cover stones

From the preceding paragraphs, it is seen that the soil under cover stones behaves differently, depending on (1) the packing density of the cover stones (loose or dense) and (2) the number of layers in the cover stones. The soil is liquefied when the cover stones are loosely packed and when they are one-layer and two-layers deep, whereas the soil is not liquefied when the cover stones are three-layers deep although they are loosely packed. It is also observed that the soil is not liquefied when the cover stones are densely packed and one-layer thick. The observed behaviour of the soil is explained as follows.

There are three "components" in the process of buildup of excess pore pressure in the case with no cover stones (the reference case):

1. The cyclic bed pressure caused by the wave passing overhead;
2. The cyclic shear strains in the soil caused by the previously mentioned cyclic bed pressure; and
3. Obviously the soil should be loose enough for soil grains to rearrange, resulting in the buildup of excess pore pressure and eventually liquefaction.

This is for the case with no stones on the bed. However we can expect that the same kind of mechanism takes place also in the case when the soil is covered with stones. Regarding Item 1 above, the present pressure measurements made at the bed just beneath the stone layer revealed that the pressure at the bed was the same as that in the no-stone case, irrespective of the packing pattern of stones (loose packing or dense packing), and therefore the first component of the process of the buildup of excess pore pressure (Item 1 above) existed also in the presence of cover stones, and this is irrespective of the packing patterns tested.

Since the bed pressure in the case of the one-layer, densely packed cover stones was exactly the same as that in the case of the one-layer, loosely packed cover stones, then the question is why the soil was not liquefied in the former case and liquefied in the latter case.

This is essentially linked to the condition in Item 2 above, namely, in the case of the densely-packed stones, there is not enough space beneath the stones for the soil to "breath". (For the effect in Item 2 to take place – i.e., for the soil to experience the cyclic shear strains – the space above the mudline must be free so that the soil is able to expand and contract in the vertical direction, i.e., the soil is able to "breath", when it is undergoing the cyclic bed pressure.) Since there is not enough space beneath the stones for the soil to "breath", not enough shear strains will be generated in the case of the densely-packed cover stones. Once the soil is prevented from undergoing the cyclic shear strains (completely or even partially), then the soil grains will fail to rearrange adequately, and therefore not enough excess pore pressure will build up, and hence no liquefaction will occur. This explains why the soil was not liquefied when the stones were densely packed.

By contrast, in the case of the loosely-packed stones, there is plenty of room beneath the stones for the soil to "breath" (when subjected to the bed pressure) so that the soil will undergo the cyclic shear strains, leading to the buildup of excess pore pressure and eventual liquefaction.

It may be noted, however, that, in the case of the densely-packed cover stones, there are two additional effects. (1) The surface loading corresponding to the densely-packed stones, p_s, is larger than that corresponding to the loosely packed stones. However, our measurements showed that p_s is even larger in the case of the two-layers, loosely packed stones, and, in this latter case, the soil is liquefied, and therefore it can be concluded that the contribution from this effect is not very significant. (2) Although our measurements are unable to resolve the relative density of the soil in the case of the densely-packed stones, this quantity is expected to be slightly larger in the case of the densely-packed stones than in the case of the loosely-packed stones, and this may, to some degree, contribute to the observed no-liquefaction response of the soil in the case of the densely-packed cover stones.

(At this juncture, it is interesting to note that, in the two experiments in Reference [3] where liquefaction did not occur, the D_{50}=3 mm coarse sand simulating the gravel cover had a depth of 1 cm in one test and 2 cm in the

other, and although no porosity data were given in the original publication, it is seen that the number of cover gravel layers (at least three or even more) was apparently too big to cause liquefaction)

D. Sinking of stones in the case of liquefaction

In the case where the soil was liquefied, cover stones sank in the liquefied soil, in precisely the same fashion as in the experiments of [8]. (In the latter work, sinking of marine objects, such as pipelines, spherical and cube-shaped bodies was studied in great detail).

In one experiment where the soil was liquefied a member of cover-stones layer was mounted to a frame which was free to move in the vertical direction; the set-up used for this experiment was the same as that used in [8]. The downward displacement of the stone was recorded, using a potentiometer. The latter showed that the stone began to sink as soon as the soil was liquefied. One interesting observation was that the stone in its downward motion came to rest not at the impermeable base of the soil box, but at about 3 cm above it (Fig. 1). This is linked to the so-called compaction process.

Stones begin to sink in the soil as soon as the liquefaction sets in. The liquefaction process spreads downwards very rapidly, and is followed by the compaction process. The compaction process first begins at the impermeable base and gradually progresses in the upward direction as the pore water is drained out of the soil. The downward motion of the stones eventually terminates when the stones, on their way, meet the compaction front. The stones will be "arrested" completely as the compaction front continues to progress upward. (Note that the complete sequence of events from the buildup of pore pressure, to the resulting liquefaction, to the behaviour of the two-layered system of liquid of different density (the water column and the liquefied soil), to the compaction of the soil (starting from the impermeable base and progressing upwards until it reaches the mudline, and to the formation of ripples on the "hardened", dense sediment bed) is described in Reference [6].)

IV. Remarks on Practical Applications

Use of select backfill (which will not liquefy) may probably be the only counter measure if there is a potential for liquefaction for a given soil (hydraulic fill or naturally deposited). Although surface protection by cover gravel/riprap over the backfill soil is a method recommended to protect the backfill soil against scouring (as mentioned previously), the present study has demonstrated that this method can also prove to be an option to protect soil against liquefaction, a result also obtained by [3]. The present results have shown that, with the implementation of this method, a liquefiable soil may be protected against liquefaction provided that cover stones are designed properly. To this end, the following recommendations may be made.

1. Stones need to be placed on the bed so that the porosity is small. The cover stones in the present study with dense packing corresponding to a porosity of 0.36 prevented the soil from liquefying even with a single cover layer.

2. Considering that such small porosities may not be easily achieved in practice (reported values for porosity being 0.38-0.40 for quarry stones, 0.47 for cubes, 0.50 for tetrapods and 0.63 for dolos, Reference [11]), it is recommended that multi-layer cover stones be implemented. The present study showed that loosely-packed (with a porosity of 0.62), three- (or more) layers cover stones prevented the soil from liquefying.

3. The above observations essentially appear to be the general guidelines from the present study. However it is recommended that an assessment study be carried out whether or not there is a liquefaction potential of the soil, given the cover-stones characteristics (the stone size, the porosity and the number of layers).

V. Conclusions

1. A liquefiable soil covered by gravel/stones/riprap may or may not be liquefied beneath a progressive wave, depending on the packing density of the cover layer; and the number of stone layers among other factors such as the relative density of the soil, the wave characteristics, etc.

2. The present experiments showed that soil under a loosely-packed stone layer (with a porosity of 0.57-0.63) was liquefied when the cover stones were one-layer and two-layers deep. Soil covered with three-layers stones (or more) was not liquefied at all.

3. The present experiments also showed that soil with densely-packed (with a porosity of 0.36) cover stones was not liquefied either even when the cover stones were one-layer deep.

4. In the case of soil liquefaction, cover stones sink in the liquefied soil. The experiments showed that the downward motion of the cover stones comes practically to a complete stop when the stones meet the compaction front travelling upwards. As the compaction front continues to travel upwards, the cover stones are completely "arrested" in the compacted soil.

5. The present results demonstrate that cover stones could be an option as a counter measure to protect soil against liquefaction. Recommendations are made as to how to implement the preceding finding.

Acknowledgment

This study was partially funded by the Danish Research Council for Technology and Production Sciences (FTP, formerly STVF) Research Frame Program "Exploitation and Protection of Coastal Zones" (EPCOAST). Dr. Figen Hatipoglu's stay at the Technical University of Denmark (on leave from the Istanbul Technical University, ITU) has been supported by EPCOAST and ITU.

References

[1] G.J.C.M. Hoffmans and H.C. Verheij, *Scour Manual*, A.A. Balkema., 1997.

[2] B.M. Sumer and J. Fredsøe, *The Mechanics of Scour in the Marine Environment*, 2002, World Scientific.

[3] H. Sekiguchi, S. Sassa, K. Sugioka and J. Miyamoto Wave-induced liquefaction, flow deformation and particle transport in sand beds. *Proc. Int. Conf. GeoEng2000*, Melbourne, Australia, 2000, Paper NO. EG-0121 (CD-ROM Proceedings).

[4] J. Fredsøe and R. Deigaard, *Mechanics of Coastal Sediment Transport*, World Scientific, 1992.

[5] J. Miyamoto, S. Sassa and H. Sekiguchi, "Progressive solidification of a liquefied sand layer during continued wave loading". *Geotechnique*, vol. 54, No. 10, 2004, 617-629.

[6] B.M. Sumer, F. Hatipoglu, J. Fredsøe, and S.K. Sumer The sequence of soil behaviour during wave-induced liquefaction. *Sedimentology*, 2006, In print.

[7] W.G. McDougal, Y.T. Tsai, P.L-F Liu,. and E.C. Clukey, Wave-induced pore-water pressure accumulation in marine soils. *J. Offshore Mechanics and Arctic Engineering*, ASME, 1989, vol. 111, 1-11.

[8] B.M. Sumer, J. Fredsøe, S. Christensen and M. T. Lind, Sinking/Floatation of pipelines and other objects in liquefied soil under waves. *Coastal Engineering*, vol. 38, 1999, 53-90.

[9] Sassa, S., Sekiguchi, H. and Miyamoto, J. (2001): Analysis of progressive liquefaction as a moving-boundary problem. *Geotechnique*, vol. 51, No. 10, 847-857.

[10] B.M. Sumer, S. Cokgor and J. Fredsøe, Suction of sediment from between armour blocks. *J. Hydraulic Engineering*, ASCE, vol. 127, No. 4, 2001, 293-306.

[11] *Shore Protection Manual* U.S. Army Coastal Engineering Research Center, vol. II, Department of the U.S. Army Corps of Engineers, 1977.

Unexpected morphological effects due to postponed maintenance of river groynes

M.A. van Heereveld[*], M. van der Wal[**]
[*] Royal Haskoning, Consulting, Architecture, Engineering, Nijmegen, The Netherlands
[**] Rijkswaterstaat, Dienst Weg- en Waterbouwkunde, Delft, The Netherlands

I. INTRODUCTION

River training works along the Dutch river Rhine branches mainly consist of series of groynes. The groynes (some 3.600 in total) are needed to 1) provide sufficient nautical depth during periods of low discharges and 2) to stabilize the main channel in plan for accommodation of floods. Postponed maintenance affects either function, although it is clearly seen that if nautical depth is compromised through damage, the discharge capacity may benefit from the damage and vice versa.

The nautical depth, however, is critical in many locations and hence, the performance of the groynes is important.

The current maintenance strategy is to upkeep the structural integrity of groynes. It occurs that the execution of these maintenance works has to be delayed due to insufficient budget and approval procedures. As a consequence maintenance is often postponed for several years leaving many groynes damaged. Inevitably, their performance is affected resulting in increased current attack on the unprotected banks and necessity for additional maintenance dredging or loss of nautical depth with all its economical consequences.

Here, the first step towards a rationalized approach for groyne maintenance is presented with focus on the nautical depth function of groynes. The rationalized approach balances maintenance costs of damaged groynes, including the development of vegetation on groynes, with the costs of reduced performance. This way the optimum of the required maintenance budget can be determined yearly. Clearly the maintenance strategy should include the often neglected effects of damaged and repaired groynes on the river bed morphology.

The rationalized approach requires reliable and detailed insight into morphological effects of (postponed) maintenance. In this study, insight was gained through the use of a one-dimensional morphodynamic model, which brought to light some unexpected morphological effects that need to be taken into account in the maintenance strategy, apart from the already complex scour and erosion processes.

II. GROYNE DAMAGE

A. *Relevant types of damage to groynes*

The nautical depth function is directly affected through postponed maintenance of damaged groynes. Examples of different types of such damage are [1]:

- steepening of the groyne head;
- general sinking of the crest;
- outflanking.

The discharge function is affected mainly through vegetation growth on the crest of groynes.

Steepening of the groyne head is usually caused through undermining or the autonomous erosion process of the river main channel. Typically, groyne heads are designed with a slope of 1:2 to 1:3. Steepening of the groyne heads results in slopes between 1:1 and 2:3.

Crest sinkage is either inflicted by a general and gradual settling of the groyne itself or through collision with ships during high water when the groynes are submerged. Typically, crest sinkage through settling is 10 – 20 cm in size.

Outflanking is a type of damage that occurs during a flood when groynes are submerged for a prolonged period of time. If the landward end of a groyne is not built properly or has become damaged, erosion may start at the attachment point. The shortcut in the flow then allows outflanking to further progress. This type of damage tends to occur more frequently nowadays which is possibly due to intensified inland navigation. Because outflanking develops rapidly and the consequential increase in flow cross section is typically very large (10 – 60 m^2), the effect on the nautical depth function is also significant.

Although not strictly a form of damage, the postponed maintenance of vegetation growth on the crests of the groynes limits the discharge capacity of the river significantly. Despite the significant effect of vegetation growth on the crests on the discharge capacity during floods, it is generally not taken into account. This type of damage was not explicitly considered in the research project and will not be discussed in detail in this paper. It is, however, important and necessary to incorporate the vegetation maintenance required for this type of damage in a maintenance strategy for groynes such as the one discussed here.

B. *Outflanking at Dodewaard*

Near the village Dodewaard a groyne on the right bank of the river Waal (km 900.330) experienced severe outflanking in the nineties. This groyne is referred to as the Dodewaard groyne hereafter. The Dodewaard groyne is located on the Middle Waal which is a relatively straight stretch of river (Fig 1). Groyne length is 100 m typically for the Middle Waal; groyne spacing is generally 200 m [2].

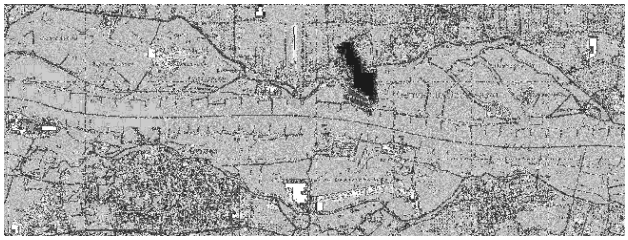

Figure 1. The Middle Waal and location of the Dodewaard groyne

In December 1996, initial outflanking was discovered after the passing of a peak discharge. In order to study the optimal intervention limit for repair of this groyne, it was decided not to repair damage immediately and allow the outflanking to further progress for some time. Over a period of approximately 1.5 years, the outflanking increased apparently gradually (Fig 2.) until a final width of outflanking of 30 m and a depth of 2 m relative to the crest was reached (Fig 3.) by summer 1998. Until the repair of the groyne in December 2000, no significant further growth took place.

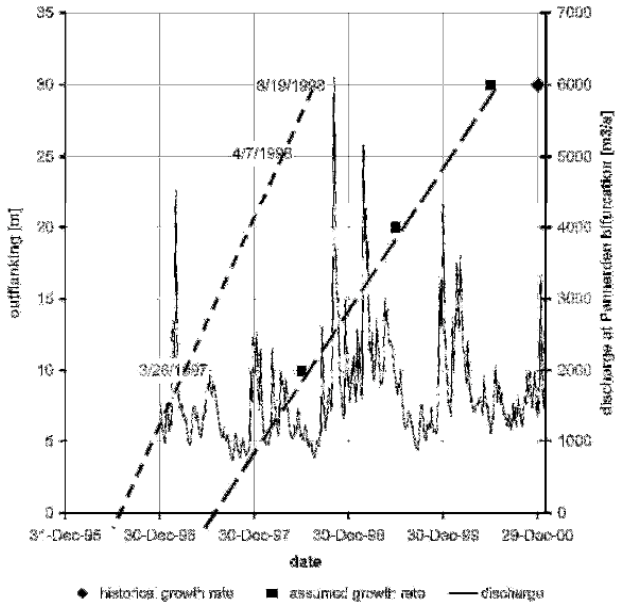

Figure 2. Progression of outflanking of the Dodewaard groyne

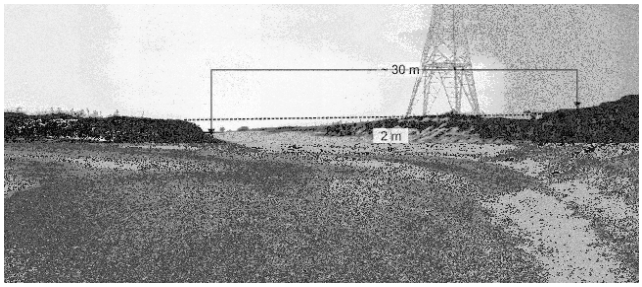

Figure 3. Outflanking of the Dodewaard groyne (approx. December 2000)

Throughout the period of growth of outflanking the bed level was monitored in plan in the Dodewaard groyne section and several sections up- and downstream.

Functional repair took place relatively quickly due to the method of repair in which wooden sheet piles are placed between the detached groyne and the floodplain after which the groyne is rebuilt into its original shape. Monitoring continued after the repair for another year.

III. INITIAL RECONAISSAINCE OF EFFECTS ON BED LEVEL FROM VARIOUS TYPES OF DAMAGE

Using a SOBEK one-dimensional morphodynamic model, the effect of three types of damage was investigated, e.g.: steepening of the head, crest sinkage and outflanking. In the model, the Waal River was schematized with one single cross section for the entire 90 kilometers of river. Damage was schematized through local alteration of the cross section.

For the initial reconnaissance of effects on bed level, constant discharges of 1,467 m^3/s (Q_{50}) and 2,400 m^3/s (Q_{90}) were used as well as a representative flood hydrograph from 2,000 m^3/s – 3,000 m^3/s. The results of the reconnaissance were extensively discussed in Akkerman, Van der Wal et al [3]. Figure 4 shows the effect on the average bed level in relation to the increased flow cross section due to groyne damage.

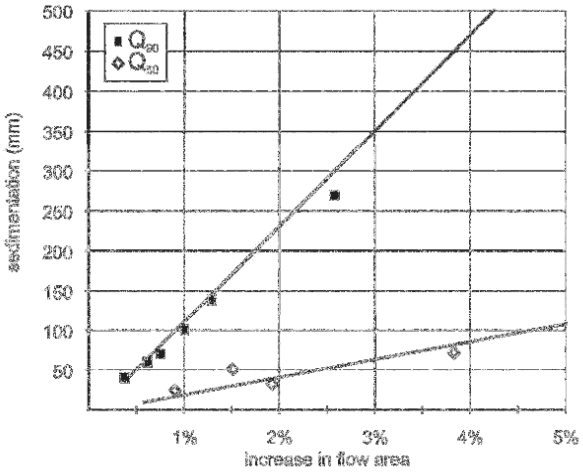

Figure 4. Effect of groyne damage (as a change in cross section) on bed levels

Furthermore, it was found that the passing of a flood wave caused a momentary peak to occur on top of the already increased bed level, which would cause significantly higher sedimentation than found from a simulation with a constant discharge.

The repair of the detached groyne was also included in the simulation. From this, it was possible to determine the manner of displacement of the sedimentation caused by groyne damage in the downstream direction. The diminution rate of the displacing sand wave was found to be very slow. Reference is made to Akkerman, Van der Wal et al [3] for a detailed discussion. Hence, hindrance from a bed level increase after repair of damage will occur for a prolonged period of time and nautical depth limitation is not immediately solved.

IV. DODEWAARD CASE AND MODELLING RESULTS

Since the initial results from the reconnaissance were found to be promising, the Dodewaard case was further investigated. The growth rate of outflanking was modeled at a rate of 10 m per year from December 1997 to the moment of repair in December 2000. The more realistic growth-rate of the outflanking as described in the previous section was not yet known, hence, this assumption was made. The one-dimensional model was run using the historical discharge (again, Fig 2.) of the same period so as to allow for comparison with the monitoring data.

Figure 5 shows the computed change in bed level due to the growing outflanking from 10 m, 20 m and 30 m from initial outflanking until the moment of repair. Bed level increase is computed proportional to depth. Because it is a one-dimensional model, the actual bed level increase may vary in plan form location and height.

The influence of peaks in the discharge is readily seen. Table 1 shows the average sedimentation per year and size of outflanking, as well as the minimum and maximum values found. The maximum values found in the simulation with the historical discharge compare rather well with the results of a simulation with a constant discharge (Q_{90}).

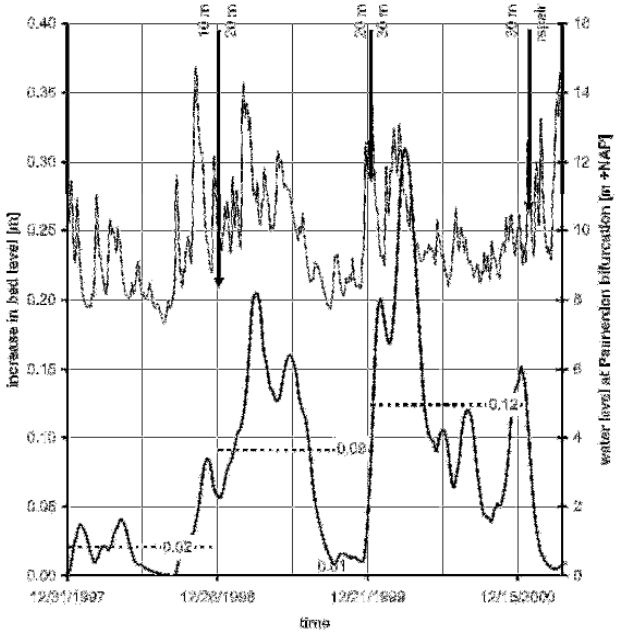

Figure 5. Computed increase in bed level due to outflanking and historical water levels. The arrows mark the schematized growth of outflanking; the dotted lines give the average increase in bed level per degree of outflanking.

Outflanking [m]	Q_{90}	$Q_{historical}$		
		min	avg	max
10	0,095	0,000	0,022	0,075
20	0,190	0,012	0,090	0,191
30	0,270	0,029	0,126	0,289

TABLE I. COMPUTED BED LEVEL INCREASE AT DODEWAARD, COMPARISON OF CONSTANT DISCHARGE (Q_{90}) COMPARED TO HISTORICAL DISCHARGE

Additionally, Fig. 5 also gives insight into the time-lag that exists between the response of the bed level increase and the peak in discharge: the maximum bed level occurs 3 to 4 weeks after the peak has passed.

This means that the water level will have lowered while the bed level is still increasing. In the last year before the outflanked groyne was repaired, the 30 m outflanking causes a bed level increase of 0,29 m, 4 weeks after the peak in discharge has passed; the water level has then dropped with 0,10 m, so that a loss of water depth of 0,39 m occurs. Again, this is an average value proportional to the depth in the cross-section and local values may be even higher. This may cause hindrance to shipping where available depth is critical, which is the case on the larger part of the Waal river.

On the Middle Waal, a survey is carried out daily to determine the Least Measured Depths. The information is passed on to shipping companies whom alter the degree of loading of their vessels to avoid the ships running aground. Hence, the hindrance does not present itself in nautical sense alone but also in an economical way because ships can carry less cargo.

In a further step, the dissolving of the local bed level increase was investigated after repair of the outflanked groyne. In the Dodewaard groyne section, the bed level returns to its original level within approximately 2 months. The sand wave has started to travel downstream. An important result was that it takes approximately 7 months for the height of the sand wave to decrease 50 percent. The problem of nautical hindrance is therefore not solved instantaneously after repair, but will persist for a long period of time. Since the peak discharges are likely to occur during winter when water levels are high, hindrance may increase significantly during summer when the traveling sand wave reaches shallow areas downstream and water levels are low, despite the fact that it may have decreased in height.

V. COMPARISON OF MODEL RESULTS WITH MONITORING DATA

The results found from the modeling of the Dodewaard case have been compared with monitoring data. The monitoring data, however, consisted of bed levels in two dimensions. In order to allow for comparison with one-dimensional model results, bed levels were averaged for each groyne section in longitudinal as well as transverse direction.

The dataset consisted of large sets of bed levels, taken at irregular intervals. Sometimes, bed levels were surveyed only on the lefthandside of the river axis, rather than across the full width.

The change in measured bed levels have been compared with the change in computed bed levels (Figure 6). In terms of trends in bed development, the model seems to yield good results. Because the model was simplified to one cross-section and a constant bed gradient, results do not match in absolute values.

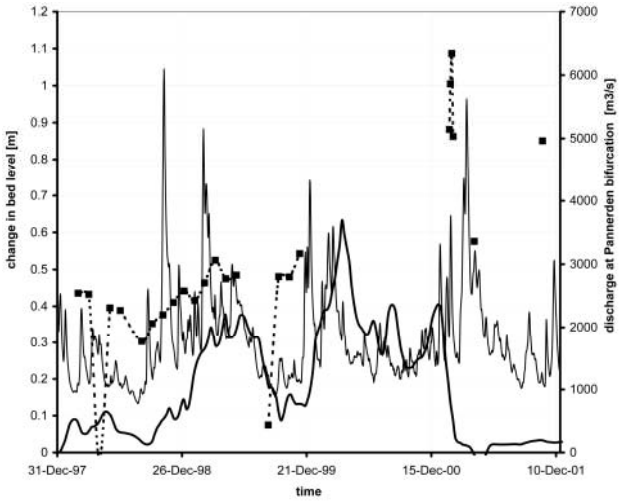

Figure 6. Change in measured and computed bed levels

The difference near the end of 2000 is probably due to the fact that it was later discovered that the development of the outflanking had taken place faster than initially assumed. Additionally, in this period, only one side of the river main channel was surveyed, so that difference may occur.

VI. CONCLUSIONS AND FUTURE WORK REGARDING MODELLING GROYNE DAMAGE

In a qualitative way, the one-dimensional model seems to predict changes in bed level due to outflanking rather well when compared with monitoring data, despite the deficiencies in the available dataset for exclusive verification.

In order to further verify the model quantitatively, measurements taken at the Haaften test location of Rijkswaterstaat where three groynes along the Waal River will be altered provide a good starting point. Additionally, comparison of changes in bed level found from a two-dimensional model may allow for verification of the one-dimensional approach adopted here.

If the model is quantitatively verified, other types of groyne damage can be investigated in greater detail and band width analysis can be carried out.

In the project Room for a River the lowering of groyne crests along a major stretch of the Waal River is considered as a promising measure to increase the safety against flooding. A lowering of about 1 m in the case of a typical groyne for the Waal River is comparable with the maximum outflanking in the Dodewaard groyne. Hence, the observed 0.4 m reduction in water depth may also apply for this measure. Operational mitigation via additional dredging may be rather complex and deserves additional study.

The one-dimensional approach itself allows for developing a good understanding of the processes that occur due to groyne damage, as well as extensive sensitivity analysis in terms of loss of nautical depth. In particular, the one-dimensional model gives excellent insight into important instationary phenomena that occur.

Schematization of the model may be improved when compared to two-dimensional models and future work includes comparing schematization of groynes and groyne damage. Although the two-dimensional models give good insight in plan form changes in bed level, it should be recognized that these models provide less insight into the instationairy effects that have proven to be very important if one is to maintain nautical depth.

VII. A NEW APPROACH TO MAINTENANCE

A. *(Unexpected) morphological effects due to postponed maintenance*

As found from the research, the relation between damage to groynes and river bed morphology and loss of nautical depth is a highly complex erosion and sedimentation problem, both on a local as well as on a larger scale.

Locally, the groyne head scour hole varies in size due to variations in discharge, as does the deposition downstream of the scour hole. In itself, this forms a potential depth limitation. Possibly, this depth limitation becomes more critical due to postponed maintenance. Whereas on a larger scale, the bed level between opposite groynes increases, causing a potential depth limitation in the main channel itself.

In both cases, the influence of peak discharges must be taken into account because sediment transport increases dramatically during the peak discharges. After the peak has passed, the water level decreases faster than the bed level decreases, causing a potentially more severe nautical depth limitation than expected.

Additionally, if the damaged groynes are repaired, the sand wave will progress downstream and local equilibrium depth (between opposite groyne sections) is re-established. Although the height of the sand wave will diminish as it travels downstream, it may again cause a nautical depth limitation when it passes already critical locations in terms of available water depth.

B. *Maintenance strategy*

Currently, the aforementioned complex and unexpected scour and erosion processes caused by groyne damage are not taken into account in the maintenance strategy, which focuses primarily on maintaining the structural integrity of the groynes, rather than focusing on the upkeep of their functioning. Although this is a good strategy in itself, shortage of maintenance budget requires that repair works are well considered since many groynes are damaged.

This implies that possibly, maintenance may need to be postponed on some groynes whilst damage on other groynes is given priority. Alternatively, anticipative dredging may have to be carried out to prepare for future sedimentation. Either way, loss of performance of groynes and hence, available nautical depth must be accepted. Hence, detailed and reliable insight into the scour and erosion processes caused by postponed maintenance is a prerequisite.

The one-dimensional approach as discussed here allows establishing a relationship between the state of

maintenance of groynes and the consequences for the available water depth or the need for anticipative dredging.

It is easily developed into a decision support system that allows the river warden to prioritize maintenance work and budgeting and whilst maintaining an optimum available water depth on the river. Also, the decision support system may assist in finding an optimum in the order in which maintenance to groynes is carried out whilst minimizing hindrance for shipping, taking into account the effect of the traveling sand waves after repair and depth limitations downstream.

REFERENCES

[1] Royal Haskoning, 'Onderzoeksproject WBKI-kribben: onderhoudsparameters kribben'. 9M2761.A0/R0002/MAVH/NIJM, 2002.

[2] Royal Haskoning, 'Onderzoeksproject WBKI-kribben: modelmatige onderbouwing onderhoudsstrategie'. 9R6047.A0/R0002/MAVH/SEP/Nijm, 2005.

[3] Akkerman, Van der Wal et al, 'Groyne optimization and river hydrodynamics', Riverflow 2004.

Minimizing River Training for Flood Control, a Dynamic Concept

M.A. van Heereveld*, G.J. Akkerman**
* Royal Haskoning, Nijmegen, The Netherlands
** Royal Haskoning, Nijmegen, The Netherlands

I. INTRODUCTION

This paper presents a generalized approach for minimizing river training works, as elaborated from the design activities for protection works for the Border Meuse Project in the Netherlands. The approach focuses on minimization of the training works which adds to nature restoration and sustainable usage of protection materials, whilst the same time maintaining sufficient scour control during extreme floods (i.e. safety). The new concept is presented, as well as its application in the Border Meuse Project.

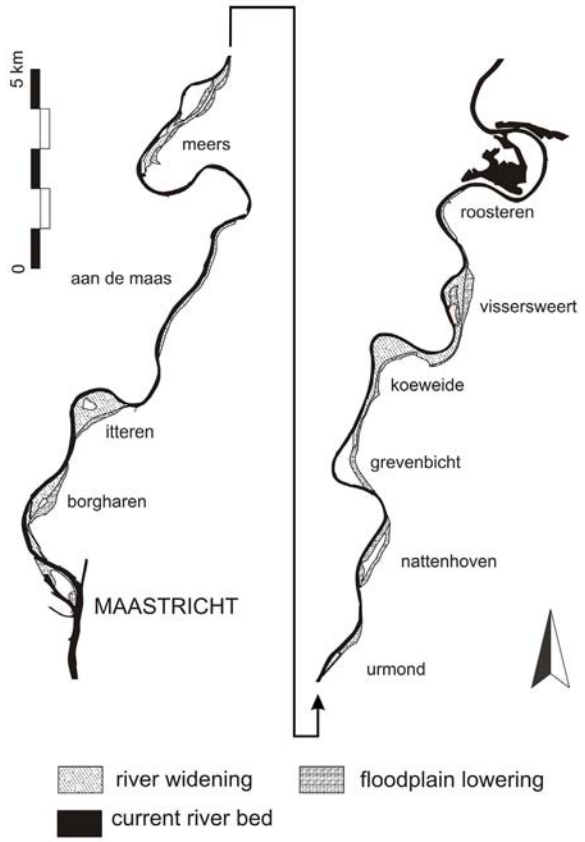

Figure 1. A schematic view of the Border Meuse project

II. BACKGROUND

The new approach was developed within the Border Meuse Project, which is shown in Figure 1. In this project the river will be altered significantly during the coming decade to accommodate higher design discharges, whilst not increasing flood levels, in combination with nature restoration. The alteration will be realized by widening the Border Meuse at gravel mining locations, the revenue of which allows the project to be carried out almost cost-neutral.

The Border Meuse is Netherlands' most natural river, with a (narrow) gravel bed and relatively high flow velocities. Especially in the remaining bottlenecks, in between the widened areas, flow velocities will further increase and erosion will intensify. Hence, the challenge was posed to the design team to minimize the protection works as much as possible and, at the same time, maintaining sufficient scour control to ensure safety.

III. PRINCIPLES OF DYNAMIC RIVER TRAINING

The conventional approach of the problem of ensuring safety against flooding through river widening is illustrated in the diagram below. Generally, the most dynamic locations are known from experience in the past. This knowledge leads to the decision that at those particular locations, regardless of the presence of important infrastructure (i.e. flood banks, bridge piers and other infrastructure of importance), river training works are required. Conservative design of river training works requires a minimum of knowledge of flow velocities and loads on bed and banks, so generally a minimum effort is put into studying these aspects. As a result, extensive river training works are often introduced. This line of thinking is illustrated in Figure 2a.

Because of the extensive river training works, such a conventional ('stable') approach also leads to high initial costs of construction. It is acknowledged that these require little monitoring and maintenance but, on the downside, this approach is not particularly sustainable altogether.

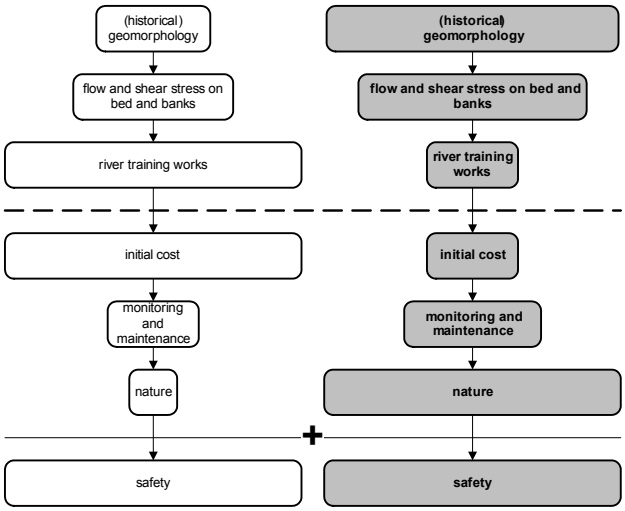

Figure 2. Schematic view on the conventional (a) and dynamic (b) approach in designing river training works to achieve a certain degree of safety.

Gradually, during the design process for the Border Meuse, a dynamic concept was arrived at, in a sense that river training works are only designed at locations where scour of bed and/or banks pose a direct threat to safety. Where no immediate threat is posed, generally the river is allowed maximum freedom [1,2]. Additionally, if scour and bank protection are needed, it is attempted to minimize protection works as much as possible. Nature development will certainly benefit from the increased river dynamics.

Such a dynamic approach requires that the emphasis is laid on different aspects of the design process as well as certain aspects after completion of the stabilization works. This is illustrated in Figure 2b.

Contrary to the stable approach, emphasis is laid on a more thorough assessment of the geomorphology of a river to begin with, rather than focusing on the actual design of river training works too early. After a thorough study of the rivers' geomorphology, the flow and loads on the bed and banks of the rivers bed are investigated in-depth. The combination of these two aspects and knowledge of the location of important infrastructure, such as flood banks and bridge piers, make that it is possible to identify locations where river training works are really a pre-requisite to ensure safety. Hence, the length of river section to be stabilized is minimized, contrary to the conventional approach.

Having minimized the extent and composition of river training works, the initial cost of construction will be much lower as well. However, it is important that more effort be put into future monitoring and maintenance of the river. An important advantage is that a more dynamic river adds significantly to nature development. Most importantly, with the dynamic approach the same degree of safety is achievable as the safety with a conservative protection works at lower (lifecycle) costs. As Figure 2 already suggests, the dynamic approach is much more balanced and sustainable.

In summary, the following three principles of the dynamic concept are:

1) Identification of areas potentially at risk, whilst maximizing river dynamics as much as possible. This is done through assessment of the geomorphologic behavior of the river where relevant for the safety against flooding.

2) Flow field and shear stress data collection and prediction. In order to obtain a detailed prediction of the hydraulic and morphologic structure of the present and – where relevant – the future river configuration at areas potentially at risk.

3) Introduce 'lean' dimensioning of the river training works. This implies using the relevant information of 1) and 2) and state-of-the-art dimensioning tools. Where possible, the principle of dynamic stability is applied.

Hereafter, these principles will be explored in detail.

IV. PRACTICAL APPLICATION OF THE DYNAMIC CONCEPT ON THE BORDER MEUSE

A. Identifying areas potentially at risk

Bed and bank protection works are only introduced where important infrastructure such as bridge piers or flood banks are found within a certain distance from the river bank. The critical range between infrastructure and ultimate river bank position must be chosen on a sound basis of knowledge of (historical) and anticipated geomorphologic behavior of the river.

The amount of outflanking that can occur within the passing of the design flood wave is a good measure. For the Border Meuse, a relatively conservative distance of 50 meters was adopted: Study of the historical erosion of river bends [3] learned that in 15 years, a maximum outflanking of 5 to 10 meters at maximum could be expected. If important infrastructure is found outside the 50 meters zone, its stability will not be affected due to the design flood event. It may, however be necessary to repair damage to the banks afterwards so as to keep the river at a reasonable distance from the infrastructure.

A typical aspect of the Border Meuse as arose from geomorphological analysis, is the fact that generally the inner bends tend to erode much faster than the outer bends. This is due to the hard points in the outer bends and to the flood plains near the inner bends that overflow during flood events and direct the flow towards the inner bank.

B. Flow field and shear stress data collection and analysis

Having identified spatial limitations, flow velocities in the old and new situations are analyzed using a hydraulic model (see also section VI for specific issues regarding the use of hydraulic models). If flow velocities do not increase significantly, bed and bank protection works are not necessary (implicitly assuming the existing bank (protection works) to be in a well maintained condition and stable). If not, the actual flow patterns for design conditions are assessed as a next step.

Assessing the flow velocities in the new situation requires thorough knowledge of the hydraulic and geomorphologic behavior of the river and knowledge of bed and banks (whether protected or not).

Next, shear stresses acting on the bank and bed are analyzed. In the Border Meuse case, most of the bed

consists of the coarse gravel ('toutvenant'), a type of gravel that is very resistant to current attack and has a low mobility at increasing loads. The characteristic flow resistance of the material in terms of critical shear stress is approximately 27 N/m^2. This corresponds roughly to a critical current velocity of 2 m/s. In the initial design it was therefore decided to adopt this critical shear stress for the full length of river.

Knowing the flow field at design conditions from the hydraulic model, it is possible to assess the level of exceedence of critical shear stress in the identified areas at risk. Next, on locations where critical shear stresses are exceeded, the equilibrium scour of the river bed can be determined.

If the above three criteria related to flow and shear stresses are met, it is likely that at the identified location, flow conditions may result in erosion of the river bank to such an extent that important infrastructure can be damaged. It is then necessary that the identified location is considered in greater detail to assess whether bed and/or bank protection works are required to ensure safety. In Fig. 3, the result of the identification of areas potentially at risk and analysis of flow and tractive forces is shown for the location Meers [5]. The black line around the model results represents the distance of 50 meters. It is readily seen that the flood bank lies within the chosen distance.

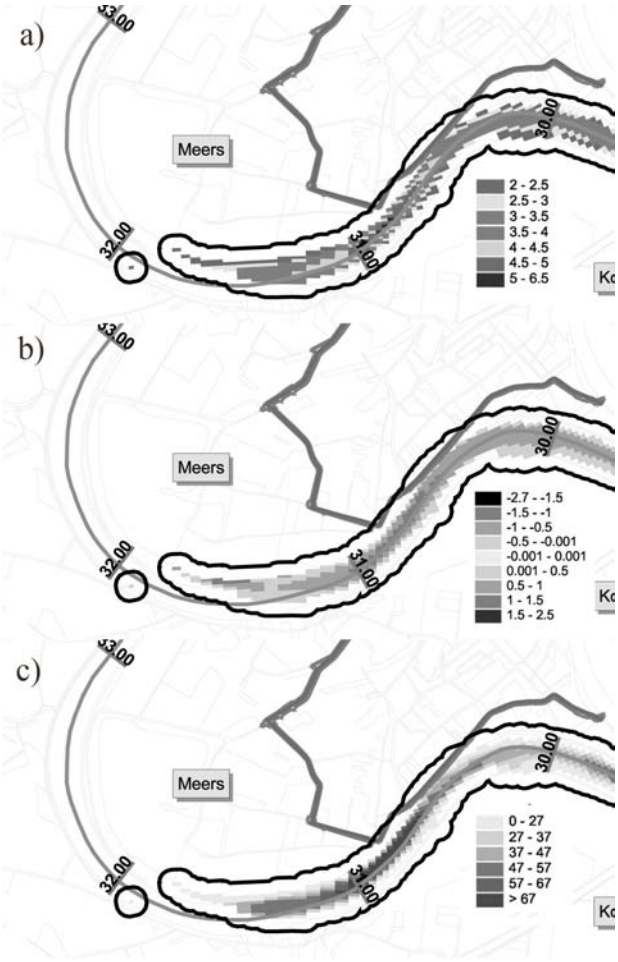

Figure 3. Result of identification of areas potentially at risk for Meers: a) flow velocities in the new situation [m/s], b) increase in flow velocity relative to the reference [m/s], c) critical shear stress [N/m^2].

All areas that do not meet the three criteria simultaneously , principally do not require strengthening of bed and banks. However, it is of great importance that, since the river is still allowed freedom on these locations to alter its flow, monitoring of planform changes after significant floods is carried out. Monitoring is necessary to ensure that safety is maintained not only immediately upon completion of the river works, but also for the medium and long term. Adequate monitoring is a key activity when maintaining scour control in a natural river.

C. Lean dimensioning of river training works

If the river banks of the identified area at risk are protected it is required to assess their resistance to the current attack. Dealing with a substantial length of river of which a large part is covered with bank protection works, the exact nature of the construction is often unknown at many locations. Not only is it very unpractical, but also very costly to investigate all banks to such an extent that it is possible to properly determine their resistance to current attack. It has therefore been decided that if the banks in the identified areas at risk are unprotected or if uncertainty had arisen regarding its construction, new protection works are necessary.

Obviously, if the nature of the existing bank protection works is adequately known, it is possible to determine threshold levels in terms of a critical velocity that should not be exceeded so as to ensure bank stability. In the Border Meuse case, the banks have historically been protected with rock armour of 10 – 60 kg or 40 – 200 kg. These are resistant to flow velocities of 3.0 m/s and 3.5 m/s respectively. If these threshold levels are exceeded, a new design must be made. If they are not exceeded, monitoring will still be necessary to ensure stability for the future.

In hydraulic bottlenecks, extreme flow velocities on the bed and the lower parts of the banks do generally not exceed 4.0 m/s, except for some locations where velocities up to around 5.0 m/s are found (Fig. 3a). In these more extreme cases other types of bank protection are required in stead of conventional rock. Particularly since it is not desirable to use extremely large sized rock because of the nature restoration objective of the Border Meuse as well as the narrow cross section that is restricted further when applying extremely large rock.

Further up the slope of the river banks, however, velocities decrease rapidly and smaller size of rock suffices to ensure bank stability. In the Border Meuse, toutvenant is abundantly present in the higher layers of soil and thus at the top end of the river bank. This allowed us to use the naturally present material for bed protection,, rather than to introduce rock on the top of the slopes.

The flow resistance of the toutvenant compares to 40/100 mm rock. Since slopes are generally steep along the Border Meuse, it was possible to limit the impact on the natural banks.

An important part of the design of bank protection works is a proper toe construction at the bottom of the slope. Hence, bed stability is also an important issue, since significant scour in the river bed may lead to damage to bank protection works. If scour potential of the bed is considered relatively low, say up to 5 meters, a falling

apron may suffice. However, at some locations a much higher scour potential is expected and the river bed must be stabilized across its full width.

Bed stabilization is necessary if the bed material is highly erosive in the new situation, if a positive gradient in the sediment transport occurs and when the equilibrium depth scour depth is large. This is typically the case in the bed section in the hydraulic bottlenecks that are inherently created when widening the river immediately downstream.

If these conditions do not apply, however, it may not be necessary to stabilize the bed. Clearly, adequate monitoring will still be necessary in this case.

V. SOME SPECIFIC DESIGN CONSIDERATIONS

A. Choosing a significant discharge for design of river training works

Along the Border Meuse, flood banks were originally designed for a flood discharge of 1/50 years. After completion of the project, the level of safety should meet the 1/250 standard. This would imply that the bed and bank protection works should meet the same standard. However, applying this standard criterion does not guarantee safety during floods with a lower frequency of occurrence, as followed from hydraulic computations. These computations showed that hydraulic circumstances of less extreme events should be taken into account locally, for instance the 1/50 flood discharge, at which the shear stresses at bed and banks were higher. This causes the design flood event to vary along the river and hence, a longitudinally varying design limit may be necessary.

It was found that the 1/50 flow velocities exceeded the 1/250 flow velocities in 12 of the 18 areas at risk with averagely 0.40 m/s. In extreme cases, flow velocities may exceed the 1/250 circumstance with 1.0 m/s – 1.5 m/s. This results in flow velocities up to 4.5 to 6.0 m/s at normative conditions [3].

In the Border Meuse case, only the 1/250 design flood has been taken into account as a first step in the design. More detailed study is yet to be carried out.

Additional to deciding on the normative discharge for bank protection design, attention should be given to the construction phases of the river adaptation works. Inherently to the scale of these works, a large period of construction with many intermediate situations may exist. In the Border Meuse case, a total of 13 locations are widened in 14 years. The order in which the locations are widened are not hydraulically and morphologically optimized (which would probably mean to start downstream and gradually work in the upstream direction). In fact, since the project is largely funded by the revenue from mining gravel in the process of widening the Border Meuse, the order is governed by other considerations, such as economics.

In terms of river training works, the above implies that during the 14 years of construction, the areas at risk may differ from the areas at risk once the entire project is completed. Still, safety must be guaranteed not only at the end of the project and afterwards, but also during the construction. It is expected that the intermediate hydraulic circumstances that occur during the construction phase, may require the use of temporary bed and bank protection works and / or result in higher design criteria where bed and bank protection works were already expected after completion [3].

Needless to say, the significant discharge for the design of bed and bank protection works after the project has been completed – and which varied for different locations along the river – may well vary from the significant discharge during construction at the same location.

The latter issue of intermediate circumstances is not yet fully addressed and requires further work.

The above shows that deciding on the normative discharge is not an easy issue.

B. The use of hydraulic models

In order to properly assess scour potential and design criteria for bed and bank protection works, reliable flow information is required. In the Border Meuse case, the flow patterns were derived from a curvi-linear WAQUA model. This state-of-the-art model provides sufficiently reliable results where the river bed is relatively level in cross-section. Due to the relatively steep slopes of the river of the Border Meuse, results are less reliable near the banks. The diagram below shows a typical cross-section of the Border Meuse [5]. It is readily seen that the flow velocity from the bed towards the bank drops dramatically according to the WAQUA model. This could lead to underestimating flow velocities on the bank.

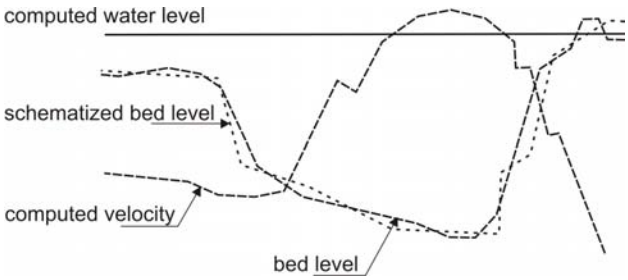

Figure 4. Cross-section with water levels and flow velocities

This problem was solved using the last reliable result near the toe of the bank as a reference. The flow velocity may then be computed assuming the water level gradient at the slope (i_{bank}) to be equal to the water level gradient in the channel (i_{bed}). This requires that a slope roughness be assumed also. Here, a Nikuradse roughness of k_s = 0,2 m was assumed. As the slope roughness depends on the applied grade of rock in the bank protection works, flow velocities on the river bank need to be solved via iteration.

Another important aspect which is not represented in steady-state flow computations is the Jones' effect [7]. The Jones' effect is the effect that during the rising stage of a flood wave, flow velocities are higher than the flow velocities with a corresponding water level after the passing of a flood wave. However, using a hydrodynamic model to incorporate this effect is generally not practical and cost-effective due to the required high resolution (on average 10 x 40 meters in the river bed) and the large number of simulations to must be run for different normative discharges and construction stages.

From theoretical analysis it was found that in the case of the Border Meuse, actual flow velocities can be some 5 percent higher than computed with the steady-state

hydraulic model for the 1/250 design flood. In the case of less extreme events, the Jones' effect will be stronger and actual flow velocities may even be 10 percent higher than computed. .

C. Maintenance & unpredictability

Having minimized bed and bank protection works through the above methodology, verification is still required. The bed and bank protections need to be included in the hydraulic model, so as to see whether the influence of these works lead to a significant change in potential areas at risk, flow velocities and so forth. In the Border Meuse case, it has been found that the flow pattern is influenced significantly and may lead to more protection works in order to establish the required safety. Rough estimates for the Border Meuse have lead to several kilometers of additional bed and bank protection works [6].

VI. CONCLUSIONS

Using the dynamic concept and methodology, it is very well possible to maintain a natural and (relatively) free flowing river after the alterations. This means: minimum bed and bank protection works whilst maintaining safety. Such a dynamic design concept adds value to nature development in the flood plains.

Normative (design) discharges need to be chosen carefully. Extreme events in terms of flooding do not necessarily result in the most extreme loads on bed and banks of rivers. It may be necessary to use different normative discharge on different stretches of the river. Moreover, when dealing with a large scale river alteration project, many intermediate hydraulic circumstances should be considered during the construction phase, during which design loads may vary. This could also lead to the need for temporary bed and bank protection works or alteration of the final works.

Hydraulic models are of the utmost importance for identification of areas at risk and for delivering boundary conditions for the design of bed and bank protection works. The results, however require careful consideration and use as well as engineering sense, especially where sudden discontinuities exist in the cross-sectional geometry. Verification of computations with an initial design of bed and bank protection works is always necessary. The influence of bed and bank protection works on the flow patterns is thus that greater lengths of bed and bank protection works may be required (using the methodology developed) because current attack increases in new areas.

In all of the above problems that face the design engineer, thorough knowledge of the geomorphology is key to minimizing protection works. Inherently attached to minimization of the protection works, monitoring of morphodynamic behavior is an important aspect of river maintenance. Rather than focusing on the upkeep of massive bed and bank protection works, focus should be put on monitoring hydraulic and morphologic changes – preferably combined with an updated hydraulic model to assess changes in (the location of) areas at risk – to support maintenance. This will add to a sustainable river development where its freedom is only limited when safety is threatened.

References

[1] Royal Haskoning, "Methodiek ontwerp rivierkundige werken Grensmaas ten behoeve van standzekerheid kaden", 2001

[2] Rijkswaterstaat Bouwdienst, "Ontwerpershandleiding granulaire oeververstерkingen Grensmaas", 2003

[3] Royal Haskoning, "Ruw Theoretisch Ontwerp, Bodem- en oeververstерkingen Grensmaas", 2005

[4] Iwaco, "Monitoringsplan Maas", 2001

[5] Royal Haskoning, "Proefproject Meers", 2001

[6] Meander Advies / Royal Haskoning, "Uitwerking RTO bodem- en oeververstерking", 2005

[7] Royal Haskoning, "schatting hysterese effect Grensmaas", 2002

[8] Rijkswaterstaat De Maaswerken, "MER Grensmaas – rivierkunde", 2003

The use of geosynthetics in scour protection

M. H. Heibaum*
* Bundesanstalt für Wasserbau (Federal Waterways Engineering and Research Institute)
Karlsruhe, Germany

I. INTRODUCTION

If scour development exceeds a tolerable limit, countermeasures are needed. Either the action has to be reduced ("active" measures) or the resistance has to be increased ("passive" measures). In both cases, geosynthetics can be rather beneficial. Changing the action means to alter the flow pattern in such a manner that scouring is stopped. This can be done for instance by river training works. Such structures may incorporate geotextiles as filter, reinforcement, containment. Increasing the resistance might be the better way if no alteration of actions can be realised, or the comparison of costs leads to such a decision.

The main application of geotextiles in scour protection is the use as filter below an armour layer that is placed to resist the hydraulic actions. But there are also geosynthetic solutions that go without armour or provide the armour themselves. A rather young and developing field are geosynthetic containers for scour protection measures. The term geosynthetic containers – Pilarczyk uses the name "geosystems" [1] – summarises all elements that use a geosynthetic fabric as containment. To improve the strength of an active or passive scour prevention structure, fill material can be reinforced by geosynthetics. Geotextiles and geogrids are increasingly used for that purpose and have proven its long lasting ability.

II. GEOSYNTHETIC SURFACE PROTECTION

The use of permanent geosynthetic surface protection nearly always incorporates geosynthetic containers, i.e. mattresses, tubes and geotextile containers

Mattresses (Fig. 1) are able to form continuous layers, usually filled with concrete or mortar. Theoretically also sand-filled mattresses can be used as it is done for landfill protection, but no worked example does exist to date to the author's knowledge. Mattresses can be placed "endless", since the fabric is sewn together as needed and then the sections of the mattress are filled. To keep the upper and the lower cloth parallel to each other, spacers are needed. These spacer strings need sufficient tensile strength (as does the warp where they are fixed) to bear the load when the mat is filled. It must not be forgotten that e.g. a concrete fill of a mattress on a slope will produce considerable hydraulic pressure inside the mattress at the toe. Mattresses of uniform thickness are inflexible and impermeable.

Figure 1. Geosynthetic mattress (Hydrotex)

To achieve a certain flexibility and permeability, mattresses consisting of columns and rows of "pillows" are used. The seams between the concrete filled pillows provide a certain permeability of the layer, if needed, and the desired flexibility for good adjustment to deformations of the subsoil. One has to consider that the dewatering capacity of these mattresses is limited, since the filtration area is restricted to the area between the corners of the pillows which might not be wide enough to guarantee an unhindered flow through the system and may cause excess water pressure below the layer. There are also limits for the mass per unit area.

Placement under water is rather difficult, since the geotextile will float before being filled. Therefore prefabricated mattresses are used that are placed by special cranes. Care has to be taken that all joints are sufficiently tight to avoid winnowing or erosion.

Figure 2. Geotextile tube for coastal scour protection (to be covered by sand) (Bradley)

Other elements that can be manufactured and placed "endlessly" are geosynthetic tubes (Fig. 2). In scour protection they can be used as toe-protection of riverbanks and coastal dikes, as core of levees, groynes and longitudinal dikes. For these applications, the geosynthetic tubes are filled hydraulically with sand or with mortar. Sand-filled tubes provide a certain flexibility. To achieve higher structures, the tubes may be stacked. Usually such defending structures are covered by sand or top soil, creating e.g.

a beach. Only during flooding or storm surges, when the beach is washed away, the protective strength of the structure is needed.

Tubes made of strong impermeable material are used as temporary flood protection. Such tubes filled with water are applied as temporary barriers to protect roads and buildings from being flooded and eroded.

Another well known scour protection of river banks is the use of gabions. Originally the casing of a gabion was made of wire mesh or steel bars. Today also geosynthetic meshes are taken as containment of the gabion (geogrids or ropes). In any case abrasion is a thread to all gabion containment.

Very successful coastal scour protection was achieved by a "wrapped wall" structure on the German island of Sylt. Layers of sand were wrapped in nonwoven geotextiles. After completion this "soft" wall was covered by sand. During one of the following storm surges, all sand was washed away and the coastline was set back several meters. Only the protected area remained in place (Fig. 3).

Figure 3. Wrapped wall protection of the Sylt coastline (Naue)

III. SURFACE PROTECTION USING GEOTEXTILES AND VEGETATION

Vegetation can and should be used for scour protection, if the hydraulic action is not too strong to destroy such natural barriers. Geosynthetics can be helpful to increase the resistance.

Grass is the most usual cover of dikes and levees. A geotextile can significantly increase the strength of a grass cover. There are various systems available, made of woven geotextiles, geogrids, geonets, geomats or geocells. In cases of very high hydraulic actions when the grass and the top soil are eroded, the surface will remain protected if the right fabric and system is used.

If other vegetation then grass is chosen that needs support against hydraulic impact, pre-planted gabion-like structures are used with success. An example is the use of elements, where the core is made of heavy stones to guarantee stability in combination with lava material to keep sufficient moisture during dry periods. To protect the (small) lava particles and the small plants from being washed away, a filter is wrapped around the unit and the strength is achieved by a confinement of geosynthetic mesh (Fig. 4). Such structures may be used for active protection (e.g. groynes, longitudinal dikes) or passive measures (e.g. bank protection).

Figure 4. Pre-planted rope gabions

Very strong protection can be build combining stacked gabions, containers or tubes with plants in between, predominantly willows (brushlayering). The geosynthetic elements provide erosion protection of the subsoil while the plants act as "ground anchors" of the whole system and grant the protection of the geosynthetic fabric against weathering. Additionally – and also for protective structures without vegetation – geosynthetic reinforcement in combination with tubes or gabions can increase the stability of such structures significantly.

IV. GEOSYNTHETIC FILTERS

If a permeable scour protection system is used, one has to pay special attention to the design of the filter between the subsoil and the armour layer. A main demand for all permeable protection systems is the increasing permeability from the subsoil to the surface. Any deviation from that principle results in more or less excess water pressure below the less permeable layer and damage may occur.

In rivers and at the coast, granular filters can be placed under water only if there is no current or only a low one. Also placing a geosynthetic filter cloth will be impossible in many cases because of the depth of the water, the flow or the wave action. The stability of the geotextile filter can be increased by certain measures. While in former times iron chains or spreaders have been used, today a geocomposite is used, namely a "sandmat", where a sand fill (or metal slag with higher specific weight) up to 9 kg/m² is confined between two geosynthetic layers. The two layers are sewn or needlepunched to keep the sand in place. Special equipment is needed for the placement of the sandmat due to its weight. Stability can be achieved up to a flow velocity of ca. 1 m/s.

On several sites sandmat solutions proved their ability. One example is the placement of a geotextile filter on the sea bottom of the Baltic Sea to build up a breakwater. Waves and currents did not agitate the filter sheet and only a storm surge resulted in some displacements. Tests proved stability when loaded by currents up to 0.6 m/s. Sandmats were also used for scour protection measures at bridge piers in rivers. The filter sheets could resist the flow successfully until the final armour layer was placed upon.

Placement difficulties were often the reason that no filter at all was used. In former times, a layer of brushwood and willow bundles has been used as a filter, when it was

not possible to place a granular filter correctly and geotextile filters had not been invented yet. This was costly and a time consuming process. Furthermore, brushwood will not function as a filter, only coarse soil may be retained efficiently. Modern fascine mattresses (or willow mats) usually comprise a base woven geotextile with willow bundles fastened on it (Fig. 5). The fascines ensure the spreading of the geotextile and the floating of the mattress whereas the geotextile acts as a filter. Today the filter can be improved by using a combined geotextile of woven and nonwoven fabric. Fascine mattresses are prefabricated according to the desired geometry on land, then they are pulled to the desired position and sunk by dumping the armour material upon.

Figure 5. Preparing a fascine mattress

Filters in scour protection measures are loaded by unsteady, turbulent, pulsating and reversing flow. Most of the design rules for geosynthetic filters are developed for unidirectional flow. Only few are reliable in case of dynamic hydraulic loading [2]. The development of excess pore water pressure in the subsoil due to the fast change in the hydraulic head complicates the proper filter design [3]. So often performance tests may be necessary, e.g. turbulence tests [4] through which it has to be proven that the amount of soil washed through the geotextile is limited and is decreasing with time when loaded by a turbulent reversing flow. Filter rules basing on the opening size (e.g. [5]) may be used as a first estimate and may be sufficient when the hydraulic load at the interface of soil and geotextile is only low, e.g. due to energy dissipation by thick armour layers.

A combined armour and filter system is provided by certain mattresses, e.g. concrete blocks cast on a woven geotextile or concrete cushion mattresses. Such block mattresses usually are assembled in the dry and placed by special cranes.

V. GEOSYNTHETIC CONTAINERS

To overcome the placement problems of filters, elements are needed that combine filter capacity and sufficient weight to withstand the hydraulic action. The protection system also should be able to adapt at any subsoil geometry (including existing scour holes) and it should be flexible to follow further scouring, e. g. at the edges of the scour protection. For such purpose, geosynthetic containers are used successfully. The container fabric can be designed as a filter, but also granular filter can be installed safely using geosynthetic containment. The container hinders the segregation of the filter fill. If the container fabric is needed only as a temporary confining material, fabric can be used that will degrade after the placement, e. g. natural fibres.

Geocontainers are really multi-purpose elements. They can be manufactured according to any demand, concerning raw material, size, shape, filtration capacity, strength etc. They are prefabricated, but filled on site (Fig. 6). The smallest size of containers, sand bags, can be used as a temporary cover layer, for instance for immediate protection of a scoured bank .

Figure 6. Filling plant for geosynthetic containers (1 m³)

In 1997 geocontainers of 1 m³ volume were used for scour protection at bridge piers in an estuary in Germany. Placement was successfully done in spite of the maximum flow velocity of 2 m/s. Around the bridge piers, the geocontainers were covered by an armour layer, but around some dolphins near the bridge, the geocontainers were left without armour. Even there till today no erosion and no degradation of the fabric has been detected.

The possibilities of geocontainers can be judged from the stabilisation of maybe the largest scour at the German coast [6]. 1m³-geocontainers were used to build up the filter layer on the slopes of a scour hole as deep as 23 m below the sea bottom (Fig. 7). In the upper part the slope was as steep as 1:1. During the works, the tidal currents had a flow velocity up to 2.5 m/s, the final revetment had to sustain flow velocities up to 5 m/s. To obtain a double line of defence concerning the filter, the fill of the geocontainer was chosen according to grain filter rules.

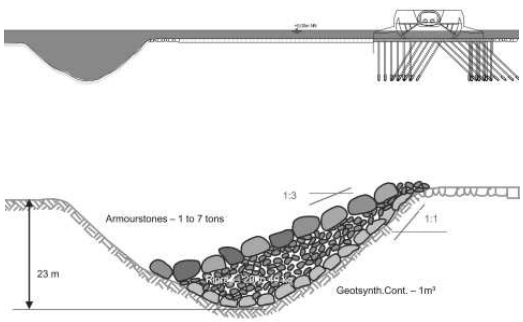

Figure 7. Scour at Eider storm surge barrier.
Cross section of scour and barrier (top)
Slope protection of scour howl (bottom)

Single geocontainers up to 2,5 m³ usually are placed by an excavator, if necessary with special clamshells or grapples (Fig. 8). Numerous geocontainers also may be dumped by side dumping vessels or split barges. Care has to be taken that the area to be protected is covered completely and no gaps remain between the containers through which the subsoil will be eroded. Special equipment allows for very precise placement of geocontainers to a depth up to 25 m.

Figure 8. Filling and transport of 2,5m³ containers in special buckets (Geofilters Australia)

The size of geosynthetic containers has to be chosen according to the hydraulic demands and to operational restrictions. From the hydraulic point of view they should be as large as possible, since the larger the lesser they are displaced. This is impressively shown by the large containers (400 tons sand fill) that are used to build artificial reefs off the Australian coast [7]). But such elements can only be placed by special equipment, e.g. split barges.

For a safe placement, for high serviceability and for sufficient long term resistance, the container material has to be chosen such that it will resist all mechanical loads. Usually there is a choice of wovens and nonwovens. The first have the advantage of high tensile strength, the second the advantage of large straining capacity. If the containment is damaged, a woven cloth might be more susceptible to crack propagation (the zip effect) than a nonwoven. Nonwoven fabric usually has a high straining capacity, so the tensile strength may be less to provide a similar resistance against mechanical impact. By allowing large deformations it will be able to withstand the impact load when hitting the ground as well as when the stones are dumped upon. For nonwoven containers of ca. 1 m³ volume, a minimum mass per unit area of 500 g/m² and a minimum tensile strength of 25 kN/m are recommended, the strain at rupture should be larger than 50%.

Since the container has to sustain abrasive forces due to rocking armour stones or due to bedload transport, any geosynthetic material used for containers needs a high resistance against abrasion. This requirement is fulfilled more easily by nonwoven fabric. The elements of any cover layer will rock and/or move in the immediate period after installation due to dynamic hydraulic loads and due to deformation of the subsoil caused by the new load. Abrasion resistance is of high importance when geotextile containers are used without armour and sediment and bedload transport is acting. If containers are additionally exposed to sunlight for at least some time, the fabric has to show a sufficient resistance against weathering in general and against UV radiation in particular. Today long lasting solutions are possible as for example groynes in Australia that did not show degradation after 10 years 879 (Fig. 9).

Figure 9. Sea groyne of geotextile containers (Hornsey)

VI. SUMMARY

Geosynthetics, predominantly geotextiles, play a major role in scour countermeasures. The most important use of geotextiles in scour protection is the installation as filter to avoid erosion ("winnowing") through the armour layer. Geotextile surface protection systems filled with concrete or mortar provide high resistance against hydraulic actions. Geotextile containers are multi purpose elements that can be used as fill (filling scour holes in flowing water, core of spurs, dikes and breakwaters), as filter (if waves of strong current hinder the placement of conventional filter layers) and as armour (filed with concrete as "hard" protection or filled with sand to provide flexible "soft" protection). Woven and nonwoven fabric may be used. Woven geotextiles can be manufactured with very high strength; nonwovens provide a high straining capacity and high abrasion resistance.

REFERENCES

[1] Pilarczyk, K.: Geosynthetics and Geosystems in Hydraulic and Coastal Engineering. Rotterdam, The Netherlands: A. A. Balkema Publishers 2000

[2] Heibaum, M.: Geotechnical filters - the important link in scour protection. In: Proceedings ICSE-2 (Second International Conference on Scour and Erosion), Singapur, 14.-17. Nov. 2004.

[3] Köhler, H.-J.: The influence of hydraulic head and hydraulic gradient on the filtration process. In: Brauns, Heibaum, Schuler (Ed.): Filters in Geotechnical and Hydraulic Engineering, pp 225-240. Rotterdam: Balkema 1993. pp.225-240.

[4] MAG: Code of Practice "Use of Geotextile Filters on Waterways (MAG)". Karlsruhe, Germany: BAW -Federal Waterways Engineering and Research Institute, 1993.

[5] Holtz, R.D., Christopher, B.R., Berg, R.R.: Geosynthetic Engineering. Bitech Publishers, Richmond, Canada, 1997.

[6] Heibaum, M.: Coastal Scour Stabilisation Using Granular Filter in Geosynthetic Nonwoven Containers. In Geotextiles & Geomembranes, Vol.17, 1999, pp.341-352.

[7] Hornsey, W..: Case studies showing the growth and development of geotextile sand containers – an Australian perspective. In: Geotextiles & Geomembranes, Vol.20, No.5. Elsevier, Oktober 2002

Turbulence Model Relation For Stability Of Bed Particles

Gijs J.C.M. Hoffmans
Ministry of Transport, Public Works and Water Management, Rijkswaterstaat, DWW, Delft, The Netherlands
(email is g.j.c.m.hoffmans@dww.rws.minvenw.nl)

ABSTRACT

For non-uniform flow conditions, the Shields diagram no longer holds because it neglects the increased turbulence intensities and fluid accelerations. The initiation of movement of individual particles is dependent on a variety of factors. Here the load is discussed in relation to the flow velocity and turbulence intensity, both depth-averaged values, and the strength is characterized by the particle diameter, the relative density and the gravity. The measure of transport or the measure of damage is expressed by the critical mobility parameter that is termed the Shields parameter. The maintenance of hydraulic structures such as bridge piers, abutments, sills, or underflow (i.e. flow under a gate) is strongly influenced by the bed stability. A model relation for predicting the stability of bed particles that includes turbulence is argued and validated by using experimental data from Aguirre Pe (2006) on uniform flow, Delft Hydraulics (1982) and Hofland (2005) on flow downstream of a backward facing step and of Escarameia and May (1992) on flow downstream of a sluice gate.

RECENT DEVELOPMENTS

As a superintendent of dikes and hydraulic engineer, Brahms (1767) tested the initiation of motion of particles experimentally. His results with respect to flow velocity and size of the particles are summarized in Figure 1. After a time period of about 150 years Shields (1936) introduced his well-known stability diagram for bed particles (Figure 2). Several model relations have been developed to improve the classical approach of Shields to bed stability, and to predict erosion in non-uniform flow regions, e.g. Izbash (1970) and Pilarczyk (1993). However, no satisfactory physical model relation has been established to provide a definite answer to the question of bed stability for practical engineering purposes.

Usually when the bed shear stress (τ_0) is close to its critical value, moving particles can be observed. Shields relation is based on the dimensionless ratio between load and strength that can be derived from considering the equilibrium of the forces on a stone.

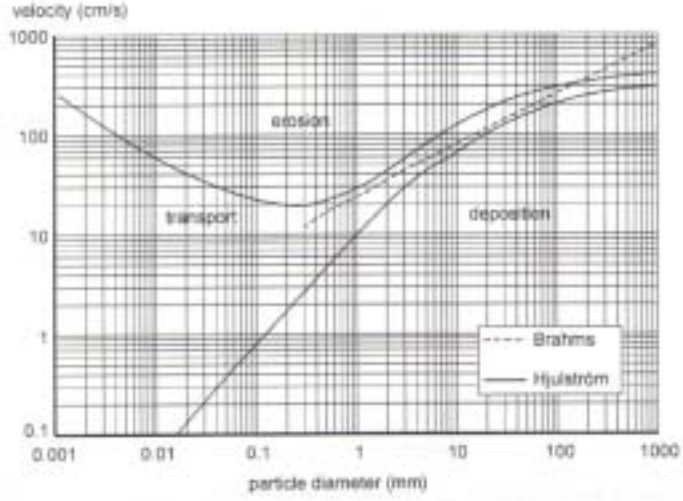

Figure 1 Initiation of motion according to Brahms (1767) and Hjulström (1935)

$$\Psi = \frac{load}{strength} = \frac{\tau_0}{(\rho_s - \rho)gd} \text{ with } \tau_0 = \rho u_*^2 \qquad (1)$$

in which Ψ is the mobility parameter, ρ_s is density of particle, ρ is density of water, g is acceleration of gravity, d is particle diameter and u_* is the bed shear velocity. Although the bed particles remain motionless when the load is less than the strength, the observation of particle movement is difficult in nature. This difficulty is a consequence of a phenomenon which is random in both time and place.

In the Shields diagram, the influence of fluctuating shear stresses on bed particles is not directly specified. In the sixties WL|Delft Hydraulics studied the initiation of movement of bed particles in detail and distinguished 7 qualitative criteria from “occasional bed particle movement at some locations” to “general transport”. These introduced criteria all lie in the broad belt originally given by Shields, thus confirming the earlier research activities of Shields.

For large particles he found a value of $\Psi_c = 0.06$. In such situations general transport will occur, however in prototype situations this must be prevented. When some damage can be accepted, a value which is half of this (or criterion 1 or 2 according to Delft Hydraulics, 1972) should be taken. When riprap structures are loaded up to design conditions more frequently, regular maintenance is necessary. Sometimes a lower value of Ψ_c ($\Psi_c < 0.02$) could be more appropriate. However, this depends on the costs on the one hand and the risk of failure of the hydraulic structure on the other hand. A cost-benefit analysis must be made to support a decisive answer.

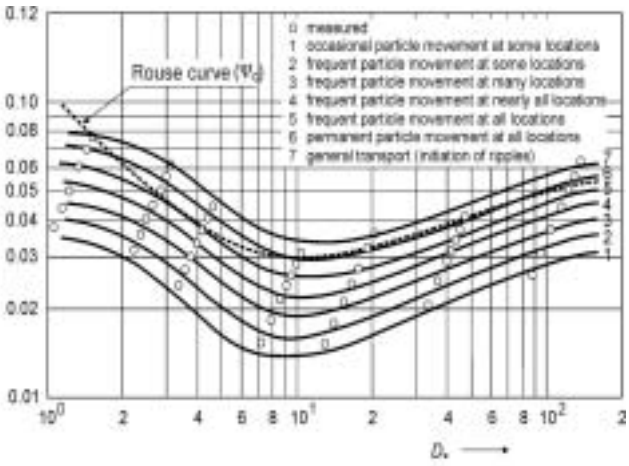

Figure 2 Diagram of Shields (1936) $D_* = d(\Delta g/\nu^2)^{1/3}$ Δ is the relative density, ν is the kinematic viscosity

The forces acting on a bed particle under turbulent flow conditions are its self weight, friction, hydraulic forces characterized as fluctuating drag and lift forces. Since the submerged weight (F_g) of the bed particle and the lift force (F_l) are most important for stone stability, they will be considered in greater detail (Booij, 1998).

$$F_l = \tfrac{1}{4}\pi d^2 p_{\max} \tag{2}$$

$$F_g = \tfrac{1}{6}\pi d^3 (\rho_s - \rho) g \tag{3}$$

in which $p_{\max}$ is the difference between the positive and negative pressure peaks. Following Hinze (1975) the standard deviation of the fluctuating pressure σ_p = (2.58 to 3.44)τ_0, which means that the pressure fluctuation on the bed in turbulent flow is about three times the bed shear stress. Emmerling (1973) found that the positive and negative pressure peaks could be up to $6\sigma_p$. With the estimate of $p_{\max}/\sigma_p \approx 6$ and $\sigma_p \approx 3\tau_0$, the maximum pressure peaks can reach up to $p_{\max} \approx 18\tau_0$. Consequently, loads from $p_{\max}$ gives:

$$\frac{F_l}{F_g} = \frac{1}{\Psi}\frac{\tau_0}{(\rho_s - \rho)gd} \quad \text{with} \quad \Psi = 0.037 \tag{4}$$

Papanicolaou (2000), investigated the characteristics of near-bed turbulence experimentally. Incipient flow conditions prevailed throughout the experiments. From his experiments he concluded that the turbulent normal stress (= $\rho\sigma_w^2$, see also equation 9 and figure 11) should be considered as the most dominant stress responsible for particle entrainment.

Unsteady eddying motions that are in constant motion with respect to each other characterize turbulent flow. At any point in the flow, eddies produce fluctuations in the flow velocity and pressure and exchange momentum and energy. Kalinske (1947) proposed the first model of bed load transport that incorporated fluctuations in the bed shear velocity.

Grass (1970) hypothesized that the value of instantaneous bed shear stress follows a Gaussian distribution. The overlapping region between the two distributions defines the critical shear stress values that correspond to particles' initiation of motion (Figure 3).

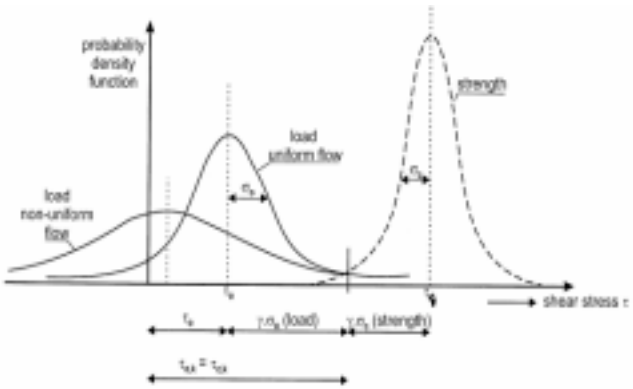

Figure 3 Probability functions of the load and strength parameters, σ_0 is the standard deviation of the instantaneous shear stress, σ_c is the standard deviation of instantaneous critical shear stress (Grass, 1970)

In the sixties Raudkivi showed that movement of a bed particle is governed by the bed shear stress (steady part) and the turbulence intensity (fluctuating part) near the bed (I_t). A bed particle could be moved by τ_0 alone (no extra bed turbulence from e.g. a mixing layer) or by I_t alone, as for example at the re-attachment point where the mean flow velocity equals zero. The two effects are not superimposed linearly, but more probably (Raudkivi, 1992, 1998).

$$f(\Psi) = \frac{\tau_0}{\rho U_0^2} + I_t^2 \tag{5}$$

where U_0 is the depth-averaged flow velocity. Jongeling *et al*. (2003) introduced a new mobility parameter (Ψ_{WL}):

$$\Psi_{WL} = \frac{\left(u_\ell + \alpha \sqrt{k_\ell}\right)^2}{\Delta g d} \quad (6)$$

in which u_ℓ is the local mean velocity near the bed, k_ℓ is the turbulent kinetic energy near the bed (see also equation 10) and α is a coefficient. Calculations with the turbulence model CFX showed that for different overflow and underflow conditions α is about 6 and the order of magnitude $O(\Psi_{WL}) = 10$. Note that $O(\Psi)$ is 0.01.

Hofland (2005) studied a single stone under non-uniform flow conditions in detail. He found that besides the classical drag force (horizontal direction) there were also turbulent wall pressures in the flow attributable to the stone movement (vertical direction). These results are consistent with other reported turbulent measurements in flow conditions well above those corresponding to particle incipient conditions. He extended equation (6) by assuming that the mobility parameter is also correlated to a characteristic length scale.

In the nineties Annandale established a model relation between stream power (load) and erosion index (strength) by analysing published and field data for a wide variety of types of earth material (Annandale, 2000, 2006).

In this study the resultant force is correlated to the turbulent kinetic energy (equation 10), so the steady part in equation (5) is assumed to be related to its fluctuating part. This hypothesis will be elaborated in the following modelling.

MODELLING UNIFORM FLOW

Nezu (1977) investigated the turbulent structure in open channel flows. Systematic measurements of turbulent open-channel flows over both smooth and rough beds were carried out using hot-film anemometers and hydrogen bubble tracers. For uniform flow Nezu found the following model relations (Figure 4):

$$\sigma_u(z) = \gamma_u\, u_* \exp\left(-z/h\right) \quad \text{for } zu_*/\nu > 70 \quad (7)$$

$$\sigma_v(z) = \gamma_v\, u_* \exp\left(-z/h\right) \quad \text{for } zu_*/\nu > 70 \quad (8)$$

$$\sigma_w(z) = \gamma_w\, u_* \exp\left(-z/h\right) \quad \text{for } zu_*/\nu > 70 \quad (9)$$

in which, σ_u , σ_v and σ_w are the standard deviations of the fluctuating velocities in the x, (= longitudinal), y (= transverse) and z (= vertical) directions respectively, h is the flow depth and γ_u (≈ 1.92), γ_v (≈ 1.06) and γ_w (≈ 1.34) are coefficients. Combining the relations for predicting fluctuating velocities and the definition of the turbulent kinetic energy, k as a function of z reads (for $zu_*/\nu > 70$):

$$k(z) = \tfrac{1}{2}\left(\sigma_u^2(z) + \sigma_v^2(z) + \sigma_w^2(z)\right) = \\ = \omega_k u_*^2 \exp(-2z/h) \quad (10)$$

in which $\omega_k = \tfrac{1}{2}(\gamma_u^2 + \gamma_v^2 + \gamma_w^2) \approx 3.3$. Hence, the depth-averaged turbulent kinetic energy is:

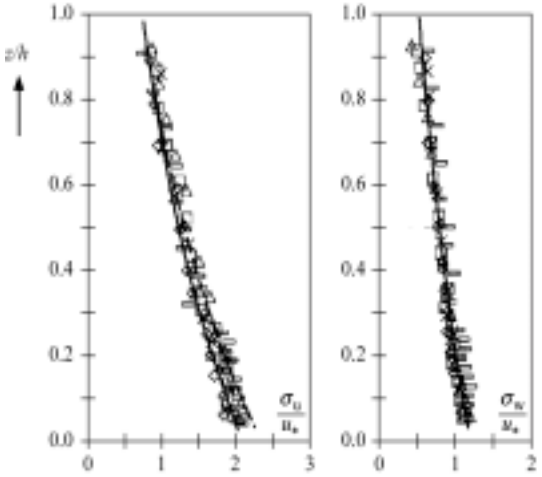

Figure 4 Distributions of turbulent flow fluctuations in uniform flow

$$k_{ave} = \frac{1}{h}\int_0^h k(z)\,dz = c_0^2\, u_*^2 \quad (11)$$

with $c_0 \approx 1.2$. The depth-averaged turbulence intensity (r_0) can be rewritten with the equation of Chézy $u_*/U_0 = \sqrt{g}/C$:

$$r_0 = \frac{\sqrt{k_{ave}}}{U_0} = c_0 \frac{u_*}{U_0} = c_0 \frac{\sqrt{g}}{C} \quad (12)$$

where C is the Chézy coefficient. For hydraulically smooth conditions (C = 75 m$^{1/2}$/s) $r_0 \approx 0.05$ and for hydraulically rough conditions (C = 25 m$^{1/2}$/s) $r_0 \approx$ 0.15. Rewriting equations (12) and (1) yields:

$$\Psi = 0.7 \frac{\left(r_0 U_0\right)^2}{\Delta g d} \quad (13)$$

Hinze (1975) had already pointed out that for uniform flow the turbulent fluctuation is related to the turbulent kinetic energy: $\sigma_p = (0.4 - 0.5)\rho k_{\max}$, with $k_{\max} \approx 6.5(u_*)^2$ resulting $\sigma_p = (2.6 - 3.4)\tau_0$. Grass (1970) found a model relation between the standard deviation of the instantaneous bed shear and the bed shear stress, σ_0/τ_0 = constant, see also Figure 3. Following Hinze and Grass, the transport or measure of damage could be modelled by only fluctuating parts. Consequently, equation (13) is valid for all types of uniform flow to predict particle stability. Note that the mobility parameter in equation (13) represents the transport or measure of damage due to a combination of a steady and fluctuating part. The advantage of equation (13) with respect to all other stability predictors is that the designer can estimate easily the strength of the top layer of the bed protection provided he knows both the load ($r_0.U_0$) and the permissible damage (e.g. Ψ_c = 0.02, see Figure 2).

VALIDATING UNIFORM FLOW

In the seventies Aguirre Pe conducted laboratory experiments to determine the influence of the bed shear stress on the sediment transport rate for different materials near the critical threshold for motion. These experiments for large relative roughness lie in the range of $0.2<h/d<30$ (Table 1).

TABLE 1
EXPERIMENTAL OVERVIEW OF AGUIRRE PE (2006)

Series	U_0 (m/s)	h (m)	Δ	d (m)	i (%)
3	0.27 – 1.03	0.06 – 0.21	0.99 – 5.90	0.05	0.5 – 9.0
4	0.22 – 0.88	0.05 – 0.21	0.99 – 5.90	0.05	1.0 – 9.0
8	0.59 – 1.01	0.12 – 0.20	1.43 – 1.92	0.064	0.92 – 5.66
11	0.60 – 0.97	0.12 – 0.21	1.65	0.055	1.13 – 4.00
12	0.31 – 0.66	0.07 – 0.19	1.65	0.037	0.25 – 5.90
15	0.63 – 1.24	0.04 – 0.12	1.62 – 1.68	0.011–0.023	1.00 – 3.00
16	0.40 – 1.16	0.02 – 0.12	1.40 – 1.54	0.023	1.00 – 3.00

In this study these experiments are used to validate equation (13). The depth-averaged turbulence intensity is calculated by applying equation (12), where the Chézy coefficient is determined by $C = U_0/\sqrt{(Ri)}$ in which R is the hydraulic radius and i is the energy slope. About 90% of the experiments lie in the range of $0.02 < \Psi < 0.05$ (Figure 5), which confirms the earlier results of Aguirre (Aguirre Pe, 1993). However, there is one difference. The vertical and horizontal axes give information on load and strength respectively. Figure 8 shows the influence of both turbulence and velocity on the movement of bed particles, which will be explained later. Usually, for uniform flow the depth-averaged turbulence intensity varies from 0.05 to 0.15, however, Aguirre Pe carried out experiments in which the ratio of flow depth and particle diameter is approximately 10, resulting high turbulence intensities ($0.2 < r_0 < 0.6$).

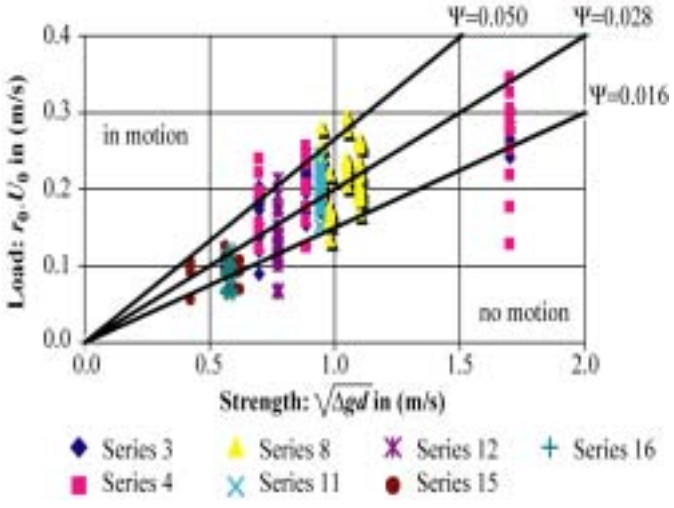

Figure 5 Initiation of motion, experimental data from (Aguirre Pe, 2006)

MODELLING OF NON-UNIFORM FLOW

The centre of the mixing layer has a very definite curvature increasing with the distance from the top of the sill (Figure 6). In the reattachment point in particular the curvature is strong. In the relaxation zone the turbulence decreases in the downstream direction e.g Hoffmans (1988). After the point of reattachment a new wall-boundary layer develops which spreads in the relaxation zone. The flow is more or less in equilibrium (uniform flow), if this boundary layer thickness equals the local flow depth. The point of reattachment is mainly determined by the magnitude of the initial slope of the scour hole and the ratio of the height of the sill and the flow depth.

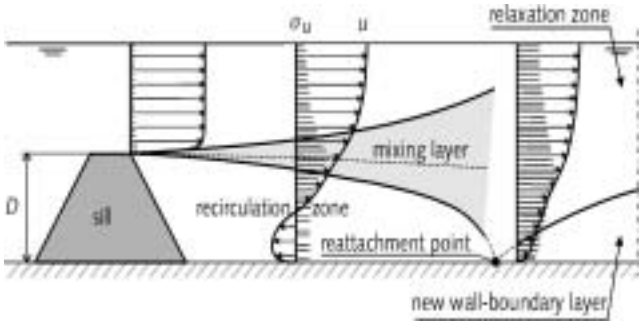

Figure 6 Flow pattern downstream of a backward facing step

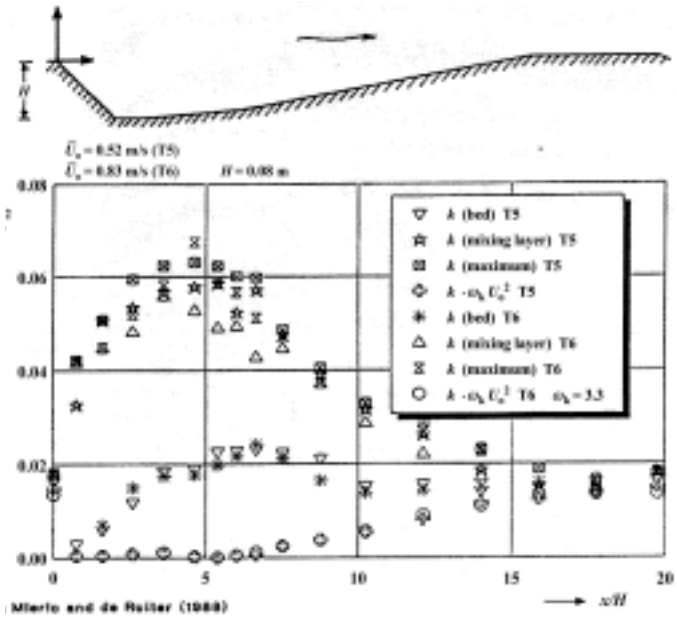

Figure 7 Calculated and measured k as function of x above an artificial dune

Non-uniform flow measurements of Van Mierlo and De Ruiter (1988) showed that the turbulence energy (k_m) in the centre of the mixing layer (with horizontal axis) grows rapidly to a maximum and vanishes where the new wall-boundary layer is well developed (Figure 7). The turbulence energy (k_0) then approaches an equilibrium value, which consists largely of turbulence generated at the bed.

Downstream of the point of reattachment, the turbulence energy (k_η) in the relaxation zone decreases gradually and becomes small compared to the bed turbulence energy (k_0) for uniform flow conditions. Earlier studies of Hoffmans (1992) have shown that in a scour hole the turbulence energy (k_b) near the bed can be represented by a combination of a certain part of the turbulence energy (k_η) and the turbulence energy (k_0) caused by the bed roughness.

$$k_b(x) = \omega k_\eta(x) + k_0(x) \quad \text{with} \qquad k_0(x) = \omega_k u_*^2(x) \tag{14}$$

Remark that in the re-circulation zone $k_0 << \omega k_\eta$ ($\omega \approx 0.3$), which can be ascribed to the small flow gradients close to the bed. To analyse the decay of the turbulence in the relaxation zone, an analogy with the decay of the turbulence energy and the dissipation in grid turbulence can be used (Launder and Spalding, 1972). When the zone downstream of the point of reattachment is considered and the production and diffusion terms in the transport equations of the turbulence energy and the dissipation are neglected, k_η can be given by (Booij, 1989):

$$k_\eta(x) = k_m \left(\frac{x - x_R}{\lambda} + 1 \right)^{\alpha_k} \tag{15}$$

where x_R ($\approx 6D$) is the x-coordinate where the flow reattaches the bed, D is the height of the sill, λ ($\approx \frac{1}{2} c_\lambda h/\beta_m$) is a relaxation length, c_λ (≈ 1.2) is a relaxation coefficient, β_m (≈ 0.09) is the angle of the mixing layer and α_k (≈ -1.08) is a coefficient that is directly related to the turbulence coefficients used in k-ε-models.

The hypothesis of self-preservation (Townsend, 1976) requires constant turbulence energy in the mixing layer up to the point where the boundaries have reached the surface and the bed. An appropriate value is (Figure 7):

$$k_m = C_k \overline{U}_0^2 \tag{16}$$

in which C_k (≈ 0.045) is a coefficient and $\bar{U}_0$ is the depth-averaged flow velocity above the sill. For a backward facing step the value of C_k is approximately equal to 0.045, whereas for a sill with gradually slopes C_k is smaller than 0.045. In fact the value of C_k depends on the configuration of the sill. However, this dependency is not examined here.

In analogy of (11) the turbulence energy averaged over the depth, from which r_0 can be determined downstream of a sill, can be given by:

$$\frac{1}{h} \int_0^h k(x,z)\,\mathrm{d}z = \beta_k k_\eta(x) + c_0^2 u_*^2(x) \tag{17}$$

where β_k (≈ 0.5) is a coefficient. If the geometry of the tests consists of a horizontal bed where the flow is sub-critical above a sill, the following relation for r_0 can be deduced for $L > 6D$ (equation 18):

$$r_0 = \sqrt{0.0225 \left(1 - \frac{D}{h}\right)^{-2} \left(\frac{L - 6D}{6.67\,h} + 1\right)^{-1.08} + 1.4 \frac{\sqrt{g}}{C}}$$

For reasons of safety the length L of the bed protection will always extend beyond the point of reattachment. More than 250 experiments were used to calibrate and verify (18). In these laboratory experiments both the hydraulic conditions and the geometrical parameters were varied (Hoffmans, 1993). In the re-circulation zone the load is at maximum. In this region the contribution of the steady part (equation 5) is neglect able with respect to the fluctuating part, see also Figure 7, so equation (18) simplifies to:

$$r_0 = \sqrt{0.0225 \left(1 - \frac{D}{h}\right)^{-2}} \tag{19}$$

The turbulence intensity increases when the height of the sill increases in relation to the tail water depth. Equation (19) yields reasonable results if the ratio between D to h is smaller than 0.7 ($r_0 < 0.5$). Note that for uniform flow the steady part is not neglected but correlated to the fluctuating part.

VALIDATION FOR NON-UNIFORM FLOW

Within the framework of the Dutch Delta Works, experience was obtained in predicting the dimensions of rock fill closure dams under tidal conditions. At Delft Hydraulics (1982) several experiments were performed on broad-crested weirs in which the discharge was constant in time. Variable parameters were the height of the sill D, the tail water depth h, the discharge, the form of the sill, the density of the bed particles and the size of the particle diameter. The objective here is to verify equation (13) for non-uniform flow conditions. Since no turbulence parameters were measured, r_0 is calculated using (19).

TABLE 2
EXPERIMENTAL OVERVIEW OF DELFT HYDRAULICS (1982)

Serie	U_0 (m/s)	h (m)	Δ	d (m)	D (m)
Criteria 1-2	0.21 – 0.92	0.10 – 0.40	1.63 – 1.68	0.01 – 0.03	0.04 – 0.25
Criteria 5-6	0.28 – 1.13	0.10 – 0.40	1.63 – 1.68	0.01 – 0.03	0.04 – 0.25

Figure 8 shows the results for both uniform and non-uniform flow. Although in the experiments of Aguirre Pe (2006) and Delft Hydraulics (1982), criteria 5-6 show scatter, all these experiments lie in the same broad belt: $0.04 < \Psi < 0.06$. The

experiments of Delft Hydraulics (1982) representing the smaller damage, criteria 1-2, also indicated a trend. Raudkivi (1992) stressed this phenomenon qualitatively, equation 5. Though the experiments do not confirm his hypothesis in a quantitative way, the results are promising.

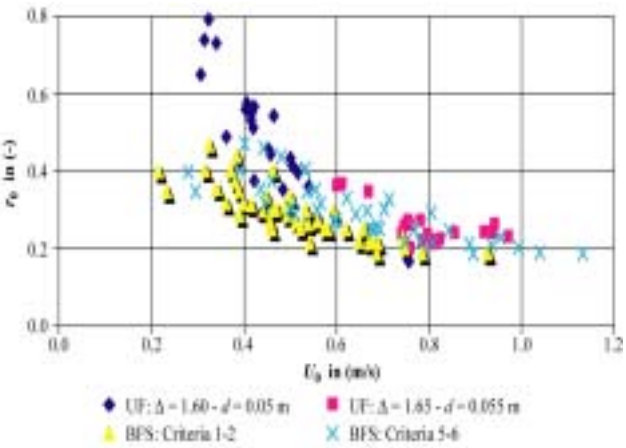

Figure 8 r_0 as function of U_0 for critical conditions of movement UF (= Uniform Flow), experimental data series 3, 4 and 11 from Aguirre Pe (2006) see also Figure 5, BFS (= Backward Facing Step), experimental data from Delft Hydraulics (1982)

Escarameia and May (1992) examined the effects of flow velocity and turbulence level on the stability of riprap placed on horizontal channel beds and sloping banks in highly turbulent environments. Experiments were carried out in a large flume where a sluice gate was installed to produce a hydraulic jump with associated turbulence upstream of the test section. Tests were carried out with several different stone sizes (d varied between 4.6 and 11.8 mm) on a flat bed, and at various turbulence levels (0.3 m/s < U_0 < 1.2 m/s; 0.15 m < h < 0.35 m).

Figure 9 shows the load as a function of the strength. The scatter of the measurements represents the measure of transport. To calculate the Shields mobility parameter using (13) two assumptions have been made. The local turbulence intensity Ti(10%), which is defined as Ti(10%) = σ_u/u(10%) with σ_u(10%) is the standard deviation of the fluctuating flow velocity at 10 % of the flow depth, u is the local mean flow velocity at 10% of the flow depth, is assumed to be equal to the depth-averaged turbulence intensity, thus Ti(10%) ≈ r_0 and secondly, u(10%) equals U_0.

Hence, the Shields mobility parameter depends on both the turbulence intensity near the bed and the bed shear stress. Again the results shown in Figure 10 support the hypothesis of Raudkivi (1992), equation (5).

Hofland (2005) described experimental series in which the stability of a single stone under uniform and non-uniform flow is studied in detail, Figure 11. He used a 2D-PIV (= Particle Image Velocimetry) technique and three piezometric pressure sensors on top of a rough bed of stones at the threshold to instability. They were able to correlate the movement of a single stone to a mechanism of small-scale lift fluctuations followed by a large-scale drag force.

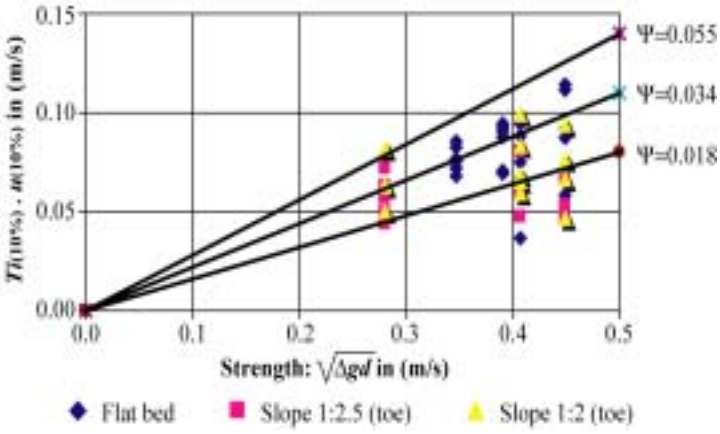

Figure 9 Initiation of motion, experimental results of Escarameia and May (1992)

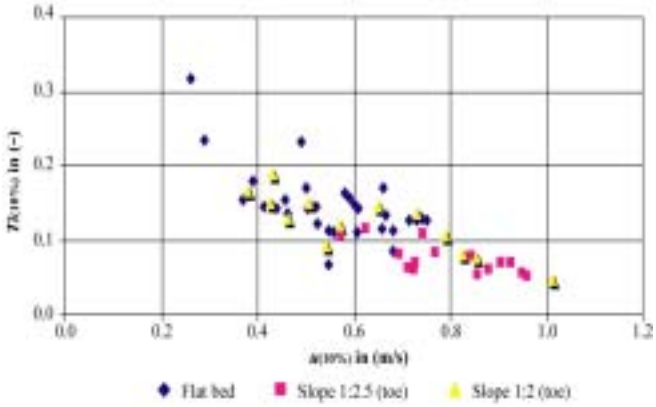

Figure 10 Ti(10%) as function of u(10%) for critical conditions of movement experimental results of Escarameia and May (1992)

When integrated over a stone the Turbulent Wall Pressure (TWP), will result in a net force on the stone and therefore contribute to the fluctuating force on a stone (vertical axis). The Quasi Steady Forces (QSF) are caused by pressure difference due to streamline curvature and represent the acceleration of water in the stream wise direction (horizontal axis). Hofland showed that the QSF account for the drag force (or bed shear stress) on exposed stones. Since the experiments of Escarameia and May (Figure 10) and the measurements of Hofland (Figure 11) are expressed by different turbulence parameters, assumptions will be made when discussing them. The local mean flow velocity at 10% of the flow depth is assumed to be equal to the characteristic flow velocity in the vicinity of the stone, thus u(10%) ≈ u_A. Moreover, the fluctuating flow velocities in

both the longitudinal and vertical directions are of the same order, thus $\sigma_u \approx \sigma_w$ or $Ti(10\%) \approx \sigma_w/u_A$. For uniform flow Hofland found that u_A lies in the range of $\sqrt{0.2} < u_A < \sqrt{0.5}$ with $\sqrt{0.01} > \sigma_w > \sqrt{0.003}$. The experiments of Escarameia and May (1992) show that the turbulence intensity $Ti(10\%)$ varied from 0.10 to 0.18 for $0.45 < u(10\%) < 0.77$. When the same velocity range was considered Hofland found $0.08 < Ti(10\%) < 0.22$, which is a remarkable good result. In addition the results of Hofland show a trend for non-uniform flow, the TWP tend to a maximum value for small values of QSF, which confirms the hypothesis of Raudkivi in a qualitative way.

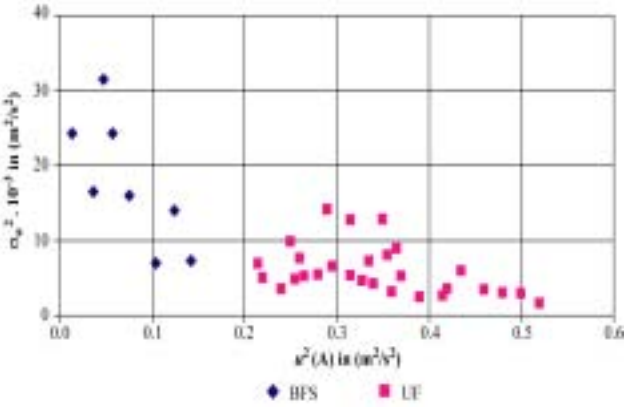

Figure 11 Classification of events. $u^2(A)$ and σ_w^2 indicate QSF and TWP forces respectively, $u(A)$ is a characteristic flow velocity near stone. The measurements were obtained just before stone movement, BFS: Backward Facing Step, UF: Uniform Flow (Hofland, 2005).

CONCLUSIONS

The previous analysis has shown that to make an accurate determination of the size of bed protection in non-uniform flow it is necessary to take explicit account of the influence of turbulence. Downstream of hydraulic structures the flow velocity profile differs from both the standard logarithmic profile and also from the profiles of the turbulent kinetic energy. A wide variety of velocity and turbulence profiles may occur (Figure 6).

The depth-averaged method discussed in the present paper has to be considered as a useful tool for designers. The influence of turbulence is given by the parameter r_0. For sills an analytical expression can be used to estimate the depth-averaged turbulence intensity (equation 18).

The depth-averaged flow velocity represents the magnitude of the drag force in the horizontal direction. The depth-averaged turbulence intensity is representative for the hydraulic characteristics in the vertical direction. Consequently, equation (13) supports the hypothesis of Raudkivi (equation 5) for both uniform and non-uniform flow.

For uniform flow conditions equation (13) confirmed earlier investigations. Though the simplified model assumptions for a backward facing step still present a challenge, the validation of equation (13) using the experiments of Delft Hydraulics (1982) are promising. For other hydraulic structures such as bridge piers, abutments and underflow, information about turbulence intensities can be gained from sophisticated turbulence models, by performing specific flow experiments or by deriving analytical solutions based on the transport equations of the turbulence energy and the dissipation, for example, equation (18).

The best ways to relate critical stone size to the flow conditions near the bed have been proposed by Jongeling *et al.* (2003) and Hofland (2005). However, at present their results have to be validated for prototype situations. Moreover, they still have to establish precise criteria for designing the bed protection in the vicinity of hydraulic structures, see Shields diagram, criteria 1 to 7.

References

[1] Aguirre Pe, J. and R. Fuentes, 1993, Stability and weak motion of riprap at a channel bed, Proc. River, Coastal and Shoreline Protection, John Wiley Sons, New York.

[2] Aguirre Pe, J. 2006, Personal Communications.

[3] Annandale, G.W., Smith, S.P and Tamara Butler, 2000, Scour of rock and other earth materials at bridge pier foundations, Proceedings ISSMGE, TC33, Melbourne.

[4] Annandale, G.W., 2006, Scour technology, Mechanics and engineering practice, McGraw Hill, New York.

[5] Booij, R., 1989, Depth-averaged k-epsilon model in Odyssee, Report No. 1-89. Technical University of Delft, Delft.

[6] Booij, R., 1998, Erosion under a geometrical open filter, Report 2-98 (in Dutch), Technical University of Delft, Delft.

[7] Brahms, A., 1767, Anfangsgründe der Deich und Wasserbaukunst, Herausgegeben vom Marschenrat bei Schuster in Leer, (in German) Aurich (Provincial Library Fryslan).

[8] Delft Hydraulics, 1972, Systematical investigation of two- and three dimensional local scour, Investigation M648/M863 (in Dutch), Delft Hydraulics, Delft.

[9] Delft Hydraulics, 1982, Stability of bed protection downstream of hydraulic structures,Investigation M1834/S543, part I and II (in Dutch), Delft Hydraulics, Delft.

[10] Emmerling, A.,1973, The instantaneous structure of the wall pressure under a turbulent boundary layer flow (in German), Max-Plank-Institut für Strömungsforschung, Bericht 9.

[11] Escarameia, M. and R.W.P. May, 1992, Channel protection; turbulence downstream of structures, Report SR 313, HR Wallingford.

[12] Grass, A.J., 1970, Initial instability of fine bed sand, Hydraulic Division, Proceedings of the ASCE, Vol.96, No.HY3, p.619-632.

[13] Hinze, J.O., 1975, Turbulence, Second edition, McGraw-Hill Book Company, New York.

[14] Hjulström, F., 1935, The morphological activity of rivers as illustrated by River Fyris, Bull. Geol. Inst. Uppsala, Vol. 25, Ch III.

[15] Hoffmans, G.J.C.M., 1988, Damping of turbulence parameters in relaxation zone, Report No.10-88, Technical University of Delft, Delft.

[16] Hoffmans, G.J.C.M., 1992, Two-dimensional mathematical modelling of local scour holes, Doctoral thesis, Technical University of Delft, Delft.

[17] Hoffmans, G.J.C.M., 1993, A study concerning the influence of the relative turbulence intensity on local scour holes, Ministry of Transport, Public Works and Water Management, Delft.

[18] Hofland, B., 2005, Rock & Roll, Turbulence-induced damage to granular bed protections, Doctoral thesis, Technical University of Delft, Delft.

[19] Izbash, S.V. and Kh.Yu. Khaldre, 1970, Hydraulics of river channel closure, Buttersworths, London.

[20] Jongeling, T,H,G., Blom, A. Jagers, H.R.A, Stolker, C. and Verheij, H.J., 2003, Design method granular protections. Technical Report Q2933/Q3018 (in Dutch), Delft Hydraulics, Delft.

[21] Kalinske, A.A., 1947, Movement of sediment as bed load in rivers, Transactions, American Geophysical Uninion, Vol.28, No.4.

[22] Launder, B. E. and D.P. Spalding, 1972, Mathematical models of turbulence, Academic Press, London.

[23] Mierlo, van M.C.L.M., and J.C.C. de Ruiter, 1988, Turbulence measurements above dunes, Report Q789, Vol. 1 and 2, Delft Hydraulics, Delft.

[24] Nezu, I., 1977, Turbulent structure in open-channel flows (translation of doctoral thesis published in Japanese), Department of Civil Engineering, Kyoto University, Kyoto.

[25] Papanicolau, A.N., 2000, The Role of Near-Bed Turbulence in the Inception of Particle Motion, International Journal of Fluid Dynamics (2000), Vol. 4, Article 2.

[26] Pilarczyk, K.W., 1993, Simplified Unification of stability formulae for revetments under current and wave attack, Proc. River, Coastal and Shoreline Protection, John Wiley Sons, New York.

[27] Raudkivi, A.V., 1992, Personal Communications.

[28] Raudkivi, A.V., 1998, Loose Boundary Hydraulics, Balkema, Rotterdam.

[29] Shields, A., 1936, Anwendung der Aehnlichkeitsmechanik und der Turbulenzforschung auf die Geschiebebewegung, Mitteilungen der Preusischen Versuchsanstalt für Wasserbau und Schiffbau, (in German) Heft 26, Berlin NW 87.

[30] Townsend, A.A.,1976, The structure of turbulent shear flow, Cambridge University Press

Numerical Modeling of Damage to Scour Protections

Bas Hofland[*,**], Rob Booij[*]
[*] Delft University of Technology / Env. Fluid Mechanics Section, Delft, The Netherlands.
[**] Presently: WL | Delft Hydraulics, Delft, The Netherlands. Email: Bas.Hofland@wldelft.nl.

I. INTRODUCTION

Granular scour protections of rock or stone are often applied near hydraulic structures like groins, weirs, sluices, etc. The flow near these structures is usually non-uniform. However, the stability parameter of Shields [1], which is the basis of most design formulae, was derived for uniform flows. Therefore physical modeling is still necessary for the design of bed protections in new configurations. Otherwise large safety factors have to be used. Contrary to this lack of knowledge, the computation of the hydrodynamics has increased immensely during the last decades. In this chapter we try to make the link between the output of such computer models and the stability of bed protections. Hereto a methodology for designing bed protections is developed, which is partly based on the approaches developed by References [2,3,4]. This model is intended in first instance for stationary, non-uniform flows.

In this paper first the general form of the stability model is described. The flow attack is assessed in a Shields-like parameter. The bed response (i.e. damage) is described by the (dimensionless) entrainment of bed material. The aim is to find a stability parameter that can predict the entrainment rate for various flow conditions. Next, the numerical method that is to be used to calculate the flow attack is assessed. The method that will be used is a 3D, Reynolds-averaged Navier-Stokes (RANS) model with k-ε turbulence closure. The turbulence intensity, which is an output of such a model, is needed for the estimation of damage to scour protections. Then the formulation of the stability parameter is determined. The parameter weights the velocity sources in the water column above the bed using a turbulence length scale. Then the relation between the new stability parameter and the entrainment rate is calibrated. To this end existing measurements are reanalyzed. Lastly it is evaluated how (already available) computations with a RANS model can predict the entrainment, and how the method can be used in design procedures.

II. THE MODEL

A. Flow attack

A stability parameter of the form of the Shields parameter is used to quantify the hydraulic attack on the bed. Its general form is:

$$\Psi_{gen} = U^2 / \Delta g d \quad , \qquad (1)$$

where Δ is the dimensionless submerged density of the rock, ρ_r/ρ - 1, ρ_r is the density of rock, ρ the density of water, g the gravitational acceleration, and d the stone diameter (usually the median nominal diameter d_{n50} is used for this). U is a typical velocity scale. For uniform flows the shear velocity u_* is typically used in the Shields parameter. Reference [4] use a stability parameter of the form:

$$\Psi_{WL} = < (\bar{u} + \alpha\sqrt{k})^2 >_{h/5+5d} / \Delta g d_{n50} \quad , \qquad (2)$$

where $\bar{u}$ is the mean flow velocity, α is an empirical parameter, k is the turbulence kinetic energy, and $<\ldots>_{h/5+5d}$ is a spatial average over a distance of $h/5+5d$ above the bed.

Here a new parameter Ψ_{new} with a new velocity term is used

B. Bed response: Entrainment parameter

The numerator in the parameter Ψ_{gen} is a measure of the flow attack on the bed. If the mechanisms causing stone displacement are correctly represented in Ψ_{gen}, with properly calibrated coefficients, then the value of Ψ_{gen} should determine the bed response for a variety of flow conditions – uniform and non-uniform. To check whether this is the case, or to which extent, a clearly defined and quantified measure of the bed response is required. This quantity should be dependent on the local hydrodynamic conditions, and should represent damage to bed protections.

No clearly defined measure of damage is available at present. In physical model tests an arbitrary number of stones moving from an arbitrarily sized area of the bed protection is usually chosen as the initiation of damage. Also a time dependence should be added. Damage to a bed protection under a steady flow increases in time as due to turbulence fluctuations a stone is moved sporadically. The quantity that represents the volume (or the number) of stones that is picked up from a bed protection per unit of bed area and time is the entrainment rate of stones, E. This is a clearly defined quantity, which

This research was financially supported by Royal Boskalis Westminster and Van Oord.

can be compared between different investigations in its dimensionless form:

$$\Phi_E = E / \sqrt{\Delta g d_{n50}} \quad , \qquad (3)$$

The entrainment rate has the advantage that it is completely dependent on the local hydrodynamic parameters. Conversely, the transport and the deposition of bed material are dependent on hydraulic loads upstream; all the stones passing a certain cross section (i.e. transport) have been entrained upstream of this cross section. This means that it is fundamentally impossible to make a transport or deposition formula for non-uniform flow based on the local hydrodynamic forces only.

To clarify this we can regard the sediment continuity equation – which was used by Reference [2] to estimate the evolution of damage in time. It can be rewritten as:

$$\mathrm{d}y_b / \mathrm{d}t = -(E-D) / (1-n) \quad , \qquad (4)$$

where y_b is the bed level, n is the porosity of the rock, and D is the deposition rate. Per definition $D \geq 0$ and $E \geq 0$. At places with maximum damage (high hydraulic loads), the deposition rate will be small. Therefore, if the non-local parameter D is omitted, the following time-dependent damage indicator is obtained:

$$\Delta y_{b,t1,max} = 1/(1-\varepsilon) \int_0^{t1} E \, \mathrm{d}t \quad , \quad (5)$$

where the bed protection was constructed at $t = 0$, and $\Delta y_{b,t1,max}$ is the maximum lowering of the bed at $t = t_1$, which is per definition larger than or equal to the real lowering of the bed. For a thin protection layer $\Delta y_{b,t1,max}$ will probably have to be less than a few percent of the stone diameter to achieve a safe design. By neglecting the deposition of the stones a conservative (safe) estimate of the damage level is obtained. It was already mentioned that at places with maximum damage the deposition is expected to be small. Therefore $\Delta y_{b,t1,max}$ will be close to the real lowering of the bed, $\Delta y_{b,t1}$.

Using eq. (4) to estimate damage could lead to a false sense of safety. For example, if we imagine a stretch of bed protection with large and equal entrainment and deposition rates, we would not expect any damage according to eq. (4). Still many stones are picked up and deposited over time, increasing the chance that holes will develop in the bed protection, which could lead to failure of the protection layer.

Also when a more classical critical-value stability approach is adopted, a low threshold value of the dimensionless entrainment parameter Φ_E can be used as the mobility of the bed that is regarded as 'initiation of motion'. The stability parameter corresponding to that Φ_E can subsequently be determined. This critical stability parameter can then be used for designing bed protections.

C. Aim

The aim of this paper is to find a damage predictor for non-uniform flows. From the preceding it follows that this can be accomplished if an expression for Φ_E is found, that includes the hydraulic forces in a representative way. The expression for Φ_E should govern the bed response, expressed by the (dimensionless) entrainment rate. Hence there should be a unique relation:

$$\Phi_E = f(\Psi_{gen}) \quad . \qquad (6)$$

It must be determined which flow parameters can be used in the numerator of Ψ_{gen} and how they can be obtained from a numerical calculation. Measured entrainment-flow combinations for a range of non-uniform flows will be used to find the formulation of Ψ_{gen} that gives a relation with the least scatter. If calibrated and verified, this relation can be the basis for a method of designing bed protections using numerical flow calculations.

III. Numerical model

The use of turbulence resolving simulations like large eddy simulations (LES) for the design of scour protections is computationally rather expensive, as flow during a long time has to be modeled, so the use of a Reynolds-averaged Navier-Stokes (RANS) model is preferred. These models directly compute the mean flow field, but need a closure to determine the turbulence viscosity. The k-ε model (k is the turbulence kinetic energy and ε is the turbulence dissipation) is widely used for this in the civil engineering practice, which makes it a logical choice to use. The k-ε model is a semi-empirical model with some fundamental shortcomings. The major one is that the k-ε model gives one turbulence length scale per point, so one cannot distinguish between different scales of turbulence at one position, e.g. scales connected to bottom turbulence and free turbulence. Still, in certain cases it can give a fair estimate of the mean flow and turbulence properties. However, assuming that the model gives the exact values for mean flow velocity $\bar{u}$, k, ε, and pressure p, still some problems remain.

1. when knowing k, the ratios $\sigma(u)^2:\sigma(v)^2:\sigma(w)^2$ (i.e. resp. the standard deviation of the streamwise, upward and transversal velocity components) are still unknown.
2. the exact shape of the probability distribution of the velocity and therewith the probability of occurrence of extreme forces on the bed material, is not known (as k only describes the second-order moment of the velocity fluctuations).
3. the usual boundary value for the near-bed value of k is: $k \sim u_*^2$. So using this k in the stability parameter in the form of eq. (1) will effectively yield the classical Shields parameter without turbulence effects. And this is what we wanted to avoid in the first place.

The latter problem can be solved by using velocity sources from higher up in the flow. Reference [4] use this method. The problem with using sources away from the bed, however, is that the main (quasi-steady) forces are determined by the flow velocity very close to the stones, so it appears that velocities from higher levels in the water column cannot be used.

A. Why use non-local parameters?

Only near-bed velocities cause the quasi-steady forces on bed material. Therefore it does not seem correct to use

velocities higher up in the flow. However, it has just been mentioned that using k obtained from a k-ε model at the grid point nearest to the bed will give a trivial answer that does not solve the problem of explicitly modeling the effect of turbulent fluctuations. But if we regard another previously mentioned 'problem' – that k only represents the second-order moments of the velocity components – it becomes possible to justify the use of values of k and $\bar{u}$ from other positions in the vertical. The velocities at higher levels in the flow, where the length scale of the turbulence usually is of the order of the water depth, can determine the higher-order moments of the near-bed velocity fluctuations. A large length scale at a certain elevation implies that the turbulence structures from that elevation will have a greater chance of reaching the bed sporadically, bringing velocities of the order of magnitude of the velocity at that depth to the bed. These fluctuations may be rare and intermittent, and therefore hardly alter the intensity (i.e. $\sigma(u)^2$) of the turbulence near the bed, while the probability of extreme forces on the bed is increased. This makes it plausible that parameters at different depths can – or rather should – be used to determine the extreme values of u near the bed.

In light of the above the stability model based on the output of a hydrodynamic RANS model with a k-ε turbulence closure is developed in the next section.

IV. NEW STABILITY PARAMETER USING RANS OUTPUT

In this section possible ways to use the computed turbulence parameters in the estimation of damage are discussed. A new model is developed which estimates a representative 'maximum velocity' near the bed, and hence the 'maximum' quasi-steady force on the bed. An important new element is that the relative importance of velocity sources above the bed is determined using the relative length scale of the turbulence.

A. Incorporating the length-scale of the turbulence

A simple physical argument is used to determine a way to incorporate the turbulence length scale in the stability parameter. Both in uniform flows and non-uniform flows large-scale structures with increased u with a vertical size of the order of the water depth were seen to be present at the time of entrainment of the stone [5,6]. This is a rationale for using velocity sources from the whole water column for estimating the quasi-steady forces. Figure 1 shows a simplified flow structure. This is used to obtain a relation between the computed parameters at a certain elevation and the (extreme) velocities that are subsequently caused near the bed.

If we assume that the large-scale vertical velocity fluctuation at height y above the bed is proportional to $\sqrt{k}$, and has a certain horizontal length scale, L_H, and we further assume that this is part of a large rolling structure with a vertical size equal to $2y$, then conservation of mass ($y\,u'_b \approx \tfrac{1}{2} L_H v'$) leads to the approximate relation:

$$u'_b \sim \sqrt{k}\, L_H / y \quad . \qquad (7)$$

As the flow structure also transports the mean momentum to the bed, we pose that the following velocity estimate could be used in a stability parameter:

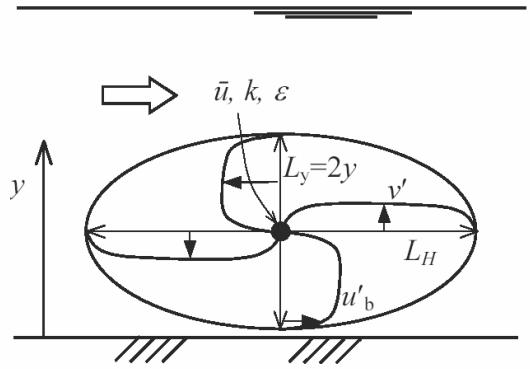

Figure 1. Model of large-scale eddy that causes damage.

$$u_b \sim (\bar{u} + \alpha\sqrt{k})\, L_H / y \quad . \qquad (8)$$

Here $(\bar{u} + \alpha\sqrt{k})$ is an estimate of the temporal 'maximum' of the local velocity, consisting of the mean velocity plus a few times the standard deviation, as expressed in the term $\alpha\sqrt{k}$, in which α is a calibration factor. As these 'maximum' velocities only sporadically reach the bed (they do not influence k near the bed), the spatial maximum over the depth of this temporal 'maximum' is taken to represent the extreme velocity near the bed governing the low-mobility entrainment:

$$u_{b,max} \sim \max\,[(\bar{u}+\alpha\sqrt{k})\, L_H/y] \quad . \qquad (9)$$

The horizontal length scale is dependent on the kind of turbulence that is present.

In addition it is necessary to restrict the intensity $\sqrt{k}$ to the *large-scale* fluctuations, as only these fluctuations will reach the bed. For instance, it is not likely that a beginning mixing layer – that gives an intense small peak in the turbulence intensity – influences the stability of the bed.

In case we use a k-ε model, we do not obtain information in the spectral domain, but we do obtain spatial information. We can argue that if a large-scale structure exists at a certain height, it will influence the turbulence intensities at all places surrounding this height that are not more than half its length-scale away from this point. Therefore, for the estimate of the large-scale intensity at height y we take the mean value of the turbulence intensities over a height between y +/- $L_H/2$ to be the turbulence sources from that height that influence bed stability. In other words: the vertical turbulence intensity profile will be filtered by taking the moving average over the (variable) width of L_H, written as $<\ldots>_{LH}$.

After this filtering operation we multiply the resulting 'maximum velocity' with L_H/y in order to obtain the influence of the turbulence at height y on the bed. As a final step the velocity source causing the largest 'maximum velocity' near the bed is taken as the velocity that governs the damage to the bed. Therefore the (vertical spatial) maximum of the (temporal) 'maximum velocity' $(\bar{u} + \alpha\sqrt{k})\, L_H/y$ above the bed is chosen as the velocity to be used in the numerator of the new stability parameter:

$$\Psi_{new} = \max\left[<\bar{u}+\alpha\sqrt{k}>_{LH} L_H/y\right]^2/\Delta g d \quad . (10)$$

Next we need an expression for L_H.

B. *Determination of the length scale*

Two methods were tried to obtain the appropriate length scale of the turbulence, L_H:

1. Using the dissipation length, L_ε
2. Using the Bakhmetev mixing length

From the calculated parameters k and ε, the dissipation length scale:

$$L_\varepsilon = k^{3/2}/\varepsilon \quad , \quad (11)$$

can be obtained. This length scale might be used as L_H in eq. (9). It is calculated by the flow model, so it is potentially a good length scale to use. In order to check whether this length scale can be used, it was compared to a measured length scale, the measured integral streamwise length scale, which is defined as [7]:

$$L_x = u_c \int_0^\infty \rho_{uu}(\tau)\, d\tau \quad , \quad (12)$$

where $\rho_{uu}(\tau)$ is the auto covariance of u, τ is a time lag, and u_c the convection velocity of the flow structures. This can be determined from measurements. This length scale seemed to be entirely not proportional to the calculated length scale L_ε (see for instance Figure 3 further on), so its use was aborted.

As the use of the calculated length scale L_ε was aborted, another length scale is used. This is the mixing length according to the Bakhmetev distribution, which is not dependent on the calculated turbulence field. This distribution is derived for a uniform open-channel flow but will be used for all flows. It reads:

$$L_m = \kappa h \gamma\sqrt{(1-\gamma)} \quad , \quad (13)$$

where $\gamma = y/h$, h is the water depth and κ is the Von Karman constant. As we use this length scale distribution for non-uniform flows, it is more an estimate of the largest possible structure due to the geometrical constraints of the bed and the free surface than an exact relation for the (integral) length scale. If we make this length scale dimensionless with the height we obtain the simple relation:

$$L_m/y = \kappa\sqrt{(1-\gamma)} \quad , \quad (14)$$

This has a maximum near the bed, so when this is used in the stability parameter in eq. (9) it corresponds to fully taking into account the velocity sources near the bed, with a reduction towards the free surface. Intuitively this seems a very reasonable weighting function for the velocity sources.

As the Bakhmetev mixing length is chosen as the length scale to use, the new stability parameter is formulated as:

$$\Psi_{Lm} = \left(\max\left[<\bar{u}+\alpha\sqrt{k}>_{Lm} L_m/y\ \right]\right)^2 / \{\Delta g d\} \ . \quad (15)$$

The different steps in finding the dominant velocity near the bed using this model are illustrated in Figure 2 for a uniform flow with an extra turbulence source at mid depth ($\gamma = 0.5$). The uniform flow is given by the law of the wall:

$$\bar{u}/u_* = 1/\kappa \ln(y/y_0) \quad , \quad (16)$$

where y_0 is the roughness length. The turbulence intensity is given by the empirical relation [7]:

$$k/u_*^2 = 4.8 \exp(-2\gamma) \quad . \quad (17)$$

V. PERFORMANCE OF THE METHODS

Two methods for the description and prediction of flow attack on bed protections (i.e. the numerator of Ψ_{gen}) are checked against measurements in the following sections. These are:

- An existing parameter Ψ_{WL} [4]: this uses $(\bar{u}+\alpha\sqrt{k})$, averaged over a certain interval above the bed, eq. (2).
- The present parameter Ψ_{Lm}: this uses the maximum over the depth of the local values of $(\bar{u} + \alpha\sqrt{k})$ weighted with the relative distance L_m/y [eq. (15)].

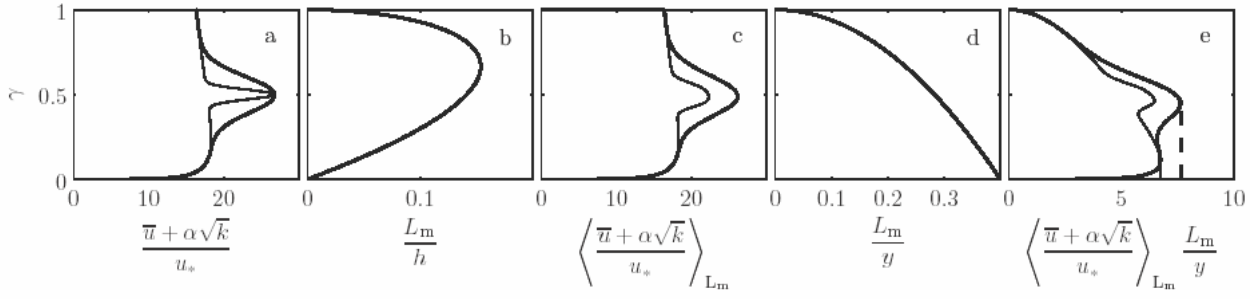

Figure 2. a) Vertical 'maximum velocity' distribution according to eqs. (16) and (17) with Gaussian bumps of two sizes, b) Bakhmetev mixing length. c) Estimate of the large-scale 'maximum' velocity. d) Relative influence of velocity at a certain elevation. e) The estimated influence of the large-scale turbulence on the bed. The vertical lines indicate the two maximum values.

The classical stability parameter, the Shields parameter Ψ, which assumes that the turbulence velocity fluctuations are proportional to the shear velocity (eq. (1) with $U = u_*$ [1]), was not originally meant for non-uniform flows, but it is used as reference.

Measurements of bulk entrainment are needed in order to find a quantitatively valid relation between a flow parameter and the stone entrainment rate; preferably for a range of flow configurations with a large range of relative turbulence intensities and types of turbulence.

A. Data used

In order to check the possible approaches for predicting damage outlined above, data are used of a number of different configurations measured at WL | Delft Hydraulics [4] and measurements at the Delft University of Technology of a backward-facing step [8], referred to as WL and DUT respectively. Velocity profiles (mean and fluctuating), as well as stone entrainment were measured for these configurations. The bed had a low mobility. All configurations have no variations in the transversal direction, which corresponds to the way the entrainment rate is measured. Furthermore, both free turbulence and wall turbulence are present with various values of the relative turbulence intensity. The following nine configurations are used (see also Figure 3).

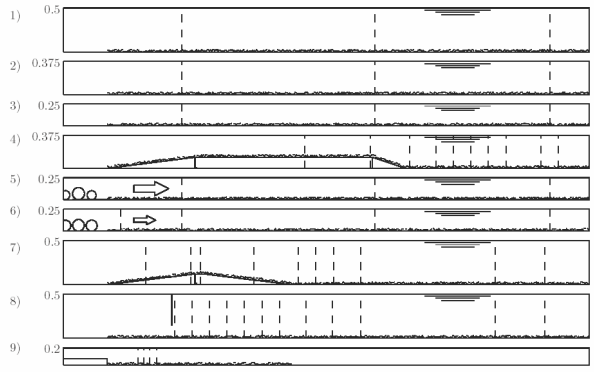

Figure 3. Longitudinal sections of the geometries used. Dashed lines are velocity-measurement locations.

1–3: Uniform flow, h=0.25, 0.375 and 0.50 m (WL).
4: Long sill, 1:3 lee-side, h= 0.375 m (WL).
5–6: Increased large-scale turbulence, Q=83.4 and 68.4 l/s (WL).
7: Short sill, 1:8 lee-side (WL).
8: Gate (WL).
9: Backward-facing step (DUT).

Reference [4] calculated the flow characteristics of some of these configurations with a numerical model (CFX) using the k-e turbulence model, so the suitability of using a RANS model for determining stone stability can be evaluated.

Next we briefly describe the data of the different measurements and calculations.

1) Velocity data

In the WL measurements the u and w velocities were measured using a two-component (x,z), forward scatter, 6 mW laser-doppler velocimeter (LDV). An electro-magnetic flow meter (EMF) was placed above the small measuring volume of the LDV, giving the x and y velocity components. As the measuring volume of the EMF is larger, the fluctuating velocities were underestimated. Therefore σ(v) was corrected using the ratio between σ(u) measured by the LDV and the EMF. The sampling frequency was 100 Hz. The calculations of the flow were done using the commercial CFX4 package. This uses a collocated grid and combined Cartesian and σ grid cells. The free surface option was used for all computations, except for the gate where it did not give stable results. The long sill was 5 mm too low, compared to the measurements. See Reference [4] for an elaborate description of the measurements.

In the measurements by Reference [8] a rigid lid was put on the water surface. Only the u and w velocity components were measured, using an LDV similar to the one used by WL. The sampling frequency was 100 Hz. The data were obtained from the graphs in the report. The velocity was measured at a lower discharge (Q_{meas}) than the discharge at which the entrainment was measured (Q_E). Therefore the mean velocities were multiplied by the correction factor Q_E/Q_{meas} and the turbulence kinetic energy by $(Q_E/Q_{meas})^2$.

2) Stone data

The specifications of the stones that were used during the WL and DUT experiments are given in Table I.

Now the determination of the entrainment rates from the measurements is described.

In physical models damage to bed protections is usually measured by applying the stones in the protection layer in transversely oriented strips with uniformly colored stones. The stones of a certain color that leave their strip of origin during a certain time-span stand out on the differently colored background and can easily be counted. A first estimate of the average entrainment rate in a strip, E_{meas}, is obtained by:

$$E_{meas} = n d_{n50}^3 / AT \quad , \qquad (18)$$

where n is the number of stones that have been removed from the strip, A is the area of the strip, and T is the duration of the measurement.

These kinds of measurements can be used to obtain the required relation between a stability parameter Ψ_{gen} and the entrainment parameter Φ_E. As the mobility of the bed and the hydrodynamic load both change in the flow direction, one configuration with several strips thus yields

TABLE I.
STONE CHARACTERISTICS

Research	d_{n50} [mm]	d_{n85}/d_{n15} [-]	Δ [-]	strip width [mm]
WL	6.2	1.51	1.72	100
DUT	10.8	1.32	1.70	100

several measurements of the required relation.

However, the local entrainment rate is not determined exactly from these measurements, as some entrained stones will deposit in their strip of origin. This will lead to an underestimation – that turns out to be significant – of the entrainment rate. This underestimation should be corrected for in order to end up with a quantity that can be compared between different investigations. Reference [6] derived a correction method for this. Input to the method is the probability distribution of the displacement lengths of the stones. Using this method for the DUT data, where also the displacement lengths were measured, a corrected entrainment of $E_{tot} = 1.93E_{meas}$ is found for the DUT data. Assuming that the displacement lengths scale with d gives a correction for the WL data – where the strips were wider compared to the stone diameter – of $E_{tot} = 2.83E_{meas}$. These corrected entrainment rates are used. At places where the entrainment rate was low the entrainment rate was averaged over a number of adjacent strips in order to reduce the measurement error.

For cases 1, 2, 3, 5, 6 and 8 the entrainment in the first period was a few times larger than in the periods afterwards. This indicates that water-working occurred in this period. The real 'strength' of the scour protection can only be evaluated after water-working. Therefore the data of the first period were not used in the cases where water-working was observed. For the other configurations the total number of entrained stones was measured only once. Here this total is simply used.

B. Comparing measured and calculated flow fields

As an example a typical calculated flow field is compared to the measurements. Figure (4) depicts the calculated and measured profiles of $\bar{u}$ and k for the long sill calculation (case 4). Also the calculated length scales L_ε are compared to two estimates of the integral length scale L_x from measurements [see eq. (12)]. One uses:

$u_c = \bar{u}(z)$ (third panel in the figures), and one uses:

$u_c = <\bar{u}>_h$ (<..>$_h$ is the depth-average, bottom panels).

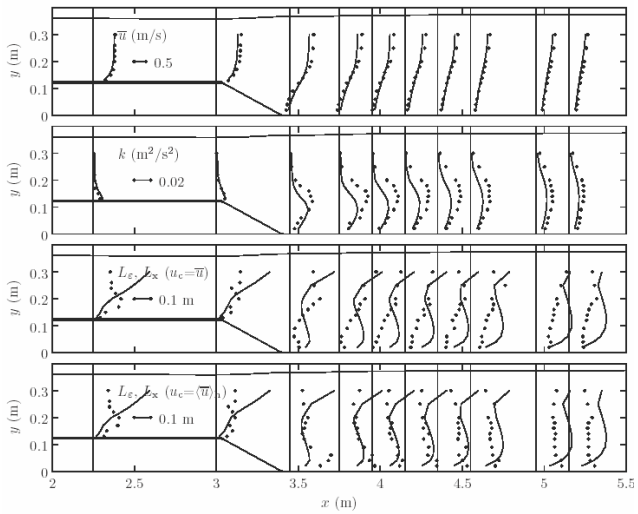

Figure 4. Profiles of calculated (lines) and measured (dots) flow parameters over the long sill. The lower two panels show the length scales determined from the calculations (L_ε, dots) and from the measurements (L_x, lines).

1) Long sill

Figure 4 shows the flow profiles for the long sill. The mean flow is calculated well, the turbulence intensity is reproduced reasonably. The turbulence intensity in the mixing layer is underestimated, and the maximum is situated too low. This leads to errors of the local 'maximum' velocity, $\bar{u} + 6\sqrt{k}$, of roughly +/-30%, see Figure 5. A value of $\alpha = 6$ is used, obtained from Reference [4]. The circles in this figure denote the positions of the measurements 1 m downstream of the sill and below the level of the sill crest. The diamonds show a comparison of the maximum values per longitudinal location, in order to see whether, besides a shift of the maximum value, also the magnitude of the vertical maximum is under-predicted by the calculation. It can be seen that the underestimation of the values cannot be explained completely by the shift of the maximum, but the underestimation of the maximum is less than when the velocity is compared at fixed locations.

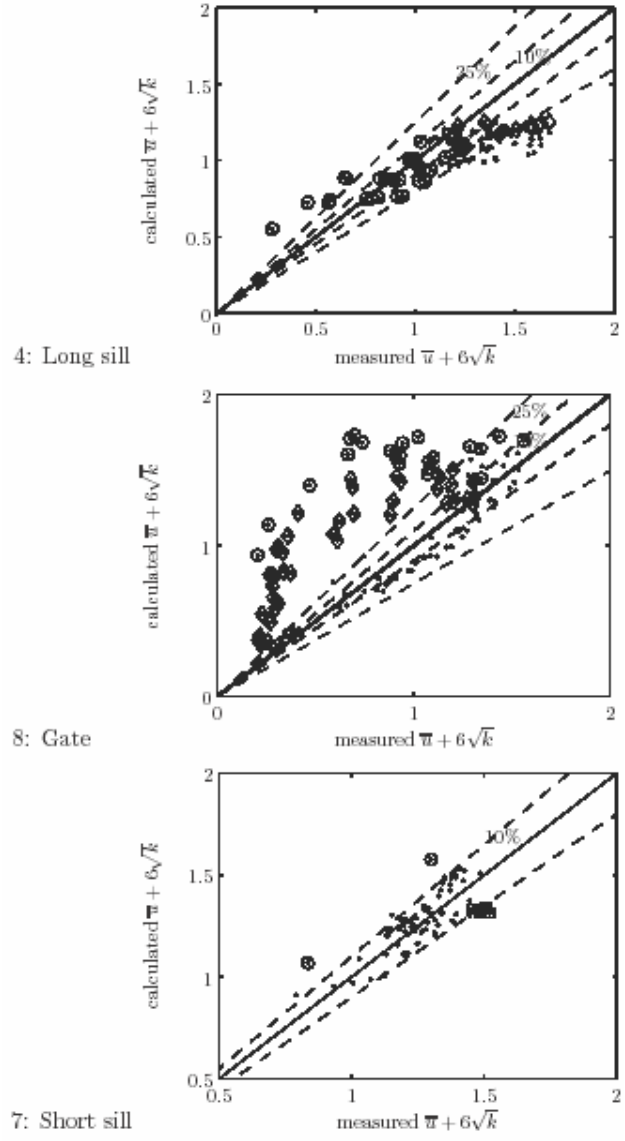

Figure 5. Profiles of calculated (lines) and measured (dots) flow parameters over the short sill. The lower two panels show the length scales determined from the calculations (Lε, dots) and from the measurements (Lx, lines).

2) Gate

The mean flow for the gate configuration (not shown) is simulated reasonably, although the mixing layer widens more quickly than measured. The turbulence intensity is not calculated very well. The origin of this error lies just upstream of the gate. This is an acceleration area with almost potential-flow-like behavior, so no turbulence production is expected here. However, in the acceleration area a high production of turbulence is calculated. Therefore, at the first measurement transect the turbulence profile is already completely wrong. This leads to an overestimation of the local 'maximum' velocity by more than 100%, see Figure 5. Applying a different grid upstream of the gate might solve this problem.

3) Short sill:

This simulation gives very good results (not shown), both for the mean flow and for the turbulence intensity. This leads to values of the local 'maximum' velocity with an error within +/- 10%, see Figure 5. The overestimated values with the circles are the lowest points of the transects on the sill, and are probably caused by the boundary condition. The underestimated values with the squares are in the deceleration area downstream of the sill.

C. Entrainment under uniform flow

First the entrainment curve from the uniform flow experiments (WL) will be established. The entrainment rate E was determined for all strips as explained in Reference [6]. In order to get a reliable estimate of E all these rates had to be averaged over a number of strips (this is possible as the flow is nearly uniform). For the experiment with $h = 25$ cm the average entrainment was determined over the first and the last 28 strips. For the other two uniform-flow experiments E was averaged over all 56 strips, as E was lower. The shear stresses for the first experiment were obtained from the CFX calculations. The flow velocity is slightly increasing due to the horizontal bed, therefore multiple 'measurements' can be obtained from one uniform flow configuration. The shear stresses for the other two measurements were obtained from the integrated log-law – eq. (16) – and the measured Q. The resulting E – shown in its dimensionless form in Figure 6 – has a strong dependence on Ψ, comparable to the Paintal curve for the sediment transport rate [9].

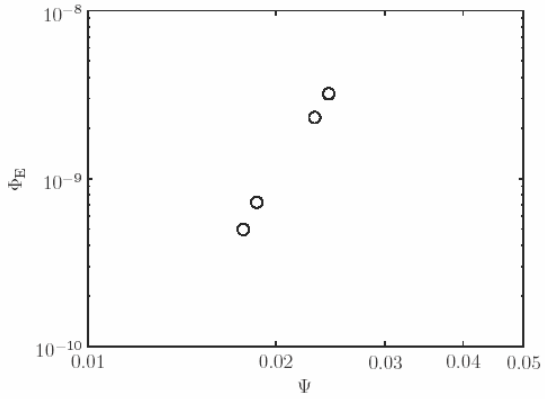

Figure 6. Measured entrainment under uniform flow (WL) as a function of Ψ.

Under uniform flow, the entrainment parameter is correlated to all three stability parameters (Ψ, Ψ_{WL}, and Ψ_{Lm}) in a similar way. Only the absolute value of the parameters is different due to the different implementation of the velocities in the different stability parameters. It. appears that all stability parameters describe entrainment (and hence damage) of stones well for uniform flow – at least for the present range of the relative depth, h/d that was used. An examination of the influence of h/d is given later.

D. Entrainment under non-uniform flow

As the calculated velocity and turbulence kinetic energy are only accurate for some cases, and are not available for all cases, we will use the Ψ_{WL} or Ψ_{Lm} based on *measured* flow properties for comparison to observed values of Φ_E for the various (non-uniform) flows. This will show which stability parameter is suited best for the prediction of entrainment of bed material, and hence damage to bed protections.

First, for reference, the plot of the Shields parameter, Ψ, against the entrainment parameter for all cases is shown in Figure 7. The shear stress was evaluated using the first velocity point near the bed and the law-of-the-wall. Note the wide range of Ψ values, down to extremely low values (10^{-5}) for which no motion would be expected in uniform flow. It is clear that no correlation exists between the two parameters. As the points with a high turbulence intensity give a large entrainment, but have a low mean shear stress, we can see a large number of points with a high Φ_E and a low Ψ. Clearly there is no sensible relation between Ψ and Φ_E for this variety of flow conditions.

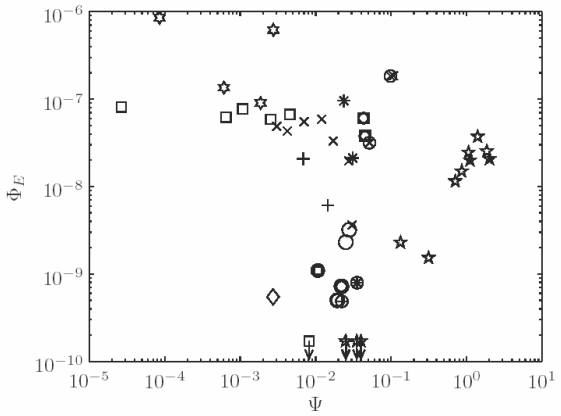

Figure 7. Measured Φ_E versus the measured Ψ for a variety of flow conditions. For legend see next figure. The markers with arrows have $\Phi_E = 0$.

Next we consider the possible relation between Ψ_{WL} and Φ_E, the top plot in Figure 8. These variables are correlated, although still a large amount of scatter is present. The points with markers which have a (partly) circular shape can be regarded to represent rather uniform flow cases (i.e. the flow on the long sill and far away from the disturbance is regarded as almost uniform), although some cases are still slightly non-uniform. It is clear that these points give a reasonable trend. The points of the flow downstream of the long sill and just downstream of the large stones in the increased turbulence case are still

on the high side of the data cloud. In these cases the entrainment increases for decreasing Ψ_{WL}. This indicates that the turbulence is still not incorporated very well.

Finally the outcome of the new method is shown in the bottom panel of Figure 8. A few values for α were tried, but $\alpha = 6$ yielded the best collapse of data. Note that no further fit coefficients are used in the determination of the maximum velocity used to predict the damage.

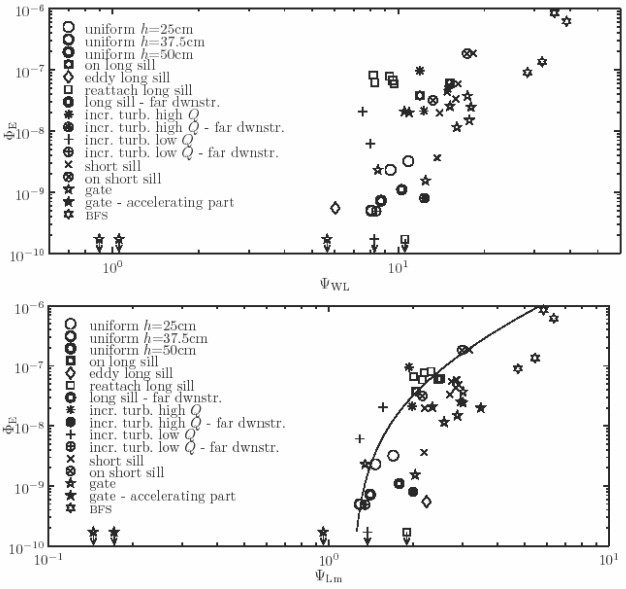

Figure 8. Top: measured Φ_E versus the measured Ψ_{WL} for a variety of flow conditions. Bottom: measured Φ_E versus the measured Ψ_{Lm} for the same flow conditions. The markers with arrows have $\Phi_E = 0$.

It can be seen that the points with high turbulence intensity that were relatively far on the left side of the data cloud in the top panel are now situated more in the neighborhood of the other points, although the scatter is still considerable. It seems that the new way of determining the quasi-steady forces is slightly better than the WL-method. It also turns out that the DUT data (BFS, case 9), which were also meant to be representative of 'initiation of movement', actually had a larger entrainment parameter. This shows that using a subjective definition of initiation of movement will not yield consistent design criteria. As the correction of the entrainment rate is derived for uniform flow, the estimated entrainment rate might be slightly different. However, without correction the relative difference between the DUT and WL entrainment rates would even be larger.

A tentative power law has been drawn more or less as an upper envelope of the data points for the new stability parameter in Figure 8:

$$\Phi_E = \Phi_{E,0}\,(\Psi_{Lm}-\Psi_{Lm,c})^p, \quad \text{for} \quad \Psi_{Lm,c} < \Psi_{Lm} < 7\,, \qquad (19)$$

with $\Phi_{E,0} \approx 5\cdot10^{-8}$, $\Psi_{Lm,c} \approx 1.2$, $p \approx 2$.

The coefficient $\Phi_{E,0}$, the threshold value $\Psi_{Lm,c}$, and the exponent p represent a conservative fit through the present data. As they have no clear physical meaning they cannot be used outside the present range of Ψ_{Lm}. Still this gives the required relation between a stability parameter (including turbulence effects) and the entrainment rate. This can be used for the (preliminary) design of bed protections. Further validation of the technique and the values is still advised.

E. Evaluation of new approach

The *measured* values of Ψ_{Lm} and Φ_E show a clear correlation, although the scatter is still large. A plot of the *calculated* Ψ_{Lm} and the measured Φ_E is given in Figure 9. It shows that the calculated values of Ψ_{Lm} are still correlated to Φ_E. The scatter has obviously increased compared to Figure 8 (bottom panel).

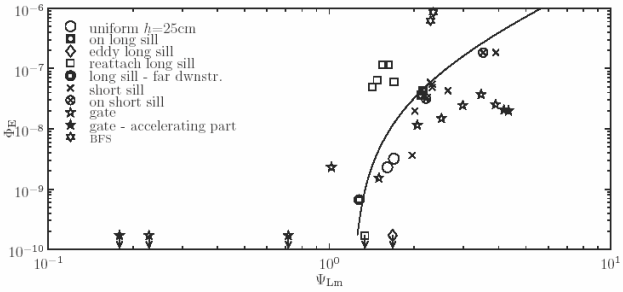

Figure 9. Measured Φ_E versus the *calculated* Ψ_{Lm} for a range of flow conditions.

In Section V-B some calculations of the 'maximum velocity' $\bar{u} + \alpha\sqrt{k}$ were evaluated. The best computation gave local 'maximum velocities' that differed less than ten percent from the measured ones. This means that – with inclusion of the uncertainty in the ratio $\sigma(u)/\sqrt{k}$ – the best model results show an accuracy of roughly 15%. This is equivalent to an accuracy in the stability parameter of about 30%.

Despite the enhanced scatter in the relation between Ψ_{Lm} and Φ_E in Figure 9, due to shortcomings of the applied computational models, it is believed that the calculations – if properly executed – can be used to obtain a fair estimate of the stability of a bed protection. This stability can for instance be plotted as the safety factor $\Psi_{Lm,c}/\Psi_{Lm}(x,y)$, which will have to be sufficiently larger than one at all positions on the bed protection. It will thus be possible to obtain an estimate of the location, size and shape of possibly damaged areas.

This kind of information can also be used to predict a stone size that will be stable, $d_{optimum}$, using a safety factor s:

$$d_{optimum} = s\,\Psi_{Lm} / \Psi_{Lm,c} d_{design}\,, \qquad (20)$$

where d_{design} is the diameter of the top layer of stone in the (preliminary) design. Based on the accuracy of the computational models, the safety factor has to be at least about 1.5, but in practice larger than 2. Note that if the stone size of the bed protection is changed, the calculation should be executed again, as a new stone diameter will

also change the flow pattern. Reference [4] states that one iteration is sufficient.

When we further regard the steep slope of the entrainment curve then we must come to the conclusion that the 'gradual damage' approach using eq. (4) or eq. (5) is not yet feasible.

If the calculation accuracy increases, however, the gradual stability approach can be applied with increasing reliability. Care must be taken with the implementation of the grid and the boundary values of the computational model.

VI. INFLUENCE OF THE RELATIVE DEPTH

For uniform flows, the present model and the WL model give different results than the Shields approach for a changing relative depth. This is discussed in this section. The parameter Ψ_{Lm} is evaluated by substituting eqs. (16) and (17), using $y_0 = d/15$.

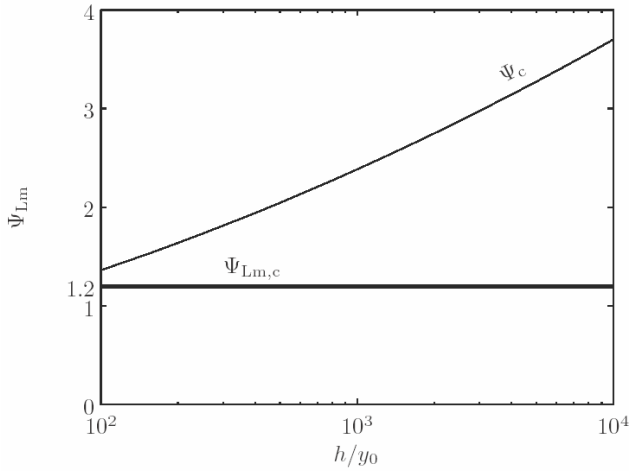

Figure 10. Ψ_{Lm} for uniform flow at critical conditions $\Psi c = 0.03$, $\Psi_{WL,c} = 1.2$, as a function of h/y_0.

It turns out that this ratio is a function of the relative depth, h/y_0 . For a realistic range of values of $h/y_0 = 10^2$–10^4, it increases by a factor of about 2.5. Using eq. (15) it is possible to see which value of the new stability parameter corresponds to the critical value of the Shields parameter, as a function of h/y_0 . This is plotted in Figure 10 for a value of Ψ_c of 0.03. It can be seen that Ψ_{Lm} corresponding to Ψ_c is higher than the critical limit of $\Psi_{Lm,c} = 1.2$. This means that the present method offers a conservative approach for uniform flow, especially for large water depths (low relative roughness).

The ratio of the existing stability parameter Ψ_{WL} to the Shields parameter was analyzed as well. This ratio shows a very similar trend as the ratio Ψ_{Lm}/Ψ. So in this respect the existing approach and the present approach are comparable.

It is generally accepted that the critical Shields parameter remains constant for particle Reynolds numbers, Re_*, larger than a certain value (≈ 500). However, the present model predicts an influence of the relative depth h/d on the critical shear stress for $Re_* >> 500$. Therefore it seems that the stability parameters are not correct for uniform flows. Note however that the usual assumption that the critical Shields parameter is constant for very high Re_* has not been proven empirically yet. Empirical evidence of these quantities is scarce and imprecise [10]. Furthermore, the critical Shields parameter is notoriously difficult to determine and its value is influenced by the method of determination [10].

The influence of the relative depth on the new models can be explained as follows. We regard a uniform flow. We slowly increase the water depth, maintaining a constant shear stress by increasing the discharge. In this situation the Shields parameter is constant. As the shear stress remains equal, the velocity profile near the bed remains the same (law of the wall). However, the profile is extended towards the new water surface. This means that the maximum and bulk mean velocity of the flow increase. When fluid with high velocity originating from near the water surface is transported to the bed by large-scale turbulence, then the maximum velocity magnitudes occurring near the bed might increase.

There is empirical evidence corroborating the above. Examinations of smooth wall flows show an increasing near-bed streamwise turbulence intensity with an increasing global Reynolds number Re [11, 12], which is due to extra large-scale velocity modes that appear in the flow. Note that $Re = Re_* \; h/d \; U/u_*$ and that U/u_* is an increasing function of h/d. Therefore an increasing h/d is equivalent to an increasing Re at a fixed Re_*.

The above is valid when the flow and the turbulence have adjusted to the roughness of the bed protection (i.e. developed turbulence). This occurs after a length of at least 30 water depths. Consequently this will hardly ever be the case for real bed protections, which usually have limited dimensions. Here usually the case of a roughness transition occurs. However, many prototype applications do have a relative depth that is much larger than the largest relative depth that can be realized in a flume. For instance, typical dimensions of an estuary are a velocity of 1 m/s and a depth of 20 m. When gravel of about 5 cm would be applied here, this yields $h/d = 400$, compared to a typical $h/d = 40$ for flume situations. Therefore, although the uniform flow problem as described above is not expected to occur in reality, an influence of the relative depth could occur. Whether the newly proposed model is correct should therefore be checked at prototype scale as well.

VII. CONCLUSIONS

A method for evaluating the stability of bed protections under non-uniform flows (i.e. near structures) based on output of a 3D Reynolds Averaged Navier Stokes (RANS) model has been formulated. The profiles of the mean velocity and turbulence kinetic energy in the water column above the bed are used to formulate a local stability parameter [eq. (15)], which basically is a Shields parameter, adapted to account for turbulence of varying relative intensity. The entrainment rate is used as a measure of damage. The entrainment can be made dimensionless in an entrainment parameter [eq. (3)] which can be used to compare different investigations. It can be

determined from conventional measurements (using colored strips) when a correction is made for the transport within a strip, and the increased entrainment rate during the initial water-working of the bed is not incorporated in the measurement.

The measured values of the new stability parameter are correlated to the entrainment parameter. This indicates that the stability parameter represents the flow attack to the bed. A tentative relation between the stability parameter and the entrainment parameter is given by eq. (19). The existing stability parameter Ψ_{WL} was also correlated to the entrainment parameter with slightly more scatter, while the conventional Shields parameter could not predict the entrainment rate at all.

The stability parameter was calculated reasonably well by the CFX model for most configurations.

The relatively large influence of the turbulence (high value of α) in the stability parameter – which is based on the quasi-steady force mechanism – indicates that a different force generating mechanism (turbulence wall pressures) may be aiding in the entrainment of stones.

ACKNOWLEDGMENT

Thanks to Bert Jagers and Tom Jongeling who provided most experimental data uses in this paper.

REFERENCES

[1] Shields, A. (1936). Anwendung der Aehnlichkeitsmechanik und die Turbulenzforschung auf die Geschiebebewegung. Mitteilungen der Preussischen Versuchsanstalt fuer die Wasserbau und Schiffbau, Heft 26.

[2] Hoffmans, G.J.C.M. & Akkerman, G.J. (1998). Influence of turbulence on stone stability. 7th international conference on River Sedimentation. Hong Kong.

[3] Mosselman & Akkerman, G.J. (2000). Low-mobility transport of coarse-grained material. Tech. rept. Q2395.40. WL | Delft Hydraulics

[4] Jongeling, Blom, Jagers, Stolker, and Verheij (2004). Design method granular protections. Tech. rept. Q2933/Q3018. WL | Delft Hydraulics (in Dutch).

[5] Nelson, Shreve, McLean and Drake (1995). Role of near-bed turbulence structure in bed load transport and bed form mechanics. Water Resources Research, 31(8), 2071–2086.

[6] Hofland, B. (2005). Rock & Roll – Turbulence-induced damage to granular bed protections. PhD thesis. Delft UT.

[7] Nezu & Nagakawa (1993). Turbulence in open-channel flows. Rotterdam: Balkema.

[8] De Gunst (1999).Stone stability in a turbulent flow behind a step. MSc thesis Delft UT.

[9] Paintal, A.S. (1971) Concept of criticalk shear stress in loose boundary open channels. Journal of Hydraulic Research, 9(1), 91–113.

[10] Buffington & Montgomery (1997). A systematic analysis of eight decades of incipient motion studies, with special reference to gravel bed rivers. Water Resources Research, 33(8), 1993–2029.

[11] DeGraaff & Eaton (2000). Reynolds-Number scaling of the flat-plate turbulent boundary layer. Journal of Fluid Mechanics, 422, 319-346.

[12] Jiménez , Del Alamo, Flores (2004). The large-scale dynamics of near-wall turbulence. Journal of Fluid Mechanics, 505, 179–199

Laboratory and Field Measurements of Bridge Contraction Scour

S. Hong[*], A. Gotvald[**], T. W. Sturm[*], and M. Landers[**]
[*] Georgia Institute of Technology, School of Civil and Environ. Engrg., Atlanta, GA 30332–0512, USA
[**] U.S. Geological Survey, Atlanta, GA 30360–2824, USA

While some field studies of bridge contraction scour have been undertaken in the past as well as laboratory studies of scour in long contractions, somewhat less attention has been paid to hydraulic modeling of contraction scour using the full bridge geometry and river bathymetry, not to mention the interaction between contraction scour and local pier scour. This study focuses specifically on contraction scour at a bridge on the Ocmulgee River in Macon, Georgia. A 1:45 scale model of the bridge, its embankments, and the approach and exit river bathymetry were constructed in the Hydraulics Laboratory at the Georgia Institute of Technology in 2005. Several flow rates were modeled including the 50–year peak flood discharge and the 100–yr peak flood discharge as well as a 1998 historical flood discharge for which field measurements were made by the U. S. Geological Survey. Comparisons are made between contraction scour measurements in the laboratory and in the field, and a procedure for hydraulic modeling of contraction scour is suggested.

I. INTRODUCTION

While flood damages typically involve widespread inundation of agricultural land, destruction of homes and businesses, and disruption of economic activity, a less obvious threat is the vulnerability of bridges over waterways that cause flow obstruction and scour around the bridge foundations leading to possible bridge failure during floods. Two types of scour that can lead to bridge failure are local scour, which occurs at the base of abutments and piers and is attributed to flow obstruction, downflow, and formation of a horseshoe vortex that wraps around the obstruction, and contraction scour, which occurs across the entire channel and is attributed to the flow contraction caused by the bridge opening and deflection of floodplain flow into the main channel.

In recent years, flood waters have closed many highways and local roads as well as interstate highways in the United States and caused scour that damaged many bridges and even resulted in loss of life. For example, intense thunderstorms in Iowa in 1992 caused 6 m of contraction scour at the State Highway 14 bridge over Wolf Creek [1]. One thousand bridges have collapsed over the last 30 years in the United States, and the leading cause is hydraulic failure which has resulted in large financial losses. In Georgia, the total financial loss from tropical storm Alberto in 1994 was approximately $130 million because more than 100 bridges had to be replaced and repaired due to flooding [2]. During the 1993 upper Mississippi River basin flooding, more than 258 million dollars in federal assistance was requested for repair and/or replacement of bridges, embankments, and roadways [3]. Bridge failures can also lead to loss of life such as in the 1987 failure of the I–90 bridge over Schoharie Creek near Albany, New York, the U.S. 51 bridge over the Hatchie River in Tennessee in 1989, and the I–5 bridges over Arroyo Pasajero in California in 1995 [4].

The engineering design of a hydraulic structure such as a river bridge requires consideration of both safety and cost with respect to the depth of the foundation relative to predicted scour depths. Engineering experience seems to indicate that computation of scour depth using current scour formulas tends to overpredict scour in comparison to field measurements. The result can be overdesigned bridge foundations that increase the cost of the bridge. In fact, achieving a balance between safety and cost is a very difficult problem which is one reason why the Federal Highway Administration in the U. S. has mandated the use of scour prediction formulas that have a large factor of safety to compensate for a lack of complete understanding of the complex physics of the scour process. These scour prediction formulas are based primarily on idealized laboratory experiments in rectangular flumes (steady, uniform flow and non–cohesive sediments). To predict more accurate scour depths and to suggest more economical methods of designing bridge foundations, physical models that reproduce the pier and abutment geometry as well as the river bathymetry can be used but only in a few cases has this been done [5].

In addition to idealized laboratory experiments, another possible reason for scour depth overprediction is the current practice of adding separate estimates of contraction scour and local scour when in fact these processes occur simultaneously and interact. Local scour occurs at the location of a bridge pier or abutment due to obstruction of the flow and the development of complex, three–dimensional horseshoe vortices at the base of the foundation that entrain and carry sediment away. Contraction scour, on the other hand, tends to occur across the entire bridge section due to contraction of the flow. During a flood, velocities increase as depths increase but they are also affected by changes in the distribution of discharge between the main channel and floodplain, especially within the contracted bridge section. In addition, the time history and time development of contraction scour and local scour are not the same. As a result, the influence of local scour on contraction scour, for example, is time dependent. Some researchers have studied the relationship between local scour and contraction scour [6, 7]. However, those studies were

limited to the interaction between abutment scour and contraction scour and so did not consider the relationship between pier scour and contraction scour. In fact, very few hydraulic modeling studies have been conducted on contraction scour which is the focus of this paper.

Many contraction scour prediction formulas are based on the theory of an idealized long contraction in which sediment continuity is satisfied between the approach and the contracted sections for equilibrium scour in the case of live–bed scour, while for clear–water scour, critical conditions for incipient motion are assumed to have been reached in the scoured contracted section at equilibrium [8, 9, 10]. Laursen [11] also developed contraction scour formulas based on this conceptual model for both the live–bed and clear–water scour cases, and these formulas are currently recommended by the Federal Highway Administration (FHWA) for estimating contraction scour. Laursen's live–bed scour formula includes the effect of contraction of the approach floodplain flow due to the bridge embankments as well as the contraction in the channel width itself.

Several laboratory studies have been performed on long contractions in laboratory flumes. Formulas for contraction scour prediction have been proposed based on the experimental results as a function of approach Froude number, the width contraction ratio, and the nonuniformity of the sediment size distribution, for example [12, 13].

Mueller and Wagner [14] have summarized available field data on contraction scour and have compared scour prediction results from formulas such as those of Komura and Laursen with field observations. Overall, the results were mixed with several cases of overprediction and even severe overprediction, while some cases resulted in underprediction of contraction scour. Their conclusion was that application of contraction scour formulas based on idealized long contractions or experimental data from long contractions in rectangular flumes were difficult to apply in the field partly because of difficulties in assessing nonuniform flow distributions in the approach and contracted channels and in separating contraction and local scour.

In this study, a 1:45 scale model of the bridge, its embankments, and the approach and exit river bathymetry for the Ocmulgee River bridge in Macon, GA were constructed in the Hydraulics Laboratory at the Georgia Institute of Technology in 2005. Several flow rates were modeled including the 50–year peak flood discharge and the 100–yr peak flood discharge as well as a 1998 historical flood discharge for which field measurements were available from the U. S. Geological Survey (USGS). The laboratory model measurements were taken in the clear–water scour range up to the maximum clear–water scour case with Froude number similarity and compared with measured live–bed contraction scour in the field. Local pier scour was separated from the measured cross sections in both the model and the field to obtain values of contraction scour alone. In addition, the contraction scour was determined relative to a reference scour surface. Continuous field measurements of scour at the main bridge pier bent were obtained with fathometers attached to the piers. These data were analyzed and compared with cross sections measured during floods to better understand the dynamic nature of the live–bed scour process.

II. Experimental Procedure

A. Laboratory Model

The experimental studies were conducted in an undistorted geometric scale model constructed in a laboratory flume, which is 24.4 m long, 4.3 m wide and 0.8 m deep. The existing flume consists of a level concrete bed with vertical steel walls bolted to the floor and water–sealed. All of the prototype data, including discharge, stage, velocity distributions and river bathymetry were measured by the USGS. Dynamic similarity was obtained by equating Froude numbers in the model and prototype. A geometric scale ratio of 1:45 was selected based on the limiting dimensions of the flume. The model sediment size of d_{50} = 1.1 mm with σ_g = 1.3 was chosen such that the ratio of pier size to sediment size, b/d_{50}, was in the range of 25–50 where it has negligible influence on pier scour [15]. In addition, the value of the sediment mobility parameter, given by the ratio of approach velocity to critical velocity for incipient sediment motion, V/V_c, was close to unity for the occurrence of maximum clear water scour [16].

The complete river bathymetry was modeled with a fixed–bed approach channel followed by a mobile–bed working section in which the bridge piers, embankments and abutments were placed. The approach section was approximately 9.1 m long with a 6.1 m long mobile–bed section followed by an approximately 3.1 m long exit section for sediment deposition. In the approach section, river bathymetry was modeled by cutting plywood templates that reproduced the surveyed cross sections. The bed material was leveled carefully by hand to match the templates. The templates were left in place in the fixed–bed section, but in the mobile–bed section, they were installed and removed after the bed was shaped for each experimental run. To accomplish this task in the mobile–bed section, the river bathymetry was molded to thin aluminum panels that could be extracted without disturbing the bed. The fixed–bed approach and exit sections were formed from a 3.3 mm gravel bed that was fixed with polyurethane.

Water enters the flume from a 0.305–m diameter pipe, which discharges vertically into the forebay section of the flume. Turbulence at the pipe outlet is reduced by two rolls of chain link fence. An overflow weir, baffles and a perforated steel plate serve to minimize entrance effects and produce a uniform inlet velocity distribution. At the downstream end of the flume, there is an adjustable flap tailgate for controlling the tailwater elevation. The water supply is provided by a constant–head tank. Water flows through the flume and recirculates through the laboratory sump where it is continuously pumped by two pumps with a total capacity of 0.3 m^3/s to the head tank which overflows back to the sump. Discharge is measured by an electromagnetic flow meter.

Adjustable rails on the top of the flume walls provide a level track for an instrument carriage. The instrument carriage is moved along the rails by a system of cables driven by an electric motor. An acoustic Doppler velocimeter (ADV) is used for velocity and bed elevation measurement, and water surface elevation measurements are made by a point gage. Both are mounted on the carriage and can be positioned in three dimensions.

The first set of experiments was conducted with a fixed bed. To determine the initial velocity distribution throughout the flow field before scour, the entire mobile–bed section was fixed by spraying polyurethane on the surface. Point velocities were measured at 8 positions above the bed at each location, and then the depth–averaged velocity at each measuring location was calculated by regression analysis using the logarithmic velocity distribution. An ADV sampling duration of 2 minutes was used at each measuring point.

After completion of the velocity measurements over a fixed bed, the mobile bed was installed, and scour experiments were conducted. The flume was slowly filled with water from a downstream supply hose so that the sand was saturated slowly and the initial bottom contours were unchanged. After complete saturation, the initial bottom elevations of the entire working mobile–bed section were measured by the ADV and point gage in detail. The required discharge was then set using the magnetic flow meter. A flow depth larger than the target value was set by the tailgate so as to prevent scour while the test discharge was established. Then the tailgate was lowered to achieve the desired depth of flow. The scour depth as a function of time at a fixed point was measured with the ADV to determine when equilibrium had been reached. Then the flow rate was greatly reduced, and the bed elevations were measured by the ADV and a point gage.

Experimental flow conditions in prototype units include the flow events shown in Table I. An additional flow rate was tested in Run 4 to achieve maximum clear–water scour (Max. CWS) as will be discussed subsequently. For comparison, the peak discharge of the flood having a 2–year recurrence interval is 807 m^3/s, and the 25–year peak discharge is 1,970 m^3/s. The maximum peak discharge of record is 3,030 m^3/s which occurred in July 1994 due to Tropical Storm Alberto.

Pier scour depths and contraction scour bed elevations between the pier bents were measured during the course of the experiment to determine when equilibrium was reached. Although pier scour reached equilibrium in approximately 2 days, contraction scour required 4 to 5 days so all experiments were run continuously for the longer duration.

TABLE I. EXPERIMENTAL DISCHARGES

Experimental Run No.	Discharge (m^3/s)	Water Surface Elev. (m)	Description
1	1,840	91.37	1998 flood
2	2,242	91.87	50–year
3	2,500	92.32	100–year
4	2,152	91.37	Max. CWS

B. *Field Measurements*

The field site chosen for this study of contraction scour is the Fifth Street Bridge over the Ocmulgee River at Macon, Georgia. The USGS has been gaging stage and streamflow at this site since 1895. The drainage area at this site is 5,800 km^2. The river channel is relatively straight for about 300 m upstream of the bridge and for about 450 m downstream of the bridge. The streambed is sandy with a median particle size of 0.8 mm at the bridge and with a geometric standard deviation, σ_g = 1.8. The right bank is high and is not subject to overflow. The left bank is subject to overflow at high stages, but the highway embankment confines all flow to the bridge opening. Seven cross sections were surveyed throughout the channel reach and were used to construct the physical model in the laboratory.

The bridge pier bents consist of four cylindrical columns that rest on concrete footings, which are buried below the streambed. The main bridge pier bent, which is shown in Fig. 1, is located in the center of the channel with one bridge pier bent on either side at each of the river banks. All three bridge pier bents are aligned with the flow. The pier columns have a diameter of 1.83 m.

Fixed field instrumentation was deployed at the bridge site to continuously measure bed elevations and stage. Bed elevations were measured by fathometers that were attached to the central bridge pier bent in the main channel in order to monitor the changes over time (30–minute intervals) in bed elevation around the bridge piers. The fathometers measured the bed elevations at a lateral distance of 0.6 m from the pier. With reference to the four cylindrical columns shown in Fig. 1, one fathometer is located on the left side (looking downstream) of the second column. Another fathometer is located on the right side of the third column. A third fathometer is located on the left side of the fourth column. A total of six fathometers were originally attached to the pier bent including one at the pier nose; however, three of the fathometers were damaged due to an abundance of logs and debris floating in the stream during high flows.

Stage and bed elevation data were collected during multiple moderate highwater events from 2001 through 2005. Before the fathometers were deployed in October of 2001, a peak discharge of 1,840 m^3/s occurred in 1998, which is near the 25–year peak discharge for this site. The highest peak discharge during the monitoring period occurred in May of 2003 and had a value of 722 m^3/s, which is just less than the 2–year flood peak.

III. RESULTS

A. *Laboratory Model*

In order to analyze contraction scour, it is necessary to first separate local pier scour from the measured cross section at the bridge and to establish a reference scour

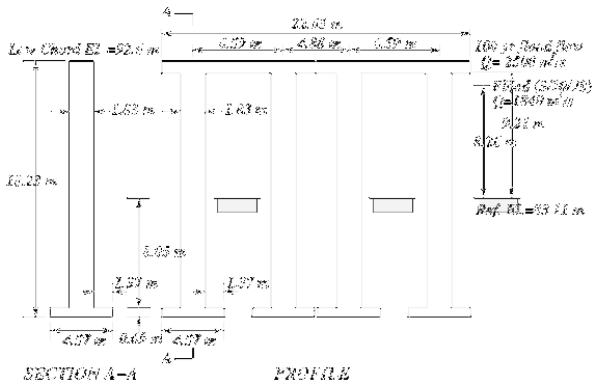

Figure 1. Dimensions of central pier bent in Ocmulgee River at Macon, GA

surface to eliminate residual contraction scour. The local pier scour was eliminated from cross sections at the upstream face of the bridge by the method of concurrent ambient bed level in which average bed elevations are established on each side of the scour hole in the unscoured region [17]. Establishing a reference scour surface for contraction scour is somewhat more difficult because the reference bed level is intended to be the bed elevation that would exist without the bridge obstruction. Historical streambed profiles prior to construction of the bridge were unavailable. Instead, the method used was to establish an average streambed profile from an upstream uncontracted reach to a downstream uncontracted reach using concurrent cross sections that were measured in 2002 as the initial river bathymetry for the laboratory physical model [17]. The reference surface and corresponding flow depths at the upstream face of the bridge were calculated in terms of average or hydraulic depths rather than maximum depths.

The approach cross section for contraction scour was established as the cross section upstream of the bridge with the largest width and smallest velocity at which flow acceleration began into the contracted bridge section. This cross section, referred to as river section 5 (RS 5) was located a distance of approximately 85 m upstream of the bridge.

The laboratory results for contraction scour are summarized in Table II using prototype values. The approach Froude number, $\mathbf{F}_1$, at RS 5 is the same in model and prototype except for Run 4 in which the prototype approach flow depth, y_1, is modeled for the 1998 flood but at a higher velocity. The result is a higher Froude number in order to obtain the contraction scour depth for maximum clear water scour. Because the Froude number is small, the resulting minor increase in Froude number is not likely to affect the results. All of the laboratory results are in the clear–water scour regime since the approach values of velocity in ratio to critical velocity, V_1/V_c, are ≤ 1.0. The reference hydraulic depth at the bridge is given in the table as y_{2ref} which is subtracted from the measured hydraulic depth y_2 at the bridge to produce the measured average contraction scour depth, $d_{sc} = (y_2 - y_{2ref})$.

TABLE II. LABORATORY MODEL RESULTS

Run No.	$\mathbf{F}_1$ *model*	V_1/V_c *model*	y_1 (m)	y_2 (m)	y_{2ref} (m)	d_{sc} (m)	y_2/y_1
1	0.234	0.793	8.15	9.18	8.24	0.94	1.12
2	0.246	0.843	8.60	9.81	8.68	1.13	1.14
3	0.248	0.868	9.14	10.67	9.23	1.44	1.17
4	0.285	0.964	8.15	9.89	8.24	1.65	1.21

B. Field Data

Before the fathometers were deployed in October of 2001, the last high water event greater than the 2–year peak discharge of 807 m^3/s occurred in March of 1998. This event peaked at a discharge of 1,840 m^3/s, which is near the 25–year peak discharge for this site. The channel cross section at the upstream side of the bridge was surveyed during this event. The channel cross section was also surveyed in February, 1998. Comparing these two channel cross sections, both contraction scour as well as local scour were occurring during the March 1998 event as shown in Fig. 2. The channel cross section at the upstream side of the bridge was also surveyed in December 2000. This cross section still showed a remnant pier scour hole from the March 1998 flood.

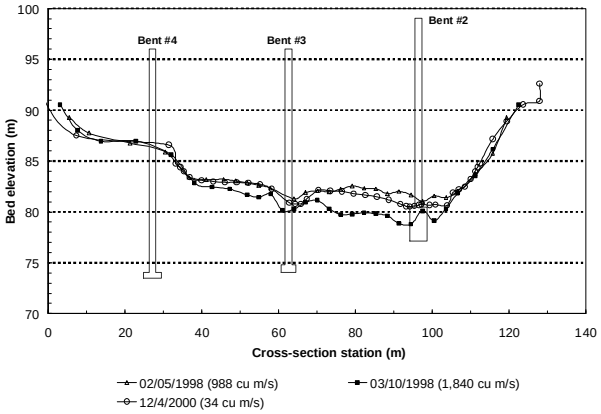

Figure 2. Comparison of bridge cross sections in the field before and after 1998 flood peak of 1,840 m^3/s.

During the period of data collection from October 2001 to July 2005, all the high water events were less than the 2–year peak discharge of 807 m^3/s due to a drought. Fig. 3 shows the fathometer data collected during the period March 12, 2003 to May 29, 2003 on the right side of the third pier column. The other two fathometer locations indicated in the figure inset show very similar results. During the first event of this time record, which occurred on March 22, 2003, all three fathometers measured nearly 1.0 m of fill. A cross section was also surveyed during this event at the upstream side of the bridge as shown in Fig. 4. This cross section verified additional fill of the remnant scour hole from the March 1998 event. From March 22, 2003 to July 10, 2003, the fathometers showed a gradual increase in bed elevation over time that can be seen in Fig. 3. Channel cross sections obtained in July 2003 and October 2005 at the upstream side of the bridge verify the gradual increase in bed elevation throughout the channel cross section as shown in Fig. 4. However, during the high water events above approximately 600 m^3/s for the period of data collection, local scour of nearly 1.0 m was measured by the fathometers. This local scour can be seen in Fig. 3 during the last two events. The local scour hole was immediately filled during the recession of the peak and the gradual fill of the channel cross section continued.

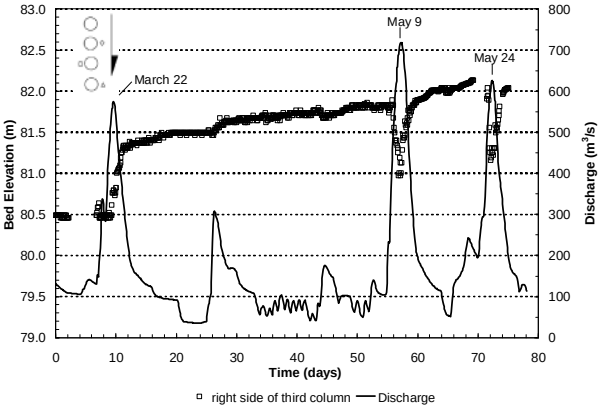

Figure 3. Continuous fathometer record of bed elevation at the right side of the third pier column from March 12 to May 29, 2003.

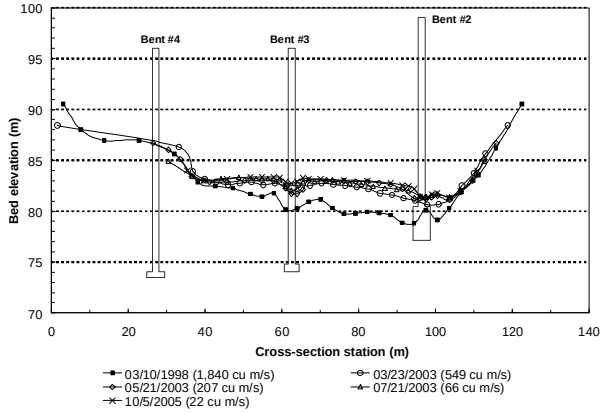

Figure 4. Bridge cross sections during the continuous monitoring period from 2001 to 2005 after the 1998 flood.

C. Comparison of Laboratory and Field Results

In Fig. 5, the model and prototype velocities are compared at the upstream face of the bridge for the 1998 flood discharge of 1,840 m^3/s. The prototype velocities were measured just after the peak discharge and so are slightly smaller than the model velocities for the peak flood discharge, but the comparison is consistent with the measured decrease in velocity with stage for the cross section.

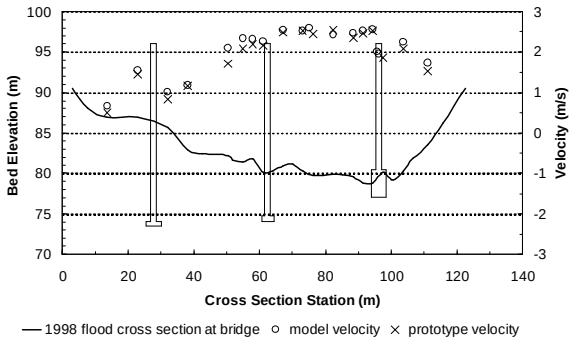

Figure 5. Comparison of measured velocities in the laboratory model and in the field at the upstream face of the bridge for the 1998 flood.

The cross section immediately upstream of the bridge is shown in Fig. 6 at the end of laboratory model run number 1 and as measured in the field for the 1998 flood. For this laboratory run, exact Froude number similarity was used to determine the discharge, and the water surface elevation measured in the field at the downstream face of the bridge was reproduced in the model. However, as shown in Table II, the value of the flow intensity factor for this model run was V_1/V_c = 0.79 which is obviously short of maximum clear–water scour. The bed elevations in Fig. 6 show very good agreement for the local pier scour, while the contraction scour is clearly underestimated in the laboratory model. The good comparison with local scour measured in the field is consistent with previous model studies [16]. These studies show that live–bed local scour in the field can be reproduced in the laboratory model by choosing a sediment size such that $V_1/V_c < 1$ to compensate for the decrease in scour observed with large values of the ratio of pier width to sediment size characteristic of field measurements [18].

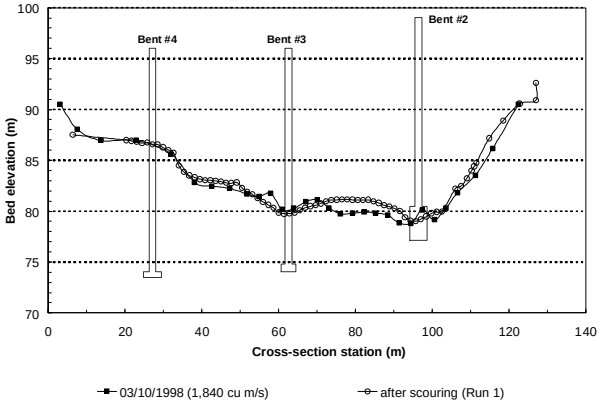

Figure 6. Comparison of laboratory and field cross sections at upstream face of the bridge for 1998 flood.

The laboratory and field contraction scour measurements can be placed in perspective by considering the comparisons shown in Fig. 7. Experimental run 4 as shown previously in Table II was a reproduction of the 1998 flood maximum water surface elevation but at a higher velocity that approached maximum clear–water scour. This should be considered a good estimate of the field live–bed contraction scour for small width contraction ratios [15]. The laboratory value of y_2/y_1 is 1.21 as shown previously in Table II compared with the field value of 1.24. In terms of the reference scour surface, the model value of mean contraction scour is 1.65 m in comparison to the field value of 2.06 m for a difference of about 20 percent. The Laursen contraction scour formulas do a reasonable job of estimating the clear–water contraction scour, but the live–bed contraction scour is underestimated.

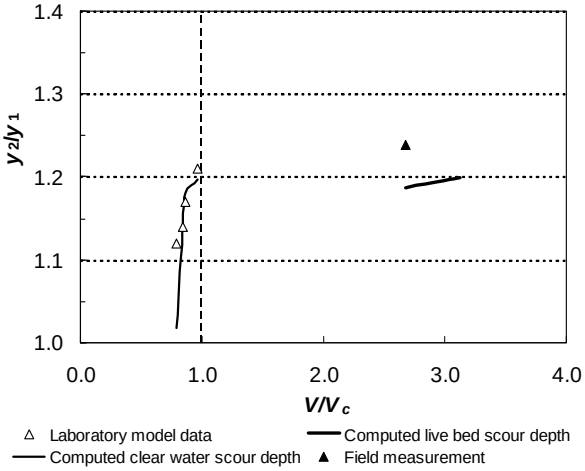

Figure 7. Comparison of laboratory and field measurements of contraction scour along with Laursen formula predictions.

The actual measured cross section upstream of the bridge for laboratory model run 4 and the field cross section for the flood of 1998 are shown in Fig. 8 after removing the local pier scour using the concurrent ambient bed level. This figure gives a better idea of the distribution of contraction scour throughout the cross

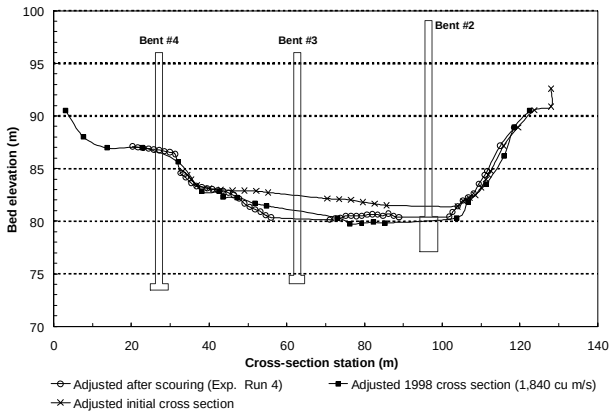

Figure 8. Comparison of adjusted cross sections upstream of bridge with local pier scour removed for 1998 flood.

section. It is not uniformly distributed, but the laboratory model results follow the general trend of the field contraction scour.

IV. SUMMARY AND CONCLUSIONS

A laboratory model study of a bridge over the Ocmulgee River in Macon, GA has been conducted, and the results have been compared with detailed field measurements of contraction scour. Model tests were run for the 1998 flood event having a peak discharge of 1,840 m^3/s as well as for the 50−year and 100−year recurrence interval flood events. Although the prototype contraction scour is live−bed, the model was run in the clear−water regime with a sediment size that resulted in flow intensity values, V_1/V_c, in the range of 0.79−0.96 while maintaining Froude number similarity. Good comparisons were obtained for the prototype values of local pier scour for the 1998 flood at the lowest experimental value of V_1/V_c with exact Froude number similarity in confirmation of a previous model study of a different river bridge [16]. Contraction scour for the 1998 flood, however, was modeled in the laboratory at a discharge approaching maximum clear−water scour, and good agreement was obtained between the laboratory and field values of mean contraction scour depth. This required slight violation of Froude number similarity, but not enough to affect the final results.

Measured field cross sections upstream of the bridge and continuous measurements of scour depths next to the piers illustrate the dynamic nature of the live−bed scour process. Subsequent to the 1998 flood peak of 1,840 m^3/s, no flood discharges in excess of the 2−year recurrence interval discharge of 807 m^3/s occurred. As a result, the contracted section experienced a slow infilling process from 2001 through 2005. The local pier score holes alternately filled and scoured back out for several small floods provided that a threshold discharge of about 600 m^3/s was reached.

Because of the continuously changing streambed at the bridge, occasional snapshot cross−section surveys may not be sufficient to assess live−bed contraction scour. Continuous measurements of scour at the bridge show that the bed responses are quite sensitive to the temporal flow record. Furthermore, both pier scour and contraction scour occur in concert with the flow time history. Under these circumstances, a hydraulic model can be quite helpful in determining contraction scour for realistic field conditions provided that the sediment size is chosen carefully such that Froude number similarity is not seriously violated for maximum clear−water scour conditions, and provided that the pier scour and contraction scour are properly separated relative to reference scour surfaces.

ACKNOWLEDGMENTS

This study was supported by the Georgia Department of Transportation.

REFERENCES

[1] E. E. Fischer, “Scour at a bridge over the Weldon River, Iowa,” Proc., *Hydraulic Engineering* ‘93, ASCE, San Francisco, CA, pp.1854−1859, 1993.

[2] E. V. Richardson and S. R. Davis, *Evaluating Scour at Bridges*, 4th edition, Hydraulic Engineering Circular No. 18, Federal Highway Administration, U.S. Department of Transportation, Report No. FHWA NHI 01−001 HEC−18, 2001.

[3] A. C. Parola, D. J. Hagerty, D. S. Mueller, B. W. Melville, G. Parker, and J. S. Usher, “The need for research in scour at bridge crossings,” Proc. of XXVII IAHR Congress, *Managing Water: Coping with Scarcity and Abundance*, San Francisco, CA, pp. 124−129, 1997.

[4] J. L. Morris and J. E. Pagan−Ortiz, “Bridge scour evaluation program in the United States,” *Stream Stability and Scour at Highway Bridges*, E.V. Richardson and P.F. Lagasse, eds., ASCE, pp.61−70, 1999.

[5] B. E. Hunt, L. N. Triandafilou, P. A. Carreras, Jr., D. A. LaBella, and G. R. Price, “Scour monitoring of the Woodrow Wilson Bridge,” *Water Resources Engineering ‘98*, S. R. Abt, J. Young−Pezeshk, and C. C. Watson eds., ASCE, Memphis, TN, pp.57−62, 1998.

[6] S. L. Niezgoda and P. A. Johnson, “Abutment scour at small severely contracted bridges,” Proc., Conf. on Cold Regions Engineering, *Putting Research into Practice*, ASCE, Lincoln, NH, pp.600−611, 1999.

[7] M. Schreider, G. Scacchi, F. Franco, and C. Romano, “Contraction and abutment scour in relief bridge in a flood plain,” Proc., *Wetlands Engineering and River Restoration*, ASCE, Reno, NV, pp.1375−1386, 2001.

[8] L. G. Straub, “Effect of channel contraction works upon regimen of movable bed streams,” *Trans., Am. Geophys. Union*, (Part 2), pp. 454−463, 1934.

[9] M. A. Gill, “Bed erosion in rectangular long contraction,” *J. Hydraul. Div.*, ASCE, Vol. 107, No. 3, pp. 273−284, 1981.

[10] S. Y. Lim and N. S. Cheng, “Scouring in long contractions,” *J. of Irrig. And Drain. Engrg.*, ASCE, Vol. 124, No. 5, pp. 258−261, 1998.

[11] E. M. Laursen, “Scour at bridge crossings,” *J. Hydraul. Div*., ASCE, Vol. 86, No. HY2, pp. 39−54,1960.

[12] S. Komura, “Equilibrium depth of scour in long constrictions,”*J. Hydraul. Div.*, ASCE, Vol. 92, No. 5, pp. 17−38, 1966.

[13] S. Dey and R. V. Raikar, “Scour in long contractions,” *J. Hydraul. Engrg.*, ASCE, Vol. 131, No. 12, pp. 1036−1049, 2005.

[14] D. S. Mueller and C. R. Wagner, “Field observations and evaluations of streambed scour at bridges,” Federal Highway Administration, U.S. Dept. of Transportation, Report FHWA−RD−03−052, 2005.

[15] B. W. Melville and S. E. Coleman, *Bridge Scour*, Water Resources Publications, Highlands Ranch, Colorado, 2000.

[16] S. Lee, A. Gotvald, T. Sturm, and M. Landers, “Comparison of Laboratory and Field Measurements of Bridge Pier Scour, *Proc. 2nd Int. Conf. on Scour and Erosion*, Y. M. Chiew, S. Y. Lim, and N. S. Cheng, eds.,Vol. 1, pp. 231−239.

[17] M. N. Landers and D. S. Mueller, “Reference surfaces for bridge scour depths,” Proc., *Hydraulic Engineering* ‘93, ASCE, San Francisco, CA, pp. 2075−2080, 1993.

[18] D. M. Sheppard, M. Odeh, and T. Glassser, “Large-scale clear−water local pier scour experiments,” *J. Hydraul. Engrg.*, ASCE, Vol. 130, No. 10, pp. 957-963, 2004.

A Laboratory Study on Incipient Motion of Nonuniform Sediment Mixtures

M.Monowar Hossain[*], Liton Kumar Sarker[**]
[*] Professor, Department of Water Resources Engineering, BUET, Dhaka, Bangladesh
[**] Assistant Engineer, Bangladesh Water Development Board, Comilla, Bangladesh

ABSTRACT

Experiments have been conducted at the Hydraulics and River Engineering laboratory of BUET in a mobile bed facility with a view to further improving the knowledge of incipient motion of non-uniform sediments. Four sediment mixtures with different gradations were used in the experiments. Sediment mixtures were made by adding different size fractions with varying proportions. A reference transport method is used to define the beginning of bed material movement. The experiments demonstrate that the incipient motion of individual size fractions within a mixture is largely controlled by their relative size with respect to median size. The $\frac{\tau^*_{ci}}{\tau^*_{c50}}$ versus $\frac{d_i}{d_{50}}$ for the experimental sediment mixtures fall into a single line, from which it may be inferred that all fractions move predominantly at the same shear stress. Functions developed for the calculation of critical shear stress of different sizes in sediment mixtures have close proximity with the previous methods.

The critical shear stress of median sized sediment of the present investigation was found to be slightly lower than the stress computed from the Shields' diagram. The value of critical shear stress was found to be dependent on its absolute size and mixture sorting. A semi empirical method has been developed for the computation of critical shear stress of median sized sediment by rearranging the dimensionless parameters of grain Reynolds number and mixture sorting. By regression with the experimental data sets the derived parameters result in functions of the form of $R^*_{c50} = 0.09\left[\sigma_g^{1/2} d_{50}^{3/2} \frac{\sqrt{(s-1)g}}{\upsilon}\right]^{1.05}$. This function can be a useful tool in determining critical shear stress of median sized non-uniform sediment mixtures. Previous investigators advocated either Shields' threshold curve or a particular value for the critical shear stress of median sized sediment in case of non-uniform sediment mixtures. The functions developed here will make the calculation of critical shear stress for other sediment sizes more simple and representative.

I. INTRODUCTION

The flow condition under which the sediment particles of given characteristics just start moving is known as the condition of critical motion or the condition of incipient motion of the sedimentary particles. The condition of incipient motion or the threshold of movement is best described by shear stress. The shear stress at which the sediment particles just start moving is known as the critical shear stress or critical tractive stress. Determination of the critical shear stress for incipient motion of streambeds is of considerable interest to river engineers, geomorphologists and stream ecologists. Natural streambeds are invariably nonuniform in character, and their behavior differs from that of the beds composed of uniform sediment. As a result of extensive investigations for nearly six decades, the critical shear stress for incipient motion of uniform sediments is reasonably well understood. The critical shear stress of any size fraction in case of a nonuniform sediment bed is, however, influenced by the other sizes on account of the sheltering and exposure effects in such beds.

It is generally accepted that in sediment mixtures, smaller particles are shielded by coarser grains and need a higher shear stress for mobilization compared with uniform sediment of the same size. Conversely, larger particles in mixtures are entrained at lower shear stress than in a bed of uniform sediment because of increased exposure and instability [12].

It has been demonstrated that the relative variation of the critical value of dimensionless bed shear stress for different grain sizes d_i within a mixture is largely controlled by their relative size with respect to a central value of the grain-size distribution, commonly the median size d_{50}.

$$\tau^*_{ci}/\tau^*_{c50} = \text{function}\ (d_i/d_{50}) \qquad (1)$$

Where τ^*_{ci} and τ^*_{c50} are critical values of the Shields' dimensionless shear stress for sizes d_i and d_{50}

respectively. Several attempts have been made by different researchers to account for the relative variation of the critical value of dimensionless bed shear stress for different grain sizes within a mixture. However, the character of the "hiding function" equation (1) has been found to differ markedly in different studies. Many laboratory and field studies have demonstrated near-equal entrainment mobility of different size fractions where most sizes begin to move at about the same shear stress [9, 10, and 19]. In other cases, significantly different degrees of size-selective entrainment have been observed [2, 7, 17, and 18]. Comparison of some of the hiding functions proposed in the literature is presented in Fig. 1 and Fig. 2 for a typical range of d_i/d_{50} found in natural gravel bed streams. It is seen that there is a considerable discrepancy in the results with almost a tenfold difference in the critical Shields' stress for the end size fractions [12]. The observed variations have been attributed to the difference in methods used to define the critical stresses [15], as well as to the character of the bed material size distribution [7, 11 and 16]. However, the cause of the variation in the reported τ^*_{ci}/τ^*_{c50} values is still poorly explained [12]. Therefore there is a need to further quantify the factors controlling relative mobility of different fractions in sediment mixtures.

There is also no generally accepted method for predicting the value of τ^*_{c50} which is needed for fractionwise calculations while using a hiding function of the form of equation (1). Attempts have been made to relate τ^*_{c50} to the Shields' threshold curve derived for uniform sediment [7, 19, and 20].

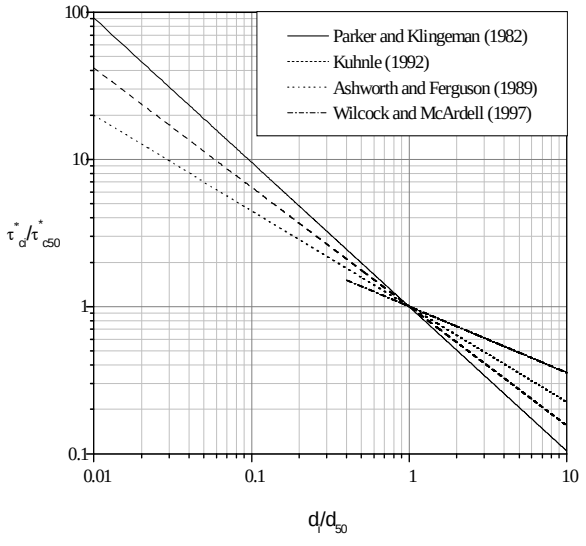

Figure 1. Comparison of $\frac{\tau^*_{ci}}{\tau^*_{c50}}$ with $\frac{d_i}{d_{50}}$ for different equations [12]

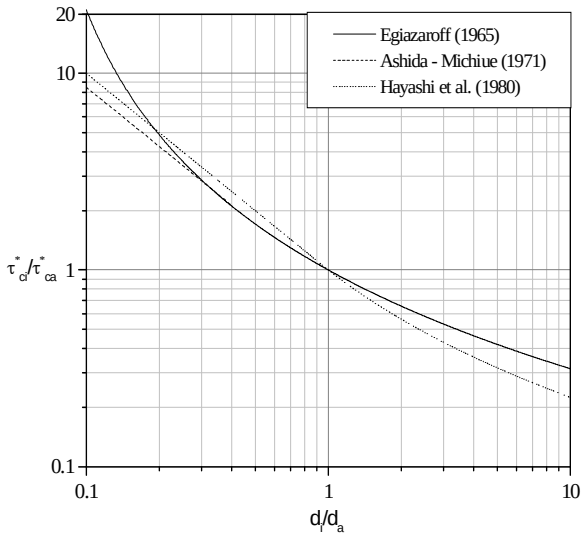

Figure 2. Comparison of $\frac{\tau^*_{ci}}{\tau^*_{ca}}$ with $\frac{d_i}{d_a}$ for different equations [12]

In many studies, however, large departures of τ^*_{c50} from the Shields' curve have been observed [e.g., 1, 2, 8, 9, and 11]. Values of τ^*_{c50} obtained by different researchers are plotted on the Shields' diagram in Fig. 3 and compared with the shields' thresholds curve [14]. It is seen that the scatter of the reported data is considerable and is hardly acceptable for practical use. Thus the development of a method predicting τ^*_{c50} requires further research.

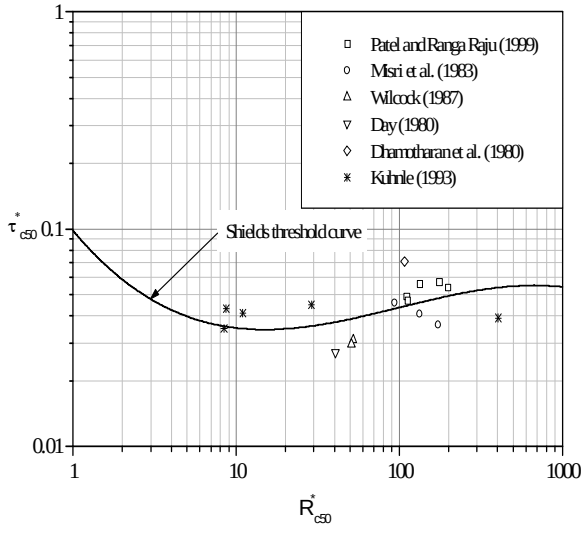

Figure 3. Comparison of critical shear stress τ^*_{c50} for median size d_{50} in sediment mixture of different researchers with the Shields threshold curve [3]

From the literature it appears that most of the studies were conducted with gravel or sand-gravel mixtures whose median size ranges from 1.62 mm to 6.4 mm. However, in Bangladesh, the coarse sand, commonly known as Sylhet sand is nonuniform in character whose median size is around 0.7 mm. Thus much research is needed for better understanding of the incipient motion of such fine sediments.

II. EXPERIMENTAL SETUP AND METHODOLOGY

A. Bed Materials

Natural sands of density 2650 kg/m^3 is being sieved into different size ranges and added in required proportions to get mixtures of the required gradations. The grain size distribution of the four mixes used in the present experiments is shown in Fig. 4 and their characteristics are summarized in Table 1. In Table 1, d_{50} = median size of the sediment, d_g = geometric mean size, d_a = arithmetic mean size and σ_g = geometric standard deviation, these being defined as,

$$d_a = \frac{1}{100}\sum \Delta p_i d_i \tag{2a}$$

$$\log d_g = \frac{1}{100}\sum \Delta p_i \log d_i \tag{2b}$$

$$\sigma_g = \sqrt{\left(\frac{d_{84}}{d_{16}}\right)} \tag{2c}$$

in which Δp_i is the percentage by weight corresponding to the size d_i. The value of d is being calculated as the geometric mean of the size ranges chosen, i.e. $d_i = \sqrt{d_{s1}.d_{s2}}$, in which d_{s1} and d_{s2} are the extreme sizes of the chosen range. Also d_{84} and d_{16} are sizes such that 84% and 16% of the material respectively, by weight, are finer than these sizes. The sediment mixtures designated by S1, S2, S3 and S4 having log – normal distribution and narrow range of median size and mixture sorting.

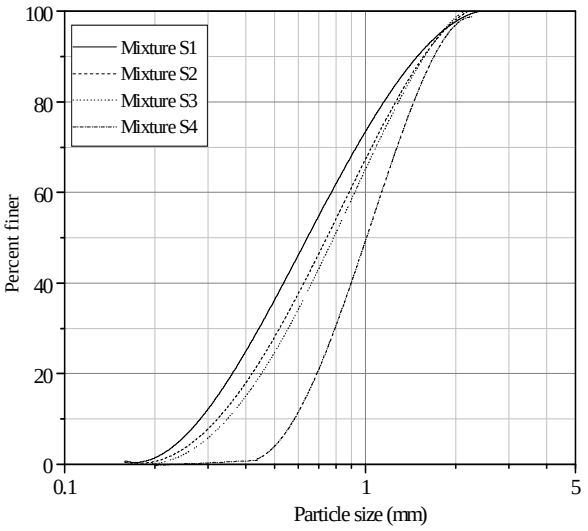

Figure 4. Grain – size distribution for the experimental sediment mixtures

TABLE 1 PROPERTIES OF SEDIMENT MIXTURES USED IN THE EXPERIMENT

Mixture Designation	d_a (mm)	d_g (mm)	d_{50} (mm)	σ_g (mm)	n_b
S1	0.78	0.66	0.64	1.96	0.0128
S2	0.85	0.72	0.74	1.90	0.0131
S3	0.88	0.75	0.79	1.84	0.0132
S4	1.09	1.00	1.02	1.53	0.0136

B. Experimental Work

The experiments were carried out in a straight 11m long channel having a width of 1.0m and a depth of 0.6m. The sides of the channel were made of concrete with enamel painted and thus much smoother than the bed, thereby making the influence of sidewall rather small. Water was allowed to flow smoothly from the upstream reservoir through the pipes placed horizontally at the inlet. A tailgate was located at the downstream end of the channel. For a particular discharge, if the tailgate is raised it increases the water level and vice versa. A Rehbok weir was attached at the end of the channel that delivers water to the downstream reservoir. The Rehbok weir was calibrated to measure the discharge directly by observing the head above the weir only. The water level and bed level were measured with the help of a point gauge. A removable sediment trap at the downstream end of the channel was used to collect the transported material.

C. Methodology of Experiment

For each sediment type at least four runs with different hydraulic conditions have been made in the present study. For each run, sand was placed in the flume bed by giving a pre-determined slope to bed and filled with the required sediment mixture to a uniform depth of 15 cm or more. Care was taken to avoid segregation of the material during placements and it was ensured that the composition of the surface layer was practically the same as that of the entire mixture. A very low discharge was allowed into the flume at first, so that the sediment bed becomes fully saturated.

After filling with water the run began by gradually increasing flow to the desired value. The tailgate was adjusted when necessary to maintain uniform flow in the flume. Several slopes were used and a number of runs were being done with the flow varying between a very low one with almost no sediment transport and one which moves a substantial portion of the bed material. A total of 19 runs were carried out in the experiment. The duration of single run was governed by sediment transport rate (the larger the transport rate is, the shorter is the run and vice versa) and varies from 3 hrs to 8.30 hrs. Care had been taken to ensure that the flow was uniform and that constant rate of sediment transport condition was attained. Constant rate of sediment transport was supposed to have been attained when three successive samples collected yields a sediment transport rate that is practically invariant with time. Sediment was feed in the flume at upstream with the help of a board placed at upstream and this was done manually by measuring the

TABLE 2. MEAN HYDRAULIC AND TRANSPORT PARAMETERS FOR THE EXPERIMENT

Run No.	Total Runtime (hr)	Sed. Collection Time (hr)	Mixture Type	Avg. Discharge, Q (m^3/s)	Avg. Depth, d (cm)	Avg. Velocity, U (cm/s)	Slope,S $\times 10^4$
1	3:45	3.00	S1	0.05071	15.12	33.53	3.199
2	3:40	0.5	S1	0.06373	17.33	36.76	3.336
3	3:15	2.00	S1	0.07062	21.47	32.88	2.151
4	4:00	3.00	S1	0.04764	15.24	31.26	2.759
5	3:30	0.58	S1	0.03454	10.37	33.31	4.78
6	3:00	1.25	S1	0.02754	8.98	30.67	4.781
7	5:00	3.00	S1	0.05047	15.73	32.09	2.81
8	6:45	5.00	S2	0.05065	15.97	31.72	2.888
9	5:00	3.00	S2	0.04337	13.48	32.17	3.563
10	4:00	1.50	S2	0.03527	10.72	32.90	4.81
11	8:30	8.25	S2	0.06252	20.01	31.24	2.22
12	4:00	1.75	S3	0.03527	10.78	32.72	4.79
13	4:00	3.00	S3	0.06254	18.32	34.14	2.937
14	4:30	2.00	S3	0.05008	14.74	33.98	3.658
15	3:45	1.00	S3	0.04688	13.68	34.27	4.16
16	4:00	1.00	S4	0.04939	14.00	35.28	4.386
17	4:00	1.50	S4	0.0435	12.15	35.80	5.285
18	7:00	6.00	S4	0.04513	14.20	31.78	3.201
19	4:00	3.00	S4	0.04631	14.14	32.75	3.416

transported sediment for the time period of 5 or 10 minutes. After attainment of equilibrium conditions, sediment had been collected for desired purpose. The collected sediment was dried, weighed and sieved to get the fractional transport rate. All the runs were conducted in such a condition that there was no pronounced bed form.

III. Analytical Method

Methodological problems have always haunted the study of incipient motion of sediments. Even in the relatively simple case of sediments that are nearly uniform in size, it has long been realized that different methods, or even variations of the same method, give different values of the critical shear stress for initiation of grain motion [15]. It has long been recognized that a basic problem encountered when determining the critical shear stress is that, it can be estimated only with data from flows with some grain motion, for which the bed shear stress already exceeds critical. A second and more fundamental problem is that the bed shear stress is a fluctuating quantity, and one can not precisely define a value below which there is no motion. Both problems lead naturally to a definition of τ_c in terms of a small but finite number of grains in motion. But the number of grains displaced depends on the area of the bed examined and the length of time over which grain displacements may occur. An initial-motion criterion must therefore be defined so that the critical shear stress determined for different sediments, or for different fractions in a sediment mixture are comparable, so that empirical data on critical shear stress can be combined into a general model or compared to theoretical results.

There are two general methods for determining the critical shear stress for individual fractions in mixed-size sediment. One associates the critical shear stress with the largest grain in the mixture that can be moved by a given flow. The other approximates the critical shear stress as that shear stress that produces a small reference transport rate of a given fraction. The former is known as the Largest Grain Method (LGM) and the latter as Reference Transport Method (RTM).

Parker et al.'s Reference Transport criterion is used in the present analysis. In this method the CTS is estimated from a fitted relationship of the dimensionless bed load parameter, W_i^*, and the dimensionless grain shear stress, τ'_{*_i}, as the shear stress corresponding to $W_i^* = 0.002$, wherein

$$W_i^* = \frac{i_B q_B (G-1)}{i_b \gamma_s \sqrt{g\left(R_b' S\right)^3}} \tag{3}$$

in which i_B, i_b - proportions of size fraction d_i in the transported material and the sediment bed respectively, q_B = total bed load transport rate per unit width by weight, γ_s = unit weight of sediment, γ_f = unit weight of water, G = relative density of sediment $= \gamma_s / \gamma_f$, g = acceleration due to gravity, R_b' = hydraulic radius corresponding to grain resistance, and S = longitudinal slope of the channel bed. The use of the grain shear stress in preference to the total shear stress is logical because the former is the effective shear stress for bed load transport in case of an undulated bed. The dimensionless grain shear stress, τ'_{*i}, is defined as

$$\tau'_{*i} = \frac{\tau'_0}{\Delta \gamma_s d_i} \tag{4}$$

in which $\Delta\gamma_s = \gamma_s - \gamma_f$, and τ_0' is the grain shear stress which can be computed using the equation

$$\tau_0' = \gamma_f R_b' S \quad (5)$$

Here R_b' is the corrected hydraulic radius corresponding to grain resistance. A sidewall correction is applied to R_b to get the corrected hydraulic radius, R_b'. S is the slope of the energy line. Computation of the reference shear stress for individual fractions requires a number of choices concerning the appropriate technique for fitting the data. Not only must a reference transport criterion be chosen, but also an appropriate curve of transport rate versus shear stress must be fitted to the data, and the method of fitting the curve to the data must be chosen. The relation chosen here is a power approximation of the Einstein (1950) bed load function at low stresses derived by Parker (1979)

$$W_i^* = 11.2\left(1 - \frac{0.8531\tau_{ci}^*}{\tau_i^*}\right)^{4.5} \quad (6)$$

A typical plot of W_i^* and τ_{*i}' for computing dimensionless critical shear stress of individual fractions in case of sediment mixtures is shown in Fig. 5.

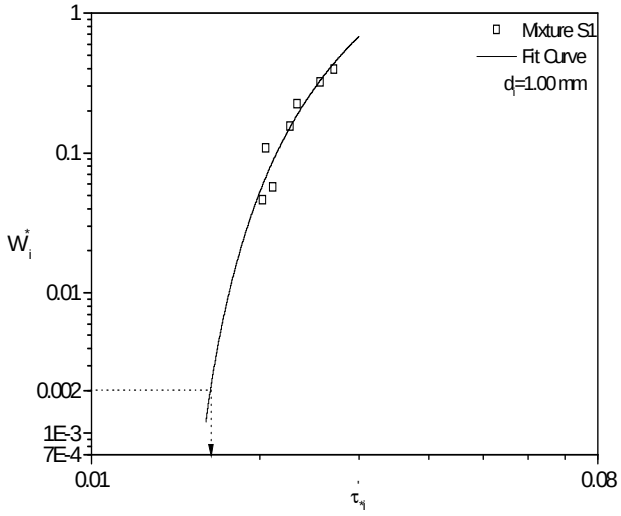

Figure 5. Variation of W_i^* with τ_{*i}'

IV. DATA FROM OTHER SOURCES

The present analysis uses both experimental results from this study and data from previous investigations. The main objective to select the additional data is that the fractional transport rates were measured over a wide range of bed mobility, including very low transport rates near to incipient motion and the data should cover a wide range of bed material gradings and median sediment sizes. Although the data were collected using different operational and measurement procedures and differ in accuracy and reliability, all refer to the transport of sand/ gravel mixture on a reasonably flat bed by steady, uniform flow.

TABLE 3. SUMMARY OF OTHER DATA SETS USED IN THE PRESENT ANALYSIS

Mixture Designation	d_a (mm)	d_g (mm)	d_{50} (mm)	σ_g	Reference
M1	4.15	3.39	3.35	1.79	Patel and Ranga Raju (1999)
M2	5.57	3.89	3.70	2.29	do
M3	3.16	2.59	2.59	1.73	do
M4	4.79	3.02	2.65	2.61	do
M5	6.10	3.55	2.80	2.90	do
MIT- 1ϕ	2.34	1.85	1.83	1.99	do
MIT- ½ϕ	1.94	1.82	1.83	1.41	do
Day- B	1.81	1.15	1.62	3.26	do
SAF	2.90	2.11	2.16	2.60	do
Misri- N1	3.00	2.41	2.37	2.00	do
Misri- N2	6.00	3.83	3.85	3.00	do
Misri- N3	5.70	4.00	3.12	2.36	do
Day- A			1.82	3.41	Wilcock and Southard (1988)

V. ANALYSIS OF RESULTS

A. *Relative Size Effect*

Variation of τ_{ci}^* with d_i/d_{50} is shown in Fig. 6 for all the sediment mixes. A consistent trend of $\tau_{ci}^* - \frac{d_i}{d_{50}}$ is being found for the experimental sediment mixes. Sediment mixtures of S2 and S3 having close median size of 0.74 mm and 0.79 mm and geometric standard deviation of 1.9 and 1.84 respectively is plotted separately in Fig. 7 shows the fact that τ_{ci}^* values for each d_i/d_{50} nearly identical. For mixtures S1 and S4 with median values as 0.64 mm and 1.02 mm and geometric standard deviation of 1.96 and 1.53 respectively shows a variation in the τ_{ci}^* vs d_i/d_{50} plotting, which is shown in the Fig.8 .

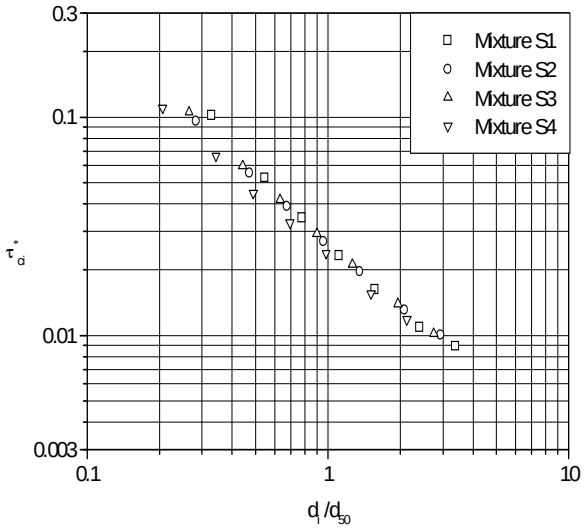

Figure 6. Variation of τ_{ci}^* with $\frac{d_i}{d_{50}}$ for the experimental data sets

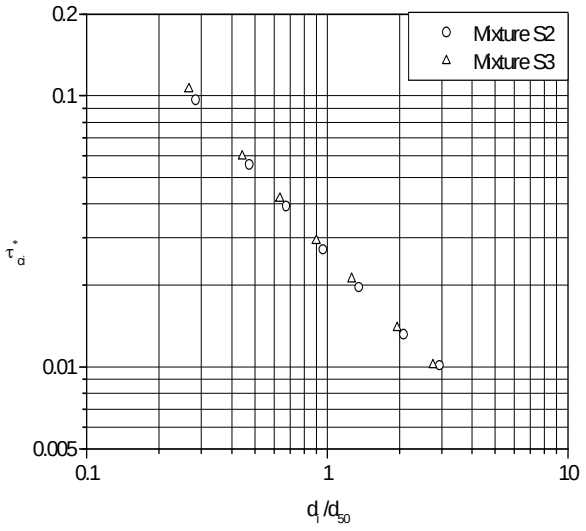

Figure 7. Variation of τ_{ci}^* with $\frac{d_i}{d_{50}}$ for sediment mixture S2 and S3

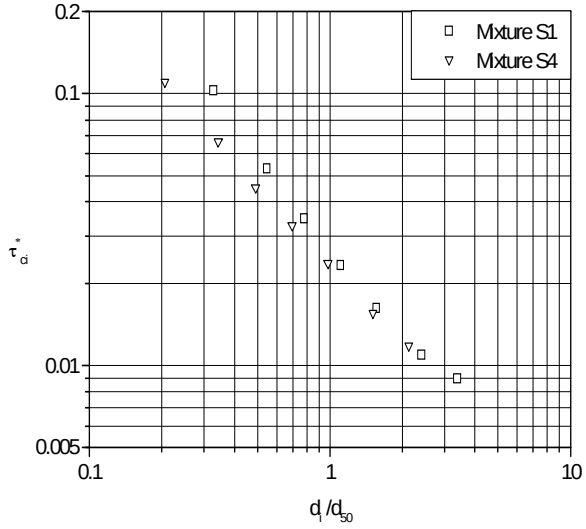

Figure 8. Variation of τ_{ci}^* with $\frac{d_i}{d_{50}}$ for sediment mixture S1 and S4

For all the experimental data and other available data shows a consistent trend of τ_{ci}^* vs di/d_{50} and can be expressed as $\tau_{ci}^* = \alpha\left(\frac{d_i}{d_{50}}\right)^{\beta}$. The trend of τ_{ci}^* vs d_i/d_{50} for all the experimental sediment mixtures are very similar and fall in the narrow range of –0.962 to –1.055, even though mixture standard deviation ranges from 1.53 to 1.96. The trends for all the sediments including present experiment fall in the narrow range of –0.92 to –1.1. Like ref. [19] the present experimental data strongly support that relative size of sediments contribute significantly to variation in τ_{ci}^* rather than mixture sorting. Values of α and β for the experimental data and other available data is being determined from the fitting of these data and is given in table 4.

TABLE 4. LEAST SQUARES FIT TO $\tau_{ci}^* = \alpha\left(\frac{d_i}{d_{50}}\right)^{\beta}$ FOR THE SEDIMENT MIXTURES.

Mixture Type	α	β	Reference
S1	0.0282	-1.055	Experiment
S2	0.0269	-0.970	do
S3	0.0269	-0.997	do
S4	0.0234	-0.962	do
Patel M1	0.0593	-1.041	Patel and Ranga Raju (1999)
Patel M2	0.0578	-1.028	do
Patel M3	0.0498	-0.979	do
Patel M4	0.0559	-1.100	do
Patel M5	0.0622	-1.002	do
MIT ½ ϕ	0.0301	-1.006	Wilcock and Southard (1988)
MIT 1ϕ	0.0356	-0.970	do
DAY B	0.0368	-0.953	do
MISRI N1	0.0475	-0.997	do
MISRI N2	0.0415	-0.953	do
MISRI N3	0.0371	-0.920	do
Oak Creek	0.0732	-0.979	do

B. *Effect of Grain Reynolds Number (Absolute Size Effect)*

To show the effect of grain Reynolds number on critical shear stress, values of dimensionless critical shear stress for each fractions of sediment mixtures is being plotted against the corresponding values of grain Reynolds number and is shown in Fig. 9. It is seen that for the finer fractions, similar sizes of different mixtures move at almost the same Reynolds number wherein for the coarser fractions it differs significantly. It tells the fact that the absolute size effect is significant for coarser fractions than the finer ones in these experimental data sets.

C. *Development of a New Relationship*

To find a relationship for the calculation of critical shear stress of any size fraction for the experimental sediment mixtures, the values of τ_{ci}^* determined from the reference transport method are normalized using reference stresses for median-sized fractions τ_{c50}^* and plotted against $\frac{d_i}{d_{50}}$. The reason behind using τ_{c50}^* rather than other values (i, e., mean value, geometric mean value) is that it is widely used and Shields' threshold curve is related with this. For sediment mixture S3 the plotting of $\frac{\tau_{ci}^*}{\tau_{c50}^*}$ vs $\frac{d_i}{d_{50}}$ is shown in Fig. 10. A least square fit to $\frac{\tau_{ci}^*}{\tau_{c50}^*} = \alpha\left(\frac{d_i}{d_{50}}\right)^{\beta}$ of these data can be made. The coefficients and exponents of straight lines fitted to these data are given in table 5.

The slopes of the $\frac{\tau_{ci}^*}{\tau_{c50}^*}$ - $\frac{d_i}{d_{50}}$ relations fall within a fairly small range of –0.962 to –1.05 and the correlation coefficient for each mixture is almost 1.0, which represents a good correlation. The coefficient of $\frac{\tau_{ci}^*}{\tau_{c50}^*}$ - $\frac{d_i}{d_{50}}$ relations also closes to unity.

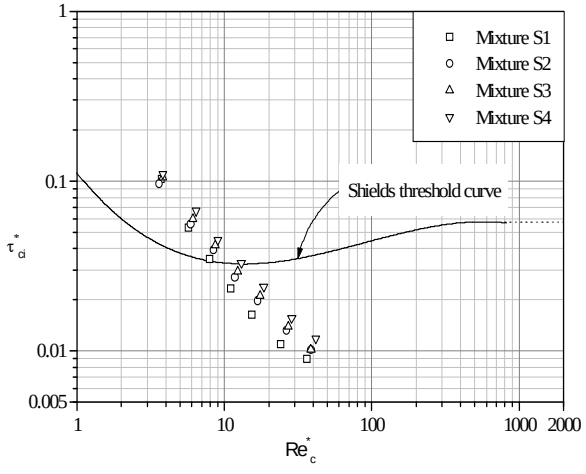

Figure 9. Variation of τ_{ci}^* with grain Reynolds number

TABLE 5. LEAST SQUARE FIT TO $\frac{\tau_{ci}^*}{\tau_{c50}^*} = \alpha\left(\frac{d_i}{d_{50}}\right)^{\beta}$ FOR THE EXPERIMENTAL SEDIMENT MIXTURES

Mixture Type	α	β	R^2
S1	1.09	-1.05	0.989
S2	1.05	-0.97	0.998
S3	1.03	-0.996	0.999
S4	1.04	-0.962	0.999

All these values tell the fact that all sediment fractions move at almost the same shear stress. This is the manifestation of the common feature of nonuniform sediment mixture that in sediment mixtures, smaller particles are shielded by coarser grains and need a higher shear stress for mobilization and larger particles are entrained at lower shear stress because of increased exposure and instability than in a bed of uniform sediment. The variations of the exponent values of $\frac{\tau_{ci}^*}{\tau_{c50}^*}$ - $\frac{d_i}{d_{50}}$ relations are due to mixture sorting, skewness and modality. Plot of $\frac{\tau_{ci}^*}{\tau_{c50}^*}$ vs $\frac{d_i}{d_{50}}$ can also be made for the whole sediment mixtures. In Fig. 11 the experimental data is being plotted and least square fit to these data shows a consistent trend. It can be represented by an equation that can be used to calculate critical shear stress of different size fractions in a sediment mixture. Experimental data along with the available data sets also fall into a straight line, which is shown in Fig. 12. Equations representing these two lines can be compared and it is shown below

For experimental data:

$$\frac{\tau_{ci}^*}{\tau_{c50}^*} = 1.05\left(\frac{d_i}{d_{50}}\right)^{-0.99} \tag{7}$$

For experimental and all available data:

$$\frac{\tau_{ci}^*}{\tau_{c50}^*} = 1.06\left(\frac{d_i}{d_{50}}\right)^{-0.98} \tag{8}$$

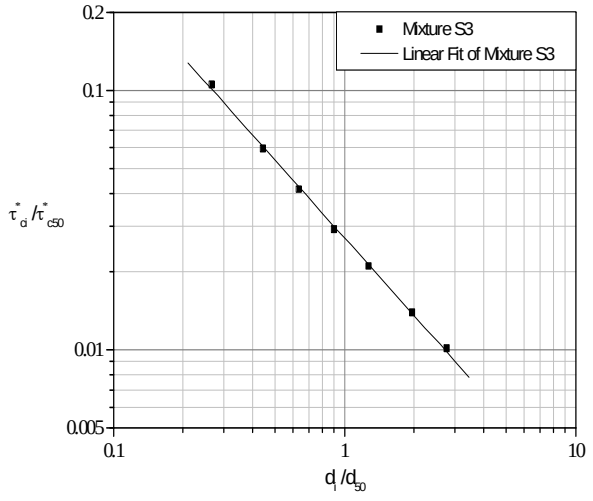

Figure 10 Variation of $\frac{\tau_{ci}^*}{\tau_{c50}^*}$ with $\frac{d_i}{d_{50}}$ for sediment mixture S3

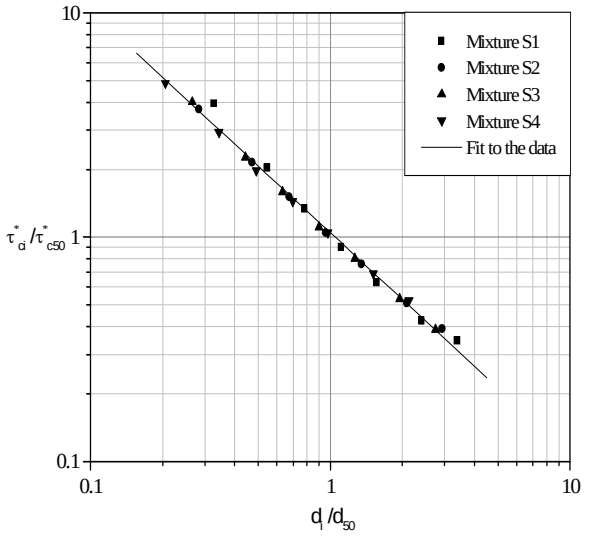

Fig. 11 Variation of $\frac{\tau^*_{ci}}{\tau^*_{c50}}$ with $\frac{d_i}{d_{50}}$ for the experimental sediment mixes

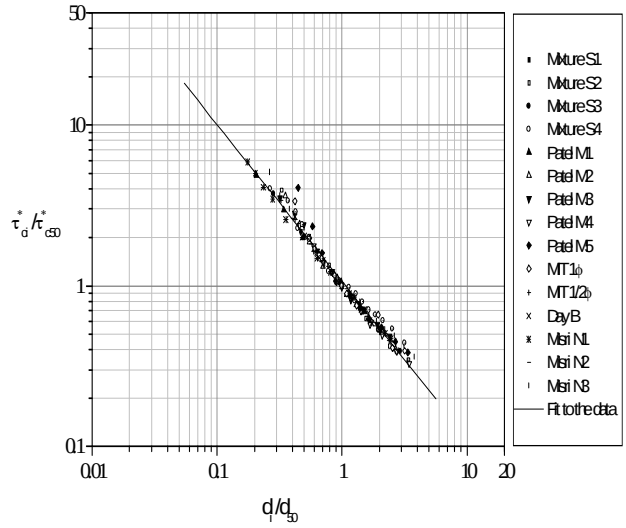

Figure 12. Variation of $\frac{\tau^*_{ci}}{\tau^*_{c50}}$ with $\frac{d_i}{d_{50}}$ for all available data sets

Comparison of these two equations shows a very similarity to each other. This result tells the fact that the results of experimental sediment mixtures are consistent with the results of other sediment mixtures. The relative variation of dimensionless critical shear stress for each size fraction with respect to a central value (median size) is consistent for different sediment mixtures. So, either of the equations can be used to represent the critical shear stress of individual fractions for sediment mixtures.

D. A New Approach to the Calculation of Critical Shear Stress of Median-Sized Sediment

Values of τ^*_{c50} are necessary for the calculation of critical shear stress of different fractions in sediment mixtures. The mobility of median – sized fraction is being compared with the Shields' threshold curve derived for uniform sediments in Fig. 13. Scatter from the Shields' threshold curve is found for the experimental sediment mixtures and for other values available in the literature. Different researchers have recommended different ideas for the computation of the value of τ^*_{c50}. Among those ref. [10] recommended τ^*_{c50} = 0.0876. Some investigators like ref. [16 and 19] recommended that τ^*_{c50} be calculated using Modified Shields' method or 88% of the above value. But the actual values of τ^*_{c50} found to be departed significantly from the above values.

We know that nonuniformity of sediment affects τ^*_{c50} and the measure of nonuniformity of sediment is the geometric standard deviation, σ_g.

By taking these two parameters, we can write,

$$\tau^*_{c50} = F(\sigma_g) \tag{9}$$

from the definition of grain Reynolds number, R^*_c

$R^*_c = \frac{u_{*c}d}{\upsilon}$, where u_{*c} is the shear velocity. From which it can be derived

$$\tau^*_{c50} = \frac{R^2_{*c}\upsilon^2}{(s-1)gd^3} \tag{10}$$

Replacing τ^*_{c50} from equation (10) into equation (9) gives,

$$\frac{R^2_{*c}\upsilon^2}{(s-1)gd^3} = F(\sigma_g)$$

$$\text{or, } R_{*c} = F\left[\left(\sigma_g^{1/2}d^{3/2}\right)\sqrt{\frac{(s-1)g}{\upsilon^2}}\right] \tag{11}$$

Regression with the available data sets as shown in Fig. 14, equations of the form of 11 found as,

$$R^*_{c50} = 0.09\left(\sigma_g^{1/2}d_{50}^{3/2}\frac{\sqrt{(s-1)g}}{\upsilon}\right)^{1.05} \tag{12}$$

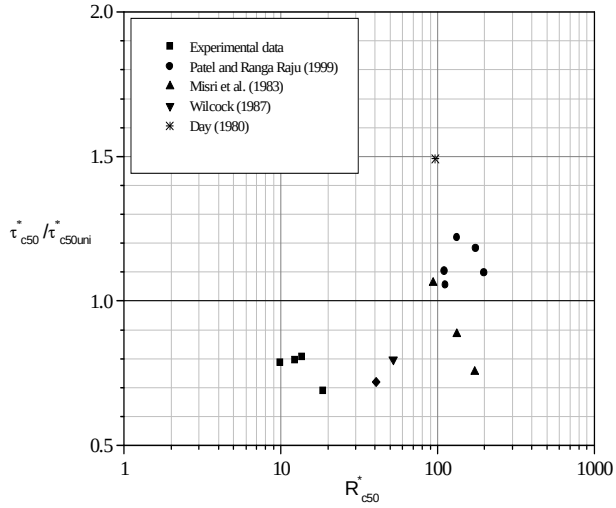

Figure 13. $\frac{\tau^*_{c50}}{\tau^*_{c50uni}}$ versus grain Reynolds number R^*_{c50}

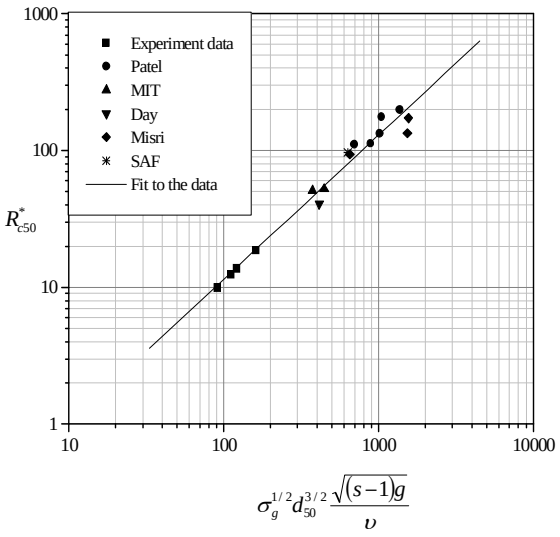

Figure 14. R^*_{c50} versus $\sigma_g^{1/2} d_{50}^{3/2} \frac{\sqrt{(s-1)g}}{\upsilon}$

VI. CONCLUSION

From analysis of experimental data sets along with those available from earlier investigations, the following conclusions can be drawn.

The critical shear stress of individual fractions depends largely on relative size and absolute size of different fractions with respect to median size. A relation has developed for calculation of critical shear stress of different fractions in sediment mixtures. The relationship reveals the fact that all sediment fractions move at almost the same shear stress, i.e., smaller particles are shielded by coarser grains and need a higher shear stress for mobilization and larger particles are entrained at lower shear stress because of increased exposure and instability than in a bed of uniform sediment.

Present analysis shows inadequacy of using Shields' diagram for the value of critical shear stress of median sized sediment (τ^*_{c50}). A new relationship has developed here for the value of τ^*_{c50} .

ACKNOWLEDGMENT

The authors are greatly indebted to Bangladesh University of Engineering and Technology (BUET) for allowing the laboratory facilities and providing necessary financial assistance. Comments and suggestions for various colleagues are also gratefully acknowledged.

REFERENCES

[1] Andrews, E. D., 1994, Marginal Bed Load Transport in A Gravel Bed Stream, Sagehen Creek, California, *Water Resources Research*, 30 (7), 2241-2250.

[2] Ashworth, P. J., and R. I. Ferguson, 1989, Size-Selective Entrainment of Bed Load in Gravel Bed Streams, *Water Resources Research*, 25(4), 627-634.

[3] Buffington, J. M., 1999, The Legend of A. F. Shields, *Journal of Hydraulic Engg*., ASCE, 125 (4), 376 – 387.

[4] Buffington, J. M. and D. R. Montgomery, 1997, A Systematic Analysis of Eight Decades of Incipient Motion Studies, With Special Reference to Gravel – Bedded Rivers, *Water Resources Research*, 33 (8), 1993 – 2029.

[5] Chang, H. H., 1988, Fluvial Processes in River Engineering, John Wiley and Sons Inc., USA.

Chow, V. T., 1986, Open Channel Hydraulics, McGraw Hill Book Company, International Edition.

[6] Garde, R. J., and K. G. Ranga Raju, 1985, Mechanics Of Sediment Transportation and Alluvial Stream Problems, Second Edition, Wiley Eastern Ltd., New Delhi, India.

[7] Kuhnle, R. A., 1994, Incipient Motion of Sand-Gravel Sediment Mixtures, *Journal of Hydraulic Engg.*, ASCE, 119 (12), 1400-1415.

[8] Misri, R. L.,R. J. Garde, and K. G. Ranga Raju, 1984, Bed Load Transport of Coarse Nonuniform Sediment, *Journal of Hydraulic Engg*., ASCE, 110 (3), 312-328.

[9] Parker, G., and P. C. Klingeman, 1982, On Why Gravel Bed Streams Are Paved, *Water Resources Research*, 18 (5), 1409-1423.

[10] Parker, G., P. C. Klingeman, and D. G. Mclean, 1982, Bed Load and Size Distribution in Paved Gravel Bed Streams, *Journal of Hydraulic Engg*., ASCE, 108 (4), 544-571.

[11] Patel, P. L., and K. G. Ranga Raju, 1999, Critical Tractive Stress of Nonuniform Sediments, *Journal of Hydraulic Research*, 37 (1), 39-58.

[12] Shvidchenko, A. B., G. Pender, and T. B. Hoey, 2001, Critical Shear Stress for Incipient Motion of Sand/Gravel Streambeds, *Water Resources Research*, 37 (8), 2773-2783.

[13] Vanoni, V. A., 1975, Sedimentation Engineering, ASCE Manuals and Reports on Engineering Practices, No. 54, 91-114, ASCE, New York.

[14] Vanoni, V. A., P. C. Benedict, D. C. Bondurant, J. E. McKee, R. F. Piest, and J. Smallshaw, 1966, Sediment Transportation Mechanics; Initiation of Motion, *Journal of Hydraulic Engg*., ASCE, 92 (2), 291-314.

[15] Wilcock, P. R., 1988, Methods for Estimating the Critical Shear Stress of Individual Fractions in Mixed Size Sediments, *Water Resources Research*, 24 (7), 1127-1135.

[16] Wilcock, P. R., 1993, Critical Shear Stress of Natural Sediments, *Journal of Hydraulic Engg*., ASCE, 119 (4), 491-505.

[17] Wilcock, P. R., and B. W. McArdell, 1993, Surface-Based Fractional Transport Rates: Mobilisation Thresholds and Partial Transport of A Sand-Gravel Sediment, *Water Resources Research*, 29 (4), 1297-1312.

[18] Wilcock, P. R., and B. W. McArdell, 1997, Partial Transport of A Sand/ Gravel Sediment, *Water Resources Research*, 33 (1), 235-245.

[19] Wilcock, P. R., and J. B. Southard, 1988, Experimental Study of Incipient Motion in Mixed-Size Sediment, *Water Resources Research*, 24 (7), 1137-1151.

[20] Wilcock, P. R., and J. B. Southard, 1989, Bed Load Transport of Mixed Size Sediment: Fractional Transport Rates, Bed Forms, and The Development of A Coarse Bed Surface Layer, *Water Resources Research*, 25 (7), 1629-1641.

Protecting canal banks and pipeline crossings against scour in the Hartelkanaal, Rotterdam

G. van der Hout*, T. Blokland*
* Rotterdam Public Works, Rotterdam, Netherlands

In november 1997, the Beerdam, at the seaward end of the Hartelkanaal in Rotterdam, was opened to create a free route for inland navigation. This paper gives an overview of the design and realisation of protection works before opening the Beerdam and shows in the severe scour and erosion which occurred in the western part of the canal.

I. INTRODUCTION

The Hartelkanaal in the harbor area of Rotterdam is 20 km long canal for inland navigation. Until 1997 the Hartelkanaal was dead ended by a dam, the Beerdam, in the western, seaward end of the canal. At the eastern, landward end, the canal has an open connection with a tidal river, the Oude Maas. The tidal water volume of the Hartelkanaal and the connected harbor basins was entering and leaving the canal from the Oude Maas.

In November 1997 an opening was excavated in the Beerdam, which resulted in a drastic change of hydraulic conditions. The aim of the so called “Open Beerdam” was to provide an open connection for inland navigation to the Maasvlakte, were increasing activities in bulk and container transport take place.

From this moment, the tidal water volume was entering and leaving the canal mainly from the seaward end of the canal. This resulted in an increase of flow velocities and caused heavy erosion in some parts of the canal.

This paper focuses on the most western part of the Hartelkanaal, between the Beerdam and the Dintelhaven.

This part of the canal is relatively narrow, while the passing tidal volume here became relatively large. Before opening the Beerdam, extensive studies were worked out to predict the increase of flow velocity and the erosion rate. Because heavy erosion was expected here, extensive bottom protection works were realized.

The southern bank of the Hartelkanaal is part of the foreshore of the Brielse Maasdijk, a primary water retaining structure. In order to guaranty the safety level of this structure, an extensive program was started for monitoring the bottom level of the canal and scour of the underwater slopes of the southern bank.

II. SITUATION BEFORE OPENING THE BEERDAM

The western part of the Hartelkanaal, between the Beerdam and the Dintelhaven, has a relatively small cross section profile compared to other stretches of the Hartelkanaal. The canal is at NAP-level approximately 140 m wide in this area. The bed level varies between 6 and 8 m below NAP (Dutch Ordnance Datum, which is approximately equal to the local mean water level), with an average depth of NAP -7,25 m. The guaranteed depth for the navigation is NAP -6,10 m, based on the required depth for a push barge combination at extreme low water conditions. The discharging surface of a cross section is about 763 m^2 below NAP. The discharge in the most western part of the Hartelkanaal, lies around 100 m^3/s for both ebb and flood period.

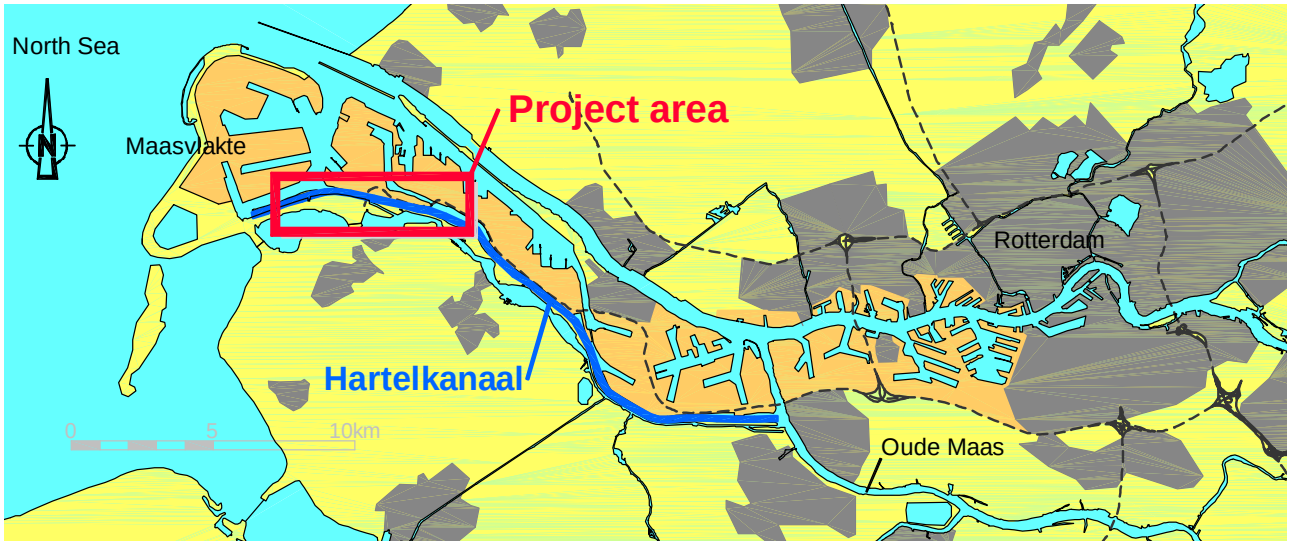

Figure 1: Map of project area

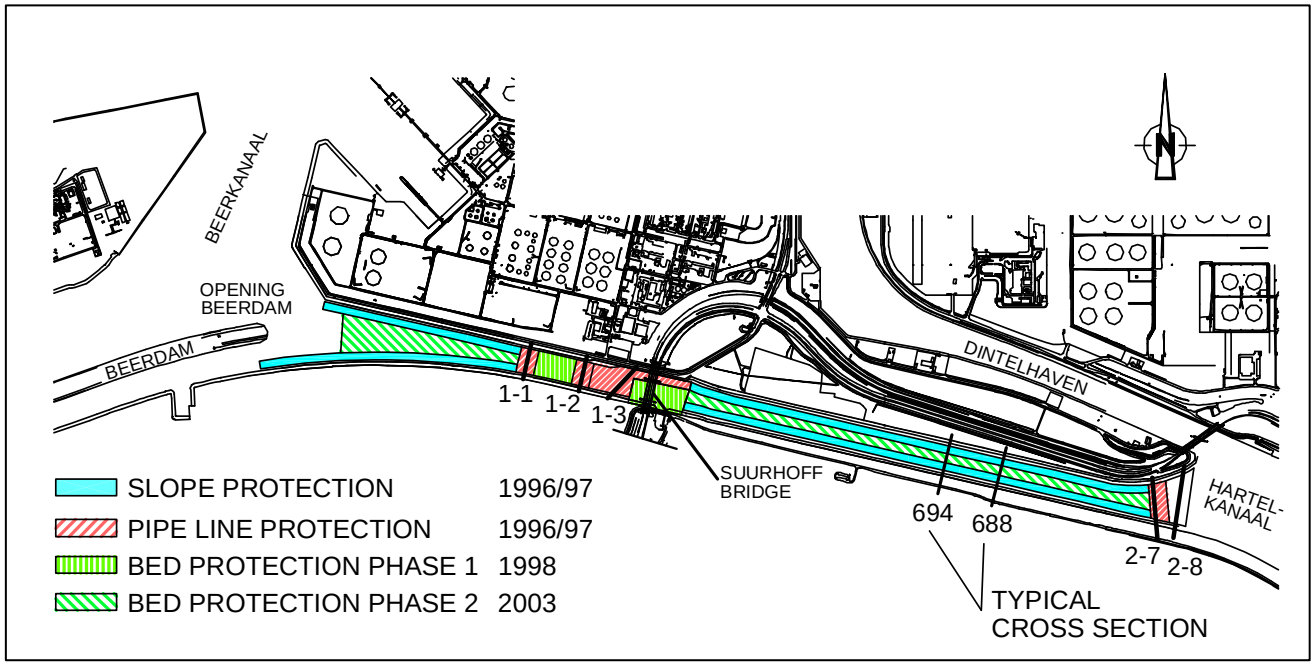

Figure 2: Project area

The banks are protection with rubble and hand placed stone from crest until NAP -4 m. The under water slope gradient is 1:4. Figure 3 gives a typical cross section for this part of the Hartelkanaal.

The Hartelkanaal is situated in the former delta of the river Rhine. Due to this fact some former flow channels are found here. From ground level till NAP -20 m the underground consist of sand which is strongly stratified with clay layers, dating from the Holocene period (Duinkerken, Calais). These Holocene layers are characterized by an irregular pattern of sand and thin, sandy clay layers of varying width.

III. PREDICTED HYDRAULIC AND MORFOLOGIC CHANGES

A. *Hydraulic conditions*

Until 1997 the tidal water volume of the Hartelkanaal and the connected harbor basins was entering and leaving the channel from the Oude Maas. As a result of opening the Beerdam, the main tidal water volume is entering and leaving the channel mainly from the seaward end of the channel. Also part of the river discharge from the Oude Maas is transported towards the sea through the Hartelkanaal. This means that, after excavating the Beerdam, the Hartelkanaal changed from a “dead ended channel” into a water discharging river “branch” with a relatively strong tidal flow. The maximum tidal discharge is about 7 times larger than the river discharge, and the river discharge volume is about 30% of the total tidal volume through the opening in the Beerdam. The tidal volume changes relatively strong along the Hartelkanaal: at the opening in the Beerdam the tidal volume is 2 times larger than the tidal volume at the debouchments at the Oude Maas.

The tidal discharge and currents in the western part of the Hartelkanaal depend on the local bed level. A lower bed level due to erosion will result in smaller tidal current velocities and meanwhile in an increase of tidal discharges, due to a decrease of hydraulic resistance.

The tidal discharges and the current velocities (averaged over a cross section) are calculated by the 1-dimensional model ZWENL for different bed levels. The result of these calculations for the original bed level (NAP-7,25 m) en for a strongly eroded canal bed (NAP-15 m) are presented in table I.

B. *Morphological modelling*

In general, river branches are characterized by a typical cross section which is related to a morphological equilibrium state. After changes in the hydraulic conditions, a river bed will reach a new equilibrium profile by erosion or sedimentation. In a tidal river, the equilibrium profile is strongly related to the total volume of water passing the river during a tidal period, i.e. the sum of water volume during ebb and flood period. Excavating the Beerdam will result in morphological changes of the bed of the Hartelkanaal in order to reach the equilibrium profile. In the most western part of the Hartelkanaal, between the Beerdam and the Dintelhaven, the tidal volume and therefore the equilibrium profile is the largest, while the cross section is relatively narrow. This means that a this part of the channel, strong erosion can be expected.

The western part of the Hartelkanaal lies in between two channel sections which a (much) larger cross profile. Westwards of opening in the Beerdam there is the Beerkanaal, which is 25 m deep and a 400 m wide entrance to several harbor basins for large seagoing vessels. The Beerkanaal has – contrary to the Hartelkanaal – a silty bed with very small current velocities near the bed, thus no sediment will be transported from the Beerkanaal into the Hartelkanaal. Eastward of the Dintelhaven there is a 2 km long relatively wide section of the Hartelkanaal. The width of this section is 500 m at NAP. Current velocities are smaller here than in the western section, so the amount of sediment which entering the western part of the canal during ebb is much smaller than the sediment transport capacity in the western section. This, combined with the fact that no sediment

enters the canal from the Beerkanaal – means that the western section will erode at least until the cross section of the western part is as large as the cross section of the Hartelkanaal eastward of the Dintelhaven. This cross section is about 3.200 m.

The most conservative prediction of the equilibrium profile is that the canal bed will erode until the current velocities are reduced below the threshold for "start of movement" for the sand particles. With the predicted discharges from the ZWENDL model, this results in a equilibrium profile of 3.000 m^2.

Table 1 gives the actual surface of a cross section, using the original width of the channel at still water level and bank slopes of 1:4.

TABLE I.
MAXIMUM FLOW VELOCITIES AND DISCHARGES BEFOR E AND AFTER OPENING THE BEERDAM

	Before 1997 bed level NAP -7,25 m	Directly after opening bed level NAP -7,25 m	End situation bed level NAP -15 m
U_{max} [m/s]	0,2	1,25	1,0
Q_{max} [m^3/s]	136	1.004	1.120
Q_{min} [m^3/s]	-96	-1.200	-1.416
Surface of cross section [m^2]	763	763	1.106

It is very clear that in the end situation, with a bed level of NAP -15 m, the actual surface of a cross section is much smaller than the equilibrium profile. The equilibrium profile cannot be reached in between the original banks of canal. Increasing the width of the river was considered as a non-realistic option, taken into account the cost of dredging, replacing bank protection and "space" in the main port area. This implied that, in the future, the canal bed at a certain level, around NAP -15 m, should be protected for further erosion.

For a more detailed prediction of the morphological changes, a numerical model was build. Results of this model showed that directly west of the eastern pipeline protection, the minimum bottom level of NAP -15 m would be reached between 0,8 and 7,7 years. Directly east of the western pipeline protection (close to the Suurhoffbrug) the minimum bed level would be reached within 2,9 and more than 10 years.

C. Geotechnical stability

Before the opening of the Beerdam, an extended geotechnical survey was done, in order to check the failure rate of the Brielse Maasdijk, the primary water retaining structure at the southern bank of the Hartelkanaal According to Dutch legislation, the failure mechanisms of instability of the outer and inner slope, piping and overflow of the crest were taken into account.

The stability of the crest was calculated using the Bishop method. This was done for the original situation (bottom level NAP -7,25 m) and for the situation with a improved dike (crest height enlarged from NAP +5,70 m to NAP +6,20 m), related to the increased water level in the Hartelkanaal. Because severe scour of the bottom was expected due to the increase in flow velocity, also a situation with an under water slope of 1:4 and bottom level NAP -15 m, was investigated.

For the characteristic cross section 692 (see Figure 2) the stability factor is 1,40 for both the original cross section and the improved dike [x]. In the situation with the eroded river bed the stability factor is 1,37, which shows that erosion of the under water slope has an marginal effect on the stability. The stability factor must be at least 1,12, according to the safety level of the Brielse Maasdijk.

TABLE II.
STABILITY FACTORS IN CROSS SECTION 692

Situation	**Stability factor (Bishop)**
original situation	1.40
new situation: increased water level and improved dike	1.40
new situation: increased water level and improved dike eroded banks and bed level NAP -15 m	1.37
critical value	1.12

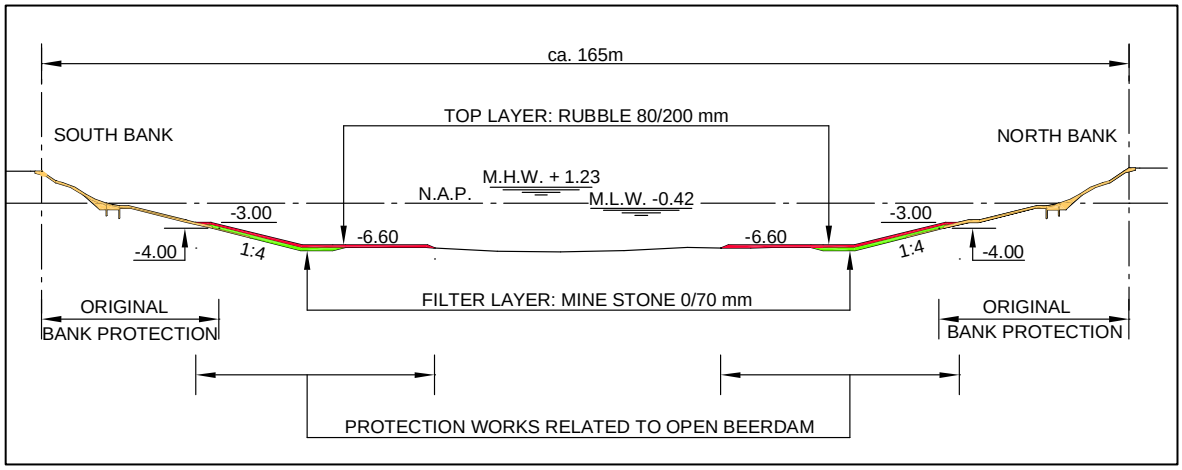

Figure 3: Typical cross section of the western part of the Hartelkanaal

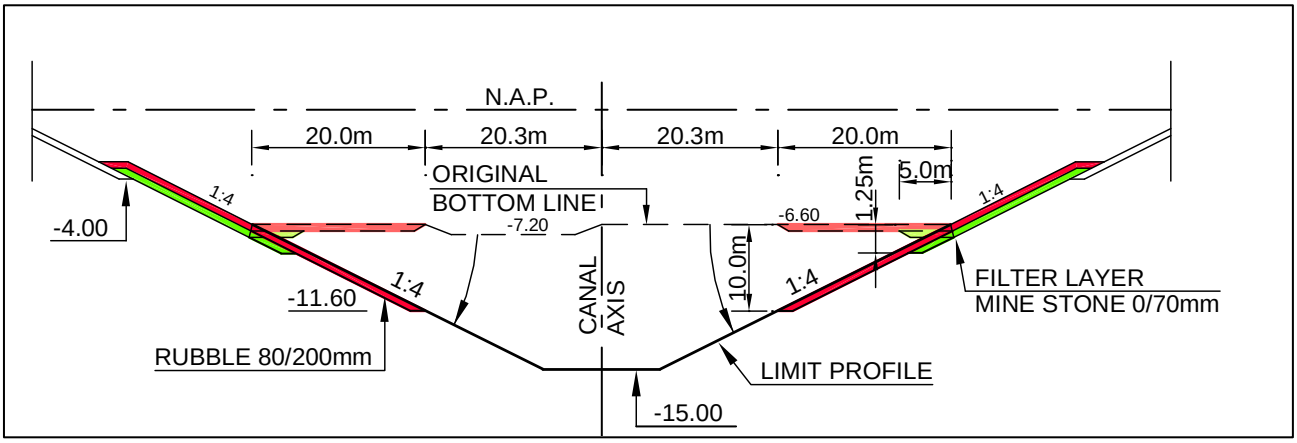

Figure 4: Slopeand toe protection with predicted settlement of toe

IV. CANAL BANKS AND TOE PROTECTION

To guarantee the stability of the canal banks, the under water slope from the toe of the original protection at NAP -4 m to the canal bed and the adjacent 20 m of the flat canal bed were protected with a rubble layer.

A. *Design method for the top layer*

The design of the top layer of the protection works is rather special, because it is not based on a stability formulae with one maximum design load. The design is based on a quasi-probabilistic calculation of movement of stones using the Shields parameter and the transport relation of Paintal. The expected maintenance works, related to the movement of stones, are estimated.

The hydraulic loads which were taken into account are a combination of maximum ebb current, a seiche current and a return current caused by a full loaded push barge combination sailing in upstream direction, eccentric from the canal axis. The return current *under* the bow of the barge is taken into account, which is about two times larger than the mean return current *around* the ship. The stability of the stones is calculated in a quasi-probabilistic way, using the Shields-parameter, in which the bottom shear stress is caused by a combination of ebb, seiche and return current. Also variations in the current velocities are taken into account. Transport of the stones is calculated with the relations of Paintal. In a situation without ships, a rubble layer of standard sort 80-200 mm would be stable, without moving stones. In combination with a return current, at the slope and also at the 20 m width toe protection, the movement of stones is almost none. Only in more negative scenario where the current velocities are higher than the expected value, substantial movement of stones occurs. Under some circumstances in these scenarios one passing ship can move almost all stones in the upper layer. Because the stones mainly remain in the protected area, the damage is limited, although frequent monitoring is required. In the years after opening the Beerdam the flow velocities will decrease which reduces the movement of stones in the protection layer.

The rubble top layer consist of broken stone standard sort 80-200 mm. On the bank and the adjacent 5 m of the flat bed the 0,40 m thick top layer is placed at a filter layer, which consists of mine stone 0-70 mm with a layer thickness of 0,50 m. For the remaining 15 m toe protection the top layer was put directly on the canal bed.

This part of the bed protection was aimed to settle along with the erosion of the unprotected bed, until a stable slope gradient was reached.

B. *Imperfect filter and falling apron mechanisms*

For the settlement of the toe protection, two settlement mechanisms were taken into account: the “imperfect filter” and the “falling apron” mechanism.

In case of an imperfect filter, sand can wash out through the stones of a protective rubble layer because of the absence of a filter layer. Theoretically the permeable rubble layer should settle with the erosion of the unprotected bed uniform over the full stretch of the protection. Due to the settlement of the bed level protection the flow velocities reduce to a rate were no sand will be washed out and no further settlement occurs. There were no reliable relations available to predict the hydraulic loads at which a rubble layer of standard sort 80-200 mm is non sand permeable. Extrapolation of data for geometrically open filter layers of relatively fine stone, indicate that already in the situation with a non eroded bed and thus high velocities, the top layer will be almost sand tight. As this extrapolation is not verified, it is quite unreliable. Also the impact of water movements caused by ships is hard to quantify.

In case of a falling apron the settlement is due to local instabilities at the edge of a protection layer, caused by small scale slides or movement of stones. The settlement of the protection layers involves sideward movement of stones, which reduces the layer thickness and thereby effects the sand permeability and thus intensifies the imperfect filter mechanism. Laboratory test indicated a resulting slope of 1:3, for a situation of a rubble layer, 1 – 2 times D_{50}, placed on loosely packed sand.

Whereas in the Hartelkanaal the bed material is not loosely packed but contains a certain amount of clay, and the top layer is 2,7 stones thick, it is uncertain what the slope in the end situation will become.

It was expected that, with the relatively large layer thickness used for the slopes, the falling apron mechanism would dominate the imperfect filter. When also the falling apron mechanism; would not react as predicted, a steep slope could develop directly adjacent to the toe protection, which caused the risk of large scale slope instabilities (slides). To reduce this risk, the layer thickness of the toe protection was reduced, compared with the slope protections, to 0,30 m ((2 * D_{50}).

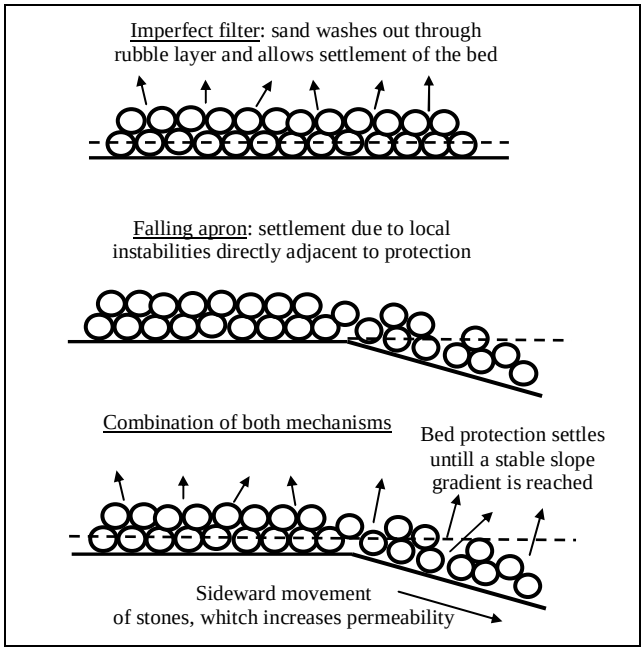

Figure 5:
Theory of "imperfect filter" and "falling apron"

The geotechnical stability of a steep slope directly adjacent to the toe protection was calculated using the Bishop method. In case of a slope gradient of 1:3, the stability factor is 1,39; for slope gradients steeper than 1:3 the stability factor reduces to 1,20 for a gradient of 1:2. The critical stability factor is 1,12.

When the bed in the middle of the canal would reach a level below NAP -15 m, it would be protected over the full width of the canal in order to prevent further erosion and instability of the slopes.

C. Pipeline crossings

In the western part of the Hartelkanaal at 4 locations, bundles of pipelines and cables cross the Hartelkanaal in one or more pipelines. The locations are indicated on the map in Figure 2 and are numbered 1-1, 1-2, 1-3 and 2-7/2-8. The expected bed level after the opening of the Beerdam is a few meters below the level of the pipelines. Protective rubble layers at these locations should prevent erosion of the canal bed. The minimum soil cover on the pipelines depends on the burial depth of the anchors of push barges and the tolerance in construction depth of the pipe lines. Laboratory tests performed in the 80s showed that the burial depth for a Danforth anchor can be as much as 1,40 m in a sand bed. With a 0,3 m tolerance in construction height for the pipeline itself, the minimum ground cover on a pipeline must be 1,70 m. This height includes the rubble protection layer.

During the process of the design of the protection works, the choice is made to protect the canal bed in between the pipeline protections *after* opening the Beerdam, when the canal bed is eroded to a certain level. The main reason for this choice is financial: due to the reduction in flow velocities caused by a lower level of the canal bed, the required dimensions of the rubble layer are less and thus the protection is cheaper. Some years of delay of investment cost, depending on the erosion rate of the canal bed, is financially attractive. On the other hand, it requires intensive monitoring to reduce the risk of instability of pipeline protections and slopes. Another negative consequence is the fact that the bed level of the pipeline protections becomes relatively high compared to the eroded, unprotected bed. This causes local changes in flow velocities, which effects the inland navigation. Also hydraulic loads on the pipeline protection itself increase.

In the first phase, three pipeline protections were realized: one protection for pipeline1-1, a protection for pipelines 1-2 and 1-3 and a protection for 2-7/2-8 (the so-called eastern protection). The protection for 1-3 is combined with the protection of the pier of the Suurhoffbrug. A few years after opening the Beerdam, in 1998, the area in between pipe lines 1-1 and 1-2 is covered with mine stone 10-125 mm. The slopes are covered with a variable layer thickness, in a way that the slopes are 1:3,5 until the level of the eroded canal bed. The flat bed is covered with a 0,30 m thick layer. Together with pipe lines 1-1 and 1-2 this is called the western pipeline protection. The area under the Suurhoffbrug is also protected with the same type of stone in this phase.

For the eastern pipeline protection, the choice is made to protect only pipeline2-7 with a new rubble layer. At the location of pipeline2-8, an existing rubble protection (sort 10-60 kg) shall give enough protection for a first phase. Dredging away this existing protection layer will give a high risk of damaging the pipelines, while the ground cover above the pipeline and cables has a critical thickness. Directly after the opening of the Beerdam, sedimentation is expected at this location, because of the supply of sediment from the narrow western part of the Hartelkanaal, where heavy erosion is expected. Monitoring the development of the bed level should indicate at which time erosion at the location of pipeline 2-8 brings the bed level at a critical level of NAP -6,75 m.

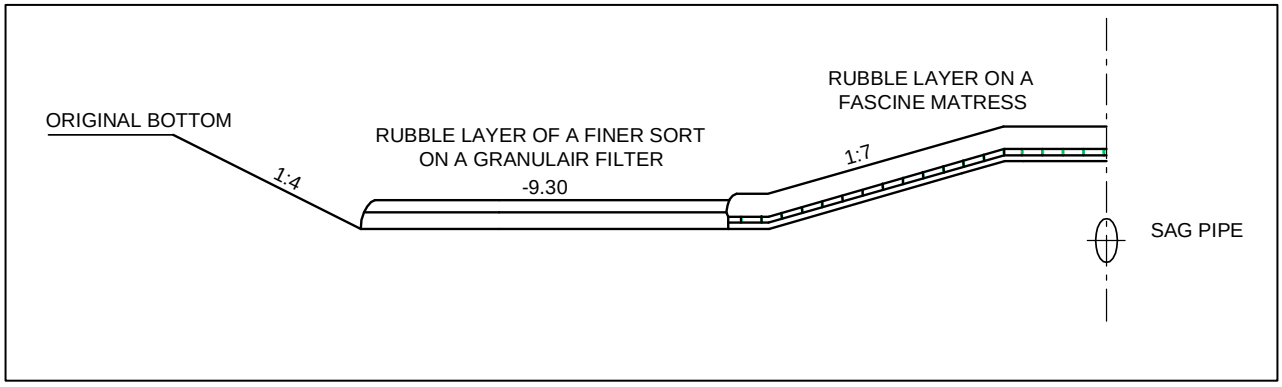

Figure 6: General design of pipeline protection

Figure 6 gives a general design of a pipeline protection. Directly above the pipeline, it consist of a rubble layer on a fascine mattress with a geotextile. The area in between the pipeline protections is covered with a rubble layer of a finer sort, on a granular filter layer. The transition area from the pipeline protection to the unprotected canal bed has a gentle slope gradient of 1:7, to prevent the separation of flow at the slope. Adjacent to the slope there is a horizontal bed protection ,10 – 20 m wide, at a level of NAP -9,30 m.

Comparable to the design of the bank protection works, the hydraulic loads are a combination of maximum ebb current, a seiche current and a return current caused by a full loaded push barge. The design is made for the morphological "end situation", in which the bed of the Hartelkanaal is eroded until a level of NAP -15 m. In this situation the largest loads occur on the edges of the pipeline protection, caused by the difference between the bed level at the pipeline protections and the level of the unprotected canal bed. This extra load is calculated by multiplying the ebb and seiche current with factor 1,2.

The dimensions of the top layer are designed by calculating the movement of the stone for different scenario's, and the expected maintenance, i.e. the volume of stones which is needed every year to prevent severe erosion of the top layer. The inaccuracies in both hydraulic conditions and the applied calculating methods, are calculated by a safety factor in the expected maintenance.

The western protection has a top layer consisting of broken stones of standard sort 10-60 kg (60 cm layer thickness) above pipeline1-1, and a top layer of standard sort 40-200 (70 cm layer thick ness) above pipeline1-2 and 1-3. The area between 1-2 and 1-3 is covered with standard sort 10-60 kg and 80-200 mm (30 cm layer thickness). Due to a wider cross section, at the eastern protection occur smaller flow velocities. At this pipeline protection, the top layer consists of broken stone 80-200 mm (layer thickness 30 to 40 cm), on a granular filter consisting of mine stone 0/70 mm. The expected amount of maintenance for the western protection varies between 10 – 1000 ton/year, for the eastern protection it is 0-80 ton/year.

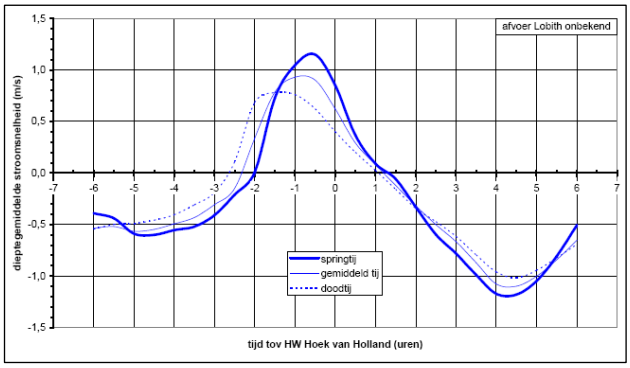

Figure 7: Average measured flow velocities at Suurhoffbrug

V. Scour and Erosion After Opening the Beerdam

A. *Measured hydraulic conditions*

On 8 November 1997, the Beerdam was excavated. At that moment, an extensive program of monitoring started, to be aware of possible erosion and possible risks for slope instability.

The velocities in the western part of the Hartelkanaal are measured at the Suurhoffbrug. The average velocities during one tidal motion, for spring, mean and neap tide are given in figure 1. The figure shows that the maximum velocity for both ebb and flood current is 1,2 m/s, slightly lower that was predicted.

B. *Erosion of the unprotected canal bed*

Figure 8 and 9 show the erosion process of the unprotected bed in cross sections 688 and 694 (Figure 2 gives a map for the location of this cross sections).

The most striking aspect in these figures is the very steep slope gradient which develop directly adjacent to the toe protection (20 m from the transition of the slope to the flat canal bed). Figure 10 and 11 give a closer look to the slopes for cross section 688. Within a period of a few months, very steep slopes develop, which move in the direction of the banks for only a few meters during the first two years, and by then remain completely stable. Directly from the start of the scour process, the slope gradient is very steep, between 1:1,5 and 1:2. It seems to be not at all related to the bed level, which continues to go down. This typical pattern can be seen in almost all cross sections in the western part of the Hartelkanaal.

The toe protection did not settle in the way it was expected. The top of the eroded slope moves back for a few meter towards the canal banks; this length could be a small part of the toe protection which does settle. The reason why the toe protection does not settle at all, or only a small part settles with the erosion of the bed, is not clear.

The flat bed between the steep slopes eroded very quick. In cross section 688 in the first half year, the canal bed eroded from NAP -9,0 m to NAP -14,5 m, with a maximum of 1,5 m/month, an average rate of almost 1 m/month. In the next years, the erosion continued at a lower rate until a level of NAP -16 m in 2003. The erosion is quite symmetric along the canal axis. The cross section 694 shows somewhat lower erosion rates. Here, the bed eroded from NAP -8,5 m to NAP -11,5 m in half a year. In 2003 the bed level was also NAP -16,5 m. The pattern of erosion looks slightly different especially at the southern bank, where an eroded "trench" seems to move sideward to the southern slope. The differences in both cross section are not examined but might be caused by differences in the cohesion of the bed material, due to local clay layers. In 2003, the unprotected bed was fixated with LD-slag, to prevent it from further erosion.

The geotechnical stability of the eroded slopes is investigated by the same way as was done before the opening of the Beerdam, using the Bishop method. In cross section 720 the stability factor in the original situation was 1,18. Using the measured depths of 1998, the stability factor is still 1,18, which is higher than the minimum of 1,12. The stability factor is not influenced by the bed level. Only in case of a slope with a steeper the gradient than 1,2, the stability factor reduces under the

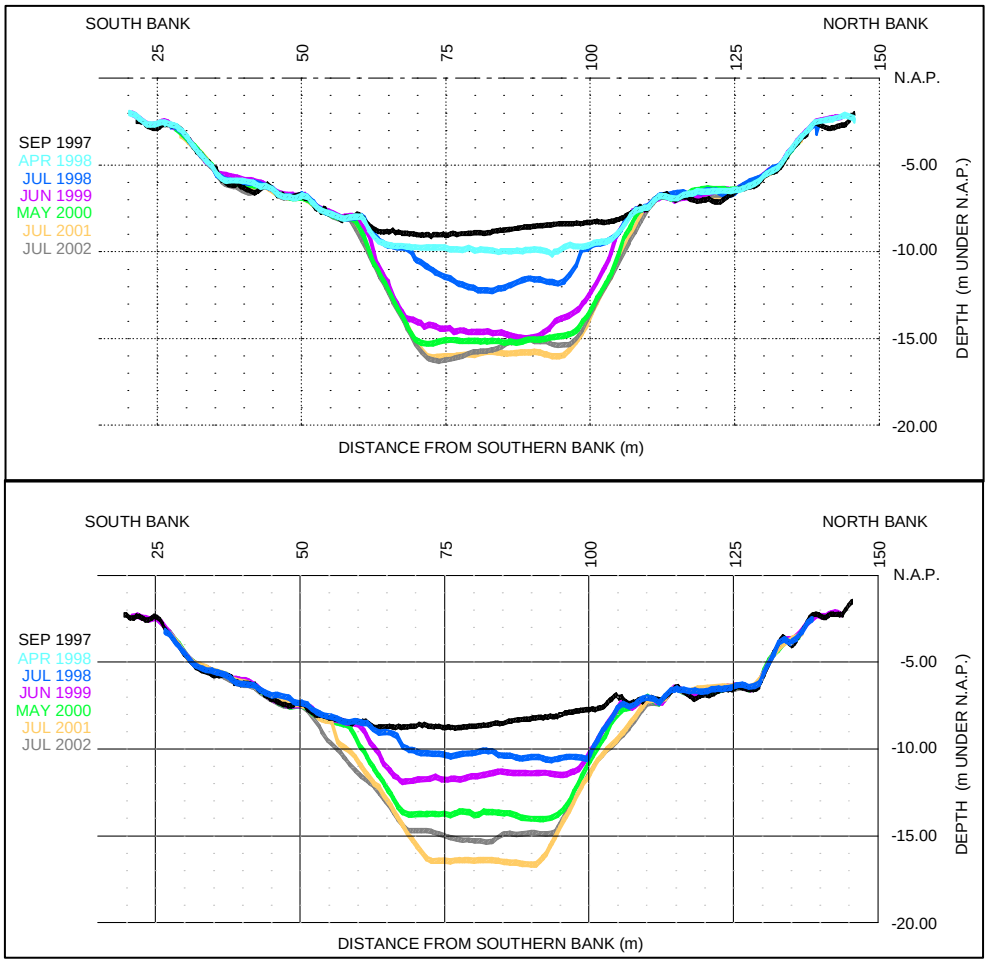

Figure 9: Eroded profile at cross section 688 (upper) and 694 (lower)

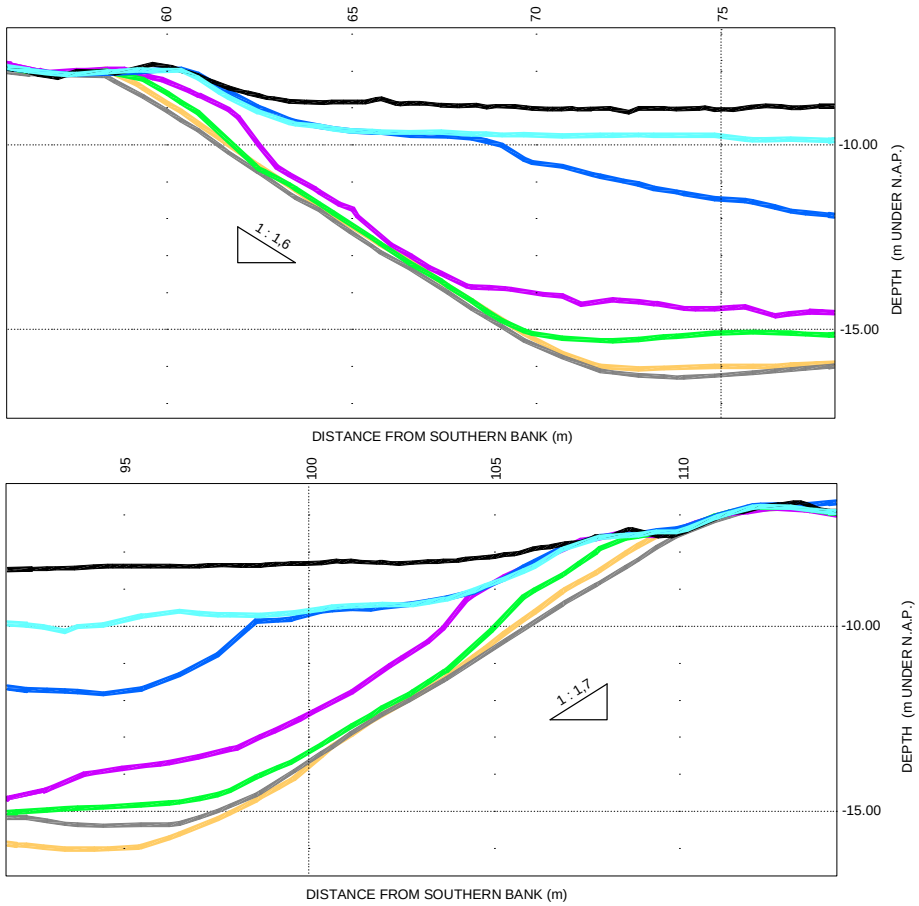

Figure 10 and 11: Eroded slopes at cross section 688

critical value.. The echo soundings shown in the cross sections, do never show a sign of slope instability or slides, despite the continuing erosion of the bed.

Figure 12 (not in draft version) gives a longitudinal profile for this part of the Hartelkanaal, and show the erosion process along the whole section. The erosion process does not start with a higher rate at the eastern or western end, but has a is quite constant along the length of this part of the canal. There are some sections which show less erosion. These differences might be caused by local clay layers, which are more resistant and cohesive. Also the "ridges" which develop but in later echo soundings are suddenly disappeared, must be due to the presence of clay.

C. Scour adjacent to pipeline protections

The longitudinal profile in figure 12 shows very clear the location and geometry of the pipeline protections. It shows that the protections itself and the protected slopes towards the unprotected bottom, are not eroded at all. The unprotected bed in between pipeline1.1 and 1-2 is eroded until a level of around NAP –13 m. In 1998, this part is protected, together with the unprotected bed around the Suurhoffbrug.

Directly east of the pipe line protection at pipeline2-7, within a few months a very deep scour hole developed. A detailed look at the echo soundings is given in figure 13. Within 3 months, the bed level lowered from NAP -7,2 m to NAP -13,4 m, and within a year to NAP – 16 m. The protection at pipeline2-8 remained stable, but the scour hole was close to it and was filled up for some meters with slag to prevent instability of the pipe lines.

The area directly east of pipeline2-8 is a transition area from erosion to sedimentation, because the width of the canal increases in landward direction. The flood current will not follow the strong curve in the Hartelkanaal, but go straightforward and decrease in velocity more eastward. On the other hand, the ebb current will accelerate when entering the western canal section due to the narrowing of the canal profile. During both ebb and flood current, there will occur erosion at this location. Due to the large differences in depth and salinity, at some moment during a tide cycle, waves occur at the surface.

VI. Conclusions

During the erosion process in the western part of the Hartelkanaal, when there is not a morphological equilibrium state, a typical profile develops in all cross sections. The canal bed in the centre of the canal is almost horizontal and sinks with a high rate as a result of erosion. At the same time at both sides of the canal, directly adjacent to the toe protections, very steep slopes develop, with slope gradients between 1:1,5 and 1:2,5. The slopes are in an almost stable position, independent of the depth of the flat canal bed.

Directly eastward of the pipeline protections works in the western section, a very deep scour hole (> 16 m) developed with a period of a year. The scour hole has a width in east-west direction of almost 70 m. At the western side it has a stable slope of around 1:2; at the eastern side the slope is much more gentle. The slope seems to be independent of the depth of the scour hole.

The toe protection of rubble 80/200 mm (D_{50} = 150 mm) with a of layer thickness of 0,30 m, directly placed on a sandy bottom shows no settlement in a situation with average tidal currents of 1,2 m/s in combination with return velocities below push barges of 1,5 to 2,1 m/s.

Acknowledgment

We hereby thank the division "Hydrografie" and Mr. Lodewijk Nijsse from the Port of Rotterdam NV for providing multibeam echo sounding data.

References

[1] E.A. Vermeer, 28 november 1995, Morfologische ontwikkeling van het westelijk deel Hartelkanaal, Project Europoortkering met open Beerdam, Studiegroep Hydraulica en Morfologie

[2] T. Blokland, 12 januari 1996, Monitorings/ onderhoudsplan Brielse Maasdijk westelijk Hartelkanaal, Gemeentewerken Rotterdam

[3] J.M. Smit, 19 mei 1995, Oeverbescherming Hartelkanaal, Stabiliteit en zettingsvloeiingen talud, Gemeentewerken Rotterdam

[4] T. Blokland, 17 juni 1996, Optimalisatie definitief ontwerp zinker- en teenbescherming en overige bodembeschermingen in westelijk Hartelkanaal, Gemeentewerken Rotterdam

[5] M. de Vries, 7 mei 1999, Stabiliteit oever Hartelkanaal, Suurhoffbrug, Gemeentewerken Rotterdam

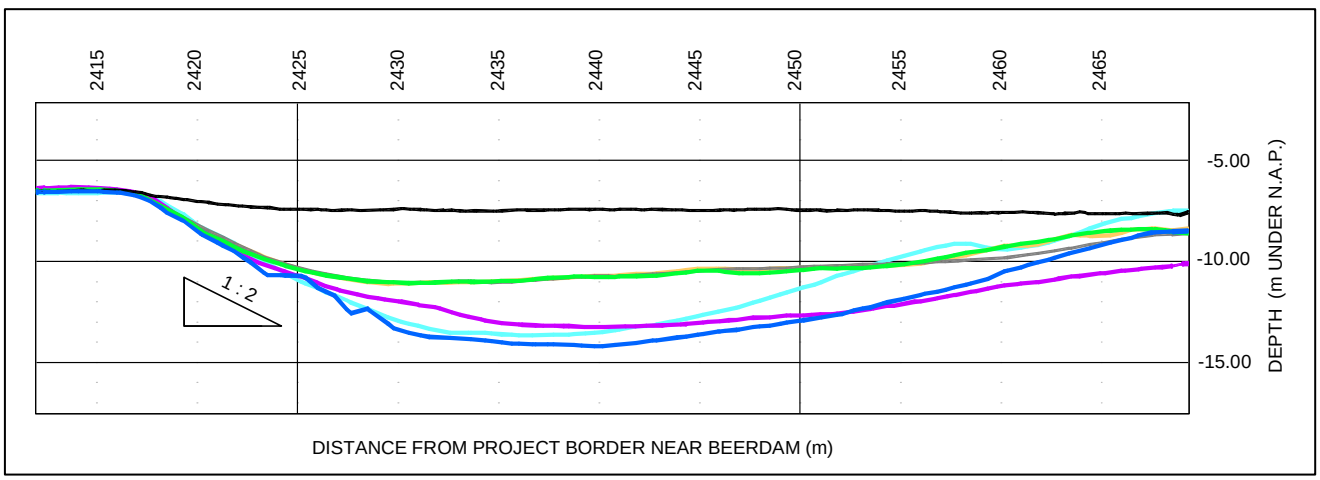

Figure 13: Scour hole at Dintelhaven, directly east of pipeline protection

Design of granular bed protections using a RANS 3D-flow model

T.H.G. Jongeling*, dr. H.R.A. Jagers*, and C. Stolker*
* WL | Delft Hydraulics, Delft, The Netherlands

This paper presents a numerical method that can be used to design the top layer of a granular bed protection near hydraulic structures. On the basis of the computed flow pattern and turbulence level both the required weight of the stones (the strength) and the extent of the protection can be determined.

I. INTRODUCTION

In the framework of a basic-research project [Ref. 1] the authors have studied the possibilities to design a granular bed protection applying the results of a numerical flow computation. Starting point for our research was that a RANS code with standard turbulence model should be used.

Experiments were carried out in a scale model for different geometries and flow conditions, including flow over a flat horizontal bed, flow over a flat bed with a transverse slope, different sill configurations with overflow, and flow through openings in a vertical plate. In all cases the bed was protected with stones and the flow conditions were such that individual stones were now and than moved by the flow ('incipient motion' condition). In this situation flow patterns, flow velocity profiles and turbulence profiles were measured.

Next, these experiments were simulated in the numerical flow model and the results of experiments and simulations mutually compared. A flow force quantity, composed of computed flow velocity and turbulence level, was such defined that it represents the dynamic load on the top layer of the protection. The flow force quantity was computed in the entire flow field and averaged over a representative part of the water body above the bed, thus taking into account relevant flow and turbulence phenomena.

Finally, we have established a new stability parameter similar as the well-known Shields parameter, that relates the flow force quantity to the strength of the granular bed protection. The value of this stability parameter at incipient motion of the stones ('critical value') was derived from our experiments. The critical value of the parameter is in principle independent of the considered geometry and bed layout.

With the help of the developed numerical method a designer can compute the required weight of the stones of the top layer (expressed in terms of the nominal stone diameter) and decide on the extent of the protection.

The new method has been applied to a fictitious case of a sluice in a dike, that discharges surplus water into the sea. The bed protection at the downstream side of the sluice was computed and compared with the results of an analytical design method.

In next sections we will explain the numerical design method more into detail.

II. EXPERIMENTS IN A SCALE MODEL

Experiments in a scale model were executed in a 0.5 m wide, glass-walled flume with effective length of 23 m. The water in this flume wais circulated by means of a pump in a return conduit underneath the flume.

The considered geometries inclusive the stone-protected bed, were constructed after a distance of about 14 m from the inflow. The entire bottom of the flume in the approach section to the model was covered with a fixed layer of stones, with mean diameter of 7.4 mm (nominal stone diameter D_n = 6.2 mm). At the location of the model similar, loosely packed stones were applied in a 40 mm thick layer. These stones were laid down in bands with different colors, which enabled the observation and counting of moving stones. Fig. 1 presents an overview of the various modeled geometries.

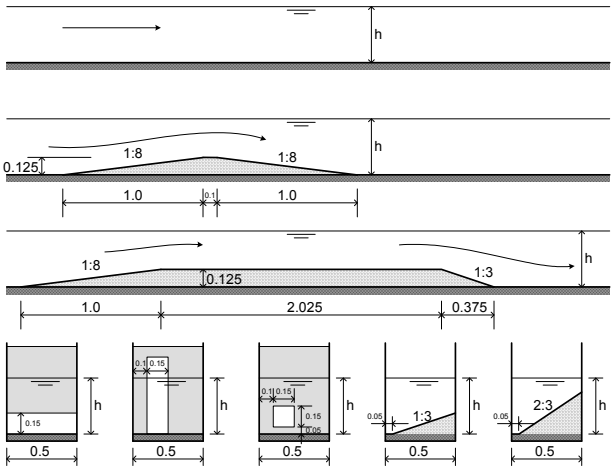

Figure 1. Experiments in scale model: overview of modeled geometries (flat bed, short-crested sill, broad-crested sill, underflow gate, plate with vertical slit, plate with square opening, transverse slope 1:3, transverse slope 2:3)

The initial geometry consisted of a flat horizontal bed without any structure. Than a short-crested sill with upstream slope 1:8, downstream slope 1:8, and height of 125 mm was modeled, followed by a broad-crested sill with upstream slope 1:8, steep downstream slope 1:3, height of 125 mm and crest width of 2.0 m. Next, a

vertical plate was fit in the flume with the lower edge at 150 mm above the stone protected bed ('underflow gate'). A second plate had an eccentrically, 150 mm wide, vertical slit, and a third plate was provided with an eccentrically, square opening, with sides of 150 mm and lower edge 50 mm above the bed. All edges of the openings in the plates were beveled, with the sharp angle at the downstream side. Finally, also a flat bed with a transverse slope 1:3 and 2:3 successively was modeled.

The flow conditions during the tests were such that individual stones of the bed protection were occasionally moved and transported by the flow. This 'incipient motion' flow condition was found by a stepwise increasing of the flow velocity in the flume and counting the number of displaced stones as a function of the flow velocity. The quantity of displaced stones per unit of time was chosen as a measure to assess the flow conditions that are representative for incipient motion.

Vertical flow velocity profiles were measured in the centre line of the flume and in lines parallel to the centre line. The three flow velocity components u, v and w along a Cartesian x, y and z coordinate system (x in longitudinal direction of flume, z in vertical direction) were measured using a Laser Doppler anemometer (u and w components) and an electro-magnetic flow meter (u and v components). The mean values $\overline{u}$, $\overline{v}$ and $\overline{w}$ were used to analyze flow patterns, while the standard deviations σ_u, σ_v and σ_w, which were combined in the quantity

$$k = 0.5*(\sigma_u^{\,2} + \sigma_v^{\,2} + \sigma_w^{\,2}) = a.\sigma_u^{\,2} \qquad (1)$$

, were used to compute turbulence intensity profiles. An example of the measured flow velocity and turbulence intensity profiles is shown in Fig. 2a/b for the case of flow over a broad-crested sill.

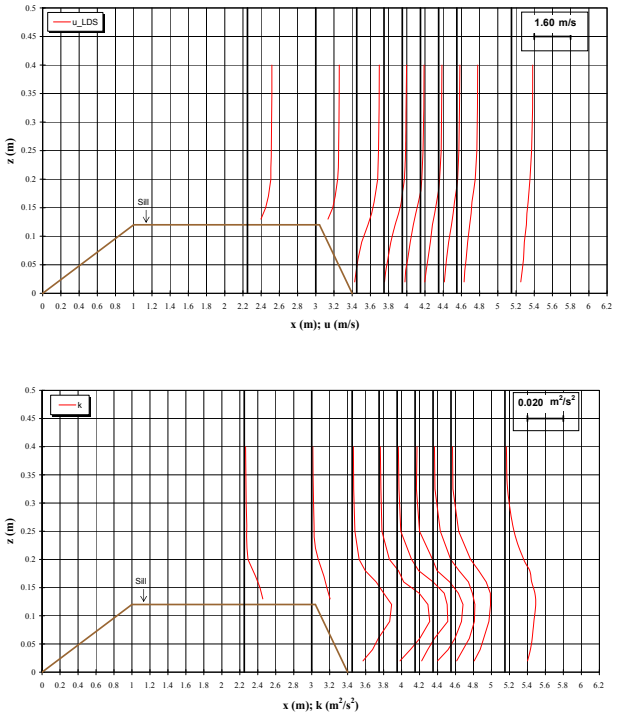

Figure 2. Experiment: flow over broad-crested sill, water depth 0.5 m; top (a): horizontal flow velocity u, bottom (b): turbulence intensity k; center line of flume

Fig. 3 gives an impression of the flow through a square opening in a vertical plate, that expands above the granular bed.

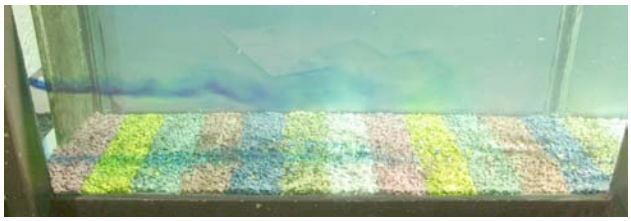

Figure 3. Experiment: flow through square opening in a vertical plate; the jet expands above the granular bed

It is interesting to note that, in the case of a fully developed flow over the stone-protected flat horizontal bed, σ_u in the zone near the bed was about a factor 2.2 as high as σ_v and σ_w, while the ratios σ_u / σ_v and σ_u / σ_w reduced to about 1.3 towards the water surface. When we assume a ratio of 2.2 in the region above the bed, the application of Equation (1) leads to a value a = 0.7. Towards the water surface the factor a increases to 1.1. In the case of jet flows through openings in the vertical plate the ratios of these standard deviations were almost equal to 1.0 in the core of the jet (a ≈ 1.5), but outside the jet, in the turbulent region, the σ_u component was strongly dominant compared to the σ_v and σ_w components (ratio between 1.5 and 2.0).

III. NUMERICAL SIMULATIONS

The experiments in the flume have been simulated using the RANS code CFX, version 4.4. This code has different turbulence models, among others the standard k-ε model and the RNG k-ε model. Both turbulence models have been applied in the simulations. With the parameters k (turbulent kinetic energy) and ε (dissipation of turbulent energy) the development and decay of the turbulence of the flow is described. Both the flow velocity and the turbulence level, which vary throughout the flow field, are used in our design method.

Lift and drag forces acting on individual stones of the protection are related to the local flow velocity; force fluctuations are related to perturbations in the flow field above the bed. In particular vortices with dimensions greater than the stone diameter (characteristic size ranging from the stone diameter up to the water depth) are relevant. Since the dynamic component of the flow force contributes to a large extent to the destabilizing load on the stones, it is of utmost importance that the turbulence quantity k of the numerical model adequately represents the turbulent nature of the flow in space and time. Much attention was therefore paid to compare the quantity k of the numerical model with the quantity k as defined with Equation (1). Especially, those regions of the flow where significant turbulence is generated such as the region near the rough, stone-protected bed and the free shear layer region near jet flows and in wakes behind structures were mutually compared.

The mesh of the numerical model was built up as a structured grid, with a refinement in regions where steep velocity gradients occur (near walls, flow openings, stone-

protected bed). Geometries with uniform properties in transverse direction of the flume (flat bed, sills, underflow gate) were modeled as a quasi 2DV grid with symmetry boundary conditions at the sides. This simplification implied that transverse flow phenomena, if any, were neglected and not simulated.

The free water surface was either modeled as a rigid lid with free-slip condition or as a moving water surface with adaptation of the thickness of the top layers of the grid. Attention was also paid to a correct modeling of the roughness of the stone-protected bed in the numerical model. From a comparison of experiments and simulations it appeared that with a roughness height corresponding to $2.D_n$ (D_n = nominal stone diameter) the best results in terms of flow velocity and turbulence gradients were obtained. This roughness height was selected in further simulations.

The comparison of experiments and simulations led to the next conclusions:

- Uniform flow over a flat, stone-protected bed. The flow is well computed when the k-ε model is applied; velocity profiles and turbulence profiles (k) show a satisfactorily similarity with measured profiles. The turbulence levels are at the high side when the RNG k-ε model is applied.
- Flow over a stone-protected short-crested sill with mild slopes 1:8; flow over a broad-crested sill with steep downstream slope 1:3. In the case of a mild downstream slope the flow remains attached, while in the case of the steep slope the flow detaches from the crest and remains detached. These flow patterns are in general correctly simulated. When the k-ε model is applied flow velocity and turbulence profiles above the downstream slope and downstream bed are reasonably well computed. With the RNG k-ε model flow patterns are well computed but the turbulence level at the downstream side of the sill is somewhat too low. Some results for flow over the short-crested and broad-crested sill are shown in Fig. 4a/b and Fig 5a/b.
- Flow through openings in a plate with stone-protected bottom at upstream and downstream side (underflow gate, vertical slit, square opening). Generally, the development of jet flows and attachment at flume walls and bottom is reasonably well predicted, but when the k-ε model is applied the jet flow widens faster in the simulation than in the experiments. In addition, the turbulence level in the free shear layer region is too high, in particular near the outflow opening in the plate. Better results are obtained when the RNG k-ε model is applied: the widening of the jet is better predicted, but as a consequence the turbulence level is somewhat too low. Fig. 6a/b present some results for the flow through a slit in a vertical plate.
- Flow over a flat, stone-protected bed with transverse slope. Similar as for a horizontal bed the flow is well computed, but with the RNG k-ε model turbulence levels are at the high side.

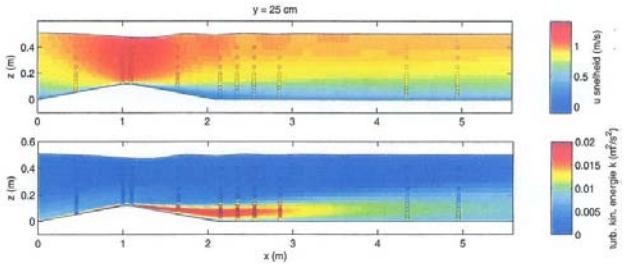

Figure 4. Simulation: flow over short-crested sill, water depth 0.5 m; top (a): horizontal flow velocity u, bottom (b): turbulence intensity k; vertical center-line plane; RNG k-ε turbulence model

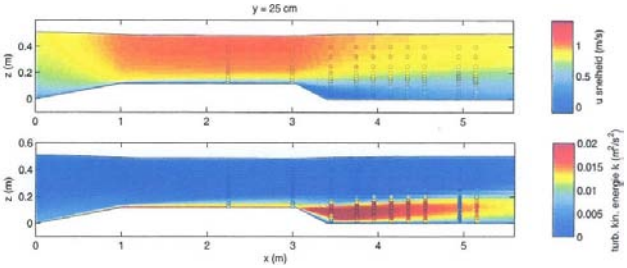

Figure 5. Simulation: flow over broad-crested sill, water depth 0.5 m; top (a): horizontal flow velocity u, bottom (b): turbulence intensity k; vertical center-line plane; RNG k-ε turbulence model

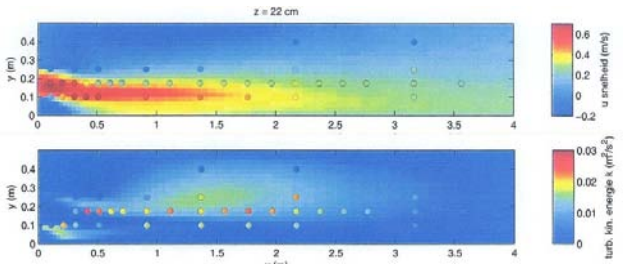

Figure 6. Simulation: flow through slit in vertical plate, water depth 0.5 m; top (a): horizontal flow velocity u, bottom (b): turbulence intensity k; horizontal plane at 0..22 m above bed; RNG k-ε turbulence model

The properties of the turbulence model influence the flow velocity profiles and turbulence distribution. The RNG k-ε model predicts better the gradual widening of jets, but the corresponding turbulence level of the free shear layer region is somewhat too low. The standard k-ε model produces satisfactorily results for flow over a flat, stone-protected bed as well as the RNG k-ε model, but the latter model overestimates the turbulence level. Since a correct simulation of the flow pattern is important in the numerical design of a granular bed protection we will use the results of simulations with the RNG k-ε model in next analysis. The effect of turbulence is accounted for through a combination of the turbulent kinetic energy k and a turbulence magnification factor α. The factor α can also be used to improve the computed turbulence level.

We have not studied flow situations where local, strong energy dissipating effects occur (such as the energy loss in a hydraulic jump).

IV. DEFINITION OF FLOW FORCE QUANTITY AND STABILITY PARAMETER

It is common practice in an analytical approach to describe the flow forces that are acting on the bed protection in terms of flow velocity and turbulence intensity. The required strength of the granular protection is assessed using a stability predictor, for example the well-known

Shields parameter Ψ. This parameter relates the flow force and the strength; the classical relationship for uniform flow over a flat bed reads:

$$\Psi = \frac{\overline{\tau}_b}{\rho g \Delta D_n} = \frac{\overline{u}_*^{\,2}}{g \Delta D_n} = \frac{\overline{U}^2}{C^2 \Delta D_n} \qquad (2)$$

where:

τ_b	= bed shear force
Δ	= relative density = $(\rho_{stone} - \rho) / \rho$
ρ	= density of water
g	= gravitational acceleration
D_n	= nominal stone diameter
u_*	= bed shear velocity
C	= Chézy coefficient related to the roughness of the stones
U	= flow velocity

Time-averaged quantities in the formula are indicated with a horizontal bar. The Shields parameter is a function of the Reynolds number (Re = $u_*.D_n/\nu$). For Reynolds numbers greater than about 600 the Shields parameter tends to a constant value; in practice this corresponds to a flow over a bed with particles greater than about 5–10 mm diameter. The value of the Shields parameter depends on the transport condition: a value of 0.032 is usually selected for incipient motion of stones. Particular geometrical, flow and turbulence phenomena are included in the analytical approach by multiplication of the flow velocity $\overline{U}$ with empirical coefficients.

In a numerical approach the effect of the geometry is already included in the flow computation and it is convenient to express the quasi-static and dynamic components of the flow force in terms of flow velocity U and turbulent kinetic energy k only. Since it is not feasible to simulate the dynamic flow force on each individual stone of the bed protection, we define the flow force as a generalized, global force per unit of area of protected bed. This force varies as a function of space.

A granular bed protection is generally designed to remain stable under the action of the hydraulic loads which occur during the anticipated lifetime of the protection, inclusive extreme loads with small probability. The flow force is roughly proportional to the velocity squared and fluctuates as a function of time. Small and large scale turbulence contributes to the flow force in a more or less chaotic way, but in particular the low-frequency part of the turbulence, corresponding to vortices with dimensions of the same order of magnitude as the stone diameter or larger, leads to a significant fluctuation of the flow force. From experimental research [Ref. 2] it is known that individual stones of the top layer become unstable and are moved when strong vortices pass.

The flow velocity can be expressed as:

$$U(t) = \overline{U} + U'(t) \qquad (3)$$

where $\overline{U}$ = local, time-averaged component and $U'(t)$ = fluctuating component. In the numerical approach with the RANS model the mean flow component $\overline{U}$ is computed, but not the fluctuating component $U'(t)$; instead the turbulent kinetic energy k, a scalar quantity, is computed. This quantity represents the mean dynamic character of the flow, and is selected in our numerical approach as base variable, together with the mean velocity $\overline{U}$. To account for peak values that occur in the real flow we define:

$$U_{peak} = \overline{U} + \alpha.\sqrt{k} \qquad (4)$$

whereas the flow force on the bed related to this peak flow is assumed to be proportional to:

$$\rho.\left(\overline{U} + \alpha.\sqrt{k}\right)_d^{\,2} \qquad (5)$$

The coefficient α in this generalized flow force quantity can be regarded as a turbulence magnification factor. The subscript d denotes that the flow force quantity is averaged in a representative region above the bed.

The relationship between the generalized flow force quantity based on the numerical variables $\overline{U}$ and k, and the strength of the bed protection is defined with the help of a new, dimensionless stability parameter $\Psi_{u\text{-}k}$, similar as the Shields parameter:

$$\Psi_{u-k} = \frac{\rho.\left(\overline{U} + \alpha\sqrt{k}\right)_d^{\,2}}{\rho g \Delta D_n} \qquad (6)$$

For design purposes we rewrite this expression as:

$$D_n \geq \frac{\left(\overline{U} + \alpha\sqrt{k}\right)_d^{\,2}}{g\Delta.\left(\Psi_{u-k}\right)_{crit}} \qquad (7)$$

The value of $(\Psi_{u\text{-}k})_{crit}$ corresponds to incipient motion of the stones. For a fully stable bed protection a smaller value than $(\Psi_{u\text{-}k})_{crit}$ may be selected or a safety factor applied to the design flow velocity.

V. CRITICAL VALUE OF STABILITY PARAMETER

The stability parameter $\Psi_{u\text{-}k}$ relates the generalized flow force on the bed protection to the 'under-water weight' of the stones. The critical value $(\Psi_{u\text{-}k})_{crit}$ marks the flow condition with incipient motion of stones; this critical value is in principle independent of flow pattern and bed layout, provided that all relevant phenomena are included in either the generalized flow force quantity or the under-water weight of the stones. This is however, generally not the case and one may expect that a certain range of values is obtained for $(\Psi_{u\text{-}k})_{crit}$ when experiments and computations are done for bed protections with different layout and flow conditions, depending also on the criterion that is used to define the transport condition of the stones. Similar as the Shields parameter Ψ the stability parameter $\Psi_{u\text{-}k}$ is a function of the Reynolds number. The dependency fades above a Reynolds number of about 600, which in practice is applicable to almost all design cases.

In our study we have concentrated on the value of the stability parameter $\Psi_{u\text{-}k}$ at incipient motion of the stones. The value of $\Psi_{u\text{-}k}$ as a function of space was computed from the location-depending variables $\overline{U}$ and k of the

numerical simulations (the RNG k-ε turbulence model was applied). To get insight in the sensitivity of the generalized flow force quantity $\rho.\left(\bar{U}+\alpha.\sqrt{k}\right)_d^2$ to a variation of the fluid control volume above the bed and the turbulence level, we have systematically varied the averaging depth d and the turbulence magnification factor α. From the analysis it appeared that the turbulence factor α is generally a much more important factor than the averaging depth d. The latter was eventually selected as:

$$d = 5D_n + 0.2h \le h \qquad (8)$$

where h = local water depth, and d = thickness of water layer directly above the bed.

The selection of d as a combination of stone diameter D_n and a fraction of the local water depth h followed from the practical consideration that the flow velocity and the turbulence level in the region near to the bed are particularly of importance for the stone stability. The turbulence level in the RANS model is related to flow gradients, which are highest near the bed or near free shear layers. In general it is true: the rougher the bed (modeled as $2.D_n$ in the simulations), the more turbulent kinetic energy is produced and the thicker the layer above the bed with an increased turbulence level. With the sum $5D_n + 0.2h$ we have in a pragmatic way accounted for the effects of stone diameter and increased turbulence level. We appreciate that other averaging depths or weighing functions for the flow force quantity may also be defined, but in RANS models the effect of other choices is expectantly only small.

In the analysis we have searched for combinations of α and d where at incipient motion of stones the stability parameter $\Psi_{u\text{-}k}$ had more or less an equal value for all considered geometries. An example of this analysis is shown in Fig. 7a/b/c. These figures present the value of the parameter $\Psi_{u\text{-}k}$ as a function of x and y at the downstream side of a plate with a vertical slit. The averaging depth d is selected as $5.D_n + 0.2h$ and the computed $\Psi_{u\text{-}k}$ -values are shown for α = 3, 6 and 10 respectively.

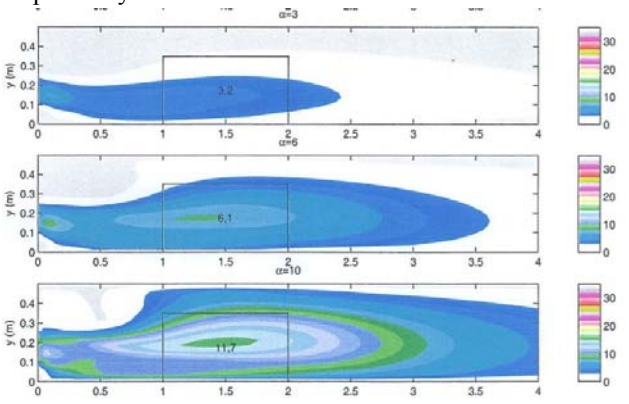

Figure 7. Simulation: flow through slit in vertical plate, water depth 0.5 m; stability parameter $(\Psi_{u\text{-}k})_{crit}$; top (a): α = 3, middle (b) α = 6, bottom (c): α = 10; rectangles indicate areas with damage in experiment; RNG k-ε turbulence model

The rectangle in the plots indicates the location where transport of stones occurred in the corresponding scale model test; the number in the rectangle corresponds to the $\Psi_{u\text{-}k}$ –value of that location.

After a mutual comparison of the various geometries it appeared that the variation of the stability parameter $\Psi_{u\text{-}k}$ is smallest when a value α = 6 is selected. This relatively high value of the turbulence magnification factor is an appropriate value considering that at the incipient motion flow condition individual stones are only moved as a result of incidental, strong flow and turbulence events. Expressed in terms of the standard deviation σ_u of the main flow component u we find with Equation (1) and k = a*σ_u^2 = 0.7*σ_u^2 for the case of uniform flow over a flat bed:

$$u + \alpha\sqrt{k} = u + \alpha\sqrt{0.7*\sigma_u^2} = u + 5.\sigma_u \qquad (9)$$

when a turbulence factor α = 6 is applied. This result indeed expresses that only the strongest flow variations are responsible for the incidental transport of stones at the incipient motion flow condition.

Application of the RNG k-ε turbulence model in combination with α = 6 and $d = 5D_n + 0.2h$ revealed critical values for the stability parameter $\Psi_{u\text{-}k}$ in the range 9 – 14, with a mean value of 12.0. An exception appeared to be the situation with flow over a transverse slope 1:3; in this situation a value $(\Psi_{u\text{-}k})_{crit}$ = 17.5 was found (notice that the steeper transverse slope 2:3 revealed a value $(\Psi_{u\text{-}k})_{crit}$ = 11.8).

For design purposes we recommend that a safe value $(\Psi_{u\text{-}k})_{crit}$ = 8.0 is used (in combination with the RNG k-ε turbulence model, α = 6 and $d = 5D_n + 0.2h$). When more data has become available and experience with the new method has been built up a more economic, somewhat higher value for $(\Psi_{u\text{-}k})_{crit}$ may be selected.

VI. CASE STUDY

The new design method has been applied to the case of a discharge sluice. This sluice spills surplus storm water from a lake into the sea. The sluice consists of five gated flow openings, see Fig. 8, each opening having a width of 33 m between the piers. The horizontal floor at a level of 6.5 m below NAP (= datum) has a downward step at the downstream side of the sluice, see Fig. 9. The design flow velocity amounts to 6.7 m/s between the piers (gates fully lifted above the water surface); this velocity corresponds to a design discharge of 1060 m^3/s per flow opening. Two breakwaters which protrude into the sea, shield the sluice from the incoming waves.

The bed at the sea side of the sluice is protected with stones. The required stone diameter was preliminary estimated using Shields stability parameter. The estimated flow velocity $\bar{U}$ was multiplied by a specific turbulence amplification factor. This resulted in a stone grading of 300 – 1000 kg, 60 – 300 kg and 10 – 60 kg, laid down in successive bands behind the 40 m wide concrete slab at the downstream side of the sluice.

A full three-dimensional model was set up that covered three adjacent flow openings, including the left side opening. A simulation was done for design flow conditions using the RNG k-ε turbulence model; the computed flow pattern in a horizontal plane at a level of 2 m below datum is shown in Fig. 10.

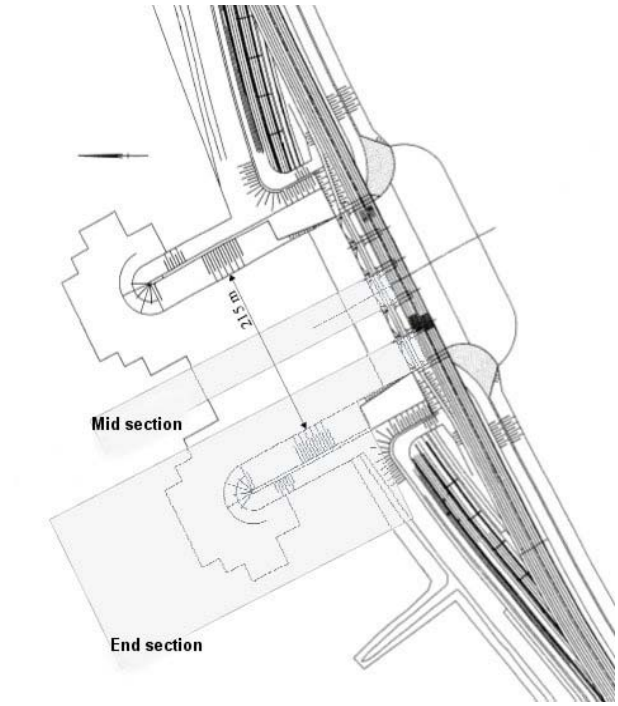

Figure 8. Case study: bed protection downstream of sluice; situation of sluice with indication of applied sub-models

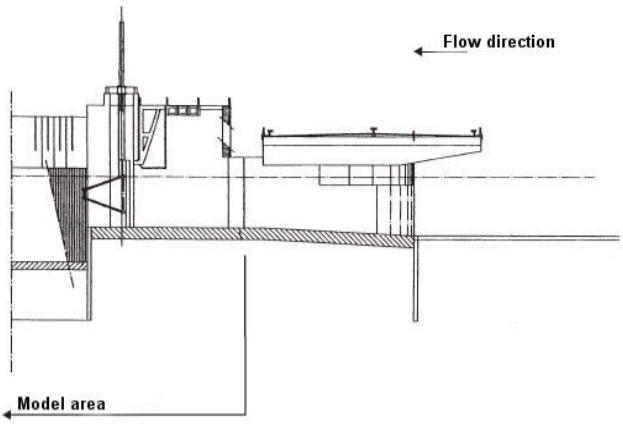

Figure 9. Case study: bed protection downstream of sluice; vertical section of sluice

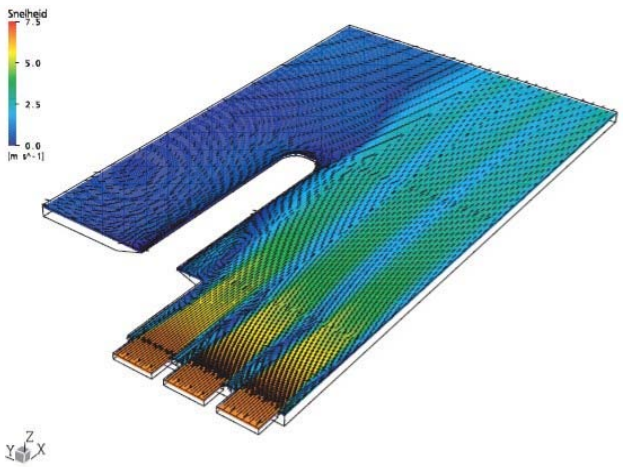

Figure 10. Case study: bed protection downstream of sluice; model of three flow openings; computed flow pattern in plane z = -2 m

From this simulation we could conclude that the flow pattern is symmetrical about a longitudinal axis through a pier between two adjacent flow openings. This enabled the set up of sub-models for individual flow openings only, using symmetry boundary conditions along the sides. One sub-model was built for the central flow opening, one sub-model for the left flow opening (see Fig. 8).

We started with the central opening and modeled the roughness of the bed as $2.D_{n50}$, with D_{n50} corresponding to the mean nominal diameter of the preliminary estimated stone grading. The computed horizontal flow component u, the turbulent kinetic energy k and flow vectors in a vertical longitudinal plane are shown in Fig. 11a/b/c. As can be seen, high turbulence levels are computed in the region of the free shear layer, immediately downstream of the downward step in the floor. The jet widens and attaches to the bed, and simultaneously the turbulent kinetic energy k spreads over the water depth and dampens; eventually the turbulence level adapts to the local bed roughness. The widening of the flow occurs also in a transverse horizontal direction.

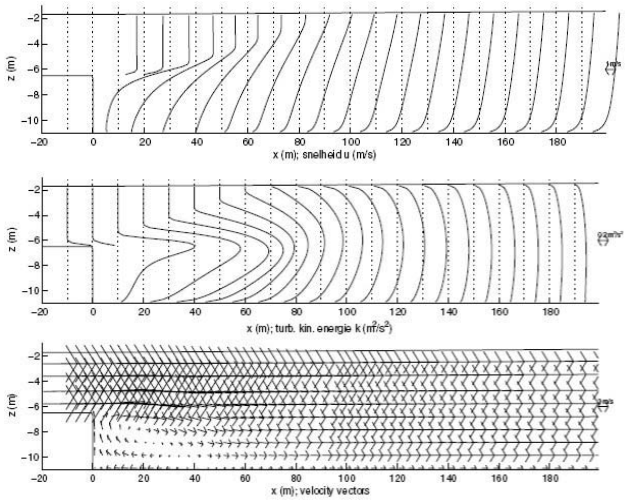

Figure 11. Case study: bed protection downstream of sluice; model of central flow opening; top (a): horizontal flow velocity u, center (b): turbulence intensity k, bottom (c): velocity vectors

Using Equation (7) and the location-dependent variables $\bar{U}$ and k, and selecting the values $(\Psi_{u\text{-}k})_{crit} = 8.0$, $\alpha = 6$ and $d = 5D_n + 0.2h$, we have computed the required mean stone diameter D_{n50} of the protection at the downstream side of the sluice. The results are shown in Fig. 12a/b/c; (a): computed stone diameter, (b): first-estimated stone diameter that was used to model the bed roughness, (c): comparison between computed and first-estimated stone diameter in the central axis of the model. The comparison shows that the difference between first-estimated stone diameter and computed stone diameter is already small. In the next iteration-step we have used the computed stone diameter to improve the bed roughness of the model. The results of the second simulation are shown in Fig. 13a/b/c; (a): computed stone diameter, (b): first-iteration stone diameter that was used to improve the bed roughness, (c): comparison between computed stone diameter and first-iteration stone diameter in the axis of the model. Fig. 13c demonstrates that the computed stone diameter is only slightly different compared to the stone diameter of the first iteration. It appears also that the stone

diameter decreases continuously from the slab behind the sluice to the downstream side of the model. With these computational results a designer is now able to define the extent of the area that has to be protected, and to select the stone grading that corresponds best with the computed stone diameter.

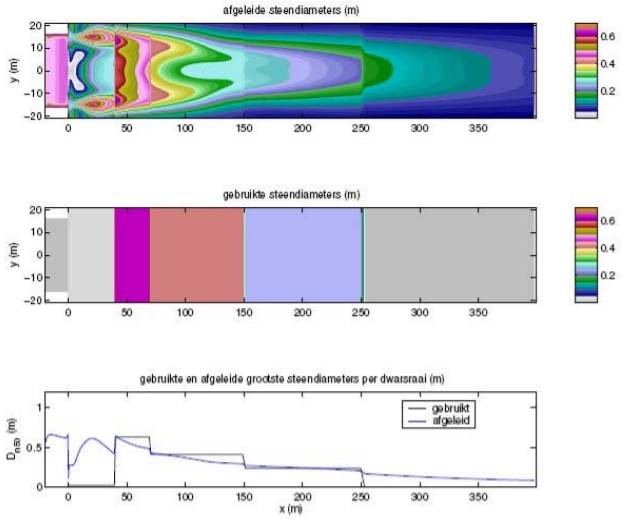

Figure 12. Case study: bed protection downstream of sluice; model of central flow opening; 1st iteration; top (a): computed stone diameter, middle (b): stone diameter used to model the bed roughness, bottom (c): comparison of initial and computed stone diameter, center line of model

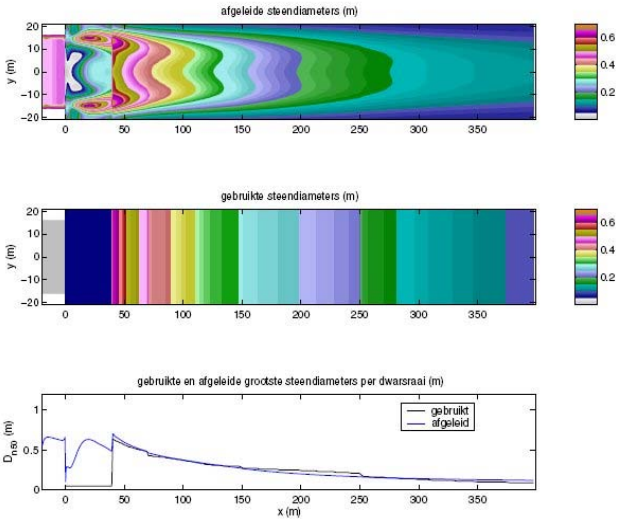

Figure 13. Case study: bed protection downstream of sluice; model of central flow opening; 2nd iteration; top (a): computed stone diameter, middle (b): stone diameter used to model the bed roughness, bottom (c): comparison of initial and computed stone diameter, center line of model

A similar procedure has been used to compute the required stone diameter of the bed protection behind the side opening. The stone diameter of the central opening was used to model the bed roughness. The results of the first simulation run are shown in Fig. 13a/b; (a): computed stone diameter, (b): stone diameter used to model the bed roughness. In a second iteration the stone diameter was only slightly adapted.

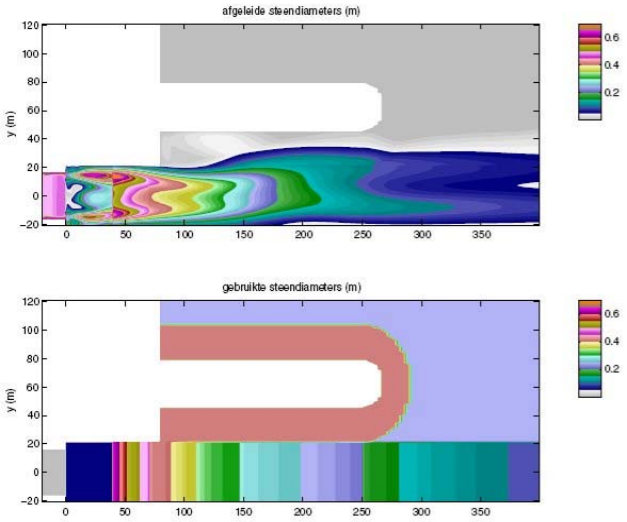

Figure 14. Case study: bed protection downstream of sluice; model of left flow opening; 1st iteration; top (a): computed stone diameter, bottom (b): stone diameter used to model the bed roughness

VII. CONCLUSIONS

A numerical method has been developed for the design of a granular bed protection near hydraulic structures. The method is based on a three-dimensional flow computation applying a RANS code and standard turbulence model. The location-depending variables $\bar{U}$ (time-averaged flow velocity) and k (turbulent kinetic energy) are used to compose a flow force quantity, that represents the dynamic load on the bed protection. A stability parameter relates the flow force to the required stone weight.

The method is found to be reliable as long as the numerical flow model is able to correctly predict the flow pattern, in particular at the downstream side of structures. The latter is, however, not always a trivial matter. Designers therefore should be aware of possible shortcomings of RANS flow models. In any case, insight in the real hydraulic processes is required and a thorough knowledge of modeling techniques. The method has not yet been tested for super-critical flows.

ACKNOWLEDGEMENTS

The Dutch Ministry of Public Works is gratefully acknowledged for their financial support in several stages of the research project.

RFERENCES

[1] WL | Delft Hydraulics; “Ontwerpmethodiek granulaire verdedigingen”, Report Q2933/Q3018, December 2003 (in Dutch)

[2] Hofland, B.; “Rock & Roll; Turbulence-induced damage to granular bed protections”, Thesis Delft University of Technology, December 2005.

Application of Sacrificial Piles to Control Scouring Around Bridge Piers

Ş.Y. Kayatürk* and M. Göğüş**
* State Hydraulic Works /Hydraulics Lab, Ankara, Turkey
** Middle East Technical University /Civil Engineering Department, Ankara, Turkey

Statistical studies have shown that the most common cause of bridge failures has resulted from the removal of bed material around bridge foundations. The researchers usually have tried to investigate the maximum scour depth around the bridge piers. As bridge failures result in costly and potentially fatal, in last decades some investigators have studied on scour countermeasures to reduce the maximum scour depth around the bridge structures [2, 5, 6, 10].

Various methods have been attempted to control scouring around bridge foundations, such as using riprap, slots through the bridge structures, a group of small piles in front of the bridge structures, and collars. In this study the effectiveness of collars placed on the sacrificial piles and also sacrificial piles placed upstream of the bridge piers on the local scour around the bridge piers were investigated.

Experiments were carried out near the threshold of sediment motion with two circular piers having diameters of D=5 cm and 10 cm. The size of the sacrificial piles are d=1 cm, 2 cm, 3 cm, 4 cm and 8 cm for D=10 cm and d=1 cm, 1.5 cm, 2 cm, 3 cm and 4 cm for D=5 cm. The distance between the pier and sacrificial pile from center to center, L=30 cm and 20 cm for D=10 cm, and 15 cm for D=5 cm. Some additional experiments were also performed to see the effect of the collar placed on sacrificial piles on reducing the maximum scour depth around the pier.

It was observed that when the sacrificial pile placed at a distance of 2D and 3D, it could reduce the maximum scour depth around the pier about 35% and 25% compared to the unprotected pier, respectively. When the collar is placed around the sacrificial pile, its protecting capacity of the pier is increasing significantly.

I. INTRODUCTION

Scour at a pier can cause damage or failure of bridges and result in excessive repairs, loss of accessibility, or even death [15]. So, after selecting the dimension of the pier, additional arrangements must be considered to prevent the formation of the excessive scour hole thereby permitting smaller foundation depths.

Successful applications of collars and sacrificial piles to reduce the local scour depth have been investigated by several researchers [3, 11]. In 1992, Reference [14] studied the effect of slot and a collar. He showed that, the collar has the effect of shielding the sediment particles from erosion by the down flow. Reference [7] tested sacrificial piles as a protective device around the pier and found that a pile having a diameter of 0.36D placed at a distance of 2D could reduce the maximum scour depth about 32% compared to the unprotected pier. Reference [13] investigated that collars of larger diameter at or nearer the bed are more effective. Reference [8], obtained 91% reduction of scour by using a collar of twice diameter of the pier and elevation of 0.1D below the average bed level. Reference [9] studied development of scouring around a rectangular pier with and without a collar. He observed that in addition to reduction of the scour depth, collar was very effective in slowing down the development of scouring. Reference [1] obtained 35% reduction of the scour by using a collar with a width equal to pier width at bed level at the skewed aligned rectangular bridge piers.

The primary objective of the present study is to investigate the effect of sacrificial piles placed upstream of the pier and collars placed on the sacrificial piles at the bed level on the reduction of the scour depth around the bridge piers.

II. MECHANISM OF SCOURING AROUND THE PIER

The vortex system and the down flow, along with the turbulence, are the principal causes of the local scour [12]. At the upstream face of the structure, the approach flow velocity goes to zero, called stagnation point. This causes an increase in pressure. Due to this phenomenon the water surface increases in front of the structure and named bow wave. As the flow velocity decreases from the surface to the bed, the dynamic pressure on the structure face also decreases downwards. Once a scour hole is formed, the scouring mechanism is dominated by the vortex system and an associated down flow. The down flow digs a hole in front of the foundation, rolls up and by interaction with the coming flow forms a complex vortex system (Fig. 1).

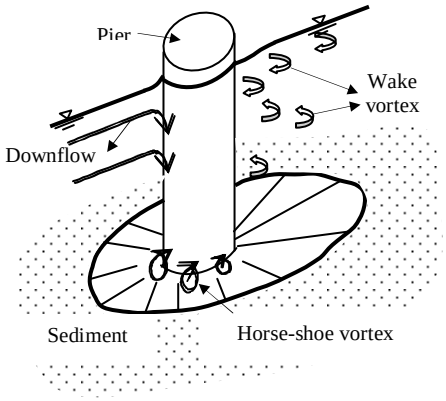

Figure 1. general view of pier scour

III. MECHANISM OF SCOURING AROUND THE PIER – SACRIFICIAL PILE ARRANGEMENT

Sacrificial piles are the piles placed upstream of the bridge pier for the purpose of protecting it from scour. The sacrificial piles protect the pier from scour by deflecting the high velocity flow and creating a wake region behind them [3]. The effectiveness of this method is dependent on the number of sacrificial piles, and their diameters and also the distance between the bridge pier and sacrificial pile [11].

IV. MECHANISM OF SCOURING AROUND THE PIER – COLLAR ARRANGEMENT

Local scour around a solid pier results from the down flow at the upstream face of the pier and the subsequent development of horse-shoe vortex at its base [4]. Hence, one way of reducing scour is to weaken and possibly prevent the formation of the down flow and the horseshoe vortex.

A collar at the bed level or below the bed level reduces the strength of the down flow and principal vortex. If it is placed around the sacrificial pile, it prevents the pier by changing the direction of the streamlines away from the pier field. However, the efficacy of a collar depends on its size and the location on the sacrificial pile with respect to the bed level.

V. EXPERIMENTAL SETUP

All tests were conducted under the clear water flow conditions at $U_*/(U_*)_c<1$, where U_* is the shear velocity of the approach flow and $(U_*)_c$ is the value of U_* at the threshold of grain motion. The threshold of bed material motion was found by experiment (the flow discharge Q=0.055 m^3/s and the flow depth y=10 cm) when the pier was not installed. The critical shear velocity, which leads to sediment motion, was calculated from Shield's diagram. A rectangular channel having a slope of S=0.001 with transparent walls, 30 m long and 1.5 m wide, was filled with erodable uniform sediment having a median diameter of d_{50}=1.48 mm with a standard deviation of particle size distribution, σ_g=1.28. The depth and length of the sand layer in the working reach were 0.50 m and 10 m, respectively. The general view of the channel is shown in Fig. 2.

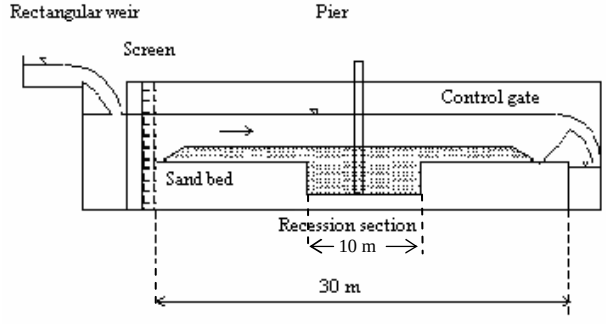

Figure 2. General view of the experimental setup

The flume had a closed-loop water system and the flow to the flume was supplied from a constant-head water tank by a pump. A gate was mounted at the tail end to adjust flow depths. The flow discharge was measured with a sharp-crested rectangular weir having the width of 1 m and the height of 0.30 m mounted at the upstream section of the flume. By means of bricks and sheet-iron strainer between them placed at the entrance of the channel as a filter, turbulence of the flow was reduced, and the uniform flow conditions were maintained which were required for upstream head measurements. The scour depths were also measured with a pointgage to an accuracy of ±0.1 mm. The scour holes were obtained by performing 6-hours continuous runs under clear-water conditions and both maximum scour depths and temporal developments of the scour holes around the piers were investigated. At the end of each experiment, the flume was carefully drained and sand bed level was straightened for the next experiment with a special apparatus, which was made of steel plate welded on a steel frame.

Fig. 3 shows a definition sketch for a sacrificial pile-pier arrangement. Sacrificial piles were placed at the upstream of the pier at a distance of 2D and 3D for piers of D=10 cm and D=5 cm. Diameters of the sacrificial piles were d=1 cm, 1.5 cm, 2 cm, 3 cm and 4 cm for pier of D=5 cm, and d=1 cm, 2 cm, 3 cm 4 cm and 8 cm for pier of D=10 cm.

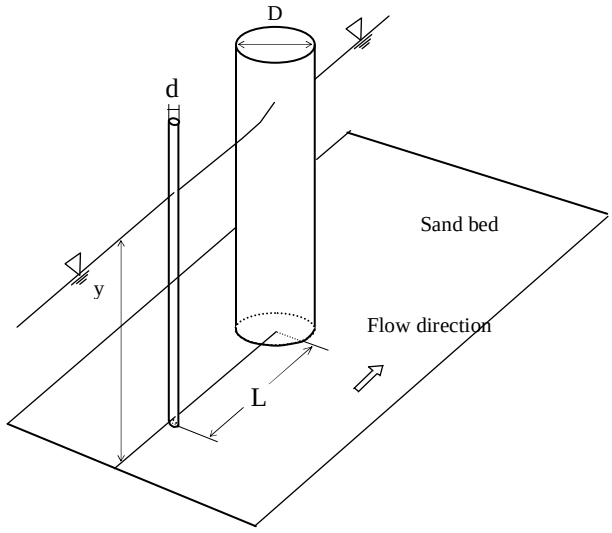

Figure 3. Definition sketch of a sacrificial pile-pier arrangement

Fig. 4 shows a definition sketch for a collar-sacrificial pile arrangement at the upstream of the pier. Collars were cut out of 3- mm thick plexi-glass sheet. The collar was placed around the sacrificial pile at the original bed level. Collar diameters, D_c, were selected as equal to the three times of the sacrificial pile diameter, D_c=3d.

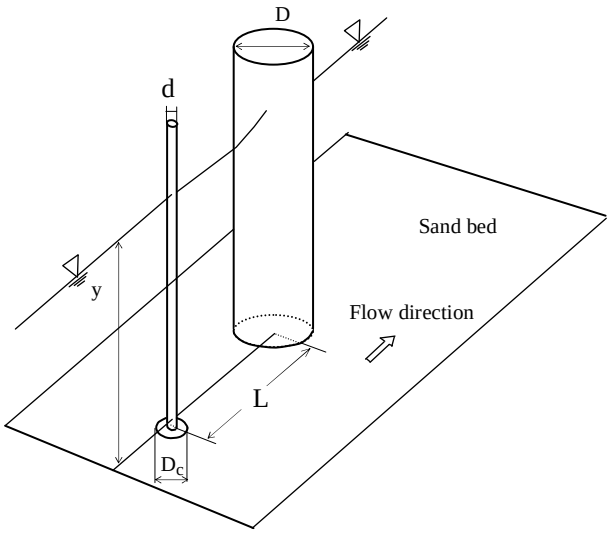

Figure 4. Definition sketch of sacrificial pile-collar arrangement at the upstream of the pier

VI. DISCUSSION OF RESULTS

A. Effect of Sacrificial Piles on the Maximum Scour Depth at Bridge Piers

In the first part of the experiments the maximum scour depths around the piers were recorded. Later on, sacrificial piles were placed upstream of the pier with intervals of 2D and 3D. The results of these experiments were compared with those having no sacrificial piles. Fig. 5 shows the effect of sacrificial pile diameter on the maximum scour depth at bridge piers for different D and L values. It is obvious from this figure that, while the distance between the sacrificial pile and the pier is increasing, the scour countermeasure effect of the sacrificial pile is decreasing for both pier diameters.

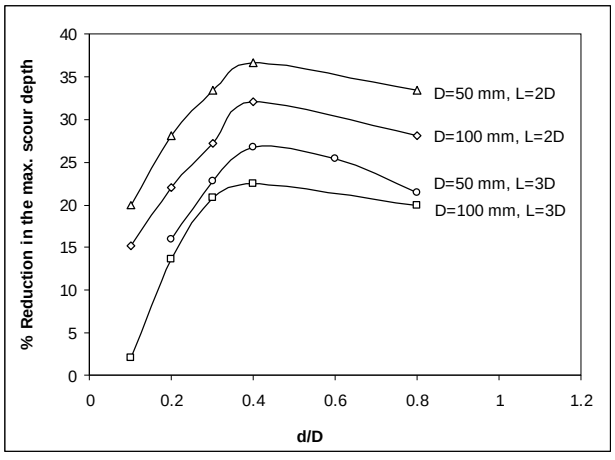

Figure 5. Variation of % reduction in the maximum scour depth with d/D as a function of L and D

In this figure, the trend of the data of piers D=50 mm and 100 mm reveals that for a given pier diameter the percent reduction in the maximum scour depth increases with increasing d/D up to about d/D=0.4. For d/D values between 0.4 and 0.8 a slightly decreasing trend is observed. It may be stated that there might be an optimum % reduction in the maximum scour depth around 0.5. From Fig. 5 it is also clearly seen that as the pier diameter increases, the effect of the sacrificial pile on reducing the maximum scour depth decreases, for a given d/D. The maximum percentage reduction in the maximum scour depth obtained in this study is about 35% for the pier of D=50 mm at d/D=0.4 where the distance between the pier and sacrificial pile is L=2D.

B. Effect of Collar Placed Around the Sacrificial Piles on the Maximum Scour Depth at Bridge Piers

In the second part of the study, in order to see the effect of the collar on reducing the maximum scour depth around the pier, the collar was placed around the sacrificial pile on the bed level with a diameter of D_c=3d. Fig. 6 shows the variation of % reduction in the maximum scour depth with d/D as a function of pier diameter. The trend of the data of piers D=50 mm and 100 mm reveals that for a given pier diameter the percent reduction in the maximum scour depth is increases with increasing d/D and attains the values of about 50% and 40 %, respectively. In this case, where collar placed around the sacrificial piles, it is seen that, the pier of smaller diameter is protected more compared to the pier of larger diameter for a given d/D.

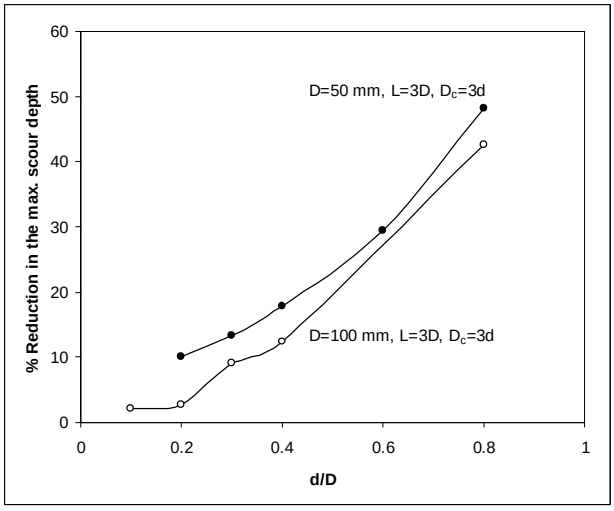

Figure 6. Variation of d/D with respect to % reduction in the maximum scour depth for various sacrificial piles rounded with collar

In order to see clearly the effect of sacrificial piles having collar on the reduction of the maximum scour depth around the piers compared to sacrificial piles having no collar Fig. 7 was presented. Referring to this figure one can state that the data of the same pier-sacrificial pile arrangement having a collar and no collar show absolutely different trends which had been explained in Figs. 5 and 6. Regardless of the pier diameter, the % reduction in the maximum scour depth at the bridge pier is inversely affected by the presence of collar around the sacrificial pile for values of d/D up to about 0.5. For d/D values larger than about 0.5 the

positive effect of the collar on the % reduction in the maximum scour depth is observed. In this zone while the % reduction in the maximum scour depth decreases with increasing d/D for the pier-sacrificial pile arrangement having no collar, with a maximum value of about 20%, at d/D=0.8, a rapid increase is seen in the % reduction in the maximum scour depth for the pier-sacrificial pile arrangement having collar with a maximum value of about 40-45 % at d/D=0.80.

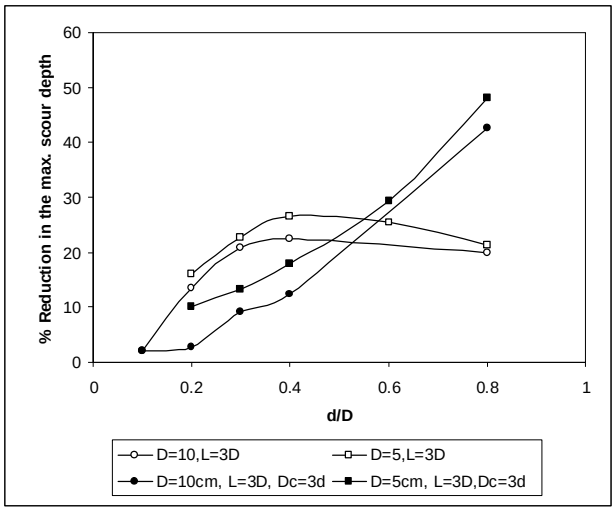

Figure 7. Variation of d/D with respect to % reduction in the maximum scour depth for various sacrificial piles rounded with collar

However, it is clear from this figure that, the scour countermeasure effect of the collar-sacrificial pile arrangement gives incredibly high values with 30% difference while the d/D ratio approaches 0.8 with compared to without collar case.

VII. CONCLUSIONS

The following conclusions can be drawn from this study.

An increase in the distance between the pier and the sacrificial pile results in a decrease in the maximum scour depth at the pier for a given d/D. As the pier diameter increases, the effect of the sacrificial pile on reducing the maximum scour depth decreases for a given d/D.

Piers of smaller diameters are protected more against scour than those of larger diameters when they are tested with sacrificial piles having collars around them at the bed level for a given d/D. Regardless of the pier diameter sacrificial piles having collars protect the piers against scour at an increasing trend with increasing d/D.

d/D=0.5 may be considered as a limit value for the effect of sacrificial piles having collar and no collar on the reduction of the maximum scour depth around bridge piers. For d/D; less than 0.5 the pier-sacrificial pile arrangement having no collar, and greater than 0.5 the pier-sacrificial pile arrangement having collar results in maximum reduction in the scour depth.

REFERENCES

[1] A.R. Zarrati, "Application of collar to control scouring around rectangular bridge piers," *J. Hydraulic Research*, vol. 42, No. 1, pp. 97-103, 2004.

[2] H.N.C. Breusers, G. Nicollet, and H.W. Shen, "Local scour around cylindrical piers,", *J. Hydraulic Research*, vol. 15, No. 3, pp. 211-252, 1977.

[3] B.W. Melville and S.E. Coleman, *Bridge Scour*,2nd ed., Water Resources Publications, LLC, Colorado, U.S.A., 2000.

[4] C.P. Singh, B. Setia, and D.V.S. Verma, "Collar-sleeve combination as a scour protection device around a circular pier," *29th IAHR Congress*, Beijing, China, vol. 2, pp. 202-210, 2001.

[5] D.B. Simons and F. Şentürk, *Sediment Transport Technology*. Water Resources Publications, Colorado, 1992.

[6] H.N.C. Breusers, G. Nicollet, and H.W. Shen, "Local scour around cylindrical piers," *J. Hydraulic Research*, vol. 15, No. 3, pp. 211-252, 1977.

[7] K.K. Singh, D.V.S. Verma, and N. K. Tiwari, " Scour protection at circular bridge pier," *Proc. 6th Int. Symposium on River Sedimentation*, New Delhi, India, pp. 1057-1068, 1995.

[8] K.K. Singh, D.V.S. Verma, and N.K. Tiwari, "Collar-sleve combination as a scour protection device around a circular pier,"29th IAHR Congress, Beijing, China, vol.2, pp.202-210, 2001.

[9] M.B. Mashahir and A.R. Zarrati, "Effect of collar on time development of scouring around rectangular bridge piers," *Proc. 5th Int. Conf. on Hydro Science and Engineering*, Warsaw, Poland, 2002.

[10] S. Dey, "Local scour at piers, Part I: A review of developments of research," International *J.Sediment Research*, vol. 12, No.2, pp. 23-45, 1997.

[11] S.Y. Kayaturk, M.A.Kokpinar, and M. Gogus, "Application of collars and sacrificial piles to control scouring around the piers," Proc. of 31th IAHR Congress, South Korea, Seul, vol. 1, pp. 2991-2999, 2005.

[12] U.C. Kothyari, R.J. Garde,and K.G. Ranga Raju, "Live-bed scour around cylindrical bridge piers," *J. Hydraulic Research*, vol. 30, No. 5, pp. 701-714, 1992.

[13] V. Kumar, K.G.R. Raju, and N. Vittal, "Reduction of local scour around bridge piers using slots and collars," *J Hydraulic Engineering*., vol. 125, No. 12, pp. 1302-1305, 1997.

[14] Y.M. Chiew, "Local scour and riprap stability at bridge piers in a degrading channel," *J. Hydraulic Engineering*, vol. 130, No. 3, pp. 218-226,1992.

[15] Y.M. Chiew, "Mechanics of riprap failure at bridge piers," *J Hydraulic Engineering*, vol. 121, No. 9, pp. 635-643, 1995.

Experimental study of flow field and sediment transport around bridge abutments

A. Khosronejad*, and C.D. Rennie**
*Tarbiat Modares University/ Department of Civil Engineering, Tehran, Iran
** University of Ottawa/Department of Civil Engineering, Ottawa, Canada

I. Introduction

A common phenomenon at the bridge site of a river is localized scour around bridge piers and abutments which may cause serious problem for foundations of these structures. The flow field around abutments, which includes flow separation and developing three-dimensional vortex flow, is an extremely complex turbulent flow and the complexity increases with the formation and development of the scour hole. This turbulent flow around the abutments leads to a cone-shape scour hole with a maximum scour depth that depends on the strength of turbulence and vortexes and the flow Froude number. The acceleration and separation of the flow as it moves past the upstream face of the abutment creates a vortex trail that moves downstream in a direction roughly perpendicular to the structure. The result is that the bed around the structure is eroded locally.

The studies on the abutments has been done in two different areas; flow field characteristics and scour hole characteristics near the abutments. Detailed studies of the flow characteristics around the abutment, have been conducted by [1 to 5]. Among these limited studies, the last study [5] is the only one in which the three-dimensional flow field around a vertical–wall and semicircular abutments has been investigated. Regarding the studies of scour hole properties, [6,2,7-9,3] have conducted experimental studies to predict abutment scour hole properties (mainly maximum scour depth) due to different flow conditions.

The present study has two main objectives. First, Measuring and investigating the three-dimensional flow field for two vertical wall semicircular abutments (in front of each other) under clear water regime, using the Acoustic Doppler Velocimeter (ADV). Second, measuring the consequently scour hole characteristics using a digital laser altimeter [10]. Also using a parametric study, the effects of flow conditions such as Froude number, flow discharge, and flow depth on the scour depth has been investigated.

II. Dimensional Analysis

In order to find the effective parameters on the scouring process at an abutment, a dimensional analysis has been performed. Based on the dimensional analysis the maximum non-dimensional scour depth depends on the following non-dimensional parameters (Lim, 1997):

$$\frac{d_s}{h} = f(Fr, F_o, \frac{h}{D}, \sigma_s, K_s) \quad (1)$$

Where d_s is maximum equilibrium scour depth; Fr is flow Froude number; h and D are respectively the flow depth and semicircular abutment diameter; σ_s is geometric standard deviation of the sediment size distribution; K_s is an abutment shape factor; and F_o is sediment densimetric Froude number:

$$F_o = \frac{u}{\sqrt{((S-1)gd_{50})}} \quad (2)$$

Where u is average flow velocity; $S = \rho_s / \rho$ is specific density of sediment particles; ρ_s and ρ are sediment particle density and fluid density, respectively; g is gravitational acceleration; and d_{50} is median diameter of sediment particles by weight.

A parametric analysis on scour process near abutments can be done in terms of the characteristic parameters in equation (1). In this paper, because of the use of only one sediment type and one abutment shape on flume bed, it was clear that the geometric standard deviation of the sediment size distribution and the shape factor of abutments didn't have any effect on the scour depth and scouring process. Hence, a parametric study using the first three non-dimensional parameters on the right hand side of equation (1) has been done.

III. Experimental procedure

Experiments were conducted in a 30 m long, 1.5 m wide and 0.8 m deep laboratory flume in the Civil Engineering Hydraulics Laboratory at the Ottawa University. As illustrated in Figure 1, a movable bed test section was constructed in the flume. The movable bed test section was 7.32 m long, with a recessed 0.25 m deep layer of quasi-uniform non-cohesive sediments with $d_{50} = 0.646$ mm and angle of repose of 42°. The semicircular abutments with a radius of 20 cm were made with a wood core and a stainless steel cover with a

smooth surface. Abutments were embedded in the sediment-bed of the movable portion of flume, and attached to the concrete side-wall of the flume. The flow discharge was measured by a sharp edge rectangular weir installed downstream of the flume. The flow depth was measured by a point gauge with an accuracy of ± 1 mm. The experiments were run under a clear water scour regime for five different inflow discharges. The flow properties related to each experiment are shown in Table 1. The development of scour depth and bed topography was monitored until an equilibrium scour condition was established. The time required to achieve this condition was about 3.5 hours, depending on the flow condition.

After the equilibrium state was achieved, the time-averaged components of flow field velocity in Cartesian coordinate (x, y, z) were measured using a trio of Acoustic Doppler Velocimeters (ADV) operated synchronously. The velocity measurements were taken at two flow depths, one near the free surface and one near the bed, at different sections around the abutment (Figure 2). Because the flow between the two abutments was symmetrical, the measurements were taken between the side wall and centerline of the channel (around one abutment).

Table 1 Flow condition for different runs

Run	Flow Discharge (lit/s)	Inflow velocity (cm/s)	Flow depth (cm)
1	70.0	24.6	19.0
2	58.0	21.4	18.0
3	123.0	36.0	22.8
4	150.3	40.9	24.5
5	131.6	31.0	28.3

The scour depths around the abutment were measured at two different representative perpendicular sections (Peng et al., 2002) with a digital laser altimeter. These two sections (AB and CD) are shown in Figure 3. Also the maximum scour depth (d_s) for each flow condition was measured.

IV. Flow Field

As mentioned above, the flow field was measured in different sections (Figure 2) and at two depths. The measured flow velocities at different depths are shown in Figures (4) to (8). As shown in these figures, close to the abutment the velocity magnitude increases, and the maximum value occurs at the section 4 (the section with maximum constriction in the flow section (Figure (2))) near the edge of abutment. The variation of longitudinal component of velocity shows an increasing trend from upstream toward section 4 and again from section 4 toward downstream it decreases with a maximum at section 4. The transverse velocity component tends to zero at section 4 and its high value occurs at sections of 3 and 5 (see Figure (6)).

This arrangement of flow around abutments leads to three-dimensional vortexes, which are formed at the edge of the abutments and travel downstream roughly in the longitudinal direction (Barbhuya and Dey, 2003).

V. Bed Topography

For all cases in this study (run 1 to 5) the position of maximum scour depth was roughly at the intersection point of lines AB and CD in Figure 3. The greatest scour occurred at this location because the vortexes in this area were the strongest and also the flow velocity and consequently the bed shear stresses in this area were the highest. Figures 9 and 10 show the bed profile along AB and CD lines of Figure (3) for run number 5. As shown in these figures, the maximum scour depth occurs at the intersection of lines AB and CD, and scour depth tend to zero near the centerline of the flume channel.

As seen in Figure 10, the scoured sediments from the scour hole in front of the abutment are deposited at the downstream face of the abutment, where the sediment transport capacity of the flow is reduced (Dongol, 1994).

VI. Parametric Study

The variation of maximum scour depth around abutments versus flow and sediment characteristics in equation (1) has been investigated through Figures (11) to (13). As show in Figure (11) the non-dimensional maximum scour depth (d_s/h) increases linearly with flow Froude number (Fr). A linear regression on these experimental data yields a coefficient of determination (r^2) of 0.94.

Figure (12) shows that the non-dimensional maximum scour depth (d_s/h) also increases linearly with the sediment densimetric Froude number (F_o), with a regression coefficient of determination (r^2) of 0.81 for these data. However, all experimental runs utilized the same sediment, thus (F_o) depended only on flow velocity. Thus, the observed correlation between dimensionless scour depth and (F_o) is due to a linear dependence of scour depth on flow velocity.

The influence of non-dimensional flow depth (h/D) on the non-dimensional maximum scour depth is shown in Figure (13). As can be seen, d_s/h varies non-linearly with non-dimensional flow depth. Again, only one pier diameter was tested in this study. Further, the influence of flow depth is accounted for in the flow Froude number, thus the observed linear relation between dimensionless scour depth and (Fr) is the most meaningful and useful. Several previous studies have utilized flow Froude number to predict abutment scour (see [12] for review).

VII. CONCLUSION

In this study, the flow field and sediment transport around a couple of semicircular abutments have been studied experimentally. The three-dimensional turbulent flow field for five different flow conditions around abutments has been measured using a trio of Acoustic Doppler Velocimeter (ADV) operated synchronously. Depending on the strength of turbulent flow and flow conditions around the abutments, different shapes of bed topography around the abutments emerged. The bed profiles related to five different flow conditions were measured in two perpendicular directions in front of the abutment with a digital laser altimeter. The data of run number 5 for both flow field and bed profile have been depicted in Figures 4 to 10.

Using a parametric approach based on experiments data of five different flows, the effects of non-dimensional water depth, sediment densimetric Froude number and flow Froude number on the maximum scour depth around the semicircular abutments were investigated. The maximum scour depth was linearly related to Froude number.

VIII. REFERENCES

[1] Kwan, T. F., (1984), Study of abutment scour. Rep. No. 328, Scool of Engineering, University of Auckland, Auckland, New Zealand.

[2] Rajaratnam, N., and Nwachukwu, B. A. (1983a). "Flow near groin-like structures." Journal of Hydraulic Engineering, ASCE, 109(3), 463-480.

[3] Lim, S. Y. (1997). "Equilibrium clear-water scour around an abutment." Journal of Hydraulic Engineering, ASCE, 123(3), 237-243.

[4] Ahmed, F., and Rajaratnam, N., (2000) "Observation on flow around bridge abutment", Journal of Hydraulic Engineering, ASCE, Vol. 126, No. 1, pp. 51-59.

[5] Barbhuiya, A. K., and Dey, S., (2003) "Vortex flow field in a scour hole around abutments", International Journal of Sediment Transport Vol. 18, No. 4, pp. 310-325.

[6] Rajaratnam, N., and Nwachukwu, B. A. (1983b). "Erosion near groyne structures." Journal of Hydraulic Engineering, ASCE, 109(3), 463-480.

[7] Kandasamy, J. K., (1989), Abutment scour. Rep. No. 458, School of Engineering, University of Auckland, Auckland, New Zealand.

[8] Melville, B. W., (1992), "Local scour at bridge abutments." Journal of Hydraulic Engineering, ASCE, 118(4), 615-631.

[9] Dongol, D. M. S., (1994), Local scour at bridge abutments. Rep. No. 544. School of Engineering, University of Auckland, Auckland, New Zealand.

[10] Peng, J., Tamai, N., Kawahara, Y. and Huang, W., (2002) "Numerical modeling of local scour around spur dikes", International Journal of Sediment Transport, No. 1, pp. 1-7.

[11] Muntuneau. A., (2004) "Scouring around a cylindrical bridge pier under partially ice-covered flow condition", Master of Science Thesis, Civil Engineering Department, Ottawa University.

[12] Melville, B.W. and S.E. Coleman, 2000, Bridge Scour, Water Resources Publications, Denver, CO."

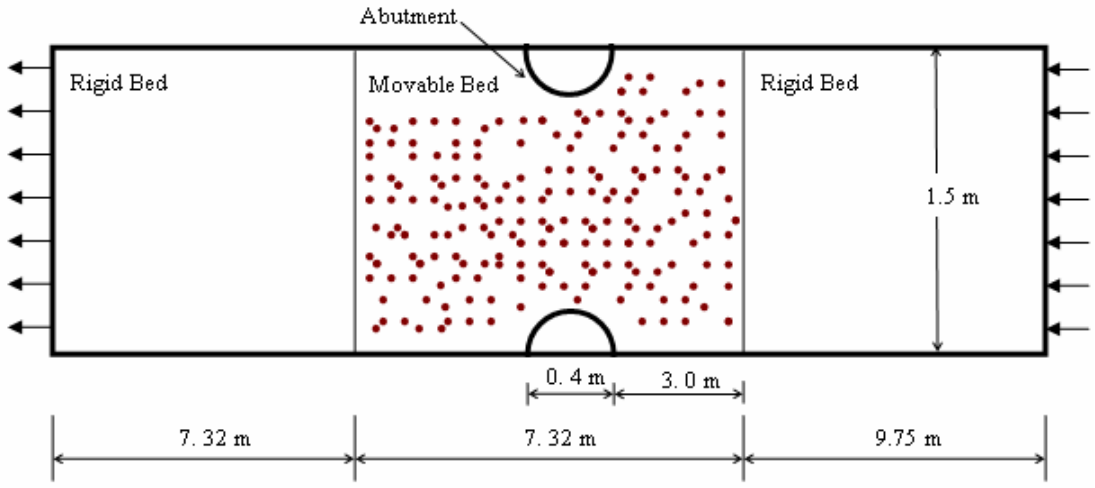

Figure 1 Schematic plan view of the laboratory flume.

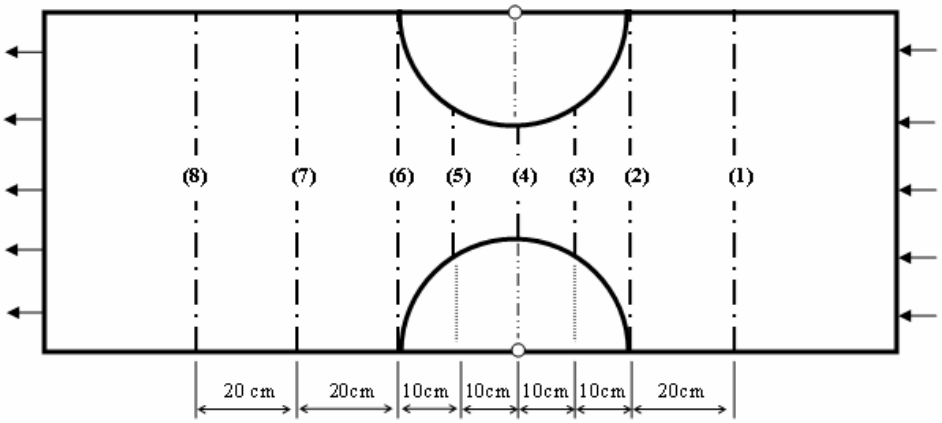

Figure 2 The sections of flow field measurements

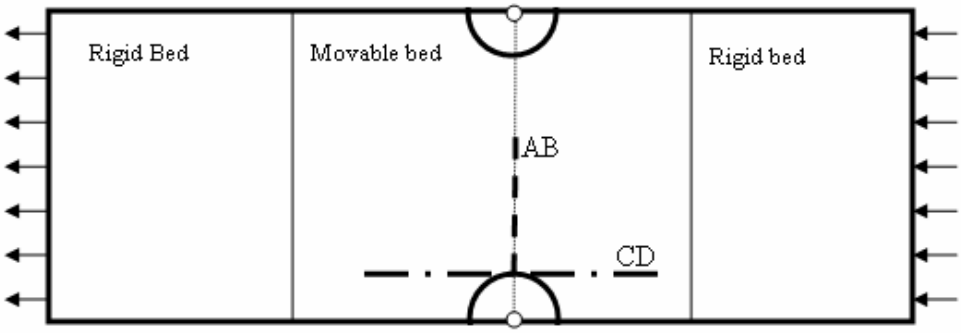

Figure 3 The scour depth measuring sections

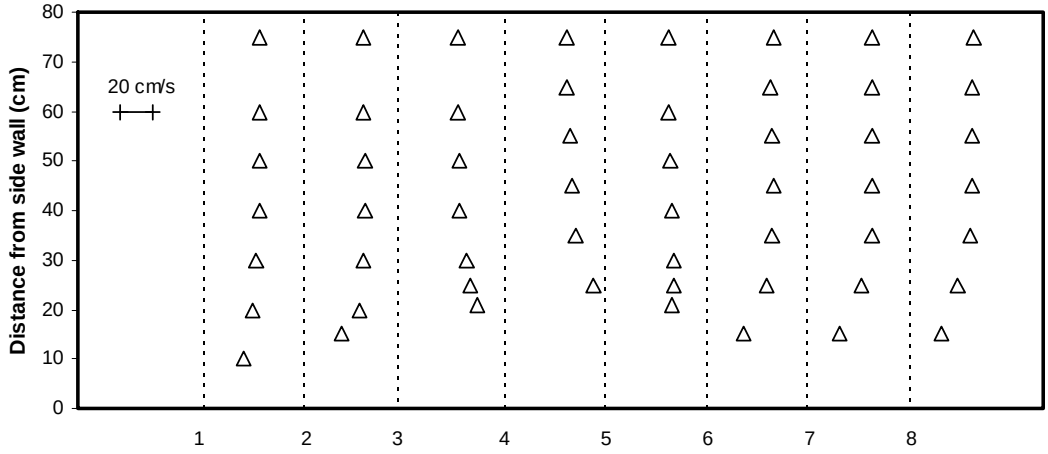

Figure (4) Velocity magnitude in run number of 5 and at the depth of 6.3 cm under free surface for different sections

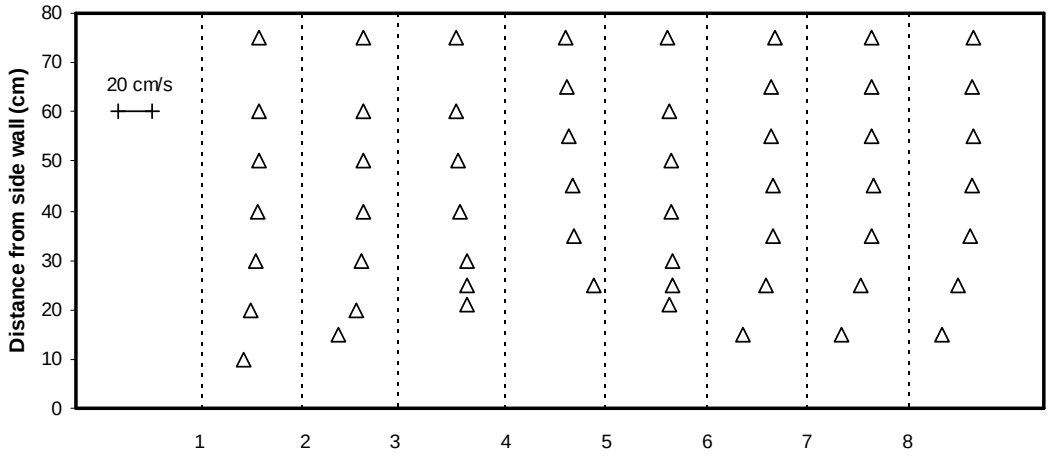

Figure (5) Longitudinal component of velocity in run number of 5 and at the depth of 6.3 cm under free surface for different sections

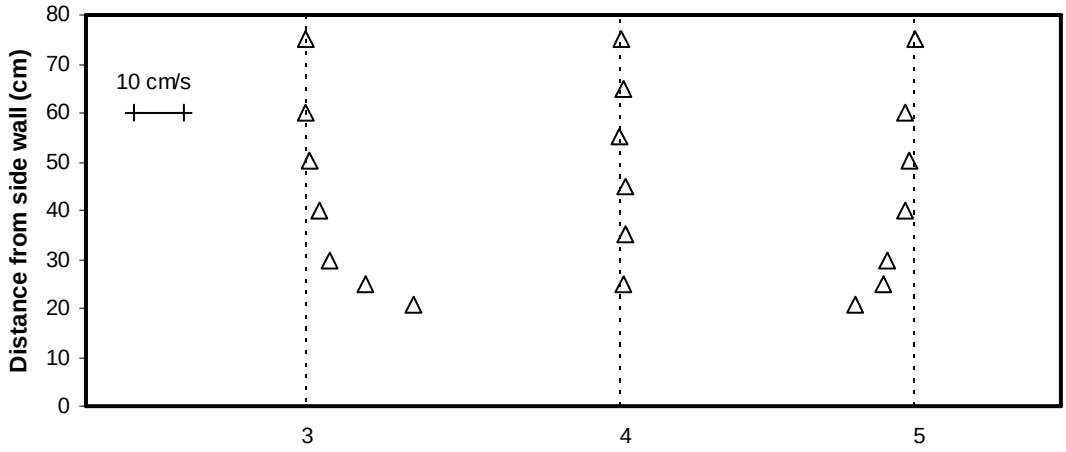

Figure (6) Transverse component of velocity in run number of 5 and at the depth of 6.3 cm under free surface for different sections

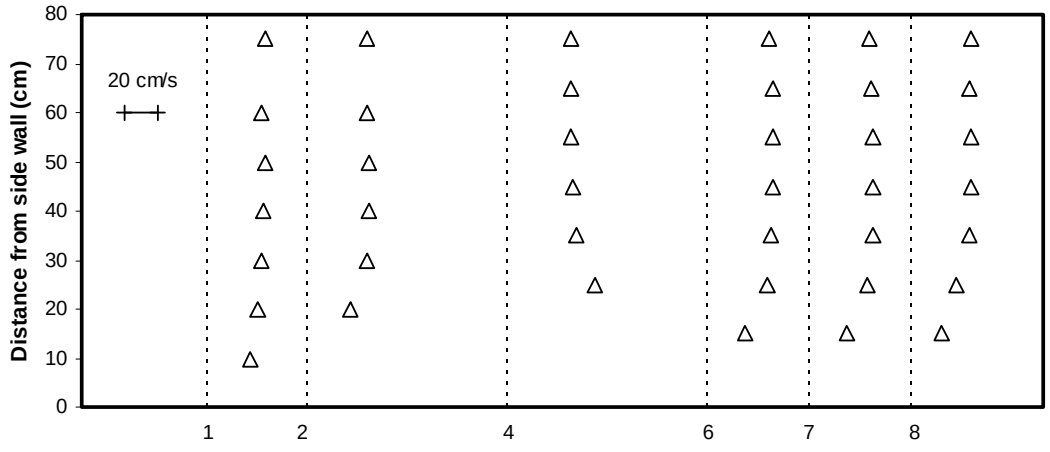

Figure (7) Velocity magnitude in run number of 5 and at a depth 5.0 cm above the bed at different sections

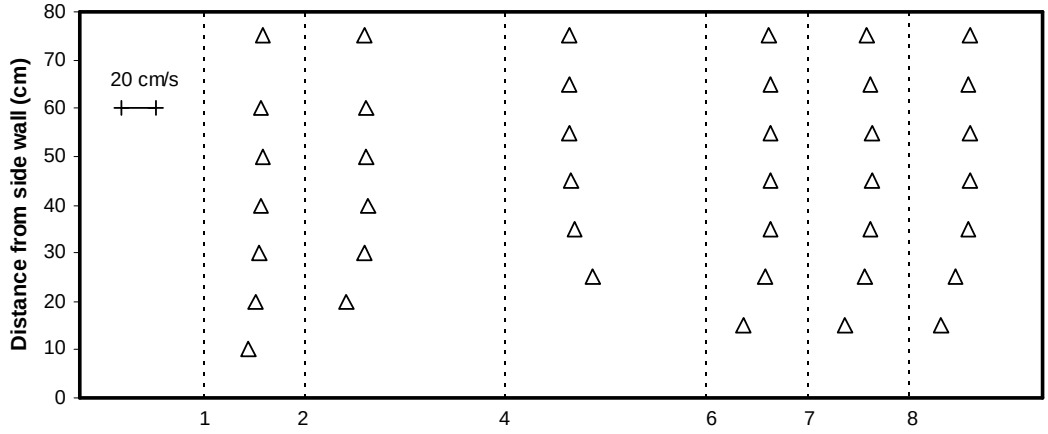

Figure (8) Longitudinal component of velocity in run number of 5 and at a depth 5.0 cm above the bed at different sections

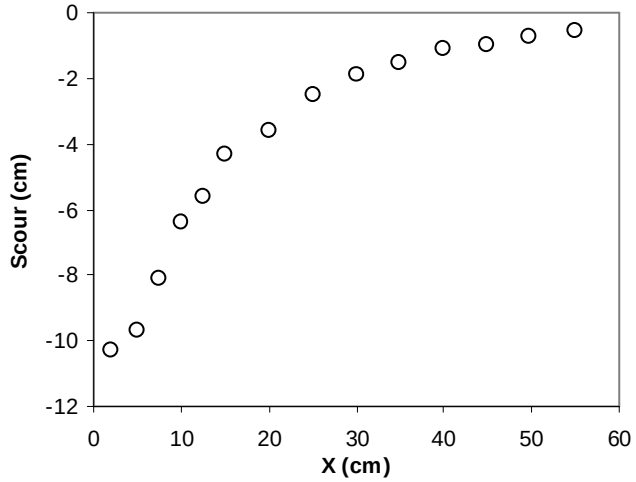

Figure (9) Scour depth and bed profile along AB line for run number 5. The origin is at the intersection of lines AB and CD.

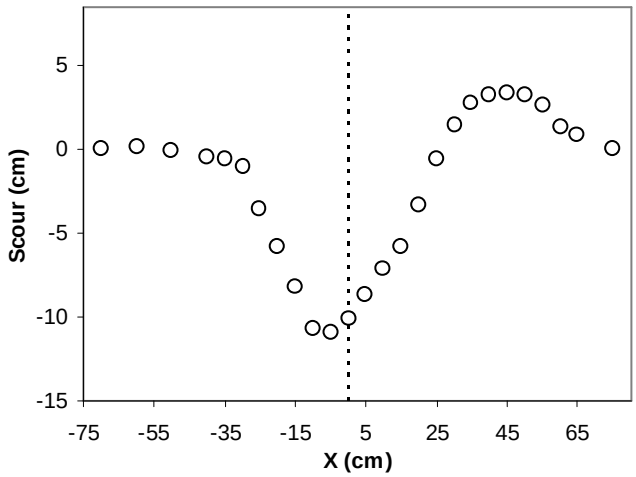

Figure (10) Scour depth and bed profile along CD line for run number of 5 (the dashed line shows the position of intersection point of AB and CD lines)

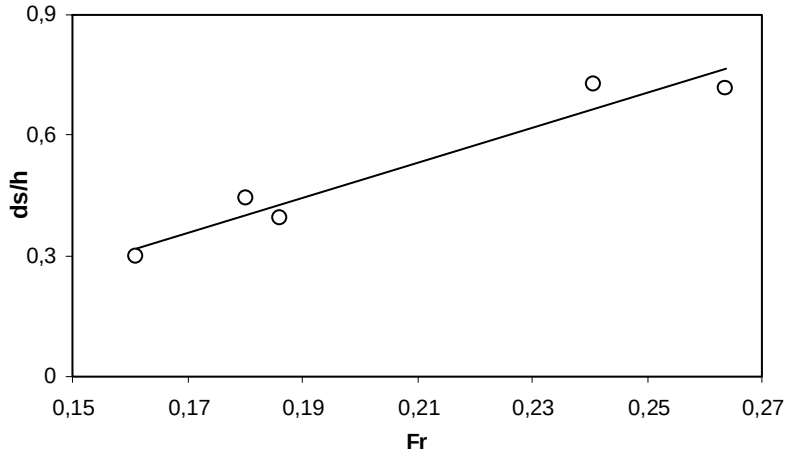

Figure 11 Variation of non-dimensional maximum scour depth versus flow Froude number. Regression equation is $y = 4.3351x - 0.3788$, with $r^2 = 0.94$

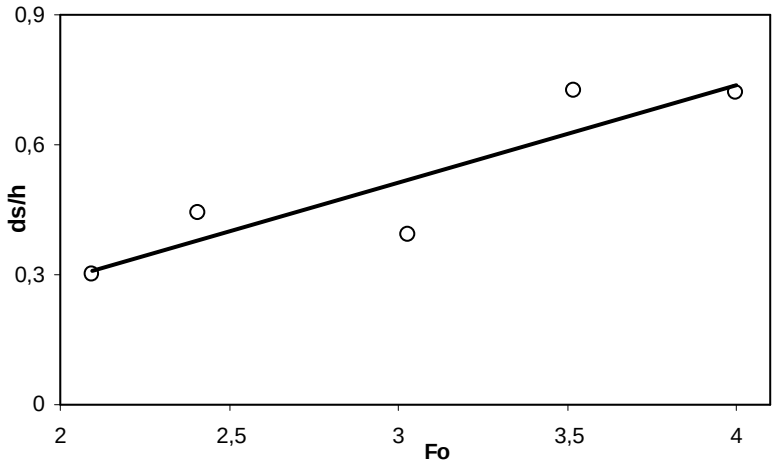

Figure 12 Variation of non-dimensional maximum scour depth versus sediment densimetric Froude number. Regression equation is $y = 22.38x - 0.158$, with $r^2 = 0.81$

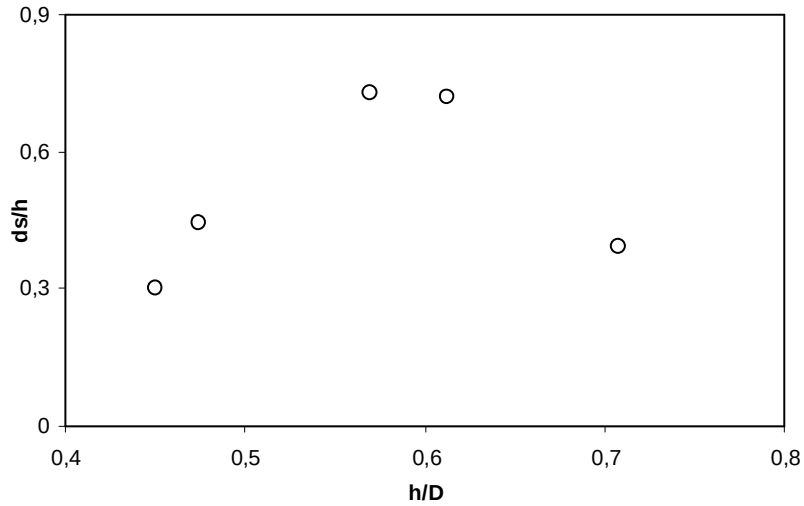

Figure 13 Variation of non-dimensional maximum scour depth versus non-dimensional flow depth.

Interaction of horseshoe vortex, detached shear layers, and near-wall turbulence during scour at a bridge pier

G. Kirkil, G. Constantinescu and R. Ettema
Department of Civil & Environmental Engineering, IIHR-Hydroscience and Engineering,
The University of Iowa, Iowa City, IA 52242; USA

I. INTRODUCTION

Local scour around a bridge pier located in a man-made channel with an erodible bed or a natural river is a common phenomenon that poses lots of practical problems related to the structural integrity of bridges. If the incoming flow is turbulent, which is practically always the case in applications of practical interest, a wide range of turbulent scales are present around the cylinder and control the transport process. The flowfields around these structures are dominated by the presence of relatively organized coherent structures in the form of necklace vortices at the base of the pier, large scale rollers in the wake behind the pier and smaller vortex tubes in the detached shear layers (DSL). Thus, to understand the scour mechanism, one has first to be able to qualitatively describe the structure of these large-scale eddies and their interactions at the different stages of the evolution of the scour process. As the time scales associated with the life and interactions among these structures is much smaller than the time scales over which significant changes in the scour hole geometry take place, when using numerical models one can perform this study under fixed bed conditions. The bathymetry at a particular stage of the scouring process can be obtained from experimental measurements.

Regardless of the exact form of the bridge pier, the main mechanism ([2], [4]) that drives the formation and evolution of the scour hole is the formation of a horseshoe vortex (HV) system at the base of the pier due to the separation of the incoming boundary layer induced by the adverse pressure gradients generated by the pier. As a consequence of this boundary layer-pier interaction, the turbulence reorganizes around the upstream side of the pier base into a number of necklace like structures. These vortical structures are stretched as they fold around the pier because of the lateral pressure gradients. In the case f a circular isolated pier, their legs are approximately parallel to the mean flow direction in the channel. In the case of an incoming turbulent flow, the location, size and intensity of the HV eddies are observed to be highly varying in time ([3], [8]). Additionally, a sharp increase of the turbulent kinetic energy (tke), pressure fluctuations levels and bed shear stress is observed within / beneath the HV region. This large amplification was related to the presence of bimodal aperiodic chaotic oscillations inside the HV region ([15], [18]). This phenomenon, which consists of the flow in the HV region switching between two modes at times intervals whose probability density function is likely Markovian, was first observed by Devenport and Simpson [5] in the study of the flow past a surface mounted wing shaped cylindrical body at very high Reynolds numbers ($Re \sim 10^6$). The switching was observed to take place at a relatively low frequency compared to the oscillation (passage frequency) of the vortices inside the HV system.

In a related Large Eddy Simulation (LES) investigation of the flow over a circular bridge pier at the start of the scouring process [5] we showed that these bimodal oscillations are present at much lower Reynolds numbers ($Re_D=UD/v \sim 1.8*10^4$, where U is the incoming mean flow velocity and D is the diameter of the circular pier) if the incoming flow is fully turbulent. It was observed that the main horseshoe vortices were oscillating randomly between two modes, one in which the vortex is far from the cylinder due to the presence of a strong wall-attached jet and one in which the main vortex was close to the cylinder and in which the wall attached jet is weaker and separates earlier.

Most of the experimental studies of scour phenomena around bridge piers were conducted in laboratory flumes. Their main goal was to investigate the temporal evolution of the scour geometry and the maximum scour depth at equilibrium conditions. Based on these experimental studies, numerous semi-empirical equations of the maximum scour depth were proposed in the literature [17]. In a recent study, Ettema et al. [6] showed that the over-prediction of the maximum scour depth by these formulas when applied to field conditions may be due in part to the fact that these formulas neglect the scaling of the large-scale coherent structures present in the region surrounding the pier. They found that the shedding frequency of the large-scale rollers and the amount of vorticity in the wake of the pier influence the scour development and the maximum scour depth at equilibrium.

Several experimental studies (e.g., see [4]) showed that scour is initiated in the accelerating flow on the sides of the cylinder and in the wake of the cylinder, before the scouring produced by the HV system at the base of the

cylinder becomes dominant. Experimental investigations of the temporal evolution of the scour around piers demonstrated that once the initial ripples start forming, the HV system becomes more stable, with most of the scouring taking place at the base of the cylinder, both upstream and on the sides of the pier. As the size of the scoured region around the upstream base of the pier increases, the overall size of the HV system is growing but the bed stress values are decaying. When these stresses are reduced to levels corresponding to the threshold for sediment entrainment, the large-scale scouring process ceases and the flow is at equilibrium conditions. In reality, even at equilibrium conditions local scouring as well as entrainment and deposition of sediment are still present but, in the mean, the geometry of the scour hole can be considered not to change in time. In most cases a deposition-dune or a hill (e.g., see Fig. 1a) is formed downstream of the pier ([4]) due to the deceleration of the sediment particles entrained in the regions of high bed shear stress and pressure fluctuations.

Dargahi ([2], [3]) performed several studies that focused on the visualization of the vortical structures around a bridge pier placed in an incoming fully turbulent flow. He identified several factors that appear to contribute to the scour process. Among them, the main ones are the rotational velocity of the HV system, the reduction in the local pressure around the sediment particles, the high turbulence levels in the incoming flow and inside the HV region, and a quasi-periodical motion associated with the horseshoe vortices.

Though recent experimental investigations using highly accurate Particle Image Velocimetry (PIV) and Laser Doppler Velocimetry (LDV) techniques (e.g., [5], [20]) have increased considerably our understanding of the intricate structure of the HV system in the symmetry plane, a detailed quantitative description of the HV system around the cylinder base and of the turbulent near-wake region is still lacking. One should emphasize that most experimental investigations have focused only on the detailed study of the HV system in the symmetry plane and have made only qualitative observations on its variation around the body (e.g., with the polar angle for the flow around a circular cylinder) and on its interaction with the scoured bed and the DSLs.

Unfortunately, detailed and accurate measurements of the mean velocity field for the flow around a bridge pier at the different stages of the scouring process are not generally available. Graf and Yulistiyanto [8] and Graf and Istiarto [9] measured the mean velocity components and turbulent Reynolds stresses using ADVP both upstream and downstream a circular pier for flat bed and equilibrium scour conditions, respectively. The mean extent of the HV region was measured but no attempts were done to visualize the coherent structures inside the HV system or downstream the cylinder.

Another approach that can be used toward understanding the fundamental dynamics and structure of the HV system is based on eddy resolving numerical techniques. In particular, the structure of the HV system around an isolated circular pier on a flat bed (start of the scouring process) or on a deformed bed (equilibrium conditions) with an incoming fully developed turbulent flow was investigated by Kirkil et al. ([13], [14], [15]). The LES simulations showed that regardless of the stage of the evolution of the scour hole, the HV system region around the base of the pier is characterized by the presence of large r.m.s. pressure fluctuations and tke levels.

Another area that did not receive much attention in previous scour studies of the flow past piers is the wake region. For instance, Dargahi [4] found that the scouring mechanism in the wake region is closely related to the shedding of wake vortices. He concluded that sediment particles were ejected when pockets of low-pressure and high velocity fluctuations associated with the convection of large-scale coherent structures were present in the near-bed region.

The flow past infinitely long cylinders was studied extensively over the last decades (see reviews by [21], [22]). The attached boundary layer on an infinite cylinder or on a surface mounted cylinder away from the bed interacts with the free-stream and, at a certain point, separates to form the DSLs. If the boundary layers are laminar at separation and the Reynolds number is high enough (Re_D>1,000), the Kelvin-Helmholtz instabilities in these DSLs will grow into vortex tubes that will be shed at a frequency that is strongly dependent of the Reynolds number and is independent of the one associated with the large scale vortex shedding frequency. If the level of the incoming free-stream turbulence is increased, than the shear layer entrainment is enhanced [1]. Transition will take place in these DSL, the flow inside the wake will be turbulent and characterized by the shedding of large spanwise vortices (rollers). The relationship between the turbulence length scales and vorticity distribution in the rollers is determined by the vorticity transport mechanism, in particular by the presence of vortex stretching.

End disturbances in the spanwise (relative to the cylinder) direction (e.g., the presence of a free surface or of a solid wall at the ends of the cylinder) will alter the predominantly two-dimensional fashion in which the predominantly spanwise vortices are shed in the case of an infinitely long cylinder and trigger what is generally called oblique shedding. In the case of a long circular cylinder mounted on a flat bed in a channel at Re_D~ 28,000, Inoue et al. [12] observed higher frequencies and more organized coherent structures near the free surface compared to mid-level depths.

The same flow at lower Reynolds numbers (1,700 to 6,000) was investigated by Vlachos [19] using several experimental techniques including PIV. Most of the focus of the investigation was on the flow structure between the free surface and the channel mid depth (the total depth was 12.8D). Laser sheet visualizations over the whole depth showed that the HV system at the base of the cylinder had some influence on the axis of the spanwise shed rollers. Vlahos [19] observed that bottom wall effects lasted until channel half depth. Past that point, the axis of the rollers became approximately parallel to the vertical cylinder axis. At lower depths, the angle between the vertical direction and the roller axis was different from 0^0, indicating the presence of oblique shedding and of a non-negligible vorticity component parallel to the free-stream direction. He found that changes in the inclination of the roller axis occurred inconsistently, in a chaotic way. One of the related effects observed in the wake was the decrease of the amplitude associated with the large-scale shedding near the free surface even though the Strouhal number was practically constant and equal to 0.25 over the upper half of the channel depth. This phenomenon

was attributed to the role of the free surface which does not allow the three-dimensional instabilities present in the DSLs to grow in a natural way.

II. Present Approach

In the present paper, the database from a highly resolved LES simulation [13] is used to investigate the dynamics of the instantaneous coherent structures associated with the HV system around a circular vertical cylinder placed in a sand bed, and their interaction with the DSLs and the near wall turbulence at the end of the scouring process (equilibrium scour conditions). The overall goal of the ongoing project is to use numerical techniques capable of accurately capturing the dynamically important coherent structures in a bridge pier flow to understand the fundamental flow physics. To achieve that, a related requirement is the use of fine enough meshes to capture the energetic structures in relevant flow regions. As this requirement increases strongly with the value of the Reynolds number, we decided to simulate a flow with a relatively low Reynolds number (Re_D=16,000, Re_H=18,000 where H=1.12D is the channel depth) but for which the turbulence characteristics of the (fully turbulent) incoming flow are not qualitatively different than those observed at much larger Reynolds numbers.

Eddy resolving techniques such as LES have the advantage that the whole 3D instantaneous flow fields, and not only the 2D fields in a certain plane, are available as part of the solution. This is important especially for flows dominated by random interactions among highly 3D coherent structures. It also allows an in depth investigation not only of the HV system, but also of the unsteady shedding of vortex tubes in the DSL and their interactions with the bed and the legs of the horseshoe vortices which are responsible to a large degree for the bed scour and deposition patterns behind the cylinder. In parallel, flow visualizations using dye and Large Scale Particle Image Velocimetry (LSPIV) techniques are used to educe the coherent structures around the cylinders and to validate the numerical results.

The equilibrium scour bathymetry is obtained from experiments conducted in a re-circulating flume. In simulation and experiment the incoming flow is fully turbulent. This insures that the present test case is relevant for practical applications in which the Reynolds numbers are higher. The only limitation is that the horseshoe vortex (HV) – detached shear layer (DSL) interactions are representative of cases in which the large-scale vortex shedding in the wake of the pier is subcritical. This is the regime where most of the scaled model experimental investigations are conducted.

III. Description of Experimental Techniques Used for Flow Visualizations

Experiments were conducted using a 27.40m-long, 0.91m-wide and 0.45m-deep sediment flume. A uniform layer of sediment with a median diameter of 0.68mm was placed as a 0.23m thick bed layer along the test section of the flume. A circular cylinder with diameter of 0.09m was placed at centerline of the flume, far from the inflow section to ensure that the flow was fully developed before it reached the pier. The water depth was H=0.1m, the average velocity was U=0.18m/s, the slope of the flume was S=0.01%, the critical shear velocity ratio was $u_\tau/u_{\tau c}$ =0.42, where $u_{\tau c}$ was estimated based on Shields diagram. The experiment was run until equilibrium scour conditions were obtained. Detailed measurements of the bed bathymetry (on a grid with the characteristic size of 0.01m) were transferred digitally to generate the scoured bed surface used in the numerical simulation (Fig. 1a). Same figure contains a topographic map of the scoured region. The measured bathymetry is almost symmetric around the $\phi=0^0$ plane (the polar angle ϕ is measured from the upstream polar plane oriented in the streamwise direction). The scour and deposition patterns are similar to the ones observed to form in previous experimental studies of scour around bridge piers of circular section (e.g., [4], [9]). The maximum scour depth occurred in the $\phi=0^0$ plane. The shape of the upstream part of the scour hole contained two regions of different slopes. The slope of the lower region was steeper (slope=33^o) than the one of the upper region (slope=31^o). Downstream of the pier, a sediment deposition region was present due to accumulation of sediment transported from the scour hole.

To visualize the dynamics of the large-scale coherent structures in the HV region and DSLs, a non-dispersive dye tracer was injected using a hypothermic tube inside the scour hole and inside the attached boundary layers on the cylinder at different elevations above the bed. The dye tracer consisted of a shear-thickening, high extensional viscosity mixture designed to disperse slowly. This property allowed the dye filament to resist breakup in turbulent flow and be able to visualize large scale vortical motions ([10], [11]). A digital video camera was used for recording the flow features as educed by the tracer paths (Sony TVR3-320). Still photos were then selected from the video recording.

LSPIV was used to determine the mean streamline patterns at the free surface in the near wake and the size of the recirculation eddies behind the cylinder. LSPIV employs much simpler illumination and larger particles compared with conventional PIV while covering considerably larger fields of view. This is an important advantage for our experiment. The variant developed by Fujita et al. [7] which was previously applied and validated for similar flow studies was used. Saw dust floating particles were used to seed the flow at the free surface. The seeding material was introduced in an uniform and continuous fashion upstream of the pier. This type of seeding particles did not stick together thus allowing individual tracking. Image recording was done by means of a digital video camera (Sony TVR 320) that produced geometrically non-distorted images. The camera was mounted at an approximate height of 1m above the water surface. The digitized images contained 640x480 pixels of 8-bit, gray-level resolution after capturing. Image processing was performed with a commercial software LSIV v.5.0. which allowed calculation of the mean velocities, etc.

IV. Description of Flow Solver, Boundary Conditions and Test Case Conditions

A massively parallel LES flow solver [16] was used to generate the LES database. The finite-volume solver uses a predictor-corrector formulation which discretely conserves energy on unstructured grids. This property

insures robustness at high Reynolds numbers without introduction of numerical dissipation (central discretizations are used for all terms including the convective ones in the momentum equations). Implicit time-stepping is performed using a Crank-Nicholson scheme. The dynamic Smagorinsky sub-grid scale (SGS) model is used to account for sub-grid scale effects on the resolved flow fields. Thus, the model does not contain any adjustable constant and keeps the SGS viscosity at a minimum level compared to the one predicted by the classical constant-coefficient Smagorinsky model. The numerical model does not employ the logarithmic law of the wall assumption (wall-functions approach) due to the known deficiencies of this method in the case in which separation and adverse pressure gradients dominate the flow field in the regions of interest (HV system, DSLs, etc.).

The computational domain (Fig. 1a) extends 5D upstream of the cylinder and 10D downstream. The domain width is 16D. The depth of the channel is H=1.12D in the flat region. The cylinder Reynolds number is identical to the one in the experiment used to determine the scour bathymetry at equilibrium. The inflow conditions are obtained from a separate LES simulation in a periodic channel of identical section. The LES velocity fields containing the realistic turbulent fluctuations are fed in a time-accurate way through the inflow section.

The grid density is varied such that the mesh is very fine in the regions containing the HV system, the DSLs and the near-wake. A detail view of the mesh in a horizontal plane around the cylinder is shown in Fig. 1b. Though the mesh contains only hexahedral cells to insure maximum quality, the mesh is unstructured. A paving technique was used in surfaces parallel to the bed. The mesh contains over 4 million cells. The first row of cells is situated at 0.001D away from the solid surfaces, corresponding to 0.5-1 wall units.

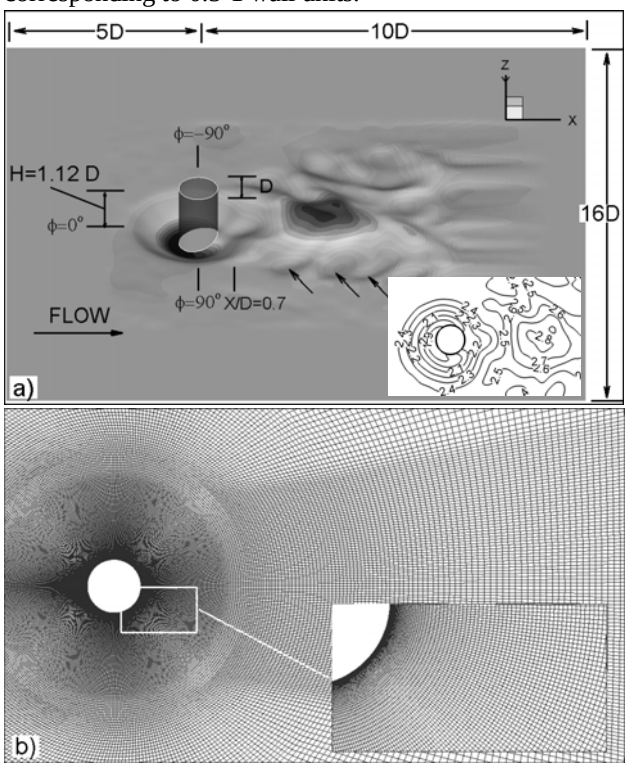

Figure 1. Computational domain. a) bathymetry at equilibrium scour conditions; b) unstructured mesh near the cylinder in a horizontal plane.

Typical computational cell dimensions in the three directions inside the HV system region, away from the walls, and inside the DSLs are 8-20 wall units. Near the free surface, which is treated as a shear-free rigid lid, the spacing in the normal direction is close to 45 wall units. At the outflow, a convective boundary condition that allows the coherent structures present in the wake to exit the domain in a time accurate fashion and without producing unphysical oscillations was used. The time step was 0.002 D/U. Simulations were run on 24 processors of a Xeon PC Cluster.

V. RESULTS

The general pattern of the 2D mean-velocity streamlines at the free surface (z/D=1.12) in the region behind the cylinder are compared in Fig 2. The LSPIV measurements are shown in frame a and the LES simulation results are shown in frame b. Observe that the mean flow is not exactly symmetrical with respect to the streamwise axis going through the center of the cylinder as would be expected for an infinite-length cylinder or for a cylinder mounted on a flat surface. The reason is that the equilibrium scour and deposition patterns around the cylinder are not exactly symmetrical in experiment (same bathymetry was used in the numerical simulation). The result of this non-symmetry is that a unique vortical eddy is observed on the left side (relative to the incoming flow direction) of the near-wake region, behind the cylinder. This eddy is associated with an upwelling motion toward the free surface which feeds fluid into the center of the eddy. From there the fluid is convected in the free surface plane towards the cylinder and the DSLs. The center of this eddy is situated at (x_v, y_v)=(0.84D, 0.44D) in experiment and at (0.9D, 0.42D) in the simulation. Its mean size is also very similar in simulation and experiment. The only difference between experiment and simulation is the slightly larger inclination angle of the limiting streamlines originating in the attached boundary layer, on the right side of the cylinder, in the experiment compared to simulation.

More information on the flow dynamics in the free surface region is provided by the distributions of the instantaneous and mean vorticity magnitude in Fig. 3.

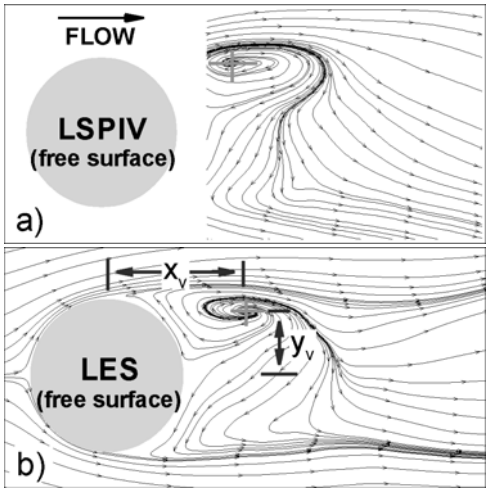

Figure 2. Mean streamline patterns at the free surface in the region behind the pier. a) LSPIV; b) LES.

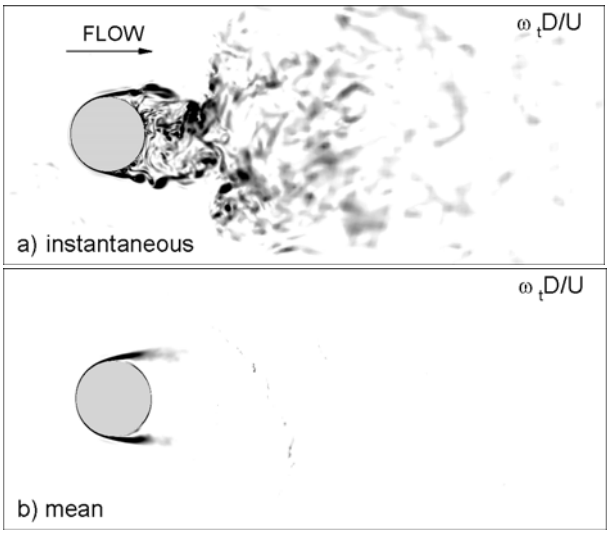

Figure 3. Vortical structure of the flow at the free surface. a) instantaneous vorticity magnitude contours; b) mean vorticity magnitude contours.

As expected, in the mean flow the vorticity is concentrated in the two DSLs on the two sides of the cylinder. At the Re_D=16,000 the boundary layers are laminar at separation. However, the flow in the downstream part of the DSLs is turbulent, as the flow transitions over a small distance from the separation line due to the amplification of the Kelvin-Helmholtz (KH) instabilities into small quasi-2D billows (vortex tubes) and to the interaction with the small-scale turbulence convected from upstream (the incoming flow is fully turbulent). The distribution of the mean vorticity inside the two DSLs is practically symmetrical.

The instantaneous flow offers a very different picture. A wide range of energetic turbulent eddies is observed over considerable distances outside the main recirculation region behind the cylinder. Inside the DSLs, the formation and shedding of KH billows is clearly observed. The instantaneous vorticity magnitude contours do not suggest the presence of a very organized large-scale shedding similar to the one generally observed in the case of an infinite cylinder at similar Reynolds numbers. In fact, results of a LES simulation done for the same flow conditions considered in the present work but with a flat bed showed that large-scale rollers were shed in the wake quasi-regularly in that case. It appears that the hump that forms due to sediment deposition behind the cylinder interacts with the instability responsible for the large-scale shedding and induces interactions with the free surface (strong upwelling and downwelling motions). This makes the wake region, especially for x/D>1.5, to be wider and the large-scale motions less organized compared to what is generally observed in the case of an infinite cylinder or in the case of a pier placed in a deep current (H/D>>5).

In the instantaneous frame sequence (a to f) in Fig. 4 showing the out-of-plane vorticity contours at a time interval of 0.2D/U in LES, the alternate shedding of vortex tubes from the DSLs is clearly observed. The separation angle, which is defined as the polar angle between the symmetry plane and the point where the boundary layer detaches from the cylinder surface oscillates around 85^o between the free surface and mid-depth levels. In the same frames one can observe that a merging event between two successively shed vortices takes place inside the DSL on the right. The patches of vorticity denoted V6 and V7 in frame a start to merge in frame b. The merging is practically complete in frame c, where a new eddy denoted V8 has formed. At other time instances, as the vortex tubes are advected away from their formation region, they can be stretched and mix with the free-stream fluid or with the fluid in the recirculation region. Eventually, these vortex tubes will break into smaller 3-D structures and force transition to turbulence not only of the flow in the downstream part of the DSL region but also of the flow inside the near wake region. Due to the fact that in the present test case the incoming flow is fully turbulent and quite shallow, the effects of turbulence burst phenomena are felt in the upper layers of the flow and the random jittering of the KH billows inside the DSLs is much higher compared to infinite cylinders. This strongly increases the production of small scales and makes that the instantaneous structure and strength of the shear layers on two sides of the cylinder can be quite different. At times, the length of these shear layers and the level of coherence of the vorticity patches inside them can be similar (frames a to c), at other times one shear layer can be much longer than the other (frames e and f where the DSL on the right side is much stronger) because of the different level of coherence of the KH billows.

The dye visualizations in frames g to i confirm the presence of merging events inside the DSLs. The tracer is introduced inside the attached boundary layer in a plane close to the free surface. Observed that the larger billow B in frame g is disturbed due to interaction with the smaller eddies inside the recirculation eddies. As a result the next billow, denoted A, starts approaching B in frame h. In frame i the two billows start moving one around the other due to forces induced by the two patches of vorticity. The merging is practically complete in frame j.

Another phenomenon that is observed in experimental visualizations and in animations of the out-of-plane vorticity contours obtained from LES is that, from time to time, as a result of the jittering of the DSL or due to an interaction between one of the KH billows with an eddy from the recirculation region, one of the KH billows is entrained inside the recirculation region. Once there, the billow is stretched by the small and medium sizes eddies that populate the recirculation region before breaking itself into smaller eddies. In most of the cases this event corresponds to a strong decay in the strength and coherence of the DSL from which the KH billow has detached. Such an even is illustrated in frames a to d of Fig. 5. In frame a the downstream part of the DSL on the right side is strongly curved toward the interior, and V12 starts detaching. In frame b, V12 has separated and started interacting with the main (co-rotating) eddy present at that moment in the recirculation region (V11) while being stretched by the surrounding smaller eddies. In frame c, V12 has disappeared as part of it has merged with V11, whose circulation and size have increased, and part of it decomposed into smaller eddies. Eventually, the DSL on the right side recovered its usual structure (frame d). A similar sequence of events is also observable in experimental visualizations in which dye was infected

near the free surface in the attached shear layer on one of the sides of the cylinder. For instance, in frame e one can observe several billows corresponding to the vortex tubes shed inside the DSL. The one closest to the separation, indicated by the arrow, has already started moving toward the back of the cylinder. In frame f the billow is entrained into that region and has stopped interacting with the other eddies inside the DSL. The dye filament associated with the billow has separated from the main streak of tracer in frame g and part of it is convected vertically away from the free surface due to intense vertical motions present in the recirculation region (see also discussion of Fig. 8). Finally in frame h, the filament of dye associated with the billow that was drawn into the recirculation region has dissipated while the main streak of tracer recovers its usual shape in which several vortex tubes that are convected parallel to the mean flow direction inside the DSL can be identified. The time intervals at which this phenomenon occurs are randomly spaced. We were not able to identify a clear frequency associated with the entrainment of patches of vorticity from the DSL into the recirculation flow behind the cylinder.

The next region of interest is the near bed region around the base of the pier. The deepest part of main scour hole occupies the upstream and the sides of the pier base (see Figs. 1a and 6f). The scour hole is not as deep behind the cylinder but it extends to larger distances away from the cylinder for polar angles close to 180^0. In the central region behind the cylinder a deposition region in the form of a dune whose axis is oriented streamwise is present. It starts immediately downstream the scour hole. On the two sides of this elongated deposition area, several contiguous regions where the bed is eroded are present. The arrows in Fig. 1a point toward the ones on the right side of the cylinder. They appear to be separated by ripple-like bedforms.

Animations of the LES instantaneous flow fields [13] and dye visualization experiments show that the HV region is populated by necklace like eddies whose extent in the polar direction is highly variable in time. However, at most time instances a larger relatively stable necklace like vortical structure is present around the upstream part of the cylinder and oscillates randomly. Random formation and shedding of "new" small necklace vortices from the separation region, upstream of the cylinder, is observed. Some of these vortices will merge with the primary vortex that is being stretched, and form a "new" primary vortex, others will loose their coherence rapidly. This makes that the intensity of the overall HV system can vary substantially in time. This is especially true for the two legs of the primary necklace vortex.

Besides the sources of randomness discussed before, random interactions among the legs of the necklace vortices, the lower part of the vortex tubes shed in the DSL and the near bed turbulent eddies convected from upstream are observed.

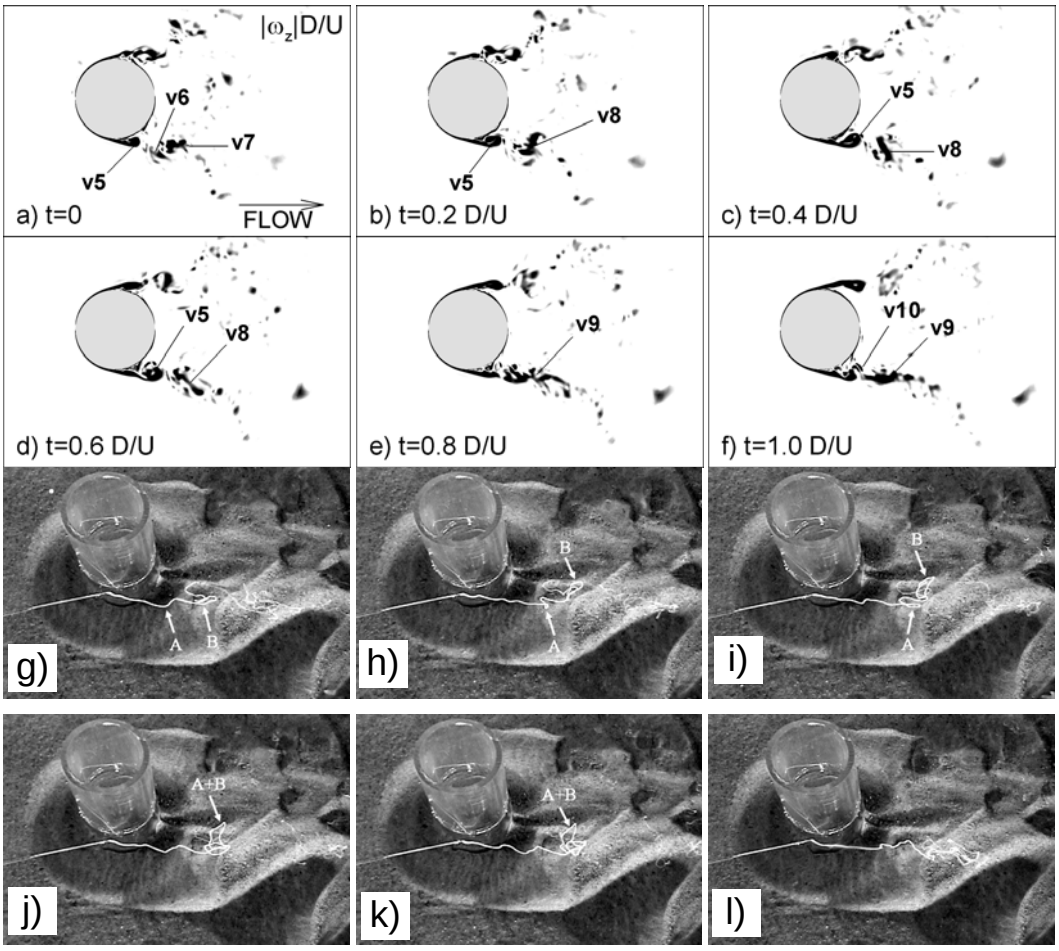

Figure 4. Visualization of the structure of DSLs using instantaneous vorticity magnitude contours. a) t=0D/U; b) t=0.2D/U; c) t=0.4D/U; d) t=0.6D/U; e) t=0.8D/U; f) t=1.0D/U; g)-l) dye visualizations.

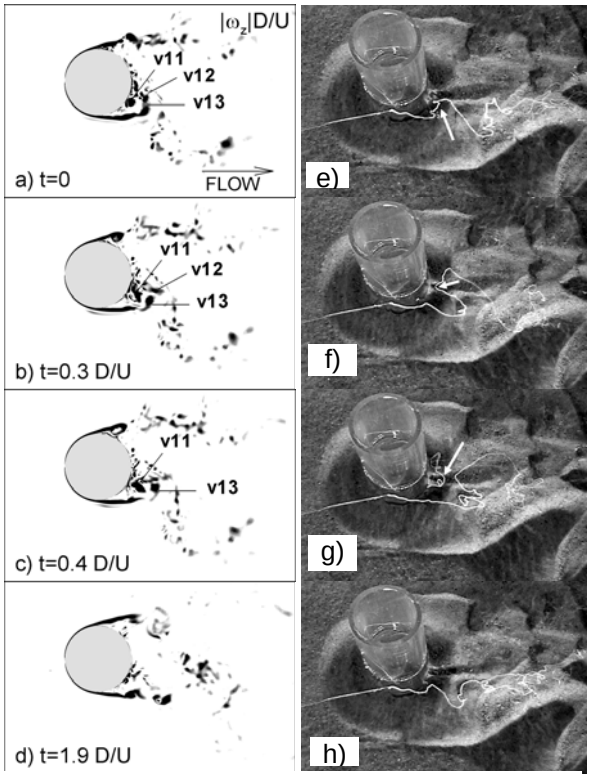

Figure 5. Visualization of the interactions between the vortex tubes in the DSLs and the recirculating flow at the free surface. a)-d) instantaneous vorticity magnitude contours from LES; e)-h) dye visualizations.

When one of the legs of a necklace vortex moves too close to the DSL, the vortical structure of the flow on that side of the cylinder in generally strongly affected. In many cases the end result is a significant loss in the coherence of the HV system on the side on which the interaction took place. Eventually, the HV system will recover its relatively symmetric shape with fairly elongated legs on the two sides of the cylinder.

A phenomenon that was not discussed in great details in previous studies is the role of the coherent structures in the evolution of the bathymetry outside the upstream part of the cylinder base where the process is controlled by the main necklace vortices of the HV system. To investigate this process in the late stages of the scouring process, snapshots in time of the vertical velocity contours are plotted in Figs. 6a to 6e in a surface parallel to the deformed bed situated everywhere at $\Delta z/D=0.13$ from the bed. This deformed surface approximately cuts through the core of the main HV that wraps around the upstream side of the cylinder and then orients itself parallel to the flow direction. Though vorticity is generally a more appropriate quantity to educe vortical structures, in the present case the vertical velocity contours appear to better isolate the large-scale vortical structures (the centerline of the core of a vortex is situated in between the parallel streaks of positive and negative vertical velocity).

Frames a to c in Fig. 6 illustrate a phenomenon also observed in dye visualizations in which the downstream part of the legs of the main necklace vortex which is oriented most of the time in a direction parallel to the flow (e.g., see frame d) is sometimes attracted toward the back of the cylinder (see arrow pointing toward the leg on the right side of the cylinder in frame b). At this point that streak of vorticity becomes oriented at an angle of around $\pm 45^0$ with the streamwise direction. The streak then detaches from the leg of the HV and is then convected downstream (frames c) by the mean flow. Before loosing its coherence due to the interaction with the small scale turbulence in the bed region (frame d), this eddy remains fairly parallel to the bed and can strongly increase the value of the bed shear stress beneath it.

Another situation arises when coherence in one of the legs of the HV becomes quite high and the end of the region over which the circulation is high is situated well past x/D=0. Such a case is illustrated in frame e where the right leg maintains its coherence up to x/D~1.7. In this case the vorticity inside the leg is oriented mainly in the streamwise direction, the right leg (see arrows) undergoes lateral oscillatory motions during which sediment is entrained from the deeper regions and carried laterally against the slope of the bed in the regions situated on the sides of the cylinder. This partially explains the growth of the scour hole in the lateral direction in the later stages of the scouring process.

These kinds of phenomena are also captured in the dye visualizations in frames g to k of Fig. 6. Similarly to the scenario observed in frames a to c, a streak containing mainly horizontal vorticity (see white arrows) is detaching from the leg of the main necklace vortex on the right side and starts advancing mostly laterally against the slope of the scoured region on the side of the cylinder. In frame h, the streak of vorticity is still very compact and is situated practically on the crest of the scoured region. Concomitantly, a second streak (black arrows) starts also being convected away from the cylinder base. This second streak travels initially mostly in the streamwise direction (compare its position in frames h and i) and then laterally, against the slope of the scoured region on the side of the cylinder (frame j).

It appears that the sediment is carried out from the deeper region not just by turbulence burst phenomena associated with the dynamics of regular turbulence structures that populate the near bed region of a fully turbulent channel flow, but primarily by the large-scale structures that detach from the legs of the primary necklace vortices part of the HV system. We were also being able to show using the LES flow fields that the sweeping motions associated with these streaks of vorticity oriented parallel to the bed can induce significant instantaneous values of the bed shear stress and thus sediment ejection. Thus, these eddies can carry sediment from the deeper regions both laterally and downstream. Once these structures start loosing their coherence as they interact with the small scale turbulence in the near bed region and dissipate, the sediment will deposit again.

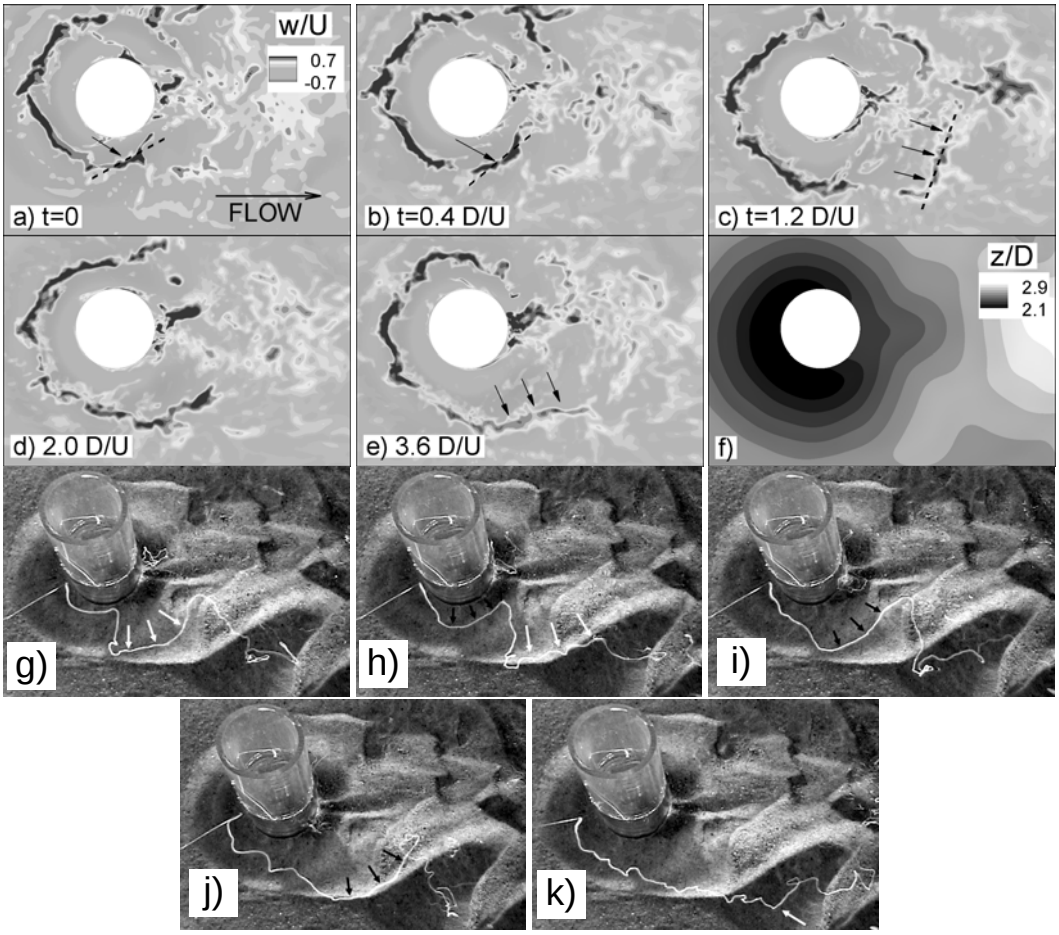

Figure 6. Visualization of the dynamics of the legs of the main necklace vortices. a)-e) instantaneous vertical velocity contours from LES in a deformed surface situated at 0.13D from the bed; f) bed elevation map around the pier; g)-k) dye visualizations.

Finally, in frame k, we illustrate a situation in which the leg of the necklace vortex is strong enough to maintain its coherence over large streamwise distances. Its axis is situated at larger distances from the bed then usual. In this case the instabilities acting on the leg of the necklace vortex will still induce the formation of streaks of vorticity that will separate and scour the bed as they are convected downstream. However, the regions over which these streaks will be active is situated on the two sides of the streamwise oriented mound of sediment where bed deformations in the form of ripples are observed (see arrows in Fig. 1a).

We think that these phenomena along with the shedding of vortex tubes in the DSLs (see discussion of Fig. 7) are responsible in a large measure for the scouring that occurs around the cylinder in the region between x/D=0 and x/D=2 before equilibrium conditions are reached.

The mean shape of the DSL is found to vary considerably as one approaches the bed. This is illustrated by the tke contours in Fig. 7a shown in a vertical plane situated at x/D=0.7D downstream of the cylinder axis. The large values of the tke and pressure fluctuations inside the DSLs are due to the shedding of energetic vortex tube-like structures at a high frequency. Observe that the DSLs are curving toward the symmetry axis of the cylinder as they approach the bed. In fact this oblique shedding phenomenon is present even at the start of the scouring process when the bed is flat, but becomes somewhat stronger as the scour evolves toward equilibrium conditions. This is because the polar angle at which these layers detach from the cylinder surface is increasing as the bed surface is approached. This is evident from the comparison of frames b, c and d in Fig. 7 in which the mean total vorticity contours from LES are shown in two deformed surfaces parallel to the bed situated at 0.04D and 0.3D from it and in a horizontal plane situated at0.5D from the free surface.

The separation angle of the boundary layer on the cylinder between the free surface and the mid depth region (frame d) is practically constant and close to 85^0, similar to the case of the flow over an infinite cylinder at the same Reynolds number. The separation angle becomes larger then 90^0 in frame c in which the distance to the bed is 0.3D. Very close to the bed (0.04D from the deformed bed surface) the separation takes place at a polar angle of 165^0. This makes that the vortex tubes from the DSLs on the two sides of the cylinder are relatively close to each other between the back of the cylinder (x/D=0.5) and x/D~1.5 which corresponds to the start of the main deposition region.

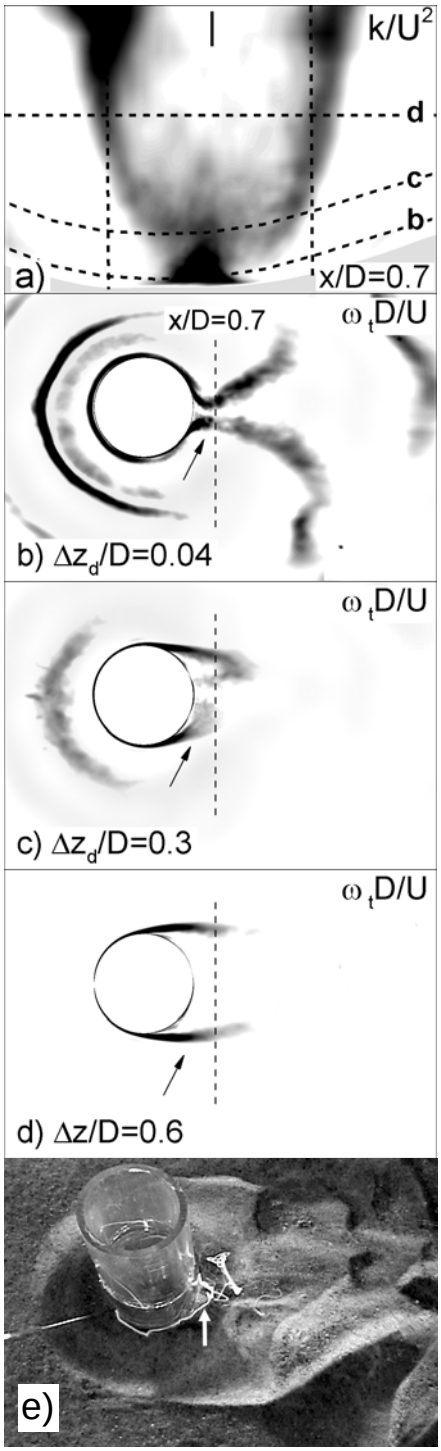

Figure 7. Visualizations of the DSLs. a) tke in x/D=0.7 plane; b) mean vorticity magnitude contours in a plane situated at 0.04D from the bed; c) mean vorticity magnitude contours in a plane situated at 0.3D from the bed; d) mean vorticity magnitude contours in a plane situated at 0.5D from the free surface; e) dye visualization of a vortex tube in the near bed region.

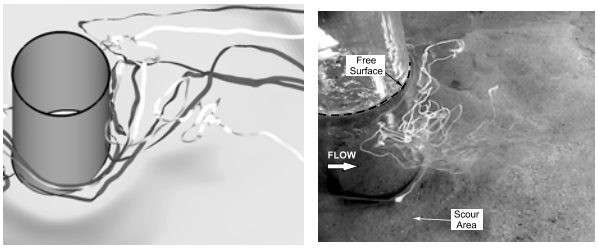

Figure 8. Visualization of uplift phenomena in the recirculation region behind the cylinder. a) 3D instantaneous streamlines from LES; b) dye visualizations.

As these highly energetic structures are convected over the bed in the region situated behind the cylinder, close to its symmetry axis, they can entrain sediment away from the bed due to the large instantaneous pressure fluctuations and bed shear stress values they induce. The mean path of these coherent structures can be inferred from Fig. 7b. This explains why scouring occurs in this region where one would otherwise expect to see deposition of sediment. In fact, as one can see from Fig. 6f, the form of the scour hole is also elongated in the streamwise direction for polar angles close to 180^0. As these vortex tubes are convected downstream they grow in size but the overall vorticity levels inside the core of these structures is decaying. Thus, past a certain distance from their formation region they will not be able to entrain sediment. Evidence of the separation delay in the near bed region is also shown in Fig. 7e in which the streak of tracer injected inside the attached boundary layer is partially entrained into one of the vortex tubes moving along the $\phi=180^0$ direction in the near bed region and from there upwards toward free surface in the recirculation region.

Instantaneous 3D streamlines (frame a) and particle path visualizations (frame b) in Fig.8 suggest that the region situated behind the cylinder in between the two DSLs is characterized by strong momentum transfer in the vertical direction. In experiment and simulation the origin of the streamlines was situated close to the base of the cylinder. Some of the streamlines in Fig. 8a are entrained in the region just behind the pier and from there they are advected toward the free surface by intermittent sweeping motions present in the near wake region close to the bed. As the channel depth is comparable to the pier diameter in the test case considered in the present work, these motions are strong enough to convect these fluid particles very close to the free surface as observed in both frames in Fig. 8. Eventually, they will be convected into regions where down-welling motions are present near the free surface and eventually will deposit some distance downstream the pier.

VI. SUMMARY

The influence of large scale coherent structures on scour at conditions close to equilibrium was investigated using a combination of numerical and experimental techniques. The bed geometry was obtained from a laboratory experiment. The present study focused on the interactions between the legs of the necklace vortices part of the HV system and the near wake, in particular the vortex tubes that are shed at a relatively high intensity inside the DSLs. The dynamics of the interactions between the legs of the horseshoe vortices and the deformed

scoured bed around the cylinder was investigated using the database from a highly resolved LES simulation and experimental visualizations. The present simulations showed that streaks of vorticity from the legs of the main horseshoe like structures can detach and then be convected downstream or laterally against the slope of the scoured region. As they travel, these patches of vorticity remain approximately parallel to the bed and can locally increase the bed shear stress values beneath them above the threshold entrainment value. This phenomenon is different from the usual bursting events present in the near bed region of a fully turbulent channel flow. The separation of the DSL in the near bed region is delayed substantially compared to the layers situated away from the bed. The DSLs on the two sides of the cylinder curve toward the centerline as they approach the bed. Consistent with dye visualization experiments, strong ejections and uplifting phenomena were observed in the region just behind the cylinder.

LES simulation results were validated by comparing the predicted free surface streamline patterns in the wake of the cylinder with those obtained using LSPIV. Though most of the vorticity in the mean flow was contained into the DSLs on the two sides of the pier, the vorticity distribution in the recirculation and near-wake regions in the instantaneous flow was shown to be very complex and to contain a wide range of turbulent scales. Phenomena such as merging of the vortex tubes inside the DSLs and entrainment of patches of vorticity from the DSLs into the recirculation region were observed to occur randomly.

All these mechanisms involving interaction among large-scale coherent structures or between them and the bed were highly intermittent and occured in a random fashion. They explain, at least partially, how the scour hole is growing in time in the regions situated laterally or behind the pier and illustrate the very complex interactions between the near-wake region and the HV system.

ACKNOWLEDGMENT

The authors would like to thank Dr. M. Muste from IIHR-Hydroscience and Engineering, The University of Iowa for his insightful advice related to the experimental part of the study and for his help in applying the LSPIV technique he developed to the present study.

REFERENCES

[1] Castro, P. and Haque, A., 1988, The Structure of a Shear Layer Bounding a Separation Region. Part2: Effects of Free-stream Turbulence, Journal of Fluid Mechanics, 192, 577-595.

[2] Dargahi, B., 1987, Flow Field and Local Scouring around a Cylinder, Bulletin No: TRITA-VBI-137, Royal Institute of Technology, Hydraulics Laboratory, Stockholm, Sweden.

[3] Dargahi, B., 1989, The Turbulent Flow Field around a Circular Cylinder, Experiments in Fluids, 8, 1-12.

[4] Dargahi, B., 1990, Controlling Mechanism of Local Scouring, Journal of Hydraulic Engineering, 116 (10), 1197-1214.

[5] Davenport, W. J. and Simpson, R. L., 1990, Time-dependent and Time-averaged Turbulence Structure Near the Nose of a Wing-body Junction, Journal of Fluid Mechanics, 210, 23-55.

[6] Ettema, R., Kirkil, G. and Muste, M., 2006, Similitude of Large-Scale Turbulence in Experiments on Local Scour at Cylinders, Journal of Hydraulic Engineering, 132 (1), 33-40.

[7] Fujita, I., Muste, M., and Kruger, A., 1998, Large-scale Particle Image Velocimetry for Flow Analysis in Hydraulic Applications, Journal of Hydraulic Research, 36(3), 397-414.

[8] Graf, W. H. and Yulistiyanto, B., 1998, Experiments on Flow around a Cylinder, the Velocity and Vorticity Fields, Journal of Hydraulic Research, 36(4), 637-653.

[9] Graf, W. H. and Istiarto, I., 2002, Flow Pattern in the Scour Hole around a Cylinder, Journal of Hydraulic Research, 40(1), 13-19.

[10] Hoyt, J. W. and Sellin, R. H. J., 2000, A Comparison of Tracer and PIV Results in Visualizing Water Flow around a Cylinder close to the Free Surface, Experiments in Fluids, 28, 261-265.

[11] Hoyt, J. W. and Sellin, R. H. J., 2001, Three-dimensional Visualization of Large Structures in the Turbulent Boundary Layer, Experiments in Fluids, 30, 295-301.

[12] Inoue, M., Baba, N. and Himeno, Y., 1993, Experimental and Numerical Study of Viscous Flow Field around an Advancing Vertical Circular Cylinder Piercing a Free Surface, J. Kansai Soc. Naval Archit. of Japan, 220, 57-64.

[13] Kirkil, G., Constantinescu, S.G., and Ettema, R., 2005, The Horseshoe Vortex System around a Circular Bridge Pier on Equilibrium Scoured Bed, World Water and Environmental Resources Congress, Alaska.

[14] Kirkil, G., Constantinescu, S.G. and Ettema, R., 2005, The Horseshoe Vortex System around a Circular Bridge Pier on a Flat Bed, XXXIst International Association Hydraulic Research Congress, Seoul, Korea.

[15] Kirkil, G., Constantinescu, S.G. and Ettema, R., 2006, Investigation of the Velocity and Pressure Fluctuations Distributions inside the Turbulent Horseshoe Vortex System around a Circular Bridge pier, Proc. River Flow 2006.

[16] Mahesh, K., Constantinescu, S.G., and Moin, P., 2004, A Numerical Method for Large Eddy Simulation in Complex Geometries, Journal of Computational Physics, 197 (1), 215-240.

[17] Melville, B. W., 1997, Pier and Abutment Scour: Integrated Approach, Journal of Hydraulic Engineering, 123 (2), 125-136.

[18] Simpson, R. L., 2001, Junction Flows, Annual Review of Fluid Mechanics, 33, 415-443.

[19] Vlachos, P. P., 2000, An Experimental Spatio-Temporal Analysis of Separated Flows over Bluff Bodies using Quantitative Flow Visualization, Ph.D. thesis, Virginia Polytechnic Institute and State University , Blacksburg, VA.

[20] Wei, Q. D., Chen, G. and Du, X. D., 2001, An Experimental Study on the Structure of Juncture Flows. Journal of Visualization, 3(4), 341-348.

[21] Williamson, C. H. K., 1995, Vortex Dynamics in the Wake of a Cylinder, Fluid vortices, S. I. Green (ed.), 155-234.

[22] Williamson, C. H. K., 1996, Vortex Dynamics in the Cylinder Wake, Annual Review of Fluid Mechanics, 28, 477-539.

Trial and Scour; Scour and Bed Protection at the Discharge Sluices in the Afsluitdijk, The Netherlands

W.C.D. Kortlever
Ministry of Transport, Public Works and Water Management, Civil Engineering Division (Rijkswaterstaat), Utrecht, The Netherlands

I. Introduction

Anticipating the rising sea level and the increasing rainfall, both attributed to climate changes, plans are made for the construction of a new, third discharge sluice in the Afsluitdijk. The design of this new sluice will be part of a Design and Construct contract. In this paper a preliminary design of the bed protection in the discharge channel is presented, which has been based on the experience gained after the construction of the two existing sluices that have been completed in 1932.

The Afsluitdijk is the dam that closes the IJsselmeer basin, the former Zuiderzee, in the northwest of The Netherlands and has a length of about 30 km (Fig. 1). Outside the dam lie the Waddenzee and the North Sea. The River IJssel and the River Vecht run into the IJsselmeer. Also, the excess rainwater from the surrounding lowlands, i.e. from the polders protected by dikes, is sluiced into the IJsselmeer. Now, in winter the target water level in the IJsselmeer is often exceeded, and is expected to be exceeded more and more often in the future. In the Afsluitdijk two discharge sluices have been built to maintain the water level at the target water level and to guarantee the safety of the surrounding polders. At the completion of these sluices the bed protection in the discharge channels consisted of a concrete apron with a stilling sill at the end. The total length of the bed protection was 18 m. The unprotected seabed at the end of the bed protection consisted of boulder clay or sand. However, in a process of lengthening the protection and monitoring the new scour at the end of the protection (trial and scour), which lasted to 1964, the bed protection had to be extended to a length of about 200 m. The scour holes reached a depth of 25 to nearly 30 m below sea level, with an original water depth of 5 m.

In the new sluice project one of the aims is to predict the scour more accurately and to design a bed protection that reduces the scour and keeps the scour away from the sluice. First, in this paper the extension of the bed protections of the existing sluices is reviewed, on the basis of [1] and [2]. Second, a preliminary design of the bed protection is presented. Third, the requirements for the new sluice are derived, on the basis of the review and the preliminary design.

II. Existing sluices

A. Present Seabed Level

The discharge sluice near to Kornwerderzand (KWZ) consists of two clusters, with five sluice channels in each cluster. The discharge sluice close to Den Oever (DO) consists of three clusters, also with five sluice channels per cluster. The situation of the sluices is shown in Fig. 1.

Recent depth measurements at the seaside of the Afsluitdijk show a large depression in the seabed next to the sluice of KWZ and three large depressions next to the sluice of DO. At KWZ the maximum depth in the depression is about 28 m below mean sea level (MSL), at a distance of about 200 m from the sluice structure. At DO the maximum depth in the depressions is about 26 m below mean sea level (MSL), at a distance of about 140 m from the sluice structure. At KWZ the steepest under water slopes, which are found at 125 m from the sluice structure, are 1:2 to 1:3. These slopes lie between depths of 14 m and 24 m below MSL. At DO the steepest under water slopes, which are found between 90 m and 140 m from the sluice clusters, are 1:2 to 1:3. These slopes lie between depths of 10 m and 24 m below MSL. Closer by and further away slopes are 1:4 or less [3,4].

Depth measurements at the IJsselmeer side of the Afsluitdijk show that the inflow channel at KWZ bends around the extremity of the western breakwater. This is explained by the fact that the inflowing water, particularly at higher discharges, flows through the deeper channels of the Middelgronden, original tidal channels at the west side of the sluice. The measurements also show that the inflow channel at DO lies south of Robbenplaat and is oblique to the flow direction through the sluice. This oblique direction is explained by, first, the location of the original tidal flow channels in the IJsselmeer and, second, the under water ridge of boulder clay that reaches to a height of 2 m below still water level (SWL). The steepest slopes, to the south of Robbenplaat, are about 1:2,5 and are found between 2 and 6 m below SWL [3,4].

B. Bed Protection History

At the completion of the discharge sluices in 1932 the total length of the bed protection in the discharge channel was 18 m. However, due to scour the bed protection had to be extended. A broad overview of these extensions behind two of the center sluices, which is derived from [1] and [2], is given in Table I [3,4].

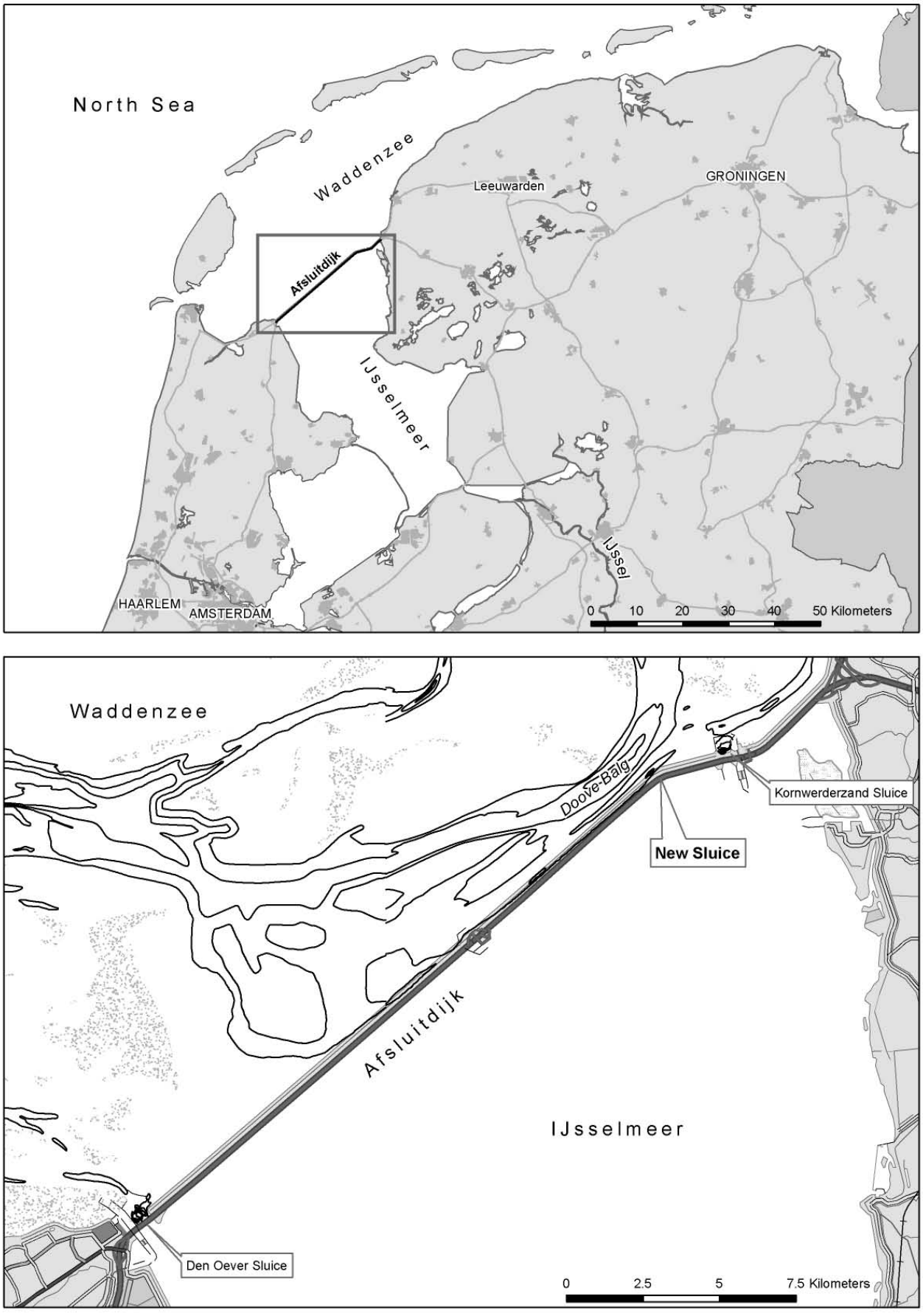

Figure 1. Situation Afsluitdijk, Den Oever sluice, Kornwerderzand sluice and new sluice

TABLE I.
BROAD OVERVIEW PROTECTION EXTENSION KWZ AND DO [3,4]

KWZ: Center Sluice Cluster 5		
Period	Distance between Sluice and Outer End Bed Protection	Bed Protection Extension
May 1932	18 m	Concrete apron with stilling sill
Dec. 1932	128 m	3 rock mattresses 80-200 kg
1933-1937	145 m	Rock mattress 80-200 kg + rock filled with concrete over 50 m from stilling sill
1945-1954	173 m	Rock mattress 80-200 kg
1955-1964	210 m	Rock mattress 80-200 kg
DO; Center Sluice Cluster 2		
May 1932	18 m	Concrete apron with stilling sill
Oct. 1932	128 m	3 rock mattresses 80-200 kg
1933-1937	140 m	Heavy rock 500-1000 kg over 25 m from stilling sill + light rock filled with concrete over 50 m from stilling sill + rock mattress 80-200 kg
1938-1944	160 m	Rock mattress 80-200 kg
1955-1964	205 m	Rock mattress 80-200 kg

The bed protection extensions were not made on the original seabed at 5 m below MSL. After the formation of a new scour hole at the end of the bed protection, this hole was partly filled with sand and a layer of boulder clay, on top of which a rock mattress was placed. The initial slope of the first three mattresses was 1:10 to 1:8. In 1964 the deepest part of the bed protection lay at a depth of 25 m below MSL.

The greater the distance is to the sluice and the deeper the bed protection lies, the lower are the flow velocities and turbulence above the seabed. At a distance of about 200 m from the sluice, the unprotected bottom seemed to resist the hydraulic loads exerted by the flow.

Fig. 2 and Fig. 3 are rough cross-sections of the seabed and the bed protection in the discharge channels behind two of the center sluices, at different points in time. From Fig. 2 and Fig. 3 it is concluded that the present level of the seabed roughly corresponds to the level of 1964. The bed protections, which have been placed before 1964 and the maintenance that has been carried out later seem to prevent subsequent scour. However, according to Fig. 3, it is possible that rock on the steep slopes between 10 m and 24 m below MSL has been transported by the flow. On the condition that maintenance will be carried out, any further scour will be limited.

In 1932 the first bed protection in the inflow channel consisted of a concrete floor, 20 m wide, and a willow mattress, also 20 m wide. After completion of the sluice the bed protection has been extended with a rock mattress, 25 m wide. In 1934 the willow mattress has been filled with concrete [1]. Now, at the end of the bed protections scour holes have been found 1 tot 3 m deep. It is possible that these scour holes will grow in the future.

C. *Safety Check*

In 2004 the stability of the sluice structures in the Afsluitdijk, given the design hydraulic conditions, has been tested according to VTV 2004 [5], a Dutch regulation to check the safety of the main dikes and other primary water-retaining structures. This test included a check of the risk of shear and flow slides in the scour holes, which can endanger the structures [3,4]. As the under water slopes close to the sluices are largely protected by bed protections, this aforementioned risk is sufficiently low.

At KWZ, at the location where one of the discharge channels touches the northeastern breakwater, the flow has caused steep under water slopes. The same holds for the inflow channel and the extremity of the southwestern breakwater. At these locations the risk of shear and slides is too high and measures should be taken. At DO, the inflow channel lies next to the south point of Robbenplaat, which is part of the Afsluitdijk. Also here, measures to prevent sliding have to be taken.

D. *Stability in Discharge Flow*

Using depth measurements, the area of the flow has been determined, perpendicular to the flow, at several cross-sections at different distances from the sluice structures. The maximum discharges have been estimated from measured discharges [6]. From those flow area's and maximum discharges the maximum averaged flow velocities at the cross-sections have been estimated. Then, using the stability formula of Pilarczyk, the required bed protection has been calculated. In Table II both the calculated and the existing bed protections are presented. From this table it is concluded that most of the existing protections are stable at the maximum flow conditions. However, locally at the breakwaters and at the edge of the protection in the IJsselmeer inspection and protection measures are necessary.

TABLE II.
CALCULATED AND EXISTING BED PROTECTION [3,4]

KWZ		
Location	Calculated	Existing
Waddenzee, distance to sluice piers (flow velocity): 0 m (6,6 m/s) 50 m (2,8 m/s) 100 m (1,5 m/s) 210 m (0,8 m/s)	 Concrete apron 60-300 kg 10-60 kg 30/60 mm	 Concrete apron Mattress and concrete 80-200 kg End of protection
Northeastern breakwater 1-1,5 m/s	80/200 mm	No protection
IJsselmeer, distance to sluice piers: 20 m (2,6 m/s) 90 m (1,9 m/s)	 5-40 kg 50/150 mm	 Concrete apron No protection
Extremity southwestern breakwater 1-2 m/s	80/200 mm	No protection
DO		
Waddenzee: 0 m (6,6 m/s) 50 m (2,8 m/s) 100 m (1,5 m/s) 210 m (0,8 m/s)	 Concrete apron 60-300 kg 10-60 kg 30/60 mm	 Concrete apron 500-1000 kg/mattress and concrete 80-200 kg End of protection
Northwestern breakwater 1-1,5 m/s	80/200 mm	80-200 kg
IJsselmeer: 20 m (2,7 m/s) 90 m (1,6 m/s)	 5-40 kg 40/100 mm	 Concrete apron No protection
South point Robbenplaat 1,7-2 m/s	80/200 mm	Partly no protection

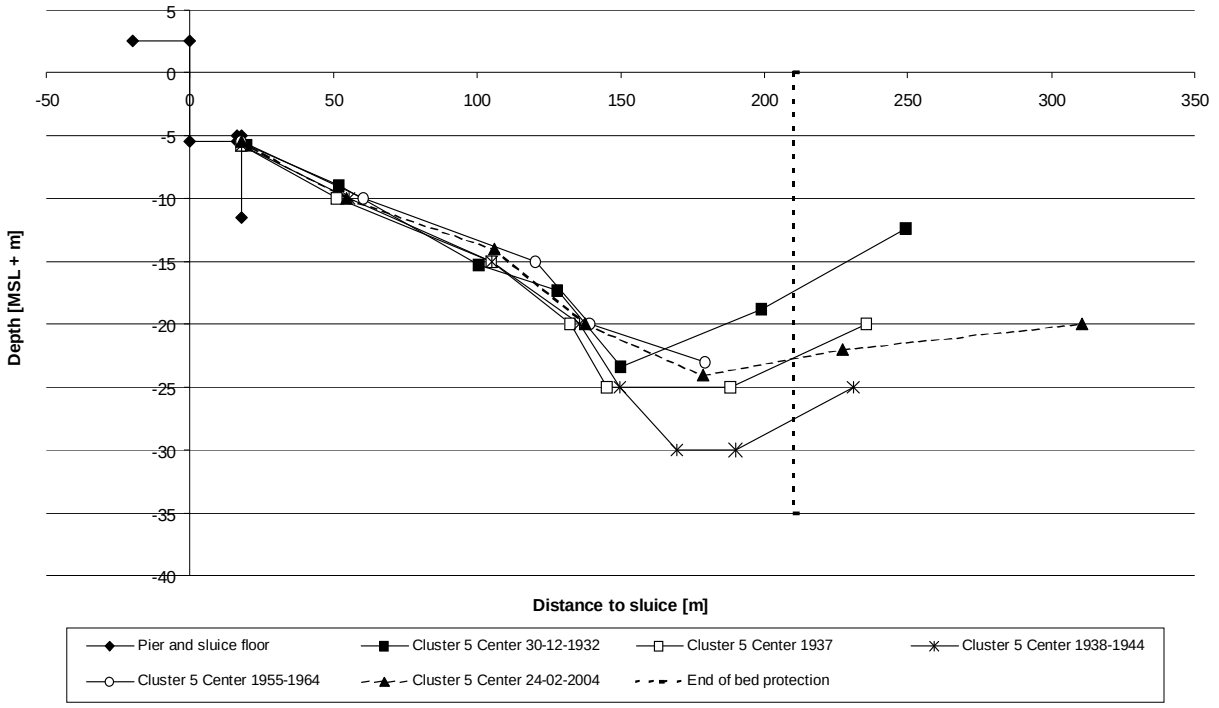

Figure 2. Cross-section of seabed and bed protection in discharge channel; Kornwerderzand

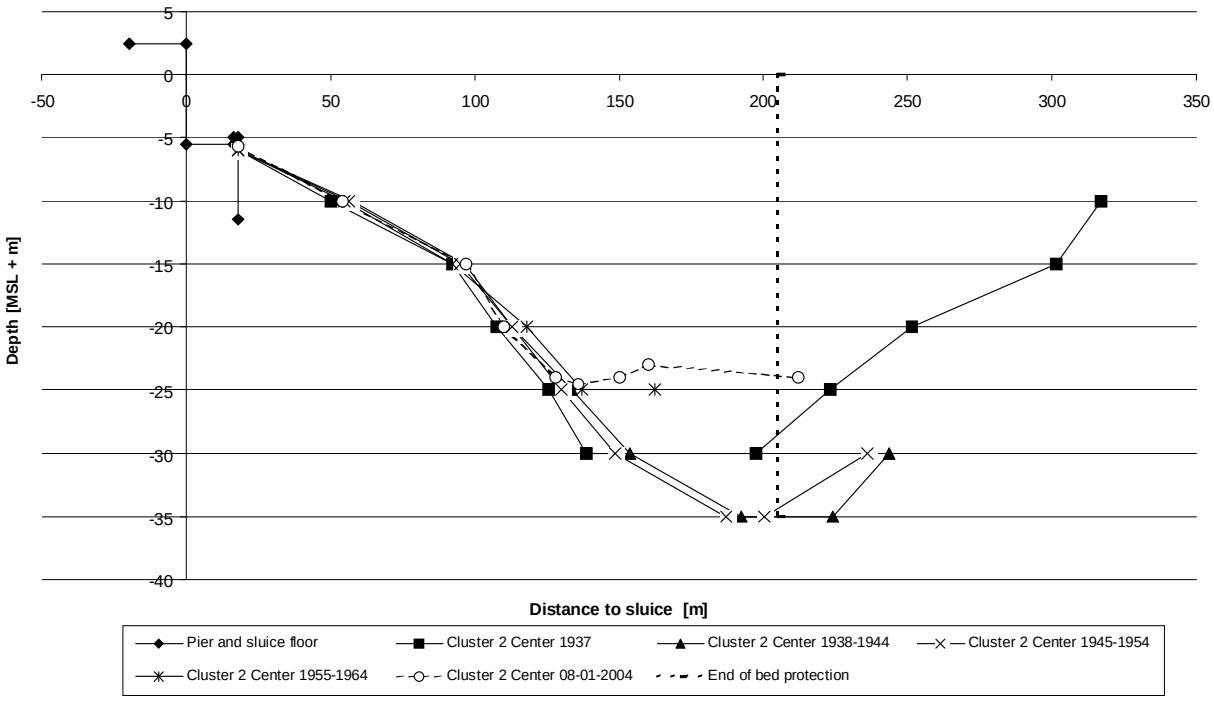

Figure 3. Cross-section of seabed and bed protection in discharge channel; Den Oever

E. Sluicegates Refuse to Close

If the sluice gates refuse to close and at high tide the flow direction turns towards the IJsselmeer, the flow velocities can become extremely high (Froude > 1), especially when it starts to storm and the wind is coming from the northwest. In this case the bed protection at the IJsselmeer side of the sluice is most probably insufficient. Large scour holes will form and part of the bed protection will be flushed away. The height of the risk that bed protection and sluice will be damaged depends on the chances of the gates refusing to close and of the Waddenzee rising to high levels simultaneously.

F. Recommendations Existing Sluices

With regard to the seabed next to the sluices, the following is recommended:

- The large bed protections on both sides of the sluice gates have to be maintained to prevent the formation of new scour holes and under water slope slides. Inspections at a maximum interval of one year.
- At the locations where the flow channels are close to the breakwaters measures have to be taken to prevent the shear and sliding of the steep under water slopes. For example, first, the under water slopes have to be measured. Then the steepening slopes have to be replenished with sand and/or boulder clay. Finally, rock mattresses have to be placed.

  Once the flow touches a rough surface, like a bed protection, the turbulence of the flow increases and this increases the transport capacity of the flow. This must be remembered if it is decided to protect the slopes only locally. In other words, protection can introduce scour.
- To maintain the bed protection at the IJsselmeer side, the scour at the edge of the protection has to be stopped. This means inspection and the aforementioned measures. It is emphasized that the speed of the erosion is limited as long as the seabed consists of boulder clay.

III. A NEW DISCHARGE SLUICE

A. Location and global features

For the present the new sluice will be built at the bend in the Afsluitdijk, less than two kilometers west of the existing sluice at KWZ (Fig. 1). At this location old tidal channels, in the IJsselmeer, and new tidal channels, in the Waddenzee, are close to the Afsluitdijk.

The preliminary design of the new sluice is an open concrete structure, 200 m wide (parallel to the Afsluitdijk). It has five channels, each of which is 30 m wide and 35 m long (perpendicular to the Afsluitdijk). In between the channels are piers, each of which is 10 m wide. Every channel is closed by a single sluice gate. The gate sill is at 6,5 m below MSL.

The new sluice will be built in the crest of the Afsluitdijk, i.e. at the seaside, which means that the inflow channel is closed in, at two sides, by the large inner berm. The seabed of the inflow channel, which is 200 m wide, lies 8 m below MSL. A discharge channel will be dug between the sluice structure and the tidal channel in the Waddenzee, the Doove Balg, to a depth level of 11 m below MSL. At the gate sill the seabed drops vertically to this depth. Given this relatively large depth, flow velocities will decrease significantly, before the flow reaches the seabed.

At the seaside, along the discharge channel, two breakwaters will be constructed, which must answer the following demands:

- Keep the flow and flow eddies away from the Afsluitdijk.
- Guide the flow to increase the efficiency of the sluice.
- Guide the flood currents away from the Afsluitdijk, leading to an enlargement of the shallow water area, east of the sluice, being beneficial for water animals and plants.

B. Scour Predictions and Protection Length

1) The Discharge Channel

The sea edge of the bed protection in the discharge channel has to lie at a minimum distance to the sluice structure. Then, when the flow reaches the unprotected seabed, flow velocities have already decreased and scour holes will be less deep. The distance has to be larger than the part of the bed protection, which possibly can slide down into the scour hole. Thus the functioning and the stability of the sluice are guaranteed.

The required length of the bed protection has been derived from the scour predictions, which are given in Table III [7]. The prediction formula of Breusers and the formula of Dietz [8] have been applied, and an average flow velocity of 1 m/s has been assumed.

TABLE III.
SCOUR PREDICTIONS, PRELIMINARY [7]

Distance between Sluice and Outer End Bed Protection [m]	Maximum Scour Depth, t = 1 year (Breusers) [m]	Maximum Scour Depth, t = 20 years (Breusers) [m]	Equilibrium Depth, t = ∞ (Dietz) [m]
100	7,7	25,7	26,2
150	6,9	22,8	24,2
200	6,3	21,0	22,9
250	6,1	20,1	22,2

The predictions in Table III say that the maximum scour depth, even at 200 m from the sluice, can be about 20 m below the original seabed, which is comparable to the scour depths at the existing sluices. As with the existing sluices, finally, the flow turbulence and the velocities in the scour hole will decrease and the scour hole will stop growing. The upstream slope of the scour hole will reach a value between about 1:2 and about 1:4, before parts of the slope start sliding down. The actual slope before sliding and the final slope after sliding strongly depend on the characteristics of the soil. Flow slides can be expected in natural sand layers, which have been deposited quickly, as a result of which the sand is less compact. Flow slides start occurring when slopes are about 1:4. The final slope after a flow slide will be 1:15-1:20. Shear will start at a steeper slopes, closer to 1:2. The final slope after a shear slide will be 1:6-1:8. The required length of the bed protection is calculated with (1) as in [8]:

$$L = \frac{1}{2} y(\cot(\gamma) - \cot(\beta)), \qquad (1)$$

in which: L = failure length (m),
y = maximum scour depth (m),
γ = upstream slope after sliding (°),
β = upstream slope before sliding (°).

The required length varies from about 60 m, in case of shear, to about 160 m, in case of flow slides. In the preliminary design, first, a protection length of 150 m has been chosen. However, in that case the scour holes at the end of the bed protection can lead to the sliding down of breakwater slopes at both sides of the discharge channel. Instability of the breakwater slopes has to be prevented by applying a toe protection, with a minimum length of about 60 m. As the scour will continue more rapidly in the small, unprotected area that is left, it has been decided to protect the entire seabed area in between the breakwaters.

The extremities of the breakwaters are at the edge of a flood channel, which lies parallel to the Afsluitdijk. At these extremities scour holes will develop as a result of both flood currents and discharge flows. Therefore, the seabed around the extremities has to be protected against sliding, by applying a bed protection, which is about 60 m wide. The total area of bed protection is shown in Fig. 4.

2) The Inflow Channel

The bed protection in the inflow channel has to withstand very high flow velocities, when the sluice gates refuse to close and the high water level of the Waddenzee rises high above the IJsselmeer level. A maximum head difference of 4 m has been assumed.

The flow over the sill will be supercritical (Froude > 1). There will be a hydraulic jump in the inflow channel, close to the sill, and the maximum flow velocities will be about 11 m/s. After the hydraulic jump velocities and hydraulic loads will be lower, but still comparable to the maximum velocities in the discharge channel. As the width of the flow increases only gradually, velocities remain high in the entire inflow channel. Scour holes at the end of the bed protection, given a hydraulic load lasting 12 hours, can reach a depth of 15 m below the seabed. The freeway on the Afsluitdijk, the A7, is guided over the inflow channel by a traffic bridge, of which the piers are standing in the inflow channel. It is concluded that the bed protection has to be extended about 75 m south of the traffic bridge. The total length of the bed protection on this side of the sluice is 170 m. The total area of bed protection is shown in Fig. 4.

C. Stability in Discharge Flow

First, the maximum averaged flow velocities have been estimated, for the maximum discharges, at several cross-sections at different distances from the sluice structures. Then, using the stability formula of Pilarczyk [9], the required bed protections have been calculated, of which the top layers are given in Table IV and shown in Fig. 4 and Fig. 5.

TABLE IV.
DISCHARGE FLOW: CALCULATED BED PROTECTION [7]

Location	Estimated Maximum Flow Velocity [m/s]	Required Top Layer (Pilarczyk)
Waddenzee, distance to sluice piers [m]		
0-40	4,7-4,3	Concrete apron / 300-1000 kg
40-70	4,3-3,5	300-1000 kg
70-150	3,5-2,8	60-300 kg / 40-200 kg
150-300	2,8-2,5	40-200 kg / 10-60 kg
IJsselmeer	3,5	5-40 kg

TABLE V.
GATES REFUSE TO CLOSE: CALCULATED BED PROTECTION [7]

Location	Required Top Layer (Pilarczyk)
IJsselmeer, distance to sluice piers [m]	
0-35	Concrete apron
35-125	1-3 ton / 300-1000 kg
125-155	300-1000 kg / 60-300 kg
155-170	60-300 kg

D. Sluice gates Refuse to Close

The bed protection in the inflow channel has to withstand the flow velocities caused by an estimated head difference of 4 m, at high tide on the Waddenzee. The top layers of the bed protection, based on estimated flow velocities, are given in Table V and shown in Fig. 4 and Fig. 5. In the discharge channel the flow velocities are maximal at the maximum discharge.

IV. DESIGN AND CONSTRUCT

A. Introduction

The design of the new discharge sluice will be part of a Design and Construct contract. To prepare this contract, first, the principal has to define the objects, which are part of the sluice. The main object of the new sluice is the sluice structure in the crest of the Afsluitdijk. Other objects are the inflow and the discharge channel, the breakwaters along the discharge channel, and the traffic bridge across the inflow channel.

Second, the functional requirements of these objects have to be formulated. With the new sluice, it has to be possible to maintain the water level of the IJsselmeer at the summer and winter target levels. As the sluice will be part of the Afsluitdijk, the sluice has to retain the water of the Waddenzee. The flow channels have to provide space for the flows to pass through. The breakwaters have to answer the requirements, which are mentioned in paragraph III.A, and the traffic bridge has to maintain the traffic connection.

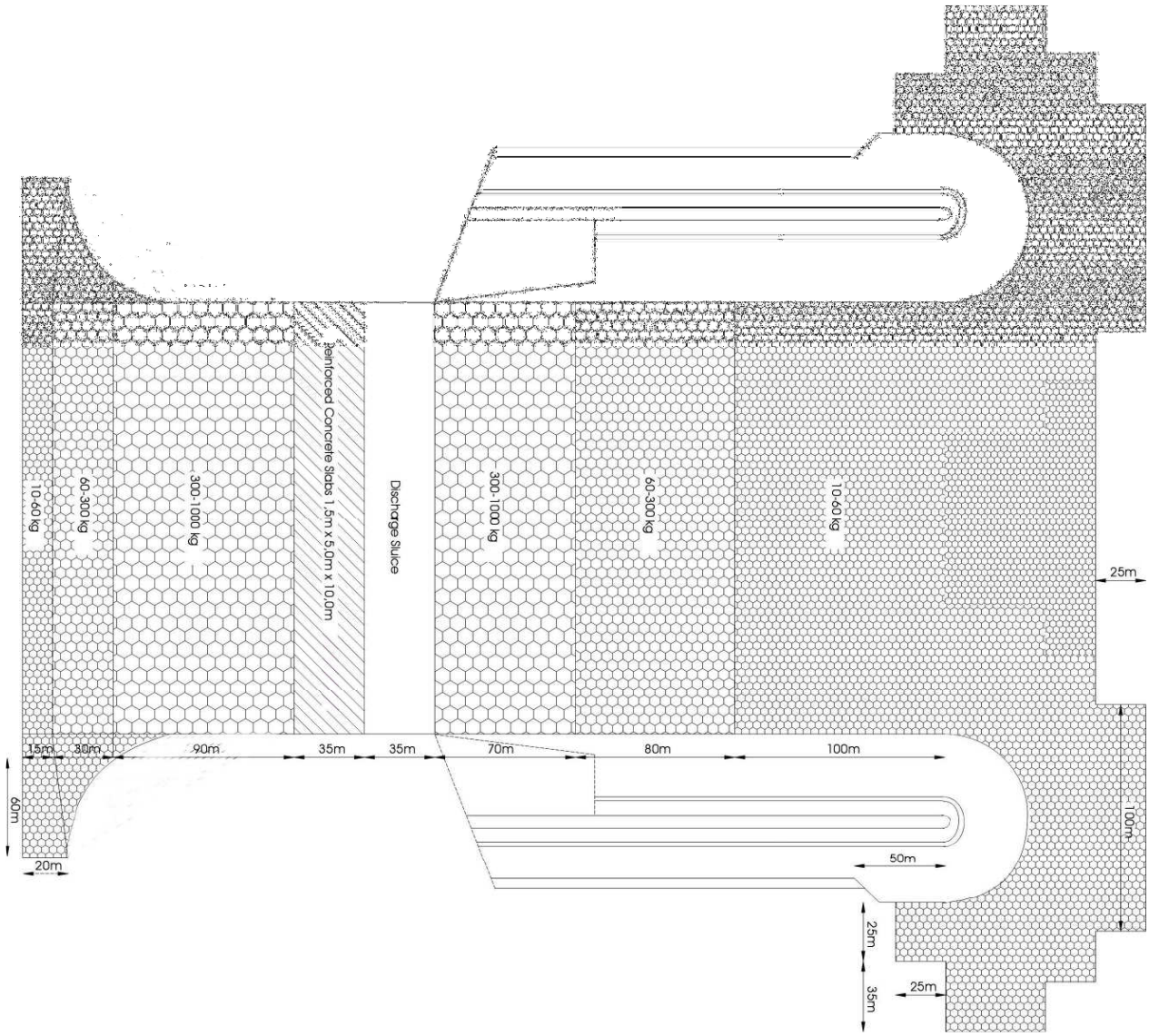

Figure 4. Upper view preliminary design bed protection

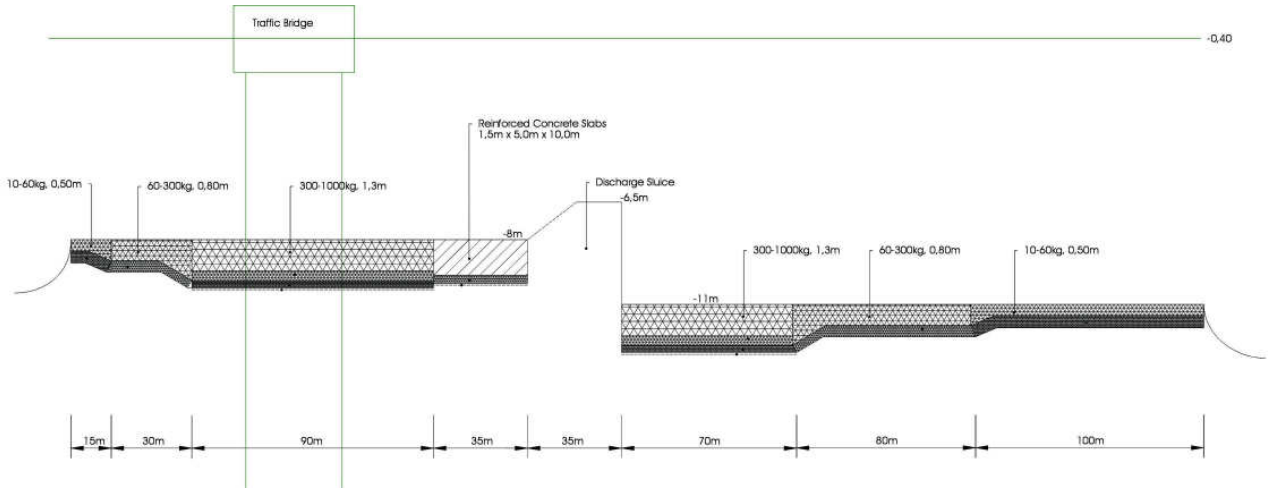

Figure 5. Cross-section preliminary design bed protection

Contrary to the usual Construct contracts, the principal does not provide the contractor with the design of the bed protections, including top layers, filter layers and protection lengths. Only the functional requirements are given, from which the contractor has to draw up the design. In the next paragraph the general requirements, which are related to scour and bed protection, have been summarized.

B. General Requirements Related to Scour

The general requirements in this paragraph have been derived from the experiences with the existing sluices and the preliminary design of the new sluice. The corresponding functions are given in the headings, between brackets.

1) Probability of Failure (To Retain Water)

The overall probability of failure of the new sluice is prescribed. From this the designer has to derive the allowed probabilities of failure for the individual objects, including any soil slope, bed protection or breakwater. These probabilities determine the measures which have to be taken to limit or to prevent scour and thus to maintain the stability of the structures.

2) Stability Afsluitdijk (To Retain Water)

The stability of the Afsluitdijk, i.e. the geotechnical stability of the foreshore and the dike body, is not allowed to decrease as a result of the new sluice structure and its morphological effects (erosion).

3) Temporary Structures (To Retain Water)

Temporary structures, which during realization take over the water-retaining function of the Afsluitdijk, have to be just as reliable as the Afsluitdijk. During the realization of any bed protection, the reliability has to be guaranteed.

4) Operating Conditions (To Retain Water, Target Water Levels)

The principal supplies the hydraulic conditions, i.e. water levels and waves, and the maximum discharges, which have to be realized. From this, the designer has to calculate the maximum hydraulic loads and flow velocities on the seabed. The designer has to determine whether measures are necessary to prevent scour and erosion, so that the sluice satisfies the maximum probability of failure and fulfills its functions. Hydraulic research in a laboratory is compulsory, to check hydraulic loads and any bed protection which has been designed.

5) The Discharge Channel (To Retain Water, Target Water Levels)

At the location where the protected part of the seabed ends and the unprotected part begins, scour holes will form, as a result of both the discharge flows and the tidal currents around the extremities of the breakwaters. It has to be prevented that shear or flow slides into the scour holes lead to the malfunctioning or even failure of the sluice and the breakwaters.

6) Inflow Channel (To Retain Water)

The designer has to determine the dimensions and the weight of the bed protections in the inflow channel from the following conditions:

- water level statistics concerning the IJsselmeer and the Waddenzee;
- the overall probability of failure;
- the chance that the sluice gates refuse to close.

The bed protection design has to be tested by hydraulic research in a laboratory.

7) The Discharge Channel (Target Water Levels, Mitigation of Morphological Effects)

A discharge channel has to be dug between the sluice structure and the large tidal channel in the Waddenzee, the Doove Balg. By prescribing this channel, it is expected that erosion and other morphological effects can be limited to the location of the channel.

8) Maintenance (Life, Maintenance)

As the design hydraulic conditions can occur in the first year of operation, any bed protections have to be robust. The amount of damage has to be very limited, i.e. without maintenance, which will hinder the operation of the sluice. Any bed protection has to be tested by hydraulic research in a laboratory.

9) Life (Life)

The new sluice has to fulfill the aforementioned requirements during the entire, prescribed life.

V. Recommendations

At the preparation of a new discharge sluice, the existing sluices are an important source of information, to draw up the requirements that are related to scour and bed protection.

The overall probability of failure of the new sluice has to be prescribed. From this the designer has to derive the allowed probabilities of failure for the individual objects, including any soil slope, bed protection or breakwater (reliability study).

The main hydraulic loads on the seabed of the inflow channel are caused by the inward flow from the Waddenzee. The height of these loads depends on the chances that the sluice gates refuse to close after the discharge period (reliability study).

If requirements lead to the construction of bed protections, these requirements have to imply robust designs, because large maintenance works will hinder operation of the sluice.

At the locations where the flows from the discharge sluice and/or tidal currents skirt the breakwaters, which are situated along the flow channels of the sluice, measures should be taken to prevent sliding down of the breakwater slopes. Under water slopes can become steep and scour holes can develop.

Shear and flow slides depend on the characteristics of the soil. A soil investigation has to be carried out to determine the probability of flow slides. Probably, flow slides are restricted to certain soil layers.

More effort has to be made to gain insight into the morphological consequences of the digging of a discharge channel towards the Doove Balg. This new channel can attract tidal currents. The combination of discharge flows and an increase of tidal currents, i.e. an increase of sediment transport capacities, can speed up scour and erosion, not only at the sluice, but also along the Afsluitdijk. In the new Design and Construct contract it has to be defined clearly how far the responsibilities of the principal and the contractor go.

Looking back at the existing sluices, it is clear that only when the unprotected seabed lies deep enough the soil can resist the hydraulic loads exerted by the flow. This is a missing element in the preliminary design. At the end of the bed protection flow velocities and turbulence are still high and scour is only shifted from the sluice to the end of the bed protections, where large scour holes will form that eventually will damage the protections. This is not a stable situation.

ACKNOWLEDGMENT

The author is grateful to M. Rikkers and D. de Wilde for their helpful comments and advices, and to G. Jimmink, L. Koot and R. Kuijpers for their drawings.

REFERENCES

[1] K.A. Bazlen, *Strijd zonder Eind (I t/m III), de Invloed van de Spuistroom op de Ontvang- en Stortebedden van de Uitwateringssluizen in de Afsluitdijk*, *Land + Water*, no. 6/66, no. 1/67, no. 2/67.

[2] J.Th.Thijsse, *Een Halve Eeuw Zuiderzeewerken, 1920-1970*, Tjeenk Willink B.V., Groningen, 1972.

[3] W.C.D. Kortlever, *Spuisluis te Kornwerderzand, Toetsing van Voorland op Afschuiving en Zettingsvloeiing (VTV 2004), Toetsing van Bodembescherming op Stabiliteit*, Bouwdienst Rijkswaterstaat, juni 2004, unpublished.

[4] W.C.D. Kortlever, *Spuisluis te Den Oever, Toetsing van Voorland op Afschuiving en Zettingsvloeiing (VTV 2004), Toetsing van Bodembescherming op Stabiliteit*, Bouwdienst Rijkswaterstaat, oktober 2004, unpublished.

[5] Rijkswaterstaat DWW, *De Veiligheid van de Primaire Waterkeringen in Nederland, Voorschrift Toetsen op Veiligheid voor de tweede toetsronde 2001-2006 (VTV)*, Rijkswaterstaat DWW, januari 2004.

[6] T. Broersma and A.J. Ponger, *Resultaten IJkmetingen aan de Spuisluizen te Den Oever*, Rijkswaterstaat Directie IJsselmeergebied, mei 2003.

[7] W.C.D. Kortlever and R. Kuijpers, *Bodemverdediging, Geleidedammen en Verbreding Afsluitdijk, Voorontwerpnota Deel 10*, Bouwdienst Rijkswaterstaat, juni 2004, unpublished.

[8] G.J.C.M. Hoffmans and H.J. Verheij, *Scour Manual*, A.A.Balkema Publishers, Rotterdam, 1997.

[9] CUR/RWS, *Manual on the Use of Rock in Hydraulic Engineering, CUR 169*, 1995.

Riprap Design Criteria, Specifications, and Quality Control

P.F. Lagasse*, L.A. Arneson**, P.E. Clopper* and L.W. Zevenbergen*
*Ayres Associates Inc, 3665 JFK Parkway, Bldg. 2, Suite 200, Fort Collins, CO, USA
**Federal Highway Administration – Resource Center, Lakewood, CO, USA

I. Introduction

In the United States, many different techniques are currently used to determine the size and extent of a riprap installation, and existing techniques and procedures for design of riprap protection can be confusing and difficult to apply. Depending on the technique used to size riprap, the required size of stone can vary widely. Most state Departments of Transportation (DOTs) have their own specifications for classifying riprap size and gradation and there is not a consistent classification system or set of specifications that can be used when preparing plans or assembling a specification package for a project. In addition, various construction practices are employed for installing riprap; many of them are not effective and projects requiring the use of riprap historically have suffered from poor construction practices and poor quality control. National Cooperative Highway Research Program (NCHRP) Project 24-23 "Riprap Design Criteria, Specifications, and Quality Control" [1] was a synthesis study to develop a unified set of guidelines, specifications, and procedures that can be accepted by the state DOTs. The effort was similar in intent to the European Union's recently adopted unified standard for riprap, a standard that transcends geographic and institutional boundaries [2].

The basic objectives of NCHRP 24-23 were to develop design guidelines, material specifications and test methods, construction specifications, and construction, inspection and quality control guidelines for riprap for a range of applications, including: revetment on streams and riverbanks, bridge piers and abutments, and bridge scour countermeasures such as guide banks. A fundamental premise of this study is that riprap is an integrated system and that successful performance of a riprap installation depends on the response of each component of the system to hydraulic and environmental stresses throughout its service life.

This paper presents an overview of the philosophy that underpins the recommendations of NCHRP Project 24-23. Then, those recommendations are summarized as they relate to: (1) riprap design equations, (2) filter requirements, (3) material and testing specifications, (4) construction and installation guidelines, and (5) inspection and quality control.

II. Riprap – an integrated system

A. Overview

Since riprap is a natural material composed of stone or boulders and is readily available in many areas, it has been used extensively in erosion protection works. In some areas, riprap is produced by quarrying hard, durable rock. In other areas, riprap is collected from talus or by excavating large river cobbles from alluvial deposits. Riprap, when properly designed and used for erosion protection, has an advantage over rigid structures because it is flexible when under attack by river currents, it can remain functional even if some individual stones may be lost, and it can be repaired relatively easily. Properly constructed riprap can provide long-term protection if it is inspected and maintained on a periodic basis as well as after flood events.

A properly designed, installed, and maintained riprap system has a functionality that is greater than the sum of its parts, i.e., successful performance depends on the system responding to hydraulic and environmental stresses as an integrated whole throughout its service life. Design of a riprap scour control system requires knowledge of: river bed, bank, and foundation material; flow conditions including velocity, depth and orientation; riprap characteristics of size, density, durability, and availability; location, orientation and dimensions of piers, abutments, guide banks, and spurs; and the type of interface material between riprap and underlying foundation which may be geotextile fabric or a filter of sand and/or gravel.

Designing riprap as an integrated system requires a life-cycle approach to the design, production, transport, installation, inspection, and maintenance of the system. The efficacy of rock riprap depends on quality of the rock; weight, shape, or size of individual rocks; slope of the embankment or

channel; thickness of the riprap layer; and stability of the bedding or filter on which the riprap is placed. Because of the size and weight of riprap, transport and placement is generally by mechanical means. Failure of riprap often is the result of poor construction techniques and poor quality control relating to weight or size. Quality control begins at the quarry. Inspection must ensure correct weight or size, density, and gradation. Transportation can be by truck, train, or barge where segregation can occur. Stockpiles at the job site should be checked for segregation and adjustments made to ensure that proper gradation is maintained.

Thus, uniform specifications and/or guidelines for riprap must be developed considering production capabilities and control at the quarry as well as at the job site and during transportation, handling, moving, and placement. Guidelines and procedures for on-site inspection and monitoring riprap also should be developed providing reasonable limits and tolerances for materials and workmanship that can be expected as construction industry standards. Constructability issues must be considered so as to accommodate site constraints, permit conditions, and the physical characteristics of the system. Additionally, the placement of ancillary system components, including filter and/or bedding requirements must be addressed for various riprap applications.

B. Life-Cycle Approach

Conceptually, a life-cycle approach, as applied to an erosion or scour countermeasure such as riprap, would incorporate a host of factors into a framework for decision making considering initial design, construction, and long-term maintenance. These factors could include engineering judgment applied to design alternatives, materials availability and cost, installation equipment and practices, and maintenance assumptions. Life cycle costs for a riprap project are influenced by three major components:

- Initial construction materials and delivery costs
- Initial construction installation costs associated with labor and equipment
- Periodic maintenance during the life of the installation

Obviously, quantity and unit cost of alternative materials will vary depending on the specific project conditions, as well as local and regional factors. Some issues to consider when developing a life-cycle cost estimate would include:

- Availability of materials of the required size and weight
- Haul distance
- Site access
- Equipment requirements
- Construction underwater vs. placement in the dry
- Environmental and water quality issues and permitting requirements
- Habitat mitigation for threatened and endangered species
- Traffic control during construction and/or maintenance activities
- Local labor rates
- Construction using DOT resources vs. outside contract
- Design life of the installation
- Anticipated frequency and extent of periodic maintenance and repair activities

While it was not the intent of NCHRP 24-23 to develop a life-cycle "formula" for riprap projects, the life-cycle concept emphasizes the need to consider riprap as an integrated system where the performance of all system components is considered throughout the design life of the project.

C. Risk and Failure

The risk of failure should be considered when evaluating the performance of riprap as an integrated system to prevent erosion or scour. There are a number of methods available for assessing the causes and effects of a wide variety of factors in uncertain, complex systems and for making decisions in the light of uncertainty. One approach, failure modes and effects analysis, is a qualitative procedure to systematically identify potential component failure modes and assess the effects of associated failures on the operational status of the system [3].

Applying a failure modes and effects analysis to a riprap installation emphasizes the integrated nature of the riprap system, and provides a method to identify system failure as a basis for evaluating riprap performance. In developing a risk-based method for selecting bridge scour countermeasures, reference [3] developed a failure modes and effects analysis for riprap similar to Table 1.

D. Service Life and Safety

When selecting a "service life" criterion for various types of bank protection measures for transportation facilities, safety must be a primary consideration. To assume that bank protection is installed to protect a facility (bridge, roadway embankment, etc.)

overlooks the mission and design goals of the highway agency. For DOTs in the U.S. safety of the traveling public is the first priority when setting service-life standards for riprap protection. Concurrent goals are protection of public and private property, protection of fish and wildlife resources, and enhancement of environmental attributes. A riprap system does not protect a facility, but rather the lives of the public who use that facility [4].

TABLE 1.
FAILURE MODES AND EFFECTS ANALYSIS FOR RIPRAP REVETMENT

Failure Modes	Effects on Other Components	Effects on Whole System	Detection Methods	Compensating Provisions
Translational slide or slump (slope failure)	Disruption of armor layer	Catastrophic failure	Mound of rock at bank toe; unprotected upper bank	Reduce bank slope; use more angular or smaller rock; use granular filter rather than geotextile fabric
Particle erosion (rock undersized)	Loss of armor layer, erosion of filter	Progressive failure	Rock moved downstream from original location, exposure of filter	Increase rock size; modify rock gradation
Piping or erosion beneath armor (improper filter)	Displacement of armor layer	Progressive failure	Scalloping of upper bank; bank cutting; voids beneath and between rocks	Use appropriate granular or geotextile filter
Loss of toe or key (under designed)	Displacement or disruption of armor layer	Catastrophic failure	Slumping of rock, unprotected upper bank	Increase size, thickness, depth, or extent of toe or key

Thus, service-life for a riprap installation should be based on the importance of the facility to the public, that is, the risk of losing the facility and how that loss may directly or indirectly affect the traveling public, as well as the difficulty and cost of future repair or replacement. The conditions that constitute an "end of service life" for a riprap installation are largely dependent on the confidence one has that a degraded condition will be detected and corrected in a timely manner (e.g., during a post-flood inspection). Generally, for facilities that are rarely checked or inspected a very conservative (i.e., shorter) service life would be appropriate, while a less conservative standard could be used for facilities that are inspected regularly.

Service life for a riprap installation can be considered a measure of the durability of the total, integrated bank, pier, abutment or countermeasure protection system. The response of a riprap system over time to typical stresses such as flow conditions (floods and droughts) or normal deterioration of system components must also be considered. Response to less typical (but plausible) stresses such as fire, vandalism, seismic activity or accidents may also affect service life. Maintenance during the life cycle of a riprap installation where such work does not constitute total reconstruction or replacement, should not be considered as the end of service life for the riprap system. In fact, a life-cycle approach to maintenance may extend the service life of a riprap installation and reduce the total cost over the life of the project.

III. RECOMMENDATIONS - NCHRP PROJECT 24-23

Conclusions and recommendations for each of the functional areas investigated for the riprap applications of interest to NCHRP 24-23 (revetment, bridge pier and abutment, and countermeasures) are summarized in the following paragraphs.

A. Riprap Design Equations

Design equations for sizing riprap were evaluated with sensitivity analyses using laboratory and/or field data, where available, for the applications of interest to this study. Based on the sensitivity analyses, the following design equations or design approaches are recommended for each application.

1. For revetment riprap, the U.S. Army Corps of Engineers EM1601 equation is recommended as the most comprehensive approach for sizing riprap considering the ability of the basic equation to discriminate between stable and failed riprap, bank and bend correction factors, and the reasonableness of safety/stability factors [5] [6].

2. For pier riprap, the HEC-23 [7] equation is recommended as the most reliable design equation for sizing riprap. The velocity multiplication factors for round and square nose piers were confirmed using available laboratory data [8].

3. For abutment riprap, the FHWA Set Back Ratio method as presented in HEC-23 [7] was confirmed, using 2-dimensional computer modeling, as an accurate approach for

estimating flow velocity and sizing riprap at an abutment. It is recommended, however, that the computed characteristic average velocity not exceed the maximum velocity in the channel [8].

4. For guide bank riprap, the abutment riprap design equations can be used [7]. The recommended velocity for computing riprap size at a guide bank is 0.85 times the velocity estimated using the Set Back Ratio method for an abutment [8].

B. Filter Requirements

In the U.S., filter design criteria is the most overlooked aspect of riprap design. More emphasis must be given to compatibility criteria between the filter (granular or geotextile) and the soil. Correct filter design reduces the effects of piping by limiting the loss of fines, while simultaneously maintaining a permeable, free-flowing interface. Filter processes and existing methods for design and placement were thoroughly investigated and discussed. Design and placement guidance for both granular and geotextile filters is provided.

1. Historically in the U.S., the Terzaghi criteria have been used for design of granular filters. It is recommended that an alternative approach, widely used in Europe, which follows the Cistin-Ziems methodology be considered as a practical alternative for filter design. As a rule of thumb, the gradation curve of the granular filter material should be approximately parallel to that of the base soil. Parallel gradation curves minimize the migration of particles from the finer material into the coarser material. Reference [9] summarizes the procedure originally developed by Cistin and Ziems whereby the d_{50} size of the filter is selected based on the coefficients of uniformity (d_{60}/d_{10}) of both the base soil and the filter material. With this method, the grain size distribution curves do not necessarily need to be approximately parallel. Figure 1 provides a design chart based on the Cistin-Ziems approach.

2. For many applications, placing a geotextile filter under water is a challenge. For low-velocity applications a product similar to that used in Germany, the SandMat™, is recommended. The SandMat™ is essentially a blanket of two non-woven geotextiles (or a woven and a non-woven) with a layer of sand in between. The composite blanket has a high specific gravity so it sinks readily. For higher velocity or deep water applications, European practice calls for use of sand-filled geocontainers. For specific project conditions, geosynthetic containers can be chosen that combine the resistance against hydraulic loads with the filtration capacity demanded by the application. Geosynthetic containers have proven stable against erosive forces under a range of conditions, including wave-attack environments. There are many applications where adoption of these approaches to filter placement in U.S. practice would be highly beneficial.

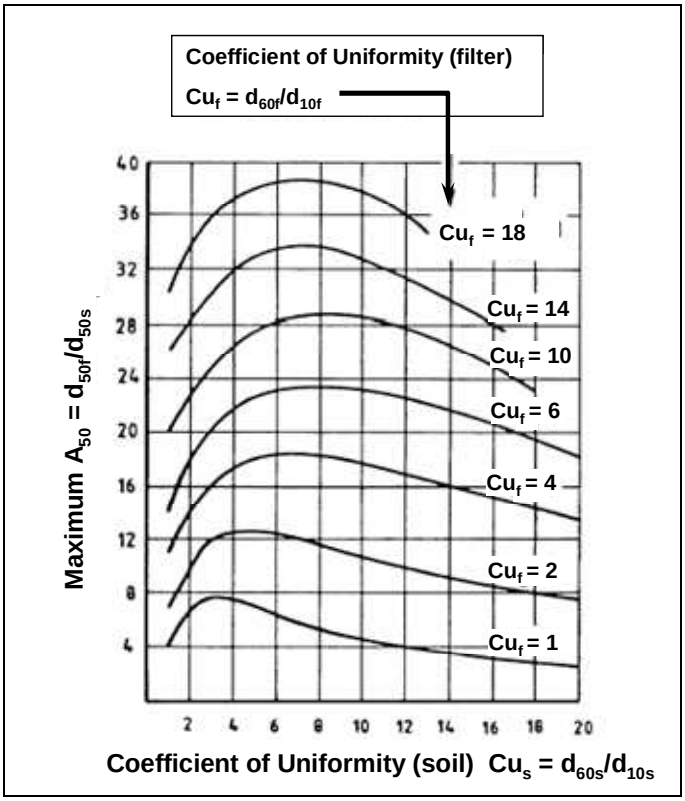

Figure 1. Filter design chart according to Cistin – Ziems [9].

3. The laboratory testing phases of NCHRP Projects 24-07(1) and 24-07(2) included evaluation of riprap as a pier scour countermeasure [10] [11]. For this application, it was found that granular filters performed poorly in the riverine case where bedforms are present. Specifically, during the passage of dune troughs past the pier that are deeper than the riprap armor, the underlying finer particles of a granular filter are rapidly swept away. The result is that the entire installation becomes progressively destabilized beginning at the periphery and working in toward the pier (see Figure 2). It is strongly recommended that only geotextile filters be used at bridge piers in riverine systems where dune type bedforms may be present during high flows. These laboratory studies also resulted in the finding that geotextile filters at piers should not be extended to the periphery of the riprap, but instead should terminate at two-thirds the riprap extent. With these two exceptions, the remainder of the guidance provided for filters for revetment riprap is appropriate for riprap installations at bridge piers.

4. The guidance provided for filters for revetment riprap is generally appropriate for riprap installations at bridge abutments located on floodplains and set back from the main channel. In the case where the abutment is integral with the bank of the main channel, the same concern regarding the use of granular filters exists as for pier riprap. That is, if dune troughs passing the abutment are deeper than the riprap apron thickness, the underlying finer particles of a granular layer can be rapidly swept away. The result is that the entire riprap installation becomes progressively destabilized beginning at the periphery and working in toward the abutment. For this reason, it is strongly recommended that only geotextile filters be used at bridge abutments in riverine systems where dune type bedforms may be present during high flows, and where the abutment and/or abutment riprap apron extend into the main channel. In addition, where the abutment and/or abutment riprap apron extend into the main channel, the geotextile filter should not be extended to the periphery of the riprap, but instead should terminate at two-thirds the riprap extent.

5. The guidance provided for filters for revetment riprap is generally appropriate for countermeasures constructed of or armored by riprap, such as guide banks or spurs. Scour at the nose of the guide bank or spur is of particular concern. Additional riprap should be placed around the upstream end of the guide bank or spur to protect the embankment material

from scour as this is the most likely failure zone for these countermeasures.

C. Material and Testing Specifications

Currently, material and testing specifications for riprap available in the U.S. (e.g., AASHTO, ASTM) are generally adequate for determining riprap quality. However, there is little consistency in specifications for riprap gradation properties. For example, many gradation specifications can be interpreted to result in an essentially uniform rock size where a more widely graded mixture was intended by the designer. In addition, the wide variety of size designations (classes) among agencies results in confusion and, potentially, increased project cost. A standardized methodology was developed and is recommended for U.S. practice. The method considers both the rock size and slope of the riprap particle distribution curve, as well as typical rock production methods.

1. Riprap gradations from six methods most often used in the U.S. and Europe were examined and compared. A gradation classification system that meets the needs of the designer, producer, and contractor was developed. A classification system consisting of ten standard classes is proposed (Tables 2 and 3). Recommended gradation criteria were developed based on a target d_{50} and a target uniformity ratio that produces riprap that is well-graded. For the recommended gradation, the range of acceptable d_{50} is 5% smaller to 15% larger than the target value. This results in a range of acceptable W_{50} of approximately minus 15% to plus 50%. The target uniformity ratio (d_{85}/d_{15}) is 2.0 and the range is from 1.5 to 2.5 (± 25%). For a target d_{50} of 51 cm (20 inches) the recommended gradation is illustrated in Figure 3.

2. Material properties and testing requirements for both field and laboratory from American Society for Testing of Materials (ASTM), Office of Surface Mining (OSM), American Association of State Highway and Transportation Officials (AASHTO), Centre for Civil Engineering Research and Codes (CUR), and the European Committee for Standardization (CEN), were investigated and specific recommendations adapted to the revetment riprap application are provided in [1].

3. The requirements for the quality and characteristics of riprap materials, and the associated tests to support those requirements for revetment riprap installations are suitable for use with riprap used to protect bridge piers and abutments and to construct or armor scour countermeasures.

a. Test 5d, riprap with geotextile filter.

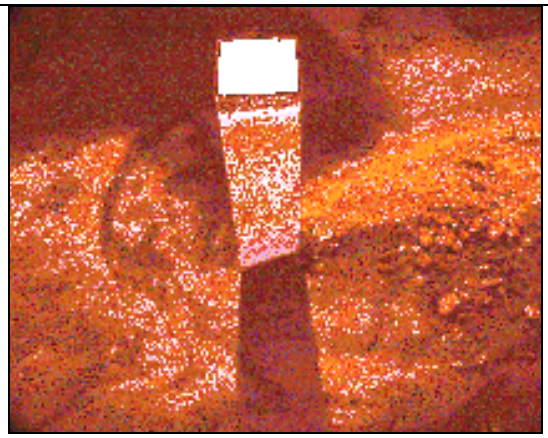

b. Test 5d, riprap with granular filter. Note displacement of riprap.

Figure 2. Riprap as a pier scour countermeasure, NCHRP Project 24-07(2). Flow is from left to right in these photographs [11].

TABLE 2.
MINIMUM AND MAXIMUM ALLOWABLE PARTICLE SIZE IN INCHES

Nominal Riprap Class by Median Particle Diameter		d_{10}		d_{15}		d_{50}		d_{60}		d_{85}		d_{100}
Class	Diameter	Min	Max	Min	Max	Min	Max	Min	Max	Min	Max	Max

I	6 in	3.5	5.0	3.7	5.2	5.7	6.9	6.3	7.5	7.8	9.2	12.0
II	9 in	5.2	7.6	5.5	7.8	8.5	10.5	9.5	11.5	11.5	14.0	18.0
III	12 in	7.0	10.0	7.3	10.5	11.5	14.0	12.5	15.0	15.5	18.5	24.0
IV	15 in	8.7	12.5	9.2	13.0	14.5	17.5	16.0	19.0	19.5	23.0	30.0
V	18 in	10.5	15.0	11.0	15.5	17.0	20.5	19.0	22.5	23.5	27.5	36.0
VI	21 in	12.0	17.5	13.0	18.5	20.0	24.0	22.0	26.5	27.5	32.5	42.0
VII	24 in	14.0	20.0	14.5	21.0	23.0	27.5	25.0	30.0	31.0	37.0	48.0
VIII	30 in	17.5	25.0	18.5	26.0	28.5	34.5	31.5	37.5	39.0	46.0	60.0
IX	36 in	21.0	30.0	22.0	31.5	34.0	41.5	38.0	45.0	47.0	55.5	72.0
X	42 in	24.5	35.5	25.5	36.5	40.0	48.5	44.0	52.5	54.5	64.5	84.0

TABLE 3.
MINIMUM AND MAXIMUM ALLOWABLE PARTICLE WEIGHT IN POUNDS

Nominal Riprap Class by Median Particle Weight		W_{10}		W_{15}		W_{50}		W_{60}		W_{85}		W_{100}
Class	Weight	Min	Max	Min	Max	Min	Max	Min	Max	Min	Max	Max
I	20 lb	3	10	4	12	15	27	20	34	39	64	140
II	60 lb	12	35	13	39	51	90	69	120	130	220	470
III	150 lb	27	83	32	93	120	210	160	270	310	510	1100
IV	300 lb	54	160	62	180	240	420	320	540	600	1000	2200
V	1/4 ton	93	280	110	310	410	720	550	950	1050	1750	3800
VI	3/8 ton	150	450	170	500	650	1150	850	1450	1650	2800	6000
VII	1/2 ton	220	670	260	740	950	1700	1300	2200	2500	4100	9000
VIII	1 ton	430	1300	500	1450	1900	3300	2500	4300	4800	8000	17600
IX	2 ton	740	2250	860	2500	3300	5800	4400	7400	8300	13900	30400
X	3 ton	1200	3600	1350	4000	5200	9200	7000	11800	13200	22000	48200

Note: Weight limits for each class are estimated from particle size by: $W = 0.85(d^3\gamma_s)$ where d corresponds to the intermediate ("B") axis of the particle, and particle specific gravity is taken as 2.65.

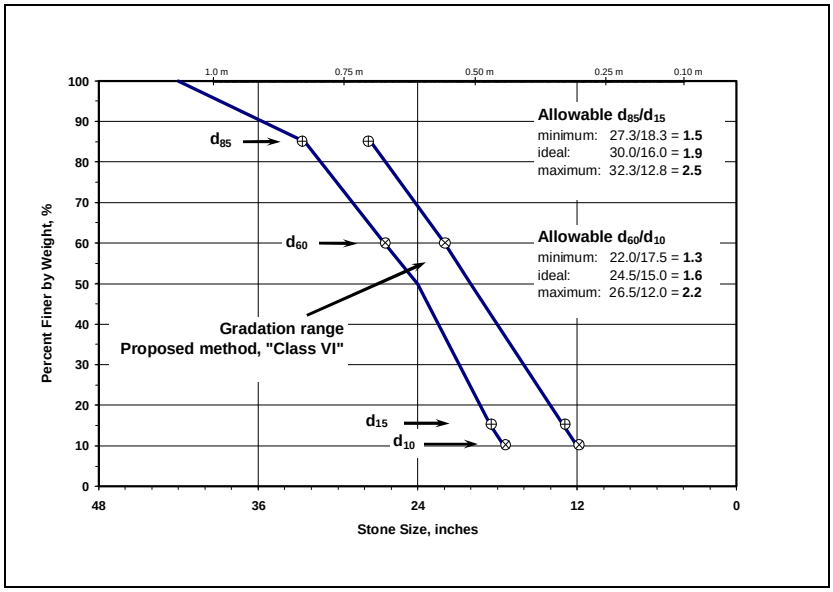

Figure 3. Recommended "well-graded" riprap with target d_{50} = 51 cm (20 inches).

4. It was apparent from the survey of current practice in the U.S. that very little field testing during construction or inspection is done on a programmatic basis. A simple methodology developed by the Office of Surface Mining is recommended to facilitate a decision to accept or reject a rock product at the quarry or on site [12]. In addition, a "pebble count" approach for verifying size distribution of riprap at the quarry or construction site is suggested for U.S. practice [13] [14].

D. Construction/Installation Guidelines

A generalized overview of riprap construction methods and placement techniques was developed for installations both in the dry and under water. Topics considered include:

- Quarry operations
- Equipment overview
- Loading and transportation of riprap
- Placing riprap and the filter
- Terminations and transitions
- Site considerations
- Measurement and payment

A set of Design Guidelines which include detailed application-specific construction and installation guidance were developed and are included as stand-alone appendices to reference [1].

E. Inspection and Quality Control

Based on a survey of current practice in the U.S., very little guidance is being promulgated by the DOTs for riprap inspection and quality control either during construction or for long-term monitoring. A field test procedure described by [14] is presented as an example of a simple, practical approach to ensuring that an appropriate riprap size distribution is achieved during construction, and that the stone has not deteriorated over the long term. In addition, riprap failure mechanisms are identified as a basis for developing inspection guidance, and selected case studies of failures are used to emphasize the need for post flood/post construction inspection.

A suggested riprap inspection code was developed. This code parallels the format of Item 113 "Scour Critical Bridges" of the U.S. National Bridge Inspection Standards (NBIS) [15] and would be applicable to all riprap installations including revetments and riprap at bridge piers, abutments and countermeasures. The form provides a numeric ranking scheme based on both the observed condition of the entire riprap installation as well as the condition of the riprap particles themselves. The form is intended to serve for underwater inspections as well as for installations that can be observed in the dry. Action items associated with the coding guidance are also provided on the inspection form.

IV. SUMMARY

NCHRP Project 24-23 was a synthesis study to develop a unified set of guidelines, specifications, and procedures that can be accepted by the State DOTs in the U.S. for the design, installation, and inspection of riprap for a range of applications. These include riprap at streams and river banks, at bridge piers and abutments, and on countermeasures such as guide banks. This research effort was

comparable in intent to the recent work by the European Union that resulted in adoption of a unified standard for riprap that transcends geographic and institutional boundaries.

To guide the practitioner in developing appropriate riprap designs and ensuring successful installation of riprap armoring systems for bankline revetment, at bridge piers, and at abutments and guide banks, the findings and recommendations of the study are combined to provide an application-specific set of design guidelines as stand-alone appendices.

These application guidelines are presented in a standard three part format using the Federal Highway Administration's Hydraulic Engineering Circular (HEC) 23 [7] as a guide. Each guideline includes:

- Part 1 – Design and Specification
- Part 2 – Construction
- Part 3 – Inspection, Maintenance, and Performance Evaluation

ACKNOWLEDGMENT

This work was sponsored by the American Association of State Highway and Transportation Officials, in cooperation with the Federal Highway Administration (FHWA), and was conducted through the National Cooperative Highway Research Program (NCHRP), which is administered by the Transportation Research Board (TRB) of the National Research Council (NRC).

This paper is based on an uncorrected draft as submitted by the authors to the TRB. The opinions and conclusions expressed or implied in the report are those of the authors. They are not necessarily those of the Transportation Research Board, the National Research Council, the Federal Highway Administration, the American Association of State Highway and Transportation Officials, or the individual states participating in the National Cooperative Highway Research Program.

REFERENCES

[1] P.F. Lagasse, P.E. Clopper, L.W. Zevenbergen, and J.F. Ruff, "Riprap Design Criteria, Specifications, and Quality Control," Preliminary Draft Final Report, NCHRP Project 24-23, Transportation Research Board, National Academy of Science, Washington, D.C., February 2006.

[2] European Committee for Standardization (CEN), "European Standard for Armourstone," Report EN 13383-1, Technical Committee 154, Brussels, Belgium, 2002.

[3] P.A. Johnson and S.L. Niezgoda, "Risk-Based Method for Selecting Bridge Scour Countermeasures," ASCE, Journal of Hydraulic Engineering, Vol. 30, No. 2, pp. 121-128, 2004.

[4] J.A. Racin, T.P. Hoover, and C.M. Crossett-Avila, "California Bank and Shore Rock Slope Protection Design," Final Report No. FHWA-CA-TL-95-10, Caltrans Study No. F90TL03 (Third Edition - Internet), California Department of Transportation, Sacramento, CA, 2000.

[5] U.S. Army Corps of Engineers, "Hydraulic Design of Flood Control Channels," Engineering Manual No. 1110-2-1601 (revised), Washington, D.C., 1991.

[6] L.W. Zevenbergen, P.F. Lagasse, and P.E. Clopper, "Comprehensive Approach for Riprap Design, Installation, and Maintenance," Sixth International Bridge Engineering Conference, Transportation Research Board, National Research Council, Boston, MA, February 2005.

[7] P.F. Lagasse, L.W. Zevenbergen, J.D. Schall, and P.E. Clopper, "Bridge Scour and Stream Instability Countermeasures," Hydraulic Engineering Circular No. 23 (HEC-23, Second Edition), Report FHWA NHI -01-003, Federal Highway Administration, Washington, D.C., 2001.

[8] L.W. Zevenbergen, P.E. Clopper, and P.F. Lagasse, "Riprap Sizing for Bridge Pier and Abutment Countermeasures," Proceedings of the EWRI/ASCE World Water and Environmental Congress 2006, Omaha, NE, May 2006.

[9] M.H. Heibaum, "Geotechnical Filters – the Important Link in Scour Protection," Federal Waterways Engineering & Research Institute, Karlsruhe, Germany, 2nd International Conference on Scour and Erosion, Singapore, 2004.

[10] G. Parker, C. Toro-Escobar, and R.L. Voigt, Jr., "Countermeasures to Protect Bridge Piers from Scour," Users Guide (revised 1999) and Final Report, NCHRP Project 24-07, prepared for Transportation Research Board by St. Anthony Falls Laboratory, University of Minnesota, MN, 1998.

[11] P.F. Lagasse, P.E. Clopper, and L.W. Zevenbergen, "Countermeasures to Protect Bridge Piers from Scour," Preliminary Draft Final Report, NCHRP Project 24-07(2), Transportation Research Board, National Academy of Science, Washington, D.C., 2006.

[12] Office of Surface Mining, "Design Manual for Water Diversions on Surface Mine Operations," prepared by Simons, Li & Associates, Inc, under OSM Contract No. J5101050, 1982.

[13] M.G. Wolman, "A Method of Sampling Coarse Bed Material," American Geophysical Union, Transactions, 35: pp. 951-956, 1954.

[14] V.J. Galay, E.K.Yaremko, et al., "River Bed Scour and Construction of Stone Riprap Protection," Sediment Transport in Gravel-Bed Rivers, John Wiley & Sons Ltd., pp. 353-383, 1987.

[15] Federal Highway Administration, "Recording and Coding Guide for the Structure Inventory and Appraisal of the Nation's Bridges," Report No. FHWA-PD-96-001, U.S. Department of Transportation, Washington, D.C., 1995, also, see errata sheet, October 2001.

Flow Patterning Associated with Three-Dimensional Obstacles: a Proxy for Scour

D.O. Lambkin*, J.K. Dix* and S. Turnock**

* School of Ocean and Earth Science, University of Southampton, Southampton, UK.

** Department of Ship Science, University of Southampton, Southampton, UK.

Understanding the patterning of near bed flow around an obstacle is the first step towards understanding the processes that control the depth and extent of any resulting scour. Both newly collected and previously published data are used to describe flow patterning around a wide variety of 3D obstacles in unidirectional flow. The extent, location and asymmetry of wake features are shown to vary considerably with obstacle size, shape and orientation. The along flow extent of affected flow regions is also shown to scale with the Reynolds number, up to a critical value ($Re \approx 10^4$), with implications when modelling flow interaction and hence scour at small scales in the laboratory.

I. INTRODUCTION

A. The Problem

Of primary concern to engineers placing structures in environments susceptible to scour is the maximum scour depth, typically located adjacent to the obstacle. Research previously undertaken has tended to focus upon flow and scour patterning around two-dimensional (2D) obstacles (e.g. horizontal and upright cylinders, e.g. pipelines and piles/foundations; sea walls). In comparison, flow and scour patterning associated with three-dimensional (3D) obstacles, (e.g. short gravity structures; truncated cylinders, e.g. anti-ship mines; shipwrecks; or natural features, e.g. aeolian or sub-aqueous dunes) is relatively poorly understood.

B. Motivation and scope of the study.

It is known that primary scour adjacent to obstacles in unidirectional flow is the equilibrium response of the mobile bed to localised regions of accelerated flow, elevated turbulence and/or the setup of pressure gradients within a porous bed, [39]. It follows that the depth, extent and location of primary scour are related also to the magnitude, extent and orientation of affected flow regions. The extent of scour or flow disturbance is of increasing interest to engineers, particularly within groups of structures (e.g. wind farms) where interaction might potentially increase maximum local scour depths.

As has been the case in research towards understanding scour in 2D systems, further knowledge regarding the flow is required first in order to better understand the process that control 3D site geomorphology. It is also therefore important to be aware of any potential differences in flow patterning when modelling at scales smaller than the prototype, especially when the extent, location or orientation of the flow features are affected.

The nomenclature relating to 3D obstacles in unidirectional flow will be defined and previously used experimental techniques will be summarised. Both previously and newly collected data describing flow patterning around such obstacles will be compared, to illustrate the effect of variation in key parameters and the relative importance of the effects of scale. Such information might be used in future research as a planning tool for experiments or as an approximation of flow fields that control scour patterning around 3D obstacles.

C. Nomenclature

Experiments may be subdivided into groups or types of obstacles that produce similar responses. In the first instance, obstacles are divided in terms of shape and angle of attack. Obstacle shape refers collectively to the general dimensions (L, H, W [see Figure 1] and diameter, D) which may be grouped as the aspect ratio (W_h=W/H). The angularity of the object is typically described rounded or bluff (upright faces with sharp vertices). It should be noted that these variables may not always be obvious or continuous across the whole of an obstacle, particularly in the field.

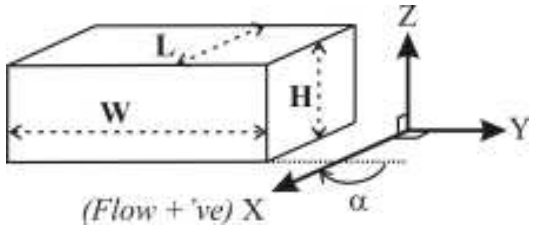

Figure 1. Definition of dimensions and α for 3D objects.

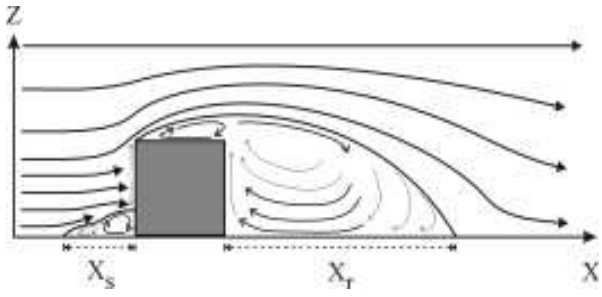

Figure 2. Schematic cross-section of streamlines in the along flow direction around a block at α=90°. Definition of separation (X_s) and reattachment (X_r) lengths. Not to scale.

The angle of attack (α) is the relative orientation of the long axis of the obstacle to the flow. For consistency in the present study, in the case of a cube or a pyramid, α=90° is defined as when one bluff face is perpendicular to the flow; this same convention is not necessarily used by other researchers. The base or tip angle of a pyramid refers to the angle formed between the faces of the prism at the specified location.

In the context of the present study, flows around obstacles are charachterised broadly by key length scales, namely, the upstream separation and the downstream reattachment lengths. The definition of the separation length, X_s and the reattachment length, X_r for cubes at α=90° is shown in Figure 2. These are typically presented relative to the obstacle height or diameter. It should be noted that, in the literature there is commonly a difference in convention, whereby, in the case of cylinders and in some cases for pyramids, distances are measured from the center of the cylinder or apex of the pyramid, whereas, in the case of cuboids at α=90°, distances are measured from the upstream and downstream edges, on the centerline of the obstacle. These conventions will cause lengths reported in the literature for cylinders and pyramids to appear greater (by 0.5 X/H) in comparison to cuboids. Herein, data referring to pyramids and cylinders have been modified as necessary to the method quoted for cubes. In the case of cuboids (W/H>1) at $\alpha \neq 90°$, X_s is measured instead from the point on the obstacle furthest upstream, to a line intersecting the separation point, perpendicular to the flow; X_r is measured as the mean distance from the downstream edge to the line of separation (typically near-parallel to the object axis).

Apart from actual shape and angularity (e.g. cuboid vs cylinder vs pyramid, etc.) obstacles are also typically separated by the relative scale of the three main dimensions, i.e. long and slender (two-dimensional) or short, truncated (three-dimensional) objects. The literature concerning scour and engineering in the marine environment consider typically flow and/or scour features around: vertical cylinders (e.g. wind turbine foundations, moorings or foundation piles, etc); horizontal cylinders (e.g. pipelines; submarine cables, etc); walls (e.g. breakwaters, groynes, etc). As objects of quasi-infinite

Example situation	**Representative length scale (m)**	**Representative velocity scale, U (ms^{-1})**	**Prototype Reynolds number**	**W_h or D:L**
Laboratory:				
Water channels	0.2	0.5	10^5 ***(max)***	1-20?
Wind tunnels	0.5-1	30-50	7.5×10^5 - 2.5×10^6 ***(max)***	1-20?
Prototype:				
Anti-ship mines	D = 0.5	0.2-2	10^5-10^6	4-5
Shipwrecks	H = 2-5	0.2-2	4×10^5-10^7	2-50
Piles and pipelines	D = 0.5	0.2-2	10^5-10^6	∞
Wind turbine and short foundations	D = 5-10	0.2-2	10^6-2×10^7	∞
Buildings	H = 50	20	5×10^7	1→∞
Bridge piers	D = 10-30	0.2-5	2×10^6-1.5×10^8	∞

Table 1. Example length, velocity and Re scales, for selected prototype situations (unidirectional flow). Laboratory entries indicate an estimate of the maximum values available from a large facility whilst other (prototype) values are estimates of the typical range of values. Key: H=height; W=cross flow width; L=pile length or along flow length; D=diameter.

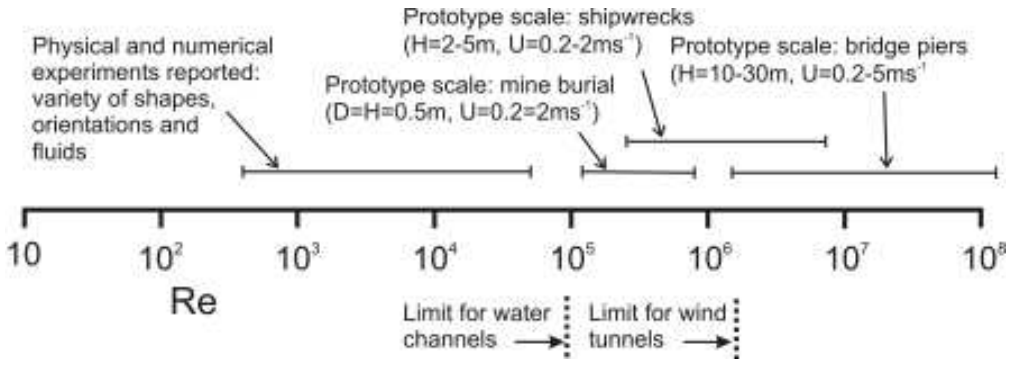

Figure 3. General location of selected prototype situations listed in Table 1. 'Physical and numerical experiments' represent the range of Re covered by the majority of the literature describing, in an accessible format, qualitative and quantitative observations of flow around wall mounted objects.

length, these characteristically produce flows that are two-dimensional along much of their length. A significant proportion of these studies are also undertaken with the focus on oscillatory (wave driven) rather than unidirectional (tidal or fluvial) flows. The typical length, velocity and Re scales of these systems are summarised in Table 1 and Figure 3. If an object were to interact significantly with the free fluid surface, then the Froude number (another dimensionless quantity) might better represent the system as a whole when modelling; in this case, the Reynolds number may be only of secondary importance.

Outline conditions in Table 1 and Figure 3 also include studies and experiments that consider objects of finite height/length, typically including: short upright cylinders (e.g. spud cans and short foundations); short horizontal cylinders (e.g. anti-ship mines and partially undercut pipelines); spheres suspended above a bed (prototype application unknown); rectangular cuboids and square based pyramids (e.g. buildings). Because fluid is able to pass more easily around such 3D objects in more than one plane, the flow tends to be characteristically three-dimensional also (eddies and recirculation in a combination of horizontal and vertical planes). The 3D term applies up to a critical [height:width:length] configuration, at which point, the central flow region may return to a more two-dimensional pattern, but may display 3D characteristics at any terminal points on the structure. It is shown in later Sections that flow characteristics vary also with the angle of attack of the flow to the obstacle faces and to the object as a whole.

II. PREVIOUS APPROACHES

A wide variety of approaches have been employed in the characterisation of the interaction between unidirectional flow and 3D obstacles. These include scaled physical modelling, numerical modelling and prototype scale observations, described with examples in more detail below. Some methods measure flow modification directly whilst others (e.g. observation of scour) can provide proxy indicators on the basis of the link between flow patterning and scour. The data reported in the following studies have been extracted where possible and form the basis of Section IV.

A. Physical Models

Scaled physical models in wind tunnels or flume tanks allow processes and patterns to be investigated at spatial and temporal scales smaller than the prototype (1:1). This has advantages in the ease and cost of setup, also the speed and practicality of making observations and manipulating the model variables. Apart from issues of scaling, other than those associated with the Reynolds number (discussed in more detail elsewhere e.g. [12],[45]), such models make fewer assumptions about the physical interaction between the flow and the obstacle (and potentially also a porous, mobile bed) than some numerical models. Hence, prior to the development of efficient numerical modelling resources, research previously undertaken to characterise the interaction between obstacles and flow will typically (and might still) employ some form of scaled physical model.

Previously published studies of flow around three-dimensional bluff objects present a variety of data and information, both quantitative and qualitative. The flow response to cubic obstacles (W_h from 1 to 24) has been observed at a variety of orientations (typically α from 90° to 45°) and over a range of Reynolds numbers (5×10^2 to 7×10^4).

Studies have considered the two- and/or three-dimensional effect for square cross-section cuboids of varying W_h ([7],[21],[24],[10],[35]) and the effect of varying α ([13],[34],[35],[36]). However, the total volume of data is relatively small and combinations of variables tested are discontinuous over the full range. A better overall impression is gained by considering other shapes also, including square based pyramids (e.g. [1],[14]), short cylinders (e.g. [2],[32],[40]) and bedforms, in either 2D ([3] ,[5] ,[9],[15],[27],[28],[43]) or 3D configurations (e.g.[22],[23]). Extensive reviews of literature relating to flow around dunes from laboratory, field and numerical studies are presented in [4] and [29].

Laboratory studies typically use either air or water as the fluid medium and a variety of flow measurement or visualisation techniques. In most studies, a smooth, fixed bed was used. It is anticipated that a large quantity of data may potentially be available from the 'gray literature', e.g. commercial reports of wind tunnel testing of cars, ships or other complex structures. These data are less easily accessed and the more complex shapes make direct comparison with other data difficult.

B. Prototype Measurements

Observations have been made previously of airflow around large 3D obstacles at full scale. These include measurements of air flow in the lee of buildings ([26],[41]) and over desert dunes ([11],[20],[42]). Studies typically used multiple cup or hot-wire anemometers mounted on poles to provide discrete measurements of wind velocity and direction in vertical and/or horizontal profiles. Observations of the occurrence/rate and direction of sediment transport are also sometimes presented as proxy evidence of flow structure and character. In the marine environment, studies have been published to describe flow over sub-aqueous dunes ([16],[17],[30]) and shipwrecks ([19]). Recent studies typically use Acoustic Doppler Profilers (ADPs) to measure flow along a profile from the instrument in either a ship- or seabed-mounted configuration although some earlier studies used a manually profiled single point current meter.

The observation of scour patterning using side scan sonar or multi-beam swath bathymetry techniques might be used to infer local changes in flow strength, direction or turbulence that has resulted in changes in bed surface texture or measurable sediment accretion or erosion.

C. Numerical Models

A number of studies are available in the literature to demonstrate the relative merits and example output from numerical models. Such studies typically report Re as being 'high', presumably indicating that the flow is fully turbulent; however, the actual value is not always reported. One reason for the avoidance of 'very high' Re may be that such models become computationally intensive and 'expensive' (i.e. they require either substantial computing power and/or long periods of time to iterate), [44]. Studies have described aspects of flow around cubes ([18],[25]), also over 2D dunes ([31]),

seamounts ([37]) and vertical piles ([33],[39]). The highest value studied was $Re \approx 10^8$, using a Computational Fluid Dynamics (CFD) model to simulate strong unidirectional flow around two adjacent bridge piers by [8]. Results are qualitatively similar to flow measured directly in the laboratory however, direct quantitative comparison is rarely presented.

The output of numerical models is typically summarised visually as 2D (slices) or 3D diagrams of streamlines or turbulent intensity and relies upon the author to present separately, any derived quantities or length scales. Slices made away from the bed and at oblique viewing angles mean that key information may be difficult to extract from the published work alone. Hence, only limited data from numerical models are included in the following Sections.

III. NEARBED FLOW PATTERNING

Given the number of possible combinations of the key variables, there are extensive gaps in the published data. There was also considered to be a lack of detailed flow mapping at the level of the bed, the region most important to any subsequent interaction with mobile bed material. To address these in part, a number of additional observations were made using a wind tunnel at the University of Southampton, UK.

The wind tunnel working section had dimensions 0.6m wide × 0.4m tall × 2m long. The velocity applied was $16ms^{-1}$, measured using a pitot tube in the center of the tunnel. Square cross section blocks ($3.8cm^2$ and $6.3cm^2$) of varying W_h (1-10) were placed onto a long flat plate mounted at mid-height in the working section. This corresponds to $Re = 5.3\times10^4$ and 8.8×10^4 for the two block sizes, respectively. A printed grid (2×2cm) was used with short thread tufts to visualize the flow patterns at the bed resulting from various combinations of W_h and α. Still photographs and video were then used to map the resulting flow patterns. Examples of the data collected are shown in Figure 4. Key length scales have been taken from these interpretive diagrams where possible and included in the following Section. Error bars have been placed on the data, on the basis of the resolution of the tuft grid used to visualize the flow.

Although not shown, in most cases where $\alpha \geq 45°$, generally elevated turbulence was observed downstream of the obstacle to the extent of the working section. The mean flow direction in this distal turbulent wake region was dominantly aligned to the X axis.

Whilst relationships presented in previous Sections indicate the response of key length scales in the flow field to variation in the key parameters, these graphical representations of the full flow field (at the bed) provide a more detailed description of the likely patterns of sediment transport that will eventually determine site geomorphology. Information can be inferred about the relative shape and size of areas of recirculation and the general location of regions of elevated turbulence. More traditional methods of dye visualisation to determine values of X_s and X_r are thought to correspond closely to those streamlines that provide continuous flow around the margins of the wake region. However, if dye is introduced at a significant proportion of the obstacle height above the bed, then the wake region would be apparently reduced in size.

For blocks at $\alpha=90°$, the extent of the wake region (X_r/H) increases with W_h whilst flow structures become resized and reoriented within this boundary. The recirculation regions located downstream of each end of the obstacle are typically ellipsoidal, progressing gradually from a flow parallel long-axis orientation for $1 \leq W_h \leq 5$, subsequently becoming more rounded and then nearly flow perpendicular axis at $W_h \approx 10$. The width of the central region or column of flow reversal increases in proportion to H but decreases in proportion to W.

Patterns of flow are qualitatively similar to that observed around a rough wing of equivalent chord and camber, at angles of attack to the flow. From $\alpha=90°$, the wake responds quickly to decreasing α, becoming asymmetric for obstacles of $W_h=5\&10$ by the first rotation increment at $\alpha=67.5°$. At shallower angles of attack ($\alpha<45°$), points of flow separation and reattachment become less distinct using the chosen method of visualisation, as flow is preferentially diverted around, rather than over the obstacle and full flow reversal is no longer observed. In this case, the boundary between flow in the ambient direction and regions of strong flow deflection is used. This position is thought to correspond also to the boundary detected by dye or smoke visualisation techniques.

The extent and intensity of turbulence is also visibly reduced at shallow α, however, deviation of this steadier flow was observed at relatively greater distances downstream than at larger values of α. At $\alpha=0°$, wake regions become localised, charachterised by flow deflection and elevated turbulence at the downstream end.

IV. SCALING OF WAKE FEATURES

Key length scale data were extracted from the flow maps presented in Section III and from the variety of literature described in Section II. Variation in the key flow length scales are charachterised in response to changes in the obstacle dimensions and orientation. It is suggested that the flow maps might provide a template for flow patterning, which is then scaled using the following relationships. The importance of working at a sufficiently high Reynolds number in order to properly scale the wake region is highlighted.

A. The separation length

The upstream separation distance (X_s) represents the stagnation line at the bed where flow from upstream is deflected upwards to meet the top of the primary vortex on the upstream face of the object. The primary vortex is therefore located and confined within the flow-perpendicular area formed by the upstream separation streamline, the bed and the wall of the obstruction. The size of this region controls, to some extent, the size and shape of vortical structures along the upstream face and the transfer of fluid around the sides of the obstacle with implications downstream for flow acceleration, bed shear stress distribution, flow structures, etc. It is also considered to be the most important region in the formation of scour around upright cylinders and so has received closer attention from researchers in this field.

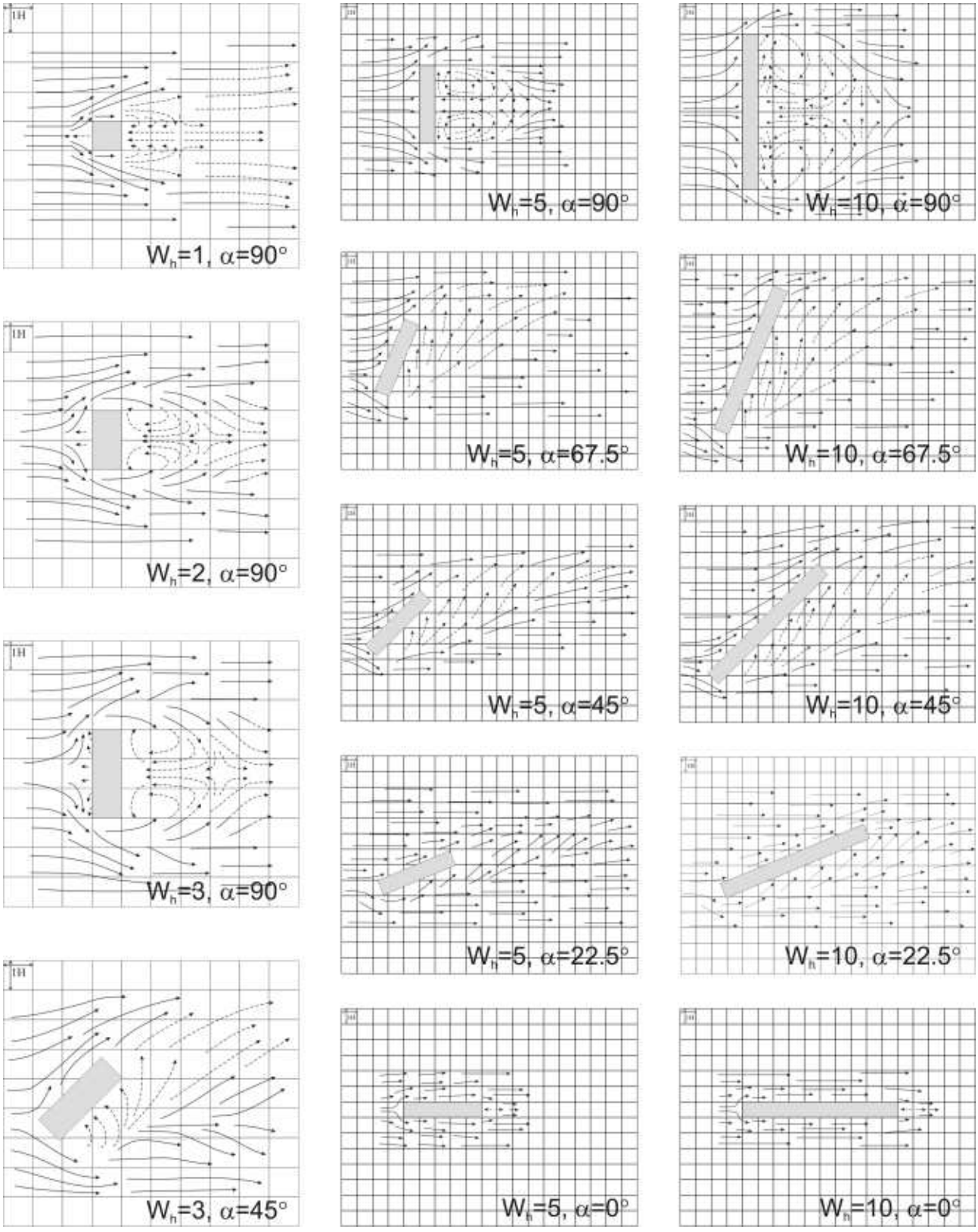

Figure 4 - Flow vectors at the bed interpreted from video imaging of flow around square cross-section cuboids at angles to the flow, $Re=1.37\times10^5$. Grid spacing is H×H. Solid lines indicate steady flow; dashed lines indicate particularly turbulent flow. For $1\leq W_h\leq3$, $Re=8.8\times10^4$. For $5\leq W_h\leq10$, $Re=5.3\times10^4$.

The variation in separation distance with Re, upstream of a vertical, rounded, slender pile of quasi-infinite length (i.e. H/D>2 [39]) was studied using a numerical model by [33]. They suggest (see Figure 5) that, once in the transitional turbulent regime ($Re \approx 5\times10^2$), the separation distance decreases with increasing Re, up to a critical value ($Re \approx 10^5$), after which the reattachment length becomes independent of Re at $X_s/D=0.5$. Measured values from two previous laboratory studies on truncated and infinite upright cylinders and data for bluff objects are also shown for comparison.

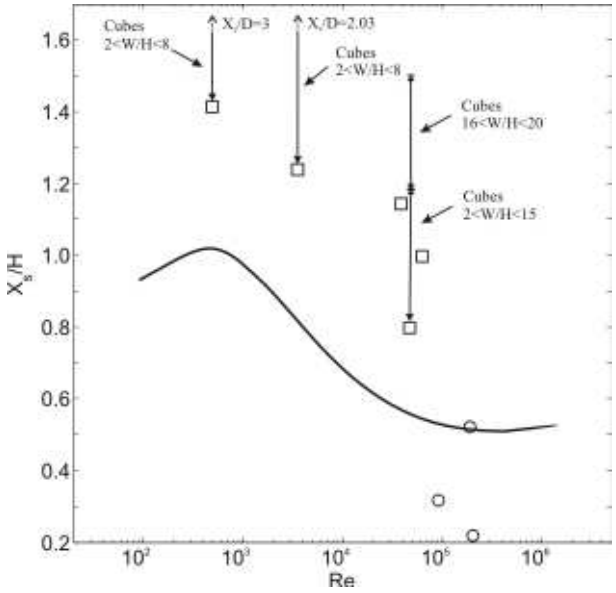

Figure 5. Influence of the Reynolds number. Separation distance X_s/D or X_s/H . Key: solid curve - model results for a cylinder ([33]) [smooth rigid-bed, $\delta/D=8$]; circles – measured data for cylinders ([32], and [2]) ; squares and arrows – measured data for cubes [W/H=1 and effect of varying the W/H ratio, respectively], various sources.

The critical Re for rounded objects is theoretically higher than for bluff objects, due to the delayed transition to super-critical turbulent flow (following migration of the lateral separation point to the rear of the cylinder). The cause of decreasing X_s with Re in all cases is attributed to increased momentum input at higher Re, compressing the upstream stagnation point.

In previous studies, it has been suggested that at high Re, X_s/H increases linearly with W_h, up to a critical value ($W_h=5$ [21]; $W_h=4$ [24]), subsequently becoming approximately constant. For the case of square cross section rectangular prisms mounted on a flat wall, results from a number of previous studies are combined in Figure 6. Here, it is confirmed that the normalised upstream separation distance (X_s/H) increases at first with W_h, up to a critical value $W_h \approx 4$-5. Beyond this, data collected at relatively high Re does possibly then follow a constant value ($X_s \approx 1.2H$) although there is significant scatter in the data. The asymptotic value for upright slender piles at 'high' Re is smaller ($X_s \approx 0.5H$). An asymptotic lower value of X_s/H should exist for infinitely long obstacles but could not be determined from the available data.

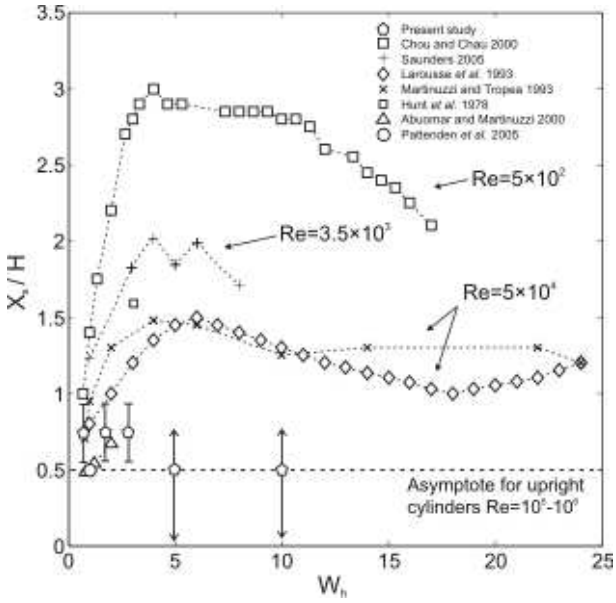

Figure 6. The variation in upstream separation length (X_s/H) with aspect ratio (W_h), at different values of Re, for rectangular cuboids at 90° to the flow. Also shown, the asymptote for upright cylinders ($W/H=\infty$) from [33], see Figure 5. After [7].

The effect of increasing Re is also illustrated in Figure 6 where observations made at lower Re are of progressively higher X_s/H. The Reynolds number independence law in modelling suggests that the relationship between X_s/H and W_h should be similar for $Re>10^4$ but insufficient data at greater Re was available to validate this here. The asymptotic separation length for vertical cylinders ($X_s/H=0.5$) is achieved at a higher value of Re ($>10^5$) ([33]), due to the corresponding migration of the separation point for cylindrical obstacles. On the basis of data shown in the Figure at $Re=5\times10^4$, it is thought that the asymptotic value for bluff objects at $Re>10^4$ may lie closer to $X_s/H=1.2$.

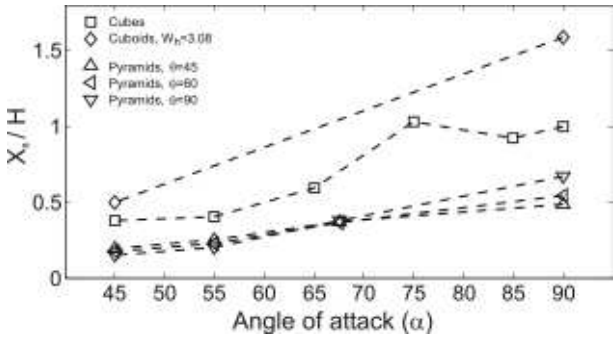

Figure 7. The variation in upstream separation distance with angle of attack: square based pyramids of various tip angle ([1]); cubes ([34]); cuboids, W:H=3.08 ([13]).

A number of studies have provided photographic information of the location of X_s for cuboids placed at angles to the flow. These data were extracted and are compared in Figure 7 with the separation distance upstream of bluff, wall-mounted square based pyramids of varying tip angle. The Figure shows that for a variety of bluff obstacle shapes, the upstream separation distance is reduced when the upstream face is presented at increasingly oblique angles to the flow. The separation

distance is maximized when the upstream face is perpendicular to the flow. Generally lower values of X_s/H measured for pyramids at similar α is attributed primarily to reduced resistance to flow over the obstacle due to the inclined upstream face(s).

In combination, three main points are demonstrated: 1) X_s is reduced at progressively higher Re; 2) the upstream stagnation point is smaller for obstacles with rounded or inclined faces; 3) increasing W_h causes X_s/H to increase also (α=90°); and 4) a smaller value of α reduces X_s.

B. The reattachment length

The nature of the wake behind an object determines locally, the amplitude and direction of velocity, shear stress and fluid/sediment transport vectors in that region. The downstream extent of the principally affected wake region is described by the reattachment length (X_r), defined as the length between the object and the flow stagnation point at the bed downstream (see Figure 2). Stream lines start typically at or just above the apex or highest part of the downstream end of the obstacle and intersect the bed at X_r. At the top of this region, momentum is transmitted vertically downwards through a turbulent shear layer and a recirculation cell is developed, with corresponding regions of flow reversal close to the bed and regions of ascending and descending flow. At lower values of α, full recirculation is not established and X_r refers instead to the width of the region of strong flow deflection (also bounded vertically by a strong shear layer). Beyond X_r, the flow direction returns to ambient but at a reduced velocity magnitude and with increased turbulence (at high α). A wide variety of studies into aeolian and sub-aqueous dunes have estimated the distance needed for full flow recovery at between 10 to >75H, but more typically 25-30H, beyond X_r.

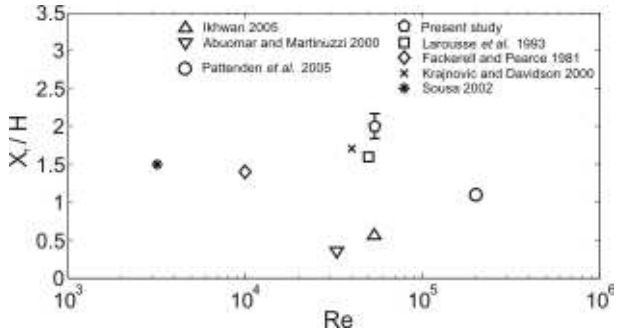

Figure 8. Reattachment length varying with Reynolds number. All data for unit dimension cubes (W=H=L) except for Ikhwan [14] for pyramids and Pattenden ***et al***. [32] for a short upright cylinder (H=D).

Only limited data is available to describe the effect of the Reynolds number on the downstream flow extent; the data found for unit dimension objects are shown in Figure 8. An upper limit for cubes at $Re>10^4$ is proposed of $X_r \approx$1.5-2.0H. The limited data demonstrate a slight increase in X_r/H for cubes with increasing Re, however, insufficient data is available for directly comparable cases (of the same W_h) to comment with any confidence on changing patterns of X_r with Re. However, it can be observed that X_r/H is generally smaller for obstacles with rounded or inclined upstream (and downstream) faces.

The effect of increasing W_h is shown in Figure 9 for a range of Reynolds numbers and a variety of object shapes (cuboids, pyramids and cylinders) perpendicular to the flow. The reattachment length increases with W_h, becoming nearly constant for W_h>10-15 ($X_r/H\approx$7-8); this corresponds closely to the point at which two-dimensional flow is established in the central section. Increasing the along flow aspect ratio (L/H) for a bluff obstacle W_h=10 results in decreasing X_r/H according to previously collected data reported in [14]. As this was the only data set found, it has not been considered in detail herein.

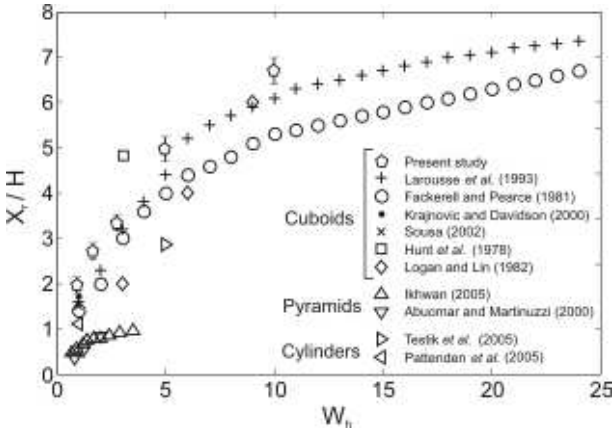

Figure 9. Reattachment length with object aspect ratio. Data representing a range of $Re>10^4$ around cuboids, except Sousa [38] ($Re=3.21\times10^3$), Ikhwan [14] and Abuomar & Martinuzzi [1] (pyramids), Testik et al. [40] (short horizontal cylinder, $Re=3\times10^2$-3×10^3) and Pattenden et al. [32] (short vertical cylinder).

Data for pyramids follows a similar pattern to cuboids but at a lower overall value. Hence, the shape and inclination of the faces of an obstacle also control, to some degree, the reattachment length of the flow. In regions of essentially 2D flow within the system (i.e. the central wake region of objects with large W_h and at $\alpha\rightarrow$90°), lee side flow intensity and direction are relatively uniform but may vary subtly due to the formation of cells in the upstream primary vortex and the development of preferential paths for fluid transfer over the obstacle. In comparison, lee side streamlines in 3D flow regions (at the ends of the obstacle, or, at smaller W:H or α) contain stronger cross-flow components of velocity. Patterning becomes more sensitive to the plane of observation and also to the object dimensions and orientation.

Around objects with large W:H and at smaller values of α, the down stream flow direction and intensity may be sensitive to physical parameters in a similar manner to an aeroplane wing stalling, i.e. stream lines are affected by the 'wing' chord, camber and roughness. This may manifest as large scale attachment of flow around long objects, or, as smaller scale flow features around individual faces or edges of obstacles. As an example of the latter, [6] liken the flow around a cube at α=45°, to the flow around a delta-wing. They also describe that the near wake and pressure field are dominated by strong vortices shed from the top of the cube; this has a marked effect on the axial components of velocity but appears then to decay rapidly, becoming similar to those behind a cube at α=90° at around 6H downstream.

The effect of angle of attack on a bluff object is to modify the shape, cross-section area and attitude of the obstruction face(s) presented to the flow; this affects flow aligned pressure gradients and may promote preferential flow channels along any inclined upstream faces. Presenting the results of wind tunnel tests of flow around cubes, [34] summarise that the value of α influences strongly: the position of the stagnation point on the cube surface; the positions of reattachment and separation; and the magnitude and distribution of pressure on the [obstacle] surface. [34] present a sequence of eight images of flow around a unit cube at $Re=6.3\times10^4$, where α is varied between 90° and 45°. These show that the distribution of flow around the object is symmetrical when the shape presented to the flow is also symmetrical (for rectangular prisms at 90° and 0°, also at 45° in the case of cubes and pyramids). Likewise, the flow (4-6H downstream) becomes asymmetrical at intermediate α; the greatest asymmetry was observed in this case at α=65°. In plan view, the larger or more dominant downstream vortical flow structure is observed on the side of the obstacle presenting a leading edge furthest upstream.

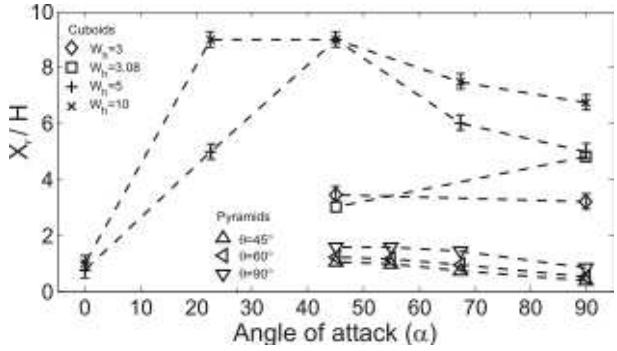

Figure 10. Reattachment length with angle of attack. Data from flow visualisation experiments: pyramids at varying tip angles, Abuomar and Martinuzzi [1]; and cuboids (W/H=3.08), Hunt ***et al***. [13].

[1] and [14] describe a number of wind tunnel experiments, investigating the flow around wall-mounted square base pyramids at 3.3×104 and 1.2×104-9×104, respectively. In the experiments undertaken by the latter, the pyramid base length and the flow rate was held constant, making the pyramid height and corresponding Re, proportional to the slope angle. Results from these studies indicate that pyramids with shallower slope angles have a shorter reattachment length. This seems more likely to be related to decreasing slope angles, rather than to varying Re.

In [1] it is also shown that by normalizing to the projected area of a square-based pyramid to the flow, flow separation and reattachment lengths for pyramids of different base angle collapse onto almost one curve. This removes the effect of obstacle face slope but not the angle of attack.

V. Summary and Conclusions

Combining previously reported data (including photographic data, not shown herein) with the results of the present study, the following general observations can be made:

The presence of a 3D obstacle to flow cases localised flow disturbance, including deviation of flow direction, regions of elevated turbulence and likely also regions of modified mean velocity (measurements not shown here). For cubic obstacles, the location, extent and character of these regions are a function of the object aspect ratio, orientation and possibly the Reynolds number. The along flow aspect ratio (L/H) is also thought to have some effect, typically decreasing X_r/H. Cuboids with bluff faces result in the most extensive wake both up and down stream of the obstacle. Rounded obstacles (e.g. cylinders) or obstacles with inclined faces (e.g. pyramids) of similar dimensions will be less extensive.

The flow field may be qualitatively reconstructed by using a template flow pattern for a given orientation, scaled then by using W_h and Re to estimate key length scales of X_s and X_r. Flow field prediction around proposed full scale 3D structures may be used to infer likely patterns of bedload transport, regions of potential erosion or deposition and the extent and location of wake regions further downstream that may interact with other nearby structures.

Scaled physical models investigating interaction of unidirectional flow with obstacles for purposes of flow or scour modelling will typically operate at a lower value of Re than the prototype case. This may potentially affect the relative scaling of flow structures with implications for the scaling of any resulting bed morphology.

Changes in the key length scales associated with varying the aspect ratio are most rapid for objects $W_h<10$. Changes in the key length scales associated with varying the orientation are most rapid at $70°\leq\alpha\leq90°$ and $20°\leq\alpha\leq0°$. Extensive local modification of the flow direction is seen in all cases except that of flow parallel (α=0°). In most cases, turbulence is visibly increased in the wake region, however, longer obstacles at lower angles of attack may not demonstrate this.

Acknowledgment

The present study is part of the 'Modelling Exclusion Zones for Marine Aggregate Dredging' project which is funded by English Heritage through the Aggregate Levy Sustainability Fund (project PD3365). The authors would also like to thank Matthew Thomas for his assistance in the preparation and execution of the laboratory work.

References

[1] Abuomar, M.M., Martinuzzi, R.J., 2000. '***An Experimental Investigation of the flow around a Surface Mounted Pyramid***', 6th Triennial International symposium on Fluid Control, Measurement and Visualization, August 13-17, 2000, Sherbroke, Canada.

[2] Agui, J.H., and J. Andreopolous, 1992. 'Experimental investigation of a three-dimensional boundary layer flow in the vicinity of an upright wall mounted cylinder'. ***Transactions of the ASCE***, **114**, p566 - 576.

[3] Bennett, S.H.J. and Best, J. 1995. Mean flow and turbulence structure over fixed, two-dimensional dunes: implications for sediment transport and bedform stability. Sedimentology, 42: 491 - 513,

[4] Best, J. 2005. The fluid dynamics of river dunes: a review and some future research directions. Journal of Geophysical Research, 110, doi: 10.1029/2004JF000218.

[5] Best, J. and Kostaschuk, R. 2002. An experimental study of turbulent flow over a low angle dune. Journal of Geophysical Research, 107, doi:10.1029/2000JC000294.

[6] Castro I.P. and Robins A.G., 1977. 'The flow around a surface-mounted cube in uniform and turbulent streams'. ***Journal of fluid mechanics***, **79**, p307-335.

[7] Chou, J.H., and S.Y. Chao, 2000. 'Branching of a horseshoe vortex around surface- mounted rectangular cylinder'. ***Experiments in Fluids***, ***28***, p394 - 402.

[8] Debus, K. Berkoe, J., Rosendall, B. Shakib, F., 2003 '***Computational Fluid Dynamics Model for Tacoma Narrows Bridge Upgrade Project***'. Proceedings of FEDSM'03: 4th ASME. JSME Joint Fluids Engineering Conference, 6-11 July, 2003, Honolulu, Hawaii.

[9] Engel, P. 1981. Length of flow separation over dunes. Journal of the Hydraulics Division, ASCE., 107: 1133 - 1143,

[10] Fackrell, J.E. and Pearce, J.E., 1981 '***Parameters affecting dispersion in the wake of buildings***'. CEGB Report No. RD/M/1179/N81.

[11] Frank, A.J. and Kocurek, G. 1996b. Toward a model for airflow on the lee side of aeolian dunes. Sedimentology, 43: 451 - 458,

[12] Hughes, S.A., 1993 '***Physical Models and Laboratory Techniques in Coastal Engineering'***, Vol. 7, Advanced series in Coastal Engineering. World Scientific, Singapore. 568 pp.

[13] Hunt, J.C.R., Abell, C.J., Peterka, J.A. and Woo, H., 1978 'Kinematic studies of the flows around free or surface-mounted obstacles applying topology to flow visualization'. ***Journal of Fluid Mechanics***, **86** 1, p179-200.

[14] Ikhwan, M., 2005 '***Investigation of Flow and Pressure Characteristics around Pyramidal Buildings'.*** Dissertation, Institute of Hydromechanics, University of Karlsruhe, Germany. 163pp.

[15] Jerolmack, D. and Mohrig, D. 2005. Interactions between bed forms: Topography, turbulence and transport. Journal of Geophysical Research, 110, doi: 10.1029/2004JF000126.

[16] Kostaschuk, R. and Best, J. 2005. Response of sand dunes to variations in tidal flow: Fraser Estuary, Canada. Journal of Geophysical Research, 110, doi: 10.1029/2004JF000176.

[17] Kostaschuk, R. and Villard, P. 1996. Flow and sediment transport over large subaqueous dunes: Fraser River, Canada. Sedimentology, 43: 849 - 863,

[18] Krajnovic, S., and L. Davidson, 2000. Flow around a three-dimensional bluff body. In: ***Proceedings of the 9th International Symposium on Flow Visualisation***, Heriot-Watt University, Edinburgh, UK.

[19] Lambkin, D.O. and Dix, J.K. (In preparation). 'Measurements of flow structure around a large submerged 3D object'.

[20] Lancaster, N. 1989. The dynamics of star dunes: an example from the Gran Desierto, Mexico. Sedimentology, 36: 273 - 289,

[21] Larousse A, Martinuzzi R.J, Tropea C., 1991. 'Flow around surface mounted, three-dimensional obstacles'. ***Turbulent Shear Flows 8: 8th International Symposium***, September 1991, Munich, Germany, selected revised papers. Springer Verlag, Berlin. p127-139.

[22] Maddux, T.B., McLean, S.R. and Nelson, J.M. 2003b. Turbulent flow over three-dimensional dunes: 2. Fluid and bed stresses. Journal of Geophysical Research, 108, doi: 10.1029/2003JF000018.

[23] Maddux, T.B., Nelson, J.M. and McLean, S.R. 2003a. Turbulent flow over three-dimensional dunes: 1. Free surface and flow response. Journal of Geophysical Research, 108, doi: 10.1029/2003JF000017.

[24] Martinuzzi R.J., Tropea C., 1993. The Flow around surface-mounted, prismatic obstacles placed in a fully developed channel flow. ***ASME Journal of Fluids Engineering***, **115**, p85-92.

[25] Mason, P.J. and Morton, B.R. 1987. Trailing vortices in the wakes of surface mounted obstacles. Journal of Fluid Mechanics, 175: 247 - 293,

[26] McEligot, D.M., McCreery, G.E. and Pink, R.J. Physical and computational modelling of airflow around buildings.

[27] Nakagawa, H. and Nezu, I. 1987. Experimental investigation on turbulent structure of backward-facing step flow in an open channel. Journal of Hydraulic Research, 25: 67 - 88,

[28] Nelson, J.M., McLean, S.R. and Wolfe, S.R. 1993. Mean flow and turbulence over two-dimensional bed forms. Water Resources Research, 29: 3935 - 3953,

[29] Nickling, W.G. and McKenna-Neuman, C. 1999. Recent Investigations of Airflow and Sediment Transport Over Desert Dunes. In: Aeolian Environments, Sediments and Landforms (Eds A.S. Goudie, I. Livingstone and S. Stokes), pp. 15-47. John Wiley and Sons, Ltd., Chichester.

[30] Parsons, D.R., Best, J., Orfeo, O., Hardy, R.J., Kostaschuk, R. and Lane, S.N. 2005. Morphology and flow fields of three-dimensional dunes, Rio Paraná, Argentina: Results from simultaneous multibeam echo sounding and acoustic Doppler current profiling,. Journal of Geophysical Research, 110, doi: 10.1029/2004JF000231.

[31] Parsons, D.R., Walker, I.J. and Wiggs, G.F.S. 2004. Numerical modelling of flow structures over idealized transverse aeolian dunes of varying geometry. Geomorphology, 59: 149 - 164, doi: 10.1016/j.geomorph.2003.09.012.

[32] Pattenden, R.J., Turnock, S.R. and Zhang, X. 2005. Measurements of the flow over a low-aspect-ratio cylinder mounted on a ground plate. Experiments in Fluids, 39: 10 - 21, doi: 10.1007/s00348-005-0949-9.

[33] Roulund, A., Sumer, B.M., Fredsøe, J. and Michelsen, J., 2005 'Numerical and experimental investigation of flow and scour around a circular pile'. ***Journal of Fluid Mechanics***, **234**, p351-401.

[34] Sakamoto, H., and M. Arie, 1982. '***Flow around a cubic body immersed in a turbulent boundary layer***'. Journal of Wind Engineering and Industrial Aerodynamics, **9**, p275 - 293.

[35] Saunders, R.D., 2005. '***Seabed scour emanating from submerged three-dimensional objects: Archaeological case studies'***. PhD Thesis, Department of Civil and Environmental Engineering, University of Southampton, UK.

[36] Schofield W.H., Logan E., 1990. Turbulent shear flow over surface mounted obstacles. ***ASME, Transactions, Journal of Fluids Engineering***, **112**, p376-385

[37] Skyllingstad, E.D. and Wijesekera, H.W. 2004. Large-eddy simulation of flow over two-dimensional obstacles: High drag states and mixing. Journal of Physical Oceanography, 34: 94 - 112,

[38] Sousa, J.M.M., 2002 'Turbulent flow around a surface mounted obstacle using 2D-3C DPIV'. ***Experiments in Fluids***, **33**, p854-862.

[39] Sumer, B. M. and Fredsøe, J., 2002 '***The Mechanics of Scour in the Marine Environment'.*** Vol 17, Advanced Series on Ocean Engineering. World Scientific, Singapore. 536pp.

[40] Testik, F.Y., Voropayev, S.I. and Fernando, H.J.S. 2005. Flow around a short horizontal bottom cylinder under steady and oscillatory flows. Physics of Fluids, 17,

[41] Vaucher, G.-T., Cionco, R. and Bustillos, M. Forecasting stability transitions and aire flow around an urban building - Phase 1.,

[42] Walker, I.J. 1999. Secondary airflow and sediment transport in the lee of a reversing dune. Earth Surface Processes and Landforms, 24: 437 - 448,

[43] Walker, I.J. and Nickling, W.G. 2003. Simulation and measurement of surface shear stress over isolated and closely spaced transverse dunes in a wind tunnel. Earth Surface Processes and Landforms, 28: 1111 - 1124, doi: 10.1002/esp.520.

[44] Wang, M., Catalano, P and Iaccarino, G., 2001 'Prediction of high Reynolds number flow over a circular cylinder using LES with wall modeling.' Centre for Turbulence Research, Annual Research Briefs, 2001. p45-50.

[45] Whitehouse, R., 1998. 'Scour at marine structures', Thomas Telford, London. 198 pp.

Characterization of Leaching Behavior of Recycled Concrete Used for Scour Prevention

Juhyung LEE*, Kiseok KWAK*, Jaehyeon PARK* and Moonkyung CHUNG**
* Korea Institute of Construction Technology/Geotechnical Engineering Research Department, Koyang, Korea
** Korea Institute of Construction Technology/International Cooperation & Public Information Division, Koyang, Korea

A series of leaching test was conducted to assess the potential environmental risk of recycled concrete produced in Korea when it is utilized as a material for protecting bridge piers against scour. Recycled concrete can be used economically to fill the scour hole directly, as granular filters of riprap or as filling materials of gabions, geocontainers, stone mattresses and so on when natural material is not enough. These applications using recycled concrete are especially effective in the side of resources saving and environmental preservation. In this study, several methods were included such as continuous batch test(DIN 38414-S4), availability leaching test(NEN 7341), pH-stat test(CEN/TC 292/WG6) and tank diffusion test(NEN 7345). On all of the tests, nearly all the trace elements were found to be low in their concentrations while some elements were recorded under detection limits. There are no criteria for environmental risk in methods we used in this study. However, conditions such as contact time, pH and so on were much more rigorous than other commonly adapted method including TCLP and domestic testing method for solid waste, the trace elemental concentrations are under the criteria for hazardous material set by the TCLP and domestic method. Based on the test results, it may be concluded that the use of recycled concrete as a scour countermeasure would be an acceptable practice as far as trace elements are concerned.

I. INTRODUCTION

The construction and demolition waste is the necessary consequences occurred during the redevelopment and reconstruction and it shows the rapidly increased amount, among which waste concrete accounts for about 67%. Advanced countries such as Japan and US have made every effort to recycle the waste concrete and especially, concentrated their effort on the development of advanced utilization technology to utilize the recycled aggregates obtained from demolition of waste concrete and other procedures as highly value-added materials such as road repairing material, compound for concrete and raw material of cement as well as simple process such as reclamation. At present, the country has tried to utilize the construction and demolition waste highly and the recycled aggregates are gradually utilized and commercialized as road base material, road sub-base material and recycled concrete block.

Before utilizing the recycled aggregates, it is important to clearly characterize the recycled aggregates environmentally and technologically and to secure the safety. Especially, the recycled aggregates containing cement may produce heavy metals and harmful mineral ions when contacting with water, probably resulting in environmental risk. This study was intended to evaluate the environmental risk of the recycled aggregates with leaching test as the basic research to utilize the recycled aggregates as the scour-protective aggregate of bridges. Recycled concrete can be used economically to fill the scour hole directly, as granular filters of riprap or as filling materials of gabions, geocontainers, stone mattresses and so on when natural material is not enough. These applications using recycled concrete are especially effective in the side of resources saving and environmental preservation.

Especially, this study deals with the environmental assessment to the recycled aggregates used as a scour-protective aggregate, which is to contact water for a long time daily over several tens of years, so the prerequisite research is to analyze the leaching characteristics of elements quantitatively and qualitatively. Solid Waste Process Test and TCLP test most used when assessing the leaching characteristics of solid waste may advantageously assess the short-term effects qualitatively as relatively simple tests costing reasonably but both tests have limitations to assess the long-term and comprehensive risk in accordance with physically and chemically environmental changes. To overcome the shortcomings, this study is to draw out a more qualitative model applicable to fields by adopting various leaching methods to simulate leaching reactions in various environments. The purposes of this study is to 1) determine whether leaching degree of a certain material complies with the environmental standards through various proven leaching tests and 2) assess the potential effects to the environment quantitatively by verifying the leaching characteristics under various physical and chemical conditions when the recycled aggregate contacts water.

II. TEST METHODS

1. Test Materials

The recycled aggregates are categorized into two types; type 1 recycled aggregate and type 2 recycled aggregate and this study chose the type 2 recycled aggregate, which is easy to process and economical, to research. Table 1 shows the general physical properties of type 1 & 2 recycled aggregate and natural aggregate. As seen in the table, it is found that there is no significantly physical difference between type 1 recycled aggregate and natural

TABLE 1.
PHYSICAL PROPERTIES OF RECYCLED AGGREGATES AND NATURAL AGGREGATE

Property	type 1 recycled aggregate	type 2 recycled aggregate	natural aggregate
Unit weight(kg/m^3)	1,579	1,406	1,509
Specific gravity(g/cm^3)	2.61	2.43	2.64
Water absorption(%)	1.14	3.12	1.13
Unit cost($/m^3)	6	3	18

aggregate and that type 2 recycled aggregate is very economical. The type 2 recycled aggregate used as test materials was offered by a waste concrete recycling company in Korea, and it shows 30~70mm of grade and 35~52% of abrasion loss.

2. *Leaching Test*

The conditions when utilizing the recycled aggregate as a scour-protective aggregate are 1) that it continues to contact water and, 2) that it flows, not a lake without stream, so leached materials are diluted and spread over, instead of sedimentation. Therefore, the maximum leaching possibility of elements was calculated by executing availability leaching test. At the moment, to apply worse condition when assessing the leaching possibility of element, the recycled aggregates have been crushed smaller than 125μm. That's why smaller particles may facilitate more leaching because of increased surface area. In addition to availability leaching test with the crushed samples, the serial batch test has been also performed with the raw(not crushed) samples.

In addition, considering that river water does not have uniform pH at positions and that pH might be changed due to acid rain or changes in the neighboring environment, pH-stat test has been performed to examine the changes in leaching characteristics depending on pH. Unlike the availability leaching test in which particle size has been adjusted, the leaching degree of elements has been calculated in other conditions by using serial batch test without any adjustment of particles.

With the above test, it is reasonably determined that the diffusion of leaching of the recycled aggregate would depend on a function of the surface area. Therefore, to examine the leaching characteristics due to the surface diffusion when it continues to contact water for a long time, the accumulative leaching characteristics of elements has been examined by using a tank test. It is available as long as the particle diameter is 40mm and larger.

A. *Serial batch leaching test - modified after DIN 38414-S4*

The serial batch leaching test is a test leaching elements continuously simply by exchanging a solution without a sample to leach exchanged, with which the reaction time of the batch test may be extended. After adding 200g of the raw(not crushed) sample and 600mL(LS ratio 3:1) of distilled water to a 1000mL polyethylene bottle, the mixture has been agitated at a speed of 30rpm/h by a rolling mixer for 24 hours. Once the first 24 hours agitation is finished, the solution is removed by 0.45μm filter and then, the bottle is filled with distilled water and agitated for 24 hours. The procedure is repeated for four times. The recycled aggregate samples used in the serial batch leaching test was performed by dividing into cleaned one and not cleaned one. That is, the cleaning procedure is to clean it with flowing water for a minute as it is normally cleaned in the fields while the other one(not cleaned) is not processed with the above process.

B. *Availability leaching test - Dutch availability leaching test NEN 7341*

It consists of processes to crush the recycled aggregate smaller than 125μm, mix 8g of the crushed aggregate and 800ml distilled water in a 1,000mL beaker and agitate them with a magnetic bar. At the moment, for the first four hours, the pH is adjusted to 7, the solution is removed in 4 hours, it is filled with distilled water again and then, it is agitated for 18 hours with pH set to 4. After mixing a sample of pH4 and a sample of pH7 and filtrating the mixture with a 0.45μm filter, it is readily analyzed. For the adjustment of pH, a peristaltic pump and a controller were used and 0.1M diluted nitric acid was used to adjust pH because the recycled aggregate itself is 11~13, which is strong alkali.

C. *pH-stat leaching test - CEN/TC 292/WG6, EU standard method of pH dependence test*

For the test, 30g of the recycled aggregate crushed smaller than 125μm and 300mL of distilled water were mixed into a 500mL beaker(LS ratio 10:1) and its pH is adjusted at 9 steps of 4, 5, 5.5, 7, 8, 9, 10, 11 and 12 by using a magnetic bar(Fig. 1). Then, it was agitated for each pH level for 24 hours. For pH adjustment, 0.1M diluted nitric acid and 0.1M diluted sodium hydroxide were used, in which pH has been uniformly maintained with a peristaltic pump and a controller.

D. *Tank diffusion test - NEN7345, Dutch diffusion leaching test*

While the above-mentioned tests were performed for pulverulent body, the tank diffusion test examines the diffusion leaching characteristics depending on the area, so a sample of which particle is small is to be formed and solidified in a certain shape before the test. Therefore, the results of the tank diffusion test are presented as the leaching of element depending a on surface area function.

Figure 1. pH-stat leaching test

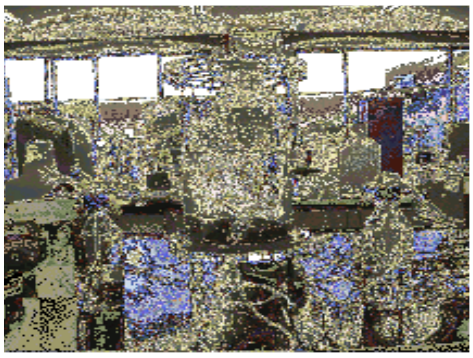

Figure 2. Tank leaching test

However, the accurate surface area of the recycled aggregate is not possible because of the diverse grading and ununiform shape, so a certain amount of the sample was inserted to a reaction cell and it is presented with the leaching of element results depending on the weight. The test is applied to solid waste of which diameter is 40mm and larger. Unlike availability leaching test or pH-stat leaching test, 1,000g of the raw recycled aggregate and 5,000mL distilled water were put into a reaction cell and mixed together(Fig. 2). In 8 hours of the reaction, the reacted water was removed from the cell and the same amount of distilled water was filled again. In 24 hours after the test started, the second reacted water was collected and like this, the accumulative reacted water was collected for 8 times; in 48 hours, 56 hours, 4 days, 9 days, 16 days, 36 days and 64 days.

3. Element Analysis

A. Recycled Aggregate

After crushing the recycled aggregate with an iron mortar at first, the crushed aggregate was re-crushed smaller than 125μm by using agate-mortar and then, the 200mg of sample was taken. The crushed sample was sealed up in Teflon bomb with 1mL of aqua regia(HNO_3 : HCl 3:1) and heated up at 80℃ for 2 hours. After then, it was cooled down at ambient temperature and neutralized by adding 10mL distilled water and 29mL saturated boric acid solution. Then, it was filtered with a 0.45μm filter and analyzed with an atomic absorption spectrometer (Shimadzu AF 6601F).

TABLE 2.
CHEMICAL COMPOSITION OF RECYCLED AGGREGATE (Unit:mg/kg)

Ca	Mg	Na	**K**	**Cd**	Pb	Cr
50800	2574	866	8720	7	33	<1ppb
Ni	Zn	Cu	As	Hg	Fe	
22	5852	17	<1ppb	<1ppb	3018	

B. Ion Analysis

The reacted water gained from the leaching test was filtered with a 0.45μm filter. After then, the positive ions including heavy metals have been analyzed by using an atomic absorption spectrometer(Analytikajena AAS Vario 6) while the negative ions have been analyzed by using an Ion chromatography (Dionex DX-120).

III. RESULTS AND DISCUSSION

1. Chemical Properties of the Recycles Aggregate

The chemical composition of the recycled aggregate is shown in Table 2. Amont major elements, Ca was the most content and followed by Mg, Fe, K and Na. For microelements, Cu and Pb were relatively high content, and Zn was the most contained.

2. Leaching Test Results

A. Serial batch leaching test

Table 3 shows the results of the batch test using distilled water. pH was relatively high between 10 ~ 11 in both cleaned/not cleaned samples. It is expected that in general, not cleaned sample would have higher concentration of element and especially, much element would be emitted during the initial leaching procedure.

TABLE 3.
LEACHATE CHEMISTRY COLLECTED FROM SERIAL BATCH LEACHING TEST (Non-washed/washed, Unit: mg/l, conductivity: μS/cm)

No. of leachings	**Ca**	**Mg**	**Na**	**K**	**Cd**	**Pb**	**Cr**	**Al**
1	17.6/9.1	0.05/0.16	12.2/18.3	22.2/20.6	0.01/<1 ppb	<1ppb/<1ppb	0.009/0.007	0.06/0.14
2	18.4/10.1	0.05/0.10	4.3/5.5	13.4/13.2	0.02/<1ppb	<1ppb/<1ppb	0.004/0.007	0.04/0.07
3	17.3/11.5	0.05/0.09	2.7/3.6	10.1/10.6	0.02/0.01	<1ppb/<1ppb	0.003/0.003	0.11/0.19
4	19.3/11.5	0.05/0.08	2.0/2.8	8.2/8.8	0.03/0.01	<1ppb/<1ppb	0.003/0.002	0.10/0.10
	Ni	**Zn**	**Cu**	**As**	**Hg**	**Fe**	**Mn**	
1	0.007/0.071	<1ppb/0.006	<1 ppb/0.437	<1ppb/<1ppb	<1ppb/<1ppb	<5 ppb/<5ppb	0.17/0.16	
2	0.009/0.080	<1ppb/<1ppb	<1 ppb/0.032	<1ppb/<1ppb	<1ppb/<1ppb	<5 ppb/<5ppb	0.17/0.16	
3	0.009/0.083	<1ppb/<1ppb	<1 ppb/0.030	<1ppb/<1ppb	<1ppb/<1ppb	<5 ppb/<5ppb	0.17/0.17	
4	0.011/0.077	<1ppb/<1ppb	<1 ppb/0.021	<1ppb/<1ppb	<1ppb/<1ppb	<5 ppb/<5ppb	0.18/0.17	
	pH	**Conductivity**	**F^-**	**Cl^-**	**NO^{3-}**	**PO^{3-}**	**SO_4^{2-}**	**HCO^{3-}**
1	11.14/10.64	418.0/270.5	1.1/1.1	6.7/3.1	6.2/4.7	0.14/<10ppb	28.2/31.9	52.6/67.1
2	11.30/10.67	309.0/180.3	0.3/0.2	2.1/0.3	1.8/1.2	<10	5.3/7.7	39.2/38.9
3	11.20/10.68	325.0/178.6	0.2/0.2	1.3/0.5	0.9/0.7	<10	3.2/5.2	31.7/31.6
4	10.94/10.54	292.5/176.4	0.1/0.1	1.2/0.31	0.8/0.5	<10	2.9/2.9	29.1/28.2

That is, elements would be much dissolved during the initial leaching as the corpuscles attached on the surface contact water. At this moment, contamination load would be reduced by eliminating the element through prior clean-up process.

Ca, K, Na, Cl^- and NO^{3-} were leached more in not cleaned sample, which is supported by the fact that the first leaching sample showed a higher concentration. However, Mg and SO_4^{2-} were showed reverse results, which means the concentrations were higher in the cleaned sample. In case of microelement, the concentration of Cd and Cr was higher in the not cleaned sample, but Ni and Cu showed higher concentration in the cleaned sample. Meanwhile, Mn showed similar concentration in both samples. The other microelements such as Pb, Cu, As and Hg had very low values of concentration under the analysis limitation. The reason why there is the concentration difference between cleaned sample and not cleaned one is probably depending on the locations of elements. That is, the elements(Ca, K, Na and etc) mainly existing on the surface are leached as soon as they contact water. Especially, in case of Cl^- or NO^{3-}, it is not a major component of the recycled aggregate and instead, it is expected that the elements are leached as being absorbed on the particles of aggregate. It is also supported with the fact that the concentration of two elements was sharply reduced after the first leaching(Table 3). However, in case of elements existing inside the particles, not on the surface, they would be leached in a certain time when they contact water. Mg and SO_4^{2-} would the latter case.

The leaching of element depends on the leaching of the element itself as well as the position. In the serial batch test, the leaching procedure of elements, depending on the leaching frequency, is divided into 1) increase(Ca, Cd, Ni), 2) reduction after the max. concentration at first(Mg-washed, Na, K, Cr-washed, Cu-washed, F^-, Cl^-, NO^{3-}, SO_4^{2-}) and 3) maintenance of the relatively proper concentration(Mn). In case the concentration of element is sharply reduced, it is determined that pre-treatment process would reduce the impact on the environment because the concentration would be reduced after the initial leaching. On the other hand, regarding that the concentration increases or maintains as the leaching frequency increases, it is estimated that the element exists inside the aggregate or the balanced concentration is maintained by solid materials to limit the solubility. The solid material to limit element leaching is calculated by earth science modeling. As such, the location of element is the primary cause to affect the leaching characteristics and the reduction by clean-up would be effective only for element existing on the surface.

TABLE 4.
CHEMICAL COMPOSITION OF LEACHATE FROM AVAILABILITY LEACHING TEST (Unit: mg/l)

Ca	Mg	Na	K	Cd	Pb
209.60	2.71	28.1	35.6	<1ppb	0.01
Ni	**Zn**	**Cu**	**As**	**Hg**	**Cr**
0.12	0.95	<1ppb	<1ppb	<1ppb	<1ppb
Fe	**Mn**	**F^-**	**Cl^-**	**PO_3**	**SO_4^{2-}**
0.13	<5 ppb	0.10	1.34	0.15	9.23

B. Availability leaching test

The test is performed to calculate the maximum value of sample to be leached. A great quantity of Ca is leached and the other major elements(Mg, Na, K, SO_4^{2-}) are also leached. Regarding microelement, the microelements(Cd, Cu, As, Hg, Cr, Mn) but Pb, Ni and Zn showed the concentration lower then the detection limit(Table 4). Even not under the same conditions, the availability leaching test results showed that all the elements were within the criterion although they were tested under worse condition than the domestic process test or TCLP

TABLE 5.
RESULTS FROM PH-STAT LEACHING TEST (Unit: mg/l)

pH	Ca	Mg	Na	K	Cd	Pb	Cr
4	580.6	3.0	17.0	48.1	0.01	0.14	<1ppb
5	276.0	0.3	20.5	493.5	0.01	0.04	<1ppb
5.5	557.3	4.9	147.8	35.3	0.02	0.01	<1ppb
7	1003.3	23.8	26.8	75.4	0.02	0.04	<1ppb
8	977.3	22.8	17.1	85.4	0.03	<1ppb	<1ppb
9	666.6	4.8	21.2	63.2	0.04	<1ppb	<1ppb
10	555.6	2.3	32.1	57.7	0.00	<1ppb	<1ppb
11	292.4	0.3	6.8	40.0	0.01	<1ppb	<1ppb
12	172.9	0.1	23.0	48.1	0.02	<1ppb	<1ppb
pH	**Ni**	**Zn**	**Cu**	**As**	**Hg**	**Fe**	**Mn**
4	0.16	0.08	0.02	<1ppb	<1ppb	0.30	<5ppb
5	0.15	0.07	0.02	<1ppb	<1ppb	0.13	<5ppb
5.5	0.14	0.08	0.01	<1ppb	<1ppb	0.12	<5ppb
7	0.29	0.08	0.01	<1ppb	<1ppb	0.13	<5ppb
8	0.38	0.08	0.01	<1ppb	<1ppb	0.07	<5ppb
9	0.14	0.08	0.06	<1ppb	<1ppb	0.11	<5ppb
10	0.14	0.09	0.05	<1ppb	<1ppb	0.13	<5ppb
11	0.16	0.09	0.04	<1ppb	<1ppb	0.03	<5ppb
12	0.15	0.09	0.05	<1ppb	<1ppb	0.06	<5ppb

method(lower pH, longer agitation time). Therefore, it is reasonably determined that the recycled aggregate would be a resource to be reclaimed or recycled, not one to be reclaimed as a harmful waste.

C. pH-stat leaching test

pH is an important adjustment factor to affect the solubility of metal elements including microelement. The leaching degree of the recycled aggregate also depends on pH(Table 5, Fig. 3). In case of the microelement, the only Zn, Cu, Cd and Ni were detected and the other microelements showed the concentration lower than the analysis limit. In addition, the max. leaching concentration was also recorded less than the criteria of the domestic waste process test or TCLP. Most heavy metals have more leaching degree as the pH is lower, but the test showed that the only Fe had lower leaching degree as its pH increaes and that Ni and Cd had the most leaching degree when the pH was between 6 ~ 8. On the other hand, it was also found that the leaching degree of Cu sharply increased.

D. Tank Diffusion Test

The results of the reaction totally for 64 days show the following 3 cases; the leaching degree of element is reduced, maintained or slightly increased(Table 6). In the former case, the most element exists on the surface, is leached at first as it contacts water and then, eliminated in a time. However, the case that the leaching degree is maintained may be understood that the leaching of element is adjusted by diffusion.

Fig. 4 shows the changes in the concentration by times of leaching test are compared with the cumulative concentration, total concentration calculated from the analysis of the solid recycled aggregate and the availability leaching test results. The bold line in Fig. 4 shows the total concentration contained in the solid while the thin line means the concentration calculated by the availability leaching test. If an element is leached by diffusion, the element leaching would occur at a uniform speed and may be expressed as a linear equation close to 1.0. However, as seen in the almost elements in the test results, the leaching concentration is reduced every time it is performed and the elements approach to equilibrium status. It may be interpreted that the element is leached much at the initial time and leaching amount of it is reduced as it is gradually exhausted. On the other hand, it is determined that the case(i.e. Zn) the initial leaching is maintained but the speed increases after a point of time would be affected by the changes in the chemical

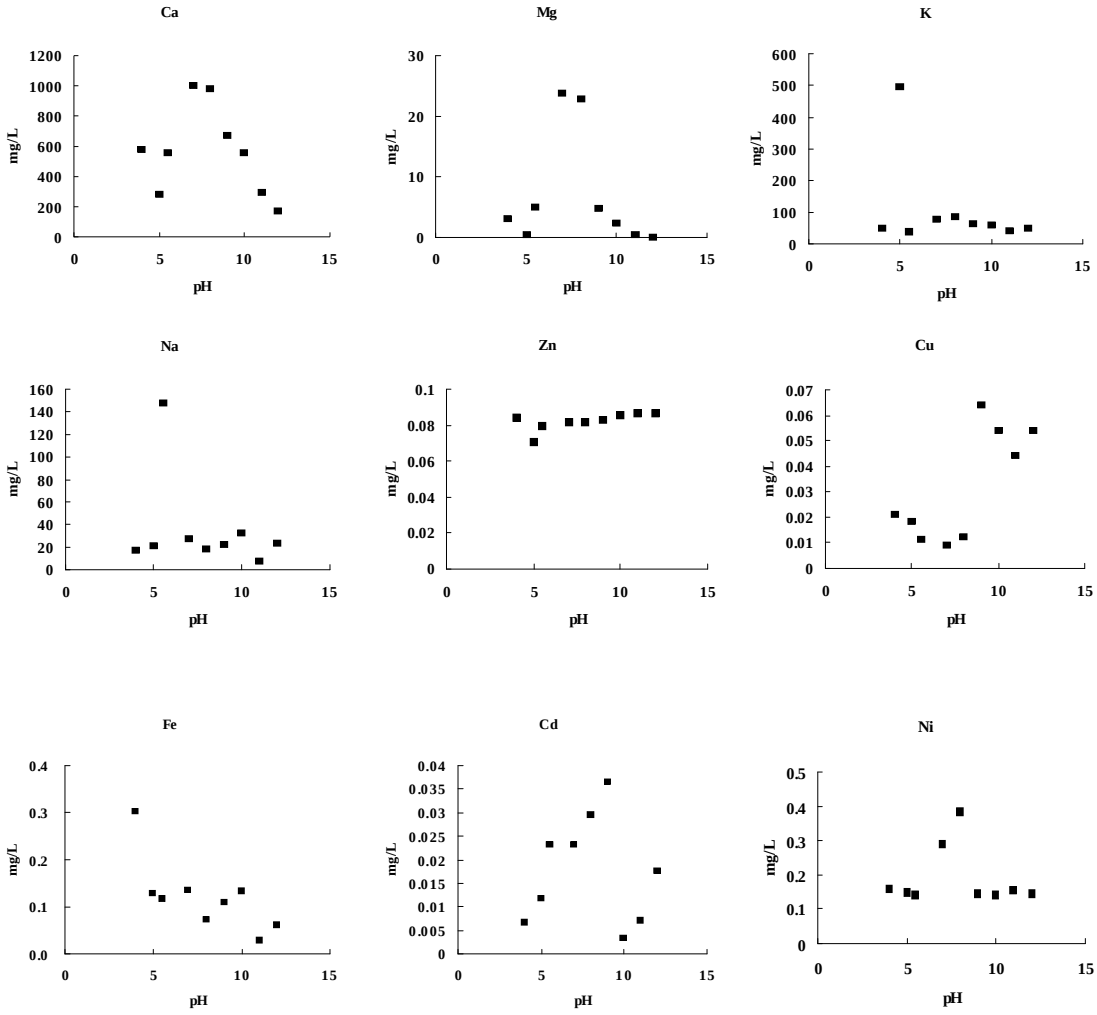

Figure 3. Elemental variation with pH (pH-stat leaching test)

TABLE 6.
AMOUNT OF DIFFUSED ION FROM TANK TEST (Unit: mg/l, conductivity: μS/cm)

Duration (hr)	Ca	Mg	Na	K	Cd	Pb	Cr
8	14.49	0.30	4.72	26.67	<1ppb	0.015	<1ppb
24	12.66	0.13	2.59	43.09	<1ppb	<1ppb	<1ppb
56	18.97	0.17	1.88	38.23	<1ppb	<1ppb	<1ppb
96 (4 days)	0.78	0.06	7.05	31.56	<1ppb	<1ppb	<1ppb
216 (9 days)	6.11	0.07	1.65	12.99	0.021	<1ppb	<1ppb
384 (16 days)	23.87	0.07	6.95	13.73	0.029	<1ppb	<1ppb
864 (32 days)	22.65	0.04	2.07	12.40	0.019	<1ppb	<1ppb
1536 (64 days)	54.89	0.01	1.32	7.42	0.023	<1ppb	<1ppb
Total amount(mg/kg)	770.10	4.22	153.81	930.44	0.46	0.08	N/A
	Ni	**Zn**	**Cu**	**As**	**Hg**	**Fe**	**Mn**
8	0.108	0.062	0.079	<1ppb	0.004	0.08	<5ppb
24	0.100	<1ppb	0.064	<1ppb	0.005	0.10	<5ppb
56	0.140	<1ppb	0.090	<1ppb	0.004	0.19	<5ppb
96	0.052	0.035	0.038	<1ppb	0.004	0.15	<5ppb
216	0.135	0.057	0.051	<1ppb	<1ppb	<5ppb	<5ppb
384	0.098	0.040	0.045	<1ppb	<1ppb	<5ppb	<5ppb
864	0.164	0.025	<1ppb	<1ppb	<1ppb	<5ppb	<5ppb
1536	0.168	0.024	<1ppb	<1ppb	<1ppb	<5ppb	<5ppb
Total amount(mg/kg)	4.83	0.78	1.84	N/A	0.08	3.71	N/A
	pH	**Conductivity**	**F-**	**Cl-**	**NO3**	**PO3**	**SO4**
8	9.78	84.1	0.02	1.12	4.37	0.30	21.88
24	9.42	33.5	0.02	0.66	1.85	<10ppb	13.83
56	9.19	23.2	0.06	0.70	1.82	<10ppb	16.27
96	9.29	22.3	0.01	0.40	0.84	<10ppb	9.00
216	9.26	80.5	0.01	0.32	0.75	<10ppb	9.63
384	8.97	105.6	0.01	0.35	0.50	<10ppb	8.66
864	9.28	48.7	0.02	1.23	0.41	<10ppb	10.31
1536	9.42	33.5	0.01	0.13	0.59	<10ppb	10.00
Total amount(mg/kg)	N/A	N/A	0.80	24.55	55.80	1.50	497.90

conditions having an influence on leaching process(i.e. changes in pH). The mobility of Zn contained in cement may be limited by the mixture of Ca-Zn. The delayed leaching in this test must depend on the leaching of Ca.

Classifying the leaching characteristics of each element, it may be 1) surface leaching: Na, Ni, NO^{3-}, Cl^{-}, 2) elimination of leaching part: Mg, K, Cu, Hg, Pb, 3) diffusion leaching: Ca, Fe, F^{-}, SO_4^{2-} and 4) changes in leaching condition: Zn. Since most micro heavy metals had too low concentration, it was difficult to examine the cumulative leaching characteristics. It was found that most elements but SO_4^{2-} in the tank test showed lower concentration than the availability leaching test, which means that more elements than the results leached in such tests may be leached. However, in case of microelement harmful to the environment(incl. heavy metals), it was determined that the contamination possibility resulting from the leaching of the recycled aggregate would be little because the leached amount was almost as same as the availability leaching test results in case of major elements.

IV. CONCLUSIONS

In conclusion, it may be said that the recycled aggregate would not cause the environmental risk due to leaching of microelement with high environment risk as it contact water. Although the leaching range of element was diverse depending on test methods, the concentration was not beyond the criteria of the waste process test or TCLP of which conditions were not worse than the tests performed in this study. Furthermore, the ratio of water to the recycled aggregate was 3:1 in this study but actually, a river will have a higher ratio between water and solid materials if it flows, almost reaching the unlimited ratio. Therefore, it is also expected that the leached element will be diffused, moved and diluted finally in river water. However, it is determined that the high pH of the recycled aggregate would affect the environment. Fortunately, it was found that the ratio of water: the recycled aggregate which was 3:1 in the serial batch leaching test dropped up to 9 in the tank test, in which the ratio of water: waste was 5:1. Considering that as a difference between both tests, the former was a test agitating at 360° but the latter left it without agitation and that the recycled aggregate used as a scour-protective aggregate in river water would not have any artificial agitation, the pH would be possibly lowered at fields. In addition, Ca and S that significantly contribute to the pH are exhausted slowly than any other element and the leaching is typically limited by diffusion, so the pH would be gradually reduced.

Without any separate harmfulness criteria, the tests in this study have been compared with TCLP test and the domestic waste process test. However, it is probable that

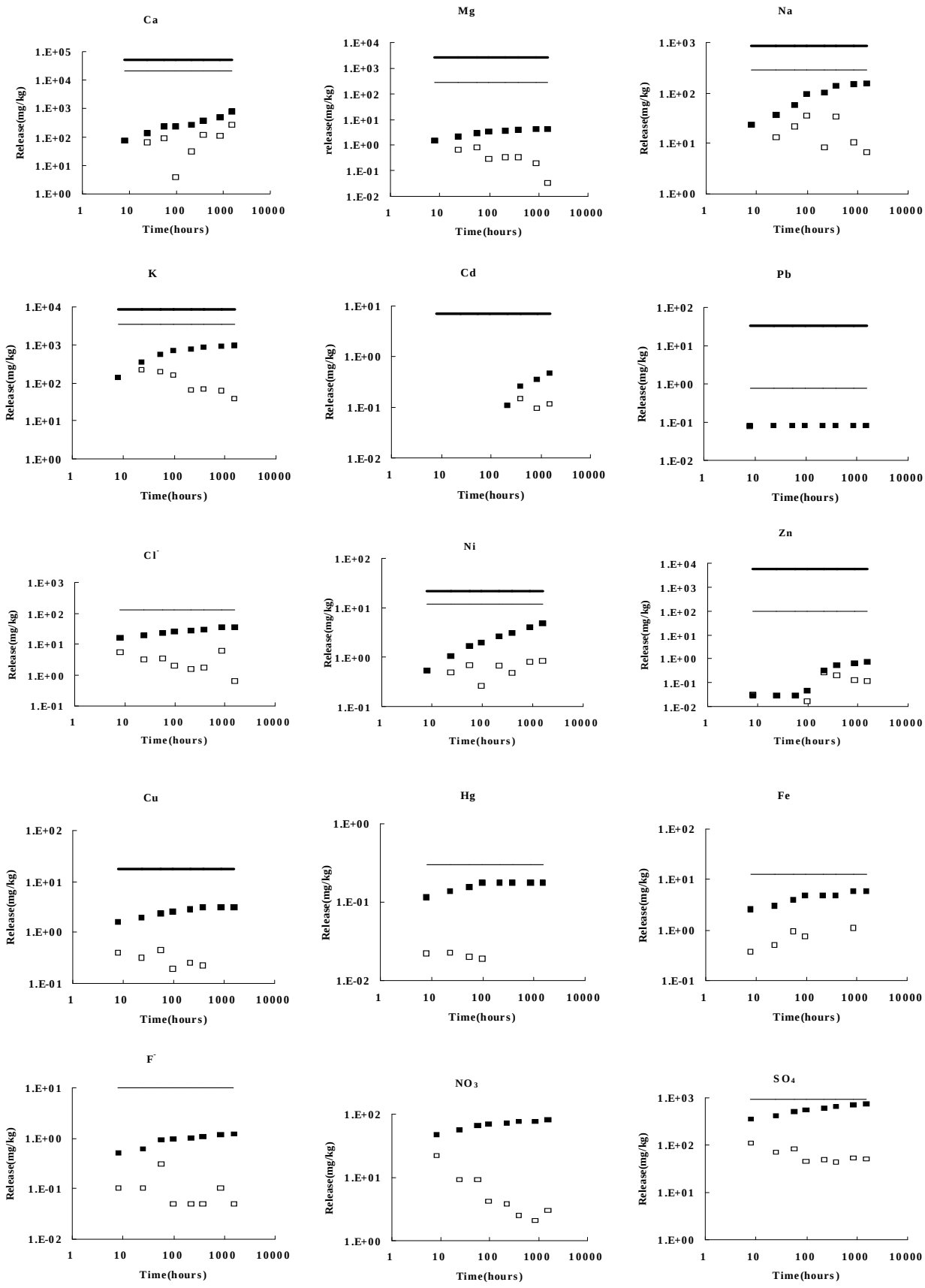

Figure 4. Elemental release from tank leaching test (thin line: availability leaching test, bold line: total contents, open square: leaching from each session, closed square: cumulative release)

little environment risk would be measured or detected as long as the current is much enough. At this case, it is more meaningful to compare the recycled aggregate with other material based on the leaching amount of unit weight, not on the environment risk of the material itself. The total cumulative amount see in Table 6 means the total amount leached from 1kg the recycled aggregate in the tank diffusion test. Based on it, it is possible to assess the leaching potentiality of elements depending on the recycled aggregate used in a river and it may be determined whether the qualitative risk exists under the conditions of a field.

Among the potential environmental occurred when the recycled aggregate is used as a material for protecting bridge foundation against scour, it seems that the environmental risk resulting from the leaching of microelement is little and the use of the recycled aggregate would be reasonable. Despite of no environmental criteria in this study, it is determined that conditionally, the assessment of safety in the aquatic ecosystem affected by minerals when Ca and Mg are plentifully leached should be necessarily considered.

REFERENCES

[1] Fallman, A. M., 1997, "Performance and design of the availability leaching test for measurement of potentially leachable amounts from waste material," Environ. Sci. Technol.

[2] Hage, J.L.T. and Mulder, E., 2004, "Preliminary assessment of three new European leaching tests," Waste management.

[3] Hohberg, I., de Groot, G. J., van der Veen, A. M. H., and Wassing, W., 2000, "Development of a leaching protocol for concrete," Waste management.

[4] K. Kwak, J. H. Lee, J. H. Park, M. Chung, S. D. Cho, H. S. Woo, 2004, Development of Technology for Extended Duration of Bridge Foundation, Korea Institute of Construction Technology.

[5] Kylefors, K., Andreas, L., and Largerkvist, A., 2003, "A comparison of small-scale, pilot scale and large scale tests for predicting leaching behaviour of landfill wastes," Waste management.

[6] Tiruta-Barna, L., Imyim, A., and Barna, R., 2004, "Long-term prediction of the leaching behaviour of pollutants from solidified wastes," Advances in Environmental Research.

[7] Todorvic, J. and Ecke, H., 2004, "Leaching tests for assessment of mobility of inorganic contaminants from solidified incineration residues – Literature review. Report No. 2004:01," Division of Waste science and technology, Lulea University of Technology, Swenden.

[8] van der Sloot, H. A., 2002, "Characterization of the leaching behaviour of concrete mortars and of cement-stabilized wastes with different waste loading for long-term environmental assessment," Waste management.

[9] Wahlstrom, M., Laine-Ylijoki, J., Maattanen, A., Luotojarvi, T., and Kivekas, L., 2000, "Environmental quality assurance for use of crushed mineral demolition wastes in road constructions," Waste management.

Automatic Non-intrusive Measurement of Scour-Hole Geometry

O. Link*, F.Pfleger** and U. Zanke*
* Institut für Wasserbau und Wasserwirtschaft, Technische Universität Darmstadt, Germany
** Fachgebiet Hydromechanik, Technische Universität München, Germany

I. INTRODUCTION

Measurement of scour-hole geometry around piers is usually limited to records of scour depth at the pier front as e.g. in references [1, 2, 3, 4]. The possible reason is partially attributed to the fact that point-measurement techniques are not fast enough to record scour-hole geometry without ocurrence of significant bed changes during the measurement. Optical measuring-systems are able to record scour-hole surface instantaneously as presented in reference [5] but this technique present difficulties working underwater also disturbing the flow [6]. Even though knowledge of scour depth at the pier front is usefull in development of predictive formulas for pier design and foundation soil maintenaince.

Information of scour-hole geometry is crucial for estimation of refilling rip-rap material and for comparison with results of numerical simulation, calibration and validation of three-dimensional morphodynamic-numerical models. Although scour-hole geometry has been measured at selected scour conditions i.e. at equilibrium stage as given in references [7,8] a systematic study of measurement of time-dependent scour-hole geometry during scouring remains undetected.

In this paper an automatic non-intrusive method for measurement of scour-hole topography is presented. Results provide information on evolution of scour-hole volume as a function of maximum scour depth, scour-hole slopes, etc. evidencing interaction patterns between flow and sediment particles i.e. the scour mechanism.

II. EXPERIMENTATION

A. Facilities

Scour experiments were conducted in a rectangular flume with glass side-walls, 26 m long, 2 m wide and 1 m deep, at the Institute for Hydraulic and Water Resources Engineering, Darmstadt University of Technology, Germany.

A plexiglas cylindrical pier having 20 cm diameter was mounted in the middle of a working section with movable bed. This is located 16 m downstream of the flume entrance, having a length of 4 m, width of 2 m and depth of 0.5 m.

A false bottom made of concrete plates was installed outside the working section in order to avoid filling the whole flume with sand. The plates rested on bricks, 0.5 m over the original flume bottom. The sides of the working section were coated with absorbing material in order to avoid secondary flows.

Inflow was controlled by a magnetic inductive discharge flowmeter and regulated by an electronic inlet valve. The flow depth, adjusted by a tailgate, was controlled by ultrasonic gages with a precision of ±0.5 mm. Fig. 1 shows the experimental set-up schematic.

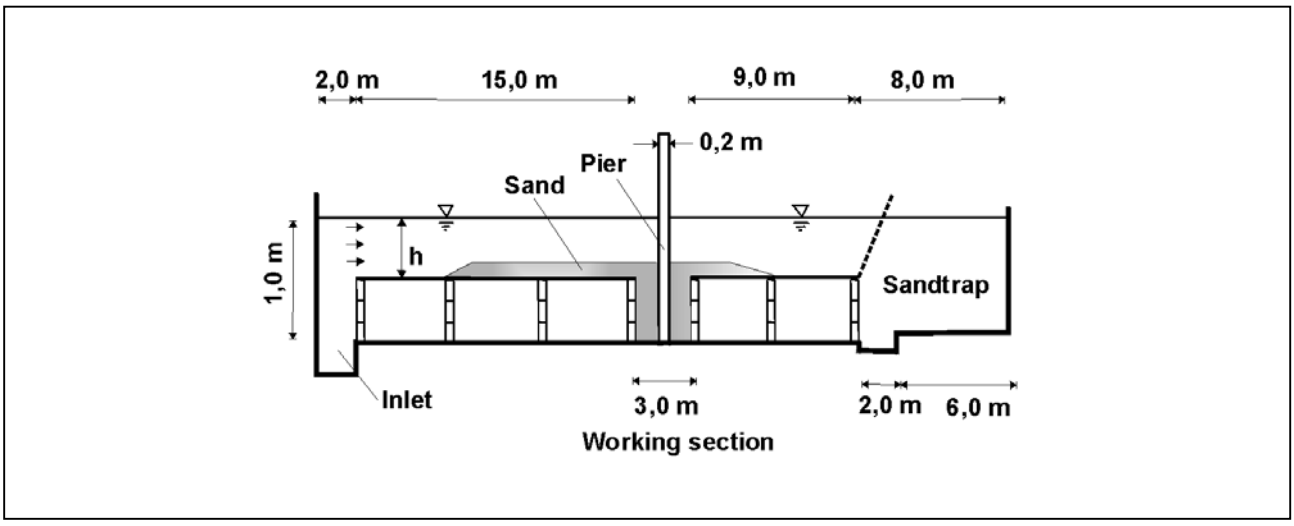

Figure 1. Experimental Setup

B. Bed-Material

The bed material was a mixture of sand with grain sizes ranging between 0.06 and 2.00 mm and having a representative particle diameter d_{50} = 0.25 mm. The geometric standard deviation $\sigma_g = (d_{84.1} / d_{15.9})^{0.5}$ of the particle size distribution was 1.37 with particle diameters $d_{84.1} = 0.35$ and $d_{15.9} = 0.19$.

The critical velocity for the initiation of motion of isolated sediment particles, in the following called critical velocity, u_{cr} was determined experimentally considering critical condition when about 10% of the surface particles become in motion. The critical velocity was equal to 0.26 m/s.

The natural repose angle of sediment particles ϕ was 30°.

The sand was filled in the working section up to 5 cm over the false bottom level having 10 m upstream and 2 m downstream of the pier also covered with a 5 cm thick sediment layer.

III. MEASURING-TECHNIQUE

A. The Laser Distance Sensor

A laser distance sensor was used to measure scour-hole radius i.e. the distance between the pier and the scour-hole surface at different points.

The measuring principle of the device base upon triangulation to perform distance measurements between the transmitter and the surface on which the laser beam is reflected.

The laser distance sensor has a measurement range of 35 cm with an accuracy of ±0.3 mm.

Calibration curves has been taken underwater for different radial directions around the pier. An excellent linearity of the sensor signal with the measured distance over the entire measurement range was observed.

Measurement data were aquired with a frequency of 70 Hz, thus allowing a very fast measurement of the scour-hole surface.

The distance sensor was located in the plexiglas pier and was driven by high-precision step-motors in the vertical and radial directions.

The accuracy of the motor-steps was ±0.1 mm and ±0.5° in the vertical and radial directions respectively.

The laser distance sensor could be positioned to measure the scour-hole radius at any point of the scour-hole.

In this way a non-intrusive measuring system was developed for the continuous measurement of the complete scour-hole geometry during running experiments. Figure 2 shows the measuring system inside the plexiglas pier.

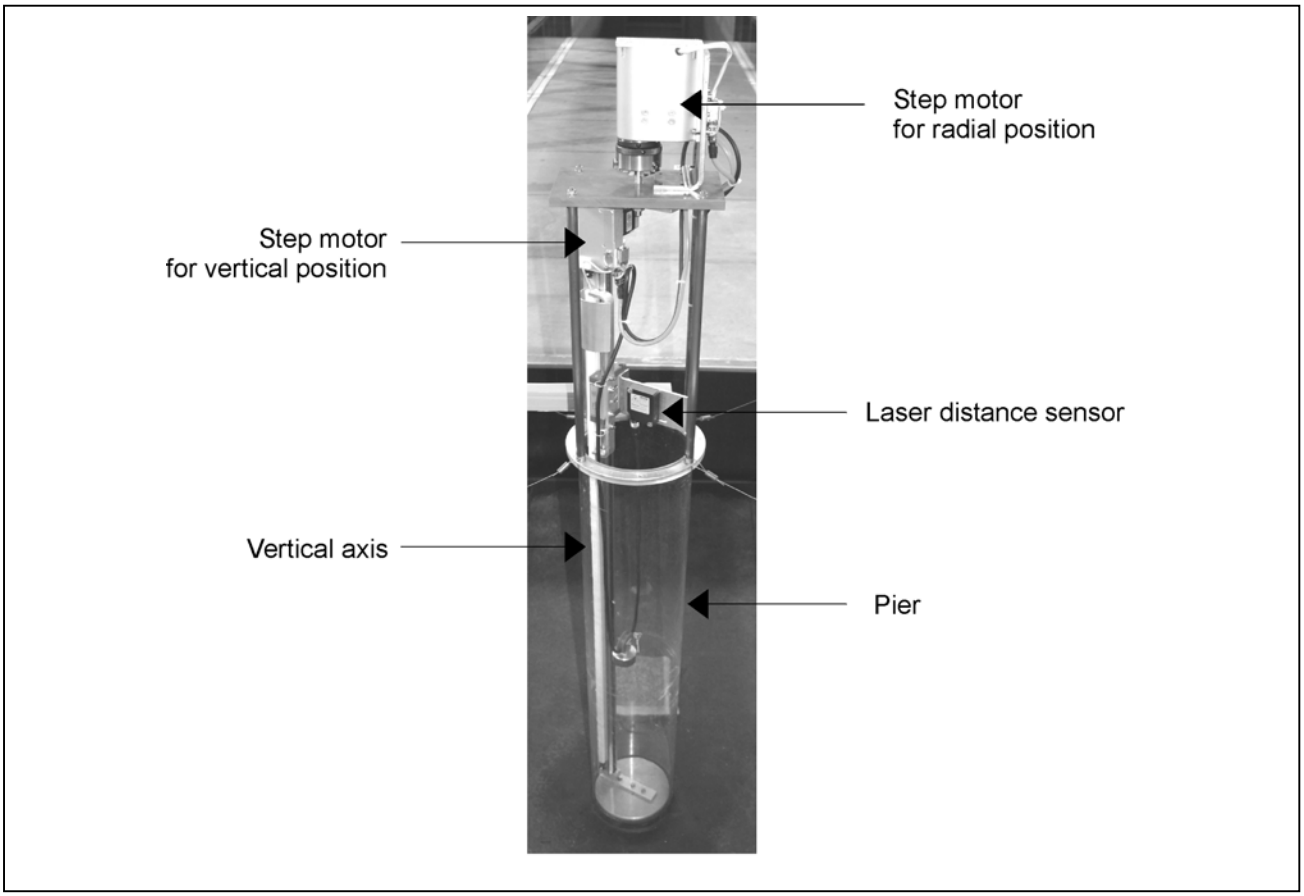

Figure 2. Measuring system inside plexiglas pier.

B. Procedure

Vertical profiles containing about 20-30 points were taken in 24 different directions around the pier by turning the distance sensor in steps of 15 degrees around its vertical axis. With these number of measuring directions scour-hole surface was satisfactory well aproximated.

Figure 3 shows the coordinate systems for the measurement of vertical profiles.

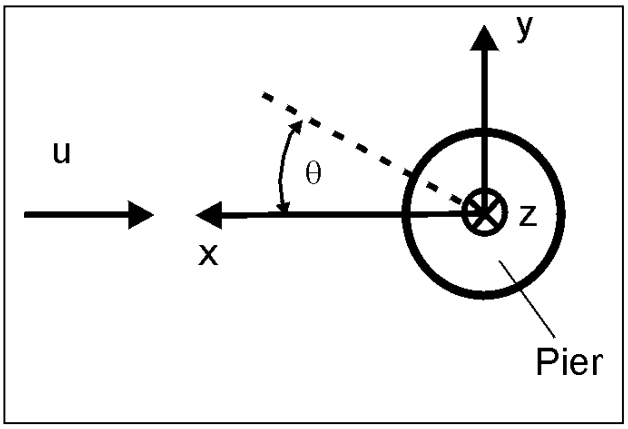

Figure 3. Coordinate system for the measurement of vertical profiles.

In order to compute maximum scour depth at each profile automatically, vertical steps were adjusted according to the actual radius measured by the laser distance sensor. In this way, when the sensor approached the scour-hole bottom, the vertical step was continuously reduced to a minimum value of 0.4 mm.

Point-data were aquired with a frequency of 70 Hz averaging 20 measurements per recorded surface-point. This technique allow a fast measurement of the complete scour-hole.

For instance, a measurement of the whole scour-hole topography took about 30 seconds at the beginning of the experiments and about 2 minutes at the end of them.

For determination of the coordinates of the measured surface-points position of the step-motors and time coordinate were recorded. Thatfore a real-time control and data acquisition system was implemented.

Since under the experimental conditions semi-equilibrium stage of scouring was reached after about 20 hours for the employed bed material, approximately 600 measurements of the entire scour-hole surface has been performed during a single scour experiment.

IV. MEASUREMENTS

Experiments with different section-average flow velocity, u_∞ have been carried out. Experimental runs were taken until quasi-equilibrium was reached, i.e. when maximum scour depth increased at a rate of about one representative particle diameter d_{50} per hour. Scour was studied under both, clear-water and live-bed conditions.

A. Vertical Profile in the Symmetry Axis at the Pier Front

Figure 4 shows typical vertical profiles in the symmetry axis at the pier front taken at different scour stages.

As reported by others, see e.g. reference [4] average angle of scour-hole slope is about 10 - 15% steeper than the natural repose angle of sediment particles. More

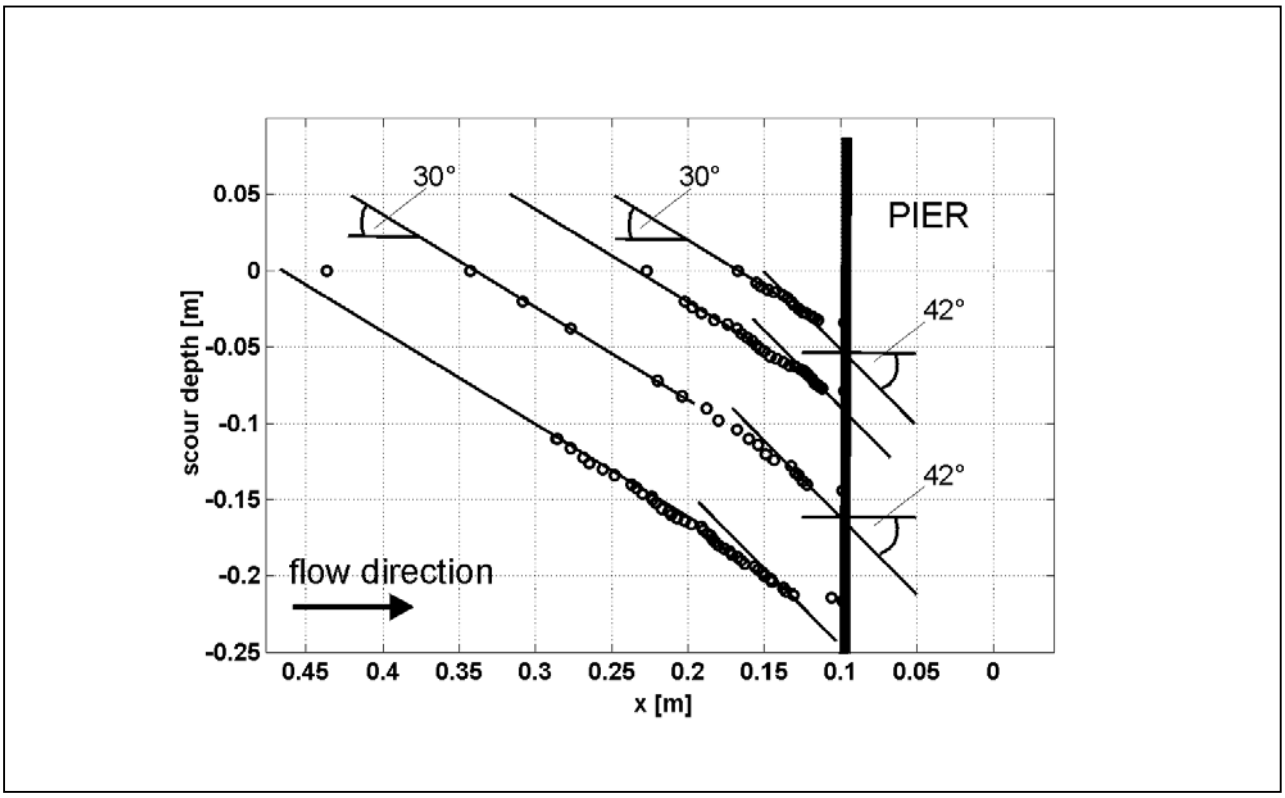

Figure 4. Vertical profiles in the symmetry axis at the pier front.

precisely, the scour-slope changes from the natural angle of repose to a steeper slope with an angle of 42°, i.e. about 40% higher than the natural angle of repose. This fact was confirmed in numerous scour experiments under different hydraulic conditions.

Surrounding the pier there is another change in scour-hole shape. In figure 5 this region is called scour-bottom.

Observation of scouring shows that sediment particles are transported upward in the steep slope region. Nevertheless, this transport is not a controlling scour mechanism.

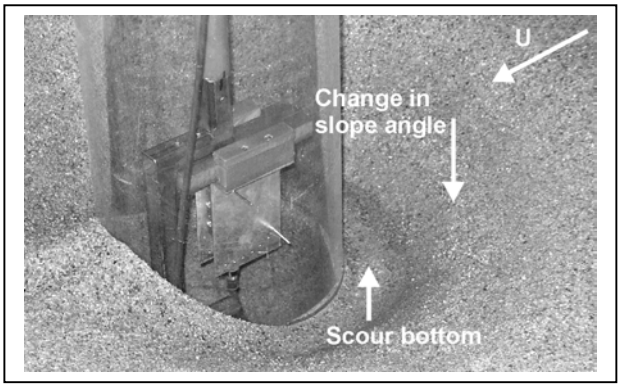

Figure 5. Scour shape.

Upward transport shows that vortex are present in the scour hole, as reported in references [9, 10]. The main action of these vortex on slope is not erosion, but stabilisation. Thus slope exhibit a steeper angle than thus of repose.

Figure 6 show the scour mechanism. Vortex V2 are neither stationary nor atached to a certain place in scour hole. They act along the steep slope region intermittently. When vortex intensity decrease, slope becomes unstable and failures i.e. side-slides take place constituting the dominant scour mechanism.

At the pier face contrarily, sediment transport due to direct vortex action of V1 dominate scouring, deepening scour hole and thus contributing to make steep slope unstable.

B. Scour-Hole Geometry

Figure 7 shows measurements of complete scour-hole during a 22 hours scour experiment with the developed technique. Measurements has been taken after time 0, 0.23, 0.36, 0.62, 0.87, 1.07, 1.42, 1.70, 1.92, 2.20, 2.57, 3.85, 4.62, 6.75, 8.67, 10.42, 11.83, 17.27, 18.00, 19.00, and 22.00 hours from scour begin.

Remarkably is that maximum scour depth takes about 50% of the time to reach equilibrium to move from the sides of the pier to the pier front.

Thus, scour monitoring in real sites should take position of maximum scour depth into account during scour development. If only pier front is monitored, maximum scour depth will not be detected and unexpected failure can occure.

Morover, laboratory experiments show that position of maximum scour depth will take a very long time to reach the pier front at relative low flow velocities i.e. below the critical velocity.

V. CONLCLUSION

An automatic non-intrusive measuring system for the measurement of the entire scour-hole geometry during running experiment has been presented.

The measuring system is composed by a laser distance sensor placed inside a plexiglas pier. The laser distance sensor is positioned in the vertical and in radial directions by two precision step-motors allowing the measurement of the scour radius at any point of the scour-hole.

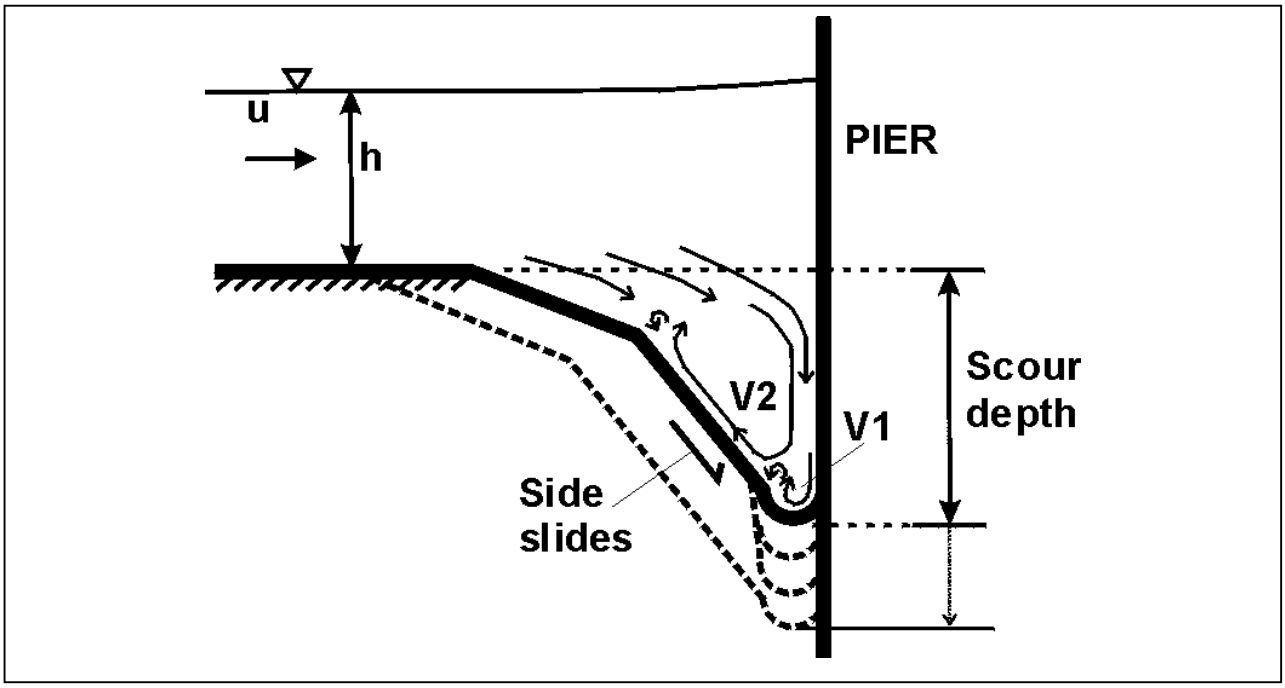

Figure 6. Scour mechanism.

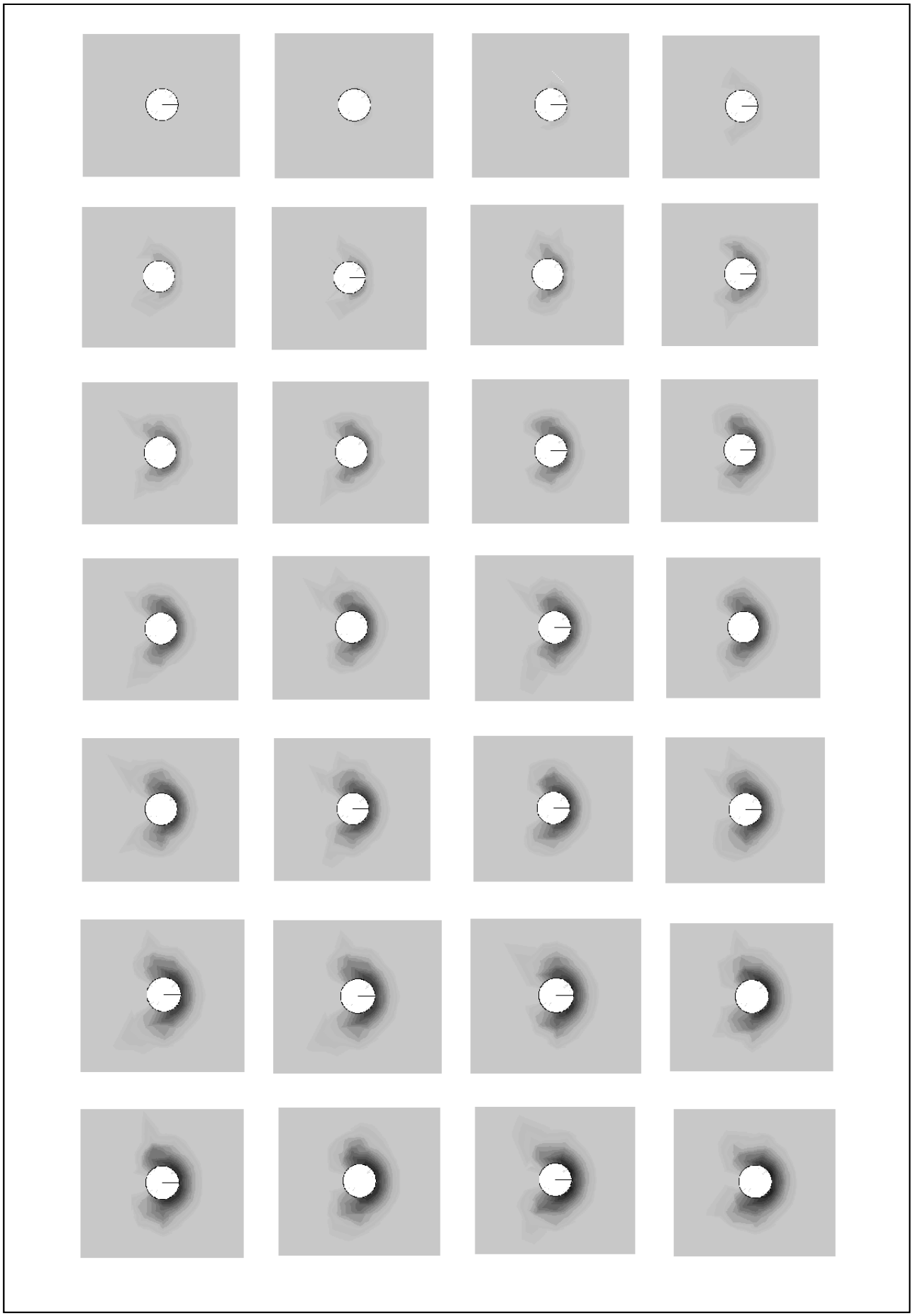

Figure 7. Measurement of scour depth during 22 hours.

The high data acquisition frequency of the measuring device allow to consider the measurments of the complete scour-hole instant measurements. Thus, time evolution of scour-hole geometry can be achieved.

Results show geometric properties of the scour hole. The slopes of the vertical profiles in the symmetry axis at the pier front evidence scour mechanism.

ACKNOWLEDGMENT

The first author thanks the financial support of the german academic exchange service DAAD through a PhD scholarship.

This study is part of the research project ZA 93/14-1 “Messung der Kolkentwicklung an Brückenpfeilern in sandigem Boden” (“Measurement of time-dependent scour at bridge piers in non-cohesive sediment”) founded by the German Research Council DFG.

.

REFERENCES

[1] Zanke, U., 1982, Grundlagen der Sedimentbewegung, Springer Verlag, Berlin.

[2] Oliveto, G. and Hager W., 2002, Temporal evolution of clear-water pier and abutment scour. *Journal of Hydraulic Engineering*. Vol. 128. Nr. 9. pp: 811-820.

[3] Oliveto, G. and Hager, W., 2005, Further results to time-dependent local scour at bridge elements. *Journal of Hydraulic Engineering*. Vol. 131. Nr. 2. pp: 97-105.

[4] Dey, S., 1999. Time-variation of scour in the vecinity of circular piers. *Proc. Instn. Civ. Engrs. Wat., Marit. & Energy*. Vol. 136. pp: 67-75.

[5] Müller, G., Mach, R. and Kauppert, K., 2001. Mapping of bridge pier scour with projection moiré. *Journal of Hydraulic Research.* Vol. 39. Nr. 5. pp: 1-7.

[6] Ballio, F. and Radice, A., 2003. A non-touch sensor for local scour measurements. *Journal of Hydraulic Research.* Vol. 41. Nr. 1. pp: 105-108.

[7] Olsen, N. and Melaaen, M., 1993, 3D calculations of scour around cylinders. *Journal of Hydraulic Engineering*, 119(9): 1048-1054.

[8] Yen, Ch., Lai, J. and Chang, W., 2001, Modeling of 3D flow and scouring around circular piers. *Proc. Natl. Sci. Counc. ROC(A).* Vol. 25. Nr. 1. pp: 17-26.

[9] Muzzammil, M. and Gangadhariah, T., 2003, The mean characteristics of horseshoe vortex at a cylindrical pier. *Journal of Hydraulic Research.* Vol. 41. Nr. 3. pp: 285-297.

[10] Unger, J. and Hager, W., 2005, Discusion of the mean characteristics of horseshoe vortex at a cylindrical pier. *Journal of Hydraulic Research.* Vol. 43. Nr. 5. pp: 584-587.

.

Unsteady bridge scour monitoring in Taiwan

J.Y. Lu, J.H. Hong, J.J. Li and C.C. Su
Nat. Chung Hsing Univ., Dept. of Civ. Engrg., Taichung, Taiwan, R.O.C.

Abstract

Fully understanding of bridge pier scour process during floods is very helpful for ensuring public safety and minimizing the repairing cost of vulnerable bridges. Many research papers have been published on the local scour of non-cohesive sediment around a pier based on the laboratory experiments with steady uniform flows. However, reliable field data for bridge scours during unsteady flows are still limited.

In this study, a field bridge scour experiment was conducted at Si-Lo bridge in the lower Cho-Shui River, the longest river in Taiwan. Total scour depths were successfully measured near a pier in the main channel using a sliding magnetic collar (SMC). In addition, a column of "numbered bricks" was installed about 100 m upstream of the bridge pier to measure the general scour. During Typhoon Mindulle (2004), the time variation of total scour was monitored continuously for about 24 hours. Emphasis was placed on the separation of general and local scours.

Many existing local scour formulas were selected to compare with the measured data. The local scour at a pier is time dependent. It was found that most of the existing local scour formulas tended to overestimate the pier scour. The "numbered bricks" and SMC were proved to be powerful tools for measuring the general and total scours near the bridge pier.

Keywords : Local scour, general scour, sliding magnetic collar, unsteady flow

I. INTRODUCTION

Bridge scour has an increasing worldwide awareness over the past decade. Scour is the erosion of the soil surrounding bridge piers and abutments by water. Scour around bridge foundation is the leading cause of bridge failure. In the US, Reference [1] reported that scour has been associated with 95% of all seriously damaged and failed highway bridges over waterways. Aggressive river scour has been blamed for the collapse of a river pier on a major bridge on the A12 motorway linking Munich and Verona near Kufstein in Austria in 1990 [2]. In Taiwan, several important bridges, including the Tou-Chien-Shi bridge, Chu-Tung highway bridge, Li-Kang bridge, and Kao-Ping bridge, collapsed seriously during Typhoon Herb in 1996. To avoid these failures, it is necessary to fully understand the causes and processes of bridge scour, especially during floods.

Most of the research on bridge scour has been conducted in the laboratory with equilibrium conditions, and with limited field data validation, e.g. [3, 4, 5]. As the floods in the natural rivers are unsteady flows, one may overestimate the scour depth if it is estimated based on the peak flow discharge. Many researchers also investigated the time variations of the scour depth under steady flows, e.g. [6, 7, 8].

Reference [9] measured the three-dimensional velocities, flow depths and streambed near bridge piers during floods on the Mississippi River, Brazos River and Sacramento River during 1993~1995 using a remote-control boat with ADCPs. The remote-control boat was proved to be an efficient and viable tool for data collection on small streams. However, this system may not applicable to rivers with highly turbulent or rapid flows. Instead of measuring the bridge scour for a particular flood event, Reference [10] installed sliding collar and sonar upstream of bridge piers in New York between August 1994 and February 1995 for a long term bridge scour observation. The transducer sometimes gave inaccurate data when exposed to air or because of the debris problem. Reference [11] observed the bridge scour using a ring with magnet sensor and found that the maximum scour occurred near the flood peak. It has to be pointed out that these three field studies only focused on total scour (local scour plus general scour) around the bridge piers. The separation of local scour from total scour was not considered.

Recently, pier scour subject to flood waves was investigated in the laboratory for clear-water scour conditions in reference [12]. A computational procedure for pier scour evolution under unsteady flow was proposed.

So far field measurements during the entire flood events for the live-bed scour conditions are still limited. During the floods, high sediment concentration and the debris problem are important characteristics for the ephemeral rivers in Taiwan. After careful consideration of the safety, reliability and the cost of instruments, a sliding magnetic collar probe (SMC) and the "numbered bricks" were used for measuring the total and general scours, respectively in this study. With proper separation of the general scour from the total scour, one can then calculate the local scour indirectly. This paper describes the scour monitoring system for collecting the scour data during floods. Results calculated from different existing local scour formulas were also compared and discussed based on the collected field data.

II. SITE DESCRIPTION

The abvoe-mentioned technique was applied to Si-Lo bridge, located downstream of Cho-Shui river, the longest river in Taiwan. Fig. 1 presents the location of the Si-Lo bridge as well as the Cho-Shui river basin. There is a groundsill about 100 m downstream of the Si-Lo bridge, where no riprap or gabion countermeasure was used to protect the piers. The drainage area upstream of the bridge is 2988 km^2. There is a stream-gauging station

named Hsi-Chou bridge located about 1 km upstream of the Si-Lo bridge. As there is no tributary between the Si-Lo bridge and the Hsi-Chou bridge, the flow discharge measured at the Hsi-Chou bridge is fairly close to that for the Si-Lo bridge. The channel slope at the site is about 0.001. Bed material samples indicate a median size d_{50} of 2 mm, with a geometric standard deviation σ_g of about 7.8. The 1.94 km long Si-Lo bridge, built in 1952, consists of 31 elliptical reinforced-concrete piers, with 62.5 m spans. The pier width and length are 3.5 m and 11 m, respectively.

III. DATA COLLECTION TECHNIQUE

It is very difficult and dangerous to collect hydraulic and sediment data in sufficient detail for bridge scour study during floods. Unfortunately, the scour occurs mainly during high flow conditions. A scour monitoring system consisting of numbered bricks and a sliding magnetic collar was applied to measure the time variations of the general scour and total scour, respectively in this study. With proper separation of the general scour from the total scour, one can then calculate the local scour indirectly. The detailed procedures are discussed in the following sections.

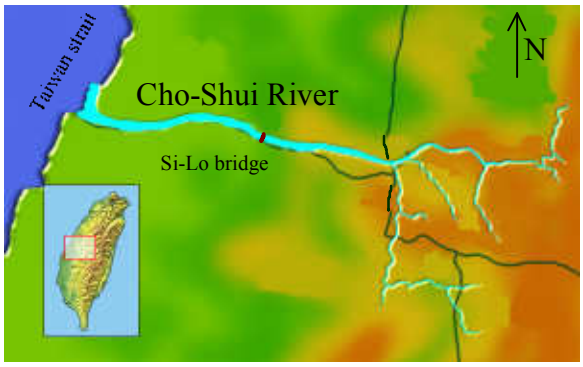

Figure 1. Location map of Cho-Shui River basin

A. *Total scour measuring equipment - sliding magnetic collar*

The sliding magnetic collar (SMC) measuring system was developed by the ETI Inc. for measuring the maximum total scour depth at piers. Both manual and automated-readout devices are available. An automated-readout device eliminates the need for a manual probe. However, it is not suitable for the high flow conditions during the floods since the junction of the wiring and the sliding collar pipe is vulnerable to damage from debris in the rapid flows. The manual-readout system consists of a stainless-steel support pipe, sliding collar and measurement probe. The steel pipe was placed vertically into the riverbed with the sliding collar that drops as the bridge pier scour progresses.

As shown in Figure 2, the sliding magnetic collar has cylindrical shape (165 mm in diameter, 178 mm high), with three round-bar magnets (22 mm in diameter, 76 mm long) fully enclosed in three stainless-steel housing to prevent corrosion. Also, a stainless-steel plate was added outside the SMC to minimize the possible damages due to debris impact. This modification is especially important for steep rivers with rapid flows such as those in Taiwan.

To determine the position of collar, a measurement probe consisting of a magnetic switch attached to a battery and buzzer on a long graduated cable was fabricated. In operation, the cable and probe was lowered through the center of the support pipe until the sensor was adjacent to the magnetic collar and activate a buzzer. The sliding magnetic collar position was located by using the cable to determine the distance from an established datum near the top of the support pipe to the magnetic collar. The graduation was added for a length of 10 m near the annunciator housing. The stainless-steel support pipe was manufactured in Taiwan. The upper end of the pipe was terminated with a locking cap near the handrail of the bridge sidewalk. The installation was completed by inserting the stainless-steel pipe into a predrilled hole. A staff gauge was set up on pier P15 for the observation of water level from the river bank or the bridge deck. Figure 3 shows a completed installation of a manual-readout sliding magnetic collar scour monitor at P16.

Figure 2. Sliding collar

Figure 3. Completed installation of the manual-readout SMC scour monitor

B. *General scour measuring equipment - numbered bricks*

A column of numbered bricks was placed at about 100 m upstream of pier P16 to measure the general scour. The bricks used in this study were the commercially available red bricks, 22 cm long, 9 cm wide and 5.5 cm thick. The top surface of each brick was continuously numbered with white paint. The top surface of the brick column was flushed with the initial riverbed. The location of the center of the brick column was accurately measured with a total-station transit. After the flood, again the center of the brick column was identified with accurate survey

using the total-station transit. The deposited material above the brick column was carefully removed with an excavator. The number on the first brick of the brick column was read and recorded. Therefore, the number of the bricks which was washed out with the flood and the general scour depth can be calculated. Figure 4 is a sketch showing the general and total scour measuring system at Si-Lo bridge.

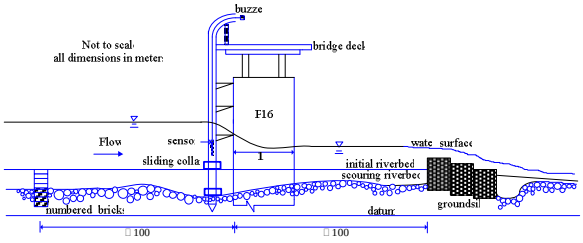

Figure 4. Schematic diagram of general and total scour measuring system at Si-Lo bridge

IV. FIELD MEASUREMENT DURING FLOODS

A stream-gauging station, namely, Hsi-Chou bridge was located at about 1 km upstream of the field measurement site, Si-Lo bridge. The flow discharge was about the same at these two stations as there is no tributary in between. During the period of observation (2003~2004), two flood events (Typhoons Dujuan and Mindulle) were investigated. For Typhoon Dujuan (Sept. 2 2003), it only rained in the upper Cho-Shui river basin, and no rainfall occurred near the field measurement site (Si-Lo bridge). Therefore, the maximum total scour depth at pier P16 and the maximum general scour at about 100 m upstream of Si-Lo bridge were only measured after the flood. On the other hand, the total scour depth was monitored continuously for about 24-hr using a SMC during Typhoon Mindulle (July 2~6, 2004). Fig. 5 shows the stage hydrographs at Hsi-Chou bridge for Typhoons Dujuan (Sept. 2, 2003) and Mindulle (July 2~6, 2004).

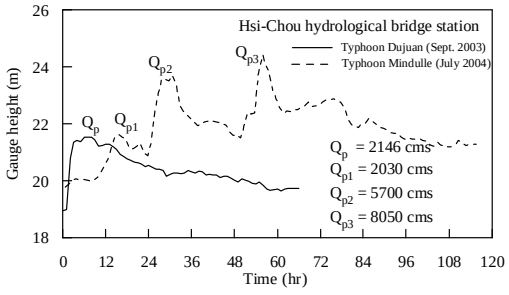

Figure 5. Stage hydrographs at Hsi-Chou bridge during Typhoons Dujuan and Mindulle

Typhoon Dujuan had a single peak flow discharge of 2146 cms, whereas Typhoon Mindulle had multiple peak flow discharges (2030, 5700 and 8050 cms). The duration of the peak flow for Typhoon Dujuan was longer than each of the three peak flows for Typhoon Mindulle. The slope of the rising limb for Dujuan was greater than that for the first peak discharge Q_{p1} of Mindulle, though they had very close flow discharge values. Also, the duration of the recession limb increased with the increase of the peak flow discharge for Mindulle.

Fig. 6(a) shows the temporal variations of flow stage at Hsi-Chou bridge and Si-Lo bridge for Typhoon Mindulle. Both stage hydrographs are fairly consistent as there is no tributary between these two bridges. Fig. 6(b) shows the temporal variations of total scour depth measured by the SMC at the pier P16.

Since the SMC was damaged at the largest peak flow (8050 cms), Fig. 6 only shows the results related to the first two peak flows (2030 and 5700 cms). The effect of the third peak flow (8050 cms) on the scour depth will be further discussed later.

As regards the relationship between the water stage and the scour depth measured by SMC, initially the scour depth increased rapidly (from 0.7 m to 2.7 m) during the first rising limb. After the first peak flow (Q_{p1} = 2030 cms), the scour rate decreased significantly during the first recession limb ($d_{TS} \cong 2.94$ m ~ 3.2 m). For the first flood peak, as shown in Fig. 6, the maximum scour depth occurred about 1 hr after the peak of the flow. The scour depth increased slightly during the second rising limb ($d_{TS} \cong 3.2$ m ~ 3.35 m), while it remained almost unchanged during the second recession limb.

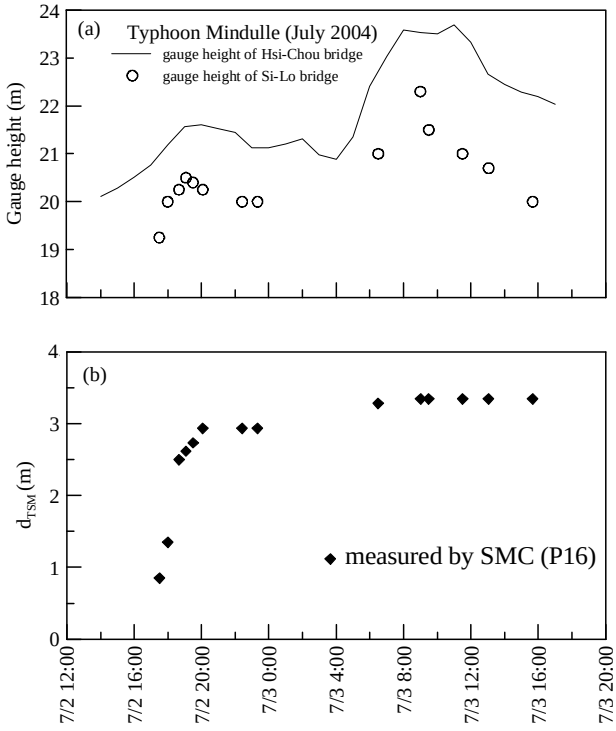

Figure 6. Relationship between measured scour depth and gauge height at Cho-Shui river near Si-Lo and Hsi-Chou bridge during Typhoon Mindulle

As mentioned before, SMC can only be used to measure the cumulative scour depth. It cannot detect the deposition of sediment since it dosen't move upward. The variation of total scour depth d_{TS} during the first recession limb can be further explained. For the first hour after the peak flow (Q_{p1} = 2030 cms), the approach flow decreased, but the intensity of the horseshoe vortex inside the scour hole was still high enough to move the sediment near the bottom of the scour hole. For the next 3.7 hrs [as shown in Fig. 6(b)], the approach flow further decreased, and the intensity of the horseshoe vortex inside the scour hole was too weak to move the sediment near the bottom of the

scour hole. The deposition might have occurred in the scour hole.

The first rising limb lasted about 2 hrs, and the first recession limb lasted about 4.7 hrs. A total scour depth of 2.94 m was associated with the first peak discharge. The scour action of the downflow associated with the second peak discharge (Q_{p2} = 5700 cms) was significantly damped out due to the "cushion effect" (increase of the flow depth).

V. COMPARISON OF MONITORING RESULTS WITH EMPIRICAL FORMULAS

After the floods induced by Typhoons Mindulle and Dujuan, general scour depths of 1.65 m and 1.10 m were measured at about 100 m upstream of P16 by excavating the pre-installed scour-brick column, respectively. Table I gives a summary of the measured and calculated data. There was a groundsill about 100 m downstream of Si-Lo bridge as shown in Fig. 4. It is reasonable to assume that the general scour depth was negligibly small near the groundsill. Therefore, the general scour depth at Si-Lo bridge can be obtained by linear interpolation. The net local scour depth caused by the pier can then be obtained.

TABLE I. SUMMARY OF MEASURED AND CALCULATED DATA

Si-Lo bridge	Typhoon Dujuan (2003)	Typhoon Mindulle (2004)
Peak discharge	Q_P = 2146	Q_{P3} = 8050
V	1.25	1.85
y	3.10	5.70
y/b	0.89	1.63
d_{TS}	2.92	3.35*
d_{GSU}	1.10	1.65
d_{GS}(at P16)	0.55	0.83
d_{CS}	0.125	0.230
d_{LS}	2.220	2.290
d_{GS}/ d_{TS}	0.188	0.248
d_{CS}/ d_{TS}	0.042	0.069
d_{LS}/ d_{TS}	0.770	0.683

Q_P, Q_{P1}, Q_{P2} = peak flow discharges (cms)
V = main channel approach flow velocity (m/s)
y = main channel approach flow depth (m)
* assume reached equilibrium condition.
d_{TS} = total scour depth at pier nose (measured by SMC at P16)
d_{GSU} = general scour depth measured at about 100 m upstream of P16 by brick column
d_{GS} = general scour at P16 by linear interpolation (assume no general scour at groundsill)
d_{CS} = contraction scour depth near pier (Laursen [13])
d_{LS} = local scour depth at pier nose [= d_{TS}-d_{GS}-d_{CS}]

As shown in Table I, the general scour depths 100 m upstream of Si-Lo bridge are 1.1 m and 1.65 m for Typhoon Dujuan and Mindulle, respectively. Although the maximum peak discharge of Typhoon Mindulle was about 4 times that for Typhoon Dujuan, the difference of general scour depth was only 0.55 m. This was mainly caused by the groundsill downstream of the Si-Lo bridge. The groundsill could restrict the lowering of the river bed for flows below a critical value. It can be noted that since the ratio of pier width to the pier centerline separation is very small (0.056), the calculated contraction scour depths were also very small in our study.

For Typhoon Mindille, the gauge height of the third peak was higher than the second peak for about 1 m when the flow discharge increased for about 2350 cms (see Fig. 5) because of the overflow of the floodplain. As shown in Table 1, the ratio of water depth to pier diameter (y/b) at the third peak flow during Typhoon Mindulle was about 1.63. Fig. 7 is a relationship between the dimensionless local scour depth d_{LSE}/b and the dimensionless flow depth y/b based on the experimental data collected by Melville and Coleman [14]. As shown in the figure, the increase of the the local scour rate significantly reduces when y/b exceeds about 1.5. A fitted curve is also added by the writers to more clearly demonstrate the trend. In the natural river, the live-bed scour occurs frequently, where the sediment particles fill into the scour hole and reduce the net local scour depth. Therefore, the local scour increasing rate reduces even faster with an increase of y/b for the live-bed scour condition. Even though the scour monitoring equipment was damaged after the second flood peak during Typhoon Mindulle, the difference between the total scour depths at the third and the second flood peaks was probably fairly limited.

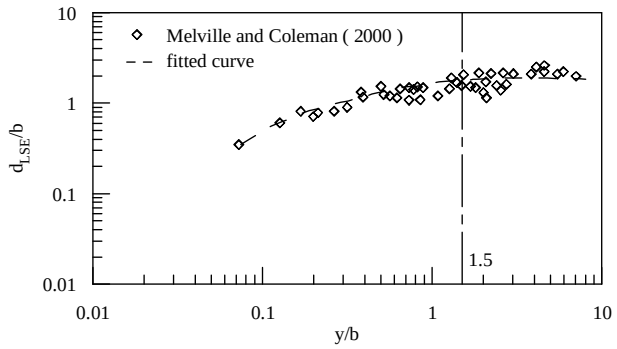

Figure 7. The influence of flow shallowness on local scour depth

With the assumptions of linear change of general scour and zero scour at groundsill, the general scour at P16 can be estimated. The net local scour depth can then be obtained by the proper separation. Table 1 indicates that the ratio of the local scour to total scour decreases with an increase of the flow.

The interaction between channel environment and bridge is so complex that even with considerable laboratory and prototype studies, estimation of scour depth and its geometry in a generalized and accurate form are still very difficult. Based on the peak flow discharges (as was assumed by most of the local scour estimations), the differences between the observed and computed local scour depths for the selected formulas are listed in Table II. None of the formulas consistently computed a scour depth that closely matched the observed scour depth for the measured conditions. In general, most formulas overestimated the local scour. Shen et al. [4], Jain and Fischer [15] and HEC-18 [1] gave better predictions (value of d_{LSE}/d_{LSM} closer to 1). However, it has to be point out that the comparison was based on the peak flows, which may also somehow overestimate the local scour depth.

References [14, 16] indicated that many laboratory experiments have been undertaken using sands to model sand bed rivers. In general, water depth/pier diameter ratio y/b, dimensionless flow intensity V/V_c, sediment characteristic variables (b/d_{50} and geometric standard deviation σ_g) are the most important parameters in local

scour. Both parameters y/b and V/V_c are relatively easier to model in the laboratory. For comparison, data ranges of the parameters for different studies are summarized in Table III. As shown in Table III, the σ_g value in our field experiment ($\sigma_g = 7.8$) was higher than those for all of the laboratory studies listed in Table III. When the gradation of the bed material is large for a natural river, the bed armoring (or sheltering effect) may occur during a flood. Among the local scour formulas compared in this study, HEC-18 [1] was the only one considering the bed armoring effect. As a result, it was also one of the most accurate formulas for predicting the local scour depth based on our field data. Furthermore, the overestimations were also affected by the flood durations since the flows were not under equilibrium conditions for peak discharges.

TABLE II. COMPARISON WITH LOCAL SCOUR FORMULAS

Investigators	Typhoon Dujuan d_{LSM} = 2.22 m Q_p = 2146 cms		Typhoon Mindulle d_{LSM} = 2.29 m Q_{p3} = 8050 cms	
	d_{LSE}	$\frac{d_{LSE}}{d_{LSM}}$	d_{LSE}	$\frac{d_{LSE}}{d_{LSM}}$
Neill [3]	5.15	2.32	6.08	2.66
Shen et al. [4]	2.94	1.32	3.67	1.60
Breusers et al. [5]	4.63	2.09	5.83	2.55
Jain and Fischer [15]	3.01	1.36	4.75	2.07
Froehlich [16]	4.55	2.05	6.51	2.84
HEC-18 [1]	3.30	1.49	4.62	2.02
Melville and Coleman [14]	6.79	3.06	8.40	3.67
Note: $d_{LSM} = d_{TS}-d_{GS}-d_{CS}$, d_{LSE} = calculated by formulas				

TABLE III. SUMMERY OF DATA RANGES FOR DIFFERENT STUDIES

Data source	y/b	V/Vc	b/d_{50}	σ_g	Note
Shen et al.[4]) & HEC-18[1]	0.67~ 2.33	0.54~ 5.14	331~ 1988	1.37~ 2.18	Lab
Jain and Fischer [15]	2.01~ 4.86	0.79~ 3.00	20~ 406	1.25~ 1.34	Lab
Melville and Coleman [14]	0.67~ 11.81	0.50~ 4.56	4~ 1000	1.30~ 5.50	Lab
Sheppard et al. [17]	0.19~ 11.14	0.75~ 1.21	143~ 4155	1.21~ 1.51	Lab
Landers and Mueller [18] - data only	0.12~ 23.0	0.70~ 49.6	9~ 17929	1.30~ 12.1	Field
Typhoon Dujuan (2003) Q_p	0.89	0.87	1750	7.8	Field
Typhoon Mindulle (2004) Q_{p3}	1.63	0.92	1750	7.8	Field

VI. CONCLUSIONS

Based on this case study, the following conclusions can be drawn:

1. The sliding magnetic collar (SMC), and the numbered brick column are useful tools to measure the total bridge pier scour and the general scour in ephemeral rivers. With proper separation of the general scour and contraction scour from the total scour, the true local scour at the pier nose can be obtained. The above bridge scour monitoring system had been successfully applied to continuously measure the bridge scour depth for about 24 hrs in the lower Cho-Shui River, the longest river in Taiwan, during Typhoon Mindulle.
2. In this study, the general scour depth at about 100 m for upstream of the bridge pier was measured and used to estimate the general scour at the bridge pier by linear interpolation. The local scour depth at the pier was then calculated by subtracting this estimated general scour depth and the contraction scour depth from the total scour depth. This strict procedure is a more reasonable estimation of the "pure local scour depth." The ratio of the local scour to the total scour decrease with an increase of the flow discharge.
3. Based on the peak flow discharge, Shen et al. [4], HEC-18[1], Jain and Fischer[15] gave reasonably good predictions ($1 < d_{LSE} / d_{LSM} < 2$) for our field data. Calculations based on the peak flow discharges tended to overestimate the scour depths. For practical applications, one may select the proper formulas based on his safety requirement.
4. When the gradation of the bed material is large for a natural river, the bed armoring (or sheltering effect) may occur during a flood. Among the local scour formulas compared in this study, HEC-18 [1] was the only one considering the bed armoring effect. As a result, it was also one of the most accurate formulas for predicting the local scour depth based on our field data.

ACKNOWLEDGMENT

This work was supported by the Water Resource Agency of R.O.C. The writers would like to express their appreciation to Prof. Chang Lin, Nat. Chung Hsing Univ., and Prof. Chuan-Yi Wang, Feng Chia Univ. for their valuable suggestions and technical assistance.

REFERENCES

[1] E. V. Richardson and S. R. Davis, "Evaluating scour at bridge." FHWA-IP-90-017, U.S.A, 1995.

[2] M.C. Forde, "Not destructive evaluation bridge of research in progress." In : Recent Advances in Engineering Bridge, Barcelona, 1996.

[3] C. R. Neill, ***River–bed scour***, Research council of Alberta Contribution no. 281, Canadian Good Roads Association, 1964.

[4] H. W. Shen, V. R. Schneider, and S. S. Karaki, "Local scour around bridge piers." ***J. Hydr. Div.,*** ASCE, vol. 95, no.6, pp. 1919-1940, 1969.

[5] H. N. C. Breusers, G. Nicollet, and H. W. Shen, "Local scour around cylindrical piers." ***J. Hydraul. Res.,*** IAHR, vol. 15, no. 3, pp. 211-252, 1977.

[6] R. Ettema, ***Scour at bridge piers***, New Zealand : University of Auckland, School of Engineering, Rep. no. 216, 1980.

[7] A. M. Yanmaz and H. D. Altinbilek, "Study of time-dependent local scour around bridge piers." ***J. Hydr. Eng.***, ASCE, vol. 117, no. 10, pp. 1247-1268, 1991.

[8] B. W. Melville and Y. M. Chiew, "Time scale for local scour at bridge piers," ***J. Hydr. Eng.***, ASCE, vol. 125, no.1, pp. 59-65, 1999.

[9] D. S. Mueller, "Scour at bridge-detailed data collection during floods." ***Proc., Sixth Federal Interagency Sedimentation Conf., FISC-6,*** Las Vegas, Nevada, U.S.A., vol. 4, pp. 41-48, 1996.

[10] G. K. Butch, "Evaluation of selected instruments for monitoring scour at bridges in New York." ***Proc., Sixth Federal Interagency Sedimentation Conf., FISC-6,*** Las Vegas, Nevada, U.S.A., vol. 4, pp. 33-39, 1996.

[11] J. Fukui and M. Otuka, "Development of new inspection method on scour condition around existing bridge foundations." ***Proc., ICSF-1, Texas A&M Univ***., College Station, Texas, U.S.A., pp. 410-420, 2002.

[12] G. Oliveto and W.H. Hager, "Further results to time-dependent local scour at bridge element," ***J. Hydr. Eng.,*** ASCE, vol. 131, no. 20, pp. 97-105, 2005.

[13] E. M. Laursen, "Scour at bridge crossings." Bulletin No.8, Iowa Highway Research Board, Ames, Iowa, U.S.A, 1958.

[14] B. W. Melville, and S. E. Coleman, ***Bridge Scour***, Water Resources Publications, LLC, Highlands Ranch, Colorado, 2000.

[15] S. C. Jain and E .E. Fischer, "Scour around bridge piers at high flow velocities," ***J. Hydr. Div***., ASCE, vol. 106, no. 11, pp.1827-1842, 1980.

[16] R. Ettema, B. W Melville, and B. Barkdoll, "Scale effect in pier-scour experiments." ***J. Hydr. Eng.,*** ASCE, vol. 124, no. 6, pp. 639-642, 1998.

[17] D. M. Sheppard, M. Odeh, and T. Glasser, "Large scale clear-water local pier scour experiments." ***J. Hydr. Eng***., ASCE, vol. 130, no.10, pp. 957-963, 2004.

[18] M. N. Landers and D. S. Muller, ***Channel scour at bridges in the United States,*** FHWA-RD-95-184, U.S.A, 1996.

Pairing riverbanks instability and fluvial hydraulics for the prediction of risk zones on a river undergoing dam break flooding

T. Mahdi
Ecole Polytechnique de Montréal (Québec), Canada

ABSTRACT: The safe operation of dams requires a good assessment and understanding of the involved risks of their failure. The direct consequences are usually considered to be limited to the maximum flooding zone created downstream. However, considering the magnitude of the dam-break flows, the riverbed could undergo deep changes. The simulation of the evolution of river reaches resulting from such catastrophic events is performed by coupling the hydraulic and sediment transport numerical model GSTARS with a slope stability model that is based on the Bishop's simplified method, which we recently developed. This paper presents a novel methodology for the delimitation of the veritable safety zone along river banks by taking into consideration not only the flood risks but also the possible induced landslides. Validation tests are performed on specific reaches of the Outaouais River (Quebec).

1 INTRODUCTION

Dams, especially those of significant height and large reservoirs' capacity were always subject in Quebec to careful inspection, monitoring and management. However, some recent events (such as Lake Beloeil, Chicoutimi River, Ha! Ha! River, Quebec, Canada) are a clear reminder that dam failures, piping failure breaches, and overtopping due to insufficient spillway capacity during large outflows are quite possible. Precipitation-runoff floods and dam failure floods result in an unusual rapid water surface elevation, and high velocity outflow through the downstream river. The inundation of river banks may cause significant erosions, important landslides and creates potentially unstable embankments, as those observed in the aftermath of the Saguenay floods in 1996. As the main goal is the protection of life and property, it is difficult to restrict the hazard potential to the only inundation zone, without considering the final extension of the larger damaged area. This wider zone may include areas with elevation higher than the maximum water level reached by the flood. The delineation of the evacuation zone of the population should be therefore extended.

The simulation of dam-break floods are essentially carried out using numerical models with fixed bed assumption (except MIKE 21 and TELEMAC models). The bathymetry and the topography of the river valley are then considered invariant and the erosion of river bed and river banks with sediment depositions are all neglected. However, the river beds and their banks are movable and sometimes unstable. Under these conditions, can one really assume that the forecasted impact and damage generated in the downstream river valley by a possible dam failure would be limited to the only consequences of the rise of waters?

The problem addressed in this paper is the definition of risk zones that are potentially at risk during a dam break by taking globally into account the maximal water level, sediment transport at the river bed and eventual induced landslides. Unlike inundation studies, our approach to the problem is based on a careful analysis of the geotechnical and topographical characteristics of the floodable zone and its neighbourhood. Such analysis allows an accurate characterisation of the erodible zones and zones of reduced stability. The solution method requires a further analysis of the flood flow in order to evaluate the potential of soil wrenching and local transport and also requires a stability analysis of river banks to identify the zones of potential landslides and include them in the risk zones.

The proposed solution uses advanced knowledge of the hydraulic and geotechnical aspects of the problem and their combination is fundamental for the comprehension of the processes involved and for the methods used to achieve the analysis. The methodology suggested in the sequel outlines our approach to the problem. To accurately study the evolution of the river bed and river banks under the impact of a dam-break flood wave, it is necessary to implement an incremental procedure and include to the hydraulic simulations the riverbanks analyses and the latest modifications of the bathymetry. It is therefore necessary to take into account the new bathymetry at the next time step and continue the hydraulic calculation. The details of the calculation scheme are explained in the following sections. This procedure is applied to a reach of several kilometres of Outaouais River upstream of Notre-Dame-du- Nord (Quebec).

2 METHODOLOGY

The phenomenon of erosion and landslide are complex processes because they depend on several characteristics such as geological, geotechnical and hydraulic conditions and involve various parameters which are seldom considered simultaneously. Moreover, the lack of the fundamental knowledge of the phenomena could hinder its realistic simulation. The complete gathering of the field data and detailed numerical modeling of the phenomena require considerable resources, especially if one is interested in studying a long reach of the river valley.

The large outflows associated with the dam-break flood wave can cause in various zones significant modifications to several sections of a river. The average slope of the bank profiles of these sections, in equilibrium before the failure, can exceed the angle of repose of the talus slope following erosion resulting from the rupture.

The adopted approach is based on a sediment transport model, able to evaluate the evolution of the river's sections under the effects of erosion, coupled with a slope stability calculation model for the river banks. The stability of the banks can be assessed at any time of the dam failure hydrograph. The valuable information regarding the erosion and bank stability is therefore available for all the sections of the river. The approach is based on a combination of two models GSTARS (river erosion) and BISHOP (slope stability), which will be presented in the following sections. After a short description of the models coupling, the algorithm for the simulations will be discussed in more details.

2.1 GSTARS model

The Generalized Stream Tube model for Alluvial River Simulation (GSTARS, Yang et al., 1998) is a one-dimensional hydraulic and sediment transport model for use in natural rivers and manmade canals. The model was developed by the U.S. Bureau of Reclamation.

The sediment transport calculations are carried out after the evaluation for each flow, of the backwater curve obtained using a one dimensional model along the river reach being studied. This hydraulic model allows the computation of quasi-steady flows for which the discharge hydrographs are approximated by bursts of constant discharge. The hydraulic computations allow therefore the use of conceptual stream tubes along the whole river reach while adapting locally to the existing conditions at some sections. A sediment routing and transport calculations are then performed for each stream and sediment size fractions. GSTARS offers various formulae of sediment transport depending on the existing soil conditions and sediment types of the section along the reach. For each section, GSTARS takes into account the balance of the volumes of bed sediment erosion and deposition. This allows the detection of the sections which may undergo erosion or global accretion.

One of the features that GSTARS offers is the capability of varying and adjusting the form of the section. In the event of total erosion, GSTARS will not systematically deepen the section to remove the necessary volume. Other adjustments can also be achieved by widening the cross section. The choice of deepening or widening of the section is commanded by the minimization of the total stream power of the reach.

2.2 BISHOP model

The BISHOP model was developed in order to carry out and automate the stability analyses of river banks. This model, which is subsequently coupled to the model GSTARS, is capable of taking into account the groundwater level distribution and the hydrostatic pressure of water in the river. Landslides calculation with the BISHOP model are based on circular slip surfaces

Program BISHOP determines a safety factor evaluating the potential risk of a landslide a long the river bank using the Bishop's simplified method (Phillipponnat and Hubert, 1997). For each river bank (two banks per hydraulic section), this model determines automatically the slip-circle having the minimal safety factor. It is thus possible to determine the length of retreat of the edge of the bank following a landslide. This allows the calculation the setback length of the edge of the river bank after a landslide. The setback length is subtracted from the edge position of the river bank determined by GSTARS. In this regard, the maximum extent of the soil erosion-landslide is determined at every moment and after the flooding, which allows the delineation of the safety zone as a preventive approach in the event of dam break.

2.3 Coupling GSTARS/BISHOP

The model GSTARS is launched by setting the conditions before the dam-break and using the flood's hydrograph. One of the results files of GSTARS describes the time dependent evolution of the sections. Several possibilities of data processing can be considered.

It is possible to transfer the characteristics of the sections and water levels at regular intervals to the BISHOP model in order to test the stability of the river banks during the flood event. This approach allows the monitoring of the evolution of the river banks stability and the assessment of the onset of bank instability which require an intervention of the civil authorities.

In the event of bank failure, the new geometry of the sections will be taken into account and the numerical simulations are carried out for the next time step using GSTARS. The transfer can also be only applied to the conditions after the passage of dam failure hydrograph. The assessment of stability in this case should be rather perceived for long-term.

2.4 Flow chart of calculations

The flowchart depicted in fig.1 explains the various logical steps leading to the predictions. The first step is the input of the hydraulic and geotechnical data (stratigraphy, cracking formation on the slope top, talus actual height and natural angle of river banks), which are supplemented by the test results carried out on some collected samples (granulometry, liquid limits and plasticity limits, cohesion and critical shear stress). An assessment of the state of natural stability is obtained.

In the second step, we consider successively the various possible scenarios of dam failure for which the following procedures will be reiterated. Analyses of hydraulic calculations specific to each scenario and to each zone being studied provide the evolution of the flow, the water level and velocity speeds and therefore the evolution in time of the shear stresses that are applied to the river bed.

In our approach, we simulate step by step the time evolution of the river reach subjected to the potential dam-break flow. We take into account simultaneously the hydraulic and geotechnical aspects and their coupling. Indeed, each section of this river reach undergoes changes caused not only by the river hydraulics, mainly sediment erosion and deposition but also by the possible landslides which eventually change the river bank profiles. Both mechanisms develop in parallel.

The initial hydraulic and geotechnical characteristics are first defined and then will be used for testing the slope stability for various sections that are representative of the river reach before the dam-break. The hydraulic and sediment transport model GSTARS determines the flow characteristics and the erosion potential of the bed for each time step. In the absence of erosion, the analysis is advanced for the next time step. If the erosion occurs, at least around one river bank, the new sections representing the bed at the end of the time step are tested for the stability of their slopes. Stability is evaluated for drained conditions for the first potential profile slide and with none drained conditions afterwards. The Bishop's simplified method is adopted for the analysis of stability and the search for the location of the centre of the slip-circles is automated. In the absence of rupture for all the sections, the simulation is advanced to the next time step. If there is rupture, the profiles representing the unstable slopes are modified based on a distribution rule of the mass wasting deposits of the unstable talus of the section being studied and the calculation are carried on (for the next time step) using the hydraulic-sediment transport model. The simulation is ended by a long-term stability analysis using the river sections obtained after the passage of the dam failure hydrograph.

Using this approach, we can draw a map delineating the zones of ultimate limits of instability, i.e. by extending the zone of instability which may develop in the long term, even when the condition are back to normal.

Although this methodology is based on recent and reliable models which are in routinely improved, when analyzing the results it is always important to bear in mind the inherent random aspects that are specific to the geotechnical characteristics and the fact that the solid transport laws are essentially valid in a steady state regime. Their extension to unsteady flood flow regimes is not straightforward.

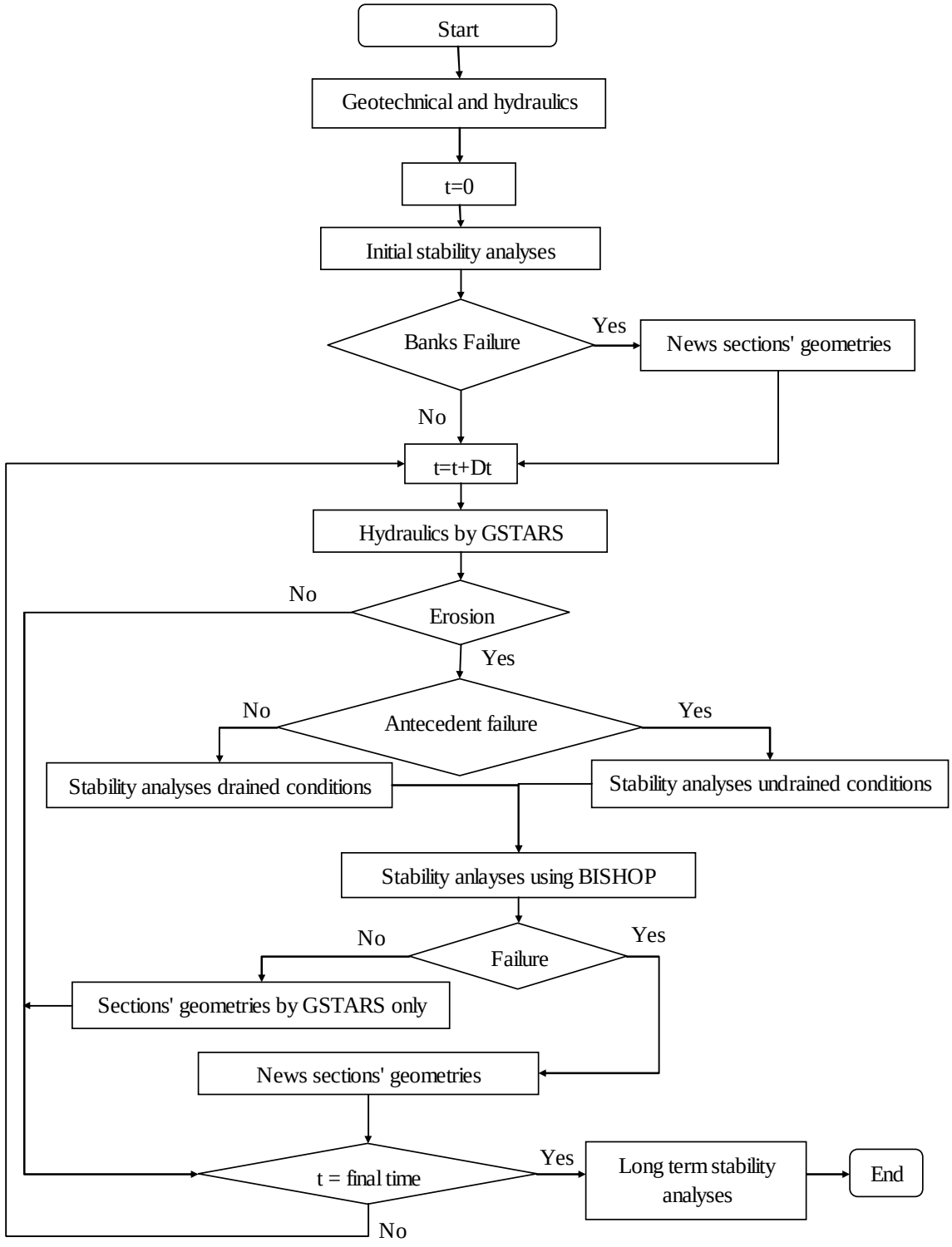

Fig.1. Detailed analysis methodology.

2.5 Definition phase of risk zones:

Once the simulations are completed, the cumulative results obtained using this approach allows a cartographic characterization of the risk zones, which may

be unstable according to the prescribed conditions and assumptions. The risk zones can be drawn on a digital map representing the river reach being studied. A legend representing the setbacks and depicting the position, color and line thickness along the initial river bank edges allows a better visualization of the risk zones.

3 APPLICATION TO THE OUTAOUAIS RIVER REACH

A river reach located between the Dam "Première Chute" and lake "Témiscamingue" was selected as a demonstration site for the proposed approach. The presence of cohesive sediments along the river and the steepness of slopes of the local banks make this location an ideal study site.

3.1 Site description

The reservoir "Première Chute" is the last constructed dam on the "Outaouais supérieure" before the river mouth discharge in the "Lake Témiscamingue". Approximately seven kilometres separate the dam from the northern entry of the "lake Témiscamingue" by the Outaouais River. Just after the dam exit, where the flow is westward, the river undergoes an elbow change in direction towards the north then returns along a gradual curve to the south-west direction. At the exit of the dam, the river bed is broad and one notices the presence of an island made up primarily of rock and debris. Afterwards, the river narrows gradually and then remains almost of constant width until the bridge "Notre-Dame du Nord" at 3.3 kilometres. Finally it widens towards the "lake Témiscamingue" at the junction of "la Pointe Miller". On most parts of the reach, the river banks are high, abrupt and susceptible to erosion.

The data characterizing the river banks is collected from several sources. Two technical reports were published by Hydro-Quebec: St-Arnaud (1981) and Lalonde el al. (1981). Thibault (2000) summarized the data available by compiling information obtained from Hydro-Quebec and the Transport Department. Aerial photographs were used to carry out a photo-interpretation of the studied reach. Geotechnical drillings were also carried out in the area. Observations and field studies on the ground were conducted to assess the vegetation cover, the height and the angle of the slopes. Soil samples were collected and used for geotechnical measurements and analysis. To validate and update these data, a field visit to the study area was organized by researchers from École Polytechnique (Quebec) and the Laval University (Quebec) between the 4 and September 8, 2000. During this period, comprehensive information was collected regarding the geometry of the river banks, the active erosion zones, the recent slips and landslides. Soil samples of were collected for further analysis and the bathymetry of the river was updated and completed. Finally, several technical reports regarding landslides were consulted during a visit to the city hall of the municipality of "Notre-Dame-du-Nord". A first compilation of this data will be presented in the next section.

3.1.1 Characteristics of the soil of the river banks

The area of the river being crosses a zone of clay deposits that were formed after the retreat of the glaciers. The major parts of the river banks therefore consist of clay with sand layers at the surface (0.5 to 1.5 m) in several locations. Drillings show the presence of a layer of granular soil of several meters of thickness beneath the layer of clay. The height of the talus slopes decreases towards downstream. Several elements control the river course or limit the bank and bed erosion. For instance, an increase in the width of the river downstream the bridge would be caused by the proximity of a rock base under the western abutment of the bridge. The deviation of the river at 1500 m upstream of the bridge could be explained by the presence of a bottom rock base at a lower depth under the sand point of the left bank. The observed clay is varved and characterized by the alternation of dark layers (very argillaceous) and pale layers (fairly silted). Table 1 presents a summary of results obtained from laboratory and field tests. The low values of the shear stress strength show that clay is sensitive to remolding, but not low enough to produce quick clay flow. However, erosion at the talus toe is more obvious on most parts of the river.

Table 1. Geotechnical data

Parameters		Results	
Granulometry (< 2 □ m)	Clay layer	80% to 90%	
	Silt layer	35%	
Moisture content (W)	Clay layer	60% (<I_l)	
	Silt layer	25% to 35% (~ I_l)	
Vane test Nilcon	Undrained cohesion (Cu)	Near the surface	90 kPa
		6.5 m	45 kPa
		> 6.5 m	Increase by 2 to 3 kPa/m
	Remold undrained cohesion Cur	2 to 4 kPa for 6 m of depth	
Swedish fall cone test	Remold undrained cohesion Cur	4 to 12 kPa	

3.1.2 River bank topography

The height of the river banks decreases in the downstream from 25 m, near the power station, to reach 5 m at the mouth of Lake Témiscamingue. The average slopes are about 20 to 25 degrees. Only the right bank area, close to the old camp-site, presents an almost vertical slope (see Figure 6). The depth of the thalweg and the angles of the river banks were determined.

The banks do not go downwards with a mild slope into the river. There is often a terrace of approximately 1 m. After this terrace, the banks ascent up according to the average slope. Breaks on the slope can be observed in the cases of former circular slip surfaces.

Observations regarding the height and the average slope angles were made for many sections of the Outaouais River, for both sides of the river banks. It is noticed that in general, the right bank is higher than the left bank, the river having crossed a tilted plateau and going downward the South-East. Moreover, the steep angles observed towards the right bank lake are probably due to the erosive action of the wind generated waves by the winds on the lake.

3.1.3 Normal hydraulics conditions

The hydraulics turbines at the hydroelectric power plant of "Première Chute" need a maximum flow rate of 630 m³/s and the maximum capacity of the spillway is 3033 m³/s. The maximum flow rate at the site will never exceed 3663 m³/s. The water level of "Lake Témiscamingue" influences the downstream reach of the river. This water level (maximum of 179 m) depends on the flow rate and the lake management.

3.1.4 Dam break's hydraulic conditions

The scenario used for this application corresponds to the cascading failure of the upstream dams of ''Rapide des Quinze'' and ''Rapide des Iles'' causing the dam break of "Première Chute". Fig.2 illustrates the dam break hydrograph at "Première Chute" with a maximum of 9780 m³/s.

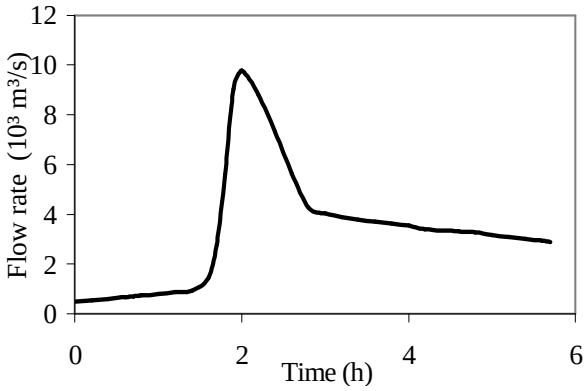

Fig.2. Dam break flood hydrograph at ''Première Chute''.

3.2 Results

Fig.3 shows the evolution of river bottom at a typical section (section 46) during the passage of the dam break flood. After 8 hours, the average erosion stabilized around 0.5 m.

Fig.4 illustrates the right bank retreat evolution at the same section. As long as the safety factor is greater than 1, the retreat is nil and it starts after 3 hours to stabilize around 4.25 m after 8 hours.

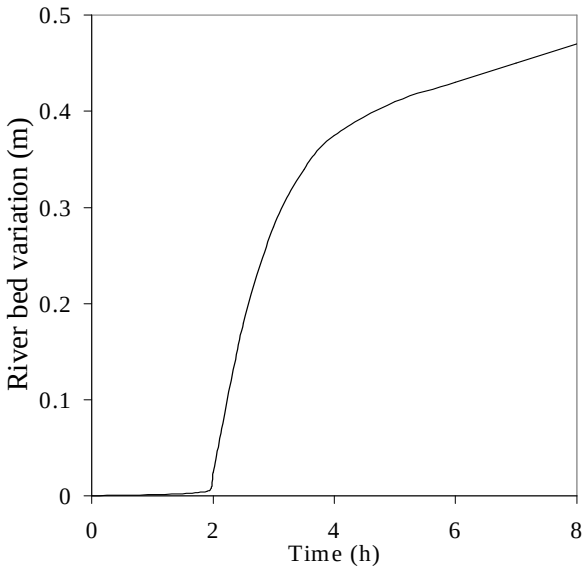

Fig.3. River bed Variation at section 46 during the dam break flood.

This methodology allows the monitoring of the safety factor of all the hydraulics sections along the Riverbanks. Fig.5 shows an example.

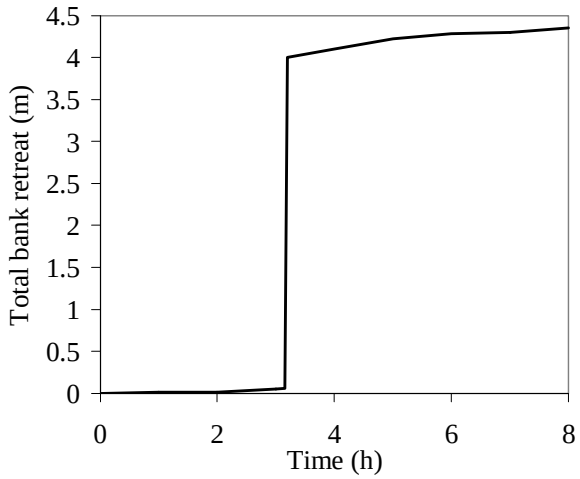

Fig. 4. Right bank retreat evolution at section 46 during the dam break flood.

3.2.1 Definition of risk zones:

A map of the risk zone is presented in fig.6 (exaggerated graphically by ten folds). The zone the most potentially affected would be out located at the right bank at the mouth outlet of the river into the lake. Setbacks reaching 80 m are predicted, but this are is unpopulated. Around the bridge of Notre-Dame-du-Nord, setbacks ranging from 6 to 8 m are predicted at the left river bank. Setbacks could reach over 10 to 12 m at the right bank. This river bank, from the power station until the bridge, is affected extensively and could present retreats ranging from 15 to 17 m at several locations.

4 CONCLUSIONS

In a dam break flood event, most rivers undergo important inundations. The limits of the potentially inundated area define actually the risk zones. The security of the habitants of those zones and the properties are the present preoccupations in the emergency plans conducted by the dam proprietors and the cities.

However, in some cases, the dangerous zone may be larger than the inundated one which is established under a fix topography hypothesis. The erosions and dam breaks induced landslides may extend significantly the risk zones.

The proposed methodology in this article allows the delimitation of the veritable safety zone along river banks by taking into consideration not only the flood risks but also the induced landslides. Indeed , each section of the river reach is subject to changes caused by the river hydraulics via the associated erosion or sediment deposition and also undergoes profile changes caused by possible landslides. This methodology produces on every riverbank a limit of potential impact.

KNOWLEDGMENT

The previous results are the fruit of research accomplished due to the support of Hydro-Québec to whom we express our heartfelt thanks.

REFERENCES

Lalonde, J. et Lavoie, A. (1981). *Première-Chut : Description des berges en aval de la centrale*. Direction Projets de Centrales, Service Géologie et Géotechnique, Hydro-Québec, décembre 1981.

Philipponnat G. et Hubert B. (1998). *Fondation et Ouvrages en Terre*. Eyrolles. France.

St-Arnaud, G. (1981). *Étude des berges entre la centrale Première-Chute et le lac Témiscaming*. Direction Projets de Centrales, Service Géologie et Géotechnique, Hydro-Québec, décembre 1981.

Thibault, C. (2000). *Résumé des données disponibles entre la centrale Première-Chute et le lac Témiscaming, Rivière des Quinze*. Étude d'érosion des berges en cas de rupture de barrage. Université Laval, Québec.

Yang, C.T., Trevino, M.A., Simoes, F. J. M. (1998). *User's Manual for GSTARS 2.0 (Generalized Stream Tube model for Alluvial River Simulation version 2.0).* US Department of the Interior, Bureau of Reclamation, Technical Service Center, Sedimentation and River Hydraulics Group, Denver, Colorado, March 1998.

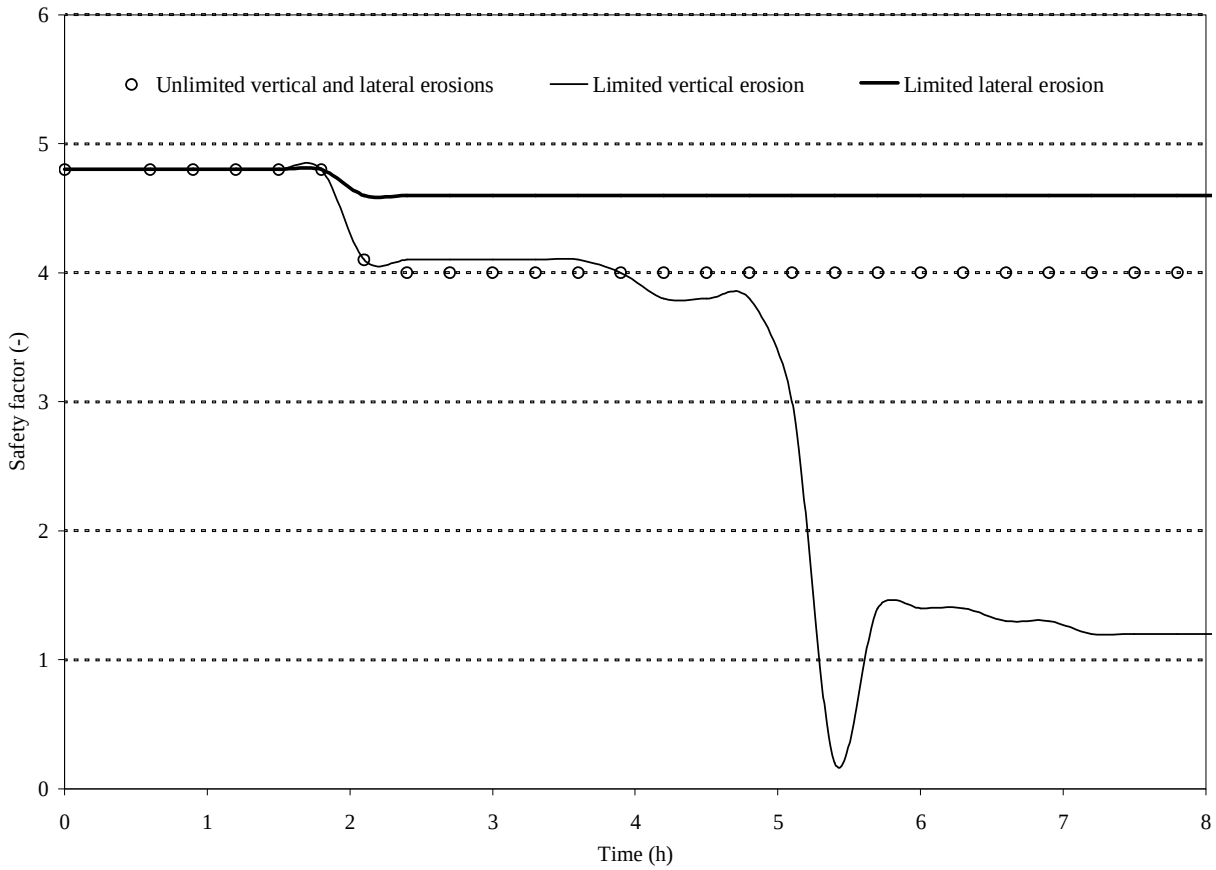

Fig.5. Comparison of the evolution of the safety factor of a bank for 3 scenarios: unlimited vertical and lateral erosions, limited vertical erosion and limited lateral erosion.

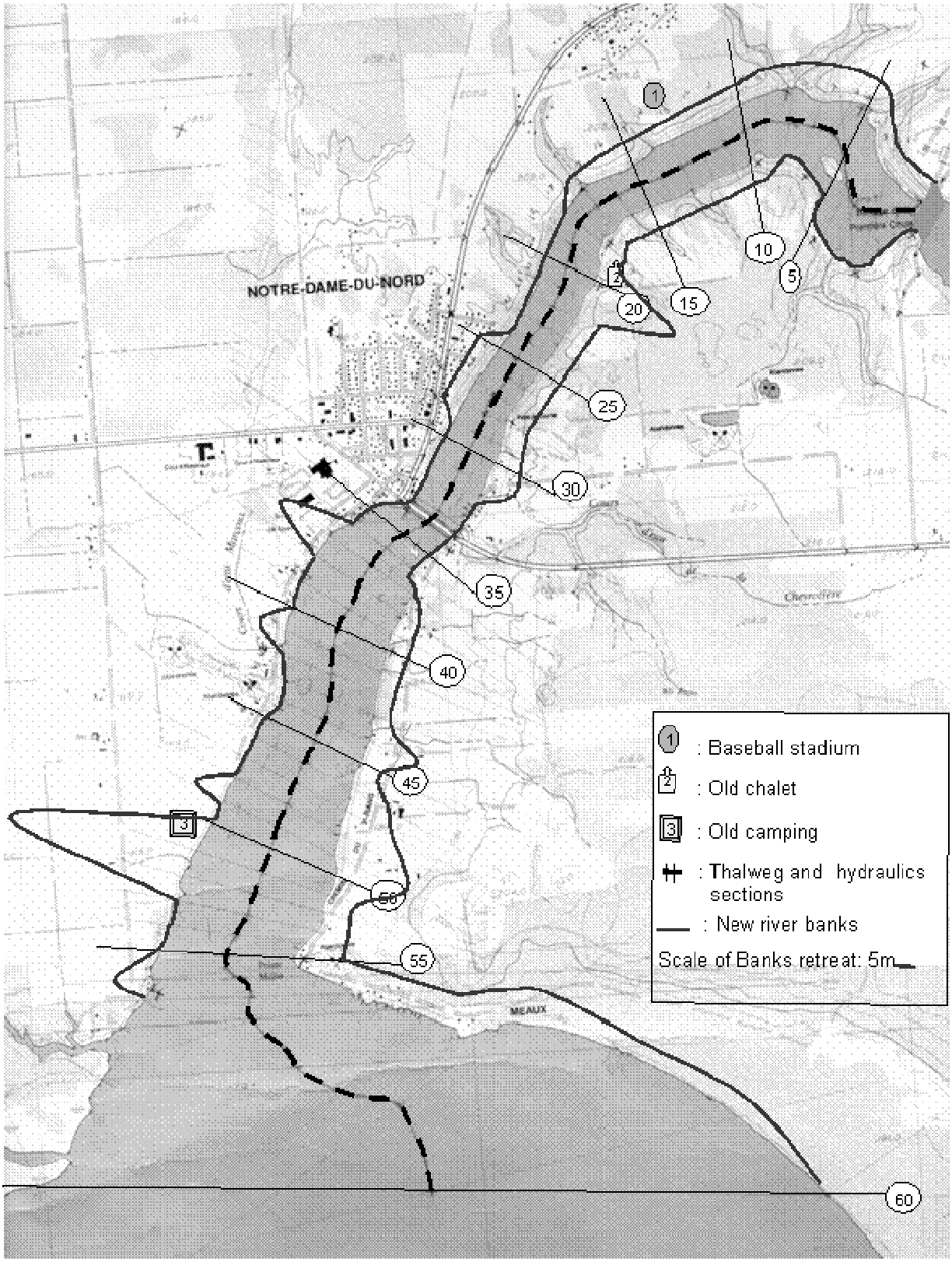

Fig.6. Riverbanks retreats after dam break occurrence (retreats are 10 times exaggerated)

Foreshore erosion and scour induced failures of sea dikes

C.V. Mai[1, 3] , K.W. Pilarczyk[2] and P.H.A.J.M. van Gelder[1]

1) Section of Hydraulic Engineering, Faculty of Civil Engineering and Geosciences
Delft University of Technology, Stevinweg 1, 2628 CN Delft, The Netherlands
2) RWS. Delft, Dutch Public Works Department, Road and Hydraulic Engineering Institute, Delft, Netherlands
3) Faculty of Coastal Engineering, Hanoi Water Resources University, 175 Tayson, Dongda, Hanoi, Vietnam

Correspondence Address: Section of Hydraulic Engineering, Faculty of Civil Engineering and Geosciences,
Delft University of Technology, P.O. Box 5048, 2600 GA DELFT
Email:c.maivan@tudelft.nl; Tel: +31- (0)15-278 4735; Fax: +31-(0)15-278 5124

Abstract: This paper aims at investigation of sea dikes failures and its mechanism due to foreshore erosion and scour in front of coastal dikes. The case of Namdinh sea dikes in Vietnam is introduced and selected for analysis. Some methods to estimate scour dimensions will be reviewed and applied for the Namdinh case in determination of suitable dimensions for dike's toe and bed protection. Namdinh coastal zone is a low-lying area which has been protected by sea dikes. In the region typhoons arrive on average four to six times each year at the coastline and the typhoons generate storm surges and waves, both attacking severely the sea dikes along the coast. As the result the sea dike system frequently suffer from damages and failures. One of the main reason for failures of the sea dikes is due to collapse of the dike's toe structures, which often causes by foreshore erosion and scour holes in front of the toe. Due to failures of the dikes and foreshore erosion coastal defensive lines of Namdinh usually has to be retreated 200m inland every 10 years. In order to mitigate the problem the dikes must be well protected. Studies on the erosion and scour induced failures of sea dikes and suggestion of proper toe/foot protection for the dikes, in this case, are important and need further research.

Key words: Foreshore erosion, scour, sea dike, failure, coastal, sea defence, stability, NamDinh, Vietnam

I. INTRODUCTION

A. General background of sea dike failures

In the low-lying coastal regions sea dikes are usually the most important coastal structures along their coastlines. The main function of sea dikes is to protect low-lying coastal areas which are highly vulnerable to coastal flooding. In general the design of these coastal structures is often based on actual boundary conditions deterministically.

The design hydraulic boundary condition of such structures is normally based on the averaged water depth front with a certain design waves under an design extreme condition of the actual cross shore profile. However, coastal dikes are usually under impacts of many coastal processes and natural phenomena which happens randomly both in time, space, their intensity and amplitude, thus the boundary situation can change subsequently compare to the design situation.

Due to the action of sea boundaries and their changes the failure of sea dikes may presented in variety of mechanisms. Some of the most possible failure mechanisms are: overtopping, instability of slope protected element, sliding of outer and/or inner slope, piping, erosion of outer and/or inner slopes, dike's toe instability, etc.. The relation between the failure mechanisms in a dike section and the unwanted consequence flooding can be schematised with a fault-tree (see Figure 1.).

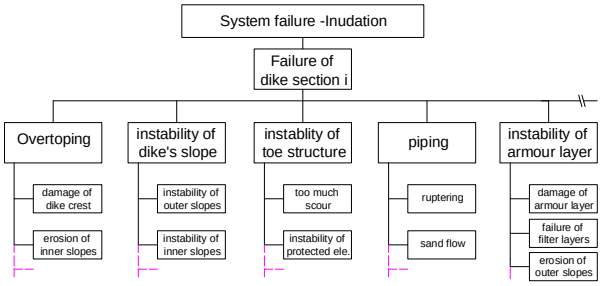

Figure 1. Example of consecutive failure mechanisms of a dike and consequence

On the other hand these failures of sea dikes can be presented in relation to their functional elements (see Figure 2.).

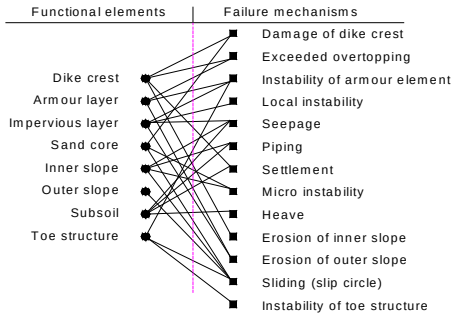

Figure 2. Functional element in relation to failure mechanism of a sea dikes

In sea dike design, it is therefore important to take in to account the future changes of boundary condition during dike design process to bring closer proper outcomes. In order to reduces the bad effects of foreshore erosion and scour, studies on the erosion and scour induced failures of sea dikes are necessary. Prediction of scour pattern (scour depth and width) and suggestion of proper toe/foot protection for the dikes, in this case is also necessary.

B. Erosion and scour induced dike's failures

Foreshore erosion and scour may cause direct and indirect effects to the safety of sea dikes and revetments. It can be explained that, firstly when the foreshore erosion takes place, the bathymetry of the sea bed in front of the dikes changes as well. This leads to the changes of hydraulic boundary condition of design situation comparing to current situation. Consequently, the loads on the dikes change (usually increases). Secondly foreshore erosion occurs near the toe of the dikes. It concentrates and forms scour holes there. When the scour depth reached at certain depth (near the level of toe foundation) the toe structure can not be stable under action of waves and currents. The failures happen to the upper structures when the toe is collapsed as consecutive consequences. Regarding to effect of erosion and scour of sea bed near the toe of a dike, four possible failure mechanisms are schematized in Figure 3. They are separated in two groups: Direct and indirect failures

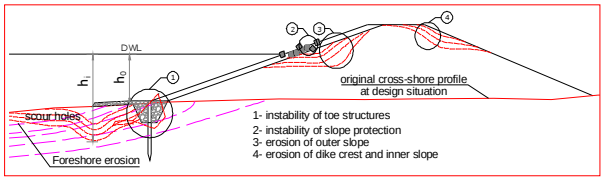

Figure 3. Schematisation of possibe erosion and scour induced dike failure modes

Direct failure: the failures which are caused by direct effect of occurring foreshore erosion and scour. Many cases in practice, due to occurring of local scour holes in front of the dikes, sand is taken away around the toe of the dikes. This sand is important for supporting the toe to remain stable. In the case heavy erosion and local scour take placed the toe structures is exposure to the sea water. The sand support is no longer available when the scour depth is exceeded depth of toe protection. This initially results in instability of toe structures by either sliding or overturning modes. Subsequently, the lower part of outer slopes of the dikes may not be stable. Overall slope stability of outer part of the dikes may be in danger also. These consecutive failure mechanisms may leads to collapse of the dikes. The series pictures in Figure 4. can be a practical expression.

Figures 4. shows the heavy damage of the dikes at Hai Chinh section 1996. First scour occurred at the toe of the dikes (Fig. 4.a) cause toe instability, after that riprap revetments was collapsed at lower and upper parts (Fig. 4.b) . After a design storm, the situation was getting more seriously. Then the dike body and revetment were collapsed after some days. The remained dike body was washed out under impact of waves and currents. Referring to the situation it is possible to say that the final failure occurred under sliding mode of outer slope

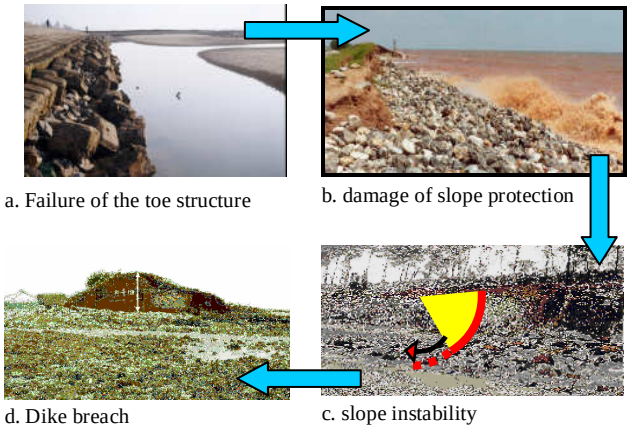

a. Failure of the toe structure

b. damage of slope protection

d. Dike breach

c. slope instability

Figure 4. Failures presented at NamDinh sea dikes [Namdinh 1996]

Regarding to erosion induced direct failure, in this study, instability of toe structures is investigated. Instability of the toe is considered with two different failure modes: sliding and overturning.

Indirect failure: Near-shore bathymetry has important influence in hydraulic loads on a coastal structures**.** In a eroded coastal region very often the sea bed levels in front of dike structures are lowering due to foreshore erosion process. This leads to increase in the water depth in front of the dikes. As the consequence, for a certain design climate condition, the near-shore waves is larger than that at the original bathymetry (at design situation). Subsequently, the others hydraulic loads (e.g wave run-up and wave overtopping...) increase as well. It therefore may cause the dikes failures. This is , in this study, defined as indirect failures. In principle when loads on the dikes are larger than the design loads, various failure modes may present and need to examined. In this case the following modes is mentioned: instability of protective armour layers at outer slopes; erosion of outer slope; erosion and damage dike crest and inner slopes.

Sensitivity analysis on rock stability of outer slope protection base on Pilarczyk 2nd formula for rock armour show that due to 50% water depth increase, the depth limited wave height increase by factor 1.5. As the result the new requirement of rock diameter increase by factor 1.4 or the safety factor decrease by factor 0.7 (see Figure 16.). Other sensitive impact analysis will be discussed with Namdinh case study at the below section.

Due to exceeded wave run-up and wave overtopping the following failures could be occurred:

- Erosion of dike crest.

- Erosion of inner slope
- Damage of crown wall, outer slope protection and upper part of revetment due to the overtopped seawater return flow.
- Washing material of filter layer, where the dike body was not well protected by cover layers.

Figure 5. shows the impression of failures at sea dikes in Hai Phong 2005 due to action of waves, wave run-up and wave overtopping. The damages of the dike in that picture included failures of crest wall and upper parts of revetments.

a. damage of armour layer and erosion upper part of outer slope

b. Damages of crest-wall and erosion of inner slopes

Figure 5. Failures of Hai Phong sea dikes 2005

Discussion

In coastal structure design in general and sea dike design in particular it is necessary to know in advance all kind of possible failure modes of such structures and their causes. Obviously, foreshore erosion and scour contribute a considerable effect to the failure by either direct or indirect ways. It is possible to analyze these effects by analytical method or setting up physical and/or numerical models. In term of foreshore erosion and scour induced failures of sea dikes, these consecutive failure mechanisms can be modelled conceptually as in Figure 6.

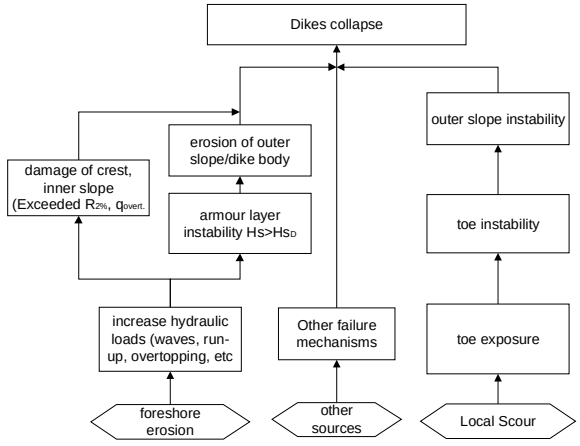

Figure 6. Consecutive failure mechanisms due to foreshore erosion and scour at a sea dikes

II. SEA DIKES FUNCTION FOR FLOOD DEFENCES IN AN ERODED COAST- A NAM DINH CASE

A. General situation of Namdinh coastal defences

The NamDinh Province constitutes part of the Red River Delta in Vietnam. The total length of Namdinh coastline is about 90 km suffering from severe erosion and serious damages of coastal defences. Along the coastline sea dikes and revetments have been the prevalent defensive system protecting the coastal areas from seawater flood and waves attacks. This system was established and has been developed continuously since thousand years ago. It suffered from many times of heavy damage, failure and breaches by attacks of severe storms, which often accompanied surges and high tidal level. This can be considered as the representative for coastal problems in Vietnam.

The failure of the sea dikes and revetments occurs frequently due to actions of severe typhoons, strong waves in combination of high tides while their design parameters were not sufficient. Moreover due to the action of waves and currents the foreshore erosion has occurred seriously which also leads to the collapse of the dikes and their revetments.

In response the central and local authorities have undertaken some efforts in order to restrain the possible adverse consequences and as future defensive measures, some sections of new sea dikes had been built. However, such efforts still remain limited to reactive and temporary measures.

The dike system is characteristically positioned as shown in Figure 7. with two defensive lines and separated section by section with sub-crossing dikes. When a breach takes place at the main dikes, the sub-crossing dikes can limit flooding areas and the second dikes will be a new first line of the system. The distance between two defensive lines is about 200 meters.

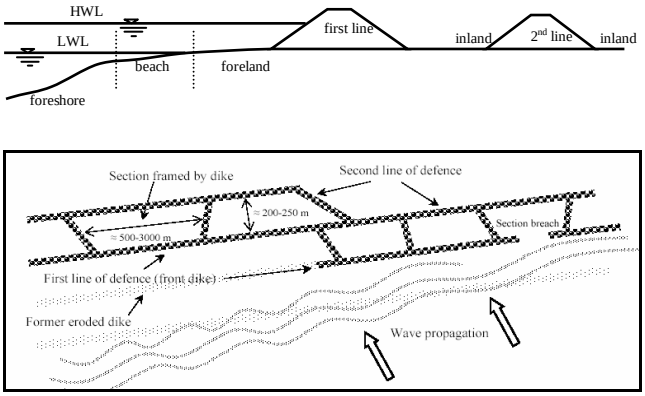

Figure 7. Schematisation of Namdinh sea dike system.

Due to budget constrains, lack of information on the sea boundary conditions and suitable design methodology as well as strategic and long-term solutions, the dike system was usually designed and constructed in poor conditions. As the consequence, the system could be destroyed once in every 10 years. Therefore the cost of dike maintenance is finally very expensive. Statistically, for maintenance of Namdinh sea dikes system it is represented nearly 95 percent of the total coastal defence budget of Vietnam. Figure 8. show the fast retreat of coastline as well the sea defence lines at Hai Trieu village, Hai Hau district in Namdinh province.

a. HaiTrieu Village in 1995

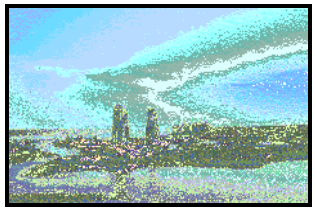

b. Abandoned HaiTrieu in 2001

Figure 8. Fast coastline retreat at HaiTrieu Village, Hai Hau, Namdinh

B. From historical development to future prediction

Historical development of coastal protection in Namdinh is available since 1890. In period from 1890 to 1972 it should be noted that there were no observation and measured records. These reports included only the major events of dike's breaches and reconstruction. More extensive information on development of the dike system is available since 1972. The observation on cross-shore profiles of Namdinh dikes were made at several locations therefore the situation can be analysed in more detail. From 1972 to 1990 the profile measurement took placed once in every 4 to 5 years. Since 1990 on the measurements of cross-shore profiles were performed at least once every year.

According to the historical information, during period of 65 years from 1890 to 1971, due to dike weakening because of erosion process and dike breaches after severe typhoon, the dikes system was shifted inland about 850 meters. There were six 6 times dike breaches and then reconstructions.

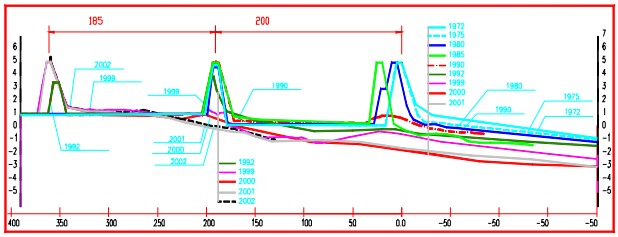

Figure 9. Overlap cross shore profiles from 1972 to 2003

During period of 30 years from 1972 to 2003, there was 6 times of dikes breach and 3 times of reconstruction of the dikes which shifting inland. The retreat of coastline during this period was around 400m inland. The dike breach and retreat of coastline for the time being because of the mentioned reasons. These processes can be summarized as following:

Since 1972 the sea dike system in Namdinh had 2 defensive lines (see Figure...). The first line was in good condition with crest level of +5.0 CD, and outer slope of 1 over 3 and inner slope of 1 over 2. Composition of dikes cross section was sandy clay body and moderated clay for outer armour layer. The toe of the dike was protected by extending under part of the outer slope with a flatter slope of 1 over 10. Foreland and beach in front of the dike was at level from -0.5 to +1.0 and around 150 m wide. The second line stood at 200m landward of the first line. The dimension of cross section was smaller than that of the first line. The crest level was at +4.5 m CD, outer slope is one over 2 and inner slope is one over 1.5. The profile of cross section is shown on Figure 9. *line label 1972*.

Three years later, in 1975, the erosion of near shore zone started. The foreland and beach along the dikes was lowered approximately 40 cm annually. The erosion depth was even more near the toe of the dikes, about 65 cm a year. Due to this erosion the toe was in danger of instability. The erosion of the lower part of outer slope was started. The first line of defensive system was in threatened. The profile (line label 1975, Figure 9.) was deeper offset in comparison to 1972's.

During period of next 5 years, from 1975 to 1980, the erosion became more heavily. Continuous erosion occurred near water line due to the actions of waves dike body's material was taken away and washed out. In front of the toe the sand was also taken away forming scour holes. The cross section of the dikes was getting smaller and thinner. Instantly, the first line was upgraded by the local people by widening the cross section at inner side. There was no recognisance of occurring of foreshore erosion and scour. The cross section then looked like *line label 1980* in Figure 9. .

In 1984 the erosion of near shore zone was still going on and the scour holes were getting deeper. The toe of the dikes was collapsed first after that sliding mode occurred as the failure of the outer slope. At the end of storm season in 1984 the first line was breached over the length of 1500 meters.

During quiet period of the sea in 1985 the breached gap was closed by new first dike section temporarily. At the same time the second line was upgraded for intention of becoming the first line later. The temporary first dike (closured section) was constructed at position of the old dikes in order to reduce the risk at the second line and kept dry area in front of that for being construction site. After upgrading, the second line became new first lines. Establishment of the new second line was started.

From 1985 to 1990 the closured section, which was constructed temporary in 1985, was eroded and had been getting weaker. At the end of storm season in 1990 this dike cross section remained only a small area with the shape of triangular (*see line label 1990*, Figure 9.). The remain material was spread out by interaction of waves and currents forming a foreshore of the new dike system.

The foreshore around the first dike toe of the new dike system was at averaged level of about +0.50. The averaged erosion rate of was about 0.30 m per year. By the end of November 1992 due to a severe storm occurred the cross shore erosion increased and scour holes appeared at approximately 0.8 meters in front of the toe and caused collapse of toe. As the consequence lower parts outer slope of the dike was damaged as well. Maintenance works were started with the outer parts of the dikes by filling rock at the dike toe and reinforcement outer slope wit riprap revetments. This maintenance work could withstand dikes until November 1995. After a typhoon with wind strength of 10 Beaufort the whole dike section mainly collapsed. The remained part had a triangle shape. It was not considered as a dike any more. At that moment the position of first dikes had to move again inland to the second dikes which stood 200 meters behind.

During the period from 1996 to 2000, busy re-reinforcement and reconstruction works of third new dikes system were going on. The upgrading works were finished temporary in 2000. New first line of dikes had crest level of +5.5m. The outer slope was one over four which was protected by rock revetments. The toe of the dikes was at level of +0.5 m with one or two lines of cylindrical concrete block. In front of the dikes the protection of scour holes was provided (see also FAO/UNDP 525 project report, Design documents for upgrading Namdinh sea dikes).

After 3 storm seasons from 2001 to 2004 the defensive system functions well in a good condition. However the observation showed that erosion process was still going on. Foreshore was narrowing and deepening year after year as the consequences.

Recently, in 2005, the Damrey typhoon, which occurred from 25th to 28th September 2005, attacked coastal areas in Northern Vietnam caused many serious damages of the coastal defence system and heavy lost for coastal regions. The wave run up was as high as 3-4 meters, high storm surge in combination with high tide led to too much overtopping of sea water at sea dikes in almost all affected regions. It broke certain sea dike sections in Thinh Long town, Hai Hau district in Nam Dinh province despite great local efforts for protection. In total, 25 kilometers of Vietnam sea dikes were broken and nearly totally destroyed. In Nam Dinh a stretch of 800m sea dikes was completely washed out.

Discussion

Based on analyses of historical development of Namdinh sea dikes the main reasons for dike failures and breaches can propose as follows:

Heavy foreshore erosion led to lowering the sand beach and foreland, formed scour holes in front of the dikes. As the consequences the toe of the dikes could not be stable. The failures of the toe resulted in series of consecutive damages of upper components of the dikes.

Increase in water depth in front of the dikes, as consequence of foreshore erosion, caused higher waves height (compared to the design wave height at the design situation) attacking directly on dike outer slope. On the other hand, the outer slope of most old dikes was not protected. That could lead to many damages of the outer slope.

During storm, high water level often accompanied with a surge and wave run-up caused too much overtopped water. This led to many damages of the dike components such as inner slope, outer slope and dike crest

Future prediction

The retreat of coastline during the period of 30 years is shown in Figures 4.3. In this Figure, the retreats of foreland levels of -0.50, 0.0, +0.50 meters (+MSL) are indicated. The based point is the position of foreland level 0.0 in the year 1972.

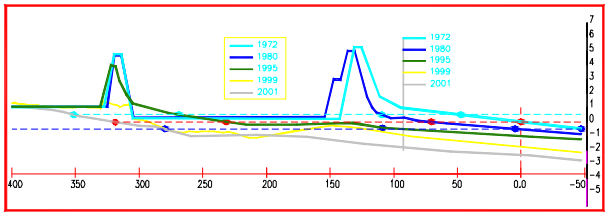

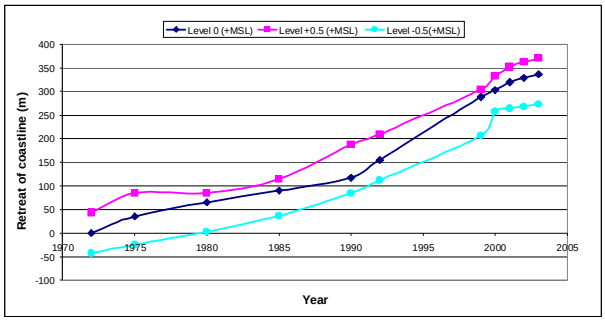

Figure 10. Retreat of coastal defences from 1972 to 2003

Based on the above analysis, if no proper measures for upgrade and protection of the dikes are undertaken, the situation will go on by similar trend of the last period. After every 10 years the retreat of coastline will be around 150 meters inland, see also Figure 10. According to the current trend, the location of the dikes will shift 200 meters landward after every 10 years.

C. Morphological changes and beach erosion of along Namdinh coast

This section concentrates on studying of sea boundary from deep ocean to near shore zone, includes waves and sediment transport processes along the coast. Advanced mathematic models - SWAN[1], and UNIBEST[2] - were used to simulate these problems. The models are setup and calibrated based on available collected data and historical map. The outputs of this section allowed, firstly, for establishment of hydraulic-sea boundaries which directly impact on the sea defensive system, and secondly, predicted statement of trend and rate of coastline changes. The wave result from SWAN model was derived and used as input data for morphological model UNIBEST. For calculation of long-shore sediment transports different sandy transport formulae were used (Bijker formula, Van Rijn formula and CERC formula). The coastline was divided into 8 sections with 9 cross section, relatively (see Figure 15.a). Simulation of coastline changes at HaiHau district by using UNIBEST-CL model was developed. The results of 24 years model are presented in Figure 15.c&d.

According to the model output, the net sediment transport direction is from north to south along the coastline. Obviously, the whole project areas are subject to erosion. The maximum erosion rate is at Hai Ly, about 22.4 meters/year (Van Rijn formula) and 21.5 meters/year (Bijker formula) which is situated in the northern part of the project, and then the erosion rate decreases southward. In order to calibrate the coastline model the simulation results are compared with the available collected data, which were deduced from the erosion map in period 1972 - 1996 (see Figure 15 b.). The comparison is shown in the Figure 15c with a acceptable fit. This result gives quite good agreement with the future prediction in the previous section.

[1] Simulating Waves Nearshore model, developed by Delft University of Technology, Rijkswaterstaat

[2] Uniform Beach Sediment Transport model, developed by WL| Delft Hydraulics

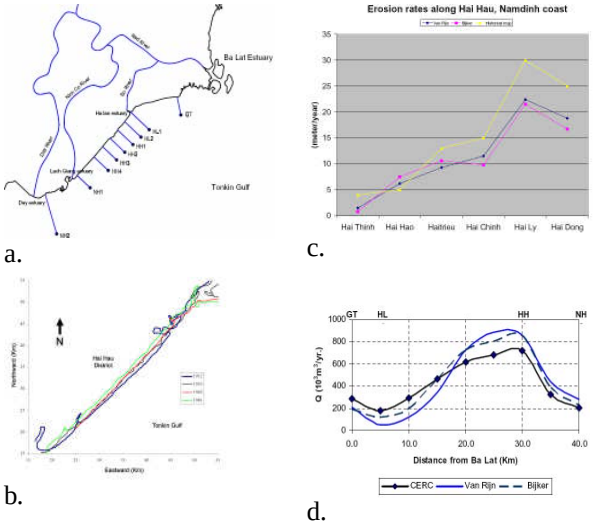

Figure 11. Longshore sediment transport and beach erosion simulation a long Namdinh coast

D. Investigation of foreshore erosion and scour induced failures of Namdinh sea dikes

From the earlier section it could be stated that most of the failures of Namdinh sea dikes are caused by under estimation of boundary condition. The possible failure modes of Namdinh sea dikes are various. For more detail on failure description of all possible failure mechanisms, see also in Mai et al, 2004. In this paper only failure modes which were direct or indirect influent by erosion and scour are examined.

The following representative cross section of Namdinh sea dikes is introduced for the assessment:

Dike crest level: +5.5 CD; Outer and inner slope : 1/4 and 1/2; Outer slope is protected by rip-rap rock with thickness of 0.40. Inner slope is exposure (non protected).

Dike body: sand core cover by 50 cm thickness clay layer.

Toe of revetment: Toe crest level: -0.5; One line of cylindrical concrete block, diameter of 100 cm and length of 150 cm, rock filled inside. Protected depth is 1.5 meters.

1) Failure of toe foot protection

a) Scour depth prediction

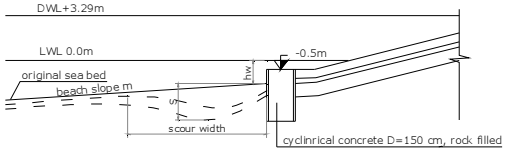

Figure 12. Schematisation of toe foot structure of NamDinh sea dikes

Scour due to waves actions is predicted at situation of occurring lowest water level. In this situation, the gentle outer dike slope is neglected; the vertical cylindrical concrete can be considered as a vertical wall. Schematisation of problem is shown in Figure 12. Maximum scour depth S can be determined by the three difference methods below.

- McDonugal Method

The scour depth in front of vertical seawall on a beach slope of m is:

$$\frac{S}{H_o} = 0.42m^{0.85}\left(\frac{Lo}{Ho}\right)^{0.2}\left(\frac{h_w}{H_o}\right)^{0.25}\left(\frac{H_o}{d}\right)^{1/3}$$

Where S is the scour depth at the seawall; Ho, Lo is wave characteristics in deep water, h_w is depth of the toe of structure and d is the sand grain size, see the schematized Figure 13.

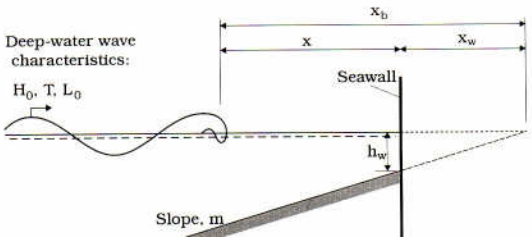

Figure 13.

- Method of Xie, 1981 (for vertical sea wall)

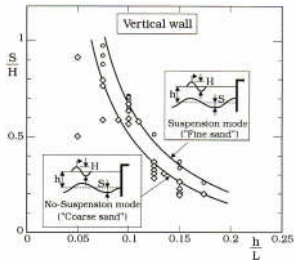

Figure 14.

According to Xie 1981, the maximum scour depth is given by the curves in Figure 14. In which H, L: local wave characteristics; h : local water depth;

- Method of Sumer and Fredsoe(2001) (developed for armour breakwater)

This method given by series of graph on Figure 15. . However it is applied for slope angle in the range of 30^o to 90^0. It suggests that when applied for the gentler slope of 30^0, the curve of $\alpha=90^0$ should be applied scour depth then should be reduced by a certain appropriate factor.

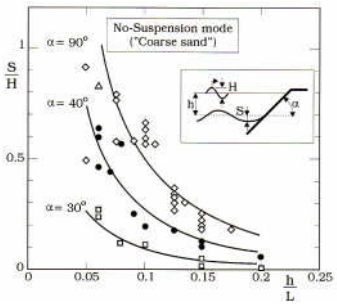

Figure 15.

$$\frac{S}{H} = \frac{f(\alpha)}{\left[\sinh\left(\frac{2\pi h}{L}\right)\right]^{1.35}} \quad \text{in which} \quad f(\alpha) = 0.3 - 1.77e^{-\frac{\alpha}{15}}$$

Applied the above methods for Namdinh sea dikes with the input parameter in TABLE I. and the results are in TABLE II.

TABLE I. INPUT PARAMETER

Parameter	unit	value

low water level	m	0.0 CD
Toe level	m	-0.5
Design wave height (in deep water)	m	2.0
Wave period	s	8.5
Sea bed level	m	-1.6
depth limited wave height	m	0.55*Depth
Shallow wave length	m	$T*(gh)^{1/2}$
calculated depth D	m	1.6
grain size	m	0.00025
sea bed slope	%	1

TABLE II. MAXIMUM SCOUR DEPTH

Method	Unit	Value
McDonugal	m	1.2
Xie 1981	m	0.9
Sumer and Fredsoe(2001	m	1.3

- Discussion

By applying various methods the different results of scour depth were given. The method of *McDougal* deals with deep water characteristic of waves while *Xie*'s, and *Sumer&Fredsoe* prefer local wave characteristic. In equation of McDougal, the grain size of sand near the toe was included. This may give more appreciate mechanism of scour.

For initial design the maximum protective depth for toe structure should be selected by the largest value of maximum scour depths by applying these various methods then multiplies safety factor. For the case of Namdinh revetment, the initial depth for toe protection should be equal to: *1.2* S_{max}*=1.2 *1.3=1.6m* from the calculated bed level of *-1.6m CD*. Therefore the protected level should be at *-1.6-1.6=-3.2m CD.*

b) Stability of the toe structures

Due to occurrence of scour hole the toe structure may lost its stability by the two modes: Sliding instability; and overturning stability. Problem is schematized for two situation: Before and after occurrence of scour hole (see Figure...). The safety factor of two interested failure modes is calculated follows the critical state conditions.

- Sliding criteria:

$$SF = \frac{n_q E_2 + n_g G_W f}{n_q E_1}$$

- Overturning criteria (around point A)

$$SF = \frac{n_q E_2 r_2 + n_g G_W r_G}{n_q E_1 r_1}$$

in which:

E_1 - Total active pressure component

E_2 - Total passive pressure component

G_W - Gravity force of the cylindrical concrete block in water

f- friction coefficient of rock with foundation at assumed sliding plane.

n_q;n_g- multiple loading factor

SF : Safety factor

r_i : moment radius of related force

More detail of stability analysis can be found in Tran, T.T. & Mai, C.V 2005. The analysis result is summarized in TABLE III. It can be concluded that due to occurrence of local scour holes, with maximum scour depth of around 1 meter, the toe of Namdinh sea dikes is totally collapsed. The overall safety factor is very low at 0.32.

TABLE III. SAFETY OF TOE STRUCTURE AT PRE&POST SCOUR

failure modes of toe structure	*safety factor*	
	before scour	*after scour*
Sliding	2.25	0.67
Overturning	2.63	0.32

2) Indirect failure modes at Namdinh dikes due to erosion and scour

As the result from scour calculation, the water depth in front of the dikes increase possibly 1.2 meters due to scour hole in comparison to the original situation. This means that the wave height acting on the dikes may increase also, ΔHs = 0.55*1.2= 0.66 meter (according to depth limited wave height).

Regarding to safety criteria of slope protection, wave run-up and wave overtopping, wave height is a dominant parameter in the equation. With the given increase of wave height, ΔHs, the reduced factor of safety of the above criteria can be estimated by sensitivity analysis (see summary result in Figure 16. and TABLE IV.

TABLE IV. EXCEEDED SAFETY CRITERIONS DUE TO SCOUR

Criteria	*original design value Hs=2.0m*	*present require value Hs=2.7m*	*reduced factor of safety*
wave run up (Van der Meer)	2.35	3.36	0.70
wave overtopping (Van der Meer)	8.5	17	0.5
Stability of rock armour layer (Pilarczyk)	0.8	1.1	0.72
Stability of rock armour layer (Van der Meer)	0.5	0.68	0.73

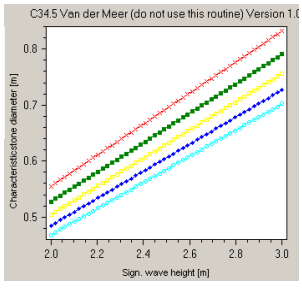

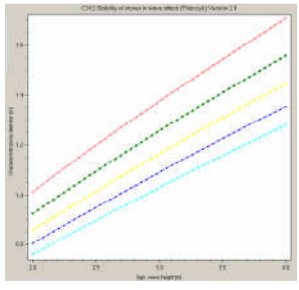

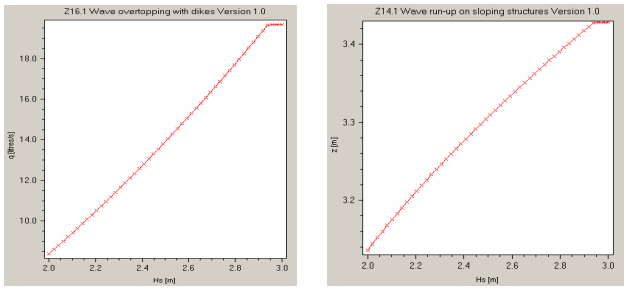

Figure 16. Sensitivity analysis of wave height related criterion

Obviously the result shows that due toe increase of 1.2 meters water depth (approximately 50% original depth) in front of the dikes, the actual safety of the dikes is decrease by factor of 0.7 in term of wave run up and stability of amour layer, and wave overtopping reduce safety factor by 0.5. This can be explained for the actual low safety level of Namdinh dikes (extensive analysis see also Mai, C.V. 2004) and what happens there during last ten years.

III. WHAT INFORMATION DO WE NEED FOR A REHABILITATION OF SEA DIKE IN VIETNAM

A. General needed information

Year 2005 can be treated as a historical year in respect to disastrous impact of typhoons on sea defences in Vietnam. Totally 8 typhoons has hit Vietnamese coast in this year resulting in human casualties and large economic damage. Typhoons No.2 and No.7 (Damrey) were of exceptional strength and belong to the heaviest typhoons in the last 3 decades.

Typhoon No.2, on 31 July, hit mainly the coastal area of Haiphong resulting in a number of kilometers of damaged sea dikes, especially on the island Cat Hai, where 8 km dikes were broken and/or heavily damaged and need total rehabilitation.

Typhoon N0.7, on 27 September, hit three provinces, Thai Binh, Nam Dinh and Thanh Hoa. The damage was enormous; 25 kilometers of dikes were broken and nearly totally destroyed. In Nam Dinh a stretch of 800m sea dikes was completely washed out.

However, it is to hoop that year 2005 will also be a turning point in national approach to sea defences in Vietnam, similar as the year 1953 was a turning point for the Netherlands in formulating the new policy and safety standards for protection the country against flooding.

The rehabilitation of these damaged or broken dikes will take a number of years and will be implemented under guidance of Department of Dike Management and Flood Control (DDMFC). It is evident that the old dikes were to weak and usually designed based on outdated design criteria, including rather poor hydraulic boundary conditions (waves, storm surges, design water levels).

To overcome the existing problems of the old dike design and come up with more proper outcomes, it is necessary to establish relationships and/or models for hydraulic boundary conditions in front of the dike as input for the design. The following issues are needed to be examination:

- **frequency distribution of water extreme levels** (historical storms/typhoons) based on data from the existing monitoring stations. However, the number of stations is too limited to cover the whole coast. The results can only be used for areas neighbouring the stations. However, these results can be also used for verification of results obtained through other methods (typhoon simulation and storm surge estimation in combination with astronomic tide)

- **simulation of historical typhoons up to end 2005** using typhoon simulation models (Vietnamese one and one provided by Delft Hydraulics in 2002). This simulation can be extended for other possible wind fields to simulate conditions exceeding historical storms to obtain some sensitivity information when extrapolating the frequency curves beyond the observed range.

- **frequency analyse of storm surges** subtracted from the measured water levels and typhoons simulations for various location along the Vietnamese coast, and estimating the value of the representative annual tidal high water (average from astronomic high water spring). Combination of the storm surges and tidal high water provides the water level per location. For location of existing measuring stations the estimated water levels can be compared with the water levels from direct observations.

- **deep water wave prediction**; comparison of standard prediction methods with waves induced by typhoons. Preparation of recommendations concerning the method which should be used, and possibly, preparing diagrams for wave prediction.

- **transformation of waves from deep water to shallow water, up to the toe of the structure;** this very crucial component for design because it defines the wave height (H) and period (T) as to be used in design of structural elements of the dike. The wave height depends on the water depth in front of the structure. Therefore the eventual erosive tendency of the foreshore should be taken into account (the wave height may increase in time). For shallow foreshore the depth limited wave height (H) can be applied: H=a h, where h is the local depth and 'a' is a coefficient, which should be determined from local measurements (usually between 0.4 and 0.6).

- **morphological development of erosion areas.** As mention above, the morphological changes may influence the wave prediction. Especially for Nam Dinh it is known that it is erosion coast. The foreshore is gradually eroded and at certain moment the deep water and high waves are approaching the dikes leading often to their destruction. The morphological maps and cross profiles should be analysed in combination with some morphological models to establish the tendency and speed of erosion. Yearly monitoring/survey at critical sections, especially after the typhoons, should be incorporated in standard management activities.

B. Information needed in term of erosion and scour

The outcome of last issue could bring relatively sufficient information in dike design process to reduce probability of erosion and scour induced sea dike failures which is focused in this paper. In this term the following specific information is proposed to have in hands before implementing a sea dike design:

1- Long-term erosion rate and trend: First the large scale longterm simulation of morphological processes should be implemented. The expected outcomes should be the nearshore erosion rate and direction, the trend of coastline changes and finally the information on predicted

equilibrium coastline shapes. This information need for a layout design in large scale of a dike system. Two questions need to be answered are: Can we still protect a low-lying area behind an eroded coastline by a sea dike system stand alone or it need to combine with other measures? Where would be the position of defensive lines and in which alignment?

For these study the hydro-morphodynamic models will be good tools. Mathematical models are available for this purpose for example MIKE21, DELFT-3D, UNIBEST, etc.

2- Short-term morphological change: The seabed level changes may influence the wave prediction. The short-term morphological change is not usually taken into account during the design and evaluation of sea defences because its effect is difficult to predict. At present, it is capable to use cross-shore transport models for this purpose. A conceptual equilibrium cross-shore profile can be predicted by either physical or numerical models. Based on that a conceptual optimal cross shore shape of coastal dikes can be suggested. Available UNIBEST-CT model could be an useful tools for scale of a coastline section.

3- Dimensions of maximum local scour and toe foot protection: Scour is natural phenomena caused by the action of waves, currents and their interaction. Scour occurs naturally as a part of morphological changes of coastal areas and as the result of artificial coastal structures such as sea dikes. Once the coastal structures are presented, the natural situation of waves and currents will be disturbed. Due to the action of waves, currents and their interaction with structures the scour is often being developed near the toe of these structures. In sea dike and coastal structure design, it is necessary to predict the scour patterns in order to provide a proper bed, toe foot protection.

Actually the determination of geometrical dimensions (protected depth and width; required size of protected elements) is based upon on the scour prediction and stability of element under attack of currents and wave-induced currents. There have been already several researches on development of scour near coastal and marine structures (e.g. McDougal et al 1994, Fewler 1992, Xie 1981, Fredsoe & Sumer 2001, Hoffmans 1992, etc.). Some empirical formulae were derived which can be used in a conceptual design stage. For more important stage of design, multi-dimensional physical and mathematical models should be applied.

IV. CONCLUDING REMARKS AND FURTHER STUDIES

This paper starts with some background information of sea dikes design, general design boundary condition of the dikes and their possible failure mechanisms, which need to account for during a design process. Dike failures, which may cause by foreshore erosion and scour are discussed and formulated conceptually in a consecutive mechanism. Subsequently a case study of a typical coastal protection of Vietnam is introduced. Investigation on the effect of scour and erosion problems to the NamDinh dike failures is figured out. The necessary information for more proper rehabilitation of sea dikes in Vietnam is presented. However, due to limited time and lack of data and information the study is just in a general state. Every indicated point may need some further studies. Nevertheless, this study allows giving the following remarks for the sea dike design and management:

Selection of design boundary condition should not only be taken at the present design situation but also count for the future changes (during serviced-life time). Because sea dikes are usually under impacts of the coastal processes and randomly natural phenomena in which their impact parameters varies both in time, space, intensity and amplitude, thus the boundary conditions of the dikes can change subsequently compare to the design situation.

Morphological changes will influence the wave prediction and change of hydraulic boundary condition. Especially for an eroded coast of Nam Dinh, the foreshore is gradually eroded and at certain moment the deep water and high waves are approaching the dikes leading often to their destruction. The morphological maps and cross profiles should be analysed in combination with some long-term, short-term morphological models to establish the tendency and speed of erosion. Based on that an optimal layout design of whole defensive system and optimal shape of the dikes can be archived.

Foreshore erosion and scour cause direct and indirect effects to the safety of sea dikes and revetment. Failures of the dikes due to these problems are obviously indicated in the case study of sea dikes in Vietnam. Given result shows that when possible scour holes occurs the safety of the dikes decrease considerably. Since the maximum scour depth of 1.2 meters (approximately 50% original depth) presents in front of the dikes, the actual safety of the dikes is decrease by factor of 0.7 in term of wave run up and stability of amour layer, and wave overtopping reduce safety factor by 0.5. The overall safety factor of the toe structure is very low at 0.32. A conceptual model of consecutive failure mechanisms in Figure 6. described these effects to the failure of sea dikes.

Using dikes in combination with other coastal defensive measure should be considered for the heavy eroded coastal region such as Namdinh. The studies and/or pilot projects on the effectiveness of the combined measures should be carried out before decision is made for the whole system.

Bed protection at the toe of sea dikes is another important aspect. When scour occurs continuously, it leads to forming of scour holes in front of the structures and may cause consecutive damages and failures of structural components. In this sense, bed protection provides functions of keeping sand in places to avoid forming scour holes and increase stability of the toe structures. It is necessary to predict the scour patterns in order to have a proper bed, toe foot protection.

To avoid consecutive failure mechanisms at existing sea dike system, a good and management strategies must be carried out. Monitoring program must be set up to ensure that all the initial damages of the dikes are aware and be repaired in time. The observation from small to a system scale is needed during any whether conditions. Based on the observation the maintenance can be provided in proper way annually. Measurement of cross-shore profiles before and after severe condition is advised in order to see the trend of profile development.

ACKNOWLEGMENT

This work has been carried out under the framework of the co-operational project between Delft University of

Technology and Hanoi Water Resources University. The project is funded by the Royal Embassy of the Netherlands.

REFERENCE

[1] Anonymous, 1992, Design document of Namdinh sea dikes and revetments, DDMFC, Namdinh.

[2] Anonymous, 1998, Design document of Namdinh sea dikes and revetments, DDMFC, Namdinh.

[3] Anonymous, 2000, Prediction and prevention of shoreline erosion at northern part of Vietnam. Research project report. Institute of Mechanics, National Center Nature Science and Technology of Vietnam.

[4] Bas Wijdeven, 2002, Coastal erosion on a densely populated delta coast – A case study of Namdinh province, Red River Delta, Viet Nam. Msc thesis, Delft University of Technology, The Netherlands.

[5] Booij, N., Haagsma, IJ.G., Kieftenburg. A.T.M.M., Holthijsen, L.H., 2000, SWAN implementation manual, Version 40.11. http://swan.ct.tudelft.nl/

[6] Cuong, N.T, Thang N.M, 2002, Annual report of situation of sea dikes in Namdinh province.

[7] CUR/CIRIA, 1991, Manual on application of rock in shoreline and coastal engineering, CUR report 154, CIRIA special publication 83, Gouda/London, 1991

[8] CUR/TAW, 1994, Manual on the use of rock in Hydraulic engineering, CUR report 169, RWS/TAW, Gouda, The Netherlands, 1994.

[9] Disaster management working group (DMWG) Joint Assessment of Disaster needs, Rapid Needs Assessment in Thanh Hoa, Ninh Binh and Nam Dinh provinces, hit by typhoon Damrey (STORM No. 7), 28-29 September 2005.

[10] Fowler, J.E., 1992, Scour problems and methods to prediction of maximum scour at vertical seawalls, Technical report CERC-92-16. US Army Engineering Waterways Experiment Station, CERC, Vicksurg, Miss. 1992

[11] HE.B-IHE, 2002, Coastal erosion analysis of Namdinh coast and proposed solutions. Final report for Group work at IHE Delft 2002.

[12] Häglund, M., Svensson, P., 2002, Coastal erosion at HaiHau beach in the Red River delta, Vietnam. MSc Thesis, Lund University, Sweden.

[13] Hoffmans, G.J.C.M., 1992, Two-dimensional mahtematical modelling of local scour holes, Doctoral thesis, Faculty of Civil Engineering and Geosciences, Delft University of Technology, Delft, 1992.

[14] Hoffmans, G.J.C.M. & Verheij, H.J. 1997, Scour Manual, A.A.Balkema, Rotterdam, Brookfied, 1997.

[15] Mai, C.V.,2004, Safety assessment of sea dike in Vietnam, M.Sc thesis, Unesco-IHE, Delft, The Netherlands, June 2004.

[16] Mai, C.V., 2005, Probabilistic safety assessments of toe foot protection at sea dikes, Journal of Scientific and technological Information, Ministry of Agricultural and Rural Development, 2005 (in Vietnamese).

[17] Mai, C.V., Pilarczyk, K.W., 2005, Safety aspect of sea dikes in Vietnam-A Namdinh case study, Conference Proceeding of International Symposium on Stochastic Hydraulics, IAHR Paseo Bajo Virgen del Puerto 3, 28005 Madrid, Spain 2005.

[18] Pilarczyk, K.W., 1990, Coastal protection, Rijkswaterstaat, A.A.Balkema/Rotterdam/Brookfield, 1990

[19] Pilarczyk, K.W., Zeidler, R.B. 1996, Offshore breakwaters and shore evolution control. Balkema, Rotterdam.

[20] Pilarczyk, K.W, Eversdijk P.J and G.Kant, 1996, Sea dikes northern part of Vietnam (red reiver delta), Mission report, DWW

[21] Pilarczyk, K.W., 1998, Dikes and revetments, Design, maintenance and safety assessment, Rijkswaterstaat, A.A.Balkema/Rotterdam/Brookfield, 1998

[22] Pilarczyk , K.W. 1998, Rehabilitation of sea dikes in Vietnam.

[23] Sumer B.M, Fredsoe J., 2002, The mechanics of scour hole in the marine environment, Advanced series on ocen engineering, Volume 17, World Scientific, 2002.

[24] Vrijling J.K., van Gelder P.H.A.J.M, Proabilistic design, Lecture notes, HH465/04/1, IHE, 2001.

[25] Vinh, T. T., Kant, G., Huan, N. N., Pruszak, Z., 1996, Sea dike erosion and coastal retreat at Nam Ha Province, Vietnam. Proceedings of the Coastal Engineering Conference, v. 3, p. 2820-2828.

[26] Xie, S.L., 1981, Scouring patterns in front of vertical breakwaters and their influences on stability foundation of the breakwaters, Delft University of Technology, Delft, 1991.

[27] WL| Delft Hydraulics, 1992. UNIBEST, A software suite for simulation of sediment transport processes and related morphodynamics of beach profiles and coastline evolution. Model description and validation. Report H454.14

Depth of Scour at Groups of Two Bridge Piers

M.B. Mashahir*, A.R. Zarrati**, and E. Mokallaf
* Amirkabir University of Technology, Tehran, Iran
** Amirkabir University of Technology, Tehran, Iran

Local scour around bridge piers occurs by the action of a complex vortex system. Local scour around bridge piers, has been extensively studied from different points of view and under different flow conditions. However, most of the previous studies were focused on a single pier. In addition to parameters affecting scouring around a single pier, for a pier that is a part of a group of piers, group effects are also important. In the present study the scour depth at groups of two piers is investigated in long term experiments. Piers aligned with the flow and transverse to the flow were considered with spacing "S/b" of 2, 3 and 4, where S is the space between the piers and b is diameter of the piers. Ratio of maximum scour depth to pier diameter (Ys/b) at upstream face of the front pier for two piers in line was measured 2.58, 2.55 and 2.53 for piers with S/b of 2, 3 and 4 respectively. For the rear pier in the same spacing Ys/b was 2.3, 2.28 and 2.25 respectively. Depth of the scour hole measured at the rear pier was more than previously reported. For two piers transverse to the flow the results of the present study showed Ys/b = 3.25, 2.88 and 2.7 for S/b= 2, 3 and 4 respectively which are also deeper than what reported before. Deeper scour holes measured in these studies are attributed to longer time of experiments and higher stresses imposed.

I. INTRODUCTION

A high percentage of bridge failures in recent years have been attributed to scouring [1]. Pier scour is the erosion of the streambed in the vicinity of pier foundations due to a complex vortex system. Researchers have extensively studied local scouring from different points of view and in different flow conditions [2,3,4,5]. Briefly, Local scour around a solid pier results from the down flow at the upstream face of the pier and the horseshoe vortex (HSV) at the base of the pier. The horseshoe vortex deepens the scour hole in front of the pier until the stresses on the bed material become less than their critical shear stress. Separation of the flow at the sides of the pier also creates so-called wake vortices. These vortices are unstable and shed alternatively from each side of the pier. They act as little tornadoes lifting the sediment from the bed and form a scour hole downstream of the pier (Fig 1).

Most of the previous studies were focused on a single pier. In addition to parameters affecting scouring around a single pier, for a pier that is a part of a group of piers, group effects are also important. For two piers in line (aligned with the flow), reinforcement and sheltering, are additional parameters, which affect the depth of the local scour. Reinforcement is when a downstream pier is placed so that piers' scour holes overlap. This aids in removal of the sediment from around the upstream pier increasing its scour depth. The presence of the upstream pier causes a sheltering effect and reduction of the effective approach

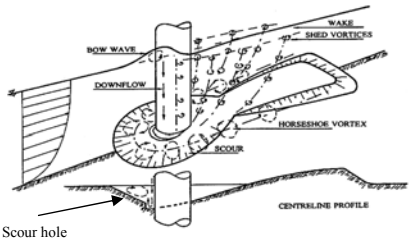

Figure 1. Vortex system around a cylindrical bridge pier [7].

velocity for the downstream pier. This effect reduces the scouring of the downstream pier.

When piers are placed transverse to the flow, compressed arms of the HSV play a vital role in local scouring. In this case, each pier will have, except for very close spacing, its own HSV. The interaction between piers in the group intensifies the strength of HSV arms and therefore the depth of the scour hole [6].

Useful insight into the local scour processes at pier groups was provided by studies of Hannah (1978) [7] which are also reported by Raudkivi (1998)[6]. Hannah used cylindrical piers in a steady flow to study the depth of scour at bridge pier groups. Bed material in Hannah experiments was uniform sand with 0.75mm diameter. According to [6] Hannah tests were performed in condition where u*/u*c was 0.72 where u* is bed shear velocity and u*c is the threshold of bed material motion found from the shields diagram. With performing a long-term test in 24 hours with a single pier, Hannah showed that with a single pier, 80% of scour depth occurred in first 7 hours. All tests with pier groups were therefore performed in 7 hours and results were extrapolated to find the maximum depth of scour hole.

The primary objective of the present study was to estimate maximum depth of the scour hole at groups of two piers in long term experiments and at near threshold of bed material motion. Piers aligned with the flow and transverse to the flow were tested.

II. EXPERIMENTAL SETUP

Experiments were carried out in a 10m long, 0.6m deep and 0.74m wide horizontal glass-sided flume. A triangular weir and a manometer were used to measure the flow discharge. A point gauge was used to measure flow and scour depth in the flume. The piers used in this study were a 0.04m diameter Perspex pipe. The flume had a working section in the form of a recess below its bed which was filled with sediment and was located 6m downstream from the flume entrance. Median size of the sediment was 0.95mm, with geometric standard deviation of sediment

grading, less than 1.2. All tests were conducted at about threshold of sediment motion where maximum depth of scour hole is expected [7].

The threshold of sediment motion was found by experiment. Threshold of sediment motion was defined as flow condition at which the bed elevation, while the pier was not installed, does not change more than 2 to 3mm after a long period of experiment (for example 5 to 10 hours). Tests showed that with 0.13m flow depth and 0.030m3/s discharge bed materials would be at initiation of motion. Therefore, this condition was selected for all experiments. In these experiments, the ratio of shear velocity to the critical shear velocity, calculated from the shields' diagram was about 0.923. Shear stress at the working section was determined by calculating the water surface profile and slope of the energy line.

In a preliminary experiment, single circular pier was tested. In the next stage, two piers aligned with the flow and transverse to the flow were considered with spacing "S/b" of 2, 3 and 4, where S is the space between the piers and b is diameter of the piers.

III. TIME OF EXPERIMENTS

To find the maximum depth of scouring, experiments were continued until the equilibrium condition, that is when the variation of scour depth was negligible. This time was assumed based on Melville and Chiew [8] definition. According to this definition when depth of the scour hole does not change by more than 5% of the pier diameter over a period of 24 hours, equilibrium condition is achieved. About 40 hours was necessary in experiments of the present study to reach the equilibrium condition.

IV. EXPERIMENTAL RESULTS

A. Single cylindrical pier

In the first experiment, a long-term test on a single pier was performed to compare its results with group of two piers. Scouring around the pier started simultaneously at the upstream face of the pier due to the down flow and HSV and downstream of the pier under the action of wake vortices. The ratio of maximum scour depth at the upstream face of the pier to pier diameter Ys/b was measured equal to 2.4. The maximum depth of scour hole measured in this experiment was in good agreement with empirical equations such as Melville and Sutherland (1988).

B. Two Piers in line

In these experiments, three different spacing S/b= 2, 3 and 4 were tested for groups of two piers in line. At the beginning of experiments, similar to a single pier, the vortex system including horseshoe and wake vortex excavated scour holes around the piers. Down flow at the upstream face of the piers impinged the streambed and dug a hole in front of the piers. Also, flow separation downstream of the piers formed the wake vortices. Except for the case with S/b=2, scour holes around the piers were independent. The ratio of maximum scour depth at the upstream face of the front pier to the pier diameter was measured 2.58, 2.55 and 2.53 for S/b= 2, 3 and 4 respectively (Table 1). Also, Ys/b at the upstream face of the rear pier was measured 2.3, 2.28 and 2.25 for S/b= 2, 3 and 4 respectively.

Considering depth of the scour hole at the front pier, results are similar to Hannah (1978) work. For the rear pier however, scour depths reported by Hannah (1978) are less than what measured in the present experiments (Table 1). Longer experiments and higher stresses imposed could be the reason for deeper scour holes measured at the rear pier in the present work. Since the front pier scour depth similar to what reported by Hannah [7] in shorter time experiments, it can be concluded that a longer time has been necessary for the rear pier, being in the shelter of the front one, to reach equilibrium condition.

Comparing with a single pier, it can be concluded that reinforcement and sheltering effects were dominant factors in the local scouring process for two piers in line. The reinforcement effect caused an increase in the local scour depth of the front pier by 7% for S/b=2, which decreased in more spacing. The sheltering effect caused reduction of local scour depth at the rear piers up to about 6% (Table 1).

C. Two Piers transverse

In these experiments also the three different spacing S/b=2, 3 and 4 were tested for groups of two piers transverse. In these experiments, similar to pervious tests, down flow and wake vortices caused the scour holes around the piers. In this arrangement sediment material that placed between the piers was removed faster than other places. With spacing S/b=2, 3 and 4 the ratio of maximum scour depth which was at the upstream face of the pier to pier diameter Ys/b was 3.25, 2.88 and 2.7 respectively.

Comparing with Hannah (1978) (Ys/b=2.71, 2.62 and 2.48 for S/b=2, 3 and 4) deeper maximum scour depth were measured in the present work (Table 1). Based on these results, time of experiment in Hannah (1978) (7 hours and extrapolating to 24 hours based on single pier experiment) was not enough for achieving the maximum scour depth. Moreover, higher stresses were imposed on bed material in the present study. It can also be seen from Table 1 that the difference between the present results and Hannah (1978) increases as piers spacing decrease. Where at S/b=4, the present experiments shows 8% deeper scour hole comparing with Hannah, for S/b=2, 16% deeper hole was measured. This shows that time of equilibrium and effect of bed shear stresses increases at closer spacing of the piers.

Comparing with a single pier, the pier spacing and HSV compression were a dominant factor in local scouring for two piers transverse. For the S/b=2, the HSV compression

TABLE I.
SUMMARY OF RESULTS OF THIS STUDY AND HANNAH (1978)

	Two piers in line (Ys/b)				Two piers transverse (Ys/b)	
	Hannah (1978)		This study		Hannah (1978)	This study
S/b	Front Pier	Rear Pier	Front Pier	Rear Pier	-	-
2	2.57	2.03	2.58	2.3	2.71	3.25
3	2.59	2.03	2.55	2.28	2.62	2.88
4	2.48	2.07	2.53	2.25	2.48	2.7

effect increased the local scour depth by 35%. With increasing the pier spacing, effect of this factor was decreased up to 12% for S/b=4 (Table 1).

V. CONCLUSION

In the present study, the scour depth around groups of two piers was investigated. Piers aligned with the flow and transverse to the flow were tested with spacing "S/b" of 2, 3 and 4, where S is the space between the piers and b is piers' diameter. In these experiments the ratio of shear velocity to the critical shear velocity of bed material calculated from Shields' diagram was 0.923. All tests were carried out for 40 hours to satisfy Chiew and Melville criteria of equilibrium condition [8]. Results showed that the scour depth at the rear pier of two piers aligned with the flow were greater than that reported before by Hannah (1978), while the scour depths at the front pier were similar. Deeper scour hole measured in the present study compared with previous works is attributed to longer time of experiment and higher stresses. Comparing with a single pier in the range of spacing tested, results show an increase of about 7% in scour depth at the front pier under reinforcement and 6% reduction in scouring at the rear pier under sheltering effect. For two piers transverse to the flow also the results of the present study showed deeper maximum scour depth compared with previous works, especially at lower spacing. This is again due to long time of experiment at the present work. Comparing with a single pier, compression of horse shoe vortex caused the scouring to be more in group of two piers. Comparing the result with pervious work on groups of two piers shows that time of equilibrium and effect of bed shear stress are more to the rear pier in two piers in line and transverse piers with closer spacing.

REFERENCES

[1] B. W. Melville, and S. E. Coleman, Bridge Scour, *Water Resources Publications LLC*., Colorado, 2000.

[2] J. Chabert, and P. Engeldinger. "Etude des Affouillements Autour des Piles des Ponts," (Study on Scour Around Bridge Piers). *Laboratoire National d'Hydraulique*, Chatou, France, 1956.

[3] P. Hjorth, "Study on the Nature of Local Scour," *Water Resources Eng*, Bulletin Series A, No. 46, Dept.., Lund Inst. of Tech., 1975.

[4] B. W. Melville, and A. J. Raudkivi, "Flow Characteristics in Local Scour at Bridge Piers," *Journal of Hydraulic Research*, Vol. 15, , pp. 373-380, 1977.

[5] B. Dargahi, "Controlling Mechanism of Local Scouring," *Journal of Hydraulic Engineering,* ASCE, Vol. 116, No. 10, pp. 1197-1214, 1990.

[6] A. J. Raudkivi, Loose Boundary Hydraulics, *A. A. Balkema publisher*. Rotterdam, Netherlands, 1998.

[7] C. R. Hannah, "Scour at pile groups," *University of Canterbury*, NewZealand, Civil Eng., Res. Rep. No. 78-3, 1978.

[8] B. W. Melville, and Y. M. Chiew, "Time Scale for Local Scour at Bridge Pier," *Journal of Hydraulic Engineering*, ASCE, Vol. 125, No. 1, pp. 59-65, 1999.

[9] B. W. Melville, and A. J. Sutherland, "Design method for local scour at bridge piers," *Journal of Hydraulic Engineering*, ASCE, Vol. 114, No. 10, pp. 1210-1226, 1988.

Key Words

Scouring, bridge pier, two piers in line, two piers transverse, time of equilibrium, bed shear stress.

Time Development of Scour in a Cohesive Material due to a Submerged Circular Turbulent Impinging Jet

K.A. Mazurek*, N. Rajaratnam** and D.C. Sego**

* University of Saskatchewan/Department of Civil & Geological Engineering, Saskatoon, Canada

** University of Alberta/Department of Civil & Environmental Engineering, Edmonton, Canada

This paper presents some results of experiments performed to examine the time development of scour in cohesive soil caused by a submerged circular turbulent impinging jet. The growth of the maximum depth of scour, the scour depth at the jet centerline, and the volume of scour was observed in one cohesive soil consisting of 40 % clay, 53 % silt, and 7 % fine sand. The jet diameter used was 4 or 8 mm, the height of the jet above the sample was 40–116 mm, and the jet velocity was in the range of 4.97–25.9 m/s. It was seen the material eroded primarily by removal of small to large chunks of material, called mass erosion. Although erosion occurred by mass erosion, the scour holes grew in an approximately linear relation with the logarithm of time and reached an asymptotic state. Two models for predicting the time development of scour are compared. It is seen that it may be difficult to predict the early part of the scour process well. Mass erosion appears to be a difficult scour process to model due to the discrete nature of the process.

I. Introduction

The prediction of scour by flows in the form of turbulent water jets is of considerable importance for the design of stable hydraulic structures such as dams, culverts, weirs, and drops. Many investigations have been performed to study scour by jets in a variety of configurations. These studies have been primarily carried out in clean, coarse grained or "cohesionless" materials. Much less studied has been scour in fine-grained or "cohesive" soils. The case of scour by submerged circular turbulent impinging jets in fine-grained materials has particularly received some attention [1,12,14,15]. There has been interest in using this form of jet to assess the erodibility of soils [4,5,6,7,9] and to evaluate the erosion of channel banks produced by ship propellers and thrusters [8]. Nonetheless, scour by these jets in fine-grained materials is still not well understood.

This lack of progress for cohesive materials is partly because there are more than one form of erosion and the type of erosion that will be observed for a particular soil under given flow conditions cannot yet be predicted. Erosion can occur by the removal of individual particles or aggregates from the surface of the soil, called "surface erosion" [13]. Erosion can also occur by the removal of large lumps or chunks of soil of various size [12,14, 15], called "mass erosion". For the time development of scour in mass erosion, if the maximum depth of scour is plotted against the logarithm of time there will be in sudden jumps or discontinuities that correspond to the removal of large chunks [15]. It is the most common form of erosion for lower void ratio materials, where the void ratio $e=V_v/V_s$, and V_v and V_s are respectively the volume of voids and solids in the soil. With respect to erosion, a low void ratio soil has a void ratio less than about 1 [16].

This paper discusses the results of an experimental study of the time development of scour of a low void ratio (e=0.73), fine-grained soil composed of 40 % clay, 53 % silt, and 7 % fine sand. The model for assessing the time development of scour by vertical impinging jets developed by Rajaratnam and Beltaos [17] for cohesionless soil, is compared to the models for predicting scour by these jets used by Ansari et al. [1] for cohesive materials. Potential difficulties in developing these type of models for cohesive soils are also discussed.

II. Experimental Setup and Experiments

For each experiment, a soil sample of 224 m length, 175 mm width, and 85 mm depth was submerged within a octagonal tank of 610 mm height and 570 mm diameter made of 19 mm thick clear acrylic. The experimental setup is shown in Fig. 1. A vertical circular turbulent jet impinged on the sample from a height of 40–116 mm. The jet of velocity U_o of 4.97–25.9 m/s was created by flow through a 830 mm long, 120 mm diameter plenum and then a well-designed nozzle of diameter d of 4 or 8 mm. This gave jet Reynolds numbers R of 26000–98500, where $R = \rho U_o d/\mu$, and ρ and μ are the density and dynamic viscosity of the eroding fluid. The relative impingement height H/d, where H is the height of the jet above the sample, thus ranged from 8.1–29.0, so that for all experiments the jet was set at a large impingement height [3]. The flow was provided by a 1/2 hP jet pump and fed from a 880 L fiberglass tank containing City of Edmonton tap water, which itself was fed from a city water supply line. A magnetic flow meter was used to measure the flow rate. Water was not recirculated in the apparatus to avoid an increasing sediment concentration, and temperature through an experiment. The details of the experiments are given in Table 1. Note that the experiments presented here are part of a more comprehensive data set given in Mazurek [10].

Only one type of soil was used for testing. This soil was a pottery clay obtained from Plainsman Clays Ltd of Medicine Hat, Alberta, Canada. This was done so that a

Figure 1. Experimental setup

large number of samples of similar characteristics could be tested under varied flow conditions. The samples were periodically tested for homogeneity for their vane shear strength, water content, grain size distribution, Atterberg Limits, and activity and contained about 40 % clay sized particles (less than 2 μm), 53 % silt (2 to 60 μm) and 7 % sand (60 μm to 2 mm). They consistently had a vane shear strength, S_v, of about 20 kPa, a liquid limit of 36 %, a plastic limit of 18 %, a dry density of 1540 kg/m^3, and an activity of 0.4. The water content of samples prior to submergence of the sample, w_c, averaged 26.0 % with a 97 % saturation. After testing, the water content, w_f, increased to a depth-averaged value over the top 30 mm of the sample of 27.7%. Electron micrographs, as seen in Fig. 2, showed the clay had an aggregated fabric with random particle orientations. An X-Ray diffraction test showed that the clay component of the soil consisted of kaolinite and illite.

The samples were prepared for testing by first pushing a 0.5 mm thick rectangular band of galvanized sheet metal into the sample. This was done to help prevent the block from splitting apart during testing and to ease placement of the samples within the apparatus. The surface of the soil was then cut with a very thin metal wire using a guide to ensure that all of the samples were the same height. After this preparation, the sample was submerged in tap water and jet flow was initiated.

For each test, the maximum scour depth ε_m, centerline scour depth ε_{cl}, and volume of scour ξ, were measured at times of approximately 2 min, 5 min, 15 min, 1 h, 2 h, 4 h, 8 h, 24 h, 48 h, 72 h, and 96 h, and then at 24 h intervals until asymptotic state was reached. This was when there was no significant change in the scour hole volume over 24 h (less than 0.5 mL). For each measurement, the flow was stopped, the tank drained, and the water was carefully vacuumed from the scour hole. The maximum and centre-

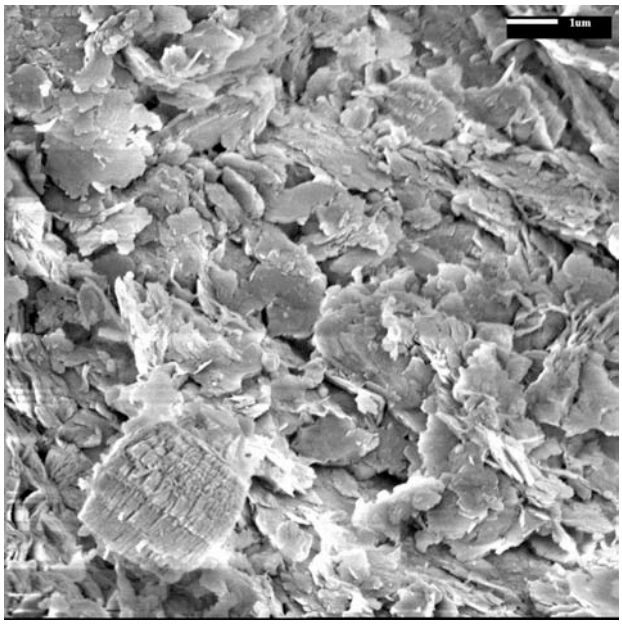

Figure 2. Electron micrograph of the soil at 7500X magnification

line depths of scour were measured using a thin wooden rod that was adapted for use as a point gauge. This rod had a blunt end, as it was observed in preliminary experiments that mass erosion might be initiated at a location where there were even small marks on the sample. To find the scour hole volume, a small graduated cylinder was used to refill the scour hole with water. During each test, measurements were taken of the eroding water conductivity, pH, and temperature. At the end of each test, the sample was removed from the tank and detailed measurements of the scour hole profile were taken along two perpendicular sections through the jet centerline using a point gauge. These measurements were relative to the unscoured soil surface.

III. OBSERVATIONS

A. Forms of Erosion

During some initial trials to investigate the characteristics of erosion of the soil used for the experiments, three forms of erosion were observed. At lower shear stresses (less than a maximum shear stress on the sample surface of about 15 Pa), erosion occurred only on the surface of the sample by the removal of circular flakes of 1 to 3 mm diameter and thickness of less than 0.5 mm. This "flake erosion" did not produce a significant amount of scour in the sample.

At higher shear stresses (greater than about 48 Pa), the erosion of chunks or lumps of soil occurred intermittently by mass erosion. A small chunk tended to be cubical in shape and was about 3 mm long, 2 mm thick, and 2 mm wide. The large chunks tended to be more angular in shape and could be up to 130 mm by 40 mm by 20 mm in size. Fig. 3 shows some typical larger eroded chunks. Mass erosion appears as if the particles are being ripped by the flow from the sample surface. This process was intermittent and there was no obvious pattern to timing of the removal of chunks or their size. In general, however, larger chunks tended to be eroded near the start of a test

TABLE 1. Details of Experiments

Expt.	H	d	U_o	w_c	w_f	S_v	χ	$(\chi-\chi_c)/\chi_c$	R	Temp	t_e	t_{80}	t_{50}	t_{35}
	(mm)	(mm)	(m/s)	(%)	(%)	(kPa)	(Pa)		10^4	(°C)	(h)	(h)	(h)	(h)
8/8.1/6.1/1	65	8	6.17	26.50	28.09	20.5	576	0.92	4.3	14.9	84.43	35.39	12.91	6.47
8/8.1/7.0/1	65	8	6.96	26.18	27.41	20.8	734	1.45	5.4	18.9	117.95	37.14	2.30	0.82
8/8.1/7.4/1	65	8	7.44	26.20	27.55	18.9	839	1.80	5.6	18.3	117.43	31.21	1.69	0.40
8/8.1/8.4/1	65	8	8.36	24.43	-	19.6	1058	2.53	5.9	15.6	93.75	8.69	0.22	0.09
8/8.1/9.0/3	65	8	8.95	25.52	27.41	20.2	1214	3.05	7.0	19.9	92.00	28.46	1.74	0.37
8/8.1/9.0/4	65	8	8.95	26.50	27.26	16.1	1214	3.05	6.3	11.8	104.89	27.84	0.48	0.27
8/8.1/9.0/5	65	8	8.95	25.50	27.54	21.7	1214	3.05	4.7	4.8	95.35	30.57	4.78	3.36
8/8.1/9.0/6	65	8	8.95	25.81	27.56	22.6	1214	3.05	4.7	4.8	154.43	101.54	23.54	16.48
8/8.1/9.9/1	65	8	9.93	26.85	28.59	18.4	1493	3.98	7.3	16.9	93.42	15.09	0.03	0.02
8/14.5/9.0/1	116	8	8.95	26.06	27.83	17.5	381	0.27	7.0	20.1	97.47	7.64	4.37	0.95
8/14.5/9.0/4	116	8	8.95	-	27.17	19.6	381	0.27	7.5	22.2	58.60	7.11	0.54	0.35
8/14.5/10.9/1	116	8	10.94	26.43	27.56	21.7	569	0.90	5.9	6.4	82.08	33.33	1.87	1.68
4/10.0/9.9/1	40	4	9.95	25.51	-	-	989	2.30	2.6	4.8	141.83	90.25	50.08	25.44
4/10.0/15.9/1	40	4	15.92	25.05	27.35	25.6	2533	7.44	4.2	5.4	81.77	20.54	1.57	0.45
4/29.0/25.9/2	116	4	25.86	25.37	-	-	795	1.65	8	15.4	106.55	69.90	22.16	15.51

and removal of chunks tended to become more infrequent as a test progressed.

Another type of erosion observed was the removal of individual particles, or surface erosion. This was seen in two tests at very high bed-shear stresses (260 and 400 Pa). It occurred only at the start of the tests and lasted at most 4 h before mass erosion occurred. This type of erosion resulted in a symmetrical shape of the scour hole through the scouring process.

Note that the bed-shear stresses reported above were calculated from the equation given by Beltaos and Rajaratnam [2] for a submerged vertical circular impinging jet on a smooth, rigid bed. They found the maximum shear stress τ_{om} created by a jet at a large impingement height (H/d>8.1) is

$$\tau_{om} = 0.16\rho U_o^2 \left(\frac{d}{H}\right)^2 \qquad (1)$$

where ρ is the density of the fluid. For the present work, since the particle size of the material tested was very fine and the surface was cut with a wire before testing, it was assumed that the soil surface could be taken to be smooth. The reported bed shear stress corresponds to the initial conditions of a test (a flat bed a distance H from the origin of the jet).

B. Time Development of Scour Holes

Since mass erosion was the only type of erosion that produced a significant amount of scour, the experiments were run under conditions to produce mass erosion. Due to the intermittent nature of mass erosion, the scour holes tended to be quite irregular in shape early on in a test (Fig. 4), but looked more symmetrical and smooth as they neared asymptotic state (Fig. 5). As well, with mass erosion of large particles, the maximum depth of scour did not necessarily fall along the jet centerline. The maximum depth of scour would remain constant for some time during a test when this occurred. This gave

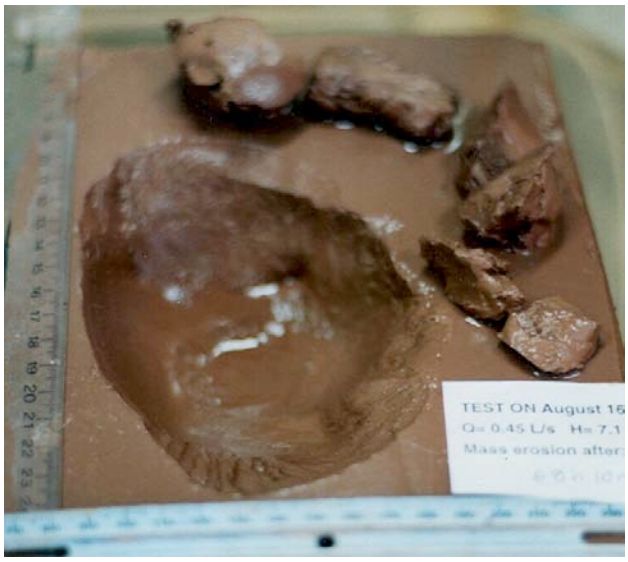

Figure 3. Larger chunks removed during an experiment with H= 65 mm, d=8 mm, and a U_o=8.95 m/s over 68 h of testing

Figure 4. Scour hole growth (in plan view) after 15 min for test with H=65 mm, d=8 mm, and U_o= 8.95 m/s.

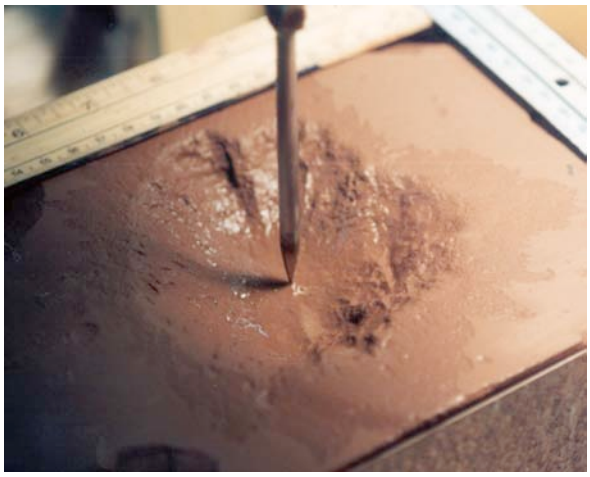

Figure 5. Typical shape of scour hole at asymptotic state (Expt. 8/14.5/10.9/1 after 93 h).

discontinuities in a plot of the maximum depth of scour with time, which was also seen by Moore and Masch [15]. Fig. 6 shows the observations from three experiments of the growth with time of the maximum depth of scour ε_m, centerline depth of scour ε_{cl}, and cube root of the scour hole volume $\sqrt[3]{\xi}$. It would appear from Fig. 6c that for Expts. 8.0/8.1/7.0/1 and 8.0/8.1/7.4/1 the centerline scour depth did not reach asymptotic state. However, this continued growth in the centerline depth of scour was attributed to the disturbance of the sample due to repeated measurements in that area, which would sometimes result in a small amount of erosion.

There were also two series of tests where there were repeated tests under the same hydraulic conditions. The observations from these experiments are shown in Mazurek [11]. The scour holes produced by the same hydraulic conditions had approximately the same volume at asymptotic state, but there was substantial variation in the maximum and centerline scour depths. Also, the time evolution of the scour holes between experiments was quite different and appeared to depend mostly on the size particles eroded early in a test.

IV. ANALYSIS OF TIME EVOLUTION OF SCOUR

A. Rajaratnam and Beltaos (1977)

Rajaratnam and Beltaos [17] developed a method to analyze the time evolution of scour by a vertical circular turbulent impinging jet in cohesionless materials. Their experiments were performed with air jets impinging on a bed of either sand or polysterene particles. They evaluated the growth of the radius of the scour hole and maximum depth of scour. Note that the maximum depth of scour occurred along the jet centreline for all but very early times. It was shown that the data from the experiments could be collapsed onto one curve if the dimensionless scour depth $\varepsilon_m/\varepsilon_{m\infty}$ was plotted against a dimensionless time t/t_+. Here ε_m is the maximum depth of scour, $\varepsilon_{m\infty}$ is the maximum depth of scour at asymptotic state, t is the time from the start of the experiment, and t_+ is the time scale for scour. For their experiments, the most effective time scale for collapsing

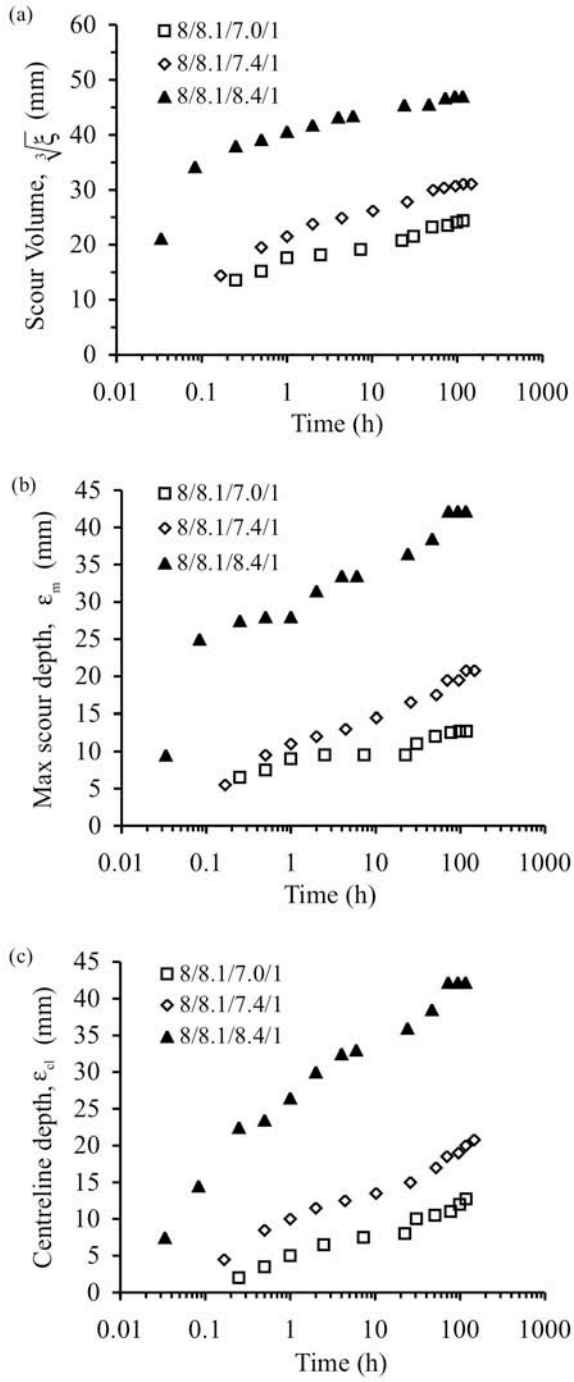

Figure 6. Examples of the growth of the (a) cube root of the scour hole volume (b) maximum depth of scour and (c) centerline depth of scour.

the data was the time to scour 50 % of the maximum depth of scour at asymptotic state.

To test this method of analyzing time evolution of scour for cohesive soils, the data for the growth of the centerline scour depth were plotted in dimensionless form as $\varepsilon_{cl}/\varepsilon_{cl\infty}$ against t/t_+. A number of different time scales were tried for t_+, including t_{80}, t_{50}, and t_{35}, where t_n is the time to n % of the centerline scour depth at asymptotic state. These times scales were determined by one of two methods. First, if a linear fit data of the data for each experiment of the centerline scour depth to the logarithm

of time did not show a lot of scatter, the curve fit was used to estimate the time to n % of the asymptotic state value. Otherwise, linear interpolation was used between data points. The estimates for these time scales are given in Table 1.

Fig. 7 shows the growth of the dimensionless centreline scour depth $\varepsilon_{cl}/\varepsilon_{cl\infty}$ with t/t_{80}, t/t_{50}, and t/t_{35}. The time scale corresponding to the time to 80 % of the asymptotic scour depth appears to provide the best fit to the overall data. It was seen the smaller time scales collapsed the data from the early part of the scour process effectively, but there was much scatter for later into the scouring process. Thus, for the present work, the analysis of the data will continue only for t_{80}. It was found the data was best fit by

$$\left(\frac{\varepsilon_{cl}}{\varepsilon_{cl\infty}}\right) = 0.10\ln\left(\frac{t}{t_{80}}\right) + 0.79 \qquad (2)$$

with an r^2=0.82 and the fit of Eq. 2 to the data is shown in Fig. 7a.

To use the dimensionless curves presented in Fig. 7(a), one would need to predict both the asymptotic depth of scour and the time scale. Methods for predicting $\varepsilon_{cl\infty}$ are presented in Mazurek et al. [12] and Ansari et al. [1]. For t_{80}, one might write

$$t_n = f_1\left\{M_o, \rho, H, \mu, \tau_c\right\} \qquad (3)$$

where $M_o = \pi\rho U_o^2 d^2/4$ is the momentum flux of the jet, and τ_c is the critical shear stress of the soil. Eq. 3 is based on the analysis of Mazurek et al. [12], who found that when assessing scour by vertical circular jets in cohesive soils at asymptotic state, M_o, ρ, H, and μ could be used to describe the properties of a jet at large impingement height and the critical shear stress τ_c can be used to represent the erosion resistance of the soil. By dimensional analysis, it is then found

$$\frac{t_{80}U_o}{H}\left(\frac{d}{H}\right) = f_2\left\{\frac{\rho U_o^2}{\tau_c}\left(\frac{d}{H}\right)^2, R = \frac{\rho U_o d}{\mu}\right\} \qquad (4)$$

For jets with Reynolds number R greater than about 10000, the Reynolds number on scour at asymptotic state can be neglected [12,17]. It is assumed here that that is also the case for the time development of scour. Also, following Mazurek et al. [12], let $\chi = \rho U_o^2\left(d/H\right)^2$. The parameter χ/τ_c represents the ratio of the shear stress on the bed to the critical shear stress of the soil. Since it can be shown that $\tau_c = 0.16\chi_c$, where χ_c is the value of χ below which (mass) erosion does not occur, χ/τ_c is proportional to χ/χ_c. Finally, χ/χ_c can be rewritten in the form of an excess stress $(\chi - \chi_c/\chi_c)$, so that

$$\frac{t_{80}U_o}{H}\left(\frac{d}{H}\right) = f_3\left\{\frac{\chi - \chi_c}{\chi_c}\right\} \qquad (5)$$

From plots of the variation of the volume of scour at

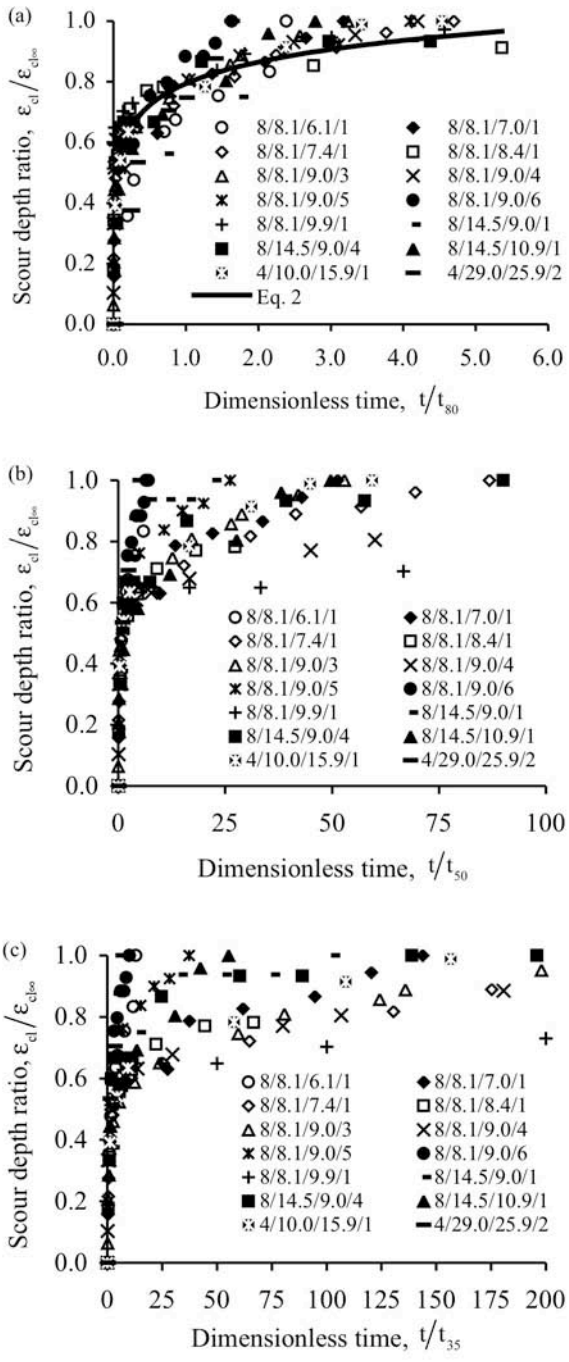

Figure 7. Dimensionless centerline scour depth with dimensionless time using a time scale corresponding to (a) 80 % (b) 50% and (c) 35 % of the asymptotic depth.

asymptotic state with χ, it was found that $\chi_c = 300$ Pa [12]. This corresponds to a critical shear stress for this soil of 48 Pa.

Fig. 8 shows the variation of the dimensionless time scale $(t_{80}U_o/H)(d/H)$ with the dimensionless excess stress $(\chi - \chi_c)/\chi_c$. Although there is a lot of scatter, an estimate for t_{80} might be made from

$$\frac{t_{80}U_o}{H}\left(\frac{d}{H}\right) = 788500\left(\frac{\chi - \chi_c}{\chi_c}\right) \qquad (6)$$

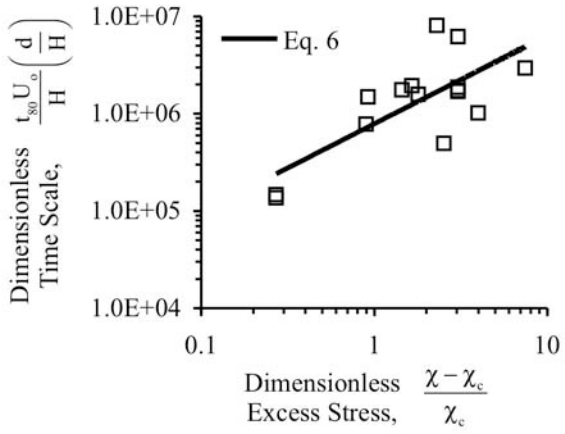

Figure 8. Variation of the dimensionless time scale with excess stress.

which gave an r^2=0.54.

An advantage of the method of Rajaratnam and Beltaos [17] is that an estimate for the time to asymptotic state is not needed, as this can be difficult to determine. This is because of the small changes in the scour hole size over long times at the late in the scouring process. Prediction of the time scale t_{80} however, at least for the current experiments, seems to be somewhat problematic. This is likely because tests under the same hydraulic conditions did not show that same rates of scour hole development. There was a 73 h variation in the estimates for t_{80} for the experiments all carried out with U_o=8.95 m/s, d=8 mm, and H=65 mm. It is unlikely that the relatively small variation in soil properties could account for a variation this large. As well, although the time to 80 % of the centerline scour depth at asymptotic state the entire scour process to asymptotic state, ultimately what time scale is most appropriate is a function of the situation considered. A smaller time scale may be more appropriate for practical situations where the duration of scour is also short-term.

It should also be noted that a smooth curve to represent the time evolution of scour in cohesive soil will miss the discontinuities in the growth of the scour hole due to mass erosion. It is difficult to model a discrete process with a continuous function. An example of this is shown in Fig. 9 for Expt. 8/8.1/7.0/1. This is a particular problem early on in the scour process when the scour hole is small and the eroded chunks tend to be large.

B. Ansari et al (2003)

Ansari et al. [1] presented a method to analyze the time evolution of scour in cohesive soils. He suggested that the scour hole growth follows the following relation

$$\frac{\varepsilon_{cl}}{\varepsilon_{cl\infty}} = \left[\sin\left(\frac{\pi t}{2t_e}\right)\right]^m \qquad (7)$$

where t_e is the time to asymptotic state. Ansari et al. [1] suggested the t_e and the power in Eq. 7, m, and t_e are a function of the soil antecedent moisture content, liquid limit (for soils with a plasticity), plasticity index, and dry unit weight. However, they did not have enough data to develop a relation to predict t_e and m.

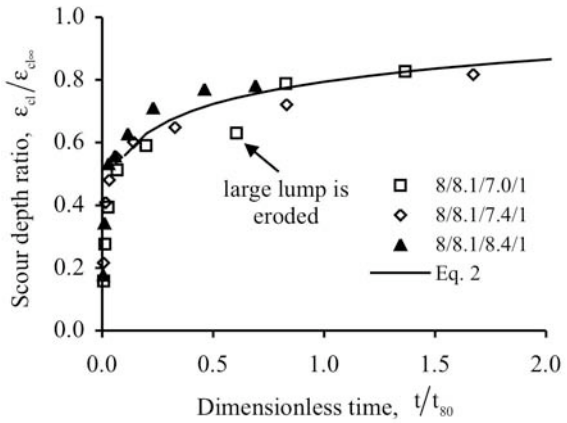

Figure 9. Variation in scour depths at early times due to mass erosion.

Fig. 10 shows the fit of the current experiments to Eq. 7. Note the time to asymptotic state was determined for each experiment from the change of slope on plots of the cube root of the scour volume with the logarithm of time, as it was constancy of the scour hole volume was used as the criteria for asymptotic state. For Eq. 7, an m=0.16 provided the best fit to the data. It is seen in Fig. 10 that there is more scatter than for Rajaratnam and Beltaos [17] method, likely due to the previously mentioned difficulties in assessing t_e.

V. CONCLUSIONS

For the time development of scour in a cohesive soil, mass erosion should be the expected scour process. Since this is the intermittent erosion of chunks or lumps of material, it is a discrete process. Modeling mass erosion by a continuous function can give a reasonable fit to the data for the time development of scour over the entire scour process. However, at very early times when the eroded chunks tend to be large and the scour hole is small

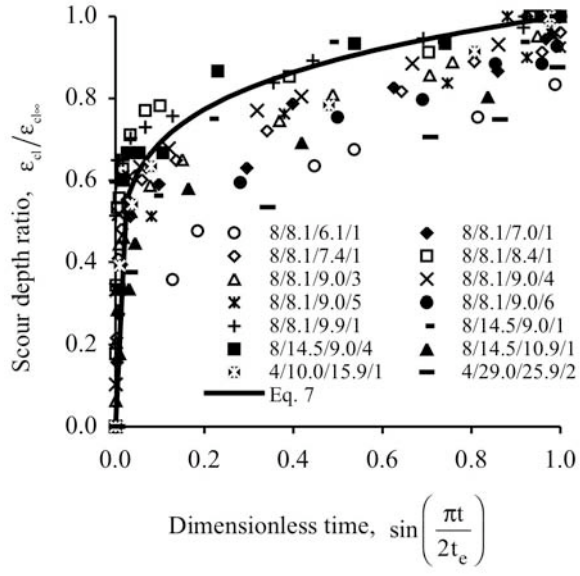

Figure 10. Time evolution of scour data based on Ansari et al. [1]

good prediction by a continuous model is less likely. A better understanding of the mechanics of mass erosion is needed for improved assessment of the time development of scour in cohesive material.

ACKNOWLEDGMENTS

The writers acknowledge financial support of the Natural Sciences and Engineering Research Council of Canada for this work. The writers are also thankful to P. Fedun for his help in the construction, maintenance, and operation of the experimental apparatus. This work was carried out in the former T. Blench Hydraulics Laboratory at the University of Alberta.

REFERENCES

[1] Ansari, S.A., U.C. Kothyari, and K.G. Ranga Ragu, 2003, Influence of cohesion on scour under submerged circular vertical jets, *J. Hydr. Engrg.*, ASCE, 129(12), 1014-1019.

[2] Beltaos, S., and N. Rajaratnam, 1974, Impinging circular turbulent jets, *J. Hydr. Div.*, ASCE, 100(HY10), 1313-1328.

[3] Beltaos, S., and N. Rajaratnam,1977, Impingement of axisymmetric developing jets, *J. Hydr. Res.*. IAHR, 15(4), 311-326."

[4] Dash, U., 1968, Erosive Behavior of Cohesive Soils, Ph.D. Thesis, Purdue University, West Lafayette, Indiana, USA.

[5] Dunn, I.S., 1959, Tractive resistance of cohesive channels, *J. Soil Mechanics and Foundations Div.,* 85(SM3), ASCE, 1-24.

[6] Hanson, G.J., 1991, Development of a jet index to characterize erosion resistance of soils in earthern spillways, *Trans. ASAE*, 34(5), 2015-2020.

[7] Hanson, G.J., and K.R. Cook, 1997, Development of excess shear stress parameters for circular jet testing, ASAE Paper No. 972227, St. Joseph, Michigan, USA.

[8] Hedges, J.D., 1990, The Scour of Cohesive Soils by an Inclined Submerged Water Jet, M.Sc. Thesis, Texas A & M University, College Station, Texas, USA.

[9] Hollick, M., 1976, Towards a routine assessment of the critical tractive forces of cohesive soils, *Trans. ASAE*, 19, 1076-1081.

[10] Mazurek, K.A., 2001, Scour of Clay by Jets, Ph.D. Thesis, University of Alberta, Edmonton, Alberta, Canada.

[11] Mazurek, K.A., 2005, Discussion of "Influence of Cohesion on Scour under Submerged Circular Vertical Jets," by S.A. Ansari, U.C. Kothyari, and K.G. Ranga Ragu, *J. Hydr. Engrg.*, ASCE, 131(8), 737-738.

[12] Mazurek, K.A., N. Rajaratnam, and D.C. Sego, 2001, Scour of cohesive soil by submerged circular turbulent impinging jets, *J. Hydr. Engrg.,* ASCE, 127(7), 598-606.

[13] Mehta, A.J., 1991, Review notes on cohesive sediment erosion, *Coastal Sediments '91*, 1, 40-53.

[14] Mirtskhulava, Ts.E., I.V. Dolidze, and A.V. Magomedova, 1967, Mechanisms and computation of local and general scour in non-cohesive, cohesive soils, and rock beds." Proceedings of 12th Congress of the IAHR, Fort Collins, Colorado, September, 1967, 3, 169-176.

[15] Moore, W.L., and F.D. Masch, Jr., 1962, Experiments on the scour resistance of cohesive sediments, *J. Geophys. Res*., 67(4), 1437-1449.

[16] Perigaud, C., 1984, Erosion of cohesive sediments by a turbulent flow: Part II - High mud concentration, *J. Mecanique Theorique et Appliquee*, 3(4), 505-519.

[17] Rajaratnam, N., and S. Beltaos, 1977, Erosion by impinging circular turbulent jets, *J. Hydr. Div.,* ASCE, 103(HY10), 1191-1205.

Empirical Modeling of the Evolution of the Coastline behind the Breakwaters (Tunisia)

MEDHIOUB. Samir*, RONDAY. François**
* Higher Institute of Technology Studies/Civil and Mining, Gafsa, Tunisia
** University of Liège/Oceanography, Liège, Belgium

Breakwaters are at the same time protective and menacing. These works create disruptions to the natural balance of transport of sediment not only locally but also to the surrounding beaches that will evolve in order to recover a new state of equilibrium.

The implementation of breakwaters result in the creation of tombolos in the zones relatively quiet and sheltered and in an erosion of the coastline on either sides. In this paper, a « parabolic » empirical model is applied to the small bay of Tunis (from Rades to Sliman) in order to predict the changing coastline position behind the implemented breakwaters or even their impact on the coast so much regressive that progressive.

The applied model could predict the new state of equilibrium of the coastline behind the implemented breakwaters, reasonably well compared to the natural curvature of the coastline behind the erosion control structures.

I. INTRODUCTION

Coastal zones are always under the threat of intensive and worrying activities of various economic and social entities.

The southern beaches of Tunis from the suburb of Rades to the village of Sliman (Fig. 1) account among the coastal zones which were seriously affected by marine erosion and by the degradation of its marine ecosystem due mainly to the anthropic pressure [1]. Beside swell and currents, the human actions which caused this regression of the shoreline were:

- the reduction of the river contributions estimated to 2,34 Million ton per annum after the construction of a number of dams on the main rivers, Médjerda and Méliane, wich used to be the two large providers of the coast in sediments [2].
- increasing urbanization near the coastline.
- the stop of the North-South sediments transit, coming from the North beaches of Tunis, because of installation of the port of Goulette [2] (Fig. 2).

These problems were the subject of a vast construction schedule of protection works in the southern beaches of Tunis. Since 1984, 19 emergent breakwaters at 6 locations hardly urbanized are constructed (Fig. 2) to protect more than 2200 m linear of littoral [3] (Table 1). These protections works constituted a direct obstacle for the transport of materials and influenced indirectly the littoral drift. They created, following the phenomena of the swell diffraction, a zone relatively calm and sheltered in their shade resulting in a material deposit which sometimes ends up connecting the breakwater to the coast by an effect of tombolo. Nevertheless, in case of a weak littoral drift, this material deposit is done with the detriment of the close zones while doing appear an erosion pits [4].

The goal of this work consists in applying an empirical shoreline model to predict the so-called of precarious balance behind the breakwaters of the Southern beaches of

Figure 1. Location plan of the fringe coastline from Rades to Sliman (Tunisia)

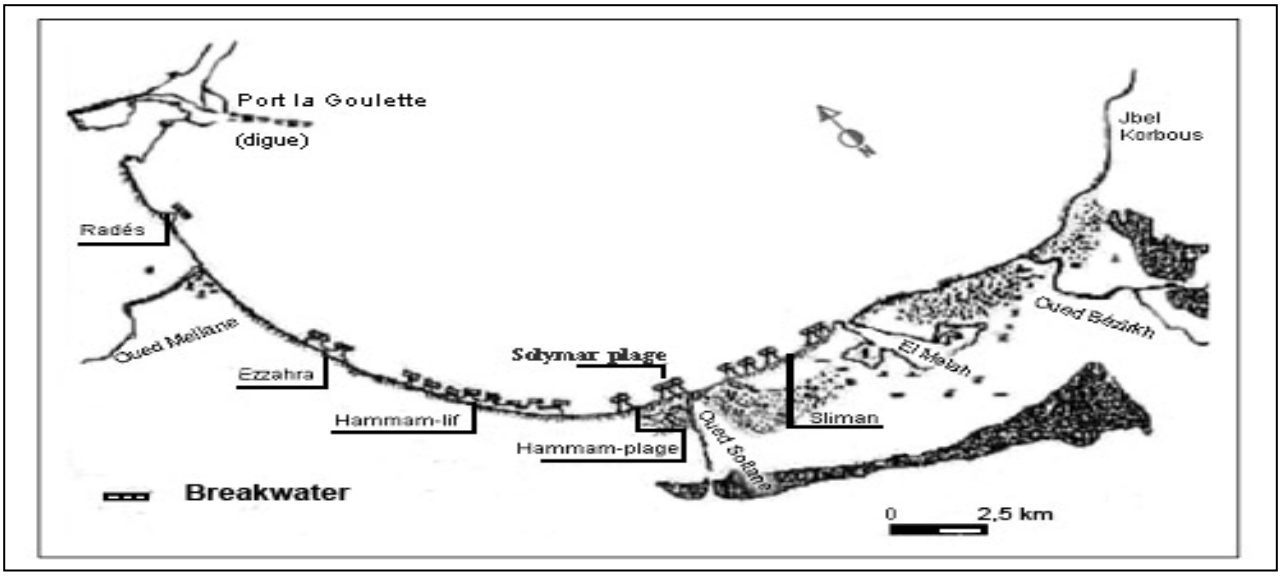

Figure 2. Emergent breakwater realized in the Gulf of Tunis [3]

TABLE I.
SUMMARY OF IMPLANTED BREAKWATERS IN THE GULF OF TUNIS

Coastal area	Number of segments	Date of construction	Medium segment length (m)	Medium gap length (m)	Water depth (m)	Offshore Distance (m)
Rades	1	1985	123	-	1,55	108
Ezzahra	2	1986-1987	135	35	2	75
Hammam-lif	8	1985-1986	150	55	2,5	100
Hammam-plage	1	1987	100	-	1,75	80
Solymar	2	1989	130	65	2,5	185
Sliman	5	1989-1990	150	40	2	116

Tunis, the limit of saturation of the tombolo and the generated erosion pit.

The model is of type “parabolic” in reference to the parabolic shape of shore observed from a natural safe headland.

II. HYDRODYNAMIC CARACTERISTICS OF THE STUDY AREA

A. Tide

The marnage in the Gulf of Tunis varies from 0,2 m to 0,3 m, either 0,24 m in weever water and 0,12 m in dead water [2]. It is considered negligible and without notable effect on coastal morphology.

B. Courantology

In the Gulf of Tunis, the currents of tide are generally very weak (less than 0,2 m/s) and masked by those related to the swells [2]. In the same way, the general currents have little influence on harbor and coastal installations: they intervene at 5 km from the coasts [5]. However the shoreline currents generated by the swell are very important in the sedimentary dynamics of the coasts [2].

C. Rise in the marine level

The signs of a variation of the sea levels are varied in Tunisia. The increase of the marine level is estimated 1,5mm/year [6]. This increase remains without perceptible effect on the Tunisian coasts.

D. Significant wave climate

Information on wave climate is necessary for understanding littoral processes. The action of waves is the primary agent producing erosion and transport impinging on the shore [7].

Several forecasting approaches have been made to estimate the wave condition in deep water including the SMB method. This method is used to determine the significant height and period for each direction. It needs as input data, the wind velocity and the stretch of water “Fetch”, that it crosses to the coast [7].

The computation results of the characteristics of the significant swell are recapitulated in Table 2.

E. Wave refraction and shoaling

Once the wave conditions in deep water have been estimated, the next step is to determine the characteristics of refracted waves before breaking occurs. The study of the refraction of the swell is based on the following simplifying assumptions [7]:

TABLE II.
SIGNIFICANT WAVE CLIMATES

Direction	Fetch	Wind velocity = 3 (m/s)			Wind velocity = 8 (m/s)			Wind velocity = 13 (m/s)		
	(km)	Occurrence %	Period Ts(s)	Height Hs(m)	Occurrence %	Period Ts(s)	Height Hs(m)	Occurrence %	Period Ts(s)	Height Hs(m)
N	***605,0***	3,10	2,25	0,26	1,40	5,37	1,68	0,00	7,70	3,69
NNE	***497,0***	2,70	2,24	0,26	1,10	5,27	1,64	0,00	7,50	3,52
NE	***510,0***	2,50	2,24	0,26	0,70	5,28	1,64	0,00	7,53	3,54
NNW	***255,0***	2,40	1,88	0,21	1,20	3,72	0,87	0,10	5,00	1,60

- Wave energy between wave rays or orthogonals remains constant.
- Waves are long-crested, constant period, small-amplitude, and monochromatic.
- The refraction analysis is based on Snell'S law which considers isobaths are parallel to the line of coast presumed linear.

Using (1), we calculate the height of the refracted wave (H_r).

$$k_s * k_r = H_r / H_0 \quad (1)$$

Where:

k_r is termed the refraction coefficient.

k_s is the shoaling coefficient.

H_0 is the deep water wave height.

The angle (α) between the refracted wave in the considered depth and the normal to the shoreline is calculated using (2)

$$\sin\alpha = \left(C_k / C_0\right)\sin\alpha_0 \quad (2)$$

Where:

C_k is the wave velocity in the considered depth. It's given by $C_k = C_0 \tanh\left(2\pi d_K / L_K\right)$.

Where:

C_0 is the deep water velocity equal to $\left(L_0 / T_s\right)$.

α_0 is the angle between the direction of the wave approach and the normal to the shoreline in deep water.

d_k is the considered water depth.

L_k is the wave length in the considered depth.

L_0 is the deep water wave length.

A typical refraction-shoaling calculation is given in the table 3.

F. The dominant wave

The weighting of each significant refracted wave by its percentage of occurrence gives the dominant wave whose characteristics are given by the following expressions [8]:

- Equation (3) is used to calculate the direction of the dominant wave (angle α_{dom}) compared to the north geographic:

$$\tan\alpha_{dom} = \frac{\sum_{j=1}^{m}\sum_{i=1}^{n} P_{i,j} Hr_{i,j}^2 Ts_{i,j} \sin\alpha_j}{\sum_{j=1}^{m}\sum_{i=1}^{n} P_{i,j} Hr_{i,j} Ts_{i,j} \cos\alpha_j} \quad (3)$$

Where

$P_{i,j}$ is the occurrence of the swell (Table 1).

n is the number of swell classes (each class corresponds to an intensity of wind velocity).

m is the number of swell directions.

- Equation (4) is used to calculate the period of the dominant swell (T_{dom})

TABLE III.
TYPICAL CALCULATION OF REFRACTED WAVE CHARACTERISTICS

Direction of wave ***North North East***									
Period, Ts = 5,27 s									
H_0 = 1,64 m			L_0= 44,2 m			C_0= 8,2 m/s			
α_0= 22,5°									
d_k (m)	d_k/L_0	d_k/L_K	tanh(2*pi*d_k/L_k)	C_K (m/s)	α	K_r	K_S	K_r*K_S	H_r (m)
10,0	0,2265	0,24760	0,91	7,67	20,9056	0,9945	0,9162	0,9111	1,4942
9,0	0,2038	0,22850	0,89	7,49	20,3827	0,9928	0,9102	0,9036	1,4820
8,0	0,1812	0,20920	0,87	7,26	19,7299	0,9907	0,9059	0,8975	1,4718
7,0	0,1585	0,19040	0,83	6,98	18,9514	0,9883	0,9043	0,8937	1,4657
6,0	0,1359	0,17160	0,79	6,65	18,0087	0,9856	0,9066	0,8936	1,4655
5,0	0,1132	0,15220	0,74	6,23	16,8396	0,9825	0,9151	0,8990	1,4744

$$T_{dom} = \sum_{j=1}^{m}\sum_{i=1}^{n} P_{i,j} Ts_{i,j} \Big/ \sum_{j=1}^{m}\sum_{i=1}^{n} P_{i,j} \qquad (4)$$

- Equation (5) is used to calculate the height of the dominant swell H_{dom}

$$H_{dom} = \left[\sum_{j=1}^{m}\sum_{i=1}^{n} P_{i,j} Hr_{i,j}^{2} Ts_{i,j} \Big/ T_{dom} \right]^{1/2} \qquad (5)$$

The obtained period, height and angle of the dominant swell are 2,968 s, 0,422 m and 3,4° compared to the north geographi***c,*** respectively**.**

G. Littoral transport

The littoral transport of sediments in the Gulf of Tunis, is classified as onshore-offshore transport and as longshore transport. The typical rate for onshore-offshore range from 1,5 to 3 million cubic meters per year [2]. The longshore transport rates, carrying from west to east, range from 15000 to 20000 cubic meters per year [2].

III. EMPIRICAL SHORELINE MODEL

In nature, many sections of coastline which are situated in the lee of a natural or artificial headland have a curved shoreline geometry. Where sections of coastline are situated between two headlands, and particularly when there is a single dominant wave direction, the shoreline may likewise assume a curved or a « scalloped » shape (see Figure 3a) [9]. Because of their geometries, these shorelines are also sometimes termed « parabolic ». The shape results from longshore transport processes which move sediment in the downdrift direction along the down-wave section of the shoreline, and from processes associated with wave diffraction which move sediment in the opposite direction in the immediate lee of the up-wave headland [9].

A new empirical approach has been developed by Hsu, Silvester, and Xia ([10], [11], [12]). This approach is based on physical models and on shoreline data from prototype bays assumed to be in static equilibrium. They presented the alternative expression (6) for parabolic model to approximate the shoreline in the lee of headland-type features

$$R/R_o = C_o + C_1 * (\beta/\theta) + C_2 * (\beta/\theta)^2 \qquad (6)$$

Where the geometric parameters R, R_o, β and θ are as shown in Figure 3a, and values for the coefficients C_0, C_1, and C_2 are shown in Figure 3b. The distance R_0 corresponds to a control line drawn between the ends of the headlands that define a given section of shoreline.

In the case of a single, upcoast, headland, the distance R_0 is the length of a control line drawn from the end of the headland to the nearest point on the downcoast shoreline at which the shoreline is parallel with the predominant wave crest.

The distance R measured from the end of the upcoast headland, defines the location of the shoreline and angles θ measured from the predominant wave crest. The angle β is that between the predominant wave direction and the control line R_0.

The data upon which equation (6) assume β to be higher than 22°.

Furthermore, Equation (6) is intended for application for θ between β and 180°, and assumes that a predominant wave direction exists at the site of interest.

For θ higher than 180°, the distance R may be assumed

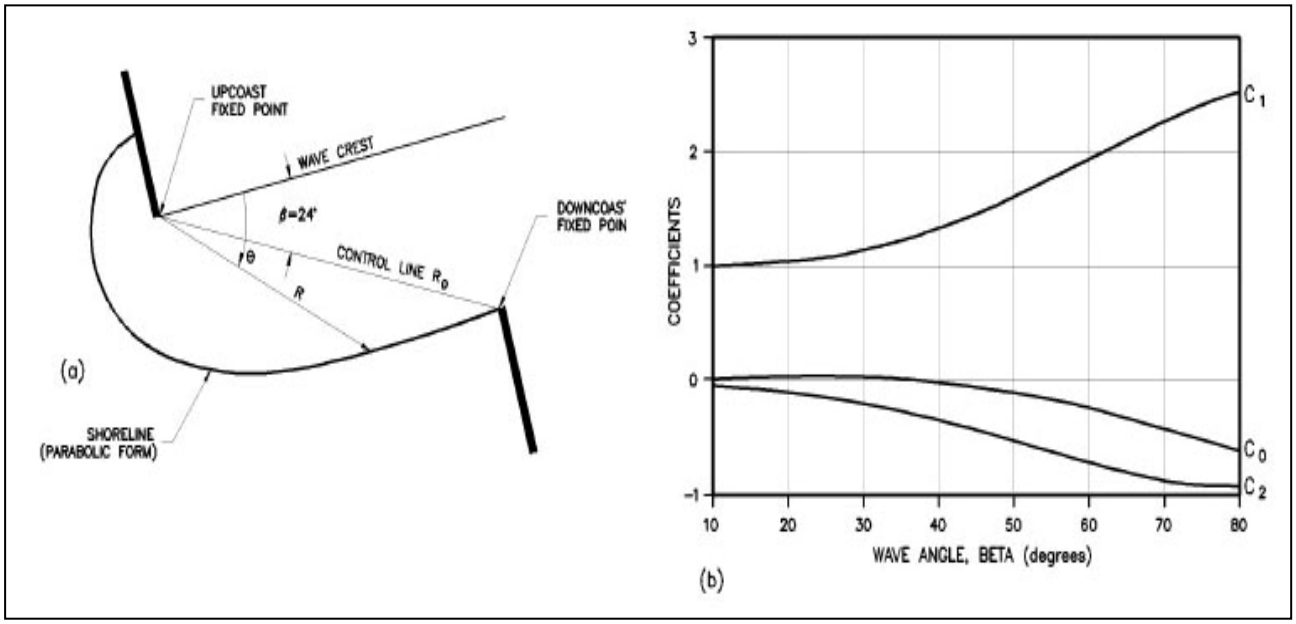

Figure 3. Spiral bay geometry: (a) definition sketch and (b) coefficients describing parabolic shoreline shape [13].

to be constant and equal to the value of R computed at θ equal to180°.

IV. Results and Discussion

Predicting shoreline changes following the construction of offshore breakwaters is predominantly governed by the resulting alterations in the longshore transport of material in the vicinity and, to a lesser extent, by the onshore-offshore transport rate. The placement of a breakwater causes the shoreline to adjust to the new conditions and seek an equilibrium state.

The applied empirical parabolic model has permit to predict the evolution of coastline behind the breakwaters. The predicted shoreline was superimposed with coastline raised by SOGREAH in 1992 [14], as well with that raised by Zeggaf in 1996 [3] to provide idea of the spatial-temporal response of the shoreline.

The whole results obtained and, presented below shows, on the one hand, that the shape of the coastline given by the empirical model is curved or was a "parabolic" form. It could not only reproduce the natural shape taken by the shoreline behind the breakwaters but also the shape of the tombolo. The tombolo would have a symmetric (Figure 4, 5 and 7) or asymmetric (Figure 6, 8 and 9) shape function of the incident dominant wave crest, i.e., if the dominant wave crests is parallel to the original shoreline, the diffracted waves into the offshore breakwaters would transport sand from the edges of this region into the shadow zone. This process would continue until the shoreline configuration is essentially parallel to the diffracted wave. When the dominant is relatively oblique, the longshore transport rate in the lee of the structure would initially decrease, causing deposition of the longshore drift. A cuspate spit is formed which will continue to grow either the longshore transport rate past the structure is reestablished or a tombolo is formed. The cuspate spit that results from oblique dominant wave attack could be expected to be asymmetric with its shape dependent on the structure length and the offshore distance [9].

On the other hand, it has been revealed that the development of the tombolo is very variable according to the arrangement and the water depth implantation of the breakwater as well as their location compared to the coastline. More the breakwaters are located close to shore and relatively impermeable (high crest and small gaps), the more the final balance state of the coastline, delimits a formation of tombolo that is enough developed (Fig. 4, 5 et 6).

As illustrated in Figures 7, 8 and 9, the predicted shoreline, showed the presence of erosion pit. In fact, the tombolo detached breakwater functions like a teeshaped groin by blocking longshore transport and promoting sediment mouvements offshore in rip-currents through the gaps. Although the longshore transport can occur seaward of the breakwater, the interruption in the littoral system may starve downdrift beaches of their normal sediment supply, causing erosion [9].

Reference to the natural evolution of the fringe littoral from Rades to Sliman behind the beakwater from 1992 to 1996, the table 4, give an estimate of a predicted medium time, counted from 1996, to reach the predicted position of the precarious equilibrium state (relative to the accretion of tombolo or to the erosion pit resulting).

The given values in table 4 supposed a linear evolution of the coastline. It appeared from these values, that, the shore protection measures in the Gulf of Tunis, are relatively well planned. They resulted in some modifications of the physical environment through the attained desired protection in a reduced time. However, thorough planning and design require that the full impact of the adverse effect must be fully considered and understood. If feasible, the expected shoreline adjustment behind the breakwaters should be artificially placed to reduce starvation of the downdrift beach.

V. Conclusion

The applied empirical shoreline model of the type « parabolic » allowed to predict the evolution of the coastline behind the breakwaters located in the fringe littoral from Rades to Sliman. The precarious balance and the erosion pits generated on either sides by these defense works were well simulated. Nevertheless, this approach outlined above may be useful for rough, preliminary calculations and estimates of « static » shoreline equilibriums when the assumptions necessary for application of the approach are fulfilled, where detailed dynamics of the changing shoreline area not sought, and where time and/or budget constraints preclude a more detailed approach. For detailed prediction of shoreline change due to longshore gradients in sand transport or otherwise complicated geometries, a preferred approach would be utilize a physical model and/or a numerical model, as appropriate to the scale of the study area.

Acknowledgment

We acknowledge the help given by the Chaâbane and Cie Company and Tunisien Underseas Works Company in all stages of this works. We also wish to thank the Development University Commission of Belgium for the financial offer to this works. Finally, we wish to thank Fahmi Naîfer for his constructive comments in his reviews of the manuscript.

TABLE IV.
VALUES OF PREDICTED MEDIUM TIME TO REACH THE PREDICTED SHORELINE TAKING THE 1996 SHORELINE POSITION AS REFERENCE

Coastal area		Rades	Ezzahra	Hammam-lif	Hammam-plage	Solymar	Sliman
Predicted medium time (year)	Accretion tombolo	8	6	2	14	5	56
	Erosion pit	17	-	18	-	-	14

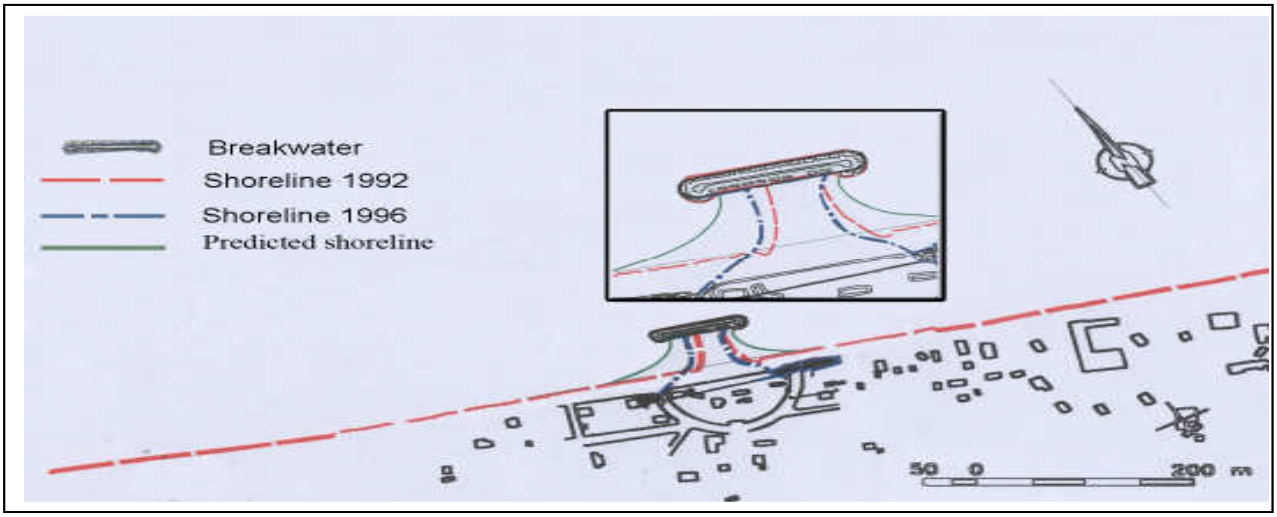

Figure 4. Predicted shoreline behind the breakwater of Hammam-plage site [15]

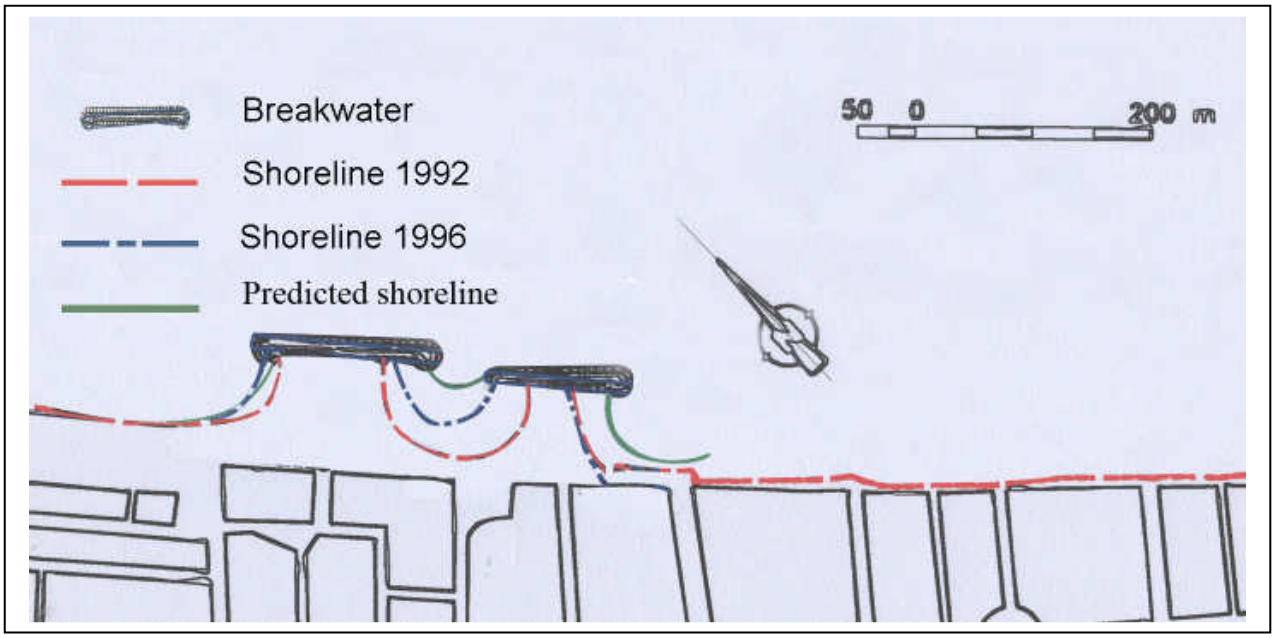

Figure 5. Predicted shoreline behind breakwaters of Ezzahra site [15]

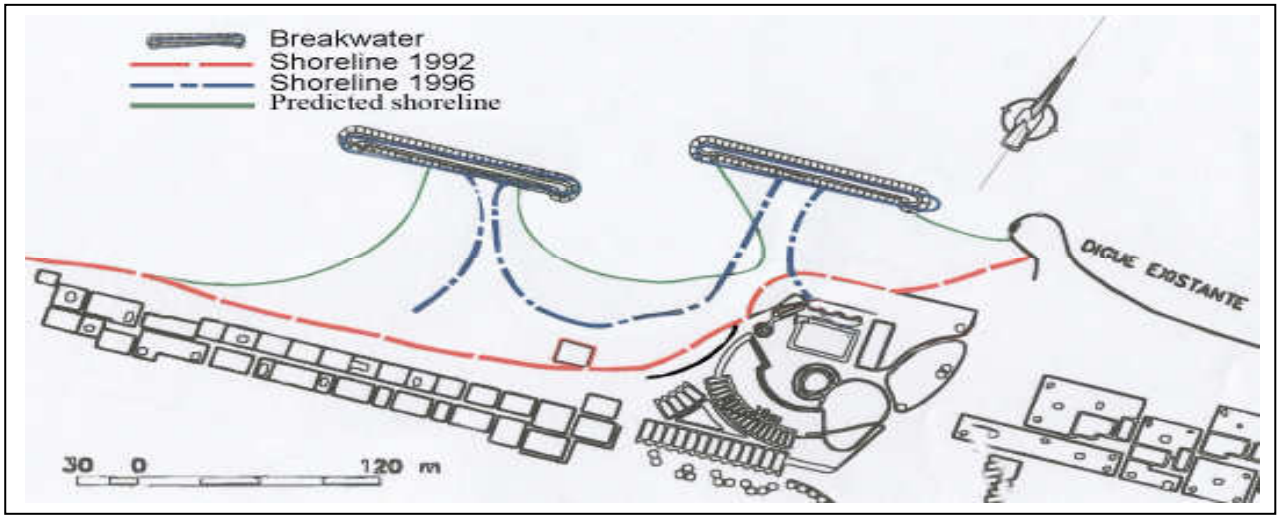

Figure 6. Predicted shoreline behind the breakwaters of Solymar site [15]

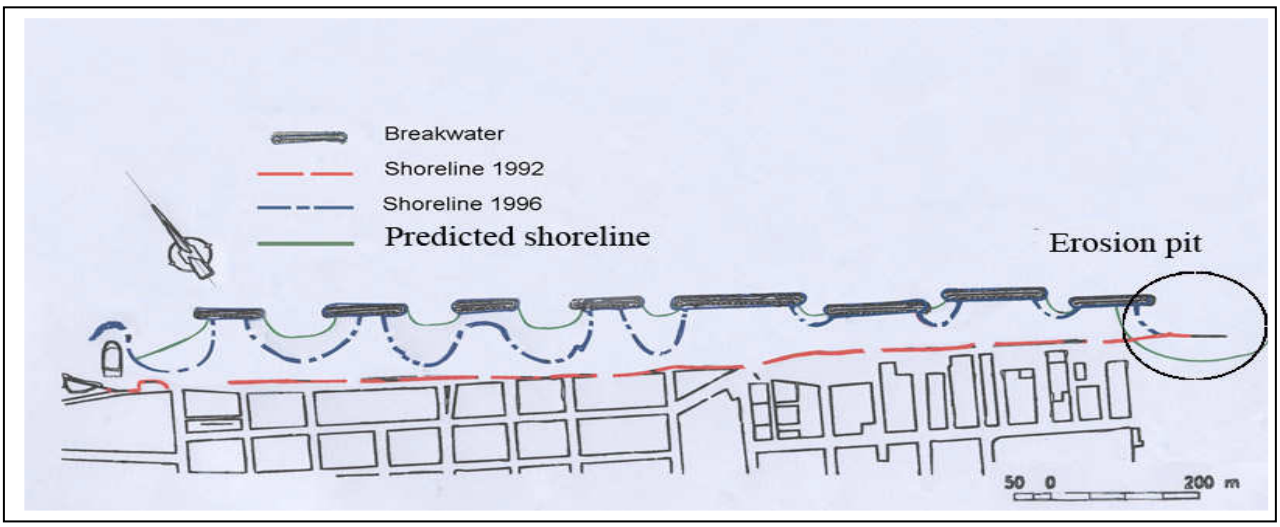

Figure 7. Predicted shoreline behind the breakwater of Hammam-lif site [15]

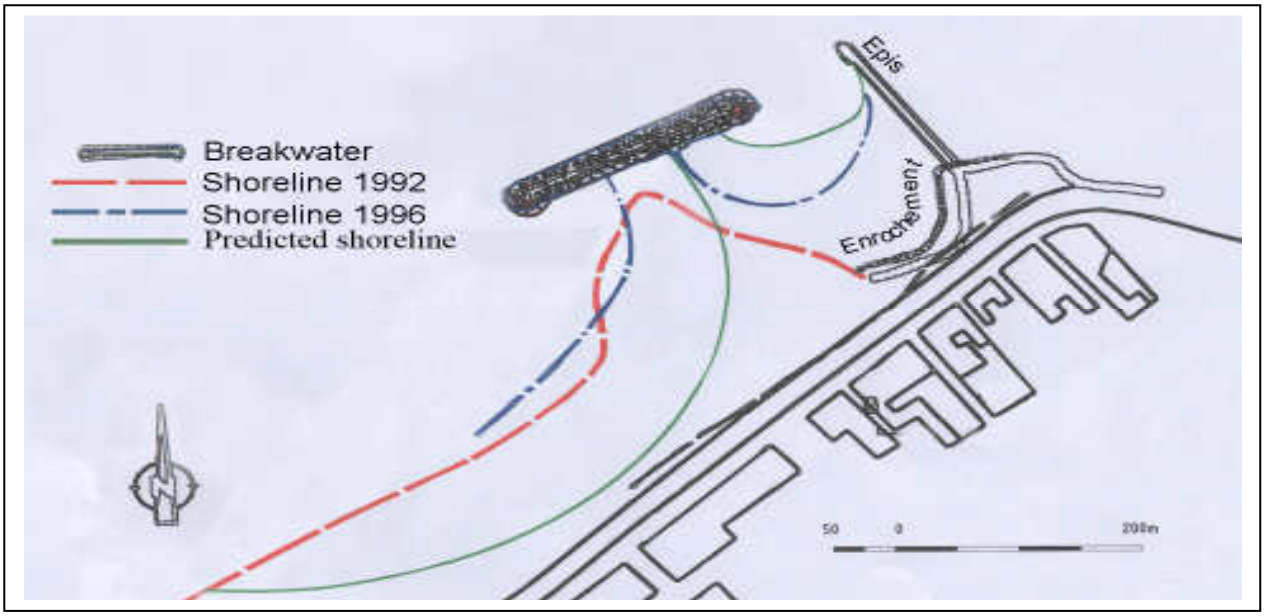

Figure 8. Predicted shoreline behind breakwaters of Rades site [15]

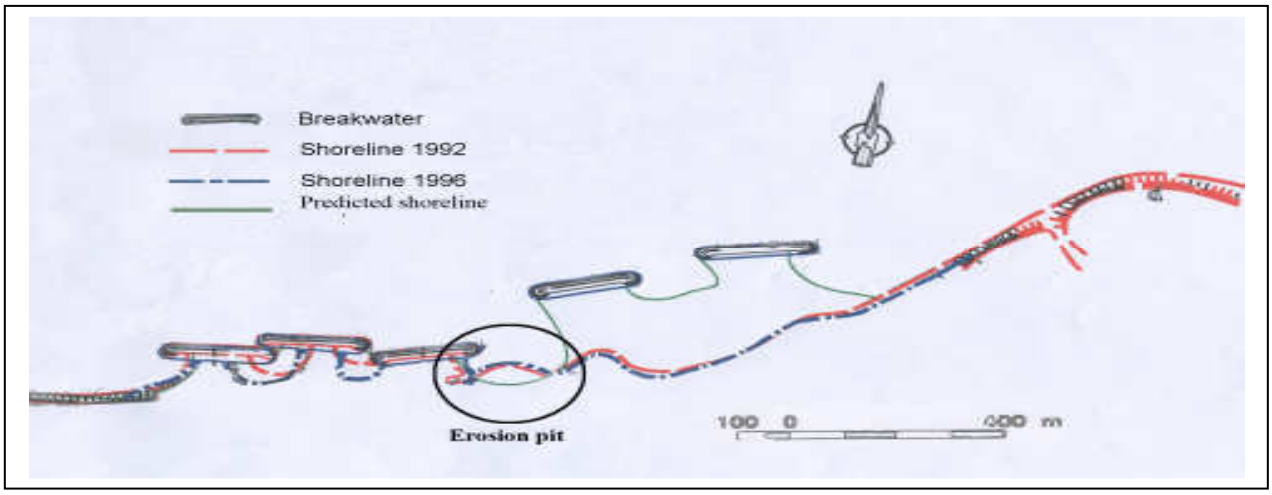

Figure 9. Predicted shoreline behind the breakwaters of Sliman site [15]

REFERENCES

[1] Oueslati, A., 2004, Littoral et aménagement en Tunisie, Faculté des Sciences de Tunis.

[2] Hidrotechnica Portuguesa (HP), 1995, Etude générale de la protection du littoral tunisien contre l'érosion marine, Ministère de l'Equipement et de l'Habitat, Tunisie.

[3] Zeggaf, T. M., 1996, Etude d'impact des ouvrages de protection sur l'environnement du littoral du petit Golfe de Tunis, Thèse de Doctorat en Géologie, Université de Tunis.

[4] Sliti, M., 1990, Fonctionnement des brise-lames dans le système marin littoral du Golfe de Tunis, Thèse de 3^{éme} cycle, Uni. Bordeaux, France.

[5] Société Tunisienne d'Etudes et d'Ingénierie (STUDI), 1991, Etude de dix ports de pèches côtiers, Ministère de l'Equipement et de L'Habitat, Tunisie.

[6] Oueslati, A., 1998, Les côtes de la Tunisie morphologie et caractéristiques de l'évolution récente du rivage, Faculté des Sciences de Tunis.

[7] Coastal Engineering Reasearch Center (CERC), 1984, Shore protection manual.

[8] Bejaoui, B., 1997, Evolution et protection du littoral dans le Golfe de Tunis, Projet de fin d'études, Ecole Nationale d'Ingénieurs de Tunis (Tunisie)

[9] Coastal Engineering Reasearch Center (CERC), 1998, Coastal engineering manual.

[10] Hsu, J.R.C., Sivester, R., et Xia, Y., M., New characteristics of Equilibrium Shaped Bays, Proceedings, 8th Augt. Conference on coastal and Ocean Eng., 140-44, 1987

[11] Hsu, J.R.C., Sivester, R., et Xia, Y., M., Static Equilibrium Bays : New Relationships, ***Journal waterways, Port, Coastal and Ocean Engineers***,115(3),p.p. 285-98, 1989 a

[12] Hsu, J.R.C., Sivester, R., et Xia, Y., M., Generalities on Static Equilibrium Bays, ***journal Coastal Engineering***,12, p.p. 353-369, 1989 b

[13] Silvester, R. et Hsu, J.R.C. Coastal stabilization : Innovative Concepts, Printice Hall, Inc., Englewwood Cliffs, NJ., 1993.

[14] SOGREAH, 1992, Réhabilitation de la protection des plages sud de Tunis et de Mahdia, Ministère de l'Equipement et de l'Habitat.

[15] Medhioub,S., 2005, Réponse dynamique aux facteurs naturels et anthropiques de la frange littorale allant de Hammam-lif à Solymar (Tunisie), Université de Liège, Belgique.

Riprap Protection of Spill-through Abutments on Laterally Sloping Floodplains

B.W. Melville*, and L.G. Fletcher*

* The University of Auckland/Department of Civil and Environmental Engineering, Auckland, New Zealand

Experimental data of local scour at spill-through abutments on laterally sloping floodplains are presented. The experiments extend an earlier study of riprap protection at bridge crossings featuring wide flood channels. This study applies to situations where the flood channel slopes laterally towards the main channel (rather than being rectangular) and the bridge crossing is skewed (rather than being perpendicular to the river channel); both equilibrium and non-equilibrium scour data are presented. Comparisons with existing design equations are given and recommended modifications to these equations are suggested to predict scour depths. Minimum apron widths to avoid failure are also given. Tests were conducted under clear-water conditions. The data show that equilibrium scour depth increases with increasing abutment length. Typically wider riprap aprons deflect scour further downstream from the abutment toe. Laterally sloping floodplains encourage riprap apron erosion with larger apron widths necessary for a given scour depth than for non-sloping floodplains of the same scour depth. Skewed abutment data show increased scour depth with increasing skew angle. This study is discussed in relation to previous data and suggested design equations and experimental limitations are also outlined.

I. INTRODUCTION

Protection of abutments through armoring and stabilization of the abutment slope, or by re-aligning the flow upstream of the abutment, is a necessary part of abutment and bridge approach design.

Riprap protection is one of the most common methods of protecting bridge abutments as it is readily available in many areas and therefore an economic solution for scouring problems. Riprap protection comprises an apron or layer of broken rock that is either dumped or placed in position as a preventative measure against scour. Typically riprap is used on the embankment side-slopes and ideally apron protection is placed at the toe of the abutment; riprap from the apron falls into the scour hole inhibiting further scour and deflecting the scour away from the abutment.

The large sizing of riprap and increased weight compared with the bed material means that increased flow velocities and turbulence created by the presence of the abutment are resisted. Riprap aprons are easy to construct, have the advantage of flexibility if settlement occurs, are easily repaired and maintained, and are durable. Individual riprap stones are recoverable should the need arise [6].

There are many design guidelines for the use of riprap as a scour countermeasure [1, 11, 16], including rock sizing, stable embankment slope, and protective apron width. These criteria are designed to prevent the common failure modes of abutments described as:

- erosion of riprap particles as a result of insufficient sizing, uniform gradation, or steep embankment side-slopes.
- riprap translational slide down the embankment because of channel scour, excess pore water pressure or steep embankment side-slopes.
- slump failure of riprap, due to channel scour, excess pore water pressure or steep embankment side-slopes.
- slump failure of the abutment due to excess pore water pressure or non-uniform material creating failure planes.

These failure mechanisms can be avoided by ensuring the riprap stones are large and heavy enough to resist movement, providing a riprap layer greater than at least one stone thick, underlying the riprap with a filter fabric to protect the side-slope material, providing a riprap apron in areas prone to scour, and reducing the angle of embankment side-slopes.

Required riprap properties are outlined in [1, 16], which state that the use of hard, durable, dense and angular rock is preferable. The riprap must be able to withstand some movement and weathering and a high density is desirable because, for a given stone size, the riprap will be able to withstand higher flow velocities prior to motion. Angular rocks are more stable on embankment side-slopes and provide a more cohesive protection apron than rounded riprap. Well graded riprap also provides stability and cohesion as the individual stones interlock.

There are many design equations that can be used to find suitable values for these parameters, however these are primarily based upon laboratory experiments or theory and often result in large sizes for individual rocks.

There have been numerous experimental studies relating to riprap protection at bridge abutments. Research on skewed wing-wall abutments was performed by [8] on a plane bed at equilibrium, finding perpendicular abutments had the deepest scour depth of any skew angle for clear-water conditions. Reference [12] studied the effectiveness of scour countermeasures and followed typical construction practice for testing. Laboratory experiments were run under clear-water conditions in an idealized channel geometry. It was found that significant riprap protection is required on the upstream face of an abutment, high velocities damage the abutment structure, and piers adjacent to abutments require special protection as they could be sited in a scour hole. As an extension of this work, [3] conducted experiments under clear-water conditions using square-edged riprap aprons with pre-

excavated scour holes. Equations for stable riprap size on embankments, and an embankment slope modification factor are derived in [3]. The study of vertical-wall and spill-through abutments to find stable riprap sizes for these abutment types was undertaken by [14]. It was found that the location of the failure zone is at the upstream corner of vertical wall abutments, and downstream of the contraction near the toe for spill-through abutments.

Design procedures for scour protection of bridges, including inspection techniques and installation techniques for countermeasures are presented in [15].

Studies of riprap protection for spill-through abutments on horizontal floodplains [4] were run under clear-water conditions for time periods shorter than equilibrium. It was found that the larger the riprap sizing, the narrower the riprap apron could be to offer sufficient scour protection to the abutment.

Further research on vertical wing-wall abutments of varying lengths under clear-water conditions was performed by [2]. Experiments were run to equilibrium on a plane bed surface with results defining the time to equilibrium relative to both abutment length and flow intensity.

Experiments performed by [18] under clear-water conditions on an idealized channel shape were run to equilibrium using riprap protected spill-through abutments crossing perpendicular to the floodplain and channel. Reference [18] derived design equations for the minimum apron width required for abutment protection and for the expected equilibrium scour depths relative to abutment length, riprap apron width, and floodplain geometry.

These previous studies used idealized channel geometries to introduce scour relationships which may not be applicable for all situations. The aim of this study is to investigate the scouring action at spill-through abutments on laterally sloping floodplains. Scour data, both in terms of scour depth and scour hole geometry are presented and compared with currently used design equations. Previous research on spill-through abutment scour is verified; riprap apron width is evaluated for this channel geometry and the effects of skewness of abutments on scour depth are also discussed [4, 8, 18].

II. Experimental Methodology

Experiments were conducted in a 2.44m wide and 0.3m deep recirculating flume with flow depths ranging from 0.1m at the abutment to 0.25m at the deepest point. The 13.0m flume test section has a sediment recess 2.8m long and 0.45m deep across the flume. A floodplain and channel slope of 0.07 was used over the entire section and was constructed from quartz silica sand with a median sediment diameter, d_{50}=0.82mm. The sediment is considered to be uniform with a geometric standard deviation, σ_g=1.30.

Abutments were constructed with the same silica sand used for the bed material, and moulds were used to achieve the desired geometry for the spill-through abutments. The moulds allowed for the variation in abutment length whilst keeping the same shape and a side-slope of 1:1. The abutment side-slopes were covered with a filter paper to improve riprap stability with riprap overlaid on the filter paper. The riprap has a median stone size, D_{50},=0.02m and σ_g=1.08 [5]. Riprap sizing was based on [7], which outlines methodology to calculate riprap sizing for these tests based on flow depth, Froude number Fr, and specific gravity S_s, of the riprap. The sediment and riprap parameters are listed below in Table 1.

Riprap was also placed over the bed material near the channel section where velocities were higher than critical for sediment entrainment. The riprap in the channel section inhibited premature scouring. As the scour hole encroaches on the channel section the riprap 'falls' into the scour hole. These riprap stones were promptly removed so as not to hinder the total scour.

Layers of aluminum sheet metal were coated with the same silica sand to provide a comparable roughness to the bed material and were laid upstream of the recessed test section to eliminate upstream scour. After each experiment, the silica sand was smoothed to a flat surface with an accuracy of ±2mm. An inlet tank was designed to provide enough head to distribute flow evenly across the flume and to eliminate excess energy; the downstream tail-gate was used to ensure uniform flow at the required depth during the entire experiment.

The flume was slowly filled to the required flow depth; this eliminated the action of sheet flow generated by insufficient flow depth. Once the required depth was reached the discharge was increased by adjusting the butterfly valves on each of the pipes. Experiments were run for 72hours which was deemed sufficient length of time to reach equilibrium and allowed for comparison with previous research [8], [18].

Measurements were taken every 0.5 hr for the first 4 hours, and every hour for the next 4 hours. Subsequent measurements were taken at 24 hr, 30 hr, and 72 hr.

An initial experiment was run with no abutment present in order to find the pipe and flume settings for uniform flow and to gauge the suitable velocities required for V/V_c of 0.80-0.90, where V is the mean flow velocity and V_c is the critical mean velocity for particle entrainment. Particle Tracking Velocimetry (PTV) analysis was performed. Flow velocities were measured under ultra-violet (UV) light, using fluorescent particles placed upstream of the test section. The particles were recorded on video as they floated downstream.

Several sets of experiments were run during this study. The first experiments were undertaken to verify previous results from [18] and provide additional scour data for the entire duration of the experiments. Equilibrium data are shown in Table II. Previous studies recorded scour depth and scour depth locations at equilibrium [18], whilst this study includes an additional focus on the temporal development of scour. As an extension to previous research, a further 18 experiments were performed using a laterally-sloped floodplain with abutment lengths (L) of 0.4m, 0.6m, and 0.8m and riprap apron widths (W) of 0.0m, 0.1m, 0.2m, 0.3m, 0.4m, and 0.5m. The data are also shown in Table II.

Floodplain setup and measured parameters are shown in Fig. 1.

TABLE I. Bed Material and Rock Riprap Properties

Description	d_{16} (mm)	d_{50} (mm)	d_{84} (mm)	σ_g	S_s
Silica Sand	0.62	0.82	1.04	1.30	2.65
Riprap	18	20	21	1.08	2.65

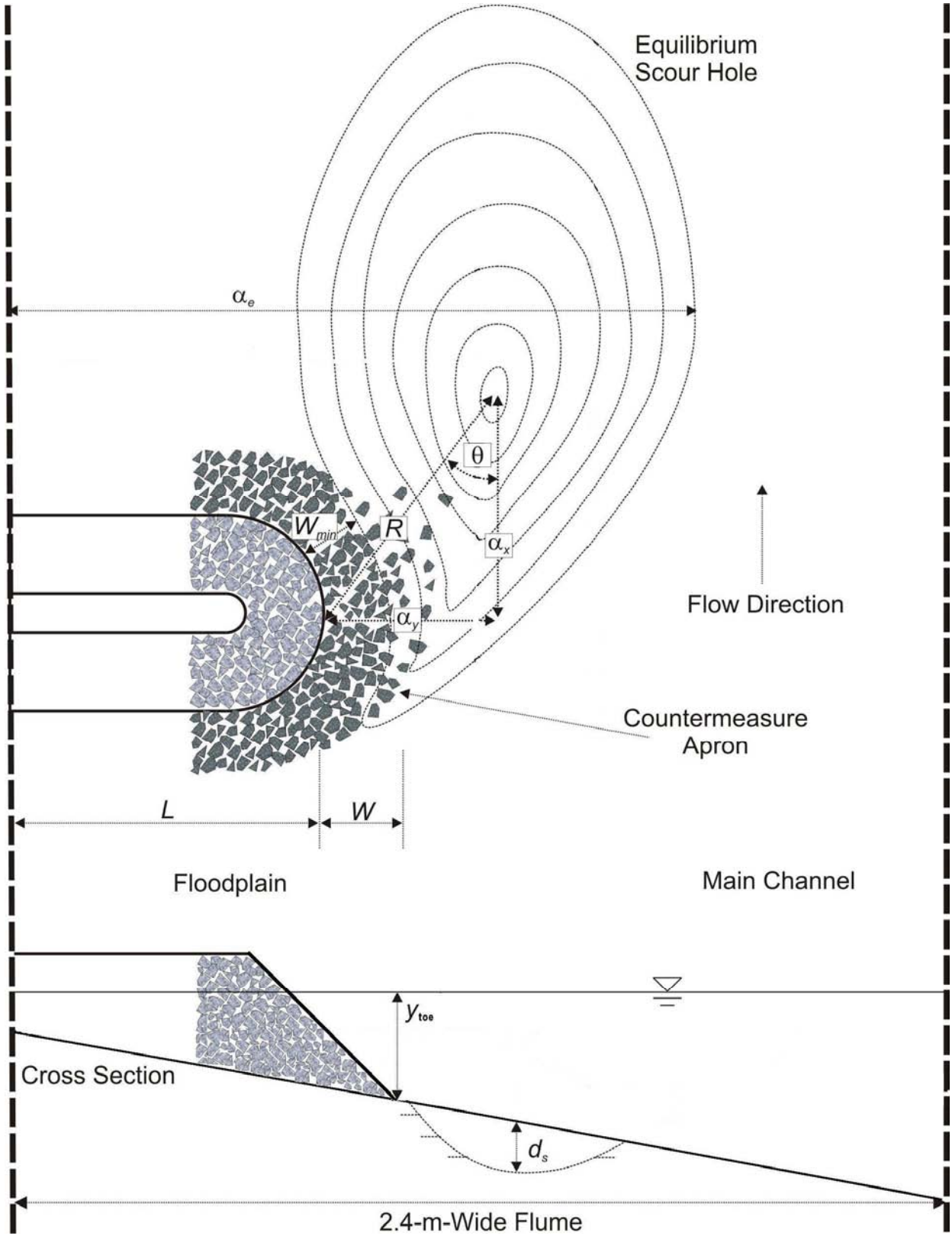

Figure 1. Floodplain setup with scour hole parameters shown. Adapted from [18].

Finally, 8 experiments were conducted with the same laterally-sloped floodplain and L=0.6m and W=0.3m for skew angles, θ, between 30° and 150 from the downstream abutment boundary. Scour data are shown in Table II.

Throughout the experiments transverse profiles of scour depth were recorded using an acoustic depth sounder mounted on a mobile trolley with an accuracy of 0.1mm. At the conclusion of each experiment a series of profiles was taken every 50.0mm across the scour hole enabling construction of a digital contour map of the scour hole. At each measurement the minimum apron width (W_{min}), the transverse (α_y) and longitudinal (α_x) location of the deepest scour from the toe of the abutment, and the outer edge of the scour hole (α_e) were recorded, each with an accuracy of ±5.0mm. From this information the progression of the scour hole was mapped in terms of the resultant distance (R) from the toe of the abutment where

$$R = \sqrt{\alpha_x{}^2 + \alpha_y{}^2} \tag{1}$$

Digital photographs were taken of the abutment layout prior to commencing the experiments and again at equilibrium, with contour lines laid at 50.0mm intervals. The contour lines were constructed using white cotton string laid at the measured depths from a straight edge of the same lateral slope as the floodplain. The contour levels depict the depth of scour from the original floodplain, d_s.

The depth of scour d_s was measured along with the location of the scour hole relative to the abutment toe (α_x, α_y, α_e), and the proximity of the scour to the abutment toe, W_{min}.

III. Discussion / Results

A. Scour Depth

Table II includes equilibrium scour data from this study and scour data for all abutment lengths, L=0.4, 0.6, 0.8m. Maximum scour depths for all apron widths W, are plotted in Fig. 2, with both equilibrium and non-equilibrium data for L=0.4, 0.6, 0.8m. The trendline shown represents the following equation

$$\frac{d_s}{L} = 0.5\left(\frac{t}{t_e}\right)^{0.28} \tag{2}$$

where d_s is the depth of scour below the original floodplain, L is the projected abutment length, t is the time elapsed, t_e is the time to reach equilibrium scour depth, and the coefficients were determined by regression (R^2=0.95). Equation (2) can be simplified for equilibrium scour depth, when t/t_e=1, giving

$$d_s = 0.5L \tag{3}$$

The equation applies to abutments protected with riprap aprons and is limited to the range of parameters investigated in this study.

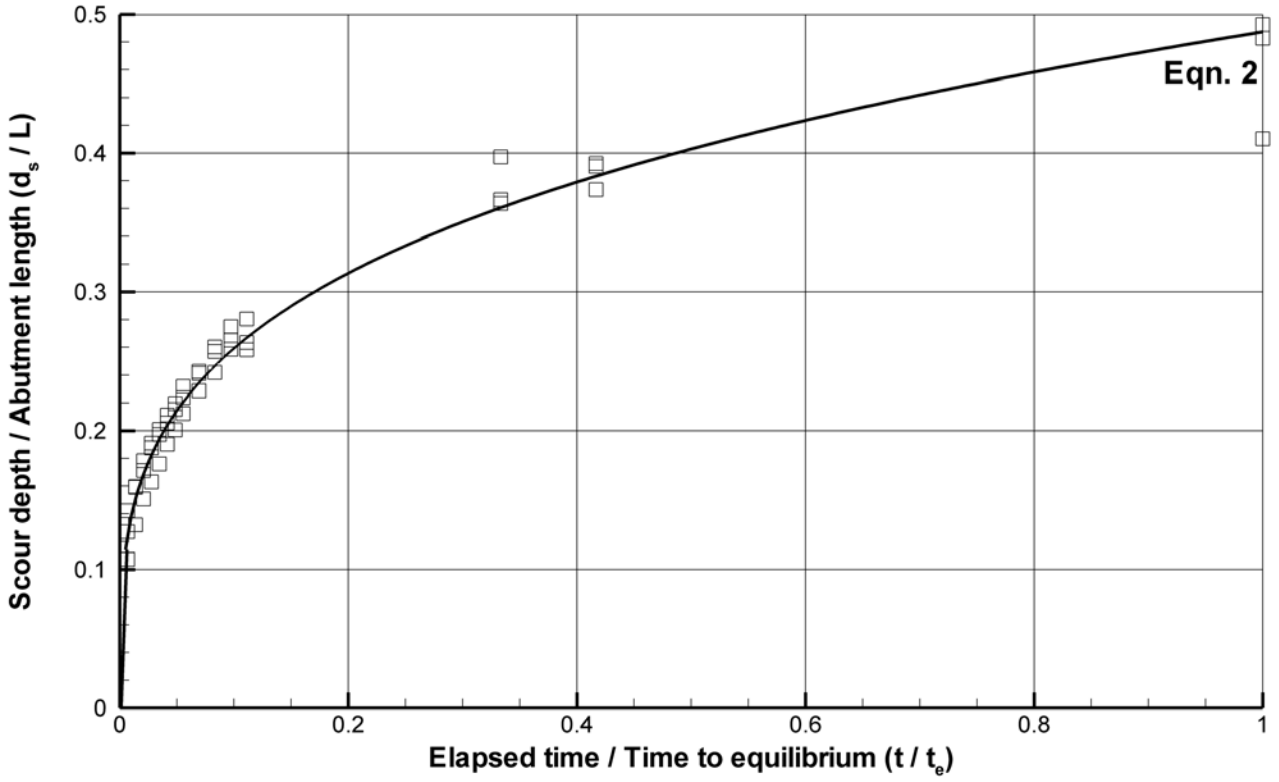

Figure 2. Normalised scour depth as a function of the proportion of elapsed time.

TABLE II. EQUILIBRIUM SCOUR DATA FOR IDEALIZED CHANNEL GEOMETRY, SLOPING FLOODPLAIN GEOMETRY, AND SKEWED ABUTMENTS.

Geometry	L	W	d_s	W_{min}	α_x	α_y	α_e
Non-Sloping B_f							
0.8	0.4	0.2	0.244	0.060	0.750	0.407	1.111
1.2	0.6	0.3	0.273	0.175	0.750	0.448	1.439
2.0	0.8	0.4	0.257	0.235	0.760	0.240	1.201
Sloping							
	0.4	0.0	0.179		0.490	0.204	0.870
	0.4	0.1	0.197	0.048	0.570	0.210	0.958
	0.4	0.2	0.177	0.163	0.710	0.265	0.968
	0.4	0.3	0.198	0.230	0.760	0.348	1.059
	0.4	0.4	0.166	0.373	0.890	0.312	1.040
	0.4	0.5	0.174	0.445	0.910	0.362	1.130
	0.6	0.0	0.277		0.640	0.339	1.317
	0.6	0.1	0.264	0.018	0.700	0.439	1.435
	0.6	0.2	0.290	0.050	0.745	0.406	1.454
	0.6	0.3	0.281	0.125	0.910	0.539	1.554
	0.6	0.4	0.280	0.250	0.880	0.533	1.567
	0.6	0.5	0.269	0.370	1.020	0.541	1.583
	0.8	0.0	0.258		0.710	0.352	1.525
	0.8	0.1	0.329	0.005	0.780	0.303	1.538
	0.8	0.2	0.311	0.038	0.960	0.425	1.668
	0.8	0.3	0.320	0.021	0.950	0.407	1.770
	0.8	0.4	0.307	0.093	1.000	0.504	1.838
	0.8	0.5	0.310	0.248	1.060	0.510	1.843
Skewed θ=							
30°	0.6	0.3	0.269	0.195	0.711	0.485	1.429
45°	0.6	0.3	0.269	0.158	0.740	0.475	1.581
60°	0.6	0.3	0.308	0.154	0.794	0.586	1.660
75°	0.6	0.3	0.275	0.105	0.719	0.518	1.496
90°	0.6	0.3					
105°	0.6	0.3	0.282	0.121	0.961	0.479	1.500
120°	0.6	0.3	0.316	0.115	0.966	0.509	1.610
135°	0.6	0.3	0.291	0.130	1.050	0.511	1.533
150°	0.6	0.3	0.296	0.127	1.319	0.534	1.639

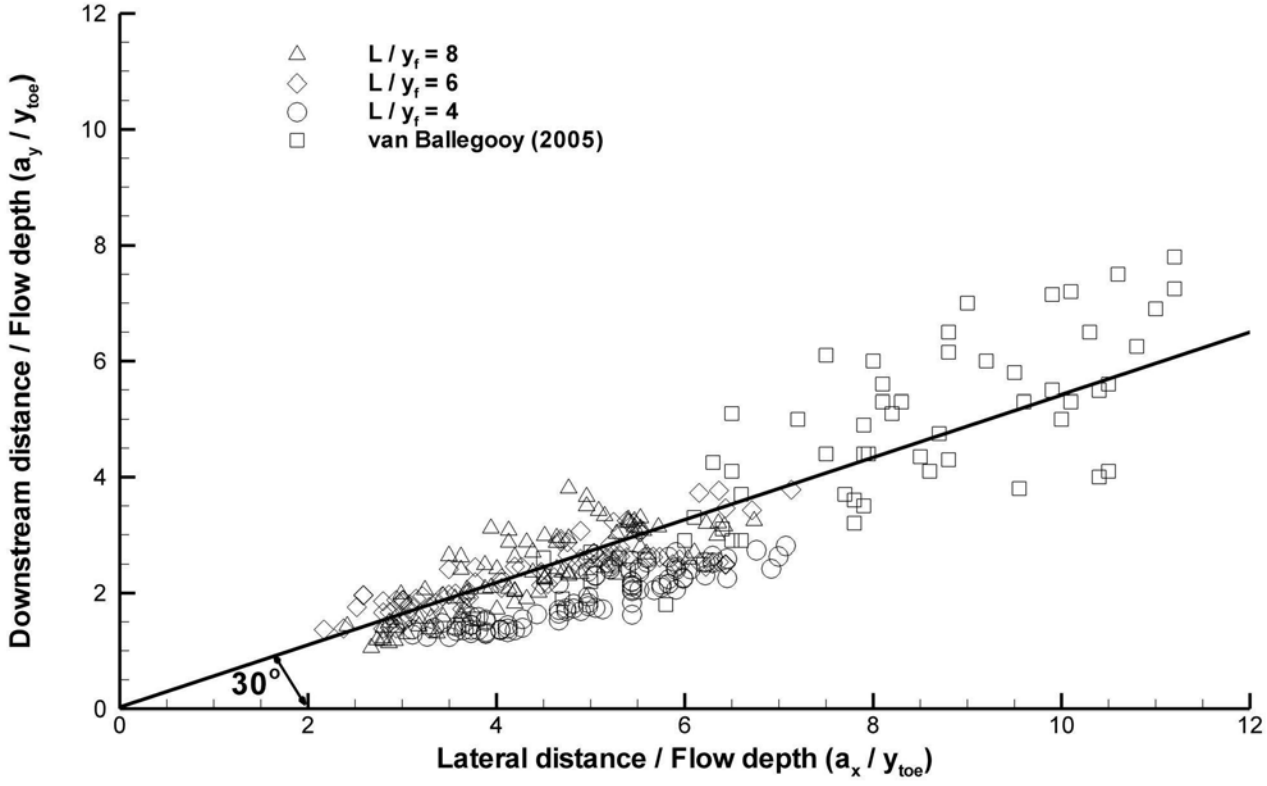

Figure 3. Distance to deepest scour from abutment toe, normalized against flow depth at the abutment toe.

B. Scour Hole Geometry

The proximity of the scour hole to the abutment is important for countermeasure design and was recorded during each experiment. Fig. 3 shows the locations of the deepest scour normalized in terms of the flow depth at the toe of the abutment throughout the development of the scour hole. Equilibrium data from [18] are also plotted for comparison. The plot indicates that the deepest scour is consistently located at $\theta \approx 30°$; where θ is defined in Fig. 1.

It is noted that for smaller L/y_{toe} (L/y_{toe} =4) the downstream deflection (α_y) of the scour hole is less than that for longer abutments, and produces a smaller resultant angle. This indicates the location of scour is dependent upon the length of the abutment, both in its downstream location and lateral position. It was observed that the velocities are slower at the tip of the abutment for shorter *L*, which in turn lessens the vortex scouring action at the abutment encouraging scour closer to the abutment tip.

The equilibrium distance of the scour hole from the toe of the abutment *R*, is plotted in Fig. 4. The following equation is valid for the data in Fig. 4 (R^2=0.81)

$$\frac{R}{y_{toe}} = 5.73\left(\frac{W_0}{y_{toe}}\right)^{0.23} \quad (4)$$

Equation (4) shows that the position of the scour is directly dependent on W_0, rather than *L*, at equilibrium. However, during the initial stages of tests (*time<24hr*), the scour hole developed further from the abutment toe, and exhibited a dependence on *L*. The higher flow velocities at the tip of longer abutments increased the magnitude of vortex scour action and also increased the range of influence of the vortex, initiating the scour hole further downstream. Once the scour hole was established, *R* followed a similar trend regardless of *L*.

C. Skewed Abutments

Tests with skewed abutments with angles between θ=30° and θ=150° were performed for projected abutment length, *L*=0.6m and *W*=0.3m. Scour results are shown in Table II. The results show that scour depth increases with increasing θ, as found by [10, 17, 19] and others. Conversely, [9] and [8] both found that scour depth decreases when abutments face upstream (θ>90°).

Scour depths are plotted for the various abutment inclinations and are normalized against perpendicular abutment scour depths in Fig. 5. Equilibrium and non-equilibrium scour data for wing-wall and vertical wall abutments are also included from [8, 9] for comparison.

Of particular interest from this study are the higher than expected scour depths obtained at both θ=60° and θ=120°. Velocity analysis using PTV shows no noticeable increase in velocity for these experiments. Stream-traces for θ=60°, 90°, and 120° are shown in Fig. 6. These also show no significant difference between the stream-trace for the perpendicular abutment and the two inclined abutments. Each stream-trace features similar approach angles upstream of the abutment and a similar vortex pattern downstream.

The additional scour experienced at the 60° skewed abutment is attributed to the limitations of the recessed test section. Scour at this angle exposed the edge of the recessed test section and a significant portion of impermeable boundary. Digital photographs taken at equilibrium scour depths indicate significant upstream elongation of the scour hole toward the skewed abutments (θ=60° and θ=120°) compared with the scour hole geometry from the perpendicular abutment.

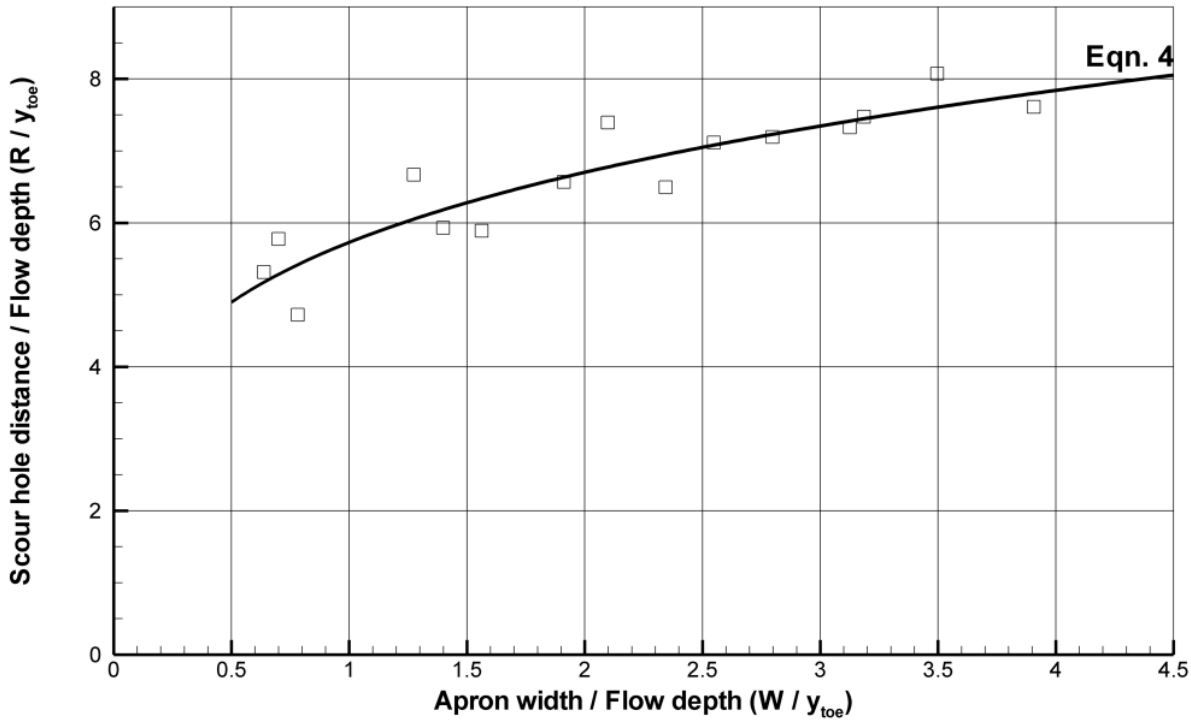

Figure 4. Scour hole position as a function of riprap apron width

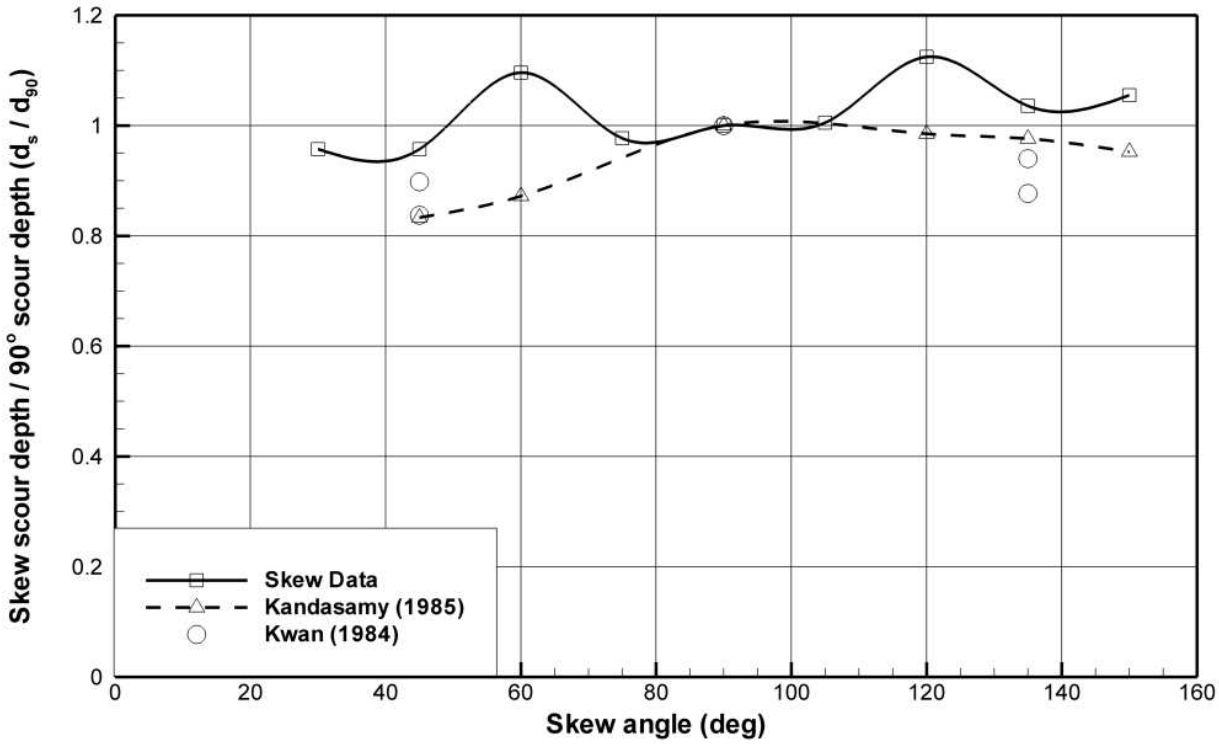

Figure 5. Skewed scour depths proportional to perpendicular scour depth as a function of skew angle.

Whilst the experiments produce these anomalies, a slight increase in scour with increasing θ is apparent.

References [8] and [9] noted the development of a secondary scour hole at θ=135° which inhibited d_s. Previous research has shown that at these skew angles (θ>135°) the downflow interferes with the principal vortex creating the secondary scour hole, which reduces the available energy available for scour of the primary scour hole [9]. This was not found to be the case for this data set and the development of a secondary scour hole is assumed to be limited by the presence of the apron.

D. Apron Width

The parameter (W-W_{min}) represents the eroded width of protective apron at equilibrium scour (Fig. 7), where W is the initial protective apron width, and W_{min} is the minimum apron width from the toe of the abutment after erosion.

When W_{min}=0, the apron is just wide enough to prevent undermining of the abutment slope, i.e. the apron erodes to the toe of the abutment. This minimum apron width to protect the abutment is termed W_0. Hence $W \equiv W_0$ when $W_{min}=0$ and $(W-W_{min}) \equiv W_0$. Fig. 7 is a plot of the data in terms of W_0 and scour depth below the floodplain level, d_s. For the case when $W>W_0$, i.e. $W_{min}>0$, the edge of the scour hole is deflected away from the toe of the abutment, and W_0 is approximated by (W-W_{min}). The envelope curve depicted in Fig. 7 has the equation

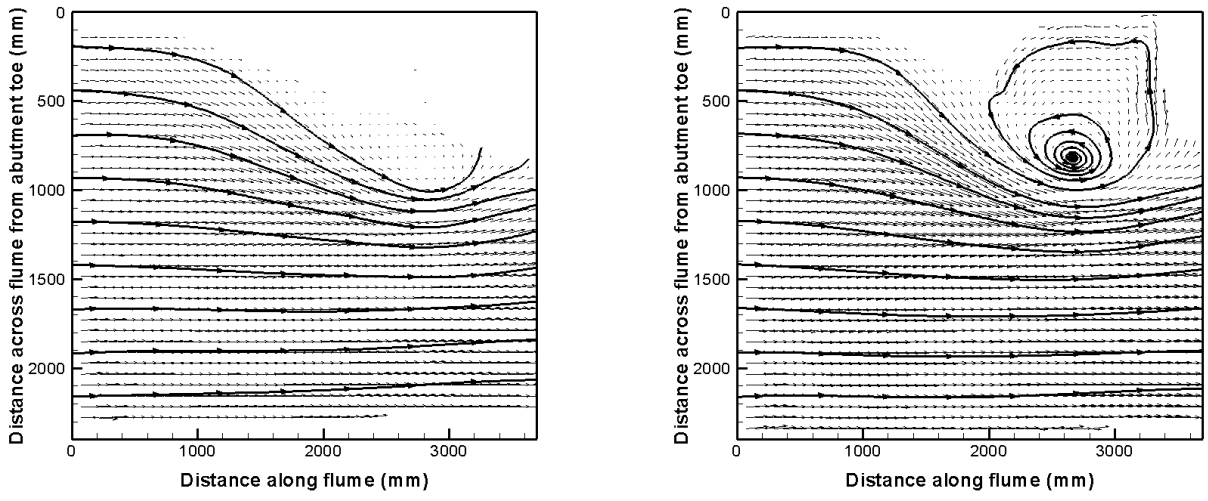

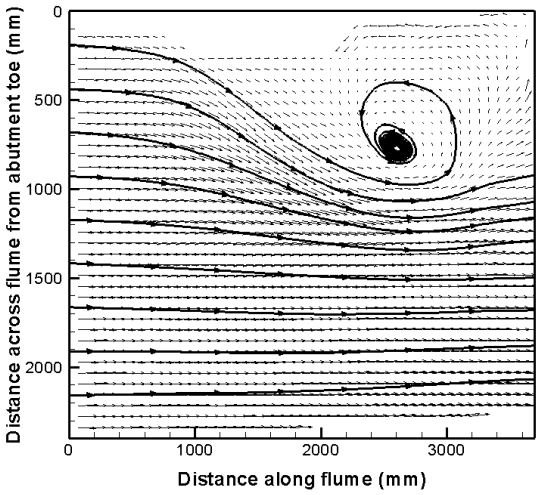

Figure 6. Stream-traces for skewed abutments with L=0.6m and W=0.3m; previous page from left to right, 60° skewed, and 90° skewed (perpendicular). Above, 120° skewed. Flow is from left to right

$$\frac{W_0}{y_{toe}} = 0.75\left(\frac{d_s}{y_{\text{toe}}}\right)^{1.25} \quad (5)$$

$$\frac{W_0}{y_f} = 0.5\left(\frac{d_s}{y_f}\right)^{1.35} \quad (6)$$

where W_0 is the minimum apron width to ensure failure does not occur, and y_{toe} is the flow depth on the floodplain at the toe of the abutment. Equilibrium and non-equilibrium scour data from this study and from [4, 18] are included in Fig. 7. Equation (5) is valid for all channel geometries studied for both equilibrium and non-equilibrium conditions. An earlier study [18] identified the relationship (6) as an envelope curve to data for non-sloping (level) floodplain experiments.

where the coefficients C_2=0.5 and λ=1.35, y_f is a constant flow depth over a level floodplain. Hence $y_{toe} \equiv y_f$ when y_f is measured at the toe of the abutment [18]. Based on the non-sloping channel geometry used in the earlier study, (6) represents a reasonable envelope. However, the

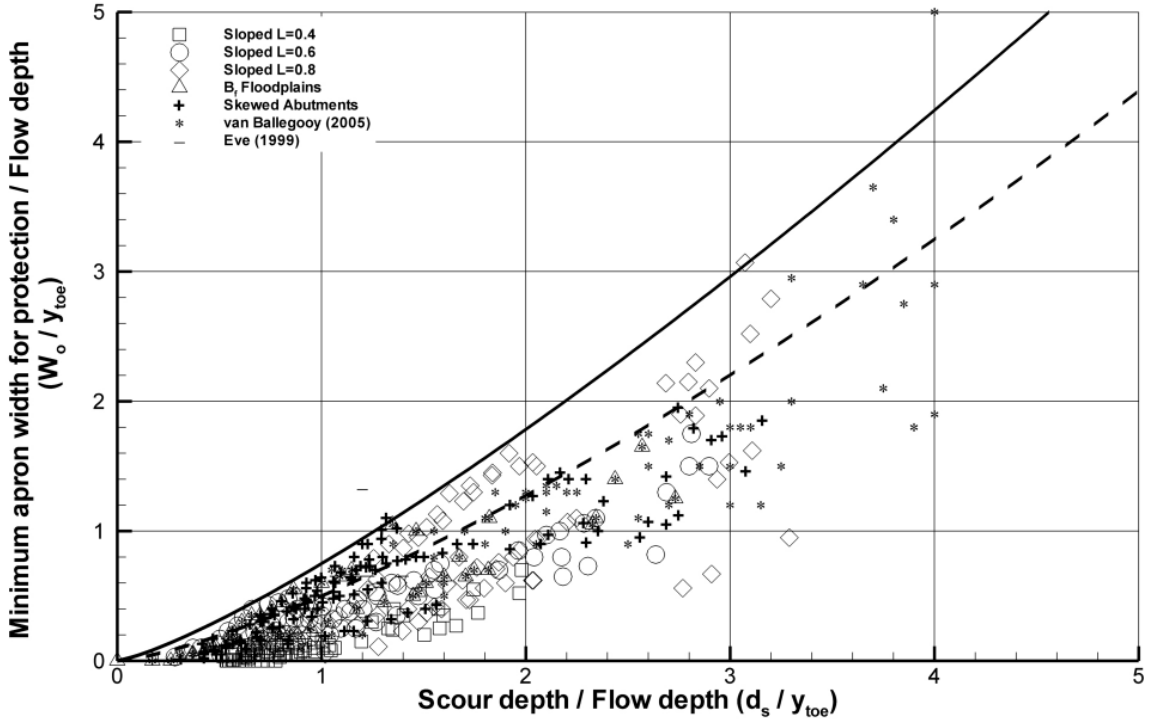

Figure 7. Minimum apron extent (W0) as a function of scour depth

modified geometry used in this study and the scour data from [4] yield significantly smaller W_{min} values for a given scour depth.

The assumption here is that erosion of the riprap apron is increased by the lateral slope of the floodplain towards the developing scour hole. The scour hole geometry is significantly different under laterally-sloping floodplain conditions. Due to the lateral slope of the floodplain, the angle at the edge of the scour hole is greater than for a level floodplain. This lateral slope encourages apron erosion closer to the abutment toe.

IV. Conclusions

Abutment length dictates the final equilibrium scour depth (2), and it can be concluded that the flow velocity is a significant factor in scour. Increased flow velocities at the toe of long abutments increase the scouring potential of the principal vortex and result in greater d_s values.

The geometry of the scour hole as defined by R is found to be dependent upon the riprap apron width. Larger apron widths deflect the scouring action away from the abutment toe. While abutment length influences the initial location of scour, equilibrium scour locations remain consistent regardless of abutment length.

Skewed abutments influence scour depth and follow the trend suggested in previous studies [13]. Scour depth is seen to increase slightly with skew angle. Significant elongation of the scour hole toward the skewed abutments (θ=60° and θ=120°) compared with the scour hole geometry for the perpendicular abutment was also evident.

Greater riprap apron width is required for protection of laterally sloping floodplains than for non-sloping channels; the lateral slope of the floodplain encourages apron erosion. A new relationship, given as (5), allows for calculation of the minimum protection apron width for sloping and non-sloping floodplains.

V. Notation

B_f	=	*width of floodplain*
C_2	=	*coefficient in (5, 6)*
d_{16}	=	*material size where 16% is finer by weight*
D_{50}	=	*median diameter of riprap*
d_{50}	=	*median diameter of bed material*
d_{84}	=	*material size where 84% is finer by weight*
d_s	=	*equilibrium scour depth*
d_{sf}	=	*scour depth from floodplain level*
Fr	=	*Froude number based on mean velocity*
L	=	*projected abutment length*
R	=	*resultant distance to centre of scour hole*
S_s	=	*specific density of material*
t	=	*elapsed time*
t_e	=	*time taken to reach equilibrium scour depth*
V/V_c	=	*mean flow intensity*
W	=	*riprap apron width*
W_{min}	=	*minimum riprap apron width*
W_0	=	*minimum riprap apron width to ensure failure does not occur*
y_f	=	*flow depth on the floodplain*
y_{toe}	=	*flow depth at the toe of the abutment*
α_x	=	*distance downstream from the toe of the abutment to the centre of the scour hole*
α_y	=	*distance across the flume from the toe of the abutment to the centre of the scour hole*
α_e	=	*distance from the toe of the abutment to the outer edge of the scour hole*
θ	=	*resulting angle from the toe of the abutment to the centre of the scour hole*
σ	=	*geometric standard deviation*

VI. References

1. Brown, S.A. and E.S. Clyde (1989). "Design of riprap revetment" *Report FHWA-IP-39-016,* Hydraulic Engineering Circular 11 (HEC 11). Federal Highways Administration, McLean, VA
2. Coleman, S.E., C.S. Lauchlan, and B.W. Melville (2003). "Clear-water scour development at bridge abutments." *Journal of Hydraulic Research*, **41**(5): p. 521-532.
3. Croad, R.N. (1989). "Investigation of the pre-excavation of the abutment scour hole at bridge abutments" *Report 89-A9303*, Central Laboratories, Works and Development Services Corporation (NZ) Ltd., Lower Hutt, New Zealand
4. Eve, N.J. (1999). "Riprap protection of bridge abutments". *ME thesis*, Department of Civil and Environmental Engineering, University of Auckland, Auckland
5. Gregorius, B.H. (1985). "Waterway design procedures - Guidelines." Civil Division Publication, Ministry of Works and Development, Hamilton, New Zealand
6. Hamil, L. (1999). "Bridge Hydraulics". London: E & FN Spon.
7. Isbash, S.V. (1936). "Construction of dams by depositing rock in running water". in *Transactions, Second Congress on Large Dams*. 1936. Washington D.C., USA:
8. Kandasamy, J.K. (1985). "Local scour at skewed abutments". Department of Civil and Environmental Engineering, University of Auckland, Auckland
9. Kwan, T.F. (1984). "Study of abutment scour". *ME thesis*, Department of Civil and Environmental Engineering, University of Auckland, Auckland
10. Laursen, E.M. and A. Toch (1956). "Scour around bridge piers and abutments" *4*, Iowa Highway Research Board Bulletin,
11. Li, R.M., R. MacArthur, and G. Cotton (1989). "Sizing riprap for the protection of approach embankments and spur dikes and limiting the depth of scour at bridge piers and abutments" *Report FHWA-AZ89-260,* Arizona Department of Transportation, Phoenix
12. Macky, G.H. (1986). "Model testing of bridge abutment scour protection" Central Laboratories, Ministry of Works and Development, Lower Hutt, New Zealand
13. Melville, B.W. (1992). "Local Scour at Bridge Abutments" *ASCE Journal of Hyraulic Engineering*, **118**(4): p. 615-631.
14. Pagan-Oritz, J.E. (1991). "Stability of rock riprap for protection at the toe of abutments located at the floodplan" *FHWA-RD-90-057,* Federal Highway Administration, USDOT, Washington, D.C
15. Richardson, E.V. and S.R. Davis (1995). "Evaluating scour at bridges" FHWA-IP-90-017, 3rd,
16. Richardson, E.V., D.B. Simons, and P.Y. Julien (1990). "Highways in the river environment" *Report FHWA-HI-90-016*, National Highways Institute/Federal Highways Administration, McLean, VA
17. Sastry, C.L.N. (1962). "Effect of spur-dike inclination on scour characteristics". *ME thesis*, University of Roorkee, India
18. van Ballegooy, S. (2005). "Bridge Abutment Scour Countermeasures". *PhD thesis*, Department of Civil and Environmental Engineering, University of Auckland, Auckland
19. Zaghoul (1983). "Local scour around spur dikes" *Journal of Hydrology*, **60**.

Barbs (Submerged Groynes) for River Bend Bank Protection: Application of a Three-Dimensional Numerical Model

B. Minor*, C.D. Rennie* and D.R. Townsend*
* University of Ottawa/Department of Civil Engineering, Ottawa, Canada

INTRODUCTION

Barbs are low-profile linear structures that are primarily used to prevent the erosion of stream banks. They are a variation of a groyne, similar to spur dikes and bendway weirs. Historically, groyne structures have been built such that the groyne emerges out of the water and is overtopped only at the highest flows. More recently, there has been interest in low-profile submerged groynes, such as barbs, because they require less material to construct and are less obtrusive. Barbs are typically anchored, in series, to the outside bank in stream bends and extend in an upstream direction from the bank into the flow. A unique feature of barbs is that they have trapezoidal cross-sections and that the top of the barb gently slopes downward as it extends away from the bank [1]. A series of barbs is designed to redirect flow away from the outer stream bank and disrupt the velocity gradient and shear stress distribution close to the outer bank. As a result of this disruption the location of the thalweg shifts away from the outside bank. Furthermore, a zone of subcritical flow is generated upstream of the barb structure along the outer bank. Thus a series of barbs, installed correctly, protects the outer bank from erosion and promotes sediment deposition. In addition to this, it has been observed that vortices are generated at the tips of the barbs creating local scour holes that can enhance aquatic habitat [2].

Many field installations of these structures have been performed using good judgment and experience rather than following specific criteria. In addition, there is limited documentation of the design criteria that have been used for the field installation of barbs and for the long-term performance of these structures. Recently there has been an effort to provide recommendations and guidelines for the design of barbs (e.g. [1]). However, it must be noted that these are only suggestions. There remains a need for studies to identify the optimum barb dimensions, spacing, and orientations in the bend flow field for different bend geometries and hydraulic conditions. Furthermore, an understanding of the interaction between the complex flow field and the sediment transport through the channel bend is required in order to predict the long-term performance of these structures.

There have been both laboratory and numerical studies performed on groyne structures. However, most of these studies have been limited to the examination of a single, emergent groyne perpendicular to the stream bank in a straight channel (e.g. [3], [4], [5], and [6]). The studies which have been conducted on groyne fields typically investigate only groynes perpendicular to the flow field. Reference [7] examined flow patterns in a series of emergent perpendicular groynes in a straight channel. Reference [8] described changes in bed morphology due to the installation of a series of groynes in the field. Scour around a single submerged spur dike in a straight channel has recently been studied for orientations perpendicular to the bank [9] and angled upstream [10]. Recently, [11] analyzed flow around a single submerged weir in a channel bend. In 2004 a laboratory study was conducted that examined the scour patterns, in a hydraulically narrow channel, of barb fields in 90^o and 135^o bends with varied spacing and angles of barbs [12].

A three-dimensional numerical model was used to simulate the turbulent flow field and associated scour and deposition of the bed sediments due to a series of barbs in both a 90^o channel bend and a 135^ochannel bend. The numerical model was calibrated to the scour measurement data obtained from the physical laboratory experiments described in [12]. The parameters that were varied for each experiment were channel bend angle, barb alignment, and the location of the barbs in channel bend. This paper aims to: (i) validate the application of a three-dimensional numerical model to moveable-bed bend sections of a hydraulically narrow rectangular channel containing barbs; (ii) simulate the effects of different arrangements of barb groups in the bend section; and (iii) analyze the data to determine the relation of the flow field to associated scour and deposition in a complex fluvial environment. This novel data is useful for improved analyses of the bank protection capabilities of these structures and for the development and improvement of design guidelines.

NUMERICAL MODEL

The three-dimensional numerical model used for this study was Sediment Simulation in Intakes with Multiblock option (SSIIM), Version 1.1. This model, developed at the Norwegian University of Science and Technology [13], uses a three-dimensional structured and non-orthogonal grid. The model utilizes a rigid-lid by default. The three-dimensional Reynolds-averaged Navier-Stokes equations are solved to calculate the water flow. The SIMPLE method [14] is used to solve the pressure term. The Reynolds stresses are solved using the k-ε model, and the suspended sediment transport is calculated with the convection-diffusion equation. The volumetric bedload transport is calculated using van Rijn's bedload transport formula [15].

EXPERIMENTAL DATA

The scour measurement data that is presented in [12] was collected in the Engineering Hydraulics Laboratory at the University of Ottawa. The channel that was used for the testing was comprised of three rectangular-shaped sections; the entrance section was 0.460 meters wide by 0.254 meters deep by 9.75 meters long; the exit section was 0.460 meters by 0.406 meters by 2.44 meters long; and there were two exchangeable bend sections 0.460 meters wide by 0.406 meters deep which were installed separately. The two bend angles used were 90^o and 135^o. The exit sections and the bend section were 0.152 meters deeper than the rest of the channel. This allowed for a 0.152 meter deep sand bed to be placed in the bend and exit sections.

The experimental procedures were largely based on design recommendations by [16]. The parameters that were varied for each experiment were channel bend angle, barb alignment, and the location of the barbs. Judging the effectiveness of the different barb groups in promoting long term stability of the outside bank region was based on two criteria: (i) percent reduction achieved in scouring in the vicinity of the outside bank and (ii) degree to which the channel thalweg was moved from the outside bank region towards the center of the channel. Scour tests were performed separately with the 90^o channel bend section and the 135^o channel bend section. For each channel bend section there were three different barb alignment angles ($\theta = 20^o, 30^o, 40^o$) assessed, where θ is defined as the angle between the tangent line to the bank and the barb. For the 90^o channel bend three different group-types (A, B, and C) were evaluated. Two different group-types were examined in the 135^o channel bend. The group-types (A, B, and C) were defined by the location of the first barb in the group.

The height of the barbs at the bank was half of the mean flow depth and decreased with a 10^o slope away from the bank. The sand placed in the 0.152 meter deep bend and exit sections had a median diameter of 0.85 millimeters with a geometric standard deviation of approximately 1.3. Throughout the experiments, a constant discharge of 0.0132 cubic meters per second was maintained with an average flow depth of 0.102 meters. Further details of the experimental methods and data are available in [12] and [17].

NUMERICAL SIMULATION

90^o Channel

The three-dimensional numerical model was initially used to simulate the sediment transport and flow through the 90^o channel bend without barbs in place. This was performed to calibrate the model before adding the barbs to the channel. A structured grid containing 123 cells in the longitudinal direction, 18 cells in the transverse direction, and 12 cells in the vertical direction was used. In order to remain consistent with the experimental data, the channel geometry, discharge, flow depth, channel slope, and sediment grain size were the same as those measured in the laboratory. For the 90^o channel without barbs the laboratory experiments were run for approximately 26 hours. A simulation time of 15 hours was used for the numerical modeling. The parameters varied to calibrate the numerical model to the experimental data were the bed roughness and the time step. A Manning number of 0.0167 and a time step of 50 seconds proved to yield favorable results. Please note that in all figures the direction of flow is from left to right.

Figure 1 presents a contour map of the predicted bed elevations in meters. These results compare favorably to the bed elevations measured in the laboratory. The laboratory bed elevations are shown in Figure 2. The distribution of boundary shear stress across a channel bend section is complex due to the transverse shear produced by the secondary currents. The secondary flow cell is typically directed vertically down towards the toe of the outside bank. There is an increase in the shear stresses in the outer bank region which results in erosion in the outer bank region. Conversely, there is a decrease in velocity and shear stress along the inside bank which encourages deposition of sediment and the formation of point bars. The laboratory results presented in Figure 2 clearly show these features. From Figure 1 it can be seen that these patterns of sediment deposition and erosion through the bend are sufficiently simulated by the numerical model. The location and magnitude of the measured and predicted point bar are observed to be comparable. The predicted scour hole is of similar magnitude to the observed scour hole. However it is located closer to the outside bank and its shape is elongated. Furthermore, it is noticed that the predicted point bar was of slightly lower magnitude than the observed value. It is possible that these discrepancies are due to an underestimation of the transverse bed load.

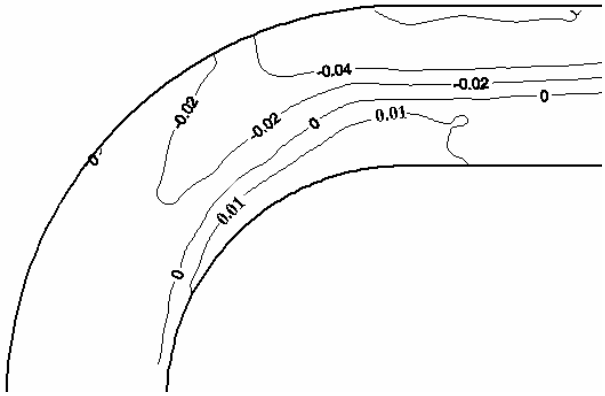

Figure 1. Predicted bed elevation contours (in meters) for 90^o channel bend without barbs

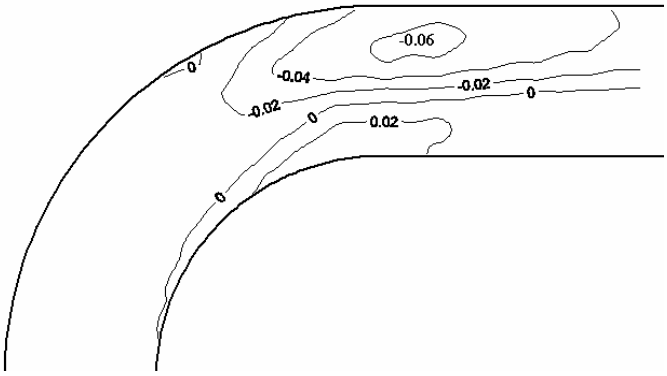

Figure 2. Measured bed elevation contours (in meters) for 90^o channel bend without barbs

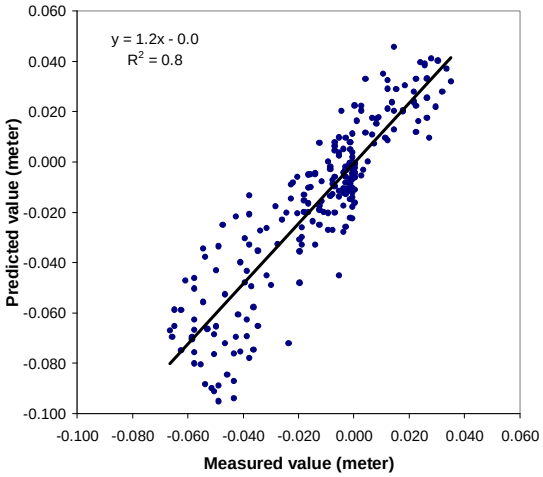

Figure 3. Predicted versus measured bed elevation for 90° channel without barbs (in meters)

A statistical comparison of the measured and predicted bed elevations for the 90° channel bend is presented in Figure 3 gives a regression coefficient of determination (r^2) of 0.8. The mean absolute deviation (M.A.D) of predicted from measured bed elevations is 0.011 meters, with a standard deviation of absolute deviation (S.D.A.D.) of 0.01 meters.

As a result of the laboratory experiments the optimum barb arrangement for the 90° and 135° channel bends was found to be Group B with a barb alignment angle of 30°. For the 90° channel this arrangement consisted of three barbs, with the first barb located 1.41 meters from the bend entrance. The three-dimensional model was used to simulate the 90° channel containing this arrangement of barbs. All parameters remained the same as the initial calibration simulation of the channel without barbs, except the simulation time was reduced to 5 hours to correspond to the time frame used during laboratory tests. Using the procedure described in [13] cells were blocked out where the barbs were located. The height, length, and slope of the barbs remained consistent with the structures used in the laboratory experiments (i.e. a height of one-half the flow depth, a length of 0.196 meters, and a 10° downward slope). However, due to limitations of the grid the width of the barbs was wider than those used in the laboratory experiments. The bed elevations, in meters, measured in the laboratory are presented in Figure 4. In comparison to Figure 1, it can be observed that the location of the thalweg has shifted away from the outer bank and the location of the deepest scour hole is located off the tip of the third barb. The bed elevations computed by the numerical model are shown in Figure 5. This figure shows similar results. In comparison to Figure 2, it can be observed that the location of the thalweg has shifted away from the outer bank and, comparable to Figure 4, the location of the deepest scour hole is located off the tip of the third barb. A statistical comparison of the measured and predicted bed elevations for the 90° channel bend containing Group B with a 30° barb alignment angle is presented in Figure 5. Figure 6 shows a regression coefficient of determination (r^2) of predicted from measured bed elevations of 0.8. The mean absolute deviation (M.A.D) of predicted from measured bed elevations is 0.008 meters, with a standard deviation of absolute deviation (S.D.A.D.) of 0.007 meters.

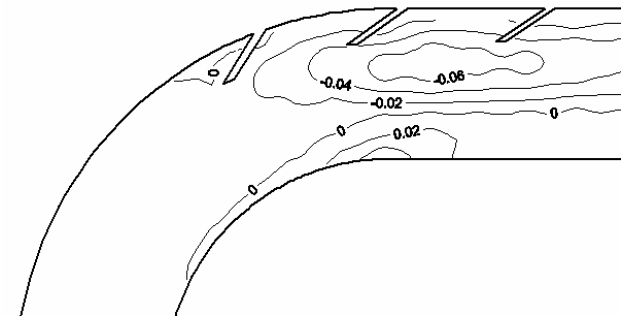

Figure 4. Measured bed elevation contours (in meters) for 90° channel bend with barbs

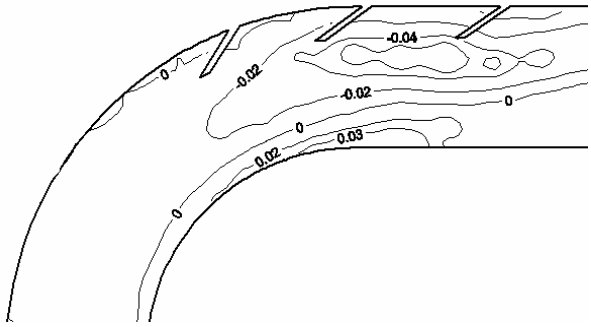

Figure 5. Predicted bed elevation contours (in meters) for 90° channel bend with barbs

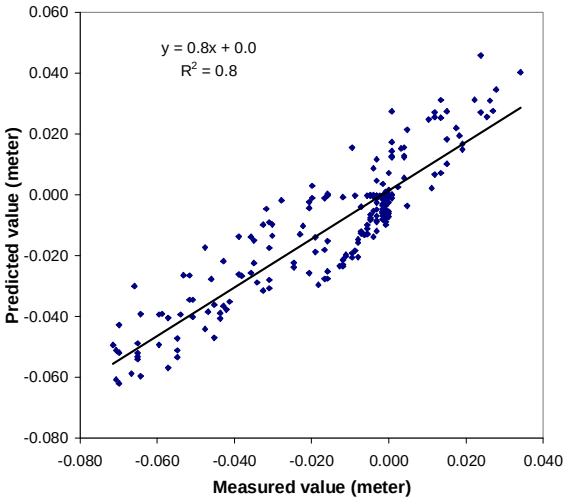

Figure 6. Predicted versus measured bed elevation for 90° channel with barbs (in meters)

Detailed measurements of the velocity field were not taken during the laboratory experiments. However, the computed velocity field for the 90° channel containing barbs was analyzed and compared to the computed velocity field for the 90° channel without barbs to observe trends in the data.

A contour map of the depth-averaged horizontal velocities, in meters per second, for the 90° channel without barbs is presented in Figure 7. It can be seen from this figure that as the flow enters the bend the location of the maximum velocity is near the center of the channel. As the flow continues through the bend, the location of the maximum velocity shifts towards the outside bank and the magnitude of velocity along the inner bank is much lower.

Figure 8 shows the depth-averaged horizontal velocity distribution for the 90° channel containing the Group B arrangement of barbs with a barb alignment angle of 30°. The location of the maximum velocity is located off the tips of the barbs, closer to the center of the channel. Therefore, with the addition of the barb arrangement to the channel, the maximum velocity does not connect with the outer bank of the channel bend. It is noted that experimental data were not available to compare to the values presented. Therefore, Figure 7 and Figure 8 are presented to suggest possible trends that relate the flow field to associated scour and deposition in a complex fluvial environment.

135° Channel

A similar procedure was used for the 135° channel bend. As a first step, the three-dimensional model was used to simulate the sediment transport and flow through the 135° channel bend without barbs in place. The structured grid for this channel bend contained 164 cells in the longitudinal direction, 18 cells in the transverse direction, and 12 cells in the vertical direction. The discharge, flow depth, channel slope, and sediment grain size remained the same as for the 90° channel bend. A simulation time of 26 hours was used. And again, a Manning number of 0.0167 and a time step of 50 seconds proved to yield favorable results. The predicted and measured bed elevations are presented in meters in Figure 9 and Figure 10, respectively. Similar to the 90° channel bend, it can be observed that sediment is being deposited along the inner bank while erosion is occurring along the outer bank. Both the measured and predicted data illustrate this trend. It can be observed that the predicted scour hole along the outer bank of the bend is smaller, and located further downstream, than the location of the measured scour hole.

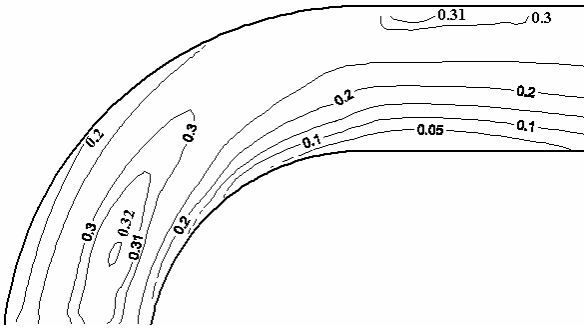

Figure 7. Depth-averaged horizontal velocity contours (in meters per second) for 90° channel bend without barbs

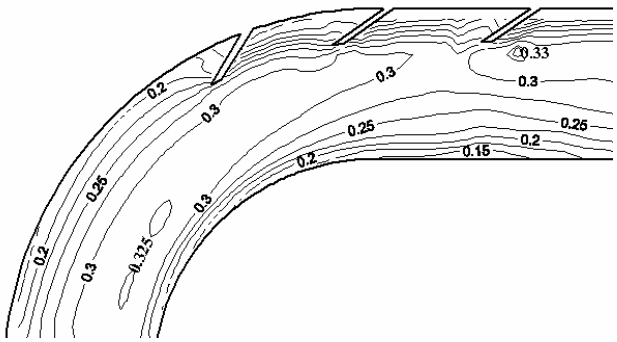

Figure 8. Depth-averaged horizontal velocity contours (in meters per second) for 90° channel bend with barbs

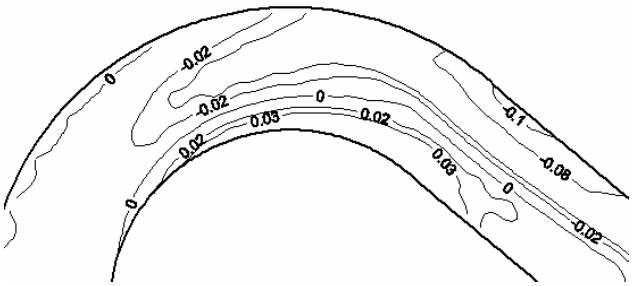

Figure 9. Predicted bed elevation contours (in meters) for 135° channel bend without barbs

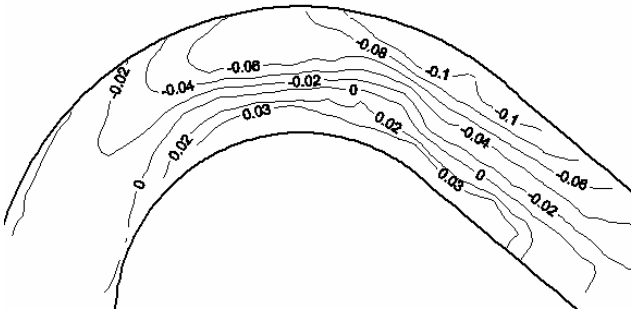

Figure 10. Measured bed elevation contours (in meters) for 135° channel bend without barbs

A statistical analysis, Figure 11, of the predicted and measured data gives a regression coefficient of determination (r^2) of predicted from measured bed elevations of 0.8, a mean absolute deviation (M.A.D) of predicted from measured bed elevations of 0.01 meters, and a standard deviation of absolute deviation (S.D.A.D.) of 0.01 meters.

The Group B arrangement of barbs with a 30° barb alignment angle consisted of 5 barbs. The first barb was located 1.41 meters from the bend entrance. The three-dimensional model was used to simulate the 135° channel containing this arrangement of barbs. All parameters remained the same as the initial calibration simulation of the channel without barbs, except the simulation time was reduced to 5 hours to correspond to the time frame used during laboratory tests.

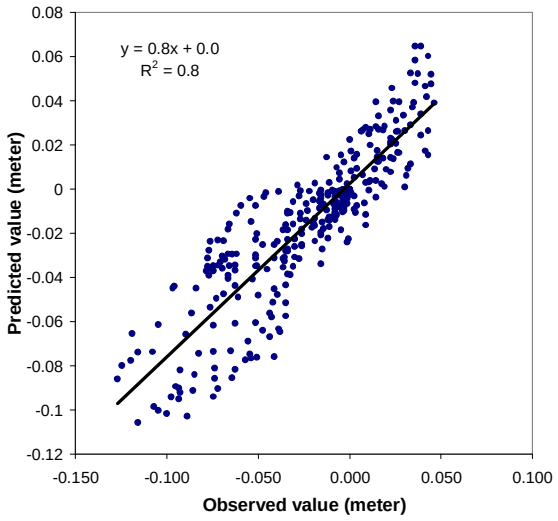

Figure 11. Predicted versus measured bed elevation for 135° channel without barbs (in meters)

The height and length of the barbs remained consistent with the structures used in the laboratory experiments (i.e. a height of one-half the flow depth, and a length of 0.196 meters). However, due to limitations of the grid the width of the barbs was wider than those used in the laboratory experiments. Furthermore, with five barbs in the channel it was not possible to replicate the slope of the barbs with the numerical model.

The measured bed elevations, in meters, are presented in Figure 12. Once again, we can see that the addition of barbs to the channel causes the thalweg to shift away from the outer bank. The location of the deepest scour hole is observed to be off the tip of the second and third barb in the grouping. The simulated bed elevations are shown in Figure 13. Similar trends can be observed in this figure. It can be seen that the thalweg has shifted towards the center of the channel. The deepest scour hole in this figure is located off the tip of the fourth barb in the grouping. The downward slope of the barbs is an important feature for their functionality. The lack of this feature for the numerical simulation could be the reason for discrepancies between the measured and predicted data. From Figure 14, the regression coefficient of determination (r^2) of predicted from measured bed elevations is 0.7. The mean absolute deviation (M.A.D) of predicted from measured bed elevations is 0.01 meters, with a standard deviation of absolute deviation (S.D.A.D.) of 0.01 meters.

A contour map of the depth-averaged horizontal velocities, in meters per second, for the 135° channel without barbs is presented in Figure 15. The depth-averaged horizontal velocities for the 135° channel with the Group B arrangement of barbs with a 30° barb alignment angle are shown in Figure 16. As with the 90° channel it can be observed that by adding the barb arrangement to the channel the location of the maximum horizontal velocity shifts away from the outer bank and towards the center of the channel. Once again it is noted

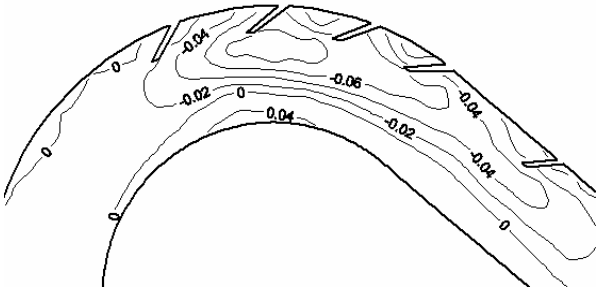

Figure 12. Measured bed elevation contours (in meters) for 135° channel bend with barbs

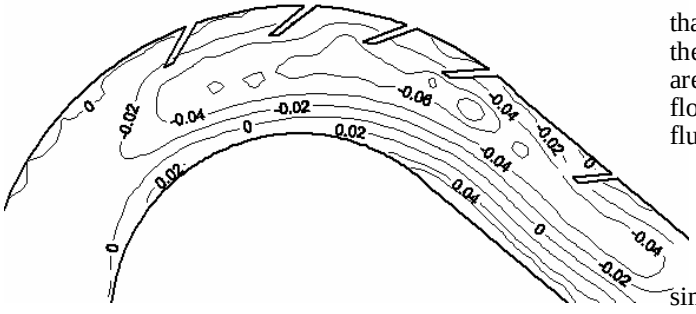

Figure 13. Predicted bed elevation contours (in meters) for 135° channel bend with barbs

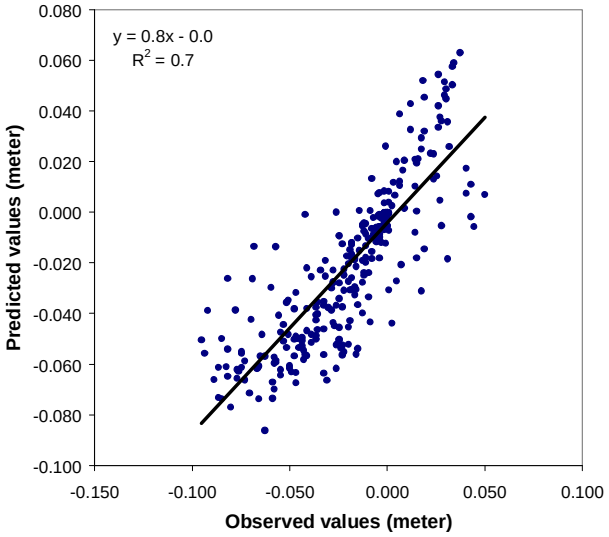

Figure 14. Predicted versus measured bed elevation for 135° channel with barbs (in meters)

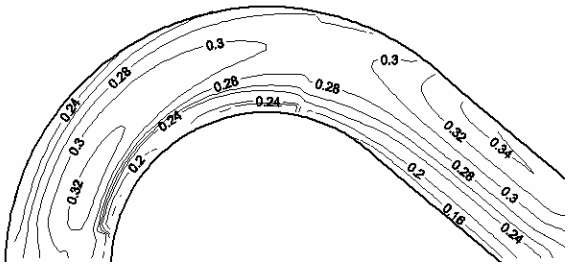

Figure 15. Depth-averaged horizontal velocity contours (in meters per second) for 135° channel bend without barbs

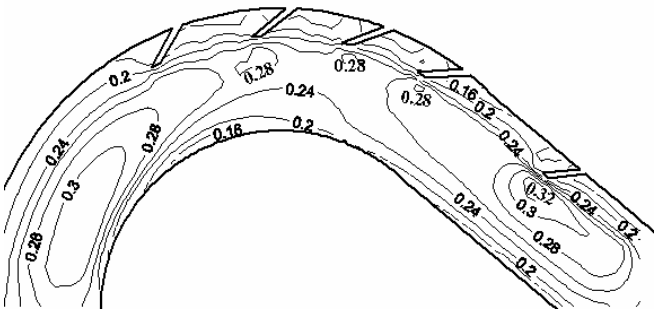

Figure 16. Depth-averaged horizontal velocity contours (in meters per second) for 135° channel bend with barbs

that experimental data were not available to compare to the predicted values. Therefore, Figure 15 and Figure 16 are presented to suggest possible trends that relate the flow field to associated scour and deposition in a complex fluvial environment.

CONCLUSIONS

A three-dimensional numerical model was used to simulate the turbulent flow field and associated scour and deposition of the bed sediments due to a series of barbs in both a 90° channel bend and a 135°channel bend. It was

observed that the results simulated by the numerical results showed good agreement with the measured data. Statistical analysis of the sediment transport results for the 90^o channel bend found a regression coefficient of determination (r^2) of predicted from measured bed elevations of 0.8 for both the channel containing the barbs and the channel without barbs. A regression coefficient of determination (r^2) of predicted from measured bed elevations of 0.7 was found for the 135^o channel containing barbs and 0.8 without barbs. The numerical model adequately simulated the important features of sediment transport through both the 90^o and 135^o channel bends (without barbs). The location and magnitude of the measured and predicted point bars and scour holes were observed to be comparable. In addition, the numerical model was able to reasonably simulate the effects of different arrangements of barb groups in the bend section. Similar to the measured results, it was observed that the location of the thalweg shifts away from the outer bank with the addition of barbs to the channel bend section. The simulated flow field data showed that the location of the maximum depth-averaged horizontal velocity moves away from the outside bank with the addition of barbs to the channel. It was observed that the maximum scour depth and horizontal velocity were located off the tips of the barbs.

There are several possible explanations for the discrepancies between the measured and predicted data. The model performed reasonably well at simulating the flow field and sediment transport through the 90^o and 135^o channel bends. However, these are complex flow fields and the three-dimensional Reynolds-averaged Navier-Stokes equations can not fully replicate secondary currents, particularly in narrow channels, due to turbulence closure. Furthermore, it was necessary to use a rigid-lid for stability of the model. Thus, it was not possible to simulate the super-elevation of the fluid along the outer bank of the channel bend. This would also reduce replication of the secondary currents due to channel curvature and pressure imbalances from the super-elevation of the fluid. As a result, it is possible that the numerical model was underestimating the transverse sediment transport.

The geometry (i.e. height, length, width, and slope) of the barbs contributes directly to its performance. It was not possible to replicate the width precisely in the model and the slope of the barbs was not included in the 135^o channel bend section. These inconsistencies in barb geometry would have contributed to discrepancies between the measured and predicted data.

REFERENCES

[1] USDA. Technical Note 23: Design of Stream Barbs. U.S. Department of Agriculture, Natural Resources Conservation Service, Portland, Oregon, April 2005.

[2] F. D. Shields, S. S. Knight, and C. M. Cooper, "Addition of spurs to stone toe protection for warmwater fish habitat rehabilitation," *J. American Water Res. Ass.*, vol. 34, pp. 1427-1436, December 1998.

[3] N. Rajaratnam and B. A. Nwachukwu, "Flow near groin-like structure," *J. Hydraulic Eng.*, vol. 109, pp. 463-480, 1983.

[4] T. Tingsanchali and S. Maherswaran, "2-D depth averaged flow computation near groyne," *J. Hydraulic Eng.*, vol. 116, pp. 71-86, January 1990.

[5] A. Molinas and Y. I. Hafez, "Finite element surface model for flow around vertical wall abutments," *J. Fluids Structures*, vol. 14, pp. 711-733, 2000.

[6] S. Ouillon and D. Dartus, "Three-dimensional computation of flow around groyne," *J. Hydraulic Eng.*, vol. 123, pp. 962-970, November 1997.

[7] W. S. J. Uijttewaal, D. Lehmann, and A. van Mazijk, "Exchange processes between a river and its groyne fields: model experiments," *J. Hydraulic Eng.*, vol. 127, pp. 928-936, November 2001.

[8] A. Sukhodolov, W. S. J. Uijttewaal, and C. Engelhardt, "On the correspondence between morphological and hydrodynamical patterns of groyne fields," *Earth Surf. Process. Landforms*, vol. 27, pp. 289-305, March, 2002.

[9] R. A. Kuhnle, C. V. Alonso, and F. D. Shields Jr, "Geometry of scour holes associated with 90º spur dikes," *J. Hydraulic Eng.*, vol. 125, pp. 972-978, September 1999.

[10] R. A. Kuhnle, C. V. Alonso, and F. D. Shields Jr., "Local scour associated with angled spur dikes," *J. Hydraulic Eng.*, vol. 128, pp. 1087-1093, December 2002.

[11] Y. Jia, S. Scott, Y. Xu, S. Huang, and S. S. Y. Wang, "Three-dimensional numerical simulation and analysis of flows around a submerged weir in a channel bendway," *J. Hydraulic Eng.*, vol. 131, pp. 682-693, August 2005.

[12] T. Matsuura, and R. Townsend, "Stream-barb installations for narrow channel bends-a laboratory study," *Can. J. Civ. Eng.*, vol. 31, pp. 478-486, June 2004.

[13] [N. R. B. Olsen, *A Three-Dimensional Numerical Model for Simulation of Sediment Movements in Water Intakes with Multiblock Option: User's Manual*. Department of Hydraulic and Environmental Engineering, Norwegian University of Science and Technology, Trondheim, Norway, 2004.

[14] S. V. Patankar, *Numerical Heat Transfer and Fluid Flow*. Hemisphere Publishing Company, Washington, USA, 1980.

[15] L. C. van Rijn, "Sediment transport. Part I: Bed load transport," *J. Hydraulic Eng.*, vol. 110, pp. 1431-1456, 1984.

[16] [USDA. Technical Note 23: Design of Stream Barbs. U.S. Department of Agriculture, Natural Resources Conservation Service, Portland, Oregon, 1999.

[17] [T. Matsuura, *Stream-Bank Protection in Narrow Channel Bends Using 'Barbs': A Laboratory Study*. M. A. Sc. Thesis, Department of Civil Engineering, University of Ottawa, Ottawa, Canada, 2004..

Field Study on Bank Erosion due to a Crank Flow in a River Channel which has Divergence Convergence Meandering System

Tomokazu MISHINA* and Nyosen SUGA**

*Chief-Eng. Chuohteck. Co. Ltd, 310-0902, Watari3082, Mito city, Ibaraki, JAPAN

** Prof. Emeritus, Univ. of Utsunomiya, 276-0023, Katsutadai4-2-4, Yachiyo city, Chiba, JAPAN

I. INTRODUCTION

This paper deals with a new concept of bank erosion in a river caused by bank attacking concentrated flow at sharp angle due to crank flow as was introduced in Ref. [1] and [7].

Definition and characteristics of crank flow are shown below. Crank flow is a flow pattern which has plain shape of crank. And after development, crank flow becomes to a bank attacking concentrated flow at sharp angle to the bank, and brings large scale bank erosion. Development process of crank flow is divided into two categories; the one by natural condition and the other by artificial condition.

This paper treats the case of crank flow developed by the deformation of morphological meandering shape divergence convergence channel system. This kind of crank flow occurs frequently according to the increase of artificial actions recently. Divergence-convergence meandering system which was also introduced in Ref. [5] and [6] develops under the condition of bed material sifting during flood flow. And the phenomena are mainly characterized to rivers which have graded large bed materials. In this case, formation of jam-up deposit of large stones promote to make flat and wide channel up-stream, and also steep and narrow channel down stream.

Practically in many rivers in Japan, the developments of various types of crank flow are recently becoming remarkable. As for the damages, the suffering cases of bank erosion caused by crank flow increase quantitatively and some of then are recognized beyond sufferance qualitatively. For example, length of damage of bank erosion exceeds 100m (about one-third of channel wide) laterally in a flood time (one day) occurred in Kinu-river 2001.

In this paper, main causes of development and the classification of crank flow are discussed based on field investigation in such rivers as Kinu and Watarase River. In those rivers, typical strong bank attacking concentrated flows at sharp angle to the bank due to the development of crank flow are appearing, according to the degree of deformation of meandering system mainly by artificial action. In this case, the meandering system in the fan shape land of Kinu and Watarase river is characterized by the divergence convergence meandering channel system.

Thus, the recent remarkable bank erosion caused by crank flow in a river which has divergence-convergence system is elucidated based on field study. Results of this study are expected to contribute to practical application and offer suggestions to farther development of the study. And also as countermeasures, mitigated relieved method and restoration of the channel meandering system are proposed besides the hither to direct protection as revetment method.

II. ACTUAL CONDITION OF CRANK FLOW

A General feature of Crank flow

Three items are mentioned as main characteristics of crank flow as follows. a) plane shape of thal-weg is crank-like. b) bank attacking concentrated flow at sharp angle to the bank. c) crank flow brings large-scale bank erosion. Typical example of crank flow is shown in Photo. 1. And also, Ref. [1] and [7] shows that characteristics of crank flow and introduction of several types of crank flow.

Development process of crank flow is divided into two classified categories based on the natural condition and artificial condition. As natural conditions, meandering river at mountain alluvial land is mentioned as an example. In this case, the importance of existence of many large stones is indicated as that the channel meandering is easily occurred where jam-up deposit of large stones and the local scour around it develop, or in the case of gravel bed without large stones, crank flow is formed as straight flow from edge to edge of rock bank in the width of forced meandering alluvial land. Above-mentioned results were

Photo 1. A typical example of crank flow (Down stream alluvial reaches of Naka river)

obtained by the field investigation of natural meandering pattern at mountain alluvial land in Yosasa-river, as stated in Ref. [2] and [3].

As artificial conditions for the development process of crank flow deformation of the meandering features the construction by channel works in the divergence-convergence meandering river is mentioned. The river bed degradation is an alternate bar channel is also one of the important additional causes as shown in photo. 1.

In this paper, the cases of divergence-convergence channels where the development of crank flows are remarkable are investigated. The objected rivers are Kinu-river and Watarase-river, tributaries of the Tone River. Basic structure of divergence convergence channel system is described later. Concerning the power of crank flow for bank erosion, relationship between discharge/water depth and velocity was shown in Fig.1.

Velocity increased near the bank occurs even during small flood when the water level is below the surface of sand bars, under the condition of development of deformation of meandering system. Those phenomena occur, corresponding to middle scale flood and also decreasing term of discharge in big flood , in accordance with the development of bed degradation of the thal-weg. But, the velocity near the bank is moderate, and the maximum velocity during large scale flood appears at the center of the channel laterally, before the deformation of meandering system occurs, maintaining the original two lane meandering channel pattern. As stated in Ref. [4], two lane meandering system is stable under the natural condition, and even big flood flows do not exert influence on river bank due to the moderate velocity near the bank.

But recently, meandering pattern is gradually deforming. Among various way of deformation, primary item is the development of flow velocity near the bank and the extension of thal-weg to the down system side along and in front of the newly constructed straight works. This brings the development of extension of distinct straight channel along and in front of the bank which is protected by rigid revetment. Though there are many causes for the change of channel pattern such as dredging, decrease of sediment run off, change of bed material, change of flood scale and flood duration, or vegitation, construction of straight revetment, among them, is considered to be the direct cause by artificial action. Concerning extension of the straight thal-weg, the meandering shape deforms, abrupt change of flow direction occurs in the thal-weg to the other side of the bank across the river, and the bank attacking concentrated flow at sharp angle to the bank develops.

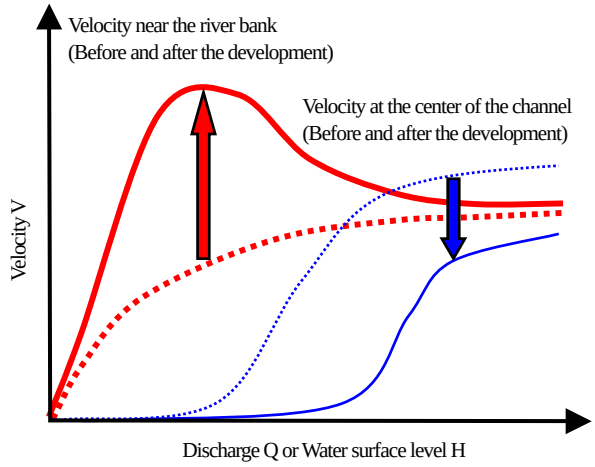

Figure 1. Change of velocity pattern

(Before and after the development of deformation of meandering system)

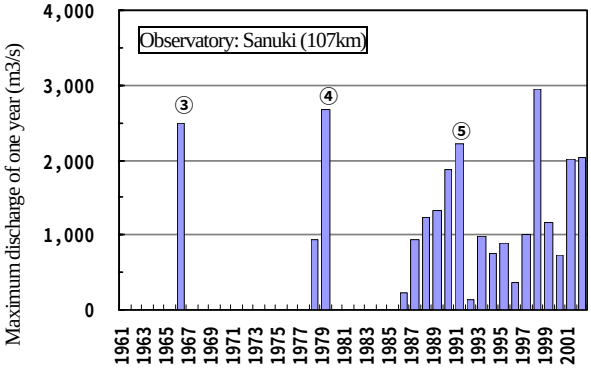

Figure 3. The rate of maximum discharge in Kinu-river

(No data shows non-observation value.)

B Relation between the Revetment and Crank flow

Fig. 2 shows relationship between extension of revetment and existent of crank flow in Kinu-river. The number of existent crank flow is in increasing tendency. 14 crank flows existed as maximum in 2002. After the war, large-scale disaster restoration works were enforced 5 times as, 1) 1950. 2) 1958-1960. 3) 1966-1967. 4) 1977-1982. 5) 1990-1995. And the maximum rate of flood discharge in those case are shown in Fig. 3. Result of decipherment, shows the increasing of the existence of crank flow after restoration works, and number of crank flows

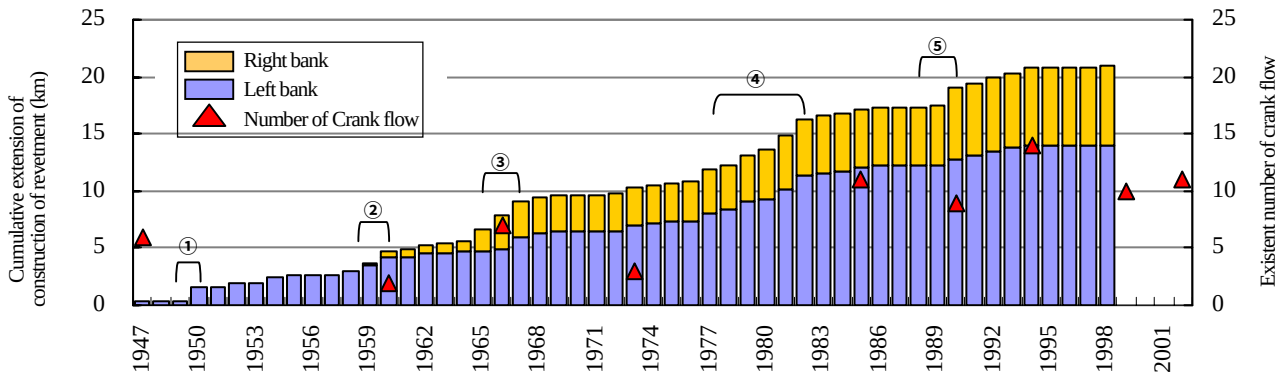

Figure 2. Cumulative extension of revetment works of and Existent number of crank flow in Kinu-river

(Section: 83-101.5k (L=18.5k), Existent number of crank flow is judged from Aerial photo.)

gradually decreases afterwards in each case. Furthermore number of existent crank flow increases again after the large-scale disaster restoration works.

C Suffering case by Crank flow

Examples the suffering cases in Kinu-river due to crank flow are picked up. The location belong to the reach where bed slope abruptly changes from 1/500 to 1/1,500, longituanaly. The size of bed material also changes from stones to the sand and gravel. Since the channel stability is not enough in this reach, lateral fluctuation of the thal-weg is remarkable compared to the upstream reaches. Photo.2 shows the development of the crank flow between 1994 and 2002, and two pictures of bank erosion of 30m lalerally, 250 m longitudinally, caused by bank attacking concentrated flow during a small flood in 2003. Photograph lot and direction are shown in the serial photograph below right.

In this case, main cause of development of crank flow is considered to be the influence of construction of straight revetment at the left bank. Flow angle at the right bank changed a little and bank materials are also loose composed of sands, gravels and stones. Disaster outbreak first by destruction of existed old revetment, and then erosion of loose bank. The wreckage of old revetment is seen in the picture above left.

D Velocity of Crank flow

Concerning velocity of crank flow at bank attacking concentrated flow does not comprehend sufficiently which some case rivers of really existence of crank flow. Therefore,

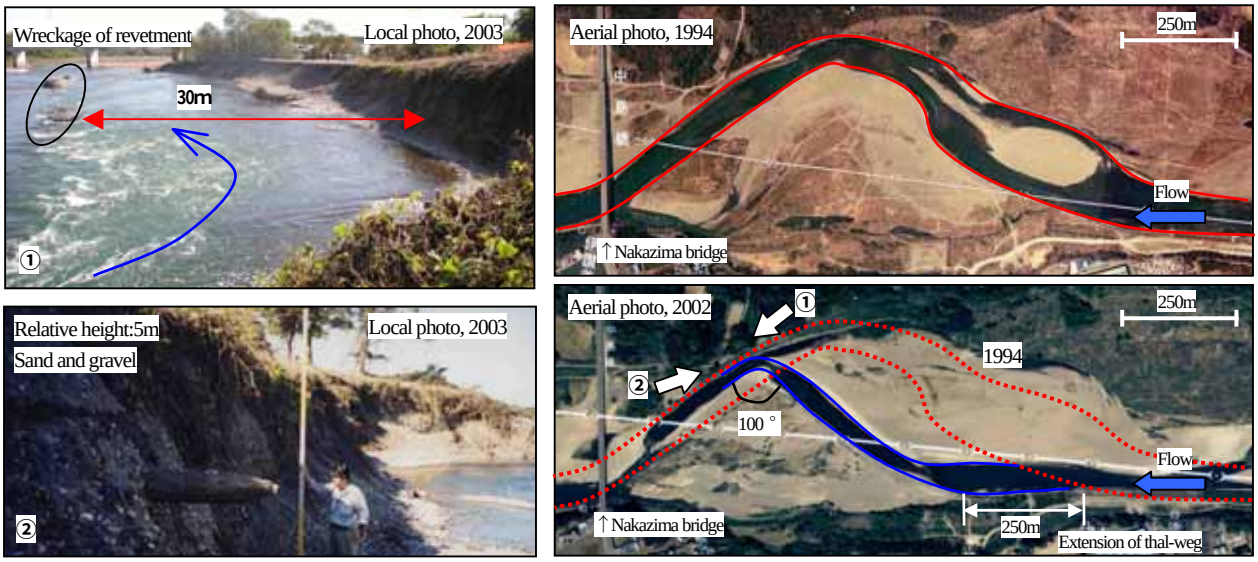

Photo 2. Development of crank flow between 1994 and 2002,

and river bank erosion after suffering (2003) in Kinu-river

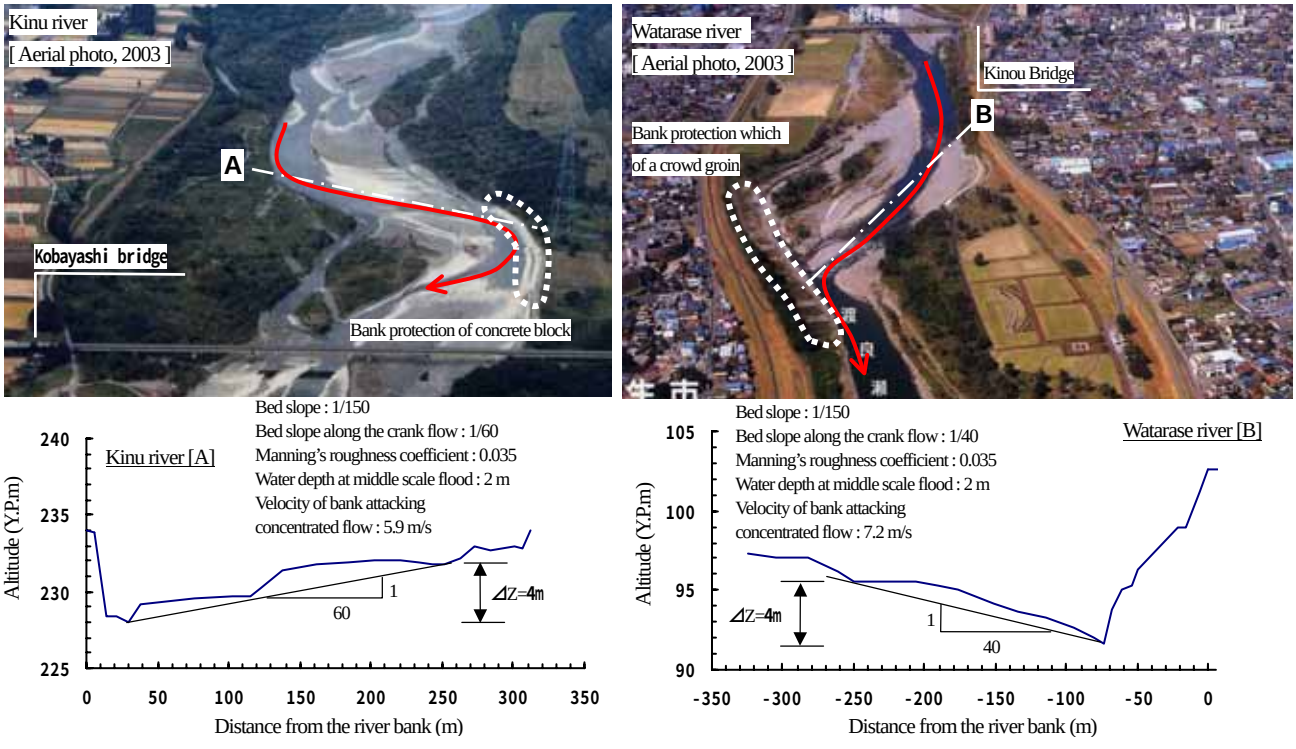

Figure 4. River bed topography along the crank flow [Cases of the Kinu-river and Watarase-river]

field investigation of crank flow is enforced in Kinu-river and Watarase river. Fig. 4 shows the topography of the crank flow in Kinu-river and Watarase-river.

The channels of crank flow in Kinu-river was investigated by field measurement. The results show that the difference of elevation of the bed of the thal-weg at right and left bank is 4m, bed slope of crank flow channel is 1/60, speed of bank erosion between 1999 and 2002 is approximately 17m/year. After disaster suffering caused by the bank attacking concentrated flow due to this crank flow, concrete block revetment is recognized to be constructed as shown in Flg. 4.

On the other hand, many parks and playgrounds were constructed alternatively in the channel of Watarase-river. Though, the original channel of Watarase had also divergence –convergence meandering system, sub lanes of two lane meandering channel were buried to make new land including central bar area, and the two-lane meandering system thus changed into alternate bar meandering system in order to use the land in the channel artificially. And the thal-weg in the alternate bar system has gradually developed to become stable crank flow system. The locations of bank attacking concentrated flow in stable and were found to coincide with the historical location of lateral deposition of jam-up large stones.

Results of topographical field measurement about the crank flow in Watarase-river show that the bed elevation difference of the channel of bank attacking concentrated flow at the positions of left and right bank is 4m, and the slope is 1/40. Large-scale groins is now constructed along the bank as direct protection countermeasure.

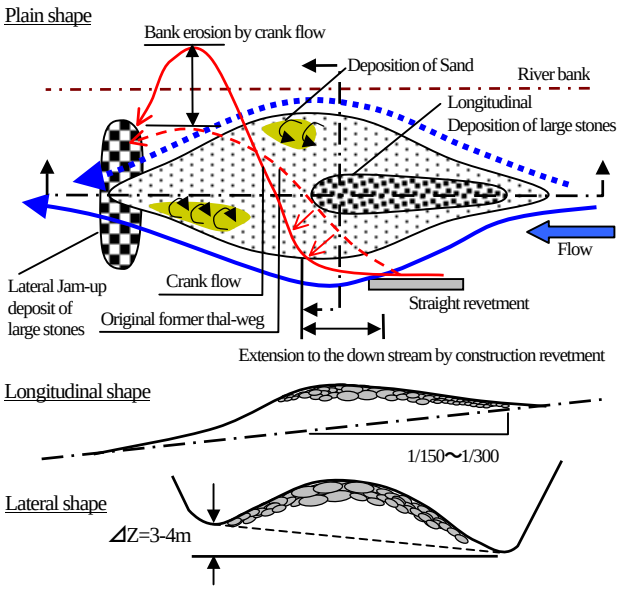

Figure 6. A schematic figure basic structure based on jam-up deposit of large stones and development of crank flow

In this connection, velocity was assumed by calculation as its maximum, based on such assumptions as uniform flow, Manning's formula and water depth 2m, which corresponds to the height of crank flow channel below the top of the surrounding sand bars. According to trial simple 2D calculation in Ref. [9] and [10], this water depth is considered to be suitable

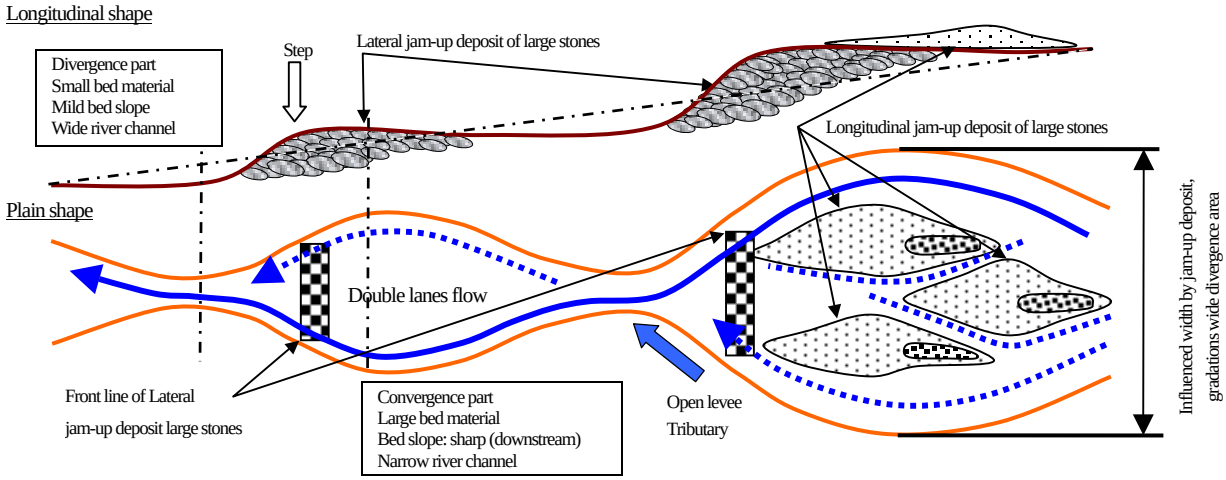

Figure 5. A schematic figure of jam-up deposit large stones and divergence convergence channel

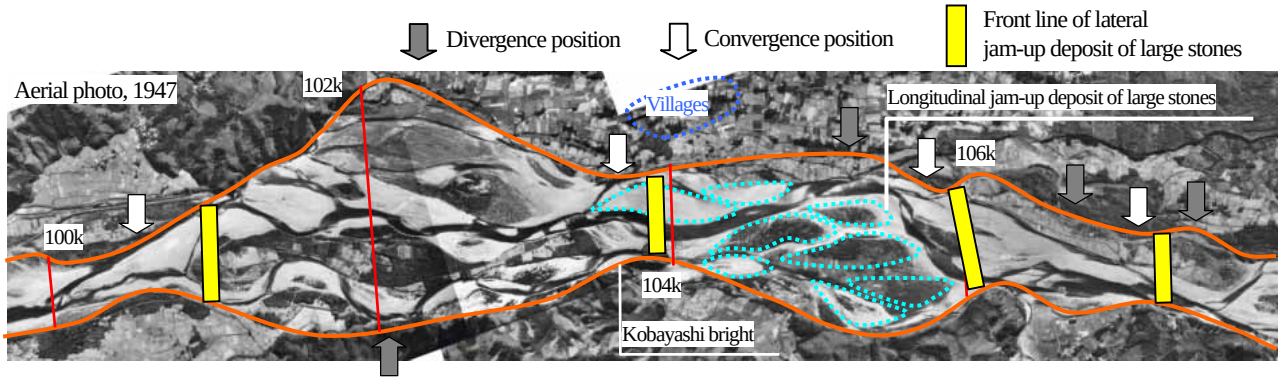

Photo 3. Divergence Convergence channel in Kinu river [Aerial photo, 1947 before construction of levee]

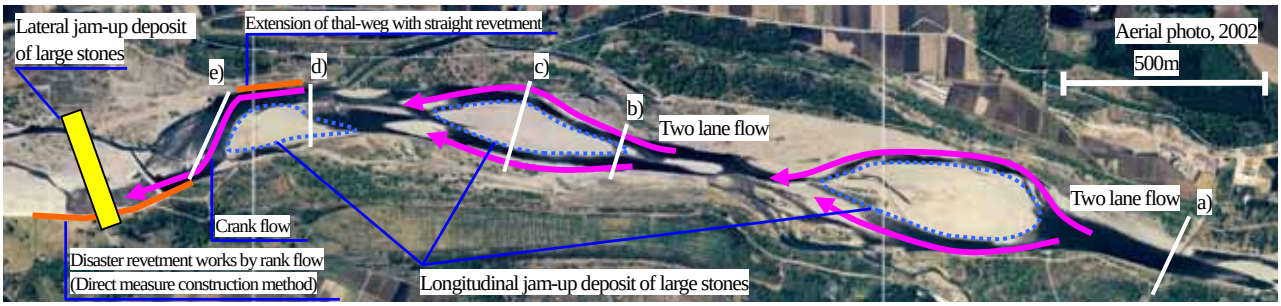

Photo. 4 Two lane meandering channel with the development of longitudinal jam-up deposit of large stones

to the condition that the strength of the crank flow becomes to its maximum during a flood. Calculated results of velocity are 6m/s in the bank attacking concentrated flow at sharp angle at Kinu River, and 7m/s in that of Watarase-river respectively.

III. DIVERGENCE CONVERGENCE MEANDERING SYSTEM

Among various meandering patterns, typical divergence convergence meandering system in Kinu-river and Watarase-river was selected for field investigation. The basic structure of divergence-convergence meandering system based on stable condition of jam-up deposit of large stones, is discussed in Ref. [5] and [6].

Morphological concept of river channel structure has been formed based on bed material sifting during flush flood flows. Those phenomena are mainly characterized to a river which has graded large bed materials. Fig. 5 shows schematic figure of divergence convergence meandering system. Formation of jam-up deposit of large stones causes flat and wide surface up-stream divergence reach, and also steep and narrow convergence reach down stream. Photo. 3 shows that plane shape of divergence convergence channel is watched as in example of aerial photograph at Kinu-river in 1947.

Especially, at the downstream side of jam-up deposit of large stones, open levee and confluence of small tributary are usually exist, and is judged to be the stable deposition.

In this paper, the positions of highly stable lateral jam-up deposit as shown in Fig. 5, are defined according to such items as longitudinal size of bed material, change of bed slope, change of channel width, existence of open levee and confluence of small tributary, existence of step in the protected land, and also direct investigation of bed material by dredging around the proposed position. Fluctuations of the shift and change of thal-weg were investigated too in Ref. [6].

Position of flow channel at divergence area locates to the center of the channel where supercritical flow occasionally occurs at near the peak of big flood, when the big stones are transported and deposited just down stream of the step longitudinally. This deposit forms longitudinal jam up deposit, makes the lateral bed profile convex and becomes the main causes to stabilize the two lane meandering system at convergence reach, as is shown Fig. 6.

Photo. 4 shows that typical two lane meandering channel in

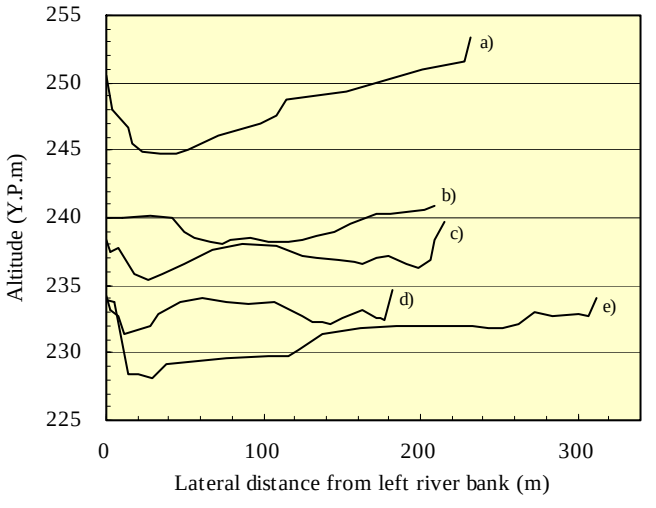

Figure 7. Lateral shape at divergence reach in Kinu river

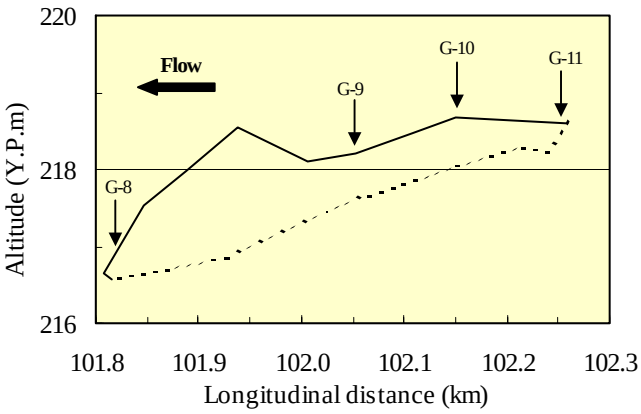

Figure 8. Longitudinal shape of longitudinal jam-up deposit of large stones

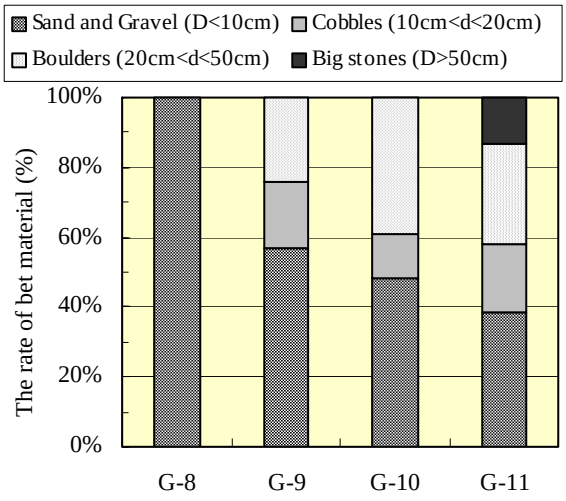

Figure 9. The rate of bed material on the surface of river-bed material rate of longitudinal jam-up deposit of large stones

Kinu-river, and lateral shape in this area shows Fig. 7 at some case of divergence reach. Fig. 8. and Fig. 9. shows that longitudinal shape and bed material at longitudinal jam-up deposit of large stones. Bed material rate appears on the surface river bed by field investigation.

In this area, longitudinal jam-up deposits clearly at the divergence reach, and thal-weg of two lane develops along the right and left bank in channel. In this case, divergence reach with flat and wide is formed by stabled lateral jam-up deposit of large stones. Basic lateral shape of longitudinal jam-up deposit of large stones becomes convex shape, and size of bed material differenced each position as longitudinally. Large-size bed material (cobbles, boulders, big stones) deposit at upper reach, and Small-size bed material (sand or gravel) deposit at down stream, as relatively.

Concerning of formation of longitudinal jam-up deposit of large stones promote to make convex shape laterally at the divergence reach. Point a) exist down stream reach of lateral jam-up deposit of large stones, as a lateral shape is concave. Formation of concave shape is stabled which basic of lateral jam-up deposit of large stones stability. The flow pattern gradually changes from mono lane flow to double lane flow is shown point b) and c). Especially, point c) is formed convex clearly with condition below, degradation of thal-weg at near the both bank developed, and stability of longitudinal jam-up deposit of large stones is high. Also point d) is convex same as point c), presently flowing at the right bank is flowed higher than flowing left bank. Crank flow at this point e) is caused by flow condition of point d), it is described below. Main cause of development of crank flow at the point e) is considered to be the influence of straight revetment at the right bank. In this case, extension of thal-weg to the down stream side is become by straight revetment. Relative height of the thal-weg between right and left banks is 2m at point d) of Fig. 6. Relative height of river bed in crank flow is 4m at point e) of Fig. 7. Damage of bank erosion by crank flow of point e), left bank was eroded 17m in 2001.

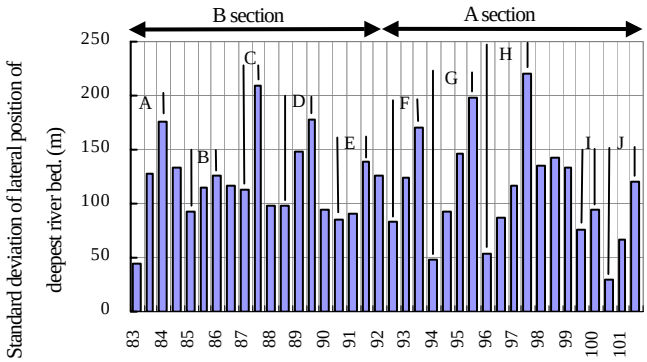

Figure 11. Standard deviation of lateral position of deepest river bed at 83k-101.5k in Kinu-river

This numerical value is the standard deviation of distance to the maximum river bed from the left bank annually. The measurements were done 13 times during 1963-2001.

IV. DEVELOPMENT PROCES OF CRANK FLOW

The crank flow treated here develops at divergence reach in the divergence-convergence channel. This area is rather flat and wide, and the stability of the channels on it depends mainly on the scale, number, and their stability of longitudinal jam-up deposits of large stones. Artificial actions such as construction of straight revetment, are another causes to decrease stability as stated in Ref. [7].

Basic structure of divergence area is constituted with several longitudinal jam-up deposits of large stones. And lateral shape is convex. Fig. 6 shows the outline of the structure of deposition of sifted materials, lateral and longitudinal shape, and low water thal-weg in the divergence reach. The occurrence point of crank flow is near the peak of longitudinal bed shape at center. It is illustrated in this case that the construction of straight revetment causes extension of thal-weg along river bank. This extension promotes development of crank flow and also bank attacking

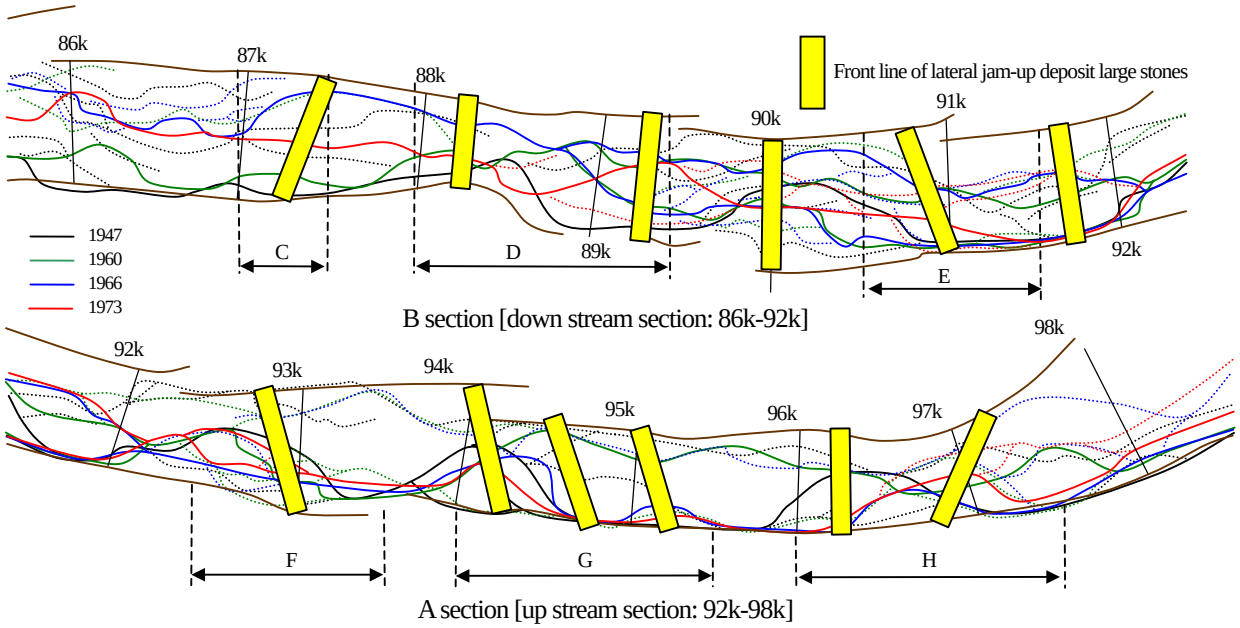

Figure 10. Change of thal-weg at up stream section and down stream section in Kinu-river.

(C-H in the figure shows decrease section to minimum value from the maximum value)

concentrated flow at sharp angle at the other side bank.

There is some difference in stability of thal-weg fluctuation between upstream section and down stream section of Kinu-river. Fig. 10. shows that change of thal-weg up stream section and down stream section in Kinu-river.

The up stream section (A section : 92k-98k) has been formed on the original fan shape land and the stable lateral jam-up deposits of large stones are clarified to be stable. On the other hand, down stream section (B section: 86k-92k) was considered to be created about 7,000 years ago by channel shift and has been developing by eroding ash accumulated lager mainly laterally. Lateral jam-up deposits also developed at some interval longitudinally. According to the field investigation, most of them have enough stability but some are found to move 100~200m down stream due to the large scale dredging of the bed after the War.

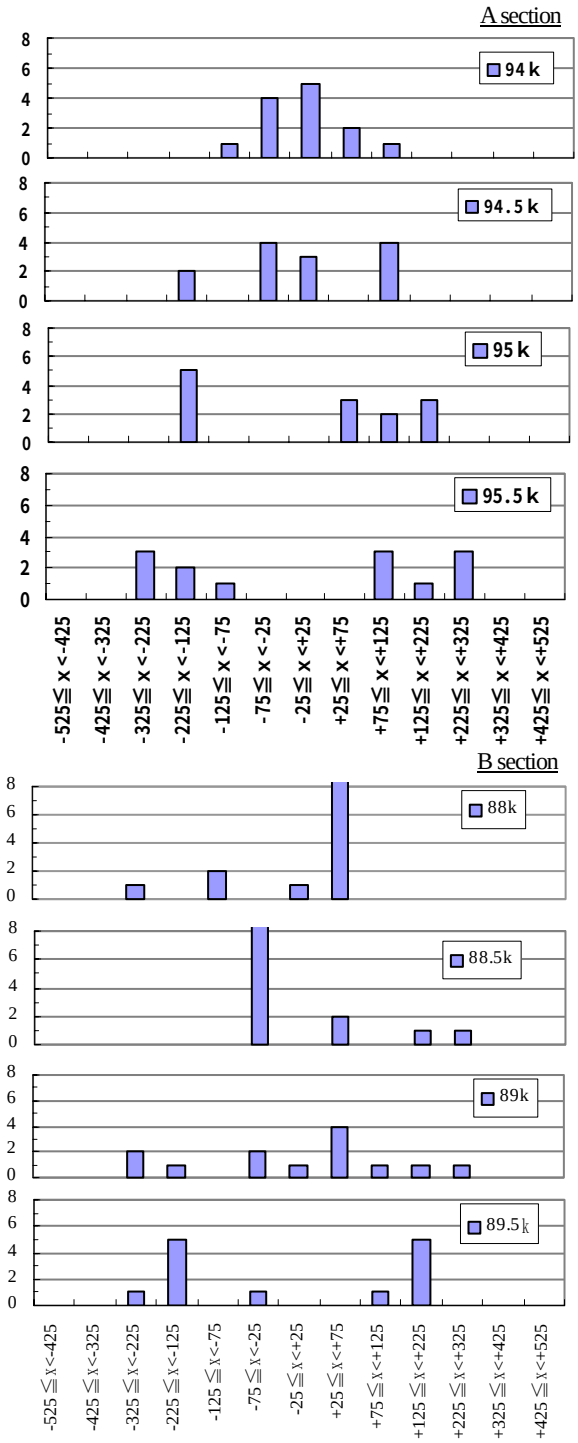

Figure 12. Frequency distribution of the position of deepest river bed in Kinu-river.

Lateral axis is a difference from the mean distance from left bank to the deepest riverbed. Vertical axis is frequency within each range. The measurements were done 13 times during 1963-2001.

Standard deviation of lateral position of deepest river bed between 83k-101.5k using 13 data from 1963 to 2001 is shown in Fig. 11. And it is found from Fig. 11 that the lateral change of thal-weg is little in up-stream section (A section) and large in down-stream section (B section). The figure of thal-weg in A section divides cleanly focus positions and emission positions, and it can be recognized that there are divided reaches, continuously connecting each reach longitudinally, where maximum value of deviation appears at upstream point of one reach and minimum value at down stream point of the same reach. In fact these down-stream points correspond to the existing positions of the stable lateral jam up deposits of large stone. In the down-stream section (B section), above tendency is not clear than that in A section.

As stated above, these causes are related to the scale and the stability of longitudinal jam-up deposit of large stones. Thal-weg in A section are formed under the condition of stable longitudinal deposits composed of larger stones, than those in B section. Fig. 12. shows frequency distribution of the position of the deepest bed in Kinu River.

In A section, the positions of thal-weg at 94k are stable near at center part and then approaches to right and left direction according to shift down stream. This tendency means the developments of thal-weg along right and left bank, and fluctuations of the flowing position also become large due to the changes of stability of longitudinal jam-up deposit of large

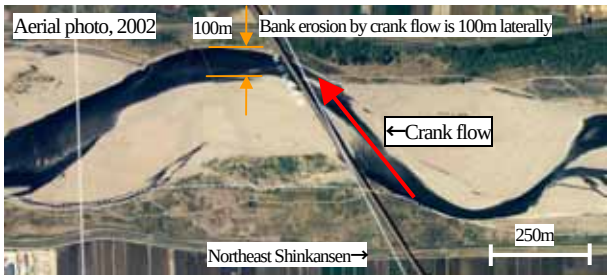

Photo 5. Crank flow of Kinu-river

[Northeast Shinkansen area, 94km]

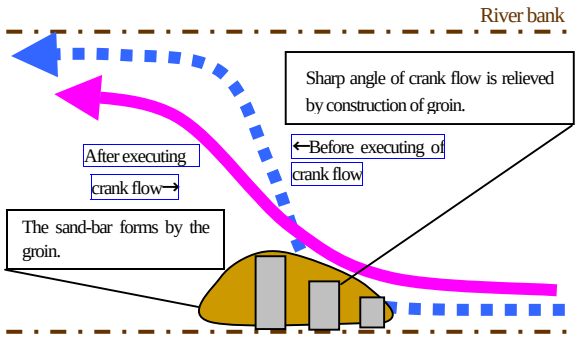

Figure 13. Jetty construction method for relief against crank flow

stones, according to shift down-stream.

Because the scale of the phenomena are larger in up stream section (A section), the scale of crank flow and also the strength of bank attacking concentrated flow becomes larger in A section than in B section.

For example in Kinu-river, at northeast shinkansen area of A section, bank erosion of 100 m laterally in a flood of one time (1day) occurred. Photo. 5 shows the crank flow at northeast shinkansen in Kinu-river. Direct causes of this area are considered as follows; 1) Existence of large-scale lateral jam-up deposit of large stones. 2) Development of thal-weg caused by the construction of straight revetment at left bank. 3) Stability of longitudinal jam-up deposit of large stones is high, and lateral shape is convex clearly. 4) Difference of elevation between left and right bank is large.

In this case, stability of longitudinal jam-up deposit of large stones and two lane flow are recognized even in Fig. 12. As result of description above, severe change of flow to the right bank from left bank is occurred after the extension of thal-weg down stream at left bank and the strong crank flow at developed along and in front of the lateral jam-up deposit of large stones.

V. MEASURE OF CRANK FLOW

Direct bank protection method was adopted in Watarase-river because local erosion came lose to the levee. But the structure of jetty was too heavy, and the straight of bank attacking concentrated flow at sharp angle to the bank aid not to be mitigated. Moreover, environmental problem becomes severe.

Countermeasure for local erosion and environment is urgent to discuss, because the developments of crank flow has recently increased quantitatively and also qualitatively, as discussed Ref. [8]. Basically, then methods are considered as countermeasure for crank flow as shown in Table I.

VI. CONCLUSION

This paper dealt with a new type local erosion along a river bank caused by crank flow which has powerful bank attacking concentrated flow at sharp angle to the bank. Among various patterns of crank flow, crank flow which develops by deformation mainly due to artificial actions is investigated. As original meandering channel system, divergence convergence morphological system was adopted.

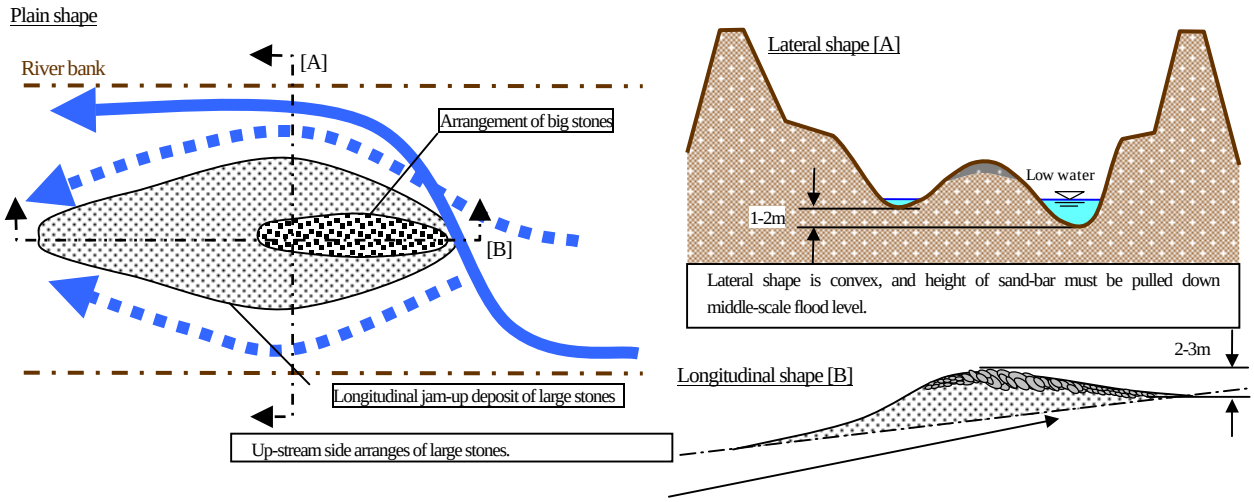

Figure 14. Restoration of double lanes meandering system

Table I. Countermeasures for crank flow

Countermeasures	Construction method	Point of construction method
Direct measure for river bank	Groin, Jetty Revetment, Foot protection, et al	1) These construction method is effective for bank erosion by crank flow. 2) The groins at the bank attacking concentrated points are effective. It is possible to move position of from the front of river bank to the central part of the river.
Relief of cause of crank flow	Relief of sharp angle of the flow	1) Change of shape of a little by using groin, is shown Fig. 13. (Angle of crank flow from sharp angle to loose angle modification.) 2) Small-scale groin system to form sandbar, and loose angle.
Restoration of river channel system	Double lanes meandering system (Longitudinal jam-up deposit of large stones)	1) The restoration of longitudinal jam-up deposit of large stones is examined. 2) Change of flow pattern to two lane meandering from single lane. Velocity at the river bank will be decreased. 3) The large stones are deposited at the upstream side of longitudinal jam-up deposit in other to get stability, is shown Fig. 14.

In Japan recently, channel characteristics has been changing and new type disaster due to bank erosion is increasing, especially by crank flow developed in divergence convergence meandering channel. Therefore, revetment works as the countermeasure for disaster are now constructed at several rivers. Those direct works change the characteristics of the river channel furthermore and promote to change again.

In order to contribute to improve above mentioned urgent practical conditions, field investigation was considered to be important in the study and was made mainly in Kinu and Watarase River. Then, general consideration was made and get following results. Suggestions were also added for the idea of countermeasure, including further problems for studies.

1) General concept of the development of crank flow was clarified in the case of divergence convergence morphological meandering channel system.
2) Local erosion along river bank caused by bank attacking concentrated flow at sharp angle to the bank is a new type phenomenon. This phenomenon has lose relation with the development of crank flow. Especially crank flow caused by deformation of meandering system in a stable divergence convergence channel develops the power to the bank attacking concentrated flow at sharp angle to the bank, in the ways to increase angle, velocity and rate of crank flow discharge.
3) The causes of increase of power to crank flow are as follows; a) degradation by dredging, enlargement of channel and decrease of sediment run off, b) development of thal-weg, extension of thal-weg down stream along constructed straight revetment, c) increase of relative height of bar and its development, growth of grasses and trees on the bar, d) decrease of disturbance due to dam construction, e) destruction of lateral and longitudinal jam up deposit, decrease of big bed materials, decrease of meandering mode from double lane meandering to mono meandering, deformation of original meandering system.
4) Basic structure of divergence convergence channel meandering system is formed based on bed material sifting during flush flood flows. And main characteristics have graded large bed material. Formation of jam-up deposit of large stones causes flat and wide surface up-stream divergence reach, and also steep and narrow convergence reach down stream. Especially, divergence side is constituted with several longitudinal jam-up deposit of large stones, and lateral shape is convex.
5) Crank flow develops mainly in the divergence reach. Scale and power of crank flow depend on the stability of longitudinal jam up deposit of large stones and the scale of convex bar of 3D (at three dimensional) curved surface, these condition bring long extension of thal-weg, big bed elevation difference, and abrupt change when deformation exceeds its critical states.
6) Countermeasure of clank flow is needed to discuss both direct construction method at bank attacking concentrated position and relief of cause of sharp angle of the crank flow. This paper proposed new construction method at relief of cause of crank flow. The other measure is characterized restoration of longitudinal jam-up deposit of large stones in order to recover the double lanes from single lane. This method is also evaluated in the sense of environment such as stone and gravel river beach simultaneously.
7) This study is expected to offer fundamental idea of measure for crank flow.

REFERENCE

[1] N. Suga, ”A study on the basis of crank flow which has power to bring big bank erosion,” *Annual Jour. Hy. Eng. JSCE. Japan*, Vol.49, pp955-960, February 2005. (In Japanese)

[2] T. Mishina, N. Suga, et al, ”Changes of channel characteristics of yosasa-river after disaster restoration,” *Annual Jour. Hy. Eng. JSCE. Japan*, Vol.46, pp343-348, February 2002. (In Japanese)

[3] T. Mishina, N Suga, et al, ”Fielding investigation on bank protection of natural meandering river at mountain allvial land,” *Advances in River Eng. JSCE. Japan*, Vol.9, pp131-136, June 2003. (In Japanese)

[4] K.Suga, ”Stable condition of double track meandering channel,” *Annua Jour. Hy. Eng. JSCE. Japan*, Vol.33, pp397-402, February 1989. (In Japanese)

[5] N. Suga, ”Basic structure of river morphological channel pattern in case of graded large bed materials,” *Advances in River Eng. JSCE. Japan*, Vol.10, pp95-100, June 2004. (In Japanese)

[6] T. Mishina, N Suga, et al, ”Comprehensive field investigation including protected land about jam-up deposit composed of large stones formed in divergence-convergence channel,” *Advances in River Eng. JSCE. Japan*, Vol.11, pp375-380, June 2005. (In Japanese)

[7] N. Suga, T. Mishina, et al, ”Crank flow and bank attacking concentrated flow at sharp angle in a river channel of divergence-convergence meandering system,” *Annual Jour. Hy. Eng. JSCE. Japan*, Vol.50, pp979-984, February 2006. (In Japanese)

[8] N. Suga, ”Fundamental idea on individual river method in high regard of river characteristics and reflection of social and natural environment based on new river law,” *Advances in River Eng. JSCE. Japan*, Vol.11, pp203-208, June 2005. (In Japanese)

[9] Y. KOGAWA, N. SUGA, H. IKEDA, F. IWASAKI, ”Structure of the open channel flow with hydraulic jump on sand bar front” *Annua Jour. Hy. Eng. JSCE. Japan*, Vol.49, pp523-528, February 2005. (In Japanese)

[10] Y. KOGAWA, H. IKEDA, F. IWASAKI, N. SUGA, ”Plane angle of sand bar front and side wall roughness exerted influence on structure of the open channel flow with hydraulic jump” *Annua Jour. Hy. Eng. JSCE. Japan*, Vol.50, pp643-648, February 2006. CD-R. (In Japanese)

Development of the Fully Functional Stilling Basin in Extreme Geological and Spatial Conditions - HPP Moste III

Jure Mlacnik*, Sabina Misigoj**
* Institute for Hydraulics Research, Ljubljana, Slovenia
** Institute for Hydraulics Research, Ljubljana, Slovenia

I. INTRODUCTION

The company SEL d.d., which owns all the HP plants on the Sava River in Slovenia plans to increase the installed power in the Moste HPP, which was built in the beginning of the fifties. The Moste HPP is situated on the Sava River approximately 4km north from the well-known tourist centre Bled. The construction of an additional machine hall (Moste II HPP) and a compensation basin, which is to enable full peak energy production for both hydroelectric plants, is planned. The project also includes a small 4MW Moste III HPP, situated in the body of the compensation basin dam.

The hydraulic model tests of spillway sections and stilling basins of the Moste III HPP were performed by the Hydroinstitute in Ljubljana. The basic demand of this research was to ensure a complete dissipation of water flow energy inside the stilling basin in every possible operating mode up to Q100. Since there are only two spillway sections, in case of one blocked gate there is only a single section operating, which entails very large specific loads of the stilling basin. This appeared to be the main problem to be solved by this research.

The original design was a 25m long standard stilling basin with one row of baffle blocks ending with one step end sill. The originally designed version shown on Fig. 1, as also all known usual variants, which could possibly lead us to a positive solution, were tested on a hydraulic model built in a model scale 1:35. By the model tests it was established that all tested variants had the same weakness, which was explicitly asymmetric flow over the end sill (Fig. 3). Therefore, in all studied cases the part of the stilling basin situated behind the blocked spillway section was inactive. The consequence was a very large specific discharge in the active part of the stilling basin. In such conditions, only a part of energy dissipation can be performed inside the stilling basin, the rest of it is

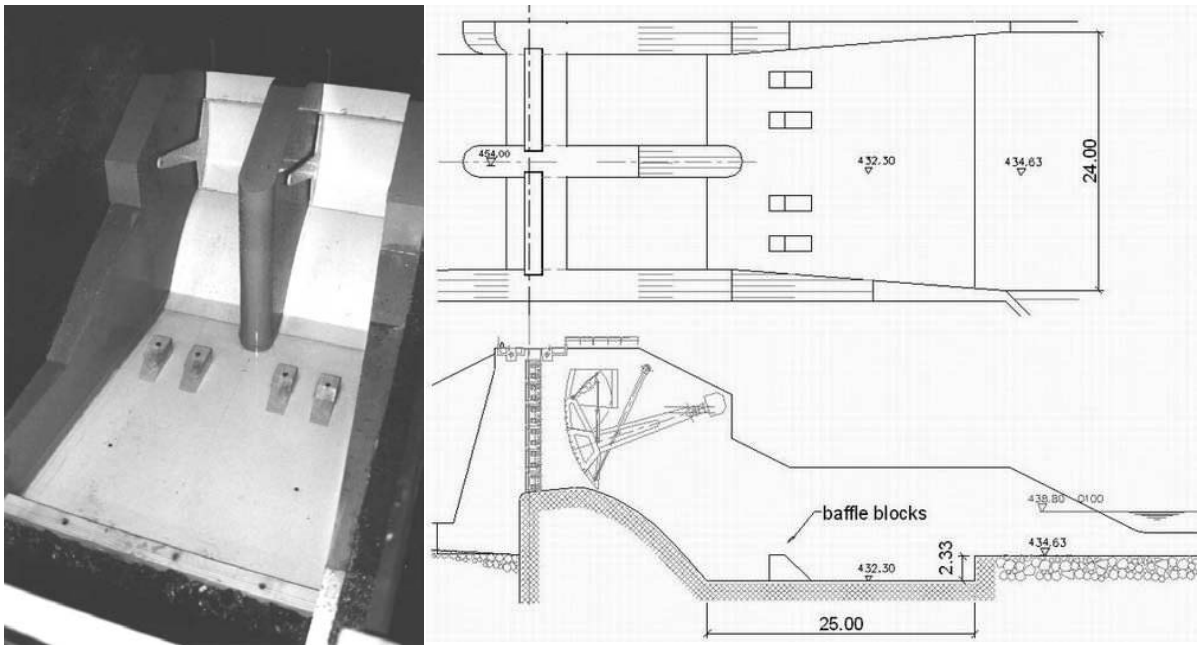

Figure 1. Spillways and stilling basin of the Moste III HPP – original design

transmitted into the downstream channel.

In order to accomplish the effective dissipation inside the stilling basin it would be necessary to diminish specific discharge over the spillways, which is possible only with increasing the number of spillway sections. This requires a newly designed and much larger building than the original design, construction in two phases and also increase of construction time (costs!) for a whole season.

As the only possible solution, which can keep the construction in some reasonable limits according to technical and economic criteria, we developed a stilling basin, which is unusual for the present type of the spillway section. The given solution provides very good water flow arrangement over the end sill and excellent energy dissipation using the combination of bottom sills and scum boards. After extensive tuning of shape and disposition of all dissipative elements we reached a highly effective solution, which practically meets the originally designed construction limits. The result of the research enables construction in only one construction phase without extending the time of construction.

II. INITIAL DESIGN RESEARCH

According to the original design the stilling basin is a 25m long joint structure for both spillway sections (Fig. 1). The middle spillway pier ends at the beginning of the stilling basin with a semicircular vertical ending. The stilling basin bottom is horizontal, equipped with one row of baffle blocks and a solid end sill, which should be able to ensure a full dissipation within the stilling basin.

A. Geometric, Hydraulic and Hydrologic Conditions

The stilling basin belongs into a group of short stilling basins; its length is reduced for about 40% regarding the theoretical length of the stilling basin, calculated according to the geometrical and hydraulic parameters. On the graph below (Fig. 2) we can see that, in our case, in almost all operating conditions the comparable values lie under the theoretical limit of stabile stilling basin operation. This demands a use of baffle blocks and other dissipating elements, which must be optimized on a hydraulic model.

Froude number F_1, which is one of the main criteria to be respected by shaping of the stilling basin and its elements, is in our case in the range between 3.7 and 6.4, depending on the operating mode. This is a very unpleasant situation because it is very difficult to optimize the stilling basin when we can not determine the exact hydraulic regime of the structure. Therefore, only a hydraulic model can give us an optimized solution.

The decisive hydrological values in our case were: Q_{100}=474m^3/s, $Q_{1.000}$=806m^3/s, $Q_{10.000}$=1185m^3/s.

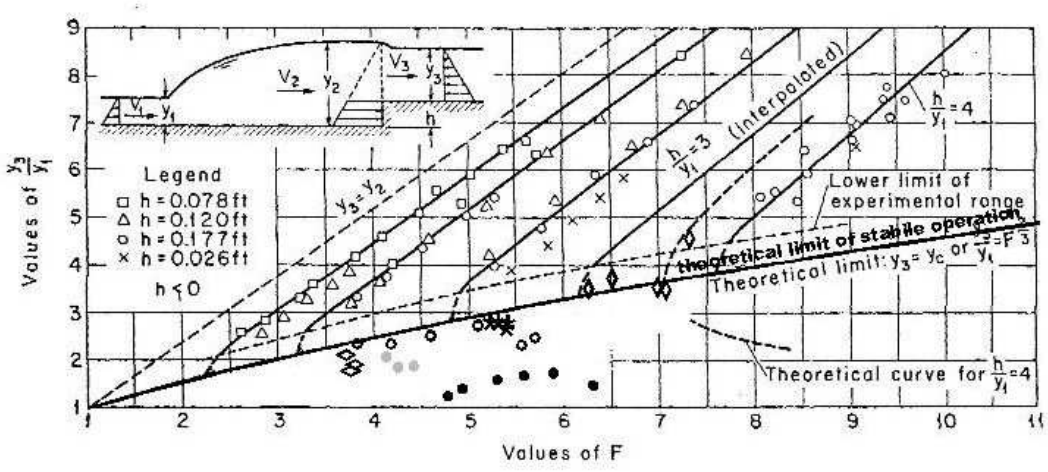

FIG. 15-13. Experimental relations among F, y_3/y_1, and h/y_1 for an abrupt rise. (*After Forster and Skrinde* [23].)

- ○ paralell free surface discharge over both spillways
- ● free surface discharge over single spillway
- ◊ paralell flow through gate a=1m
- ✱ paralell flow through gate a=2m
- ▪ paralell flow through gate a=3m
- ◇ paralell flow through gate a=4m

Figure 2. Diagram which characterizes the initial efficiency of the stilling basin (source: Open-Channel Hydraulics, Ven Te Chow 1959 – after Forster and Skrinde)

B. Operating Conditions

The designer's claim was that the object has to be operating stably in all possible operating conditions within the discharge range up to Q_{100}. This includes also asymmetrical operation (one blocked spillway) with discharges into the tail water lower than normal tail water level for a handled discharge. Such requirement implies almost excessive operating conditions, which are not usual in the hydro-energetic projects design.

A final solution of the spillways should be able to pass:

- Q_{100} through a single spillway not higher than the normal top water level,
- $Q_{1.000}$ through both spillways not higher than the normal top water level,
- $Q_{10.000}$ through both spillways lower than the dam crown.

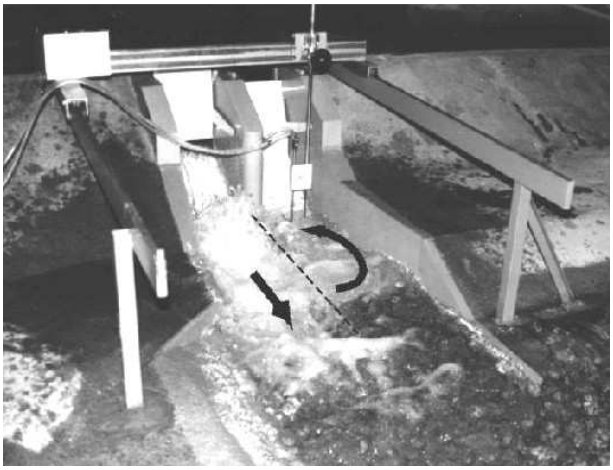

Figure 3. Original Design – Flow over a single spillway section, Q=312 m3/s, HTW = 437.7 m a.s.l. (regular tailwater level), gate opening a=4.0 m; the left margin of the main flow and a dominant vortex in an inactive half of the stilling basin can be clearly seen.

C. Research Tasks

For the originally designed shape of the stilling basin the research should:

- Determine the range of stabile operation,
- Determine the necessary measures to fulfill the above conditions.

If the original design of the stilling basin can not be fully optimized, the researcher should develop a new stilling basin, fulfilling all the above-mentioned conditions and, additionally, the following ones:

- The stilling basin width should stay unchanged,
- The bottom level and length of the stilling basin should be as close to the originally designed ones as possible,
- A uniform velocity distribution of subcritical flow over the end sill should be attained.

D. Results of the Original Design Research

When operating symmetrically with equal discharge through both spillways, the stilling basin operates correctly up to discharge Q_{100}. However, in consequence of the too small water depth above the end sill, the flow over the end sill becomes in many cases critical.

When operating asymmetrically with total discharge through a single spillway, the hydraulic conditions in the stilling basin and downstream of the end sill become very rough. The water jet through the stilling basin remains undispersed, which causes overloading of the active half and a reverse secondary flow in the other half of the stilling basin (Fig. 3). The Froude numbers downstream of the end sill exceed 1.2, which brings us fully into a supercritical flow regime.

During further investigation many different variants of the dissipating elements (buckets, baffle blocks, end sill) and dimensions of the stilling basin were tested. Every variant was subject to the operating conditions mentioned above.

The final conclusion of an extensive experimenting is that the originally designed stilling basin, even deepened and bearably prolonged, no matter which type or combination of known and normally used dissipating elements we choose, is not able to function properly under the directed operating conditions.

There are only two solutions to achieve adequate efficiency of the stilling basin, either:

- diminishing of the third spillway of the same width as the specific discharge by increasing the width of the spillways or by adding existent two, which is a very costly solution, or
- designing a new type of a stilling basin, which would be able to bear the directed operating conditions.

III. Development of a New Stilling Basin

After completion of a research of the originally designed stilling basin and its variants, both possibilities were offered to the investor. Since it would still be possible to come to the same problems as at the originally designed spillway, the second possibility, that is development of a new type of a stilling basin, was a logical choice.

A. *Basic Directions*

When deciding about the type of a stilling basin, a major guidance was the investor's requirement that the stilling basin must be able to function properly under all operating conditions up to a discharge Q_{100} over a single spillway section. According to the designer's limitations, the guiding rules during the development were:

- minimum possible length of the stilling basin,
- minimum possible depth of the stilling basin,
- practicability of the civil structure,
- economic suitability of the project.

Considering the distinctly asymmetric flow over the spillways into a joint stilling basin it was assumed that the only possible solution is a cascade type of a stilling basin. This is not the type that is usual in the hydro engineering practice and therefore there are no widely known recipes for it's dimensioning. There are also some cogent reasons for avoiding such structures in the hydro energetic practice, which have mostly practical background. But in some cases like ours, there are exactly such practical reasons, which can be strong enough to study such a solution. Namely, if we want to calm down the distinctly asymmetric flow, it is necessary to catch it into some sort of a basin and then establish the control over the outflow.

B. *Resulting Stilling Basin*

On the basis of conclusions of the original design research it became apparent, that for the attainment of sufficient energy dissipation within the stilling basin it is necessary to investigate the dissipation elements such as vertical hanging baffles, bottom sills and their combinations. This concrete structure should be able to convert the asymmetric flow into a uniform flow pattern on the outlet of the stilling basin in all the possible operating conditions for a very wide range of tail water levels.

After testing some simpler shapes of the stilling basin the resulting solution containing two vertical hanging baffles, combined with two bottom sills and an end sill appeared to be the only effective shape of a stilling basin, able to function properly even with almost no tail water. The final design can be seen in Figure 4.

The elements of the stilling basin seem to be of very complex shapes. Of course in the early stage of the investigation this wasn't the case, but if all the conditions were to be fulfilled, also all the elements needed to be investigated and optimized.

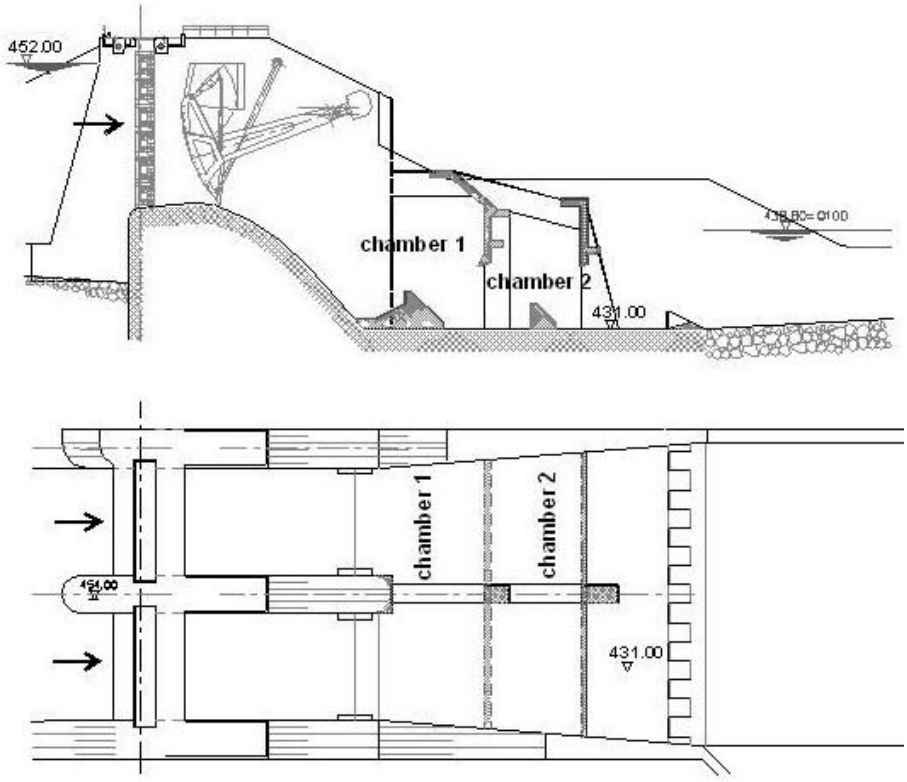

Figure 4. Final Design – Stilling basin, equipped with dissipating elements

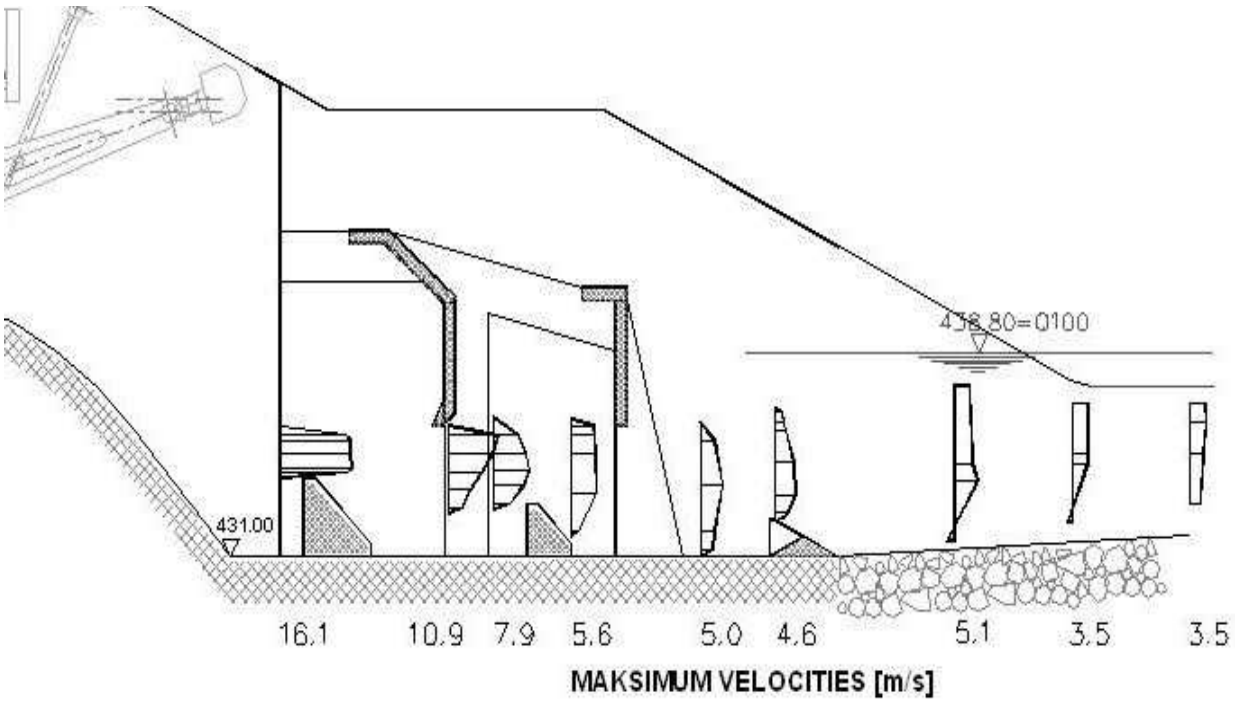

Figure 5. Intermediate Design – Velocity profile changing alongside the stilling basin

The emergency operation was also investigated during the model tests. Regarding the demands stated in chapter 1.2 the spillways and the stilling basin must be able to pass the discharges $Q_{1.000}$ and $Q_{10.000}$ without any damage to the object or the surrounding structures. In order to fulfill this condition, some adjustments of the sidewall height had to be made. The greatest effort however was to

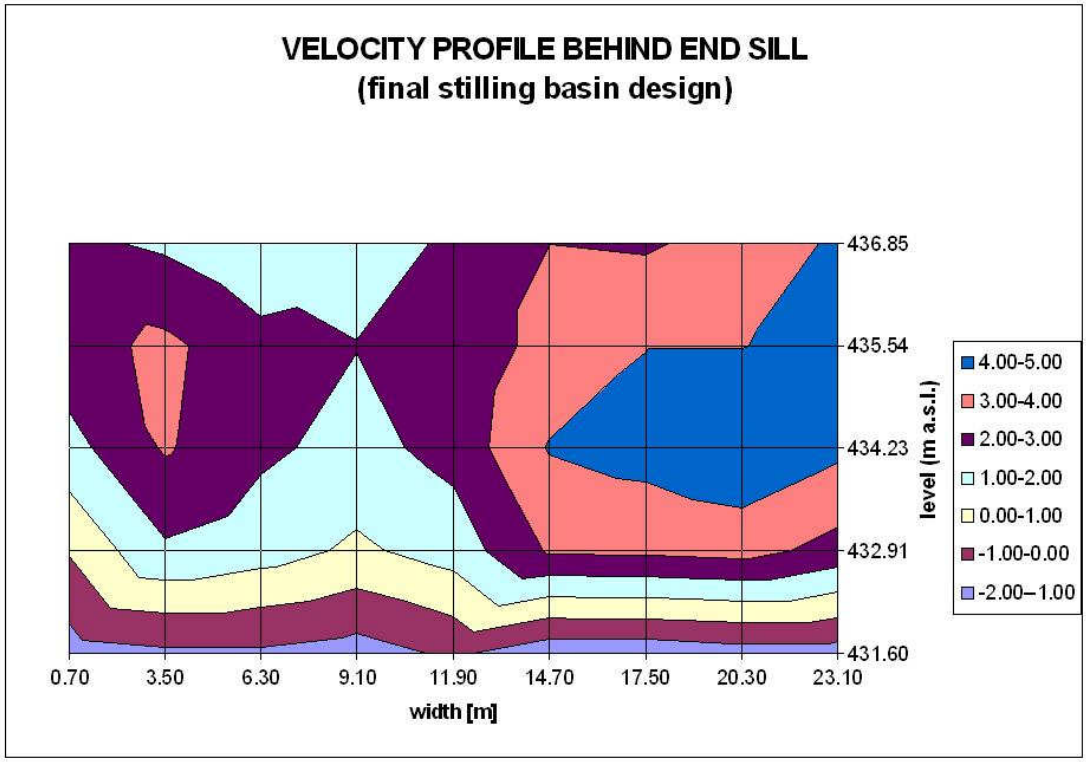

Figure 6. Final Design –Velocity profile in cross-section immediately downstream of the end sill; Flow over a single spillway section, Q=312 m3/s, H TW = 437.7 m a.s.l. (regular tail water level), gate opening a=4.0 m, right spillway in operation;

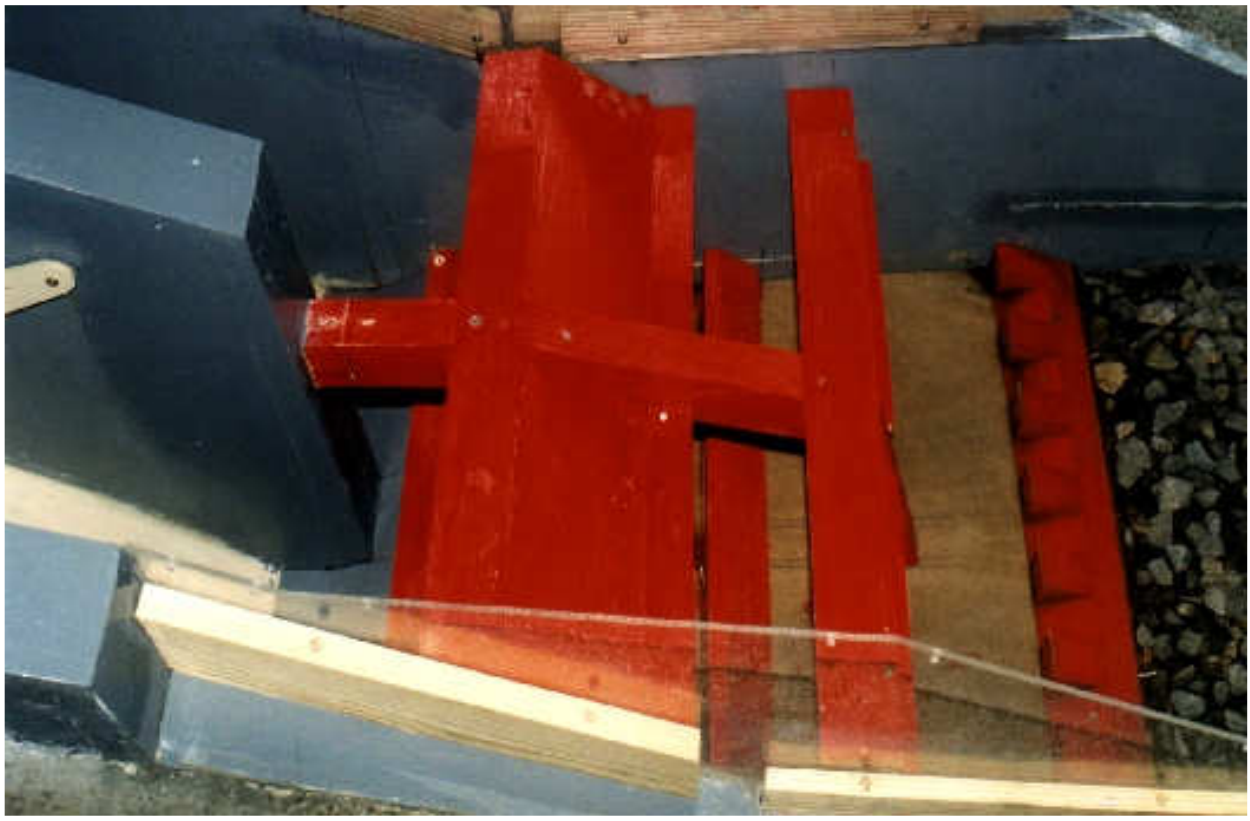

Figure 7. Final Design –The final shape of the stilling basin

reach the lowest possible water resistance of the vertical hanging baffle ceiling. The purpose of the ceiling is to diminish or even prevent the sprinkling from both chambers outside the stilling basin and also to direct the surface flow inside the chambers into the upstream direction. This way a recurrent vortex around a horizontal axis appears which enables sufficient energy dissipation inside each chamber. During emergency operation the energy dissipation inside the stilling basin still performs and the overflow passes over baffles top.

In Figure 5 it can be seen that the velocity profile changes intensively alongside the stilling basin. From a very nonuniform velocity distribution at the beginning of the stilling basin (v_{max}>16m/s) it changes step by step after each dissipation element and reaches a practically uniform vertical distribution of the velocities 10 – 15m downstream of the end sill. The cross distribution immediately downstream of the end sill (Fig. 6) shows very uniform velocity profile. The only area with negative velocities lies close to the bottom and the velocities near the bottom do not exceed 2m/s, while the difference in maximum velocities between right and left half of the cross section amounts only 1m/s.

IV. CONCLUSIONS

The newly developed stilling basin is designed on a principle of a cascade. The stilling basin wholly meets the requirements from the beginning of the research. At the same time it has no negative influence on the discharge capacity. According to the tests, even in case of larger occlusion by debris (30 – 40%), it still operates with no influence on the top water level. It was however suggested to the investor to reinvestigate the presence of debris during the flood waves. In case of a distinctive debris discharge it should be better to consider the solution with more than two spillway sections to avoid such severe hydraulic conditions in the stilling basin.

REFERENCES

[1] Mlacnik, J., “Hydraulic Model Tests of a spillwy sections HPP Moste III”, Final research report, 2003.

[2] Chow Ven Te, “Open-Channel Hydraulics ”, 1959

Study on Local Scour around Spur Dikes in the Akashi River

A. Morita*, K. Kanda**and M. Kishihara***
* Akashi National College of Technology /Advanced course, Akashi, Japan
** Akashi National College of Technology/ Civil Engineering, Akashi, Japan
*** Okayama University /Environmental and Civil Engineering, Okayama, Japan

Recently, traditional river methods of construction have been reconsidered from a river landscape and ecological environment perspective. A spur dike is one such method of construction. However, the influence and character of spur dikes are not usually understood. This study uses a model for experiments to examine flows around spur dikes. Moreover, we have observed riverbed levels and flow velocities at a location 8.8 km from the mouth of the Akashi River. We examined the adaptability of the spur dikes to this river.

I. INTRODUCTION

In Japan, where death and injury frequently occur by flooding attributable to geographical and meteorological reasons, diversified banking and bank protection works have been provided from ancient times to protect human lives, property and agricultural crops from flood damage. The nation coexists well with rivers. Although flood control safety has been improved since the Meiji Era together with progress in modern civil engineering technology, in heavily populated urban districts where rivers are artificially straightened, fish and aquatic organisms lose their habitats, thereby accelerating destruction of natural environments. For this reason, today, a trend exists by which river construction methods are richly endowed with natural materials, numerous stones and wooden materials, to retain rich natural environments provided by rivers [1].

The Akashi River flowing through western part of Kobe City and Akashi City is a typical example of this sort of river. Many natural environment type constructions such as stone-lined bank protections, spur dikes and submerged wooden beds are structured from upstream to the river mouth. However, these structures are based mostly on experience and technologies gained centuries ago. Sufficient investigations to see if these river structures are adopted and functioning effectively in the highly developed modern society from flood control and environment viewpoints, have not been carried out yet. Many areas remain badly affected by flooding [2].

In this study, we attempted to clarify characteristics of flows and river bed deformations around spur dikes using field observations and model experiments that specifically examine stone-lined spur dikes constructed downstream from the Hirano bridge of the Akashi River. We investigated a method for reducing and controlling local scouring that occurs during floods to establish a reasonable design and work execution method for stone-lined spur dikes.

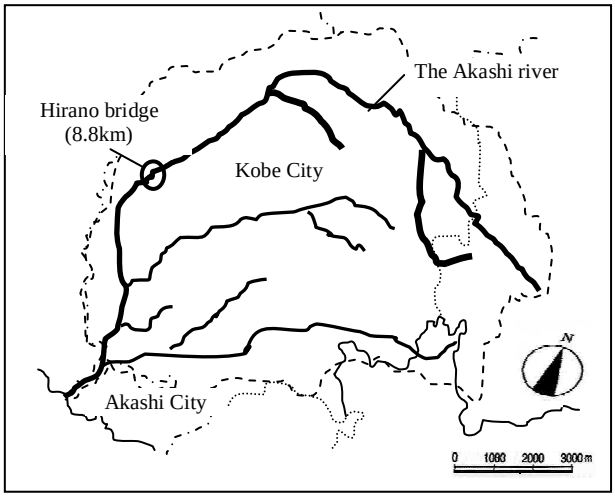

Figure 1. Outline of the Akashi River

II. SPUR DIKES IN AKASHI RIVER

The Akashi River is a main stream of the Akashi River system. Its source is in Kita-ward, Kobe City. Most of its watershed is in Nishi-ward, Kobe City. It is a class B river with river channel length of 26 km and a basin area of 126.7 km^2 (Figure 1).

Spur dikes provided in the Akashi River are of stone-lined impermeable overflow dikes constructed on the right bank downstream from the Hirano bridge located 8.8 km from the river mouth. Before these spur dikes were constructed, the foot protection block provided at the root of the high-water revetment was exposed as the concealed bank protection. Consequently, river bank water protection spur dikes were provided, which were aimed primarily at water turbulence to deepen channel erosion, providing current foot protection to the dike front edge, thereby suppressing velocity along the river bank. These spur dikes are expected to protect green vegetation of areas between spur dikes and provide diversified flow conditions around spur dikes, which engender good effects on ecological systems and water amenity.

In all, 11 sets of spur dikes are installed outside the bends of the river channel downstream from the Hirano great bridge of the Akashi River (Figure 2). Of those, the current study examines five sets located at downstream division at the jog. To elucidate spur dike hydraulic characteristics, results of hydraulic experiments using scale models are compared with field observations after flooding.

Figure 2. Spur dikes of the Akashi River

III. OUTLINE OF EXPERIMENTS

A. Experimental apparatus

Figure 3 shows an outline of the experimental apparatus. The water channel has a rectangular section that is 6.3 m total long, 0.8 m wide and 0.4 m high. Its sands are almost uniformly shaped, with average particle diameter of d = 0.088 cm, which were placed to form a 15 cm thick river bed of materials. Water suctioned from the underground water tank using a pump is introduced to the water channel via an electromagnetic type flow meter. It flows down the water channel and returns to the underground water tank. A current straightening part using filter materials is provided at the upper stream end of the water channel and a water level regulating plate that can be adjusted to an arbitrary angle is provided at the downstream end. The water channel gradient of the bed is adjustable using a jack, and four spur dike models are placed on the left bank 2 m from the upper stream end at 80 cm intervals.

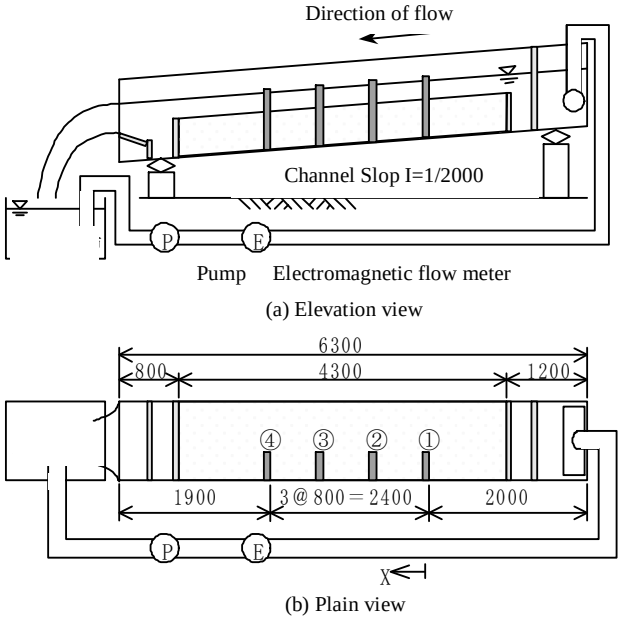

Figure 3. Outline of the experimental apparatus (Unit: mm)

For data arrangement reasons, the origin of the coordinates is placed at 2 m from the upper stream end in the down flowing direction (upper stream end of the first spur dike). The x-axis is set in the flow down direction and the y-axis is set from left bank wall to right bank. The z-axis is set in a vertical direction. The water channel floor bottom is considered as the origin.

B. Spur dike model

The spur dike model is made of impermeable material. The basic profile of this model is a rectangular section, as shown in Fig. 4(a). It is 18 cm wide, 20 cm high and 5 cm thick. This basic profile of the spur dike was sloped (1 : 1.5), as shown in Fig. 4(b) to represent actual sections of spur dikes used in the Akashi River. Experiments were carried out using this model.

C. Experimental conditions and Experimental Method

Experiments were conducted for seven cases while the flow rate and spur dike profile were changed as parameters. Details of experiments are shown in TABLE Ⅰ. The time for water flowing is 90 min for Run 4 and 120 min. for other cases.

For analyses of surface flow conditions, images taken from an oblique direction were corrected to perpendicular images and then subjected to Large Scale Particle Image Velocimetry (LSPIV) analysis developed by Fujita et al[3]. In the current study, punched refuse of 5 mm diameter was used as the tracer to investigate the relationship between river bed deformations around the spur dikes and surface flow velocity. The surface flow velocity around spur dikes was measured using LSPIV.

IV. RESULTS OF EXPERIMENTS AND DISCUSSIONS

A. Critical friction velocity

Local scouring around spur dikes falls into two categories. One is static scouring, by which the drag force is greater than the moving limit of river bed only around spur dikes; only river bed sands around spur dikes are moved. In addition, dynamic scouring occurs, in which the drag force is excessive and quicksand is created over the entire river channel. The moving limit friction speed of river bed materials (average particle diameter d = 0.088 cm) evaluated by Iwagaki's formula is U_{*cr} = 2.201 (cm/s).

TABLE Ⅰ
EXPERIMENTAL CONDITIONS

Run No.	Flow rate Q(l/s)	Time for water flowing t(min)	Overflow conditions	Profile of Spur dike
Run 1	18.20	120	Overflow	Basic profile
Run 2	8.25		Non-overflow	
Run 3	11.75		Partially overflow	
Run 4		90		
Run 5	18.20	120	Overflow	Basic profile + slope
Run 6	8.25		Non-overflow	
Run 7	11.75		Partially overflow	

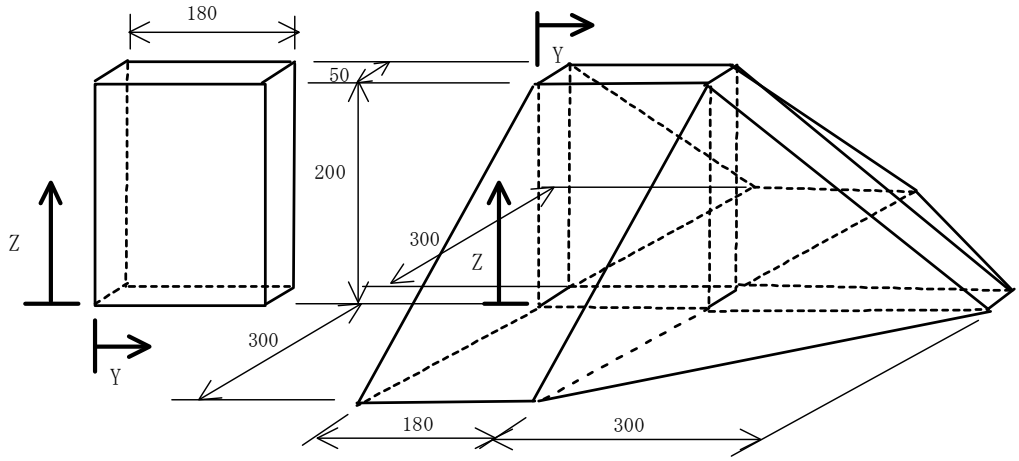

(a) Basic profile (b) Basic profile + Slope

Figure 4. Profile of model (Unit: mm)

Results of calculation of friction velocity U_*, based on the uniform flow depth h_0, are shown in TABLE Ⅱ. The uniform flow depth used here is an average at the center of water channel (y = 40 cm), which does not traverse the levee crown of the spur dike longitudinally. The TABLE shows that $U_* < U_{*cr}$ in all cases and all are of static scouring.

B. Water Surface Profile

Figure 5 shows the water surface profile of Run 1, Run 2 and Run 3. Figure 6 shows water surface profile of Run 4, Run 5 and Run 6, in which a slope is provided to the basic profile. Measurements were taken at a section traversing center of the levee crown (y = 9 cm) of the spur dike longitudinally 120 min after commencement of water flowing.

Figure 5 shows that for flows overflowing the spur dikes, water splash effects are relaxed as the flow rate increases. It might be said that effects of roughness of the spur dikes are reduced because of the increased flow rate. In addition, for flows not overflowing the spur dikes, reduction of the water level is recognized at the rear of the spur dikes. Comparison of Figure 5 and Figure 6 reveals that when a slope is provided to the basic profile, water splash effects upstream from the spur dikes are relaxed. It might be said that this is attributable to the fact that flows are not concentrated in the upper stream portion of the spur dikes, but are rather dispersed by the slope. The water level in the downstream from the spur dikes is lowered rapidly because of the slope effects.

TABLE Ⅱ
UNIFORM FLOW DEPTH AND FRICTION VELOCITY

Run No.	Flow rate Q(l/s)	Uniform flow depth h_0(cm)	Friction velocity U_*(cm/s)
Run 1	18.20	5.97	1.60
Run 2	8.25	4.29	1.38
Run 3	11.75	5.34	1.52
Run 4			
Run 5	18.20	6.66	1.67
Run 6	8.25	4.44	1.40
Run 7	11.75	5.27	1.51

C. Scouring Characteristics around Spur Dikes

Deformations of the river bed from its initial state for each case 120 min after commencement of water flow are shown in Figure 7 in the form of a contour map. Each contour map shows measurement results: the black area signifies scouring and white areas denote deposition. The darker the color, the more scouring or deposition is generated. The following findings are apparent from Figure 7.

With the basic profile, the maximum scouring depth is developed at the front edge of the first spur dike in an inverted cone shape. It is always generated along with wall surface at upstream from the first spur dike. Scouring around each spur dike maintains a nearly identical shape between spur dikes regardless of the flow rate while its magnitude is decreased. Simultaneously, the maximum scouring depth becomes smaller with spur dikes located more on the downstream side. The maximum scouring depth and range of scouring around each spur dike become greater as the flow rate and time for water flowing increase. The maximum scouring depth of the first spur dike is always approximately twice that of the second spur dike and has a smaller flow rate. Scouring does not occur, except at the front edge of the third spur dike and onward. The maximum scouring depth of the first spur dike at the maximum flow rate (overflow conditions on spur dikes) is approximately twice that of the minimum flow rate (non-overflow conditions on spur dikes). The maximum scouring depth of the first spur dike reaches as deep as 75% of the spur dike height.

When a slope is provided to the basic profile, the maximum scouring depth is developed downstream from the front edge of the first spur dike and at the bottom of slope of the spur dike in inverted cone shape. It is generated along with the slope at front edge of the spur dike. Scouring around each of spur dikes maintains a similar shape regardless of the flow rate, but its magnitude is decreased. The maximum scouring depth becomes less with spur dikes located more on the downstream side, while it is stabilized on the third spur dike and onward regardless of flow rate. Therefore, at least three sets of spur dikes are necessary to form a group.

The maximum scouring depth of the first spur dike is reduced by about two times if the rectangular section is

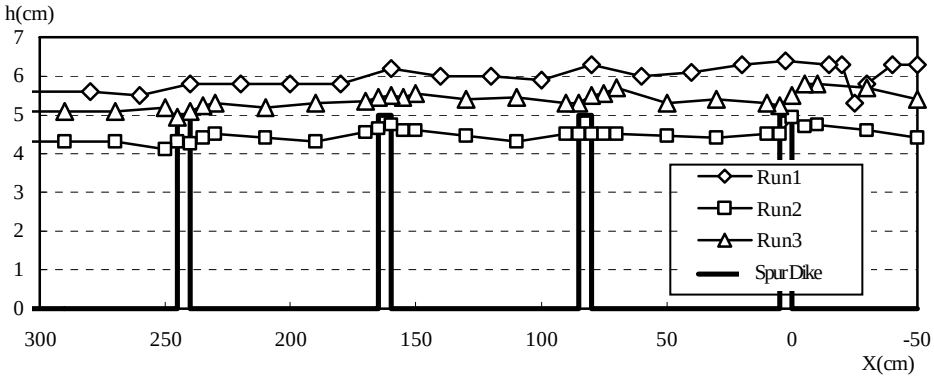

Figure 5. Water surface profile (Basic model, T=120min, Y=9cm)

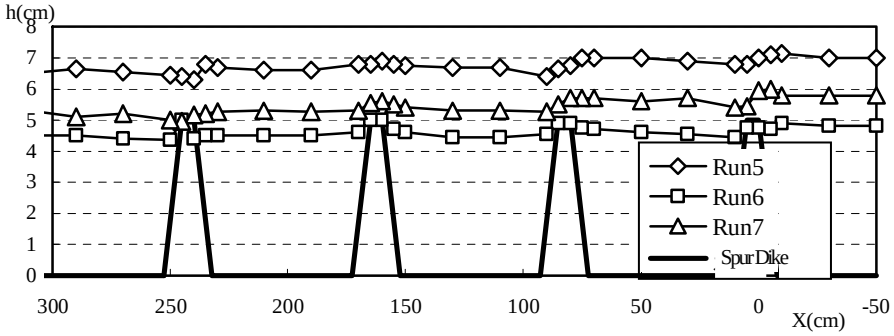

Figure 6. Water surface profile (Basic model+ slope, t=120min, Y＝9cm)

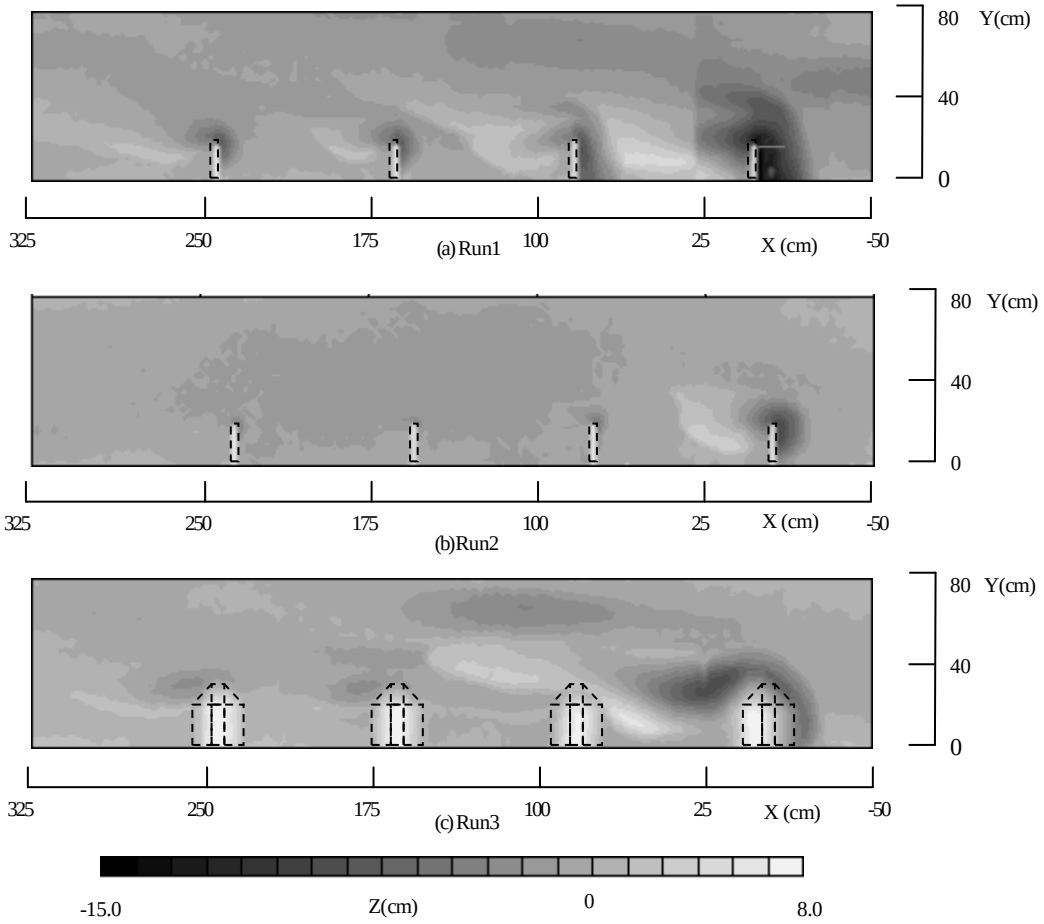

Figure 7 . Contour maps showing river bed deformation from initial state

replaced with trapezoidal section and is stabilized as constant regardless of the flow rate, indicating that scouring is reduced if the front edge angle of the spur dike is reduced. When the flow rate is increased, the maximum scouring depth is increased along with the slope. Accordingly, it is preferable that the downstream gradient should be made more gentle than that of upstream to allow gentle water flow and to prevent scouring downstream.

D. Surface Flow Velocity around Spur Dikes

For flow characteristics of the surface flow in the case of basic profile of spur dike plus slope, the following findings are apparent from Figure 8.

At the main stream part, the flow velocity is high and the direction of flow is nearly constant. Between spur dikes, flow velocity becomes slow and the direction of flow is not constant, thereby causing vortex flow. Upstream from the spur dikes, flow velocity is reduced because of the water splash effect and the maximum scouring depth that occurs on the extension line of fast flow generated along with the upstream slope. Accordingly, relaxation of the angle at front edge of the spur dike is useful for reducing scouring because it prevents the flow from being concentrated in one direction.

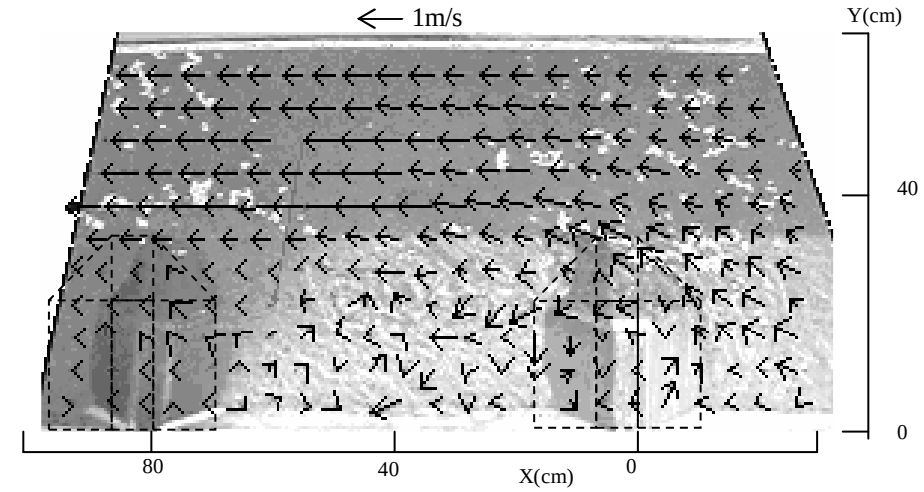

(a) Analytical result of surface velocity of Run5

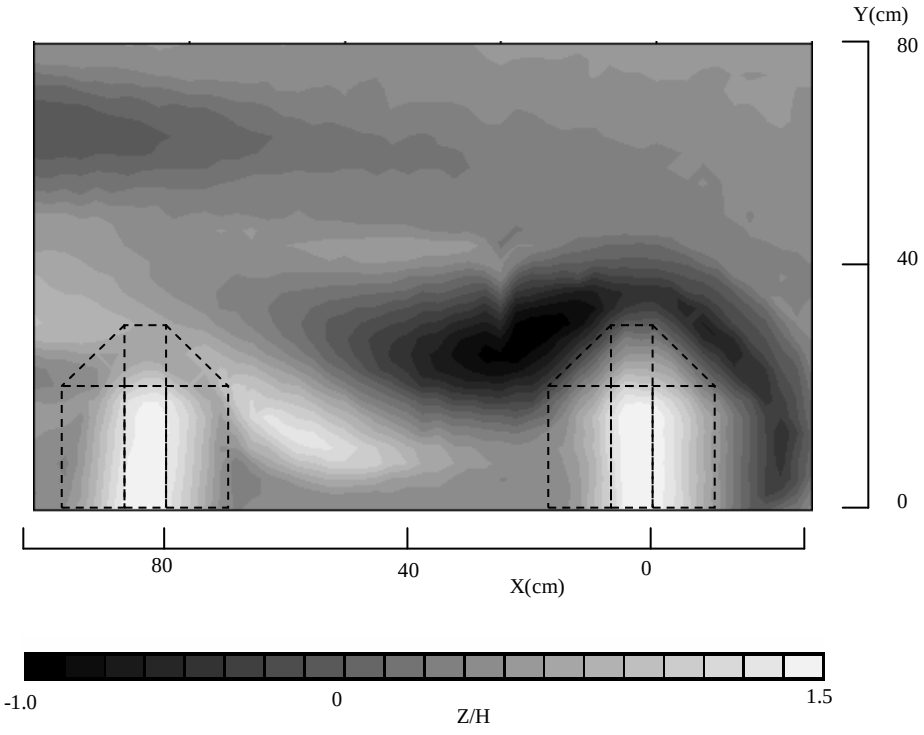

(b) Contour maps showing river bed deformation from initial state in Run 5 (Unit: cm)

Figure 8. Results of LSPIV analysis and contour maps in Run 5 (Around the1-2nd spur dike)

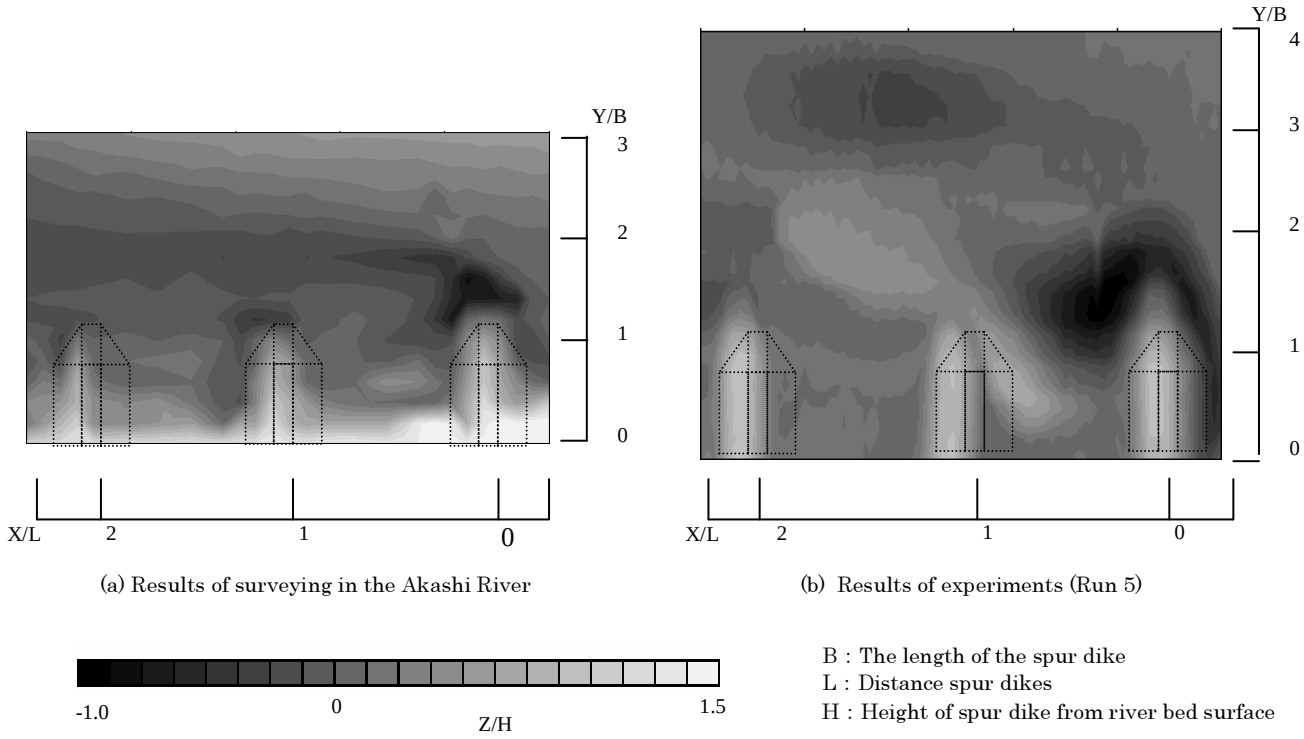

(a) Results of surveying in the Akashi River

(b) Results of experiments (Run 5)

Figure 9. Comparison of dimensionless river bed profile (Around the1-3rd spur dike)

E. Comparison with Results of Surveying in Akashi River

Before our field observations, the Akashi River was heavily damaged by No. 23 typhoon, which hit this area in October 2004. Remarkable scouring phenomena resulting from flooding were apparent around spur dikes downstream from the Hirano greater bridge. The peak flow rate at flooding was calculated using water level data obtained at the Fujiwara observation station located about 4 km upstream from the Hirano greater bridge. The peak flow rate was calculated from the water level and length of the flood channel using Manning's flow rate formula as approximately 350 m^3/s. Meanwhile, the river bed gradient was 1/180 and the roughness coefficient in Manning's formula was set as 0.03.

If Froude's similarity rule is used, the flow rate of 350 m^3/s corresponds to the flow rate 18.20 l/s (actual flow rate 322 m^3/s), which is a condition for overflowing for all spur dikes in model experiments. Subsequently, comparison was made with experimental results (Run 5) relating to river bed deformation for spur dikes with a slope. Figure 9 shows results of the observation of the river bed profile around spur dikes in the Akashi River and experimental results (Run 5) expressed in dimensional form. For initial river bed height of spur dikes in the Akashi River, the average of the river bed height downstream was used; it was considerably less affected by spur dikes in the Akashi River.

Contour maps showing river bed deformation of the Akashi River shown in Figure 9(a) revealed that the maximum scouring depth was caused downstream from the front edge of the first spur dike. The maximum scouring depth in dimensionless form is Z/H = 1.0 while the same obtained from experimental results is Z/H = 1.5. Therefore, an identical tendency as that noted with model experiments was obtained. Reasons for that position of deposition and scouring configurations are different are attributable to that shape and materials of the river bank differ, sands are supplied constantly from upstream in the Akashi River. Furthermore, the river bed configuration is changed because of flooding that occurred in the past. Consequently, we infer that river bed deformation around the spur dikes can be predicted to a certain extent by model experiments in which local hydraulic conditions are examined.

V. CONCLUSIONS

In this study, for prediction of flow around stone-lined spur dikes and river bed deformation, river bed deformation because of the flow was elucidated using experiments with scale models. The relationship between flow and scouring characteristics was elucidated from surface flow velocity obtained by LSPIV method. For discussion, results of experiments were compared with results of observations of the actual river (Akashi River). Experimental results of position of scouring and dimensionless scouring depth exhibit similar characteristics to those observed with the river at the site, considering flow rate conditions and uncertainty.

REFERENCES

[1] S. Yamamoto, "Spur Dikes Used in Japan", Sankaido Publishing, pp. 393–395,1996.

[2] Kobe Public Works Office, Hyogo Prefecture, "Reference Data for Designing Rivers Richly Endowed with Nature", pp. 3.36–3.42, 2004.

[3] I. Fujita, et al. ," Large-scale particle image velocimetry for flow analysis in hydraulic engineering applications 、 Journal of Hydraulic Research Vol.36, No.3、 pp.397-414,1998.

Scour around Vertical-wall Abutments in the Floodplain of A Two-stage Channel

Joko Nugroho* and Lim Siow-Yong**

* School of Civil and Environmental Engineering – Bandung Institute of Technology, Bandung, Indonesia

** School of Civil and Environmental Engineering – Nanyang Technological University, Singapore

I. INTRODUCTION

Most of the information for scour around abutment was obtained for the case of abutment which is placed in a rectangular channel. As the geometry of a natural river usually consists of a main channel with one or two sides floodplain, some efforts has been done to take into account the effect on abutment scour in two-stage channel. The study on the effect of two-stage channel geometry itself is complicated and the topic has been studied by many researchers to obtain its flow characteristics or parameters such as total discharge and component discharge. This paper first gives a brief review on the previous approaches in formulating the prediction on depth of scour around an abutment terminated in floodplain of a two-stage channel. A model is developed which uses the bulk parameter of the approach flow in a semiempirical analysis to predict the equilibrium scour depth in case of abutment terminating on a floodplain under clear water scour condition. The applicability of the proposed relationship is tested using the data collected by the authors and available published data.

II. LITERATURE REVIEW

Reference [1] seems to be the first attempt on the experimental work on the scour around abutment terminating on a floodplain. Experimental works in [1] were done on a horizontal flume. The scouring experiments lasted only 10 to 12 hours and visual observations were used to determine the state of scouring process. According to the authors' experiences, the rate of scour depth development at near equilibrium phase is usually very slow; hence it is possible that the increase of scour depth at this phase was not easily noticeable over a short testing period.

In [1], it is emphasized that the scour depth does not directly depend on abutment length but depends on the effect of the abutment on the flow redistribution at the contracted section. Hence a contraction parameter, M, was proposed in [1]; where M = (Q-Q_{obst})/Q, Q = total discharge in compound channel, and Q_{obst} = obstructed discharge in the approach section. The result of a least-square regression analysis, based on the important variables obtained using dimensional analysis, was:

$$\frac{d_{se}}{d_f} = 7.70\left(\frac{F_f}{MF_c} - 0.35\right) \tag{1}$$

where d_{se} = equilibrium scour depth; d_f = floodplain flow depth, F_f = Froude number of the floodplain flow; F_c = Froude number of flow in the floodplain at critical condition of sediment motion. The parameter, M, may represent the flow condition in a two-stage channel, but its relationship as function of the geometry of two-stage channel as well as approach flow characteristics would be much more applicable in field applications.

A similar formulation to the one proposed in [1], which is valid for setback and bankline abutment was proposed in [2]. The proposed formulation is:

$$\frac{d_{se}}{d_f} = C_r\left(\frac{q_{f1}}{Mq_{f0c}} - C_0\right) \tag{2}$$

where, C_r and C_0 = coefficients, q_{f1} = flow rate per unit width in the approach floodplain, and q_{f0c} = critical flow rate per unit width in floodplain at normal depth.

Reference [3] shows that the ratio of flow obstructed by abutment, Q_a, to flow at a specific width near the tip of the abutment, Q_w, was a significant parameter in estimating the equilibrium scour depth. The formulation of the functional relationship is based on:

$$\frac{d_{se}}{d_f} = f\left(F_c, F_f, \frac{Q_a}{Q_w}, S\right) \tag{3}$$

This is similar with formulation in [1], except for the additional shape factor term, S.

Experiments in [3] were done on an adjustable-slope symmetrical two-stage channel. The measured scour depth was based on fixed test duration of 5 hours and subsequently extrapolated up to the equilibrium scour depth. The extrapolation was based on several short and long period of scouring experiments which indicated that the scour depth at 5 hours was approximately 60% and 65% of equilibrium scour depth for d_{50} = 0.5 mm and 0.7 mm, respectively. The flow depth ratios in their experiments were in the range of 0.22 to 0.29. The final formulation was obtained from regression-analysis by using their experimental data.

$$\frac{d_{se}}{d_f} = 13.5\left(\frac{Q_w}{Q_a}\right)^{3.9} F_f^{\,1.17} F_c^{\,-0.25} \tag{4}$$

where Q_w = specific discharge for a certain width "w" near the abutment tip, Q_a = discharge for width "w" at the approach section, F_f = Froude number of at approach section and F_c = Froude number when the sediment is at incipient motion condition.

The Q_w quantity is also related to the abutment length as well as the geometry of the two-stage channel. The value of Q_w/Q_a in [3] ranges from 0.78 to 0.85. With this

small range, probably this ratio can be substituted with a proper constant. This gives the impression that the two-stage channel geometry effect is constant. This makes generality of the formulation questionable.

Reference [4] presents results of study on the effects of time and channel geometry on scour at bridge abutments in a two-stage channel. Their study focused on abutments which were terminated in the floodplain. They analyzed the maximum scour depth and the scour development with time. According to their data, [4] confirmed hypothesis in [5] which mentioned that scour of abutment terminating on a floodplain can be considered as a special case of abutment placed in rectangular channels.

III. SEMI EMPIRICAL ANALYSIS

At the abutment site cross section the flow distribution across the cross section will be redistributed. There are two main effects of flow distribution due to the abutment. The abutment may only affects the floodplain flow distribution or the effect may propagates to the main channel. In the beginning of the scour process where the size of scour hole is relatively small, the component discharge at the main channel will be higher than that at the approach section. During the scouring process it is possible that the flow distribution will change as the scour geometry evolves. After the scouring process reaches its equilibrium state, the final flow distribution at the abutment site cross section has two possibilities, i.e. same as at initial condition or different to that. Two possible cases may occur. First, the flow is diverted towards the main channel and second, the flow direction is towards the floodplain after the scour hole is developed. For the 1st case, the equilibrium scour depth will be less than of that in a rectangular channel case, and for the 2nd case it will be deeper.

As the scour around abutment is localized, it is clear that the local flow characteristic is the main parameter in the scouring process. However, the local flow information is difficult to get, especially in the real case, hence bulk flow characteristics at the approach section are preferred to be used in a formulation. There are many parameters which may be involved in the scouring process around abutment terminated in a floodplain. The parameters typically used in scour model in rectangular channels are of the approach flow properties, sediment properties and abutment dimension and shape.

This paper shows the flow interaction between the floodplain and the main channel which affects the scouring process. Comparison of the flow distributions for the flat bed conditions at the approach section and the cross section at the abutment site in experiments 20-60-03 and 20-80-04, are shown in Figures 1 and 2, respectively. The figures show an increase in the main channel discharge and a decrease in the floodplain discharge.

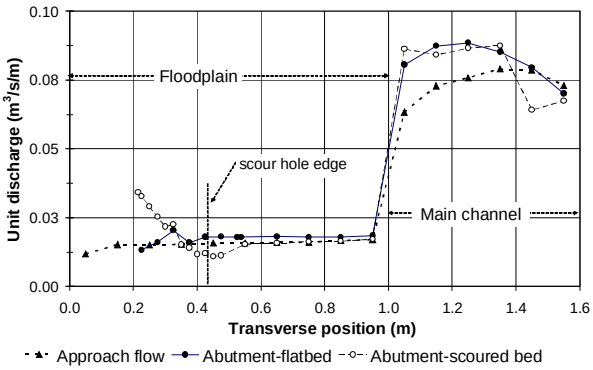

Figure 1. Unit discharge at approach section and abutment-site cross-section, Experiment 20-60-03.

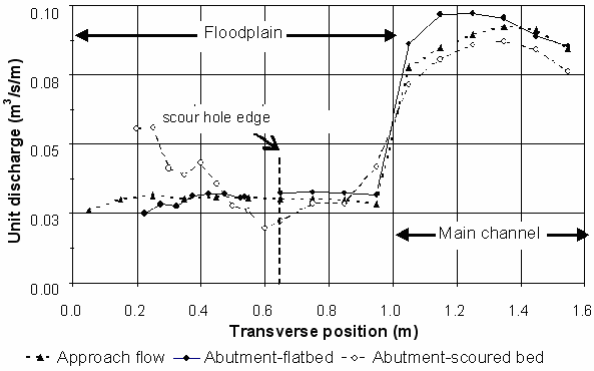

Figure 2. Unit discharge at approach section and abutment-site cross-section in Experiment 20-80-04.

At the initial condition the flow in the floodplain will be diverted towards the main channel. The strength of the diverted flow due to blockage by the abutment should be dependent on the abutment length (L), floodplain flow depth (d_f), floodplain width (B_f) and the flow velocity in the floodplain (u_f) and main channel (u_m).

That partial flow diversion due to the abutment reduces the flow in the floodplain and it may affect the scouring processes around abutment terminated in this region. In a rectangular channel there is no possibility for the flow to divert to other part. Hence, the scour depth around an abutment in the floodplain of the two-stage channel should be less than that in a rectangular channel of the same flow characteristics given in the approach section. However it should be noted that there is momentum exchange between the flow in the main channel and on the floodplain which will also impose on the flow condition. Hence the scour process is affected by these two flow mechanisms besides the factor contributed by the sediment properties.

The mechanism of scouring inside the scour hole for a case of an abutment terminated in a floodplain can be assumed to be similar to that in a rectangular channel. The difference from the case in rectangular channel is believed to be caused by the redistribution the flow due to the combined effect of the presence of the abutment and two-stage channel geometry. Hence, it is possible to develop a formulation for two-stage channel case by modifying the established formulation of scour around abutment sited in a simple rectangular channel.

In general, scour prediction formulas can be grouped into three types. They are: the regime approach [6] which formulate the scour depth as a function of discharge; the dimensional approach ([5], [7], [8], [9]); and analytical or semiempirical approach ([10], [11], [12], [13]) based on the increase of the sediment transport due to the increase of shear stress caused by the abutment. Lim's (1997) model in [11] was based on the premise that the obstruction in a channel would increase the shear stress at the area adjacent to the structure. The increase of the shear stress will increase the sediment transport capacity in the locality. A semiempirical approach as a function of the flow-continuity, scour geometry and a generalized form of the power-law formula for flow resistance in an alluvial channel was developed according to that premise.

Formulation in [11] had been tested on 252 data of clear water scour case in rectangular channels and employs general properties of sediment and flow. These points provide generality of the formula to be improved towards the case of abutment terminating in a floodplain. The formula proposed in [11] is

$$\frac{d_{se}}{d_f} = K_s \left\{ 2\left(\frac{u_{*1}}{u_{*c}}\right)^{0.75} \left[0.9\left(\frac{L}{d_f}\right)^{0.5} + 1 \right] - 2 \right\} \qquad (5)$$

where K_s = abutment shape coefficient, u_{*1} = shear velocity at approach section, u_{*c} = critical shear velocity.

The shear velocity can be expressed as a function of mean velocity, Manning's n roughness coefficient, gravitational acceleration, g and hydraulic radius, R, as follows:

$$u_* = \sqrt{\frac{\tau}{\rho}} = \sqrt{gRS_f} = \sqrt{\frac{gU^2 {n_M}^2}{R^{1/3}}} = U\, n \sqrt{\frac{g}{R^{1/3}}} \qquad (6)$$

As the shear velocity is proportional to the mean velocity and assuming that the rest of the parameters have same value, the ratio of the approach and critical value of shear velocity can be substituted by their corresponding mean velocity as in (7). Equation (7) is preferred as it uses bulk parameters of the flow and abutment which are more practical to use in practice.

$$\frac{d_{se}}{d_f} = K_s \left\{ 2\left(\frac{U_f}{U_c}\right)^{0.75} \left[0.9\left(\frac{L}{d_f}\right)^{0.5} + 1 \right] - 2 \right\} \qquad (7)$$

The performance of (7) towards the present data and further improvement based on the two-stage channel effect is given after the Experimental Works section.

IV. Experimental Works

The two-stage channel used was 19 m long, 1.6 m wide (1 m wide floodplain and 0.6 m wide main channel) and had sidewall of 1 m high measured from the bed of the main channel. The channel had a longitudinal bed slope of 0.00116. There was a 2.5 m long sand recess section, from 11 m downstream of the flume entrance. The sand-recess of the floodplain and main channel part was separated by a steel plate at the interface between the floodplain and the main channel. The main channel bank height was 0.15 m. At the downstream end of the channel there was a tail-gate which can be moved vertically by two electric-motors. A sump below the floor provided water for the test. A 22 kW submersible pump was used to pump the water from the sump to deliver continuous flow to the channel. The water passed through a header tank before it flowed into the flume. The header tank was equipped with perforated steel plates, sponge layer and cloth to reduce surface water undulation.

The dimension of the sand recess was 1m wide for the floodplain and 0.6 m wide for the main channel. They were 2.5 m long and the depth was 0.40 and 0.25 m in the floodplain and main channel, respectively. The sand recess in the main channel was covered by a piece of sand-coated aluminum plate to keep it in the flat bed condition.

The sand used in the experiment had a median size, d_{50} of 0.9 mm and a geometric standard deviation, σ_g of 1.05. The sand was of the quartz type, and was a non-ripple forming size and considered uniform as $\sigma_g < 1.5$.

Immediately downstream of the sand recess was a sediment trap to catch the sediment which was scoured from the sand bed. Sand was coated on the channel floor for 2m length of the floodplain bed upstream of the sand recess. This coating was expected to make the flow fully developed before it reached the sand recess.

The vertical-wall abutments used in the experiments were 0.20 m, 0.35 m and 0.50 m long (protruding perpendicularly across the flume) and 0.07 m wide. The abutments were made from 10-mm thick perspex. It was placed 1 m after the upstream edge of the sand recess and was firmly attached to the sidewall using silicon glue.

In the present experiments, the scouring process was allowed to proceed until the equilibrium scour depth was attained and this process lasted many days. Scour depth observations were done and recorded at different time intervals depending on the scouring rate. Observation time interval In the beginning, the depth was recorded in the range of 2 to 10 minutes, while after the scouring rate decreased the interval could be extended to 2 to 6 hours. The flow velocity, flow depth and discharge at the approach section were also measured to provide flow data related to the scour experiment.

V. Analysis of Experimental Results

The application of (7) on the present experimental data of scour around abutment terminating at the floodplain of two-stage channel is presented in Figure 3. The K_s value was taken as 1.0 for vertical-wall abutment. Equation (7) is valid only for:

$$\left(\frac{u_f}{u_c}\right)^{0.75} \left[0.9\left(\frac{L}{d_f}\right)^{0.5} + 1 \right] \geq 1,$$ so that $d_{se}/d_f = 0$ when

$$\left(\frac{u_f}{u_c}\right)^{0.75} \left[0.9\left(\frac{L}{d_f}\right)^{0.5} + 1 \right] = 1.$$

In Figure 3, the flow depth ratios, d_f/d_m of the present tests ranges from 0.2 to 0.5. To test the applicability of (7), data with relatively high $d_f/d_m = 0.5$ and 0.6 from [15] and [16] were also used. The experimental works in [15] and [16] were done at the school of CEE, NTU, Singapore. Figure 3 shows certain agreement between the predicted scour depths to the measured ones even though (7) is formulated for rectangular channels. The one data

point for experiment 20-50-02 which is marked with a circle in Figure 3 was conducted with very low flow and low flow depth ratio, and it is possible that the viscosity effect is more dominant in this case. Hence the model, which is based on the flow inertia, could not deliver reasonable result. This data will not be used in subsequent analysis. Further examination of Figure 3 shows the data may be grouped into three clusters, marked I for d_f/d_m = 0.2, II for d_f/d_m = 0.3 and III for d_f/d_m = 0.4. At flow depth ratio of 0.2, equation (7) over-predicts the equilibrium scour depth, while for the flow depth ratio of 0.4, it tends to under-predict. The second cluster, d_f/d_m = 0.3, shows better agreement between the predicted and the measured equilibrium scour depth.

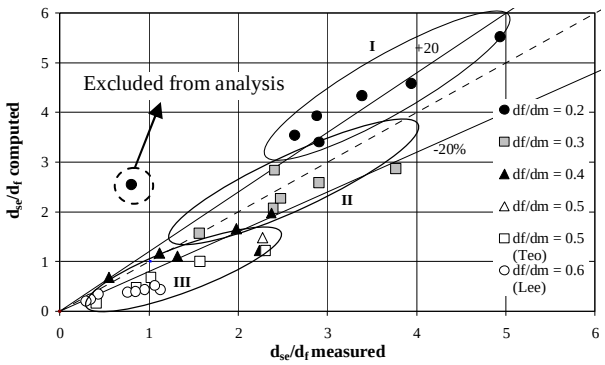

Figure 3. The plot of computed d_f/d_m using (7) compared to the measured data.

As discussed earlier, it is agreed that the two-stage geometry would affect the scouring process, and hence (7) needs to be modified in order to accommodate the geometrical effect of the channel. The degree of interaction between floodplain and main channel flow is closely related to the interface between them [14], and the floodplain and main channel depths are important parameters affecting the flow interaction. This suggests that the approach mean floodplain flow velocity in (7) should be modified to account for the effect of floodplain-main channel flow interaction. Therefore, an adjustment factor, α, is introduced into (7), as follows

$$\frac{d_{se}}{d_f} = K_s \left\{ 2\left(\frac{\alpha u_f}{u_c} \right)^{0.75} \left[0.9\left(\frac{L}{d_f} \right)^{0.5} + 1 \right] - 2 \right\} \qquad (8)$$

To determine α, a least square analysis was done for every cluster of data in Figure 3 such that the sum of square error in each cluster is minimized. It was found that the adjustment factor is mainly a function of the flow depth ratio d_f/d_m as follows (see Figure 4),

$$\alpha = 1.55\left(\frac{d_f}{d_m} \right)^{0.35} \qquad (9)$$

Equation (9) used data with d_f/d_m between the ranges of 0.2 to 0.6, corresponding to the range of α from 0.88 to 1.30. Substitution of this relationship into (8) gives

$$\frac{d_{se}}{d_f} = K_s \left\{ 2.78\left(\frac{d_f}{d_m} \right)^{0.13} \left(\frac{u_f}{u_c} \right)^{0.75} \left[0.9\left(\frac{L}{d_f} \right)^{0.5} + 1 \right] - 2 \right\}$$

(10)

For vertical-wall abutment, K_s = 1, and (10) becomes

$$\frac{d_{se}}{d_f} = 2.78\left(\frac{d_f}{d_m} \right)^{0.13} \left(\frac{u_f}{u_c} \right)^{0.75} \left[0.9\left(\frac{L}{d_f} \right)^{0.5} + 1 \right] - 2 \qquad (11)$$

The application of (11) to the present data is shown in Figure 5 and good agreement between the measured and the predicted equilibrium scour depth is obtained. The data in Figure 5 are for scour holes that did not encroach to the bank of the main channel.

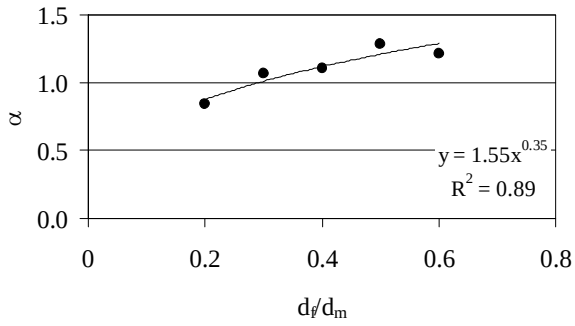

Figure 4. Adjustment factor of approach flow velocity as the function of flow depth ratio.

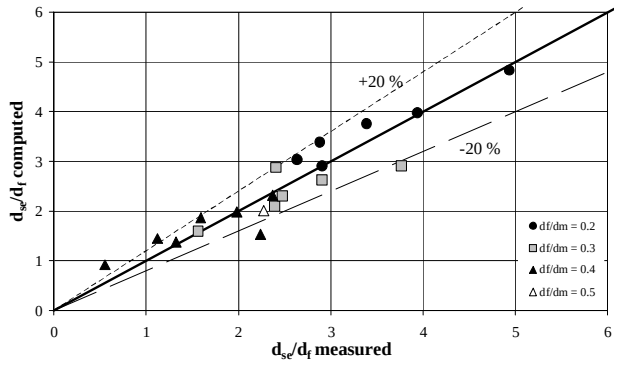

Figure 5. The plot of calculated d_f/d_m against measured d_f/d_m of present data.

The proposed formula is then applied to three published data with abutments terminating on a floodplain. Data in [1], [3] and [4] were used to assess the generality of the formulation. In terms of testing time, the data in [4] is superior to the others in terms of test duration as their tests were conducted up to the equilibrium scour stage. In [1], the test duration was between 10 to 12 hours. In [4], the data were extrapolated to the equilibrium stage, as discussed in Section II. The comparisons of the measured and computed scour depth for these datasets are presented in Figures 6 to 9.

The data in [1] may be re-analyzed based on the experience from the present study. For 10 and 12 hours scouring duration, we observed that the average scour depth for our data is about 68% and 70% that of the equilibrium scour depth, respectively (see Table 1). If we used the average 69% for the data in [1] and adjusted upwards to the equilibrium value, Figure (7) shows that the agreement between the data of [1] and equation (10)

improves to within the ±30% lines compared to Figure 6 where the scour depth data in [1] is used without extrapolation.

TABLE I. MEASURED SCOUR DEPTHS AT 5, 10 AND 12 HOURS, AS A PERCENTAGE OF EQUILIBRIUM SCOUR DEPTH BASED ON PRESENT DATA.

Expts.	% depth		
	5 hrs	10 hrs	12 hrs
20-50-02	n.a.	n.a.	n.a.
20-60-02	95	95	96
20-70-02	94	97	97
20-50-03	50	58	61
20-60-03	49	56	58
20-70-03	71	76	78
20-50-04	n.a.	n.a.	n.a.
20-60-04	47	57	60
20-70-04	44	46	47
20-80-04	68	77	79
20-100-05	41	48	50
35-50-02	49	51	54
35-60-02	87	94	95
35-50-03	51	63	65
35-60-03	54	60	62
35-50-04	47	55	59
35-60-04	52	62	64
50-50-02	65	78	80
50-60-02	75	85	88
50-50-03	67	72	74
50-50-04	45	57	61
average	61	68	70
min	41	46	47
max	95	97	97

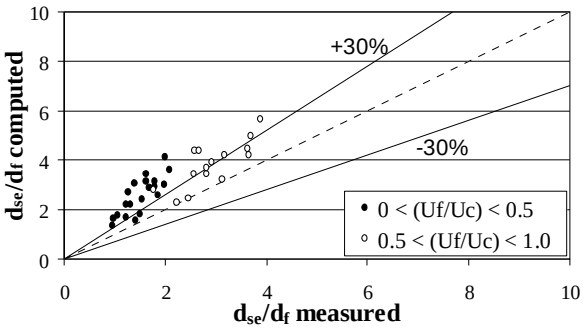

Figure 6. Comparison between scour depth of data in [1] with computed equilibrium scour depth.

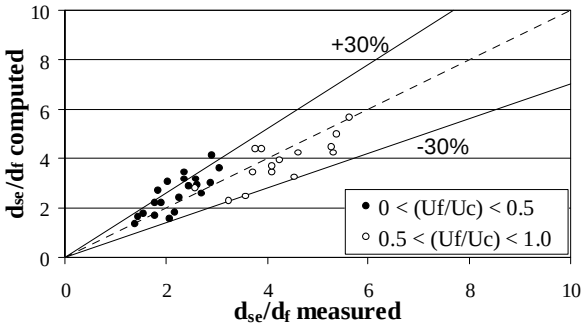

Figure 7. Comparison between extrapolated equilibrium scour depth of data in [1] with computed equilibrium scour depth.

In reference [3], the U_f/U_c for all the tests were close to the threshold condition. Comparison between the extrapolated equilibrium scour depth and the computed equilibrium scour depth for d_{50} = 0.5 mm and 0.7 mm are presented in Figures 8 and 9, respectively. The assumption on the extrapolation that the scour depth at 5 hours duration is about 60 to 65 of the equilibrium is acceptable (see Table 1). The effect of the abutment shape has been included in the computed equilibrium scour depth. Figure 9 shows a better predicted result compared to Figure 8. The discrepancy between the computed and extrapolated equilibrium scour depth, especially in Figure 8, may be due to unnoticeable sediment transport into the scour hole. This argument is based on the magnitude of approach velocities which are close to and some of them are slightly higher than the critical value of sediment motion. Another possible reason is due to the size of the sediment. The sediment with d_{50} = 0.5 mm can be grouped into the ripple forming sediment. Hence if there is ripple formation, the transported sand may have reached the scour hole and reduce the equilibrium scour depth.

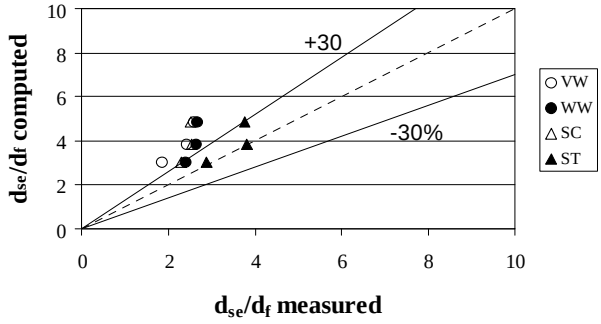

Figure 8. Measured and computed equilibrium scour depth of Kouchakzadeh and Townsend's (1997) data, for d_{50} = 0.5 mm. (VW=vertical wall, WW=wing-wall, SC=semi-circular, ST= spill-through)

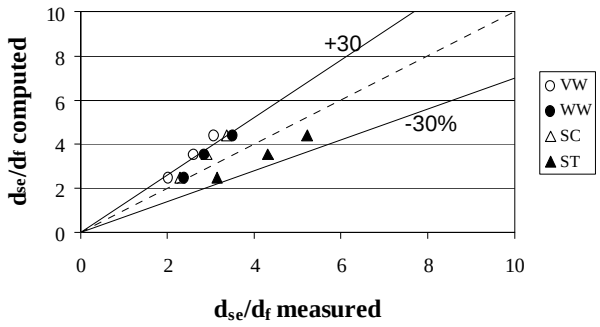

Figure 9. Measured and computed equilibrium scour depth of Kouchakzadeh and Townsend's (1997) data, for d_{50} = 0.7 mm.

The plot of measured and computed data from [4] is shown in Figure 10. The data used here are those with abutment lengths of 0.147, 0.270, 0.400 and 0.530 m, where the scour hole does not encroached into the main channel. Reference [4] showed that the U_f/U_c values in their experiments are close to the critical value of sediment motion. However, the computed values of U_c based on logarithmic velocity distribution and Shields criterion on critical condition of sediment motion gave lower value of U_f/U_c. The white circle data points in Figure 10 are based on U_f/U_c provided in [4]. The computed equilibrium scour depths (black circles in Figure 10) using U_c obtained from computed U_f/U_c show reasonably good agreement to the measured ones.

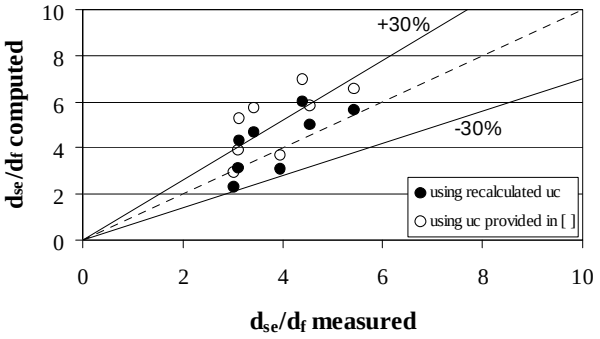

Figure 10. Comparison between extrapolated equilibrium scour depth of Cardoso and Bettess's (1999) data with computed equilibrium scour depth.

VI. CONCLUSIONS

Based on a semi-empirical formulation on scour around abutment in rectangular channel [12], a formulation for scour around abutment placed in two-stage channels is proposed. An adjustment for velocity in the floodplain is proposed to accommodate the effect of flow interaction between the floodplain and main channel. The adjustment factor was defined as the function of the ratio of floodplain flow depth to the main channel depth. The adjustment factor for the floodplain velocity was obtained from the experiments done by the author. The application of the proposed formula to the published data of [1], [3] and [4] shows a good agreement. Of those three published data, only data in [4] that had done until equilibrium scour depth is achieved. Despite the limited data used to verify the formulation, the formula shows that two-stage geometry affects the scouring process around abutment terminating on floodplain. The formula includes flow and two-stage channel characteristics to predict equilibrium scour depth.

REFERENCES

[1] Sturm, T. W. and Janjua, N.S. (1994), "Clear water scour around abutments in floodplains", *Journal of Hydraulic Division*, American Society of Civil Engineers, Vol. 120, No. 8, pp. 956-972.

[2] Sturm, T. W. (2005), "Scour around bankline and setback abutments in compound channels," *Journal of Hydraulic Division*, American Society of Civil Engineers, Vol. 132, No. 1, pp. 21-32.

[3] Kouchakzadeh, S. and Townsend, R. D. (1997b), "Maximum scour depth at bridge abutments terminating in the floodplain zone", *Canadian Journal of Civil Engineering*, Vol. 24, pp. 996-1006.

[4] Cardosso, A. H. and Bettes, R. (1999), "Effects of time and channel geometry on scour at bridge abutments," *Journal of Hydraulics Engineering*, American Society of Civil Engineers, Vol. 125, No. 4, pp. 443-452.

[5] Melville, B. W. (1992), "Local scour at bridge abutments", *Journal of Hydraulic Engineering*, American Society of Civil Engineers, Vol. 118, No. 4, pp. 615-631.

[6] Ahmad, M. (1953), "Experiments on design and behavior of spur dikes," Proceeding, *International Hydraulics Convention*, American Society of Civil Engineers, New York, N.Y., pp. 145-159.

[7] Garde, R. J., Subramanya, K., and Nambudripad, K. D. (1961), "Study of scour around spur dikes," *Journal of Hydraulics Division*, American Society of Civil Engineers, Vol. 87, No. 6, pp. 23-28.

[8] Liu, H. K., Chang, F. M., and Skinner, M. M. (1961), "Effect of bridge construction on scour and backwater." *CER 60 HKL 22*, Colorado State University, Civiel Engineering Section, Ft. Collins, Colo.

[9] Froechlich, D. C. (1989), "Local scour at bridge abutments," *Proceeding*, American Society of Civil Engineers National Hydraulics Conference, American Society of Civil Engineers, New York, N.Y., pp 13-18.

[10] Laursen, E. M. (1960), "Scour at bridge crossings", *Transactions*, American Society of Civil Engineers, Vol. 127, Part I, pp. 166-209.

[11] Gill, M. A. (1972), "Erosion of sand beds around spur dikes", *Journal of Hydraulics Division*, American Society of Civil Engineers, Vol. 98, No. HY9, pp. 1587-1603.

[12] Lim, S.Y. (1997), "Equilibrium clear water scour around an abutment", *Journal of Hydraulic Engineering*, American Society of Civil Engineers, Vol. 123, No. 3, pp. 237-243.

[13] Rahman, M. M. (1998), "Study on deformation process of meandering channels on local scouring around spur-dike-like structures", *PhD Dissertation*, Kyoto University, Japan.

[14] Bhowmik, N. G. and Demissie, M. (1982), "Carrying capacity of flood Plains," *Journal of Hydraulics Division*, American Society of Civil Engineers, Vol. 108, No. HY3, pp. 443-452.

[15] Lee, M. H. (2000), *Scouring around bridge abutment in floodplain and main channel of a two stage channel*, A Final Year Project Report, School of Civil Engineering, Nanyang Technological University, Singapore.

[16] Teo, C. Y. (1999), *Bridge abutment scour in a two-stage channel*, A Final Year Project Report, School of Civil Engineering, Nanyang Technological University, Singapore.

Geobags for Riverbank Protection

K. Oberhagemann *, M.A. Stevens**, S.M.S. Haque***, and M.A. Faisal***
* Northwest Hydraulic Consultants Ltd., Edmonton, Canada
** River Consultant, Boulder, USA
*** Bangladesh Water Development Board, Dhaka, Bangladesh

INTRODUCTION

The large rivers in the deltaic country of Bangladesh are up to 30 m deep in places, and scour even deeper. Strong river currents erode the fine sand from the toe of the riverbank, steepening its slope. The upper bank then fails as a wedge slide or in some cases as a flow slide. The river removes the slide material from the toe of the slope and the erosion process repeats. In the Jamuna River, banks have receded locally by more than 1 km in a single year. In addition, there are numerous small rivers with the same sandy banks. In this nation, bank erosion is pandemic.

The traditional bank erosion protection is too expensive for almost all applications in the large rivers. Costs ranged from USD 29 M to 6 M per kilometer of bank protected with revetments [1]. There are shortages of local aggregate for concrete; no suitable rock for riprap; no heavy marine equipment for construction; troublesome river currents; and great depths to protect.

Instead, the resources of the country are sand, labor, and experience with simple floating equipment. Geobags – geotextile bags filled with fine river sand – serve to reduce costs to feasible level for protection. About half the cost for the slope protected with geobags is the purchase of the geotextile material. Initially, the geotextile fabric was imported in large rolls. Now, it is also produced locally.

Here, the ongoing efforts to protect the Padna Irrigation and Rural Development Project (PIRDP) with geobags adjacent to the Jamuna River are described. Another project at the confluence of the Padma and Upper Meghna Rivers was protected in the same way at the same time, but is not reported here.

THE SITE AT THE PIRDP

The PIRDP is a Flood Control, Drainage, and Irrigation (FCDI) Project protected from Brahmaputra/Jamuna River flooding by earthen embankments, and is drained and irrigated by sluice gates and aided by pumping. There are 35,000 ha and 250,000 people inside the embankments. The Project was put into operation in the late 1980's and became threatened by riverbank erosion in the late 1990's.

The site is approximately 25 km upstream from the Jamuna-Ganges confluence. The rates of bankline erosion are in the order of 100 m per year and vary along a 14-km reach starting upstream where the small Hurashagar River joins the Jamuna from the west (Fig. 1). A section of embankment was retired from the immediate riverbank in 1997/98 just before it would have disappeared into the river. Since erosion was continuing, efforts changed from moving the embankment to stopping the erosion. Moving the embankment again was not socially or politically acceptable.

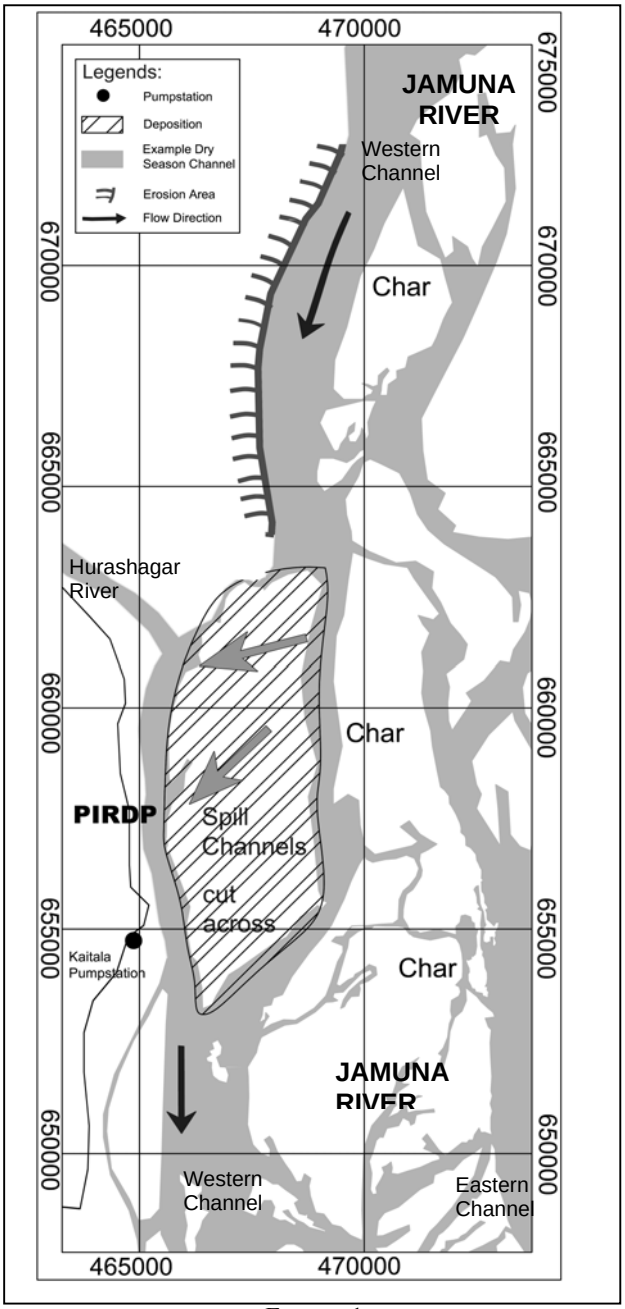

FIGURE 1
RIVER SITUATION ALONGSIDE THE PIRDP. NOTE THAT PROTECTIVE WORKS HAS BEEN BUILT FROM KAITALA TO THE HURASHAGAR RIVER.

By the time a feasibility study had been completed a crises had been reached. An emergency placing of geobags was begun to save the Project and a disaster plan was conceived in case the bank protection was not adequate.

RIVER MORPHOLOGY

The Jamuna River is braided with generally two major channels on the east and west sides, islands in the middle and smaller channels cross-connecting the east and west sides. The Hurashagar River adds a complexity to the west bank hydrodynamics, creating a small but influential confluence with its mammoth neighbor. The bankfull depth in the area of deep scour is approximately 30 m at times and is marked on the surface during low flow by an upwelling of brown water in the clearer current.

Flow along the eroding bank is essential north-south, and parallel to the bankline during the flood season but angles towards the bank during the dry season. The lowest scoured bed level can be during low-flow. The morphology is now well understood. The bankline movement at the Project is the result of bankline erosion upstream of the Hurashagar delivering an extra large load of sediment to the sandbars next to the Project (Fig. 1).

The Jamuna River carries as much as 85,000 m^3/s during large floods but that discharge is spread on average across a 12.5-km wide expanse of major and minor channels and island floodplain. It is the water that travels immediately adjacent to the Project bankline at speeds up to 3 m/s that define the protection works underwater. Eroding bank slopes are on average 1 vertical to 2 horizontal (1V:2H). At the surface strong winds cause 1-m high waves that erode the exposed bankline so protection is needed for that as well.

DEVELOPMENT OF GEOBAG PROTECTION

The riverbank protection concept developed in phases:

1. Initial experimentation during the mid-1990
2. Suggested for emergency protection alongside the PIRDP in 2000
3. -Feasibility level designs in 2002
4. Modified designs implemented since 2004.

a. Initial Experimentaiton during the mid 1990

Several projects used geobags as alternatives for mostly temporary works as emergency protection or as falling aprons. Little systematic reporting on these developments exist even though in some places work has withstood all loads since 10 years now.

b. Emergency Proetction in 2000

The DHV Consultants [1] proposed to fill geotextile bags (geobags) with local sand and place them on the eroding bank as a feasible emergency measure. The case for this solution is that sand and labor are in plentiful supply and inexpensive. The bagsize was 250 kg.

Initial placement of geobags in 2001 was done along the riverbank as an emergency measure – it was a case of "do it now or lose the project." At the same time, a disaster plan was prepared in case the river should breach the flood-control embankment. To the extent that the Project is still intact, it can be claimed that protection with geobags has been a success.

c. Feasibility Level Design in 2002

Halcrow and Associates [2, 3, 4] conducted the feasibility study of geobag protection and recommended that bank-slope revetment of geobags was viable. However, there were questions about the technical feasibility. Certain basic assumptions about geobags could not be proven either theoretically or by experience, in-country or elsewhere. The proposed geobags design was essentially experimental, based on knowledge of "trench-filled" revetment behavior in the USA (Fig. 2). Plans were made to accommodate changes for the geobag revetment if they appeared necessary or advisable. This need for change became known as the "adaptive approach." Adaptation would be necessary because the behavior of the bags on the eroding bank was not certain and the river is prone to change in ways that are not entirely predictable, even in the short term.

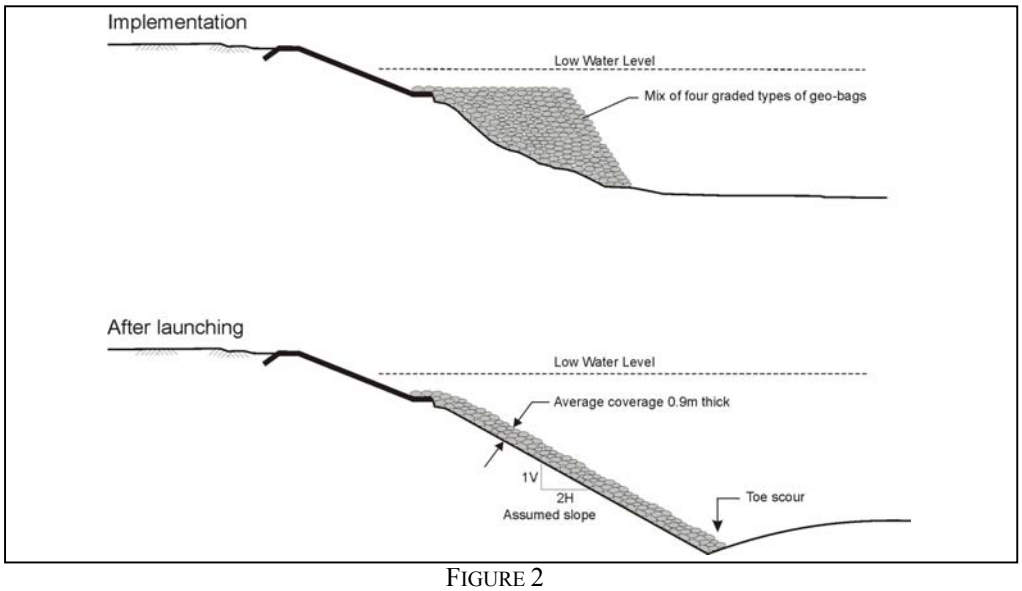

FIGURE 2
FEASIBILITY DESIGN CONCEPT: A HEAP OF BAGS DUMPED FROM THE BANKLINE LAUNCHES DOWN THE SLOPE PROVIDING AN AVERAGE 0.9 M THICK PROTECTIVE LAYER ON A SLOPE OF 1V:2H

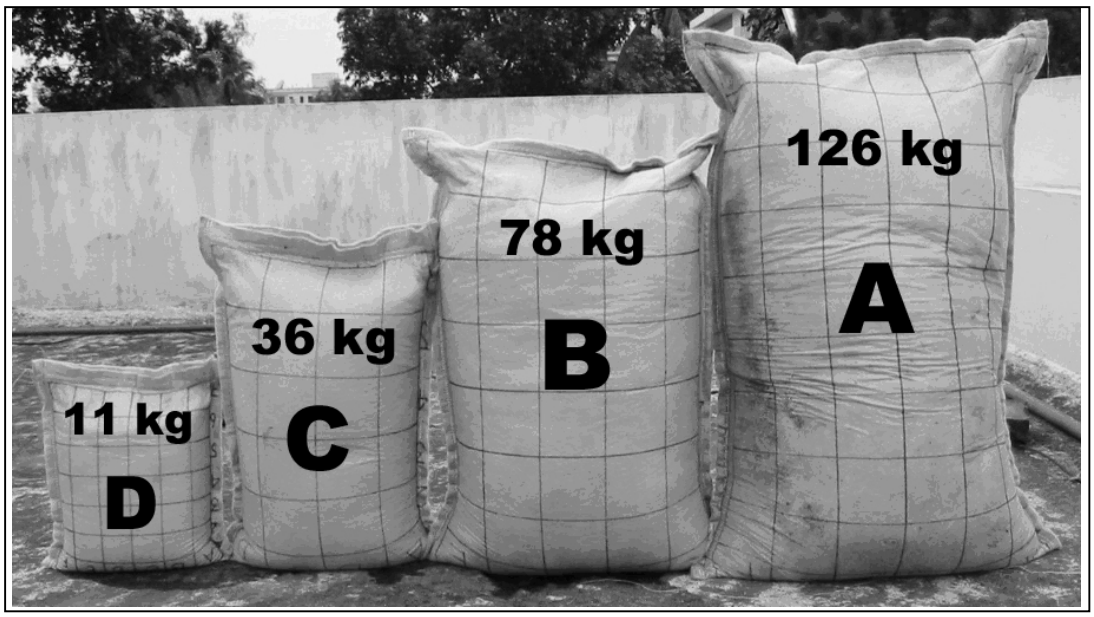

FIGURE 3
GEOBAGS. THE GRID ON THE THREE LARGEST BAGS IS 10 CM BY 10 CM, AND 5 CM BY 5 CM ON THE SMALLEST. THE 126-KG BAG IS APPROXIMATELY ONE METER HIGH.

In the feasibility assessment [3] a gradation of geobags was proposed based on that had been recommended for quarry rock [5] in the USA. The proposed sizes were later modified after field experience in 2002 [4]. The adopted masses of the bags became 11, 36, 78, and 126 kg when filled with dry sand (Fig. 3). All sizes were combined into mix each comprising 25 percent of the total mass. The density of fill sand was taken as 1500 kg/m^3.

d. Modified Designs Implemented since 2004

The first major adaptation based on field experience was to eliminate the two smallest sizes from any more consideration (Tab. I). Now, either one of the larger sizes is judged adequate. This finding was later reconfirmed by hydraulic model tests [6]. For stability against currents, the larger bags are better. As yet, there is no evidence that sand-filled geobags for revetment protection in Bangladesh should be heavier than 126 kg.

A bag filled to 80% of capacity (flatter shape) covers 80% of its unfilled area (length x width), whereas when filled to 100 % (rounded shape) it covers only 75 % of its unfilled area. Based on observations, the latest specifications call for 100% filling with dredged sand. Underwater consolidation reduces the volume to approximately 85 %. There is discussion about the shape still. At this time, there is no compelling reason to change the empty-bag shape.

TABLE 1.
MASS AND SIZE OF EMPTY GEOBAGS

Designation Type	Dry mass (kg)	Length (m)	Width (m)	Length/ Width
A	126	1.03	0.70	1.47
B	78	0.83	0.60	1.38
C	36	0.68	0.45	1.51
D	11	0.40	0.20	1.33

The original feasibility specifications called for non-plastic, non-saline sand free from silt, clay, roots, and other organic materials. The minimum grain size was 0.074 mm, meaning no silt. Experience has indicated that such sand does not leak from the geobags. Moreover, no damage to properly seamed geobags has been experienced when bags are dropped from the water surface.

Diving investigations on the first implemented works indicated that geobags launch down the slope and protect the bank from further erosion. The launching, however, does not result in a multiple layer coverage as assumed during the feasibility study but mostly in a one-layer thick protection. Consequently, the implementation concept was modified to arrive at a stable multiple layer coverage.

Life forms use the geobags as substrate on which to live and grow. Some small tubes built from mica flakes and inhabited by worms about 1 cm long are attached to the surface of geobags. At some places, small snails are attached to the bags; at others, there are fungi on the bag surface.

When the opportunity arises, a 126-kg geobag will be weighed field dry, and then submerged into water. The weight will be monitored until such time as it becomes constant. This will give an indication of how fast the air is expelled. The final weight is the submerged weight of the bag and its sand.

Geobags are manufactured from polypropylene or polyester textile fabric, which is non-woven and needle-punched and not solely thermally bonded. The textile has a density of about 400 g/m^2 and a tensile strength of more than 20 kN/m. It is UV stabilized to ensure retention of at least 70% of its original tensile strength before exposure. The porosity (ratio of the volume of voids to the total volume of fabric) of the geotextile is required to be at least 80%. After observing the unraveling of certain used geotextile materials, abrasion tests have been specified to assure the long-term stability (Fig. 4). There are tests specified for other properties of the geobag material, the bag, and its seams.

FIGURE 4
DIFFERENT TYPES OF GEOBAGS PLACED AS TEMPORARY WAVE PROTECTION. NOTE THE ABRASION OF THE BAG SURFACE OF THE BAG ON TOP

KEY ELEMENTS OF GEOBAG REVETMENTS AT THE PIRDP

a. General Considerations

In the geobags revetment, the geobags form a thin layer over the natural (unprepared) bank slope. No filter is required. The design calls for placing geobags only below low-water level. Above low water, concrete blocks or other hard material are used to provide the additional stability to resist wave attack and to guard against vandalism. Waves produce a significant pounding action on the bags [7] and have moved heavy geobags. When left unchecked, waves cut a vertical notch in the more cohesive top bank. Also, geobags above water have been sliced, drained of sand and the fabric taken was to serve such functions as drapery for doors.

On the revetment, the geobags are subjected to fluctuating hydrodynamic forces of pressure and shear caused by the water flowing over them. Gravity is the main stabilizing force acting to hold the geobags in place against hydrodynamic forces - provided that the bank is not too steep, in which case gravity can become a de-stabilizing force.

Beneath the thin layer of geobags is the natural bank material consisting of sand, silt, or clay, which also must be stable in a geotechnical sense.

Riverbed scour at the toe of the bank is a most important factor affecting bank slope stability. The river bed at the Project consists of fine and very fine sand, with median diameters of 0.1 to 0.3 mm. Almost any river flow can disturb this material, and floods move great masses of bed material eroded from the bank and picked up from the bed and sandbars. A local rate of scour deepening of 5 m/day has been measured at the lead spur for protection works in the Jamuna River at Sirajganj [8].

In hydrodynamic stability assessment, it is assumed that the bank slope behind the geobag skin is stable and that the bags do not slide on the bank material, only on each other. The hydrodynamic forces tend to move the bag downstream. The gravity force has an against-slope component tending to keep the bag in place and a down-slope component tending to move it down the slope. Adjacent bags can affect stability depending on their own stability and orientation and on the points or areas of contact.

b. Physical Hydrulic Model Tests

The hydrodynamic behavior of geobags was investigated by hydraulic model testing at a geometric scale of 20 to 1 (prototype to model) in the laboratory of nhc in Vancouver, Canada [6]. Model geobags, consisting of permeable cloth fabric filled with fine sand, were placed on banks formed in crushed walnut-shells at slopes of 1V:1.5H and 1V:2H. They were displaced at the incipient motion velocities shown in Table 2. The tabulated bag masses are sand-filled dry scaled-up prototype values, and the "bank" velocities represent scaled-up depth-averaged values at a point one-third of the slope length inshore from the initial toe of the slope.

TABLE 2.
INCIPIENT MOTION VELOCITIES (PROTOTYPE VALUES)

Mass of Geobag (kg)	Bank Velocity (m/s)
Slope 1V:1.5H	
126	2.6
90	2.4
38	1.7
Slope 1V:2H	
126	2.9

Incipient motion velocities for angular rock (22 kg), rounded rock (50kg) and concrete blocks (65 kg) were determined in the model as well. Incipient motion velocities were practically the same for all three *and* for the 126-kg geobags.

The model information was analyzed in the context of the U.S. Army Corps of Engineers' design equation [5,9] for rock riprap used as bank protection:

$$\frac{D_{30}}{Y} = S_f C_S C_V C_T \left(\frac{V^2}{K_1 g Y} \quad \frac{\gamma}{\gamma_s - \gamma} \right)^{1.25} \qquad (1)$$

where

V = local vertically-averaged velocity
S_f = safety factor, minimum recommended value for riprap design = 1.1
C_s = 0.30 for angular rock and 0.36 for rounded
C_V = coefficient for vertical velocity distribution, range 1.0 to 1.28 for straight channels to abrupt bends
C_T = coefficient for riprap layer thickness, 1.0 or less with increasing thickness
K_1 = side slope correction factor
D_{30} = size of stone for which 30 % by weight is finer
Y = depth of flow
γ = specific weight of water
γ_s = specific weight of stone

Key values recommended for the side slope correction factor K_1 are as follows (Table 3):

TABLE 3.
CORRECTION FACTORS FOR SIDE SLOPES

Slope	Slope angle (degrees)	Correction Factor K_1
1V:1.5H	33.5	0.71
1V:2.0H	26.5	0.88
1V:3.0H	18.0	1.00
Flatter than 1V:3.0 H	-	1.00

From the experimental results it was determined that a value of 0.77 should be used for the shape factor C_s for the two largest model geobags bags on 1V:2H and 1V:1.5H slopes. The diameter of a geobag was taken as the cube root of the volume.

It has been reported [10] that when the flow velocity exceeds 1.5 m/s or so, sand can move inside a bag from the upstream to the downstream side. In special cases a bag could roll because of this movement. Such sand movement could not occur in the model geobags, and has not been observed to date in the field. Velocities at or adjacent to the bags on the revetment are generally not this high.

Model geobags slide over each other on bank sloes of approximate 52 degrees. Prototype bags are just slightly less stable, sliding over each other on slopes of 47 degrees

Model 90-kg geobags were dropped into a 10-m depth of water flowing at 1.7 and 3.3 m/s (scaled-up prototype values). It was difficult to achieve complete coverage even when the bank was visible and bags were dropped to cover an observed bare spot. Bags tended to cluster in random piles surrounded by bare patches. Mixtures of bags achieved even more precarious coverage.

c. Geotechnical Studies

Geotechnical aspects discussed in this report include movements in the riverbank soil and on the interface between geobags and bank material. This includes geobags sliding on sand, and bags and sand bonded so that bags plus underlying sand slide on sand.

Before the installation of geobag protection, eroding banks at the Project were characterized by erosion of sand from the bank slope and river bed by currents, followed by geotechnical failure of the more cohesive upper layer, extending from the top of the bank down to low-water. Wave erosion was also an important factor.

In the feasibility study [2,3], it was recommended that the upper slope of the bank be dressed to 1V:2H before placing the geotextile filter and concrete blocks. The launching heap would consist of a graded mixture of geobags dumped below low water. The width of the heap, normal to the bank, would be based on the design scour depth. The riverward slope of the heap was set at 1V:1.25H (approximately 39 degrees to the horizontal). The angle of repose for model geobags is 52 degrees, but the bags could be heaped at a steeper slope by piling them. The launched slope was considered stable.

Model tests at BUET [3] indicated that if a slope failure occurs for one reason or another - for example, the loose state of the soil - the geobags have no chance to launch. Rather, they fail as a whole, the heap sliding down the slope as a unit.

Considerable geotechnical investigation has been done for the Project, including drilling and logging boreholes, and estimating soil strength properties. At the Project, the slopes are generally stable. For inclinations steeper than 1V:2H (Fig. 5), slope stability where it exists results from"hidden stabilizing influences," that is, geotechnical factors that are not taken into consideration in common practice. The steep parts of the natural slopes are considered to be at the "ultimate limit of stability."

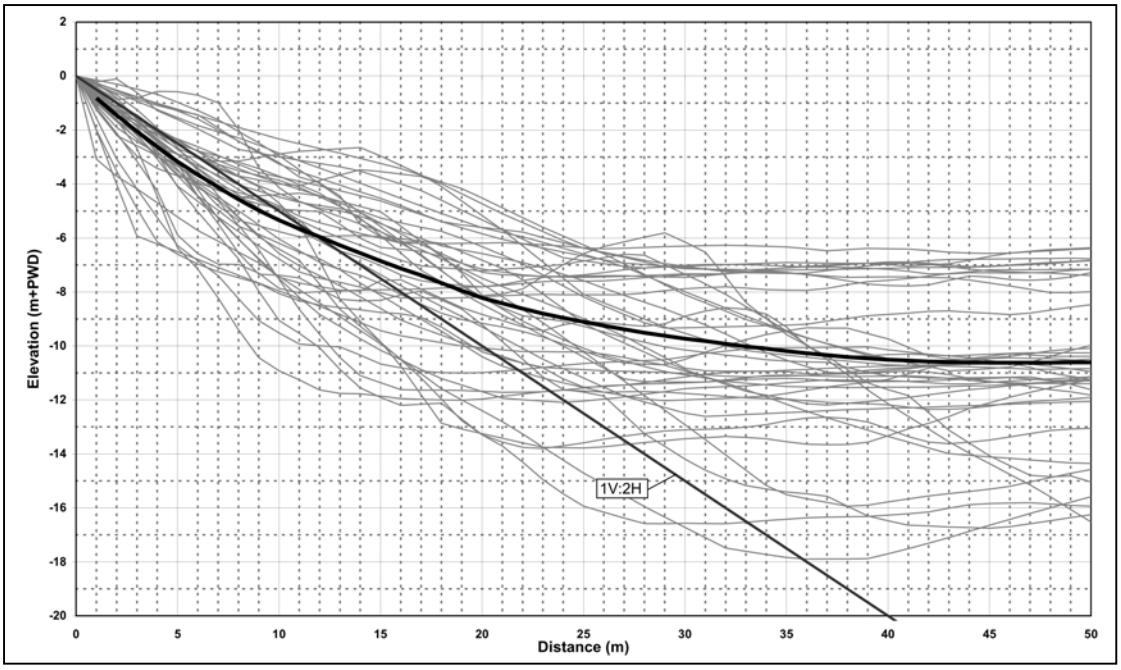

FIGURE 5
BANK PROFILES TAKEN AT THE ERODING SECTION IN APRIL 2004 WHEN THE WATER LEVEL WAS APPROXIMATELY +5.0 M PWD.

There is an upper layer, 5 to 6 m thick, of floodplain soil consisting of clay and clay-silt with low plasticity. The clay layer reaches down from floodplain level to approximately low-water level. Below this upper clay layer, the bank consists of fine-grained and poorly graded sand of medium compactness. The specific weight of the sand grains is taken as 26.5 kN/m^3. The effective shear strength of the clay allows for vertical faces up to 4 to 5 m high.

Sand dominates the overall stability. It can fail below the clay, and then the clay collapses afterwards. Sand usually fails more or less on a flat plane, the movement being in the form of a wedge translation. Slip circle failures are uncommon.

For the flatter slopes of 1V:2H to 1V:2.5 H, the angle of internal friction is 28 to 30 degrees. For slopes of 1V:1.5H and steeper, the angle of internal friction is 32 to 35 degrees.

There are three geotechnical ways the slope can fail. They are: geo-mechanical; flow slide of sand; and liquefaction due to dredging or earthquakes. Scour (erosion of bed and lower bank material by flowing water) is an important factor triggering the slope failure process. Scour is considered a hydrodynamic issue.

The slopes are prevented from such failures by protecting the toe and lower bank erosion that would steepen the slope, preventing rapid changes in soil stress levels at the toe of the bank, and stabilizing the top bankline.

d. The Adaptive Approach

In the feasibility study it was conceived that a heap of geobags of different sizes placed along the bank just below low water would launch when undercut by erosion and cover the eroding area with a 0.9 m thick layer of protection. Divers' observations clearly showed that this did not happen. The coverage was either by single bags or sometimes lumpy with bare patches. The smallest bags disappeared. Clearly adaptations were needed.

For predominantly construction purposes, single-size geobags are favorable so only 126 kg bags will be used for future work in Jamuna River. The smaller size of 78 kg is proposed for smaller rivers. If there is to be a mix, it will be with the 78- and 126-kg bags.

The protective system was to remain geobag revetment protection below low water level and concrete blocks or interconnected systems such as grout-filled mattresses above low water.

A multi-step implementation system combining a fast response to erosion threat and an optimized use of bags has been developed and implemented that has provided satisfactory protection.

Immediate Protection: Imminent river erosion requires a fast response. This is provided through mass dumping of bags along the eroding bank, allowing the bags to launch down the slope (Fig. 6). The result is a commonly one-bag thick cover layer, which substantially reduces erosion rates but is not stable in the long run. During this initial stage only temporary wave protection above low water level, consisting of geobags, can be provided.

First level protection: A three-bag layer is placed over the launched bags making, on the average, a four-layer thickness on the slope after completion of this first level protection (Fig. 7). In addition, a thin and wide falling apron for the expected future scour is placed at the toe of this protection. Lately, 12 to 15 m wide falling aprons are built consisting of three layers of bags. This falling apron can cover up to 15 m scour depth.

FIGURE 6
IMMEDIATE PROTECTION IMPLEMENTED AT THE PIRDP IN 2002.

FIGURE 7
1ST LEVEL PROTECTION DUMPED FROM POSITIONED BARGES

Adaptation: The river response to protection commonly results in toe scour along revetments. For this purpose falling aprons are placed along the toe. These falling aprons may have to be upgraded to first level protection after their deployment. In addition to depth changes, the erosion can shift in upstream or downstream direction. In these cases, immediate and first level protection will be repeated for areas under new attack.

Second level protection: The river reacts to the bank protection during the initial years and there are changes to the overall morphology. Settlements and adjustments of the unprepared uneven bank will occur. Scour might reach deeper levels and the falling apron at the toe starts deploying. The second level protection is designed to improve the protective layer of first level protection and subsequent adaptation works and to arrive at a more uniform surface. It is planned to place 1.5 layers of bags after reaching deepest scour depths.

Maintenance: Regular maintenance is a long-term operation during the lifetime of the protective system. The normal maintenance is expected to start about 5 to 10 years after implementation and after completion of second level protection to deeper scour levels.

Phased Construction and Monitoring: To obtain sustainable bank protection several phases of construction in the same area are required. A period of monitoring and adaptation follows the initial immediate and first-level protection construction. The phased implementation concept requires plenty of resources for monitoring and supervision.

FIGURE 8
CONSTRUCTION OF PERMANENT WAVE PROTECTION ABOVE LOW WATER LEVEL DURING THE ADAPTATION PHASE

SUMMARY

The hastily designed and constructed emergency geobag revetment prevented the PIRDP from becoming a disastrous failure. It was a success! To date, more than five million geobags have been placed here and at the Padma-Upper Meghna confluence. Nearly all phases of the initial concept have been modified based on field (most importantly, diving inspections) and laboratory experience. This adaptation method is used to adjust the works to suit conditions that cannot be predicted and to make improvement to any aspect of the works deemed deficient, whether it is in design, construction, management, scheduling, or other issue. The revetment derived at is the most cost effective solution at estimated cost of around USD 2 M per kilometer on average.

ACKNOWLEDGMENT

The Jamuna-Meghna River Erosion Mitigation Project under which the described work is being developed is supported through Asian Development Bank Loan No 1941 BAN (SF).

REFERENCES

[1] DHV Consultants DV, 2000, River Erosion Prevention and Morphology Study of Pabna Irrigation and Rural Development Project (PIRDP). Final report prepared for the Bangladesh Water Development Board and Asian Development Bank, Nov.

[2] Halcrow and Associates, 2002, Feasibility Study - Final Report, Jamuna-Meghna River Erosion Mitigation Project, Volume 1 (Phase II). Main Report prepared for Bangladesh Water Development Board and Asian Development Bank, May.

[3] Halcrow and Associates, 2002, Feasibility Study - Final Report, Jamuna-Meghna River Erosion Mitigation Project, Volume 2 (Phase II). Report prepared for Bangladesh Water Development Board and Asian Development Bank, May.

[4] Halcrow and Associates, 2002, Feasibility Study - Final Report, Addendum, Jamuna-Meghna River Erosion Mitigation Project, Volume 2 (Phase II). Report prepared for Bangladesh Water Development Board and Asian Development Bank, May.

[5] US Army Corps of Engineers, 1991, Hydraulic Design of Flood Control Channels, EM 1110-02-1601.

[6] [6] nhc (northwest hydraulics consultants), 2006, Jamuna-Meghna River Erosion Mitigation Project, Physical Model Study (Vancouver, Canada). Final report prepared for Bangladesh Water Development Board, Jan.

[7] Individual Consultants, 2003, Geobags Protection, Project Concept, Experience, Future, Jamuna-Meghna Erosion Mitigation Project, Part A. Report prepared for Bangladesh Water Development Board and Asian Development Bank, June.

[8] Oberhagemann, K. and Noor, Abdun, 2004, Scour and Erosion alongside Bank Protection work: Case Studies from Bangladesh. Paper presented at Singapore meeting of ICSE.

[9¦ US Army Corps of Engineers, 1994, Channel Stability Assessment for Flood Control Projects, EM 1110-2-1418.

[10] Pilarczyk, K.W., 2000, Geosynthetics and Geosystems in Hydraulic and Coastal Engineering, A.A. Balkema, Rotterdam.

Abutment Scour in Cohesive Soil: Initial Results

Seung Jae Oh, Xingnian Chen, Kuang-An Chang, Hamn-Ching Chen, and Jean-Louis Briaud
Department of Civil Engineering, Texas A&M University, College Station, Texas, 77843-3136, U.S.A.

I. INTRODUCTION

The blockage in a channel caused by a structure such as a pier or an abutment decreases the flow area while increases both the water velocity and shear stress at the water-soil interface. The increment of flow velocity and shear stress leads to scour around the structure on the channel bed. Abutment scour is the decrease of the channel bed elevation due to the acceleration of the water around the abutment at the end of the approach embankment. Abutment scour weakens the foundation of abutment and therefore destabilizes the channel-crossing structure such as a bridge.

Most researches studied abutment scour using cohesionless soil. Among them, Laursen (1960) found that the diameter of scour hole is approximately 2.75 times the scour depth. The study estimated the maximum clear water scour ($\tau_1/\tau_c<1$) depth is 10% deeper than the live bed scour ($\tau_1/\tau_c>1$) depth. Eqs. 1 and 2 are Laursen's abutment scour equations for clear-water and live-bed condition, respectively.

$$\frac{L_a}{y_1}=2.75\frac{z_a}{y_1}\left[\left(\frac{z_a}{11.5y_1}+1\right)^{7/6}/\left(\frac{\tau_1}{\tau_c}\right)^{1/2}-1\right] \quad (1)$$

Fout! Objecten kunnen niet worden gemaakt door veldcodes te bewerken. (2)

Gill (1972) found that the maximum scour depth for both the clear-water and live-bed conditions around spur dikes is the same. He assumed that the maximum scour depth depends on the contraction ratio and the ratio of the sediment size to flow depth. Gill found that an approximately 90% of the maximum scour depth is reached within 15 hours for both fine sand and coarse sand. Gill's clear water scour depth equation is

$$\left(\frac{z_a}{y_1}\right)+1=8.375\left(\frac{D_{50}}{y_1}\right)^{0.25}\left(\frac{L-L_a}{L}\right)^{6/7}\left(\frac{\tau_1}{\tau_c}\right)^{3/7} \quad (3)$$

Based on a database of 170 live-bed scour experiments and 164 clear-water scour experiments, Froehlich (1989) developed both live-bed scour and clear-water scour equations to predict the scour depth around an abutment, expressed in Eqs. 4 and 5, respectively.

$$\frac{z_a}{y_1}=2.27K_1K_2\left(\frac{L_a}{y_1}\right)^{0.43}Fr^{0.61} \quad (4)$$

$$\frac{z_a}{y_1}=0.78K_1K_2\left(\frac{L_a}{y_1}\right)^{0.63}Fr^{1.16}\left(\frac{y_1}{D_{50}}\right)^{0.43}\sigma_g^{-1.87} \quad (5)$$

Melville (2000) investigated the effect of channel geometry on abutment scour in a compound channel. Four parameters were found to be influential to the abutment scour depth - flow, sediment, geometry, and time. He constructed a relationship between the scour depth and these parameters by assuming a constant sediment density and an absence of viscous as:

$$z_a = K_{yL}K_IK_dK_1K_2K_GK_T \quad (6)$$

Even though many researches have conducted research on abutment scour, little has been done using cohesive soil. The reasons may be due to the hurdles of preserving the material property and installation, in addition to a much time consuming test period due to its erodibility in comparison with the use of cohesionless soil.

An effective and accurate prediction of abutment scour is very important for the design and construction of bridges. The prediction of scour depth is often based on the results obtained using cohesionless soil which may be too conservative. In the present study, three clear water scour experiments were performed to investigate abutment scour in cohesive soil using a large-scale model. The results were compared with that in several previous studies. In addition, numerical computation was performed and the results were compared with the experiments.

II. EXPERIMENT SETUP

The experiments were conducted in a large two-dimensional flume that is 45.7 m (150 feet) long, 3.7 m (12 feet) wide, and 3.4 m (11 feet) deep located in the Haynes Coastal Engineering Laboratory at Texas A&M University. Water is discharged from a large cross-tank pipe with a long strip of opening located at the upstream end of the flume. An adjustable gate is located at the other end of the flume to control the water level in the flume. The flume also includes a 7.6 m (25 feet) long by 1.5 m (5 feet) deep sediment pit starting at about one-half the flume length.

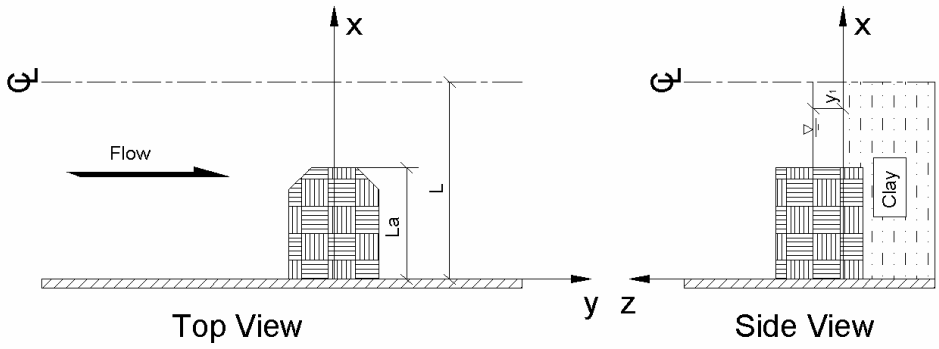

Figure 1. Geometry and coordinate system of experiments
(not to scale, the right panel was rotated 90 degree counterclockwise)

TABLE I. TEST CONDITIONS

Case	L (m)	L_a (m)	y_1 (m)	v_{avg} (m/s)	Fr	Q (m^3/s)
B1	3.66	1.01	0.37	0.33	0.58	0.446
B2	3.66	1.62	0.37	0.33	0.58	0.446
B3	3.66	2.23	0.37	0.33	0.58	0.446

The sediment pit was used as the test area for abutment scour. It was filled with sand up to 0.9 m (3 feet) height from the bottom of the pit. The remaining 0.6 m (2 feet) in the pit was filled with Porcelain clay. The clay has a median particle diameter of D_{50} = 0.003 mm, plastic index PI = 14%, critical velocity v_c = 0.95 m/s and critical shear stress τ_c = 1.7 N/m^2. The property of clay mentioned above was determined following the ASTM standard test procedures and the EFA test procedure (Briaud et al., 1999).

A vertical wall abutment with a 45° wing wall, 0.46 m (18 inch) wide crest, 1.12 m (44 inch) height, and 2.29 m (90 inch) width was used in the tests. The length of the abutment was varied in the tests, adjusted using several wooden embankments. Fig. 1 shows the experiment setup and the definition of geometry and coordinate system. The test conditions are shown in Table I.

The water elevation, bed elevation, and flow velocity were measured every 24 hour during the tests using a point gauge, a bed profiler, and an ADV. The point gauge is designed to detect the difference in electrical conductivity. Once the needle-shaped gauge touches the interface between two different materials, a sudden conductivity change occurs. This enables the gauge to determine the free surface and soil bottom. The bed profiler consists of 23 rulers with a 15.24 cm (6 inch) constant spacing between the adjacent rulers. The rulers are allowed to move vertically only. The profiler is capable of measuring 23 bed elevations at once, while the point gauge measures only one bed elevation at a time. The profiler was used to obtain the channel bed profile and to find the position of the maximum scour depth. Note that the bottom was not visible during the test due to the muddy circulated water in the flume.

III. NUMERICAL SIMULATION

Two numerical models, RMA2 and CHEN 3D, were used to help the measurements by providing the detailed flow field. RMA2 is a two-dimensional depth-averaged finite element hydrodynamic model for computing water surface elevations and horizontal velocity components in a subcritical free-surface flow (King, 2003). CHEN 3D is a three-dimensional Reynolds-averaged Navier-Stokes (RANS) model in conjunction with a flexible chimera domain decomposition technique to predict the flow around obstacles and resolve in the turbulent boundary layer. CHEN 3D solves the mean flow and turbulence quantities on embedded and overlapped multiblock grids. Within each computational block, the finite-analytic method of Chen et al. (1990) is employed to solve the RANS equations in a curvilinear body-fitted coordinate system. The overall numerical solution is completed by the hybrid PISO/SIMPLER pressure solver of Chen and Korpus (1993) that satisfies the continuity equation at each time step. The present method was used in conjunction with the PEGSUS program of Suhs and Tramel (1991) that provides the interpolation information between different grid blocks.

Fig.2 shows the 2D grids in Case B1 with a total of 6778 elements and 20785 nodes used in the RMA2 simulation. A constant eddy viscosity of 0.8 lb-s/ft^2 and Manning's n value of 0.035 were used in the simulation. Fig. 3 shows the 3D grid system in Case B1 used in CHEN 3D simulation. The grids were divided into six blocks as shown in the figure. The grid points in the x, y and z directions in each block are: Block 1, 40×80×31; Block 2, 53×23×31; Block 3, 165×41×31; Block 4, 80×80×31; Block 5, 80 ×16×31; and Block 6, 12×11×31. In both numerical models, only one-half of the channel was covered in the computation by assuming that the channel and abutment are symmetric.

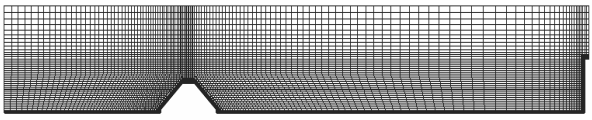

Figure 2. Grid system in 2D simulation for Case B1
(flow direction from left to right)

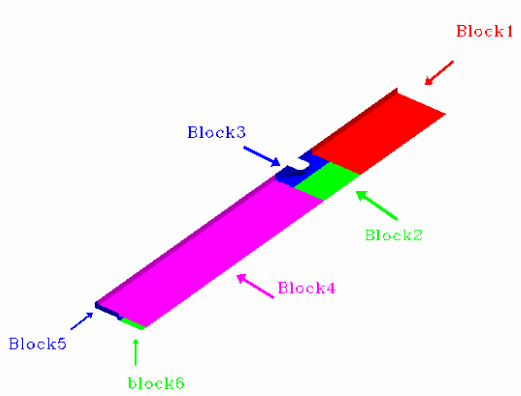

Figure 3. Grid system in 3D simulation for Case B1 (flow direction from Block 1 to Block 6)

IV. Results and Discussion

Water elevation along the flume was measured every 24 hours at the middle of the opening section. The measurements for all three cases were shown in Fig. 4. Fig. 4(a) shows that the contraction ratio (L_a/L) does not influence the initial water level upstream, while a higher contraction ratio results in a greater water level change around the abutment. Fig. 4(b) shows that the water level around the abutment decreases as time progresses due to the abutment scour and contraction scour that increase the cross sectional area at the contracted section. The change is quite remarkable in the higher contraction cases. Note that the flow rate was kept constant at 0.45 m^3/s during the tests with only a negligible variation.

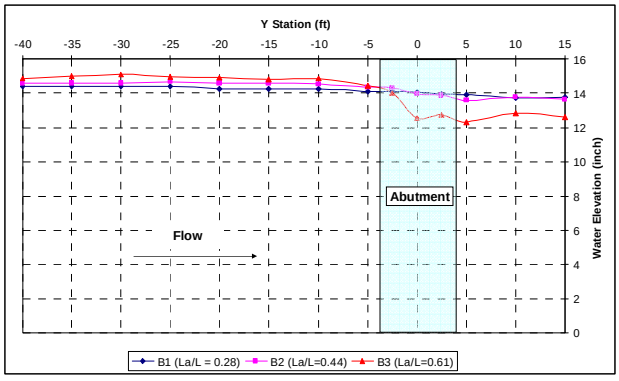

(a) Initial water elevation along the flume

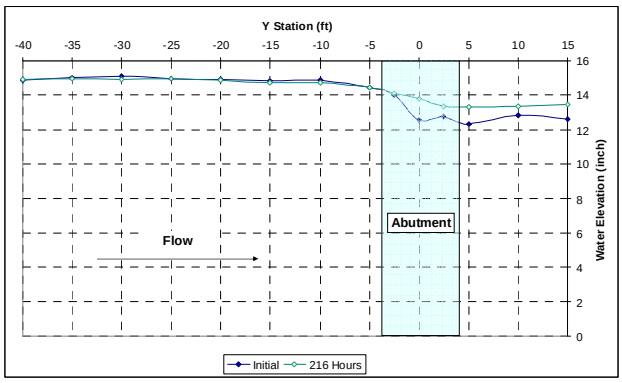

(b) Water elevation during the experiment in Case B3

Figure 4. Water elevation measured at the center of the opening along the flume

The scour depth was measured every 24 hours throughout the test. The measurement covered the entire test area (i.e., the sediment pit). We found the center of scour hole located at the end of abutment near either the middle section (y = 0 ft for Case B1) or slight downstream (y = 0.75 ft for Case B2 and y = 1.5 ft for Case B3). Fig. 5 shows the measured bed contour in Case B2. Note that the center of scour hole in cohesionless soil was observed to locate at the upstream corner of abutment regardless the shape of abutment and test condition (Laursen and Toch, 1956), indicated in Fig. 6.

Fig. 7 shows the cross sectional plots along the cross-tank direction of bed profile at three locations close to the maximum scour hole. The along-tank direction bed profile is shown in Fig. 8. From the plots, the frontal slope of the scour hole was much steeper than the rear slope. Moreover, the higher the contraction ratio (L_a/L) is, the more significant slope difference was observed between the front and the rear.

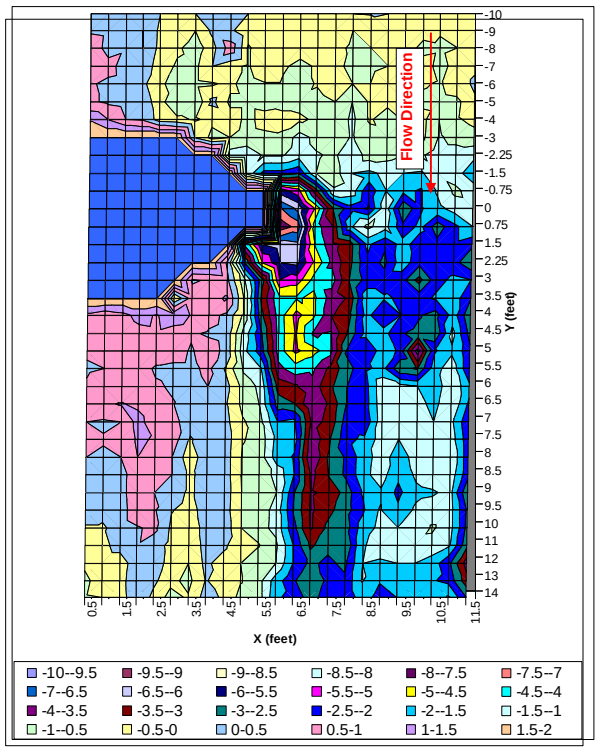

Figure 5. Contour of channel bed elevation after 240 hours in Case B2

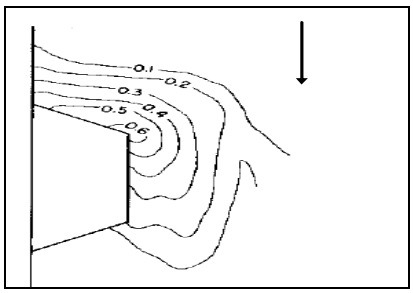

Figure 6. Top view of scour pattern around a wing wall abutment in cohesionless soil (Laursen and Toch, 1956). The flow direction is indicated by the arrow.

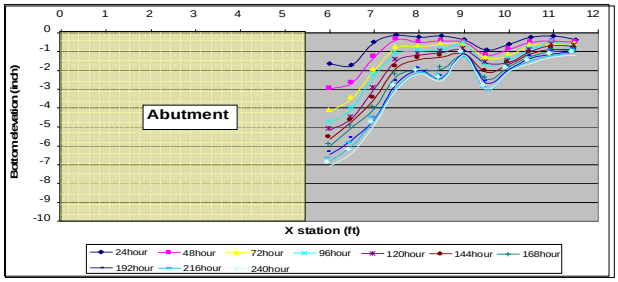

(a) y = 0.0 ft

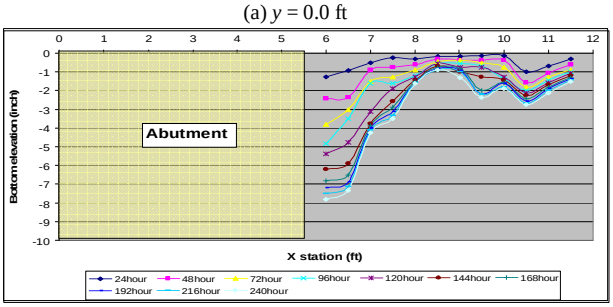

(b) y = 0.75 ft

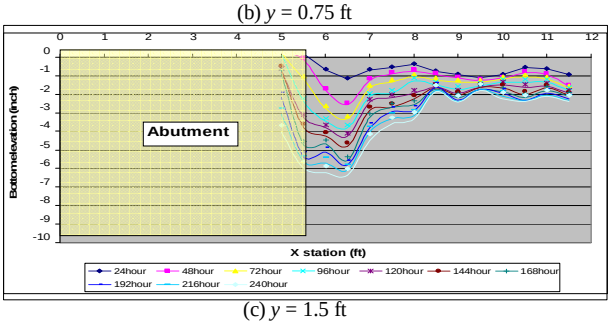

(c) y = 1.5 ft

Figure 7. Scour development in the x direction for Case B2

The scour rate at the beginning of test was high and then gradually decreased with time. Fig. 9 shows the amount of eroded clay calculated using the measured bottom contour. The figure shows that the contraction ratio is an important parameter in the analysis of abutment scour. Fig. 10 shows the abutment scour depth in all three cases. Although it is obvious in Fig. 9 that the high contraction ratio Case B3 has a much larger scour volume in comparison to the lower contraction ratio Case B2, the maximum scour depth between these two cases is about the same, as shown in Fig. 10. This may indicate that there exists a critical scour depth; the scour hole will not continue to deepen but simply widen. This is very different from results found in cohesionless soil. More tests need to be conducted to confirm this preliminary finding. Fig. 10 and Table II show that the measured scour depth can be fitted with a hyperbolic function in all three cases. Using the hyperbolic fits Cases B1 to B3 reached between 60% and 70% of the equilibrium scour depth after 240 hours in this study. The time to reach 90% of equilibrium scour depth using the hyperbolic model is 923 hours, 1459 hours and 1319 hours for Cases B1, B2, and B3, respectively. In contrary, the approximated 90% equilibrium scour depth occurred within 15 hours in both fine and coarse sand (Gill, 1972). Note that the calculated critical velocity for the Porcelain clay used in the present study using Laursen's (1963) equation is 0.076 m/s while the velocity used in this study is 0.33 m/s. The velocities indicate that the experimental condition in this study is not clear water scour but live bed scour.

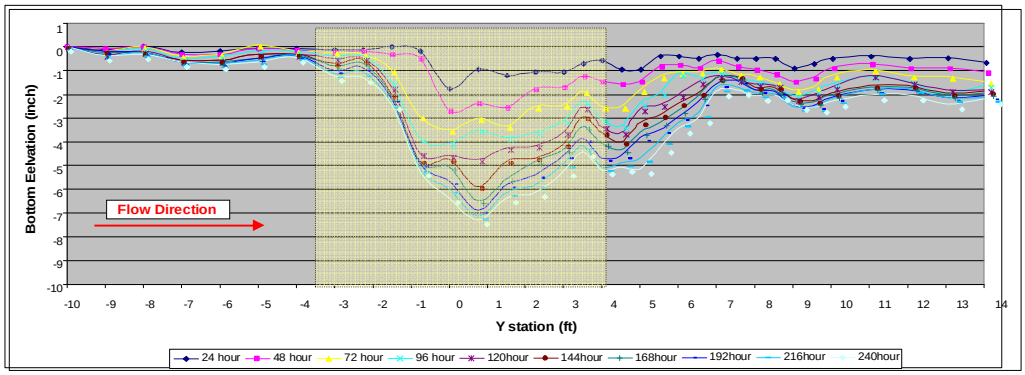

(a) x = 6.0 ft

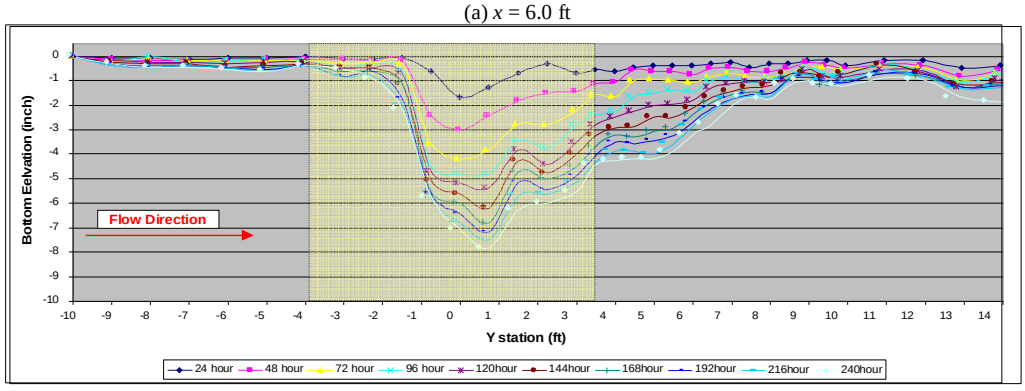

(b) x = 6.5 ft

Figure 8. Scour development along the flow direction in Case B2

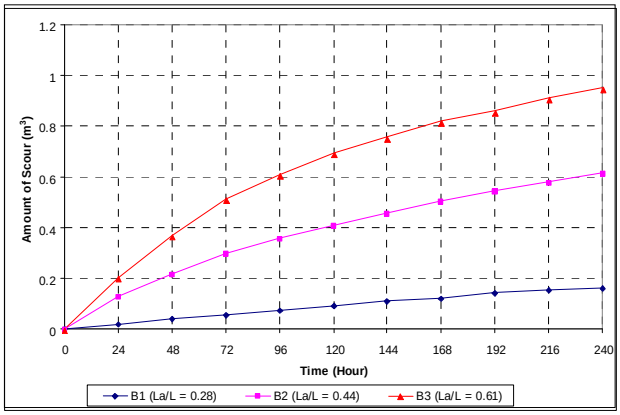

Figure 9. Amount of eroded clay versus time

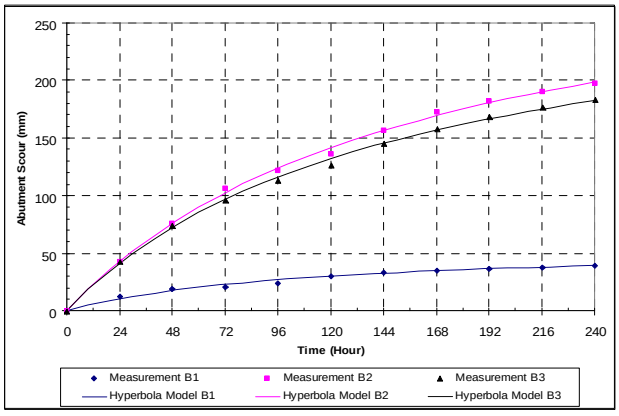

Figure 10. Abutment scour depth versus time

TABLE II. HYPERBOLIC MODEL OF ABUTMENT SCOUR DEPTH

Case	L_a/L	Hyperbolic Model for Abutment Scour Depth (mm)	Equilibrium Scour Depth (mm)	R^2 value
B1	0.28	$z_a = \frac{t}{0.0179t + 1.8349}$	55.9	0.97
B2	0.44	$z_a = \frac{t}{0.003t + 0.4866}$	333	0.99
B3	0.61	$z_a = \frac{t}{0.0034t + 0.4984}$	294	0.99

Table III shows the comparison among several previous studies and this study under the test condition. In the table, Melville's shape factor (K_1 = 0.75) was incorporated into the equations of Laursen (1960) and Gill (1972) to account for the geometric variation of abutment. The results obtained using cohesionless soil are either of the opposite trend (deposition rather than scour) or too conservative to predict the scour depth in cohesive soil.

Fig. 11 depicts the comparison of water elevation between the measurement and numerical simulations for Case B1. Very good agreement was found for both the numerical models used in the study. Fig. 12 presents the streamwise velocity distribution across the flume at the contacted section at y = 0.0 ft and at the expanded section behind the abutment at y = 15.0 ft. The figure shows that only the 3D simulation agrees well with the measurement. The calculated velocity using 2D model has a very significant deviation in the vicinity of abutment and behind the abutment.

TABLE III. COMPARISON WITH PREVIOUS STUDIES

Case	Abutment Scour Depth (mm)				
	Laursen (1960)	Gill (1972)	Froehlich (1989)	Melville (1992)	This Study
B1	694	-183	761	917	56
B2	871	-202	932	1161	333
B3	1015	-222	1069	1363	294

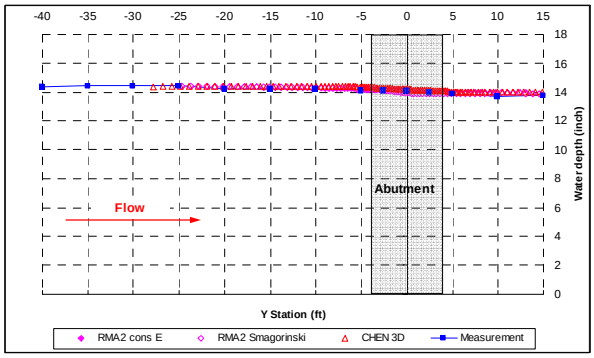

Figure 11. Comparison of water elevation between measurement and numerical simulations for Case B1

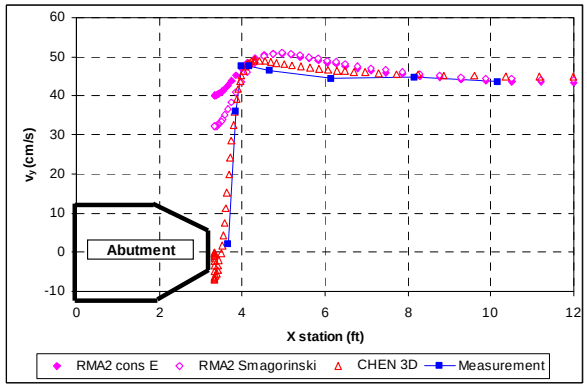

(a) Middle section at y = 0.0ft

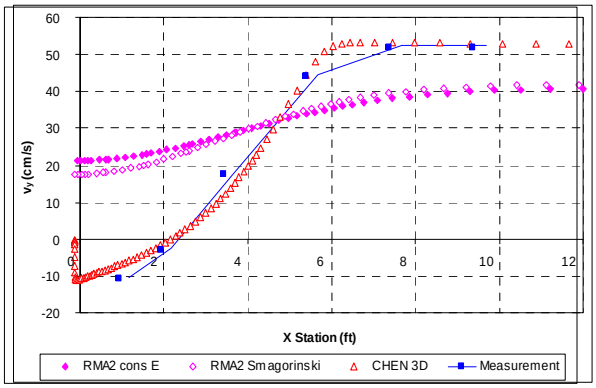

(b) Downstream at y = 15.0 ft

Figure 12. Comparison of streamwise velocity distribution between measurement and numerical simulations for Case B1

Fig. 13 is a picture taken in Case B2 at the moment after the flume was filled but before the test was started. Fig. 14

was taken after the test was completed with water drained in the same case.

Figure 13. Top view of test area in Case B2 before the test started

Figure 14. Image taken after 240 hours of run time in Case B2 (looking at the upstream direction)

V. Conclusion

Three large-scale laboratory tests were performed to investigate the abutment scour process in cohesive soil. Results in these experiments were compared with that in previous studies using cohesionless soil. The following is the findings:

- The scour pattern in cohesive soil is very different in comparison with the pattern in cohesionless soil. The location of scour hole in cohesive soil is at the middle or slight downstream of the abutment section. However, previous studies using cohesionless soil showed that the location is at the upstream corner of abutment.
- The hyperbolic function may be a good approximation for scour depth prediction in cohesive soil.
- Time needed to reach the equilibrium scour depth in cohesive soil is one order of magnitude longer than that in cohesionless soil.
- Predictions of scour depth using methods developed for cohesionless soil are too conservative to predict scour in cohesive soil.
- 3D numerical simulations may be necessary to compute the detailed flow field in the study.

Notation

D_{50}	median diameter of soil particle
Fr	Froude number based on upstream velocity and depth
K_{yL}	depth-size factor (m)
K_I	flow intensity factor
K_1	shape factor
K_2	alignment factor
K_G	approach channel geometry factor
K_T	time factor
L	width of channel
L_a	length of abutment
Q	discharge
t	time (hour)
v_{avg}	average velocity at up stream
v_c	critical velocity
y_1	water elevation at upstream
z_a	Calculated abutment scour depth (mm in this study)
σ_g	geometric standard deviation of sediment $=\sqrt{D_{84}/D_{16}}$
τ_1	shear stress at upstream
τ_c	critical shear stress

References

[1] Briaud, J.-L., Ting, F.C.K., Chen, H.C., Gudavalli, R., Perugu, S., Wei, G., 1999, "SRICOS: Prediction of Scour Rate in Cohesive Soils at Bridge Piers", Journal of Geotechnical and Geoenvironmental Engineering, 125, 237-246.

[2] Chen, H.C. and Patel, V.C., and Ju, S., 1990, "Solutions of Reynolds-Averaged Navier-Stokes Equations for Three-Dimensional Incompressible Flows," Journal of Computational Physics, 88, 305-336.

[3] Chen, H.C. and Korpus, R., 1993, "A Multi-block Finite-Analytic Reynolds-Averaged Navier-Stokes Method for 3D Incompressible Flows," ASME FED-Vol. 150, pp. 112-121, Proceedings of the ASME Fluids Engineering Conference, Washington, D.C., June 20-24

[4] Froehlich, D.C., 1989, "Local scour at bridge abutments", Journal of Hydraulic Engineering, ASCE, Proceedings of the 1989 National Conference on Hydraulic Engineering: New York, American Society of Civil Engineering, 13-18

[5] Gill, M.A., 1972, "Erosion of Sand Beds Around Spur Dikes", Journal of Hydraulic Division, ASCE, 98, 1587 – 1602

[6] King, I. P., 2003. "RMA2 Users Guide 4.5x." US Army Corps of Engineers –Waterways Experiment Station Hydraulics Laboratory.

[7] Laursen, E.M., Toch, A. 1956, "Scour Around Bridge Piers and Abutments", IOWA Highway Research Board Bulletin No 4

[8] Laursen, E.M., 1960, "Scour at bridge crossings", Journal of Hydraulics Division, ASCE., 86, 39-54

[9] Laursen, E.M., 1963, "An analysis of relief bridge scour", Journal of Hydraulics Division, ASCE., 89, 93-118

[10] Melville, B.W., 1992, "Local Scour at Bridge Abutments", Journal of Hydraulic Engineering, 118, 615-631

[11] Suhs, N.E. and Tramel R.W., 1991, "PEGSUS 4.0 Users Manual," Report AEDC-TR-91-8, 1991, Arnold Engineering Development Center, Arnold Air Force Station, TN.

Effects of Pile Caps on Local Scour at Bridge Piers

G. Oliveto*, B. Onorati* and V. Comuniello*
* University of Basilicata - Dipartimento di Ingegneria e Fisica dell'Ambiente, Potenza, Italy

The most existing pier-scour equations mainly apply to uniformly shaped piers (i.e. piers with a constant horizontal cross-section geometry over their length). However, actual bridge piers have composite shapes. Typical examples are piers founded on plinths, caissons, or piles. Pier footings may often project above the streambed because of scour. This may be caused by either long-term bed degradation or local scour. In such cases, the computation of the local bridge scour depth becomes complicated because of the difficulty in choosing an appropriate pier dimension. Referring to piers founded on piles, in previous papers (references [7] and [8]) some outcomes were achieved, mainly on the quasi-equilibrium scour depth. Based on additional experiments, this paper would like to come up with a deepening of the previous findings and provide new insights on the temporal evolution of the river-bed morphology around the pier. Tests typically lasted some days to provide a more effective interaction between the flow and the complex pier-plinth-piles. The results could provide useful tools in design, numerical modeling and field investigations.

I. INTRODUCTION

Bridge piers are often founded on piles mainly due to geotechnical and economic reasons. This kind of foundation is commonly considered a guarantee for the safety of the bridge structure against any scouring problems. However, pier footings may often project above the streambed as result of either long-term degradation, lateral shifting of the stream, contraction scour, or local scour during a runoff event. For such cases piles should be designed to resist to a certain exposure to the flow and the footing location should be designed on structural and hydraulic bases. Moreover, when general scour produces a significant bed lowering, the safety reassessment of the bridge requires a new local scour prediction that must consider the combined pier/foundation pile geometry. Figs. 1 and 2 provide two field examples of local and general scour around piers founded on piles.

Papers dealing with the effects of such a combined geometry on scour depth are rare in literature. Based on a laboratory study, the Authors of reference [3] evaluated how the effect of footing location can be taken into account in scour prediction equations that use a single characteristic pier size. They found that a weighted width technique provides simple and accurate estimations. Their analysis did not account for the scour-arresting effects for footings located below the streambed. HEC-18 [10] provides some guidelines for evaluating local scour at exposed pile caps. It is recommended that the pier width should be used in a scour equation if the top of the pile cap is at or below the streambed. If the pile cap is placed into the flow, its width should be considered instead of the pier width. However, the HEC-18 procedure is based on few data and many engineers consider it conservative, especially for large piers. An experimental investigation of scouring at rectangular piers founded on two circular cylindrical piles is [4]. That research was thus focused on a pure two-width problem, while disregarding more complex geometries. Preliminary results on physical models composed by pier, pile cap and pile group were given in [2]. A detailed references list is provided in [5]. More recently, a new methodology to predict local scour depth at a complex pier was presented in [1]. In particular, the method distinguishes the different scouring processes for different pile-cap elevations.

Figure 1. River Basento (Italy): Local scour around the plinth of a pier founded on piles

Figure 2. River Basento (Italy): General scour around a pier with consequent exposure of the piles

All these studies are mainly focused on conditions of quasi-equilibrium scour depth. Moreover, the proposed design procedures are specific and preliminary because of

the complexity of the problem and the large number of parameters involved.

In this context, a research project was initiated at University of Basilicata for developing general and straightforward design criteria. This paper would like to provide some results on the temporal evolution of the scour depth around the pile cap and, in particular, upstream and downstream of it. This, by highlighting differences with uniform cylindrical piers.

II. EXPERIMENTAL SETUP

Experiments were conducted in a 1 m wide and 20 m long rectangular straight channel at the Hydraulic Engineering Laboratory, University of Basilicata, Italy. The working section was about 10 m. The bed material was a nearly uniform sand with density ρ_s = 2.65 t/m^3, grain size d_{50} = 1.7 mm and sediment gradation σ = $(d_{84}/d_{16})^{1/2}$ = 1.5. The scour elements were three-width models consisting of a cylindrical pier of diameter D, a square pile cap of width B and thickness T, and 4 cylindrical piles of diameter d, spaced each other by s. A definition sketch is given in Fig. 3.

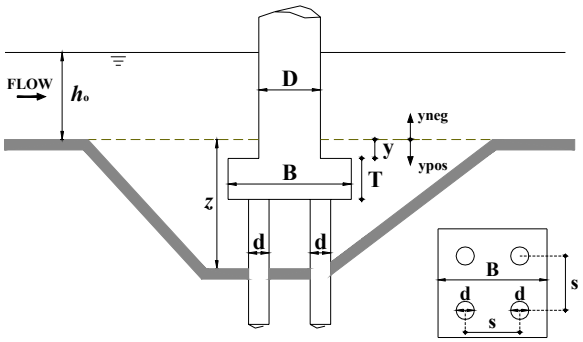

Figure 3. Definition sketch of the scour element and hydraulic variables

Two models were tested. One had D = 0.12 m, B = 0.24 m, T = 0.08 m, and d = 0.04 m. The other had D = 0.06 m, B = 0.12 m, T = 0.04 m, and d = 0.02 m. All model dimensions were multiples of the piles diameter.

All the experiments were run under plane bed conditions, steady flow, and clear-water scour regime. Moreover, the models were always set with the top elevation of the pile cap placed at the initial bed level.

Discharges Q were measured with an orifice plate with ±3% of accuracy. Water surface was surveyed with a conventional point gage, typically ±0.5 to 1 mm, whereas the bed morphology was surveyed with a so called shoe gage having 4 mm by 2 mm wide horizontal plate at its base. The tests were of long duration, typically 2 days up to 13 days, to ensure an adequate interaction between flow and the complex pier-plinth-piles and to get conditions of quasi-equilibrium. Measurements during the test were carefully taken in extensive regions around the pile cap.

The approach flow depth was controlled by an adjustable sharp-crested weir located at the channel downstream end. Once the bed was accurately leveled the experiment initiated submerging the working section by setting the sharp-crested weir up. This was lowered within 10 to 20 seconds to the pre-selected flow depth and the temporal start of the experiment was set at scour inception. Photograph in Fig. 4 is an upstream view of the experimental stand.

Figure 4. Upstream view of the experimental stand

Test conditions and measured scour depths are presented in Tab. I, with h_o = approach flow depth, F_d = $V_o/(g'd_{50})^{1/2}$ = approach densimetric Froude number, V_o = approach velocity, g = gravitational acceleration, , g' = $[(\rho_s-\rho)/\rho]g$, ρ = fluid density, z = maximum scour depth at the experiment's end, and t_t = test duration.

TABLE I. TEST CONDITIONS AND MEASURED SCOUR DEPTHS

Run	D	B	h_o	F_d	z	t_t
-	cm	cm	cm	-	cm	hours
1	12.0	24.0	5.6	1.99	9.8	47.8
2	12.0	24.0	11.6	2.36	18.5	313.2
3	12.0	24.0	13.3	2.05	14.2	66.7
4	12.0	24.0	21.8	2.22	13.1	52.5
5	12.0	24.0	29.2	3.01	22.4	21.5
6	6.00	12.0	5.5	2.35	10.8	43.0
7	12.0	24.0	10.6	2.63	18.3	271.3
8	6.0	12.0	10.8	2.37	12.0	216.4

III. EXPERIMENTAL EVIDENCES

Fig. 5 provides a typical evolution of the scour area around a pier founded on piles. At the beginning of the scour process the maximum scour depth tends to be located at the downstream edge of the pile cap. Successively, it migrates toward the pile cap front so that the exposition of the piles to the flow occurs first upstream and only after a long time downstream.

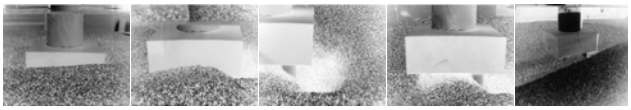

(a) (b) (c) (d) (e)

Figure 5. Run 2: Temporal scour evolution around a pier founded on piles after (a) 10 hours, (b) 20 hours, (c) 4 days, (d) 10 days, and (e) 12 days

Fig. 6 refers to the typical bed morphologies observed in the laboratory and in the field at the first phase of the scour process. Conditions encountered in the field were similar to those observed during the experiments.

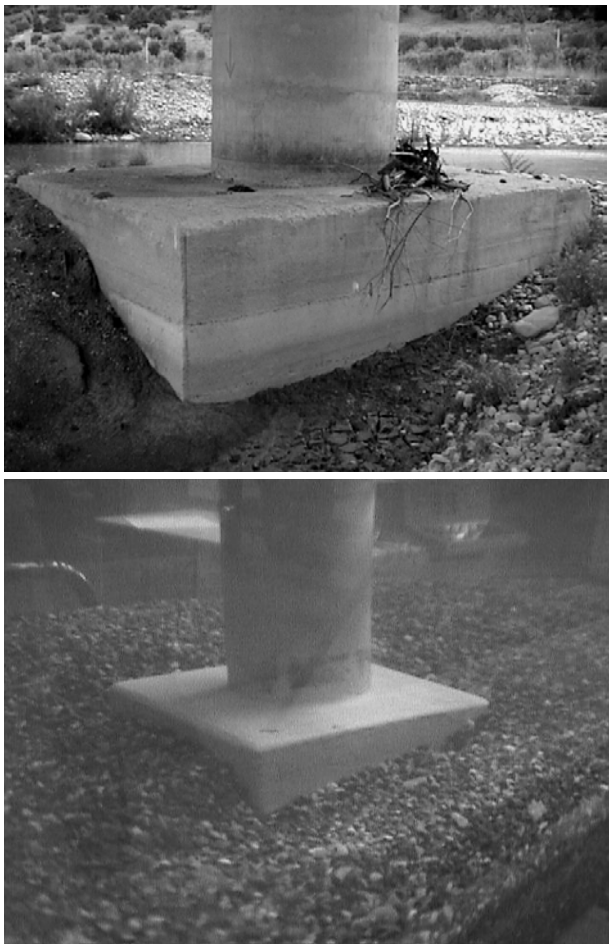

Figure 6. Local scour observed around a pile cap in the field (above) and in the laboratory (below)

Fig. 7 provides the bed contours during and at the end of the two runs 7 and 8. The first three plots show the bed morphology for the run 7 at 23, 142, and 271 hours after the run-start. It can be noted as the scour region tended to elongate downstream of the pile cap as two distinct and divergent ogival-shaped areas. The upstream part of the scour hole developed with slope almost equal to the angle of repose of the bed material. The bed configuration appeared to be satisfactorily symmetric. Similar bed morphologies were observed, but with less distinctness, also for the run 8. The second set of plots refers to this run at 0.5, 48, and 216 hours after the run-start. The aggradation zone tended to growing up axially downstream of the pile cap becoming shallow or even disappearing when the scour process approached its quasi-equilibrium phase. In both runs the maximum observed longitudinal extension of the scour region was remarkable and equal to about 6 times the pile cap width B. The hole's edges spanned significantly also in the transverse direction by about $4B$.

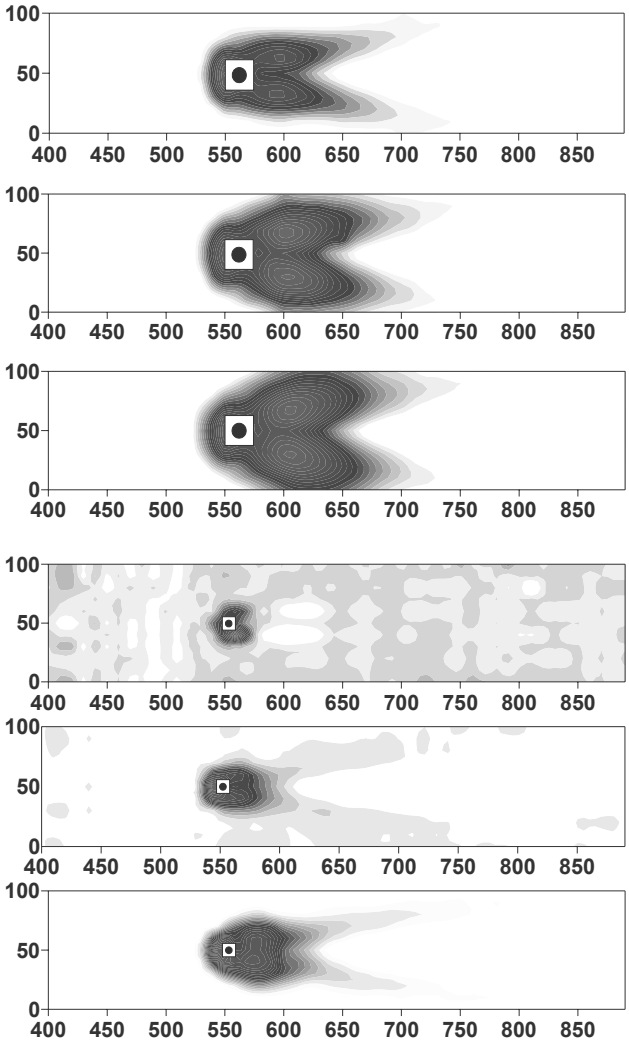

Figure 7. Bed contours during and at the end of the runs 7 (first three plots) and 8 (second set of plots)

IV. Data Analysis and Conclusions

The scour equation suggested in [6] for the temporal progress of scour at uniformly shaped piers was assumed as framework for this analysis. This equation was supported by an extensive experimental work. Tests were performed in two rectangular channels of width 1.0 and 0.5 m. Using three uniform and three non-uniform sediments of average grain sizes d_{50} between 0.5 and 5 mm, pier diameters D between 5% and 50% of the channel width, and approach flow depths h_o between 10 and 500 times the average grain size, the temporal scour evolution $z(t)$ around cylindrical bridge piers under clear-water conditions was investigated. It was found that the maximum scour depth z depends on three main parameters, namely the reference length $L_R=D^{2/3}h_o^{1/3}$; the densimetric Froude number $\mathsf{F}_d=V_o/(\mathrm{g}'d_{50})^{1/2}$; and the relative time $T=[\sigma^{1/3}(\mathrm{g}'d_{50})^{1/2}/L_R]t$ as

$$Z = 0.068\sigma^{-0.5}\mathsf{F}_d^{1.5}\log(T) \qquad \mathsf{F}_d > \mathsf{F}_{di}. \qquad (1)$$

Here $Z=z/L_R$ and F_{di} is the value of F_d for sediment entrainment around the pier. For square-shaped piers the second member of (1) should be multiplied for a shape factor N=1.25.

More recently, the following equation interpreting the temporal trend of the scour depth at rear of a cylindrical pier has been proposed in [9]

$$\frac{Z_r\sigma^{0.5}}{\mathsf{F}_d^{1.5}} = 0.086\log(T) - 0.16 \quad \mathsf{F}_d > \mathsf{F}_{di} \tag{2}$$

with subscript r = rear. Equation (2) applies for flows in transitional regime (i.e. $15<D^*<150$, where $D^*=(g'/\nu^2)^{1/3}d_{50}$ is the dimensionless grain size and ν is the fluid kinematic viscosity).

In the following the ratio $Z\sigma^{0.5}/\mathsf{F}_d^{1.5}$ will be denoted as ζ. More specifically ζ_D and ζ_B will denote the values of ζ when D and B are assumed as effective pier width, respectively.

With reference to the run 2 lasted 13 days, Fig. 8 shows the temporal trend for the scour depth upstream and downstream of the pile cap.

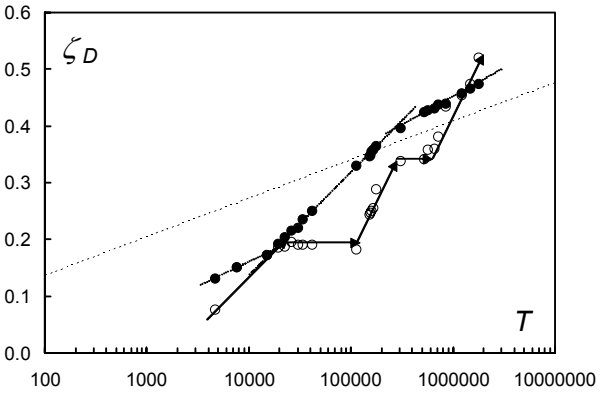

Figure 7. Run 2: $\zeta_D=Z\sigma^{0.5}/\mathsf{F}_d^{1.5}$ as a function of dimensionless time T by assuming D as the effective pier width. Temporal evolution of scour depth upstream (●) and downstream (○) of the pile cap. (·····) Equation (1)

The analysis of the plot would involve the following considerations. With reference to the scour progress upstream of the pile cap one can observe that:

- Scour starts after a certain delay compared to a uniform cylindrical pier of the same diameter D, owing to the collar-like protection exerted by the plinth;

- Then, the scour process develops until about $T=2\cdot10^4$ at a similar rate as that of a uniform cylindrical pier of the same diameter D;

- Successively ($2\cdot10^4<T<2\cdot10^5$), the scour rate increases owing to the exposure of the plinth that would determine an increasing of the effective element width;

- Lastly ($T>2\cdot10^5$), the scour rate would tend to decrease again owing to the exposure of the piles with a consequent reduction of the effective obstacle width.

While, the scour evolution downstream of the pile cap exhibits a two-step trend probably connected to the upstream piles exposure first and to the exposure of the complete pile group afterwards. This exposure would imply a compression of the flow between the piles thus creating higher velocities and greater scour potential.

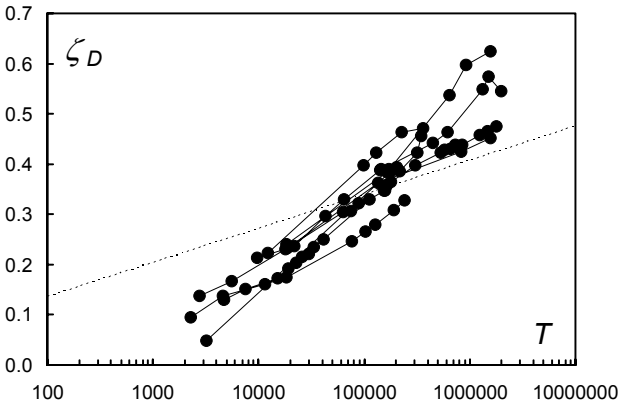

Figure 8. $\zeta_D=Z\sigma^{0.5}/\mathsf{F}_d^{1.5}$ as a function of dimensionless time T by assuming D as the effective pier width. (·····) Equation (1)

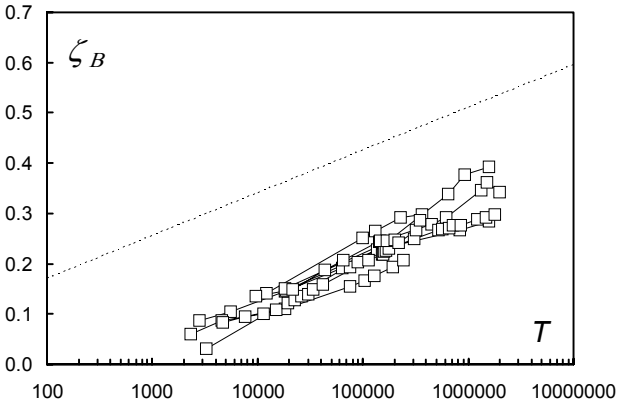

Figure 9. $\zeta_B=Z\sigma^{0.5}/\mathsf{F}_d^{1.5}$ as a function of dimensionless time T by assuming B as the effective pier width. (·····) Equation (1) multiplied for the shape factor 1.25

The plot in Fig. 8 refers to the temporal trend of the maximum scour depth. Typically, such scour depth was located just upstream of the pile cap except for the initial phase of the process in which it localized at the lateral of the pile cap and for very high values of T ($T>10^6$) when it localized even downstream of the pile cap mainly because of the exposure of the piles. It can be observed that:

- For $T<10^3$ the pile cap performs as a good protection so that the scour process appears completely inhibited;

- For $10^3<T<10^5$ the pile cap performs as a scour mitigator because the scour depths tend to be smaller than those that would occur for a uniform cylindrical pier at the same flow conditions;

- For $T>10^5$ the pile cap is significantly exposed to the flow and thus the scour depths are greater than those for a uniform cylindrical pier of the same diameter D because of an increasing of the effective pier width;

- Lastly, for $T>10^6$, as above said, the maximum scour depth would tend to localize downstream of the pile cap mainly because of the pile group exposure.

The plot in Fig. 9 shows the discrepancies between observed and computed scour values when, as usual, data are interpreted by assuming the plinth width as the effective element width. Differences tend to be attenuated

for T increasing. Nevertheless, overall such kind of method would appear too conservative.

Finally, the plot in Fig. 10 shows the temporal evolution of the scour depth downstream of the pile cap.

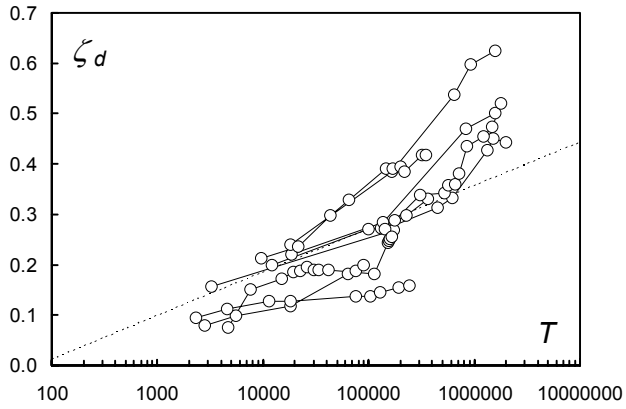

Figure 10. $\zeta_d=Z\sigma^{0.5}/F_d^{1.5}$ as a function of dimensionless time T downstream of the pile cap and by assuming D as the effective pier width. (·····) Equation (2)

In general, scour depths are significantly greater than those at uniform cylindrical piers with divergences increasing as T increases. The trend in the plane (ζ, log$T$) is manifestly not linear because the changing in the time of the effective element width would significantly affect the features of scour mechanisms.

ACKNOWLEDGMENT

The Authors would to thank Arcangelo Imperiale and Giovanni Falconieri for their help during the experimental phase.

REFERENCES

[1] Coleman, S.E., 2005, Clearwater local scour at complex piers, *Journal of Hydraulic Engineering*, ASCE 131(4): 330-334.

[2] Jones, S.J. and D.M. Sheppard, 2000, Local scour at complex pier geometries, In Hotchkiss and Glade (eds), *Joint Conference on Water Resources Engineering and Water Resources Planning & Management; Proc. intern. conf., Minneapolis, July 30-August 2 2000*. Reston, Va: ASCE.

[3] Jones, S.J., Kilgore, R.T. and M.P. Mistichelli, 1992, Effects of footing location on bridge pier scour, *Journal of Hydraulic Engineering*, ASCE 118(2): 280-290.

[4] Martin-Víde, J.P., Hidalgo, C. and A. Bateman, 1998, Local scour at piled bridge foundations, *Journal of Hydraulic Engineering*, ASCE 124(4): 439-444.

[5] Melville, B.W. and S.E. Coleman, 2000, Bridge Scour, Water Resources Publications, Denver, CO.

[6] Oliveto, G. and W.H. Hager, 2002, Temporal evolution of clear-water pier and abutment scour, *Journal of Hydraulic Engineering*, ASCE 128(9): 811-820.

[7] Oliveto, G. and A. Rossi, 2003, Some evidence on local scour at non-uniform piers, *Proceedings of the 3rd IAHR Symposium on River, Coastal and Estuarine Morphodynamics (RCEM)*, Barcelona, Spain, Vol. I., pp. 272-278.

[8] Oliveto, G., Rossi, A. and W.H. Hager, 2004, Time-dependent local scour at piled bridge foundations, In Yazdandoost and Attari (eds), *Hydraulics of Dams and River Structures*, Taylor & Francis Group, London, pp. 305-310.

[9] Oliveto, G., Hager, W.H. and A. Di Domenico, 2005, Additional results on scour at bridge piers, In J. Byong-Ho Jun, Sang-II Lee, II Won Seo and Gye-Woo Choi (eds), *Proc. of XXXI IAHR Congress, Seoul, Korea, September 2005*, 2005 Korea Water Resources Association: Seoul. Paper D09-2: 2964-2972.

[10] Richardson, E.V. and S.R. Davis, 1995, Evaluating scour at bridges, *Publ. No. FHWA-IP-90-017*, Washington, D.C.: Federal Hwy. Admin.

Structural defence for plunge pool scour

S. Pagliara*, M. Palermo*
* Department of Civil Engineering , Pisa, Italy

Plunge pool scour is a major topic in presence of hydraulic structures that foresees the production of jets. The scour hole is a function of several variables including the tailwater, the densimetric Froude number, the sediment granulometry, the water discharge. The maximum scour depth is of great interest in the design process. Aim of the paper is to analyze the effect of structures, inserted in the scour hole, in order to mitigate the scour geometry. About 300 tests have been carried out in the Hydraulic laboratory of the University of Pisa (Italy) in order to assess the advantages and the problems connected with the insertion of a rigid structures in the river bed. In this paper a first description of the phenomena is presented.

I. INTRODUCTION

The study of jets due to hydraulic structures is an important research topic in engineering practice. In fact, the impact of a jet on the basin downstream of the hydraulic structures can cause a scour phenomenon whose main geometrical parameters has to be foreseen in order to avoid structural instability. It was seen that the main parameters on which the scour process depends are the hydraulic characteristics of the jet, the water level in the basin downstream of the structure and the granulometric characteristics of the basin bed material.

The scour process is characterized by the formation of both a scour hole and a ridge. The phenomenon is characterized by the concomitance of three different phases: basin material disruption, formation of a vortex and deposit of material downstream of the scour hole.

When the jet stops, the basin material, which is let into suspension by the vortex, falls down and deposits in the scour hole. The dynamic configuration of the downstream face of the scour hole becomes static reducing its slope because of the ridge sliding. This occurrence puts in evidence that there are two typical configurations. The dynamic configuration is characterized by a relevant quantity of basin material which is in suspension in the vortex. Moreover, the jet pressure on the downstream face of scour hole is able to increase its natural slope, partially carrying the weight of the ridge. It means that when the jet stops, there are no dynamic forces and there is a partial ridge collapse. The phenomenon reaches its static configuration in which the slope of the downstream face of the scour hole becomes equal to the natural basin material friction slope and the suspended material deposits in the scour hole.

With these considerations it is evident that during the dynamic phase the scour hole is deeper than in the static phase [5]. This occurrence has to be taken in serious consideration in structures design. The measurements of bed profile during the dynamic phase showed that there can be also a great increase of the scour depth. Plunge pool scour is a phenomenon which constitutes a significant structural risk.

Many Authors studied this phenomenon. Reference [1], [2] and [6], gave a contribution to understand the main hydraulic and geometrical parameters which characterize the scour mechanism. Pagliara et Al. [4] proposed an experimental formula to evaluate the dimensionless maximum scour depth $Z_m=z_m/D$ in which z_m is the maximum measured scour depth and D is the jet diameter. The following relation is valid in absence of any type of structural defence,

$$Z_m = f_1(F_d)\cdot f_2(\alpha)\cdot f_3(\beta)\cdot f_4(T_W)\cdot f_5(\sigma)\cdot f_6(F_u) \quad (1)$$

The previous relation shows that Z_m is a function of the densimetric particle Froude number (F_d), the jet impact angle (a), jet air content (b), relative tailwater depth (T_w), sediment non uniformity parameter (s) and upstream Froude number (F_u), where $F_d=V_w/(g'd_i)^{1/2}$ with $V_w=Q_w/(pD_w^2/4)$ as the water velocity, $g'=[(r_s-r)/r]g$ as the reduced gravitational acceleration with the densities r_s and r of sediment and water, respectively, and d_i as the determining grain size. The significant length scale is either the conduit diameter D or the black-water jet diameter $D_w=[(4/p)(Q_w/V_w)]^{1/2}$. The air content b is equal to Q_A/ Q_w, where Q_A and Q_w are air and jet water discharge, respectively. T_w is equal to h_0/D , where h_0 is flow depth as shown in Fig. 2; s is equal to $(d_{84}/d_{16})^{1/2}$, in which d is the sediment size and the subscript indicates the percentage of passage across a sediment net. $F_u=V_u/(gh_0)^{1/2}$, in which V_u is the upstream velocity.

Aim of this paper is to analyze the effects of structures, inserted in the scour hole, in order to mitigate the jet scour.

II. EXPERIMENTAL SETUP

All the experiments were carried out in the same rectangular channel. This channel was 25 *m* long, 0.80 *m* wide and 0.90 *m* high. For the present study, the transversal section of the previous channel was divided longitudinally into two parts in order to assure the two dimensionality of the phenomenon. In fact, the model built inside the channel had a width of 0.20 *m* and a length of about 3 *m*. The channel narrowing was obtained using a vertical impermeable wood wall, which had the same height of the channel. At least the physical model built inside the channel had the following geometrical characteristics: 0.20 *m* wide, 3 *m* long and 0.90 *m* high. A certain quantity of granular material was put in this experimental model in order to simulate the mobile bed downstream of a dam spillways. The basin material employed in this study has the following granulometric

characteristics: d_{84} = 11.4 mm, d_{16} = 9.0 mm, d_{90} = 11.63 mm and s = 1.13.

Before starting each experiment, channel bed material was levelled in order to maintain the same fixed level. To simulate a dam spillway, a movable pipe was fixed on the channel. The extremity of this pipe could be changed in order to vary the jet section. Moreover, the pipe could slide in an iron guide in order to regulate the distance of the outlet from the water surface and could rotate in order to change the jet impact slope. Two pipe sections were employed whose diameters were 27 *mm* and 35 *mm* respectively. Some different fixed discharges ranging between 2.50 *l/s* and 5.65 *l/s* were investigated. In all the tests the impact angle was 30°. Fig. 1 shows the model used in experiments.

The channel bed was measured in some fixed points both transversally and longitudinally before starting each experiment. As to confront the results of various tests executed with different pipe diameters, let us define the dimensionless parameter T_w as h_0/D, where h_0 is the water level and D is the jet diameter, as shown in Fig. 2.

Four different values of T_w were investigated: 1, 5, 7 and 9. The water level in the channel was regulated using a gage in order to maintain the value of T_w constant during each test. To clarify the effects of protection works on the geometry of the scour due to the impact of jet four different structures were employed (i.e. *S*, *SF*, *SG10* and *SG17*). Fig. 3 shows the different used structures. Structure *S* is a 3 mm thick iron sheet; *SF* is an iron sheet on which 10 mm diameter holes were made and the percentage of vacuum is 54; *SG10* is an iron grid with 10 mm side square holes. Its percentage of vacuum is 66.8; *SG17* is an iron grid with 17 mm side square holes with a vacuum percentage of 70.

Figure 1. View of the physical model employed for the experiments.

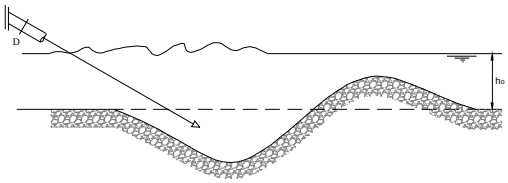

Figure 2. Definition sketch.

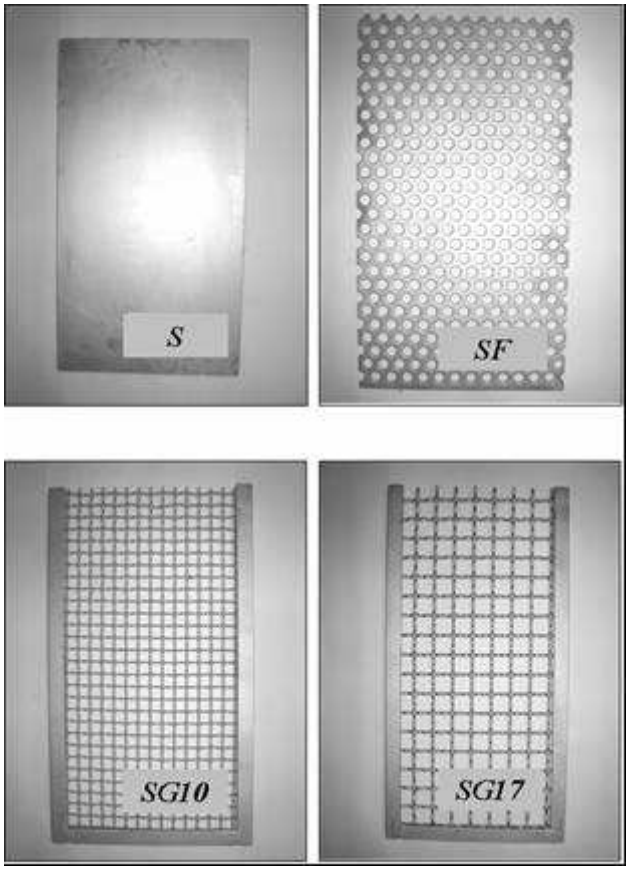

Figure 3. Scour protection structures

III. EXPERIMENTAL RESULTS

To understand the effects of the different protection works on scour mechanism, some reference tests were carried out. Namely, for each tested combination of discharge and tailwater, a reference test was carried out in order to find the longitudinal length L_0 and the maximum depth z_m, of the scour hole. These reference tests were carried out without any protection structure, as shown in Fig. 4.

Having found the reference values of L_0 and z_m, a control grid, constituted of fifteen different "control points", was fixed in order to individuate the optimal longitudinal and vertical protection structure positions which had to be tested. For each test, according to the reference frame, the longitudinal positions were fixed in $L_0/2$, $3/4L_0$, L_0, $5/4L_0$ and $3/2L_0$, while the three vertical positions were fixed in $+z_m/3$, 0 z_m and $-z_m/3$, as shown in Fig. 5.

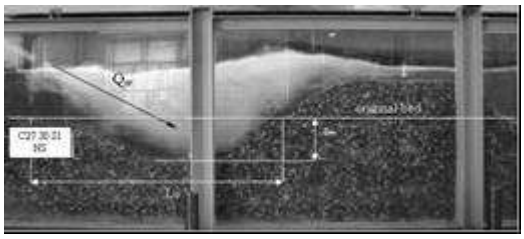

Figure 4. Example of a reference prove (Q_w=4.50 l/s; T_w=7).

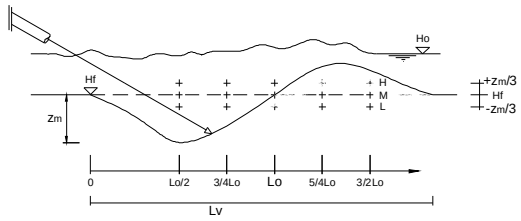

Figure 5. Control grid.

Considering all the geometrical and hydraulic parameters, a systematic investigation of all control points for each type of structure was avoided and, after having done some preliminary tests, the structures and the control positions which had to be preferred in order to minimize the scour were individuated and investigated systematically.

For each prove, including the reference one, the bed channel profile was measured at four different fixed times (1, 5, 20 and 50 minutes after the beginning of the test) in order to understand the dynamic evolution of the scour mechanism. Moreover, channel bed was measured after stopping the jet in order to analyze the final static configuration and highlight the differences with the dynamic one. The two dimensionality of the phenomenon was verified doing some transversal measurements of the maximum scour section. A thorough study of the longitudinal position $L_0/2$ was not interesting to be deepened because of the direct impact of the jet on the protection structure. In fact, for a real structure located in this position, the impact wall would be damaged by the jet energy. Moreover, for example, if a *S* type structure is located at $L_0/2$ and its upper upstream edge is at $+z_m/3$, a significant scour depth can be noted, as shown in Fig. 6. Fig. 7 shows that the same occurrence happens if the *S* type structure is located at $L_0/2$ and $-z_m/3$. The last structure settlement causes a division of the jet which directly impacts the superior part of the structure and two different vortexes are generated, one upstream and the other downstream of the structure. It means that two scour holes are present if the structure is located in this position, as shown in Fig. 7.

As also in this position the scour is deeper than in the relative reference test, this structure settlement was not considered efficient in order to minimize scour depth and this longitudinal position was not analysed further.

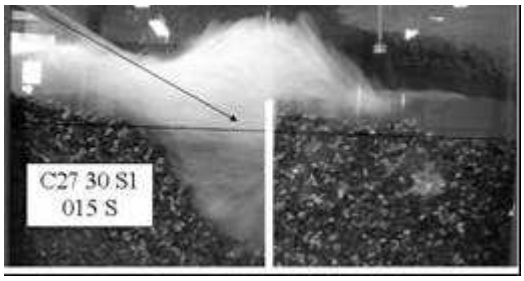

Figure 6. Scour profile in presence of S type structure located at $L_0/2$ and $+z_m/3$.

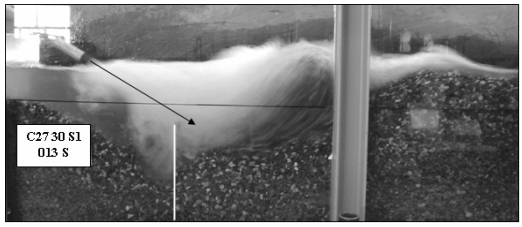

Figure 7. Scour profile in presence of S type structure located at $L_0/2$ and $-z_m/3$.

When the different structures are located at longitudinal distances ranging between $3/4L_0$ and $3/2L_0$, the jet loses a certain quantity of its energy first impacting the basin upstream of the structure. The presence of a structure, when its longitudinal position is $3/2L_0$, does not have significant effects on reducing scour depth because of the formation of a ridge downstream of the scour hole which entirely covers the structure vanishing every beneficial effect of it. Based on these considerations and on several other experimental deductions and observations, finally the positions which were considered most efficient in scour depth reduction are shown in Fig. 8 and Fig. 9 with a bold point. Fig. 8 shows the systematically investigated control positions in absence of an upstream flow, whereas Fig. 9 shows the same aspects when there is an upstream flow (Q_u) in the channel. Then they were systematically investigated further for each one of the four types of structures employed in this study.

Experimental tests, conducted with different structures, showed that one of the most important parameters which influences scour mechanism is the percentage of vacuum of the structure. Generally, maintaining constant all the other geometrical and hydraulic variables, an increase of the percentage of vacuum in the structures lets to a reduction of the scour depth. Fig. 10 shows the variables used to compare the efficiency of different structures in reducing scour depth.

z_{ms} is the maximum scour depth in presence of a protection structure, L_v is the length of the scour hole and of the ridge in the reference test, L_{vs} is the length of the scour hole and of the ridge in presence of a structure, L_0 is the length of the scour hole in the reference test, L_{0s} is the length of the scour hole in presence of a structure, h_s is the distance between water level and structure along jet direction, h_L is the distance between water level and downstream scour face along jet direction.

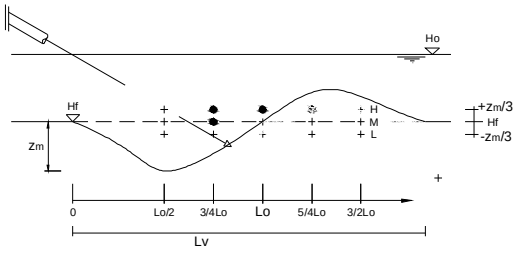

Figure 8. Systematically tested control positions in absence of an upstream channel discharge.

Figg. 11 and 12 confirm the influence of the permeability of structure on the scour mechanism and show the ratio of the maximum scour depth in presence of a protection structure to the one in absence of any type of structure. The dimensionless scour depth Z_m in absence of defence structures can be foreseen, as reported in [4], with (1) in which $f_1(F_d) = F_d$, $f_2(\alpha) = -[0.38 \cdot \sin(\alpha+22.5°)]$, $f_3(\beta) = (1 + \beta)^{-m}$, $f_4(T_w) = [0.12 \cdot \ln(1/T_w) + C_r]/0.30$, $f_5(\sigma) = -[0.33 + 0.57\sigma]$ and $f_6(F_u) = 1 + F_u^{0.50}$, with C_r=0.45 for ridge presence, and C_r=0.52 when the ridge is artificially removed and m = 0.75 for the unsubmerged and m = 0.50 for the submerged jet configuration.

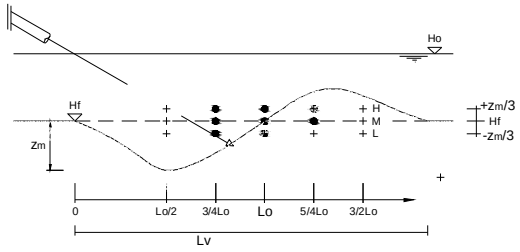

Figure 9. Systematically tested control positions in presence of an upstream channel discharge Qu.

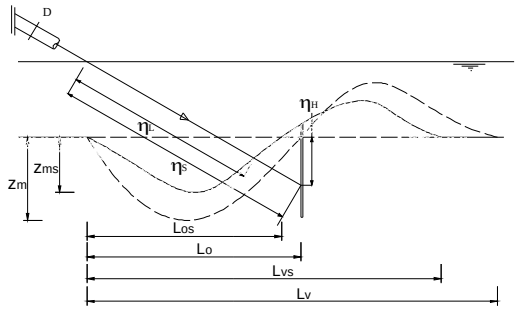

Figure 10. Schematic definition of the geometrical parameters.

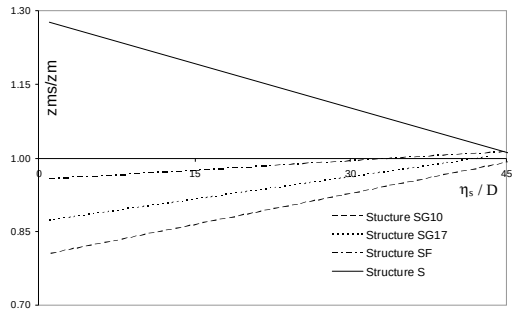

Figure 11. Comparison of the efficiency of different structures at $+z_m/3$.

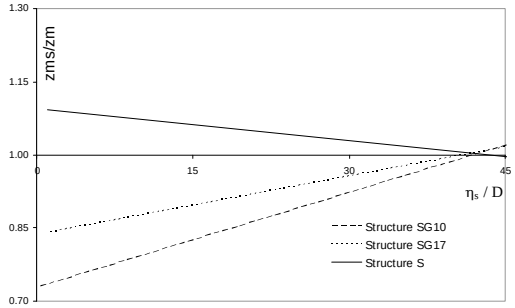

Figure 12. Comparison of the efficiency of different structure at $0z_m$.

SG10 type structure results to be the most efficient one in reducing scour depth whereas the presence of the impervious structure *S* causes an increase of the scour depth (z_{ms}/z_m>1). As mentioned above, the scour reduction efficiency of the structure is generally proportional to its percentage of vacuum, but, as can be seen in the previous figures, *SG10* results to be more efficient than *SG17*. In fact, as basin material d_{90} is 11.63 mm, *SG17* allows the passage of many particles and this occurrence reduces structure efficiency.

Let us examine both the qualitative jet hydraulic behaviour and the scour mechanism that occurs in presence of the two "extreme protection structures", *S* type and *SG10* type, respectively, whose upper upstream edge is located at $+z_m/3$. For each control position, one sketch which illustrates the phenomenon is proposed. During its path, the jet diameter increases and when it impacts the structure jet enlargement takes the shape of an "umbrella". Scour profile remains two dimensional but jet behaviour is three dimensional. Generally, as the most relevant differences of the scour mechanism and jet behaviour are due to the variation of the structure longitudinal position, rather than the vertical one, the following sketches can be considered well representative of the qualitative phenomenon behaviour which occurs also if the upper upstream edge of structure is located both at $-z_m/3$ and $0z_m$. The only case in which there is a great difference in jet flow behaviour is when the structure is located at $L_0/2$. Especially for the *S* type structure, the vertical position influences the dynamic behaviour of the phenomenon. As shown in Fig. 13, because of the partial direct impact on the structure, the jet is divided into two parts generating two different vortexes, one upstream the structure and the other one downstream. This particular flow behaviour, which is most evident in this structure configuration, is due to the imperviousness of the *S* type structure. In fact, if a *SG10* type structure is located in the same spatial configuration, there is no partial reflection of the water flow on the upstream part of structure. The permeability of the structure allows water to pass through its holes and thereby no vortex is formed on the upstream side of this structure, as shown in Fig. 14.

As mentioned above, if, in the same longitudinal position $L_0/2$, the upper upstream edge of the *S* type structure is located at $+z_m/3$, the scour profile completely changes. The jet totally and directly impacts the structure being reflected. Both vortex and scour hole are present only upstream of the structure and the jet energy dissipation causes a deep scour and the formation of two different ridges, as shown in Fig. 15. Fig. 16 shows the scour profile that occurs when a *SG10* type structure is

located at $L_0/2$ and $+z_m/3$. There is no ridge formation upstream of the structure and the scour profile is less deep then in the previous case.

This longitudinal position causes a great dissipation of energy on the structure. In practical applications it is not convenient to put a protection structure at $L_0/2$ because of the great jet impact strength that has to be opposed to dynamic forces. For this reason, this longitudinal position was not systematically investigated in the present study.

If a *S* type structure is located at $3/4L_0$ and $+z_m/3$, the jet behavior is quite similar to case in which the same structure is located at $L_0/2$ and $+z_m/3$. There is a formation of a scour hole upstream but the basin material is deposited only downstream of the structure forming a ridge, as shown in Fig. 17. This structure configuration causes the maximum observed scour depth.

The settlement of a *SG10* type structure at $3/4L_0$ and $+z_m/3$ gave interesting results. In fact, in this structure configuration there is the minimization of the scour depth. Moreover, scour volume results to be the minimum and the quantity of the material put in rotation is maximum. Fig. 18 shows scour profile and jet behavior in this configuration.

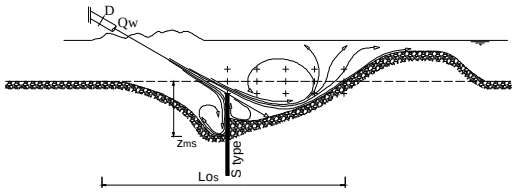

Figure 13. Qualitative scour and flow behavior in presence of a S type structure at $L_0/2$ and $-z_m/3$.

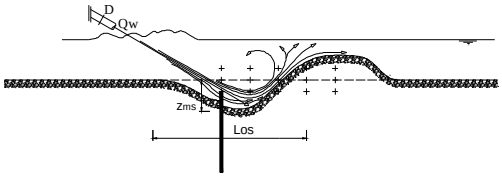

Figure 14. Qualitative scour and flow behavior in presence of a SG10 type structure at $L_0/2$ and $-z_m/3$.

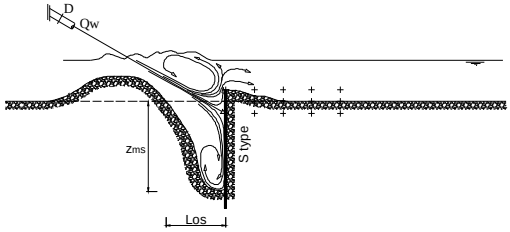

Figure 15. Qualitative scour and flow behavior in presence of a S type structure at $L_0/2$ and $+z_m/3$.

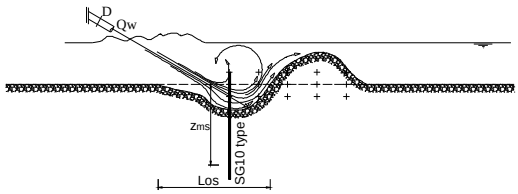

Figure 16. Qualitative scour and flow behavior in presence of a SG10 type structure at $L_0/2$ and $+z_m/3$.

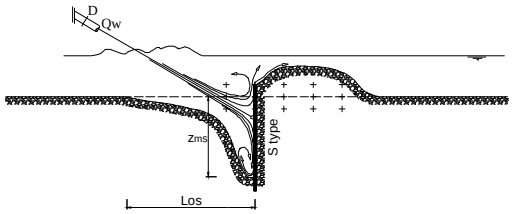

Figure 17. Qualitative scour and flow behavior in presence of a S type structure at $3/4L_0$ and $+z_m/3$.

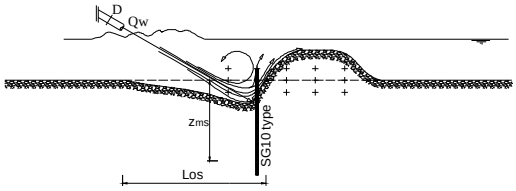

Figure 18. Qualitative scour and flow behavior in presence of a SG10 type structure at $3/4L_0$ and $+z_m/3$.

If a *S* type structure is located at L_0 and $+z_m/3$, the maximum scour volume occurs because the jet, before reaching the structure has enough energy to put in motion a great quantity of basin material. Fig. 19 shows the scour profile that occurs in this case.

As shown in Fig. 20, the same thing happens if a *SG10* structure is located in the same spatial configuration. Moreover, through the structure holes, a certain quantity of jet air content is able to pass, reducing its erosive energy. For this reason, the basin material at the structure toe becomes more stable and the material volume put in motion by the jet flow is less than in the previous case.

When a *S* or *SG10* type structure is located at $5/4L_0$ and $+z_m/3$, the scour profile is quite similar and depends on tailwater T_w. In fact, for low tailwater values (T_w=1), both the structures support the ridge downstream and the solid transport does not easily pass over the structure. This occurrence obliges the basin material to remain in scour hole reducing the scour depth. Fig. 21 shows the scour profile that occurs in presence of a *S* type structure when T_w=1.

When both *S* and *SG10* type structures are located in the same previous spatial configuration ($5/4L_0$ and $+z_m/3$), if the tailwater increases (T_w>1), the jet does not impact directly the structure which is submerged by the basin material. The structure permeability does not influence the scour mechanism and scour profile tends to be similar to that one that occurs without any protection structure. Fig. 22 and Fig. 23 show the scour profiles that occur in presence of a *S* and *SG10* type structure, respectively.

When a *S* or *SG10* type structure is located at $3/2L_0$ and $+z_m/3$, the structure is practically not influential on scour mechanism and the scour profile is almost the same of the reference test, as shown in Fig. 24.

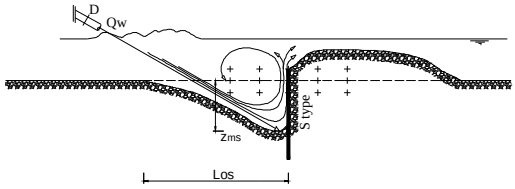

Figure 19. Qualitative scour and flow behavior in presence of a S type structure at L_0 and $+z_m/3$.

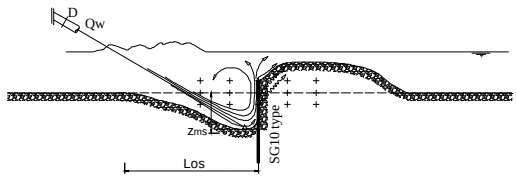

Figure 20. Qualitative scour and flow behavior in presence of a SG10 type structure at L_0 and $+z_m/3$.

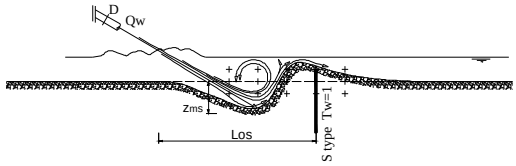

Figure 21. Qualitative scour and flow behavior in presence of a S type structure at $5/4L_0$ and $+z_m/3$ when T_w=1.

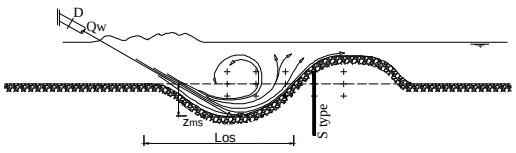

Figure 22. Qualitative scour and flow behavior in presence of a S type structure at $5/4L_0$ and $+z_m/3$ when T_w>1.

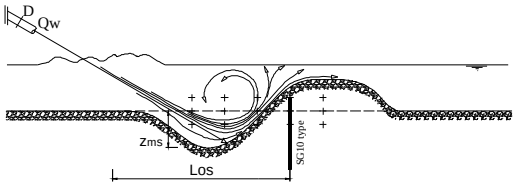

Figure 23. Qualitative scour and flow behavior in presence of a SG10 type structure at $5/4L_0$ and $+z_m/3$ when T_w>1.

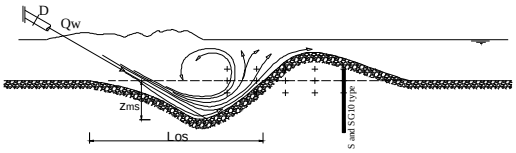

Figure 24. Qualitative scour and flow behavior in presence of both S and SG10 type structure at $3/2L_0$ and $+z_m/3$.

The previous qualitative description of different scour profiles that occur for different structure positions shows that the scour mechanism, in presence of a protection structure, is mostly influenced by the longitudinal position and permeability (percentage of vacuum) of the structure. Four different scour mechanisms and profiles can be individuated.

The scour typology called "Type 0" occurs when the presence of the structure is negligible and the scour mechanism is the same of the reference test. This scour typology typically occurs when the longitudinal position of the structure is too far from the scour hole.

The scour typology called "Type A" occurs when the jet, after hitting the structure, goes down its toe. This typology typically occurs when the structure is located near the jet outflow and the scour depth upstream of the structure becomes maximum. This phenomenon is most evident in presence of impervious structures (S type).

The scour typologies called "Type B_1" and "Type B_2" occur when the jet does not have enough energy to reach the structure toe. The difference between these two typologies is that in the former case (Type B_1) the jet directly impacts the structure whereas in the latter (Type B_2) the jet cannot impact on the structure directly due to the formation of a ridge which covers the structure.

Fig. 25 shows the scour typology classification, where *Ps(x)* is the dimensionless longitudinal position of the structure and *I* is its percentage of vacuum (permeability). No indications about vertical structure position are given in this classification. It does not mean that the vertical position of the structure does not have an influence on scour depth, but it means that the qualitative scour typology depends on the longitudinal position of the structure. The same considerations can be made for variable T_w. Figg. 26-29 show the different scour typologies that where observed in the present study.

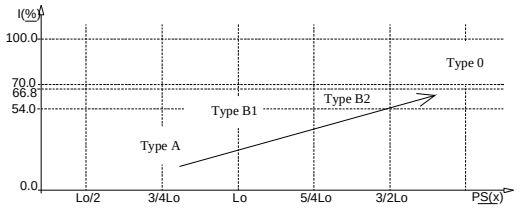

Figure 25. Scour typology classification.

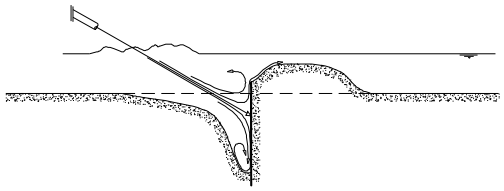

Figure 26. "Type A" typology.

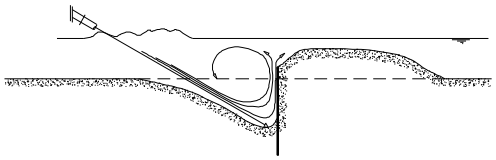

Figure 27. Type B_1" typology.

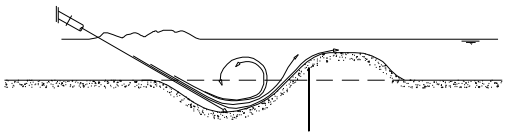

Figure 28. Type B_2" typology.

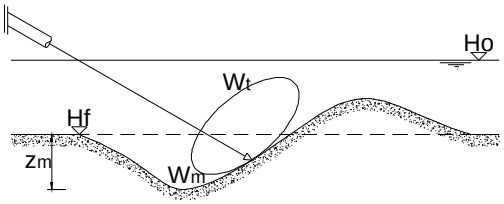

Figure 29. "Type 0" typology.

IV. CONCLUSIONS

This experimental study investigated the effects of the presence of different types of structures in order to mitigate the jet scour geometry. The parameters that were varied in order to understand their influence on the phenomenon are: jet discharge, jet diameter, tailwater T_w and selected vertical and horizontal positions of the structure. The different percentage of vacuum (permeability) of the employed structures has a significant effect on the scour mechanism. Tests in which a *S* type structure was employed show that the presence of this structure typology generally causes an increase of the scour depth compared to the reference test which is carried out in the same hydraulic conditions, whereas in presence of a *SG10* type structure the scour depth is generally less. The effect of the tailwater is to reduce the jet impact energy on stilling basin. It means that an increase of the tailwater causes a reduction of the scour depth and transported bed material volume. In presence of an upstream channel discharge, with all the other parameters constant, the scour depth increases because of the removal of a certain quantity of bed material from scour hole and ridge. The maximum reduction of the scour depth and of material volume removed by jet energy was observed in presence of a *SG10* type structure located at $3/4L_0$, whereas, in presence of a *S* type structure located in the same longitudinal position, the maximum scour depth was observed. A scour typology classification, depending on *I* and *Ps(x)* parameters, is proposed and it consents to classify the jet scour typology.

REFERENCES

[1] Canepa, S. and Hager, W.H., 2003, Effect of Air Content on Plunge Pool Scour, *Journal of Hydraulic Engineering* 129(5), 358-365.

[2] Mason, P.J., 2002, Review of Plunge Pool Rock Scour downstream of Srisailam Dam, Rock Scour due falling high-velocity jets, A.J. Schleiss & E. Bollaert eds Balkema: Lisse.

[3] Minor, H.E., Hager, W.H. and Canepa, S., 2002, Does an Aerated Water Jet Reduce Plunge Pool Scour, Rock Scour due falling high-velocity jets, A.J. Schleiss & E. Bollaert eds Balkema: Lisse

[4] Pagliara, S., Hager, W.H. and Minor, H.E., 2006, Hydraulics of Plane Plunge Pool Scour, *Journal of Hydraulic Engineering.*

[5] Pagliara, S., Hager, W.H. and Minor, H.E., 2004, Plunge Pool Scour in Prototype and Laboratory, Conf. Hydraulics of dams and river structures, Teheran: 165-172, Balkema: Leiden.

[6] Rajaratnam, N. and Mazurek, K.A., 2002, Erosion of a Polystyrene Bed by Obliquely Impinging Circular Turbulent Air Jets, *Journal of Hydraulic Research* 40(6), 709-716.

Design and Protection of Artificial Underwater-Sand-Depots in the Elbe Estuary

K. Peters*, P. Ruland*, A. Gaulke* and J. Osterwald**
* IMS Ingenieurgesellschaft mbH, Hamburg, Germany
** Wasser- und Schifffahrtsdirektion Nord, Kiel, Germany

I. INTRODUCTION

The Elbe estuary is a very important waterway for whole Germany and consists of economical, environmental, ecological and habitation spheres. The Elbe connects the important Port of Hamburg with the approx. 100 km long waterway with the North Sea (see map in Figure 1).

The Port of Hamburg belongs to the most important harbours in the world with respect to transshipment capacities and infrastructure. Especially the growing container traffic is the reason for the further increasing transshipment rates of the Port of Hamburg. Nearly 12.000 seagoing ships and 12.000 inland vessels reach and pass the Port of Hamburg every year. In the year 2005 for the first time more than 8 Million TEU [4] were transshipped at several container terminals in Hamburg. In the northern Europe Hamburg competes at the second position after Rotterdam.

So far the navigational depth of the Elbe is a limiting factor for ship traffic, especially for large container vessels. The navigational depth of the Elbe allows ships with a maximum draught of 12.5 m to reach the Port of Hamburg independent from tidal conditions. Ships with a larger draught than 12.5 m have to consider the tidal conditions [4].

With respect to the raising container transshipment especially with ports in Asia and China and the design of the next generation of container ships a deepening of the 100 km long access channel of the Elbe between the North Sea and the Port of Hamburg is intended by German federal authorities. This measure has the aim to guaranty best economical and therefor navigational conditions for future developments of the Port of Hamburg, which is competing with other European and international ports. For further information it is referred to [4].

This aim can only be gained with a detailed planning concept, where all economical and environmental aspects have to be considered. As part of this planning process a detailed hydraulic and dredging concept concerning the hydraulic conditions along the river Elbe and management of dredged materials was elaborated by the responsible project group commissioned by the responsible German Ministry (Bundesministerium für Verkehr, Bau und Stadtentwicklung, BMVBS) and the federal state Hamburg.

One aim of this concept is the deposition of dredged sand material at several locations along the river Elbe below still water level in so called underwater-sand-depots, which have a certain hydraulic function within the estuary. This concept was already applied within the last dredging measure in the last. So these underwater-depots enable on the one hand the controlled deposition of dredged material and on the other hand a softening of the daily incoming tidal energy. Figure 1 gives an overview of the proposed locations of the underwater-depots for the coming deepening measure.

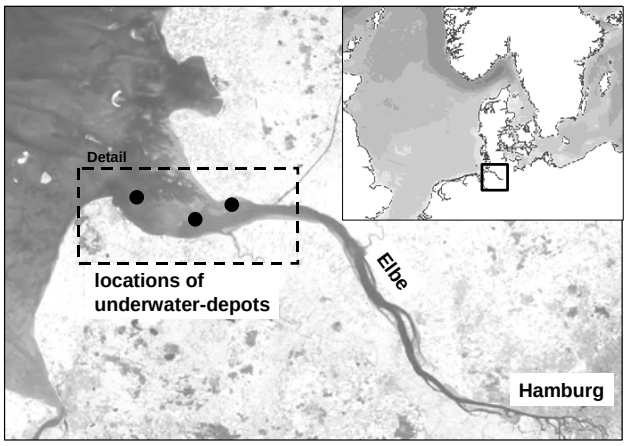

Figure 1: Map of northern Germany with the Elbe estuary and proposed locations of underwater-depots

With the placement of these underwater-depots in the western entrance of the Elbe estuary it is further intended to compensate negative consequences according to a deepening or dredging measure in the Elbe river, like reduction of the lowering of low water levels and heightening of high water levels (increase in tidal range).

This paper presents different construction methods for underwater-depots and gives explanations on their design dependent on spatial circumstances and hydraulic conditions. Finally recommendations for the construction of underwater-depots are given.

II. PAST AND PRESENT DEEPENING MEASURES IN THE ELBE ESTUARY

A. *Deepening measures of the Elbe estuary in the past and hydraulic consequences*

In the past the river Elbe has been deepened several times. 200 years ago Hamburg had to conduct dredging measures for increasing drafts of ships and against ongoing sedimentation in the Port of Hamburg. Since 1834 the dredging work was done by steam dredgers. Until 1897 ships with a draught of 4.3 m (7.9 m at high water) could reach Hamburg, but sedimentation was still going on. Therefor a further deepening of the Elbe of 10 m below low water level was conducted, accompanied by additional construction measures (like groins) along the river. The historical development of the deepening measures is described by Keil (1985). The latest deepening measures of the Elbe are summarized in Table 1.

TABLE 1: LATEST DEEPENING MEASURES OF THE ELBE BETWEEN HAMBURG AND THE NORTH SEA

depth below chart zero (LAT)	period of dredging works
11.0	1956 – 1961
12.0	1964 – 1969
13.5	1974 – 1978
14.5	1997 - 2000

With each dredging and deepening measure of the Elbe estuary in the past the hydraulic conditions, namely water levels and tidal range, were changed apart from natural influences and changes. The deepening measure reduces the hydraulic roughness of the estuary which leads to a reduction of tidal energy dissipation and an amplification of the tidal amplitude in the estuary. This effects generally increased tidal currents in the main river channel after dredging works, while sedimentation increased in flat areas and branches of the Elbe river caused by reduced currents and increased sedimentation. For further explanations concerning deepening measures in estuaries and their hydrodynamic effects it is referred to Flügge (2002).

B. *Aim of the elaborated dredging measure and hydraulic concept*

It is the aim of the elaborated dredging measure for the next dredging campaign to increase the navigational depth downstream of Hamburg for larger vessels and at the same time to reduce the consequences on hydraulic conditions to a minimum with the help of the deposition of dredged material.

The hydraulic concept proposes therefore an increased hydraulic roughness and tidal energy dissipation, which will be gained with the help of underwater-sand-depots in the western end of the Elbe estuary, and a resultant reduction of the hydraulic changes in water levels and currents along the access channel. A potential variant of underwater-depots is illustrated in Figure 2.

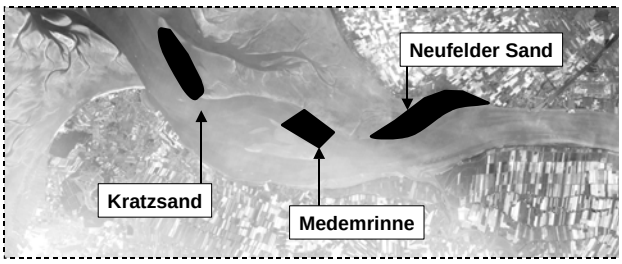

Figure 2: Location of three planned underwater-sand-depots in the Elbe estuary as detail to Figure 1

In the estuary mouth the navigational channel shifts to the southern coastline. The underwater-depots, placed closely to the access channel, reduce the cross section significantly in the entrance to the estuary, which leads to an increase of shear stresses and a loss of incoming tidal energy in upstream direction. This energy reduction results in a reduction of proposed water level changes in case of the deepened Elbe river. This effect is mostly expected with the depot *Kratzsand*.

Additionally the currents are concentrated in the deeper river channel parts. The depot *Medemrinne* will guide the flow along the navigational channel and not go apart through the *Medemrinne*, which results in increased currents in this area in the navigational channel.

The hydraulic function of the depot *Neufelder Sand* is also the guidance of the tidal flow and concentration of the currents in the main river parts in order to avoid the deflection of the tidal currents towards the tidal flats *Neufelder Sand* and *Neufelder Watt*.

III. CONSTRUCTION OF UNDERWATER-SAND-DEPOTS

A. *General*

With regard to the construction of the underwater-sand-depots it has to be investigated how mobile this depot has to be and is allowed to be because of its hydraulic function and durability in a morphodynamic active environment. Considering the impacting currents and waves in the Elbe estuary it is evident that an underwater-depot consisting of dredged material has to be built and protected in a certain way that its function is guarantied for a certain life time. More information on the hydraulic design conditions are given in chapter IV. In the following different construction methods are presented and discussed based on [5].

B. *Construction methods for underwater-sand-depots*

Underwater-depots generally change the cross section geometry of the river and influence the flow. The resulting influence on the hydraulic conditions can be minimized if the depot is adopted, smoothened and integrated into the given topography. The following construction types of underwater-depots are summarized and illustrated in Figure 3:

- natural slopes with protection layer (riprap),
- bordering dams and backfilling with protection layer and
- bordering dams with new front slope and backfilling with protection layer

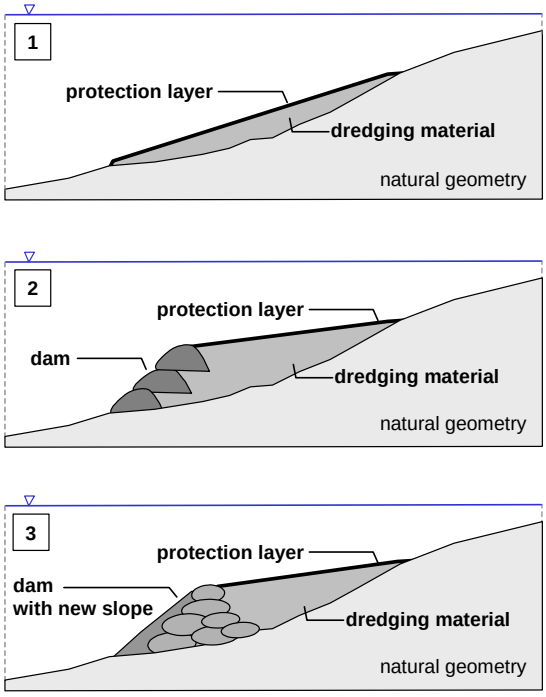

Figure 3: Construction types for underwater-depots (schematized)

If possible the dredged material can be deposited within the underwater profile (adopted to the natural geometry) without changing the cross section significantly (case 1 in Figure 3). Normally the possible volume of the material deposition is very limited. In comparison to the surface, which has to be protected dependent on the hydraulic impact, the deposition volume is quite small, which results in higher deposition costs.

In the second case (case 2 in Figure 3) bordering dams, i.e. made of stones, can be built and used during the dredging and deposition works in such a way that the backfilling material will not be transported out of the working field, which is common practice for dredging works. The material of the bordering dam varies between stones and geotextile tubes or any other stable construction element. The bordering dams have the function to define a certain stable underwater dam, which surrounds the deposition area and reduces the mobilization and transport of the deposited dredging material. The bordering dam can be constructed with a quite steep slope that the backfilling volume will be larger than in case 1 of Figure 3.

Parallel to the ongoing construction works the bordering dam is increased in height. If necessary a protection layer is finally constructed, which covers and protects the deposition area. This protection layer has the task to resist against the hydraulic impact and guaranty for the shape and geometry as well as for the hydraulic function of the underwater-depot. In case of reduced hydraulic impact or coarser grain sizes of the dredged and deposited material the protection layer can be neglected.

As a third case the bordering dam with additional front slope and backfilling with protection layer is illustrated in Figure 3. In comparison to case 2 an additional front slope covers the bordering dam. This could be necessary for geotechnical or hydraulic reason.

The volume of the dredged material, the given topography at the location as well as the hydraulic conditions have influence on the proposed geometry of the underwater-depot. If a certain hydraulic function is intended with the underwater-depot each component of the construction has to be designed for the boundary conditions.

C. Construction of the bordering dam

The bordering dam can be built with different materials and methods as summarized and illustrated in Figure 4:

- quarrystones
- gabions
- geotextile containers with filling
- geotexile tubes with sand filling
- sheet piling

Figure 4: Construction types for the bordering dam

The most common method to build a bordering dam is the use of quarrystone, because of the flexibility, the easy handling and the construction costs. Gabions are possible to use but not the common case.

In case of the use of geotextile container more effort is necessary to fill, transport and displace the container at the

location. For geotextile tubes detailed experience for the filling is important.

Sheet piling is cost intensive and only economically effective if there is not enough space to build a dam or a slope.

All construction types have to be compared with regard to the suggested building, also in combination with the construction types for the protection layer in order to find the best solution. For further information it is referred to [11] and [12].

D. Construction of the protection layer

The necessity of a protection layer is a function of the hydraulic impact and the definition on the acceptable mobility of the depot material.

The protection layer has to be designed considering filter stability (geotechnical design) and erosion by hydraulic impact (hydraulic design). In general the protection layer can consist of different layers (see Figure 5) with corresponding functions as

- filter layer,
- armour layer or
- combined construction types.

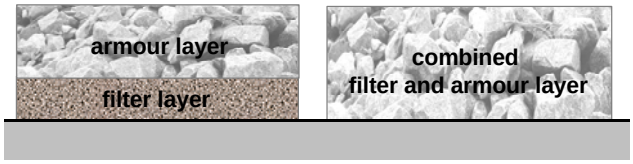

Figure 5: Construction types of the protection layer

Possible materials are stone materials with certain grading, weight and stone sizes or geotextile layers, also in combination with concrete blocks. In the following the above mentioned construction types are shortly discussed.

1) Filter layer

Filter layers consist of different natural or artificial stone mixtures with different grading. The corresponding sieving curve has to be designed for the soil material (lower border) and armour stones (upper border). The filter layer can also consist of a geotextile mattress, like illustrated in Figure 6.

Figure 6: Geotexile layer before controlled sinking process

2) Armour layer

The armour layer has the task to resist against the hydraulic impact like tidal and wave-induced shear stresses and has to be designed for this. In most cases armour stones are used for the armour layer. In cases with extreme hydraulic conditions it can be necessary to interlock the stones with underwater concrete.

Figure 7: Armour stones

3) Combined construction types

Combined construction types fulfill two requirements according to the filter and armour layer, which means filter stability against the soil and hydraulic stability against the impacting current and wave forces. Construction types can be

- single layer stone mixtures,
- geotextile mattress with sand or concrete filling,
- geotextile mattress with concrete blocks or
- material mattress made of tires

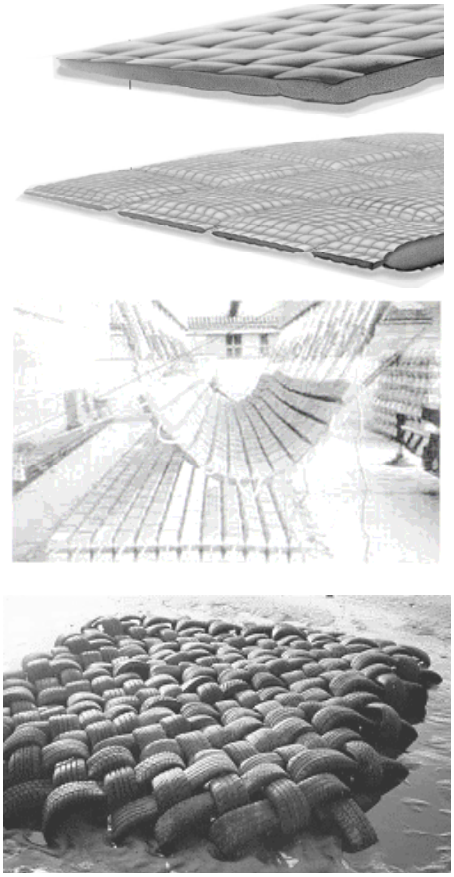

Figure 8: Combined construction types: mattress with sand/concrete filling (top), mattress with concrete blocks (middle) and mattress of tires (below)

The most used combined construction type is the single layer stone mixtures because of its flexibility, easy construction and small construction costs. For certain applications also other construction types are used as illustrated in the Figure 8.

E. Recommendations for construction of bordering dam and protection layer

For the decision of the perfect method for construction of the bordering dams and protection layer many project specific boundary conditions have to be investigated and evaluated for the project.

The decisive points are the stability of the construction under the hydraulic conditions, the flexibility in case of necessary modifications on the repositories and the economy of the chosen construction. The construction time is an important fact as well as ecological aspects and the necessary effort for maintenance of the construction.

In the specific project the criteria were weighted separately for all underwater depots (see Figure 2).

IV. DESIGN OF UNDERWATER-DEPOTS IN THE ELBE ESTUARY

A. Design requirements

The underwater-depots are placed in the complex area of the Elbe estuary, which underlies continues morpho-dynamic processes and resulting changes of the morphology. This depot area is open for incoming tidal movement as well as for wind and ship waves, which means that also the underwater-depots have to be designed for these hydraulic conditions.

Caused by the proposed depot geometry and position in the dynamic estuary different hydraulic impacts scenarios have to be considered for the protection design as well as requirements for the long-term stability of the depot. Therefore a detailed analysis of the hydraulic impact and the abbreviated design conditions was carried out.

As a geometrical boundary condition the top of the depot *Kratzsand* is particularly below the mean low water level in order to achieve the intended hydraulic behaviour and function.

B. Hydraulic boundary conditions

With regard to the design of the necessary protection layer of the underwater-depots numerical simulations of the wave and current conditions have been conducted by the Federal Waterways Engineering and Research Institute (BAW). The hydraulic design conditions were further extracted and defined for the design of the protection layer.

Especially the underwater-depots *Kratzsand* and *Medemrinne* located in the river mouth will be stressed by fairly high wind and ship induced waves as well as tidal currents. The depot *Medemrinne* with a schematic cross section is exemplary illustrated in Figure 9.

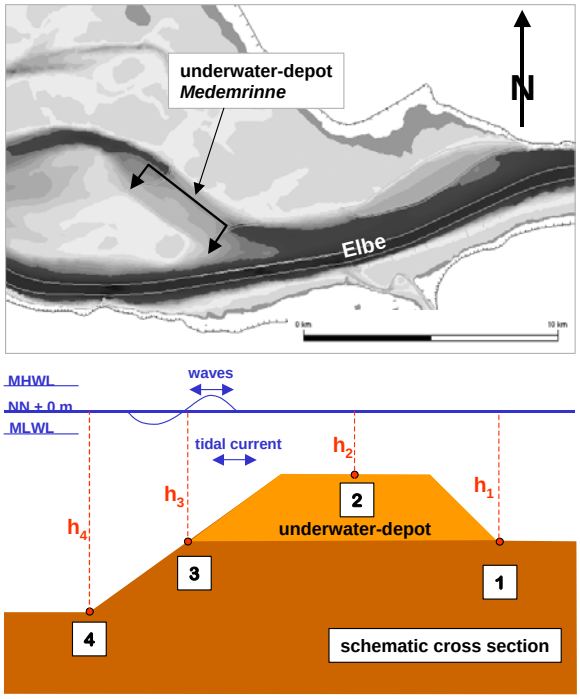

Figure 9: Underwater-depot *Medemrinne with* schematic illustration of the cross section

Investigations showed that the most relevant scenarios are low water levels in combination with relatively high waves, which resulted in highest shear stresses at the slope and the top surface of the depot. With increasing water level the resultant bed shear stresses reduce significantly compared to the shear stress increase by to increased wave parameters. Therefor the following range of design conditions have been considered for the depot *Kratzsand* and *Medemrinne* in the design scenarios :

- minimum water depth below LAT: 1.0 m – 2.0 m
- maximum tidal currents:1.6 m/s – 3.0 m/s
- max. wind waves H_s/T_m for LAT: 1.15 m / 3.7 s
- max. ship waves H_s/T_m for LAT: 1.0 m / 4.0 s
- underwater-depot slopes: 1:3 – 1:10

C. Hydraulic design

In general these underwater-depots influence the tidal dynamic of the Elbe estuary. According to the hydraulic impact mainly by waves and tidal currents an adequate protection of the underwater-depots is necessary in order to guaranty the essential local stability of the depot in the dynamic estuary and maintain the intended and corresponding hydraulic function. The most relevant design scenarios are low water levels in combination with relatively high waves.

1) Approches for protection layer design

For the design of the depot protection different engineering solutions were investigated. With regard to the preferred solution as grain filter or riprap with larger stones, if necessary, a comparison of different existing formulas and approaches for stone size design has been conducted and led to a wide bandwidth of protective measures. An overview of existing calculation methods is given in [7], [8], [9], [10], [11] and [12]. The calculated stone diameters varied with a factor of 10 to 15.

The major input for the practical use of such formulas is the correct and adequate description of the current profile and the turbulence (see Figure 10), which has a significant influence on the design of necessary stone sizes and finally the construction costs. Additionally the acceptable mobility of the stone has to be defined.

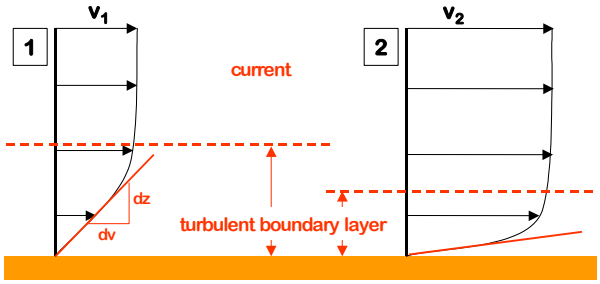

Figure 10: Current profiles with low turbulence (1) and high turbulence (2)

It has to be differentiated between current profiles with low turbulence intensity in the boundary layer and current profiles with high turbulence, which can mobilize grains or stones which would be stable under conditions with low turbulence intensity.

In case of tidal currents and undisturbed flow a current profile with low turbulence intensity is expected, which means that grains or stones at the bed have to resist a quasi constant hydraulic impact. In this case the calculation method of Shields or Hjulström (in Zanke, 1982) can be applied to calculate the necessary stone diameter against erosion.

In case of a current profile with higher turbulence intensity in the boundary layer, calculation methods of Isbash or Pilarczyk have to be applied.

2) Application of the Shields concept

While composing all information and calculation results the Shields concept was applied for the design of the scour protection of the underwater-depots in the Elbe estuary under the given hydraulic conditions considering different slopes and current impacts as well as wave induced shear stresses. For detailed description of the scientific background it is referred to Soulsby (1997), Pilarczyk (1998) or CIRIA/CUR (1991).

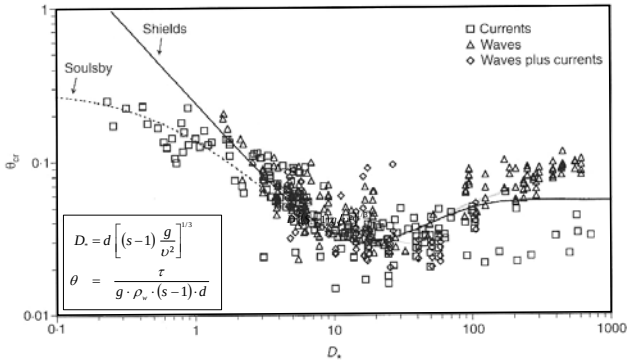

Figure 11: Critical Shields parameter as a function of the dimensionless grain size (after Soulsby, 1997)

The Shields diagram defines the critical Shields parameters for grains or stones larger than D* = 150 (equivalent to grain diameter of 7,5 mm) with a constant value of 0.055 (Soulsby, 1977) or 0.060 (Pilarczyk, 1998). For larger stones no detailed information is available to define the critical Shields parameter. It can be assumed that the critical Shields parameter increases with increasing stone diameter and angle of repose, but more research has to be done in order to gain engineering and calculation approaches.

3) Results

As a result necessary stone sizes were calculated for all underwater-depots dependent on the given boundary conditions. The protection layer was designed as single grain filter layer with the mentioned advantage that a self-armouring effect establishes which means smaller stones are carried away and larger stones of the mixture protect the dredged material. Exemplary a possible protection strategy for the underwater-depot *Medemrinne* is illustrated in Figure 12.

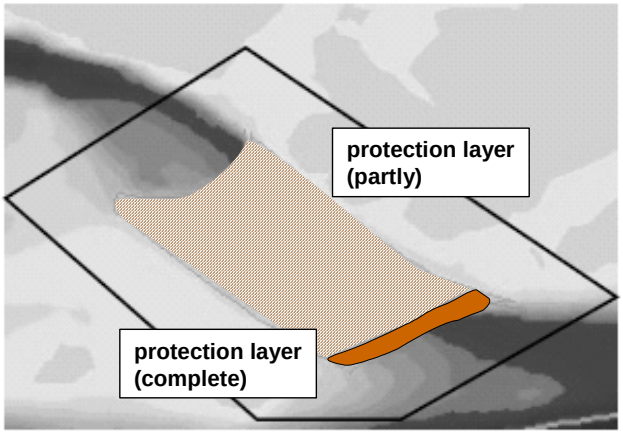

Figure 12: Possible protection strategy for the underwater-depot *Medemrinne*

V. RECOMMENDATIONS

For choosing the best fitting construction method for bordering dams and protection layers the hydraulic conditions have to be examined very detailed for the specific locations.

With the knowledge of the hydraulic conditions the correct design concept has to be chosen in order to find a design which is on the one hand stable for the hydraulic conditions and on the other hand as cost effective as possible.

The applied hydraulic design concept has to be verified with the expected, measured or calculated hydraulic conditions. The characterization and correct description of the flow including the turbulence intensity has to be done intensively with respect to the deposition and protection costs of the dredged material. With regard to all boundary conditions the acceptable freedom of movement of the protection layer or unprotected deposition areas has to be investigated and finally defined. Small changes in the design results have great influences on the construction costs.

With all this boundary conditions a detailed engineering and design for the repositories has to be made in order to optimize the construction.

ACKNOWLEDGMENT

Investigations on feasibility, construction and protection of underwater-depots in the Elbe estuary [5] have been conducted on behalf of the Wasser- und Schifffahrtsamt Hamburg.

REFERENCES

[1] Keil G.W. (1985) Die schrittweise Anpassung der Elbe an die Entwicklung des Seeschiffsverkehrs. Jahrbuch der Hafenbautechnischen Gesellschaft, Band 40

[2] Flügge, G. (2002) Ausbauvorhaben in Tideästuaren – Erläuterung der wirksamen hydromechanischen Prozesse. Jahrbuch der Hafenbautechnischen Gesellschaft, Band 53

[3] Soulsby, R. (1997) Dynamics of Marine Sands. Thomas Telford

[4] Projektbüro Fahrrinnenanpassung, Wasser- und Schifffahrtsamt Hamburg, www.zukunftelbe.de

[5] IMS Ingenieurgesellschaft mbH (2006) Feasibility study on underwater-depots (unpublished). On behalf of the Wasser- und Schifffahrtsamt Hamburg

[6] CIRIA/CUR (1991) Manual on the use of rock in coastal and shoreline engineering, CIRIA special publication No. 83, CUR report No. 154, Balkema

[7] Bundesanstalt für Wasserbau (2004) Grundlagen zur Bemessung von Böschungs- und Sohlensicherungen an Binnenwasserstraßen. Federal Waterways Engineering and Research Institute, Mitteilungsblatt Nr. 87

[8] Zanke (1982) Grundlagen der Sedimentbewegung. Springer Verlag

[9] DVWK (1997) Maßnahmen zur naturnahen Gewässerstabilisierung. DVWK-Schriften, Heft 118

[10] Hansen (1987) Wasserbausteine im Deckwerksbau. Westholsteinische Verlagsgesellschaft Boysen & Co.

[11] Pilarczyk, K.W. (1998) Dikes and revetments – design, maintenance and safety assessment. Balkema

[12] Przedwojski, B and Pilarczyk, K.W. (1998) River training techniques – fundamentals, design and application. Balkema

.

Studies to Determine Dimensions for River Training Works in the Hanoi Segment of the Red River

PHAM DINH
Vietnam Institute for Water Resources Research (VIWRR), Hanoi, Vietnam

Based on the natural laws and adverse impacts of the human activities on the Red River, this Paper will present applied studies as a basis for determining dimensions of river training works in the Hanoi segment of the Red River.

I. INTRODUCTION

The Red River plays an important role in the multi-faceted sustainable development of the Red River Delta in general, and the capital city of Hanoi in particular. The Red River's segment running through Hanoi has the length of about 40 km and is a factor causing direct effects on every economic, social and environmental activities of the city. This factor is becoming more crucial in the context that the Red Rivermailto:cora.hoogeveen@cur.nl will soon run through the center of the city, as a result of the city development planning until 2020.

The Red River is considered the cradle of the Vietnam nation. It brings up the Vietnam people and helps to enlarge the territory. It also created the ancient capital city of the country, Thang Long (or "ascending dragon" citadel), which has become Hanoi nowadays. But, on the other hand, it is a source of many unexpected and unwanted disasters, the most dangerous of which possibly is flooding. The flood water level in the Red River may reach up to 14 m while the landside elevation is only 6.5 m. Therefore, the whole city of Hanoi will be under deep water if the dyke is broken. Another kind of disasters that may happen in the Red River is landslide. Due to the instability of the flow, the floodplain of the Red River is usually eroded, causing frequent landslide and endangering the safety of local people and structures. Sedimentation and erosion also cause a lot of obstructions to water supply and drainage as well as navigation. Thus, to have the Red River running at the center of the city, we must ensure that its morphology is stable and any changes of the flow are kept under control (see Fig. 1).

The Red River segment in Hanoi has very complicated features as if there are so many channels and effluent. Such the complicatedness is exacerbated by the human unplanned and strong impact on the river, making the river under coercive rater than natural, factor. However, in spite of these complicated developments of the Red River, it still keeps its original spatial position; its width and water depth are still within certain limits and even sedimentation and erosion follow some certain cycle and a cause - and - effect relation. This is the issue that needs to be studied further for determining dimensions for the river training works. Within the frameworks of this Paper, the author will only focus on one of the basic aspect of river dynamics, which is, in particular, the law of applied morphology. This law itself is determined by other component laws, namely the law of flow, the law of sediment transport in natural conditions and in the "with river training works" conditions.

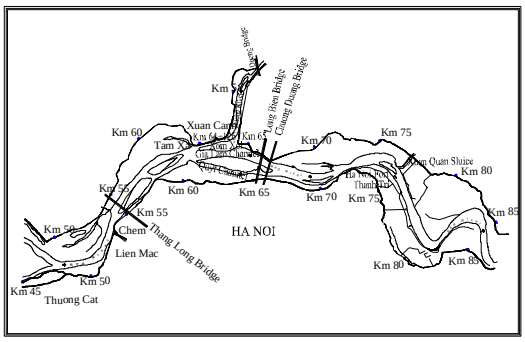

Figure 1. The Hanoi Segment of the Red River

II. GENERAL STUDIES AND REQUIREMENT ON RIVER TRAINING WORKS IN THE HANOI SEGMENT OF THE RED RIVER

A. *Requirements*

The Red River channel must ensure safe flood discharge through Hanoi city at the designed dyke water level of 13.40 m in Hanoi, according to the national elevation system.

As a matter of fact, the Red River has an effluent on its left, which is Duong River. The Duong River dike is rather weak, therefore the river training solution must maintain the current regime of flow distribution between the Red River and Duong River in the flood season so as no additional water goes into the Duong River.

In addition, it is necessary to maintain stable conditions for navigation, avoid sedimentation at Hanoi Port and other new port and berths already specified in the city master plan.

Good planning of the flood plain is also required for proper use of land on the flood plain, for development of the city and "beatification" of the riverside landscape.

B. *General Studies*

Sediment Transport Capacity: In Vietnam, the well-known formula of Truong Thuy Can is usually used for this purpose. Other authors, namely Vi Van Vy, Hoang Huu Van, Luong Phuong Hau, etc., have defined

coefficients and powers for this formula when applied for the rivers in the northern delta of Vietnam [5].

Stability and morphological relation: this aspect was analyzed by many authors in their studies in the 1970s-1980s, e.g. the ones carried Nguyen Thoi Giap, Le Ngoc Bich and Luong Phuong Hau. Luong Phuong Hau assuming that the morphology of the river channel would follow the principle of "minimum channel variation", has suggested a formula to determine the morphological relation of the cross section [1], [5].

Channel stabilization: Since the 1980s, the Ministry of Transport has launched a number of projects on channel stabilization and sedimentation prevention at Hanoi Port. In three years 2001-2003, JICA also conducted a study on the Red River Inland Waterway Transport System [2], [3].

Flood discharge Capacity: Since 1971, there have been many projects and research programs studying the issue of flood discharge for the Red River in general, and for its Hanoi segment in particular. However, there has not been yet any answer to the question due to its complexity. This issue is becoming more pressing now as the law on dike management is being drafted.

Achievements and outstanding issues: The dyke system has been safely protected for a long time and so far. The river training works have appeared to be effective for preventing sedimentation at Hanoi Port [2].

Apart from these achievements, however, there are still outstanding issues on this river segment, such as unstable channels, unplanned arrangements of structures, uncontrollable river channel alignment, and unreasonable dimensions of structures.

III. Main Bases in the Studies Methods

A. Hydrological data

Data on daily mean discharge and water level are the real values measured at Son Tay and Hanoi Stations on the Red River and Thuong Cat station on the Duong River during the period 1960-1998. There are also data showing high water level and discharge, reflecting the extreme values of maximum floods. These data on discharge and water level are used to analyze the water level rising. Data on suspended sedimentation, hourly water level and discharge from 1993 to 2001 are also available and data on sedimentation are used to calculate the volume of sediment transport in the Red River.

B. Methodology

This study combines, in a reasonable manner, the method of analyzing the real data series and method of examining the physical model. Subjects of the study are also combined with the national level research project on "Development of river training plan to increase the flood discharge capacity and stabilize the river channel in the critical Hanoi segment of the Red River," conducted by the author himself. For the purpose of the study, 2 models have been developed:

Rigid-bed model, length scale 1/400 and depth scale 1/80: its coverage includes the whole studied area, i.e. the Red River in the Hanoi segment and the Duong River from the Duong River mouth to Duong Bridge. The model has been designed with similar characteristics of the flow, Froude and Reynolds numbers in order to ensure the hydraulic regime in the area of rough and turbulent flow.

Movable-bed model, length scale 1/200 and depth scale 1/100: the function of this model is limited by the requirement of studying the bed transformation in the area of critical works. Therefore the coverage of the model is defined from Chem to Long Bien Bridge, including the Duong River mouth. This model design follows the method of M. De. Vries [9], using light material Keramzit, and ensures similar transport and flow parameters and sediment load.

IV. Analyzing and Determining Dynamic Factor Effecting the Morphology Development in the Red River Through Hanoi

A. Bankfull discharge

Of the hydrological data series from 1990 to 1998, the year 1997 has been chosen as the base year for calculating the bank full discharge corresponding to the water level 9.50 m in Hanoi. The bank full discharge, calculated according to Makkaveep method [6], is 10,750 m^3/s on the Red River segment, upstream of the Duong River mouth, and 7,650 m^3/s on the segment downstream of the Duong River mouth.

B. Changes of flow distribution between effluents

The flow distribution to the Duong River has calculated for different periods of time in comparison with the discharge at Son Tay and on the basis of hydrological data of Son Tay and Hanoi stations on the Red River and Thuong Cat Station on the Duong River from 1960 to 1998. Calculations show that during the period 1961-1969, the flow in the Duong River accounted for about 24.9 % of the discharge of at Son Tay which was 20,000m^3/s. It was 29.5 % during the period 1991-1998.

C. Discharge and stage relation in Hanoi

Analyses of discharge and stage relations show that, at the same water level, the river channel cannot discharge the same discharge as in the past. This situation reflects the decreased discharge capacity of the river channel, which is dangerous for flood control. Particularly in Hanoi, with the same flood discharge as 30 years ago, the water level during the period 1991-1998 was increased by 63 cm.

D. Total sediment transport formulas

Introduction: Total sediment transport formulas of Rottner, Meyer - Peter Muller, Engelund and Hansen, Van Rijn, Ackers and White can put in the form of two parameter relations as follow [7]:

Transport parameter (dimensionless):

$$\psi_t = X = \frac{s_t}{\sqrt{g\Delta D_{50}{}^3}} \quad (1)$$

Flow parameter (dimensionless):

$$\theta = \frac{h.i}{\Delta D_{50}} \quad (2)$$

In which:

s_t: volumetric total transport of bed ($m^3/m/s$)

g: gravitational acceleration (m/s^2)

Δ: relative density $(\rho_s-\rho)/\rho$ (-)

ρ: density of water (kg/m^3).

ρ_s: density of sediment (kg/m^3).

D_{50}: Mean grain size of bed material (m)

h: average water depth (m)

i: average water-surface slope (-).

The total sediment transport (s_t) is a sum of the bed-load transport (s_b) and the suspended-load transport (s_s). In the case that the bed load is unknown, it can be calculated using Meyer-Peter Muller formula. Suspended-load transport can be determined from measured data at hydrographical stations

$$s_t = s_b + s_s \tag{3}$$

In general, the form of Englund - Hansen formula:

$$\psi_t = \alpha \frac{C^2}{g} \theta^{\beta} \tag{4}$$

In which: α is the coefficient and β is the power determined from measured data.

Formula (4) in the actual condition of the Red River: For the Red River (4) can be adapted by adjusting the coefficient (α) and the power (β). Based on the measured data of Son Tay, Thuong Cat and Hanoi Stations in the period 1993-2001, it can be determined the coefficient and power of (4) for transport of solid material:

$$s_t = \alpha \sqrt{g\Delta D_{50}{}^3} \frac{C^2}{g} \left(\frac{hi}{\Delta D_{50}} \right)^{\beta} \tag{5}$$

The results on the total sediment transport (3), then ψ_t and θ are basis to plot the Engelund - Hansen relation for the Red River (see Fig. 2). After that, the coefficient and the power have been determined:

$\alpha = 0.284$ and $\beta = 2.18$

Substituting α and β into (5), the total sediment transport formula for the Red River for solid material can be written:

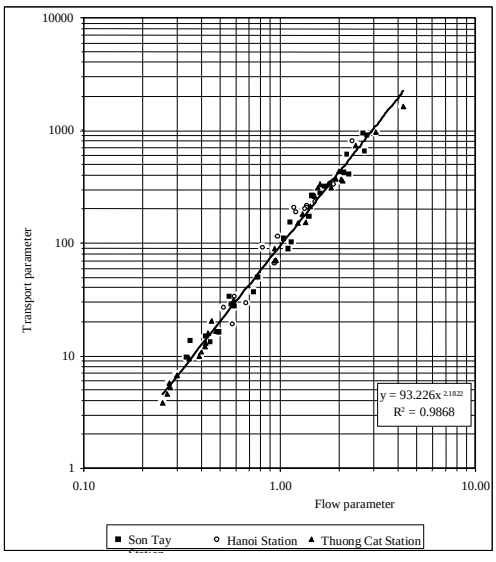

Figure 2. Relationship between Ψ_t and θ for the Red River

$$s_t = 0{,}284 \sqrt{g\Delta D_{50}{}^3} \frac{C^2}{g} \left(\frac{hi}{\Delta D_{50}} \right)^{2{,}18} \tag{6}$$

Formula (6) is basic to determine dimensions for the proper alignment of the river training works for the Red River in general and the Hanoi Segment of the Red River in particular.

V. Evolutions of River Channel and Mechanism to Control the Morphology Development of River Channels of the Studies River Segment

The Red River segment in Hanoi has had a lot of changes. Since the XI century, when this place was selected to be the capital city of the country, nearly one thousand years have been over, and the human being, during that long period time, have a lot of impacts (of different levels) on the Red River, for the sake of their livelihood. As a result, the river has lost many of its movements and developments, which should have followed the natural laws. Nevertheless, studying the historical evolution of this river segment, we still find basic characteristics of the semi-natural laws (i.e. with the presence of coercive factors such as dyke, river training works etc.)

A. Evolutions on plan

Stable factors on the river plan: Though there have been very complicated evolutions, affected by many natural and man-made factors, the studied river segment still maintains quite stable features on its plan, in particular:

- The river - bank configuration in the season of medium water level is hardly changed.

- The river sections determining the river channel alignments are quite stable, such as the sections Lien Mac - Chem, Tam Xa - Xom Xoi and the section from Hanoi Port to Thanh Tri.

- The Duong River mouth: Analyzing the river site plan since 1958, we can see that the position of the Duong river mouth has not been changed at all, as this river mouth is located in the area of good geological conditions, formed of layers of inerodible clay materials.

- There are controlling "bottlenecks" on this river segment, such as Chem, Chuong Duong and Thanh Tri. The River channel with is 960 m at Chem, 880 m at Chuong Duong and 800 m Thanh Tri. With these bottlenecks, transversal changes are limited.

Transversal fluctuations of channels: According to the analyses of river evolutions, we see that the main channel of the section from Chem to the Duong River mouth has very strong fluctuations, from being very close to the left side dyke to being close to the right side dyke and vice - versa, with the fluctuation amplitude of about 3,800 m. These fluctuations endanger the both dykes and make navigation become difficult. Furthermore, these unwanted and uncontrolled movements even go further to the downstream part of the Duong River mouth, causing sedimentation at the Hanoi port and Xuan Quan sluice.

Major river channel alignments: Based on the changes of the main channel from 1986 until now, it can be noted that in general, the Hanoi segment of the Red River has 3 major channel alignments, of which Alignment A as described in Fig. 3 [2], [3] is a favorable curve, desirable for the purposes of irrigation /drainage, navigation and

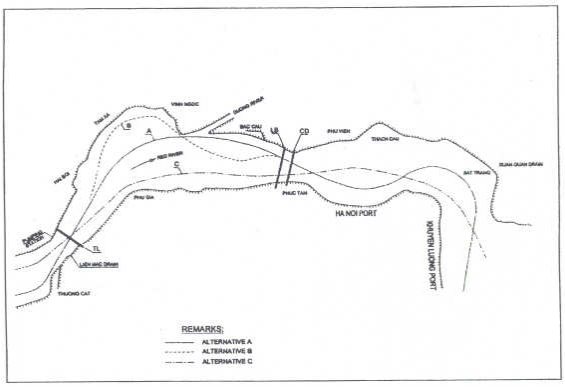

Figure 3. Historical Evolution of Channel Alignment and Alternatives

urban development. The channel alignment A has been noted in the two periods of time, 1959-1964 and more recently 1995-2005.

B. Changes of the flood plain

Comparing the elevation of the river floodplain in 2000 with that in 1976, we see that the Hanoi segment of the Red River has had elevation of the flood plain increased by 0.86 m. This is one of the causes making the flood water level become higher.

C. Relationship between transverse and vertical factors of the channel

On the river longitudinal profile, there usually deep scour holes where the river width is narrowing and abrupt curve is formed [4]. The depth of the scour hole has correlation with the configuration of the river plan, represented by the ratio of the minimum radius of curvature to the river width. This is a typical feature reflecting the relations between the transverse and vertical factors of a river. Data on the scour hole - depth (h_{max}) and the ratio of the minimum radius of curvature to river width (R_{min}/B) on the Red River are topographical data in 1997.

The graph shows the depth of the scour hole in the Hanoi segment of the Red River in a general broad picture governed by a quite clear law. According to this relation (h_{max}-R_{min}/B), the Red River can be divided into 2 sections - ahead and behind river mouth.

- The sections ahead of the Duong River mouth often have large width and small depth. Corresponding to the bank full water level, the river width (B) is within the range of 960-2,000 m. The smallest radius of curvature (R_{min}) is within the range of 4,000-8,000 m. The maximum depth (h_{max}) varies between 12.85 m and 21.36 m.

- The sections behind of the Duong River mouth often have small width and high depth. With typical features as with the bank full water level, the width of water surface is within the range of 443-1,243 m. The radius of curvature (R_{min}) is within the range of 900-5,000 m. The maximum depth (h_{max}) varies between 10.60 m and 30.24 m.

On the Red River, the most abrupt curves are the 2 sections at Duong Tao, corresponding to the bed elevation - 22.22 m, and at Quang Lang, corresponding to the deepest bed elevation - 23.73 m. The radius of curvature at this location is only 900 m. These are also 2 positions where the ratio R_{min}/B is smallest on the Red River. From the topographical data in 1997, the relation between h_{max} and R_{min}/B is shown on Fig. 4 and in accordance with the approximate relation as follow:

$$h_{max} = 47.26\left(\frac{R_{min}}{B}\right)^{-0.762} \quad (7)$$

Relation (7) correlates to the elevation of the foundation of training works, bank protection works, groins, bridge piers, berths, etc., and to the stability of the structures on the river.

D. Relation between B and h

The Channel of narrow river section will be stable when a relative balance is achieved, which is expressed by the following basic equations [9]:

For the water flow: $Q_0=Q_1$ (8)

$$Q=BCh^{3/2}i^{1/2} \quad (9)$$

For sediment: $S_1=S$ (10)

$$S=Bau^b \quad (11)$$

In which: values of the original parameters corresponding to the natural status have the indicator '0', and those of the new parameters corresponding to the "with river training works" conditions have the indicator '1', a represents coefficient, b represents the power.

The current balancing status and the final future balancing status, assuming: $C_1 \approx C_0$ and $D_1 \approx D_0$

a and b do not change in the both balancing situations.

The equations (8)-(11) bring the following results:

$$\frac{h_1}{h_0} = \left(\frac{B_0}{B_1}\right)^{\frac{b-1}{b}} \quad (12)$$

and

$$\frac{i_1}{i_0} = \left(\frac{B_1}{B_0}\right)^{1-\frac{3}{b}} \quad (13)$$

Using (11), the power b doubles the power β in (5). For the Red River in particular, Using (6) has determined β equal to 2.18 therefore b is 4.36. Put this value of b in (12) and (13), we have the following formulas:

$$\frac{h_1}{h_0} = \left(\frac{B_0}{B_1}\right)^{0,771} \quad (14)$$

and

$$\frac{i_1}{i_0} = \left(\frac{B_1}{B_0}\right)^{0,312} \quad (15)$$

Then, using (14) and (15), we can predict the average depth of the flow (h) and slope (i) within the context of narrowing river channel by river training works.

E. Impacts of structures and construction works

Dykes: The Hanoi dyke was constructed in the XI century and further developed throughout the period of nearly one thousand years. Apart from the Hanoi dyke, there are also many layers of ring levees surrounding the residential zones. The smallest and largest distance has the gap of 3.2 times.

Bridges across river, and river training works: On the studied river segment, there are 3 bridges: Long Bien (built in 1902), Thang Long (built in 1984), and Chuong

Duong (built in 1985). The bridge piers occupy the area for water drainage, diminish the flow in the main channel and the flood plain, marking the water level increase and causing local erosion. Experiments done on the physical model with the discharge of 29,000 m^3/s have identified that the difference water levels upstream and downstream of Thang Long Bridge is 12 cm; that between water levels at Long Bien is 26 cm, and at Chuong Duong 16 cm.

E. Analysis of flood plain impacts on flood discharge capacity

General analysis: To analyze the flood plain impacts on the stage-discharge relations, we have made reference to studies by Myers and Brennan (1990), Wormleaton and Merrett (1990) in experimental flumes (Fig. 5A and Fig. 5B). There is difference in the stage-discharge relations in the "main channel" and the "flood plain". Fig. 5A indicates that when the flood plain is narrow the stage-discharge relation is line 4 in the case of smooth tests, which has the "main channel" in the "stretched out" form though the stage-discharge relation is in the "flood plain". Similarly, in Fig. 5B, when there is no the flood plain, the depth-discharge relation curve is line 4 in the case of smooth tests too. In both cases, corresponding to the same water level, the discharge is the smallest, or in other words, the flood discharge is the lowest.

Impacts from residential zones: Impacts from the residential zones on the flood plain have made the water level increase. The rise of the water level has been determined on the rigid-bed model. After removing all the residential zones on the flood plain and with the total discharge of 29,000m^3/s, the water level has been decreased by 20 cm.

Impacts of the rise of flood plain elevation: (see Fig. 6)

To determine the level impacts by the rise of the flood plain elevation (ΔZ) on the water level, we have made reference to studies by Bray [8] and start from the stage-discharge relations (H-Q) in the "main channel" and the "flood plain" as follows:

- In the "main channel": $Q_1=a_1H_1^{\alpha 1}$ (16)
- In the "flood plain": $Q_2=a_2H_2^{\alpha 2}$ (17)

In which: a_1, a_2, α_1, α_2 are the coefficients and powers determined from real measurement data or from experiments on the physical model. The B-D_1 line illustrates the relations in the "flood plain" at present, i.e. with impacts from the residential zones. The B-D_2 line represents the relations in the "flood plain" after the removal of all the residential zones on the flood plain. Using the real measurement data, we can only define the B-D_1 line and the point (Z*, Q_2) on it. The B-D_2 line must be based on the model. The rise of the water level (ΔH) determined according to the B-D_2 line is completely due to the rise of the flood plain elevation, and corresponds to the point (Z**, Q_2) on the line.

Equations (16) and (17) have the intersection at coordinates (Z_0, Q_0), where $Q_1=Q_2=Q_0$; $H_1=H_2=Z_0 \Rightarrow a_1Z_0^{\alpha 1}= a_2Z_o^{\alpha 2}$, therefore:

$$Z_o = \left(\frac{a_1}{a_2}\right)^{\frac{1}{(\alpha 2-\alpha 1)}} \quad (18)$$

When the flood plain elevation rises by ΔZ, use (16) at the point ($Z_0+\Delta Z$, Q_1), we have:

$$Q_1= a_1 (Z_0 +\Delta Z)^{\alpha 1} \quad (19)$$

When the flood plain does not yet rise up and the discharge is the same ($Q_1=Q_2$), use (17) at the point (Z*, Q_2) we have:

$$Q_2 = a_2Z^{*\alpha 2} \quad (20)$$

Use (19) and (20) calculate the elevation Z*:

$$Z^* = \left\{\frac{a_1(Z_0 + \Delta Z)^{\alpha 1}}{a_2}\right\}^{\frac{1}{\alpha 2}} \quad (21)$$

So, with the same discharge, the water level rise (ΔH) when the flood plain elevation rises (ΔZ) is:

$$\Delta H = (Z_0+\Delta Z)-Z^*$$

$$\Delta H = (Z_0+\Delta Z) - \left\{\frac{a_1(Z_0 + \Delta Z)^{\alpha 1}}{a_2}\right\}^{\frac{1}{\alpha 2}} \quad (22)$$

In which: Z_0 is calculated according to (18)

From hydrological data in 1996, in the period 1991-1998 and experiments on the model, we can determine (16) and (17), and relevant coefficients and powers a_1, a_2, $\alpha 1$, $\alpha 2$.

Calculate the flood plain elevation with ΔZ equal to 86 cm, use (18) and (22) to identify the rise of the water level due to the rise of the flood plain elevation. For example, Fig 7 is drawn to identify a_1, a_2, $\alpha 1$ and $\alpha 2$ according to 1996 data. Use (18) and (22), we can identify the rise of the water level being 25 cm. Similarly, if the hydrological data of the 1991-1998 period are used, the rise of the water level will be 24 cm, and if the data from experiments on the physical model are used (in case of removal of all houses in the residential zones), such value will be 27 cm.

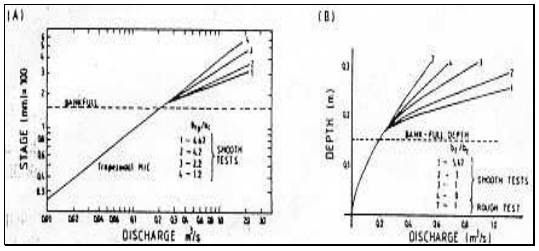

Figure 5. Depth - discharge curves for different geometric of the compound cross-sections. (A)- After Myers' and Brennan's flume experiments (B) - After Wormleaton's and Merrett's flume experiments (1990)

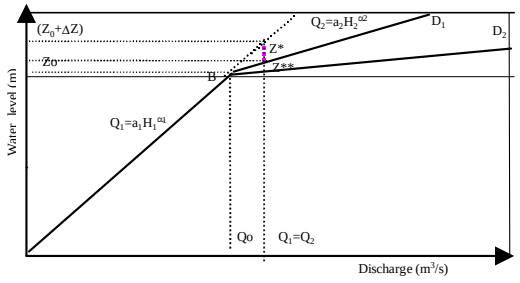

Figure 6. The rise of the water level due to the rise of flood plain elevation

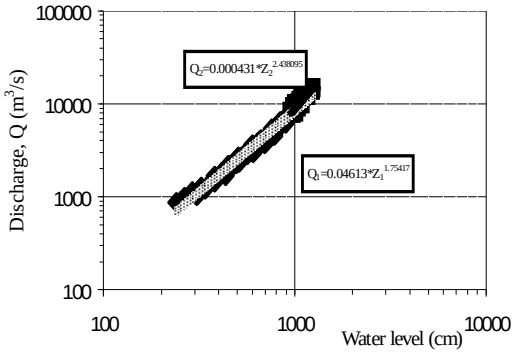

Figure 7. Stage - discharge relation in 1996 at Hanoi Hydrological Station

The flood plain elevation has risen due to the impacts of the human activities, such as raising the ground elevation to build up houses or construct roads, etc. This in turn makes the water level go up. If the flood plain continues to rise up by 1 or 2 m, the flood water level will become 30-60 cm higher. Therefore, the river training solution absolutely needs to refer to the elevation of the flood plain, and any bank protection or groin works must be designed in such a way to have an adequate crest elevation.

VI. Application of Studied Results to Determine Dimensions for Alignment and River Training Work in Hanoi Segment of th Red River

The major objective of river training in Hanoi Segment of the Red River is, first of all, to increase the flood discharge capacity, overcome constraints to navigation and beatify the environmental landscape and build up a modern and civilized urban appearance. From the studied results, we see that premise for regulating this river segment is to stabilize the channel alignment in the season of medium water level, stabilize the flow distribution to the Duong River and remove man-made obstructions on the flood plain. For this purpose, the first thing to do is determine specific dimensions of the river training works on a scientific basis.

A. Objects of river training and objects of impact

For the Hanoi segment of the Red River, there are two objects of the river training works, which are objects of training works for flood discharge, and the object of training works for channel stabilization.

For effective flood discharge, it is necessary to make impacts on obstructions in the main channel and flood plain. However, the bridge piers are un-removable obstructions. The objects of the training works for flood discharge therefore will be mainly the obstructions in the flood plain, such as the ring levees, houses and the parts of flood plain where the elevation has risen. For the immediate purpose, it is essential to clear away obstruction within the 50 m - wide belt along the banks, and remove houses at the bottles necks, as well as avoid, raising the flood plain elevation.

To stabilize the river segment, it is necessary to focus the flow on the main channel under the desirable alignment and guide the flow to the direction of Gia Lam channel.

B. Dimensions of alignment and Training works

Use (12) to calculate the dimensions of the training alignment - see results in Table1, then draw out the alignment and locate the groins - After that, carry out experiments on the physical model to determine specific dimensions for each groin.

There are 2 alternatives to arrange the works: CT1 (B_1=940 m) and CT2 (B_2=880 m). Both alternatives have the same alignment width in the downstream of the Duong River mouth.

The two alternatives are tested on the models in terms of the velocity distribution and flow distribution in Gia Lam and Quyt channels as well as in the effluent to the Duong River. On this basic, analyses are done to choose the suitable alternative.

CT2 alternative: This alternative can be the best to stabilize the channel as desired. However, the flow distribution to the Duong River will increase by a small volume, compared to the current situation. At the discharge levels of 27,500 and 29,000 m^3/s, the increased flow entering the Duong River will account for about 1.8-1.9 % of the total flow.

CT1 alternative: This alternative can ensure quite good stability for the channel alignment A, and stability for new port at Tam Xa, and more important, it will meet requirement of not increasing the flow in to Duong River during the flood season. Therefore, CT1 alternative has been selected.

VII. Conclusions and Recommendations

A. Conclusions

1. This study has been conducted on basis of materials and basic data collected from reliable sources and edited according to consistent criteria.
2. Specific values have been determined for the Red River conditions for coefficients and powers in the Engelund-Hansen formula to calculate the sediment load (6), as the basic to determine dimensions for the river training works (14), (15).
3. The author has suggested formula (22) to calculate the rise of water level during the flood season due to the rise of flood plain elevation. Therefore, the river training solution absolutely needs to refer to the elevation of the flood plain, and any bank protection or groin works must be designed in such a way to have an adequate crest elevation.
4. The author has analyzed the effect of channel stabilization of controlling bottlenecks and guiding bank sections. On this basis, the channel alignment A, which is the current alignment for river training

TABLE I.
LONG- TERM WIDTHS AND DEPTHS

River section	B_0 (m)	h_0 (m)	B_1 (m)	h_1 (m)
The Red River, upstream of Duong River mouth	1520	5.82	940	8.40
	1520	5.82	880	8.90
The Red River, the downstream of Duong River mouth	1150	6.12	709	8.90

works, as well as calculate the dimensions of the alignment and training works for maintaining the stable flow distribution for the Hanoi segment of the Red River.

B. Recommendations

1. It is recommended that the flood plain elevation should be decreased to increase the flood discharge capacity of the channel. This solution is worth of considering and will certainly bring about obvious effects.
2. Along with the requirements on the main channel, the food plain and urban management in Hanoi city, there should be a consistent guidance among the sectors in order to study and work out a river training master plan for the Hanoi segment of the Red River.
3. For the immediate time, it is necessary to remove soon houses at the bottlenecks and remove the obstructions within the 50 m - wide belt along the banks to facilitate the current measures of channel stabilization.

ACKNOWLEDGMENT

The Author would like to thank the River Engineering Research Center (RERC) of VIWRR for creating good conditions of his study. He is also indebted to the following for information, comment and help provided: Prof. Luong Phuong Hau (Hanoi University of Civil Engineering) and Dr. Tran Xuan Thai (VIWRR). The Author wishes to thank Dr. Nguyen Van Toan (VIWRR) for giving useful suggestions.

REFERENCES

[1] Le Ngoc Bich, "Studies on Channel Morphology Relation of downstream part of the Red River," Selected Works of Studies on the Red River sedimentation and channel hydraulic, Vietnam Institute for Water Resources Research, Hanoi, pp. 245-260, 1984 ["Nghi^an cøu quan hÖ h×nh th¸i lßng s«ng cña h¹ du s«ng Hång," TuyÓn tËp c«ng tr×nh, ViÖn KHTL, Hµ Néi, 1984].

[2] Nguyen Van Phuc, "Some Problems on the River Training Work System in the Hanoi Segment of the Red River," Selected Research Works of TEDI PORT, pp.74-81, 1998 [Mét sè vÊn ®Ò vÒ hÖ thèng c«ng tr×nh chØnh trÞ s«ng Hång ®o¹n Hµ Néi, TuyÓn tËp b¸o c¸o khoa häc, C«ng ty TVXD C¶ng - §-êng thuû, 1998].

[3] Japan International Cooperation Agency (JICA), "Plan for Channel Stabilization in the Hanoi Segment of the Red River," pp. 14, December 2002.

[4] Maunsell PTY LTD in association with Nor consult International, Flagstaff Consulting, Coffer MPW, Monash University, ID&A, TEDI, AIC Maunsell, "Final Report on River Studies," My Thuan Bridge Project - Vietnam, pp. 25-26, 1996.

[5] Luong Phuong Hau, "River Dynamics," Textbook in Hanoi University of Civil Engineering, ["§éng lùc häc dßng s«ng," Gi¸o tr×nh tr-ên §¹i Häc X©y Dùng, Hµ Néi, pp.121-136, 1992].

[6] Nguyen Van Cung, Vo Phan, Luu Cong Dao, Quan Ngoc An, Do Tat Tuc, "River Dynamics," Textbook in Water Resources University, Hanoi, Vietnam, pp.172-175, 1981 ["§éng lùc häc s«ng ngßi," Gi¸o tr×nh tr-ên §HTL, Hµ Néi, Viet Nam].

[7] Delft Hydraulics, "Wendy Manual," version 3.00, vol. 1&2, pp. 43-45, 1991.

[8] Przedwojsky B. & Blazejewsky R., Pilarczyk K. W., River Training Techniques, Fundamentals, Design and Applications, A.A. Balkema / Rotterdam, Netherlands / Brookfield, USA pp. 48-54, 1995.

[9] Termes A. P. P, "The Hanoi Lecture Notes on River Morphology" Delft Hydraulics, pp.3.30-35, 4.31-34 and 7.64-73, 1989.

Experimental Study of Scouring in the vicinity of Lateral Intake in U-Shape Channels

M.R. Pirestani [*], M.R.M Tabatabai [**] and A.A. Salehi Neyshabouri [***]

[*] Assis. Prof., Islamic Azad University - South Tehran Branch, Dept. of Civil Engineering, Tehran, Iran

[**] Assis. Prof., Power and Water University of Technology, Tehran, Iran

[***] Assoc. prof., Tarbiat Modarres University, Dept. of Civil Engineering, Tehran, Iran

ABSTRACT: The effect of hydraulic and geometric parameters on scouring in the vicinity of lateral intakes is significant to identify stability of the structure. These also enable us to facilitate flow in to diversion channel, moreover, to exclude sediment transport in to the intake. The transverse pressure gradients in the vicinity of the intake induced regions of mean-velocity gradients, depth-varying surface of flow diversion and separation zone at the intake entrance in the diversion channel.

A number of researchers have shown that rate of scouring at the entrance of lateral intake is dependent upon discharge in the main channel Qm, depth of flow y, type of flow regime Fr, Diversion angle ϕ, radius of curvature in the bend R, intake location in the bend θ, width of the main channel B and width of diversion channel b.

However, in this research, experiments were carried out in a U-shape flume with a rectangular cross section of a moveable bed. The U-shape channel is 0.6 m wide, 0.6 m high and 2.6 m radius of curvature, diversion channel is also characterised by a rectangular moveable bed channel 0.25 m wide, 0.35 m high and 1.1 m long. In addition, intake channel is located at second half of the bend (θ=115˚). Median diameter of bed sediment was selected 1.3 mm. These experiments showed that the variations of the scour hole at the entrance of the lateral intake depends on the main channel hydraulic parameters and diversion angle of the intake channel in bends.

I. INTRODUCTION

Some of the most substantial factors that should be taken into consideration in designing lateral intakes are to facilitate water conveyance into the intake channel as well as exclusion of sediment inflow and its deposition at intake entrance. This can remarkably increase the efficiency of the intake [1].

Reference [2] carried out some experiments on a lateral intake at 90˚ with a straight channel. They concluded that the formation of diversion flow is due to the presence of transverse hydraulic gradient at intake entrance. They also found out that the pressure variation at intake entrance is such that to decrease at the inner intake entrance and increase in outer intake entrance. It is also proportional to the water level variation at intake entrance. The diversion flow rate is dependent on the surface of the dividing stream-flow. The equilibrium between longitudinal pressure gradient as well as shear and centrifugal forces causes a secondary clockwise flow in the outer entrance of the diversion channel. The flow pattern in lateral intakes is so that there is a possibility of particle accumulation and sedimentation near the inner entrance of the diversion channel [2].

Investigations carried out along bend cross-sections of the curved channels revealed that the flow velocity decreases as the depth increases. The transverse slope also decreases from the outer bend towards the inner bend direction. This occurs due to pressure gradient in the bend. Therefore, the boundary layer is affected by a dynamic pressure gradient which leads to the formation of a spiral flow in the bend. The existing conditions cause the sediments to migrate from outer bend towards the inner bend [3]. Those who have studied on the bend channels suggest using a U-shape (180˚) channel when experimenting on the secondary flow, as the secondary flow can be fully developed in such conditions [3, 4 and 5].

Considering the flow pattern in the bends, many researchers suggest the preferable location for the intake to be the outer bend [1, 6, 7 and 8]. Reference [7] has preferred intake location in 3/4 of central angle in the second half of the bend channel (Figure. 1).

In addition, diversion angle of the intake has been the subject of some studies. Reference [9] concluded that optimum diversion angle varies with diversion rate ($Q_r=Q_D/Q_m$) and intake location in channel bend. Reference [7] defined the best diversion angle as where separation zone in the intake is a minimum value.

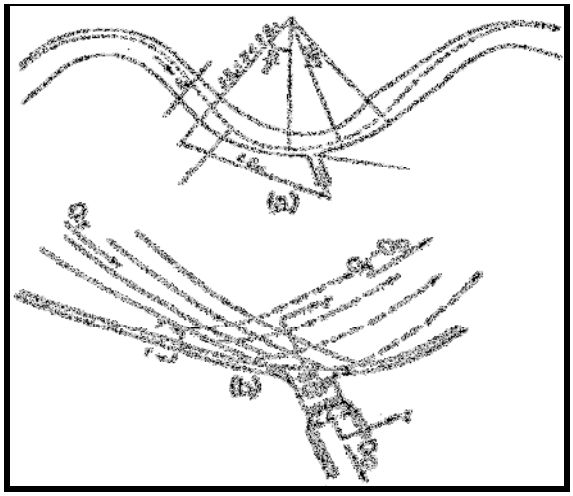

Figure 1. Intake Location without Dam in the Bend Channel (Razvan, 1989).

Optimum diversion angle was also determined experimentally by some investigators and proved to vary a wide range of 30-65˚ [7].

The water-intake sediment problem is illustrated a lateral intake adjoining the Ohio River. The sandbar formed in the intake for bay is an indication that the intake is withdrawing a significant amount of sediment and that the performance of the plant is diminished because of the resulting non-uniform approach flow. One strategy to mitigate such a problem is to separate mechanically the sediment from the water and eject it from the intake. Such an approach is rather expensive and may impact adversely the river environment by disturbing the local sediment regime [2 and 10].

As the above investigations show the flow pattern can be complex and three dimensional in the vicinity of the lateral intakes in straight channels. The complexity of the flow greatly increases and entails more investigations to have a better understanding of scouring where the lateral intakes are located in curved channels.

II. Dimensional Analysis

In order to study the effects of the hydraulic parameters, it is necessary to be familiar with the dimensional analysis. It is possible to approach and study a phenomenon and its characteristics by utilizing dimensional analysis. Applying the dimensional analysis to a problem is based on the assumption that, it can be expressed through introduction of some compatible equations which express the relationship of different parameters with each other. The first procedure in dimensional analysis is to specify the contributing parameters. Thereafter, existing techniques are applied to find the relationship between these parameters. The obtained relationship should be meaningful, easily applicable and compatible with any unit systems. After specifying the contributing parameters in the dimensional analysis, the number of the dimensionless parameters can be obtained by using existing theories. In this research, the effective parameters on the geometry of the dividing zone and diversion flow were considered as follows: water density ρ, dynamic viscosity μ, depth of flow in the main channel y, flow velocity V, acceleration of gravity g, width of the main channel B, the width of diversion channel b, θ, ϕ, the main channel radius of curvature R, mean bed material size D_{50} and bed material density ρ_S. Dimensionless parameter for maximum scour hole depth H_S was obtained by applying the dimensional analysis and π theory [11]:

$$\frac{H_S}{B} = f(Fr, Fr^*, \mathrm{Re}^*, \frac{y}{B}, \varphi, \theta) \qquad (1)$$

Where:

$$Fr^* = \frac{u_*^{\,2}}{g(G_S - 1)D_{50}} \qquad (2)$$

$$\mathrm{Re}^* = \frac{\rho u_* D_{50}}{\mu} \qquad (3)$$

$$G_S = \frac{\rho_S}{\rho} \qquad (4)$$

u*= shear velocity (m/sec). Fr* and Re* are negligible by considering a constant value for D_{50} and also intake location is constant, therefore (1) is simplified as:

$$\frac{H_S}{B} = f(Fr, \frac{y}{B}^{\mathrm{R}}, \varphi) \qquad (5)$$

III. Experimental Setup

The main objective of the current study is to investigate the effect of constant intake location θ=115˚, different diversion angles (ϕ= 45˚, 60˚, 75˚ and 90˚) and various flow conditions, under different flow depths and discharge values, on the scour hole in the vicinity of the lateral intake. As secondary current is fully developed in 180˚ channel, experiments were carried out in a U-shape rectangular flume of rigid bed and boundaries; as such models simulate the most critical condition [3].

Flume dimensions are: 0.6 m wide B, 0.6 m high and 2.6 m radius of curvature to the centerline R with a ratio of R/B equals 4.3. A straight rectangular channel with dimension of 0.6 m wide, 0.6 m high and 7.2 m long is located upstream of the bend section. In addition, to remove gate effect on the water level in bend channel, a straight rectangular channel built with the same cross section and 3.5 m long downstream of the bend section (Figure. 2).

Reference [1] suggested the width ratio of diversion channel to the main channel to be in the range of 0.4-0.5. Therefore, horizontal diversion channel designed with

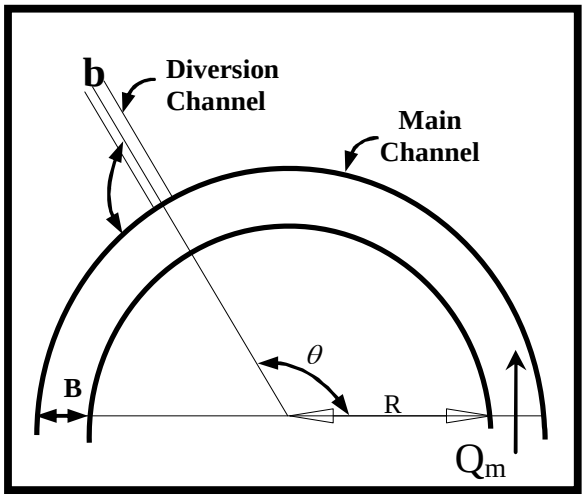

Figure 2. Geometrical details of bend channel and lateral intake.

rigid bed rectangular cross section of 0.25 m wide (b), 0.35 m high and 1.1 m long (Figure. 2). Discharge of main channel is measured by ultrasonic flow meter and a triangular sharp crested weir was used to measure the flow in diversion channel.

Experiments were conducted to investigate scour hole variations adjacent to the lateral intake for 10 and 15 cm water depths under 10, 15 and 20 lit/sec discharge values (i.e. Fr= 0.09, 0.14, 0.18, 0.25 and 0.34) for clear water condition (Table. I). This was based on the ratio of the mean and critical velocities to be less than one, where critical velocity is a function of median bed material size [12]. Bed material size was selected to have uniform distribution with median D_{50} of 1.3 mm and standard deviation of 1.31 [13].

After installing the intake channel for each diversion angle, bed material, with a thickness of 20 cm and zero slope, were placed along the diversion and in the main channels (3 m upstream and downstream of diversion channel).

With the start of experiments, bed materials near the intake entrance began to scour, this took approximately about 5 hours to reach an equilibrium state (Pirestani, 2004), after which experiment was ceased to measure the bed profile variation by a digital point gauge.

IV. Results and Discussions

To investigate flow pattern in the vicinity of lateral intake, two dimensional near bed velocity measurements were made.

In the main channel, as flow approaches the entrance of the intake, hydraulic gradient increases and streamline is influenced by diversion channel. This leads to gradual flow diversion toward the intake. Likewise, streamline is even more affected by the intake in the outer bend (Figure. 3).

TABLE I.
VARIABLE PARAMETERS IN THE EXPERIMENTS

ϕ	y (cm)	Q_m (lit/sec)	Fr	Re
90	15	10	0.09	11033.9
90	15	15	0.14	16550.8
90	15	20	0.18	22067.7
90	10	15	0.25	12413.1
90	10	20	0.34	16550.8
75	15	10	0.09	11033.9
75	15	15	0.14	16550.8
75	15	20	0.18	22067.7
75	10	15	0.25	12413.1
75	10	20	0.34	16550.8
60	15	10	0.09	11033.9
60	15	15	0.14	16550.8
60	15	20	0.18	22067.7
60	10	15	0.25	12413.1
60	10	20	0.34	16550.8
45	15	10	0.09	11033.9
45	15	15	0.14	16550.8
45	15	20	0.18	22067.7
45	10	15	0.25	12413.1
45	10	20	0.34	16550.8

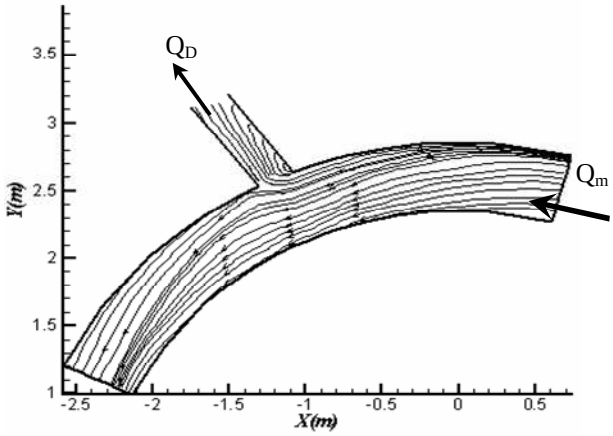

Figure 3. Flow pattern near bed in the vicinity of lateral intake (θ=115˚, ϕ=75˚, Fr=0.27, y=15 cm).

Variation of water surface profile drown in figure (4) illustrates that it is resulted by hydraulic gradient, which is actually reduced near inner entrance of the diversion channel so that it could reach its minimum level approximately in the middle of the entrance where separation zone initiates in the diversion channel. Thereafter, it tends to have a rising trend where it reaches its maximum level near outer entrance. This is stagnation point in the main channel where it is the end of dividing streamline, velocity head reaches its minimum value approximately to null hence energy level equals to the flow depth. From this point, water surface begins a decreasing trend so far from intake in the main channel, where the influence of the intake on water surface profile disappears [14]. This condition effectively plays an important role in separation zone formation while inciting about reverse flow near channel bed in downstream corner of intake entrance directed from the main towards the diversion channel [15]. These factors are effective in bed elevation variations, which ultimately lead to form scour hole [14]. As a result, some of the washed out sediments are transported downstream of the main channel as some other diverted into the intake, through which some deposited in the separation zone and the rest downstream.

Plots of Fr versus ratios of maximum depth H_S and Length L_S of scour hole to the main channel width B for each diversion angle were sketched by observed data

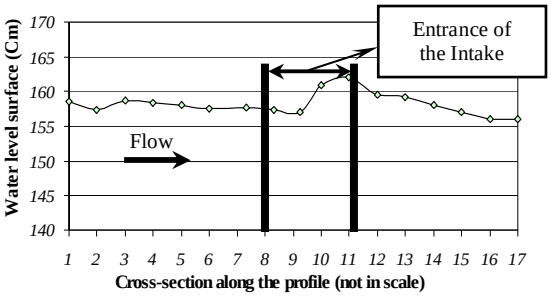

Figure 4. Water surface profile variations near the lateral intake in the main Channel (not in scale).

(Figures. 5 and 6). These shows that in all diversion angles, H_S/B and L_S/B have an increasing trend with an increase Fr values. However, a discontinuity is noticeable where $0.18<Fr<0.25$, this illustrates the effect of upstream flow depth, in the main channel, on scour hole dimensions.

Diversion angle ϕ and H_S/B values were also plotted for different Fr values (Figure. 7). These represent diversion angle of 60˚ in comparison to the others has generated the deepest scour hole under constant depth of 15 cm upstream, which corresponds to the maximum diversion flow rate Q_r under the same condition (Figure 8). However, when flow depth is decreased to 10 cm, Figure (8) tends to follow an increasing trend which reflects the significance of flow depth on the dimensions of the scour hole.

For all the experiments under different y/B, ϕ and Fr values, the following relationship was optimized by using Solver menu in Excel Software.

$$\frac{H_S}{B} = 0.7314 Fr^{0.691} \phi^{0.231} \left(\frac{y}{B}\right)^{0.293} \qquad (6)$$

In which, ϕ is in radians, y, B and H_S are in metres.

Equation (6) was obtained by trial and error, as the computed values from the equation and observed data proved to have the minimum root mean square values in comparison with applying other mathematical forms in equation (6). Observed values of (H_S/B) was plotted against the computed ones (Figure. 9).

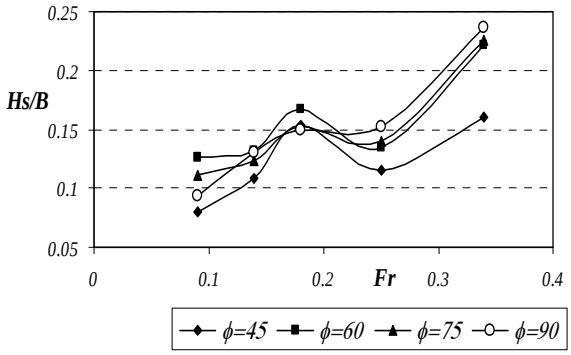

Figure 5. Variation of measured (H_S/B) for different (Fr) under different (ϕ) values.

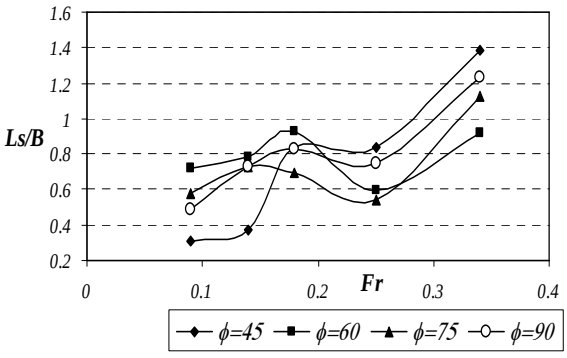

Figure 5. Variation of measured (L_S/B) for different (Fr) under different (ϕ) values.

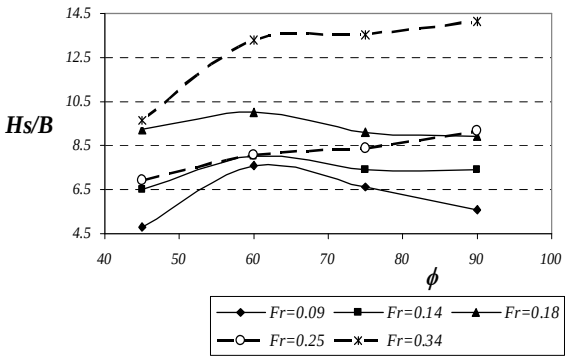

Figure 7. Variation of measured (H_S/B) for different (ϕ) under different (Fr) values.

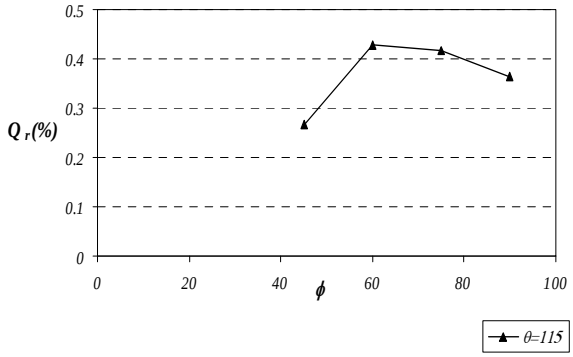

Figure 8. Variation of measured (Qr) for different (ϕ) under $\theta=115^{\circ}$.

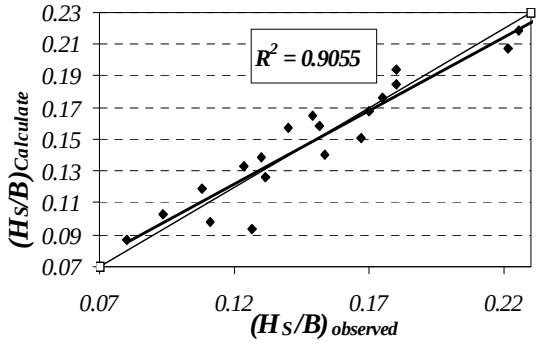

Figure 9. Observed and calculated maximum scour hole depth

V. CONCLUSION

Based on observations were made from analysis of the data, the following concluding remarks were obtained:

- As streamline approaches the intake in the main channel, it is diverted party by it. The effect of this on water surface profile is in such a way that it profile has a decreasing trend from the inner wall of the diversion channel to the mid-point of the entrance where it reaches its least value, thereafter an increasing upwards trend begins so that it should reach its most value at the outer wall of the diversion channel where tangential velocity is approximately equal to zero at this point which is called stagnation point.

- For all different diversion angles, H_S/B and L_S/B are directly related to the Fr values.
- Flow depth variations upstream of the intake, in the main channel, plays a significant role in the scour hole dimensions.
- By analysis observed data experimental, empirical relationship was presented to estimate the maximum scour hole depth for lateral intakes in U-shape channels.

ACKNOWLEDGMENT

This investigation was carried out in Tarbiat Modares laboratory according to the enacted research program (no. Riv3-79423) in Iran Ministry of Power and Water.

REFERENCES

[1] A. J. Raudkivi, "*Sedimentation, Exclusion and Removal of Sediment from Diverted Water*," IAHR, Balkema, The Netherlands, 1993, pp. 63-87.

[2] V. Neary, F. Sotiropoulos, and A. J. Odgaard, "Three-Dimensional Numerical Model of Lateral-Intake Inflows," *Journal of Hydraulic Engineering*, Vol. 125, No. 2, 1999, pp. 126-140.

[3] M. A. Bergs, "*Flow Processes in a Curved Alluvial Channel*," Unpublished, Ph. D Thesis, University of Iowa, 365 pp, 1990.

[4] R. Booij, "Modeling of the Secondary Flow Structure in River Bends," *River Flow*, Bousmar & Zech (eds), ISBN 90 5809 509 6, 2002, pp. 127-133.

[5] K. Blanckaert, "Analysis of Coherent Flow Structures in a Bend Based on Instantaneous-Velocity Profiling," *Third International Symposium on Ultrasonic Doppler Methods for Fluid Mechanics and Fluid Engineering EPFL*, Lausanne, Switzerland, 2002, pp. 51-58.

[6] J. C. A. Russel, "*The Optimum Location for a Canal Sediment Extractor*," Report OD/TN 55, HR Wallingford, Oxford shire, UK, 1991.

[7] E. Razvan, "*River Intakes and Diversion Dams*," Amsterdam, 1989.

[8] P. Novak, A. Morfett, and C. Nalluri, "*Hydraulic Structures*," Pitman, London, 546 pp, 1990.

[9] J. L. Boillat, and G. De Cesare, "Dichtestrmungen im Bereich des Grundablasses des Stausees Luzzone-Modellversuche," *Tagungsband (proceeding) des Symposiums "Betrieb, Erhaltung und Erneuerung von Talsperren und Hochdruckanlagen"*, Graz, Austria, 1994, pp. 183-192.

[10] P. J. Kerssen, and A. Urk, "Experimental studies on sedimentation due to water withdrawal," *J. Hydr. Engrg.*, ASCE, 112(7), 1986, pp. 641-656.

[11] E. Buckingham, "Model experiments and the forms of empirical equations," Trans, ASME, (37), 1915, pp. 263-296.

[12] C. R. Neill, "Mean velocity criterion for scour of coarse uniform bed material," *12th IAHR Congress*, Fort Collins, Colorado, 1968.

[13] D. B. Simons, "*Sediment transport technology*," Water Resource Publications, USA, ISBN 0-918334-66-7, 897 pp., 1992.

[14] M.R. Pirestani, "*Investigation of flow pattern and scour in the vicinity of lateral intakes at bend channels*," Unpublished, Ph. D Thesis, Islamic Azad University, Research and Science Campus, Iran, 176 pp, 2004, *(Persian)*.

[15] M. R. Pirestani, M. R. M. Tabatabi and A. A. Salehi Neyshabouri, "Investigation of dividing streamline in lateral intake of U-shape channel," *XXXI IAHR Congress*, Seoul, Korea, 2005, pp. 405-411.

The analysis of factors inducing and inhibiting morphological changes of the Warta river reach downstream of the Jeziorsko reservoir (Poland)

B. Przedwojski, J. Wicher-Dysarz, M. Wierzbicki and T. Dysarz
Agricultural University of Poznan, Department of Hydraulic Engineering, Poznan, Poland

The main goal of the presented research is the analysis of morphological changes in the Warta river downstream of the Jeziorsko dam (Poland). The longitudinal erosion and local scours have been observed there since the dam was built in 1983. These processes were induced by the water management in the Jeziorsko reservoir and significant change of hydraulic and hydrologic conditions in the Warta river. The main factor determining the intensity of the erosion is type of soil in the river bottom and banks. However, other factors as local channel configurations or bottom armoring may accelerate or inhibit the process intensity. In the paper long series of the data collected since the reservoir was built are presented and discussed. The several factors influencing the intensity of erosion process in the Warta river reach under consideration are analyzed. Finally the prediction of the Warta river bottom is presented.

I. INTRODUCTION

The process of intensive longitudinal and local river bed erosion is often observed downstream of dams and weirs. The phenomenon is especially important in the case of large reservoirs. The main factor inducing the analyzed process is the change of hydraulic conditions in the river related to the dam performance. Since the dam is built the previous balance in sediment deposition and erosion is no longer kept. The particles are accumulated in the reservoir located upstream of the dam. The sediment transport continuity is interrupted. The main features of river stream flowing from stilling pool to river bed are very intensive turbulence and almost no load. The water starts to take the particles from the bottom just below the stilling pool or other bottom protecting structures.

The intensity of the river bed erosion depends on the factors mentioned above. In addition bottom and banks material characteristics as alluvium layer thickness and grain size play important role. The assessment and management of risk linked to local and longitudinal erosion of river bed downstream of the dams is crucial for the performance and safety of many hydraulic structures installed in the river including dams themselves.

The main purpose of the conducted research is to present and discuss the problem of local and longitudinal erosion of river bed observed in the Warta river reach downstream of the Jesiorsko Reservoir Dam. The paper consists of several sections. First the Jeziorsko Reservoir Dam and hydrological conditions in the water system are presented. Then the field measurements and bottom material characteristics are described and shortly discussed. The model used for the analyses is presented in section no. 5. Next section includes the analysis of simulation results and forecast of bed changed due to the erosion process. Last section includes summary and concluding remarks.

This research is supported by Polish Committee for Scientific Research, project no. 2 P06S 034 30

II. DESCRIPTION OF THE JEZIORSKO RESERVOIR

Jeziorsko reservoir was built in 1986 in central part of Poland. It is located in the Warta river, between the Sieradz (upstream) and Uniejow (downstream) gauge stations. The dam is located in the Warta river at km 484+090 (fig. 1). The Jeziorsko reservoir is relatively new object. First time it was filled up to the admissible maximum water level (121,50 m a.s.l.) in 1991. The hydropower plant was put into operation in 1995.

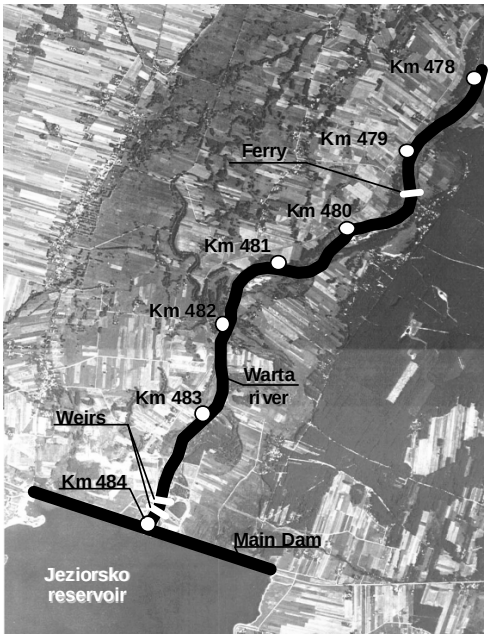

Figure 1 Map of the Warta river reach downstream of the Jeziorsko reservoir

The Jeziorsko reservoir is multipurpose reservoir performing in the annual working scheme. During the months from October to December the water stages are kept on the minimum level of 116 m a.s.l.. In spring months the reservoir is filled with water. The maximum water level 121.5 m a.s.l. is hold during April – June

period. In the period from July to August the water stored at the reservoir is used and the reservoir water stages gradually come back to the minimum level. The main purpose of the reservoir performance is the flood protection during wet season. The reservoir is also the source of water for the big cities in Great-Poland province: Poznan, Kolo, Srem and Konin. The water stored is also used for irrigation purposes and to preserve biological life below the dam. The Patnow-Konin and Adamow power plants used the water from the reservoir for cooling. Other goal of the Jeziorsko performance is production of hydro-power, though, this is not significant due to the small difference between upper and lower water levels in the dam (about 10 m). The reservoir is also used for recreation and inland fishery.

Before the dam started to perform the protecting elements had been installed in the tailwater to prevent from negative effect of erosion. The length of protecting structures were 90 m. The basic element of erosion protection is stilling pool. Downstream of the stilling pool the river banks and bottom were protected by the concrete slabs of the length 40 m and the thickness 1 m. The elevation of the concrete slab crest was 109.06 m a.s.l.. Below the slabs the fascine and stone mattresses protected the river bottom and banks. The mattress was 1 m thick and 50 m long.

III. River Hydrology

The Warta river catchment area in the dam cross-section is 9021.8 km^2. The hydrologic characteristics of the Warta river in this region may be assessed on the basis of records from the Sieradz gauge station. The gauge station is located upstream of the reservoir in the km 521. The catchment area ratio is $F_z/F_s = 1.108$, where F_s is catchment area in Sieradz and F_z – in the dam cross-section. The specific discharges in Sieradz gauge station determined for the period 1951-1998 were presented in ref. [5]. They are also shown in tab. I.

In the river reach downstream of the Jeziorsko reservoir there are four gauge stations. These are two gauge station

TABLE I.
CHARACTERISTIC FLOWS IN THE SIERADZ GAUGE STATION

Description	Notation	Value (m^3/s)
absolute observed maximum flow	*Max Q*	397.5
absolute observed minimum flow	*Min Q*	10.5
average flow	Q_a	48.9
median flow, flow related to probability of excedance 50 %	$Q_{50\%}$	187.0
flow related to probability of excedance 10 %	$Q_{10\%}$	353.0
flow related to probability of excedance 1 %	$Q_{1\%}$	557.0

located just below the dam: W.D. I in km 483+860 and W.D. II in km 483+330 and two gauge stations located near towns Ksieze Mlyny (in km 479+400) and Uniejow (km 465+850). Intensive longitudinal erosion of Warta river bed in the reach from weir no. 2 (km 483+710) to gauge station Ksieze Mlyny (km 479+400) caused large decrease of water surface elevation. It is especially visible for medium and low discharges. Due to that fact it is impossible to control water stages at gauge stations W.D. II and Ksieze Mlyny now. The mentioned gauge stations are used only during short period of time in the year when high water flow occur in the analyzed river reach. Because of the discussed river bed changes only two gauge stations installed in the system may be used to observe and control the discharges from the dam. These are W.D. I and Uniejow.

IV. Analysis of Data from Field Measurements

Presented analyses of bottom and water surface elevations changes were done on the basis of field measurements made in period 1987-2004 (ref. [4], [6], [7], [8], [9], [11], [12]). A range of the observed river reach is from the dam tailwater to the Koscielnica village. This is the river reach from km 484 to km 465 (total distance is 19 km). The field measurements consist of longitudinal water surface leveling, the hydrometric measurements of 52 cross-sections and bed material sampling. During the field measurements the constant outflows from the reservoir were kept. The discharge intensity differs slightly between 31.5 and 33.0 m3/s.

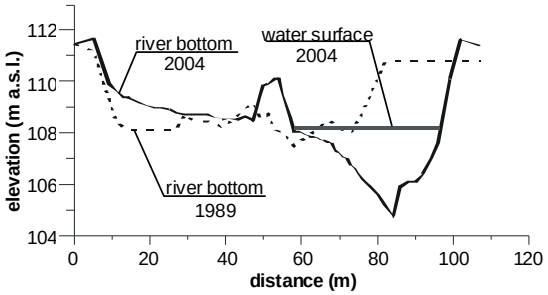

Figure 2. Observed bottom elevation in cross-section P5/1' (km 483+220)

The map of the system is presented in fig. 1. In the map there are denoted the main elements in the system as river reach kilometers, reservoir, dam, weirs and ferry rack. The river reach shown in the map includes the area of the most intensive bed morphology changes. The transverse contours of two selected cross-sections are drawn in fig. 2 and 3. In fig. 4 the longitudinal profile of the river is shown.

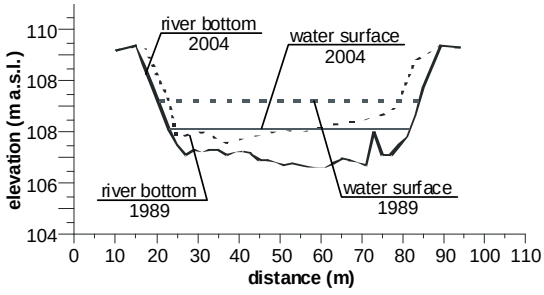

Figure 3. Observed bottom elevation in cross-section P6 (km 483+012)

The cross-sections presented in fig. 2 and 3 are denoted as P5/1' and P6. The field measurements done in July 12-17, 2004 are compared with the cross-section contours observed in July 17th, 1975. The thick continuous line

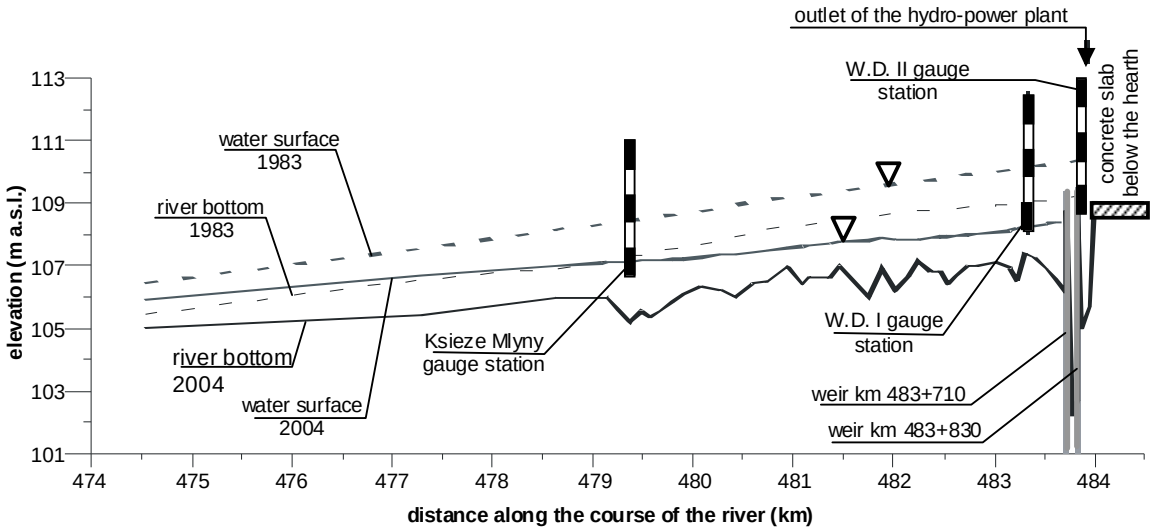

Figure 4. Water surface and bottom elevation changes in the Warta river downstream of the Jeziorsko Reservoir Dam

TABLE II.
RESULTS OF FIELD MEASUREMENTS IN SELECTED WARTA RIVER CROSS-SECTIONS (JULY 12-17, 2004, DISCHARGE Q = 32.5 m^3/s)

cross-section	km	water surface (m a.s.l.)	bottom (m a.s.l.)
P4'	483+657	108.37	106.37
P5	483+514	108.35	106.92
P5/3	483+300	108.25	107.40
P6	483+012	108.11	107.11
P7	482+821	108.02	107.02
P7/5	482+358	107.90	106.81
P8	482+130	107.85	106.65
P8/3	481+656	107.80	106.01
P9'	481+169	107.65	106.65
P10	480+740	107.48	106.49
P11	480+080	107.27	106.35
P11/1	479+906	107.21	106.10
P12'	479+376	107.13	105.30
P13	478+630	107.01	105.96
P15	474+530	105.90	105.00
P17	470+140	104.33	103.14
P19	467+170	103.17	102.37
Uniejów	465+850	102.67	101.52

represents the data taken in 2004 for each cross-section. The past situation is denoted as thin dashes line. In addition the observed water surface elevations are also shown in fig. 2 and 3.

The longitudinal profiles of water surface and average bottom elevations in the reach range from km 484+000 to km 474+530 (fig. 4). The average bottom elevation are determined as the difference between the water surface level and the average depth measured along the bottom width. As it results from practical observations of natural river flows the later characteristic, average depth along bottom width, is almost always equal to depth evaluated in the channel axis. The thick continuous and dashed lines represent the river bottoms measured during July 12-17, 2004 and in July 17th, 1975, respectively. In the same figure there are corresponding water surface profiles denoted by thin lines. The measurements in the period July 12-17, 2004 were done during the discharge 32.5 m3/s. The historical data from July 17th, 1975 were taken during the discharge 33.0 m3/s. The thin and dashed gray lines represent maximum banks elevations.

The longitudinal profiles of water surface and average bottom elevations measured in 1975 are taken as the description of initial conditions in the system. In the fig. 2, 3 and 4 one may notice that the changes of the river bottom elevation are significant.

The basic cross-sections hydraulic properties with water surface and average bottom elevations measured in July 12-17, 2004 are presented also in tab. 2

The specific grain sizes of bed sediment were determined on the basis of sieve analysis. The samples of bottom material taken from Warta river bed were used. The results of the analysis are shown in tab. 4. This table presents the data measured in July 12-17, 2004. The presented specific grain sizes are D_{10}, D_{35}, D_{90} and D_{95}. These factors are frequently used for the description of bottom material characteristics.

Although, the tab. 3 presents only current measurements, the grain sizes in the analyzed river reach have been controlled since the dam was built. In the natural conditions before the dam was built the largest

specific grain sizes (D_{95}) varied between 0.60 and 1.00 mm. After 14 years of reservoir performance, in 1997 the same indicators increased to the range from 1.20 to 10.0 mm. The values presented in the table are related to the conditions in 2004, after 21 years since the reservoir started to perform. Now the specific grain size is varying from 3.80 to 36.0 mm.

TABLE III.
GRAIN SIZES OF BOTTOM MATERIAL IN THE WARTA RIVER BED
(JULY 12-17, 2004)

cross-sect.	km	specific grain sizes (mm)				
		D_{10}	D_{35}	D_{50}	D_{90}	D_{95}
P5	483+514	0.29	0.65	3.80	20.0	28.0
P5/2	483+390	0.27	0.44	6.70	32.0	36.0
P6	483+012	0.34	0.49	1.25	15.0	18.5
P7	482+821	0.32	0.48	0.73	8.40	15.5
P8/1	482+019	0.34	0.58	0.78	2.30	3.80
P8/2	481+887	0.32	0.49	0.63	6.50	9.40
P8/3	481+656	0.21	0.36	0.54	10.0	18.5
P8/4	481+369	0.30	0.50	0.70	12.0	20.0
P9'	481+169	0.34	0.60	0.73	1.35	1.90
P10	480+740	0.21	0.27	0.34	0.70	1.50
P10/2	480+425	0.32	0.48	0.56	3.00	8.00
P11	480+080	0.30	0.53	0.74	11.5	19.0
P12'	479+376	0.26	0.37	0.42	0.79	0.90
P13	478+630	0.32	0.47	0.50	0.93	1.30
P16	472+190	0.33	0.47	0.53	1.10	1.35
P17	470+140	0.34	0.57	0.73	2.10	3.90
P18	468+280	0.30	0.33	0.48	0.90	1.25
P22	465+920	0.37	0.52	0.60	1.35	1.75

The changes in time of the specific grain sizes for the selected cross-sections are also presented in fig. 5. The increase of the bottom material grain sizes is especially visible in the period 1997-2004. The largest changes were observed in the river reach ranging from weir no. 2 (km 483+700) to Ksieze Mlyny gauge station (km 479+400). In this period the specific grain sizes D95 increased almost 4 times, from 10.0 to 36.0 mm.

Although the increasing tendency is clearly visible in the grain sizes changes in time, several factors may inhibit this process. Two of them are the most important namely bank erosion and earth works performed to install the weirs (fig. 1). However, the temporary inflow of smaller material is not able to stop intensive bottom material segregation caused by the bed erosion. The substantial increase of the largest grain sizes caused so called bottom armouring in the Warta river. In the cross-sections where the increase of grain sizes is largest the decrease of average bottom elevations is small during the last 3 years. It varies from 3 to 15 cm in the reach from weir no. 2 to Ksiezę Mlyny gauge station. The result of bottom armouring is increase of river bed resistance to outwash.

The analysis of field measurements data shows the significant longitudinal bed erosion with local bed and banks washouts. The changes of bottom and water surface elevations in time for the selected cross-sections are presented in fig. 6 and 7. During the period of first 4 years since the dam was built (1983-1987) the erosion process occurred in the reach ranging from km 484+000 to km 481+500 (length 3.5 km). The intensive bed erosion was observed just below the stilling pool in the reach of length 300 m. In 1987 the maximum depth of local scour was 1.70 m.

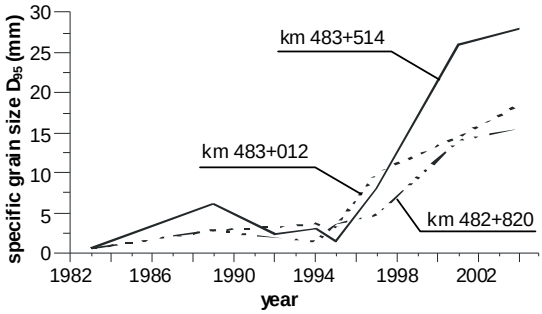

Figure 5. Changes of particles specific diameter during the observation period

In 1991, after the 8 years of sediment transport continuity interruption, the longitudinal erosion was observed in the reach of length 7.0 km. The maximum local scour depths occurred below the concrete protection elements of stilling pool. The scours depths were 3.0 m and 3.2 m. They occurred in the river reach of length 100 m. The secondary effect of erosion was the significant decrease of water surface elevation. The observed decrease of water surface elevation was 1.3 m in the cross-section located just below the concrete protection elements of stilling pool during the discharge 30 m3/s.

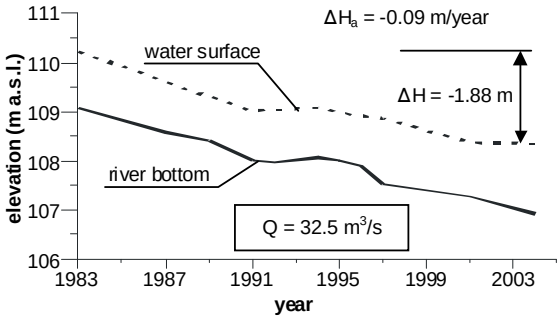

Figure 6. Bottom and water surface elevation changes at cross-section P5 (km 483+574)

In order to restore initial water surface elevations, conditions of hydraulic jump inundation and protection elements stability below the stilling pool two weirs were built in the period 1993-1994 (fig. 1 and 4):

- weir no. 1 located in km 483+830, the overfall crest 109.50 m a.s.l.
- weir no. 2 located in km 483+710, the overfall crest 109.40 m a.s.l.

The construction and earth works related to the installation of weirs caused local increase of bottom elevation below weir no. 2 (fig. 6). The secondary effect of this activity was temporary decrease of bed sediment grain sizes.

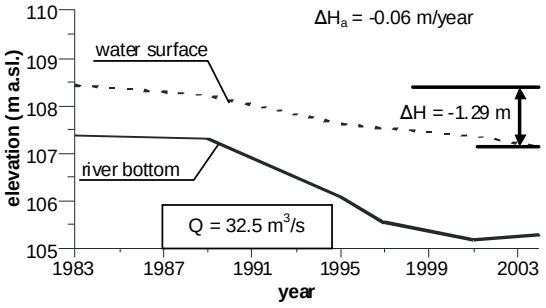

Figure 7. Bottom and water surface elevation changes at cross-section P12 (km 479+400)

V. WATER AND SEDIMENT TRANSPORT MODEL

Due to the complex cross-sections geometry in the analyzed Warta river reach, the basis for the simulation model are St. Venant equations in conservative form. For the sake of sediment transport simulation the equations may be written in the form explicitly indicating the changes of cross-section area related to river bed elevation variations.

$$dA = Bdh - Pdz_b , \tag{1}$$

where A is cross-section area, B – surface width, P – wetted perimeter. dh and dz_b are infinite changes of water depth and bed elevation, respectively. Taking into account (1) the mass balance equation is written in the following form

$$B\frac{\partial h}{\partial t} - P\frac{\partial z_b}{\partial t} + \frac{\partial Q}{\partial x} = q , \tag{2}$$

where t is time and x indicates the distance measured along the river reach. Q is discharge and q is lateral inflow to the reach.

The assumed momentum equation form is as follows

$$\frac{\partial Q}{\partial t} + 2\frac{Q}{A}\frac{\partial Q}{\partial x} - B\frac{Q^2}{A^2}\frac{\partial h}{\partial x} + gA\frac{\partial h}{\partial x} = \\ = gA\left(i_b - I_f\right) + q\left(u_q - \frac{Q}{A}\right) + \frac{Q^2}{A^2}\frac{\partial A_h}{\partial x} , \tag{3}$$

where i_b and I_f are bottom and energy slopes, respectively. u_q is component of the lateral inflow velocity in the channel direction. The term $\partial A_h/\partial x$ describes the changes of cross-section related to the changes of river bed geometry. This term is important only in the case of large geometry changes along the open channel.

The sediment transport continuity equation is taken in the below form

$$P\left(1-p\right)\frac{\partial z_b}{\partial t} + \frac{\partial\left(AC_s\right)}{\partial t} + \frac{\partial S_t}{\partial x} = 0 , \tag{4}$$

where p is the bed porosity, S_t is total sediment transport intensity and C_s is the average volumetric concentration of sediment over a cross-section. The last two variables are linked according to the relationship

$$S_t = C_s Q , \tag{5}$$

The initial conditions for the system of partial differential equations (2) – (4) are written below

$$\begin{aligned} Q(x, t=0) &= Q_P(x), \\ h(x, t=0) &= h_P(x), \\ z_b(x, t=0) &= z_{bP}(x), \end{aligned} \tag{6}$$

where Q_P, h_P and z_{bP} are the scalar functions determined along the river reach $0 \le x \le L$ (L – the length of the reach). Assuming that the Froude number along the analyzed river reach is much lower than 1 the boundary conditions are as follows

$$\begin{aligned} Q(x=0, t) &= Q_0(t), \\ h(x=L, t) &= h_L(t), \\ z_b(x=0, t) &= z_{b0}(t). \end{aligned} \tag{7}$$

The functions Q_0, h_L and z_{b0} are determined for time $t \ge 0$.

The energy slope I_f in the case of flow with movable bed is linked to the variables describing water flow (Q, h, A, etc.) as well as to the features of bed material (ρ_s, D_{35}, etc.) and bed forms. According to the analyses presented in [3] the bed forms identification is related to the Shields' parameter and additional variable defined as follows

$$\theta = \frac{RI_f}{\left(\frac{\rho_s}{\rho} - 1\right)D_{35}}, \qquad Z = \frac{R}{D_{35}} , \tag{8}$$

where R is hydraulic radius, D_{35} is characteristic sediment particles diameter, ρ and ρ_s are water and sediment particles densities, respectively. The energy slope is calculated as

$$I_f = C \cdot Z^m \cdot Fr^{2n} , \tag{9}$$

where Fr is Froude number and C, m and n are parameters determined on the basis of (8). The procedure is described in details in [3].

For the evaluation of the volumetric concentration of sediment Ackers and White formula ([1]) is used. The formula describes the total concentration of suspended and bed load. Its basis is the set of two dimensionless parameters, mobility number F_{gr} and sediment transport relationship G_{gr}, defined as follows

$$F_{gr} = \frac{u_*^{N_1}}{\sqrt{gD_{32}\dfrac{\rho_s - \rho}{\rho}}}\left[\frac{u}{\sqrt{35}\log\left(\dfrac{10h}{D_{35}}\right)}\right]^{1-N_1}, \qquad (10)$$

$$G_{gr} = C_w\left(\frac{F_{gr}}{A_1} - 1\right)^{M_1},$$

where u_* is shear velocity

$$u_* = \sqrt{gRI_f}\ . \qquad (11)$$

The coefficients N_1, A_1, M_1 and C_w depend on the water flow around the particles and they are defined on the basis of so called dimensionless particle diameter

$$D_{gr} = D_{35}\left(\frac{\rho_s - \rho}{\rho}\frac{g}{\nu^2}\right)^{1/3}, \qquad (12)$$

where ν is kinematic viscosity coefficient. The total volumetric concentration of sediment in the cross-section is evaluated as follows

$$C_s = \frac{G_{gr}D_{35}}{h\left(\dfrac{u_*}{u}\right)^{N_1}}. \qquad (13)$$

The presented model consists of partial differential equations (PDEs) (2) – (4), the additional formulae (5), (9), (13) and initial and boundary conditions (6), (7). This is the system of nonlinear hyperbolic PDEs. The domain of the problem is $0 \le x \le L$ and $t \ge 0$. If the formulae (5), (9), (13) are substituted into equations (2) – (4) the system consists of three PDEs with three dependent variables: $Q(x, t)$, $h(x, t)$, $z_b(x, t)$. The application of the accurate analytical methods to solve the problem is practically impossible due to the complex nature of the presented mathematical model. The approximate numerical methods have been used for the simulation of many physical processes for long time. In the analyzed case the decomposition of the PDEs' system and application of a few different numerical methods is forced by the complexity of the problem. The first step is the separation of the water flow and sediment transport equations. Such approach is consistent with different dynamic of these two processes. The changes of the water flow parameters as discharge and depth are much more faster than changes of bed elevations.

The basis of the numerical solution is digitizing of the domain in time and space with integrations steps Δt and Δx, respectively. The domain is covered by the grid with $L/\Delta x + 1$ nodes is 0x direction and a number of nodes in 0t direction. Next the terms in the equations are approximated by the algebraic formulae. In this way the system of three PDEs is replaced by the number of algebraic equations, which is the discreet form of the considered mathematical model. The choice of the digitizing method and numerical scheme is of the crucial importance. In the case of unsteady flow modeling the Preissmann scheme is recommended for many researchers (e.g. ref. [2], [14], [10], [13]). This is one of the finite difference method approximations. The Preissmann scheme is relatively simple, but the accuracy of the results is huge. Due to above reasons the mentioned scheme is used for the implementation of the mathematical model presented earlier.

VI. Simulation Results

The field measurement data are used to prepare the mathematical model described in the previous part of the paper. The unsteady flow and longitudinal erosion process occurring downstream of the weir no. 2 (km 483+650) is analyzed. The river reach length is 17.807 km. The river reach is divided into several cross-sections. The average distance between cross-sections is Δx = 500 m.

The initial condition is the current stage of the analyzed system. Two elements are used as boundary conditions. The average annual scheme of the Jeziorsko reservoir performance is imposed in the inlet of the river reach. The second boundary condition is the rating curve determined for the Uniejow gauge station located in the outlet.

The chosen time step is Δt = 24 h. This value guarantee the stability of computations and prevents from too long time of simulation.

On this basis the forecast of river bottom changes is elaborated. The unsteady flow and sediment transport in the analyzed river reach is simulated. The simulation begins in current stage, what means year 2004. The time horizon is year 2010. The final results of the simulation are presented in fig. 8.

The forecast is not restful. The river reach vulnerable to erosion changes will be longer. In fig. 8 one may notice that bottom and water decrease will be greater in the future. The flow conditions will degrade. This will result in greater difficulties with inland sailing and water use. The actions preventing from longitudinal erosion are necessary.

VII. Conclusions

The longitudinal and local erosion process in Warta river reach ranging from the dam tailwater to the Uniejów gauge station was analyzed. The presented investigations were done on the basis of field measurements done in the period 1987-2004 and numerical forecast for the period 2004-2010. The measurements were compared with the initial conditions in the system which were changed in 1983. The main features of the investigated process is significant variability in time and along the reach. The main factors influencing the process are the outflows from the reservoir and the bed material segregation resulting in the increase of grain sizes.

The reservoir started to perform 21 years ago (in 1983). The process of Warta river bed erosion occurred in the reach ranging form the tailwater of weir no. 2 (km 483+650) to the ferry rack in Kościelnica town (km 465+000). The most intensive bed erosion is observed in the 9.0 km reach located downstream of the dam. In this area the decrease of the bottom elevations is varying from 2.60 m in the tailwater of weir no. 2 to 0.5 m in km 474+530. In downstream of this reach the bottom elevations decrease is varying from 0.50 m to 0.25 m. The

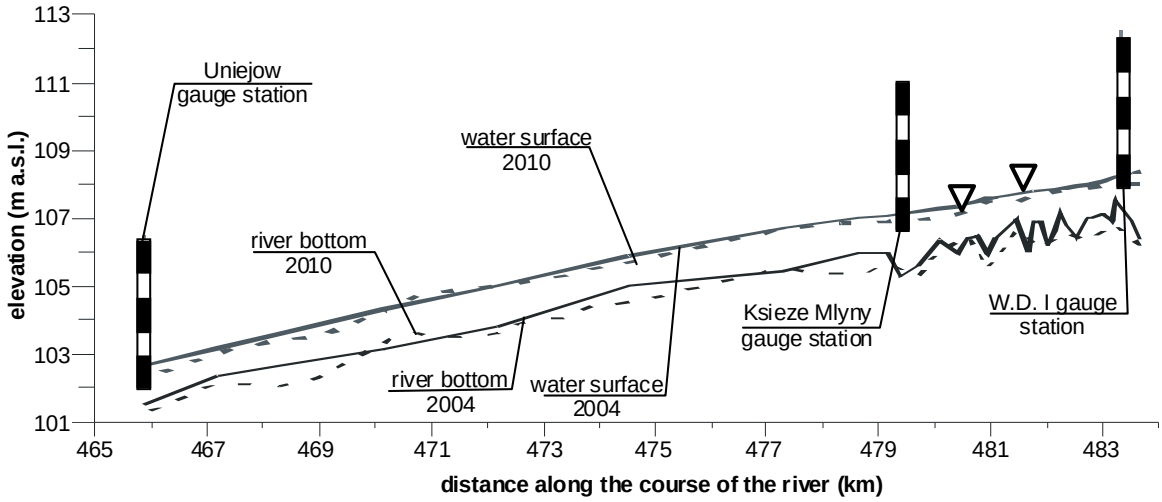

Figure 8. Current (2004) and forecasted (2010) water surface and bottom elevation changes in the Warta river downstream of the Jeziorsko Reservoir Dam

simulation performed indicated that the process of longitudinal erosion is moving further. It is expected that the bed changes reach the Uniejow gauge station until 2010.

Especially intensive bed erosion occurred in the river reach located downstream of the dam in the distance 4.2 km. The water surface elevations measured during the discharge 32.5 m^3/s in 2004 were lower than the average bottom elevations in 1989.

The increase of bed material grain sizes was observed. The effect of this process is the increase of bottom resistance to outwashes. The most intensive increase of grain sizes occurred in the river reach located just below the weir no. 2 (fig. 4 and 8).

The secondary effect of erosion process is the decrease of water surface elevations. After the period of 21 years since the reservoir started to perform the decrease of water surface elevations is varying from 1.88 m (km 483+510) to 0.56 m (km 474+530). These values were determined during the discharge 32.5 m3/s. The average annual decrease of water surface elevation is changing from 9.0 cm/year in km 483+510 to 6.1 cm/year in km 479+400.

Due to the erosion process in years 1983-1992, the water surface elevations in the tailwater of the dam was decreased to the elevation 109.06 m a.s.l.. This elevation is equal to the elevation of the concrete slab crest installed below the dam stilling pool. In order to restore the water surface elevations in the dam tailwater two weirs were built in km 483+860 and km 483+710.

NOTATION

Δt	time step of numerical simulation, (s) or (min, hours)
Δx	step of spatial integration in numerical computations, (m)
ρ	water density, (kg/m^3),
ρ_s	sediment particles density, (kg/m^3),
ν	kinematics viscosity coefficient, (m^2/s),
$\partial A_h/\partial x$	changes of cross-section related to the changes of river bed geometry, (m^2/m),
A	cross-section area, (m^2),
A_1	parameter,
B	surface width, (m),
C	parameter,
C_s	average volumetric concentration of sediment over a cross-section, (-)
C_w	parameter,
D_{35}	characteristic sediment particles diameter, (m) or (mm),
dh	increment of water depth, (m),
dz_b	increment of bed elevation, (m),
G_{gr}	sediment transport relationship, dimensionless,
F_{gr}	mobility number, (-),
Fr	Froude number, (-),
h_L	depth changes in the outlet cross-section imposed as boundary condition, (m),
h_P	initial depth in the river reach varying along the channel, (m),
i_b	bottom slope, (-),
I_f	energy slope, (-),
L	the length of the river reach, (m),
m	parameter,
M_1	parameter,
$Max\ Q$	maximum observed flow, (m^3/s),
$Min\ Q$	minimum observed flow, (m^3/s),
n	parameter,
N_1	parameter,
q	lateral inflow to the reach, ($m^3/(ms)$),
Q	discharge, (m^3/s),
Q_0	flow changes in the inlet cross-section imposed as boundary condition, (m^3/s),
$Q_{1\%}$	flow related to probability of excedance 1 %, (m^3/s),

$Q_{10\%}$ flow related to probability of excedance 10 %, (m^3/s),

$Q_{50\%}$ median flow, probability of excedance 50 %, (m^3/s),

Q_a average flow, (m^3/s),

Q_P initial flow in the river reach varying along the channel, (m^3/s),

p bed porosity, (-),

P wetted perimeter, (m),

R hydraulic radius, (m),

S_t total sediment transport intensity, (m^3/s)

t time, (s) or (min, hours),

x distance measured along the river reach, (m),

u_q component of the lateral inflow velocity in the channel direction, (m/s),

u_* shear velocity, (m/s)

z_{b0} bottom elevation changes in the inlet cross-section imposed as boundary condition, (m),

z_{bP} initial bottom elevation in the river reach varying along the channel, (m),

REFERENCES

[1] P. Ackers, W.R. White, "Sediment transport: new approach and analysis", *Proc. ASCE*, 99, HY 11, 1973

[2] J. Kubrak, "One-dimensional model for unsteady flow bed-load transport in lowland river", (in polish), *XI Polish School of Hydraulics*, 1991

[3] M. Kuroki, T. Kishi, "The bed roughness configuration of alluvial streams", Task Committee on the Bed Configuration and Hydraulic Resistance of Alluvial Streams, Committee on Hydraulics and Hydraulic Engineering, The Japan Society of Civil Engineers., 1974

[4] J. Nowak, R. Nowicki, "The field measurements of the Warta river cross-sections in the reach from Ksieze Mlyny to Uniejow" (in polish), ODGW Poznan, 1999, (typescript)

[5] W. Orłowski and B. Gajewski, "Water management directive for the Jeziorsko Reservoir in the Warta river" (in polish), Regional Board of Experts SITWM NOT in Poznan, 1999, (typescript),

[6] B. Przedwojski, "The consequences of erosion in the Warta river bed downstream of the Jeziorsko Reservoir" (in polish), *XII Polish School of Hydraulics*, September 1992

[7] B. Przedwojski, T. Naskręt, "The investigation of changes in the Warta valley and river reach downstream of the Jeziorsko Reservoir; Task 1 The prediction of bottom decrease in Warta river reach downstream of the Jeziorsko Reservoir; Part 1 Cross-sections measurements and bottom material analysis" (in polish), Poznan, 1989, (typescript)

[8] B. Przedwojski, J. Nowak, "The Jeziorsko Reservoir – The assessment of river bed erosion downstream of the dam" (in polish), Poznan, 1995, (typescript)

[9] B. Przedwojski, "Assessment of bed erosion in the Warta river reach downstream of the Jeziorsko Reservoir Dam; The concept of weir no. 3 location" (in polish), Poznan, 1997, (typescript)

[10] B. Przedwojski, "River morphology and forecasting of river processes", (in polish), *Publishing of Agricultural Univ. of Poznan*, Poznan, 1998

[11] B. Przedwojski, "Assessment of bed erosion in the Warta river downstream of the Jeziorsko Dam and hydro-power plant" (in polish), Poznan, 2001, (typescript)

[12] B. Przedwojski, J. Wicher-Dysarz, M. Wierzbicki, "The investigations of bed erosion in the Warta river reach for the preservation of minimum water levels in the Jeziorsko hydro-power plant tailwater" (in polish), Poznan, 2004, (typescript)

[13] R. Szymkiewicz, "Mathematical modeling of flows in open channels", (in polish) Polish Scientific Publishing, Warsaw, 2000

[14] B. Wosiewicz, Z. Sroka, I. Laks, "System for analysis and forecasting of unsteady flow in the Warta river", (in polish) *Gospodarka Wodna*, 10, 1996

Scour development and sediment motion at rectangular and trapezoidal abutments

A. Radice[*], F. Ballio[*], V. Armenio[**] and S. Franzetti[*]
[*] Politecnico di Milano, Dept. I.I.A.R., Milan, Italy
[**] Università degli Studi di Trieste, Dept. Of Civ. Eng., Trieste, Italy

We present results of abutment scour experiments in a pressurized rectangular duct. Two obstacles of different shape were tested: a vertical plate and a 45° trapezoidal abutment. During the experiments, scour depths were measured all around the abutments; both tests were repeated several times to verify repeatability of the erosion trends. Sediment motion was filmed from the top via a digital CCD; concentration and velocity of the moving grains were measured by image processing. The measured scour trend at the vertical plate is not different from those measured in previous experiments with a free surface, showing that the pressurized flow does not significantly influence the erosion development and the scour hole shape. Maximum scour depths at the trapezoidal abutment were almost 25% less than those at the vertical plate; the shape effect is consistent with the results from literature free surface experiments. For both the abutment types, sediment activity is intense in the first part of the process, it then becoming weaker as time proceeds. Measurements of the instantaneous values of sediment concentration and velocity show that variability in space and time of the solid discharge magnitude and direction increases in the meantime; unsteadiness of grain kinematics indicates similar features of the scour inducing flow field. The obstacle shape influences the intensity of sediment motion: experimental results show that the absence of a blunt obstruction to the mean flow in case of a trapezoidal abutment determines a weaker sediment activity than that for the vertical plate.

I. INTRODUCTION

Local scour at bridge structures has been extensively studied over the past fifty years, mainly by means of laboratory experimentation (see for example [1] and [2]). Such approach allows for individuating the effect of the system control parameters on the erosion trend, without exploring in detail the dynamics of the scour process at a small scale. Thus, little scale phenomenological studies may be a good complement to the large scale ones.

Both experimental and numerical studies of the three dimensional flow field that develops in the proximity of bridge structures can be found in the scientific literature (see for example ref. from [3] to [7]). Visualization of the instantaneous flow field showed the presence of unstable coherent structures of significant dimension in comparison to that of the obstacle. Analysis of the average structure of the flow field highlighted the presence of the horseshoe vortex and of the principal vortex system, that are generally considered the main scouring agents at bridge piers and abutments, respectively.

In this paper we focus on sediment motion around a bridge abutment. Particle entrainment and transport is direct consequence of the action of the scouring flow field; therefore, analyzing the kinematics of the solid phase can considerably support the study of the flow field in investigating the dynamics of the scour process at the particle scale. Some previous works by the Authors (ref. from [8] to [11]) showed that availability of data on the sediment motion can help the interpretation of the process features.

We measured sediment kinematics by filming the scour phenomenon in process and then applying some recent image processing techniques to the acquired movies. We performed the experiments in a closed transparent duct to allow for a clear vision of the process.

We used two obstacles, a vertical plate and a 45° trapezoidal abutment. It is well known that trapezoidal abutments lead to smaller scour depths than vertical ones having the same width (see for example [12]).

We compared the sediment kinematics we obtained for the two abutment shapes, in order to infer similarities in the scouring flow fields for the two cases, as well as discrepancies that could be responsible for the differences in the scour depth trends. Prior to analysis of the sediment motion, we verified that our scour reduction factor was consistent with that given in the literature, in order to check for any possible distortion due to the absence of a free surface.

II. EXPERIMENTAL SETUP

The experimental duct is 5.8 m long, with a rectangular transversal section having width and height equal to 40 and 16 cm, respectively. The whole duct is made of plexiglass to assure complete transparency of the walls. An upstream and a downstream tank complete the experimental installation; the hydraulic head in the duct is imposed by a Bazin weir posed in the outlet tank. Water entrance in the duct is guided by a streamlined inlet to avoid wake effects in the flow.

The test reach of the duct is deeper than the other parts; it was filled with PVC cylinders having median equivalent diameter d_{50} = 3.6 mm, a uniformity coefficient very close to 1 and specific gravity $\Delta = (\rho_s-\rho)/\rho = 0.43$, where ρ_s and ρ are the densities of sediments and water, respectively. In the upstream and downstream reaches, the same bed roughness is obtained by gluing the PVC grains to steel sheets posed onto the duct bottom; as a result, the effective duct height is h = 15.5 cm.

The abutment model is located at about 3.4 m from the duct inlet; we used two different abutments, being the first

a vertical plate and the second a 45° trapezoidal abutment. Both obstacles were made of transparent PVC. Abutment length was b = 10 cm and b = 8 cm for the rectangular and trapezoidal abutments, respectively (Fig. 1).

Water discharge is measured by a magnetic flowmeter posed on the delivery pipe.

The scour depth d at the abutment nose (see Fig. 1) was continuously measured by a laser distance sensor posed just over the duct ceil. The scour depth at the channel wall was visually measured by a rule on the same wall. During the test, the scouring process was filmed via a black and white CCD capable of 50 fps with a resolution of 576 x 763 pixel. Duration of every movie was equal to 20 s. Profiles of transversal and longitudinal sections of the scour hole were surveyed one or two times during the tests, in order to measure also the scour hole shape.

We performed some experimental runs with the same water discharge (Q = 18.5 l/s), to verify repeatability of the experimental procedure. The selected water discharge corresponded to the incipient motion of the bed particles.

The characteristics of the experimental tests are given in Table 1. Only for experiments 1 to 8 the scour depth was measured via the laser distance sensor; in the remaining experiments (tests 9 and 10) the laser was not used to guarantee a good visibility for the CCD and thus a large focus area. The CCD and the laser were used jointly during the other experiments with a vertical plate (1, 2, 6 and 8), but the visualization area was considerably smaller than that we will present in this work (see [10] and [11]).

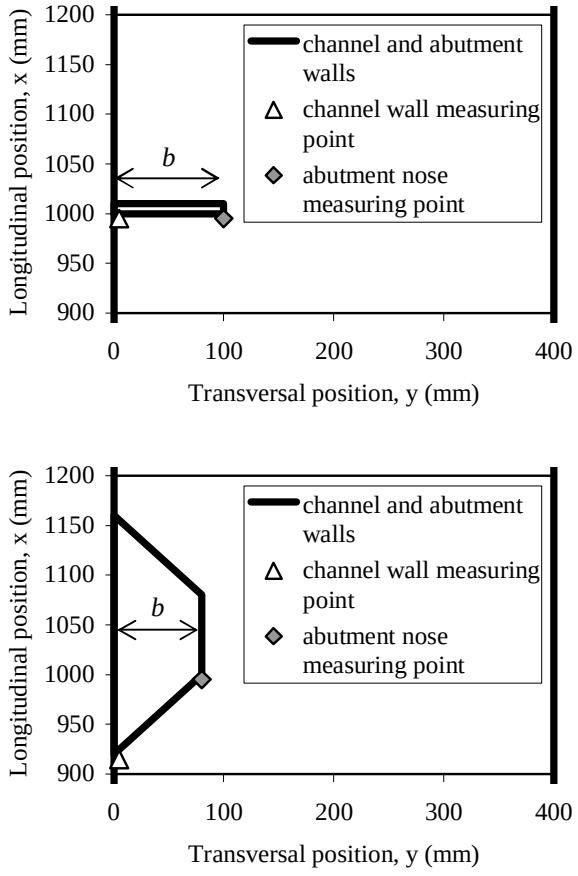

Figure 1. Definition sketch. Vertical wall (up) and 45° wing wall (down) abutments. Water flow is from bottom to top

TABLE I. EXPERIMENTAL TESTS

Test	Abutment
1, 2, 6, 8	Vertical plate
3, 4	Trapezoidal
9	Trapezoidal
10	Vertical plate

III. SCOUR DEVELOPMENT

The temporal development of the scour depth at the vertical plate is shown in Fig. 2. Local erosion trend presents the classical features that are typically observed during experiments with a free surface; scour depth continuously grows with time, but at a decreasing rate. The temporal trend at the abutment nose can be approximated by two straight segments having different slopes in the semi-logarithmic plane; the temporal trend at the channel wall starts later than at the nose, and it is approximated by a straight line of similar slope to that of the first line for the abutment nose. As a consequence, maximum scour depth is initially located at the abutment nose, but later it moves towards the channel wall; intersection between the two scour trends occurs for a time T of about 800 s, corresponding to a dimensionless time $\tau = TU/b \cong 2.4 \cdot 10^3$, where U is water velocity and b is the abutment length.

Fig. 3 presents the temporal trends of the scour depth at the trapezoidal abutment. Also in this case the scour depth continuously grows with time. The rate of the erosion depth in the semi-logarithmic plane is variable till a time $T \cong 3000$ s, corresponding to a dimensionless time $\tau \cong 1.1 \cdot 10^4$; then, the scour trend can be approximated by a straight line. The scour depth at the channel wall follows a similar evolution, even if the activation is later and the rate is larger than that at the abutment nose. Differently from the vertical wall abutment, no intersection between the two scour trends was observed for the final dimensionless time, $\tau \cong 9 \cdot 10^5$. Thus, the abutment shape influences the location of the maximum scour depth around the obstacle.

The dimensionless evolution of the maximum scour depth is presented in Fig. 4 for all the experimental tests where the laser sensor was used. The local scour depth d was normalized via the abutment length b. The superimposition of all the curves shows the good repeatability of the experiments.

The scour depth at the vertical abutment is larger than that at the trapezoidal one. Ref. [12] defined a scour reduction factor K_s depending on the abutment shape, indicating 0.75 as the K_s value for a 45° wing wall abutment. Even if the shape coefficient was defined by [12] with reference to the equilibrium scour depth and not to the temporal trend of the erosion, present results are substantially in agreement with previous findings: for the dimensionless time $\tau = 10^4$, for example, the ratio between the scour depths at the trapezoidal abutment and at the vertical plate is equal to the literature value of K_s.

Data from the surveys of the longitudinal and transversal sections of the scour hole were processed via a kriging interpolator to obtain the contour lines of the hole; these are showed in Fig. 5. The scour hole shape at the vertical wall abutment is consistent to that found for example by [13]: the maximum scour depth is located upstream of the abutment, in the proximity of the channel

wall, with the upstream part of the scour hole being similar to an inverted cone. Upstream of the abutment nose a sort of sediment hill is present, whose existence is highlighted by the irregular shape of the contour line corresponding to $-d/b = -1.8$ for $x \cong 950$ mm, $y \cong 90$ mm. In the downstream part of the hole, two parallel channels develop, that are separated by a sediment ridge. For the trapezoidal abutment, the maximum scour depth is located near the abutment nose; the upstream part of the scour hole is similar to an inverted cone, but in this case the sediment hill upstream of the abutment nose is hardly present. Also the downstream part is significantly different from that at the vertical plate, in that only one sediment channel is present. One possible reason for this feature may be the fact that the flow reattachment to the lateral wall is progressively guided by the streamlined abutment shape in case of the trapezoidal obstacle; this would indicate the larger wake as responsible of the formation of the left sediment channel for the vertical plate. Contour lines of the scour hole are consistent with previous literature findings (see [14] and [15]).

Present results demonstrate that scour experiments in a pressurized duct are similar to those for a free surface stream; thus, our results for sediment motion around the obstacles will be good indicators also for the dynamics of the scour process in free surface experiments.

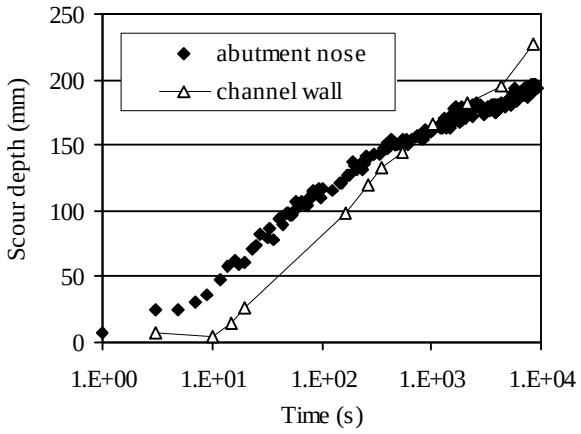

Figure 2. Time development of scour depth at the vertical plate (test 1)

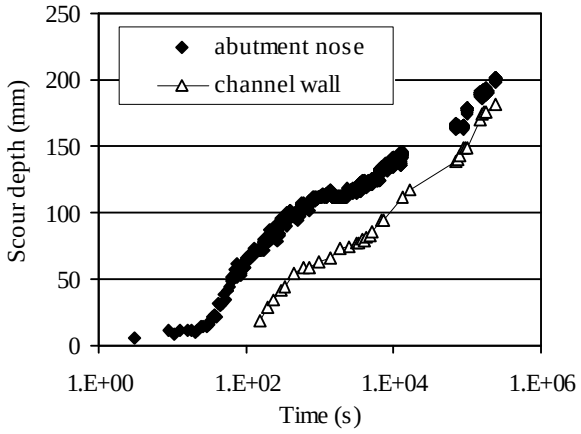

Figure 3. Time development of scour depth at the trapezoidal abutment (test 4)

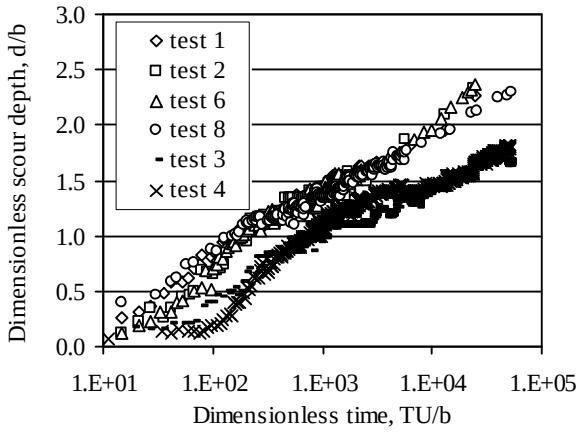

Figure 4. Dimensionless time development of maximum scour depth for the experimental tests

IV. IMAGE PROCESSING

Measurement of concentration and velocity of the moving particles allows for evaluation of the sediment fluxes around the obstacles. In fact, the vector solid discharge per unit width (hereafter simply called solid discharge) can be calculated as $\boldsymbol{q_s} = C \cdot \boldsymbol{v_s} \cdot d_{50}$, where C is the aerial sediment concentration and $\boldsymbol{v_s}$ is sediment velocity.

Sediment concentration (see [8]) was measured via an image difference technique: consecutive frames in a movie were subtracted to highlight the occurred movements; the difference images were then thresholded and filtered to eliminate the noise and to obtain the final image of the displaced particles. After counting the number of displaced particles N, the corresponding sediment concentration could be easily calculated as $C = (N \cdot W_g)/(\Delta x \cdot \Delta y \cdot d_{50})$, where W_g is the volume of a single particle, and Δx and Δy are the dimensions of the measuring cell. Sediment velocity was measured by applying a Particle Image Velocimetry algorithm to a couple of successive difference images (see [9]).

Measures of both grain concentration and velocity require definition of spatial and temporal support scales, that have to satisfy opposite requirements. The spatial measuring scale has to be large enough in comparison to grain dimension, to allow for an eulerian representation of movement; on the contrary, it has to be small enough to allow observing the spatial variability of grain motion. The temporal measuring scale has to be large enough to observe non vanishing grain movements between one instant and the next; on the contrary, a too long temporal scale compromises the measures due to dispersion of the grains. In this work, we used spatial measuring cells whose dimension was 2 cm x 2 cm, while the time sampling interval was the maximum allowed by the CCD, i.e. 0.02 s. Effect of variation of the support scales on the measure are described in [16].

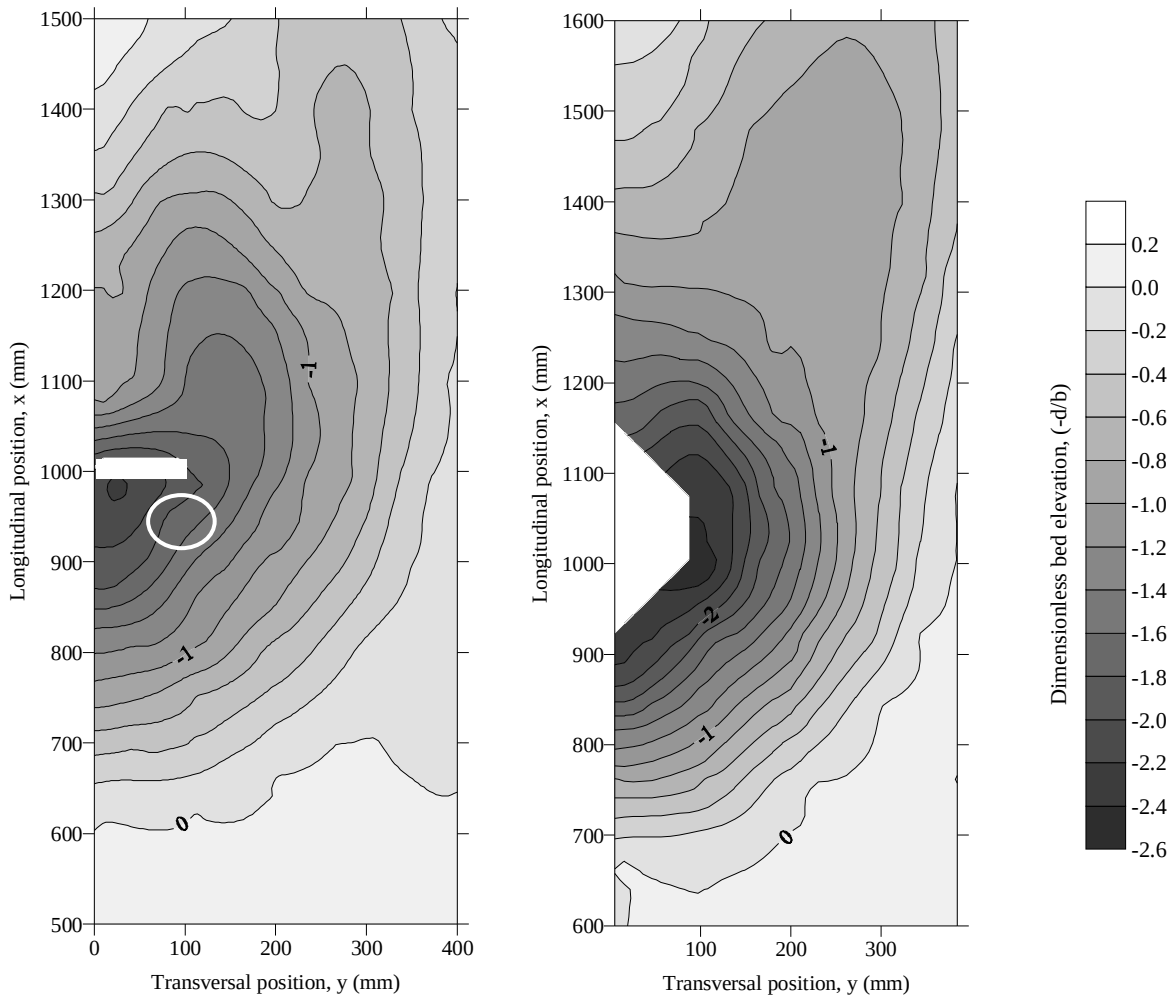

Figure 5. Contour lines of the bed elevation around the vertical plate (left) and the trapezoidal abutment (right), for similar scour levels. For the vertical plate test 1 is considered at time T = 9900 s; for the trapezoidal obstacle one test 4 is considered at time T = $2.4 \cdot 10^5$ s. Colour scale is proportional to dimensionless bed elevation measured from the original non-scoured bed. Water flow is from bottom to top; the sediment hill upstream of the vertical plate nose is highlighted

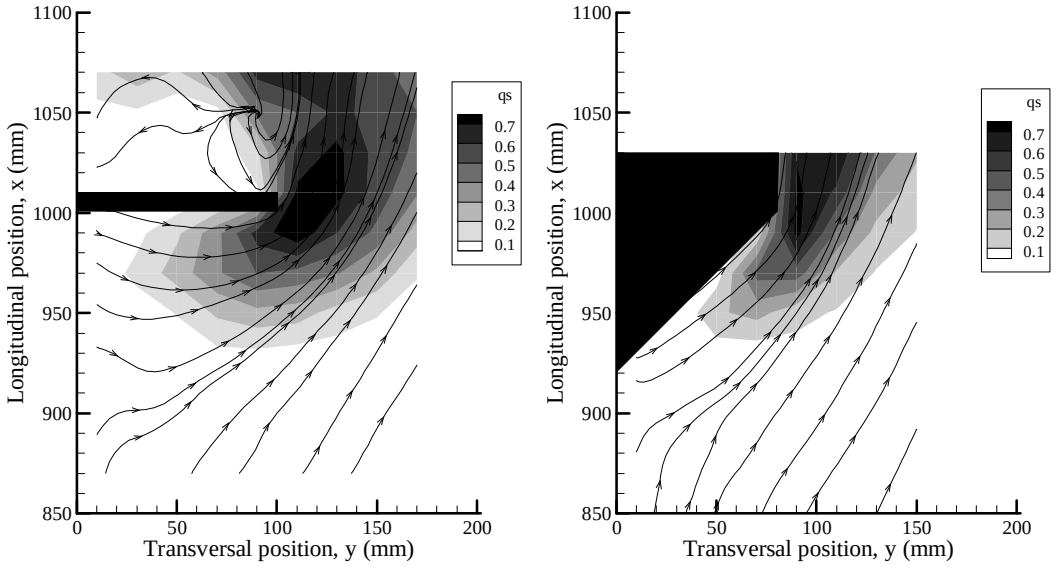

Figure 6. Mean solid discharge fields for the test start (T < 20 s) at the vertical plate (test 10, left) and at the trapezoidal abutment (test 9, right). Colour scales are proportional to the module of average solid discharge (q_s) in cm^2/s

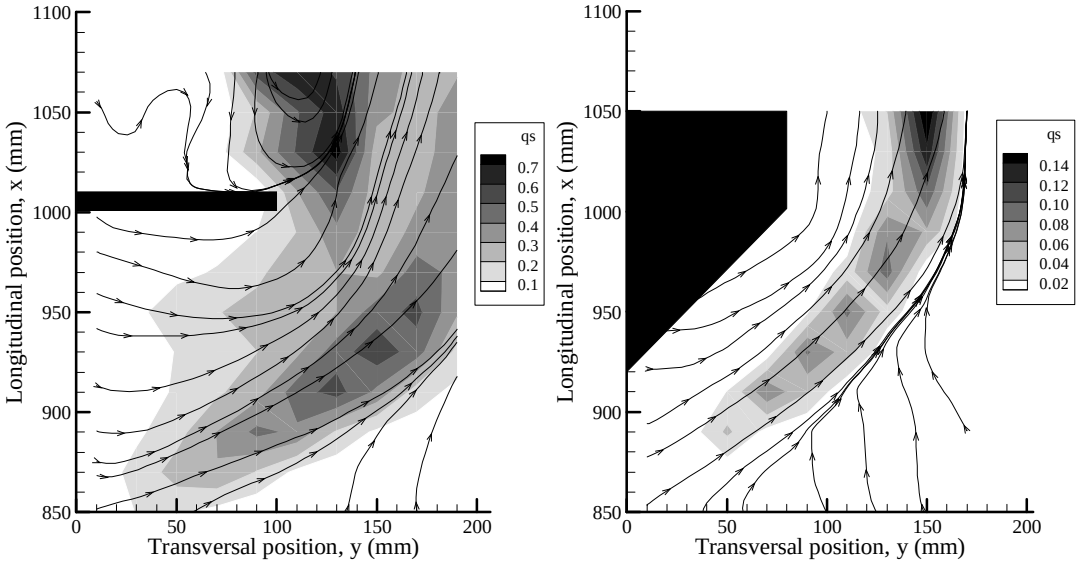

Figure 7. Mean solid discharge fields for d/b ≅ 1.20 at the vertical plate (test 10, T = 100 s, left) and at the trapezoidal abutment (test 9, T = 420 s, right). Colour scales are proportional to the module of average solid discharge (q_s) in cm^2/s

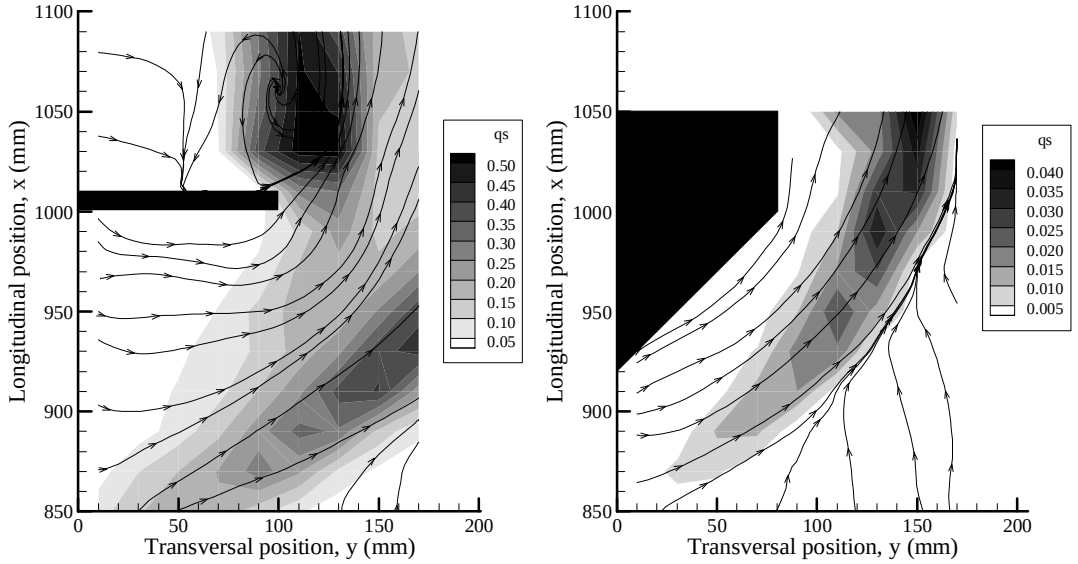

Figure 8. Mean solid discharge fields for d/b ≅ 1.40 at the vertical plate (test 10, T = 270 s, left) and at the trapezoidal abutment (test 9, T = 18000 s, right). Colour scales are proportional to the module of average solid discharge (q_s) in cm^2/s

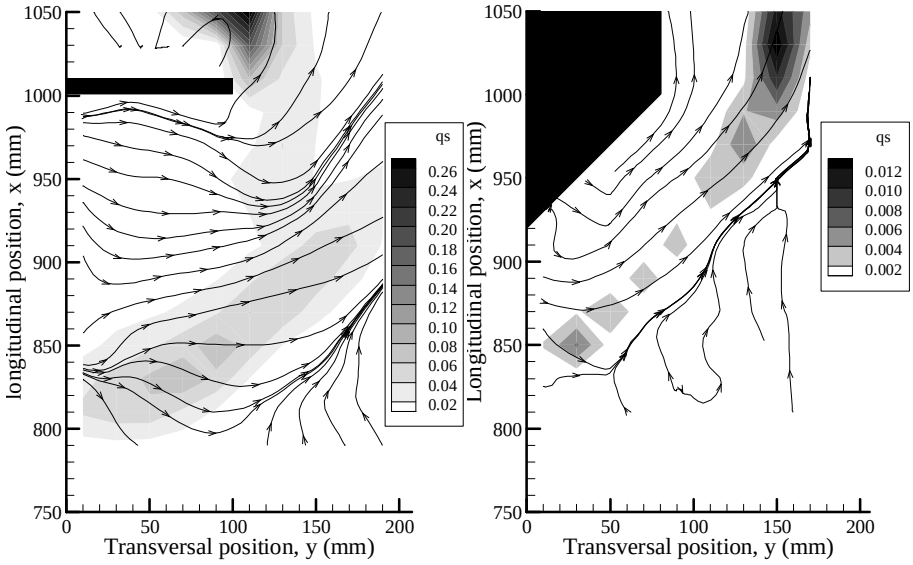

Figure 9. Mean solid discharge fields for d/b ≅ 1.80 at the vertical plate (test 10, T = 2900 s, left) and at the trapezoidal abutment (test 9, T = 14000 s, right). Colour scales are proportional to the module of average solid discharge (q_s) in cm^2/s

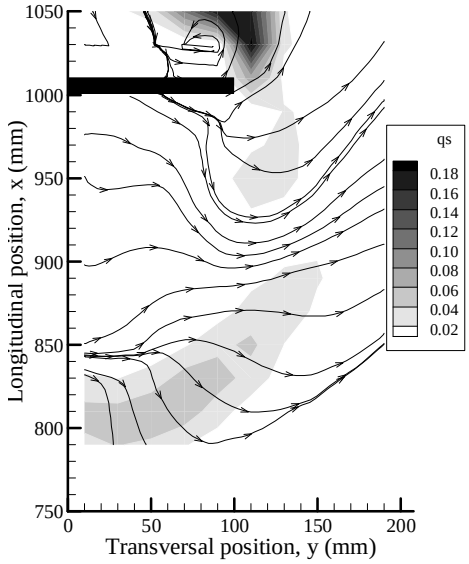

Figure 10. Mean solid discharge at the vertical plate (test 10, T = 7500 s). Colour scale is proportional to the module of average solid discharge (q_s) in cm^2/s

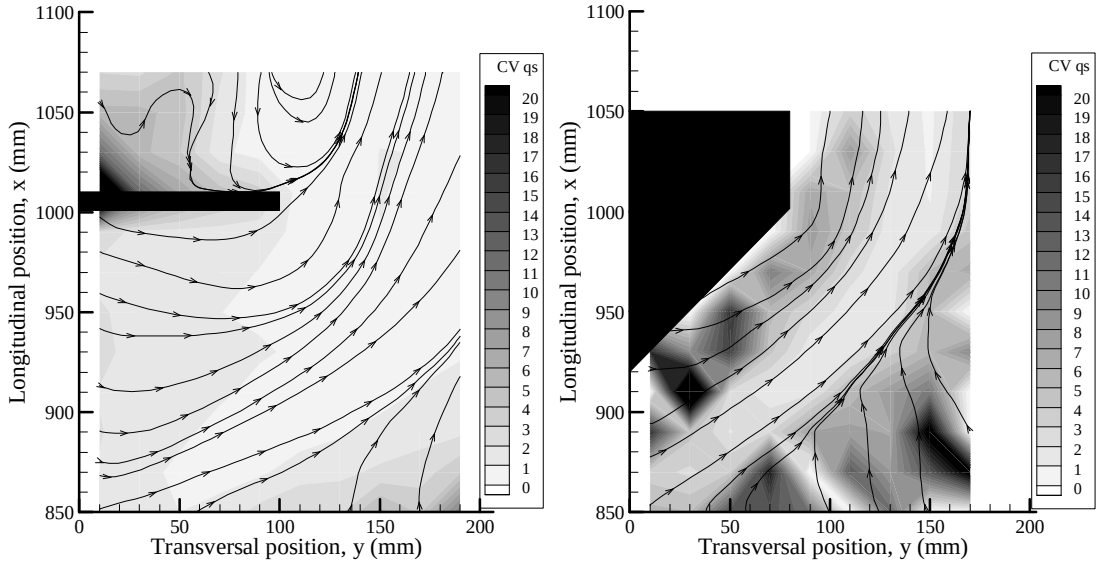

Figure 11. Variation coefficient of solid discharge for d/b ≅ 1.20 at the vertical plate (test 10, T = 100 s, left) and at the trapezoidal abutment (test 9, T = 420 s, right). The corresponding solid discharge fields are presented in Fig. 7

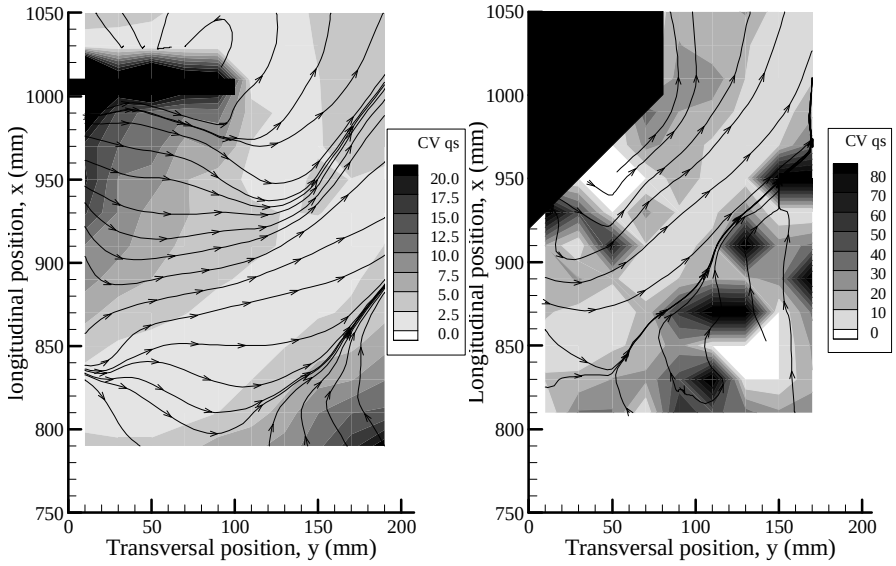

Figure 12. Variation coefficient of solid discharge for d/b ≅ 1.80 at the vertical plate (test 10, T = 2900 s, left) and at the trapezoidal abutment (test 9, T = 14000 s, right). The corresponding solid discharge fields are presented in Fig. 9

V. SEDIMENT MOTION

Analysis of the sediment motion will be made through observation of the spatial distribution of the time average solid discharge. The latter can be computed in two ways:

$$q_{s(1)} = \sqrt{\left(\sum_{i=1}^{n} \frac{q_{sx,i}}{n}\right)^2 + \left(\sum_{i=1}^{n} \frac{q_{sy,i}}{n}\right)^2} \qquad (1);$$

$$q_{s(2)} = \frac{1}{n} \sum_{i=1}^{n} \sqrt{q_{sx,i}^2 + q_{sy,i}^2} \qquad (2).$$

In (1) and (2), q_{sx} and q_{sy} are the components of the solid discharge along the coordinate axes, n is the sample dimension, q_s is the average solid discharge. Evaluating the latter by (1) gives the magnitude obtained by the time average components of the vector solid discharge, while (2) furnishes the time average magnitude of the instantaneous solid discharges. The information one

obtains from the two quantities is different: (1) is related to the resulting structure of the solid discharge field, while (2) is proportional to the average intensity of sediment motion regardless of the direction. Typically the solid discharge evaluated by (1) is smaller than that obtained via (2), since the presence of movements having different directions reduces the average components of the final vector. For a comparison between the spatial distributions of the two quantities see [10]. In the following, spatial distributions of the time average magnitude of solid discharge by (2) will be shown, together with average streamlines obtained via the solid discharge calculated via (1).

Fig. 6 presents the average sediment fluxes around the obstacles for the initial stage of the experiments (time T < 20 s). In this phase the scour rate is maximum, as it is shown in Figs. 2 and 3. Maximum sediment activity is located in the proximity of the abutment nose in both cases, with similar maximum values of the solid discharge. Spatial distribution of the average sediment flux is consistent with previous literature indications on the average shear stress distribution around the obstacles (see for example [17] and [18]), which presents a maximum at the abutment nose due to the flow concentration in the same position. Higher solid discharges span a wider area in the case of the vertical wall abutment, indicating a larger intensity of the flow field, that is reasonably due to the bluntness of the obstacle. The large solid discharges around the abutments are not directly linked to the great erosive power in this phase, since the scour rate is related to the spatial variation of the sediment flux and not to the maximum flux values; yet it is reasonable that larger solid discharge values will result in a larger divergence of the vector flux, and thus in a larger erosion depth.

The average streamlines turn around the obstacles, with increasing solid discharge as the streamlines are travelled; this effect is due to the progressive entrainment of new sediments, that join to those coming from upstream. Sporadic upward direction were measured for both the abutments near the channel lateral wall. Literature visualizations of the scouring flow field around rectangular and trapezoidal abutments in the flat bed condition ([18] and [19]) showed the presence of the principal vortex structure, that would result in diffuse upward sediment movements. Present findings show that the principal vortex is, on average, highly stretched along the mean flow direction, and upward movements are limited to the wall region. For the rectangular abutment the recirculation area downstream of the obstacle was filmed; the wake vortex, whose trace is evident from the observation of the average streamlines, appears to be responsible for high solid fluxes.

As the scour depth increases, the sediment pattern around the obstacles varies. We show the average sediment movement fields at the two obstacles for similar values of the dimensionless scour depth, regardless of the time needed to reach such erosion levels. The effect of the abutment shape on the temporal development of the erosion depth was already shown (Fig. 4); now we intend to investigate the effect of the abutment shape in determining the flow field and thus the sediment pattern on a similar scour hole. Results are presented in Figs. 7 and 8. The average solid discharge decreases at both the obstacles as larger scour levels are achieved, due to the flow field weakening that is consequent to the increase in the area available for the flow conveyance. Sediment fluxes at the trapezoidal abutment are smaller than those at the vertical plate, owing to the fact that the streamlined obstacle produces a weaker recirculation of the flow. The area where sediment activity is larger spans a sort of circumference around the obstacle nose; it is remarkable to note that near the obstacle walls the solid discharge flux is weak, indicating that the flow field is inhibited by the corner between the abutment face and the bed. Actually shear distributions on a scoured bed around bridge piers present a maximum in a region that is qualitatively consistent to that where we observed the maximum sediment fluxes (see [20]). The large activity region delimits two parts of the scour hole; in the inner one (that closer to the abutment) the sediments are moved by the flow field and conveyed downstream around the obstacle. In the outer one the sediments either slide along the scour hole or are displaced by occasional transport events, with a longitudinal direction; as they arrive at the active zone, they are entrained by the principal movement. The above effect is more evident for the trapezoidal abutment thanks to the small dimension of the inner area, that instead covered nearly all the image for the vertical plate. The average solid discharge increases along the streamlines, as was previously noticed for the initial phase of the erosion process. In this phase the action of the principal vortex is clearer for the vertical plate, where upward movements were measured upstream of the abutment nose. The effect of the wake downstream of the vertical plate is still clearly identifiable.

Figure 9 presents the solid discharge fields for a more developed condition (dimensionless scour depth d/b is equal to 1.80). For the vertical plate, the focus area of the CCD was shifted upstream to capture the upstream part of the scour hole; as a consequence, the recirculation downstream of the abutment is no more visible, even if the direct observation of the phenomenon in process showed it was similar to the previous instants. It can be seen anyway that the wake is responsible for the largest sediment fluxes.

The activity regions are similar to those previously described; yet there is no systematic increase of the solid discharge along the streamlines. This would indicate the presence of movements that do not result in real migration of the sediments, but rather in displacements that are not effective for the sediment leaving the hole and thus for the scour depth increase. This is particularly evident for the trapezoidal abutment. For the latter, the action of the principal vortex is now evident from some upward movements near the channel wall. The sediment pattern around the vertical plate is more complicated: there are two zones of relatively considerable activity (near the channel wall for $x \cong 830$ mm and upstream of the abutment nose, $x \cong 940$ mm and $y \cong 120$ mm), where the solid discharge assumes relatively high values and the sediment streamlines are considerably directed upstream. This is particularly evident also for the successive stages of the erosion process, as is shown in Fig. 10. This observation can be interpreted with the existence of two vortical systems, the first of which is larger and localized near the channel wall, while the second is smaller and located upstream of the abutment edge. It is interesting to note that the smaller vortex is reasonably responsible for the formation of the sediment hill in the same position

(compare Figs. 10 and 5, even if they are for different scour levels). The larger vortex is present also upstream of the trapezoidal abutment, while the smaller is typical of the vertical plate, again due to the bluntness of such obstacle.

Figs. 11 and 12 present some spatial distributions of the variation coefficient CV of the solid discharge (CV is defined as the ratio between the standard deviation and the mean value of the solid discharge sample). It can be seen that irregularity of the scour process increases for growing scour depth (and thus for smaller sediment activity), as was found also in previous works ([8] and [10]). Comparison between the maps for the vertical plate and the trapezoidal abutment shows that irregularity of the scour process is larger for the streamlined obstacle, indicating again that there is a correspondence between small activity and large irregularity. The last consideration is enforced by the observation that, for both the experimental times we show, the areas where there are the maximum flux are also those where the coefficient of variation is minimum. This was interpreted admitting that in all the locations the flow field can reach similar maximum intensity, but this leads to high irregularities where the mean intensity is rather weak.

VI. Conclusions

In this work we analyzed the scour development and the sediment motion around bridge abutments. The experiments were run in a pressurized duct to allow for optimal vision conditions, essential for acquiring films of the sediment motion to be processed to obtain quantitative indicators. We tested two types of abutment, a vertical plate and a trapezoidal obstacle, to investigate similarities and discrepancies in the scour process due to the abutment shape.

The scour depth evolution is consistent with those obtained during experiments with a free surface; dimensionless maximum scour depth at the trapezoidal abutment is about 75 % of that at the vertical plate.

Data on the sediment kinematics were analyzed to infer the description of the scouring flow field. The average solid discharge for certain locations and evolution stages was assumed as an indicator of the sediment activity and of the erosive power of the flow field. The sediment activity decreases for both the obstacles as the process develops.

The sediment patterns at the obstacles are rather similar in the initial phase of the process, where the principal vortex system is highly stretched along the main direction in both cases. Next, bluntness of the vertical plate determines a larger evidence of the three-dimensional vortical systems: the principal vortex is present at both the abutments, even if it is weaker in the trapezoidal case; in the vertical plate, a second vortex system develops upstream of the abutment nose, that is not present in the trapezoidal case. Some features of the scour hole shape were interpreted on the basis of the observations on the sediment motion.

Irregularity of the sediment motion is inversely proportional to sediment activity. Thus, the variation coefficient of the solid discharge increases in time, being much larger in case of the trapezoidal abutment than in that of the vertical plate.

References

[1] G. Oliveto and W.H. Hager, "Temporal evolution of clear water pier and abutment scour", *J. Hydraul. Eng.*, vol. 128, pp. 811-820, 2002.

[2] S.E. Coleman, C.S. Lauchlan and B.W. Melville, "Clear-water scour development at bridge abutments", *J. Hydraul. Res.*, vol. 41, pp. 521-531, 2003.

[3] B. Dargahi, "The turbulent flow field around a circular cylinder", *Exp. Fluids*, vol. 8, pp. 1-12, 1989.

[4] R.T.F. Kwan and B.W. Melville, "Local scour and flow measurements at bridge abutments", *J. Hydraul. Res.*, vol 32, pp. 661-673, 1994.

[5] F. Ahmed and N. Rajaratnam, "Observations on flow around bridge abutment", *J. of Engineering Mechanics*, vol. 126, pp- 51-59, 2000.

[6] M.H. Tseng, C.L. Yen and C.C.S. Song, "Computation of three-dimensional flow around square and circular piers", *Int. J. Numer. Meth. Fl.*, vol. 34, pp. 207-227, 2000.

[7] A. Chrisohoides, F. Sotiropulos and T.W. Sturm, "Coherent structures in flat-bed abutment flow: computational fluid dynamics simulations and experiments", *J. Hydraul. Eng.*, vol. 129, pp. 177-186, 2003.

[8] S. Malavasi, A. Radice, and F. Ballio, "Study of Sediment Motion in a Local Scour Hole through an Image Processing Technique", *River Flow 2004, II Int. Conf. on Fluvial Hydraulics, Naples, Italy*, 2004, vol. 1, pp. 535-542, 2004.

[9] A. Radice, S. Malavasi, and F. Ballio, "PIV Analysis of Sediment Kinematics in an Abutment Scour Hole", *ICSE 2004, II Int. Conf. on Scour and Erosion, Singapore*, vol. 2, pp.359-366, 2004.

[10] A. Radice, S. Malavasi, and F. Ballio, "Time Evolution of Erosion Depth and Sediment Motion for Abutment Scour in a Pressure Duct", *River Flow 2006, III Int. Conf. on Fluvial Hydraulics, Lisbon, Portugal*.

[11] A. Radice, S. Franzetti, and F. Ballio, "Prove Sperimentali di Erosione Localizzata in un Condotto Rettangolare in Pressione (Local Scour Experiments in a Rectangular Pressurized Duct)", *XXX Convegno di Idraulica e Costruzioni Idrauliche, Roma* (in italian).

[12] B.W. Melville, "Pier and Abutment Scour: Integrated Approach", *J. Hydraul. Eng.*, vol. 123, pp. 125-136, 1997.

[13] F. Ballio and E. Orsi, "Time evolution of scour around bridge abutments", *Water Engineering Research*, vol. 2, pp. 243-259, 2001.

[14] W. H. Wong, "Scour at bridge abutments", *Report n. 275, University of Auckland, Auckland, New Zealand*, 1982.

[15] R.T.F. Kwan, "A study of abutment scour", *Report n. 451, University of Auckland, Auckland, New Zealand*, 1988.

[16] A. Radice, "Cinematica dei Sedimenti in un Fenomeno Erosivo Localizzato (Sediment Kinematics in a Local Scour Phenomenon)", *PhD Thesis, Politecnico di Milano, Milan, Italy*, 2005 (in italian).

[17] S. Ouillon and D. Dartus, "Three-dimensional computation of flow around groyne", *J. Hydraul. Eng.*, vol. 123, pp. 962-970, 1997.

[18] A. Teruzzi, S. Salon, F. Ballio and V. Armenio, "Numerical investigation of the turbulent flow around a bridge abutment", *River Flow 2006, III Int. Conf. on Fluvial Hydraulics, Lisbon, Portugal*.

[19] V. Armenio, E. Caroni and V. Fiorotto, discussion to "Equilibrium clear-water scour around an abutment", *J. Hydraul. Eng.*, vol. 124, pp. 1069-1070, 1998.

[20] B.W. Melville and A. J. Raudkivi, "Flow characteristics in local scour at bridge piers", *J. Hydraul. Res.*, vol. 15, pp. 373-380, 1977.

Erosion in the Foundation of Abshineh Dam (Iran)

M. Rajabalinejad First author*,**, M. H. Baziar Coauthor*, A. Noorzad Second coauthor*, and J.K. Vrijling Third coauthor**

* Iran University of Science and Technology (IUST)/ Civil engineering faculty, Tehran, Iran
** Delft University of Technology (TUDelft)/ Civil engineering faculty, Delft, Netherlands

Almost 75% of dams in the world are constructed from soil and rock [1]; and, they can easily be damaged by seepage and piping. Earth fill dams usually suffer from this problem more; and, only a short time after the first impounding several embankment dams have collapsed [1,3, 4].

Abshineh dam, located in the west of Iran, is an earth fill dam with a clay core in which a complicated seepage has appeared through its foundation. Though, insufficient insitu testing and incomplete geotechnical investigations has led this situation, yet the highly weathered rock of foundation, insufficient depth of cut-off wall, and a fault and a Qanat[1] crossing its foundation are the most important elements which must be considered in its seepage analysis.

SEEP2D, a well-known program in the underground seepage analysis, has been used to analyze the seepage flow and find the most eroded areas in the foundation of Abshineh dam. To make seepage model with a two-dimensional program, the dam body and its foundation has been divided into several sections; and, for each section uniform soil properties are assumed. Then, the model has been updated with the insitu data which are mainly drilling, grouting, and piezometric data.

Outcomes of the analysis show a very good agreement between the calculated results and measured data. Moreover, the results prove that a high rate of erosion has been occurred in an extended zone of the dam's foundation. Moreover, the analyses of one line grouting, the method used to get the weathered foundation of Abshineh dam watertight, shows that this method does not provide a permanent remedial pattern.

In fact, the efficiency of (a very condensed) one-line grouting in a limited zone of the foundation of Abshineh dam has been analyzed and estimated maximum 60% (for seepage reduction) by the finite element program; therefore, the past experiences and conclusions[2] declaring that the reliability of one line grouting system is not as much as engineers can trust on it as the only system for seepage's controlling is certainly certified.

Moreover, the conclusions of this research must be considered for the optimized selection of the remedial method.

This research is sponsored by Water Resource Management, Ministry of Power, Islamic Republic of Iran.

[1] Qanat is a continued underground aqueduct (small tunnel without lining) which was invented in Persia and used to transit water from mountains to flat areas. Also, vertical shafts with equal distances were used to access to Qanat and dredge it. More information can be found on www.Qanat.info.

[2] Prof. Terzaghi and Prof. Casagrande, First rankine lecture, Geotechnique, 1961.

FIGURE 1. ABSHINEH DAM AND ITS RESERVOIR, HAMADAN, IRAN

I. INTRODUCTION

The Abshineh dam is a clay core dam located in Hamadan, one of the provinces of Iran, on the Abshineh River and downstream from Ekbatan dam. A picture taken over the crest of Abshineh dam is presented in Fig 1. The Abshineh dam was constructed in 1996 to secure the water supply and irrigation needs of Hamadan city. Moreover, the discharged water of Ekbatan dam accumulates behind Abshineh dam. Table 1 presents the main characteristics of the Abshineh dam.

Fig 2 shows a typical cross section of Abshineh dam, which is comprised by three main parts: rock fill, clay core, and filter. The double filter at the downstream side is used to prevent piping or transportation of clay particles from the core into the rock-fill zone. It is

TABLE 1
THE MAIN CHARACTERISTICS OF ABSHINEH DAM

	Abshineh Dam's Characteristics	
1	Maximum height of dam	18 M
2	Abshineh dam's crest level	MSL+1818
3	Maximum water level	MSL+1818
4	Normal water level	MSL+1815
5	Crest length	660 M
6	Crest width	8 M
7	Normal reservoir capacity	5,000,000 M^3
8	Area of reservoir	750,000 M^2
9	Length of reservoir	1200 M

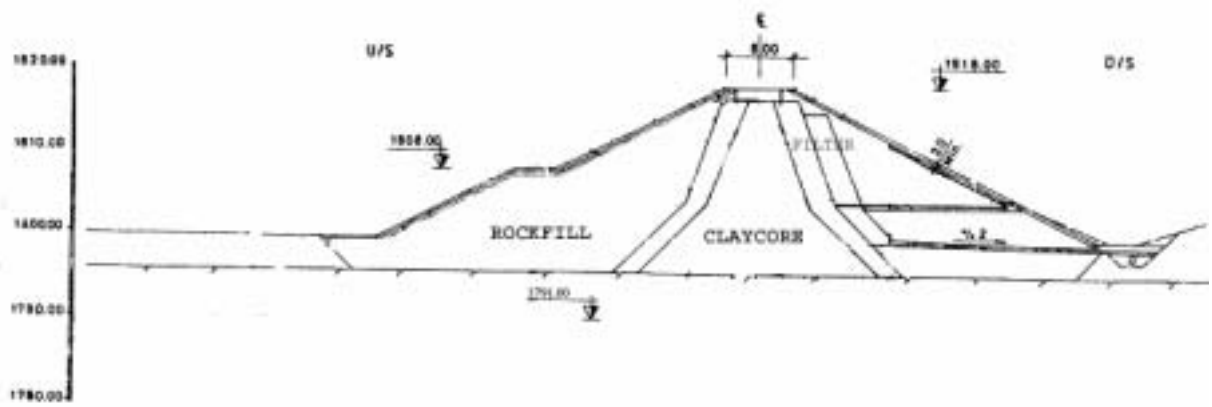

FIGURE 2. TYPICAL CROSS SECTION OF ABSHINE DAM

important to notice that an appropriate design of filter and its material size can perfectly prevent piping through the dam's body [2]. Also, a short cut-off wall with a constant depth of two meters had been designed, yet because of differing depths of the constructed cut-off wall, varying from 0.35 to 2 meters, it is not included in this Figure, neither in the seepage analysis. Nevertheless, it must be considered that in a weathered rock foundation like Abshineh dam's, a cut-off wall is an important element which can change the underground flow path, and especially prevent piping through the contact layer and foundation.

Fig. 3 represents a plan view of the Abshineh dam. Its right embankment is extended to make a higher reservoir capacity. In addition, the concrete structure[3], being used to discharge reservoir water, is displayed in this figure. Letters accompanied with numbers (C38, C37…) over the crest of the dam signify the primary grouted boreholes in an effort to get the foundation watertight; some of them, however, are not grouted.

The interest is focused on the difficult foundation of this dam: a complex site, both in a geological and geotechnical matters. For instance, the combination of karstic limestone and silt in the highly weathered foundation rock is clearly an indicator of a potential seepage problem, and generally cause to wash out the silts and clay particles through the limestone fissures.

It is not possible here to elaborate on the design process of Abshineh dam, but it is important to mention that this project has a lack of basic investigation; only one exploration borehole was drilled at the dam's location [1, 7-9]; in other words, the geological profiles of foundation are schematic. In fact, this case is a clear example that the underground condition cannot be guesstimated, and *geotechnical examinations are a very important part of the design processes of infrastructures* [10]. Accordingly, the Qanat and fault which cross through the foundation of Abshineh dam were not considered in the first design.

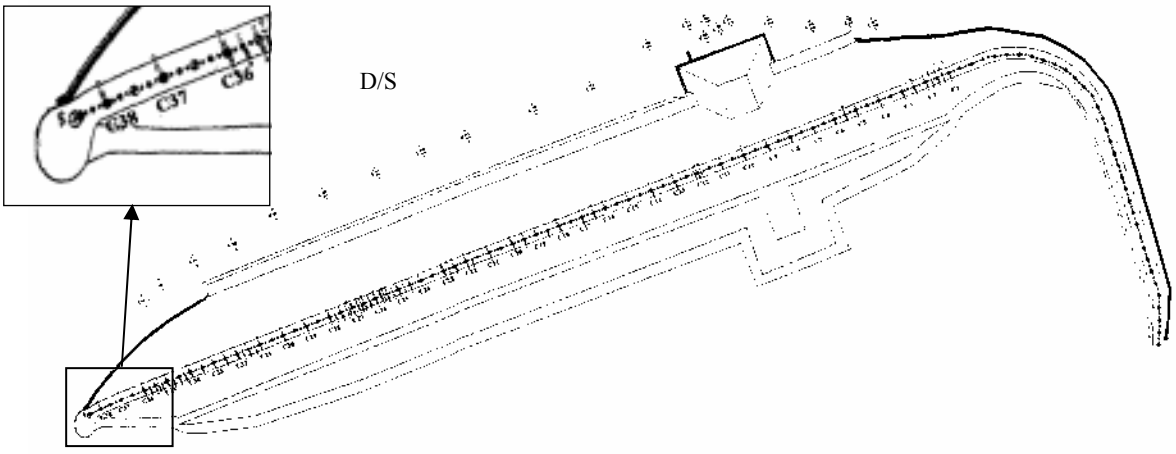

FIGURE 3. PLAN VIEW OF ABSHINEH DAM, *STATION E, WHICH IS MAGNIFIED, IS LOCATED ON* THE LEFT BANK WERE THE HEIGHT OF CLAYCORE IS ZERO

[3] Because of the probability of piping, it is suggested avoiding design of a (concrete) structure passing through the clay core; and, in the case of Abshineh dam regarding the highly weathered foundation, presence of this structure means an *unacceptable risk of failure*.

II. DAM SITE GEOLOGY

The valley of Abshineh dam is almost symmetrical. The left abutment has a slope of around 4.5%, and the right abutment has a 13.6% slope below 1814 +MSL and 3.3% above that level. The site is located at Sanandaj-Sirjan[4] zone, expanding overall the northeast of Hamadan, one of the provinces of Iran.

The formations under dam are a composite of shale, marl-shale and sand-shale in the color of gray-dark to gray-light blue followed by layers of lime sand-stone with medium sand size; and, the main composite is marl-shale. The mineral combination of the main bedrock is marl-shale, clay-silicate, quartz, and carbonate combination. In addition, some metal minerals such as Fe_2O_3 can be found in the field. Shale is highly weathered, and sandstone layers are in better situation [7].

The insitu data which includes boring, testing, and grouting displays a highly cracked zone within 2 to 3 meters depth under the base of Abshineh dam, and its uniaxial strength is close to 12 MPa. Medium and high weathered rocks are at a depth of 2-6 meters below the base. And, in deeper places, there are usually better rocks, and the uniaxial strength gets up to 32 MPa or more. On the other hand, all samples of surface rock saturated in a limewater solution for 48 hours changed to clay phase.

III. HISTORY OF PROBLEMS AND GROUTING

During the construction of Abshineh dam, a high rate of water flow passing through the foundation was detected when the rain water accumulated behind Abshineh dam could easily flow through the foundation; therefore the consultant[5] company tried to suggest a cure pattern for sealing the foundation; to evaluate one line grouting as a cure method, a grouting test was proposed and accomplished in a limited region over the half-constructed clay core (the height of the dam was maximum 5m from its base). The grouting test was applied at 0+430m from station E, located in the left abutment as it is presented in Fig. 3. In the grouting pattern, boreholes A1 and A2 (with distance of 6 meters) were drilled and grouted first; then A3, and in the next step A4 and A5 were drilled and grouted. Finally, two checking boreholes, named CH1 and CH2, were drilled to evaluate the performance of grouting in seepage reduction. A schematic draw of this pattern is shown in Fig. 4.

The main conclusions of this (grouting) test were: 1- Permeability of clay core was acceptable. 2- The highest permeable zone was under the cut-off wall. 3- Grouted cement decreased permeability of the foundation. 4- Contact zone between clay core and its foundation had a permeability of 10^{-4} cm/s [11].

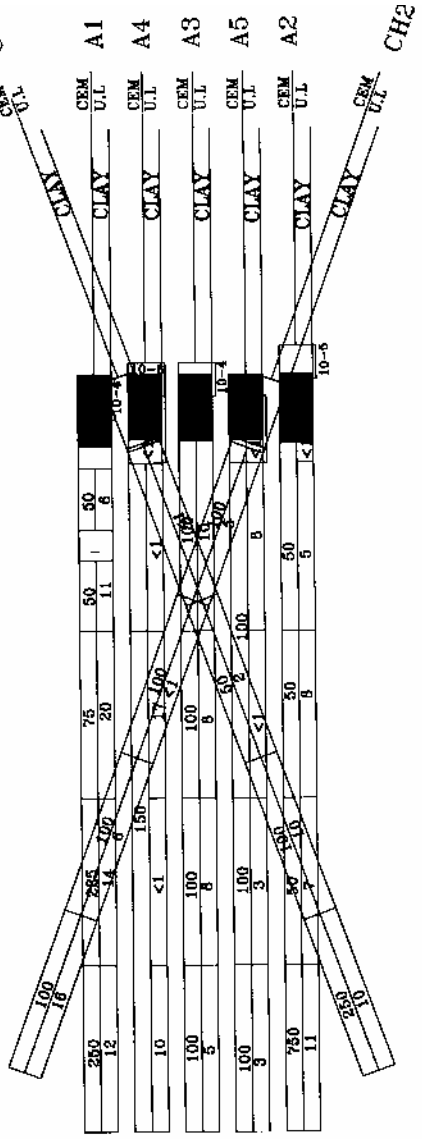

FIGURE 4. DETAILS OF TRIAL GROUTING IN 0+430 FROM LEFT OF THE DAM

Then, one-line grouting of mixed cement[6] along the top of the crest in permeable areas of foundation was suggested as a remedial plan, in which at first the distance between boreholes was 16 m and this could reduce to 2 meters by the dividing method. In this manner, the permeable boreholes were grouted, and the low permeable ones were filled with cement.

However, considering the fact that only one-line grouting was possible because of limited width of the clay core on the top and bearing in mind the past experiences of one line grouting, [1, 3, 4, 12], and conclusions of some experts[7] that *the maximum efficiency of a grout curtain can usually cause a reduction of seepage by maximum 30%,* some questions about the

[4] Sanandaj-Sirjan is one of the most dynamic (seismic) zones of Iran; and, this zone has registered diverse phases of magmatism, metamorphism and deformation. More information about this zone can be found in: http://www.ngdir.ir/States/

[5] Mahabe Ghods engineering company.

[6] Combination of cement, bentonite, and water.

[7] Prof. Terzaghi and Prof. Casagrande, First Rankine Lecture, Geotechnique, 1961.

capability of this curative method come to the mind: How effective is this method? Or, is this a permanent remedial scheme?

After first impounding in 1996, seepage was observed at the downstream side, and so was grouting restarted in the areas that had not been grouted before (low permeable boreholes). Then, at second impounding in 1999 when water depth behind the dam was not more than 6 meters, water flow was observed at three locations of downstream side: right, center, and left. The rates of discharges flowing over the downstream were estimated 20 lit/s at right and almost 4 lit/s at left; yet, the seepage rate in central part was low. As a matter of fact, development of seepage faced Abshineh dam with internal erosion; and, in as much as it might cause instability of dam, the impounding was interrupted, the reservoir water was completely discharged, and grouting was seriously restarted.

It is important to notice that the reservoir was discharged in a dry season and caused economic damages especially for the farmers of downstream side.

In this time, even grouting more than 7.5 tons mixed cement in C1, a borehole at the right abutment of dam, it did not fill, so was a shaft with diameter of 70 cm bored from the crest, and the excavation exposed a fault under the foundation. Fig 5 shows some pictures related to this borehole and fault. To close this fault, it was filled with concrete and rock in one-meter thickness, and then it was grouted with mixed cement.

Meanwhile, the primary boreholes, C11, C12, C13, C14, C27, and C34, intersected with cavities under the concrete cut-off wall; these cavities clearly show the karstic nature of the foundation. In addition, close to left abutment, borehole C27 crossed an old Qanat, (Qanat term is explained in the first page).

IV. MODELING

Seepage of Abshineh dam has been analyzed using SEEP2D, a two dimensional (2D) finite element program produced by Fred Tracy. Seep2D is a valid program for seepage analysis; and, many international projects have been analyzed by this program.

Nevertheless, using a two dimensional program provides some restrictions. For instance, making a model including different zones of a foundation, Qanat, or fault is not possible. To overcome the limitations, the dam is divided into eight different zones by length, and each zone is modeled separately; 8 zones totally have been defined, and information of these zones are summed up in Table 4. In addition, the analyses have been done for two reservoir water levels: 1809 and 1818 which represent the water level of existing data and full supply level, respectively.

Figure 6 shows the basic model used for seepage analysis of Abshineh dam. The main elements constructing the model are a clay core, grout curtain, weathered rock, and fresh rock. The cut-off wall, with varying depth, and rock-fills are not included in the model.

FIGURE 5. BORING A MANHOLE OVER THE CREST, C1 CROSSED THE FAULT THROUGH THE FOUNDATION

The grout curtain, being a zone with lower permeability, is modeled by low permeable elements, and its permeability and thickness is estimated by using the information of grouted boreholes and some checking boreholes. Furthermore, the Qanat which passes through the foundation of Abshineh dam is modeled as a small tunnel. Figure 8 presents the results of the analyses of the full reservoir water level. In this case, the outcomes of the analyses have been used for evaluation of the sealing approach used in the Qanat and fault passing through the foundation of Abshineh dam.

The data which are used for updating the model can be divided into two categories: the data of drilling boreholes including insitu testing and grouting, and the piezometric data. The first group of data, in this case, is used as a base of modeling, and the second group is used for controlling and updating the model.

In other words, the average of insitu testing and grouting data in each zone defines the permeability of the clay core, weathered rock, fresh rock, and grouted area.

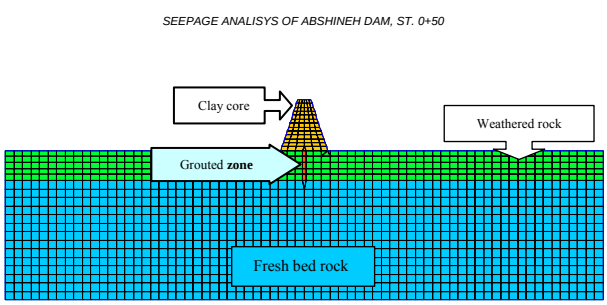

FIGURE 6. ABSHINEH DAM'S BASIC MODEL USED FOR SEEPAGE ANALYSIS

Therefore, this is a practical modeling that is completely based on the insitu data. Meanwhile, the piezometric data can effectively help updating the model; every piezometer, moreover, can act like an alarm announcing the internal erosion or increasing seepage energy. Unfortunately, at the first impounding of Abshineh dam, no pizometer was installed; although, it had been designed. However, at the second impounding in 1999 several piezometers were installed in three typical areas: clay core, contact zone, and foundation rock to measure local pore pressures. The 5th column of Table 4 presents the name of piezometers.

V. Analysis Results

As it is previously explained, in order to utilize the SEEP2D, the dam body and its foundation is divided to eight zones, and the average properties of each zone is applied to the model. The information of defined zones and the analysis results are summarized in this Table 4.

A. The Fist Zone

The first zone, is the first 40 meters of dam's length from left bank (station E), where the height of clay core is zero, as it is depicted in figure 3. The first row of the Table 4 presents the information of this zone.

However, there are no data to calibrate model for this zone; yet, the high permeability of C34, located in the border of this zone, and flowing water at the downstream side after grouting of the second zone signifies high permeability of this zone. In other words, the water flow in the left part of downstream side comes from this zone.

B. The Second Zone

In the second zone, including main boreholes, C35, C36, and several intermediate boreholes, no grouting had been done before first impounding. Yet, after seepage flow at the downstream side, this zone was completely grouted. The seepage has been analyzed on the base of data coming from drilling boreholes, insitu testing, and grouting; and the results show that both highest velocity of underground water flow and the volume of seepage have been reduced by nearly 60%. Table 2 presents the results of the analysis of seepage before and after grouting. Meanwhile, the area of high velocity seepage has been decreased as it is shown in Figure 7; so grouting does reduce seepage through the foundation and the contact layer.

TABLE 2.
Results of The Seepage Analysis Before and After Grouting in The Second Zone

MSL +	Before grouting		After grouting	
	Seepage (lit/day)	Max. velocity (m/day)	Seepage (lit/day)	Max. velocity (m/day)
1809	430	0.092	143	0.026
1815	1436	0.031	480	0.089

C. The Third Zone

The main boreholes of the *third zone*, also, had divulged a low permeability before impounding. However, the piezometric data revealed a higher permeability. In fact, backward analysis of seepage shows that erosion has been occurred in the foundation of Abshineh dam.

In order to find the rate of erosion, backward analyses were done; in this case different value of permeability has been tested as input data for the analysis. A brief of this process is summed up in Table 3; and it results a higher permeability almost 5.5 times more than the time before impounding (for duration of near two years) which proves a high rate of erosion. The total seepage volume estimated for entire of this zone is presented in Table 4.

TABLE 3.
To Get Equivalent Pore Pressure (water-level), Backward Analysis Has Been Done With The Assumed Permeabilities

MSL +1809	Piezometer A4		Piezometer A5	
	measured water level	calculated water level	measured water level	calculated water level
1ST	70.1807	1805.4	1802	1802.5
2ND	70.1807	1807.63	1802	1800.75
3RD	70.1807	1807.17	1802	1801.67

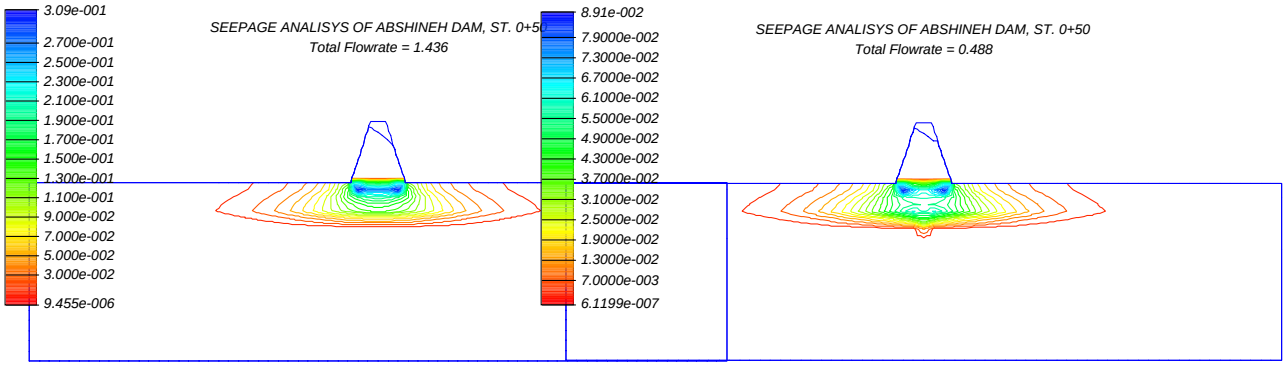

FIGURE 7. GROUTING HAS REDUCED BOTH VOLUME AND VELOCITY OF SEEPAGE; LEFT PICTURE SHOWS CO-VELOCITY CONTOURS BEFORE GROUTING AND RIGHT PICTURE PRESENTS THE SAME CONTOURS AFTER GROUTING

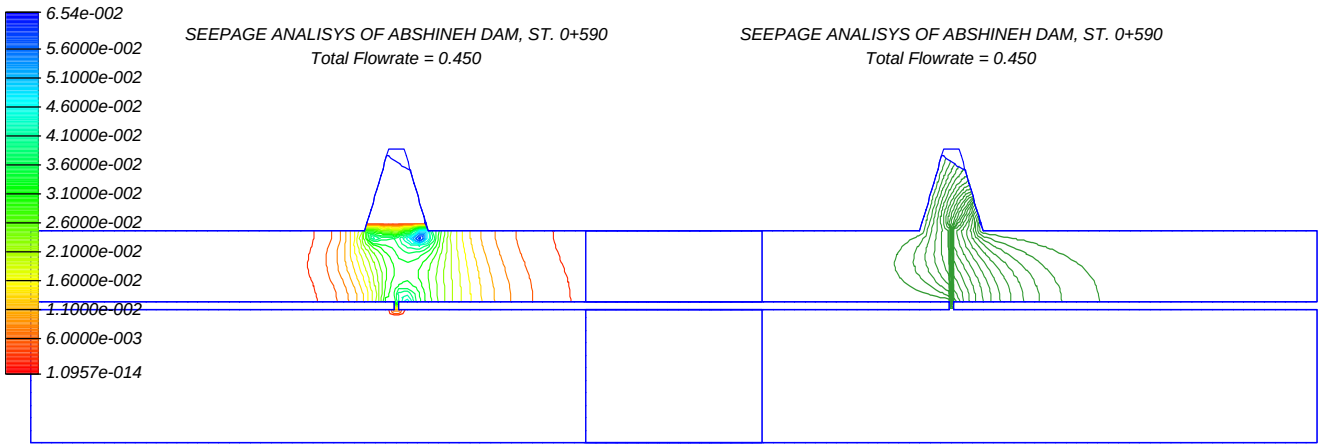

FIGURE 8. THE MODEL OF QANAT IN FOUNDATION OF ABSHINEH DAM. THE LEFT PICTURE SHOWS THE CO-VELOCITY CONTOUR, AND THE RIGHT ONE PRESENTS CO-POTENTIAL CONTOURS.

D. The Fourth Zone

In the fourth zone, half of the drilled boreholes had disclosed a permeability of 10^{-3} cm/s during insitu testing. In C27, one of the most permeable boreholes, a manhole was bored, and met an old Qanat. To close the Qanat flow path, it was filled with concrete and rock in one-meter thickness, and then it was grouted with mixed cement. This method is, also, was used to close C1 (see Fig. 5).

In order to check the performance of this closing method and its effects on the surrounded areas, a separate modeling is done. Fig 8 shows the results of model analysis used for Qanat and closing approach. As shown in this figure, concentration of high velocity seepage is an undesirable consequence of this closing method; as a result a high rate of erosion over the full length of grout curtain especially in weathered rock near the contact layer will be happened, and this case can seriously encourage piping; *so this closing approach does not provide a permanent remedial method at all!*

E. The Fifth Zone

In the fifth zone, no grouting had been done before the first impounding because of the fact that permeability of this area was reported very low by drilling of boreholes and insitu testing; nevertheless, after impounding, the out flow of water at the downstream side showed a high permeability. Meanwhile, the piezometers of this zone had many things to tell; in other words, analysis of the data of piezometers A7d and A10, located at the weathered rock of foundation, showed that a high rate of erosion has occurred after impounding. In fact, there is a big difference between the data before and after impounding. As a matter of fact, the backward seepage analysis demonstrates that if $K_x = K_y = 10^{-4}$ cm/s, the pore pressure is in agreement with the data of piezometers which do very well correspond with each other; so has high rate of erosion occurred in this zone. This fact confirms the result of the other zones, and proves the erosion-able nature of the Abshineh dam's foundation. Accordingly, three important conclusions can be drawn from the analysis of this zone: *first, no grouting in this zone caused fast erosion in the foundation. Second, a high rate of erosion is expected in weathered foundation of Abshineh dam; so will not grouting have a long lasting effect. The third conclusion is a high probability of piping in the contact layer.* The estimated seepage volume of this zone is presented in Table 4.

F. The Sixth Zone

The sixth zone spreads over 75m along the dam axis whereas the last 30 meters is located on the right abutment. This zone, also, was reported to be a low

TABLE 4.
CALCULATED RATE AND VOLUME OF SEEPAGE FOR DIFFERENT ZONES OF ABSHINEH DAM IN 1818 +MSL

Zone number	Start from	End to	Boreholes	Piezometers	Max. Velocity (cm/day)	Seepage (lit/m/day)	Seepage (lit/day)
1	0+0 (station E)	0+40	----		---	---	---
2	0+40	0+60	C29 to C36		8.90	480	9600
3	0+ 60	0+170	C26 to C33	A1u, A1d, A2, A4, A5	1.76	93	10،230
4	0+170	0+230	C24 to C28		4.69	247	14،820
5	0+230	0+410		A7u, A7d, A10, A11	4.68	316	56،880
6	0+410	0+585	C2 to C12	A13u, A13d, A14	2.10	121	21،175
7	0+585	0+600	C1		9.47	865	12،975
8	0+600	0+678		A21u, A21d	---	---	---
Total calculated seepage from Abshineh dam and it's foundation							125،680

permeable area before impounding, and it includes boreholes C2 to C12. Piezometers, named A13u, A13d, and A14 are located in this zone, and the model was updated with the piezometric data. The backward analysis of this zone, also, demonstrated internal erosion in the foundation. The estimated seepage volume of this zone is presented in Table 4.

G. The Seventh Zone

The seventh zone contains borehole C1, having a permeability of more than 100 Lugeon (1 Lugeon unit = 1 litre/m/minute at 150 psi) over its full length. This borehole intersected a fault crossing dam axis through the foundation. In order to make this borehole watertight, more than 7.5 tons of mixed cement was grouted without getting any result. Then, boring a manhole from the crest, it crossed a horizontal highly cracked fault with north to south direction. Therefore, it was closed in the same manner as C27; so can the analysis approach of Qanat (see Figure 8) also be applied for this zone. The analysis results of this zone are presented in table 4.

H. The Eighth Zone

There is a lack of data in the last zone, *eighth zone*. However, some piezometers have been installed, yet the fault can act like a drainage system; it easily affects on the piezometric data. Meanwhile, the possibility of erosion must also be considered.

CONCLUSIONS

1. The efficiency of (a very condensed) one-line grouting in a limited zone of the foundation of Abshineh dam has been estimated maximum of 60% of seepage reduction by a finite element program, and regarding the past experiences [1, 3, 4, 12] and conclusions[8], it is concluded that the reliability of one-line grouting system is not as much as engineers can rely on it as the only system for seepage's controlling.
2. The in-situ and piezometric data proves that a high rate of erosion has been occurred in the foundation of Abshineh dam estimated almost 5.5 times more than the time before impounding for the two years period.
3. Since concentration of seepage with higher velocity occurs in the grouted zones, its performance in the grouted zones will be reduced by seepage; so the one-line grouting does not prepare a permanent remedial method.
4. The analysis of method which was used to seal the Qanat and fault shows that the surrounding area of the Qanat (or fault), grouted zone, and especially the contact layer are faced with a high probability of erosion. It means that there is a high risk of piping for that area; in this case, the repairing procedure will be a very difficult task.

[8] Prof. Terzaghi and Prof. Casagrande, First rankine lecture, Geotechnique, 1961.

RECOMMENDATIONS

1. It is recommended that *engineers do not rely on the one-line grouting system as the only system for seepage's controlling.*
2. Evaluation of *the reliability of one line grouting* is an important research subject for dam engineers.
3. As far as a reliable remedial method has not been applied, developing a risk assessment system for this project, including the economical model of downstream fields is recommended.
5. The results of this research should be considered for the selection of the optimized remedial method.

ACKNOWLEDGMENT

The Organization of Water Resource Management, one of the national organizations of The Ministry of Power of Islamic Republic of Iran, has sponsored this research.

Also, the helps of Dr. Hans van Duivendijk, Dr. Pieter Van Gelder, and Dr. Wilfred Molenaar from civil engineering faculty of TUDelft for improving this article are kindly appreciated.

REFERENCES

[1] M. Rajabalinejad, M.H. Baziar, Ali Noorzad, *Investigations In To the Seepage of Dams, a Case Study Abshineh Dam*. Ministry of power, 2001: Tehran. P. 300.
[2] ICOLD, *dam foundations*, (2005), Bulletin No. 129.
[3] Seed, H.B. And J.M. Duncan, *the Failure of Teton Dam.* Engineering Geology, 1987. **24**(1-4): P. 173-205.
[4] Leps, T.M., *Failure of Teton Dam, 1976 - Response.* Engineering Geology, 1987. **24**(1-4): P. 217-220.
[5] Golabchi, I., *the Report of Abshineh Dam's Grouting*, Mahab Ghods Eng. Company.
[6] Lecture, F.R., *Control of Seepage through Foundations and Abutments of Dams by Arthur Casagrande.* Geotechnique, 1961.
[7] Mahabe-Ghods, *Geology Report of Abshineh Dam and Its Reservoir*, Mahab Ghods Eng. Company.
[8] Golabschi, I., *Geotechnical Exploration and Grouting of Abshineh Dam*. 1999, Mahab Ghods Eng. Company: Tehran.
[9] Mohammadreza Rajabalinejad, *Investigations In To the Seepage of Abshineh Dam*, In *Civil Engineering Faculty*. 2000, Iran University of Science and Technology: Tehran. P. 270.
[10] ICOLD, *Rock Foundation for Dams*, In *Bulletin No. 88*. 1993.
[11] Mahabe-Ghods, I., *Results of Grouting Test on the Abshineh Dam's Foundation*. 1997, Mahab Ghods Engineering Company: Tehran.
[12] *Darwin Dam Design and Behavior of an Embankment on Karstic Foundations*. In *International Commission on Large Dams*. 1999. Antalya: ICOLD.
[13] A. M. Scuero, G.L.V. *Remedial Works for Seepage and Aar Control by Using Watertight Geomembranes*. In *International Commission on Large Dams*. 1999. Antalya: ICOLD.
[14] A. Veiga Pinto, A.Q., A. Silva Gomes, Ana Maria Coelho. *Beliche Dam; Study of a Foundation Leakage*. In *International Conference on Large Dams*. 1999. Antalya: ICOLD.
[15] C.E. Schneeberger, T.I., Y. Pigeon. *The Use of Slurry Wall and Jet Grouting Techniques to Repair Existing Cofferdams*

at Lg-1. In *International Commission on Large Dams*. 1999. Antalya: ICOLD.

[16] Vrijling and Van Gelder, *the Effect of Inherent Uncertainty in Time and Space on the Reliability of Flood Protection*, In: Safety and Reliability, 1998b. Vol. 1, Pp. 451-456 Trondheim.

[17] Dan Dobrescu, C.T., Adrian Popovici, Radu Sârgltiuta. *Problems Related To Water-Tightness of A Dam Foundation Consisting of A Thick Alluvial Layer*. In *International Commission on Large Dams*. 1999. Antalya: ICOLD.

[18] Enrique Cifres, J.A.B. *Design of Embankment Dams Upon Highly Karstified Rock Foundation to Prevent Internal Erosion, Algar Dam Case (Spain)*. In *International Commission on Large Dams*. 1999. Antalya: ICOLD.

[19] ICOLD, *Grouting*: Bulletin No. 76.

[20] J.K. Can, L.A.M. *Mardi Dam - A Case Study Of A Dam on Permeable Foundations*. In *International Commission on Large Dams*. 1999. Antalya: ICOLD.

[21] Juan Antonio Bustinza, A.P., Juan Carlos Schefer. *Paso De Las Piedras Dam - Repair of Foundation Problems*. In *International Commission on Large Dams*. 1999. Antalya: ICOLD.

[22] Michal Lukac, M.L. *Design, Construction and Operation of Earth-fill and Concrete Gravity Dams on Permeable Soils and Rocks*. In *International Commission on Large Dams*. 1999. Antalya: ICOLD.

[23] Morando Dolcetta, G.R., Mauriz (Cavalli, Italy). *The Behaviour of Zoccolo Dam, Built on Permeable Soils*. In *International Commission on Large Dams*. 1999. Antalya: ICOLD.

[24] S.Y. Li, S.J.P., F.L. Kinstler. *A Concrete Faced Rock-fill Dam Constructed on a Deeply Weathered Foundation*. In *International Commission on Large Dams*. 1999. Antalya: ICOLD.

[25] Naeini, S. And M. Baziar, *Effect of Fines Content on Steady-State Strength of Mixed and Layered Samples of A Sand.* Soil Dynamics and Earthquake Engineering, 2004. **24**(3): P. 181-187.

Investigation for the Process-Oriented Development of Stability Formulae for Structures made of Geotextile Sand Containers

[1)]Juan Recio and [2)]Hocine Oumeraci
[1)]PhD Student, [2)]University Professor Leichtweiß-Institute for Hydraulic Engineering
Technical University, Braunschweig, Germany. j.recio@tu-bs.de, h.oumeraci@tu-bs.de
Bethoven st. 51a Braunschweig 38106, Germany

I. INTRODUCTION

The hydraulic stability of geotextile sand containers (GSCs) subject to wave action has been studied within an ongoing extensive research program at Leichtweiß Institute on the use of geotextile structures for coastal structures, including artificial reefs, revetments, sea walls as well as dune reinforcement.

Although the effect of the deformations of the sand containers on the hydraulic stability is significant, no stability formula is available to account for those deformations. To achieve a better understanding of these processes and to analyze the influence of the deformation on the stability of GSC-coastal structure, large scale model tests have been performed which are being complemented by: (i) VOF-modeling (volume of fluid) to simulate the outer and inner wave-induced flow field, including the resulting loads on the containers (validation and verification provided by the experimental data) and (ii) a Finite Element and Discrete Element modeling (FEM-DEM) to simulate the deformations and displacements of the containers. The paper will primarily focus on the results from scale model tests, including: (i) wave-induced forces on the sand containers, (ii) internal movement of sand in the containers and its effect on the stability and (iii) underlying processes leading to the deformations and displacement of the containers. Based on the model test results a better understanding of the processes which affect the stability of the revetment has been achieved, including the effect of the deformations of the sand containers and their mutual interaction.

In this paper, it is shown that the deformations of the geotextile sand containers strongly influence the stability of a GSC-revetment. The final goal of the project is to develop a generic hydraulic stability formula taking into account the effect of the deformations and that can be applied to a class of protective structures such as seawalls, revetments, breakwaters as well as dune and beach reinforcement.

II. EXPERIMENTAL SET-UP AND PROCEDURE

The model tests have been performed in the wave flume of the Leichtweiss Institute for Hydraulic Engineering and Water resources (LWI). At one end waves were generated. At the other end a revetment made of geotextile sand containers was built (figure 1).
The 2m-wide flume was divided in two sections. In the first section at the glass window, PIV measurements of the wave-induced flow are performed using the large-scale PIV system proposed by Bleck and Oumeraci [1]. The main characteristics of the PIV set-up are summed up in figure 3. The general PIV characteristics consisted in a measurement area of 2 x 1 meters, ("PIV-section") lighted with halogen lamps and using seeding particles having approximately the same density as water. Using the common commercially available PIV system with laser-light only a "PIV-section" of 0.25m2 (instead of the 2m2 with white light) can be obtained.

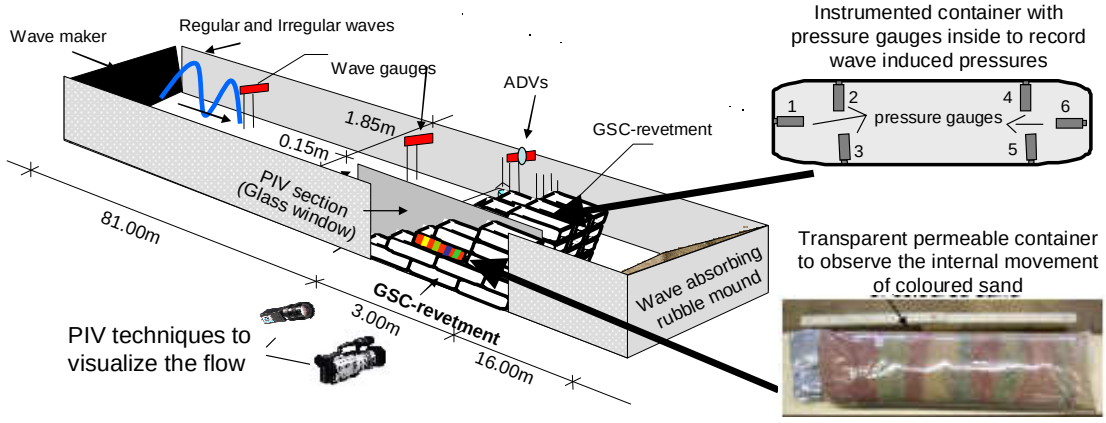

Figure 1: Experimental Set-Up

Inside the "PIV section", a single column GSC-revetment was installed (figure 2) and subjected to different wave conditions. Over the "PIV-section" two vibrating trays were constructed, from where the amount of seeding particles in the flow was controlled. To visualize the flow, the "PIV section" was illuminated using halogen lamps and the flow was recorded using a CCD-chip-camera (DMP-60-H13). This camera and the PIV section were covered with a black textile "tent" to avoid disturbance from other light (and noise) sources. After the images were recorded, the "DaVis PIV software" was used to process the velocity vectors.

Figure 2: GSC-revetment in the PIV-Section

(a) PIV General Characteristics

- Measurement Area: 2.0 x 1.0m over a width of 0.15m (black training wall parallel to glass window)
- Seeding Particles: PA12 Mix with ρ_s=1.01t/m³, d_s=3mm(≅1.3 Pixel) and w_{S0}=4.9cm/s
- Lightening: White light (2 x 1500 W and 1 x 500 W)
- Time interval between PIV-Pictures: Δt=1/10s

(b) CCD-Camera Characteristics

Camera	The Imaging Source DMP 60H13
CCD-Chip	Sony ICX084AL: 1/3", 659x494 Pixel, Pixel size 7.4x7.4 µm
Sampling Frequency	30 Hz and 60 Hz
Scanning Mode	Interlaced or Progressive Scan
Shutter	Electronically: off ÷ 1/10,000 s
Amplification	0-25 dB
Lens	f_n = 4.8 mm k_n = 1.8-16

Figure 3: Main Characteristics of PIV-Set-Up According to Bleck and Oumeraci [1]

In addition, a permeable transparent container was filled with colored sand and placed within the revetment to investigate the sand movements inside the container. The sand movements were recorded using digital video cameras.

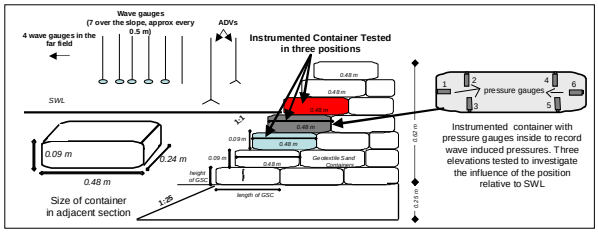

Figure 4: GSC-Revetment in the Wave-Flume (Adjacent to PIV Section)

In the other section, adjacent to the PIV section, pressure measurements on instrumented container are performed to record wave induced loads (figure 4). This instrumented container was laid at different elevations in the revetment to investigate the location of the still water level on the wave induced pressures. Then, by integrating the pressures around the containers, the total wave-induced forces and moments were derived.

Surface elevations were recorded in front of the revetment and along the flume using common resistance type wave gauges (figure 5). The gauges directly in front of the revetment were combined with pressure cells and ADV-probes (Acoustic Doppler Velocimeters) in order to measure the energy components simultaneously. In addition, ADV-probes were used to calibrate PIV-measurements. The revetment was also instrumented with four additional pressure gauges on its seaward face to record wave-induced pressure distribution. The GSC-revetment was subject to both regular and irregular wave trains with wave heights varying from 0.08 to 0.20 m and wave periods from 1.5 to 4 seconds by using three constant water depths (0.52, 0.61 and 0.70m).

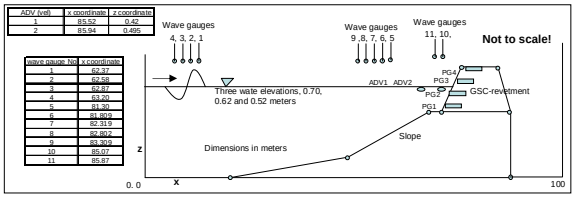

Figure 5: Location of the Measurement Devices

III. Experimental Results

3.1 Wave Loading of Instrumented Sand Container

Among the three tested elevations of the instrumented container, the largest wave-induced pressures are recorded at the container placed just below the still water level (figure 6). For all three locations, the temporal development over each wave cycle of the pressure distribution around the container as well as the resulting wave-induced force and overturning moment have been determined, showing that the most critical situation for the hydraulic stability of the revetment clearly occurs during wave down rush (figures 6 and 7).

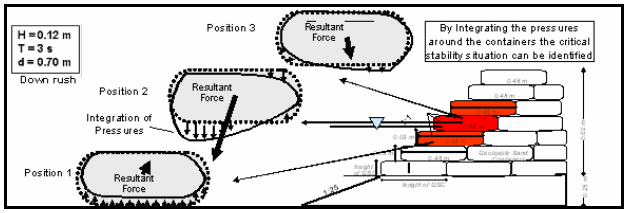

Figure 6: Wave Induced Pressures on Instrumented Sand Container

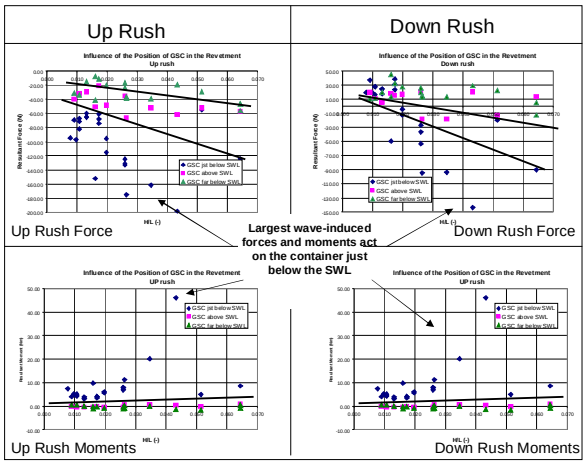

Figure 7: Total Forces and Moments Induced by Waves on the Instrumented Container at Three Tested Elevations

3.2 Wave-Induced Flow on GSC-Revetment

To get an insight into the coherent structure of the flow next to the revetment and to obtain pertinent data for validation of a VOF-model (Volume of Fluid) a PIV-technique was used.

The images obtained from the CCD camera where processed to get velocity vectors and from the images and flow vectors, global and local effects could be determined.

a) Global effects

For each model test, several waves were recorded and the velocity fields were obtained. The velocity fields as well as the visualization of the particles help to clarify the flow processes on the revetments. A better insight in these processes is achieved when the images are observed in rapid succession ("movie"). However, the photographs (figure 8) show clearly how the flow varies at every phase of the wave cycle. It was found that the flow in front of the revetment is initially orbital (induced by wave motion). During up and down rush, it was observed that the flow consists in a main flow running up/down and in local flows that are "trapped" between the containers (see next section "local effects" for details). The velocity vectors of the main flow are approximately parallel to the revetment slope. During up rush an "uplift" deformation of the containers is induced. During down rush, the velocity vectors of the main flow will increase the return of the up-lifted part to a "normal" position and will also induce a seaward force on the containers.

Under breaking waves the containers behave as flexible structures. They are uplifted and deformed at the front part by the impact of the breaking waves. The entire wave breaking process (figure 10) was recorded by PIV-techniques. However, after breaking, clear velocity vectors could be hardly obtained due to the extremely strong vortices and turbulence.

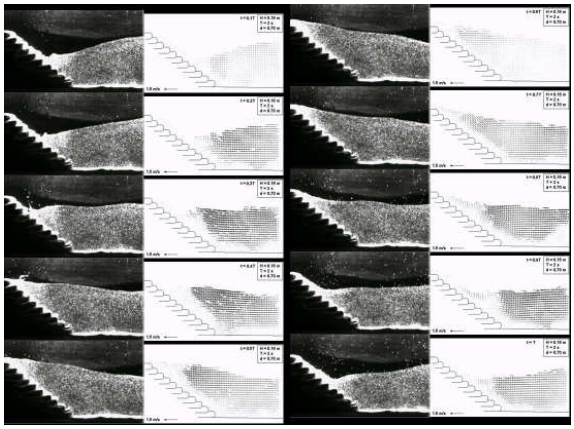

Figure 8: Flow Visualization for a Wave Cycle (H=0.16m, T= 2s) with Between Successive Images

b) Local effects

Among the local effects at the revetment vortex generation was also investigated. During wave action two different types of vortices were observed:

(i) Well structured vortices. The motion is characterized by fluid particles moving around a common centre. These vortices are generated during up and down rush and appear in the areas between containers. These vortices may affect the stability of the structure by applying a small rotational force on the container. (figure 9).

(ii) Non-structured vortices. They occur during up rush induced by higher waves (higher than 0.12m) which break before reaching the revetment (figure 11).

Figure 9: Vortices Appearance During Wave Up and Down Rush

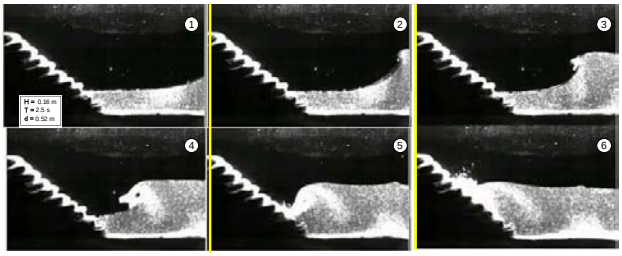

Figure 10: Breaking Waves Recorded with PIV-Techniques

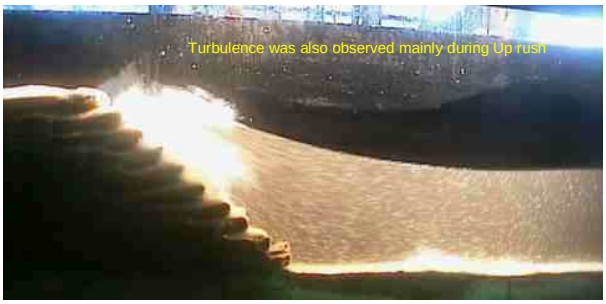

Figure 11: Turbulence During Wave Up and Down Rush of High Waves

3.3 Internal Sand Movement in the Container

The internal movement of sand inside the containers was based on the video records investigated. The observations of the colored sand in the transparent container subject to wave attack have shown that (figure 12):

a) Similar pattern of the sand motion occur for different wave conditions. As expected, noticeable movements of sand are only induced by larger incident waves.

b) The largest sand movements occur during the first 30 wave cycles which then rapidly decrease. This means that the sand fill re-accommodates due to the wave induced forces on the container.

c) During wave up rush the dominant sand movement is rather rotational and directed upward (figure 12a).

d) During wave down rush the movement is essentially translatory rotational and directed seaward (figure 12b). At this stage, a displacement of the container occurs as soon as a certain critical wave height is exceeded.

e) After some wave cycles, the sand accumulates at the seaward end of the container causing a deformation of the latter and reducing the contact areas with neighboring containers (figure 12c). These conditions prevails as long as no further horizontal displacement of the container occurs, internal movements of sand are triggered by an incremental horizontal displacement of the container. These movements of sand occur because the contact areas of the GSC with the neighboring containers are reduced. As a result, the entire process of sand movement will again repeat itself in a similar way as during the first wave cycles (figure 12d).

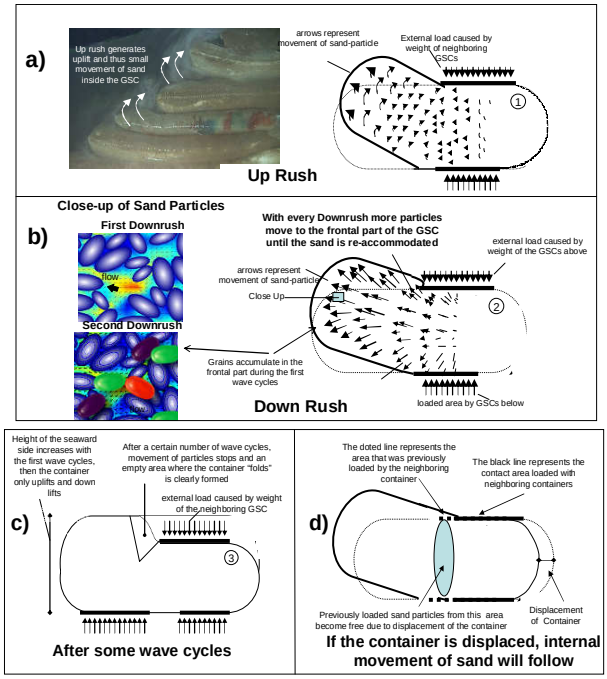

Figure 12: Internal Movement of Sand in a GSC During Wave Action

3.4 Effect of Internal Sand Movement on the Stability of the Geotextile Sand Container

During the model tests the effect of sand movement inside the container on the stability of GSC-revetments was investigated.

To understand the effect of the internal movement of the sand fill on the hydraulic stability of GSC, it is necessary to consider the force balance on the container (figure 13).

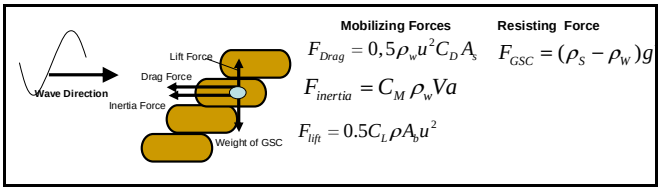

Figure 13: Force Balance on a GSC

The hydraulic loading (mobilizing forces) due to wave action on the revetment can be defined as:

Drag force: $F_D = 0,5\rho_w u^2 C_D A_s$ (1)

Inertia force: $F_M = \rho_w \frac{\partial u}{\partial t} C_D V_{GSC}$ (2)

Lift force: $F_L = 0,5\rho_w u^2 C_L A_T$ (3)

where:

FD is the drag force, Fm is the inertia force, FL is the lift force, the density of water, CD, CL and CM are empirical coefficients, u the wave-induced horizontal

particle velocity, $\frac{\partial u}{\partial t}$ is the associated horizontal particle acceleration, is the volume of the container, AS the projected area of the containers normal to the wave direction and AT is projected area in wave direction (figure 14).

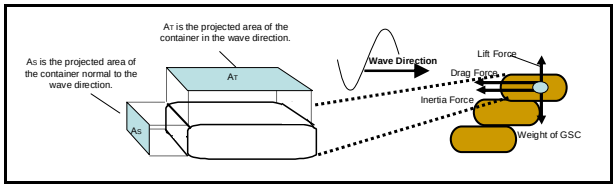

Figure 14: Definition of Projected Areas AS and AT of a GSC

The resisting force of the submerged container can be defined as:

Resisting Force: $F_{GSC} = (\rho_S - \rho_W) g V_{GSC}$ (4)

where:

ρ_s is defined as the density of sand, g is the gravity and V_{GSC} is the volume of the container.

Depending on the way the containers are placed on a coastal structure, on the geometry and on the hydrodynamic processes acting on the containers two kinds of displacements are possible. The container can either slide or overturn.

a) Sliding

The condition of stability against sliding of the container can be described as (figure 15):

$$\mu\left[F_{GSC} - F_L\right] < F_D + F_M \qquad (5)$$

where μ is the friction coefficient between containers

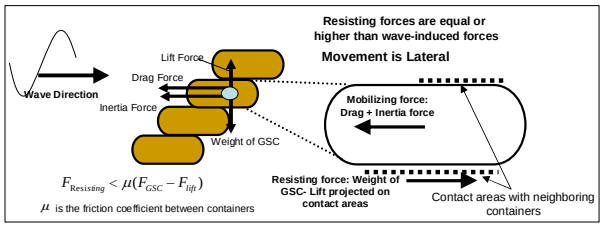

Figure 15: Stability of a GSC Against Sliding

When internal movement of sand in the container occurs, the frontal part of the container will increase while the rear part will decreased. This means that the projected areas (AS and AT) will change. If we recall equations 1 and 2, the mobilizing forces FD and FL which are a function of the projected areas will increased. Now, if the deformed container is uplifted, the contact areas with the neighboring containers are smaller than before sand movements leading to a reduction of the resisting forces. Thus, the stability of the container is reduced by the internal movement of sand (figure 16).

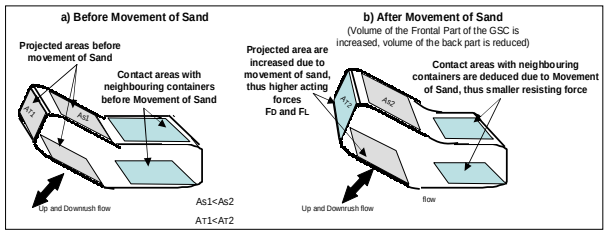

Figure 16: Effect of the Movement of Sand on the Stability of a GSC (Sliding Displacement of GSC)

b) Overturning

The condition of stability against overturning of the container can be described by the relation (figure 17):

Resisting Moments > Mobilizing Moments

$$F_{GSC} \cdot r \geq (F_D + F_M) m + F_L \cdot r \qquad (6)$$

where r is the horizontal projection of the distance between the centre of gravity of the container and the rotation point and m is the vertical projection of the distance between the centre of gravity of the container and the rotation point.

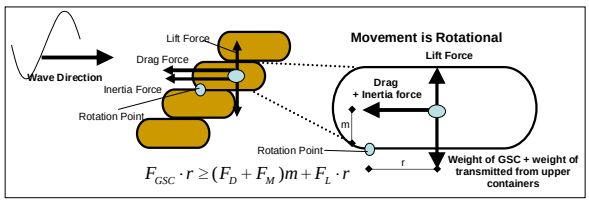

Figure 17: Stability of a GSC Against Overturning

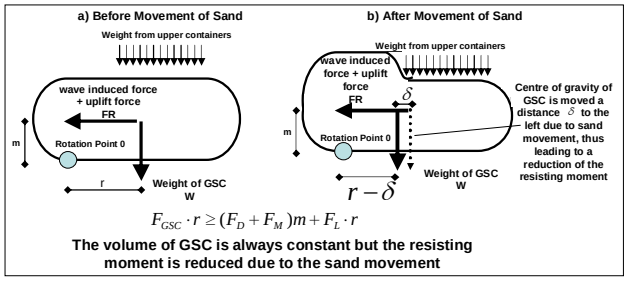

Figure 18: Effect of the Movement of Sand on the Stability of a GSC (Overturning Displacement of GSC)

When the movement of sand in the container occurs, the centre of gravity of the container will move seaward due to the fact that the frontal part of the container will be heavier (accumulation of sand in the frontal part) than before the sand movement started. This means, the resisting moment of the container decreases (due to the fact that centre of gravity has moved a distance) and thus the stability of the container is also reduced (figure 18).

3.5 Variation of the Contact Areas During Wave Action

During the model tests, the variation of the contact areas among neighboring containers was observed during wave action. It was seen that the contact areas among neighboring containers are reduced due to the uplifting of containers. Recalling that the resisting force of GSC is the weight projected on the contact area, a reduction of these contact areas will thus reduce the stability of the revetment (figure 19).

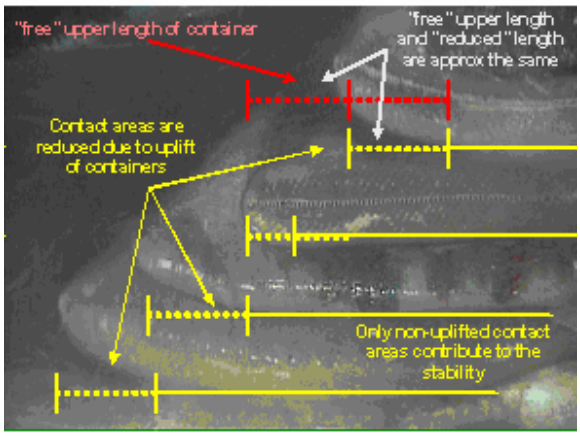

Figure 19: Variation of the Contact Areas Between Neighboring Containers

3.6 Effect of the Deformation on the Stability of a GSC-Revetment

The experimental results have shown that the deformation of the containers strongly affects the hydraulic stability of the revetment.

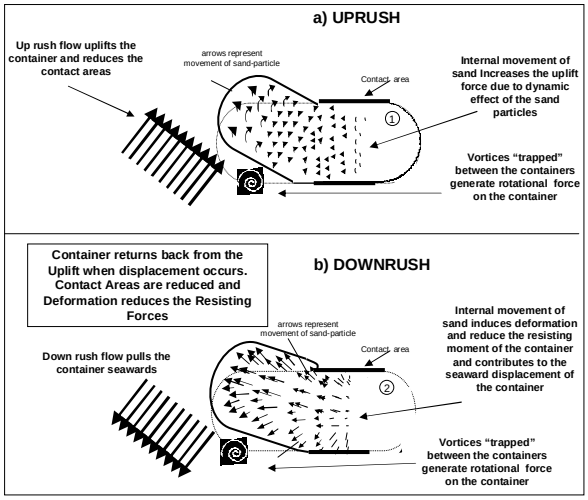

Figure 20: Influence of the Deformation on the Stability of the Container

During up rush the wave-induced flow uplifts the frontal part of the containers (figure 20a). Moreover the local vortex flow between the containers induces an overturning moment on the container. Uplift of the containers reduces the contact areas and thus the stabilizing forces.

During down rush (figure 20b), the uplifted container returns down, while its contact areas are still reduced and the internal movement of sand has reduced its contact areas and resisting moment. The return flow in front and behind the container induces seaward forces, resulting in a critical situation for the stability of the containers (figure 21).

Figure 21: Displacement of Containers Observed During the Large-Scale Model Tests

3.7 Types of Displacements of a GSC in the Revetment

From the model tests two types of displacements of the slope containers were recorded:

a) When the wave height is large enough to induce displacement of the loaded container, the displacement of the container is rather rotational in the upward direction.

b) The most common displacement of a GSC occurs during down rush, when the uplifted container is released at maximum run up level. This displacement is progressive and only becomes noticeable after several wave cycles (for example, with a wave height of 0.12m and period of 3 seconds, a displacement of couple of centimeters was recorded after approx. 100 wave cycles).

IV. Concluding Remarks

Based on (i) the detailed measurements of wave-induced loads on the instrumented sand container, (ii) on the PIV-measurements of the flow field in front of the GSC-revetment, and (iii) the video observations of the internal movement of colored sand in a transparent container, a much better understanding of the processes which affect the hydraulic stability of the revetment has been achieved, including the effect of the deformation of the sand containers and their mutual interaction. With this understanding it can tentatively be concluded that:

a) The most critical location on the seaward slope with respect to the hydraulic stability is for the containers located just below the still water level;

b) The most critical phase for the stability of the revetment occurs during wave down rush;

c) The deformation of the container strongly affects the stability of GSC-revetments. Deformation reduces the resisting contact areas and thus the resisting forces on the containers;

d) The internal movement of sand inside the container induces deformation of the container and therefore substantially affects the stability of the revetment;

e) Breaking waves are not as critical as originally expected for the hydraulic stability of GSC-revetments

The experimental results will be used for the validation of a VOF-model and an FEM-DEM model, which will be run to further improve the understanding of the aforementioned processes. This improved understanding will then allow to develop HUDSON-like stability formulae that can be applied to GSC-made seawalls, revetments and reefs and scour protection systems, but additionally including the effect of the deformation of the sand containers and further related effects. This is the ultimate objective of the PhD-Thesis of the first author which is to be completed in March 2007.

ACKNOWLEDGMENT

The financial support of the first author by DAAD (German Academic Exchange Service) is gratefully acknowledged. The model tests, however, were fully financed by the Leichtweiss Institute (LWI). The Geotextile for the model tests and technical advice on the use of Geosynthetics were kindly provided by NAUE GmbH & Co. KG. This cooperation is also gratefully acknowledged.

REFERENCES

[1] Bleck, M. and Oumeraci, H. 2004. Hydraulic Performance of Artificial Reefs: Global and Local Description, Proceedings of the 28th ICCE 2002, pp. 1778-1790, Cardiff, Wales

[2] Dean, R. G., and Dalrymple R. A. 1998 Water Wave Mechanics for Engineers and Scientists. World Scientific, Advanced Series on Ocean Engineering, Singapore.

[3] Fuerboeter, A, 1991, A.: Wave Loads on Sea Dykes. In: M.B. Abbott and W.A. Price Coastal, Estuarial and Port Engineer's.

[4] Marth R., Mueller G and Wolters G, 2005. Damages of blockwork coastal structures due to internal wave impact induced pressures, Proceedings of the International Coastal Symposium, Ireland 2005 (in print)

[5] Oumeraci H.; Hinz, 2004 M.: Geotextile sand-filled container as innovative measures for shore protection, Technical paper, Proc. EuroGeo 2004, Vol 1, p. 175-180.

[6] Oumeraci, H.: Review and Analysis of Vertical Breakwater Failures - Lessons learned. Coastal Engineering, Special Issue on "Vertical Breakwaters", Amsterdam, The Netherlands: Elsevier Science Publishers B.V., vol. 22, nos. 1/2, pp 3- 29

[7] Recio J. and Oumeraci H. 2005 Analyse der Stabilitätsgefährdenden Prozesse von Deckwerken aus Geotextilen Sandcontainer, 5.FZK Kolloquium „Seegang, Küstenschutz und Offshorebauwerke“ Hannover, pp 83-87.

[8] Recio J. and Oumeraci H. 2005b Processes Affecting the Stability of revetments made with geotextile Sand Containers. International Conference of Coastal Engineering, ICCE 2006, (Abstract submitted)

[9] Recio J. and Oumeraci H. 2005c, Experimental Results obtained from Model Tests, Wave-induced Forces, PIV visualization and Internal Movement of Sand of a Revetment made with Geotextile Sand Containers, Leichtweiß Institute for Hydraulic Engineering, Progress Report

[10] Roeckelein S., 2004. Erosion of blockwork coastal structures and rock cliffs. Master Thesis, Queen’s University Belfast/University of Kalsruhe

[11] Wouters, J. (1998) Open Taludbekledingen; stabiliteit van geosystems (Stability of Geosystems) Deftt Hydraulics Report H1930, Annex 7 (in Dutch).

.

Comparative study of superficial and internal erosion tests

P. Reiffsteck*, T. L. Pham*, R. Vargas*, S. Paihua*
* French Public Works Laboratory (LCPC), Soil Mechanics Division, Paris, France

I. INTRODUCTION

Since the last catastrophic floods appeared in the southeast of France, the state, land planning agencies and urban planners worry about the susceptibility of dikes and road embankments to floods [5]. The internal phenomenon of piping is often estimated in projects and expertises using finite elements software through the evolution of the calculated gradient. The theoretical values of critical head gradient, used as reference in France, results from relatively old research of the Thirties. To revalue the relevance of this criterion very much used in practice, it is necessary to study the initiation of erosion within soil material.

The research program presented in this paper is interested in the process of erosion of the argillaceous matrix of structured soil using various types of tests:

- surface erosion tests with the LPC mobile water jets test apparatus developed by reference [7]. The characteristic of this test is to be able to characterize the surface erosion of soil under a gauged water flow. It can be carried out on site. This apparatus is similar to the jet erosion test developed by reference [6].
- dispersity tests with the pinhole test: it acts of a rather qualitative test which makes it possible to evaluate the dispersiveness of a soil subjected to a given hydraulic gradient [1,2].
- internal erosion test with Hole Erosion Test (HET). This test, which is the most recently developed, is carried out for a given hydraulic gradient and gives the variation of the rate of erosion versus time. This apparatus allows to follow the evolution of the geometry of the cavity in which water circulates [14]. A parametric study has been initiated by French Public Works Laboratory (Laboratoire Central des Ponts et Chaussées, Paris, France) with this new experimental device to provide more values of internal erosion characteristics.

The complementarity of these techniques to estimate stability of soil to internal erosion, makes it possible to dissociate the mechanisms due to dispersion, with the shear stress to the soil-fluid interface due to water flow. The triaxial erosion test, which is an alternative, was not elected. It is a more sophisticated version of the last cited apparatus where confinement allows the exploration of another dimension of the problem. However the absence of hole totally or partially traversing the sample makes the analysis more difficult as suffusion is superimposed to erosion [3,10,13].

A work of interpretation of the results of these experiments is presented. A first approach of an application to well documented pathologies was carried out.

The capacity to carry out the modelling of internal erosion is one of the finalities of this study. This is an important repercussion towards the practice necessary to the engineers to evaluate a priori the stability of geotechnical works on which they carried out leak detection surveys [4].

II. EXPERIMENTAL DEVICE

A. *Description*

The device consists in a modified Hole Erosion Test apparatus [14]. The main body is composed of three cells with an internal diameter of 72 mm: a first cell filled with glass beads or gravel, a second cell in which the soil sample is compacted and a third cell including measuring devices. A Hengstler turbine flow rate sensor placed between the fluid supply tank and the apparatus measures the flow rate. As during the test, we measure the pressure upstream and downstream using Honeywell miniature pressure transducers (0-100 kPa), we can calculate the gradient. We propose to make the exact measurement of eroded material quantity by the monitoring of turbidity (ATI turbidimeter) caused by fine particles suspended in the water downstream the eroded zone (fig. 1). All the transducers are connected to a HBM spider 8 datalogger. Measurements are displayed and recorded by a software developed under Labview from National Instruments.

The control of the water head is obtained by the use of an air compressor regulator connected to the fluid supply tank.

Figure 1. Photograph of the experimental device

Figure 2. Detail of the three cells

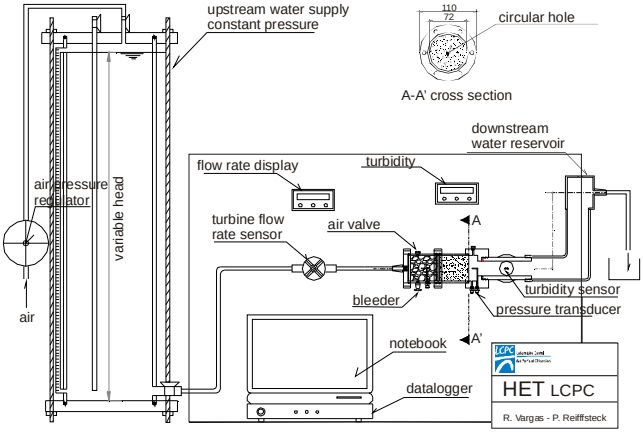

Figure 3. Schema of the experimental device

B. *Materials used*

To achieve our parametric study we have planned to test mixtures of textbook soils (kaolin, silt, sand), which would correspond as much as possible to a class of classical textural classification of original and altered grounds. We made this choice because the aim of the study is to connect under conventional test conditions in laboratory or on site, the erodibility of a soil to the classification of the GTR design guide (i.e. Guide for Road Earthworks) familiar for French public works actors in dyke and embankment construction [9].

When the characteristics of each mixture are determined, the proportion of each component is calculated using a graphical method [13]. The entry parameters observed are particularly the porosity, expressed in term of texture, and void ratio, as well as the water sensibility of the fine fraction evaluated via the physicochemical characterization of the soil and the fluid.

C. *Preparation of sample*

The preparation of soil sample is divided into three steps:

- First step, the soil is placed in a drying oven during 24 hours then it is weighted in order to determine the water quantity necessary to obtain the desired water content. We gradually introduce water into the soil during mixing. Then we soak the samples during 24 hours, after having covered it with a plastic film to avoid evaporation.

- Second step, we take a mass of soil which when it has been compressed to the height of the test-cell, will give the projected dry density. The dry density required corresponds to 95% of the Proctor optimum density. The compression is realized in four layers using a hydraulic jack.

- Third step, a vertical drilling machine is used to create a hole of 4 mm of diameter along the longitudinal axis of the soil sample to simulate a concentrated leak.

D. *Test procedure*

After having connected the pipes, we open gently the water flow in order to avoid soil sample movement. At this stage, the air valves must stay open. While water goes up in the cell, we pour the water in the tank downstream in order to balance the pressure, still to avoid a displacement of the sample. When the cell is filled, we close the air valves after having checked that there does not remain any air bubbles. We use the air pressure regulator to maintain the water head at the desired height. The test begins at the same time we start the specific software to monitor the different measuring devices. In the test, time, flow rate, upstream pressure, downstream pressure, turbidity are measured automatically every 30 seconds. We conventionally realized the test in three hours with the initial gradient and initial flow rate chosen after few trial tests.

III. TEST AND ANALYSIS

We have already tested 35 soils with mobile water jet and pinhole tests [11] but the delay for the design and validation process of our apparatus only allow us to test 16 samples of 4 different textures up to now. We present here the results of three tests made with two different textures. Table 1 summarizes the soils used and their classification.

TABLE I .

Different texture tested

Type	Desired mix design (%)			W_l (%)	Wp (%)	I_p	Wopn (%)	γ_{opn} (t/m^3)
	clay	silt	sand					
1.1	25	5	70	18,1	14	4,1	11	2
1.3	35	25	40	25,6	16,7	8,9	13,81	1,927

A. *Test for texture 1.1*

This texture corresponds to clayey sand. In this test, the initial gradient is equal to one, and the initial flow rate to about 700 ml/min. During the test, the diameter of the hole increases as a result the flow rate rises and the gradient decreases (fig. 4 and fig. 5). In the 50 initial minutes, the flow rate increases sharply, the gradient decreases dramatically, the cumulated turbidity rise considerably (until 4000 ppm) and then it grows moderately (at the end of test, the turbidity is only about 5000 ppm) (fig. 6). Thus, the erosion goes up significantly in the initial time and then it improves slightly before having the tendency stabilized.

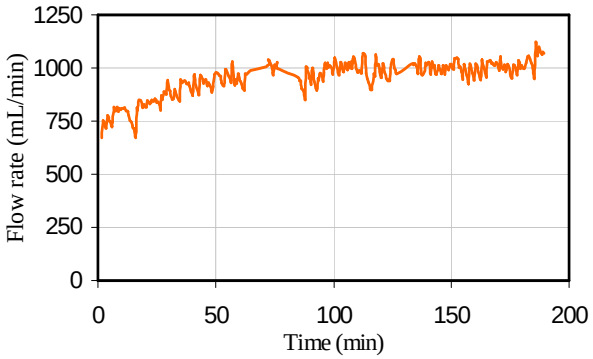

Figure 4. Flow rate vs. time for sample 1.1.3

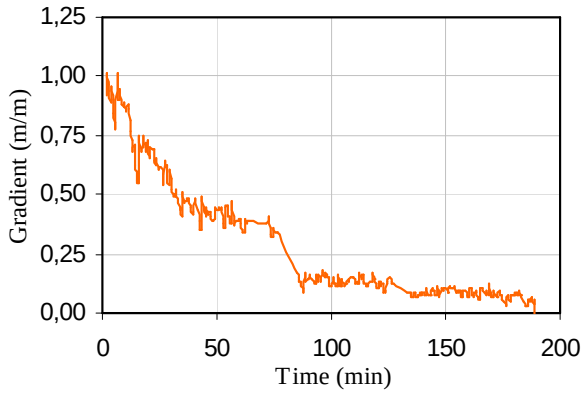

Figure 5. Gradient vs. time for sample 1.1.3

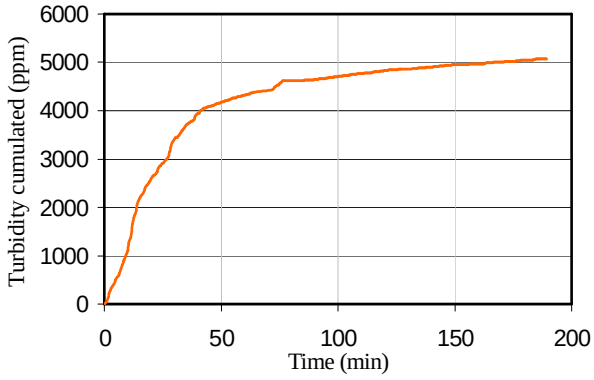

Figure 6. Cumulated turbidity vs. time for sample 1.1.3

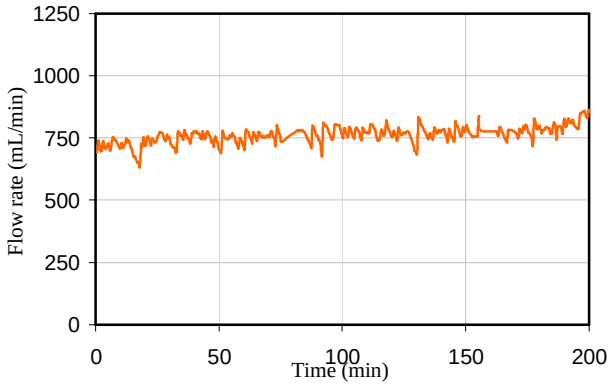

Figure 7. Flow rate vs. time for sample 1.1.6

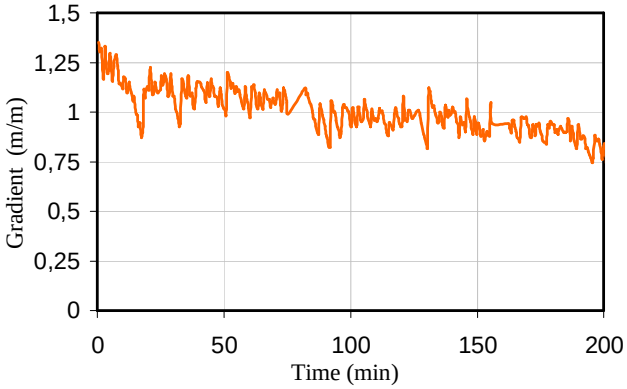

Figure 8. Gradient vs. time for sample 1.1.6

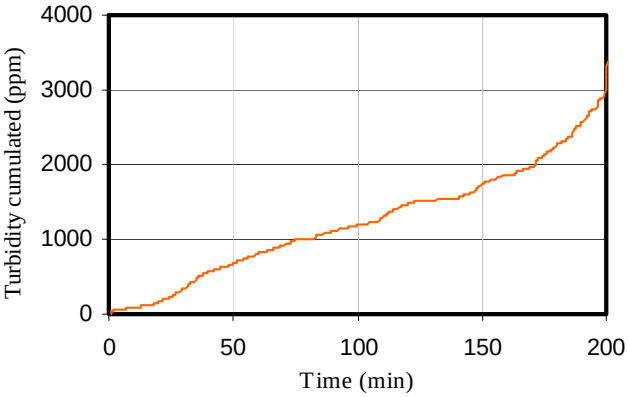

Figure 9. Cumulated turbidity vs. time for sample 1.1.6

B *Influence of compaction*

For the sample 1.1.3 described above, the most compacted layer was placed downstream. For the sample 1.1.6, we changed the orientation so that the least compacted layer was downstream.

It can be seen that for the sample 1.1.6 the flow rate increases slightly (fig. 7), the gradient decreases moderately (fig. 8) and the cumulated turbidity grows not much in the 50 initial minutes (only 800 ppm) (fig. 9). It is noticeable that the sample is more difficult to erode because the most compacted layer, limiting the erosion, is placed in upstream position so it needs more time to increase the diameter of the hole. At the end of test the flow rate goes up not much (about only 800 mL/min), the gradient is still high (about 0,8 m/m) and the cumulated turbidity is slightly more than 3000 ppm. It is spot on that the compaction plays a very important role in the erosion of soil.

It implies also that in this particular case, the apparition of erosion takes more time: almost 2 hours, than in the first test presented. The choice of the conventional test duration has to be revised. Some trial tests have been done using duration of 6 hours and gave interesting results. We decide for some texture to use this duration preferentially.

C. *Test for texture 1.3*

This texture corresponds to sandy clay. Although we start the test with a high gradient (s=5) (for the sample 1.1.3 and 1.1.6 we start with s is around 1), the cumulated turbidity increases very moderately (after 50 initial minutes, the turbidity is only 360 ppm and at the end of test it is 650 ppm) (figure 11). We can observe eight times less erosion than for texture 1.1. Soil with a high

fraction of clay is less eroded than a soil with a small clay fraction.

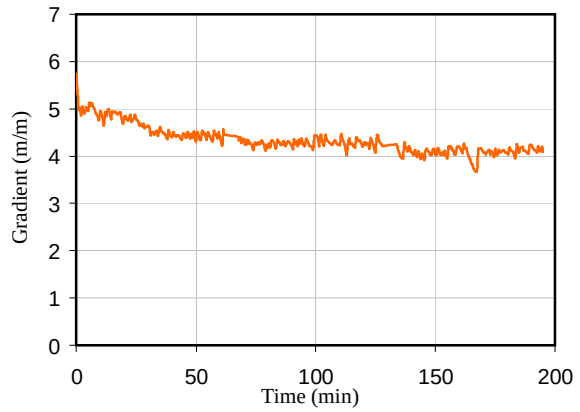

Figure 10. Gradient vs. time for sample 1.3.1

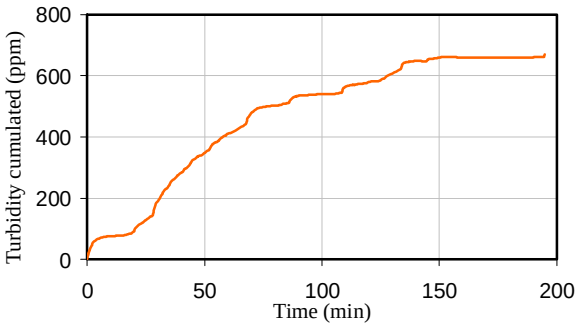

Figure 11. Cumulated turbidity vs. time for sample 1.3.1

D. *Synthesis of test results*

All the results of performed tests underline very different magnitude of erosion rate (cumulated turbidity), the turbidity vary from hundred ppm (sample 1.3.1) to thousand ppm (sample 1.1.3 and 1.1.6).

The comparison of the erosion rate index I_{HET} defined by [14] made in table II indicates that the texture 1.1 erode very rapidly and that the texture 1.3 erode moderately rapidly. These results are in very good accordance with the mobile water jet apparatus results [11]. For this test, the results are separated in three classes proposed by previous studies: solid loads higher than 150g and from 150g to 50g are respectively classified as soils with low and moderate resistance to erosion. Lower values of solid load are obtained for soil having a good resistance to erosion.

TABLE II.

Comparison of results

Type	Desired mix design (%)			E_{10}	E_{67}	Dispersivity	I_{HET}
	clay	silt	sand				
1.1	25	5	70	58.5	141.5	D	2.48
1.3	35	25	40	48	70	SD	3.30

The dispersivity obtained with the pinhole test show a similar trend.

The compaction is an important parameter to influence the erosion rate. With the same sample, if we change the position of the more compacted layer at downstream to upstream, we have an erosion rate about two times lower.

The time factor is another remarkable parameter. For the sandy soil type (sample 1.1.3), major erosion occurs in the 100 initial minutes and then erosion rate is relatively low. For the clayey soil type, after 200 minutes the erosion rate is very small. It is obvious that it takes much more time to erode a clayey soil compared to a sandy soil. Therefore the test procedure and more particularly the test duration must be adapted

The fine grain faction appears as a strong influence for soil erodibility. The performed tests tend to underline that for 30% of fine samples the erosion rate is about seven times higher than for 70% of fine although the gradient is five times less.

IV. MODELLING

The application to a well-documented case study and pathology was carried out using the finite element software CESAR-LCPC. We were interested to understand the behaviour of a dyke build along the Loire river in the middle age and improved at the end of the XIXth century. The dyke made with alluvium sand and silt has an average height of 5 m, a with of 10 m at the crest and around 30 m at the toe (figure 12). We consider three cases:

- a single-layered fill subjected to an increasing hydraulic load and respecting the critical head gradient suggested by Lane and observed in the HET.
- a multi-layer embankment comporting a contrast of permeability subjected to a hydraulic load. In this model, the Lane gradient criterion is maintained but it is necessary to take into account other important criteria, like the flow rate and the flow, which determines the direction of erosion.
- a multi-layer fill identical to the previous one and subjected to an overflow. The criterion relates to the rate of flow and the shear stress due to flow (critical tractive speed).

During the calculation, the zone of the mesh where the critical head gradient is reached vanishes and the stability of the structure is checked. So at each step, a geometry of the erosion process is obtained, a velocity field can be observed and a factor of safety analysed. For these three different structures of embankment, the water head, the width at the crest and the slope have been varied. Finally in this parametric study, more than 130 cases have been calculated to produce abacus. This study showed us the capacity to obtain realistic mechanisms of rupture with a simple modelling and a standard calculation procedure of the finite element method while waiting to be able to implement a piping model fitted on the experiments presented before. For example, reference [8] developed a piping model for levees resting on clayey foundations within the framework of a Darcy's law-based critical head model.

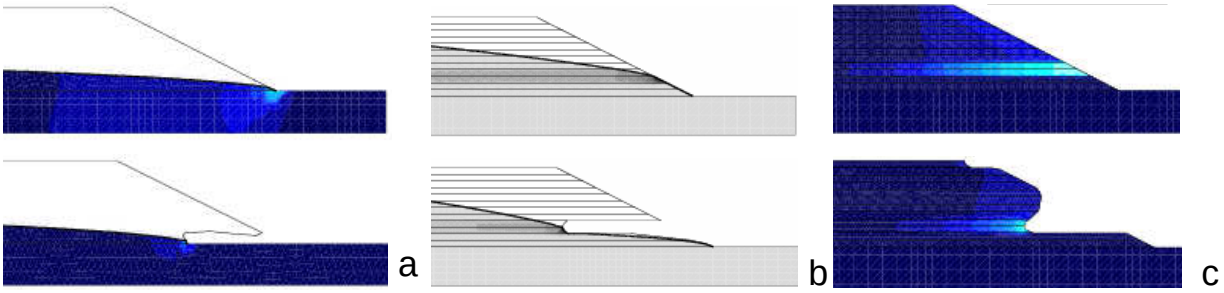

Figure 12. Result of modeling showing flow field on (a) a single-layered fill (b) a multi-layer fill subjected to an increasing hydraulic load and (c) a multi-layer fill subjected to an overflow

IV. CONCLUSIONS

The first results obtain with our modified hole erosion test are rich and promising. In the near future, tests on a large panel of soil texture are needed to build a database.

This research focuses on the influence of the soil texture on the erosion characteristics of soils. This first set of tests doesn't take into account the clay mineralogy of the fine fraction of the soil, which has been point out to be a major factor of influence [1,13]. This will be done in the second part of the program.

This comparative study of testing techniques is supplemented by a multi-scale analysis including the analysis of the susceptibility of the various types of colloids composing the matrix of the ground (silt, kaolinite, illite or smectite) to be dispersed in a fluid charged with cations with various valences.

The modelling of internal erosion gives realistic results and need to be improved by the use of empirical laws fitted on experimental results.

These different goals are in the objectives of a four years national research program founded in France by the French Ministry of Research, Science and Technology and manage by the French energy company EDF. This research program is called ERINOH. A lot of the French authors listed in the references involve in this program.

ACKNOWLEDGEMENT

The writers wish to acknowledge the support of the French Ministry of transportation. The writers would like to thank J.-L. Tacita for his help in the development of the different apparatus and the realization of the experimental work.

REFERENCES

[1] Arulanandan, K. Gillogley E., Tully R., 1980. Developpement of a quantitative method to predict critical shear stress and rate of erosion of natural undisturbed cohesive soils, Tech Rep. GL-80-5 , U.S. Army Engineers, Waterways Experiment Station, Viksburg, MS EU.

[2] ASTM, 1993, Identification and classification of dispersive clay soils by the pinhole test, standard test method D4647-93, Annual book of ASTM standards, Vol 04.08, pp801-810

[3] Bendahmane, F.2005, Influence des interactions mécaniques eau-sol sur l'érosion interne, PhD Univ. Nantes, 153 pages

[4] Fauchard, C. Mériaux, P. (2004), Méthode géophysique et géotechniques pour le diagnostic des digues de protection contre la crue, guide pour la mise en œuvre et l'interprétation, Ed. CEMAGREF

[5] Guiton, M. 1998, Ruissellement et risque majeur, Phénomènes, exemples et gestion spatiale des crues, Études et recherches des LPC, Série Environnement et Génie Urbain EG13, 315 pages

[6] Hanson, G.J. 1991, Development of a jet index to characterize erosion resistance of soils in earthen spillways ASAE paper N° 34(5), 2015-2020.

[7] Hénensal P., Duchatel F. 1990 L'érodimètre à jets mobiles. Bulletin des LPC n°167, p. 47-52.

[8] Khilar, K. C., Folger, H. S., and Gray, D. H. (1985). ''Model for piping plugging in earthen structures.'' J. Geotech. Engrg., ASCE, 111(7), 833–846.

[9] LCPC, SETRA, 1992 Guide pour les Terrassements Routiers. Vol 1 et 2, 98 pages

[10] Marot, D. Bendahmane, F. and Alexis A. 2005, Parametric study of internal erosion on sand-clay samples, ALERT Geomaterial Workshop, Aussois

[11] Reiffsteck, P. 2005, Evaluation of erosion of earth embankment subjected to overtopping by laboratory testing, Workshop on internal erosion, Aussois

[12] Reiffsteck, P. Nguyen Pham, P.T. 2005, Influence de la répartition granulométrique sur le comportement mécanique d'un sol, 16th International Conference on Soil Mechanics and Foundation Engineering, Osaka, Balkema,

[13] Sanchez, R.L. Strutynsky, A.I., Silver M.L., 1983, Evaluation of the erosion potential of embankment core materials using the laboratory triaxial erosion test procedure, Tech Rep. GL-83-4, U.S. Army Engineers, Waterways Experiment station, Viksburg, MS EU, 51 pages.

[14] Wan C.F. Fell R., 2004, Investigation of rate of erosion of soils in embankment dams, Journal of Geotech. And Geoenv. Eng., 30(4) : 373-380

Scour Countermeasures At Long Bridge Abutments

M.L. Reynares[*], M. Roca Collell[**], G. B. Scacchi[*] and M.I. Schreider[*]
[*] Universidad Nacional del Litoral, Santa Fe, Argentina
[**] Universidad Politécnica de Catalunya, Barcelona, España

I. INTRODUCTION

The most common cause of a bridge failure is found in the local scour produced at its piers and abutments. The scour mechanisms round the piers have been extensively treated in the scientific literature, which has allowed to develop estimation methods of the maximum scour depth and the scour evolution in time, quite acceptable according to certain parameters. In the case of abutments, Ref. [7] observed, that out of 383 bridge failures, 25% was due to pier problems while 72% involved the abutments. According to [3] out of 108 bridge failures observed in New Zealand during the period 1960-1984, 29 were caused by abutment problems.

The study of local scour, both at piers and abutments, involves highly complex phenomena and a great number of variables which could be grouped in hydraulic, geometric, sediment and obstacle ones.

In order to minimize these local scour effects and guarantee the abutment safety, the adequate design of abutment revetment is of key significance. Regardless the type of revetment used, the design variables are the same: material size, stratum thickness and plant dimensions, both in flow and cross direction. To dimension the size of revetment material, it is necessary to know the flow velocity, and depth and the dimensions of the pier, the abutment or obstacle, among other variables ([7], [1], [6], [4], [2]). Concerning the plant design, there are some recommendations on the revetment suggested in the technical literature. For example, in [5], it is recommended that the width should be equal to the estimated maximum local scour and extended in all directions round the obstacle. In the case of pier protection, although the recommended extension is between 1.5 and 6 times the pier width, these values are frequently increased.

Once built, the presence of the revetment prevents the development of scours at the abutment area. This produces a change in the flow pattern and, as a result, in the bed topography. Therefore, the revetment is subjected to different actions from the ones it was formerly designed for.

The experimental sequence presented here had as an objective to make an exploratory and introductory analysis of the resulting erosive effects at locating a bed protection by an abutment of a brief bridge, specially the interaction between the revetment, discharge distribution and scour development, ye.

Considering a specific bridge width, the presence of revetment and a non-erodible area at the abutment, can affect the in discharge distribution in the area. The revetment width becomes a fundamental variable as it defines the percentage of the opening liable to be scoured and the one remaining invariable. Another parameter analysed is the revetment´s roughness. Even if the riprap revetment is one of the most commonly used as protection, other types of material are also frequent such as concrete slabs, geotextile stratum with concrete blocks, etc., each one with a different surface roughness.

II. EXPERIMENTAL DESIGN

The experience was performed in a laboratory flume, 20m long, 10.2m wide and 0.8m deep, belonging to the Hydraulics Laboratory of the Facultad de Ingeniería y Ciencias Hídricas (FICH) – Universidad Nacional del Litoral, specially adapted for the aims of this investigation. The experimental flume has an initial 5 m long fixed-bed followed by a 10 m long erodible bed and a final section with another 5 m long fixed-bed. The erodible bed consists of a uniform sand streambed, which is 0.60 m thick, with a mean diameter, d_{50}, of 0.001 m and a standard deviation, σ_g, of 1.3. The cross-section development to the flow coincides with the one of the flume.

A 3.6 m long partial closure was placed in the erodible bed sector, 11 m downstream from the inlet section, this closure is achieved by means of a 0.12 m thick vertical-wall abutment on the right bank and was kept constant in all the test (Fig. 1).

The laboratory experiences detailed below have one of the geometric and hydraulic conditions developed by [8], where the scour hole was freely developed at the abutment, thus becoming a reference or model test (Fig. 2). The parameters related with the test were:

- Geometrical: Opening width (B): 4 m.

- Hydraulic: Total discharge (Q): 0.144 m^3/s, Opening unit discharge (q): 0.036 m^2/s

- Geometry of the scour hole at the abutment: Maximum scour depth (ye): 0.348 m, width: 0.84 m

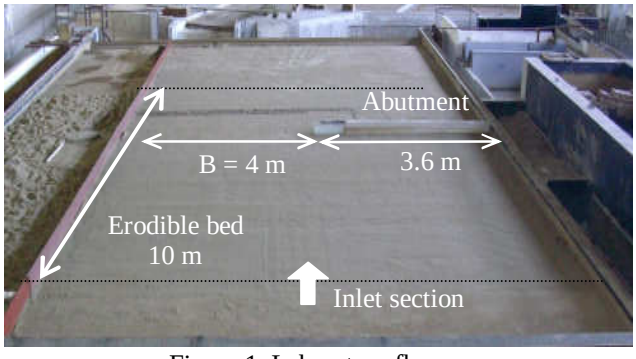

Figure 1. Laboratory flume

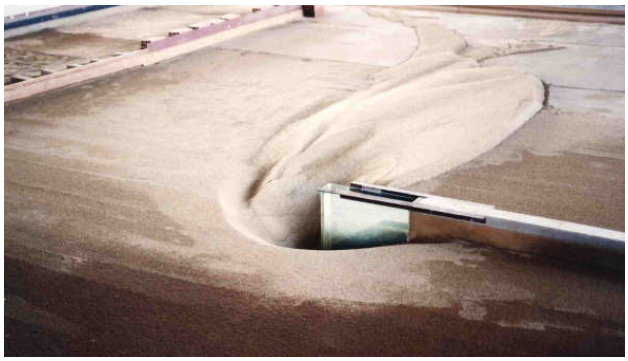

Figure 2. Scour hole in the reference test without protection [8].

The protection was made of a group of concrete slabs. The tests were performed varying the revetment width (b), while length in the flow direction (l) was kept constant (Fig. 3). The width was considered as the revetment extension, cross-section to the flow from the abutment. The tested b were 0.5 m, 1 m, 1.5 m, 2 m, 3 m and 4 m metres, for that case the opening section was completely protected.

Two different types of roughness were used for each revetment width, so as to observe in what way the resulting scour is affected by the flow structure in relation to the change of revetment material. The first type of roughness, considered as smooth, was obtained by placing a layer of sand similar to the rest of the flume (d_{50} = 0.001 m). The increase of roughness was achieved pouring broken stone directly onto the concrete slabs. The mean diameter of this material was 0.02 m (Fig. 4). It is worth mentioning that scale factors related to roughness are not taken into account as the study objective is the analysis of the qualitative effect of the revetment material size in the local scour produced by the presence of the abutment.

A 0.10 m wide boulder belt was placed acting as a transition between the rigid revetment and the surrounding erodible bed so as to avoid local perturbations (Fig. 3).

Since this was a preliminary study, the deformation of the revetment was not introduced as another element for analysis, by which reason only concrete slabs were used. This variable will be incorporated in a subsequent stage, with further details on the topic, including various types of flexible revetments.

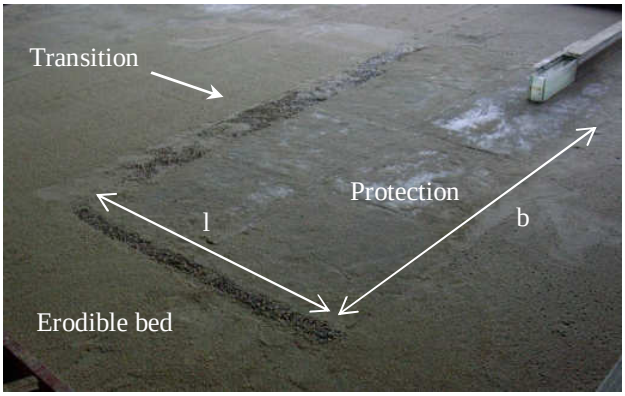

Figure 3. Location of boulder transition area in a protection, width b = 3 m

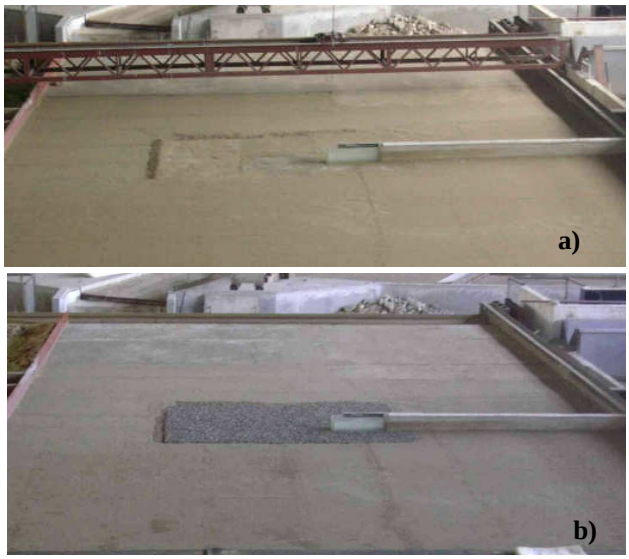

Figure 4. Revetments configuration for a protection width of 2 m. a) Sand roughness and b) Broken stone roughness

The sequence of the tests performed is presented in Table I. It shows the cross-section dimension of the revetment and the roughness used in each test. It is noted that the references to each test consists of a letter followed by a number; the letter identifies the type of roughness used, S for “smooth”, with sand, and R for “rough”, with broken stone, while the number shows the revetment width, b, in metres. In every case the tests lasted 24 hours.

Once the scours developed, the bed and water surface levels and velocity were measured in the following places:

- a cross section coinciding with the upstream side of the abutment.

- a cross section coinciding with maximum scour depth, generally located downstream of the opening section.

TABLE I.
SCHEDULE TESTS PERFORMED

Test	Protection width b (m)	Protection roughness
S 0.5	0.5	Sand
R 0.5	0.5	Broken stone
S 1	1.0	Sand
R 1	1.0	Broken stone
S 1.5	1.5	Sand
R 1.5	1.5	Broken stone
S 2	2.0	Sand
R 2	2.0	Broken stone
S 3	3.0	Sand
R 3	3.0	Broken stone
S 4	4.0	Sand
R 4	4.0	Broken stone

The bed and water surface levels were measured by means of a point gauge with a vernier scale, together with an optical level of precision. The three velocity components were measured in each of the mentioned sections with an Acoustic Doppler Velocimeter (ADV).

Once the test was finished and the flume was drained, a detailed survey was performed of the sector where the revetment and the developed scour hole were located. The measurements were taken in different verticals across the section´s width.

III. ANALYSIS OF RESULT

The results of the test are separately analysed below, in relation to the influence of the two studied parameters, the width and roughness of the bed protection. The aim is to understand which were the physical phenomena defining the problem and provide qualitative ideas about the design of bed revetment.

A. Influence of the protection width

First of all the analysis will concentrate on the results of the tests when its protections were covered with sand (called "smooth") especially those related to the characteristics of the resulting scour holes (their maximum depth, geometry and location) as much as the associated distributions of discharges. In this way we try to identify the answer of the phenomenon being studied only as regards the change in the length of the protection used. A posteriori it will be incorporated the effect introduced by the superficial roughness which will be watched comparing the previous results with the ones obtained in the experiences performed with those bed revetments whose roughness was represented by broken stone.

1) Maximum scour depth

The maximum scour values, y_{ep}, measured in the different tests were quite similar, when the width of revetment surpassed the metre. In every case, the scour value is smaller than the model test (y_e = 0.348 m) and was observed between 0.30 m and 0.70 m downstream from the end of the revetment, slightly varying its position in relation to the test (Fig. 5). The curves corresponding to revetments width less than the metre have a quite different behaviour from the others, this is because the hole was developed on one side of the revetment. The maximum scours are clearly higher than the other tests, although they are still smaller to the values obtained in the reference test.

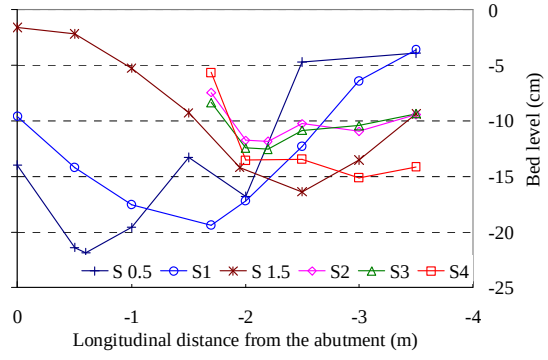

Figure 5. Longitudinal profile over maximum sour values

Considering the results obtained, it could be concluded that the protection is effective in reducing the maximum depth in the scour hole. However, it should be born in mind that, even if smaller, the scour shifted and affected other sectors which, without the revetment, would not be scoured.

2) Geometry and location of the scour hole

The width of the protected area in the abutment section does not only determine the maximum depth values but also define its location. When "b" is large, the presence of the revetment prevents the development of scours in the opening section. This is observed in the test S4, where the revetment covers the total flow section, and the complex three-dimensional configuration of the flow originated by the presence of the abutment makes it evident its removal capacity approximately 1.70 m downstream from the abutment section (Fig. 6a)

In tests S2 and S3 the results were similar, both as regards maximum scour values and location (Fig. 6b). Only when the revetment width is smaller than 1.5 m (S0.5, S1 and S1.5) there is a substantial change in the scour development. In this case, the flow was able to erode the material in the area next to the lateral limit of the revetment so that the hole was located upstream and had a greater extension in the direction of the main flow (Fig. 6c).

The scour hole geometry was significantly different if it placed totally downstream of the revetment instead of by its. In the cases located downstream of the revetment, the maximum depth value was kept almost constant in the flow direction, producing an elongated hole (Fig. 5), which differs from the typical cone-shape of most scour holes at the abutment (Fig. 2). When the hole was placed to one side of the revetment (S0.5, S1 and S1.5), after reaching its maximum depth, the bed quickly recovers downstream (Fig. 5).

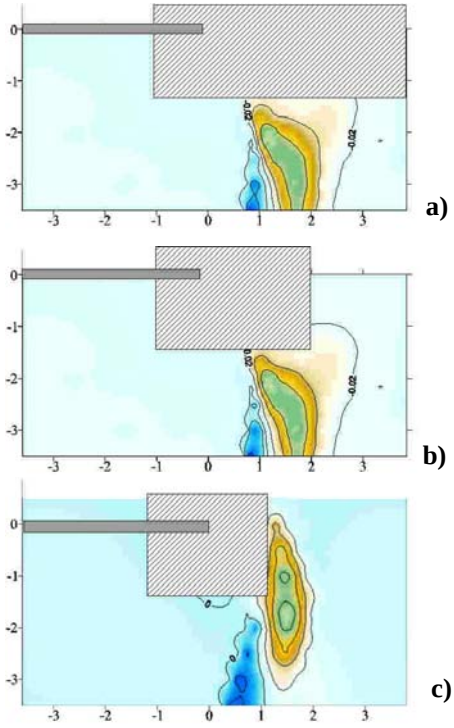

Figure 6. Bed level in the area near the abutment.

The appearance of the cross sections corresponding to the scour hole is characterised by the V-shape in the area of maximum scours, with steep slopes on the bank near the revetment (Fig. 7a). In some of them, the scour development is observed in the area next to the previous one, farther from the lateral limit of the revetment, but with a less steep cross-section slope (Fig. 7b). In some cases, there is a second hole in this area (Fig. 7c).

3) Unit discharges

From the velocities measured in different points of verticals strategically placed in the cross sections, the cross distributions of unit discharges were represented. This parameter was calculated as the product of the average velocity in the vertical and the depth of the flow in that point. The analysis of such results corresponding to the section of the opening shows that when the width of the protection was larger than 1.5 m the final distribution of unit discharges is similar to the ones obtained at the beginning of the tests, before the development of the scour holes. In effect, the unit discharges are uniformly distributed throughout the section, except in a small zone where there are values whose magnitude decreases as it approaches the abutment. This behaviour coincides with the one informed by [8] in reference to the initial distribution of the flow observed in the section of the abutment location without any protection.

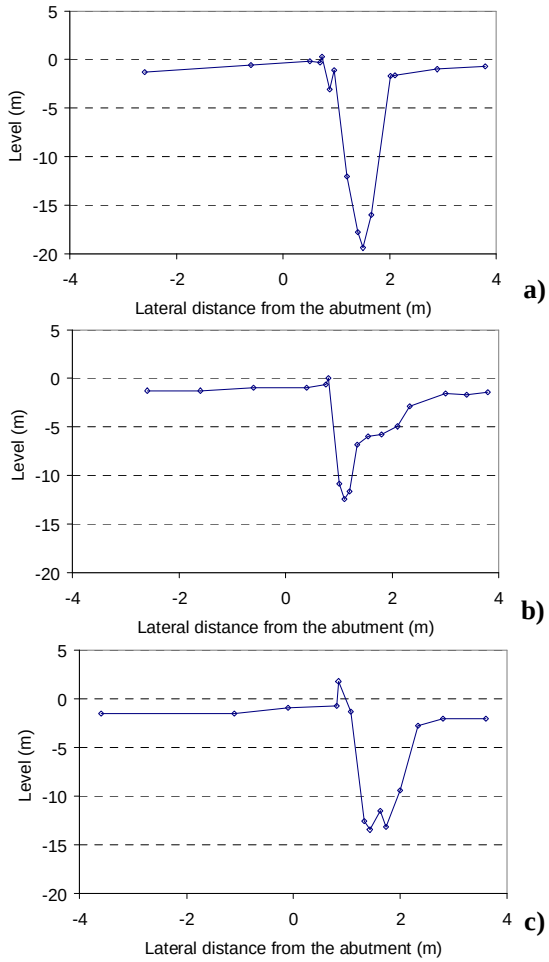

Figure 7. Cross sections of maximum depths a) in S1 at -1.7 m downstream abutment, b) in S3 at -2m and c) in S4 at -2.5m

As it is shown in Fig. 8, the cross distributions of unit discharges showed a special behaviour in the experiments where the width of the protection was smaller than 1.5 m, that is to say that in those situations in which deepenings of the bed were developed at the side of the protection. In Fig. 8a the curves corresponding to S0.5 y S1 show an important concentration of discharges in agreement with the sector of maximum scour and a more uniform distribution, with remarkably inferior unit discharges, for the rest of the section that, without any revetment, does not show to have been exposed to significant scour processes. This situation could be comparable with the one verified in the case of a long abutment without any protection [8], as it is shown in Fig. 8b.

Fig. 9 show the discharge distribution along the sections where the largest scour was located also shows a higher concentration in the areas of bigger scours. However, the matching between the maximum unit discharge and maximum depth is not exact. Instead, the greatest discharge is found slighted displaced to the left bank, opposite the abutment´s location (Fig. 9). Once again, on comparing the tests with a revetment width of over 1 metre, it was observed that the discharge distribution was quite similar in all of them.

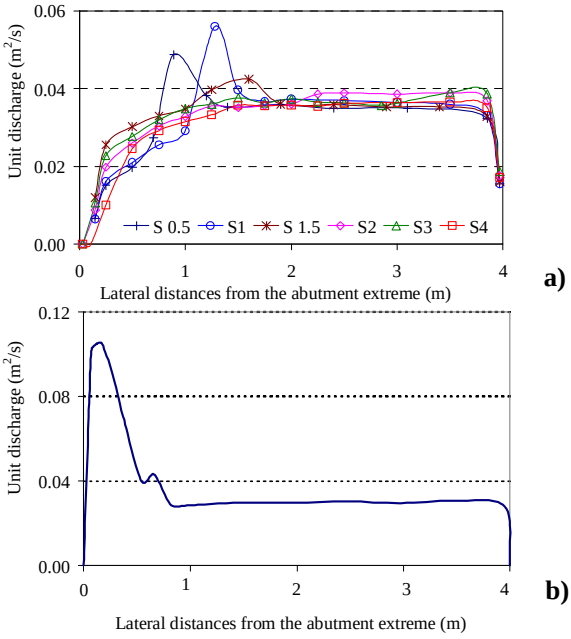

Figure 8. Unit discharge distribution along the opening section for: a) Tests with revetment; b) Reference test without revetment, [8].

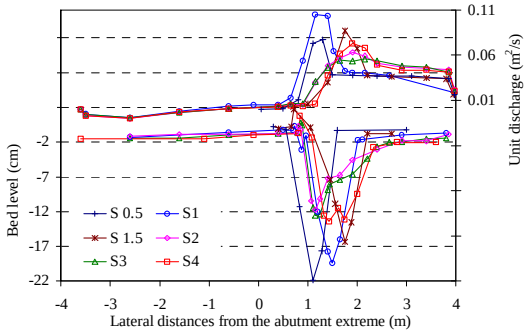

Figure 9. Unit discharge distributions and bed levels, in the maximum scour area.

B. *Influence of roughness*

1) Maximum scour depth

Fig. 10 shows a comparison between the tests that had protections covered by sand and those that had broken stone, in terms of the maximum scour depths that were reached. As there can be seen, both curves have the same tendency, but the one corresponding to the rough revetment shows deepenings slightly inferior, this fact is probably attributed to the greater dissipation of the flow energy due to the greater roughness of the bed in that sector. Notice that the depth differences decreased as the protection width was smaller.

2) Geometry of the scour hole

The behaviour of maximum depths within the resulting holes was similar to the tests in which the roughness was smooth. Once again, there is a clear difference between the geometry of the holes corresponding to narrower than 1.5 m revetment in relation to wider ones (Fig. 11).

3) Unit discharges

The behaviour of unit discharges in the opening section does not show significant changes when compared to the case in which sand provided the revetment roughness. It can be noticed how the discharge distribution is affected by the bed topography (Fig. 12). There are also significant increases in unit discharges in relation to smaller revetments (R0.5 and R1). The curves observed in tests R2 and R4 show a slight increase in the unit discharges, coinciding with the lateral extreme of the revetment, which remained constant along the adjoining sector liable to be scoured. This would show a lateral deviation of discharges from the protected to the unprotected area, originated by the strong resistance to the flow due to the presence of stones. It is worth mentioning that in such cases the scour holes were developed downstream from the revetment, approximately between the cross lateral distances 1 and 2 m from the abutment.

On comparing the discharge distribution with equal revetment's widths but different roughness, it is to be observed that in the section with the biggest scour, the distributions of unit discharges show the same tendency (Fig. 13). In the case of rough surface tests, the curve smoothes, probably as a consequence of energy loss produced by the increase in roughness, thus generating a much more uniform scoured section, where the limits of the hole in R4 are not so marked as in S4.

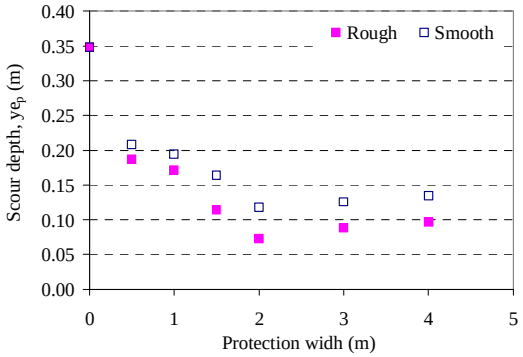

Figure 10. Maximum scour depth values, y_{ep}, grouped by type of roughness.

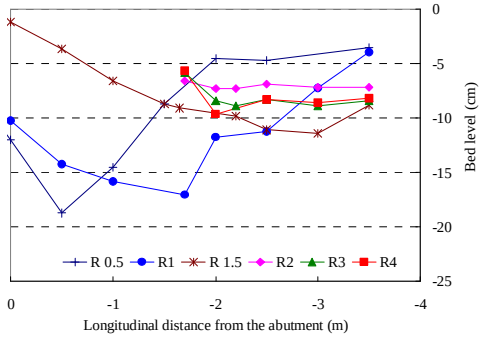

Figure 11. Longitudinal profile of scour holes for rough revetments.

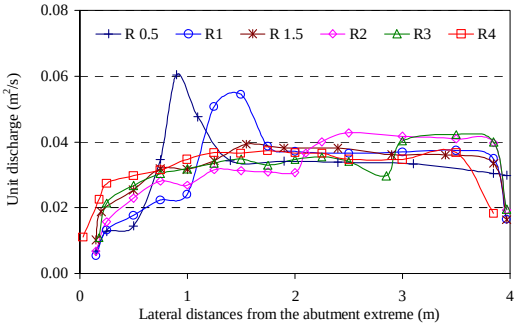

Figure 12. Unit discharge distribution along the opening section for rough revetments

Finally, it is worth noticing how the revetment becomes an important factor to be considered in the analysis of scouring processes at the abutment. Clearly, the complex three-dimensional flow pattern at the abutment, together with the disturbances due to the presence of the revetment, need to be adequately considered to understand the resulting phenomenon more accurately.

One way of observing the three-dimensional flow is to analyse the velocity component vectors. Figs. 14a and 14b show the deviation of velocity vectors in relation to the main flow direction along the opening cross section α, considering both the initial conditions as well as the final pattern, i.e., once the scour hole has developed.

In all of the tests performed, the velocity component in cross direction, v_y, at the beginning of the scouring process had significant values at the abutment, with angles over 50 degrees in relation to the main flow (Fig. 14a). Such values exponentially decreased as the analysis target was focused farther way from the abutment.

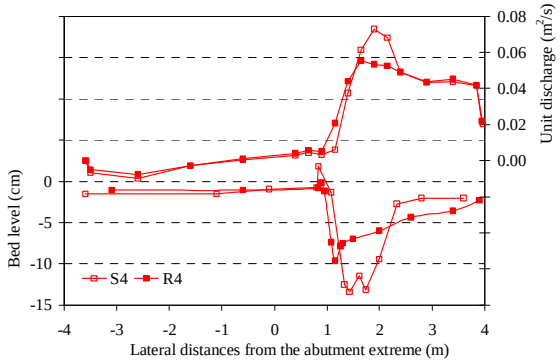

Figure 13. Unit discharge distribution and bed level in the maximum scour section.

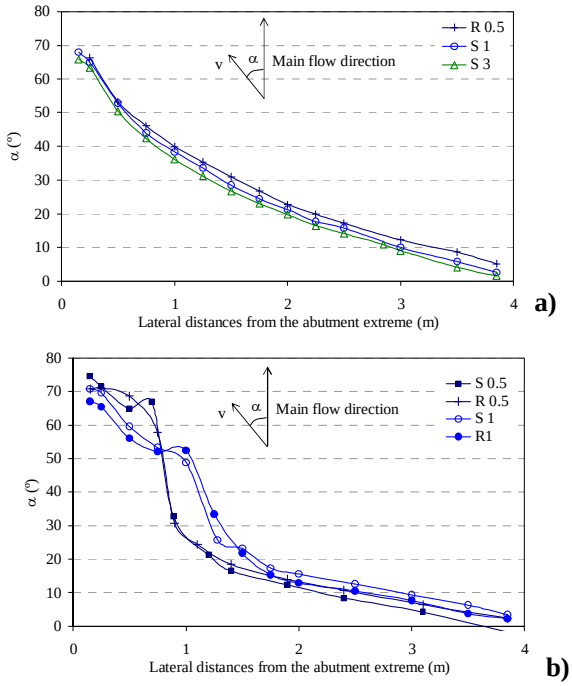

Figure 14. Deviation of velocity vector in relation to the main flow direction in the opening cross section: a) in initial conditions and b) after the development of the scour hole.

Once the scour hole had developed (Fig. 14b), the values of angles α, increased and noticeably moved away from the general tendency. These differences are observed in the lateral distances where the scour hole was located, thus matching the resulting scouring patterns.

IV. CONCLUSIONS

The laboratory tests performed constitute an exploratory analysis and a first approximation to the influence of a bed revetment at the abutment of a relief bridge on the flow pattern and the development of local scours next to it.

The results show that the presence of the revetment reduces, as expected, the maximum scours at the abutment but does not palliate the problem. On the contrary, it produces a displacement of the scour hole to areas which were not previously affected by the presence of the abutment, like the bridge piers. These observations warn about the importance of the correct design of an abutment revetment.

The location of the scour hole is clearly influenced by the revetment width. If it is big, the hole is shifted downstream and when it is small, it locates at one side upstream, nearer the abutment section. The existence or non-existence of a scour hole at the side would be related to the flow pattern at the abutment and the presence of developing cross flows.

The increase in roughness on the revetment surface for the range of the variables considering, produced a decrease in the maximum scours of about 15%.

ACKNOWLEDGMENT

We would like to express our gratitude to the Universidad Nacional del Litoral (Santa Fé, Argentina), which provided the funds for the Research Project, through CAID+D (Courses of Action for Investigation), within which this study was developed.

REFERENCES

[1] Chiew, Y.M., 1995, "Mechanics of riprap failure at bridge piers," *Journal of Hydraulic Engineering*, A.S.C.E., 121(9), pp 635-643.

[2] Lauchlan, C.S. and Melville, B.W., 2001, "Riprap protection at bridge piers". *Journal of Hydraulic Engineering*, A.S.C.E., 127(5), pp 412-418.

[3] Melville, B.W., 1992, "Local Scour at bridge abutments", *Journal of Hydraulic Engineering*, A.S.C.E., 118(4), pp 615-630

[4] Melville, B.W. and Coleman, S.E., 2000, "Bridge Scour", Water Resources Publications, LLC.

[5] Ministerio de Obras Públicas y Urbanismo (MOPU), 1988, "Control de la erosión fluvial en puentes", Madrid, Spain.

[6] Przedwojski, R., Blazejewski, R. and Pilarczyc, K.W., 1995, “River training techniques, fundamentals, design and applications”. A.A. Balkema Ed. Rotterdam.

[7] Richardson, E.V., Harrison, L.J., and Davis, S.R., 1993, "Evaluating scour at bridges". Report No FHWA-IP-9-017, Hydraulics Engineering Circular No 18 (HEC 18), Federal Highway Administration (FHWA), Washington, D.C., U.S.A.

[8] Scacchi, G.B., 2003, “Abutment Scour at Relief Bridges in Floodplains”. Master Thesis (in Spanish) Engineering of Hydric Resources. Universidad Nacional del Litoral. Santa Fe, Argentina.

Scour around a monopile under combined wave-current conditions and low KC-numbers

DANIEL RUDOLPH[1], KLAAS JAN BOS[2]
[1] *WL | Delft Hydraulics, P.O. Box 177, 2600MH Delft, The Netherlands; daniel.rudolph@wldelft.nl*
[2] *WL | Delft Hydraulics, P.O. Box 177, 2600MH Delft, The Netherlands; klaasjan.bos@wldelft.nl*

Abstract
This paper describes selected results of scale model tests on scour around an unprotected monopile under combined wave and current conditions with oblique direction. Physical modelling experiments were carried out using structures with two different diameters and variable hydraulic conditions. The choice of the model scale was guided by typical situations of offshore monopiles in the southern North Sea (monopile diameter 3-6m, water depth up to 30m). The results were compared with published data. An improved formula is presented for the prediction of scour around monopiles in non-cohesive material (sand) which is valid for wave and current dominated situations.

1 Introduction

Recently numerous monopile foundations have been planned and installed in connection with the development of offshore wind energy. The assessment of the scour potential and the design of scour protection has become subject to discussion. The present knowledge on the development of scour has been mainly based on rules of thumb derived from model scale tests under flow only conditions. Little research has been carried out on scour in waves (e.g. Sumer & Fredsøe, 1992) and scour under combined current and wave conditions (e.g. Sumer & Fredsøe, 2001). However, these works do not necessarily cover the typical range of situations for which the potential of scour needs to be estimated in practice. The range of results for the maximum scour depth based on the currently available formulae and rules of thumb indicate a range of S_{max}=0.1...2.5*D_{pile}. Such a wide range is unsatisfactory for both researchers and designers.

Therefore, a research project was set up in order to improve the understanding and to clarify on scour prediction for monopiles in an offshore environment.

The choice of the model set-up and the test conditions was guided by the typical range of prototype conditions to be studied:

- Normal conditions, i.e. tidal current and low to moderate waves: The hydraulic conditions are characterised by flow-only situations or flow domination.
- Extreme conditions, i.e. high waves in combination with wind-driven and tidal currents. The hydraulic condition can be characterised by "wave-domination". The situation "waves only" hardly occurs in prototype.

Typical prototype conditions are summarised in Table 1. These ranges were used to guide the choice of the model set-up and the test programme.

parameter	symbol [unit]	minimum value	maximum value
water depth	h_w [m]	10	30
significant wave height	H_s [m]	0	9
spectral peak wave period	T_p [s]	0	13
depth-averaged current velocity	u_c [m/s]	0.5	1.2
pile diameter	D_{pile} [m]	3	6
seabed material	d_{50} [mm]	(fine sand)	(coarse sand)
Keulegan-Carpenter number	KC [-]	0	10

Table 1 Basis for model-set-up: Typical prototype conditions for offshore monopiles

This paper includes a short literature review on scour around a monopile in combined waves and current (Chapter 2) and it describes recently conducted scale model tests (Chapter 3). In Chapter 4 the results are presented. An interpretation of available data together with a new scour formula is given in Chapter 5. Finally, conclusions are presented (Chapter 6).

2 Published experimental results

A recent summary on research on scour around monopiles is given in Sumer & Fredsøe (2002). Among the published experiments on scour around a slender pile we mainly found the results presented by Sumer & Fredsøe (2001) conclusive and sufficiently described to use them in a re-analysis and to compare those with the results obtained from our own experiments.

Sumer & Fredsøe (2002) presented the following scour depth prediction formula for the experimental data presented in Sumer & Fredsøe (2001):

$$\frac{S}{D_{pile}} = \frac{S_c}{D_{pile}} \cdot \left[1 - \exp\left\{-A \cdot \left(KC - B\right)\right\}\right] \qquad KC \geq B \quad (1)$$

$$A = 0.03 + 0.75 \cdot U_{cw}^{2.6} \quad (2)$$

$$B = 6 \cdot \exp\left(-4.7 \cdot U_{cw}\right) \quad (3)$$

$$U_{cw} = \frac{u_c(z = 0.5 \cdot D_{pile})}{u_c(z = 0.5 \cdot D_{pile}) + U_w} \quad (4)$$

$$KC = \frac{U_w \cdot T_p}{D_{pile}} \quad (5)$$

with
S … scour depth [m]
D … pile diameter [m]
S_c … scour depth due to current only situation, average $S_c/D=1.3$
KC … Keulegan Carpenter number
U_{cw} … relative velocity [-]
u_c … current-induced velocity at a height $z=0.5D_{pile}$ above the bed
U_w … maximum bed orbital velocity
A … empirical coefficient representing the effect of the relative velocity U_{cw}
B … empirical coefficient representing the KC-threshold when scour starts to develop

This formula is valid for single slender piles. The criteria for a slender pile are

- the wave length is large relative to the pile diameter ($L_{wave}/D_{pile}>5...10$)
- the water depth is large relative to the pile diameter ($h_w/D_{pile}>4$)

We have identified a few aspects to be considered in further research:

- The typical range of offshore monopile foundations is 0<KC<10. Only very little scale model test data are available for this range of KC values. Therefore, scale model tests were conducted to obtain additional data for the practically important range of KC<10.
- The formula presented by Sumer & Fredsøe (2002) leads to unexpected results in flow-dominated conditions. In case of relatively low waves on a moderate current (e.g. h_w=20m, u_c=0.6m/s, H_s=2m, T_p=6s, D_{pile}=5m) the formula predicts negligible scour (KC=0.2, U_{cw}=0.7; S/D_{pile}=0.01) whereas the expected scour is significant because situation is flow dominated, therefore similar to "current only".
- A comparison of measurements (Sumer & Fredsøe, 2001) and hindcast (equation 1) indicated that the data fit is not optimal. The formula generally overpredicts the maximum scour depth measured in the laboratory by on average 50% (see Figure 4 at the end of this paper).

These points were addressed in the model set-up and in the analysis of data.

3 Scale model set-up and test conditions

All tests were carried out in Delft Hydraulics' Scheldt basin (see Figure 1). The angle between waves and current was between 60º (D_{pile}=0.08m) and 90º (D_{pile}=0.12m). The pile surface was very smooth (material: PVC). The bed of the facility was covered with a 20cm non-cohesive sand layer (d_{50}=0.13mm). Irregular waves were used in all tests (Jonswap spectrum with γ=3.3). The cross-current was generated by a continuous discharge from a pumping system. Velocity and wave height measurements were performed at various positions in the test section. The scour depths were measured after drainage of the basin using a ruler. The maximum scour depth was defined as the maximum vertical difference between the bed level close to the pile and the surrounding undisturbed bed level.

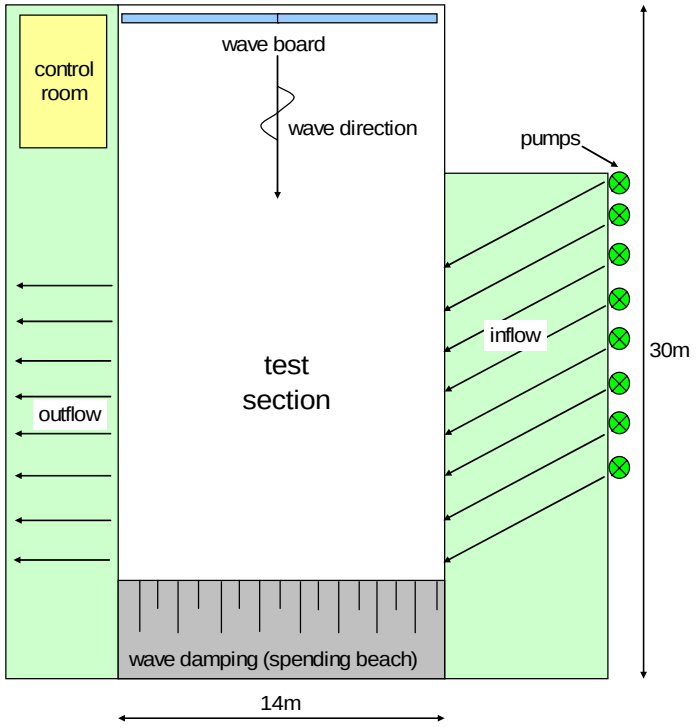

Figure 1 Schematisation of the test facility layout

The hydraulic conditions and scour measurements are summarised in Table 2.

4 Interpretation of model test results

Figure 2a and 2b give impressions on scour which occurred under current dominated conditions (left side) and wave-dominated conditions (right side). In case of the flow dominated situation, the edges of the scour hole could be clearly distinguished from the surrounding undisturbed seabed. The upstream extent of the scour hole was about 1-1.5*D_{pile} (slope about 30-40º), the downstream extent was about 2*D_{pile} (slope 25-30º). This is in agreement with typical values found in literature. In case of wave dominated situations, the scour hole became much more shallow. The transition between the local scour hole and the surrounding bed was rather continuous. The side slopes were in the order 1:5 to 1:10. Sand ripples also occurred in the scour hole. The ripple texture was locally slightly affected around the pile.

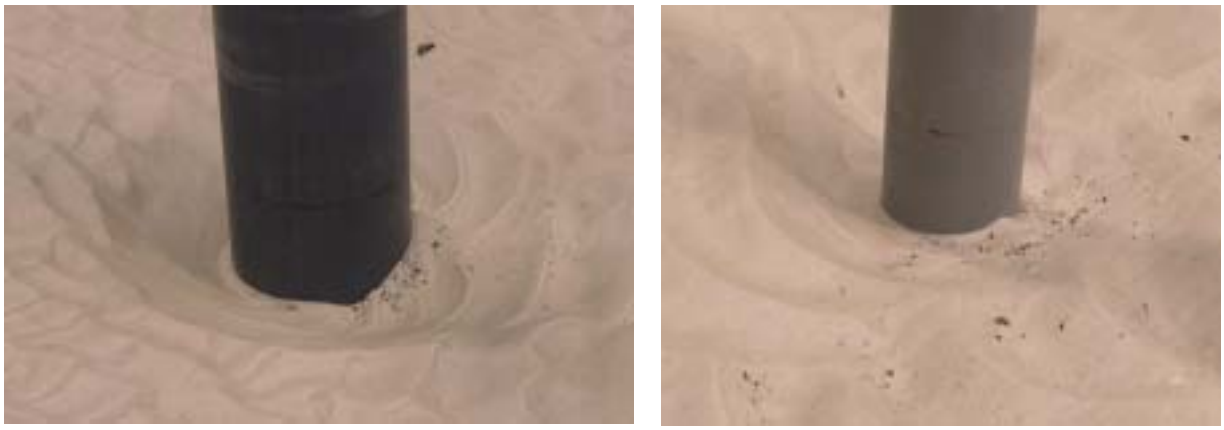

Figure 2 Photo taken after execution

Left side: pile 1 (D_{pile}=120mm; KC=1.5, U_{cw}=0.7; S_{max}=6.5cm)
Right side: pile 2 (D_{pile}=80mm; KC=10.2; U_{cw}=0.3; S_{max}=5.4cm)

The accuracy of the scour depth measurements was estimated at about 5mm which is in the order of 5% of the pile diameter. The scour depths given in Table 2 refer to the maximum scour depth and the time equilibrium found at the piles. Two test runs were repeated in order to obtain an impression on the scatter of the maximum scour depths. It was found that scour depth differences among comparable test runs were in the order of 1-1.5cm. This might be explained by a model effect: The migration of sand ripples (which have a height of about 1cm) leads to depth variations of the (relatively shallow) scour holes, especially in the case of wave dominated situations. This leads to a time dependent variation of the maximum scour depths of about 0.1…0.2*D_{pile}. This is taken into account in the interpretation and analysis of the data summarised in Table 2.

5 Data analysis

Key parameters

The following definitions were applied:

- Pile Reynolds number (constant flow)
- Keulegan-Carpenter number according to Equation (5)
- Mobility parameter
- Relative flow velocity

The flow regime around a cylindrical pile in constant flow is commonly expressed in terms of the Reynolds number. According to Sumer & Fredsøe (1997), vortex shedding starts for Re>40 and the wake is turbulent for Re>300. Typical prototype Reynolds numbers are in the order of 10^6 to 10^7. The pile-Reynolds numbers (constant flow) in the scale models were generally between $0.5*10^4$ and $3*10^4$. In our analysis we have assumed that the Reynolds number beyond Re=300 has little influence on the equilibrium scour depth. Since all test were carried out with Re>$0.5*10^{\wedge 3}$, the scour depth was not expressed in terms of the Reynolds number. However, the parameters affecting the flow regime (pile diameter, flow velocity) were taken into account in the analysis.

Under the presence of waves, the hydrodynamic regime is typically described in terms of the Keulegan Carpenter number KC. In the considered range (KC<10), the flow regime changes from „no separation“ (KC<1) to „vortex shedding“ (KC>7). Therefore, the parameter KC was considered as one of the key parameters in the analysis.

The mobility of the bed material was assessed by using the bed shear stress concept as presented by Soulsby (1997). The computed mobility parameters were above 0.2, while the critical mobility parameter of sand was about 0.068. It was concluded that the bed material was mobile during all tests („live-bed“).

Current profiles were constructed from velocity measurements at different height levels. It was found that the current profile followed a typical logarithmic-relation with a seabed roughness of k_s=0.01m and $z_0=k_s/30$. The current velocity was taken at $z=D_{pile}/2$ with an upper limit of $z=0.5\delta$ (δ…thickness of bed boundary layer). The relative flow velocity U_{cw} was defined as in Equation 4.

Based on these parameters, a new formula for the estimation of the maximum scour depth at a single circular pile under combined waves and currents was derived.

Data applied in the analysis

The following data were applied:

- Test results as presented in Table 2.
- Data as presented by Sumer & Fredsoe (2001).

Sumer & Fredsoe (2001) concluded that the effect of the angle between flow and waves on the maximum scour depth around a slender circular pile appears to be very low. Based on our experience and engineering judgement we agree with this conclusion. Therefore, we have taken into account available data with codirectional waves and currents and oblique direction.

Physical boundaries

The following criteria were introduced to satisfy physical boundaries:

- no waves, no flow: Scour does not occur (S/D=0)
- waves, no flow: Scour is a function of KC, the relation fits to data published by Sumer & Fredsøe (1992): S/D=f(KC)
- no waves, flow: In case of current only, it is assumed that S_c/D=constant
- waves, flow: scour depends on KC and U_{cw}

Improved data base and scour prediction formula

The main parameters determining the non-dimensional scour depth S/D_{pile} were assumed to be the Keulegan-Carpenter number (KC) and the relative nearbed velocity (U_{rel}). This is in agreement with the parameterisation chosen by Sumer & Fredsøe (2002).

The analysis of the chosen data led to the following *best-fit* expression

$$\frac{S}{D_{pile}} = 1.3 \cdot \left[1 - \exp\left\{ -A \cdot (KC - B) \right\} \cdot \left\{ 1 - U_{cw} \right\}^{C} \right] = 1.3 \cdot K_{wave} \qquad KC \geq B \tag{6}$$

$$A = 0.03 + 1.5 \cdot U_{rel}^{\ 4} \tag{7}$$

$$B = 6 \cdot \exp\left(-5 \cdot U_{rel} \right) \tag{8}$$

$$C = 0.1 \tag{9}$$

The definitions of KC and U_{cw} were given in Equation 4 and 5. This formula is valid for a single circular pile, live-bed situation and narrow-graded bed material. It is based on a best fit and does not include safety factors. An indication on the dependency of the non-dimensional scour depth from the relative flow velocity and the KC-number is shown in Figure 3. The black symbols represent the measurements including the estimated accuracy range.

Quality of data fit

Equation 6 represents a best fit of the available data. The quality of the data fit was assessed by comparing non-dimensional scour depth measurements and hindcasts (see Figure 4b). The variation from the "perfect fit" was analysed in terms of the standard deviation. The standard deviation of the ratio measurement/hindcast was about 50%.

The data fits were also compared with respect to the Keulegan Carpenter number (Figure 5) and the relative velocity (Figure 6). The differences between hindcast and measurement are more or less normally distributed and do neither depend on KC nor U_{rel}.

In order to obtain significant scour in flow-dominated situations (and very low KC numbers), an additional factor $(1\text{-}U_{cw})^C$ was introduced. However, no data were available to check the accuracy of this assumption for KC<1.

Interpretation for design purposes

For design purposes a safety factor and additional correction factors should be applied to account for the effect of a limited water depth (h_w<4D_{pile}). The design formula then reads:

$$\frac{S}{D_{pile}} = \gamma \cdot 1.3 \cdot K_{wave} \cdot K_{h_w} \tag{10}$$

with

γ	safety factor, depending on design process and acceptable risk, typically γ=1.5
K_{wave}	wave reduction factor, relation see Equation 6
K_{hw}	correction factor for limted water depth, according to Breusers et al. (1977) $K_{hw}=\tanh(h_w/D_{pile})$

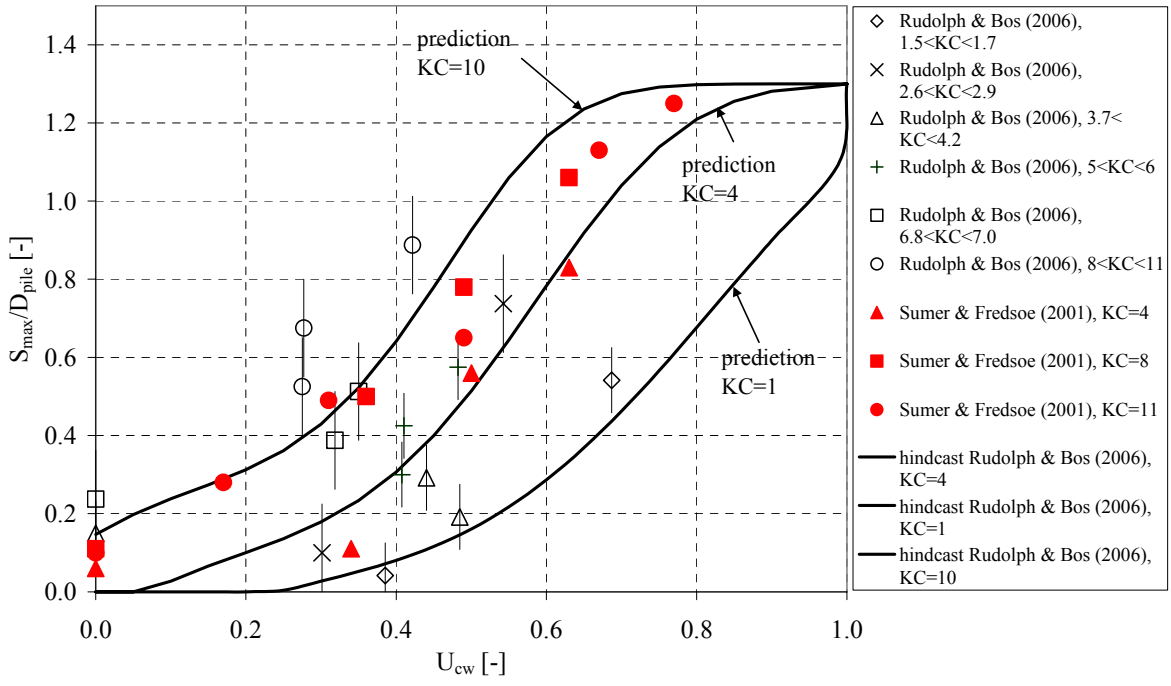

Figure 3 Comparison of measurements with predictions, data based on Table 2 and Sumer & Fredsoe (2001)

The principal set-up of Equation (10) is well known and has been published earlier, e.g. Melville & Sutherland (1988). The innovation of this formula is the improved correction factor for the effect of waves, especially for low Keulegan Carpenter numbers. K_{wave} satisfies the demands of physical boundaries: little scour in case of wave-dominated conditions, maximum scour in case of flow-dominated situations.

We suggest not to apply equation (10) including the K_{wave}-factor for structures with a different shape. Local hydrodynamic conditions (vortex shedding) and the onset of scour differ from circular piles, especially in wave-dominated situations. In wave-dominated situations and low KC numbers, scour will be significant at angular structures while scour is generally low in case of monopiles.

Additional remarks on the use for design purposes

Practically, it is of interest how scour develops with time and under a sequence of hydraulic conditions. This aspect was not considered in this study. All test results refer to the equilibrium scour depth under a given combination of hydraulic conditions.

Care must be taken in connection with the use for design purposes. Although it is believed that the data and formulae presented in this paper give a good indication on expected scour in prototype situations, several scale effects might be present. Without further study (scale model tests) or relevant field measurements it is proposed to apply a safety factor. The choice of the safety factor should depend on the specific situation. Suggestions by various authors are summarised for example by Breusers et al. (1977), Melville & Sutherland (1988), Hoffmans & Verheij (1997) and Whitehouse (1998).

6 Conclusions

Scale model tests were carried out to study the scour development around monopile structures in combined wave and current situations. It was focussed on the range 1<KC<10. Although this range is typically found in shallow-water offshore projects (say up to 30m water depth), little research has been published so far.

The test results generally confirmed the trends published by Sumer & Fredsøe (2002). The analysis of the new test data and data published in literature led to a new scour prediction formula for a single pile in a live-bed situation. It was found that the relative velocity (describing wave or flow domination) and the KC-number are the predominating factors for the prediction of the scour depth.

Compared with existing formulae the improved formula contains the following improvements:

- In case of flow dominated situations with moderate waves, scour depth predictions orientate at the current-only situation.
- The scour prediction is based on an extended data set which covers the typical range of applications of shallow water offshore projects, such as offshore windparks (1<KC<10)

In case of a design study, the scour depth prediction should take into account an appropriate safety factor and project-specific correction factors (sediment gradation, structure shape, limited water depth etc.).

Acknowledgements

The authors are thankful to the Dutch Ministry of Foreign Affairs for co-financing this research project.

References

Breusers, H.N.C., Nicollet, G., Shen, H.W. (1977): Local scour around cylindrical piles", Journal of Hydraulic Research, Delft, The Netherlands, 15 (3), 211 – 252.

Hoffmans, G.J.C.M., Verheij, H. (1997): Scour manual, Balkema, Rotterdam, The Netherlands

Melville, B.W., Sutherland, A.J. (1988): Design method for local scour at bridge piers, Journal of Hydraulic Engineering, ASCE, 114(19), 1210-1226.

Soulsby, R.L. (1997): Dynamics of Marine Sands – A Manual for Practical Applications, Thomas Telford Publications, London

Sumer, B.M., Fredsøe, J. (1997): Hydrodynamics around cylindrical structures, Avanced series on ocean engineering, Volume 12, World Scientific Publishing Co. Pte. Ltd., Singapore

Sumer, B.M., Fredsøe, J. (2001): Scour around pile in combined waves and current, Journal of Hydraulic Engineering, , published by ASCE, Vol. 127, No. 5, pages 403 – 411

Sumer & Fredsoe (2002): The Mechanics of Scour in the Marine Environment, Advanced Series on Ocean Engineering, Vol. 17, World Scientific Press, New Jersey/Singapore/London

Sumer, B.M., Fredsøe, J., Christiansen, N. (1992): Scour around a vertical pile in waves, Journal of Waterway, Port, Coastal and Ocean Engineering, ASCE, Vol. 117, No. 1, 15-31

The improved formula represents a best fit and reads:

$$\frac{S}{D_{pile}} = 1.3 \cdot K_{wave} = 1.3 \cdot \left[1 - \exp\left\{ -A \cdot \left(KC - B \right) \right\} \cdot \left\{ 1 - U_{rel} \right\}^{C} \right] \qquad KC \geq B$$

Figures

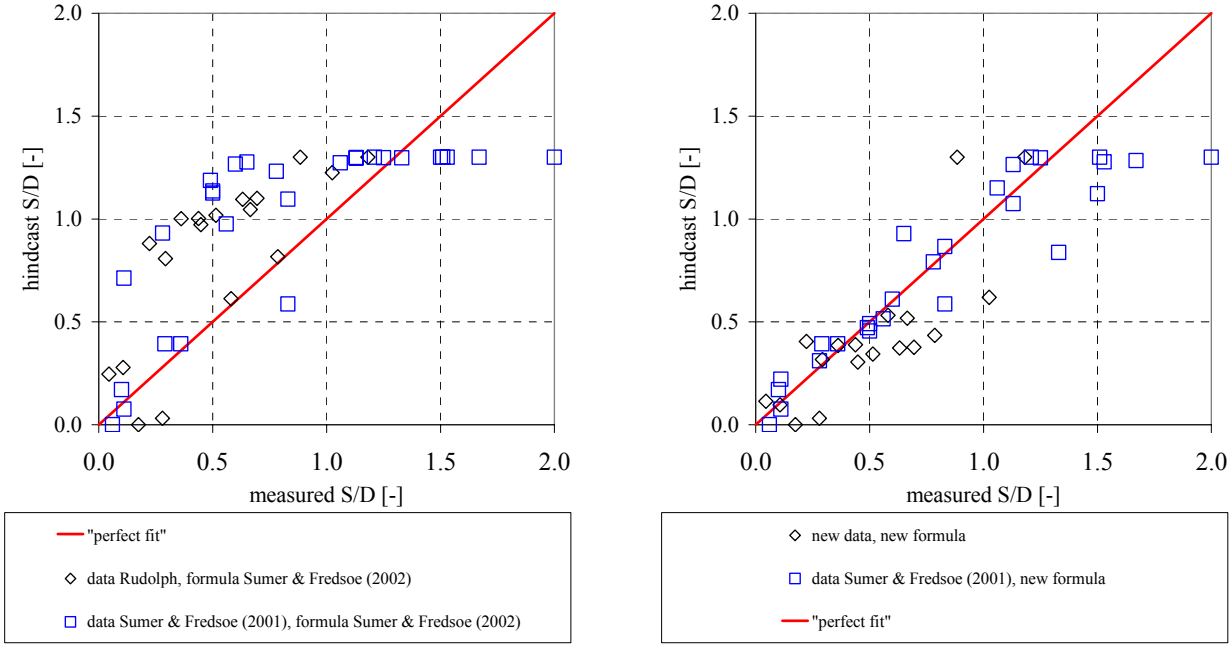

Figure 4 **Comparison of measured and predicted scour depths, left: formula Sumer & Fredsoe (2002), right: Rudolph & Bos (2006)**

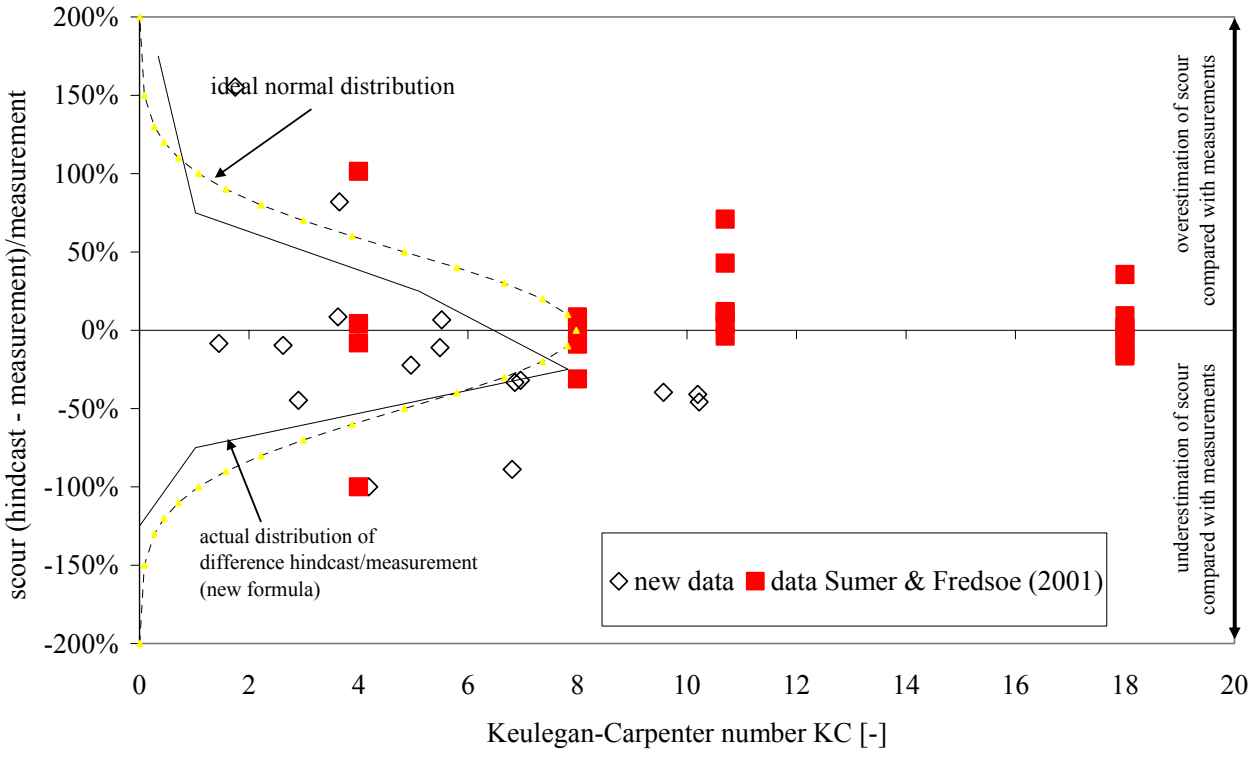

Figure 5 **Comparison of measured and predicted scour depths, depending on Keulegan-Carpenter number**

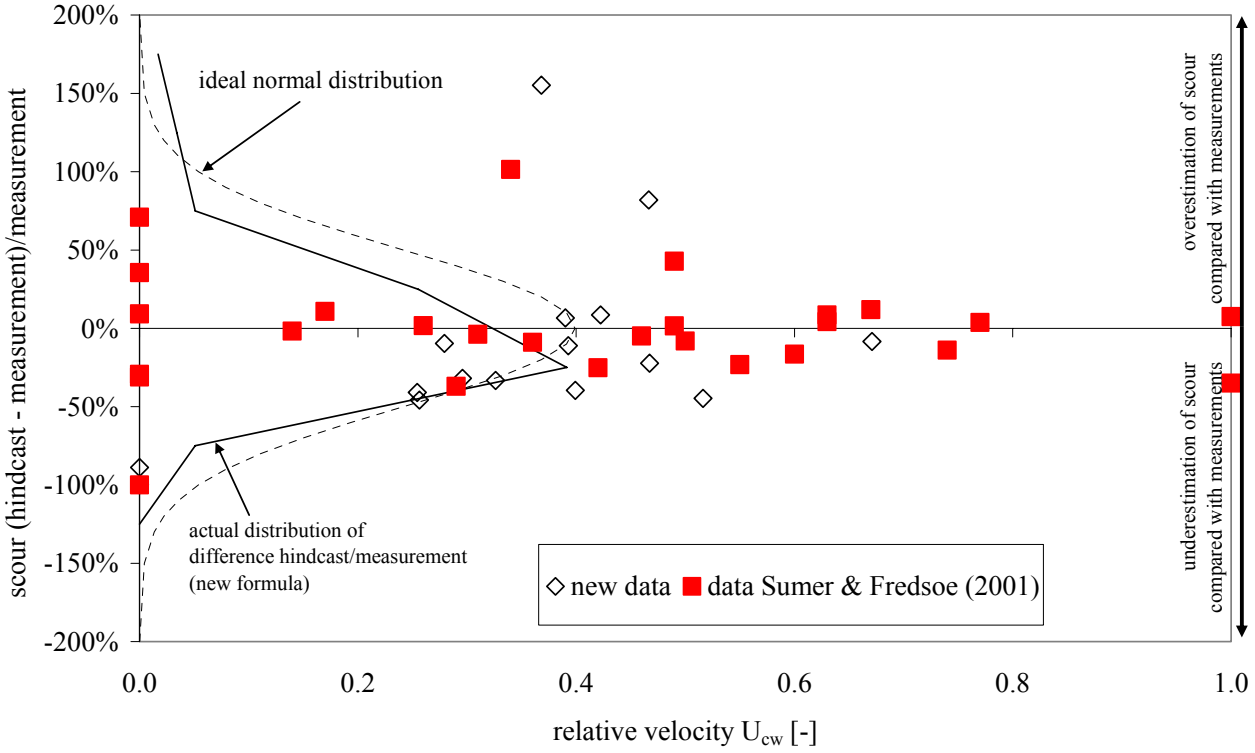

Figure 6 **Comparison of measured and predicted scour depths, depending on relative flow velocity**

Tables

test id	D_{pile} *[m]*	h_w *[m]*	H_s *[m]*	T_p *[s]*	U_{bed} *[m/s]*	u_c *[m/s]*	*u(z=D/2) [m/s]*	*KC [-]*	*Θ [-]*	U_{rel} *[-]*	Re_D *[-]*	S/D_{pile} *[-]*
1-3	0.120	0.50	0.150	1.82	0.28	-	-	4.2	5.3	0.00	-	0.17
1-1	0.120	0.50	0.135	1.82	0.24	0.26	0.23	3.7	5.0	0.48	$2.4*10^4$	0.22
1-2	0.120	0.50	0.135	1.81	0.24	0.21	0.19	3.6	5.0	0.44	$2.0*10^4$	0.29
1-6	0.120	0.50	0.096	1.33	0.13	0.32	0.29	1.5	4.4	0.69	$3.0*10^4$	0.58
1-7	0.120	0.50	0.115	1.34	0.16	0.11	0.10	1.7	4.7	0.39	$1.0*10^4$	0.04
1-9	0.120	0.50	0.166	2.03	0.33	0.34	0.31	5.0	5.9	0.48	$3.2*10^4$	0.66
1-10	0.120	0.50	0.165	2.03	0.33	0.26	0.23	5.5	5.4	0.41	$2.4*10^4$	0.36
1-11	0.120	0.40	0.152	1.80	0.33	0.34	0.23	5.5	5.4	0.41	$2.4*10^4$	0.44
1-4	0.120	0.40	-	-	-	0.29	0.26	-	0.2	1.00	$2.8*10^4$	0.88
2-3	0.080	0.50	0.153	1.89	0.29	-	-	6.8	5.3	0.00	-	0.28
2-1	0.080	0.50	0.171	1.80	0.31	0.17	0.15	7.0	5.7	0.32	$1.0*10^4$	0.45
2-2	0.080	0.50	0.169	1.79	0.31	0.20	0.17	6.9	5.7	0.35	$1.2*10^4$	0.51
2-6	0.080	0.50	0.138	1.29	0.18	0.25	0.21	2.9	5.3	0.54	$1.5*10^4$	0.79
2-7	0.080	0.50	0.121	1.31	0.16	0.08	0.07	2.6	4.8	0.30	$0.5*10^4$	0.11
2-9	0.080	0.50	0.205	1.79	0.43	0.36	0.31	9.6	6.8	0.42	$2.2*10^4$	1.03
2-10	0.080	0.50	0.209	2.02	0.40	0.18	0.15	10.2	6.1	0.28	$1.1*10^4$	0.63
2-11	0.080	0.40	0.209	2.02	0.40	0.18	0.15	10.2	6.1	0.28	$1.1*10^4$	0.69
2-4	0.080	0.40	-	-	-	0.38	0.33	-	0.3	1.00	$2.3*10^4$	1.18

Table 2 Overview on hydraulic conditions and scour measurements

Scour around a triangular fully submerged structure under combined wave and current conditions

DANIEL RUDOLPH[1], TIM RAAIJMAKERS[2], KLAAS JAN BOS[3], KLAAS RIETEMA[4], RUPERT HUNT[5]

[1] WL | Delft Hydraulics, P.O. Box 177, 2600MH Delft, The Netherlands; daniel.rudolph@wldelft.nl
[2] WL | Delft Hydraulics, P.O. Box 177, 2600MH Delft, The Netherlands; tim.raaijmakers@wldelft.nl
[3] WL | Delft Hydraulics, P.O. Box 177, 2600MH Delft, The Netherlands; klaasjan.bos@wldelft.nl
[4] Amec Jacobs Nederland & Stork, Radarweg 60, 1043NT Amsterdam
[5] Shell UK Exploration and Production, 1 Altens Farm Road, Aberdeen, AB12 3FY

Abstract
This paper describes selected results of the scale model tests on scour around a triangular spud can under combined wave and current conditions with oblique direction. Physical modelling experiments were carried out using structures with two orientations, three different heights and variable hydraulic conditions. The observed scour depths were analysed. A new formula was developed for the prediction of scour around a triangular structure in non-cohesive material (sand) for typical North Sea design conditions.

1 Introduction

In connection with the site evaluation for jack-up drilling rig operations, scour assessments are usually carried out. The scour assessment comprises the potential of scour and a scour depth prediction for given hydraulic design conditions. Often, some scour is allowed depending on the spud can penetration depth. If the predicted scour depth is too high (more than penetration depth), scour protection measures need to be applied. As these measures are time and money consuming, the decision making on the necessity of scour protection measures must be based on a reliable and not too conservative scour depth prediction.

In principle, scour depth predictions can be based on a comparison with similar field cases, empirical scour depth prediction formulae and scale model testing. In general, field experiences are difficult to transfer to new situations and the degree of uncertainty of scour development remains high. Empirical scour prediction formulae do not exist for spud cans. Spud cans have different shapes, dimensions and penetration depths. Typical spud can designs are summarised by Rapoport & Young (1987).

In cooperation with Shell Netherlands, NAM and AJS a research project was set-up in order to investigate the scour development around triangular spud cans. The triangular spud cans represent the footings of a jack-up rig which is under contract in the North Sea. Jack-up operations are characterised by different operation periods, hydraulic design conditions and spud can penetration depths.

Scale model tests were carried out in order to investigate the effects of spud can orientation, hydraulic design conditions and penetration depth on the maximum scour depth for typical situations in the southern North Sea. Based on the test results a scour prediction formula was derived.

In this paper we first present typical prototype conditions which were considered (Chapter 2). Then we shortly summarise available literature for the prediction of spud can scour (Chapter 3). Next, the model set-up (Chapter 4) and selected test results are presented (Chapter 5). In Chapter 6 the data analysis and the scour prediction formula are provided. Finally, conclusions and an outlook are given (Chapter 7).

2 Typical prototype conditions

The model set-up and the validity range of the scour depth prediction formula were guided by typical prototype conditions. The considered jack-up is operated in water depths of about 20 to 40m in the southern North Sea. The leg and footing structure are schematised in Figure 1.

For the purpose of scale model tests, the structure was schematised by a fully submerged block with triangular base. The spud can forms a huge flow obstruction with a width of b_{obst}=10m and a height depending on the penetration depth. The leg bracings and the chords were not considered further, since it was judged that these structural members do not contribute significantly to the scour development.

The seabed of the southern North Sea generally consists of fine, medium dense to dense non-cohesive sand. Typical hydraulic design conditions are usually in the range between the 1/1 year condition and 1/100 years condition, depending on the operation period and scour management philosophy.

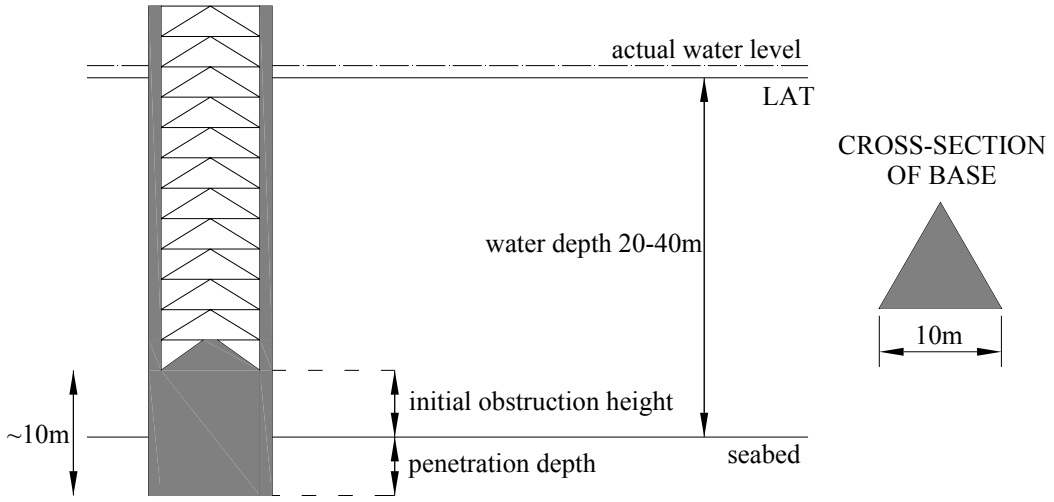

Figure 1 Leg and footing structure of the considered jack-up unit

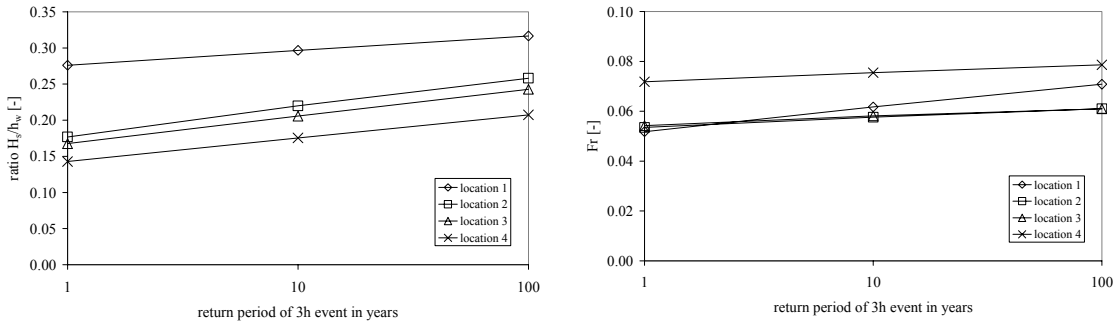

Figure 2 Typical prototype conditions (non-dimensional). Left: return period versus H_s/h_w; Right: Return period versus Froude number

A selection of typical non-dimensional hydraulic design conditions are presented in Figure 2. The significant wave height H_s was related to the water depth h_w, the depth-averaged current velocity was expressed in terms of the Froude number $Fr=u_c/(g*h_w)^{0.5}$. The central peak wave period T_p can often be approximated by $T_p=3.6\ldots4.6*H_s^{0.5}$.

These prototype conditions were used to improve the understanding of scour development around triangular structures and to derive a scour prediction formula for fully submerged triangular structures in general.

3 Short literature review

Literature on scour around angular and especially triangular fully submerged structures is very scarce. Melville & Sutherland (1988) give shape factors for triangular emerged piles in current-only situations for design purposes. Sweeney et al. (1988) carried out two scale model tests with triangular fully submerged structures in current only situations. Rudolph et al. (2005) analysed inhouse data from scale model tests and field experiences and developed a rule of thumb for a rough estimate of the maximum scour depth for spud cans. Assuming that the obstruction height is smaller than the obstruction width, scour is determined by the shape and the obstruction height. The rule of thumb reads:

$$S_{\max} = K \cdot h_{obst}$$

with

K … influence factor, mainly depending on spud can shape [-]

h_{obst} … initial obstruction height of the structure [m]

For angular structures (blocks, triangles) a K factor between 1 and 2 was found for the available data.

Based on the available literature it was concluded that there are no data on scour around a fully submerged triangular structure under offshore conditions.

4 Model set-up

All tests were carried out in Delft Hydraulics' Scheldt basin (see Figure 3). Irregular waves were used in all tests (Jonswap spectrum with γ=3.3). The cross-current was generated by a continuous discharge from a pumping system. The angle between waves and current was between 60º and 90º. Velocity and wave height measurements were performed at various positions in the test section.

Scaling of spud can dimensions was guided by the Froude law with a scale factor of 1:50. In each test run we investigated 6 triangular spud cans at the same time. The applied structures were fixed at the floor of the facility and had a width of $b_{obst,m}$=0.20m. The obstruction height varied between $h_{obst,m}$=0.06m, $h_{obst,m}$=0.18m and $h_{obst,m}$=0.30m above the undisturbed surrounding seabed. The water depth was h_w=0.50m.

The spud can surface was smooth (material: wood). The bed of the facility was covered with a 0.20m non-cohesive sand layer (d_{50}=0.13mm). The scour depths were measured after drainage of the basin using a ruler. The maximum scour depth was defined as the maximum vertical difference between the bed level close to the structure and the surrounding undisturbed bed level.

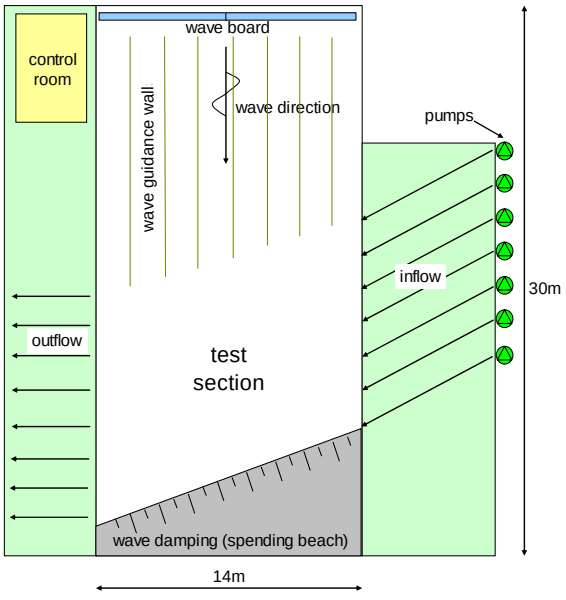

Figure 3 Schematisation of the test facility layout

The hydraulic conditions varied between

- H_s/h_w=0.2…0.4
- T_p=4.5*$H_s^{0.5}$
- Fr=0.04…0.2

As a measure of the relative magnitude of the current compared with the wave orbital velocity, the relative velocity U_{rel} was defined:

$$U_{rel} = \frac{u_c}{u_c + U_w} \qquad \text{(Equation 1)}$$

with

U_{rel} … relative velocity [-]

u_c … current velocity at z=0.5*h_{obst} [m/s] but with a maximum of z=b_{obst} or z=δ with δ being the height of bed boundary layer

U_w … peak orbital velocity at the bed as a function of H_s, T_p, h_w [m/s]

Under the considered hydraulic design conditions, the relative velocity U_{rel} is usually in the order of 0.3 to 0.4. The tests focussed on this range of U_{rel}. In addition to this narrow U_{rel} range, tests were carried out with variable U_{rel} (U_{rel}=0…1) in order to check the effects of waves only (U_{rel}=0), current dominated situations (U_{rel}>0.5) and flow only (U_{rel}=1).

All test conditions represented the live-bed situation (undisturbed wave and current induced bed shear stress > critical bed shear stress).

Prior to the test runs, the current velocity profile was determined for a range of conditions. It was found that in case of current only, the velocity profile follows a logarithmic shape with a bed roughness of k_s=0.01m and z_0=k_s/30.

5 Visual impressions of test results

After test execution and drainage of the basin, the scour patterns were inspected visually and scour depths were measured along several rays depending on the scour pattern and the scour extent. Figure 4 shows typical test results of current only situations. If the current hits at first the tip (here: point B), little scour occurs. If the current hits the face (here: face A-B), significant scour occurs. The spud can dimensions and the Froude numbers were the same.

In case of waves only, the scour pattern and scour depths were the same for waves hitting the tip and waves hitting the face. An image from a test with waves only hitting the tip at first is shown in Figure 5, left side. The difference with the current only situation can be explained by the oscillatory water particle motion: in every wave cycle, the flow hits the face in perpendicular direction which causes a much higher disturbance at the bed than hitting the tip at first.

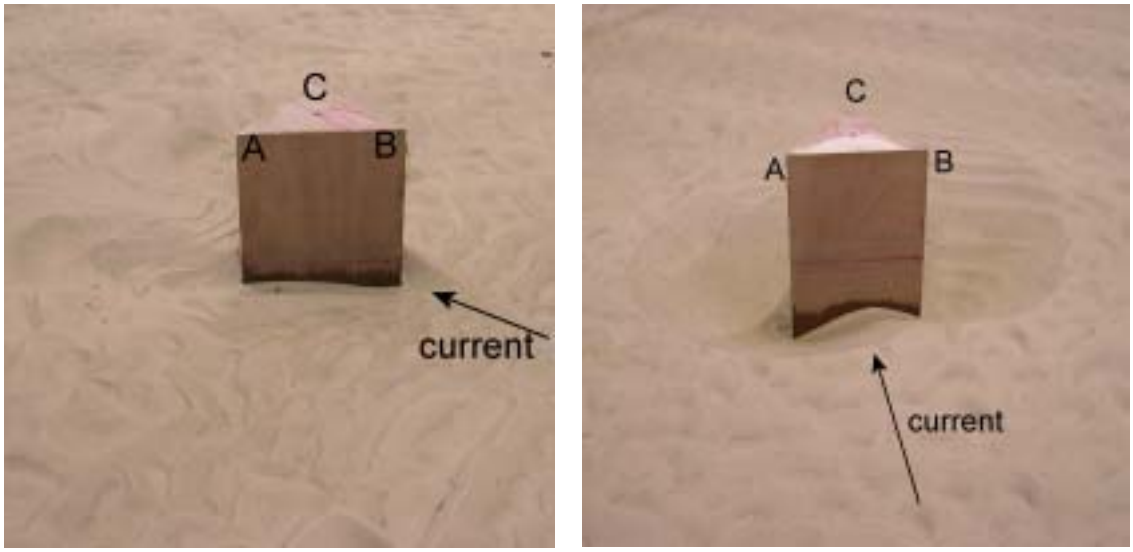

Figure 4 Scour patterns in case of current only; Left side: current against tip leads to little scour; Right side: current against face leads to significant scour. Note: Very high current velocities (Fr=0.15) were used to generate significant scour patterns. These are not representative for the considered typical design conditions.

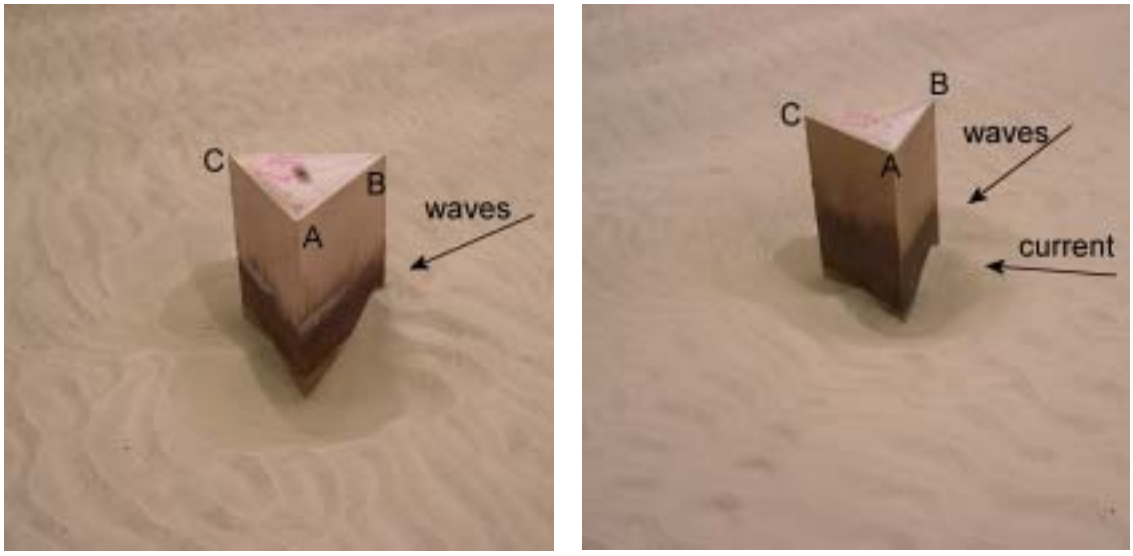

Figure 5 Scour patterns in case of waves only (left side) and wave dominated (right side)

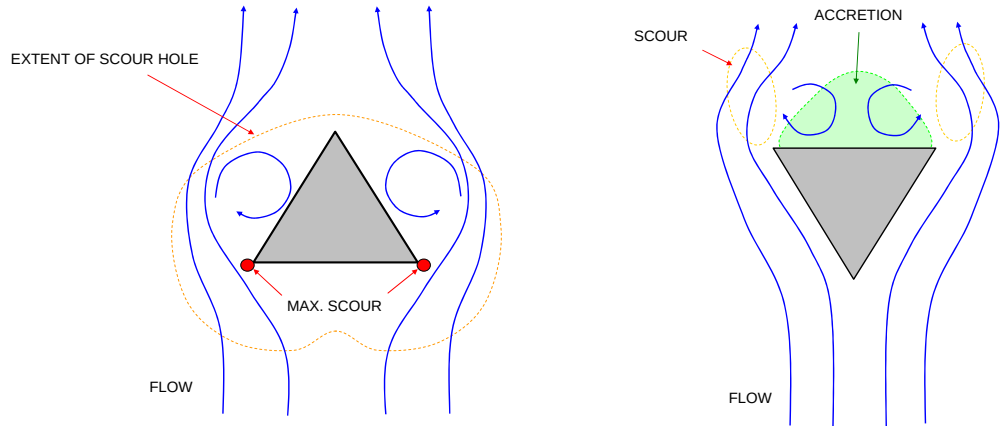

Figure 6 Schematisation of flow patterns and scour patterns in case of flow perpendicular to the face (left side) and flow hitting the tip (right side)

In case of a current superimposed on waves, the scour pattern starts to change. In case of wave domination, the change of scour depths at the corner points is marginal. A scour pattern of a wave dominated situation is shown in Figure 5, right side. The applied conditions are representative for typical prototype conditions (U_{rel}=0.4). A further increase of the current velocity (wave conditions constant) leads to scour patterns gradually changing towards the flow-only scour pattern with flow hitting the face. However, the maximum scour depths did not change significantly in the tests.

Schematisations of typical flow and scour patterns are indicated in Figure 6. In case of wave dominated conditions, the flow patterns are expected to be similar to current only, however, the flow patterns and scour patterns reverse during each wave cycle. In case of wave dominated situations, an accretion zone does not build up.

6 Analysis

Data selection

In total, 10 test runs were carried out with 6 structures each (3 heights, 2 orientations). In the analysis we focussed on the maximum and time-equilibrium scour depths measured around the perimeter. The scour hole extent and the scour hole slopes were not analysed in detail. The scour development in time was investigated by interrupting selected tests and measuring the scour depth. The development with time followed an exponential curve. The characteristic number of waves was determined at about $N_{char}\approx1200$.

$$\frac{S}{S_{eq}} = 1 - \exp\left(-\frac{N_{waves}}{N_{char}}\right) \qquad \text{(Equation 2)}$$

with

S … scour [m] measured after N waves

S_{eq} … time-equilibrium scour depth, maximum around perimeter [m]

N_{waves} … number of waves [-]

N_{char} … characteristic number of waves [-], for $N_{waves}=N_{char}$ about 63% of the equilibrium is reached

Choice of non-dimensional parameters

The following general trends were expected which also determine boundary conditions for the set-up of the scour prediction formula.

- The scour depth generally increases with the width of the structure b_{obst}. If b_{obst} reaches the order of magnitude of the water depth, the effect of b_{obst} on S reduces and reaches an equilibrium. A further increase in b_{obst} does not lead to a further increase of S.
- The scour depth generally increases with h_{obst} but less than linearly. The increase of h_{obst} from e.g. $h_{obst}=0.1h_w$ to $0.3h_w$ has more effect on scour than the increase between $h_{obst}=0.8h_w$ to $h_{obst}=1h_w$.
- If $h_{obst}<b_{obst}$ then h_{obst} is the most important structural dimension affecting scour. If $b_{obst}<h_{obst}$ then b_{obst} is the most important structural dimension affecting scour.
- Scour generally increases with wave conditions. The wave conditions are best represented by the amplitude of the wave orbital motion.
- Scour generally increases with the current velocity.

In the analysis the following non-dimensional parameters were chosen:

- Dimensionless equilibrium scour depth S_{eq}/b_{obst}.
- Keulegan-Carpenter number KC. The KC number as defined in Equation 4 describes the relation between wave-induced load and a characteristic dimension of the structure. It was chosen to relate the amplitude of the wave orbital motion A to the spud can width.
- Relative structure height h_{obst}/h_w.

The current velocity was not considered in this analysis because of limited data with current only. Furthermore, test results indicated that the current velocity did not increase the wave-induced scour significantly within the range of interest ($U_{rel}<0.5$). Of course, theoretically, it would be more sound to define a combined wave and current parameter instead of the wave dependent KC number. In the near future, it is envisaged to obtain additional current-only data and to extend the validity to current-only and current-dominated situations as well.

Data fitting

Based on the above given considerations, the following principal formula set-up was chosen:

$$\frac{S_{\max}}{b_{obst}} = c_1 \cdot \left\{1 - \exp\left[-c_2 \cdot KC \cdot \left(\frac{h_{obst}}{h_w}\right)^{c_3}\right]\right\} \qquad \text{(Eq.3)}$$

$$KC = 2 \cdot \pi \cdot \frac{A_w}{b_{obst}} \qquad \text{(Equation 4)}$$

with

S_{max} … maximum scour depth [m]

b_{obst} … width of structure [m]

KC … Keulegan Carpenter number [-]

h_{obst} … obstruction height [m], $h_{obst}\leq h_w$

h_w … water depth [m]

c_1, c_2, c_3 … empirical coefficients [-]

Based on the analysis of the selected data, the best fit was obtained if all three coefficients equal unity (c_1=1, c_2=1, c_3=1).

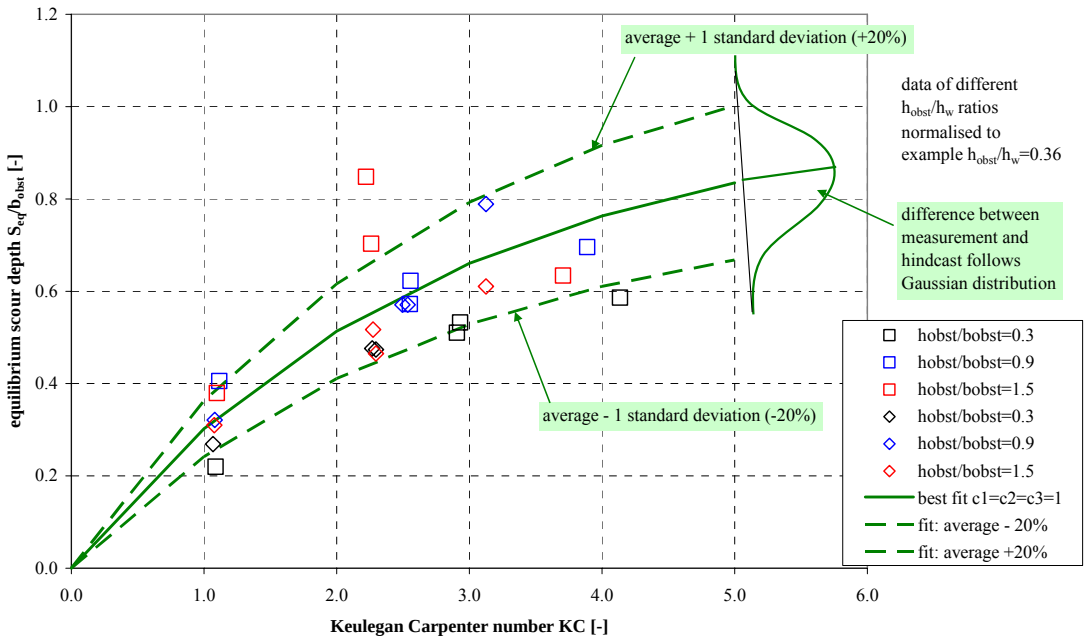

Figure 7 Relation between KC and scour depth prediction for an arbitrarily chosen example (h_{obst}/b_{obst}=0.9, h_{obst}/h_w=0.36)

For illustration of the data fit and the accuracy range, an example is provided in Figure 7. The scour depth prediction (green line) is given in terms of the KC-number for arbitrarily chosen values of h_{obst}/h_w=0.36, h_{obst}/b_{obst}=0.9.

Quality of data fit

The empirical coefficients presented above correspond with a standard deviation of about 20% for the ratio scour depth hindcast/ scour depth measurement (S_{hind}/S_{meas}). The 95% confidence interval was about 7%.

The quality of the data fit was assessed by comparing scour depth measurements with scour depth hindcasts for the test conditions. The results are presented in Figure 8.

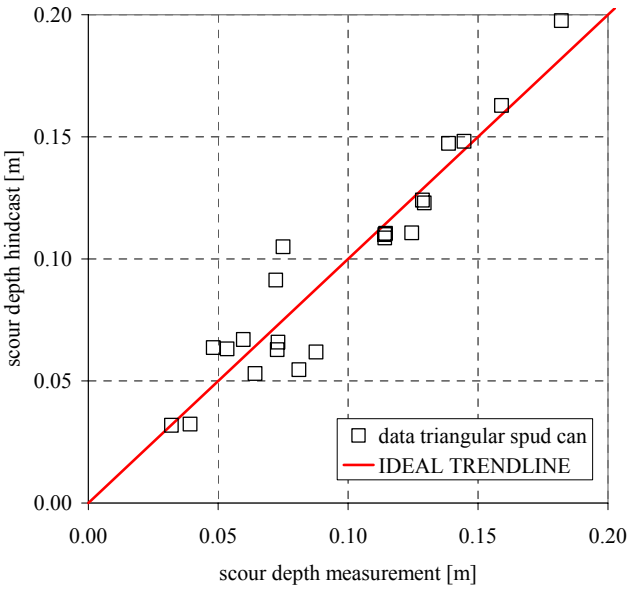

Figure 8 Quality of data fit: measurement versus hindcast, based on selected test results

Validity range of new formula

The new formula was derived based on scale model test data representing typical North Sea design conditions. The range of validity is approximately:

- $0<KC<5$
- $U_{rel}<0.5$
- $b_{obst}/h_w<1$; $h_{obst}/h_w<0.6$
- seabed material: non-cohesive mobile sand ("live-bed situation")
- shape of structure: triangular base

Recommendations for application for design purposes

Various scale factors may exist which should be taken into account when using the results of this study for design purposes: In practice, waves and currents might also approach from the same direction which might increase the hydrodynamic load and consequently the scour depth. Taking also into account the standard deviation of the measurements, we suggest applying a safety factor γ.

7 Conclusions and outlook

Scale model tests were carried out to study the scour development around a triangular fully submerged structure in combined wave and current situations. The tested situations were representative for typical design conditions of the southern North Sea. The practical application of the scale model tests is related to triangular footings of jack-up drilling rigs (spud cans).

The analysis of the test results led to a scour prediction formula for a fully submerged structure with triangular base in a live-bed situation. It was found that the KC-number, the structure height and the structure width are the dominating factors for the prediction of the scour depth. The orientation of the structure and the current velocity were of minor importance in the considered range of conditions.

The new formula represents a best fit and reads:

$$\frac{S_{\max}}{b_{obst}} = \gamma \cdot c_1 \cdot \left\{ 1 - \exp\left[-c_2 \cdot KC \cdot \left(\frac{h_{obst}}{h_w} \right)^{c_3} \right] \right\} \quad with\ KC = \frac{2 \cdot \pi \cdot A_w}{b_{obst}} \quad and\ c_1 = c_2 = c_3 = 1$$

For design purposes it is recommended to apply a safety factor γ in order to account for scale effects and limitations of the model set-up (e.g. tests: current perpendicular to waves; prototype: current and waves possibly unidirectional).

The test results indicated that significant scour can occur around a triangular structure in wave dominated situations. The scour development differs from the situation with a cylindrical pile (for cylindrical piles see e.g. Sumer & Fredsøe, 2002; Rudolph & Bos, 2006).

Therefore, we suggest not to apply a general shape factor on scour prediction formulae for cylindrical piles to account for the difference in shape between triangular structure and cylinder.

For more general use of this scour prediction formula, additional scale model tests need to be carried out. These tests should focus on:

- Current and waves unidirectional
- Variation of structure width (b_{obst})
- Scour in flow dominated situations ($0.5<U_{rel}<1$)

Acknowledgements

The authors are thankful to the Dutch Ministry of Foreign Affairs for co-financing this research project.

References

Melville, B.W., Sutherland, A.J. (1988): Design method for local scour at bridge piers, Journal of Hydraulic Engineering, ASCE, 114(19), 1210-1226.

Rapoport, V., Young, A.G. (1987): Foundation performance of jack-up drilling units, analysis of case histories, In: Mobile Offshore Structures, Edited by L.F. Boswell, C.A.D'Mello, A.J. Edwards, published by Elsevier Applied Science, London and New York

Rudolph, D., Bijlsma, A., Bos, K.J., Rietema, K. (2005): Scour around spud cans – analysis of field measurements, 15th International Offshore and Polar Engineering Conference, June 19-24, 2005, Seoul, Korea

Sweeney, M., Webb, R.M., Wilkinson, R.H. (1988): Scour around jack-up rig footings, Proceedings of the 20th Offshore Technology Conference, Paper No. 5764, Houston, Texas, USA

Numerical computation of seepage erosion below dams (piping)

J.B. Sellmeijer
GeoDelft, Delft, The Netherlands

I. Introduction

In delta areas the land is protected from floods and high tides by dikes. In general these are constructed of impervious clays and built on a sandy aquifer as subsoil. Such structures are vulnerable to an erosion effect called piping.

The actual word 'piping' refers to the development of shallow channels in the sand below the dike, which begins at the downstream side of the structure. Here often a ditch is situated with a burst bottom due to excess water pressures. The subsequent erosion process develops backwards to the high head side. The natural non-homogeneity in the soil causes the shallow channels to be irregularly shaped.

Below a critical value of the hydraulic head over the structure the erosion process eases down until water only is transported through the channels. It is common to observe sand boils behind the dike, which produce water alone. However, if a critical head difference is reached, the erosion process continues and the structure may in the end collapse.

II. Historical Notes

During the beginning of the previous century the piping phenomenon has been intensively studied. References [1] through [5] show in its perspective the way piping was considered and understood. Simple empirical rules for the critical gradient were applied with some theoretical backup.

TABLE I.
SOME EXAMPLES OF SIMPLE PIPING RULES

Bligh $\frac{H}{L} = \frac{1}{C_{\text{Bligh}}}$	fine silty sand moderate fine sand course sand fine gravel course gravel		C_{Bligh} 18 15 12 9 4
Lane $\frac{H}{L_h} = \frac{\frac{1}{3}+\frac{L_v}{L_h}}{C_{\text{Lane}}}$	fine silty sand moderate fine sand course sand fine gravel course gravel		C_{Lane} 8.5 7 5 4 3
Sellmeijer $\frac{H}{L} = GRSF$	geometry factor rolling equilibrium sand properties 4 force factor	$G = \left(\frac{D}{L}\right)^{\frac{0.28}{\left(\frac{D}{L}\right)^{2.8}-1}}$ $R = \frac{\gamma'_p}{\gamma_w}\tan\vartheta$ $S = \eta\frac{d}{\sqrt[3]{\kappa L}}$ $F = 0.68 - 0.1\ln(S)$	D: aquifer height H: hydraulic head L: dike width γ_p: unit weight particles γ_w: unit weight water ϑ: bedding angle η: Whites constant d: particle diameter κ: intrinsic permeability

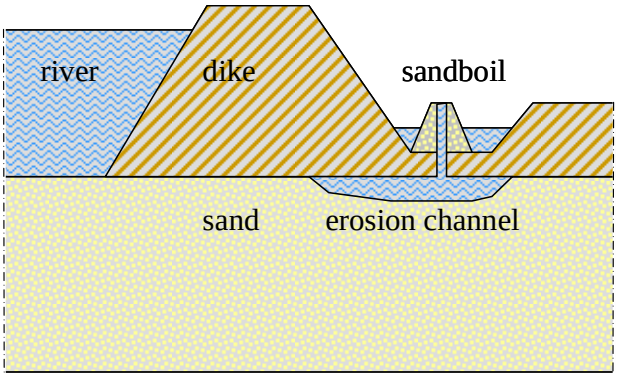

Figure 1. Geometry of the standard dike

In the second half of the previous century extended programs of visual tests were carried out. Based on these observations numerical models were developed. References [6] through [16] represent the activities during this period.

The simple piping rules for the critical gradient are meant for ordinary consultancy. These rules are easy to handle and provide results instantaneously. They are applicable to a standard dike, shown in Figure 1. The sand is considered to be homogeneous and the geometry consists of a horizontal layer with a clay dike on top. Note that the dimensions of the erosion channel and sand boil are exaggerated in order to view them properly.

Examples of the simple rules are collected in Table I. The first two are empirical. They specify the role of the soil properties by a characteristic factor. This factor is read from a table after classification of the sandy material.

The third rule is obtained by calculation by a conceptual model. A number of specific results is curve fitted and collected into the rule. This has the advantage that the soil properties are involved by their parameter values. These values may be measured or determined by correlation.

III. Advanced Numerical Piping Modelling

The simple piping rules are fine for standard consultancy. However, they are insufficient for complicated problems, where risks are high. Then, a more refined approach is required.

For instance, the rules do not consider the effect of a course gravel sublayer below the sandy layer. Nor a sloping bottom of the dike, the role of a partially covered river bottom by slurry, the effect of varying layer thickness, etc. .

For these cases a versatile numerical tool is required. Such a model is described in reference [12]. In fact it is used for the derivation of the third simplified piping rule. The groundwater flow, here, was modeled by the analytical technique of conformal mapping. For simple geometries this is possible.

For more complex geometries an analytical approach is no longer feasible. A numerical model will be presented.

A. *Numerical piping program*

The conceptual piping model consists of three areas: the groundwater flow in the layers, the water flow in the erosion channel and the state of limit equilibrium of the particles at the bottom of the channel.

The last two areas together form the boundary condition for the first area. That means that the problem of piping may be determined by ordinary groundwater flow computation with a special piping boundary condition.

However, this is a cumbersome condition. It is highly non linear. It is not operative in a single point of the boundary, but affects the boundary on aggregate. By implication, only iteratively this condition may be applied.

B. *Condition of continuity in the erosion channel*

The erosion channel appears to be very shallow. This is observed in the visual tests; see [8], [10], [11], [14], [15]. Results by computation also show extremely shallow channels; see [12]. Apparently, quite a lot of seepage water may flow off through a small open channel.

The flow in the channel may be modeled by the laminar Navier Stokes equations. For a sandy sublayer the flow is laminar; for course gravel it might tend to become turbulent. Since the channel is so shallow, the solution of the Navier Stokes equations is not unlike the formula for pipe flow. It reads:

$$a^3 p = 12\,\kappa \frac{Q}{k}. \qquad (1)$$

a is the height of the channel; p is the gradient in the channel; Q is the discharge in the channel; κ is the intrinsic permeability and k the hydraulic permeability. The hydraulic and intrinsic permeabilities are linked by the viscosity.

The solution supplies also the shear stress along the bottom of the channel. This stress is caused by the momentum of the flow through the channel. It reads:

$$\tau = \tfrac{1}{2}\gamma_w\, p\, a. \qquad (2)$$

This stress is required to determine the limit stress state of the particles.

C. *Limit stress state of the bottom particles*

The question of limiting stability at the interface of soil and water cannot be solved by regarding the soil as a continuum. This is due to the fact that continuum mechanics allow the effective vertical stresses to vanish near the bottom of the slit. The shearing stress which is associated with the near parabolic velocity profile in the slit itself, therefore, cannot be dealt with then in a Coulomb manner.

Conversely, the condition of limiting equilibrium must be imposed to the balance of forces on a particle. This yields a connection for the forces for a given mode of motion. Two modes of motion are feasible: translation and rolling. Koenders [17] showed that the rolling mode is preferred. The result is a rule not unlike a Coulomb criterion.

In the original work of [12] four distinct forces are considered for the force balance for a grain at the top of the interface. The horizontal ones are the drag force due to channel flow and the horizontal seepage gradient. The vertical ones are the weight of a particle and a force associated with the vertical seepage gradient.

However, heterogeneous mixture in steady state shows a landscape where the large grains stick out and the small ones are well buried. Between the large grains substantial open space occurs. The forces due to the seepage gradients by no means can affect the grain at the top of the interface.

By implication, two forces should be balanced, see **Figure 2.** The force along the sloping channel is the shear stress (2) times the equivalent area d^2/η. White's constant η takes care of the substantial open space between the top grains. The vertical force is the weight of a spherical particle. The rolling mode balance of these two forces follows from the sine law in geometry:

$$\frac{\gamma'_p \frac{\pi}{6} d^3}{\cos\vartheta} = \frac{\frac{1}{2}\gamma_w\, p\, a\, d^2}{\sin(\vartheta+\alpha)\,\eta}. \qquad (3)$$

α is the slope of the erosion channel.

D. *Boundary condition along the erosion channel*

An appropriate expression for the boundary condition along the erosion channel follows from (1) and (3). If the yet unknown height of the channel is eliminated, an expression remains with flow features only. It reads:

$$\sqrt[3]{\frac{Q}{k\,L}\,p^2} = \frac{\pi}{3}\eta\,\frac{\gamma'_p}{\gamma_w}\,\frac{\sin(\vartheta+\alpha)}{\cos\vartheta}\,\frac{d}{\sqrt[3]{12\,\kappa\,L}}. \qquad (4)$$

This is a suitable boundary condition for the flow. It relates the discharge on aggregate to the gradient. The

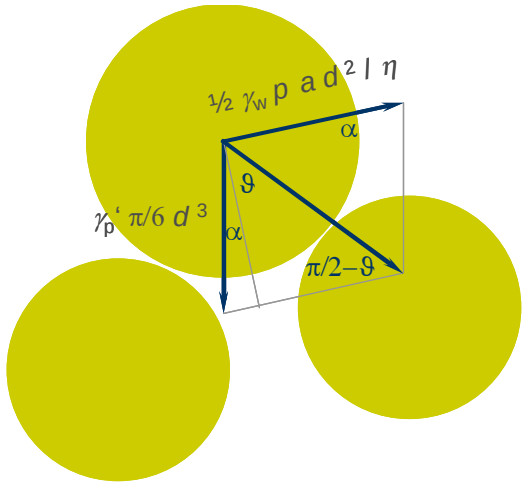

Figure 2. Two force balance of a top grain

right hand side is a constant. The erosion channel needs not to be straight. It may consist of several parts with different angles α.

E. Groundwater flow computation

It appeared that piping may be described as boundary condition in a groundwater flow program. That does not imply that such a program may be run to make predictions for piping design. Since the condition is non linear and is applied on aggregate over the boundary, a special iteration module is required.

Therefore, a shell is developed in order to control the iteration. If needed, the groundwater flow computation is called, where the current head or discharge in the piping boundary is applied. The shell examines how accurate the piping condition is met and adjusts the current head or discharge.

The head or discharge along the boundary is simulated by a number of shape functions. A few shape functions is sufficient, since the gradient is rather smooth. At the inflow point the gradient buckles, since the discharge tends to zero.

Despite the smooth character of the gradient the iteration process is a struggle. The reason is not the buckle at the inflow point. It is the fact that a change of the discharge easily compensates the one of the gradient without apparent improvement of the accuracy, see left hand side of (4).

A useful remedy for this problem is to pin down the incremental expression for the discharge at the inflow point. This expression reads:

$$\Delta Q_j = \sum \frac{\partial Q_j}{\partial S_i} \Delta S_i + \frac{\partial Q_j}{\partial H} \Delta H \cdot \qquad (5)$$

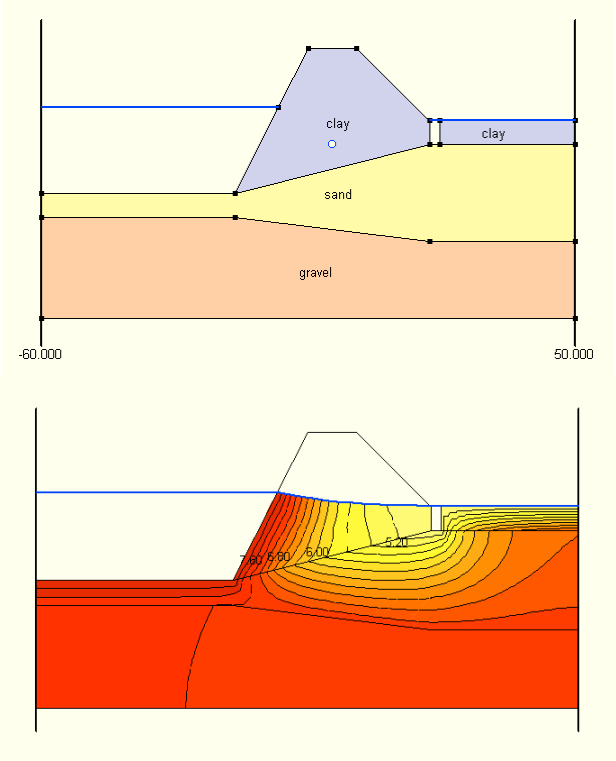

Figure 3. Example advanced piping design

S is the strength of the shape functions. The derivatives of the discharge are delivered by the groundwater flow program. Often the groundwater flow is linear, so that the incremental notation may be omitted. In the inflow point the discharge theoretically vanishes. However, since the gradient buckles, it is better to apply a small positive value, which is fixed by minimizing the inaccuracy.

Pinning down the discharge at the inflow point introduces some inaccuracy so as to make the process stable and fast. Since the outcome is calibrated by precise large scale testing results, this is justified.

An example of advanced piping design is presented. In **Figure 3** the geometry is shown at the top. The dike is sloping and situated on a two-layer subsoil. It slopes upwards, which reduces the danger for piping, since particles must roll upwards. The opposite would endanger the piping thread and should be avoided.

The upper layer is sand and the lower one gravel. The presence of the very permeable gravel endangers the piping thread. The river water flows directly downwards through the thin sand layer to the gravel. At a minimum of head loss it flows though the gravel until down under the outflow point. There it flows upwards to the erosion channel. In this way more water reaches the channel than in the case of sand alone.

In **Figure 4** the effect of the gravel is illustrated. In the top picture the gravel has the same permeability as the sand. The critical hydraulic head appears to be 4.4 m. In the bottom picture the gravel is 100 times more permeable than the sand. The critical hydraulic head appears to be 2.7 m. In the bottom picture of **Figure 3** the contour lines of the head are shown for the permeable gravel. The minimum head loss is clearly observed.

The left side of the curves in **Figure 4** represents the safe and steady state of the piping phenomenon. A small

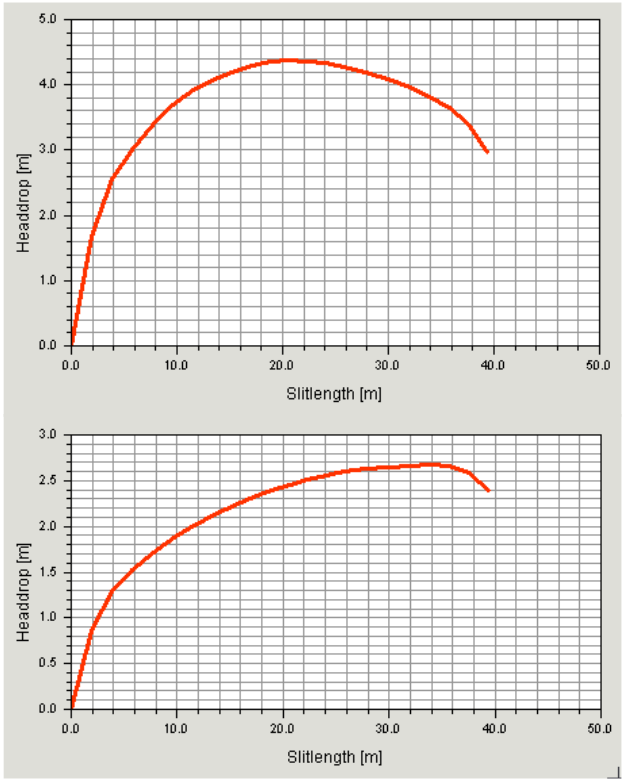

Figure 4. Output advanced piping design

disturbance is compensated by a small increase of the channel length. However, in the right side this would lead to progressive erosion. The maximum of the curves is associated with the critical head.

IV. Piping Neural Netwerk

Numerical piping computations last between dozens of seconds to a dozen of minutes. If the goal of piping design is probabilistic of nature, this takes too long. A computation requires ample preparation, while consultancy prefers ready made approaches. Therefore, acceleration is sought in the design process.

The answer is the development of a new advanced piping rule, like the third one in Table I. An appropriate means to facilitate this is the use of an Artificial Neural Network. Neural networks are meant for pattern recognition, [18]. The pattern to be recognized could be a handwriting, fingerprint, but also results of piping computations. The advantage is that results of laborious computation are available at snapping one's fingers.

To set up a proper network the degrees of freedom must be limited as much as possible. Every freedom multiplies the required number of data by a factor depending on its complexity. Therefore, the piping parameters are first grouped together into meaningful clusters.

A single piping computation determines the critical head as function of the geometry and soil parameters. The Result, however, may be interpreted as the critical width of the dike as function of the head over the dike and geometry and soil parameters. Therefore, two useful types of neural networks may be derived: one for the classification of the critical head and one for the critical width of the dike.

Engineers prefer the last one, since the head occurs according to river discharge and the width of the dike may be designed.

A. Clustering parameters in the piping model

The aim is to obtain a network for a geometry with a sloping dike and two sublayers, shown in **Figure 5**. The layer heights are denoted by h with a two letter index. 'g' indicates 'granular' and 's' 'sublayer'; 1 refers to river side and 2 to polder side.

Two important scaling operations are possible: for the geometry and for the outcome. On one hand the geometry

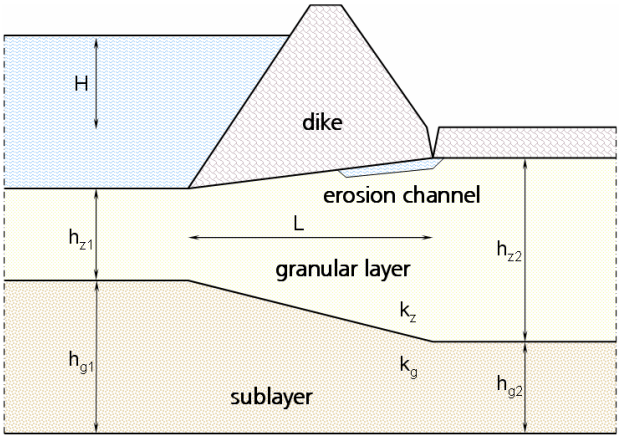

Figure 5. Geometry for the neutral network

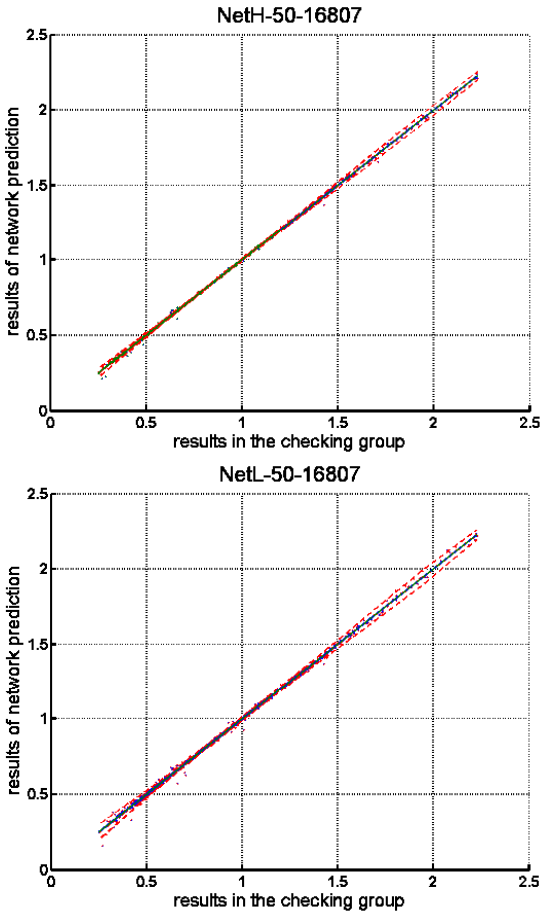

Figure 6. Neural network accuracy

may be scaled by the width of the dike, when the critical head is sought. On the other hand it may be scaled by the hydraulic head, when the critical width of the dike is sought.

The outcome (the critical head or the critical width of the dike) may be scaled by the right side of (4). It contains the width of the dike, which is better replaced by one of the neutral heights of the layers.

Thus, the general solution is specified in the following fashion:

$$\frac{1}{\beta}\frac{H}{L} = \mathrm{F}\left(\frac{h_{z1}}{L}, \frac{h_{z2}}{L}, \frac{h_{g1}}{L}, \frac{h_{g2}}{L}, \frac{k_z}{k_g}\right) \quad . \qquad (6)$$

$$\beta\frac{L}{H} = \mathrm{G}\left(\frac{h_{z1}}{H}, \frac{h_{z2}}{H}, \frac{h_{g1}}{H}, \frac{h_{g2}}{H}, \frac{k_z}{k_g}\right)$$

where,

$$\beta = \frac{\pi}{3}\eta\frac{\gamma'_p}{\gamma_w}\frac{\sin(\vartheta+\alpha)}{\cos\vartheta}\frac{d}{\sqrt[3]{\kappa h_{z2}}} . \qquad (7)$$

The factor β is a multiplier and need not to be incorporated in the neural network. Both networks have 5 degrees of freedom, 4 heights and the permeability contrast of the layers.

B. *Network training*

A neural network consists of layers of nodes. There are three types: input layer, hidden layers, output layer. The data in every node of a layer are passed by weight factors to all nodes of the next layer. In the nodes the data are transformed. The input nodes are filled with input. The output node(s) contain(s) the outcome. The number of hidden layers may be more than one, but this does not necessarily improve the result.

The number of hidden nodes affects the behavior of the network. Few nodes have a smoothing effect on irregularities. However, the result will be inferior for an abrupt course of the outcome. Many nodes facilitate a precise pattern recognition without too much smoothing. Here, 5 input nodes, 50 hidden nodes and 1 output node are applied.

Both networks are trained by the results of in total 18674 piping computations. 90% (16807) is used for the training, the remaining ones are applied for checking. The accuracy is shown in **Figure 6.**

Here, the input value is plotted against the result of network prediction. For a perfect fit a line under 45° would be found. The dotted lines represent the standard deviation of the difference. The top picture reflects the network for the critical head; the bottom picture for the critical width of the dike.

The agreement is rather good. The differences are very small, as may be expected for well performed computations. In some corners of the parameter space the behavior is more abrupt of nature, resulting occasionally in a minor hop.

The training data cover only that part of the parameter space, where computations are carried out. The network is applicable in that area alone. Beyond, preposterous predictions would be obtained, which are of no use and should be avoided.

C. *Advanced piping rule applied to standard dike*

The accuracy of the network prediction looks promising according to the results for the checking group in **Figure 6.**

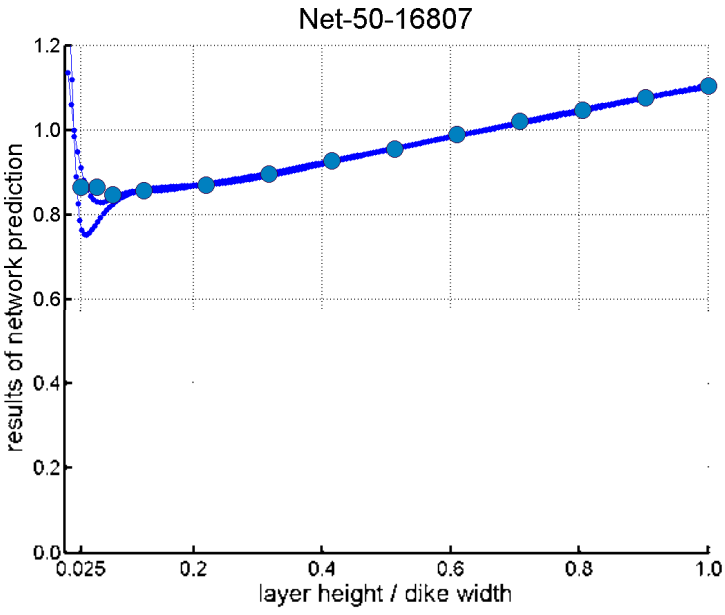

Figure 7. Advanced piping rule applied to standard dike

However, the few incidental hops are a source of concern. Therefore, it makes sense to observe the behavior in a specific range. A suitable range is the geometry of the standard dike.

Figure 7 shows the predictions by both networks (solid lines). The ones for the critical height are directly determined for the ratio of layer height and dike width. The ones for the critical dike width are determined for the ratio of layer height and hydraulic head. They are presented in the same fashion as the critical height.

For reference, the outcome of individual computations is added as large dots. In the range $h_{g2} / L > 0.1$ the agreement is excellent. For thin layers there appears to be a complication.

The problem is that the finite element groundwater flow calculation requires a few elements over the layer height in order to facilitate accurate computation. For thin layers this is not possible anymore. Very thin layers have one element only, often distorted.

No computations in the range $h_{g2} / L < 0.025$ have been made. Therefore, in that area no predictions are possible. Due to poor computation results for the smaller layer heights the predictions in the area $0.025 < h_{g2} / L < 0.1$ are less accurate.

The predictions by the neural networks still must be multiplied by the factor β in (7). For thin granular layers this factor is high, so that the risk for piping is small. However, accurate calculations must be possible also for thin layers.

V. Conclusion and Summary

For the design against piping, simple rules are used to specify the critical gradient over the dike. These rules apply to a standard dike. They do not facilitate advanced calculations.

The mechanism of piping is embodied into a conceptual model. This model is incorporated into a numerical program. By this program advanced piping computations may be carried out.

For an advanced geometry consisting of two granular layers with a sloping dike on top, a large amount of random computations is carried out. Neural networks are trained by the results of these computations. The networks in fact are a new advanced piping rule. There is a network for prediction of the critical head and one for the critical width of the dike.

The performance of the neural networks is excellent, as long as proper numerical computations are available. At present the granular height is by the dike width, the subsoil height by half the dike width.

For very thin granular layers the computations are not yet accurate enough. By implication, the networks must be used with care. The first priority is to assure detailed accuracy of the numerical flow calculation for the entire range of engineering practice, especially for very thin layers.

VI. UNITS

D	[m]	:	aquifer height
H	[m]	:	hydraulic head
L	[m]	:	dike width
Q	[m^2/s]	:	erosion channel discharge
a	[m]	:	erosion channel height
d	[m]	:	particle diameter
h	[m]	:	layer height
k	[m/s]	:	hydraulic permeability
p	[-]	:	erosion channel gradient
γ_p	[kN/m^3]	:	unit weight particles
γ_w	[kN/m^3]	:	unit weight water
α	[DEG]	:	erosion channel angle
ϑ	[DEG]	:	bedding angle
η	[-]	:	Whites coefficient
κ	[m^2]	:	intrinsic permeability

REFERENCES

[1] J. Clibborn and J.S. Beresford, "Experiments on the Passage of Water through Sand", *Govt. of India, Central Printing Office*, 1902.

[2] W.G. Bligh, "Dams Barrages and Weirs on Porous Foundations", *Engineering News*, p. 708, 1910.

[3] W.M. Griffith, "The Stability of Weir Foundations on Sand and Soil Subject to Hydrostatic Pressure", *Minutes of Proceedings J.C.E.* , Vol. 197 pt III, p. 221, 1913.

[4] L.F. Harza, "Uplift and Seepage under Dams on Sand", *Proceedings ASCE*, Paper no. 1920, 1935.

[5] E.W. Lane, "Security from Under-Seepage Masonry Dams on Earth Foundations", *Transactions ASCE*, Vol. 100 , Paper no. 1919, 1935.

[6] D. Miesel, "Rückschreitende Erosion unter Bindiger Deckschicht", Vorträge der Baugrundtagung, Berlin, *Deutsche Gesellschaft für Erd- und Grundbau E. V.*, 1978.

[7] H. Müller-Kirchenbauer, "Zum Zeitlichen Verlauf der Rückschreitenden Erosion in Geschichtetem Untergrund unter Dämmen und Stauanlagen", *Beitrag zum Talsperrensymposium*, München, 1978.

[8] J.M. de Wit, J.B. Sellmeijer, A. Penning, "Laboratory Testing on Piping", *Proceedings of the 10th International Conference on Soil Mechanics and Foundation Engineering*, Stockholm, Part 1 , p. 517, 1981.

[9] D. Van Zyl, and M.E.Harr, "Seepage Erosion Analysis of Structures", *Proceedings of the Tenth International Conference on Soil Mechanics and Foundation Engineering*, Stockholm, Part 1, p. 503, 1981.

[10] U. Hanses, H. Müller-Kirchenbauer, S. Stavros, "Zur Mechanik der Rückschreitenden Erosion unter Deichen und Dämmen", *Bautechnik 5*, pp. 163-168, 1985.

[11] I. Kohno, M. Nishigaki, Y. Takeshita, "Levee failure caused by seepage and preventive measures", *Natural Disaster Science*, V. 9, No. 2, pp 55-76, 1987.

[12] J.B. Sellmeijer, "On the Mechanism of Piping under Impervious Structures (Thesis)", *LGM-Mededelingen*, No. 96, October 1988.

[13] J.B. Sellmeijer, E.O.F. Calle, J.W. Sip, "Influence of Aquifer Thickness on Piping below Dikes and Dams", *Proc. CIGB ICOLD*, Copenhagen, July 1989, pp. 357 – 366.

[14] J.B.A. Weijers and J.B. Sellmeijer, "A new model to deal with the piping mechanism", *Filters in Geotechnical and Hydraulic Engineering*, Brauns, Heibaum & Schuler (eds), © 1993 Balkema, Rotterdam, ISBN 90 5410 342 6, 1993.

[15] J.H. Schmertmann, "The no-filter factor of safety against piping through sands", *ASCE special volume*, 2000.

[16] Xing Zheng Wu, "Probabilistic Risk Analysis and Safety Evaluation of Dikes", *Research Centre of Flood and Drought Disaster of the Ministry of Water Resources in China (RCDR) China Institute of Water Resources and Hydropower Research (IWHR)*, 2003.

[17] M. A. Koenders, "Hydraulic Criteria for Protective Filters", *private communication*, 1987.

[18] C.M. Bishop, "Neural Networks for Pattern Recognition", *Oxford University Press*, ISBN 019853864, 1995.

Internal erosion – state of the art and an approach with percolation theory –

O. Semar* and K. J. Witt*
* Bauhaus University Weimar/Department of Geotechnical Engineering, Weimar, Germany

During groundwater flow fines can move inside the grain skeleton and suffosion occur. In previous investigation mostly the problem is reduced into a normal filtration or contact erosion problem. The criteria to control if suffosion take place or not don't take into account that the pore structure play an important role in suffosion processes. With percolation theory, which is a branch of probability theory dealing with properties of random media, it is possible to build up a model of the pore structure. Characteristic quantities can be determined to describe suffosion. Therefore certain input parameters are necessary. The determination of these will be topic of further research.

I. INTRODUCTION

The vulnerability of river basins as referring to extreme flood events has increased over the past years. This is a consequence of climatic changes and the more and more intensive usage of rivers and their environment, e.g. for industrialisation, land use and shipping. One of the negative results is that any change in flow conditions in river basin scale is a potential impact for erosion in subsurface. One kind of erosion is the internal erosion. Internal erosion of soil structures induced by seepage forces is also a main problem for the stability of water engineering structures. Dam failures statistical analysis taken from ICOLD [14] [15] show that the reasons for dam failures are 18 % internal erosion of the dam body and 12 % internal erosion of the subsurface. Only overtopping of dams has a higher responsibility for dam failures. River embankments and hydraulic structures are not considered in this statistic.

During groundwater flow fines in the grain skeleton can be displaced by seepage forces. The kind of erosion where the displacement of fines in the grain skeleton is taking place is called suffosion. When suffosion occur than the permeability and the porosity will increase while the bulk density decrease ([4] and [11]). The consequences are less resistance against external load and settlement as well as significant change in state of pore pressure. The probability for scour, landslides and hydraulic heave will increase.

In dependency of the location where suffosion occur Ziems [25] distinguish between three kinds of suffosion i. e. internal suffosion, external suffosion and contact suffosion (Fig. 1). The focus in this paper is located at the phenomena of internal suffosion. Therefore external and contact suffosion will no longer be discussed. Good reviews to several kinds of internal erosion were published among others in [4] [14], [16] and [17]. Internal suffosion can be in the best case a local phenomena where the fines will be trapped in dependency of particle size and hydrodynamic forces (colmatation). But also suffosion can be maintained when contact erosion at different layers or external erosion follow.

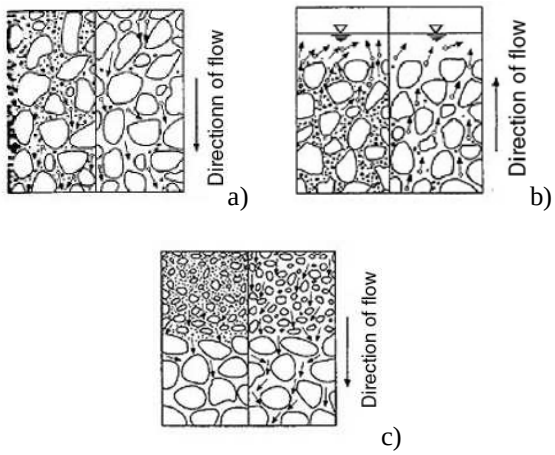

Figure 1. a) internal suffosion b) external suffosion and c) contact suffosion [25]

To exclude that internal suffosion or internal erosion of soils can occur it is necessary to satisfy two criteria. The fundamental criterion is the proof if it is possible that fine material can pass through void throats without clogging (geometrical criteria). The sufficient criterion is satisfied when it can be excluded that the hydrodynamic load in the void structure provides a critical energy needed to mobilize the fines inside the void structure (hydraulic criteria). The most important criteria for suffosion used in German engineering practice will be summarized.

II. GEOMETRICAL CRITERIA

The proof of the geometrical criteria, especially for non-uniform soils with steady and concave grain size distributions or soils with an omitted-size fraction, are based mostly on studies focused on filter materials for embankment dams [3]. Burenkova [3] found a empirical solution (Fig. 2) after numerous studies on different soils. Schneider et al. [20] formulated that this empirical relationship is very useful to predict if a risk for suffosion exist or not.

The Federal Waterways Engineering & Research Institute (BAW) in Germany recommend in [13] to first separate the grain size distribution into a finer and coarser part and to proof the geometrical criterion of Cistin/Ziems (Fig. 3) afterwards. The criterion of Cistin/Ziems were initially developed to analyse contact erosion phenomena. The geometrical criterion – i. e. no filtration – is satisfied if the d50-relation A50 = d_{50II}/d_{50I} is less than the ultimate-relation A50,ult. given at the y-axis of the chart in Fig. 3.

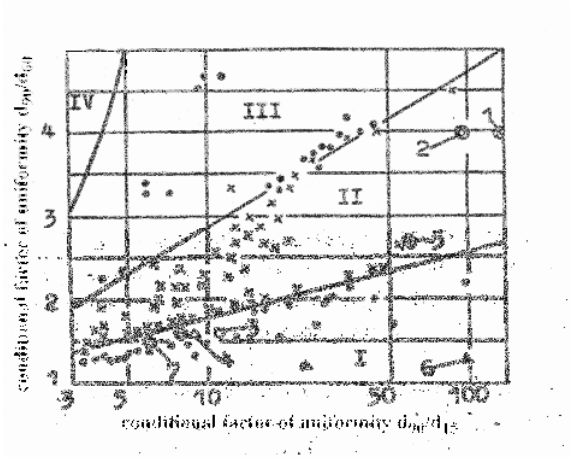

Zone I and III: suffosive
Zone II: non-suffosive
Zone IV: zone of artificial soils

Figure 2. Criterion of Burenkova [3]

Other fundamental investigations to geometrical criteria were performed by e.g. Terzaghi (1948) [22], Patrašev (1938), Sichardt (1928), Istomina (1957), Pavčič (1961), (cited in [25]), Lubočkov [12] and Kenney and Lau [10]. The study of these criteria permit to characterise in advance which soils are definitely not at risk that suffosion occur and which kind of soil has to be analysed. Therefore characteristical non-suffosive soils are ([4], [17]):

- Soils with a factor of uniformity $C_U = d_{60}/d_{10} \approx 1$ (d_{60} and d_{10} - diameters of particles for which 60 % or 10 % are smaller by weight).

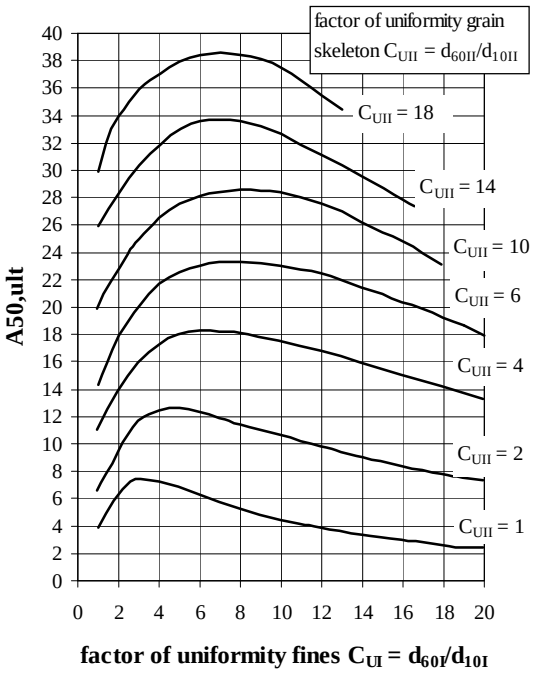

Figure 3. Criterion of Cistin/Ziems (cited in [4])

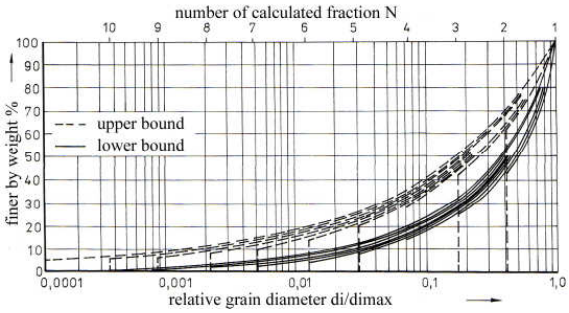

Figure 4. Limits of grain size distributions for non-suffosive soils [12]

- Soils with a rather linear grain size distribution in semi-logarithmic scale with $C_U < 10$ irrespective of density index

$$D_r = \frac{e_{max} - e}{e_{max} - e_{min}}. \qquad (1)$$

- Non-uniform soils with $C_U > 10$ and $D_r < 0.6$.
- Steady curved grain size distribution with $C_u < 8$ irrespective of D_r.
- Non-uniform soils which are very close to the Fuller or Talbot grain size distribution.
- After Lubočkov [12] non-uniform soils with $D_r = 0.3$ till 0.6 and steady curved grain size distribution in border area of Fig. 4 .

III. HYDRAULIC CRITERIA

The hydraulic criteria for suffosion compare the existing hydraulic gradient i to the allowable hydraulic gradient i_{ult}. The hydraulic criterion is exceeded when the fines inside the grain skeleton begins to move. To guarantee that the suffosion criteria are satisfied the BAW MSD 2005 [13] defined the ultimate condition

$$\eta = \frac{i_{ult}}{i} \geq 2. \qquad (2)$$

For the determination of the ultimate hydraulic gradient Busch et al. [4] and the BAW MSD 2005 [13] recommend, for the case that the grain size distribution is steady, the following formula:

$$i_{ult} = \varphi_0 \cdot \sqrt{\frac{n \cdot g \cdot d_s^2}{\nu \cdot k}} \qquad (3)$$

$$\varphi_0 = 0.6 \cdot \left(\frac{\gamma_d}{\gamma_w} - 1\right) \cdot \mu^* \cdot \sin\left(30 + \alpha/8\right) \qquad (4)$$

$$\mu^* = 0.82 - 1.8 \cdot n + 0.0062 \cdot (C_U - 5) \qquad (5)$$

$$d_s = 0.27 \cdot \sqrt[6]{C_U} \cdot \frac{n}{1-n} \cdot d_{17} \qquad (6)$$

The definition of the angle α which characterize the direction of flow is:

$$\alpha = \begin{cases} \rightarrow 90° \\ \downarrow 0° \\ \uparrow 180° \end{cases} . \qquad (7)$$

α	angle between acceleration of gravity and direction of flow
n	Porosity
k	Permeability
ν	kinematic viscosity
γ_d	dry specific weight of soil
γ_w	specific weight of water
d_s	largest suffosive grain diameter

For a non-steady grain size distribution and α= 180° (upward directed flow) the BAW MSD 2005 [13] and Busch et al. [4] recommend the approximate formula of Istomina (1957).

$$i_{crit} = \frac{n \cdot k_F}{n_F \cdot k} + f\left(\frac{d_{10,Sk}}{d_{10,F} \cdot \tan\varphi_F}\right). \qquad (8)$$

n, k	Porosity and permeability of soil sample
n_F, k_F	Porosity and permeability of filling
$d_{10,Sk}$	d_{10} of grain skeleton (matrix)
$d_{10,F}$	d_{10} of filling

The border of filling and matrix is chosen by Istomina at the 1 mm grain size diameter. For the second term of the criterion there exist a graphical description (Fig. 5) and the value tan φ_F can be taken from Tab 1.

Another criterion for two component mixtures of sand and gravel and α = 180°can be found in the dissertation of Wittmann [24]. He put the velocity of the fluid inside the voids in opposite to the decantation rate after Zanke (cited in [24]). This criterion allows also the examination of suffosion under turbulent flow in the void structure.

IV. Valuation of the Criteria

In the existing criteria there is assumed that only a transport of the skeleton filling obey while the grain skeleton don't have further structural change. This assumption stands in contradiction to observations in nature. Already first investigations of Leussink et al. [11] at artificial soils show clearly a interrelationship of structural change and soil-mechanical characteristics. The fundamental of geometrical criteria are the simplification that the grains are spheres. The determination of the controlling grain diameter is going back to a sphere packing in two dimensions

TABLE I.
VALUES TAN φ_F [17]

Filling	Silt	Fine Sand	Medium Sand
tan φ_F	0,57	0,6	0,7

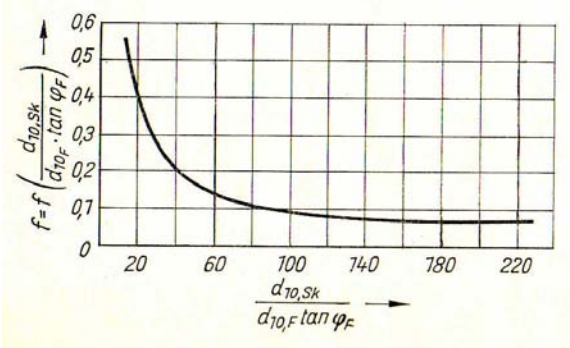

Figure 5. Graphical description of the Istomina-function f=f() [4]

without an extrapolation to 3-D (e. g. [14], [18], [19] or [24]). An observation in randomly chosen two dimensional slices don't represent the true void or void throat size distribution (Fig. 6). In two dimensions it is not possible to differentiate if the space between the grains are voids or void throats. The void size distribution determined with these approach represents a mean opening size but not the distribution of the minima, i.e. the throats, which are responsible for filtration.

The criteria are mostly practicable in a short range inside a factor of uniformity between C_U = 3 – 65. Without Schuler [18] and Witt [23] the investigations for geometrical criteria don't take into account that with increasing thickness of the layers the probability that a particle can be trapped increase, too. Therefore the factor of safety is very high. New investigation were not developed because the mathematical and physical relationships and the technical facilities to rebuild and understand the transport and fluid flow inside the complex void structure were only partially given or not at all.

V. Percolation Theory

A modern approach to comprehend flow and transport mechanisms inside a void structure is the percolation theory which is a branch of probability theory dealing with properties of random media ([1]). Large advances to understand complex relationships concerning transport and flow in porous media were developed in the last 15 years with this theory. Broadbent and Hammersley [2] can be named as originators for the use of percolation theory to study fluids in a maze. Percolation theory is used in several disciplines dealing with complex structures like petrophysics, hydrology, chemistry and statistical physics. Hence there were published several reviews to percolation theory in general (e. g. [6] and [21]) and particular in relation to porous media (e. g. [5], [7] and [15],). Schuler [18] used a percolation model to simulate the penetration length into a filter. He realised for his studies a very sim-

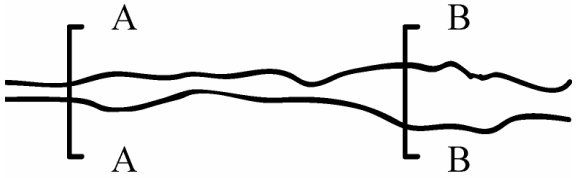

Figure 6. Void channel with random slices A-A and B-B

ple percolation model. He simulated the void throat sizes on a simple square lattice without correlations between voids, void throats and their interrelationship in the void structure. The consequence is a misinterpretation of the penetration depth. All investigations with percolation theory concerning flow and transport processes in porous media demonstrate that percolation theory is a helpful tool to analyse also internal erosion phenomena like suffosion.

The huge advantage of percolation models to previous investigations concerning geometrical suffosion criteria is that a transformation of the void structure, very close-to-the reality, is possible. This allows detailed analysis of transport phenomena inside the void structure. The rearrangement and transportation of fines can be analysed. Percolation theory deals with three kinds of models namely bond, site and continuum percolation models. Exemplary and most important to suffosion processes bond percolation is explained below.

In this approach the void structure will be transferred randomly to a given two or three dimensional grid (lattice). In this lattice the knots (sites) represent voids and the connections (bonds) represent the void-throats.

A very simple percolation model is the bond percolation model on a two dimensional square lattice (Fig. 7). Bond percolation means that only the void throats were simulated on a square lattice. A grain can pass from one void (site) to a neighbouring void if the void throat (bond) is big enough. In this case the bond is called occupied and the sites are connected. The connected nearest neighbour sites form a cluster. A spanning cluster is a cluster of occupied bonds from one border of the lattice to the opposite border. All other clusters are called finite clusters. Each void has a coordination number z = 4 which means that each void has four neighbouring voids. The randomly placed void throats are with occupation probability p occupied or with q = 1 - p not. If p = 1 all bonds are occupied and if the lattice is very large and the occupation probability p is small there are only small finite clusters (Fig. 7). Dependent of the kind of lattice (e. g. cubic, square, triangular) one well defined value p_c (p_c = percolation threshold), below which there is no spanning cluster, exist [21]. In the case that no correlations are allowed several exact solutions for different lattices of the bond percolation threshold p_c can be denoted (Tab 2).

The determination of the percolation threshold is identical with the determination of the biggest suffosive grain diameter which can be transported by seepage forces irrespective of the layer thickness. Additionally suffosion

TABLE II.
SELECTED BOND PERCOLATION THRESHOLD P_C BOND FOR DIFFERENT UNCORRELATED LATTICES [15]

Lattice Type	Coordination Number z	p_c bond
Honycomb	3	$1-2\sin(\pi/18)$
Square	4	0.5
Triangular	6	$2\sin(\pi/18)$
Diamond	4	0.388
Simple Cubic	6	0.2488
BCC	8	0.1795
FCC	12	0.119

properties can be characterized by several other quantities. The most important of which are:

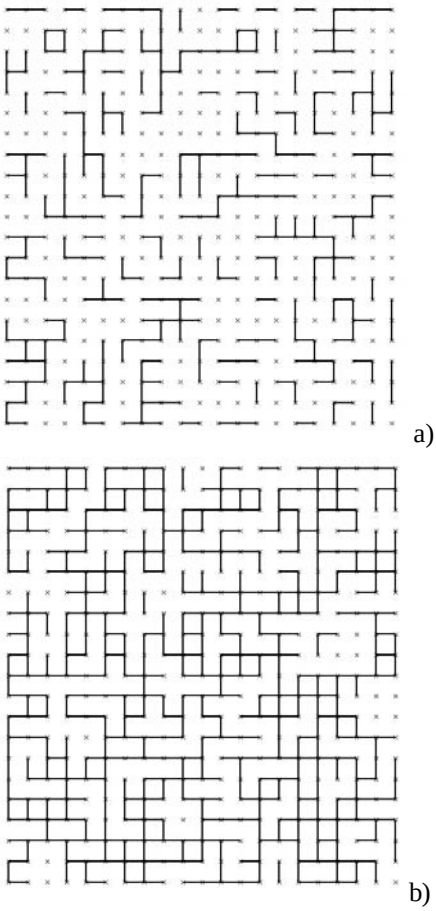

Figure 7. Bond percolation clusters on a square lattice with bond occupation probability a) p = 0.30 and b) p = 0.60.

- The percolation probability P (p) , which describes the probability that a site belongs to the spanning cluster when the occupation probability for bonds is p.
- The backbone fraction X^B (p), which is the fraction of occupied bonds participating in the transport of fines in the examined lattice at bond occupation probability p. This fraction take into account that some voids are dead-end i.e. that suffosion processes will be stopped as a reason of clogging.
- The correlation length ξ (p), which is a factor for the Representative Element Volume (REV). It describes the typical radius of a finite cluster for $p < p_c$ and the length scale over which a lattice is macroscopically homogeneous for $p > p_c$ [15]. The discretisation L of the lattice, i. e. the number of sites per direction in space, have to be larger than ξ (p) to be independent of L.
- The average size of a finite cluster per site, which is the weighted average of cluster sizes. The average cluster size S (p) is the average cluster size per open bond. This fraction is an information about local structural changes in the examined lattice.
- The fractal dimension D, which is a factor of self-similarity of the system.

A very important characteristic of the percolation theory are the universal scaling laws. Independent of the particular lattice some of the percolation properties obey scal-

ing laws near the percolation threshold. They depend only on the Euclidian Dimensionality d of the system. Referring to the above mentioned percolation quantities the following scaling laws can be specified.

$$P(p) \propto (p - p_c)^{\beta} \text{ für } p > p_c \tag{9}$$

$$S(p) \propto (p - p_c)^{-\gamma} \tag{10}$$

$$\xi(p) \propto (p - p_c)^{-\nu} \text{ if } p < p_c \tag{11}$$

$$X^B(p) \propto (p - p_c)^{-\beta B} \text{ if } p < p_c \tag{12}$$

The exponents are universal constants, which can be used as control parameters for the lattice considered.

A first simple bond percolation model has been developed at the Bauhaus – University Weimar. The general suitability to use percolation theory to understand filtration phenomena could be demonstrated. For a broader explication realistic pore structures are needed. The determination of the relevant largest suffosive grain diameter and the segregation behaviour is not analysed till now. This will be the topic of current research.

VI. Conclusions

A further development of geometrical suffosion criteria is necessary because previous investigations do have numerous assumptions which are in parts even false.

The percolation theory provides a new approach for a realistic analyse of suffosion. To use a realistic percolation model and to determine a realistic percolation threshold and the important quantities it is necessary to simulate adequate the real pore-structure of natural and manmade soil layers. Therefore secured void and void throat size distributions as well as their correlations in the void structure have to be determined. Important correlations are e. g. the number of void-throats per void, the number of voids at unit length or the dependency between void size and size of the adjacent void throats. The density dependency of the void structure and their change during suffosion have to be understood in detail. It is important to study the void structure by e. g. structure images (e. g. Synchrotron Tomography or X Ray tomography) or with modelling of 3 D sphere packing. The segregation and the derive of the relevant largest suffosive grain diameter have to be analysed. The determination of these important input parameters are topic of the current research at the Professorship Geotechnical Engineering of the Bauhaus – University Weimar.

References

[1] B. Berkowitz and R. P. Ewing, "Percolation theory and network modeling applications in soil physics," *Surveys in Geophysics 19*, Kluwer Academic Publishers, Printed in the Netherlands, pp. 23 – 72, 1998.

[2] S. R. Broadbent and J.M. Hammersley, "Percolation processes." *I. Crystals and Mazes*, Proceedings of the Cambridge Philosophical Society 53, pp. 629–641, 1957.

[3] V. V. Burenkova, "Assessment of suffosion in non-cohesive and graded soils," in Brauns et al. (eds.), *Proceedings 1st Int. Conf. Geo-Filters*, pp. 357-360, Balkema, Rotterdam, 1992.

[4] K.-F. Busch, L. Luckner and K. Tiemer, *Geohydraulik: Lehrbuch der Hydrologie*, 3rd ed., Ferdinand Enke Verlag, 1974.

[5] F.A.L. Dullien, *Porous Media: Fluid Transport and Pore Structure*, 2nd ed., Academic Press, San Diego, 1992

[6] G. Grimmet, *Percolation*, 2nd ed., Springer Berlin, 1999

[7] A. Hunt, *Percolation theory for flow in porous media*, Springer Heidelberg, 2005.

[8] ICOLD (1995): *Dam failures statistical analysis*,Bulletin 99.

[9] ICOLD (1997): *Dams less than thirty metres high*,Bulletin 109.

[10] T. C. Kenney and D. Lau, "Internal stability of granular filters," *Can. Geotech. J.*, vol. 22, pp. 215–225, 1985.

[11] H. Leussink, T. G. Visweswaraiya and H. Brendlin, *Beitrag zur Kenntnis der bodenphysikalischen Eigenschaften von Mischböden*, Veröffentlichung des Institutes für Bodenmechanik und Felsmechanik, Universität Karlsruhe, Heft 15, 1964.

[12] E. A. Lubočkov, "Grafičeskie i anallitičeckij sposoby opredelenija suffozionnych svojsto nesvjaznych gruntov," Leningrad, *Izv. VNIIG*, vol. 78, 1965.

[13] BAW MSD, Merkblatt: *Standsicherheit von Dämmen an Bundeswasserstraßen (MSD)*, Bundesanstalt für Wasserbau, 2005;

[14] P. Muckenthaler, *Hydraulische Sicherheit von Staudämmen*, Dissertation TU München, 1989.

[15] M. Sahimi, *Flow and Transport in Porous Media and Fractured Rock*, VCH, Weinheim. 1995

[16] U: Saucke, "Nachweis der Sicherheit gegen innere Erosion für körnige Sedimente," *Geotechnik*, Organ der Deutschen Gesellschaft für Geotechnik, vol. 1, 2006, pp. 43-53.

[17] H. J. Schaef, *Örtliche Standsicherheit (Suffosion und Erosion) bei Sickerwasserströmungen*, Erläuterungen zum Bodenmechanischen Arbeitsblatt 4.4 der ehemaligen Obersten Bergbehörde Leipzig, Institut für Geotechnik der TU Bergakademie Freiberg, 1995.

[18] U. Schuler, *Bemessung von Erdstoff-Filtern unter besonderer Berücksichtigung der Parameterstreuung*, Veröffentlichungen des Institutes für Bodenmechanik und Felsmechanik, Universität Karlsruhe, Heft 143, 1997

[19] A. F. Silveira, "An analysis of the problem of washing through in protective filters," Proceedings 6th *Int. Conf. on Soil Mechanics and Foundation Engineering*, Montreal, vol. 2, pp. 551-555, 1965.

[20] H. Schneider, U. Schuler, K. Kast and J. Brauns, "Bewertung der geotechnischen Sicherheit von Hochwasserschutzdeichen und Grundlagen zur Beurteilung von Sanierungsmaßnahmen," *Mitteilungen Abteilung Erdammbau und Deponiebau am Institut für Bodenmechanik und Felsmechanik*, Universität Karlsruhe, Heft 7. 1997.

[21] D. Stauffer and A. Aharony, *Introduction to Percolation Theory*, revised 2nd ed., Taylor and Francis, London, 1994.

[22] K. Terzaghi, R. B. Peck and G. Mesri, *Soil Mechanics in Engineering Practice*, 3rd ed., Wiley-Interscience, 1996.

[23] K. J. Witt, "Reliability study of granular filters," in Brauns et al. (eds.), *Proceedings 1st Int. Conf. Geo-Filters*, pp. 35-42, Balkema, Rotterdam, 1992.

[24] L. Wittmann, *Die analytische Ermittlung der Durchlässigkeit rolliger Erdstoffe unter besonderer Berücksichtigung des nichtlineraren Widerstandgesetzes der Porenströmung*, Veröffentlichungen des Institutes für Bodenmechanik und Felsmechanik, Universität Karlsruhe, Heft 87, 1981.

[25] J. Ziems, *Beitrag zur Kontakterosion nichtbindiger Erdstoffe*, Dissertation TU Dresden, 1969.

REVISITING THE STUDY TO ASSESS SCOUR AROUND A PROTOTYPE BRIDGE IN MALAYSIA

Faridah Jaffar Sidek* and Ahmad Khairi Abdul Wahab**
* Coastal & Offshore Engineering Institute, Universiti Teknologi Malaysia City Campus, Kuala Lumpur, Malaysia
** Faculty of Civil Engineering, Universiti Teknologi Malaysia, Johor, Malaysia

This paper will focus on a Study which has been carried out to evaluate scour development around piers supporting an existing bridge which plies 13.5 km across coastal waters ten years on after construction. The Study was first undertaken in 1996. It was also the first of its kind to be executed in Malaysia at that time, where computer simulation exercises using the computer model TELEMAC to evaluate the hydrodynamic processes at the site and projections concerning bridge pier stability were made.

Generally, the paper will outline several work components that have been undertaken for the Study which covers tasks such as field data collection works and data appraisal, hydrographic survey works of the area, computer simulations to evaluate the hydrodynamic processes at the site and projections made to predict potential scour evolutions around the bridge over a specified period of five years. The paper will then present a summary of the results yielded and highlight several recommendations which have been drawn to ensure hydraulic stability of the bridge in light of limitations faced and assumptions made to complete the Study.

I. INTRODUCTION

The long term functioning of bridges require that bridge owners continually attend to hydraulic safety issues in particular the stability of bridge abutments and piers that are perpetually in contact with the water. Attention is needed not only prior to bridge construction but also during bridge operation and their maintenance periods. When bridges have been planned to traverse water, bridge engineers will need to make early evaluations to determine potential scour severity in the pre-design and design stages of the bridge supports; assess whether there exist instability from scour of its piers and foundations after construction and also during bridge operation or maintenance stages; and likewise identify other future threats which may affect bridge safety apart from that which could be caused by potential scour related failures mentioned. On top of this if signs of concern existed, engineers may be required to recommend and implement remedial measures in the event of protecting the hydraulic structures from damage.

In order to substantiate decisions with regards to confirmations of bridge stability, it is essential that bridge engineers well-plan the bridge operation and maintenance works. The engineers could opt for operations to send divers for underwater inspections as is the norm, or choose to carry out computer simulations to provide the needed information to support their engineering judgments, or even use both options to complement each other. If computer simulating exercises were chosen, then the engineers will need to first establish the hydraulic parameters present in the surrounding water regime. These parameters could include that which describe the existing flow processes namely, wave climate (wave heights, wave periods and water depths) in the coastal area, water level fluctuations, flow characteristics (velocities and discharges), bathymetric information which characterizes the flow pattern and shoreline dynamics which may affect bridge abutments. This will be continued with the conduct of a detail hydraulic data analysis of the compiled data and also the need to choose as well as use relevant computer models to simulate the hydrodynamic processes in the project area and subsequently make projections to gauge the extent of potential bed movement around the bridge supports. Only after undertaking these activities would the engineer be more technically equipped to identify factors which could potentially destabilize the bridge and to recommend mitigating measures to minimise potential damage. If underwater inspection is selected as a means of evaluation, then the engineer must be able to identify the particular support of the bridge requiring the attention. When the bridge is particularly long and is supported by many piers, this could be a more expensive exercise.

This paper highlights an investigation which has been undertaken to determine potential scour magnitudes that might have evolved around the piers of an existing bridge

which traverses a coastal strait in Malaysia. As part of the routine tasks that has been undertaken by the bridge owner to maintain and safeguard the bridge, the owner has opted to apply a computer model as a tool to evaluate the stability of the prototype bridge. Information described in this paper has been obtained from experiences derived by the authors from the conduct of the Study [1] which was carried out to evaluate potential scour evolutions around the bridge supports so as to confirm that the developed scour holes have been designed-for ten years after their construction.

II. PROJECT BACKGROUND

Penang Straits is an elongated water channel of about 25 km which is bounded by Peninsular Malaysia to its east and Penang Island to the west. The Straits is connected to the Straits of Malacca to its north and south. An existing bridge that is, the Penang Bridge, a significant landmark in Malaysia, forms the only physical link between the two land masses. The bridge has been constructed as an elevated cable stayed concrete girders, with a dual carriageway and three lanes at the Main Span. Figure 1(a) and (b) illustrate the location of the bridge.

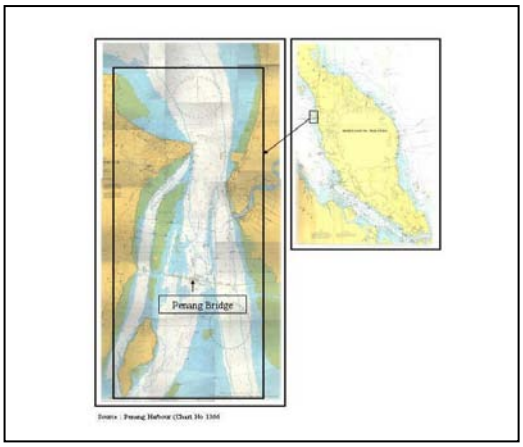

Figure 1(a). Extend of the Study Area

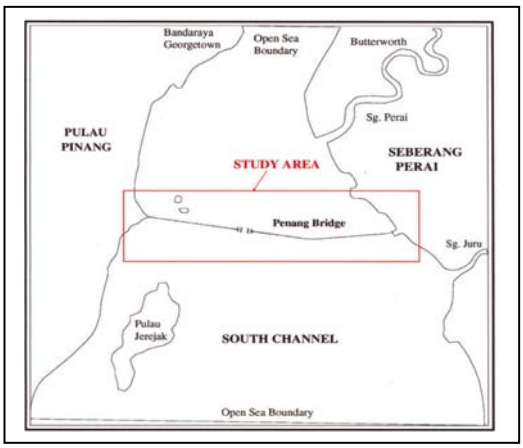

Figure 1(b). Location of the Bridge in the Straits

The crossing was built in 1985 as an alternative to using the ferry as a mode of transfer to cross the Straits. It was also built to escalate economic development on the Island. The bridge is supported by 517 piers with approximately 197 of the supporting piers lying in the straits water. The Main Span is about 225 m in length. It is supported by 4 main piers. The other piers are in turn supported by individual groups of raker piles ranging in number from 11 to 40, which have been well embedded into the sea bottom at various reduced levels. Four of the piers in the Main Span are each covered and protected by rock berms. Exact depths to which each of the individual piles was founded into the bed was not known with certainty at the time the scour assessment study was carried out in 1996. It has been reported that they could have been piled down to more than the recommended RL-49.7 m and potential scour related failure of the piers has been accounted for in the design. In spite of this, it was decided in 1996 that a scour assessment study be undertaken as part of routine checks to confirm bridge support stability by the bridge owner.

III. THE SCOUR ASESSMENT STUDY

Three work stages were adopted to evaluate scour development around the piers. They were :

- Stage 1 – Initial Scour Assessment Works
- Stage 2 – Detail Scour Assessment Works
- Stage 3 - Recommendations and Suggestions for Future Works

The first stage involved examining past and existing reports, information and drawings for gathering of general information and details of activities relating to the construction of the bridge and other related works. Initial identification of piers showing indications of local bed lowering was evaluated from the many hydrographic survey drawings produced by surveyors who carried out survey works especially for the project in 1996.

The second stage included works to execute computer models to describe the flow conditions in the straits and quantitative magnitudes of potential scour around the bridge. In this stage, extensive data collection of environmental parameters in the water body making up the Straits was required and planned for. Thereafter, the morphological module of the computer model was applied to yield computer simulated outputs to identify potential piers at risk to scour and also project potential scour hole magnitudes around each individual pier.

The final stage of the Study documented recommendations which should be adopted by the bridge

owners. This was to ensure that consistent hydraulic checks were made and that they form part of the routine inspection works for the bridge.

Overall, the completed Study was deemed to be useful in assembling baseline hydraulic information and generating initial estimations and projections of scour hole magnitudes a decade after bridge completion. It assisted in recognizing and identifying the piers which should be constantly inspected more regularly than others along the bridge length. The Study also resulted in laying out recommendations for monitoring works which should be undertaken by the bridge owners to confirm overall stability of the bridge from the hydraulic aspects in particular.

IV. ESTABLISHING THE TOPOGRAPHIC AND HYDRAULIC PARAMETERS

A review of past and present data, records, reports, drawings, chronological information available with respect to the pre-design, design and construction stages of the bridge were important in order to generate a comprehensive understanding of the events that took place over the past ten years prior to the Study being undertaken. Some information on early feasibility study reports [2] and [3], an underwater inspection report and a set of structural drawings were found available for use for the Study. Compiled hydraulic data were not readily available for the second stage of works which required the set-up of a computer model for the surrounding waters where the bridge was located.

The authors were faced with several difficulties to initiate the Study in the early stages. This arise particularly from the lack of information made available to describe the flow conditions in the straits, the absence of past survey drawings of the area to provide reference details of the seabed levels in relation to the location of the piers underwater that is, during the before- and after-bridge construction periods, and there was no clear indication of what allowable maximum scour hole depth values have been finally used in the design of the supporting structures. These reasons therefore justified the necessity to plan and carry out hydrographic survey works of the surrounding area particularly in the vicinity of the bridge in order to initiate the Study. Survey information was also required for use in the computer model to establish first the flow pattern in the existing area before projections of bed movement could be made. Thus, an extensive field data collection program was implemented. Data collected from the field measurements were used to serve as the boundary conditions to execute the computer model. The data collection task therefore consisted of collecting the following much needed environmental parameters.

A. Hydrographic Survey Works

The site was surveyed using side scan sonar with an approximately 5 metres sounding interval very close to the piers and at greater intervals further away from the bridge area. The drawings were useful in providing the exact locations of the bridge supports underwater and an early description of immediate bed lowering details around individual supports.

From visual evaluations of the drawings, it was noted that the sea bed has been lowered down to depths of 0.6m to 0.9 m around some piers when compared to the surrounding bed. Review of limited past structural drawings made available to the authors indicated that most piers have been founded very deeply in the sea bottom. It has also been reported in [2] and [3], that beds should be expected to be lowered in total by about 5 m to 6 m as a result of bridge construction. It was not possible to confirm the significance of the values shown by the drawings due to the absence of previous reference levels of the seabed. From limited data made available and the knowledge that the piles have been founded to more than the RL-50m, it was safe to assume that the value has not exceeded the maximum pre-designed and designed value.

B. Water Surface Elevations

For the Study, two tidal gauges were setup in the field in order to capture water level variations over the spring and neap tidal cycles. The data collected compared well with published predictions made for the area. They were then used as inputs to drive the computer model used in the simulations. The reliability of computed water surface elevations produced by the model was also checked against measured water levels generated over a time series in the field. Comparisons made gave good agreement.

C. Tidal Currents

There were no readily available current data for use for the Study and thus on-site measurements were made. Three current meters were deployed to obtain records of simultaneous readings of current magnitudes at several locations during spring and neap tides. Readings were recorded at every 15 minutes interval. Since tidal current data is important to generate flow distribution and bed movement in the area, sufficient data is needed to calibrate and verify the computer model to simulate the current distribution pattern characterizing the coastal strait. Good agreement of the field measured and computed currents was to be found when calibration and

verification works were carried out by the computer model.

From in-situ readings obtained, flood currents were recorded to flow southwards with a peak current reaching 0.85 m/s during spring tide in the straits. Lower currents ranging from 0.3 m/s to 0.5 m/s were recorded during neap. Ebb currents were comparatively lower and flowed northwards.

D. Wave Climate

The bridge lie in a sheltered area of the straits from offshore waves and is relatively unaffected by the offshore wave climate. Thus, wave data was excluded from the Study.

E. Bed Material

Bed samples were measured for use to define bottom roughness in the computer model. Twenty-two samples were collected around the site, coarse sand with a maximum d_{50} size of 1.0 mm was found to occur around the central regions of the water channel and finer materials ranging from 0.001 to 0.06 mm (fine silt to fine sand) were found along the coastlines. Sensitivity tests were applied in the model computation works using several roughness values in order to ensure that outputs of bed movement obtained did not vary too widely.

V. COMPUTER SIMULATION WORKS

In order to obtain a description of the flow conditions and quantitative estimates of bed lowering around the piers, the computer model TELEMAC 2D and its sediment module were used. TELEMAC 2D is a two-dimensional finite element model developed by *Laboratoire Nationale d' Hydraulique, Electricite de France*. There existed several assumptions and limitations which the authors have had to accommodate during the application of the two-dimensional computer model to simulate bottom bed movement. One of them as mentioned earlier was the absence of original sea bed level description before or after bridge construction to use as reference to compare and justify the lowering captured in the 1996 survey drawings. Therefore, actual scouring extent of the bed and the piles could not be ascertained from the period of bridge completion up to 1996 when the Study was initiated. Due to these uncertainties, the authors have had to execute the computer model based on the assumption that the bed description provided by the 1996 survey works was the existing bed condition to be found in the area. Potential projections of bed depressions over a period of five years were then initiated from there henceforth. Other assumptions made in the Study are described in the sub-sections below.

A. Computer Model Set-Up, Execution and Assumptions

The model boundary covered an area of about 15 km by 14.2 km. In the modeling exercise, the size of the pile cap of each pier was used as an effective pier width to depict the dimensions of each of the individual piers supporting the length of the bridge as several big columns due to model limitations. It was anticipated that this assumption could result in more conservative scour magnitudes. Each raker pile which supported the bridge pier was less than 1 metre in size and was inclined in various numbers and grouping arrangement. They were not possible to be modelled individually in the computer model to gauge bed movement. A comparison of modelled and observed current measurements obtained from the current pattern output generated by the model indicated good agreement and that the model has been well calibrated and validated.

B. Generated Computer Model Outputs

Samples of computational outputs produced by the model are illustrated in Figures 2 to 6. Figure 2 shows the mesh generated by the computer model. The element size of the mesh varied from 1 km in the study area to approximately less than 5 m around the bridge piers. Figure 3 shows a close up of the digitized bed bathymetry adjacent to selected bridge piers. Flow pattern in the surrounding bridge area is illustrated in Figure 4. Samples of the projected bed movement around the piers are shown in Figure 5. Projected maximum bed stresses in the model domain are illustrated in Figure 6.

From the exercise, it was possible to identify piers which were expected to be more susceptible to greater scour capability. These identified piers were located mainly in the areas which possessed the higher bed stress values and flow strengths. These piers were then used to quantify estimates of scour magnitudes that might develop around the piers in a five years time frame.

C. Results and Analysis

In the Scour Assessment Study, flow was shown to be influenced by the tidal cycle in the Straits. Water movement around the piers (discharge and velocity magnitudes) have been well computed and can be used as a basis for comparison should there be flow variations in the straits. It was found that generally currents moved

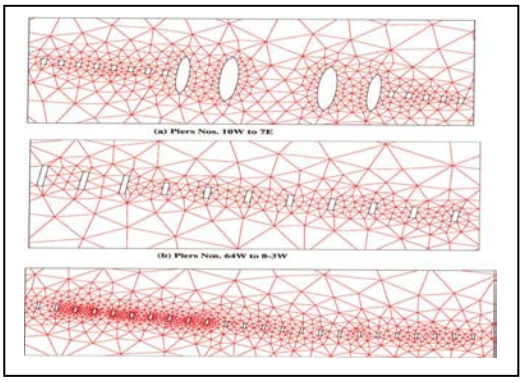

Figure 2. Mesh Generated by the Computer Model

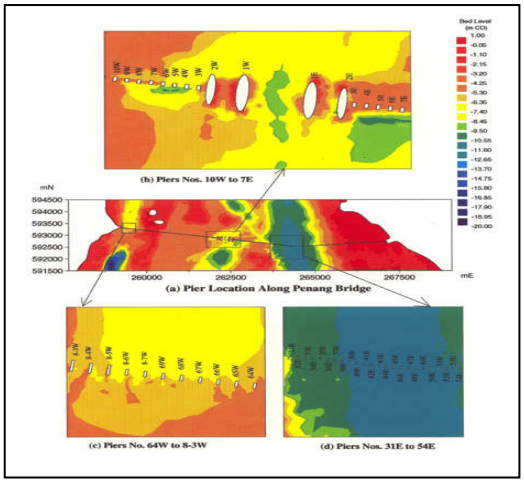

Figure 3. Digitised Bed Bathymetry

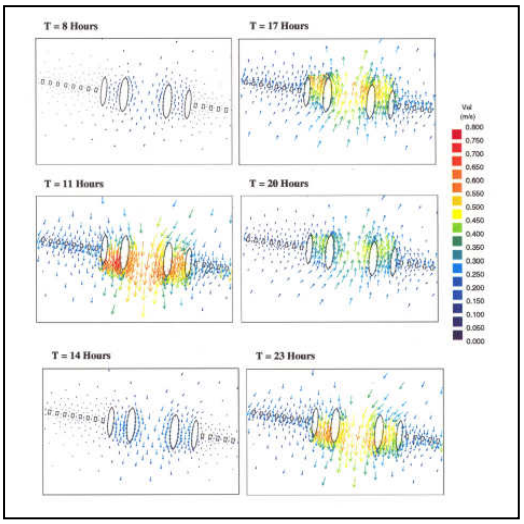

Figure 4. Flow Distribution Around the Piers

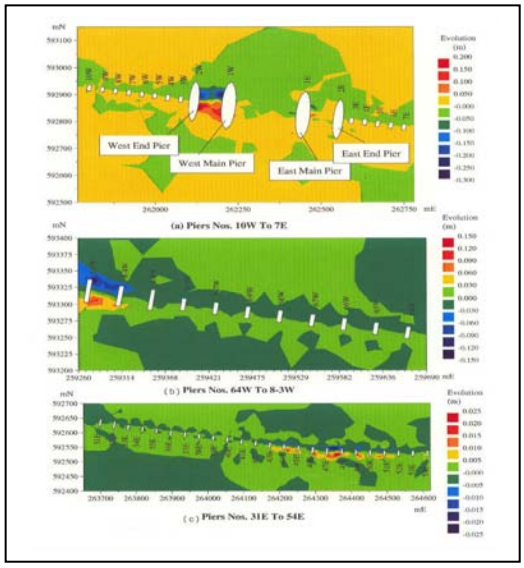

Figure 5. Projected Maximum Bed Stresses in Model Domain

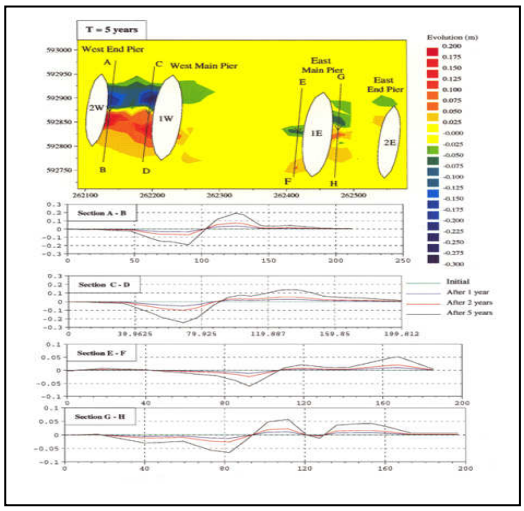

Figure 6. Projected Bed Evolution around the Main Piers

northwards during ebb and the reverse upon flood tide. A peak of 0.75 m/s in speed was attained in the deeper sections of the Straits and also at bridge mid-span. Lower values of 0.55 m/s was reached during ebb tide at the same location. Flow distribution around mid-span moved smoothly around the streamline shaped of the rock berms. At other locations, flow around piers in the deeper water developed stronger currents than those located in the shallower areas.

Bed shear stresses were computed in order to determine potential sediment transport around the piers. Peak stresses were observed to occur in the deeper sections of the water channel with lower stress values generated in shallower regions. In the tests conducted to simulate scour development, it was assumed that the 1996 survey drawings were taken as the reference to describe the original bed level to start the potential scour projections over a five years period. From the results of the bed evolution, it was found that maximum erosion could potentially occur towards the northern end of the piers reaching a magnitude of 0.3 m. Accretion tended to occur on the southern end reaching a value of 0.2 m. A rate of 0.3 m in five years could be generated around the edges of the rock berms at mid-span. From analysis made, the values obtained from the computations were considered to be insignificant to cause risks since the piers were reported to be generally well embedded and founded in the seabed. With information made available then, the authors have concluded that the piers were not expected to undergo excessive scouring. However, it was advisable to monitor potential of the piers to scour over the long term and a review be made whenever new data become available so that predictions made in this Study could be confirmed through further computational exercises.

The computer simulation outputs were treated as that providing a baseline from which future investigations on scour projections could be initiated from. Detail information of flow was important in providing the basis for comparison in a changed scenario. Information obtained from the documented Scour Study could also be used as a reference to determine potential risks afforded by new changes in the coastal straits making up the bridge surroundings in future. Identified bridge piers which were embedded in locations with higher capability to scour could then be routinely checked through regular underwater inspections and scour monitored periodically to confirm stability.

D. Recommendations and Future Computations

It is always advisable to ensure that checks and appropriate measures have been undertaken to ensure that there existed some level of security in order to avoid high risks when operating and maintaining a bridge. In the scour assessment study, some recommendations have been made to safeguard the bridge. These included the following:

- the conduct of another study in the near future for example, within an ideal span of the next three to five years to confirm local bed movement around the piers; or when new data become available; or in the event of changes in the straits from activities such as future dredging or sand extraction works which may change the flow distribution pattern.

- to undertake further hydraulic investigations for example, before reclamation activities along the coastline are planned since these may constrict flow movement in the straits or before the construction of other infrastructures namely, a new bridge or underwater tunnel which may indirectly impact the existing bridge.

- to carry out regular inspection for scour related failures accordingly not longer than a period of one year and shorter when the need arise. It has been recommended that all information collected and monitored be properly archived for future use. These included information made available by divers, surveyors or bridge engineers through routine checks of piers namely, reports/drawings/charts/data etc. by providing full details of structure foundation and levels, sea bed material, hydraulic parameters, details of previous and future inspection checks.

- the need for underwater divers to work very closely with the bridge engineers to note if any, for example the nature and location of any serious defects, the extent of defects for comparison with previous and subsequent reports, existing extent of scour, information of the location and value of horizontal and vertical reference datums, data of previously measured bed levels, etc. so that appropriate action could be followed up by the engineers if necessary.

- the need for specialist surveyors to provide reports to bridge engineers such as to include location and contour plans of associated bridge structures, cross-sections of seabeds especially around the piers which have been identified in the priority checklist from the present study, photographs or multi-media display of evidences to confirm bed depressions which could create concern

- piers that were especially noted to be higher up in the priority risk checklist as provided in the study should be periodically checked.

- regular updating of the information archived and computer model already set-up for the straits should be made.

- a long term monitoring study so that scour risks could be more meaningfully rated should be periodically undertaken by the bridge owners.

VI. ADAPTATION OF THE COMPUTER MODEL TO INCORPORATE FUTURE PHYSICAL CHANGES AROUND THE BRIDGE

It has been reported by the local media that there might be on-going physical changes in the Straits in the future. It is expected that the coastline on both sides of the Straits may undergo changes where plans to build coastal roads on new reclaimed coastal land could materialize. There is the possibility of a new bridge being constructed to support the traffic congestion already being felt daily during peak periods on the existing bridge. Also, bridge expansion of the existing link is to be anticipated. With such plans, it is envisaged that there will be new data available. Thus, there arises the need to provide further detail information of the physical impact of these projected new developments in the straits to the existing bridge structure.

A model of the straits has been set-up from the Scour Assessment Study described herein. It is therefore not difficult to include the new features into the model to gauge these changes and predict their potential impacts on the existing bridge. It is reassuring to know that a hydraulic data baseline is already in existent and is accessible for use whenever required.

VII. CONCLUSIONS

The following conclusions have been drawn :

- Computer models can be used as decision tools during bridge maintenance works to project scour development around piers. Outputs generated by the models could aid engineers in identifying piers which needed more regular inspection.

- In the scour assessment study undertaken, it has been shown that though data made available was found to be limited, evaluations carried out were useful in providing general information on the hydraulic stability of bridge supports up to a certain extent. However, continual monitoring of the bridge should be undertaken periodically over the long term so that more new data could become available for use to confirm findings already made in the present study.

- A baseline for the gauging of future physical impacts near the bridge surroundings have been derived through the setting up of the computer model for the straits.

ACKNOWLEDGMENT

The authors wish to acknowledge the Coastal and Offshore Engineering Institute of Universiti Teknologi Malaysia for allowing the use of the computer modelling outputs. We wish to extend our gratitude to the same organizations also for providing the financial support to present this paper at the Conference. Our utmost appreciation is especially extended to Penang Bridge Sdn. Bhd for having the confidence to engage the authors to undertake the Scour Assessment Study.

REFERENCES

[1] Coastal & Offshore Engineering Institute, October 1996, Final Report on Penang Bridge Scour Assessment Study, Report submitted by Propel Bhd. to Penang Bridge Sdn. Bhd.

[2] Christiani & Nielsen A/S, Danish Hydraulic Institute, Hoff and Overgaard and Malysian International Consultants Sdn. Bhd., October 1974, Final Report on Full Feasibility Study of a Fixed Linkage between Penang Island and Province Wellesley

[3] Christiani & Nielsen A/S, Danish Hydraulic Institute, Hoff and Overgaard and Malysian International Consultants Sdn. Bhd., October 1972, Interim Report on the Full Feasibility Study of a Fixed Linkage between Penang Island and Province Wellesley

[4] Tan Sri Datuk Professor Ir. Chin Fung Kee, 1988, The Penang Bridge - Planning, Design and Construction by. Published by Lembaga Lebuhraya Malaysia.

[5] Faridah Jaffar Sidek, Ahmad Khairi Abdul Wahab and Hadibah Ismail, June 2006, The Need for Hydraulic Data Archival and Computer Simulation to Safeguard Bridge Stability, Proceedings of the First International Conference on Advances in Bridge Engineering, In press.

Flood-induced scour in the Nile by modified operation of High Aswan Dam

C.J. Sloff* and I.A. El-Desouky **

* WL | Delft Hydraulics and Delft University of Technology, Delft, Netherlands

** Hydraulics Research Institute (HRI), Delta Barrage, Cairo, Egypt

Due to climate-change it is anticipated that the hydrological regime of many river basins is gradually changing. This requires a revision of operation rules of the affected hydropower, flood control and water-supply reservoirs, as well as the impacts of modified operation on the downstream reach. The Lake Nasser Flood and Drought Control (LNFDC) Project has addressed these issues for the Nile River and Lake Nasser in Egypt. As part of this project the impact of man-induced increased flood releases on scour in the lower Nile River have been investigated. In the past 30 years, since Nile flows are regulated by the High Aswan Dam, the river channel has changed to such an extent that risk of damage by scour and flooding has increased significantly. Most relevant risks are related bridge-pier scour, scour at barrages, and bank erosion. Predictions based on analytical methods and scale model experiments show at three barrages protection is needed to deal with possible scour. Also bank erosion at a number of locations requires initial protection works.

I. INTRODUCTION

In historic times the sand-bed of the Nile River in Egypt was sensitive to local scour phenomena such as bank erosion (notably bend scour), scour at bridge piers, and scour downstream of the main barrages in the river (located along the Nile as shown in Figure 1). Scour holes of tens of meters, and annual shifts of bank lines of hundreds of meters have been reported. However, after construction of High Aswan Dam (HAD) the flood discharges in the lower Nile River in Egypt have significantly been reduced. Due to the absence of these floods the local-scour phenomena also have become inconsiderable.

HAD is by far the most important structure to regulate the water flow of the river Nile in Egypt. This dam is a rock fill dam with a total length of 3,600 m and a maximum height above the Nile bed of 111 m. The amount of water stored behind the dam at a level of 183 m+MSL (the maximum in case of an emergency situation) is 169 BCM (BCM = 10^9 m^3), which is about twice the average annual yield of the River Nile at Aswan. The length of the reservoir is 500 km with an average width of 12 km.

If the reservoir level exceeds a height of 178 m, water is spilled to the Toshka depression (see Figure 1). This occurred the last four years year after year, to an average annual amount of 10 BCM. The Toshka canal and spillway were designed to convey some $250 \cdot 10^6$ m^3/day (i.e., 250 MCM/day = 2,900 m^3/s) at a level of 182.7 m. Its capacity amounts only 150 MCM/day at a level of 182 m. Plans have been made to upgrade the Toshka canal by deepening and widening it. At present the water release to the Nile is limited to 270 MCM (3125 m^3/s) as more discharge is believed to cause serious degradation of the bed of the river Nile and may endanger the stability of the riverbanks, bridge piers and other structures. Furthermore, because the discharge through the Nile has been low since HAD was put into operation, at various locations constructions have been built in the floodplain. Hence, flood damage may be experienced if the Nile conveys a too large discharge.

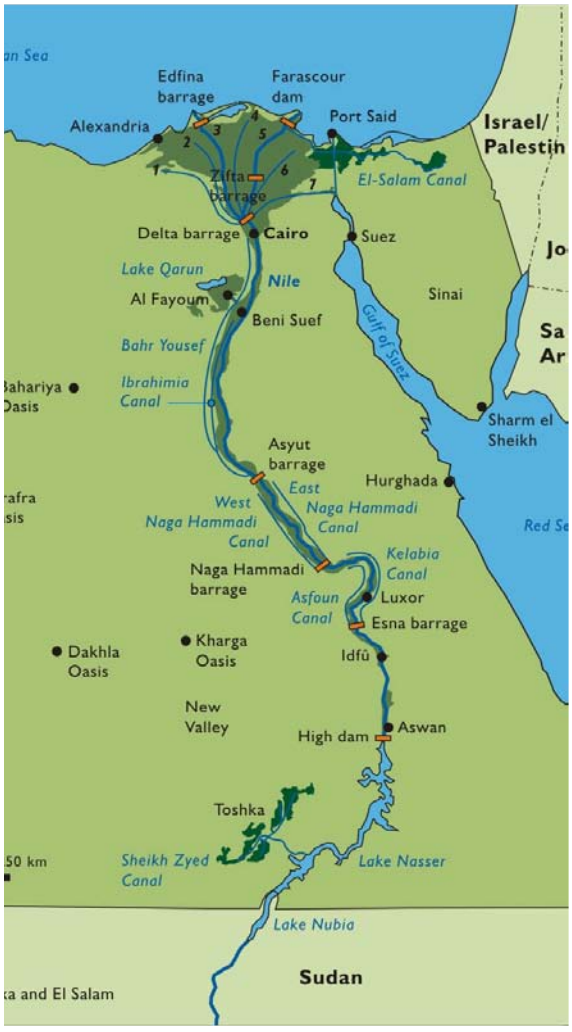

Figure 1 Overview of water resources system of Egypt, showing the main barrages and irrigation canals

In the year 2001 Egypt indeed experienced a flood from

the River Nile for the first time since the construction of the High Aswan Dam. Although the discharges were not more than 270 MCM/d, the flood caused damage in the lower parts of Egypt. The vulnerability for flood damage at these relatively low peaks lies mainly in the changed land use resulting from the perception of the people that the Egyptian Nile is fully under control. The inflow in Lake Nasser was however so high for a number of consecutive years, that Lake Nasser operation had to be adjusted.

Considering the expected climate change, the changes in the upstream catchment and change of land use and water resources demands downstream, a need for reconsidering the operation of HAD was born. In the year 2005 the National Water Resources Plan (NWRP) was approved by the Cabinet. In this plan an outlook for the management of the water in Egypt up to the year 2017 is presented. It gives a strategy to develop the country's water resources and to cope with many of the effects of the growing Egyptian economy on the natural resources system. One of the proposed measures was to look into the operation of Lake Nasser.

These developments form the stage for the Lake Nasser Flood and Drought Control (LNFDC) Project. The aim of the project is to strengthen the capability of the Ministry of Water Resources and Irrigation (MWRI) to analyse these developments and to answer some key-questions. One of the key questions relevant for scour in the Nile has been: should excess water be spilled over the Toshka spillway or should excess water be released to the Nile?

This release will increase flood discharges up to 400 MCM/day for a period of several weeks through the lower Nile reach. The most important damage caused by these manmade floods is expected to be caused by local scour, and particularly scour at bridge piers, barrages and erosion of river banks. As a subcomponent of the LNDFC project vulnerable locations have been identified, and predictions have been made using semi-analytical approaches as well as a scale model study. In the following sections the approach for scour assessment is presented for separate scour phenomena in the Nile River.

II. LOCAL SCOUR IN THE NILE IN THE PRESENT AND THE PAST

Local scour at the hydraulic structures located across the Nile River constitutes a major concern. The two main types of hydraulic structures on the Nile River are bridges and barrages. In table II an overview of the main barrages in the Nile is given. It can be seen that most barrages are constructed and designed in pre-HAD conditions, except for the New Esna barrage.

The morphological processes in the Nile River have significantly changed by the change of regime after construction of HAD. It can be seen in Figure 2 that the reservoir fully controls the Nile flows; the high flows during August and September are completely eliminated and maximum discharges are now limited to 270 MCM/day, i.e. less than 1/3 of the earlier peak values. Note that bankfull discharge of the lower Nile is in the order of 600 MCM/day, and therefore the discharge is completely conveyed through the main channel.

TABLE I.
GENERAL DATA ON RIVER NILE STRUCTURES

Name of structure	Construc-ted	Chain-age (km)	Design Head (m)
Aswan Dam	1898-1902	0	33.0
Esna Barrage	1906-1908	166.65	5.0
New Esna Barrage	1990-	167.85	7.0
Nag Hammadi Barrage	1927-1930	359.45	4.5
Asyut Barrage	1898-1902	544.75	4.3
Mohamed Ali Delta Barrages	1843-1863	952.92	2.0
-Damietta		952.92	2.0
-Rosetta			
Delta Barrages	1936-1939		
-Damietta		953.20	3.8
-Rosetta		953.76	3.8
Zifta Barrage (Damietta)	1901-1903	1,046.7	4.0
Damietta Dam (Fariskour)	1985-1988	1,161.0	2.2
Idfina Barrage (Rosetta)	1951	1,159.0	2.7

source: River Regime of the Nile in Egypt, NRI, 1992

.

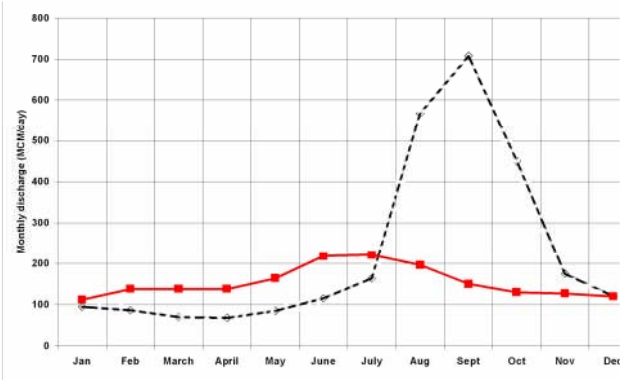

Figure 2 Average monthly flow of the Nile at Aswan before (dashed line) and after (drawn line) the construction of HAD (data 1938-1962 and 1969-1988)

Furthermore the HAD has a huge effect on the transport of sediments. The supply of sediment is interrupted as sediment from upstream is captured by the reservoir, and the transport capacity of the lower Nile has been reduced because of the reduced discharges. For instance in 1967 in Dongola a peak concentration of 8900 mg/litre was measured, whereas downstream Aswan the peak value was less than 100 mg/litre. Downstream Aswan the mean annual suspended load transport prior to HAD amounted 129 Mt/yr against 2.27 Mt/yr after 1967, which is only 2% of the original value. Under the post HAD conditions further downstream the mean annual suspended load transport doubles almost to 4.23 Mt/yr. If the bed-material transport is assumed as 50% of the suspended load (NRI,

[6]), then there is a difference of nearly 3 Mt/yr between the upstream and downstream reaches, which would mean, in absence of other sources, bed degradation. Part of the difference may be due to some influx of wind-blown sediment: the river is in direct contact with the desert in the reaches 1 and 2 over a total length of 43 km. Assuming that these influxes are small (wind direction is generally north, i.e. parallel to the river), the data would lead to an average bed degradation of 4 mm/yr. In the first 5 years after the implementation of HAD the bed levels in the reaches 1 to 3 dropped by 40 to 50 cm, whereas no changes occurred downstream Asyut. Thereafter, in sections the bed level drop continued and in other sections rose.

Since the construction of the HAD the number of islands in the river between Aswan and Cairo reduced drastically from 150 to 36 in 1989, due to infilling of secondary channels. In 1988 along 567 km of 2033 km of riverbanks between Aswan and Cairo bank protection in the form of revetments and spur dikes was available. Bank erosion took place along some 242 km of riverbanks.

Below the HAD the Nile flows in a northerly direction over a distance of 950 km before the river bifurcates at the apex of the Nile Delta into the Damietta and Rosetta branches to reach the Mediterranean Sea respectively 250 and 240 km further downstream (see Figure 1). From Aswan to the head of the Nile delta, a distance of 943 km, the river bed drops from 79 m to 11 m+MSL. This implies an average bed slope of 7.2 cm/km. It appears though that the bed slope increases from less than 5 cm/km in the upper reaches to over 8 cm/km further downstream. The bed slope of the Damietta branch is about 6 cm/km and of the Rosetta branch 8 cm/km. The top width of the river varies from 640 in the upper reaches to 540 towards Cairo. The flow depth ranges between 4 and 6 m under the present river regime.

The bed material consists of medium to fine sands with D_{50} (median grain size) values of 0.31, 0.25, 0.42 and 0.43 mm. and D_{90} of 0.80, 0.70, 0.90 and 0.90 mm. in the first four river reaches respectively. With this type of fine sediment the river bed is very susceptible to local scour. Scour can be quite significant if no protection is provided. In the following sections is shown what the impact of increased discharges will be.

III. LOCAL SCOUR AT BRIDGE PIERS

Various empirical relations for bridge pier scour have been applied, e.g., Shen et al. [7], Colorado State University (CSU) [2], Jain and Fischer [5] and others. In addition, the applicability of a newly developed analytically based equation by Youssef Hafez [4] from Hydraulics Research Institute (HRI) based on an energy balance theory is investigated. Because the latter has been derived for Nile data, it is obvious that the new equation by Hafez performs best to the bridges across the Nile and is therefore used in the final estimation of scour depths. The equation of Hafez expresses equilibrium bridge scour depth, and reads:

$$\left(\frac{D_s}{h}\right)^3 = \left(\frac{3\tan\phi}{(S_G-1)(1-\varepsilon)}\right)\left(1-\frac{b}{B}\right)^{-2}\left(\frac{\eta^2 u^2}{g\,h}\right)\left(1+\frac{D_s}{h}\right)$$

in which

B = the channel width (if one pier) or bridge span (if multiple piers at equal distances)
b = obstruction width or pier width
D_s = equilibrium scour depth
g = gravitational acceleration
h = approach water depth
S_G = the sediment specific gravity
u = local flow velocity
ϕ = the bed material angle of repose,
η = a coefficient reflecting momentum transfer,
ε = the bed material porosity,

The factor η has been found to vary between 0.56 and 1.00 (based on tests). The parameter must be calibrated to reduce the inherent uncertainty of this equation. For the hydraulic parameters the 1D hydraulic model, using the SOBEK modeling system [8], has been applied.

The local scour has been observed around bridge piers of the following bridges:

1. El-Tahrir Bridge at Cairo (built pre-HAD). Contains 7 piers with intermediate of distance 50 m. Current stable scour-hole depth is about 3.5 m. Predicted scour depth with formula of Hafez [4] for 270 MCM/d is 1.73 m, and for 400 MCM/d is 2.35 m.

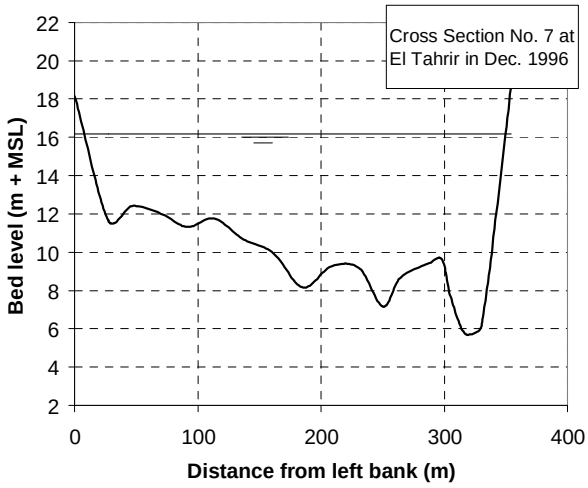

Figure 3 Cross Section No. 7 at El Tahrir showing scour holes at the Bridge Piers

2. Imbaba Bridge at Cairo (built pre-HAD). Contains 8 piers with intermediate of distance 65 m. Current stable scour-hole depth is about 5.25 m. Predicted scour depth with formula of Hafez [4] for 270 MCM/d is 1.76 m, and for 400 MCM/d is 2.41 m.
3. El Marazek Railway Bridge at Marazek near Helwan (built pre-HAD). Contains 8 piers with intermediate of distance 90 m. Current stable scour-hole depth is about 6 m. Predicted scour depth with formula of Hafez [4] for 270 MCM/d is 2.10 m, and for 400 MCM/d is 2.95 m.
4. Edfina Railway Bridge at the end of Rosetta Branch. Contains 4 piers with intermediate of distance 80 m. Current stable scour-hole depth is between 4 and 9 m.

Predicted scour depth with formula of Hafez [4] for 270 MCM/d is 2.13 m, and for 400 MCM/d is 4.34 m.

5. Desouk Railway Bridge at Rosetta Branch. Contains 6 piers with intermediate of distance 70 to 35 m. Current stable scour-hole depth is about 2 m. Predicted scour depth with formula of Hafez [4] for 93 MCM/d (Rosetta) is 1.25 m, and for 261 MCM/d is 2.24 m.
6. Rahmania Railway Bridge at Rosetta Branch. Contains 2 piers with intermediate of distance 60 m. Current stable scour-hole depth is about 2 m.
7. Zefta Railway Bridge at Damietta Branch. Contains 4 piers with intermediate of distance 35 to 70 m. Current stable scour-hole depth is about 5 m. Predicted scour depth with formula of Hafez [4] for 59 MCM/d (Damietta) is 1.93 m, and for 139 MCM/d is 3.58 m.
8. Mansoura Railway Bridge at Damietta Branch. Contains 4 piers with intermediate of distance 35 to 70 m. Current stable scour-hole depth is about 4 m. Predicted scour depth with formula of Hafez [4] for 59 MCM/d (Damietta) is 1.35 m, and for 139 MCM/d is 2.57 m.
9. Kafr el-Zayat Railway Bridge at Rosetta Branch (see Figure 4). Contains 4 piers with intermediate distance of 35 to 70 m. Current stable scour-hole depth is about 4.5 m. Predicted scour depth with formula of Hafez [4] for 93 MCM/d (Rosetta) is 2.26 m, and for 261 MCM/d is 3.95 m.

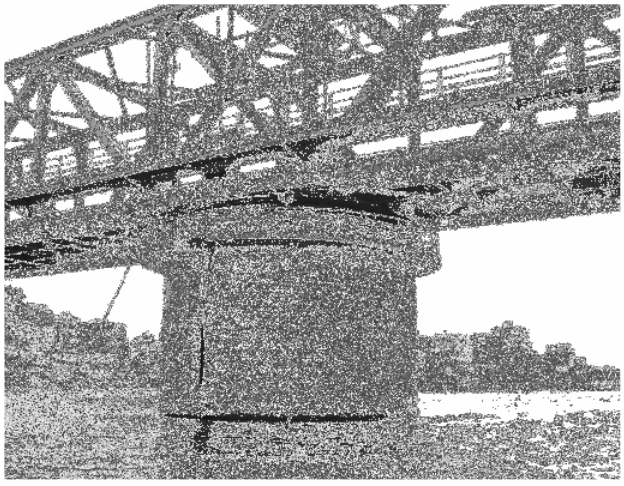

Figure 4 Central (largest circular) pier of Kafr el-Zayat railway bridge

From this list it can be observed that the predicted scour depths are generally smaller or in some cases equal to the current scour depths. It is concluded that the local scour around bridge piers at the bridges listed above is in a stable condition under the current flow conditions as well as for discharges up to 400 MCM/day at HAD.

IV. LOCAL SCOUR AT BARRAGES

Scour at barrages occurs downstream of the gates. The Nile barrages are designed to with-stand local scour under working conditions that are less severe than the expected flood scenarios in LNFDC Project. On basis of computations and scale model tests it is assessed whether scour can become a threat for the barrages.

Before the construction of High Aswan Dam (HAD) in 1964 all barrage gates during the flood season were completely opened with the barrage acting as a bridge section with constriction scour only expected. In the rising period of the flood, scour occurred while in the falling period filling of the scoured holes occurred by the flood sediment laden water. In the present situation, after HAD, the observed scour holes are due to conditions where the water is almost clear of sediment. Scour is presently resulting from high velocity jets either from high head difference on the barrage or high unit width discharge due to gate operation schemes. Maximum scour occurred when most of the discharge was forced in a few gates of the barrage causing a highly concentrated jet attacking the bed protection and natural-river-bed. This type of scour is not related to the discharge but rather to improper gate management.

The water jet is controlled by the head difference on the barrage, gate dimensions (width and height), stilling basin characteristics and the downstream water level. When gates are operate such that the whole discharge is concentrated to a few gates, the downstream protective layer or the unprotected bed further downstream can become damaged. Note that the existence of significant scour holes downstream a barrage causes undermining of the bed material below the barrage foundation. This might cause a collapse of the barrage.

The two types of methods that have been applied are:

1. Analytical (empirical) approaches have been used to calculate the expected scour depth for increased discharge conditions. Existing equations for predicting scour depths downstream barrages or low head structures are limited to laboratory studies using coarse sediments, i.e. Breusers and Raudkivi [1]. Therefore, a new analytical equation for predicting scour downstream low head structures has been developed by Hafez [4].
2. Scale model tests have been carried out for local scour prediction downstream of Rosetta barrage for high releases at HAD

ANALYTICAL APPROACH

Prediction of scour in case of higher releases from HAD have been made using the Hafez [4] equation developed for estimating equilibrium scour depth downstream of low head hydraulic structures. The equation is based on the same principles of the energy balance theory that was used for predicting bridge pier scour:

$$D_s^3 = \frac{6\eta^2 q^2}{g\left(S_G - 1\right)\left(1-\varepsilon\right)\left(\frac{1}{s_1}+\frac{1}{s_2}\right)\sin\phi_1}\left(1+\frac{D_s}{H_j}\right)$$

in which

D_s = equilibrium or maximum scour depth
H_j = the water depth of the incoming jet
q = the unit width discharge of the jet

S_2 = the upstream and downstream slopes of the scour hole respectively

ϕ_1 = the angle of the upstream slope of scour hole,

η = a momentum transfer coefficient,

In case of unavailability of data about q, the maximum jet velocity as an under flow could be calculated from the formula $V=\sqrt{(2gH)}$. For example, from a model study for the New Nag Hammadi barrage a jet velocity in the order of 9.45 m/s for flow under a sluiceway radial gate at normal conditions has been reported. This jet could be an underflow jet that in the absence of a weir downstream the barrage keeps its momentum till it meets the unprotected bed. The value of η is taken equal to unity for maximum scour depth. As the method is designed for Nile conditions, it performs better for the Nile barrages than other general empirical formulas for local scour.

In Table II an overview is given of observed scour (at current conditions) and predicted scour (at increase flow releases of HAD) at the main barrages that are investigated by HRI. The barrages built before HAD have about 100 gates (or about 50 gates in the delta branches) of about 5 to 8 m width. The New Esna barrage consists of a power house with 6 gates and a flood sluiceway with 11 gates, of 12 m width each. It can be seen that the predicted scour depths reach quite significant values when only a limited number of gates is operated. For Asyut, Rosetta and Damietta barrages the possibility of undesirable conditions during gate closure requires a rip-rap protection over the full width of the barrage.

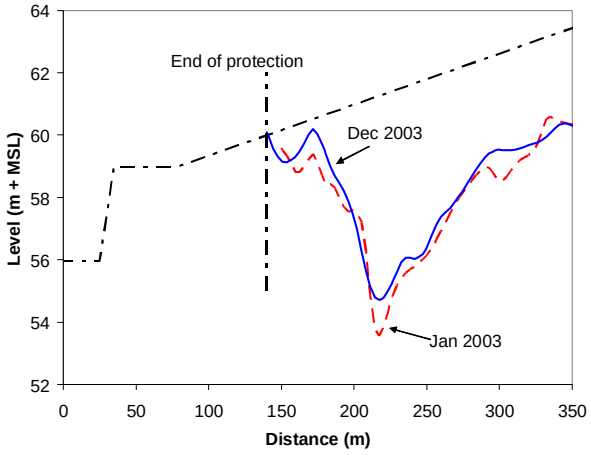

Figure 5 Scour Hole Downstream the New Esna Barrage at Turbine Gate No. 1

In Figure 5 the observed scour a New Esna barrage downstream of turbine gate 1 is plotted, with a scour depth up to 8 m. Its shape is typical for the scour holes at this barrage and the new Naga Hammadi barrage. The upstream slope of the scour hole S_1 = 0.11 and the downstream slope S_2 = 0.05. For predictions we used the jet depth H_j = 3 m, and at a flood discharge of 400 MCM/day the unit discharge q = 35.1 m^2/s from the sluiceway gates. For the sluiceway gates this results in a scour depth of 9 m (see Table II).

TABLE II.
LOCAL SCOUR AT BARRAGES, OBSERVED AND PREDICTED BY HRI

Name of structure	Condition (flood = 400 MCM/d)	Observed (m)	Predicted (m)
New Esna sluice-	current	3 – 6.5	5.7
way	flood		9
Nag Hammadi	current	< 10	8.7 -11
	fld, 100 gates		2.91
	fld, 50 gates		5.15
	fld, 20 gates		11.5
Asyut Barrage	current	< 7.5	8.4
	fld, 111 gates		3.1
	fld, 55 gates		5.6
	fld, 20 gates		13.5
Delta Barrage on	current	4 – 4.7	4.75-5
Rosetta	fld, 46 gates		4.3
	flood, 46 gates+d/sweir		3.8
Delta Barrage on	current	2 – 3.3	4
Damietta	fld, 34 gates		2.3
	flood, 34 gates+d/sweir		2.5
Zefta (Damietta)	current	3.5	4.2
	fld, 50 gates		2.4
	flood, 50 gates+d/sweir		2.4

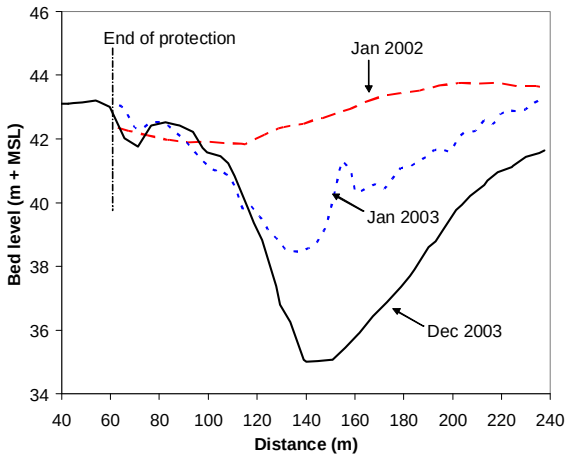

Figure 6 Scour Hole Downstream the Asyut Barrage at Vent No.58

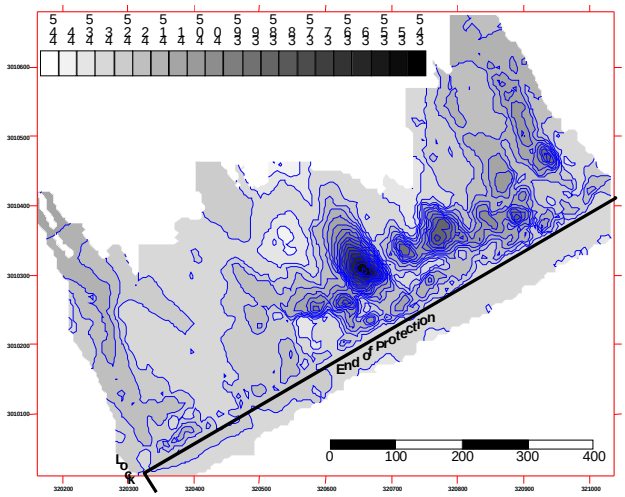

Figure 7 Bed Topography of the Scour Holes Downstream Asyut Barrage, December 2003

In Figure 6 and Figure 7 some observations of scour holes downstream of Asyut barrage (from HRI) are plotted. A particularly large scour hole has developed below vent No. 58. In Figure 6 it is shown that this scour hole developed in stages in the period between Dec 2002 and Dec 2003, up to a scour depth of 7.5 m. With the formula of Hafez [4] a scour depth of 8.4 m is predicted for this situation, which agrees reasonable with the data.

For Delta barrage at Rosetta branch (see Figure 9) it is shown in Table II that the predicted scour for floods is less than the current scour depth provided that all gates are open. For this prediction it is assumed that during a 400 MCM/day flood about 70% of the total discharge will pass through the Delta barrage at Rosetta branch (the rest will pass through Damietta branch). Distinction is made between the scour directly below the structure, and that below the downstream weir. The downstream weir is applied to reduce the jet-velocities (of about 9 m/s) with about 40%, and a scour depth below the weir of 3.8 m is predicted for flood conditions.

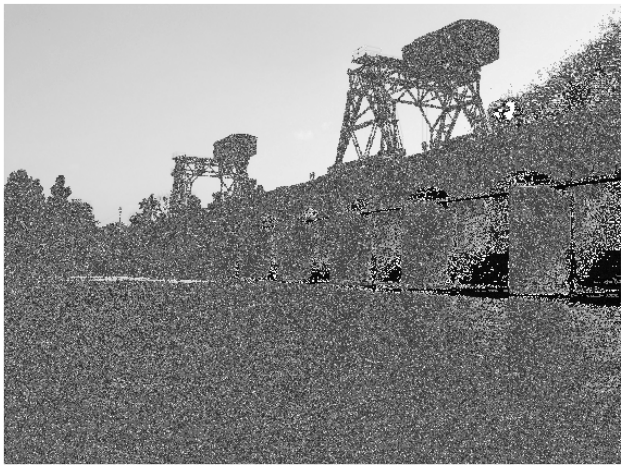

Figure 8 Delta barrage (d/s) in Rosetta branch

SCALE MODEL

The analytical model provides reasonable estimates of the maximum scour depth. However, more detailed imformation is required for design of the bed protection and scour-hole characteristics. Therefore movable-bed scale model tests have been carried out at HRI. Tests were run for a range of discharges between 150 to 400 MCM/day at the barrage (i.e. up to releases of 605 MCM/day at HAD). A geometrical scale of 1:32 was selected for best simulation of hydraulic phenomena with smallest possible scale effects. The model represents 100 m of the river bed upstream, 5 of the gates, the stilling basin, and 150 m of the downstream river bed (see Figure 9).

Figure 9 Scale model test for Rosetta Barrage: construction of the model at HRI

The experiments show that the maximum scour depth at 275 MCM/day (all 5 gates open) is 3.10 m, with scour length of 43 m. Compared to the analytical value for this condition, 4.3 m, this value is slightly lower. For a discharge of 400 MCM/day the maximum scour depth becomes 5 m if all 5 gates are opened, and 7 m if one of the gates is closed (see Figure 10, middle gate closed). The experiments confirm that as long as the flow is evenly distributed (all gates opened) the scour will not form a threat (it does not exceed the present scour depth).

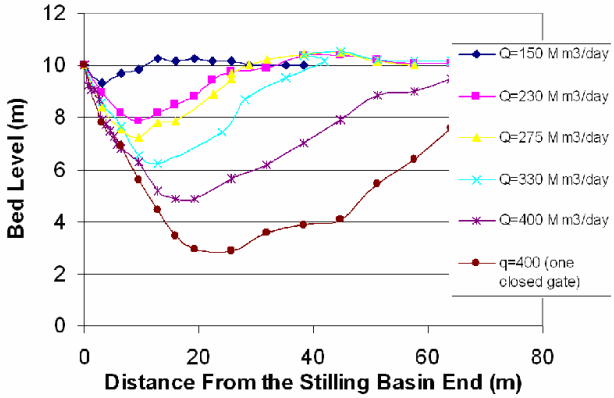

Figure 10 Bed levels downstream at section 9 (right side of flume)

To anticipate on an unequal opening of the gates, a rip-rap protection has been designed that will withstand these undesirable conditions. It requires a sand-base filling of the present scour hole, two filter layers with particle size 3 and 30 mm, and a rip-rap layer with thickness of 0.6 m over the full length of the scour hole.

V. BANK EROSION

The process of bank erosion in the lower Nile is related to both meandering and to general scour or river-bed-degradation. Currently bank erosion processes are limited to the absence of floods due to operation of HAD, degradation processes initiated by HAD have more or less diminished. Areas that used to be threatened by scour and bank erosion, such as islands and outer bends of meanders are now cultivated and developed, and have become much more vulnerable.

Figure 11 Bank erosion near Beni Suef (Nile main branch)

River banks in the lower Nile are cohesive and rather steep. Bank failure usually shows as sliding of bank section after undercutting. An example of failure that occurred during the flood release of 2001 is shown in Figure 11.

At most locations vulnerable for bank erosion the banks are already protected. Nevertheless, six locations have been identified which may suffer from bank instability during high floods. At these locations bank protection works have been designed.

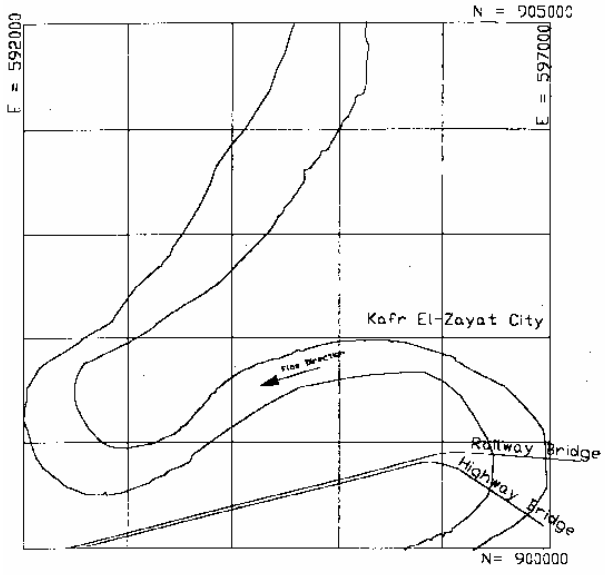

Figure 12 River bend at Kafr el-Zayat (Rosetta branch)

For the river bank at Kafr el-Zayat, located in a sharp bend at the Rosetta branch (see Figure 12) in the Nile delta, a detailed study has been carried out to improve the existing (inadequate) bank protection for resisting the flood releases from HAD. In Figure 13 is shown how currently the city is protected by rip-rap toe and a concrete slab.

Figure 13 Protected bank in river bend at Kafr-el-Zayat (Rosetta branch) just downstream of the railway bridge (right bank)

The detailed design for improvement of the bank protection is based on modelling study by HRI using a 2D hydraulic model. For different flood discharges the relevant flow conditions near the river bank have been determined.

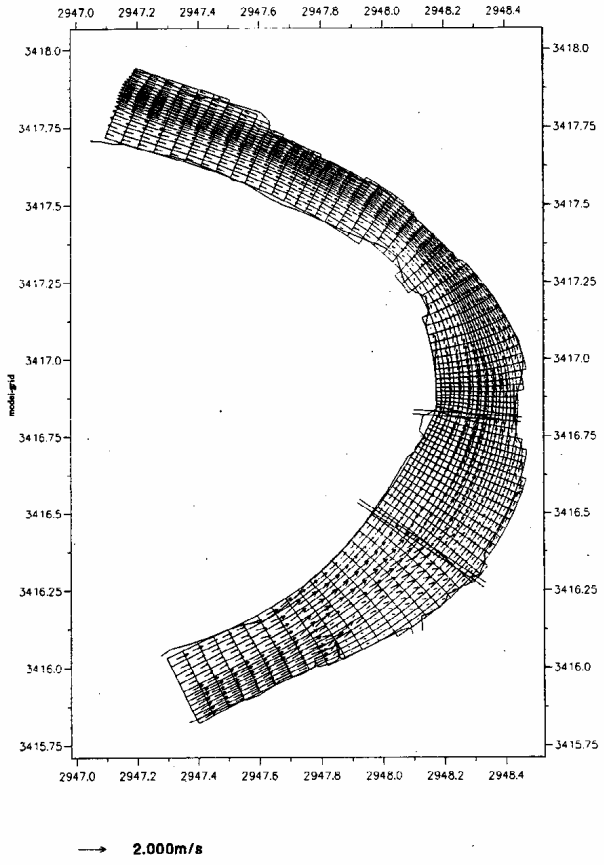

Figure 14 Velocity vectors in the modeled reach Kafr-el-Zayat

The hydraulic simulations were carried out using the Delft3D modelling system of WL | Delft Hydraulics [3].

In Figure 14 the velocity vectors are shown on the curvi-linear grid following the alignment of the main river. The model has been calibrated on basis of field measurements in 1999 for two cross-sections. The model results show that the maximum velocity occurs in the cross-section at 850 m downstream of the railway bridge. The maximum velocity ranges from 0.9 m/s (Rosetta discharge 150 MCM/d, i.e. 240 MCM/d at HAD), 1.5 m/s (Rosetta discharge 275 MCM/d, i.e. 432 MCM/d at HAD), to 2 m/s (Rosetta discharge 440 MCM/d, i.e. 605 MCM/d at HAD). To protect the river bank against the resulting bend scour at Kafr El-Zayat several types of retaining walls have been proposed. They are founded well below the expected scour depth that is associated to the flow velocities computed for floods.

VI. Discussion

The regulation of Nile discharges by HAD has removed the threat of flooding and scour. In the past decades the area around the river (flood plains) and within the river (islands) has gradually been developed and has become more vulnerable. Furthermore, the river has incised significantly at several reaches, such that river banks have become relatively high and steep with potential risk of failure. Although most of the structures (bridges and barrages) existed already before HAD, and therefore have strong protections, it was found that this does not mean that presently these can still withstand the flood discharges. It requires a careful operation of gates at barrages (e.g., following pre-HAD rules) and protection of river banks that have become critical with respect to stability. The problems and conditions in the lower Nile can be considered representative for many other reservoirs as well. The modifications in rivers downstream of high dams (both anthropogenic and natural) can become significant after some decades, resulting in an increased risk of damage by scour. The Nile example shows that protection against scour may be an important issue for the future reservoir management.

VII. Conclusions

Anticipating on climate change the operation of reservoirs may be modified in such a way that periodic flood discharges have to be released to the downstream reach. For the Nile this means an expected release of flood discharges for a period of several weeks through the lower reach. Damages in the downstream reach are to be expected as the (use of the) river-channel has changed significantly after floods have been diminished by the High Aswan Dam.

The most important damage caused by these manmade floods is expected to be caused by local scour. For the main Nile branches the most vulnerable locations have been determined, and the expected conditions have been predicted from analytical, numerical and laboratory scale modelling results. Particularly bank-erosion and bridge-pier scour processes have been estimated using mathematical modelling approaches designed for the Nile conditions. Whereas most bridge piers are already sufficiently protected, it has been concluded that only the river banks require an additional protection at several locations, and require inspection after each flood.

Furthermore laboratory experiments have been carried out to assess the scour downstream of Rosetta barrage which is governing the discharge distribution to the Nile delta. The mobile-bed model results appeared to agree with observations very well, and can be used for improvement of the theoretical models. It has been found that only by distributing the flood discharge over all the vents (instead of a few vents as is common practice) the scour depth will not exceed the present scour depth. Nevertheless it is necessary to protect three of the main barrages against local scour, as their present protection appears to be insufficient to withstand the high floods.

Acknowledgment

The scour study for the Nile River was commissioned by the Ministry of Water Resources and Irrigation within the framework of the Lake Nasser Flood and Drought project. The project was funded by a grant from the Royal Netherlands Embassy in Cairo. The work has been carried out together with various staff members of the Hydraulics Research Institute (HRI) in Cairo and staff members of WL | Delft Hydraulics, for which they are gratefully acknowledged. Furthermore the writers like to express their gratitude to the support and coordination of the project by staff members of the Planning Sector of the Ministry of Water Resources and Irrigation and the Nile Forecasting Centre.

References

[1] Breusers and Raudkivi, 1991, *Scouring*, IAHR Hydraulic Structures Design Manual 2 A.A. Balkema/Rotterdam/Brookfield.

[2] Colorado State University, 1975, "Highways in the River Environment: Hydraulic and Environmental Design Considerations," prepared for the Federal Highway Administration, U.S. Department of Transportation, May 1975.

[3] Delft3D modelling system, Software, WL | Delft Hydraulics, The Netherlands.

[4] Hafez, Youssef, 2004, A New Analytical Bridge Pier Scour Equation. Proc. of the Eighth International Water Technology Conference (IWTC 2004), March 2004, Alexandria, Egypt.

[5] Jain, S.C. and Fischer, E. E. (1979). "Scour around circular bridge piers at high Froude numbers." Rep. No.FHwa-RD-79-104, Federal Hwy. Administration (FHwa), Washington, D.C.

[6] NRI, 1992., River Regime of the Nile in Egypt.

[7] Shen, H.W., Schneider, V. R., and Karaki, S. S., 1969, " Local Scour Around Bridge Piers,", J. Hydraul. Div. ASCE, 95 (HY11), pp. 1919-1940, November 1969.

[8] SOBEK modelling system, Software, WL | Delft Hydraulics and Rijkswaterstaat RIZA, The Netherlands.

Laboratory Tests of Scour at a Seawall

J. Sutherland[*], C. Obhrai[*], R.J.S. Whitehouse[*] and A.M.C. Pearce[**]
[*] HR Wallingford Ltd., Wallingford, Oxfordshire, OX10 8BA, UK
[**] University of Southampton, Southampton, SO17 1BJ, UK

A set of medium-scale laboratory tests of wave-induced scour at seawalls has been performed in a flume at HR Wallingford. The methodology is presented along with test conditions and summarized results. The scour depth at the toe of the seawall is highly dependent on the form of wave breaking onto the structure. Sea states where waves plunge directly onto the wall generate jets of water that may penetrate to the seabed and cause a local scour hole immediately adjacent to the seawall. This is a different scouring mechanism to that observed in deeper water and is also absent when the seawall is well within the surf zone and most of the large waves have broken before they reach the seawall. Theoretical limitations are discussed.

I. INTRODUCTION

Toe scour is believed to be the most common cause of seawall failure in the UK [1] yet some of the empirical predictors of toe scour derived from laboratory tests give results with opposite dependence on relative depth [2, 3, 4]. Moreover many of the existing laboratory experiments on scour in front of seawalls were performed at relatively small scales, leading to tests dominated by bedload transport [2]. The pattern of sediment erosion and accretion varies with the mode of sediment transport, so bedload transport gives a different bed profile to suspended load transport [2, 5].

In many circumstances scour problems in the field will be dominated by suspended sediment transport. The results from physical model results are likely to be misleading unless the most important scaling parameters are satisfied. Therefore, laboratory tests should to be done with a justification of the scale used and with an awareness of the ambiguities that have arisen in previous experiments done at small-scale. As a minimum it is recommended that the dominant transport mode (bedload or suspended) is reproduced in the laboratory. In many cases when considering sand beaches this will require suspended sediment transport to be produced in the laboratory for a significant proportion of the time. This will require experiments to be performed at a medium to large scale.

A number of wave flume experiments on toe scour at seawalls that were conducted at medium to large-scale, used fine sand and were conducted with irregular waves have been identified and their results collated. This database has been extended and gaps in it filled by devising and performing a set of medium-scale experiments of toe scour in front of smooth seawalls in a new wave flume in the Froude Modelling Hall at HR Wallingford. The laboratory tests looked at the longshore-uniform case of normal wave incidence only.

Funded by UK Department of Environment, Fisheries and Rural Affairs (Defra) under R&D project FD1927

II. PREDICTION OF SUSPENSION

Scaling rules have been developed for bedload [6] and suspended load [7] tests. In cases where suspended sediment is predominant the Shields parameter does not have to be preserved [7, 8] as the wave breaking and turbulence are more dominant mechanisms in determining sediment mobility than the wave shear stress. In this case an undistorted model with Froude scaling using the same value of the Dean fall speed parameter in model and prototype is recommended. The Dean fall speed parameter, D_{ws}, is given by:

$$D_{ws} = \frac{H_s}{w_s T_p} \qquad (1)$$

Here H_s is the significant wave height, w_s is the fall speed of the median sediment and T_p is the spectral peak wave period. Various formulae have been derived that distinguish between suspended and bedload hydrodynamic regimes. The following criterion has been proposed [9] for the initiation of suspension under waves :

$$\frac{U_w - U_{cr}}{w_s} \geq 16.5 \qquad (2)$$

where U_w is the maximum value of orbital velocity at the bed and U_{cr} is the critical velocity for incipient sediment transport.

Simple Froude scaling rules exist for the fall velocities of both small and large particles (if the same density material is used in model and prototype) but not for intermediate values. Therefore, Equation 3 [10] was used to determine the sediment fall speed, w_s as:

$$w_s = \frac{\nu}{d}\left[\left(10.36^2 + 1.049 D_*^3\right)^{1/2} - 10.36\right] \qquad (3)$$

Where D_* is the dimensionless grain size given by:

$$D_* = \left[\frac{g(s-1)}{\nu^2}\right]^{1/3} d \,. \qquad (4)$$

Here ν is the kinematic viscosity, d is the grain diameter, g is gravitational acceleration and $s=\rho_s/\rho$ is the relative density with ρ_s the sediment density and ρ the water density.

The critical velocity for incipient transport, U_{cr} [11] is given by Equation 5:

Fout! Objecten kunnen niet worden gemaakt door veldcodes te bewerken. (5)

The maximum near-bed wave velocity, U_w, can be calculated from linear theory for a representative wave. Substituting U_w, U_{cr} and w_s back into Equation 2 allows one to determine if a test should generate suspended sediment transport.

III. Existing Datasets

Results from the tests reported here are intended to be comparable to those from the following datasets on toe scour that had suspended sediment transport and were conducted with irregular waves.

Xie [9] included a number of tests that generated scour in a flat bed in front of a vertical seawall that were in the suspension mode. Most of the tests used regular waves but three irregular wave tests were also conducted in suspension mode. Scour profiles were provided from two of those tests.

Fowler [3] performed mid-scale (wave heights between 0.2 and 0.3m) laboratory tests of the scouring of a 1:15 sloping sand bed in front of a vertical wall, which was always placed close to the intersection of the beach and mean water line. All 18 irregular wave tests were conducted in the ranges $-0.011<h_t/L_0<0.025$ and $0.015<H_s/L_0<0.040$ where h_t is the initial water depth at the toe of the seawall and L_o is the linear theory deep water wavelength. Ottawa sand, with d_{50}=0.13mm and a specific gravity of 2.65 was used in all cases.

The SUPERTANK Data Collection Project was performed at the O.H. Hinsdale Wave Research Laboratory (WRL), Oregon State University [12, 13]. The WRL flume is 104.2m long, 3.66m wide and 4.57m (15 feet) deep. The beach was made of very well-graded sand trucked from the Oregon coast with a median diameter, d_{50} = 0.22mm. Waves were run in relatively short bursts to provide data for numerical model calibration. Only in one toe scour test, ST_C0, were about 3,000 waves of the same spectrum run. Test ST_C0 was the only one directly comparable to these tests.

IV. Experimental Setup

The new tests were performed in a 45m long wave flume at HR Wallingford [14, 15]. The internal cross-section of the flume is 1.2m wide by 1.7m high. Waves were generated using a piston-type wavemaker with a maximum stroke of ±0.6m and a maximum operating depth of 1.4m. The wavemaker has an absorption system for absorbing wave energy reflected from the seawalls. The test setup had a 19.2m long 1:30 smooth concrete slope from the flume floor up to an elevation of 0.64m. The test section was a 5.14m long sand bed filled with Redhill 110 sand. The sand bed was 0.3m deep at the offshore end. Tests 1 to 14 all started from a screeded 1:30 slope. The sand bed level at the wall was therefore approximately 0.80m above the flume floor. Tests 15-34 started from a screeded 1:75 slope where the sand bed level at the wall was approximately 0.7m above the flume floor.

Redhill 110 sand has typically 98.80% SiO_2, 0.09% Fe_2O_3, 0.21% Al_2O_3 and 0.14% loss on ignition. The results of a sieve analysis of Redhill 110 are shown in Table I. Assuming d_n is the sieve size that n percent of the sand by weight passes through, common percentiles are d_{16} = 0.087mm, d_{50} = 0.111mm and d_{84} = 0.154mm. Settling velocities are also given using (3) and (4) for fresh water (salinity = 0) at a typical temperature in the tests of 11ºC, giving calculated density of water ρ = 999.5kgm^{-3} and a kinematic viscosity $\nu = 1.272\times10^{-6}$m^{2}s^{-1}. In addition, a sediment density ρ_s = 2650kgm^{-3} was assumed – appropriate for silica sand.

Waves were measured by 10 wave gauges. A group of 4 wave gauges was situated over the flat flume bed before the start of the beach slope and were used to separate out incident and reflected wave spectra using a least-squares technique. A second group of 4 wave gauges was situated at the offshore end of the sand bed to separate out incident and reflected wave spectra over the sand bed. Variations in the standard deviation in the surface elevation at these gauges could also be used to provide information on the partial standing wave pattern in front of the seawall. A further two wave gauges were placed 1.00m and 0.10m in front of the seawall, where local variations in the water level were greater due to the stronger partial standing wave pattern.

The profile of the sand bed was measured using the touch sensitive, 2D bed profiling system developed at HR Wallingford. The profiler consists of a probe which can move up and down and is mounted on a carriage which moves horizontally along a support beam. On the bottom of the probe is a sensor which consists of a lightweight "finger" that can move freely up and down inside a 20mm cylinder. The cylinder rests either on a small ball that is pulled along the bed by a lever arm mounted on the probe or on a foot that takes small steps (see Fig. 1).

The resolution of the bed profiler was ±1mm in the horizontal direction and ±0.5mm in the vertical direction. However even though the finger is very light it did cause a slight deformation (approximately 1-2mm) of the sand bed. This meant that the profiler tended to smooth out some the finer features of the bed. Bed profiles were interpolated onto a regular spacing of 1mm.

Each test started from an initial slope of either 1:30 or 1:75 which was achieved using wooden templates installed on each side of the flume. The initial profile was then measured using the bed profiler.

TABLE I. Sieve analysis of Redhill 110 sand

Percent by weight passing sieve			Soulsby w_s (ms^{-1})
(%)	*(mm)*	*(Phi)*	
5	0.064	3.97	0.0026
10	0.074	3.75	0.0035
16	0.087	3.53	0.0048
25	0.095	3.40	0.0057
50	0.111	3.17	0.0077
75	0.135	2.89	0.0111
84	0.154	2.70	0.0141
90	0.167	2.58	0.0163
95	0.177	2.50	0.0180

Figure 1. Bed profiler and wave gauges 5 to 8

V. Test Conditions

A total of 34 tests were performed. Details of the test conditions are given in Table II.

- Test type is either V = vertical, or S = sloping (1:2) with T added if test had varying water level;
- H_{si} is the measured incident offshore significant wave height (m) calculated by the least squares technique using gauges 1-4;
- T_p is the measured spectral peak wave period (s);
- h_t is the initial water depth at the structure toe (m);
- Cr is the bulk reflection coefficient;
- S_t is the scour depth at the toe of the seawall (m) with negative values being accretion;
- S_{max} is the maximum scour depth (m);
- X_{sm} is the distance from the toe of the structure to the location of S_{max} (m);
- A_{max} is the maximum increase in bed level (m);
- X_{am} is the distance from the toe of the structure to A_{max} (m).

19 tests were performed with a vertical wall. 13 of these were with a beach slope of 1:30 and 6 were with a beach slope of 1:75. Details of these are given in Table 2. A total of 6 scour protection tests were carried out, but are not reported here. A sloping wall at 1:2 was used in 9 of the tests with a beach slope of 1:75.

The majority of tests used a constant incident significant wave height, period and depth to measure the time development of scour. In these tests a bed profile was taken before the test and after 300, 1000, and 3000 spectral peak wave periods.

In the second type (tests 10, 17 and 34a) the water depth was varied to simulate part of a tidal cycle and in these tests a new profile was taken after each of the 300 wave bursts. Test 10 started with a water depth at the wall close to zero, increasing the depth in steps to a maximum depth of 0.3m then decreasing the depth in steps down to -0.1m at the seawall. However test 17 started from a higher water depth of 0.2m and decreased the depth in steps down to -0.05m, while in test 34a the water was slowly drained from the flume during the test.

VI. Bed Level Changes for a Vertical Wall

Bed level changes (final – initial elevation) at the end of Tests 7, 12, 4 and 11 (i.e. after 3,000 waves) are provided in Fig. 2. All the tests were performed with a vertical seawall. Negative values represent scour, while positive values represent accretion. These four tests had the same initial bed profile, wave period (T_p=3.24s) and incident wave height (H_s=0.2m) but different water depths (h_t=0.0m, 0.1m, 0.2m and 0.4m respectively). A comparison has been drawn between these four tests as they resulted in very different breaking wave conditions at the wall and hence different bed profiles.

During test 7 (h_t=0.0m) the waves broke offshore and the wave energy was largely dissipated before the waves reached the wall in the swash zone. As a result there was a slight accretion at the wall but a general lowering throughout the rest of the profile. The vertical seawall was situated within the surf zone during Test 12 (h_t=0.1m) and some breaking occurred onto it, although most of the larger waves had already broken by the time they reached the seawall. The resulting scour profile includes a small dip at the toe of the seawall caused by turbulence and a deeper scour hole at about 0.5m from the structure toe.

However during Test 4 (h_t=0.2m) the waves tended to break onto the structure and the impacts sent water high up above the seawall (see Fig. 3). In these cases water plunging down the face of the seawall to the bed, resulted in suspended sediment transport at the toe, and this mechanism generated the deepest scour depths. Fig. 2 shows that the maximum scour occurred at the wall (0.158m) with significant accretion (0.056m) occurring 1.3m offshore.

In deeper water (test 11, h_t=0.4m) the waves did not break onto the seawall as plunging breakers, but tended to reflect more energy. The scouring pattern (shown in Fig 2) in these cases was closer to the classic Xie type standing wave pattern. The maximum scour of 0.117m occurred away from the wall and was significantly less than the plunging breaker case shown in Fig. 2 (0.158m).

TABLE II. DETAILS OF EXPERIMENTS PERFORMED

Test no.	Test type	Beach slope	H_{si} [m]	T_p (s)	h_t [m]	C_r [-]	S_t [m]	S_{max} [m]	X_{sm} [m]	A_{max} [m]	X_{am} [m]
1	V	1:30	0.193	1.55	0.200	0.50	0.057	0.057	0.031	0.006	0.660
2	V	1:30	0.193	1.87	0.200	0.49	0.065	0.065	0.031	0.023	0.680
3	V	1:30	0.198	2.29	0.200	0.47	0.130	0.130	0.031	0.044	0.950
4	V	1:30	0.194	3.24	0.200	0.46	0.158	0.158	0.031	0.056	1.369
5	V	1:30	0.197	4.58	0.200	0.44	0.140	0.143	0.049	0.073	2.449
6	V	1:30	0.204	1.87	0.000	0.09	-0.031	0.025	0.731	0.033	0.016
7	V	1:30	0.196	3.24	0.000	0.13	-0.011	0.032	1.513	0.026	0.082
8	V	1:30	0.197	1.87	0.100	0.26	0.110	0.111	0.006	0.009	0.731
9	V	1:30	0.202	1.87	0.400	0.82	-0.013	0.035	0.327	0.013	0.009
10	VT	1:30	0.195	1.87	-0.1 to 0.2	0.31	0.067	0.067	0.001	0.001	4.077
11	V	1:30	0.217	3.24	0.400	0.84	0.040	0.117	0.414	0.069	1.881
12	V	1:30	0.197	3.24	0.100	0.27	0.088	0.114	0.469	0.030	2.106
13	V	1:30	0.295	2.29	0.150	0.28	0.093	0.125	0.415	0.013	1.925
14	V	1:75	0.280	1.87	0.300	0.49	0.036	0.052	0.354	0.027	1.005
15	V	1:75	0.196	1.87	0.200	0.40	0.027	0.048	0.295	0.009	2.085
16	V	1:75	0.197	3.24	0.200	0.39	0.089	0.102	0.404	0.022	1.342
17	VT	1:75	0.193	1.87	0.2 to -0.1	0.16	0.014	0.034	0.191	0.004	3.617
18	V	1:75	0.191	4.58	0.200	0.37	0.062	0.119	0.495	0.055	2.662
19	V	1:75	0.215	3.24	0.400	0.77	0.050	0.100	0.417	0.067	1.901
26	S	1:75	0.190	1.87	0.200	0.31	0.063	0.068	0.165	0.010	4.590
27	S	1:75	0.192	3.24	0.200	0.36	0.104	0.105	0.232	0.024	3.729
28	S	1:75	0.194	1.55	0.200	0.28	0.062	0.072	0.155	0.009	3.565
29	S	1:75	0.241	1.87	0.300	0.49	0.063	0.052	0.203	0.014	3.232
30	S	1:75	0.243	3.24	0.400	0.64	0.043	0.064	0.124	0.055	3.652
31	S	1:75	0.201	1.87	0.000	0.07	-0.001	0.010	2.480	0.015	0.488
32	S	1:75	0.206	3.24	0.000	0.12	-0.006	0.023	2.640	0.068	0.069
33	S	1:75	0.192	1.87	0.400	0.50	0.014	0.024	0.066	0.014	3.384
34	S	1:75	≈0.20	3.24	0.100	-	0.069	0.079	0.201	0.006	2.682
34a	ST	1:75	≈0.20	3.24	0.1 to -0.1	-	0.074	0.081	0.210	0.002	2.642

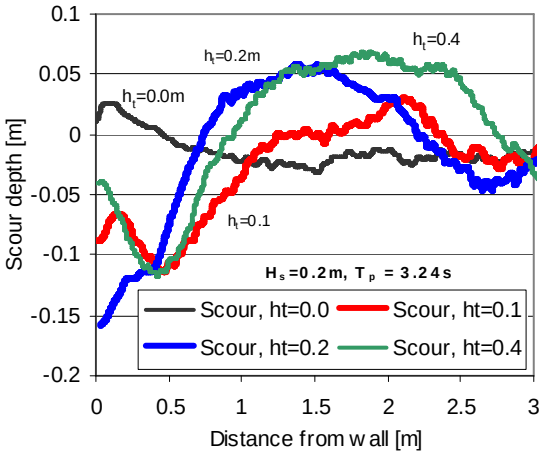

Figure 2. Bed level changes after tests 4, 7, 11 and 12

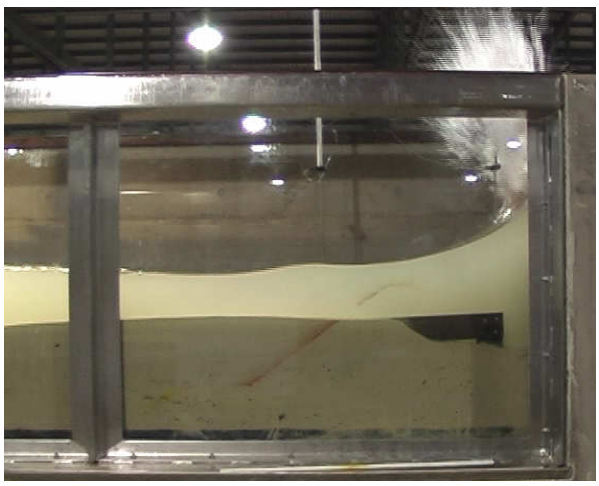

Figure 3. Wave breaking against a vertical wall. Metre stick gives scale

VII. EFFECT OF BEACH SLOPE

Four pairs of tests were performed where the same incident wave height, wave period, water depth and structure were used but in the first case the initial beach profile was at 1:30 while in the second case the initial beach slope was 1:75. The four pairs of tests were:

- 2 and 15 (H_{si}=0.195m, T_p=1.87s and h_t=0.20m);
- 4 and 16 (H_{si}=0.195m, T_p=3.24s and h_t=0.20m);
- 5 and 18 (H_{si}=0.194m, T_p=4.58s and h_t=0.20m);
- 11 and 19 (H_{si}=0.216m, T_p=3.24s and h_t=0.40m).

The scour depths for the 1:75 beach slope are plotted against the scour depths for the 1:30 beach in Fig. 4, which shows the toe scour depths and the maximum scour depths. It is clear that the 1:75 beach slope gave much lower scour depths than the 1:30 beach slope. Best-fit straight lines through the origin gave toe scour depths in the 1:75 beach as 52% of those in the 1:30 beach, while maximum scour depths were 75% of those in the 1:30 beach. The reason for this is believed to lie in the way the waves broke on the beach in front of the seawall.

The waves tended to break as spilling breakers on the 1:75 beach, where for the 1:30 case there were more breakers plunging onto the seawall causing turbulent jets to reach the seabed, resulting in scour.

VIII. BED LEVEL CHANGES FOR A SLOPING WALL

Bed level changes (final – initial elevation) at the end of Tests 32, 27 and 30 (i.e. after 3,000 peak wave periods) are provided in Fig. 5. All the tests were performed with a 1:2 (V:H) smooth sloping seawall. Negative values represent scour, while positive values represent accretion. These three tests had the same initial bed profile, wave period (T_p=3.24s) and similar offshore incident wave height (H_s=0.19m to 0.24m) but different water depths (h_t=0.0m, 0.2m and 0.4m respectively). A comparison has been drawn between these three tests as they resulted in very different breaking wave conditions at the wall and hence different bed profiles.

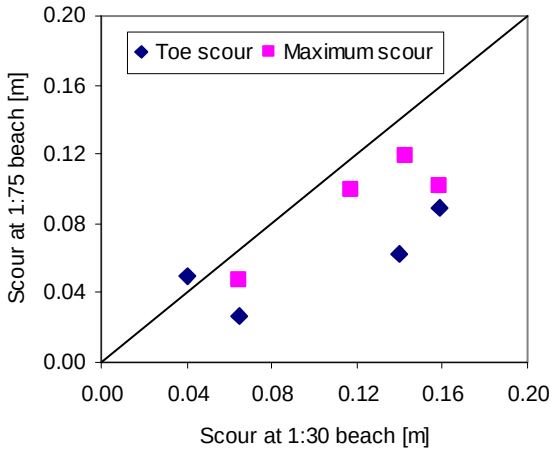

Figure 4. Scour depths in a 1:75 beach versus scour depths in a 1:30 beach

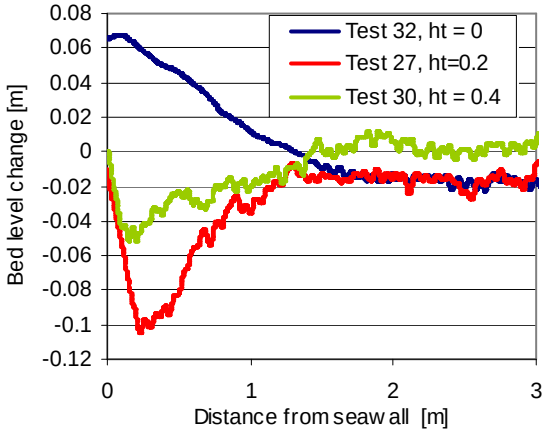

Figure 5. Bed level changes in front of a 1:2 sloping wall

The distance from the seawall is taken as the cross-shore distance from the point where the seawall emerged from the initial screeded bed profile. Test 32, with an initial toe depth of 0.0m again showed accretion. The largest scour depth again occurred for a toe depth of 0.2m (Test 27) while the scour depth for the higher toe depth of 0.4m (Test 30) was again lowered. In each of the latter two cases the initial part of the bed profile follows the line of the sloping seawall. Minor differences between the bed level changes from Tests 27 and 30 where both tests measured the sloping seawall are due to minor differences in the initial bed levels and to some small sand ripples that were left on the seawall at the end of the tests.

Three tests were performed with an incident significant wave height of 0.2m, peak period of 3.24s and water depth at the toe of 0.20m. These were Test 4 (vertical wall, 1:30 slope, S_t = 0.158m, S_{max} = 0.158m), Test 16 (vertical wall, 1:75 slope, S_t = 0.089m, S_{max} = 0.102) and Test 27 (sloping wall, 1:75 slope, S_t = 0.104m, S_{max} = 0.105m). This shows that reducing the initial beach slope reduced the toe and maximum scour depths. Changing the seawall from a vertical to a 1:2 slope increased the scour depths slightly. The differences between using a sloping and vertical seawall are investigated further in the next section.

IX. VARIATION IN SCOUR DEPTH WITH WALL SLOPE

Four pairs of tests were performed where the same incident wave height, wave period and water depth were used but in the first case a vertical wall was present while in the second case a sloping wall was present. In all cases an initial bed slope of 1:75 was used. The four pairs of tests were:

- 15 and 26 (H_{si}=0.20m, T_p=1.87s and h_t=0.20m);
- 16 and 27 (H_{si}=0.20m, T_p=3.24s and h_t=0.20m);
- 14 and 29 (H_{si}=0.26m, T_p=1.87s and h_t=0.30m);
- 19 and 30 (H_{si}=0.23m, T_p=3.24s and h_t=0.40m).

The sloping wall scour depth is plotted against the vertical wall scour depth in Fig. 6, for the scour depth at the structure toe and the maximum scour depth. The diagonal line plotted is the line of equivalence. Fig. 6 shows that for the four cases tested the scour depths were not, on average, reduced by replacing a vertical seawall with a 1:2 sloping seawall. This runs contrary to many

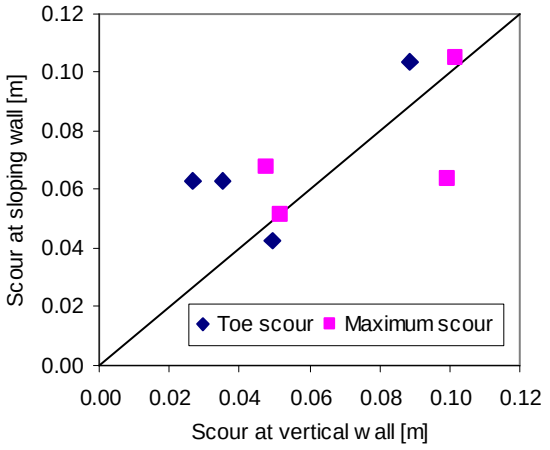

Figure 6. Scour depths at sloping wall versus scour depths at vertical wall. Diagonal line is line of equivalence

people's expectations [1] that reducing the wall slope reduces the scour depth as it reduces the reflection coefficient.

As with a vertical wall the scour depth reached partly depends on the way the wave runs down the seawall slope and interacts with the following wave. Deep scour depths appear to correlate well with wave run-down reaching the structure toe, which continued as a 1:2 slope under the beach.

X. Variation in Scour Depth with Relative Water Depth

Fig. 7 shows the variation of relative scour depth, S/H_{si} with relative toe depth, h_t/L_p where $L_p = gT_p^2/(2\pi)$ is the deep water linear theory wavelength for the wave peak period, T_p at the toe depth h_t. Fig. 7 (top) shows the scour depth at the toe, S_t/H_{si} while Fig. 7 (below) shows the relative maximum scour depth, S_{max}/H_{si}. Fig. 7 shows the highest relative scour depth occurring for relative toe depth of $h_t/L_p \approx 0.01$ in both cases.

The trend of decreasing relative scour depths with increasing relative depth (for $h_t/L_p > 0.012$) fits with the form of the scour prediction formulae devised in [4] and [9] where measurements were made within this range. The trend of increasing relative scour depths for increasing relative depth (for $h_t/L_p < 0.012$) fits with the form of the scour prediction formulae devised in [3] where experiments showed increasing relative scour depths for $h_t/L_p \leq 0.015$. Some authors, such as [16] had considered that the variation of scour depth with relative depth in [3] ran contrary to expectations and other scour formulae.

These tests have reproduced the form of the results in [3] within the expected range. This illustrates the fact that scour occurs by different mechanisms in different hydrodynamic regimes. The different scouring mechanisms should not be expected to exhibit the same variation in scour depth with relative water depth. These tests have helped to reconcile the approaches of [3], [4] and [9].

Fig. 7 (top) shows that accretion occurred for the lowest and in one case for the highest relative water depths. Accretion occurred at the toe of the vertical structure for $h_t/L_p \approx 0$ due to swash zone processes. At high relative

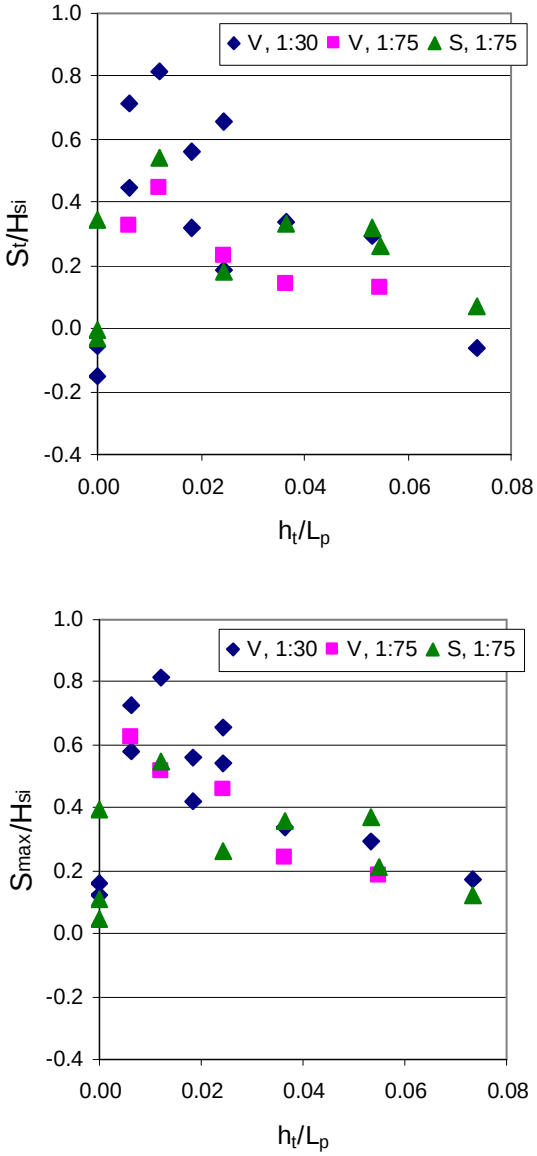

Figure 7. Variation of relative toe scour depth (top) and maximum scour depth (below) with relative toe depth

depths the lack of wave breaking resulted in a scouring pattern dominated by streaming and similar in form to those in [9]. In these cases accretion at the toe of the structure can occur.

Fig. 7 illustrates the differences between maximum and toe scour depths, which are shown over the same ranges and at the same scale to aid comparison. Maximum scour depths are all positive and are always larger than or equal to the toe scour depth. The maximum relative scour depth recorded was $S/H_s = 0.82$.

XI. Variation in Scour Depth with Iribarren Number

The observed dependency of the scour depth on the form of wave breaking on the structure indicates that there might be a relationship between scour depth and Iribarren number [17] (or surf similarity parameter as it is also known) defined in Equation 6 and including the beach slope, $\tan(\alpha)$.

$$\mathrm{Ir} = \frac{\tan(\alpha)}{\sqrt{H_{si}/L_p}}. \qquad (6)$$

On a uniformly sloping beach without a seawall the breaker type has been categorized as spilling for Ir < 0.5 and plunging for 0.5 < Ir < 3.3 [18] although there is no abrupt limit from one breaking state to the other for irregular waves. In this case the wave breaking in front of the structure was heavily influenced by the reflections from the structure (with reflection coefficient in excess of 0.8, see Table II). This has resulted in waves plunging onto the seawall for Iribarren numbers less than 0.5. Fig. 8 shows the variation of relative scour depth with Iribarren number for toe scour (top) and maximum scour (bottom).

There is a stronger apparent link between the relative maximum scour depth and Iribarren number than there is between the toe scour depth and the Iribarren number. A number of simple best-fit curves were calculated to show the link between relative maximum scour depth and Iribarren number. The simple linear fit given in (7) had the equal lowest mean absolute error of 0.134.

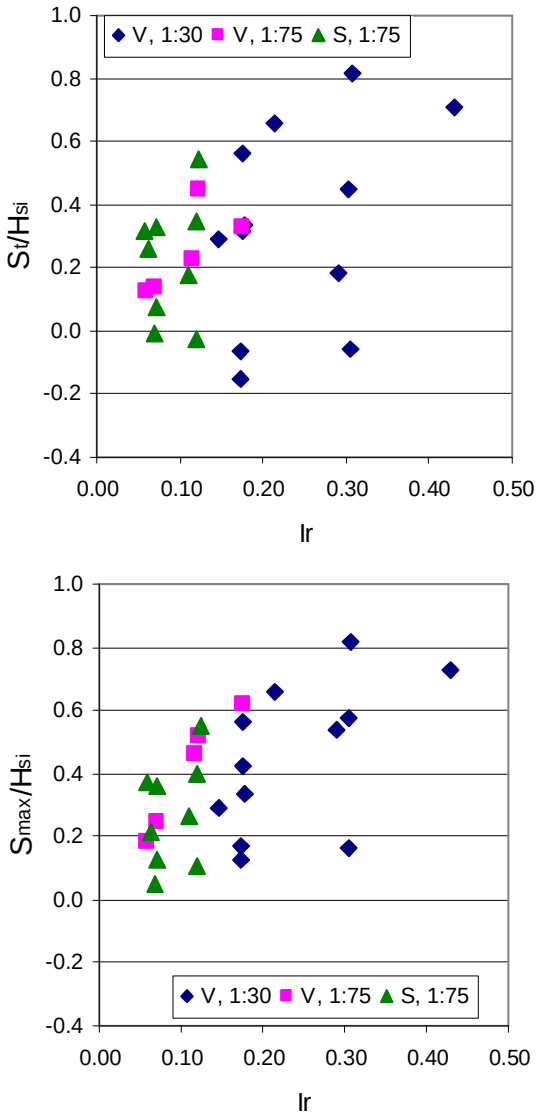

Figure 8. Variation of relative scour depth with Iribarren number for toe scour (top) and maximum scour (below)

$$\frac{S_{max}}{H_{si}} = 1.30 \times \mathrm{Ir} + 0.169. \qquad (7)$$

However, there is a considerable variation in scour depths for similar values of Iribarren number. For example Tests 4, 7, 11 and 12 all have Iribarren numbers between 0.29 and 0.31 but have relative maximum scour depths between 0.16 and 0.82. All four tests have incident significant wave heights between 0.194m and 0.217m, peak periods of 3.24s and were performed with a vertical seawall and an initial beach slope of 1:30. The difference lies in the toe depth, which governs where the seawall is in relation to the position waves start to break and hence which hydrodynamic processes dominated. See section VI for a discussion of these tests and Fig. 2 for their final bed profiles.

XII. Variation of Relative Scour Depth with Iribarren Number and Relative Toe Depth

Section X and XI have shown how scour depths vary with relative depth and Iribarren number. Fig. 9 shows relative scour depth plotted against relative toe depth, with the data arranged into three ranges of Iribarren number:

- Ir < 0.08;
- 0.1 < Ir < 0.2; and
- Ir > 0.2.

Fig. 9 shows that for any given relative depth, h_t/L_p, the greatest scour depths tend to occur for the larger Iribarren numbers. The trend appears more visibly obvious for the maximum scour depth than for the toe scour depth. This opens up the possibility of developing a scour predictor that is a function of relative toe depth and Iribarren number.

XIII. Ranges of Parameters and Logical Limits to Scour Depth at High and Low Toe Depths

The tests performed at HR Wallingford were within the following ranges:

1 $0.000 \le h_t/L_p \le 0.073$;
2 $0.059 \le \mathrm{Ir} \le 0.430$;
3 $0.00 \le h_t/H_{si} \le 2.08$;
4 $0.006 \le H_{si}/L_p \le 0.052$;

Moreover, not all sections of these ranges were covered equally. Therefore, as with any set of experimental results, any extrapolation outside these limits (and for some cases within these limits) carries a risk. Nevertheless, some limits can be placed on the expected behaviour due to our understanding of the physical processes involved. If the beach extends above the maximum runup limit for a particular seastate, the waves will not reach the seawall so the scour depth at the wall is expected to be zero. Note however, that wave activity seawards of the beach toe may cause scour that may, in time, extend to the seawall toe.

At the other extreme of very deep water the wave orbital velocity will tend towards zero and again no scour would be expected to occur. For relatively deep water and low (or flat) bed slopes accretion also occurs at the seawall for suspended load sediment transport [9].

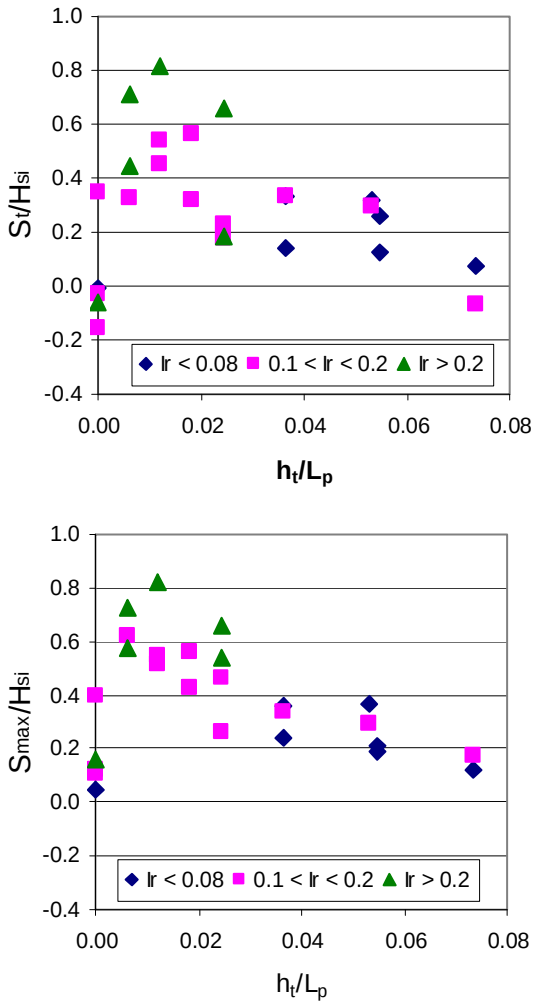

Figure 9. Variation of relative scour depth with relative toe depth for toe scour (top) and maximum scour (bottom)

XIV. Modelling of Tidal Half Cycle

Measurements of toe scour at seawalls in the inter-tidal zone [19, 20, 21] show that scour holes can often form and refill within a single tide, leaving the beach level after the event similar to, or the same as, the beach level before the event. The full extent of such events cannot be determined from beach profiles.

Test 10 modeled a half tidal cycle using bursts of 300 peak wave periods at a series of discrete water levels, starting at 0.05m above the intersection of the vertical seawall and the initial 1:30 bed profile. The water level was then increased in steps of 0.05m to 0.30m before decreasing in steps of 0.05m to a level of -0.10m. Two additional bursts were then added, at levels of -0.08m and -0.09m to see if more infilling of the scour hole would occur.

The same offshore wave conditions were used for all water levels, with a target significant wave height of 0.20m, and spectral peak period of T_p = 1.87s. The gains on the wavemaker and the wave absorption system were tuned to the water depth before running each burst of waves to ensure that the wave conditions were as uniform as possible.

The bed level change profiles from Test 10 are shown in Fig. 10, which is split into three sections. Fig. 10a shows the scour profiles from the rising water levels. The scour depth at the wall increased up until 1200 waves (with a water depth at the toe of 0.20m above the initial bed level) then decreased as the water level rose to 0.30m after 1800 waves. This is compatible with the results from Section VI and the observations that the greatest scour depths are achieved when waves break directly onto the seawall. This was observed to occur at a depth of 0.20m than at higher or lower depths. The position of the maximum accretion (within 1.5m of the seawall) moves offshore from the seawall as the water depth and hence wavelength increases.

Fig. 10b shows the scour profiles from the greatest water depth of 0.30m (the last profile shown in Fig. 10a) down to a depth of 0.05m, after 3300 peak wave periods. Here the scour depth at the wall did not increase noticeably as the water level dropped from 0.30m to 0.20m, but it did increase as the water depth dropped from 0.20m to 0.10m. At the same time the location of maximum accretion (within 1.5m of the seawall) moved towards the seawall and decreased in elevation as the water level dropped, until after 3300 waves there was no accretion within 1.5m of the wall and the whole section of the seabed exhibited erosion. Between about 2m and 3m offshore a second area of accretion remained above the initial bed level.

Figure 10c shows the scour profiles from a water depth of 0.05m down to -0.10m then 2 after 2 further bursts of waves at -0.08m and -0.09m. At these low water levels the further offshore mound (between 2m and 3m from the seawall) became gradually washed out and the bed profiles became smoother. The toe scour in front of the seawall also started to fill in by a small amount. The water depths for the final two bursts were chosen so that the offshore mound was just exposed as it seemed to be periodic swash events over this outer mound that contributed most to the infilling.

Figure 10c shows that the nearly complete infilling of scour holes seen in the field was only partially reproduced in the medium scale laboratory tests. Scale effects and the discrete representation of changes in water level as well as the longshore non-uniformity of bed levels are all likely to have contributed to the differences between the results in the laboratory and measurements made in the field.

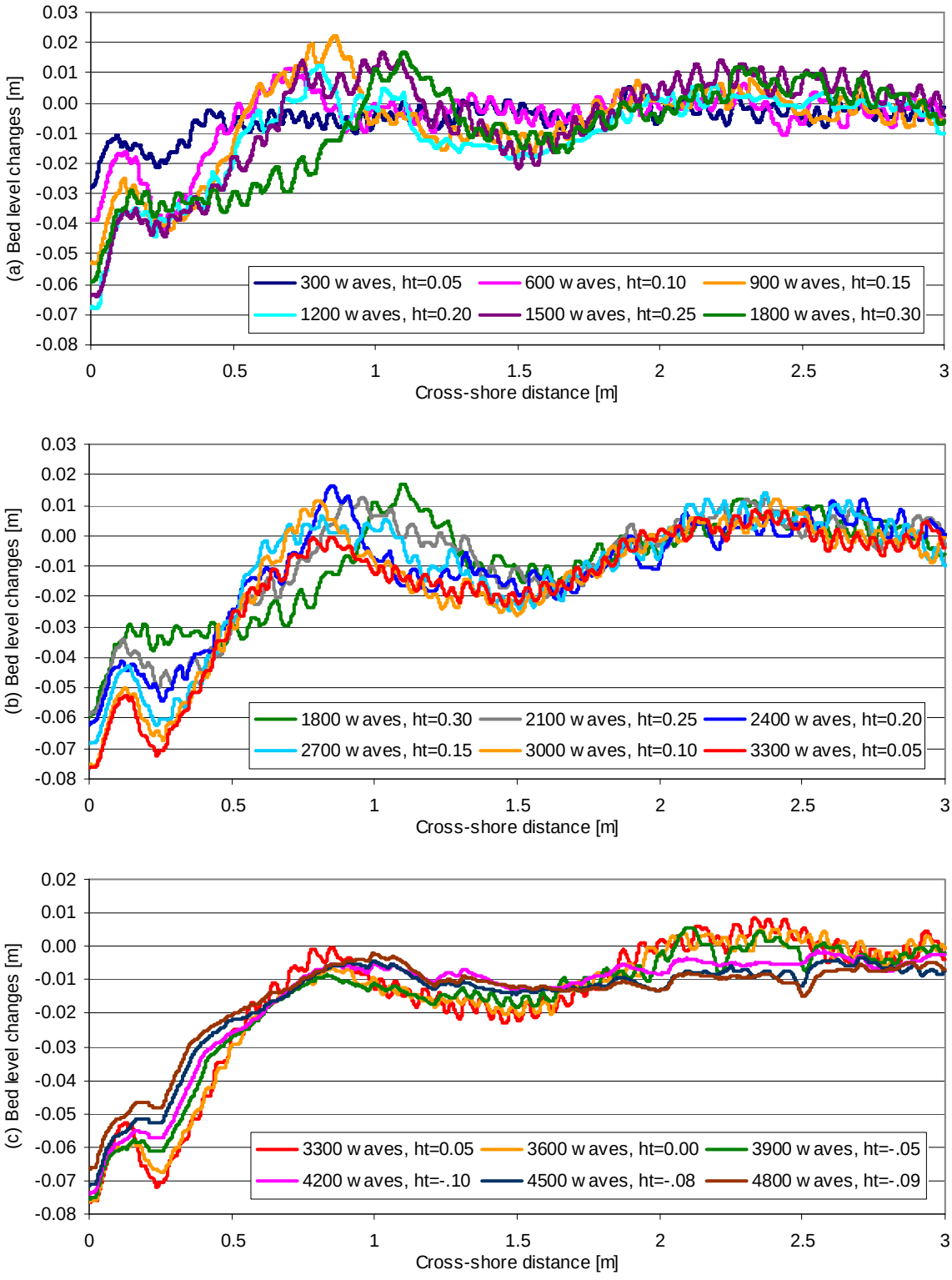

Figure 11. Bed level changes (from initial bed level) after a series of bursts of 300 waves at different levels to simulate half a tidal cycle

XV. SUMMARY AND CONCLUSIONS

A set of thirty-four medium-scale laboratory tests of toe scour at seawalls has been performed. The tests were all intended to generate suspended sediment transport within the laboratory flume and suspension was often observed during the tests. The tests were all carried out with irregular waves. The results are complementary to other medium-to-large scale laboratory tests that also used irregular waves, particularly 2 tests of [9], 1 of [13] and 18 of [3].

Two scour depths were determined: S_t the scour depth immediately adjacent to the toe of the structure and S_{max} the maximum scour depth measured at any point in the test section. Both are of interest in considering the stability of coastal structures. The presence of a deep scour hole at the toe of a structure may allow fill material to escape under the seawall, leaving a void behind the seawall that may cause its sudden collapse. A deep scour hole at the toe of the structure also means that the toe may slide outwards – another form of failure. A scour hole away from the structure toe is also of interest as its presence may shorten any slip surface, thereby increasing the risk of structural failure by sliding.

The relative scour depth was found to depend on the relative water depth at the structure toe, h_t/L_p and the Iribarren number (6). It was relatively insensitive to the slope of the seawall, with a 1:2 slope giving similar scour depths to a vertical seawall.

An attempt was made to reproduce the formation and in-filling of a scour hole during a half tidal cycle, as observed in the field. Only partial infilling occurred, probably as a result of scale effects and the discrete changes in water level made during the test.

REFERENCES

[1] J. Sutherland, A. Brampton, G Motyka, B. Blanco and R. Whitehouse, Beach lowering in front of coastal structures. Research Scoping Study. Report FD1916/TR1, 2003. INTERNET: available from http://sciencesearch.defra.gov.uk/ (page accessed 05/04/06).

[2] B.M. Sumer and J. Fredsøe, The mechanics of scour in the marine environment. World Scientific, 2002, pp.536.

[3] J.E. Fowler Scour problems and methods for prediction of maximum scour at vertical seawalls. Technical Report CERC-92-16, U.S. Army Corps of Engineers, Waterways Experiment Station, 3909 Halls Ferry Road, Vicksburg, MS, 1992.

[4] B.M. Sumer and J. Fredsøe. Experimental study of 2D scour and its protection at a rubble-mound breakwater. Coastal Engineering, vol 40, pp. 5-87, 2000. Elsevier Science.

[5] I. Irie and K. Nadaoka, Laboratory reproduction of seabed scour in front of breakwaters. *Proc 19th Int Conf on Coastal Engineering*, Houston. ASCE, pp. 1715-1731, 1984.

[6] J.W. Kamphuis, On understanding scale effect in coastal mobile bed models. In *Physical Modelling in Coastal Engineering*, AA Balkema, Rotterdam, pp. 141-162, 1985.

[7] R.G. Dean, Physical modelling of littoral processes. In *Physical Modelling in Coastal Engineering*, AA Balkema, Rotterdam, pp. 119-139, 1985.

[8] S.A. Hughes and J.E. Fowler, *Midscale physical model validation for scour at coastal structures*. Technical Report CERC-90-8, US Army Corps of Engineers, CERC, Vicksburg, Miss., 1990.

[9] S-L. Xie, *Scouring patterns in front of vertical breakwaters and their influence on the stability of the foundations of the breakwaters.* Department of Civil Engineering, Delft University of Technology, Delft, The Netherlands, 61p. 1981.

[10] R.L. Soulsby, *Dynamics of Marine Sands.* Thomas Telford, London. ISBN 07277 2584 X, 1997.

[11] P.D. Komar and M.C. Miller, Sediment threshold under oscillatory water waves. *J. Sediment. Petrol.* Vol 43, pp. 1101-1110, 1974.

[12] N.C. Kraus, J.M. Smith and C.K. Sollitt, SUPERTANK Laboratory Data Collection Project, *Proc 23rd Int Conf on Coastal Engineering*, American Society of Civil Engineers, pp 2191 – 2204, 1992.

[13] N.C. Kraus and J.M. Smith (editors), *SUPERTANK Laboratory data collection project. volume 1: Main text*. Technical report CERC-94-3, US Army Corps of Engineers Waterways Experiment Station, Coastal Engineering Research Center, Vicksburg. Miss., 1994.

[14] HR Wallingford, *Design of physical model scour tests*. HR Wallingford Technical Note CBS0726/02, 2005.

[15] HR Wallingford, *Medium scale 2D physical model tests of scour at seawalls*. HR Wallingford Technical Note CBS0726/06, 2006.

[16] W.G. McDougal, N. Kraus and H. Ajiwibowo, The effects of seawalls on the beach Part 2: numerical modeling of SUPERTANK seawall tests. *Journal of Coastal Research* Vol 12(3) pp. 702 – 713, 1986.

[17] J.A. Battjes, Surf similarity. *Proceedings of the 14th Int Conf on Coastal Engineering*, ASCE, pp. 466-480, 1974.

[18] J.M. Smith, Surf zone hydrodynamics. Part 2, Chapter 4 of the *Coastal Engineering Manual*, USACE EM 1110-2-1100, 2003.

[19] J. Sutherland and A.M.C. Pearce, *Beach lowering and recovery at Southbourne (2005*). HR Wallingford Technical Note CBS0726/01, 2006.

[20] HR Wallingford, *Scour monitor deployment at Blackpool*. HR Wallingford Technical Note CBS0726/04, 2005.

[21] A.M.C. Pearce, J. Sutherland, G. Müller, D. Rycroft and R.J.S. Whitehouse, Scour at a seawall – field measurement and physical modeling. Paper accepted for *30th Int Conf Coastal Engineering 2006*.

Influence of Grain Size on the Direction of Bed-Load Transport on Transverse Sloping Beds

A.M. TALMON [*], J.-U. WIESEMANN [**]
[*] Delft Hydraulics, P.O. BOX 177, 2600 MH Delft, the Netherlands
[**] Institute of Hydraulic and Water Resources Engineering, Darmstadt University of Technology
Rundeturmstraße 1, 64283 Darmstadt, Germany

There is an intimate link between sediment transport and 3D-scour. In particular the role of transverse bed slope on the direction of sediment transport is determining 3D bed topographies. Hydraulic conditions, particle diameter and scale of the flow are important to the transverse slope effect. The present analysis focuses on the mechanical balance of particles travelling over ripples and dunes (grain size range: 0.09 to 0.9 mm). Fluid shear stresses on the grains, the average travelling height of particles in the turbulent boundary layer and drag coefficients of particles are considered. It is concluded that the transverse slope effect for fine grains is subject to viscosity, while for coarse grains it is not. It is shown how grain size is to be accounted for in the mathematical formula for transverse bed slope.

I. INTRODUCTION

The direction of bed-load transport over transverse sloping bed plays an important role in the calculation of the morphology of rivers, Struiksma et al. 1985. On a sloping bed, bed-load transport experiences a gravity component parallel with the bed surface, van Bendegom 1947. This is brought about by mechanical contact with the bed surface.

If this transverse bed slope effect is modelled too strong the calculated bed topographies will be flattened. If modelled too weak an unrealistic steep variation of bed topography will result. So calculated depths of 3D-scour holes, channel systems and hypsometry of estuaries will turn out to be wrong. Recent Delft3D calculations for Westerscheldt revealed such difficulties. It should be realized that a factor two difference in transverse slope coefficient will double the amplitude of calculated bed-topography variations.

World wide, the number of true data-points for transverse slope effect is worrying small (about 15, until Univ. Darmstadt commenced testing three years ago). Only dedicated well executed bed levelling experiments in straight flumes, see Figure 1, classify as true data points. Under such conditions one can focus on sediment transport processes without complications by 3D flow effects (secondary flow).

The force balance of transport in longitudinal and transverse direction specifies the actual sediment transport direction.

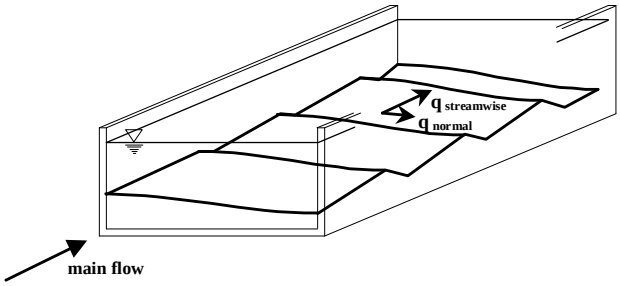

Figure I-1: Sand bed in bed-levelling experiment. For prolonged flow the bed levels horizontally.

The forces affecting a grain on a transverse bed slope are depicted in Figure I-2. In addition to the fluid drag force, the gravity force and the inclined bed turn the resulting force in downslope direction.

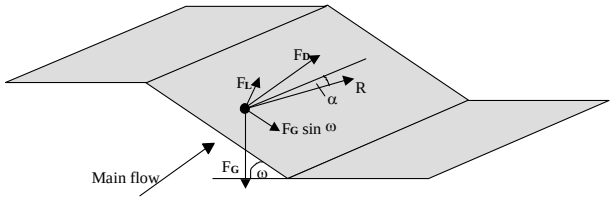

Figure I-2: Forces acting on grain on a transverse sloping bed: F_G=gravity, F_D=fluid drag, F_L=fluid lift, R=resulting force (transport direction), ω=angle transverse inclination.

In this paper it is shown that measured longitudinal and transverse bed-load transport in the laboratory, on different scales and different regimes, can be unified (fine and coarse sand). Account is given to grain stresses, the vectored force balance of particles on sloping beds, the transport velocity of bed-load and variation of drag coefficients. Discrepancies regarding the influence of grain diameter on the transverse slope effect, reported on in Talmon et al. 1995, are thus solved.

Unrightfully, the transverse slope effect has become a tuning parameter in the art of conducting numerical computations. This bad habit has to be eradicated as quickly as possible. Developers and users of mathematical models are provided an alternative by the release of these new findings.

The bed-load transport rate in transverse (***y***) direction on transverse sloping beds is modelled by:

$$q_{bed\,y} = -q_{bed\,x} G \frac{dz_b}{dy} \qquad (1)$$

with: G = transverse bed slope coefficient, q_{bedx} = bed-load transport rate in longitudinal (***x***) direction, per unit width and q_{bedy} = bed-load transport rate in transverse (***y***) direction, per unit width, z_b = bed surface level.

Longitudinal and transverse bed-load transports are governed by a mechanical balance of forces of particles traveling over the sloping bed surface. The transverse bed slope coefficient (***G***) is a function of flow conditions and grain size. In general the ***G***-value may range between 2 á 3 (theoretical maximum: from angle of repose: Engelund 1976) to 0.2 á 0.3 (smallest value, measured by Hasegawa 1981). The general accepted functional dependency is:

$$G \sim 1/\sqrt{\theta} \qquad (2)$$

with: θ = Shields parameter.

In bed leveling experiments the transverse slope parameter is determined from measured transverse transport (bed leveling rate) and measured longitudinal bed-load transport. In flume tests it is easier to measure the total transport rate than to measure the bed-load transport rate. If no distinction is made between bed-load transport and suspended-load transport the formula for transverse slope effects reads:

$$q_{bed\,y} = -q_{totalx} G_{total} \frac{dz_b}{dy} \qquad (3)$$

with: G_{total}= transverse bed slope coefficient to total load, q_{totalx} = total transport rate.

Though, from a mechanical point of view, suspended load is not involved in the transverse slope process, Eq.(3) is useful to compare results of different tests.

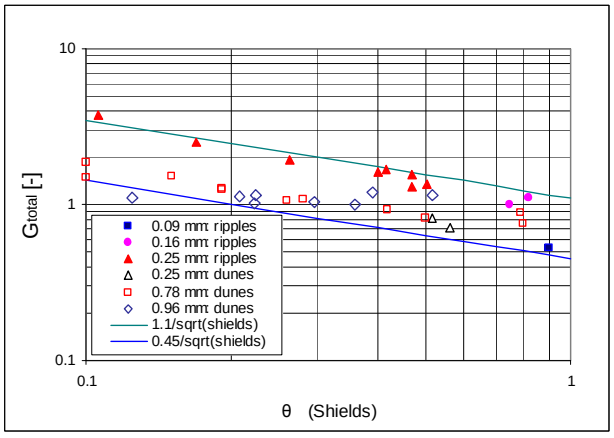

Figure I-3: Transverse slope parameter, related to total transport, for fine to coarse sands in Delft and Darmstadt bed levelling experiments as a function of Shields parameter.

Results of bed-leveling experiments in Darmstadt and Delft, with G calculated on basis of total load transport (Eq. 3) are compiled in Fig. I-3. These experiments are described in Talmon et al. 1995, Wiesemann et al. 2004 and Wiesemann et al. 2006ab.

Figure I-3 shows that the transverse slope parameter, based on total load, is found between two lines: $0.45/\sqrt{\theta} < G_{total} < 1.1/\sqrt{\theta}$. Fine sands of 160 and 250 µm behave different than 780 µm sand. These fine sands are found along the upper boundary. Their bed was rippled, and suspended-load occurred. For θ<0.5 their transverse slope effect is a factor two stronger than that of coarse 780 µm sand, which did not involve suspended-load transport. Amongst the fine sands of 160 & 250 µm and the finest sand of 90 µm the transverse slope effect is distinctly different (a factor of two). The transverse slope parameter of the very recently released Darmstadt 960 µm data is similar to that of 780 µm Delft data for 0.2< θ<0.4. Delft data is referenced by median grain size: d_{50}=90, 160 and 780 µm. Darmstadt data is referenced by mean grain size: d_m= 250 and 960 µm. Median grain sizes of the Darmstadt tests are d_{50}=230 and 830 µm.

The formula being employed in calculations for natural rivers is (see Talmon et al. 1995):

$$G = \frac{1}{9}\left(\frac{h}{d}\right)^{0.3} \frac{1}{\sqrt{\theta}} \qquad (4)$$

with: d = particle diameter, h = water depth, $\theta \equiv \frac{\tau}{(s-1)\rho g d}$ = Shields parameter, τ = total bed shear stress, g = gravity, s = relative density (sand 2.65), ρ = fluid density.

This is a formula based on integral parameters (water depth h and Shields parameter including form drag of bed features).

In the present contribution it is focused on processes at the surface of the bed. The formulae being employed are known from earlier studies on bed-load transport and bed slope effects (Ashida and Michiue 1972, Engelund and Fredsoe 1982, Hasegawa 1981). Numerical values of parameters are re-evaluated by considering regime influences, measured longitudinal transport and measured transverse transport.

II. DATA

Typical conditions in the Delft bed levelling experiments are summarised in Table II-1. Bed-load transport was measured by gathering sand at the end of the flume and suspended-load transport was subtracted, if present. The transverse slope parameter (***G***) was determined by the levelling rate of initially prepared transverse beds. The driving force of bed-load transport is difficult to measure. A measurable property of bed-load transport is the transport rate. The measured transverse slope parameter is shown in Figure II-1 as a function of the dimensionless transport rate of bed-load:

$$q_b^* = \frac{q_{bed\ x}}{\sqrt{(s-1)gd^3}} \qquad (5)$$

Experiments labelled T1-T11 are coarse grain, bed-load only, conditions (dunes). The experiments labelled run2, run4 and run5 are experiments involving suspended-load transport and rippled beds.

Suspension concentrations were measured by iso-kinetic sampling. Suspended load was about 50% of total transport. Examples of suspended load profiles are shown in Figure II-2. The scatter in the data points is attributed to distortion of the flow by the presence of ripples. The flow was rather shallow. The ripples typically extended about 1 cm above mean bed level.

Table II-1: Characteristic conditions Delft bed levelling experiments

Experiment	d_{50} [µm]	h [m]	U [m/s]	θ [-]
T1-T11	780	0.14-0.44	0.39-0.75	0.1-0.8
run 2	90	0.07	0.22	0.90
run 4	160	0.07	0.28	0.82
run 5	160	0.033	0.22	0.75

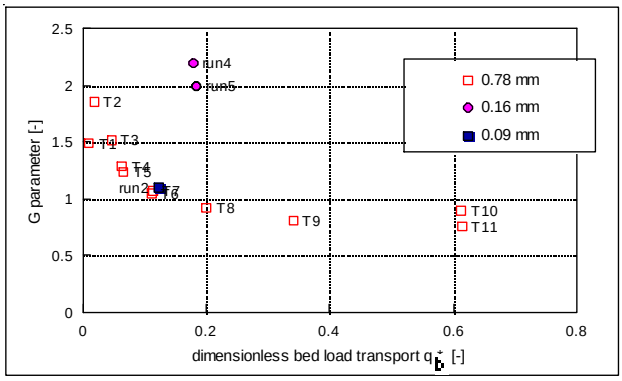

Figure II-1: Dimensionless bed-load transport and transverse slope parameter in Delft bed levelling experiments.

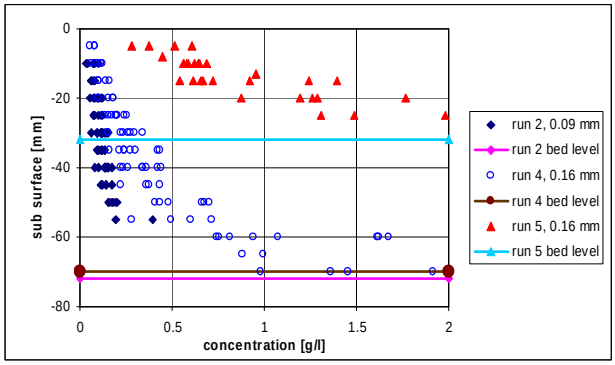

Figure II-2: Concentration profiles measured in Delft suspended load tests.

The conditions in the Darmstadt bed levelling experiments are summarized in Table II-2. The 250 µm tests had ripple covered beds, except for the two highest transport rates where dunes occurred. All 960 µm tests had dune covered beds. In both series the longitudinal transport rate was measured by gathering the sand at the end of the flume too, but there were no measurements conducted which lead to information about the suspended-load concentrations. Additionally to the measurements of a sand trap set-up the longitudinal transport rates were evaluated by considering the movement of the bed forms/dunes in the measuring section. This led to more reliable results regarding to the correlation of Shields parameter to the transport rate. To make these results comparable to the series with the fine sand a small factor was used to shift the bed-load results in the region of the measurements conducted by using the sand trap at the end of the flume. So the total amount of longitudinal transport was measured with a comparable method to the fine sand experiments but the correlation of the transport rates of the dune-experiments was increased by using the bed form-travelling method (Wiesemann et al. 2006b).

The measured transverse slope parameter (to total transport) is shown in Figure II-3 as a function of the dimensionless total transport rate. For coarse material this equals the dimensionless bed-load transport rate.

Figure II-1 shows that fine sand (90 µm) and coarse sand (780 µm) lie within a lower band of ***G***-values. Material in between, 160 µm, shows a stronger bed slope effect.

Figure II-3 shows that at the lowest transport rates, the transverse slope parameter of 960 µm sand is somewhat lower than for 250 µm sand if evaluated on basis of total transport. If 250 µm sand would have been evaluated on basis of longitudinal bed-load transport (for which no data is available), a similar trend to that shown in Figure II-1 would result, giving distinctly higher G-values for 160 and 250 µm sands.

Table II-2: Characteristic conditions Darmstadt bed levelling experiments

experiment	d_m [µm]	h [m]	U [m/s]	θ [-]
Series R0	250	0.30	0.22-0.64	0.11-0.57
Series R1	960	0.30	0.48-0.77	0.12-0.53

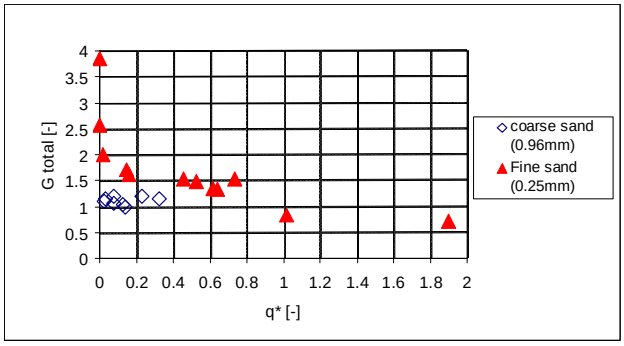

Figure II-3: Dimensionless total transport and transverse slope parameter (to total transport) in Darmstadt bed levelling experiments.

The results of all bed levelling experiments (***G*** parameter) are compared to the empirical field equation for natural rivers (Eq. 4) in Figure II-4 and Figure II-5. It is to be mentioned that the equation for natural rivers was derived from field experience in combination with results of the 780 µm data-set. Figure II-4 shows major differences between the suspended-load experiments (run4, 5 versus run2) and a major deviation of the experiments run4 and run5 from Eq. (4).

Figure II-5 shows that the Darmstadt coarse sand data, corresponds reasonable to the formula for natural rivers

Eq. (4). If the 250 μm experiments would be corrected for suspended-load transport, these points would shift upward, and the same tendency would emerge as for run 4 and run 5 shown in Figure II-4.

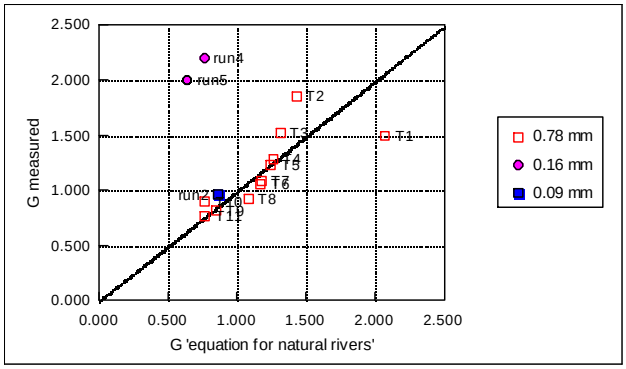

Figure II-4: Comparison of the transverse bed slope parameter for natural rivers (Eq. 4) with the results of Delft straight flume bed levelling experiments.

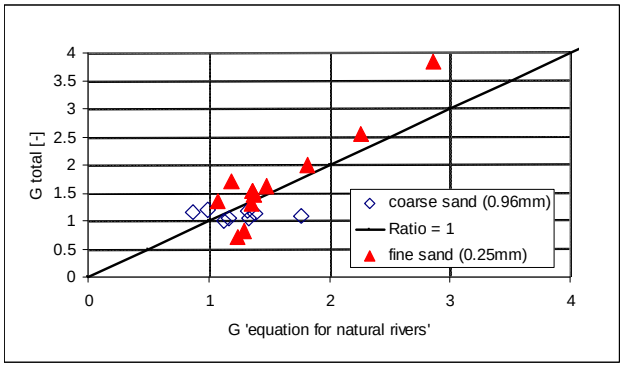

Figure II-5: Comparison of the transverse bed slope parameter for natural rivers (Eq. 4) with the results of Darmstadt straight flume bed levelling experiments (to total load).

III. FLAT BED THEORY: MATHEMATICAL MODELLING OF TRANSVERSE SLOPE EFFECTS

Bed-load transport follows from a mechanical balance of travelling bed-load particles. The employed formulas for longitudinal transport and transverse slope effect do not differ much from the mechanical approach followed by Engelund and Hansen 1967 and Ashida and Mitchieu 1972 (a description is given in Kovacs and Parker 1994). Assumptions are: 1) Mechanical processes at the bed surface determine the bed slope effect (equilibrium of forces and continuity). 2) Suspended load transport is not influenced by bed slope. 3) Time-average modelling of transport processes suffices to capture governing physics (no need for dynamic simulation of saltations). 4) Lift forces are negligible. 5) The influence of density driven flow along transverse slopes is negligible. Concentration measurements given in Talmon 1991 show that the transverse variation of concentration is small. The dimensionless transport rate of bed-load is:

$$q_b^* \equiv \frac{q_{bed\,x}}{\sqrt{(s-1)gd^3}} = \frac{\sqrt{a}}{\mu_c}(\theta' - \theta_{cr})\left(\sqrt{\theta'} - \sqrt{\theta_0}\right) \qquad (6)$$

with: $u^* \equiv \sqrt{\tau'/\rho}$ = friction velocity to the grains, μ_c= dynamic granular friction coefficient, τ' = shear stress on the grains, θ_{cr} = critical Shields parameter (at incipient erosion),

$$\theta' \equiv \frac{\tau'}{(s-1)\rho g d} = \text{Shields parameter to the grains,} \qquad (7)$$

$$\theta_0 \equiv \frac{4}{3}\frac{\mu_c}{aC_d} = \text{dynamic granular friction / fluid drag,} \qquad (8)$$

with: C_d = drag coefficient particles

$$\sqrt{a} \equiv \frac{U}{u_*} = \text{fluid velocity ratio} \qquad (9)$$

with: U = fluid velocity at particle height

Transverse bed-load transport on a sloping bed follows from a two-dimensional force balance of bed-load transport. The coefficient in the transverse slope formula is:

$$G = \frac{1}{\mu_c}\sqrt{\frac{\theta_0}{\theta'}} \qquad (10)$$

The same variables emerge in the formulae for both q_b^* and G, because the formulae stem from one force balance. The variables in these equations are: flow velocity at particle height, friction velocity, drag coefficient and dynamic friction coefficient. Appropriate values pertaining to governing flow regimes have to be established. Regimes are determined by particle Reynolds number and consideration of the average vertical position of travelling bed-load in the turbulent boundary layer.

The particle diameter is an important factor:

- In case of coarse sands bed-load travels in the buffer region of the velocity profile. The flow above the sand bed is hydraulically rough. In hydraulically rough flow the travelling height of the particles scales with the particle diameter (Ashida & Michieu 1972). In case of fine sand, the flow is hydraulically smooth and bed-load travels at the edge of the laminar sublayer. At this level the flow velocity is less.
- The drag coefficient of particles is influenced by particle diameter. The microscopic flow around coarse particles is turbulent. The flow around fines is laminar, consequently higher drag coefficients apply and vary with the particle-Reynolds number.

The average velocity difference (***U-V***= slip velocity) between the fluid and the particle is important to particle drag regime. This velocity difference follows from a balance of forces (hydrodynamic drag, submerged weight of particles, bed-grain friction):

$$U - V = U\sqrt{\frac{4}{3}\frac{\mu_c}{aC_d\theta'}} = U\sqrt{\frac{\theta_0}{\theta'}} \qquad (11)$$

with: V = particle velocity parallel with the bed.

Viscosity influences the drag of small particles. The Reynolds number of fluid drag of these particles is:

$$Re = \frac{(U - V)d}{\nu} = \sqrt{\frac{4}{3}\frac{\mu_c}{C_d}d^{*3}} \qquad (12)$$

with:

$$d^* = d\left(\frac{(s-1)g}{\nu^2}\right)^{1/3} \qquad (13)$$

Particle and fluid properties are accommodated in the dimensionless particle diameter d^*. Fluid and flow properties are accommodated in the drag coefficient C_d. At Re < 1, the Stokes regime, the drag coefficient is given by C_d = 24/Re. At high Reynolds number the C_d is constant: for a smooth sphere, at high Reynolds: C_d = 0.4, for irregular spheres at high Re: C_d = 1.25, Chien (1994). The transitional and Stokes regimes, which are applicable to our conditions, might be described by one formula (Shiller & Naumann 1933):

$$C_d = \frac{24}{Re}(1 + 0.15\,Re^{0.687}) \text{ , valid for } Re<800 \qquad (14)$$

Examples of numerical values are: C_d = 24 at Re = 1 (laminar regime), C_d = 4.15 at Re = 10 (transitional regime), C_d = 1.09 at Re = 100 (transitional regime). Combining Eq. (12) and Eq. (14) leads to the conclusion that the 90 μm and 160 μm sands of the Delft experiments are within Stokes range. Reynolds numbers are respectively Re ~0.15, and Re ~1. The 780 μm sand is within the turbulent drag regime.

Another parameter is the fluid velocity (U) at average particle transport height. The average transport height of particles was assumed proportional to particle diameter:

$$z = nd \text{ , } (n = 2, \text{ Ashida Michieu}) \qquad (15)$$

Particle diameters are non-dimensionalised the same way as the profile coordinate of turbulent boundary layer flow:

$$d^+ = \frac{u^* d}{\nu} \quad , \quad z^+ = \frac{u^* z}{\nu} \qquad (16)$$

At a transport level of n=1 á 2 the 90 μm sand will be transported in the laminar sublayer (z^+<11) region; because d^+= 1.2 at θ'= 0.15 which is a typical value. The 160 μm sand will also be transported in the laminar sublayer region: d^+= 3.2 at θ'= 0.15. The 780 μm sand is transported in the logarithmic fully turbulent (z^+>70) region: d^+=39 á 137 , at 0.05<θ'<0.15.

At 960 μm the sand will be transported in the fully turbulent region, because all the different runs have values of d^+ which are larger than 70. The 250 μm sand lead to values which are in the transitional buffer region. Only two experiments in the R0 series, in which dunes were present, might lead to larger values in the fully turbulent region.

In Section IV the appropriate numerical values for C_d and $a = (U / u^*)^2$ will be identified by consideration of the above theory and available data.

IV. Transverse Bed Slope Effect in Ripple and Dune Regime

To calibrate the parameters-values in the transverse slope theory, it is noticed that longitudinal and transverse transports are governed by the same fundamental physical processes. This means that sediment transport in both transport directions is governed by one and the same bed-load transport model. It must be possible to obtain fair agreement between available data on both transports and mathematical formulation.

For longitudinal bed-load transport a generalized form of Eq. (6) is used, with a multiplication factor A to accommodate typical conditions in ripple and dune regime:

$$q_b^* = \frac{q_{bed\,x}}{\sqrt{(s-1)gd^3}} = A\frac{\sqrt{a}}{\mu_c}(\theta_{eff} - \theta_{cr})\left(\sqrt{\theta_{eff}} - \sqrt{\theta_0}\right) \qquad (17)$$

in which: A = constant to accommodate bed form properties. θ_{eff} = effective Shields number to the grains. The formula for the transverse slope coefficient is generalized to:

$$G = B\frac{1}{\mu_c}\sqrt{\frac{\theta_0}{\theta_{eff}}} \qquad (18)$$

with: B = constant to accommodate bed form properties.

Bed-load transport processes are governed by fluid mechanical stresses acting on the grains. In case of dunes, the bed shear stress at the top of the dune is calculated by assuming a fully developed turbulent flow above the dune top. The bed shear stress distribution over the face of the dune is calculated on the assumption of similarity of dune-shape profiles, Talmon 1997. Bed-load transport in longitudinal and transverse direction is

calculated by integration of shear stress over one dune. The grain shear stress at the top of the dune is substituted for the effective Shields number in Eq. (17) and (18): $\theta_{eff} = \theta'_{top}$ Integration of bed-load transport in longitudinal and transverse direction over dune profile gives theoretical values of A=2/3 and B=1.05. The grain shear stress at the top of the dune is then calculated from $k_s = 3 * d_{90}$, local water depth above the dune and flow velocity above the dune. In the analysis of the 780 μm T1-T11 experiments, measured dune height were used to determine θ'_{top}. For field conditions the dune height predictor by van Rijn might be applied.

In the ripple regime such a type of integration method is not applicable because the flow is different and saltation lengths are greater. The shear stress at the grains is calculated from $\theta_{eff} = \theta' = 0.2\,\theta$ for the 90 and 160 μm experiments. This relation was established by evaluation of realistic parameter values for the variables in Eq. (17) and Eq. (18). The overall Shields value was calculated from the measured hydraulic energy gradient. A quasi flat bed is assumed by default: A=1 and B=1.

Of these Delft experiments, first the coarse grain 780 μm experiments were analyzed. At $\sqrt{\alpha} = 6.8$[1] and C_d = 0.8 a fair agreement of longitudinal transport and transverse slope parameter is obtained, see Figure IV-1, is employed. For the fine sands investigated, a suitable ratio of the local flow velocity and friction velocity u_* is $\sqrt{\alpha} = 2.5$. For 90 and 160 μm sand values of C_d = 6 respectively C_d =15 apply well. In the average C_d value of bed-load, account was made for the dynamical character of bed-load transport. The velocity difference with the fluid is larger than the theoretical value, because of saltation of the grains. Consequently in the laminar drag regime, on the average, smaller C_d values have to be employed than theoretically because the actual Re particle number is larger. For coarse grains C_d =0.8 value is appropriate (non-spherical particle in turbulent drag regime). An overview of employed parameter values in calculations is given in Table IV-1.

The Darmstadt 250 data can not be analysed similarly because the suspended-load transport was not measured. So there is no information on longitudinal bed-load transport.

In the 960 μm experiments dunes were present. The relevant Shields parameter is nevertheless calculated from roughness height $k_s = 3 * d_{90}$ and mean flow depth. This series leads to A=0.72 and B=1.06. The results are shown in Figure IV-2. The parameters are comparable to those in the 780 μm T1-T11 experiments, even though this time mean flow depth and mean flow velocity were used.

[1] this is smaller than Kovacs and Parker 1994 who use $\sqrt{\alpha} = 11$.

Table IV-1: Overview of parameter values in analysis of transverse bed slope influence.

model parameters	90 μm	160 μm	780 μm	960 μm
d^*	2.13	4.05	19.9	24.1
θ_{eff}	0.17	0.15	0.02-0.14	0.04-0.10
d^+	1.5	3.2	12.6 - 90	69.5-111
μ_c	0.3	0.3	0.4	0.3
$\sqrt{\alpha}$	2.5 (z^+=2.5)	2.5 (z^+=2.5)	6.8 ($z=k_s/2$)	7.8
C_d	6	1.5	0.8	0.8
Re	0.8	4.2	72	83.8
θ_0	0.0107	0.042	0.014	0.01
θ_{cr}	0.12	0.066	0.029	0.03

Measured and calculated longitudinal bed load transport of Delft tests is shown in Figure IV-3 (including all suspended load experiments of Talmon 1992 in 180° bend flume).

Measured and calculated transverse slope parameter of Delft tests are shown in Figure IV-4. This graph shows that fair agreement between theory and measurement is achieved when regime influences for fine and coarse sand are accounted for.

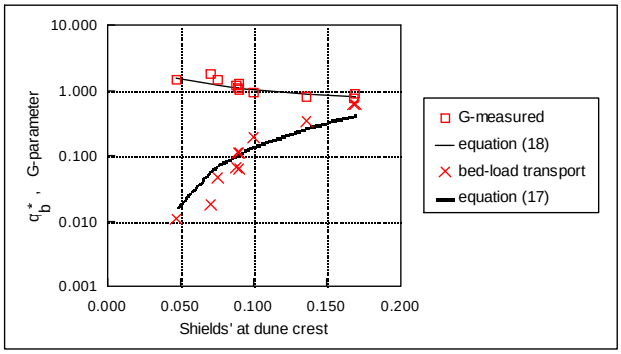

Figure IV-1: Bed-load transport and transverse slope parameter in dune-regime: 780 μm sand data and calculations by Eq.(17) and Eq.(18).

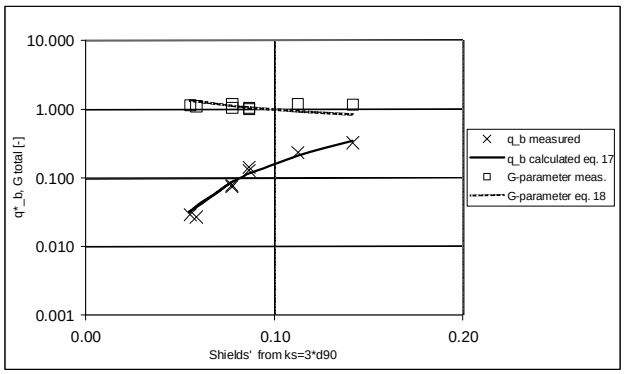

Figure IV-2: Bed-load transport and transverse slope parameter in dune-regime for 780 μm series R1: laboratory data of Wiesemann and calculations by Eq.(17) and Eq.(18).

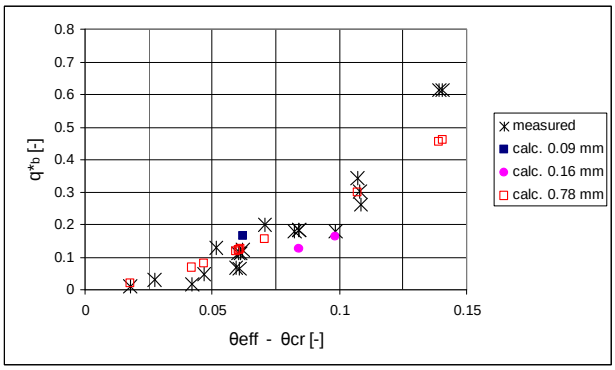

Figure IV-3: Measured and calculated dimensionless longitudinal bed load transport of 90, 160 and 780 μm sands as a function of the dimensionless shear stress at grains minus critical shear stress (ripples: $\theta_{eff}=0.2\ \theta$, dunes: $\theta_{eff}=\theta'_{top}$).(97Tmod05.xlw)

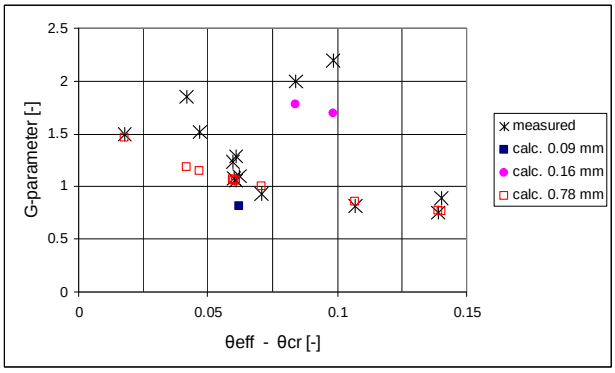

Figure IV-4: Measured and calculated transverse bed slope parameter of 90, 160 and 780 μm sand as a function of the dimensionless shear stress at grains minus critical shear stress (ripples: $\theta_{eff}=0.2\ \theta$, dunes: $\theta_{eff}=\theta'_{top}$). (97Tmod05.xlw)

V. CONCLUSIONS

The measured values for the transverse slope coefficient related to bed-load, for 90-960 μm sand, are within a range of $0.7<\boldsymbol{G}<4$.

By using the force balance of bed-load particles, an unification of longitudinal and transverse bed-load transport has been achieved for the fine grain ripples regime and the coarse grain dune regime. This way numerical values for the transverse slope parameter ($\boldsymbol{G}$) are found for different conditions. It is concluded that account has to be made for flow conditions at the traveling height of the particles and particle drag conditions.

Grain shear stresses have to be predicted beforehand. In the dune regime dune height has to be predicted also (which might explain the role of $\boldsymbol{d_{50}/h}$ in the equation for natural rivers). The model should be tested further against recent field experience.

Further laboratory tests are advised, because more data on the transverse bed slope influence, under conditions of fully developed bed forms, is needed urgently. Specifically in the regime of 100 to 600 μm sand more data is needed. In such experiments, suspended load transport has to be measured also. This has to be deducted from measured total transport for determination of bed-load transport. Such strategic data will serve to improve confidence in the outcome of numerical models.

ACKNOWLEDGMENT

Thanks to Dr Erik Mosselman, Dr Kees Sloff and Dr Peter Mewis for bringing parties together within a framework of coordination of river-bound transverse bed slope activities. Thanks to Dirk Jan Walstra and Kees Kuijper for sharing experience on estuary and sea research. Thanks to Prof. Dr Leo van Rijn for inspiring discussions on transverse slope effects. This work was partly funded the by the National Institute for Coastal and Marine Management (RIKZ) of the Dutch Ministry of Transport, Public Works and Water Management.

NOTATIONS

$\boldsymbol{a}$	square of velocity ratio $\boldsymbol{a}=(\boldsymbol{U/u^*})^2$
$\boldsymbol{A}$	constant to accommodate bed form properties
$\boldsymbol{B}$	constant to accommodate bed form properties
$\boldsymbol{C_d}$	drag coefficient particles
$\boldsymbol{d}$	particle diameter
$\boldsymbol{d_{50}}$	median sand diameter
$\boldsymbol{d^*}$	dimensionless particle diameter
$\boldsymbol{d^+}$	particle diameter in boundary layer coordinates
$\boldsymbol{g}$	gravitational acceleration
$\boldsymbol{G}$	transverse bed slope coefficient
$\boldsymbol{G_{total}}$	transverse bed slope coefficient to total load
$\boldsymbol{h}$	local water depth
$\boldsymbol{k_s}$	equivalent (Nikuradse) sand-roughness
$\boldsymbol{n}$	porosity
$\boldsymbol{n}$	constant in travelling height particle
$\boldsymbol{q}$	sediment transport rate per unit width (volume, incl. pores)
$\boldsymbol{q_{bed\ x}}$	bed-load transport in $\boldsymbol{x}$-direct. (incl. pores)
$\boldsymbol{q_{bed\ y}}$	bed-load transport in $\boldsymbol{y}$-direct. (incl. pores)
$\boldsymbol{q^*}$	dimensionless total transport rate
$\boldsymbol{q_b^*}$	dimensionless transport rate bed-load
$\boldsymbol{q_{total}}$	total transport rate
$\boldsymbol{Re}$	Reynolds number particle
$\boldsymbol{s}$	relative density
$\boldsymbol{U}$	fluid velocity at mean particle height
$\boldsymbol{u^*}$	friction velocity
$\boldsymbol{V}$	particle velocity parallel to the bed
$\boldsymbol{x}$	coordinate in streamwise direction
$\boldsymbol{y}$	coordinate transverse direction
$\boldsymbol{z_b}$	bed surface level
$\boldsymbol{z^+}$	coordinate boundary layer flow
μ_c	dynamic granular friction coefficient
ν	kinematic viscosity
θ	Shields parameter
θ'	Shields parameter to the grains
θ_{cr}	critical Shields parameter
θ_{eff}	effective Shields parameter to the grains

θ_0	parameter in transport model (ratio of Coulomb friction and fluid drag)
ρ	density water
ρ_s	density sediment
τ	total shear stress
τ'	grain shear stress
ψ	direction bed load transport

REFERENCES

[1] Ashida K. & Michiue M, 1972, Study on hydraulic resistance and bedload transport rate in alluvial streams, ***Trans. Japan Soc. Civ. Engrg.***, Vol 206, pp.59-69.

[2] Bendegom, L. van, 1947, Eenige beschouwingen over riviermorphologie en rivierverbetering, De Ingenieur, Vol.59, No.4, pp.B1-B11, in Dutch, English translation: Some considerations on river morphology and river improvement, Nat. Res. Council of Canada, Tech. Transl. 1054, 1963.

[3] Chien, S.F., 1994, Settling velocity of irregularly shaped particles, SPE Drilling and Completion, paper 26121

[4] Engelund, F., 1976, Experiments in curved alluvial channel, part 2, Progress Rep.38, Tech. Univ. Denmark, pp.13-13.

[5] Engelund, F. and E. Hansen, 1967, A monograph on sediment transport in alluvial streams, Teknisk Forlag, Copenhagen, Denmark, pp.62.

[6] Engelund, F. and J. Fredsºe, 1982, Hydraulic theory of alluvial rivers, Advances in Hydroscience, Vol.13, pp.187-215.

[7] Hasegawa, 1981, Bank-erosion discharge based on a non-equilibrium theory, Trans. JSCE, Vol.13, pp202-205 (in Japanese).

[8] Kovacs, A. & G. Parker, 1994, A new vectoral bed load formulation and its application to the time evolution of straight river channels, J. Fluid Mech., Vol.267, pp.153-183.

[9] Shiller J. and A Naumann, 1933, Uber die grundlegende berechnungen bei der schwerkrachtaufbereitung, Ver. Deunt. Ing. vol 77, p318.

[10] Struiksma N., Olesen, K.W., Flokstra, C. and H.J. de Vriend, 1985, Bed deformation in alluvial channel bends, J. Hydr. Res., IAHR, Vol.23, No.1, pp.57-79.

[11] Talmon, A.M., 1991, Suspended sediment transport in axi-symmetric river bends , in Soulsby & Bettess (eds), Sand Transport in rivers estuaries and the sea, proc. Euromech 262, Wallingford, England, Balkema publ.

[12] Talmon, A.M., 1992, Bed topography of river bends with suspended sediment transport, Doctoral thesis, Delft Univ. of Technol., (also: Communications on Hydr. and Geotechnical Engrg., Delft Univ. of Technol., Dept. of Civil Engrg., Rep.92-5, ISSN 0169-6548).

[13] Talmon, A.M., 1997, Sediment transport in dune regime and transverse slope effect (in Dutch, sediment transport bij duinen en invloed dwarshelling), Delft Hydraulics, J1234.

[14] Talmon, A.M., M.C.L.M. van Mierlo & N. Struiksma, 1995, Laboratory measurements of the direction of sediment transport on transverse alluvial-bed slopes, J. Hydraulic. Res., vol.33, no 4, pp.495-517.

[15] Wiesemann, J.-U., Mewis, P., Zanke, U., 2004, Laboratory measurements of sediment transport on transverse sloped beds, Singapore, Second International Conference on Scour and Erosion, Proceedings, Volume 2, pp. 252-259.

[16] Wiesemann, J.-U., Mewis, P., Zanke, U, 2006a, Bed Levelling Investigations on Transverse Sloped Beds, **submitted** for the International Conference of River Hydraulics - Riverflow 2006, Lisboa, Portugal.

[17] Wiesemann, J.-U., Mewis, P., Zanke, U, 2006b, Sediment Transport Rate in the Dune Regime in Bed Levelling Experiments, **submitted** to the International Conference on Scour and Erosion ICSE3 2006, Netherlands.

Scour effects on Coastal Defense Structures Examples from the Portuguese West Coast

F. Taveira-Pinto*, F. Veloso-Gomes* and P. Rosa-Santos*

* Faculty of Engineering of the University of Porto – IHRH, Porto, Portugal

I. INTRODUCTION

Different types of coastal defense structures are used to protect shoreline against coastal erosion and flooding. Many of these structures were built on sand or soil material that can be easily removed or eroded by the action of waves, currents or combined waves and currents.

The loss of bed material, either from beneath the structure or nearby the structure, can occur rapidly, over short time spans (during a storm event), or gradually, during a lengthy time span (months to years), [1]. In both cases, scour can significantly affect the structure functionality and stability and, in some situations, may lead to an imminent collapse and failure of some sections or all the coastal defense structure.

The physical processes involved in scour are quite complex and usually are significantly influenced by the characteristics of the structure, the local wave climate and water depth, the currents regime and the bed material characteristics in the vicinity of the structure.

Because scour related damages on coastal structures is often difficult and expensive to repair, the possibility of damage resulting from scour should be addressed during its project. Regarding this issue some limitations of available design guidance are pointed out [2]. During the structure lifetime periodic inspections should be carried out.

In this paper, several scour related damages on coastal defense structures located on the highly energetic Portuguese West coast will be reported and analyzed. The (potential) mechanisms of failure will be identified and possible measures to reduce the consequences of that phenomenon will be presented.

II. WAVE CLIMATE

The wave climate in the Portuguese West coast is highly energetic. The main storms come from the North Atlantic, mainly between the months of October and March.

The most frequent significant wave heights are in the range of 2 to 3m but during storms significant wave heights may exceed 8m (maximum wave heights up to 1.7 times the significant wave heights).

The most frequent wave periods are in the range of 8 to 12s, reaching 16 or 18s during storms. The dominant wave direction is the Northwest, Fig.1.

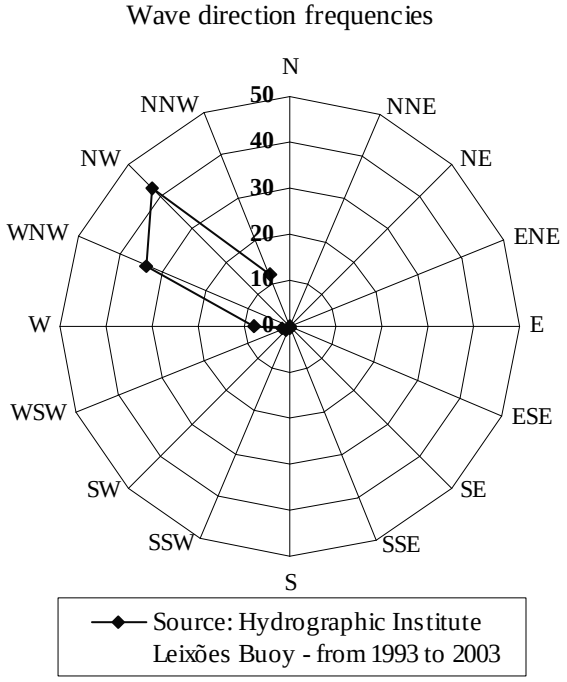

Figure 1. Wave direction frequencies in the Portuguese West coast, [3].

Tides are of the semi-diurnal type, reaching a range between 2 and 4m during spring tides. Meteorological tides outside enclosed water bodies are small (0.2m to 0.6m).

III. SCOUR EFFECTS ON COASTAL DEFENSE STRUCTURES

Coastal defense structures built on sand or soil material are often submitted to coastal erosion and scour effects.

In the Portuguese West coast, groins or adherent longitudinal revetments are the most used types of coastal defense structures. Several cases of erosion or structure induced phenomena can be reported along the Portuguese West coast, namely Espinho, Cortegaça, Maceda and Costa da Caparica. Fig.2 presents the location of the most important coastal defense structures in the Portuguese coast, namely groin fields (67 large structures).

Groins are rubble-mound structures that assure a certain level of flexibility due to its ability to withstand severe wave conditions and continuing to function when original design conditions are exceeded. A certain level of damage

can therefore be experienced without total loss of their functioning ability.

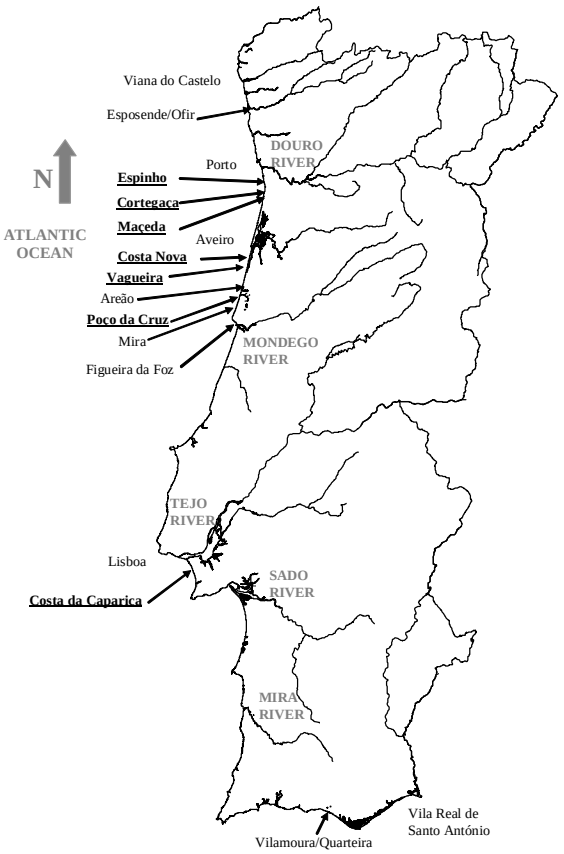

Figure 2. Location of the most important coastal defense structures in the Portuguese coast.

The used groins have a typical symmetrical trapezoidal cross section with an armor layer, underlayer and a core (Fig.3). The armor layer is in general composed of natural stones and/or concrete blocks.

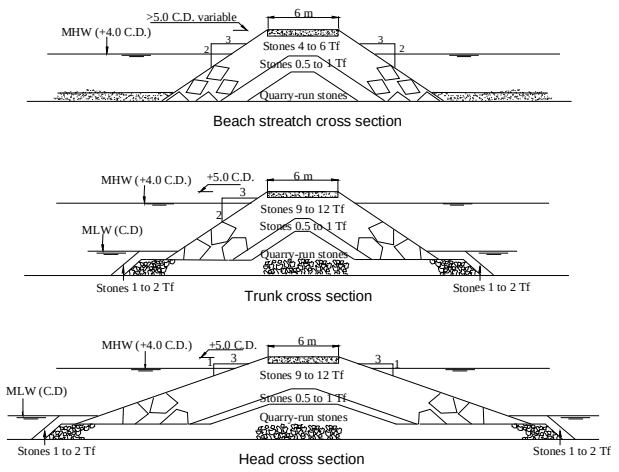

Figure 3. Generic cross sections of the Costa da Caparica groins.

The groins plant configuration is usually linear, as the Costa da Caparica groins, Fig.4, but sometimes these structures have a more complex configuration like the two S shaped groins located near the city of Espinho and the curved groin located in Poço da Cruz. These latter configurations allow the creation of a diffraction beach downdrift.

Some of these structures can reach more than 500m of length, having dimensions and structural components similar to harbor breakwaters. Fig.4 presents the dimensions of the Costa da Caparica groin field after the 2005/2006 repair program, as well as the bathymetry in the vicinity of these structures.

The magnitude of scour effects at the toe of a sloping structure is considered to be a function of the structure characteristics, incident wave conditions, water depth, currents regime and the characteristics of the bed material in the vicinity of the structure.

Due to the slope, roughness and permeability of the rubble-mound coastal defense structures, their reflection coefficient is expected to be somewhat less than the one expected for a vertical smooth and impermeable structure, at the same place under the same wave conditions.

Nevertheless some wave reflections are expected to occur at the rubble-mound structure, which may lead to an increase of the local wave heights, flow velocity and turbulence, promoting the occurrence of wave induced scour in the vicinity of the structure.

The highly energetic wave climate in the Portuguese West coast and the construction of long groin structures, which can easily reach depths of -5m bellow chart datum, Fig.4, expose these coastal structures to significant forcing loads.

The mobile sand foundation of these structures is also an important drawback issue. At the groin's head, bathymetry can change between -1 and -4m, bellow tide datum, during the year, [5].

A scour depth of -11m has been measured in 2005 near the head of groin EV2 at Costa da Caparica. The bathymetric changes in the vicinity of the Costa da Caparica groin field, between September 2001 and September 2005, are presented in Fig.5.

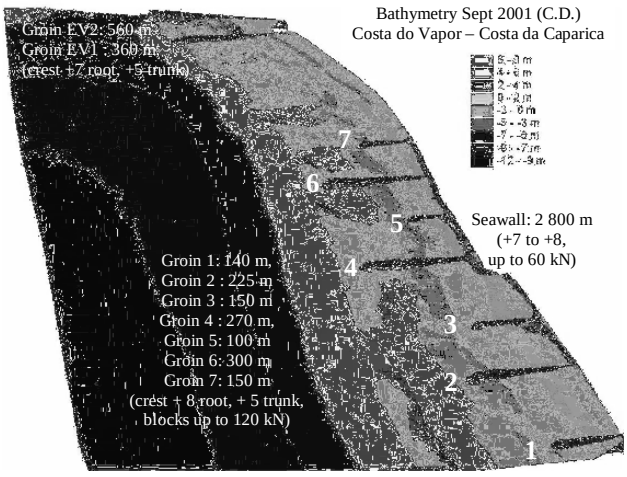

Figure 4. Costa da Caparica groin field after reconstruction (2006) and before the artificial sand nourishment [4].

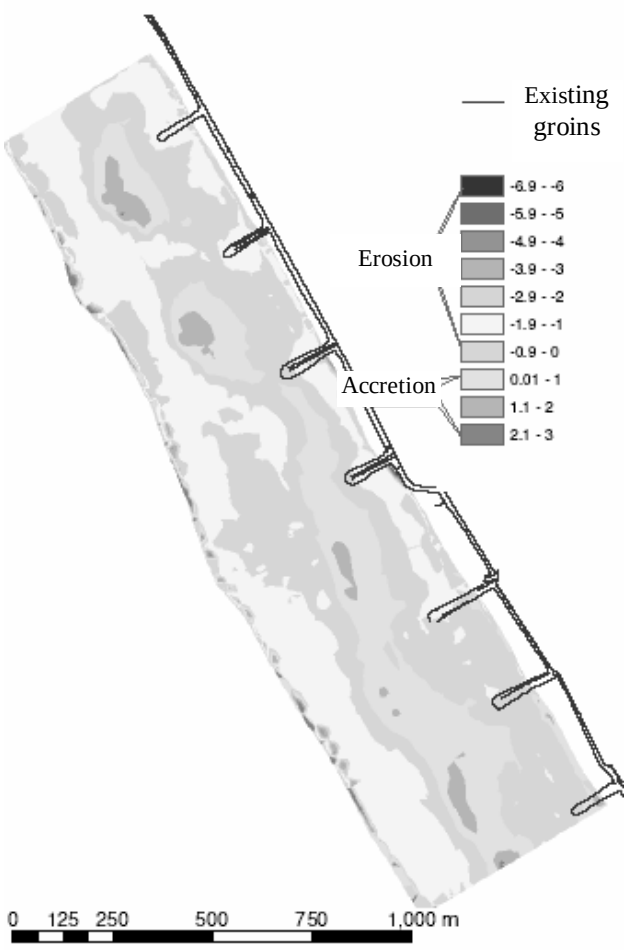

Figure 5. Bathymetric changes between Sept. 2001 and Sept. 2005 at Costa da Caparica groin field.

Along the most critical waterfronts of the Portuguese West coast several coastal defense structures have been built through the years. Despite the care taken in their design and construction, and the repairing actions that have been carried out, some important damages on these structures can be observed. Interventions that were carried out on the Portuguese coastal defense structures are summarized in Fig.6.

In the Espinho seafront two S shaped groins are located; the North groin with a length of 350m and the central groin with a length of 400m. Both structures have an armor layer mainly composed by 300kN tetrapod concrete blocks.

The repair actions on the Espinho North groin, carried out in 1997, are presented in Fig.7. These actions included replacement of 250 tetrapod blocks, replacement of displaced armor and filter stone units, increase of the weight of stone units, increase of the crest width and consideration of submerged berms.

Despite the repairing actions that were carried out on the two S shaped groins of Espinho, some damages can be observed in Fig.8 and Fig.9, which present the conditions of these structures in the year of 2005. Both groins present damages at the structure head. However the damages were more severe on the central groin, whose head almost disappeared completely.

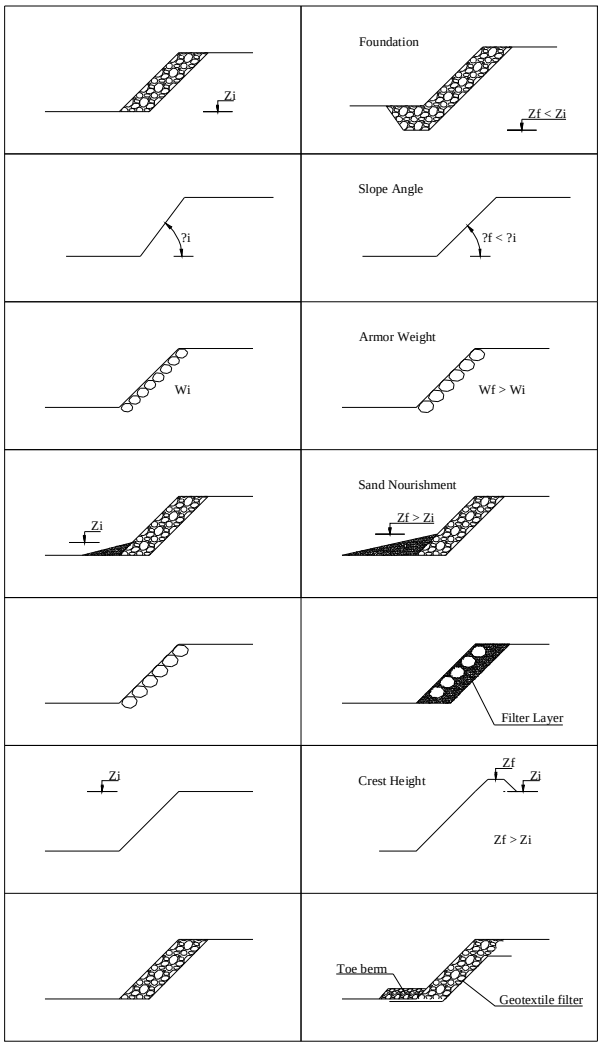

Figure 6. Situation before and after technical actions on damaged coastal defense structures [5].

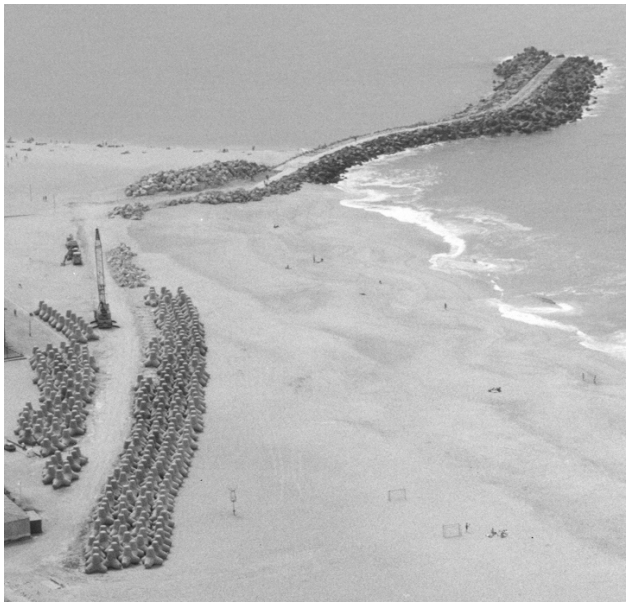

Figure 7. Reconstruction of the North groin of Espinho, 1997.

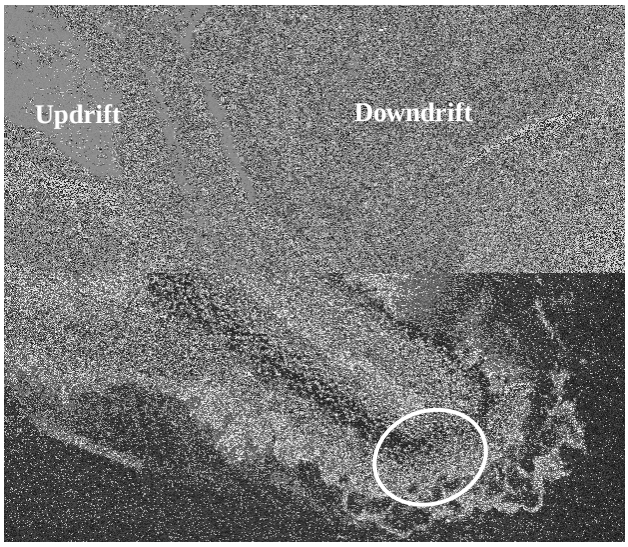

Figure 8. North groin of Espinho, 2005.

Figure 9. Central groin of Espinho, 2005.

The groin presented in Fig. 10 is located near Cortegaça. The structure armor layer is composed by stone blocks with weights up to 12t and the length of the structure is approximately 170m. The photograph shows important damages at the structure head and at some localized sections along the trunk, either in the updrift side or in the downdrift side of the groin.

The new groin located in Poço da Cruz, Fig.11, presents a curved plant configuration and is approximately 230 m long. The armor layer is composed by stone blocks of 12t. At the head of the structure a toe berm, partially covered by sand, can be observed and in the downdrift side of the groin a diffraction beach has been created. There is no evidence of damages on this structure.

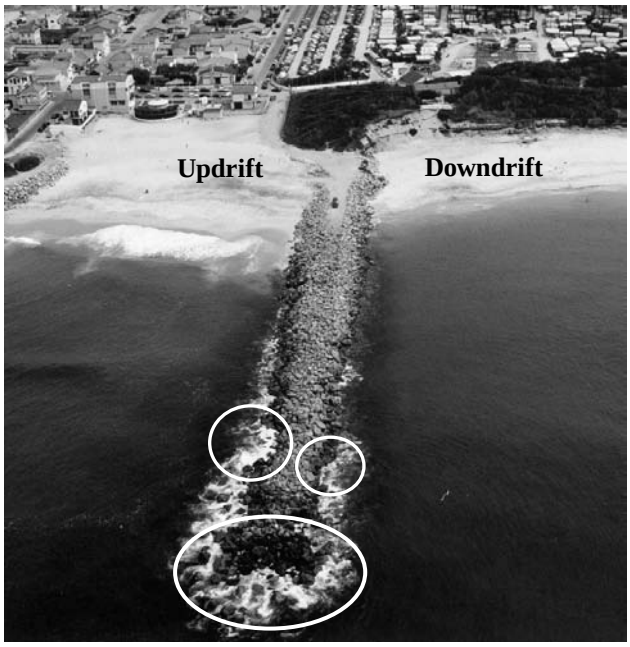

Figure 10. Groin of Cortegaça.

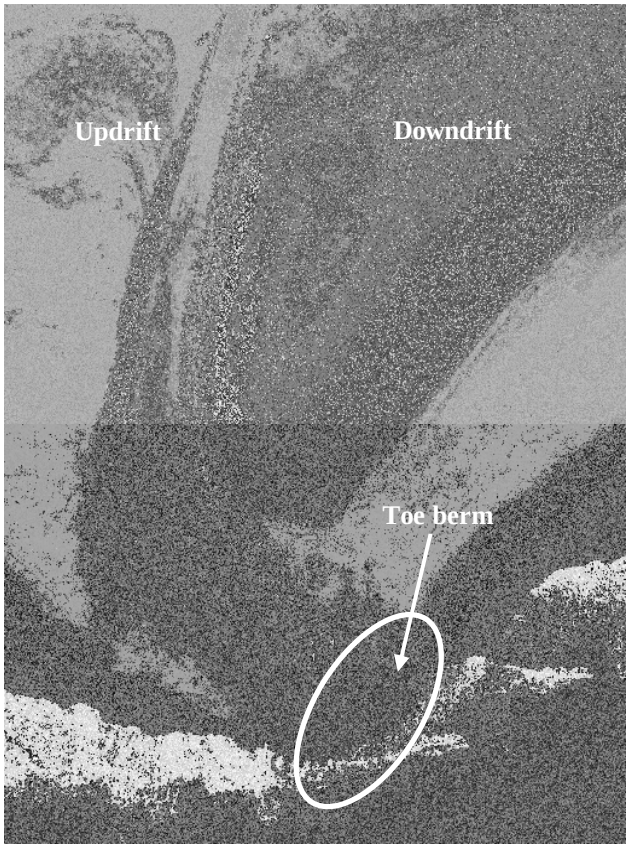

Figure 11. New groin of Poço da Cruz, 2005.

At the head of groins, the combination of wave breaking with local currents around the groin's head may lead to the generation of scour holes at the toe of the structure and undermining, which may destabilize the structure. The interaction of incident with reflected waves may increase the magnitude of these phenomena.

Destabilization of the structure armor layer support may lead to the sliding of the amour layer blocks into the seabed, which then may come to rest at the structure toe or the at toe berm (if it exists).

Displaced armor blocks usually contribute to the improvement of the structure toe scour protection as they may fill any existing scour hole at that location or form a more stable protection apron around the structure toe. Scour effects on the structure will then be attenuated or even stopped at that location. The resulting smoother slope of the structure is advantageous to its stability under the wave action.

The failure of a rubble-mound structure is usually progressive, having therefore a "flexible" behavior (some damage can occur without functional failure). Because of this, design is usually made for waves with a relatively low return period (significant wave height) [6].

This design approach can explain, to some extent, why some damage is expected to occur during the structure lifetime, when design conditions are exceeded. In Portugal a design wave height equal to the maximum wave that can reach the coastal structure without breaking is being adopted.

Damage on a groin structure with an armor layer composed of relatively fragile concrete blocks can be worsened by the breaking of these units. This often occurs with tetrapod concrete blocks exposed to severe wave conditions (Espinho case).

Either the sliding down of the armor layer tetrapod blocks due to scour effects at the toe of the structure or the dynamic actions induced by waves can break these units into smaller parts. These tetrapod fragments, with a reduced weight, are then projected by wave action against intact units leading to their breaking. Fragments of broken tetrapods are often observed at the head of the structure.

Arrestment of the alongshore drift material in the updrift side of the groin structure will lead to downdrift side beach erosion with lowering of the beach/seabed level and retreat of the shoreline. This effect usually occurs gradually, during a lengthy time span.

These bathymetric changes near the structure may be precursors of a functional or structural failure. This effect can occur together with localized scour on the structure toe, which worse the scour problem. Fig.10 presents damage at some locations in the downdrift side of the groin that can be associated with these effects and with diffraction currents around the structure head.

The shoreline retreat and the beach lowering can also lead to the situation presented in Fig. 12, in which the root of a groin structure located near Maceda, Portugal is being flanked in the downdrift side. The groin has been extended landward about 60m. This situation is a cumulative impact of shoreline retreat due to an overall negative sediment balance along the coastal zone and the local impact induced by the structure itself.

Figure 12. Groin of Maceda, 2005.

At this stage it is important to refer that despite the importance of the scour and erosion effects on the structures stability other effects could have also played an important role in the damage presented in the previous figures.

The hydrodynamic forces due to the action of waves above design levels on the armor blocks can by themselves originate important damages on the structure armor blocks.

Overtopping of the structure is another important phenomenon that can easily originate problems to the structure.

Due to the highly energetic wave climate in the Portuguese West coast, the sand foundation of most of these coastal defense structures, and the design approach, damages as well as settlements of the structure can be expected during the structure life span. Settlements are especially significant during the first 5 years.

According to [5] it is expected that every eight to twelve years a large repair action will be needed on the Portuguese coastal defense structures and every two years a maintenance procedure will be necessary depending on the intensity and frequency of the storms.

IV. SCOUR PREDICTION AND SCOUR PROTECTION

Most of the scour prediction tools are based on empirical equations derived from results of small scale laboratory tests and from past successful field experience.

As stated in [1], there are no generally accepted techniques for estimating maximum scour depth or planform extend of scour at sloping structures, despite the considerable research already carried out.

For obliquely incident waves on coastal defense structures there are no accurate design relationships available to scour prediction [7]. The use of empirical equations, developed to normally incident waves, can be implemented but do not take into account important issues of the phenomenon.

The usual approach to the problem is often practical and empirical, often based on the experience of past successful and similar works. However, the complexity and importance of some projects may require 2D or 3D physical model studies.

Taking into account the flexible behavior of a rubble-mound structure, an alternative to deal with the problem is to build an appropriate scour protection, only after realizing that scour has actually occurred near the structure. However this approach can lead to significant damage on the structures, especially if they are located on a very exposed coast.

If nothing is done in due time to stop the scour progression, damage on the structure may increase significantly. This is an important issue that must be taken into account because legal constrains that have to be overcame in order to allocate financial resources to the repair intervention, tender schedules and the difficulty of carrying out works on groins during the winter time, may delay the repairing intervention on the structure.

Rules of thumb are generally used to guide engineers in the design of scour protection solutions for coastal defense structures. Generally these rules consist of qualitative information about the extent and preferential location of the scour damage on the structure as well as the influence of some design parameters on the magnitude of scour effects.

Some semi-empirical formulations can also be used to estimate scour depth and the width of the scour hole near the sloping structure.

Ref. [8] present empirically developed formulas to estimate the maximum scour depth and the width of the necessary scour protection layer, for the case of wave-induced scour at the round head of a slopping-front breakwater. The tests were performed with the breakwater structure aligned parallel to the incident irregular waves and the majority of the tests were carried out for an impermeable and smooth breakwater surface, having a slope of 1:1.5.

Two different mechanisms were identified to be responsible for the scour phenomena around the head of the structure: steady streaming of flow occurring around the breakwater head in the plan view, and plunging breaker taking place at the head of the breakwater. For each mechanism an empirical equation to predict the maximum scour depth was developed.

The maximum depth of scour holes caused by the steady streaming in front of the breakwater head, seaward, can be estimated by the following equation:

$$\frac{S}{B} = 0.04\, C_1 [1 - e^{-4.0(KC - 0.05)}], \qquad (1)$$

in which S is the maximum scour depth, B is the base diameter of the breakwater head, C_1 is an uncertainty factor with a mean value of 1 and a standard deviation of 0.2, and KC is the Keulegan-Carpenter number, defined as,

$$KC = \frac{U_m T_p}{B}, \qquad (2)$$

in which U_m is the maximum value of the undisturbed orbital velocity at the sea bottom and T_p is the peak spectral wave period.

The maximum depth of scour holes caused by waves breaking across the sloping front of the breakwater head can be estimated by the following equation:

$$\frac{S}{H_s} = 0.01 C_2 \left(\frac{T_p \sqrt{g H_s}}{h} \right)^{\frac{3}{2}}, \qquad (3)$$

in which $C2$ is an uncertainty factor with a mean value of 1 and a standard deviation of 0.34, H_s is the significant wave height, h is the water depth at the structure head and g is the acceleration due to gravity.

2D scour at the trunk section of a rubble-mound breakwater was experimentally investigated in [7] for regular and irregular waves and two breakwater models with slopes of 1:1.2 and 1:1.75. It was found that the scour depth decreases with the decreasing of the breakwater slope and in the case of irregular waves. The 2D scour/deposition pattern was found to be similar to the case of a vertical–wall breakwater, with alternating scour and deposition areas lying parallel to the breakwater.

The protection against scour damage on sloping structures is usually assured by the construction of a protection apron, which should be designed to resist to the action of waves and currents. This protection layer has the additional function of supporting the main armor layer and must be flexible enough to conform to the irregularities of the seabed.

The protection layer does not avoid scour and thus some scour holes are expected to occur at the edge of the toe berm. Armor blocks from the protection layer will then slump down into the scour hole leading to the formation of a protective slope which helps to stabilize scour progression.

Scour also occurs underneath the toe berm of the structure. According to [7] this phenomenon is the result of the combined action of two effects: the stirring up of sand material underneath the protection apron by waves, which is then brought up into suspension, and the action of the existing steady streaming near the bed that carries these sediments away, leading to significant settlements of the toe berm.

The design of the toe berm is therefore of vital importance to the structure and its instability can trigger or accelerate the instability of the main armor layer. The width of the toe berm should be large enough to ensure that some portion of it will remain intact in order to avoid instability of the main layers of the groin. According to [8] the toe berm width should be about the same length as the scour hole that would develop at the structure toe in the absence of the protection apron. The width, L, of the necessary protection layer can be estimated using the following equation:

$$L = \frac{A H_s}{\sinh(kh)}, \qquad (4)$$

in which k is the wave number, and A is 3.3 for a complete scour protection and 2.4 for an allowed maximum scour depth of 1% of the base diameter of the breakwater head.

Due to the settlement of the toe berm and the already referred mechanisms, the number of layers and the toe berm elevation are also important design issues.

Stones used in the toe berm can have the same dimensions as the armor layer, in order to remain stable under the wave action, however, in most cases, one wants to reduce the size in such way that construction costs will be reduced.

Size of the toe berm stones can be determined using the toe stability formulas for waves given in [1]. These formulas are based on the stability number related to the depth ratio, which is the quotient between the depth of the toe bellow still water level and water depth just in front of the structure toe. The standard toe berm sizes are of about 3-5 stones wide and 2-3 stones high.

Typical toe berm solutions are also presented in [1], which distinguishes three different cases, according to the relative water depth at the structure. In very shallow water conditions, with depth limited design wave heights, the toe protection can be ensured by one or two extra rows of main armor units at the toe of the slope, Fig.13.a. In shallow water conditions it is usually possible to use smaller stones or blocks than in the main armor, Fig.13.b, and for deep water conditions the toe berm can be constructed at a level above the seabed, Fig.13.c.

The use of geotextile filters under the toe berm, as sketched in Fig. 14, can be also an additional measure to improve its stability.

Portuguese groin structures are now constructed and repaired with protection toe berms having a high toe berm elevation in order to compensate the anticipated settlement and sliding of the toe berm blocks, due to scour effects and dynamic behavior of the forcing loads.

The toe berms of groin structures are clearly visibly during the first years after construction. This can have some negative visual impacts on the beach users; however these impacts will disappear with time. Fig.15 presents the elevated toe berm protection of a groin structure located near Costa Nova. Fig. 11 shows a toe berm partially covered by sand.

Short term prevention against flanking of the groin root, Fig.12, can be assured, to some extend, by the extension of the downdrift rubble-mound slope of the structure, following the coastline alignment as presented in Fig.16.

Additionally the groin superstructure can be constructed with a reduced crest elevation in order to allow the transposition of sand material from the updrift side to the downdrift side of the structure.

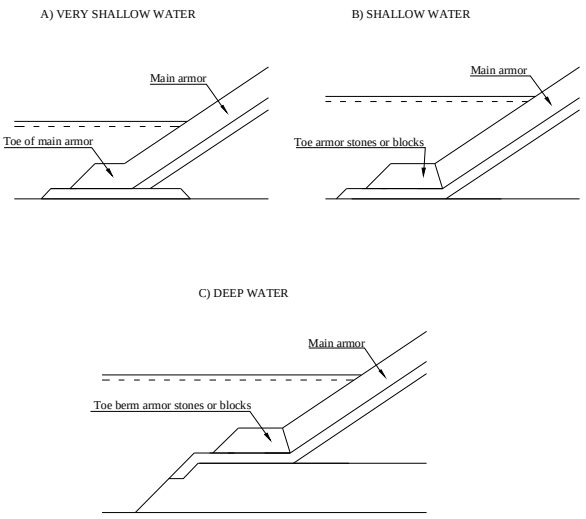

Figure 13. Typical toe berm solutions, [1].

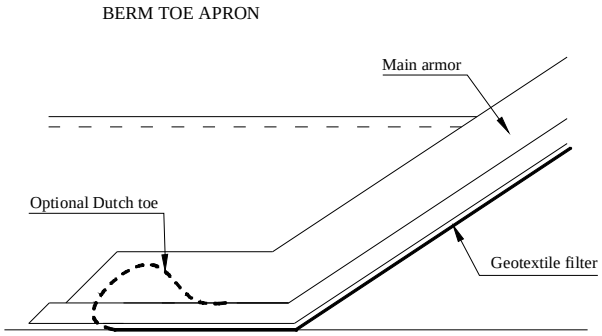

Figure 14. Toe berm apron with a geotextile filter, adapted from [2].

The curved head configurations of groins, which allows the creation of a diffraction beach in the downdrift side of the structure (Fig.8 and Fig.11), can also be an important measure in the prevention of damage at the groin root.

Due to the limitations of the scour prediction techniques and the characteristics of this kind of structures, damage is expected to occur during the structure lifetime. Therefore periodic inspections should be carried out.

The frequency of these inspections should be defined according to the type of the project, physical environment at site and scope of the project. This way, interventions can be prepared previously avoiding the worsening of the damage extent on the structure that obviously would increase the reconstruction costs.

Regarding this issue is important to point out the short-living characteristics of the toe scour phenomena, with the scour holes being filled in within a few hours after the storm that had originated them, leaving a little trace of its existence. Therefore routine surveys are unlikely to reveal toe scour. This stresses the importance of designing an adequate scour protection apron to the coastal defense structure.

The beach/seabed lowering in the vicinity of the structure, occurring over a more lengthy time span can more easily be detected.

Figure 15. Toe berm of a groin at Costa Nova, 2003.

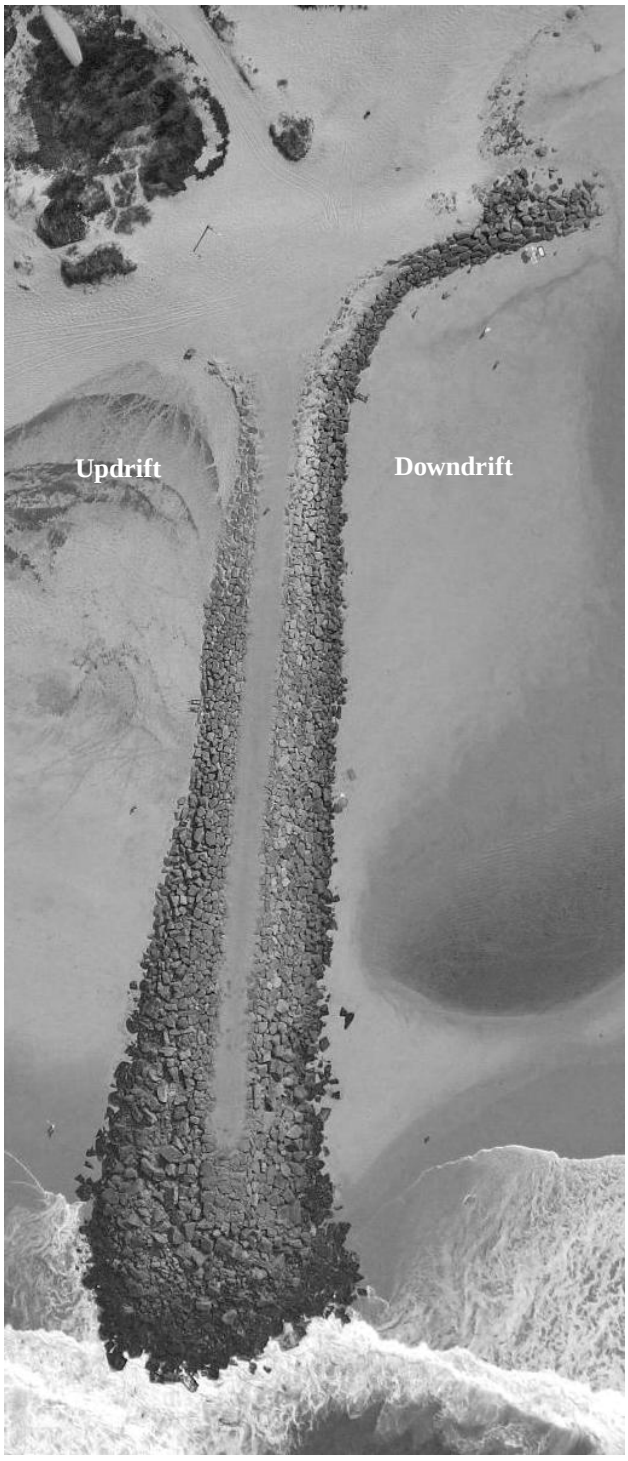

Figure 16. Groin of Vagueira Sul, 2005.

In coastal zones where erosion phenomena are very important due to human action (dams, harbor breakwaters, navigation channels, dredging works) and sea level rise, modeling of the seabed and the coastline should include: medium to long term evolution (up to 100 years) for different scenarios of sea levels, meteorological tides, storm distributions, sediment inputs and outputs (rivers supply, artificial nourishment, dredging works); and local scour effects induced by the coastal structures.

A long term configuration model is now being used [9] to forecast the medium to long term evolution and the results present evidence of the problems that should be expected in a near future to maintain the coastal structures in Portugal.

V. CONCLUSIONS

Due to the highly energetic wave climate in the Portuguese West coast and the sand foundation, important damages often occur on coastal defense structures, which can be associated with scour and coastline evolution landwards, due to strong erosion phenomena.

Damages on Portuguese coastal defense structures were reported and analyzed. The potential mechanisms of failure were identified and current practices to deal with these problems were presented.

Despite the work already carried out, there is still much more to be done in the development of scour prediction techniques generally accepted by the technical community and easily applicable to current design. Experience on successful and similar works still have an important role in the design of scour protection.

Adequate toe berm solutions should be used to prevent and reduce the consequences of scour and erosion on coastal defense structures.

Periodic inspections should be carried out during the structure lifetime according to the type and scope of the project, and physical environment at site.

Long term configuration models incorporating local effects induced by the presence of coastal structures, can be a useful tool to deal with the scour and erosion phenomena.

ACKNOWLEDGMENTS

Instituto da Água, Ministério do Ambiente, namely to Dr. Orlando Borges, Eng.º João Costa and Eng.º António Rodrigues.

REFERENCES

[1] Burchart, H.F. and S.A. Hughes, 2001, Fundamentals of Design, Part VI, Design of Coastal Project Elements - Chapter 5 in Coastal Engineering Manual, 1110-2-1100, US Army Corps of Engineering, Washington, DC.
[2] Burgess, K., 2003, Current Practice and Problems in Designing Rubble Structures on Beaches. [Internet] available from <http://cozone.org.uk.
[3] Coelho, C., 2005, Riscos de Exposição Ambiental de Frentes Urbanas para Diferentes Intervenções de Defesa Costeira, PhD thesis, Universidade de Aveiro, Portugal. In Portuguese.
[4] Veloso Gomes, F., F. Taveira Pinto and J. Pais Barbosa, 2004, Rehabilitation Study of Coastal Defense Works and Artificial Sand Nourishment at Coasta da Caparica, Portugal, Proceedings of ICCE2004, Lisbon, Portugal, pp.3429-3441.
[5] Veloso Gomes, F. and F. Taveira Pinto, 2000, Reconstruction and Repair of Portuguese Coastal Defense Structures, Costal Structures '99, Vol.2, pp.977-984.
[6] ASCE, 1994, Coastal Groins and Nearshore Breakwaters, Technical Engineering and Design Guides as adapted from the US Army Corps of Engineers, nº6.
[7] Summer, B. M .and J. Fredsøe, 2000, Experimental Study of 2D Scour and its Protection at a Rubble-Mound Breakwater, *Coastal Engineering*, Vol. 40, pp.59-87.

[8] Fredsøe, J. and B.M. Summer, 1997, Scour at the Head of a Rubble-Mound Breakwater, *Coastal Engineering*, Vol. 29, pp.231-262.

[9] Coelho, C., F. Veloso-Gomes and R. Silva, Shoreline Coastal Evolution Model: Two Portuguese Case Studies, 30th ICCE, San Diego, USA, 2006 (accepted).

Advances in One-dimensional Numerical Breach Modeling of Sand Barriers

Thieu Quang Tuan*, Henk Jan Verhagen** and Paul Visser**
* Faculty of Coastal Engineering, Water Resources University, Hanoi, Vietnam
** Faculty of Civil Engineering and Geosciences, Delft University of Technology, Delft, the Netherlands

A hydrodynamic numerical model is formulated to describe the breach erosion process of sandy barriers. The breach flow is based on the system of unsteady shallow water equations, which is solved using a robust upwind numerical approach in conjunction with the Finite Volume Method (FVM). The hydraulic jump is considered as part of the breach flow, which escalates the scour hole development in the breach channel during the early stages. To reliably capture the jump, additional source terms are added to enhance the momentum balance in the flow equations. A three-layer refined scheme is used to compute the current profile and the associated sediment transport rate under the effects of the jump. A new approach to model the breach morphological development is proposed, which involves several new morphologic factors such as the channel characteristic width and the channel growth index. The model is capable of predicting the breach growth in both lateral and vertical directions, including the development of the scour hole. Some understanding of breach growth in coastal sand barriers in general can be drawn out based on the results of model simulation.
The model is calibrated using the laboratory dike breach data of Caan [2] and is verified against the field experimental data of the Zwin's 94 [20].

I. INTRODUCTION

Coastal breaching can occur at narrow landmasses such as dikes, barrier islands, spits, and lagoonal barriers, etc. Unintended breaches can be catastrophic, causing losses of human lives and properties, and damages to infrastructures. Quantitative understanding of coastal breaches is therefore of great importance to the vulnerability assessment of protection works as well as spatial planning against flooding hazards (see [20] and [8] for reviews).

In spite of numerous historical events, reliable predictive tools are still lacking. Scarceness of quantitative data and ambiguity in the processes involved have greatly hampered the development of breach models. Apart from hydrodynamic factors, properties of the breach materials largely contribute to the complexity of the problem. A breach in a cohesive dike would be far more complex than that occurs in a sand dike. Recently, some progress has been made in the latter case, which is also the issue we discuss in this paper, i.e. breach modeling of sand barriers or of similar types. For breach modeling of other soil types such as clay or mixed clay in earth-dams and fuse-spillways, a comprehensive review can be found in [13] and [20].

In principle, breaching is regarded as a gradual erosion process starting with an initial (or pilot) channel. Whereby, the breach modeling is, in fact, to describe the enlargement of this channel both vertically and laterally.

Visser [20] developed a mathematical model for breaching in sand-dikes, namely BRES, in which five evolutional stages of the breach erosion process are defined. In each stage, the breach discharge is calculated using a weir formula. As the model ultimate goal is to quantify the discharge through a breach, the scour hole is neglected in the vertical breach growth. In the first two stages, the breach width is assumed to be constant and equal to the initial value. From stage III, the channel width starts to increase linearly with the reduction of the breach sill level. The BRES model was calibrated through a field experiment (the Zwin'94, see [20]) and then validated against a small scale laboratory test (Caan's experiment see [2]). Good agreement between measurements and model predictions for the increase of the breach width was found. However, the vertical breach growth observed in the laboratory tests does not comply much with the five defined stages. This is because a scour hole develops in the breach channel, which appears to take out a large part of the dike even in the first stage. The development of the scour hole should therefore be accounted for in the breach modeling.

Kraus [8] derived a heuristic analytical model for breaching of coastal sand barriers. It follows that an idealized rectangular breach evolves gradually towards an equilibrium situation in an exponential manner. The model reveals that the breach growth in sand barriers is stipulated by seven variables, including the initial and equilibrium channel dimensions (depth and width). However, it is disadvantageous that the model relies heavily on empirical estimates, which are hard to know in advance such as the maximum transport rates and the equilibrium breach dimensions.

Busnelli [1] argues that hydraulic jumps tend to disappear in mobile beds so one-dimensional hydrodynamic model is plausible for modeling the breach growth, provided that the increase of channel width must be someway quantified. A semi-implicit numerical scheme was used to resolve the breach flow and a total sediment transport approach was adopted to compute the transport rate. The first two stages of the laboratory dike breach [2] were successfully simulated, however keeping a constant breach width.

In this paper, we present the formulation of a new numerical breach model of sand barriers. The model is hydrodynamic and capable of simulating the breach growth in both lateral and vertical directions, without defining stages. The scour hole development is also incorporated. The model is calibrated and verified through

the laboratory dike breach data [2] and the Zwin'94 field measurement.

In the following sections, we first discuss the flow modeling that includes the jump turbulent terms in the horizontal momentum equation. Next, the current profile and the sediment transport under the effects of the jump turbulence are discussed. For the morphological computation, the governing equation of the breach growth and several new morphologic parameters used in the breach modeling such as the characteristic (volumetric) channel width and the growth index are then introduced. Finally, the result of model simulation and some evaluation are given.

II. FLOW MODEL WITH TURBULENT JUMP

The hydraulic jump usually takes place at the downstream side of the breach, where there is a transitional state between the upstream supercritical and downstream subcritical flow. The jump position is governed by the hydraulic conditions as well as the breach geometry and bed roughness. During the breaching process, the jump can progress upstream as the downstream water level increases. Once a turbulent jump exists, the current profile as well as the surface profile is substantially modified. Extraordinarily, the maximum velocity is found very close to the bed (see [5]) that is in contrast to the logarithmic profile of open channel flows without jump, where the maximum velocity is at the surface. Much more sediment is therefore agitated and brought into transport by the high turbulence of the jump. As a consequence, a scour hole which is a noticeable morphologic feature observed in the vertical breach development, may develop around the jump (see Fig.1). The scour hole in the breach channel is dynamic as the jump can move back and forth during the breaching.

From the foregoing arguments, the flow model should be able of reliably predicting both the location and the length of the jump as a part of the breach flow conditions. Most models of shallow flows (e.g. St. Venant equations) with shock-capturing techniques are able to predict well the jump position [15]. The jump length, however, is dependent of the spatial discretization, typically is of the order of several grid intervals. This drawback is mainly attributed to the depth-integrated effects, because of which information on the vertical velocity profile is lost. As a consequence, turbulent stresses and dissipation of turbulent energy across the jump cannot be fully accounted for in the horizontal momentum balance. Based on this implication, a relatively simple approach to improve the jump modeling is proposed as follows.

We start with the two dimensional Reynolds averaged Navier-Stokes (RAN) equations, which for incompressible fluid are:

Equation of continuity:

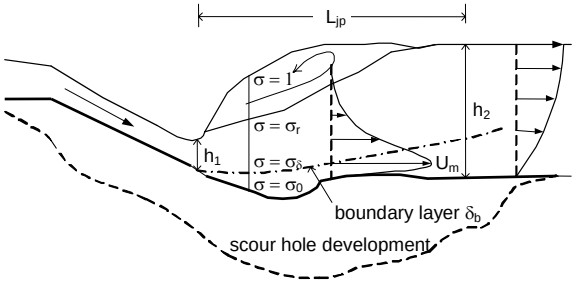

Figure 1. The hydraulic jump in the breach channel

$$\frac{\partial u}{\partial x}+\frac{\partial w}{\partial z}=0. \tag{1}$$

Equation of horizontal momentum:

$$\frac{\partial u}{\partial t}+u\frac{\partial u}{\partial x}+w\frac{\partial u}{\partial z}=-\frac{1}{\rho}\frac{\partial p}{\partial x}+\frac{1}{\rho}\frac{\partial \tau_{xx}}{\partial x} +\frac{1}{\rho}\frac{\partial \tau_{xz}}{\partial z}+\nu\left(\frac{\partial^2 u}{\partial^2 x}+\frac{\partial^2 u}{\partial^2 z}\right). \tag{2}$$

Neglecting vertical acceleration terms, the pressure distribution across the jump is assumed to be hydrostatic (as showed in [11] that this assumption is eligible):

$$p=\rho g(h-z). \tag{3}$$

Multiplying the equation of continuity by u and adding it to the horizontal momentum equation yields:

$$\frac{\partial u}{\partial t}+\frac{\partial u^2}{\partial x}+\frac{\partial uw}{\partial z}=-\frac{1}{\rho}\frac{\partial p}{\partial x}+\frac{1}{\rho}\frac{\partial \tau_{xx}}{\partial x} +\frac{1}{\rho}\frac{\partial \tau_{xz}}{\partial z}+\nu\left(\frac{\partial^2 u}{\partial^2 x}+\frac{\partial^2 u}{\partial^2 z}\right). \tag{4}$$

After rearranging we get:

$$\frac{\partial u}{\partial t}+\frac{\partial}{\partial x}\left(u^2+\frac{p}{\rho}-\frac{1}{\rho}\tau_{xx}-\nu\frac{\partial u}{\partial x}\right) =\frac{\partial}{\partial z}\left(-uw+\frac{1}{\rho}\tau_{zx}+\nu\frac{\partial u}{\partial z}\right). \tag{5}$$

Where, ν and ν_t are molecular and eddy viscosities, respectively; τ_{xx} and τ_{zx} are turbulent (Reynolds) stresses. These stresses can be determined based on the Boussinesq relations and the eddy-viscosity concept as follows.

$$\tau_{xx}=-\rho\overline{u'u'}=\rho\nu_t\frac{\partial u}{\partial x}.$$
$$\tau_{zx}=-\rho\overline{u'w'}=\rho\nu_t\frac{\partial u}{\partial z}. \tag{6}$$

Integrating (2) over the flow cross-section A and neglecting the effect of molecular viscous stresses, the momentum equation is transformed into:

$$\frac{\partial U}{\partial t}+\frac{\partial}{\partial x}\left((1+\beta)U^2+\frac{1}{\rho}\int_A p dA-\frac{A}{\rho}T_{xx}\right) =\frac{1}{\rho}\int_A\frac{\partial}{\partial z}\tau_{zx}dA. \tag{7}$$

In which, the averaged quantities are:

The energy correction factor: $\beta=\int_A\left(\frac{u}{U}\right)^2 dA-1$. $\beta = 0$ for uniform flow.

Depth-averaged velocity: $U=\frac{1}{A}\int_A u dA.$

Depth-averaged normal stress: $T_{xx}=\frac{1}{A}\int_A\tau_{xx}dA=\rho\bar{\nu}_t\frac{\partial U}{\partial x}.$

with $\bar{\nu}_t$ being the depth-averaged eddy viscosity.

Equation (7) can be rewritten as:

$$\frac{\partial Q}{\partial t}+\frac{\partial}{\partial x}\left(\frac{Q^2}{A}+gI_{1P}\right)=\frac{\partial}{\partial x}\left(\frac{A}{\rho}T_{xx}\right)+\frac{1}{\rho}\int_A\frac{\partial}{\partial z}\tau_{zx}dA. \qquad (8)$$

Where we have substituted $\frac{\partial}{\partial x}(\beta)\approx 0$ and I_{1P} is the hydrostatic pressure force term

$$I_{1P}=\int_A(h-z)dA.$$

The second term on RHS of (8) accounts for the effects of the turbulent shear stress (hereinafter designated R^*). Without the presence of a discontinuity (e.g. a jump) in the flow, this term can be quantified in the following

$$R^*=\frac{1}{\rho}\tau_{zx}\Big|_{z=0}^{z=Z_s}=\frac{1}{\rho}\overline{B}(\tau_{zx}\big|_{z=Z_s}-\tau_{zx}\big|_{z=Z_b}). \qquad (9)$$

Where, Z_s and Z_b stand for the elevations at the surface and the bottom, respectively.

If the shear stress is assumed zero at the surface, R^* retains only the bed shear stress, i.e. the second term on RHS of (9). Further simplification by neglecting the contribution from the normal stress T_{xx}, (8) reduces to the ordinary shallow water equation (or St. Venant). It is worth noticing, on mathematical grounds, that the integration in (9) is only viable as long as τ_{zx} is differentiable at any arbitrary elevation z over the flow depth domain. In other words, τ_{zx} must be first continuous and then $\partial\tau_{zx}/\partial z$ must exist or be bounded at any z.

However this may not be the case over a vertical section in a turbulent hydraulic jump, where a part of the roller slides against the incident flow (see e.g. [14]). In the mechanical sense, along the lower limit of the roller there exists sliding stresses against the flow underneath. These sliding forces make τ_{zx} discontinuous along this boundary and thus indifferentiable. Further, as the flow structure in the roller is violently turbulent with entrained air bubbles and vortices, it is uncertain that whether τ_{zx} is continuous over the roller.

From the above, R^* resulting from the integration over the entire water depth including the roller may result in errors in the horizontal momentum balance. Therefore, the roller should be treated separately as a turbulent source regardless of its internal turbulent structure. Following this approach, R^* is integrated until the lower limit of the roller and then supplemented with the shear stress imposing by the roller:

$$R^*=R_{jp}-\frac{1}{\rho}\frac{A}{h}\tau_b=\frac{1}{\rho}\frac{A}{h}(\tau_r-\tau_b). \qquad (10)$$

Where the subscript ($_r$) denotes the lower limit of the roller, τ_r is the shear stress imposing by the roller. R_{jp} is the stress term arising from the roller:

$$R_{jp}=\frac{1}{\rho}\overline{B}\tau_{zx}\big|_{z=Z_s}=\frac{1}{\rho}\frac{A}{h}\tau_r. \qquad (11)$$

As we regard the roller as an independent source of turbulent energy that transmits into the flow underneath. Mechanically, τ_r can therefore be estimated through the work done by the roller.

$$\tau_r=\rho\frac{D_t}{u_r}=\rho\frac{D^*}{\varepsilon_j u_r}. \qquad (12)$$

In which D_t is the production of the turbulent energy by the roller or loss of the mean flow energy to turbulence, D^* is the dissipation of the turbulent energy, which is unnecessarily equal to D_t, u_r is a nominal relative velocity between the roller and the incident flow, ε_j is an energy efficiency factor, ε_j =1 implies a local equilibrium.

In a turbulent flow, loss of the mean flow energy is first converted to the turbulent kinetic energy (via production) and then gradually dissipated into heat (via dissipation). It is therefore rational, in a jump, to relate the dissipation D^* to the head loss (energy loss expressed in water head) across the jump:

$$D^*(x)=\beta_h\frac{gq\delta h}{L_{jp}}. \qquad (13)$$

In which $D^*(x)$ is the space-varying energy dissipation, δh is a local head loss, L_{jp} is the length of the jump, q is the unit discharge, and β_h is an energy correction factor. With (13) substituted, (12) can be rewritten:

$$\tau_r=\left(\frac{\beta_h}{\varepsilon_j}\frac{U}{u_r}\right)\times\frac{\rho gh\delta h}{L_{jp}}=\beta_j\beta_u\frac{\rho gh\delta h}{L_{jp}}. \qquad (14)$$

Where we have substituted $q=U*h$, U and h are the depth-averaged flow velocity and the mean flow depth, respectively, $\beta_j=\beta_h/\varepsilon_j$ and $\beta_u=U/u_r$ are empirical coefficients to be specified later.

Physically, β_j stipulates the spatial distribution of the dissipation D^* in relation with the production D_t, and β_u is a nominal relative velocity factor.

Now the jump source term in (11) turns into:

$$R_{jp}=\beta_u gA\frac{\delta h(x)}{L_{jp}}=\beta_u gAS_{jp}. \qquad (15)$$

Where $\delta h(x)=\beta_j*\delta h$. The term $S_{jp}=\delta h(x)/L_{jp}$ represents the slope of the head loss across the jump.

The inclusion of the above jump source term in the momentum equation requires the spatial distribution of $D^*=D^*(x)$ or $\delta h=\delta h(x)$. Preceding studies of turbulent jumps (see e.g. [11]) indicate empirical distributions of the dissipation D^* can be adopted, realizing some characters of the jump turbulence. Then, the spatial distribution of δh is as follows.

$$\delta h(\lambda)=\Delta h.f(\lambda). \qquad (16)$$

Where Δh is the total head loss across in a classical hydraulic jump, $f(\lambda)$ is a shape function of the energy loss.

To specify $f(\lambda)$, some relevant characters of a turbulent jump are followed. These are the turbulent production is mostly generated within the roller length, but the dissipation spreads over a distance of several times the jump length. Also, the largest dissipation occurs at the central region of the roller (see e.g. [11], [14]).

Mathematically, the following properties of this function are realized from the above (see also Fig.2):

$$f=0. \quad \text{for} \begin{cases}\lambda=0 & (x=x_1)\\ \lambda\to\infty & (x\to\infty)\end{cases} \qquad (17a)$$

$$f=f_{\max}. \quad \text{for } \lambda=1\ (x=x_1+1/2L_{jp})$$

$$f_\lambda>0. \quad \text{for } \lambda<1 \qquad (17b)$$

$$f_\lambda<0. \quad \text{for } \lambda>1$$

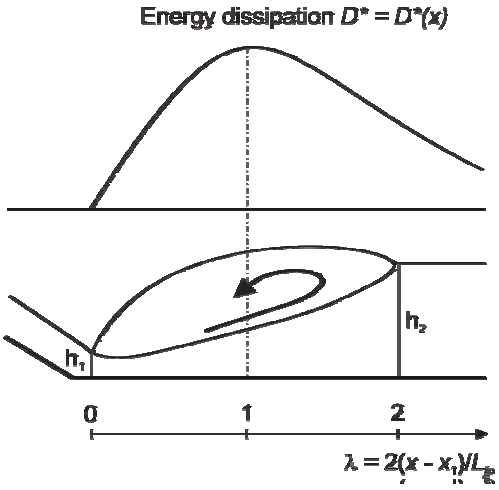

Figure 2. Spatial distribution of the energy dissipation

$$\int_0^{\infty} f(\lambda)d\lambda = 1. \tag{17c}$$

Where, λ is a dimensionless length parameter $\lambda = \dfrac{2(x-x_1)}{L_{jp}}$.

The following function is just found that satisfies fully the above criteria (17a) through (17c):

$$f(\lambda) = \lambda e^{-\lambda}. \tag{18}$$

Finally, the horizontal momentum equation (8) can be rewritten as follows:

$$\frac{\partial Q}{\partial t} + \frac{\partial}{\partial x}\left(\frac{Q^2}{A} + gI_{1P}\right) = \frac{\partial}{\partial x}\left(\bar{\nu}_t A \frac{\partial U}{\partial x}\right) + gA(S_{bx} - S_f + \beta_u S_{jp}). \tag{19}$$

Where S_{bx}, S_f, and S_{jp} are the bottom, friction, and jump head loss slopes, respectively.

The equation of continuity reads:

$$\frac{\partial A}{\partial t} + \frac{\partial Q}{\partial x} = 0. \tag{20}$$

Omitting unnecessary high order terms O(2), the first term on the RHS of (19) can be approximated as:

$$\frac{\partial}{\partial x}\left(\bar{\nu}_t A \frac{\partial U}{\partial x}\right) \approx \bar{\nu}_t \left(\frac{Q}{A^2}\frac{\partial A}{\partial x} - \frac{1}{A}\frac{\partial Q}{\partial x}\right)\frac{\partial A}{\partial x}. \tag{21}$$

Where $\bar{\nu}_t$ is specified based on the relation between the gradient of the near bed velocity profile with the bed shear stress.

The equation system of (20) and (19) can be written in a conservative form and solved using an upwind (shock-capturing) numerical scheme. In the present model, the well-known first order Roe's numerical scheme solved in conjunction with the finite volume method (FVM) is adopted (see e.g. [15]). To resolve numerical difficulties, such as arising from source terms induced by abrupt bed level variations and presence of hydraulic jumps, the source terms on the RHS of (19) are also upwinded according to the approach of Varquez-Cendon [19].

The laboratory experimental data of the jump surface profile of Gharangik documented in [4] is selected to calibrate the empirical coefficient in the jump source term (β_u). The experiment was carried out in a rectangular and horizontal flume with Froude numbers between 2.30 and 7.0.

Good agreement of the surface profiles between the model simulation and the measurement is found for a fixed value of the nominal relative velocity factor $\beta_u = 2.0$. Because of space limited, only two representative cases of Froude numbers of 7.0 and 2.3 are reported here as shown respectively in Figs. 3 and 4. In the simulations the Manning coefficient was varied in the range between 0.008 and 0.010, which is in conformity with [4].

It is worth mentioning that the present study disregards undular jumps (waves), i.e. Froude number less than 2.0, because of their insignificant effects on the sediment transport. Also, the shallow water equations are not able to model this specific type of short waves.

III. FLOW STRUCTURE AND SEDIMENT TRANSPORT

A. The Flow Structure in Hydraulic Jumps

The turbulence and flow structure in hydraulic jumps have been studied extensively given their importance in the design of hydraulic works. In morphological modeling they are also crucial to the computation of the sediment transport rate. From literature, modeling of the flow in hydraulic jumps can be tentatively classified into two different levels of hydrodynamics. In the first level, viz. full hydrodynamics, the RAN equations (or similar type) coupled with the standard turbulent closure k-ε model are used to resolve the flow structure. Models of this type are, for example, as described in [1], [9] and [10]. In the second level, which is simpler and less hydrodynamic, the shape of the velocity profile is empirically specified in several zones over the vertical or is based on a simplified turbulent closure model (e.g. one or zero equation). Some typical models are described in [14] and [11].

The flow structure in turbulent hydraulic jumps is highly complex. A more hydrodynamic model does not always mean more reliable as our descriptions of the processes involved are also limited. Hence, in many cases

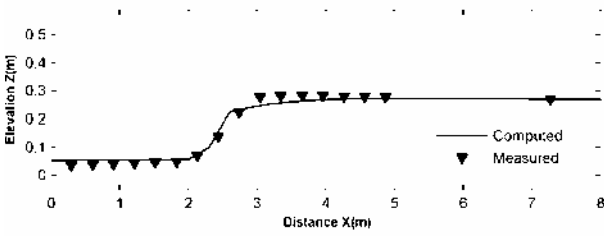

Figure 3. Surface jump profile for Froude = 7.0

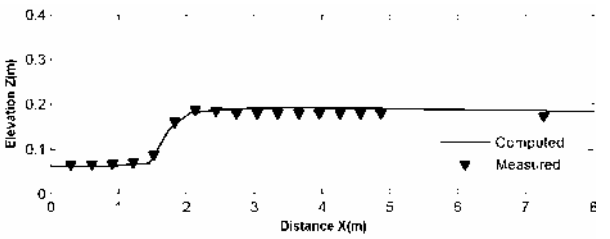

Figure 4. Surface jump profile for Froude = 2.3

of engineering practice, the latter approach is more efficient, providing that the level of reliability is sufficient.

To be more efficient and in consistent with the jump modeling discussed in the previous section, a three-layer approach is used here to specify the flow structure in the hydraulic jump. Whereby, the flow depth domain in the hydraulic jump is divided into three layers as follows (see also Fig.1). The shape of the velocity profile follows the approach of Ohtsu as reported in [3], which is commonly used for the jump modeling. Other similar formulations can be found in [5].

1) The boundary (or near wall) layer ($Z_o \le z \le \delta_b$): from the bottom to the elevation of the maximum horizontal velocity U_m. The velocity in this layer follows the law of the wall jet, increasing away from the bed in a power manner:

$$\frac{u}{U_m} = \left(\frac{\sigma}{\sigma_b}\right)^{\alpha} \text{. with } \alpha = 1/7 \tag{22}$$

2) The mixing (middle) layer ($\delta_b \le z \le Z_r$): between the boundary layer and the surface roller. The velocity distribution in this zone is quadratic exponential.

$$\frac{u}{U_m} = \exp\{-[\eta(\frac{\sigma}{\sigma_b} - 1)]^2\}. \tag{23}$$

3) The roller layer ($Z_r \le z \le h$): is treated as a "dead" layer, only providing the shear stress boundary to the incident flow. The flow structure in this zone is disregarded since it is irrelevant to the breach sediment transport.

The boundary layer gradually grows in the streamwise direction, starting from the toe of the jump. The thickness (δ_b) of the boundary layer can be deduced from Hager [5], using the dimensionless length λ and $L_{jp} = mL_r$ (L_r is the length of the surface roller).

$$\frac{\delta_b}{h_2 - h_1} = 0.06\left[1 + 5\left(\frac{m\lambda}{2} - \frac{1}{4}\right)^2\right]. \quad \frac{0.1}{m} \le \lambda \le \frac{2.8}{m} \tag{24}$$

In the above formulations, σ is the dimensionless vertical ordinate $\sigma = z/h$, $\sigma_0 = Z_0/h$, $\sigma_b = \delta_b/h$, $\sigma_r = Z_r/h$, $U_m = u(\sigma = \sigma_b)$, $\eta = 0.44$ deduced from the formulation of Ohtsu [3], and $m \approx 1.25$.

The maximum velocity at the top of the boundary layer can be determined by averaging over the vertical domain $[\sigma_0, \sigma_r]$:

$$\frac{1}{\sigma_r} U = \frac{1}{\sigma_r}\left(\int_{\sigma_o}^{\sigma_b} u d\sigma + \int_{\sigma_b}^{\sigma_r} u d\sigma\right). \tag{25}$$

It is noted that $1/\sigma_r$ on the RHS of (25) is the correction to the depth-averaged velocity as in the flow model the mean velocity U is averaged over the entire depth domain including the roller. After some algebraic manipulation, (25) becomes:

$$U_m = \frac{U}{\sigma_b\left(\frac{\sqrt{\pi}}{2\eta}\text{erf}(\eta(\frac{\sigma_r}{\sigma_b} - 1)) + \frac{1}{1+\alpha}\right)}. \tag{26}$$

Where *erf*(•) is the error function. This function is asymptotic to unity (*erf*(•)→1.0) as $\sigma_r/\sigma_b \ge 5$, which is always the case within the jump as can be seen from (24). Hence, (26) can be further simplified to:

$$U_m = \frac{U}{\sigma_b\left(\frac{\sqrt{\pi}}{2\eta} + \frac{1}{1+\alpha}\right)}. \tag{27}$$

The effect of the roller height in the determination of U_m is therefore eliminated.

Knowing the depth-averaged velocity U from the flow model, the velocity profile over the flow depth is fully determined using (22) and (23) together with (24) and (27).

B. Breach Sediment Transport

In terms of sediment transport, the breach channel is split into two parts as the transport in that under the effects of the hydraulic jump is exceptional.

Outside the jump, a suitable transport approach can be just used. An investigation of various formulae for this purpose is shown in [20]. In the present model, the formulae of Van Rijn ([17] and [18]) are used. These formulations are widely used in practice, especially eligible for purposes of numerical morphological modeling.

To the authors' knowledge, there has been no study on the sediment transport under turbulent hydraulic jumps, for which more physical insights into the sediment bursting processes are needed. In the present model, based on the above flow structure, we propose in the following a computational approach for this manner.

We consider the total transport load as the sum of the suspended load and the bed load.

The suspended load is calculated as the integration of the product between the velocity *u(z)* and the sediment concentration *c(z)* over the water depth.

$$q_s = \int_a^{Z_r} u(z)c(z)dz. \tag{28}$$

The concentration profile follows the diffusion model and can be determined numerically:

$$c(z)w_s + \varepsilon_s(z)\frac{dc}{dz} = 0. \tag{29}$$

Where w_s is the sediment fall velocity, ε_s is the sediment mixing coefficient at height z above the bed. $\varepsilon_s(z)$ is adopted here as a parabolic-constant distribution [18].

In the jump, the maximum horizontal velocity is located near the bottom. Therefore, the shear stress exerts on the bed is high and the bed load transport is expected to occur under the sheet flow conditions. Bed-load formulae, in which the bed shear stress is based on the depth-averaged velocity such as in [17], appear to underestimate the transport. For this reason, the general bed load formulation of Ribberink [12] is selected.

$$\frac{q_b}{\sqrt{g\Delta d_{50}^3}} = M_b(\theta' - \theta_{cr})^n. \quad \text{for } \theta' > \theta_{cr} \tag{26}$$

Where $M_b \approx 11.0$ is an empirical constant, *n=1.65* is the dimensionless transport exponent, d_{50} is the median sediment diameter, Δ is the relative sediment bulk density, θ' and θ_{cr} are the effective and the critical Shields numbers, respectively.

The magnitude of q_b depends largely on the determination of the effective Shield number θ' or of the bed shear stress.

$$\theta' = \frac{\tau_b}{\rho g \Delta d_{50}} = \frac{u_*^2}{\Delta g d_{50}} \tag{27}$$

Where u_* is the bed friction velocity.

In steady flows, the bed shear stress τ_b can be related to the depth-averaged velocity U, assuming a logarithmic profile over the entire water depth:

$$\tau = \frac{1}{2}\rho\frac{U^2}{C^2} \qquad \text{with } C = 18\log\left(\frac{12h}{k_s}\right) \tag{28}$$

$$\begin{aligned} k_s &= 3\theta' d_{90} \qquad \text{for } \theta' > 1 \\ k_s &= 3d_{90} \qquad \text{for } \theta' < 1 \end{aligned} \tag{29}$$

Where C is the Chezy coefficient, k_s is the effective roughness according to Van Rijn [17].

Alternatively, following the law-of-the-wall, τ_b can be determined using the velocity at a prescribed level above the bed in the logarithmic layer [12].

$$\tau_b = \frac{1}{2}\rho f_c u_b^2. \tag{30}$$

$$f_c = 2\left(\frac{0.4}{\ln Z_\delta / Z_0}\right)^2 \tag{31}$$

In which f_c is the friction coefficient, Z_δ is an arbitrary level, $Z_0 = k_s/30$ is the zero velocity level, u_b is the velocity at Z_δ.

The determination of the bed shear stress according to the latter approach is generally more valid than the former one since only a small logarithmic layer near the bed is assumed.

In the current model, to avoid unnecessary iteration procedures in the determination of the effective Shields number as k_s is also a function of θ' in the jump ($\theta'>1$), we estimate the bed shear stress at height $Z_\delta = k_s$. From (31) this results in a constant friction coefficient f_c (~0.02). Using (22) for u_b, (29) for k_s and then substituting into (30) yields:

$$\frac{\tau_b}{\rho} = u_*^2 = \frac{1}{2} f_c' U_m^2. \tag{32}$$

with f_c' being another friction coefficient:

$$f_c' = f_c\left(\frac{3\theta' d_{90}}{\delta_b}\right)^{2\alpha}. \tag{33}$$

The effective Shields number then follows:

$$\theta' = \left(\frac{1}{2} f_c U_m^2 \left(\frac{3d_{90}}{\delta_b}\right)^{2\alpha}\right)^{1/(1-2\alpha)}. \tag{34}$$

It is noted that although we have estimated the friction coefficient at Z_δ (i.e., $u_b = u(Z_\delta)$), the relations (32) through (34) allow the explicit determination of the bed shear stress using the maximum velocity U_m at the top of the boundary layer.

IV. THE BREACH GROWTH

In this section we briefly introduce the new approach and its associated parameters for the numerical computation of the breach growth. The detail of this elaboration can be found in the previous work of the authors [16].

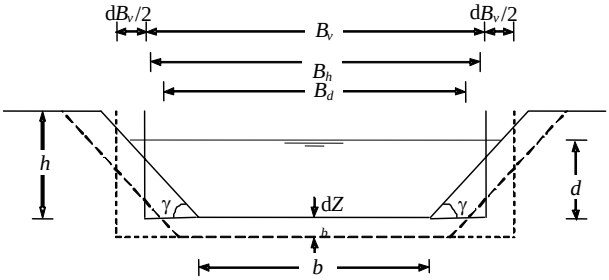

Figure 5. The schematized breach section and the channel characteristc width

A. Governing Equation of The Breach Growth

The breach growth follows the principle of mass conservation, in which the changes of both the bed and the banks of the channel are simultaneous:

$$\frac{\partial Z_b}{\partial t} B_h - \frac{\partial B_h}{\partial t} h + \frac{1}{(1-p)}\frac{\partial (q_{st} B_d)}{\partial x} = 0. \tag{35}$$

with:

$$B_h = b + \frac{h}{\tan\gamma}. \qquad B_d = b + \frac{d}{\tan\gamma}. \tag{36}$$

Where it is assumed that the cross-section of the breach channel is trapezoidal (see Fig. 4), q_{st} is the total transport rate per unit width, p is the bed porosity, B_h and B_d ($B_h \geq B_d$) are channel widths averaged over the cross-section height (h) and over the water depth (d), respectively, b is the bottom width, γ is the side slope.

For the case of wide channels, i.e. $B_d \approx B_h$, (35) reduces to the conventional equation for the bed level change only.

Equation (35) is just a point-wise equation that does not present the channel as a whole in quantifying the width increase. As Z_b varies along the breach, B_h and B_d also varies accordingly. In one dimensional morphological modeling, it is necessary to seek for a unique breadth quantity that can characterize the channel width as a whole. To do this, integrating (35) with respect to the distance x over the entire channel length L yields:

$$\frac{\partial B_v}{\partial t} h_L - \left(\frac{\partial Z_b}{\partial t}\right)_L B_v = \left(\frac{\partial A}{\partial t}\right)_L. \tag{37}$$

In which we have defined the averaged quantities as follows.

Channel characteristic width (volumetric) B_v:

$$B_v = \frac{\int_L B_h h dx}{\int_L h dx} = \frac{V_c}{\int_L h dx}. \tag{38}$$

Where V_c is the total channel volume, $\partial B_v/\partial t$ is the rate of the channel lateral growth.

The averaged vertical growth rate $(\partial Z_b/\partial t)_L$:

$$\left(\frac{\partial Z_b}{\partial t}\right)_L = \frac{\int_L \frac{\partial Z_b}{\partial t} dx}{L}. \tag{39}$$

The averaged rate of change of the channel cross-sectional area $(\partial A/\partial t)_L$:

$$(\frac{\partial A}{\partial t})_L = \frac{\frac{1}{(1-p)}\int_L \frac{\partial (q_s B_d)}{\partial x} dx}{L}. \quad (40)$$

The averaged channel depth h_L:

$$h_L = \frac{\int_L h dx}{L}. \quad (41)$$

Geometrically, B_v in (38) is in fact the volume-averaged width. In general, B_v is of the order of B_h and is equal to B_h for regular channels.

Equation (37) is used later on to quantify the channel lateral enlargement using the new characteristic B_v.

B. The Channel Growth Index K_{vl}

Equation (37) contains two unknown growth variables, i.e. the lateral ($\partial B_v/\partial t$) and the vertical ($(\partial Z_b/\partial t)_L$) growth rates. To solve the equation, an additional parameter, namely the growth index K_{vl}, is introduced and defined as the growth rate ratio of the vertical to the lateral as follows:

$$K_{vl} = \frac{-(\frac{\partial Z_b}{\partial t})_L}{\frac{\partial B_v}{\partial t}}. \quad (42)$$

It is worth mentioning that this parameter is valid only for erosional channels, viz. as a whole $K_{vl} \geq 0$ and thus $(\partial Z_b/\partial t)_L$ is negative and $\partial B_v/\partial t$ is positive.

In a homogenous erosional channel, the growth index generally expresses the relative strength between the transport capacity along the bottom and the sides of the channel. In this sense, in [16] we have formulated and calibrated this parameter using the laboratory data of the overwash channel experiments. Interestingly, it is found, as shown below, to depend mainly on the instantaneous channel geometry and the transport exponent n.

$$K_{vl} = \frac{1}{\frac{B_v}{h_L}\tan\gamma - 1}\left((n+1) - \frac{2}{\cos\gamma}\right). \quad (43)$$

Equation (43) reveals some physics of the channel growth in general. Apart from the power of transporting sediment (the exponent n), geometric factors considerably affect how the channel grows, e.g. a flatter cross-section (large B_v/h_L) tends to have a stronger lateral growth and vice versa. Also, a cross-section of steep side slopes (large $\tan\gamma$ and small $\cos\gamma$) slows down the vertical growth as can be explained physically that bank avalanching feeds extra sediment into the flow.

C. Computation of The Lateral and Vertical Growth

Manipulating (40) and substituting (42) into (37) yields:

$$\left(h_L + K_{vl} B_v\right)\frac{\partial B_v}{\partial t} - \frac{1}{(1-p)}\frac{q_s^*}{L} B_v = 0. \quad (44)$$

Where q^*_s is the net sediment transport rate over the channel.

Since K_{vl} is related to B_v through (43), (44) can be solved numerically with respect to B_v using a simple discretized scheme.

The updating of the bed level follows a slightly modified version of (35):

$$-\frac{\partial}{\partial t}(B_h h) + \frac{1}{(1-p)}\frac{\partial (q_s B_d)}{\partial x} = 0. \quad (45)$$

Where B_h and B_d can be calculated via the use of the characteristic width B_v:

$$B_h \cong B_v - \frac{1}{\tan\gamma}(h_L - h).$$
$$B_d \cong B_v - \frac{1}{\tan\gamma}(h_L - d). \quad (46)$$

To avoid a spurious discontinuity of the bed due to an abrupt increase of the transport rate at the toe of the jump, the calculated transport field is smoothed out using a response function before it is used in (45) to update the bed level change.

$$\frac{dq_{st}}{dx} = \frac{q_{st,c} - q_{st}}{L_a}. \quad (47)$$

Where $q_{st,c}$ is the total sediment transport rate obtained directly from the transport module, q_{st} is the transport after smoothing and is used for updating the bed change, L_a is a adaptation length for the sediment transport. L_a is of the order of several jump lengths and is found using a trial and error procedure.

It notes that the smoothing procedure is widely accepted and considered rational in numerical morphological modeling since by nature the flows need some transitional distance before they can fully adapt to the local conditions (see e.g. [6]).

Behind the downstream end of the breach channel, the flow is complexly three dimensional with horizontal circulations. The breach sediment spreads out widely. Therefore, the mass balance equation for the channel growth ((44) and (45)) is no longer valid at this location. To overcome this problem, a non-depositing bed boundary is applied. From the laboratory observation, this assumption seems reasonable.

V. MODEL CALIBRATION AND VERIFICATION

The breach model formulated so far needs empirical calibration and verification. For this purpose, we utilize the existing data from the two breach experiments, viz. the (field) Zwin'94 and the laboratory experiment of Caan, which were used to calibrate and validate the BRES model [20]. The laboratory experiment is selected for the model calibration since the measurement is the most complete, including the scour hole development. The model is then verified against the data of the field experiment.

Detail of the experimental procedures and the measurements can be found in [20] and [2]. In the following only a brief description is given.

In both experiments, the breach was initiated by a small pilot channel on the dike crest and the breach erosion process was then followed.

The Zwin'94, a field test, was carried out in 1994 in the Zwin tidal channel. The dike crest was 8.0m wide and was 3.3m above the mean sea level. The test was purposefully elaborated to measure the complete breach erosion process. Unfortunately, due to a technical failure during the experiment very limited data of the breach level were logged and only those of the channel lateral development were fully measured. Because of the incident, the experiment still left some ambiguity in the scour development and in the reliability of the breach level

observation. It was then decided to perform an additional laboratory experiment. The Caan's experiment consisted of two tests of small dike constructed in a wave basin. Video and photo cameras were used to capture the vertical and lateral breach development. The breach profile was videoed through a glass-wall which acts as the central axis of the breach. Initially, water flowed through a pilot channel of 3cm deep and 20 cm wide notched on the dike crest. The flow spilled downstream into a dry sand polder. The first test was less successful because the sand bed was so thin that the basin bottom was exposed shortly after the start of the breaching. From this experience, the dike geometry and the sand bed were adjusted and the breach was successfully occurred in the second test.

Figs. 6 through 9 show the calibration results for the laboratory dike breach growth of Caan (1996). The model predictions for the Zwin'94 breach growth are given in Figs. 10, 11, and 12. In general, the scour development in the breach channel is successfully simulated. Fair resemblance with the measurement is found.

VI. Discussion of Results

The present model successfully simulates the breach growth in both vertical and lateral directions, including the development of the scour hole in the breach channel. The scour development during the first three stages is in agreement with the measured data (see Fig. 10 with a limited number of observed scour depths). However, the final scour depth is still underestimated (in the Zwin'94 experiment, the maximum scour depth was claimed to be about 2.3m beneath the breach bottom while the present model predicts that of about 1.7m as shown in Fig. 11). This may be, in part, because the mechanism for the scour development during the last two stages is unrelated to the hydraulic jump and therefore is not yet covered by the model. For this, another turbulence-induced scouring mechanism as described in [7] might be used. Nevertheless, it is worth mentioning that the profiles were captured along the glass wall (in the laboratory case) or along the central breach axis (in the field experiment), where the maximum gully depth is expected. Further, there are uncertainties, e.g. inhomogeneous porosity due to uneven compaction, which are not able to be accounted for in the breach model. The laboratory experiment [2] showed appreciable differences in the breach profile between two control tests with the same testing conditions except for the sand compaction that was definitely not the same everywhere and for every test. This may explain the sudden increase of the scour depth observed in the tests. The scour depth was sometimes even larger than the mean flow depth and the breach flow was "poured" into a deep hole. For this reason, the scour depth in the laboratory experiment was in fact exaggerated by small-scale effects (geotechnical-related) phenomena.

Unlike the BRES model, the pilot channel plays a role in the present breach model as a part of the initial conditions. The significance of the channel geometry can be understood via the growth index as mentioned earlier. In general, a bigger initial breach would result in a faster breaching and vice versa. Since the hydraulic boundary conditions are dynamic during breaching, the effects of the initial breach dimensions on the breaching process are generally complex. Fig. 9 shows the increase of the breach width in the first stages (up to 71 sec.) of Caan's

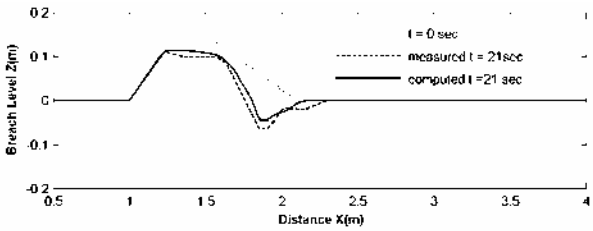

Figure 6. Caan's test 2 - the breach profile at t = 21sec.

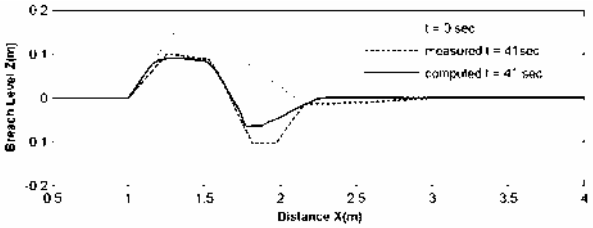

Figure 7. Caan's test 2 - the breach profile at t = 41sec.

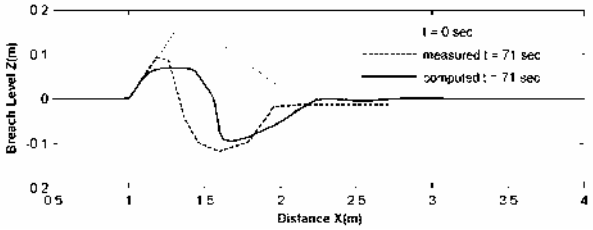

Figure 8. Caan's test 2 - The breach profile at t =71 sec.

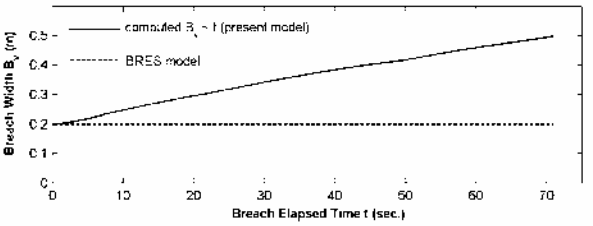

Figure 9. Caan's test 2 - The breach lateral growth

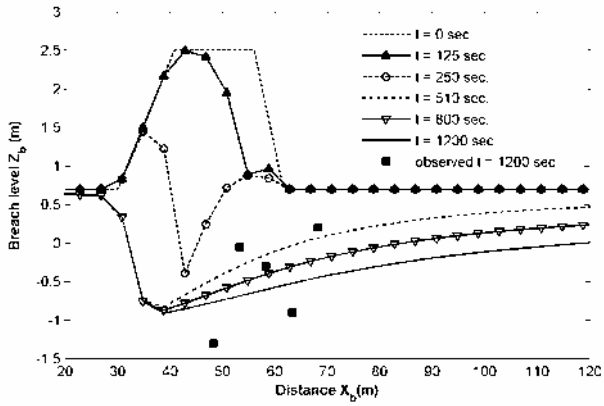

Figure 10. Zwin94 field experiment – Computed development of the breach profile up to t = 1200 sec.

experiment. The present model predicts an increase from 0.20 m to about 0.5 m, whereas the BRES model assumes an unchanged width for this period. The latter result seems

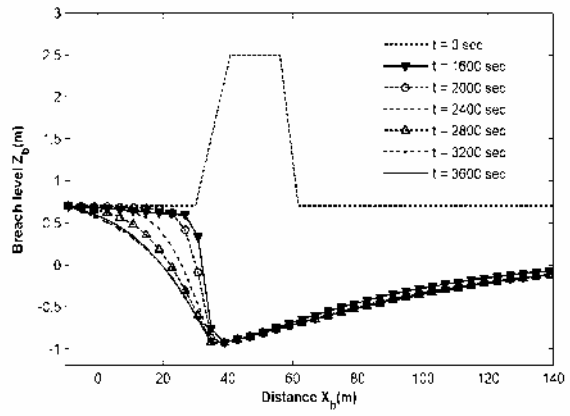

Figure 11. Zwin94 field experiment – Computed development of the breach profile up to t = 3600 sec.

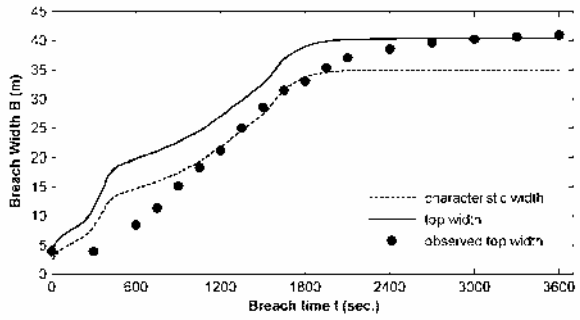

Figure 12. Zwin'94 field experiment – Development of the breach width: computed versus measured

doubtful since it is unlikely that the breach was not widened when about two third of the dike was completely washed out (see Fig. 8). Likewise, Fig. 12 shows the model prediction for the breach (top) width increase in comparison with that measured in the Zwin'94 experiment. Fair agreement is found. It should be noted that this is the average top width determined from the characteristic width B_v and the channel depth h_L (since in the model it is variant along the breach), while in both the experiments this width was measured at a fixed section on the breach crest.

The laboratory data and the model simulation reveal some insights into the dynamics of the scour hole. The scour hole starts to form in the breach channel at the location of the turbulent hydraulic jump, where the sediment transport capacity under the jump prevails over the sediment supply from the upstream breach flow. The scour hole is highly dynamic as it associates with the jump location and the jump turbulence, which is largely stipulated by the instantaneous relative strength between the upstream flow and the downstream water level as well as the bed roughness. In the above case of the laboratory experiment, i.e. the polder breach, the jump progresses upstream as the retrograde erosion process takes place and the downstream water level increases. The scour hole thus expands gradually upstream. In general, it is expected that breaching with low (or dry) downstream water level certainly leads to a more pronounced scour depth.

Also, it appears from the laboratory data as well as the model results that the scour attains a major part of its final depth during the first stages of the breaching process before the complete washing out of the remaining sand plug. After that (say after stage III of Visser [20]) the scour slows down its development in depth considerably, while expanding in both upstream and downstream directions. This is because the jump weakens or even disappears as the driving water head difference tends to neutralize in the last stages. This somewhat disagrees with the breach profile development described in [20], where the scour is assumed to develop only in the last two stages.

VII. Conclusions

The development of the scour hole in the breach channel phases out noticeably the breach growth in comparison with the five-stage erosion process defined by Visser [20]. The turbulent hydraulic jump is responsible for the scour hole formation and development during the first stages of breaching. The incorporation of the jump modeling in breach models is the key to improve model predictions for the vertical breach growth, allowing simulation of the scour formation. However, better understanding of the sediment transport under turbulent hydraulic jumps is crucial to further improve the modeling.

The new morphologic factors, i.e. the growth index and the characteristic channel width, which are introduced in association with the general equation for breach growth, allow the hydrodynamic computation of the breach growth in both vertical and lateral directions. It follows from the growth index that apart from the flow capacity of carrying sediment, the channel geometry (depth, width and side slope) plays an important role in the breach development.

The simulation results help gain some understanding of the dynamics of the scour in the breach channel. Under effects of the jump turbulence during the first stages of the breach erosion process, the scour hole is found to develop vigorously and attains major part of its final depth. In the last stages, the continuation of the scour hole development is unrelated to the jump and thus should be modeled with another scouring mechanism such as that of "local-scour holes" by Hoffmans [7].

In conclusion, the present model is capable of simulating the breach erosion process of sand barriers under arbitrary hydraulic conditions. Both the vertical breach growth including scour development and the lateral breach growth are successfully modeled without defining any evolutional stages.

Acknowledgment

The research was carried out under the framework of the coastal engineering cooperation project funded by the Royal Netherlands Embassy in Hanoi between Delft University of Technology and Hanoi Water Resources University.

References

[1] Busnelli, M.M., Numerical simulation of free surface flows with steep gradients, *Communications on Hydraulic and Geotechnical Engineering*, Report No. 01-3, 2001, Delft Univ. Techn., Delft, the Netherlands, 180 pp.

[2] Caan, C.P., Bresgroei: een experimental onderzoek naar de ontwikkeling van de ontgrodingskuil (Breach growth: an experimental investigation of the development of the scour hole), Master thesis, Hydraulic and Geotechnical Eng. Div., Dept. Civ. Eng., Delft Univ. Techn., Delft, the Netherlands, 1996.

[3] Chanson, H. and Brattberg, T., Experimental Study of the Air-Water Shear Flow in a Hydraulic Jump, *Int. J. Multiphase Flow*, 2000, 26, pp. 583-607.

[4] Gharangik, A. M. and Chaudhry, M. H., Numerical Simulation of Hydraulic Jump, *J. Hydr. Engrg.*, ASCE, 1991, 117, 9, pp. 1195-1211.

[5] Hager, W. H. , Energy Dissipators and Hydraulic Jumps, Kluwer Academic Publishers, Water Science and Technology Library, Dordrecht, the Netherlands, 1992, 288 pp.

[6] Jorgen Fredsoe and Rolf Deigaard, Mechanics of Coastal Sediment Transport, *Advanced Series in Ocean Engineering*, V. 3, 1992, World Scientific, 369 pp.

[7] Hoffmans, G.J., Two Dimensional Mathematical Modeling of Local-scour Holes, Ph.D Thesis, Delft Univ. Techn., Delft, the Netherlands, 1992, 198 pp.

[8] Kraus, N.C., Analytical Model of Incipient Breaching of Coastal Barriers, *Coastal Engineering Journal in Japan*, World Scientific, 2003, 45(4), pp.511-531.

[9] Liu Qinchao and Uwe Drewes, Turbulence Characteristics in Free and Forced Hydraulic Jumps, *J. Hydr. Research*, 1994, 32, 6, pp. 877-898.

[10] Long, D., Steffler, P. M. and Rajaratnam, N., A numerical study of submerged hydraulic jumps, *J. Hydr. Research*, IAHR, 1991, 29, 3, pp. 293-308.

[11] Madsen, P.A. and Svendsen, I.A., Turbulent Bores and Hydraulic Jumps, *J. Fluid Mech.*, 1983, 129, pp. 1-25.

[12] Ribberink, J. S., Bed-load Transport for Steady Flows and Unsteady Oscillatory Flows, *Coastal Engineering*, 1998, 34, pp. 59-82.

[13] Singh, V.P. (ed.), Dam Breach Modeling Technology, 1996, Kluwer, Dordrecht, the Netherlands.

[14] Svendsen, I. A., Veeramony, J., Bakunin, J. and Kirby, J. T., The Flow in Weak Turbulent Hydraulic Jumps, *J. Fluid Mech.*, 2000, 418, pp. 25-57.

[15] Toro, E.F. (ed.), Riemann solvers and numerical methods for fluid dynamics: a practical introduction. Springer-Verlag, Berlin, 1997, 624 pp.

[16] Tuan, T.Q., Verhagen, H.J., Visser, P., Numerical modeling of wave overwash at low-crested sand barriers, *Proc. 30th Coast. Engrg. Conf.*, USA, 2006, unpublished.

[17] Van Rijn, L.C., Sediment Transport, Part I: Bed Load Transport, *J. Hydr. Eng.*, ASCE, 1984, 110, pp. 1431-1456.

[18] Van Rijn, L.C., Sediment Transport, Part II: Suspended Load Transport, *J. Hydr. Eng.*, ASCE, 1984, 110, pp. 1613-1641.

[19] Varquez-Cendon, M.E., Improved Treatment of Source Terms in Upwind Schemes for the Shallow Water Equations in Channels with Irregular Geometry. *Journal of Computational Physics*, 1999, 148, pp. 497-526.

[20] Visser, P.J., Breach Growth in Sand-Dikes, *Communication on Hydraulic and Geotechnical Engineering*, Report No. 98.1, Delft Univ. Techn., Delft, the Netherlands, 1998, 172 pp.

KEY WORDS

Breach, Breach Growth, Lateral Growth, Vertical Growth, Breach channel, Breach profile, Growth index, Scour hole, Characteristic Width, Hydraulic Jump, Jump modeling, Numerical Modeling.

Design of Scour Protection for Sutong Bridge, P.R. China

C. Truelsen*, W. Shouchang**, O. Juul Jensen***, and Z. Gao****

* Ph.D., Coastal Engineer, COWI A/S, Parallelvej 2, DK-2800 Kgs. Lyngby, Denmark

** Deputy Chief Engineer of the Site Commanding Department of Sutong Bridge, Nantong, P.R. China

*** Director, Marine and Coastal Engineering, COWI A/S, Parallelvej 2, DK-2800 Kgs. Lyngby, Denmark

**** Professor, Nanjing Hydraulic Research Institute, Nanjing, P.R. China

This paper presents the results of scour assessment and conceptual design of scour protection structures for the Sutong Bridge, P.R. China. The SuTong Bridge, to date the Worlds Largest Cable-Stayed Bridge, is presently being constructed in the Yangtze River near the city of Nantong, P.R. China. The main pylons and approach piers are founded in the river and as a result they are susceptible to scouring of the erodible river bed. State-of-the-art methods have been used in the assessment and the design of scour protection for the SuTong Bridge. The designed scour protection primarily consists of quarry stones and is separated into three areas, Central Area, Outer Area and Falling Apron Area. During construction, extensive surveys using Multi-beam echo sounder were made in order to control and verify the amount of materials dumped. When finished, the scour protection is still a flexible structure that will be subject to some displacement of material. Therefore a detailed monitoring programme was prepared.

I. INTRODUCTION

The Sutong Bridge in the lower Yangtze River will be a cable stay bridge with approach bridges on both sides. It will thus cross the river with quite a number of bridge piers founded into the river bed. The main bridge will with its span of 1088 m be a world record cable stay bridge. The exact location of the Sutong Bridge is shown in Fig. 1.

The river is alluvial and highly volatile with large morphological changes. Further the river is subjected to the combined effect of the astronomical tide and the fresh water run-off and flow velocities can be very high exceeding 3.0 m/s in extreme conditions.

Therefore the river bed will respond almost immediately when introducing man-made structures such as bridge piers and pylons.

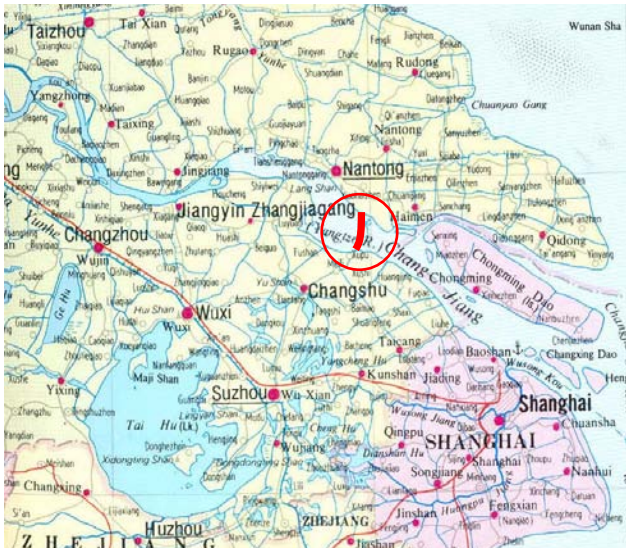

Figure 1. Location of Sutong Bridge, P.R. China

The present paper focuses on COWI's conceptual design of scour protection for the foundation structures of the two main pylons. Part of this work has been presented in [1].

II. HYDRAULIC DESIGN DATA

Design parameters are a combination of the current, water level and in some cases waves acting at the same time. To be conservative a 1/100 year return period wave has been combined with a 1/100 year current and the Mean Low Water Spring (MLWS). Details are outlined below.

Worst case for the scour protection is at low water level. The MLWS has been applied in the analysis:

MLWS: 1.0 m

The water depths at the two pylon locations are shown in Table 1.

The significant wave height for North and South Pylons are found in Table 1 where H_{max} can be taken as 1.8 x H_s. Corresponding wave periods have been assessed and also given in Table 1.

The design currents being a combination of tidal current and fresh water discharge are found in Table 1.

TABLE I.
SUMMARY OF HYDRAULIC CONDITIONS

Location	Water depth, h [m]	Significant Wave Height, H_s [m]	Peak Period, T_p [s]	Current Velocity, U [m/s]
North Pylon	30 m	2.24	9.0	3.06
South Pylon	16 m	2.52	9.2	3.18

III. RIVER MORPHOLOGY

A. *River bed and geotechnical conditions at the site(s)*

At the southern pylon, in about 20 m water depth the bed mainly consists of sandy materials. At the northern pylon, in about 30 m water depth the bed material is mainly silty loam and silty clay.

The natural material have approximately d_{50} = 0.1 mm in the main channel and lower elsewhere.

B. *Future morphology development without the bridge*

Without the bridge in place, the river may erode the river bed and change the position of the thalweg and river bank erosion may occur.

It appears from the bathymetric map, see Fig. 2, that there is a hardpoint immediately upstream of the bridge on the right bank. In Fig. 2 also two areas with potential for bank erosion have been marked.

Channel meanders have a bend radius of the order of 20 km. The main channel crosses from one bank to the other between bends. It seems the seawards flow is dominant in forming the river morphology. If an upstream bend is eroding, this may cause a shift in the channel pattern downstream.

The channel location at the bridge alignment seems controlled by the hardpoint immediately upstream on the right bank.

The river is the main waterway to the entire Yangtze Basin and the traffic by barges & boats etc. is very heavy. The banks of the river are controlled by river training works. The authorities regularly monitor the waterway, water depths and morphological development of the river and its bank protection. This is important to secure that the main thalweg stays in place under the main bridge.

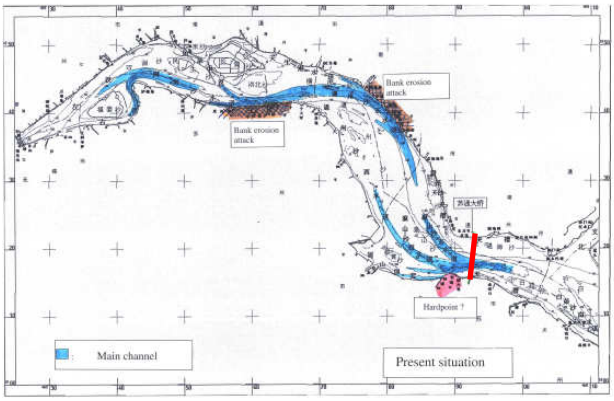

Figure 2. Present situation of the flow in the river

IV. BRIDGE PYLONS

A plan and cross-sectional view of the main bridge are shown in Fig. 3. The two main pylons consist of a pile cap located on top of a pile group. Horizontally the pile cap is approximately 48 m wide and 112 m long.

The following data applies for the piles:

Pile diameter: 2.5 m - 2.8 m
Distance between piles: 4 m - 5 m

V. DEVELOPMENT OF SCOUR PROTECTION CONCEPT

A. *Scour assessment*

As mentioned above, the Yangtze River is highly alluvial and carries a lot of sediment due to the high flow velocities. Therefore any man-made intervention obstructing the flow in any way will result in morphological changes, i.e. erosion or accretion of river bed material.

Table II and Table III are based on the results of the hydraulic model study made at Nanjing Hydraulic Research Institute for SuTong Bridge. They show results from the scour studies for different solutions including the solution now adopted using a foundation on large pile groups.

The scour depth is about 19 to 22 m and 17 to 19 m respectively for the S-pylon and N-pylon respectively. The differences reflect the difference in initial water depth of about 16 and 30 m at the pylons respectively, see Table II.

Besides the depth of scour for the no scour-protection situation an important aspect is the extent of the scour.

Table III shows the results of the studies.

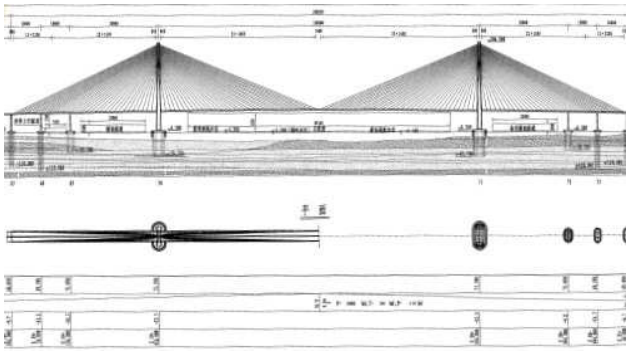

Figure 3. Plan and Cross-sectional view of main bridge

TABLE II.
MAXIMUM LOCAL SCOUR DEPTH

Position	Foundation type	Return period (year)			
		300	100	20	5
Main Bridge, South Pylon	Cofferdam	45.3	40.2	29.3	21.5
	Caisson (40 m x 88 m)	33.4	29.0	25.7	20.7
	Pile	21.9	19.1	16.2	13.5
Main Bridge, North Pylon	Cofferdam	41.2	35.5	27.4	20.4
	Caisson (40 m x 88 m)	30.4	27.1	22.7	18.7
	Pile	19.2	17.1	14.3	11.8

If again as an example, focus is made on the S-pylon and the solution for piles and 100 year Return Period, the extension of the scour from the centre of the pile group is 170 and 230 m in the N-S and E-W directions respectively. The extension is defined to where the scour depth is limited to 10 m.

Knowing that the pile group has a width of about 48 m and a length of about 112 m the extension of the scour from the structure is found as:

Extension, N-S Direction: (170-48)/2 = 61 m

Extension, E-W direction: (230-112)/2 = 59 m

It is interesting that the extension from the structure is about the same in all directions. This indicates that a scour protection structure should also in the first approximation have about the same width in all directions.

It is clear that it will be possible to design the bridge pylons to allow for such deep scour.

However, it was decided after geotechnical and structural calculations to include scour protection on the two main pylons, but not on all the other piers.

TABLE III.
MAXIMUM EXTEND OF SCOUR DEPTH OF 10 M

Position	Foundation type	Return period (year)	
		100	
		Width (m)	Length (m)
Main Bridge, South Pylon	Cofferdam	290	600
	Caisson (40 m x 88 m)	180	390
	Pile	170	230
Main Bridge, North Pylon	Cofferdam	260	580
	Caisson (40 m x 88 m)	170	350
	Pile	160	200

VI. CONCEPTUAL DESIGN

The ideas presented for scour protection have been developed based on COWI´s experience in combination with our understanding of the very difficult conditions in Yangtze River with deep water, high currents and high sediment transport as presented by the Client from other studies.

The major problem associated with the scour protection is its construction. The scour protection in itself shall be made in a way that it is not too difficult to construct and also that it will prevent scour during construction. It was assessed that if the bridge piers are made without prior scour protection the development of scour will be so rapid that it will be difficult to construct the scour protection later on and the bed level would have eroded to such a low level, that the advantage of the existing bed levels would have disappeared.

Therefore the scour protection has been designed in such a way, that it will allow for the construction of the piles through the central part of a temporary scour protection and then later on the final scour protection can be introduced.

It is further clear that due to the very high flow velocities and high sediment transport, the adopted scour protection scheme should be relatively simple and robust and not require very accurate dredging levels before placing of the material in the scour protection.

It should further be possible to construct the protection in smaller sections that together will constitute the protection. The final protection should be robust and able to function also with these unavoidable inaccuracies.

COWI has on the basis of this analysis refrained from the use of large prefabricated mattresses, gabions or large bamboo/willow mattresses, etc. Such solutions could be used but would be difficult to handle and place in the very high currents prevailing at the site.

The principal ideas for the scour protection of the Pylons of the Sutong Bridge include the use of three distinct areas or zones.

1. **The Central Area or Inner Zone**
   This zone includes the central area where the bridge piles for the main pylons and temporary structures are present. The area extends 20 m away from the structures. In this area the river bed shall be temporary protected by use of layers (3 nos.) of geotextile bags. The idea behind this concept is that by this action the river bed will be protected but it will still be possible to bore the piles through the protection. After completion of the piling the final protection is constructed with a filter layer of quarry-run and minimum 2 layers of armour stones (rock).

2. **Outer Area**
   Outside this the Outer Area is situated. It extends about 40 m further out from the Central Area, thereby the distance from to the edge to the structure is 60 m. This was based on a combined geotechnical and hydraulic assessment of the stability of the pile group. The scour protection consists of one layer of sand bags covered with a

layer of quarry-run on top of which is placed the same type of rock armor as for the central area.

3. **The Falling Apron Area**
Outside the Central and Outer Area is the Falling Apron area. Its width is varying according to an estimate of the scour depth and the width is set at 1.5 times the actual maximum expected scour depth. The material in this area consists of quarry-run on top of which layers of quarry stones are dumped.
The concept of the falling apron has been used in many countries for river training structures where the scour is expected to reach to a level significantly below the level at which the structure is/can be built. The principle is that the material in the falling apron will launch itself down the scoured slope that will thereby stabilize itself. It is previously been studied and used in [2].

The ideas developed have been turned into a conceptual design plan and cross-section for the S-pylon given in Fig. 4 and Fig. 5. This formed the basis for subsequent detailed design by Jiangsu Provincial Communication, Planning & Design Institute.

VII. SUPPORTING CALCULATIONS

A. ASSUMPTIONS

1) Amplification of flow

The presence of the structure under water will increase the flow velocity. This is taken into account through an amplification factor on the bed shear stress. The amplification depends upon the shape of the structure [3]. For a square-shaped structure the amplification of the bed shear stress is up to 3 for a 90 degree rotation and up to 9 for a 45 degrees rotation.

2) Critical Shields parameter

Incipient motion of stones resting on the river bed is characterized by a critical Shields parameter. A critical Shields parameter of the material used in the scour protection is shown in Table IV

Included in the critical Shields parameter value is a security that the stones is resting with no motion on the seabed for the inner and outer area. For sand bags in the temporary protection, it is not critical if there is a slight movement of the bags. For the falling apron it is emphasised that the materials are planned to mix and move down the slope.

B. CALCULATION METHODS

A short description of the method used for calculating the dimensions of the scour protection material is presented below. The Shields criterion is used to satisfy the stability of the top layer; namely, the Shields parameter calculated for scour protection material defined by

$$\theta = \frac{\left(U_{fm}\right)^2}{(s-1)gd_{50}}$$

must be smaller than θ_{cr}, the critical value of the Shields parameter corresponding to the initiation of motion at the top layer of the protective layer. In the above equation, s is the relative density of the protection material, g is the acceleration due to gravity and d_{50} is the mean particle size.

TABLE IV.
CRITICAL SHIELDS PARAMETERS FOR SCOUR PROTECTION MATERIAL

Item	Location	Critical Shields parameter, θ_{cr} [-]
Stones	**Inner area**	0.025
Sand bags		0.040
Stones	**Outer area**	0.025
Sand bags		0.040
Stones	**Falling apron**	0.035
Stones at slope		0.025

U_{fm} is the friction velocity for the combined action of the steady current and waves. U_{fm} can be calculated from the following expression ([4] and [5]).

$$U_{fm} = \sqrt{U_{fw}^2 + U_{fc}^2\left(1 + 1.2\left(\frac{U_{fw}^2}{U_{fc}^2 + U_{fw}^2}\right)^{3.2}\right)}$$

U_{fc} is the friction velocity based on the mean current velocity given by

$$U_{fc} = \frac{V}{\frac{1}{\kappa}\left(\ln\left(\frac{30h}{k}\right) - 1\right)}$$

Here κ is the von Karman constant equal to 0.4, h is the water depth and k is the grain roughness. The grain roughness, k, is taken as d_{50} for the stone material and for bed material it can be taken as $2.5d_{50}$. U_{fw} is the friction velocity based on the maximum orbital velocity at the bed, U_m, calculated by

$$U_{fw} = \sqrt{\frac{f}{2}}U_m$$

where f is the wave friction factor.

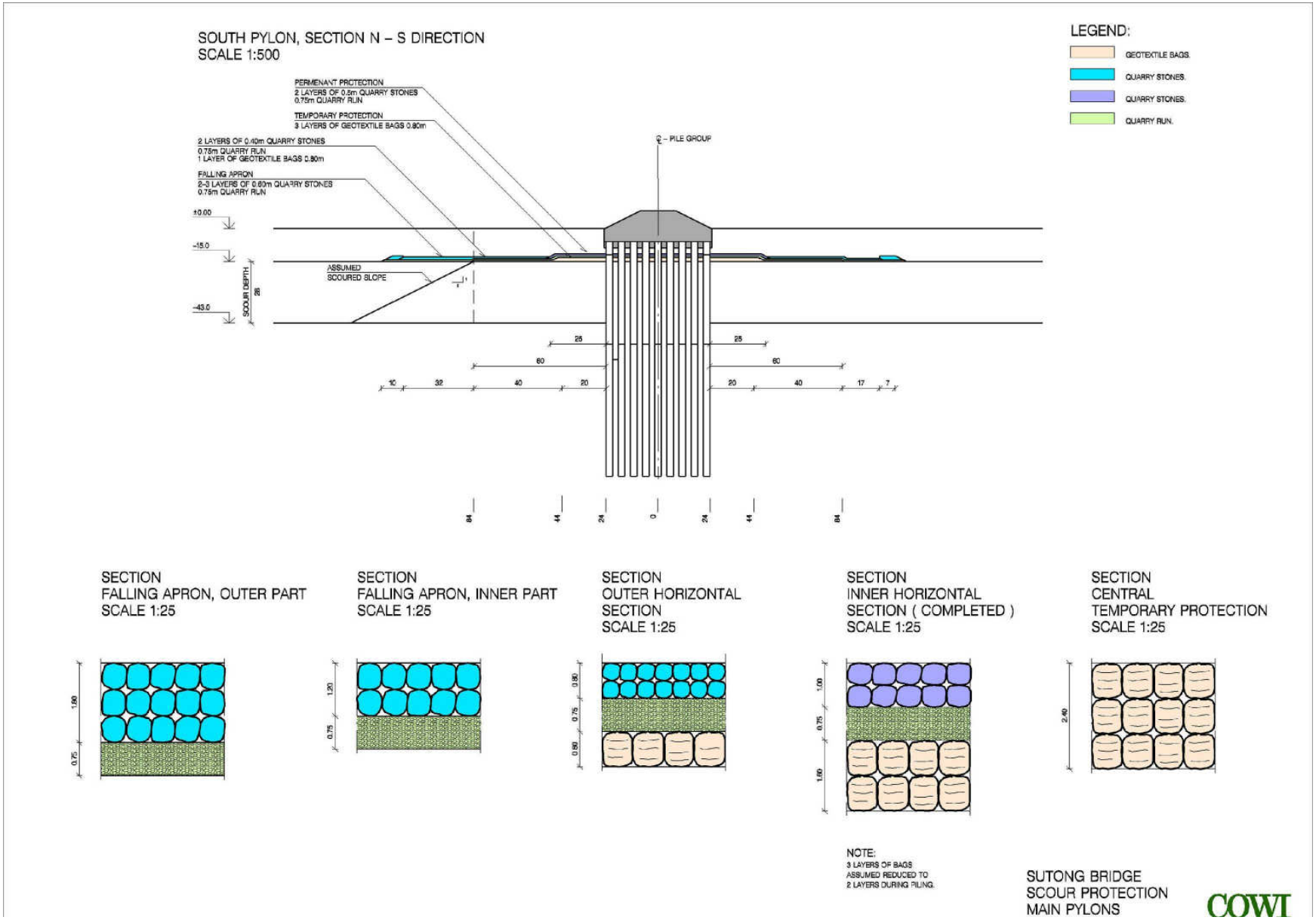

Figure 4. Scour protection layout - cross-section - South Pylon

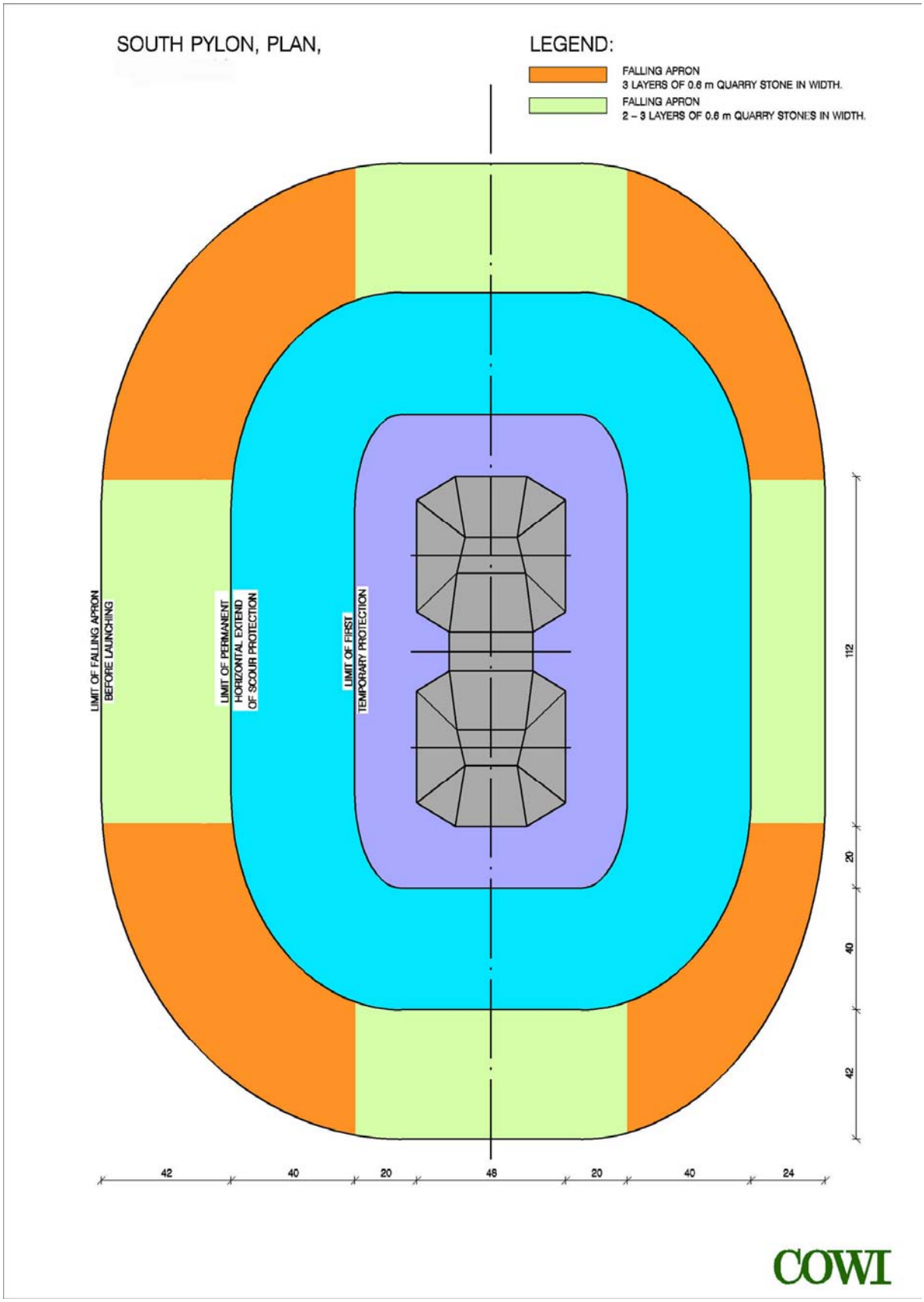

Figure 5. Scour protection layout - plan view - South Pylon

In case of sloping river bed the critical Shields parameter will be reduced by the following equation.

$$\theta_{cr,slope} = \theta_{cr} \cdot \cos(\beta)\sqrt{1 - \frac{\tan(\beta)}{\tan(\phi_s)}}$$

Here β is the river bed slope and ϕ_s is the material friction angle. The river bed slope has been taken to 26 degrees (1:2) and the material friction angle has been estimated to 30-35 degrees.

For verification of the stone size the Izbash Equation has been used and the stones were found to be in the same order of magnitude.

C. RESULTS

Table V shows the stone sizes of the scour protection for the North and South Pylon. The table also shows sizes of sand bags, which are exposed in the temporary protection during construction and later on covered with stone material.

It is found that the stone material is largest for the south pylon.

Further, the practical design should adopt the same size of bags all over and the same stone size for the outer area and falling apron. The actual sand bags used were of size: 1.6 x 1.6 x 0.6 m^3.

1) *General Scour Protection Material*

Grading of the material for the general scour protection shall comply with:

$$W_{15} = \frac{W_{50}}{1.5}$$
$$W_{85} = W_{50} \cdot 1.5$$
$$\overline{W} \approx W_{50}$$

Here W is the weight of the stone material for the fractiles 15%, 50% and 85%, respectively.

Below the stones a layer of filter material (quarry-run) characterised by d_{50} = 0.15 m (between 0.05 m and 0.25 m) shall be placed with a layer thickness of 0.75 m.

TABLE V.
STONE AND SAND BAG SIZE FOR THE SCOUR PROTECTION MATERIAL AT THE NORTH AND SOUTH PYLON

Item	Location	Density [t/m^3]	d_{50} [m]	
			North pylon	South pylon
Stones	Inner area	2.65	0.40	0.50
Sand bags		2.00	0.50	0.60
Stones	Outer area	2.65	0.30	0.40
Sand bags		2.00	0.30	0.40
Stones	Falling apron	2.65	0.30	0.40
Stones at slope		2.65	0.40	0.60

2) *Falling Apron Material*

The falling apron stones shall be graded as given above. References [6], [7] & [8] recommend the following on the design of the falling apron:

- Maximum predicted depth of scour, Y_s (m)
- Thickness of rock on slope face, T (m)
- Assumed scoured slope: 1V:2H (1:2)
- Length of apron on slope: 2.24Y_s (m)
- Assumed deployed apron thickness: 1.5 T (m)
- Volume of material: 3.35TY_s (m^3/m)
- Width of apron: WA = 1.5Y_s (m)
- Average thickness of apron: 2.24T (m)

Various authors suggest that the thickness of the apron be made larger towards its outer edge. COWI suggests that the above average 2.24 layers be distributed as follows. This is to make construction easier. Due to the critical conical shape of the corners more apron material is needed here. On these areas, see Fig. 6, three layers of stones should be used in the full width of the apron.

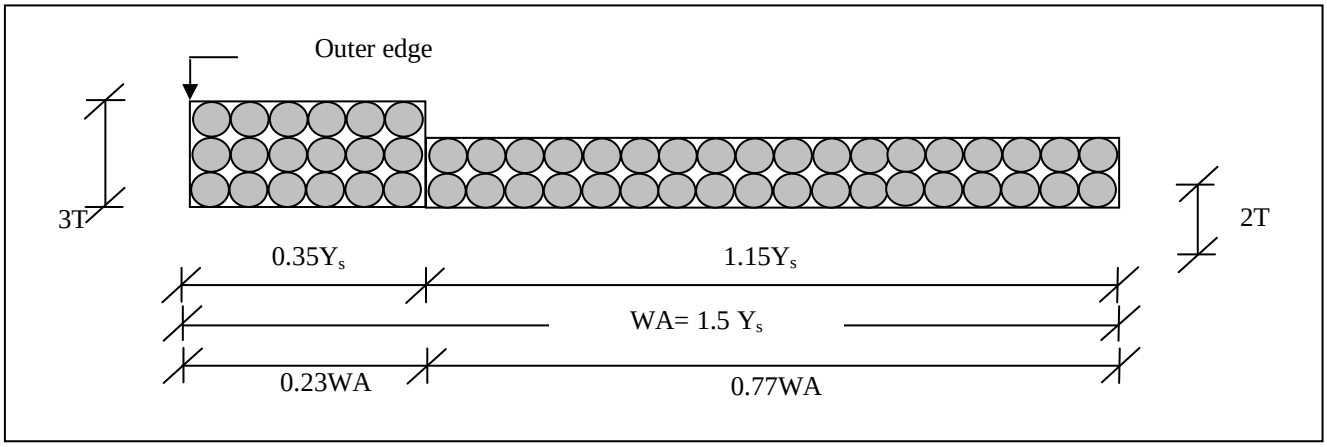

Figure 6. Falling apron details

VIII. EXPERIENCE FROM CONSTRUCTION

Extensive surveys using multi-beam echo sounder were made in order to control and verify the amount of materials dumped. The dumping of material was performed by split-barges using a grid with 28 x 26 cells (see Fig. 7) for the North Pylon and 16 x 16 cells for the South Pylon. Fig. 7 shows an example of the registration of volumes [m^3] in the protection of dumped sand bags within each control area. In connection with the distribution of the scour protection material acceptance criteria were established depending on two things, namely: (1) the type of material (sand bags, quarry-run or armour stones) and (2) the location of dumping.

Since the sand bags are a temporary protection, no criteria should be applied for acceptance. The experience from dumping of sand bags directly on to the river bed showed quite some penetration. Only half the volume of the sand bags was detected by the survey. Further due to the high currents and turbulence, the sand bags were displaced somewhat downstream from the barge and spread over a significantly area of the split barge itself.

The next layer of the structure, the graded stones has a design thickness of 1.0 m, meaning that the volume of material to be dumped should as a minimum correspond to 1.0 m of material. In reality the forming rate (recovery percentage) is less than 1.0 due to penetration of the graded stones in between the sand bags. It is therefore not required that 1.0 m thickness is present in the survey measurements. An absolute minimum for such filters is normally corresponding to 2 times d_{50} or 0.30m assuming that d_{50} = 0.15m as specified in the design. It was on this basis decided that the minimum requirements in the measurements should be 0.4 m for all the Areas: Central, Outer and Inner section of the Falling Apron Area. For the Outer section of the Falling Apron no Criteria should be applied, because here the apron might be eroding during construction due to scour at the edge and this is a natural process for which the apron is designed. The control for this outer section of the Falling Apron Area is thus that strict control is exercised on the volume of material to be dumped as well as the distribution of the material.

With respect to the armor stones, it was essential that the structural integrity was obtained. Therefore it would be crucial that 2 layers of armor stones are present in all areas. In layer thickness this corresponds to 1.0m for the Central Area and the Outer Area. For the inner section of the Falling Apron Area it corresponds to 1.2m thickness.

The above thicknesses have been determined as the difference between the in-survey (before dumping) and the out-survey (after dumping).

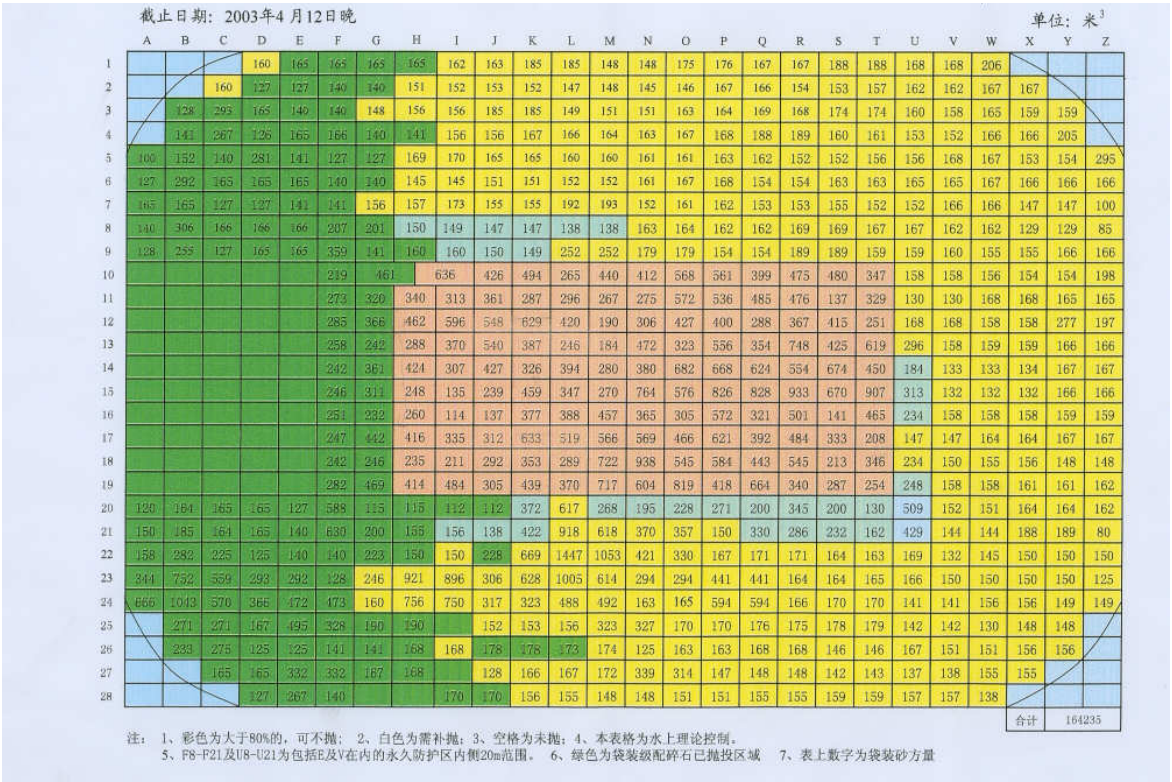

Figure 7. Volume of sand bags dumped at each control area

IX. RECOMMEDED MONITORING PROGRAM

The scour protection is a flexible structure that will be subject to some displacement of material. Especially the Falling Apron will be moving during launching when scour occur at its edges. Therefore a detailed monitoring program has been prepared. The program covers the entire bridge from the N to the S river bank.

In Fig. 8, the two survey areas are shown. Area A corresponds to a survey of the entire riverbed along the bridge alignment. Area B corresponds to a detailed survey of the scour protection around the main pylons. The recommended interval between each of the survey areas are presented in Table IV below.

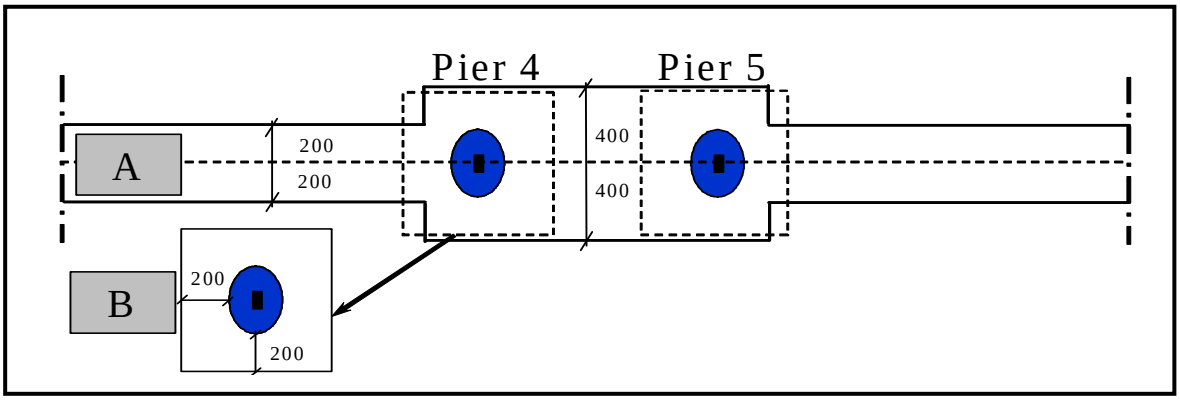

Figure 8. Survey area for monitoring program

TABLE VI.
RECOMMENDED MONITORING PROGRAM

Year	Month	Area A	Area B
2004	5	X	
	6		X
	7		X
	8		X
	9		X
	10	X	X
	11		
	12		
2005	1		X
	2		
	3		
	4	X	X
	5		
	6		X
	7		
	8		X
	9	X	
	10		X
	11		
	12		
2006	1		X
	2		
	3		
	4	X	
	5		X
	6		
	7		X
	8		
	9		
	10	X	X
	11		
	12		

Year	Month	Area A	Area B
2007	1		X
	2		
	3		
	4		
	5		X
	6		
	7		X
	8		
	9		
	10	X	X
	11		
	12		
2008	1		X
	2		
	3		
	4		
	5		X
	6		
	7		
	8		
	9		X
	10	X	
	11		
	12		

X. CONCLUSION

The paper presents the scour protection design for the Sutong Bridge in the Yangtze River. The solution adopted, with sand bags and stone layers dumped from the water surface, was found to be the most feasible under the given difficult circumstances with water depth up to 30 m, high currents and zero visibility. The future erosion at the edges of the protection will be prevented from progressing close to the bridge piers by the use of the Falling Apron concept for the outer edge of the scour protection.

REFERENCES

[1] Jensen, O. Juul and Truelsen C.: *Scour Assessment and Conceptual Design of scour protection for Sutong Bridge, P.R. China* (section in book published by the client for Sutong Bridge), 2004.

[2] Jensen, O. Juul: River training structures and scour depth prediction in the Brahmaputra River, Bangladesh., Proc. Hornafjördur Int. Coastal Symp., Iceland, June 1994.

[3] Sumer, B. M. and Fredsøe, J.: The mechanics of scour in the marine environment. World Scientific, xiii+536pp., 2002.

[4] Soulsby, R.. L.: Bed shear-stresses due to combined waves and currents. Advances in coastal morphodynamics. Delft Hydraulics, Delft, 1995

[5] Soulsby, R.. L.: Dynamics of marine sands. A manual for practical applications. Thomas Telford, London, 1997.

[6] Joglekar, D.V.: Manual on River Behaviour Control and Training. Central Board of Irrigation and Power, Publication no. 60, New Dehli, India, 1971.

[7] Hoeven, M. A. van der: Behaviour of falling apron. M. Sc Thesis Delft University of Technology (DUT), January 2002.

[8] Ciria (C551): Manual on scour at bridges and other hydraulic structures, 2002.

The Interdependent Effects of Wave Reflection and Seabed Erosion

ir. H. Vastenholt
Offshore Contractors (CI) Ltd,
Sleeuwijk, The Netherlands

INTRODUCTION

This paper presents the occurrence of severe coastal erosion, which was suffered during the installation of a new offshore gas pipeline near the town of Miri, Sarawak. From the shore line a trench was dredged out into the sea to accommodate this offshore pipeline. When the trench was dredged it appeared that waves were reflected by this trench. This resulted in more wave energy being projected on a short section of the coast.

This paper discusses the phenomena that occurred, identifies the possible causes and describes the remedial actions that were taken to mitigate the adverse effects of the erosion. An adequate solution was selected: a dyke was designed and built in the time span of a few months.

The author of this paper was at the time of these events acting on behalf of the oil company as the project sponsor and as such was directly involved.

DESCRIPTION OF THE PROJECT

During the second half of the eighties and first part of the nineties the Malaysian oil company Petronas Carigali, with the technical support from Shell Petroleum Development Company, undertook the refurbishment of the existing Baram Delta oil fields. These fields are situated offshore Miri, a town in Sarawak, close to Brunei. Sarawak is a state on the island of Borneo and is part of the Malaysian Federation. Figure 1 shows the location and layout of the field.

Shell discovered oil around the town of Miri early in the twentieth century. After the second world war oil exploration also commenced offshore. In the eighties the concession of the Baram Delta oil fields was handed over to the state oil company Petronas Carigali. Shell however initially continued the operator-ship of the field, handing over its activities on a gradual basis.

Oil fields generally produce large quantities of associated gas that is produced with the oil. Up to the middle eighties quite a large portion of the gas in Baram was exported to Miri, but most was vented in the atmosphere due to lack of customers. It was realized however that a valuable commodity was lost. Therefore, when the concession was handed over, Shell and Carigali undertook a general refurbishment of the Baram fields.

Gas that was allowed to escape at the various platforms is now gathered and sent by pipelines to a newly built central gas gathering platform at Baronia, where it is compressed. Most of the gas is then exported via a new pipeline to the Luconia gasfields, which lie 120 km further west. The gas is commingled there with the Luconia gas and exported to Bintulu, which lies a few hundred kilometres south from Miri. There the gas is liquefied and sold on the international gas market as LNG.

A fair portion of the Baram gas is also exported directly to the ever expanding town of Miri. The field development plan thus included the laying of a 16 inch (400mm) gas export pipeline to that town. The pipeline was to follow a route from the offshore Baram field directly to the Miri crude oil terminal [fig 1].

MIRI COAST

The coast at the pipeline landfall comprises a sandy beach. There are no dunes, which are a tell tale of limited sediment transport along the coast. Little sediment transport also means that in case of beach erosion, self restoration can be expected to be slow. On earlier and similar pipeline construction activities nearby on the beach and directly offshore, coastal erosion had been reported. But nature had always shown to quickly restore itself and in a year’s time signs of any human activities had disappeared.

The foreshore of the coastline shows a flat and featureless seabed, comprising sands, silts and soft clays. The seabed slopes down very gradually; a few metres per kilometres only. Directly behind the beach runs the Pan Sarawak Coastal Highway, which interconnects the main towns of Sarawak and nearby Brunei.

Some ten kilometres to the north of the pipeline landfall the Baram river flows out into the sea. Sediment production of that river is fairly small. Sands that are deposited by the river offshore are removed to a great extend by dredgers for the development of Miri and its surrounding towns. Note that Malaysia has a high

economic growth-rate and living standards for its population are quickly improving.

Malaysia has a monsoon climate. The weather generally is calm. Strong winds are the result of thunderstorms. Cyclones, which pass over the Philippines, may cause gales in the area. The mouth of the Baram river and the banks, which lie in front of it, provide shelter from the north. Only winds from the west generate appreciable waves. As a result the seas at Miri are generally calm. The waves come in perpendicular to the coastline. Because of the gradual sloping seabed, larger waves die out before reaching the shore due to friction with the seabed. Hence the surf is small; an ideal beach for children.

During the dredging of the trench for the installation of the 16 inch pipeline across its landfall section, severe seabed erosion occurred locally. Also about one kilometre of beach became affected. From the air a particular wave pattern became apparent, which could be attributed to the dredging activities. Figure 2 is a photograph of the area taken from a helicopter. It now is opportune to explain the pipeline construction method, the occurrence of the particular wave pattern and the effects it had on the environment.

PIPELINE CONSTRUCTION

Offshore pipe laying is a large and capital intensive business. Many work vessels and a large crew are involved. The 16 inch gas pipeline was installed with the pipelay/ derrick barge, DB 26, which was operated by McDermott. The barge has an overall length of 120 m and is 33 m wide. The barge also has a large 800 tonne crane, with which platforms can be installed offshore. A picture of the barge is attached as figure 3. The barge provides living quarters for 270 persons. The crew works in two shifts covering the full 24 hours a day and seven days per week. The vessel is accompanied by two tug boats, which assist in the deployment of the twelve barge anchors. The barge is held in position with these anchors and it is moved along the pipeline route by hauling in on its front anchor wires and paying out concurrently on its stern wires. A survey vessel monitors where and how the pipeline is laid on the seabed. A small fleet of supply vessels, tugs and barges bring sections of pipe and other supplies to the barge.

The 12 metres long pipe sections are already coated when brought to the barge. On board, the pipes are joined sequentially using an automatic welding process. The pipe welds are then inspected with radiography. The pipe string thus formed is guided over the stern of the barge and a supporting stinger towards the seabed. Lay rates in the order of several kilometres per day can be achieved.

Where pipelines have to cross a shoreline, the following technique is generally applied. The barge is turned with its stern to the beach. On shore a winch is installed and its pull cable is run towards the laybarge. Here it is connected to the pipe string being welded. As pipe welding continues on the barge, the pipeline end is pulled on the beach. Figure 4 shows the DB 26 whilst the above work activity is in progress. When the pipeline end has been pulled ashore, the lay barge then starts moving ahead on its anchors along the pipeline route and pipe laying continues.

In the North Sea generally the smaller diameter pipelines have to be trenched, for instance to protect these against trawl fishing. In Malaysia such fishing is not conducted and pipelines can remain exposed on the seabed. Near shore pipelines have to be buried however to protect these against the breaking surf, large waves and currents.

The conventional approach is to dredge a trench from the deeper water towards the shore, using a cutter suction dredger. The excavated spoil is dumped nearby. Since the dredger has to find its way to the beach, when making the trench, the trench has to be wide and deep to provide access to the dredger. When the trench has been made, the pipelay barge enters the trench and the pipeline is installed. Figure 2 shows the cutter suction dredger at work and figure 5 gives a view from the shore towards the pipelay barge. To protect the trench in the surf zone a twin row of sheet piles is driven on the beach to keep the trench open. Figure 5 shows us these sheet piles and in the foreground, part of the pipe pull winch is visible as well. The DB 26 is several hundred metres offshore.

When the pipeline has been pulled ashore, the cutter suction dredger returns to the construction site, recovers the spoil and backfills the trench. It is evident that a large trench near shore causes beach erosion. However experience has shown that the coast always restores itself. A few months later, someone walking the beach, will hardly notice what happened.

ANALYSIS OF THE EVENTS

For the installation of the 16 inch gas line the construction method as explained above was followed. Mc Dermott laid the pipeline and Dredging International dug the trench and later back filled it. Other pipelines along the Miri coast had been installed in previous years in a similar way. Due to the trenching activities coastal erosion had always occurred. Employees recounted that on one of the last pipelines the beach had to be protected locally by the installation of wire mesh baskets filled with rocks. It was reported that in the following season the beach had fully restored itself.

This time the seabed erosion was much more pronounced and thus one may question why this happened.

In hindsight a few things become apparent. The beach near the landfall runs more or less north - south. The trench for the pipeline was dredged towards the north-west under an oblique angle with the shore line. When trenching had been completed it became apparent that to the south of the trench waves had become significantly

higher, showing a confused pattern. To the north of the trench the waves had abated to a great extent. From helicopters this picture [fig 2] became much clearer. It seemed as if the trench was working as a break-water.

In wave mechanics, it is known that seawalls reflect waves. However, to reflect waves it is not necessary that obstructions protrude the water surface. Waves are also reflected by sudden changes on the seabed and therefore straight trenches in an otherwise flat seabed can reflect waves quite effectively. The coastal bathymetry near Miri had the ideal form to demonstrate this effect.

On our project the oncoming waves were reflected against the trench and were diverted in a south-easterly direction towards the shore. These reflected waves also crossed with the other oncoming waves, forming a very distinct interference pattern. Refer to figure 6 for a situation sketch. Where waves cross each other, the coinciding wave tops increase in height and in the shallow water breaking surf is formed at these wave tops. The photograph of figure 2 shows these distinct breaking wave tops. In a gradual sloping seabed higher waves will start breaking further from the coastline and the photograph shows that clearly.

The oncoming waves combined with the reflected waves project more energy onto the beach immediately to the south of the trench. A very rapid and severe coastal erosion developed there. Since the interference pattern caused breaking surf further offshore, quite a large area of coastline and foreshore was affected. Since the coast comprised sand and soft soils, a drastic response was thus required. Figures 7 and 8 show the erosion of the beach. An existing buried pipeline lying nearby became exposed and the level of the beach had dropped about one metre and the coastline was swept back. One issue became alarming: the Pan Sarawak Coastal Highway is here within less than a hundred metres from the shoreline.

REMEDIAL ACTION

Fortunately, in the Netherlands sufficient knowledge is available to design sea defenses. Such expertise was called in from Witteveen and Bos and for Miri an effective solution was found. Along the beach a dyke about eight hundred metres in length was designed, procured and built in less than three months.

A base cloth filter was laid, covered with an intermediate layer of 10-60 kg rocks, to provide a firm footing [fig 9]. On top selected rock boulders with weights in the range of 100-1000 kg were laid in a dense packing. It was anticipated that the dyke would to have to last a few years, enough for the beach to restore itself. Figure 10 shows the completed dyke.

CONCLUSION AND CLOSE OUT

One may question: why was the beach erosion more pronounced this time. Perhaps that the notable oblique angle of the trench with the coastline was the root cause.

When the trench had been backfilled, the peculiar wave pattern did not abate immediately and still a lot of seabed had to restore itself. As the water depth of the foreshore had deepened, higher waves could now also reach the shore. The natural backfill was expected to last a few years because of the limited natural supply of sediments. One can report now that the beach has restored itself.

Could the remedial action not be claimed under the usual construction all risk insurance? That was not the case. The loss adjuster had to report on behalf of his management that only the costs for repair of damage is insured. Expenses to prevent damage are not covered. In effect we should have been standing by, watching the loss of public land and a coastal road and then calling the insurance company to pay for the repairs. However all parties agreed that responsible people do not act that way.

What can we learn from this? Although wave reflection is a well-understood phenomenon, none of the experts consulted had ever seen this event before. So a statement that more studies should have been conducted is therefore somewhat misplaced. This paper is more of a reminder for other pipeline engineers to be alert for the unusual.

Often incidents happen during projects one never foresees. It is then important that the project sponsor has a management structure, which can adapt to changes in a coherent way and where key members of staff do not lose their nerve and provide each other the necessary back up to systematically analyze the problem and do what is required. The author wishes to thank his management in Carigali and Shell for standing by him when these difficulties arose. Also the valuable and dedicated support from Mc Dermott, Dredging International and Witteveen and Bos is appreciated. One may report that financially the work was closed out in a transparent way and in a short time span.

Why is this paper presented only now? In the oil industry focus is generally not on coastal engineering. Papers presented at offshore oil and gas conferences cover pipelines, platforms and sub-sea structures in ever-deeper water. The author worked most of his life in that industry overseas and just learned of the existence of this conference, considered it the perfect platform for this topic and felt that civil and coastal engineers should share this special experience.

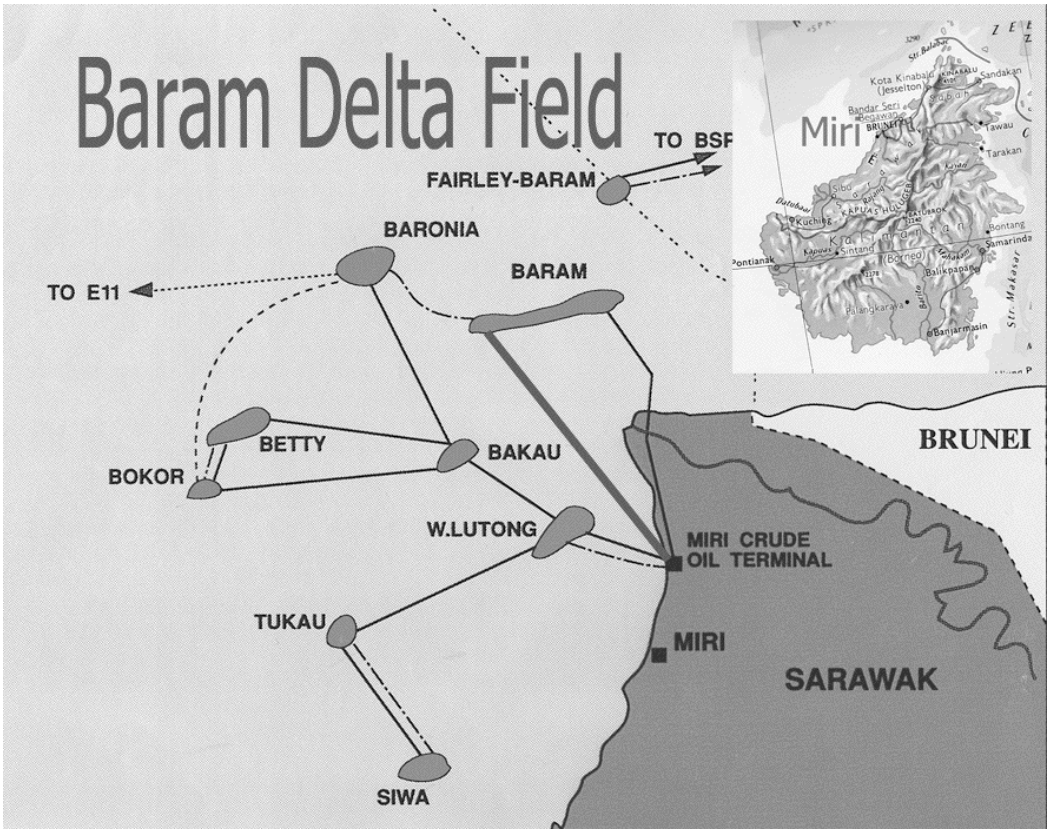

Fig 1. Location map of Baram Delta Oil and Gas Fields. The new gas pipeline is from Baram to the Miri crude oil terminal (heavy line)

Fig 2. Dredging of the pipe trench with cutter suction dredging in progress; on shore is the pipeline landfall; in the foreground is the Pan Sarawak Coastal Highway, behind the dredger is the wave interference pattern with breaking waves.

Fig 3. Pipelay barge LB 26
Pipes are welded along the starboard side of the barge

Fig 4. LB 26 pulling pipe to shore

Fig 5. View from the beach

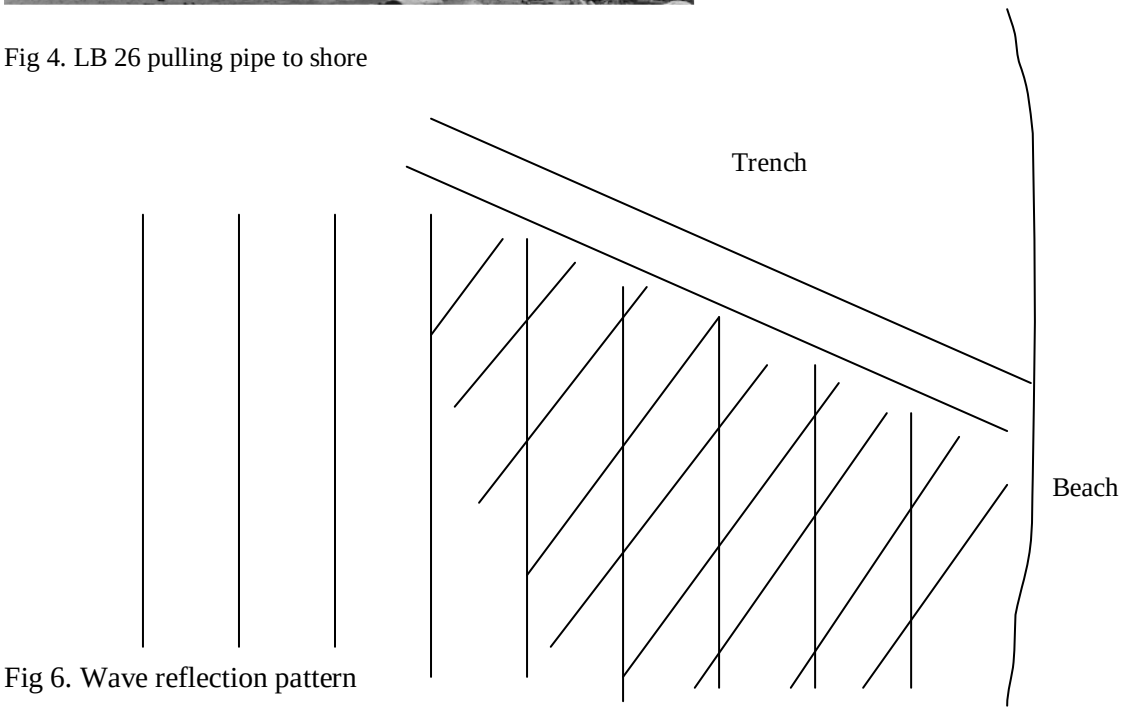

Fig 6. Wave reflection pattern

Fig 7. Exposed pipeline

Fig 8. Eroded beach with drift wood

Fig 9. Filter overlain with rock

Fig 10. Beach with dyke

Flood Risks in Red River Basin, Vietnam

H.J.Verheij* and J.K.G.Rohde**

* WL | Delft Hydraulics, Delft, The Netherlands
** SWECO Gröner AS, Lysaker, Norway

ABSTRACT

The flood risks in the Red River delta in Vietnam, in particular for the Bac Hung Hai polder are determined. The risk analysis includes aspects such as hydraulics, hydrology, morphology, geotechnics as well as socio-economic evaluations of the dike system and is based on the formula: risk = failure probability x damage. Failure mechanisms as overflow, geotechnical slope stability and piping have been taken into account, resulting in failure probabilities for each dike kilometre. Also the consequences of a dike breach which respect to inundation are shown.

INTRODUCTION

Floods occur almost every year in the Red River delta in Vietnam causing large scale inundations leading to serious damages and loss of human lives. The most serious recorded flood in modern times occurred in 1971 when more than 500 people were killed, approximately 2,71 million people and 250,000 ha of land were affected. The estimated damage was approximately US$ 1 billion.

A water level at Hanoi of 14.80 m would have been attained if the dikes had not failed. Some 648 dike segments over a length of 74 km were distorted; at 307 places the crests were overtopped or nearly so and inundation depths up to 3.5 m were reported.

Obviously, improvement of the flood protection system is required. As part of the 2nd Red River Basin Sector Project, Part A for Water Resources Management a Flooding Risk Assessment (FRA) has been carried out. The FRA activity has the following objectives:

1. ranking of flood protection projects for the rehabilitation of dikes and irrigation structures;
2. demonstrating the FRA methodology to the Department of Dyke Management and Flood Control of MARD (Ministry of Agriculture and Rural Development).

The project has been carried out in Vietnam by WL | Delft Hydraulics and SWECO Groner under an ADB loan and includes aspects such as hydraulics, hydrology, morphology, geotechnics as well as socio-economic evaluations of the dike system [1].

THE RED RIVER BASIN

General

The Red River Basin in Vietnam is shown in Figure 1. It has a catchment area of 169,000 km^2, of which 86,000 km^2 is situated within the Vietnamese borders, 81,240 km^2 in China and 1,100 km^2 in Laos. From about 50 km upstream of Hanoi near Viet Tri the Red River flows in south-easterly direction to reach the Gulf of Tonkin over a distance of 214 km. The basin downstream of Viet Tri until the Gulf of Tonkin forms the Red River delta. The Red River delta measures 12,700 km^2.

In the delta the Red River is linked with the Thai Binh River through the Duong River and more downstream by Luoc River.

Figure 1. Vietnam with the Red River delta

Hydrology

The average annual rainfall varies from 1,500 to locally 4,800 mm, where the highest values are recorded near the Vietnamese-Chinese border. A clear seasonal pattern is apparent in the rainfall with the highest values in June-September.

About 5 typhoons on average cross annually the north and middle part of Vietnam. From June till September typhoon tracks cross the Red River. Particularly in August and September the occurrence rate is high with an average of 1.0-1.7 typhoons/month each year. Typhoons bring heavy rains with high wind speeds. Maximum wind speeds are up to 40 m/s.

The average inflow to the Red River delta amounts roughly 3,800 m3/s. The runoff from Da River is since 1988 controlled by the operation of Hoa Binh reservoir. The lower Red River basin is affected by tide.
Characteristics of largest floods on the Red River in the last century are presented in Table 1 It gives the peak discharge Q_{max} (m^3/s), date of occurrence and 8-day flood volume at Son Tay.

TABLE 1
Characteristics of the 5 largest floods in the Red River at Son Tay

Year	H_{max} Hanoi (m)	Son Tay		
		day-month	**Q_{max} (m^3/s)**	**8-day flood volume (10^6 m^3)**
1945	13.90	20-08	33,500	18,800
1968	12.23	15-08	24,000	12,960
1969	13.22	18-08	28,300	16,500
1971	14.80	21-08	38,000	19,600
1996		21-08	19,800	11,250

It is observed that the largest floods have all occurred between 15 and 21 August. In Figure 2 return periods of instantaneous natural flood peaks at Son Tay with and without the influence of the Hoa Binh reservoir are presented.

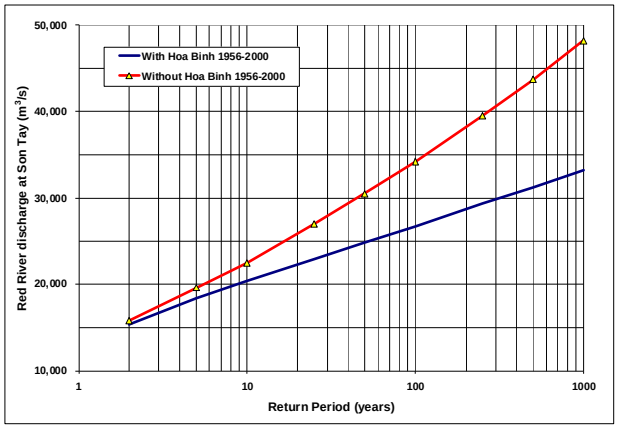

Figure 2. Frequency distribution of flood peaks (daily average discharges) with and without effect of Hoa Binh reservoir, period 1956-2000

Dikes and structures

In general, a flood control system consists of the physical control infrastructures, a flood forecasting system as well as an institutional or management infrastructure. The physical flood control infrastructure in the Red River delta contains the following elements:

- River and sea dikes, inclusive sluices and pumping stations;
- Reservoirs: Thac Ba, and Hoa Binh;
- Flood diversions;
- Retention areas.

At present, the river dike system in the delta consists of 2,417 km of dikes of which 1,667 km is in the Red River system and 750 km in the Thai Binh River system. River dikes attain heights up to 10 m.

More than 952 revetments and groins are built to protect the dikes. Furthemore, 2985 sluices are present for present and irrigation purposes.

The dike system in the Red River delta has a long history. There is archaeological evidence that already in the 3rd century BC dikes were constructed in the delta. However, significant dike building has likely commenced in the 10th century after Vietnam regained independence, further accelerated by the transfer of the capital to Hanoi in 1010 AD. In the last century several times in the aftermath of a serious flood (1915, 1924, 1926, 1945) the dikes strengthening and heightening programs were amended. In 1960 the design flood level for Hanoi amounted RL 13.0 m, with the crest level at RL 14.0 m. In 1971, however, flood levels reached RL 14.15 at Hanoi but would have reached RL 14.80 had not the dike on the left bank upstream of Hanoi breached. Thereafter, the 1971 flood conditions have been taken as the design criterion for the Red River dike system.

FRA METHODOLOGY

Approach

In this section the FRA calculation method based on failure probabilities of the various failure mechanisms will be described. The method is based on the philosophy that the safety of a polder depends on the weakest spot in the dike ring around the polder. The safety is historically derived from the probability that an area might be flooded, because the water defense around that area (the dike ring) fails at one or more locations.
A dike ring is considered, i.e. an area surrounded by a water defense system, Figure 3. This protection system may fail because the design water level exceeds the crest levels of the dikes and hydraulic structures, but it may fail well before the design water level is exceeded by structural incapacities or operational flaws.

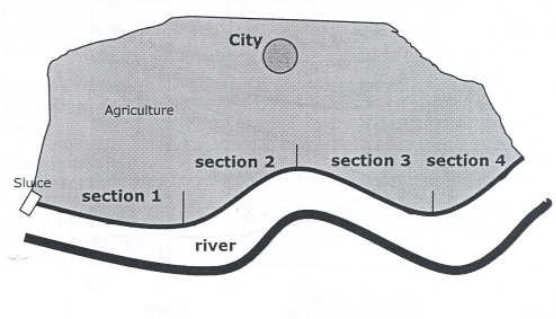

Figure 3. Example of a dike ring

For flood management in addition to flooding probability also the consequences of flooding have to be assessed. When the probability of flooding of a certain area is high but if the damages are small then from a flood management point of view there is little to gain with measures which reduce the probability as the risk is low. Therefore, to estimate the safety of the flood protection system and to determine in what sequence rehabilitation works can best be carried out to improve safety at minimum cost a flooding risk assessment should be carried out. Flooding risk is defined as:

$$\textit{flooding risk} = \textit{probability of flooding} * \textit{damage due to flooding} \quad (1)$$

So a flooding risk assessment has two elements:

- estimation of the probability of failure of the dike, when the river is in flood; this may be due e.g. to poor design, lack of maintenance or improper operation of hydraulic structures, and
- estimation of the losses due to flooding, tangible and intangible.

The FRA methodology will be used to rank flood protection projects in the Red River delta. To demonstrate the FRA methodology it has been applied to the Bac Hung Hai polder, hust south-east of Vietnam's capital Hanoi. This activity resulted in a quantitative assessment of priorities regarding dike sections, presented as Average Annual Damage (AAD) values for the different sections. The AAD values are essentially a translation of both potential damage and flooding probability into a single figure for expected annual costs due to flooding. The AAD values are part of a cost-benefit analysis to assess economic viability of flood projection investments.

Probabilistic computations use the reliability function and the probability density functions of the variables in the reliability function as the base for the determination of failure probabilities. The reliability function Z is the difference between the strength (R = resistance) and the load (S = Solicitation) of a particular failure mode: Z = R - S. Wherever Z < 0 the load exceeds the strength and the system will fail.

Many failure mechanisms might be considered, for instance, failure due to: overflow of water over the crest of the dike, overtopping due to waves, piping, macro-instability of the outer slope during the flood, macro-instability of the outer slope after a rapid fall of the flood levels, macro-instability of the inner slope during the flood, structural strength of hydraulic structures, not closing the gates of the structure before a flood.

In principle, a reliability function for each mechanism should be defined. Hereafter, the reliability functions for the following failure mechanisms are presented:

1. overflow, including wave overtopping and settlement
2. piping, including soil rupture and sand transport, and
3. macro-instability, including instability of the inner and outer slope of the dike.

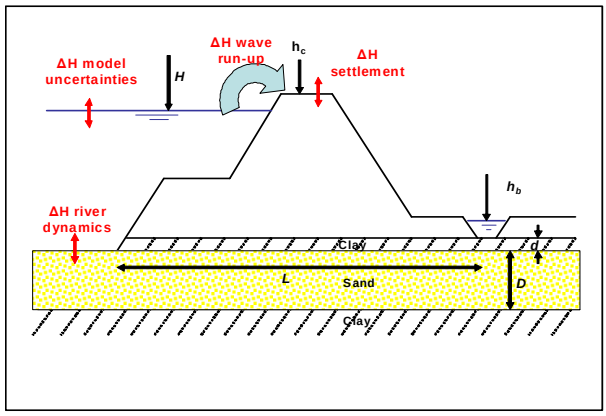

Figure 4. Reliability function for mechanisms overflow, overtopping and piping

Failure mechanism overflow

The reliability function applied for the failure mechanism overflow has the following form, with reference to Figure 4:

$$Z = (h_{crest\ level} - \Delta H_{settlement}) - (H_{flood} - \Delta H_{river\ dynamics} - \Delta H_{runup} - \Delta H_{model\ uncertainty}) \quad (2)$$

with: $\Delta H_{riverd\ ynamics} = \Delta H_{fluctuations} + \Delta H_{trend}$

where: $h_{crest\ level}$ = crest level of the dike (m), $\Delta H_{settlement}$ = uncertainty in the crest level due to settlement of the dike (m), H_{flood} = flood water level (m), $\Delta H_{river\ dynamics}$ = water level trend and uncertainty due to river dynamics (m), $\Delta H_{fluctuations}$ = uncertainty in the bed level variations due to dunes, bed ripples (m),

ΔH_{trend} = assessing the trend in bed level changes, i.e. morphology and encroachment (m), ΔH_{runup} = wave run-up (m), $\Delta H_{model\ uncertainty}$ = uncertainty in water level due to model imperfections (m).

Failure mechanism piping

The reliability function for piping consists of two sub-mechanisms, soil rupture and transport of sand, (see also Figure 4):

1. sub-mechanism soil rupture:

$$Z_1 = \rho_c g d - \rho_w g\,(H - h_b) \qquad (3)$$

2. sub-mechanism transport of sand:

$$Z_2 = \left(\frac{L}{c_1} + \frac{d}{c_2}\right) - \left(H - h_b - d\right) \qquad (4)$$

where: h_b = water level at the inner or field side of the dike (m), d = thickness of the clay layer (m), ρ_c = density of wet clay (kg/m^3), ρ_w = density of water (kg/m^3), g = gravity acceleration (m/s^2), L = seepage path length (m), c_1, c_2 = constants, depending on the soil type (m).

Both conditions must be satisfied for piping: soil rupture, i.e. the clay layer under the dike must be ruptured (in case of the presence of a clay layer) and there must be continuous transport of sand. So, Z_1 as well as Z_2 must be negative at the same time at the same location. The piping probability then reads:

$$P\{piping\} = P\{Z_1 < 0\} \cap P\{Z_2 < 0 \mid Z_1 < 0\} \qquad (5)$$

Above equations also apply for piping at hydraulic structures. In that case there is no clay layer, e.g. d = 0 m.

Failure mechanism macro-instability

For the computation of the failure probability due to macro-instability either the river side or the field side slope of the dike has been considered. The actual macro-stability can be computed for both sides using the Bishop method (see Figure 5 for a definition sketch) for different conditions. In the Bishop method the actual safety factor is computed from:

$$F_{actual} = f_0 \frac{\sum \frac{\left[c + (p-u)\,tg\varphi\right]\Delta x}{n_\alpha}}{\sum \Delta W \cdot tg\alpha + Q} \qquad (6)$$

where: F_{actual} = actual factor of safety (-), f_0 = correction factor (-), c = cohesion (N/m^2), p = overburden pressure (N/m^2), u = pore pressure (N/m^2), φ = friction angle (degrees), Δx = width of segment (m), n_α = factor of iteration (-), ΔW = weight of segment (kg), α = angle of slide circle to horizontal (degrees), Q = external horizontal load (N).

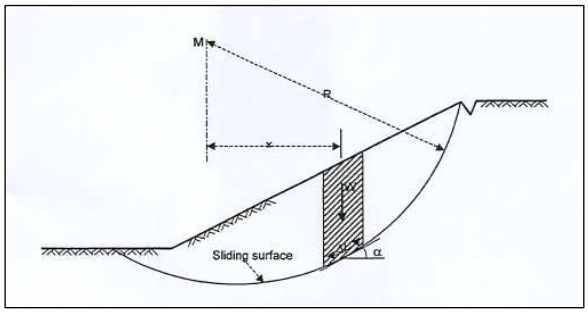

Figure 5. Reliability function for mechanism macro-stability

Combined failure probability

Reliability functions can be solved by different methods, like Monte Carlo simulations or by linearization of the limit state function. The actual failure probability for a dike section then reads:

$$P_{f,actual} = P_{f,overflow} \cup P_{f,piping} \cup P_{f,sliding} \cup P_{f,termites} \cup etc \qquad (7)$$

The probability of failure of a dike ring is to be derived by combining the failure probabilities for the various dike sections, where the lower and upper bound follows from complete correlation and full independence between the sections.

Flood damages

The following damage types are distinguished:

1. Direct damages,
2. Indirect losses,
3. Intangible effects, and
4. Macro-economic effects.

The damage types are elaborated below.

a) Direct damages

Direct damages occur at the time of the actual disaster. The main items include:

- The total or partial destruction of physical infrastructure:
- The destruction of crops ready for harvest
- Farm equipment and stock.

b) Indirect losses

Indirect losses refer to the flows of goods and services that will not be produced or rendered over a time span that begins after the disaster and may extend throughout the rehabilitation and reconstruction periods.

Some examples of indirect losses that can be measured in monetary terms:

- Higher operational costs: due to the destruction of physical infrastructure and inventories or losses to production and income (e.g., losses in sales of perishable goods; unexpected costs incurred in the replacement of lost records in the health care system);
- Diminished service provision: due to the total or partial paralysis of activities (e.g., damages due to the loss of a full school term);
- Added cost of alternative means of production: or provision of essential services (e.g., greater costs arising out of the use of longer or low standard roads (detours) and the construction of emergency roads;
- Cost of budgetary reorientation or reassignment;
- Income reduction: due to the non-provision or partial provision of services by public utilities (power; drinking water); reduction in personal income owing to loss of employment or being forced to work part-time;
- Costs during the emergency stage;
- Cost of situations arising from a disaster: (e.g., health campaigns to prevent epidemics);
- "Forward" or "backward" linkage effects (e.g., the destruction of a factory reduces the economic activities of suppliers who have no alternative markets or of clients who have no other suppliers);
- Costs or benefits of external factors: (e.g., any disaster repercussion or side effect whose costs (or benefits) are absorbed by third parties who are not direct victims (or beneficiaries) of the disaster).

c) Intangible Effects

Disasters may produce indirect effects, some of them major effects, that may be difficult to identify and impossible to quantify. These effects lead to "intangible" damage (or benefits) such as: human suffering, insecurity, a sense of pride or antipathy at the way in which authorities have faced the disaster's consequences, solidarity, altruistic participation, the impact on national security and many other similar factors that have an effect on well-being and the quality of life.

d) Macro-economic effects

If the disaster is large enough, it may affect prices and employment nationally and internationally. Macro-economic effects reflect the manner in which the disaster modifies the performance of the main economic variables of the country. The magnitude of the disaster is important for defining the time-frame for which macroeconomic effects are to be estimated. Experience shows that a "reasonable" time is normally the remainder of the year in which the disaster occurs plus another one or two additional years.

FAILURE PROBABILITIES

Bac Hung Hai polder

First, the failure probabilities of each kilometer along the river dikes have been determined. Results will be discussed of the left Red River dike protecting the Bac Hung Hai polder. Also the consequences of a dike breach which respect to inundation will be shown.

Secondly, it will be shown in this paper how local scour at the toe of a dike due to river flow velocities in combination with an incorrect bank protection results in slip circle instability. The interaction of disciplines as hydraulics, morphology, geotechnics and statistics resulted in failure probabilities for particular dike sections.

The Bac Hung Hai irrigation and drainage system is located south-east of Hanoi in the lower area of the Red River Delta and surrounded by Duong River in the north, Red River in the west, Thai Binh River in the east and Luoc River in the south (Figure 6).

The dikes protect 2.8 million people (year 2003) most of them living in small villages. The polder itself is about 225,000 ha of which most is agricultural land situated within Ha Noi, Bac Ninh, Hung Yen, Hai Duong provinces, including Hai Duong and Hung Yen cities. The land use in the polder is mostly rice production. In the western part along the river some annual crops are grown. Residential land also consumes a considerable amount of space.

The National Highway no 5 and the National Railway both connecting Ha Noi via Hai Duong with the port city of Hai Phong cross Bac Hung Hai polder. This major transportation axis is part of the "Industrial Corridor" along which many (international) factories and businesses are located.

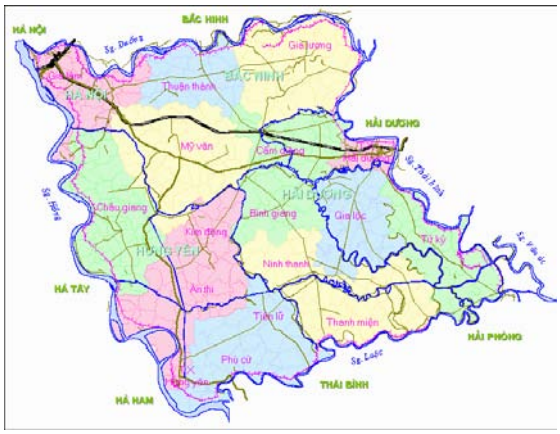

Figure 6. Map of Bac Hung Hai polder with important infrastructure

The elevation of the polder ranges between 10 and 0 meters, with the highest parts in the north-west and the lowest parts in the south-east.

The irrigation and drainage of Bac Hung Hai polder is regulated mainly by three main gates; one intake and

two outlets. The main water inlet is the Xuan Quan Inlet located along the Red River left dyke at km 77.200. The total width is 19 m divided over 4 gates (each 3.5 m width x 4 m high) and 1 lock (5.0 m width x 8.5 m high). The inlet is designed for a discharge of 75 m^3/s. The main drainage sluices are located in the south-east of the polder.

In addition, the polder is connected with the surrounding rivers with many small inlet conduits and numerous pumping stations. The small inlet conduits have openings of about 1.0 m x 1.5 m. These conduits are built in the dike body at levels much lower than the dike crest level. Therefore, overflow is no failure mechanism. The conduits were built in the end of 1950s and in 1960s. Most of the conduits are in a good condition, although some conduits show cracks in the concrete.

Hydraulic boundary conditions

In the FRA extreme situations are studied for which appropriate observations do not exist, and the data are available only on a very limited number of stations in the project area. From these restraints it has been concluded that the complexity of the Red River Basin hydraulic behavior for this project cannot be assessed adequately from simple empirical relations.

Therefore, for quantitative predictions of the water levels and discharges during flood conditions state-of-the-art hydraulic modeling tools have been used that account for the dynamics and variations in geometry in the system, and that have been calibrated on the limited observations.

For the Red River delta a calibrated 1D model is already available. In Figure 7 results of computations are presented, in particular water level relation curves for the Red River at km 92, at Hanoi and at Son Tay for a certain discharge.

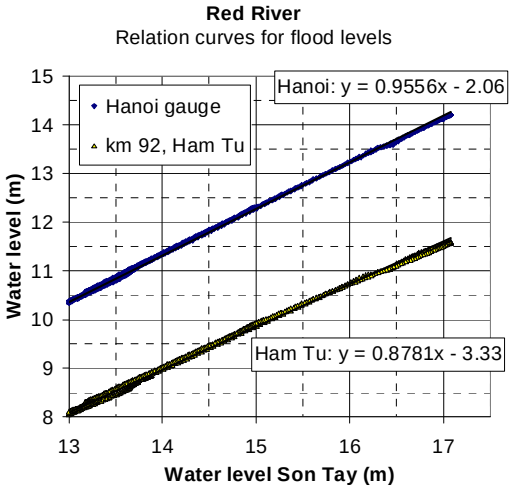

Figure 7. Relation curves for flood levels for the Red River computed from 1D hydraulic model simulations

Recurrence intervals for piping

Recurrence intervals (or failure probabilities) of dike sections were computed with a so-called "crude Monte Carlo" method. In this approach the random nature and uncertainties of the physical variables involved, are taken into account. Other variables are described in a deterministic way. Random variables are assumed to be normally distributed, except some variables, such as for instance the water level in the river (H) which is expressed as a relation with recurrence interval by a table of values and settlement of the dike body. Figure 8 shows the water levels in the Red River and in ditches at the inland side of the dike.

The average value d = 4.62 m of the thickness of the clay layer is determined on the basis of the available geotechnical data. For some locations a less thick clay layer is observed, for instance between km 90 and 100 only 3.3 m. The resulting recurrence intervals are presented in Figure 9.

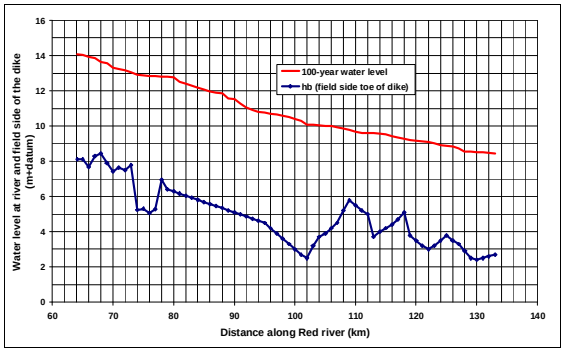

Figure 8. Water level in Red River (H = $H(T_{100})$) and water level at the inland side of the dike (h_b).

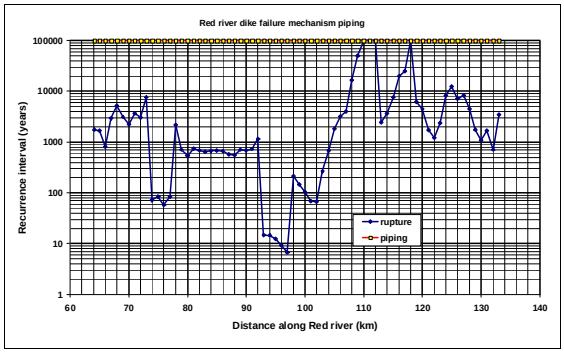

Figure 9. Recurrence intervals for the failure mechanism 'piping' along Red River

It is observed that soil rupture or sand boils can be expected during major floods. However, the reliability function for the sub-mechanism sand transport does nowhere lead to negative values. Hence, based on the failure probability analyses, it is concluded that dike failure due to piping is unlikely for the dikes along Bac Hung Hai polder.

Recurrence intervals for macro-instability

The slip circle computations have been carried out for different flood levels, but as the design flood level is related to the 100 year flood, the actual safety level computed for the 100 year flood has been selected. Besides, the differences between the safety levels for the different flood levels are small. The selected actual safety levels take into account the occurrence of a small flood some days/weeks before the extreme flood, which will result in a saturated dike body and water in the cracks.

The failure probability due to macro-instability for that dike is shown in Figure 10. It is observed that between km 90 and km 115 due to insufficient stability of the field side slope of the dike problems may be expected.

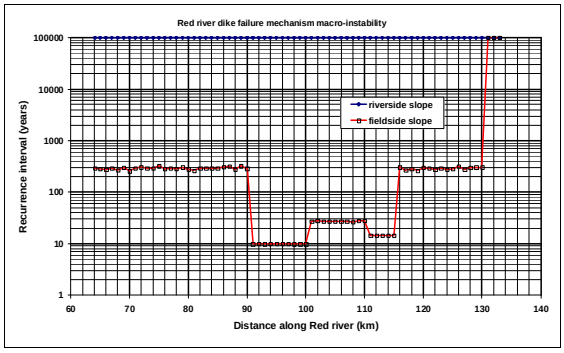

Figure 10. Recurrence intervals for mechanism macro-instability along Red River

Combined recurrence intervals

The probability of failure (or recurrence interval) of a dike ring is to be derived by combining the failure probabilities for each river kilometre, where the lower and upper bound follows from complete correlation and full independence between the sections.

Figure 11 shows that the combined recurrence intervals more or less equals the minimum value of the recurrence intervals due to the overflow or the macro-instability mechanisms. Basically, the dominant mechanism everywhere is overflow, except at the Red River reach km 90 to km 115, where the instability of the field side slope of the dike determines the overall failure probability.

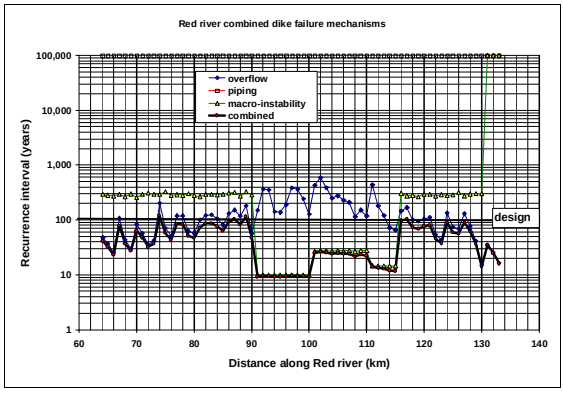

Figure 11. Combined recurrence intervals along the left Red River

Ultimately, the weakest locations can be determined on the basis of the combined failure probabilities. For the Bac Hung Hai polder they are shown in Figure 12.

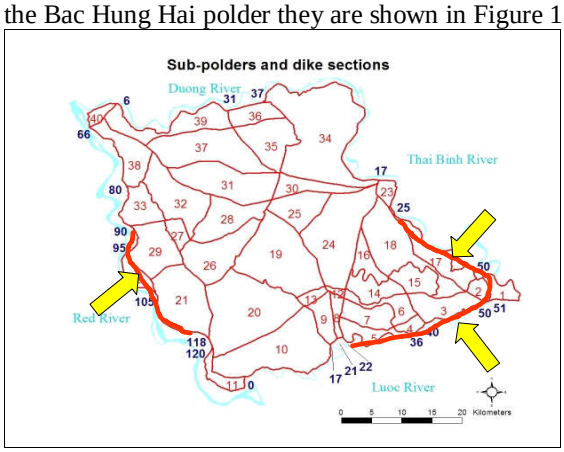

Figure 12. Overview of location of the weakest sections in the Bac Hung Hai polder dikes

Example of the consequences of a weak section

The combined recurrence interval or failure probability as computed above for each dike kilometre, includes the uncertainties in the river dynamics, in particular the trend in the vertical movement of the bed level. It is observed that the bed levels and water levels of the Red River downstream of Son Tay (down till the sea) are lowering with a rate of 1 to 2 cm/year in the long term. They seem to have changed even more in the period 1996 – 2000. It is most likely that the ongoing trend will persist, leading to an approximate degradation (of cross-section averaged bed levels) of about 1 meter in 2050 compared to the present situation.

In addition, river dynamics also refers to the horizontal movement of the river and this may form a major threat to the stability of the dikes. Hence, channel fixation by revetments at various locations has been carried out to maintain or improve safety. At the toe of the revetments in outer bends, however, bend scour due to the high flow velocities occur if the

revetment has not been designed properly. In sequence, the following phenomena may occur:

- General scour of the bed level due to the bed lowering trend;
- Scour of the river bed in the outer bend;
- Erosion below the revetment resulting in a steepening of the under water slope (sometimes even steeper than 1 vertical to 2 horizontal);
- Loss of stability of dike material along a slip circle;
- Visible sliding (Figure 13).

Figure 13. Example of a sliding due to toe scour in an outer bend

Slip circle computations have been made using the available, very limited data regarding river bend scour and soil characteristics. Ground investigations and laboratory tests have not been carried out. The stability analysis was a common α-φ-analysis and even for moderate values for cohesion and friction angles, it resulted at some locations in values of the safety factor F in the range of 1 to 1.5, where 1.35 is the minimum requirement in Vietnam.
Figure 14 shows the damage to houses as a consequence of a sliding after a flood.

Figure 14. Damage to a house due to a sliding

DAMAGE ASSESSMENT

The flood-damage assessment for Bac Hung Hai is carried out by combining and aggregating spatial varying information using GIS-tools, hence spatially varying inundation depths and impacts are required. For that reason the inundation simulations are carried out using a two-dimensional (depth-averaged 2D) model that simulates the spreading of the inflow and filling of the polders dynamically and spatially.

In the simulations it has been assumed that dike failure occurs during the moment of maximum water level. This is the situation with highest pressure on the dikes, but also generates the highest inflow discharges (causing the highest damage).

On basis of a more detailed inspection of the topography 5 breach locations were selected that were expected to represent sufficiently the inundation process in each zone for breaches anywhere in large reaches of the adjacent dike-sections.

The inundations are representative for a 1/100 year median sized flood (maximum daily average discharge Son Tay = 26,700 m3/s). The moment of failure is assumed to be on August 21. Dike failures in the north-west along the Red River result in flooding of almost the entire Bac Hung Hai polder (Figure 15), whereas dike failures in the north-eastern result in partly flooding,

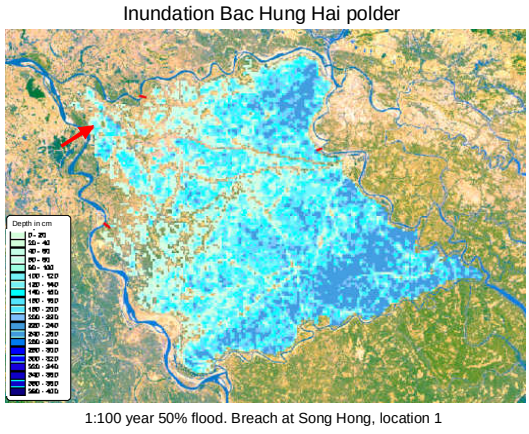

Figure 15. Computed inundation due to a breach in the most north-west part of the Bac Hung Hai polder

As an example, water levels as function of time for Hung Yen are shown in Figure 16. As can be seen in this figure, the water level reaches values up to 3 m. This is close to the inundation depth of 3.5 m observed at some locations during the 1971 flood, as reported by Ministry of Agriculture and Rural Development [2]. It is also observed from this figure that there will be severe flooding till several weeks after the breach, creating large damages, affecting people for a very long time and will have considerable environmental impact.

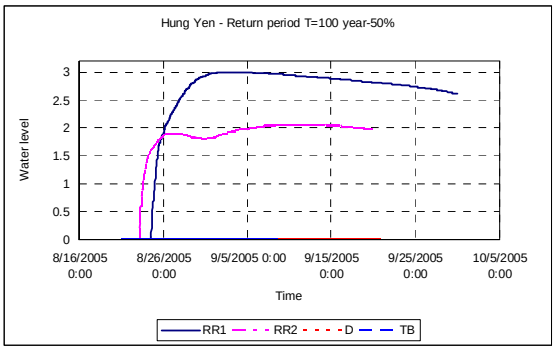

Figure 16. Water levels at Hung Yen as result of dike breaches at different rivers

Flooding risk is defined as the product of the probability of flooding and the damage of flooding. To assess the damage of flooding first the physical damage has to be determined and subsequently economic valuation of this damage should be carried out. The physical damage is determined by calculating areas of different types of land use that are inundated while valuation of the damage is done using an economic model. For ranking purposes a cost-benefit analysis of dike improvements is carried out. The ranking is further carried out using a composite index that includes an index for affected population, affected poor and volume inundated.

The final step in the economic valuation of flood damage is a cost-benefit analysis. The cost-benefit analysis is used as input for the priority ranking of the different dike sections. Additional information required for the cost-benefit analysis is the improvement costs of dike sections.

The outcomes of the damage assessment shows the largest damage if dike section 40 fails, followed by dike section 38 (Figure 12). Failure of these sections, located in the north-west region of the Bac Hung Hai polder, cause the whole polder to flood.

The calculated damages are based on the volume of water that entered the polder from two dike breach scenarios at 5 locations: due to a 25-year flood and a 100-year flood. From Figure 17 it is observed that a distinct relationship between flood volume and damage exists.

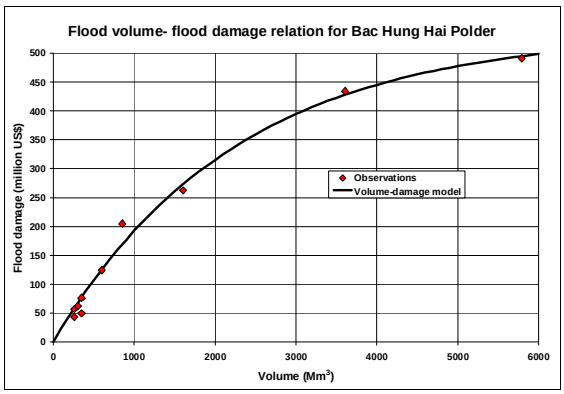

Figure 17. Relationship between flood volume and damage

CONCLUSIONS

Based on the Flooding Risk Assessment for the Bac Hung Hai polder in the Red River delta south-east of Hanoi the following conclusions can be drawn:

- The dike failure mechanisms overflow (including wave overtopping), piping and macro-instability have been considered. The analyses indicate that only overflow and macro-instability play a role for the dikes along Bac Hung Hai polder.
- Simulations based on the 1/25 and 1/100 year flood scenarios indicate that breaches particularly in the Red River dike will create inundation depth of up to about 3 m. Similar depths were observed during the inundations caused by the dike failure of 1971 flood event. The simulations also indicate that the flooding will continue for some months.
- Consequently, such dike failures will create enormous damages, affecting a large number of people and will have severe environmental impacts. The combination of the high flooding probability and the large damage costs in case of flooding make the average annual damage value large. Since the costs for dike repair and improvement are comparatively small, dike improvement projects will have a large benefit-cost ratio.

It can be concluded that a full FRA is a strong tool for ranking projects, e.g. weak spots along the dikes that require improvements. Obviously, there is a strong need for accurate predictions of water levels, river bed levels and detailed knowledge of geotechnical characteristics of the dikes.

ACKNOWLEDGMENT

The authors wish to thank Asian Development Bank, Ministry of Agriculture and Rural Development of Vietnam, SWECO Groner and WL|Delft Hydraulics for their permission to publish results of the study.

REFERENCES

[1] Ogink, H.J.M., et al, 2005, Flooding Risk Assessment for Bac Hung Hai polder – ranking of flood protection projects, Sweco Groner & WL | Delft Hydraulics, Technical Report prepared for ADB, Hanoi, October 2005.

[2] Marshall Silver & Associates Ltd., 2001, Feasibility Study for Flood Protection Projects in the Red River Delta of Vietnam, final report, June 2001.

An Innovative Ballasted Geocomposite Filter for the Stabilisation of the Seabed in the Venice Lagoon: Field and Laboratory Test Results

Marco Vicari , Francesco Ferraiolo
Officine Maccaferri S.p.A., Bologna, Italy
francesco.ferraiolo@maccaferri.com
marco.vicari@maccaferri.com

ABSTRACT

In order to assure the complete defence of all inhabited centres of the Venice lagoon from high waters, including exceptional occurrences, the solution based upon the temporary closure of all the three Venice lagoon inlets through a line of mobile flood barriers, has eventually emerged as the only solution able to fully respond to the required objectives.
The mobile flood barriers are made up of lines of flap-gates built into the inlet canal beds: in normal tide conditions they are full of water and lie flat in their housings built into the inlet canal bed. When tides exceeding predetermined levels are forecast, an emission of compressed air empties the flap-gates of water until they emerge, thus temporarily isolating the lagoon from the sea thereby blocking the flow of the tide. The system is dimensioned to resist a difference in level of up to 2 m between the sea and the lagoon and it will thus also be effective in the event of the predicted significant rise in sea level during the next century.
Similarly to other interventions carried out in the world to regulate tidal floods (Thames, Scheldt), the selected solution for the seabed protection involves a prefabricated mattress, assembled in a plant, wound onto a floating cylinder and transported to the site where it is laid on the seabed by means of a special pontoon.
The 40 mm thick ballasted filtering mattress consists of three basic elements:

- a lower filtering polypropylene, spun-bonded, nonwoven geotextile;
- a polypropylene geomat, reinforced with double twist steel wire mesh, to entrap the ballasting gravel;
- an upper polypropylene, spun-bonded, nonwoven geotextile to contain the material, the total structure is interconnected by steel crews.

The main performance characteristics the filter has to assure are: a submerged weight capable to resist to the pressure gradients due to waves occurring between its installation and the further rockfill covering; the granular material inside the mattress must not be allowed to move during transport and installation; to maintain its tensile strength and filtering properties after the rockfill installation.
In order to verify the hydraulic characteristics of the filtering mattress, a series of laboratory and in-situ tests has been carried out both on the single components and the whole mattress, covering the following aspects: hydraulic properties before and after different energy impact tests carried on 2 soil types (silt and sand); tensile properties (MD, XD) before and after different energy impact tests; lifting tests on assembled units to verify the resistance of both longitudinal and transversal joints.
The paper presents the required characteristics, the test methodology and results which have allowed to select the materials to be eventually adopted for the installation.

I. INTRODUCTION: THE INTERVENTIONS FOR THE SAFEGUARDING OF VENICE

The objective of the legislation to safeguard Venice is to guarantee the complete defence of all built-up areas in the lagoon from high waters of all levels, including extreme events. Ever more frequently, Venice, Chioggia and other historic towns and villages in the lagoon are flooded with water and the lowest lying zones - usually the oldest and most valuable - are now flooded almost daily, particularly during the winter.

The risk of an event representing a danger to the city, such the dramatic flood of 4 November 1966, is ever greater. The so-called MOSE protection system has been designed to protect the whole Venice lagoon and includes mobile flood barriers, realised at the lagoon inlets (fig. 1) in order to isolate the lagoon from the sea in the case of tides higher than the pre-established height of 110 cm, whose frequency is approx. 12 times per year, together with complementary measures capable of abating the level of the most frequent tides. Furthermore, at the Malamocco inlet, a navigation lock is under construction to allow the transit of large ships [1], [2], [3].

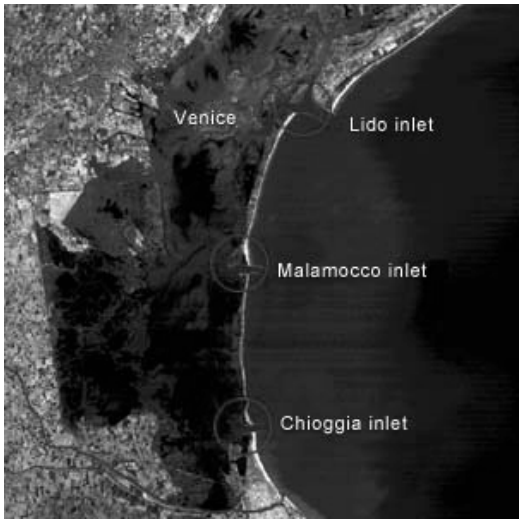

Figure 1. The Venice lagoon

The mobile flood barriers are made up of lines of flap-gates built into the inlet canal beds. They are "mobile" because in normal tide conditions they are full of water and lie flat in their housings built into the inlet canal bed (fig. 2).

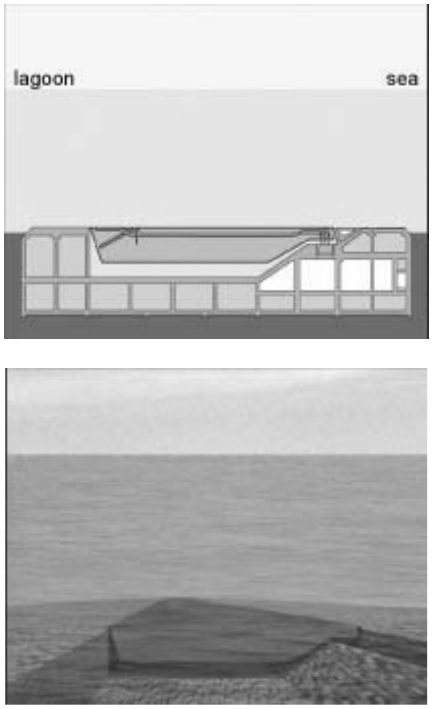

Figure 2. The floodgates at rest

When tides exceeding predetermined levels are forecast, an emission of compressed air empties the flap-gates of water until they emerge (fig. 3).

The inlets remain closed for the duration of the high water and for the time it takes to manoeuvre the flap-gates. The system is designed to resist a difference in level of up to 200 cm between the sea and the lagoon, thus being effective also in the event of the predicted significant rise in sea level during the next century.

Each oscillating buoyant floodgate consists of a box-shaped metal 'flap' attached to its housing by two hinges;,at rest they are "folded-away" into their housings buried at the bottom of the lagoon inlets. The housing consists of prefabricated concrete caissons which are located into the sill, built up of graded layers of stones installed above a mattress filter applied to protect against erosion by scour and migration.

The total amount of approx. 600.000 m^2 surface of filter mattress, to be installed on the 3 inlets within 2008, is therefore an essential part of the whole foundation structure, which is designed to prevent settlement of the caissons.

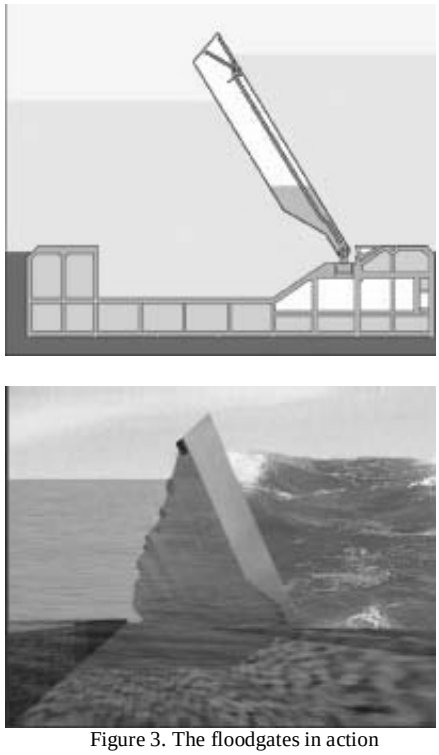

Figure 3. The floodgates in action

Similarly to other interventions carried out in the world to regulate tidal floods such as the Eastern Scheldt Project [4], [5] the selected solution for the seabed protection involves a prefabricated mattress, assembled in a plant, wound onto a floating cylinder and transported to the site where it is laid on the seabed by means of a an accurately positioned pontoon (fig. 4).

Immediately after the start of the ebb-tide the mattress is unwound from the cylinder in a direction parallel to the current at a speed of approx. 4 m per minute in the same direction as the current. At both end of the mattress ballasting beams are fitted to assure the required stability with respect to currents and waves.

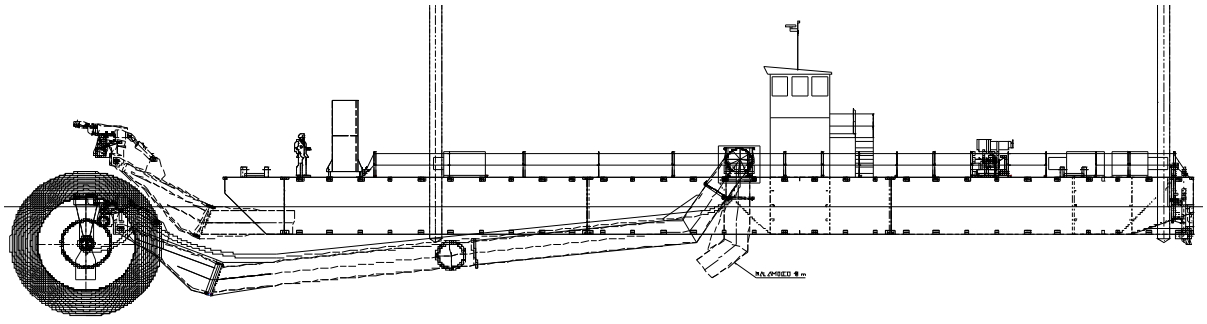

Figure 4. The pontoon for the mattress installation

II. THE FILTER MATTRESSES

The solution of the problem has requested the study, the design, the realization and the execution of performance tests of a brand new product, suitable for the bathymetric and meteomarine conditions of the Venetian site, characterized by a water depth variable between 6 and 15 m, a maximum wave height of 1.5 m and a current on the seabed up to 1.5 m/s.

For such scope, the Client has requested a solution with an optimal filtration capability, flexibility, resistance, durability with respect to the mechanical stresses imparted during the rip-rap installation.

A. Design of the Filter Mat

The fundamental role of the geotextile filter is to prevent the erosion of the existing soil foundation while allowing easy dissipation of hydraulic pressures and avoiding that pressures which can force up the filter should develop (uplift criterion).

The equation used to design the ballasting of the filter layer is the one used for the calculation of the unit lifting force p_w through the surface of the geotextile:

$$P_w = i\, k_s\, t_g / k_g \qquad (1)$$

where:

- i is the hydraulic gradient on the soil
- t_g is the geotextile thickness
- k_g is the geotextile permeability
- k_s is the soil permeability

In the case of the Venice inlets, the lifting force on the surface unit results:

$$p_w(\Delta H) = 8.2 \text{ daN/m}^2$$

By applying a safety factor equal to 3 we obtain a minimum design value for the ballasting in submerged conditions equal to 25 daN/m^2.

In relation to the long term performance of the geotextile, a further check has been conducted through a finite element modelling, which allows to analyze the fields of filtering motion under saturated and not saturated conditions, both as steady or as transitory.

Considering a configuration in which the rocks are sunk in the water (fig. 5) and that the filter settles as represented in fig. 6, the tension induced by the filter settlement has been calculated assuming that the under-pressure resultant ΔU, produced by the passage of the wave, is balanced by the stress generated in the geotextile N (fig. 6).

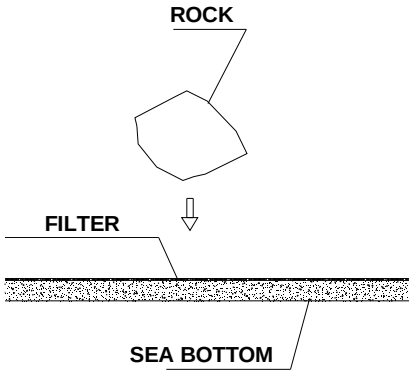

Figure 5. Rip-rap installation

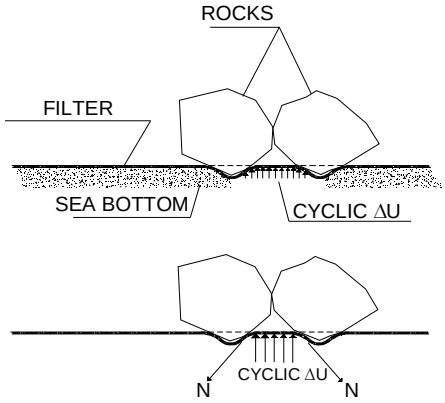

Figure 6. Filter settlement and corresponding reaction force N

B. Composition of the filter mat

The 40 mm thick ballasted filtering mattress (BFM) consists of the following basic elements (fig. 7):

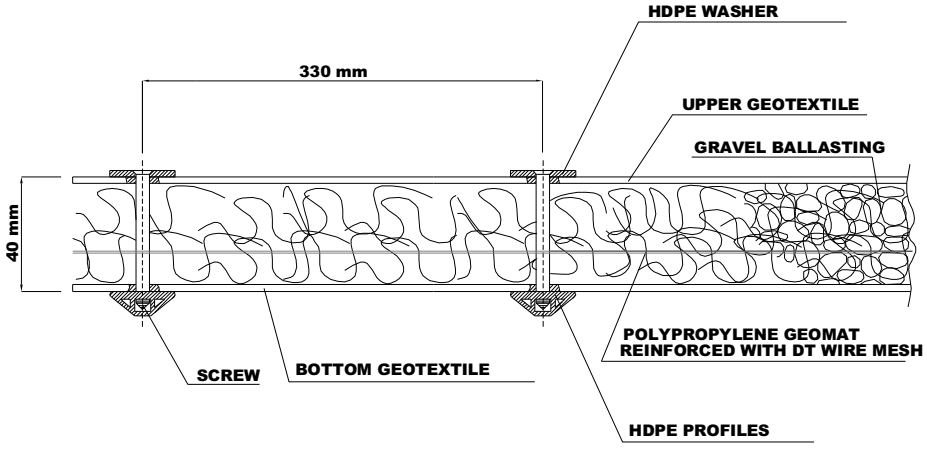

Figure 7. Cross-section of the filter mattress

- a geotextile as bottom filter;
- a central body consisting in a geomat in polypropylene filaments, internally strengthened with a double twist wire mesh;
- a ballasting of the central body with small crushed rock , grading 4-8 mm;
- a geotextile for the upper closure;
- a side band in filtering geotextile;
- a quilting with HDPE profiles and steel screws.

The total weight of the mattress in air is approx. 50 daN/m^2, such to guarantee a submerged weight not less than 25 daN/m^2. The filter mattresses are 11.20 m wide and their length is 150/200/250 m depending upon the inlet zone to be protected.

Bottom geotextile

The bottom layer, with the main function of filtering element and containment of the crushed rock, is made of a 350 g/m^2 spun-bonded, non woven, polypropylene geotextile without added resins and adhesives, resistant to the attack of bacteria and fungi, and UV rays.

Central body

It has the function to contain the ballasting material, preventing its migration and is constituted by a geomat in polypropylene filaments extruded on a double twist 6x8 wire mesh, wire diameter 2.2 mm with Zn/Al corrosion coating and external protection in PVC. The pre-assembled product (fig. 8) used for the site production is constituted by a geocomposite formed by the bottom geotextile coupled, by thermal welding, to the reinforced geomat having a nominal thickness of 40 mm.

All the geocomposite rolls are protected from rain and UV by a cover with a black PE film both during the transportation and the storage in the yard.

Ballasting inerts

The inerts, whose principal function is to ballast the mattress, is a calcareous crushed rock with apparent specific weight 14.4 kN/m^3 and a 4-8 mm granulometry, (fig. 9) which responds to both the requirements of easily penetrating inside the geomat and of avoiding segregation during the installation.

Upper geotextile

The upper geotextile, with the main function to contain the inerts, is a spun-bonded, non woven polypropylene geotextile with the same characteristics of the bottom one. To minimize the sewing operations, the rolls of the upper geotextile are 5.20 m wide.

Quilting

The mechanical connection of the upper geotextile layer to the ballasted mattress is realized by profiles in HDPE with trapezoidal section, placed transversally every 33 cm on the lower side of the mattress, with washers of the same material on the top side, and joined with metal screws (fig. 10).

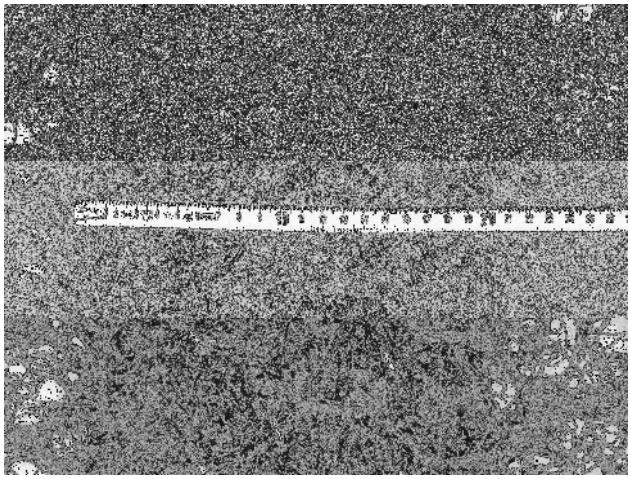

Figure 8. The PP geomat reinforced with wire mesh

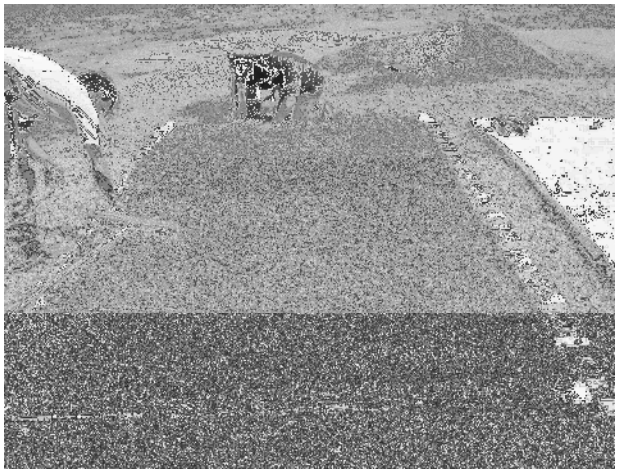

Figure 9. The mats ballasted with 4-8 mm gravel

Side band

The side band 1.20 m wide (fig. 10) is present for the whole length of the mattress and is realized with the same type of geotextile used for the bottom filter layer and its functions are:

- to guarantee the resistance to the impact due to the high tenacity of the filter geotextile;
- to supply a transversal rigidity against the lifting actions through the transverse HDPE section placed with a 33 cm spacing;
- to avoid the need of doubling the thickness of the filtering mattress at the overlaps;
- to reduce the weight of the mattress on the launching roll assembly, with equal surface, minimizing the loading problems.

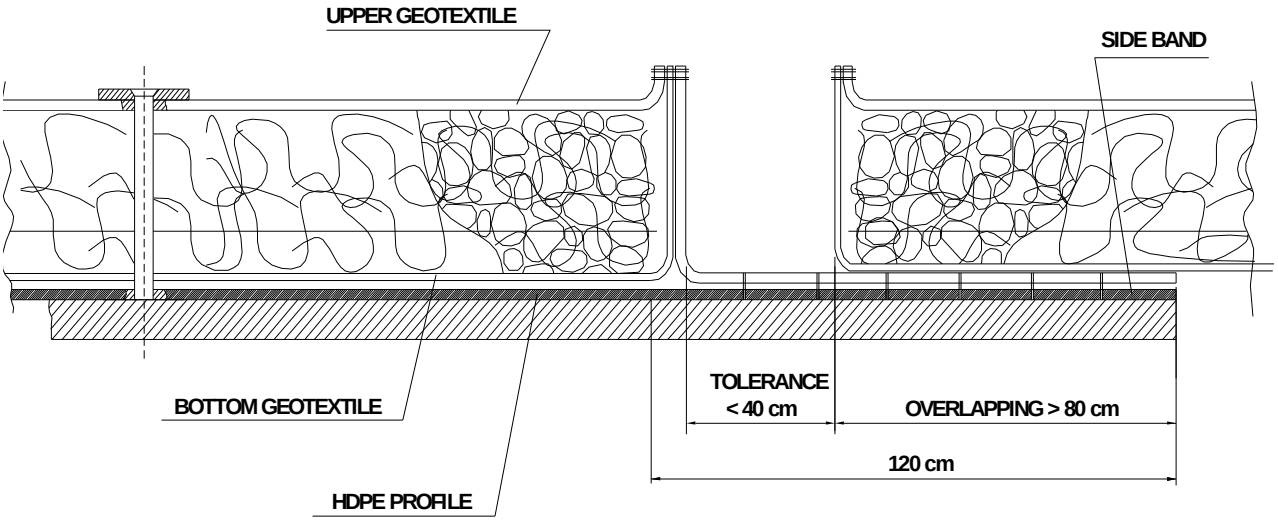

Figure 10. Overlapping of the mattress onto the side band

The band can be placed on the right or left side of the mattress, depending on the laying direction.

In order to verify the hydraulic characteristics of the filtering mattress, laboratory and in-situ tests have been carried out both on the single components and the assembled mattress, covering the following aspects: hydraulic properties before and after different energy impact tests carried on 2 soil types (silt and sand); tensile properties (MD, XD) before and after impact tests; lifting tests on assembled units to verify the resistance of both longitudinal and transversal joints.

III. REQUIRED CHARACTERISTICS OF THE FILTER MATTRESSES

The main performances the filter has to assure are:

- a submerged weight capable to resist to the pressure gradients due to waves occurring between its installation and the further rockfill covering;
- the granular material inside the mattress must not be allowed to move during transport and installation;
- to maintain its tensile strength and filtering properties after the dumped rock installation.

The specific required characteristics are shown hereafter.

A. Filter properties

To prevent the migration of the subsoil particles (sands and silts) through the filter layer and to assure the retention of the base material without the generation of unacceptable excess pore water pressure, at the dredging water depth, a maximum geotextile pore size O_{90} = 60 μm was required.

B. Resistance to uplift

The submerged weight of the filter mattress must be adequate to prevent its uplift due to the wave cyclic loads occurring after the filter installation and before its complete covering with the rock layers.

The permeability of the seabed silts and sands is approx 10^{-5}-10^{-6} m/s, while the permeability of the filter had to be at least equal to 10^{-3} m/s. Therefore the uplift pressures occurring during the installation period with frequent waves and calculated with equation 1, are in the range of 8 daN/m^2 and applying a safety factor of 3 the required submerged weight became 25 daN/m^2.

C. Resistance to impact

The application of the seabed rip-rap protection can pose a severe threat to the condition of the filter mattress, as stones, whose mean weight can is in the range 60-300 daN, are dumped from barges directly onto the mattress. Consequently, a 300 daN stone has been assumed to evaluate the impact energy in water and a test where the stones are dumped dry by modifying the dry fall height was required.

The geotextile must be elastic enough to deform and stretch along the contact surface soil rock to maintain the tensile forces far from breaking, thus assuring its filter properties. For this reason the required elongation at peak strength of the geotextile was set to 50%.

Furthermore, the main characteristics of the filter geotextile after impact had to be checked to assure their acceptability as follows:

Pore size after impact	≤ 1.05 x 60 μm
Tensile strength after impact	>70% NBL
Permeability after impact	$>10^{-3}$ m/s.

D. Resistance to installation forces

The ballasted filter mattress is subjected, during the phases of construction, wounding and final placement onto the seabed, to forces which could cause elongations or breakages. For this reason, the reinforcement placed in between the mattress shall have a minimum tensile strength of 35 kN/m.

Furthermore, the granular material inside the mattress must not be allowed to move. To verify its stability, a lifting test of a fully assembled mattress 10x2 m, to check the possible stone movement inside its thickness, was required.

E. Durability

All the materials composing the ballasted filter mattresses have to comply with a minimum required lifetime of 100 years.

IV. TEST METHODOLOGY

In order to verify the compliance of the adopted mattress with the performance requirements, a series of laboratory and in-situ tests has been carried out, both on the single components and the mattress.

A. Hydraulic properties

To evaluate the hydraulic properties before and after energy impact tests, a semi-dry test was set up where the design stone 300 kg weight was dumped onto the mattress from various fall heights (fig. 11).

The tests were done using two soil types (silt and sand) commonly found in the inlets seabed and placed in two trenches 8x8x1 m. The impact test on the sand soil has been carried out with two different water content conditions (dry and saturated), for a total of 3 test conditions (table 1 and 2).

Figure 11-a. Impact tests on sand before impact

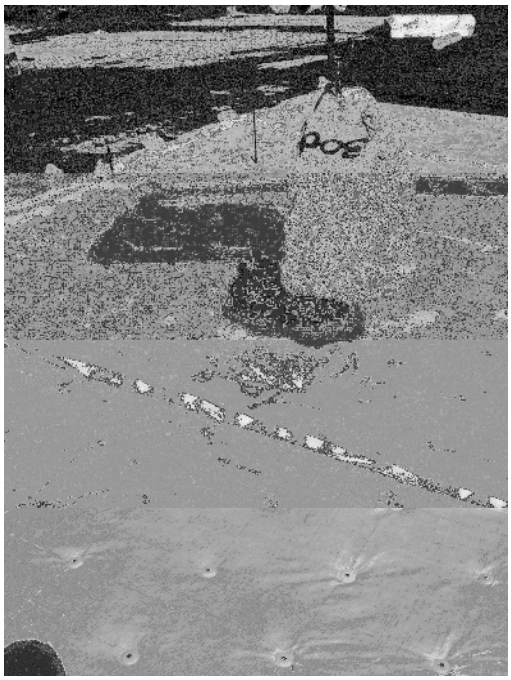

Figure 11-b. Impact tests on sand after impact

For each falling test, a thorough survey of the impact area has been registered, both in terms of superficial size and depths, to finally evaluate the elongation of the geotextile (fig. 12).

To compare the hydraulic properties after impact with those of the virgin material, 5 samples for each of the 3 test conditions have been extracted for a total of 15 samples. As per the specific test methodologies, reference has been made to the following standards: EN ISO 12956 for the pore size under hydraulic loads, EN ISO 11058 for the permeability.

TABLE 1.
Impact test: soil types

Test condition	Soil type	Water content %	D_{50} (mm)
A	Sand	5.3	0.125
B	Silt	112.4	0.040
C	Sand	100	0.125

TABLE 2.
Falling heights of the dumped 300 daN stone

Falling height (m)	Simulated weight (daN)
0.10	75
0.26	150
0.66	300
0.93	390
2.84	900

B. Submerged weight

Some BFM samples 0.8x0.8 m have been weighed by immersing them in a water tank, to check their actual submerged weight, obtaining 28 and 48 daN/m^2 respectively for the submerged and the dry conditions (fig. 14).

C. *Tensile strength*

For all the mattress components tensile strength tests have carried out, in compliance with EN ISO 10319; for the wire mesh, due to its specific geometry and opening size, a specific methodology has been adopted.

All the materials have proven to be well above the required values both before and after impact.

D. *Lifting and shaking tests*

To verify both the resistance of the reinforcement and the stability of the ballasting gravel within the mattress, when placed vertically, a sample 10x2 m has been completely lifted and subjected to shaking movements (fig. 15).

The BFM has showed no visible movements of the infill material, confirming the suitability of the chosen gravel D_{50} and the positive effect provided by the quilting system adopted to mechanically join the components.

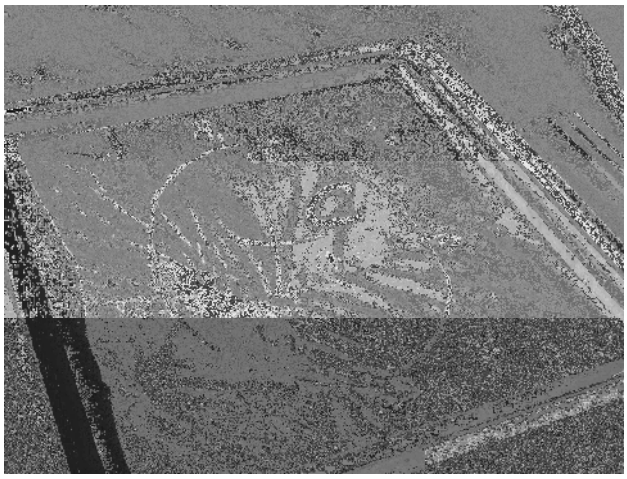

Figure 12. Measurements on the deformed area after impact

Figure 13. Extraction of samples for laboratory testing

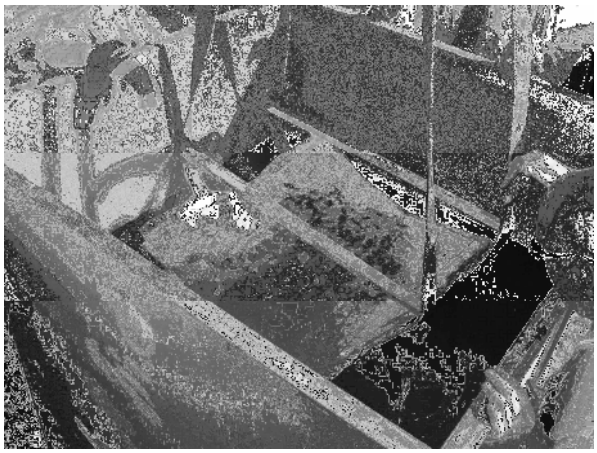

Figure 14. Determination of the BFM submerged weight

Figure 15. Lifting test on a 10x2 m sample

At the end of the test campaign on virgin and damaged samples, it has been verified that all the components comply with the requirements (table 3).

Table 3: main characteristics of the BFM components

Material	Mass per unit area	Tensile strength	Permeability	Pore size
	EN 965	EN 10319	EN 11058	EN 12956
	g/m^2	kN/m	m/s	μm
Filter GT	350	26.5 18.7 [(a)]	0.0012 0.0018[(a)]	59.5 49[(a)]
Geomat	650	1	-	-
Wire mesh	1490	36 [(b)]	-	-
Upper GT	150	10.3 8.6 [(c)]	0.0018	76.5

(a) = value after impact tests (900 daN) on silt

(b) = for the wire mesh a specific methodology has been used

(c) = value after impact tests (900 daN) on saturated sand

Breach Erosion in Dikes

Paul J. Visser* and Yonghui Zhu*/**
* Faculty of Civil Engineering and Geosciences, Delft University of Technology, Delft, the Netherlands
** College of Water Conservancy and Hydropower Engineering, Hohai University, Nanjing, China

A model for breach erosion in dikes is outlined. The model is based on the five-stage breach erosion process as described in [1] and [2]. For the final two stages three breach types are distinguished in the model, depending on the erodibility of the base of the dike, the presence (or absence) of a solid toe protection on the outer slope and the presence and erodibility of a high foreland. The model version for sand-dikes has been calibrated with the data of a field experiment and tested to the data of a 3D laboratory experiment, yielding good agreement. The confrontation of the model with the data of the failure of a prototype dike in the Netherlands yields results more or less in agreement with an eye-witness report. The model version for clay-dikes has been calibrated and tested with the data of a 2D laboratory experiment, the data of the laboratory experiment of the EC IMPACT Project and the data of a prototype dike-burst in China. The agreements between model predictions and the data are fairly good.

I. INTRODUCTION

The Netherlands has many kilometers of dikes to protect the land against flooding. Construction of dikes started some 1000 years ago and since then new dikes have been built and existing dikes have been strengthened to cope with the ongoing processes of land-subsidence and sea-level rise. Nevertheless, the Netherlands has a long history of flooding, with about 200 major floods reported, both along the rivers and in the coastal areas, some of these with many deaths (e.g. the St. Aagten Flood of 1287 with tens of thousands people drowned, the St. Elisabeth Flood of 1404 and the Storm Surge of 1953, both with thousands of deaths). Very surprisingly, until recently, the knowledge of the process of breaching of dikes was very poor, not only in the Netherlands but worldwide. Also prototype data of dike breaching are scarce and far from complete. Most information has been based on eye-witness reports of past dike-bursts.

Modeling of the dike breaching process, so also knowledge of this process, is of importance to both the design method of dikes based on a risk-norm and the development of evacuation plans for polders in case of a dike failure. In the Netherlands preparations are going on to substitute the present design method for dikes (based on an exceedance frequency of the water level) by an inundation risk approach. In this new method safety levels will be expressed in terms of risks (combinations of inundation chances with the consequences of flooding), see [3]. In order to determine the consequences of inundation, it is necessary to be able to predict the development of the breach. Evacuation plans have to be made in the Netherlands for all dike ring areas since the near flooding of polders along the river Rhine in 1995. The present evacuation plans were determined using a very simple description for the breach growth; a better breach erosion model is required to improve these evacuation plans.

The process of dike-breaching has similarities to breaching in earth dams and coastal sand-barriers. Earth dams (to make a distinction with dikes) are relatively high embankments, with relatively short lengths, having in general water on both sides, that are constructed with earth and rock to create reservoirs for water supply, hydro-electric power generation, flood control, etc. During the last forty years, and particularly since the 1980's, progress has been made in modeling of earth dam breaching and consequently also in flood forecasting. Many numerical models are available now for the simulation of breach erosion in earth dams (see the overview given in [4]). The calibration and validation of these models remains, however, problematic due to the lack of good empirical data.

Breaching of coastal barrier islands and spits is a common natural feature. Breaches in sand-barriers can be initiated in four ways: (1) inundation from the sea combined with wave action, (2) elevation of the water level in the lagoon, (3) narrowing of a barrier island by reduction of sediment supplied through longshore transport and (4) artificially for flood protection and to increase the water quality (see [5]). Breaching of some coastal barriers in the USA and Australia has been documented in [6], [7], [8], among others. For some years also some relatively simple models exists to simulate coastal barrier breaching, see [9] and [5].

Research on dike breaching has been initiated in the last few decades, see e.g. [10], [11], [12], [13], [14], [15], [1], [16]), [17], [18] and [2]. The results obtained so far are encouraging: good insight into the breaching process (see also Chapter III) has been obtained and some models are available for the simulation of breach growth in both sand-dikes and clay-dikes (see also Chapter IV). As for earth-dams, the calibration and validation of these models is still a major problem due to the lack of good empirical data. This applies especially to the models for clay-dikes (see Chapter V).

This paper summarizes the results of the research work on breaching of sand-dikes (see [1]) and clay-dikes (see [2]) performed at Delft University of Technology (DUT) in the period 1986-2006.

II. OBJECTIVE

The aim of the present investigation is a mathematical model that predicts the breach development and the discharge through the breach in case of a dike-burst as function of relevant parameters as the cross-section of the dike, the structure of the dike and the hydraulic conditions. The first version (see [1]) has been focused on the breach erosion process in sand-dikes. The present model has also a version for clay-dikes (see [2]).

It is assumed that the body of the dike is homogeneous

and that it consists of sand, or clay, or a mixture of sand, silt and clay, and that, after the formation of an initial breach at the top of the dike the revetments on the slopes do not decelerate the erosion process. As yet possible effects of waves have not been included in the model.

III. BREACH EROSION PROCESS

It is assumed that the breach erosion starts (at time $t = t_0$) with the flow of water through a small initial breach at the top of the dike with a trapezoidal cross-section. In general five stages (see Fig. 1) can be distinguished in the process of breach erosion, both for sand-dikes (as described in [1]) and clay-dikes (see [2]). In Stages I and II ($t_0 < t \leq t_2$), the breach eats its way into the dike, decreasing gradually the width and the height of the dike in the breach. In Stage III ($t_2 < t \leq t_3$) the breach growth accelerates, and consequently also the discharge through the breach. After the wash-out of the dike in the breach at the end of Stage III, the breach grows further in Stage IV ($t_3 < t \leq t_4$), mainly laterally. In Stage V ($t_4 < t \leq t_5$) backwater in the polder decelerates the flow in the breach, and consequently also the increase of the breach width. Raising backwater ultimately stops the flow of water through the breach.

In Stage I ($t_0 < t \leq t_1$), erosion occurs along the inner slope of the dike and, depending on the flow velocity, possibly also along the dike crest. The flow along the inner slopes accelerates, consequently the erosion along this slope increases, steepening the slope until a critical slope angle is achieved at $t = t_1$. This critical gradient is held later on by the inner slope throughout Stages II and III. In sand-dikes the breach erosion process in Stages I, II and III is dominated by shear erosion (see [1]), which leads to a gradual and relatively uniform retreat of the inner slope. However, in clay-dikes, when the inner slope of the dike has been steepened to the critical gradient, the steep slope acts as a headcut. Headcut erosion, including flow shear erosion, fluidization of the headcut slope surface, impinging jet scour of the dike foundation and discrete soil mechanical slope mass failure from the headcut dominates the breach development (see [19], [20] and [2]). In principle, in Stages I, II and III the breach develops mainly vertically with only ignorable widening, for both sand-dikes and clay-dikes.

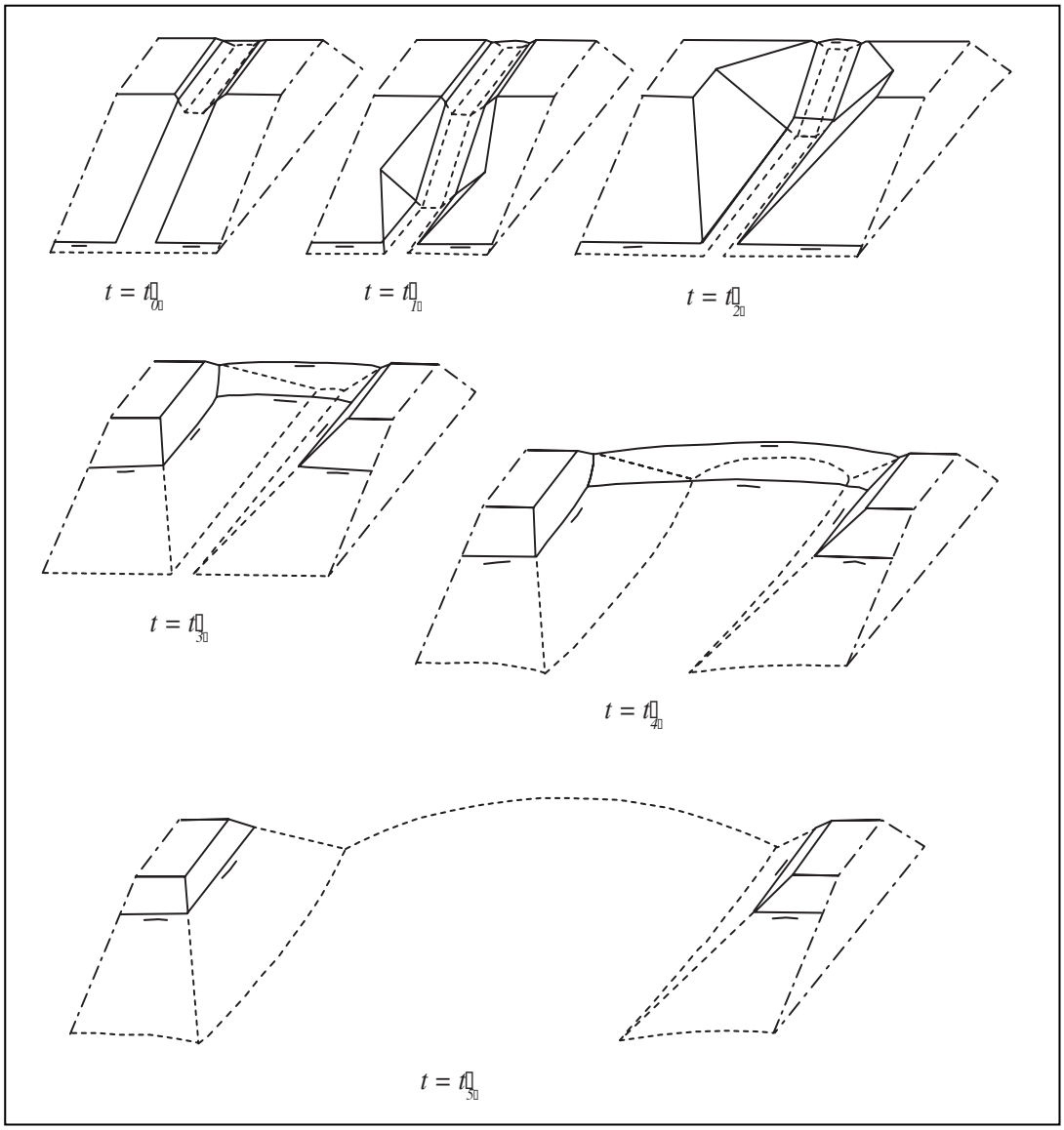

Figure 1. Schematic illustration of breach development in a sand-dike.

The breach erosion process in Stages IV and V depends on the erodibility of the foundation of the dike, and on the stability of the toe protection on the outer slope of the dike (if any) or the height and erodibility of the foreland in cases where the dike foundation has low resistance against erosion. Hence, three types of breaches (Types A, B, and C) can be distinguished in Stages IV and V, depending on these geometrical and material conditions (see [1], [2] and [20]). Generally, the dominating mechanisms of breach erosion in Stages IV and V are the flow shear erosion along the side-slopes of the breach and the resultant discrete soil mechanical breach side-slope instability. Fig. 2 shows the breach development in Stages IV and V with a toe protection on the outer slope of the dike.

IV. Mathematical Model

The model is based on the five-step breach erosion process shortly outlined above.

The flow through the breach and the flow velocities in the breach are calculated with broad-crested weir formulae (see (1) and (2)), i.e. for critical discharge in Stages I through IV and for subcritical discharge in Stage V.

$$Q = m\left(\frac{2}{3}\right)^{3/2}\sqrt{g}B\left(H_w - Z_{br}\right)^{3/2} \quad \text{for } t_0 < t \le t_4 \qquad (1)$$

$$Q = m\sqrt{2g}B\left(H_w - H_p\right)^{1/2}\left(H_p - Z_{br}\right) \text{ for } t_4 < t \le t_5 \qquad (2)$$

in which Q is the discharge through the breach (m^3/s), m is the discharge coefficient (non-dimensional), g is the gravity acceleration (m/s^2), B is the breach width averaged over the water depth (m), H_w is the outer water level (m), Z_{br} is the height of the breach bottom (m), and H_p is the level of the backwater in the polder (m). The discharge coefficient m is about 1 for Types A and C breaches and about 1.5 for a Type B breach. In a Type B breach the erosion of the relatively high foreland creates a circular or elliptical spillway with a length that is a factor m larger than the breach width.

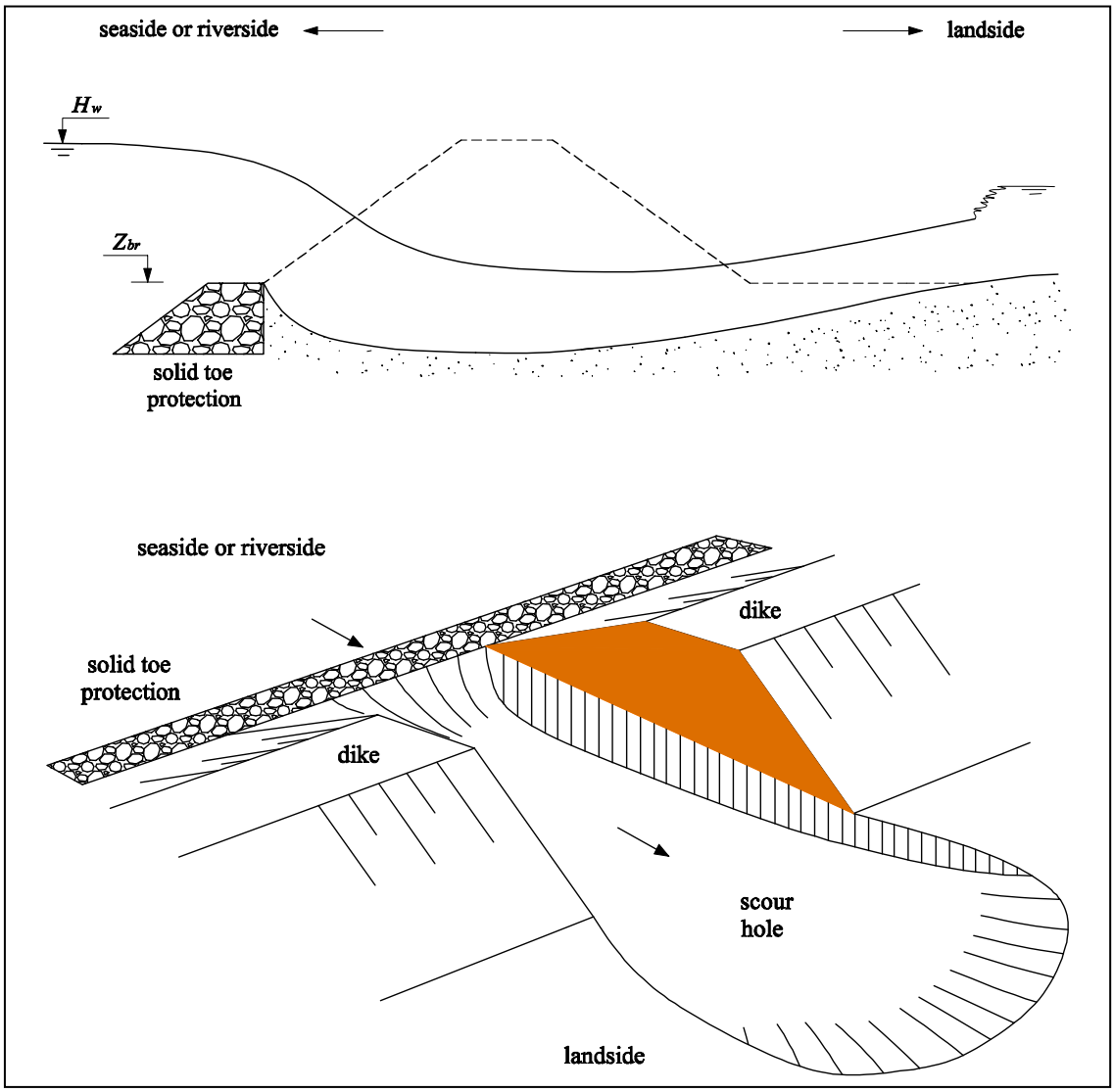

Figure 2. Breach development in Stages IV and V when vertical erosion at the breach inflow is obstructed by a toe protection on the outer slope of the dike (Type A breach).

An essential part of a breach erosion model is the description of the entrainment of sediment, both for sand-dikes and clay-dikes. For each stage separate descriptions for the erosion rate can be implemented. However, up-to-date best results have been obtained:

- for sand-dikes with Galappatti's (see [21] and [22]) description for the pick-up of sediment combined with the sediment transport formulae of Bagnold-Visser ([12], see also [1]) or Van Rijn (see [23] and [24]) in Stages I, II and III, and Van Rijn ([23], [24]) in Stages IV and V (see [1]);
- for clay-dikes with the frequently used excess shear stress equation representing the detachment process of cohesive sediment: $E = M\left(\tau_b - \tau_c\right)$, in which E is the erosion rate (m/s), M is a material-dependent coefficient describing the soil erodibility (s-m^2/kg), τ_b is the bed shear stress (N/m^2), and τ_c is the critical shear stress for erosion of the soil (N/m^2), see [2] and [20].

The erosion at a headcut during the breach erosion process of clay-dikes, including the impinging jet scour of the dike foundation (if any), headcut undermining and discrete slope mass failure, etc, is simulated through the mathematical model developed in [19] (see also [2] and [20]).

The breach growth and the breach discharge in Stages IV and V are computed by the model depending on the geometrical and material conditions of the foundation and the foreland of the dike. Fig. 3 shows the breach growth of a Type A breach in sand-dikes. In this situation, the vertical erosion at the breach inflow is prevented by a solid dike foundation, or by a solid toe protection on the outer slope of the dike, or by a solid, relatively high foreland (solid here means: with relatively high resistance against erosion).

The increase in time of the breach width at the top of the dike in Stages IV and V in a sand-dike is described by (see [1])

$$\frac{\mathrm{d}B_t}{\mathrm{d}t} = \frac{2}{\tan\gamma_1} E_{sl} \tag{3}$$

in which B_t is the breach width at the dike top (m), γ_1 is the critical value of the angle of the breach side-slopes (^{o}), and E_{sl} is the erosion rate in vertical direction at the toe of the side-slopes (m/s).

For clay-dikes, the breach width increase in Stages IV and V is given by (see [2])

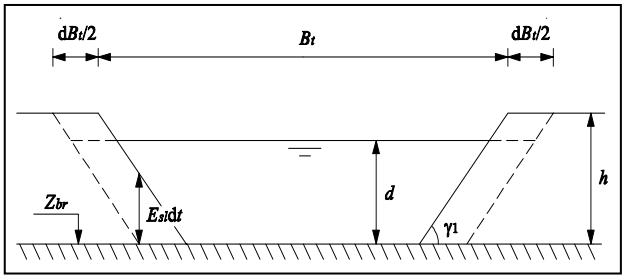

Figure 3. Growth of breach width in a Type A breach in sand-dikes in stages IV and V.

$$\frac{\mathrm{d}B_t}{\mathrm{d}t} = \frac{2}{\sin\gamma_1} E_{sl} \tag{4}$$

in which E_{sl} is defined as the erosion rate at the toe of the side-slopes perpendicular to the slope (m/s).

V. EXPERIMENTS

For the calibration and validation of the model the following experiments were executed:

A. The Zwin'94 field experiment

The Zwin'94 experiment was performed in October 1994 in the Zwin Channel, a tidal inlet at the Dutch-Belgian border connecting the nature-reserve the Zwin with the North Sea (see [1]). The Zwin area measures about 1.5 km^2; the mean tidal prism is about 350000 m^3. The experiment was done in quiet autumn weather, with negligible wave heights against the sand-dike.

A sand-dike closing of the Zwin Channel was built with a height of 2.6 m above the channel bottom, a width at the crest of 8 m and a total length of about 250 m. The inclination of the outer slope was 1 : 1.6, that of the inner slope 1 : 3. A small trapezoidal pilot channel, 0.8 m deep and with a width of about 1 m at the breach bottom and about 3.6 m at the dike crest was made in the upper part of the dam to ensure breaching near the middle of the Zwin Channel.

The experiment started at $t = t_0 = 0$, about 20 minutes before high water, with the flow of water through the pilot channel. At three locations upstream and three locations downstream from the breach , current velocity meters (Ott propeller type) and pressure probes measured continuously horizontal flow velocities and water elevations, respectively. The breach development was both video-taped and photographed (marks put in the dike-top allowed the observation of the dimensions of the breach at different times from the video-images, slides and photos). A total number of 40 vibration probes, buried in the sandy bottom of the Zwin Channel, detected the development of the breach under water in Stages IV and V. Each probe acted as a burglar-alarm: by measuring its own rate of vibration it could detect when the erosion process had exposed it to the flowing water. The signals of all vibration probes were recorded on the hard disks of personal computers. At $t = t_5 \approx 60$ min the flow velocities in the breach had become so small that the erosion process stopped.

The Zwin'94 field experiment has clearly confirmed the five-step breach erosion mechanism as described in Chapter III. The development of the breach width in time is shown in Fig. 4.

The data set of the Zwin'94 experiment is very useful for the validation of mathematical breach erosion models. Reference is made to [1] and [14] for details about the data set resulting from this experiment.

B. 3D laboratory experiment in basin of DUT

The 3D laboratory experiment was performed in 1996 in the 34.0 m long, 16.6 m wide and 0.7 m deep (wave) basin of the Laboratory of Fluid Mechanics of Delft University of Technology. The experiment was prepared by C.P. Caan as part of his MSc thesis project at the Delft University of Technology, see [25]. In the Zwin'94 experiment the scour hole could only be measured in a limited number of points. Hence, the laboratory experiment

was especially aimed at an accurate observation of the development of the scour hole and its upstream spillway in Stages IV and V.

The small-scale sand-dike was built normal to a 9.0 m long and 0.75 m high glass-wall on a 0.50 m thick sand-bed. The D_{10}, D_{50} and D_{90} of the sand of both the dike and the bed are D_{10} = 0.070 mm, D_{50} = 0.088 mm and D_{90} = 0.120 mm, respectively. The laboratory dike had a height of 15 cm and a width at the crest of 20 cm. The inclination of the outer slope was 1 : 2 and that of the inner slope 1 : 4. A small pilot channel was made in the upper part of the dike at the glass-wall to ensure breaching started near the glass-wall.

Water was pumped into the inflow section of the basin through two pipes at a maximum capacity of 0.66 m^3/s. The water level against the dike in the upstream section was kept constant as good and long as possible by increasing the rate of inflow to the basin.

Water level measurements were done with wave height probes in three positions in the upstream part of the basin and in one position in the downstream section. Flow velocity measurements were done using electromagnetic flow velocity meters in two positions upstream of the breach and one in the breach. The data of these instruments were recorded on a personal computer. The breach development was both video-taped (through the glass-wall) and photographed (from above). The increase of the breach width in time is shown in Fig. 5.

C. 2D laboratory experiment in flume of DUT

The 2D laboratory experiment was performed in 2005 in a 35.5 m long, 0.80 m wide and 0.85 m deep flume of the Laboratory of Fluid Mechanics of Delft University of Technology. The aim of this experiment has been to observe the breach erosion process in clay-dikes in Stages I, II and III. The small-scale dike had a height of 75 cm, a width of 40 cm and a length of the crest of 60 cm. The inclination of both slopes was 1 : 2.

Water level measurements were done with wave height probes in four locations (three upstream and one downstream from the dike). Flow velocity measurements were done using electromagnetic flow velocity meters in two locations upstream of the breach and in one downstream from the breach. The breach development was both video-taped (through the glass-wall) and photographed (from above and through the glass-wall).

In this experiment five tests were done, one with a small-scale sand-dike, four with clay-dikes constructed with different mixtures of fine sand, silt and clay. Much attention was paid to get a proper sand-silt-clay mixture. For details of this experiment readers are referred to [2].

VI. Model Validation

The model version for sand-dikes has been calibrated with the data of the Zwin'94 field experiment and validated against the data of the laboratory experiment (see [1]). The agreement of the model predictions with the data of these two experiments is good (see e.g. Fig. 4 and Fig. 5). Fig. 4 shows the model prediction for the breach width increase in the Zwin'94 experiment by applying Bagnold-Visser ([12]) in Stages I, II and III and Van Rijn (1984, see [1]) in Stages IV and V. Fig. 5 shows the model prediction for the growth of the breach width in the 3D laboratory experiment by applying Bagnold-Visser ([12]) in Stages I, II and III and Van Rijn (1984) in Stages IV and V. The confrontation of the model with the failure of the Noord Dike in Papendrecht (a sand-dike) in the Netherlands during the 1953 Storm Surge indicates that the final breach width $B_t \approx 110$ m was present after about 2.5 hr, which is more or less in agreement with a rough eye-witness report (see [1]).

The model version for clay-dikes has been calibrated with the data of two 2D DUT laboratory experiments and two 3D EC IMPACT (Investigation of Extreme Flood Processes and Uncertainty) Project laboratory experiments on clay-dike breaching (see [2]). The model predictions are in good agreement with the experimental data (see e.g. Fig. 6). Validation of the model with the data of other two 2D DUT laboratory experiments yields reasonable agreement between the model predictions and the measurements (see e.g. Fig. 7, see also [2]). Finally, the model has been confronted with a prototype dike failure in China in 1998 (see [2]). The predicted final breach width 274 m is about 39.7% smaller than the observed 390 m. The predicted 5.6 $\times$ 10^8 m^3 of diverted floodwater volume is close to the investigation-based estimation of 5.2 $\times$ 10^8 m^3.

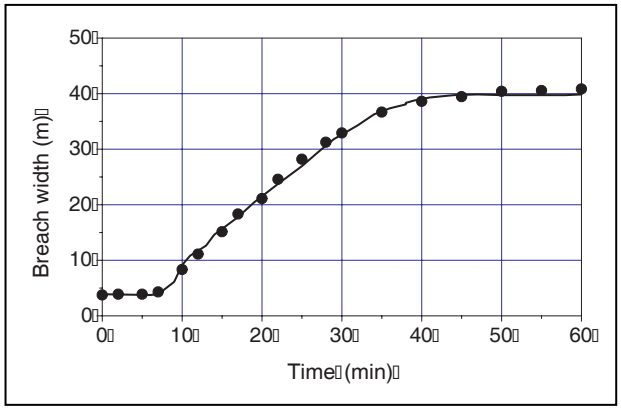

Figure 4. Comparison of predicted (solid line) and observed (dots) breach width at the dike crest for the Zwin'94 sand-dike experiment.

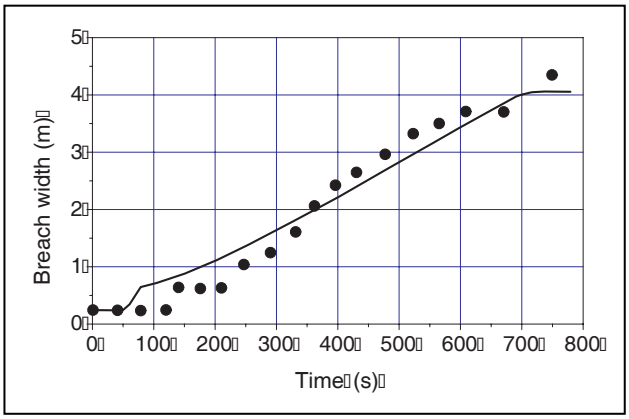

Figure 5. Comparison of predicted (solid line) and observed (dots) breach width at the dike crest for the laboratory sand-dike experiment.

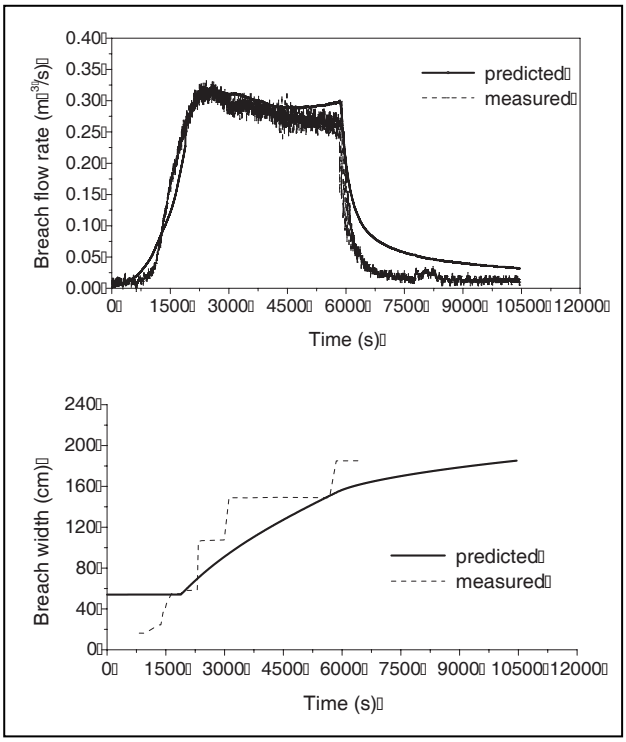

Figure 6. Comparison of predicted and measured breach flow rate (upper panel) and breach width increase (lower panel) for test no.10 of the EC IMPACT Project laboratory clay-dike experiment.

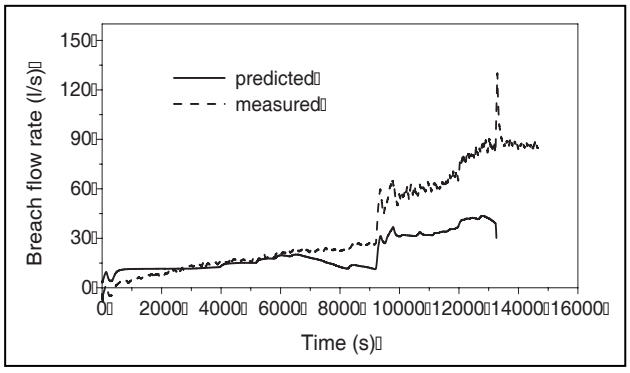

Figure 7. Comparison of predicted and measured breach flow rate for test T_3 of the DUT laboratory clay-dike experiment.

VII. DISCUSSION

After suitable calibrations, the agreement of the model predictions for sand-dikes with the data of both the Zwin'94 experiment and the 3D laboratory experiment is good. Also the confrontation of the model with a rough eye-witness observation of the breaching of the Noord Dike in Papendrecht yields reasonable agreement.

The model version for clay-dikes has been calibrated with the data of four laboratory tests and validated against other two laboratory tests and one prototype dike failure in China. The agreements between the model predictions and the data are fairly good. More reliable data, from both laboratory and/or field experiments as well as prototype dike failures are needed for the further calibration and validation of the model.

ACKNOWLEDGEMENT

Younghui Zhu's PhD study was supported by the European Community's Sixth Framework Programme through the grant to the budget of the Integrated project FLOODsite, Contract GOCE-CT-2004-505420. This paper reflects the authors' views and not those of the European Community. Neither the European Community nor any member of the FLOODsite Consortium is liable for any use of the information in this paper.

REFERENCES

[1] Visser, P.J., 1998. Breach Growth in Sand-Dikes. PhD thesis, Delft University of Technology, Delft, the Netherlands.

[2] Zhu, Y., 2006. Breach Growth in Clay-Dikes. PhD thesis, Delft University of Technology, Delft, The Netherlands.

[3] Kraak, A.W., Bakker, W.T, Graaff, J. van de, Steetzel, H.J. and Visser, P.J., 1995. Breach-Growth Research Programme and Its Place in Damage Assessment for a Polder. Proc. 24th Int. Conf. Coastal Eng., Kobe, Japan, 1994, pp. 2197-2206.

[4] Singh, V.P., 1996. Dam Breach Modeling Technology, Kluwer, Dordrecht, the Netherlands.

[5] Kraus, N.C., 2003. Analytical Model of Incipient Breaching of Coastal Barriers. *Coastal Engineering Journal*, vol. 45, no. 4, pp. 511-531.

[6] Dent, E.J., 1935. Establishing a Permanent Inlet at Ocean City, Maryland. *Shore and Beach*, vol. 3, no. 3, pp. 89-94.

[7] Gordon, A.D., 1991. Coastal Lagoon Entrance Dynamics. Proc. 22nd Int. Conf. Coastal Eng., Delft, the Netherlands, 1990, pp. 2880-2893.

[8] Kraus, N.C., Militello, A. and Todoroff, G., 2002. Barrier Breaching Processes and Barrier Spit Breach, Stone Lagoon, California, *Shore & Beach*, vol. 70, no. 4, pp. 21-28.

[9] Basco, D.R. and Shin, C.S., 1999. A One-Dimensional Numerical Model for Storm-Breaching of Barrier Islands, *Journal Coastal Research*, vol. 15, no. 1, pp. 241-260.

[10] Fujita, Y. and Tamura, T., 1987. Enlargement of Breaches in Flood Levees on Alluvial Plains. *Journal of Natural Disaster Science*, vol. 9, no. 1, pp. 37-60.

[11] Ralston, D.C., 1987. Mechanics of Embankment Erosion During Overflow. Proc. 1987 ASCE National Conf. Hydraulic Eng, Williamsburg, Virginia, USA, 1987, pp. 733-738.

[12] Visser, P.J., 1989. A Model for Breach Growth in a Dike-Burst. Proc. 21st Int. Conf. Coastal Eng., Malaga, Spain, 1988, pp. 1897-1910.

[13] Temple, D.M. and Hanson, G.J., 1994. Headcut Development in Vegetated Earth Spillways. *Applied Engineering in Agriculture*, vol. 8, no. 2, pp. 237-242.

[14] Visser, P.J, Kraak, A.W., Bakker, W.T, Smit, M.J., Snip, D.W., Steetzel, H.J. and Van de Graaff, J., 1996. A Large-scale Experiment on Breaching in Sand-Dikes. Proc.

Coastal Dynamics'95, Gdansk, Poland, 1995, pp. 583-594.
[15] Steetzel, H.J. and De Vroeg, J.H., 1998. Extension and Validation of the BREACH-model. Technical report A094R1r2, Alkyon/Delft Hydraulics for Rijkswaterstaat, Delft, the Netherlands.
[16] Hahn, W., Hanson, G.J. and Cook, K.R., 2000. Breach Morphology Observations of Embankment Overtopping Tests. Proc. 2000 Joint Conf. Water Res. Eng and Water Res. Planning and Management, Minneapolis, USA (CD-Rom).
[17] Mohamed, M.A.A., Samuels, P.G., Morris, M.W., 2002. Improving the Accuracy of Prediction of Breach Formation through Embankment Dams and Flood Embankments. In: Bousmar & Zech (Eds), River Flow 2002, Swets & Zeitlinger, Lisse, the Netherlands, pp. 663-673.
[18] Mohamed, M.A.A., Morris, M., Hanson, G.J. and Lakhal, K., 2004. Breach Formation: Laboratory and Numerical Modeling of Breach Formation. Proc. Dam Safety 2004, ASDSO Phoenix, AZ, USA (CD-Rom).
[19] Zhu, Y., Visser, P.J. and Vrijling, J.K., 2005. A Model for Headcut Erosion during Embankment Breaching. In: Parker & Garcia (Eds), River, Coastal and Estuarine Morphodynamics: RCEM 2005, Taylor & Francis Group, London, UK, pp. 1183-1190.
[20] Zhu, Y., Visser, P.J. and Vrijling, J.K., 2006. A Model for Breach Erosion in Clay-Dikes. Proc. 5th Int. Conf. Coastal Dynamics (in press), Barcelona, Spain, 2005.
[21] Galappatti, R., 1983. A Depth-Integrated Model for Suspended Sediment Transport. Comm. on Hydraulics, Rep. 83-7. Dept. Civil Eng., Delft University of Technology, Delft, the Netherlands.
[22] Galappatti, R. and Vreugdenhil, C.B., 1985. A Depth-Integrated Model for Suspended Sediment Transport. *Journal Hydraulic Research*, IAHR, vol. 23, no. 4, pp. 359-377.
[23] Van Rijn, L.C., 1984a. Sediment Transport, Part I: Bed Load Transport. *Journal Hydraulic Engineering*, ASCE, vol. 110, no. 10, pp. 1431-1456.
[24] Van Rijn, L.C., 1984b. Sediment Transport, Part I: Suspended Load Transport. *Journal Hydraulic Engineering*, ASCE, vol. 110, no. 11, pp. 1613-1641.
[25] Caan, C.P., 1996. Breach Growth: an Experimental Investigation of the Development of the Scour Hole (in Dutch). MSc thesis, Hydraulic and Geotechnical Eng. Div., Dept. Civ. Eng., Delft University of Technology, Delft, the Netherlands.

Seabed Scour Assessment for Offshore Windfarm

R.J.S. Whitehouse[*], J. Sutherland[**] and D. O'Brien[*]
[*] HR Wallingford Ltd, Howbery Park, Wallingford, OX10 8BA UK
[**] Scott Wilson, Basing View, Basingstoke, RG21 4JG, UK

The prediction of scour at offshore windfarm foundations in areas with mobile seabeds is a challenging topic. In areas with strong currents and wave action, and in areas with shallow water with the additional process of wave breaking to consider, it is necessary to complete laboratory testing. The work described in this paper examined the scour at foundations for a coastal site with waves and strong currents crossing at an oblique angle. The scour in the sand bed was tested for a range of current dominated and extreme wave conditions. The detailed scour profiles were used to determine the depth and extent of scour for a range of water levels, currents and boundary conditions for waves. The testing confirmed the need for scour protection to be installed.

A careful design of the scour protection was required to ensure performance of the foundations. The information on scour depth and extent for the design conditions was used to value engineer the scour protection design. A range of options was tested and the most appropriate one was selected based on a quantified and acceptable level of damage and the degree of interaction of the scour protection design with the surrounding seabed.

Following installation of the offshore wind turbines data was collected on the depth and extent of scour in the field. A reasonable agreement was found between the laboratory results and site observations of the scour hole. This added confidence to the scour protection design that was selected and installed.

The OPTI-PILE design tool gave the correct form of behaviour for rock stability but should be recalibrated for use in such shallow water with such fast currents.

I. INTRODUCTION

The Arklow Bank Wind Park is now operational, with 7 of GE's 3.6MW wind turbines generating clean power for the people of Ireland. Arklow Bank is a shallow water sandbank situated between 10km and 12km offshore from the eastern coast of Ireland and has some of the best wind resources in the British Isles. The project is co-owned by GE and Airtricity, who commissioned Scott Wilson to design the scour protection system for the monopiles[1]. Scott Wilson commissioned HR Wallingford Ltd to perform physical model tests of scour around the monopiles and of the stability of and scour around various scour protection designs[2].

Arklow Bank is subject to overall seabed movement, such as movement of the sandbank, channel migration and overall erosion and accretion. In addition the installation of the monopile foundations for the wind turbines was predicted to (and did) cause local scour around the monopiles. Scour was caused by the strong currents, often over $2ms^{-1}$ that flow over the sandbank and design wave heights that approach 6m on the offshore side (see Section II). The water depth is as low as 5m over the crest of the bank so depth-limited wave breaking occurs during severe storms.

The prediction of local scour at offshore windfarm foundations in areas like Arklow Bank with mobile seabeds is a challenging topic that requires laboratory testing to optimize the design. This paper describes two sets of physical model tests performed by HR Wallingford with Scott Wilson to assist in the scour protection design.

The first set of tests comprised five scour tests of the sand bed around the 5m diameter monopile. These tests were aimed at determining the maximum depth and extent of scour around the monopile under extreme conditions and confirmed the need for scour protection to be installed.

A careful design of the scour protection was required to ensure performance of the foundations. Therefore a second set of ten tests was conducted with scour protection in place to assess the damage to the scour protection and the scour at the edge of the scour protection. Details of the scour protection designs are presented in Section VI. The most appropriate option was selected based on a quantified and acceptable level of damage and the degree of interaction of the scour protection design with the surrounding seabed.

Following installation of the offshore wind turbines data was collected on the depth and extent of scour in the field and was compared to the experiments in Section X.

After the completion of these tests, HR Wallingford derived the OPTI-PILE design tool [3] which aids the preliminary design of scour protection works for offshore monopile wind turbines located on a sandy seabed. The OPTI-PILE design tool was calibrated against a different set of laboratory tests and has been verified against field data from Scroby Sands Offshore Wind Farm [4]. It has been applied to the Arklow tests in Section XI.

II. SCALING OF THE PHYSICAL MODEL

Practical considerations led to the choice of a geometric length scale of 1:36 for the physical model. The hydrodynamics were scaled using Froude scaling [5] so velocities were a factor of 6 lower in model than prototype. However, the situation is complicated by the need to model the mobility of the scour protection rock and sand, and the flow around the monopile.

The wave-induced scour around circular cylinders depends on the Keulegan-Carpenter, KC, number [6]. This occurs as the Keulegan-Carpenter number represents the way in which the wave flow interacts with the

monopile. Froude scaling preserves the Keulegan-Carpenter number for the monopile.

If Froude scaling is applied to the rock protection also, the Keulegan-Carpenter number of the rock will be scaled correctly and hence the pressure gradient term for the rock will also be scaled correctly.

A. Scaling of sand

The mobility of sand and rock is commonly determined using its Shields Parameter, which is the ratio of the force exerted by the bed shear stress on the grain to the submerged weight of the grain counteracting this [7]. The Shields parameter, θ, is defined as:

$$\theta = \frac{\tau}{g(\rho_s - \rho)d} \qquad (1)$$

Where τ is the bed shear stress (Nm^{-2}), $\boldsymbol{g}$ is gravitational acceleration (ms^{-2}) ρ_s is the density of the sediment (kgm^{-3}), ρ is the density of the water (kgm^{-3}) and $\boldsymbol{d}$ is the sediment diameter. The wave skin friction shear stress, τ_w, is given by:

$$\tau_w = \tfrac{1}{2}\rho f_w U_m^2 \qquad (2)$$

Where f_w is the wave friction factor and U_m is the near-bed wave orbital velocity (ms^{-1}). This friction factor is a function of $\boldsymbol{U_mT/d}$ for rough turbulent flows. As Froude scaling gives the same values for $\boldsymbol{U_mT/d}$ in model and prototype, (where T is the wave period) it follows that the wave friction factor will be the same in model and prototype, providing both are rough turbulent flows.

The limit on grain size and rock, for which the same model and prototype Shields parameter (due to wave skin friction) can be obtained from Froude scaling, is at the transition from rough turbulent to smooth-turbulent flow. The transition was obtained from Equations 62a and 63 of [7] and was found to be around 0.05mm for typical model values.

However, a scaled version of the Arklow Bank sand would have been so small it would have been a cohesive sediment and would not behave like a sand. Therefore a larger, but fine, washed sand, was used in the model. In this case Redhill 110 with median grain diameter 0.11mm was used.

The interaction of the rock protection and surrounding seabed in terms of scour will still be reproduced in the model if the same sediment transport regime exists in the model and prototype. In order for sediment to remain in suspension its fall velocity, $\boldsymbol{w_s}$, must be smaller than the turbulent component of velocity which is related to the skin friction shear velocity, $\boldsymbol{u_{sts}}=(\tau_w/\rho)^{0.5}$. Therefore, the relative skin friction velocity = $\boldsymbol{u_{sfs}/w_s}$ should both be greater than one in model and prototype, for suspended sediment. Preliminary results calculated using linear wave theory and equations in [7] indicate that both model and prototype storm conditions will produce suspended sediment transport.

An alternative criterion for suspended sediment transport [8] was also met in model and prototype storm conditions. Therefore the mechanism of sand transport will be similar in model and prototype so the interaction of the rock protection and surrounding seabed in terms of scour will be reproduced in the model, but not at the same rate. The model does not, however, reproduce geotechnical effects.

B. Scaling of rock

The rock used in the physical model had a density of $2710kgm^{-3}$, while the prototype rock had a density of $2650kgm^{-3}$. The fluid used in hydraulic model tests was fresh water, the prototype sea water had a greater density. These variations in densities mean that, without compensation, the rock in the model would be more stable than in the prototype. Such a model would underestimate movement and, hence, the damage that might occur. The size of the rock to be used in the model was corrected using the Hudson equation, so that it exhibited the same stability characteristics as the prototype.

III. PHYSICAL MODEL

The physical model was constructed in a wave basin and consisted of:

- Wave paddle to generate irregular waves with the required spectral properties;
- Eastern and western wave flumes, with bathymetry representative of eastern and western sides of Arklow Bank, starting at the -14mCD contour. These ensured that there was realistic wave shoaling and breaking in the model;
- Sand bed with enough space for monopiles and scour protection schemes;
- Model monopile, constructed in two sections: the lower section was attached to the bed of the wave basin and extended just above the sand bed, while the upper section extended above the water surface;
- Wave absorber for the wave flume not in use;
- Re-circulating current input with control structures to widen and steady the flow and ensure that there was a smooth transition onto the sand bed; and
- Sediment trap and sump area where sediment transported from the model can settle out and the current can be re-circulated from.

The monopile was installed in the sand bed in front of the centre of the wave flume to be used in testing (east or west). Testing was performed in one wave flume at a time as the flumes required different wave conditions. A wave absorber was installed in the flume not being used as otherwise waves entered the sand bed at different times from the different flumes as the shoaling was different.

Wave heights were measured in front of the wave paddles and at the end of the moulded bathymetry, before the waves entered the sand bed. The eastern moulded bathymetry had its high point before the sand bed as the modeled monopile was to be on the western side of the Bank's crest. Currents were measured using a current meter just before they entered the sand bed.

Bed profiles were measured along 8 radial lines from the monopile suing a touch-sensitive bed profiler. The top section of the monopile was removed and the profiler head (shown in Fig. 1) was positioned on the edge of the monopile to provide a known starting locations. Measurements were made every 15mm from there.

Figure 1. Bed profiler measuring scour hole

The layout of the test section is shown in Fig. 2, which also shows the numbering scheme adopted for the profiling lines. Dimensions in Fig. 2 are given in model scale. Results given in the paper are presented at full or prototype scale.

IV. HYDRODYNAMIC CONDITIONS

A design current speed of 2.3ms^{-1} was specified for all tests. Wave conditions with return periods of 50 years and 200 years were provided by Scott Wilson at the 14m CD contour on the east side and west side of Arklow Bank, as shown in Table I. The wave conditions in the western flume were calibrated until the measured wave conditions at the -14mCD contour matched the target conditions. The wave heights in the eastern flume were increased until the point where increasing the wave height generated failed to increase the measured wave height at the sand bed due to depth-limited wave breaking over the crest of the sandbank, which was offshore from the monopile location.

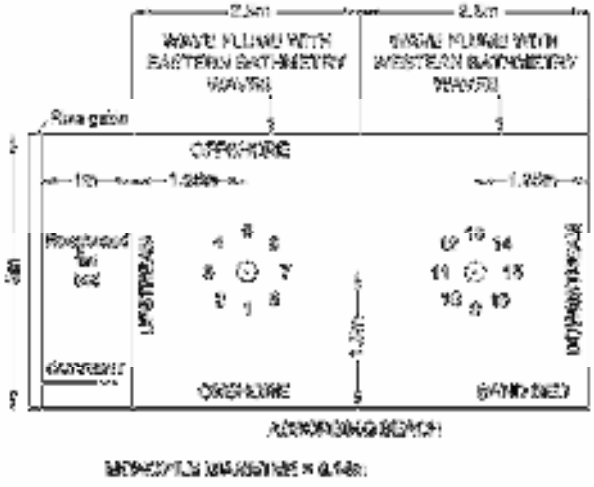

Figure 3. Sketch of test section showing current and wave flumes, sand bed, monopile positions and profiling line numbers

	Bank side	Wave return period [years]	Hs [m]	Tm [s]	Tp [s]	Water depth [m]	Current speed [ms^{-1}]
A	East	50	5.1	10.2	13.1	8.2	2.3
B	East	200	5.8	10.7	13.7	10.2	2.3
C	West	50	3.2	10.3	13.2	8.2	2.3
D	West	200	3.9	10.7	13.7	10.2	2.3

TABLE I. TARGET HYDRODYNAMIC CONDITIONS

V. SCOUR TESTS

Five tests were carried out of scour around a monopile: a current only test with the current speed, U_{cr}, just above the threshold of motion, then four wave plus current tests representing 50- and 200-year return period conditions from the east and west (conditions A to D in Table I). The threshold current test was run for 24 prototype hours, while the wave plus current tests were run for 6 prototype hours.

The sand bed was screeded flat and eight radial profiles of the initial sand bed level were measured before the start of each test. The current was started and the current speed checked using a current meter, before starting the waves (in tests 2 to 5). Scour depths around the monopile were measured using a metre stick throughout the tests. At the end of the test the waves and currents were stopped, the water was drained from the basin, photographs were taken and the same 8 radial lines were re-profiled.

The sand bed at the end of the first, current only, test is shown in Fig. 1. The time-development of the scour during this test is shown in Fig. 4 at prototype scale. A fitting routine that minimised the mean absolute difference between the measurements and the curve was used to determine values for the equilibrium scour depth and timescale of scour to a curve of the following form:

$$S(t) = S_{eq}\left(1 - e^{-t/T}\right) \qquad (3)$$

where S(t) is the scour depth at time t, S_{eq} is the equilibrium scour depth and T is the timescale of the scour. The average value of S_{eq} = 4.8m and the average value of T = 2.4 hours. The maximum scour depth for any of the points was close to one monopile diameter.

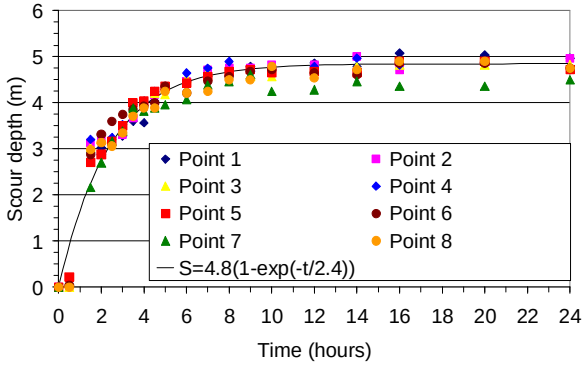

Figure 4. Time development of scour from current-only test

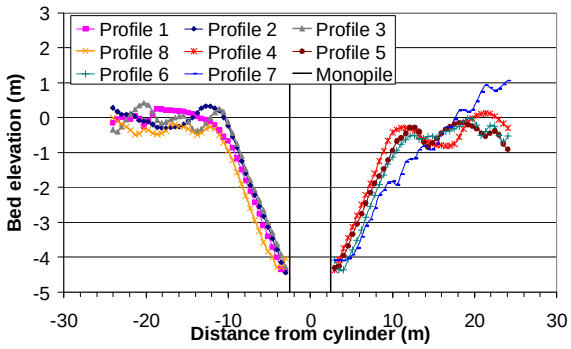

Figure 5. Radial bed profiles after sand bed Test 1

The 8 radial bed profiles measured at the end of Sand Bed Test 1 are shown in Figure 5, with zero in the vertical being the original bed level. Measurements made before the test showed that the original bed was typically within 0.04m (prototype) of zero. Figure 5 shows that the sides of the scour pit generally had a fairly constant bed slope of around 30°to 32°.

The same procedure was repeated for the four wave and current tests (sand bed Tests 2 to 5) except that the 200-year return period condition tests followed on from the bathymetry left by the 50-year return period tests. Therefore the bed was screeded flat after sand bed Test 1, 3 and 5, but not after Tests 2 and 4.

The resulting equilibrium scour depths, S_{eq} and timescales, T are presented with their standard deviations, σ_S and σ_T respectively in Table II., which shows that all the sand bed scour tests produced substantial scour pits. The scour pits had smooth, almost conical walls with side slopes of around 30° to 32°. The base of the scour pit was generally flatter and the side slopes were generally less steep at the top, in the region where the scour pit started to interact with the bedforms that covered the whole of the sand bed.

Test 1 was conducted because current-only scour tests have been observed to give the greatest scour depth, in tests using a smaller diameter pile. That was not the case here with the greatest scour depths coming from wave & current Tests 2 and 3, which gave a relative scour depth of S_{eq}/D = 1.4, where D is the monopile diameter. The largest measured scour depth was 6.5m.

Test 1 was also run for longer than the other tests (24 prototype hours) to investigate the timescale of the scouring. Test 1 showed that conducting a test for six (prototype) hours will amount to approximately 2.5 times the timescale so the scour will be just over 90% of the equilibrium scour depth.

Test	Cond-ition	S_{eq} [m]	σ_S [m]	T (min)	σ_T (min)
1	Ucr	4.8	0.1	143	16
2	A	7	0.5	230	7
3	B	7	0.4	178	30
4	C	6.3	0.4	155	52
5	D	5.9	0.2	88	33

TABLE II. EQUILIBRIUM SCOUR DEPTHS AND TIMESCALES OF SCOUR WITH STANDARD DEVIATIONS FOR SAND BED TESTS

Although the timescale has been converted to a prototype equivalent value using Froude scaling, in practice the timescale in the field will be different (probably shorter) as the sand in the field under storm is relatively smaller and more mobile, with a higher ratio of mean shields parameter over threshold shields parameter.

VI. SCOUR PROTECTION TEST SETUP

The ten scour protection model tests were carried out using different combinations of four scour protection schemes and three environmental conditions. The four scour protection designs are described below and their cross-sections are provided in Fig. 6.

A. Two layers of armour stone over 1m deep filter layer in a 20m wide ring around the monopile (plus 1:2 side slopes). The prototype armour rock weight was in the range 1 tonne to 3 tonnes and the filter layer prototype median weight was 200kg. More detailed specifications for armour rock and filter material are given in Table III. A geotextile was placed under the 200kg rock.

B. Two layers of armour stone over 1m deep filter layer in a 20m wide ring around the monopile (plus 1:2 side slopes). The prototype armour rock weight was in the range 0.3 tonne to 1 tonne and the filter layer prototype median weight was 65kg. More detailed specifications for the armour stone and filter material are given in Table IV. A geotextile was placed under the 65kg rock.

C. One metre deep filter layer in a 10m wide ring around the monopile (plus 1:2 side slopes) in an excavated pit so that the top of the filter layer was flush with the top of the sand bed. The filter layer prototype median weight was 200kg (as used in design A). No geotextile was used.

D. Two layers of armour stone (1 tonne to 3 tonnes) over 1m deep filter layer, sunk into the sand bed so that the top of the filter layer was flush with the top of the sand bed. There was a 10m wide ring of filter and armour around the monopile. The filter layer had a 1:2 slope at the outer edge. The prototype armour rock weight was in the range 1 tonne to 3 tonnes and the filter layer prototype median weight was 200kg (as for design A). No geotextile was used.

The three environmental conditions were:

i. 50-year return period wave and water level conditions for the western side of Arklow Bank, plus 2.3m/s depth-averaged current, (i.e. Hs = 3.2m, Tm = 10.3s, water level = +2.8m CD.

ii. 200-year return period wave and water level conditions for the western side of Arklow Bank, plus 2.3m/s depth-averaged current, (i.e. Hs = 3.9m, Tm = 10.7s, water level = +4.8m CD.

iii. Low water condition with depth limited waves for the western side of Arklow Bank, plus 2.3m/s depth-averaged current, (i.e. Hs = 3.0m, Tm = 10.3s, water level = -1.4m CD.

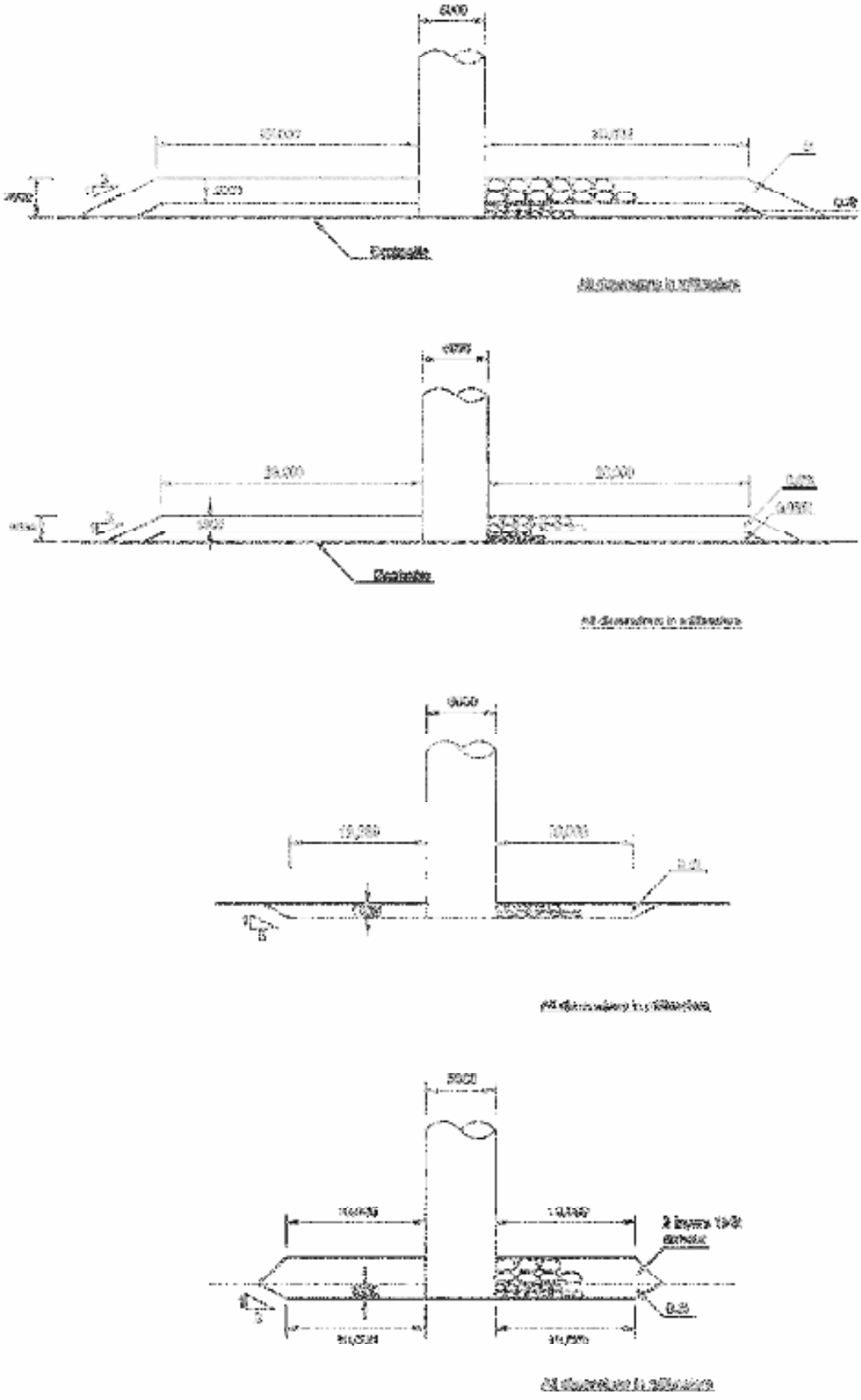

Figure 6. Prototype cross-sections for scour protection designs A, B, C and D (from top to bottom)

	Armour stone		Filter layer	
% finer	Prototype mass (tonne)	Model Mass (kg)	Prototype mass (tonne)	Model mass (kg)
0	0.93	0.016	0.09	0.002
10	1.08	0.019		
25	1.36	0.023	0.14	0.0031
50	2	0.034	0.2	0.0045
75	2.93	0.051	0.29	0.0064
90	3.69	0.064		
100	4.3	0.074	0.43	0.0095

TABLE IV. SCOUR PROTECTION DESIGN A, C AND D ARMOUR STONE AND FILTER WEIGHTS

	Armour stone		Filter layer	
% finer	Prototype mass (tonne)	Model Mass (kg)	Prototype mass (tonne)	Model mass (kg)
0	0.28	0.005	0.028	0.0006
10	0.33	0.006		
25	0.43	0.007	0.043	0.001
50	0.65	0.011	0.065	0.0015
75	0.99	0.017	0.099	0.0022
90	1.27	0.022		
100	1.51	0.026	0.151	0.0033

TABLE III. SCOUR PROTECTION DESIGN B ARMOUR STONE AND FILTER WEIGHTS

The ten scour protection (SP) tests were model representations of:

SP Test 1. Scour protection design 'A' with environmental condition 'i' (50-year return period conditions). The test was run from a flat bed for six hours.

SP Test 2. Scour protection design 'A' with environmental condition 'ii' (200-year return period conditions). The test was run from the final bathymetry of the previous test, for six hours.

SP Test 3. Scour protection design 'A' with environmental condition 'iii' (low water conditions). The scour protection was rebuilt on a flat bed. The test was run for six hours.

SP Test 4. Scour protection design 'B' with environmental condition 'i' (50-year return period conditions). The scour protection was built on a flat bed and the test was run for six hours.

SP Test 5. Scour protection design 'B' with environmental condition 'i' (50-year return period conditions). The test was run from the final bathymetry of the previous test, for thirty hours.

SP Test 6. Scour protection design 'B' with environmental condition 'iii' (low water conditions). The scour protection was rebuilt on a flat bed and the test was run for six hours.

SP Test 7. Scour protection design 'C' with environmental condition 'iii' (low water conditions). The scour protection was built starting with a flat bed and the test was run for six hours.

SP Test 8. Scour protection design 'D' with environmental condition 'iii' (low water conditions). The scour protection was built starting with a flat bed and the test was run for six hours.

SP Test 9. Scour protection design 'D' with environmental condition 'iii' (low water conditions). The test was run from the final bathymetry of the previous test for thirty hours.

SP Test 10. Scour protection design 'C' with environmental condition 'ii' (200-year return period conditions). The scour protection was built starting with a flat bed and the test was run for six hours.

VII. RESULTS OF SCOUR PROTECTION TEST 1

Overhead photographs of Scour Protection Test 1 are shown in Fig. 7. Note that the top part of the monopile has been removed and that the camera is at an angle to the flow. The brick wall on the bottom, left hand side of the photograph is the downstream edge of the sand bed.

The damage caused during Scour Protection Test One can be seen by comparing the two photographs in Fig. 7. Fig. 7 shows that the sand bed is rippled throughout (so sediment transport is occurring throughout) with the ripple

Figure 7. Before (top) and after (below) Scour Protection Test 1

crest direction predominately perpendicular to the current direction on the upstream and onshore sides of the model (implying development is current dominated). The ripple patterns are more three-dimensional on the offshore side, showing the influence of waves. There is a small area downstream of the model where the ripple crests are parallel to the incident wave crests showing that their growth is wave dominated.

Bed profiles at the end of the test are shown in Fig. 7 (top). The scour (negative values) and deposition (positive values) were calculated by subtracting initial profiles from final profiles and are shown in Fig. 7 (below) for Scour Protection Test 1. Fig. 7 shows that there were some changes in elevation between the edge of the monopile and displacement of stones (at 2.5m radial distance) and about 15m radial distance. This may have been due to flow acceleration around the monopile. Note however, that changes in elevation between 'before' and 'after' may occur due to slightly different displacement of the probe in the two deployments or to minor rotations or displacements of armour stones. Consistent changes over two or three points are a more reliable indication of movement than differences at a single point.

The profile showing the greatest changes in elevation close to the monopile is profile 13, which points directly offshore (into the waves). It is therefore likely that the environmental conditions could cause some stone movement on the flat top of the model, close to the monopile. Little movement can be detected from the changes in bed elevation at the edge of the protection, shown in Fig. 8. However, the photographs (Fig. 9) reveal that some stones have moved out from the edge of the model, off the geotextile.

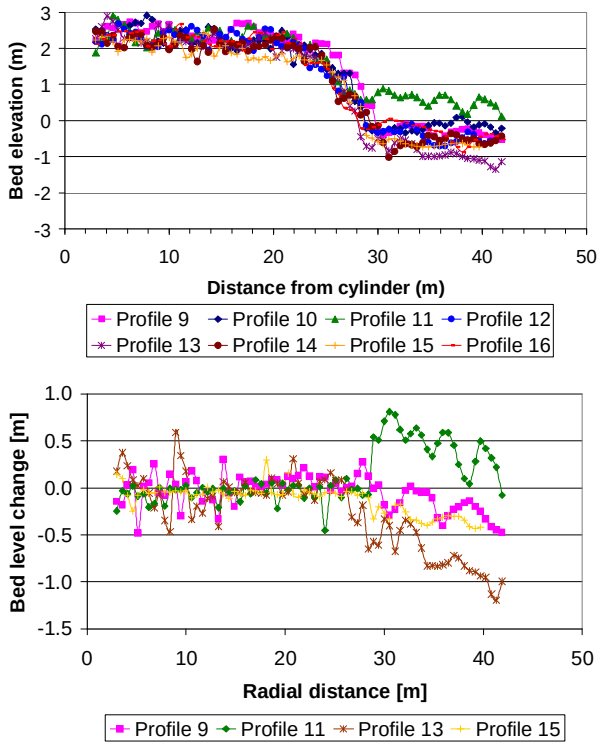

Figure 9. Bed levels at the end of Scour Protection Test 1 (top) and bed level changes during the test (below)

VIII. Results From Other Scour Protection Tests

Scour Protection Test 1 was presented in some detail to show the type of data collected for all the scour protection tests. Examples are given below from the other scour protection tests. Fig. 8 (top) shows scour protection design B before SP Test 4, while Fig. 8 (below) shows the same design at the end of SP Test 5, after 36 hours of environmental condition ii.

Two rows of armour stones were added to the downstream edge of the model before Scour Protection Test 5 was run which minimized the depth of the scour pit that had formed at the hard edge of the sand bed during SP Test 4.

The photographs in Fig. 8 reveal that some stones have moved out from the edge of the model, off the geotextile. Where this has occurred, there is often a strip of geotextile visible between the remaining stones in the model and those that have slipped down and out from the edge of the model. This movement is associated with bed lowering and shows that the model is unraveling by movement away from the model. The radial profiles showed that steep slopes typically occur between 23m and 25m radial distance, with a flatter area where the displaced stones have settled between 25m and 27m radial distance.

Equivalent sets of photographs for SP Design C are shown in Fig. 9, before and after SP Test 10. Here the upper surface was spray-painted in concentric rings so that

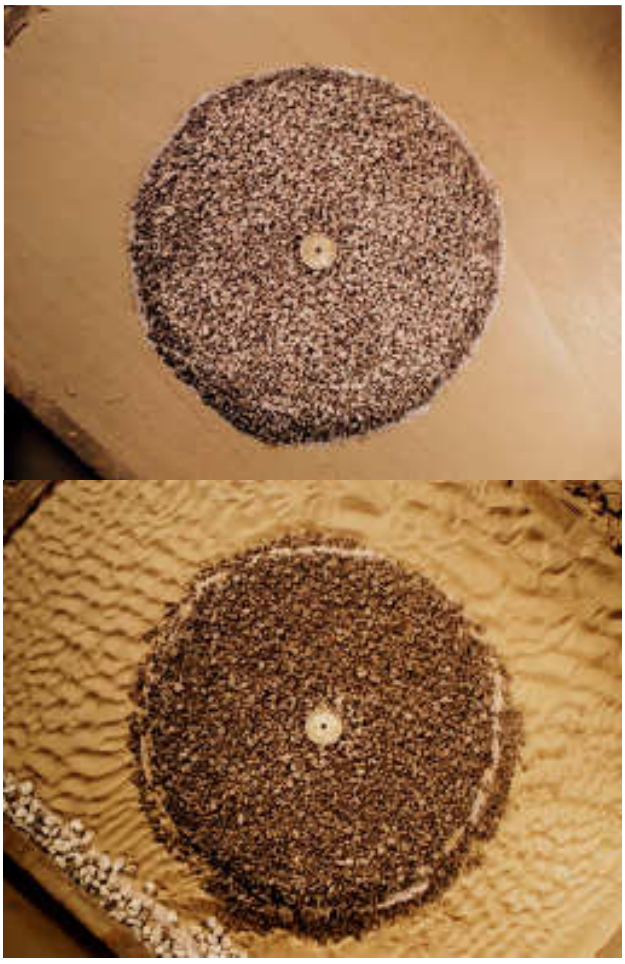

Figure 8. Scour protection Design B before SP Test 4 (top) and after SP Test 5 (below)

Figure 10. Scour Protection Design C before (top) and after (below) SP Test 10.

movement could be assessed at different distances from the monopile. Fig. 9 shows that there was relatively little movement of scour protection material during the test, although some occurred along profile 11 close to the monopile and some occurred at the edge of the model, where the seabed lowered. Fig 10 shows overhead photographs of Design D after SP Test 9.

IX. DAMAGE ANALYSIS

Damage was defined as the numbers of armour stones that were displaced by more than one diameter, expressed as a percentage of twice the total number of armour stones visible in the top layer of armour (as the models had two nominal armour layers). Damage calculations were made by printing 'before' and 'after' overhead photographs of the scour protection system onto acetates and overlaying them. This method allows the stones that had moved to be identified, marked and counted.

Damage was calculated for each of the following four quadrants:

Figure 11. Model after Scour Protection Test 9

- scour profile 9 (beach) to scour profile 11 (upstream)
- scour profile 11 (upstream) to scour profile 13 (offshore)
- scour profile 13 (offshore) to scour profile 15 (downstream)
- scour profile 15 (downstream) to scour profile 9 (beach).

For breakwaters and similar marine structures to breakwaters, accepted practice within the industry is to consider damage to the whole structure of between 2% and 5% as 'onset of failure' and damage between 6% and 10% as 'failure' [9]. These figures are for stone movement of more than one diameter. Ref [9] recommends that tests are run for six hours at design conditions, as here.

Damage statistics from the Scour Protection Tests with larger armour stones are given in Table V, which shows that most damage occurred in the two offshore quadrants between profile lines 11 and 15 (Fig. 2). Designs A, B and C all showed damage of over 10% in one of the offshore quadrants, although SP Tests 5 and 9 were unusually long (at 30 hours each). Therefore the structure as a whole may be said to be on the onset of failure. However, two factors should be borne in mind:

1. Damage was predominantly limited to the edge of the structure, well away from the monopile that the scour protection was designed to protect. The scour protection suffered an insignificant amount of damage close to the monopile.
2. Damage mainly took the form of armour stones moving down and out from the edge of the armour in locations where the bed lowered around the protection. The armour stone is expected to reach a stable condition in time, through the formation of a falling apron, even though the maximum lowering is about 3m.

Scour protection Design C, which used the filter layer from Design A as its main armour was not assessed in the same way as the stones were too small. It was used in SP Tests 7 and 10. Bed level changes from the bed profiling were used to assess damage here. Erosion of up to 0.5m was measured right against the monopile in SP Test 7, which otherwise showed relatively low changes in bed level. The maximum erosion close to the monopile in Sp Test 8 was less than 0.25m and again there were relatively small changes in the sand bed level around the model, with a maximum lowering of just under 1m immediately downstream (profile 15).

Test	**Design**	**Lines 9-11**	**Lines 11-13**	**Lines 13-15**	**Lines 15-9**
One	A	1	3.4	5.1	0.5
Two	A	0.3	1.4	2.4	0.3
1+2	A	1.3	4.8	7.5	0.8
Three	A	3.2	9.8	12.2	2.5
Four	B	1.5	1.9	3.3	2
Five	B	4.4	9.3	8.1	5.6
4+5	B	5.9	11.2	11.4	7.6
Six	B	3.2	7.9	7.4	2.3
Eight	D	0	0	0	0.6
Nine	D	0	11	2	0
8+9	D	0	11	2	0.6

TABLE V. DAMAGE STATISTICS FROM DIFFERENT QUADRANTS

X. INSTALLATION AND OBSERVED SCOUR

Installation of the initial 7 wind turbines was achieved in only 9 weeks during late summer and early autumn in 2003 using a jackup barge fitted with a 1,200 tonne crane [10] as shown in Fig 11. There was a short delay between installation of the monopiles and the scour protection, which was sufficient for scour holes to develop around the monopiles, due to the tidal current alone.

Side scan sonar was used to measure the size of the scour holes and an example of a contour plot derived from side-scan sonar is shown in Fig. 12. The scour hole is fairly symmetrical, with smooth sides and is about 4m deep. It has a similar form to the scour hole measured in the laboratory current-only test, shown in Fig. 1.

Scour protection was installed using a back-hoe on the side of a jackup barge. The scour protection design, as built, was based on Design C, but included filling up the naturally-occurring scour hole, so extended deeper than shown in Fig. 5, providing a greater level of scour protection.

XI. APPLICATION OF OPTI-PILE SPREADSHEET

The OPTI-PILE design tool is a spreadsheet that calculates the main parameters needed for a conceptual scour protection design for an offshore monopile wind turbine on a sandy seabed [3]. The spreadsheet calculates the depth, extent and volume of the predicted scour hole. The stable rock size for scour protection, the extent of protection and the mass of rock required can also be calculated for both a static design and a dynamic design.

A number of key parameters were calibrated using a set of physical model tests of the scour protection around an offshore wind turbine in the Dutch sector of the Southern North Sea. The OPTI-PILE design tool was subsequently verified [4] against field data obtained from the Scroby Sands Offshore Wind Farm, off the East Anglian coast.

The conditions at Arklow are rather different from those used to calibrate the OPTI-PILE design tool: the current speed is over twice as fast, the wave heights are just over half the size and the water is less than half the depth. The comparison between the predicted and observed rock stability will indicate whether the OPTI-PILE design tool can be used outside the original limits of its calibration.

Figure 12. Installation of wind turbines at Arklow. © Airtricity

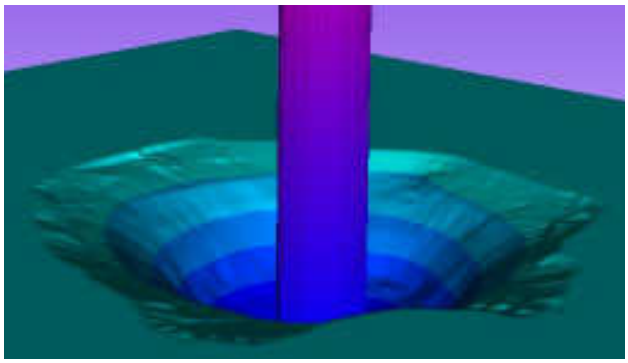

Figure 13. Scour hole measured at Arklow between installation of monopile and scour protection

The OPTI-PILE design tool calculates a stability parameter, $\text{Stab} = \theta_{max} / \theta_{cr}$ where θ_{max} is the maximum Shields parameter and θ_{cr} is the critical Shields parameter for the inception of motion. The value θ_{cr} =0.056 (for stone diameters greater than 0.01m) was taken in conjunction with the maximum bed shear stress. Higher values of Stab are less stable. Critical values of Stab were set based on the experimental tests. The test results were classified into the following three categories:

1) No movement of rocks;
2) Some movement of rocks, but not sufficient to cause failure;
3) Failure.

Here, different failure criteria were used so the results are not directly comparable to the damage statistics given in Table V. The failure criteria were:

- Static scour protection has failed when a section of top layer armour has disappeared completely, exposing the filter layer over a minimum area of four armour units;
- Dynamic scour protection has failed when a volume of rock has eroded that is equivalent to the volume of rock that had to be eroded for a static failure.

Table VI lists the ten scour protection tests with the scour protection design and environmental condition used. The OPTI-PILE stability parameter, Stab, is then given with the damage category the stability parameter falls into. Three values for measured damage are then given:

1) Maximum damage from Table V;
2) E_{max}/d_{50}, where E_{max} is the maximum erosion measured using the bed profiler over the flat top of the model (excluding lowering at the edges) and d_{50} is the median armour diameter;
3) E_{max}/AD where AD is the armour depth from Figure 6.

Table VI shows that the stability parameter, Stab is not closely related to the maximum damage. It is related to the damage statistics E_{max}/d_{50} and E_{max}/AD, as shown in Figure 14, which also shows best-fit straight lines through the data. These lines were used to predict damage from Stab to obtain a relative mean absolute error of 0.19 in both measures of damage.

The OPTI-PILE design tool stability number increases with increasing measured damage: the correct behaviour for a stability predictor. However, the different measures of damage used in [3] and here have made the

SP Test	Design	Environment	STAB	Oti-Pile Category	Max Damage (%)	E_{max}/d_{50}	E_{max}/AD
1	A	i	0.277	N	5.1	0.44	0.24
2	A	ii	0.301	N	2.4	0.49	0.27
3	A	iii	0.426	S	12.2	0.64	0.35
4	B	i	0.302	N	3.3	0.74	0.42
5	B	i	0.302	N	9.3	0.40	0.23
6	B	iii	0.461	F	7.9	0.77	0.44
7	C	iii	0.493	F		0.96	0.48
8	D	iii	0.426	S	0.6	0.37	0.20
9	D	iii	0.426	S	11	0.60	0.33
10	C	ii	0.35	N		0.44	0.22

comparison more difficult. The Arklow experiments only measured changes in the armour level along 8 radial profiles and it would be possible for greater levels of damage to occur in between. The definition of failure for a static model used in OPTI-PILE implied a maximum erosion, $E_{max} = 1$, a condition that was not observed in the tests. The OPTI-PILE design tool would need to be recalibrated for design use in similar circumstances.

XII. Summary and Conclusions

A set of laboratory experiments were conducted to investigate scour depths and the stability of scour protection around a monopile foundation in relatively shallow water (sometimes less than the monopile diameter) with high current speeds and breaking waves.

The scour tests showed that equilibrium scour depths of up to 7.5m (1.5 pile diameters) were possible under the wave plus current conditions tested. The timescale of scour in the model indicated that 80% to 90% of the equilibrium scour could occur in the course of six hours. The scour pits produced had smooth side slopes of around 30°, which were elongated in the downstream direction.

The flow acceleration around scour protection designs 'A' and 'B' (Fig. 6) which stood 3m and 2m above the bed caused substantial lowering of the sand bed around them. This trend was particularly pronounced at low water condition, when the initial water depth was only 4m and bed lowering of up to 3m was observed. Although there is some evidence of armour stone movement on the flat tops of these models (particularly close to the monopile where there would have been higher than ambient shear stresses due to local flow accelerations) the majority of the damage occurred at the edge of the model, where the bed had lowered.

The percentage damage determined in the tests were high enough to be considered as the onset of failure or as failure itself, according to the criteria [9] for coastal breakwaters. However, the scour protection designs tested are a different type of structure, which will not collapse if a few stones are moved in the interior or at the edges, but

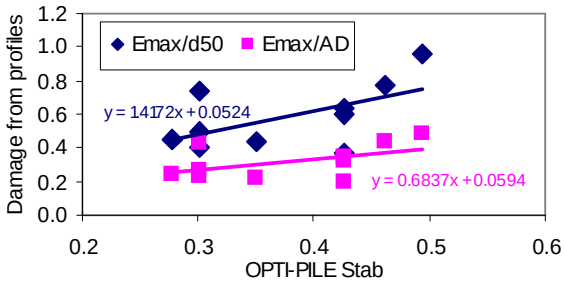

Figure 14. Measured damage against predicted damage

which will gradually unravel at the edges. A higher percentage damage can therefore be tolerated.

The results for scour protection design 'D' (Fig. 6) were of a similar form to the results from design 'A' and 'B'. The lower structure caused less flow acceleration and bed lowering around it. Damage levels were correspondingly lower as well (compare the results from Test 8 with those from tests 3 and 6 which used the same environmental conditions with designs A and B).

The two tests with design 'C' (Fig. 6) showed little apparent damage, although only filter material was used. This design had its top surface flush with the bed, so it did not disrupt the flow.

The OPTI-PILE design tool was used outside its calibrated range and gave the correct form of behaviour for a stability protector but should be re-calibrated for use at such low depth and high current speeds.

Acknowledgments

The authors thank Airtricty and GE Wind Energy for permission to publish their data.

References

[1] D. O'Brien, "Scour protection for offshore windfarms," ***British Wind Energy Association 25, 2005.***.

[2] HR Wallingford, "Arklow Bank physical model scour tests." HR Wallingford Report EX 4789 (confidential) July 2003.

[3] J.H. Den Boon, J. Sutherland, R. Whitehouse, R.L. Sousby, C.J.M. Stam, K. Verhoeven, M. Høgedal and T. Hald, "Scour protection and scour behaviour for monopile foundations of offshore wind turbines." ***Proceedings of the European Wind Energy Conference,*** London, UK. UWEA, pp14 [CD-ROM].

[4] M. Høgedal and T. Hald, "Scour assessment and design for scour for monopile foundations for offshore wind farms". ***Proceedings of Copenhagen Offshore Wind Conference***, 2005.

[5] S.A. Hughes, "***Physical Models and laboratory techniques in coastal engineering***." World Scientific, Advanced Series on Ocean Engineering – Volume 7. pp 568, 1993

[6] B.M. Sumer, J. Fredsøe and N. Christiansen, "Scour around vertical piles in waves." Journal of Waterway, Port, Coastal and Offshore Engineering, ASCE, 118(1): 15 – 31, 1992.

[7] R.L. Soulsby, "Dynamics of marine sands". Thomas Telford, pp. 249, 1997.

[8] I. Irie and K. Nadaoka, Laboratory reproduction of seabed scour in front of breakwaters. Proc 19th Int. Conf. Coastal Engineering, Houston, USA. ASCE, pp. 1715-1731, 1984.

[9] British Standards Institution, "Maritime Structures - Part 1: Code of practice for general criteria. BS 6349-1:2000.

[10] http://www.airtricity.com/england/. Accessed 28/04/2006.

Field Observations of Scour Around a Rock Berm Over a Subsea Pipeline on a Clay Seabed

R.J.S. Whitehouse[1], J.S. Damgaard[1,2], and J. Parkes[3]

[1] HR Wallingford Ltd, Howbery Park, Wallingford, OX10 8BA, UK.
[2] Now at: WorleyParsons, Al Masaood Tower (8th Floor), Najda Street, PO Box 44169, Abu Dhabi, United Arab Emirates.
[3] Saipem Asia Sdn. Bhd, 4th-5th Floor Ritratana Bldg., 5 Ramkhamhaeng Road, Hua-Mark, Bangkapi, Bangkok 10240, Thailand.

The evaluation of scour in shallow water for a pipeline installed and covered with engineered rock-dump has been analysed based on survey data. The 3km long shore approach section of the 10" pipeline was installed in a trench and backfilled with rock dump. Due to the rapid siltation of the trench there was no trench to deposit the rock in and the rock formed a berm. Scour was found to occur either side of the berm due to the fast, turbulent near bed tidal currents. The magnitude of scour that occurred could be as large as the initial water depth in the shallowest depths of around 10m. The time series of scour is analysed and the characteristic timescales are determined.

I. INTRODUCTION

A significant proportion of the world's hydrocarbon pipelines are routed through areas with clay seabeds. However, despite the obvious importance of the stability design of pipelines in clay, there is very little engineering guidance or data in existence. One of the important design issues is scour, or rather prevention of scour, especially in areas with high current speeds.

Whereas scour in sandy seabeds is well studied and relatively straightfoward to predict the situation is very different when it comes to clay seabeds. The scour behaviour is very different to that of a sandy seabed and the magnitude of scour can be much larger because the soil, once eroded, can be removed from the local area by the currents.

In this paper we present a data set obtained during a pipeline project carried out by Saipem for CNOOC on the Pinghu oil and gas field in the East China Sea. Because an extensive monitoring programme was initiated it was possible to study the spatial and temporal development of scour that took place in the clay seabed, and to derive some engineering recommendations about how to deal with pipelines in this type of area.

II. PROJECT DESCRIPTION

The shore approach at Daishan Dao island for a 10" (254mm) oil pipeline is located approximately 140km south of Shanghai transporting product from the offshore Pinghu Field some 300km southeast of Daishan Dao. The first three kilometers of the pipeline passes offshore from the landfall to a water depth of around 10m below local datum TDDL, Theoretical Depth Datum Level, which was approximately Chart Datum (Fig.1). The tidal range is approximately 1.4m on neap tides and 3.4m on spring tides. The remainder of this section provides more details of the hydrodynamics and bed sediments with some details summarized from the report by COGC [1].

In terms of hydrodynamic forcing the area is dominated by tidal currents with extremely high currents of up to six knots. The tidal current in the shallow water off the northeast coast of Daishan Dao is very turbulent and a tidal race was observed less than 1km to the southeast of KP2.00. This is generated by the fast tidal flow around the headland to the south of the pipeline and the shallowing water depth. The axis of the bidirectional currents lies approximately northwest to southeast and hence perpendicular to the pipe route. Measurements of maximum velocities near the seabed for the ebb and flood tidal flows made in October 1995 were reported by COGC [1] as 2.67m/s and 1.94m/s respectively; the maximum values of surface velocity were higher. The flood current direction in the measurements lay between NNW and N and the ebb current between SSE and SE.

In addition to the prevailing tidal forcing, there are occasionally significant swell waves, mainly generated by typhoons. The one-year return period significant wave height is 3.2m. Therefore in terms of hydrodynamic forcing for pipe stability, engineered backfill stability and sediment transport both tidal currents and waves have to be considered.

The soils are characterized by soft, siltey, clayey sediments. A borehole (P18) at KP2.125 showed an upper sediment unit of 7.4m thickness comprising very soft olive grey clay with silty partings and pockets. The design value of undrained shear strength from testing was 7kPa, the submerged unit weight 6.6kN/m^3, and natural water content was 50%. For design purposes these parameters were taken to be constant over the depth of the soil unit. The clay was classified as inorganic and of medium to high plasticity. Inshore of P18 the boreholes showed presence of a silt unit overlying the clay. Over the 640m between P18 and P17 at KP1.485 the silt unit increased to a thickness of 2.5m. The median grain size of the surficial bed sediments along the pipeline was in the range 0.01 to 0.022mm.

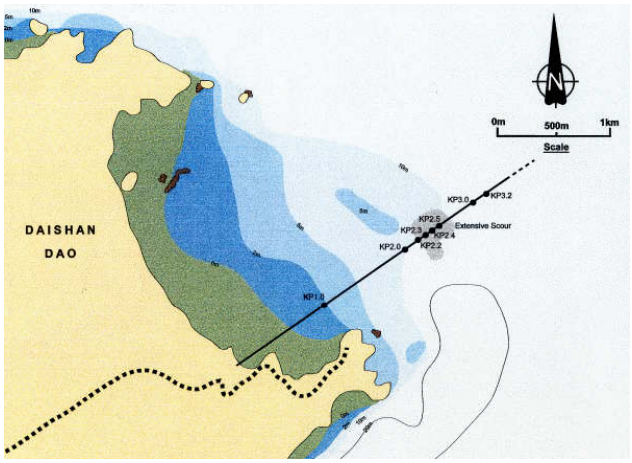

Figure 1 Location map of pipeline landfall section at Daishan Dao in East China Sea

The assumed maximum erosion or migration of the natural seabed at the landfall was limited to 1m over the 30 year design life of the pipeline. The pipeline was pre-trenched to a target depth of 3m below seabed level between the landfall and KP3.00 and the trench depth decreased from full depth to the seabed surface over the 100m between KP3.00 and KP3.10. The dredged trench profile had a bottom width of about 18m and side slopes in the range 1:10 to 1:15. Due to the dynamic nature of the site the trench filled in totally during dredging and before the pipe lay-barge arrived. The pipe was therefore laid on the backfilled trench, effectively at seabed level. The pipeline was lowered post-lay to the required 3m (bottom of pipe) by mobilizing a jetting machine. The trench backfilled almost completely during and immediately after the jetting process. Following jet lowering to comply with the rock armour requirements the pipeline was covered with a three-layer engineered backfill, as far as KP3.00. Firstly an inner layer of fine gravel (4mm) was placed, then an intermediate layer of graded gravel (50mm) and finally an armour layer of graded rock (200mm to 500mm). The armour layer was selected to withstand the combined action of 100 year waves and currents. In the trench transition zone no armour was applied to allow the post-lay trenching of the pipeline to a minimum depth of 1.5m BOP (Bottom Of Pipe) from KP3.00 onwards.

Following installation of the engineered backfill extensive scour was observed on either side of the pipeline between KP2.20 and KP2.60 where the backfill formed a berm which was higher than the adjacent seabed level. This was because the trench in that zone of shallow water had almost completely infilled with sediment during the post lay jetting and in the period between jetting and dumping of the rock. Additionally the rock dumping tended to form peaks rather than form a shallow uniform thickness protection to the pipe. The scour development along this section of the pipeline is assessed in this paper.

III. SCOUR RESPONSE OF BED

The pre-dredge survey of the seabed along the pipeline alignment showed the bed levels along the pipe route as indicated in Table I. The seabed topography around KP 2.00 was quite complex with a strong gradient in bed level from north to south of the pipeline associated with a deeper channel to the south of the pipe route at this location as indicated on Fig. 1. Beyond KP 2.55 the water depth becomes deeper.

The post-rock-dump surveys in the deeper water at KP2.00 showed the bed levels were reasonably stable but that the seabed at other KP points listed in Table I experienced scoring both north and south of the pipeline. The bed level changes from repeat surveys at the KP points in Table I were analysed as the project was underway and an example of the results have been plotted in Fig. 2.

TABLE I. PRE-DREDGE SEABED LEVELS MAY 1998

KP	Initial Depth S_0 (m)
2.00	16.0
2.10	13.5
2.20	11.0
2.35	9.5
2.45	9.5
2.55	10.5

Fig. 2 shows the pre-dump seabed level and the presence of the 1.5m high rock berm. The seabed survey shown for 21/06/98 was taken approximately 18 days after installation of the rock armour and at that time the seabed north of the pipeline had scoured by 6m and on the south side by about 8m.

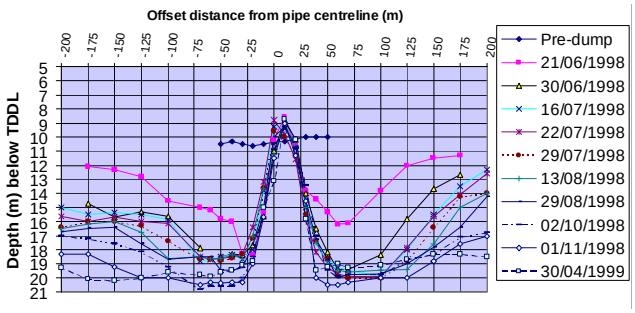

Figure 2 Seabed evolution at KP2.55. Survey profile lines run south and north of pipeline and show evolution of the seabed. South is represented by negative distances and TDDL is effectively local Chart Datum

The scouring continued over the following nine days to depths of 10m on the north side whereas on the south side the depth did not increase but the extent of scour did. By the end of April 1999 the scour areas had extended at least 200m from the pipeline but the depths of the scour pits adjacent to the rock berm were relatively stable and had shown a reduction in depth of a metre at this location. This is indicative of the long-term fluctuation in bed levels due to natural variations in flow and sediment supply adjacent to the pipeline.

The side slopes of the exposed rock berm were found to remain close to the theoretical angle of 25° (1V:2.1H) out to KP2.75 even in areas with scour such as those shown in Fig. 2.

The local scour response was attributed to the flow interaction with the rock berm structure giving rise to the generation of separated flow and high turbulence levels downstream of the berm. This produces a higher potential

for sediment transport in the bed region immediately downstream of the berm which causes scour. Also with the fine sediment present at the site the rock berm will present a blockage to sediment transport from the upstream direction. The influence of the rock dump on the sediment transport is illustrated in Fig 3. With the strong bidirectional flow at the site this process leads to an alternating erosion on either side of the rock berm and hence the development of scouring leading to the reduction in sediment thickness Z above a given horizon with time. The increase in scour depth with time to an equilibrium level is illustrated in Figure 4.

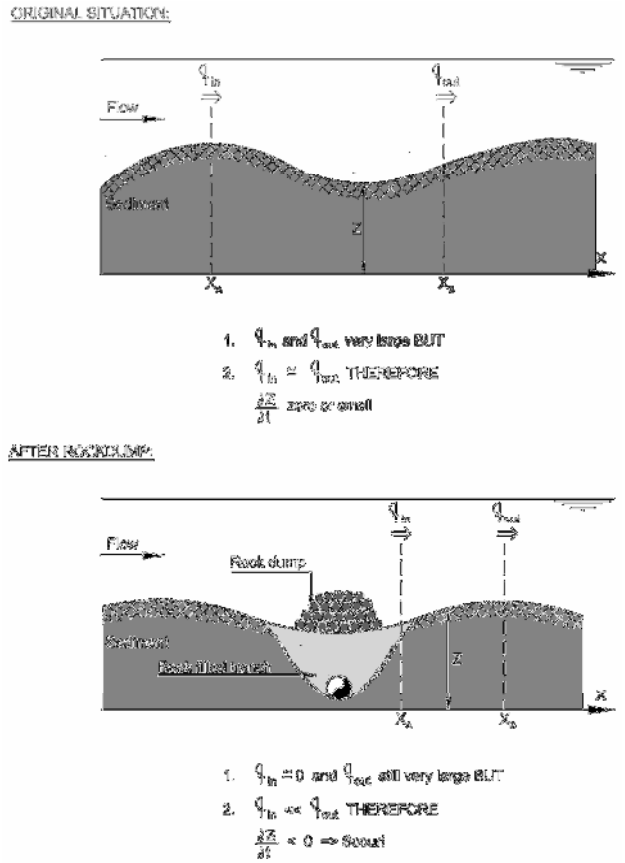

Figure 3 Schematic illustration of the influence of a rock berm on seabed sediment transport and scour development

The scour data was analysed for locations 50m north and south of the pipeline and the time histories of water depth below TDDL for KPs 2.1 to 2.55 were plotted (Figs. 5 and 6). The time of the main rock dump is shown on each of the figures and at those locations where remedial rock dump was carried out these are also shown on the Figures. The observed increase in water depth after the main rock dump is similar in form to the scour development curve sketched in Fig. 4. The scour development north and south of the pipeline at each KP follows a similar trend despite some differences in levels being observed at various times.

The maximum water depths recorded 50m north or south of the pipeline are listed in Table II and the increase in water depth is listed in Table III. Table III shows that at the two shallowest locations KP2.35 and 2.45 the water depth can increase by up to a factor of 2 from the initial values.

TABLE II. MAXIMUM WATER DEPTHS END APRIL 1999

KP	Max. Depth (m)
2.00	17.0
2.10	20.5
2.20	19.0
2.35	19.5
2.45	18.5
2.55	19.5

TABLE III. INCREASE IN WATER DEPTH MAY 1998 TO APRIL 1999

KP	Scour (m)	Ratio Scour to Initial Depth
2.0	1	0.063
2.1	7	0.519
2.2	8	0.727
2.35	10	1.053
2.45	9	0.947
2.55	9	0.857

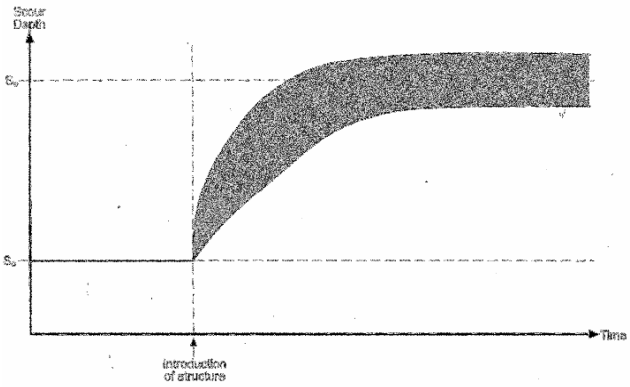

Figure 4 Illustration of scour depth evolution

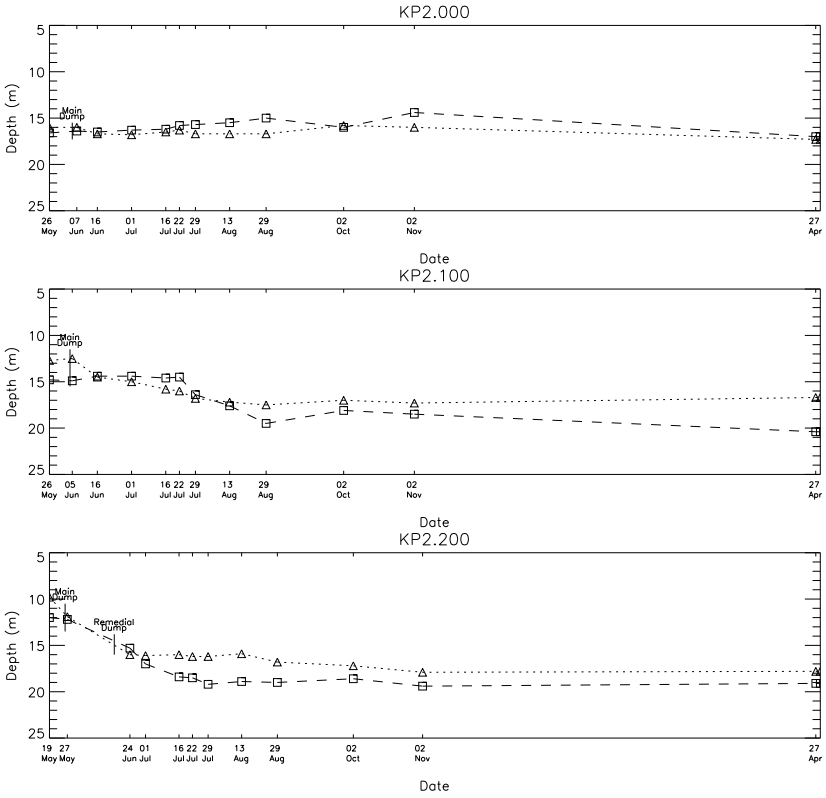

Figure 5 Seabed evolution at locations 50m either side of the pipeline (KP2.00 to 2.20)

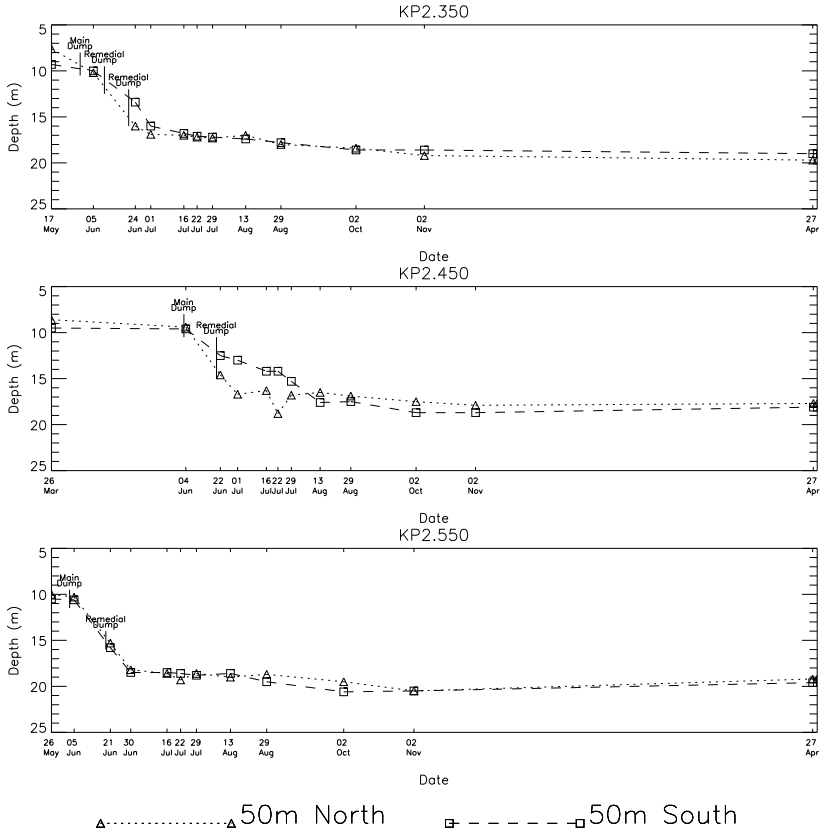

Figure 6 Seabed evolution at locations 50m either side of the pipeline (KP2.35 to 2.55)

IV. ANALYSIS OF SCOUR RESPONSE

The data was analysed to determine the characteristic response times for scour. This was carried out assuming the evolution of the depth of the scour hole with time S(t) at a particular location is adequately described by the equation:

$$S(t) = S_0 + S_{eq}\left(1 - \exp^{-t/T}\right) \qquad (1)$$

Where S_0 is the initial depth before scouring occurs, S_{eq} is the equilibrium value of scour depth and T is the timescale of the scour process. The physical meaning of T is as follows: after a period of length T, the scour depth relative to the initial depth S(t) $-S_0$, is 1-1/exp or 63% of the equilibrium value. After a period of 2 times T the depth is 87% of the equilibrium value. Another way of viewing this is that approximately 90% of the equilibrium scour depth is reached after a time period of length equal to 2.3 times T. It is convenient to consider this time period as being the time taken for the scour to develop within 10% of the equilibrium value. The equilibrium value will fluctuate with time owing to natural variations and it is probably sensible to take 10% as being the level of precision that is achievable. In the present study the variation in scour depth after the initial period of scour development shown on Fig. 2 is of the order of 1m which equates to approximately 10% of the maximum scour depth. Differentiating the scour equation (1) with respect to time allows the initial rate of scour development to be estimated from the ratio S_{eq}/T.

An analysis of the data was made during the project (November 1998) using the data obtained up to October 1998. The results of that analysis are presented in Table IV based on the initial phase of scour development.

TABLE IV. INITIAL ANALYSIS OF SCOUR RESPONSE

KP	S_0 (m)	S_{eq} (m)	T (days)	S_{eq} / T (m/day)
2.00	16	0	0	0
2.10	15	3	14	0.21
2.20	12	6	46	0.13
2.35	10	9	35	0.26
2.45	10	9	44	0.21
2.55	11	10	30	0.33

Based on the results in Table IV for KP2.10 to 2.55 the values of 2.3 times T are 32, 106, 81, 101 and 69 days respectively. By comparison of these timescales with the elapsed time of approximately 125 days between the main rock dump and the date of the October survey it was concluded that the scour development was close to an equilibrium state.

Since more survey data was collected between October 1998 and April 1999 it has been possible to make an assessment of how close those predictions were in the light of this additional data. The scour equation has been fitted to the time series data of Figs. 5 and 6 to evaluate the scour coefficients obtained in Table IV. The equation provides a general form for the scour depth evolution for comparison with Table IV. The plots in Figs. 7 and 8 are obtained by plotting scour development curves using the estimates presented in Table V.

Based on the estimates using the scour equation, after 11 months the early assessments of S_{eq} are within a metre of the value of S_{eq} specified in Table V, and within 1 to 2 metres of the maximum recorded values (Table II). The comparison can be seen on Fig. 7 for KP2.20 where the scour depth for the south side at the end of April 1999 is slightly greater than the value obtained using equation (1) with the coefficients given in Table IV. The data for KP2.20 has also had a curve with S_{eq} of 8m and timescale of 51 days plotted to evaluate the sensitivity to the parameters selected. This overestimates the scour on the north side. It is interesting to note that in some cases the scour depth has reduced compared with the predicted curve, as can be seen in Fig. 8 at KP2.45 and KP2.55. This indicates some infilling of the scour hole has taken place at these locations after the October 1998 survey.

This exercise indicates the value of survey data in assessing the evolution of scour morphology through the application of a scour prediction equation such as (1). The coefficients can be estimated from the initial phase of scouring to make an assessment of the final scour depth and time to reach equilibrium.

TABLE V. FINAL ANALYSIS OF SCOUR RESPONSE PLOTTED IN FIGS. 6 AND 7

KP	S_0 (m)	S_{eq} (m)	T (days)
2.00	N/A	N/A	N/A
2.10	N/A	N/A	N/A
2.20	12.0	6* 8	46* 51
2.35	9.2	9.8	38
2.45	9.3	9.7	47
2.55	10.0	11	34

N/A Not Analysed

*Values from Table IV

The scour response is considered to have been mainly due to tidal current forcing, it was relatively calm in May and June 1998, although it may have been sped up slightly by wave action had severe weather occurred. A period of severe weather did occur in Autumn 1998 resulting from typhoon activity and the resulting wave conditions were examined. Wave hindcast data for the period between 19 September and 19 October showed five storm events exceeding 1.5m significant wave height in that period, of which the most severe had a peak significant wave height up to 2.2m and associated period 5.7sec. Examination of the scour time series showed no evidence for the scour depth that had already been reached as being significantly affected by the action of the waves.

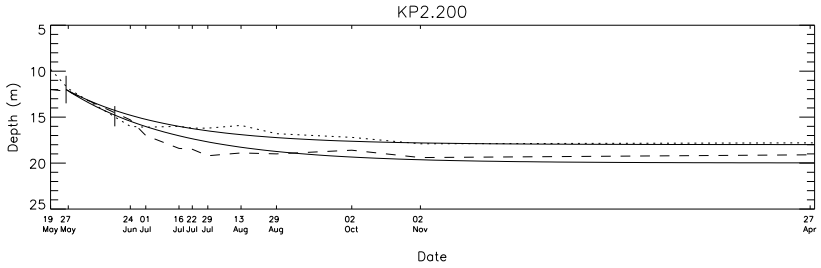

Figure 7 Scour curve fitted to seabed evolution data at KP2.20

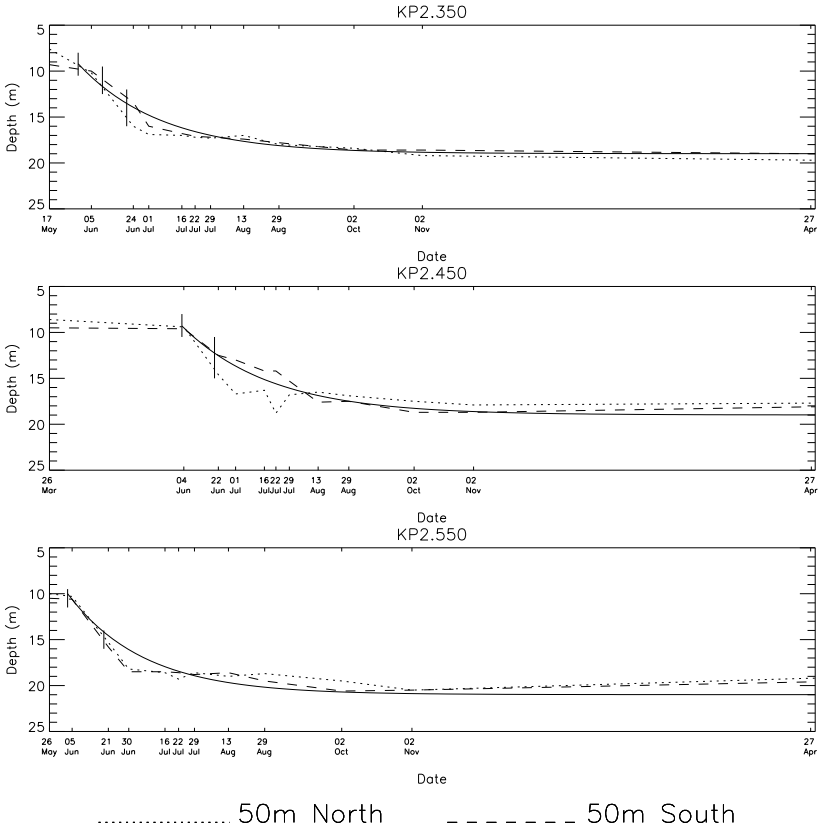

Figure 8 Scour curve fitted to seabed evolution data at KP2.35 to 2.55

In addition to the scour either side of the rock berm it is worth recording that significant scour occurred at the offshore end of the berm. This was attributed to the flow interaction with the rock berm structure giving rise to the generation of separation flow and high turbulence levels. The berm acted as a subsea dam and the flow acceleration round the end of the dam caused scour. It was this scour which gave rise to subsequent problems with the Pinghu pipeline, which is not the subject of this paper.

V. Final Remedial measures

During the end of August and in early September 1999 a remedial pipe protection was installed in the areas affected by scouring. This comprised a low height engineered solution laid over the pipeline alignment with a gravel dump (80mm to 10mm grading) armoured with an array of 0.5m thick 10m x 5m geotextile mattresses, filled with a gravel/sand mix, with their long axis installed perpendicular to the pipeline. The extensive scour that occurred at the offshore end of the berm was rectified with geotextile bags.

VI. Conclusions

The combination of the soft soils and fast tidal flows in an area with varying seabed topography led to the extensive scouring of the seabed soils either side of the engineered rock armour installed over a trenched pipeline. The scour development was rapid and led to a doubling of the original water depth over a period of about four months. Repeat surveys of the seabed topography were used to monitor the scour development and to inform appropriate measures relating to remedial rock dumping

and the installation of geotextile mattresses some 11 months after installation.

For pipelines in soft soils with high current speeds in shallow water it is recommended that the engineered rock armour is placed over the pipeline within the depth of the trench. If rock armour cannot be placed within the depth of the original trench (i.e. so the finished level is flush with the seabed) then it is recommended that the need for and advantages of the rock armour are reconsidered. However, if the rock armour is unavoidable, the experiences on this project show that a rock berm can be used to protect the pipeline provided a sufficient volume of rock is used to account for scouring that will occur. It is recommended that the rock berm height is minimized and the rock berm is extended significantly each side of the pipeline location, rather than increasing the height. If rock armour is not required an alternative approach would be to consider enhanced self-burial of the pipeline with spoilers providing it was demonstrated that the flow and soil conditions were suitable to generate the tunnel erosion under the pipeline for this method to work. This has been proven effective on the recently completed offshore section of the Hangzhou Bay crossing in water depths of 10m, bottom currents of 0.8 to 1.6m/s and higher and loose, silty sands [2]. Engineered backfill was not adopted as a solution at that site because of the large range of natural bed level changes up to 6m that can occur.

ACKNOWLEDGEMENT

The authors acknowledge the permission of China National Offshore Oil Corporation for permission to publish the information presented in this paper.

REFERENCES

[1] COGC Engineering Survey Company, "Geotechnical investigation and environmental study – pipeline route survey area OA-OB section, Pinghu Oil and Gas field, East China Sea, P.R. China". A report submitted to Pinghu Project Group, CNOOC, December 1995.

[2] Xia Yu Fei, Gu Jian Ning, Ng Eng Bin, Janardanan Kizhikkilod, Tan Sin Le and Daniel Zhao, "The Hangzhou Bay pipeline crossing project – use of spoilers to initiate pipeline self-burial and re-initiate future re-burial. Proceedings 2nd International Conference on Scour and Erosion, 14-17 November, Singapore, eds.Y-M. Chiew, S-Y. Lim and N-S. Cheng, 506-521, 2004.

Sediment Transport Rate in the Dune Regime in Bed Levelling Experiments

JENS-UWE WIESEMANN, PETER MEWIS and ULRICH C.E. ZANKE
Institute of Hydraulic and Water Resources Engineering, Darmstadt University of Technology,
Rundeturmstraße 1, 64283 Darmstadt, Germany.
email: wiesemann@ihwb.tu-darmstadt.de

In this paper different methods of determining the sediment transport rate in the laboratory are presented. Different methods regarding investigations of bed levelling experiments on a transverse sloped bed are discussed and correlated. The studies were carried out in a straight flume in the Hydraulic laboratory at Darmstadt University of Technology. For morphodynamic model computations, particularly with scours, the natural development of the river geometry and for simulations of alternating bars, the knowledge of the transport processes in longitudinal and transverse direction are important. In two- and threedimensional morphological models the transverse transport is of much higher importance then in the classical one-dimensional coputations. Regarding the high relevance of the transverse transport the number of measurements is insufficient. There is a need for more detailed information supported by experimental data.
Investigations on sediment transport on a transverse sloped bed were conducted under different flow conditions. The analysis of the transverse transport relies on the knowledge of the longitudinal transport. The transport rates were determined by the propagation of present bed forms, observed in longitudinal bed profiles and by gathering the transported bed material at the end of the flume. A comparison of the aforementioned methods will be given. These are discussed with respect to the determination of transport rates.

I. INTRODUCTION

In investigations of hydraulic engineering topics the morphological evolution of the channel bed is often one important component. The river morphology, and in the laboratory the flume bed morphology, depends on the behaviour of the moving bed material. Therefore it is very important to know exactly how much material is transported and in which paths (direction) the sediments travel. To quantify the transported material it is inevitable to measure transport rates under various conditions to find representative approaches of sediment transport prognoses. In field observations normally some point measurements are conducted to quantify representative transport rates of the natural area of observation. Mostly these measurements are taken in addition to some common transport formula to get substitutional transport rates for the considered area. Contemporary morphodynamic-numeric models contain such expressions and are able to simulate the transported quantities under the knowlegde of the prevailing sedimentologic parameters. But the morphodynamic-numeric models need some calibration data too, in order to find the right amount of transported sediments. Here the aforementioned point measurements, sometimes coupled with a non contact measuring method, are useful.

In the laboratory the measurement of the transported material of a bounded area is common. Here the regional conditions make an integrated consideration of the transported material possible.

For measuring the amount of the bed load transport a separation of common methods could be made by differentiating in gravitational, volumetric and non contact (acoustical, tracer using or optical) methods. The most accurate method to get the quantity of the transported material is an integrated weight measurement. The weighing of the total transported material which was transported out of a flume with a movable bed arranged over the total length of the flume up to the outflow region yield an accurate total transport rate. If the bed morphology and its changing with time is known, then the different volumina of the bed form and its propagation gives agood estimate of the total transported volume. By knowledge of the porosity the sediment transport rate can be calculated. These two methods are applied in this investigation.

II. BED LEVELLING EXPERIMENTS IN THE LABORATORY

A current investigation in which the knowledge of sediment transport rates is necessary deals with the observation of bed levels in a channel section with a movable bed (*Wiesemann, Mewis, Zanke* 2004 [4]). This investigation, conducted in a 60m long tilting flume, includes experiments with prevailing bed-load transport and dunes (bed forms). The mobile bed was preformed previous to each experiment with a cosine in cross-section. The investigated sediment was a coarse sand with an representative diameter $d_m = 0.96$mm. The grading curve of the flume bed sand is given in Figure II-1.

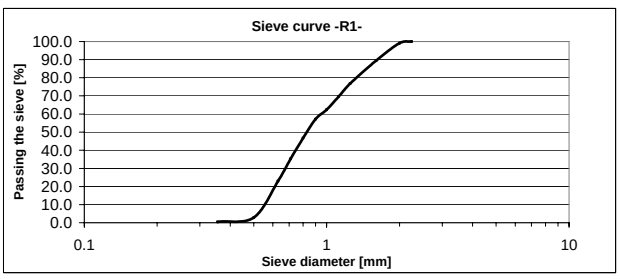

Figure II-1: Results of sediment analysis (sieve analysis).

The amplitude of the preformed cosine function decreases with time. This decay is observed by measuring longitudinal bed profiles at different positions in the cross section of the flume. The decaying amplitude was measured under the presence of bed forms. This decay is a degree for the transverse transport caused by the inclination of the bed and the affecting gravity component.

The experiment was controlled by adjusting the tilt of the flume, adjusting the flow discharge and positioning the sliding panel at the outlet of the flume. Possible disturbances caused by the inflow and the outflow conditions affect the evolution of bed morphology. By locating the measurement section in sufficiently long distance from the boundaries these interferences can be regarded as negligible.

Each run is short because the main goal was the bed levelling. No feeding of sediment at the inflow was necessary.

Every run includes several measurements of longitudinal bed profiles of 30m length, which were measured by moving the Laser Distance Sensors (LDS) on a measuring carriage with mean flow velocity to minimize the disturbances to the flow conditions. This setup of devices enables a high resolved simulation of the movable flume bed (see Figure III-1).

The evolution of bed forms continues until the geometry of bed forms is fully developed or reaches a quasi-equilibrium-condition.

The aim of the described bed levelling investigation is to formulate a new approach for describing the transverse transport. Because of the correlation of longitudinal transport and transverse transport the knowledge of the longitudinal transport rate is essential for this experimental investigation. The longitudinal transport rate includes important information about the prevailing hydraulic and sedimentologic parameters. For an accurate formulation of the transverse transport the longitudinal transport component should be known. In the described bed levelling investigation the aim was to evaluate the sediment transport direction, therefore both components the longitudinal and the transverse one are necessary.

III. SEDIMENT TRANSPORT MEASUREMENTS

A. Measurements in the laboratory

The determination of the transport rates was conducted by weighing the transported material and by observing the morphology of the bed, checking the evolving and propagating bed forms.

Weighing the transported material by collecting the material at the end of the flume and determining its submerged weight leads to an exact total transport mass. This magnitude could be transferred with the known duration of the experiments into a transport rate. So this method does not give information about potential present time variations in the transport rate. If bed forms are present the gathered sediment mass at the end of the flume is subject to fluctuations caused by the propagating bed form crests (dune shape). On a 3D ripple bed this influence is not dominant but on a 2D dune bed the transport rate differs significantly with a propagation period of a single dune. This leads to a fluctuation in the total transport weight against the point of time when the experiment is stopped: Stopping the experiment before or after the dune crest is travelling out of the flume affects the total transport rate, because of the small number of dunes travelling out of the flume.

To avoid these dependencies the transport behaviour within the measurement section of the bed levelling has to be measured. By considering the propagation of the bed forms the transported volume could be determined. The measurement of longitudinal bed profiles yields the geometry of the travelling dunes. With an adequate algorithm the bed profiles could be analyzed. With known geometric parameters the propagation of the bed forms and hence the transport rate could be calculated.

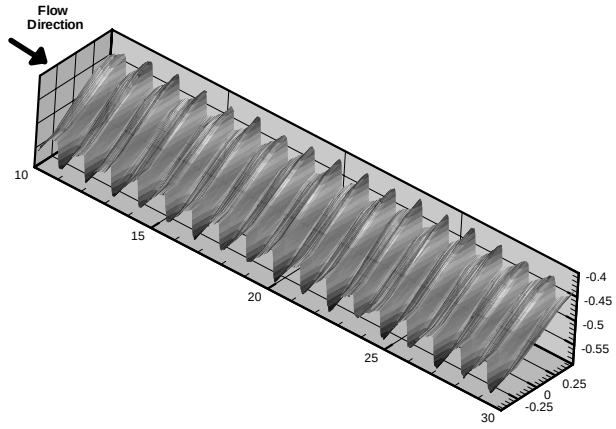

Figure III-1: Threedimensional depiction of measured flume bed. The dunes that developed are shown.

Figure III-1 shows the three-dimensional flume bed measured with five Laser-Distance-Sensors. The bed forms, here two-dimensional dunes, are depicted. At various time steps the bed levels at five transverse located points were measured. The evolution and rearrangement of the flume bed could be observed with this technique. For a more simple determination of the prevailing morphology the profiles were plotted in 2D as shown in Figure III-2.

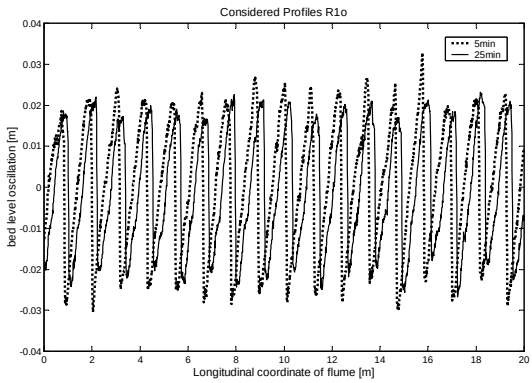

Figure III-2: Plotted longitudinal bed profiles.

In Figure III-2 the propagation of the dunes can be observed. A longitudinal bed profile at two different time steps is depicted. Beside the propagation of the bed forms the variation of bed form height is given, but the characteristic form of the bed forms remains the same.

B. Analyzing the transported material

For an explicit consideration of various methods an exact analysis of the transported material is necessary. In addition to the density of the grains the porosity of the bed layer is important to evaluate the transported mass from the measured volumina. For this purpose the non-compacted density of the bed layer is the basis for the assumed porosity of a travelling dune. This approach seems to be the obvious one because of the poured condition of the dune bed. Whether the primary inserted bed layer was possibly compacted, the continuing rearrangement of the bed layer leads to a loose fill.

C. Bed form geometry

For a complete consideration of the transported volumina in addition to the bed form propagation speed the knowledge of the length and the height of the bed forms is necessary. The applied zero up- and down-crossing method to the zero crossing of the longitudinal bed profiles yield information about the geometry of the dunes. With known length of the profiles and the number and positions of zero-crossings the length and height are given. It is important to know whether the dune form is nearly a triangle or a more rounded one.

By determing the rms-values of each bed profile the the volume of the dunes can be determined in a more direct way.

A more detailed analyzis concerning maxima and minima between the zero-crossings lead to the bed form height. With an adequate algorithm the profiles could be analyzed with respect to these aims. In Figure III-3 a longitudinal bed profile is shown. The average bed level value is the basis to apply the zero-crossing method.

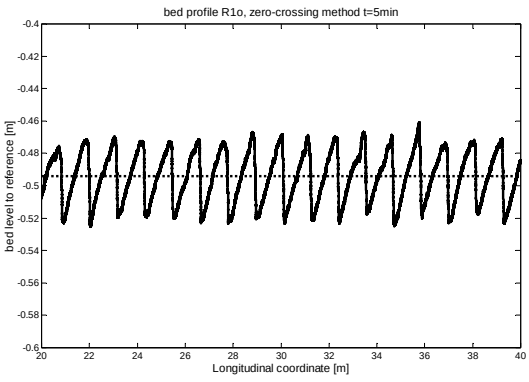

Figure III-3: Longitudinal bed profile R1o, t = 5min. Oscillating bed levels. The dotted line is the average bed level value.

The applied measurement technique yields high resolved data. So it is possible to evaluate the typical dune profile by summing up all values multiplicated with the longitudinal distance for each value of the bed profile. For that purpose the average value of the minima values of the bed profile has to be indentified.

The determined typical dune profile of this investigation is characterized with a factor $\beta_F = 0.55$.

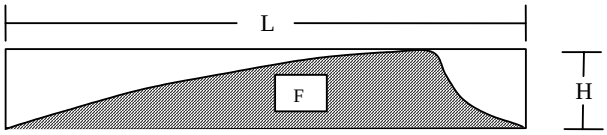

Figure III-4: bed form (dune). Sketch of determination of the form faktor β_F.

The dune form factor β_F , proposed by *Führböter* 1967 and here applied according to *Zanke* 1982 [6] is formulated as

$$\beta_F = \mathrm{F}/(\mathrm{H}\cdot\mathrm{L}), \tag{1}$$

in which H = bed form height, L = bed form length, F = cross section (area) of dune.

is the relation of the present dune profile to the product of length and height. Hence the form factor for a triangle form is 0.5 and with a present parabolic form the dune about 0.66. Other investigations which dealed with sediment transport determination from dune profile propagation used different form factors due to the prevailing bed form properties. Calculations described in *Zanke* 1982 [6] were conducted with a form factor of 0.6 for a good agreement. With the flume width of 0.5m the calculated dune height and length is transferred into the sediment transport volume.

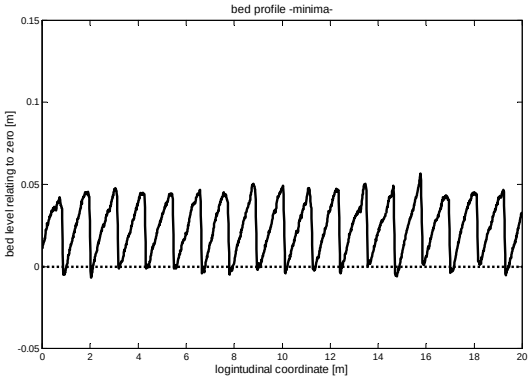

Figure III-5: Shifted bed profile R1o, t = 5min. Average minimum value is set to zero.

In Figure III-5 the average value of the minima is set to zero. The area above this zero line was evaluated.

Another method to determine the bed form geometry is the Fast Fourier Transformation (FFT). For application of this method a couple of algorithms exist. In this case a MatLab-implemented routine was used to find the periodic components of the bed profile.

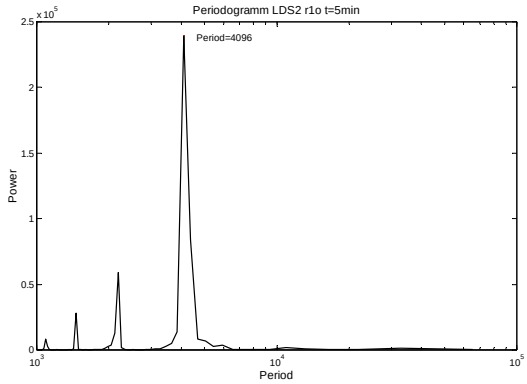

Figure III-6: From FFT determined period of measured longitudinal bed profile.

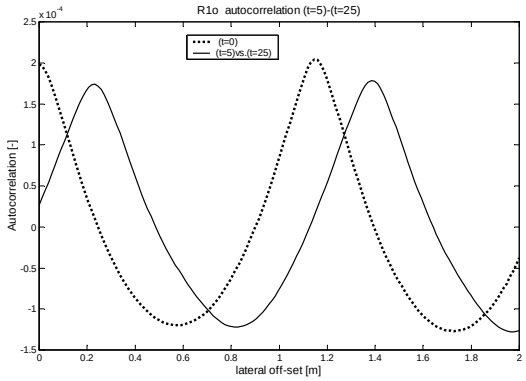

Figure III-7: Auto-correlation function of two bed profiles. Time 5min versus 25min.

In Figure III-6 the results of the FFT of the bed profile is shown. The FFT lead to a main period of 4096 data points. This number of data points could be converted in the length of the prevailing bed forms and results in a dune length. For the Laser Distance Sendor LDS2 in run R1o at running time t = 5min the dune length was 1.06m. The length of the dunes resulting from the FFT-analysis is comparable to the length of the auto-correlation and the zero-crossing method, but the resulting length from zero-crossing and auto-correlation do correlate better, here a dune length of 1.15m was evaluated. The resulting bed form length shows significant variations in the consideration of all measured bed profiles of an experiment. Because of the leaping variation in length by considering all bed profiles over the whole time period of one experiments the FFT was not applied in the analysis of the bed levelling experiments.

D. Determination of dune propagation velocity

Based on the investigations of *Kühlborn* 1993 [1] the bed form propagation velocity could be determined from auto-correlation of adjacent longitudinal bed profiles of one time step of bed levelling measurements. The auto-correlation is expressed as:

$$R_{yy}(\Gamma) = \frac{1}{n-m-1} \sum_{i=1}^{(n-m)} \left[y(x_i, t) \cdot y(x_i + \Gamma, t + \Delta t) \right] \quad (2)$$

Ryy (Γ) =	autocorrelation at position Γ
n =	number of measuring points
m =	number of measuring steps of lateral offset
Γ =	lateral offset of autocorrelation
x, y =	coodinates of height and horizontal location Δt = time interval

The auto-correlation yields the period of the lateral staggered profiles (see Figure III-7). A maximum in the auto-correlation indicates that the staggered profile is in accordance to that one at the beginning of the considered time interval.

With the knowledge of the time step and the lateral distance belonging to the maximum value in the auto-correlation function the propagation velocity is given. With the known dune propagation velocity the transport volumina can be evaluated.

For a simple procedure to verify the evaluated propagation velocities, the longitudinal bed profiles are in depicted Figure III-8. The ordinate in Figure III-8 is the time. The bed profiles are depicted with the average value to the belonging time, so the oscillations of the profiles still exist, but their average value is set to the associated time of measurement. By connecting the dune crests a straight lines with a specific inclination result. This inclination yields the propagation velocity of the bed forms as well.

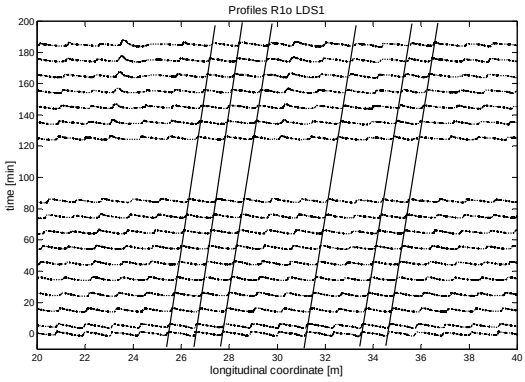

Figure III-8: Plotted longitudinal bed profiles of LDS1 (run R1o), straight line connection for progation velocity determination

A comparison of randomized testings of plotted profiles and auto-correlations with associated dune propagation velocity lead to a good conformance. So the dune propagation method to determine the velocity is verified.

E. Transport rate

The comparison of the different methods in the investigation of the bed form geometry favourite the application of the auto-correlation method coupled with the zero-crossing method. In addition to these operations the transport rates q_G could be determined by using a method proposed by *Führböter* 1967. The following method was applied according to *Zanke* 1982 [6]:

$$q_{G,average} = H \cdot u \cdot \beta_F \tag{3}$$

in which H = bed form height, u = propagation velocity and β_F = form factor, due to prevailing bed forms (eq. 1).

Including the density and porosity of the bed layer the analysis leads to transport rates corresponding to the aforementioned technique. In Figure III-9 the evaluated transport rates from the dune propagation method considering the rms-values are shown. The dimensionless transport rates (eq. 4) are depicted versus the dimensionless shear stress Θ, the integral Shields parameter.

$$q^*_{bed} = \frac{q_{bed\,s}}{\sqrt{(s-1)gd^3}} \tag{4}$$

$$\Theta \equiv \frac{\tau}{(s-1)\rho g d} \tag{5}$$

here are d = diameter of particles, τ = total bed shear stress, g = gravity, s = relative density of sand, ρ = fluid density, $q_{bed\,s}$ = longitudinal sediment transport rate. This is a formula based on integral parameters (water depth h, Shields parameter including form drag of bed forms, water level gradient).

A good agreement of determined transport rates over a range of increasing dimensionless shear stress is given. The good correlation of the determined transport rates is another argument for the verification of this method. In order to get a similar transport rate to other results the total values of the dune propagation with the rms-analysis were modificated with a small parameter. So the quantatitive magnitude of the sediment transport is in the same range as the sand trap measurements but the correlation of all considered experiments is better.

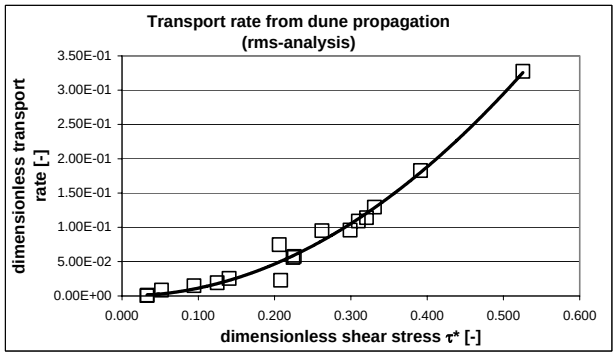

Figure III-9: Evaluated transport rate values versus the dimensionless shear stress values (Shields parameter).

Because of the fairly good correlation the dune propagation method should compared to other methods. In addition to the determination of the dune propagation velocity the analysis of the bed form geometry, based on observations of minimum and maximum value between the zero-crossing points, yields the transported volumina.

In the bed levelling investigation the evaluation of the sediment transport direction of the series R1 (coarse sand, d_m = 0.096mm) was conducted with the data of eight experiments. The sediment transport data of these experiments, determined with the dune propagation, with the transport formula of Zanke 1999 [7] and with weighing up the sediments collected in the sand trap, are compared in Figure III-10, Figure III-11 and Figure III-12.

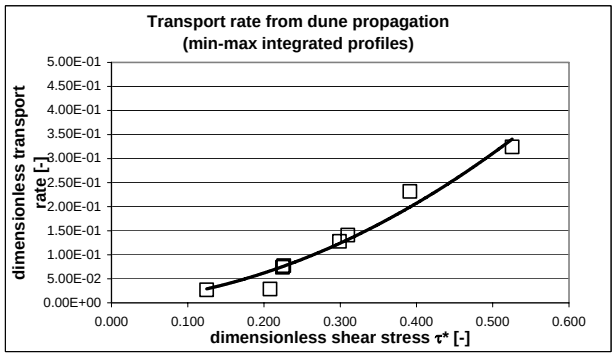

Figure III-10: Dimensionless transport rate versus dimensionless shear stress. Transport rates evaluated from dune propagations.

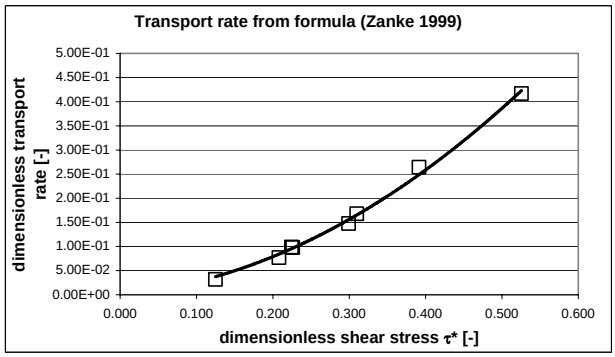

Figure III-11: Dimensionless transport rate versus dimensionless shear stress. Transport rates evaluated from transport formula of Zanke 1999.

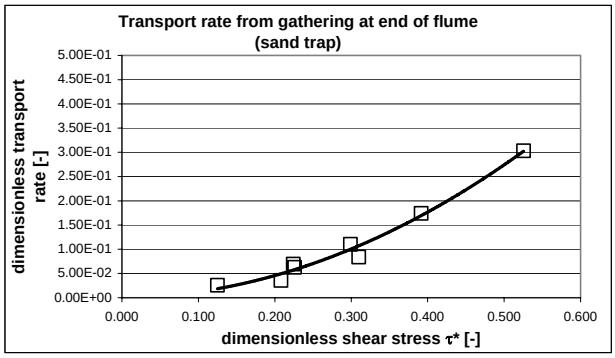

Figure III-12: Dimensionless transport rate versus dimensionless shear stress. Transport rates evaluated from the gathered total sediment transport mass (sand trap).

A comparison of the three different methods of sediment transport rate determinations is given in Figure III-13. Both methods, the dune propagation method and the sand trap (weighing) method vary from the calculations with the formula of *Zanke* 1999.

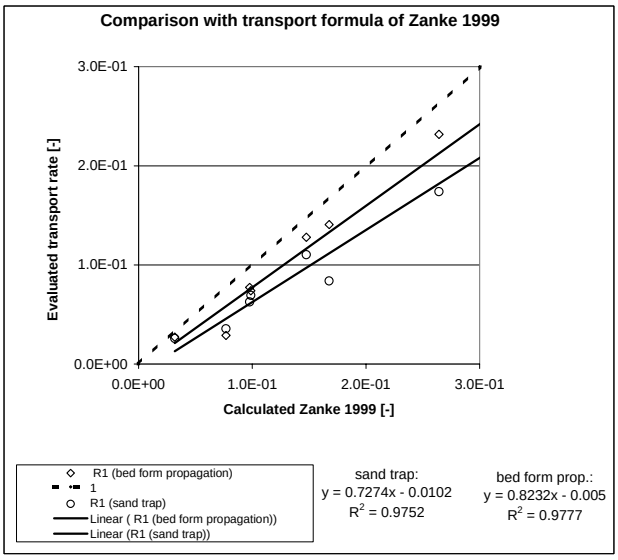

Figure III-13: Comparison of transport rate determination methods.

With regard to the bed levelling experiments and the combined determination of transverse transport rates the dune propagation method yields better results concerning the correlation of a transverse transport approach (cp. Wiesemann, Mewis, Zanke 2006 [5]). This could be attributed to the location of analyzing the bed profiles. In that case the longitudinal transport rate and the transverse transport rate are determined from the same measurement section and both from analyzing the bed profiles.

Further experiments must be conducted to get more data which support the concluded results.

IV. Conclusion

In the presented investigation it was shown that sediment transport rates could be determined by considering the prevailing bed forms and their propagation successfully. In experimental investigations with a movable bed and with the need for determining the transport rates gathering the transported material at the end of the flume is an accurate procedure. These integral measurements do not give information about the variation of transport rates and include the conditions of the total experimental setup with all disturbances at inflow and outflow sections. By considering the transport rates within the section where different but associated measurements are conducted the results of the transport rate determination could be better referred to that process which is measured too. In the present investigation the measured bed levels and hence the decay of a previous formed transverse slope was measured. The dune propagation method enables a direct association of measured longitudinal transport rates and the evolution and rearrangement of the bed morphology in the same measurement section.

V. Application of Sediment Transport Analysis

The described determination of sediment transport rates considering the dune propagation is suitable for all laboratory experiments in which bed forms are present. To get reliable results the prevailing bed forms should have two dimensional character and should be stable in their characteristic form. Increasing dune heights do not lead to sigificant inaccuracies but a similarity of the dunes (stability of profile form) should be present.

References

[1] Kühlborn, J., 1993, Wachstum und Wanderung von Sedimentriffeln, Technische Berichte über Ingenieurhydrologie und Hydraulik, Nr. 49, TH-Darmstadt.

[2] Mewis, P., 2002, Morphodynamisch-numerische Modellierung von Flußkurven, Dissertation, Mitteilungen des Institutes für Wasserbau, Heft 126, TU Darmstadt.

[3] Talmon, van Mierlo, Struiksma, 1995, Laboratory measurements of the direction of sediment transport on transverse alluvial-bed slopes, Journal of Hydraulic Research, Vol. 33, No. 4.

[4] Wiesemann J.-U., Mewis P., Zanke U., 2004, Laboratory measurements of sediment Transport on transverse sloped beds, Second International Conference on Scour and Erosion, Proceedings, Volume 2, 252-259, Singapore.

[5] Wiesemann, J.-U., Mewis, P., Zanke, U., 2006, Bed Levelling Investigations on Transverse Sloped Beds, **submitted** for the International Conference of River Hydraulics - Riverflow 2006, Lisboa, Portugal.

[6] Zanke, U., 1982, Grundlagen der Sedimentbewegung, Berlin; Heidelberg; New York: Springer-Verlag.

[7] Zanke, Ulrich C.E., 1999, Zur Physik von strömungsgetriebenem Sediment (Geschiebetrieb), Mitteilungen des Instituts für Wasserbau und Wasserwirtschaft, Technische Universität Darmstadt, , Heft 106.

A Static Analysis of Hydraulic Heave in Cohesive Soil

Robert-Balthasar Wudtke* and Karl Josef Witt*
* Bauhaus-University Weimar, Dep. Geotechnical Engineering, Germany

I. INTRODUCTION

During percolation of soil the forces of resistance are getting activated within a soil body. This leads to a reduction of the hydraulic potential in direction of flow. Hydraulic heave initialised by an ultimate hydraulic gradient occurs as a sudden base failure if flow forces exceed the soil resistance i. e. dead load and shear forces.

In non cohesive soils the expansion of the pore microstructure precedes hydraulic heave in a state of liquefaction if there is no grain-to-grain contact pressure during the different states. When developing hydraulic heave a movement of single sand particles occurs at first followed by a temporary abrupt lifting of the upper soil layers what can finally lead to a selective "boiling" like a viscous fluid (see Fig. 1).

To estimate the safety against hydraulic heave in non cohesive soil, different calculation methods have been developed. The most conventional methods are presented by Terzaghi [8] and Davidenkoff [2]. A comparison of both methods shows that the crucial difference is based on the soil volume in consideration to define the representative seepage force. Terzaghi uses in his theory a quasi static equilibrium of acting flow forces and resisting dead load related to a defined soil continuum. Davidenkoff relates his theory to the maximum possible hydraulic gradient acting along the sheet pile. In any case his approach gives the most conservative assumption due to the fact that the limit state is reached with a weightlessness of a single grain ($\sigma_{eff} < 0$) when a local liquefaction of soil occurs.

Considering cohesive soils both methods are suitable to only a limited extent. To guarantee a feasible consideration of cohesion as the relevant parameter the following questions have to be answered:

- How does cohesion influence the failure process? Does the simple model of the failure process in non cohesive soil meet the conditions?
- Is the failure mechanism more a liquefaction of the soil or is the model of a wedge failure more adequate?
- At which stress state and at which location a crack will be initiated?
- How does the change of the shear properties influence the change of the effective stresses and the pore water pressure in the state of failure?

Based on known theories to estimate the stability against erosion a limitation of the range of application in connection with hydraulic failure in form of liquefaction and through wedge failure in consideration of the parameter cohesion will be introduced. To show an application of wedge failure a mechanic sensible basic approach will be presented in order to estimate the safety against hydraulic heave. To document the effect of a variable hydraulic influence on stress distribution along a sheet pile wall results of calculations will be presented. To detect the failure type mentioned above experiments were carried out. The method and first results are reported

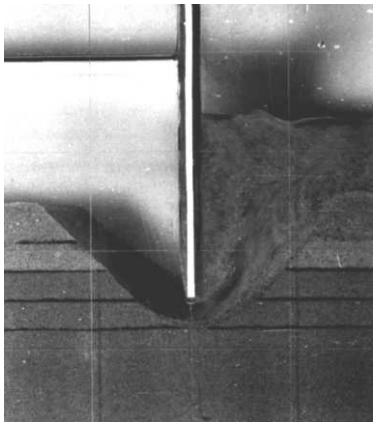

Figure 1. Hydraulic heave of a two layer soil system with relative impervious top layer [4]

II. HYDRAULIC HEAVE IN COHESIVE SOIL

To prove the safety against hydraulic heave two different failure scenarios of the ultimate state are possible: A failure due to erosion of particles and a wedge failure mechanism. A failure due to erosion can be characterised as liquefaction in dependence on the local hydraulic gradient. During wedge failure a soil continuum breaks into single parts. The failure is initiated by a discrete crack that will arise in a pre-failure state or can be produced by exceeding the tensile strength. Liquefaction as well as wedge failure occurs if the effective stress in a soil becomes zero. Main difference between them is the additional tensile strength within a cohesive soil. Consequently in a non cohesive soil hydraulic heave occurs typically by liquefaction as consequence of a structure collapse due to dilatancy while wedge failure can only occur when a tensile strength of the soil is activated or if a shear resistance arises in inner shear zones.

The different types of calculation have to be analysed in order to estimate the effect of cohesion on limit state conditions. An analysis of different approaches to estimate the stability against erosion leads to the following criteria for erosion of single grains or grain aggregates expressed by the global factor of safety FoS.

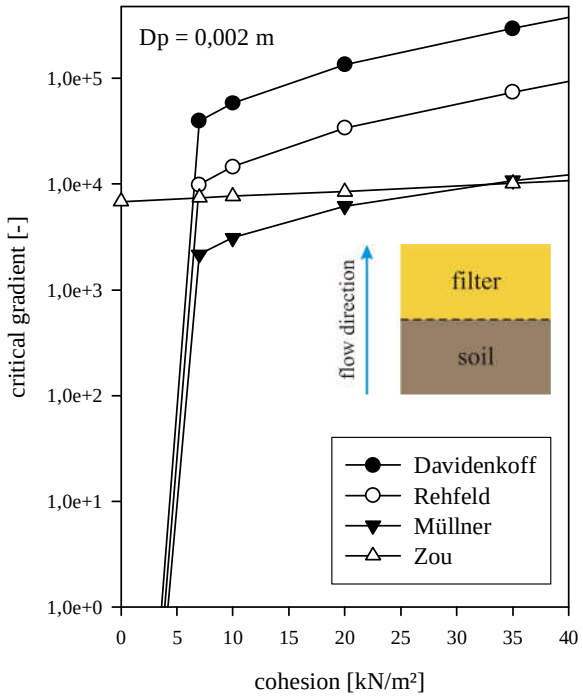

Figure 2. Comparison of erosion criteria according to Davidenkoff [3], Rehfeld [5], Müllner [6] and Zou [10]; different percolated material and constant filter material

Davidenkoff [3]

$$FoS = \frac{6\,c'}{tan\,\varphi' \cdot D_p \cdot \left(\gamma_w \cdot i + \gamma' \cdot cos\,\alpha\right)} \quad (1)$$

Rehfeld [5]

$$FoS = \frac{3\,c'}{2 \cdot tan\,\varphi' \cdot D_p \cdot \left(\gamma_w \cdot i + \gamma' \cdot cos\,\alpha\right)} \quad (2)$$

Müllner [6]

$$FoS = \frac{6.2\,c'}{D_p \cdot i \cdot \gamma_w} \quad (3)$$

Zou [10]

$$FoS = \frac{4\,c' + \left(\sigma_{x0} - \gamma_w \cdot D_p \cdot i\right) \cdot tan\,\varphi'}{2 \cdot \zeta\ p + \left(\frac{\gamma_w}{T_1} \cdot i - \gamma' \cdot cos\,\alpha\right) \cdot D_p} \quad (4)$$

While the derivation of their erosion criteria the authors consider in [3], [5] and [6] the shear parameters φ' and c', the equivalent pore diameter of the filter soil D_p and the gradient of the contact plane between the cohesive material and the filter soil relative to horizontal line, represented by the angle α. According to the approach of Zou a consideration of the pressure state is possible. In formula 4 he considered the effective lateral pressure σ_{x0} and the shearing stress within the erosion capillary $\zeta \cdot p$. A factor T_1 is defined to consider the fabric of the soil.

Assuming a safety factor of FoS = 1 the erosion criteria mentioned above are plotted in Fig. 2 in term of a critical gradient in dependence of the cohesion for an upward directed flow. The limit state of the evaluation was calculated under the condition of a filter layer (medium gravel). The safety against erosion and the resulting critical gradient are valid for the surface of contact between the percolated soils as well as for the filter layer. At the same time the weight of the filter layer causes a stress in the contact plain.

The comparison of the presented criteria shows a strong increase of the critical gradient even with moderate rising cohesion. The functions show partially large differences in values of cohesion c' > 10 kN/m² but a unique tendency relating to the influence of cohesion in general. Zou's erosion criterion is recognisable due to its different shape (see Fig. 2). In a range of small cohesion (c' ≤ 5 kN/m²) the critical hydraulic gradient is much higher compared to the other erosion criteria under the state of stress considered in his paper.

Calculations were executed to describe the effect of the equivalent pore diameter of the filter on the critical hydraulic gradient. Different values of D_p were assumed for the calculations: D_p = 2 mm representing medium gravel as filter, D_p = 20 mm representing a stone filter layer and D_p = 10 m represents a state when no filter is hydraulically active. The results are shown in Fig. 3. The effect of the pore size of the filter on the critical gradient within the base soil is obvious when comparing the results. The smaller the pore size of the filter material the higher the critical gradient for initialling erosion.

Within the scope of different experiments Leussink [5] studied the influence of a varying fine particle content of soils with small cohesion (c' < 5 kN/m²) with regard to strength and stiffness of soil mixtures. Besides the examination of the shear strength and the pore pressure in

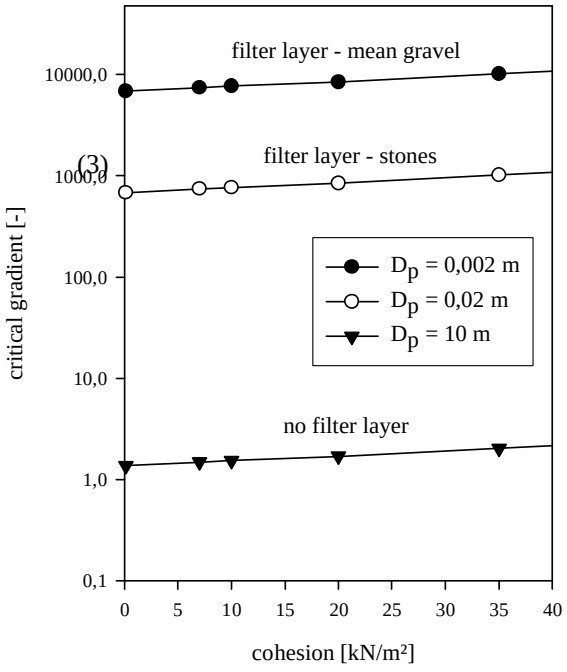

Figure 3. Erosion criterion according to Zou [10], different filter layers

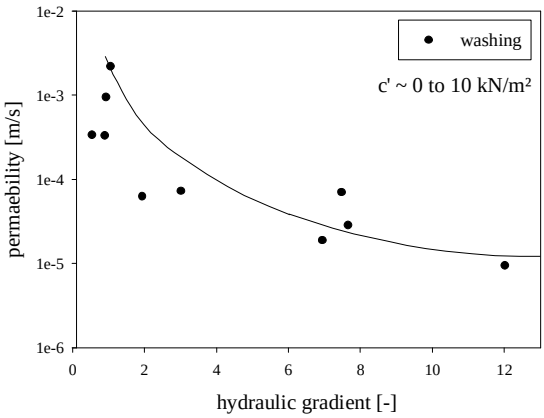

Figure 4. Correlation between permeability and critical gradient of soils with small cohesion [5]

wide graded soils the experiments were focused on the safety against erosion. Fig. 4 shows experimental investigated failures according to the permeability and the hydraulic gradient. In detail the points in the figure mark a partially or total failure of the soil body by erosion of the fine particle content. They are generalised as a function. Assuming that cohesion and permeability are related indirect proportional it can be derivated that soils with less or quasi zero cohesion respectively relative pervious soils will fail in range of a comparatively small hydraulic gradient, while the critical gradient increases over proportional with a rising cohesion.

All of the mentioned investigations indicate that erosion failure due to a drop of hydraulic potential is only probable in soils with low cohesion. Already in cohesive soils a wedge failure mechanism with discrete elements or clods will be relevant. As demonstrated in Fig. 5, soils with low cohesion will qualitatively fail as a certain kind of erosion (liquefaction) while soils with higher cohesion will fail due to a development of discrete shear planes and as wedge failure mechanism or as a uplift of discrete cracked layers. A semi quantitative analysis shows that up

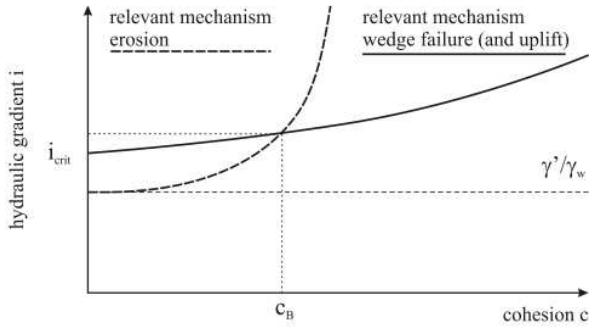

Figure 5. Different failure modes in cohesive soils [9]

to a cohesion of c' $\leq$ 2,5 kN/m² a failure due to erosion will be dominant, while higher cohesive soils will fail in a more complex dimension. Nevertheless for initiating a wedge failure, discrete shear zones or initial cracks are necessary to develop a pre-failure state.

Therefore in cohesive soils a wedge failure mechanism can be described by using the theory of effective stresses with the simplified formula:

$$p^* = \sigma' + \sigma_t \tag{5}$$

According to that failure occurs if there is no effective stress σ' and the excess pore water pressure p* is greater than the tensile strength σ_t within the soil continuum.

Fig. 6 shows three different shaped failure bodies to find an upper bound or limit state due to a wedge failure mechanism on a sheet pile wall as a support of an excavation. Besides from the consideration of rectangular, triangular and parabolic shaped bodies (I, II and IIIa) there are two different ways to build equilibrium of forces. At first the undrained cohesion c_u can be considered as the representative resistance in a slip plane at limit state (see failure body I to IIIa). On the other hand the resistance at the stadium right before failure can be assumed by taking

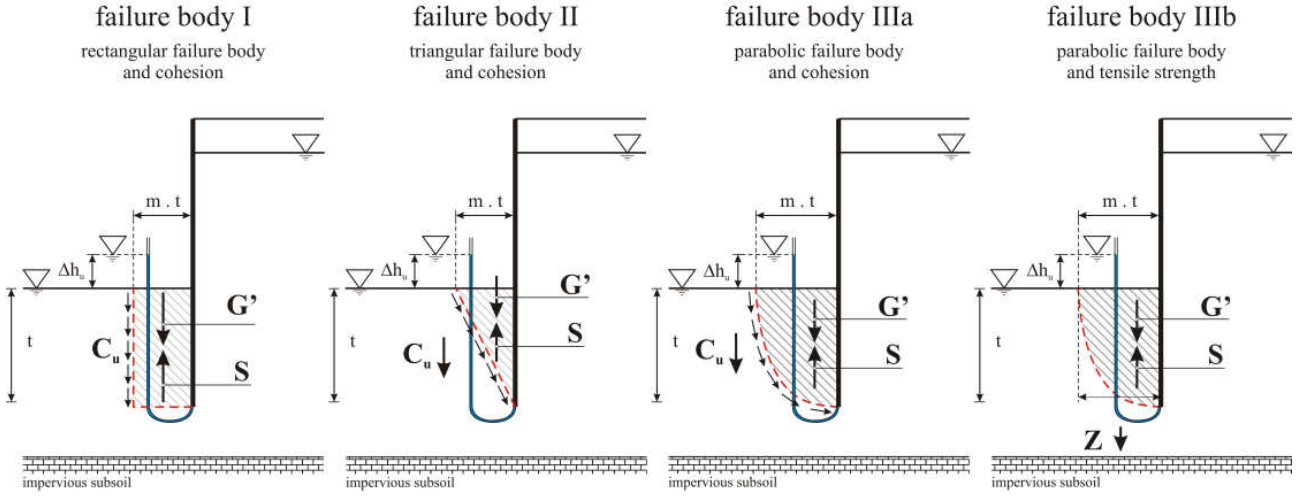

Symbols: C_u – vertical part of the force from undrained cohesion, G' – dead load under uplift, S – streaming force, Z – tensile force over width of the failure body, Δh_u – potential difference, m · t – width of the failure body

Figure 6. Different types of wedge failure [9]

the achievable tensile strength of the soil into consideration. The resulting equilibrium of forces is illustrated in Fig. 6 as failure body III b.

The thickness of a failure body with the slightest safety against hydraulic heave is described by the factor b = m · t. The shape and therefore m depends significant on the flow net. Assuming a small embedding and a corresponding flat shape of the flow net a relative broad area of influence will be developed. Reason for that is the inclination of the flow forces. In such a case the thickness complies with m = 1/2 suggested by Terzaghi respectively b = 1/2 · t. If the embedding reaches deeper into the ground the flow net will be orientated more vertical and the values of the parameter will be from approximately m = 1/3 to m = 1/4.

The failure body IIIa shown in Fig. 6 describes the failure mechanism of a hydraulic heave in the most probable way. The parabolic surface of the failure body corresponds with the flow lines of the flow net and therefore with the direction of flow induced shear forces. In case of shear planes the residual shear strength represented by the undrained cohesion c_u will be activated. At the base of a wall the hydraulic gradient on a supporting sheet pile wall of an excavation reaches the highest values. The realisable potential difference at the base of the wall Δh_u is the excess head related to the deepest part of the sheet pile wall and can be estimated with formula 6:

$$\Delta h_u = \frac{t \cdot \gamma' + 1{,}5 \frac{c_u}{m}}{\gamma_w} \qquad (6)$$

γ' = submerged unit weight and γ_w = unit weight of water.

III. Analysis of Stress State

In engineering practice there are two typical situations known for failure due to hydraulic heave, the downstream foot of a relative impervious dam or a weir above a pervious soil and an excavation with a impervious support (sheet pile). Referring to both the seepage forces oppose the forces of gravity, neutralizing a part or the whole weight of the soil. Thus the effective stress and the shear strength decrease. To analyse the changes of stress and the deformation in a cohesive soil the inflow of an excavation was simulated by using the program PLAXIS and a briefly calculation of hydraulic pressures by PLAXFLOW. The geological circumstances are characterised by a cohesive soil located under a 10 m thick layer of non cohesive material.

Referring to Fig. 7 the cross section of the system is characterised by gravel with its typical shear parameters, deformation behaviour and permeability. Under this relative permeable sediment there is a dense layer of silty and clayey sand. This soil shows typical low cohesive behaviour. The permeability of the gravel is more than 100 times higher than those of the cohesive material. In general there is no activation of flow forces within the gravel in comparison to the overlying silt. For reasons of calculation there is no difference taken into account between horizontal and vertical permeability within both layers.

In the first step the excavation and the installation of the supporting elements, thus the sheet pile wall and anchors, were inserted. Before raising the water level, it was defined at a depth similar to the bottom of the excavation. Fig. 7 illustrates an overview of the geological and hydrological conditions used within the calculation.

Aim of the numerical analysis was the determination of the change of the stress state and the resulting deformation around the sheet pile wall due to a rise of the water level, as depicted in Fig. 7 points 1 to 4. The rise of water level was executed using the steady state algorithm of the program tool PLAXFLOW.

To show the change of the stress state of the soil the effective stresses before and after the rise were documented in Fig. 7 details 3 and 4. But due to the lateral load from the support the effective stresses in final state don't became zero. This fact leads to the result that failure due to hydraulic heave didn't happen during the calculation. The relative strong fixation of the sheet pile base in the soil abutment was partially loosened. Nevertheless in general an significant decrease of the effective stresses on the excavation sided wall can be determined.

Due to the fact that failure didn't occur by hydraulic heave, the determination of a failure body could not be

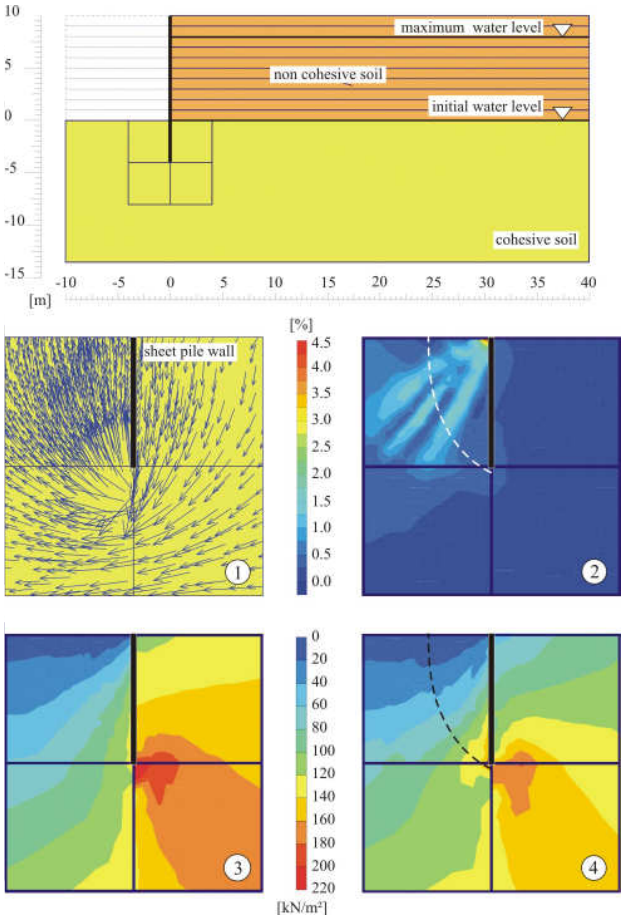

1 – seepage forces, 2 – total shear stains, 3 – effective stress before rise of the water level, 4 – effective stress after rise of the water level

Figure 7. Distributions of pore pressure, total and effective stresses

executed. But by evaluating the total shear strain plot (see Fig. 7 point 2) a spacious expansion of the excavation sided soil were ascertained. The maximum value of shear strain deformations were reached in direct contact to the sheet pile. This result indicates that the ratio of seepage forces and dead load under uplift is comparatively small in this area. Regarding the whole soil expansion and the points of maximum values a failure body with a width of $b \approx ½ \cdot t$ (according to Terzaghi's suggestion) can be derivated.

To estimate the validity of formula 6 calculations of the safety factor and the possible critical hydraulic potential difference were executed. In case of a maximum water level behind the wall and a thickness of the failure body of ca. 2 m, thus according to Terzaghi m = 1/2, a safety of FoS = 3,5 is indicated. This result corresponds with the FEM calculations. According to formula 6 the calculated result represents exclusive the safety against hydraulic heave. The result of the computational calculation contains in contrast to this effects of embedding the wall and material properties of the wall, i. e. stiffness and strength.

The most important result of this analysis is the documented influence of the flow direction on the probable shape of the failure body. In case of an almost continuous flow without any influences due to redirection on layer planes or constructions a flat soil will be uplifted. This result corresponds with observations made in similar cases. On the other hand the results of the sheet pile wall example show the strong influence of a direction change of the flow net. In such cases the shape of the failure body will significantly be influenced by the permeability of the percolated soils and the thickness of such layers.

The more concentrated a percolation occurs the thinner the failure body shape will be.

IV. Visualising of the Failure Initiation

Experiments were executed to visualise the failure process and to characterise the failure type in dependence on the cohesion. Furthermore the experiments should document the initiation and the development of the failure process. The experimental study should demonstrate weather the failure in cohesive soil is more characteristic for liquefaction or for wedge uplift and how large is the value of the limiting parameter cohesion c_B between both failure types.

The experimental equipment simulates a sheet pile wall as supporting element on an excavation. To minimize the necessary potential difference within the experimental box different material were installed on the upstream and the downstream side. The embedding of the wall on the upstream side consists of 10 mm clay and 90 mm coarse grained filter material. On the downstream side the wall is fully embedded in the cohesive clay (see Fig. 8). By installing different permeable material on the sides of the wall most of the seepage forces were activated on the downstream side within the clay. Bažant carried out investigations (see [1]) to show that the deformations on the upstream side of a wall are comparatively smaller than those on the downstream side when reaching hydraulic heave. The embedding in the clay can be installed as small as possible thus very small deformations are expected on the upstream side of the wall.

Figure 8. Experimental box with installed clay and filter material

Figure 9. Result after failure (white line = slip plane)

After installation of the soil layer a saturation of the soils have to be executed. To increase the velocity of saturation the hydraulic stress level on both sides of the wall was continuously raised and held constant at a backpressure of approximately 50 kN/m². Through a slow minimization of the stress down to zero the saturation was accelerated.

Due to a following raise of the hydraulic head on the upstream side of the wall an expansion of the soil continuum on the downstream side were observed. The process was followed by the initiation of a crack at the end of the wall foot on the downstream side. The first crack don't lead automatically to a failure of the soil. The range of the crack first increases when the acting stress level rises up. Finally the crack reaches the downstream surface. The consequence was a short term uplift of a discrete clod followed by a compensation of the different stress levels on both sides of the wall. During the compensation the clod was destroyed and teared apart into small aggregates and even particles of the soil. The result after the compensation is shown in Fig. 9.

The failure due to hydraulic heave occurs in the strong cohesive clay as a wedge mechanism. The initial crack was realised when a total hydraulic stress difference of 25 kN/m² forces the soil. That is the excess hydraulic head related to the base of the wall was about Δh_u = 2 m. Aim of the experimental work is not to determine the stress at limit state, but to study the development of the failure in

cohesive soils. Nevertheless the first results correspond with formula 6.

Fig. 9 shows the shape of the failure clod in a cross section (white line). The dimension of the failure body leads to a value of $m \approx 2$. The result doesn't correspond with the expected value of $m = 1/2$. Reason for the investigated shape could be the soil installation technique, which produces a horizontal layered soil continuum and anisotropic conditions concerning density and permeability. When installing the soil in a way that quasi isotropic properties are existent during the experiment a change of the failure body shape will be expected.

As things will develop another question has to be answered. How does the stress state at the wall base change the soil conditions during increasing of the total potential difference? Thus a comparison of the failure time with the change of pore water pressure on the wall foot will be estimated.

Alternatively to the static approach (formula 6) the initiation of cracks can be defined as limit state. This approach matches the conditions of hydraulic fracturing to define a limit state. From a mechanical point of view the initiation of the crack will always be orthogonal to the direction of the smallest principle stress. In case of a starting failure due to hydraulic heave this would be under consideration of soil decompression which leads finally to a lifting of the bottom of the excavation. According to the documented results of the first experiments an increasing pore water pressure would force the expansion of the crack till the failure due to hydraulic heave occurs.

V. SUMMARY

Aim of the present research is the examination of the failure type, in detail liquefaction and wedge failure, due to hydraulic heave on a supporting wall of an excavation. To answer the question the problem was analysed theoretically by comparison of the critical hydraulic gradient in dependence of different erosion criteria, by computational calculations to validate the presented safety criteria of a wedge failure mechanism and by experiments to recognize the deformations pre and post failure.

The influence of the cohesion on the failure process could be shown based on the comparison of different erosion criteria. To reach erosion in cohesive soils a very high local hydraulic gradient would be necessary. This leads to the assumption that a wedge failure mechanism is valid even in low cohesive soils.

The introduced shapes of failure clods leads to the conclusion that the failure body on a sheet pile wall can be modelled as a parabolic clod in a first static approximation. The width of the mechanism depends significantly on the geological behaviour in the sphere of influence. In this context layering and non isotropic permeability got the strongest influence on the shape. The presented formula to estimate the hydraulic potential difference at limit state can be used estimating the shape of the wedge. Generalising the thickness of the failure body will be half of the embedding, if isotropic conditions will be present. When using the formula to estimate the safety it is essential to realize that energy conversion while deformation and liquefaction of the soil as well as the horizontal fixation of the supporting are unconsidered.

Summarising the first results of the study hydraulic heave in cohesive soils will arise as a wedge failure. Only soil with very low small cohesion (ca. $c' < 5$ kN/m²) will fail in the manner described in the common formula by Terzaghi. The course of failure in highly cohesive soils is dominated by the development of cracks. If they are already existent genetically failure will occur in a certain type of uplift. The principle which leads to cracks due to pressure can be described by the phenomenon of hydraulic fracturing using an approach that considers the energy needed for deformation and the propagation of cracks.

ACKNOWLEDGEMENT

The results presented in this contribution are part of an ongoing research-work in the order of the German Federal Waterways Engineering and Research Institute – BAW. The funding assistance provided by the BAW in support of this project is gratefully acknowledged.

REFERENCES

[1] Z. Bažant, „Grundbruch unter einer Spundwand“, *„Bautechnik“* (18), pp. 595 – 599, 1940

[2] R. Davidenkoff, “Unterläufigkeit von Stauwerken,” *Werner-Verlag GmbH*, 1970.

[3] R. Davidenkoff, „Anwendung von Filtern im Wasserbau“, *Verlag Ernst & Sohn*, 1976

[4] W. Knaupe, „Aushub umschlossener Baugruben unter besonderer Berücksichtigung des hydraulischen Grundbruches im schichtweise gelagerten Baugrund“, *Dissertation - Hochschule für Bauwesen Leipzig*, 1972

[5] H. Leussink, T. G. Visweswaraiya, H. Brendlin, „Beitrag zur Kenntnis der bodenphysikalischen Eigenschaften von Mischböden“, Veröff. Des Institutes für Bodenmechanik und Grundbau der Techn. Hochschule Fridericiana in Karlsruhe, 1964

[6] B. Müllner, „Beitrag zur Untersuchung der Erosionssicherheit bindiger Mischböden bei vertikaler Durchströmung“, *Mitt. des Fachgebietes Grundbau, Boden- und Felsmechanik Gesamthochschule Kassel – Universität*, 1991

[7] E. Rehfeld, „Die Erosionsbeständigkeit bindiger Lockergesteine“, *Wiss. Zeitschrift der TU Dresden*, 5/67, pp. 1431 – 1437, 1967

[8] K. Terzaghi, R. B. Peck, “Soil Mechanics in Engineering Practice,” *John Wiley & Sons*, 1. Corrected printing, 1968.

[9] K. J. Witt, R.-B. Wudtke, „hydraulisch bedingte Versagensformen in der Sohle von Baugruben“, *BAW & Bauhaus-Universität Weimar*, 2006

[10] Y. Zou, „Der vom Spannungszustand und vom Bodengefüge abhängige Erosionsdurchbruch bindiger Böden“, *Wasserwirtschaft* (90), pp. 554 – 559, 2000

Maximum Migration Distance of a Meandering Channel

P.-H. Yeh, N. Park, K.-A. Chang, H.-C. Chen, and J.-L. Briaud
Department of Civil Engineering, Texas A&M University, College Station, Texas, 77843-3136, U.S.A.

I. Introduction

The erosion of streambank is an old yet very complicated problem for geotechnical and hydraulic engineers. Being able to predict the migration distance of a river is crucial because it provides the information for planning, design, and protecting the structures such as bridges, buildings, and bank revetment near a meandering river. Several attempts have been made to estimate the river bankline retreat. Notable are those by Brice [1], Hooke [2], Hickin [3], Hickin and Nanson [4], Keady and Priest [5], Lagasse, Zevenbergen, Spitz, and Thorne [6].

The objectives of this study are to simulate river meandering using large-scale physical models and to develop a simple formula involving the associated physical properties affecting the meander processes to estimate the maximum distance of river meander migration.

II. Experiment Setup

The experiments were conducted in a large basin that is 36 m long, 23 m wide, and 1.5 m deep located in the Haynes Coastal Engineering Laboratory at Texas A&M University. The test area is 27m long, 14m wide and 30cm deep in the basin which was filled with sand. An idealized curved channel was dig from the sand bed to investigate the natural river erosion process. A constant head reservoir was connected to the entrance of the channel to provide the desired constant flow rate. A weir at the end of the channel was used to control the water depth in the channel. The experimental setup and test matrix with different geometric and hydraulic parameters is shown in Fig. 1 and Table I, respectively. The channel has an initial trapezoidal cross section with a bottom width of 40 cm, top width of 74.6 cm, bank slope of 30 degree, and depth of 15.6 cm. The channel slope was carefully controlled by adjusting the slope of the sand bed to maintain a constant initial water depth of h = 10 cm along the channel in each test case. Sand with a median particle diameter D_{50} = 0.32mm was used in the tests. Three most important parameters were varied in the tests: The width to radius ratio, R/W, the angle of the channel bend, Φ, and the Froude number, $Fr = U/\sqrt{gh}$ with U being the mean water velocity in the channel. The temporal and spatial variations of water-bank interface, the channel cross-section, and the water elevation were recorded.

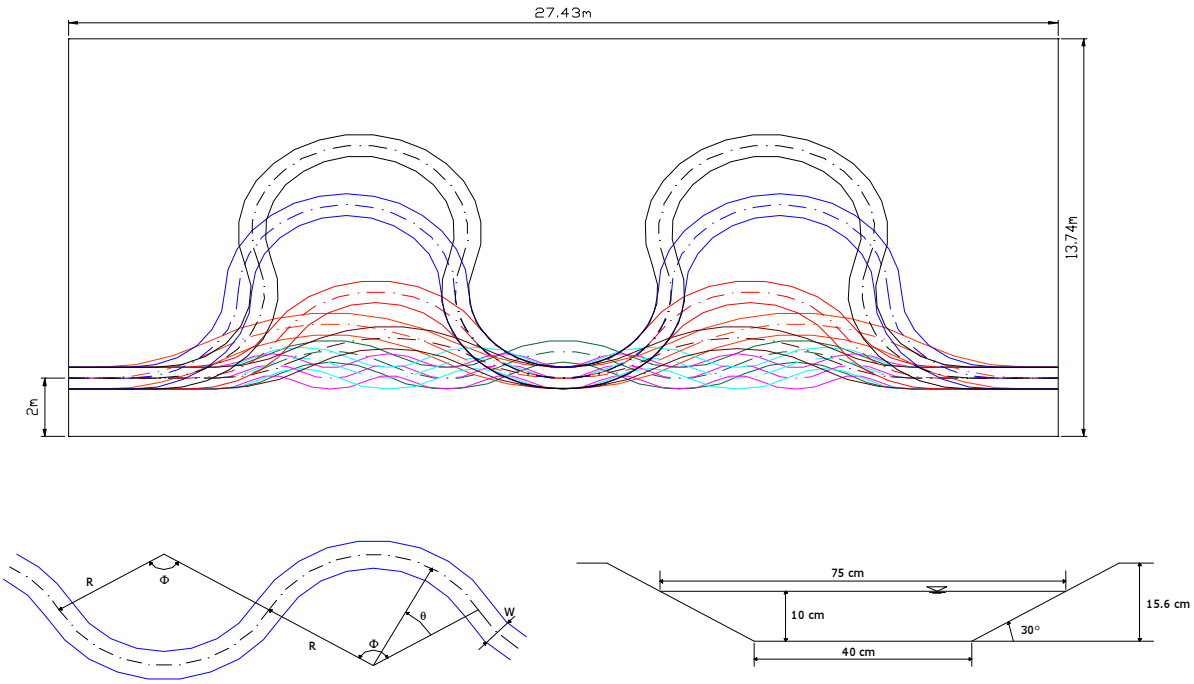

Figure 1. Experimental setup and channel configuration

Table I. Test Conditions

CASE No.	R / W	Φ	Fr No.
01	2	65˚	0.29
02	3	65˚	0.29
03	4	65˚	0.29
04	6	65˚	0.29
05	8	65˚	0.29
06	4	120˚	0.29
07	4	180˚	0.29
08	4	220˚	0.29
09	4	120˚	0.29
10	4	120˚	0.29

III. METHODOLOGY AND RESULTS

Figs. 2~4 show the variations of the channel plain form for three representative test cases with a different width to radius ratio, R/W, and bend angle Φ. From these figures, it is observed that the channel migrates in both the lateral and downstream directions; the channel bankline expands laterally and translates to the downstream. The location of maximum erosion distance is behind the channel apex. Figs. 5~6 plot the channel cross sectional profiles at two cross sections within the curved bend in CASE 03. Flow within the curved channel makes deep scour holes along the channel outer bank and sand deposits as the point bar in front of the toe of the inner bank. Due to the sediment supply from upstream and the bank erosion which aggrades the channel bed elevation and the bankfull flow rate running in the experiment, the bankline moves outwards on both sides of the bend with a larger distance at the outer bank. It is clearly seen that if the flow rate were to reduce, the water would flow in the deeper and lower sections of the channel and the water-bank interface would shift to the outer bank.

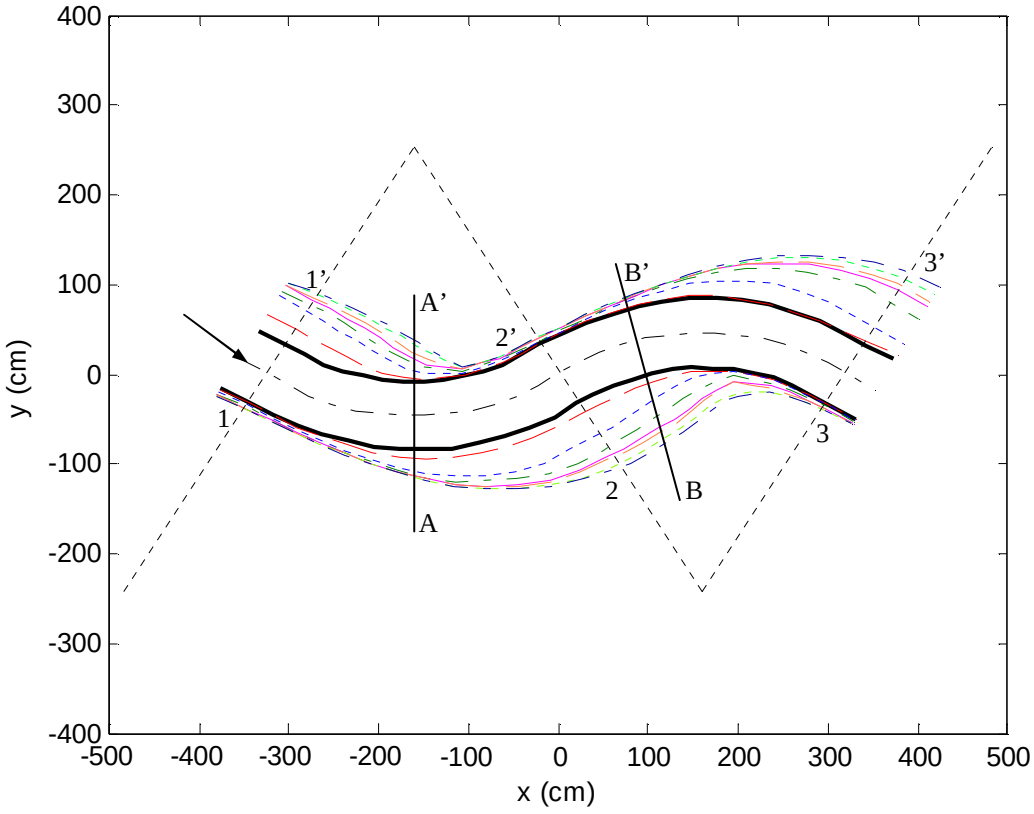

Figure 2. Channel plain form variations of CASE 03

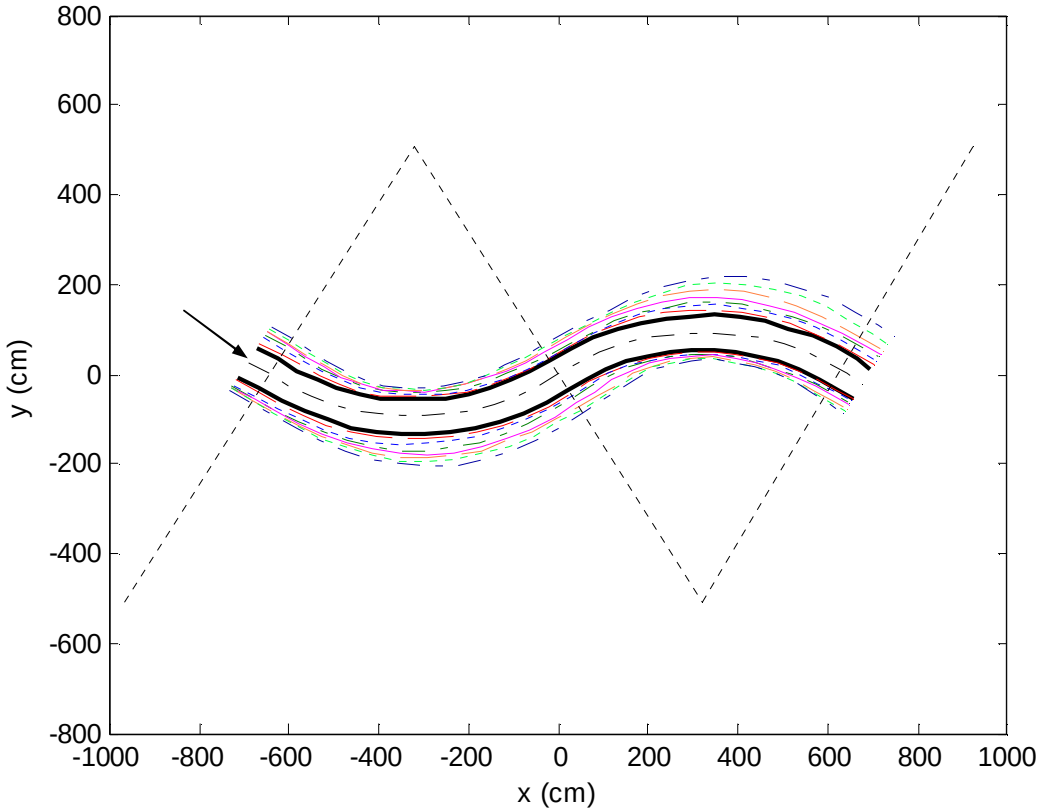

Figure 3. Channel plain form variations of CASE 05

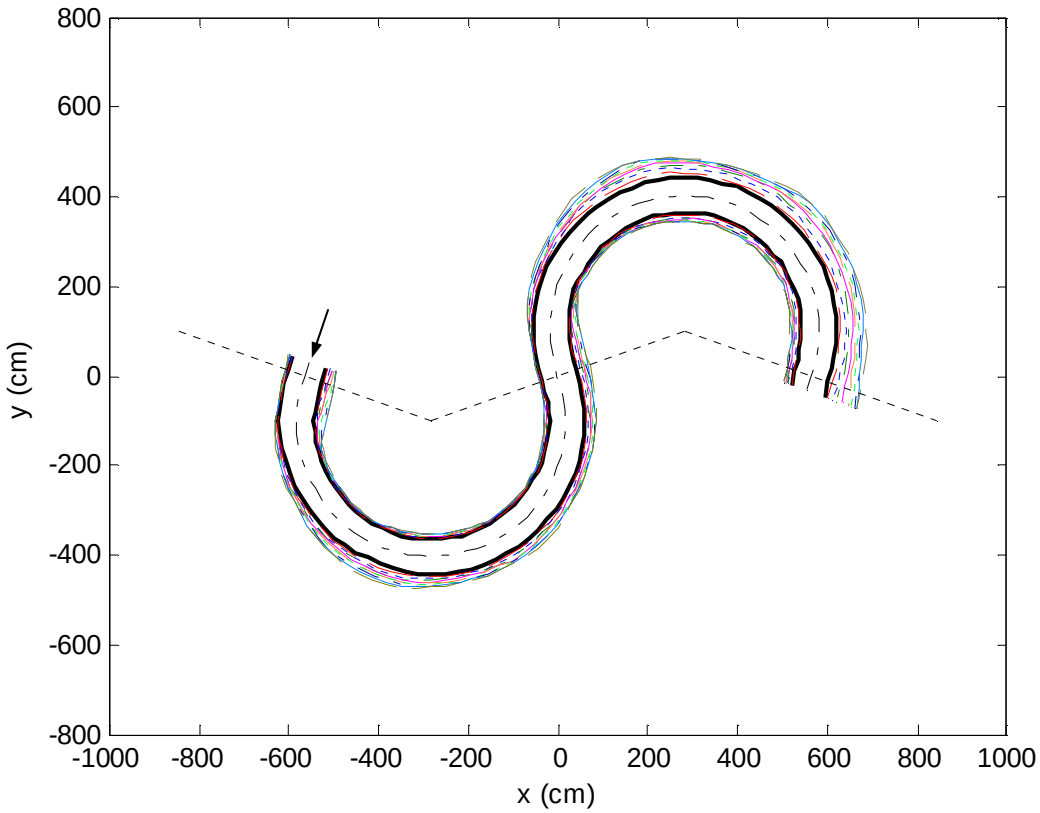

Figure 4. Channel plain form variations of CASE 06

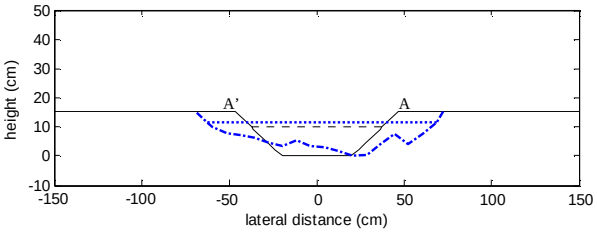

Figure 5. Cross sectional profile of section A-A' in Fig. 2

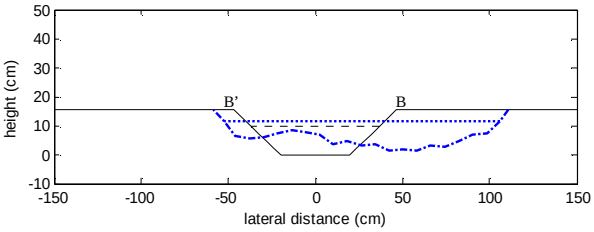

Figure 6. Cross sectional profile of section B-B' in Fig. 2

The erosion of a meander channel cross section underwent a constant flow rate may be expressed by a hyperbolic function. It has a higher initial erosion rate and gradually attains an equilibrium maximum displacement as follow:

$$m = \frac{t}{a + bt} \tag{1}$$

where m is the channel migration distance, t is time, and a and b are constants. The reciprocals of these two constants are indeed the initial migration rate, $\dot{M}_i$, and the maximum migration distance, $M_{\max}$, respectively, i.e., $1/a = \dot{M}_i$ and $1/b = M_{\max}$.

Figs. 7~9 show the bank erosion process in three different cross sections in CASE 03. When the flow starts to erode the bank, the erosion rate (slope) is greater in the earlier stage; the channel migration distance increases abruptly within a short time period. The erosion rate then decreases gradually as the process continues. Finally, the bankline stops moving and the cross sectional erosion reaches an equilibrium state. Figs. 7~9 also show that using the hyperbolic function may be a valid assumption on the description of the meander erosion of soil.

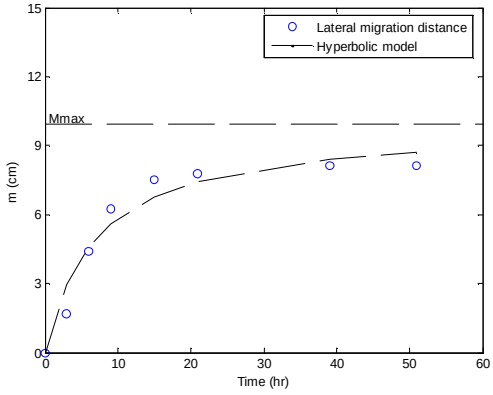

Figure 7. Bank erosion process of section 1-1' in Fig. 2

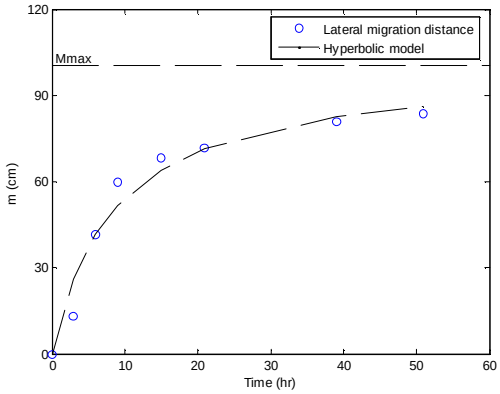

Figure 8. Bank erosion process of section 2-2' in Fig. 2

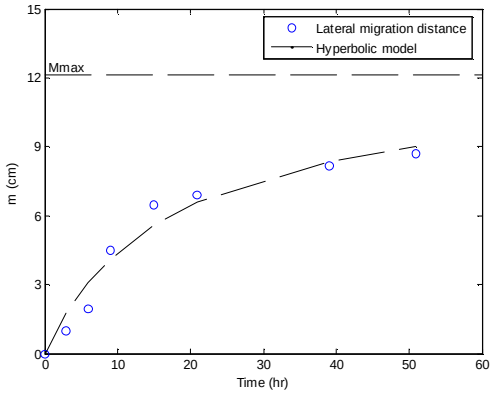

Figure 9. Bank erosion process of section 3-3' in Fig. 2

The maximum migration distance, $M_{\max}$, at each cross section was obtained by curve fitting the measured data points using the hyperbolic model. In the experiment, the data from the second outer bank of the channel and the following third inner bank were used. This is to make sure that the fully-developed secondary current in the channel was accounted for and the back water effect from the channel exit was negligibly small there. The non-dimensional result from one test case is shown in Fig. 10. The result shows $M_{\max}$ along the channel demonstrates a Gaussian distribution function with an obvious phase lag to the channel curvature.

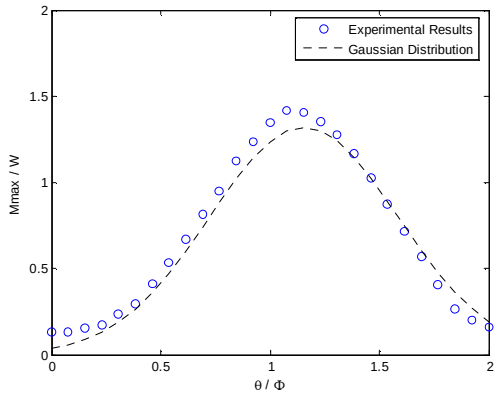

Figure 10. $M_{\max}$ measurement through curve fitting for Case 03

Since the fitted curve in Fig. 10 is close to a Gaussian distribution, the Gaussian distribution function was used

to calculate the values of M_{max} along the channel. The function can be expressed as

$$\frac{M_{max}}{W} = A\exp\left[-0.5\left(\frac{\theta/\Phi - \mu}{\sigma}\right)^2\right] \quad (3)$$

in which A, μ, and σ are three undetermined coefficients and θ/Φ is the normalized angle. Note that $\theta/\Phi > 1$ denotes the following inner bank from the target outer bank. The three parameters in the Gaussian distribution function then were correlated with the width to radius ratio, R/W, the bend angle, Φ, and the Froude number, Fr, using the multi-regression technique. A simple form of the relationship is chosen as:

$$\begin{aligned} A &= k_1(R/W)^{a_1}(\phi)^{b_1}(Fr)^{c_1} \\ \mu &= k_2(R/W)^{a_2}(\phi)^{b_2}(Fr)^{c_2} \\ \sigma &= k_3(R/W)^{a_3}(\phi)^{b_3}(Fr)^{c_3} \end{aligned} \quad (4)$$

where k_i, a_i, b_i, c_i are unknown coefficients. After taking logarithm on both sides of (4), it becomes three linear equations. The coefficients can then be determined using the least-square-error method. After fitting all the 10 cases in the study, the final equations for three parameters in the Gaussian distribution function are expressed as

$$\begin{aligned} A &= 24.2684(R/W)^{0.1457}(\phi)^{-0.5593}(Fr)^{0.7165} \\ \mu &= 32.5558(R/W)^{-0.5981}(\phi)^{-0.5828}(Fr)^{0.1188} \\ \sigma &= 0.3747(R/W)^{0.0888}(\phi)^{-0.0284}(Fr)^{-0.1480} \end{aligned} \quad (5)$$

With the use of Eqs. (3) and (5), M_{max} can be obtained along the channel. Fig. 11 shows a typical comparison between the prediction equations and the measurement in CASE 02. The result demonstrates that the predicted values of M_{max} are in good agreement with the measurement.

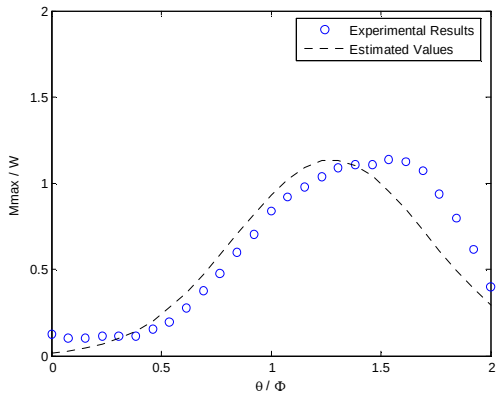

Figure 11. Comparison between prediction and measurement for CASE 02

IV. SUMMARY

Experiments were conducted to investigate the channel meandering migration by varying three important geometric and hydraulic conditions. The results show that the cross sectional erosion process could be modeled by a hyperbolic function. From this hyperbolic model, each cross section would attain an equilibrium state while the total erosion distance from the initial position to this equilibrium state was defined as the maximum migration distance, M_{max}. The magnitude of M_{max} along the channel bend displays a Gaussian distribution. The peak value of this Gaussian distribution appeared to be behind the apex of the original channel so creating a phase lag. A set of equations were obtained with the three parameters in the Gaussian distribution function determined using the experimental data by varying the initial geometric and hydraulic conditions. The equations were validated by comparing the M_{max} values with the experimental data.

REFERENCES

[1]. Brice, J. C., "Stream Channel Stability Assessment," *Rep. FHWA/RD-82/021*, 42 pp., Fed. Highway Admin., U.S. Dep. of Transp., Washington, D.C., 1982.

[2]. Hooke, J. M., "Magnitude and Distribution of Rates of River Bank Erosion," *Earth Surface Processes and Landforms*, Vol. 5, 1980, pp. 143-157.

[3]. Hickin, E. J., "The Development of Meanders in Natural River-Channels," *American Journal of Science*, Vol. 274, 1974, pp. 414-442.

[4]. Hickin, E. J., and Nanson, G. C., "Lateral Migration Rates of River Bends," *Journal of Hydraulic Engineering*, Vol. 110, 1984, pp. 1557-1567.

[5]. Keady, D. M., and Priest, M. S., "The Downstream Migration Rate of River Meandering Patterns," *Proceedings, 12th Mississippi Water Resources Conference*, Jackson, MS., 1977, pp. 29-34.

[6]. Lagasse, P.F., Zevenbergen, L.W., Spitz, W.J., and Thorne, C.R., "Methodology for Predicting Channel Migration," *NCHRP Project No. 24-16*, Ayres Associations for National Research Council, Transportation Research Board, National Cooperative Highway Research Program, Washington, D.C., 2003.

Prediction of scoured bed and sediment transport at equilibrium conditions in curved alluvial channels using advanced near wall models

J. Zeng, G. Constantinescu and L. Weber
Department of Civil & Environmental Engineering, IIHR-Hydroscience and Engineering,
The University of Iowa, Iowa City, IA 52242; USA

I. INTRODUCTION

Strongly curved alluvial river reaches and channels are especially affected by scour phenomena over time due to the presence of strong secondary motions in transverse sections. These secondary motions generate highly irregular bed profiles. As a consequence, the channel navigability and bank stability are strongly dependent on the evolution of the bed deformations in time. Additionally, sediment erosion and deposition in time can have important environmental repercussions for the river. Presence of hydraulic structures in regions of strong flow curvature tends to amplify local scour phenomena around these structures. Thus, prediction of the bathymetry and scour at equilibrium conditions is of great interest for river engineering applications.

Before considering complex applications involving river reaches of complex bathymetry, it is important to focus on simpler problems that retain most of the complexity of real applications, but allow to separate the effects of some of the main factors contributing to the bed evolution in real applications. In this paper we consider only curved channel bends of rectangular section with non-erodible banks in which a uniform thick layer of sand is originally present on the bottom of the channel.

In the region of strong channel curvature, due to the action of the centrifugal forces, the fluid particles follow a helical motion. As a consequence of the action of these forces, a pressure gradient is induced between the two banks in the region of high curvature such that the fluid and sediment particles move from the outer bank toward the inner bank in the near bed region. The main characteristic of the bed scouring in these bends is the formation of a point sand bar near the inner bank and of a pool at the outer part of the bend. The transversal distribution of the streamwise velocity is also affected by this strong secondary flow which induces a vertical velocity component in the transversal section and locally modifies the magnitude and direction of the bed shear stress. In the outer regions, where the bed shear stress is strongly amplified, local scour phenomena develop in time. The transversal slope increases until the force induced by the secondary current against the transversal slope is balanced by the (downwards) component of the gravitational force acting on the sediment particles in the same direction. At this point the flow and sediment transport are at equilibrium.

In the present paper, we try to predict the equilibrium flow, sediment transport and bathymetry using a fully three-dimensional (3D) Reynolds-Averaged Navier-Stokes (RANS) non-hydrostatic numerical model using advanced turbulence models ([1], [2]). The use of such a sophisticated model is needed because of the strong transverse non-uniformity of the flow in regions of high channel curvature and of the non-local nature of the sediment entrainment / deposition processes. The model is fully coupled. The bed changes induced by deposition / erosion phenomena affect the flow which, in turn, influences not only the advection of the suspended sediment but also the distribution of the bed shear stress. Thus, the distribution of the bed load component will also change.

II. BACKGROUND ON NUMERICAL MODELING OF FLOW AND SEDIMENT TRANSPORT IN ALLUVIAL CHANNELS

Due to their obvious limitations, 1D models are clearly not appropriate to predict bathymetry changes in curved alluvial channels in which large variations of the bed profiles are present in the transverse direction. Two-dimensional (2D) model are much more successful and are presently the most common approach used to predict flow and sediment transport in curved bends with movable beds. Duc et al. [3] gives a good description of some of the most popular of these 2D models based on finite differences, finite volume or the finite element approach ([4], [5]). Because of the information lost through the depth-averaging process, these 2D models are limited, to a degree or another, by the fact that they cannot account correctly for the effects of strong secondary currents on the flow and sediment transport, or for non-equilibrium effects. The usual way to account for some of these three-dimensional effects in 2D depth-averaged models is to introduce empirical secondary flow corrections. However, these corrections typically assume fully developed flow in the bend, require additional assumptions about the radius of curvature of the flow streamlines and do not account for the coupling between the primary and secondary flows. Thus, these models are in fact limited to flows with moderate streamline curvatures. Even in these cases, to obtain accurate results using these models lots of calibration of the empirical model constants is needed.

A more complex variant of these 2D models that tries to incorporate more of the original 3D characteristics of the

secondary flow into the depth-averaged model ([6], [7]) uses additional conservation equations for the moment of the momentum equations. These quasi-3D models can account in a physically more correct way for the redistribution of the bed shear stress magnitude caused by the momentum transfer between the streamwise and the transversal flows along the channel. Another quasi-3D model was proposed by van Rijn [8]. In his model the sediment transport was calculated in 3D while the horizontal mean flow was obtained using a 2D depth-averaged model. The vertical velocity profile needed in the sediment transport module was assumed to be logarithmic.

The next level of modeling is the use of fully 3D hydrostatic models. Gessler et al. [9] integrated a complex mobile-bed module into a 3D hydrostatic code CH3D that uses the σ-stretching technique in the vertical direction. Their mobile-bed module developed for sand-rivers included several processes such as aggradation and scour, bed-material sorting, and accounted for the movement of non-uniform sediment mixtures as bed load and suspended load. Though clearly incorporating more physics than 2D depth averaged models, the accuracy of the flow and sediment predictions using 3D hydrostatic models in strongly curved river reaches or channels, where strong secondary motions are present and separation may occur, is also limited.

One of the first successful applications of a fully 3D non-hydrostatic finite-volume model for movable bed applications was reported by Olsen [10]. The model successfully predicted the formation of the meandering pattern in an initially straight alluvial channel and accounted for wetting and drying caused by channel erosion / deposition. Both the suspended load and the bed load were simulated. The k-ε model with wall functions was used. The same code was used in [11] to predict flow and sediment transport in a narrow 90^0 curved bend. Another 3D non-hydrostatic finite-volume model that was used to calculate the equilibrium flow, sediment transport and bathymetry in curved channel bends was proposed by Wu et al. [12]. Their modeling of the bed load was more sophisticated and was based on the non-equilibrium method proposed in [8]. The water surface deformation was calculated from a 2D Poisson equation for the surface height obtained from the depth-averaged 2D momentum equations. The k-ε model with wall functions and corrections for rough surfaces was used. The model was subsequently used in [13] to predict the flow and suspended sediment transport for the reservoir generated by the dam of the Three Gorges Project on the Yangtze River.

Because of the empiricism related especially to the bed load transport modeling, model validation and a certain degree of calibration (though much more reduced than the one required by 2D depth-averaged or quasi-3D models) is necessary even in fully 3D models. Thus, comparison of computed results with experimental data corresponding to well-controlled laboratory experiments is essential before application of the model to predict equilibrium flow, sediment and scoured bed geometry in realistic river reaches.

III. FLOW SOLVER

The incompressible RANS and turbulence transport equations are first transformed in generalized curvilinear coordinates. However, the primitive variables (Cartesian velocity components, V_i) for which the momentum equations are solved are left unchanged (partial transformation approach). The continuity and momentum equations are:

$$J\frac{\partial}{\partial \xi^j}\left(\frac{V^j}{J}\right) = 0 \tag{1}$$

$$\frac{\partial Q}{\partial t} + A_j\frac{\partial Q}{\partial \xi^j} - J\frac{\partial E_{vj}}{\partial \xi^j} + H_p = 0 \tag{2}$$

where x_i are the Cartesian coordinates and ξ^j are the curvilinear coordinates. In equation (2), $Q=(V_1,V_2,V_3)^T$ is the Cartesian velocity vector; J is the Jacobian $J=\partial(\xi^1,\xi^2,\xi^3,)/\partial(x_1,x_2,x_3)$, $V^i = V_j\xi^j_{x_i}$ are the contravariant velocity components, A_j= diag(V^1, V^2, V^3) and $E_{vj} = (E^1_{vj}, E^2_{vj}, E^3_{vj})$ are the vectors containing the viscous and turbulence fluxes and, finally, H_p is the pressure gradient vector

$$H_p = \left(\xi^k_{x1}\frac{\partial \psi}{\partial \xi^k}, \xi^k_{x2}\frac{\partial \psi}{\partial \xi^k}, \xi^k_{x3}\frac{\partial \psi}{\partial \xi^k}\right)^T . \tag{3}$$

The governing equations are non-dimensionalized using a length scale H_0 (water depth at the inlet) and a velocity scale U (bulk velocity in the inlet section) such that formally the Reynolds number ($Re=UH_0/\nu$) replaces the molecular viscosity ν, and the Froude number ($Fr=U/(gH_0)^{0.5}$) is used to scale the free surface deformations. The modified pressure χ is defined as $\chi=p+2/3k$ and the effective piezometric pressure P is defined as $P=p/\rho+z/Fr^2-2/3k$, where p is the pressure, z is the free surface elevation and k is turbulence kinetic energy. The Froude number enters the solution through the free-surface boundary condition assuming that the deformable free surface model is turned on (for more details on the free surface module see [1]). The velocity components are set equal to zero on all solid surfaces. At the outflow all variables are extrapolated from the interior. The pressure is extrapolated from the interior of the domain on all boundaries except at the free surface.

The eddy viscosity in the simulations discussed in the present paper is provided by the k-ω (SST) model. As the standard form of the k-ω (SST) model was used, only the implementation of the boundary conditions is discussed. The turbulence kinetic energy k is set equal to zero at the walls. For smooth surfaces, ω is calculated as $\omega = 800\nu/(\Delta n_1^2)$ where Δn_1 is the normal distance to the wall of the first grid point off the wall. For rough

surfaces, $\omega = 2500\nu/(k_s)^2$ for $k_s^+ < 25$ and $\omega = 100u_*/k_s$ for $25 < k_s^+$, where k_s is equivalent roughness height ($k_s^+ = u_* k_s/\nu$) and u_* is the friction velocity.

The equivalent bed roughness is estimated using a formula proposed by van Rijn [8] in the case in which small bed forms are present:

$$k_s = 3d_{90} + 1.1\Delta(1 - e^{-25\psi}) \tag{4}$$

where the first term accounts for the sand grain roughness contribution and the second term represents the bed form contribution. In equation (4), $\psi = \Delta/\lambda$ where Δ and λ are the height and length of the sand waves, respectively. Following Wu et al. [12], the length λ is assumed to be $\lambda = 7.3H$ and the parameter ψ is estimated from:

$$\psi = \Delta/\lambda = 0.015(d_{50}/H)^{0.3}\left(1 - e^{-0.5T}\right)(25 - T) \tag{5}$$

in which H is the local water depth, d_{50} and d_{90} are the median and 90% diameters of the bed material, and T is the non-dimensional excess shear stress. Its expression is given in [8] and [1].

A fractional step method is used to solve the RANS equations. All terms in the pressure Poisson equation are discretized using second-order accurate central differences. The momentum and turbulence transport equations are discretized using second order accurate upwind differences for the convective terms. All other operators are calculated using second-order central discretizations. All terms are treated implicitly, including the source terms in the transport equations for turbulence quantities. To accelerate the convergence of the resulting system of equations toward steady state (equilibrium), local time-stepping techniques are used. An approximate factorization technique is used to simplify the inversion of the discrete form (left hand side) of the momentum, pressure-Poisson and turbulence transport equations. The equations are solved implicitly using the alternate-direction-implicit (ADI) method. The implementation of the deformable free surface module in which the proper kinematic and dynamic boundary conditions are applied at the top boundary is described in [1].

IV. SEDIMENT TRANSPORT AND MOVABLE BED MODELS

An advection-diffusion scalar transport equation with an additional settling-velocity source term is solved to determine the local sediment concentration C and the suspended sediment fluxes at the top of the bed load layer for simulations in which the suspended sediment load cannot be neglected. The equation is not solved up to the wall, as are the momentum equations, but rather up to the interface with the bed load layer ($\delta(x,y)$) which typically corresponds to a k=constant surface in the computational domain. In curvilinear coordinated, the equation is:

$$\frac{\partial C}{\partial t} + V^j \frac{\partial C}{\partial \xi^j} - \omega_s \delta_{3i} \frac{\partial C}{\partial \xi^j}\frac{\partial \xi^j}{\partial x_i} - J\frac{\partial}{\partial \xi^j}\left(\frac{g^{ij}}{J}\left(\frac{\nu + \nu_t}{\sigma_c}\right)\frac{\partial C}{\partial \xi^i}\right) = 0 \tag{6}$$

where ω_s is the setting velocity of the sediment, δ_{3j} is the Kronecker delta symbol with $j=3$ indicating the vertical direction and σ_c is the Schmidt number. Its role is to relate the sediment (turbulent) diffusivity to its (eddy) viscosity. At the free surface, the total vertical flux of suspended sediment is set to zero:

$$\left(\frac{\nu + \nu_t}{\sigma_c}\right)\frac{\partial C}{\partial \xi^j}\frac{\partial \xi^j}{\partial x_3} + \omega_s C = 0 \tag{7}$$

At the interface between the suspended sediment and the bed load layers situated not far, but not necessarily at the reference level $z=a$, following van Rijn [8] and Wu et al. [14], the entrainment rate is assumed to be equal to the one under equilibrium conditions. The total vertical sediment flux at the interface is equal to the net sediment transport (deposition minus entrainment) across the interface. This can be written as

$$\left(\frac{\nu + \nu_t}{\sigma_c}\right)\frac{\partial C}{\partial \xi^j}\frac{\partial \xi^j}{\partial x_3} + \omega_s C = D_b - E_b = \omega_s C - \omega_s C_{b**} \tag{8}$$

where C_{b**} is the equilibrium concentration at $z=\delta$, $D_b = \omega_s C_b$ is the deposition rate and $E_b = \omega_s C_{b**}$ is the entrainment rate at the top of the bed layer. The value of C_{b**} can be calculated assuming Rouse formula to be valid between the reference level where $C=C_{b*}$ ($z=a$) and the interface between the bed and the suspended load layers ($z=\delta(x,y)$). There is no unique way to choose the reference level a. In some cases it is taken equal to the bed roughness, in other cases it is taken as a percentage of the total depth. At the inlet section a concentration profile needs to be prescribed, while at the sidewalls and outlet a zero gradient boundary condition is imposed.

The empirical formulas proposed in [8] are used to estimate the equilibrium concentration at the reference level (C_{b*}) needed to calculate C_{b**} in (8), the equilibrium bed load transport rate (Q_{b*}) and the non-equilibrium adaptation length (L_s). Their detailed expressions are also given in [1] and [2] along with several methods to numerically estimate the local bed shear stress τ_*. The

equilibrium bed load transport rate and the non-equilibrium adaptation length are needed to close the non-equilibrium bed transport model (see (10) below). Following [12], the mass balance equation for the sediment within the bed load layer, in which the storage term is neglected, is:

$$(1-p')\frac{\partial z_b}{\partial t} - D_b + E_b = -\nabla Q_b = \\ -J_b\left(\frac{\partial}{\partial \xi}\left(\frac{Q_{b\xi}}{J_b}\right) - \frac{\partial}{\partial \eta}\left(\frac{Q_{b\eta}}{J_b}\right)\right) = 0 \quad (9)$$

In the above equation p' is the porosity, J_b is the Jacobian of the geometric transformation in the bed load layer, $(J_b = \partial(\xi, \eta)/\partial(x, y))$, z_b is the bed level above a datum, $Q_{b\xi}$ and $Q_{b\eta}$ are the components of the bed-load transport in the two directions. Then, in the present model we use the same non-equilibrium bed-load model as in [12] in which the relation between the bed change due to deposition from the bed load layer and the bed load transport rate is:

$$(1-p')\frac{\partial z_{b\_bed\_load}}{\partial t} = \frac{1}{L_s}(Q_b - Q_{b*}) \quad (10)$$

such that the total change in the bed elevation is:

$$(1-p')\frac{\partial z_b}{\partial t} = D_b - E_b + \frac{Q_b - Q_{b*}}{L_s}. \quad (11)$$

The equation for the bed load rate Q_b is derived from (9) in which we made the substitution corresponding to the model assumed in (11):

$$\frac{(Q_b - Q_{b*})}{L_s} + \nabla Q_b = 0 \quad (12)$$

Equation (12) which is solved to determine the bed load Q_b is the same for the case when the suspended sediment transport module is active and for the case when the suspended sediment transport can be neglected.

To close the model, one has to express $Q_{b\xi}$ and $Q_{b\eta}$ in (9) and (12) as a function of Q_b. When the bed becomes sloped, the gravitational force on the particles will resist the shear force to further carry the particles to the upper part of the slope. The sediment transport direction will deviate from the local direction of the bed shear stress. Especially for simulations in which the suspended sediment load becomes comparable or larger than the bed load, it is important to account for bed slope effects on the total load Q_T and not only on the bed load component, as it is generally done. To do that, in our model we define the total load (considered as a vectorial relationship in the horizontal directions) as simply:

$$Q_T = Q_b + Q_S \quad (13)$$

where Q_S is the suspended sediment load flux in the local water column from the top of the bed layer to the free surface. By taking the divergence of (13) we obtain, using the mass conservation equation in the water column corresponding to the suspended sediment domain (between z=δ(x,y) and free surface) and neglecting the storage term,

$$\nabla Q_T = \nabla Q_b + \nabla Q_S = \nabla Q_b - D_b + E_b. \quad (14)$$

Then, we rewrite (12) for the total load using (13) and (14) as

$$\frac{1}{L_s}(Q_T - Q_S - Q_{b*}) + \nabla Q_T + D_b - E_b = 0. \quad (15)$$

As the new variable in (15) is Q_T, we rewrite (11) as

$$(1-p')\frac{\partial z_b}{\partial t} = -\nabla Q_T \quad (16)$$

where use was made of (9) and (14). At this point the model is closed, provided that we are able to estimate Q_S from the concentration field and a formula to split Q_T after the two horizontal directions (ξ, η) is available.

To evaluate Q_S, one simply has to apply the definition to calculate the two components of the flux of suspended sediment in the two horizontal directions (x,y) as

$$Q_{Sx} = \int_\delta^h \left(uC - \frac{\nu + \nu_t}{\sigma_c}\frac{\partial C}{\partial x}\right)dz' \quad (17)$$

$$Q_{Sy} = \int_\delta^h \left(vC - \frac{\nu + \nu_t}{\sigma_c}\frac{\partial C}{\partial y}\right)dz'. \quad (18)$$

The magnitude of the suspended sediment flux is:

$$Q_S = \sqrt{\left(Q_{Sx}^2 + Q_{Sy}^2\right)}. \quad (19)$$

To introduce bed slope effects directly for Q_T, the formula proposed by Sekine and Parker [14] for bed slope effects affecting the bed load transport is used, but with Q_b replaced by Q_T:

$$Q_{T\eta} / Q_{T\xi} = \left(\sin\theta_b - \beta \frac{\partial z_b}{\partial l_\eta} \right) / \left(\cos\theta_b - \beta \frac{\partial z_b}{\partial l_\xi} \right) \qquad (20)$$

where $\theta_b = \tan^{-1}(\tau_{*\eta} / \tau_{*\xi})$ is the angle between the bed shear stress vector and the streamwise direction, $\beta = \beta^*(\tau_c^*/\tau_L^*)^m$, τ_L^* is the nondimensional longitudinal Shield stress $\tau_L^* = \tau_* \cos\theta_b / \rho R g d_{50}$, $R = \rho_s/\rho - 1$, ρ_s is the sediment density, ρ is the water density, the critical shear stress $\tau_c^* = \rho u_{*cr}^2$ is given by Shields diagram, m is a coefficient (m=1), $\beta^* = \alpha_G / \tau_c^*$, $\partial z_b/\partial l_\xi$, $\partial z_b/\partial l_\eta$ are the streamwise and transverse bed slopes, and α_G is a coefficient typically in the range 0.45-0.7. In the present simulations we used α_G=0.6.

Thus, the divergence operator ∇Q_T can be calculated in curvilinear coordinates (ξ,η). Once z_b is calculated from (16), the grid points between the bed level and the free surface are redistributed vertically based on the new positions of the water surface and bed level elevations.

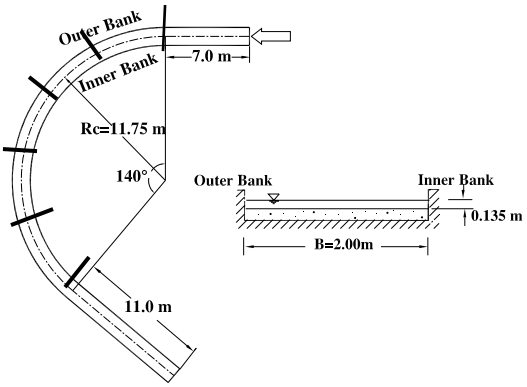

Figure 1. Flume layout and cross section geometry at the start of the 140^0 curved bend experiment of Olesen [15].

V. RESULTS

The equilibrium flow, sediment transport and scoured bed in the 140^0 curved bend of rectangular section (see sketch in Figure 1) studied experimentally by Olesen [15] are computed in the present study. Specifically, we validate our method by computing the flow corresponding to the experimental conditions in test case T4 in [15]. The curvature radius of the flume in the curved region was 11.75m. Both ends of the curved region (bend) were connected to straight channels toward the inflow and outflow sections. Their lengths were 7m and 11m, respectively. The width of the channel was B=2.0m wide. The inflow discharge was $0.118 m^3/s$. The mean inlet velocity was U=0.44 m/s and the water depth at the inlet was H_0=0.135m. The Froude and Reynolds numbers upstream of the curved region were 0.38 and 59,400, respectively. The incoming flow was fully turbulent. The flume bed in the experiment was initially leveled with a layer of relatively uniform sand whose thickness was 0.3m. The mean sand diameter was d_{50}=0.80mm (d_{90}=1.61mm). The main parameters of the experiment are summarized in Table 1. The experiment was run for approximately 72 hours to reach equilibrium steady state. In the experiment it was observed that the sediment moved mainly as bed load. The bathymetry and water levels were then measured at several selected sections. These measurements are used for validation of the present numerical model.

The flow was simulated on a computational mesh with close to 350,000 grid points (99x101x35 mesh points in the streamwise, spanwise and vertical directions, respectively). Two simulations were performed using the k-ω (SST) model. In the first simulation the contributions of both the bed load and the suspended sediment transport were considered (kω_total_load). In the second simulation only the bed load transport was considered, and the suspended sediment module was turned off. One of the goals of the present study is to investigate if the predictions of the equilibrium scour bathymetry are closer to experiment when considering both modes of sediment transport for a test case in which the suspended sediment transport is not thought to be important.

In both simulations the bottom roughness was estimated by using (4) and (5) in the initial straight part of the channel. The value of the bottom roughness k_S was found to be close to 0.0185m (~$20d_{90}$), corresponding to $k_S^+ \sim 920$ (well into the fully rough regime). The mean nondimensional value of the friction velocity at the bed was close to 0.11 in the same initial region. The side walls were considered smooth. The first points off the side-walls and channel bottom were situated at $\Delta n/H_0 \sim 0.0002$ ($\Delta n^+ \sim 0.7$).

Fully developed turbulent flow was specified at the inflow section. The profiles of the streamwise velocity and turbulent quantities were obtained from a preliminary simulation of the flow at the same Reynolds number in a straight periodic channel of identical section to that of the curved channel at its inlet section. Non-gradient conditions were used at the outlet to impose the velocity, concentration profile above the bed load layer and the value of the bed load transport rate.

The experimentally measured value of the bed-load transport rate (Q_b=0.0205 Kg/(ms)) was used to specify the inlet boundary condition for bed load transport. The suspended sediment concentration at the inlet was set equal to zero over the whole section as no measurements were available and the incoming flow is assumed to contain very little sediment above the bed load layer. The Schmidt number was equal to 0.85. The reference level corresponding to the thickness of the bed load layer (a) was assumed to be close to $3d_{90}$. This made that 16 mesh points were contained in the vertical direction inside this

TABLE 1. THE MAIN PARAMETERS OF THE EXPERIMENT CONDUCTED BY OLESEN [15]

Test Case	B (m)	H_0 (m)	U (m/s)	C (Chezy) ($m^{0.5}/s$)	I (surface slope)	d_{50} (mm)	d_{90} (mm)	Fr	Re
T4	2.0	0.135	0.44	29.9	$1.58x10^{-3}$	0.80	0.855	0.38	59,400

layer. This is different from models employing wall functions in which the bed load transport is generally assumed to occur within the first layer off the wall.

Similarly to the experiment, the simulations started from an initial flat bed and continued until equilibrium flow and bathymetry were reached in the curved channel. However, as we are using a steady state model in which local time stepping techniques are used to accelerate the convergence of the solution toward steady state, the transient in our numerical simulation is not expected to follow the evolution of the flow and bathymetry in the experiment. Only the steady state solution is expected to be close to the flow and bathymetry observed at equilibrium conditions in the experiment.

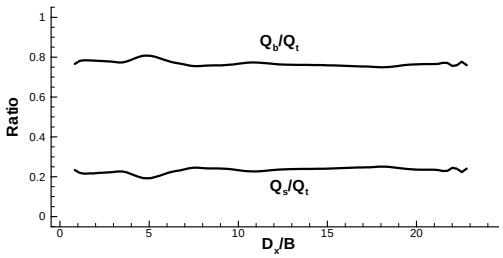

Figure 2. Predicted ratios of suspended sediment load and bed load to the total load along longitudinal direction in the kω_bed_load simulation.

Figure 2 shows the variation of the ratio of the cross-section averaged suspended sediment load to the total load (Q_s/Q_t) in the longitudinal direction for the kω_total_load simulation. The average value of this ratio for the simulated flow conditions is close to 0.2 over the whole length of the curved bend, confirming the fact that the suspended sediment component does not play an essential role in the overall sediment transport process.

The streamwise variation of the relative water depth at three positions situated 0.15B from the two banks and along the center line of the channel is shown in Figure 3. The longitudinal distance D_x, nondimensionalized by the width B of the channel, is measured along the centerline from the entrance in the straight reach of the channel. The entrance into the curved bend is situated at D_x=3.5B and the entrance into the downstream straight reach is situated around 18B. As no significant differences were observed in the distributions predicted by the two simulations, only the kω_total_load simulation results are shown. Overall, the predictions of the longitudinal water depth levels within the bend are in good agreement with measurements. In particular, the predictions near both banks are very close to the experiments in the region around the bend end ($15<D_x/B<20$). At the location situated 0.15B from the outer bank, the deepest scour is observed to occur in the experiment at $D_x/B\sim7$. The water depth at that location is $1.7H_0$. In the simulation the maximum scour occurs slightly downstream at $D_x/B\sim7.6$ and the water depth is somewhat underpredicted ($1.55H_0$). At the inner bank side, where a deposition sand bar has formed, the minimum water depth is observed to occur at $D_x/B\sim8.2$ in both simulation

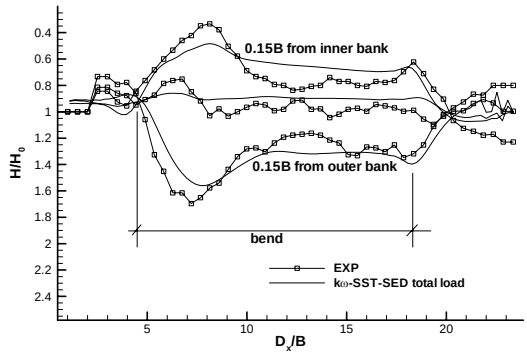

Figure 3. Comparison of longitudinal relative water depths at three positions inside the channel bend. H is local water depth. Only the results of simulation kω_bed_load are shown.

and experiment. However, at that location the flow is shallower in the experiment ($H=0.45H_0$) compared to simulation ($H=0.5H_0$). A second region, where some disagreement is observed between the simulation and experiment, is situated between D_x=10B and D_x=15B. Over this region the scour at the outer bank and the deposition at the inner bank are larger in experiment compared to simulation by about $0.1H_0$.

The numerical predictions of the water depth levels are compared with the measurements in Figure 4 at 12 cross-sections along the channel. The cross-sections cover the entire curved region of the channel, starting at its entrance (D_x/B=3.5), and the first 3.5B of the downstream straight reach (Figure 1). The transverse (lateral) slope gradually increases from zero at the bend entrance, to a maximum value that occurs at streamwise locations at which $9<D_x/B<10$. This region corresponds to the location of the highest sand bar and deepest scour hole (maximum water depth variation in the section is approximately 20cm in the experiment). The slope then slowly decays until $D_x/B\sim15$ and then remains almost constant until the end of the bend region (D_x/B=18.5). Once the flow enters the downstream straight reach, the

lateral slope returns quickly to horizontal and then becomes slightly negative. For example, in the section somewhat underpredicted in the simulations. For example, the maximum scour depth at the outer bank is

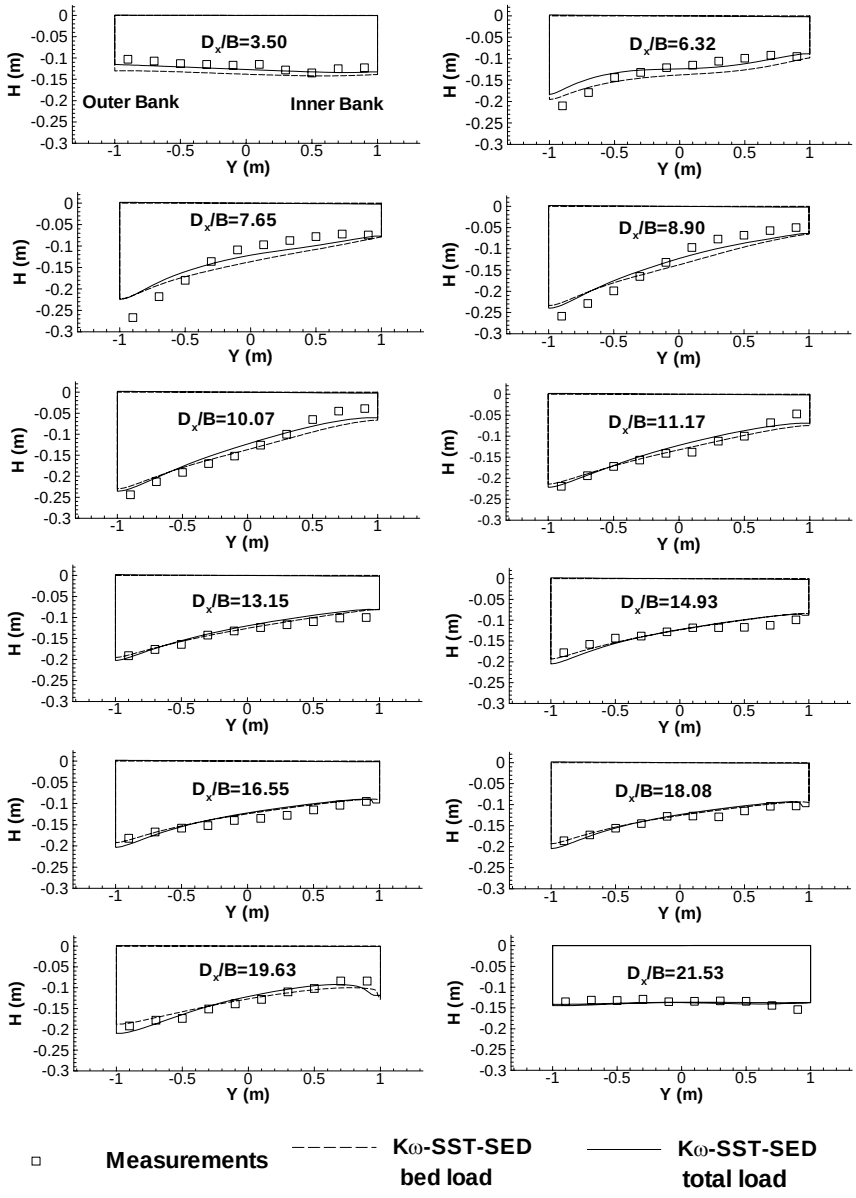

Figure 4. Comparison between predicted (kω_total_load and kω_bed_load simulations) and measured water depth levels at equilibrium conditions at different cross sections along the curved bend.

situated at $D_x/B=21.53$ the water depth is slightly higher near the inner bank, as the scour and deposition patterns switch to the opposite bank.

The variations of the water depth profile in the transversal direction predicted by the two simulations are found to be in good agreement with the ones obtained from experiment over the whole bend. The only region where some noticeable disagreement is observed is situated between $D_x/B=6$ and $D_x/B=11$. Over this region the largest differences in elevation between the two banks are observed in experiment. Though this is also true for the simulations, the maximum difference between the water depths in the regions close to the two banks is underpredicted by 1.5cm at $D_x/B=6.32$, by 4cm at $D_x/B=7.65$ and by 2.5cm in the section at $D_x/B=8.9$. Though the prediction of the maximum scour depth is very close to the experimental value at $D_x/B=10.07$, the water depth starts being overpredicted at the inner bank, where the level of the sand bar is about 1.5cm lower compared to the experiment.

As expected, the inclusion of the suspended sediment transport in the model did not have a large effect on the final equilibrium bathymetry. Still, the water depths predicted by the kω_total_load simulation appear to be slightly closer to the experiment in the middle of the channel ($-0.3m<Y<0.7m$) in the sections situated at

$D_x/B=7.65$ and $D_x/B=8.9$ where both simulations underpredicted the overall bed slope in the transversal section. The kw_bed_load simulation appears to overpredict by about 1cm the water depth at the entrance in the bend ($D_x/B=3.5$) over the whole section compared to experiment and to the kω_total_load simulation results.

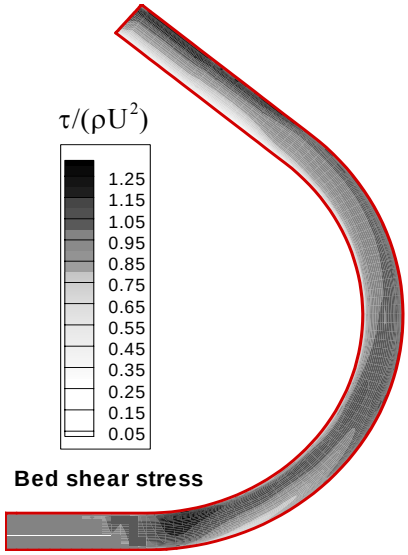

Figure 5. Distribution of the non-dimensional bed shear stress ($\tau/\rho U^2$) at equilibrium conditions in the kω_total_load simulation.

Figure 5 shows the contours of the predicted bottom shear stress ($\tau/\rho U^2$) inside the channel bend at equilibrium for the kω_total_load simulation. This distribution can not be obtained in an easy and accurate way from experiment. The distribution for the case in which only the bed load transport is considered was found to be quite similar and is not shown. The values of the bed shear stress in Fig. 4 are non-dimensionalized by the mean value of the bed shear stress at the inlet section obtained from the periodic straight channel simulation. As expected, a patch of relatively high bed shear stress values is present at the entrance into the bend closer to the inner wall. This happens because the position of the maximum streamwise velocity in sections close to the entrance into the curved region is situated closer to the inner wall. In fact, this effect, observed around the upstream part of the curved channel region in our simulation at equilibrium conditions, is present even for flat bed channels and was explained, among others, by Henderson [16] using Euler equations. As one moves downstream, the area of high bed shear stress gradually switches toward the deeper outer wall region inside the bend region.

For polar angles larger than 100^0 inside the bend, the maximum bed shear stress is observed to occur close to the outer bank. Interestingly, the maximum value in cross sections situated past the end of the curved region continues to increase for some distance in the downstream straight reach due to the transverse momentum acquired by the flow inside the bend. As one moves further downstream, the position of the maximum bed shear stress starts moving again toward the center of the section. Sane is true for the depth averaged streamwise velocity distribution (not shown). However, as observed from Fig. 4 this process is very slow and the distance needed for the distributions of the (depth-averaged) streamwise velocity and bed shear stress to recover the symmetrical shapes corresponding to fully developed flow in a straight channel is estimated to be of the order of 15-20B.

VI. SUMMARY

A fully 3D non-hydrostatic model developed by Zeng et al. [1,2] to predict the flow, free surface deformation, bed load, suspended sediment transport and bed morphology in open channels at equilibrium conditions was tested for the case of the flow in an 140^0 curved bend studied experimentally by Olesen [15]. One of the novelties of the present model is the use of RANS closures in versions that do not necessitate the use of wall functions and in which the small-scale bed roughness effects are incorporated via the specification of the wall boundary conditions.

The simulations confirmed the experimental observations that showed that most of the sediment moves as bed load. The suspended sediment load was estimated to contribute only 20% to the total sediment load for the flow and geometrical conditions considered in the test case. Consequently, the inclusion of the suspended sediment module in the numerical model did not affect significantly the equilibrium flow and bathymetry predictions. Comparison of the simulation results with the experimental data showed that the model was able to predict reasonably well the water depth levels over the whole length of the channel. A slight underprediction of the mean transverse bed slope was observed in the upstream part of the bend around the region where maximum scour occurs. The reason was an underprediction of the maximum scour depth at the outer bank, or an overprediction of the minimum water depth at the inner bank.

The model is being applied to predict flows in curved open channels with substantial amounts of suspended sediment transport and with very strong curvature in which three-dimensional effects are expected to be even more important than the ones present in the application considered in the present paper. Eventually, the goal will be to use the present model to predict equilibrium bathymetry in straight and curved channels containing hydraulic structures (e.g., bridge piers, bridge abutments, spur dikes, intakes, etc.) where local scour phenomena are important.

ACKNOWLEDGMENT

The authors would like to thank Professor A. Jacob Odgaard from IIHR-Hydroscience and Engineering, The University of Iowa for his insightful advice related to different aspects of this study.

REFERENCES

[1] Zeng, J., Constantinescu, G. & Weber, L.J. 2005a, A fully 3D non-hydrostatic model for prediction of flow, sediment transport and bed morphology in open channels, XXXIst International Association Hydraulic Research Congress, Seoul, Korea.

[2] Zeng, J., Constantinescu, S.G. and Weber, L.J. 2005b. Validation of a computational model to predict suspended and bed load sediment transport and equilibrium bed morphology in open channels. River and Coastal Estuarine Morphology Conference, The University of Illinois, Urbana Champaign, Illinois.

[3] Duc, B.M., Wenka, T and Rodi, W. 2004, Numerical modeling of bed deformation in laboratory channels, *J. Hydraulic Engineering*, 130(9), 894-904.

[4] Ghamry, H.K. and Steffler, P.M. 2005, 2D depth-averaged modeling of flow in curved open channels. *J. Hydraulic Research*, IAHR, 43(1), 44-55.

[5] Choi, S.U., Kim, T.B. and Min, K.D. 2005, 2D finite element modeling of bed elevation change in a curved channel, River and Coastal Estuarine Morphology Conference, The University of Illinois, Urbana Champaign, Illinois.

[6] Kassem, A.A. and Chaudhry, M.H. 2002, Numerical modeling of bed evolution in channel bends. *J. Hydraulic Engineering*, ASCE, 128(5), 507-514.

[7] Vasquez, J.A., Millar, R.G. and Steffler, P.M. 2005, Vertically-averaged and momentum model for alluvial bend morphology, River and Coastal Estuarine Morphology Conference, The University of Illinois, Urbana Champaign, Illinois.

[8] van Rijn, L.C. 1987, Mathematical modeling of morphological processes in the case of suspended sediment transport, *Delft Hydraulics Communication* No. 382, The Netherlands.

[9] Gessler, D, Hall, B., Spasojevic, M., Holly, F., Pourtaheri, H, Raphelt, N. 1999, Application of a 3D mobile bed, hydrodynamic model, *J. Hydraulic Engineering*, ASCE, 125(3), 737-749.

[10] Olsen, N.R. 2003, 3D CFD modeling of self-forming meandering channel, *J. Hydraulic Engineering*, 129(5), 366-372.

[11] Ruther, N. and Olsen, N.R. 2005, 3D modeling of sediment transport in a narrow 90^0 channel bend, *J. Hydraulic Engineering*, 131(10), 917-920.

[12] Wu, W., Rodi, W. and Wenka, T. 2000, 3D numerical modeling of flow and sediment transport in open channels, *J. Hydraulic Engineering*, 126(1), 4-15.

[13] Fang, H. and Rodi, W. 2003, 3D calculations of flow and suspended sediment transport in the neighborhood of the dam for the Three Gorges Project Reservoir in the Yangtze River, *J. Hydraulic Research*, 41(4), 379-394.

[14] Sekine, M. and Parker, G. 1992, Bed load transport on transverse slope, *J. Hydraulic Engineering*, 118(4), 513-535.

[15] Olesen, K.W. 1985, Experiments with graded sediment in the DHL curved flume, Report R 657 – XXII M 1771, Delft Hydraulics Laboratory.

[16] Henderson, F.M. 1966, Open Channel Flow. The Macmillan Company, New York.

Effects of Debris on Bridge Pier Scour

L.W. Zevenbergen*, P.F. Lagasse*, P.E. Clopper*, and W.J. Spitz*
*Ayres Associates Inc, 3665 JFK Parkway, Bldg. 2, Suite 200, Fort Collins, CO, USA

I. Introduction

Waterborne debris (or drift), composed primarily of tree trunks and limbs, often accumulates on bridges during flood events. Debris accumulations can obstruct, constrict, or redirect flow through bridge openings resulting in flooding, damaging loads, or increased scour at bridge foundations. The size and shape of debris accumulations vary widely, ranging from a small cluster of debris on a bridge pier to a near complete blockage of a bridge waterway opening. The effects of debris accumulation can vary from minor flow obstructions to severe flow contraction resulting in significant bridge foundation scour. Currently, there is only limited guidance available on which to base critical public safety decisions during flooding on debris-prone rivers. There is a need for accurate methods of quantifying the effects of debris on scour at bridge-pier foundations for use in the design, operation, and maintenance of highway bridges.

This paper provides a preview of the results expected from National Cooperative Highway Research Program (NCHRP) Project 24-26. The project was started in July 2004 and is scheduled for completion in December 2007. It is expected that this research project will produce results on two related problems: (1) predicting the accumulation characteristics of debris from potentially widely varying source areas, in rivers with different geomorphic characteristics, and on bridges with a variety of substructure geometries, and (2) developing improved methods for quantifying the depth and extent of scour at bridge piers considering both the accumulation variables and the range of hydraulic and geomorphic factors involved.

The project involves literature review, survey of bridge owners in the U.S., limited field reconnaissance, extensive hydraulics laboratory studies, and development of both debris accumulation guidelines and improved bridge scour prediction methods under debris loading. An early product of this research was a photographic archive of more than 700 debris accumulations on 106 streams and rivers in the U.S. This paper illustrates the scope of the problem, summarizes preliminary findings, and outlines the laboratory testing phase of the project and anticipated results.

The following specific tasks are planned to accomplish the objectives of NCHRP Project 24-26.

Phase I

Task 1 – Review The Technical Literature
Task 2 – Conduct Survey and Site Reconnaissance
Task 3 – Develop Preliminary Guidelines
Task 4 – Develop Phase II Laboratory Plan
Task 5 – Interim Report

Phase II

Task 6 – Finalize Task 3 Guidelines
Task 7 – Laboratory Studies
Task 8 – Develop Scour Prediction Methods
Task 9 – Submit Final Report

As of April 2006, Phase I was complete and preparations were being made for the initial Task 7 laboratory studies.

II. Literature Summary and Survey

A. Literature Review

Both the Federal Highway Administration (FHWA) [1] and the National Cooperative Highway Research Program (NCHRP) [2] have published recent debris-related studies that have excellent reference source lists. These sources were screened and a preliminary working bibliography of the most relevant references was assembled. Then a thorough literature search of national and international literature on vegetative debris (drift) and debris impacts on bridges was completed.

This effort produced a working bibliography of 240 references. These references were screened and an annotated bibliography of the most relevant documents considering the objectives of this study were developed into a bibliography of 110 citations. Based on the annotated bibliography, a detailed literature summary was prepared to include the following topics:

- Debris source, loading, distribution, and recruitment
- Debris transport
- Debris deposition, accumulation, and storage
- Debris accumulation at bridges
- Modeling debris induced hydrodynamic forces and scour
- Managing debris accumulations at bridges

B. Survey

Since the late 1970s there have been at least three studies related to debris that conducted surveys and/or visited state Departments of Transportation (DOTs) and other agency bridge sites. FHWA's 1979 study of "Debris Problems in the River Environment" [3] presents a literature review, a survey of debris hazards for FHWA regions and state DOTs, a debris hazard map, and a statistical analysis and observations resulting from the survey. Diehl's 1997 [1] study for FHWA compiles detailed information and maps on sources of drift (debris), Diehl also identifies debris field study sites and presents a generalized map of debris sites based on publications and written and oral communications. While Parola's [2] study for NCHRP did not include an independent survey, he relied on and interpreted the results of Diehl's [1] work; and Parola's [4] NCHRP report on "Highway Infrastructure Damage caused by the 1993 Upper Mississippi River Basin Flooding" contains specific information on debris problems and bridge failures for that region.

To supplement and update results of earlier surveys, a detailed survey to investigate regional characteristics of debris accumulations and typical bridge-related debris problems facing State DOTs was sent to 93 agencies. Surveys were returned from 88 respondents, representing 30 states including Alaska and Hawaii. In addition, two responses were returned from Puerto Rico; therefore, 84 responses representing the continental United States were received. A breakdown of responses in accordance with five geographic regions is shown in Table 1 (note that some states may be split into more than one geographic region):

TABLE 1.
SURVEY RESPONSES BY GEOGRAPHIC REGION

Geographic Region	Responses	States Represented
Pacific Coast	8	2
West	10	7
Midwest	29	11
South	20	5
East	17	8

The survey was partitioned into seven categories. Five of the seven categories asked respondents to rank debris-related questions on a scale of 0 to 5 in terms of importance/severity of problem. Responses to all the questions in each of these five categories were examined using the Analysis of Variance (ANOVA) method to determine if statistically significant differences in the responses could be assigned to geographic regions.

In general, responses from different geographic regions tended to be similar in nature, indicating that there are relatively insignificant regional differences regarding the nature of drift accumulations at bridges. Similarly, the types of drift-related problems reported tended to show very few regional differences. In some instances, however, regional differences were found to be statistically significant. Based on the 84 surveys received from five regions representing the continental United States, a qualitative interpretation of the survey responses combined with an analysis of variance statistics indicates the following:

- Drift material is primarily derived from unstable stream banks.
- It is most common for drift problems to occur at pile bents compared to other pier configurations. A possible exception may be in the Eastern region, where wall-type piers are reported to have the most problems.
- Large logs are not necessary for drift to begin accumulating at bridge piers. Most commonly, drift accumulation is initiated by logs 7.6 m (25 ft) or less in length, or, in the Western region, by shrubs and brushy vegetation (e.g., willows, Tamarisk).
- Nationwide, the most common drift configuration at bridges is that of an individual cluster of material on a single pier.
- Drift is most likely to exacerbate scour at bridges by either: (a) local scour at an individual pier, or (b) stream instability due to flow redirection.
- Highway departments typically do not collect cost data associated with drift removal and associated bridge repairs. Maintenance needs are sporadic in nature and are most often related to larger flood events. A reasonable range of cost estimates might be 0.5 to 1% of the DOTs total annual maintenance budget in years with little flooding, and perhaps 2 to 5% in years that experience one or more significant events.
- The relatively high standard deviation from the mean numerical responses within each region indicates that it is possible to experience the full range of drift-related problems in any given region; however, ranking the responses does provide an indication that some problems or issues are more common than others, as noted above.

III. DEBRIS PHOTOGRAPHIC ARCHIVE

To supplement the survey and support a regional analysis of debris accumulations, a photographic archive was compiled to assess typical debris geometry relationships. Photos of debris at bridges were acquired from a number of contributors. The photos in the archive provided the primary source used for evaluating debris accumulation characteristics and debris geometry from a wide range of sites located throughout the United States.

The primary contributor of debris photos was Debris Free, Inc. (almost 50% of the photos) [5]. Numerous photos were provided by state DOT personnel in response to the survey. The remaining photos were acquired from in-house sources, Internet sites, and from referenced publications. A total of 1,155 photos were acquired from the various sources. After screening and consolidation, the debris photo archive contains 736 photographs of debris-prone bridge sites on 106 rivers in all geographic regions of the United States.

IV. Regional Analysis Of Debris

One might infer from previous studies, experience with debris problems nationally, the geomorphic characteristics of rivers in different Physiographic Regions, and the distinctly different characteristics of woody vegetation and river bank erosion processes that there should be some regional bias in debris characteristics and in debris impact on bridges. Based on the literature search, the debris photo archive, and the survey, an attempt was made to identify common (or typical) debris characteristics that might be distinguishable by major Physiographic Region or Ecoregion of the U.S.

Several studies have suggested the potential for regionalized debris generation characteristics. Reference [3] developed a depiction of a national distribution of debris problems from severe, to moderate, to minor or no problem. The distribution was based on a state-specific survey of debris problems at highway bridges nationwide and indicated that the Pacific Northwest and the upper and lower Mississippi River Valley experience the most severe debris problems. Reference [1] mapped debris sites reported by DOTs, distribution of debris field-study sites, and debris sites referenced in publications or personal communications. Diehl suggests that watersheds of high or low debris generation can be identified based on watershed characteristics such as proximity of vegetation to the stream, rate of bank erosion, and/or channel instability resulting form natural properties, climate change, fire, or human modification.

An examination of the debris characteristics and accumulation geometry from the various debris site photographs in the archive, relative to their locations on Physiographic Region and Ecoregion maps reveals that there is no identifiable or well-defined relationship with regard to the individual Physiographic Regions or Ecoregions. Instead, the typical debris accumulations can be identified and appear to be common throughout the United States, and any river or stream with a riparian corridor along its banks is susceptible to debris problems. For example, a common debris accumulation geometry was found at five different sites from various parts of the county that are in distinctly different Physiographic Regions and Ecoregions. With regard to vegetation types, only general relationships exist. In most of the eastern half of the United States, large woody debris delivered to streams and rivers is primarily from riparian forests or corridors along those streams and rivers. In the arid southwest and west, vegetation can be limited to small trees and shrub-like vegetation, and the debris accumulation sizes and geometry in these areas often reflects this type of vegetation. In the Pacific Northwest, large conifers are the dominant tree species and are the controlling factor in the size of the debris accumulations and the debris geometry in this region.

V. Debris Accumulation Characteristics

As a basis for developing a laboratory test plan, typical debris accumulation characteristics were identified from the literature review and from an examination of the photo archive. At bridges, debris characteristics at a minimum might include a single pier floating cluster, a floating raft bridging two or more piers, and submerged or sunken variations of these configurations. The debris accumulations shown in the debris photo archive database were evaluated for specific geometric characteristics and guided identification of the specific geometries described below. The photos were also used to identify typical geometries of the debris piles and provide rough estimates of debris accumulation length upstream of the pier and debris accumulation width relative to pier width.

Debris was observed accumulating at bridge piers as single logs, multiple logs, or a mass of logs. The single log accumulation was comprised of one or two logs that had become trapped on a pier or between spans. The multiple log accumulation consisted of several logs that were loosely intertwined and had no filling of the interstices or matrix with finer debris, detritus, and sediment. The mass of logs accumulation was composed of a cluster of logs and other debris tightly interlocked with almost all of the matrix or interstitial openings filled with smaller debris, detritus, and sediment. Unlike the mass of logs accumulation, in almost all cases, the single log and multiple log types of accumulations did not extend upstream for any significant distance. Figure 1 shows a schematic of the mass of logs accumulation, as well as example photos for this accumulation type.

Dongol [6] used triangular, rectangular, and elliptical planform shapes in his modeling of debris related scour. Most debris accumulations observed in the photo archive could be considered either triangular or rectangular in planform. Triangular debris accumulations tend to have a conical shape in profile, while rectangular accumulations tend to have

a cylindrical profile. Figures 2 and 3 present schematics and photographs of the triangular and rectangular planforms, respectively. Both conical and cylindrical profile geometries were identified. Figure 4 provides a photograph of what is thought to be a debris pile with a conical geometry after the water has receded and the pile has collapsed upon itself. All types of debris accumulation profiles can evolve from being a surface accumulation to being partially or fully submerged, depending on flow depth.

A third type of profile geometry is the inverted conical profile, which generally has a triangular planform. This type of accumulation is very common and usually occurs following one or more floods when an accumulation with a triangular-conical geometry settles onto the bed of the channel. The lower portion of the accumulation then becomes embedded in the bed. This condition leads to a fourth profile, a collapsed buried wedge. When the next flood occurs, the debris accumulation remains trapped on the bed, but can grow in size because of trapping of additional debris. As more debris is trapped by the existing debris pile during subsequent flows, a rectangular-cylindrical geometry may develop.

VI. Laboratory Test Plan

A substantial laboratory testing program using the Hydraulics Laboratory of Colorado State University is planned for Phase II (Task 7). The goal of the laboratory testing will be to provide sufficient data for a range of debris accumulations to develop adjustment factors to the HEC-18 pier scour equation [7]. The adjustment factors could be a correction factor to the overall equation (such as the K_w factor for wide piers) or an adjustment to the pier width used as an input variable to the equation (similar to the HEC-18 complex pier approach). The goal of the laboratory plan is to develop a series of tests for a wide range of debris configurations that can be run quickly and efficiently. Initially, the tests will be performed for single debris clusters at individual piers, which is the primary type of debris accumulation identified by all regions in the survey. These tests will then be supplemented to address specific issues related to other factors that cannot be incorporated into the initial runs. For example, other pier shapes will be tested under conditions of debris loading, including pile bents and skewed wall piers. The majority of the testing will be performed for clear-water sediment transport conditions (approach flow velocity less than the critical velocity to initiate sediment transport) for durations much less than would be required to achieve ultimate scour. The duration will, however, be sufficient to achieve at least 60% of ultimate scour. This approach to the laboratory testing will maximize the number and range of debris configurations that can be tested within the laboratory budget.

The testing will include a range of debris characteristics including debris accumulation shape, thickness, width, and length. The range of debris accumulation size that will be tested in the laboratory is related to actual debris accumulations observed in the field or from the survey sources and the photo archive. Figures 5, 6, 7, and 8 illustrate the debris shapes (rectangular, conical, collapsed inverted cone, and collapsed buried wedge) that will be modeled and define the dimensions for the various shapes. The dimensions will be varied in order to model the range of conditions typically seen in the field.

The majority of the physical modeling will be conducted in the 2.4 m (8 ft) wide flume under clear-water flow conditions using 10 cm (4 inch) square piers. This scale and flow condition is recommended to maximize the number of debris conditions that can modeled because scour should develop rapidly at this scale and clear-water runs are also less time consuming. Table 2 shows a summary of the observed debris dimensions from the photo archive from the photo archive and the recommended range of debris dimensions for the laboratory physical modeling. All of the dimensions have been normalized by the pier width so the field conditions can be used to develop a realistic range of laboratory runs. The range of debris dimensions was selected to encompass the range observed in the field +/- one standard deviation around the mean.

VII. Scour Prediction Methods

Based on the results of laboratory testing, methods for predicting the depth, shape, and lateral and longitudinal extent of scour at bridge piers resulting from debris accumulations will be developed. The methods will be suitable for incorporation into FHWA Hydraulic Engineering Circular 18, "Evaluating Scour at Bridges," 4th Edition [7].

For local pier scour, the concept of effective pier diameter is included in the HEC-18 complex pier scour approach. The complex pier scour approach includes the pier stem, pile cap and pile group scour amounts as independent scour components [8]. This complex pier approach is similar to the effective pier diameter approach suggested by [9].

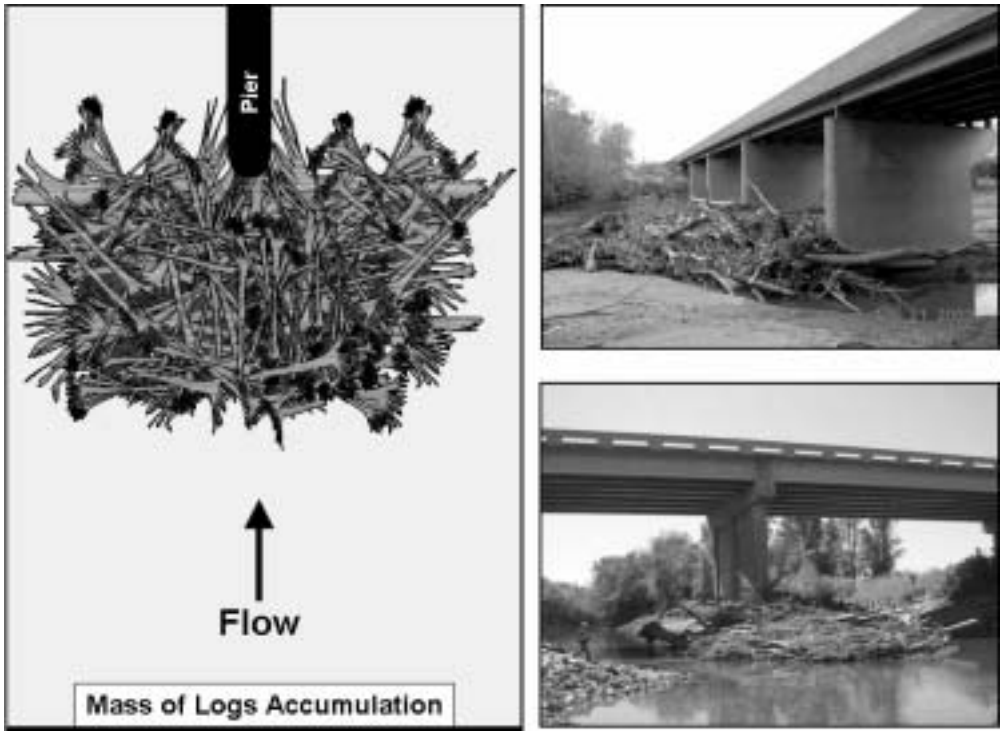

Figure 1. Mass of logs debris accumulation.

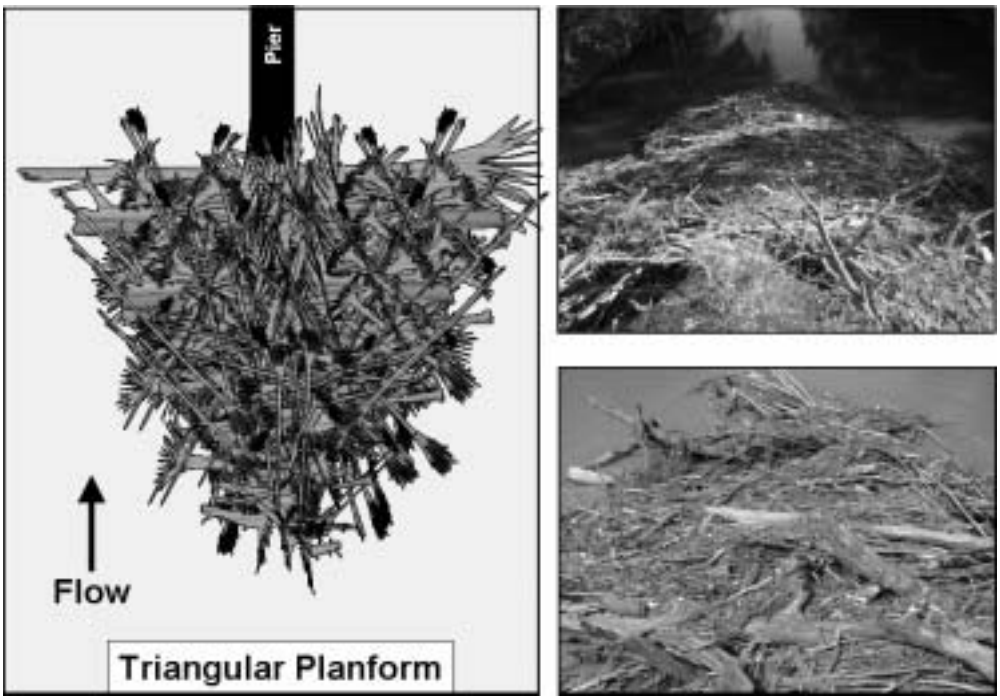

Figure 2. Triangular debris pile planform.

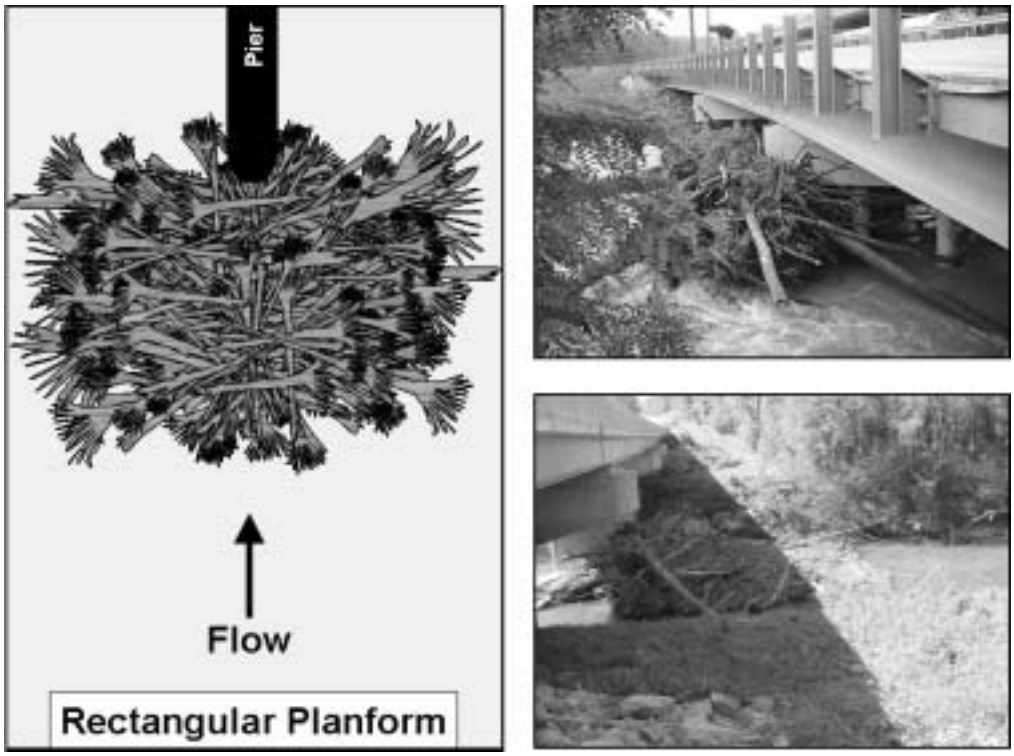

Figure 3. Rectangular debris pile planform.

Figure 4. Debris pile with conical profile geometry.

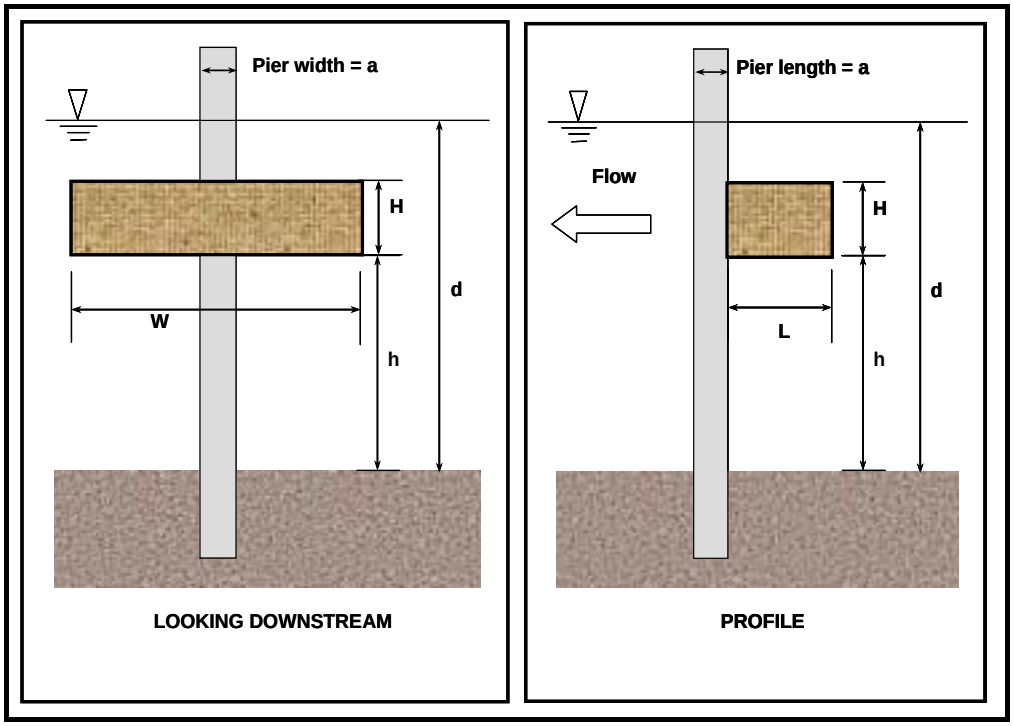

Figure 5. Rectangular shape definition sketch.

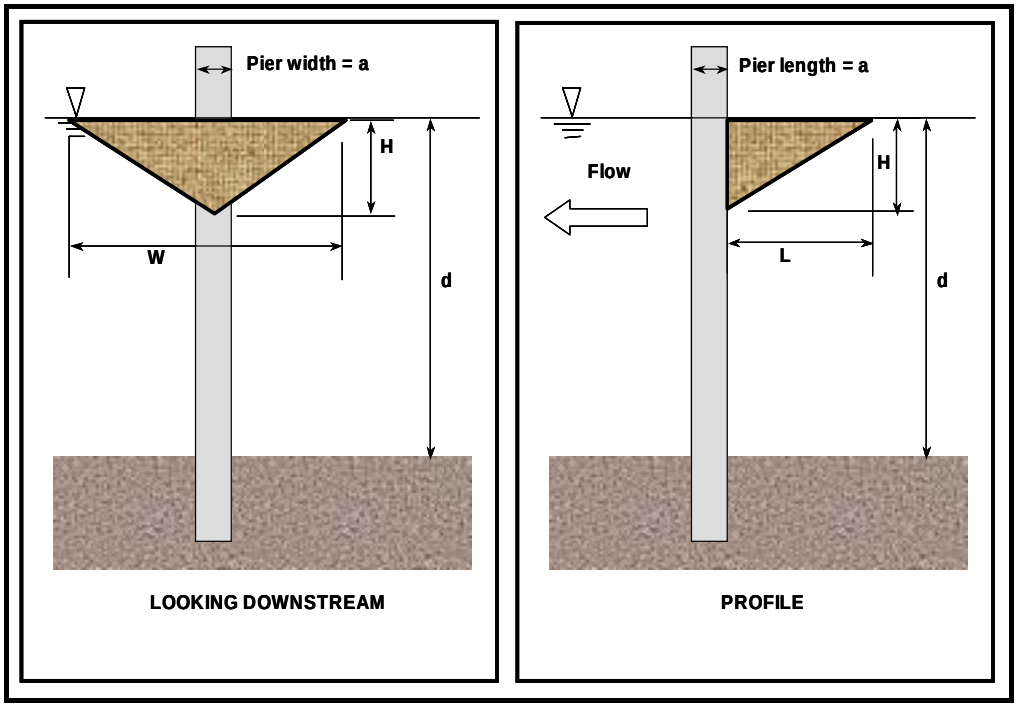

Figure 6. Conical shape definition sketch.

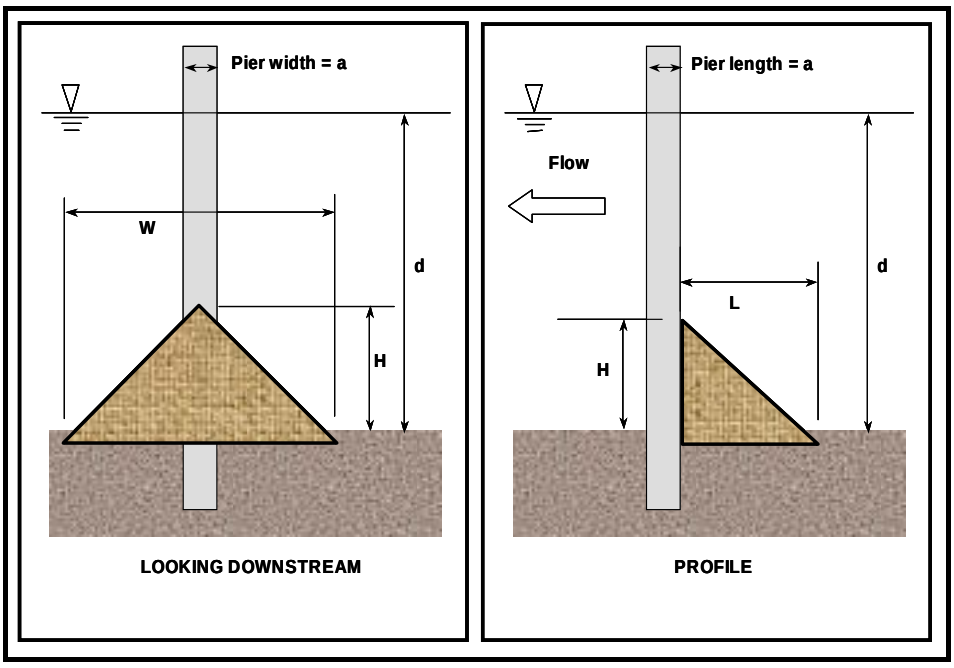

Figure 7. Collapsed inverted cone definition sketch.

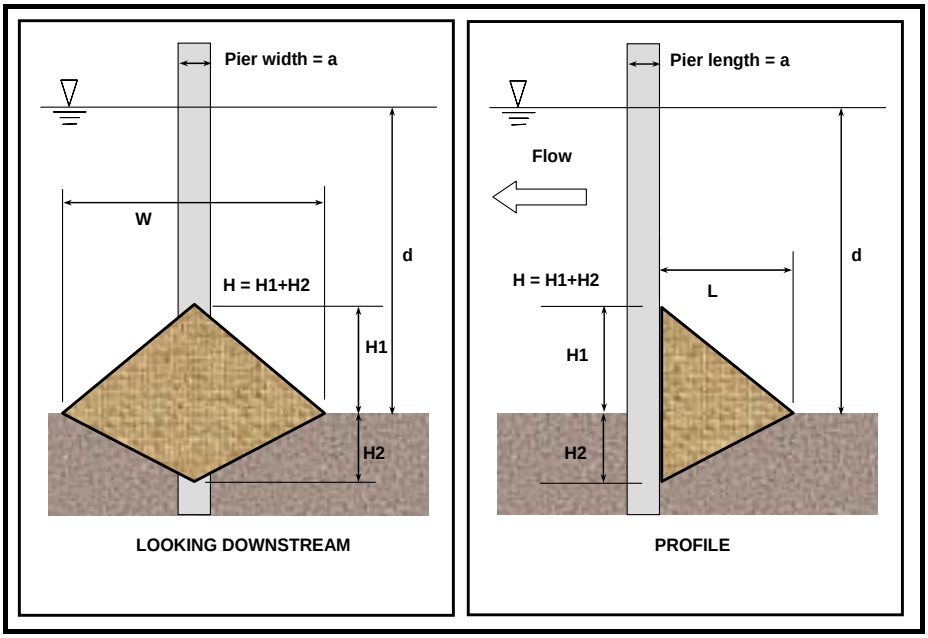

Figure 8. Collapsed buried wedge definition sketch.

TABLE 2.
FIELD AND LABORATORY DEBRIS DIMENSIONS

	W/a	L/a	L/W
Field and Photo Measurements			
Average	15.1	12.4	0.9
Range	5.2 – 43	3 – 48	0.2 – 2.7
St. Dev.	8.2	9.2	0.5
-/+ St. Dev.	6.9 – 23.3	3.2 – 21.5	0.4 – 1.3
Recommended Laboratory Tests			
Range	6 – 24	3 – 24	0.5 – 1.5

If the effective pier diameter approach is used, the local pier scour equation in HEC-18 would remain unaltered but the effective diameter (a^*_{debris}) would be substituted for the pier width (a). Another approach would be to add another correction factor (K_d) to the local HEC-18 pier scour equation. The correction factor approach may be more easily applied but may not be as applicable to the debris condition as the effective diameter. This is because for some debris conditions the debris may totally dominate scour and the original pier diameter may have little or no contribution.

Functionally, the relationship for either K_d or a^*_{debris} will be related to the range of conditions tested in the laboratory. The functional relationship is:

$$K_d \text{ or } \frac{a^*_{debris}}{a} = fn\left(\text{shape}, \frac{L}{a}, \frac{W}{a}, \frac{H}{d}, \frac{h}{d}, \frac{H_1}{H_2}, \theta\right) \qquad (1)$$

The dimensions a, L, W, H, h, d, H_1, and H_2 are shown for the various debris shapes in Figures 5 through 8 and θ is the flow angle of attack at the pier. If some of the variables or variable groupings prove to be insignificant in comparison to others, they could be eliminated from consideration.

VIII. Anticipated Research Results

As a result of this research, it is anticipated that State DOTs and other bridge owners will have documentation, guidelines, and analytical procedures to quantify the effects of debris-induced scour on bridges including:

- Fully documented data base on debris and case studies, photographs, and data related to debris generation, movement, accumulation and scour at bridges that can be used to inform and train design and maintenance personnel on debris-related hazards.
- Necessary guidelines for predicting the size and geometry of debris accumulations at bridge piers.
- Identification of geomorphic channel types where debris delivery can be expected to be low, even during flood events.
- Methods for quantifying scour at bridge piers resulting from debris accumulations suitable for incorporation in the next edition of FHWA's HEC-18.
- Guidance for incorporating debris effects in 1- and 2-dimensional hydraulic modeling.

The end result will be practical, implementable guidance for bridge owners that will enhance their ability to predict debris-related hazards at bridges and design, operate, inspect, and maintain bridges considering those hazards.

Acknowledgment

This work was sponsored by the American Association of State Highway and Transportation Officials, in cooperation with the Federal Highway Administration (FHWA), and was conducted through the National Cooperative Highway Research Program (NCHRP), which is administered by the Transportation Research Board (TRB) of the National Research Council (NRC).

This paper is based on an Interim Report as submitted by the authors to the TRB. The opinions and conclusions expressed or implied in the report are those of the authors. They are not necessarily those of the Transportation Research Board, the National Research Council, the Federal Highway Administration, the American Association of State Highway and Transportation Officials, or the individual states participating in the National Cooperative Highway Research Program.

References

[1] T.H. Diehl, "Potential Drift Accumulation at Bridges," Report FHWA-RD-97-28, U.S. Department of Transportation, Federal Highway Administration Research and Development, Turner-Fairbank Highway Research Center, McLean, VA (1997).

[2] A.C. Parola, C.J. Apeldt, and M.A. Jempson, "Debris Forces on Highway Bridges," NCHRP Report 445, National Academy Press, Washington, D.C. (2000).

[3] F.F.M. Chang and H.W. Shen, "Debris Problems in the River Environment, Federal Highway Administration Report No. FHWA-RD079-62, 67 p. (1979).

[4] A.C. Parola, D.J. Hagerty, and S. Kamojjala, "Highway Infrastructure Damage Caused by the 1993 Upper Mississippi River Basin Flooding," Transportation Research Board Report 417, Washington, D.C. (1998).

[5] Debris Free Inc. Bridge Systems, http://www.debrisfree.com (2005).

[6] M.S. Dongol, "Effect of Debris Rafting on Local Scour at Bridge Piers, Report No. 473, School of Engineering, University of Auckland, Auckland, NZ (1989).

[7] E.V. Richardson and S.R. Davis, "Evaluating Scour at Bridges, Fourth Edition, Hydraulic Engineering Circular No. 18, Federal Highway Administration Publication No. FHWA NHI 01-001, Washington, D.C. (2001).

[8] J.S. Jones and D.M. Sheppard, "Local Scour at Complex Pier Geometries, Proceedings ASCE 2000 Joint Conference on Water Resources Engineering and Water Resources Planning and Management, July 3 – August 2, Minneapolis, MN (2000).

[9] B.W. Melville and D.M. Dongol, "Bridge Pier Scour with Debris Accumulation, Journal of Hydraulic Engineering, Vol. 118, No. 9, pp. 1306-1310 (1992).

PERFORMANCE OF SHALLOW FLOW STRUCTURES IN PREVENTING SCOUR

Alan K. Zundel, Ph.D., Michael Fazio, P.E.

Brigham Young University, Department of Civil & Environmental Engineering, Provo, Utah

Utah Department of Transportation, Salt Lake City, Utah

I. ABSTRACT

An interest in using natural in-stream structures to protect bridge embankments from erosion and scour has prompted the Utah Department of Transportation (UDOT) to study the performance of these structures in order to evaluate from an engineering point of view how these structures withstand higher than average flows.

Shallow flow structures are man-made in-stream features that generally help concentrate the flow in specific parts of the stream, thus reducing the energy (erosion and scour) on other parts of the stream. This study focuses on the so-called w-weirs, cross vanes and j-hooks. The names are descriptive of the shape these features form in the stream. Their function is also relative to their shapes.

These shallow-flow structures were introduced by David Rosgen, author of "Applied River Morphology" a book on his theory on river morphology. In the book, Mr. Rosgen introduces his concept of river training, showing how to apply these structures to improve the stream stability and enhance some other characteristics. The shallow flow structures are often made with large rocks, root barbs and dead trees or other natural occurring materials that can resist stream forces. Many agencies in the US that are responsible to maintain the natural lands have adopted these methods for protecting river embankments, enhance fish habitats and maintain a healthier stream.

Critics have pointed out that many of these structures may not produce the promised results, and that in certain cases are failing or showing adverse effects to the streams.

The objective of the study is to define conditions for which these non-traditional engineering approaches can be successfully applied. The goal is to provide design engineers with another tool to provide the most economical and efficient methods for resolving various types of channel stability and training problems as well as scour problems at bridges.

Brigham Young University is the principal researcher. They are investigating the performance of existing structures, modeling selected structures with two-dimensional hydraulic models to assess stresses, and developing guidelines for this modeling process.

In the last two years, several in-stream structures installed in five rivers (the Spanish Fork River, the Provo River, the San Pitch River, Thistle Creek and Weber River) in Utah have been surveyed, monitored and modeled. Multiple surveys were completed to verify movement of the structure elements due to successive flood seasons. All the acquired data is being organized in a database to help the researchers understand the modes of failure and success of these structures. The findings, though preliminary, are revealing. Specifically, the results show how sensitive these structures can be to several factors, including workmanship, types of flow, and stream-types. They also show that current design and construction methodologies must change in order for these structures to be used as permanent protection of civil infrastructure**.**

The peak runoff experienced by the surveyed structures in the past two years is much less than the typical design flow for bridge scour (one percent or 100-year flow and the overtopping flow), but they are sufficient to give information for the research. These structures were affected by spring runoff flows of twenty to five percent annual recurring magnitudes, sometimes referenced as the five to twenty-year flood event. Several structures surveyed failed after the 2005 spring runoff. Failure occurs when elements of the structure are displaced and no longer function as intended or designed.

Structure designers point out that these structures are not designed to withstand the forces from peak stream run-off, and failure may be the result of poor installation rather than limited applications or techniques. Both of these points illustrate limitations of the current practice when viewed with civil infrastructure needs in mind.

Field measurements and two-dimensional models illustrate that these structures do have an impact of the stream forces for normal flows. Both data types show how the stream forces concentrate in parts of the stream because of the position of the structure elements. Shear forces increase greatly in the elements interstices. The large majority of structures included in the study indicate a susceptibility to failure do to the removal of materials from in between and at the base of the elements until they are undermine and displaced by the currents.

The model also showed that these structures become invisible as the flow in the stream/river increases.

It is very difficult to set parameters for an engineering design because of the variability of shape and the location of the elements in the stream. Initial results show the importance of providing a solid foundation for the structures to prevent premature failures.

II. INTRODUCTION

Utah Department of Transportation (UDOT) is responsible for over 1800 bridge, of which more than 800 hundred are over water. Many of these bridges span over morphologically unstable streams and rivers. Some of these bridges are vulnerable to the scour forces of periodic, violent flows. Most of the bridges that were built more than 30-years ago are not properly protected against scour. Many of these bridges have a high potential to be damaged by scour.

The most common methods to protect these bridges from scour damage and failure are rock rip-rap, grout bags, cable-tied blocks, gabions, spurs, guide banks and other man-made armoring products. Other scour revetments methods that are more conscious of river environments, form, and aesthetics are becoming prevalent. These methods are known as shallow-flow structures and they consist of installations of rock and other natural materials, positioned to train the river to concentrate forces from flowing waters to protect vulnerable banks and other channel elements.

A recent emphasis has been made by several agencies to utilize natural stream stability enhancement measures instead of more traditional engineering responses to stabilize river and streambeds against scour. These measures include the construction of shallow flow control structures, sometimes referred to as Rosgen countermeasures, across all or part of the river. Structure types include cross-vanes, w-weirs and j-hooks. This emphasis comes in response to studies that indicate such vanes can be designed to control the location of scour and protect bridge abutments (Johnson et.al. 2001, Odgaard, 1990, Odgaard, 1991)).

While claims have been made that these structures are durable, cost effective, and provide scour stability, the necessary case studies have not been documented. Several studies indicate a need for more work to understand the processes involved (Parola 1997, Yanmaz 2004).

Natural stream stabilization methods are particularly attractive in Utah. Utah has four major National Parks/Monuments that are visited annually by millions of people from all over the world. The desire is to keep the streams attractive and maintain the habitat they are famous for.

UDOT requested Dr. Zundel, from Brigham Young University to study the properties of these shallow flow structures, by surveying and modeling existing structures in two and three dimensional hydraulic computer programs. The objective is to understand how these structures perform, how they dissipate the river energy and under what range of conditions they can protect the bridges from scour damage. The final objective is to write a manual for designing these structures for protecting riverbanks and bridges.

A. Definition

Shallow flow structures studied in this research are:

- W Weir
- Cross-vanes
- J-hook vane

Following is an engineering description and definition of these structures:

The "Cross-Vane" is a weir structure constructed of rock riprap. In plan view it is always curved upstream. The structures are most commonly intended to reduce flow velocity and shear stress at the stream banks by concentrating the flow to the center of the channel.

The "W Weir" is a doubled up form of the Cross Vane Weir and in plan view, as it's name implies, takes the form of a "W". The points on the bottom of the W face upstream and twin scour holes develop just downstream of these points. It could also be described as a labyrinth weir constructed of rock riprap. As with the Cross Vane the upstream curvature is meant to reduce flow velocity and shear stress at the stream banks by concentrating the flow to the center portions of the channel.

The "J hook Vane" is a variation of a barb or spur dike and in plan view, as it's name implies, takes the form of a "J". The curved end of the J faces upstream while the straight portion of the J is embedded into the bank. The J hook is generally constructed of rock riprap elements although Rosgen suggests that it can include logs and root wads as well. The curved portion consists of what used to be called "fish boulders" and exist in the channel as individual elements. The rock elements making up the straight portions of the J in the J hook are intended to rest tightly against one another or to be made of a log. If a root wad is included it is meant to face upstream.

III. OBJECTIVES

The research objective is to study existing shallow flow installations to develop guidelines for designing and installing shallow flow structures as a method of stream stabilization and scour protection at or near bridge crossings and to define conditions for which these non-traditional engineering approaches can be applied. These conditions could be formulated into design guidelines to allow engineers to use these structures appropriately and with numerical and empirical data justifying their use. Specific methods used include:

1. Literature Search to learn from other research on this subject.
2. Evaluate of the performance of shallow flow structures in Utah stream reaches. This will be accomplished by monitoring of 1) one cross-vane and one j-hook structure on Thistle Creek, 2) a series of structures on the Left Fork Hobble Creek (designed and built by David Rosgen) and 3) a control group selected form sites throughout Utah which vary in classification, age, and stream type.

3. Initiate the specification of quantitative methodologies for the application of shallow flow type scour countermeasures. This will include the determination of the normal failure modes and associated critical points for shallow flow structures.

4. Illustrate the evaluation procedure methodology on a specific site.

5. Preparing guidelines for selecting and designing shallow flow structures in streams and rivers next to highway crossings.

A. Literature Search

The literature review revealed several applications of shallow flow structures for scour control. However, long term results including life span of those structures were not available. Further, specific research on shallow flow structures is not extensive.

The literature further accentuated that the processes that influence scour are many, varied, and not completely understood. The major parameters that affect the selection of a structure and that structure's performance include the river type, stream width, bend radii, flow velocity, bed material, ice and debris loads, bank conditions and floodplain width (Lagasse 1998). Not only is this list long, but many of the items in the list vary drastically over time and over the space included in a scour counter measure project. Fairly recently the Federal Highway Administration has updated the Hydraulic Engineering Circulars 18, 20 and 23 based on extensive literature searches from around the world. These provide very good methodologies to evaluate the scour, and stream stability (HEC-18 and 20) and design appropriate countermeasures (HEC-23). However, research to understand these processes continue, and our understanding of scour countermeasures is evolving. The literature stresses a need for more data to be compiled and studies to be conducted. No definitive resources are available to determine which scour countermeasure is most appropriate for a specific situation, nor one set of design guidelines to follow once a countermeasure is chosen.

Any scour revetment method chosen, may or may not work depending on the unique hydrologic and hydraulic circumstances where the countermeasures are placed. Several design guidelines have been developed for scour revetment and a variety of tools and resources available to designers of scour protection. Johnson et al. (2001) proposed using a risk base system for choosing the best countermeasure.

The literature review also clearly documents that river training structures are a sound engineering approach when designed correctly and applied in the correct locations and with the correct goals in mind. However, evaluation processes that are proposed for applying these structures are general guidelines and lack detail. Significant risk exists that the correct structure may not be chosen, and even if the correct structure is chosen design guidelines may not be suitable to the specifics of the site in question.

Detailed design specifications for the structures apply to similarly detailed conditions. It is difficult to install shallow flow structures according to design. Some design variables are too sensitive and when installed, the structure may not perform as expected. If an appropriate structure is chosen and installed correctly, it is still necessary to monitor them. In fact, Richardson (1991) proposes the idea that the most important and cost effective countermeasure for scour and stream instability is monitoring and inspection. Initially, this monitoring confirms that the application and performance of the structure satisfy the goals of the installation. Later on this monitoring allows for early detection of structure failure and correction of problems.

IV. WORK AND RESULTS

A. Database

As part of this research, a database of all installation in Utah was completed. The database provides information on the location and eventual performance of the installations. The database includes a description of each structure, notes on performance, and a time series of pictures of the structure. The design of the database also includes the ability to store surveys of the site to track bathymetric changes and numerical models of the site used for design or analysis.

Database Information. The database is a tool to store shallow flow structure data in an organized way. There are two primary types of data stored in this database. The first is spatial and the second is event driven data. It also contains secondary or supporting data. These data are located in a central location where users can access the data. Event driven data is data gathered over time. An example would be a descriptive note as to the functionality of a specific structure over a several year period. From these observations, a list of entries about the same structure over the observation period would be generated. Information gathered during the monitoring process is event driven data. This data is organized and tracked in Access. The event driven data that we are collecting are photos, observations, bathymetric surveys and pin point surveys. ArcMap is also used to organize spatial data pertaining to the structures. The extent of the project is limited to the state of Utah. The layers included are:

- Structures in Utah (location)
- Watersheds of Utah
- County Boundaries of Utah
- Streams of Utah
- Topographic Maps or Arial Photographs (limited to the site)

ArcMap is used to combine the spatial data with the event driven data. The tables created for use in access can be imported to ArcMap and analyzed. Analyses that can be made are:

Graphical representations of attributes of SFS ex. types of structures

Graphical representations of failures each year

B. Detailed Topographic Surveys

As part of this research, several shallow flow structures installation in rivers and stream in Utah, were selected for survey and study. The intention of this part of the work is: 1. to capture any physical movements of the structures, 2. to have data points for statistical analysis in the performance of the structures, and 3. to set-up two-dimensional models to analyze forces acting on these structures.

The selected structures are on regulated and unregulated rivers. Following is a description on the work performed on these rivers.

Provo River

Three installations were selected on this river. Using a total station, a velocity meter, and range rod, data points were gathered for the following:

Using the bathymetric and bank data, two finite element meshes were created for the three reaches. Boundary conditions of flow rate and a downstream water surface elevation were computed from the velocity and depth measurements.

These initial finite element meshes were analyzed using the FESWMS-2DH finite element package which is sponsored by the FHWA. The results indicated that although, we could predict flow rates, these sites had several weaknesses. Namely:

1. The structures in these sites were not designed according to Rosgen methodology.
2. The flow in this reach of river, while variable, is restricted and would never see high flow rates that should be analyzed when considering the use of Rosgen structures as engineering structures in general.
3. The data gathered was not highly enough resolved to represent the complex nature of the flow.

Thistle Creek

The structures on this creek closely match the design methodologies defined by Rosgen. The section of the stream has seen many reclamation works over the past few years and work continues. This area is also of interest, because it has had erosion problems historically.

The goal for the topographical survey was to gather high-resolution geometry to accurately model the site in FESWMS. Permanent survey points were identified, and cross sections measured at one-foot intervals through the area of a selected Cross-Vane and J-Hook structure. Cross sections were also gathered upstream and downstream of the two structures. In addition, velocity and depth measurements were taken and approximately twenty-five locations to be used for boundary condition computation and model verification/calibration. The site chosen for modeling includes many structures including two Cross-Vanes one J-Hook and a number of spurs.

Weber River at Rockport Reservoir

This site is the location of a scour critical bridge for which a shallow flow structure was proposed as a scour countermeasure. A detailed survey of the site was performed after the structure had been in place for approximately one year.

The goal for this site is similar to that of Thistle Creek. In addition, this site may be used as a case study for the use of shallow flow structures for bridge protection.

C. Monitoring Program

During the literature review, it was noted that the performance of shallow flow structures varied over application an time. It was also noted that the durability and life span of the structures may be much lower than traditional scour countermeasures. Therefore, part of this study was to initiate a monitoring program of several structures. This program serves several purposes including:

1. Providing general understanding of structure performance in a range of conditions over multiple years.
2. Providing data to be used as a prototype data base to track structure performance.
3. Provide evaluation data points for structure durability and efficiency.

There are various levels of monitoring that we have implemented. Types of monitoring methods include:

- Sketching a site map
- Using a GPS to obtain coordinates for a structure
- Conducting high density bathymetric surveys
- Installing fixed points where photos are taken
- Using photos to document the site
- Installing pins in rocks and surveying those rocks
- Numerical models
- Scour analysis.

High density bathymetric surveys were used to create 3D renderings of the site in SMS. Once the surveys were in SMS they were used to evaluate scour and to create meshes used with a FESWMS analysis.

As part of the research, 16 sites are being monitored that have 98 structures associated with them.

D. Two-Dimensional Numerical Modeling

The Thistle creek site that we have modeled includes two separate finite element meshes. They represent two reaches of the stream that are very close together. The first includes a Cross-Vane structure and the second includes a J-Hook.

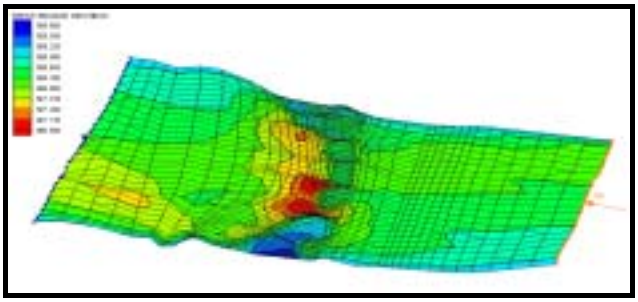

Figure 1. Layout of mesh for the Cross-Vane Structure.

Figures 1 and 2 show the meshes constructed around the Cross-Vane and the J-Hook respectively. The color keys in the upper left hand corners indicate elevations. These finite element grids were constructed to represent each structure element. By using elements down to six inches on a side, the meshes define the elevation and shape of each boulder, the chutes between the boulders and the pools that have formed on both the upstream nad downstream sides of the structures.

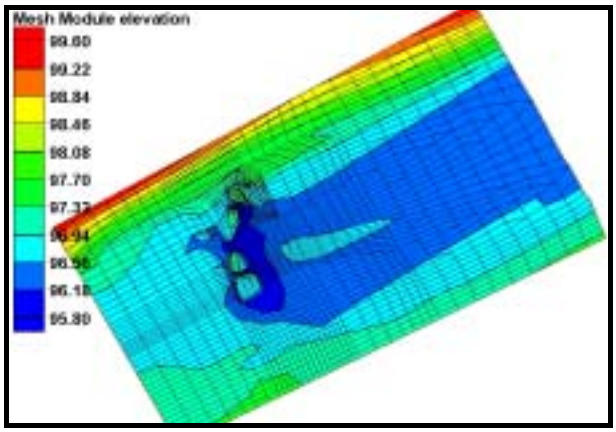

Figure 2. Layout of mesh for the J-Hook Structure.

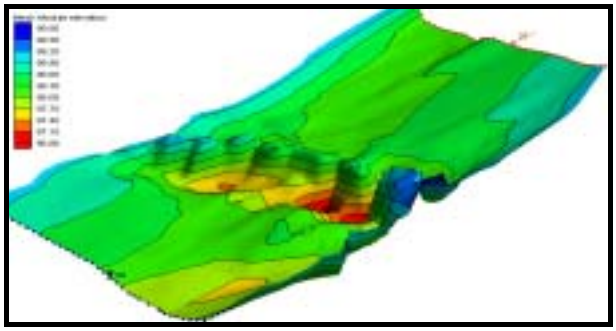
Figure 3 Oblique view of geometry of the Cross-Vane structure.

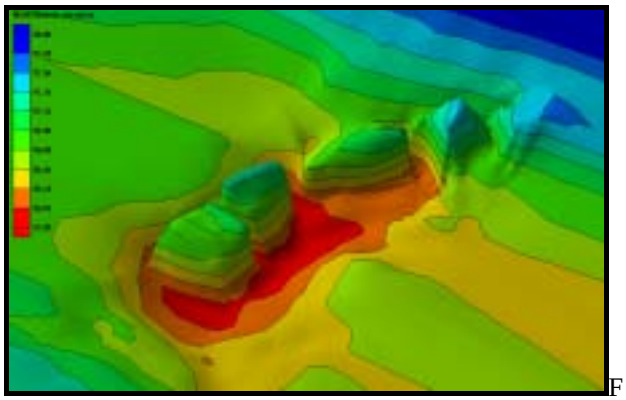
Figure 4. Oblique view of the geometry of the J-Hook structure.

Figure 3 and Figure 4 show the geometry of the meshes from an oblique view. These views accentuate the scour holes that are developing downstream of the structures. We have monitored these holes over a two year period. After two years, we came to the conclusion that significant, detrimental scour is occurring and structure failure is eminent. On a side note, we observed scour that is occurring upstream on the J-Hook. This scour upstream was mentioned during one of the interviews with structure designers. Evidence supports that failure of these structures occurs not only by downstream scour, but also by upstream scour.

V CONCLUSIONS

We wish to clearly state that the results of this work are far from final. Our understanding of the benefits and effectiveness of shallow flow structures continues to evolve. It is clear that these structures are capable of modifying the flow of river (Odgaard 1990, Makowski 1989 and Johnson 2001). However, due to the wide range of conditions and applications, a structure may be perfectly reasonable for one purpose, while only a part of the solution, or even unreasonable for another purpose.

A. Uncertainty

A critical question that must be resolved when determining the applicability of a scour counter measure is the level of uncertainty associated with that situation, and the level of uncertainty that can be tolerated with a solution. In the case of shallow flow structures, our research has reiterated several potential areas of uncertainty that were also identified in the literature review. Some of the uncertainties associated with shallow flow structures are:

- "Non-transferability" of design criteria. Design criteria that are developed in one geographic setting may not be successful in another location (Harman 2001). Trial and error design processes and criteria may produce successful applications of the scour countermeasure, but also require increased cost due to structure failures and repairs. Implicit to this design method is the need for extra monitoring throughout the life of the structure.
- No definitive selection or design methodology.
- Evolving understanding of scour and scour countermeasures.
- Severity and frequency of debris loads, snags and ice.
- Variability in flow ranges affect what scour counter methodologies may apply. Traditionally, shallow flow structure designs only treat two to five year recurrence intervals. In some situations, this may be the design flows needed for critical scour situations. However, when larger recurrence intervals apply, design processes must be altered accordingly.
- Traditional scour counter measures require only average workmanship (Yanmaz 2004). However, shallow flow structures require for high quality workmanship and high quality control (Harman 2001).

- Variable failure modes (Johnson 2004), need for higher quality control and post construction monitoring (Richardson 1991) reduce the cost effectiveness of the structures. In many cases, it may even be impossible to determine total costs because of unpredictable life spans.
- Acceptability of concept of sacrificial structures
- Cost for high workmanship requirements
- Cost and availability of high quality specific dimension rocks

Generally speaking, for all practical purposes the FHWA HEC-18, 20 and 23 are the most up to date and complete methodology for evaluating river stability and scour and choosing an appropriate structure. While using the documents it should be kept in mind that not all the structures available are addressed directly therein. Structures are evolving and changing through the trial and error method and are usually just small variations on more well-known and studied structures. Shallow flow structures are addressed in the HEC documents

Structures should be installed based on sound principles and then be monitored after installation with the intent to adjust and maintain the structures over the period of their lifetime.

C. Failures – Modes and Frequency

During the course of this research it has become evident that shallow flow structures can fail in a variety of ways. In just two years of monitoring between 50-100 structures, the following have been observed:

- Movement of structure elements due to scour. Observations have been made of scour occurring both upstream and downstream of the structure element. Design specifications include the creation of a foundation for each structure element. It appears that these principals are either inadequate, or are not being followed.
- Movement of structure elements due to debris. In one example a fifty foot log caused the failure of three successive structures.
- Burial of structures due to deposition.
- River morphology causing the flow to bypass the structure entirely.

While all of these failure mechanisms are to be expected, the rate of failure over the past two years has been alarming. It is our conclusion that quality control in all phases of a scour countermeasure project is crucial for application success. This includes higher than standard controls on all phases from design to material selection, to construction to monitoring. At the same time, it must be understood that even the highest quality control, will not prevent the some failure mechanisms such as debris flows.

C. Applicability

At this point in time it is not recommended that shallow flow structures be used as the principle method of scour prevention. Two primary reasons are the basis for this recommendation. First, the design flood for these structures is generally a bank full situation. This is traditionally a two- to five-year recurrence event. While this type of event may be the critical flow condition in some cases, engineering structures are usually designed for higher flow, lower frequency events. The impact of these structures changes significantly for larger flow. In some situations, the impact the structure makes to protect against scour is reduced, while in others, the structure may even increase scour. When installed, these structures should be continually monitored throughout their service.

Long term performance of shallow flow structures remains a major question. Our monitoring has shown a high failure rate for the structures. Over a two year period, all three sites of previous interest (7 structures) were significantly impacted. The two structures on Thistle creek, monitored as part of phase 1 of this study both failed. One failed as the stream actually migrated away from the structure and the other was buried. Structures on the upper Provo and Rockport were severely damaged due to debris flow.

BIBLIOGRAPHY

Harman,W.A, et al., *Lessons Learned from Designing and Constructing In-Stream Structures*, Proceedings of the 2001 Wetlands Engineering and River Restoration Conference, 2001, pg 765-773.

Johnson, P.A. and Niezgoda, S.L. *Risk-Based Method for Selecting Bridge Scour Countermeasures*, Journal of Hydraulic Engineering, ASCE, Feb 2004, pg. 121-128.

Johnson, P.A., Hey, R. D. Hey, Tessier, M. and Rosgen, D.L. *Use of Vanes for Control of Scour at Vertical Wall Abutments*, Journal of Hydraulic Engineering, ASCE, September 2001, pg. 772-778.

Lagasse,P.F., Byars,M.S., and Zevenbergen, L.W. *Bridge Scour Countermeasures*, International Water Resources Engineering Conference-Proceedings, 1998, V1 pg. 5-14.

Laursen, E.M. *Sediment Management with Submerged Vanes.II: Applications*, Journal of Hydraulic Engineering, ASCE, May 1992, pg. 827-830.

Makowske, P.B., Thompson, P.L. and Yew, C.P., *Scour Assessment at Bridges*, Proceedings National Conference of Hydraulic Engineering, 1989, pg. 1-6.

Odgaard, A. Jacob (Univ of Iowa); Wang, Yalin, *Sediment Management with Submerged Vanes*, Hydraulic Engineering, Proceedings of the 1990 National Conference, pg. 963-968.

Odgaard, A. Jacob (Univ of Iowa); Wang, Yalin, Sediment *Management with Submerged Vanes. I: Theory*, Journal of Hydraulic Engineering, ASCE, March 1991, pg. 267-283.

Odgaard, A. Jacob (Univ of Iowa); Wang, Yalin, *Sediment Management with Submerged Vanes. II: Applications*, Journal of Hydraulic Engineering, ASCE, March 1991, pg. 284-302.

Parola, A.C. (Univ of Louisville); Hagerty, D.J.; Mueller, D.S.; Melville, B.W.; Parker, G.; Usher, J.S., *Need for Research on Scour at Bridge Crossings*, Proceedings, Congress o fhte International Association of Hydraulic Research. 1997, pg. 124-129.

Richardson, J.R. and Wacker, A.M. *Bridge Scour and Stream Instability Countermeasures*, Proceedings-National Conference on Hydraulic Engineering, 1991, pg. 317-322.